CODEN: JASMAN

ISSN: 0001-4966

The Journal of the Acoustical Society of America

Vol. 117, No. 5 May 2005

(Continued)

THE JOURNAL OF THE ACOUSTICAL SOCIETY OF AMERICA VOL. 117, NO. 5, MAY 2005

CONTENTS—*Continued from preceding page*

(Continued)

THE JOURNAL OF THE ACOUSTICAL SOCIETY OF AMERICA VOL. 117, NO. 5, MAY 2005

CONTENTS—*Continued from preceding page*

(Continued)

THE JOURNAL OF THE ACOUSTICAL SOCIETY OF AMERICA VOL. 117, NO. 5, MAY 2005

CONTENTS—*Continued from preceding page*

ACOUSTICAL NEWS—USA

Elaine Moran
Acoustical Society of America, Suite 1NO1, 2 Huntington Quadrangle, Melville, NY 11747-4502

Editor's Note: *Readers of this Journal are encouraged to submit news items on awards, appointments, and other activities about themselves or their colleagues. Deadline dates for news items and notices are 2 months prior to publication.*

New Fellow of the Acoustical Society of America

K. Anthony Hoover—For contributions through the practical application and teaching of principals of architectural acoustics in the design of buildings.

Medwin Prize in Acoustical Oceanography awarded to Svein Vagle

Svein Vagle

The 2005 Medwin Prize in Acoustical Oceanography was awarded to Svein Vagle on 18 May at the Acoustical Society of America meeting held in Vancouver, Canada. Dr. Vagle received the award ''for development of experimental techniques to probe the upper ocean boundary layer'' and presented the 2005 Acoustical Oceanography Prize lecture titled ''Acoustic explorations of the upper ocean boundary layer.''

Dr. Vagle is a research scientist at the Institute of Ocean Sciences in Sidney, British Columbia, Canada. His fields of interest include instrumentation for passive and active detection of marine mammals and their habitat, novel acoustical instruments for *in situ* and remote sensing of the upper ocean, and acoustical measurements of near-surface microbubbles in ship wakes.

The Medwin Prize in Acoustical Oceanography was established in 2000 from a grant made to the Acoustical Society Foundation by Herman and Eileen Medwin to recognize a person for the effective use of sound in the discovery and understanding of physical and biological parameters and processes in the sea. It is awarded annually to an individual who is under 46 years old. Recipients have been: 2001—Timothy J. Leighton, 2002—Bruce D. Cornuelle, 2003—Jeffrey A. Nystuen, 2004—Stan E. Dosso.

Further information about the Medwin Prize is available from the Acoustical Society of America, Suite 1NO1, 2 Huntington Quadrangle, Melville, NY 11747-4502. Phone: 516-576-2360; Fax: 516-576-2377; E-mail: asa@aip.org; Web: asa.aip.org/fellowships.html.

Third CHRG Summer Institute planned for Aspen, CO in August 2006

Planning is underway for the third Concert Hall Research Group Summer Institute in Aspen, CO during the third week in August 2006, coinciding with the world-renowned, annual Aspen Music Festival. Noted faculty from the acoustical consulting, theater consulting, architectural, and academic communities will present topics on concert hall design, construction, and evaluation to practicing acoustical consultants and university students. Similar to the previous institutes at Tanglewood in 1999 and at Saratoga Springs in 2003, the format will be intimate, with faculty and students mixing together for meals, happy hours, and informal discussions throughout.

Two general subject categories are planned for Aspen—variable acoustic design and special design for sound isolation and noise control. Along with technical presentations, tours and/or evening concerts are planned at the Harris Concert Hall (Aspen), the Benedict Tent (Aspen), and Vilar Hall (nearby Beaver Creek). Most of the acoustical consultants, architects, and theater consultants responsible for the design of these three halls have been invited and are currently planning to participate in the Institute. ''New features'' at Aspen 2006 will include a *design challenge* (amongst faculty/

FIG. 1. Aspen's Harris Concert Hall

 0001-4966/2005/117(5)/2671/2/$20.00

student teams) and *presentations of listening notes* (by a panel of faculty members) each morning after a concert performance.

The organizing committee currently consists of Carl Rosenberg, Bob Coffeen, Gary Siebein, Michael Yantis, and Bill Dohn. Assistance is also being provided by the organizers of the first two institutes—Bill Cavanaugh and Tim Foulkes at Cavanaugh Tocci Associates and Robin Glosemeyer and Clare Hurtgen at Jaffe Holden Acoustics. As in the past, the Aspen 2006 CHRG Summer Institute will be sponsored by the Concert Hall Research Group with the support of the Technical Committee on Architectural Acoustics (TCAA) of the Acoustical Society of America, the National Council of Acoustical Consultants (NCAC), and the Robert Bradford Newman Student Award Fund.

Additional announcements for the Aspen 2006 CHRG Summer Institute will be mailed to ASA members interested in architectural acoustics and printed in ASA meeting programs through the spring of 2006. Applications for attendance, including a limited number of full and partial scholarships for students registered at accredited universities, will be available at that time.

For further information, contact Bill Dohn by email at ⟨bill.dohn@gte.net⟩ or by telephone at 805-771-8434. Send your contact information to Bill to be sure you will be included in the Aspen 2006 mailing list for future announcements and for applications. Clear your calendar (if you have one yet) for the week beginning Monday, 13 August 2006! Stay tuned!

USA Meetings Calendar

Listed below is a summary of meetings related to acoustics to be held in the U.S. in the near future. The month/year notation refers to the issue in which a complete meeting announcement appeared.

2005

16–20 May	149th Meeting joint with the Canadian Acoustical Association, Vancouver, Canada [Acoustical Society of America, Suite 1NO1, 2 Huntington Quadrangle, Melville, NY 11747-4502; Tel.: 516-576-2360; Fax: 516-576-2377; E-mail: asa@aip.org; WWW: http://asa.aip.org].
16–19 May	Society of Automotive Engineering Noise & Vibration Conference, Traverse City, MI [Patti Kreh, SAE International, 755 W. Big Beaver Rd., Ste. 1600, Troy, MI 48084, Tel.: 248-273-2474; E-mail: pkreh@sae.org].
23–26 May	For Whom The Decibel Tolls: Reducing the Impact of Noise Banff, Alberta [Dr. Daryl Caswell, Tel.: 403-220-5160; E-mail: djcaswel@ucalgary.ca].
18–22 July	17th International Symposium on Nonlinear Acoustics, State College, PA [Anthony Atchley, The Pennsylvania State University, 217 Applied Research Lab Building, University Park, PA 16802; Tel.: 814-865-6364 E-mail: ISNA17@outreach.psu.edu; WWW: http://www.outreach.psu.edu/c&i/isna17/].
17–21 October	150th Meeting joint with Noise-Con, Minneapolis, MN [Acoustical Society of America, Suite 1NO1, 2 Huntington Quadrangle, Melville, NY 11747-4502; Tel.: 516-576-2360; Fax: 516-576-2377; E-mail: asa@aip.org; WWW: http://asa.aip.org].
27–29 Oct.	5th International Symposium on Therapeutic Ultrasound, Boston, MA [www.istu2005.org; E-mail: info@istu2005.org}.

Cumulative Indexes to the *Journal of the Acoustical Society of America*

Ordering information: Orders must be paid by check or money order in U.S. funds drawn on a U.S. bank or by Mastercard, Visa, or American Express credit cards. Send orders to Circulation and Fulfillment Division, American Institute of Physics, Suite 1NO1, 2 Huntington Quadrangle, Melville, NY 11747-4502; Tel.: 516-576-2270. Non-U.S. orders add $11 per index.

Some indexes are out of print as noted below.

Volumes 1–10, 1929–1938: JASA and Contemporary Literature, 1937–1939. Classified by subject and indexed by author. Pp. 131. Price: ASA members $5; Nonmembers $10.

Volumes 11–20, 1939–1948: JASA, Contemporary Literature, and Patents. Classified by subject and indexed by author and inventor. Pp. 395. Out of Print.

Volumes 21–30, 1949–1958: JASA, Contemporary Literature, and Patents. Classified by subject and indexed by author and inventor. Pp. 952. Price: ASA members $20; Nonmembers $75.

Volumes 31–35, 1959–1963: JASA, Contemporary Literature, and Patents. Classified by subject and indexed by author and inventor. Pp. 1140. Price: ASA members $20; Nonmembers $90.

Volumes 36–44, 1964–1968: JASA and Patents. Classified by subject and indexed by author and inventor. Pp. 485. Out of Print.

Volumes 36–44, 1964–1968: Contemporary Literature. Classified by subject and indexed by author. Pp. 1060. Out of Print.

Volumes 45–54, 1969–1973: JASA and Patents. Classified by subject and indexed by author and inventor. Pp. 540. Price: $20 (paperbound); ASA members $25 (clothbound); Nonmembers $60 (clothbound).

Volumes 55–64, 1974–1978: JASA and Patents. Classified by subject and indexed by author and inventor. Pp. 816. Price: $20 (paperbound); ASA members $25 (clothbound); Nonmembers $60 (clothbound).

Volumes 65–74, 1979–1983: JASA and Patents. Classified by subject and indexed by author and inventor. Pp. 624. Price: ASA members $25 (paperbound); Nonmembers $75 (clothbound).

Volumes 75–84, 1984–1988: JASA and Patents. Classified by subject and indexed by author and inventor. Pp. 625. Price: ASA members $30 (paperbound); Nonmembers $80 (clothbound).

Volumes 85–94, 1989–1993: JASA and Patents. Classified by subject and indexed by author and inventor. Pp. 736. Price: ASA members $30 (paperbound); Nonmembers $80 (clothbound).

Volumes 95–104, 1994–1998: JASA and Patents. Classified by subject and indexed by author and inventor. Pp. 632. Price: ASA members $40 (paperbound); Nonmembers $90 (clothbound).

Volumes 105–114, 1999–2003: JASA and Patents. Classified by subject and indexed by author and inventor. Pp. 616. Price: ASA members $50; Nonmembers $90 (paperbound).

OBITUARIES

William C. Meecham • 1925–2003

William C. Meecham, a Fellow of the Acoustical Society of America who made many important contributions to theoretical and applied acoustics, passed away on 11 March 2003. At the time of his death, he was Professor of Mechanical and Aerospace Engineering at the University of California at Los Angeles.

Professor Meecham was born in Detroit, MI on 17 June 1925. His father, William E. Meecham, was in the construction business, and his mother, Catherine, was a schoolteacher. He attended Grosse Pointe Senior High School and graduated in June of 1942. As many young Americans did during that time, he enlisted in the Army. When he was in high school, he had learned to operate instruments for detecting vacuum leaks; therefore, when he completed boot camp, he was sent to Oak Ridge National Laboratory in Tennessee to assist in the process of purifying uranium for the atom bomb.

After his military service, he attended the University of Michigan and received a Bachelor of Science Degree in Physics in 1948. The following six years were spent at the University of Michigan and at Brown University, resulting in 1954 in a Ph.D. from the University of Michigan. In his thesis, he developed a statistical model for the propagation of radiation in refraction ducts bounded by rough surfaces; the model was subsequently used for the study of the effects of surface reflections in the propagation of underwater sound, and the thesis has been frequently cited by workers in underwater acoustics.

Following the completion of his thesis, Professor Meecham held a succession of appointments, including that of an Assistant Professor at the University of Michigan, a visiting scientist at the Scripps Institute of Oceanography, University of California, a Professor at the University of Minnesota, and a Senior Research Scientist at Lockheed Research Laboratories. Meecham's first paper in the *Journal of the Acoustical Society of America*, which appeared in May 1956 when he was at Michigan, was an important contribution to the theory of reflection from rough surfaces. Another paper, in April 1958 with G. W. Ford, applied and extended Lighthill's ideas on aerodynamic sound to the radiation of sound from isotropic turbulence. A related paper, in December 1960, addressed the problem of scattering of sound by isotropic turbulence. Then, in 1963, a provocative letter, written when Meecham was at Minnesota, addressed controversial aspects of the theory for the mechanisms by which sound was radiated by turbulent boundary layers. This was followed by an exchange of opinions in letters by John Ffowcs-Williams and Meecham in the June 1963 issue. A subsequent paper in March 1965 gave a fuller account of Meecham's ideas and addressed apparent paradoxes in the estimation of sound radiation from boundary layers. Also in 1965, Meecham addressed the still important problem of low-frequency sound (infrasound) in the atmosphere, especially the ducted propagation of acoustic-gravity waves over long distances. This work appeared in a Rand Corporation memorandum and was subsequently published in the *Proceedings of the IEEE*. (Professor Meecham published many papers over his lifetime; those mentioned above are only a representative sample of his early work that will be remembered by the acoustics community.)

In 1967, Meecham joined the University of California at Los Angeles as a Professor in the School of Engineering and Applied Sciences. Between 1969 and 1970, he was Chairman of the Mechanical and Aerospace Engineering Department. A principal achievement during his years at UCLA was the development of a simple source model for the quantification of jet noise. The work included both theoretical and experimental research and included several Master and Ph.D. students, the most recent achievement being a method for CFD-based calculation of jet engine exhaust noise. A major focus of his professional activities was the effects of jet noise on the general population. His studies of such effects for the flight-path corridor near Los Angeles International Airport resulted in the discovery that there was a higher rate of cardiovascular deaths, strokes, suicides, and murders among the 200 000 people who lived in this flight path than in the rest of Los Angeles. He partly attributed this to the effects to the prolonged exposure to loud noise. From 1990 to 1992, he was a member of the Citizens Advisory Committee of the Los Angeles Airport Commission.

In addition to his participation in the Acoustical Society of America, Professor Meecham was a founding member of the Institute of Noise Control Engineering (INCE), a member of Tau Beta Pi, Sigma Xi, and the American Physical Society. He was an Associate Fellow of the American Institute of Aeronautics and Astronautics and a member of the New York Academy of Science.

He is survived by his wife, son, and daughter.

PATRICK M. HURDLE
DENNIS REGAN
DAVID SCHEIN
NEIL SHAW
okc Penrod *et al.*Obituary

Claude Wendell Horton, Sr. • 1915–2002

Claude Wendell Horton, Sr., a Fellow of the Society, a leading figure in underwater acoustics research, and a recipient of the Society's Pioneers in Underwater Acoustics Medal, died in Austin, Texas, on March 2, 2002, following a long illness.

Horton was born in Cherryvale, Kansas, on September 23, 1915, grew up in Houston, and attended the Rice Institute (now Rice University). He received a B.A. (Honors) with a major in physics in 1935 and an M.A. in 1936, both from Rice. The following year he worked as an Assistant Seismologist for the Shell Oil Company, and this initiated an enduring interest in seismology and geophysics. Subsequent graduate studies were at Princeton in the academic year 1937–1938. On November 23, 1938, he married Louise Charlotte Walthall of Houston. He returned to Shell Oil in 1938, and was there chief of a group in exploration geology, and he held this position until January 1943, when he resigned to undertake efforts in support of World War II.

In May of 1943, he joined the staff of the Harvard Underwater Sound Laboratory (HUSL) and there carried out analytical studies on several aspects of underwater acoustics. He was then very heavily involved in the design of scanning sonars.

At the end of World War II, C. P. Boner, the Associate Director of the Harvard Underwater Sound Laboratory, initiated the establishment of the Defense Research Laboratory (DRL), now the Applied Research Laboratories, at the University of Texas, and Claude Horton was especially asked to be one of its founding staff members. As part of the DRL work in the development of a radar homing system for the new series of surface-to-air guided missiles, Horton in his early years at DRL made significant theoretical contributions to the theory of electromagnetic horn antennas and dielectric waveguides and antennas. He completed his graduate work at Texas and received a Ph.D. in Physics in 1948, the thesis being on the subject of the theory of horns.

When the Defense Research Laboratory moved into the field of underwater acoustics, Dr. Horton shifted his activities to this field and over the subsequent years made many significant contributions, especially in the general area of echo structures. Analytical and experimental work by Horton and his students progressed to a strong physical understanding of acoustic scattering from complex targets. This understanding of echo formation, coupled with the recognition of when and how statistical treatment is needed, culminated in the successful implementation of a device to automatically classify echoes. This also led to the development of innovative designs for transducers, especially of transducers–reflector combinations. Another accomplishment was a detailed understanding of the nearfield properties of directional transducers, so that one could predict the farfield performance of large transducers from near-field measurements.

 0001-4966/2005/117(5)/2677/2/$20.00

Related work was carried out on the echo structure caused by the ocean surface, bottom, and volume. Horton was a major leader in the use of statistical ideas for the treatment of such effects. The extent of the progress made over a period of 20 years is described in a paper, ''A review of reverberation, scattering, and echo structure'' [J. Acoust Soc. Am., **51**, 1049–1061 (1972)].

In 1980, Horton received the Pioneers of Underwater Acoustics Medal from the Acoustical Society of America; he was the 7th person to receive this award, which was instituted in 1959. The citation read as follows: ''For his contributions in underwater acoustics in the field of propagation, reflection, and scattering, signal processing, particularly methods in acoustic data treatment and interpretation, and especially for his contribution as a teacher and friend of scientists.''

As suggested by the last part of the citation, his activities as an educator at the University of Texas were especially significant. He joined the faculty of the Physics Department in 1946 and progressed to full professor in 1953, served as department chair from 1957 through 1962, and was instrumental in leading that department to the prominent place it holds today in the world of physics. He taught courses in acoustics and was a leading educator in the field at a specially critical time when there was a great need for highly trained professionals in acoustics. He supervised the work of 27 students for the Ph.D. degree and of 30 students for the Master's degree, and these students comprise an impressive list, which includes Chester McKinney and Loyd Hampton, both former Directors of the Applied Research Laboratory, Richard Lane, the founder of Tracor, and James Truchard, a co-founder of National Instruments. Horton also helped with the geophysics program at Texas, teaching a course during 1972–1975 and serving on doctoral committees in that field.

Horton retired in 1976, after 31 years as a professor. His research accomplishments are documented in some 69 published papers (of which 18 are in J. Acoust. Soc. Am.), in numerous technical reports, and in 4 patents. In 1978, the Applied Research Laboratory published a volume, ''The published papers of Claude W. Horton, Sr.: with listings of laboratory reports, dissertations, and theses,'' which can be found in various libraries. A significant publication was a book, ''Signal processing of underwater acoustic waves,'' which was sponsored by the Naval Ship Systems Command; it was published in 1969 and is distributed by the U.S. Government Printing Office.

Dr. Horton is survived by his wife Louise, by their son Wendell Horton and daughter Margaret Elaine Morefield.

CLARK S. PENROD
CHESTER M. MCKINNEY
LOYD HAMPTON

OBITUARIES

Claude Wendell Horton, Sr. • 1915–2002

Claude Wendell Horton, Sr., a Fellow of the Society, a leading figure in underwater acoustics research, and a recipient of the Society's Pioneers in Underwater Acoustics Medal, died in Austin, Texas, on March 2, 2002, following a long illness.

Horton was born in Cherryvale, Kansas, on September 23, 1915, grew up in Houston, and attended the Rice Institute (now Rice University). He received a B.A. (Honors) with a major in physics in 1935 and an M.A. in 1936, both from Rice. The following year he worked as an Assistant Seismologist for the Shell Oil Company, and this initiated an enduring interest in seismology and geophysics. Subsequent graduate studies were at Princeton in the academic year 1937–1938. On November 23, 1938, he married Louise Charlotte Walthall of Houston. He returned to Shell Oil in 1938, and was there chief of a group in exploration geology, and he held this position until January 1943, when he resigned to undertake efforts in support of World War II.

In May of 1943, he joined the staff of the Harvard Underwater Sound Laboratory (HUSL) and there carried out analytical studies on several aspects of underwater acoustics. He was then very heavily involved in the design of scanning sonars.

At the end of World War II, C. P. Boner, the Associate Director of the Harvard Underwater Sound Laboratory, initiated the establishment of the Defense Research Laboratory (DRL), now the Applied Research Laboratories, at the University of Texas, and Claude Horton was especially asked to be one of its founding staff members. As part of the DRL work in the development of a radar homing system for the new series of surface-to-air guided missiles, Horton in his early years at DRL made significant theoretical contributions to the theory of electromagnetic horn antennas and dielectric waveguides and antennas. He completed his graduate work at Texas and received a Ph.D. in Physics in 1948, the thesis being on the subject of the theory of horns.

When the Defense Research Laboratory moved into the field of underwater acoustics, Dr. Horton shifted his activities to this field and over the subsequent years made many significant contributions, especially in the general area of echo structures. Analytical and experimental work by Horton and his students progressed to a strong physical understanding of acoustic scattering from complex targets. This understanding of echo formation, coupled with the recognition of when and how statistical treatment is needed, culminated in the successful implementation of a device to automatically classify echoes. This also led to the development of innovative designs for transducers, especially of transducers–reflector combinations. Another accomplishment was a detailed understanding of the nearfield properties of directional transducers, so that one could predict the farfield performance of large transducers from near-field measurements.

Related work was carried out on the echo structure caused by the ocean surface, bottom, and volume. Horton was a major leader in the use of statistical ideas for the treatment of such effects. The extent of the progress made over a period of 20 years is described in a paper, ''A review of reverberation, scattering, and echo structure'' [J. Acoust Soc. Am., **51**, 1049–1061 (1972)].

In 1980, Horton received the Pioneers of Underwater Acoustics Medal from the Acoustical Society of America; he was the 7th person to receive this award, which was instituted in 1959. The citation read as follows: ''For his contributions in underwater acoustics in the field of propagation, reflection, and scattering, signal processing, particularly methods in acoustic data treatment and interpretation, and especially for his contribution as a teacher and friend of scientists.''

As suggested by the last part of the citation, his activities as an educator at the University of Texas were especially significant. He joined the faculty of the Physics Department in 1946 and progressed to full professor in 1953, served as department chair from 1957 through 1962, and was instrumental in leading that department to the prominent place it holds today in the world of physics. He taught courses in acoustics and was a leading educator in the field at a specially critical time when there was a great need for highly trained professionals in acoustics. He supervised the work of 27 students for the Ph.D. degree and of 30 students for the Master's degree, and these students comprise an impressive list, which includes Chester McKinney and Loyd Hampton, both former Directors of the Applied Research Laboratory, Richard Lane, the founder of Tracor, and James Truchard, a co-founder of National Instruments. Horton also helped with the geophysics program at Texas, teaching a course during 1972–1975 and serving on doctoral committees in that field.

Horton retired in 1976, after 31 years as a professor. His research accomplishments are documented in some 69 published papers (of which 18 are in J. Acoust. Soc. Am.), in numerous technical reports, and in 4 patents. In 1978, the Applied Research Laboratory published a volume, ''The published papers of Claude W. Horton, Sr.: with listings of laboratory reports, dissertations, and theses,'' which can be found in various libraries. A significant publication was a book, ''Signal processing of underwater acoustic waves,'' which was sponsored by the Naval Ship Systems Command; it was published in 1969 and is distributed by the U.S. Government Printing Office.

Dr. Horton is survived by his wife Louise, by their son Wendell Horton and daughter Margaret Elaine Morefield.

CLARK S. PENROD
CHESTER M. MCKINNEY
LOYD HAMPTON

 0001-4966/2005/117(5)/2678/1/$20.00

REVIEWS OF ACOUSTICAL PATENTS

Lloyd Rice
11222 Flatiron Drive, Lafayette, Colorado 80026

The purpose of these acoustical patent reviews is to provide enough information for a Journal reader to decide whether to seek more information from the patent itself. Any opinions expressed here are those of reviewers as individuals and are not legal opinions. Printed copies of United States Patents may be ordered at $3.00 each from the Commissioner of Patents and Trademarks, Washington, DC 20231. Patents are available via the Internet at http://www.uspto.gov.

Reviewers for this issue:

GEORGE L. AUGSPURGER, *Perception, Incorporated, Box 39536, Los Angeles, California 90039*
JOHN M. EARGLE, *JME Consulting Corporation, 7034 Macapa Drive, Los Angeles, California 90068*
SEAN A. FULOP, *California State University, Fresno, 5245 N. Backer Avenue M/S PB92, Fresno, California 93740-8001*
IBRAHIM M. HALLAJ, *Wolf Greenfield & Sacks P.C., 600 Atlantic Avenue, Boston, Massachusetts 02210*
JEROME A. HELFFRICH, *Southwest Research Institute, San Antonio, Texas 78228*
MARK KAHRS, *Department of Electrical Engineering, University of Pittsburgh, Pittsburgh, Pennsylvania 15261*
DAVID PREVES, *Starkey Laboratories, 6600 Washington Ave. S., Eden Prarie, Minnesota 55344*
DANIEL R. RAICHEL, *2727 Moore Lane, Fort Collins, Colorado 80526*
CARL J. ROSENBERG, *Acentech Incorporated, 33 Moulton Street, Cambridge, Massachusetts 02138*
NEIL A. SHAW, *Menlo Scientific Acoustics, Inc., Post Office Box 1610, Topanga, California 90290*
WILLIAM THOMPSON, JR., *Pennsylvania State University, University Park, Pennsylvania 16802*
ERIC E. UNGAR, *Acentech, Incorporated, 33 Moulton Street, Cambridge, Massachusetts 02138*
ROBERT C. WAAG, *Univ. of Rochester, Department of Electrical and Computer Engineering, Rochester, New York 14627*

6,796,182

43.20.Dk METHOD FOR TESTING STUDS AND CORRESPONDING DEVICE

Joachim Wagner and Walter Schappacher, assignors to Agfa NDT GmbH
28 September 2004 (Class 73/588); filed in Germany 13 July 2000

A pair of ultrasonic transducers **A** and **B** is placed at an angle to the surface of a piece of sheet metal to which a bolt **8** is to be welded. By measuring the relative intensity of the ultrasonic signal and translating the pair of transducers across the location of the weld, the size of a weld spot **10** can be determined, and thereby a determination of the quality of the weld can be made.—IMH

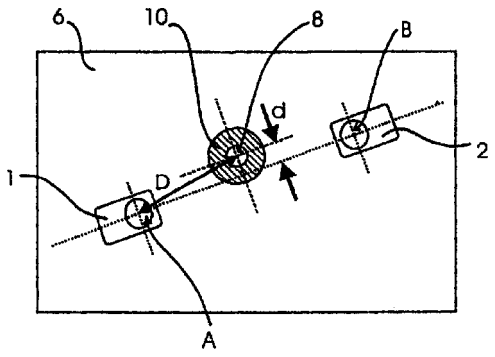

6,811,630

43.20.Ks ULTRASONIC VIBRATION METHOD AND ULTRASONIC VIBRATION APPARATUS

Morio Tominaga and Shinji Iwahashi, assignors to Sony Corporation
2 November 2004 (Class 156/73.1); filed in Japan 20 November 2000

A method is described for exciting a composite ultrasonic vibration in a structure. Two coupled, intersecting, ultrasonic horns **11**, **12** are driven in their respective longitudinal dimensions to excite a respective transverse vibration, each in the other horn. The point at which the horns are joined is thus driven in a composite vibration, which can be transmitted to another member (not shown in figure) or used to perform an operation, such as ultrasonic welding.—IMH

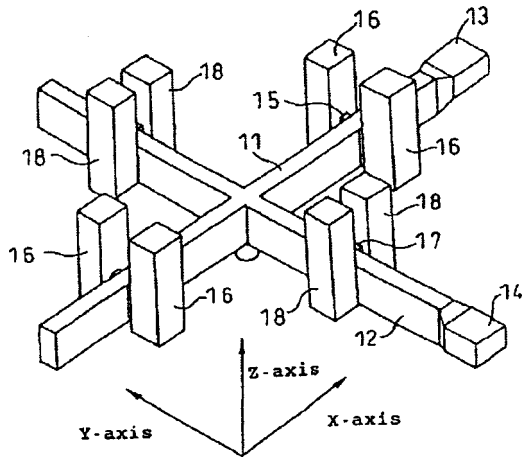

 0001-4966/2005/117(5)/2682/21/$20.00

6,798,716

43.20.Px SYSTEM AND METHOD FOR WIRELESS ELECTRICAL POWER TRANSMISSION

Arthur Charych, assignor to BC Systems, Incorporated
28 September 2004 (Class 367/119); filed 19 June 2003

The patent presents a wireless electrical power transmission technique in which an electrically driven acoustic transducer array projects a focused beam onto a second transducer apparatus, which converts the acoustic energy back into electrical energy. This can be used to charge an electrical device (e.g., a battery of a portable device). The patent describes the power transmitting array as being capable of spatially scanning a space to locate a device to power, or even more than one device, through known beam-steering techniques.—IMH

6,829,197

43.30.Gv ACOUSTICAL IMAGING INTERFEROMETER FOR DETECTION OF BURIED UNDERWATER OBJECTS

Kenneth R. Erikson, assignor to BAE Systems Information and Electronic Systems Integration INC
7 December 2004 (Class 367/88); filed 30 July 2003

A technique for the underwater detection of fully or partially buried objects, such as mines or cables, is discussed. An acoustical camera mounted aboard a maneuverable underwater vehicle produces initial images of some target area. An acoustical pulse radiated by another onboard transducer is then directed at that target area with the purpose of disturbing loose particulate matter overlaying the area. Second images of the target area taken by the acoustical camera are compared with the first images for evidence of buried objects.—WT

6,831,876

43.30.Xm ACOUSTIC WINDOW

Craig L. Cartwright, assignor to Goodrich Corporation
14 December 2004 (Class 367/152); filed 9 July 2003

This invention is concerned with improving the acoustic transparency of underwater sonar windows, especially at non-normal angles of incidence. A sandwich construction is described in which a low-impedance core material is bonded to at least one ply of a different material having specified acoustic characteristics. The patent includes formulas for determing preferred specifications for the two materials. Relatively uniform transmission can be achieved over an incidence angle greater than $\pm 40°$.—GLA

6,822,535

43.35.Pt FILM BULK ACOUSTIC RESONATOR STRUCTURE AND METHOD OF MAKING

Qing Ma *et al.*, assignors to Intel Corporation
23 November 2004 (Class 333/187); filed 28 March 2002

This patent discloses a method of fabricating Al-N thickness-mode resonators. The novel feature is that it uses the 1-3 mode of actuation, with piezo parts formed of layers deposited on the sidewalls of trenches.—JAH

6,822,785

43.35.Sx MINIATURE, NARROW BAND, NON-COLLINEAR ACOUSTIC OPTICAL TUNABLE FILTER FOR TELECOM APPLICATIONS

Raymond R. Chu and Qing Jiang, assignors to Acceeze, Incorporated
23 November 2004 (Class 359/308); filed 4 June 2003

This patent describes a method for providing a tunable filter for optical fiber signal communication systems. The device includes an acousto-optical tuning device which uses TeO_2 in share mode, is non-collinear, and in a high-radio-frequency range (or a large Bragg's deflection region). It is said that it achieves a telecom-worthy tunable filter that provides high tuning speed, no moving parts, very narrow filter line-widths (on the order of 0.2 nm), and miniaturization sufficient for incorporation in a telecom-active module. Other than the TeO_2 crystals, a tunable filter can also be created with AsS_3 and GeAsBe crystals based on the same acousto-optical interaction processes in the higher rf range.—DRR

6,811,631

43.35.Zc DEVICE AND METHOD FOR WELDING THIN-WALLED WORK PIECES USING ULTRASOUND

Hartmut Möglich, assignor to Herrmann Ultraschalltechnik GmbH & Company KG
2 November 2004 (Class 156/73.1); filed in Germany 30 March 2002

Here is an ultrasonic welding tool that secures a portion of thin work

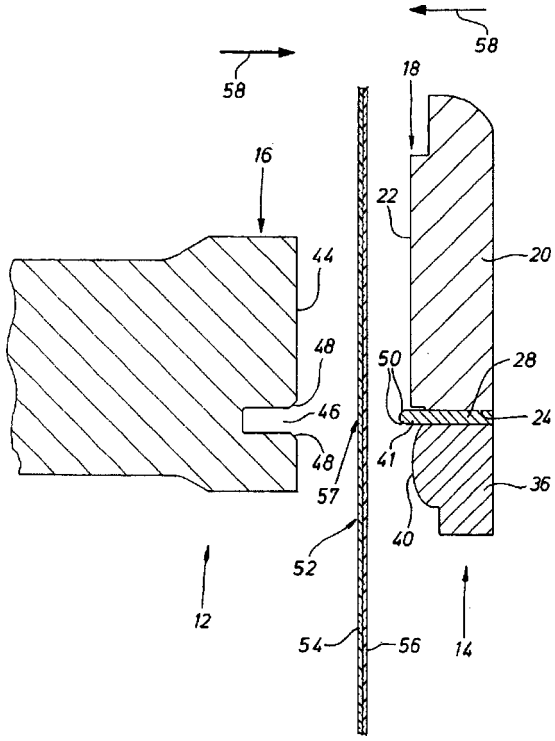

pieces **54**, **56** within a mating projection **41** and recess **46**.—IMH

6,796,184

43.35.Zc ULTRASOUND SORTING OF WEANLINGS AND IDENTIFICATION OF TENDERNESS INDICATORS

Rethel C. King, Harrison, Arkansas
28 September 2004 (Class 73/602); filed 9 July 2003

This is essential reading for meat eaters and will perhaps also be informative for vegetarians looking for affirmation of their lifestyles. According to the patent, ultrasonic ''carcass measurement'' is used in the cattle industry to assist in optimizing ''harvest time'' and quality of meat, and therefore provides ''maximum financial gain'' to meat producers. Here, 3.5-MHz transmit-receive devices are used to determine tenderness according to National Cattlemen's Beef Association standards. For example, measuring the length of the longissimus dorsi muscle (rib eye) has been conducted to arrive at a rib eye shape (RES). Also, the RES of a ''weanling'' age calf is found to be a useful parameter for predicting the yield grade potential of its meat. Furthermore, it is found that the relative angle between the centerline of an animal and the connective tissue of the longissimus dorsi muscle is inversely related to its tenderness, with angles less than 27° being ''tender.'' Breeding decisions can be informed by the results of such testing. Bon apetit.—IMH

6,802,920

43.35.Zc ULTRASONIC WAVE SEALING METHOD FOR CONTAINER

Mitsuhiko Shinohara and Michio Ueda, assignors to Shikoku Kakoki Company, Limited
12 October 2004 (Class 156/73.1); filed in Japan 12 March 2001

The patent describes sealing a container by applying pressure using an ultrasonic horn while simultaneously applying a rotational ultrasonic vibration that seals the edges of the container.—IMH

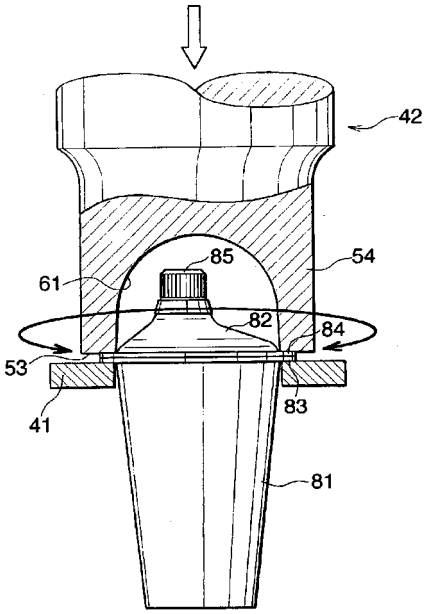

6,813,950

43.35.Zc PHASED ARRAY ULTRASONIC NDT SYSTEM FOR TUBES AND PIPES

David Glascock *et al.*, assignors to R/D Tech Incorporated
9 November 2004 (Class 73/633); filed 25 July 2002

This is a system for nondestructive testing of solid tubes. The system includes a phased ultrasonic array **2** having a curved face to match a tube being tested **4**. Defects in three dimensions (longitudinal, transverse, oblique) are detected by refraction of incident waves in a transmit-receive configuration of the array.—IMH

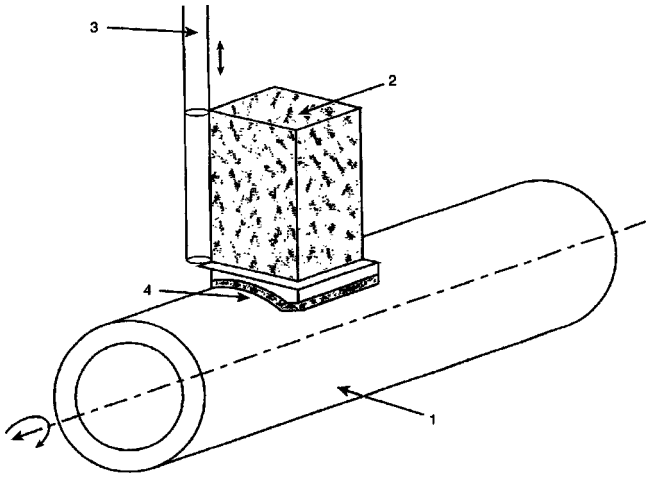

6,818,098

43.35.Zc ULTRASONIC BONDING MACHINE

Shigeru Sato and Seiya Nakai, assignors to Ultex Corporation
16 November 2004 (Class 156/580.2); filed in Japan 3 October 2002

This is a device for ultrasonic welding of layers (sheets) of overlapped work pieces. The device includes a roller coupled to an ultrasonic source that can project into the workpieces while being rotated with a handle. The workpieces are pressed between the roller and a table to ensure good coupling of ultrasound between the source and the workpieces.—IMH

6,825,592

43.35.Zc VIBRATORY MOTORS AND METHODS OF MAKING AND USING SAME

Bjoern Magnussen *et al.*, assignors to Elliptec Resonant Actuator AG
30 November 2004 (Class 310/323.02); filed 22 October 2003

This lengthy patent covers the principles of operation of a piezo-actuated ultrasonic motor that operates in two frequency ranges through the use of separately tuned resonances. The patent refers to over 80 previous patents, and the claims are quite specific. There is no mention of a MEMS application here, although the geometries depicted are quite generally applicable to any length scale.—JAH

6,827,724

43.35.Zc ULTRASONIC VIBRATOR CAPABLE OF INFALLIBLY PREVENTING DROPS OF WATER FROM ENTERING THE INSIDE OF A CASING OF THE VIBRATOR EVEN IF AUTOCLAVE STERILIZATION WITHOUT A DRYING PROCESS IS PERFORMED

Norikiyo Shibata, assignor to Olympus Corporation
7 December 2004 (Class 606/169); filed in Japan 8 June 1999

The object of this bolt-fastened, Langevin-type, ultrasonic vibrator is to provide waterproofing against water droplets from entering its casing, even if autoclave sterilization is performed without the benefit of a drying process. The patent essentially describes sheathing over the vibrator mechanism (which contains a transducer for driving a plurality of vibrating elements) so as to prevent water leakage into the system.—DRR

6,819,946

43.38.Ar APPARATUS AND METHOD FOR CONTROLLING SOURCE OF SOUND EMITTED FROM A MOBILE TERMINAL

Magnus F. Hansson, assignor to Sony Ericsson Mobile Communications AB
16 November 2004 (Class 455/569.1); filed 4 October 2002

The patent deals with the application of a single transducer in a portable communications device such as a cell phone for both alerting the user of an incoming call as well as providing at-the-ear reception. The two basic conditions call for different signal levels. Prior technology has included using a pair of transducers, as well as use of a mechanical cowl that directs the transducer's output where needed. This patent describes further improvements, including automatic operation of the cowl.—JME

6,821,252

43.38.Ar HARMONIC TRANSDUCER ELEMENT STRUCTURES AND PROPERTIES

Kjell Arne Ingebrigtsen and Arne Ronnekleiv, assignors to G.E. Medical Systems Global Technology Company, LLC
23 November 2004 (Class 600/459); filed 26 March 2002

An embodiment of this device consists of a transducer element for ultrasound transmission and reception. One active transducer layer is connected to a receiver and transmitter. A second layer is laminated to the first and is connected to a second receiver and a second transmitter. The transducer element may incorporate passive circuitry in which a pulse pair is processed so as to have differing amplitudes, time delays, and pulse shapes prior to being combined into a single ultrasound pulse.—DRR

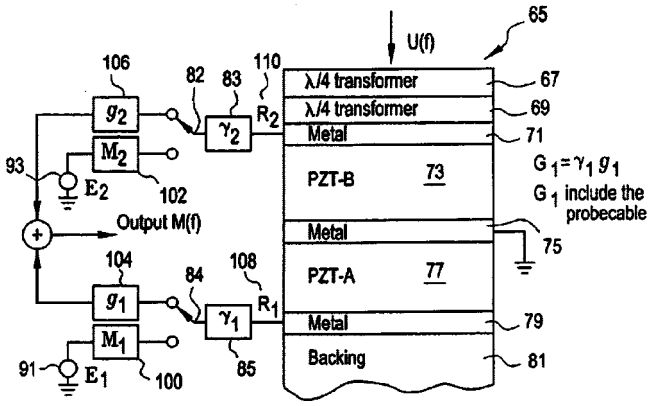

6,823,073

43.38.Ar DIRECTIONAL MICROPHONE ASSEMBLY

Dion Ivo de Roo, assignor to Sonionmicrotronic Nederland B.V.
23 November 2004 (Class 381/92); filed in Denmark 19 January 2000

The patent describes the synthesis of forward-oriented, first-order directional patterns through combination of the outputs of two small fore-aft omnidirectional elements via polarity inversion and time delay. The array can operate in an omni mode in quiet surroundings, switching to a directional mode when higher ambient noise levels are detected.—JME

6,831,987

43.38.Ar DIRECTIONAL MICROPHONE ASSEMBLY

Mead C. Killion *et al.*, assignors to Etymotic Research, Incorporated
14 December 2004 (Class 381/313); filed 19 May 2003

Certainly the most beneficent and humane industry in acoustical engineering is that which deals with devices for the hearing impaired. This finely written patent goes into great detail on the design of small directional microphone elements for hearing aid application, covering a broad range of topics, including relevant measurements, circuit component values, and discussion of hearing loss itself. The authors of this patent are surely experts in their field, and this patent may contain just about everything most readers might ever want to know about the art.—JME

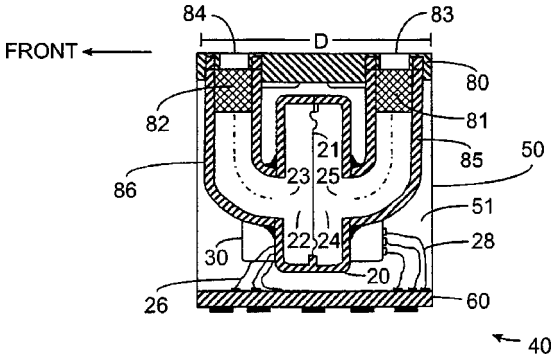

6,817,244

43.38.Bs METHODS AND SYSTEMS FOR ACTIVELY CONTROLLING MOVEMENT WITHIN MEMS STRUCTURES

William P. Platt, assignor to Honeywell International Incorporated
16 November 2004 (Class 73/504.16); filed 6 January 2003

This patent describes an electronic control system for certain types of interdigitated (comb-drive) actuators, which separates and controls the common mode (out of plane) and differential mode (in plane) motions separately. The disclosure goes into detail on how this is done for a MEMS gyroscope structure, with schematics and electrode geometries given.—JAH

6,818,959

43.38.Bs MEMS DEVICES WITH VOLTAGE DRIVEN FLEXIBLE ELEMENTS

Lars G. Montelius *et al.*, assignors to BTG International Limited
16 November 2004 (Class 257/415); filed in the United Kingdom 12 March 2002

This patent discloses a design for MEMS devices consisting of many lateral fingers of silicon that are individually electrostatically controlled. The focus of the patent is on optical applications (variable reflectivity screens,

variable polarizers, etc.), but claims are also made for molecular sensors and rf filter applications. The discussion is clear and interesting with some data to back it up.—JAH

6,819,769

43.38.Bs ELECTROLYTIC LOUDSPEAKER ASSEMBLY

Claus Zimmermann, Newbury Park, California
16 November 2004 (Class 381/152); filed 1 December 1999

Loudspeakers for ''high fidelity'' audio systems, according to the patent, are generally categorized as either magnetic moving coil or nonmagnetic electrostatic. Many electrostatic loudspeaker designs require a high dc bias voltage, which can be as high as 3500 VDC, to operate. In this error-filled and confusing patent, a means of improving the electret properties of the diaphragm (to eliminate the dc bias voltage), an improved means of

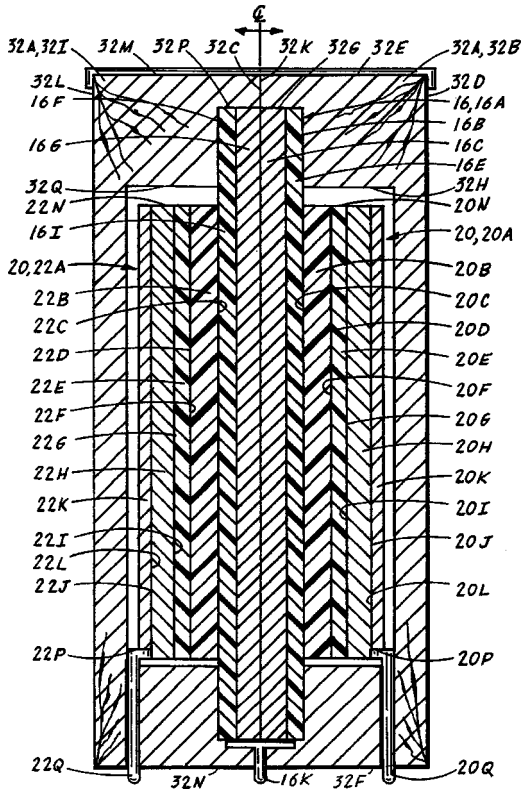

building the composite diaphragm (for cost effectiveness), as well as a design for an acoustic wave diffusing, reflecting, and absorbing structure, and an acoustic baffle structure are presented. The inventor is associated with a company that manufactures and markets electrostatic loudspeakers. Many of the concepts disclosed in the patent could find use in other than high-end electrostatic systems.—NAS

6,829,131

43.38.Ew MEMS DIGITAL-TO-ACOUSTIC TRANSDUCER WITH ERROR CANCELLATION

Wayne A. Loeb *et al.*, assignors to Carnegie Mellon University
7 December 2004 (Class 361/234); filed 13 September 1999

This odd little patent claims to have invented the ''micromachined membrane fabricated on the substrate and a layer of material sealing said substrate.'' That is a pretty broad claim for an earphone. The novelty claimed is that all of the fabrication steps are done in CMOS-compatible process, so that there is room left for an A/D converter, a sensor amplifier, a DSP core for filtering, and a PWM amplifier. The microphone diaphragm is of an unusual slotted design to allow for flexibility and reduce manufacturing steps. It is also supposed to operate reversibly as a speaker, using only capacitive drive and sensing. There are no data to quantify the performance of this device as a sound emitter, but it is probably very poor. Also thrown in for good measure are motional feedback and PCM to PWM conversion. There are some design expressions thrown in, but the whole thing is just a jumble of blocks added to a flexible suspension for a diaphragm.—JAH

6,816,295

43.38.Fx MEMS VARIABLE OPTICAL ATTENUATOR

Jung Hyun Lee *et al.*, assignors to Samsung Electro-Mechanics Company, Limited
9 November 2004 (Class 359/227); filed in the Republic of Korea 7 April 2003

This patent describes a variable knife-edge optical attenuator fabricated from a comb-drive actuator in silicon. The parts can all be surface micromachined, but it calls for some metal deposition on parts at acute angles. It is basically a micron-sized mechanical shutter.—JAH

6,819,029

43.38.Fx VIBRATION WAVE DRIVING APPARATUS

Yuuji Ohno *et al.*, assignors to Canon Kabushiki Kaisha
16 November 2004 (Class 310/323.17); filed in Japan 12 March 2001

This patent describes a device for translating and rotating an object (such as a ball or flat plate) placed upon it. The device is a sort of four-legged pedestal with piezoelectronic actuators driving the legs individually. The outcome is pretty easy to imagine, but there is a lot of analysis of the vibration modes of the base, as described in the patent, to show how to execute various motions. Little or no mention of MEMS fabrication methods or applications is made, and the device does not depend on size for its functionality.—JAH

6,831,985

43.38.Fx PIEZOELECTRIC SPEAKER

Toshitaka Takei, Fujisawa-shi, Kanagawa-ken, Japan
14 December 2004 (Class 381/190); filed in Japan 13 July 2000

Diaphragm 1 is a piezoelectric bimorph formed from two or more layers of film, pleated into a serpentine shape. Its operation is that of a Heil ''air motion transformer'' in which forward-facing cells contract while rearward facing cells expand, and vice versa. In this design, the serpentine edges

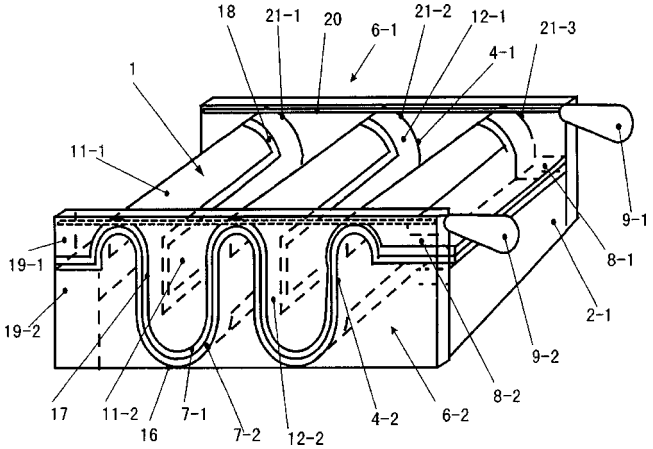

are clamped between two pairs of side blocks, which is said to simplify assembly and maintain constant tension over time. Also, the etched-circuit electrodes are designed to minimize the chance of electric shock or burnout.—GLA

6,813,362

43.38.Ja LOUDSPEAKER AND METHOD OF MAKING SAME

Andrew D. Bank *et al.*, assignors to New Transducers Limited
2 November 2004 (Class 381/152); filed in the United Kingdom 5 April 2001

Distributed mode loudspeakers lend themselves to some novel implementations. The patent describes a multitude of these that can be called folded panel and multiple panel. In one instance, a cardboardlike material is folded into a tilted truncated pyramid to which two exciters **88** are attached to the front face **82** and one exciter each are attached to side faces **84**. One benefit claimed is that the set of modes of one subpanel can be calculated to be substantially different from that of another panel, and the resulting sets of modes can then be constructively interleaved, thereby improving the response of the assembly. Various materials are described which can be used

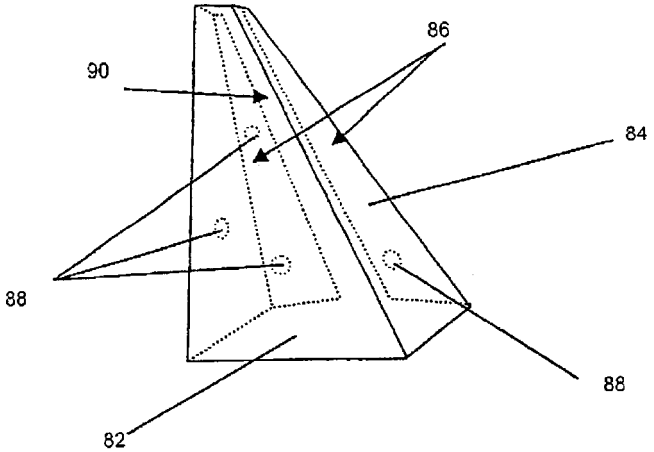

for the ''cardboard material'' and the patent includes an extensive review of how the base material can be grooved or otherwise manipulated to form the hinges. Some of the various materials that can be used to join separate panels together and the benefits of these are presented. A formula and graph are included to help in determining the panels' optimum aspect ratios. One could see how the material could be printed with a message and used for point-of-purchase applications, themed for an event, among other uses.—NAS

6,820,718

43.38.Ja ACOUSTIC REPRODUCTION DEVICE WITH IMPROVED DIRECTIONAL CHARACTERISTICS

Emanuel LaCarrubba, Novato, California
23 November 2004 (Class 181/155); filed 4 October 2002

In the original Voigt corner horn, sound waves were conducted upward then bounced off a complicated reflector to emerge in a horizontal fan-shaped pattern. Western Electric used a similar reflector in certain right-angle, high-frequency horns. Now, more than 50 years later, experimenters continue to exploit the possibilities of specially shaped reflecting surfaces.

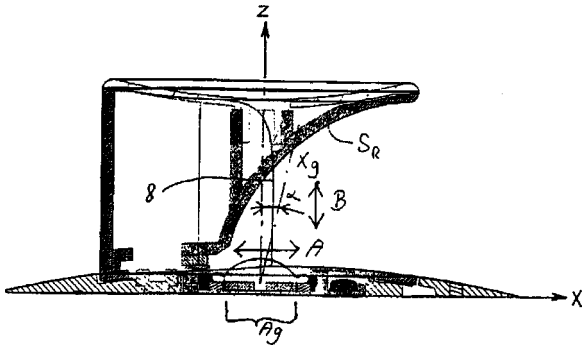

In earlier United States patents 5,615,176, 6,068,080, and 6,435,301, the inventor described a clever design employing intersecting ellipsoidal surfaces. This latest update suggests that additional pattern control can be achieved by scaling size in relation to wavelength, adding absorptive areas, and using different kinds of acoustic generators for different frequency bands.—GLA

6,826,285

43.38.Ja BENDING WAVE LOUDSPEAKER

Henry Azima, assignor to New Transducers Limited
30 November 2004 (Class 381/152); filed in the United Kingdom 3 August 2000

The inventor holds a number of patents dealing with panel-type, bending wave loudspeaker designs. Most of these deal with distributed mode operation, i.e., exploiting panel resonances to achieve nondirectional, wideband response. But what happens if such a panel is critically damped so that no energy is reflected from its edges? Such damping can be achieved through a combination of panel construction, edge damping, and additional damping applied to specific areas of the panel. This patent asserts that such a device exhibits a number of desirable features not found in other types of loudspeakers or microphones. The patent includes interesting background information, theoretical development, and test results. Those interested in the field will want to obtain a copy.—GLA

6,819,773

43.38.Ja LOUDSPEAKER WITH A THREE-DIMENSIONAL DIAPHRAGM

Guido Odilon Maurits D'Hoogh, assignor to Koninklijke Philips Electronics N.V.
16 November 2004 (Class 381/396); filed in the European Patent Office 10 August 2001

Various kinds of inside-out loudspeakers have been designed to reduce depth or provide more efficient cooling. In this case, the goal is to reduce the

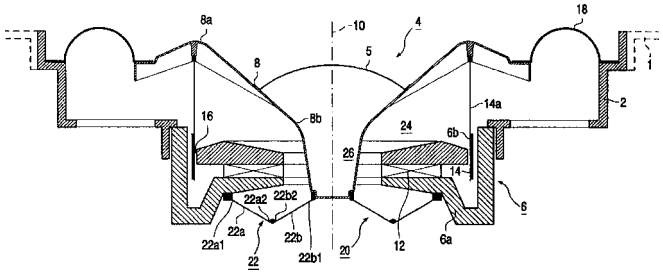

(wasted) air volume occupied by a conventional conical diaphragm, yet provide for large excursions over an extended period of time.—GLA

6,818,815

43.38.Md PHONOGRAPH TURNTABLE WITH MIDI OUTPUT

Laurent Cohen, assignor to Stanton Magnetics Incorporated
16 November 2004 (Class 84/645); filed 6 May 2002

Today, there are turntablists who are artists in their own right. This reviewer has seen them perform solo, where they are colloquially referred to as DJs, and as part of a modern music performance group. The patent describes a way in which the turntablist can use the instrument, the turntable

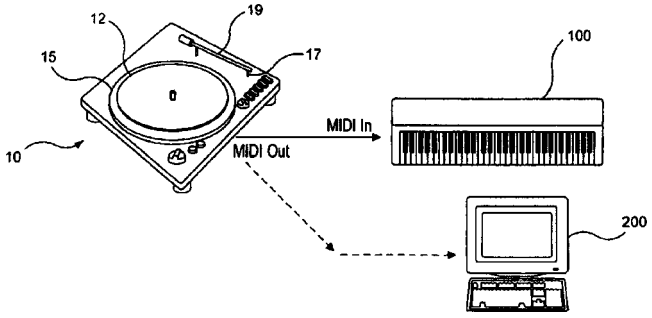

10, to control other devices, such as **100** and **200**, that accept MIDI time code and control information. The assignee is a well-known manufacturer of turntables, phonograph cartridges, and other DJ equipment and this patent portends new products to come. The patent itself is short and easy to read.—NAS

6,829,360

43.38.Md METHOD AND APPARATUS FOR EXPANDING BAND OF AUDIO SIGNAL

Kazuya Iwata *et al.*, assignors to Matsushita Electric Industrial Company, Limited
7 December 2004 (Class 381/61); filed in Japan 14 May 1999

Given a band-limited signal, the question is how to expand the signal to fill the rest of the spectrum. The solution outlined here is to use a nonlinear function (absolute value with dc bias removed) to generate harmonics

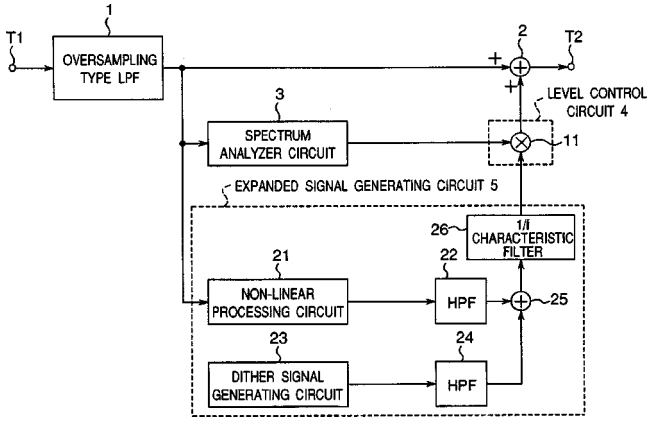

and a weighted dither. These are weighted by a simple $1/f$ filter before being added in by a bandweighted filter.—MK

6,817,440

43.38.Si MULTI-CHANNEL HEADPHONES

Sung-Il Kim, assignor to MM Gear Company, Limited
16 November 2004 (Class 181/128); filed in the Republic of Korea 26 February 2000

How is it possible to convey front- and rear-channel surround sound information to a listener wearing headphones? A number of inventors have

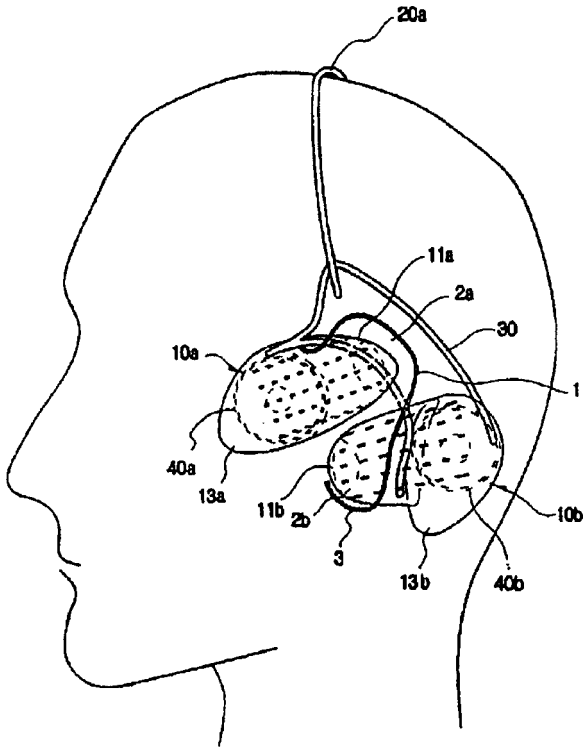

patented double-transducer headphones that convey front-channel information to the front portions of the user's ears, and rear-channel information to the rear portions. What could be more logical? However, this patent takes a different approach—front-channel information is conveyed to the upper portion of the user's ears and rear-channel information is conveyed to the lower portions.—GLA

6,832,663

43.38.Si EAR COUPLER

Jessica Ash Warring and Alfred Christian Walton, assignors to Natus Medical Incorporated
21 December 2004 (Class 181/129); filed 27 August 2001

This device is a transparent, one-piece coupler with an internal chamber that creates a tuned acoustic environment in the immediate vicinity of the subject's ear. It has a port to accommodate a transducer and a flange positioned around the periphery of the coupler for mounting the unit over the subject's ear. The goal is to provide an ear coupler that is more usable for

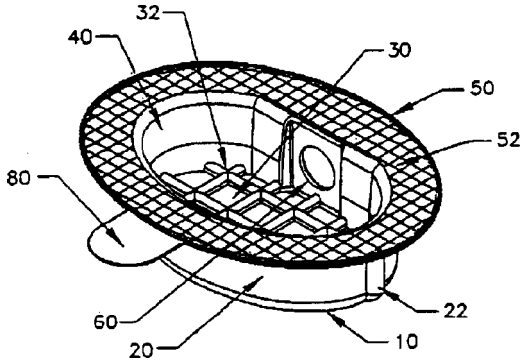

monitoring infants' hearing and one that is not subject to being tugged off the head by forces acting on the transducer housing. It is also said that this coupler can be manufactured inexpensively by injection molding or other suitable processes.—DRR

6,825,593

43.38.Si PIEZOELECTRIC TYPE ELECTRIC ACOUSTIC CONVERTER

Tetsuo Takeshima, assignor to Murata Manufacturing Company, Limited
30 November 2004 (Class 310/330); filed in Japan 19 April 2000

This patent describes a design for a piezo-bimorph speaker element suitable for cell phones and other portable applications. The central part of the claims concerns the electroding scheme and the encapsulation so as to make it easy to fabricate and shatter resistant as well. There is no mention of its application to MEMS-scale devices.—JAH

6,829,365

43.38.Si MP-3 PLAYER

Cheon-Kuk Kim, assignor to I & C Company, Limited
7 December 2004 (Class 381/370); filed in the Republic of Korea 18 January 2000

Today's technology allows several thousand musical compositions to be stored and replayed from a device not much larger than a cigarette lighter. Simply plug in a lightweight headset and you have a complete stereo reproduction system. Well, why not include the electronics in the headset itself?

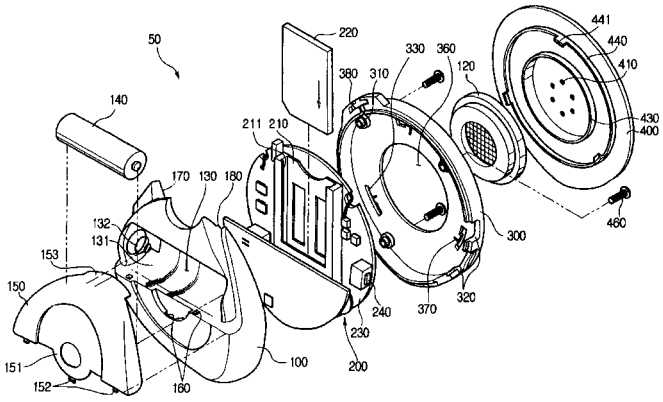

The patent at hand describes a practical implementation of this general concept.—GLA

6,819,767

43.38.Vk SPEAKER UNIT AND SOUND REPRODUCTION APPARATUS USING THE SAME

Osamu Funahashi and Hiroyuki Morimoto, assignors to Matsushita Electric Industrial Company, Limited
16 November 2004 (Class 381/27); filed 14 September 2000

In automotive sound systems, it is common practice to use a dual voice-coil loudspeaker as a subwoofer, allowing left and right signals to be summed without the need for an additional power amplifier. This 23-page patent suggests that the same trick can be used to drive a vocal-range center speaker.—GLA

6,829,361

43.38.Vk HEADPHONES WITH INTEGRATED MICROPHONES

Ronaldus Maria Aarts, assignor to Koninklijke Philips Electronics N.V.
7 December 2004 (Class 381/309); filed in the European Patent Office 24 December 1999

This patent assumes that each earcup of a pair of headphones can be fitted with a microphone such that the microphone accurately registers the sound produced by the headphone and also that produced by an external source such as a loudspeaker. (This is a formidable assumption.) The patent

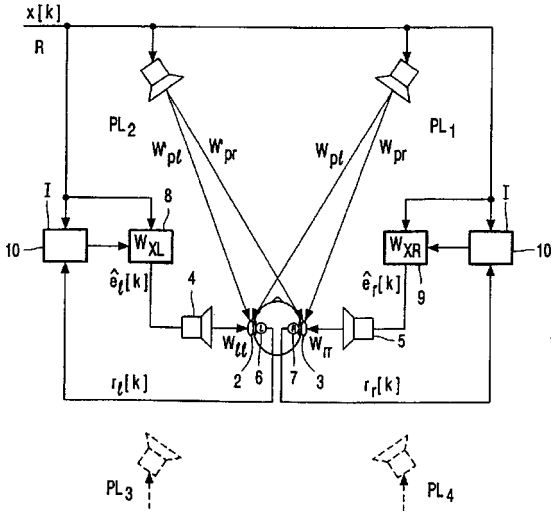

teaches that, with a little digital processing, relationships between the various signals can be used to derive reasonably accurate head-related transfer functions for a particular listener. Known techniques can then be employed to calculate suitable correction filters.—GLA

6,820,985

43.40.Dx DISPLAY PANEL AND PRODUCTION METHOD THEREFOR

Masafumi Ookawa *et al.*, assignors to Matsushita Electric Industrial Company, Limited
23 November 2004 (Class 359/513); filed in Japan 19 April 2000

Under normal drive conditions, some plasma display panels may produce noise due to panel vibration that may be a nuisance to close-in users. The patent describes design and manufacturing methods for minimizing this problem and maintaining noise levels in the range of 30 dB L_p or lower.—JME

6,805,244

43.40.Ey ULTRASOUND QUALITY INSPECTION OF AVIAN EGGS

L. Taizo Toelken, assignor to Ultra Hatch, Incorporated
19 October 2004 (Class 209/510); filed 16 July 2002

An ''endless succession of avian eggs'' is passed through a testing station that includes an opposing ultrasonic transducer pair capable of testing the quality of the egg shells. Grading into categories can then be accom-

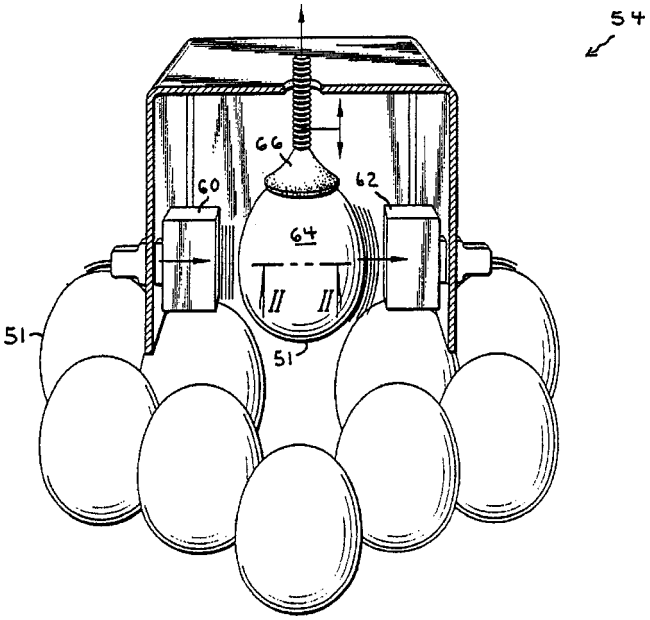

plished and the eggs can be classified as being suitable for people to eat, animals to eat, or rubbish.—IMH

6,828,020

43.40.Tm SELF-ADHESIVE VIBRATION DAMPING TAPE AND COMPOSITION

Dennis K. Fisher and Siddhartha Asthana, assignors to Adco Products, Incorporated
7 December 2004 (Class 428/355 EN); filed 14 August 2002

A damping tape consists of a dissipative adhesive layer topped by a relatively stiff layer. The tape described in this patent is intended to be adhered to automotive sheet metal components to increase their damping. This is said to produce relatively high damping in the temperature and frequency ranges of interest and can be made of comparatively inexpensive materials.—EEU

6,827,551

43.40.Tm SELF-TUNING IMPACT DAMPER FOR ROTATING BLADES

Kirsten P. Duffy *et al.*, assignors to The United States of America as represented by the Administrator of the National Aeronautics and Space Administration
7 December 2004 (Class 415/119); filed 1 February 2000

A spherical mass fits loosely into a cavity located near the tip of each blade of a compressor or turbine so that rattling of the mass against its confining surfaces can damp the vibrations of the blade. The cavity is shaped so that the mass' rattling distance changes as the centrifugal force changes with machine speed, thereby tuning the damping.—EEU

6,817,456

43.40.Tm DYNAMIC DAMPER FOR STEERING SYSTEM

Rentaro Kato and Takahiro Aoi, assignors to Tokai Rubber Industries, Limited
16 November 2004 (Class 188/380); filed in Japan 30 March 2001

Dynamic absorbers, each consisting essentially of a spring and a mass, are attached to the steering wheel of an automotive vehicle. One of these absorbers is tuned to the idling frequency band of the engine, and another is tuned to the natural frequency band of the steering system.—EEU

6,827,156

43.40.Tm VIBRATION SUPPRESSING DEVICE FOR AIR HAMMER

Wen-Liang Hsiao, Taipei, Taiwan, Province of China
7 December 2004 (Class 173/212); filed 22 September 2003

An air volume, rather than a mechanical spring, is used to provide a cushion between the housing of this air hammer and impacts of the hammering mechanism. This cushioning serves to reduce the vibrations to which the operator's hand is exposed and also to increase the fatigue life of the hammer.—EEU

6,830,351

43.40.Tm ELECTRONIC VIBRATION DAMPENING CENTRAL REARVIEW REINFORCING ASSEMBLY

Jonathan Force Newcomb, Livingston, New Jersey
14 December 2004 (Class 359/871); filed 21 March 2003

Vibrations of a vehicular rearview mirror are suppressed by mounting the mirror resiliently and by providing it with piezoelectric elements. When the mirror's structure is deformed these elements generate currents that are rectified and dissipated in light-emitting diodes. All circuits are housed in the mirror support.—EEU

6,832,143

43.40.Vn DRIVE TRAIN VIBRATION CONTROL SYSTEM

Curtis A. Trudeau and Robert D. Sorum, assignors to Hadley Products
14 December 2004 (Class 701/37); filed 30 July 2002

Vibration, torque, and other parameters of a vehicle drive train are sensed and used to adjust the vehicle's suspension elements, controlling the ride height of the vehicle and alignment of the drive train.—EEU

6,825,635

43.40.Vn VIBRATION ISOLATOR, DEVICE MANUFACTURING APPARATUS AND METHOD, SEMICONDUCTOR MANUFACTURING PLANT AND METHOD OF MAINTAINING DEVICE MANUFACTURING APPARATUS

Hiroaki Kato, assignor to Canon Kabushiki Kaisha
30 November 2004 (Class 318/649); filed in Japan 27 March 2001

The precise vibration control required in micro-manufacturing is provided by an active vibration isolation system that uses servo-type acceleration sensors mounted on an isolation platform. These precise sensors, however, are sensitive to the platform's inclination relative to gravity. Therefore, inclination sensors are added to the platform, and their signals are used to correct those from the acceleration sensors, so that only the pure acceleration signals are employed to control the vibration-reducing actuators.—EEU

6,828,887

43.40.Yq BISTABLE MICROELECTROMECHANICAL SYSTEM BASED STRUCTURES, SYSTEMS AND METHODS

Joel A. Kubby *et al.*, assignors to J.P. Morgan Chase Bank
7 December 2004 (Class 335/78); filed 10 May 2002

This patent discloses the idea of using a bistable beam of micron dimension to create various types of switches. The novelty in it resides in the concept of using etched, deformed beams, rather than prestressed beams, to do the job. The authors do not go into the specifics about how such a thing would be actuated or how the chosen dimensions and materials would affect the performance of the device. The emphasis is on operation as an optical (fiber) switch.—JAH

6,832,519

43.40.Yq VIBRATION DETECTING APPARATUS

Seung Taek Baek, assignor to LG Electronics Incorporated
21 December 2004 (Class 73/514.31); filed in the Republic of Korea 20 February 1999

In drum-type washing machines, the water level generally is sensed by means of a Colpitts oscillating circuit arrangement, in which a bobbin is moved by the water pressure along a cylindrical coil and the change of the coil inductance is measured. The present patent shows various configurations of the same bobbin-and-coil system that also detects the machine's vibrations.—EEU

6,811,372

43.50.Gf DEVICE AT AN ACOUSTIC LINER

Urban Emborg and Sohan Sarin, assignors to A2 Acoustics AB
2 November 2004 (Class 415/119); filed in Sweden 7 December 1999

Gas turbines, like other engines, generate noise. When the gas turbine is a jet engine, the noise can disturb people, both in the airplane and on the ground, and can also cost an airline more to operate the aircraft (due to increased landing fees). Acoustic liners **9** and **11** at the intake **3** and outlet **4**

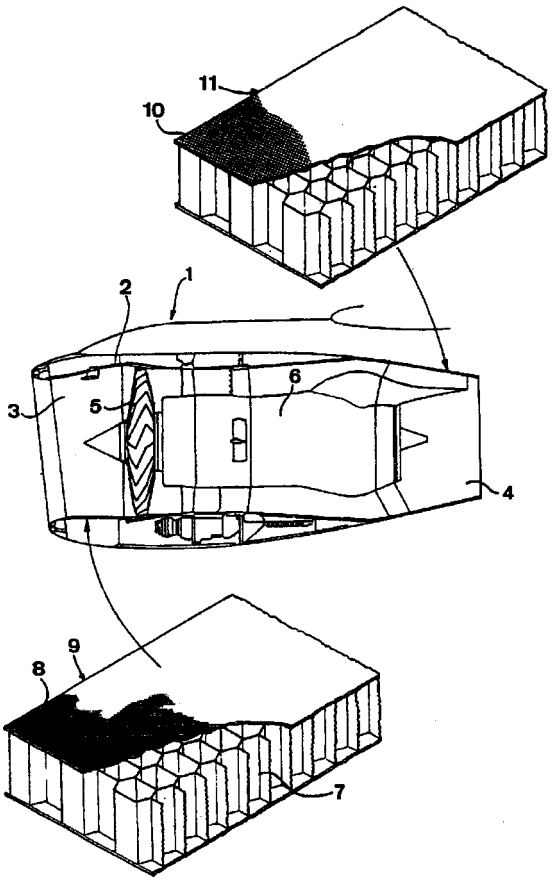

of an engine **1** are commonly used to partially mitigate the noise and these are, at least partially, gas permeable. The cover layer **8** of the liner **9** at the intake typically has very small perforations, on the order of **10** microns, so that the acoustic impedance is more or less linear. As the gases at the outlet can be on the order of 500–600 °C, the cover layer **10** of the liner 11 at the outlet typically uses a perforated sheet. With larger perforations the acoustic impedance is nonlinear and is dependent on the gas temperature and pressure. ''It is particularly advantageous that the liner is a nonlinear acoustic liner, since the disadvantages with respect to the sensitivity of the acoustic impedance for the flow and air pressure of such a liner may be converted into advantages, since it will be possible to regulate the acoustic impedance of the liner through said means so that this is advantageous in most different operating situations.'' The patent does, thus, in sometimes tortured prose and poor grammar, describe several means of varying the acoustic impedance of these output liners by using streams of cold gases, heating the liners, and changing the flow resistance of the liners, among other means, to increase their effectiveness.—NAS

6,827,179

43.50.Gf SOUND BARRIER SYSTEM

Christina M. Drake *et al.*, assignors to Commonwealth Industries, Incorporated
7 December 2004 (Class 181/290); filed 25 March 2003

These lightweight, aluminum-skin, modular panels can be supported between poles to form a highway noise barrier that meets necessary sound reduction requirements. The panels can be embossed or painted with coatings to resist graffiti. The top and bottom edges have a tongue-and-groove

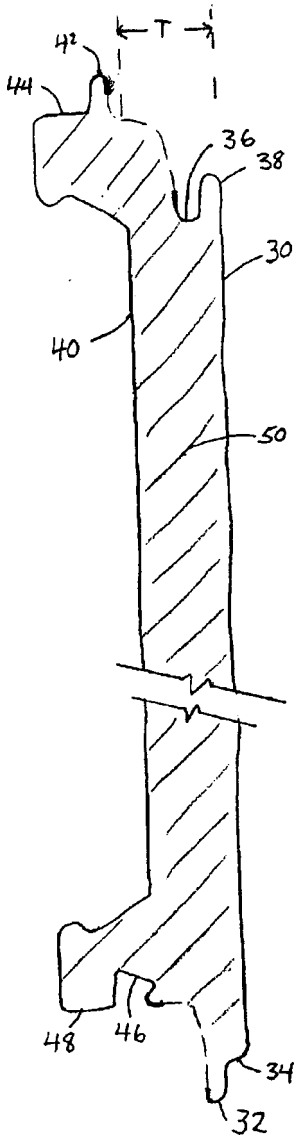

fitting for ease of stacking. There is an inner layer of closed-cell polyurethane foam between the two outer faces.—CJR

6,820,720

43.55.Dt SOUND-ABSORBING ARTICLE EFFECTIVE OVER A BROAD FREQUENCY RANGE

Norbert Nicolai *et al.*, assignors to Clion Irland Limited
23 November 2004 (Class 181/292); filed in Germany 11 August 1999

This sound-absorbing liner might be used as the roof panel in an automobile. It is a layered structure of microperforated sheets stacked over foam absorbers.—CJR

6,830,796

43.55.Ev ACOUSTIC BOARD WITH AN IMPROVED COMPOSITE STRUCTURE

Paul Murray and Massimo Battini, assignors to Aermacchi S.p.A.
14 December 2004 (Class 428/73); filed in Italy 17 January 2001

This honeycomb structure reduces the sound of jet aircraft engines by incorporating a fabric of metal, graphite, or nylon with appropriate flow resistance.—CJR

6,816,846

43.55.Ka METHOD FOR GENERATING RICH SOUND ENVIRONMENTS USING GENETIC OR SHAPED ALGORITHMS

Maribeth J. Back and Maureen C. Stone, assignors to Xerox Corporation
9 November 2004 (Class 706/13); filed 12 November 1999

Genetic algorithms are now used for all types of optimization problems. In this application, they are used to create a ''sonic environment'' (cf. Shafer and Xenakis) by changing the sound parameters in real time. The patent includes VRML code for the truly inspired.—MK

6,813,927

43.58.Dj LOG TESTING APPARATUS

Paul David Harris and Michael Kenneth Andrews, assignors to Carter Holt Harvey Limited
9 November 2004 (Class 73/12.12); filed in New Zealand 30 July 1999

''The timber industry faces a need to efficiently utilize its rather variable forest resource. Timber classification, for example, machine stress grading, is currently done at the end of the production chain. This process results in wastage from the processing which ultimately proves to have been inappropriate. Clearly, it would be more efficient to measure log properties early

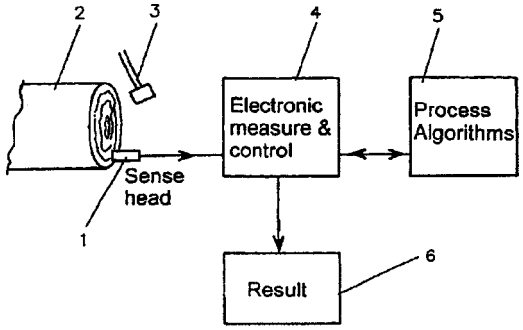

in the chain and process the logs accordingly.'' As such, the patent discloses a means of using a sensor **1**, processing means **4** and **5**, a display (which one assumes is indicated by **6**), and impact device **3**, all of which can be used in the field to determine the plane wave speed *V* and other indicators in specimen **2** to classify the log.—NAS

6,832,344

43.58.Jq MONITOR SYSTEM

Peter Lin *et al.*, assignors to Winbond Electronics Corporation
14 December 2004 (Class 714/48); filed in Taiwan, Province of China 23 February 2001

Over 25 years ago machines had modems for distant service experts to examine the machine internals. Now, this team thinks you'd be better off storing the alarm tone sequence and playing it back later. You get what you pay for.—MK

6,822,929

43.58.Kr MICRO ACOUSTIC SPECTRUM ANALYZER

W. Kent Schubert *et al.*, assignors to Sandia Corporation
23 November 2004 (Class 367/181); filed 25 June 2003

This patent describes three variants on a MEMS-mechanical-wave filter bank to be used for frequency analysis. The physical argument and fre-

quency relationships are clearly laid out, and some experimental data are given to support the claims. Interesting use is made of the Lorentz force to act as a mixer that brings acoustic signals up into the range of resonance with the xylophone and cantilever bar structures described. There seem to be shortcomings in this scheme in comparison to an all-electronic implementation in the size and power consumption of the device.—JAH

6,819,635

43.58.Wc PORTABLE CLOCK WITH CHIME SIGNAL

Stephen Ian McIntosh *et al.*, assignors to Now & Zen, Incorporated
16 November 2004 (Class 368/273); filed 30 May 2003

Anyone who has stayed in or near a zen monestary will recall the sound of gongs before and during meditation. The inventors eschew recorded chimes and offer instead a portable, battery-powered chime (attached to a digital clock). Unfortunately, the chime pitch is inversely proportional to the length of the bar, thereby restricting the pitch range.—MK

6,831,552

43.58.Wc VOCAL CONTAINER CAP

Ted Lin, Taishan Shiang, Taipei, Taiwan, Province of China
14 December 2004 (Class 340/384.7); filed in Taiwan, Province of China 26 July 2001

The title is misleading—it's really just a screw-top container with audio output. There's nothing really exciting in the description. By separating the cap **11**, a spring **60** allows the switch **70** to close, thereby energizing the

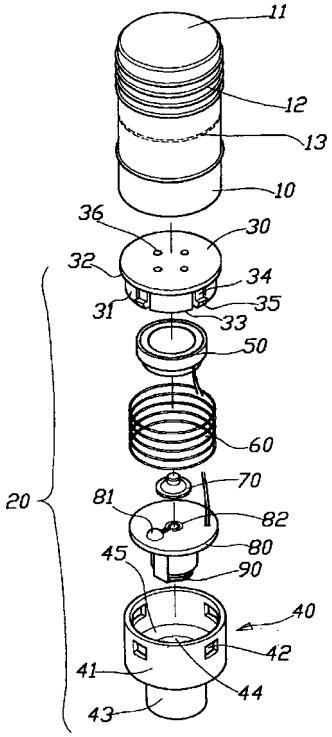

sound circuit **81** that is connected to the mini-transducer **50**. But think of the excitement when you open the container.—MK

6,826,284

43.60.Jn METHOD AND APPARATUS FOR PASSIVE ACOUSTIC SOURCE LOCALIZATION FOR VIDEO CAMERA STEERING APPLICATIONS

Jacob Benesty *et al.*, assignors to Agere Systems Incorporated
30 November 2004 (Class 381/92); filed 4 February 2000

The relative acoustic delays sensed at a three-dimensional array of microphones can define the bearing angle of a sound source in terms of both

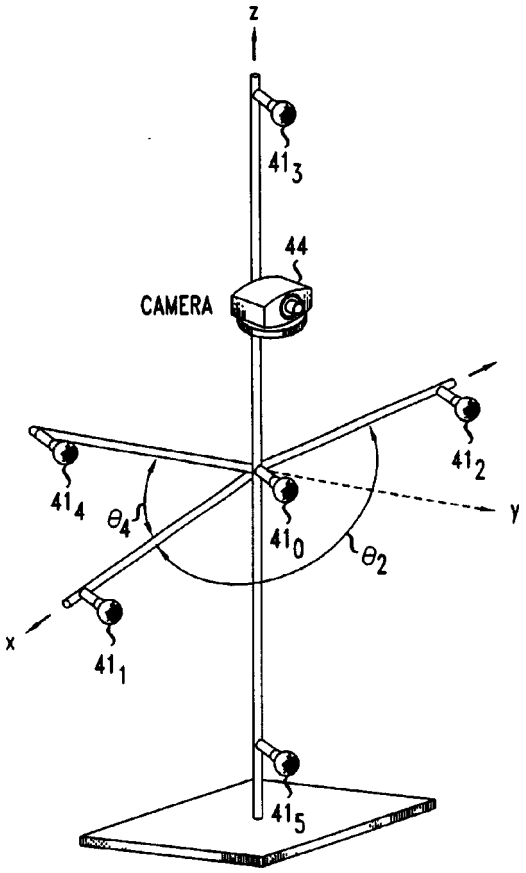

azimuth and elevation. This information can then be used to steer a video camera in the direction of the source. The apparatus is intended for hands-free operation in video conferencing systems.—JME

6,829,017

43.60.Jn SPECIFYING A POINT OF ORIGIN OF A SOUND FOR AUDIO EFFECTS USING DISPLAYED VISUAL INFORMATION FROM A MOTION PICTURE

Michael E. Phillips, assignor to Avid Technology, Incorporated
7 December 2004 (Class 348/738); filed 1 February 2001

The patent discusses in broad terms a method of indicating, via a graphic user interface, the on-screen (or off-screen) source directions for prerecorded, multichannel sound accompanying a motion picture. The system, which is intended as an aid for editors in motion picture and video post-production, allows the user to identify a specific source for computing the actual panning (directional) coefficients.—JME

6,829,018

43.60.Jn THREE-DIMENSIONAL SOUND CREATION ASSISTED BY VISUAL INFORMATION

Yun-Ting Lin and Yong Yan, assignors to Koninklijke Philips Electronics N.V.
7 December 2004 (Class 348/738); filed 17 September 2001

Among audio professionals, the ''unwrapping'' of a two-channel stereo program into artificial surround sound is very suspect—even though there may be valid commercial reasons for wanting to do this. What about generating artificial surround sound from monophonic sources? Scandalous, you

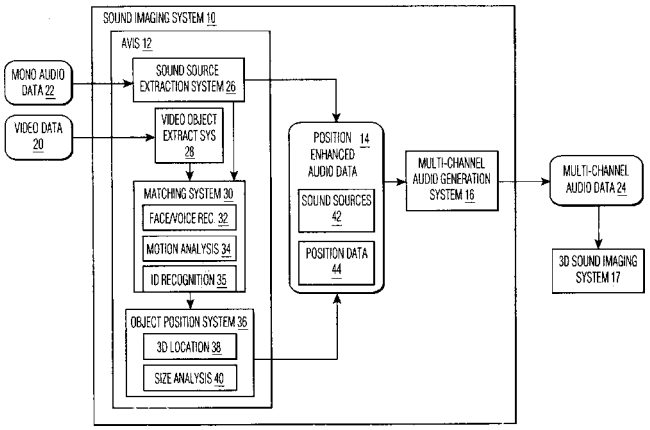

may say, but for the reprocessing of mono soundtracks from older motion pictures there may be enough in the way of on- and off-screen cues to make it all work! The figure shown describes an operational process for doing just this.—JME

6,829,359

43.66.Qp MULTISPEAKER SOUND IMAGING SYSTEM

Juan Serrano, assignor to Arilg Electronics Co., LLC
7 December 2004 (Class 381/17); filed 8 October 2002

Some years ago while attending a consumer high-fidelity show, this reviewer saw a setup, referred to as a ''polyphonic isolator,'' that fed a two-channel stereo program to a frontal array of four loudspeakers. The signal processing was linear time invariant, and the effect was a pleasant spread of sound from left to right. This patent proposes much the same

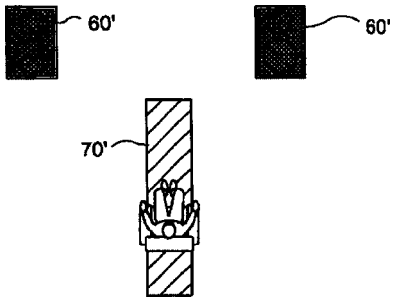

through a combination of simple stereo stage widening (through the use of careful antiphase crosstalk) and gradual signal panning from left to right over a number of adjacent loudspeakers. The details of this are clearly apparent from the figure.—JME

6,820,004

43.66.Qp OPERATION SUPPORTING APPARATUS

Daisuke Arai *et al.*, assignors to Mitsubishi Denki Kabushiki Kaisha
16 November 2004 (Class 701/211); filed 2 January 2003

The patent describes the use of stereophonic imaging to enhance the visual cues that are inherent in vehicular navigational systems. The basic premise is an excellent one in that, in judging locations and directions, the

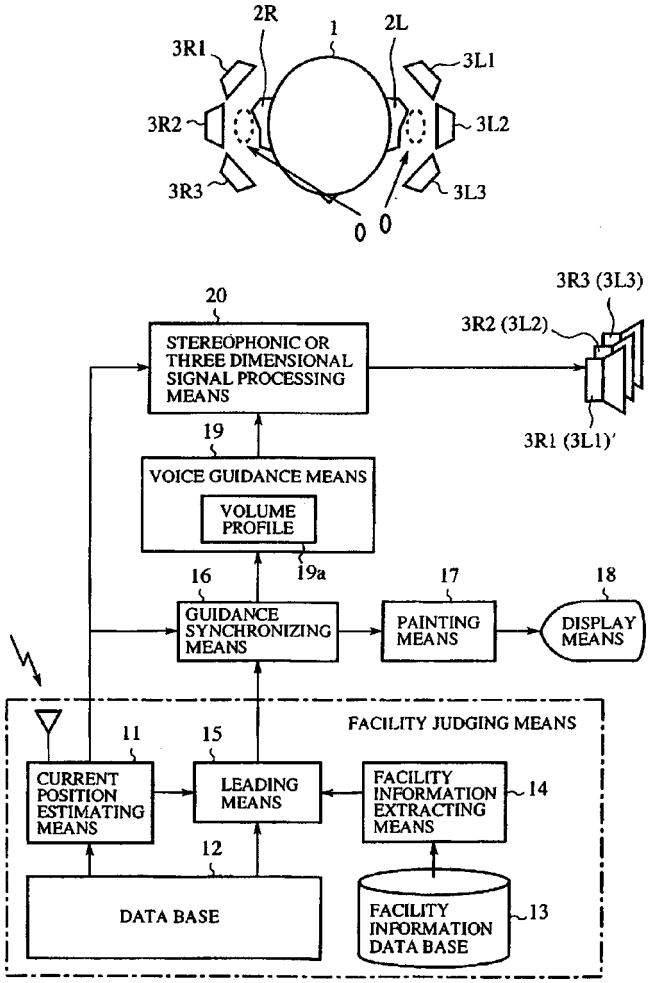

visual field is likely to be dominated by more cues, both on- and off-screen, than can be reasonably, and safely, assimilated by the driver. The patent is sound and well written.—JME

6,816,599

43.66.Ts EAR LEVEL DEVICE FOR SYNTHESIZING MUSIC

Thilo Volker Thiede and Carl Ludvigsen, assignors to Topholm & Westermann APS
9 November 2004 (Class 381/314); filed in the European Patent Office 14 November 2000

Tinnitus can be extremely distracting and uncomfortable. The inventors propose using fractal sequences to control a musical tone generator that creates ''pleasant'' sounds to mask the tinnitus.—MK

6,816,600

43.66.Ts REMOTE CONTROL FOR A HEARING AID, AND APPLICABLE HEARING AID

Andreas Jakob and François Marquis, assignors to Phonak AG
9 November 2004 (Class 381/315); filed 13 January 2000

An inductively coupled remote control for a hearing aid is implemented in a variety of constructed wrist watch case constructions. A coil acting as the transmitter antenna produces a magnetic dipole at the wrist

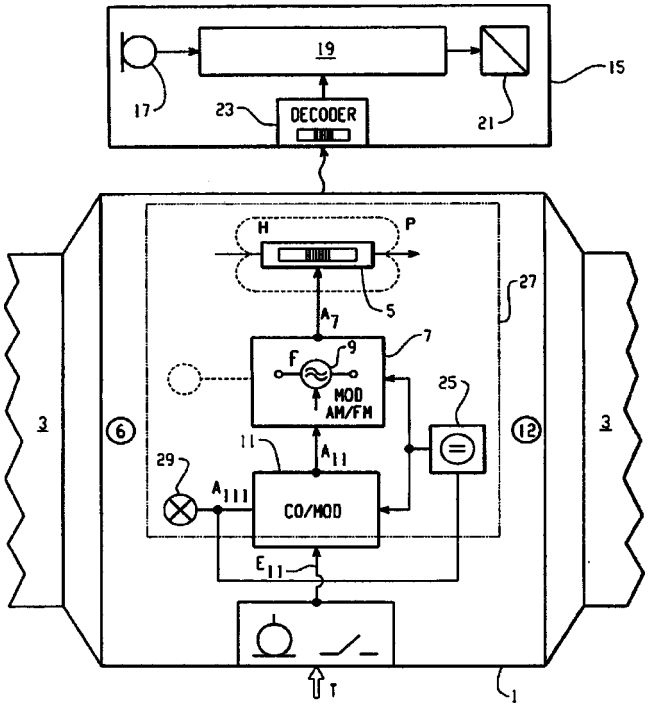

watch with an axial direction parallel to the wrist band. The remote control accepts inputs such as voice control commands, capacitive touch sensors, and other manually operated keys.—DAP

6,816,601

43.66.Ts MICROPHONE AND BATTERY CONFIGURATION FOR HEARING INSTRUMENTS

Shin Chai Mark Lin and Oleg Saltykov, assignors to Siemens Hearing Instruments, Incorporated
9 November 2004 (Class 381/322); filed 7 March 2002

To minimize the depth occupied by microphones of custom hearing aids, the microphone is positioned in a pocket that orients it at an angle rather than perpendicular to the plane of the hearing aid's faceplate.—DAP

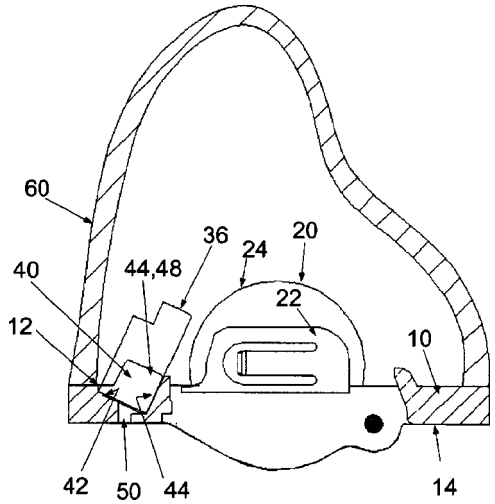

6,819,770

43.66.Ts HEARING AID WITH PORTION THEREOF INSERTED IN AUDITORY CANAL, WITH AUDITORY CANAL VENTILATION

Torsten Niederdränk, assignor to Siemens Audiologische Technik GmbH
16 November 2004 (Class 381/322); filed in Germany 27 August 2001

To improve ear canal ventilation and wearer comfort, two aeration

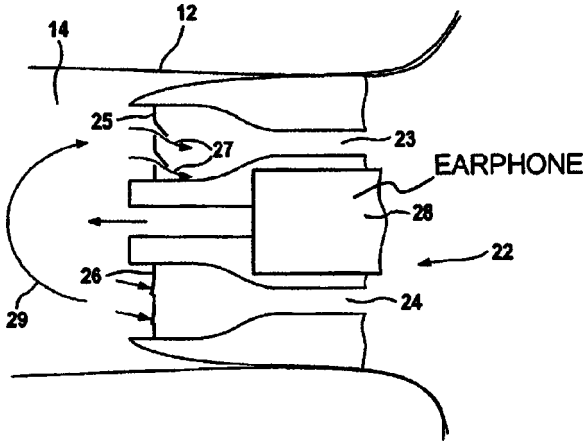

channels are provided for an earmold or an in-the-ear hearing aid.—DAP

6,823,171

43.66.Ts GARMENT HAVING WIRELESS LOOPSET INTEGRATED THEREIN FOR PERSON WITH HEARING DEVICE

Juha Kaario, assignor to Nokia Corporation
23 November 2004 (Class 455/41.1); filed 12 March 2001

Electrically conductive fibers are implanted into an article of clothing to form an induction loop designed to function like, but not be as cumbersome as, an inductive neckloop. Communication from a portable electronic

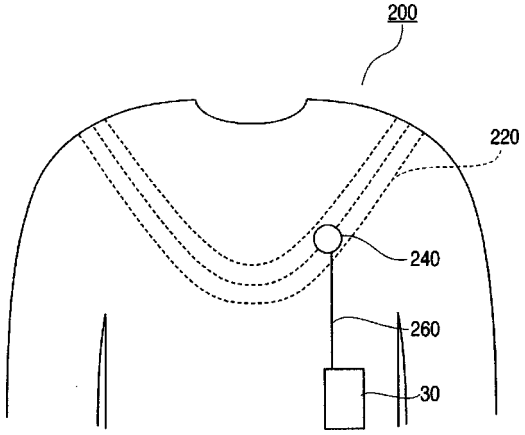

device, such as a cell phone, to the hearing device is via magnetic induction.—DAP

6,818,816

43.66.Ts PERSONAL AMPLIFICATION SOUND SYSTEM

Theodore Roberts and Brian E. Ainsworth, assignors to Theodore Roberts
16 November 2004 (Class 84/723); filed 21 November 2002

This is a sort of a rudimentary hearing aid designed to function as a kind of personal PA system. The system includes a microphone adapted to receive sound and convert it into an original source signal and an amplifier

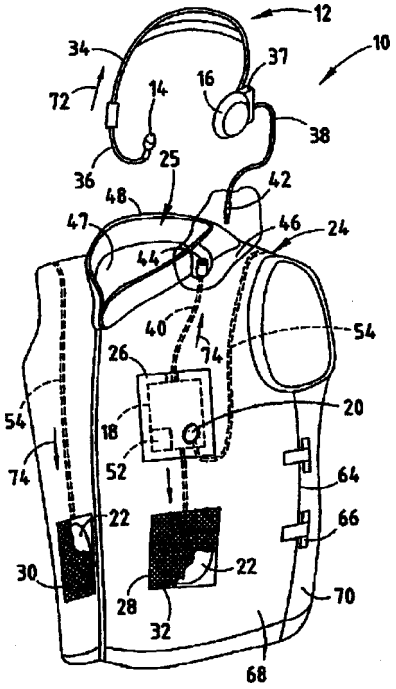

to increase that signal, which is then relayed to a speaker (possibly in the form of a headset). A vest worn by the user contains the amplifier.—DRR

6,829,364

43.66.Ts HEARING AID WITH A CAPACITOR HAVING A LARGE CAPACITANCE

Henning Haugaard Andersen and Ole Erik Toft, assignors to Topholm & Westermann APS, NY
7 December 2004 (Class 381/323); filed 22 June 2001

To prevent voltage ripples and transients on the hearing aid power supply line caused by the current demands of pulsed digital circuitry and to thereby reduce distortion and extend the usable life of the battery, at least one fast supercapacitor with value up to 22 mF is added in parallel to the battery. The physical size of the supercapacitors was not specified.—DAP

6,831,986

43.66.Ts FEEDBACK CANCELLATION IN A HEARING AID WITH REDUCED SENSITIVITY TO LOW-FREQUENCY TONAL INPUTS

James M. Kates, assignor to GN ReSound A/S
14 December 2004 (Class 381/312); filed 20 August 2002

A feedback reduction system is described in which desired low-frequency tonal signals are removed in the error signal in a first adaptive filter block, thereby preventing the system from canceling them along with undesired high-frequency tonal signals. A second adaptive filter block produces an adaptively modeled feedback signal that may be subtracted from the input signal in the forward path of the hearing aid.—DAP

6,826,286

43.66.Ts AUDIO AMPLIFICATION DEVICE WITH VOLUME CONTROL

Horst Arndt and Andre Vonlanthen, assignors to Unitron Hearing Limited
30 November 2004 (Class 381/312); filed 26 September 2003

An audible tone is produced when the user of an amplification device

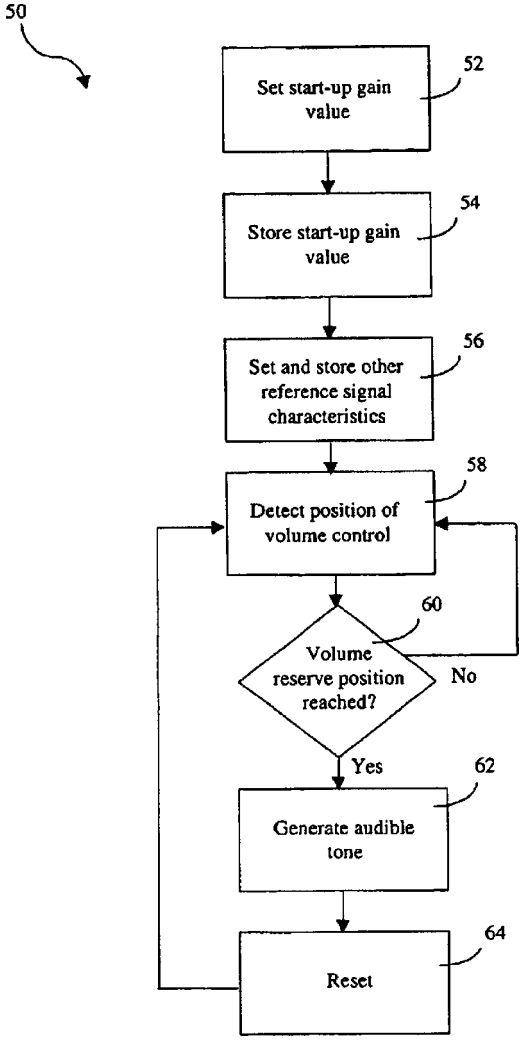

such as a hearing aid has adjusted the volume control to a preset preferred level from another volume control position.—DAP

6,827,178

43.66.Ts METHOD FOR MANUFACTURING AN EAR DEVICE AND EAR DEVICE

Christoph Widmer and Joydeep Dutta, assignors to Phonak AG
7 December 2004 (Class 181/135); filed 25 February 2003

A hearing aid or ear protection device is constructed from a three-dimensional scan of the wearer's ear geometry. Casings are constructed via ''rapid prototyping'' by repeatedly depositing thin layers of a thermoplastic

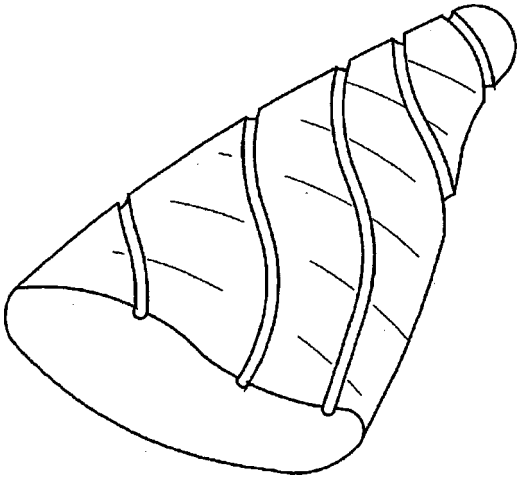

material and solidifying them with a laser. Additional features such as venting slots, not easily formed when using traditional earshell pouring methods, may be added to the casings with the additive build-up processes.—DAP

6,831,988

43.66.Ts BEHIND-THE-EAR HEARING AID AND ATTACHMENT MODULE FOR SAME

Andi Vonlanthen, assignor to Phonak AG
14 December 2004 (Class 381/323); filed in Switzerland 16 June 1999

A removable hinged module that is part of a behind-the-ear hearing aid case normally contains either a primary or rechargeable cylindrical battery

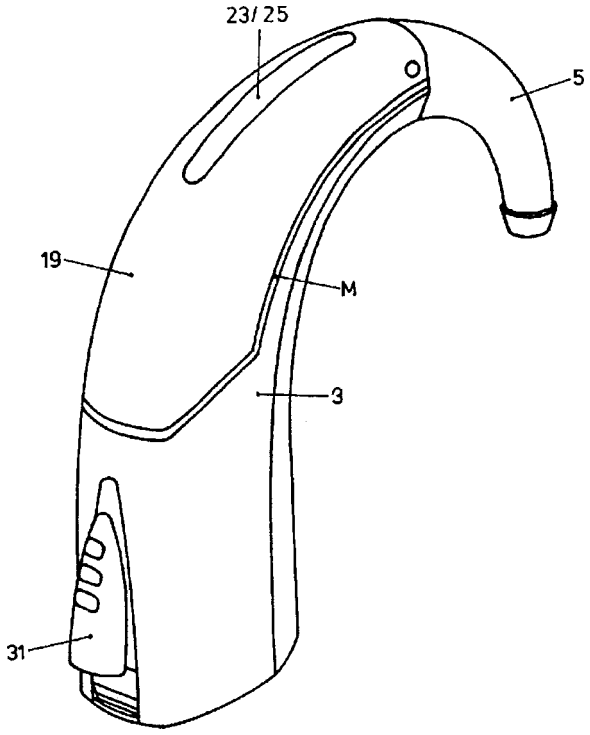

and a voltage regulator. The module lid, which may be color coded, has a locking feature to prevent children from accessing the hearing aid battery.—DAP

6,829,363

43.66.Ts HEARING AID WITH TIME-VARYING PERFORMANCE

Mike K. Sacha, assignor to Starkey Laboratories, Incorporated
7 December 2004 (Class 381/315); filed 16 May 2002

New hearing aid wearers typically require a period of adjustment to get used to sounds they have not been hearing. In order to prevent repeated visits to the audiologist or dispenser to optimize their hearing aid performance, a system is described that initially programs the hearing aid with suboptimal parameter values, such as lower gain, than initially thought appropriate. After the initial fitting, timers in the hearing aid signal-processing circuitry or firmware automatically trigger periodic increases in gain and other adjustable parameters proportionally with wearing time.—DAP

6,829,939

43.66.Yw METHOD AND APPARATUS FOR MEASURING SOUND THAT TAKES HEARING CHARACTERISTICS INTO CONSIDERATION

Kenji Kurakata and Yasuo Kuchinomachi, assignors to National Institute of Advanced Industrial Science and Technology; Kenji Kurakata
14 December 2004 (Class 73/585); filed 29 April 2002

A method and apparatus are described for measuring a sound corresponding to the hearing characteristics of a given age group. Hearing data are read from a memory by age group and used to correct input sounds for

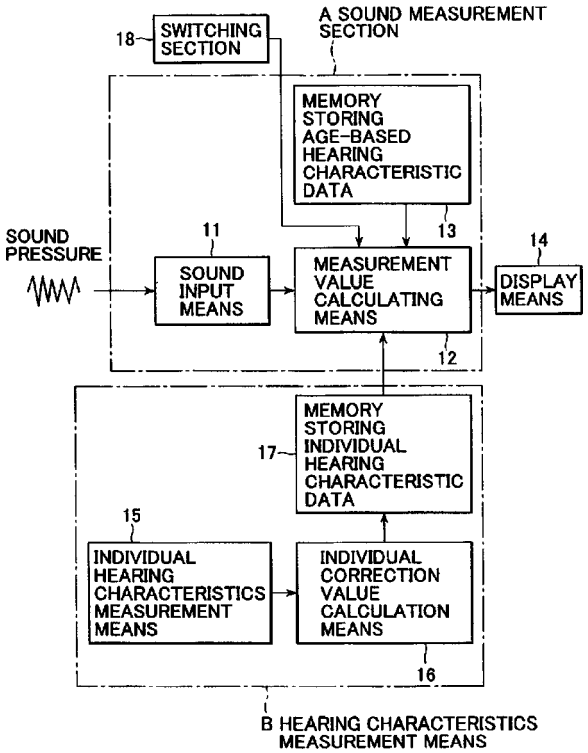

that group. The hearing of an individual is compared with those of his/her age group.—DRR

6,820,053

43.72.Dv METHOD AND APPARATUS FOR SUPPRESSING AUDIBLE NOISE IN SPEECH TRANSMISSION

Dietmar Ruwisch, assignor to Dietmar Ruwisch
16 November 2004 (Class 704/232); filed in Germany 6 October 1999

A method is promised by which ''a moderate computational effort is sufficient to identify a speech signal by its time and spectral properties and to remove audible noise from it.'' To those well-versed in the art, such a statement is recognizable as a pipe dream, and so the possible success of the patent's hopelessly vague proposals is suspect. The basic outline of the proposal, no details of which are ever provided, involves a frame-by-frame neural network filtering scheme consisting of a ''minima detection layer,'' a ''reaction layer,'' supposed to distinguish speech from audible noise by entirely mysterious means (we are told there is a ''nonlinear reaction function *r* used by the reaction-layer neurons to compute the relative spectrum''), a ''diffusion layer,'' which smooths the filter derived from the reaction layer, and finally an ''integration layer,'' which integrates the derived filter function over all frequencies for the current frame and ''feeds the integration signal so obtained back into the reaction layer.'' These neural nets are illustrated with uninformative schematic diagrams. A graph is provided showing the performance of the method on AM white noise—hardly applicable to speech signals. This patent promises a lot but comes up short on methods and details. It is difficult to even determine just what has been patented here—the idea of neural net filtering?—SAF

6,819,863

43.72.Gy SYSTEM AND METHOD FOR LOCATING PROGRAM BOUNDARIES AND COMMERCIAL BOUNDARIES USING AUDIO CATEGORIES

Serhan Dagtas and Nevenka Dimitrova, assignors to Koninklijke Philips Electronics N.V.
16 November 2004 (Class 386/46); filed 22 December 2000

An audio controller classifies audio segments into such categories as silence, music, noise, and speech and determines the rates of change of the audio categories to locate the boundaries of programs and commercials.—DAP

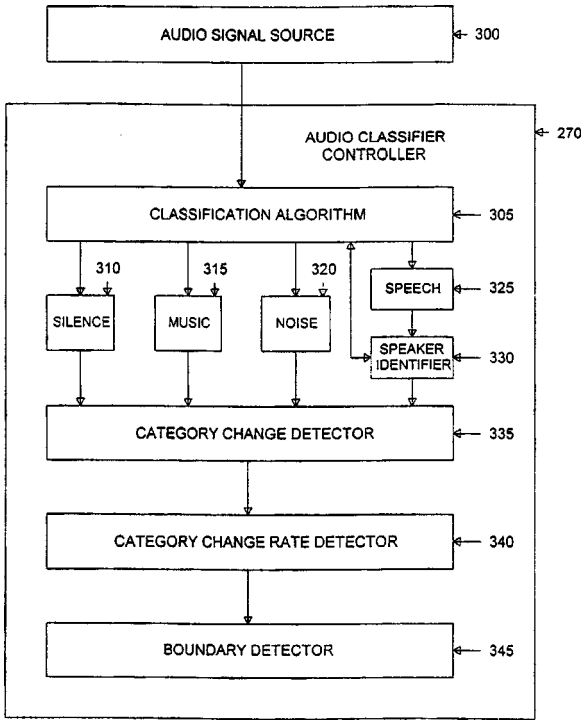

6,829,578

43.72.Ne TONE FEATURES FOR SPEECH RECOGNITION

Chang-Han Huang and Frank Torsten Bernd Seide, assignors to Koninklijke Philips Electronics, N.V.
7 December 2004 (Class 704/211); filed in the European Patent Office 11 November 1999

This patent outlines a scheme by which a feature vector for lexical tone can be added to the customary kind of acoustic feature vector in a HMM-based speech recognition system for a tone language. A wide variety of extant techniques are thoughtfully cobbled together to yield a purportedly excellent pitch extraction and tracking scheme, including the measurement of pitch by subharmonic summation and adaptively pruned beam search for the optimal contour. The inventors also add to the features a measurement of the degree of voicing present in the frame, using the coefficients of the second-order regression of the short-time autocorrelation contour. It is hard to distinguish the new techniques from the old in the numerous subcomponents of this complicated scheme, but the most important new idea appears to be that of using a weighted moving average of the estimated pitch contour for an entire utterance to represent the ''phrase intonation effect,'' which can then be removed from the pitch contour assuming superposition, leaving the lexical tone pitches unscathed. The patent is sufficiently detailed to permit one to reproduce its methods, and the performance of the system's manifold improvements to the feature vectors for Mandarin Chinese are nicely evaluated. The grand average Chinese character error rate is improved by 27.3% by the inclusion of the various tone features in a bigram recognition system.—SAF

6,832,190

43.72.Ne METHOD AND ARRAY FOR INTRODUCING TEMPORAL CORRELATION IN HIDDEN MARKOV MODELS FOR SPEECH RECOGNITION

Jochen Junkawitsch and Harald Höge, assignors to Siemens Aktiengesellschaft
14 December 2004 (Class 704/255); filed in Germany 11 May 1998

This patent proposes to modify the usual hidden Markov models of a speech recognition system by making each acoustic observation probability partially dependent on the preceding state sequence. This, by admission, is not an idea unique to this patent. Specifically, it is proposed that a suitable calculation of the conditional probability of an observation given the preceding sequence of p states can be effected by means of linear prediction (thus accounting for temporal correlation) over a number of uncorrelated sequences of length p drawn from the preceding p observations. The uncorrelated values at each frame in the sequence are to be obtained from the output of a discriminant analysis of the feature vector in the observation sequence. The conditional probability so computed is then combined with the standard observation probability by a novel technique of some complexity, the details of which seem to be amply described. It is an interesting

proposal, but no indication is given that the inventors have implemented it, so its effectiveness cannot be evaluated. In particular, the question of how to train a hidden Markov model with such unwieldy observation probabilities remains unanswered. It seems unlikely that standard expectation maximization would any longer be appropriate.—SAF

6,815,599

43.75.Fg MUSICAL INSTRUMENT

Yasuhiko Asahi, assignor to Yamaha Corporation
9 November 2004 (Class 84/485 R); filed in Japan 8 May 2002

An electronic trumpet features an air vibration sensor **24**, a series of pistonic switches **61–63**, and an output loudspeaker **27**. The air sensor is piezoelectric, which is then converted, and pitch detection is used to find the

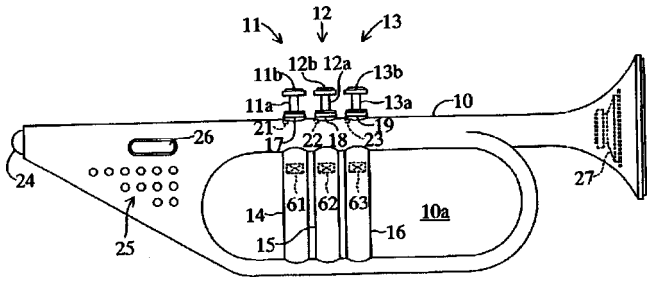

open pitch. The patent also includes a discussion of LED sensors for the ''valve'' keys. Notably missing is a discussion of the importance of the cup of the mouthpiece on the player.—MK

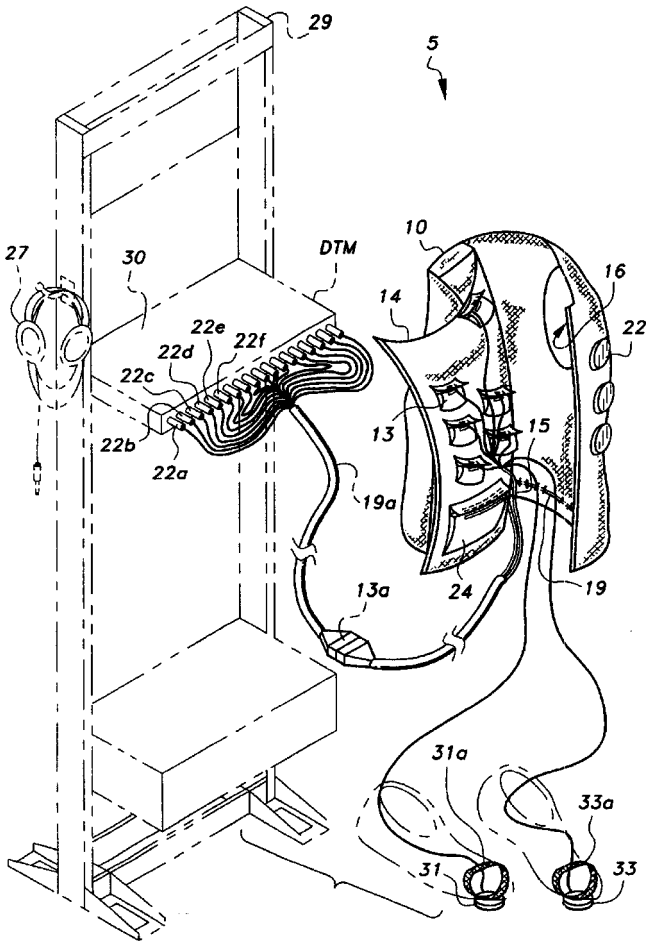

(especially the pockets), season with toe tapping sensors **31** and **33**, and then connect them to a rack of sound synthesizers.—MK

6,822,147

43.75.Gh ARRANGEMENT OF A SOUND HOLE AND CONSTRUCTION OF A SOUND BOARD IN AN ACOUSTIC GUITAR

Mathew McPherson, Norwalk, Wisconsin
23 November 2004 (Class 84/291); filed 9 May 2000

This author believes (without substantiation) that acoustic guitar sounds are better the closer they are to the body edge. Accordingly, he proposes moving the sound hole to the edge of the body. Nothing more, nothing less.—MK

6,819,771

43.75.Hi VEST WITH PIEZOELECTRIC TRANSDUCER FOR PRACTICING MUSIC

Kenneth S. Menzies, Mechanicsville, Virginia
16 November 2004 (Class 381/333); filed 6 May 2003

Bobby McFerrin uses his torso as a musical instrument, so why can't you? Take a vest **16**, add piezoelectric sensors **22** liberally over the surface

6,815,604

43.75.Kk ELECTRONIC PERCUSSION INSTRUMENT

Jiro Toda, assignor to Yamaha Corporation
9 November 2004 (Class 84/746); filed in Japan 24 April 2002

A high hat can be hit in a number of different ways. The challenge is to capture all the nuance. Specifically, a cymbal can be hit on the cup (the upper part of the top cymbal) **11b**, the base **11a**, or edge **11c**. Further, a pedal

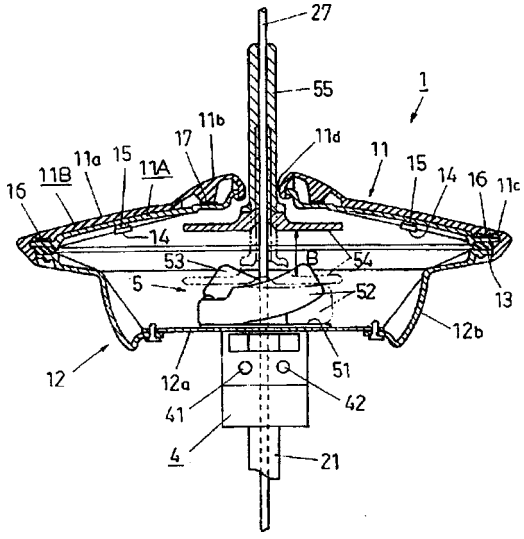

can cause the plate to move. Towards an electronic high hat—to use a high hat as a musical sensor—sensors are added to different surfaces including the backside of the cymbal **14**, edge sensor **16**, and cup sensor **17**.—MK

6,822,148

43.75.Kk ELECTRONIC PAD

Hiroyuki Yanase, assignor to Roland Corporation
23 November 2004 (Class 84/422.1); filed in Japan 27 December 2000

This is an electronic high hat. As shown, the hit sensor **1** is near the

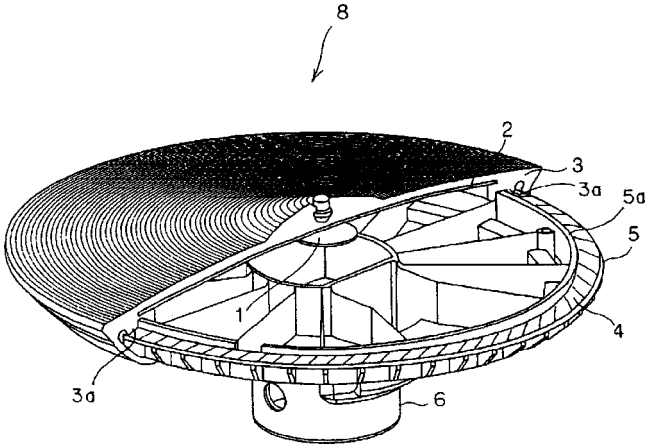

bell and the sheet sensor **4** detects hits on the rim.—MK

6,832,574

43.75.Pq BICYCLE WHISTLE

James Gregory Coconas, Sebastopol, California
21 December 2004 (Class 116/58 R); filed 20 March 2003

A reed **28** is held inside a horn **24**. This generates a sound when the

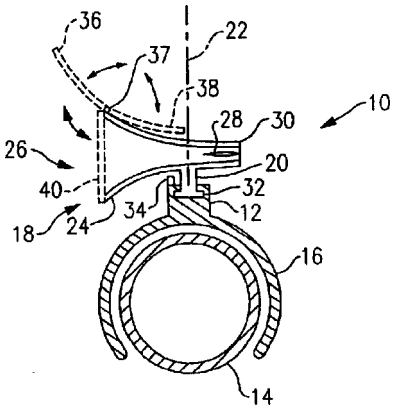

bicycle is moving, thereby warning errant sidewalk consumers that trouble is heading in their direction.—MK

6,316,710

43.75.Wx MUSICAL SYNTHESIZER CAPABLE OF EXPRESSIVE PHRASING

Eric Lindemann, assignor to Eric Lindemann
13 November 2001 (Class 84/609); filed 27 September 1999

The main problem with looping synthesizers is the lack of expressiveness. In a typical implementation, a waveform is stored in attack, sustain, decay, and release (ASDR) segments. Now think of the opening clarinet glissando in ''Rhapsody in Blue''—it smoothly increases in both amplitude and frequency. How can this be synthesized? This disclosure extends the ASDR gestures as shown in the table. The patent also describes how to determine these gestures from raw audio input. The writing is lucid and segues into the inventor's other patents on vector quantization representations.—MK

gesture type	gesture subtype	gesture symbol
attack	breathy_attack	BA
	soft_attack	SA
	medium_attack	MA
	hard_attack	HA
release	breathy_release	BR
	soft_release	SR
	medium_release	MR
	hard_release	HR
	falloff_release	FR
transition	small_downward_slur	SDS
	large_downward_slur	LDS
	small_upward_slur	SUS
	large_upward_slur	LUS
	run_up_slur	RUS
	run_down_slur	RDS
sustain	flat_sustain	FS
	vibrato_cycle	VP
	lip_down_sustain	LD
	bend_down	BD
	bend_up	BU
silence	silence	S

6,805,129

43.80.Gx APPARATUS AND METHOD FOR ABLATING TISSUE

Benjamin Pless *et al.*, assignors to Epicor Medical, Incorporated
19 October 2004 (Class 128/898); filed 27 October 2000

Two tissue ablation probes **20**, **22** are inserted into the body of a patient through 2–5-cm-wide incisions below the sternum. Acoustic energy (150 W at 500 kHz) is then used to ablate myocardial tissue at temperatures

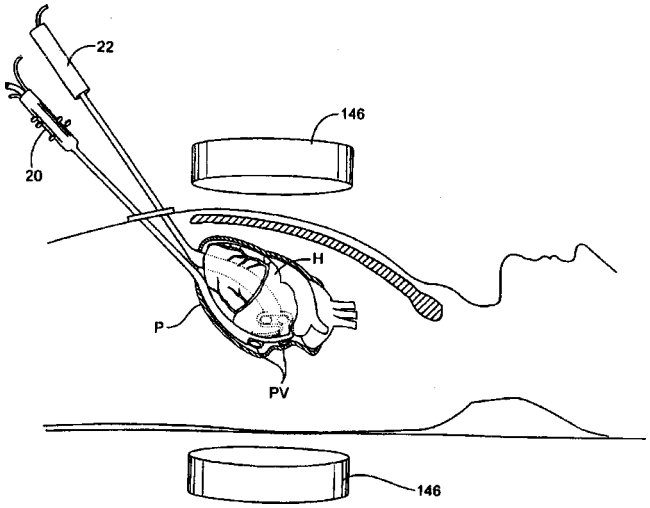

of 45–95 °C. This technique avoids cutting or puncturing the pericardial reflections in the vicinity of the pulmonary veins. Imaging apparatus **146** may be used to monitor and guide the process.—IMH

6,805,132

43.80.Qf PERFORMING ULTRASOUND RANGING IN THE PRESENCE OF ULTRASOUND INTERFERENCE

N. Parker Willis, assignor to SciMed Life Systems, Incorporated
19 October 2004 (Class 128/899); filed 6 August 2002

An ultrasonic ranging and tracking technique and filter are presented. A first reference element **1120** (e.g., a medical catheter) with ultrasonic

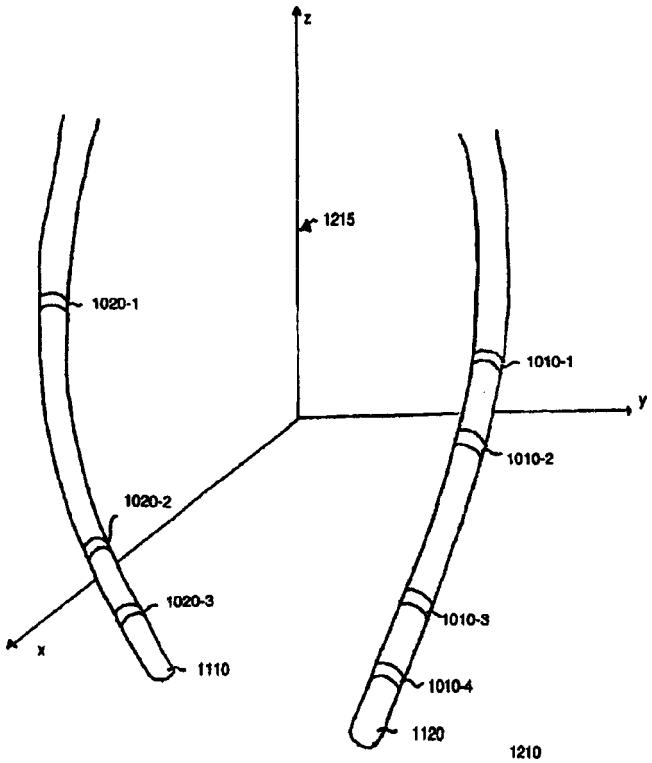

transducers thereon can detect ranging signals from a second element **1110** (e.g., another medical catheter). A number of ranging signals are received and processed by a filter to account for multiple signal interference.—IMH

6,815,951

43.80.Qf MAGNETIC RESONANCE APPARATUS WITH MULTIPLE MICROPHONES FOR IMPROVING CLARITY OF AUDIO SIGNALS FOR A PATIENT

Andrea Schwarz, assignor to Siemens Aktiengesellschaft
9 November 2004 (Class 324/307); filed in Germany 16 October 2001

The aim of this device is to provide a magnetic resonance apparatus in which the signals coming from a patient undergoing examination can be picked up in such a manner that these signals can be separated from the

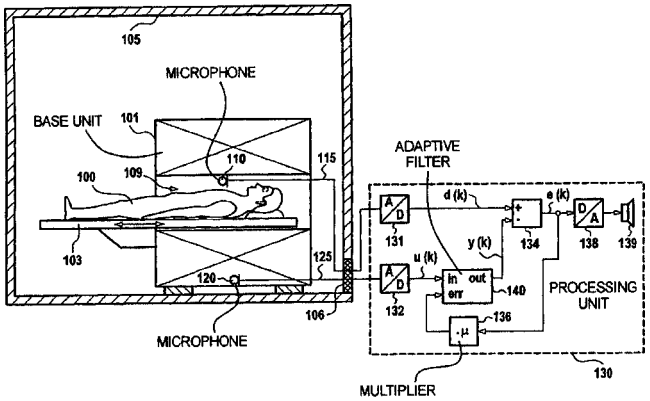

magnetic resonance noise that also tends to be picked up. The object is achieved by arranging one microphone **110** to pick up acoustic signals from the patient and a second microphone **120** to be as free as possible from picking up the patient's signals. The two microphone signals are processed to eliminate the magnetic resonance apparatus noise, extracting the desired signals for evaluation.—DRR

6,824,519

43.80.Qf HEART-SOUND DETECTING APPARATUS

Kiyoyuki Narimatsu and Toshihiko Ogura, assignors to Colin Medical Technology Corporation
30 November 2004 (Class 600/528); filed in Japan 20 June 2001

This is a version of a heart-detecting apparatus that detects sound by extraction from a physical signal containing a heart-sound component. The apparatus includes a memory device that stores heart-sound information characterizing the heart sound of a patient, a heart-sound sensor adapted to be worn on a body portion of the patient that is distant from the patient's chest, and a heart-sound analyzer for determining the characteristics of the heart sound picked up by the sensor.—DRR

6,821,274

43.80.Sh ULTRASOUND THERAPY FOR SELECTIVE CELL ABLATION

Anthony Patrick McHale and Anna Maria Rollan Haro, assignors to Gendel Limited
23 November 2004 (Class 606/41); filed in the United Kingdom 7 March 2001

This device combines electric field energy and ultrasound energy for the selective ablation of tissues, such as tumors, and cells in an organism. A method of sensitizing target cells to ultrasound energy uses a stimulus such as an electric field. This ''electrosenitization'' prepares target cells to be disrupted by ultrasound at frequencies and energies that do not cause dis-

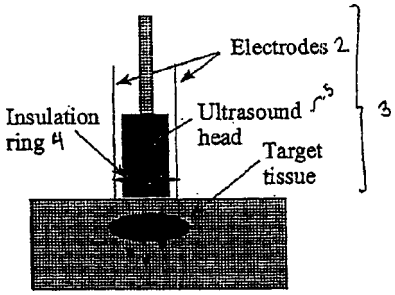

ruption of nonsensitized (i.e., nontarget) cells. It is said that this method increases the selectivity of the ultrasound therapy by providing a way to ablate malignant cells while minimizing damage to neighboring, benign cells. In another embodiment, ultrasound can be used to sensitize cells while the electric field is applied to disrupt them.—DRR

6,824,514

43.80.Vj SYSTEM AND METHOD FOR VISUALIZING SCENE SHIFT IN ULTRASOUND SCAN SEQUENCE

McKee D. Poland and Karl E. Thiele, assignors to Koninklijke Philips Electronics N.V.
30 November 2004 (Class 600/437); filed 11 October 2002

Two ultrasound images are used. A border in the first image and a corresponding border in the second image are found. The borders are overlayed to show misalignment.—RCW

6,824,517

43.80.Vj ULTRASOUND QUANTIFICATION IN REAL-TIME USING ACOUSTIC DATA IN MORE THAN TWO DIMENSIONS

Ivan S. Salgo and Bernard J. Savord, assignors to Koninklijke Philips Electronics N.V.
30 November 2004 (Class 600/443); filed 25 June 2002

A two-dimensional array is used to acquire orthogonal (bi-plane) images simultaneously. The images are segmented individually to determine the borders of a region. The borders are combined and used to compute the volume. A number of simultaneous two-dimensional images in a volume can be also be used to find the border for the volume computation.—RCW

6,824,518

43.80.Vj HIGH TRANSMIT POWER DIAGNOSTIC ULTRASOUND IMAGING

Patrick L. Von Behren *et al.*, assignors to Siemens Medical Solutions USA, Incorporated
30 November 2004 (Class 600/443); filed 26 November 2002

High-power ultrasonic pulses are temporally or spatially interleaved with zero-power, low-power, or normal-power ultrasonic pulses to provide a better signal-to-noise ratio or to allow imaging at higher frequency for difficult-to-image patients. A means is provided to monitor temperature to prevent tissue or transducer damage.—RCW

6,827,685

43.80.Vj METHOD OF ULTRASONIC SPECKLE REDUCTION USING WIDE-BAND FREQUENCY COMPOUNDING WITH TISSUE-GENERATED HARMONICS

Feng Lin *et al.*, assignors to General Electric Company
7 December 2004 (Class 600/437); filed 31 December 2002

Echoes from two or more transmissions are combined coherently to extract tissue-produced harmonic components. Echoes from one or more of the individual transmissions are also detected. The detected outputs are combined to form a compound image. Unlike other frequency compounding methods, both transmit and receive signals are wideband. Narrow-band filters are not needed.—RCW

6,827,686

43.80.Vj SYSTEM AND METHOD FOR IMPROVED HARMONIC IMAGING

Thomas L. Szabo *et al.*, assignors to Koninklijke Philips Electronics N.V.
7 December 2004 (Class 600/458); filed 21 August 2002

Transducer sensitivity in an ultrasound imaging system is improved by selecting a desired transmit pulse spectrum, determining the transmit-channel impulse response, calculating a drive signal that produces the desired transmit spectrum, and applying the drive signal to the transducer.—RCW

A unified view of imaging the elastic properties of tissue

Kevin J. Parker, Lawrence S. Taylor, and Sheryl Gracewski
School of Engineering and Applied Sciences, University of Rochester, P.O. Box 270126, Rochester, New York 14627-0127

Deborah J. Rubens
Department of Radiology, University of Rochester Medical Center, 601 Elmwood Avenue, Rochester, New York 14642-8648

(Received 8 April 2004; revised 24 January 2005; accepted 28 January 2005)

A number of different approaches have been developed to estimate and image the elastic properties of tissue. The biomechanical properties of tissues are vitally linked to function and pathology, but cannot be directly assessed by conventional ultrasound, MRI, CT, or nuclear imaging. Research developments have introduced new approaches, using either MRI or ultrasound to image the tissue response to some stimulus. A wide range of stimuli has been evaluated, including heat, water jets, vibration shear waves, compression, and quasistatic compression, using single or multiple steps or low-frequency (<10 Hz) cyclic excitation. These may seem to be greatly dissimilar, and appear to produce distinctly different types of information and images. However, our purpose in this tutorial is to review the major classes of excitation stimuli, and then to demonstrate that they produce responses that fall within a common spectrum of elastic behavior. Within this spectrum, the major classes of excitation include step compression, cyclic quasistatic compression, harmonic shear wave excitation, and transient shear wave excitation. The information they reveal about the unknown elastic distribution within an imaging region of interest are shown to be fundamentally related because the tissue responses are governed by the same equation. Examples use simple geometry to emphasize the common nature of the approaches.
[DOI: 10.1121/1.1880772]

PACS numbers: 43.80.Qf, 43.80.Ev, 43.80.Jz [FD] Pages: 2705–2712

I. INTRODUCTION

The biomechanical properties of tissues, particularly the stiffness or tactile hardness of tissues, are inextricably linked to the function, the composition, and the relative state of the tissue with respect to inflammation or pathology.[1] Thus, a number of approaches have been proposed to develop estimates of *in vivo* tissue elasticity. Significant among these in the late 1980s were Krouskop *et al.*, using an M-mode Doppler analysis of muscle tissue during externally applied vibration,[2] and Sato *et al.*, using full B-scan imaging of muscle during vibration to follow the propagating shear waves and thus make a regional estimate of Young's modulus (E).[3] The milestone of creating an actual image of a region of interest, demonstrating the detection of a region of high stiffness, surrounded by softer material, was reached in 1988.[4] This was extended to real-time imaging using slightly modified color Doppler scanning to image a vibration field, and finite element models were employed to demonstrate the sonoelastic void produced by a relatively hard abnormality in an otherwise soft background material that contains a propagating shear wave.[5,6] These general results were later refined and applied to a variety of anatomical and clinical tasks[7] along with expansions of the theoretical basis for vibration sonoelastography.[8,9] Meanwhile, Levinson, who had collaborated with Krouskop and Sato on the key muscle elasticity experiments, applied a number of vibrational and quasistatic techniques to create localized estimates of muscle elasticity, even during active contraction.[10,11] Independently, Ophir and colleagues developed an approach in which tissue was imaged before and after a step compression[12,13] to determine local estimates of strain. Strain imaging of tissue proved to be capable of displaying the relative responses of hard and soft regions at high resolution.[14,15]

Compression can be applied as a single step or as a series of steps.[16] Additional techniques include single-step shear[17] and cyclical, quasistatic harmonic excitation[18] with frequencies on the order of 5–10 Hz.[19]

Magnetic resonance imaging has also been combined with shear wave excitation to perform magnetic resonance elastography (MRE).[20–23] Inverse solutions have been applied to the three-dimensional vector displacement field available in MRE experiments to solve for unknown local elastic parameters.

Another approach is to use a transient tone burst of shear wave excitation, instead of steady-state excitation.[24,25] The excitation stimuli can also be provided directly by acoustic radiation force (ARF) from the ultrasound itself,[26,27] which can be used to create transient[28,29] or harmonic tissue displacements.[30,31] Together, these different approaches provide a diverse and creative set of stimuli that produce measurable changes in tissue. We seek to understand any commonality that may exist among the set of approaches.

In the next sections, we examine a simple homogeneous isotropic linear viscoelastic material under excitation by a progressive set of displacements: compression, shear, quasistatic cyclic shear, and vibration. The material is considered with and without a small inclusion that has a slightly elevated Young's modulus (E) with respect to the surrounding

material. It is shown that the elastic response within the material under the different stimuli all belong within a common spectrum of elastic behavior, and some information concerning the inclusion can be derived from each of the responses to the stimuli.

II. OVERVIEW OF GOVERNING EQUATIONS

Following the methods of continuum mechanics, the governing equations for a deformable medium can be obtained by applying, to any part of the medium, conservation of linear momentum, given by

$$\frac{d}{dt}\int_V\int\int \rho\dot{\mathbf{u}}\,dV=\int_S\int\mathbf{T}^{(\mathbf{n})}\,dS+\int_V\int\int\rho\mathbf{b}\,dV. \quad (1)$$

This equation states that the rate of change of linear momentum is equal to the resultant applied surface and body forces. In this equation, ρ is the density, $\mathbf{u}$ is the displacement vector (with the superposed dot indicating a time derivative), $\mathbf{b}$ is the body force per unit mass vector, and $\mathbf{T}^{(\mathbf{n})}$ is the traction vector on the surface S (with outward unit normal $\mathbf{n}$) of volume V.

Writing the traction vector in terms of the stress tensor σ as

$$\mathbf{T}^{(\mathbf{n})}=\sigma\cdot\mathbf{n}, \quad (2)$$

we can use the divergence theorem to obtain the differential form of conservation of linear momentum,

$$\rho\ddot{\mathbf{u}}=\boldsymbol{\nabla}\cdot\sigma+\rho\mathbf{b}. \quad (3)$$

In measurements of elastic properties, the body forces (such as gravity) are either negligible or their effects can be subtracted from the measured response. Therefore, the last term will not be considered further in this discussion.

To complete the problem statement, the material behavior must be specified. If the deformation is small enough, it can be expressed in terms of the infinitesimal strain tensor,

$$\epsilon_{ij}=\frac{1}{2}\left(\frac{\partial u_i}{\partial x_j}+\frac{\partial u_j}{\partial x_i}\right). \quad (4)$$

Then, the constitutive relation relating stress and strain for a linear-elastic, isotropic medium can be written as

$$\sigma_{ij}=(2\mu\epsilon_{ij}+\lambda\epsilon_{kk}\delta_{ij})=\frac{E}{(1+\nu)}\left(\epsilon_{ij}+\frac{\nu}{1-2\nu}\epsilon_{kk}\delta_{ij}\right), \quad (5)$$

where λ and μ are called the Lamé constants, μ is also the shear modulus, E is the elastic or Young's modulus, and ν is Poisson's ratio. In this equation, the summation convention has been used and δ_{ij} is the Kronecker delta equal to 1 if $i=j$ and 0 otherwise.

In homogeneous regions, where λ and μ are constant, Eqs. (3)–(5) can be combined to obtain an equation in terms of the displacement vector alone as

$$(\lambda+\mu)\frac{\partial^2 u_j}{\partial x_j\,\partial x_i}+\mu\frac{\partial^2 u_i}{\partial x_j\,\partial x_j}=\rho\ddot{u}_i,$$

or

$$(\lambda+\mu)\boldsymbol{\nabla}(\boldsymbol{\nabla}\cdot\mathbf{u})+\mu\,\nabla^2\mathbf{u}=\rho\ddot{\mathbf{u}}, \quad (6)$$

where the body forces, such as gravity, have been assumed negligible. This equation, with given boundary and initial conditions, governs the general dynamic response of a homogeneous, isotropic, linearly elastic material to a force or displacement excitation. If loads are applied slowly (quasistatically) or if the displacement response to a constant load is measured after all the motion has stopped, then the right-hand side of this equation is negligible and set equal to zero. Therefore, this equation governs the static, quasistatic, and dynamic (transient, harmonic, and wave propagation) responses that can occur in response to applied loads.

The lossy nature of biological tissues is often modeled using a viscoelastic model. Such a model can be implemented in these equations for a time-harmonic excitation by assuming that λ and μ are complex. In this case, the wave or vibration amplitude will decay with distance from the excitation point, and the loss will generally increase with increasing frequency. For a more in-depth presentation of the derivation and solution of the elastic and viscoelastic equations, see Kolsky[32] and Achenbach.[33]

At times, it is convenient to represent the response in terms of waves propagating within the tissue. Two types of plane wave, shear waves and pressure waves, propagate independently in the bulk material, interacting only at boundaries. The shear wave equation can easily be obtained from Eq. (6) by noting that there is no volume change as layers of material move in shear, transverse to the direction of propagation, so the dilatation $\boldsymbol{\nabla}\cdot\mathbf{u}=0$. The shear wave equation is then

$$\nabla^2\mathbf{u}=\frac{1}{c_s^2}\ddot{\mathbf{u}}, \quad (7)$$

where the shear wave speed is

$$c_s=\sqrt{\frac{\mu}{\rho}}. \quad (8)$$

This equation can either be solved in terms of standing waves or propagating waves, depending on the particular conditions.

Propagating plane pressure waves are irrotational, that is, $\boldsymbol{\nabla}\times\mathbf{u}=\mathbf{0}$ so $\mathbf{u}$ can be written in terms of a potential as $\mathbf{u}=\boldsymbol{\nabla}\psi$. Using the vector identity $\nabla^2\mathbf{u}=\boldsymbol{\nabla}\boldsymbol{\nabla}\cdot\mathbf{u}-\boldsymbol{\nabla}\times\boldsymbol{\nabla}\times\mathbf{u}$, we can obtain the wave equation for $\boldsymbol{\nabla}\psi$ as

$$\nabla^2(\boldsymbol{\nabla}\psi)=\frac{1}{c_p^2}(\ddot{\boldsymbol{\nabla}\psi}), \quad (9)$$

and the pressure wave speed is

$$c_p=\sqrt{\frac{\lambda+2\mu}{\rho}}. \quad (10)$$

For typical biomaterials, the pressure wave speed is orders of magnitude faster than the shear wave speed. Consistent with this statement, biological tissues are nearly incompressible with $0.49<\nu<0.5$. In the limit, as ν approaches 0.5, the shear modulus $\mu=E/2(1+\nu)\rightarrow E/3$. Therefore, for a nearly incompressible material, a measurement of the shear

wave speed $c_s \approx \sqrt{E/3\rho}$ can be used to obtain information about the stiffness of the material. Therefore, in elastographic imaging experiments, the focus of attention is typically on the shear wave properties and not on pressure wave properties, which have already been investigated extensively in ultrasonic tissue characterization studies.

Equation (6) can also be a starting point for the consideration of step-compression elastography experiments. For static displacement or very low-frequency cyclic motion, the inertial terms are negligibly small. And for nearly incompressible biomaterials, the divergence (or dilatation) $\nabla \cdot \mathbf{u}$ is nearly zero, so Eq. (6) reduces to Laplace's equation,

$$\nabla^2 \mathbf{u} = \mathbf{0}. \tag{11}$$

Solutions to Laplace's equation depend on and reach their extrema on the boundary values of $\mathbf{u}$. For simple geometry, as will be shown in the next section, the solution for $u_x(x)$ is linear with x, a fact that is assumed to be true in most step-compression elastographic imaging experiments.

III. PROPOSED TECHNIQUES FOR ESTIMATING ELASTIC PROPERTIES OF TISSUES

A. Step-compression imaging

For convenience we consider a two-dimensional case of a linear viscoelastic, homogeneous, isotropic material with tissue mimicking properties: E_0 in the kPa range, ρ (density) near 1.0 g/cm^3, and ν (Poisson's ratio) in the range $0.49 < \nu < 0.5$, that is, nearly incompressible. This block of tissue-mimicking material is of a rectangular cross section and is rigidly constrained along one face and further constrained by a parallel plate used for compression or other enforced displacements. We further assume that the tissue mimicking material is allowed to slip freely along the two constraining plates so that the displacement and stress fields will be independent of position in the y direction. Body forces due to gravity are assumed to be negligible. The example is shown in Fig. 1.

We assume that compression is applied at time t_0, and that images are obtained using some ideal imaging system, before and after the compression step. In the case of viscoelastic or poroelastic materials, the state of the material response and its image will be time dependent until sufficient relaxation has occurred. Assuming that a dense field of displacements can be estimated from the two images, in the homogeneous case, Eq. (11) predicts that the displacement $u_x(x)$ will be linear with x, as shown in Fig. 1(b) (solid lines). In the case where a small inhomogeneous region of $E' > E_0$ (assumed here to be of relatively small contrast $E'/E_0 < 2$), is present, a plot of displacement taken on a line bisecting the inhomogeneity will produce a local deviation from the linear slope. The exact details depend on the precise geometry and the stress concentration effect,[34] but the general trend is shown in Fig. 1(b) (dotted lines).

Although the presence of the inhomogeneity can be detected from inspection of the displacement estimates (assuming reasonable elastic contrast and very high imaging signal to noise), it is convenient to display a strain image, $\epsilon_{xx} = du_x/dx$, as this produces a more intuitive result. Homogeneous regions undergo constant strain in this example, and hard inclusions result in locally reduced strain, except for stress concentration effects that are localized near the boundaries. This is demonstrated graphically in Fig. 1(c). The terms elastography and elastographic imaging generally refer to strain images produced in this way. As long as the overall stress produced by the compression is approximately constant over the imaging region, the strain image values will correlate with local relative values of E.

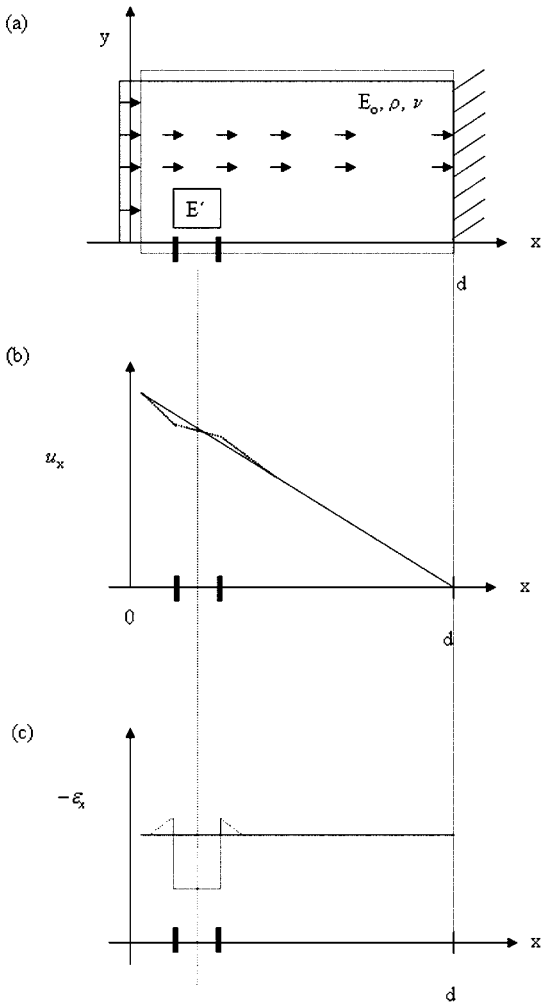

FIG. 1. Schematic of static compresson experiment on a rectangular block of viscoelastic material constrained at position d, containg a small block of material. The larger block has Young's modulus E_0, density, ρ, and Poisson's ratio, ν, while the smaller block has an elevated Young's modulus $E' < 2E_0$. (a) Block before (solid lines) and after (dotted lines) compression in the positive x direction by a rigid plate. (b) General trend of the resulting displacement field (u_x; vertical axis) along a line parallel to the x-axis through the small rectangular inclusion. (c) Strain field ($-\epsilon_x$; vertical axis) along this same line. The dotted lines indicate the perturbation caused by the presence of the inhomogeneity.

B. Shear step imaging

As an alternative to a single compression step, one can apply a single shear step, obtaining images before and after the deformation with some suitable imaging system. The displacement information is similar to that gained by compression, as shown in Fig. 2. Barbone and colleagues have shown[17] that the shear experiment creates a result that is

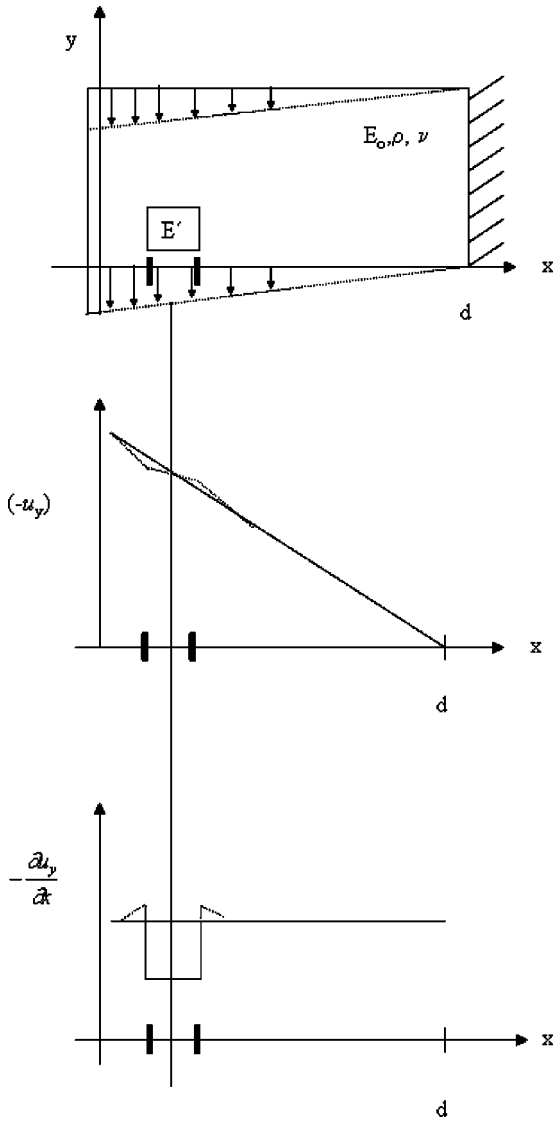

FIG. 2. Static shear experiment on a same block shown in Fig. 1: (a) Block before (solid lines) and after (dotted lines) shear by a rigid plate. (b) Shear displacement field (u_y; vertical axis) along a line parallel to the x-axis through the small rectangular inclusion. (c) Shear strain field along this same line. The dotted lines indicate the perturbation caused by the presence of the inhomogeneity.

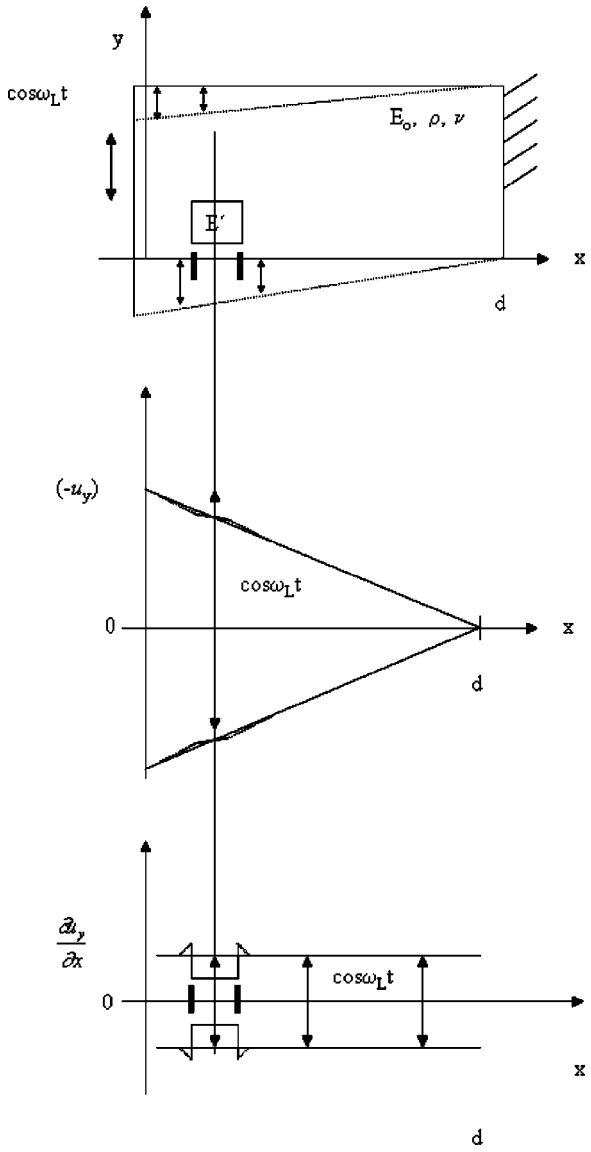

FIG. 3. Cyclical quasi-static shear experiment on the block shown of Fig. 1: (a) Block before (solid lines) and at peak (dotted lines) shear. The applied shear is sinusoidal at low frequency. (b) Peak shear displacements (solid line), along a parallel to the x-axis through the small rectangular inclusion, are linear but slowly time-varying. (c) Peak shear strain along this line is also slowly time-varying. The dotted lines indicate the perturbation caused by the presence of inhomogeneity.

complementary to the compression result when one considers the uniqueness of inverse solutions from these experiments. However, the details of that subject are beyond the scope of this discussion. As in the compression step results, Eq. (11) predicts that for a homogeneous medium displacement, $u_y(x)$ will be linear with x, which can be perturbed by an inclusion. As before, the exact details of the shear in the vicinity of the inclusion require treatment of the exact geometry and elastic contrast of the inclusion. However, stress concentration effects are highly localized in the surrounding medium. As demonstrated in Fig. 2, a spatial derivative can be employed to produce a more intuitive display where homogeneous regions exhibit constant shear strain, $\epsilon_{xy}=(1/2)[\partial u_y/\partial x+\partial u_x/\partial y]$. However, it must be understood that constant strain image values correlate with constant E only under certain idealized, low-contrast conditions.

C. Cyclic, quasistatic imaging

If a shear step is repeated sinusoidally at a relatively slow rate (e.g., at less than five cycles per second), then for most practical cases of tissues and organs, the inertial terms of the governing equations can still be neglected. The behavior can be described in the same functional form as the static case, but modified by the addition of a sinusoidal time-varying term. Thus, if the shear plate of Fig. 2 is moved as $u_y(x=0)=U_0\cos\omega_L t$, where ω_L is low frequency, then $u_y(x)=U_0(1-x/d)\cos\omega_L t$ for $0<x<d$, and the resulting strain is similarly time varying. This is shown schematically in Fig. 3. The practical advantages of cyclic quasistatic methods over single-step methods are primarily due to the ability to average and automate, thereby reducing noise and artifacts.[16,35]

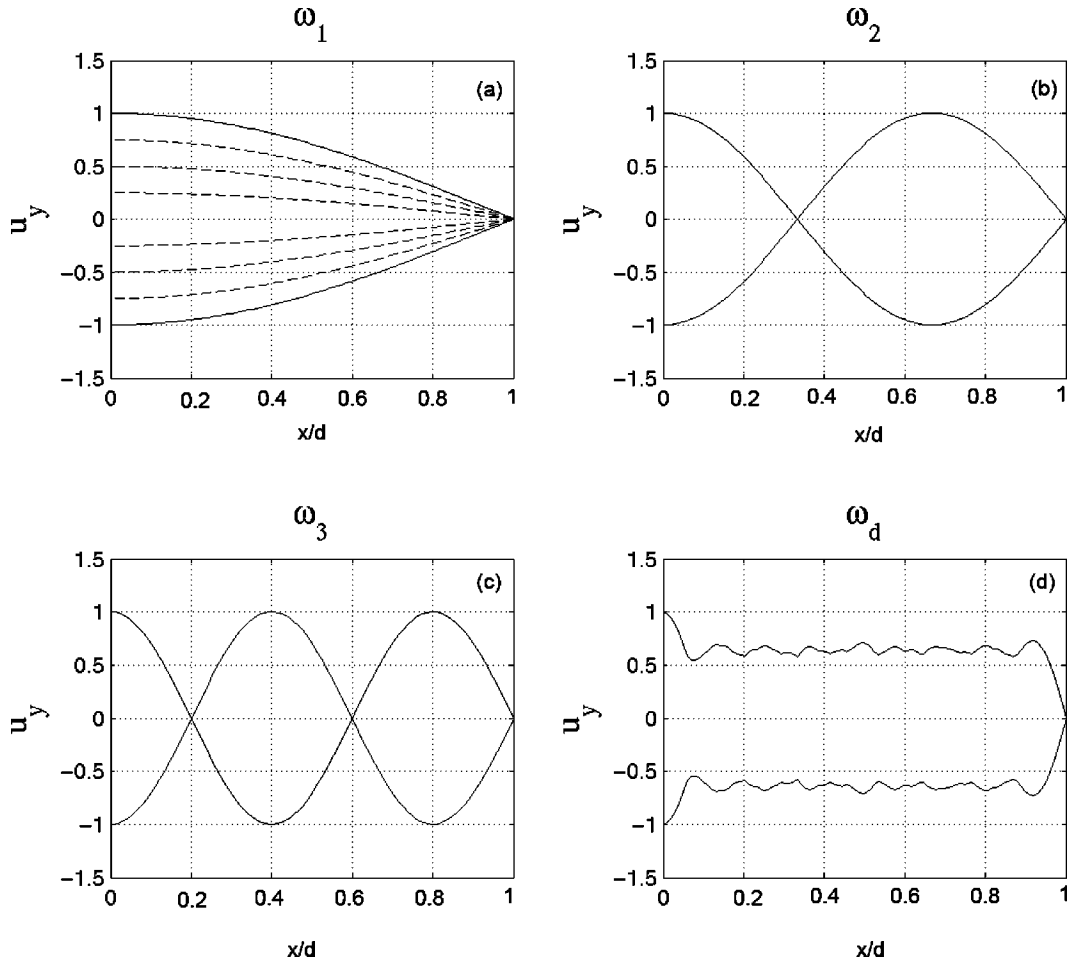

FIG. 4. Displacement fields at the block surface (see Fig. 1) during application of a sinusoidal shear with frequencies above the quasi-static range. (a) First mode. (b) Second mode. (c) Third Mode. (d) Result of many modal frequencies applied simultaneously as ''chords.''

D. Shear wave vibration

As the left vertical plate of Fig. 3 is displaced at higher frequencies, the time-varying inertial terms of the governing equation cannot be ignored and the behavior of the medium obeys the classic wave equation.

For a plane wave propagating in the x direction with particle motion in the y direction [$u_y = u_y(x,t)$ and $u_x = u_z = 0$], the shear wave equation [Eq. (7)], reduces to a one-dimensional equation of the form

$$\frac{\partial^2 u_y}{\partial x^2} = \frac{1}{c_s^2}\frac{\partial^2 u_y}{\partial t^2}. \tag{12}$$

For regular geometries and simple conditions, with low loss or attenuation, the response of the medium will peak at specific eigenfrequencies, with standing wave or eigenmodal patterns produced within the interior. Specifically, these occur when the frequency is such that odd multiples of quarter-wavelengths in the x direction are created. These frequencies are given by

$$f = \frac{2n-1}{4}\left(\frac{c_s}{d}\right), \quad \text{where}$$

$$c_s = \sqrt{\frac{E}{3\rho}}, \quad \text{the shear wave speed.}$$

In this case, we are explicitly treating the resonance as a one-dimensional problem for simplicity. For example, this would be equivalent to having the medium extend for a great length in the y axis compared to the dimension d.

The first few eigenmodes are sketched in Figs. 4(a), 4(b), and 4(c). Note the presence of nodes and antinodes within the eigenmode patterns at higher eigenfrequencies. These modal patterns are observed in regularly shaped phantoms and even in organs such as the liver at low frequencies (lowest eigenmode).[36] These eigenmode patterns can make it more difficult to visually identify regions of different elasticity.

However, the eigenmode patterns are unlikely at higher eigenfrequencies, where the irregular shape of organs, imperfect boundary conditions, and loss all conspire against modal pattern. In any event, the orthogonal nature of the successive eigenmodes makes it possible and beneficial to combine different frequencies into a multiharmonic excitation, which tends to produce a uniform vibration field, free of nulls. These multifrequency excitations are represented in Fig. 4(d), and have been referred to as ''chords.''[37] Regions of inhomogeneity would then cause variations in the vibration

patterns that can be more easily identified when using multifrequency excitations.

These vibration patterns can be imaged in real time using modified color Doppler techniques and are generally referred to as vibration sonoelastography, or simply, sonoelastography. Specifically, the Doppler spectral variance has been shown to be proportional to the vibration displacement amplitude in a sinusoidal steady state.[38] This can be displayed as a color scale overlay on the B-scan image. It has been shown by theory, by finite element modeling, and by experiments that hard inclusions present as a void or local reduction in the vibration pattern.[9] These are illustrated in Fig. 5. In this example of sonoelastography, it is not necessary to take a spatial derivative, particularly in the case where more uniform vibration patterns have been formed in the background. However, in the case where lower frequencies are employed, a derivative operation can be useful to enhance the detectability of lesions.[8]

E. Transient elastography

Transient elastography utilizes a short tone burst of vibration. This can be related to sinusoidal steady-state excitation by the use of Fourier transform relations. However, in transient experiments the forward propagating wave can be resolved and analyzed separately from the reflected waves, and this can be advantageous in some situations. In either case, the effect of an inhomogeneity is governed by the elastic-Born approximation[9] for those cases where the inhomogeneity has limited elastic contrast with respect to the surrounding background medium.

F. Detectability and resolution of issues

Of great concern in the lesion detection problem is the practical limit on the detectability of a low elastic contrast, small lesion in tissue, and the resolvability of multiple discrete small lesions. We assume in this discussion a high signal-to-noise ratio within the displacement field estimates such that derivative operations are practical and we further assume that background uniformity is nearly ideal.

For strain imaging, the general concept has already been introduced: after a derivative operation on the displacement estimations, hard inclusions will be displayed as a local region of lower strain, surrounded by localized stress concentration effects in many cases. However, it is clear from the sequence of operations that a hard inclusion must be larger than the resolution scale of the imaging system. Otherwise, it is not possible to estimate displacements, and then spatial derivatives of displacements, that fall exclusively within the inclusion. If this is satisfied, and ignoring any stress concentration effects, the strain contrast $\epsilon_{xx}(\text{lesion})/\epsilon_{xx}(\text{background})$ is directly proportional to $E_0(\text{background})/E'(\text{lesion})$, the inherent elastic contrast. The resolvability of multiple inclusions as discrete small lesions is similarly tied to the imaging system resolution plus any localized effects of stress concentration. In practice, additional practical considerations of noise, decorrelation, and displacement estimates, all complicate the issue of contrast.[39]

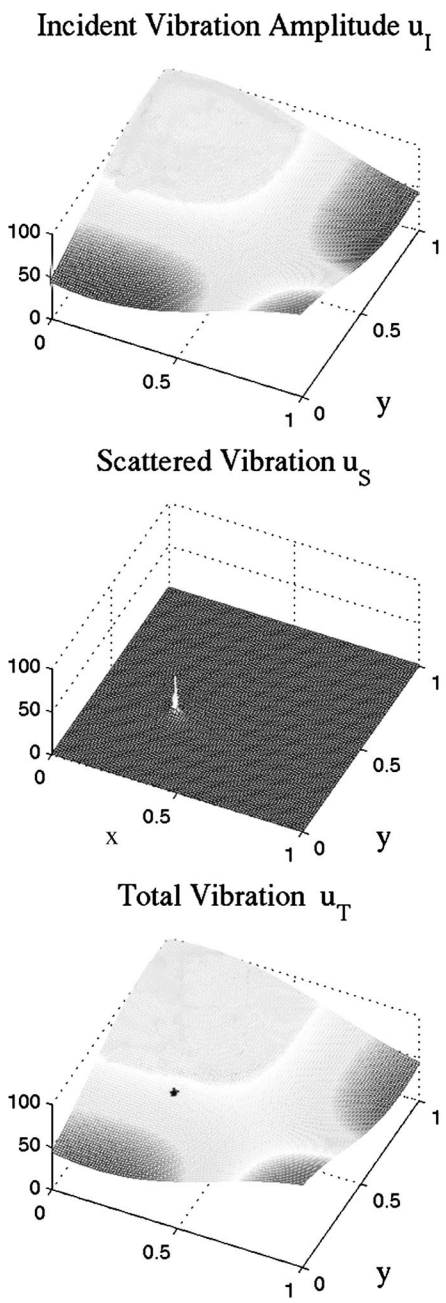

FIG. 5. Detectability and point spread function for a subresolvable elastic inhomogeneity. (top) Incident peak vibration amplitude field in a 2D region containing a small inhomogeneity with Young's modulus $E'>E_0$. (middle) The vibration field resulting from scattering by the inhomogeneity. (bottom) Total observed vibration which is the sum of a and b.

For shear wave excitation in sonoelastography and MRE, the detectability and resolution issues are recast as wave phenomena. The incident shear wave must satisfy the shear wave equation [Eq. (7)]. In the elastic-Born approximation[9] a small elastic inhomogeneity at position x' acts as a source of a scattered shear wave, and the strength of this source is proportional to the elastic contrast, $(E'-E_0)/E'$, times the wave number squared, times the strength of the incident shear wave A:

$$\nabla^2\mathbf{u}+k^2\mathbf{u}=Ak^2\left(\frac{E'-E_0}{E'}\right)\delta(\vec{x}-x'). \tag{13}$$

Within the elastic-Born approximation, the resulting so-

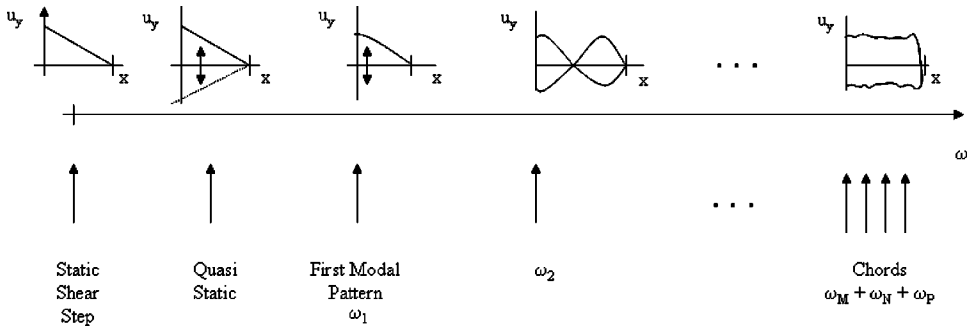

FIG. 6. Summary image showing the continuum from step displacement through dynamic vibration and multiple tones. The displacement field u_y is given in each case. The solution for displacement in homogenous object is linear for the static case, sinusoidal for modal patterns at eigen-frequencies, and approaches a constant for multiple, simultaneous ''chord'' excitation.

noelastic vibration image will be comprised of the addition of a homogeneous solution to Eq. (13) (right-hand side equal to zero) plus the scattered wave. This is depicted in Fig. 5.

Conceptually, this means that even a very small point inhomogeneity, even one well below the resolution of the imaging system, can be detected as a localized disturbance in the form of a free space Green's function, that is a $1/r$ falloff, as depicted in Fig. 5. This is similar to a small point source of light detected (and then blurred) by an optical imaging system, even though the point source aperture may be below the nominal resolution of the imaging lens. However, the strength of the inhomogeneity's signature increases with increasing frequency. Simulations and experiments have demonstrated that the sonoelastic image contrast of lesions increases with increasing frequency[8] until other frequency-dependent effects, such as lossy behavior, present a practical upper frequency limitation.[40]

This wave behavior limits the resolvability of two small neighboring points since the Green's function scattered waves pattern produced by each has an inherent type of blur, which will add coherently when the two points are closely spaced. Thus, no general claim for subresolution resolvability can be made, even though a general claim for subresolution detectability can be made.

IV. DISCUSSION AND CONCLUSION

A plethora of techniques for estimating and imaging the elastic properties of tissue have been proposed, each one employing a unique excitation function to create displacements in tissue. We demonstrate, however, that the most commonly utilized methods, from step-compression elastography through vibration (sono) elastography, fall on a continuum of elastic behavior. The information that can be derived from an ideal imaging system can be used, in each case, to identify an inclusion that is defined by some elastic contrast compared to the background. However, the particular details of preprocessing, detectability, and resolvability do change from static and quasistatic to dynamic systems where wave behaviors are exhibited. Figure 6 compares the shear behavior of a simple homogeneous system as it is excited by different displacement functions along the continuum of frequencies.

As a practical matter, the imaging system (typically ultrasound or MRI) resolution and noise characteristics will limit the performance of elasticity imaging and reconstruction schemes, along with the other practical limits from tissue motion and loss mechanisms. Specifically, on the static and low-frequency side of the continuum, tissue motion out-of-plane, noise, and speckle decorrelation artifacts from rotations all limit the displacement and derivative of displacement estimations.[39] At the other end of the continuum, the high losses or attenuation of shear waves above 200–400 Hz creates a practical limitation on whole organ penetration and potential increases in lesion contrast that would otherwise be predicted from Eq. (12). Lower bounds on correlation-based displacement estimates[40] and Doppler estimates of vibration amplitudes,[38] and MRE detection of vibration[23] have demonstrated very fine scale (micron or below) possibilities given an adequate signal-to-noise ratio.

There is another important topic of exact inverse solutions (of unknown elastic properties from the imaging data) that is beyond the scope of this paper. However, a few general remarks can be made. The exact inversion of static and quasistatic cyclic compression cases requires knowledge of boundary conditions that in most cases lie outside of the imaged region of interest. Solving for the unknown stress field (including localized stress concentrations) is difficult but necessary to utilize the local stress–strain behavior to solve for elastic parameters. In shear wave propagation, however, local estimates of displacement and wave behavior can be used to generate localized estimates of elastic properties, either through direct inversions or through forward iterative approaches. In all cases, the problem of noise in estimating spatial (or temporal) derivative terms can be a major limiting factor.

In this paper we have emphasized the common groundwork, and common information, that is obtainable over a wide range of experimental approaches to elastography.

ACKNOWLEDGMENTS

This work was supported in part by NIH 5 R01 AG16317-03, ''3D sonoelastography imaging for prostate cancer.''

[1] A. P. Sarvazyan, O. V. Rudenko, S. D. Swanson, L. B. Fowlkes, and S. Y. Emelianov, ''Shear wave elasticity imaging: a new ultrasonic technology of medical diagnostics,'' Ultrasound Med. Biol. **24**, 1419–1435 (1998).
[2] T. A. Krouskop, D. R. Doughtery, and S. F. Levinson, ''A pulsed Doppler ultrasonics systems for making noninvasive measurements of the me-

chanical properties of soft tissues,'' J. Rehabil. Res. Dev. **24**(2), 1–8 (1987).
[3] Y. Yamakoshi, J. Sato, and T. Sato, ''Ultrasonic imaging of internal vibrations of soft tissue under forced vibration,'' IEEE Trans. Ultrason. Ferroelectr. Freq. Control **37**, 45–53 (1990).
[4] R. M. Lerner, K. J. Parker, J. Holen, R. Gramiak, and R. C. Waag, ''Sonoelasticity: Medical elasticity images derived from ultrasound signals in mechanically vibrated targets,'' *Proceedings of the 16th International Acoustical Imaging Symposium (Plenum)*, 1988, Vol. 16, pp. 317–327.
[5] R. M. Lerner, S. R. Huang, and K. J. Parker, ''Sonoelasticity images derived from ultrasound signals in mechanically vibrated targets,'' Ultrasound Med. Biol. **16**, 231–239 (1990).
[6] K. J. Parker, S. R. Huang, R. A. Musulth, and R. M. Lerner, ''Tissue response to mechanical vibrations for 'sonoelasticity imaging','' Ultrasound Med. Biol. **16**, 241–246 (1990).
[7] L. Gao, K. J. Parker, R. M. Lerner, and S. F. Levinson, ''Imaging of the elastic properties of tissue—A review,'' Ultrasound Med. Biol. **22**, 959–977 (1996).
[8] K. J. Parker, D. Fu, S. M. Gracewski, F. Yeung, and S. F. Levinson, ''Vibration sonoleastography and the detectability of lesions,'' Ultrasound Med. Biol. **24**, 1937–1947 (1998).
[9] L. Gao, K. J. Parker, S. K. Alam, and R. M. Lerner, ''Sonoelasticity imaging: Theory and experimental verification,'' J. Acoust. Soc. Am. **97**, 3875–3880 (1995).
[10] S. F. Levinson, M. Shinaguwa, and T. Sato, ''Sonoelastic determination of human skeletal muscle elasticity,'' J. Biomech. **28**, 1145–1154 (1995).
[11] F. Yeung, S. F. Levinson, D. Fu, and K. J. Parker, ''Feature-adaptive motion tracking of ultrasound image sequences using a deformable mesh,'' IEEE Trans. Med. Imaging **17**, 945–956 (1998).
[12] J. Ophir, I. Cespedes, H. Ponnekanti, Y. Yazdi, and X. Li, ''Elastography: A quantitative method for imaging the elasticity of biological tissues,'' Ultrason. Imaging **13**, 111–134 (1991).
[13] J. Ophir, B. Garra, F. Kallel, E. Konofagou, T. Krouskop, R. Righetti, and T. Varghese, ''Elastographic imaging,'' Ultrasound Med. Biol. **26**, s23–29 (2000).
[14] R. Righetti, F. Kallel, R. J. Stafford, R. E. Price, T. A. Krouskop, J. D. Hazle, and J. Ophir, ''Elastographic characterization of HIFU-induced lesions in canine livers,'' Ultrasound Med. Biol. **25**, 1099–1113 (1999).
[15] P. Chaturvedi, M. F. Insana, and T. J. Hall, ''Ultrasonic elasticity imaging to model disease-induced changes in soft-tissue structure,'' Med. Image Anal **2**, 325–338 (1998).
[16] M. O'Donnell, A. R. Skovorada, B. M. Shapo, and S. Y. Emalianov, ''Internal displacement and strain imaging using ultrasonic speckle tracking,'' IEEE Trans. Ultrason. Ferroelectr. Freq. Control **41**, 314–325 (1994).
[17] A. Oberai, N. Gokhale, and P. E. Barbone, ''Direct reconstruction of elastic modulus images from ultrasound images'' (Abstract), *Proceedings of the 2nd International Conference on the Ultrasonic Measurement and Imaging of Tissue Elasticity*, 2003, Vol. 2, p. 69.
[18] T. J. Hall, Y. Zhu, and C. S. Spalding, ''In vivo real-time freehand palpation imaging,'' Ultrasound Med. Biol. **29**, 427–435 (2003).
[19] B. Brendel, S. Siebers, M. Scholz, C. Welp, J. Werner, A. Lorenz, A. Pesavento, and H. Ermert, ''Intraoperative applications of elasticity imaging using vibrography,'' in Ref. 17.
[20] R. Muthupillai, D. J. Lomas, P. J. Rossman, J. F. Greenleaf, A. Manduca, and R. L. Ehman, ''Magnetic resonance elastography by direct visualization of propagating acoustic strain waves,'' Science **269**, 1854–1857 (1995).
[21] R. Sinkus, J. Lorenzen, D. Schrader, M. Lorenzen, M. Dargatz, and D. Holz, ''High-resolution tensor MR elastography for breast tumour detection,'' Phys. Med. Biol. **45**, 1649–1664 (2000).
[22] M. M. Doyley, J. B. Weaver, E. E. W. VanHouten, F. E. Kennedy, and K. D. Paulsen, ''Thresholds for detecting and characterizing focal lesions using steady-state MR elastography,'' Med. Phys. **30**, 495–504 (2003).
[23] D. B. Plewes, J. Bishop, A. Samani, and J. Sciarretta, ''Visualization and quantification of breast cancer biomechanical properties with MRE,'' Phys. Med. Biol. **45**, 1591–1610 (2000).
[24] S. Catheline, F. Wu, and M. Fink, ''A solution to diffraction biases in sonoelasticity: The acoustic impulse technique,'' J. Acoust. Soc. Am. **105**, 2941–2950 (1999).
[25] L. Sandrin, S. Catheline, M. Tanter, X. Hennegin, and M. Fink, ''Time-resolved pulsed elastography with ultrafast ultrasonic imaging,'' Ultrason. Imaging **21**, 259–272 (1999).
[26] T. Sugimoto, S. Ueha, and K. Itoh, ''Tissue hardness measurement using the radiation force of focused ultrasound,'' *IEEE 1990 Ultrasonics Symposium Proceedings*, 1990, pp. 1377–1380.
[27] F. L. Lizzi, R. Muratore, C. X. Deng, J. A. Ketterling, S. K. Alam, S. Mikaelian, and A. Kalisz, ''Radiation-force technique to monitor lesions during ultrasonic therapy,'' Ultrasound Med. Biol. **29**, 1593–1605 (2003).
[28] W. F. Walker, F. J. Fernandez, and L. A. Negron, ''A method of imaging viscoelastic parameters with acoustic radiation force,'' Phys. Med. Biol. **45**, 1437–1447 (2000).
[29] K. R. Nightingale, M. L. Palmeri, R. W. Nightingale, and G. E. Trahey, ''On the feasibility of remote palpation using acoustic radiation force,'' J. Acoust. Soc. Am. **110**, 625–634 (2001).
[30] M. Fatemi and J. F. Greenleaf, ''Ultrasound-stimulated vibro-acoustic spectrograpy,'' Science **280**, 82–85 (1998).
[31] M. Fatemi and J. F. Greenleaf, ''Application of radiation force in noncontract measurements of elastic parameters,'' Ultrason. Imaging **21**, 147–154 (1999).
[32] H. Kolsky, *Stress Waves in Solids* (Dover, New York, 1963).
[33] J. D. Achenbach, *Wave Propagation in Elastic Solids* (North-Holland, Amsterdam, 1984).
[34] I. Shames, *Mechanics of Deformable Solids* (Prentice–Hall, Englewood Cliffs, NJ, 1964).
[35] M. M. Doyley, J. C. Bamber, F. Fuechsel, and N. L. Bush, ''A freehand elastographic imaging approach for clinical breast imaging: system development and performance evaluation,'' Ultrasound Med. Biol. **27**, 1347–1357 (2001).
[36] K. J. Parker and R. M. Lerner, ''Sonoelasticity of organs: Shear waves ring a bell,'' J. Ultrasound Med. **11**, 387–392 (1992).
[37] L. S. Taylor, D. J. Rubens, and K. J. Parker, ''Artifacts and artifact reduction in sonoelastography,'' *2000 IEEE Ultrasonics Symposium Proceedings*, 2000, pp. 1849–1852.
[38] S. R. Huang, R. M. Lerner, and K. J. Parker, ''On estimating the amplitude of harmonic vibrations from the Doppler spectrum of reflected signals,'' J. Acoust. Soc. Am. **88**, 310–317 (1990).
[39] Srinivusan, R. Righetti, and J. Ophir, ''Tradeoffs between axial resolution and signalto-noise ration in elastography,'' Ultrasound Med. Biol. **29**, 847–866 (2003).
[40] W. F. Walker and G. E. Trahey, ''A fundamental limit on delay estimation using partially correlated speckle signals,'' IEEE Trans. Ultrason. Ferroelectr. Freq. Control **42**, 301–308 (1995).

LETTERS TO THE EDITOR

This Letters section is for publishing (a) brief acoustical research or applied acoustical reports, (b) comments on articles or letters previously published in this Journal, and (c) a reply by the article author to criticism by the Letter author in (b). Extensive reports should be submitted as articles, not in a letter series. Letters are peer-reviewed on the same basis as articles, but usually require less review time before acceptance. Letters cannot exceed four printed pages (approximately 3000–4000 words) including figures, tables, references, and a required abstract of about 100 words.

Ultrasonic relaxation and internal rotation in butyl formate (L)

S. Z. Mirzaev,[a] Z. S. Bakaeva, P. K. Khabibullaev, and V. S. Kononenko
Heat Physics Department, Uzbekistan Academy of Sciences, Katartal 28, Tashkent 700135, Uzbekistan

(Received 10 October 2004; revised 1 February 2005; accepted 24 February 2005)

The acoustic spectra of liquid butyl formate have been investigated in the frequency range from 0.1 to 150 MHz and at the temperatures 20 °C, 50 °C, and 80 °C. The ultrasonic spectra of pure butyl formate show a single relaxation term in the frequency range between 200 kHz and 2 MHz. The relaxation process has been assigned to the cis and trans molecular conformations. © *2005 Acoustical Society of America.* [DOI: 10.1121/1.1893425]

PACS numbers: 43.35.Bf [RR] Pages: 2713–2715

I. INTRODUCTION

In the past years ultrasonic methods as well as T-jump P-jump,[1] nuclear magnetic resonance (NMR),[1] electron paramagnetic resonance, and stopped flow techniques[1] have been extensively used to study the kinetics of monomolecular reactions in liquids. Rotational barriers in a two-isomer system are most accurately measurable with the ultrasonic relaxation method, when the isomer is presented in unequal amounts.[2] Sound waves traversing liquids induce periodic perturbations in pressure and temperature, which can shift equilibria, resulting in characteristic sound attenuation and velocity dispersion spectra. A time lag between pressure and density in the sound field leads to a dissipation of acoustic energy.

On the other hand, it is difficult to extend the NMR method to two-isomer systems where the ratios of the two isomers are much smaller than ca. $\frac{1}{20}$. Therefore, in the study of rotational barriers the techniques of ultrasonic relaxation and NMR are largely complementary.[3]

This work is part of a series dealing with internal rotation (change of configuration between the two isomers) and low-frequency ultrasonic relaxation[4,5] behavior in pure liquids. The kinetics and mechanisms of the processes occurring in liquid formate during thermal movement have been inadequately studied. The study of the kinetics of relaxation processes has proved useful, apart from their independent scientific and practical interest, for a more detailed understanding of the mechanism of the internal rotations in liquid formate.

In this paper we focus on the relaxation process caused by internal rotation in pure butyl formate [$HCOO(CH_2)_3CH_3$, synonyms: formic acid butyl ester]. Butyl formate may exist in two rotational isomers *cis*(I) and *trans*(II) Fig. 1. At room temperature there will be a fast dynamical equilibrium between these two isomers. The isomers (I) and (II) are presented in unequal amounts and their ratio varies with temperature. The relaxation processes associated with these processes are usually characterized by relaxation times ~ 1 μs, and for exact estimating of the relaxation parameters a low-frequency ultrasonic technique ($f < 1$ MHz) must be used. Unfortunately precise ultrasonic attenuation measurements at frequencies below 200 kHz, as would be required, are practically experimentally inaccessible due to diffraction losses.

The rotational equilibrium of butyl formate has been the subject of numerous investigations.[6–8] The dispersion of the quantity α/f^2 in formates has been observed and attributed to the internal rotation relaxation processes by Lamb.[2] Pancholy and Mathur[6] suggested the existence in liquid butyl formate of a single low-frequency region ($f_r < 1.5$ MHz) of acoustic dispersion associated with ''trans'' and ''cis'' isomers. The attenuation of sound α/f^2 and velocity was studied in the frequency ranges $f = 3-20$ MHz at temperatures 10 °C, 20 °C, 30 °C, 40 °C, and 50 °C. The relaxation frequency lies outside the experimental frequency range and analysis of the data is difficult. Therefore the relaxation parameters were estimated within an uncertainty of ca. ±50%. Several years later, Burundukov and Yakovlev[7] investigated the attenuation of ultrasonic waves in butyl formate in the frequency range from 0.3 to 74.2 MHz and at one fixed temperature 21.5 °C. More recently, Sharipov *et al.*[8] performed measurement of acoustic spectrum in butyl formate by the reverberation and pulse methods in the frequency range 0.03–1100 MHz. The dispersion of the quantity α/f^2 at $-70\,°C < t < -50\,°C$ and at $0.03\,\text{MHz} < f < 100\,\text{MHz}$ was not observed in the investigated frequency region. The sound

[a]Electronic mail: mirzaev@web.de

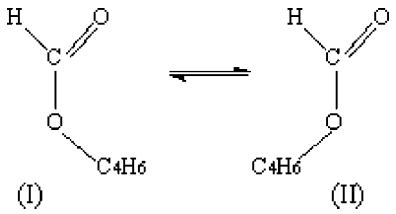

FIG. 1. The rotational isomers of butyl formate.

velocity was found to vary linearly with temperature and the velocity dispersion was negligible.

The above studies dealt mostly with the investigation of the acoustic properties of butyl formate over relatively narrow frequency and temperature ranges, and there are significant discrepancies between the results of different researchers. In no case was a low enough frequency attained to permit direct experimental determination of the relaxation term in the expression for the attenuation coefficients. Further experimental investigations of the acoustic spectra of butyl formate and their detailed analysis are therefore necessary.

II. METHODS

The acoustic spectra of liquid butyl formate have been investigated in the frequency range from 0.1 to 150 MHz and at the temperatures of 20 °C, 50 °C, and 80 °C. The ultrasonic spectrum of the butyl formate has been measured by a cavity resonator method using two different specimen cells to cover the frequency range between 100 kHz and 20 MHz[9,10] and further developed versions of pulse-modulated wave transmission techniques[11] in the frequency range from 20 to 150 MHz. The procedure for the measurement of sound attenuation and velocity is described in our earlier work.[5,9,11] For automatic measurements a computer connected to a commercial network analyzer (NWA HP E5100B) is used. It performs a sophisticated evaluation of complete transfer functions and allows fast and reliable measurement procedures. The temperature of all specimens cells was controlled to within 0.05 K. The error in the attenuation data was smaller than 3% at $f<20$ MHz and smaller than 2% at $f>20$ MHz. Butyl formate was purchased from REAHIM (Erevan, purity >97%) and was subjected to additional distillation.

III. RESULTS AND DISCUSSION

Figures 2 and 3 show results of the ultrasonic attenuation measurements and data analysis. As seen from these figures, as the temperature is increased, the relaxation frequency moves toward higher frequencies. Analyzing the data, we have found that the curves are described by identical relaxation processes of the form

$$\frac{\alpha}{f^2}=\sum_{i=1}^{n}\frac{A_i}{1+(\omega\tau_i)^2}+B, \tag{1}$$

where f is the frequency, A is the relaxation amplitude, τ_i is the relaxation time of the characteristic processes, B is a contribution to attenuation of other factors which do not depend on the considered relaxation process, and $\omega=2\pi f$ is

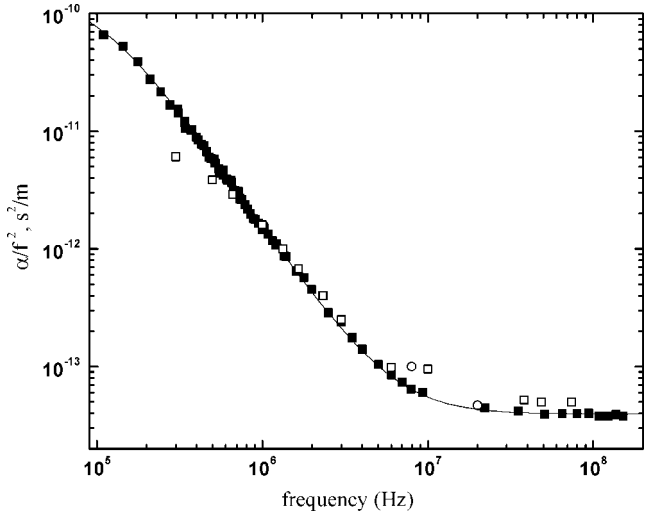

FIG. 2. Ultrasonic attenuation as a function of frequency for butyl formate at 20 °C: ● our data; ○ Pancholy and Mathur,[6] and □ at 21.5 °C Burundukov and Yakovlev.[7] The solid line represents the calculated relaxation spectra from a single relaxation equation.

the cyclic frequency. The experimental data at each temperature were analyzed by using the least-squares method. The approximate results are the solid curves shown in Figs. 2 and 3. It is apparent that a single relaxation equation is required to adequately fit the experimental data obtained, and this holds for all of the ultrasonic relaxation spectra obtained in this study. For the temperature 80 °C, measurements in the frequency range between 1 and 10 MHz were impossible. Therefore, in Table I values A and τ can have uncertainty exceeding a standard value. The coefficients resulting from these calculations and sound velocity measured at 20 MHz are given in Table I.

On the other hand, the relaxation parameters A and τ are in qualitative agreement with[7] those of determined in this study. It has been suggested that this single relaxation term in the excess attenuation of formates reflects a rotational isomerization of the chain molecules.[2] This would be a

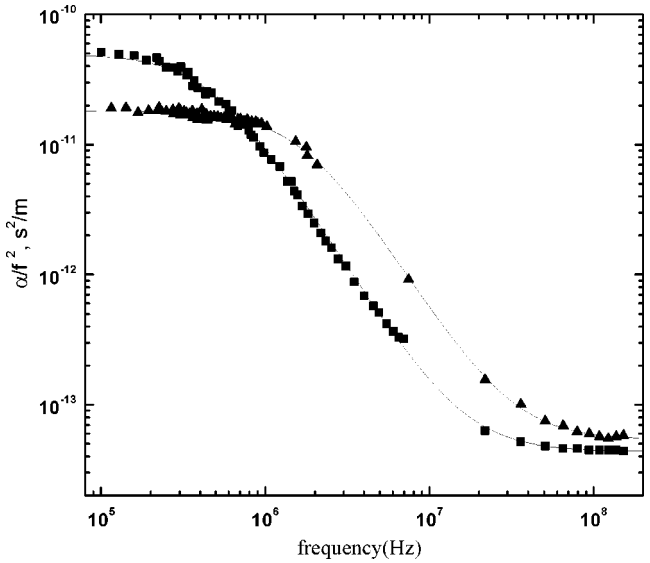

FIG. 3. Ultrasonic attenuation as a function of frequency for butyl formate at 50 °C (■) and 80 °C (▲). The solid lines represent the calculated relaxation spectra from a single relaxation equation.

TABLE I. Ultrasonic relaxation parameters for pure butyl formate [Eq. (1)].

Temperature (°C)	Velocity (m/s) ±0.5%	A (10^{-12} m^{-1} s^2) ±10%	τ (ns) ±10%	B (10^{-15} m^{-1} s^2) ±5%
20	1195.68	182	1600	36
50	1087.47	51	350	44
80	979.26	18	94	54
methyl formate at 60 °C			227 (Ref.12)	
ethyl formate at 60 °C			265 (Ref.12)	
propyl formate at 70 °C			220 (Ref. 4)	

monomolecular rotation, described by a rather simple reaction type $R \underset{k_{21}}{\overset{k_{12}}{\Leftrightarrow}} R^*$ with the forward and backward rate constants k_{12} and k_{21}, respectively, and the equilibrium constant $K=k_{12}/k_{21}$.

The kinetic analysis of acoustic data about conformation processes is carried out rather simply. The experimental results were analyzed for a low-frequency relaxation process by using Eyring relations.[2] We employ the expressions (the details are described in Ref. 5)

$$\frac{2\mu_{\max}}{\pi}\frac{C_P}{\gamma-1}\approx R\left(\frac{\Delta H_0}{RT}\right)^2\exp\left(-\frac{\Delta H_0}{RT}\right)F, \tag{2}$$

where

$$F=\exp\left(\frac{\Delta S_{21}^{\neq}}{R}\right) \tag{3}$$

and

$$\mu_{\max}=\frac{A_1 c}{4\pi\tau_1}. \tag{4}$$

C_P is the specific heat per unit mass and at constant pressure, $\mu_{\max}$ is the maximum value of the attenuation per wavelength at the frequency $f=1/(2\pi\tau_i)$, c is the sound velocity, $\gamma=C_P/C_V$ is the ratio of the specific heat, R is the gas constant, and T is the absolute temperature. The energy difference ΔH_0 between the activation enthalpies of ''cis and trans'' groups derived from Eq. (2) by least-square method yields $\Delta H_0=15.4$ kJ/mol.

Taking into account relations $f_r=(1/2\pi)(k_{12}+k_{21})=k_{21}(1+K)/2\pi$ and

$$k_{21}=(kT/h)\exp(-\Delta G_2/RT), \tag{5}$$

it then follows from the given expression that

$$f_r=(1/2\pi)(kT/h)\exp(\Delta S_2/R)\exp(-\Delta H_2/RT), \tag{6}$$

where h is the Planck constant, ΔH_2 is an energy barrier for the reverse reaction, ΔG_2 is the Gibbs energy change of reaction, f_r is the characteristic frequency of the relaxation process, and ΔS_2 is the entropy of activation of the reverse reaction. On the basis of the foregoing arguments and the experimental values of τ (Table I) we determine $\Delta H_2=40\pm2$ kJ/mol. This temperature behavior of τ is typical of systems in which acoustic relaxation is caused by rotational-isomeric conversions of the molecules. It may be assumed, therefore, that the low-frequency sound-attenuation interval in the butyl formate is attributable to violation of the equilibrium between *cis-trans* rotational isomers of the formate molecules, as is indeed confirmed by the results of Refs. 2, 6, and 7.

The dependence of the relaxation frequency on the number of atoms in formates C_NH_{2N+1} ($N=1,2,...$ is the homolog number) was studied in Ref. 7, which shows that the relaxation frequencies group about a straight line with slope $\Delta f_r/\Delta N\approx10^5$ Hz. As shown in Table I, it is not observed of an essential alteration of relaxation time of a depending on homolog numbers, as it was circumscribed in Ref. 7. The values of both ΔH_0 and ΔH_2 for propyl and butyl formates within the limits of experimental error coincide and are close to values for methyl and ethyl formates, obtained by other authors using an impulse method. However, outcomes of calculation of magnitudes ΔH_0 and ΔH_2, obtained in Refs. 7 and 12 with the help of the reverberation method and the method of substitution, give the underestimated values that can be related to the inaccuracy of low-frequency measurements by these methods. The small modification of magnitudes ΔH_0 and ΔH_2 depending on homolog numbers confirms the conclusions of Ref. 13 about the small influence of alkyl group length on the internal rotation of formate molecules.

ACKNOWLEDGMENTS

This work was supported by a grant from the State Committee for Science and Technology (Tashkent, Uzbekistan). We thank the Volkswagen-Stiftung (Hannover, FRG) for a grant for the purchase of the HP network analyzer.

[1] G. G. Hammes (ed.), *Principles of Chemical Kinetics* (Academic, New York, 1978).
[2] J. Lamb, ''Thermal relaxation in liquids,'' in *Physical Acoustics*, edited by W. P. Mason (Academic, New York, 1965), Vol. 2. Part A, p. 203.
[3] K. Dahlqvist and S. Forsen, ''The barrier to internal rotation in 2-furanaldehyde,'' J. Phys. Chem. **69**, 4062–4071 (1965).
[4] S. Z. Mirzaev, P. K. Khabibullaev, A. A. Saidov, and V. S. Kononenko, ''Study of the ultrasonic relaxation and cis-trans isomerization in propyl formate: evidence from low frequency spectrometry,'' J. Chem. Phys. **112**, 1057–1058 (2000).
[5] S. Z. Mirzaev, P. K. Khabibullaev, A. A. Saidov, V. Kononenko, and I. I. Shinder, ''Conformation transition and behavior of the ultrasonic attenuation in cyclohexanol and aqueous solution of cyclohexanol,'' J. Acoust. Soc. Am. **104**, 585–587 (1998).
[6] M. Pancholy and S. S. Mathur, ''Frequency and temperature variation of ultrasonic absorption in esters,'' Acustica **13**, 42–48 (1963).
[7] K. M. Burundukov and V. F. Yakovlev, ''Study of the absorption coefficient and velocity of ultrasound in the first four homologs of the series formic acid esters,'' Sov. Phys. Acoust. **15**, 254–256 (1969).
[8] Sh. A. Sharipov, M. G. Khaliulin, and P. K. Khabibullaev, ''On the mechanism of acoustic relaxation in formats,'' Sci. Notes Tashkent State Pedagogical Inst. **142**, 120 (1975).
[9] V. S. Kononenko and V. F. Yakovlev, ''Precise method for measuring sound velocity in liquids between 0.7–30 MHz,'' Ultrazv. Tekh. **1**, 78–82 (1965).
[10] V. S. Kononenko, ''Precision method for measurements of the ultrasound absorption coefficient in liquids at frequencies of 0.1–20 MHz,'' Sov. Phys. Acoust. **33**, 401–404 (1987).
[11] L. A. Davidovich, S. Makhkamov, L. Pulatova, P. K. Khabibullaev, and M. G. Khaliulin, ''Acoustical properties of certain organic liquids at frequencies from 0,3 to 3 GHz,'' Sov. Phys. Acoust. **18**, 264–266 (1972).
[12] S. V. Subrachmanyan and J. E. Piercy, ''Ultrasonic relaxation and Cis-Trans izomerization in methyl and ethyl Formates,'' J. Acoust. Soc. Am. **37**, 340–347 (1965).
[13] C. Woker, in *Internal Rotation in Molecules*, edited by W. J. Orville-Thomas (Wiley, London, 1974), p. 235.

Transmission loss measurement of consolidated granular media (L)

Giulio Pispola[a)]
Department of Industrial Engineering, University of Perugia, via G. Duranti 67, 06125 Perugia, Italy

Kirill V. Horoshenkov[b)]
School of Engineering, Design and Technology, University of Bradford, Bradford BD7 1DP, England

Francesco Asdrubali[c)]
Department of Industrial Engineering, University of Perugia, via G. Duranti 67, 06125 Perugia, Italy

(Received 25 June 2004; revised 8 February 2005; accepted 10 February 2005)

The normal incidence transmission loss of a new class of sustainable acoustic materials, i.e. consolidated granular media, has been measured to determine their sound insulating performance. Tests performed on different samples in a standing wave tube suggest that the traditional method employing an anechoic termination assumption can yield serious errors because its accuracy depends significantly on the properties of both the termination and the tested sample. Since it is not possible to implement a perfect anechoic termination over a wide frequency range, a well-developed alternative approach has been adopted. A simple theoretical analysis has been carried out to compare these two methods. It has been shown that the two-load method, based on two sets of measurements with different boundary conditions at the tube termination, can give more reliable and predictable results. Greater discrepancies have been observed in the case of the anechoic termination method applied to samples with higher values of flow resistivity. Results of the two-load method match well with predictions based on a simple model for acoustic transmission through a porous plate. [DOI: 10.1121/1.1886365]

PACS numbers: 43.20.−f, 43.20.Ye, 43.20.Mv, 43.55.Ti [DKW] Pages: 2716–2719

I. INTRODUCTION

The development of sustainable materials with improved acoustic performances, e.g. recycled materials, has progressively gained interest in recent years. Several consolidated granular media have shown good acoustic absorbing and insulating performance, together with beneficial mechanical properties. This claims both for accurate and fast measurement methods of material characterization. Recently Song *et al.*[1,2] suggested a useful bench top experimental technique to determine the normal incidence transmission loss (TL) by means of an impedance tube and one or more microphones. In this method a relatively small specimen is required so that a rapid laboratory assessment of the acoustic performance on a large selection of materials is possible. The suggested experimental setup, previously used for the characterization of fibrous media, has been adapted to carry out measurements on porous, consolidate granular samples with a relatively high compression modulus and flow resistivity, e.g. consolidated flint, recycled foam, and recycled rubber. Two different methods of data analysis were then adopted: (i) the analysis of data from the transmission loss tube with an anechoic termination and (ii) the analysis of data from the same tube, but with open and rigid terminations (two-load method). In this work we discuss the accuracy of the two methods of measurement and the prediction results.

[a)]Electronic mail: pispola.unipg@ciriaf.it
[b)]Electronic mail: K.Horoshenkov@bradford.ac.uk
[c)]Electronic mail: fasdruba@unipg.it

II. METHODOLOGY

The experimental apparatus (see Fig. 1) is a custom-made 82 mm standing wave tube divided in two 1.0 m long sections: a loudspeaker section and a section with an acoustic termination. The tube material is 8 mm stainless steel mounted on a heavy steel frame to minimize vibration transmission. Each section has been provided with three microphone holders, closed by dummy inserts when unused in the experiment. The material sample with the diameter of 99 mm is inserted and firmly tightened between the two sections using the adjustable screws on two threaded bars as shown in Fig. 1(b). Before the experiment the edge of the sample is sealed with tape and putty to minimize the flanking transmission. An uPVC sliding seal and two rubber seals [see Fig. 1(b)] are used to ensure the complete seal of the area around the sample. The spacing between microphone holders is 50 mm and positions closest to the sample are 100 mm from the surfaces on each side. A single microphone was adopted in the experiment to take sequential measurements at the four different positions along the tube: this approach avoided the need for an accurate calibration procedure and compensation for the channel mismatch. The measurement setup employed a B&K Type 4939 1/4 in. condenser microphone with Type 2670 preamplifier, B&K Nexus conditioning amplifier, AUDAX AP100Z0 speaker, ARCAM A65 signal amplifier and a PC equipped with a professional sound card (Marian Marc VIII). WinMLS 2000 software was used to control the card to generate a MLS signal and to calculate the average of 8 impulse responses. This type of the stimulus guarantees a greater than 15 dB signal-to-noise ratio throughout the

 0001-4966/2005/117(5)/2716/4/$22.50

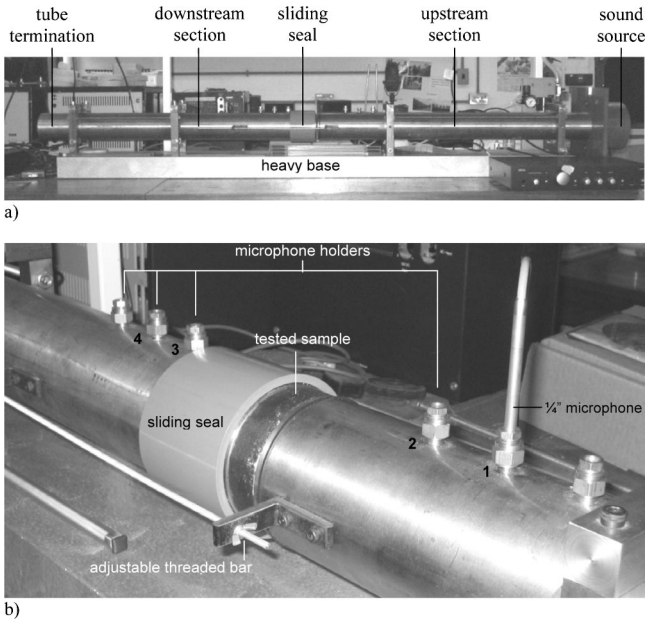

FIG. 1. Experimental setup used for the measurements: (a) view of the standing wave tube; (b) detail of the microphone locations and of the sample holder.

adopted frequency range at all the microphone positions and for all the measurement regimes. The software was operated at 22 050 Hz sampling frequency and the MLS order was set to 16. Custom-made routines have been developed in Matlab and used to carry out post-processing of the signals. Considering the tube internal diameter and microphone spacing (50 mm), the expected working frequency range of the apparatus was between 100 and 1700 Hz.

Following Song *et al.*[1,2] an approximately anechoic termination was created by stacking inside the downstream section a 150 mm layer of natural wool and a 100 mm layer of more dense fiberglass. The normal incidence absorption coefficient of this termination was measured independently in a standard 99 mm Brüel & Kjær impedance tube (Type 4206) controlled with a PULSE system. It does not fall below 0.95 in the 500–2000 Hz frequency range and is greater than 0.76 in the frequency range of 100–500 Hz. The rigid termination was simulated with a 10 mm steel lid, firmly screwed and hermetically sealed at the end of the tube.

The anechoic termination method[2] and the so-called ''two-load'' transfer function method[3,4] were adopted. In the case of the ''two-load'' method the measurement has to be repeated twice: leaving open the downstream section of the tube and terminating it with a rigid lid. This method obviously implies doubling the number of measurements. However, it can be argued that in a practical measurement setup it would be easier to simulate two independent boundary conditions, such as a rigid and an open termination, rather than an anechoic one, so that the accuracy of the measurements can be enhanced.

The theoretical principle for the transmission loss pipe experiment is schematically illustrated in Fig. 2. From the frequency responses P_1-P_4, from the microphones in positions 1–4, it is possible to calculate the complex amplitudes $A-D$ of the direct, reflected and propagated plane wave

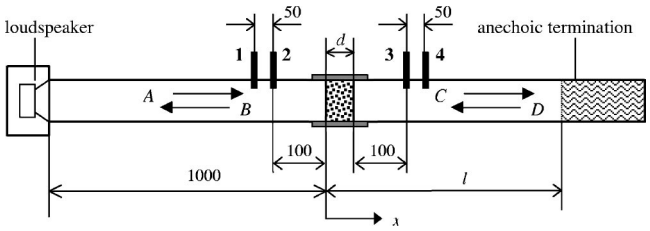

FIG. 2. Diagram of the standing wave tube showing geometry and physical dimensions (in mm). A, B, C, and D are the complex amplitudes of the plane wave components in the tube sections, l is the distance from the surface of the termination to the origin, d is the sample thickness and 1, 2, 3 and 4 are the microphone positions. The x points to the positive direction of the coordinate system.

components in the upstream and downstream tube sections. The complex amplitudes can be correlated in a matrix representation

$$\begin{Bmatrix} A \\ B \end{Bmatrix} = \begin{bmatrix} \tau & \beta \\ \gamma & \delta \end{bmatrix} \begin{Bmatrix} C \\ D \end{Bmatrix},$$

where the matrix coefficients depend just on the acoustical properties of the sample. In particular, the transmission coefficient is defined as $T=\tau^{-1}$. In the case of a perfectly anechoic termination ($D=0$), TL can then be determined from a single measurement of the four impulse responses,[2] i.e. $\mathrm{TL}=-10\log_{10}(|C/A|^2)$. Employing the two-load method,[3] two equations are available: $A_o=\tau C_o+\beta D_o$ and $A_h=\tau C_h+\beta D_h$. These lead to $\tau=(A_hD_o-A_oD_h)/(C_hD_o-C_oD_h)$, where the subscripts o and h denote the open and hard termination, respectively. Similarly, the expression for the feedback-like coefficient is given by $\beta=(A_oC_h-A_hC_o)/(C_hD_o-C_oD_h)$. In general, the open end termination may not necessarily ensure a perfect pressure release boundary condition, i.e. $C_o=-D_o$ (Ref. 5). However, if the two-load method is adopted and the boundary conditions at the far end of the pipe are sufficiently different between the two sets of measurements, e.g. rigid termination versus open termination, then the above expression should be sufficiently accurate throughout the considered frequency range. If the termination is not perfectly anechoic, i.e. has an arbitrary, complex value of the reflection coefficient, R_t, then the boundary condition at $x=l$ yields $De^{ikl}=R_tCe^{-ikl}$ so that $\tau_a=A/C=\tau+\beta R_te^{-2ikl}$, and the transmission coefficient

$$T_a=\frac{C}{A}=\frac{T}{1+\beta TR_te^{-2ikl}}=\frac{|T|e^{i\phi_T}}{1+|\beta||T||R_t|e^{i\theta}},$$

$$\theta=(\phi_\beta+\phi_T+\phi_{R_t}-2kl). \tag{1}$$

Here, the subscript a stands for the experiment with a nonperfectly anechoic termination. Thus T_a depends not just on the actual transmission coefficient of the sample T, but also on the distance to the anechoic termination (l) and on the acoustical properties of the termination (R_t) and of the sample itself (β).

Therefore, even for small values of $|R_t|$ a significant error can occur with a nonperfectly anechoic termination. In the case of materials with medium and low porosity and high flow resistivity the effect of β and nonzero phase angles [see θ in Eq. (1)] is likely to be more pronounced and should

TABLE I. Nonacoustical microscopic and macroscopic properties of the tested samples.

Material (designation)	Recycled rubber (R)	Consolidated flint (C)	Recycled foam (F)
Flow resistivity σ (Pa s m^{-2})	18 300	46 238	190 759
Open porosity Ω	0.36	0.40	0.8
Tortuosity q	1.63	1.338	2.519
Pore size standard deviation (ϕ-units)	0.35	0.31	0.31
Young's elastic modulus E (Pa)	1.7×10^6	6.2×10^7	2.3×10^7
Poisson ratio ν	0.35	0.3	0.35
Bulk density (kg m^{-3})	1050	1455	418
Plate thickness d (m)	0.02	0.02	0.021

result in oscillations of the TL spectrum across the considered frequency range. Such an effect can be observed in the results obtained by Bolton *et al.*[6] for automotive sealant materials (foams) tested using the anechoic termination method. In the case of materials with high porosity and low or medium flow resistivity, such effects may be marginal, as is evident from the results for fiber glass presented by Song *et al.*[1,2]

Both methods have been tested on samples of three different materials: a sample (C) manufactured from flint particles mixed with epoxi-resin binder (Coustone™), a sample (F) made from consolidated particles of recycled automotive foam and a sample (R) of consolidated particles of recycled tyres both mixed with polyurethane (PU) binder. The process of manufacturing of these materials has been detailed by Swift.[7] The choice of rigid frame granular porous materials with a relatively high compression modulus and the design of the tube allowed the sample to be tightly secured between the two sections in a manner which limited the effect of circumferential edge constraint reported and modelled by Song *et al.*[2] for glass fibers.

In order to compare the measured acoustic characteristics with the predictions by an established model for sound propagation in granular media, samples of the three materials were tested in the standard impedance tube to obtain the surface impedance ratios with rigid backing. The values of the relevant nonacoustic parameters were determined using standard testing methods and are summarized in Table I.

The normalized surface impedance of the hard-backed samples was predicted using the 2-parameter Padé approximation model[8] and validated against the impedance tube data. The maximum relative errors between the measured and predicted values of the impedance have been estimated as 13%, 24% and 27% for samples R, C and F, respectively. Finally, the measured and deduced values of nonacoustic parameters were used to predict the transmission loss calculated according to the expressions proposed by Horoshenkov *et al.*[9] These results were compared against the measured data.

III. RESULTS

The impedance tube data for the complex reflection coefficient, R_t, of the anechoic termination can be used to estimate its effect on the measured values of the transmission loss using Eq. (1). The experimental data show noticeable

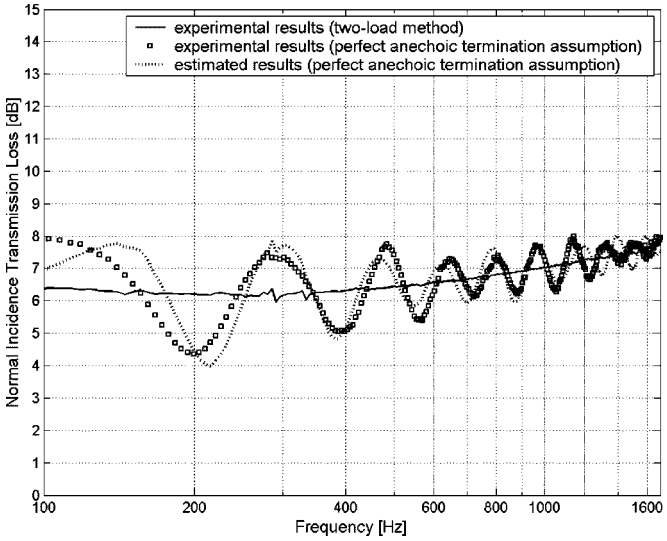

FIG. 3. A comparison of the TL measured with the two-load method and the TL measured and estimated with an approximately anechoic termination for sample C. The estimated TL is calculated using Eq. (1), accounting for results of the two-load method and for the reflection coefficient and position of the anechoic termination.

fluctuations in the TL spectrum measured with the anechoic termination method without compensation for $R_t \neq 0$ (squares in Fig. 3). Substantial discrepancies of ± 2 dB at 200 Hz, where the two-load method provides a TL of 6 dB, can be observed. If the effect of the imperfectly anechoic termination is accounted for, using Eq. (1), then an improved agreement between the two methods of measurement can be observed (dotted line in Fig. 3). These results define the theoretical limit of accuracy of the anechoic termination method for the available type of termination and the acoustic properties of material sample C. Similar results were observed for the other two material samples considered in this work.

Experimental results for the TL of the samples of rubber and consolidated foam are presented in Fig. 4, both for the two-load method and for the anechoic termination method. Significant differences between the two experimental sets of

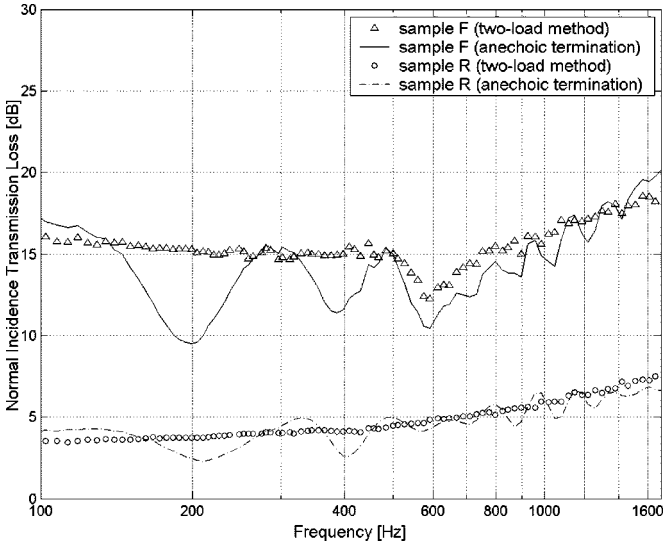

FIG. 4. Transmission loss of samples R and F measured using the anechoic termination and the two-load methods.

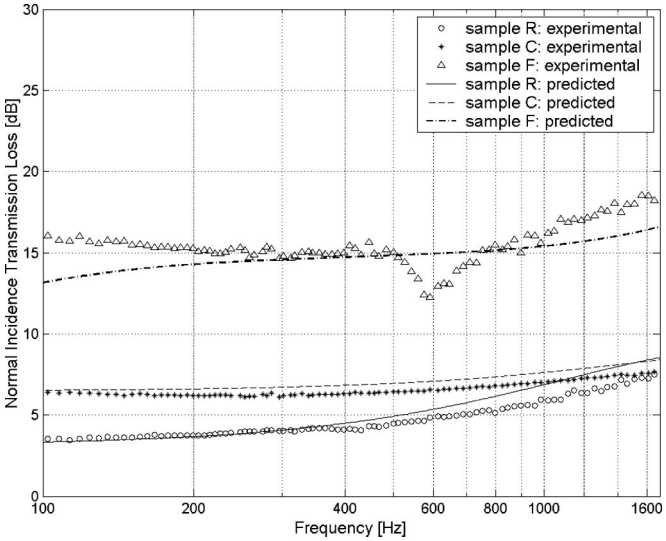

FIG. 5. A comparison between predicted and measured two-load method values of transmission loss for samples R, C and F.

data can be observed for sample F (5 dB at 200 Hz and 3 dB at 400 Hz). The data confirms that the discrepancy between the two methods becomes more significant as the material flow resistivity increases, as in the case of sample F, so that the $|T||\beta||R_t|$ term in the denominator of Eq. (1) is no longer small.

Repeating the two-load experiment ten times, the maximum standard deviation in the measured values of the transmission loss was estimated as 0.5 dB which supports well the repeatability of the two-load method. Figure 5 shows a comparison between the predicted and measured data obtained from the two-load experiment. The predicted and experimental data match closely for samples R and C, although some discrepancy in the medium and higher frequency range can be observed in the case of sample F. This phenomenon can be related to the method of support and the finite dimensions of the material sample which are not accounted for by the adopted theoretical model. It can also be linked to possible errors in measuring the flow resistivity and tortuosity, which values are relatively high in the case of sample F.

The measured data for sample F show a minimum around 600 Hz which, according to Song *et al.*,[2] is likely to be linked to the circumferential edge constraint of the sample. A proof is indirectly provided by the fact that, at low frequencies, the measured TL recovers to a finite limit of 15 dB that can be predicted, according to Song *et al.*,[2] by $T_{f\to 0}=2\rho_0 c/(2\rho_0 c+\sigma d)$, ρ_0 being the density of air, c the speed of sound and σ the material flow resistivity (see Fig. 5).

IV. CONCLUSIONS

Two bench top methods of measurement of the transmission loss coefficient have been investigated and their accuracy has been compared on three samples of consolidated granular materials. These are: (i) the transmission loss tube with an anechoic termination method; and (ii) the two-load method. It has been shown that the accuracy of method (i) can significantly depend on the quality of the anechoic termination and on the acoustic properties of the tested material. A perfect anechoic termination is difficult or impossible to implement. If the termination is not perfectly anechoic, then the accuracy of this method can be improved if the data on the impedance of the anechoic termination and the tested sample are included in the calculations. This procedure may not be required if the flow resistivity of the porous samples is limited and the porosity is high, as shown in the work by Song *et al.*[2]

The results reported here that the two-load method can provide a simple and reliable alternative to the anechoic termination method if the transmission loss measurements need to be performed on acoustic materials with a relatively high flow resistivity and limited values of porosity. This method is quick and stable over a broad frequency range and the experimental results are found to match well with the predictions based on a simple predictive model for poroelastic plates.[9]

ACKNOWLEDGMENTS

The authors would like to acknowledge the British Council and the Italian Ministry for Education, University and Research for the financial support provided to the research project ''Multi-functional Sustainable Materials for Noise Control'' within the British–Italian Partnership Program for Young Researchers. The authors are grateful to Dr. Mark Swift, Dr. Ian Rushforth, Mr. Siow N. Ting, and Professor David Hothersall for the help in preparing samples and comments on this manuscript. We acknowledge that without the technical skills and patience of our technician, Mr. Clive Leeming, this work would have been impossible.

[1] B. H. Song and J. S. Bolton, ''A transfer-matrix approach for estimating the characteristic impedance and wave numbers of limp and rigid porous materials,'' J. Acoust. Soc. Am. **107**, 1131–1152 (2000).
[2] B. H. Song, J. S. Bolton, and Y. J. Kang, ''Effect of circumferential edge constraint on the acoustical properties of glass fiber materials,'' J. Acoust. Soc. Am. **110**, 2902–2916 (2001).
[3] J. C. Young and M. J. Crocker, ''Prediction of transmission loss in mufflers by the finite-element method,'' J. Acoust. Soc. Am. **57**, 144–148 (1975).
[4] M. L. Munjal and A. G. Doige, ''Theory of a two source-location method for direct experimental evaluation of the four-pole parameters of an aeroacoustic system,'' J. Sound Vib. **141**, 323–333 (1990).
[5] L. E. Kinsler and A. R. Frey, *Fundamental of Acoustics*, 2nd ed. (J Wiley, New York, 1962), p. 199.
[6] J. S. Bolton, R. J. Yun, J. Pope, and D. Apfel, ''Development of a new sound transmission test for automotive sealant materials,'' *SAE 1997 Transactions 106*, J. Passenger Cars, 1997, Sec. 6, pp. 2651–2658.
[7] M. J. Swift, ''The physical properties of porous recycled materials,'' Ph.D. thesis, December 2000, University of Bradford.
[8] K. V. Horoshenkov and M. J. Swift, ''The acoustic properties of granular materials with pore size distribution close to log-normal,'' J. Acoust. Soc. Am. **110**, 2371–2378 (2001).
[9] K. V. Horoshenkov, K. Sakagami, and M. Morimoto, ''On the dissipation of acoustic energy in a thin, infinite, poroelastic plate,'' Acta Acust. (Beijing) **88**, 500–506 (2002).

Sound of shallow and deep water lobsters: Measurements, analysis, and characterization (L)

G. Latha,[a] S. Senthilvadivu, R. Venkatesan, and V. Rajendran
National Institute of Ocean Technology, Velachery-Tambaram Road, Campus, Pallikaranai, Chennai—601 302, TamilNadu, India

(Received 9 August 2004; revised 28 January 2005; accepted 3 February 2005)

Study of sound made by marine species aid in ambient noise studies and characterization. This letter presents the work carried out on measurement of sound made by lobsters in a controlled environment and the data processing and the spectral analysis to identify the frequency contents. Lobsters collected in the shallow waters as well as deep waters in the ocean have been used for the sound measurement. The *Panulirus Homarus* and *Palinustur Waguersis* species were kept in a tank in a laboratory and measurements were made. Their fundamental frequencies, harmonics, and peaks are analyzed in the band 3 to 100 kHz under different conditions such as molting and nonmolting states. Analysis with respect to diurnal variations is also carried out. The results show that lobsters produce sound like musical instruments, which agree with the observations of Patek [Nature (London) **411**, 153–154 (2001)].
[DOI: 10.1121/1.1893525]

PACS numbers: 43.80.Ka, 43.30.Sf [WA] Pages: 2720–2723

I. INTRODUCTION

Biological noise is the most important component of the ambient noise prevailing in the ocean in a wide frequency band from very low frequencies to very high frequencies. The sound produced by the marine animals contributes to the ambient noise in the ocean. As ambient noise masks the signals from the underwater communication systems, to improve the signal-to-noise ratio, the ambient noise needs to be characterized at the location. Though ambient noise is caused by many parameters, the contribution of biological noise is over a wide band and identification of noise by specific species is a task.

Many researchers have carried out studies on the sounds produced by different marine species.[1–12] Enough information on classification of underwater noises with details on each type of noise, their sources, and their impacts are dealt with by Wenz.[1] Noise generated by snapping shrimps was studied in detail in the literature[2,7,8] and it is reported that they produce noise over a wide band and they are dominant in shallow waters, causing serious limitations to SONAR performance. Cato[3] measured ambient noise in the Timor Sea of Australia and identified a few frequency tones and their harmonics whose sources were not known.

Sound produced by whales was examined in Refs. 4, 5, 9, 10, and 12 and it is reported that they produce distinct peaks in the band 10 Hz to 3 KHz. Kelly *et al.*[11] have studied ambient noise in the East Indian ocean region and they suspect croakers to be the source, which produces a 500-Hz peak. It is evident from the literature that identification of a biological source causing the background noise is possible only if the specific species with their noise spectrum level is known *a priori*.

Patek[13] has identified the sound produced by spiny lobsters to match with that of a musical instrument. She has studied the physical mechanism by which the sound is produced in lobsters and found that it is similar to that in a violin. A preliminary work on shallow water lobster sound has been carried out by the authors[14] of this paper. Sounds produced by musical instruments have been studied by various authors.[15–19]

This paper presents the work carried out on sound made by different species of lobsters. First, the extensive work on the analysis of sound made by spiny lobsters and the comparison of the results with the observations of Patek are presented. Second, the measurement and analysis of sound made by deep-sea lobsters are presented.

At the Lobster Breeding Center of the National Institute of Ocean Technology, lobsters have been collected from the sea and kept in a tank of required dimension. The frequency spectrum and the amplitude of the noise level of the lobster noise are studied under varying conditions. The current study focuses on the measurements and analysis of sound made by spiny lobsters (shallow water lobsters) in both the molting as well as nonmolting periods and the deep-sea lobsters during day and night time. It is observed that both the species produce harmonics.

II. MATERIALS AND METHODS

The spiny lobster *Panulirus Homarus*, which weighs approximately 200 g, has been used in the current study. The lobster undergoes a change during molting period in which it shells out its outer skin. Sound measurements have been made during molting and nonmolting periods. These lobsters were collected at a water depth of 5 m off the Chennai coast.

The deep-sea lobster *Palinustur Waguersis* is used for sound measurement both in day and night time. Three juvenile lobsters collected from 350-m depth in the channel between Andaman and Nicobar Islands were used in sound measurement. The weight at the time of recording was 3.5 g.

[a]Electronic mail: latha@noit.res.in

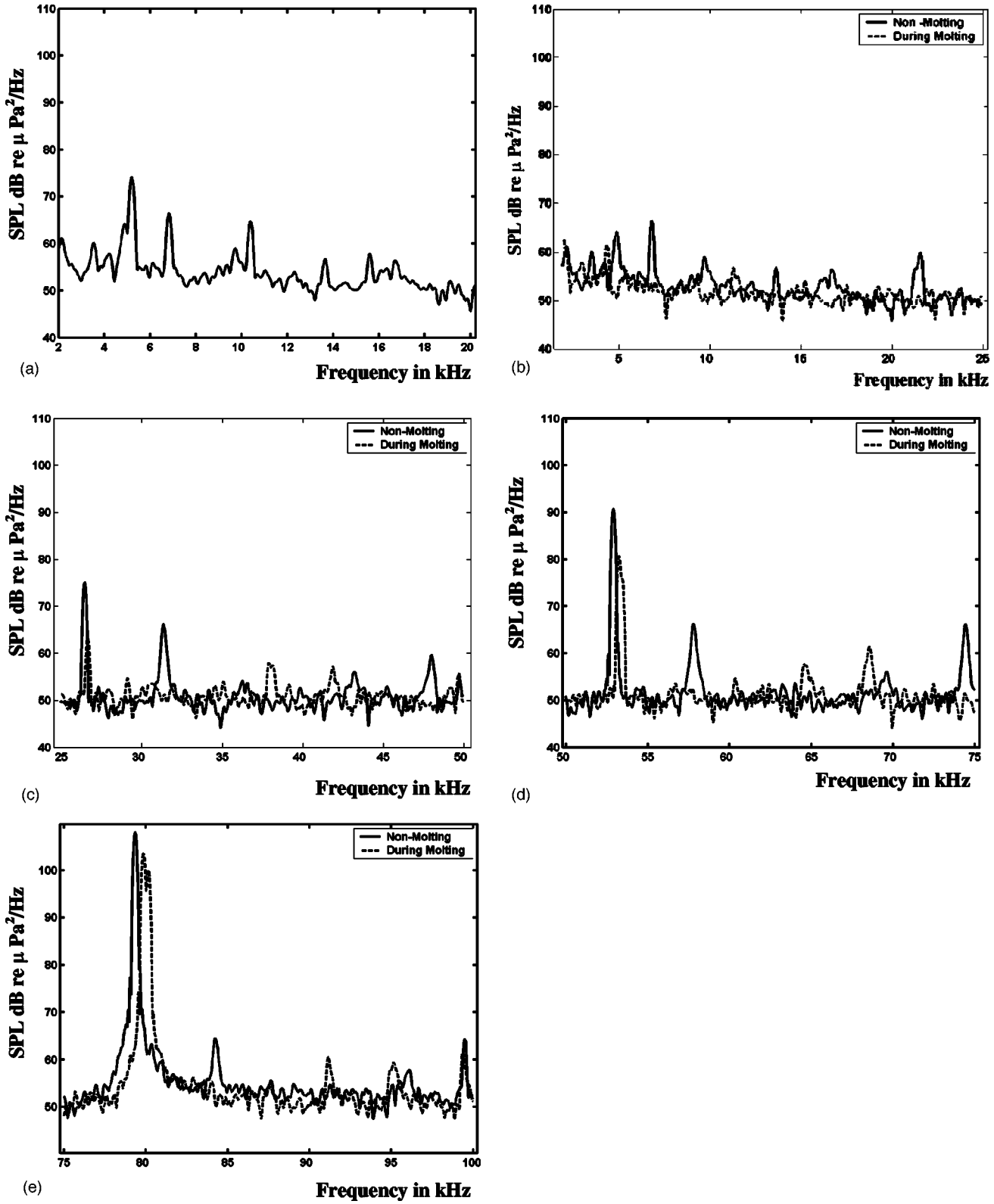

FIG. 1. Noise spectrum for shallow water lobster during molting and nonmolting. (a) Harmonic components of the fundamental frequency 5.2 kHz. (b) In the frequency band 3 to 25 kHz. (c) In the frequency band 25 to 50 kHz. (d) In the frequency band 50 to 75 kHz. (e) In the frequency band 75 to 100 kHz.

Measurements have been carried out independently for the species mentioned above. Lobsters were kept in a tank of dimension 4.3 (length)×1.3 (breadth)×1.28 (height) m^3, which was filled with water up to 1-m height. Measurements were made in the tank during night when they were molting and also during nonmolting periods. The hydrophone was immersed at 0.5-m depth and measurements were carried out and hence a minimum frequency of measurement that can be made is 3 kHz, i.e., 0.5 m of wavelength.

The tank noise is measured without the animals and spectrum analysis for the ambient noise shows no such typical peaks, which are present when the noise is measured with

the animals. The aerator and the other noise-making mechanisms were switched off and hence the tank noise and the surrounding noise is made nil. Thus the ambient noise was made nil to the maximum extent possible when these measurements were carried out.

A hydrophone with the frequency range 0.1 Hz to 120 kHz was used with a data acquisition system to collect the sound made by lobsters. The hydrophone (make: Reson, model: TC 4032) has an Omni directional flat response of −170 dB over the above said frequency band, which was calibrated and certified by the manufacturer. The hydrophone has also been calibrated at the local acoustic test facility available.

A DSP-based portable data acquisition system with 12-bit resolution with eight channels has been used for the data collection and the data were acquired at the rate of 1 MHz. The data collection experiment constitutes a continuous measurement of noise over a period of 2 days at 1-h intervals.

III. ANALYSIS PROCEDURE

Since the tank is half filled, the maximum wavelength that can be considered for the analysis is 0.5 m and hence the lower limit of the analysis band is 3 kHz. The upper limit is 100 kHz (based on the sampling rate), allowing enough margins above the Nyquist rate. The power spectrum of the voltage data is computed by using the Welch periodogram technique. The spectral averaging of a series of data sets taken over 1 s is used for the analysis. The window size chosen is 65 536 with 50% overlapping and the antileakage window used is the Hanning window.

TABLE I. Shallow water lobster noise at different frequencies during molting and nonmolting periods.

Frequency (kHz)	Shallow water lobster noise during nonmolting period (dB)	Shallow water lobster noise during molting period (dB)
6.9	68.1	52.5
9.7	69.5	50.1
13.7	57.6	51.2
21.5	59.2	50.8
31.3	66.4	51.3

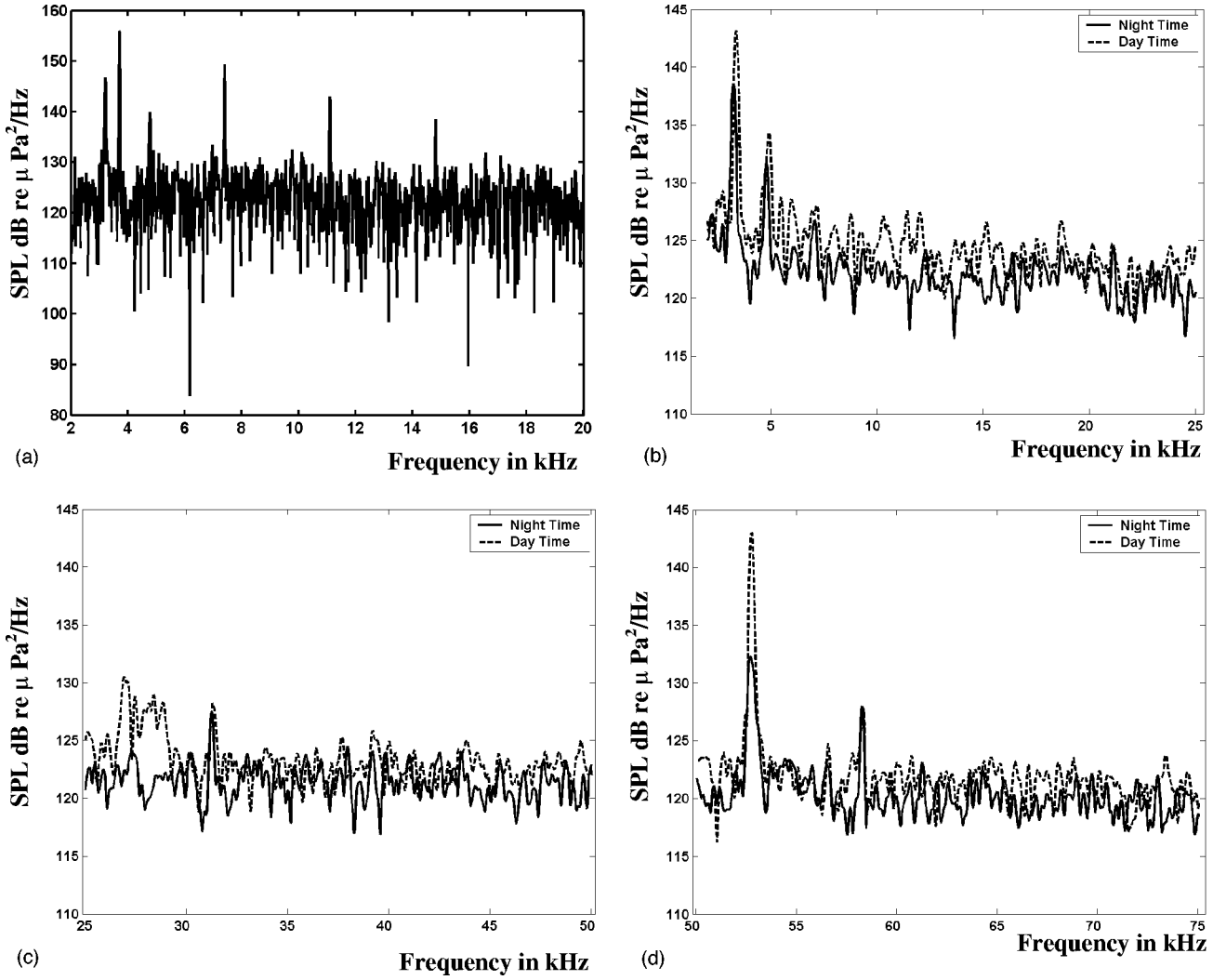

FIG. 2. Noise spectrum for the deep-sea lobster in day- and nighttime. (a) Harmonics with a fundamental frequency of 3.7 kHz. (b) In frequency band 3 to 25 kHz. (c) In frequency band 25 to 50 kHz. (d) In frequency band 50 to 75 kHz.

TABLE II. Deep-sea lobster noise at different frequencies during day- and nighttimes.

Frequency (kHz)	Deep sea lobster noise during nighttime (dB)	Deep sea lobster noise during daytime (dB)
3.3	138.2	143.16
4.9	133.5	134.4
7.1	127.1	128.3
11.9	123.13	125.1
18.7	123.9	126.8
21.1	123.9	123.9
24.9	121.5	124.2
31.8	127.5	127.5
39.8	123.2	125.1
49.8	122.1	125.1
56.5	122.9	125.2
58.3	125.2	128.1
60.9	120.1	121.2
66.0	120.2	119.1

IV. RESULTS AND DISCUSSION

The results of data analysis of sound by spiny lobsters are presented in Figs. 1(a)–(f). The first three harmonic components of fundamental frequency 5.2 kHz is observed and is shown in Fig. 1(a). The harmonics observed in the data analysis clearly show that the lobsters make sounds like musical instruments, which agrees with the results presented by Patek on her observations based on physical mechanism.

Figures 1(b)–(e) show the spectrum of the shallow water lobster noise over various frequency bands in both molting and nonmolting periods. Table I gives the frequencies in common at which the prominent peaks occur in both the molting and nonmolting periods.

The results of data analysis of sound by deep-sea lobsters are shown in Figs. 2(a)–(d). The first four harmonic components of the fundamental frequency 3.7 kHz are observed for the deep-sea lobster as shown in Fig. 2(a). Figures 2(b)–(d) show the spectrum of the deep-sea lobster noise over a frequency band of 2 to 75 kHz with each figure showing the spectrum of a 25-kHz band in both day- and nighttime. Table II gives the frequencies of prominent peaks, which occurs both in day- and nighttime and the corresponding power level in dB.

V. CONCLUSIONS

The spectral analysis shows that the shallow water and deep-sea lobsters produce sound like musical instruments, which agree with the observations made by Patek based on the physical mechanism.

It is found that for the shallow water lobsters the noise level during the molting period is less that in the nonmolting period. The sound pressure level decreases by 10–15 dB during the molting period. A positive frequency shift of around 300 Hz to 1.1 kHz is observed for the nonmolting period at the prominent peaks observed at 26.1, 52.6, and 79.1 kHz.

It has been observed that for the deep-sea lobsters the noise level in the daytime is more than that in nighttime and the difference on an average is 2 dB. There is a positive frequency shift of around 200 Hz for daytime data at the prominent peaks observed at 3.3 and 52.12 kHz.

Further the authors intend to make the measurements of sound made by the same species in the ocean and carry out similar analysis.

ACKNOWLEDGMENTS

The authors thank S. Ramji, A. Malarkodi, P. M. Rajeshwari, G. Raguraman, A. Thirunavukarasu, Dr. Senthil Murugan, and Mary Lina, for their help in measuring lobster noise.

[1] G. M. Wenz, ''Review of underwater acoustics research: Noise,'' J. Acoust. Soc. Am. (Part 2) **51**, 1010–1024 (1972).
[2] M. W. Widener, ''Ambient noise levels in selected shallow water off Miami, Florida,'' J. Acoust. Soc. Am. **42**, 904–905 (1967).
[3] D. H. Cato, ''Some usual sounds of apparent biological origin responsible for sustained background noise in the Timor Sea,'' J. Acoust. Soc. Am. **68**, 1056–1060 (1980).
[4] D. H. Cato, ''Marine biological choruses observed in tropical waters near Australia,'' J. Acoust. Soc. Am. **64**, 736–743 (1978).
[5] D. H. Cato, ''The biological contribution to the ambient noise in waters near Australia,'' Acoust. Aust. **20**, 76–80 (1992).
[6] J. F. Fish and G. C. Offutt, ''Hearing thresholds from toadfish, opsanus tau, measured in laboratory and field,'' J. Acoust. Soc. Am. **51**, 1318–1321 (1972).
[7] M. L. Readhead, ''Snapping shrimp noise near Gladstone, Queensland,'' J. Acoust. Soc. Am. **101**, 1718–1722 (1997).
[8] D. C. Bertilone and D. S. Kileen, ''Statistics of Biological Noise and Performance of Generalized Energy Detectors for Passive Detection,'' IEEE J. Ocean. Eng. **26**(2), 285–294 (2001).
[9] J. Northrop, ''20-Hz signal observed in the Central Pacific,'' J. Acoust. Soc. Am. **43**, 383–384 (1968).
[10] A. T. Corcella and M. Green, ''Investigation of impulsive deep-sea noise resembling sounds produced by whale,'' J. Acoust. Soc. Am. **44**, 483–487 (1968).
[11] L. J. Kelly, D. J. Kewley, and A. S. Burgess, ''A biological chorus in deep water in northwest of Australia,'' J. Acoust. Soc. Am. **77**, 508–511 (1985).
[12] K. R. Curtis, B. M. Howe, and J. A. Mercer, ''Low frequency ambient sound in the North Pacific: Long time series observation,'' J. Acoust. Soc. Am. **106**, 3189–3200 (1999).
[13] S. N. Patek, ''Spiny Lobsters stick and slip to make sound,'' Nature (London) **411**, 153–154 (2001).
[14] G. Latha, G. A. Ramadass, R. Venkatesan, and V. Rajendran, ''Lobster Noise Measurement and Analysis,'' Proceedings of SYMPOL 2003, Department of Electronics, Cochin University of Science and Technology, Cochin—682022, India.
[15] R. E. Berg and D. G. Stork. *The Physics of Sound* (Prentice Hall, Englewood Cliffs, 1982).
[16] N. H. Fletcher and T. D. Rossing. *The Physics of Musical Instruments* (Springer-Verlag, New York, 1991).
[17] J. G. Roederer, *Introduction to the Physics and Psychophysics of Music* (English Universities, London, 1973).
[18] T. D. Rossing, ed., *Musical Acoustics* (American Association of Physics Teachers, College Park, MD, 1988).
[19] T. D. Rossing, *The Science of Sound* (Addison-Wesley, Reading, MA, 1990).

Atypical calling by a blue whale in the Gulf of Alaska (L)

Kathleen M. Stafford and Sue E. Moore
National Marine Mammal Laboratory, Alaska Fisheries Science Center, NOAA Fisheries, 7600 Sand Point Way NE, Seattle, Washington 98115

(Received 12 October 2004; revised 21 January 2005; accepted 3 February 2005)

Worldwide, calls from blue whales share the characteristics of being long (>20 s), low-frequency (<100 Hz) signals that often exhibit amplitude and frequency modulation. Despite sharing these basic features, the calls of blue whales recorded in different ocean basins are distinct from one another, leading to the suggestion that populations and/or subspecies may be identified based on call characteristics. An example of anomalous calling behavior by a blue whale in the Gulf of Alaska is reported that may complicate this approach, and that suggests that blue whales can mimic each other's calls. [DOI: 10.1121/1.1887005]

PACS numbers: 43.80.Ka; 43.30.Sf [WA] Pages: 2724–2727

I. INTRODUCTION

Blue whales in both hemispheres were severely depleted by commercial whaling during the 20th century and now the species is listed as endangered worldwide.[1] Acoustic tools are now routinely used to investigate blue whale distribution, population stock structure, and seasonal movements.[2–4] Because blue whales commonly make geographically distinct, stereotyped calls,[4,5] it has been suggested that acoustic methods can be used to distinguish among populations and/or subspecies.[6]

Blue whale calls are recorded seasonally in varying locations in the North Pacific.[3,5] Call types have been well described and are stable within geographic regions over periods of at least 30 years.[2,7] Calls in the North Pacific are detected most often from July until January[3,5] and include two types, one each from the eastern and western sides of the ocean basin.[5]

The eastern North Pacific call type consists of an amplitude-modulated pulsive unit (the *A-unit*) followed by one or more frequency-modulated moans (the *B-unit*).[7] A short, lower frequency, lower amplitude upsweep (the *C-unit*) often precedes the comparatively higher amplitude B-units[8] [Fig. 1(a)]. Together, the A-unit and one or more succeeding B-units (and C-units, if present) are known as a *phrase*. The western North Pacific call type consists of a unit beginning with a constant-frequency tone that changes to a frequency downsweep, followed by a short gap, then a frequency up-and-downsweep that ranges over about 1 Hz [Fig. 1(b)].

Eastern and western calls are spectrographically distinct from each other, and each type is produced in long stereotyped sequences that sometimes last for hours (Fig. 1). The fundamental frequencies of the western units average higher than the eastern B-units by about 2 Hz, and the duration of individual units is about 23 s, compared to roughly 17 s for eastern A- or B-units.[5] To date, no upsweeping precursor similar to the C-unit has been associated with western phrases. Although the two call types show clear geographic separation over most of their ranges, they sometimes overlap in time and space in the Gulf of Alaska (GOA) and the central North Pacific.[9] Here we describe what we believe to be a single individual producing both call types during one of these periods of overlap.

II. METHODS

Five autonomous hydrophone instruments were deployed in the GOA to record whale calls, with data archived digitally in the instrument.[10] Only three of the instruments deployed in 2001 were recovered in 2002. Each instrument was moored such that the hydrophone was buoyed at the axis of the deep sound channel (300–500-m depth). The instrument frequency response was flat (± 3 dB) in the 10–40-Hz range of interest, with low-pass filter roll-off beginning at 440 Hz and a sample rate of 1 kHz. A random sample of 20% of all hours of available data was displayed as running spectrograms [256 point fast Fourier transform (FFT), 50% overlap, Hanning window]. To investigate blue whale calling behavior during periods of overlapping call types, spectrograms of acoustic data recorded in the GOA from May 2001 to May 2002 were visually inspected. Measurements of call characteristics, including duration, begin and end frequency, intercall interval, and peak amplitude, were made using the software program *Raven*.[11]

III. RESULTS

Series of typical eastern and western blue whale call types were detected in the GOA on all three instruments from mid-July until mid-December. Here we focus on the instrument at 50° N 135° W, on which eastern and western blue whale calls were detected on 50 and 16 days, respectively, out of 84 days examined between 26 July 2001 and 19 October 2001. Then, on 20 October 2001, six anomalous call series were detected during one of the sampled hours (0200–0259 GMT, Fig. 2). In these instances, a western-type call replaced the A-unit that usually initiates the eastern call type, and the subsequent ''variant'' B-units took on some characteristics of western calls. These anomalous series included one at 0217 in which three western-type calls came in succession, occurring with a period (~ 60 s) much closer to the typical period of eastern-type calls (~ 50 s) than to that of western-type calls (~ 130 s).[5]

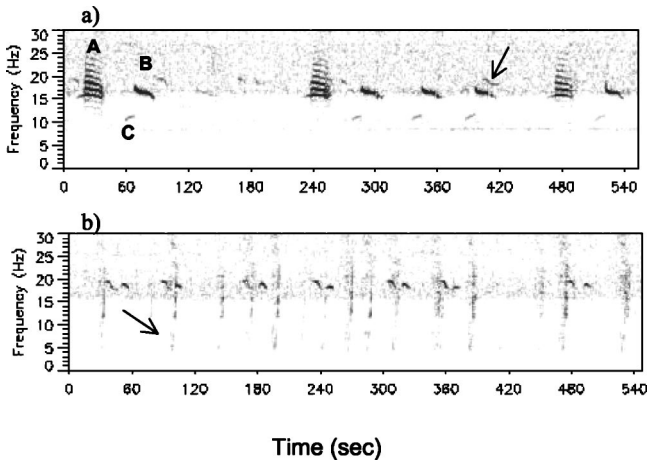

FIG. 1. a) Spectrogram of typical northeastern Pacific blue whale call series from 16 August 2000. Units are indicated in the first call as A, B, and C. The B-units continuously decrease in frequency. A solid arrow indicates an overlapping western unit. b) Spectrogram of a typical northwestern Pacific blue whale call series from 10 November 1999. 7 western units are shown here. The very low-frequency signals are volcanic seismic signals (arrow). (5 s FFT, 80% overlap, Hanning window).

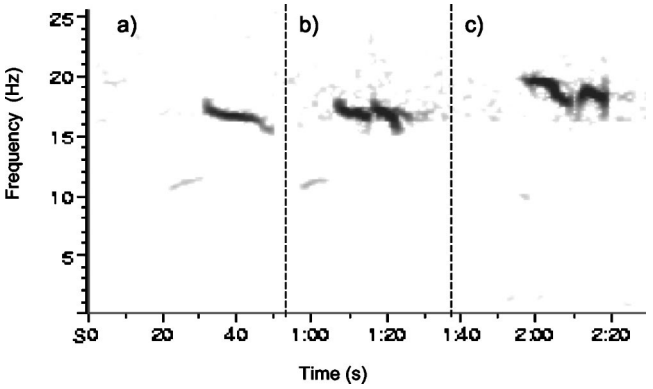

FIG. 3. Detail of frequency modulated North Pacific blue whale calls. a) Typical B-unit. The call is frequency modulated, with the frequency continually decreasing. A precursor C-unit can be seen preceding this call starting at about 10 Hz. b) An atypical B-unit recorded in the Gulf of Alaska. Note the increase in frequency in the middle of the call. A precursor C-unit can also be seen preceding this call. c) Typical western unit. (4 s FFT, 87.5% overlap, Hanning window).

To investigate the extent of this atypical calling behavior, the 5 h before and after this discovery (2100–0700 GMT) were examined for similar patterns. Measurements of acoustic characteristics were made for the 19 highest amplitude phrases between 0215 and 0346. Fifty total phrases were recorded from 2215 to 0515. Seventeen (34%) of these were anomalous phrases, 16 recorded between 2215 and 0300, followed by one 2 h later at 0513. During this same time period, there were two instances of single western units and 31 series of A-units followed by 2–7 B-units (62% of all phrases).

The clearest difference between standard B-units [Fig. 3(a)] and the variant B-units [Fig. 3(b)] was a shift up in frequency in the second part of the call. In the variant calls, the first part of the B-unit is the usual tonal that decreases rapidly in frequency and is then followed by one decreasing more slowly. There is a short gap before the call increases in frequency and again sweeps downward [Fig. 3(b)]. Variant B-units started at 18.0 ± 0.2 Hz and decreased in frequency to 16.3 ± 0.3 Hz over 9.5 ± 0.5 s before shifting up to 17.1 ± 0.5 Hz and sweeping down again to 15.4 ± 0.2 Hz over 7.5 ± 0.7 s ($n = 23$). The gap between these two sweeps lasted 1.3 ± 0.7 s for a mean call duration of 18.3 ± 0.8 s. These variant B-units were sometimes intermixed in a phrase

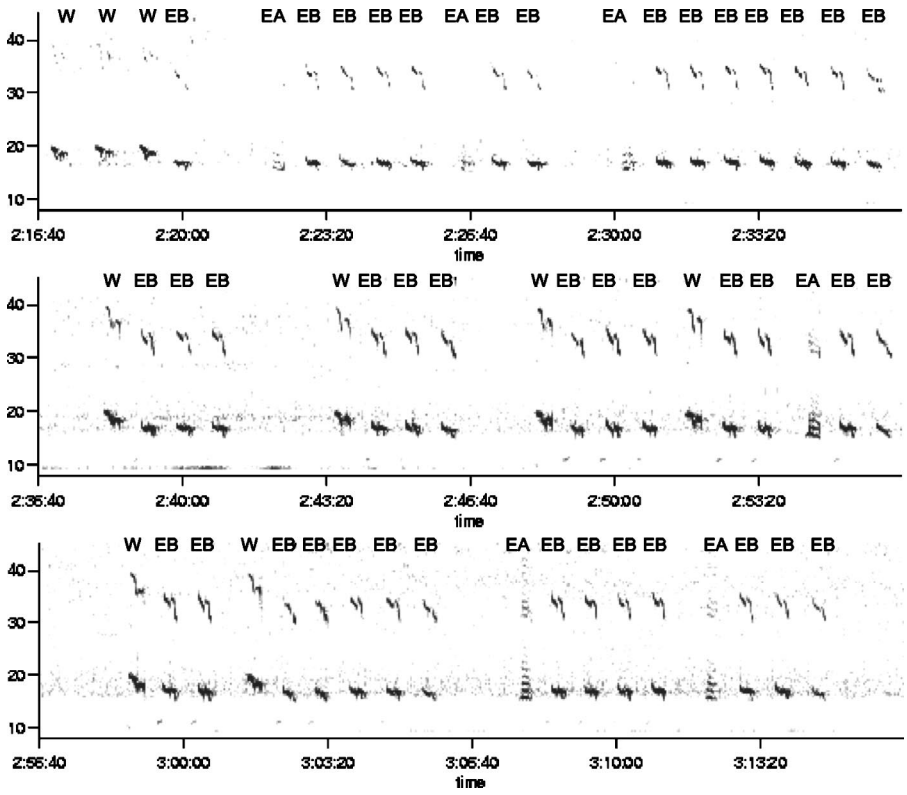

FIG. 2. Spectrogram of one hour of the atypical blue whale call series from 20 October 2001. Time is given in GMT. Western units are indicated with W, eastern B-units with EB, and eastern A-units with EA. (4 s FFT, 87.5% overlap, Hanning wndow).

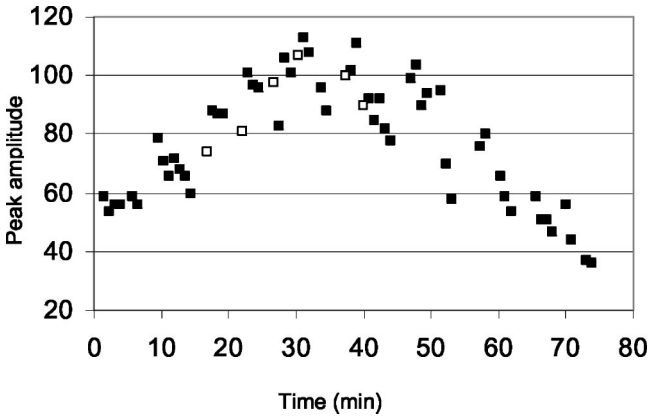

FIG. 4. Peak amplitude of calls shown in Fig. 3. B-unit amplitudes are shown as black squares, western units as white squares. Decibel units are to an arbitrary reference. The increasing and decreasing amplitudes of the FM calls indicates an animal approaching and then moving away from the hydrophone.

with standard B-units, as for example in the phrase at 0301–0306 (Fig. 2).

On average, the lowest components of A-units began at 15.6 ± 0.13 Hz and ended at 15.5 ± 0.1 Hz over 18.8 ± 2 s ($n = 13$). Standard B-units began with a slight downsweep, followed by a tonal part of nearly uniform frequency that ends with another downsweep; overall the call swept down from 17.8 ± 0.3 Hz to 15.7 ± 0.3 Hz over 17.7 ± 0.9 s ($n = 34$) [Fig. 3(b)]. Only eastern-type A-units and the variant B-units were recorded after 0315. Amplitudes of the calls from the 0215–0330 period are shown in Fig. 4. Time between A- and B-units (27.9 ± 1.7 s, $n = 13$) and western- [Fig. 3(c)] and B-units (27.9 ± 1.6 s, $n = 6$) in a phrase did not differ. The time between successive B-units in a phrase was 30.8 ± 1.9 s ($n = 39$).

IV. DISCUSSION

The type of unit substitution and call variability reported here has been seen only this once in visual inspection of over 2100 h of acoustic data during which blue whale calls were recorded from the GOA[9] or elsewhere in the eastern North Pacific.[2] Although the vast majority of calls recorded in the sampled dataset were the stereotyped calls previously described for the eastern and western North Pacific, the temporary replacement of an eastern call-type unit by a western call shows previously undescribed plasticity in blue whale calling.

Evidence that these call series were produced by a single whale includes these features that all series had in common: (1) the increasing and then decreasing amplitudes of the units as the animal(s) apparently moved toward and away from the hydrophone (Fig. 4); (2) the similarity in amplitudes of consecutive units; (3) the consistency of interunit and phrase timing; and (4) the harmonics in the western units (Fig. 2) which are seldom seen in typical western series.[5]

In addition to a single animal from one acoustic population producing call series with both eastern and western Pacific blue whale components, there are at least two other possible explanations for the anomalous call series reported here. The first is that the animal in question was the product of a hybrid mating between an animal that makes the western call and one that makes the eastern call. It is currently unknown whether or not the populations of animals that produce these two distinct call types interbreed and, if so, how interbreeding would impact calling behavior. This explanation seems unlikely because the whale discussed here resumed the stereotyped A-B calling pattern after producing call series that had the same pattern as these eastern North Pacific series but with the substitution of western units for eastern A-units. However, as currently nothing is known about the relationship, if any, between genetic relatedness and acoustic similarity in baleen whales, this possibility cannot be ruled out.

The second possibility is that the atypical calling series was produced by two whales, each producing an eastern and a western call type antiphonally. Were this the case, the animal making the eastern sounds did not produce any A-units, as these would have been visible in the spectrogram at both lower (16 Hz) and higher (90 Hz) frequencies than the western calls. Additionally, this animal would then have had to produce variant eastern B-units in response to the western call unit. Why the whale would change the character of the B-units over the course of this interaction is not clear. Further, these two whales must have exactly matched the amplitude and intercall timing of their calls. While it is possible that two whales moving together past the hydrophone produced the amplitude record shown in Fig. 4, it seems unlikely they would have produced such a close match in intercall timing, and overall the two-whale theory seems improbable.

The substitution of a western call for the eastern A-unit followed by B-units that had intermediate characteristics shows that at least one blue whale in the North Pacific can produce both call types. Vocal mimicry has been documented for other cetacean species including bottlenose dolphins (*Tursiops truncatus*), beluga whales (*Delphinapterus leucas*), and humpback whales (*Megaptera novaeangliae*).[12,13] During a long-term study of killer whale (*Orcinus orca*) vocal repertoires, whales from one pod were found to imitate call types from different pods, although this was a very rare occurrence and pods did not seem to adopt each other's calls.[14]

The results present directions for future research from behavioral, ecological, and management perspectives. Clearly, the behavioral ecology of blue whale calling requires detailed investigation to determine call function. For example, song differences in numerous bird and anuran species have been hypothesized as isolating mechanisms between potentially interbreeding congeners.[15–17] If the repetitive, stereotyped calls of blue whales serve a similar role as bird song, then the atypical ''song'' of blue whales might serve as a genetic isolating mechanism for these two populations. On the other hand, it might have an opposite effect: The copying and incorporation of elements from a western blue whale into the eastern call pattern could be used in intersexual selection by introducing novelty into the ''song'' while still retaining species recognition.[18] Novelty may drive the intra- and interseasonal changes in humpback whale song,[19] potentially increasing the fitness of heterospecific singers. However, the data here were recorded on a nominal

feeding ground of blue whales and during a season that is not known to be associated with mating behavior.[20]

The calling behavior reported here is the first documentation showing that blue whales can vary the types of calls they produce, and possibly mimic calls of their neighbors in areas where different call types overlap. Whether this behavior serves in inter- or intrasexual selection, individual identification, group recognition, or perhaps resource defense is unknown and deserves further attention. Clearly, plasticity in blue whale calling behavior should be investigated prior to diagnostic application of acoustic data to population assessment. However, the rarity of this behavior strengthens the use of acoustic detection as a reliable and important cetacean assessment tool. In addition, because the potential effects of anthropogenic noise on marine mammals are of concern,[21] baseline data on calling patterns, including anomalous behavior, must be documented.

ACKNOWLEDGMENTS

This work was performed while KMS held a National Research Council Research Associateship Award at the National Marine Mammal Laboratory, Alaska Fisheries Science Center. We are grateful to Chris Fox of NOAA/PMEL for generously providing access to the data used in this manuscript. Barbara Lagerquist, Dave Rugh, Dave Mellinger, and two anonymous reviewers provided helpful comments that greatly improved an earlier draft of this manuscript.

[1] IUCN, 2003 IUCN Red List of Threatened Species, 2003 ⟨http://www.redlist.org⟩, Downloaded on 3 March 2004.
[2] K. M. Stafford, S. L. Nieukirk, and C. G. Fox, ''Low-frequency whale sounds recorded on hydrophones moored in the eastern tropical Pacific,'' J. Acoust. Soc. Am. **106**, 3687–3698 (1999).
[3] W. A. Watkins, M. A. Daher, G. M. Reppucci, J. E. George, D. L. Martin, N. A. DiMarzio, and D. P. Gannon, ''Seasonality and distribution of whale calls in the North Pacific,'' Oceanography **13**, 62–67 (2000).
[4] D. K. Mellinger and C. W. Clark, ''Blue whale (*Balaenoptera musculus*) sounds from the North Atlantic,'' J. Acoust. Soc. Am. **114**, 1108–1119 (2003).
[5] K. M. Stafford, S. L. Nieukirk, and C. G. Fox, ''Geographic and seasonal variation of blue whale calls in the North Pacific,'' J. Cetacean Res. Manage. **3**, 65–76 (2001).
[6] D. K. Mellinger and J. Barlow, ''Future directions for acoustic marine mammal surveys: Stock assessment and habitat use,'' Report of a workshop held in La Jolla, CA, 20–22 November 2002, NOAA OAR Special Report, NOAA/PMEL Contribution No. 2557. (2003).
[7] P. O. Thompson, L. T. Findley, and O. Vidal., ''Underwater sounds of blue whales, *Balaenoptera musculus*, in the Gulf of California, Mexico,'' Marine Mammal Sci. **12**, 288–292 (1996).
[8] C. W. Clark and K. M. Fristrup, ''Whales '93: a combined visual and acoustic survey of blue and fin whales off southern California,'' Rep. Int. Whal. Commn. **47**, 583–600 (1997).
[9] K. M. Stafford, ''Two types of blue whale calls recorded in the Gulf of Alaska,'' Marine Mammal Sci. **19**, 682–693 (2003).
[10] C. G. Fox, H. Matsumoto, and T. K. A. Lau., ''Monitoring Pacific Ocean seismicity from an autonomous hydrophone array,'' J. Geophys. Res. **106**(B3), 4183–4206 (2001).
[11] R. A. Charif, C. W. Clark, and K. M. Fristrup, *Raven 1.2 User's Manual* (Cornell Laboratory of Ornithology, Ithaca, NY, 2004).
[12] L. Rendell and H. Whitehead, ''Culture in whales and dolphins,'' Behav. Brain Sci. **24**, 309–382 (2001).
[13] H. E. Winn and L. K. Winn, ''The song of the humpback whale, *Megaptera novaeangliae*, in the West Indies,'' Mar. Biol. (Berlin) **47**, 92–114 (1978).
[14] J. K. B. Ford, ''Vocal traditions among resident killer whales (*Orcinus orca*) in coastal waters of British Columbia,'' Can. J. Zool. **69**, 1454–1483 (1991).
[15] J. Martens, ''Vocalizations and speciation of Palearctic birds,'' in *Ecology and Evolution of Acoustic Communication in Birds*, edited by D. E. Kroodsma and E. H. Miller (Cornell U. P., Ithaca, NY, 1996), pp. 221–240.
[16] W. F. Blair, ''Isolating mechanisms and interspecies interactions in anuran amphibians,'' Q. Rev. Biol. **39**, 334–344 (1964).
[17] B. R. Grant and P. R. Grant, ''Cultural inheritance of song and its role in the evolution of Darwin's finches,'' Evolution (Lawrence, Kans.) **50**, 2471–2487 (1996).
[18] V. M. Janik and P. J. B. Slater, ''Vocal learning in mammals,'' Adv. Study Behav. **26**, 59–99 (1997).
[19] M. J. Noad, D. H. Cato, M. M. Bryden, M. N. Jenner, and K. C. S. Jenner, ''Cultural revolution in whale songs,'' Nature (London) **408**, 537 (2000).
[20] P. K. Yochem and S. Leatherwood, ''Blue whale, *Balaenoptera musculus* (Linnaeus, 1758),'' in *Handbook of Marine Mammals, Vol. 3*, edited by S. H. Ridgeway and R. J. Harrison (Academic, London, 1985), pp. 193–240.
[21] National Research Council, *Ocean Noise and Marine Mammals* (National Academies, Washington, DC, 2003).

Evoked-potential audiogram of the Yangtze finless porpoise *Neophocaena phocaenoides asiaeorientalis* (L)

Vladimir V. Popov[a] and Alexander Ya. Supin[b]
Institute of Ecology and Evolution, the Russian Academy of Sciences. 33 Leninsky Prosp., 119071 Moscow, Russia

Ding Wang,[c] Kexiong Wang,[d] Jianqiang Xiao, and Songhai Li
Institute of Hydrobiology, The Chinese Academy of Sciences, Wuhan, Hubei 430072, People's Republic of China

(Received 27 October 2004; revised 1 February 2005; accepted 3 February 2005)

Evoked-potential audiograms were obtained in two (one male and one female) Yangtze finless porpoises, *Neophocaena phocaenoides asiaseorientalis*. Sinusoidal amplitude-modulated 20-ms tone bursts were used as probes with recording envelope-following evoked potentials. A frequency range of 8 to 152 kHz was investigated. The range of greatest sensitivity covered frequencies from 45 to 139 kHz, and the lowest thresholds of 47.2 and 48.5 dB *re*: 1 μPa were found at a frequency of 54 kHz in the two subjects, respectively. At lower frequencies, threshold increased with a rate of around 14 dB/octave, and threshold steeply increased at 152 kHz. © *2005 Acoustical Society of America.* [DOI: 10.1121/1.1880712]

PACS numbers: 43.80.−n, 43.80.Lb [WA] Pages: 2728–2731

I. INTRODUCTION

The auditory system of odontocetes (toothed whales, dolphins, and porpoises) is known for unique capabilities with respect to sensitivity and frequency range. To date, audiograms of almost a dozen odontocete species have been obtained using both psychophysical and evoked-potential methods. Au (1993) and Supin *et al.* (2001) summarized these data through 2001; some additional data were obtained recently (Kastelein *et al.*, 2002, 2003; Au *et al.*, 2003). All these studies have demonstrated high sensitivity (thresholds down to 50–60 dB *re*: 1 μPa) and wide frequency range (well above 100 kHz) of odontocete hearing.

The finless porpoise, *Neophocaena phocaenoides*, attracts attention both as a representative of poorly investigated *Phocoenidae* family and as a species including both marine and riverine populations inhabiting different environments where the use of their sonar may be correspondingly different. There are some data about the finless porpoise vocalization and sonar signals (Pilleri *et al.*, 1980; Kamminga *et al.*, 1986, 1996; Wang, 1996; Nakahara *et al.*, 1997; Akamatsu *et al.*, 1998; Goold and Jefferson, 2002). Similarly to another *Phocoenidae* representative, the harbor porpoise (Kamminga, 1988; Kamminga *et al.*, 1996; Nakamura and Akamatsu, 2003), sonar pulses of the finless porpoise are rather long and narrow-band, looking more like high-frequency (about 100-kHz carrier) pips rather than clicks. It may be of interest to compare this feature of the finless porpoise's sonar with hearing abilities of this species. Apart from that, conservation and protection tasks dictate the necessity to know sensory abilities of this endangered species. However, data on hearing abilities of the finless porpoise are still absent.

Therefore, the motivation of the present study was to obtain a complete and detailed audiogram of the finless porpoise. For this purpose, we used the evoked-potential method since it allows performance of audiometric measurements for a short time without preliminary training of the animals (Supin *et al.*, 2001).

II. MATERIAL AND METHODS

The study was carried out in facilities of the Institute of Hydrobiology of the Chinese Academy of Sciences, Wuhan, P.R. China.

The subjects were two adult Yangtze finless porpoises, *Neophocaena phocaenoides asiaeorientalis*, a male (8 years old, body length 144 cm, body weight 38.2 kg) and a female (5 years old, body length 137 cm, body weight 37.6 kg). The animals were kept in a kidney-shaped pool ($20\times7\times3.0$ m) filled with fresh water. The care and use of the animals was performed under the Guidelines of the Russian Ministry of Higher Education on the use of animals in biomedical research. Since the animals were not trained for psychophysical measurements, the evoked-potential method was used for threshold measurements.

During the experiment, the animal was taken away from the home pool and placed on a stretcher in a wooden bath $2.25\times0.85\times0.6$ m filled with water in such a manner that the dorsal surface of the head with the blowhole remained above the water surface. For noninvasive evoked-potential recording, suction-cup sensor electrodes were used consisting of a 15-mm stainless-steel disk mounted within a 60-mm silicon suction cup. The active electrode was fixed at the vertex head surface, 5 cm behind the blowhole, above the water surface. The reference electrode was fixed at the pectoral fin. The electrodes were connected by shielded cables to

[a]Electronic mail: popov_vl@sevin.ru
[b]Electronic mail: alex_supin@sevin.ru
[c]Electronic mail: wangd@ihb.ac.cn
[d]Electronic mail: wangk@ihb.ac.cn

 0001-4966/2005/117(5)/2728/4/$22.50

the input of a custom-made EEG amplifier that provided 88-dB gain within a frequency range of 200 to 5000 Hz. The amplified signal was digitized and collected using an E-6040 data acquisition board (National Instruments) and stored in computer memory. To extract signal from noise, the digitized signal was coherently averaged (1000 original records per one averaged recording) using triggering from the stimulus onset.

Sound stimuli were sinusoidal amplitude-modulated (SAM) tone bursts of 20-ms duration, 1-kHz modulation frequency, 100% modulation depth, and variable carrier frequency. The stimuli were digitally synthesized at an update rate of 500 kHz and digital-to-analog converted by the same E-6040 board, amplified, attenuated, and played using a B&K 8104 hydrophone as a transducer. The transducer was positioned at a distance of 60 cm in front of the animal's head, near the front wall of the bath. The playback channel was calibrated both before and after the experiments by positioning a calibrated receiving hydrophone at the same location as the animal's head. Carrier frequencies varied from 8 to 152 kHz, separated by 1/4-octave steps within a range from 8 to 128 kHz, and by 1/8-octave steps within a range from 128 to 152 kHz, namely (rounded to 0.1 kHz): 8, 9.5, 11.2, 13.5, 16, 19, 22.5, 27, 32, 38, 45, 54, 64, 76, 90, 108, 128, 139, and 152 kHz. Sound monitoring near the animal's head showed that, despite sound reflections within the bath, modulation depth remained more than 70%–80%, and local sound levels varied by less than 5 dB.

For threshold evaluation, a 16-ms long part of the rhythmic evoked-potential response to the SAM stimulus, from 6 to 22 ms, was Fourier transformed to obtain its frequency spectrum. The magnitude of the 1-kHz peak was plotted as a function of sound intensity, and an oblique near-threshold part of the plot not longer than 20 dB was approximated by a straight regression line (the criteria for selection of a range for straight-line approximation are described in more detail by Supin *et al.*, 2001). The intersection of this line with the zero-amplitude level was adopted as a threshold estimate.

III. RESULTS

The recorded evoked responses and the procedure of threshold measurement are presented in Figs. 1 and 2. The amplitude-modulated tone burst evoked a sequence of evoked potentials following the modulation rate—the envelope-following response, EFR [Fig. 1(a)]. Note that both the EFR beginning and end featured a lag of around 3.5 ms. This lag, reflecting the evoked-response latency, confirms the physiological, not artifactual origin of the recorded waveform. To find the response threshold, stimulus intensity was decreased in 5-dB steps. This resulted in a corresponding decrease of the EFR amplitude, until the response disappeared in noise [in Fig. 1(a), at an intensity of 65–60 dB].

Frequency spectra of the records are shown in Fig. 1(b). These spectra were obtained by Fourier transform of a part of the record, from 6 to 22 ms. This 16-ms window contained a major part of the EFR record but did not contain the latency and the initial transient part of the response. At sound intensities of 70 dB and higher, all the spectra featured a peak at the stimulus envelope frequency of 1 kHz. At the intensity of

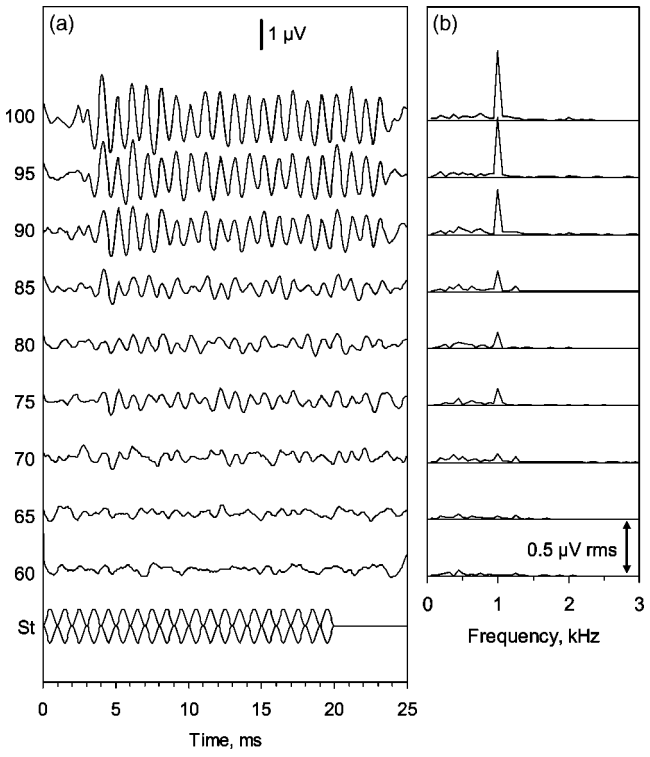

FIG. 1. (a) Waveforms of EFR recorded at various stimulus intensities, as indicated in dB *re*: 1 μPa (female, 128 kHz); St—stimulus envelope. (b) Frequency spectra of corresponding waveforms.

65 dB, this peak was comparable with the spectrum noise level, and at 60 dB it completely disappeared. The magnitude of this peak was taken as an estimate of EFR amplitude. Figure 2 plots this response amplitude as a function of sound intensity. The plot featured three branches: an oblique low-intensity one (60–75 dB), a quasihorizontal one (75–85 dB), and a steeply rising high-intensity branch (above 85 dB). Such form of the plot is typical of EFR amplitude dependence on intensity (Supin *et al.*, 2001). To evaluate the threshold, the near-threshold oblique branch, up to the inflection point but not including the zero-amplitude point, was

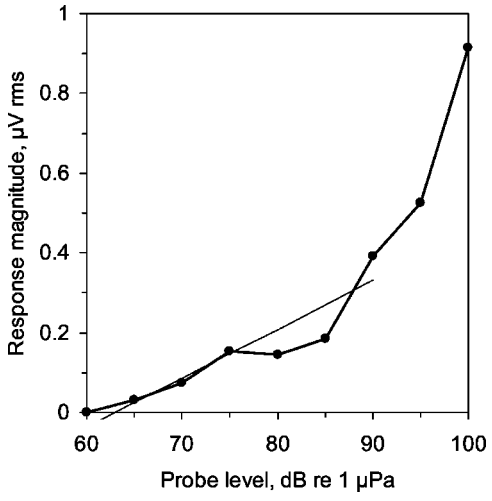

FIG. 2. Magnitude of 1-kHz component of EFR frequency spectrum as a function of stimulus intensity. Straight line—the regression line approximating a part of the function within a range of 65 to 75 dB.

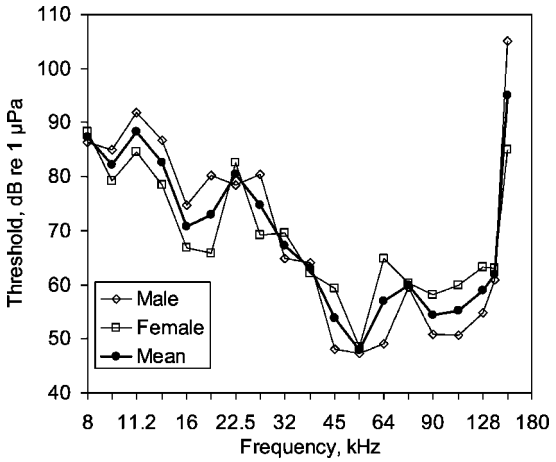

FIG. 3. Audiograms of the two subjects and the mean of two.

approximated by a straight regression line; in the presented example, this range is as short as 10 dB (from 65 to 75 dB *re*: 1 μPa). The regression line is shown along with the data plot. In most cases, approximation of this branch by a straight line was satisfactory enough (r^2 from 0.91 to 1.00, in particular, 0.97 in Fig. 2). In the presented case, the intersection of this line with the zero-amplitude level adopted as a threshold estimate was 63.2 dB.

With the use of the described procedure, thresholds were measured in both the subjects (the male and female) at frequencies indicated above (Sec. II). At each of the frequencies, three measurement runs were repeated. From run to run, threshold decreased by 2 to 15 dB at different tested frequencies. It correlated with more quiet behavior of the animals in the bath. Therefore, the lowest threshold values were adopted as the final threshold estimates.

The resulting audiograms of both subjects are presented in Fig. 3. Both audiograms demonstrated a high-sensitivity region from 45 to 139 kHz; the lowest threshold of 47.2 (in the male) and 48.5 (in the female) dB *re*: 1 μPa was found at 54 kHz. Below this high-sensitivity region, thresholds increased at a rate of around 14 dB/octave, up to 86–88 dB at 8 kHz. Above 139 kHz, thresholds increased extremely steeply, up to 105 (in the male) and 85 (in the female) dB at 152 kHz. Superimposed on this general trend, some peak–valley patterns were present in the audiograms, namely, a threshold increase at 64–76 kHz between higher-sensitivity regions of 45–54 and 90–108 kHz and a threshold decrease at 16–19 kHz between lower-sensitivity regions of 11–13.5 and 22.5–27 kHz. These patterns almost coincided in the two subjects, so they manifested themselves in the intersubject averaged audiogram.

IV. DISCUSSION

In general, the audiograms presented herein look similar to those obtained in many other odontocete species (see the references above). Among specific features of the audiogram of the finless porpoises, there may be mentioned (i) rather high sensitivity (low thresholds) in the best-sensitivity frequency range; (ii) high cutoff frequency; and (iii) some irregularities (alternating regions of higher and lower sensitivity).

Assessing the sensitivity of the finless porpoises, it must be taken into consideration that the evoked-potential method may give a little higher threshold than the psychophysical method. It may be a sequence of different conditions for temporal summation of the stimulus energy. Evoked potentials are responses to short transients in the stimulus, so they reflect accumulation of the stimulus energy for no longer than a few milliseconds or a fraction of a millisecond. In particular, to follow the stimulus modulation rate of 1 kHz used in the present study, brain responses may accumulate stimulus energy for less than 1 ms. In psychophysical measurements, stimuli of unlimited duration may be used. As shown by Johnson (1968), hearing thresholds decrease with stimulus duration increase up to hundreds of milliseconds. This was probably a reason why most psychophysical audiograms obtained in other odontocete species featured lowest thresholds down to 40–50 dB, whereas most evoked-potential audiograms ranged down to 50–60 dB (See Supin *et al.*, 2001). Therefore, thresholds as low as around 48 dB obtained in the present evoked-potential study must be considered as rather low for the present stimulation conditions.

As to the cutoff frequency, it is higher than 100 kHz in all investigated odontocetes. In many species it does not exceed 120–130 kHz; however, in the harbor porpoise *Phocoena phocoena*, a representative of the same family as the finless porpoise, the cutoff frequency was above 150 kHz (Andersen, 1970; Kastelein *et al.*, 2002). In the finless porpoise, the cutoff frequency was of the same order: at 152 kHz, thresholds were markedly increased but sounds were still perceivable. Such wide frequency range is likely characteristic of this family.

It is not clear yet how to assess a few peaks and valleys found in the audiograms. The dip at 64–76 kHz between two high-sensitivity regions of 45–54 and 90–108 kHz was not very deep, so it may be considered as a random data scatter. But, on the other hand, this dip was similar in both subjects. Similar dips in between two high-sensitivity regions were observed in audiograms of the harbor porpoise, *Phocoena phocoena* (Popov *et al.*, 1986), and much deeper dip was observed in the Amazon river dolphin, *Inia geoffrensis* (Popov and Supin, 1990). A question remains open, whether the presence of two or more high-sensitivity regions in the audiograms reflects specific biological significance of certain frequency ranges for the species.

ACKNOWLEDGMENTS

Grants provided by National Foundation of Natural Sciences of China (30170142), the Chinese Academy of Sciences (KSCX2-SW-118), the Institute of Hydrobiology, the Chinese Academy of Sciences (220103), Russian Foundation for Basic Research (02-04-39017, 03-04-48117), and Russian Ministry of Science and Education (NSh-2152.2003.4) are greatly appreciated.

Akamatsu, T., Wang, D., Nakamura, K., and Wang, K. (**1998**). "Echolocation range of captive and free-ranging baiji (*Lipotes vexillifer*), finless

porpoise (*Neophocaena phocaenoides*), and bottlenose dolphin (*Tursiops truncatus*),'' J. Acoust. Soc. Am. **104**, 2511–2516.
Andersen, S. (**1970**). ''Auditory sensitivity of the harbour porpoise, *Phocoena phocoena*,'' Invest. Cetacea **2**, 255–258.
Au, W.W.L. (**1993**). *The Sonar of Dolphins* (Springer, New York).
Au, W.W.L., Thomas, J., Western, A., and Ramirez, K.M. (**2003**). ''Evoked potential measurement of the masked hearing threshold of a Pacific white-sided dolphin (*Lagenorhynchus obliquidens*),'' J. Acoust. Soc. Am. **113**, 2306.
Goold, J. C., and Jefferson, T. A. (**2002**). ''Acoustic signals from free-ranging finless porpoises (*Neophocaena phocaenoides*) in the waters around Hong Kong,'' Raffles Bull. Zool. **Suppl. 10**, 131–139.
Johnson, C.S. (**1968**). ''Relation between absolute threshold and duration of tone pulse in the bottlenosed porpoise,'' J. Acoust. Soc. Am. **43**, 757–763.
Kamminga, C. (**1988**). ''Echolocation signal types of odontocetes,'' in *Animal Sonar, Process and Performance*, edited by P. E. Nachtigall and P. W. B. Moore (Plenum, New York), pp. 9–22.
Kamminga, C., Cohen Stuart, A. B., and Silber, G. K. (**1996**). ''Investigations on cetacean sonar: Intrinsic comparison of the wave shapes of some members of the *Phocoenidae* family,'' Aquatic Mammals **22**, 45–55.
Kamminga, C., Kataoka, T., and Engelsma, F. J. (**1986**). ''Investigations on cetacean sonar. Underwater sounds of *Neophocaena phocaenoides* of the Japanese coastal population,'' Aquatic Mammals **12**, 52–60.
Kastelein, R.A., Bunskoek, P., Hagedoorn, M., Au, W.W.L., and Haa, D.d. (**2002**). ''Audiogram of a harbor porpoise (*Phocoena phocoena*) measured with narrow-band frequency-modulated signals,'' J. Acoust. Soc. Am. **112**, 334–344.
Kastelein, R.A., Hagedoorn, M., Au, W.W.L., and Haan, Dd. (**2003**). ''Audiogram of a striped dolphin,'' J. Acoust. Soc. Am. **113**, 1130–1137.
Nakahara, F., Takemura, A., Koido, T., and Hiruda, H. (**1997**). ''Target discrimination by an echolocating finless porpoise, *Neophocaena phocaenoides*,'' Melliand Textilber. **133**, 639–649.
Nakamura, K., and Akamatsu, T. (**2003**). ''Comparison of click characteristics among odontocete species,'' in *Echolocation in Bats and Dolphins*, edited by J. Thomas, C. F. Moss, and M. Vater (University of Chicago Press, Chicago), pp. 36–40.
Pilleri, G., Zbinden, K., and Kraus, C. (**1980**). ''Characteristics of the sonar system of cetaceans with pterygoschis. Directional properties of the sonar system of *Neophocaena phocaenoides* and *Phocoena phocoena (Phocoenidae)*,'' Invest. Cetacea **11**, 157–188.
Popov, V.V., Ladygina, T.F., and Supin, A.Ya. (**1986**). ''Evoked potentials in the auditory cortex of the porpoise, *Phocoena phocoena*,'' J. Comp. Physiol., A **158**, 705–711.
Popov, V.V., and Supin, A.Ya. (**1990**). ''Electrophysiological investigation of hearing of the freshwater dolphin *Inia geoffrensis*,'' Dokl. Biol. Sci. **313**, 488–491.
Supin, A.Ya., Popov V.V., and Mass, A.M. (**2001**). *The Sensory Physiology of Aquatic Mammals* (Kluwer, New York).
Wang, D. (**1996**). ''A preliminary study on sound and acoustic behavior of the Yangtze River finless porpoise, *Neophocaena phocaenoides*,'' Acta Hydrobiol. Sinica **20**, 127–133.

Wave-induced fluid flow in random porous media: Attenuation and dispersion of elastic waves

Tobias M. Müller[a] and Boris Gurevich[b]
Department of Exploration Geophysics, Curtin University,[c] *Perth, WA 6845 Australia*

(Received 10 June 2004; revised 26 November 2004; accepted 1 March 2005)

A detailed analysis of the relationship between elastic waves in inhomogeneous, porous media and the effect of wave-induced fluid flow is presented. Based on the results of the poroelastic first-order statistical smoothing approximation applied to Biot's equations of poroelasticity, a model for elastic wave attenuation and dispersion due to wave-induced fluid flow in 3-D randomly inhomogeneous poroelastic media is developed. Attenuation and dispersion depend on linear combinations of the spatial correlations of the fluctuating poroelastic parameters. The observed frequency dependence is typical for a relaxation phenomenon. Further, the analytic properties of attenuation and dispersion are analyzed. It is shown that the low-frequency asymptote of the attenuation coefficient of a plane compressional wave is proportional to the square of frequency. At high frequencies the attenuation coefficient becomes proportional to the square root of frequency. A comparison with the 1-D theory shows that attenuation is of the same order but slightly larger in 3-D random media. Several modeling choices of the approach including the effect of cross correlations between fluid and solid phase properties are demonstrated. The potential application of the results to real porous materials is discussed. © *2005 Acoustical Society of America.* [DOI: 10.1121/1.1894792]

PACS numbers: 43.20.Jr, 43.20.Gp, 43.20.-f, 43.20.Px, 43.20.Wd [JJM] Pages: 2732–2741

I. INTRODUCTION

One major cause of elastic wave attenuation in heterogeneous porous media is wave-induced flow of the pore fluid between heterogeneities of various scales. It is believed that for frequencies below 1 kHz most important is the wave-induced flow between mesoscopic inhomogeneities, which are large compared with the typical individual pore size, but small compared to the wavelength. Various laboratory experiments in some natural porous materials provide evidence for the presence of centimeter-scale (mesoscopic) heterogeneities.[1,2] Attenuation and dispersion due to mesoscopic flow can be modeled using Biot's equations of poroelasticity with spatially varying coefficients.[3]

The simplest model of mesoscopic heterogeneities is a horizontally layered (1-D) structure. In such structures an elastic wave passing perpendicular to layers causes an ''inter-layer'' flow, that is the flow of the pore fluid from more compressible into stiffer layers during a compression cycle of the wave (and vice versa during extension). Elastic wave attenuation and dispersion due to interlayer flow were first studied for structures with periodic stratification.[4,5] More recently, Gurevich and Lopatnikov[6] and Gelinsky *et al.*[7] analyzed attenuation and dispersion for structures with random layering. These 1-D studies revealed that frequency dependencies of attenuation and velocity in periodic and random layered structures were somewhat different. In both situations attenuation and dispersion have their maximum at a frequency $\omega_{\max}$ where (typical) layer thickness equals the fluid diffusion length (that is, the wavelength of Biot's slow wave). Furthermore, at higher frequencies, $\omega \gg \omega_{\max}$ attenuation (expressed through the reciprocal quality factor Q^{-1}) for both periodic and random layers has the same asymptotic behavior $Q^{-1} \propto \omega^{-1/2}$. However, attenuation is different in the low-frequency limit $\omega \ll \omega_{\max}$: it is proportional to frequency ω for periodic layering and to $\sqrt{\omega}$ for random layering. These findings underline the importance of spatial distribution of inhomogeneities for modeling mesoscopic-flow attenuation and dispersion.

The situation is naturally more complex in porous materials with three-dimensional inhomogeneities. In such media the behavior of attenuation as a function of frequency depends on the distribution and shape of inhomogeneities. However, recently Johnson,[8] Pride and Berryman,[9] and Pride *et al.*[10] showed that in porous media with a regular distribution of identical inhomogeneities of *any* fixed shape, the reciprocal quality factor Q^{-1} scales with ω at low frequencies and with $\omega^{-1/2}$ for high frequencies. In real porous composites heterogeneities are more likely to have a random spatial distribution. Given the 1-D results quoted earlier, it is therefore natural to ask how the random distribution of inhomogeneities will influence the magnitude and frequency dependency of wave attenuation. To address this question, Müller and Gurevich[11] developed a theory for elastic wave propagation in a fluid-saturated porous medium with random distribution of 3-D inhomogeneities. Applying the method of statistical smoothing[12] to Biot's equations of poroelasticity with spatially variable coefficients, they derived an explicit expression for a complex-valued, effective wave number of a compressional wave (*P*-wave) which accounts for the effect of wave-induced flow.

In this paper we use the results of Müller and Gurevich[11] (referred below as paper I) to analyze the magnitude and

[a]Current address: Geophysical Institute, Karlsruhe University, 76187 Karlsruhe, Germany, Electronic address: Tobias.Mueller@gpi.uni-karlsruhe.de
[b]Electronic address: boris.gurevich@geophy.curtin.edu.au
[c]URL: http://www.geophysics.curtin.edu.au

 0001-4966/2005/117(5)/2732/10/$22.50

frequency dependence of attenuation and velocity dispersion caused by wave-induced fluid flow in poroelastic random media. Specifically, we derive closed-form expressions for elastic wave attenuation and dispersion as functions of the correlation properties of the inhomogeneities (Sec. II). We show that these wave field attributes are mutually related by the Kramers-Kronig relations, and therefore represent a causal pair (Sec. III). For most commonly used correlation models we obtain simple, analytic expressions for attenuation and dispersion and demonstrate their behavior using numerical examples (Sec. IV). We also analyze the low- and high-frequency asymptotic behavior of both velocity and attenuation (Sec. V). Finally, in Sec. VI we discuss our results in the light of existing theories for wave propagation in poroelastic media, in thermoelastic media, and in suspensions of solid particles in a viscous fluid. The conclusions are presented in Sec. VII.

II. ATTENUATION AND DISPERSION DUE TO WAVE-INDUCED FLOW

According to paper I, the effective *P*-wave number $\overline{k_p}$ in 3-D poroelastic random media can be written as a sum of the homogeneous background *P*-wave number k_p and a correction term which accounts for the conversion scattering from fast into slow *P*-waves due to the presence of randomly distributed inhomogeneities

$$\overline{k_p} = k_p\left(1+\Delta_2+\Delta_1 k_{ps}^2\int_0^\infty rB(r)\exp[\mathrm{i}k_{ps}r]dr\right), \tag{1}$$

where Δ_1 and Δ_2 are the dimensionless coefficients

$$\Delta_1 = \frac{\alpha^2 M}{2P_d}\left(\sigma_{HH}^2 - 2\sigma_{HC}^2 + \sigma_{CC}^2 + \frac{32}{15}\frac{G^2}{H^2}\sigma_{GG}^2 - \frac{8}{3}\frac{G}{H}\sigma_{HG}^2 + \frac{8}{3}\frac{G}{H}\sigma_{GC}^2\right), \tag{2}$$

$$\Delta_2 = \Delta_1 + \frac{1}{2}\sigma_{HH}^2 - \frac{4}{3}\frac{G}{H}\sigma_{HG}^2 + \left(\frac{4G}{H}+1\right)\frac{4}{15}\frac{G}{H}\sigma_{GG}^2, \tag{3}$$

and k_{ps} denotes the wave number of Biot's slow wave

$$k_{ps} = \sqrt{\frac{\mathrm{i}\omega\eta}{\kappa_0 N}}. \tag{4}$$

In Eqs. (2) and (3) P_d and H are respectively dry and saturated *P*-wave moduli of the background material, which are related by the Gassmann equation

$$H = P_d + \alpha^2 M, \tag{5}$$

where

$$M = [(\alpha-\phi)/K_g + \phi/K_f]^{-1}, \tag{6}$$

$\alpha = 1 - K_d/K_g$ is the Biot-Willis coefficient, ϕ is background porosity, and $N = MP_d/H$ while K_g, K_d, and K_f denote the bulk moduli of the solid phase, the drained frame, and the pore fluid, respectively. The shear modulus is denoted as G. In Eq. (4) ω is angular frequency, κ_0 is the background permeability, and η is the viscosity of the pore fluid. Equation (1) was obtained by assuming that the parameters H, G, and $C = \alpha M$ have a random component. The correlation properties of the random inhomogeneities are characterized by the normalized correlation function $B(r)$, which for the three random functions H, G, and C assumes the same functional form. The variances of the relative fluctuations are denoted as σ_{HH}^2, σ_{GG}^2, and σ_{CC}^2. The cross variance of the relative fluctuations are σ_{HG}^2, σ_{HC}^2, and σ_{GC}^2. Approximation (1) for the effective *P*-wave number has a restricted range of applicability, which can be expressed through the conditions (for a detailed analysis see paper I)

$$\max\{\Delta_1(|k_{ps}|a)^2, \Delta_2\} \ll 1 \tag{7}$$

and

$$a^2 \gg \frac{\kappa_0 N}{\eta\omega_B}, \tag{8}$$

where $\omega_B = \phi\eta/(\kappa_0\rho_f)$ is the characteristic Biot frequency with ρ_f denoting fluid density and a the correlation length, that is, a characteristic length scale of the inhomogeneities. Condition (7) expresses the weak-contrast assumption which is necessary for the derivation of the effective *P*-wave number, whereas condition (8) arises from the use of the low-frequency approximation to Biot's equations of poroelasticity.

Equation (1) for the effective wave number enables us to derive expressions for the attenuation and dispersion due to the presence of mesoscopic inhomogeneities. By definition, the real part of $\overline{k_p}$ yields the phase velocity

$$v(\omega) = \omega/\Re\{\overline{k_p}\} = v_0\left[1-\Delta_2+2\Delta_1\overline{k^2}\times\int_0^\infty rB(r)\exp[-\overline{k}r]\sin(\overline{k}r)dr\right], \tag{9}$$

where v_0 is the constant background *P*-wave velocity defined as $v_0 = \sqrt{H/\rho}$ (ρ is the bulk density) and $\overline{k}$ denotes the real part of the slow *P*-wave number k_{ps}

$$\overline{k}(\omega) = \sqrt{\frac{\eta}{2\kappa_0 N}}\,\omega. \tag{10}$$

The imaginary part of the wave number yields the attenuation coefficient γ and the reciprocal quality factor Q^{-1}, which for low-loss media can be written as

$$Q^{-1} = 2\gamma/\Re\{\overline{k_p}\} = 2\Im\{\overline{k_p}\}/\Re\{\overline{k_p}\}. \tag{11}$$

Then, from (1) we find

$$Q^{-1}(\omega) = 4\Delta_1\overline{k^2}\int_0^\infty rB(r)\exp[-\overline{k}r]\cos(\overline{k}r)dr. \tag{12}$$

From Eqs. (9) and (12) the meaning of the coefficients (2) and (3) becomes clear. The attenuation Q^{-1} and the frequency-dependent part of v are proportional to Δ_1. Thus Δ_1 is the measure of the magnitude of attenuation and velocity dispersion, that is, the dynamic effects. In contrast, Δ_2 produces a frequency-independent velocity shift in (9).

In the following we analyze general properties of velocity and attenuation as given by Eqs. (9) and (12), and com-

pute closed-form expressions for attenuation and phase velocity for several specific correlation models.

III. GENERAL PROPERTIES OF ATTENUATION AND VELOCITY DISPERSION

A. Alternative representation using the fluctuation spectrum

To gain further insight into the general properties of the results for attenuation and velocity dispersion (and to analyze their analytic structure, cf. the next section) it is useful to express the equations (9) and (12) in terms of the fluctuation spectrum (power spectrum), that is, the spatial Fourier transform of the correlation function. In statistically isotropic random media the fluctuation spectrum $\Phi(\kappa)$ and the correlation function $B(r)$ are related through the three-dimensional Hankel transform

$$B(r)=\frac{4\pi}{r}\int_0^\infty \kappa\Phi(\kappa)\sin(\kappa r)d\kappa. \tag{13}$$

Note that Eq. (13) implies that the integral over the fluctuation spectrum is finite if $B(0)$, i.e., the variance is finite. Substituting expression (13) into Eqs. (9) and (12), changing the order of integration, and integrating over r we obtain

$$v(\omega)=v_0\left[1-\Delta_2+16\pi\Delta_1\int_0^\infty \frac{\bar{k}^4\kappa^2}{4\bar{k}^4+\kappa^4}\Phi(\kappa)d\kappa\right] \tag{14}$$

and

$$Q^{-1}(\omega)=16\pi\Delta_1\int_0^\infty \frac{\bar{k}^2\kappa^4}{4\bar{k}^4+\kappa^4}\Phi(\kappa)d\kappa. \tag{15}$$

From Eq. (15) we observe that the dynamic behavior of attenuation is controlled by the integrand, that is, by the product of fluctuation spectrum $\Phi(\kappa)$ and the function

$$\Theta(\kappa,\bar{k})=\frac{\bar{k}^2\kappa^4}{4\bar{k}^4+\kappa^4}. \tag{16}$$

The function $\Theta(\kappa,\bar{k})$ acts like a filter and controls which part of the fluctuation spectrum yields a relevant contribution to attenuation. A similar filter function can be deduced from Eq. (14). In analogy to the acoustic scattering problem[13] we refer to Θ as the spectral filter function. Analyzing the product $\Phi\Theta$ in terms of the dimensionless, spatial wave number κa (a is the characteristic length scale of the inhomogeneities) we identify three different regimes for different values of $\bar{k}a$.

If $\bar{k}a\ll 1$, then $\Theta(\kappa a,\bar{k}a)$ behaves like $\bar{k}a$ and, therefore, the product $\Phi\Theta$ and, hence, the attenuation, becomes small. Since $\bar{k}$ is inverse proportional to the diffusion wavelength $\lambda_d=\sqrt{\kappa_0 N/\omega\eta}$, this case corresponds to the relaxed or low-frequency regime where the induced pore pressure is equilibrated during one wave cycle.

In the opposite case, if $\bar{k}a\gg 1$, then $\Theta(\kappa a,\bar{k}a)\approx(\kappa a)^4/(\bar{k}a)^2$. This means that the contribution of Φ at small spatial wave numbers is suppressed but its contribution at large wave numbers is amplified. However, since $\Phi(\kappa)$ becomes very small for large κ, the product of Φ and Θ becomes small again. In other words, in the high-frequency (unrelaxed) regime only the behavior of Φ at large $\bar{k}a$ is important.

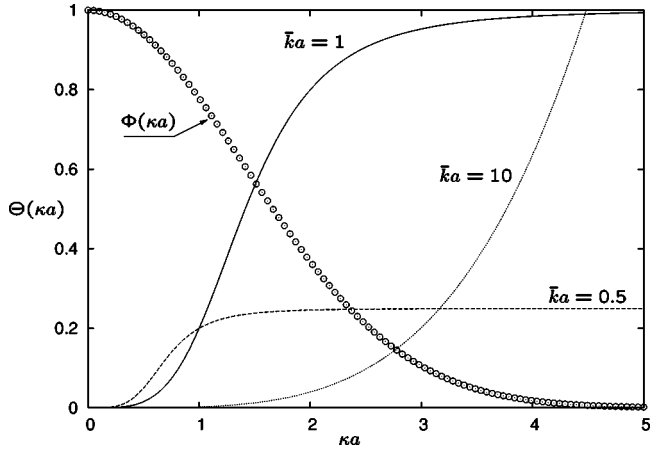

FIG. 1. The spectral filter Θ as a function of dimensionless spatial wave number κa for varying $\bar{k}a$. The general behavior of the fluctuation spectrum Φ is also shown (circles). Elastic wave attenuation due to fluid flow is proportional to the product of Φ and Θ. Maximal attenuation occurs at $\bar{k}a\approx 1$.

There is an intermediate regime with $\bar{k}a\approx 1$ where $\Phi\Theta$ (and Q^{-1}) attains its maximum. Since in our approximation attenuation due to wave-induced flow and the process of conversion scattering from fast into slow P-waves are equivalent, maximum attenuation is observed at the ''resonance'' condition $\lambda_d=a$.

The interplay between Φ and Θ is illustrated in Fig. 1.

B. The causal relationship between attenuation and dispersion

It can be shown that in any passive, linear medium the attenuation and phase of a wave are mutually related by the Kramers-Kronig relations[14] or, more generally, satisfy a dispersion relation with n subtractions (for a recent exposition of these theorems we refer to Mobley *et al.*[15]). Mathematically this means that the attenuation coefficient and the phase velocity, or the real and imaginary part of the complex wave number (1), are related through a Hilbert transform. Physically, this relation between attenuation and dispersion is a consequence of the causality of a pulse signal. The propagating pulse p can be represented as a convolution integral

$$p(z,t)=\int_{-\infty}^{\infty} h(z-z',t-t')s(z',t')dt', \tag{17}$$

where $h(L,\tau)$ is the impulse response and s is the source wavelet. Causality implies that $h(L,\tau<0)=0$.

In our model the Fourier transform of the impulse response, $\tilde{h}(L,\omega)$, is given by $\exp[ik_pL]$, where k_p is the complex P-wave number [Eq. (1)]. Instead of $\tilde{h}$, we analyze the analytic properties of its logarithmic decrement $\tilde{\gamma}(\omega)\equiv\ln\tilde{h}/L=ik_p$. The real and imaginary parts of $\tilde{\gamma}(\omega)$ form a Hilbert transform pair provided that $\tilde{\gamma}(z=\omega+iy)$ is analytic in the complex upper-half plane (minimum phase condition) and is square integrable. From Eqs. (14) and (15) we can deduce that $\tilde{\gamma}(z)$ is analytic for $y>0$. However, $\tilde{\gamma}$ is not

square integrable: Eq. (14) shows that $\tilde{\gamma}(\omega)$ diverges as ω^1 if $\omega\to\infty$. To circumvent this difficulty we use the method of subtractions[15] and form a new complex function Λ which is square integrable:

$$\Lambda(\omega)=\frac{\tilde{\gamma}(\omega)}{\omega^2}-\frac{\tilde{\gamma}(0)}{\omega^2}-\frac{1}{\omega}\frac{d}{d\omega}\tilde{\gamma}(\omega)\big|_{\omega_0=0}. \tag{18}$$

The function $\Lambda(\omega)$ is analytic in the upper-half complex z-plane. But also, $\Lambda(\omega)$ is convergent to zero as $|z|\to\infty$ and square integrable. The function Λ forms a so-called dispersion relation with two subtractions and subtraction frequency $\omega_0=0$.[15] The real and imaginary components of Λ form a Hilbert transform pair

$$\Re\Lambda(\omega)=\mathcal{H}[\Im\Lambda(\omega)]=\frac{1}{\pi}P\int_{-\infty}^{\infty}d\omega'\frac{\Im\Lambda(\omega')}{\omega'-\omega}, \tag{19}$$

$$\Im\Lambda(\omega)=-\mathcal{H}[\Re\Lambda(\omega)]=-\frac{1}{\pi}P\int_{-\infty}^{\infty}d\omega'\frac{\Re\Lambda(\omega')}{\omega'-\omega}, \tag{20}$$

where $P\int$ denotes the Cauchy principal value of the integral. Using expressions (14) and (15) the real and imaginary parts of Λ can be written as

$$\Re\Lambda(\omega)=-c\int_0^{\infty}d\kappa\Phi(\kappa)\frac{g(\kappa)}{\omega^2+g(\kappa)}, \tag{21}$$

$$\Im\Lambda(\omega)=-c\int_0^{\infty}d\kappa\Phi(\kappa)\frac{\sqrt{g(\kappa)}\omega}{\omega^2+g(\kappa)}, \tag{22}$$

where $g(\kappa)=\kappa^4\kappa_0^2N^2/\eta^2$ and $c=4\pi\Delta_1\eta/(v_0\kappa_0N)$. It is easy to verify that (21) and (22) are related through (19) and (20) if we remember the basic Hilbert transform pair $\mathcal{H}[-x/(1+x^2)]=-1/(1+x^2)$.

Thus, the attenuation coefficient and phase velocity satisfy a twice-subtracted dispersion relation. In other words, formulas (19) and (20) allow us to compute attenuation and dispersion from each other. It is important to note that this causal relationship is an intrinsic property of our model and not a prerequisite.

IV. ANALYTICAL EXPRESSIONS AND MODELING CHOICES

A. Analytical expressions

We now give explicit results for Q^{-1} and v for several correlation functions of practical interest. Ideally, the correlation function should be inferred from experimental data such as x-ray images of rock samples. In many circumstances the true correlation behavior can be well approximated by simple correlation functions such as an exponential correlation function or combinations of them. A review of frequently used correlation functions in random media is provided by Klimes.[16]

First, let us assume that the inhomogeneities are exponentially correlated so that $B(r)$ becomes

$$B(r)=\exp[-|r|/a]. \tag{23}$$

Here a denotes the correlation length, i.e., a characteristic length scale associated with the inhomogeneities. More precisely, the correlation length a is the length scale at which $B(r)$ assumes the value e^{-1}. The choice of a single correlation function $B(r)$ implies that the correlation length is the same for the three random functions $H(\mathbf{r})$, $G(\mathbf{r})$, and $C(\mathbf{r})$ (note that in general the results of paper I allow the use of different correlation lengths associated with each random function). Substituting correlation function (23) into Eqs. (9) and (12) we find

$$Q^{-1}(\omega)=\Delta_1\frac{4(a\overline{k})^2(2\overline{ka}+1)}{(1+2\overline{ka}+2\overline{k^2}a^2)^2} \tag{24}$$

and

$$v(\omega)=v_0\left[1+\Delta_1\frac{4(a\overline{k})^3(1+\overline{ka})}{(1+2\overline{ka}+2\overline{k^2}a^2)^2}-\Delta_2\right]. \tag{25}$$

For the so-called Gaussian correlation function

$$B(r)=\exp[-r^2/a^2], \tag{26}$$

we obtain

$$Q^{-1}(\omega)=2\Delta_1(a\overline{k})^2\left[1-\frac{\sqrt{\pi}}{4}\sum_{z=z_-}^{z_+}a\overline{kz}\times\exp[(a\overline{kz})^2/4]\mathrm{erfc}[a\overline{kz}/2]\right], \tag{27}$$

$$v(\omega)=v_0\left[1+\Delta_1(a\overline{k})^2\frac{\sqrt{\pi}}{4}\sum_{z=z_-}^{z_+}a\overline{kz}^*\times\exp[(a\overline{kz})^2/4]\mathrm{erfc}[a\overline{kz}/2]-\Delta_2\right], \tag{28}$$

where $z_+=1+\mathrm{i}$, $z_-=1-\mathrm{i}$, z^* denotes complex conjugation, and erfc is the complementary error function. Another widely used correlation model is the von Kármán function

$$B(r)=2^{1-\nu}\Gamma^{-1}(\nu)\left(\frac{r}{a}\right)^{\nu}\mathrm{K}_{\nu}(r/a), \tag{29}$$

where K_{ν} is the modified Bessel function of third kind (MacDonald function) and Γ denotes the gamma function. The von Kármán correlation function involves an additional parameter, the so-called Hurst coefficient ν which is assumed to be $0<\nu\leqslant 1$. For the case $\nu=\frac{1}{2}$ the von Kármán function is identical to the exponential correlation function (23). Its fluctuation spectrum is given by

$$\Phi(\kappa)=\frac{a^3\Gamma(\nu+\frac{3}{2})}{\pi^{3/2}\Gamma(\nu)(1+\kappa^2a^2)^{\nu+3/2}}. \tag{30}$$

Substituting (30) into (15) and (14) gives

$$Q^{-1}(\omega)=c_1\Delta_1\Bigg[c_2\,{}_3F_2\Bigg(1,\frac{1}{2}+\frac{\nu}{2},1+\frac{\nu}{2};\frac{1}{4},\frac{3}{4};-4(a\bar{k})^4\Bigg)$$
$$-\frac{1}{2}\Gamma\Bigg(\nu+\frac{3}{2}\Bigg)(2\nu+3)B^{-3/4-\nu/2}\cos\Bigg[\Bigg(\frac{3}{4}+\frac{\nu}{2}\Bigg)A\Bigg]$$
$$+\Gamma\Bigg(\nu+\frac{5}{2}\Bigg)B^{-5/4-\nu/2}\{2(a\bar{k})^2\cos[c_3A]$$
$$+\sin[c_3A]\}\Bigg], \tag{31}$$

$$v(\omega)=v_0\Bigg[1-\Delta_2-\frac{c_1}{2}\Delta_1\Bigg(-4c_2(1+\nu)(a\bar{k})^2\,{}_3F_2\Bigg(1,1$$
$$+\frac{\nu}{2},\frac{3}{2}+\frac{\nu}{2};\frac{3}{4},\frac{5}{4};-4(a\bar{k})^4\Bigg)$$
$$+\frac{1}{2}\Gamma\Bigg(\nu+\frac{1}{2}\Bigg)(2\nu+3)c_3B^{-3/4-\nu/2}\cos\Bigg[\Bigg(\frac{3}{4}+\frac{\nu}{2}\Bigg)A\Bigg]$$
$$+\Gamma\Bigg(\nu+\frac{3}{2}\Bigg)\Bigg(\frac{3}{2}+\nu\Bigg)B^{-5/4-\nu/2}\{2(a\bar{k})^2\cos[c_3A]$$
$$+\sin[c_3A]\}\Bigg)\Bigg], \tag{32}$$

where we used $c_1=16\sqrt{\pi}(a\bar{k})^3/(\Gamma(\nu)(2\nu+3))$, $c_2=\Gamma(\nu+1)(2\nu+3)/(2\sqrt{\pi}a\bar{k})$, $c_3=(1/4+\nu/2)$, $A=2\arctan(2a^2\bar{k}^2)$, and $B=1+4(a\bar{k})^4$. ${}_3F_2$ is the generalized hypergeometric function.

B. Modeling choices

Let us consider various scenarios how mesoscopic inhomogeneities can affect attenuation and dispersion of *P* waves. The above results allow us to model signatures of wave-induced flow due to fluctuations in the solid phase, drained frame, and fluid parameters. In all numerical examples we assume that the background material is a porous sandstone with parameters specified in Table I.

In the first example, we assume that the correlation function is of exponential type (23) with varying correlation length *a*. Further, we assume that there are fluctuations of all bulk moduli and the shear modulus specified through their variances: $\sigma^2_{K_dK_d}=0.12$, $\sigma^2_{K_gK_g}=0.02$, $\sigma^2_{GG}=0.1$, and $\sigma^2_{K_fK_f}=0.14$. The fluctuations of K_d, K_g, and G are fully correlated so that the coefficient of correlation for two different random fields $R=\sigma^2_{XY}/\sqrt{\sigma^2_{XX}\sigma^2_{YY}}$ is equal to one. In our case, the cross variances become $\sigma^2_{K_dK_g}=0.049$, $\sigma^2_{K_dG}=0.110$, and $\sigma^2_{GK_g}=0.048$. The fluctuations of porous material parameters and fluid bulk modulus are uncorrelated. Using these variances we compute the variances of the poroelastic parameters *H*, *C*, and *G*: $\sigma^2_{HH}=0.051$, $\sigma^2_{CC}=0.081$, $\sigma^2_{HG}=0.098$, $\sigma^2_{HC}=0.025$, and $\sigma^2_{GC}=0.098$. The frequency dependence of attenuation and phase velocity for this model according to Eqs. (24) and (25) is shown in Fig. 2. The frequency is normalized by Biot's critical frequency f_c. From Fig. 2 we can observe that even weak fluctuations of the bulk moduli

TABLE I. Parameters of the background solid and fluid phases used for the computation of the numerical examples.

Porous material	
K_g (GPa)	40
K_d (GPa)	4.5
G (GPa)	9
ρ_g (kg/m^3)	2650
ϕ	0.17
κ_0 (mD)	250
Pore fluid	
K_f (GPa)	2.17
η (Pa s)	0.001
ρ_f (kg/m^3)	1000
Poroelastic parameters	
P_d (GPa)	16.5
α	0.89
M (GPa)	10.4
H (GPa)	24.7
N (GPa)	6.9
ω_B (kHz)	680

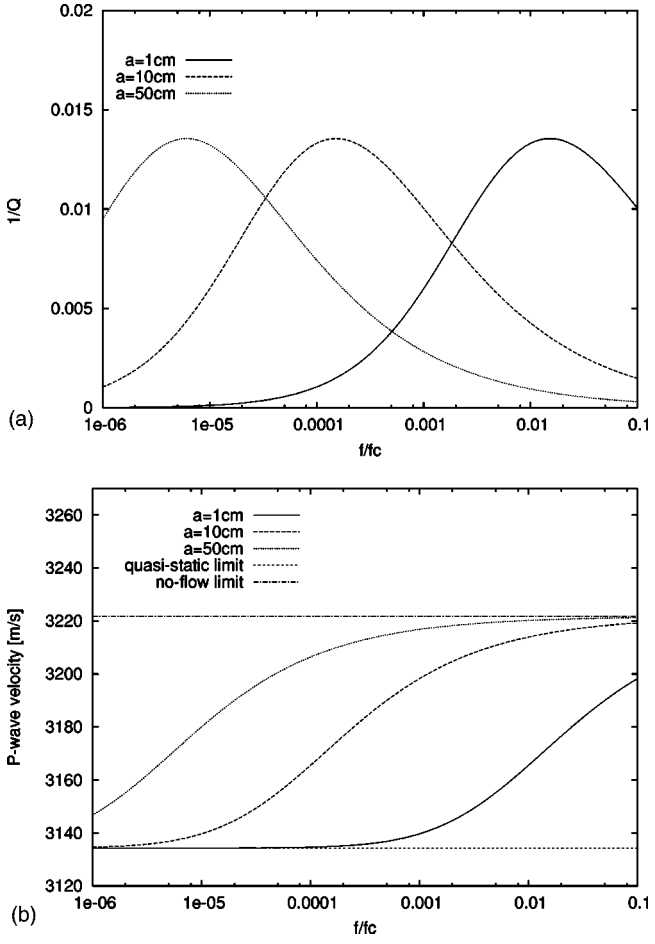

FIG. 2. (a) Reciprocal quality factor as a function of frequency (normalized by Biot's critical frequency $f_c\approx 100$ kHz) for different correlation lengths. (b) *P*-wave velocity versus frequency for the same models. It can be observed that for larger correlation lengths the dispersion curves are shifted toward lower frequencies. The horizontal curves denote the quasi-static and no-flow limits, respectively.

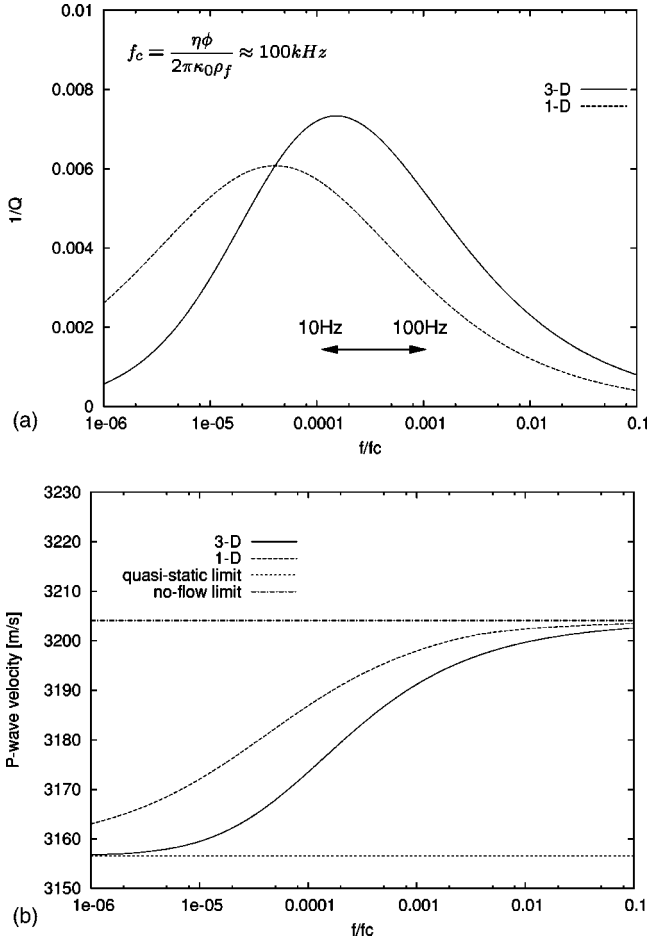

FIG. 3. Attenuation in terms of Q^{-1} (a) and velocity dispersion (b) as a function of normalized frequency for a model with fluctuations in the parameter K_f with $\sigma^2_{K_fK_f}=0.2$ and $a=25$ cm. For the same parameters the result of the 1-D poroelastic extension of the ODA theory is also shown (dashed curve).

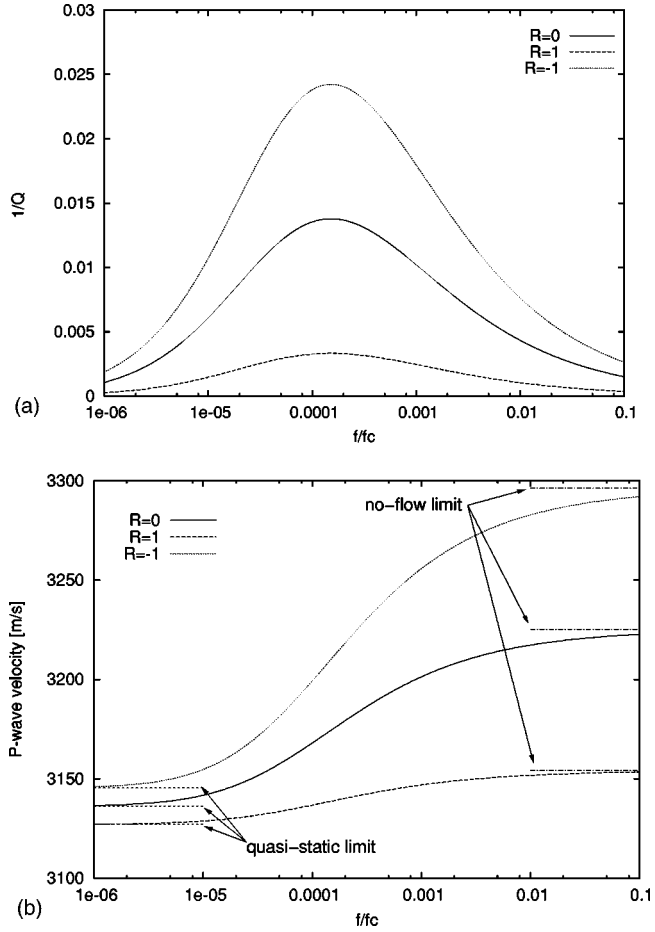

FIG. 4. (a) Q^{-1} versus normalized frequency for differently correlated fluctuations. A significant amount of attenuation ($Q^{-1}>0.01$) can be observed if the fluctuation of the solid and frame material are negatively correlated with the fluctuations of the fluid bulk modulus (that means a soft frame inhomogeneity contains a fluid with increased bulk modulus). The correlation length is constant ($a=25$ cm). (b) *P*-wave velocity for the same model. It can be observed that for negative cross correlation the dispersion effect is most pronounced.

can produce significant attenuation of the fast *P* wave ($Q^{-1}\gtrsim 0.01$).

We also compare the result for the attenuation with those obtained in the 1-D case. For this purpose we use the results of the poroelastic extension of the O'Doherty-Anstey theory [Eq. (17) in Gelinsky *et al.*[7]]. For the same sandstone model as above we compute Q^{-1} in the case that only parameter K_f exhibits fluctuations with $\sigma^2_{K_f}=0.2$ and $a=25$ cm (Fig. 3). It can be observed that the magnitude of attenuation in 1-D and 3-D random media is of the same order. However, note that the attenuation in 3-D is slightly larger. Maximal attenuation in the 3-D case is observed at

$$\omega^{3D}_{\max}=2\kappa_0 N/a^2\eta, \tag{33}$$

whereas in the 1-D case it is observed at $\omega^{1D}_{\max}=\kappa_0 N/a^2\eta$. Thus, the maximum of attenuation in 3-D occurs at a frequency twice as large as compared with the 1-D case. In our example, this difference has important implications for the observability of the attenuation mechanism: For typical seismic frequencies (10–100 Hz) the attenuation due to wave-induced fluid flow is larger in 3-D inhomogeneous structures (this is indicated by the arrow in Fig. 3). It can be also observed that the low- and high-frequency velocities coincide for the two cases. This is, however, a consequence of the constant shear modulus in this example (see also next section).

Next, we consider the influence of the cross correlations of the fluctuations. Obviously, if there is an inhomogeneity with low *P*-wave modulus but relatively high fluid bulk modulus (that is, negatively correlated fluctuations in K_d and K_f), we expect an increased wave-induced fluid flow during the compression cycle of the wave. This means that both the dispersion and attenuation characteristics should be more pronounced than in the case of uncorrelated fluctuations. Such a behavior can be observed in Fig. 4, where *P*-wave velocity and attenuation are computed for the above sandstone model with $\sigma^2_{K_dK_d}=0.10$, $\sigma^2_{K_gK_g}=0.02$, $\sigma^2_{GG}=0.08$, and $\sigma^2_{K_fK_f}=0.16$. The fluctuations of K_d, K_g, and G are positively correlated. The fluctuations of the fluid bulk modulus and those of all other fluctuating parameters are either positively (coefficient of correlation $R=1$) or negatively ($R=-1$) correlated. The case of uncorrelated fluctuations ($R=0$) between K_f and all other moduli is also displayed in Fig. 4. We note that such scenarios may produce a

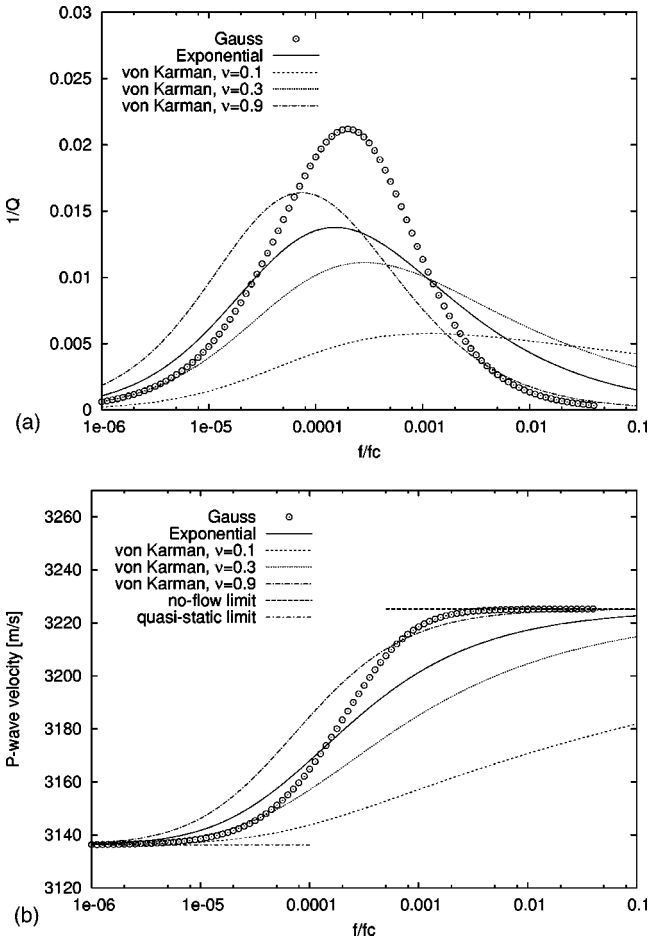

FIG. 5. Q^{-1} and *P*-wave velocity as a function of normalized frequency for Gaussian, exponential, and von Kármán (the Hurst coefficient ν is denoted in the legend) correlation functions. The model parameters are the same as in Fig. 4, where the fluctuations of K_f are uncorrelated with those of K_d, G and K_g.

significant amount of *P*-wave attenuation ($0.01<Q^{-1}<0.1$) even if the relative fluctuations in the medium parameters are small.

To demonstrate the influence of the correlation function on the frequency dependence of attenuation and velocity dispersion, in Fig. 5 we show Q^{-1} and *P*-wave velocity for exponential, Gaussian, and von Kármán correlation functions. Note that all curves are generated using the same medium parameters (those from Fig. 4). The resulting differences in magnitude and frequency dependence of attenuation are only due to the use of a different correlation model [see Eqs. (23), (26), and (29)]. Maximal attenuation is obtained for the Gaussian correlation model. Whereas at low frequencies the frequency dependence is the same for all correlation models, one can observe that at high frequencies different asymptotes are obtained. Only the Gaussian correlation model is symmetric with respect to its maximum. The asymptotic frequency behavior of our attenuation model is analyzed below. The variability of both attenuation and velocity dispersion for different correlation models indicates the importance of the geometrical shape of mesoscopic inhomogeneities for the wave-induced flow.

V. ASYMPTOTIC BEHAVIOR AT LOW AND HIGH FREQUENCIES

A. Attenuation

One goal of our study is to infer the low- and high-frequency asymptotic behavior of attenuation due to wave-induced fluid flow. At low frequencies we can approximate the exponential in Eq. (1) by 1 because $B(r)$ will vanish before the exponential term changes noticeably from its value at small arguments. Obviously, an asymptote only exists if the resulting expression $\int_0^\infty dr\, rB(r)$ has a finite positive value. This is the case for a large class of correlation functions. Then we have $\gamma \propto \omega^2$ or, in terms of the quality factor,

$$Q^{-1} \propto \omega. \tag{34}$$

It is important to note that the same low-frequency behavior is reported for 1-D and 3-D periodic structures.[5,8,10] The universality of this relation is discussed in Sec. VII.

At high frequencies only the behavior of $B(r)$ at small arguments is important. Assuming that the correlation function can be expanded in power series around the origin

$$B(r/a) = 1 - r/a + O((r/a)^2), \tag{35}$$

we can evaluate the integral in Eq. (1) and obtain

$$Q^{-1} \propto \frac{1}{\sqrt{\omega}}. \tag{36}$$

The same asymptote has been found in 1-D/3-D periodic and 1-D random structures. It is, however, important to note that the scaling (36) it not universal for any kind of disorder (see also Fig. 4). For example, the Gaussian correlation function (26) yields at high frequencies the proportionality $Q^{-1} \propto 1/\omega$, a much faster decrease of attenuation with frequency as compared to Eq. (36). The reason for this discrepancy is that the Gaussian correlation function behaves differently at small argument. Instead of (35) we have $B^{\mathrm{Gauss}}(r/a) = 1 + O(r^2/a^2)$, which means that on small scale $r \ll a$ the medium is almost homogeneous. As a consequence, at high frequencies the passing wave will create less fluid flow as compared with a medium characterized by (35) and, therefore, the decrease of Q^{-1} with frequency is stronger. In other words, the smoother the medium at small spatial scales, the less wave-induced flow takes place.

B. Velocity

Having studied the low- and high-frequency asymptotes of the wave attenuation, we now analyze the asymptotic behavior of phase velocity in the cases of low- and high frequencies. In both cases the phase velocity has a finite limit. The physical situation, however, is different for these two limits: in the low-frequency limit, there is enough time during the wave cycle to equilibrate the induced pore pressure. We refer to this relaxed limit as ''quasi-static'' and denote the corresponding phase velocity as v_{qs}. In the high-frequency limit, there is no time to develop a wave-induced fluid flow.

This situation is called the no-flow (unrelaxed) limit and we denote the phase velocity as v_{nf}. From Fig. (2) it can be observed that

$$v_{nf} \geqslant v_{qs}. \tag{37}$$

Physically, this relation can be explained by the additional stiffening of the porous frame in the no-flow limit.

From Eq. (9) it is straightforward to deduce v_{qs}. The low-frequency limit is obtained by neglecting the third term in (9). We obtain

$$v_{qs} = v_0(1-\Delta_2). \tag{38}$$

The no-flow velocity is determined if we compute the limit $\omega \to \infty$ in Eq. (9). Since in the limit $\omega \to \infty$ only the value of B at zero correlation lag yields a contribution [see Eq. (35)] we can replace $B(r)$ by $B(0)=1$. Thus the third term in (9) gives

$$2\Delta_1 \overline{k}^2 \int_0^\infty r \exp[-\overline{k}r]\sin(\overline{k}r)dr = \Delta_1, \tag{39}$$

so that

$$v_{nf} = v_0(1+\Delta_1-\Delta_2). \tag{40}$$

From Eqs. (38) and (40) it follows that the relative magnitude of the dispersion effect is

$$\frac{v_{nf}-v_{qs}}{v_0} = \Delta_1 \tag{41}$$

with Δ_1 defined in Eq. (2). It is interesting to note that the limiting velocities do not depend either on the correlation function or on the transport properties of the porous material. In other words, v_{qs} and v_{nf} are independent of the geometry of the inhomogeneities.

An independent verification of the results for the limiting velocities can be obtained by the following consideration. First, we assume that only the fluid bulk modulus K_f is fluctuating and all other parameters of the porous medium are constants. This situation may arise if the pore space is filled with different fluids. It is then expedient to change the parametrization from (H,C,G) to (P_d,α,M,G) fluctuations because in the new parametrization only the parameter M will vary. Both limiting cases must be consistent with Gassmann's equation (5) for the saturated bulk moduli K_{sat} involving some effective medium parameters:

$$K^*_{sat} = K^*_d + (\alpha^*)^2 M^*, \tag{42}$$

where the superscript * denotes the effective value of the corresponding parameter. In the quasi-static limit, the averaging of the fluid bulk modulus should be done according to Wood's formula, which leads to the following effective M^*,

$$M^* = \left\langle \frac{1}{M} \right\rangle^{-1}, \tag{43}$$

and hence

$$v_{qs} = v_0\left(1 - \frac{\alpha^2 M}{2H}\sigma^2_{MM}\right). \tag{44}$$

It is important to note that Wood's average can be applied regardless of the space dimension. Therefore, v_{qs} for 3-D random media is exactly the same as the quasi-static velocity resulting from the so-called poroelastic Backus averaging.[17] The coincidence of the quasi-static velocities in 1-D and 3-D space can be also observed in Fig. 3. In the no-flow limit the porous material behaves like an elastic composite. In the case of constant shear modulus the no-flow limit can be computed using the Hill average of the saturated *P*-wave moduli *H*:

$$H^* = \left\langle \frac{1}{H} \right\rangle^{-1}, \tag{45}$$

which in the weak fluctuation limit yields

$$v_{nf} = v_0\left(1 - \frac{\alpha^4 M^2}{2H^2}\sigma^2_{MM}\right) = v_0\left(1 - \frac{1}{2}\sigma^2_{HH}\right). \tag{46}$$

We notice that Eq. (46) is also valid in 1-D random media.[7] Again, the coincidence of both limiting velocities can be observed in Fig. 3.

The above consideration yields the same quasi-static and no-flow velocities as the 1-D approach and only requires the exact mixing laws of Wood and Hill. This could lead to the conclusion that the poroelastic Backus averaging, which provides the limiting velocities in 1-D inhomogeneous media, is also valid in 3-D inhomogeneous media. This is, however, merely a consequence due to neglecting fluctuations of the shear modulus. In general, we have to analyze the consistency of our limiting velocities with results obtained for 3-D inhomogeneous media. In the no-flow limit, we can use the results of Gold *et al.*[18] They derived an expression for the effective *P*-wave velocity in weakly inhomogeneous elastic random media (see their equation A-28):

$$v^* = v_0\left(1 - \frac{1}{2}\frac{\lambda^2}{(\lambda+2\mu)^2}\sigma^2_{\lambda\lambda} - \frac{2}{3}\frac{\lambda\mu}{(\lambda+2\mu)^2}\sigma^2_{\lambda\mu} - \frac{2}{5}\frac{\mu^2}{(\lambda+2\mu)^2}\sigma^2_{\mu\mu} - \frac{4}{15}\frac{\mu}{(\lambda+2\mu)}\sigma^2_{\mu\mu}\right), \tag{47}$$

where λ and μ denote the Lamé parameters and σ^2_{xy} the (cross) variances of the fluctuations of the Lamé parameters. The no-flow limit can be obtained from Eq. (47) by replacing the Lamé parameters with their saturated values. To demonstrate the equivalence between this result and our expression for v_{nf} we have to change from the (λ,μ) to (H,G) parametrization. Using the simple relation between the relative fluctuations in both parametrizations $\varepsilon_H = (\lambda\varepsilon_\lambda + 2\mu\varepsilon_\mu)/H$ and $H = \lambda + 2\mu$, where λ and μ are the saturated Lamé parameters, we obtain

$$v_{nf} = v_0\left(1 - \frac{1}{2}\sigma^2_{HH} + \frac{4}{3}\frac{G}{H}\sigma^2_{HG} - \frac{16}{15}\frac{G^2}{H^2}\sigma^2_{GG} - \frac{4}{15}\frac{G}{H}\sigma^2_{GG}\right), \tag{48}$$

which is exactly Eq. (40). In conclusion, the no-flow velocity according to our approach can be obtained from the effective velocity in elastic random media when the elastic moduli are replaced by their saturated counterparts.

VI. DISCUSSION

A. Applicability to real porous materials

The model proposed in this paper provides expressions for frequency-dependent attenuation and dispersion in 3-D randomly inhomogeneous porous media accounting for the effect of wave-induced fluid flow. Our results are based on perturbation theory and, therefore, are restricted to weak-contrast media. However, we think that this approximate solution reveals the exact solution's essential dependence on frequency and medium parameters. In our approach the dynamic characteristics depend on the correlation properties of the medium fluctuations. Closed-form expressions for $Q^{-1}(\omega)$ and $v(\omega)$ are obtained for several correlation functions. The form of attenuation and dispersion curves are typical for a relaxation mechanism. The low-frequency behavior of attenuation is found to be $Q^{-1} \propto \omega$, whereas at high frequencies $Q^{-1} \propto \omega^{-1/2}$. It is interesting to note that these asymptotes coincide with those predicted by the periodicity-based approaches.[8,10] Consequently, in 3-D space the observed frequency dependency of attenuation due to fluid flow has universal character independent of the type of disorder (periodic or random). This result is somewhat unexpected if we remember that in 1-D space the attenuation asymptotes are different for periodic and random structures.

Typically in the seismic frequency band attenuation is of the order[19] $0.01 < Q^{-1} < 0.1$. Despite the fact that our attenuation model is restricted to weakly inhomogeneous media, it may explain attenuation values of the order 0.01. Our model is also restricted to mesoscopic inhomogeneities (condition 1 in paper I): $\lambda \gg a \gg a_{\text{pore}}$, where a_{pore} denotes any characteristic pore-scale length. In the case $\lambda \gg a$ attenuation due to scattering on weak inhomogeneities is negligible. However, if $\lambda \gtrsim a$, scattering attenuation becomes noticeable (scattering attenuation has a maximum for $\lambda = a$). Such a case may occur at sonic or ultrasonic frequencies. Scattering attenuation can also be modeled in the framework of the statistical smoothing method (recall that the present approach is based on this approximation method). However, since the latter approximation describes signatures of the ensemble-averaged field, its application to the evaluation of scattering attenuation in heterogeneous rocks is limited.[20] Instead, a wavefield approximation valid in single realizations of the random medium[21] should be employed. An extension of the present results with proper account of scattering attenuation (i.e., to relax the restriction $\lambda \gg a$) is the subject of future research.

There are a few more issues that have to be addressed in future work. In order to construct a quantitative model for the case of partial saturation with pore fluids having large contrasts in their elastic properties, the present approach has to be modified in such a way that the low- and high-frequency limits are connected with the known (exact) bounds of Gassmann-Wood and Gassmann-Hill, respectively. For 1-D random media such a model has been recently developed and used in order to interpret laboratory data.[22]

B. Analogy with other physical systems

As discussed in more detail in paper I, attenuation and dispersion due to mesoscopic wave-induced flow can also be described as conversion scattering of the normal (fast) *P* wave (governed by the wave equation) into Biot's slow wave, which is governed by the diffusion equation. Such a situation is not unique to poroelasticity, but occurs in a number of physical situations. Two most obvious situations of this kind are conversion scattering of elastic waves into thermal waves in inhomogeneous thermoelastic materials, and scattering of acoustic waves into viscous waves in viscous suspensions and emulsions. It is thus interesting to compare our poroelastic results with those for poroelastic solids and viscous fluids, and find out whether they yield the same patterns of frequency dependence for 1-D and 3-D periodically and randomly inhomogeneous structures.

The theory of thermoelasticity is based on a system of coupled partial differential equations which has exactly the same structure as Biot's equations of poroelasticity.[23,24] Therefore, using this correspondence, results from the theory of thermoelasticity can be translated into results for poroelasticity. In thermoelasticity, dissipation of elastic waves propagating in media with varying thermal conductivity is caused by conversion into a thermal compression wave. Physically, an elastic wave causes temperature fluctuations which create a heat flux. There are numerous works on the description of the dissipation effect in randomly inhomogeneous, thermoelastic structures. For 1-D random thermoelastic media Armstrong[25] showed that attenuation in the low-frequency range scales like $Q^{-1} \propto \sqrt{\omega}$, which is the very same scaling as in the 1-D random poroelastic case. In 3-D random thermoelastic media characterized by a von Kármán correlation function Shermergor and Baryshnikov[26] showed that $Q^{-1} \propto \omega$ at low frequencies. This asymptotic behavior is the same as found in the present work for any correlation function. Thus the observed low-frequency asymptotes of attenuation in 1-D and 3-D thermoelastic structures are the same as in corresponding poroelastic structures.

It is also interesting to compare our results with those for acoustic signatures in suspensions of solid particles in a viscous fluid. Acoustic wave attenuation in suspensions is caused by the viscous drag between the fluid and the particles during a wave cycle, i.e., by the resistance to fluid flow around the solid particle.[27] Similar to the case of wave-induced flow in poroelastic structures, it is the relative motion of fluid and solid phase that controls the dissipation process. The difference is that the solid phase in suspensions is not continuous. At low frequencies one finds,[27] once again, the scaling $Q^{-1} \propto \omega$. Urick[28] presented a simple attenuation formula valid for all frequencies, which agrees with experimental results in suspensions. Urick's Eq. (5) yields $Q^{-1} \propto \omega$ at low frequencies and $Q^{-1} \propto 1/\sqrt{\omega}$ at high frequencies. This is the very same scaling as obtained in exponentially correlated poroelastic random media [Eq. (24)]. Interestingly, Urick's equation for attenuation also contains a term which accounts for scattering at the suspended particles resulting in the Rayleigh scattering dependence $Q^{-1} \propto \omega^3$. From these comparisons we can conclude that observed frequency dependencies of attenuation (and velocity) in 1-D and 3-D periodically and randomly inhomogeneous media are common for many situations where wave field energy is dissipated

due to energy transfer from the coherent component of a propagating wave mode into a highly dissipative wave mode.

VII. CONCLUSIONS

(1) Attenuation and dispersion of elastic waves due to wave-induced flow between 3-D mesoscopic inhomogeneities are given by simple linear integral expressions (9) and (12) involving the autocorrelation function of heterogeneities or, alternatively, involving the power spectrum of the heterogeneities [expressions (14) and (15)].
(2) Attenuation and dispersion given by these expressions satisfy a twice-subtracted dispersion relation, and thus form causal pair. Maximal attenuation occurs at the resonance condition $\lambda_d = a$, i.e., if the wavelength of the Biot slow wave equals the characteristic size of the inhomogeneities.
(3) For exponential, Gaussian, and von Kármán correlation functions attenuation and velocity are given by closed-form expressions.
(4) For a large class of correlation functions mesoscopic flow attenuation expressed through reciprocal quality factor scales with ω at low frequencies and with $\omega^{-1/2}$ for high frequencies.
(5) In the presence of fluid bulk modulus fluctuations only the velocities in the low- and high-frequency limit, v_{qs} and v_{nf}, are consistent with Gassmann's equation: v_{qs} is obtained by harmonic averaging of the fluctuating modulus prior to application of Gassmann's equation. v_{nf} is given by the Hill average applied to saturated moduli.
(6) Frequency dependencies of attenuation (and velocity) in 1-D and 3-D randomly poroelastic media are the same as for random thermoelastic media and suspensions of particles in a viscous fluid.

ACKNOWLEDGMENTS

This work was kindly supported by the Deutsche Forschungsgemeinschaft (Contract No. MU1725/1-1), CSIRO Petroleum, and Center of Excellence for Exploration and Production Geophysics.

[1] W. F. I. Murphy, J. N. Roberts, D. Yale, and K. W. Winkler, "Centimeter scale heterogeneities and microstratification in sedimentary rocks," Geophys. Res. Lett. **11**, 697–700 (1984).
[2] T. Cadoret, G. Mavko, and B. Zinszner, "Fluid distribution effect on sonic attenuation in partially saturated limestones," Geophysics **63**, 154–160 (1998).
[3] J. E. White, *Underground Sound: Application of Seismic Waves* (Elsevier, Amsterdam, 1983).
[4] J. E. White, N. G. Mikhaylova, and F. M. Lyakhovitsky, "Low-frequency seismic waves in fluid saturated layered rocks," Izv., Acad. Sci., USSR, Phys. Solid Earth **11**(10), 654–659 (1975).
[5] A. N. Norris, "Low-frequency dispersion and attenuation in partially saturated rocks," J. Acoust. Soc. Am. **94**, 359–370 (1993).
[6] B. Gurevich and S. L. Lopatnikov, "Velocity and attenuation of elastic waves in finely layered porous rocks," Geophys. J. Int. **121**, 933–947 (1995).
[7] S. Gelinsky, S. A. Shapiro, T. M. Müller, and B. Gurevich, "Dynamic poroelasticity of thinly layered structures," Int. J. Solids Struct. **35**, 4739–4752 (1998).
[8] D. L. Johnson, "Theory of frequency dependent acoustics in patchy-saturated porous media," J. Acoust. Soc. Am. **110**, 682–694 (2001).
[9] S. R. Pride and J. G. Berryman, "Linear dynamics of double-porosity dual-permeability materials I. Governing equations and acoustic attenuation," Phys. Rev. E **68**, 036603 (2003).
[10] S. R. Pride, J. G. Berryman, and J. M. Harris, "Seismic attenuation due to wave-induced flow," J. Geophys. Res. **109**(B1), B01201 (2004).
[11] T. M. Müller and B. Gurevich, "A first-order statistical smoothing approximation for the coherent wave field in porous random media," J. Acoust. Soc. Am. **117**, 1796–1805 (2005).
[12] F. C. Karal and J. B. Keller, "Elastic, electromagnetic and other waves in random media," J. Math. Phys. **5**, 537–547 (1964).
[13] A. Ishimaru, *Wave Propagation and Scattering in Random Media* (Academic, New York, 1978).
[14] K. Aki and P. G. Richards, *Quantitative Seismology: Theory and Methods* (Freeman, New York, 1980).
[15] J. Mobley, K. Kendall, M. Hughes, C. Hall, J. Marsh, G. Brandenburger, and J. Miller, "Kramers-Kronig relations applied to finite bandwidth data from suspensions of encapsulated microbubbles," J. Acoust. Soc. Am. **108**, 2091–2106 (2000).
[16] L. Klimes, "Correlation functions of random media," Pure Appl. Geophys. **159**, 1811–1831 (2002).
[17] S. Gelinsky and S. A. Shapiro, "Poroelastic Backus-averaging for anisotropic, layered fluid and gas saturated sediments," Geophysics **62**, 1867–1878 (1997).
[18] N. Gold, S. A. Shapiro, S. Bojinski, and T. M. Müller, "An approach to upscaling for seismic waves in statistically isotropic heterogeneous elastic media," Geophysics **65**, 1837–1850 (2000).
[19] M. Sams, J. P. Neep, M. H. Worthington, and M. S. King, "The measurement of velocity dispersion and frequency-dependent intrinsic attenuation in sedimentary rocks," Geophysics **62**, 1456–1464 (1997).
[20] H. Sato, "Amplitude attenuation of impulsive waves in random media based on travel time corrected mean wave formalsim," J. Acoust. Soc. Am. **71**, 559–564 (1982).
[21] T. M. Müller, S. A. Shapiro, and C. M. A. Sick, "Most probable ballistic waves in random media: A weak-fluctuation approximation and numerical results," Waves Random Media **12**, 223–246 (2002).
[22] T. M. Müller and B. Gurevich, "1-D random patchy saturation model for velocity and attenuation in porous rocks," Geophysics **69**, 1166–1172 (2004).
[23] M. A. Biot, "Thermoelasticity and irreversible thermodynamics," J. Appl. Phys. **27**, 240–253 (1956).
[24] A. N. Norris, "On the correspondence between poroelasticity and thermoelasticity," J. Appl. Phys. **71**, 1138–1141 (1992).
[25] B. H. Armstrong, "Models for thermoelastic attenuation of waves in heterogeneous solids," Geophysics **49**, 1032–1040 (1984).
[26] T. D. Shermergor and V. G. Baryshnikov, "Description of intercrystalline thermoelastic internal friction using the von Karman correlation function," Sov. Phys. Solid State **10**, 1709–1711 (1969).
[27] R. L. Gibson and M. N. Toksöz, "Viscous attenuation of acoustic waves in suspensions," J. Acoust. Soc. Am. **85**, 1925–1934 (1989).
[28] R. J. Urick, "The absorption of sound in suspensions of irregular particles," J. Acoust. Soc. Am. **20**, 283–289 (1948).

Energy transmission in a mechanically-linked double-wall structure coupled to an acoustic enclosure

L. Cheng,[a] Y. Y. Li, and J. X. Gao
Department of Mechanical Engineering, The Hong Kong Polytechnic University, Hung Hom, Kowloon, Hong Kong SAR, China

(Received 3 May 2004; revised 14 February 2005; accepted 16 February 2005)

The energy transmission in a mechanically linked double-wall structure into an acoustic enclosure is studied in this paper. Based on a fully coupled vibro-acoustic formulation, focus is put on investigating the effect of the air gap and mechanical links between the two panels on the energy transmission and noise insulation properties of such structures. An approximate formula reflecting the gap effect on the lower-order coupled frequencies of the system is proposed. A criterion, based on the ratio between the aerostatic stiffness of the gap cavity and the stiffness of the link, is proposed to predict the dominant transmitting path, with a view to provide guidelines for the design of appropriate control strategies. Numerical results reveal the existence of three distinct zones, within which energy transmission takes place following different mechanisms and transmitting paths. Corresponding effects on noise insulation properties of the double-wall structure are also investigated. © *2005 Acoustical Society of America.* [DOI: 10.1121/1.1886525]

PACS numbers: 43.20.Tb, 43.40.At [MO] Pages: 2742–2751

I. INTRODUCTION

Double-wall structures are widely used in noise control engineering due to their superiority over single-leaf structures in providing better acoustic insulation. Typical examples include vehicles, partition walls in buildings and aircraft fuselage shells, etc. Early work can be traced back to London,[1] who discussed the sound transmission through double-leaf panels using a simplified model consisting of two identical walls. The model was then extended by Beranek,[2] leading to the London–Beranek model for noise transmission analysis of double walls with identical mass. Since then, the topic has received a great deal of attention. Various numerical techniques, such as the statistical energy analysis and the finite element approach, have been used for transmission calculation.[3–5]

A clear understanding of the energy transmission mechanism between the two panels is of paramount importance in the design of such structures. Among other parameters, the air gap separating the two walls plays a critical role. A practical method for estimating the sound transmission loss of double walls was presented by Iwashige and Ohta[6] and was applied to analyze the popular case of light panels with an air gap. Antonio *et al.*[7] observed that the influence of the air gap on sound reduction was frequency dependent. At low frequencies a better performance was achieved using a thicker air layer, while at higher frequencies a thinner air layer was preferable. Meanwhile, filling the gap with porous sound absorbing materials to increase the sound insulation capability of such structures has also been investigated.

Double-wall structures, however, are less efficient at low frequency around the mass–air–mass resonance at which the model for infinite panels reveals an out-of-phase motion of the two walls.[8] Until quite recently, there has been a persistent effort to explore the potential of using active controls to increase the transmission loss of double-wall partitions at low frequencies.[9–14] Literature review shows that most previous studies used structures without any mechanical connections between the two walls. In such cases, sound/vibration energy is entirely transmitted through the air gap, i.e., from the acoustic transmitting path. In many applications, however, there exist mechanical links to connect the two walls. As a result, energy might also be transmitted from the link, thus forming the structural transmitting path. In this regard, Bouhioui investigated the effect of mechanical joints on double wall systems using the finite element method.[15] Bao and Pan experimentally examined the effect of the mechanical path on the active control of noise transmission into an acoustic cavity.[16] Using a given configuration, they showed that the existence of the structural transmitting path presents formidable challenges to the control, in terms of both sensing arrangement and actuation mechanism. In fact, different transmitting paths (acoustic or structural) call for different control strategies. If the acoustic transmitting path is dominant, acoustic treatment or controlling the sound field inside the gap would be a natural choice, whereas when the structural transmitting path is dominant, effort might be put on reducing structural energy transmission. In a double-wall system, the energy transmission depends on many parameters such as the gap dimension, structural details and properties of the mechanical link. For a given configuration, unfortunately, unless a complete vibroacoustic analysis is performed, which is rather complicated and computationally demanding, there exists no simple rules to assess the relative importance of each transmitting path to further guide the decision-making process in terms of control.

In this paper we attempt to bring some answers to the above mentioned problems. The configuration under investigation is a mechanically linked double-wall structure, radiat-

[a]Author to whom correspondence should be addressed. Electronic mail: mmlcheng@polyu.edu.hk

 0001-4966/2005/117(5)/2742/10/$22.50

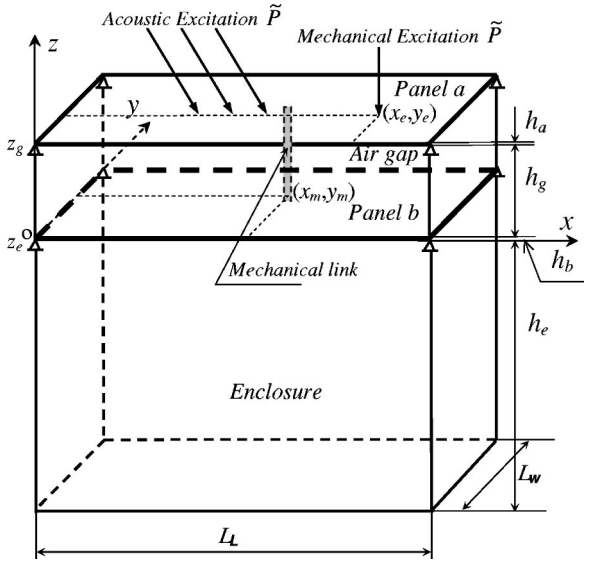

FIG. 1. Schematic representation of a mechanically linked double-wall structure.

ing sound into a rectangular acoustic enclosure. Theoretical development is first carried out, taking into account the full coupling between different components (two panels, mechanical links, the gap cavity and the enclosure). Numerical studies are then conducted to investigate the coupling characteristics of the system, providing general information on energy transmission between different components. A simple formula is derived to estimate the gap effect on the fundamental frequencies of the coupled system. Effects of the air gap and the mechanical link on energy transmission between the two walls, and the noise insulation properties are studied. It is shown that the effect of the gap can roughly be represented by an equivalent stiffness term, which is calculated using parameters related to the gap cavity. A simple criterion, based on the ratio between the aerostatic stiffness of the air gap and the stiffness of the mechanical link, is put forward to determine the dominant energy transmission path.

II. VIBROACOUSTIC MODELING

The structure under investigation, which comprises a double-wall structure connected to an acoustic enclosure and a mechanical link, is shown in Fig. 1. The double-wall structure is composed of two homogeneous and isotropic rectangular panels, which are simply supported along their boundaries and separated by an air gap cavity with a volume V_g. A mechanical link, located at (x_m,y_m), connects the two panels by its translational stiffness. The upper panel, called panel *a*, is subjected to external excitations; whereas the lower one, denoted as panel *b*, is coupled to the acoustic enclosure with a volume V_e. Apart from the surfaces occupied by the two panels, A_a and A_b, all other surrounding walls of both the air gap and the enclosure are acoustically rigid.

A brief description on the vibroacoustic modeling of the coupled system is presented. For the two panels, the equations of motion under an external excitation $\tilde{P}$ can be described as

$$D_a\nabla^4 w_a+\rho_a h_a\frac{\partial^2 w_a}{\partial t^2}=\tilde{P}-f_m\cdot\delta(x-x_m,y-y_m)-P_g(z_g=0), \quad (1)$$

for panel *a*, and

$$D_b\nabla^4 w_b+\rho_b h_b\frac{\partial^2 w_b}{\partial t^2}=f_m\cdot\delta(x-x_m,y-y_m)+P_g(z_g=h_g)-P_e(z_e=0), \quad (2)$$

for panel *b*. In the above equations, w_a, D_a, ρ_a and h_a are the transverse displacement (positive downwards), the flexible rigidity, the density and the thickness of panel *a*, respectively. Symbols with subscript *b* have the same meanings as defined above but applied to panel *b*. P_g and P_e are the acoustic pressures inside the air gap and the enclosure, respectively. $\tilde{P}$ can either be a point force or an acoustic pressure. In the former case, by neglecting the fluid loading on the emitter side of the system, a harmonic point force of amplitude F_0 applied at location (x_e,y_e) is assumed,

$$\tilde{P}(x,y,t)=F_0\delta(x-x_e,y-y_e)e^{i\omega t}, \quad (3a)$$

in which δ is the Dirac delta function. As to the latter, an oblique incident plane wave is assumed. In general, the total pressure acting on the panel can be decomposed into three parts, i.e., the incident pressure, the reflected pressure when the panel is assumed rigid and the radiated pressure due to the panel vibration. It is generally accepted that the radiated pressure is rather low compared to the other two components. Therefore, by neglecting the radiated pressure towards the outside and assuming equal magnitudes for the incident and reflected pressure waves, the excitation pressure on the panel is twice the magnitude of the incident wave, known as blocked pressure:[17]

$$\tilde{P}(x,y,t)=2P_0\exp(i\omega t-ik_0 z\cos\phi-ik_0 x\sin\phi\cos\theta-ik_0 y\sin\phi\sin\theta), \quad (3b)$$

where P_0 is the amplitude of the incident pressure, and ϕ and θ are the elevation angle and azimuth angle, respectively. $k_0=\omega/c_0$ is the wave number with c_0 being the sound speed.

In Eqs. (1)–(2), f_m is the force produced by the mechanical link, which can be simulated by a spring with a stiffness K_m as

$$f_m=K_m[w_a(x_m,y_m)-w_b(x_m,y_m)]. \quad (4)$$

In light of modal superposition theory,[18] w_a and w_b can be decomposed over their respective mode shape functions $\varphi_{a,ij}(x,y)$ and $\varphi_{b,ij}(x,y)$ of panels *a* and *b* as

$$w_a(x,y,t)=\sum_i\sum_j\varphi_{a,ij}(x,y)q_{a,ij}(t), \quad (5a)$$

$$w_b(x,y,t)=\sum_i\sum_j\varphi_{b,ij}(x,y)q_{b,ij}(t), \quad (5b)$$

where $q_{a,ij}(t)$ and $q_{b,ij}(t)$ are the modal coordinates to be determined. Substituting Eq. (5) into Eqs. (1), (2), introduc-

ing viscous damping terms and applying the orthogonality properties of shape functions yield

$$\ddot{q}_{a,kl}(t)+2\zeta_{a,kl}\omega_{a,kl}\dot{q}_{a,kl}(t)+\omega_{a,kl}^2 q_{a,kl}(t)$$
$$=\frac{1}{m_{a,kl}}\left\{\tilde{P}\varphi_{a,kl}(x_e,y_e)-f_m\varphi_{a,kl}(x_m,y_m)-\int\int P_g\varphi_{a,kl}\,dx\,dy\right\}, \tag{6}$$

$$\ddot{q}_{b,kl}(t)+2\zeta_{b,kl}\omega_{b,kl}\dot{q}_{b,kl}(t)+\omega_{b,kl}^2 q_{b,kl}(t)$$
$$=\frac{1}{m_{b,kl}}\left\{f_m\varphi_{b,kl}(x_m,y_m)+\int\int (P_g-P_e)\times\varphi_{b,kl}\,dx\,dy\right\},\quad k=1,...,\mathsf{M};\quad l=1,...,\mathsf{N}, \tag{7}$$

where $\omega_{a,kl}$ (or $\omega_{b,kl}$) and $m_{a,kl}$ (or $m_{b,kl}$) are the klth natural angular frequency and the generalized mass of the klth mode of panel a (or b), respectively.

The acoustic pressure P_g inside the gap cavity is governed by the classical wave equation,

$$\nabla^2 P_g-\frac{1}{c_0^2}\frac{\partial^2 P_g}{\partial t^2}=0, \tag{8a}$$

with the constraint of the continuity of velocity on different parts of the cavity walls,

$$\frac{\partial P_g}{\partial \mathbf{n}}=\begin{cases}\rho\ddot{w}_a, & \text{on panel } a,\\ -\rho\ddot{w}_b, & \text{on panel } b,\\ 0, & \text{on the rigid wall,}\end{cases} \tag{8b}$$

where ρ is the equilibrium fluid density and $\mathbf{n}$ the normal direction towards the outside. In general, P_g can also be decomposed on the basis of acoustic mode shapes $\psi_{g,j}$ as

$$P_g=\sum_j \psi_{g,j}p_{g,j}(t), \tag{9a}$$

with

$$\nabla^2\psi_{g,j}=-\left(\frac{\omega_{g,j}}{c_0}\right)^2\psi_{g,j}, \tag{9b}$$

$$\frac{1}{V_g}\int_{V_g}\psi_{g,i}\psi_{g,j}\,dv=\begin{cases}0, & i\neq j,\\ m_{g,jj}, & i=j,\end{cases} \tag{9c}$$

where $p_{g,j}(t)$, $\omega_{g,j}$ and $m_{g,jj}$ stand for the jth modal pressure amplitude, angular frequency and the generalized mass of the gap cavity, respectively. The following Green's theorem[19] can then be used to transform the above wave equation into a set of ordinary differential equations:

$$\int_{V_g}(P_g\nabla^2\psi_g-\psi_g\nabla^2 P_g)dv=\int_{A_a}\left(P_g\frac{\partial\psi_g}{\partial\mathbf{n}}-\psi_g\frac{\partial P_g}{\partial\mathbf{n}}\right)ds. \tag{10}$$

Substituting Eq. (9) into (10) and introducing a modal loss factor $\zeta_{g,j}$ lead to the following set of acoustic equations for the gap cavity:

$$\ddot{p}_{g,j}(t)+2\zeta_{g,j}\omega_{g,j}\dot{p}_{g,j}(t)+\omega_{g,j}^2 p_{g,j}(t)$$
$$=\frac{\rho c_0^2}{m_{g,jj}V_g}\left[A_a\sum_k\sum_l L_{j,kl}^{ag}\ddot{q}_{a,kl}(t)-A_b\sum_k\sum_l L_{j,kl}^{bg}\ddot{q}_{b,kl}(t)\right],\quad j=1,...,n_g,$$
$$n_g=n_{gx}\times n_{gy}\times n_{gz}, \tag{11}$$

where (n_{gx},n_{gy},n_{gz}) are the numbers of modes used in modal expansions for the gap cavity. $L_{j,kl}^{ag}$ and $L_{j,kl}^{bg}$ are the modal coupling coefficients between the jth cavity mode of the gap cavity and the klth structural mode of panels a and b, respectively:

$$L_{j,kl}^{ag}=\frac{1}{A_a}\int_{A_a}\psi_{g,j}\varphi_{a,kl}\,ds,\quad L_{j,kl}^{bg}=\frac{1}{A_b}\int_{A_b}\psi_{g,j}\varphi_{b,kl}\,ds. \tag{12}$$

In the absence of mechanical links, the structural–acoustic coupling occurs in a very selective way due to the orthogonality of trigonometric functions involved in mode shape functions. For instance, any symmetric mode of the panel is decoupled to an acoustic mode as long as the latter is antisymmetrical in one of the two directions parallel to the panel surface.

Similarly, the acoustic pressure P_e inside the enclosure is expressed as

$$\ddot{p}_{e,j}(t)+2\zeta_{e,j}\omega_{e,j}\dot{p}_{e,j}(t)+\omega_{e,j}^2 p_{e,j}(t)$$
$$=\frac{\rho c_0^2 A_b}{m_{e,jj}V_e}\sum_k\sum_l L_{j,kl}^{be}\ddot{q}_{b,kl}(t),\quad j=1,...,n_e;$$
$$n_e=n_{ex}\times n_{ey}\times n_{ez}. \tag{13}$$

In Eq. (13), the quantities with the subscript "e" have the same meaning as those defined before but apply to the enclosure. In the case where the harmonic excitation is assumed,

$$q_{a,kl}(t)=a_{kl}e^{i\omega t},\quad q_{b,kl}(t)=b_{kl}e^{i\omega t},$$
$$p_{g,j}(t)=c_j e^{i\omega t},\quad p_{e,j}(t)=d_j e^{i\omega t}. \tag{14}$$

Equations (6), (7), (11), (13) can be combined in matrix form:

$$\begin{bmatrix}H_{11} & H_{12} & H_{13} & 0\\ H_{21} & H_{22} & H_{23} & H_{24}\\ H_{31} & H_{32} & H_{33} & 0\\ 0 & H_{42} & 0 & H_{44}\end{bmatrix}\begin{Bmatrix}A\\ B\\ C\\ D\end{Bmatrix}=\begin{Bmatrix}F_a\\ 0\\ 0\\ 0\end{Bmatrix}, \tag{15}$$

where $H_{11},\ldots,$ and H_{44} are coefficients calculated using expressions given in the Appendix. F_a is the generalized force applied to panel a. $A_{\mathsf{MN}\times 1}=\{a_{11},\ldots,a_{\mathsf{MN}}\}^T$, $B_{\mathsf{MN}\times 1}=\{b_{11},\ldots,b_{\mathsf{MN}}\}^T$, $C_{n_g\times 1}=\{c_1,\ldots,c_{n_g}\}^T$, $D_{n_e\times 1}=\{d_1,\ldots,d_{n_e}\}^T$.

Equation (15) describes the vibroacoustic behavior of the coupled system, which can be used to calculate various coefficients for constructing the displacement of each panel and the acoustic pressures inside the air gap and the enclo-

sure. It is evident that the formulation takes the full coupling between different components of the system into account, as reflected by the presence of terms $H_{12},\ldots,H_{42}$.

Two parameters, related to the vibration of the panels and the acoustic field, are defined as follows.[20]

(1) Averaged quadratic velocity $\langle V^2\rangle$,

$$\langle V^2\rangle = \begin{cases} \langle V^2\rangle_a = \dfrac{\omega^2}{2A_a}\displaystyle\int_{A_a} w_a w_a^*\, ds, & \text{for panel } a, \\ \langle V^2\rangle_b = \dfrac{\omega^2}{2A_b}\displaystyle\int_{A_b} w_b w_b^*\, ds, & \text{for panel } b, \end{cases} \tag{16}$$

where the asterisk denotes the complex conjugate of the quantity. In the following, $\langle V^2\rangle$ is expressed in dB referenced to $2.5\times10^{-15}\,\mathrm{m^2/s^2}$.

(2) Averaged sound pressure level L_p,

$$L_p = \begin{cases} L_{p,g} = 10\log(\langle P_g^2\rangle/P_{\mathrm{ref}}^2), & \text{for air gap}, \\ \langle P_g^2\rangle = \dfrac{1}{2V_g}\displaystyle\int_{V_g} P_g P_g^*\, dv, & \\ L_{p,e} = 10\log(\langle P_e^2\rangle/P_{\mathrm{ref}}^2), & \text{for enclosure}, \\ \langle P_e^2\rangle = \dfrac{1}{2V_e}\displaystyle\int_{V_e} P_e P_e^*\, dv, & \end{cases} \tag{17}$$

where $P_{\mathrm{ref}} = 20\ \mu\mathrm{Pa}$.

III. NUMERICAL RESULTS AND DISCUSSIONS

A double-wall structure with a dimension of $L_{\mathrm{L}}\times L_{\mathrm{W}}\times h_a = 0.5\times0.35\times0.002\ \mathrm{m}^3$ for the upper aluminum plate, *a*, and of $L_{\mathrm{L}}\times L_{\mathrm{W}}\times h_b = 0.5\times0.35\times0.003\ \mathrm{m}^3$ for the lower one, *b*, is used in numerical simulations. The depth of the enclosure is set as $h_e = 0.55$ m, while the depth of the air gap h_g varies to investigate the gap effect. The modal loss factors are assumed as 0.005 for the two panels and 0.001 for the gap cavity and the enclosure.

The number of modes used for both structural displacement and sound pressure decomposition is the main factor affecting the accuracy of the solution. In general, the accuracy can be satisfied by increasing the number of modes until convergence is achieved in the frequency range of interest. In the present case, a careful convergence study was carried out by increasing the number for each variable involved in the modal expansion series, leading to the following selection: (9,7,2) for the gap cavity, (9,7,8) for the enclosure and (10,10) for the two panels.

A. Fundamental frequencies of the coupled system

Prior to detailed analyses on energy transmission, a proper estimation of the aerostatic stiffness of the air gap is necessary. A good indication of the aerostatic stiffness of the air gap is the changes in the low-order natural frequencies of the coupled system due to the variation of h_g.

Upon assuming that only the mode (0,0,0) of the air gap affects the system, the first natural frequency of a cavity-backed panel (with a hard bottom) f_{coupled} can be estimated as[20]

$$f_{\mathrm{coupled}} = \left(f_{\mathrm{in\ vacuo}}^2 + \frac{1}{4\pi^2}\frac{\rho c_0^2 A_a^2 L_{0,s}^2}{m_s V_g} \right)^{1/2}, \tag{18}$$

where $f_{\mathrm{in\ vacuo}}$ is the fundamental frequency of the panel *in vacuo*, m_s is the generalized modal mass and $L_{0,s}$ the coupling coefficient between the *first panel mode* and the mode *(0,0,0) of the cavity*.

In the case of a double-wall structure, the stiffness of the air gap, seen by both panels, is frequency dependent. As far as low frequency modes are concerned, however, the effect of mode (0,0,0) is overwhelming over other modes. Using Eq. (18), an aerostatic stiffness term K_g can be defined as

$$K_g = \frac{\rho c_0^2 A_a^2 L_{0,s}^2}{V_g}. \tag{19}$$

Since the effect of the shallow gap on structural vibration surpasses that of the enclosure, a set of truncated equations can be obtained from Eq. (15) by neglecting terms related to the enclosure, while keeping those related to the first mode of each panel and mode (0,0,0) of the air gap. This operation leads to the following frequency equation:

$$\omega^4 - (\omega_a^2+\omega_b^2+\epsilon_a^2+\epsilon_b^2)\omega^2 + (\omega_a^2\omega_b^2+\epsilon_b^2\omega_a^2+\epsilon_a^2\omega_b^2) = 0, \tag{20}$$

with

$$\epsilon_a = \sqrt{\frac{K_g}{m_{a,11}}}, \quad \epsilon_b = \sqrt{\frac{K_g}{m_{b,11}}}, \tag{21}$$

where ω_a and ω_b are, respectively, the *in vacuo* fundamental angular frequencies of panels *a* and *b*; $m_{a,11}$ and $m_{b,11}$ are their corresponding generalized masses.

Solving Eq. (20) yields

$$\omega^2 = (\omega_a^2+\omega_b^2+\epsilon_a^2+\epsilon_b^2 \pm \sqrt{\epsilon_{ab}})/2, \tag{22}$$

where

$$\epsilon_{ab} = (\omega_a^2+\omega_b^2+\epsilon_a^2+\epsilon_b^2)^2 - 4(\omega_a^2\omega_b^2+\epsilon_b^2\omega_a^2+\epsilon_a^2\omega_b^2). \tag{23}$$

Thus, for the coupled system, the *first two* natural frequencies can be calculated by

$$f_{\mathrm{coupled}} = \left(\frac{f_a^2+f_b^2}{2} + \frac{1}{8\pi^2}\cdot(\epsilon_a^2+\epsilon_b^2 \pm \sqrt{\epsilon_{ab}}) \right)^{1/2}. \tag{24}$$

Equation (24) shows that f_{coupled} depend on both the frequencies of the fundamental mode of each panel and the aerostatic stiffness of the air gap. It can been seen from Eqs. (19), (21) and (24) that a decrease of h_g leads to an increase of ϵ_a and ϵ_b, and subsequently the f_{coupled}. Figure 2 compares the *first* f_{coupled} calculated by Eq. (24) with the result obtained by the full coupling analysis based on Eq. (15) in terms of f_{coupled}/f_a ($f_a = 59.7$ Hz) using different h_g/h_e. A good agreement between the two curves shows the validity of the formula given by Eq. (24). As a special case when panel *b* is immovable, it can be mathematically shown that Eq. (24) gives the same expression as Eq. (18), the validity of which is also shown in Fig. 2. In both cases, it can be seen that the derived formula gives a very good prediction on the changes in f_{coupled} caused by the air gap. A shallow gap increases

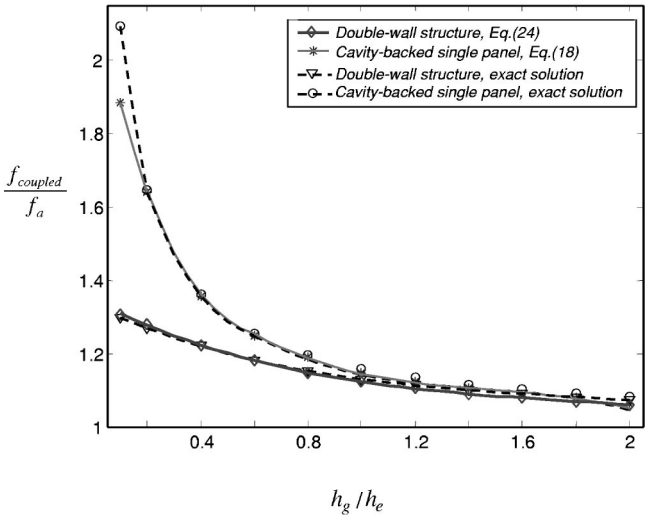

FIG. 2. Frequency variation of the *first* vibration mode of panel *a* with h_g/h_e varying from 0.05 to 2.

f_{coupled} to a lesser degree if both panels are flexible. This effect tends to be negligible when h_g becomes larger.

B. Mechanical excitation with subsections

1. General analysis

In this section, a harmonic exciting force with an amplitude of 1 N is applied to panel *a* at $(0.4L_{\text{L}},0.4L_{\text{W}})$. To gain basic understandings, a coupling analysis without mechanical links is first investigated. The depth of the air gap is set as $h_g=0.6h_e$. The natural frequencies of the coupled system, together with those of the corresponding uncoupled components (panels *a* and *b*, the air gap and the enclosure) are tabulated in Table I. A comparison between the two cases shows a significant alteration of the first two frequencies, dominated by panel *a* and *b*, respectively, in agreement with the results presented in Sec. III A. It should be pointed out that for the coupled system, the values of the natural frequencies are determined from the peak locations of the forced response curves, instead of solving the coupled eigenvalue problem. In order to identify the nature of a mode, the responses of each panel or the acoustic pressures of each cavity at the resonant frequency of the coupled system are calculated. Contributions of each subsystem can therefore be identified to determine the dominant component. The classification of different types of modes in a coupled system has been investigated previously.[21] For the sake of convenience, a mode is loosely labeled as ''mode dominated by one component'' to show the dominance of said component and the closeness of its natural frequency to its uncoupled counterpart.

As an example, the normal displacements of both panels at the first two resonant frequencies and the corresponding fluid velocities in the *z* direction in the gap cavity (contour) are illustrated in Fig. 3. It can be seen that the first mode (ω=67.3 Hz) is mainly dominated by panel *a* [Fig. 3(a)]; whereas the second one (ω=96.7 Hz) by panel *b* [Fig. 3(c)]. The two modes involve in-phase and out-of-phase motions of the two panels, respectively. The velocity contours given by Figs. 3(b) and 3(d) clearly show the phenomenon of air pumping (stiffness effect) due to the difference between the motions of the two panels.

Figures 4(a) and 4(b) show the spectra of the averaged quadratic velocity $\langle V^2\rangle$ of the two panels and the averaged sound pressure level L_p inside the air gap and the enclosure, respectively. Various peaks are marked with different sym-

TABLE I. Natural frequencies of the system in Hz ($h_g/h_e=0.6$).

Uncoupled case						
Mode\ Components	Panel *a*	Panel *b*	Mode\ Component	Air gap	Mode\ Component	Enclosure
(1,1)	59.7	89.6	(0,0,0)	0	(0,0,0)	0
(2,1)	118.6	177.9	(1,0,0)	340.0	(0,0,1)	309.1
(1,2)	179.9	269.9	(0,1,0)	485.7	(1,0,0)	340.0
(3,1)	216.8	325.2	(0,0,1)	515.2	(1,0,1)	459.5
(2,2)	238.8	358.3			(0,1,0)	485.7
(3,2)	337.0					
(4,1)	354.2					
(1,3)	380.3					
(2,3)	439.2					
(4,2)	474.5					
	Coupled case: Modes dominated by					
	Panel *a*	Panel *b*		Air gap		Enclosure
	67.3	96.7		0		0
	117.2	175.0		339.0		308.8
	178.5	266.8		486.8		341.4
	216.1	325.3				459.9
	237.5	356.5				486.8
	335.8					
	356.5					
	378.0					
	438.3					
	473.1					

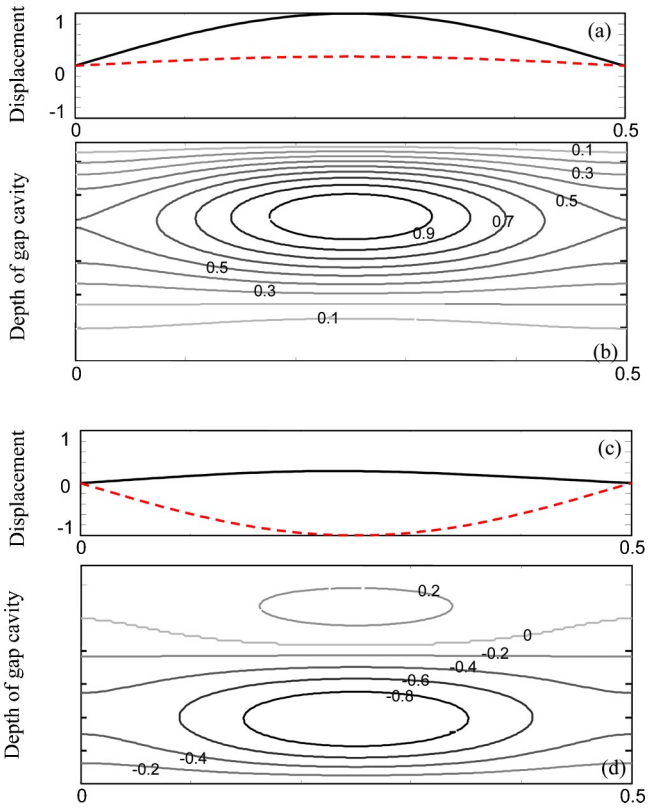

FIG. 3. Normal displacements of both panels at the first two resonant frequencies and the corresponding fluid velocities in the z direction at cross section $y=b_1/2$ in the air gap. (a) Displacements of two panels, $\omega=67.3$ Hz; (b) velocity distribution, $\omega=67.3$ Hz; (c) displacements of two panels, $\omega=96.7$ Hz; and (d) velocity distribution, $\omega=96.7$ Hz (a solid line for panel a and dashed for panel b).

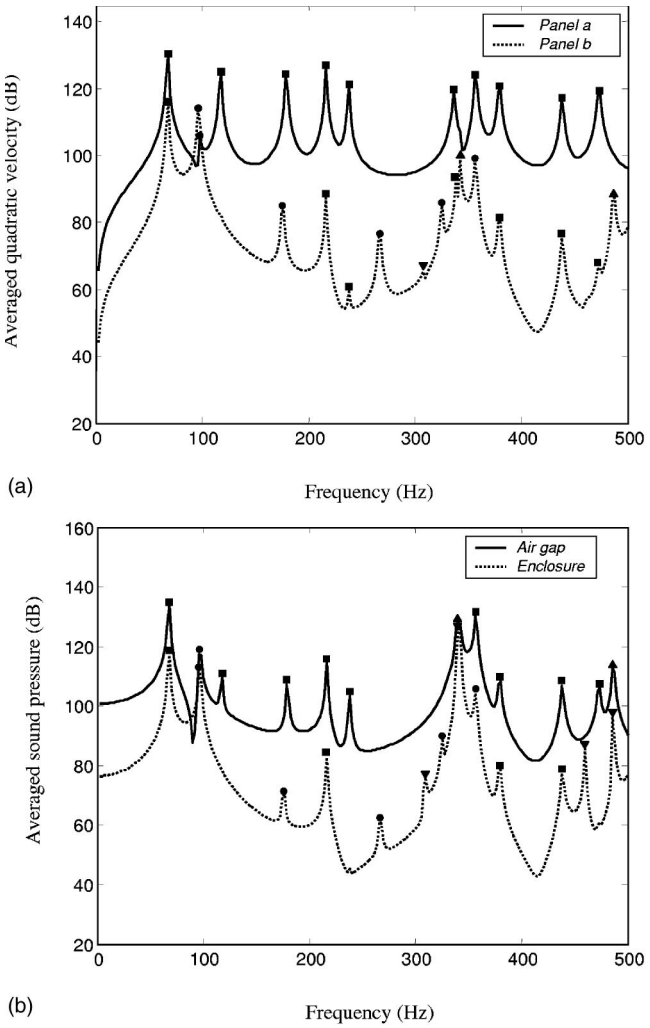

FIG. 4. (a) Averaged quadratic velocity $\langle V^2\rangle$ of panels a and b when $h_g/h_e=0.6$. ■: modes dominated by panel a; ●: modes dominated by panel b; ▲: modes dominated by the air gap; ▼: modes dominated by the enclosure. (b) Averaged sound pressure L_p inside the air gap and the enclosure when $h_g/h_e=0.6$.

bols so as to identify modes of a different nature. Figure 4(a) shows an obvious difference of around 30 dB in $\langle V^2\rangle$ between the two panels. Panel a exhibits resonances at frequencies close to its own natural frequencies. Via the air gap, the feedback effect of the panel b on a is relatively weak, since only the first mode of the panel b can be detected in $\langle V^2\rangle_a$. However, the forward energy transmission through the air gap (from a to b) is evident, because most of the resonance peaks dominated by panel a clearly appear in $\langle V^2\rangle_b$. Resonances of the air gap at 340 Hz (1,0,0) and 485.7 Hz (0,1,0) create a negligible effect on panel a, but an obvious effect on panel b. All peaks identified in $\langle V^2\rangle_a$ induce high sound pressure in the air gap, as shown in Fig. 4(b). In addition, two resonances of the air gap give raise to high acoustic energy concentration. Comparing the sound pressure levels inside the two cavities, it can be seen that the sound transmission is particularly high at the first two resonances, related to panels a and b, respectively, and also at modes (1,0,0) and (0,1,0), where both the air gap and the enclosure undergo resonances. Generally speaking, the results based on the present configuration without a mechanical link seem to imply a clear forward transmission path (panel a—air gap, panel b—enclosure) with a relatively small feedback effect.

2. Effect of the depth hg

In order to reveal the effect of the depth of the air gap h_g, the case when $h_g/h_e=0.2$ is studied and the spectra of $\langle V^2\rangle$ and L_p are plotted in Fig. 5, together with their counterparts when $h_g/h_e=0.6$ (already shown in Fig. 4) for comparison purposes. It can be seen from Fig. 5(a) that a decrease in h_g leads to an increase in the aerostatic stiffness of the air gap, consequently resulting in an obvious increase in the *first two* resonance frequencies dominated by panels a and b, respectively. For the same token, the feedback effect of the acoustic mode (1,0,0) of the air gap at 340 Hz creates an obvious peak in $\langle V^2\rangle_a$ [denoted by a "▲" in Fig. 5(a)], implying a more significant coupling and a stronger reverberation of energy when the double-wall structure has a shallow gap. Apart from these particular frequencies, the overall level of $\langle V^2\rangle_a$ is basically not affected. Subsequent energy transmissions, however, be it for $\langle V^2\rangle_b$ in Fig. 5(a), or $L_{p,g}$ and $L_{p,e}$ in Fig. 5(b), are all systematically increased to almost the same extent due to the decrease of h_g.

3. Effect of the mechanical link

A mechanical link, modeled as a punctual translational spring with a stiffness of $K_m=10^6$ N/m is assumed to connect the two panels at $(0.6L_L,0.6L_W)$. The spectra $\langle V^2\rangle$ and

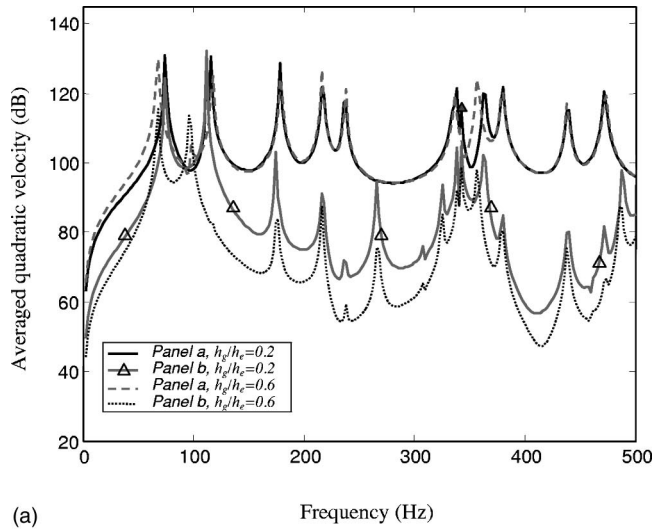

(a)

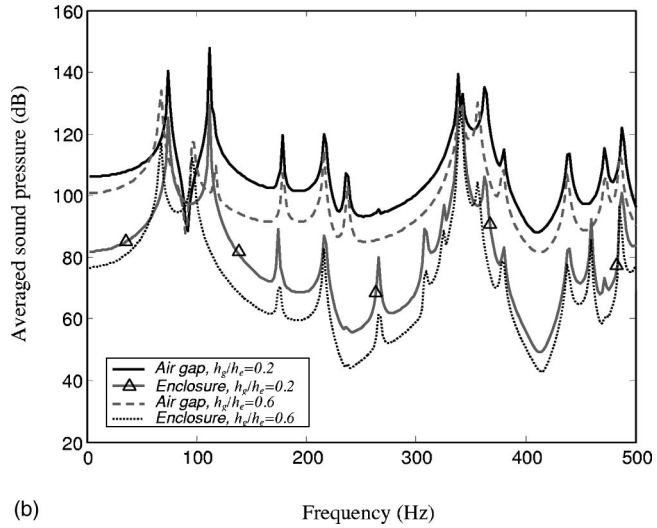

(b)

FIG. 5. (a) Averaged quadratic velocity $\langle V^2 \rangle$ of panels a and b when $h_g/h_e=0.2$ and 0.6. (b) Averaged sound pressure L_p inside the air gap and the enclosure when $h_g/h_e=0.2$ and 0.6.

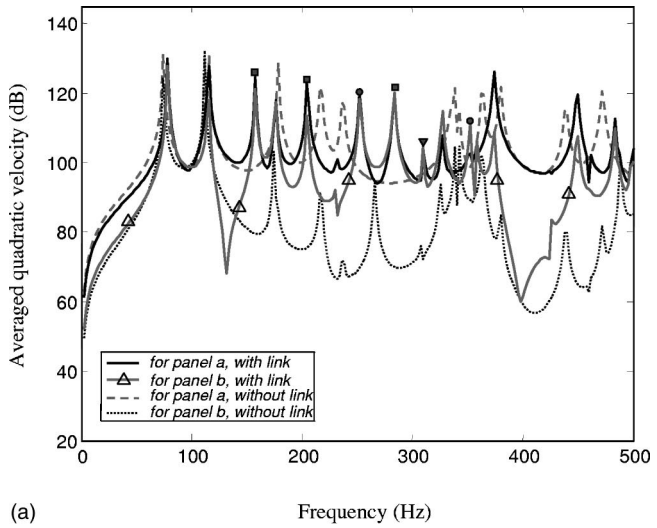

(a)

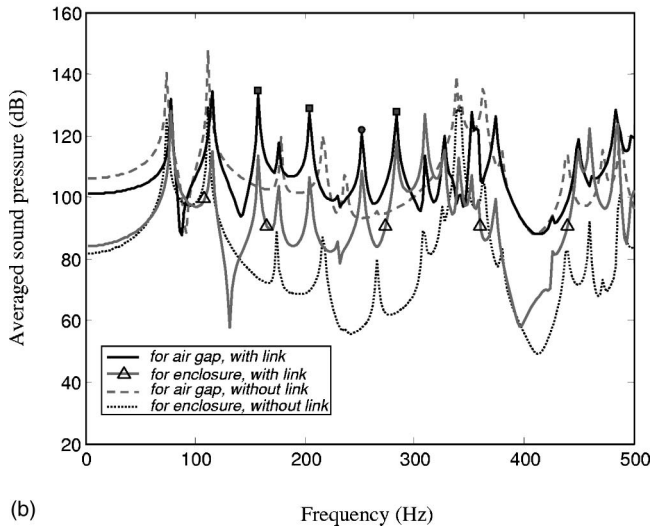

(b)

FIG. 6. (a) Averaged quadratic velocity $\langle V^2 \rangle$ of panels a and b of a double-wall structure with ($K_m=10^6$ N/m) and without ($K_m=0$) a link when $h_g/h_e=0.2$. (b) Averaged sound pressure level L_p inside the gap and the enclosure with ($K_m=10^6$ N/m) and without ($K_m=0$) a link when $h_g/h_e=0.2$.

L_p when $h_g/h_e=0.2$ with and without the link are plotted in Figs. 6(a) and 6(b), respectively. It can be seen that, compared with the case without a mechanical link, the transmission of vibration energy from panel a to b is significantly increased [Fig. 6(a)], resulting in an increase in L_p inside both cavities [Fig. 6(b)]. Although the vibration level of panel a remains more or less the same, resonance peaks are evidently altered. In addition, resonance peaks dominated by panel b can also be clearly identified in $\langle V^2 \rangle_a$ as well as in $L_{p,g}$ and $L_{p,e}$. These results indicate a strong coupling between the two panels and a more significant energy transmission due to the introduction of a mechanical link, which is quite understandable.

4. Comparison between gap effect and mechanical effect on energy transmission

Previous results show that energy can be transmitted either through the acoustic path, especially with a shallow air gap, or through the structural path with a mechanical link, which are reflected by the parameters h_g and K_m. In this section we aim at developing a criterion to predict the dominant transmission path in the presence of a mechanical link.

Based on the fact that the area under the spectrum of the averaged quadratic velocity $\langle V^2 \rangle$ can roughly represent the energy level within the analyzed frequency band, a global index characterizing energy transmission between the two panels can then be defined as

$$\gamma_{\mathrm{pl}}=E_{\mathrm{pl},b}/E_{\mathrm{pl},a}, \tag{25a}$$

with

$$E_{\mathrm{pl},b}=\frac{1}{2}\rho_b h_b A_b \overline{\langle V^2 \rangle}_b, \quad E_{\mathrm{pl},a}=\frac{1}{2}\rho_a h_a A_a \overline{\langle V^2 \rangle}_a, \tag{25b}$$

in which $\overline{\langle V^2 \rangle}_b$ and $\overline{\langle V^2 \rangle}_b$ are the areas under the spectra $\langle V^2 \rangle_b$ and $\langle V^2 \rangle_a$, respectively.

Figure 7(a) illustrates the tendency plot of γ_{pl} with different depth ratios h_g/h_e and stiffness K_m of the mechanical link. γ_{pl} decreases either with a decreasing K_m or an increasing h_g/h_e, in agreement with observations made in Figs.

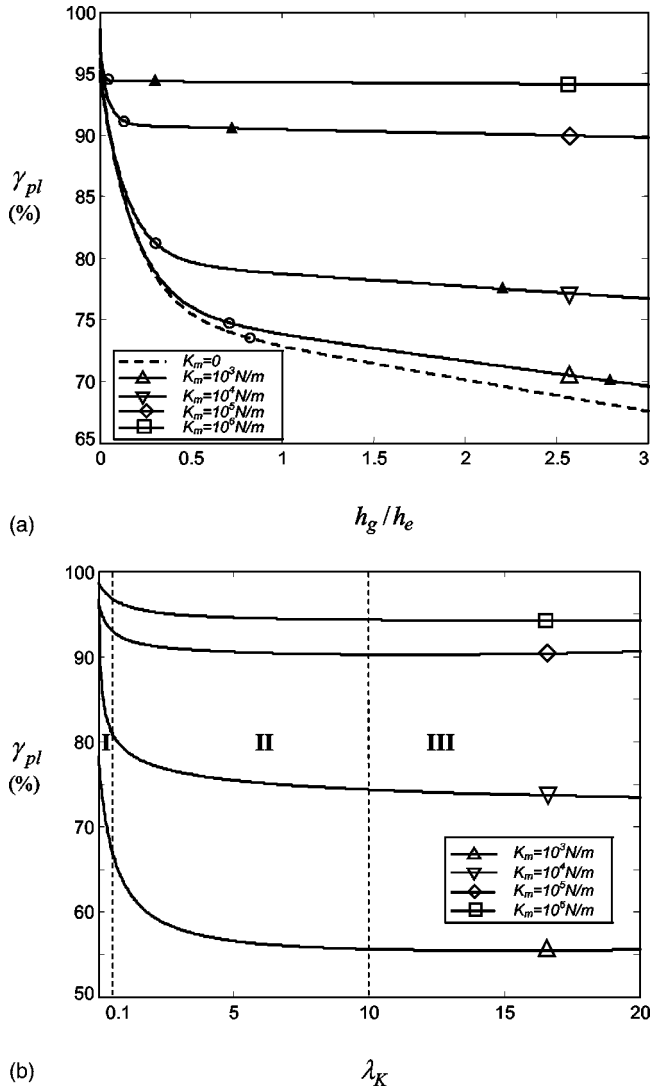

FIG. 7. Tendency plot of γ_{pl} showing the energy transmission between two walls: (a) with respect to h_g/h_e; (b) with respect to λ_K.

5(a) and 6(a). Given a K_m, γ_{pl} drops rapidly with the increase of h_g/h_e, then smoothly bends before reaching a plateau. This tendency is most obvious when K_m becomes relatively large. Obviously, the energy transmission undergoes *three* different zones. In the first fast dropping zone (before the symbol "○" in the curve), where the gap between two walls is shallow, γ_{pl} is very sensitive to h_g/h_e, meaning that a slight change in h_g has a significant impact on energy transmission between the two panels. Therefore, most energy will be transmitted from panel *a* to *b* through the air gap. The second zone is characterized by a smooth drop of γ_{pl} (ended by a "▲" in the curve), within which the gap effect on energy transmission is weakened and the air gap can be regarded as a soft spring. Energy is then transmitted simultaneously through the link and the air gap. In the plateau zone, γ_{pl} is insensitive to h_g/h_e, implying that most energy is transmitted through the mechanical link rather than the air gap. The separating points between different zones apparently depend on the value of K_m, which a stiff mechanical link reduces the *first two* zones.

The prediction of these three zones is helpful for determining the most significant energy transmitting path. To this end, a new parameter, defined as the ratio between the stiffness K_m of mechanical link and the aerostatic stiffness K_g of the air gap, is used to generalize the aforementioned phenomena:

$$\lambda_K = \frac{K_m}{K_g}. \tag{26}$$

Using this normalized parameter λ_K, the same set of results used in Fig. 7(a) is plotted in Fig. 7(b), which shows a systematic demarcation of the three different zones, irrespective of individual values of K_m and h_g/h_e. Zone I is roughly delimited by $\lambda_K < 0.1$, in which the acoustic transmitting path is dominant; zone II is confined to $0.1 < \lambda_K < 10$, within which both acoustic and structural transmitting paths play important roles in energy transmission; and zone III covers the region $\lambda_K > 10$, in which energy transmission is mainly due to the structural path. Although the demarcation lines between different zones are very vague, the use of λ_K indeed facilitates the prediction of the dominant transmitting path, since the calculation of λ_K only uses the physical and geometrical parameters related to the mechanical link and the air gap.

C. Acoustic excitation

Different energy transmission paths between two walls certainly affect the noise isolation properties of the double-wall structure. This can be examined by investigating the noise peduction (NR) index when the panel *a* is subjected to an oblique incident plane wave. A NR index is defined as the difference between the outer surface-pressure level $L_{p,\mathrm{out}}$ and averaged inner enclosure-pressure $L_{p,e}$ as

$$\gamma_{NR} = L_{p,\mathrm{out}} - L_{p,e}, \tag{27a}$$

$$L_{p,\mathrm{out}} = 10\log(\langle P_{\mathrm{out}}^2\rangle / P_{\mathrm{ref}}^2), \tag{27b}$$

where $\langle P_{out}^2\rangle$ is the mean-square pressure averaged over the outside panel surface, i.e.,

$$\langle P_{\mathrm{out}}^2\rangle = \frac{1}{2A_a}\int_{A_a} P_{\mathrm{out}} P_{\mathrm{out}}^* \, ds. \tag{27c}$$

It should be pointed out that the above definition is different from the conventional NR in that the receiving side of the sound is an enclosure. As a result, the dynamic behavior of the enclosure has an influence on the resulting NR.

Figure 8(a) shows γ_{NR} when $h_g/h_e = 0.2$, for three cases: (1) $K_m = 0$ (without a link); (2) $K_m = 10^3$ N/m; and (3) $K_m = 10^6$ N/m. The excitation is an oblique plane wave with $P_0 = 1$ Pa, $\theta = 60°$ and $\phi = 30°$. All three cases exhibit a similar tendency when frequencies vary, i.e., poor insulation at low frequencies, especially around the *first two* resonances of the double-wall structure, with an obvious increase at higher frequencies. Comparing different cases shows very little difference between $K_m = 10^3$ N/m and $K_m = 0$ cases, meaning a negligible effect of K_m on NR for a soft link. With $K_m = 10^3$ N/m, the corresponding $\lambda_K = 0.03 < 0.1$ ($K_g = 3.625 \times 10^4$ N/m), which is indeed inside zone I, where acoustic transmitting path proves to be dominate. The increase in K_m from 10^3 N/m to 10^6 N/m pushes the case into zone III (λ_K

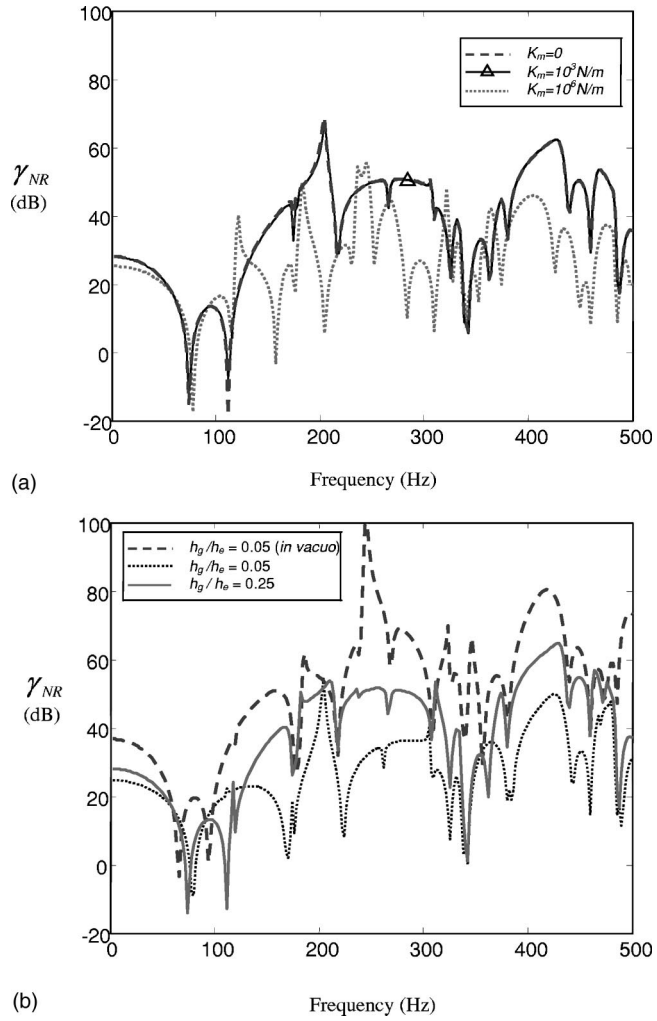

FIG. 8. Noise reduction index γ_{NR} of the double-wall structure. (a) Effect of the mechanical link; (b) effect of the depth of the gap.

$=28>10$), as evidenced by a clear decrease in γ_{NR} at frequencies above the *first two* resonances, implying a significant energy transmission through the structural path.

By keeping $K_m=10^4$ N/m, Fig. 8(b) shows the variation of γ_{NR} with two different gap depths: (1) $h_g/h_e=0.05$ (*in vacuo*, $\lambda_K=0.07$); (2) $h_g/h_e=0.05$; and (3) $h_g/h_e=0.25$ ($\lambda_K=0.34$). The difference in γ_{NR} between case (1) and case (2) shows a very significant energy transmission through the acoustic path. Increasing the depth of the air gap to $h_g/h_e=0.25$ approaches the γ_{NR} curve to that of case (1), implying a weakened acoustic transmitting path. If an even larger h_g/h_e is used (not shown), the γ_{NR} curve will converge to the *in vacuo* one, that is, a total energy transmission through the structural path.

As a final remark, the observed phenomena and the established criterion would also be useful in the modeling of the double-wall system. Most of the practical double-wall structures have closely spaced panels, which most likely fall into zones I and II. Such structures require the inclusion of the air gap into the modeling. An exception occurs when the two panels are widely separated and connected by very stiff mechanical joints (zone III). In such cases, the air gap between the panels can be ignored to simplify the modeling process.

IV. CONCLUSIONS

Based on a fully coupled vibroacoustic model, in the present paper we focus on the effect of the air gap and mechanical links on the energy transmission and noise insulation properties of a double-wall structure coupled to an acoustic enclosure. Results lead to the following conclusions.

(1) The existence of the mechanical link enhances the coupling between the two panels. As a result, the forward transmission path, the feedback effect and the reverberation of vibration energy between the two panels intensify.
(2) The depth of the air gap has significant effects on both the vibration of panels and the energy transmission. The shallow gap has a remarkable added-stiffness effect on the panels and increases the forward energy transmission. A simple formula is proposed to estimate the coupled fundamental frequencies of the double-wall structure without a mechanical link.
(3) In the presence of mechanical links, energy can be transmitted via both the acoustic path (through the air gap) and the structural path (through mechanical links). The stiffness of the mechanical link and the aerostatic stiffness of the air gap are shown to be two governing parameters. The latter can be roughly estimated using the definition given in the paper, which is based on the coupling between the first structural mode and the fundamental mode of the air gap. The ratio between the two stiffness terms forms a parameter λ_K, which can be used to identify the most dominant transmitting path in a given configuration. Numerical results reveal three different zones, which involve different transmission mechanisms. When λ_K is very small, e.g., $\lambda_K<0.1$, corresponding to a soft mechanical link or a shallow gap case, energy goes mainly through the air gap to the system. On the contrary, when λ_K is very large, e.g., $\lambda_K>10$, the mechanical link will be the main media for energy transmission. In the intermediate zone, both the air gap and the mechanical link are responsible for transmission.

It should be mentioned that the proposed demarcation values of λ_K, which are used to separate different zones, should be regarded as indicative values with a certain margin. The criterion put forward in the present study, in its simple form, provides a practical means to estimate the main energy transmission path without performing a complex vibroacoustic analysis. This information is believed to be useful for providing guide on the design of control systems.

ACKNOWLEDGMENTS

The authors would like to thank the Research Committee of The Hong Kong Polytechnic University and the Research Grants Council of HKSAR for the financial support

for this project. They are grateful to Professor J. Pan and Dr. C. Bao from University of Western Australia, for providing data used in model validation.

APPENDIX: CALCULATION OF H_{11},..., AND H_{44}

$$H_{11}=M_a+K_m\Phi_a^T(x_m,y_m)\Phi_a(x_m,y_m),$$

$$M_a=\begin{bmatrix}\ddots & & \\ & m_{a,ij}(\omega_{a,ij}^2+2i\zeta_{a,ij}\omega_{a,ij}\omega-\omega^2) & \\ & & \ddots\end{bmatrix}_{\mathrm{MN}\times\mathrm{MN}},$$

$$\Phi_a(x_m,y_m)=\lfloor\varphi_{a,11}(x_m,y_m),\varphi_{a,12}(x_m,y_m),\ldots,\varphi_{a,\mathrm{MN}}(x_m,y_m)\rfloor,$$

$$H_{12}=-K_m\Phi_a^T(x_m,y_m)\Phi_b(x_m,y_m),\quad H_{21}=H_{12}^T,$$

$$H_{22}=M_b+K_m\Phi_b^T(x_m,y_m)\Phi_b(x_m,y_m),$$

$$M_b=\begin{bmatrix}\ddots & & \\ & m_{b,ij}(\omega_{b,ij}^2+2i\zeta_{b,ij}\omega_{b,ij}\omega-\omega^2) & \\ & & \ddots\end{bmatrix}_{\mathrm{MN}\times\mathrm{MN}},$$

$$H_{13}^T=A_a\begin{bmatrix}L_{1,11}^{ag} & \cdots & L_{1,\mathrm{MN}}^{ag}\\ \cdots & \cdots & \cdots\\ L_{n_g,11}^{ag} & \cdots & L_{n_g,\mathrm{MN}}^{ag}\end{bmatrix},$$

$$H_{23}^T=-A_b\begin{bmatrix}L_{1,11}^{bg} & \cdots & L_{1,\mathrm{MN}}^{bg}\\ \cdots & \cdots & \cdots\\ L_{n_g,11}^{bg} & \cdots & L_{n_g,\mathrm{MN}}^{bg}\end{bmatrix},$$

$$H_{24}^T=A_b\begin{bmatrix}L_{1,11}^{be} & \cdots & L_{1,\mathrm{MN}}^{be}\\ \cdots & \cdots & \cdots\\ L_{n_e,11}^{be} & \cdots & L_{n_e,\mathrm{MN}}^{be}\end{bmatrix},$$

$$H_{31}=\frac{\rho c_0^2A_a\omega^2}{V_g}\begin{bmatrix}\frac{1}{m_{g,11}}[L_{1,11}^{ag}\ \cdots\ L_{1,\mathrm{MN}}^{ag}]\\ \cdots\\ \frac{1}{m_{g,n_gn_g}}[L_{n_g,11}^{ag}\ \cdots\ L_{n_g,\mathrm{MN}}^{ag}]\end{bmatrix},$$

$$H_{32}=-\frac{\rho c_0^2A_b\omega^2}{V_g}\begin{bmatrix}\frac{1}{m_{g,11}}[L_{1,11}^{bg}\ \cdots\ L_{1,\mathrm{MN}}^{bg}]\\ \cdots\\ \frac{1}{m_{g,n_gn_g}}[L_{n_g,11}^{bg}\ \cdots\ L_{n_g,\mathrm{MN}}^{bg}]\end{bmatrix},$$

$$H_{33}=\begin{bmatrix}\ddots & & \\ & -\omega^2+2i\zeta_{g,j}\omega_{g,j}\omega+\omega_{g,j}^2 & \\ & & \ddots\end{bmatrix}_{n_g\times n_g},$$

$$H_{42}=\frac{\rho c_0^2A_b\omega^2}{V_e}\begin{bmatrix}\frac{1}{m_{e,11}}[L_{1,11}^{be}\ \cdots\ L_{1,\mathrm{MN}}^{be}]\\ \cdots\\ \frac{1}{m_{e,n_en_e}}[L_{n_e,11}^{be}\ \cdots\ L_{n_e,\mathrm{MN}}^{be}]\end{bmatrix},$$

$$H_{44}=\begin{bmatrix}\ddots & & \\ & -\omega^2+2i\zeta_{e,j}\omega_{e,j}\omega+\omega_{e,j}^2 & \\ & & \ddots\end{bmatrix}_{n_e\times n_e}.$$

[1] A. London, "Transmission of reverberant sound through double wall," J. Acoust. Soc. Am. **22**, 270–279 (1950).
[2] L. L. Beranek, *Noise Reduction* (McGraw-Hill, New York, 1960).
[3] A. J. Price and M. J. Crocker, "Sound transmission through double panels using statistical energy analysis," J. Acoust. Soc. Am. **47**, 683–693 (1970).
[4] J. A. Steel and R. J. M. Craik, "Statistical energy analysis of structure-borne sound transmission by finite element methods," J. Sound Vib. **178**, 553–561 (1994).
[5] F. C. Sgard, N. Atalla, and J. Nicolas, "A numerical model for the low frequency diffuse field sound transmission loss of double-wall sound barriers with elastic porous linings," J. Acoust. Soc. Am. **108**, 2865–2872 (2000).
[6] H. Iwashige and M. Ohta, "A practical method of estimating sound-transmission loss of double walls—a proposal and its application to the popular case of light panels and air gap," Acustica **48**, 97–101 (1981).
[7] J. M. P. Antonio, A. Tadeu, and L. Godinho, "Analytical evaluation of the acoustic insulation provided by double infinite walls," J. Sound Vib. **263**, 113–129 (2003).
[8] L. Cremer and M. Heckl, *Structure-Borne Sound: Structural Vibrations and Sound Radiation at Audio Frequencies* (Springer-Verlag, Berlin, 1988).
[9] F. W. Grosveld and K. P. Shepherd, "Active sound-attenuation across a double-wall structure," J. Aircr. **31**, 223–227 (1994).
[10] P. Sas, C. Bao, F. Augusztinovisz, and W. Desmet, "Active control of sound transmission through a double-panel partition," J. Sound Vib. **180**, 609–625 (1995).
[11] C. Bao and J. Pan, "Experimental study of different approaches for active control of sound transmission through double walls," J. Acoust. Soc. Am. **102**, 1664–1670 (1997).
[12] C. Y. Wang and R. Vaicaitis, "Active control of vibrations and noise of double wall cylindrical shells," J. Sound Vib. **216**, 865–888 (1998).
[13] J. Pan and C. Bao, "Analytical study of different approaches for active control of sound transmission through double walls," J. Acoust. Soc. Am. **103**, 1916–1922 (1998).
[14] P. Gardonio and S. J. Elliott, "Active control of structure-borne and airborne sound transmission through double panel," J. Aircr. **36**, 1023–1032 (1999).
[15] H. Bouhioui, "Vibroacoustic study of a double glazing system (in French)," Université de Technologie de Compiègne, Compiègne, Ph.D. thesis, 1993.
[16] C. Bao and J. Pan, "Active acoustic control of noise transmission through double walls: Effect of mechanical paths," J. Sound Vib. **215**, 395–398 (1998).
[17] J. P. Carneal and C. R. Fuller, "An analytical and experimental investigation of active structural acoustic control of noise transmission through double panel systems," J. Sound Vib. **272**, 749–771 (2004).
[18] A. W. Leissa, *Vibration of Plates* (published for the Acoustical Society of America through the American Institute of Physics, Woodbury, NY, 1993).
[19] E. H. Dowell, G. F. Gorman, and D. A. Smith, "Acoustoelasticity: general theory, acoustic natural modes and forced response to sinusoidal excitation, including comparisons with experiment," J. Sound Vib. **52**, 519–541 (1977).
[20] L. Cheng and J. Nicolas, "Radiation of sound into a cylindrical enclosure from a point-driven end plate with general boundary conditions," J. Acoust. Soc. Am. **91**, 1504–1513 (1992).
[21] L. Cheng, "Fluid-structural coupling of a plate-ended cylindrical shell: vibration and internal sound field," J. Sound Vib. **174**, 641–654 (1994).

Contactless micromanipulation of small particles by an ultrasound field excited by a vibrating body

Albrecht Haake[a] and Jurg Dual
Swiss Federal Institute of Technology Zurich (ETHZ) Institute of Mechanical Systems—Mechanics, CH-8092 Zurich, Switzerland

(Received 20 July 2004; revised 9 January 2005; accepted 29 January 2005)

A method is presented to position and displace micron-sized particles of a diameter between 10 and 100 μm without contact to solid instruments. An ultrasound field is utilized for this purpose. It is excited in a fluid-filled gap between a harmonically vibrating body and a rigid plane surface of an arbitrary other body, e.g., an object slide or a wafer. In this ultrasound field a force field is established, which acts on the particles suspended in the fluid and moves them to certain positions. The advantage of the method is that it is possible to manipulate single particles or many particles in parallel on any surface, for example, on a structured wafer. Theoretical calculations of the force field and experimental results including three principles to displace particles with micrometer accuracy are shown. The method might be used for microassembly or cell manipulation and treatment. [DOI: 10.1121/1.1874592]

PACS numbers: 43.25.Qp, 43.25.Uv, 43.40.Rj, 43.40.Sk [MFH] Pages: 2752–2760

I. INTRODUCTION

The idea to investigate the topic of the contactless manipulation of particles arose because of problems encountered by microtweezers. After it became possible to manufacture very small tweezers, it turned out that it was easy to grab particles but very difficult to release them again. The reason is that there are adhesive forces that make objects stick to each other. Contactless manipulation means in this context to position and displace particles without contact to solid instruments such as tweezers. However, for ultrasonic positioning the particle must always be suspended in a liquid or a gas, as the acoustic forces arise in a sound field that is established in a fluid. These acoustic forces are very weak and are usually neglected, but for a small particle in a high-intensity sound field at kilohertz or megahertz frequency these forces reach a magnitude that is in the range of the particle's weight. Therefore, it is possible to use these forces to manipulate the particles.

A major field where acoustic forces have been used is in acoustic filters. One of two phases, where at least one is liquid or gaseous, can be concentrated at certain planar locations within a standing one-dimensional ultrasonic wave. From these locations a mixture of higher concentrated particles can be removed.[1] A frequently suggested method to position single or few particles is to use multiple transducers. The particle is then trapped in a sound field that is a superposition of the sound fields emitted by each of these transducers.[2] The problem is that a complicated control device is necessary to run each of the transducers independently from the others. A further principle to manipulate single particles is to trap the particle with two focused ultrasound beams.[3] The ultrasound beams are generated by piezoelectric shells and the equilibrium position of the particle is the focal point.

The novel ultrasonic micromanipulation method introduced here allows the positioning of small particles with a diameter between 10 and 100 μm. The sound field that is necessary to apply forces on the particle is excited by a vibrating body (not necessarily vibrating at a resonance frequency). For the experiments performed to obtain the results presented here, this body was a flat glass plate vibrating in bending modes. The advantage of this method is that it is possible to position and displace single or many particles over a large area, depending on the size of the vibrating body. In addition, this method is not limited to special environments in which the sound field is established. The developed device can be placed opposite any other body that has a surface of a matching profile separated by a thin fluid filled gap of between 50 μm and several hundreds of micrometers. In this gap the particles can be positioned and displaced, either with contact to the surface or levitating in the fluid.

Figure 1 shows the device that was developed for the purpose of ultrasonic manipulation. The glass plate is the vibrating body mentioned above. Excitation of one or two adjacent piezoelectric elements attached to the edges of the glass plate results in a quasi-one- or two-dimensional vibration, respectively. The piezoelectric elements perform shear deformation in the *y* direction. The glass plate and the piezoelectric elements are held by a clamp made of stainless steel.

In Sec. II we deal with the description of the sound field in a fluid layer and the deduction of the force acting on particles in that fluid. In Sec. III three principles to displace particles are introduced using the theoretical description of Sec. II and the experimental results are shown.

II. THEORETICAL ANALYSIS

A. Primary forces

In the scientific literature there are many formulas for the calculation of the acoustic forces (also termed primary

[a]Corresponding author: Albrecht Haake, ETH Zürich, IMES-Mechanik, Tannenstrasse 3, ETH Zentrum, CH-8092 Zürich, Switzerland. Telephone: +41-1-632 77 57; Fax: +41-1-632 11 45; electronic mail: a.haake@alumni.ethz.ch

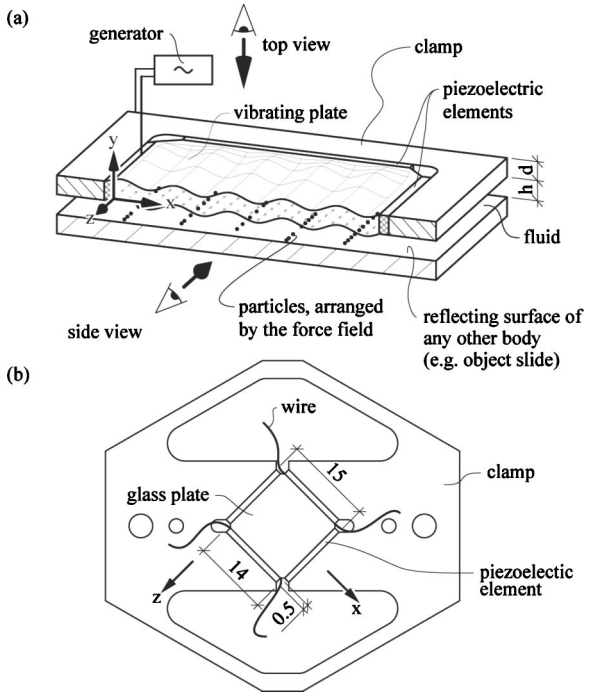

FIG. 1. Principle of the method (a) and a drawing of the developed device (b). A plate (made of glass) is excited to bending vibrations and emits a sound field into an adjacent fluid. In this sound field, forces act on particles and align them.

forces) on a particle in a one-dimensional sound field. However, the sound field that is created by the vibrating body is two- or three-dimensional. Therefore, the formulas which are often cited, for rigid[4] or compressible[5] spheres cannot be used here as they are limited to one-dimensional sound fields. For an arbitrary sound field the time-averaged force $\langle \mathbf{F} \rangle$ on a particle with radius r_S, density ρ_S, and speed of sound c_S can be calculated with $\langle \mathbf{F} \rangle = -\nabla \langle U \rangle$, where $\langle U \rangle$ is the force potential with

$$\langle U \rangle = 2\pi r_S^3 \rho_F \left(\frac{1}{3} \frac{\langle p^2 \rangle}{\rho_F^2 c_F^2} f_1 - \frac{1}{2} \langle q^2 \rangle f_2 \right). \tag{1}$$

$\langle p^2 \rangle$ and $\langle q^2 \rangle$ are the mean square fluctuations of the pressure and velocity in the sound field at the point where the particle is located, $f_1 = 1 - \rho_F c_F^2/(\rho_S c_S^2)$, $f_2 = 2(\rho_S - \rho_F)/(2\rho_S + \rho_F)$, ρ_F is the density of the fluid, and c_F is the speed of sound in the fluid.[6] Equation (1) is valid only for a particle with a longitudinal speed of sound c_S, as it is given for a fluid. However, Eq. (1) can be used for a solid sphere when in the factor f_1 instead of the compressibility of the liquid ($\beta_{Li} = 1/[\rho_S c_S^2]$) the compressibility of the solid $\beta_{S0} = 1/[\rho_S (c_1^2 - 4/3 c_t^2)]$ is used, where c_1 and c_t are the compressional and shear wave speed of the particle, respectively.[7,8]

1. Quasi-one-dimensional vibration of the plate

As previously mentioned, the sound field in the fluid gap is excited by the vibrating body. The interface between the vibrating body and the fluid is at $y = 0$. The fluid gap has in the vertical direction (y direction, Fig. 1), the height h. The reflecting surface is at $y = -h$ and has an impedance that is much greater than the impedance of the liquid. It is assumed therefore that the reflector is rigid. Furthermore, the vibrating body is assumed to perform a bending vibration with a displacement of the surface in the y direction as a harmonic function of the x direction. All values are constant as a function of the z direction. This will be termed ''one-dimensional vibration'' throughout this paper. The displacement of the vibrating body at the interface to the fluid u_{Sf} in the y direction and can be described with

$$u_{Sf} = u_{Sf0} \cos(x k_{Sf}) e^{i\omega t}, \tag{2}$$

where u_{Sf0} is the peak amplitude, x the spatial coordinate in the x direction, k_{Sf} the wave number, ω the angular frequency, and t the time. If it is assumed that the gap spreads infinitely in the x direction the velocity potential ϕ in the fluid gap between $y = 0$ and $y = -h$ becomes

$$\phi = i \frac{\Phi_F}{\sin(h k_{Fy})} \cos(x k_{Fx}) \cos((h+y) k_{Fy}) e^{i\omega t}, \tag{3}$$

where $\Phi_F = \omega u_{Sf0}/k_{Fy}$ is the amplitude and k_{Fx} and k_{Fy} are the wave numbers in the fluid with $\sqrt{k_{Fx}^2 + k_{Fy}^2} = k_F = \omega/c_F$ and $k_{Fx} = k_{Sf}$. The sound field that is excited by a one-dimensional vibration of the plate (here as a function of x) is two dimensional (as a function of x and y). The velocity $\boldsymbol{\nu}$ and the pressure p in the fluid are given by the relation $\boldsymbol{\nu} = -\nabla \phi$ and $p = \rho_F \partial \phi / \partial t$, respectively. With $\langle p^2 \rangle$ and $\langle q^2 \rangle$ calculated for the sound field of Eq. (3), the force potential $\langle U \rangle$ becomes

$$\begin{aligned} \langle U \rangle = U_0 \Bigg(& \frac{f_1}{3} k_F^2 \cos^2(x k_{Fx}) \cos^2((h+y) k_{Fy}) \\ & - \frac{f_2}{2} [k_{Fx}^2 \sin^2(x k_{Fx}) \cos^2((h+y) k_{Fy}) \\ & + k_{Fy}^2 \sin^2((h+y) k_{Fy}) \cos^2(x k_{Fx})] \Bigg), \end{aligned} \tag{4}$$

where $U_0 = \pi \rho_F \Phi_F^2 r_S^3 / \sin^2(h k_{Fy})$. From this, the two-dimensional force field acting on the particles $\langle \mathbf{F} \rangle$ due to acoustic forces can be calculated,

$$\mathbf{F} = U_0 \begin{bmatrix} k_{Fx} \sin(2x k_{Fx}) \left\{ \frac{f_1}{3} k_F^2 \cos^2((h+y) k_{Fy}) + \frac{f_2}{2} (k_{Fx}^2 \cos^2((h+y) k_{Fy}) - k_{Fy}^2 \sin^2((h+y) k_{Fy})) \right\} \\ k_{Fy} \sin(2(h+y) k_{Fy}) \left\{ \frac{f_1}{3} k_F^2 \cos^2(x k_{Fx}) + \frac{f_2}{2} (-k_{Fx}^2 \sin^2(x k_{Fx}) + k_{Fy}^2 \cos^2(x k_{Fx})) \right\} \end{bmatrix}. \tag{5}$$

The locations where the particles are collected are given by the condition $\mathbf{F}=\mathbf{0}$. It can be shown using Eq. (5) that these points are determined by $\sin(2xk_{Fx})=0$ and $\sin(2(h+y)k_{Fy})=0$, resulting in

$$xk_{Fx}=\frac{1}{2}\pi m \quad \text{and} \quad (y+h)k_{Fy}=\frac{1}{2}\pi m \quad (m=1,2,3,...), \tag{6}$$

which can be rewritten as $x=\frac{1}{4}m\lambda_{Fx}$ and $y=\frac{1}{4}m\lambda_{Fy}-h$. However, the force also vanishes when the terms in curly brackets in Eq. (5) become zero. Therefore a further condition for $\mathbf{F}=\mathbf{0}$ is

$$\cos^2((h+y)k_{Fy})=\frac{\frac{1}{2}f_2}{\frac{1}{3}f_1+\frac{1}{2}f_2}\frac{k_{Fy}^2}{k_F^2} \quad \text{and}$$

$$\cos^2(xk_{Fx})=\frac{\frac{1}{2}f_2}{\frac{1}{3}f_1+\frac{1}{2}f_2}\frac{k_{Fx}^2}{k_F^2}. \tag{7}$$

In Eq. (5) and consequently also in Eqs. (6) and (7) the gravity and buoyancy were not taken into account. These two forces are directed in the negative and positive y directions, respectively, and are constant over time and space. For the sake of simplicity and because the inclusion of gravity and buoyancy would not lead to a deeper understanding here they are ignored in this part of the analyses. These forces would only shift the entire grid given in Eqs. (6) and (7) by a constant value in the y direction.

Equation (6) and Eq. (7) are necessary conditions, because particles are collected at these points, but they are not sufficient, as these necessary conditions also specify maxima and saddle points of the force potential. As particles are only concentrated at minima of the force potential it has to be found at which of the points given by Eq. (6) and Eq. (7), $\langle U\rangle$, has a minimum. The minima of a scalar function like the force potential $\langle U\rangle$ are given by the necessary conditions that the gradient has to be zero and the sufficient condition that the Hessian is positive definite. The condition that the gradient is zero is equivalent to $\mathbf{F}=\mathbf{0}$. The Hessian H_U is the derivative matrix for the force potential from Eq. (5). It is

$$H_U=\begin{bmatrix}\frac{\partial^2\langle U\rangle}{\partial x^2} & \frac{\partial^2\langle U\rangle}{\partial x\,\partial y}\\ \frac{\partial^2\langle U\rangle}{\partial x\,\partial y} & \frac{\partial^2\langle U\rangle}{\partial y^2}\end{bmatrix}=-\begin{bmatrix}\frac{\partial F_x}{\partial x} & \frac{\partial F_x}{\partial y}\\ \frac{\partial F_x}{\partial y} & \frac{\partial F_y}{\partial y}\end{bmatrix}. \tag{8}$$

It turns out that particles are collected at $xk_{Fx}=\pi m$ or $xk_{Fx}=(1/2+m)\pi$ and $(y+h)k_{Fy}=m\pi$ or $(y+h)k_{Fy}=(1/2+m)\pi$ [the condition given by Eq. (6)]. At which of these points the particles will be collected depends on the material parameters f_1 and f_2. Particles of different materials might be collected at different points. Considering two types of particles with the material properties ρ_{S1}, c_{S1} and ρ_{S2}, c_{S2}, respectively, it is possible to find a fluid that both types of particles are collected at different positions in the sound field. In that manner it is possible to separate particles of different material properties from each other or to manipulate them differently.

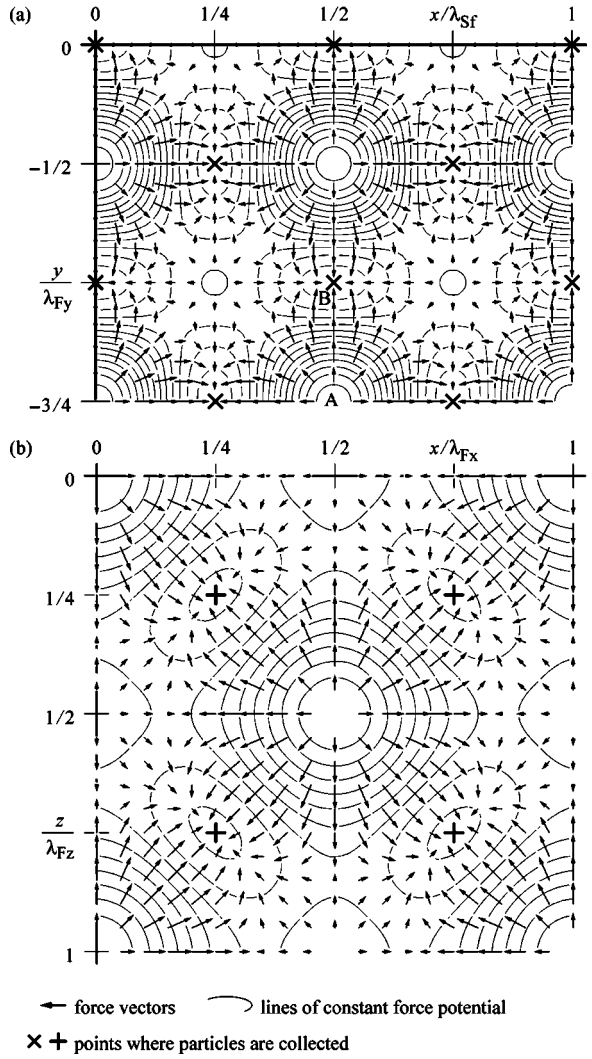

FIG. 2. Force field in the fluid gap for glass particles in water. For the two-dimensional force field (a) (side view), it was assumed that the fluid gap is 0.75 times the vertical wavelength λ_{Fy}. The particles are collected at points of minimum force potential; they can also levitate in the fluid (see cross signs). In the three-dimensional force field at the reflecting surface at $y=-h$ (b) (top view) the particles are concentrated at four points (see plus signs) in the rectangle of the dimensions corresponding to the lateral wavelengths in the fluid λ_{Fx} and λ_{Fz}.

Equation (2) gives the surface vibration for an infinite plate. However, for a real setup the vibrating body has only a finite length. Close to the edges the surface vibration can no longer be described by Eq. (2) and the sound field in the fluid will not fulfill Eq. (3). If the fluid gap is small compared to the length of the vibrating body the sound field can be approximated by Eq. (3) sufficiently far away from the edges.

Figure 2(a) shows the two-dimensional (x-y plane) force field in the fluid gap for glass particles in water. It is drawn for one horizontal wavelength in the fluid λ_{Fx}, which coincides with the wavelength of the plate vibration $\lambda_{Sf}=2\pi/k_{Sf}$. For this example it is assumed that the height of the fluid gap is 0.75 times the vertical wavelength $\lambda_{Fy}=2\pi/k_{Fy}$, i.e., the reflecting surface is at $y=-0.75\lambda_{Fy}$. The points where the force potential has a minimum, i.e., the

points where the glass particles are collected, are marked with a cross. There are points at the reflective surface [at $y=-h$, in Fig. 2(a) at $y=-3/4\lambda_{Fy}$], where the particles will be collected. But there are also points within the fluid gap where particles are held in equilibrium levitated by the force field. Particles are collected vertically and horizontally at two positions per wavelength. If there are many particles suspended in the fluid gap they will form parallel lines in the z direction [out of the plane shown in Fig. 2(a)].

2. Quasi-two-dimensional vibration of the vibrating plate

Equation (3) and Eq. (4) are only valid for a one-dimensional vibration of the body as a function of x, but the expressions can easily be expanded for a two-dimensional vibration with a harmonic displacement of the body as a function of x and z. In this case, if two piezoelectric elements at adjacent edges of the glass plate are excited, two perpendicular one-dimensional vibrations are superimposed additively. The surface displacement is then

$$u_{Sf}=\frac{1}{2}u_{Sf0}[\cos(xk_{Sf})+\cos(zk_{Sf})]e^{i\omega t}. \tag{9}$$

With this two-dimensional plate vibration the sound field in the fluid varies in three dimensions. The expression for the velocity potential ϕ and the force potential $\langle U\rangle$ changes analogously:

$$\phi=\frac{1}{2}i\Phi_F[\cos(xk_{Fx})+\cos(zk_{Fz})]\frac{\cos((h+y)k_{Fy})}{\sin(hk_{Fy})}e^{i\omega t} \tag{10}$$

and

$$\begin{aligned}\langle U\rangle=\frac{1}{4}U_0\Bigg(&\frac{f_1}{3}\frac{\omega^2}{c_F^2}(\cos(xk_{Fx})+\cos(zk_{Fz}))^2\\&\times\cos^2((h+y)k_{Fy})-\frac{f_2}{2}[k_{Fx}^2\sin^2(xk_{Fx})\\&\times\cos^2((h+y)k_{Fy})+k_{Fz}^2\sin^2(zk_{Fz})\cos^2((h+y)k_{Fy})\\&+k_{Fy}^2(\cos(xk_{Fx})+\cos(zk_{Fz}))^2\sin^2((h+y)k_{Fy})]\Bigg).\end{aligned} \tag{11}$$

The resulting force field is three dimensional and particles will not be arranged in lines, as described in the previous paragraph, but at points. In Fig. 2(b) the force field, in the plane of the reflective surface, at $y=-h$, for a rectangle with the length of λ_{Fx} by λ_{Fz}, is given, where λ_{Fx} and λ_{Fz} are the horizontal wavelengths in the fluid in the x and z directions, respectively. It can be seen that in such a unit rectangle the particles are collected at four points.

B. Secondary and external forces

Besides the primary forces there are also secondary forces in the sound field. They arise due to the interaction of particles with each other within the sound field. An important secondary force is the Bjerknes force. It is caused by the volume change of compressible particles due to the pressure variation in the fluid.[9] Another relevant interparticle force appears between two (or more) rigid particles. Depending on the alignment of the particles in the sound field this force is attractive or repulsive.[10]

In this section external forces, such as gravity or buoyancy, have not been considered. They have not been discussed as they are constant and do not, as such, change the shape of the sound field, but can easily be added to the acoustic forces.

C. Plate fluid interaction

One important issue of this method is the vibration of the plate. For the previous analysis the movement of the interface to the fluid was assumed to be sinusoidal, but the vibration itself was not considered. The glass plate of the device (Fig. 1) is excited by piezoelectric elements performing shear deformation. Without fluid this results in a bending mode, that can be described as the zeroth antisymmetrical Lamb mode. The fluid layer has only a small influence on this mode, so that for an appropriate estimation of the dispersion relation the dispersion curves for Lamb waves can be used.[11] A shorter wavelength results when the frequency is increased. For a one millimeter thick glass plate, as was used in the device, the wavelength is between two and one millimeter for a frequency range between one and three megahertz, respectively.

III. EXPERIMENTAL RESULTS

In this section the experimental results are presented. This includes four principles by which particles can be displaced. For the experiments the device shown in Fig. 1(b) was used. Either one or two piezoelectric elements were driven with a frequency between 1 and 3 MHz. The amplitude of the driving signal was approximately 30 V_{rms}. Some of the results were recorded; the AVI-videos can be reached via the webpage http://www.zfm.ethz.ch/alumni/haake/publications/jasa/ or via the EPAPS homepage.[12]

A. Experimental setup

The full experimental setup (Fig. 3) is situated on a vibration isolation table to isolate it from the vibration of the building. The device [of Fig. 1(b)] is mounted on a positioning system, so that it can be moved in all three orthogonal directions. The basin containing the liquid is positioned on a translation stage, so that it can be raised upward to the device. An object slide with the particles containing the fluid is placed in the basin. The device can be observed with a microscope and images can be made using a CCD camera.

The instruments used for micromanipulation and the way in which they are connected can be seen in Fig. 3(a). The function generator 1 (Krone Hite, KH5920) produces a signal of defined frequency and amplitude. This signal is amplified (amplifier ENI 2100L) and then applied to the piezoelectric elements of the device. The particles can be observed with a microscope (Olympus ZSH; objectives DF PLAN 0.5X, DF PLAN 0.75X and DF PLAN 2X; camera adapter NFK 2.5X LD and NFK 5X LD) and with a CCD

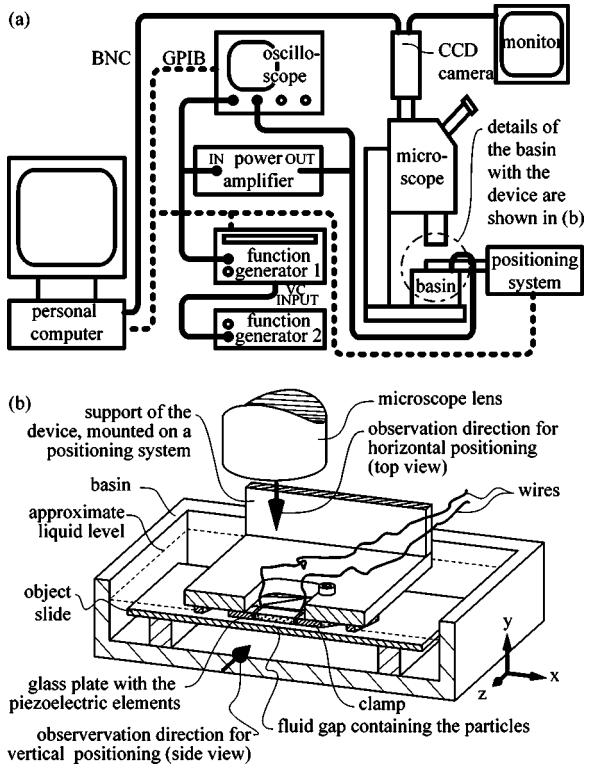

FIG. 3. Diagram of the experimental setup for the micromanipulation (a). The excitation signal comes from the function generator 1 and is amplified before being applied to piezoelectric elements. The particles are observed with a microscope and with a CCD camera images can be stored on the PC. The device and the particles are located in the basin (b). The figure shows the arrangement of the device and the object slide. The particles are located in the gap between the two. The device is mounted to a positioning system, so that it can be positioned in all three directions.

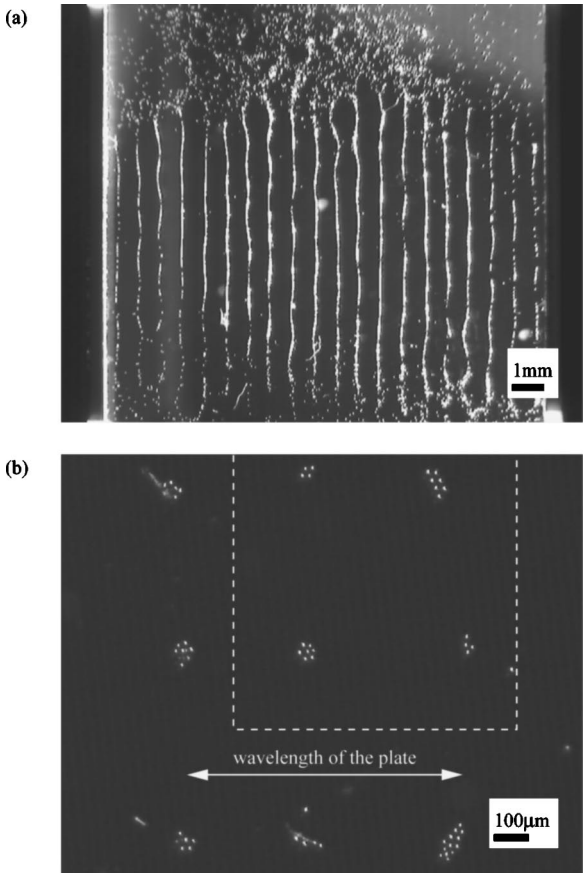

FIG. 4. Top view of the two- (a) and three-dimensional (b) concentration of particles caused by a one- and two-dimensional vibration of the plate, respectively. In the upper part of image (a) the force field is too weak to position the particles so they are still in their initial positions.

camera (Sony CCD-IRIS, Model SSC-M370CE). The camera was connected to a monitor and to a PC frame grabber card (Newport, PC-IMAQ 1408). Thus, it was possible to save images and video sequences of images on the PC. The excitation voltage was measured with an oscilloscope (LeCroy, LC3944 CM; probe PP002). The function generator 2 (Stanford Research, DS345) is only used for the frequency ramping experiments. It generates a slowly rising DC voltage that is connected to the VC input (voltage control) of the function generator 1.

The particles are manipulated in the fluid filled gap between the device and an object slide. Figure 3(b) shows the detail of this part of the experimental setup. The clamp holding the device is screwed to a support that is mounted on a positioning system (Newport, MM4006, three translatory axes). Thus it is possible to move the device in all three orthogonal directions relative to the object slide. The alignment of the device and the object slide can be adjusted independently (not shown in the figures). During the experiments the device and the clamp were immersed approximately 0.5 mm into the liquid that filled the basin. The level of the liquid is marked in the figure with a dashed line. The wire from the piezoelectric elements are connected to the amplifier via a BNC cable. The ground of the BNC cable is connected to the clamp that is in contact with the outer electrodes of the piezoelements.

B. Tracing the force field

The shape of the force field that appears in the fluid gap can be traced by the patterns that particles form, which are suspended in the fluid. Figure 4 shows two photographs of such patterns of polymer particles with a diameter of 26 μm. In Fig. 4(a), almost the whole glass plate can be seen with the left and right piezoelectric elements (the black bar at the left and right edge), the upper and lower piezoelectric elements are not on the image. The photograph of Fig. 4(a) was taken as the right piezoelectric transducer was driven with a frequency of 1 MHz. The spacing of two of the lines complies with half of the wavelength of the plate vibration. These lines agree with the prediction of the force field, as illustrated in Fig. 2(a); each cross at the reflecting surface at $y=0$ (two per horizontal wavelength λ_{Fx}) represents one of the lines in Fig. 4(a).

The two-dimensional alignment of particles is achieved by simultaneously driving two of the piezotransducers at adjacent edges of the glass plate with the same frequency. Each of them excites a quasi-one-dimensional standing wave perpendicular to the other. As can be seen in Fig. 2(b), there are four points in a rectangle of the size $\lambda_{Fx}\times\lambda_{Fz}$ where the force potential has a minimum and particles are collected. Nine of these points can be seen in Fig. 4(b). The edges of the dashed rectangle are one wavelength long; this rectangle symbolizes the same region over which the force field was

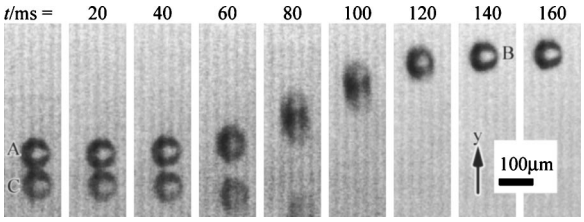

FIG. 5. Sequence of images of a particle lifted up by the force field in the fluid gap (side view, see Fig. 1). The images were separated by a delay of 20 ms. At the beginning the sound field was off, the particle is in position A (C is the mirror image). The power was turned on at $t=20$ ms and the particle raised to a position 300 μm above to position B. The images are taken from a video sequence [see VideoFig5.avi (Ref. 12)].

plotted in Fig. 4(b). Single particles would be aligned in points. When there are many particles, they cannot be concentrated in one point, instead they will be aligned in the regions of the smallest force potential. The clump of particles in the two right corners are aligned at 45°, which agrees with the theory as the minimum of the force potential is surrounded by oval shaped isolines at 45° [Fig. 2(b)].

C. Displacement of particles

1. Vertical displacement

It is possible to lift up particles from the object slide using forces produced by the sound field. Particles jump to the first equilibrium position above the slide [see the cross marked with a "B" in Fig. 2(a)] when the sound field is turned on. To do so the particle has to be placed there where the force potential has a maximum [position "A" in Fig. 2(a)]. This seems to contradict the theory, which stated that there is no vertical force at the reflecting surface at $y=-h$. However, the force on the particle at $y=-h$ (directly at the surface) is more complicated than Eq. (5) indicates (diffusion, acoustic streaming, influence of the boundary, etc.) and needs to be further investigated. If this acoustic force is greater than the weight and the contact forces this causes the particle to be lifted up. Figure 5 shows a sequence of nine images of a particle (diameter 76 μm) with an interval of 20 ms (the images are taken from the video VideoFig5.avi[12]). At the beginning the particle (A) was placed on an object slide [the mirror image can also be seen (C)]. The sound field was turned on at $t=2$ ms and it took the particle 120 ms to rise to a position 300 μm above (B). The particle was stable at the upper position. It dropped down as the sound field was turned off and could be lifted up if the sound field is turned on again.

Measurements of the maximum speed of the particle (by analyzing the video VideoFig5.avi[12] taken with the microscope camera; see Fig. 5) and the comparison with the drag force, according to Stokes law, appearing in the fluid allowed the force acting on the particle to be measured. To determine the force the velocity is taken where it is at a maximum and as such the acceleration zero. At this instance there are four forces that have to be taken into account. The equilibrium of forces in vertical direction is $F_y+F_B=F_S+F_G$, where F_y is the vertical acoustic force, $F_G=4/3\pi r_S^3\rho_S g$ the weight, $F_B=4/3\pi r_S^3\rho_F g$ the buoyancy, and $|F_S|=6\eta\pi|\nu|r_S$ the viscous force according to the Stokes law. This leads to

$$F_y=6\eta\pi|\nu|r_S+\frac{4}{3}\pi r_S^3(\rho_S-\rho_F)g, \tag{12}$$

where ν is the vertical speed of the particle taken from the video sequence, $r_S=37$ μm is the radius of the particle, $\rho_S=1050\,\mathrm{kg/m^3}$ is the density of the particle (polymer), $\eta=0.001\,\mathrm{N/m^2\,s}$ is the viscosity of the fluid (water) and $\rho_F=998\,\mathrm{kg/m^3}$ is the density of the fluid. In the experiments forces between 2.9×10^{-9} N and 3.3×10^{-9} N with an average value of 3.2×10^{-9} N were measured.

An alternative way to estimate the force acting on the particles, is to deduce it from the theoretically calculated sound field. The surface displacement of the vibrating plate u_{Sf0} was measured with a laser interferometer to be 10 nm in amplitude. The thickness of the fluid gap was $h=2.25\times10^{-3}$ m. The wavelength of the plate vibration λ_{SF} at a frequency of 1.2 MHz is of the order of 2 mm. The vertical force F_y is according to Eq. (5) is

$$F_y=U_0k_{Fy}\sin(2(h+y)k_{Fy})\left\{\frac{f_1}{3}k_F^2\cos^2(xk_{Fx})+\frac{f_2}{2}(-k_{Fx}^2\sin^2(xk_{Fx})+k_{Fy}^2\cos^2(xk_{Fx}))\right\}, \tag{13}$$

with $U_0=0.352\times10^{-18}\,\mathrm{N\,m^3}$. For $x=0$, Eq. (13) becomes (with $f_1=0.9449$ and $f_2=0.03357$) $F_y=12\times10^{-9}\sin(8012(h+y)(1/m))$ N. The maximum vertical force $F_{y\,\max}$ is then 12×10^{-9} N.

There is a deviation of a factor 4 between the two results (the video sequence of Fig. 5 and the calculated value using the measured surface displacement of the plate). This is because of simplifications made in the modeling approach and the fact that damping was not taken into account. However, both results have the same order of magnitude with the force being in the nanoNewton range.

2. Horizontal displacement

In the next paragraphs three methods to displace particles are introduced. The experimental setup is the same as that described above. The three principles are sketched in Figs. 6(b)–6(d). The initial setup is shown in Fig. 6(a).

a. Displacement of the full device The easiest way is to move the device with respect to the reflecting surface and to keep the operational parameters such as frequency and amplitude constant. This principle is shown in Fig. 6(b). For these experiments, the device was mounted on a positioning table so that it can be moved continuously in the horizontal direction. In order to displace the particles, the sound field was first turned on so that the particle moved to their equilibrium position in the force field [point "A" in Fig. 6(a)]. The device was then displaced horizontally, with the particle following the movement of the device. Figure 7 shows a sequence of images of such an experiment (the images are taken from the VideoFig7.avi[12]). The initial arrangement of the particles can be seen in the upper image (a). To highlight the movement of the particles, six photographs at intervals of 0.8 s were superimposed upon each other in the lower image (b). This illustrates how the particles move their position relative to the initial position. The device was moved 200

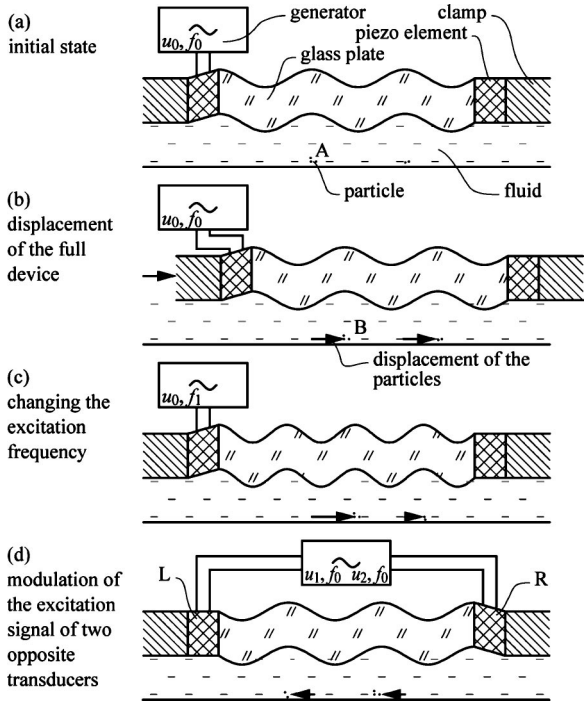

FIG. 6. Three displacement principles. The initial position is shown in the topmost figure (a). One method is to move the device (b). The particles have a fixed position relative to the device due to the force field and will follow that movement. Another possibility is to change the frequency (c). As the wavelength of the plate vibration varies as a function of the frequency, and the particles are collected at fixed positions with respect to the nodes and antinodes of the vibration, the particles can be moved by altering the drive frequency. A further principle is to excite the plate vibration with two piezoelectric elements (d). By varying the amplitude of the two excitation signals it is possible to change the positions of the nodes and antinodes of the plate vibration and the particles will follow that change.

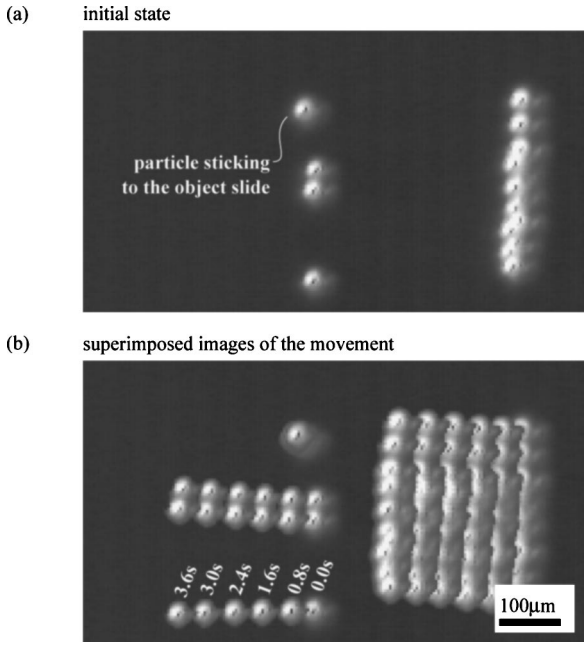

FIG. 7. The images show (top view, see Fig. 1) how particles are displaced when the device is moved. At the top (a) the initial state can be seen. In the image below (b) six photographs, taken 0.8 s after each other, are superimposed on top of each other. The particles follow the leftward directed movement of the device over a range of 200 μm [see VideoFig7.avi (Ref. 12)].

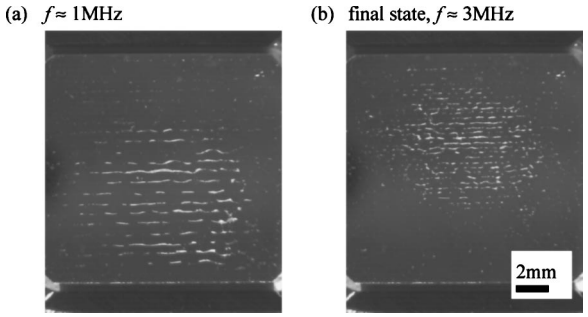

FIG. 8. The images demonstrate (top view; see Fig. 1) how particles are displaced over a long range with a frequency sweep from 1 MHz (a) to 3 MHz (b). [See VideoFig8.avi (Ref. 12)].

μm with a speed of 50 μm/s to the left. One of the particles stuck to the object slide and was not moved at all. One effect that might influence or even disturb the controlled movement is the drag force on a particle. Due to the viscosity of the fluid, there is a small drag force acting on the particle. This can either be avoided by a slower movement of the device or by a larger fluid gap. To check whether the change in position was caused by the sound field, and not, for example, by drag forces, the experiment was repeated without a sound field. Under such conditions the particles are not expected to move (VideoFig7.avi[12]). One problem of this method is that the shape of the sound field changes while the device is displaced. This can cause a change in the force field and consequently unwanted movement of the particles.

b. Frequency pamping Now a method will be introduced that avoids the relative movement between the device and the reflecting surface and is capable of larger movement. The wavelength of the plate vibration diminishes with increasing frequency. This behavior can be used to displace particles over a distance of some millimeters by changing the frequency continuously. The particles will be collected according to vibration modes of the glass plate with diminishing wavelength when the device is driven with an increasing frequency, as illustrated in Fig. 6(c). The experimental results can be seen in Fig. 8 (the images are taken from the video VideoFig8.avi[12]). The left image (a) shows the state after the sound field is excited at 1 MHz. The ramping of the frequency takes 25 s and ends at 3 MHz. This state can be seen in the right image (b). The particles moved into the upper region of the device. To concentrate the particle further the procedure can be repeated many times (not shown). What cannot be seen in the two images is that the movement is not continuous. Sometimes during the ramping the lines formed by the particles rest, jitter a bit and exchange particles with the next line and then suddenly the lines start moving and come closer to each other (VideoFig8.avi[12]). This behavior makes this method unsuitable for some applications where a smooth motion is necessary. But this method can be used when particles need to be concentrated or displaced over a large distance of many millimeters.

c. Superposition of two standing waves Now a method is introduced to position particles in the micrometer range by modulation of the plate vibration, without displacing the device. If the displacement of the surface of the plate is described by $u_{P1}=u_{P10}\sin(\alpha_{P1}+xk_{P1})e^{i\omega t}$, the nodes and anti-

nodes will change in the x direction if α_{P1} is changed. The principle of the modulation of the plate vibration can be seen in Fig. 6(d). The plate vibrations excited by two opposing transducers (''L'' and ''R'') are superimposed because of the linearity of the vibrating system. There are many possibilities to vary the parameters of the vibration with two transducers. The vibration modes of the glass plate are determined by the geometrical shape, the mechanical properties, and the excitation. An easy way to influence the vibration modes is to change the amplitude by operating the transducer with a signal of varying magnitude. Voltages of the same frequency and phase but different amplitudes are applied to two transducers (''L'' and ''R'') at opposite ends of the glass plate, using a voltage divider.

If the two piezoelectric transducers at the opposite ends are driven simultaneously with the same frequency [Fig. 6(d)] the vibrations excited by each of the transducers superimpose to a resulting vibration mode. For the following analysis it is assumed that the displacement of the surface of the plate excited by the left and right transducer can be described by $u_L = L\sin(\alpha_L + k_{P1}x)e^{i\omega t}$ and $u_R = R\sin(\alpha_R + k_{P1}x)e^{i\omega t}$, respectively, with k_{P1} being the wave number. L and R are the amplitudes and can be changed by varying the amplitude of the excitation signal. α_L and α_R define the spatial phase shift (the location of the nodes and antinodes); they are given by the parameters of the setup (e.g., geometry, material, excitation frequency) and cannot be changed easily if the frequency stays constant. The resulting plate vibration u_{P1} is given by the superposition of the two vibrations, each excited by the left and right piezotransducer, respectively, $u_{P1} = u_L + u_R$. For the following calculation $e^{i\omega t}$ will be omitted, as it appears in each of the components. The vibration of the plate is then given by

$$u_{P1} = L\sin(\alpha_L + k_{P1}x) + R\sin(\alpha_R + k_{P1}x) = u_{P10}\sin(\alpha_{P1} + xk_{P1}), \tag{14}$$

with

$$u_{P10} = \sqrt{L^2 + R^2 + 2LR\cos(\alpha_L - \alpha_R)} \tag{15}$$

and

$$\alpha_{P1} = \arctan\frac{L\sin\alpha_L + R\sin\alpha_R}{L\cos\alpha_L + R\cos\alpha_R}. \tag{16}$$

The resulting vibration u_{P1} has the same wavelength as the two initial vibrations. The angle α_{P1}, which defines the position of the nodes and antinodes of the resulting vibration, depends on the variable parameters L and R. However, a condition that α_{P1} is a function of L and R is that $\alpha_L \neq \alpha_R$ and $\alpha_L \neq \alpha_R + \pi$. If, for example, $\alpha_L = \alpha_R$, Eq. (16) reduces to $\alpha_{P1} = \alpha_R$. The amplitude of the resulting vibration u_{P10} is also a function of α_L and α_R. The theoretical analysis in this section is only an approximation, as the displacement amplitude of the plate cannot be described by a simple sine function; for example the amplitude will decrease toward the edges. Also, transducer coupling needs to be considered.

The effect described in the previous paragraph can be used to displace particles, as they are concentrated at fixed positions relative to the nodes and antinodes of the plate vibration. By increasing the amplitude of one of the two excitation signals (e.g., for transducer ''L'') from zero to maximum (the amplitude L goes form 0 to $u_{\max}$) and reducing the amplitude at the opposite piezoelectric element (transducer ''R'') from maximum to zero (the amplitude R goes form $u_{\max}$ to 0) using a voltage divider, the sound field can be switched stepwise or continuously between the sound fields excited by the two transducer alone. The maximum possible displacement is then approximately given by the distance of the lines that the particles form when each of the transducers is driven alone. The consequence for the experiments is that an excitation frequency should be chosen, where the nodes of the two initial vibrations (described by α_L and α_R), excited by each of the two transducers ''L'' and ''R,'' have a certain offset. Consequently, a necessary condition is that the two initial vibrations, each excited by one of the piezoelectric elements alone, are spatially not in phase or do not have a spatial phase shift of half a wavelength. If this were the case it would only be possible to change the amplitude of the resulting vibration, but not the position of the nodes and antinodes.

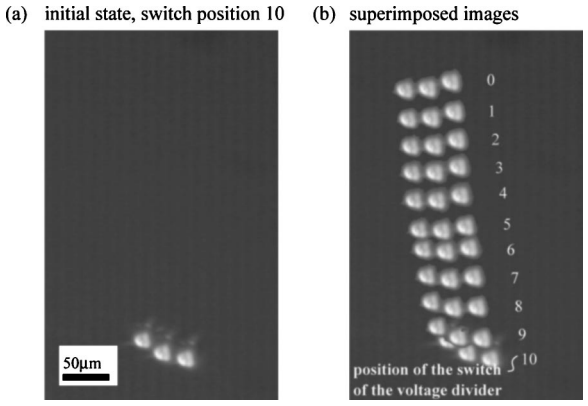

FIG. 9. The images show (top view; see Fig. 1) how particles are displaced when two opposite transducers are excited with varying amplitude. On the left (a) the initial state can be seen. In the right image (b) 11 photographs, each taken for one specific setting of the voltage at the two transducers, are superimposed on top of each other. The particles were moved by approximately 300 μm [see VideoFig9.avi (Ref. 12)].

To apply voltages of the same frequency and phase but different amplitude to each of the two transducers, a voltage divider was used. The voltage divider consists of two mechanically coupled turn switches, each with 11 positions labeled from 0 to 10, and 20 Ohmic resistors. It has one input connector (from the power amplifier) and two output connectors, one for each of the opposing piezoelectric elements. For example, for the positions 0, 3, and 10 of the turn switch the voltage at the one of the outputs (connected to the bottom transducer) is 0, 0.3, and 1 times the input voltage and 1, 0.7, and 0 times the input voltage at the other output (connected to the top transducer), respectively.

Figure 9 shows three particles that are positioned by this method (the images are taken from the video VideoFig9.avi[12]). In the left image (a) the initial stage is displayed. The right image (b) is made by superimposing 11 images into 1, each belonging to one position of the voltage divider from 10 to 0. At the beginning the switch of the voltage divider was at position 10 and was then turned step

by step to position 0. While turning the switch the particles changed their location from the bottom to the top. In the video VideoFig9.avi[12] the backward movement can also be seen. This shows that it is possible to switch discretely between the sound field that is excited by two transducers at opposite ends of the vibrating plate. The whole displacement was 300 μm and the wavelength of the plate vibration was 2 mm. For this experiment a discrete voltage divider was used but it is also possible to work with an analog one.

IV. CONCLUSION

The technical implementation of a novel ultrasonic micromanipulation method has been introduced, modeled, and experimentally verified. The developed device has a simple design implementing fundamental acoustic principles in a new way, and it is easy to operate. The sound field in the fluid layer concentrates particles in patterns that are predicted by a theoretical model. Furthermore, it was possible to displace particles in the micrometer range using three methods. The accuracy of these displacements was limited by nonuniformities of the sound field. However, it is expected that these nonuniformities can be minimized by a further development of the device and especially by miniaturization.

The method and the presented device proved their ability to position and displace particles either individually or as ensembles. Applications are seen mainly in two fields: microtechnology and life sciences. The field of microtechnology demands methods to handle small particles carefully. The positioning and the displacement of microparts using this method is straightforward. In addition, a few particles can be levitated and concentrated in single points. Attractive forces (secondary forces) might be used for self-assembly.

Life sciences is a field with increasing importance. For example, a particle such as a single cell, can be levitated in a fixed position in the sound field. By applying a fluid flow with a changing chemical composition along the length of the chamber with the fixed cell, it is possible to let the particle or cell react with many substances in succession. Also, various feeding devices (see Ref. 13) could be used to bring individual particles to desired locations in a controlled way.

[1] M. Gröschl, ''Ultrasonic separation of suspended particles—Part I: Fundamentals,'' Acustica **84**, 432–447 (1998).
[2] T. Kozuka, T. Tuziuti, H. Mitome, and T. Fukuda, ''Control of a standing wave field using a line-focused transducer for two-dimensional manipulation of particles,'' Jpn. J. Appl. Phys., Part 1 **37**, 2974–2978 (1998).
[3] J. R. Wu, ''Acoustical tweezers,'' J. Acoust. Soc. Am. **89**, 2140–2143 (1991).
[4] L. V. King, ''On the acoustic radiation pressure on spheres,'' Proc. R. Soc. London, Ser. A **147**, 212–240 (1934).
[5] K. Yosioka and Y. Kawasima, ''Acoustic radiation pressure on a compressible sphere,'' Acustica **5**, 167–173 (1955).
[6] L. P. Gorkov, ''On the forces acting on a small particle in an acoustic field in an ideal fluid,'' Sov. Phys. Dokl. **6**, 773–775 (1962).
[7] X. C. Chen and R. E. Apfel, ''Radiation force on a spherical object in the field of a focused cylindrical transducer,'' J. Acoust. Soc. Am. **101**, 2443–2447 (1997).
[8] H. J. Simpson and P. L. Marson, ''Ultrasonic four-wave mixing mediated by an aqueous suspensions of microspheres: Theoretical steady-state properties,'' J. Acoust. Soc. Am. **98**, 1731–1741 (1995).
[9] L. A. Crum, ''Bjerknes forces on bubbles in a stationary sound field,'' J. Acoust. Soc. Am. **57**, 1363–1370 (1975).
[10] W. L. Nyborg, ''Microsonation of cells under near-threshold conditons,'' Int. Con. Ser. **309**, 360–365 (1973).
[11] A. Haake and J. Dual, ''Positioning of small particles by an ultrasound field excited by surface waves,'' Ultrasonics **42**, 75–80 (2004).
[12] See EPAPS Document No. E-JASMAN-117-051504 for downloadable files containing the AVI movie animations. This document can be reached via a direct link in the online article's HTML reference section or via the EPAPS homepage (http://www.aip.org/pubservs/epaps.html).
[13] D. Baechi, R. Buser, and J. Dual, ''A high density microchannel network with interated valves and photodiodes,'' Sens. Actuators, A **95**, 77–83 (2002).

Influence of viscosity on the diffraction of sound by a periodic array of screens

Dorel Homentcovschi,[a] Ronald N. Miles, and Lin Tan
Department of Mechanical Engineering, SUNY Binghamton, New York 13902-6000

(Received 27 January 2004; revised 12 January 2005; accepted 8 February 2005)

The paper contains an analysis of the transmission of a pressure wave through a periodic grating including the influence of the air viscosity. The system of equations in this case consists of the compressible Navier–Stokes equations associated with no-slip boundary conditions on solid surfaces. The problem is reduced to two hypersingular integral equations for determining the velocity components along the slits. These equations are solved by using Galerkin's method with some special trial functions. The results can be applied in designing protective screens for miniature microphones realized in the technology of micro-electro-mechanical systems (MEMS). In this case, the physical dimensions of the device are on the order of the viscous boundary layer so that the viscosity cannot be neglected. The microfluidic model of the screen consists of a periodic array of slits in a substrate. The analysis indicates that the openings in the screen should be on the order of 10 μm in order to avoid excessive attenuation of the signal.
[DOI: 10.1121/1.1882923]

PACS numbers: 43.28.Py, 43.38.Kb [ADP] Pages: 2761–2771

I. INTRODUCTION

The reflection and transmission of a scalar plane wave through a periodic grating is a classical problem of acoustics. Thus, Lamb[1] succeeded in obtaining analytical formulas for the reflection and transmission coefficients in the low-frequency range for normal incident waves; Miles[2] obtained a one-mode approximation for small screens, in the case of oblique incidence. Achenbach and Li[3] developed a method that is appropriate for arbitrary frequencies and angles of incidence. They used a representation of the solution as an integral over the length of a screen. Finally, we mention the results in Ref. 4, where explicit analytical formulas are given for the reflection and transmission coefficients in one-mode, oblique incidence penetration.

The inclusion of viscous effects in acoustics is a subject not very often approached. The book by Pierce[5] contains a chaper discussing the dissipative processes devoted especially to explain attenuation of sound waves. Davis and Nagem, in Ref. 6, have investigated the problem of diffraction by a half plane studying the behavior of fluid velocity near a diffracting edge. The same authors analyzed, in Ref. 7, diffraction of an acoustic plane wave by a circular aperture in a viscous fluid.

The viscous dissipative processes are described by a constitutive relationship between shear stress and rate of shear involving the shear viscosity μ and the bulk viscosity μ_B. The bulk viscosity takes into account the departure of the kinematic mode of molecular motion from mutual thermodynamic equilibrium. By assuming a Newtonian constitutive relationship, the momentum equations yield the Navier–Stokes system corresponding to a compressible fluid. In the case of isentropic flow and constant viscosity (μ), the system decomposes into an acoustical (propagational) mode and a vorticity (viscous) mode. The vorticity mode dies out rapidly with increasing distances from boundaries, interfaces, and sources. Therefore, in the bulk of the atmosphere, the velocity and the pressure fields are described mainly by the propagating mode.

A simple calculation shows that the viscous mode gives, along a solid boundary, a viscous boundary layer of thickness $t_{\text{visc}}=\sqrt{\mu/(\pi f\rho)}$ (f denotes the frequency and ρ the density)[5] which has the value 223 μm at 100 Hz and 22.3 μm at 10 KHz. In the case of miniature silicon microphones, realized in MEMS technology, the linear dimensions of the device are of the order of 1 mm. Hence, the viscous boundary layer cannot be neglected anymore in determining the disturbance of the sound waves by the microphone parts. As an example, we consider the influence of a protecting system, consisting of a plane surface containing a periodic system of parallel slits (a horizontal periodic grating), placed in front of the diaphragm. This analysis is important since we are interested in protective surfaces having small holes, which will avoid the penetration of water and dust particles to the diaphragm surface. It is clear that for very narrow slits the transmission coefficient is small. Therefore, we have to find an optimum dimension of the holes which enables the penetration of the sound and at the same time does not allow the penetration of water and dust particles.

In Sec. III we give representation formulas for the pressure and velocity fields in the upper and lower half planes. The incoming wave is considered as a pressure wave characterized by the angle θ_0. As the attenuation of the sound waves in air is very small, we neglect it in the incoming plane wave and in the propagating modes. This is why, despite the viscous dissipation, we continue to use the Sommerfeld condition for selecting the proper waves in each case. The representation formulas for the scattered and transmited

[a]Permanent address: Polytechnica University & Institute of Mathematical Statistics and Applied Mathematics of Romanian Academy, Calea13 Septembrie #13, RO-76100, Bucharest, Romania. Electronic mail: homentco@binghamton.edu

pressures contain an infinite number of wave modes, each with its cutoff frequency. At the cutoff frequency, a mode converts from an evanescent mode into a propagating wave mode. At small frequences only the lower-order modes are propagating. As the frequency is increasing, more and more evanescent modes convert to propagating modes. In the case of acoustical frequences in air, only the lowest mode is propagating. This is the case we are considering in this paper. The case when other modes are also propagating can be analyzed similarly. By using the momentum equations we obtain representation formulas for velocities. These contain, besides the above-discussed modes, some viscous (vorticity) modes which are decaying exponentially with the distance to the perturbation sources.

Next, we consider as main unknown functions the velocity components along the slits. The advantage, as compared with the approach in Ref. 3, where the unknown function is related to the pressure on the screens, is that the final integral equations are simpler. All the coefficients entering into representation formulas can be determined in terms of Fourier coefficients of the velocity components on the slits. Now, the condition of continuity of velocity and its normal derivative along the slits furnishes the functional equations for solving the problem. There is one such equation for each of the velocity components. As these equations contain some divergent Fourier series, they can be interpreted properly only within distribution theory. Further on, we succeeded in transforming the distributional equations into hypersingular integral equations. The singular part of both equations is the same; the weak singular parts differ by a multiplicative constant and the regular parts contain continuous functions resulting from summing some uniform convergent Fourier series.

In Sec. V we developed a method for solving the hypersingular integral equations based on the representation of solutions in terms of a basis of functions, given by some Chebyshev functions, and using also the convenient form of the convolution equations in the spectral domain. With a Galerkin technique we succeeded in obtaining an infinite system of linear equations for each of the integral equations. The systems have good computational properties. Thus, the coefficients of the equations result from using the spectral properties of the singular operators, the FFT transform of some smooth functions (realized in fact by using the 2D discrete cosine transform of MATLAB), and the summation of some fast convergent infinite series. The finite sections of the final systems are well conditioned such that we need only a small number of terms to obtain a solution with good precision.

Section VI contains some numerical results. We computed the transmission coefficient for certain geometries important in designing miniaturized microphones. We applied the same mathematical technique to the classical (nonviscous) acoustical periodic grating problem. The results are also given in Sec. VI for comparison. We note that the numerical results obtained in the nonviscous case coincide with those calculated by Ref. 4. The graphs show that for very small slit width the influence of viscosity is very important.

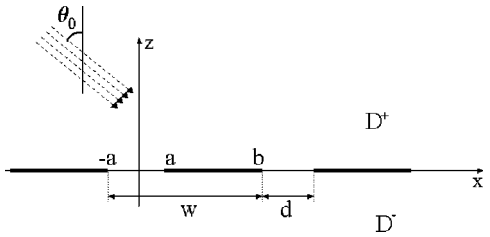

FIG. 1. The geometry of the problem.

The graphs provided can be used in designing of microphones realized in MEMS technology.

Finally, in the Appendix we give the most important formulas used in calculation of the spectral form of singular integral operators and also of the regular parts of the integral equations.

II. THE EQUATIONS OF THE PROBLEM

A. Formulation of the problem

Let us consider the penetration of a pressure wave through the array of coplanar rigid screens located at $z=0$ in Fig. 1. The screens are infinitely long in the y direction. The opening between two neighboring screens is $2a$ and the period of the grating is $T=a+b$. We denote by $\mathcal{D}^+$ the upper half plane ($z>0$) and by $\mathcal{D}^-$ the half plane $z<0$. The incident wave is located in the domain $\mathcal{D}^+$ and its propagation vector makes an angle $\theta_0-\pi$ with the z axis.

There are two periodic phenomena in this problem: one is associated with the acoustical incoming wave and the other one with the grating periodicity. To avoid possible confusions we associate a "*" with the quantities related to the acoustical incoming wave (k^* is the spatial frequency wave number of the plane incoming wave and ω^* its angular frequency). The "nonstarred" quantities T and $\omega=2\pi/T$ are the spatial period of the grating and its corresponding spatial frequency, respectively.

B. The equations of the motion of a compressible viscous fluid

The isentropic motion of a viscous fluid is described by the continuity equation

$$\frac{\partial \rho}{\partial t}+\nabla\cdot(\rho\mathbf{V})=0, \tag{1}$$

and the momentum equation

$$\rho\left(\frac{\partial}{\partial t}+\mathbf{V}\cdot\nabla\right)\mathbf{V}+\nabla\cdot\sigma=\mathbf{0}. \tag{2}$$

Here, by $\mathbf{V}$ we denote velocity, ρ is density, and the stress tensor σ has the components

$$\sigma_{ij}\equiv\sigma_{ij}[P,\mathbf{V}]=\left[P-\left(\mu_B-\frac{2}{3}\mu\right)\nabla\cdot\mathbf{V}\right]\delta_{ij} -\mu\left(\frac{\partial V_i}{\partial x_j}+\frac{\partial V_j}{\partial x_i}\right). \tag{3}$$

Also, μ and μ_B are the shear and bulk viscosities[5] and P the pressure.

Also, in the case of isentropic flow the density is a function of pressure alone such that the state equation can be expressed as

$$\rho = \rho(P). \tag{4}$$

For a viscous fluid we have the nonslip boundary condition

$$\mathbf{V}(\mathbf{x},t) = \mathbf{0}, \tag{5}$$

on any immobile solid surface.

In the case of inviscid (nonviscous) model of fluid, the viscosities μ and μ_B have to be considered zero in (3); also, the boundary condition (5) is replaced by the nonpenetration condition

$$V_n(\mathbf{x},t) = 0, \tag{6}$$

stating the cancellation of normal component of velocity on any immobile solid surface.

Besides this, we will impose that all the propagating perturbations, except for the incoming plane wave, are outgoing waves (*Sommerfeld radiation condition*).

C. The equations of the motion of a viscous fluid in linear acoustic approximation

In the case where the coordinate system is chosen so that the unperturbed fluid is at rest, the first-order equations describing the motion of the gas can be written as[8,5]

$$\frac{1}{c_0^2}\frac{\partial}{\partial t}\frac{p'}{\rho_0} + \nabla\cdot\mathbf{v}' = 0, \tag{7}$$

$$\frac{\partial \mathbf{v}'}{\partial t} + \nabla\left[\frac{p'}{\rho_0} - (\nu' - \nu)\nabla\cdot\mathbf{v}'\right] - \nu\Delta\mathbf{v}' = \mathbf{0}, \tag{8}$$

where p' and $\mathbf{v}'$ denote the pressure and velocity perturbations, respectively, and

$$\nu = \frac{\mu}{\rho_0}, \quad \nu' = \frac{\mu_B}{\rho_0} + \frac{4\mu}{3\rho_0},$$

are the kinematic viscosities.

We consider the case where all the physical variables are harmonic in time with the same angular velocity, $\omega^* = 2\pi f$. The case of general time dependence can be obtained, after analyzing each frequency separately, by Fourier superposition. In the case of simple harmonic oscillations in time, we shall write

$$\{p'(\mathbf{x},t), \mathbf{v}'(\mathbf{x},t)\} = \{p(\mathbf{x}), \mathbf{v}(\mathbf{x})\}\exp(-i\omega^* t).$$

In this case the continuity equation (7) becomes

$$\nabla\cdot\mathbf{v} = \frac{i\omega^*}{c_0^2}\frac{p}{\rho_0}. \tag{9}$$

Also, the momentum equation can be written as

$$\Delta\mathbf{v} + \frac{i\omega^*}{\nu}\mathbf{v} = \frac{1 + (\nu - \nu')i\omega^*/c_0^2}{\nu}\nabla\frac{p}{\rho_0}. \tag{10}$$

The relationships (9) and (10) give the equation for the pressure

$$[\Delta + k^{*2}]p = 0. \tag{11}$$

Here, we have used the notations

$$k^* = \frac{\omega^*}{\sqrt{c_0^2 - i\omega^*\nu'}}, \quad \mathrm{Im}(k^*) \leqslant 0.$$

Equations (10) and (11) yield the equation for velocity in the form

$$[\Delta + k^{*2}]\left[\Delta + \frac{i\omega^*}{\nu}\right]\mathbf{v} = 0. \tag{12}$$

Equation (12) is in fact the product of two operators. Consequently, the solution can be written as a sum of two terms: the first describes a propagation mode (called also the acoustical mode) and the second is a diffusion mode driven by viscosity.

III. THE REPRESENTATION FORMULAS FOR THE PRESSURE AND VELOCITY FIELDS

Let us consider now an incoming pressure plane wave in $\mathcal{D}^+$

$$p^0(x,z)/\rho_0 = c_0^2\exp\{ik^*(x\sin\theta_0 - z\cos\theta_0)\}. \tag{13}$$

It can be verified directly that (13) satisfies the pressure equation (11) and the corresponding velocity field is $\mathbf{v}^0 = u^0(x,z)\hat{\mathbf{x}} + w^0(x,z)\hat{\mathbf{z}}$, where

$$u^0(x,z) = ik^*c_0^2\delta\sin\theta_0\exp\{ik^*(x\sin\theta_0 - z\cos\theta_0)\}$$

$$w^0(x,z) = -ik^*c_0^2\delta\cos\theta_0\exp\{ik^*(x\sin\theta_0 - z\cos\theta_0)\}.$$

We have denoted

$$\delta = \frac{1 + (\nu - \nu')i\omega^*/c_0^2}{i\omega^* - \nu k^{*2}}.$$

Then, we write

$$p(x,z) = \begin{cases} p^0(x,z) + p^+(x,z), & \text{in } \mathcal{D}^+ \\ p^-(x,z), & \text{in } \mathcal{D}^- \end{cases},$$

$$u(x,z) = \begin{cases} u^0(x,z) + u^+(x,z), & \text{in } \mathcal{D}^+ \\ u^-(x,z), & \text{in } \mathcal{D}^- \end{cases},$$

$$w(x,z) = \begin{cases} w^0(x,z) + w^+(x,z), & \text{in } \mathcal{D}^+ \\ w^-(x,z), & \text{in } \mathcal{D}^- \end{cases}.$$

The functions $p^\pm(x,z)$ satisfy Eq. (11) in the corresponding domains $\mathcal{D}^\pm$ and the functions $u^\pm(x,z)$, $w^\pm(x,z)$ are solutions of Eq. (10). Since the array of scatterers is periodic over the ox axis, the pressure and velocity fields can be written as

$$p^\pm(x,z) = \exp\{ik^*x\sin\theta_0\}\tilde{p}^\pm(x,z), \tag{14}$$

$$\mathbf{v}^\pm(x,z) = \exp\{ik^*x\sin\theta_0\}\tilde{\mathbf{v}}^\pm(x,z), \tag{15}$$

where $\tilde{p}^\pm(x,z)$ and $\tilde{\mathbf{v}}^\pm(x,z)$ are periodic functions with respect to x

$$\tilde{p}^\pm(x+T,z) = \tilde{p}^\pm(x,z),$$

$$\tilde{\mathbf{v}}^\pm(x+T,z) = \tilde{\mathbf{v}}^\pm(x,z).$$

Equation (11), taking into consideration the periodicity of the function $\tilde{p}^{\pm}(x,z)$, gives

$$p^{\pm}(x,z)/\rho_0 = P_0^{\pm}\exp\{ik^*(x\sin\theta_0 \pm z\cos\theta_0)\} + \sum_{n\neq 0} P_n^{\pm}\exp(ik_n x)\exp(\mp r_n z), \tag{16}$$

where

$$k_n = n\omega + k^*\sin\theta_0, \quad \omega = 2\pi/T,$$

$$r_n = \sqrt{k_n^2 - k^{*2}}, \quad \mathrm{Re}(r_n) > 0.$$

Thus, the scattered pressure field consists of a superposition of an infinite number of wave modes. For small frequences $[0 < k^*T/2 < \pi/(1-\sin\theta_0)]$ only the lowest-order mode is propagating; all the other modes describe waves which decay exponentially with the distance to the plane $z=0$. In writing the solution (16) we considered also the Sommerfeld radiation condition. The constants $P_n^{\pm}$ will be detemined by using the boundary conditions. In the case of the viscous fluid, these conditions are written by means of velocities.

To determine the representation formulas for the velocity field we use Eq. (10), where we introduce the form (16) for the pressure. Taking into consideration also the abovementioned periodicity results in

$$u^{\pm}(x,z) = \sum_{n=-\infty}^{\infty} u_n^{\pm}(x,z),$$

$$w^{\pm}(x,z) = \sum_{n=-\infty}^{\infty} w_n^{\pm}(x,z),$$

where

$$u_0^{\pm}(x,z) = ik^*\sin\theta_0\,\delta P_0^{\pm}\exp\{ik^*(x\sin\theta_0 \pm z\cos\theta_0)\} + \frac{H_0^{\pm}}{ik_0}\exp\{ik_0 x \mp q_0 z\},$$

$$w_0^{\pm}(x,z) = \pm ik^*\cos\theta_0\,\delta P_0^{\pm}\exp\{ik^*(x\sin\theta_0 \pm z\cos\theta_0)\} \pm \frac{H_0^{\pm}}{q_0}\exp\{ik_0 x \mp q_0 z\}, \tag{17}$$

$$u_n^{\pm}(x,z) = \frac{H_n^{\pm}}{ik_n}\exp\{ik_n x \mp q_n z\} + ik_n\,\delta P_n^{\pm}\exp\{ik_n x \mp r_n z\},$$

$$w_n^{\pm}(x,z) = \pm\frac{H_n^{\pm}}{q_n}\exp\{ik_n x \mp q_n z\} \mp r_n\,\delta P_n^{\pm}\exp\{ik_n x \mp r_n z\}. \tag{18}$$

The constants $H_n^{\pm}$ have to be determined by the boundary conditions. We have also denoted

$$q_n = \sqrt{k_n^2 - i\omega^*/\nu}, \quad \mathrm{Re}(q_n) > 0.$$

We note that naturally the solution for velocity has been decomposed into two parts: a propagating mode including the P terms and a diffusive mode, driven by viscosity, including the H terms.

IV. THE HYPERSINGULAR INTEGRAL EQUATIONS OF THE PROBLEM

Let us consider the functions

$$\tilde{u}(x) \equiv \tilde{u}^-(x,0) = \sum_{n=-\infty}^{\infty} \tilde{u}_n \exp(in\omega x), \quad x\in\mathbb{R} \tag{19}$$

$$\tilde{w}(x) \equiv \tilde{w}^-(x,0) = \sum_{n=-\infty}^{\infty} \tilde{w}_n \exp(in\omega x), \quad x\in\mathbb{R} \tag{20}$$

where the Fourier coefficients are given by the formula

$$[\tilde{u}_n, \tilde{w}_n] = \frac{1}{T}\int_{-T/2}^{T/2} [\tilde{u}(x), \tilde{w}(x)]\exp(-in\omega x)\,dx. \tag{21}$$

Since the velocity is vanishing on the rigid boundaries between the openings, the functions $\tilde{u}(x)$, $\tilde{w}(x)$ are different from zero only along the apertures. Due to periodicity, it is sufficient to determine them along the interval $(-a,a)$.

The continuity of the velocity across the apertures and screens yields also the relationships

$$u^0(x,0)\exp\{-ik^*x\sin\theta_0\} + \tilde{u}^+(x,0) = \tilde{u}(x), \tag{22}$$

$$w^0(x,0)\exp\{-ik^*x\sin\theta_0\} + \tilde{w}^+(x,0) = \tilde{w}(x), \tag{23}$$

valid along the whole axis. The relationships (19)–(23) allow us to determine the constants $P_n^{\pm}$ and $H_n^{\pm}$ in terms of the Fourier coefficients $\tilde{u}_n$ and $\tilde{w}_n$ as

$$P_0^+ = \frac{q_0\tilde{w}_0 - ik^*\tilde{u}_0\sin\theta_0}{iq_0\cos\theta_0 + k^*\sin^2\theta_0}\frac{1}{\delta k^*} + \frac{iq_0\cos\theta_0 - k^*\sin^2\theta_0}{iq_0\cos\theta_0 + k^*\sin^2\theta_0},$$

$$P_0^- = \frac{-q_0\tilde{w}_0 - ik^*\tilde{u}_0\sin\theta_0}{iq_0\cos\theta_0 + k^*\sin^2\theta_0}\frac{1}{\delta k^*},$$

$$H_0^+ = ik^*\tilde{u}_0\sin\theta_0 + \delta k^{*2}(1+P_0^+)\sin^2\theta_0,$$

$$H_0^- = ik^*\tilde{u}_0\sin\theta_0 + \delta k^{*2}P_0^-\sin^2\theta_0, \tag{24}$$

$$P_n^{\pm} = \frac{\pm q_n\tilde{w}_n - ik_n\tilde{u}_n}{\delta(k_n^2 - r_n q_n)}, \quad n\neq 0,$$

$$H_n^{\pm} = \frac{\pm k_n^2 q_n\tilde{w}_n - ik_n r_n q_n\tilde{u}_n}{k_n^2 - r_n q_n}, \quad n\neq 0.$$

To obtain the equations satisfied by the functions $\tilde{u}(x)$ and $\tilde{w}(x)$, we impose the condition of continuity of the normal derivative of velocity along the aperture

$$\frac{\partial u^0(x,0)}{\partial z}\exp\{-ik^*x\sin\theta_0\} + \frac{\partial\tilde{u}^+(x,0)}{\partial z} = \frac{\partial\tilde{u}^-(x,0)}{\partial z}, \quad x\in(-a,a), \tag{25}$$

$$\frac{\partial w^0(x,0)}{\partial z}\exp\{-ik^*x\sin\theta_0\} + \frac{\partial\tilde{w}^+(x,0)}{\partial z} = \frac{\partial\tilde{w}^-(x,0)}{\partial z}, \quad x\in(-a,a). \tag{26}$$

These "boundary relationships" will be associated with the boundary conditions along the screens

$$\tilde{u}(x)=0, \quad x\in(a,b),$$

$$\tilde{w}(x)=0, \quad x\in(a,b).$$

Taking the second primitive (indefinite integral) with respect to the x variable of the relationships (25) and (26) results in

$$\alpha_1\tilde{u}_0\frac{x^2}{2}+\sum_{n\neq 0}\frac{r_n}{k_n^2-r_nq_n}\frac{\tilde{u}_n}{(in\omega)^2}\exp\{in\omega x\}$$

$$=\frac{ad_1}{2T}x^2+c_1x+c_0, \quad x\in(-a,a), \tag{27}$$

$$\alpha_3\tilde{w}_0\frac{x^2}{2}+\sum_{n\neq 0}\frac{q_n}{k_n^2-r_nq_n}\frac{\tilde{w}_n}{(in\omega)^2}\exp\{in\omega x\}$$

$$=\frac{ad_3}{2T}x^2+c_1'x+c_0', \quad x\in(-a,a), \tag{28}$$

where c_1, c_0, c_1', c_0' are arbitrary integration constants and the constants α_1, α_3, d_1, d_3 are given by formulas

$$\alpha_1=\frac{-i\cos\theta_0}{iq_0\cos\theta_0+k^*\sin^2\theta_0},$$

$$\alpha_3=\frac{q_0/k^*}{iq_0\cos\theta_0+k^*\sin^2\theta_0},$$

$$d_1=\frac{c_0^2\delta k^*T\sin\theta_0\cos\theta_0/a}{iq_0\cos\theta_0+k^*\sin^2\theta_0},$$

$$d_3=\frac{-ic_0^2\delta q_0T\cos\theta_0/a}{iq_0\cos\theta_0+k^*\sin^2\theta_0}.$$

The asymptotic developments

$$\frac{r_n}{k_n^2-r_nq_n}=\frac{|n\omega|}{A}+\frac{k^*\sin\theta_0}{A}\frac{n}{|n|}+\frac{C_1}{A}\frac{1}{|n\omega|}+O\left(\frac{1}{|n\omega|^2}\right),$$

$$\frac{q_n}{k_n^2-r_nq_n}=\frac{|n\omega|}{A}+\frac{k^*\sin\theta_0}{A}\frac{n}{|n|}+\frac{C_3}{A}\frac{1}{|n\omega|}+O\left(\frac{1}{|n\omega|^2}\right),$$

where

$$A=\frac{1}{2}\left(k^{*2}+\frac{i\omega^*}{\nu}\right), \quad B=\frac{i\omega^*k^{*2}}{2A\nu},$$

$$C_1=B-\frac{3k^{*2}}{4}-\frac{i\omega^*}{4\nu}, \quad C_3=B-\frac{k^{*2}}{4}-\frac{3i\omega^*}{4\nu},$$

also prove true.

Since $\tilde{u}_n$ are the Fourier coefficients of a continuous function, we have also $\tilde{u}_n=o(n^{-1})$ and consequently

$$\left|\frac{r_n}{k_n^2-r_nq_n}\frac{\tilde{u}_n}{(in\omega x)^2}\right|<\frac{\text{const}}{n^2}.$$

Hence, the infinite series in formula (27) is converging uniformly for $x\in[-a,a]$. According to property (*f*) in Ref. 9 (or Ref. 10) the relationship (27) can be differentiated term by term any number of times and the formulas obtained this way are valid as distributions (generalized functions).

The second derivative of relationship (27) with respect to the x variable can be written as

$$\frac{1}{A}\frac{d^2}{dx^2}\sum_{n\neq 0}\frac{|n\omega|\tilde{u}_n}{(in\omega)^2}\exp\{in\omega x\}$$

$$+\frac{k^*\sin\theta_0}{A}\frac{d^2}{dx^2}\sum_{n\neq 0}\frac{n}{|n|}\frac{\tilde{u}_n}{(in\omega)^2}\exp\{in\omega x\}$$

$$+\frac{C_1}{A}\sum_{n\neq 0}\frac{\tilde{u}_n}{|n\omega|}\exp\{in\omega x\}+\alpha_1\tilde{u}_0$$

$$+\sum_{n\neq 0}\left[\frac{r_n}{k_n^2-r_nq_n}-\frac{|n\omega|}{A}-\frac{k^*\sin\theta_0}{A}\frac{n}{|n|}\right.$$

$$\left.-\frac{C_1}{A}\frac{1}{|n\omega|}\right]\tilde{u}_n\exp\{in\omega x\}=\frac{ad_1}{T}, \quad x\in(-a,a). \tag{29}$$

Since the last infinite series in this relationship is uniformly convergent, its sum is a smooth function of x along the interval $(-a,a)$. Let us denote

$$K_1^R(x)=\alpha_1+\sum_{n\neq 0}\left[\frac{r_n}{k_n^2-r_nq_n}-\frac{|n\omega|}{A}-\frac{k^*\sin\theta_0}{A}\frac{n}{|n|}\right.$$

$$\left.-\frac{C_1}{A}\frac{1}{|n\omega|}\right]\exp\{in\omega x\},$$

$$K_3^R(x)=\alpha_3+\sum_{n\neq 0}\left[\frac{q_n}{k_n^2-r_nq_n}-\frac{|n\omega|}{A}-\frac{k^*\sin\theta_0}{A}\frac{n}{|n|}\right.$$

$$\left.-\frac{C_3}{A}\frac{1}{|n\omega|}\right]\exp\{in\omega x\}.$$

Introducing the expression of the Fourier coefficients, we obtain

$$\mathbb{I}_R(x)\equiv\alpha_1\tilde{u}_0+\sum_{n\neq 0}\left[\frac{r_n}{k_n^2-r_nq_n}-\frac{|n\omega|}{A}-\frac{k^*\sin\theta_0}{A}\frac{n}{|n|}\right.$$

$$\left.-\frac{C_1}{A}\frac{1}{|n\omega|}\right]\tilde{u}_n\exp\{in\omega x\}$$

$$=\frac{1}{T}\int_{-a}^{a}\tilde{u}(x')K_1^R(x-x')dx'.$$

The other infinite series will give the singular terms of Eq. (29). We analyze now each of the singular terms. Thus, substituting again the Fourier coefficients results in

$$\mathbb{I}_3 \equiv \sum_{n\neq 0} \frac{\tilde{u}_n}{|n\omega|}\exp\{in\omega x\}$$

$$= \sum_{n\neq 0} \frac{1}{T}\int_{-a}^{+a} \tilde{u}(x')\frac{\exp\{in\omega(x-x')\}}{|n\omega|}dx'$$

$$= \frac{1}{\pi}\int_{-a}^{+a} \tilde{u}(x')\sum_{n=1}^{\infty}\frac{\cos[n\omega(x-x')]}{n}dx'$$

$$= -\frac{1}{\pi}\int_{-a}^{+a} \tilde{u}(x')\log\left|2\sin\frac{\omega(x-x')}{2}\right|dx'. \quad (30)$$

Here, the formula

$$\sum_{n=1}^{\infty}\frac{\cos(n\omega x)}{n} = -\log\left|2\sin\frac{\omega x}{2}\right|,$$

given in Ref. 11 (formula 1.442) or Ref. 12 has been used. Therefore

$$\mathbb{I}_3 = -\frac{1}{\pi}\int_{-a}^{+a} \tilde{u}(x')\log\left|\left[\sin\frac{\omega(x-x')}{2}\right]\left[\frac{\omega(x-x')}{2}\right]^{-1}\right|dx'$$

$$-\frac{1}{\pi}\int_{-a}^{+a} \tilde{u}(x')\log|\omega(x-x')|dx'. \quad (31)$$

The first integral in this relationship is regular and the second one has a weak (logarithmic) singularity for $x'=x$.

Similarly, the second singular term in Eq. (29) becomes

$$\mathbb{I}_2 \equiv \frac{d^2}{dx^2}\sum_{n\neq 0}\frac{n}{|n|}\frac{\tilde{u}_n}{(in\omega)^2}\exp\{in\omega x\}$$

$$= -\frac{d}{dx}\frac{i}{\pi}\int_{-a}^{+a} \tilde{u}(x')\sum_{n=1}^{\infty}\frac{\cos[n\omega(x-x')]}{n}dx'.$$

Hence

$$\mathbb{I}_2(x) = i\frac{d\mathbb{I}_3}{dx} = \frac{i}{\pi}\int_{-a}^{+a}\tilde{u}(x')\left[\frac{\omega}{2}\cot\frac{\omega(x-x')}{2} - \frac{1}{x-x'}\right]dx'$$

$$+\frac{i}{\pi}\frac{d}{dx}\int_{-a}^{+a}\tilde{u}(x')\log|\omega(x-x')|dx'. \quad (32)$$

Again, the first integral in formula (32) is regular. The second one can be written as

$$\frac{i}{\pi}\frac{d}{dx}\int_{-a}^{+a}\tilde{u}(x')\log|\omega(x-x')|dx' = \frac{i}{\pi}\int_{-a}^{+a}\tilde{u}(x')\frac{dx'}{x-x'}, \quad (33)$$

and represents a finite part (or principal value) integral (see Refs. 13, 9, and 14). Finally, the second term in Eq. (29) has the form

$$\mathbb{I}_2(x) = \frac{i}{\pi}\int_{-a}^{+a}\tilde{u}(x')\left[\frac{\omega}{2}\cot\frac{\omega(x-x')}{2} - \frac{1}{x-x'}\right]dx'$$

$$+\frac{i}{\pi}\int_{-a}^{+a}\tilde{u}(x')\frac{dx'}{x-x'}. \quad (34)$$

For the first singular term in (29), performing similar transformations results in

$$\mathbb{I}_1 \equiv \frac{d^2}{dx^2}\sum_{n\neq 0}\frac{|n\omega|\tilde{u}_n}{(in\omega)^2}\exp\{in\omega x\} = -\frac{d^2\mathbb{I}_3(x)}{dx^2}$$

$$= \frac{d^2}{dx^2}\frac{1}{\pi}\int_{-a}^{+a}\tilde{u}(x')\log|\omega(x-x')|dx'$$

$$+\frac{d^2}{dx^2}\frac{1}{\pi}\int_{-a}^{+a}\tilde{u}(x')\log\left|\left[\sin\frac{\omega(x-x')}{2}\right]\right.$$

$$\left.\times\left[\frac{\omega(x-x')}{2}\right]^{-1}\right|dx'.$$

The last integral in this formula is regular and the other one can be written as a finite part. Finally, the first singular term becomes

$$\mathbb{I}_1 = -\frac{1}{\pi}\int_{-a}^{+a}\tilde{u}(x')\left[\frac{\omega^2}{4}\sin^{-2}\frac{\omega(x-x')}{2}\right.$$

$$\left.-\frac{1}{(x-x')^2}\right]dx' - \frac{1}{\pi}\int_{-a}^{+a}\tilde{u}(x')\frac{dx'}{(x-x')^2}.$$

In this formula

$$\int_{-a}^{+a}\tilde{u}(x')\frac{dx'}{(x-x')^2} = -\frac{d}{dx}\int_{-a}^{+a}\tilde{u}(x')\frac{dx'}{x-x'}$$

$$= -\frac{d^2}{dx^2}\int_{-a}^{+a}\tilde{u}(x')\log|\omega(x-x')|dx, \quad (35)$$

is a finite part integral (see Refs. 13, 15, and 14).

Bringing together all the above transformations, Eq. (29) becomes

$$-\frac{1}{\pi A}\int_{-a}^{+a}\tilde{u}(x')\frac{dx'}{(x-x')^2} + \frac{ik^*\sin\theta_0}{\pi A}\int_{-a}^{+a}\tilde{u}(x')\frac{dx'}{x-x'}$$

$$-\frac{C_1}{\pi A}\int_{-a}^{+a}\tilde{u}(x')\log|\omega(x-x')|dx'$$

$$+\frac{1}{T}\int_{-a}^{a}\tilde{u}(x')K_1^R(x-x')dx' - \frac{1}{\pi A}\int_{-a}^{+a}\tilde{u}(x')$$

$$\times\left[\frac{\omega^2}{4}\sin^{-2}\frac{\omega(x-x')}{2} - \frac{1}{(x-x')^2}\right]dx'$$

$$+\frac{ik^*\sin\theta_0}{\pi A}\int_{-a}^{+a}\tilde{u}(x')\left[\frac{\omega}{2}\cot\frac{\omega(x-x')}{2} - \frac{1}{x-x'}\right]dx'$$

$$-\frac{C_1}{\pi A}\int_{-a}^{+a}\tilde{u}(x')\log\left|\left[\sin\frac{\omega(x-x')}{2}\right]\left[\frac{\omega(x-x')}{2}\right]^{-1}\right|dx'$$

$$= \frac{ad_1}{T}, \quad x\in(-a,a). \quad (36)$$

Performing the same transformations with Eq. (28), a similar equation results for the function $\tilde{w}(x)$

$$
\begin{aligned}
&-\frac{1}{\pi A}\int_{-a}^{+a}\tilde{w}(x')\frac{dx'}{(x-x')^2}+\frac{ik^*\sin\theta_0}{\pi A}\int_{-a}^{+a}\tilde{w}(x')\frac{dx'}{x-x'}\\
&\quad-\frac{C_3}{\pi A}\int_{-a}^{+a}\tilde{w}(x')\log|\omega(x-x')|dx'\\
&\quad+\frac{1}{T}\int_{-a}^{a}\tilde{w}(x')K_3^R(x-x')dx'-\frac{1}{\pi A}\int_{-a}^{+a}\tilde{w}(x')\\
&\quad\times\left[\frac{\omega^2}{4}\sin^{-2}\frac{\omega(x-x')}{2}-\frac{1}{(x-x')^2}\right]dx'\\
&\quad+\frac{ik^*\sin\theta_0}{\pi A}\int_{-a}^{+a}\tilde{w}(x')\left[\frac{\omega}{2}\cot\frac{\omega(x-x')}{2}-\frac{1}{x-x'}\right]dx'\\
&\quad-\frac{C_3}{\pi A}\int_{-a}^{+a}\tilde{w}(x')\log\left|\left[\sin\frac{\omega(x-x')}{2}\right]\left[\frac{\omega(x-x')}{2}\right]^{-1}\right|dx'\\
&\quad=\frac{ad_3}{T},\quad x\in(-a,a).
\end{aligned}
\tag{37}
$$

Equations (36) and (37) will be solved in Sec. V by using a Galerkin-type method.

Since there are numerical methods tailored specially for finite-part integrals, we shall write also a different form of these equations. So, by using the finite-part definition for more general functions[13] and Ref. 16, pp. 64–66, problem 5, Eqs. (36) and (37) can be written as

$$
\begin{aligned}
&-\frac{\omega}{2A}\int_{-a}^{a}\frac{\tilde{u}(x')dx'}{\sin^2(\omega(x-x')/2)}\\
&\quad+\frac{ik^*\sin\theta_0}{A}\int_{-a}^{a}\tilde{u}(x')\cot\frac{\omega(x-x')}{2}dx'\\
&\quad-\frac{2C_1}{\omega A}\int_{-a}^{a}\tilde{u}(x')\log\left|2\sin\frac{\omega(x-x')}{2}\right|dx'\\
&\quad+\int_{-a}^{a}\tilde{u}(x')K_1^R(x-x')dx'=ad_1
\end{aligned}
\tag{38}
$$

$$
\begin{aligned}
&-\frac{\omega}{2A}\int_{-a}^{a}\frac{\tilde{w}(x')dx'}{\sin^2(\omega(x-x')/2)}\\
&\quad+\frac{ik^*\sin\theta_0}{A}\int_{-a}^{a}\tilde{w}(x')\cot\frac{\omega(x-x')}{2}dx'\\
&\quad-\frac{2C_3}{\omega A}\int_{-a}^{a}\tilde{w}(x')\log\left|2\sin\frac{\omega(x-x')}{2}\right|dx'\\
&\quad+\int_{-a}^{a}\tilde{w}(x')K_3^R(x-x')dx'=ad_3.
\end{aligned}
\tag{39}
$$

Notice that both integral equations have the same singular part. As the solutions are satisfying the conditions $\tilde{u}(\pm a)=\tilde{w}(\pm a)=0$ the equations can be transformed into integro-differential equations with Cauchy-type singularities. Numerical methods for solving such equations were developed by Multhopp-Kalandiya,[17] Kutt,[18] and Dragos.[19]

Remark 1. *These types of singular integral equations involving second-order "poles" arise naturally in various physical problems.*[14,15,20,21] *They are called "integral equations with strong singularities" in some papers and "hypersingular integral equations" in other papers. Since in the field of wave propagation and acoustics the last denomination is used more often, we adopted it also in the present work.*

Finally, we note that using a Rayleigh-type representation of velocity field, by means of a potential function $\phi(x,z)$ and a stream function $\psi(x,z)$ the solution of the viscous diffraction problem reduces to the same hypersingular integral equations (38) and (39). Hence, these equations characterize the viscous diffraction problem by a grating and are not the result of a particular approach.

V. REDUCTION OF THE HYPERSINGULAR INTEGRAL EQUATIONS TO INFINITE SYSTEMS OF ALGEBRAIC EQUATIONS

Instead of using collocation methods for approximating the solution of the singular integral equations (38) and (39), we prefer a Galerkin-type approach based on a special basis of the corresponding Hilbert space. The method takes advantage of the form of integral equations by using some spectral-type relationships, fast Fourier transform of some smooth function, and summation of rapid convergent infinite series.

A. Galerkin's method for solving the integral equations

In the space $\mathcal{H}^{1/2}(-a,a)$ of functions continuous on $[-a,a]$ with derivatives having singularities of order 1/2 at extremities, we consider the basis

$$
\left\{\sin\left(n\arccos\frac{x}{a}\right)\right\},\quad n=1,2,\ldots.
$$

We represent the function $\tilde{u}(x)$ as

$$
\tilde{u}(x)=\sum_{m=1}^{\infty}u_m\sin\left(m\arccos\frac{x}{a}\right).
$$

Equation (36) becomes

$$\sum_{m=1}^{\infty} u_m \Bigg\{ -\frac{2C_1}{\omega A}\int_{-a}^{+a} \sin(m\theta')\log|\omega(x-x')|\,dx' + \frac{2ik^*\sin\theta_0}{\omega A}\int_{-a}^{+a}\frac{\sin(m\theta')\,dx'}{x-x'} - \frac{2}{\omega A}\int_{-a}^{+a}\frac{\sin(m\theta')\,dx'}{(x-x')^2} - \frac{2}{\omega A}\int_{-a}^{+a}\sin(m\theta')\left[\frac{\omega^2}{4}\sin^{-2}\frac{\omega(x-x')}{2} - \frac{1}{(x-x')^2}\right]dx' + \frac{2ik^*\sin\theta_0}{\omega A}\int_{-a}^{+a}\sin(m\theta') \times\left[\frac{\omega}{2}\cot\frac{\omega(x-x')}{2} - \frac{1}{x-x'}\right]dx' + \int_{-a}^{a}\sin(m\theta')K_1^R(x-x')\,dx' - \frac{2C_1}{\omega A}\int_{-a}^{+a}\sin(m\theta')\log\left|\left[\sin\frac{\omega(x-x')}{2}\right] \times\left[\frac{\omega(x-x')}{2}\right]^{-1}\right|dx' = ad_1, \quad x\in(-a,a),$$

where we have denoted $\theta' = \arccos(x'/a)$.

Applying the *Galerkin's method* results in

$$\sum_{m=1}^{\infty}[S_{pm}^0 + C_1\hat{S}_{pm}^0]u_m + \sum_{m=1}^{\infty}[S_{pm}^R + C_1\hat{S}_{pm}^R + R_{pm}^{(1)}]u_m = \frac{d_1}{2\pi}\delta_{p,1}, \quad p=1,2,\ldots.$$

The singular terms are

$$S_{pm}^0 = \frac{-2}{\omega a^2 A}\frac{1}{\pi^2}\int_0^{\pi}\int_0^{\pi}\frac{dS}{(\cos\theta-\cos\theta')^2} + \frac{2ik^*\sin\theta_0}{\omega aA}\frac{1}{\pi^2}\int_0^{\pi}\int_0^{\pi}\frac{dS}{\cos\theta-\cos\theta'},$$

$$\hat{S}_{pm}^0 = -\frac{2}{\omega A}\frac{1}{\pi^2}\int_0^{\pi}\int_0^{\pi}\log|\cos\theta-\cos\theta'|\,dS,$$

and the regular part contains the terms

$$S_{pm}^R = \frac{1}{\pi^2}\int_0^{\pi}\int_0^{\pi}\left\{-\frac{\omega}{2A}\left[\frac{1}{\sin^2 Z}-\frac{1}{Z^2}\right] + \frac{ik^*\sin\theta_0}{A}\left[\cot Z-\frac{1}{Z}\right]\right\}dS, \tag{40}$$

$$\hat{S}_{pm}^R = -\frac{2}{\omega A}\frac{1}{\pi^2}\int_0^{\pi}\int_0^{\pi}\log\left|\frac{\sin Z}{Z}\right|dS, \tag{41}$$

$$R_{pm}^{(1)} = \frac{1}{a^2\pi^2}\int_{-a}^{a}\int_{-a}^{a}\sin(m\theta')\sin(p\theta)K_1^R(x-x')\,dx'\,dx.$$

We have denoted $\theta = \arccos(x/a)$, and also

$$dS = \sin(m\theta')\sin(p\theta)\sin\theta'\sin\theta\,d\theta\,d\theta',$$

$$Z = \frac{\omega a}{2}(\cos\theta-\cos\theta').$$

Using formulas given in the Appendix results in

$$S_{pm}^0 = \frac{m}{\omega a^2 A}\delta_{p,m} + \frac{ik^*\sin\theta_0}{2\omega aA}(\delta_{p,m+1}-\delta_{p+1,m}) \tag{42}$$

$$\hat{S}_{pm}^0 = \frac{1}{4\omega A}\begin{cases}(\delta_{p,m}-\delta_{p,m+2})/(m+1) \\ \quad +(\delta_{p,m}-\delta_{p+2,m})/(m-1), & m\neq 1, \\ (\delta_{p,1}-\delta_{p,3})/2 - 2\log(\omega a/2)\,\delta_{p,1}, & m=1\end{cases} \tag{43}$$

$$R_{pm}^{(1)} = \frac{\alpha_1}{4}\delta_{p,1}\delta_{m,1} + i^{p-m}mp\sum_{n=1}^{\infty}\frac{J_p(an\omega)J_m(an\omega)}{(an\omega)^2} \times\left[\frac{r_n}{k_n^2-r_nq_n} + (-1)^{p+m}\frac{r_{-n}}{k_{-n}^2-r_{-n}q_{-n}} - \frac{1+(-1)^{p+m}}{A}\left(n\omega+\frac{C_1}{n\omega}\right) - \frac{1-(-1)^{p+m}}{A}k^*\sin\theta_0\right]. \tag{44}$$

Finally, we obtain the infinite system of algebraic equations for determining the coefficients u_n

$$\sum_{m=1}^{\infty}[S_{pm}^0 + C_1\hat{S}_{pm}^0 + S_{pm}^R + C_1\hat{S}_{pm}^R + R_{pm}^{(1)}]u_m = \frac{d_1}{2\pi}\delta_{p,1}, \quad p=1,2,\ldots. \tag{45}$$

Similarly, we write

$$\tilde{w}(x) = \sum_{m=1}^{\infty} w_m \sin\left(m\arccos\frac{x}{a}\right),$$

and the integral equation (39) yields the infinite system of algebraic equations for the coefficients w_m

$$\sum_{m=1}^{\infty}[S_{pm}^0 + C_3\hat{S}_{pm}^0 + S_{pm}^R + C_3\hat{S}_{pm}^R + R_{pm}^{(3)}]u_m = \frac{d_3}{2\pi}\delta_{p,1}, \quad p=1,2,\ldots. \tag{46}$$

The coefficients $R_{pm}^{(3)}$ have the expression

$$R_{pm}^{(3)} = \frac{\alpha_3}{4}\delta_{p,1}\delta_{m,1} + i^{p-m}mp\sum_{n=1}^{\infty}\frac{J_p(an\omega)J_m(an\omega)}{(an\omega)^2} \times\left[\frac{q_n}{k_n^2-r_nq_n} + (-1)^{p+m}\frac{q_{-n}}{k_{-n}^2-r_{-n}q_{-n}} - \frac{1+(-1)^{p+m}}{A}\left(n\omega+\frac{C_3}{n\omega}\right) - \frac{1-(-1)^{p+m}}{A}k^*\sin\theta_0\right]. \tag{47}$$

B. Numerical realization of the method

The systems of linear equations (45) and (46) have good properties from a computational point of view. Thus, the coefficients S_{pm}^{0}, $\hat{S}_{pm}^{0}$ are given by explicit relationships (42) and (43). The coefficients S_{pm}^{R}, $\hat{S}_{pm}^{R}$ are expressed by 2D cosine Fourier transforms. The integrands in formulas (40) and (41) are smooth functions such that these integrals can be computed efficiently by using the 2D discrete cosine transform function of MATLAB. Finally, the coefficients $R_{pm}^{(1)}$, $R_{pm}^{(3)}$ can be obtained directly by summing the infinite series in formulas (44) and (47). By subtracting several terms, and summing them separately, we have transformed the initial infinite series into rapid convergent series.

In fact, by the approch used in the previous section, we have turned the convolution operators in Fourier transform domain; this transform converts the convolution to a product ''quasidiagonalizing'' the operators. Thus, the strongly singular operator contributes only on the main diagonal of the system, the principal value integral has contributions on the two diagonals next to the principal one, and the term containing the logarithmic singularity contributes in the system to coefficients lying on the principal diagonal and the four closer to it. This is why the finite sections of the resulting infinite systems of linear equations have relatively low condition numbers and the series giving the functions $\tilde{u}(x)$, $\tilde{w}(x)$ are rapidly convergent.

VI. SOUND TRANSMISSION FACTOR. NUMERICAL RESULTS

The important element in this analysis is the modulus t of the *sound transmission factor*,[22] $t=|P_0^-/c_0^2|$, which shows ''how much'' of the incoming plane wave is passing through the grating. Thus, once the solutions of the systems (45) and (46) are determined the functions $\tilde{u}(x)$, $\tilde{w}(x)$ can be introduced in formula (21) to obtain the corresponding Fourier coefficients. Finally, the formula (24) provides the value of the modulus of sound transmission factor as

$$t\equiv|P_0^-/c_0^2|=\left|\frac{q_0\tilde{w}_0+ik^*\tilde{u}_0\sin\theta_0}{iq_0\cos\theta_0+k^*\sin^2\theta_0}\,\frac{a\pi}{2(a+b)c_0^2\delta k^*}\right|. \tag{48}$$

In Fig. 2(a) we have plotted the modulus t of sound transmission factor versus slit width d for various values of the periodic spacing w by including the influence of viscosity. All the calculations assumed a value of $\pi/4$ for the angle θ_0. In Fig. 2(b) the same problem was solved for the case where the viscosity of the air is neglected. It is very clear that, especially for very narrow slits, the viscosity of the air causes significant attenuation of the transmission wave. The results of Fig. 2(b) agree very well (the first three digits are the same) with those obtained by using the formulas provided in Refs. 3 and 4. Figure 3 shows again the dependence of modulus t of sound transmission factor upon d for different values of the incidence angle θ_0.

These results indicate that, in a simplified model of the screen, treated as a periodic array of slits in a substrate, the openings in the screen should be on the order of at least 10 μm in order to avoid excessive attenuation of the signal.

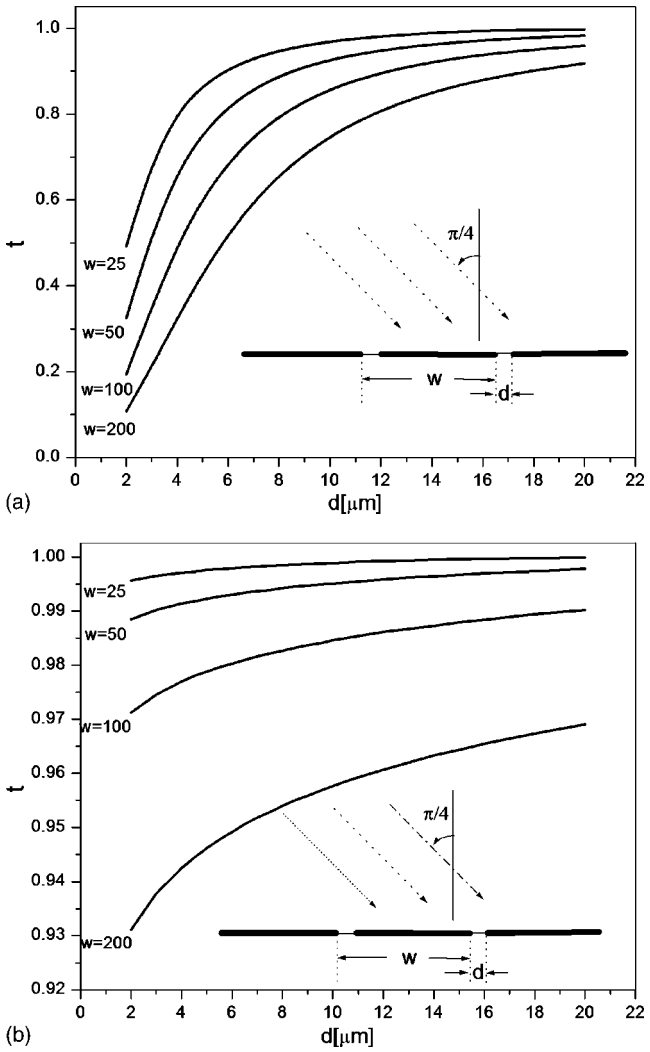

FIG. 2. (a) Modulus t of sound transmission factor versus slits' width for periodic spacing $w=25$, 50, 100, and 200 μm, $f=20$ KHz, and incidence angle $\theta_0=\pi/4$. The viscous case. (b) Modulus t of sound transmission factor versus slits' width for periodic spacing $w=25$, 50, 100, and 200 μm, $f=20$ KHz, and incidence angle $\theta_0=\pi/4$. The nonviscous case.

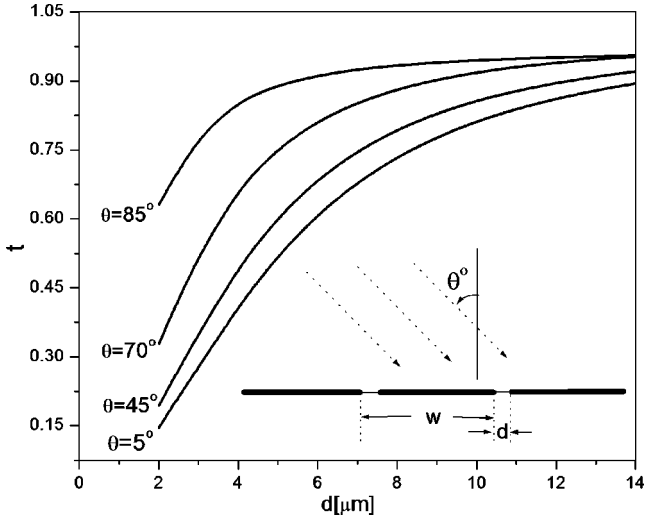

FIG. 3. Modulus t of sound transmission factor versus slits' width d for $w=100$ μm, $f=20$ KHz, and incidence angles $\theta_0=5$, 45, 70, and 85 deg.

ACKNOWLEDGMENTS

This work has been supported through NIH Grant R01 DC05762-1A1, and DARPA Grant DAAD17-00-C-0149 to R.N.M.

APPENDIX: SOME DEFINITE INTEGRALS

In the following, we evaluate some integrals used in Sec. IV. Starting with the formula[23,24]

$$-\frac{1}{\pi}\int_{-1}^{1}\frac{\cos(n\arccos x')}{\sqrt{1-x'^2}}\log|x-x'|dx' = \begin{cases}\cos(n\arccos x)/n, & n\geqslant 1\\ \log 2, & n=0\end{cases}, \tag{A1}$$

we can write also

$$-\frac{1}{\pi}\int_{-1}^{1}\sin(n\arccos x')\log|x-x'|dx' = \begin{cases}\dfrac{\cos(n-1)\theta}{2(n-1)}-\dfrac{\cos(n+1)\theta}{2(n+1)}, & n>1\\ \dfrac{\log 2}{2}-\dfrac{\cos(2\theta)}{4}, & n=1\end{cases}, \tag{A2}$$

where $\theta=\arccos x$. The derivatives of relation (A2), taking into consideration the definitions (33) and (35), give

$$\frac{1}{\pi}\int_{-1}^{1}\frac{\sin(n\arccos x')}{x-x'}dx' = \cos(n\theta), \quad n\geqslant 1, \tag{A3}$$

$$-\frac{1}{\pi}\int_{-1}^{1}\frac{\sin(n\arccos x')}{(x-x')^2}dx' = n\frac{\sin(n\theta)}{\sin\theta}. \tag{A4}$$

The change of integration variable $x'=\cos\theta'$ in the formulas (A2), (A3), and (A4) gives

$$-\frac{1}{\pi}\int_{0}^{\pi}\sin(n\theta')\sin\theta'\log|\cos\theta-\cos\theta'|d\theta' = \begin{cases}\dfrac{\cos(n-1)\theta}{2(n-1)}-\dfrac{\cos(n+1)\theta}{2(n+1)}, & n>1\\ \dfrac{\log 2}{2}-\dfrac{\cos(2\theta)}{4}, & n=1\end{cases}, \tag{A5}$$

$$\frac{1}{\pi}\int_{0}^{\pi}\frac{\sin(n\theta')\sin\theta'}{\cos\theta-\cos\theta'}d\theta' = \cos(n\theta), \quad n\geqslant 1, \tag{A6}$$

$$-\frac{1}{\pi}\int_{0}^{\pi}\frac{\sin(n\theta')\sin\theta'}{(\cos\theta-\cos\theta')^2}d\theta' = n\frac{\sin(n\theta)}{\sin\theta}, \quad n\geqslant 1, \tag{A7}$$

the last two integrals being considered singular (finite-part) integrals.

For the last integral we consider the generating function of Bessel's functions

$$\exp\left\{\frac{z}{2}\left(w-\frac{1}{w}\right)\right\} = \sum_{n=-\infty}^{\infty}J_n(z)w^n,$$

and take $w=i\exp\{i\varphi\}$. This results in

$$\exp\{iz\cos\varphi\} = \sum_{n=-\infty}^{\infty}J_n(z)i^n\exp\{in\varphi\}.$$

Using the orthogonality relationship of the complex exponentials results in

$$\int_0^{\pi}\exp\{iz\cos\varphi\}\cos(m\varphi)d\varphi = \pi i^m J_m(z). \tag{A8}$$

Then, we have

$$\int_{-a}^{a}\sin\left(p\arccos\frac{x}{a}\right)\exp\{in\omega x\}dx = a\int_0^{\pi}\sin(p\theta)\sin\theta\exp\{in\omega\cos\theta\}d\theta,$$

and, using Eq. (A8) and some properties of Bessel's functions, we finally obtain the formula

$$\int_{-a}^{a}\sin\left(p\arccos\frac{x}{a}\right)\exp\{in\omega x\}dx = \pi i^{p-1}\frac{p}{n\omega}J_p(an\omega). \tag{A9}$$

[1] H. Lamb, *Hydrodynamics* (Cambridge University Press, Cambridge, 1932).
[2] J. W. Miles, "On Rayleigh scattering by a grating," Wave Motion **4**, 285–292 (1982).
[3] J. D. Achenbach and Z. L. Li, "Reflexion and transmission of scalar waves by a periodic array of screens," Wave Motion **8**, 225–234 (1986).
[4] E. Scarpetta and M. A. Sumbatyan, "Explicit analytical results for one-mode oblique penetration into a periodic array of screens," IMA J. Appl. Math. **56**, 109–120 (1996).
[5] A. D. Pierce, *Acoustics* (McGraw-Hill, New York, 1981).
[6] A. M. J. Davis and R. J. Nagem, "Acoustic diffraction by a half plane in a viscous acoustic medium," J. Acoust. Soc. Am. **112**, 1288–1296 (2002).
[7] A. M. J. Davis and R. J. Nagem, "Influence of viscosity on the diffraction of sound by a circular aperture in a plane screen," J. Acoust. Soc. Am. **113**, 3080–3090 (2003).
[8] P. M. Morse and K. U. Ingard, *Theoretical Acoustics* (Princeton University Press, Princeton, NJ, 1968).
[9] V. S. Vladimirov, *Equations of Mathematical Physics* (Marcel Dekker Inc., New York, 1971).
[10] V. S. Vladimirov, *Methods of the Theory of Generalized Functions* (Taylor & Francis, London and New York, 2002).
[11] I. S. Gradshteyn and I. M. Ryzhik, *Table of Integrals, Series, and Products* (Academic, New York, 1994).
[12] D. S. Jones, *The Theory of Generalized Functions* (Cambridge University Press, Cambridge, 1982).
[13] J. C. Ferreira, *Introduction to the Theory of Distributions* (Addison Wesley Longman, Reading, MA, 1997).
[14] A. C. Kaya and F. Erdogan, "On the solution of integral equations with strongly singular kernels," Q. Appl. Math. **45**, 105–122 (1987).
[15] P. A. Martin, "End-point behaviour of solutions to hypersingular integral equations," Proc. R. Soc. London, Ser. A **432**, 301–320 (1991).
[16] A. H. Zemanian, *Distribution Theory and Transform Analysis* (McGraw-Hill, New York, 1965).
[17] A. I. Kalandiya, *Mathematical Methods of Two-dimensional Elasticity* (Mir, Moscow, 1975).
[18] H. R. Kutt, "The numerical evaluation of principal value integrals by finite part integration," Numer. Math. **24**, 205–210 (1975).
[19] L. Dragos, "Integration of Prandtl's equation with the aid of quadrature formulae of Gauss type," Q. Appl. Math. **52**, 23–29 (1994).
[20] M. P. Brandao, "Improper integrals in theoretical aerodynamics: The problem revisited," AIAA J. **25**, 1258–1260 (1986).
[21] G. Krishnasamy, L. W. Schmerr, T. J. Rudopphi, and F. J. Rizzo, "Hyper-

singular boundary integral equations: Some applications in acoustic and elastic wave scattering,'' Trans. ASAE **57**, 404–414 (1990).
[22] F. P. Mechel, *Formulas of Acoustics* (Springer, Berlin, 2002).
[23] G. M. L. Gladwell, *Contact Problems in Classical Theory of Elasticity* (Sijthoff and Noordhoff, Alphen aan Rijn, 1980).
[24] I. H. Sloan and E. P. Stephan, ''Collocation with Chebyshev polynomials for Symm's integral equation on an interval,'' J. Aust. Math. Soc. Ser. B, Appl. Math. **34**, 199–211 (1992).

Acoustic positioning using multiple microphone arrays

Hui Liu and Evangelos Milios[a)]
Faculty of Computer Science, Dalhousie University, Halifax, Nova Scotia B3H 1W5, Canada

(Received 16 July 2004; revised 1 March 2005; accepted 1 March 2005)

Passive acoustic techniques are presented to solve the localization problem of a sound source in three-dimensional space using off-the-shelf hardware. Multiple microphone arrays are employed, which operate independently, in estimating the direction of arrival of sound, or, equivalently, a direction vector from the array's geometric center towards the source. Direction vectors and array centers are communicated to a central processor, where the source is localized by finding the intersection of the direction lines defined by the direction vectors and the associated array centers. The performance of the method in the air is demonstrated experimentally and compared with a state-of-the-art method that requires centralized digitization of the signals from the microphones of all the arrays. © *2005 Acoustical Society of America.* [DOI: 10.1121/1.1895005]

PACS numbers: 43.28.Tc, 43.60.Gk [EJS] Pages: 2772–2782

I. INTRODUCTION

Acoustic positioning is useful in a variety of problems. Teleconferencing appliances, which use multiple microphones to localize a speaker in the room and steer a video camera to that speaker, have been proposed.[1] Localization of underwater vehicles can be accomplished through acoustic techniques. Acoustic transponders for underwater localization usually work at ultrasonic frequency range and require expensive special-purpose signal processing hardware. Various acoustic methods have been described in the literature for the localization of air and ground objects and for underwater applications. The military has been using towed arrays for a long time for detection and localization of submarines.[2] A motivation of the work presented in this paper is the acoustic localization of an underwater walking robot, on which an appropriate sound source has been mounted, by one or more floating hydrophone arrays.

One typical acoustic positioning application, which finds wide use in teleconferencing, is to localize a speaker based on her voice.[1,3,4] Reid[4] estimates the direction of arrival of sound by an omnidirectional microphone pair. The microphone pair is mounted on a pan-tilt unit with a fixed baseline and two rotational degrees of freedom. The sound direction is estimated by time delays between the microphones in different microphone pair positions. Therefore, a persistent signal is required for the direction estimation. Kapralos[1] reports a position estimation method with an array of four omnidirectional microphones mounted in a static pyramidal shape. This method uses delay and sum beamforming to determine the direction of arrival of the sound. In the absence of source direction information, it searches by focusing the beamformer to every possible source direction. Audio is combined with a panoramic camera. Voice-tracking is becoming available on high-end commercial videoconferencing systems.[5]

Rabinkin[3] proposes an algorithm using arrays of omnidirectional microphones to localize a sound source with beamforming and generalized time-delay techniques. His method requires simultaneous and synchronized recording and digitization from all microphones. Moreover, Rabinkin's algorithm is based on iterative nonlinear optimization, therefore it requires an initial source position to start the iteration.

Brandstein and Silverman[6] performed a detailed study of the estimation of the position of a speaker in a real room setting. They point out that locators based on time difference of arrival (TDOA) present significant computational advantages compared to steered beamformers or methods based on high-resolution spectral estimation. However, they are limited in that they assume a single-source model. We follow a similar two-stage procedure, where delay estimation is followed by location evaluation. For localization, they use a heuristic linear intersection algorithm, where pairs of pairs of sensors give loci of bearing lines in 3D space that intersect at the source location. Their heuristic is to determine, for each bearing line, its points that are closest to each of the remaining bearing lines. The overall location estimate is a weighted average of these points.

Once the time difference of arrival approach has been chosen, the problem of reliably estimating time differences between signals at microphone pairs arises.[7] Omologo and Svaizer[8] investigate three techniques for time delay estimation, normalized cross correlation, LMS adaptive filters, and crosspower-spectrum phase, and demonstrate that the last technique is the most suitable for time delay estimation for direction of arrival. Time difference estimation is complicated by issues such as spatially correlated noise and the presence of room reverberation. Rui and Florencio[9] have extended the generalized cross-correlation approach[7] into a two-stage process, where the first stage performs removal of correlated noise, and the second stage reduces reverberation.

In this paper, we estimate the direction of arrival from a sound-emitting object to a passive local microphone array. We use multiple microphone arrays in the audio frequency range at known positions to measure the directions of arrival of sound based on the far-field assumption, which requires the sound source to be sufficiently far from the microphones for the acoustic wave reaching the microphones to be ap-

[a)]Author to whom correspondence should be addressed. Electronic mail: eem@cs.dal.ca

 0001-4966/2005/117(5)/2772/11/$22.50

proximately planar. The sound source position is estimated at the intersection of the multiple direction lines in 3D space. Our method shares the decentralized property of Brandstein and Silverman,[6] in that each array performs its own A/D conversion and direction of arrival estimation in an asynchronous manner with respect to the other arrays. Once direction vectors have been computed, they can easily be communicated to the other arrays for localization, via wireless ethernet. Another advantage of decentralized processing is that we can add more arrays to improve the area coverage or accuracy of the localization without any problem. In Rabinkin's method, we would need ever more sophisticated centralized digitization hardware to accommodate additional microphones, and ever longer cables to transmit the analog sound to the digitization hardware. With the availability of wireless networking, acoustic positioning approaches that can be spatially distributed in wireless sensor networks gain increasing attention.[10]

The main contribution of our method is a closed-form solution for the localization of source position. Our method uses the same intuition of avoiding nonlinear optimization as Brandstein and Silverman,[6] but it avoids the heuristic of weighted averaging of point estimates, which is difficult to formally justify. We demonstrate that our closed-form solution may be superior to search-based nonlinear optimization approaches in that the latter may not converge in some cases.

The paper is structured as follows. The methodology and localization principle are discussed in Sec. II. Section III describes the signal processing mechanism for time delay estimation. The results of the simulation and of the air experiments are presented in Sec. IV. Finally, conclusions and directions for future research are presented in Sec. V.

II. SOUND SOURCE LOCALIZATION

We now present the geometric model for the sound source localization. The essence of the model is to first estimate the direction of the arrival of sound at each microphone array based on the far-field assumption, and then to determine the sound source position as the intersection of direction lines towards the source out of the multiple microphone arrays.

We have also considered other geometric models in our work. Further details about the methodology and the simulation results of those models are presented elsewhere.[11]

A. Measurement of direction of arrival of sound

The measurement of the direction of arrival of sound is based on the far-field assumption, which requires the sound source to be sufficiently far from the microphones for the acoustic wave reaching the microphones to be approximately planar. We follow the formulation by Reid.[4]

Consider two omnidirectional microphones $\mathbf{M_1}$, $\mathbf{M_2}$ with coordinates $\mathbf{M_1}=[M_{1x},M_{1y},M_{1z}]$ and $\mathbf{M_2}=[M_{2x},M_{2y},M_{2z}]$ as shown in Fig. 1. The time difference for the sound to propagate from $\mathbf{M_1}$ to $\mathbf{M_2}$ is t_{12}, which is related to the angle of arrival γ and can be be calculated by the constraint

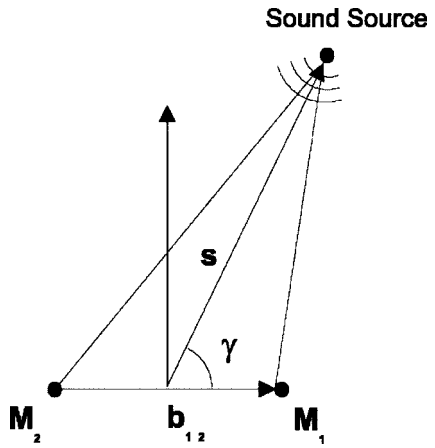

FIG. 1. Two microphones $\mathbf{M_1}$ and $\mathbf{M_2}$ form a baseline $\mathbf{b_{12}}$, listening to the same source. The direction of sound event **s** arrives at the microphones with angle γ.

$$\cos\gamma=\frac{ct_{12}}{|\mathbf{b_{12}}|}=\frac{cn_{12}}{f|\mathbf{b_{12}}|}, \tag{1}$$

where c is the speed of sound, $|\mathbf{b_{12}}|$ is the length of the baseline between $\mathbf{M_1}$ and $\mathbf{M_2}$, n_{12} is time delay in samples, and f is the sampling frequency.

Consider the unknown direction from the reference point of the microphone array to the source as a unit vector $\mathbf{s}[s_x,s_y,s_z]$. The relation between **s** and the baseline vector $\mathbf{b_{12}}[b_{12x},b_{12y},b_{12z}]=\mathbf{M_1}-\mathbf{M_2}=[M_{1x}-M_{2x},M_{1y}-M_{2y},M_{1z}-M_{2z}]$, where γ is the incidence angle of the sound wave onto the microphone array, is

$$\mathbf{s}\cdot\mathbf{b_{12}}=|\mathbf{b_{12}}|\cos\gamma \tag{2}$$

or, equivalently,

$$s_xb_{12x}+s_yb_{12y}+s_zb_{12z}=|\mathbf{b_{12}}|\cos\gamma. \tag{3}$$

Combining Eqs. (1) and (3) we obtain

$$s_xb_{12x}+s_yb_{12y}+s_zb_{12z}=ct_{12}. \tag{4}$$

Thus a set of three linear equations can be solved to uniquely determine the three unknown variables s_x, s_y, and s_z. This implies that three microphones are required in one microphone array for finding the sound direction. For arrays with more than three microphones, we have an overdetermined problem, for which an optimal solution for **s** can be computed via a least mean squares approach. The error $f_1(s_x,s_y,s_z)$ in satisfying Eq. (4) is

$$f_1(s_x,s_y,s_z)=s_xb_{12x}+s_yb_{12y}+s_zb_{12z}-ct_{12}. \tag{5}$$

There is also an implicit nonlinear constraint that $s_x^2+s_y^2+s_z^2=1$ since **s** is a unit vector:

$$f_{\text{nonlinear}}(s_x,s_y,s_z)=s_x^2+s_y^2+s_z^2-1. \tag{6}$$

Therefore, the solution for the sound direction can be obtained by solving the nonlinear minimization problem shown

in Eq. (7). An iterative nonlinear optimization algorithm is used to solve this problem,[12] where the initial solution for starting the search is obtained by solving any of the properly determined sets of linear equations mentioned:

$$\min_{s_x,s_y,s_z}\left(f_{\text{nonlinear}}^2+\sum_i f_i^2\right). \tag{7}$$

The estimation of the direction of arrival of sound is based on the far-field assumption. The error this assumption introduces is quantified in previous work.[4] It is noted there that when the ratio of r/b is greater than 3, where r is the distance from the midpoint of the two microphones to the source and b is distance between the two microphones, the error is less than 0.4°.

B. Estimation of sound source position

The position of the sound source is estimated as the intersection of multiple lines in three-dimensional space. Each line is defined by the reference point of a microphone array and the direction vector from the microphone array to the source. Due to measurement noise in the direction vectors and the microphone positions, these lines will not, in general, intersect exactly at a single point. Therefore, the optimal estimate of the source position is the point that has minimal overall distance from these lines.

Consider the center (reference point) $\mathbf{P_i}$ of a microphone array and the associated direction of arrival of sound $\mathbf{s_i}$. A line l_i in three-dimensional space can be defined by a starting point $\mathbf{P_i}$ and its direction $\mathbf{s_i}$. Every point $\mathbf{P}$ lying on l_i satisfies the following constraint for some real number λ:

$$\mathbf{P}=\mathbf{P_i}+\lambda\mathbf{s_i}. \tag{8}$$

Consider the unknown sound source position $\mathbf{P}'[x,y,z]$ and its projection $\mathbf{P_0}$ onto l_i. As a point of l_i, $\mathbf{P_0}$ also satisfies relation Eq. (8), where λ is a parameter to be determined. By solving for λ in terms of $\mathbf{P}'$, $\mathbf{P_i}$ and $\mathbf{s_i}$, we obtain

$$\mathbf{P_0}=\mathbf{P_i}+((\mathbf{P}'-\mathbf{P_i})\cdot\mathbf{s_i})\mathbf{s_i}. \tag{9}$$

The distance d_i between $\mathbf{P}'$ and $\mathbf{P_0}$, which is the distance from $\mathbf{P}'$ to l_i, can be expressed as

$$d_i^2=(\mathbf{P}'-\mathbf{P_0})\cdot(\mathbf{P}'-\mathbf{P_0}). \tag{10}$$

By applying Eq. (9) to Eq. (10), d_i^2 can be obtained by the following constraint with respect to $\mathbf{P}'$, $\mathbf{P_i}$, and $\mathbf{s_i}$:

$$d_i^2=\|(\mathbf{P}'-\mathbf{P_i})-((\mathbf{P}'-\mathbf{P_i})\cdot\mathbf{s_i})\mathbf{s_i}\|^2. \tag{11}$$

We note that d_i^2 is a quadratic function of the (unknown) coordinates x, y, z of the sound source position $\mathbf{P}'$, where the coefficients of the quadratic terms are constants determined by $\mathbf{P_i}$ and $\mathbf{s_i}$. Therefore, given a set of microphone arrays, the solution for the sound source position coordinates x, y, z can be computed through the minimization equation:

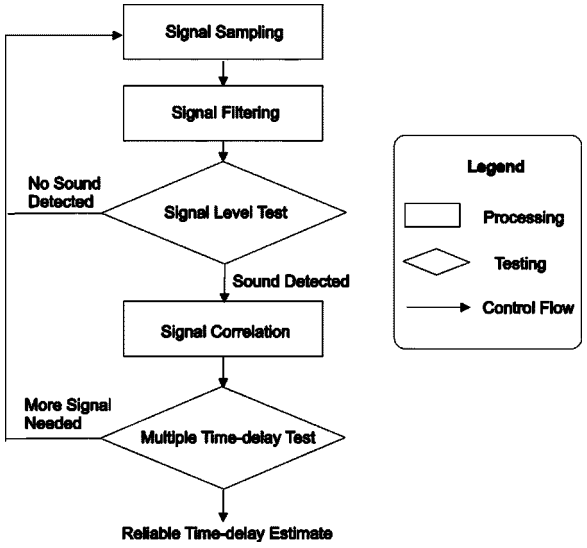

FIG. 2. Signal processing flowchart for time delay estimation.

$$\min_{x,y,z}\left(\sum_i d_i^2\right), \tag{12}$$

where the summation extends over all microphone arrays i. This is a quadratic minimization problem, reducible to the solution of a set of linear equation.

III. SIGNAL PROCESSING FOR TIME DELAY ESTIMATION

In order to calculate reliable time delay between the arrivals of the sound signals, we correlate two channels of a window of audio data from two microphones, and look for the peak of the correlation function. The location of the peak corresponds to the time-delay estimate. Before correlation, filtering is carried out to reduce noise, and a signal level test is performed to check for the presence of a sound source. In this work, we follow the same signal processing steps that are described in earlier work.[4] The flowchart in Fig. 2 is a summary of the processing on the sampled audio signals for time-delay estimation. It must be pointed out that the simplified signal processing described here is suitable for simple sounds. For more sophisticated sounds, such as speech, advanced signal processing must be used for time-delay estimation.[6–8]

A. Filtering

Most human-audible sounds lie in the frequency range from a few Hz to about 20 KHz. A 60-Hz electric interference is common in audio signals. We also want to cut off high-frequency noise that is above 4000 Hz, due to the fact that we are using fairly inexpensive microphones in the air designed for speech, while in the water higher frequencies attenuate faster. Therefore, frequencies that are not in the region of interest (200–4000 Hz) will be filtered out. This is accomplished through the use of a bandpass digital FIR filter.[1] The optimal frequency range in the air and the water needs further investigation.

```
Algorithm: Time delay estimation
Input: Two channels of audio signals,
       start and end index of correlation window.
Output: Time delay between two channel of signals.

Method:
(1):  repeat:
(2):      read audio data from two channels;
(3):      compute signalVariance of audio data;
(4):      if signalVariance > dynamicVarianceThreshold, then
(5):          for every timeShift in correlationWindow
(6):              compute correlationFunction;
(7):              if output > maxCorrelationOutput, then
(8):                  let output be maxCorrelationOutput;
(9):                  save this timeShift as indexOfPeak;
(10):         if indexOfPeak < precalculatedMaxDelay, then
(11):             timeDelay = indexOfPeak;
(12): until timeDelay is found;
```

FIG. 3. Time delay estimation algorithm.

B. Signal level test

A test is performed to determine the presence of signal. The simplest approach is based on a comparison of the signal magnitude E_{signal} to the magnitude of the background noise. If the signal is weak relative to background, the above magnitude level test may not be sufficient. A test based on *signal variance* was introduced previously.[1] Signal variance captures the overall deviation of signal samples from the mean. Signal variance may be computed with Eqs. (13) and (14):

$$\overline{s} = \frac{1}{n}\sum_{j=0}^{n-1} |s[j]|, \tag{13}$$

$$V_{\text{signal}} = \frac{1}{n}\sum_{j=0}^{n-1} (s[j]-\overline{s})^2. \tag{14}$$

Generally, the variance of a signal is greater than the variance of the background noise.

In our work, we use a threshold value V_{thresh} to determine the presence of sound. The maximum variance of the background noise $\max V_{\text{bckgrnd}}$ is dynamically measured, and V_{thresh} is computed by Eq. (15), where λ is a constant real number. The value of λ is determined experimentally:

$$V_{\text{thresh}} = (\max V_{\text{bckgrnd}}) + \lambda. \tag{15}$$

We should note that if we have additional knowledge of the signal source, for example, when we attach a known source onto an underwater vehicle for the purpose of localizing it, then a more powerful matched filtering approach can be applied for signal detection.

C. Signal correlation

The correlation function, which we use in this work, is given by

$$f(i) = \sum_{t} s_1(t+i)s_2(t), \tag{16}$$

where s_1 and s_2 are two sound channels over the time window t and i is the amount of time shift, which is the independent variable of the correlation function. The value of i that yields the maximum output of function $f(i)$ corresponds to the time delay estimate.

The maximum possible time delay between two microphones equals the length of the baseline divided by the speed of sound. We therefore require that the time delay of the maximum peak of the correlation function be under the maximum delay.

D. Multiple time delay test

The final step for the time delay estimation is to reject outliers by clustering the time delays estimated from a number of consecutive and non-overlapping signal time windows from the same microphone pair and assuming that the position of the sound source is the same. We discard outliers and compute the mean time delay value over the remaining estimates as the final time delay estimate from the given microphone pair and source position. Separate time delay estimates are obtained by repeating this process for all microphone pairs within an array and the same source position. The time delay estimates are then used to determine the sound direction of arrival at the array (a line) as described in Sec. II A. Availability of multiple arrays gives multiple lines, which are then used to determine the source position as described in Sec. II B.

Agglomerative clustering[13,14] is used. Consider we have five time delay estimates $\{t_1, t_2, t_3, t_4, t_5\}$. We initially place each number into its own group. Therefore, we start with five groups. Each of these groups contains only a single number and the initial centroid of each group is the number itself. Clustering proceeds as follows, based on a carefully selected threshold distance.

(1) Compare all centroid pairs.
(2) Compare the distance between the closest centroid pair to the threshold value.

(a) If the distance between this closest pair is less than the threshold distance, then these two groups are merged

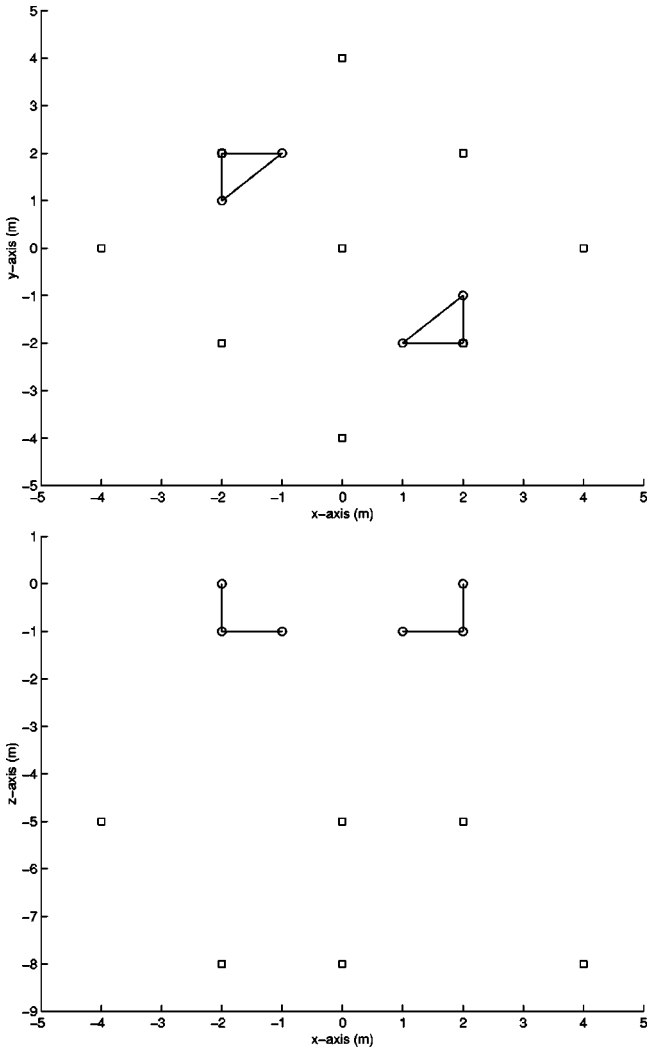

FIG. 4. Microphone and source arrangement in the simulation program. Eight microphones are represented as circles connected by line segments and the sources are represented as squares.

into a single group and a new centroid for the new group is generated. Return to step 1 to continue the clustering.

(b) If the distance between the closest pair is greater than the threshold, the clustering stops.

IV. EXPERIMENTAL RESULTS

In this section we describe our experiments, which included both simulations and experiments with real microphones in a room setting. In the real data experiments, we generated impulsive sound by hitting a metal appliance approximately once per second, and used one or more microphone arrays to estimate the location of the sound source in 3D space. The algorithm for time delay estimation is given in Fig. 3. It uses the method described in Sec. III to correlate the signals received at the listening apparatus.

A. Simulation

A simulation was implemented on Matlab6.0 to test the positioning method described in Sec. II and compare it with Rabinkin's method.[3] The coordinates of the microphones and sound sources are shown in Table I. The arrangement of the microphones and the sound sources is shown in Fig. 4. The speed of sound in the simulation was set to be $c = 1482.0$ m/s.

In order to simulate errors in the measurement of the time delay in samples between the arrival of signals, we add a random number of samples (noise) in a specific range (noise level) to the ideal time delay estimate at the each measurement. We estimate the sound source position ten times with different random generation seeds, repeat over ten different source positions, and calculate the overall average and the standard deviation of the source position estimates. Then the noise level is increased by one sample and the same process is repeated, as shown in Fig. 5. The results of both our method, as described in Sec. II, and Rabinkin's method[3] are shown in Fig. 6. The graphs on the left show the mean localization error in the same unit length as the source positions, while the graphs on the right show the standard deviations of the localization error, as a function of the noise level in the time delay estimates. The results show that the two methods have comparable accuracy, when Rabinkin's method converges.

B. Air experiments

1. Experimental setting

This experiment took place in a rectangular room 16 m long, 9 m wide, and 3 m high. The room is carpeted and has sound-absorbent ceiling tiles. The arrangement of the room and the placement of the apparatus are shown in Figs. 7 and 8.

The listening apparatus consists of two sets of microphones. Each set has four omnidirectional Genexxa 3303003

```
Algorithm: Simulation of noisy time delay estimates in source positioning.
 Input: Microphone positions, source position,
        Range of time delay estimation error in samples,
        Number of measurements.
 Output: Mean and standard deviation of source position estimates.

     for each source position measurement
         compute the time delays based on the microphone
             and the actual source positions;
         for each time delay estimate
             generate a random error (noise) in the specified range;
             add the noise to the time delay estimates;
         estimate the source position;
     compute mean and standard deviation;
```

FIG. 5. Simulation of noisy time delay estimates in source position estimation. The term *random* refers to a function which would produce a uniformly distributed random number between [−range,range].

TABLE I. The microphone and source positions used in the simulation program.

	x (m)	y (m)	z (m)		x (m)	y (m)	z (m)
M_1	−1.0	2.0	−1.0	M_5	1.0	−2.0	−1.0
M_2	−2.0	2.0	−1.0	M_6	2.0	−2.0	−1.0
M_3	−2.0	1.0	−1.0	M_7	2.0	−1.0	−1.0
M_4	−2.0	2.0	0.0	M_8	2.0	−2.0	0.0
S_1	0.0	0.0	−5.0	S_6	2.0	−2.0	−5.0
S_2	0.0	0.0	−8.0	S_7	0.0	4.0	−8.0
S_3	2.0	2.0	−5.0	S_8	−4.0	0.0	−5.0
S_4	−2.0	2.0	−8.0	S_9	0.0	−4.0	−5.0
S_5	−2.0	−2.0	−8.0	S_10	4.0	0.0	−8.0

electret condenser microphones (with diameter of approximately 8 mm) mounted at the corners of a square wooden frame with side length of 0.3 m.

In order for the far-field assumption to be applicable, the ratio of distance r to length of the baseline b must be sufficiently large. In this experiment, the sound source is placed at a minimum distance of 1.2 m which corresponds to $r/b=4$. The resulting far-field error is less than 0.23°.[4,11]

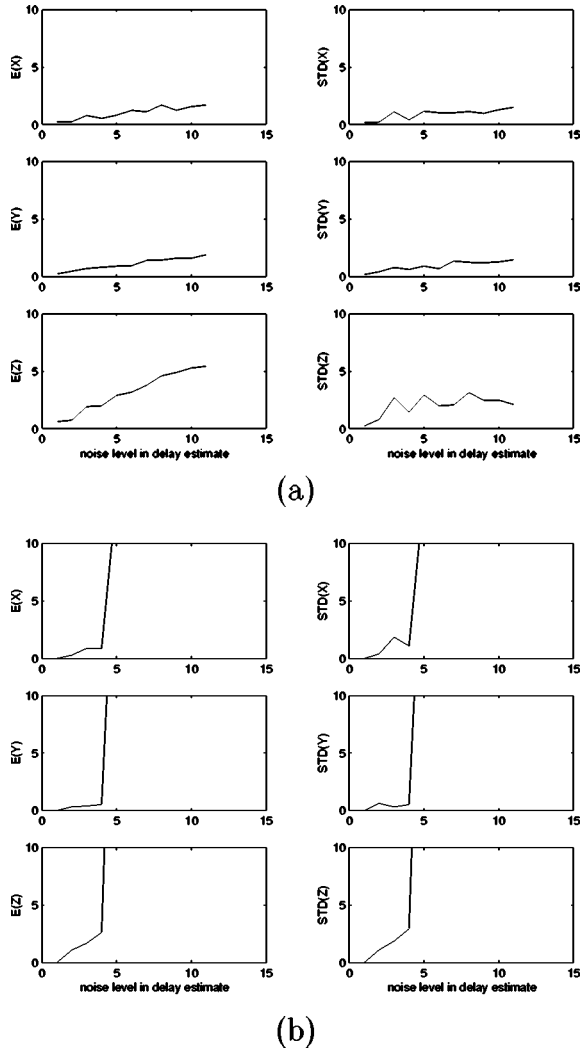

FIG. 6. The plots illustrate the performance of our approach and Rabinkin's approach in the simulation program, where random noise is added to the time delay estimate. The top six graphs (a) are the average and the standard deviations of the estimates of our approach, and the bottom six (b) are the results of Rabinkin's approach.

The main tool that we use in the measurement of ground truth is a measuring tape. To minimize measurement error, an optimal measurement method is used. Further details regarding the distance measurement and the coordinate system construction can be found elsewhere.[11]

We use an Echo Layla 24 Digital Audio Recording unit as the analog-to-digital (A/D) converter. The parameter specifications for the experiments are shown in Table II.

In our air experiments, the sound source is at a place slightly above the ground and generates an impulsive sound (hand clapping or hitting a metal appliance) approximately every 1.5-s interval. This time interval needs to be maintained in the experiments so as to keep successive impulses and their reflections apart. The spectrogram of the sound is shown elsewhere.[11] The frequency of sound lies in the range of 200–4000 Hz. In addition to the impulsive sound source, there are other sound sources. For example, there are air conditioning and ventilation fans running. This background noise is not very loud and is usually below 200 Hz. Such noise is filtered out by the bandpass filtering.

Based on our setup, the range of the time delay values in terms of samples can be determined through Eq. (1). Considering a sound source at $\gamma=0°$, and with sampling frequency $f=44\,100$, baseline length=0.3 m, and speed of sound $c=345$ m/s, Eq. (1) yields

$$\pm n = \pm \frac{f|\mathbf{b}|}{c} \approx \pm 38. \tag{17}$$

Therefore, the number of possible time delays is in the range of $[-38,38]$ samples. Since n represents the time delay as a number of samples, the value of n must be an integer. The corresponding incidence angle $\alpha=\pi/2-\gamma$ is calculated through Eq. (1). The discernible angles for α, which can be achieved with time delay values of 0 to 38, are shown in Table III. The table is symmetric for the negative time delay values.

The quantization error due to the discretization of time delays is shown in Table III. The theoretical resolution of approximately 1.5° or corresponding maximum quantization error of ±0.75° is accurate only at a time delay of 1. The error is close to that value when the time delay is within 30 samples (51.5°). Beyond that the error starts to grow. Therefore, in our setup, the error caused by the quantization dominates the far-field assumption error, since only when the distance from the source to the microphones is less than about 0.25 m, the far-field assumption error starts to be greater than the quantization error. This indicates that it is worth aiming for subsample accuracy in time delay estimation by interpolation or by estimation in the frequency domain.

It is interesting to observe the range of values of r/b (distance to baseline ratio) that give errors due to violation of the far-field assumption comparable to the quantization errors due to discretization of delay measurements. The range

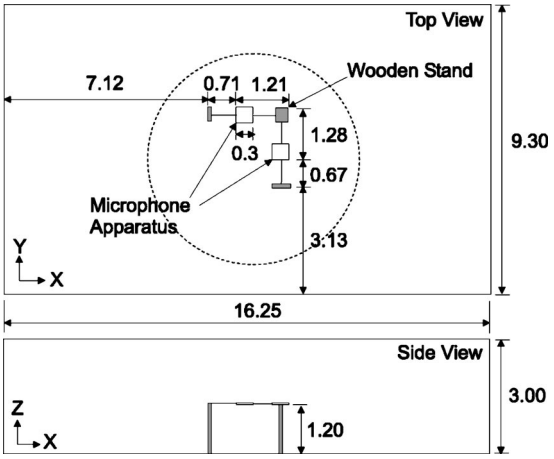

FIG. 7. Room arrangement for the air experiments. The size of the room is 16.25×9.30×3.00 m. Two microphone arrays are placed at a height of 1.2 m from the ground. The interior of dotted area represents possible positions of the sound source, which is at a height of 0.02 m above ground.

of values of r/b computed based on Table III is [0.67,1.75] for the air experiments.[11] The worst case, corresponding to the highest r/b, is in the vicinity of 45°.

2. Results

In the air experiments, the sound source is placed at a fixed position and we estimate its position ten consecutive times. Then the sound source is moved and the experiment is repeated at the new position. A total of 25 sound source positions throughout the area around the two microphone arrays are chosen and, for each sound source position, mean and standard deviation are calculated as two measures to illustrate the consistency and the accuracy of our approach.

We use the same setup and process to test our method described in Sec. II and Rabinkin's method.[3] The results of both approaches are shown in Fig. 9. The cross is centered at the average position of those measurements. The height and width of each cross represent the standard deviation along the two dimensions. We observe that the standard deviation on the z axis is generally greater than the x and y axis. This is also reported by Rabinkin[3] and explained by the fact that the baseline along the z dimension is smaller. Particularly in our geometry, we expect the z accuracy to be smaller as the source gets closer to the line (or plane) of the microphones, which happens when the source gets farther from the array.

FIG. 8. Actual photograph of the room arrangement where the air experiments took place.

TABLE II. Parameter specifications for the air experiments.

Parameter	Value
Sampling frequency	44 100 Hz
Sample resolution	16 bits
Sample size	2048
Low-pass filter cutoff frequency	4000 Hz
High-pass filter cutoff frequency	200 Hz
Filter coefficients	128 (for low and high pass)
V_{thresh}	Dynamically determined

In our method, we only compute time delays between microphones that are close to each other. Therefore, the possible time delay range is narrow and we can use small correlation windows to shut out reflections. In Rabinkin's method, which needs to estimate time delays between arrays, we have to enlarge the correlation window, making time delay estimates less robust. To address this problem, we introduce and experiment with a ''decentralized'' version of Rabinkin's method, by only estimating the time delays between the microphones within the same array. The standard deviation of the estimates is shown in Fig. 9. We observe that there are certain source positions where the ''decentralized'' Rabinkin's method fails to give a meaningful estimate, as the estimates of those source positions are over 100 m away, which exceeds the size of the room for the experiment. Those positions are represented by squares in Fig. 9.

The means of the estimated positions and the actual sound source locations overlaid on top of each other are shown in Fig. 10, offering a view of the distance between the estimates and the actual source positions. A summary of the experimental results is given in Table IV.

In our experimental results, we encountered convergence problems for some source locations with the decentralized version of Rabinkin's method.

C. Preliminary water experiments

As mentioned earlier, one of the motivations of this project is the acoustic localization of an underwater walking

TABLE III. Discernible angles for time delays in integer units for the air experimental setup: n=time delay in integer units, α=angle α in degrees, and e=maximum quantization error in degrees.

n	α	e	n	α	e	n	α	e	n	α	e
0	0.0	0.75	10	15.1	0.78	20	31.4	0.88	30	51.5	1.23
1	1.5	0.75	11	16.7	0.78	21	33.2	0.90	31	53.9	1.31
2	3.0	0.75	12	18.2	0.79	22	35.0	0.92	32	56.6	1.41
3	4.5	0.75	13	19.8	0.80	23	36.9	0.95	33	59.4	1.54
4	6.0	0.75	14	21.4	0.81	24	38.7	0.97	34	62.5	1.71
5	7.5	0.75	15	23.0	0.82	25	40.7	1.00	35	65.9	1.98
6	9.0	0.76	16	24.7	0.83	26	42.7	1.03	36	69.8	2.46
7	10.5	0.76	17	26.3	0.84	27	44.8	1.07	37	74.8	3.76
8	12.0	0.77	18	28.0	0.85	28	46.8	1.12	38	82.3	3.76
9	13.6	0.77	19	29.7	0.87	29	49.1	1.17			

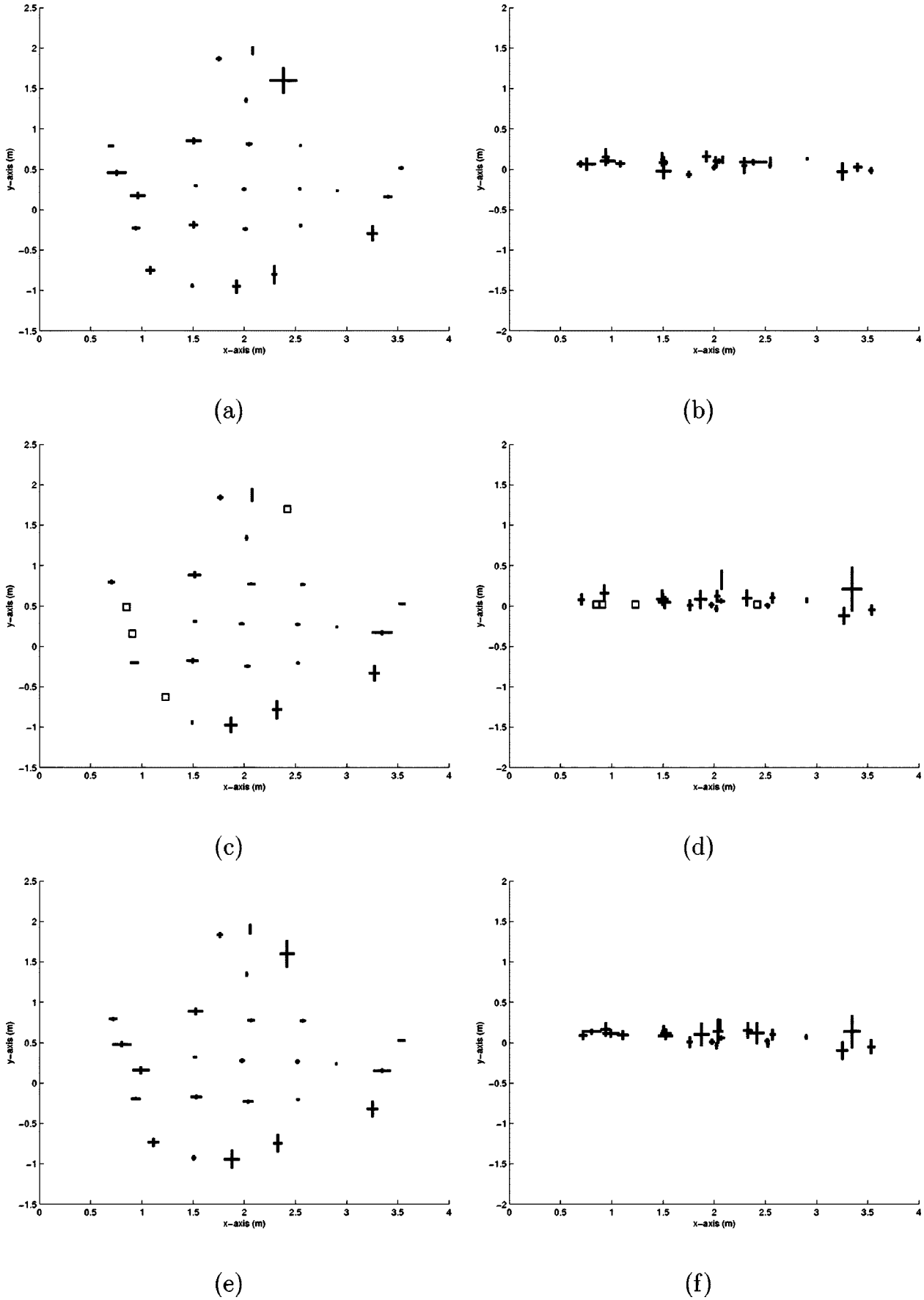

FIG. 9. The graphs show the estimated sound source position of the air experiments in the *x*-*y* plane and *x*-*z* plane, corresponding to the layout of the room as shown in Fig. 7. The size of the cross represents the standard deviation. The center of the cross is the estimated mean position of the sound source. (a) and (b) Centralized Rabinkin's method. (c) and (d) Decentralized Rabinkin's method. (e) and (f) Standard deviation on *x*, *y* and *x*,*z* axes of our approach.

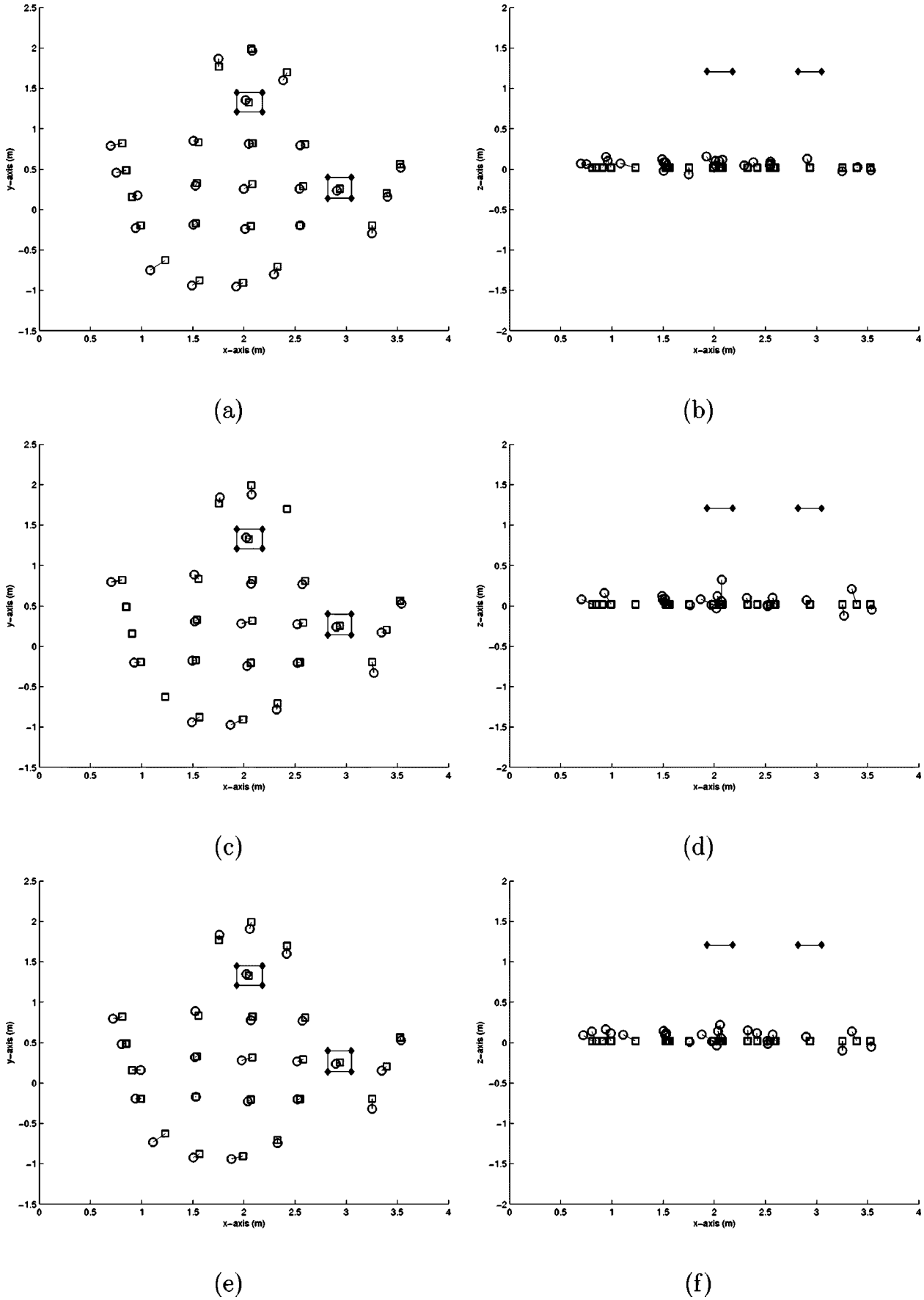

FIG. 10. The graphs overlay the actual source positions and the estimated mean positions from the air experiments, along the *x*, *y* axes and *x*, *z* axes. (a) and (b) Centralized Rabinkin's approach. (c) and (d) Decentralized Rabinkin's approach. (e) and (f) Our approach.

TABLE IV. Summary of experimental results of our approach and centralized and decentralized Rabinkin's approach, without the failed estimates: δ=average of standard deviations, ϵ=average error in estimates of source position, and $\delta(\epsilon)$=standard deviation of errors.

	Our approach			Rabinkin's approach (centralized)			Rabinkin's approach (decentralized)		
	x (m)	y (m)	z (m)	x (m)	y (m)	z (m)	x (m)	y (m)	z (m)
δ	0.043	0.043	0.074	0.035	0.039	0.053	0.042	0.041	0.074
ϵ	0.041	0.040	0.084	0.044	0.045	0.063	0.050	0.049	0.077
$\delta(\epsilon)$	0.036	0.034	0.046	0.036	0.033	0.035	0.038	0.034	0.046

robot.[15] In the context of that project, preliminary experiments were carried out on the localization of an impulsive sound source (generated in the same manner as in the air experiments) in a pool of size 20×25 m^2, with a depth of approximately 4 m at the deep end. Signals were windowed to exclude reflections off the sides of the pool. The hydrophones were placed near the surface of the water, while the sound was generated at the bottom of the pool. The results of those experiments are reported in Ref. 11. The accuracy of the position estimates in the horizontal plane was acceptable, while the position estimates in the vertical direction were grossly inaccurate. We conjecture that the reason for the poor estimates is the reflection off the water-air boundary, which was not modeled in the system. Current research is directed towards the design of a proper sound source based on a transducer. The sound source will be programmed to generate a characteristic spectrum (for example, a chirp) that should be detectable in an open water environment containing natural sounds. Hydrophones will be placed at a depth of 2 m in a tetrahedral arrangement. The open-water system will require more sophisticated signal processing for detection and time delay estimation.[8,9] Knowledge of the spectrum of the source will make frequency domain processing more appealing. Finally, explicit modeling of the unavoidable reflection off the water-air boundary will have to be included in the solution.

V. DISCUSSION

In this report, we have presented a technique that uses the far-field assumption to estimate the direction of arrival of sound at a microphone array. The optimal location of the sound source is estimated as the intersection of the direction lines from each array pointing toward the source. Our technique operates in the audio frequency range, and therefore it can be implemented using off-the-shelf audio hardware.

We tested our technique both in the water and in the air, with a setup that reflects the distances of the water experiment scaled for the difference in the speed of sound. The results of the pool experiments show extremely poor estimates of the z coordinate of the source, as reported elsewhere.[11] The average accuracy in the air experiment is 0.05 m. In order to achieve reasonably accurate results in the water experiments, an additional depth sensor needs to be assumed, which gives an estimate of the depth of the source, resulting in position accuracy of 0.8 m. Current research is addressing the open issues with applying this method in the water for the localization of an underwater walking robot.

Rabinkin's approach[3] was implemented and tested with the same setup as our air experiment, and the result is comparable to that of our method. However, it requires the synchronization and digitization of signals between microphones in different arrays, which needs centralized digitization hardware. When we tried to decentralize Rabinkin's method, the method failed to converge in the localization of some source positions.

ACKNOWLEDGMENTS

The research was supported by a grant from the The Institute for Robotics and Intelligent Systems (IRIS), a federally funded Network of Centres of Excellence managed by PRECARN Inc., and by the Natural Sciences and Engineering Research Council of Canada. Dr. Gao and Dr. Gu provided constructive comments on the manuscript. Yael Kollet, Kori MacCara, Lingyan Zhang, Liwen Zhou, and Ye Liang provided help with the logistics of the experiments. Bill Kapralos of York University provided his beamforming code.

[1] B. Kapralos, M. Jenkin, and E. Milios, "Audio-visual localization of multiple speakers in a video teleconferencing setting," Int. J. Imaging Syst. Technol. special issue on Facial Image Processing, Analysis and Synthesis **13**(1), 95–105 (2003).
[2] P. Gerstoft, W. Hodgkiss, W. Kuperman, H. Song, M. Siderius, and P. Nielsen, IEEE J. Ocean. Eng. **28**(1), 44–54 (2003).
[3] D. V. Rabinkin, Ph.D. thesis, Electrical and Computer Engineering, Rutgers University, 1998.
[4] G. L. Reid and E. Milios, "Active stereo sound location," J. Acoust. Soc. Am. **113**, 185–193 (2003).
[5] P. Inc., *Polycom ViewStation MP*, Tech. Rep. (last accessed, 13 January 2005), URL http://www.polycom.com/
[6] M. S. Brandstein and H. F. Silverman, "The generalized correlation method for estimation of time delay," Comput. Speech Lang. **11**, 91–126 (1997).
[7] C. Knapp and G. Carter, "A partical methodology for speech source localization with microphone arrays," IEEE Trans. Acoust., Speech, Signal Process. **24**(4), 320–327 (1976).
[8] M. Omologo and P. Svaizer, in *IEEE Int. Conf. on Acoustics, Speech and Signal Processing* (IEEE, New York, 1994), pp. 273–276.
[9] Y. Rui and D. Florencio, in *IEEE Int. Conf. on Acoustics, Speech and Signal Processing* (IEEE, New York, 2004).
[10] D. S. Group, *Acoustic Positioning*, Tech. Rep., Electrical Engineering and Computer Science, Univ. of California, Berkeley (last accessed 13 January 2005), URL http://sensornetworks.eecs.berkeley.edu/
[11] H. Liu and E. Milios, *Acoustic Positioning Using Multiple Microphone Arrays*, Tech. Rep. CS-2004-01, Faculty of Computer Science, Dalhousie University, Halifax, Canada (2004).
[12] W. H. Press, S. A. Teukolsky, W. T. Vetterling, and B. P. Flannery, *Nu-*

merical Recipes in C, 2nd ed. (Cambridge, U.P., Cambridge, 1992).
[13] J. Han and M. Kamber, *Data Mining: Concepts and Techniques*, 1st ed. (Morgan Kaufmann, San Francisco, CA, 2001).
[14] B. Luke, *Agglomerative Clustering* (Web reference, last accessed on 8 July 2003), URL http://fconyx.ncifcrf.gov/~lukeb/agclust.html
[15] C. Georgiadis, A. German, A. Hogue, H. Liu, C. Prahacs, A. Ripsman, R. Sim, L.-A. Torres, P. Zhang, M. Buehler, G. Dudek, M. Jenkin, and E. Milios, in *IEEE/RSJ International Conference on Intelligent Robots and Systems, IROS 2004* (Spearhead Exhibitions, Sendai, Japan, 2004), http://www.iros2004.org/

Shallow water sound propagation with surface waves

Chris T. Tindle
Physics Department, University of Auckland, Bag 92019, Auckland, New Zealand

Grant B. Deane
Marine Physical Laboratory, Scripps Institution of Oceanography, La Jolla, California 92093

(Received 14 September 2004; revised 8 February 2005; accepted 9 February 2005)

The theory of wavefront modeling in underwater acoustics is extended to allow rapid range dependence of the boundaries such as occurs in shallow water with surface waves. The theory allows for multiple reflections at surface and bottom as well as focusing and defocusing due to reflection from surface waves. The phase and amplitude of the field are calculated directly and used to model pulse propagation in the time domain. Pulse waveforms are obtained directly for all wavefront arrivals including both insonified and shadow regions near caustics. Calculated waveforms agree well with a reference solution and data obtained in a near-shore shallow water experiment with surface waves over a sloping bottom.
[DOI: 10.1121/1.1883368]

PACS numbers: 43.30.Cq [AIT] Pages: 2783–2794

I. INTRODUCTION

The efficient modeling of pulse propagation in range-dependent environments is an important problem in underwater acoustics. The PE (parabolic equation) model introduced by Tappert[1] and refined by others[2,3] readily accommodates range dependence but time-dependent or broadband problems must be handled using multiple frequencies and Fourier synthesis. The process is computation intensive and the application of the PE to time-dependent problems has been limited. Jensen *et al.*[4] have recently compared broad-band range-dependent computer codes and concluded that, at present, ray-based methods are necessary above 1 kHz. In recent work[5] the wavefront modeling method of calculating waveforms in pulse propagation was described. The method is based on ray tracing but is different from conventional ray tracing because the field is obtained as an integral over wave number derived directly from the wave equation. The method is fast because it avoids the need for Fourier synthesis by working directly in the time domain. In Ref. 5 the method was applied to range-independent deep water propagation and very close agreement with a full multi-frequency normal mode reference solution was demonstrated. A key feature of the method is that the field is expressed as a sum of phase integrals which are evaluated in terms of their points of stationary phase. The approximate evaluations are accurate even at low frequencies and lead to simple expressions for the field. Single points of stationary phase correspond to isolated ray paths. Nearby pairs and triplets of stationary phase points correspond to caustics and cusps, respectively, and describe the field in both insonified and shadow regions.

In the present work wavefront modeling is extended to handle range dependence, including variation of sound speed profile and water depth. Even though the method is based on ray tracing, the extension to allow range dependence required careful consideration of ray paths and the various derivatives necessary to calculate ray amplitudes. The resulting method is able to model sound propagation in the surf zone with variable water depth and surface waves. The motivation for the development of the model was the type of experiment described by Preisig and Deane[6] whose objective was to describe the propagation conditions relevant to acoustic communications systems in shallow water near the surf zone. Some of the modeling work described in Ref. 6 used the methods to be described in the present paper. Earlier work on diffraction corrections for caustics and shadow zones in ray-based approaches to underwater acoustics was outlined in Ref. 5 and reviews of the subject are given by Kravstov and Orlov[7] and by Brekhovskikh and Godin.[8]

Previous work on the effect of surface waves on underwater acoustic transmission treated the surface as either random or regular. A random rough surface scatters the incident sound and leads to reduction of intensity on reflection as a function of rms roughness and wavelength.[9,10] A regular periodic surface shape leads to coherent scattering and has been modeled with both theory and experiment.[11–13] Reflection from a smooth realization of a random surface was studied by Williams *et al.*[14] who found that the field was dominated by cusps and caustics due to reflection from concave sections of the surface.

The wavefront modeling method to be presented here is able to describe propagation in a shallow water waveguide with arbitrary realizations of smooth surface waves and results will be shown for measured instantaneous surface shapes in the real ocean. There is some superficial resemblance to the work of Williams *et al.*[14] as both consider reflection from smooth random surfaces and express the acoustic field as an integral which is evaluated by stationary phase approximations. However, the approaches are quite different. In the present work the acoustic field is derived from a direct solution of the wave equation which gives the field in a range-dependent waveguide as an integral over horizontal wave number. The method includes multiple reflections and expresses the phase as a power series in horizontal wave number or ray launch angle. In contrast, Williams *et al.* use

the Kirchhoff approximation to express the field as a surface integral for a single reflection and expand the phase as a power series in distance along the surface from the point of reflection.

The integral expression for the acoustic field presented here also has some similarity to the interferential integrals obtained from the eikonal equation and discussed by Avdeev *et al.*[15] The expression described in the present work is derived using *WKB* approximations in a Hankel transform solution of the wave equation in a method introduced to underwater acoustics by Sachs and Silbiger[16] and described by Brekhovskikh and Godin.[8] The method leads naturally to expressions for the acoustic field which can be evaluated everywhere including near caustics and in shadow zones.

In Sec. II the wavefront modeling method is extended to allow for range dependence. In Sec. III we illustrate the method in an idealized shallow water wedge with sinusoidal surface waves and there is good agreement with a reference solution. The focusing that occurs due to reflection of sound from the underside of wave crests is considered in detail. The method is then used to model real data obtained in a shallow water experiment. Agreement between model and experiment is good. Our conclusions are given in Sec. IV.

II. SOLUTION OF THE WAVE EQUATION

A. Hankel transform solution and ray expansion

A method of obtaining a ray expansion from a Hankel transform solution of the wave equation was described originally by Batorsky and Felsen[17] and was extended in Ref. 5 to describe pulse propagation in deep water. In the case considered in Ref. 5 all propagating rays cycled up and down about the sound speed minimum and were turned by refraction at upper and lower turning points.

In shallow water, ray propagation is determined by repeated reflections at surface and bottom and it is convenient to express the solution in terms of ray paths with reflection coefficients. The details of the derivation are similar to those in Ref. 5 and are given in Appendix A. The solution for the acoustic pressure $p(r,z_r)$ as a function of range r and receiver depth z_r measured downwards from the surface, due to a harmonic source at $(0,z_s)$ can be written

$$
\begin{aligned}
p(r,z_r) = Q(2\pi r)^{-1/2} e^{i\pi/4} \int_{-\infty}^{\infty} \left(\frac{k}{|\gamma_s||\gamma_r|} \right)^{1/2} \\
\times \left[\exp\left(i \int_{z_s}^{z_r} \gamma \, dz' \right) \right. \\
+ R_a \exp\left(i \int_a^{z_s} \gamma \, dz' \right) \exp\left(i \int_a^{z_r} \gamma \, dz' \right) \\
+ R_b \exp\left(i \int_{z_s}^{b} \gamma \, dz' \right) \exp\left(i \int_{z_r}^{b} \gamma \, dz' \right) \\
\left. + R_a R_b \exp\left(i \int_a^{z_s} \gamma \, dz' \right) \exp\left(i \int_a^{b} \gamma \, dz' \right) \right] \\
\times \exp\left(i \int_{z_r}^{b} \gamma \, dz' \right) \Bigg] \\
\times \sum_{n=0}^{\infty} \left\{ R_a R_b \exp\left[2i \left(\int_a^b \gamma \, dz' \right) \right] \right\}^n \exp(ikr) dk.
\end{aligned}
\tag{1}
$$

The acoustic pressure is given as a sum of terms, each of which is an integral over the horizontal wave number k. It will be shown below that each term corresponds to a particular ray path between source and receiver. In writing Eq. (1) we have assumed that $z_r > z_s$. There is a similar expression for $z_r < z_s$.

The phase terms in Eq. (1) contain integrals over the vertical wave number γ which is given by

$$
\gamma = \left[\frac{\omega^2}{c^2(z)} - k^2 \right]^{1/2}. \tag{2}
$$

The parameters γ_s and γ_r in Eq. (1) represent the wave numbers evaluated at source and receiver positions, respectively.

The reflection coefficients R_a and R_b are the reflection coefficients at the upper and lower turning points at $z=a$ and $z=b$, respectively. As discussed in Appendix A, the ray paths may turn by reflection at actual boundaries or by refraction within the water column.

It is convenient to write Eq. (1) as

$$
p(r,z) = \sum_{n=0}^{\infty} \sum_{j=1}^{4} p_{nj}, \tag{3}
$$

where the four values of j correspond to the four terms in the first square-bracket of Eq. (1). It is also convenient to write the reflection coefficients with an explicit phase ψ so that

$$
R_a(k) = |R_a(k)| \exp[i\psi_a(k)] \tag{4}
$$

and similarly for R_b. The acoustic pressure contribution p_{nj} of Eq. (3) can now be written

$$
\begin{aligned}
p_{nj}(r,z) = Q(2\pi r)^{-1/2} e^{i\pi/4} \int_{-\infty}^{\infty} k^{1/2} |\gamma_s \gamma_r|^{-1/2} |R_a|^{n_j'} |R_b|^{n_j''} \\
\times \exp(i\phi_{nj}) dk,
\end{aligned}
\tag{5}
$$

where the parameters n_j' and n_j'' are the number of upper and lower turning points of the associated ray and are defined by

$$
\begin{aligned}
n_j' &= n, n+1, n, n+1, \quad n_j'' = n, n, n+1, n+1, \\
&\text{for } j = 1,2,3,4.
\end{aligned}
\tag{6}
$$

The phases ϕ_{nj} are given by

$$
\phi_{nj} = \phi_{0j} + n\left(2 \int_a^b \gamma(z') dz' + \psi_a + \psi_b \right) + kr, \tag{7}
$$

where

$$
\phi_{01} = \int_{z_s}^{z_r} \gamma(z') dz', \tag{8}
$$

$$
\phi_{02} = \int_a^{z_s} \gamma(z') dz' + \int_a^{z_r} \gamma(z') dz' + \psi_a, \tag{9}
$$

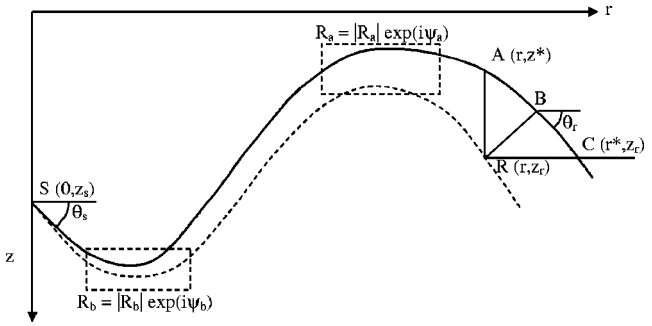

FIG. 1. The solid curve shows a representative ray path for a range-dependent sound speed profile. The ray has angle θ_s at the source and the point *B* is its point of closest approach to the receiver at *R*. The dashed ray is the eigenray with the same sequence of turning points.

$$\phi_{03} = \int_{z_s}^{b} \gamma(z')dz' + \int_{z_r}^{b} \gamma(z')dz' + \psi_b , \tag{10}$$

$$\phi_{04} = \int_{a}^{z_s} \gamma(z')dz' + \int_{a}^{b} \gamma(z')dz' + \int_{z_r}^{b} \gamma(z')dz' + \psi_a + \psi_b . \tag{11}$$

The structure of Eqs. (7)–(11) is linked to a ray path interpretation of the sound field[5,17] as detailed in Appendix B and illustrated in Fig. 1.

The solid curve in Fig. 1 shows an arbitrary ray which leaves the source *S* downwards at grazing angle θ_s and which has two turning points before passing through *B*, its closest approach to the receiver *R*. As noted above, the upper and lower turning points can be refractions or reflections and are described by reflection coefficients R_a and R_b, respectively. The dashed curve shows the corresponding eigenray from source to receiver. The point *A* with coordinates (r,z^*) in the figure marks the depth of the ray as it passes the range of the receiver. Similarly the point *C* with coordinates (r^*,z_r) marks the range at which the ray passes the depth of the receiver after the appropriate number of turning points. The parameters r^* and z^* are important in later analysis.

The phase corresponding to the ray *SB* of Fig. 1 is given by ϕ_{04} of Eq. (11). The terms ψ_a and ψ_b are the phase changes due to upper and lower turning points. The integrals over vertical wave number γ combined with the kr term gives the phase change due to the path as described in detail in Appendix C.

For a general ray with several complete cycles up and down the factor $|R_a|^{n'}|R_b|^{n''}$ in Eq. (5) and the phases ψ_a and ψ_b in Eqs. (7)–(11) show, as expected, that the ray amplitude is multiplied by the reflection coefficient at each turning point. The phase terms in Eqs. (8)–(11) represent the phase change due to the incomplete cycle in each ray path.

It is important to note that the ray paths in the phase terms ϕ_{nj} of Eqs. (8)–(11) are not eigenrays. The expressions give a phase at any receiver position (r,z_r) for any ray parameter *k*. If the ray does not pass through the receiver, the phase is the phase at closest approach as shown by the point *B* in Fig. 1 and discussed in detail in Appendix C.

It is convenient to write ϕ_{nj} in the form

$$\phi_{nj} = \int_{z_s\sim}^{z_r} \gamma(z')dz' + n_j'\psi_a + n_j''\psi_b + kr, \tag{12}$$

where the notation $z_s\sim$ indicates that the integral is taken over the whole ray path including the appropriate number of reflections.

The expressions given in Eqs. (5) and (12) give the acoustic field in a range-independent situation. They are equivalent to the expressions given in Ref. 5 where all ray reflections were due to refraction turning points well clear of boundaries with associated reflection coefficients of $\exp(-i\pi/2)$.

B. Range dependence

In order to allow range dependence of the sound speed profile it is necessary to allow the horizontal wave number *k* in Eq. (12) to be a function of range. Thus *k* becomes $k(r)$ and the vertical wave number also becomes a function of range through Eq. (2).

The phase ϕ_{nj} of Eq. (12) is readily modified to accommodate variable *k* by writing

$$\phi_{nj} = \int_{z_s\sim}^{z_r} \gamma(z')dz' + \sum_{1}^{n_j'} \psi_a + \sum_{1}^{n_j''} \psi_b + \int_0^r k(r)dr, \tag{13}$$

where the sums over ψ_a and ψ_b are necessary because the phases of the reflection coefficients can be different at each reflection.

In a range-independent situation the wave number *k* is independent of range and it does not matter whether the integral in Eq. (5) is evaluated at source or receiver. However, with range dependence the value of *k* varies along the ray path. Following Kamel and Felsen[18] we "symmetrize" the integral by replacing dk by $(dk_s dk_r)^{1/2}$ which is symmetric in source and receiver. Rearrangement then leads to

$$p_{nj}(r,z) = Q(2\pi r)^{-1/2} e^{i\pi/4} \int_{-\infty}^{\infty} k_s^{1/2} |\gamma_s \gamma_r|^{-1/2} \times \prod_{1}^{n_j'} |R_a| \prod_{1}^{n_j''} |R_b| \exp(i\phi_{nj}) \times (dk_r/dk_s)^{1/2} dk_s . \tag{14}$$

The products over $|R_a|$ and $|R_b|$ are necessary because the reflection coefficients may be different at each reflection. Strictly, the values of ψ_a and ψ_b in Eq. (13) and of R_a and R_b in Eq. (14) should have subscripts *n* and *j* but these are omitted for clarity.

Equation (14) is fully range dependent and can be evaluated to give the acoustic field at the receiver due to propagation with any sequence of reflections.

It is now convenient to convert to parametrization in terms of the ray angle using the well-known connections between horizontal wave number *k*, vertical wave number γ, and ray angle θ given by

$$k = (\omega/c)\cos\theta \tag{15}$$

and

$$\gamma = (\omega/c)\sin\theta. \tag{16}$$

The phase in Eq. (13) becomes

$$\phi_{nj} = \int_{z_s\sim}^{z} (\omega/c)\sin\theta\, dz' + \sum_{1}^{n_j'} \psi_a + \sum_{1}^{n_j''} \psi_b + \int_0^r (\omega/c)\cos\theta\, dr, \tag{17}$$

and the acoustic pressure of Eq. (14) becomes

$$p_{nj}(r,z) = Q(2\pi r)^{-1/2} e^{i\pi/4} \int_{-\infty}^{\infty} [(\omega/c_s)\cos\theta_s]^{1/2} \times \prod_{1}^{n_j'} |R_a| \prod_{1}^{n_j''} |R_b| \exp(i\phi_{nj}) \times (d\theta_r/d\theta_s)^{1/2} d\theta_s. \tag{18}$$

The integral in Eq. (18) gives the acoustic field at the point (r,z) in terms of the contribution of a fan of rays from the source, each with the same sequence of turning points. It is important to note that the integral can always be evaluated numerically and can be used at all field points including points near and on caustics and in shadow zones. However, more importantly, the integral can be evaluated semi-analytically by the method of steepest descents and the field in practical cases can be found without the need for numerical integration.

C. Isolated saddle point—geometric ray

Because the phase in Eq. (18) changes much faster than the amplitude, the integral is dominated by points of stationary phase or saddle points and these correspond to eigenrays. The field due to an isolated saddle point corresponds to an isolated eigenray which arrives with sufficient time separation from any other eigenrays with the same sequence of turning points as we now show.

In order to evaluate the integral over θ_s, the saddle points are first found by solving

$$\frac{d\phi_{nj}}{d\theta_s} = 0, \tag{19}$$

It is shown in Appendix D that this defines an eigenray from source to receiver and that the value of the second derivative at the saddle point is given by

$$d^2\phi_{nj}/d\theta_s^2 = -(dz^*/d\theta_s)(\omega/c_r)\cos\theta_r(d\theta_r/d\theta_s), \tag{20}$$

where z^* is defined above and in point A of Fig. 1 as the depth at which the ray of launch angle θ_s arrives at the range of the receiver after the appropriate number of reflections or turning points.

The integral in Eq. (18) can be evaluated approximately for an isolated saddle point using the method of steepest descents as given in Ref. 5 and the second derivative given by Eq. (20). The result can be simplified to

$$p_{nj}(r,z) = Qr^{-1/2} \prod_{1}^{n_j'} |R_a| \prod_{1}^{n_j''} |R_b| [(\omega/c_s)\cos\theta_s]^{1/2} \times [(\omega/c_r)\cos\theta_r]^{-1/2} |dz^*/d\theta_s|^{-1/2} \times \exp[i(\phi_{nj}+\delta)]. \tag{21}$$

The expression in Eq. (21) gives the phase and amplitude for the field due to an isolated saddle point. The amplitude is exactly the same as that which can be derived from geometric acoustics and energy conservation. The phase ϕ_{nj} is an accumulation of phase due to path length and reflection coefficients. The phase δ arises from a phase change of $-\pi/2$ whenever a ray touches a caustic, as noted in Ref. 5.

In the numerical applications to follow, the eigenrays are found by tracing rays of source angle θ_s to find the depth $z^*(\theta_s)$ at the range of the receiver. Simple interpolation of $z^*(\theta_s)$ to the depth of the receiver gives the eigenray angles. The derivative $dz^*/d\theta_s$ is obtained by numerical differentiation of $z^*(\theta_s)$ and the phase $\phi_{nl}(\theta_s)$ is obtained directly from the ray trace. All the parameters required to evaluate Eq. (21) are found from a simple ray trace and the phase, amplitude, and travel time of each eigenray can be calculated. The waveform expected at a receiver can be constructed by placing a pulse of the appropriate amplitude and phase at the expected arrival time. This is automatically a narrow-band approximation as the phase is calculated for the center frequency of the pulse. However, it works well, even for single-cycle pulses, and gives good agreement with a reference solution and with the experimental results presented later.

It is interesting to note that the derivative $d\theta_r/d\theta_s$, which appears in Eqs. (18) and (20), cancels out in the derivation of Eq. (21). The derivative can be evaluated numerically as part of a numerical ray trace and varies rapidly for propagation involving reflections from curved boundaries.

D. Caustics and shadow zones

Caustics occur in underwater acoustics when two rays of nearby launch angles arrive at the receiver almost simultaneously. The caustic marks the boundary between the shadow zone for which there are no ray paths and the insonified side of the caustic where there are two ray arrivals.

In the vicinity of caustics the corresponding saddle points are close by and must be treated as a pair. The second derivative of the phase vanishes on the caustic at $\theta_s = \theta_0$, say, and the integral in Eq. (18) can be evaluated by expanding the phase function as a cubic as follows,

$$\phi_{nj}(\theta_s) \approx \phi_0 + (\theta_s - \theta_0)\phi_0' + (\theta_s - \theta_0)^3 \phi_0'''/6, \tag{22}$$

where the primes indicate derivatives with respect to θ_s and the subscript zero indicates evaluation at $\theta_s = \theta_0$. There is no term in $(\theta_s - \theta_0)^2$ because $\phi_0'' = 0$ by assumption. The resulting integral leads to an Airy function expression for the field as derived in Ref. 5 and given by

$$p_{nl}(r,z_r) = Q(2\pi/r)^{1/2} e^{i\pi/4} \times \prod_1^{n_j'} |R_a| \prod_1^{n_j''} |R_b| \frac{\omega}{c(z_s)}$$
$$\times \left(\frac{\cos\theta_s |\sin\theta_s|}{\omega |\sin\theta_r| / c(z_r)} \right)^{1/2} \left| \frac{d\theta_r}{d\theta_s} \right|^{1/2} \beta$$
$$\times \exp[i(\phi_0 + \delta_0)] Ai(-|\phi_0' \beta|), \quad (23)$$

where

$$\beta = |\phi_0'''/2|^{-1/3} \quad (24)$$

and the derivative is evaluated at $\theta = \theta_0$. The expression in Eq. (23) describes the field on both sides of the caustic and smoothly extends the acoustic field into the shadow zone.

E. Reduced phase derivative

In extending the wavefront modeling approach to full range dependence a minor complication occurs for caustics. A direct cubic approximation to the phase function fails because there are zeros of the phase derivative which do not correspond to eigenrays.

The first derivative of the phase function is derived in Appendix E, [Eq. (E4)], and is given by

$$d\phi/d\theta_s \approx (r^* - r)(\omega/c_r) \sin\theta_r (d\theta_r/d\theta_s). \quad (25)$$

If there is horizontal stratification and no range dependence, $\cos[\theta(z)]/c(z)$ is constant and $d\theta_r/d\theta_s$ is readily evaluated. Equation (25) becomes

$$d\phi/d\theta_s \approx (r^* - r)(\omega/c_s) \sin\theta_s. \quad (26)$$

Zeros of the phase derivative occur when $r = r^*$ and correspond to eigenrays as noted in Ref. 5. Zeros of $d\phi/d\theta_s$ also occur when $\theta_s = 0$, but this is not an eigenray unless $r = r^*$.

If there are range-dependent curved boundaries such as ocean waves at the surface, the derivative $d\theta_r/d\theta_s$ in Eq. (25) can have zeros as θ_s varies. These zeros occur when $d\theta_r/d\theta_s$ is evaluated numerically in agreement with Eq. (25), but they do not correspond to eigenrays. Such zeros occur in the vicinity of caustics and it is found that the phase function $\phi(\theta_s)$ is approximately quartic rather than the expected cubic. A cubic approximation to the numerical phase function $\phi(\theta_s)$ is then unsuitable for finding the field near the caustic.

To overcome this difficulty we work instead with a ''reduced phase derivative'' which is obtained by ignoring the zero of $d\phi/d\theta_s$ which occurs when $d\theta_r/d\theta_s$ is zero. Instead of finding the derivatives of the phase by fitting a cubic to the phase itself, we fit a quadratic to the reduced phase derivative. The right-hand side of Eq. (25), with the $d\theta_r/d\theta_s$ term fixed at its value at θ_0, is equated to the derivative of the right-hand side of Eq. (22) to give

$$(r^* - r)(\omega/c_r) \sin\theta_r (d\theta_r/d\theta_s)_{\theta=\theta_0} \approx \phi_0' + (\theta_s - \theta_0)^2 \phi_0'''/2, \quad (27)$$

The left-hand side of Eq. (27) is found numerically from the ray trace information and fitting a quadratic determines ϕ_0' and ϕ_0''' for use in Eqs. (23) and (24). The numerical value of ϕ_0 is already known from the ray trace.

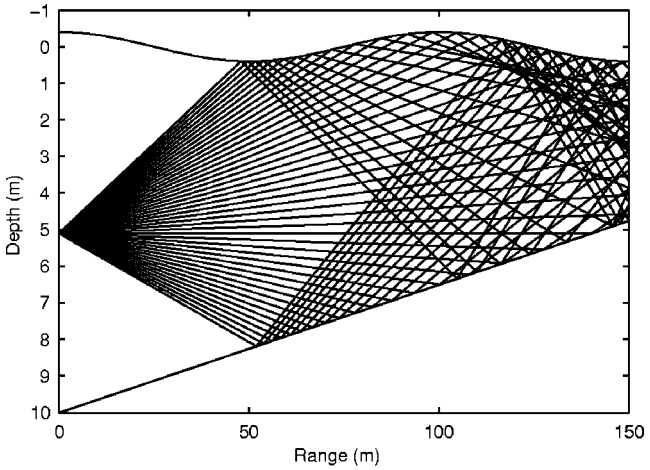

FIG. 2. Ray trace for a sinusoidal surface wave and a sloping bottom.

The field in the vicinity of the caustic found using Eqs. (23)–(27) matches smoothly on to the field when the two nearby rays can be treated separately using Eqs. (21).

III. RESULTS

A. Shallow water wedge with surface waves

As an illustrative example of wavefront modeling we consider a shallow water wedge with a bottom slope of 2° and a sinusoidal surface wave of wavelength 100 m and amplitude 0.4 m. The sound speed in the water is 1500 m/s, the sound speed in the bottom is 1757 m/s, and the density of the bottom is 2048 kg/m^3. A sound source is placed at depth 5.01 m where the water depth is 10 m.

A ray trace for upslope propagation is shown in Fig. 2 for a fan of rays between grazing angles of −5.6° and 3.4° in 0.2° increments where a positive angle means a downgoing ray. The surface and bottom reflections are treated as specular reflections at the point where the ray meets the curved interface.

The most obvious feature of Fig. 2 is the convergence of the group of rays which reflect from the underside of the wave crest at 100-m range. These rays cross over to form a focus at a depth of about 0.8 m and a range of 120 m.

The depth-time diagram at 150-m range corresponding to Fig. 2 is found numerically from the ray trace and is shown in Fig. 3. The circles mark the depth and arrival time of individual rays in 0.1° increments. The water depth is 4.75 m at this range and there is a surface wave trough at 150-m range so the water surface is at 0.4-m depth compared to the undisturbed water level. It is convenient to refer to the curve in Fig. 3 as a ''wavefront'' even though it is not strictly a wavefront but instead represents the time at which a wavefront from the source arrives at a given depth. There are multiple arrivals at any given depth because the wavefront from the source is repeatedly reflected from surface and bottom.

The section of wavefront labeled *D* in Fig. 3 corresponds to direct rays from the source which reach the range of 150 m without encountering the surface or the bottom. Similarly the sections of wavefront labeled *B* and *S* correspond to rays which have had one bottom reflection and one

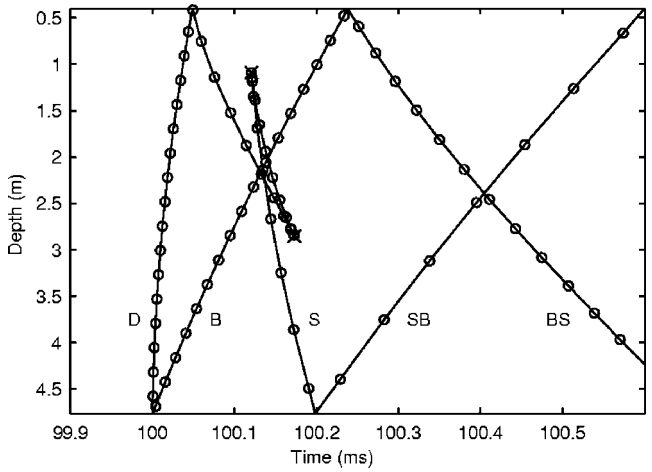

FIG. 3. Depth time diagram at 150-m range. Direct (*D*), surface reflected (*S*), and bottom reflected (*B*) branches are indicated. The labels *SB* and *BS* indicated branches reflected twice.

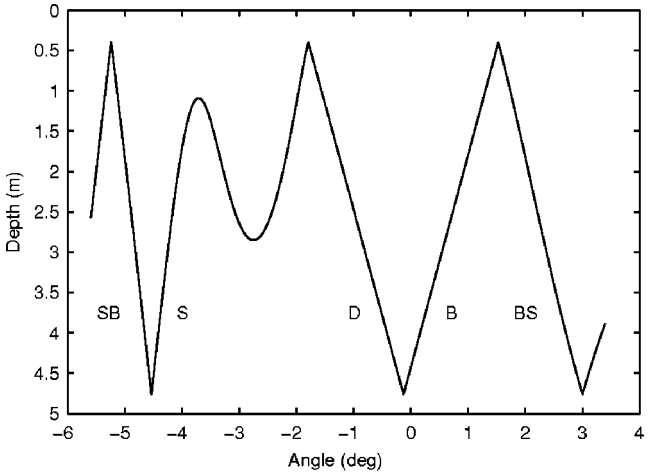

FIG. 4. Ray arrival depth as a function of launch angle.

surface reflection, respectively. The labels *SB* and *BS* indicate the sequence of reflections for the other parts of the wavefront.

The section of wavefront labeled *S* which arrives at the surface at 100.05 ms and at the bottom at 100.2 ms is folded back on itself between depths of 1.1 and 2.9 m. This folding has occurred because of the ray convergence in Fig. 2. As noted above, the convergence of rays produced a focus at a range of about 120 m. At a range just before the focus the depth-time diagram would be similar to Fig. 3 except that the surface reflected section of the wavefront would have the circles very close together but would not be folded back on itself. The circles become coincident at the focus and then as the range increases beyond the focus the wavefront folds back on itself as in Fig. 3.

Depth-time diagrams such as that shown in Fig. 3 are obtained as an intermediate step in the wavefront modeling procedure. The depth-time diagram is useful in its own right because it provides a clear physical picture of the arrival structure.

The ray arrival depth as a function of launch angle is shown in Fig. 4. The graph is equivalent to $z^*(\theta_s)$ where z^* is the depth of the ray as it passes the range of the receiver as shown in Fig. 1. The sections of the graph labeled *D*, *B*, *S*, *SB*, and *BS* correspond to the wavefront sections of Fig. 3. The maximum and minimum on section *S* of the graph correspond respectively to the upper and lower extrema of the folded wavefront in Fig. 3. Thus as the ray launch angle moves steadily between $-4°$ and $-3.4°$ the depth of the ray at 150-m range decreases to 1.1 m for a launch angle of $-3.7°$ and then increases again. The turning point at an angle of $-3.7°$ corresponds to a caustic in the acoustic field. At a caustic there are two nearby rays on the insonified side (depth$>$1.1 m) and no corresponding rays on the shadow side (depth$<$1.1 m). The caustic appears in Fig. 3 as the sharp extremum in the wavefront at a 1.1-m depth. There is a second caustic at 2.9-m depth.

The waveforms expected from a short transmitted pulse on hydrophones at a range of 150 m is readily calculated from the information in Figs. 3 and 4. Examples of waveforms are shown at successive depths in Fig. 5. The source pulse is taken as a four-period, Hanning weighted sine wave at 80 kHz with a bandwidth from 40 to 120 kHz. The wavelength at 80 kHz is about 1.9 cm so the surface wave amplitude is about 20 acoustic wavelengths. Figure 5 also shows a reference solution kindly provided by Finn Jensen and Peter Nielsen and found using the wide band PE code RAM described in Ref. 4. Agreement between the present wavefront result and the reference curve is very good.

The first pulse at each depth from 1 to 4 m comes along a direct ray path and is a replica of the source pulse. Near the surface and bottom the direct and reflected pulses are not separated in time and overlap to produce a distorted pulse.

The sequence of arrivals at a given depth is found by considering a line on the depth-time curve of Fig. 3 at the appropriate depth. Thus a line at 3.5-m depth shows that the first three pulses would be expected to begin at 100, 100.06, and 100.16 ms, respectively, corresponding in turn to direct, bottom reflected, and surface reflected ray paths. The centers of the pulses arrive 0.025 ms later. The corresponding waveform is shown at 3.5-m depth in Fig. 5. The pulse centered at 100.18 ms is inverted with respect to the direct pulse because it has been reflected at the surface and has a 180° phase shift. The pulses at 100.08 and 100.33 ms have been reflected at the bottom and have an intermediate phase shift due to the complex reflection coefficient at the bottom. The amplitude of the pulses is found from Eq. (21) and is a function of $dz^*/d\theta_s$, which is readily obtained numerically from the data of Fig. 4.

The waveforms in the vicinity of the caustics are readily calculated using the methods outlined in Ref. 5 but modified as discussed in Sec. III above. On the insonified side there are two rays with nearby launch angles. If the paths lengths of these rays differ by less than a quarter of a wavelength (at the center frequency of the pulse), they must be considered as a pair. When this occurs the corresponding stationary points of the phase function $\phi(\theta_s)$ of Eq. (13) are not isolated. The reduced phase derivative can be approximated by a quadratic and the amplitude and phase of the contribution to the acoustic field is given by an Airy function as described above. Examples of this are seen in Figs. 3 and 5 at a depth

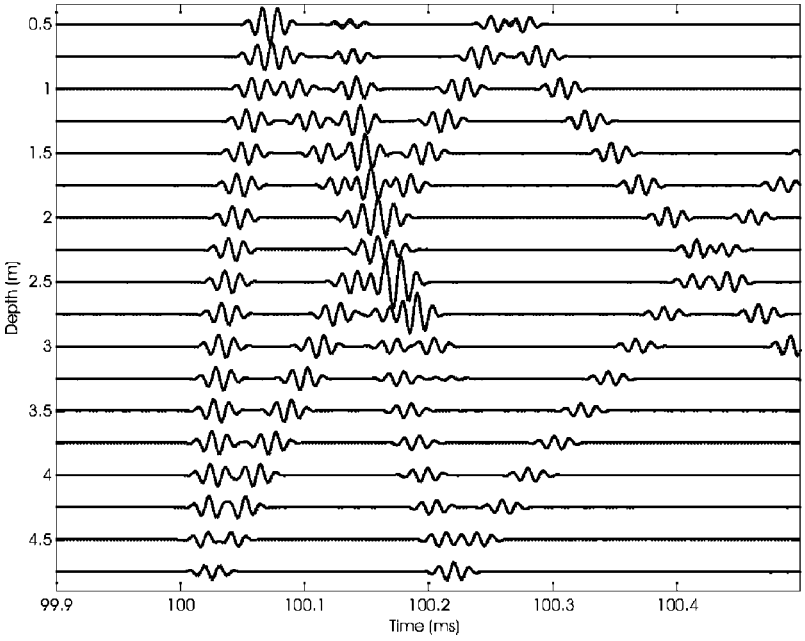

FIG. 5. Waveforms (solid lines) and reference solution (dashed lines) at successive depths corresponding to the depth-time diagram of Fig. 3.

of 1.25 m and a start time of 100.12 ms and also at a depth of 2.75 m and a start time of 100.17 ms.

On the shadow side of a caustic there are no geometric eigenrays but there is still a contribution to the acoustic field which decays exponentially with distance into the shadow. Comparison of Figs. 3 and 5 shows that the pulses centered at about 100.14 ms at depths of 0.5, 0.75, and 1.0 m and at the pulses at about 100.21 ms at depths of 3.0 and 3.25 m in Fig. 5 are all in the shadow zones of the corresponding caustics.

Pulses which arrive at the same time but which have quite different launch angles interfere normally and the corresponding contribution to the waveform is simply the sum of the individual contributions. Figure 3 shows that at 2-m depth there are four arrivals between 100.13 and 100.16 ms. Figure 4 shows that these four arrivals do not have nearby launch angles and so the corresponding pulses add independently to produce the complicated pulse at 2-m depth between 100.13 and 100.19 ms in Fig. 5.

The wavefront modeling calculations leading to Fig. 5 are fast and efficient because they take place in the time domain without the need for multiple frequency calculations and Fourier transforms.

B. Comparison with experiment

Experimental results were obtained at the Scripps Pier in December 2000. The experimental data taken on the three hydrophones showed the sequence of pulse arrivals expected from multiple reflections in shallow water and the theoretical results from the wavefront model were in general qualitative agreement. There was occasional strong signal enhancement associated with focusing due to surface waves and examples were given in Ref. 6. It was hoped that it would be possible to model all waveforms in detail, but unfortunately the surface waves were not measured well enough to allow precise modeling of any focusing or caustic events.

General features of the experimental results were presented in Ref. 6. An acoustic source was placed 2.35 m above the bottom and a three-hydrophone vertical array was placed 36 m directly shoreward. The hydrophones were 0.5 m apart and the lowest was 1 m above the bottom.

Short pulses at 10 kHz were transmitted upslope from the source in about 7 m of water to the hydrophones in about 6 m of water. Surface waves were present throughout the experiment. As successive waves pass over the system the pulses with one or more surface reflections have varying time delays with respect to the direct and bottom reflected signals. The experiment showed that the underside of a wave crest acts as a curved mirror for sound. This leads to focusing and strong increase of signal amplitude. Since the acoustic path length is longer for reflection from a wave crest the increased intensity is associated with a time delay. The experimental situation is illustrated in Fig. 6 which shows the main eigenrays from the source to the middle hydrophone. The source is on the left at 4.9-m depth and the positions of the three hydrophones are shown as circles on the right of the

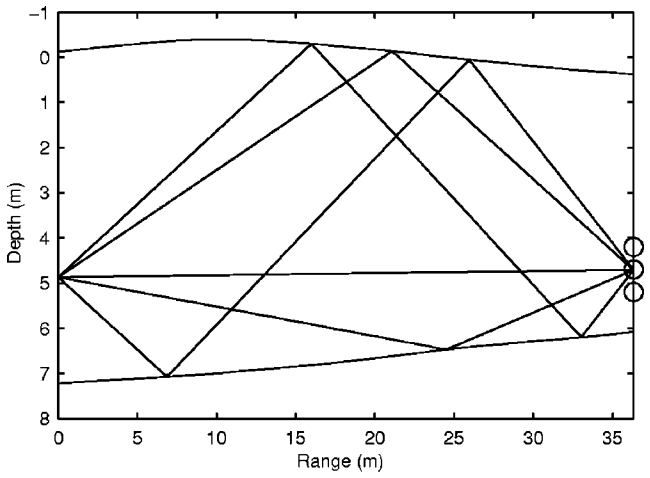

FIG. 6. Eigenrays for a wave crest at range 14 m.

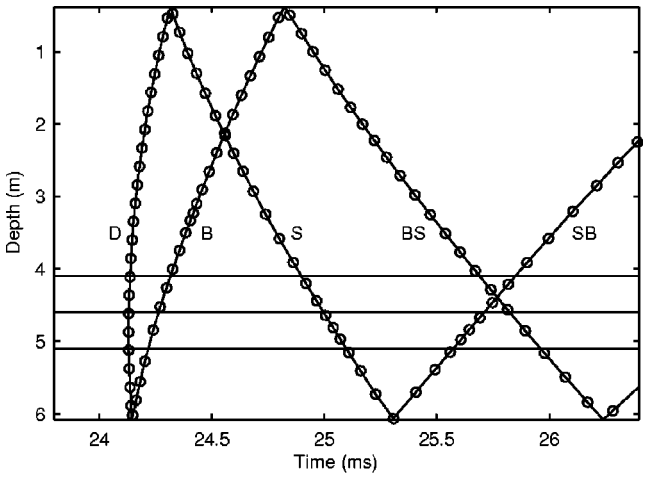

FIG. 7. The depth time diagram at a range of 36 m.

figure. The ocean bottom has depth 7.1 m at the source and slopes upward at about 1.9°.

Unbroken surface waves of amplitude about 0.8 m peak-to-trough were present during the experiment and wave data were taken on an array of nine uniformly spaced, bottom-mounted pressure sensors. The instantaneous waveform shape at a given time was deduced by interpolation of the time series for each pressure sensor. Unfortunately, sampling the pressure field at the bottom has the effect of smoothing the surface waves and the measurement of the surface shape has some uncertainty.

In the representative experimental situation shown in Fig. 6 the curved water surface shows a wave crest at about 14 m from the source. The depth-time diagram at the range of the receiving array is shown in Fig. 7 for the situation corresponding to Fig. 6. Each circle corresponds to the arrival time of a particular ray in increments of 0.5° launch angle. The labels *D*, *B*, and *S* indicate direct, bottom reflected, and surface reflected rays, respectively. The labels *SB* and *BS* similarly indicate the sequence of reflections. There is no significant focusing in this case. There is a very slight convergence near the label *B*. This would lead to a focus further in range. The three horizontal lines in Fig. 7 show the hydrophone depths and the sequence of arrivals at each hydrophone is given by the wavefront crossings at that depth. The source was excited by a one-cycle pulse at 10 kHz. The transmitted waveform sampled on a hydrophone 1 m from the source is shown in Fig. 8.

The theoretical waveforms (solid lines) are compared

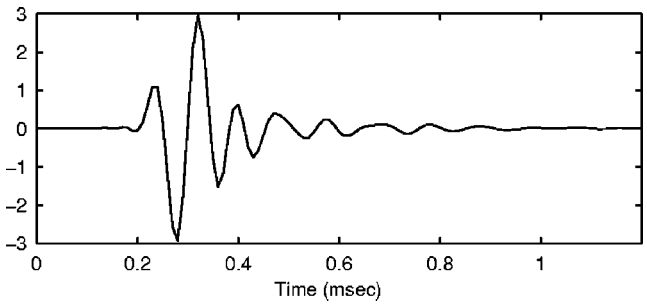

FIG. 8. Source waveform.

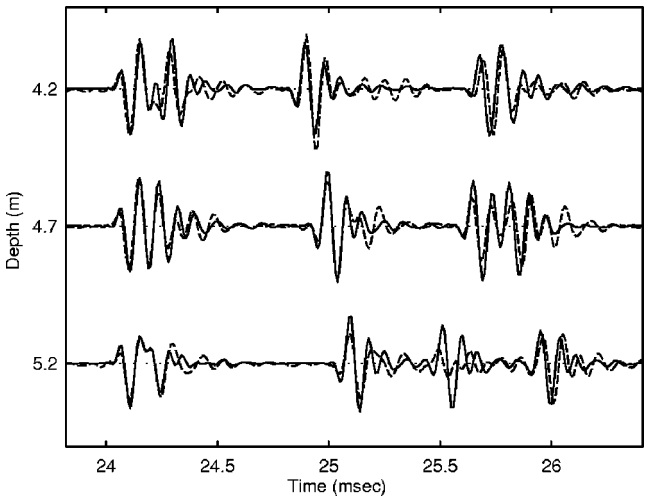

FIG. 9. Calculated waveforms (solid lines) compared with data (dashed lines). The curves have been adjusted to have the same amplitude and arrival time for the first pulse on the top hydrophone.

with the experimental data (dashed lines) in Fig. 9 for the experimental situation of Fig. 6. The waveforms correspond to the three hydrophones at the depths indicated. The two sets of curves have been adjusted to have the same arrival time and pulse amplitude for the first arrival on the top hydrophone. The total water depth has been reduced by 0.2 m from the measured water depth in order to improve the agreement of the arrival times of the surface reflected pulses.

Apart from these adjustments there are no fitted parameters. It is clear that the theoretical waveforms are in good general agreement with the data. The waveforms before 24.5 ms are given by the direct and bottom reflected rays. The corresponding pulses are almost separated on the top hydrophone but interfere to give a lengthened pulse on the middle hydrophone and a severely distorted waveform on the bottom hydrophone. These first two arrivals are unaffected by the surface waves and are identical on all data records. The waveforms for the first two arrivals are very well reproduced by the model.

The third arrival in Fig. 9 on each hydrophone, i.e., the pulses between 24.7 and 25.4 ms are due to the surface reflected eigenray of Fig. 6. There is good agreement of arrival time and pulse shape between model and experiment for these surface reflected pulses.

The pulses after 25.4 ms in Fig. 9 are due to *SB* (surface then bottom) and *BS* (bottom then surface) reflections. The *SB* and *BS* pulses are separated on the bottom two hydrophones but interfere to give a single pulse on the top hydrophone. There is good agreement of the arrival times of the pulses but some of the amplitudes do not agree, particularly for the *SB* arrival on the bottom hydrophone. It is likely that the *SB* arrival has been defocused on reflection from a curved ocean surface whose details have been lost because of the use of pressure sensors, as noted above.

The difference in modeled and measured waveforms in Fig. 9 results from the sensitivity of the model to the precise details of the ocean surface. As noted above there is some uncertainty in determination of the surface shape accounting

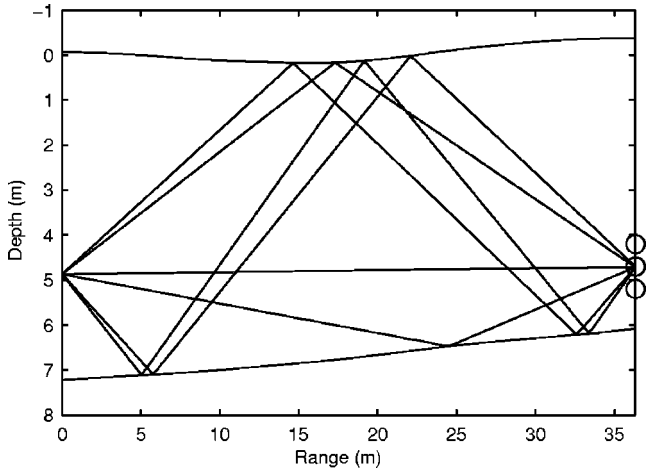

FIG. 10. Eigenrays 3.8 s after Fig. 6. Wave crest at 36-m range.

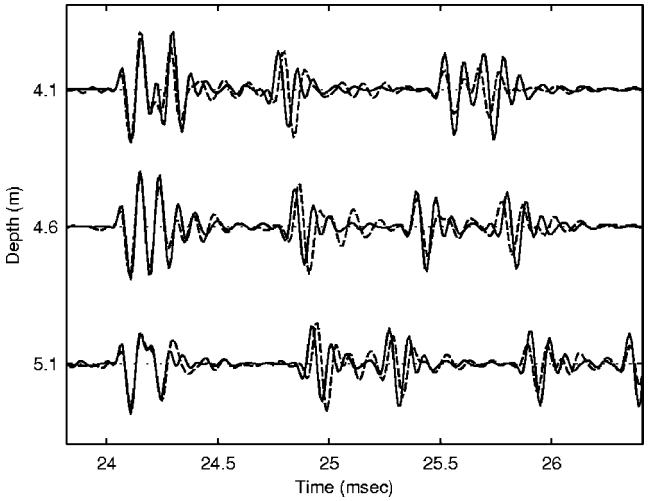

FIG. 12. As for Fig. 11 but with water depth reduced by 10 cm.

for the few disagreements between model and data in Fig. 9. Overall the agreement is good.

The situation 3.8 s later than Figs. 6 and 9 is shown in Figs. 10 and 11. The wave crest has moved to 36-m range in Fig. 10 with a wave speed of about 6.6 m/s. The ray paths in Fig. 10 show that the surface reflected rays are reflected from a trough rather than near a crest as in Fig. 6.

The waveforms for this case are shown in Fig. 11. The waveforms before 24.5 ms in Fig. 11 are the same as in Fig. 9 because they represent the direct and bottom reflected rays and are unaffected by the surface waves.

Because of the wave trough at 15-m range the surface reflected eigenray in Fig. 10 has a shorter total path than the corresponding one in Fig. 6 and so the associated pulses (between 24.7 and 25.2 ms) in Fig. 11 arrive earlier than those in Fig. 9.

For the later arrivals after 25.3 ms in Fig. 11 there is a time offset between model and experiment which indicates that the experimentally determined surface shape is not correct. The sensitivity of the calculation to the precise values of the environmental parameters is illustrated in Fig. 12. The figure is obtained using all the parameters of Fig. 11 except that the water depth has been reduced by 10 cm. The modeled surface reflected pulses now arrive a little early but the agreement of arrival times of the *SB* (25.2 to 25.6 ms) and *BS* (25.6 to 26.2 ms) pulses is much improved. In addition, the arrival time of the *BSB* pulse at the end of the waveform for the bottom hydrophone is well modeled.

In principle it would be possible to use the measured waveforms and pulse travel times to deduce the surface wave shape and improve the overall agreement between model and data. However, the results show that the computer code based on the wavefront modeling method is able to model the general features and much of the detail of the experimental data.

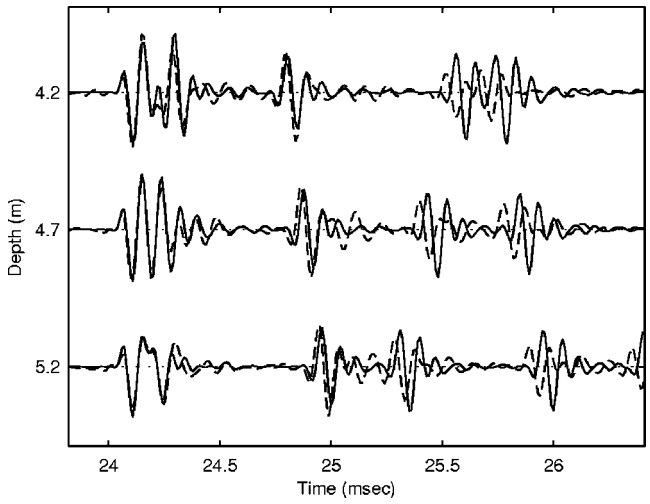

FIG. 11. Waveforms 3.8 s after those of Fig. 9.

IV. CONCLUSIONS

The wavefront modeling method has been extended to model acoustic propagation when there is rapid range dependence of the boundaries due to real surface waves in shallow water. The model gives generally good agreement with a reference solution and with experimental data. It produces all the qualitative features of the data including the sudden amplitude changes due to focusing and the formation of caustics. Unfortunately, the surface wave field was not obtained with sufficient precision to model every detail of the experimental data.

The wavefront modeling approach gives a clear physical interpretation of the propagation process. In particular, the depth time diagrams produced as an intermediate stage in the wavefront modeling method provide a very useful physical picture of the multiple reflection process and the signal enhancement due to focusing by the curved underside of surface waves crests.

ACKNOWLEDGMENTS

This work was partially supported by ONR Contract No. N00014-00-1-0138. The authors are grateful to Finn Jensen and Peter Nielsen for supplying the reference solution of Fig. 5.

APPENDIX A: RAY EXPANSION SOLUTION OF THE WAVE EQUATION

A direct ray expansion solution of the wave equations can be obtained by combining a Hankel transform solution with the *WKB* approximation in a method introduced by Batorsky and Felsen[17] and extended to wavefront modeling of deep water pulse propagation in Ref. 5.

For a cylindrically symmetric situation in which the sound speed is a function of depth, the acoustic pressure at range r and depth z due to a point source of strength Q at range $r=0$ and depth $z=z_s$ can be written as a Hankel transform in the horizontal wave number k as follows:

$$p(r,z)=-Q\int_{-\infty}^{\infty}\frac{U(z)V(z_s)}{W}H_0^{(1)}(kr)k\,dk, \quad z<z_s, \tag{A1}$$

$$=-Q\int_{-\infty}^{\infty}\frac{U(z_s)V(z)}{W}H_0^{(1)}(kr)k\,dk, \quad z>z_s. \tag{A2}$$

The Wronskian W is given by

$$W=U(z)V'(z)-U'(z)V(z), \tag{A3}$$

and the depth functions $U(z)$ and $V(z)$ satisfy the boundary conditions above and below the source, respectively. The functions $U(z)$ and $V(z)$ are linearly independent solutions of the depth-separated wave equation

$$\frac{\partial^2 U}{\partial z^2}+\gamma^2 U=0. \tag{A4}$$

The vertical wave number γ is given by Eq. (2).

We now assume that the boundary condition above the source at depth $z=a$ can be described by a reflection coefficient $R_a(k)$. The depth a does not have to be an actual boundary as the reflection coefficient can be defined as the ratio of amplitudes of downgoing and upgoing waves at the depth $z=a$. Similarly, the boundary condition below the source at depth $z=b$ is described by a reflection coefficient $R_b(k)$.

The *WKB* approximations to the depth functions $U(z)$ and $V(z)$ can now be written

$$U(z)\approx B|\gamma(z)|^{-1/2}\left[\exp\left(-i\int_a^z\gamma\,dz'\right)+R_a\exp\left(i\int_a^z\gamma\,dz'\right)\right], \tag{A5}$$

$$V(z)\approx C|\gamma(z)|^{-1/2}\left[\exp\left(-i\int_z^b\gamma\,dz'\right)+R_b\exp\left(i\int_z^b\gamma\,dz'\right)\right], \tag{A6}$$

and the Wronskian W becomes

$$W=2iBC\exp\left[-i\left(\int_a^b\gamma\,dz'\right)\right]\times\left[1-R_aR_b\exp\left(2i\int_a^b\gamma\,dz'\right)\right], \tag{A7}$$

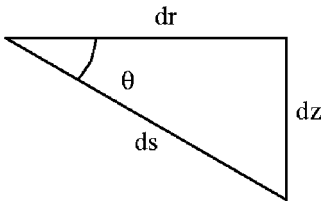

FIG. 13. An element of a ray path.

where we have neglected terms in $d\gamma/dz$ to be consistent with the *WKB* assumptions of slow parameter variation with respect to wavelength.

Following Batorsky and Felsen[17] and Frisk[19] the Wronskian in the denominator of Eq. (A2) leads through Eq. (A7) to a term of the form $(1-x)^{-1}$, which can be expanded as a power series to give

$$1/W=(2iBC)^{-1}\exp\left[i\left(\int_a^b\gamma\,dz'\right)\right]\times\sum_{n=0}^{\infty}\left\{R_aR_b\exp\left[2i\left(\int_a^b\gamma\,dz'\right)\right]\right\}^n. \tag{A8}$$

Combining this expansion, the explicit expressions for U and V in Eqs. (A5) and (A6), and the asymptotic approximation to the Hankel function

$$H_0^{(1)}(kr)\sim(2/\pi kr)^{1/2}\exp[i(kr-\pi/4)] \tag{A9}$$

and rearranging gives Eq. (1).

APPENDIX B: RAY PATH PHASE AND WAVE NUMBER INTEGRALS

The phase change ϕ along a ray path is given by

$$\phi=\int(\omega/c)ds, \tag{B1}$$

where ω is the angular frequency of propagation, s is distance along the ray path, and c is the local sound speed. An element of a ray path is shown in Fig. 13.

With the geometry of Fig. 13 we can write

$$\phi=\int(\omega/c)[\cos\theta\,dr+\sin\theta\,dz]=\int_0^r(\omega/c)\cos\theta\,dr+\int_{z_s\sim}^{z_r}(\omega/c)\sin\theta\,dz, \tag{B2}$$

where the notation $z_s\sim$ indicates that if the ray cycles up and down the corresponding sections of the integral over depth are added together.

Using the usual relations between wave numbers and ray angle given in Eqs. (15) and (16), Eq. (B2) can be written

$$\phi=\int_0^r k\,dr+\int_{z_s\sim}^{z_r}\gamma\,dz. \tag{B3}$$

For horizontal stratification the horizontal wave number k is constant and we can write

$$\phi=kr+\int_{z_s\sim}^{z_r}\gamma\,dz. \tag{B4}$$

Equations (B2)–(B4) show explicitly the link between the phase of a geometric ray and the solution of the wave equation developed in Eqs. (5)–(14).

APPENDIX C: PHASE OF AN ARBITRARY RAY

Figure 1 shows schematic ray geometry for a ray path with one lower and one upper turning point. The turning points could be refractions or reflections at boundaries which need not be horizontal. The dashed curve is an eigenray from the source S at $(0,z_s)$ to the receiver R at (r,z_r).

The solid curve shows a typical nearby ray with the same sequence of turning points as the eigenray. The ray separation is exaggerated for clarity. The ray leaves the source at angle θ_s and has angle θ_r in the vicinity of the receiver. The depth z^* is defined as the depth of the ray at the range of the receiver and so the ray passes through the point A with coordinates (r,z^*). Similarly the range r^* is defined as the range at which the ray crosses the receiver depth after the appropriate number of turning points and the ray passes through the point C with coordinates (r^*,z_r).

The line BR is perpendicular to the ray through B. Since the solid and dashed rays have nearby launch angles, the arc AB can be considered a straight line and the phase $\phi(\theta_s)$ of the ray at B is given by

$$\phi(\theta_s)=\int_{(0,z_s\sim)}^{(r,z^*)}(\omega/c)ds+(\omega/c)(z_r-z^*)\sin\theta_r+\psi_a+\psi_b, \tag{C1}$$

where ψ_a, and ψ_b are the phase changes due to reflection or refraction at the turning points. Using Eqs. (B2) and (C1) this can be written

$$\phi(\theta_s)=\int_0^r(\omega/c)\cos\theta\,dr+\int_{z_s\sim}^{z^*}(\omega/c)\sin\theta\,dz+(\omega/c)\times(z_r-z^*)\sin\theta_r+\psi_a+\psi_b, \tag{C2}$$

which simplifies to

$$\phi(\theta_s)=\int_0^r(\omega/c)\cos\theta\,dr+\int_{z_s\sim}^{z_r}(\omega/c)\sin\theta\,dz+\psi_a+\psi_b. \tag{C3}$$

The phase $\phi(\theta_s)$ is the phase of the ray at the point B in Fig. 1. However the line BR is perpendicular to the ray at B and therefore BR is a wavefront. Therefore $\phi(\theta_s)$ is the phase at the receiver of the wavefront corresponding to the ray with source angle θ_s.

It is important to note that even though the ray with launch angle θ_s is not an eigenray, the ray still has a phase at the receiver and this phase is given by $\phi(\theta_s)$.

APPENDIX D: EIGENRAYS

The phase derivative with respect to source angle can be written

$$d\phi/d\theta_s=\int_0^r(\omega/c)[-\sin\theta(d\theta/d\theta_s)]dr+\int_{z_s\sim}^{z_r}(\omega/c)\times[\cos\theta(d\theta/d\theta_s)]dz+(d\psi_a/d\theta)(d\theta/d\theta_s)+(d\psi_b/d\theta)(d\theta/d\theta_s). \tag{D1}$$

Setting $d\phi/d\theta_s$ equal to zero gives an equation which can be treated as a relationship between r, z_r, and θ_s. This equation is the equation of the eigenray, i.e., the ray of launch angle θ_s which passes through the point r, z_r after the appropriate number of turning points. This is readily shown if we assume horizontal stratification. For horizontal stratification Snell's law is satisfied in the form

$$\cos\theta/c(z)=\cos\theta_s/c(z_s). \tag{D2}$$

Using this to evaluate $d\theta/d\theta_s$, substituting in Eq. (D1) and simplifying leads to

$$r=\int_{z_s\sim}^{z_r}\cot\theta\,dz+d\psi_a/d\theta[(\omega/c_a)\sin\theta_a]^{-1}+d\psi_b/d\theta[(\omega/c_b)\sin\theta_b]^{-1}, \tag{D3}$$

which is the equation of an eigenray ray path with beam displacement. The subscripts a and b refer to values at the turning points at $z=a$ and $z=b$, respectively. The beam displacement arises when the phase change on reflection is a function of the angle of incidence.[20] The inclusion of beam displacement is unnecessary in the present high-frequency wavefront modeling, but it will be considered in future work.

APPENDIX E: PHASE DERIVATIVES

Changing the variable of integration in the second integral of Eq. (D1) using

$$\cos\theta\,dz=\sin\theta\,dr \tag{E1}$$

from Fig. 13 and ignoring beam displacement leads to

$$d\phi/d\theta_s=\int_0^r(\omega/c)[-\sin\theta(d\theta/d\theta_s)]dr+\int_0^{r^*}(\omega/c)[\cos\theta(d\theta/d\theta_s)]\tan\theta\,dr, \tag{E2}$$

which simplifies to

$$d\phi/d\theta_s=\int_r^{r^*}(\omega/c)[\sin\theta(d\theta/d\theta_s)]dr. \tag{E3}$$

It is clear that $d\phi/d\theta_s=0$ when $r=r^*$ and this corresponds to an eigenray as shown in Fig. 1. In order to evaluate the second derivative of the phase for an eigenray we can use the following approximation to Eq. (E3):

$$d\phi/d\theta_s\approx(r^*-r)(\omega/c_r)\sin\theta_r(d\theta_r/d\theta_s). \tag{E4}$$

Differentiating and setting $r=r^*$ gives for the eigenray

$$d^2\phi/d\theta_s^2=(dr^*/d\theta_s)(\omega/c_r)\sin\theta_r(d\theta_r/d\theta_s). \tag{E5}$$

Now by the geometry of Fig. 1 we have

$$dr^* \approx r^* - r \approx (z_r - z^*)\cot\theta_r \approx -dz^* \cot\theta_r, \quad \text{(E6)}$$

which gives for the eigenray

$$d^2\phi/d\theta_s^2 = -(dz^*/d\theta_s)(\omega/c_r)\cos\theta_r(d\theta_r/d\theta_s). \quad \text{(E7)}$$

[1] F. D. Tappert, ''The parabolic approximation method,'' in *Wave Propagation in Underwater Acoustics*, edited by J. B. Keller and J. S. Papadakis (Springer-Verlag, New York, 1977), pp. 224–287.

[2] D. J. Thomson and N. R. Chapman, ''A wide-angle split-step algorithm for the parabolic equation,'' J. Acoust. Soc. Am. **74**, 1848–1854 (1983).

[3] M. D. Collins, ''Applications and time-domain solutions of higher-order parabolic equations in underwater acoustics,'' J. Acoust. Soc. Am. **86**, 1097–1402 (1989).

[4] F. B. Jensen, C. M. Ferla, P. L. Nielsen, and G. Martinelli, ''Broadband signal simulation in shallow water,'' J. Comput. Acoust. **14**, 577–591 (2003).

[5] C. T. Tindle, ''Wavefronts and waveforms in deep-water sound propagation,'' J. Acoust. Soc. Am. **142**, 464–475 (2002).

[6] J. C. Preisig and G. B. Deane, ''Surface wave focusing and acoustic communications in the surf zone,'' J. Acoust. Soc. Am. **146**, 2067–2080 (2004).

[7] Y. A. Kravtsov and Y. I. Orlov, *Geometrical Optics of Inhomogeneous Media* Springer Series on Wave Phenomena, Vol. 6 (Springer, Berlin, 1990).

[8] L. M. Brekhovskikh and O. A. Godin, *Acoustics of Layered Media. II: Point sources and bounded beams*, Springer Series on Wave Phenomena, Vol. 10 (Springer, Berlin, 1992).

[9] L. Brekhovskikh and Y. Lysanov, *Fundamentals of Ocean Acoustics*, 3rd ed. (Springer-Verlag, New York, 2003).

[10] S. T. McDaniel, ''A small-slope theory of rough surface scattering,'' J. Acoust. Soc. Am. **95**, 1859–1864 (1994).

[11] W. A. Kinney, C. S. Clay, and G. A. Sandness, ''Scattering from a corrugated surface: Comparison between experiment, Helmholtz-Kirchhoff theory, and the facet-ensemble method,'' J. Acoust. Soc. Am. **73**, 183–194 (1983).

[12] D. F. McCammon and S. T. McDaniel, ''Application of a new theoretical teatment to an old problem; sinusoidal pressure release boundary scattering,'' J. Acoust. Soc. Am. **78**, 149–156 (1985).

[13] A. Purcell, ''Reflection coefficient for scattering from a pressure-release, sinusoidal surface,'' J. Acoust. Soc. Am. **100**, 2919–2936 (1996).

[14] K. L. Williams, J. S. Stroud, and P. L. Marston, ''High-frequency forward scattering from Gaussian spectrum, pressure release, corrugated surfaces. I. Catastrophe theory modeling,'' J. Acoust. Soc. Am. **96**, 1687–1702 (1994).

[15] V. B. Avdeev, A. V. Demin, Y. A. Kravtsov, M. V. Tinin, and A. P. Yarygin, ''Method of Interferential Integrals—A Review,'' Inst. General Phys., Acad. Sci. USSR, translated from Izv. Vyssh. Uchebn. Zaved., Radiofiz. **31**, 1279–1294 (1988).

[16] D. A. Sachs and A. Silbiger, ''Focusing and refraction of harmonic sound and transient pulses in stratified media,'' J. Acoust. Soc. Am. **49**, 824–840 (1971).

[17] D. V. Batorsky and L. B. Felsen, ''Ray-optical calculation of modes excited by sources and scatterers in a weakly inhomogeneous duct,'' Radio Sci. **6**, 914–923 (1971).

[18] A. Kamel and L. B. Felsen, ''Spectral theory of sound propagation in an ocean channel with weakly sloping bottom,'' J. Acoust. Soc. Am. **73**, 1421–1430 (1983).

[19] G. V. Frisk, *Ocean and Seabed Acoustics* (Prentice-Hall, Englewood Cliffs, NJ, 1994).

[20] L. M. Brekhovskikh, *Waves in Layered Media* (Academic, New York, 1980).

Simulations of optoacoustic wave propagation in light-absorbing media using a finite-difference time-domain method

Deng-Huei Huang, Chao-Kang Liao, Chen-Wei Wei, and Pai-Chi Li[a)]
Department of Electrical Engineering, National Taiwan University, Taipei, Taiwan

(Received 21 June 2004; revised 12 December 2004; accepted 22 February 2005)

Optoacoustic (OA) imaging is an emerging technology that combines the high optical contrast of tissues with the high spatial resolution of ultrasound. Taking full advantage of OA imaging requires a better understanding of OA wave propagation in light-absorbing media. Current simulation methods are mainly based on simplified conditions such as thermal confinement, negligible viscosity, and homogeneous acoustic properties throughout the image object. In this study a new numerical approach is proposed based on a finite-difference time-domain (FDTD) method to solve the general OA equations, comprising the continuity, Navier-Stokes, and heat-conduction equations. The FDTD code was validated using a benchmark problem that has an approximate analytical solution. OA experiments were also conducted and data were in good agreement with those predicted by the FDTD method. Characteristics of simulated OA waveforms and OA images were discussed. The simulator was also employed to study wavefront distortion in OA breast imaging.
 [DOI: 10.1121/1.1893305]

PACS numbers: 43.35.Ud, 43.20.El, 43.20.Bi [AJS] Pages: 2795–2801

I. INTRODUCTION

Optoacoustic (OA) effects in biological tissues have received considerable attention in recent years because of their potential applications in biomedical imaging such as depth-resolved analysis of tissues,[1] detection and localization of breast cancer,[2] and noninvasive brain functional imaging.[3] OA signals can be generated when a light-absorbing object is irradiated by modulated light. The dominant mechanism for the conversion of optical electromagnetic energy into mechanical energy in biological tissues is thermal expansion. Several algorithms have been proposed for reconstructing the internal light-absorption profile of an object,[4–8] and these algorithms can generally be categorized into three modes according to the configuration of irradiation and OA signal acquisition: (1) forward mode, with the radiation source and ultrasound detection on opposite sides of the object; (2) backward mode, with the radiation source and ultrasound detection on the same side of the object; and (3) sideward mode, with ultrasound receivers perpendicular to the direction of irradiation to detect the OA signals induced inside the object. Visualization of the OA propagation in these modes, which is currently only possible via simulations, is very important to the development of effective OA imaging methods. Current simulation methods are based on simplified conditions such as thermal confinement, negligible viscosity, and homogeneous acoustic properties throughout the object to be imaged. The thermal-confinement condition is satisfied when the duration of the light pulse is much shorter than the thermal diffusion time, which is generally the case in soft tissues. The viscosity and the variations in acoustic properties, however, are not negligible for most soft tissues (e.g., blood is very viscous, and the abdomen and breast are highly inhomogeneous). In this study we start from the general OA equations that incorporate the spatial inhomogeneities of thermal and acoustic properties. A numerical approach to solving the OA equations is formulated using a finite-difference time-domain (FDTD) method. FDTD techniques have been used extensively to simulate the propagation and scattering of electromagnetic waves[9] and acoustic waves.[10] In optoacoustics, however, no similar application has yet been proposed. The approximate analytical solutions obtained by Karabutov *et al.*[11] were then used to validate the FDTD simulator. Experimental backward OA signals from a phantom were also acquired for further validation. The characteristics of simulated OA waveforms and OA images are discussed. In addition, the simulator is employed to investigate the wavefront distortion in OA breast imaging.

In recent years considerable effort has been devoted to the study of OA effects in human breast.[2] The angiogenesis phenomenon associated with cancers makes tumors have appreciably higher optical absorption with respect to normal surrounding tissues. When such a tumor is irradiated by short laser pulses, the difference is optical absorption results in differentiable OA signals that can be used to reconstruct the optical absorption distribution.[6,8] Current OA imaging algorithms, however, are based on the assumption that acoustic properties of the medium to be imaged are uniform. Unfortunately, such an assumption is rarely valid in clinical applications. Effects of acoustic heterogeneities, including acoustic impedance mismatch and sound velocity infomogeneities, on ultrasound breast imaging have long been studied by many researchers.[12–14] It has been widely recognized that wavefront distortion and the resultant degradation in focusing quality is a major cause to prohibit breast ultrasound from obtaining the diffraction-limited resolution. In breast OA tomography, Xu and Wang[15] proposed a ray approach similar to that in geometric optics to account for the OA wavefront distortion. Using acoustic ray tracing under sim-

[a)]Author to whom correspondence should be addressed. Electronic mail: paichi@cc.ee.ntu.edu.tw

plified geometries, they inferred that amplitude distortion caused by refraction was not serious in breast OA tomography because OA signals are broadband, in a lower frequency range, and experience only one-way transmission distortion. However, *in vitro* one-way transmission experiments[14] have shown that waveform distortion was generally not negligible for broadband ultrasound. In addition, full-wave approaches such as the FDTD method[10] showed that waveform distortion was accumulative caused by acoustic impedance mismatch along all possible propagation paths, which cannot be fully described with simple ray tracing. An OA wavefront could potentially undergo less waveform distortion as compared to an ultrasonic wavefront because it suffers less distortion due to its lower frequency range, but it still remains unclear if the distortion is negligible in OA breast imaging because no counterparts of experiments or full-wave simulations as those in clinical breast ultrasound have yet been seen. Therefore, the simulator that we developed in this study can also be employed to study wavefront distortion in OA breast imaging. Numerical examples are also given in this paper to further demonstrate the usage of this FDTD simulator.

II. MATHEMATICAL FORMULATION

The equations of optoacoustics that relate sound excitation and the subsequent propagation in liquids to the thermal field change caused by light absorption can be formulated—with second-order nonlinear terms and classical dissipative effects—as follows:[16]

$$\frac{\partial \rho'}{\partial t}+\rho_0 \nabla \cdot \vec{u}=-\rho' \nabla \cdot \vec{u}-\vec{u}\cdot\nabla(\rho'+\rho_0), \tag{1}$$

$$\rho_0 \frac{\partial \vec{u}}{\partial t}+\nabla p=-\rho' \frac{\partial \vec{u}}{\partial t}-(\rho_0+\rho')(\vec{u}\nabla)\vec{u} + \frac{1}{3}\mu\nabla(\nabla\cdot\vec{u})+\mu\nabla^2\vec{u}, \tag{2}$$

$$\rho_0 T_0 \frac{\partial s}{\partial t}=\nabla\cdot(\kappa\nabla T')+W, \tag{3}$$

$$p-c_0^2\rho'=(c_0^2/\rho_0)(B/2A)\rho'^2+c_0^2(\rho\beta T/C_{\mathrm{p}})_0 s, \tag{4}$$

$$T'-(T\beta/\rho C_{\mathrm{p}})_0 p=(T/C_{\mathrm{p}})_0 s, \tag{5}$$

where ρ' is the acoustic density deviation, $\vec{u}$ is the particle velocity vector, p is the acoustic pressure, s is the acoustic entropy deviation, and T' is the acoustic temperature deviation. The constants c_0, ρ_0, and T_0 are the ambient sound speed, density, and temperature, respectively, while β, μ, κ, C_{p}, and B/A are the coefficients of thermal expansion, shear viscosity, thermal conductivity, specific heat at constant pressure, and ratio of the first two terms of the Taylor series expansion of the total pressure in terms of ρ'. W is the space- and time-dependent heating function caused by light absorption. The continuity equation (1) and the Navier-Stokes equation (2) are derived from the laws of conservation of mass and momentum, respectively, (3) is the heat-conduction equation, while (4) and (5) define the thermodynamic relations between the OA pressure and other field variables. The above equations can also be used to model acoustic propagation (without considering optoacoustic effects) in soft tissues by neglecting the heat conduction and removing the nonlinear terms and dissipative terms.[10]

Equations (1)–(5) can be rewritten as

$$\frac{\partial}{\partial t}\left(\frac{\rho'}{\rho_0}\right)+\nabla\cdot\vec{u}=N1, \tag{6}$$

$$\frac{\partial}{\partial t}(\rho_0\vec{u})+\nabla p=N2+D1, \tag{7}$$

$$\frac{\partial}{\partial t}(\rho_0 T_0 s)=D2, \tag{8}$$

$$p-c_0^2\rho'=N3+D3, \tag{9}$$

$$T'-(T\beta/\rho C_{\mathrm{p}})_0 p=D4, \tag{10}$$

where

$$N1=-\left[\rho'\nabla\cdot\vec{u}-\vec{u}\cdot\nabla(\rho'+\rho_0)\right]/\rho_0, \tag{11}$$

$$N2=-\rho'\frac{\partial\vec{u}}{\partial t}-(\rho_0+\rho')(\vec{u}\nabla)\vec{u}, \tag{12}$$

$$N3=(c_0^2/\rho_0)(B/2A)\rho'^2, \tag{13}$$

$$D1=\tfrac{1}{3}\mu\nabla(\nabla\cdot\vec{u})+\mu\nabla^2\vec{u}, \tag{14}$$

$$D2=\nabla\cdot(\kappa\nabla T')+W, \tag{15}$$

$$D3=c_0^2(\rho\beta T/C_{\mathrm{p}})_0 s, \tag{16}$$

$$D4=(T/C_{\mathrm{p}})_0 s. \tag{17}$$

In this formulation, $N1-N3$ denote the nonlinear terms while $D1-D4$ denote the dissipative terms. In general, (6)–(8) [with (9) and (10) satisfied] constitute a four-dimensional (4-D; one dimension in time and three dimensions in space) problem and can be numerically solved using a FDTD method. Given the initial conditions of ρ', $\vec{u}$, and s over the space domain, these variables (together with p and T') can be found at all future times. However, the associated large computational and storage requirements make the 4-D scheme infeasible. One realistic scheme adopted in OA investigations is to employ an axisymmetrical cylindrical coordinate system (with the z-axis parallel to the direction of irradiation), which reduces the computations to three-dimensional while remaining 4-D in physical nature. In subsequent sections we consider only the axisymmetrical configuration in all FDTD computations. More specifically, the two-step MacCormack scheme,[17] which is fourth-order accurate in space and second-order accurate in time, was adopted to implement our finite-difference code. The first-order Mur absorbing boundary conditions[18] were applied at the outer boundaries:

$$\left[\frac{\partial f}{\partial r}-\frac{1}{c}\frac{\partial f}{\partial t}\right]_{r=r_0}=0,\quad \left[\frac{\partial f}{\partial z}\mp\frac{1}{c}\frac{\partial f}{\partial t}\right]_{z=\pm z_0/2}=0, \tag{18}$$

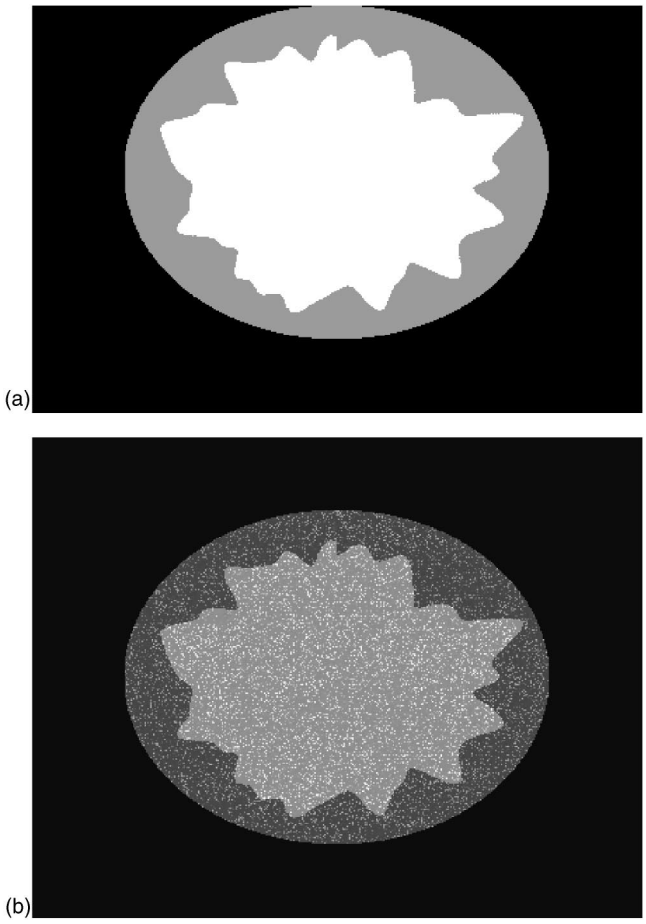

FIG. 1. Background tissue maps for the breast model. (a) Acoustic speed map. (b) Density map. Glandular parenchyma is enclosed by the irregular wall, subcutaneous fat is bounded by the irregular wall and the circular wall. Outside the circular wall is the surrounding medium used to couple the ultrasound receiver to the subcutaneous fat.

where the field parameter f may be ρ', $\vec{u}$, or s, and r_0 and z_0 are the radius and length of the simulated domain, respectively. The simulation procedure is similar to that described by Sparrow and Raspet.[19]

The background acoustic models adopted in all breast imaging simulations were constructed according to experimental results for human breast.[20,21] As shown in Figs. 1(a) and (b), the cross-sectional model consists of a zone of glandular parenchyma surrounded by subcutaneous fat. The sound speed in the parenchyma and the fat were set as 1523 and 1459 m/s, respectively. The breast model had a radius of 5 cm. The averaged radius of the parenchyma is 4 cm and the thickness was varied in such a way that the arrival time fluctuations profile for an acoustic wavefront after propagating through the parenchyma wall has a root-mean-square value of 66.8 ns and a correlation length of 4.3 mm, which was based on the *in vitro* measurements obtained by Hinkleman *et al.*[21] Figure 1(a) illustrates one such acoustic speed model. Acoustic scattering was also incorporated in our model by adding a normally distributed, zero-mean random component with a root-mean-square value of 0.1 g/cm^3 to the density map in which the density of the parenchyma and the fat were set as 0.99 and 0.94 g/cm^3, respectively. A typical density map is shown in Fig. 1(b). The acoustic speed and average density in the surrounding medium shown in Fig. 1 were the same as those in subcutaneous fat. The configuration used in this study also had a simulated tumor inside the breast model. It had a disk with a radius of 1 mm placed at its center. The absorption coefficient of the disk was set to be three times that of surrounding tissues. The sound speed inside the disk was 1550 m/s and the density was 1.12 g/cm^3. Simulations without heterogeneities were also performed by removing the subcutaneous fat and extending the parenchyma outside the tumors to all simulated domains.

In OA simulations, uniform irradiation was assumed with an intensity of 10 mJ/cm^2. The laser pulse is temporally Gaussian with a full duration at 1/e level of 10 ns. Point ultrasound detectors were placed around the breast model at an interval of 0.25° (i.e., totally 1440 points), while the radius of detection is 6 cm. Received OA signals were obtained by summing the OA waveforms received at six consecutive points (i.e., totally 240 received OA signals). In pulse-echo ultrasound simulations, a linear array with a focus at the breast center was placed 1 cm above the breast wall to be used both as a transmitter and as a receiver. A Gaussian pulse with a central frequency of 1.5 MHz and a 6-dB bandwidth of 1.5 MHz was employed as the transmitted waveform. This frequency range, which was lower than usually used in breast ultrasonography but was common in breast OA imaging, was chosen to form a fair basis for the comparison between the OA wavefront and the pulse-echo wavefront. The linear array consists of 1440 points spaced at an interval of 0.043 mm (span=6.2 cm). Also acoustic signals coming from six consecutive points were summed together to form 240 received acoustic waveforms.

III. RESULTS

The FDTD code was validated using a benchmark problem that has an analytical solution as proposed by Karabutov *et al.*[11] The problem involves calculating the backward OA signal for a single-layer object with a uniform light-absorption profile and acoustic properties, irradiated by a laser pulse that is Gaussian in both space and time:

$$p_{\mathrm{tr}}(\vartheta=\tau/\tau_{\mathrm{L}},z,r_{\perp}=0)=C\cdot\{A\exp(-A\vartheta+A^2/4)[1+\mathrm{erf}(\vartheta-A/2)]-D\exp(-D\vartheta+D^2/4)[1+\mathrm{erf}(\vartheta-D/2)]\}, \tag{19}$$

where C is a scaling factor, $A=\mu_{\mathrm{a}}c_0\tau_{\mathrm{L}}$, $D=2zc_{\mathrm{tr}}\tau_{\mathrm{L}}/a_0^2$, μ_{a} is the light-absorption coefficient, z is the normal distance between the acoustic receiver and the irradiated surface, c_0 and c_{tr} are the speed of sound in the light-absorbing and transparent media, respectively, and τ_{L} and a_0 are the time and radius (i.e., in the time and space domains, respectively) for the laser pulse intensity to reduce to 1/e of its original level. Figure 2 shows the results for two different light-absorption coefficients with $2\tau_{\mathrm{L}}=9$ ns and $D=50$. A grid spacing (Δx) of 30 μm was adopted in our FDTD code, and the grid was 1000×500. A speed of sound of 1523 m/s was chosen for both media. The time step Δt was set to 5 ns in order to meet the Courant stability condition,[22] which requires that $c_0\Delta t/\Delta x$ should be about 0.25 to obtain the ex-

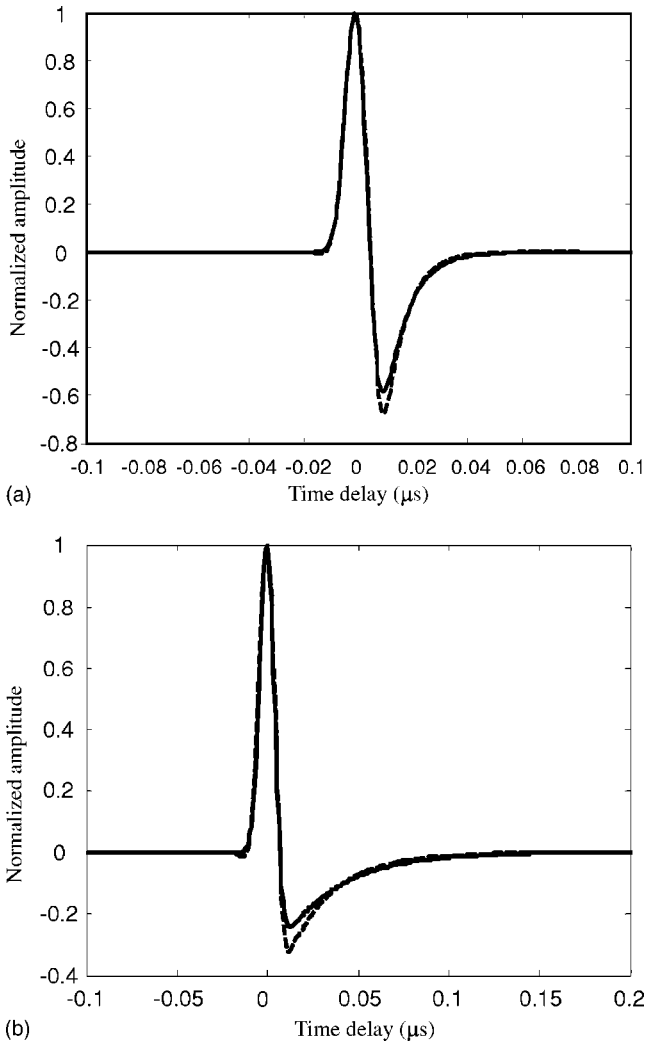

FIG. 2. Backward OA signals computed by the FDTD method (solid line) and using (19) (dashed line): (a) absorption coefficient $=160\ \mathrm{cm}^{-1}$ and (b) absorption coefficient $=600\ \mathrm{cm}^{-1}$.

pected accuracy. Figure 2(a) shows the results for $\mu_a = 160\ \mathrm{cm}^{-1}$. The solid curve refers to the OA waveform generated by the FDTD method, while the dashed curve was obtained using (19). Figure 2(b) shows the corresponding results for $\mu_a = 600\ \mathrm{cm}^{-1}$. It can be seen that our numerical results were in excellent agreement with those from the analytical solutions; the small discrepancies were mainly attributable to the errors of the paraxial approximation used when deriving (19).[23]

Experimental validation was also performed using backward OA signals induced in a light-absorbing phantom comprising gelatin mixed with commercially available black pigments (OSAMA 42, SIMBALION, ROC). Pulses from a Nd:YAG laser (LS-2132U, LOTIS TII, Belarus) (10 ns at 532 nm) provided irradiation with an incident energy density of $34\ \mathrm{mJ/cm}^2$. A broadband hydrophone (GL-200, ONDA, USA) with -3-dB cutoff frequencies of 0.2 and 20 MHz and high sensitivity (28 nV/Pa) was used to record the OA signals at 1 cm from the irradiated surface. Water was adopted as an optically transparent medium acoustically coupled to the OA phantom. The absorption coefficient was obtained by fitting (19) (i.e., the analytical solution proposed

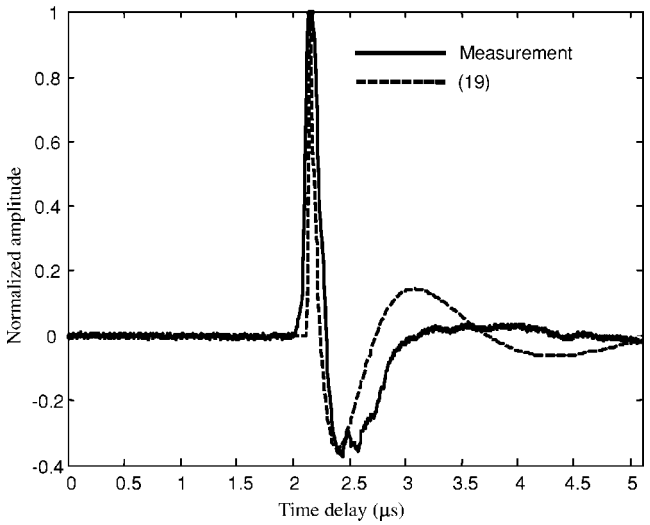

FIG. 3. Measured backward OA signal (solid line) and its curve fitting (dashed line) obtained from (19), for an absorption coefficient of $30\ \mathrm{cm}^{-1}$.

in Ref. 11) to the measured profile. The curve fitting, which was obtained by letting the measured curve and the fitted one have approximately the same amplitudes at their crests and troughs after normalization, is shown in Fig. 3 with an absorption coefficient of $30\ \mathrm{cm}^{-1}$. The solid line corresponds to the measured OA signal and the dashed line was obtained using (19) combined with a filter accounting for the impulse response of the hydrophone. The significant difference between the theoretical and experimental results is mainly attributable to (19) being less accurate at predicting extreme-near-field OA signals coming from a weakly absorbing medium (i.e., $D \ll 1$, $A \ll 1$). The experimental setup, however, had D at 0.011 and A at 0.027. The proposed simulator is based on the general OA equations and therefore not restricted to these limitations. It can be clearly seen in Fig. 4—in which the solid line is the measured OA signal and the dashed line was obtained using the FDTD method—that a significantly better agreement was reached. Another factor

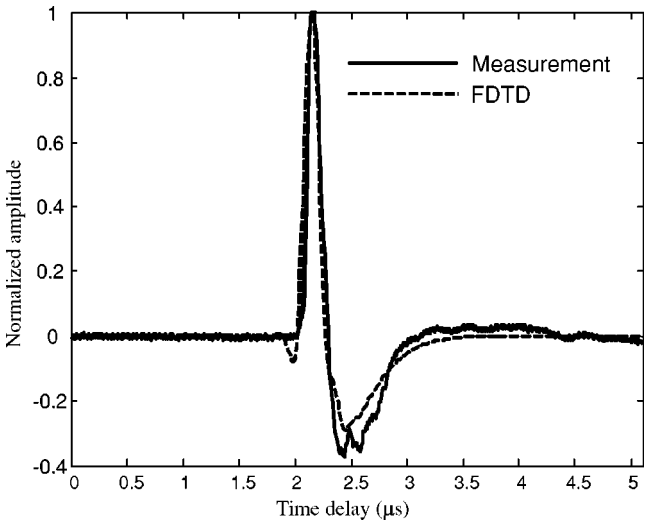

FIG. 4. Measured backward OA signal (solid line) and its curve fitting (dashed line) obtained from the FDTD method, for an absorption coefficient of $30\ \mathrm{cm}^{-1}$ and an assumed shear viscosity of 0.00086 Pa s.

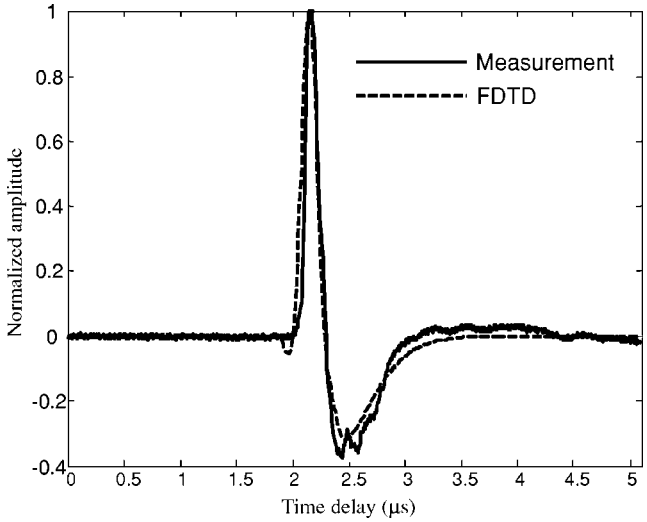

FIG. 5. Measured backward OA signal (solid line) and its curve fitting (dashed line) obtained from the FDTD method, for an absorption coefficient of 30 cm^{-1} and an assumed shear viscosity of 0.3 Pa s.

not considered in (19) that would affect the OA waveform is shear viscosity. The dashed line in Fig. 5 shows the result calculated by the FDTD method with a typical shear viscosity of 0.3 Pa s for agar gelatin, in contrast with the result in Fig. 4 for which a low viscosity equal to that of water (0.000 86 Pa s) was used. The solid line in Fig. 5 is the same as that in Fig. 4. It can be seen that a more accurate result was obtained using high viscosity, although the improvement was minor. Moreover, our approach is more flexible and practical than the analytical approach.

A typical OA wavefield inside a homogeneous light-absorbing object irradiated through a transparent medium using laser pulses with a Gaussian spatial intensity distribution is shown in Fig. 6. The transparent medium and the absorbing object had different acoustic properties. The distortion of the forward OA signal caused by the acoustic impedance mismatch at the interface[23] and the diffraction effects on both forward and backward OA signals caused by a finite laser spot size[23] are clearly visible in Fig. 6. The forward OA signal has a leading edge that suffers no shape change during propagation and can be applied directly to reconstruct the

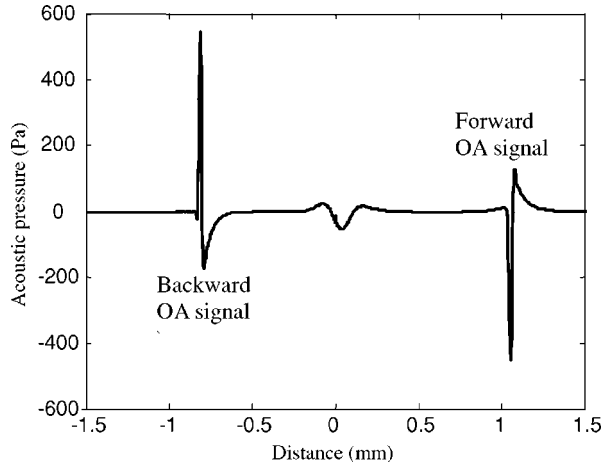

FIG. 6. OA signal profile along the axis of the laser radiation.

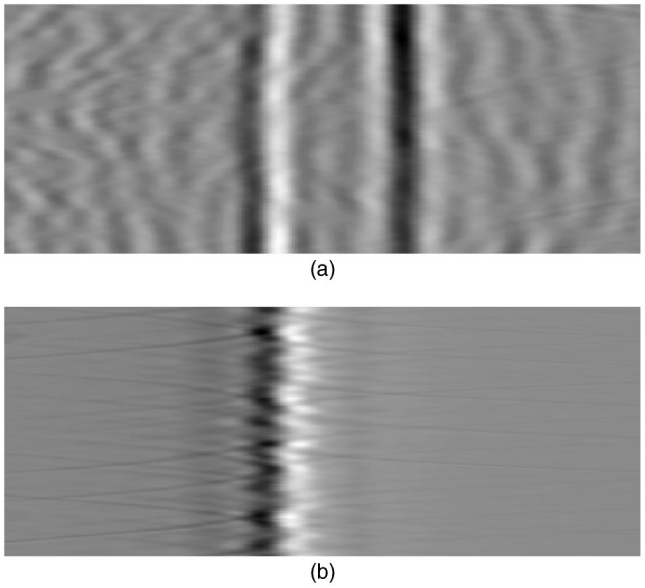

FIG. 7. (a) Pulse-echo wavefront and (b) OA wavefront for the simulated breast phantom with a tumor placed at the center. In (a), the vertical coordinate denotes the array direction and spans a distance of 6.2 cm in 0.26-mm increments. In (b), the vertical coordinate denotes the receive angle extending from 0° to 360° with an interval of 1.5°. The horizontal coordinates in (a) and (b) are time with a length of 22.7 μs and an interval of 0.03 μs. Signal amplitude is displayed on a 128 linear gray scale, with the maximum represented by white and the minimum represented by black.

light-absorption profile. However, the forward mode requires two-sided access to the object under investigation to collect the forward OA signals, which is not practical in many clinical applications. Therefore, although backward OA signals have diffraction-dependent shapes that change with the propagation distance, they are often still used to study the absorption of optical electromagnetic energy inside a medium.[11,24]

Sideward OA signals have been used extensively to reconstruct the cross-sectional absorption profile[6,8] inside an absorbing medium. Current reconstruction algorithms, however, are based on the assumption that the irradiated medium has uniform acoustic properties, which is rarely true in clinical situations. To elucidate the effects of acoustic heterogeneities (including the acoustic impedance mismatch and sound velocity inhomogeneities) on the reconstructed OA images, sideward OA signals were simulated. The pulse-echo acoustic wavefront and the OA wavefront formed by aligning the waveform for each scanning angle are displayed in Fig. 7. The relative-time delays between individual received waveforms in these wavefronts have been removed using the cross-correlation method.[25] Obvious energy level fluctuations can be seen from both wavefronts. The pulse-echo wavefront contains two stronger subwavefronts originating from the acoustic impedance mismatch between the tumor and the parenchyma. Minor wavefronts caused by random scattering are also obvious in the pulse-echo wavefront. On the other hand, the OA wavefront consists of one main wavefront only. The corresponding OA signal and the signal suffering no acoustic heterogeneities are shown in Fig. 8 by the solid curve and dashed curve, respectively, indicating that the OA signal was appreciably distorted in pulse width and

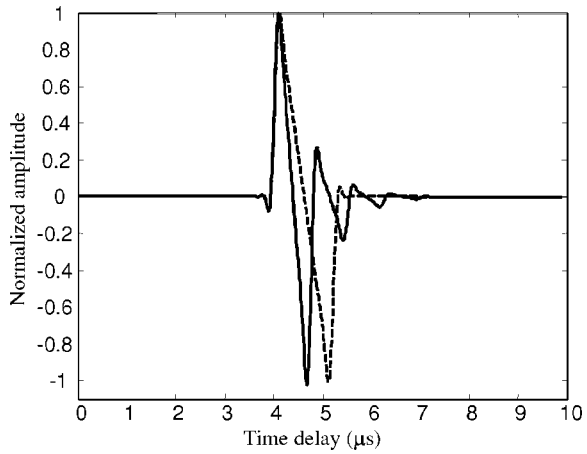

FIG. 8. Sideward OA signals for a uniformly irradiated sphere with (solid line) and without (dashed line) acoustic heterogeneities.

shape. The difference in acoustic properties between the absorbing sphere and the surrounding medium results in a series of N-shaped waveforms in addition to the main N-shaped one.[26] Similar distortion effects, usually referred to as wavefront distortion, have been studied extensively in abdomen[27] and breast[21] ultrasound images. The reconstructed absorption profile for the simulated phantom with a tumor placed at the center is shown in Fig. 9 using the time-domain algorithm proposed by Xu *et al.*[8] Figures 9(a) and (b) show the results with and without acoustic heterogeneities, respectively. The display range is $3.3\times3.3\ \mathrm{cm}^2$. The sound speeds used in the reconstructions are 1523 m/s. It can be seen that the OA image is seriously distorted when the background tissue is acoustically inhomogeneous. This indicates that an efficient reconstruction algorithm must take acoustic heterogeneities into consideration.

IV. CONCLUSIONS

A FDTD code has been developed to numerically solve the general OA equations under axisymmetrical conditions. A benchmark problem that has an approximate analytical solution was used to validate the FDTD code. Experimental validation was also performed using the OA signal from an OA phantom as measured in the backward mode. Numerical results show qualitative agreement with reported data for OA signals in the forward, backward, and sideward modes. The proposed FDTD code can be used as an aid in the design of OA imaging systems, to visual OA wave propagation in biological tissues, and to develop advanced image reconstruction algorithms.

In this study, the simulator was employed to investigate wavefront distortion in OA breast imaging. For pulse-echo ultrasound, soft tissues can be viewed as a collection of randomly distributed acoustic scatterers which result in speckle appearance in the image. On the contrary, the received wavefront in OA imaging originates from the differential thermal expansion of tissues caused by optical absorption, which is relatively a uniform property with local magnitudes that depend on the tissue types (e.g., cancerous tissue and normal tissue). Nonetheless, as demonstrated in this paper, the OA wavefront is still distorted after propagating through the breast tissue and the distortion must be corrected in order to fully realize the potential of OA imaging. In the future, the FDTD simulator described in this study will be used as an effective tool to develop and evaluate imaging algorithms that can compensate for the wavefront distortion in OA breast imaging.

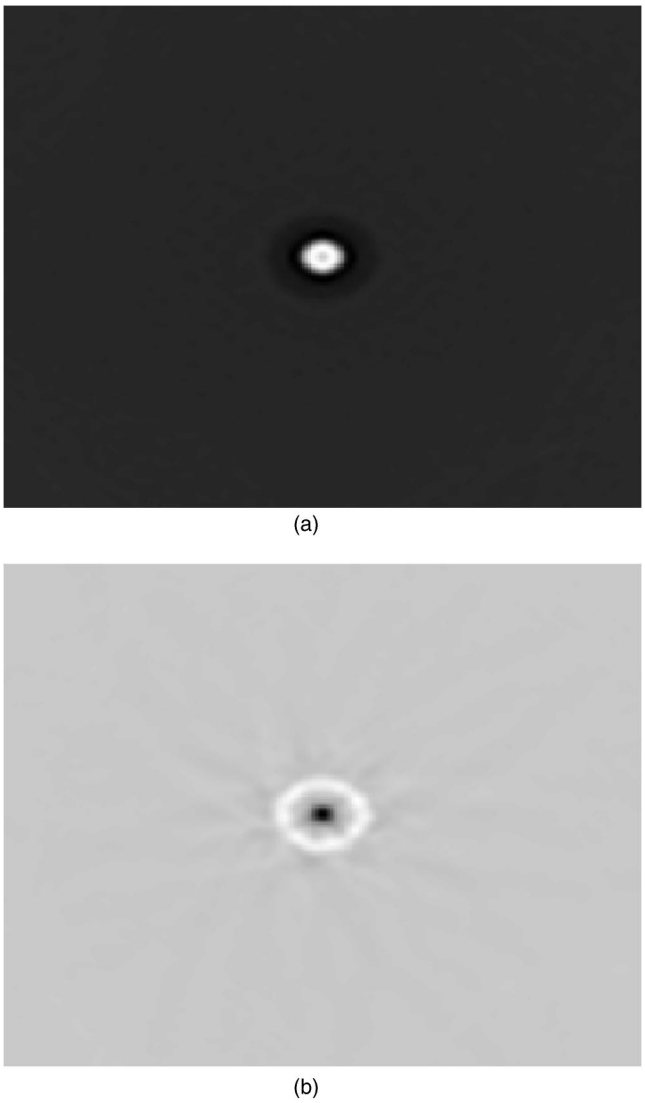

FIG. 9. Reconstructed OA images for the simulated phantom with a tumor placed at the center (a) without acoustic heterogeneities and (b) with heterogeneities. The images are displayed on a 128 linear gray scale.

[1] A. Beenen, G. Spanner, and R. Niessner, "Photoacoustic depth-resolved analysis of tissue models," Appl. Spectrosc. **51**, 51–57 (1997).
[2] A. Oraevsky, A. A. Karabutov, S. V. Solomatin, E. V. Savateeva, V. G. Andreev, D. R. Fleming, Z. Gatalica, and H. Singh, "Laser optoacoustic imaging of breast cancer *in vivo*," Proc. Int. Soc. Opt. Eng. **4256**, 6–15 (2001).
[3] X. Wang, Y. Pang, G. Ku, X. Xie, G. Stoica, and L. V. Wang, "Noninvasive laser-induced photoacoustic tomography for structural and functional in vivo imaging of the brain," Nat. Biotechnol. **21**, 803–806 (2003).
[4] A. A. Oraevsky, R. O. Esenaliev, and A. A. Karabutov, "Laser optoacoustic tomography of layered tissue: Signal processing," Proc. SPIE **2979**, 59–70 (1997).
[5] A. A. Karabutov, E. V. Savateeva, and A. A. Oraevsky, "Imaging of layered structures in biological tissues with opto-acoustic front surface transducer," Proc. SPIE **3601**, 284–295 (1999).
[6] R. A. Kruger, P. Liu, Y. R. Fang, and C. R. Appledorn, "Photoacoustic

ultrasound (PAUS)—Reconstruction tomography,'' Med. Phys. **22**, 1605–1609 (1995).
[7] K. Köstli, M. Frenz, H. Bebie, and H. P. Weber, ''Temporal backward projection of optoacoustic pressure transients using Fourier transform methods,'' Phys. Med. Biol. **46**, 1863–1872 (2001).
[8] M. Xu, Y. Xu, and L. V. Wang, ''Time-domain reconstruction algorithms and numerical simulations for thermoacoustic tomography in various geometries,'' IEEE Trans. Biomed. Eng. **50**, 1086–1099 (2003).
[9] A. Taflove and K. R. Umashankar, ''Review of FDTD numerical modeling of electromagnetic wave scattering and radar cross section,'' Proc. IEEE **77**, 682–699 (1989).
[10] T. D. Mast, L. M. Hinkelman, M. J. Orr, V. W. Sparrow, and R. C. Waag, ''Simulation of ultrasonic pulse propagation through the abdominal wall,'' J. Acoust. Soc. Am. **102**, 1177–1190 (1997).
[11] A. A. Karabutov, E. V. Savateeva, and N. B. Podymova, ''Backward mode detection of laser-induced wide-band ultrasonic transients with optoacoustic transducer,'' J. Appl. Phys. **87**, 2003–2014 (2000).
[12] P. D. Freiburger, D. C. Sullivan, B. H. LeBlanc, S. W. Smith, and G. E. Trahey, ''Two dimensional ultrasonic beam distortion in the breast: In vivo measurements and effects,'' Ultrason. Imaging **14**, 398–414 (1992).
[13] Q. Zhu and B. D. Steinberg, ''Wavefront amplitude distortion in the female breast,'' J. Acoust. Soc. Am. **96**, 1–9 (1992).
[14] L. M. Hinkelman, D.-L. Liu, R. C. Waag, Q. Zhu, and B. D. Steinberg, ''Measurements and correction of ultrasonic pulse distortion produced by the human breast,'' J. Acoust. Soc. Am. **97**, 1958–1969 (1995).
[15] Y. Xu and L. V. Wang, ''Effects of acoustic heterogeneity in breast thermoacoustic tomography,'' IEEE Trans. Ultrason. Ferroelectr. Freq. Control **50**, 1134–1146 (2003).
[16] V. E. Gusev and A. A. Karabutov, *Laser Optoacoustics* (American Institute of Physics, New York, 1993), Chap. 2, pp. 45–48.
[17] R. W. MacCormack, *Lecture Notes in Physics* (Springer-Verlag, Berlin, 1971), Vol. 8, p. 151.
[18] G. Mur, ''Absorbing boundary conditions for the finite-difference approximation of the time-domain EM field equations,'' IEEE Trans. Electromagn. Compat. **23**, 377–382 (1981).
[19] V. W. Sparrow and R. Raspet, ''A numerical method for general finite amplitude wave propagation and its application to spark pulses,'' J. Acoust. Soc. Am. **90**, 2683–2691 (1991).
[20] G. Kossoff, E. K. Fry, and J. Jellins, ''Average velocity of ultrasound in the human female breast,'' J. Acoust. Soc. Am. **53**, 1730–1736 (1973).
[21] L. M. Hinkelman, D.-L. Liu, R. C. Waag, Q. Zhu, and B. D. Steinberg, ''Measurements and correction of ultrasonic pulse distortion produced by the human breast,'' J. Acoust. Soc. Am. **97**, 1958–1969 (1995).
[22] E. Turkel, ''On the practical use of high-order methods for hyperbolic systems,'' J. Comput. Phys. **35**, 319–340 (1980).
[23] A. A. Karabutov, N. B. Podymova, and V. S. Letokhov, ''Time-resolved laser optoacoustic tomography of inhomogeneous media,'' J. Appl. Phys. **63**, 545–563 (1996).
[24] K. Köstli, M. Frenz, H. Weber, G. Paltauf, and H. Kloiber, ''Optoacoustic tomography: time-gated measurement of pressure distributions and image reconstruction,'' Appl. Opt. **40**, 3800–3809 (2001).
[25] S. W. Flax and M. O'Donnell, ''Phase aberration correction using signals from point reflectors and diffuse scatters: Basic principles,'' IEEE Trans. Ultrason. Ferroelectr. Freq. Control **35**, 758–767 (1988).
[26] G. J. Diebold, M. I. Khan, and S. M. Park, ''Photoacoustic signatures of particulate matter: Optical production of acoustic monopole radiation,'' Science **250**, 101–104 (1990).
[27] L. M. Hinkelman, D.-L. Liu, L. A. Metlay, and R. C. Waag, ''Measurements of ultrasonic pulse arrival time and energy level variations produced by propagation through abdominal wall,'' J. Acoust. Soc. Am. **95**, 530–541 (1994).

Optimal design of loudspeaker arrays for robust cross-talk cancellation using the Taguchi method and the genetic algorithm

Mingsian R. Bai,[a] Chih-Wei Tung, and Chih-Chung Lee
Department of Mechanical Engineering, National Chiao-Tung University, 1001 Ta-Hsueh Road, Hsin-Chu 300, Taiwan, Republic of China

(Received 10 August 2004; revised 13 December 2004; accepted 7 February 2005)

An optimal design technique of loudspeaker arrays for cross-talk cancellation with application in three-dimensional audio is presented. An array focusing scheme is presented on the basis of the inverse propagation that relates the transducers to a set of chosen control points. Tikhonov regularization is employed in designing the inverse cancellation filters. An extensive analysis is conducted to explore the cancellation performance and robustness issues. To best compromise the performance and robustness of the cross-talk cancellation system, optimal configurations are obtained with the aid of the Taguchi method and the genetic algorithm (GA). The proposed systems are further justified by physical as well as subjective experiments. The results reveal that large number of loudspeakers, closely spaced configuration, and optimal control point design all contribute to the robustness of cross-talk cancellation systems (CCS) against head misalignment. [DOI: 10.1121/1.1880852]

PACS numbers: 43.38.Vk [AJZ] Pages: 2802–2813

I. INTRODUCTION

Spatial audio or three-dimensional (3D) audio has received much attention in many emerging applications such as computer multimedia, home theater, video games, digital television, etc. Despite the rapid development of the technology, cross talk has been a plaguing problem when loudspeakers are used as the means of rendering. Binaural audio signals containing directional cues are to be reproduced, at the ears of a listener, that he or she would naturally hear. However, excess cross talk can smear these cues and adversely effect the localization of sound images reproduced by loudspeakers. It is thus desirable to preprocess the loudspeaker signals by using the so-called cross-talk cancellation system (CCS) so that the sound from the loudspeakers to contralateral ears is minimized, if not completely eliminated.

Several CCS have been proposed in the past. The idea of CCS was first introduced by Bauer,[1] and later put into practice by Atal and Schroeder,[2] and Damaske and Mellert.[3] The limitation of these early systems is that head movement away from the sweet spot greater than about 75 to 100 mm would significantly degrade the spatial effect. Cooper and Bauck suggested a propagation matrix based on the spherical head model.[4] A similar method by Gardner approximates the effect of the head with a low-pass filter, a delay, and a simple gain.[5] Blumlein,[6] and Cooper and Bauck[7,8] showed that, under the assumption of left–right symmetry, a ''shuffler'' filter can be used to simplify the implementation of CCS. Note that, if the position of the listener changes over time, then ipsilateral and contralateral transfer function will not be symmetrical, but will vary to reflect the head-related-transfer functions (HRTF) for the listener's new position. A head-tracking CCS was reported in the work of Kyriakakis *et al.* to cope with head movement of the listener.[9,10] Ward and Elko in Bell Labs have conducted a series of less elaborate but insightful analysis of the robustness of the CCS. In their first paper[11] on this topic in 1998, robustness of a simple 2×2 CCS was investigated using weighted cancellation performance measure (at the pass zone and stop zone, respectively). In their second paper[12] in 1999, robustness of a 2×2 CCS was again examined using a different measure that focuses more on numerical stability, as reflected by matrix condition numbers, with respect to data and/or system perturbations during matrix inversion. Both approaches wind up with optimal loudspeaker spacing inversely proportional to frequency. Parallel to the previous work, the present paper explores the robust issue in a more general context. Using multidrive array configurations, more than two loudspeakers are used to provide additional degrees of freedom for control of the sound field. In the optimization procedure, channel separation and beamwidth are employed as a more intuitive robustness measure against head misalignment. The optimization leads to an optimal loudspeaker configuration independent of frequency. An alternative approach was developed by Takeuchi and Nelson to enhance the robustness of CCS against head movement away from the sweet spot. In their system, two loudspeakers are closely spaced to form what they call the ''stereo dipole.''[13] This idea was further extended by the same researchers to be the optimal source distribution (OSD) system.[14] Their robust analysis of CCS was also based on numerical stability in relation to the errors in matrix inversion. The performance of CCS deteriorates due to these errors resulting possibly from head misalignment and the HRTF modeling variations. Inversion of an ill-conditioned system (with a large matrix condition number) leads to loss of dynamic range and lack of robustness to head misalignment. The authors attempt to pinpoint an optimal configuration of a 2×2 CCS in which loudspeaker spacing is the primary design parameter such that the trade-off among dynamic range, robustness, and control performance

[a]Electronic mail: msbai@mail.nctu.edu.tw

 0001-4966/2005/117(5)/2802/12/$22.50

are best reconciled. Their analysis also yielded optimal loudspeaker spacing inversely proportional to frequency. Since the spacing thus found is frequency dependent, a multidrive configuration of the OSD, comprising pairs of loudspeakers with different spacing, was suggested to deal with cross-talk cancellation in different frequency bands. Apart from the robustness measure and analysis techniques, the present paper differs from their approach in that our approach is a direct multidrive (more than two loudspeakers) array configuration, which requires no crossover circuits that may introduce distortions at the crossover frequencies. In this array configuration, the additional degrees-of-freedom in control of sound field provided by the beamformer can be exploited to the greatest extent.

In this paper, the performance and robustness issues of CCS for various loudspeaker configurations are examined. Traditional stereo CCS systems require that the listener is positioned in the so-called ''sweet spot'' such that the listener forms an equilateral triangle with respect to the loudspeaker pair. The loudspeakers, therefore, subtend an angle of 60° from the listener.[15] Once the listener moves away from the sweet spot, especially when moving sideway, the conditions for cancellation are no longer met and the spatial sound images are lost. The idea of sweet spot applies with different degrees not only to stereo systems but also to other loudspeaker configurations.

Following the analysis of performance and robustness analysis, this paper is focused on the development of a CCS using a loudspeaker array in an effort to best compromise performance and robustness of the system. An array focusing scheme is also exploited, based on the inverse propagation operator that relates the transducers to a set of chosen control points.[16,17] Optimal design parameters of the array are found using the Taguchi method[18] and the genetic algorithm (GA).[19,20] It has been found in Refs. 11 and 13 that cancellation is least effective because of the narrow sweet spot as the head moves sideway rather than when it moves in the other directions. Hence, only lateral misalignment is investigated in the present paper. As will be detailed later, the optimal configuration is the closely spaced array. Such system is found to be more robust to misalignment of the listener's head. This finding is in agreement with the conclusion of Ref. 21. The 3D audio system resulting from the above-mentioned optimization is then implemented on a multimedia Pentium 4 personal computer. The proposed systems are further justified by physical and subjective experiments. Feasibility of the proposed CCS will be discussed in the conclusions.

II. THEORY AND METHODS

A. The propagation matrix

Assume that the process of sound propagation from the loudspeakers to the listener's ears is linear and time invariant. Viewed as a multichannel system, a propagation matrix relates the loudspeaker inputs and a set of chosen ''control points.'' These control points are allocated along the line linking two ears, as shown in Fig. 1. These control points are crucial to the tailoring of the so-called sweet spot, which is

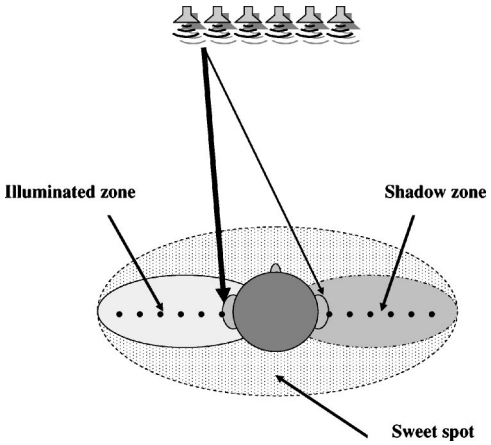

FIG. 1. Allocation of control points for the CCS.

composed of an illuminated zone for the ipsilateral propagation and a shadow zone for the contralateral propagation. The main purpose of a CCS is to minimize, if not completely eliminate, the cross talks associated with the contralateral propagation. To accomplish this, therefore, unity gains are designated to the control points in the illuminated zone, whereas nulls are designated to the control points in the shadow zone. For simplicity, we restrict ourselves to a one-dimensional array and define head-related impulse responses (HRIR), $h_{mj}(n)$, $1 \leqslant m \leqslant M$, $1 \leqslant j \leqslant J$, as the impulse responses corresponding to the mth control point and the jth loudspeaker (n being the discrete-time index). Let $v_j(n)$, $1 \leqslant j \leqslant J$, be the J input signals to the loudspeaker array. The output signals $f_m(n)$, $1 \leqslant m \leqslant M$, received at the control points are given by

$$f_m(n) = \sum_{j=1}^{J} h_{mj}(n) * v_j(n), \quad 1 \leqslant m \leqslant M, \tag{1}$$

where* denotes the convolution operator. Fourier transform of this equation leads to

$$F_m(e^{j\omega}) = \sum_{j=1}^{J} H_{mj}(e^{j\omega}) V_j(e^{j\omega}), \quad 1 \leqslant m \leqslant M. \tag{2}$$

In matrix form

$$\mathbf{f}(e^{j\omega}) = \mathbf{H}(e^{j\omega}) \mathbf{v}(e^{j\omega}), \tag{3}$$

with $\mathbf{v}(e^{j\omega}) = [V_j(e^{j\omega})]_{1 \leqslant j \leqslant J}$ and $\mathbf{f}(e^{j\omega}) = [F_m(e^{j\omega})]_{1 \leqslant m \leqslant M}$ being the column vectors of the Fourier transforms of the loudspeaker input signals and the reproduced signals, respectively. Overall, the transfer matrix $\mathbf{H}(e^{j\omega}) = [H_{mj}(e^{j\omega})]_{1 \leqslant m \leqslant M, 1 \leqslant j \leqslant J}$ represents the frequency-domain multichannel propagation process from the array loudspeakers to the control points at the sweet spot.

B. Inverse filtering with Tikhonov regularization

The CCS aims to cancel the cross talks in stereo loudspeaker rendering so that the binaural signals are reproduced at two ears like those from a headphone. This can be viewed as a model-matching problem, shown in Fig. 2. In the block diagram, $\mathbf{x}(z)$ is a vector of H program input signals (z being the z-transform variable), $\mathbf{u}(z)$ is a vector of $I = 2$ binaural

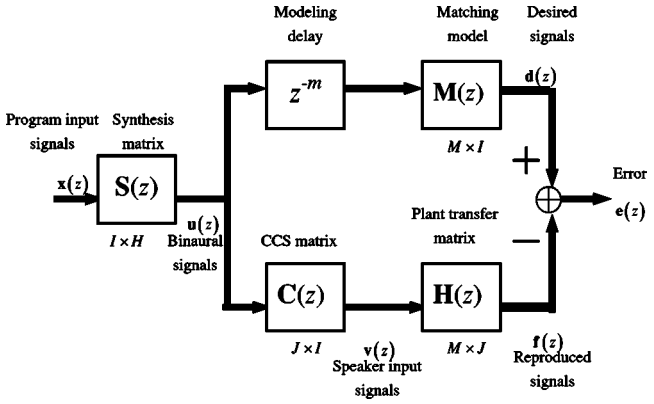

FIG. 2. The block diagram of a multichannel model-matching problem in the CCS design.

signals, $\mathbf{v}(z)$ is a vector of J loudspeaker input signals, $\mathbf{f}(z)$ is a vector of M reproduced signals, $\mathbf{d}(z)$ is a vector of M desired signals, and $\mathbf{e}(z)$ is a vector of M error signals. $\mathbf{M}(z)$ is an $M\times I$ matrix of matching model, $\mathbf{H}(z)$ is an $M\times J$ plant transfer matrix, and $\mathbf{C}(z)$ is a $J\times I$ matrix of the CCS filters. The term z^{-m} accounts for the modeling delay to ensure causality of the CCS filters. It is straightforward to establish the following relationships:

$$\mathbf{v}(z)=\mathbf{C}(z)\mathbf{u}(z), \tag{4}$$

$$\mathbf{f}(z)=\mathbf{H}(z)\mathbf{v}(z), \tag{5}$$

$$\mathbf{d}(z)=z^{-m}\mathbf{M}(z)\mathbf{u}(z), \tag{6}$$

$$\mathbf{e}(z)=\mathbf{d}(z)-\mathbf{f}(z). \tag{7}$$

Ideal model matching requires that $\mathbf{H}(z)\mathbf{C}(z)=z^{-m}\mathbf{M}(z)$. In general, $\mathbf{H}(z)$ is noninvertible because it is usually ill-conditioned and even nonsquare. To overcome this difficulty, we employ the Tikhonov regularization procedure in the matrix inversion process.[22] In the method, one seeks to minimize a frequency-domain objective function $O(e^{j\omega})$ defined as

$$O(e^{j\omega})=\mathbf{e}^H(e^{j\omega})\mathbf{e}(e^{j\omega})+\beta^2\mathbf{v}^H(e^{j\omega})\mathbf{v}(e^{j\omega}). \tag{8}$$

The regularization parameter β weighs the input power $\mathbf{v}^H\mathbf{v}$ against the performance error $\mathbf{e}^H\mathbf{e}$. The optimal solution $\mathbf{v}_{\mathrm{opt}}(e^{j\omega})$ of Eq. (8) is

$$\mathbf{v}_{\mathrm{opt}}(e^{j\omega})=[\mathbf{H}^H(e^{j\omega})\mathbf{H}(e^{j\omega})+\beta^2\mathbf{I}]^{-1}\mathbf{H}^H(e^{j\omega})\mathbf{M}(e^{j\omega})\mathbf{u}(e^{j\omega}). \tag{9}$$

Consequently, the CCS matrix can be readily identified as

$$\mathbf{C}(e^{j\omega})=[\mathbf{H}^H(e^{j\omega})\mathbf{H}(e^{j\omega})+\beta^2\mathbf{I}]^{-1}\mathbf{H}^H(e^{j\omega})\mathbf{M}(e^{j\omega}). \tag{10}$$

In our approach, the parameter β is frequency dependent and constrained by a gain threshold applied to $\mathbf{C}(e^{j\omega})$, e.g., 12 dB. This is in contrast to the approach in Ref. 16, where a constant β applied to all frequencies.

Traditionally, the desired signals $\mathbf{d}(z)$ are just the binaural signals $\mathbf{u}(z)$. The matrix $\mathbf{M}(z)$ is an identity matrix of order 2, i.e., $\mathbf{M}=\mathbf{I}$, and the frequency responses of the corresponding optimal filters are given by

$$\mathbf{C}(e^{j\omega})=[\mathbf{H}^H(e^{j\omega})\mathbf{H}(e^{j\omega})+\beta^2\mathbf{I}]^{-1}\mathbf{H}^H(e^{j\omega}). \tag{11}$$

The frequency response matrix $\mathbf{C}(e^{j\omega})$ is then sampled at N_c equally spaced frequencies with discrete-frequency index k

$$\mathbf{C}(k)=[\mathbf{H}^H(k)\mathbf{H}(k)+\beta^2\mathbf{I}]^{-1}\mathbf{H}^H(k),\quad k=1,2,...,N_c. \tag{12}$$

The impulse responses of the inverse filters can be calculated using the inverse fast Fourier transform (IFFT) of the frequency samples of Eq. (12) with appropriate windowing. Circular shifts may be necessary to guarantee the causality of CCS filters; hence, the modeling delay z^{-m} in Fig. 1.

The present method differs from the foregoing conventional approach in that, instead of ''single-point'' matching, a number of control points are distributed in the illuminated zone and the shadow zone so that the sweet spot can be widened. This is accomplished by choosing a more complex matching model akin to the window design in the time-domain digital signal processing. An example of choosing control points is illustrated as follows. Suppose we wish to choose three points in the illuminated zone and six points in the shadow zone for each ear. These control points can only be located at six discrete locations on each side of the head, as shown in Fig. 1. In this scenario, we may choose a 9×1 matching model for the left ear with the following pattern:

$$\mathbf{M}_L=[1\ \ 1\ \ 1\ \ 0\ \ 0\ \ 0\ \ 0\ \ 0\ \ 0]^T, \tag{13}$$

where the subscript L stands for the left ear, and the ones and zeros correspond to the designated control points in the illuminated zone and the shadow zone, respectively. Hence, the desired signal for the left ear is

$$\mathbf{d}_L=z^{-m}\mathbf{M}_L\mathbf{u}=z^{-m}[u_L\ \ u_L\ \ u_L\ \ 0\ \ 0\ \ 0\ \ 0\ \ 0\ \ 0]^T. \tag{14}$$

After the matching model is selected, the optimal CCS filters can be calculated according to Eq. (10). The same procedure applies to the ear on the right side. In general, more points in the shadow zone are needed than in the illuminated zone, since the performance in the former region is more critical to cancellation of cross talks. It should be noted that the increased complexity of the sweet spot widening technique lies purely in the off-line design procedure. The number of channels $(J\times I)$ of the resulting CCS filter remains the same.

III. OPTIMIZATION OF ARRAY CONFIGURATION FOR ROBUST CROSS-TALK CANCELLATION

Many design factors are involved in the CCS, e.g., array configurations, spacing and positions, number of control points in filter design, and so forth. Different configurations have effects with varying degree on the performance as well as robustness of the CCS. To minimize the effort of trial and error, a systematic design procedure of CCS based on the Taguchi method and the genetic algorithm (GA) is presented as follows.

A. Taguchi method

The Taguchi method is an experiment design procedure well suited to multivariable optimization. The method is intended for three engineering applications: system design, parameter design, and tolerance design. For our optimization

TABLE I. Parameter design using the orthogonal array of the Taguchi method. Nine observations and three factors for three levels are required.

	Factor			
Run	A	B	C	Fitness
1	1	1	1	317.35
2	1	2	2	74.653
3	1	3	3	173.62
4	2	1	2	141.81
5	2	2	3	35.169
6	2	3	1	80.04
7	3	1	3	43.49
8	3	2	1	90.706
9	3	3	2	206.65

	Level		
Factor	1	2	3
A	Closely spaced	Apart and facing ears	Apart and facing front
B	5 control points (2 points on the illuminated zone, 3 points on the shadow zone)	5 control points (2 points on the illuminated zone, 1 point at the head center, 2 points on the shadow zone)	2 control points (one at each ears)
C	2×6 CCS	2×3 CCS	2×2 CCS

problem at hand, we focus primarily on the parameter design with application in determining array configuration.

The greatest benefit of using the Taguchi method is that, instead of an exhaustive search, much fewer experiments are required in search of the optimal combination of design parameters. This is accomplished by means of orthogonal arrays which are based on statistical experimental design theory. To illustrate, we consider three factors and three levels problem. Assume that no interactions exist and the variation is very small in each observation. The orthogonal array, denoted as $L_9(3^3)$, is shown in Table I, where the numbers 1–3 correspond to three discrete levels of the design factors. According to the table, only nine runs of experiment are required, which is fewer than original 27 searches. The $L_9(3^3)$ orthogonal array is applied to the design of a robust CCS. The parameters to optimize include (A) the configurations of loudspeaker arrays; (B) the distribution of the control points; and (C) the dimension of the CCS matrix. As shown in Fig. 3, the factor (A) is categorized into three levels: (A1) represents the case in which the loudspeakers are closely spaced (six loudspeakers in a row); (A2) represents the case in which two three-element loudspeaker arrays are wide apart (subtending 60°) and facing the ears; (A3) represents the case in which two three-element loudspeaker arrays are wide apart (subtending 60°) and facing the front. The factor (B) is categorized into three levels: (B1) represents the case of five control points in which two points are placed in the illuminated zone and three points are placed in the shadow zone; (B2) represents the case of five control points in which two points are placed in the illuminated zone, one point is placed at the center of the head with 0.5 weighting, and two points are placed in the shadow zone; (B3) represents the case of two control points in which one point is placed at the ipsilateral ear and one point is placed at the contralateral ear. As shown in Fig. 4, the factor (C) is categorized into three levels. (C1) represents the case of a 2×6 CCS in which six loudspeakers are driven with different signals to reproduce the binaural signals (12 filters are needed). (C2) represents the case of a 2×3 CCS in which only a three-element array is considered in the CCS design to focus on the ipsilateral ear and nullify the beam at the contralateral ear loudspeakers. The 2×3 CCS design procedure is applied to each side of the ear to reproduce the binaural signals (six filters are needed). (C3) represents the case of a 2×2 CCS in which only two stereo loudspeakers are driven with different signals to reproduce the binaural signals (four filters are needed).

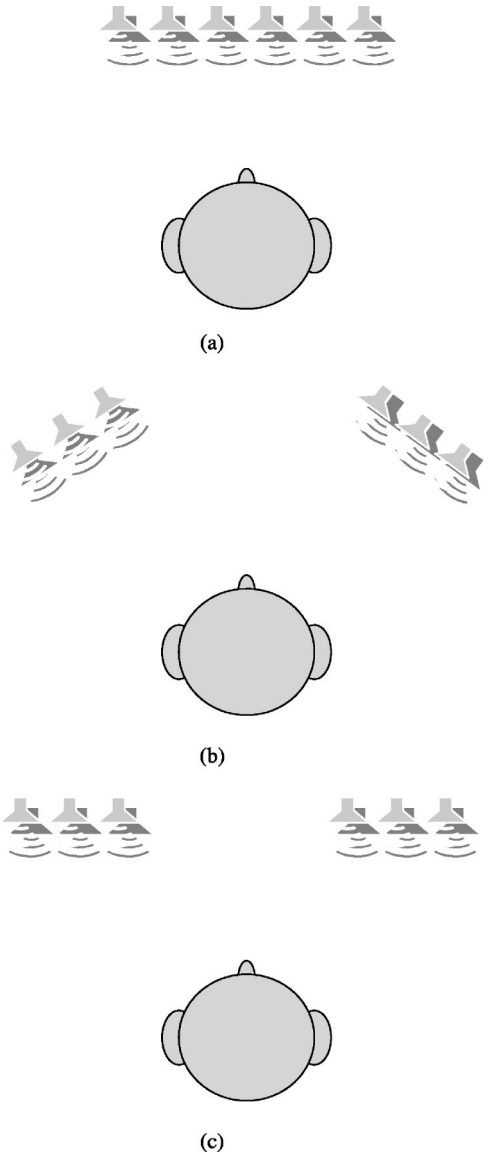

FIG. 3. Three configurations of loudspeaker arrays. (a) closely spaced loudspeakers (six loudspeakers in a row); (b) two wide-apart three-element loudspeaker arrays (subtending 60°), facing the ears; (c) two wide-apart three-element loudspeaker arrays (subtending 60°), facing the front.

Both performance and robustness are considered with appropriate weighting W in the objective function

$$f = \text{performance} + W \times \text{robustness}. \tag{15}$$

To assess the performance and robustness, the channel sepa-

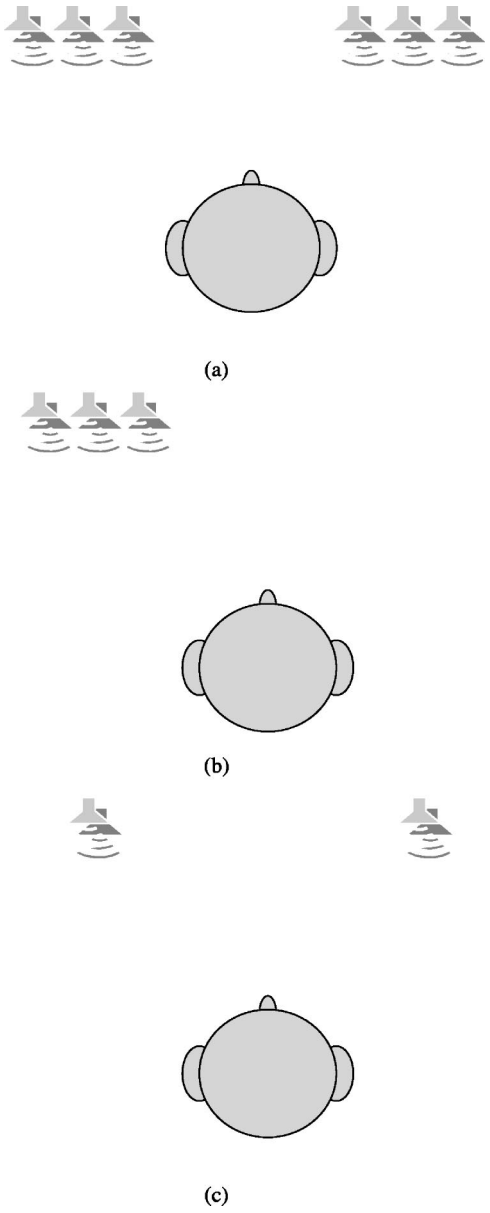

FIG. 4. The dimension of the CCS matrix. (a) a 2×6 CCS in which six loudspeakers are driven with different signals to reproduce the binaural signals. (b) a 2×3 CCS in which only a three-element array is considered in the CCS design to focus on the ipsilateral ear and nullify the beam at the contralateral ear loudspeakers. The 2×3 CCS design procedure is applied to each side of the ear to reproduce the binaural signals. (c) a 2×2 CCS in which only two stereo loudspeakers are driven with different signals to reproduce the binaural signals (four filters are needed).

ration is calculated using the interaural transfer functions (ITFs)

$$ITF_L = \frac{H_{LR}}{H_{LL}}, \quad ITF_R = \frac{H_{RL}}{H_{RR}}, \tag{16}$$

where H_{LR} and H_{RL} are the contralateral frequency responses; H_{LL} and H_{RR} are the ipsilateral frequency responses. The performance function is defined as the channel separation at the nominal position, and the robustness function is defined as the lateral beamwidth when the channel separation drops below −20 dB. The lower the channel separation, the better is the performance of cross-talk cancellation. The larger the beamwidth, the more robust is the CCS against lateral misalignment of the listener's head. The results with the weighting $W=10$ are summarized in Table II. From Table II, the optimal parameters (with maximum values of objective function) of the robust CCS are found to be closely spaced arrays, five control points (two points on the illuminated zone, three points on the shadow zone), and a 2×6 CCS matrix.

TABLE II. The results of optimal parameters obtained using the Taguchi method. The numbers in the second column are obtained by summing the fitness functions of the corresponding parameter levels. The optimal combinations of parameters of the robust CCS are closely spaced loudspeakers, five control points (with two points on the illuminated zone, three points on the shadow zone), and with an 2×6 CCS matrix.

Levels of parameters	Average of objective function	Chosen level
A1	317.35+74.653+173.62=565.623	Closely spaced
A2	141.81+35.169+80.04=257.019	
A3	43.49+90.706+206.65=340.846	
B1	317.35+141.81+43.49=502.65	5 control points
B2	74.653+35.169+90.706=200.528	(2 points on the
B3	173.62+80.04+206.65=460.31	illuminated zone, 3 points on the shadowzone)
C1	317.35+80.04+90.706=488.096	2×6 CCS
C2	74.653+141.81+206.65=423.113	
C3	173.62+35.169+43.49=252.279	

B. The genetic algorithm

The above-mentioned Taguchi method is more suited to design parameters with finite number of discrete levels. In

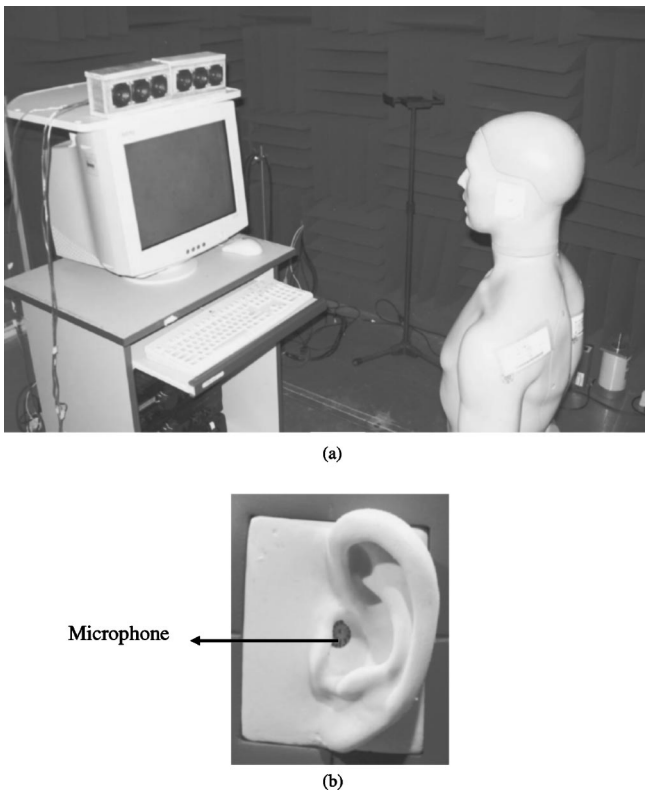

FIG. 5. The photo of the experimental arrangement. (a) The robust CCS with an loudspeaker array. (b) The 1/2-in. condenser microphone embedded in the manikin's ear.

the sequel, an alternative approach that is useful for optimization of continuous parameters is exploited to find the best configuration of the CCS.

1. Encoding and decoding

In the method of GA, all parameters are encoded into binary strings called the *chromosomes*. The resolution of a parameter is dependent on the amount of bits per string and search domain. For instance, we wish to find the optimal spacing $x \in [U_{\min}, U_{\max}]$ ($U_{\min}$ and $U_{\max}$ being the lower limit and the upper limit of the search space) of the loudspeaker array. This parameter is then mapped to an unsigned integer in $[0, 2^l]$, where l is the number of bits. Thus, the resolution of this coding scheme is

$$\Gamma = \frac{U_{\max} - U_{\min}}{2^l - 1}. \tag{17}$$

2. Fitness evaluation

In the GA optimization, the objective one seeks to achieve is termed the fitness function. A chromosome with high fitness has higher probability to survive the natural selection and reproduce offspring in the next generation. The fitness function is the performance function (channel separation) and the robustness function (beam width) with appropriate weighting W

$$f = \text{performance} + W \times \text{robustness}. \tag{18}$$

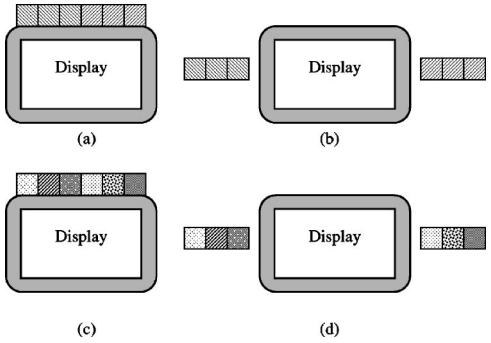

FIG. 6. Illustrations of four loudspeaker array configurations. (a) Configuration 1: closely spaced 2×2 CCS. (b) Configuration 2: wide apart (subtending 60°) 2×2 CCS. (c) Configuration 3: closely spaced 2×6 CCS. (d) Configuration 4: wide-apart (subtending 60°) 2×6 CCS.

3. Reproduction, crossover, and mutation

Reproduction directs the search of GA towards the best individuals. During the process, the reproduction probability of the chromosome is determined by the fitness function. First, the chromosome of the present population is reproduced in the next generation according to the reproduction probability S_i

$$S_i = \frac{f_i}{\sum_{k=1}^{P_l} f}, \tag{19}$$

where P_l is the population size.

Crossover exchanges the contents of chromosomes via probabilistic decision in the mating pool. It is done in three steps. First, the crossover ratio C_r is defined (in general,

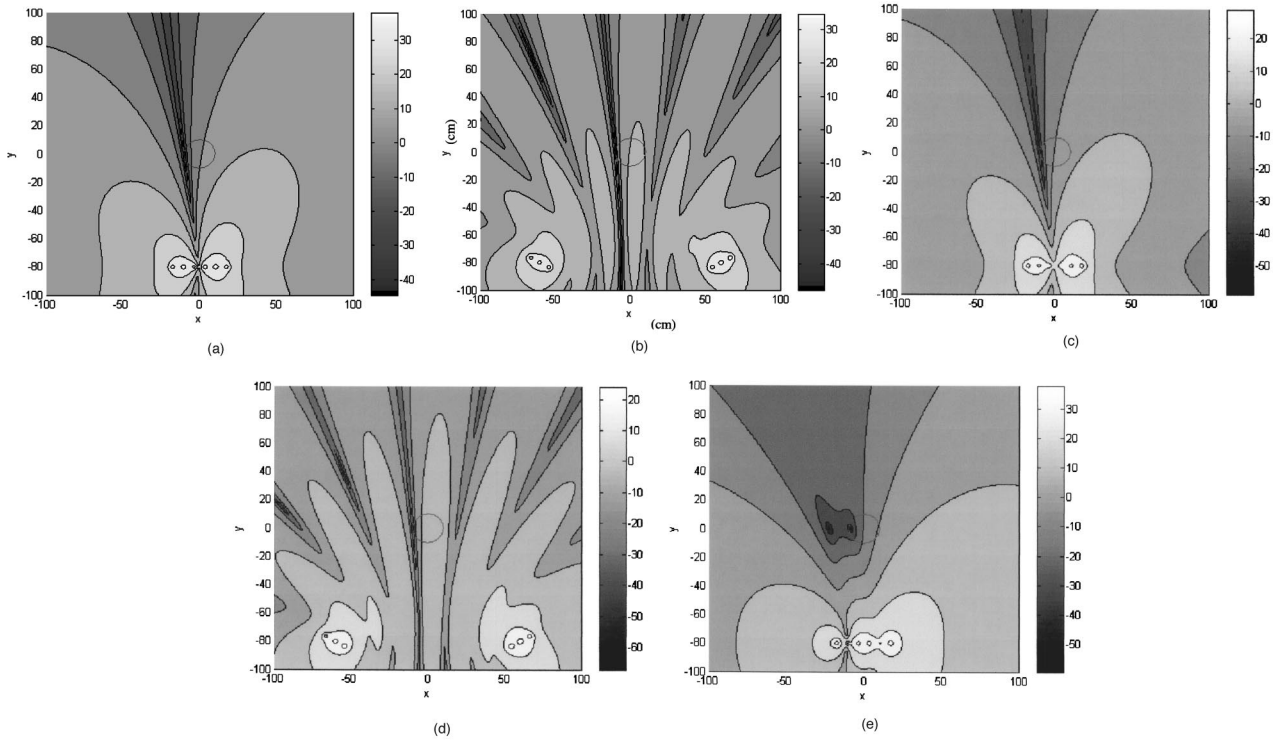

FIG. 7. The contour plots of beam patterns at 1 kHz of various CCS configurations. (a) Configuration 1. (b) Configuration 2. (c) Configuration 3. (d) Configuration 4. (e) Configuration 3 with the optimal 2×6 CCS obtained in the GA procedure.

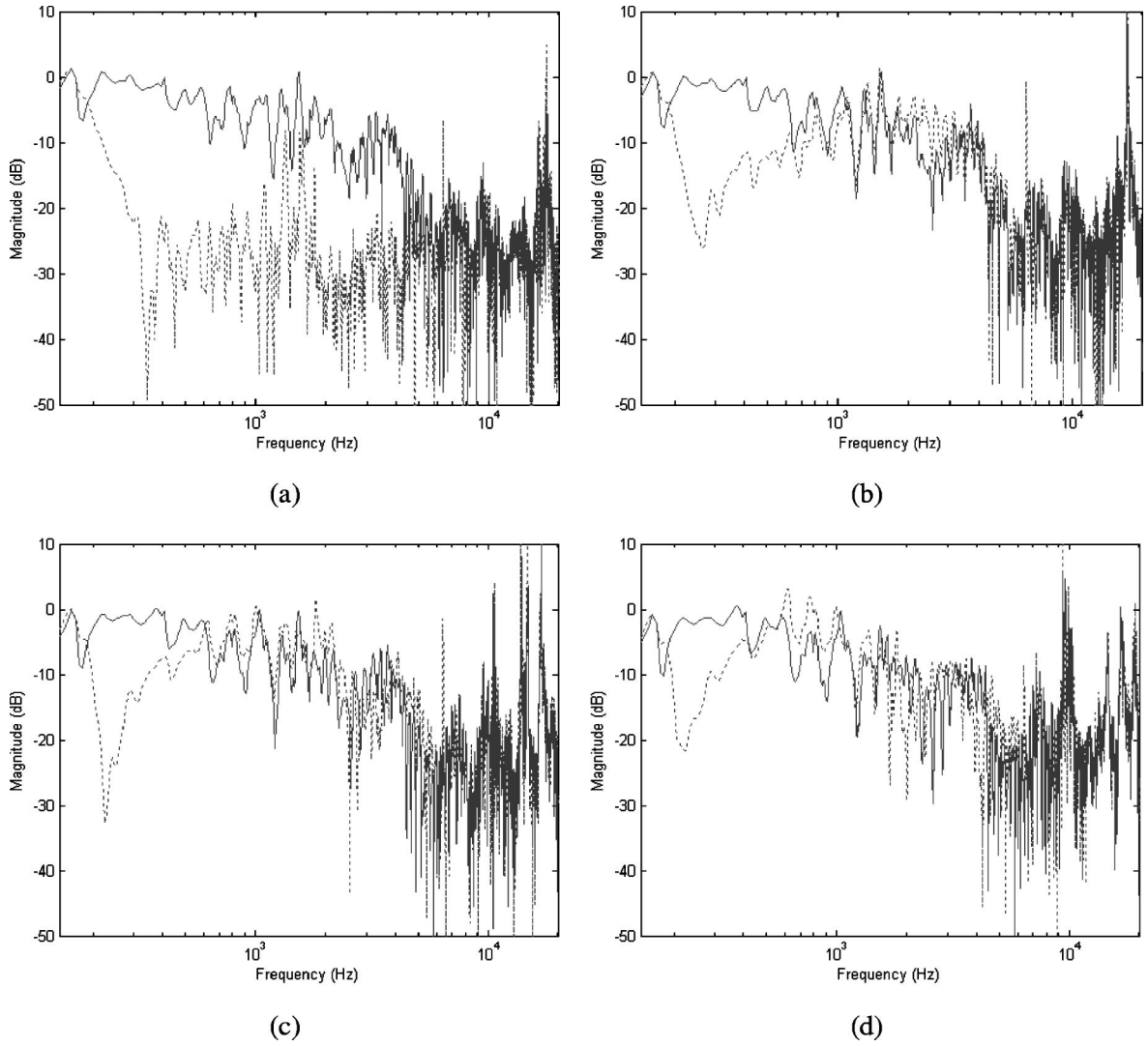

FIG. 8. Channel separations of the left ear obtained using the 2×2 CCS for the wide-apart configurations. The solid lines represent the natural separations and the dotted lines represent the separations with cross-talk cancellation. (a) The channel separation with no displacement. (b) The channel separation with 5-cm displacement to the left. (c) The channel separation with 10-cm displacement to the left. (d) The channel separation with 15-cm displacement to the left.

$0.8 \leqslant C_r \leqslant 1$ and we choose $C_r = 0.85$) and two chromosomes in the present population are selected randomly. Second, a splice point at the chromosomes is selected randomly. Third, the chromosomes codes after the splice point are interchanged.

Normally, the chromosomes become increasingly homogeneous as one particular gene begins to dominate after several generations and eventually leads to premature convergence. To obviate this problem, *mutation* is introduced into the GA procedure. Let the mutation ratio be M_r (in general, $0 \leqslant M_r \leqslant 0.01$ and we choose $M_r = 0.008$). The mutation point is determined randomly and carried out by alternating the gene from zero to 1, or vice versa. Note, however, that mutation should be used sparingly. The GA would behave like a random search if the mutation rate were too high.

The aforementioned GA procedure was applied to optimize the design of the robust CCS. The design parameters we wish to optimize are similar to those in the Taguchi method, i.e., the spacing between loudspeaker arrays, the distribution of the control points, and the dimension of CCS matrix. When the robustness weighting of fitness function is set to be 1, the optimal design parameters of the robust CCS obtained with the aid of the GA procedure are 0 cm spacing (closely spaced arrays), six control points (one point in the illuminated zone and five points in the shadow zone), and a 2×6 CCS matrix. This result is consistent with the optimal configuration obtained previously using the Taguchi method.

IV. NUMERICAL AND EXPERIMENTAL INVESTIGATIONS

In the paper, the performance of CCS and the associated robustness against head misalignment is examined via numerical and experimental investigations. Only lateral misalignment is considered because it affects the performance of the CCS more significantly than the other types of misalignment.[23,24] The objective performance index is channel separation as defined previously. The experimental arrangement is shown in Fig. 5. A loudspeaker array is mounted on a computer monitor. The distance between the array and the manikin is 80 cm. The loudspeaker array is 10 cm higher than the ears of the manikin. A 1/2-in. condenser

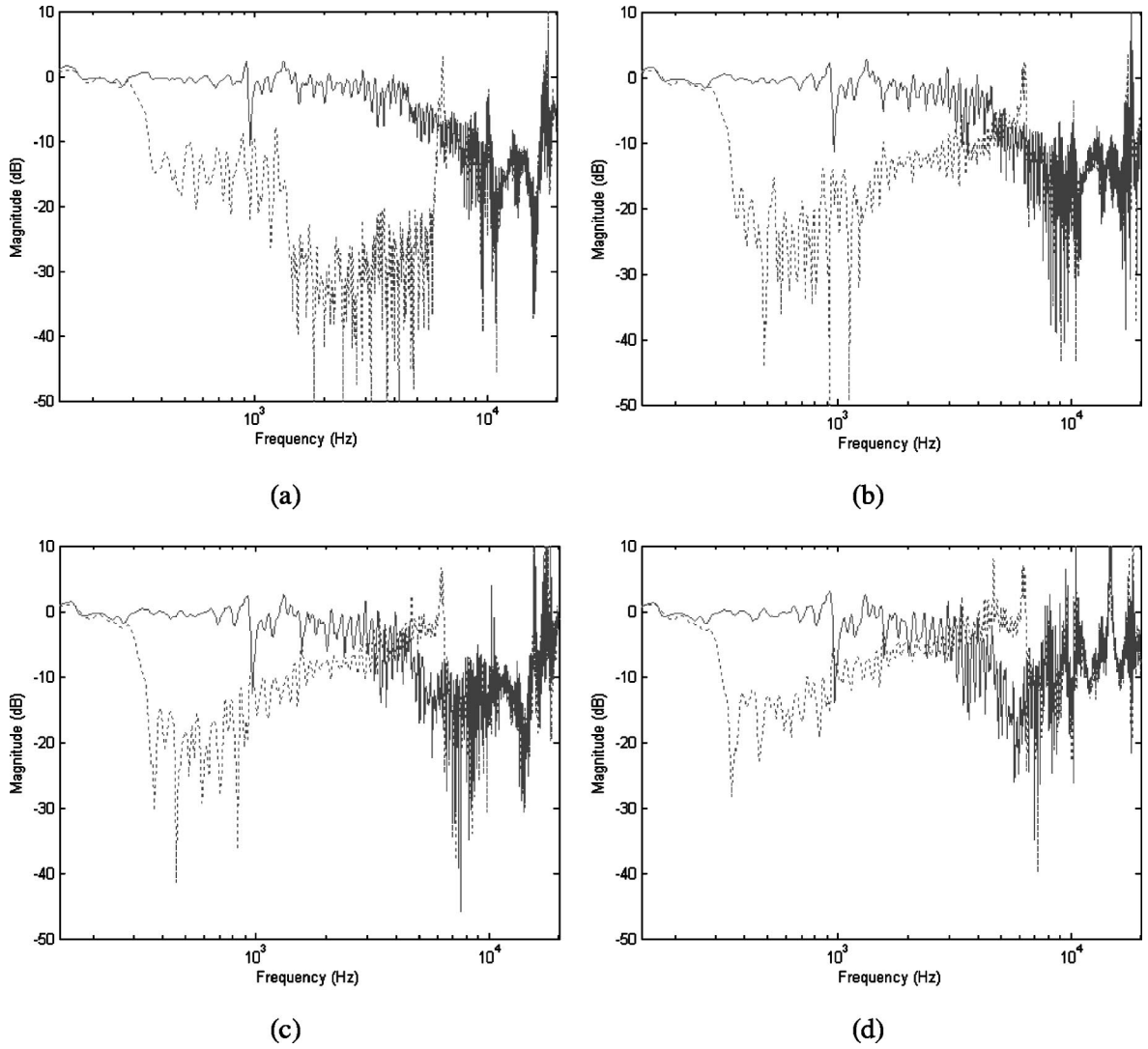

FIG. 9. Channel separations of the left ear obtained using the 2×2 CCS for the closely spaced configuration. The solid lines represent the natural separations and the dotted lines represent the separations with cross-talk cancellation. (a) The channel separation with no displacement. (b) The channel separation with 5-cm displacement to the left. (c) The channel separation with 10-cm displacement to the left. (d) The channel separation with 15-cm displacement to the left.

microphone is fitted inside the ear of the manikin. The sampling rate is 51.2 kHz. The CCS matrix of inverse filtering is calculated by using Eq. (10). The length of each filter is 512 samples and the modeling delay m is 256 samples. The *overlap-add* method is employed to perform block convolution efficiently.[25]

A. Numerical simulations

Before embarking on the experimental investigations, a numerical simulation is carried out to gain more insights into the loudspeaker array configurations in relation to the robustness issue of the CCS. The simulation is conducted for the configurations shown in Fig. 6. In configurations 1 and 2, the 2×2 CCS is simulated, where only one control point is placed in the illuminating zone and another in the shadow zone. There are six loudspeakers in each configuration, where three out of the six loudspeakers form a cluster. The loudspeakers in the same cluster are driven by the same input signal, as indicated by the same pattern of shading. The two clusters are placed side by side in configuration 1, while the two clusters are placed apart (subtending 60°) in configuration 2. In configurations 3 and 4, the 2×6 CCS is simulated. The six loudspeakers are driven by independent signals. Similar to configurations 1 and 2, the only difference between configurations 3 and 4 is whether the loudspeaker clusters are placed side by side or apart. For simplicity, the loudspeakers are assumed to be point sources and the head diffraction as well as room reflection is neglected.

The following contour plots in $x-y$ coordinates compare the beam patterns for the right-ear signals resulting from the foregoing loudspeaker configurations. Only the results of the right-side control are shown. The head and the six loudspeakers are indicated in the figures. The results of configurations 1 and 2 are shown in Figs. 7(a) and (b), respectively. The configuration when all loudspeakers are closely placed results in a wider beam. In contrast, many grating lobes with narrow beamwidth can be seen in the pattern produced by the wide-apart configuration. This shows that the closely spaced configuration is more robust than the wide-apart configuration in cross-talk cancellation, albeit the two CCS perform equally well.

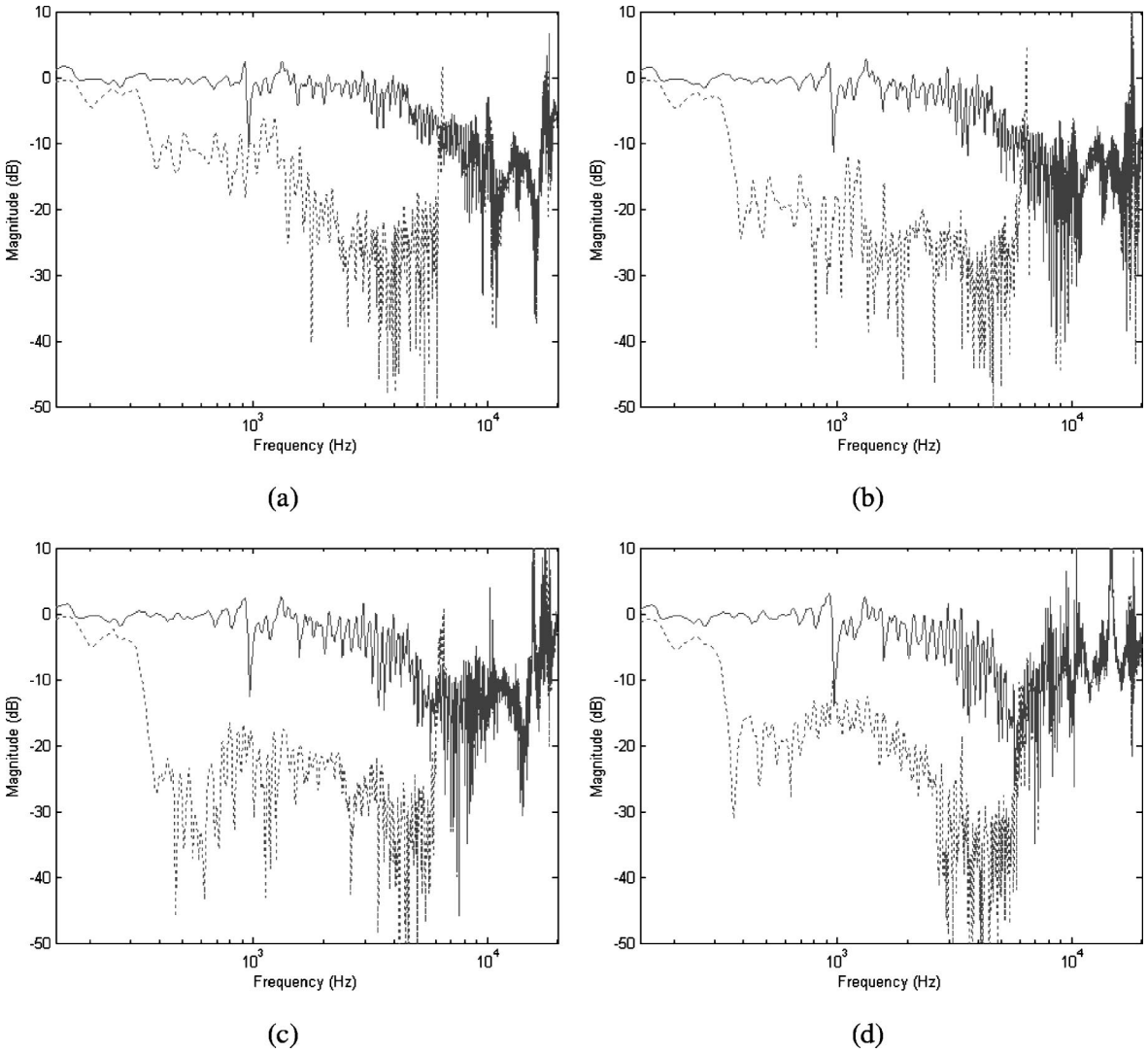

FIG. 10. Channel separations of the left ear obtained using the optimal closely spaced 2×6 configuration designed using six control points (one at the ipsilateral ear and five at the contralateral ear). The solid lines represent the natural separations and the dotted lines represent the separations with cross-talk cancellation. (a) The channel separation with no displacement. (b) The channel separation with 5-cm displacement to the left. (c) The channel separation with 10-cm displacement to the left. (d) The channel separation with 15-cm displacement to the left.

The results of configurations 3 and 4 are shown in Figs. 7(c) and (d), respectively. Inspection of these figures reveals that performance of the two CCS is better than configurations 1 and 2. The wide-apart configuration performs better than the closely spaced configuration, especially at low frequency. However, the closely spaced configuration appears to be more robust than the wide-apart configuration in cross-talk cancellation.

The last four beam patterns are based on the CCS design with only one control point at each ear. Figure 7(e) shows the beam pattern of configuration 3 for the optimal 2×6 CCS obtained in the aforementioned GA procedure. Six control points are used in the design: one at the ipsilateral ear and five at the contralateral ear. As compared to the previous configurations, the sweet spot of the CCS has been effectively widened using the control point technique without significant compromise of cancellation performance.

B. Physical tests

In this section, experiments were conducted to examine how channel separation degrades when the listener's head is laterally displaced from the nominal location in the ideal listening scenario. The experiment was performed in an anechoic room, where a CCS bandlimited to 6.4 kHz was tested.

The channel separations of the left ear obtained using the 2×2 CCS are shown in Fig. 8 and Fig. 9 for the wide-apart and closely spaced configurations, respectively. The solid lines represent the natural separations and the dotted lines represent the separations with cross-talk cancellation. In low frequencies, due to diffraction effect, there is almost no natural separation below 400 Hz in the wide-apart configuration (Fig. 8) and below 900 Hz in the closely spaced configuration (Fig. 9). Head shadowing effect becomes visible in high frequencies, where the wide-apart configuration offers better natural separation than the closely spaced configuration. The peaks at higher frequencies result from the inversion of the notches in the ipsilateral responses. Inspection of the results indicates that the 2×2 CCS is not very robust. The performance degrades by 20 dB above 1.5 kHz as the head is displaced leftward by more than 5 cm irrespective of which configuration is used. Nevertheless, the closely spaced con-

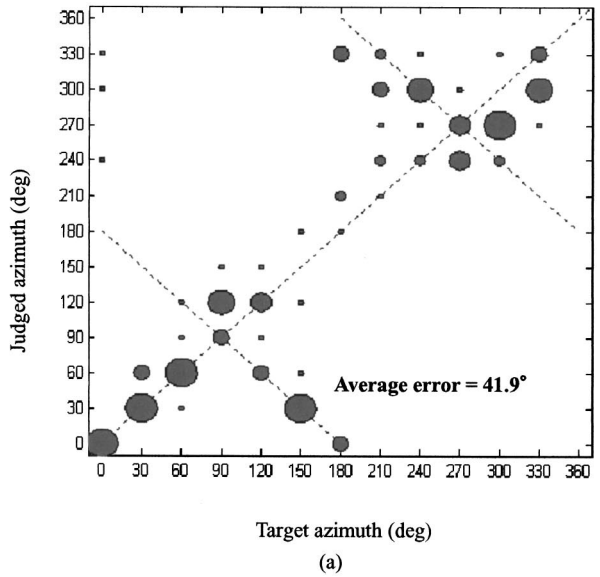

(a)

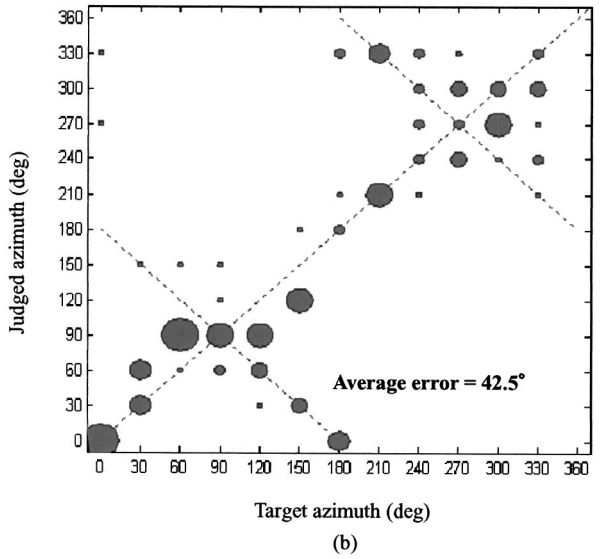

(b)

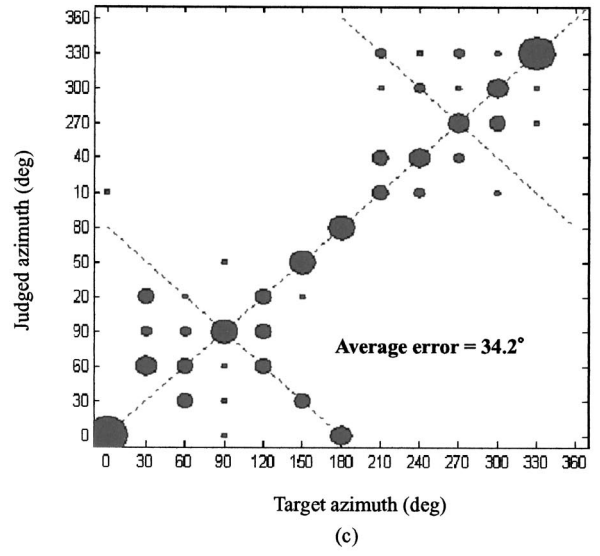

(c)

FIG. 11. Azimuth localization results of the subjective test with no head displacement. (a) wide-apart 2×2 CCS; (b) closely spaced 2×2 CCS; (c) The optimal closely spaced 2×6 configuration designed using six control points (one at the ipsilateral ear and five at the contralateral ear).

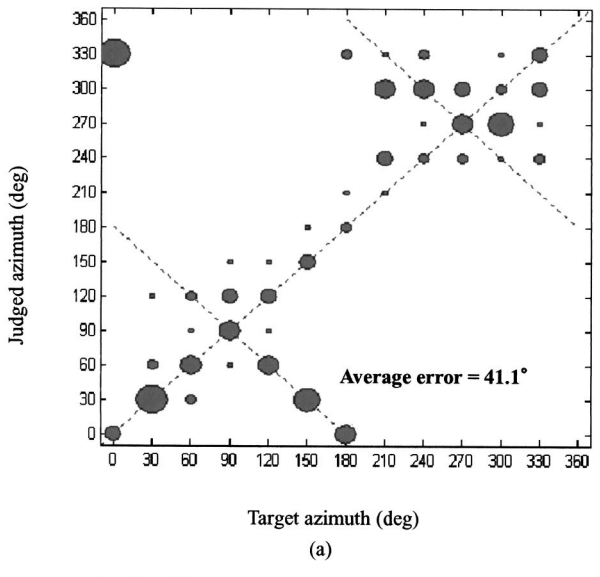

(a)

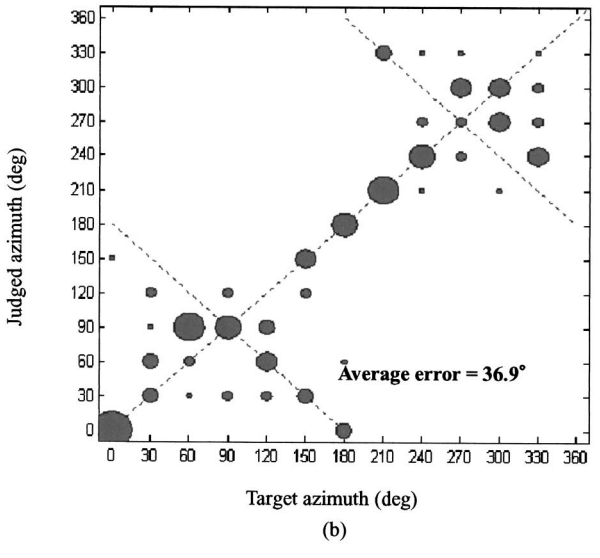

(b)

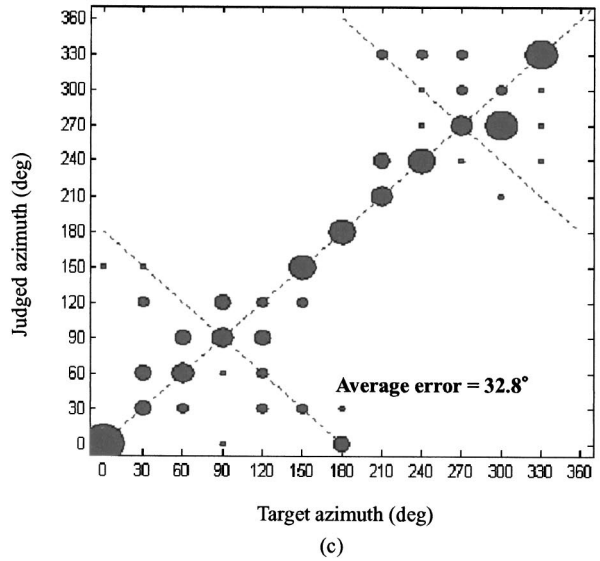

(c)

FIG. 12. Azimuth localization results of the subjective test with 5-cm head displacement to the left. (a) wide-apart 2×2 CCS; (b) closely spaced 2×2 CCS (c). The optimal closely spaced 2×6 configuration designed using six control points (one at the ipsilateral ear and five at the contralateral ear).

figuration in Fig. 9 appears to be slightly more robust than the wide-apart configuration. In Figs. 8(c) and (d), the wide-apart CCS almost lost entire performance above 1 kHz, and the channel separations are nearly the same as the natural channel separations.

In order to improve the robustness of CCS, the optimal closely spaced 2×6 configuration designed using six control points (one at the ipsilateral ear and five at the contralateral ear) was utilized in the next experiment. Figure 10 shows the channel separations obtained using this CCS. It is evident from these plots that the robustness of the 2×6 CCS has been significantly improved over the previous 2×2 CCS. Figure 10(d) shows that the channel separation of the optimal CCS remains as low as −30 dB above 2.5 kHz. The regularization parameter β is frequency dependent and constrained by a 12-dB gain threshold. Because of thus applied regularization, some peaks in Figs. 8–10 can be seen due to imperfect cancellation. From the observation of these results, it is fair to say that large number of loudspeakers, closely spaced configuration, and optimal control point design all contribute to the robustness of CCS against head misalignment.

C. Subjective listening tests

In order to compare various configurations of CCS, a subjective localization experiment was performed in the anechoic room. The test stimulus was a random noise band-limited to 20 kHz. Each stimulus was played for 5-s in duration and switched off for 2 s before the next stimulus was switched on. Virtual sound images at 12 directions on the horizontal plane with increment of 30° azimuth were generated through the filtering of head-related transfer functions (HRTFs). The CCS configurations used in the experiment were the wide-apart 2×2 CCS, the closely spaced 2×2 CCS, and the optimal closely spaced 2×6 CCS. Nine human subjects with normal hearing participated in the experiment.

The experimental results of the judged angles versus the target angles in the localization tests are shown in Figs. 11–13, corresponding to the cases of no misalignment, 5-cm misalignment, and 10-cm misalignment. In each case, all three CCS configurations were tests. The area of each circle is proportional to the number of the listeners who localized the same perceived angle. The 45-deg line represents the perfect localization. The average errors of localization are shown in the figures. As can be seen from the results, the optimal closely spaced 2×6 CCS exhibited remarkable performance and robustness among all configurations. The average localization error using this configuration is only 32.8° (approximately 1 increment of angle) for 5-cm misalignment.

V. CONCLUSIONS

Performance and robustness issues are examined through extensive numerical and experimental investigations. An array beamforming technique using control points is exploited in the design of the CCS filters. Various configurations are compared in the numerical simulations. In terms of the cancellation performance, the wide-apart configura-

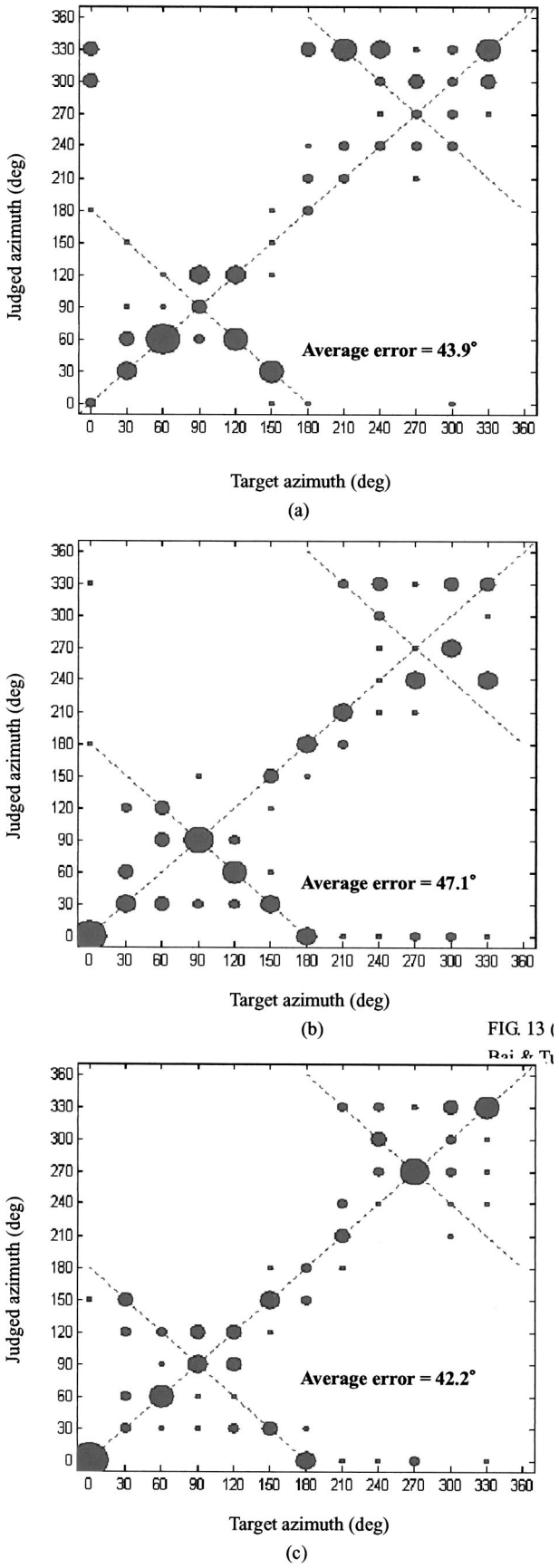

FIG. 13. Azimuth localization results of the subjective test with 10-cm head displacement to the left. (a) wide-apart 2×2 CCS; (b) closely spaced 2×2 CCS. (c) The optimal closely spaced 2×6 configuration designed using six control points (one at the ipsilateral ear and five at the contralateral ear).

TABLE III. Comparison of the CCS configurations. Performance is the average channel separation throughout 20 kHz. Robustness is the lateral displacement (in 5-cm increments) of the head that allows for decay of channel separation within 5 dB. The numbers corresponding to the rows of performance and robustness are experimental data.

	2×2 CCS close	2×2 CCS apart	2×6 CCS close	2×6 CCS apart
Performance	−20 dB	−23 dB	−15 dB	−15 dB
Robustness	±5 cm	±0 cm	±10 cm	±5 cm
Subjective localization test	good	good	excellent	fair
Number of CCS filters	4 filters	4 filters	12 filters	12 filters
Ranking	2	3	1	4

tions could achieve higher channel separation than the closely spaced configurations. However, the closely spaced configurations appear to be more robust than the wide-apart configurations against the lateral misalignment of the head. There is a trade-off that we have to reconcile between the performance and robustness. To facilitate this trade-off, a procedure based on the Taguchi method and the GA has been developed to find optimal configurations of CCS and loudspeaker arrays that attain the best compromise between the performance (channel separation) and robustness (beamwidth). Four configurations are compared by means of objective and subjective experiments. The results are summarized in Table III.

The experimental results indicate that the optimal closely spaced 2×6 CCS is the best choice in terms of performance and robustness. It is fair to say that large number of loudspeakers, closely spaced configuration, and optimal control point design all contribute to the robustness of CCS against head misalignment. Such array design is well suited to equipment that must be spatially compact, e.g., laptop computer, portable audio, mobile phone, etc. A limitation of the 2×6 design of loudspeaker array is that it is more computationally intensive than the 2×2 system. The 2×6 CCS requires 12 filters versus 4 filters in the 2×2 CCS. If computation loading is an issue, however, the closely spaced 2×2 CCS is perhaps the second best choice. Some limitations of the employed optimization methods should also be mentioned. Although the Taguohi method is well suited to problems with discrete levels, the choices must be prespecified. The number of combinations becomes exceedingly large when too many factors to investigate are involved. The same situation happens to the GA; the search requires a very long time to converge for problems with long-coded chromosomes. However, this is not a problem for the CCS in the paper since only loudspeaker spacing is the major design variable. It should be borne in mind that the configuration of the CCS suggested may not be the ultimate optimal, but is the best of the configurations considered.

The horizontally placed loudspeaker array suggested in the paper could have potential impact on the way people implement 3D sound in practical applications. For example, conventional wide-apart stereo loudspeakers are commonplace in PC multimedia and TV applications, but are not effective configurations in the context of 3D audiovisual reproduction. The new loudspeaker configuration proposed in this paper provides a useful alternative.

ACKNOWLEDGMENT

The work was supported by the National Science Council in Taiwan, Republic of China, under the Project Number NSC 92-2212-E009-030.

[1] B. B. Bauer, ''Stereophonic earphones and binaural loudspeakers,'' J. Audio Eng. Soc. **9(2)**, 148–151 (1961).
[2] M. R. Schroeder and B. S. Atal, ''Computer simulation of sound transmission in rooms,'' IEEE Conv. Record. **7**, 150–155 (1963).
[3] P. Damaske and V. Mellert, ''A procedure for generating directionally accurate sound images in the upper- half space using two loudspeakers,'' Acustica **22**, 154–162 (1969).
[4] D. H. Cooper, ''Calculator program for head-related transfer functions,'' J. Audio Eng. Soc. **30**, 34–38 (1982).
[5] W. G. Gardner, ''Transaural 3D audio,'' MIT Media Laboratory Tech. Report, 342, (1995).
[6] A. D. Blumlein, ''Improvements in and relating to sound-transmission, sound-recording and sound-reproducing systems,'' J. Audio Eng. Soc. **6(2)**, 91–99 (1958).
[7] D. H. Cooper and J. L. Bauck, ''Prospects for transaural recording,'' J. Audio Eng. Soc. **37**, 3–19 (1989).
[8] J. L. Bauck and D. H. Cooper, ''Generalized transaural stereo and applications,'' J. Audio Eng. Soc. **44**, 683–705 (1996).
[9] C. Kyriakakis, T. Holman, J. S. Lim, H. Homg, and H. Neven, ''Signal processing, acoustics, and psychoacoustics for high-quality desktop audio,'' J. Visual Commun. Image Represent **9**, 51–61 (1997).
[10] C. Kyriakakis, ''Fundamental and technological limitations of immersive audio systems,'' Proc. IEEE **86**, 941–951 (1998).
[11] D. B. Ward and G. W. Elko, ''Optimal Loudspeaker Spacing for Robust Crosstalk Cancellation,'' Proc. ICASSP 98, IEEE, 3541–3544 (1998).
[12] D. B. Ward and G. W. Elko, ''Effect of loudspeaker position on the robustness of acoustic crosstalk cancellation,'' IEEE Signal Process. Lett. **6(5)**, 106–108 (1999).
[13] T. Takeuchi and P. A. Nelson, ''Robustness to head misalignment of virtual sound imaging systems,'' J. Audio Eng. Soc. **109**, 958–971 (2001).
[14] T. Takeuchi and P. A. Nelson, ''Optimal source distribution for binaural synthesis over loudspeakers,'' J. Audio Eng. Soc. **112**, 2786–2797 (2002).
[15] A. Sibbald, ''Transaural acoustic crosstalk cancellation,'' Sensaura White Papers (1999) (http://www.sensaura.co.uk)
[16] M. Tanter, J.-L. Thomas, and M. Fink, ''Time reversal and the inverse filter,'' J. Acoust. Soc. Am. **108**, 223–234 (2000).
[17] O. Kirkeby, P. A. Nelson, and H. Hamada, ''Fast deconvolution of multichannel systems using regularization,'' IEEE Trans. Speech Audio Process. **6**, 189–194 (1998).
[18] H. C. Robert, Jr., *Fundamental Concepts in the Design of Experiments* (Saunders College Publishing, Philadelphia, 1982).
[19] J. H. Holland, ''Outline for a logical theory of adaptive system,'' J. ACM **3**, 297–314 (1962).
[20] C. T. Lin and C. S. G. Lee, *Neural Fuzzy Systems* (Prentice-Hall, Englewood Cliffs, NJ, 1996).
[21] T. Takeuchi, P. A. Nelson, and H. Hamada, ''Robustness to head misalignment of virtual sound imaging systems,'' J. Acoust. Soc. Am. **109**, 958–971 (2001).
[22] A. Schuhmacher and J. Hald, ''Sound source reconstruction using inverse boundary element calculations,'' J. Acoust. Soc. Am. **113**, 114–127 (2003).
[23] B. S. Atal, M. Hill, and M. R. Schroeder. ''Apparent sound source translator.'' U.S. Patent No. 3236949. 22 Feb., 1966.
[24] W. G. Gardner, *3D Audio using Loudspeakers* (Kluwer Academic, Dordrecht, 1998).
[25] A. V. Oppenheim and R. W. Schafer, *Discrete-Time Signal Processing*, 2nd ed. (Prentice-Hall, Englewood Cliffs, NJ, 1999).

Locally periodic Timoshenko rod: Experiment and theory

A. Díaz-de-Anda, A. Pimentel, J. Flores,[a] A. Morales, L. Gutiérrez, and R. A. Méndez-Sánchez[b]

Centro de Ciencias Físicas, Universidad Nacional Autónoma de México, A.P. 48-3, 62251, Cuernavaca, Mor., México

(Received 6 August 2004; revised 2 February 2005; accepted 4 February 2005)

The flexural vibrations of a locally periodic rod, which consists of N unit cells, are discussed both from the experimental and theoretical points of view. Timoshenko's beam theory and the transfer matrix method are used to calculate the normal-mode frequencies and amplitudes. The theoretical values are then compared with the experimental ones, which are obtained using an electromagnetic acoustic transducer (EMAT). Good agreement between the numerical results and the experimental measurements is obtained. It is shown that as N grows, a band spectrum emerges. © *2005 Acoustical Society of America.* [DOI: 10.1121/1.1880732]

PACS numbers: 43.40.Cw, 43.40.At, 43.38.Dv [ANN] Pages: 2814–2819

I. INTRODUCTION

It is well known that spatially periodic systems show a spectrum which is arranged in bands of allowed frequencies, or pass bands, separated by gaps of forbidden frequencies, called stop bands.[1] One-dimensional locally periodic systems, composed of a finite number N of identical cells, also show a spectrum in which the normal-mode frequencies are clustered in bands as N grows. This has been obtained theoretically for a variety of wave-like systems: electrons in solids,[2] elastic systems,[3,4] Love analysis of waves in rods,[5] waves in a stretched wire,[6] and compressional and torsional waves in rods.[7] It should be noted that, except for the last two references, a direct comparison with experimental data is not performed. Apart from its academic value, some of these results have applications in vibration isolation.[8]

The emergence of a banded spectrum is obtained in all these cases for systems related to second-order differential equations. Flexural vibrations, described by a more complicated fourth-order differential equation,[9] have also been analyzed from the theoretical standpoint for an infinite supported Timoshenko beam[10,11] and numerically for a multispan beam using the finite element method.[12] However, in none of these works is a comparison with experiment performed. Therefore, our main goal in this paper is to study flexural vibrations in locally periodic rods from the theoretical and experimental viewpoints.

The Timoshenko beam theory (TBT) as well as the simpler Bernoulli-Euler (B-E) approach will be analyzed. In Sec. II the transfer matrix method is used to calculate both normal-mode frequencies and amplitudes for these rods. In Sec. III the experimental setup to measure these quantities is described. An electromagnetic acoustic transducer (EMAT) is used to excite and detect the rod vibrations.[13] This EMAT is inexpensive and easy to construct with commercially available components. It is a non-contact and very versatile device which operates at low frequencies. Furthermore, this EMAT is selective in the sense that either compressional, torsional or flexural vibrations can be excited or detected with it. Finally, in Sec. IV the theoretical results are compared with the experimental ones. Since a good agreement is obtained, this result works as another check of TBT, which was formerly accomplished only for a uniform rod.[14–16]

II. TRANSFER MATRIX METHOD FOR THE TIMOSHENKO EQUATION

There are two well-known theories which describe flexural vibrations of beams, the Bernoulli-Euler and the Timoshenko beam theories.[9] In the TBT, apart from the transverse displacement ξ, another degree of freedom exists, the angular coordinate ψ.[9] The Timoshenko equation for the transverse displacement ξ of a uniform rod is given by

$$\frac{EI}{\rho S}\frac{\partial^4 \xi}{\partial z^4} - \frac{I}{S}\left(1+\frac{E}{\kappa G}\right)\frac{\partial^4 \xi}{\partial z^2\,\partial t^2} + \frac{\partial^2 \xi}{\partial t^2} + \frac{\rho I}{\kappa G S}\frac{\partial^4 \xi}{\partial t^4} = 0. \tag{1}$$

An identical equation holds for the angle ψ. Here G and E are the shear and Young's modulus, respectively, ρ is the density, S is the cross-section area, κ is the Timoshenko shear coefficient and I is the moment of inertia with respect to the axis perpendicular to the rod axis. Imposing the normal-mode condition $\xi(z,t)=\Psi(z)\exp(i\omega t)$, where $\omega=2\pi f$, f being the frequency, the Timoshenko equation can be written as a set of four linear differential equations.[16] As has been shown in Ref. 16, for a circular uniform rod the amplitude $\Psi(z)$ reads as

$$\Psi(z) = Ak_1^{-3}e^{k_1 z} + Bk_2^{-3}e^{k_2 z} + Ck_3^{-3}e^{k_3 z} + Dk_4^{-3}e^{k_4 z}, \tag{2}$$

where $z=0$ and $z=L$ correspond, respectively, to the left- and right-hand free ends of the rod. In the last equation,

$$k_j = (-1)^{[j/2]}\sqrt{\frac{\alpha+(-1)^j\sqrt{\alpha^2+4\beta}}{2}}, \quad \text{for } j=1,\ldots,4, \tag{3}$$

[a]Permanent address: Instituto de Física, UNAM, A. P. 20-364, 01000 México, D. F., México.
[b]Electronic mail: mendez@fis.unam.mx

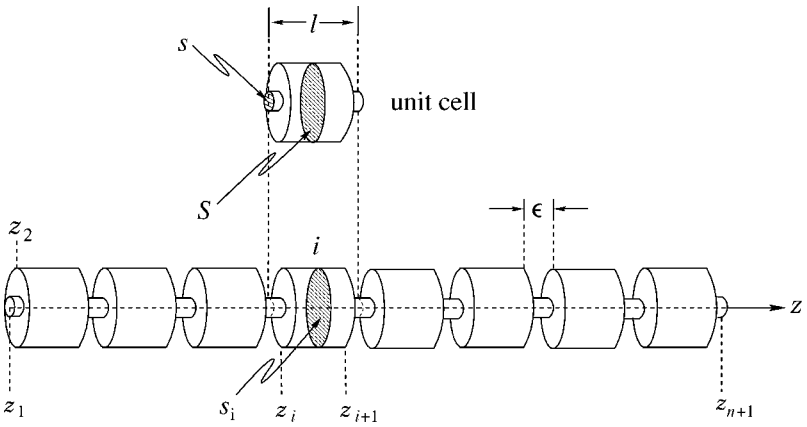

FIG. 1. A schematic diagram of the locally periodic rod formed by N unit cells of length l, with $n=2N+1$ cylinders. The total length L is Nl.

depends on the mechanical and geometrical properties of the rod through $\alpha=-\rho\omega^2/E-\rho\omega^2/\kappa G$ and $\beta=\rho S\omega^2/EI-\rho^2\omega^4/E\kappa G$. Here $[j/2]$ is the largest integer less than $j/2$.

The eigenfrequencies are obtained when the free-end boundary conditions are fulfilled. Then the bending moment,

$$M(z)=EI\Psi''(z), \tag{4}$$

and the shear force,

$$F(z)=EI\Psi'''(z), \tag{5}$$

vanish at $z=0$ and $z=L$. This leads to

$$\begin{aligned} &k_1^{-1}A+k_2^{-1}B+k_3^{-1}C+k_4^{-1}D=0,\\ &A+B+C+D=0,\\ &k_1^{-1}e^{k_1L}A+k_2^{-1}e^{k_2L}B+k_3^{-1}e^{k_3L}C+k_4^{-1}e^{k_4L}D=0,\\ &e^{k_1L}A+e^{k_2L}B+e^{k_3L}C+e^{k_4L}D=0. \end{aligned} \tag{6}$$

The eigenfrequencies f_i are then found obtaining the roots of the determinant of this system numerically.

These results are now used to deal with the locally periodic rod. The system is formed by coaxial cylinders of areas S and s with $S>s$, as shown in Fig. 1. As was done in Ref. 7, the transfer matrix method is used. There compressional and torsional waves were studied and the transfer matrix was 2×2, because these oscillations obey a second-order differential equation. Since flexural vibrations are described by a fourth-order differential equation, the transfer matrix is now 4×4.

If the notation indicated in Fig. 1 is used, the amplitude $\Psi_i(z)$ in the ith cylinder is

$$\begin{aligned} \Psi_i(z)=&A_ik_{1,i}^{-3}e^{k_{1,i}(z-z_i)}+B_ik_{2,i}^{-3}e^{k_{2,i}(z-z_i)}\\ &+C_ik_{3,i}^{-3}e^{k_{3,i}(z-z_i)}+D_ik_{4,i}^{-3}e^{k_{4,i}(z-z_i)}, \end{aligned} \tag{7}$$

which implies the use of a local coordinate system. Here $z_i\leqslant z\leqslant z_{i+1}$, $i=1,...,n$ and $k_{j,i}$ with $j=1,...,4$ is now given by

$$k_{j,i}=(-1)^{[j/2]}\sqrt{\frac{\alpha_i+(-1)^j\sqrt{\alpha_i^2+4\beta_i}}{2}}, \tag{8}$$

where

$$\alpha_i=-\rho_i\omega^2/E_i-\rho_i\omega^2/\kappa_iG_i \tag{9}$$

and

$$\beta_i=\rho_iS_i\omega^2/E_iI_i-\rho_i^2\omega^4/E_i\kappa_iG_i. \tag{10}$$

The transfer matrix for the B-E case is obtained replacing the right-hand side of Eq. (8) by $(-1)^{[j/2]}\sqrt{(-1)^j\omega\sqrt{S_i/E_iI_i}}$. Note that $k_{j,i}$ depends on the radius of each cylinder so two characteristic wavelengths exist for the rod of Fig. 1.

The conditions of continuity at the points where the cylinders of different radii join each other are as follows: continuity of the displacement, slope, bending moment Eq. (4) and shear force Eq. (5):

$$\begin{aligned} &\Psi_i|_{z_{i+1}}=\Psi_{i+1}|_{z_{i+1}},\\ &\Psi_i'|_{z_{i+1}}=\Psi_{i+1}'|_{z_{i+1}},\\ &E_iI_i\Psi_i''|_{z_{i+1}}=E_{i+1}I_{i+1}\Psi_{i+1}''|_{z_{i+1}},\\ &E_iI_i\Psi_i'''|_{z_{i+1}}=E_{i+1}I_{i+1}\Psi_{i+1}'''|_{z_{i+1}}. \end{aligned} \tag{11}$$

The amplitude $\Psi_i(z)$ and its derivatives depend on the physical and geometrical properties of cylinder i through Eqs. (8) to (10). It should be pointed that these continuity conditions are approximate.[7,17,18]

Using Eq. (7) in the continuity conditions, the coefficients A_{i+1}, B_{i+1}, C_{i+1}, and D_{i+1} in the $(i+1)$th cylinder can be expressed in terms of A_i, B_i, C_i, and D_i in the following form:

$$(A_{i+1},B_{i+1},C_{i+1},D_{i+1})^T=\mathbf{M}_{i\rightarrow i+1}(A_i,B_i,C_i,D_i)^T, \tag{12}$$

where T means taking the transpose and

$$\mathbf{M}_{i\to i+1}=\begin{pmatrix} k_{1,i+1}^{-3} & k_{2,i+1}^{-3} & k_{3,i+1}^{-3} & k_{4,i+1}^{-3} \\ k_{1,i+1}^{-2} & k_{2,i+1}^{-2} & k_{3,i+1}^{-2} & k_{4,i+1}^{-2} \\ k_{1,i+1}^{-1} & k_{2,i+1}^{-1} & k_{3,i+1}^{-1} & k_{4,i+1}^{-1} \\ 1 & 1 & 1 & 1 \end{pmatrix}^{-1} \times \begin{pmatrix} k_{1,i}^{-3}e^{k_{1,i}(z_{i+1}-z_i)} & k_{2,i}^{-3}e^{k_{2,i}(z_{i+1}-z_i)} & k_{3,i}^{-3}e^{k_{3,i}(z_{i+1}-z_i)} & k_{4,i}^{-3}e^{k_{4,i}(z_{i+1}-z_i)} \\ k_{1,i}^{-2}e^{k_{1,i}(z_{i+1}-z_i)} & k_{2,i}^{-2}e^{k_{2,i}(z_{i+1}-z_i)} & k_{3,i}^{-2}e^{k_{3,i}(z_{i+1}-z_i)} & k_{4,i}^{-2}e^{k_{4,i}(z_{i+1}-z_i)} \\ \eta_i k_{1,i}^{-1}e^{k_{1,i}(z_{i+1}-z_i)} & \eta_i k_{2,i}^{-1}e^{k_{2,i}(z_{i+1}-z_i)} & \eta_i k_{3,i}^{-1}e^{k_{3,i}(z_{i+1}-z_i)} & \eta_i k_{4,i}^{-1}e^{k_{4,i}(z_{i+1}-z_i)} \\ \eta_i e^{k_{1,i}(z_{i+1}-z_i)} & \eta_i e^{k_{2,i}(z_{i+1}-z_i)} & \eta_i e^{k_{3,i}(z_{i+1}-z_i)} & \eta_i e^{k_{4,i}(z_{i+1}-z_i)} \end{pmatrix}, \tag{13}$$

with $\eta_i = I_i / I_{i+1}$. Applying successively $\mathbf{M}_{1\to 2}$, $\mathbf{M}_{2\to 3}$, until $\mathbf{M}_{(n-1)\to n}$, it follows that

$$(A_n, B_n, C_n, D_n)^T = \mathbf{M}(A_1, B_1, C_1, D_1)^T, \tag{14}$$

where the transfer matrix $\mathbf{M}$ is given by

$$\mathbf{M} = \mathbf{M}_{(n-1)\to n}\mathbf{M}_{(n-2)\to(n-1)}\cdots\mathbf{M}_{2\to 3}\mathbf{M}_{1\to 2}. \tag{15}$$

The appropriate boundary conditions for free ends at $z_1 = 0$ and $z_{n+1} = L$ are given by the vanishing of the bending moment and the shear force. These conditions imply the following algebraic equations:

$$\begin{aligned} &k_{1,1}^{-1}A_1 + k_{2,1}^{-1}B_1 + k_{3,1}^{-1}C_1 + k_{4,1}^{-1}D_1 = 0, \\ &A_1 + B_1 + C_1 + D_1 = 0, \\ &k_{1,n}^{-1}e^{\mu_{1,n}}A_n + k_{2,n}^{-1}e^{\mu_{2,n}}B_n + k_{3,n}^{-1}e^{\mu_{3,n}}C_n + k_{4,n}^{-1}e^{\mu_{4,n}}D_n = 0, \\ &e^{\mu_{1,n}}A_n + e^{\mu_{2,n}}B_n + e^{\mu_{3,n}}C_n + e^{\mu_{4,n}}D_n = 0, \end{aligned} \tag{16}$$

where $\mu_{j,n} = k_{j,n}(z_{n+1} - z_n)$, with $j = 1,...,4$. If the coefficients A_n, B_n, C_n and D_n of Eq. (14) are substituted in Eqs. (16) the system of four homogeneous equations can be written as

$$\mathbf{P}(A_1, B_1, C_1, D_1)^{\mathrm{T}} = 0, \tag{17}$$

where the matrix $\mathbf{P}$ is given by

$$\mathbf{P} = \begin{pmatrix} k_{1,1}^{-1} & k_{2,1}^{-1} & k_{3,1}^{-1} & k_{4,1}^{-1} \\ 1 & 1 & 1 & 1 \\ \sum_{i=1}^{4} t_{i,1} & \sum_{i=1}^{4} t_{i,2} & \sum_{i=1}^{4} t_{i,3} & \sum_{i=1}^{4} t_{i,4} \\ \sum_{i=1}^{4} h_{i,1} & \sum_{i=1}^{4} h_{i,2} & \sum_{i=1}^{4} h_{i,3} & \sum_{i=1}^{4} h_{i,4} \end{pmatrix}, \tag{18}$$

with $t_{i,j} = M_{ij}k_{i,n}^{-1}e^{k_{i,n}(z_{n+1}-z_n)}$ and $h_{i,j} = M_{ij}e^{k_{i,n}(z_{n+1}-z_n)}$. Here M_{ij} are the matrix elements of $\mathbf{M}$. The normal mode frequencies are then finally obtained setting $\det(\mathbf{P}) = 0$.

III. THE EXPERIMENT

A block diagram of the experimental setup is shown in Fig. 2. The signal of an oscillator is amplified and sent to the EMAT exciter. The detector signal is converted by a lock-in amplifier into a dc voltage proportional to the amplitude. The detector is moved along the rod to obtain the amplitude as a function of z. A somewhat more detailed description of this fully automatized system is given in Ref. 16.

The EMAT used to detect or excite waves in rods consists of a coil and a permanent magnet. It employs Foucault (or eddy) currents, as indicated in Refs. 7, 13, 16. The EMAT is shown in the left lower corner of Fig. 2, where it is configured to detect the amplitude ξ of the flexural wave, without any mechanical contact with the rod.

The results obtained by measuring ξ can be verified with a different configuration of the EMAT, shown in Fig. 3. With this configuration it is possible to detect the angular coordinate ψ of the flexural mode. The two permanent magnets produce a magnetic field parallel to the X axis. Due to this field, any rotation of the rod with respect to the Y axis induces a Foucault current in the XY plane. This in turn generates a magnetic field along the Z axis. The emf induced by this field in the coil is the signal corresponding to the angular mode. It is not difficult to understand that the same configuration can be used to excite the ψ oscillation. An ac current in the coil produces a magnetic field that induces Foucault currents circulating in the XY plane. These currents interact with the magnetic field of the permanent magnets, giving rise to a torque in the direction of the Y axis. This seems to be a unique experimental setup, in the sense that it makes it possible to excite or detect the angular mode ψ along the rod

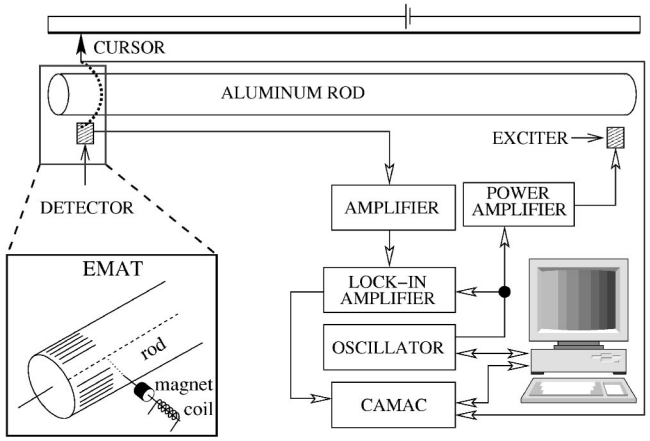

FIG. 2. Block diagram of the experimental setup. The EMATs (exciter and scanning detector) are shown shaded and in a configuration to excite or detect flexural modes. The dotted line connecting the cursor with the detector indicates mechanical coupling.

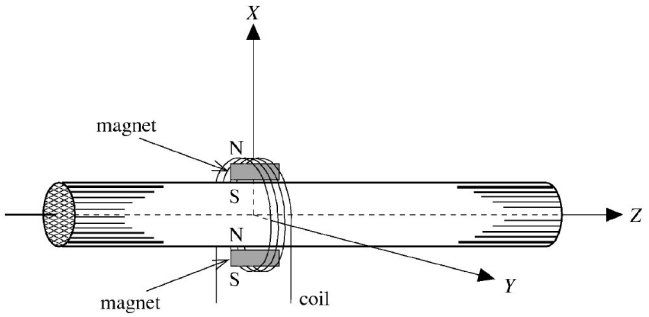

FIG. 3. The configuration of the coil and magnets of the EMAT to detect or excite the angular coordinate ψ.

without any mechanical contact between the rod and the exciter or detector.

The eigenfrequencies of a uniform aluminum rod of circular cross section have been measured with this setup. For each normal mode two very close resonances (doublets) are observed, as shown in Fig. 4. This is due to the lack of perfect circularity in the manufacturing process of the aluminum rods. The frequency difference between the two resonances of the doublet is very small, of the order of 0.2% of the frequency. This difference in frequency would correspond to a uniform rod of elliptical cross section with a difference between major and minor semi-axes of the order of 10 μm. This figure also shows the precision of our measurements. In what follows only one of the resonant frequencies will be given due to the scale used.

The measured eigenfrequencies are shown as open circles in Fig. 5 as a function of the mode number. They are compared with the TBT (triangles) and B-E (squares) predictions in the same figure. It is clearly seen that the simplest theory fails except at very low frequencies, as is well known.[9] On the other hand, the TBT results agree very well with the experimental data.

IV. COMPARISON BETWEEN THEORY AND EXPERIMENT

Normal-mode amplitudes and frequencies were measured for locally periodic aluminum rods using the experimental setup of Sec. III and the EMATs, as indicated in Figs. 2 and 3. The frequencies for $N=1$, 4, 8 and 12 unit cells are given in Fig. 6, where they are also compared to numerical values obtained both for the Timoshenko and Bernoulli-Euler theories. For each value of N the left column corresponds to the experimental values, the center column to the Timoshenko approach and the right-hand one to the B-E approximation. The numerical values were obtained using the transfer matrix method as explained in Sec. II. Except for the shear coefficient κ, the parameters entering the calculation were measured for each rod. The value $\kappa=(6+12\nu+6\nu^2)/(7+12\nu+4\nu^2)=0.925$ with the Poisson ratio $\nu=0.3$, a well known value for aluminum, was used.[19] One could say, then, that these are parameter free calculations.

It is apparent from Fig. 6 that as N grows the normal-mode frequencies are grouped forming bands separated by gaps of forbidden frequencies. This is true for experimental values as well as for both theoretical approaches. As will be seen in this figure the Timoshenko predictions fit the measured values rather well, much better indeed that the Bernoulli-Euler results. The B-E theory agrees with experi-

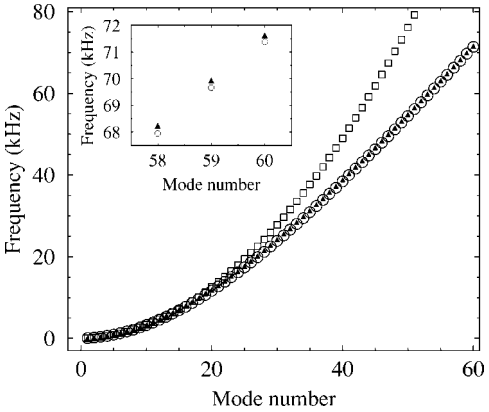

FIG. 5. A comparison between the measured normal-mode frequencies (open circles) with the Timoshenko beam theory results for $\kappa=0.925$ (triangles). The results obtained with the Bernoulli-Euler approach are given by the squares. The inset shows a zoom of some data. The same rod of Fig. 4 was used.

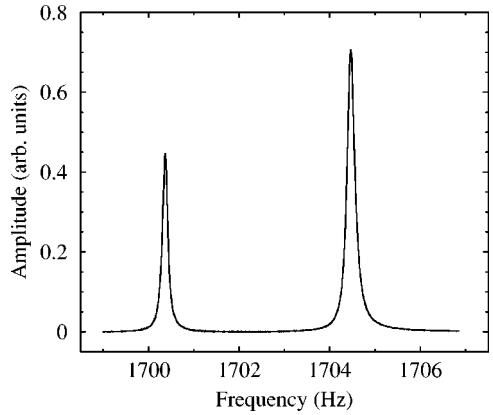

FIG. 4. Typical bending doublet measured for a uniform aluminum rod of circular cross section of radius 6.35 mm and length $L=0.9105$ m. The frequency difference is small of the order of 0.2% of the normal-mode frequency f.

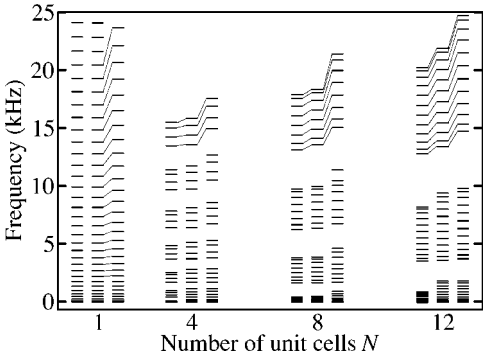

FIG. 6. Normal-mode frequencies for locally periodic rods with N unit cells. The left, center and right columns for each N correspond to the experimental values, Timoshenko and Bernoulli-Euler theoretical results, respectively. Four aluminum rods of length $L=1.005$ m and radius 6.35 mm were used. The notches were obtained machining the uniform rods and have radius $r=1.5$ mm and width $\epsilon=0.3$ mm.

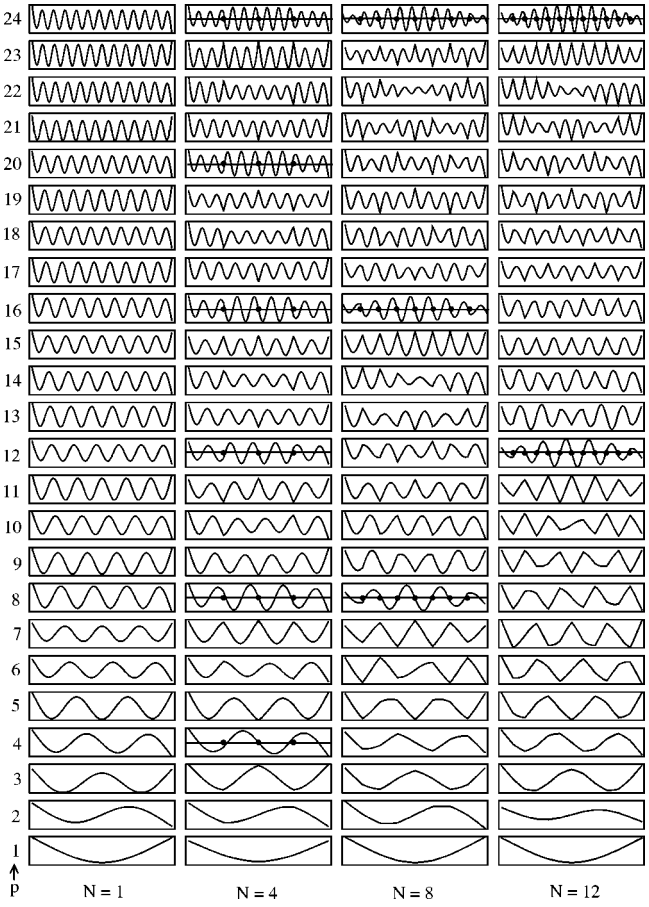

FIG. 7. Theoretical Timoshenko amplitudes for rods with $N-1$ notches. The amplitude vanishes at the position of the notches (dots) when the Bragg condition $p=mN$, m an integer, is fulfilled. The parameters of the rods are those of Fig. 6.

ment only at low frequencies, as could be expected from the results shown in Fig. 5 for $N=1$.

In Fig. 7, the theoretical amplitudes for the TBT are shown as a function of N for modes $p=1$ to $p=24$. The gap in the spectrum is produced when $p=mN$ with m an integer, i.e., when the Bragg condition $kl=m\pi$ is fulfilled. In this case, the amplitude vanishes at the location of the notches. The notches would then have a minimal effect and the corresponding state would have a normal-mode frequency very

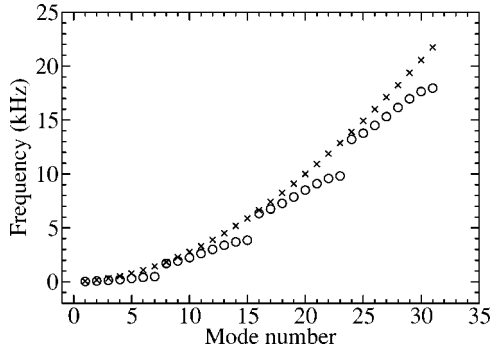

FIG. 8. A comparison of the flexural experimental frequencies of a uniform rod (crosses) with those of a rod with $N=8$ unit cells (open circles). The frequency shift is minimum when the Bragg condition is fulfilled. The parameters of the rods are the same as in Fig. 6.

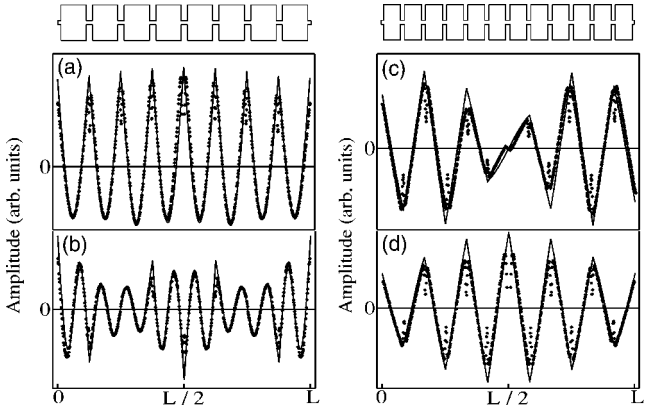

FIG. 9. Flexural amplitudes for locally periodic rods with $N=8$, (a) $p=15$, (b) $p=21$ and $N=12$, (c) $p=10$ and (d) $p=11$. Here p is the mode number. The continuous lines correspond to Timoshenko's theory and the dots to experimental measurements. The same parameters as in Fig. 6 are used. A sketch of the rod is shown in the upper part (not in scale) as a guide to the reader.

similar to the one corresponding to the $N=1$ case. This is shown to be the case in Fig. 8, where, as an example, the experimental values for $N=8$ are compared to the measurements for $N=1$. It is clear that the first mode of each band remains almost unaffected by the presence of the notches.

As mentioned before, the experimental setup makes it possible to measure the normal-mode amplitudes by moving the EMAT detector along the rod. A comparison between theoretical and experimental amplitudes is then achievable. A selection of these amplitudes are shown for $N=8$ and $N=12$ in Fig. 9. The theoretical predictions using TBT are shown as continuous lines and the measurements correspond to the dots. Except at the location of the notches, where the eddy currents detected by the EMAT are interrupted, the agreement between theory and experiment is excellent. It should be pointed out that the amplitudes arising from the B-E theory would give similar results since, as shown in Fig. 10, both theories predict very similar amplitudes, albeit different frequencies, as mentioned above.

V. CONCLUSIONS

Amplitudes for flexural vibrations in locally periodic rods were measured continuously along the rod for the first

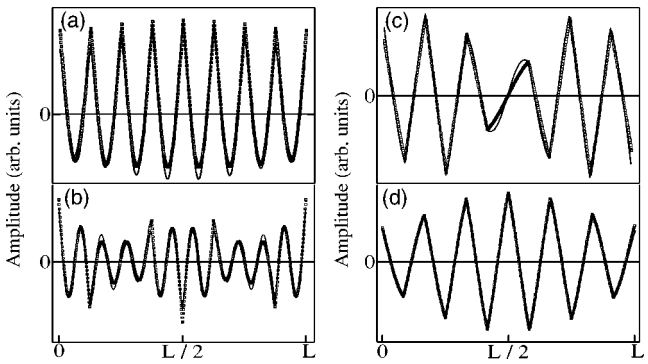

FIG. 10. The amplitudes of the Timoshenko Beam Theory (continuous line) and the Bernoulli-Euler approach (squares) are very similar. (a), (b), (c) and (d) correspond to the same cases of Fig. 9.

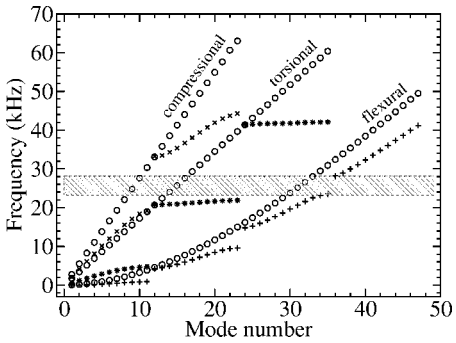

FIG. 11. Measured band spectra for compressional (crosses), torsional (stars) and flexural vibrations (plusses) of a locally periodic aluminum rod of length $L=0.9105$ m and radius 6.35 mm and $N=12$ unit cells. The notches have radius $r=1.3$ mm and width $\epsilon=0.3$ mm. The circles correspond to experimental values of a uniform aluminum rod of the same length and radius. The frequencies in the shaded band form a common stop band for the three types of vibration.

time. This was possible thanks to a noncontact electromagnetic acoustic transducer introduced recently.[13] It was shown that a banded spectrum arises as the number of unit cells grows. This turns out to be the case also from the theoretical point of view. Both Timoshenko theory and the simpler Bernoulli-Euler approach predict also a banded spectrum for the normal-mode frequencies. The fit to the experimental values is, however, much better if the first of these theories is used.

As mentioned in the Introduction, bands also emerge for locally periodic rods when dealing with compressional and torsional vibrations. The experimental results for these cases[7] are compared to the values obtained in this work for flexural vibrations for the particular case $N=12$ in Fig. 11. It is observed that the gap is produced in all types of vibrations when the Bragg condition holds. In this figure, it is also clear that a common gap (shaded region) in the frequency spectrum appears, so a very efficient isolation vibration is possible for these frequency values.

Compressional and torsional vibrations are described by second-order differential equations whereas flexural vibrations require a fourth-order differential equation, so one could conclude that bands appear due to the local invariance with respect to translations that the system shows and not to the peculiarities of the equations governing them.

ACKNOWLEDGMENTS

This work was supported by DGAPA-UNAM Project No. IN104903-3 and by CONACyT, México Project No. 41024-F.

[1] L. Brillouin, *Wave Propagation in Periodic Structures* (Dover, New York, 1946).
[2] D. J. Griffiths and C. A. Steinke, "Waves in locally periodic media," Am. J. Phys. **69**, 137–154 (2001).
[3] D. Li and H. Benaroya, "Waves, normal modes and frequencies in periodic and near-periodic rods. Part I," Wave Motion **20**, 315–338 (1994); and "Waves, normal modes and frequencies in periodic and near-periodic rods. Part II," *ibid.* **20**, 339–358 (1994).
[4] B. Ravindra and A. K. Mallik, "Harmonic vibration isolation characteristics of periodic systems," J. Sound Vib. **154**, 249–259 (1992).
[5] B. Ravindra, "Love-theoretical analysis of periodic system of rods," J. Acoust. Soc. Am. **106**, 1183–1186 (1983).
[6] C. H. Hodges and J. Woodhouse, "Vibration isolation from irregularity in a nearly periodic structure: Theory and measurements," J. Acoust. Soc. Am. **74**, 894–905 (1983).
[7] A. Morales, J. Flores, L. Gutiérrez, and R. A. Méndez-Sánchez, "Compressional and torsional wave amplitudes in rods with periodic structures," J. Acoust. Soc. Am. **112**, 1961–1967 (2002).
[8] J. C. Snowdon, "Vibration isolation: Use and characterization," J. Acoust. Soc. Am. **66**, 1245–1274 (1979).
[9] K. F. Graff, *Wave Motion in Elastic Solids* (Dover, New York, 1991), Chap. 3.
[10] D. J. Mead, "A new method of analyzing wave propagation in periodic structures: Applications to periodic Timoshenko beams and stiffened plates," J. Sound Vib. **104**, 9–27 (1986).
[11] M. A. Heckl, "Coupled waves on a periodically supported Timoshenko beam," J. Sound Vib. **252**, 849–882 (2002).
[12] S. D. Lust, P. P. Friedmann, and O. O. Bendiksen, "Free and forced response of multi-span beams and multi-bay trusses with localized modes," J. Sound Vib. **180**, 313–332 (1995).
[13] A. Morales, L. Gutiérrez, and J. Flores, "Improved eddy current driver-detector for elastic vibrations," Am. J. Phys. **69**, 517–522 (2001).
[14] J. D. Renton, "A check on the accuracy of Timoshenko's beam theory," J. Sound Vib. **245**, 559–561 (2001).
[15] N. G. Stephen, "On a check on the accuracy of Timoshenko's beam theory," J. Sound Vib. **257**, 809–812 (2002).
[16] R. A. Méndez-Sánchez, A. Morales, and J. Flores, "Experimental check on the accuracy of Timoshenko's beam theory," J. Sound Vib. **279**, 508–512 (2005).
[17] H. Sato, "Free vibration of beams with abrupt changes of cross-section," J. Sound Vib. **89**, 59–64 (1983).
[18] H. J. Petroski, "Comments on free vibration of beams with abrupt changes in cross-section," J. Sound Vib. **92**, 157–159 (1984).
[19] H. E. Rosinger and I. G. Ritchie, "On Timoshenko's correction for shear in vibrating isotropic beams," J. Phys. D **10**, 1461–1466 (1977).

Comparison of structural response and fatigue endurance of aircraft flap-like box structures subjected to acoustic loading

Y. Xiao
Lloyd's Register EMEA, 71 Fenchurch Street, London EC3M 4BS, United Kingdom

R. G. White[a)]
Institute of Sound and Vibration Research, University of Southampton, Highfield, Southampton SO17 1BJ, United Kingdom

G. S. Aglietti
School of Engineering Sciences, University of Southampton, Highfield, Southampton SO17 1BJ, United Kingdom

(Received 4 June 2004; revised 8 November 2004; accepted 9 November 2004)

The results of an extensive test program to characterize the behavior of typical aircraft structures under acoustic loading and to establish their fatigue endurance are presented. The structures tested were the three flap-like box-type of structures. Each structure consisted of one flat (bottom) and one curved (top) stiffener stiffened skin panel, front, and rear spars, and ribs that divided the structures into three bays. The three structures, constructed from three different materials (aircraft standard aluminum alloy, Carbon Fibre Reinforced Plastic, and a Glass Fibre Metal Laminate, i.e., GLARE) had the same size and configuration, with only minor differences due to the use of different materials. A first set of acoustic tests with excitations of intensity ranging from 140 to 160 dB were carried out to obtain detailed data on the dynamic response of the three structures. The FE analysis of the structures is also briefly described and the results compared with the experimental data. The fatigue endurance of the structures was then determined using random acoustic excitation with an overall sound pressure level of 161 dB, and details of crack propagation are reported. [DOI: 10.1121/1.1853934]

PACS numbers: 43.40.Hb, 43.40.At, 43.40.Qi, 43.40.Ey [ADP] Pages: 2820–2834

I. INTRODUCTION

Lightweight aircraft structures close to, or in the path of, the engine efflux experience very high acoustic loads that produce severe random vibrations that may lead to fatigue failures.[1,2] For aircraft with wing mounted engines, the flaps, when deployed, can experience particularly high sound pressure loading. Tests carried out by Airbus found sound pressure levels on flap panels of up to 155 dB.[3] In general, the stress and strain in aircraft structures induced by acoustic loading are much smaller than those caused by aircraft maneuvers or gusts. However, the random vibrations generated by acoustic loads cause stress and strain of a magnitude that can produce fatigue damage. Furthermore, as the bandwidth of the acoustic loads extends up to a few kHz, high-frequency vibrations can cause fatigue failures in a relatively short period of time due to the growth of old defects and/or formation of new cracks.[4]

This problem has been studied for several years and a certain amount of literature is available on the subject.[5–8] However, the various approaches (see, for example, Refs. 9–12) introduce simplifications that, although necessary for a convenient mathematical description of the problem, often neglect factors that can be very important in specific practical applications.

For aircraft structures, very often, a box type of configuration is used. A relatively thin skin stiffened is used that covers and encloses a skeletal structure comprising of a number of spanwise spars and fairly regularly spaced chordwise ribs. Besides the flaps that are considered in this work, wings, ailerons, fins, and rudders are examples of this type of structure. Notwithstanding the literature and guidelines available on the acoustic fatigue of typical aircraft structures, such as stiffened panels, the response of an isolated stiffened panel provides only an approximation for the overall response of a continuous box-type structure. In fact, as it is shown in the present work, the skin panels of the flap cannot be treated as panels isolated from each other and the remainder of the structure. Tests carried out by BAe have shown strong coupling between the upper and lower surface of a flap, so that acoustic excitation on one surface leads to a significant vibration of the opposite surface. Another important factor, not sufficiently represented in the existing design guides is the fact that the surface of the flaps has variable curvature. Hence, one of the motivations for this work is to provide detailed information on the dynamic behavior of this type of structure under acoustic loading.

Besides the structural configuration, the mechanical properties of the materials used for the structure play a central role in the definition of the behavior under loading. Up to now, aircraft structures have been built predominantly in aluminum alloys. However, during the last 20 years, the aircraft

[a)]Emeritus Professor (retired).

industry has seen a significant increase in the use of composite materials for aircraft structures. Due to the high strength/mass, and stiffness/mass ratio that can be achieved with these materials, composites are gradually replacing aluminum alloys and their use is extending from secondary structures to primary structures. Taking the Airbus as an example, the proportion of composites content in the Airbus A300 was only 4%, but is 17% in A340.[13] Carbon Fibre Reinforced Plastics (CFRP) are a particularly good example of composite materials that outperform standard aluminum alloys in terms of specific strength and stiffness. However, the damage resistance of composites like CFRP, such as impact resistance, is relatively low compared to monolithic aluminum alloys, and this can be a problem for aircraft constructions. As an alternative to monolithic aluminum alloys for fatigue prone areas in primary aircraft structures, Fibre Metal Laminates (FML) have been developed. These consist of alternating thin metal alloy sheets and unidirectional or cross-ply layers of fiber composites.

The first generation of these laminates was ARALL, which used aramid fibers, and the second one was GLARE (GLAssfibre REinforced) with high strength glass fibers. These laminates are constructed by stacking thin (0.2–0.4 mm) aluminum alloy sheets alternately with fiber reinforced composite layers and curing in an autoclave where the epoxy resin of the fiber composites acts as the adhesive between the layers. The resultant laminates have low specific weight, compared to aluminum alloys, and in certain conditions, they have superior properties in terms of fatigue crack initiation behavior and fatigue crack growth. In particular, crack growth rates can be much lower than those in aluminum alloys[14,15] due to a mechanism called the fiber bridging effect (i.e., a crack initiated in a metal layer is bridged by the fibers in the composite layer that impose a restraint on further opening of the crack). Due to the high failure strain of the glass fibers, GLARE can absorb a considerable amount of energy before failure. Therefore, the impact behavior of GLARE is comparable to that of aluminum alloys[16] and superior to other composites such as CFRP. Furthermore, GLARE offers various advantages over CFRP, as its ease of formability and machinability, so that often it can be handled in the same manner as monolithic aluminum.

In the field of acoustic fatigue, considerable experience has been accumulated in decades of use of aluminum alloys. In relative terms, CFRP and GLARE are new materials and, therefore, before they can be safely employed in crucial structural elements of aircraft, extensive test programs are required. Material coupon testing is necessary to determine the material characteristics.[17,18] However, it is not sufficient, and tests on structural assemblies,[19] like the flaps considered in this work, are essential to understand the behavior of real structures, and verify theoretical models.

Furthermore, the intensity of the acoustic loads very often produces a nonlinear response of the structure, which makes the computation of the dynamic response and the prediction of fatigue life even more complex.[20] Hence, acoustic tests on realistic specimens are necessary, not only to verify the computations of the structural response provided by our mathematical models, but also to provide realistic data on the fatigue endurance of the built-up structures.

In this work, the results of an extensive test program to characterize the behavior of typical aircraft structures under acoustic loading and to establish their fatigue endurance are presented. Three structures made of three different materials (aluminum alloy CFRP and GLARE) have been tested and the dynamic behavior of each structure under acoustic loads is accurately investigated and reported. The performances of the three structures are then compared, and the results of the tests are compared with FE predictions.

II. THE TEST SPECIMENS

The test specimens used in the test experimental work were three flap-like box-type structures designed and manufactured by British Aerospace Airbus Ltd. These are representatives of aircraft flaps and were constructed from three different materials: aluminum alloy, CFRP composite, and GLARE laminates. These boxes consisted of one flat (bottom) and one curved (top) stiffened skin panel together with front and rear spars and ribs that divided the structures into three bays (see Fig. 1 and Fig. 2). The three boxes were built with the same configuration and the same external dimensions, 1140 mm (stiffener wise) by 600 mm (ribwise) by 80–170 mm depth (between two skin panels). Two of the boxes (the one made of aluminum alloy and the one made of GLARE also had exactly the same internal geometry, with Z-shaped stiffeners that were connected to the skins by rivets, and only minor differences in dimensions, mainly due to the difference between the thickness of the GLARE laminate and that of the aluminum alloy. The CFRP structure was slightly different from the other two structures in the dimensions of the three bays and had integral stiffeners (flat bar). In all the boxes, the skin panels, ribs, and spars were all connected by rivets.

To easily locate a particular position on the box structures, the side A is defined as the left-hand side when the box lies on its flat skin panel with rear spar facing the observer, and side B is the opposite side. The stiffener closest to the rear spar is defined as stiffener No. 1. The number increases in the direction toward the front spar. The stiffeners next to the front spar are numbered as No. 4 or No. 5, respectively, for bottom and top skin panels. The longitudinal direction is defined as along the stiffener length, and the transverse direction as the perpendicular to stiffener length.

All three structures had the same aluminum alloy end ribs (modulus of elasticity 72 GPa, density 2700 kg/m^3) while a different type of aluminum was used for the skin of the aluminum structures (modulus of elasticity 65 GPa, density 2500 kg/m^3). The skin panels of the CFRP box were built with integral stiffeners made of 16 layers of CFRP unidirectional tape T300/924 (longitudinal module of elasticity 135 MPa, transverse 9 MPa, and density 1565 kg/m^3) with fiber volume fraction of 66% (cure schedule: 2 h at 180 °C and 700 kN/m^2 pressure, plus 2 h post-cure at 180 °C). The layup is shown in Table I with a 0° fiber direction along the stiffeners. The front and rear spars of the CFRP box were built of the same CFRP unidirectional tape but had 24 layers, and the inner ribs had 20 layers. For the GLARE structure,

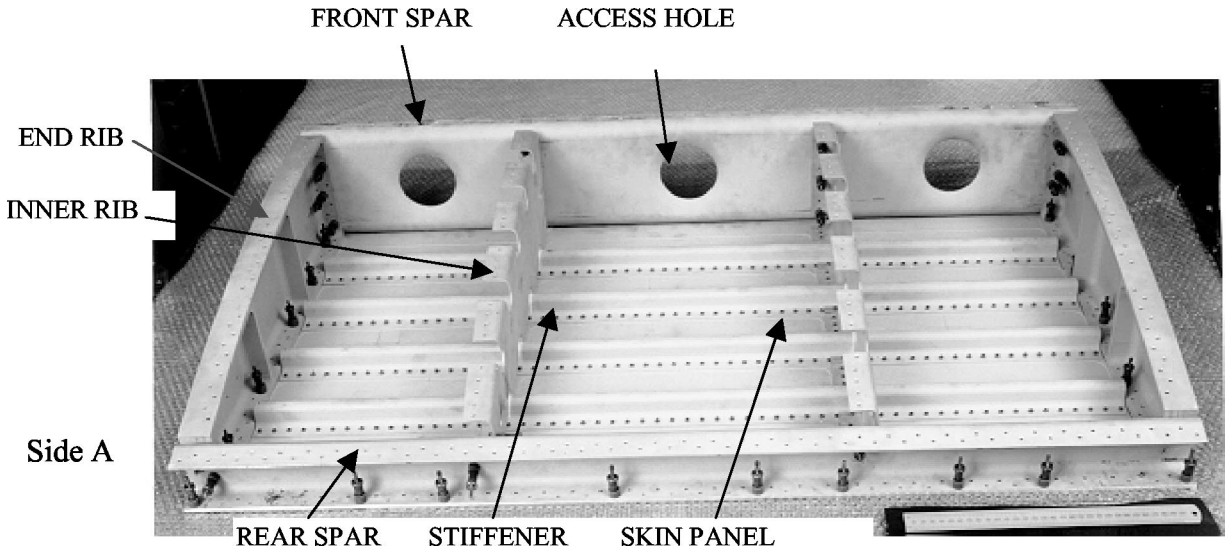

FIG. 1. Aluminum alloy and GLARE flap-like box structure before final assembly (curved panel removed to show the internal structure).

GLARE 2 and GLARE 3 (module of elasticity 58 MPa, density 2480 kg/m^3) with a configuration of 3/2 (i.e., three layers of aluminum alloy and two layers of glass fiber composite). The skin part was made of GLARE 3 (0°/90° cross-ply glass fiber reinforced plastic) and the stiffener was made of GLARE 2 (unidirectional glass fiber reinforced plastic layer) in which the fibers were along the stiffener length (longitudinal module of elasticity 65 MPa, transverse 50 MPa, and density 2480 kg/m^3). The thickness of the metallic layer and glass fibre reinforced plastic layer was 0.3 and 0.25 mm respectively, which resulted in a total thickness of 1.4 mm for both skin and stiffener. The remainder of the components of the CFRP and GLARE boxes were the same as for the aluminum alloy structure. The total mass of the structures was 25 kg for the aluminum specimen, 20.01 kg for the GLARE specimen and 16.7 kg for the CFRP specimen.

III. PRELIMINARY ACOUSTIC TESTS

The aim of this set of tests was to characterize the strain response of the structures subjected to acoustic excitation, before the final endurance acoustic tests, which are described in the next section, were carried out.

The acoustic testing was carried out using the Progressive Wave Tube (PWT) at the University of Southampton (UK). The PWT is a facility that was specially designed to simulate the acoustic loading on aircraft components in the test section where the test structure is mounted in an opening in the wall. The PWT is driven by a siren via a horn and can produce an Overall Sound Pressure Level (OASPL) of up to 163 dB. The test section of the PWT is 1.2 m long, 0.6 m high, and 0.3 m deep. The test panel, which is mounted on the side of the test section, basically replacing one of the walls, is excited by high-intensity sound waves propagating

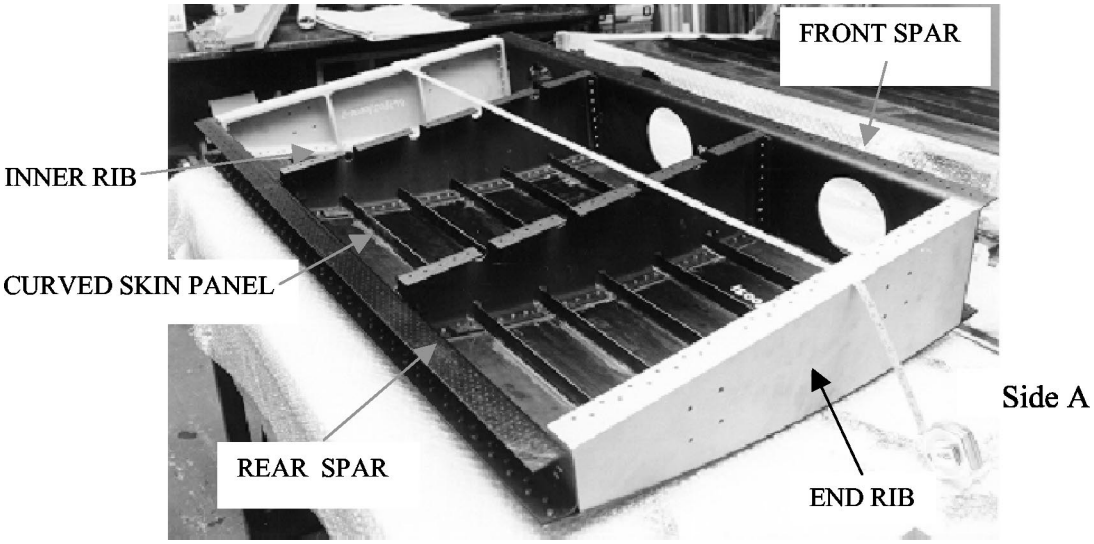

FIG. 2. CFRP flap-like box structure before final assembly (curved panel removed to show the internal structure).

TABLE I. Layup of the CFRP material.

Layer No.	Fibre Direction	Material
1	0	CFRP UD tape T300/924
2	−45	Specimen lay-up
3	+45	
4	90	
5	0	
6	−45	
7	+45	
8	90	
9	90	
10	+45	
11	−45	
12	0	
13	90	
14	−45	
15	+45	
16	0	

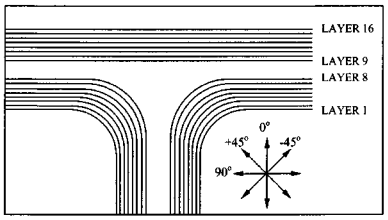

along the tube. A good description of the apparatus is given by Cunningham.[21]

The test structures (described in Sec. II) were mounted, one at a time, in the opening of the test section of the PWT on a wooden supporting frame. For each measurement run, either the top or the bottom skin panel was placed facing the inside of the PWT so it was directly excited by acoustic pressure loading. For each box structure, at least two sets of measurements were taken to record the responses. The OASPL of acoustic excitation at the test section of the PWT was measured by the reference microphone, which was fixed in the middle of the test section. The response of the structures to the acoustic loading was measured by a number of strain gauges. These gauges were installed inside the structures at the various locations of interest, and the leads from the gauges brought out from the access holes. The advantages of installing the gauges inside the boxes were to minimize the disturbance to the pressure field during the tests and to protect the gauges during transport and various other tests. The middle bay of the skin panel was heavily gauged to supply the information required. Strain gauges were attached to both curved and flat skin panels to establish the relationship of the responses of the two panels to acoustic loading. Gauges were also attached to the other two bays to investigate the response relationships between three bays. There were seven three-gauge rosettes on the curved skin panels plus another two on one of the five stiffeners and six on the flat panel with two on one of four stiffeners. Another two strain gauges were also installed on one of the inner ribs. Strain gauges of 5 mm length were used to give good strain resolution. Figure 3 shows the locations and numbering of the gauges.

A shaped broadband random signal was fed into to the siren of the PWT in order to generate the desired acoustic field in the test section. The 30 strain amplifier channels were used to take the strain measurements. The LABVIEW, which is a PC-based 16-channel data acquisition system, was used to acquire data. Data analysis was carried out using a MATLAB signal processing toolbox.

Because the data acquisition system and low pass filters had only 16 channels, 30 strain gauges were divided into two groups of 15 gauges and measurements were taken in two batches for each excitation level. For each batch, the sound signal from B&K Type 4136 microphone and signals from one of the 15 strain gauge groups were measured. A 16-channel anti-liasing low pass filter was employed to filter the signals at 1 kHz before they were digitally sampled at a sampling rate of 6000 Hz. The frequency resolution of spectral distributions was 1.2 Hz.

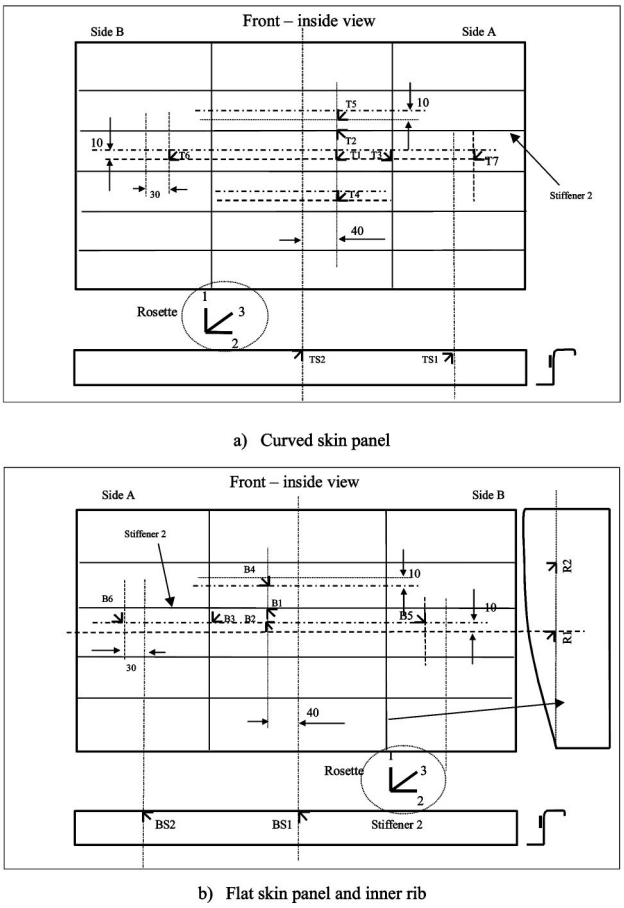

FIG. 3. Locations and numbering of the strain gauges for acoustic excitation of the box structures.

A. Measurement system and calibration

Before carrying out the tests, the reference microphone was calibrated using a B&K-Type 4220 PistonPhone that produces a signal with a SPL of 124 dB and a frequency of 250 Hz. This calibration was performed as many times as possible to ensure an accurate sound pressure level measurement.

Also, the strain gauge measurement system was calibrated before the tests using, as a reference, the known strains produced on an aluminum beam.

B. Acoustic excitation

The three test structures were excited on each skin panel at OASPL levels ranging from 140 to 160 dB (in steps of 5 dB) one at the time, and strain data acquired. An extra set of data was also collected at an excitation level of 161 dB, for

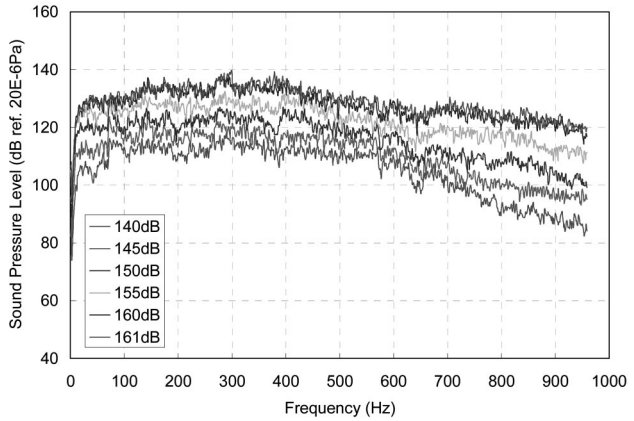

FIG. 4. Spectra of the acoustic pressure loading measured by the reference microphone.

the aluminum and CFRP structures, and at 162 dB for the GLARE one. The reason for the different maximum test levels is that the specimen under test influences, although marginally, the maximum level that can be achieved by the facility. A driving signal in the frequency range from 80 to 600 Hz was used and the OASPL was measured by the reference microphone that was located at the middle of the test section. Power spectral densities of the acoustic excitation were measured by reference microphone are shown in Fig. 4. Note that the sound energy is mainly in the frequency range of 100 to 600 Hz.

C. Strain measurement results

Measured strain results for each strain gauge are identified by the gauge number. Gauges on the top (curved) skin panels are numbered with prefix T, on the bottom (flat) skin panels with B, on the inner ribs with R, and on the stiffeners of the top and bottom panels with TS and BS, respectively. Figure 3 shows the location of the strain gauges on the structures.

1. Aluminum alloy box structure

The rms strain results for the 30 strain gauges on the structure are listed in Table II. The variations of some of the rms strains with an increase of the excitation level are given in Fig. 5. At excitation levels below 155 dB, the relationships between sound pressure and rms strain are linear, but show the tendency into nonlinear form when the excitation level is above 155 dB, especially in the locations with higher strain levels. The maximum strain was found on the stiffeners in the transverse direction. At an excitation level of 160 dB, the rms strain value at strain gauge location BS1-2 was 267 and 186 $\mu\epsilon$ at location BS2-2. For the bottom skin panel, the highest strain was 157 $\mu\epsilon$ at location B32 in the transverse direction and at the location B42 in the longitudinal direction. For the top skin panel, the maximum strain was 79 $\mu\epsilon$, measured by gauge number T6-2 in bay B. In the middle bay of the top skin, lower strain values were found. The response of the inner rib measured by strain gauge R1-1 was 51 $\mu\epsilon$ but a higher value of 117 $\mu\epsilon$ was found in the vertical direction measured by gauge R1-2. The maximum strain responses in the strain gauge rosettes on the stiffeners of both skin panels were always in the direction transverse to the stiffeners (such as TS1-1, TS2-1, BS1-2, and BS2-2), which indicates that the stiffeners responded mainly in torsion during the acoustic excitation.

TABLE II. The rms strain response of the aluminum alloy box structure to acoustic pressure loading when excited on the flat skin panel ($\mu\epsilon$).

Strain gauge	Acoustic excitation level					
	140 dB	145 dB	150 dB	155 dB	160 dB	161 dB
B1-1	5.4	7.5	12.0	20.5	33.7	36.6
B1-2	13.8	24.7	43.9	77.6	131.2	140.1
B2-1	3.7	6.3	10.8	19.2	34.0	36.8
B2-2	7.6	12.9	23.5	47.1	94.9	104.0
B3-1	3.8	5.0	7.8	13.3	24.0	26.2
B3-2	15.1	29.7	53.7	93.7	156.8	169.3
B4-1	3.8	6.5	11.4	19.8	33.7	36.2
B4-2	20.2	33.4	60.8	104.1	157.0	152.1
B5-1	3.5	5.2	8.8	15.3	26.6	28.4
B5-2	13.1	23.3	42.0	68.8	120.1	131.3
B6-1	2.1	3.8	6.9	12.4	23.1	25.9
B6-2	12.7	25.4	44.4	70.4	109.4	120.1
BS1-1	18.4	34.6	63.5	111.2	175.7	187.8
BS1-2	26.8	51.1	93.5	164.8	266.5	288.8
BS1-3	6.2	12.0	21.3	37.1	64.2	70.7
BS2-1	11.5	24.5	39.3	66.1	107.9	
BS2-2	20.5	43.1	70.0	115.9	185.8	
BS2-3	8.7	17.2	27.4	45.2	76.8	
R1-1	5.8	11.9	18.7	31.6	50.5	
R1-2	13.1	27.5	43.6	71.6	116.6	
T1-1	6.7	11.0	15.7	25.5	41.4	
T1-2	4.9	9.7	16.8	37.8	56.5	
T2-1	8.2	8.4	8.9	10.4	13.7	
T2-2	6.4	10.7	15.7	22.4	37.6	
T6-1	7.4	14.2	21.6	29.9	41.2	
T6-2	7.9	9.0	12.5	38.2	78.7	
T7-1	5.7	8.2	12.1	19.4	31.6	
T7-2	5.4	5.5	6.2	9.3	14.7	
TS2-1	10.9	18.9	29.1	42.3	63.0	
TS2-2	6.6	10.3	15.7	22.3	33.4	

A phenomenon observed with an increase of the excitation level was the ''smearing'' effect, with well-separated response frequency peaks joining together to form a wide peak.

2. GLARE box structure

The measured rms strains for 30 strain gauges are listed in Table III, and the strain results versus applied load are shown in Fig. 6. It can be seen that the relationships between excitation levels and structural response rms strain values became nonlinear as the sound pressure level of the acoustic loading increased.

As for the aluminum alloy structure, the higher strains were found on the stiffeners of both skin panels in the transverse direction. Strain responses in the side bays of the GLARE box were higher than those in the aluminum alloy structure.

When the GLARE box was excited on the bottom skin, the strain level measured by BS1-2 was 152 $\mu\epsilon$, which was much less than that of the aluminum alloy structure. The highest strain (165 $\mu\epsilon$) was found at the gauge B2-2 location in the transverse direction. The two side bays also showed a high strain response, as in the case of the aluminum alloy

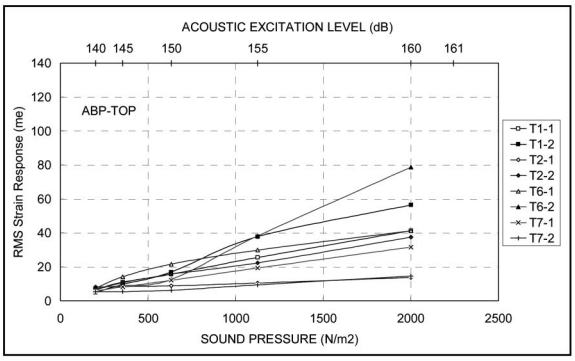

RMS strain response of the top skin panel

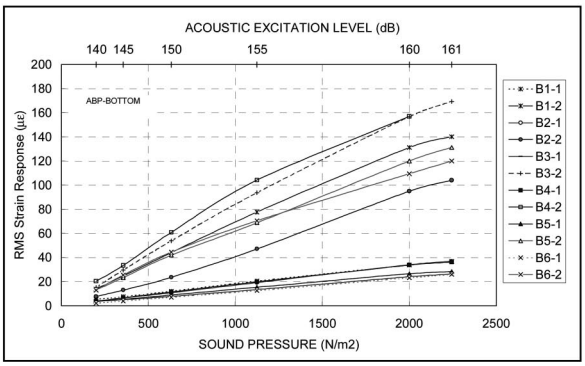

RMS strain response of the bottom skin panel

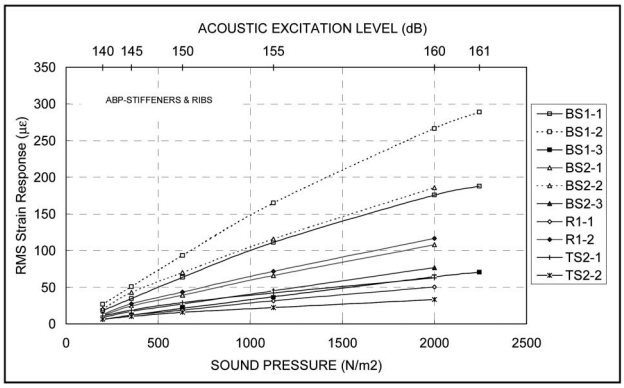

RMS strain response of the stiffeners and ribs

FIG. 5. The rms strain response of the aluminum alloy structure excited on the bottom skin.

box. The responses of the top skin panel were relatively low and similar in amplitudes to those of the aluminum alloy box. The response of the inner rib measured by the strain gauges R1-1 and R1-2 were similar to those of the aluminum alloy structure.

The strain power spectral densities have similar characteristics to those of the aluminum alloy box. The fundamental resonance frequency of the GLARE structure was lower than that of the aluminum box because the effective modulus of the GLARE 3 (58 GPa) is lower than that of aluminum alloy (72 GPa).

TABLE III. The rms strain response of the GLARE structure to acoustic pressure loading when excited on the flat skin panel ($\mu\epsilon$).

Strain gauge	Acoustic excitation level					
	140 dB	145 dB	150 dB	155 dB	160 dB	162 dB
B1-1	4.9	7.3	10.3	15.8	30.8	43.9
B1-2	15.4	29.1	43.6	65.6	120.5	143.8
B2-1	3.6	6.4	9.2	14.7	31.5	47.5
B2-2	21.8	39.9	58.5	87.0	165.0	210.2
B3-1	5.3	8.4	12.2	18.7	38.4	46.7
B3-2	6.2	10.6	16.0	24.6	50.2	69.8
B4-1	4.4	8.2	12.1	19.5	38.5	56.4
B4-2	16.2	31.2	45.6	67.3	135.1	188.0
B5-1	3.8	5.6	8.1	13.0	32.5	41.0
B5-2	27.4	45.9	62.8	83.5	137.4	214.0
B6-1	2.6	4.8	7.5	12.5	29.4	43.4
B6-2	18.3	34.0	50.2	76.0	149.4	200.3
BS1-1	12.7	24.9	39.0	59.6	119.0	160.2
BS1-2	16.4	32.7	50.8	78.1	151.7	210.2
BS1-3	4.6	9.2	14.0	22.7	44.7	61.0
BS2-1	7.1	18.2	27.4	43.6	85.0	108.1
BS2-2	12.9	32.3	47.0	74.1	143.3	185.1
BS2-3	7.0	18.1	27.4	44.9	89.0	113.9
R1-1	2.2	5.0	7.4	11.4	23.6	31.1
R1-2	8.6	22.5	34.9	55.2	118.0	155.3
T1-2	3.9	5.3	6.9	9.7	16.3	19.7
T2-1	25.9	26.0	26.3	27.0	31.4	33.6
T2-2	5.4	10.8	15.6	22.7	37.6	43.6
T6-1	5.7	11.3	16.3	23.5	46.3	67.3
T6-2	4.2	4.9	5.8	7.7	15.3	20.8
T7-1	6.4	12.8	17.2	21.8	37.7	44.8
T7-2	4.4	4.7	5.4	7.0	19.0	24.2
TS2-1	9.5	19.3	26.6	39.4	65.0	71.9
TS2-2	6.5	14.1	20.9	31.1	52.8	60.0

3. CFRP box structure

The measured rms strain results for the CFRP box structure are listed in Table IV. Much higher strain levels occurred than in the aluminum alloy and GLARE structures, especially on the stiffeners.

The relationships between sound pressure and rms strain (Fig. 7) show less of a tendency of nonlinear behavior compared with the aluminum and GLARE structures. The maximum strains were found on the stiffeners, but in the longitudinal direction rather than in the transverse direction, as for the aluminum alloy and GLARE structures. This indicated that bending dominated the deformation of the stiffeners. The maximum rms strain value was 385 $\mu\epsilon$, at strain gauge location BS1-1. In general, the strains on the stiffeners, were higher than those on the stiffeners of the aluminum alloy and GLARE structures. For the skin panels, the maximum strain responses were 111 $\mu\epsilon$ (T1-1) for the top skin and 184 $\mu\epsilon$ (B2-2) for the bottom skin. The responses of the top skin were relatively low when the excitation was on the bottom skin. The vertical strain of the inner rib (R1-2) was 196 $\mu\epsilon$, which was quite high compared with responses of other locations.

Strain spectral densities and normalized integrals across the strain PSD of the CFRP box (not reported in this paper for reasons of space) showed that multimodal contributions dominated the spectra, and the individual peaks were less distinguishable than for the other structures. Strain energy redistribution, with increasing excitation level, was more ap-

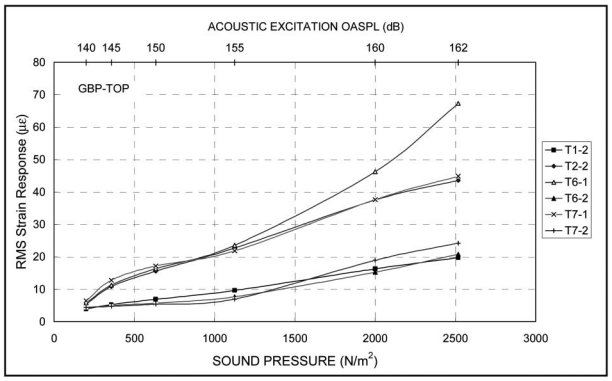

RMS strain response of the top skin panel

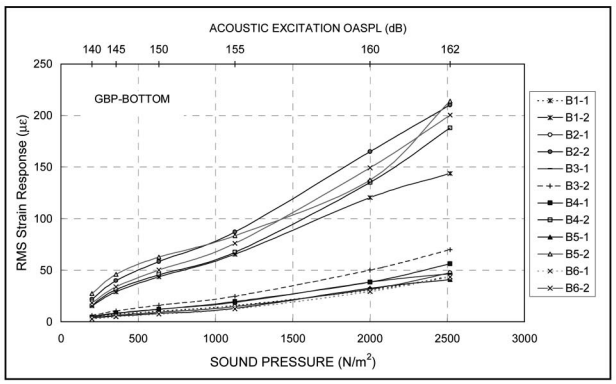

RMS strain response of the bottom skin panel

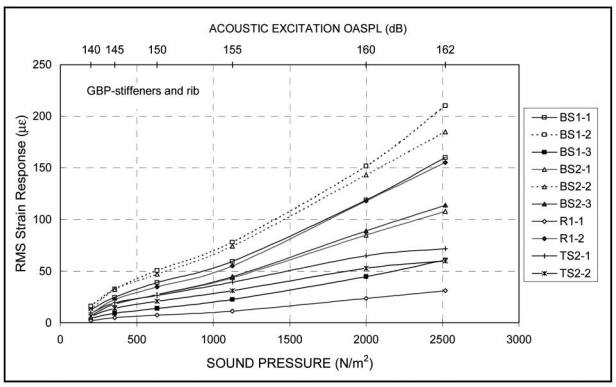

RMS strain response of the stiffeners and inner rib

FIG. 6. The rms strain response of the GLARE structure excited on the bottom skin.

parent. The response spectra of the CFRP structure had broad peaks compared with the other two boxes, which indicates the higher damping of the CFRP structure. When it was directly excited by acoustic loading, more resonance peaks appeared in the strain spectrum than in the situation of indirect excitation.

D. Characteristics of the strain response of the box structures

Among the three box structures, the CFRP structure had the highest strain response. The highest strain level was found on the stiffeners of all three structures. For the stiffeners of the aluminum alloy and GLARE structures, the maximum strain was in the direction transverse to the length of the stiffeners, which indicates that the stiffeners responded mainly in torsion during acoustic excitation. For the CFRP structure, the maximum strain on a stiffener was in the longitudinal direction along the length of the stiffener, which means that the stiffeners were mainly undergoing bending deformation during acoustic excitation.

TABLE IV. The rms strain response of the CFRP structure to acoustic pressure loading when excited on the flat skin panel ($\mu\epsilon$).

Strain gauge	Acoustic excitation level					
	140 dB	140 dB	150 dB	155 dB	160 dB	161 dB
B1-1	3.8	4.9	6.7	10.2	18.7	20.7
B1-2	8.5	17.3	28.7	47.3	90.6	101.2
B2-1	2.0	3.4	5.4	8.8	17.2	19.3
B2-2	18.2	37.3	60.5	101.4	184.0	203.5
B3-1	4.0	7.6	12.8	21.3	40.8	46.9
B3-2	10.3	22.9	39.1	65.9	121.5	137.7
B4-1	2.3	3.7	6.4	9.4	18.1	20.9
B4-2	13.2	27.1	44.8	72.7	137.0	150.6
B5-1	2.5	4.6	7.8	12.7	24.5	27.0
B5-2	13.5	29.4	51.1	82.3	156.8	170.8
B6-1	1.9	3.8	5.9	9.2	19.7	21.8
B6-2	12.3	27.7	42.9	68.1	140.6	153.1
BS1-1	33.6	70.9	120.7	201.6	384.9	431.3
BS1-2	9.4	19.9	33.9	56.3	106.7	119.7
BS1-3	12.3	25.8	43.9	73.2	140.2	157.8
BS2-1	32.6	59.2	101.8	163.3	296.4	328.7
BS2-2	9.1	16.4	28.1	45.1	81.7	90.6
BS2-3	10.7	19.6	33.3	54.1	106.9	120.1
R1-1	4.7	8.2	14.5	23.9	43.7	48.7
R1-2	23.9	37.9	67.3	106.8	196.0	213.3
T1-1	8.7	13.7	22.0	34.5	58.6	65.7
T1-2	6.4	7.0	8.3	11.1	17.7	20.3
T2-1	0.3	0.6	1.4	2.8	7.6	9.6
T2-2	7.8	10.8	16.1	24.1	40.4	46.3
T6-1	2.4	1.4	2.3	3.7	5.5	8.7
T6-2	5.6	5.7	5.7	6.2	8.2	9.1
T7-1	6.1	6.2	6.5	7.2	9.9	10.4
T7-2	8.6	11.7	17.3	25.7	45.5	51.6
TS2-1	8.7	10.9	14.4	19.8	29.6	31.0
TS2-2	17.1	30.3	49.6	74.9	127.2	135.1

The relationship between excitation levels and rms response strains at various locations of the test structures showed nonlinear behavior, especially for the aluminum alloy and GLARE boxes. When the structures were excited on one skin panel, the other skin panel and the inner ribs all showed relatively high strain response, which indicates the coupling of top and bottom skins. Therefore for a box-type structure, the skin panels should not be simply treated as isolated items.

As the excitation level increased, strain energy redistributed in the frequency band of interest, i.e., the response of higher-frequency modes enhanced, and their contribution to the total strain therefore became more significant. This is shown by the normalized integrals of the strain spectral densities. As shown, for example, in Fig. 8, for the aluminum alloy box, the contribution to the total rms value of the first two peaks between 200 and 300 Hz was around 58% at the excitation level of 140 dB, but was reduced to about 45% at 160 dB. At 600 Hz, the normalized integral was 0.91 for the

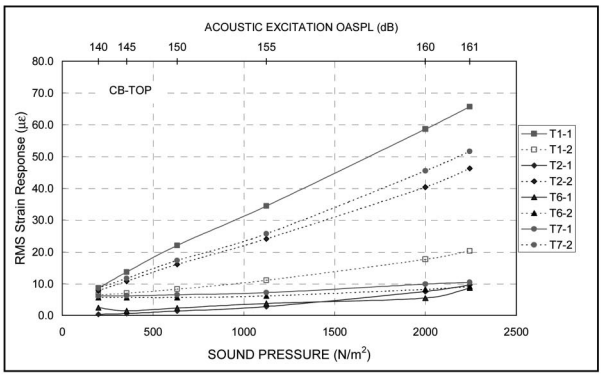

RMS strain response of the top skin panel

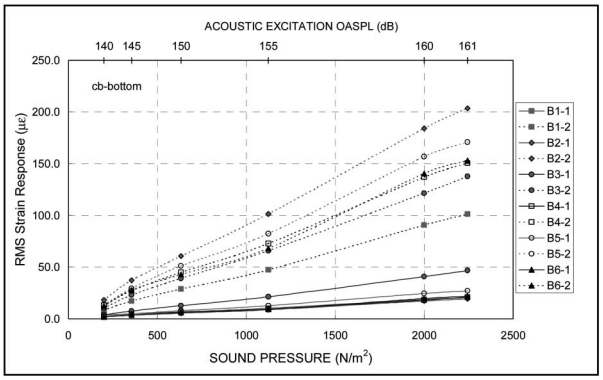

RMS strain response of the bottom skin panel

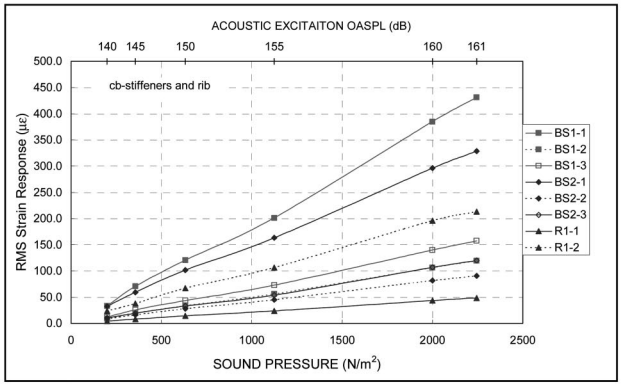

RMS strain response of the stiffeners and inner rib

FIG. 7. The rms strain response of the CFRP structure excited on the bottom skin.

excitation level of 155 dB, but decreased to 0.85 at 160 dB. In these cases the single mode approach is no longer suitable. The same type of behavior was also found in the responses of the CFRP box and was even more evident for the GLARE structures, especially when the boxes were excited on their flat skin panels. At the higher excitation levels, adjacent individual frequency peaks tended to coalesce to form broad peaks. Results from the CFRP box showed less peaky resonance peaks due to its higher damping.

The characteristics of rms strain responses of the three box-type structures were indicative of nonlinear behavior at high excitation levels. The dynamic behavior observed was very similar to that occurring in acoustically excited, plate-type structures with constrained boundaries at high response levels.[22]

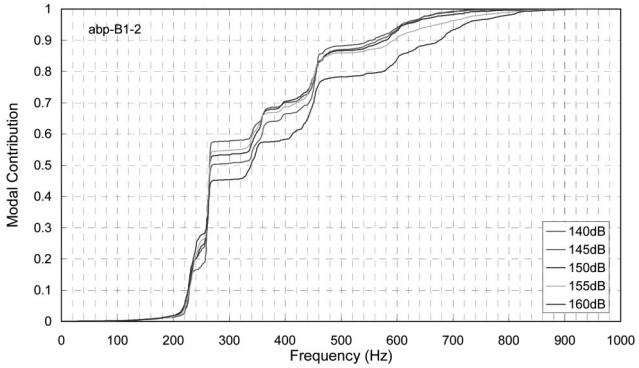

FIG. 8. Normalized integral across strain spectral density aluminum alloy box—bottom excitation—gauge B1-2.

The Statistical Characteristics of Strain Response were also investigated and the data showed nearly Gaussian distributions, with skewness values close to zero, and kurtosis values generally between 3 and 3.5.

Tests were also carried out by acoustically exciting the structures on the top panel. These tests showed results similar to those obtained by exciting the structures on the bottom panel, with strong structural coupling between top and bottom skins and strain energy redistribution in the structures. The maximum responses of the bottom skin panels were 61% (aluminum alloy, B1-2), 122% (GLARE, B2-2) and 125% (CFRP, B6-2) of the maximum strain values found on the top skin panels. Relatively low response levels were found on the top skins when excitation was on the bottom skins. Here the ratios of the highest strains between top and bottom skin panels were 50% (Al alloy box, T6-2), 28% (GLARE, T6-1), and 32% (CFRP, T1-1). These values were relatively low compared with those for bottom excitation cases, but still were not negligible. The inner ribs of the structures also exhibited high responses in the vertical direction. These proved that components, such as skins and ribs, of a box-type structure should not be treated as isolated items in the analysis.

IV. ACOUSTIC FATIGUE ENDURANCE OF BOX STRUCTURES

After all the strain measurements had been completed, the three structures were subjected to acoustic endurance tests. The excitation was applied to the flat skin panel at an overall sound pressure level of 161 dB with the spectrum shape shown in Fig. 4. The structures were inspected at regular intervals during the endurance tests using an endoscope to trace the propagation of fatigue cracks.

A. Aluminum alloy structure

This structure was excited for a total of 521 min. Most of the fatigue damage was found on the stiffeners in two side bays on the bottom skin panel.

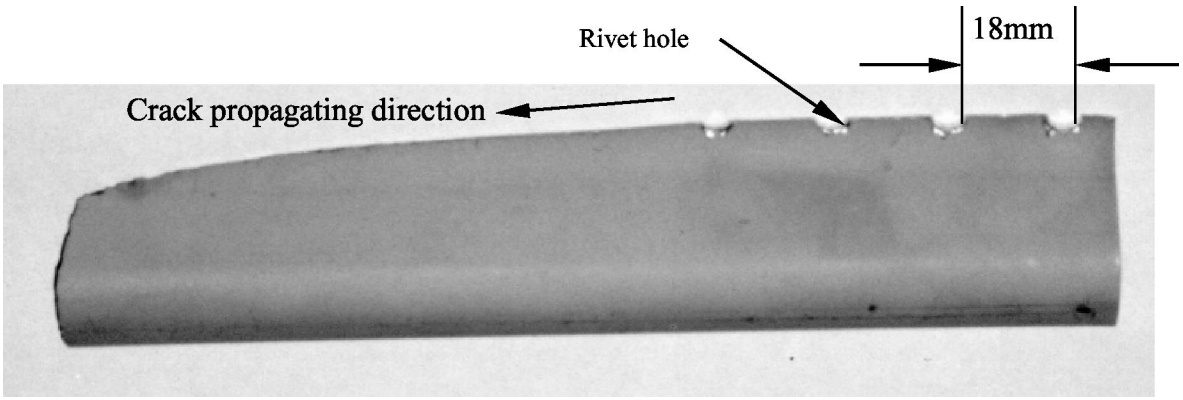

FIG. 9. End part of stiffener No. 3 on bay side B (bottom skin) broken off from the aluminum alloy structure after 50 min of acoustic endurance testing.

After the first 50 min of the endurance test, the end part of stiffener 3 on the bottom panel at side B broke off from the structure. Figure 9 shows photographs of the detached part. The crack started at the end of the stiffener and propagated along the rivet line toward the inside of the structure, and eventually toward the stiffener edge, causing the part to detach. The endoscope inspection also revealed cracks on every stiffener on both side bays (A and B) along rivet lines. As the testing continued, cracks grew quickly and two more end parts of the stiffeners on side A detached from the box at 156 and 200 min, respectively. In the total 521 min of endurance testing, no fatigue cracks were found in the top panel and ribs. A fatigue crack was found in stiffener No. 3 of the bottom middle bay at 372 min. The longest crack was 296 mm across 17 rivets on stiffener No. 2 of bay side B, which is almost across the whole length of bay side B. Figure 10 illustrates the crack propagation path.

The crack length versus test time curves are plotted in Fig. 11, which show the crack growth rates. Bay side B, which was at the ''downstream'' end of the test tunnel in the PWT, had longer fatigue cracks than bay side A. As the test time increased, the crack propagation rate decreased. Rivets connecting the inner ribs and the bottom panel started to loosen and some started to snap at 320 min. Black powder around some of the rivet's holes indicated that those rivets had experienced substantial movements.

B. GLARE structure

Acoustic endurance testing of the GLARE box lasted for 588 minutes. Before the tests, the structure was inspected internally using an endoscope. After 92 min of testing, the first cracks appeared in the side A bay. For the bay on side B, fatigue cracks were present before the endurance testing started. These cracks were induced during the strain measurement tests, which were carried out twice, and each took

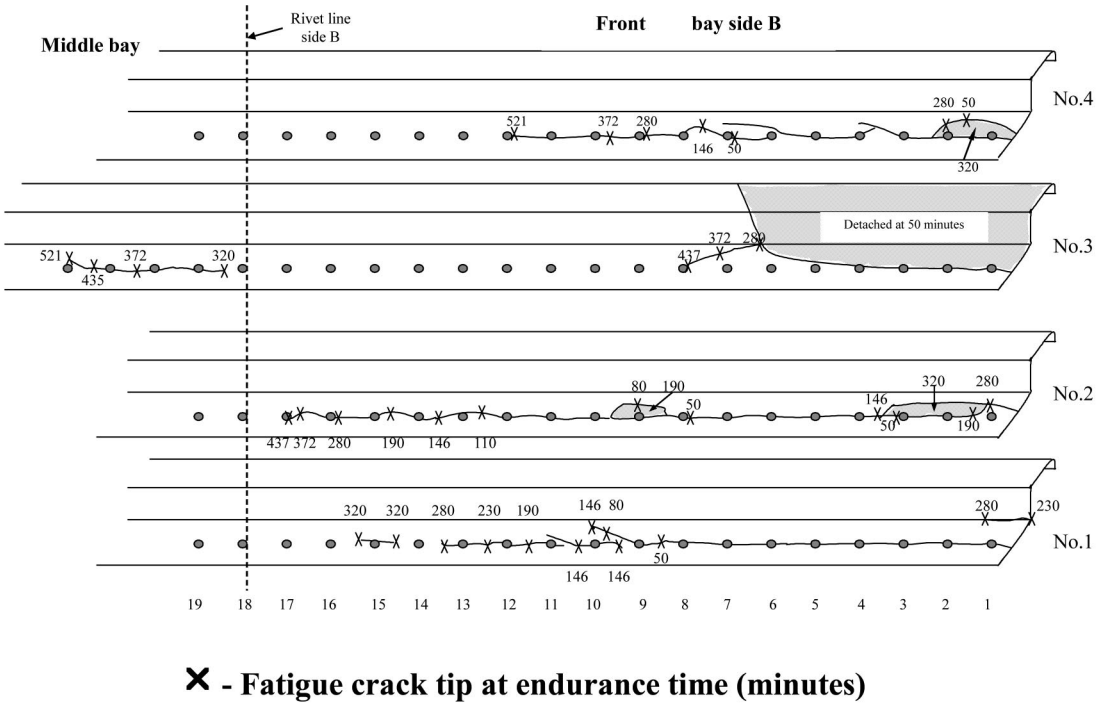

FIG. 10. Fatigue crack propagation path in the stiffeners on the bottom skin of bay side B and the middle bay of the aluminum alloy structure during acoustic endurance testing.

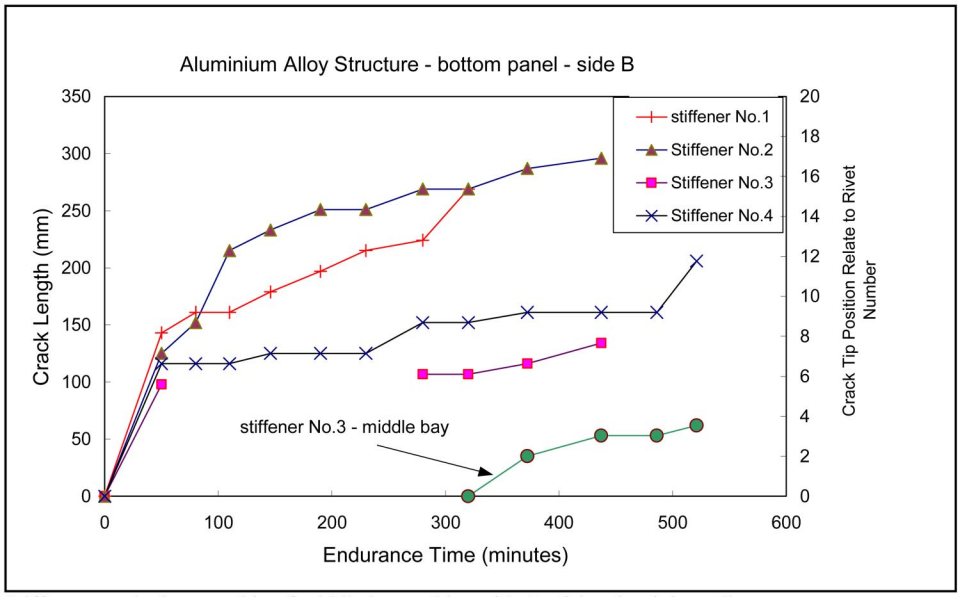

Stiffeners on the bottom skin of middle bay and bay side B of the aluminium alloy structure

FIG. 11. Fatigue crack length versus the time of endurance testing—aluminium alloy structure.

about a total of 9 min from an excitation level of 140 to 162 dB (about 3–4 min at levels of 160 and 162 dB). Fatigue crack propagation paths for both side bays are illustrated in Fig. 12. Compared with the aluminum alloy structure, the GLARE structure had shorter crack lengths at the end of the testing. For the aluminum alloy structure, when a crack initiated, it propagated rapidly through the thickness of the stiffener. But for the GLARE structure, cracks initiated in the outer metal layer and were arrested by the glass fiber composite layer, which delayed propagation. For stiffener No. 3 on bay side B, it took 362 min to see the crack through the thickness. Similar to the aluminum alloy structure, the longest fatigue crack was seen on the ''downstream'' side of the GLARE structure. Figure 13 shows the crack length against time, and indicates the lower crack growth rates compared with those in the aluminum alloy structure.

From Fig. 12, it can be observed that there were two types of cracks: one mainly along the rivet line and the other at the lower bend line of the stiffeners.

No rivet failures were found on the rib lines. But one of

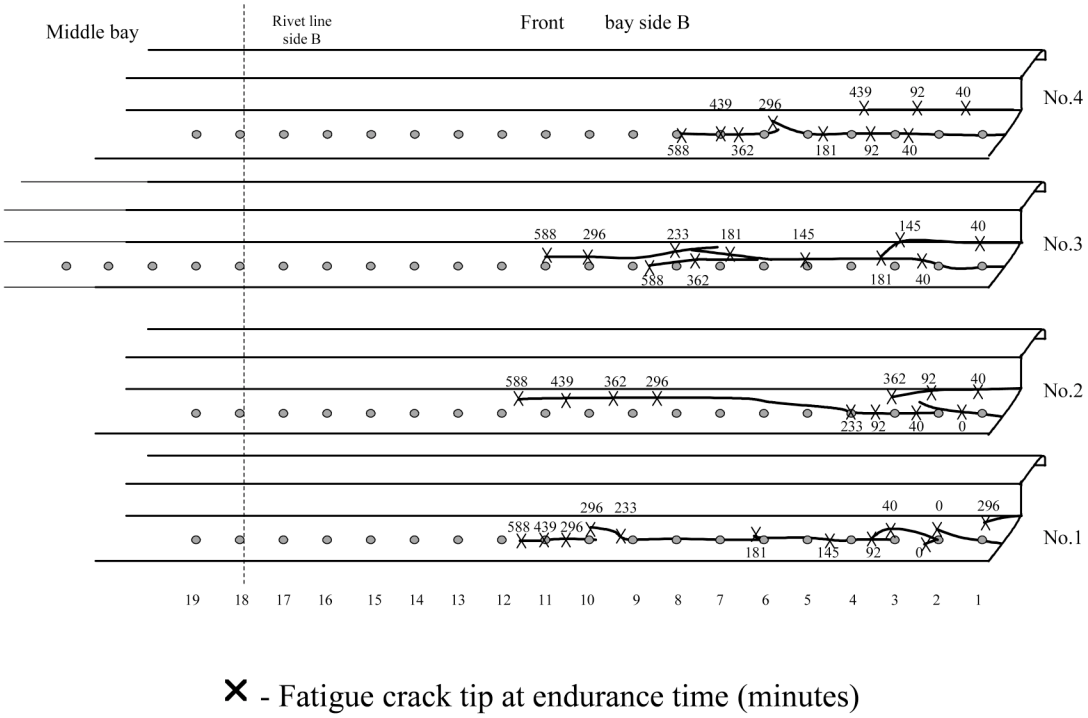

FIG. 12. Fatigue crack propagation path in the stiffeners on the bottom skin of bay side B of the GLARE structure during acoustic endurance testing.

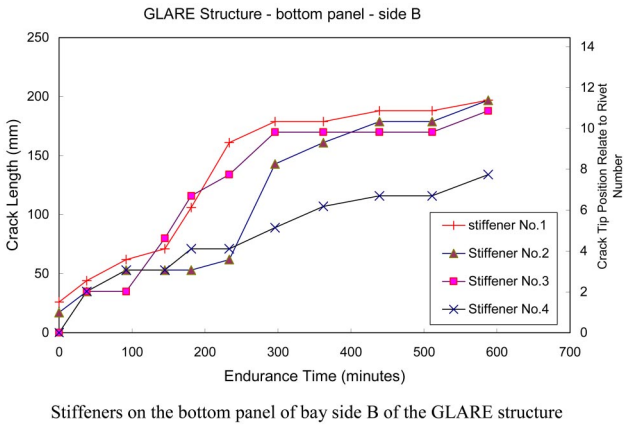

FIG. 13. Fatigue crack length versus time of endurance testing GLARE structure.

the rivets that connected the rear spar and inner rib (side B) snapped after 233 min. Cracks were also seen on the inner rib at side B (Fig. 14).

C. CFRP structure

The CFRP structure was subjected to acoustic loading for a total of 536 min. No visible structural failure was found except that three of the four rivets connecting the rear spar and inner ribs snapped after 60, 77, and 120 min, respectively. In fact, the snapped rivets were of a wrong type (hollow center) installed by the manufacturer by mistake.

To examine whether there was any undetected damage that could affect the resonance frequencies of the CFRP structure, the strain spectral densities at the four inspection times were checked and no significant changes of the resonance frequency and strain spectral shape were found.

V. FINITE ELEMENT ANALYSIS OF THE BOX STRUCTURES

Finite element analyses of the box structures were carried out to estimate the structural response to high-intensity acoustic loading and to compare the predicted responses with the results obtained during the tests. The finite element analyses reported in the next sections are carried out according to the standard working practice in this industry. However, more sophisticate finite element techniques (see, for example, Ref. 23) can be applied to these types of problems, to achieve more accurate predictions.

A. Finite element models

MSC/PATRAN was used to prepare the finite element models of the box structures. Each model was built using four-node shell elements. The stiffeners were modeled using shell elements in order to obtain the detailed strain response. For the aluminum alloy and GLARE structures, there were 26 584 elements and 27 065 nodes, and 23 343 elements and 21 823 nodes for the CFRP structure. There were at least ten elements between stiffeners in order to obtain accurate mode shape estimations. Figure 15 shows the finite element models of the aluminum and CFRP structures.

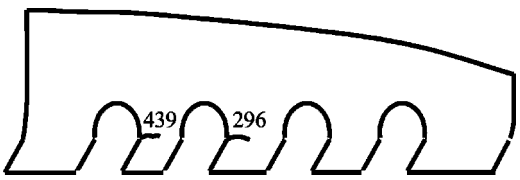

FIG. 14. Acoustic fatigue cracks found in the inner rib at bay side B of the GLARE structure during endurance testing.

The MSC.NASTRAN shell element—CQUAD4—was used for the modeling of both metallic and composite materials, using different material properties. For the aluminum parts, isotropic material properties were used (with the assumption of classical lamination theory in formulating shell behavior for composite laminate element properties). For those in a composite, laminate properties were used. The skin thickness was 1.4 mm for the aluminum alloy and 2 mm for the CFRP (details of the lay-up are reported in Table I).

B. Loading and boundary conditions

During the tests, the structures were supported by a frame that restricted the deflection of the end ribs, hence for the random response analysis of the structures to the acoustic loading, the whole of the end ribs was constrained to stop translational movements.

The response of the structures to the random pressure excitation was calculated by applying random pressure loading of overall sound pressure levels from 140 to 160 dB in steps of 5 dB to the bottom skin panel. The pressure loads are considered to have a constant amplitude but varying spatial phase angle, i.e.,

$$P(f,x) = P_0 e^{i2\pi f x/V}, \tag{1}$$

where x is the airflow distance, and $V = 340$ m/s is the speed of sound.

This type of loading recreated the conditions produced by the traveling sound wave passing over the panel skin. The types of solution implemented by the software were NASTRAN solution 103 for normal mode analysis, and solution 111 for frequency response analysis.

C. Finite element results

Because of the similarity of the aluminum alloy and GLARE structures, only the results for aluminum and CFRP structures are presented.

In Table V, the rms strain response to the random pressure at various strain gauge locations of the FE model of the aluminum alloy box structure are listed, together with their percentage difference from the test results. As an example, the strain spectral density at strain gauge locations B12 is shown in Fig. 16. It can be seen that the estimated strain levels are of the same order of magnitude and have a similar pattern to those measured. However, the FE analysis has been carried out using an average value for the damping loss factor (0.0340), while the real structures have different values of modal damping and therefore some differences in the results are to be expected.

TABLE V. FE results and comparison of rms strain responses with test data—Aluminium alloy structure (damping loss factor 0.0340).

Strain gauge No.	SPL	140 dB	145 dB	150 dB	155 dB	160 dB
B11	FEM	4.4	7.8	13.9	24.6	43.8
	% diff with tests	22.7	−3.8	−13.7	−16.7	−23.1
B12	FEM	11.2	19.9	35.3	62.8	111.7
	% diff with tests	23.2	24.1	24.4	23.6	17.5
B21	FEM	5.3	9.4	16.8	29.9	53.1
	% diff with tests	−30.2	−33.0	−35.7	−35.8	−36.0
B22	FEM	13.9	24.7	43.8	78.0	138.7
	% diff with tests	−45.3	−47.8	−46.3	−39.6	−31.6
B31	FEM	2.8	5.0	8.8	15.7	27.8
	% diff with tests	35.7	0.0	−11.4	−15.3	−13.7
B32	FEM	9.9	17.6	31.3	55.7	99.0
	% diff with tests	52.5	68.8	71.6	68.2	58.4
B41	FEM	4.6	8.3	14.7	26.1	46.4
	% diff with tests	−17.4	−21.7	−22.4	−24.1	−27.4
B42	FEM	15.0	26.7	47.5	84.4	150.1
	% diff with tests	34.7	25.1	28.0	23.3	4.6
B51	FEM	5.0	8.8	15.7	27.9	49.5
	% diff with tests	−30.0	−40.9	−43.9	−45.2	−46.3
B52	FEM	17.7	31.5	56.0	99.6	177.0
	% diff with tests	−26.0	−26.0	−25.0	−30.9	−32.1
B61	FEM	4.1	7.3	13.1	23.2	41.3
	% diff with tests	−48.8	−47.9	−47.3	−46.6	−44.1
B62	FEM	11.0	19.5	34.6	61.6	109.5
	% diff with tests	15.5	30.3	28.3	14.3	−0.1
BS11	FEM	8.5	15.1	26.8	47.6	84.6
	% diff with tests	116.5	129.1	136.9	133.6	107.7
BS12	FEM	18.5	32.9	58.6	104.1	185.2
	% diff with tests	44.9	55.3	59.6	58.3	43.9
BS21	FEM	8.6	15.2	27.1	48.2	85.7
	% diff with tests	33.7	61.2	45.0	37.1	25.9
BS22	FEM	20.0	35.5	63.2	112.4	199.8
	% diff with tests	2.5	21.4	10.8	3.1	−7.0
T11	FEM	4.5	7.9	14.1	25.1	44.6
	% diff with tests	48.9	39.2	11.3	1.6	−7.8
T12	FEM	2.2	4.0	7.1	12.6	22.3
	% diff with tests	122.7	142.5	136.6	200.0	153.4
T21	FEM	1.6	2.8	4.9	8.7	15.5
	% diff with tests	412.5	200.0	81.6	19.5	−11.6
T22	FEM	4.9	8.8	15.6	27.7	49.2
	% diff with tests	30.6	21.6	0.6	−7.9	−15.9
T61	FEM	4.0	7.1	12.6	22.4	39.8
	% diff with tests	85.0	100.0	71.4	33.5	3.5
T62	FEM	1.3	2.3	4.2	7.4	13.2
	% diff with tests	507.7	291.3	197.6	416.2	496.2
T71	FEM	3.5	6.2	11.1	19.8	35.1
	% diff with tests	62.9	32.3	9.0	−2.0	−10.0
T72	FEM	1.3	2.3	4.0	7.1	12.7
	% diff with tests	315.4	139.1	55.0	31.0	15.7
TS21	FEM	10.4	18.5	32.9	58.6	104.1
	% diff with tests	4.8	2.2	−11.6	−27.8	−39.5
TS22	FEM	1.6	2.8	4.9	8.7	15.5
	%diff with tests	312.5	267.9	220.4	156.3	115.5

TABLE VI. FE results and a comparison of rms strain responses with test data—CFRP structure (damping loss factor 0.050).

Strain gauge No.	SPL	140 dB	145 dB	150 dB	155 dB	160 dB
B11	FEM	3.2	5.6	10.0	17.8	31.7
	% diff with tests	18.8	−12.5	−33.0	−42.7	−41.0
B12	FEM	20.7	36.8	65.4	116.4	206.9
	% diff with tests	−58.9	−53.0	−56.1	−59.4	−56.2
B21	FEM	3.0	5.4	9.5	17.0	30.2
	% diff with tests	−33.3	−37.0	−43.2	−48.2	−43.0
B22	FEM	17.7	31.5	56.0	99.6	177.1
	% diff with tests	2.8	18.4	8.0	1.8	3.9
B31	FEM	4.3	7.7	13.7	24.4	43.3
	% diff with tests	−7.0	−1.3	−6.6	−12.7	−5.8
B32	FEM	6.8	12.0	21.4	38.1	67.7
	% diff with tests	51.5	90.8	82.7	73.0	79.5
B41	FEM	2.1	3.8	6.8	12.1	21.5
	% diff with tests	9.5	−2.6	−5.9	−22.3	−15.8
B42	FEM	17.0	30.2	53.7	95.5	169.9
	% diff with tests	−22.4	−10.3	−16.6	−23.9	−19.4
B51	FEM	3.0	5.3	9.4	16.7	29.7
	% diff with tests	−16.7	−13.2	−17.0	−24.0	−17.5
B52	FEM	16.4	29.1	51.7	92.0	163.6
	% diff with tests	−17.7	1.0	−1.2	−10.5	−4.2
B61	FEM	4.1	7.3	13.0	23.1	41.1
	% diff with tests	−53.7	−47.9	−54.6	−60.2	−52.1
B62	FEM	17.9	31.8	56.6	100.6	178.9
	% diff with tests	−31.3	−12.9	−24.2	−32.3	−21.4
BS11	FEM	46.5	82.7	147.0	261.4	464.8
	% diff with tests	−27.7	−14.3	−17.9	−22.9	−17.2
BS12	FEM	12.9	23.0	40.9	72.7	129.3
	% diff with tests	−27.1	−13.5	−17.1	−22.6	−17.5
BS21	FEM	28.1	49.9	88.7	157.7	280.5
	% diff with tests	16.0	18.6	14.8	3.6	5.7
BS22	FEM	7.8	13.8	24.5	43.6	77.6
	% diff with tests	16.7	18.8	14.7	3.4	5.3
T11	FEM	4.6	8.3	14.7	26.1	46.4
	% diff with tests	89.1	65.1	49.7	32.2	26.3
T12	FEM	1.3	2.3	4.1	7.3	12.9
	% diff with tests	392.3	204.3	102.4	52.1	37.2
T21	FEM	5.9	10.5	18.7	33.3	59.3
	% diff with tests	−94.9	−94.3	−92.5	−91.6	−87.2
T22	FEM	1.5	2.7	4.8	8.6	15.3
	% diff with tests	420.0	300.0	235.4	180.2	164.1
T61	FEM	3.5	6.3	11.1	19.8	35.2
	% diff with tests	−31.4	−77.8	−79.3	−81.3	−84.4
T62	FEM	0.7	1.2	2.2	3.9	7.0
	% diff with tests	700.0	375.0	159.1	59.0	17.1
T71	FEM	3.2	5.7	10.1	17.9	31.9
	% diff with tests	90.6	8.8	−35.6	−59.8	−69.0
T72	FEM	0.7	1.3	2.3	4.1	7.4
	% diff with tests	1128.6	800.0	652.2	526.8	514.9
TS21	FEM	2.8	4.9	8.7	15.5	27.6
	% diff with tests	210.7	122.4	65.5	27.7	7.2
TS22	FEM	9.9	17.6	31.3	55.7	99.0
	% diff with tests	72.7	72.2	58.5	34.5	28.5

The ''smearing'' effect is visible in Fig. 16, especially in the higher-frequency region, where strain spectral density curves became more smooth and separated peaks no longer exist due to high damping.

In the acoustic endurance tests of the box structures discussed in the previous section, fatigue damage was found at the ends of the stiffeners of both the aluminum alloy and GLARE boxes at an early stage of the endurance tests. This eventually led to the end parts of stiffeners of the aluminum alloy structure breaking away. The FE analyses [details of the FE model shown in Fig. 17(a)] carried out using an input of 160 dB, estimated transverse rms strains of 902 μ strain and 949 μ strain for sides A and B, respectively. This is because the ends of the stiffeners were not constrained to the ribs. Under the acoustic loading, the stiffener ends could vibrate in the manner of a cantilevered beam, which induced large transverse strains in the stiffener. To reduce the strain

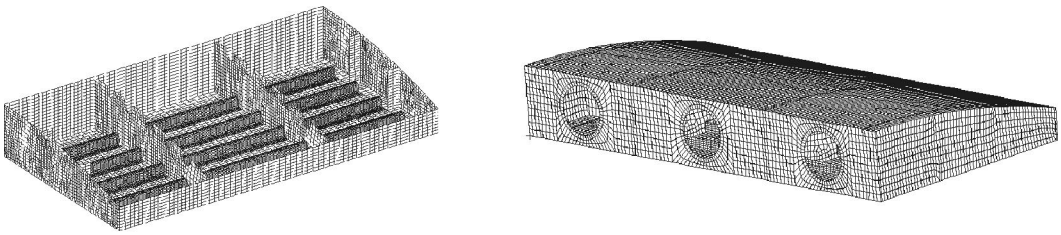

a). Aluminium alloy box without top skin b). CFRP structure

FIG. 15. Finite element models of the box structures.

level at this location, the finite element model of the aluminum box structure was modified by extending the ends of the stiffeners on the bottom skin and connecting them to the end ribs, as shown in Fig. 17(b). A normal mode analysis of this modified model showed that the first natural frequency of the box increased from 234 to 240 Hz, which indicates the increase of total stiffness of the structure. Response analysis revealed that rms strains in the modified model reduced significantly at the ends of the stiffeners. The transverse strains decreased to 77 μ strain and 129 μ strain for sides A and B, respectively. Longitudinal strains were also reduced, but less dramatically.

For the CFRP box structure, the rms strain response to the pressure loading at various strain gauge locations are listed in Table VI, together with the percentage difference from the experimental data. Some of the strains reported in the table are quite close to zero (e.g., location T72), hence the very large percentage difference between FE and experimental data.

VI. DISCUSSION OF TEST RESULTS AND FE PREDICTIONS

The natural frequencies estimated using the FE models agreed relatively well with the experimental results at low frequency, however, at higher frequency the FE models predicted many more resonances (in the frequency range from 0 to 800 Hz, 169 and 108 modes were predicted for the aluminum alloy and CFRP box structures, respectively) than actually observed in the real structures. This is in part due to the practical difficulties of exciting and detecting all modes (some of the FE predicted modes are local and can be detected only with a sensor positioned on the vibrating part, which can be unfeasible when the number of accelerometers is limited), and in part due to the fact that at high frequency, and, in particular, for higher excitation levels, the structural modes tend to merge (''smearing'' effect). Overall the FE models are able to reproduce quite correctly shape and frequency of the global modes and their response. However, many factors such as nonlinearity due to the high driving pressure, peak broadening, energy redistribution and additional acoustic damping, affect panel modes much more than the global modes. These phenomena are not properly reproduced by the current FE model, and this produces discrepancies between the computational and experimental results (for example, the discrepancies visible in Fig. 16).

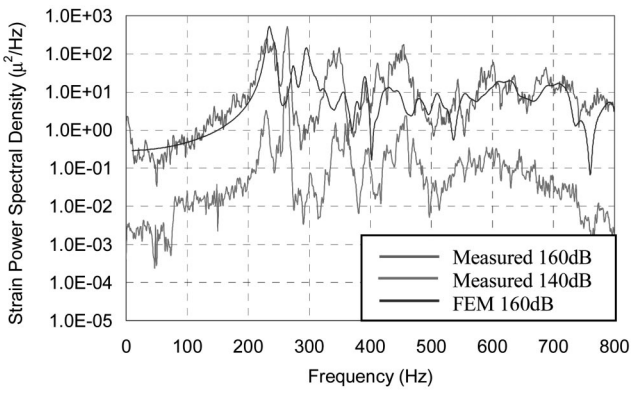

FIG. 16. Strain power spectral densities at strain gauge location B12 of the aluminum alloy structure excited on the bottom skin panel.

The modal damping ratios obtained during resonance testing carried out before the acoustic tests and not described in this article showed that the CFRP box structure had the highest damping ratios and the aluminum alloy structure had the lowest damping values among the three box structures. The average damping ratios for the CFRP, GLARE, and aluminum alloy structures were 1.14%, 0.71%, and 0.55%, respectively. Due to the high damping value of CFRP material, measured transfer functions of the CFRP structure showed wide peaks and strong modal overlap. It was found that response levels at various measurement points were higher and more evenly distributed for the CFRP structure than for other two structures due to the high stiffness and damping of the CFRP skin panels, which produced strong modal overlap and higher-energy redistribution in comparison with the other structures.

The results of the acoustic tests show that the CFRP structure had the highest strain response among the three box structures.

The highest strain level was found on the stiffeners of all three structures. For the stiffeners of the aluminum alloy and GLARE structures, the maximum strain was in the direction transverse to the length of the stiffeners, which indicates that the stiffeners responded mainly in torsion during acoustic excitation. For the CFRP structure, the maximum strain on a stiffener was in the longitudinal direction along the length of the stiffener, which means that stiffeners were mainly undergoing bending deformation during acoustic excitation.

Nonlinear relationships were found between excitation levels and rms strain responses at various locations of the test structures, especially for the aluminum alloy and GLARE boxes. When the structures were excited on one skin panel, the other skin panel and inner ribs all showed a relatively high strain response, which indicates coupling of the top and bottom skins. These results proved that components, such as

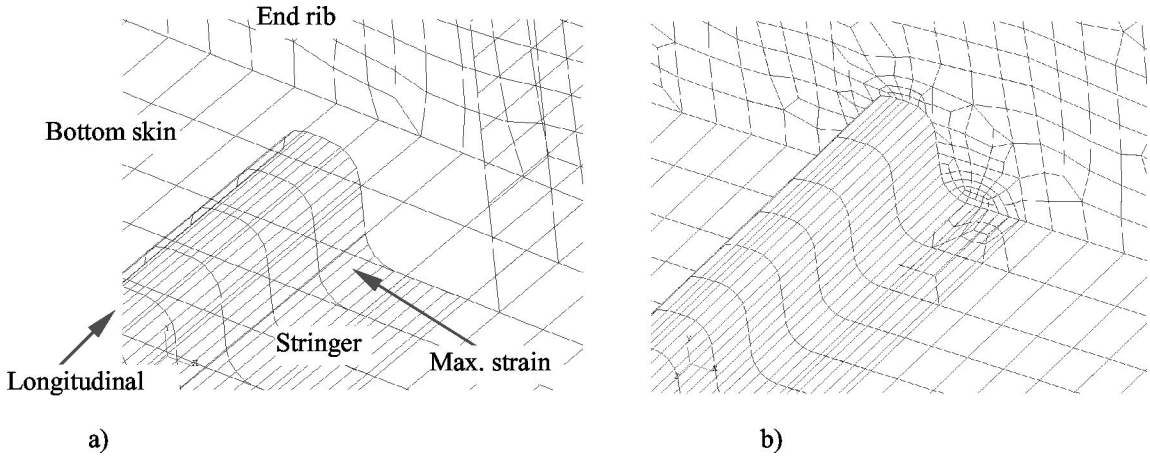

FIG. 17. Details of the FE model of the aluminum alloy structure showing the end of the stiffeners. (a) Original structure, end of the stiffener free. (b) End of the stiffener attached to the rib.

skins and ribs, of a box-type structure should not be treated as isolated items in the analysis.

Spectral densities of the strain responses have shown strain energy redistribution with increase of excitation level. As the excitation level increased, the response of higher frequency modes enhanced, and their contribution the total strain was therefore more significant. This is shown by normalized integration across the strain spectral densities. As shown, for example, in Fig. 8 for aluminum alloy box with bottom excitation, the contribution to the total rms value of the first two resonance peaks was around 58% at low excitation level, but was reduced to 45% at 160 dB. At 600 Hz, the normalized integral was 0.91 for an excitation level of 155 dB, but decreased to 0.85 for 160 dB. This phenomenon was seen for all three box structures. The single mode approach for the prediction of fatigue life is not suitable for this type of structure. At the higher excitation levels, adjacent individual frequency peaks tended to coalesce to form broad peaks. These behaviors indicate the nonlinear response of the test structures at high excitation levels.

Acoustic fatigue endurance tests had shown that CFRP has superior fatigue resistance compared with GLARE and aluminum alloy structures. There was no visible fatigue damage found in the CFRP structure apart from the failure of four rivets. For the aluminum alloy and GLARE structures, fatigue cracks located in the stiffeners of the both side bays started at the early stage of the endurance tests. Due to the existence of glass fiber composites, the growth rate of the fatigue crack in the GLARE structure was lower than that in the aluminum alloy structure. Some of rivets connecting the inner ribs and bottom skin panel of the aluminum alloy structure also failed. This behavior did not occur in the GLARE structure. For both aluminum alloy and GLARE structures, longer fatigue cracks were seen in the ''downstream'' bay (side B).

From the endurance testing carried out, it appears that for the box-type structures of the form used in this project, the CFRP structure was the most acoustic fatigue resistant followed by the GLARE structure, the aluminum alloy structure being the least fatigue resistant. It must be noted, however, that only visual inspections were carried out during the tests, no NDT examinations were made for the CFRP structure. It should also be pointed out that the ends of the stiffeners of the aluminum alloy and GLARE structures were not constrained, therefore, large deflections were induced during the acoustic excitation. This explains why the ends of the stiffeners detached from the structure at an early stage during the endurance tests.

VII. CONCLUSIONS

An extensive test program has been carried out on three flap-like box structures made of three different materials, Aluminum Alloy, GLARE, and CFRP. A comparison between FE results and test data shows that, although at low frequency the FE models give a good estimation of the resonance frequency, at high frequency the real structures exhibited far less resonances than predicted by the FE models. This is in part due to the excitation used, and in part to the ''smearing'' effect observed at high frequency.

When the structures were excited on one skin panel, the other skin panel and inner ribs all showed a relatively high strain response, which indicates coupling of the top and bottom skins. Hence, particular care must be taken when trying to examine single components (e.g., a panel surrounded by two stiffeners and two ribs) in isolation as, in reality, the strong coupling that exists with the rest of the structure affects its response.

As the excitation level increased, the response of higher frequency modes enhanced, and their contribution the total strain became more significant. The implication is that in these cases the single mode approach for the prediction of the fatigue life is no longer suitable.

Types of acoustic fatigue failures in the aluminum alloy and GLARE structures have been recorded and crack propagation rate data are also presented. From the endurance testing carried out, it appears that for the box-type structures of the form used in this project, the CFRP structure was the most acoustic fatigue resistant followed by the GLARE structure, and the aluminum alloy structure being the least fatigue resistant. It must be noted, however, that only visual

inspections were carried out during the tests; no NDT examinations were made for the CFRP structure.

[1] J. W. Miles, ''On structural fatigue under random loading,'' J. Aeronaut. Sci. **21**, 753–762 (1954).
[2] A. Powell, ''On the fatigue failure of structures due to vibrations excited by random pressure fields,'' J. Acoust. Soc. Am. **30**, 1130–1135 (1958).
[3] L. C. Chow and R. J. Cummins, ''Airbus aircraft acoustic fatigue certification,'' *Acoustics Bulletin*, November/December, 1994, pp. 5–10.
[4] P. D. Green, ''Current and future problems in structural acoustic fatigue,'' AGARD-CP-549, September, 1994, p. 1-1.
[5] E. J. Richards and D. J. Mead, *Noise and Acoustic Fatigue in Aeronautics* (Wiley, New York, 1968).
[6] ESDU Engineering Data, Acoustic Fatigue Series, Vol. 1 to 6, ISSN 0141-3961, 2002.
[7] J. S. Mixson, ''Overview of acoustic fatigue activities at NASA Langley Research Centre,'' *Proceedings of the 3rd International Conference on Recent Advances in Structural Dynamics*, July 1988, pp. 573–591.
[8] B. L. Clarkson, ''Review of sonic fatigue technology,'' NASA Contractor Report 4587, 1994.
[9] J. W. Miles, ''On structural fatigue under random loading,'' J. Aeronaut. Sci. **21**, 753–762 (1954).
[10] A. Powell, ''On the fatigue failure of structures due to vibrations excited random pressure fields,'' J. Acoust. Soc. Am. **30**, 1130–1135 (1958).
[11] B. L. Clarkson, ''Stresses in skin panels subjected to random acoustic loading,'' Aeronaut. J. **72**, 1000–1010 (1968).
[12] R. Blevins, ''An approximate method for sonic fatigue analysis of plates and shells,'' J. Sound Vib. **129**, 51–71 (1989).
[13] D. H. Middleton, in *Composite Materials in Aircraft Structures* (Longman Scientific & Technical, City, 1990).
[14] G. H. J. J. Roebroeks, ''Fibre–metal laminates, recent developments and applications,'' Int. J. Fatigue **16**, 33–42 (1994).
[15] J. B. Young *et al.*, ''Crack growth and residual strength characteristics of two grades of glass-reinforced aluminium GLARE,'' Compos. Struct. **27**, 457–469 (1994).
[16] A. D. Vlot, ''Low and high velocity impact loading of fibre/metal laminates, carbon/peek and monolithic aluminium 2024-T3,'' SAMPE European Chapter, 1992, pp. 347–360.
[17] K. Koenig, ''Acoustic fatigue testing on different materials and skin stiffener elements,'' presented at a symposium on the ''Impact of acoustic loads on aircraft structure,'' held in Lillehammer, Norway, May 1994.
[18] Y. Xiao, R. G. White, and G. S. Aglietti, ''An experimental characterization of the acoustic fatigue endurance of GLARE and comparison with that of CFRP,'' J. Composite Structures; full paper currently available on the journal website and archived as DO:10.1016/J.compstruct.2004.04.011, article in press.
[19] I. Holehouse, ''Sonic fatigue design method for the response of CFRP stiffened skin panels,'' *Proceedings of the 2nd International Conference on Recent Advances in Structural Dynamics*, April 1984, pp. 787, 798.
[20] J. Q. Sun and R. N. Miles, ''Acoustic fatigue life prediction for non-linear structures,'' J. Sound Vib. **150**, 531–535 (1991).
[21] P. R. Cunningham, ''Response prediction of acoustically-excited composite honeycomb sandwich structures with double curvature,'' Ph.D. thesis, Department of Aeronautics and Astronautics, School of Engineering Sciences, University of Southampton, February 2001.
[22] C. Mei and C. B. Prasad, ''Effects of nonlinear damping on random response of beams to acoustic loading,'' J. Sound Vib. **117**, 173–186 (1987).
[23] M. I. McEwan, J. R. Wright, J. E. Cooper, and A. Y. T. Leung, ''A finite element/modal technique for nonlinear plate and stiffened panel response prediction,'' *Proceedings of the 42nd AIAA/ASME/ASCE/AHS/ASC Structures, Structural Dynamics, and Material Conference and Exhibit*, AIAA-2001-1595, Seattle, WA, 2001.

Finite element prediction of wave motion in structural waveguides

Brian R. Mace[a)]
ISVR, University of Southampton, Southampton SO17 1BJ, United Kingdom

Denis Duhamel
LAMI, ENPC, Marne La Valle, France

Michael J. Brennan
ISVR, University of Southampton, Southampton SO17 1BJ, United Kingdom

Lars Hinke
Technische Universität Dresden, Dresden, Germany

(Received 26 June 2004; revised 9 February 2005; accepted 17 February 2005)

A method is presented by which the wavenumbers for a one-dimensional waveguide can be predicted from a finite element (FE) model. The method involves postprocessing a conventional, but low order, FE model, the mass and stiffness matrices of which are typically found using a conventional FE package. This is in contrast to the most popular previous waveguide/FE approach, sometimes termed the spectral finite element approach, which requires new spectral element matrices to be developed. In the approach described here, a section of the waveguide is modeled using conventional FE software and the dynamic stiffness matrix formed. A periodicity condition is applied, the wavenumbers following from the eigensolution of the resulting transfer matrix. The method is described, estimation of wavenumbers, energy, and group velocity discussed, and numerical examples presented. These concern wave propagation in a beam and a simply supported plate strip, for which analytical solutions exist, and the more complex case of a viscoelastic laminate, which involves postprocessing an ANSYS FE model. The method is seen to yield accurate results for the wavenumbers and group velocities of both propagating and evanescent waves.
 [DOI: 10.1121/1.1887126]

PACS numbers: 43.40.−r, 43.20.Bi, 43.40.Cw, 43.20.Mv [PEB] Pages: 2835–2843

I. INTRODUCTION

Knowledge of the wave propagation characteristics of a structure is of great value. This is particularly true at higher frequencies, where finite element analysis (FEA) models of the structure as a whole become impractically large. Wave approaches can then be used to predict the propagation of disturbances, the transmission of energy or the acoustic radiation from the structure. Methods such as statistical energy analysis also require knowledge of wavenumber, group velocity, wave attenuation, modal density, and so on.

Many structural components can be regarded as uniform waveguides: they are uniform in one direction, along the axis x of the waveguide, so that the cross-section of the waveguide has the same physical and geometric properties at all points along the waveguide's axis. Waves propagate in both directions along the waveguide, having a characteristic shape across the cross-section. The cross-section might be zero-, one-, or two-dimensional with the motion over the cross-section being a function of zero, one, or two coordinates. Examples are: a rod undergoing axial vibration, a beam in bending or a thin, infinite, isotropic medium [zero-dimensional cross-section: the displacement $u(x)$ is a function only of x]; a plate strip of uniform width in bending or a cross-section of a laminated solid [one-dimensional cross-section, $u=u(x,y)$]; a rail track, an extruded section, or an acoustic duct [two dimensional, $u=u(x,y,z)$]. Examples are shown in Fig. 1. For the tyre shown in Fig. 1(c) the axis is circular rather than a straight line, and the cross-section might be modeled as one or two dimensional (i.e., a shell or a solid) as the analyst chooses.

Simple waveguides (e.g., rods, beams, a plate strip with simply supported edges, rectangular acoustic ducts) are amenable to exact analysis (e.g., Graff[1]), with analytical expressions being available for the wavenumber, group velocity, etc., at frequency ω. For more complex examples an approximate solution might be sought, and it is here that FEA can play a useful role. Perhaps the most common approach is the ''spectral finite element'' (SFE) method.[2–8] The displacement field $u(x,y,z,t)$ at frequency ω is assumed to be separable into the form $u(x,y,z,t)=\phi(y,z)v(x)\exp(i\omega t)$. The cross-section, which lies in the (y,z) plane, is then meshed in a manner analogous to conventional FEA so that $\phi(y,z)$ is approximated by chosen shape functions. Vibrational formulations are used to write the equations of motion in the form

$$\sum_n \mathbf{K}_n \frac{\partial^n \mathbf{v}}{\partial x^n} - \omega^2 \mathbf{M}\mathbf{v} = 0, \tag{1}$$

where $\mathbf{K}_n$ and $\mathbf{M}$ are stiffness and mass matrices. The solution for free vibration (i.e., free wave propagation) is then of the form $\mathbf{v}(x)=\mathbf{V}\exp(-ikx)$, where k is the wavenumber

a)Electronic mail: brm@isvr.soton.ac.uk

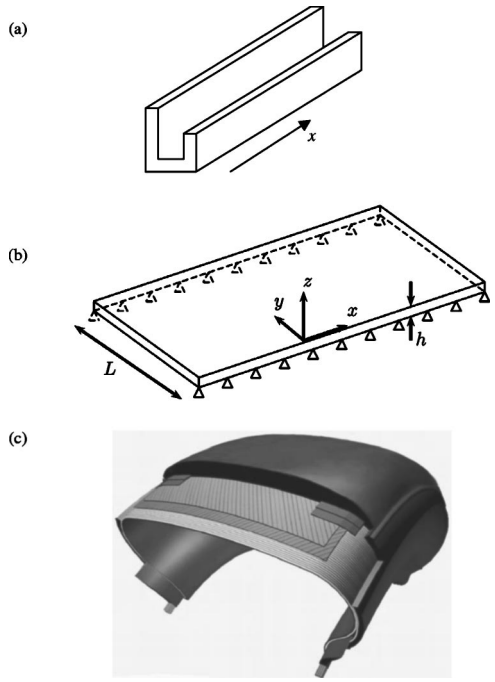

FIG. 1. Structural waveguides: (a) beam (arbitrary cross-section); (b) simply supported plate strip; (c) tyre.

and is, in general, complex. In some papers (e.g., Refs. 2 and 4) it is explicitly assumed at the outset that the motion along the waveguide is of the form $\exp(-ikx)$.

Wave propagation is consequently described by solutions to the polynomial eigenproblem

$$\sum_n \mathbf{K}_n(-ik)^n\mathbf{V}-\omega^2\mathbf{M}\mathbf{V}=0 \tag{2}$$

with $\mathbf{K}_n$ and $\mathbf{M}$ being the mass and stiffness matrices for the ''spectral'' element appropriate for the assumed wavenumber and frequency. The eigenvalues lead to the dispersion relation, while the eigenvectors describe the shape of the corresponding wave across the cross-section. Applications include rail tracks,[2] fluid-filled pipes,[3] and viscoelastic laminates,[4] while Finnveden[5] reviews the method and gives further applications and presents two applications,[6] with the emphasis being placed on the estimation of group velocity and modal density. Birgersson[7] considers the response to harmonic and random excitation.

The spectral finite element requires new, spectral stiffness matrices to be developed on a case-by-case basis, and this can be a not-insignificant task. In this paper an alternative waveguide-FE (WFE) approach is presented. In broad terms the spectral matrices follow from postprocessing the matrices produced by FEA of a short section of the waveguide, typically using a conventional FE package and existing element matrices. The method was developed[9] with particular reference to the formulation of relatively small FE models of large but finite structures and the computation of their forced response. Here the approach is applied to the prediction of the wave propagation characteristics of the waveguide. A section of the waveguide, typically, but not necessarily, one element long, is modeled using conventional FE methods, using perhaps a commercial FE package. The resulting mass, stiffness, and damping matrices are then postprocessed. A periodicity condition[10] and the periodic structure/FE method of Abdel-Rahman[11] are applied to the section, although the length of the spatial periodicity is of course arbitrary. An eigenvalue problem then yields the dispersion relation. Further computational aspects are discussed in Duhamel *et al.*[9]

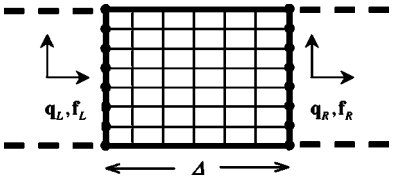

FIG. 2. FE mesh of section of waveguide.

The advantages of this waveguide/FE approach over the SFE approach include the fact that no new elements need be developed, the full power of existing element libraries can be harnessed, commercial packages can be used, and their outputs merely postprocessed. Damping and complex stiffness matrices can be included straightforwardly and real or complex solutions for k at any given ω can be found equally.

Similar approaches have been described by Thompson[12] and, in different contexts, by Gry[13] and Zhang.[14] Applications of FEA to wave propagation and forced response of periodic structures are described by Abdel-Rahman,[11] while ''scale independent elements'' (e.g., Ref. 15) involve a similar approach to the calculation of the forced response of large, finite, uniform structures, the similarity arising from the philosophy of describing the motion in terms of wavelike terms which vary exponentially along the axis of the waveguide.

In Sec. II the waveguide finite element approach is described. The dynamic stiffness matrix of the section is found, partitioned, and rearranged to find the transfer matrix relating the nodal degrees of freedom (DOFs) and nodal forces on the two sides of the sections. Wave propagation is described by the eigenvalues and eigenvectors of this matrix. Section III concerns the estimation of energy, power and group velocity, while Sec. IV contains illustrative numerical examples. These include examples for which analytical solutions are known, and an application to wave propagation in a laminated solid. Some concluding remarks are then made. Further details and applications, together with issues concerning the forced response, can be found elsewhere.[9,16]

II. FINITE ELEMENT MODELING OF WAVEGUIDES

A. Finite element analysis of a section of the waveguide

Consider a structural waveguide whose properties are constant along the waveguide axis x. The cross-section of the waveguide may be zero, one, or two dimensional (e.g., for the cases of a beam, a plate strip, or an acoustic duct). The aim is to predict the characteristics of wave motion along the waveguide for harmonic motion at frequency ω, and in particular the wavenumbers and group velocities.

A section of axial length Δ is cut from the structure as indicated in Fig. 2. The section is now meshed, as in con-

ventional FEA, with the only additional constraint being that the nodes, DOFs, and their ordering on the left- and right-hand sides of the section are identical. Normally the length Δ will be equal to the length of one finite element in the x direction. The choice of Δ should then be made bearing in mind the same criteria as in conventional applications of FEA. For example, the length must not be too large compared to the shortest wavelength in the structure or else the accuracy of the model suffers. Typically the element should be about one-tenth of this wavelength or shorter. Nor must Δ be extremely small compared to the shortest wavelength of interest, or the accuracy again suffers because of numerical problems that can arise due to machine rounding errors.

Following a conventional FE analysis, the equation of motion of the section becomes

$$(\mathbf{K}+\mathrm{i}\omega\mathbf{C}-\omega^2\mathbf{M})\mathbf{q}=\mathbf{f}, \tag{3}$$

where $\mathbf{K}$, $\mathbf{M}$, and $\mathbf{C}$ are, respectively, the stiffness, mass, and damping matrices, $\mathbf{f}$ is the vector of nodal forces, and $\mathbf{q}$ the vector of the nodal DOFs. The dynamic stiffness matrix $\tilde{\mathbf{D}}=\mathbf{K}+\mathrm{i}\omega\mathbf{C}-\omega^2\mathbf{M}$ is now introduced, and the nodal forces and DOFs decomposed into sets associated with the right (R) and left (L) cross-section and interior (I) nodes. Of course, the FEA might be such that there are no internal DOFs. For the case where there are no external forces on the interior nodes, the equation of motion can be partitioned into

$$\begin{bmatrix} \tilde{\mathbf{D}}_{II} & \tilde{\mathbf{D}}_{IL} & \tilde{\mathbf{D}}_{IR} \\ \tilde{\mathbf{D}}_{LI} & \tilde{\mathbf{D}}_{LL} & \tilde{\mathbf{D}}_{LR} \\ \tilde{\mathbf{D}}_{RI} & \tilde{\mathbf{D}}_{RL} & \tilde{\mathbf{D}}_{RR} \end{bmatrix} \begin{bmatrix} \mathbf{q}_I \\ \mathbf{q}_L \\ \mathbf{q}_R \end{bmatrix} = \begin{bmatrix} \mathbf{0} \\ \mathbf{f}_L \\ \mathbf{f}_R \end{bmatrix}. \tag{4}$$

From the first line of Eq. (4) it follows that the interior degrees of freedom are given by

$$\mathbf{q}_I=-\tilde{\mathbf{D}}_{II}^{-1}(\tilde{\mathbf{D}}_{IL}\mathbf{q}_L+\tilde{\mathbf{D}}_{IR}\mathbf{q}_R). \tag{5}$$

The interior degrees of freedom can then be eliminated from Eq. (4). This leads to

$$\begin{bmatrix} \mathbf{D}_{LL} & \mathbf{D}_{LR} \\ \mathbf{D}_{RL} & \mathbf{D}_{RR} \end{bmatrix} \begin{bmatrix} \mathbf{q}_L \\ \mathbf{q}_R \end{bmatrix} = \begin{bmatrix} \mathbf{f}_L \\ \mathbf{f}_R \end{bmatrix}, \tag{6}$$

where the partitions of the dynamic stiffness matrix are

$$\begin{aligned} &\mathbf{D}_{LL}=\tilde{\mathbf{D}}_{LL}-\tilde{\mathbf{D}}_{LI}\tilde{\mathbf{D}}_{II}^{-1}\tilde{\mathbf{D}}_{IL}, \quad \mathbf{D}_{LR}=\tilde{\mathbf{D}}_{LR}-\tilde{\mathbf{D}}_{LI}\tilde{\mathbf{D}}_{II}^{-1}\tilde{\mathbf{D}}_{IR}, \\ &\mathbf{D}_{RL}=\tilde{\mathbf{D}}_{RL}-\tilde{\mathbf{D}}_{RI}\tilde{\mathbf{D}}_{II}^{-1}\tilde{\mathbf{D}}_{IL}, \quad \mathbf{D}_{RR}=\tilde{\mathbf{D}}_{RR}-\tilde{\mathbf{D}}_{RI}\tilde{\mathbf{D}}_{II}^{-1}\tilde{\mathbf{D}}_{IR}. \end{aligned} \tag{7}$$

Because the stiffness, damping, and mass matrices are symmetric, so, too, is the dynamic stiffness matrix. Hence

$$\mathbf{D}_{LL}^T=\mathbf{D}_{LL}, \quad \mathbf{D}_{RR}^T=\mathbf{D}_{RR}, \quad \mathbf{D}_{LR}^T=\mathbf{D}_{RL}, \tag{8}$$

where the superscript T indicates the transpose. Equation (6) forms the basis for the subsequent analysis of wave motion in the waveguide.

B. The transfer matrix of a section of the waveguide

Suppose that no external forces are applied to the structure, and that the waveguide is divided into a number of identical sections such as the one described in Sec. II A. From continuity of displacements and equilibrium of forces at the cross-section between sections s and $(s+1)$ it follows that

$$\mathbf{q}_L^{s+1}=\mathbf{q}_R^s, \quad \mathbf{f}_L^{s+1}=-\mathbf{f}_R^s, \tag{9}$$

where the meaning of the superscripts is obvious. The transfer matrix $\mathbf{T}$ relates the nodal displacements and forces in cross-sections s and $(s+1)$. This matrix is defined such that

$$\begin{bmatrix} \mathbf{q}_L^{s+1} \\ \mathbf{f}_L^{s+1} \end{bmatrix} = \mathbf{T} \begin{bmatrix} \mathbf{q}_L^s \\ \mathbf{f}_L^s \end{bmatrix}. \tag{10}$$

From Eqs. (6), (9), and (10) it follows that

$$\mathbf{T}=\begin{bmatrix} -\mathbf{D}_{LR}^{-1}\mathbf{D}_{LL} & \mathbf{D}_{LR}^{-1} \\ -\mathbf{D}_{RL}+\mathbf{D}_{RR}\mathbf{D}_{LR}^{-1}\mathbf{D}_{LL} & -\mathbf{D}_{RR}\mathbf{D}_{LR}^{-1} \end{bmatrix}. \tag{11}$$

The transfer matrix $\mathbf{T}$ depends only on the dynamic stiffness of one section of the waveguide.

C. Free wave propagation: Eigenanalysis of the transfer matrix

When a free wave propagates along the waveguide, the displacements and forces at successive cross-sections are such that

$$\begin{bmatrix} \mathbf{q}_L^{s+1} \\ \mathbf{f}_L^{s+1} \end{bmatrix} = \lambda \begin{bmatrix} \mathbf{q}_L^s \\ \mathbf{f}_L^s \end{bmatrix}. \tag{12}$$

Free wave propagation is thus described by the eigenproblem

$$\mathbf{T} \begin{bmatrix} \mathbf{q}_L^s \\ \mathbf{f}_L^s \end{bmatrix} = \lambda \begin{bmatrix} \mathbf{q}_L^s \\ \mathbf{f}_L^s \end{bmatrix}. \tag{13}$$

The $2n$ eigenvalues λ_j $(j=1,2,...2n)$ are related to the phase change (or decay) over the length of the cross-section Δ and the eigenvectors $\boldsymbol{\phi}_j$ indicate the shape of the motion over the cross-section. Here n is the number of nodal DOFs on each side of the cross-section.

The eigenvector can be partitioned into $n\times 1$ vectors associated with the nodal DOFs and nodal forces, i.e.,

$$\boldsymbol{\phi}_j=\begin{Bmatrix} \boldsymbol{\phi}_j^q \\ \boldsymbol{\phi}_j^f \end{Bmatrix}. \tag{14}$$

From the first row of Eq. (13) it can be shown that

$$\mathbf{f}_L=(\mathbf{D}_{LL}+\lambda\mathbf{D}_{LR})\mathbf{q}_L \tag{15}$$

and hence

$$\boldsymbol{\phi}_j^f=(\mathbf{D}_{LL}+\lambda_j\mathbf{D}_{LR})\boldsymbol{\phi}_j^q. \tag{16}$$

If λ_j is an eigenvalue then so, too, is $1/\lambda_j$. This follows by substituting Eq. (15) in the second row of Eq. (13) leading, after some manipulation, to the relation

$$\left(\mathbf{D}_{LL}+\mathbf{D}_{RR}+\lambda\mathbf{D}_{LR}+\frac{1}{\lambda}\mathbf{D}_{RL}\right)\mathbf{q}_L=0. \tag{17}$$

The result follows by taking the transpose of this equation and noting the symmetric properties of the dynamic stiffness matrices [Eq. (8)].

Henceforth the eigenvalues of $\mathbf{T}$ are defined such that

$$|\lambda_j| \leqslant 1,$$
$$\mathrm{Re}\{\mathbf{f}_L^H \dot{\mathbf{q}}_L\} = \mathrm{Re}\{\mathrm{i}\omega \mathbf{f}_L^H \mathbf{q}_L\} < 0 \quad \text{if } |\lambda_j| = 1. \tag{18}$$

The eigensolutions therefore come in two sets whose eigenvalues and eigenvectors are $(\lambda_j, \boldsymbol{\phi}_j^+)$ and $(1/\lambda_j, \boldsymbol{\phi}_j^-)$ and which represent n positive-going and n negative-going wave types, respectively. Equation (18) implies that either the amplitude of a wave decreases in the direction of propagation or that, if the amplitude remains constant, there is time average power transmission in the direction of propagation.

The jth eigenvalue can be written as

$$\lambda_j = e^{-\mathrm{i}k_j\Delta} = e^{-\mu_j\Delta} e^{-\mathrm{i}k_j'\Delta}, \tag{19}$$

where the wavenumber $k_j = k_j' - \mathrm{i}\mu_j$ may be complex and where μ_j and k_j' are real and equal to the attenuation and phase change per unit length that is associated with the jth wave type. By the definitions in Eq. (18) $\mu_j \geqslant 0$ and usually $k_j' \geqslant 0$ if $\mu_j = 0$. In the absence of damping those eigenvalues for which $|\lambda_j| = 1$ and hence $\lambda_j = e^{-\mathrm{i}k_j'\Delta}$ (i.e., for which $\mu_j = 0$), represent freely propagating waves with wavenumber k_j', while those for which λ_j is real (i.e., for which $k_j' = 0$) represent evanescent waves. Under certain circumstances there may be a pair of (complex conjugate) eigenvalues for which λ_j is complex and $|\lambda_j| < 1$: these represent decaying but oscillatory waves. In the presence of small levels of damping the dynamic stiffness matrix is complex. A wave type is then typically either a slowly decaying propagating wave or a rapidly attenuating, but slightly oscillatory, evanescent wave. Numerical results will usually be presented in terms of μ_j and k_j' or, equally, $\mathrm{Re}\{k_j\}$ and $\mathrm{Im}\{k_j\}$.

Propagation over a distance L is such that, for motion in the jth wave mode, the nodal displacements and forces at locations x and $x+L$ are related by

$$\mathbf{q}(x+L) = \lambda_j^{L/\Delta} \mathbf{q}(x), \quad \mathbf{f}(x+L) = \lambda_j^{L/\Delta} \mathbf{f}(x). \tag{20}$$

In general the motion is a sum of wave components of amplitudes $a_j^{\pm}$ so that

$$\begin{Bmatrix} \mathbf{q} \\ \mathbf{f} \end{Bmatrix} = \sum_{j=1}^{n} (a_j^+ \boldsymbol{\phi}_j^+ + a_j^- \boldsymbol{\phi}_j^-). \tag{21}$$

1. Numerical considerations

The numerical solution of the eigenvalue problem (13) or (17) is straightforward if the number of DOFs n is small. However, for large numbers of DOFs, typically for two-dimensional cross-sections, direct application of numerical solvers can lead to difficulties because $\mathbf{T}$ may be ill conditioned. (No such problems were encountered in the numerical examples reported in the following.) The ill-conditioning arises because $\mathbf{T}$ has both very large and very small eigenvalues. Normally the eigenvalues for which $|\lambda_j| \sim 1$ are of most interest, since these either propagate over a significant distance or at least do not attenuate very rapidly. The eigenvalues which have very small or very large magnitudes are of little interest as far as wave propagation is concerned, however, since they decay so rapidly with distance.

These numerical problems can be overcome, for example by reformulating the eigenvalue problem in terms of $(\lambda + 1/\lambda)$ as proposed by Gry[13] or, with more mathematical detail, by Zhong.[14] The eigenvalue problem can be put in the form

$$\begin{bmatrix} -\mathbf{D}_{RL} & -\mathbf{D}_{LL} - \mathbf{D}_{RR} \\ \mathbf{O} & -\mathbf{D}_{RL} \end{bmatrix} \begin{bmatrix} \mathbf{q}_L \\ \tilde{\mathbf{q}}_L \end{bmatrix} = \lambda \begin{bmatrix} \mathbf{0} & \mathbf{D}_{LR} \\ -\mathbf{D}_{RL} & \mathbf{0} \end{bmatrix} \begin{bmatrix} \mathbf{q}_L \\ \tilde{\mathbf{q}}_L \end{bmatrix}, \tag{22}$$

where $\tilde{\mathbf{q}}_L = \lambda \mathbf{q}_L$. Another form is

$$\begin{bmatrix} \mathbf{D}_{LR} & \mathbf{O} \\ \mathbf{D}_{LL} + \mathbf{D}_{RR} & \mathbf{D}_{LR} \end{bmatrix} \begin{bmatrix} \mathbf{q}_L \\ \tilde{\mathbf{q}}_L \end{bmatrix} = \frac{1}{\lambda} \begin{bmatrix} \mathbf{0} & \mathbf{D}_{LR} \\ -\mathbf{D}_{RL} & \mathbf{0} \end{bmatrix} \begin{bmatrix} \mathbf{q}_L \\ \tilde{\mathbf{q}}_L \end{bmatrix}. \tag{23}$$

Summing the above and rearranging gives

$$\begin{bmatrix} \mathbf{D}_{RL} & \mathbf{O} \\ \mathbf{O} & \mathbf{D}_{LR} \end{bmatrix} \begin{bmatrix} \mathbf{q}_L \\ \tilde{\mathbf{q}}_L \end{bmatrix} = \frac{1}{\lambda + \frac{1}{\lambda}} \begin{bmatrix} -(\mathbf{D}_{LL} + \mathbf{D}_{RR}) & -(\mathbf{D}_{LR} - \mathbf{D}_{RL}) \\ (\mathbf{D}_{LR} - \mathbf{D}_{RL}) & -(\mathbf{D}_{LL} + \mathbf{D}_{RR}) \end{bmatrix} \begin{bmatrix} \mathbf{q}_L \\ \tilde{\mathbf{q}}_L \end{bmatrix}. \tag{24}$$

This has only double eigenvalues.[9] Denoting two independent eigenvectors associated with the same eigenvalue of Eq. (24) as $\mathbf{w}_1$ and $\mathbf{w}_2$, the eigenvector associated with the eigenvalue λ can be written as

$$\mathbf{w} = \alpha_1 \mathbf{w}_1 + \alpha_2 \mathbf{w}_2. \tag{25}$$

Substituting this into Eq. (22) and taking the scalar product with the complex conjugate of $\mathbf{w}_1$ gives a relation between α_1 and α_2, and hence the eigenvector $\mathbf{w}$.

An alternative is to use a solver for polynomial eigenvalue problems. While this may be simpler, it does not provide any clear theoretical advantages over the preceding formulation.

2. Consequences of symmetry

The section of the waveguide analyzed is symmetric, so that certain relations follow for the positive and negative going wave pairs and for the dynamic stiffness matrices. The symmetric problem, which follows from the substitution $x' = -x$, is such that

$$\mathbf{q}_L^s = \mathbf{S}\mathbf{q}_R, \quad \mathbf{q}_R^s = \mathbf{S}\mathbf{q}_L, \quad \mathbf{f}_L^s = \mathbf{S}\mathbf{f}_R, \quad \mathbf{f}_R^s = \mathbf{S}\mathbf{f}_L, \tag{26}$$

where $\mathbf{S}$ is a diagonal matrix whose elements are ± 1 and hence is such that $\mathbf{S}^2 = \mathbf{I}$, where $\mathbf{I}$ is the identity matrix. The superscript s denotes variables for the symmetric problem. From this it can be shown that

$$\mathbf{D}_{LL} = \mathbf{S}\mathbf{D}_{RR}\mathbf{S}, \quad \mathbf{D}_{LR} = \mathbf{S}\mathbf{D}_{RL}\mathbf{S},$$
$$\mathbf{D}_{RL} = \mathbf{S}\mathbf{D}_{LR}\mathbf{S}, \quad \mathbf{D}_{RR} = \mathbf{S}\mathbf{D}_{LL}\mathbf{S}. \tag{27}$$

Substituting these expressions into Eq. (17) and premultiplying by $\mathbf{S}$ yields

$$\left(\mathbf{D}_{LL} + \mathbf{D}_{RR} + \frac{1}{\lambda}\mathbf{D}_{LR} + \lambda \mathbf{D}_{RL} \right) \mathbf{S}\mathbf{q}_L = 0, \tag{28}$$

whereas the eigenvalue problem was originally written as

$$\left(\mathbf{D}_{LL}+\mathbf{D}_{RR}+\lambda\mathbf{D}_{LR}+\frac{1}{\lambda}\mathbf{D}_{RL}\right)\mathbf{q}_L=0. \tag{29}$$

Thus it follows that the positive-going eigenvector $\boldsymbol{\phi}_j^+$ associated with the eigenvalue λ_j and the negative-going eigenvector $\boldsymbol{\phi}_j^-$ associated with the eigenvalue $1/\lambda_j$ are symmetric partners, so that

$$\boldsymbol{\phi}_j^-=\mathbf{S}\boldsymbol{\phi}_j^+, \quad \boldsymbol{\phi}_j^+=\mathbf{S}\boldsymbol{\phi}_j^-. \tag{30}$$

3. The left eigenproblem

The left eigenproblem $\boldsymbol{\psi}_j\mathbf{T}=\lambda_j\boldsymbol{\psi}_j$ has the same eigenvalues as the right eigenproblem, while the left and right eigenvectors are orthogonal, i.e.,

$$\boldsymbol{\psi}_i\boldsymbol{\phi}_j=0, \quad i\neq j. \tag{31}$$

III. ENERGY, ENERGY DENSITY, POWER, AND GROUP VELOCITY

Energy-related quantities follow straightforwardly once the eigenproperties (wavenumbers and wave modes) are known. Consider the propagation of the jth wave mode, the eigenvector $\boldsymbol{\phi}_j$ for which is partitioned into vectors $\boldsymbol{\phi}_j^q$ and $\boldsymbol{\phi}_j^f$ corresponding to the nodal DOFs and nodal forces, respectively, as indicated in Eq. (14). Putting $\mathbf{q}=\boldsymbol{\phi}_j^q$ and $\mathbf{f}=\boldsymbol{\phi}_j^f$ for clarity, the time average kinetic and potential energy densities E_k and E_p (i.e., the energies per unit length) for the jth wave mode are

$$E_k=\frac{1}{4\Delta}\mathrm{Re}\{\dot{\mathbf{q}}^H\mathbf{M}\dot{\mathbf{q}}\}=-\frac{\omega^2}{4\Delta}\mathrm{Re}\{\mathbf{q}^H\mathbf{M}\mathbf{q}\},$$
$$E_p=\frac{1}{4\Delta}\mathrm{Re}\{\mathbf{q}^H\mathbf{K}\mathbf{q}\}, \tag{32}$$

where the superscript H denotes the Hermitian, or complex conjugate transpose. The total energy density is then

$$E_{\mathrm{tot}}=E_k+E_p. \tag{33}$$

As the wave propagates, so the time average power transmitted through the cross-section of the waveguide is

$$P=-\frac{1}{2}\mathrm{Re}\{\mathbf{f}^H\dot{\mathbf{q}}\}=\frac{\omega}{2}\mathrm{Im}\{\mathbf{f}^H\mathbf{q}\}. \tag{34}$$

The group velocity of the jth wave mode, which by definition is the speed at which energy is propagated, is therefore given by

$$c_g=\frac{P}{E_{\mathrm{tot}}}. \tag{35}$$

The dissipated power follows from the imaginary part of $\mathbf{K}$ and/or the damping matrix $\mathbf{C}$.

IV. NUMERICAL EXAMPLES

In this section three numerical examples are considered. The first, a beam, is a simple demonstration of the method. An analytical solution also exists for the wavenumbers of the second example, a simply supported plate strip, while the viscoelastic laminate, which forms the last example, is an application where the method might be used in earnest.

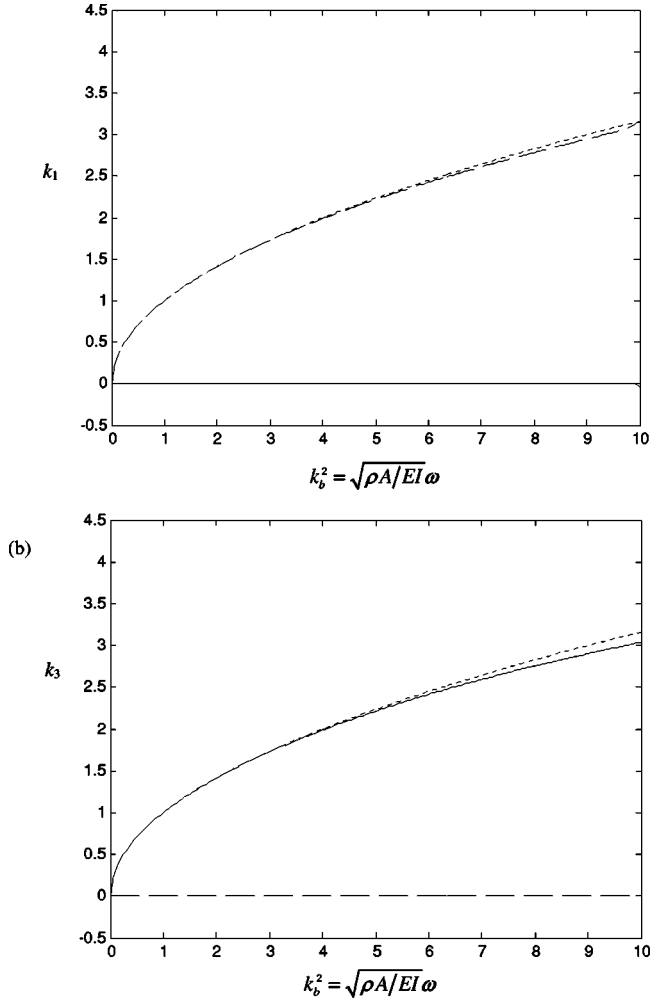

FIG. 3. Beam wavenumbers for (a) evanescent wave $k_1(\omega)$ and (b) propagating wave $k_3(\omega)$ as functions of $k_b^2=\sqrt{\rho A/EI}\omega$: — real part, --- imaginary part and $\cdots$ theoretical value k_b.

A. Uniform beam

Consider a uniform Euler–Bernoulli beam undergoing bending vibrations. The possible wavenumbers are $\pm k_b$, $\pm ik_b$ where

$$k_b=\sqrt[4]{\frac{\rho A\omega^2}{EI}} \tag{36}$$

and where EI is the bending stiffness. The waves form a pair of propagating waves and a pair of evanescent, or near field, waves.

An element of length l is now taken from the beam. There are two nodes and two DOFs at each node, displacement and rotation, and correspondingly two nodal forces, shear and bending moment. The element thus has four nodal DOFs in total. The stiffness and mass matrices for the element are[17]

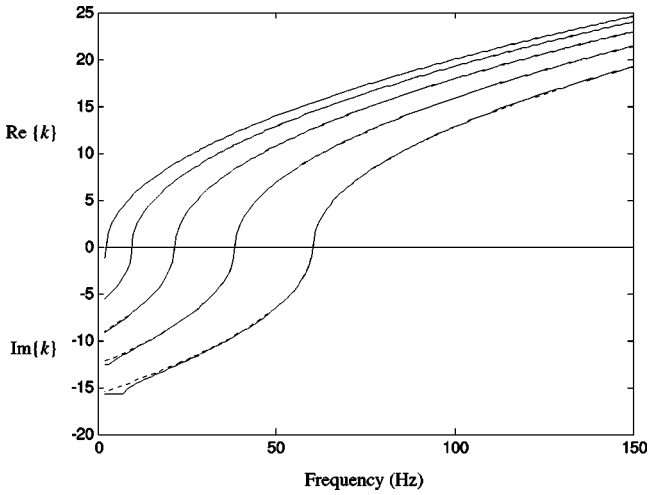

FIG. 4. Wavenumbers of the first five wave modes for simply supported plate strip: — FE, ⋯ theory [Eq. (41)]. Positive and negative values correspond to the real and imaginary parts of the wavenumbers, respectively.

$$\mathbf{K}=\frac{EI}{l^3}\begin{bmatrix} 12 & 6l & -12 & 6l \\ 6l & 4l^2 & -6l & 2l^2 \\ -12 & -6l & 12 & -6l \\ 6l & 2l^2 & -6l & 4l^2 \end{bmatrix},$$

$$\mathbf{M}=\frac{\rho Al}{420}\begin{bmatrix} 156 & 22l & 54 & -13l \\ 22l & 4l^2 & 13l & -3l^2 \\ 54 & 13l & 156 & -22l \\ -13l & -3l^2 & -22l & 4l^2 \end{bmatrix}. \tag{37}$$

Damping is neglected, although E could be complex. The analysis is straightforward but tedious.[15] The eigenvalues of the transfer matrix for the element are

$$\lambda_{1,2}=1\pm kl+\tfrac{1}{2}(kl)^2\pm\tfrac{1}{6}(kl)^3+\tfrac{1}{24}(kl)^4+O((kl)^5),$$
$$\lambda_{3,4}=1\pm ikl-\frac{1}{2}(kl)^2\mp\frac{i}{6}(kl)^3+\frac{1}{24}(kl)^4+O((kl)^5). \tag{38}$$

These expression are accurate to fourth-order terms in kl, with errors being of order $(kl)^5$. Predictions for the positive-going propagating and near field waves are shown in Fig. 3. Numerical estimates of the propagating wavenumbers from FEA are real, to within machine precision, so that FE modeling errors only produce phase errors in propagating wavenumbers, and not apparent damping, with the magnitudes of the eigenvalues being unity to within machine precision. These results are consistent with previous lumped-mass models[18] and with analysis of dispersion errors in FE models[19–21] and with results for a rod.[17–21]

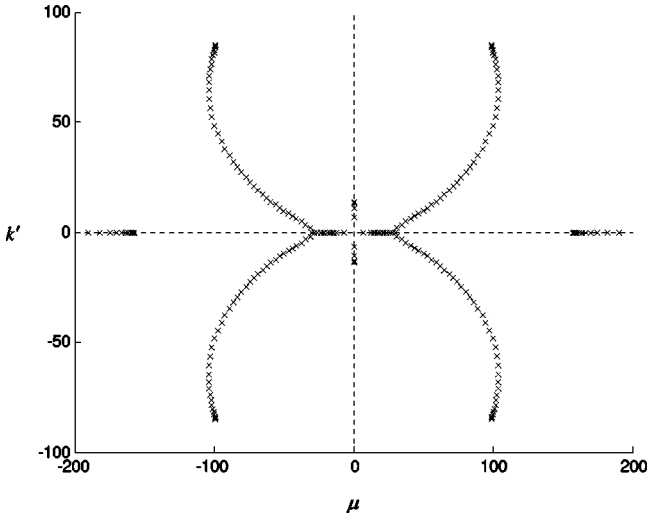

FIG. 5. Eigenvalues for plate strip in complex (μ,k') plane at 50 Hz.

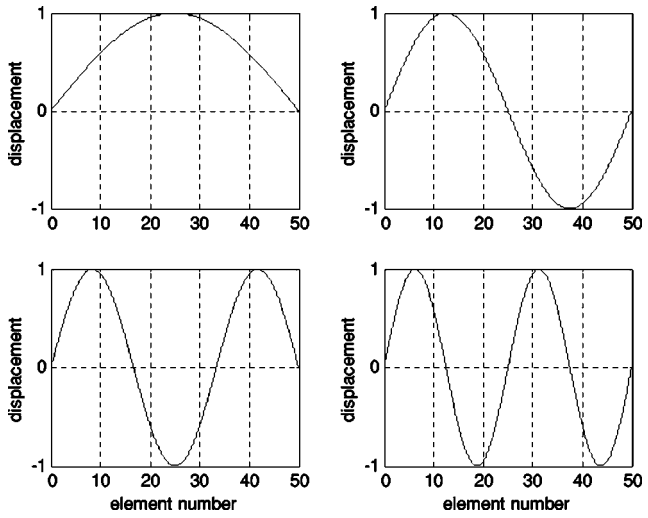

FIG. 6. Eigenvectors (transverse displacement only) for the first four wave modes at 50 Hz, wavenumbers=14, 13, 11, and 7 m^{-1}.

B. Simply supported plate strip

Consider now the thin plate strip shown in Fig. 1(b). The width L and thickness h of the plate are constant, and the edges are simply supported. In the absence of external forces, the equation of motion of the plate is

$$D\left(\frac{\partial^4 w}{\partial x^4}+2\frac{\partial^4 w}{\partial x^2\partial y^2}+\frac{\partial^4 w}{\partial y^4}\right)+\rho h\frac{\partial^2 w}{\partial t^2}=0, \tag{39}$$

where w is the transverse displacement and ρ and D are the density and bending stiffness, respectively.

For the particular boundary conditions along the edges of the plate ($w=0$; $\partial^2 w/\partial y^2=0$) waves exist with the displacement having a y dependence of the form $\sin(n\pi y/L)$; $n=1,2,3,\ldots$. The variation with x for the nth wave component is of the form $\exp(\pm ik_{p,n}x)$ or $\exp(\pm k_{e,n}x)$ where

$$k_{p,n}^2=k_p^2-\left(\frac{n\pi}{L}\right)^2,\quad k_{e,n}^2=k_p^2+\left(\frac{n\pi}{L}\right)^2. \tag{40}$$

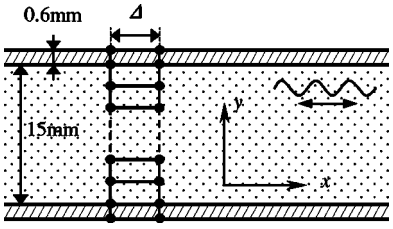

FIG. 7. Sandwich panel and FE mesh.

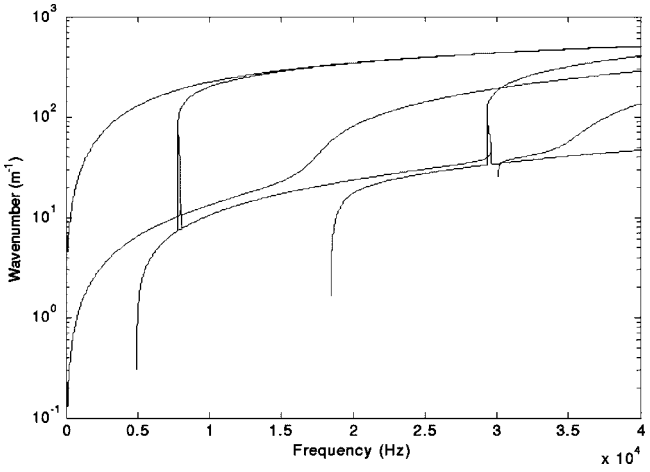

FIG. 8. Propagating wavenumbers of sandwich panel.

Here $k_p=\sqrt{\rho h\omega^2/D}$ is the free plate wavenumber. For frequencies for which $k_p>n\pi/L$ the wavenumber $k_{p,n}$ represents a propagating wave, while below that cut-off frequency it is evanescent. The wavenumber $k_{e,n}$ always represents an evanescent wave.

Numerical results are shown here for a steel plate ($E=2.1\times10^{11}$ Pa, $\rho=7.8\times10^3$ kg/m^3, $\nu=0.3$), 0.001 mm thick and of width 1 m. A strip of length 0.01 m was meshed in ANSYS using 50 rectangular shell elements. When the boundary conditions at the edges are applied and the DOFs associated with in-plane motion condensed, each cross-section has 149 DOFs, and hence 149 pairs of positive-going and negative-going waves are predicted. The vast majority of these are rapidly attenuating in the frequency ranges considered here.

Figure 4 shows the wavenumber k for the five lowest-order positive-going waves which propagate in the frequency range shown. Evanescent partners and negative-going waves are not shown. Each wave mode has a clear cut-off frequency below which $k=-i\mu$ is imaginary and negative, the wave being evanescent, and above which k is real (in the absence of damping), the wave thus propagating. Agreement with the analytic results is very good with differences only being noticeable at frequencies where μ is very large: the FE

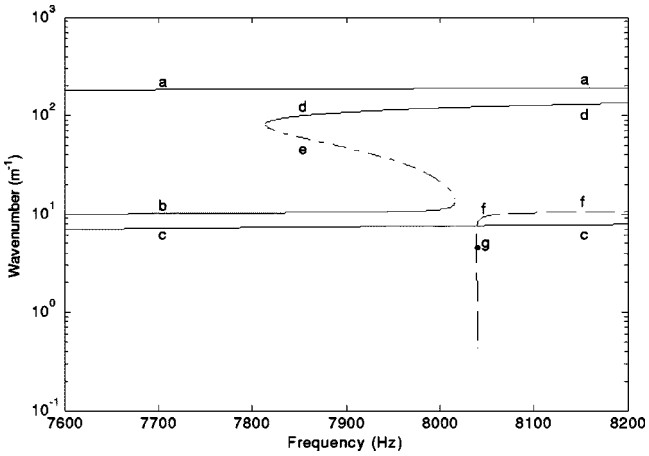

FIG. 9. Propagating wavenumbers and cut-off effects between 7600 and 8200 Hz.

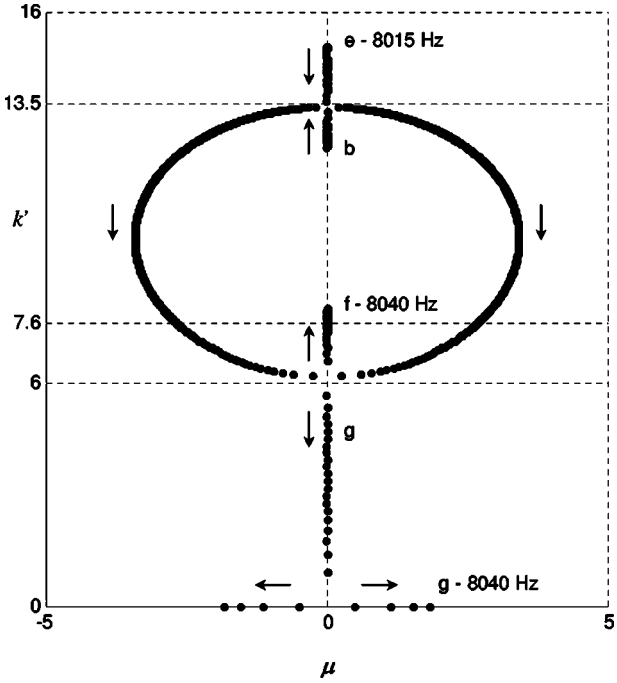

FIG. 10. Loci of eigenvalues of composite laminate in the complex (μ,k') plane from 8015 to 8040 Hz in steps of 0.02 Hz.

shape function cannot accurately model such rapidly attenuating waves. Figure 5 shows the wavenumbers $k=k'-i\mu$ at 50 Hz: there are four pairs of real wavenumbers (the propagating waves) plus many (145 pairs) which represent evanescent waves. Some of these are oscillatory (i.e., $k'\neq0$) and these eigenvalues come in complex conjugate pairs. Finally Fig. 6 shows the elements of the eigenvectors corresponding to out-of-plane displacements for the first four wave modes.

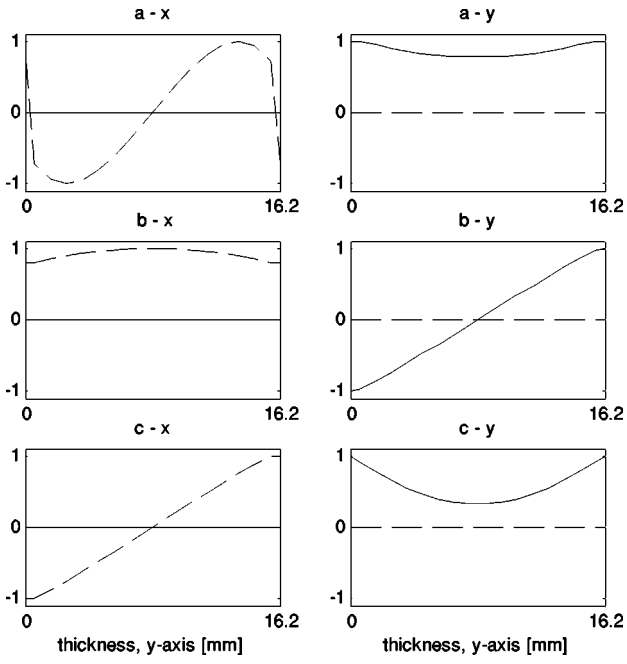

FIG. 11. Mode shapes of waves in composite laminate at 7000 Hz, wave modes *a*, *b*, and *c*. Displacements in the *x* and *y* directions across the cross-section are shown in the left- and right-hand columns, respectively.

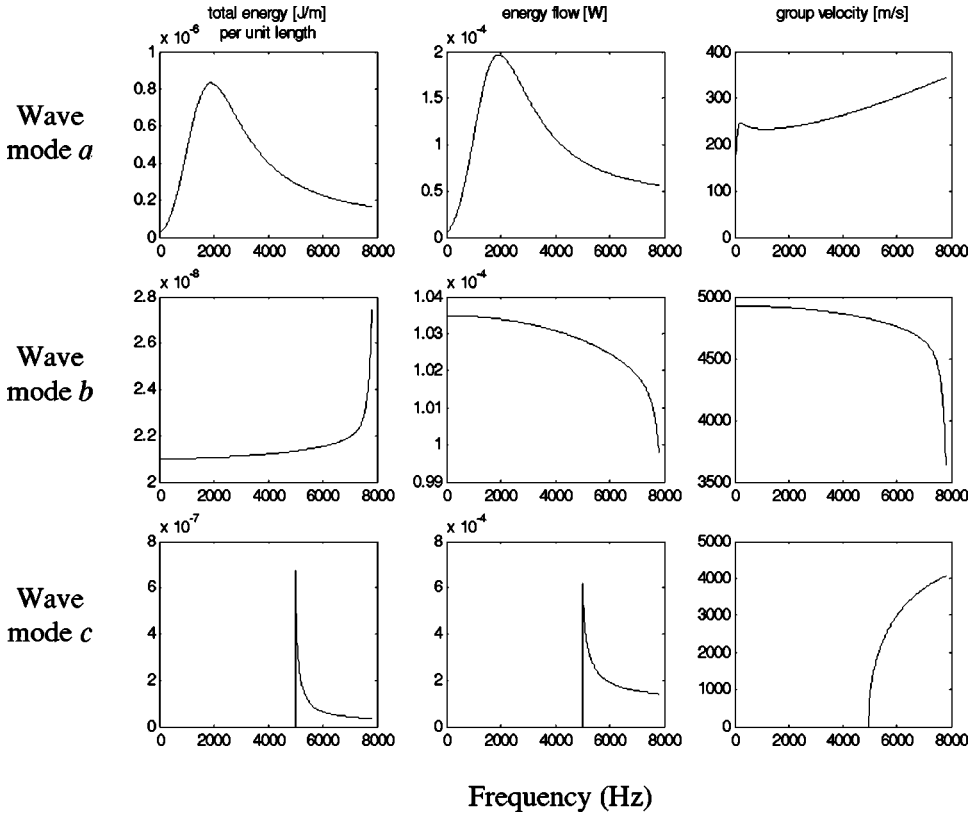

FIG. 12. Wave motion in composite laminate: energy per unit length, energy flow, and group velocity for wave modes *a*, *b*, and *c*.

These are real and have the form $\sin(n\pi y/L)$ as expected. Further results are given in Hinke *et al.*[16]

C. Viscoelastic laminate

The final example concerns a viscoelastic laminate, and is an application where the method might be used in earnest. The specific problem has been considered before[4] using the spectral FE method. Here, an ANSYS FE model was created and the resulting mass and stiffness matrices postprocessed using the above-described methods. Further details can be found in Hinke *et al.*[16]

A symmetric sandwich panel is shown in Fig. 7. The core and skins are 15- and 0.6-mm-thick, respectively. The core is isotropic with $E=3\times10^7$ Pa, $\rho=48$ kg/m^3, and $\nu=0.2$ while the skins are aluminum with $E=7.1\times10^{10}$ Pa, $\rho=2700$ kg/m^3, and $\nu=0.3296$. Damping is neglected here, but it is straightforward to include a complex elastic modulus, especially for the core. All wavenumbers are then complex. Figure 7 indicates the FE mesh of the cross-section that was used. Rectangular plane strain elements were used, one each to mesh the skins and 15 to mesh the core, giving a total of 17 elements. The elements have two nodal degrees of freedom, displacement in the x and y directions. The motion in the (x,y) plane (e.g., bending and axial extension) is thus modeled. The length of the meshed region was $\Delta=0.001$ m, which gives good accuracy for wavenumbers up to about $k=1000$/m.

Example wavenumbers are shown in Fig. 8. Below 5 kHz two propagating waves exist, these broadly being extensional and bending waves of the plate. Further propagating waves cut off at 5, 8, 18, and 26 kHz and involve higher order modes across the thickness of the sandwich panel. There are also complex cut-off effects. For example, Fig. 9 shows the dispersion curves between 7.6 and 8.2 kHz while Fig. 10 shows the loci of two of the eigenvalues in the complex k plane in the frequency range between 8015 and 8040 Hz.

Above 5 kHz three waves (a,b,c) exist. Their mode shapes (x and y displacements) at 7 kHz are shown in Fig. 11. They can broadly be interpreted as (*a*) a core-bending wave with the skins bending in anti-phase to the core, (*b*) an axial wave, with some lateral Poisson contraction, and (*c*) a bending wave with core and skins bending in-phase. Figure 12 shows the energies and group velocities of these wave modes. Mode *c* cuts-off at about 5 kHz. At 7810 Hz two waves (d,e) cut on with the same finite, nonzero wavenumber. While the wavenumber of wave *d* increases, that of *e* decreases, which means that the wave has a negative group velocity. Therefore it is a wave carrying energy in the negative x direction, but with a positive wavenumber. The motion thus somewhat resembles a Michael Jackson "Moonwalk:"[22] it goes forward but moves backwards. At 8016 Hz a bifurcation occurs: the wavenumbers of waves *e* and *b* are equal and both waves become attenuating waves and no longer propagate. At 8039 Hz, two more waves *f* and *g* cut on with the same nonzero wavenumber. While wave *g* only seems to be a propagating wave over a frequency range of 1–2 Hz, wave *f* continues to propagate over a wide frequency range and with an increasing wavenumber.

V. CONCLUDING REMARKS

This paper has presented a WFE method for the prediction of wavenumbers and group velocities for one-dimensional structural waveguides using finite element

analysis. The waveguide must be uniform along its axis, but the cross-section may be zero, one, or two-dimensional. The method involves FEA of a short section of the waveguide, typically one element long, evaluation of the dynamics stiffness matrix and transfer matrix of this section and a subsequent eigenanalysis. The eigenvalues yield the wavenumbers, which may be real, imaginary, or occur in complex conjugate pairs. Group velocities, powers, and energies can be found straightforwardly from the eigenvectors. Numerical examples were presented.

The method involves postprocessing mass and stiffness (and damping, if relevant) matrices which are found using conventional FE approaches. Thus the output of a conventional FE package can be used. This contrasts with the more commonly used approach, the SFE method, in which new, spectral stiffness and mass matrices must be developed. The advantages of the WFE approach include the fact that no new elements need be developed, so that the full power of existing element libraries and commercial packages can be harnessed, and the output merely postprocessed. Furthermore, the WFE approach also predicts imaginary and complex conjugate wavenumbers as well as the real wavenumbers that represent propagating waves. Thus it is straightforward to include damping, for which the dynamic stiffness matrix is complex.

The accuracy of the WFE method is comparable to, but somewhat less than, that of the SFE approach, since the latter requires no approximation in the x direction. For one- and two-dimensional cross-sections the accuracy difference might be quite small, however, since both approaches require a mesh across the cross-section, which hence involves FE discretization and approximation errors. In any event, accuracy can of course be improved by refining the mesh. The choice of the element size should be made using the same criteria as in conventional applications of FEA.

[1] K. F. Graff, *Wave Motion in Elastic Solids* (Dover, New York, 1975).
[2] L. Gavric, ''Computation of propagative waves in free rail using a finite element technique,'' J. Sound Vib. **185**, 531–543 (1995).
[3] S. Finnveden, ''Spectral finite element analysis of the vibration of straight fluid-filled pipes with flanges,'' J. Sound Vib. **199**, 125–154 (1997).
[4] P. J. Shorter, ''Wave propagation and damping in linear viscoelastic laminates,'' J. Acoust. Soc. Am. **115**, 1917–1925 (2004).
[5] S. Finnveden, ''Finite element techniques for the evaluation of energy flow parameters,'' Proceedings Novem, Lyon, 2000.
[6] S. Finnveden, ''Evaluation of modal density and group velocity by a finite element method,'' J. Sound Vib. **273**, 51–75 (2004).
[7] F. Birgersson, ''Prediction of random vibration using spectral methods,'' Ph.D. thesis, KTH, Stockholm, Sweden, 2004.
[8] C.-M. Nilsson, ''Waveguide finite elements applied on a car tyre,'' Ph.D. thesis, KTH, Stockholm, Sweden, 2004.
[9] D. Duhamel, B. R. Mace, and M. J. Brennan, ''Finite element analysis of the vibrations of waveguides and periodic structures,'' ISVR Tech. Memo. No. 922, 2003.
[10] D. J. Mead, ''Wave propagation and natural modes in periodic systems. II. Multi-coupled systems, with and without damping,'' J. Sound Vib. **40**, 19–39 (1975).
[11] A. Y. A. Abdel-Rahman, ''Matrix analysis of wave propagation in periodic systems,'' Ph.D. thesis, University of Southampton, 1979.
[12] D. J. Thompson, ''Wheel-rail noise generation. III. Rail vibration,'' J. Sound Vib. **161**, 421–446 (1993).
[13] L. Gry and C. Gontier, ''Dynamic modelling of railway track: A periodic model on a generalized beam formulation,'' J. Sound Vib. **199**, 531–558 (1997).
[14] W. X. Zhong and F. W. Williams, ''On the direct solution of wave propagation for repetitive structures,'' J. Sound Vib. **181**, 485–501 (1995).
[15] M. M. Ettounay, R. P. Daddazio, and N. N. Abboud, ''Some practical applications of the use of scale independent elements for dynamic analysis of vibrating systems,'' Comput. Struct. **65**, 423–432 (1997).
[16] L. Hinke, B. R. Mace, and M. J. Brennan, ''Finite element analysis of waveguides,'' ISVR Tech. Memo. No. 932 (2004).
[17] M. Petyt, *Introduction to Finite Element Vibration Analysis* (Cambridge University Press, New York, 1990).
[18] T. Belytschko and W. L. Mindle, ''Flexural wave propagation behavior of lumped mass approximations,'' Comput. Struct. **12**, 805–812 (1980).
[19] I. Babuska, F. Ihlenburg, T. Strouboulis, and S. K. Gangaraj, ''*A posteriori* error estimation for finite element solutions of Helmholtz' equation. I. The quality of local indicators and estimators,'' Int. J. Numer. Methods Eng. **40**, 3443–3462 (1997).
[20] I. Babuska, F. Ihlenburg, T. Strouboulis, and S. K. Gangaraj, ''*A posteriori* error estimation for finite element solutions of Helmholtz' equation. II. Estimation of the pollution error,'' Int. J. Numer. Methods Eng. **40**, 3883–3900 (1997).
[21] M. Ainsworth, ''Discrete dispersion relation for hp-version finite element approximation at high wavenumber,'' SIAM (Soc. Ind. Appl. Math.) J. Numer. Anal. **42**, 553–575 (2004).
[22] Michael Jackson, Thriller, Billie-Jean mini-video, Epic, 1982.

A categorization method applied to the study of urban road traffic noise

Juan Miguel Barrigón Morillas,[a] Valentín Gómez Escobar, Juan Antonio Méndez Sierra, Rosendo Vílchez-Gómez, and José M. Vaquero
Departamento de Física, E. Politécnica, Universidad de Extremadura, Avda. de la Universidad s/n, 10071 Cáceres, Spain

José Trujillo Carmona
Departamento de Matemáticas, F. Ciencias, Universidad de Extremadura, Avda. de Elvas s/n, 06071 Badajoz, Spain

(Received 8 August 2003; accepted for publication 23 February 2005)

The present work summarizes a study of the hypothesis that urban noise can be stratified by measuring street noise according to a prior classification of a town's streets according to their use in communicating the different zones of the town. The method was applied to five medium-sized Spanish towns (Vitoria-Gasteiz, Salamanca, Badajoz, Cáceres, and Mérida) with populations ranging from 218 000 down to 50 000 and with different socio-economic characteristics, climate, etc. As the initial hypothesis of the work was that traffic is the main source of urban noise and is also the principal cause of the variability of the sound levels measured in urban settings, the study focused only on the five nonpedestrian categories of streets. The continuous equivalent sound level (L_{eq}) was employed in the statistical analysis as it is commonly used as a general noise index, and other noise indicators such as L_{DN} or L_{DEN} are calculated from it. It was found that, although differences between the medians were not statistically significant in some of the towns for certain pairs of adjacent categories, the differences between pairs of nonadjacent categories were always significant, indicative of the stratification of noise in these five towns. Further studies on other medium-sized towns and on large towns and small villages would be needed to test whether the present definition of street categories is extensible elsewhere without modification. [DOI: 10.1121/1.1889437]

PACS numbers: 43.50.Rq, 43.50.Lj [DKW] Pages: 2844–2852

I. INTRODUCTION

Although there can be no doubt about the many advantages that the technological revolution has brought to human livelihood, not everything has been beneficial. Contamination of the environment is one of the most relevant problems associated with technological advance. One major kind of contamination is noise pollution, which is a notable annoyance in our daily lives and a potential health risk. Noise pollution hence needs to be characterized and, in as far as possible, minimized. Several studies have been carried out over the last decades in different towns around the world. They have focused either simultaneously (Fidell, 1978; Brown and Lam, 1987) or individually on some of the interesting characteristics of noise, such as its sources (Kumar and Jain, 1994), pollution levels (García and Faus, 1991; Chakrabarty *et al.*, 1997; Saadu *et al.*, 1998), exposure (Miedema and Vos, 1998; Job, 1988; Heinonen-Guzejev *et al.*, 2000), physiological and psychological effects (Fields, 1993, Fidell *et al.*, 1995, Ouis, 2001; Öhrström, 2004), etc.

There are different strategies for studying environmental noise in a town. Brown and Lam (1987) give an extensive review. The method that has long been most commonly used is to select sampling points by laying a grid over a map of the target zone. A review of several studies using this method is given by Brown and Lam (1987). More recent studies can be found elsewhere (Zannin *et al.*, 2001, 2002; Sommerhoff *et al.*, 2004). This strategy, though interesting, has some drawbacks. For example, the validity of the conclusions is strongly dependent on the size of the grid, and there are heavy demands made on time, equipment, and other resources. Studies using this method carried out by our research group have shown that even small grid sizes do not allow a reasonable explanation of the noise distribution to be found (Barrigón Morillas *et al.*, 2002a). Other drawbacks of this method are the difficulty in calculating the percentage of citizens exposed to a given noise level, and that any future reorganization of traffic flow in the town can significantly affect the noise map that is obtained so that, since the strategy is of no help in foreseeing the effects of such changes, the current noise map will become worthless. An alternative group of methods selects the sampling points using a prior classification of the urban noise by neighbourhoods (Glaser and Silver, 1979), uses by zones (Broderson *et al.*, 1981; Chakrabarty *et al.*, 1997), town planning characteristics (Cannelli, 1974), etc. As indicated by Brown and Lam, while strategies of this type involve fewer measurements, ''categorization of land use for noise surveys can only be used if categories are surrogates for measures of the location and intensities of roadway sources'' (Brown and Lam, 1987). Accepting this caveat, our research group has been studying a categorization method for the analysis of noise in towns

[a]Electronic mail: barrigon@unex.es

 0001-4966/2005/117(5)/2844/9/$22.50

which consists of classifying the streets according to their use in communicating different zones of the town.

Underlying the proposed method is the generally accepted assumption that traffic is the most important of the different sources of town noise. Furthermore, given the well-known relationship between the continuous equivalent sound level (L_{eq}) and the logarithm of the traffic flow (Q) that is usually found in urban noise studies, traffic can also be considered to be the main reason for the spatial variability of noise. We therefore formulate the hypothesis that this variability leads to a stratification of the noise over the entire town, and study this stratification by means of categories of streets based on their use in communicating the different zones of a town.

If the proposed hypothesis is satisfied and the method is applied properly, some important advantages accrue. First, fewer measurements are needed to characterize the noise levels over the entire town. Second, while possible future reorganization of traffic flow may mean that a street is reassigned to a different category, the new noise distribution can be easily estimated. Third, it is easier to calculate the percentage of citizens exposed to a given noise level than with the grid method.

The proposed method can be described as consisting of the following six steps. (1) Define the categories as objectively as possible (a small number of categories is desirable). (2) Assign the towns' streets to these categories. (3) Select the sampling points (several for each category); as will be described below, we used a random method of selection over the entire street length of each category. (4) Decide on the sampling schedule: the number of measurements to be made at each sampling point, the hour-of-day interval for sampling, and the sampling time. (5) Carry out the sampling. (6) Interpret the results, and verify the initial hypothesis. To the best of our knowledge, the method proposed and studied in this work is novel.

Step 1, and perhaps the main challenge of the method, is to arrive at an adequate definition of the categories. In order to minimize the number of variables involved (some of them very difficult to control), it seemed reasonable to focus the test of the method on towns that were similar in size. In particular, we chose to study five medium-sized towns in Spain which, despite their similarity in size, differ clearly in urban layout, life-style (which is closely related to geographical location and hence climate), industrialization, number of tourists, etc. Preliminary studies of three of these towns (Barrigón Morillas *et al.*, 2000a, b, 2002b) served to adapt and optimize the definition of the categories. The final definition that was established (Gómez Escobar *et al.*, 2002) consists of six categories. Five of these categories correspond to streets with traffic and one to pedestrian-only streets. The definition of these categories will be given below. Since the initial hypothesis to test in the present work is that traffic is both the main source of urban noise and the main cause of the variability of street sound levels, the study only considered the five nonpedestrian categories.

Section II describes the method and the five Spanish towns in which it was applied (Vitoria-Gasteiz, Salamanca, Badajoz, Cáceres, and Mérida). Section III presents and discusses the results; some of the statistical results were obtained from nonparametric tests, as was appropriate given the nonadditive nature of the sound levels. Finally, Sec. IV presents the most important conclusions.

II. METHODS

A. Categorization

The level and the variability of urban noise is known to be due principally to variations in traffic flow. There are also other minor factors involved: the type of traffic, vehicle speed, road width, the height of buildings, etc. In this sense, it could be useful in urban noise studies to stratify the noise on the basis of categories that take this variability into account, especially if it is found that the same categories are applicable at least to some group of similar towns.

Traffic flow is implicit in the definition of the categories used in the present work, even though it does not appear explicitly. While the other factors mentioned above were not explicitly included in the definition because this would have led to an excessive number of categories, they either are implicit at least in part (e.g., vehicle speeds and traffic type, and partially the width of the street) or will be included as an averaged effect in the statistical study (e.g., the heights of the buildings).

As a result of previous work on the stratification of noise in medium-sized towns, the following small group of categories was established, based on how the streets are used in communicating the different zones of a town:

Type 1 comprises those preferential streets whose function is to form a connection with other Spanish towns (national roads for the five towns studied) and to interconnect those preferential streets (in general, the indication of this latter type of street is its system of road signs).

Type 2 comprises those streets that provide access to the major distribution nodes of the town. For the purpose of this study, a distribution node is considered to exist when at least four major streets meet. This definition does not include any possible nodes of preferential streets as defined in type 1 above. This category also includes the streets normally used as an alternative to type 1 in case of traffic saturation.

Type 3 comprises the streets that lead to regional roads, streets that provide access from those of types 1 and 2 to centers of interest in the town (hospitals, shopping malls, etc.), and streets that clearly allow communication between streets of types 1 and 2.

Type 4 comprises all other streets that clearly allow communication between the three previously defined types of street, and the principal streets of the different districts of the town that were not included in the previously defined categories.

Type 5 comprises the rest of the streets of the town except pedestrian-only streets.

Type 6 comprises all the pedestrian-only streets. Since the assumption behind the present method of street categorization is that traffic is the most important source of noise pollution, this category was not included in the statistical study.

As can be seen, the definition of the categories includes

FIG. 1. Location of the five Spanish towns studied.

no explicit consideration of traffic flow or any characteristics of the streets (architecture, zoning, etc.) except how they are used for the movement of vehicles inside the town. One would indeed expect that with this definition of categories—except perhaps for categories 1 and 2—the higher the index of the category a street belongs to, the fewer vehicles using it, and hence the lighter the traffic flow.

All of each town's streets were assigned to one of the above categories, with sometimes different sections of the same street having to be assigned to different categories. The procedure used for this assignation was first to make a putative but objective categorization on the basis of the town map, and then to confirm or modify this assignation by visiting the town and talking with the inhabitants. This second stage was necessary because the categorization of the streets requires a detailed and in-depth knowledge of their real use, traffic restrictions, maintenance, etc.

B. The towns studied

Five towns were studied, located in different areas of Spain (Fig. 1). These towns have very different characteristics with respect to their industrial development, socioeconomic situation, zoning, meteorological conditions, and so on. The following is a brief overview of their characteristics. The meteorological data are averages for 1971 to 2000 (Instituto Nacional de Meteorología, 2001).

Vitoria-Gasteiz is approximately 22 km^2 in area and has 218 000 inhabitants. It is the second most populous town and the administrative capital of the Basque Region. It has an important industrial center, and its urban plan is conditioned by the presence of a historic zone, dating from mediaeval times. The mean temperature and rainfall are 11.5 °C and 779 mm, respectively.

Salamanca is approximately 16 km^2 in area and has 160 000 inhabitants, although this number increases during the academic year (from September to July) due to the presence of its many university students. There are also many visiting tourists throughout the year. Its altitude is 800 m above sea level. It is a UNESCO World Heritage site, with a clearly distinguishable historic part and a modern area that can be divided into several zones. The mean temperature and rainfall are 11.7 °C and 382 mm, respectively.

Badajoz is approximately 17 km^2 in area and has 140 000 inhabitants. It is on the border with Portugal and is an important commercial center in the Region of Extremadura. The mean temperature and rainfall are 16.6 °C and 463 mm, respectively.

Cáceres is approximately 10 km^2 in area and has 81 000 inhabitants, with significant increases due to tourists and students of the University of Extremadura. It is a UNESCO World Heritage site, and the need to conserve the historic part of the town has greatly influenced urban development, including the width and conformation of almost all the town's streets. The mean temperature and rainfall are 16.1 °C and 523 mm, respectively.

Mérida is nearly 7 km^2 in area and has 50 000 inhabitants. It is a UNESCO World Heritage site, and, as it was an important Roman administrative center in the past, its urban plan is conditioned by the presence of the many remains of the original Roman town. At present it is again the region's administrative center, which, together with the great number of visiting tourists, implies an major influx of people added to the permanent inhabitants. The mean temperature and rainfall are 16.9 °C and 473.6 mm, respectively.

C. Sampling point selection

For the selection of sampling points, first the total street length corresponding to each category was determined. Then a pseudo-random sequence was used to choose different sampling points along the total length of each category, and the points were located on the map. Equivalent points (two points were considered to be equivalent if they were located on the same section of street with no intersection between them) were discarded, and a new selection was made. With this protocol, all points in a given category had the same probability of being chosen; in particular, the longer the street, the more likely that one of its points would be sampled.

This selection method avoids the negative effects of other methods that use an arbitrary selection of sampling points which may lead to the noisiest points being chosen, thereby introducing a bias into the results (Mochizuki and Imaizumi, 1967).

The numbers of sampling points for each town are listed in Table I. In Cáceres and Badajoz, the number of sampling points for each category was not uniform as these two towns had been studied in the preliminary trials used to establish the final category definition. In the other towns, a similar number of sampling points was chosen for each category (although Vitoria-Gasteiz had also been studied in the preliminary trials, after the final category definition had been established, the town was studied again, with none of the old measurements being used). In Mérida and Vitoria-Gasteiz, ten sampling points were used for each category, and in Salamanca sometimes more than ten for operational reasons. In Cáceres and Badajoz, which had formed part of the preliminary studies, more measurements were made per sampling

TABLE I. Sampling points taken for the first five categories of the studied towns.

	Vitoria-Gasteiz	Salamanca	Badajoz	Cáceres	Mérida
No. of sampling points	50	55	37	56	50
No. of measurements by points (average value)	3	4	7	5	3
Total number of measurements	150	229	276	306	150

point than in the other three towns. By way of illustration, Fig. 2 shows the map of Mérida with the selected sampling points.

The total number of sampling points for the five towns and the five categories was 248 (Table I). With a grid method, the number of sampling points required for the towns of Vitoria-Gasteiz, Salamanca, Badajoz, Cáceres, and Mérida would have been around 580, 400, 440, 256, and 170, respectively, for the grid size of 200×200 m^2 that is used by some workers (Garcia *et al.*, 1990). For instance, a noise map elaborated in 1991 with the grid method required 704 points with that grid size (Vitoria-Gasteiz Council, 1991).

D. Temporal sampling procedure

The sampling procedure was based on 15-min measurements. At each point, several measurements were made in the period from 8 a.m. to 8 p.m. (working hours). The measurements were made on different days of the week (only working days were studied) and at different hours of the day. All the measurements were carried out in the years 1999 to 2002, following the ISO 1996-2 (ISO, 1987) guidelines with the use of a 2236 Brüel & Kjaer type-I sound-level meter, with tripod and windshield. Calibration was performed using a 4231 Brüel & Kjaer calibrator. The sound-level meter was located at 1 m from the curb. The volume of traffic was visually determined and classified (cars, heavy vehicles, and motorcycles) during sampling, and other relevant information (noise sources, meteorological conditions, street dimensions, road surface type, conservation of road surface, etc.) was also noted. At each measurement, L_{eq}, L_{10}, L_{50}, L_{90}, L_{max}, and L_{min}, in dBA, were recorded for subsequent analysis.

The choice of the time-of-day intervals was made on the basis of prior weekly measurements, with, when possible, one measurement per category in each town. The intervals were selected according to the behavior of the sound level over the course of the day (working hours). These weekly measurements were made with a 2260 Brüel & Kjaer type-0 sound-level meter, with tripod and windshield, placed on balconies in the selected streets.

The 15-min sampling time was chosen for operational reasons after studying the noise fluctuations obtained in the weekly measurements. Also, this is the usual sampling time employed by other workers (Glaser and Silver, 1979; Flynn and Yaniv, 1985).

E. Statistical methods

The variable chosen for the different statistical tests used to analyze the results and evaluate the quality of the category classification was the continuous equivalent sound level (L_{eq}) since this is the most commonly used in noise studies. It is also used to calculate other noise indicators such as L_{DN} and L_{DEN}, that are preferred in some of the international regulations (ANSI, 1996; European Commission, 2002).

Since L_{eq} is a nonadditive variable (it is a logarithmic variable and, therefore, not linearly additive; in particular, the increase in noise level due to a given noise source de-

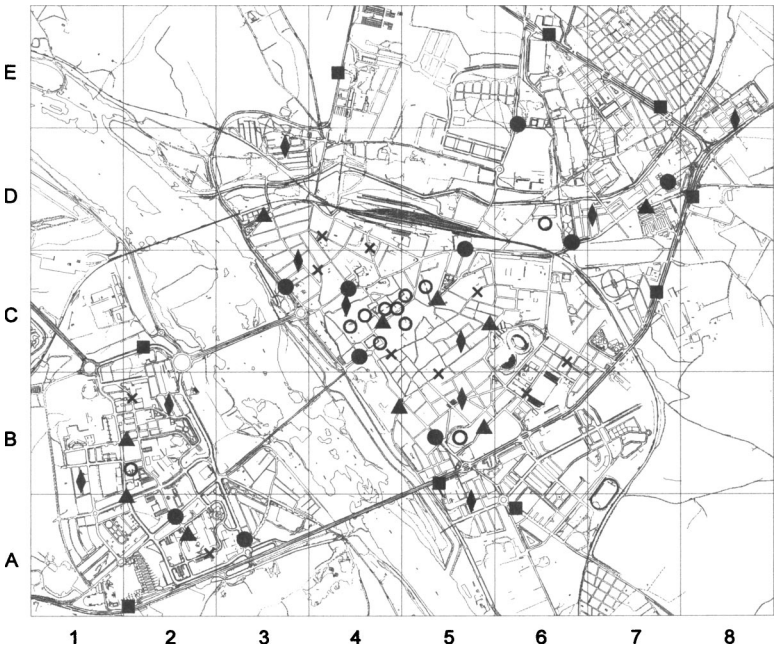

FIG. 2. City map and sampling points of Mérida. ■ Type 1. ● Type 2. ▲ Type 3. ✕ Type 4. ♦ Type 5. ○ Type 6. The size of each rectangle is 462×608 m^2.

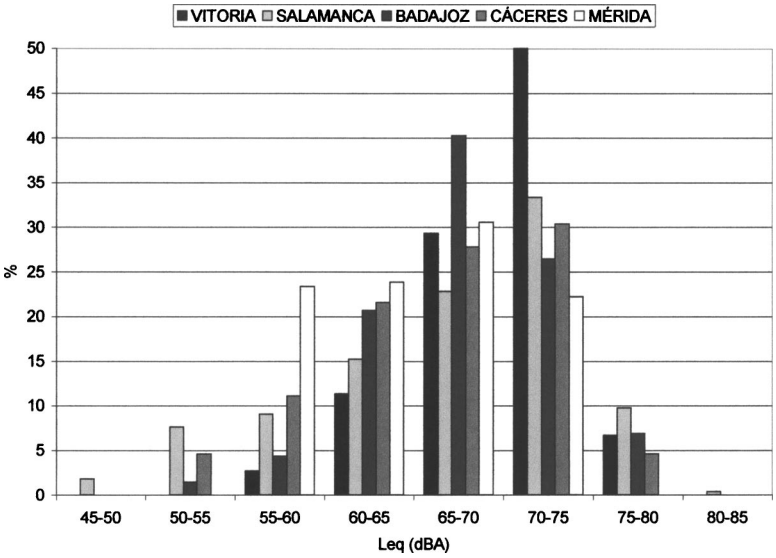

FIG. 3. Sound distribution (5 dBA bar charts) of L_{eq} (dBA) of the towns studied.

pends on the background level: the higher the background level, the less the contribution of the noise source to the total noise level), comparison of means by standard analysis of variance is inapplicable. Instead, the nonparametric Kruskal-Wallis analysis of variance test was used to test for significant differences among the medians of each category. The Tukey-type Nemenyi test was then used to analyze the significance of differences between mean ranks. This test, proposed by Nemenyi and Miller, is the nonparametric analog of Tukey's Studentized range test. Finally, the relationship between category and sound level was studied by means of Spearman's grade correlation coefficient. The Spearman coefficient was used instead of the more usual Pearson coefficient because of the noninterval nature of the category data. Information about these tests can be found in the standard literature (Nemenyi, 1963; Miller, 1966, 1981; Zar, 1999; Gibbons and Chakrabarti, 1992; etc.).

III. RESULTS AND DISCUSSION

A. Preliminary analysis

Nearly 1100 measurements were carried out overall, corresponding to 248 sampling points. The results are summarized as bar charts in Fig. 3. As can be seen, the distribution is similar for the five towns. As expected for a nonadditive variable, it is negatively skewed except for Mérida where the measurements are more uniformly distributed over the range 55–75 dB. This is possibly because Mérida is too small a town for high levels of traffic flow to be reached, and because the large numbers of visitors to the town for tourism and administrative purposes cause the background noise level to rise above 55 dB.

To check the hypothesis that traffic is the most important source of noise in the towns and the main reason for its variability, the relationship between L_{eq} and the logarithm of traffic flow was studied (Fig. 4). As can be seen, in all five towns there was a strong linear correlation between L_{eq} and the logarithm (base 10) of the traffic flow (Q) (in vehicles per hour), including heavy vehicles (vehicles with weights over 3500 kg, such as buses, trucks, vans, etc.) and motorcycles. The results of a simple linear regression are given in Table II. They are coherent with the results reported by other workers for towns in Spain and other parts of the world [summarized in Barrigón Morillas *et al.* (2002b)]. Given the values of the regression coefficient and the large number of samples taken

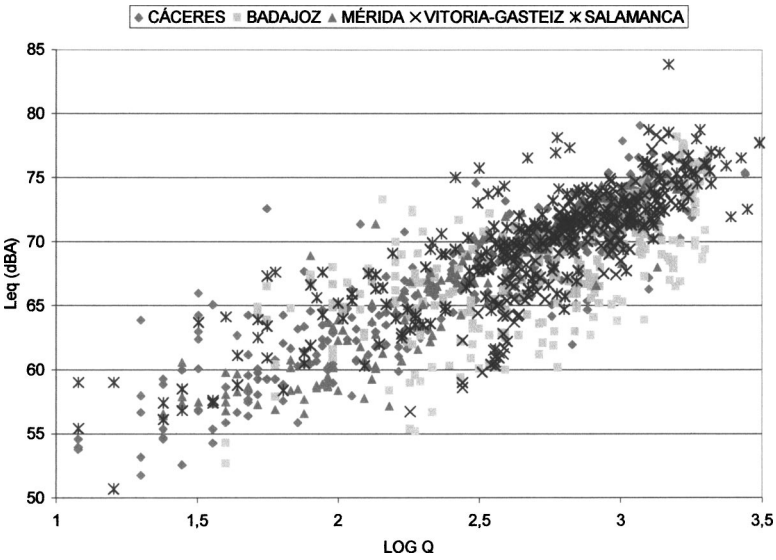

FIG. 4. L_{eq} as a function of the logarithm of the traffic flow (vehicles per hour) for the five towns studied.

TABLE II. Regression parameters between L_{Aeq} and the logarithm of the traffic flow Q (vehicles/hour) for the different towns studied.

	Vitoria-Gasteiz	Salamanca	Badajoz	Cáceres	Mérida
Slope (a)	9.39	8.94	7.28	8.80	7.84
Origin (b)	41.69	45.78	48.06	45.23	47.55
Correlation coefficient	0.83	0.89	0.69	0.90	0.80

in each town, we can conclude that there was a highly significant $[p(|r| \geq r_0|) < 1\%]$ correlation between sound level and the logarithm of traffic flow. Furthermore, the latter parameter explains much of the observed variability in the measurements of the sound events in the five towns (the percentages of the variation in sound levels explained by the linear relationship between the logarithm of traffic flow and sound levels ranged from 50% in Badajoz to 81% in Cáceres). These results are clearly in agreement with the hypothesis of the proposed method.

B. Category analysis

The results for the different categories in the five towns are summarized in the box-and-whisker plots of Fig. 5. In these plots, the edges of a box are the quartiles, the vertical thick black line is the median, and the vertical thin black lines are the maximum and minimum values [except when outliers are present—see Milton (1998)]. Outliers are shown as open circles, and extreme outliers as asterisks. As can be seen, in all the towns the lower the index corresponding to the category, the higher the value of the median (with the exception of one value in Mérida). The values of the medians are listed in Table III. One also observes that there are clear differences in the noise structure of the towns. In one group (Vitoria-Gasteiz, Salamanca, and Cáceres) the sound level decreases only gradually with increasing category index until the fifth, at which the decrease is far sharper. In Mérida this fall-off occurs in the fourth category, and in Badajoz in the

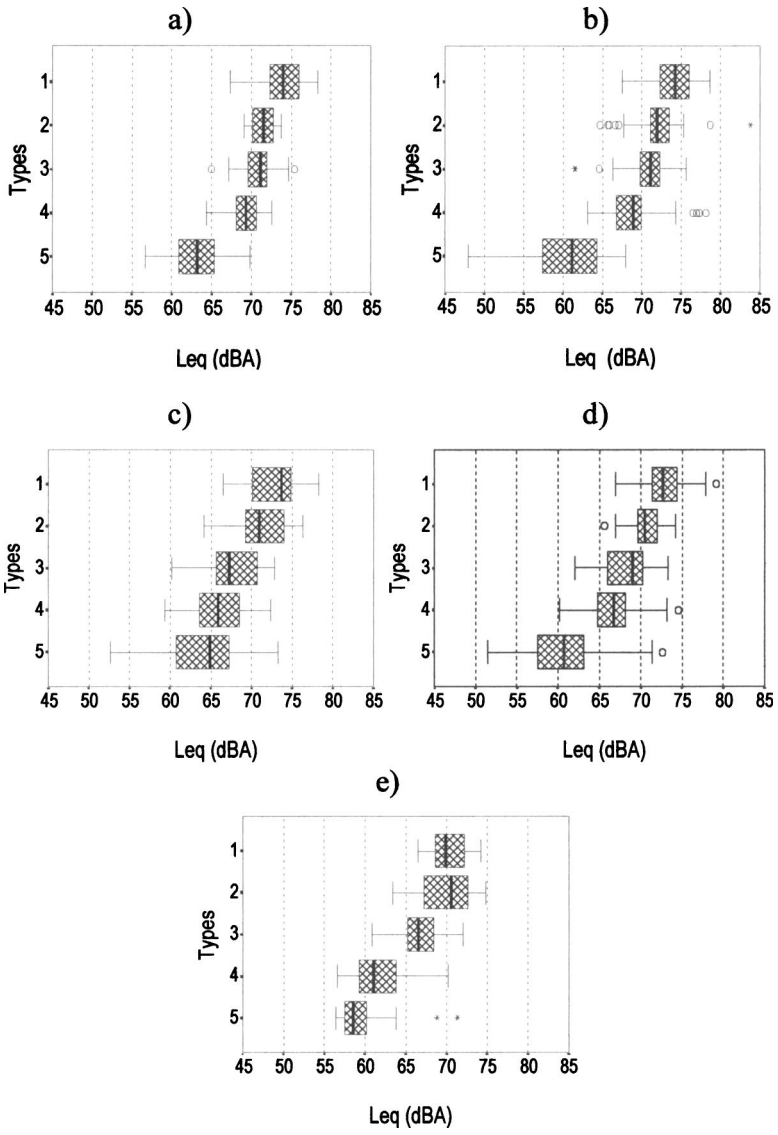

FIG. 5. Box-and-whisker diagram by categories for the different towns studied: (a) Vitoria-Gasteiz, (b) Salamanca, (c) Badajoz, (d) Cáceres, and (e) Mérida.

TABLE III. Values of the median (dBA) for each category in the different towns studied.

	Category				
	1	2	3	4	5
Vitoria	74.0	71.5	71.2	69.3	63.3
Salamanca	74.2	72.0	71.1	68.9	61.2
Badajoz	73.7	71.0	67.3	65.9	64.9
Cáceres	72.7	70.5	69	66.7	60.7
Mérida	70.0	70.6	66.6	61.1	58.6

TABLE IV. Spearman rank correlations between categories and L_{eq} (dBA) for each town. The data in the last column are Studentized values.

City	N	r_s	t
Vitoria	150	−0.782	−15.26
Salamanca	229	−0.753	−17.24
Badajoz	276	−0.653	−14.27
Cáceres	306	−0.864	−29.92
Mérida	150	−0.781	−15.21

third. In all the towns except Mérida, the fifth category has a higher variability in the measured L_{eq} than in the other categories. This can be explained by the great variability in the zoning and the architecture of the streets of the fifth category [studied in Barrigón *et al.* (2001a, b)], with some of the neighborhoods consisting of high-rise blocks of flats and others of single-family dwellings.

Table IV gives the Spearman rank correlation coefficients and their Studentized *t*-values for the relationship between category and sound level. As can be observed, all the coefficients are highly significant (the critical value of Student's *t* for more than 100 data is approximately 2). The results of the test confirm that there is a decrease in noise with increasing category index.

Kruskal-Wallis and Tukey-type Nemenyi tests were applied to study the similarities and differences between the categories in the five towns. The Kruskal-Wallis test showed significant differences between the five group medians in all the towns ($p \leqslant 0.001$). The values obtained from this test (which is approximately a Pearson chi-squared test with four degrees of freedom) were 95, 135, 125, 229, and 95, for Vitoria-Gasteiz, Salamanca, Badajoz, Cáceres, and Mérida, respectively (when the medians are all equal, the expected values of this test are near 4.0). These differences were further studied by means of the Nemenyi test. The results are listed in Table V. Some pairs of adjacent categories gave results below the critical value (these cases are presented in boldface in the table), indicating that no significant differences can be assumed to exist between them. In no case of nonadjacent pairs of categories was the result of the test below the critical value. This is an important result as it confirms the stratification of the noise in these towns, so that the categorization of streets according to their use in communicating the different zones of a town could indeed be an appropriate approach to studying urban noise.

It is also important to note that there is at least one differentiated adjacent pair of categories for every town, and likewise every adjacent pair of categories is differentiated in at least one town, thus confirming the suitability of the categories used. The differences between the towns may reflect socio-economic and urban planning differences. For example, the closeness of the values for categories 1 and 2 in Badajoz and Mérida can be explained as reflecting the open nature of their type-1 streets, with no high-rise buildings. Indeed, this may also be the explanation for the lower slope for these two towns in the regression relationship between L_{eq} and the logarithm of traffic flow (Q) (Table II).

Finally, the results given in Tables III and V show that the present method has allowed significant differences to be found between categories whose medians differ by only a few decibels. For instance, Table V shows that categories 2 and 3 in Cáceres are statistically different, even though their medians only differ by 1.5 dB (Table III). Similarly, categories 2 and 4 in Vitoria-Gasteiz are differentiated, while their medians differ by only 2.4 dB.

In sum, the statistical study of the sound level data proved that the category structure defined in the present work has shown that there is indeed stratification in the urban noise of these five towns. As these medium-sized towns have different socio-economic characteristics, climate, etc., we would expect the method to be extensible to other towns of a similar size. In any case, we consider further studies necessary to investigate the application of this definition of categories to towns in other countries and to towns different in size from those of the present study. It would also be desirable to study nonworking hours and nonworking days in future work.

TABLE V. Results of the Tukey-type Nemenyi test applied to the different categories of the five towns studied. Boldface values are below the critical value of the test. The critical value was 3.86 for all cases.

Compared types	Vitoria-Gasteiz Tukey q-statistic	Salamanca Tukey q-statistic	Badajoz Tukey q-statistic	Cáceres Tukey q-statistic	Mérida Tukey q-statistic
1-2	**2.96**	**3.60**	**1.67**	5.51	**0.51**
1-3	4.53	5.49	7.69	11.82	5.33
1-4	7.45	8.80	11.24	14.49	10.80
1-5	12.84	15.29	13.07	33.59	13.66
2-3	**1.57**	**1.94**	5.58	5.73	4.83
2-4	4.49	5.23	8.84	8.49	10.30
2-5	9.88	11.89	10.60	22.71	13.16
3-4	**2.92**	**3.23**	**3.36**	**3.01**	5.47
3-5	5.39	9.89	5.37	15.67	8.33
4-5	5.39	6.85	**2.16**	11.13	**2.86**

It seems that stratifying the traffic-bearing streets of a town could be an appropriate, rapid, and inexpensive approach to studying urban noise. Nevertheless, we believe that it is important to continue with methodological and applicability studies of this new approach, and that comparison of the results with those of other methods would also be desirable.

C. Some considerations about the magnitude of the measured sound levels

A major proportion of the samples—86.0%, 66.3%, 73.6%, 62.8%, and 52.8% for Vitoria-Gasteiz, Salamanca, Badajoz, Cáceres, and Mérida, respectively—surpassed the 65 dBA value suggested by the OECD as the daytime exposure limit (OECD, 1986). Although the different categories studied do not have a uniform weight in the real noise levels supported by the population, these percentages by themselves imply that noise must be regarded as a major problem in these five towns. This is even more the case if one takes the more conservative value of 55 dBA given by the WHO (2000) for serious annoyance in daytime, since nearly all of the samples surpassed this level—100%, 92.6%, 98.6%, 95.4%, and 100% for Vitoria-Gasteiz, Salamanca, Badajoz, Cáceres, and Mérida, respectively.

IV. CONCLUSIONS

A new method for the study of urban noise was tested in five Spanish towns with major differences in size, location, socio-economic status, climate, etc. Taking as initial hypothesis that the main source of noise in these towns is due to traffic, we designed a method of classifying the streets into six categories according to their use as transportation routes. Five categories correspond to streets with vehicular traffic, and one to pedestrian-only streets. In order to evaluate the reliability of the proposed categorization and the viability of the method for future urban noise studies, the five traffic categories were analyzed with appropriate statistical methods, using the continuous equivalent sound level as the indicator of the noise levels of each category.

The conclusions drawn on the basis of the results are as follows:

The initial hypothesis that traffic is the major source of the spatial variability of noise in the towns, on which the suitability of this kind of categorization is based, was confirmed by the finding that a major percentage of the sound level is explained by the logarithm of the traffic flow.

A Kruskal-Wallis test showed significant differences between the five group medians in all the towns ($p \leqslant 0.001$).

The null hypothesis of no significant differences was rejected by a Tukey-type Nemenyi test in all cases of nonadjacent categories and between certain of the adjacent categories in each town studied. These results indicate that the urban noise was stratified, and thus confirm the suitability of the stratification procedure used.

The study has thus shown that a town's urban noise is indeed stratified, and that an appropriate way to study this stratification is by means of a categorization method in which the streets of the town are classified according to their use as transportation routes.

ANSI (**1996**). ''Quantities and Procedures for Description and Measurement of Environmental Sound—Part 4: Noise Assessment and Prediction of Long-Term Community Response—Includes Errata (10/01/97)'' (Acoustical Society of America, New York).

Barrigón, J. M., Gómez Escobar, V., Gutiérrez Marcos, P. D., Méndez Sierra, J. A., and Ruiz de Azua, J. (**2000a**). ''Study of Vitoria-Gasteiz by categorizing roadway characteristics,'' Proceedings of Internoise, Nice, France, 2000, p. 292, CDROM—ISBN: 2-9515619-8-9, Paper IN2000/205.

Barrigón, J. M., Gómez Escobar, V., Gutiérrez Marcos, P. D., and Alejandre, L. (**2000b**). ''Study of medium-sized cities of Extremadura by categorizing roadway characteristics,'' Proceedings of the 7th International Congress on Sound and Vibration (ICSV7), Garmisch-Partenkirchen, Germany, pp. 2413–2420.

Barrigón Morillas, J. M., Gómez Escobar, V., Méndez Sierra, J. A., and Vílchez Gómez, R. (**2001a**). ''Influence of the density of population on the sound levels for some districts of the city of Vitoria-Gasteiz (Spain),'' Proceedings of the 17th International Congress of Acoustics, Roma, Italy, 2001, p. 365, CDROM—ISBN: 88-88387-02-1.

Barrigón, J. M., Pulido Guío, J., Gómez Escobar, V., Méndez Sierra, J. A., and Vílchez Gómez, R. (**2001b**). ''Caracterización acústica de las calles de barrio de la ciudad de Cáceres,'' Rev. Española Acúst. Vol. 32, CD publication (ISBN: 84-87985-05-X).

Barrigón Morillas, J. M., Gómez Escobar, V., Méndez Sierra, J. A., and Vílchez Gómez, R. (**2002a**). ''Study of noise in a small Spanish Town,'' Int. J. Acoust. Vib. **7**, 231–237.

Barrigón Morillas, J. M., Gómez Escobar, V., Méndez Sierra, J. A., Vílchez Gómez, R., and Trujillo Carmona, J. (**2002b**). ''An environmental noise study in the city of Cáceres, Spain,'' Appl. Acoust. **63**, 1061–1070.

Broderson, A. B., Edwards, R. G., Hauser, W. P., and Coakley, W. S. (**1981**). ''Community noise in twenty Kentucky cities,'' Noise Control Eng. **16**, 52–63.

Brown, A. L., and Lam, K. C. (**1987**). ''Urban Noise Surveys,'' Appl. Acoust. **20**, 23–39.

Cannelli, G. B. (**1974**). ''Traffic noise pollution in Rome,'' Appl. Acoust. **7**, 103–115.

Chakrabarty, D., Santra, S. C., Mukherjee, A., Roy, B., and Das, P. (**1997**). ''Status of road traffic noise in Calcutta metropolis, India,'' J. Acoust. Soc. Am. **101**, 943–949.

European Commission (**2002**). ''EU Directive on the Assessment and Management of Environmental Noise (END)'' (The European Parliament and the Council of the European Union, Brussels).

Fidell, S. (**1978**). ''Nationwide urban noise survey,'' J. Acoust. Soc. Am. **64**, 198–206.

Fidell, S., Pearsons, K., Tabachnik, B., Howe, R., Silvatti, L., and Barber, D. S. (**1995**). ''Field study of noise-induced sleep disturbance,'' J. Acoust. Soc. Am. **98**, 1025–1033.

Fields, J. M. (**1993**). ''Effect of personal and situational variables on noise annoyance in residential areas,'' J. Acoust. Soc. Am. **93**, 2753–2763.

Flynn, D. R., and Yaniv, S. L. (**1985**). ''Relations among different frequency rating procedures for traffic noise,'' J. Acoust. Soc. Am. **77**, 1436–1446.

García, A., and Faus, L. J. (**1991**). ''Statistical analysis of noise levels in urban areas,'' Appl. Acoust. **34**, 227–247.

García, A., Miralles, J. L., García, A. M., and Sempere, M. C. (**1990**). ''Community response to environmental noise in Valencia,'' Environ. Int. **16**, 533–541.

Gibbons, J. D., and Chakrabarti, S. (**1992**). *Nonparametric Statistical Inference*, 3rd ed. (Marcel Dekker, New York).

Glaser, E. R., and Silver, C. A. (**1979**). ''The use of stratification to improve the design efficiency of community noise surveys,'' J. Acoust. Soc. Am. **65**, 1467–1473.

Gómez Escobar, V., Barrigón Morillas, J. M., Méndez Sierra, J. A., Vílchez Gómez, R., and Vaquero Martínez, J. M. (**2002**). ''Noise study of Salamanca (Spain) by means of a categorization method,'' Acust. Acta Acust. **88**, S-64, CDROM-ISBN: 84-87985-06-8, Paper NOI-06-003.

Heinonen-Guzejev, M., Vuorinen, H. S., Kaprio, J., Heikkilä, K., Mussalo-Rauhamaa, H., and Koskenvuo, M. (**2000**). ''Self-report of transportation

noise exposure, annoyance and noise sensitivity in relation to noise map information,'' J. Sound Vib. **234**, 191–206.
Instituto Nacional de Meteorología (**2001**). ''Guía resumida del clima en España, 1971–2000 (Abridged guide to the climate in Spain, 1971–2000),'' Madrid.
ISO 1996-2: 1987 (**1987**). ''Description and measurement of environmental noise. Part 2: Acquisition of data pertinent to land use'' (International Organization for Standardization, Geneva, Switzerland).
Job, R. F. S. (**1988**). ''Community response to noise: A review of factors influencing the relationships between noise exposure and reaction,'' J. Acoust. Soc. Am. **83**, 991–1001.
Kumar, K., and Jain, V. K. (**1994**). ''A study of noise in various modes of transport in Delhi,'' Appl. Acoust. **43**, 57–65.
Miedema, H. M. E., and Vos, H. (**1998**). ''Exposure-response relationships for transportation noise,'' J. Acoust. Soc. Am. **104**, 3432–3445.
Miller, R. G., Jr. (**1966**). *Simultaneous Statistical Inference* (McGraw-Hill, New York).
Miller, R. G., Jr. (**1981**). *Simultaneous Statistical Inference*, 2nd ed. (Springer-Verlag, New York).
Milton, J. S. (**1998**). *Statistical Methods in the Biological and Health Sciences*, 3rd ed. (McGraw-Hill, Boston).
Mochizuki, T., and Imaizumi, N. (**1967**). ''City noises in Tokyo,'' J. Acoust. Soc. Jpn. **23**, 146–159.
Nemenyi, T. (**1963**). ''Distribution-free multiple comparisons,'' unpublished doctoral dissertation, Princeton University, Princeton.
OECD, Organization for Economic Cooperation and Development (**1986**). ''Report Fighting Noise'' (OECD, Paris).
Öhrström, E. (**2004**). ''Longitudinal surveys on effects of changes in road traffic noise annoyance, activity disturbances, and psycho-social well-being,'' J. Acoust. Soc. Am. **115**, 719–729.
Ouis, D. (**2001**). ''Annoyance from road traffic noise: a review,'' J. Environ. Psychol. **21**, 101–120.
Saadu, A. A., Onyeonwu, R. O., Ayorinde, E. O., and Ogisi, F. O. (**1998**). ''Road traffic noise survey and analysis of source major urban centers in Nigeria,'' Noise Control Eng. J. **46**, 146–158.
Sommerhoff, J., Recuero, M., and Suárez, E. (**2004**). ''Community noise survey of the city of Valdivia, Chile,'' Appl. Acoust. **65**, 643–656.
Vitoria-Gasteiz Council (**1991**). ''Mapa sonoro de Vitoria-Gasteiz,'' private communication.
World Health Organization (WHO) (**2000**). *Guidelines for Community Noise*, Edited by B. Berglund, T. Lindvall, D. H. Schwela, and K. T. Goh (WHO, Geneva).
Zannin, P. H., Diniz, F. B., and Barbosa, W. A. (**2002**). ''Environmental noise pollution in the city of Curitiba, Brazil,'' Appl. Acoust. **63**, 351–358.
Zannin, P. H., Diniz, F. B., Calixto, A., and Barbosa, W. A. (**2001**). ''Environmental noise pollution in residential areas of the city of Curitiba,'' Acust. Acta Acust. **87**, 625–628.
Zar, J. H. (**1999**). *Biostatistical Analysis*, 4th ed. (Prentice Hall International, London).

Effect of season and meteorological conditions on community noise annoyance

Henk M. E. Miedema[a)]
TNO Inro, P.O. Box 6041 2600 JA Delft, Netherlands

James M. Fields[b)]
10407 Royal Road, Silver Spring, Maryland 20903

Henk Vos[c)]
TNO Inro, P.O. Box 6041 2600 JA Delft, Netherlands

(Received 1 July 2004; revised 24 February 2005; accepted 3 March 2005)

More than 80 000 residents' responses to transportation noise from 42 studies conducted at different times of year provide statistical estimates of the effects of season and meteorological conditions on community response to noise. The strongest evidence for a seasonal effect comes from 7 years of continuous daily interviewing of nationally representative probability samples in the Netherlands. Long-term annoyance with noise is slightly, but statistically significantly, higher in the summer than in the winter. Analyses of 41 other surveys drawn from diverse countries, climates, and times of year also provide evidence that noise annoyance varies over the year, is increased by temperature, and may be increased by more sunshine, less precipitation, and reduced wind speeds. These findings are not sufficiently precise to determine whether the apparent relationships with meteorological conditions are only the result of seasonal variations or are also the result of differences in the climate at different locations. There is not consistent evidence that the meteorological conditions on the day of the interview or the immediately preceding days have any more effect on long-term noise annoyance measures than do the conditions over the immediately preceding weeks or months. [DOI: 10.1121/1.1896625]

PACS numbers: 43.50.Sr, 43.50.Vt, 43.50.Qp [DKW] Pages: 2853–2865

I. INTRODUCTION

More than 500 social surveys of residents' reactions to environmental noise (Fields, 2001) have provided considerable information about the relationship between noise exposure and residents' reactions in residential areas. Many of these studies have been subjected to secondary analyses to describe the variation in reactions in different studies and to provide pooled estimates of the average annoyance reactions at different noise levels for aircraft, road traffic, and railway noise (Fidell *et al.*, 1991; Miedema and Oudshoorn, 2001; Miedema and Vos, 1998). Both meta-analyses and secondary analyses have also been directed at a large range of demographic and other personal characteristics of residents. Demographic variables have generally been found to have little or no effect on noise annoyance reactions while attitudes such as self-rated noise sensitivity and fear of the noise source have been found to be strongly related to noise annoyance. (Fields, 1993; Miedema and Vos, 1999). By way of contrast relatively little is known about the effects of the more general characteristics of the locations in which respondents live. This paper examines one class of such characteristics, the seasonal and meteorological conditions in which residents live.

A simple personal noise-exposure theory provides the most common basis for hypothesizing that noise reactions vary with meteorological conditions. It is assumed that meteorological conditions affect residents' exposure to noise by influencing two behaviors: the opening of windows and the use of outdoors space. The increased noise exposure is then presumed to increase annoyance. In moderate climates it is assumed that outdoor activities become more desirable and frequent in residential areas with higher temperature, more sunshine, an absence of precipitation, and an absence of high winds. Window opening is assumed to increase for ventilation purposes as temperature increases. Window opening is presumed to decrease in higher wind and precipitation conditions as residents attempt to shelter their interior living space from the effects of high air velocity and the associated intrusion of moisture or dust through open windows. The resulting relationship between temperature and noise exposure provides the basis for hypothesizing that noise annoyance reactions will be stronger in the summer than the winter season and stronger in warmer than colder climates. Other meteorological variables such as precipitation, sunshine, and wind velocity are not uniformly higher in the winter or summer in all climates and therefore do not predict a simple, universal increase in noise exposure and annoyance in the summer season. The effect of meteorological factors on noise exposure and on noise reactions could also be modified by individual and cultural differences such as the value placed on fresh air in homes, the amount of interest in outdoors activities around the home, window opening preferences in sleeping rooms, and the usage of air conditioning during

[a)]Electronic mail: hme.miedema@inro.tno.nl
[b)]Electronic mail: fieldses@umich.edu
[c)]Author to whom correspondence should be addressed. Electronic mail: h.vos@inro.tno.nl

warm periods. For example, exposure might be reduced for some residents under the highest temperature conditions in warm climates in a culture that places a low value on ''fresh air,'' if the sufficiently wealthy members of a population use air conditioning and thus reduce noise exposure through increased window closing.

Alternative theoretical bases for meteorological and seasonal effects can be posited. General psychological well-being might be assumed to vary with season and cause a corresponding change in all types of annoyance. It might be hypothesized that there is some long-term adaptation to the base climatic meteorological conditions, so that only seasonal variations, not the stable base climatic variations, are important. Alternatively, it is known that the noise propagation and noise emissions from some noise sources vary with meteorological conditions. For example, snow and water on pavement can affect noise emissions, temperature inversions can affect noise propagation through the atmosphere, meteorological conditions can affect how absorptive the ground is for surface transportation, and seasonal vacation traffic affects some airports. Seasonal variations in emissions and propagation are commonly accounted for in noise surveys where concurrent noise exposure is measured. In addition, many such conditions are sufficiently minor, short-lived, or localized that their impact can be presumed to be of relatively little importance. For example, even a 25% seasonal increase in the number of aircraft or road traffic vehicles would create only a small, 1-dB seasonal increase in noise exposure in the equivalent continuous noise level (LAeq).

Attempts to precisely model the effects of meteorological factors might consider several additional issues. If respondents' reactions are affected by a history of noise exposures, then it is reasonable to assume that a complex model should give greater weight to relatively recent noise exposure conditions. A more highly developed model might also include threshold values for temperature or other meteorological variables that affect window opening and outdoors usage patterns and that could generate parallel thresholds in the relationship between temperature and reactions to noise.

A review of the evidence for seasonal effects summarized the evidence from seven studies (Fields *et al.,* 2000). Five of the seven surveys found seasonal differences in the expected direction; annoyance reactions were higher during warmer periods (Connor and Patterson, 1972; de Jong, 1981; McKennell, 1963; Borsky, 1978; Dunn and Posey, 1974). However, the interpretation of these findings is uncertain. It is not clear whether reporting practices may have introduced biases. The two surveys that did not find seasonal effects were the only two of the seven studies that were explicitly designed to test for such effects (García and Romero, 1987; Griffiths *et al.,* 1980). None of the five studies that did find an effect was designed to study seasonal reactions. Twelve other longitudinal studies have collected reaction data at more than one time of year, but have not reported any findings about the presence or absence of seasonal effects. It is possible that the studies contained no season effects but did not publish these negative findings.

This paper examines the evidence for seasonal effects with two strategies. First, reactions at different times of year are contrasted within a single 7-year study that was conducted at all times of year. Second, reactions are compared between 41 different studies that happened to have been conducted in various climates at various times of year. The survey data are analyzed to estimate the differences between reactions in different seasons, the effects of four meteorological variables (temperature, sunshine, wind speed, and precipitation), and the period of integration for meteorological experiences.

II. DATA FOR ANALYSES

The data for analyses in this article come from social surveys of residents' reactions to noise in residential areas. Three data sets have been compiled from two sources. One data set, the Netherlands Continuous Life Information Survey (DLO), provides measures of the Netherlands' population's reactions to community noise for the 84 months from January 1990 to December 1996. The second source of data, the TNO archive data, consists of the original social survey and acoustical data from 41 cross-sectional noise annoyance surveys in which the respondents rated a total of 48 noise sources for which noise exposure was measured. These 41 surveys are all of the surveys that TNO has been able to obtain from around the world that include data on noise annoyance, noise exposure, the season of the study, and enough information on each respondent's location to match the TNO data with independently obtained meteorological data sets. For the purposes of the analyses in this article the 41 studies from the TNO archive are referred to as the ''seasonal'' data set when all 41 studies are analyzed. Of these 41 studies with reactions to 48 noise sources, a subset of 12 studies with reactions to 16 noise sources is referred to as the ''day-linked'' data set because this data set identifies the exact day on which each interview was conducted and thus can be linked to the meteorological conditions during the interview day and the preceding days and weeks. The social survey, acoustical, and meteorological characteristics of the three data sets are compared in Table I. More information about the data and study methods is available in a NASA report (Fields, 2004).

The Netherlands Continuous Life Information Survey (DLO) is part of a long-term study that has interviewed representative probability samples of the Netherlands population continuously for a wide range of purposes. With 7 years of data spread over all 84 months this data set provides the best information about seasonal reactions. No noise data are available to estimate noise exposure-response relations. The noise annoyance data have only been released in an aggregated form. For each of the 84 months the country-wide summary of responses is available. For purposes of calculating sampling errors there are presumed to be 84 independent observations, one for each month.

The season-linked and day-linked data sets consist of studies each one of which collected data under specific meteorological and seasonal conditions. The advantage of these data sets is the wide range of meteorological conditions that are included. The disadvantage is that the data were collected with a variety of different noise and social survey data col-

TABLE I. Characteristics of the three data sets analyzed.

Characteristic	Data set: Day-linked data set	Data set: Season-linked data set	Data set: Netherlands Continuous Life Information Survey (DLO)
	Social survey characteristics		
No. of responses[a]	15 107 (7713 with precipitation data)	53 130 (47 825 with wind speed data)	35 000 (approximate)
No. of respondents	13 100 (approximate)	49 400 (approximate)	35 000 (approximate)
No. of studies	12 (16 noise sources evaluated)	41 (48 noise sources evaluated)	1 (4 noise sources evaluated)
Settings	7 countries (5 languages)	14 countries (9 languages)	Netherlands (1 language)
Reaction question	Intensity of annoyance (Diverse wordings)	Intensity of annoyance (Diverse wordings)	Frequency of annoyance[e] (1990–93 and 1994–96 versions)
Study methods	Methods differ between studies	Methods differ between studies	Uniform for data set
Noise sources studied	Road traffic Aircraft	Road traffic Aircraft Railway	Road traffic Aircraft Railway (Neighbors)
Aggregation	Individual interviews	Individual interviews	Group averages of each month's interviews
Within-study variation in weather	Small	Small	Large
	Acoustical data		
Acoustical index	DNL	DNL	(No noise data)
Estimation and measurement methods	Methods differ between studies	Methods differ between studies	(No noise data, but same population for all years)
	Meteorological data		
Aggregation in base data	Daily data	30-year averages for each month (total of 12 values)	Monthly data
Integration time (default)[b]	91 days up to and including the interview day	3 months up to and including the interview month	2 months preceding the interview month
Meteorological data (means of daily values)	Temperature (C)[c]	Temperature (C)[c]	Temperature (C)[c]
	Precipitation ($total-mm\ per\ 24\ hours$)	Precipitation *(total (mm) and number of days with precipitation)*	Precipitation *(total (mm) and number of hours with precipitation)*
		Sunshine *(minutes per 24 hours)*	Sunshine *(minutes and percent of daylight hours with sunshine)*
		Wind speed ($mean-m/s$)	Wind speed *(mean and average of hourly maximums)*
Sources[d]	UK Met office, for British sites, GDCN Version 1.0 for all other sites	Wereld Klimaat Informatie (WKI) data base from KNMI	KNMI (Web site)
	Information for linking meteorological and social survey data		
Location	City of survey or nearby city	City of survey or nearest location in the same country within the same climate zone	One central location in the Netherlands (De Bilt)

TABLE I. (*Continued*.)

Characteristic	Data set		
	Day-linked data set	Season-linked data set	Netherlands Continuous Life Information Survey (DLO)
Data on date of survey interviews	Day Month	Month (Within 3-month period)	Month

[a]If respondents are asked about two noise sources for which noise data are available, a single interview usually provides two responses in the day-linked and season-linked data sets.

[b]This ''default'' integration period is used in the analyses in this article unless otherwise noted. The interview month is excluded from the DLO data because respondents interviewed early in a month would not have experienced the entire month's conditions. The nominal ''interview'' month is included for the season-linked data set because this ''nominal'' month is sometimes in the middle of a two- or three-month interviewing period.

[c]Three measures of temperature (in Celsius) are available for all three data sets: an average of the 24 hourly values, and the maximum and minimum obtained in a day. The algorithm for combining the 24 hourly values may vary between studies.

[d]The sources of the meteorological data for the three data sets are as follows:

(1) Day-linked data set: Data for most studies come from the Global Daily Climatology Network (GDCN) Version 1.0 data set that was produced in July 2002 by the Climate Analysis Branch of the National Climate Data Center of the National Oceanic and Atmospheric Administration (NOAA). Information is available from www.ncdc.noaa.gov/gden.html. The daily weather data for the UK were specially ordered from the UK MET Office (www.meto.gov.uk).

(2) Season-linked data set: In 2003 the Wereld Klimaat Informatie (WKI) data base from KNMI (Royal Netherlands Meteorological Institute at http://www.knmi.nl) provided 30-year averages (1961–1990) for each month of the year for a large number of sites around the world in a graphic product (in Dutch).

(3) Continuous DLO survey: The KNMI data set for De Bilt also included data on mean air pressure (hPa), maximum wind gusts, wind direction, and cloud cover (octants of sky visible) that were not examined in any analyses. Definitions were obtained from http://www.knmi.nl/voor/kd/lijsten/daggem/uitleg_dagklim_en_html in January of 2003.

[e]The annoyance questions are shown in Dutch and an English translation in a NASA report (Fields, 2004).

lection methods that can interfere with comparisons of the effects of those meteorological conditions. An extensive data preparation project (Miedema and Vos, 1998) considered the differences between studies when carefully examining the social survey data gathering practices and applying uniform assumptions to estimate noise environments with the day-night noise level metric (DNL) at the noisiest facade of the residence (excluding reflections). A variety of assumptions were made to attempt to create a uniform scoring of the different studies' annoyance scales. For example, adjustments for varying numbers of scale points were made by transforming simple annoyance scales to a 100-point scale. For most studies the transformation assumed that the responses on the ordinal response scales represent the midpoints of equal-size response intervals (i) using the formula: $\text{score}_i = 100 \times (i - \frac{1}{2})/m$, where ''$m$'' is the total number of categories and ''i'' is the rank order of the category beginning with $i = 1$ for the lowest category. For example, on a four-point scale with four intervals of 25 points each, no annoyance would be scored 12.5, and the highest annoyance would be scored 87.5. Other assumptions provided the basis for adjustments for differences between unipolar and bipolar scales, scales with or without a screening question, questions about indoor and outdoor conditions, questions about weekday and weekend annoyance, extreme differences in labels for scale categories, and other variations (Fields, 2004; Miedema and Vos, 1998).

While the wording of the social survey annoyance questions vary in some respects, they do tend to be similar in containing the type of long-term or indefinite time reference that is displayed in the following survey question:

''When you are here at home, how much does the noise from aircraft bother, disturb, or annoy you: Extremely, Very, Moderately, Slightly or Not at all?''

Within the context of survey questions that provide general assessments of all aspects of a residential area, the assumption is that respondents attempt to evaluate the long-term noise environment and not only the current day or week's noise environment.

Meteorological and interview data were temporally and topographically linked as closely as feasible given the limited numbers of meteorological stations and the limited amount of temporal and locational information about interviews. The procedures are summarized in Table I. The temporal matching was performed on a quite exact daily basis for the day-linked data set, but on an approximately monthly basis for the DLO data and a 30-year average monthly basis for the season-linked data set. Topographical matching considered the position and altitude of the sites. The day-linked meteorological station data came from the city of the interview (or, in a few cases, a nearby city) while the DLO and season-linked meteorological data sometimes came from a more distant area within the same country and Köppen climate classification. While these types of linkages could generate considerable error in estimating hour-to-hour meteorological conditions, it is assumed that such errors are of relatively little importance for most analyses given the long integration periods analyzed in this study.

Since the individual interviews in the TNO data sets are clustered within countries, studies, and cities, the interview observations are not statistically independent. As a result sampling errors have been assessed using a technique, jackknife repeated replication, that recognizes the dependence between observations in the sample (Brick *et al.*, 2000; Frankel, 1983). For the purposes of sampling error calculations, each of the 41 studies in the season-linked data set is assumed to be an independent primary sampling unit (PSU). For the day-linked data set, the 15 107 responses from the 14 studies are divided into 28 primary sampling units, usually defined by cities, that are assumed to be independent. The

jackknife replication model used does not assume that the sample of PSUs is stratified. The resulting sampling errors indicated that inferential statistics such as confidence intervals are several times larger than would be estimated using incorrect simple random sampling assumptions.

The characteristics of the 41 studies (48 noise source evaluations) that constitute the season-linked data set are listed in Table II. The subset of 12 studies (16 noise source evaluations) that form the day-linked data set is listed in the first panel of the table.

Table II displays the range in climatic and meteorological conditions found in the study sites. The median difference between the summer and winter temperatures at the sites is about 15 °C. The temperatures for the survey season (3 month averages) range from −0.1 to 22.7 with 83% of the studies within the 15° range from 3.9 to 18.7 °C. The amounts of precipitation for the survey season are within the 5-mm range of 0.9 to 5.8 m/day for all but two of the surveys. The average wind speed during the season of the surveys ranged from 1.2 to 5.8 m/s.

The seasonal temperature and precipitation patterns define the climatic conditions that are characterized in Table III with the widely accepted Köppen Climate Classification System (Critchfield, 1983). With the exception of a single tropical moist climate site and two dry climate sites, the study sites are in moist mid latitudes (codes Cfa, Cfb, Cfc, Csa, Dfa, Dfb) with about half of the sites being from moist midlatitude climates with warm summers and no dry period (code Cfb).

III. EVIDENCE ON SEASONAL EFFECTS FROM THE CONTINUOUS NETHERLANDS SURVEY

Respondents in the Netherlands Continuous Life Information Survey (DLO) were asked whether they were bothered by noise from the four sources road traffic, aircraft, railway, and neighbors. They chose their answer from a card that listed the three alternatives of ''Yes, often,'' ''Yes, sometimes,'' or ''Seldom or never'' (for the 1989 to 1993 surveys) or the alternatives of ''Yes,'' ''Sometimes'' or ''No'' (for the 1994 to 1996 surveys). Figure 1 plots the annoyance scores for April through March, averaged over the 7 years for each of the four noise sources where the three annoyance scale points are scored 16.6, 50.0, and 83.3. The seasonal variation is modeled with a sine function, represented by the solid curves in the figure, defined as

$$\text{annoyance score} = a + b \sin[(\text{month} - c) \times (2\pi/12)],$$

where month=month of year (1=Jan., 2=Feb.,...12=Dec.), a=annoyance score at the midpoint of the yearly reaction cycle, b=multiplier determining the size of the variation in annoyance during the annual cycle, and C=the month in the annual cycle where annoyance rises through the midpoint of the annual reaction.

The parameters of the function have been estimated for each of the four noise sources with a Marquardt procedure (Draper, 1981). For the three transportation noise sources, the greatest annoyance occurs in July, August, or September. The function estimates that there is a rather small seasonal difference in reactions, less than a 2-point difference on the annoyance scale. However, as the parameter b is statistically significantly greater than zero, it is clear that these reactions do vary with the season. In contrast, reactions to neighbor noise, which appear in Fig. 1 to be highest in the winter months, are not statistically significantly related to season. This absence of an effect for neighbor noise, a noise source that could include both interior and exterior noise, shows that the seasonal effect is not simply explained by more general, season-related psychological characteristics.

The regression analyses in Table IV suggest that the seasonal effect is at least partially due to temperature but that sunshine, precipitation, or wind speed may also contribute. Table IV provides unstandardized regression coefficients for meteorological variables from linear regression analyses of annoyance with road traffic, aircraft, or railway noise on each of the four meteorological variables. For the univariate regressions with a single meteorological variable (first row of each noise source part of Table IV), all relationships are in the expected direction and, with the exception of precipitation, statistically significant ($p < 0.05$). Annoyance increases with temperature and sunshine and decreases with precipitation and wind speed. However, when all four meteorological variables are included in the same prediction equation in the first multivariate analysis row for each noise source, none of the regression coefficients are any longer statistically significant, many of the coefficients are substantially reduced, and some of the sunshine, precipitation, and wind speed coefficients even reverse direction. In the last row for each noise source, the sunshine variable is excluded because it is confounded with the temperature and precipitation variables (correlations of $r = 0.66$ and $r = -0.39$, respectively). Although the partial regression coefficients are now somewhat more consistent, the uncertainty about the variables' effects remains. In the three analyses of precipitation and wind speed, only one achieves or approaches significance for each source, one is in the wrong direction for each source, and the remaining one for each source would be expected to be observed by chance more than 50% of the time if there were no relationship. A forward stepwise regression analysis ($p = 0.05$ for inclusion and $p = 0.10$ for removal) selected only the temperature variable for prediction equations for road traffic noise annoyance and aircraft noise annoyance, and only the sunshine variable for a prediction equation for aircraft.

In other analyses it was found that the relationships are not consistently stronger for the meteorological variables that are based on the 2 months that include the interview month than for the 2 months preceding the interview month (the months used in these analyses) (Fields, 2004). Graphs of the relationship between noise reactions and temperature were also visually examined. No evidence for consistent temperature threshold values or consistent nonlinear relationships was found. In other analyses, precipitation was estimated to have a weaker effect when it was represented by the total amount of precipitation, rather than by the hours-of-precipitation measure reported in this section.

The seasonal variations in reactions to road traffic and railway noise that were evident in Fig. 1 are largely explained by the meteorological variables. For these two noise

TABLE II. Characteristics of the day-linked and season-linked data set.

Description of study				Conditions for survey season (30-year averages for three months)			Range in temperatures (°C) between the warmest and coldest months in the climate (Summer−Winter=Range)
Study [Catalog no.—see Fields (2001)]	Noise source	No. of responses	Climate (Köppen classification)	Temperature (°C)	Precipitation (mm/day)	Wind speed (m/s)	
Day-linked studies (also in Season-linked data set)							
1967 USA Four-Airport (Phase I Tracor) (USA- 022)	Aircraft	3499	Cfa, Csa, Dfa	15.4	3.2	5.3	24.2−2.8=21.4
1973 Los Angeles Airport Night (USA-082)	Aircraft	702	Csa	14.7	4.5	4.1	20.6−13.8=6.8
1974 Dordrecht Home Sound Insulation (NET-106)	Road	420	Cfb	5.6	1.7	5.6	16.8−2.8=14.0
1975–1976 Southern Ontario Community (CAN-121)	Road	1304	Dfb	15.1	2.2	4.1	22.1−−4.5=26.6
1979 Burbank Aircraft Noise Change (USA-203)	Aircraft	924	Csa	20.6	6.6	4.0	20.6−13.8=6.8
1984 Glasgow Combined Aircraft/Road Traffic (UKD-238)	Aircraft	598	Cfb	9.6	2.1	⋯	14.4−2.8=11.6
	Road	536	Cfb	9.6	2.1	⋯	14.4−2.8=11.6
1984–1986 French Combined Aircraft/Road Traffic (FRA-239)	Aircraft	565	Cfb	15.4	1.9	3.7	18.4−3.4=15.0
	Road	524	Cfb	15.4	1.9	3.7	18.4−3.4=15.0
1984 Schiphol Combined Aircraft/Road Traffic (NET-240)	Aircraft	573	Cfb	12.9	2.3	4.5	16.6−2.4=14.2
	Road	473	Cfb	12.7	2.3	4.6	16.6−2.4=14.2
1982 United Kingdom Aircraft Noise Index (UKD-242)	Aircraft	1993	Cfb	14.4	1.7	3.6	16.5−3.5=13.0
	Road	410	Cfb	14.1	1.7	3.6	16.5−3.5=13.0
1975 Amsterdam Home Sound Insulation (NET-258)	Road	365	Cfb	4.5	1.6	5.8	16.6−2.4=14.2
1989 Oslo Airport (NOR-311)	Aircraft	1548	Dfb	0.1	1.4	2.1	16.4−−4.3=20.7
1992–1993 Bodoe Aircraft Military Exercise (NOR-328)	Aircraft	702	Cfc	−1.5	2.8	⋯	12.5−−2.2=14.7
Subtotal		15 136		12	2.6	4.2	19.0−2.5=16.5
Other season-linked studies							
1967 Heathrow Aircraft (2nd Heathrow) (UKD-024)	Aircraft	4515	Cfb	15.5	1.8	3.3	16.5−3.5=13.0
1969 USA Three-Airport (Phase II Tracor) (USA-032)	Aircraft	1666	Aw, Cfa, Dfb	22.7	2.5	5.7	23.1−−1.8=24.9
1970 USA Small City Airports (USA-044)	Aircraft	1954	Bsk, Cfa	7.9	2.5	2.7	24.2−1.9=22.3
1971 Swiss Three-City (SWI-053)	Aircraft	3934	Cfb	8.8	3.1	3.1	16.7−−1.0=17.7
	Road	945	Cfb	11.6	3.7	3.0	16.7−−1.0=17.7
1972 Paris Area Railway (FRA-063)	Railway	344	Cfb	6.8	1.6	4.3	18.4−3.4=15.0
1972 B.R.S. London Traffic (UKD-071)	Road	2903	Cfb	11.2	1.8	3.8	16.5−3.5=13.0
1972 English Road Traffic (UKD-072)	Road	1040	Cfb	12.7	1.7	4.1	15.8−3.1=12.7
1973 French Ten-City Traffic (FRA-092)	Road	975	Cfb, Csa	17.1	1.9	3.1	20.1−3.1=17.0
1975 British National Railway (UKD-116)	Railway	1385	Cfb	8.5	1.9	4.3	15.8−3.1=12.7
1975 Western Ontario University Traffic (CAN-120)	Road	1149	Dfb	−0.4	2.3	5.9	22.1−−4.5=26.6
1977 Netherlands Railway (NET-153)	Railway	671	Cfb	13.7	2.3	3.0	16.8−2.2=14.6
1977 London Area Panel (UKD-157)	Road	364	Cfb	6.2	2.4	3.9	16.5−3.5=13.0
1978 Canadian Four-Airport (CAN-168)	Aircraft	631	Dfb	15	2.2	4.1	22.1−−4.5=26.6
	Road	568	Dfb	15	2.2	4.1	22.1−−4.5=26.6

TABLE II. (*Continued*.)

Description of study				Conditions for survey season (30-year averages for three months)			Range in temperatures (°C) between the warmest and coldest months in the climate (Summer−Winter=Range)
Study [Catalog no.—see Fields (2001)]	Noise source	No. of responses	Climate (Köppen classification)	Temperature (°C)	Precipitation (mm/day)	Wind speed (m/s)	
1981 John Wayne Airport Operation Change (USA-204)	Aircraft	601	Csa	21	6.5	4.0	20.6−13.8=6.8
1980 Australian Five-Airport (AUL-210)	Aircraft	3288	Bsh, Cfb, Csa	18.7	3.2	4.1	22.3−11.7=10.6
1983 Netherlands Tram/Road Traffic (NET-276)	Road	697	Cfb	14.7	2.1	5.0	16.8−2.8=14.0
	Railway	265	Cfb	14.7	2.1	5.0	16.8−2.8=14.0
1989 Austrian Alps Road Traffic (AUS-329)	Road	826	Cfb	10	2.0	1.2	18.7−−1.1=19.8
1990 Modena Traffic (ITL-350)	Road	908	Cfa	17.6	2.0	⋯	24.6−2.4=22.2
1993 Netherlands National Environmental (NET-361)	Road	880	Cfb	15.5	2.3	3.0	16.8−2.2=14.6
1984–1985 Arnhem Trolley Bus Introduction (NET-362)	Road	293	Cfb	8.2	2.1	4.7	16.6−1.6=15.0
1993–1994 French 18-Site Time-Of-Day (FRA-364)	Road	895	Cfb, Csa	11.2	2.2	3.2	19.0−2.7=16.3
1989–1993 Swedish Railway (SWE-365)	Railway	2532	Cfb	6.0	1.5	4.2	15.9−−2.4=18.3
1990–1991 Vaernes Aircraft Military Exercise (NOR-366)	Aircraft	391	Cfc	13.3	2.7	2.4	13.9−−3.2=17.1
1996 Istanbul Trans-Europe Motorway (TUR-367)	Road	154	Csa	22	0.9	⋯	23.2−5.6=17.6
1996 Gothenburg Road Traffic (SWE-368)	Road	1316	Cfb	−1	2.0	4.5	16.2−−1.6=17.8
1996 Kumamoto Road Traffic (JPN-369)	Road	823	Dfa	18.6	5.8	2.9	26.9−5.8=21.1
1985–1986 Ratingen Dusseldorf Road Traffic/Aircraft (GER-372)	Road	559	Cfb	3.9	2.1	⋯	18.1−2.2=15.9
1987 Dusseldorf/Ratingen Aircraft/Road Traffic (GER-373)	Road	440	Cfb	6.9	2.0	⋯	18.1−2.2=15.9
1993 Greifswald Traffic (GER-374)	Road	582	Cfb	15.5	1.8	4.9	18.1−−1.0=19.1
Subtotal		37 994		11.9	2.4	3.7	18.7−2.1=14.7
Total		53 130		11.9	2.5	3.9	18.8−2.2=15.2

TABLE III. Köppen climate classification system (first, second, and third character codes).

First	Second	Third
A=tropical moist (all months>18 °C)		
B=dry climates		h=hot (average>18 °C) k=cool (<18 °C)
C=moist mid-latitude with mild winter	w=dry winter	a=hot summer
D=moist mid-latitude with cold winter	s=dry summer	b=warm summers c=cool summers
E=polar (extremely cold winter and summer)	f=no dry period	

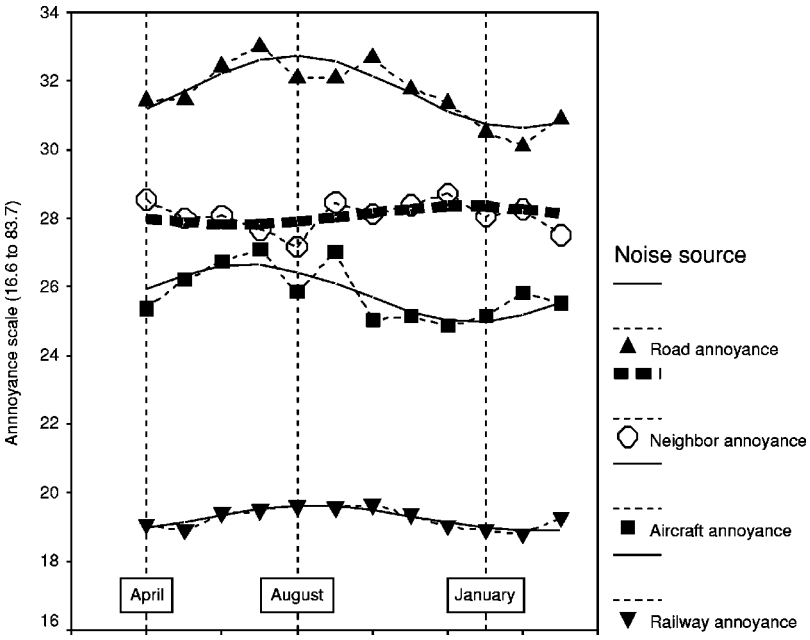

FIG. 1. Netherlands Continuous Life Information Survey (DLO): annoyance scores for April through March, averaged over 7 years for each of the four noise sources where the three annoyance scale points are scored 16.6, 50.0, and 83.3. In addition to the lines connecting the points, the model curves are shown (not significant for neighbors).

sources, the residuals from the regression of annoyance on temperature are not related to season (i.e., the parameter "*b*" in the previous equation is not statistically significant and is also reduced by at least 75%). For aircraft noise annoyance, however, this control for temperature, as well as a control for the three remaining meteorological variables, indicates that a strong seasonal effect remains and is not explained by the meteorological variables.

The consistently positive, but not always statistically significant, temperature coefficients in Table IV suggest that temperature affects noise annoyance. However, the high correlations between the major meteorological variables, especially wind speed and temperature ($r=-0.68$) within this single type of climate, set limits on the precision of the estimates and the conclusions to be drawn about the independent effects of the correlated variables. Data from a wider range of climatic conditions are needed to evaluate the independent effects of meteorological variables.

TABLE IV. Unstandardized regression coefficients for meteorological variables from linear regression analyses of noise annoyance for road traffic, aircraft, and railway (per type of noise source: univariate analyses in first row, multivariate analyses—with and without "sunshine"—in second row). An asterisk indicates that the regression coefficient is statistically significantly different from zero ($p<0.05$).

		Independent variables in the regression equation:[a]							
		Mean temperature (°C)		Sunshine (% of daylight hours)		Precipitation (hours/day)		Wind speed (m/s)	
Type of analysis	Intercept	B	Std Err (B)	B	Std Err (B)	B	Std Err (B)	B	Std Err (B)
				Part A: Road traffic noise annoyance					
Univariate[b]	[b]	0.148*	0.032	0.072*	0.018	−0.519*	0.226	−0.824*	0.248
Multiple	30.765	0.088	0.057	0.032	0.032	0.052	0.363	−0.326	0.408
meteorological variables	31.192	0.129*	0.039			−0.188	0.274	−0.137	0.362
				Part B: Aircraft noise annoyance					
Univariate[b]	[b]	0.075*	0.030	0.048*	0.017	−0.539*	0.198	−0.462*	0.228
Multiple	25.219	0.055	0.054	0.009	0.030	−0.456	0.344	0.154	0.386
meteorological variables	25.342	0.067	0.370			−0.526*	0.258	0.208	0.341
				Part C: Railway noise annoyance					
Univariate[b]	[b]	0.045*	0.013	0.012	0.008	−0.097	0.090	−0.308*	0.097
Multiple	19.724	0.035	0.023	−0.004	0.013	0.083	0.148	−0.240	0.167
meteorological variables	19.675	0.030	0.016			0.110	0.111	−0.261	0.147

[a]The definitions of the meteorological variables are given in Table II with the default meteorological integration period of the two months preceding the month of the interview. The parameters for each independent variable are B=the unstandardized regression coefficient, Std Err(B)=Standard Error of B [95% confidence interval for B=1.96*Std Err(B)].

[b]The "Univariate" rows contain the results from four univariate regressions of noise annoyance on each meteorological condition. The intercept for each of the univariate regression equations is not shown here, but is, of course, different for each of the four regressions.

TABLE V. Results from linear and logistic regressions of noise annoyance on the four meteorological variables, noise exposure, and the noise source for the season-linked data set. A single asterisk (“*”) indicates that a partial regression coefficient is significant at $p<0.05$.

Variables in equation[a]	Meteorological variable (Met. Var.) examined[b] (All meteorological values are averaged over the nominal survey month and the preceding 2 months)											
	Temperature (°C)			Sunshine (hours)			Precipitation (mm)			Wind speed (m/s)[a]		
	B	Std. Err.	Sig.	B	Std. Err.	Sig.	B	Std. Err.	Sig.	B	Std. Err.	Sig.
Part A: Individual meteorological variables—linear regression												
[Intercept]	−36.14			−34.86			−34.48			−28.81		
Met. Var.	0.23	0.166	0.18	0.15	0.618	0.80	−0.05	0.879	0.96	−0.99	1.686	0.56
DNL	1.20*	0.146	0.00	1.20*	0.142	0.00	1.21*	0.147	0.00	1.18*	0.147	0.00
Aircraft	4.70	3.173	0.15	5.03	3.383	0.14	5.26	3.284	0.12	5.06	3.516	0.16
Railway	−13.97*	2.843	0.00	−14.44*	3.118	0.00	−14.63*	3.219	0.00	−13.49*	2.845	0.00
$R^2=$	$R^2=0.186$			$R^2=0.184$			$R^2=0.184$			$R^2=0.169$		
Part B: Individual meteorological variables—logistic regression with a moderate annoyance division (50% or more of scale=1, under 50%=0)												
[Intercept]	−6.11			−6.05			−6.02			−5.64		
Met. Var.	0.01	0.012	0.24	0.02	0.042	0.60	0.01	0.048	0.79	−0.01	0.107	0.90
DNL	0.09*	0.010	0.00	0.09*	0.010	0.00	0.09*	0.011	0.00	0.09*	0.010	0.00
Aircraft	0.38*	0.177	0.04	0.39*	0.192	0.05	0.41*	0.178	0.03	0.42*	0.194	0.03
Railway	−1.32*	0.369	0.00	−1.34*	0.394	0.00	−1.36*	0.381	0.00	−1.21*	0.291	0.00
R^2 analog=	0.129			0.128			0.128			0.115		
Part C: Individual meteorological variables—logistic regression with a high annoyance division (72% or more of scale=1, “high” annoyance)[c]												
[Intercept]	−7.39			−7.32			−7.30			−7.00		
Met. Var.	0.01	0.014	0.64	−0.01	0.041	0.80	−0.03	0.070	0.67	−0.03	0.132	0.83
DNL	0.09*	0.010	0.00	0.09*	0.009	0.00	0.09*	0.010	0.00	0.09*	0.009	0.00
Aircraft	0.14	0.254	0.58	0.17	0.259	0.51	0.18	0.247	0.48	0.12	0.285	0.68
Railway	−1.38*	0.269	0.00	−1.42*	0.261	0.00	−1.42*	0.277	0.00	−1.29*	0.280	0.00
R^2 analog=	0.113			0.113			0.113			0.105		
Part D: Examination of the combined effect of three meteorological variables from a single linear regression analysis.												
[Intercept]	−30.14											
Met. Var.	0.24	0.247	0.34				−0.27	1.018	0.79	−1.11	1.709	0.52
DNL	1.18*	0.143	0.00									
Aircraft	4.51	3.726	0.23									
Railway	−12.67*	2.898	0.00									
$R^2=$	$R^2=0.171$											

[a]The aircraft and railway sources are represented by dummy variables (1=the noise source, 0=other noise source). The coefficients for the dummy variables therefore measure deviations from reactions to road traffic (the default noise source).

[b]The parameters for each independent variable are B=unstandardized regression coefficient, Std Err.=Standard Error of B, Sig.=probability that B is greater than zero. Analyses are based on 53 130 reactions except for analyses including wind speed, for which 47 825 reactions are available.

[c]Since the scale has been rescaled as explained in the text, high annoyance is defined by the top point on a 4- or 5-point scale, the top 2 points on a 6- or 7-point scale, and the top 3 on a 10- or 11-point scale.

IV. EVIDENCE ON METEOROLOGICAL EFFECTS FROM A SECONDARY ANALYSIS OF ARCHIVED SURVEYS

The most extensive evidence on meteorological effects comes from the season-linked data set formed by adding temperature, precipitation, sunshine, and wind speed data to the 41 social survey studies containing ratings of 48 noise sources with the 53 130 noise annoyance responses. These meteorological data characterize the conditions at respondents’ residences at the time of year of the interview. For most of the 41 studies the information about the interview date came from a statement in a report or from personal communication with the study designers about the month or months during which the social survey was in the field. For a few studies the year of the survey was uncertain or the survey occurred in the same months in different years. For all studies a nominal ‘‘survey month’’ was assigned to each respondent that is presumed to best represent the interviewing month(s). In most cases the interviews occurred in that nominal month and in all cases the interviews for a single nominal month were drawn from three or fewer months. Several other, otherwise satisfactory, studies were excluded because some interviews could not be placed within a 3-month period. The final meteorological indicators used in the analysis are averaged over the nominal survey month and the 2 preceding months for the 30-year period from 1961 to 1990. These aggregated meteorological data were readily available for the survey locations from the Royal Netherlands Meteorological Institute (KNMI). No other worldwide data base could be located that provided more detailed data for most of these sites. Given the imprecise specification of the interview date in most of these studies and the availability of the subset of studies in the day-linked data set, it was decided that the KNMI data were sufficient for these analyses.

An analysis of seasonal response patterns in the season-linked data set found a seasonal response pattern that is similar to the sine curve in Fig. 1 for the DLO data. For the season-linked dataset, a nonlinear regression analysis based on the sine function found that the peak annoyance, occurring in September, is about eight annoyance score points

TABLE VI. Regression analyses of noise annoyance on DNL, noise source (road traffic or aircraft), and one of two meteorological variables (temperature or precipitation) for the day-linked data set. The table shows the coefficient of the meteorological variable. [Note: None of the coefficients presented in this table (e.g., coefficients for meteorological variables) are statistically significant at $p<0.05$. The coefficients for noise exposure (not shown in this table) are always statistically significant while the coefficients for noise source are significant in some analyses but not others.]

Type of regression	Annoyance variable[a]	Earliest day from which daily meteorological data are averaged[b]								
		0	1	2	3	7	14	30	60	90
Meteorological variable: temperature (C)										
Linear	Interval scale	−0.11	−0.08	−0.06	−0.04	0.01	0.00	−0.01	0.07	0.20
Logistic	Moderate annoyance	−0.001	0.002	0.004	0.005	0.009	0.008	0.006	0.010	0.017
Logistic	High annoyance	−0.016	−0.015	−0.014	−0.014	−0.011	−0.012	−0.014	−0.010	−0.003
Meteorological variable: precipitation (mm)										
Linear	Interval scale	−0.04	−0.04	−0.06	−0.07	−0.09	−0.09	−0.10	−0.09	−0.03
Logistic	Moderate annoyance	−0.003	−0.003	−0.004	−0.005	−0.007	−0.007	−0.007	−0.010	−0.007
Logistic	High annoyance	−0.001	−0.002	−0.003	−0.003	−0.003	−0.002	−0.003	0.000	0.003

[a]Definitions of ''moderate'' and ''high'' annoyance are given in Table V.
[b]The meteorological data for day ''0'' are for the interview day. The data for day 3, for example, include 4 days, the interview day (0) and the 3 prior days.

higher than for the lowest point in March. The possibility that this seasonal effect might be explained by meteorological variables is examined in detail next.

Table V presents the results from linear and logistic regressions of noise annoyance on the four meteorological variables, noise exposure, and the noise source for the season-linked data set. Parts A, B, and C of Table V present the basic results for the analysis. The partial regression coefficients (B) are in the expected direction in every analysis for temperature and wind speed and two of the three analyses for sunshine and precipitation; noise annoyance increases with increasing temperature, more sunshine, less precipitation, and lower wind speeds. There is not a systematic tendency for more precise estimates (higher significance) for the linear regressions in part A than for the logistic regression of moderate annoyance (part B) or high annoyance (part C). Part D of Table V contains tests for the combined effects of three meteorological variables (temperature, precipitation, and wind speed) by including the three variables simultaneously in a multivariate linear regression equation. The regression coefficients for these variables are almost identical or slightly stronger than those found in part A where they were analyzed separately. The same patterns of relationships were found when analyses (not shown in Table V) were restricted to noise exposures between 45 and 75 DNL and when temperature was averaged for the 3 months prior to the interview month (i.e., not including the interview month). Other analyses did not find evidence for a significant interaction effect between noise level and meteorological variables. Still other analyses did not find evidence of nonlinear relationships or threshold effects when graphs were examined that displayed the form of the relationship between any of the four meteorological variables and the residuals from the regression of annoyance on noise level and noise source. Graphs of the relationship between noise reactions and temperature were also visually examined with similar conclusions.

Although the effects of temperature are consistent in all analyses, none of the meteorological variables' effects in Table V are statistically significant ($p>0.05$). Many alternative analyses with slightly different definitions of meteorological variables and different control variables were performed. Thirty-six of the most plausible analyses yielded only five instances (four for temperature and one for sunshine) that were statistically significant, but none of these controlled for noise source. The evidence for an effect of precipitation or wind speed is especially weak. The significance levels in the ''Sig.'' column for the precipitation and wind speed variables are all over $p=0.50$, indicating that relationships this strong or stronger would be expected more than half of the time even if no relationship existed.

Some confidence that the weak meteorological effects are not due to some more general weaknesses in the data set come from the findings for other variables that are broadly consistent with well-established findings from previous noise surveys. Regression coefficients for noise exposure in Table V are consistent and statistically significant. There is less annoyance with railway noise and the most with aircraft noise. Though the differences in reactions to aircraft and road traffic noise are not usually statistically significant ($p>0.05$), the differences are in the expected direction.

The previously observed seasonal differences (derived from the sine function) are found to be reduced by about $\frac{1}{3}$ by an adjustment for temperature and by about $\frac{1}{2}$ by an adjustment for all four meteorological variables in an analysis of the residual annoyance scores from the season-linked data set. The point of maximum reaction is still reached in September.

Analyses of the 12 studies in the day-linked data set in Table VI address the question of whether long-term noise annoyance reactions are affected by the meteorological conditions on only the day of the interview or by the conditions over a longer period. Regression analyses of noise annoyance on DNL, noise source (road traffic or aircraft), and one of two meteorological variables (temperature or precipitation) are reported for the day-linked data set in Table VI. Each row in the table contains the unstandardized partial regression coefficients from nine regression analyses that differ only in the length of the period over which the meteorological data are averaged. The first two of the three temperature analyses show the same pattern: temperature becomes more positively related to annoyance as the length of the

TABLE VII. Estimated effect of a 15 °C change in temperature from seven analyses performed on this report's three data sets. A single asterisk ("*") indicates that a partial regression coefficient is significant at $p<0.05$.

Unique features of analysis (Analyses are based on linear regressions controlled for noise source using all cases unless noted)	Regression equation			Decibel equivalent of 1 °C increase	Decibel equivalent of 15 °C increase		
	B_{DNL}	B_{Temp}	Std. Err. (B_{Temp})		Best estimate	Lower (95%)	Upper (95%)
Part A: Day-linked data set (Temperature is mean of previous 90 days)							
[Base analysis]	1.213*	0.212	0.358	0.17	3	−6	11
DNL (45–75)	1.658*	0.217	0.313	0.13	2	−4	8
Part B: Season-linked (Temperature is averaged over 30 years for 3 months)							
[Base analysis]	1.229*	0.281	0.147	0.23	3	0	7
DNL (45–75)	1.398*	0.237	0.147	0.17	3	−1	6
Logistic: Moderate annoyance	0.0804*	0.0126	0.0129	0.16	2	−2	7
Logistic: High annoyance	0.0939*	0.0148	0.0129	0.16	2	−2	6
Part C: Continuous DLO survey (Temperature is mean of previous 2 months)							
No control for noise exposure	1.15	0.090*	0.011	0.08	1	1	1

[a]Definitions of "moderate" and "high" annoyance are given in Table V.

period over which temperature is accumulated increases from the day of the interview ("0" column) to all 90 days before the interview ("90" column). For the logistic regression for high annoyance, however, all coefficients are negative although the pattern is similar to the other analyses in that the coefficients become more nearly positive as the number of accumulated days increases. The precipitation analyses generally show little difference for the number of days that are accumulated. The linear regression for precipitation shows a pattern rather similar to temperature with the relationship being a bit stronger for the 7-day to 60-day periods. Other analyses of temperature and precipitation that controlled for noise level but not noise source show a stronger tendency for both temperature and precipitation effects to increase as the number of days accumulated increased (Fields, 2004). Firm conclusions cannot be drawn from the data here since none of the meteorological variables for any of the day-linked analyses in Table VI are statistically significant ($p<0.05$). The table provides no evidence, however, that the days immediately preceding the interview are especially important.

An attempt was made to explore one remaining issue with the season-linked data set: whether reactions are a simple function of meteorological conditions (e.g., temperature), or whether reactions are somewhat moderated by the base, average climatic conditions in a location. Do residents in all climates find, for example, that summer is more annoying but adjust to the average climatic conditions so that the average of the reactions to each season (for example, summer) is the same in all climates? While there was some weak evidence that responses to meteorological conditions might be moderated by long-term climatic conditions, the correlations between the seasonal and yearly average meteorological conditions are too high in this data set to draw even tentative conclusions. The correlations between yearly and seasonal values were $r=0.93$ for precipitation, 0.91 for wind speed, 0.67 for sunshine, and 0.62 for temperature. The DLO data and the data from the other sets did not, however, contain any evidence that seasonal patterns in reactions might disappear if controlled for long term climatic conditions.

V. RANGE OF POSSIBLE TEMPERATURE EFFECTS

Analyses of all three data sets have found more consistent evidence for an effect of temperature than for the effect of precipitation or wind speed. Although the temperature is not usually estimated to have a significant effect on annoyance, it is possible to determine whether these analyses can exclude the possibility of an important temperature effect.

Table VII presents the estimated effect of a 15 °C change in temperature from seven analyses performed on this report's three data sets. Fifteen degrees is about the average difference between the coldest and warmest months of the year in the last column of Table II. About $\frac{3}{4}$ of the sites' study period temperatures are within the 15° range from 7.9 to 22.7 °C. Each of the three parts of Table VII presents the results for one data set. The first three columns of results provide the basic regression coefficients for noise level and temperature and the standard error of the temperature regression coefficient. The decibel equivalent of the 1° increase in the next column is the ratio of the temperature regression coefficient to the noise exposure coefficient. The last three columns indicate the number of decibels of change in noise exposure that are estimated to create the same increase in annoyance as a 15 °C increase in temperature. The results in the "best estimate" column thus indicate this 15° difference in temperature is estimated to produce a change in annoyance that is equivalent to that produced by a 1- to 3-dB increase in noise exposure. An approximate estimate of the 95% confidence intervals of the "best" estimate is formed in the last two columns where only the variability in the temperature regression coefficient has been considered. The DLO study results in part C suggest that the estimate is very exact: the 15 °C increase in temperature is equivalent to a 1-dB increase in noise level. However, this confidence interval does not take into account other nonsampling errors such as the fact that the estimate of the effect of noise level ($B_{DNL}=1.15$) comes from other studies, that those studies used a different type of noise annoyance scale (a degree-of-annoyance rather than frequency-of-annoyance scale), and that it is possible that the temperature effects in the Nether-

lands climatic setting may be confounded with other effects that are not present in other countries. When the results from the wider range of conditions present in the day-linked or season-linked data sets are examined, the confidence intervals for the estimates are very large. The lower 95% confidence interval is negative or zero for all estimates. The upper 95% confidence interval is from 6 to 11 dB. Other analyses, not shown here, found that the estimated size of the effect is sensitive to the temperature measure and whether or not a control for type of noise source is included. In analyses that do not include the control for type of noise source, the estimated effect of temperature is the equivalent of 1 or 3 dB higher. For the minimum daily temperature measure, the best estimates for a 15 °C difference are greater than the equivalent of 6 dB with 95% confidence intervals that exceed 10 dB. The exact values of the estimates for these and other alternatives are shown in a NASA report (Fields, 2004).

VI. CONCLUSIONS

The Netherlands Continuous Life Information Survey (DLO) provides clear evidence for seasonal differences in reactions to noise under the combination of meteorological conditions found in the Netherlands with a moist mid-latitude climate with mild winter and warm summer, without a dry period. This seasonal effect is consistent with most previous publications that discussed seasonal comparisons and found higher annoyance in the summer season. Some evidence about the meteorological conditions that may produce such a seasonal effect comes from the season-linked and day-linked data sets of 53 130 reactions to noise from 41 studies. Increasing temperature, a variable that is closely related with the amount of sunshine, is consistently associated with increased annoyance. There are some weaker indications that increased wind speed and precipitation may decrease annoyance. The best estimates from these data are that a 15 °C difference in temperature has about the same effect on noise annoyance as does a 1- to 3-dB difference in noise exposure. The estimate from the DLO Netherlands data, 1 dB, is relatively precise, but is based on the particular set of correlated climatic conditions found in the Netherlands. The estimates of meteorological effects from the combined data from the 41 season-linked studies are imprecise. They indicate that a 15 °C difference has about the same effect on noise annoyance as does a 1- to 3-dB difference in noise exposure, but confidence intervals indicate that these analyses cannot exclude either the possibility that temperature has little or no effect or that temperature has an important effect.

The results from these analyses do not directly test a theory of noise reactions. However, the results are consistent with the hypothesis that variations in window opening behavior and out-of-doors area usage behavior are related to seasonal meteorological conditions that affect personal noise exposure that in turn affects noise annoyance. This noise-exposure-based hypothesis obtains additional support from the DLO data that do not find a seasonal effect for noise from neighbors, a noise source that could have a very different seasonal exposure pattern than does transportation noise. Some additional support is provided by the analyses that found that controls for meteorological conditions explained most of the cyclical seasonal variation for two of the three noise sources in the DLO Netherlands data and explained about half of the cyclical seasonal variation for the season-linked data set. It should be noted that the effects of small seasonal differences in noise emissions or propagation have been largely controlled for in these analyses because many studies are based on noise measurements made outside residents' homes during the season of the survey.

The analyses of the day-linked data set finds no evidence that long-term reactions are more strongly influenced by meteorological conditions on the interview day or the immediately proceeding days than by the meteorological conditions that prevailed in the weeks and months preceding the interview. Examinations of the form of the relationship between annoyance and temperature did not provide evidence of threshold effects for temperature.

The existing data were not sufficient to test some hypotheses, such as the possibility that annoyance might be reduced at the highest temperatures for residents who own air conditioning. It is possible that the relationship between annoyance reactions, especially short-term reactions, and the concurrent meteorological conditions are more complex due to, for example, threshold values of meteorological variables or complex weightings for the period of integration. However, it seems unlikely that such complexities would be of importance for long-term annoyance because of the apparently long integration time for meteorological conditions, the large amount of variation in meteorological conditions during this period, individual variation in threshold values, and the possibility of considerable variation between residents in their personal window-opening and outside-usage behaviors.

It is also possible that stronger relations between annoyance and meteorological conditions are being partially obscured by approximations introduced by the linkages between the meteorological station data and residences that are described in Table I. While these types of linkages could generate considerable error in estimating hour-to-hour meteorological conditions, it is assumed that such errors are of relatively little importance for most meteorological measures for the long integration periods used here. An analysis of variation between six sites in the Netherlands, for example, found little variation between the sites in temperature, precipitation, and sunshine, but did find more variation in wind speed.

Most previous surveys of noise reactions have not considered the possibility of seasonal differences in reactions. This is a potentially serious problem for studies that compare reactions to changes in noise environments (for example, from a new airport) if the interview data come from different times of year and thus meteorological conditions are correlated and confounded with the primary study variable (i.e., a change in noise exposure). Such seasonal effects are probably of little practical significance for most noise-impact studies that base their conclusions upon contrasts between interviews that are all conducted in the same time period. The possibility of seasonal effects does, however, suggest that previous studies' estimates of long-term noise annoyance reactions may have been affected by the time of year when residents were interviewed.

The most direct interpretation of these studies' results is that for the same noise level, noise annoyance is greater in warmer seasons. In these data, the meteorological conditions at the time of the interview are highly correlated with yearly average meteorological conditions. As a result, the findings are not sufficiently precise to reject the possibility that while there are seasonal variations in response to meteorological conditions, the responses to meteorological conditions that vary between climatic regions may be moderated by adaptations to long-term climatic conditions.

Information about transitory reactions to noise could come from studies in a small number of locations that limit respondents' attention to the immediately preceding events under varied meteorological conditions. Better information about the effects of meteorological conditions on considered, long-term noise reactions cannot be obtained from a study conducted in a single climate under a limited range of meteorological conditions. Better information could be developed from studies that include noise exposure data and date of interview for all respondents; closely link each respondent's location with permanent weather stations; include a wide range of meteorological conditions that are not highly correlated; and use uniform noise assessment procedures, social survey methods, and noise annoyance measures at different sites.

ACKNOWLEDGMENTS

This work was supported by the Netherlands Ministry of Environment and by the National Aeronautics and Space Administration Langley Research Center (Contract No. NAS1-19061).

Borsky, P. N. (**1978**). ''Community Annoyance Before and After Concorde Operation at J.F.K. Airport,'' Noise Research Unit, Columbia Univ., New York.

Brick, J. M., Morganstein, D., and Valliant, R. (**2000**). *Analysis of Complex Sample Data Using Replication* (Westat, Rockville, MD).

Connor, W. K., and Patterson, H. P. (**1972**). ''Community Reaction to Aircraft Noise Around Smaller City Airports,'' NASA CR-2104, National Aeronautics and Space Administration, Washington, DC.

Critchfield, H. J. (**1983**). *General Climatology* (Prentice Hall, Englewood Cliffs, NJ).

de Jong, R. G. (**1981**). ''Nederlands Onderzoek naar Geluidhinder door Vliegtuigen—een overzicht'' (''Research on Noise Annoyance by Planes in the Nederlands—an overview''), (an English translation of this paper is available as: Some Highlights from the Dutch Aircraft Noise Studies. IMG-TNO document no. 765), Geluid en Omgeving (Noise and the Environment), Vol. 3, pp. 228–232.

Draper, N. (**1981**). *Applied Regression Analysis* (Wiley, New York).

Dunn, B. E., and Posey, M. H. (**1974**). *Calgary Noise Survey Vol. II: The Human Response to Noise* (Calgary Univ., Calgary).

Fidell, S. A., Barber, D. S., and Schultz, T. J. (**1991**). ''Updating a dosage-effect relationship for the prevalence of annoyance due to general transportation noise,'' J. Acoust. Soc. Am. **89**, 221–233.

Fields, J. M. (**1993**). ''Effect of personal and situational variables on noise annoyance in residential areas,'' J. Acoust. Soc. Am. **93**, 2753–2763.

Fields, J. M. (**2001**). ''An Updated Catalog of 521 Social Surveys of Residents' Reactions to Environmental Noise (1943–2000),'' NASA/CR-2001-211257, National Aeronautics and Space Administration, Washington, DC.

Fields, J. M. (**2004**). ''Effects of meteorological conditions on reactions to noise exposure,'' NASA/CR-2004-213249, National Aeronautics and Space Administration, Washington, DC.

Fields, J. M., Ehrlich, G. E., and Zador, P. (**2000**). ''Theory and design tools for studies of reactions to abrupt changes in noise exposure,'' NASA CR-2000-210280, National Aeronautics and Space Administration, Washington, DC.

Frankel, M. (**1983**). ''Sampling theory,'' In *Handbook of Survey Research*, edited by P. H. Rossi, J. D. Wright, and A. B. Anderson (Academic, New York), pp. 21–68.

García, A. M., and Romero, J. (**1987**). ''A Social Survey on the Effects of Road Traffic Noise in Urban Areas,'' Federation of Acoustical Societies of Europe, FASE 87, pp. 173–176.

Griffiths, I. D., Langdon, F. J., and Swan, M. A. (**1980**). ''Subjective Effects of Traffic Noise Exposure: Reliability and Seasonal Effects,'' J. Sound Vib. **71**(2), 227–240.

McKennell, A. C. (**1963**). ''Aircraft Noise Annoyance Around London (Heathrow) Airport,'' S.S.337. The Government Social Survey, Central Office of Information, London.

Miedema, H. M. E., and Oudshoorn, C. G. M. (**2001**). ''Annoyance from Transportation Noise: Relationships with Exposure Metrics DNL and DENL and Their Confidence Intervals,'' Environ. Health Perspect. **109**(4), 409–416.

Miedema, H. M. E., and Vos, H. (**1998**). ''Exposure-response relationships for transportation Noise,'' J. Acoust. Soc. Am. **104**(6), 3432–3445.

Miedema, H. M. E., and Vos, H. (**1999**). ''Demographic and attitudinal factors that modify annoyance from transportation noise,'' J. Acoust. Soc. Am. **105**(6), 3336–3344.

Time reversal of noise sources in a reverberation room

Guillemette Ribay,[a] Julien de Rosny, and Mathias Fink
Laboratoire Ondes et Acoustique, CNRS/ESPCI/Université Paris VII, UMR 7587, 10 rue Vauquelin, 75005 Paris, France[b]

(Received 8 September 2004; revised 10 February 2005; accepted 10 February 2005)

Usually, time reversal is studied with pulsed emissions. Here, the properties of time reversal of the acoustic field emitted by noise sources in a reverberation room are studied numerically, theoretically, and experimentally. A time domain numerical simulation of a two-dimensional enclosure shows that the intensity of a time-reversed noise is strongly enhanced right on the initial source position. A theory based on the link that exists between time reversal of noise and the ''well-known'' time reversal of short pulse is developed. One infers that the focal spot size equals half a wavelength and the signal to noise ratio only depends on the number of transceivers in the time reversal mirror. This last property is characteristic of the time reversal of noise. Experimental results are obtained in a $5\times3\times3$ m^3 reverberation room. The working frequency range varies from 300 Hz to 2 kHz. The ability of the time reversal process to physically reconstruct the image of two noise sources is studied. To this end, care is given to the technique to separate two close random sources, and also to the influence of temperature fluctuations on the focusing quality. [DOI: 10.1121/1.1886385]

PACS numbers: 43.55.Br, 43.50.Yw, 43.20.Ye [RLW] Pages: 2866–2872

I. INTRODUCTION

For 15 years, the properties of time reversal (TR) of acoustic fields generated by pulsed sources have been extensively studied in many different areas.[1] Schematically, the experiments follow always the same sketch. In a first step, a source emits a short pulse. The transient acoustic wave propagates through a reflecting-scattering medium that spreads the wave front. One or several microphones record the time dependence of the pressure field. Each signal is sampled and stored in a digital memory. In a second step, the set of recorded signals is read in the reverse order and sent back into the medium by a set of loudspeakers that now replace the previous microphones. Then, due to the time reversal invariance, the wave back-propagates and finally refocuses at the initial source: the initial short pulse is recovered. TR was first experimentally demonstrated in weakly aberrating media such as liver. Later, it has been shown that TR still works in complex media such as a strong multiple scattering medium made of thousands of vertical rods,[2] a chaotic 2D-silicon cavity[3] or a reverberant room.[4]

Nevertheless, until now, only short-transient emitted signals were considered and no attention has been paid to more complex signals. In this article, the properties of TR of noise are studied. The TR of noise sources is of great interest because it makes connections with various problems such as time reversal communication.[5] Actually, a random signal is a model of message to transmit. Hence, time reversing a noise can be regarded as an attempt to send a message to a receiver. The TR of noise is also linked to the Green's function correlation technique.[6–9] This technique consists in recovering the Green's functions from correlations of ambient noise. Derode *et al.* have shown that it can be reinterpreted within the framework of time reversal.[10]

In this article, the TR of noise is investigated numerically, theoretically, and experimentally inside a reverberation room within the audible frequency range. First a time-domain-finite-difference (TDFD) code is used to simulate the acoustic wave propagation inside a two-dimensional (2-D) reverberant room. It shows that a time reversed-wave still focuses at the initial noise source location. A theory is then developed. The main part of this theory consists in showing the relation that exists between the TR of a short pulse and the TR of a noise. From this formalism, it is proven that the hyper-resolution property is still obtained.[2,11] However, the signal to noise ratio only depends on the number of transceivers and not on the bandwidth of the initial source signal. This important result forms one of the main differences between pulse and noise time reversal. In a third part, we present experimental data obtained in a reverberation room within a 300 Hz–2 kHz bandwidth. We focus our attention on the ability of the TR to separate two close sources. Finally, we study the sensitivity of the technique to temperature fluctuations.

II. NUMERICAL SIMULATION

A time-domain finite-difference (TDFD)[12] is used to simulate the acoustic propagation in a bidimensional (2-D) reverberation room whose surface is 5×3 m^2. The impedance of the wall is chosen about three times as large as the impedance of air (see Fig. 1). This relatively small impedance mismatch has been chosen in order to get about 15 wave reflections before the wave vanishes. Due to two major computational limitations, the code stability and computing time, the number of reflections cannot be much larger. However, we introduce a rough wall profile (see Fig. 1) so that the diffuse field is reached more quickly. The boundary con-

[a]Electronic mail: Guillemette.ribay@loa.espci.fr
[b]URL: www.loa.espci.fr

 0001-4966/2005/117(5)/2866/7/$22.50

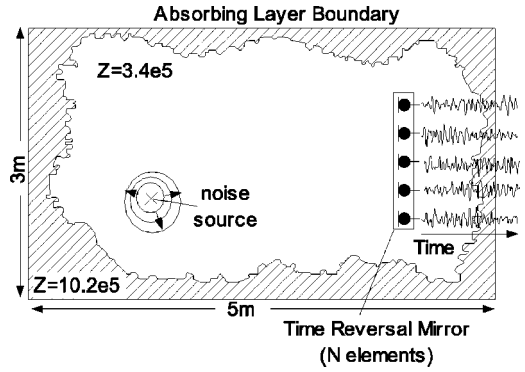

FIG. 1. Simulation configuration.

ditions of the simulation mesh are totally absorbing. The first step starts with the emission of a Gaussian noise spanning from 1400 Hz to 1900 Hz (λ from 17.9 to 24.3 cm) at a point of the grid (see Fig. 1). At the same time the amplitude of the field is recorded at N grid points. These N points make up the time reversal mirror (TRM). The recording lasts more than ten times the reverberation time of the room so that the transient regime due to the beginning of the noise emission is insignificant. During the second step, the recorded signals are re-emitted by the TRM in the reverse order; meanwhile, the pressure amplitude is recorded at a 60 cm spanning vertical line centered at the initial source location. Obviously, unlike pulse time reversal, there is no temporal focusing: after time reversal, the sound pressure is still a random noise. Nevertheless, there is still a spatial focusing effect. This is clearly observed in Fig. 2, where the time-averaged intensity $I(x)$ (i.e., time-integrated squared field) distribution is clearly peaked around the initial source.

We then define a signal to noise ratio, noted SNR, as the ratio of the focused time-averaged intensity at the initial random source to the spatially averaged time-averaged intensity far from the focal spot. The SNR is plotted with respect to the number N of elements of the time reversal mirror in Fig. 3. It seems that the SNR is approximatively equal to N. In

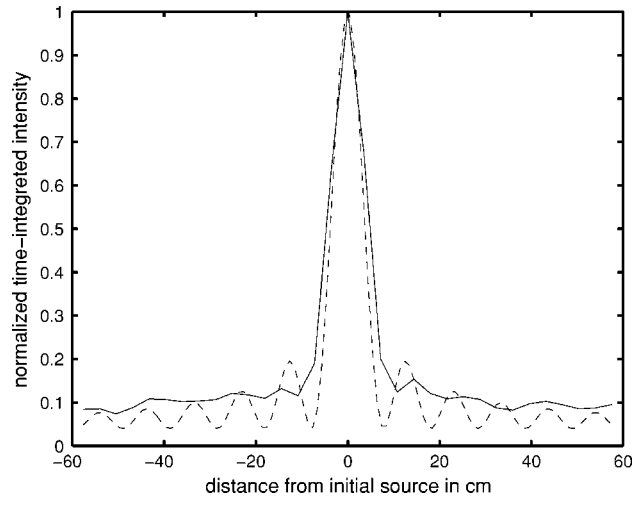

FIG. 2. Solid line: normalized mean-time intensity $I(x)$ versus abscissa x of the recording point during the second step of the Time Reversal Process ($N=24$) obtained with the simulation; dashed line: the same quantity obtained with the theory in two dimensions.

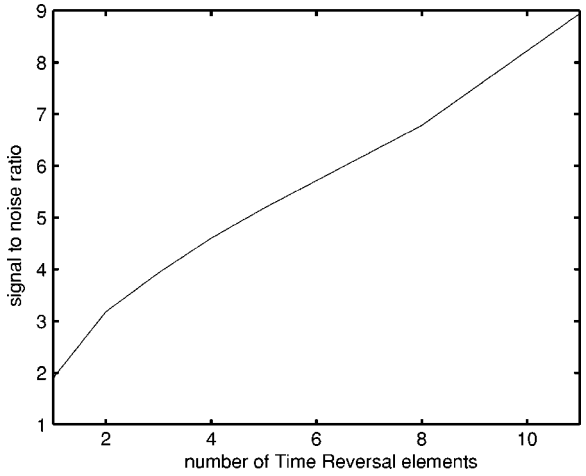

FIG. 3. SNR versus the number of Time Reversal elements N. The frequency of the noise spans between 1400 and 1900 Hz (a linear scale has been chosen instead of a logarithmic one because of the linear relation between the SNR and the number of elements).

case of the TR of pulses, the SNR is also proportional to N, but it is also proportional to a factor that is equal to the pulse bandwidth divided by the frequency correlation length.[13] Hence, the TR of noise corresponds to TR of an almost monochromatic emission.

In Fig. 4 the focal spot width is represented with respect to the central frequency. The width is measured at the half maximum value of $I(x)$. The resolution limit is reached: the focal spot width is about half a wavelength.

III. THEORY

The cornerstone of the theory is the demonstration of the link between pulse time reversal and time reversal of a noise with an identical bandwidth. Thanks to this relation, the properties of pulsed TR found in previous works can be applied to the case of random noise sources.

A. Formal link between transient and noise time reversal

In the first step, a signal $e(t)$ is emitted by a source located at point S. The resulting field is recorded on the Time

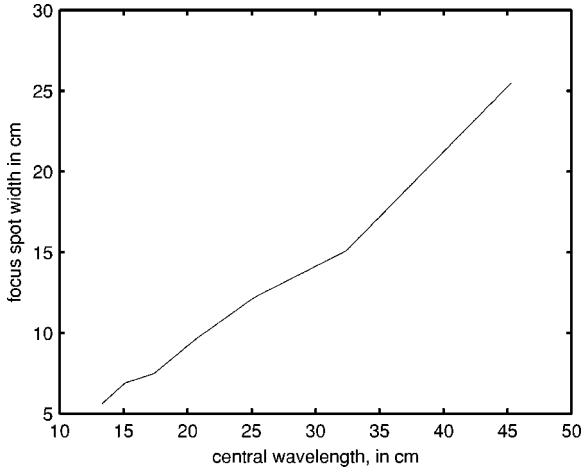

FIG. 4. Focal spot width with respect to the central wavelength ($N=24$). The bandwidth of the noise equals 500 Hz.

Reversal Mirror (TRM), made of N transceivers. On the ith element of the TRM, the recorded field is written as $G(S,\mathbf{r}_i;t)\otimes e(t)$, where $\mathbf{r}_i$ is the position of the ith TRM element, $G(S,\mathbf{r}_i;t)$ is the Green's function between point S and $\mathbf{r}_i$, and $\otimes$ is the convolution operator. In a second step, each signal is time reversed and sent back into the medium. The theory of linear systems and the spatial reciprocity lead to the following expression for the time-reversed field $P(M;t)$ recorded at point M:

$$P(M;t)=K(S,M;t)\otimes e(-t), \tag{1}$$

where

$$K(S,M;t)=\sum_{i=1}^{N} G(S,\mathbf{r}_i;-t)\otimes G(M,\mathbf{r}_i;t). \tag{2}$$

Now, we assume that $e(t)$ is a random signal with $\langle e(t)\rangle = 0$. Experimentally, we record the time-averaged intensity, i.e., $\overline{I(x)}=\int P(M;t)^2\,dt$. This time-averaged intensity can be rewritten as $\overline{I(M)}=P(M;t)\otimes P(M;-t)|_{t=0}$. The introduction of the convolution operator leads to

$$\overline{I(M)}=K(S,M;t)\otimes K(S,M;-t)\otimes e(t)\otimes e(-t)|_{t=0}. \tag{3}$$

One can show that, if the acquisition window is large enough, $I(M)$ is a self-averaging quantity, i.e., $\langle\overline{I(M)}\rangle = \overline{I(M)}$. Let us introduce a function $\gamma(t)$, defined by the way of its Fourier transform, $\tilde{\gamma}$, such as $\tilde{\gamma}(\omega) = \sqrt{\langle|\tilde{e}(\omega)|^2\rangle}$, where $\tilde{e}$ is the Fourier transform of e. Then $\gamma(t)\otimes\gamma(-t)=\langle e(t)\otimes e(-t)\rangle$. We assume that the power spectrum of the colored noise e is a smooth Gaussian-like function with a width W. Then $\gamma(t)$ is a short pulse of duration $\tau_0=1/W$. Equation (3) becomes

$$\overline{I(M)}=\int [K(S,M;t)\otimes\gamma(t)]^2\,dt. \tag{4}$$

Hence, we deduce from Eq. (4) that the time-averaged intensity after time reversal of a noise [on the left-hand side of Eq. (4)] can be simply interpreted as the time-integrated intensity after the Time Reversal of a short pulse $\gamma(t)$ [on the right-hand side of Eq. (4)].

B. Theoretical results on the time reversal of a pulse

The time-reversed field of a pulsed source is made of two contributions: the field that exactly backpropagates toward the initial source location, and the field that does not backpropagate. The last contribution is a "deterministic noise." Indeed, when the TR experiment is performed twice, these noise contributions are identical. Nevertheless, the wave field does not show a coherent structure, and this contribution is uniformly distributed all over the cavity, except close to the boundaries. A schematic representation of the time dependence of the time-reversed wave field recorded at the initial source location is drawn in Fig. 5. The brief and strong peak corresponds to the "perfect" backpropagating contribution, and the lower but longer time evolution corresponds to the "noise." The characteristic amplitude and duration have been computed within a diffusive model.[2,13] They depend on the number of TR transceivers, N, the reverberation time of the enclosure, τ, and the duration of the pulse, τ_0 (see Table I). A diffusive approach is justified here, because there are more than ten reflections on the boundaries before the wave vanishes. Computing the signal to noise ratio means evaluating the respective energies (i.e., the time integration of the square of the field) of the peak and the "deterministic" noise. The exact calculus is fastidious and we prefer to give a more intuitive approach here. The peak energy is given by $N^2\tau^2/\tau_0$ while the energy of the noise is equal to $N\tau^2/\tau_0$. Hence, the signal to noise ratio at the initial source location equals $I_{\text{peak}}/I_{\text{noise}}=N$. As for the spatial dependence of the peak, it has been shown that in the diffusive model, as the wave focuses from every direction, the focal spot is given by a Bessel function of the first kind, $J_0(kr)$, in two dimensions and a cardinal sine, $\text{sinc}(kr)$ in three dimensions,[13] where k is the wave number and r is the distance from the initial source position. It is assumed here that the initial excitation is narrow band, i.e., that the central frequency is much larger than the bandwidth. Finally, the normalized mean intensities in two and three dimensions are, respectively,

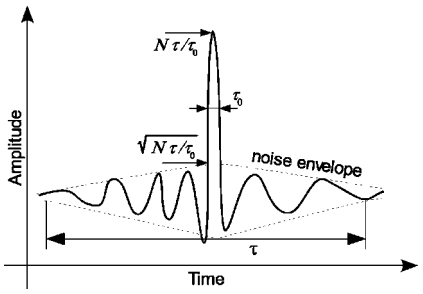

FIG. 5. Schematic representation of the time dependence of a field time reversed by a TR mirror made of N transceivers. Here the initial source emitted a short pulse lasting τ_0 in an enclosure whose reverberation time equals τ.

$$\overline{I(M)}/I_{\text{noise}}\approx 1+NJ_0^2(k\|\mathbf{r}_M-\mathbf{r}_S\|), \tag{5}$$

$$\overline{I(M)}/I_{\text{noise}}\approx 1+N\,\text{sinc}^2(k\|\mathbf{r}_M-\mathbf{r}_S\|). \tag{6}$$

Equation (5) is in agreement with the numerical results (see Figs. 2, 3, and 4) that confirm our theoretical approach.

To be exhaustive, one should mention that the previous theoretical results are only valid when the reverberation time of the room is lower than the Heisenberg time τ_{H} associated with the room.[13] τ_{H} equals the modal density of the room, that is, the number of modes per frequency unit. When τ is greater than τ_{H}, it has been shown that the signal to noise ratio of the pulse compression for transient time reversal reaches a plateau $\sqrt{N\tau_{\text{H}}/\tau_0}$, while the ratio of the duration of noise to the pulse duration increases as τ/τ_0. Hence, the SNR is given by $N\tau_{\text{H}}/\tau$ when considering the time reversal of noise. Thus, surprisingly, when $\tau>\tau_{\text{H}}$, the signal to noise

TABLE I. Respective amplitude and duration of the pulse compression and the deterministic noise generated by the TR.

	Pulse compression	Noise background
Amplitude	$N\tau/\tau_0$	$\sqrt{N\tau/\tau_0}$
Duration	τ_0	τ

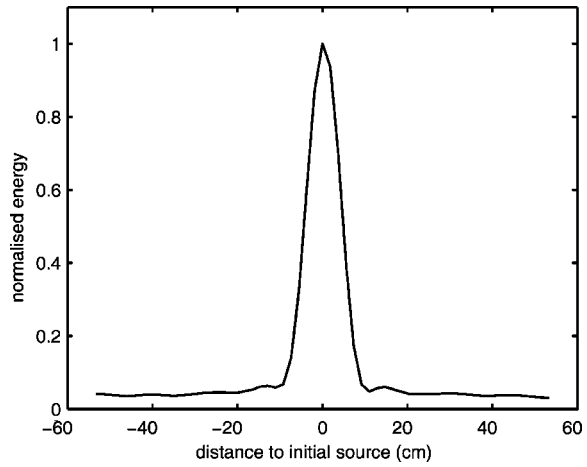

FIG. 6. Time-averaged intensity after the TR of the noise ($N=32$).

ratio degrades as the room becomes more and more reverberant. However, in the article, we only deal with reverberation rooms with Heisenberg time much higher than their reverberation time ($\tau \ll \tau_H$).

IV. EXPERIMENTS

Experiments have been performed in a $5\times3\times3$ m^3 reverberating room with a reverberation time (Sabine time) T_{60} of 3 s. The time reversal mirror is made of N digital recorders and N digital emitters coupled to N transceiver devices. One transceiver is composed of a loudspeaker with a small electret microphone in front of it. The sampling frequency is 20 kHz. The time-reversed wave is recorded by a microphone fixed on a one-axis motor bench. The initial random source (one loudspeaker) is set at the center of the motor bench. It emits a Gaussian noise with a frequency band spanning from 300 to 2000 Hz. The noise emission and time-reversed signals must last more than the reverberation time of the room in order to reach a steady-state regime. A focusing is observed (see Fig. 6). However, the focal spot width is not exactly equal to $\lambda/2$ (see Fig. 7). Actually, the limit of resolution [see Eq. (6)] is only reached when considering a point-like initial source. Our initial loudspeaker is baffled in a wooden box, leading to an extended source and therefore to an extended focusing.

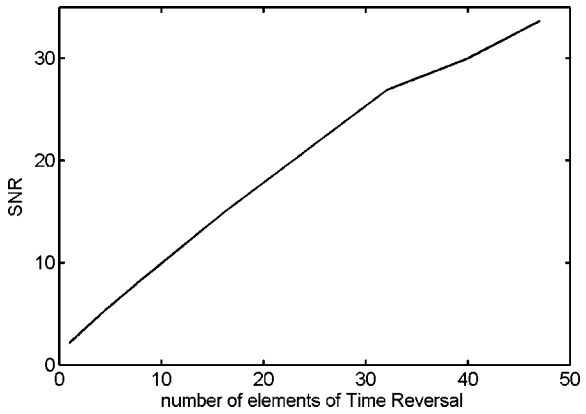

FIG. 8. SNR versus the number of transceivers in the TR mirror (central frequency=1650 Hz).

A. SNR

At 1650 Hz, the signal to noise ratio is linear with respect to the number of transceivers (Fig. 8). However, the slope is a bit smaller than 1, as expected by the theory.

Actually, if two TRM transceivers are separated by less than half a wavelength, they contribute to the SNR as if there were only one element, because in this case, they record and time-reverse quasi-identical signals. More generally, a group of transceivers within half a wavelength acts as one transceiver. As a consequence, knowing that there are N equidistant elements separated one from another by a distance d, the effective number N_{eff} that now replaces N in the mean intensity expressions [see Eqs. (5) and (6)] is given by

$$N_{\text{eff}} \approx \begin{cases} 2Nd/\lambda, & \text{when } \lambda/2 > d, \\ N, & \text{when } \lambda/2 < d. \end{cases} \tag{7}$$

Besides, the source used in the first step of the TR process is a common loudspeaker, and because of the working frequency range and the diaphragm size, it cannot be considered as a point-like source. This has to be taken into account

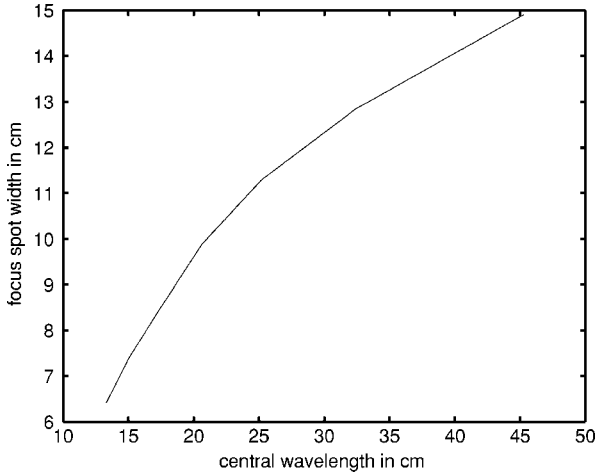

FIG. 7. Width of the focal spot versus the central frequency of the noise ($N=47$).

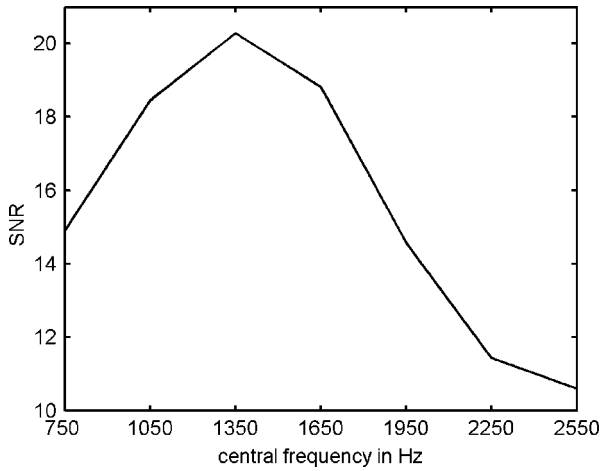

FIG. 9. Experimental SNR versus the central frequency of the emitted noise. The TRM transceiver number is fixed ($N=27$).

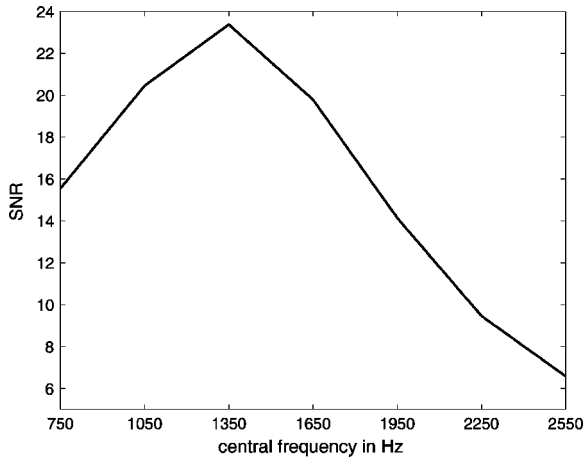

FIG. 10. Theoretical SNR versus the central frequency of the emitted noise. The TRM transceiver number is fixed ($N=27$).

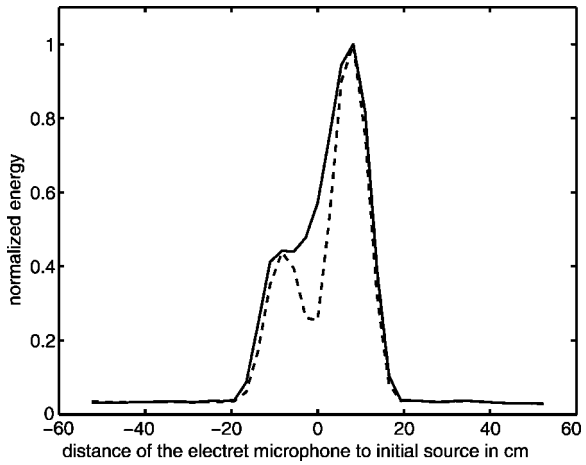

FIG. 11. Experimental normalized energy recorded after the time reversal of two random sources separated by 15 cm that are uncorrelated (dashed line) and correlated (solid line).

in the calculus of the SNR. To evaluate the time-averaged acoustic field intensity, we assume that the signals are ergodic. We consider a two dimensional apodized source. The apodization function is noted as $w(\mathbf{r}_s)$ and its width is a. Within the diffusive assumption, in a 3-D model, the SNR equals

$$\mathrm{SNR}=1+N_{\mathrm{eff}}\frac{(\int w(\mathbf{r}_s)\mathrm{sinc}(k\|\mathbf{r}-\mathbf{r}_s\|)d\mathbf{r}_s)^2}{\int\int w(\mathbf{r}_s)w(\mathbf{r}_{s'})\mathrm{sinc}(k\|\mathbf{r}_{s'}-\mathbf{r}_s\|)d\mathbf{r}_s\,d\mathbf{r}_{s'}}. \tag{8}$$

This effect is confirmed experimentally: for a given number of transceivers ($N=27$), when a is equal to 10.6 cm and d is around 12 cm, the evolution of the SNR with respect to the central frequency (Fig. 9) given by the theoretical model is the same as the evolution observed experimentally (Fig. 10).

The theoretical SNR level is a little greater than the experimental one, because some parameters that can influence the SNR have not been taken into account, such as the directivity pattern of the loudspeakers of the time reversal mirror. Moreover, in the experiments, the measured acoustic field is made of a diffusive part and a nondiffusive part. The latter corresponds to the first reflections. Actually, the theory we develop here does not take into account the nondiffusive part, and therefore the experimental results depend a little on the experimental configuration. However, provided the number of TR elements is great enough, even with a non-point-like source, the TR can build the acoustic image of the initial source with a high signal to noise ratio.

B. Resolution

Since the TR naturally builds the acoustic image of the initial source (Fig. 6), it may be an original holographic technique in order to physically construct the image of a set of random sources. One of the main issues in holography is the resolution, i.e., the ability of the technique to separate two close random sources. In order to evaluate the resolution capacities, two sources separated by 15 cm emit the same noise (correlated sources) or two different noises (uncorrelated sources). The corresponding focusing are plotted in Fig. 11. Obviously the resolution is better when the emitted noises are uncorrelated. As in the previous section, one can show within the diffusive assumption that when dealing with two point-like sources of amplitudes α_1 and α_2 and positions $\mathbf{r}_1$ and $\mathbf{r}_2$, the averaged intensity is, respectively, in the case of uncorrelated and correlated sources:

$$\frac{\overline{I(M)}}{I_{\mathrm{noise}}}\approx\begin{cases}1+N_{\mathrm{eff}}\dfrac{\alpha_1^2\,\mathrm{sinc}^2(k\|\mathbf{r}_M-\mathbf{r}_1\|)+\alpha_2^2\,\mathrm{sinc}^2(k\|\mathbf{r}_M-\mathbf{r}_2\|)}{\alpha_1^2+\alpha_2^2}, & \text{uncorrelated},\\ 1+N_{\mathrm{eff}}\dfrac{(\alpha_1\,\mathrm{sinc}(k\|\mathbf{r}_M-\mathbf{r}_1\|)+\alpha_2\,\mathrm{sinc}(k\|\mathbf{r}_M-\mathbf{r}_2\|))^2}{\alpha_1^2+\alpha_2^2+2\alpha_1\alpha_2\,\mathrm{sinc}(k\|\mathbf{r}_1-\mathbf{r}_2\|)}, & \text{correlated}.\end{cases} \tag{9}$$

The theory (Fig. 12) correctly describes the experimental results (Fig. 11).

C. Sensitivity to medium modification

Fluctuations of the acoustical properties of the medium between the forward and backward steps can spoil the TR focusing because it breaks the reciprocity. Here the influence of the room temperature variation during the time reversal process is studied. The time reversal is performed with a TRM made of 47 transceivers. The central frequency and the bandwidth of the emitted noise are, respectively, equal to 1750 and 500 Hz. The set of N signals recorded during the

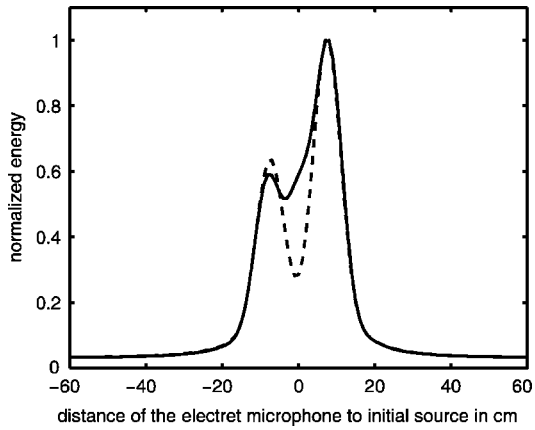

FIG. 12. Theoretical prediction of the normalized energy after time reversal of two random sources separated by 15 cm that are uncorrelated (dashed line) and correlated (solid line).

first step of the TR process is repetitively time reversed for various room temperatures. In Fig. 13 is shown the evolution of the SNR with respect to the room temperature. The initial room temperature is 22.15 °C. First the room was heated to 25.4 °C and then cooled to 20.9 °C. Obviously, degradation of the SNR is due to the decreasing of the averaged intensity peak. With a variation of one degree, the acoustic properties of the room have changed enough so that the focusing vanishes. Another phenomenon is observed: when the room is cooled, as the temperature reaches its initial value, the SNR does not reach the initial maximum. This is probably due to temperature inhomogeneities in the room. Indeed, during the heating phase, at T equal to 22.15 °C, the heaters and the walls are cold; during the cooling phase, as the thermometer comes back to 22.15 °C, the heaters are still hot and the walls are a little bit warmer than before. As a consequence, the reciprocity of the medium is not completely restored and the amplitude of the peak only partially restored. One may wonder whether the temperature-caused degradation of the refocusing could not be compensated by stretching or compressing the signals before re-emitting them. Some works (e.g., Ref. 14), dealing with the temperature dependence of ultrasonic field correlations inside reverberant cavity, successfully compensate the temperature effect by stretching the signals.

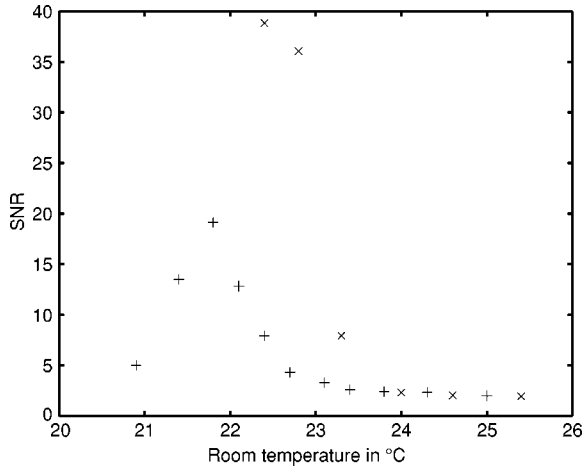

FIG. 13. SNR versus room temperature during the second step.

It will work similarly when a field generated by a short pulse is time reversed. However, in our case, it is not possible to make use of this sort of compensation because we work with a continuous source. The emitted noise lasts a few seconds, and thus the pressure at a given time results in a sum of contributions emitted at different times. There is no more link between the recording time of the field and the distance covered by the wave.

V. CONCLUSION

Since time reversal through complex media has been studied, it is commonly admitted that the larger is the bandwidth of the initial signal, the higher is the signal to noise ratio. In this article, it is paradoxically shown that the signal to noise ratio is independent of the noise bandwidth. Actually, in the previous works, the form of the initial signal, generally a short pulse, was of prior knowledge. Now, when a noise source is time reversed, the time dependence of the signal that refocuses is unknown. Only a signal to noise ratio in terms of time-integrated intensities that does not depend of the bandwidth can be defined. This result is fundamental in the theory of time reversal. Indeed, until now, it was known that the spatial and temporal diversity help to refocus spatially a short pulse. However, the respective role of each of them was not clearly identified. Here, with a point-like noise source, there are no effects due to the frequency diversity, even when the noise is wide band. Thus, only the spatial diversity plays a role in the spatial focusing.

One potential interest of the method is, like holography, to rebuild the image of a noise source (Ref. 15), such as the noise of a car or a plane. Whereas holography requires the computation of the Green's functions of the room and thus has to be used in anechoic or at least weakly reverberant chambers, our technique allows the use of strong reverberant rooms. Moreover, the reverberation leads to a very good resolution, about half a wavelength, with only a few transceivers. However, TR imaging is much more cumbersome, since it needs to scan the acoustic pressure at many locations around the source. Another potential interest of the technique is its application to TR communications inside complex media. To this end, the survey of the Time Reversal of noise has to be extended to open-multiple scattering media.

ACKNOWLEDGMENTS

Many thanks to Mickael Tanter for his numerical code called "ACEL" that we used to perform our simulations and to Arnaud Tourin for helping us to improve the English in the manuscript.

[1] M. Fink, "Time reversed acoustics," Phys. Today **50**, 34 (1997).
[2] A. Derode, A. Tourin, and M. Fink, "Limits of time reversal focusing through multiple scattering: Long range correlation," J. Acoust. Soc. Am. **107**, 2987 (2000).
[3] C. Draeger and M. Fink, "One-channel time reversal of elastic waves in a chaotic 2D-silicon cavity," Phys. Rev. Lett. **79**, 407–410 (1997).
[4] S. Yon, M. Tanter, and M. Fink, "Sound focusing in rooms: The time reversal approach," J. Acoust. Soc. Am. **113**, 1–11 (2003).
[5] G. F. Edelmann, T. Akal, W. S. Hodgkiss, S. Kim, W. A. Kuperman, and H. C. Song, "An initial demonstration of underwater acoustic communi-

cation using time reversal,'' IEEE J. Ocean. Eng. **27**, 602–609 (2002).
[6] M. Campillo and A. Paul, ''Long-range correlations in the diffuse seismic coda,'' Science **299**, 547–549 (2003).
[7] R. L. Weaver and O. I. Lobkis, ''On the emergence of the Green's function in the correlations of a diffuse field,'' J. Acoust. Soc. Am. **110**, 3011–3017 (2001).
[8] O. I. Lobkis and R. L. Weaver, ''Ultrasonics without a source, thermal fluctuation correlations at MHz frequencies,'' Phys. Rev. Lett. **87**, 134301 (2001).
[9] B. A. van Tiggelen, ''Green function retrieval and time-reversal in a disordered world,'' Phys. Rev. Lett. **91**, 243904 (2003).
[10] A. Derode, E. Larose, M. Campillo, and M. Fink, ''How to estimate the Green's function of a heterogeneous medium between two passive sensors? Application to acoustic waves,'' Appl. Phys. Lett. **83**, 3054–3056 (2003).
[11] P. Blomgren, G. Papanicolaou, and H. Zhao, ''Super-resolution in time-reversal acoustics,'' J. Acoust. Soc. Am. **111**, 203–248 (2002).
[12] The code was developed by M. Tanter, Laboratoire Ondes et Acoustique, France.
[13] C. Draeger and M. Fink, ''One-channel time-reversal in chaotic cavities: Theoretical limits,'' J. Acoust. Soc. Am. **105**, 611 (1999).
[14] R. L. Weaver and O. I. Lobkis, ''Temperature dependence of diffuse field phase,'' Ultrasonics **38**, 491–494 (2000).
[15] J. D. Maynard, E. G. Williams, and Y. Lee, ''Nearfield acoustic holography: I. theory of generalized holography and the development of n.a.h.,'' J. Acoust. Soc. Am. **78**, 1395–1413 (1985).

Acoustic analysis in Mudejar-Gothic churches: Experimental results

Miguel Galindo,[a] Teófilo Zamarreño,[b] and Sara Girón[c]
Departamento de Física Aplicada II, Universidad de Sevilla, ETS de Arquitectura, Avda. Reina Mercedes 2, 41012-Sevilla, Spain

(Received 11 June 2004; revised 8 November 2004; accepted 28 February 2005)

This paper describes the preliminary results of research work in acoustics, conducted in a set of 12 Mudejar-Gothic churches in the city of Seville in the south of Spain. Despite common architectural style, the churches feature individual characteristics and have volumes ranging from 3947 to 10 708 m^3. Acoustic parameters were measured in unoccupied churches according to the ISO-3382 standard. An extensive experimental study was carried out using impulse response analysis through a maximum length sequence measurement system in each church. It covered aspects such as reverberation (reverberation times, early decay times), distribution of sound levels (sound strength); early to late sound energy parameters derived from the impulse responses (center time, clarity for speech, clarity, definition, lateral energy fraction), and speech intelligibility (rapid speech transmission index), which all take both spectral and spatial distribution into account. Background noise was also measured to obtain the NR indices. The study describes the acoustic field inside each temple and establishes a discussion for each one of the acoustic descriptors mentioned by using the theoretical models available and the principles of architectural acoustics. Analysis of the quality of the spaces for music and speech is carried out according to the most widespread criteria for auditoria. [DOI: 10.1121/1.1894789]

PACS numbers: 43.55.Gx, 43.55.Mc, 43.58.Gn [NX] Pages: 2873–2888

I. INTRODUCTION

The acoustic aspects of places of worship have been affected throughout history by the dominant architectural style and by the type of religion, as shown by several authors.[1–3] Until auditoria emerged in the western world, the church stood out from other types of buildings as the place which witnessed the birth and performance of musical compositions. Sendra *et al.*[4] have made a detailed historical investigation of the evolution of acoustic conditions in Christian churches from their origins to the Late Baroque period. By consulting numerous documentary sources on the history of architecture and the history of music they have found hardly any evaluations of, nor references to, acoustics in churches. It seems that form has long taken precedence over function, even liturgical function, in the development of church architecture.

Over recent decades there has been an increase in the literature, and performance to conciliate both functional aspects (music and speech) is being considered as much in the construction of new liturgical buildings[5] as in the study of the acoustics of existing worship enclosures.[6] These spaces are sometimes renovated, sometimes reused with other cultural aims, or are even shared with the liturgical use.

This recent interest in the acoustic behavior of places of worship is common to all religious creeds. Without trying to be exhaustive it is possible almost chronologically to emphasize in this sense the early study of Raes *et al.*[7] in 1953 of the acoustic properties of two Roman basilicas, and the reverberation study in an extensive range of Spanish, French, and English churches of different creeds and architectural styles made by Fearn[8] in 1975. In the 1980s the measurements of reverberation times, sound pressure levels, and tests of articulation were carried out by Lewers *et al.*[9] in 1984 in St. Paul's Cathedral in London, and in 1985 the experimental work of Recuero *et al.*[10] was based in a Spanish church.

The last decade has seen work published on speech intelligibility reported by Hammad[11] in 30 mosques of Amman in 1990 and on the acoustics of a huge mosque in Amman carried out by Abdelazeed *et al.*[12] in 1991. In 1996 Klepper[6] studied the electroacoustic system at Holy Cross Cathedral in Boston to reconcile musical and oral uses. At the end of the decade in Switzerland the work of Desarnoulds *et al.*[13] appeared in 1998 which analyzed geometric parameters and the results of objective acoustic measurements for about 200 Swiss churches. There are also the research programs on the acoustics field in Catholic churches in Portugal coordinated by Carvalho,[14] the European project CAHRISMA on Sinan's mosques and Byzantine churches,[15] and, more recently, the work in Italian Romanesque churches due to Magrini *et al.*,[16] the papers of Cirillo *et al.*[17] on the acoustics of the Apulian-Romanesque churches, and the measurements of acoustic characteristics of mosques in Saudi Arabia by Adel,[5] among others.

The importance of this topic is also manifested in some of the latest international congresses such as in Rome[18] and Seville, Spain[19] showing a specific session for worship building acoustics inside the more general field of architectural acoustics.

[a]Electronic mail: mgalindo@us.es
[b]Electronic mail: teofilo@us.es
[c]Electronic mail: sgiron@us.es

FIG. 1. Wooden timber roofs in San Isidoro church (a), stone apse in San Esteban church (b), Santa Marina church lateral nave (c), interior views of Santa Marina church (d), San Marcos church (e), and Santa Catalina church (f).

II. MUDEJAR CHURCHES

When the Christians recovered southern Spain from the Arabs in the 13th century, they decided to build their temples over the mosques, thus symbolizing the new authority. However, this power had to allow and even to favor the coexistence of three linguistic, religious, and cultural groups: the Christians, the most numerous group; the Jews, fewer in number and located in a kind of separate city; and the Moors, the smallest colony since most of the Arabs had emigrated to Islamic kingdoms.

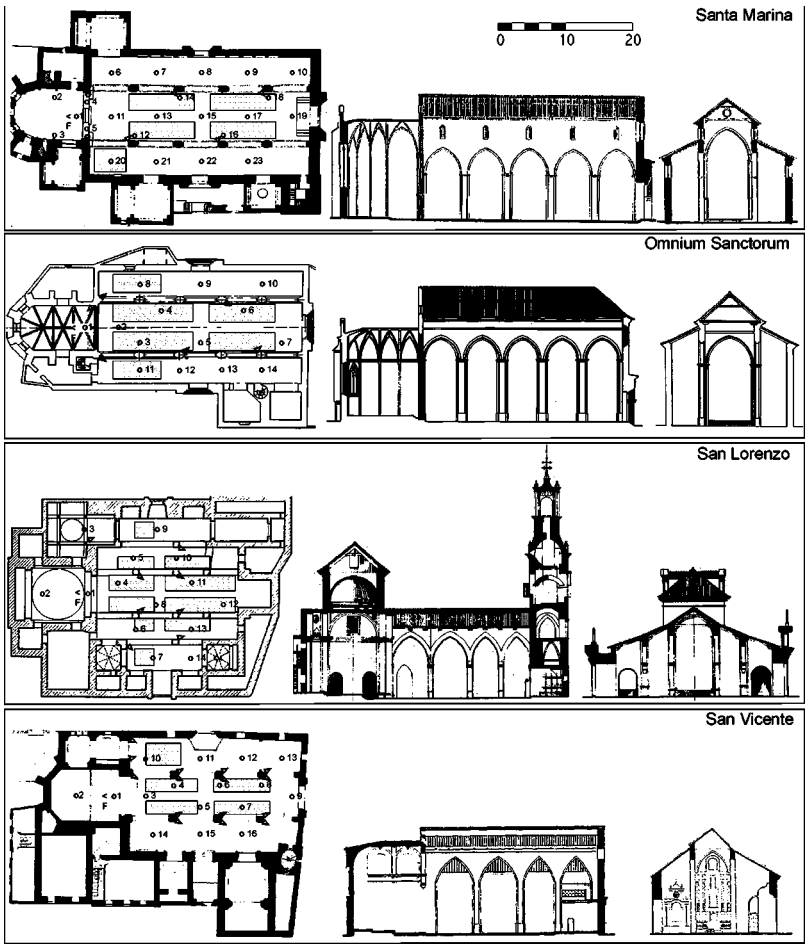

FIG. 2. Ground plan with the source ($\tilde{F}$) and receiver positions (○) for measurements, locations of loudspeakers (▷), and pew zone (darker area); longitudinal and cross sections for Santa Marina church, Omnium Sanctorum church, San Lorenzo church, and San Vicente church.

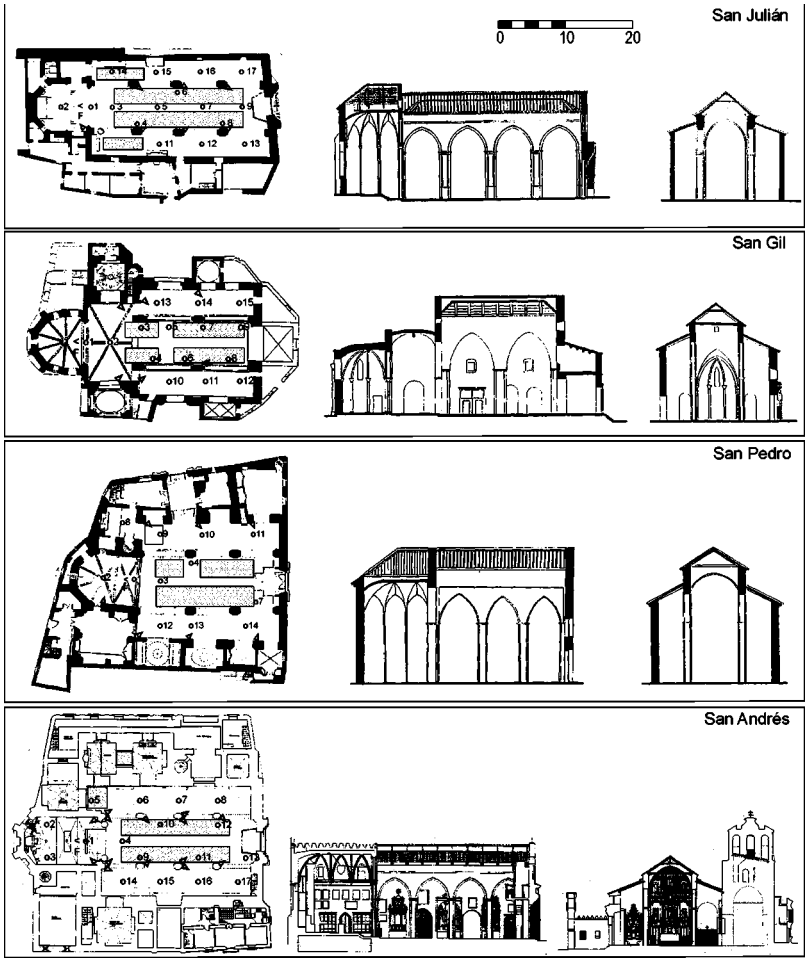

FIG. 3. Ground plan with the source ($\tilde{F}$) and receiver positions (○) for measurements, locations of loudspeakers (▷), and pew zone (darker area); longitudinal and cross sections for San Julián church, San Gil church, San Pedro church, and San Andrés church.

For their buildings they decided to follow the so-called *proto-Gothic* which at that time was the highest form of artistic expression in the Christian western world.

There immediately arose an artistic confrontation between the Gothic Castilian culture and the Muslin Andalusian culture; this conflict gave birth to the most distinctive artistic movement in medieval Spain: the Mudejar style. The Mudejar style cannot be understood as Islamic art or as Western Christian art, but rather as a link between the two; it is a uniquely Spanish artistic movement.

The Mudejar churches in Seville are morphologically characterized by a stylistic dualism: a vaulted Gothic apse and a body of three naves with a wooden timber roof (collar beam in the main nave) of Moorish origin. The brick walls are complemented with portals and a stone apse. The supports are also clearly Islamic, with quadrangular or sometimes octagonal pillars and with raised brick mouldings as decoration. Pointed, round, or segmental arches rest on these supports (Fig. 1).

Among other elements of particular interest, funeral chapels are found which have been added successively to the side naves and which, on some occasions, are housed in remaining sections of preexisting mosques. Funeral chapels do not exist in San Julián, San Esteban, and San Marcos churches (Figs. 2–4).

According to the specialist Angulo,[20] the first Mudejar church built in Seville was Santa Marina; this church established the so-called *Seville parish type*.

The 12 temples analyzed in the city of Seville are all located in its historical center. Figures 2–4 shows each church's ground plan with source and receiver positions for measurements, the seating zone for the congregation and the location of loudspeakers, and its longitudinal and cross sections.

The measurements are taken in accordance with the Catholic liturgy after the Second Vatican Council: the priest is facing the parishioners and not with his back to the congregation as before; currently the native language is used for ceremonies instead of Latin; a larger seating area has been incorporated in the churches; and the altar is nearer the congregation.[21]

Other complementary information of the churches is included in Tables I and II. Table I summarizes some geometric data of interest: volume V, length L, width W, average height H, central nave ground surface S_C, lateral nave ground surface S_L, and total ground surface S_T for the 12 churches studied. In Table II, surface materials and furnishings are presented for a better understanding of their acoustic behavior.

The present work describes a part of Galindo's Ph.D. thesis.[22] The acoustic measurements of these churches are given in detail and a previous diagnosis is carried out by taking into acount the monoaural acoustic parameters of room quality. Finally, an evaluation is presented which uses auditorium criteria in relation to audibility, intelligibility, and conditions for music perception. These churches play an im-

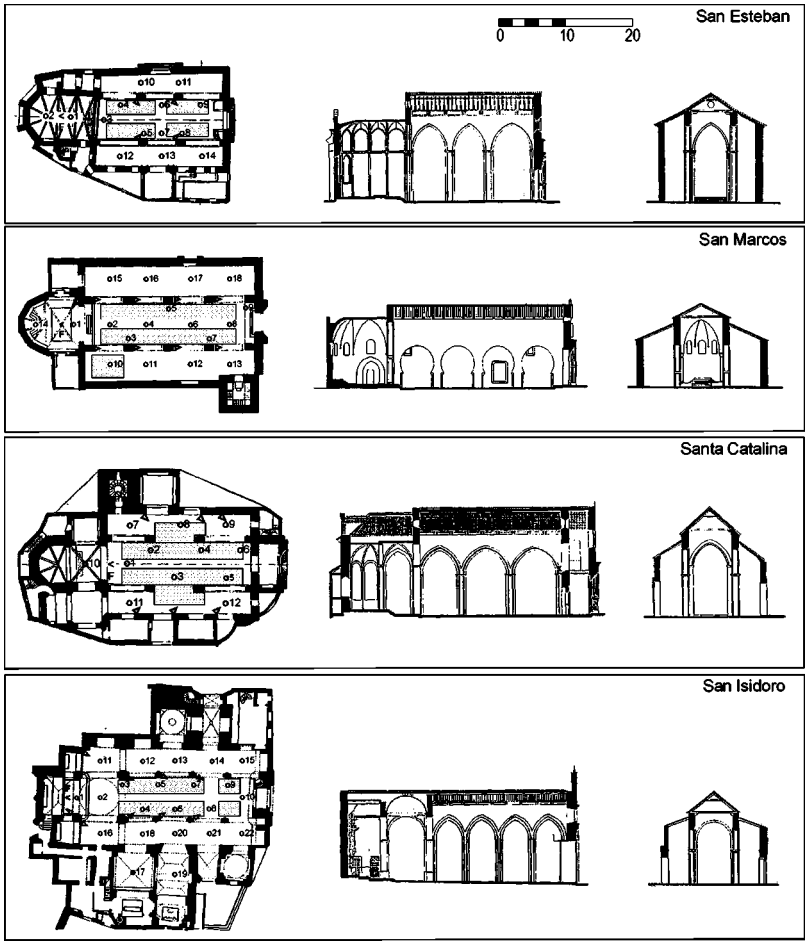

FIG. 4. Ground plan with the source ($\vec{F}$) and receiver positions (○) for measurements, locations of loudspeakers (▷), and pew zone (darker area); longitudinal and cross sections for San Esteban church, San Marcos church, Santa Catalina church, and San Isidoro church.

portant role in the architectural and artistic patrimony of the city.

III. EXPERIMENTAL METHOD

The procedures employed here are those established in the ISO 3382 standard and all measurements have been taken in unoccupied churches. Temperature and relative humidity have been measured with a precision electronic thermohygrometer and a barometer determines the atmospheric pressure. The range of variation is 22.6–27.4 °C for the temperature, 35.7%–65.7% for the relative humidity, and 101.7–102.5 kPa for the atmospheric pressure, respectively. Monaural impulse responses and other room responses to stationary signals have been measured to determine the following parameters for each frequency band and in all receiver positions: reverberation time (RT) and early decay time (EDT) for the evaluation of reverberation characteristics; sound strength (G) to explore the sound level distribution within the measuring area; center time (Ts), clarity for speech (C_{50}), clarity (C_{80}), definition (D_{50}), and lateral energy fraction (LF) as energetic parameters related to the early to late sound energy ratio obtained from the impulse responses, and, finally, the STI-RASTI indices to evaluate the intelligibility from the degradation of the modulation transfer function.

To quantify the background noise in the churches the

TABLE I. Geometric data in Mudejar-Gothic churches.

Church	Reception	V (m^3)	L (m)	W (m)	H (m)	S_C+S_L (m^2)	V/S_T (m^3/m^2)
Sta. Marina (MN)	23	10 708	34	19	15	250+279	20.24
O. Sanctorum (OM)	14	8180	29	16	16	194+219	19.81
S. Lorenzo (LO)	14	7040	24	24	16	132+267	17.64
S. Vicente (VI)	16	6915	26	18	11	144+180	21.34
S. Julián (JU)	17	6226	27	15	13	187+150	18.47
S. Gil (GI)	15	6200	22	15	14	170+148	19.50
S. Pedro (PE)	14	6180	20	17	16	123+154	22.05
S. Andrés (AN)	17	5955	23	15	11	132+154	20.82
S. Esteban (ES)	14	4746	20	14.5	14	141+134	17.26
S. Marcos (MC)	18	4623	26	17	10	144+226	12.49
Sta. Catalina (CA)	12	4362	22	15	12	121+102	19.56
S. Isidoro (IS)	22	3947	26	14.5	11	133+144	14.25

TABLE II. Surface materials and furnishings in Mudejar-Gothic churches.

Church	MN	OM	LO	VI	JU	GI	PE	AN	ES	MC	CA	IS
Ground plan	3n	3n	5n	3n	3n	3n	3n	3n	3n	3n	3n	3n
n=nave, s=section	5s	5s	4s[a]	4s	4s	2s[b]	3s[c]	4s	3s	4s	3s[d]	4s[e]
Lateral walls	b	pb	pb	pb	pb	pb	pb	pb	b	p	pb	pb
b=visible brick with thick mortar; pb=plastered and painted; p=directly painted brick												
Intermediate walls, arches, pillars	iap	ap	⋯	ia	⋯	ap	a	ip	iap	ap	a	ip
i=intermediate walls in visible brick; a=arch edges in visible brick; p=pillars in visible brick												
Baseboard	⋯	mc	th	⋯	th	th	th	⋯	⋯	⋯	⋯	mc
mc=in the major chapel; th=throughout the whole church												
Decoration	s	p	p	f	f	f	p	f	p	s	p	f
s=scarce; p=profuse; f=fair												
Ceiling	w	w	w	w	w	w	t	w	w	c	w	w
w=wooden framework in three naves; t=tiles substitute the wooden board in the laterals; c=rough ceramics substitute the wooden boards in the central nave												
Apse	ms	ms	ng	st	ms	ms	ms	ms	ms	ms	ms	f
ms=mortared and painted ribs in stone; ng=non-gothic; st=stucco; f=fresco												
Major chapel	na	ac	ba	ba	ba	ac	ba	ba	a	na	ba	ba
na=no high altar; a=with high altar; ba=Baroque high altar; ac=high altar with canopy												
Textile	a	⋯	c	⋯	p c	a c	c	c	cu	⋯	c a	cu
a=apse walls; p=pennant on pillars; cu=curtains on a lateral chapel door, or on windows; c=carpet in presbytery												
Floor	c	m	m	m	m	m	m	m	m	c	m	m
c=ceramic; m=marble												
Inner doors	3s	2d	2d	2d1s	1d	2d	2d	2d1s	1d1s	2s	2d	1s
s=simple; d=double												
Apertures	wrg	wrg	⋯	wr	wr	wr	wr	wr	wr	wr	wr	wr
w=windows; r=rosettes; g=glass window in presbytery												
Choir	⋯	b	g	⋯	⋯	b	b	b	b	⋯	b	b
b=in a balcony; g=on the ground floor												
Organ	⋯	o	o	⋯	⋯	⋯	o	o	⋯	⋯	⋯	⋯
Loudspeakers (see Figs. 2–4 for positions)	4	6	8	15	7	6	7	14	4	8	6	9

[a]Non-gothic head+choir.
[b]Ante presbytery+atrium.
[c]Vestibule.
[d]Atrium+vestibule.
[e]Ante presbytery.

NR (noise rating) indices will be indicated corresponding to the spectrum measured in each church, linearly averaged for at least 6 min.

The impulse response, the fundamental descriptor of a linear system from which a wide range of important acoustic indicators can be deduced, has been obtained using MLS (maximum length sequence) signals. The analyzer used is the MLSSA based on a full-length ISA card of data acquisition housed in a slot of a PC with the corresponding software which runs under MS-DOS.

The omnidirectional source B&K 4296 is placed at the most usual point of location of the natural source: the altar at a height of 1.70 m from the floor. The microphone is located at the approximate height of the head of a seated person, which is 1.20 m above the finished floor, in a predetermined number of positions distributed in the central and lateral naves ranging from 12 reception points at Santa Catalina church to 23 at Santa Marina (Table I).

When the aim is to measure the impulse response in order to obtain the decay curves and the sound energy parameters, then the MLS spectrum must be conditioned to that of pink noise before being fed to the amplifier. This is done here by means of the filter CWF-1 from One-on-One Technical Products. In order to improve the signal-to-noise ratio at low frequencies, the signal captured by the microphone is inverse filtered before entering MLSSA for its analysis.

On the other hand, if the aim is to measure the impulse response to obtain the modulation transfer function (MTF)

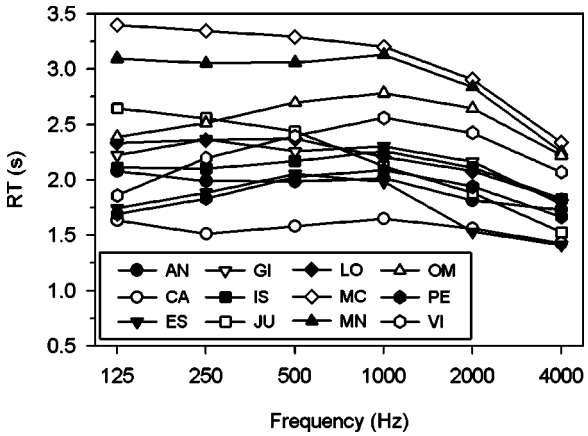

FIG. 5. Reverberation times versus frequency for all churches.

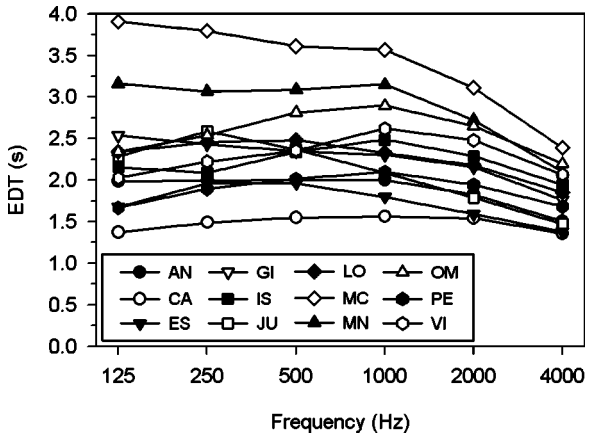

FIG. 6. Early decay times versus frequency for all churches.

and thereby calculate the values of the STI-RASTI indices, the filter is altered to the position STI with the purpose of conditioning the MLS spectrum to that of the human voice.

The microphone used is the Audio-Technica AT4050/CM5 whose amplifier and polarization source is of Earthworks LAB1 which, by means of a simple switch, allows its directivity pattern to change from omnidirectional to bidirectional in a figure-of-eight. This pattern is necessary for the measurement of parameters involving the fraction of lateral energy.

In order to study sound pressure levels, two different techniques have been used for the calculation of sound strength. The first technique uses the emission of a stationary signal, later corrected with the level produced by the source, at a 10-m distance under free field conditions. The other technique is derived from the impulse response generated from the MLS signals, by means of calculating the reference level from the direct sound of this impulse response and from its source-receiver distance. This distance is calculated from the initial flying time of the impulse responses. The results coming from these two techniques have been compared through lineal regression and a slope near to one has been obtained. In this work the data of the stationary signal is presented as a more reliable and clearer method of determining the spectral variation when a calibrated source is available.

The stationary levels are produced by the B&K 4296 omnidirectional source which emits pink noise and they are measured using MLSSA configured in Scope mode. The power level of emission is adjusted to 111 dB *re* 1 pW. A $\frac{1}{2}$-in. B&K 4190 microphone was used with a 2669 preamplifier which is connected to the microphone power supply B&K 2804, thereby allowing calibration *in situ*.

The background noise measurements are carried out by following the same procedure but by substituting the calibrated source with the background noise in each case. As for measurements in the frequency domain, using MLSSA the average of more than 400 spectra is taken over a period of approximately 6 min. These measures are carried out at one/several representative reception points (avoiding the vicinity of the entrance or other positions near potential noise disturbance sources).

To obtain the modulation transfer function two types of experiments have been performed with the B&K 3361 equipment, which uses the modulated stationary noise technique,[23] and by means of the MLSSA, which determines the MTF from the impulse response.[24]

In the first case the emission is adjusted to ref +10 dB, which implies a sound pressure level of 69 dB in the 500-Hz band and 60 dB in the 2-kHz band [67 dB(A)].

Whenever possible, the electroacoustic reinforcement existing in each church has been taken into account. In these cases the complete transmission system is considered including the microphone, which was located at an approximate distance of 50–60 cm from the B&K 4225 emitter. In gen-

TABLE III. Standard error for spatial distribution of RT (upper row) and EDT (lower row) in octave bands for each church.

Frequency	AN	CA	ES	GI	IS	JU	LO	MC	MN	OM	PE	VI	Average
125 Hz	0.05	0.03	0.13	0.06	0.03	0.05	0.05	0.09	0.07	0.06	0.06	0.09	0.06
	0.10	0.13	0.14	0.18	0.09	0.17	0.16	0.17	0.16	0.15	0.16	0.17	0.15
250 Hz	0.04	0.03	0.07	0.06	0.03	0.03	0.03	0.05	0.06	0.04	0.05	0.07	0.05
	0.11	0.09	0.15	0.14	0.08	0.15	0.15	0.18	0.16	0.18	0.14	0.17	0.14
500 Hz	0.03	0.02	0.15	0.05	0.01	0.02	0.03	0.04	0.07	0.03	0.05	0.07	0.05
	0.11	0.13	0.15	0.19	0.06	0.12	0.10	0.17	0.16	0.17	0.15	0.18	0.14
1 kHz	0.02	0.02	0.13	0.04	0.01	0.03	0.02	0.03	0.05	0.04	0.03	0.04	0.04
	0.08	0.11	0.12	0.13	0.06	0.14	0.14	0.16	0.20	0.22	0.14	0.15	0.14
2 kHz	0.03	0.01	0.05	0.05	0.01	0.02	0.01	0.04	0.06	0.04	0.03	0.05	0.03
	0.08	0.06	0.11	0.15	0.06	0.12	0.14	0.13	0.17	0.19	0.14	0.16	0.13
4 kHz	0.05	0.02	0.05	0.05	0.01	0.03	0.02	0.05	0.07	0.04	0.03	0.05	0.04
	0.08	0.06	0.11	0.12	0.05	0.10	0.13	0.11	0.14	0.15	0.12	0.13	0.11

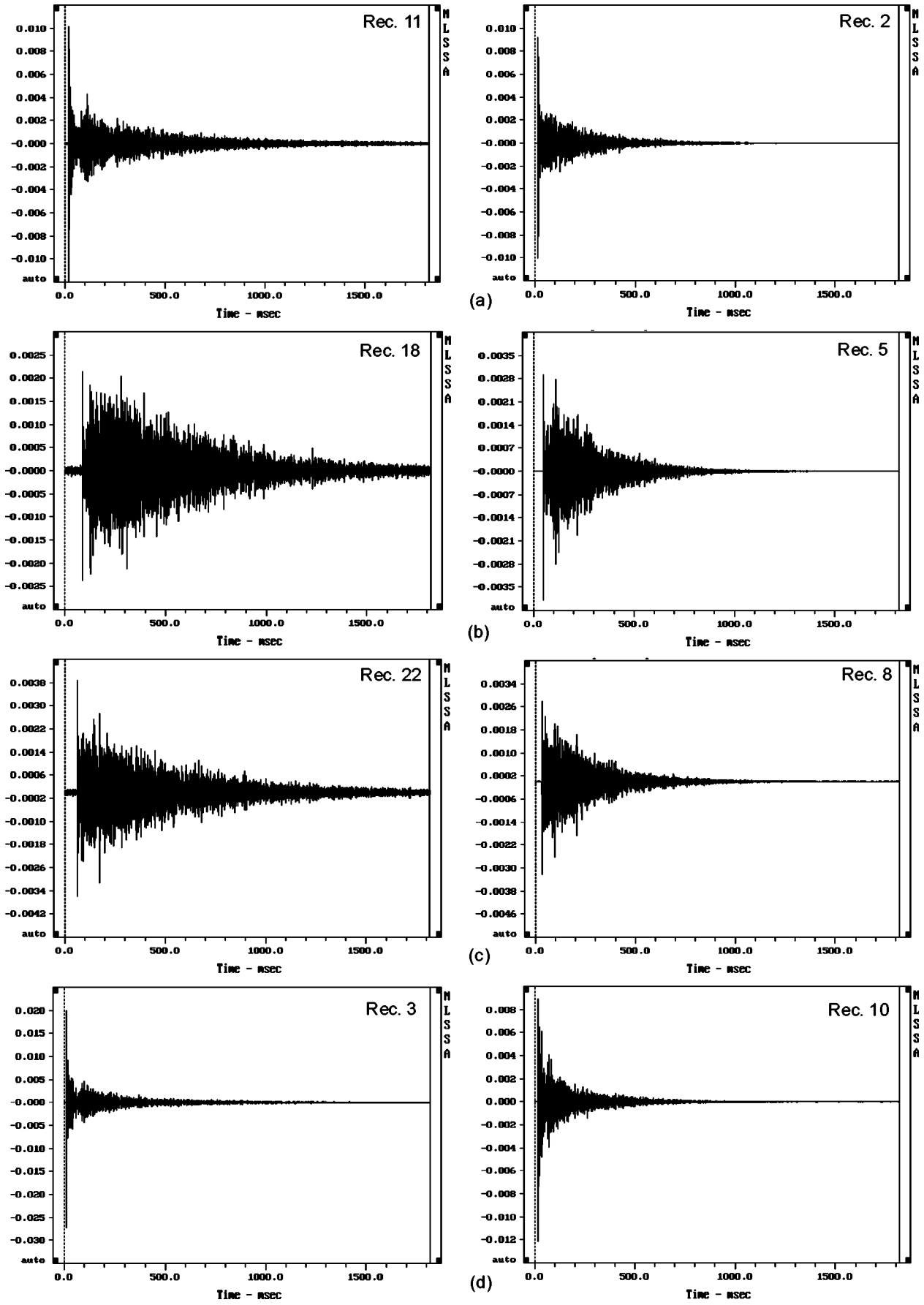

FIG. 7. Impulse response that has been octave filtered at 1 kHz for Santa Marina (left) and Santa Catalina (right) at several reception points: forward position of central nave (a), rear of central nave (b), at lateral nave (c), and at the apse (d). The vertical scales have been adjusted for better views.

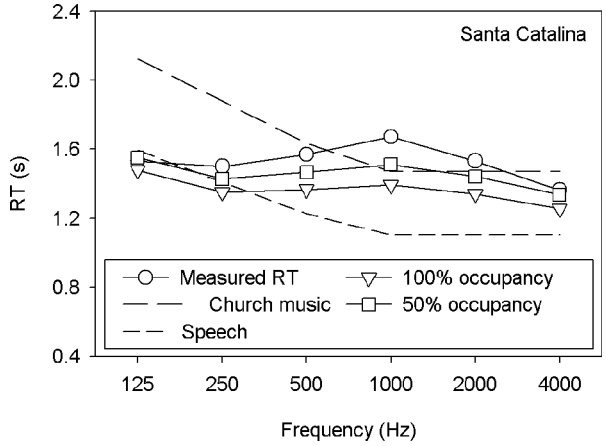

FIG. 8. Comparison of measured, estimated, and desirable values of the reverberation times for Santa Catalina church.

eral the level is also adjusted to ref +10 dB, even if in some cases the reference emission is considered.

In the second case, for the correct determination of the STI (alternatively RASTI) index, some precautions must be taken: adjusting the exit of MLSSA (once the spectrum is conditioned) to 67 dB (A) at 1 m from the emitter, checked by the B&K 2231 sound level meter; conditioning the spectrum by putting the CWF-1 filter switch in the STI/RASTI position; and using a small loudspeaker mounted on a box of the dimensions of a human head and adjusting the measurement conditions to register a band width up to 12 kHz, in order to obtain the STI index that uses a band width up to 8 kHz.

IV. EXPERIMENTAL RESULTS AND DISCUSSION

A. Reverberation

Figures 5 and 6 show the reverberation time and the EDT as a function of frequency in octave bands for all the churches studied. In the following sections, figure captions and tables appear in alphabetical order. Since the standard error is a biased and nonefficient estimator it is used to assess the spatial dispersion of the acoustic parameters. Table III gives the values for the reverberation time and EDT in octave bands for each church and the last column shows the

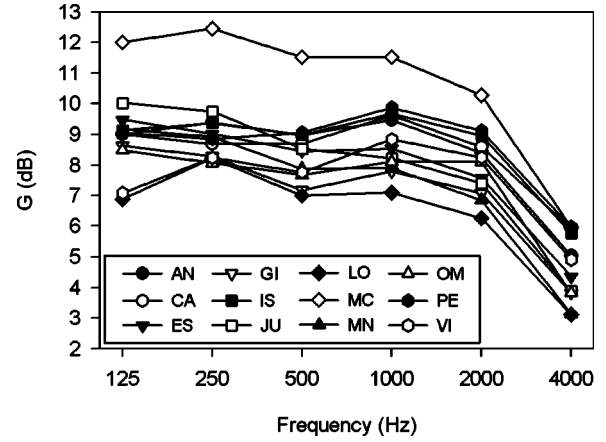

FIG. 9. Sound strength as a function of frequency for all churches.

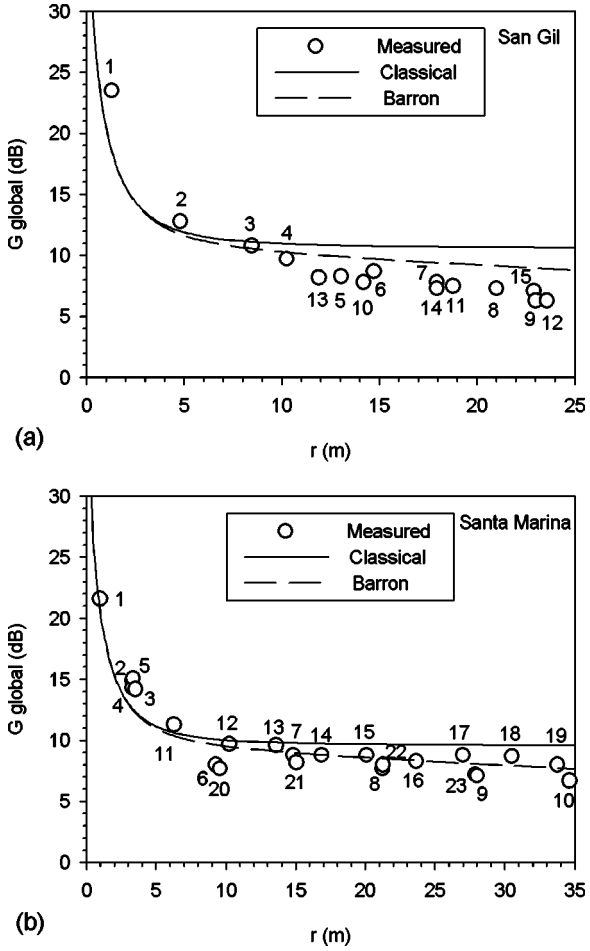

FIG. 10. Global sound strength versus distance for San Gil church (a) and Santa Marina church (b). The measurement points are shown.

average value assigned to this typology for each frequency. In all the following tables the last column labeled ''Average'' corresponds to the typological average of the parameter studied in each case.

In view of the data it is necessary to highlight that the two parameters present the same tendency in the frequency in almost all the churches. A wider spatial dispersion throughout the values of EDT is also observed, associated in all cases to the nonhomogeneity in the sound absorption in the adornments and the decoration of the temples and to the small lateral chapels that exist in nine churches. The EDT values are greatly influenced by the first reflections and these in turn are strongly influenced by the close geometry to the source and the relative position of the source-receiver. It causes a bigger dispersion in the values of the EDT. When evaluating RT, the significance of these early reflections is smaller than the energy of the late reflections, which incorporates global information of the enclosure geometry.

Similar justification holds for the sound energy parameters related to early-to-late sound energy. The LF parameter is especially sensitive to positioning since initial lateral reflections are selected. In this respect it is useful to compare the impulse responses given in Fig. 7, for the largest church (Santa Marina) and one of the smallest (Santa Catalina) at several representative points.

Bearing the different curves of the churches in mind, two groups can be observed (Fig. 5). The first group consists

TABLE IV. Standard error for the spatial distribution of G in octave bands for each church.

Frequency	AN	CA	ES	GI	IS	JU	LO	MC	MN	OM	PE	VI	Average
125 Hz	1.2	1.4	1.2	1.1	1.9	1.5	1.2	1.3	1.6	1.8	2.3	1.7	1.5
250 Hz	1.0	1.5	0.9	1.1	1.6	1.2	1.2	1.5	0.9	1.7	1.9	1.3	1.3
500 Hz	1.4	2.7	1.3	1.9	2.0	1.4	1.0	1.4	1.3	1.9	1.5	1.6	1.6
1 kHz	1.2	2.1	1.2	1.8	2.1	1.7	1.3	1.2	1.2	2.0	1.4	1.3	1.5
2 kHz	1.3	2.0	1.4	1.8	2.1	1.8	1.1	1.0	1.3	2.0	1.5	1.2	1.5
4 kHz	1.6	2.2	1.5	2.3	2.3	2.4	1.2	1.4	1.6	2.4	1.5	1.4	1.8

of San Marcos, Santa Marina, Omnium Sanctorum, and San Vicente churches, which register the longest reverberation times, longer than 2.4 s at 1000 Hz. The remaining churches form the second group. This first group corresponds to the largest spaces and includes San Marcos, which does not have a wooden roof and features austere interior decoration and a treatment of plastic painting on its brick walls that diminishes their porosity (Table II). The closest acoustic behavior to optimum according to the recommended RT values suggested by Knudsen *et al.*[25] corresponds to Santa Catalina church (see Fig. 8). This is attributed to the fact that it has one of the smallest volumes, abundant interior decoration, and pew areas in the three naves.

In all the graphs an acute decrease in reverberation times is also found as the frequency increases above 1000 Hz, which is a greater drop than expected to result from the absorption solely by air for these volumes, thus revealing the presence of absorption which is probably associated to the porosity of the walls in many cases. For instance, in Santa Marina church, the total absorption calculated from RT measured at 4000-Hz frequency is about 750 metric Sabines and the air absorption calculated as 4 mV from Cremer *et al.*[26] is approximately 230 metric Sabines, which represents slightly less than a third of the absorption. The decoration in this church is austere, the largest surface is of visible brick with thick porous mortar, and there are no coupled lateral chapels. These data suggest the possibility of carrying out absorption measurements *in situ* throughout the technique proposed by Mommertz.[27] The widespread increment of absorption at low frequencies (especially in the band of 125 Hz) shows the presence of a membrane-type absorbent. The most important absorbents are the wooden roofs, which are the main characteristic of these enclosures, and the pew zones. If there is also interior decoration based in wooden panels or wooden altars, this increment of absorption is more pronounced (Omnium Sanctorum, San Vicente, and San Pedro in Fig. 5). This fact is related to the reverberant ceiling effect studied by Carvalho,[28] but in this case the presence of both elements (wooden ceiling and pew zones) is generalized, hence the low-frequency effect is emphasized.

In all the temples studied, the experimental results deviate from the optimum reverberation times suggested in the bibliography for this type of enclosure, as much for music as for speech, although better approximations to the recommended values are reached for music. The degree of occupation would also improve the conditions of the enclosure to obtain better behavior. Figure 8 presents, as a sample, the experimental reverberation time values, the values estimated with different degrees of occupation, and the optimal spectral values for church music and speech in Santa Catalina church.

B. Sound levels

In Fig. 9 the results of the sound strength spatially averaged as a function of frequency for the different octave bands and in all the studied churches are shown. In Table IV its standard errors are expressed, giving information of the spatial dispersion. The high values of this parameter, especially in San Marcos church, are in correspondence with the long reverberation times of these enclosures. The spatial dispersion of this parameter is significant, as revealed by Table IV.

In Fig. 10(a) the global sound strength is represented against the distance and the measurement points for San Gil church. As a reference, two theoretical curves have been superimposed: the classic equation [Eq. (1)] (continuous line), admitting a perfectly diffuse sound field in the enclosure,

TABLE V. Spatially averaged values of T_S in ms (upper row) and their standard errors (lower row) in octave bands for each church.

Frequency	AN	CA	ES	GI	IS	JU	LO	MC	MN	OM	PE	VI	Average
125 Hz	146.6	92.3	119.3	170.7	150.3	153.1	167.9	290.7	215.0	145.0	114.6	126.5	157.7
	10.4	8.7	13.3	12.6	7.8	11.5	12.7	18.5	13.5	11.4	13.3	10.6	12.0
250 Hz	160.4	102.8	149.1	174.7	164.0	187.5	178.0	301.1	216.9	186.4	145.1	163.6	177.5
	12.5	10.2	13.5	12.7	7.0	14.0	13.5	20.7	15.2	15.5	15.7	13.9	13.7
500 Hz	162.3	108.7	157.3	182.2	193.4	179.0	188.0	288.2	228.2	212.1	153.7	190.2	186.9
	13.5	14.8	15.3	15.5	7.6	14.6	14.6	18.6	19.9	17.9	16.8	16.8	15.5
1 kHz	153.4	104.9	135.0	168.0	195.1	151.4	168.5	277.2	221.2	215.9	150.2	196.6	178.1
	11.3	12.8	13.7	14.0	7.9	13.6	13.9	16.6	19.1	18.9	15.8	16.0	14.5
2 kHz	137.5	99.0	116.2	150.0	179.2	124.7	159.8	242.5	191.1	195.1	139.7	182.4	159.8
	11.3	11.8	12.1	13.8	7.9	12.1	13.4	14.9	16.3	18.1	15.8	15.8	13.6
4 kHz	115.0	90.0	105.8	122.6	154.1	102.9	137.0	189.8	148.5	159.5	122.0	155.5	133.6
	10.1	11.7	12.4	11.5	6.9	10.7	11.9	11.6	13.2	15.4	14.1	14.2	12.0

TABLE VI. Spatially averaged values of C_{80} (dB) (upper row) and their standard errors (lower row) in octave bands for each church.

Frequency	AN	CA	ES	GI	IS	JU	LO	MC	MN	OM	PE	VI	Average
125 Hz	−1.3	2.4	0.4	−1.6	−1.2	−0.4	−1.7	−6.2	−2.8	0.1	0.5	0.6	−0.9
	0.9	1.0	1.1	0.9	0.6	0.8	0.9	0.9	0.7	0.8	1.1	0.9	0.9
250 Hz	−3.0	1.1	−1.5	−2.3	−2.6	−2.6	−2.2	−7.0	−3.2	−2.6	−1.9	−1.4	−2.4
	1.1	1.0	1.1	0.9	0.4	0.9	1.0	1.0	0.8	1.2	1.3	1.1	1.0
500 Hz	−3.4	0.7	−2.2	−3.1	−4.7	−2.7	−3.3	−6.5	−4.0	−3.8	−1.8	−3.2	−3.2
	1.2	1.4	1.1	1.2	0.5	1.1	1.1	1.0	1.1	1.2	1.4	1.3	1.1
1 kHz	−2.2	1.3	−0.5	−2.3	−4.0	−1.3	−2.0	−5.8	−3.0	−3.5	−1.5	−3.0	−2.3
	0.9	1.2	1.2	1.0	0.5	1.1	1.1	0.8	1.1	1.4	1.2	1.1	1.1
2 kHz	−1.3	1.3	0.3	−1.0	−3.4	0.2	−1.9	−5.0	−2.1	−2.8	−1.0	−2.4	−1.6
	1.0	1.1	1.3	1.1	0.5	1.1	1.1	0.8	1.0	1.4	1.3	1.2	1.1
4 kHz	−0.1	2.0	1.2	0.1	−2.7	1.2	−1.0	−3.7	−0.9	−1.5	−0.4	−1.6	−0.6
	1.0	1.2	1.3	1.1	0.5	1.1	1.1	0.7	1.0	1.3	1.4	1.2	1.1

$$G = 10\log\left(\frac{100}{r^2} + \frac{31\,200\mathrm{RT}}{V}\right), \tag{1}$$

and Barron's revised theory,[29] Eq. (2) (dashed line),

$$G_B = 10\log\left(\frac{100}{r^2} + \frac{31\,200\mathrm{RT}}{V}e^{-0.04r/RT}\right). \tag{2}$$

The measured levels, except in the cases of San Andrés and Santa Marina churches [Fig. 10(b)], which approach the tendency suggested by Barron, all move away from the theoretical predictions by presenting an attenuation with distance greater than expected for both models. It may be considered that this behavior is due to the lack of diffusion. Some of the reasons for nondiffuse conditions were pointed out by Carvalho:[28] simple geometric shapes and nonuniform distribution of absorption. In the analyzed sample nondiffuse conditions occur in general through the concentration of absorption in the ceiling (wooden), the floor (wooden pews), and in some cases the lateral altars. Essentially, the basis of Barron's revised theory implies a nondiffuse acoustic field. Although the reasons for the nondiffusivity are different, the acoustic field in the churches may be considered nondiffuse.

The behavior is also more pronounced when the analysis in the frequency domain[30] is carried out, with sensitive differences between the different octave bands. Due to the extensive nature of the data, these results are omitted here but constitute part of a later analysis under development.

C. Early to late sound energy parameters

In Fig. 11(a) the experimental results are shown for San Julián church of center time against frequency in octave bands together with their standard errors associated to spatial dispersion. Figure 11(b) shows the results of the center time (averaged at 500-, 1000-, and 2000-Hz octave bands) as a function of source-receiver distance.

For almost all the temples, the spectral results of the center time reveal an increase in this parameter at low and middle frequencies such as is shown in Fig. 11(a) for the church of San Julián, which indicates lower clarity of sound at these frequencies. In some temples the frequency of 2000 Hz is also deficient.

The spatial distribution of center time with distance reveals a strong dependence on position and also reveals that this distribution does not fit according to the diffused sound field behavior, Ts=RT/13.82, whose value is shown in the plotted graph. The results for the other temples and their standard errors in octave bands appear in Table V.

In the literature no recommended values of this parameter exist for these types of enclosures. In auditoria it is suggested not exceeding 140 ms. In accordance with this approach, the clearest is Santa Catalina church and later San Pedro, San Esteban, and San Andrés, and the most notoriously faulty is again San Marcos.

Four graphs are presented for San Marcos church in Fig. 12. Figure 12(a) shows the clarity index for speech (C_{50}) and the clarity index (C_{80}) versus frequency with a measure of the spatial dispersion expressed by their standard errors. In Fig. 12(b), the clarity averaged at 500-, 1000-, and 2000-Hz bands ($C_{80\mathrm{av}}$) versus source-receiver distance is shown. As

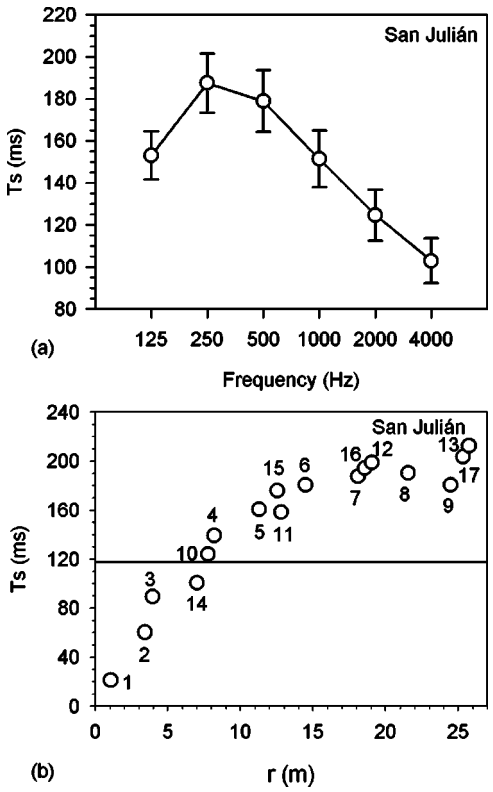

FIG. 11. Center time as a function of frequency (a) and distance (b) for San Julián church. The measurement points are shown.

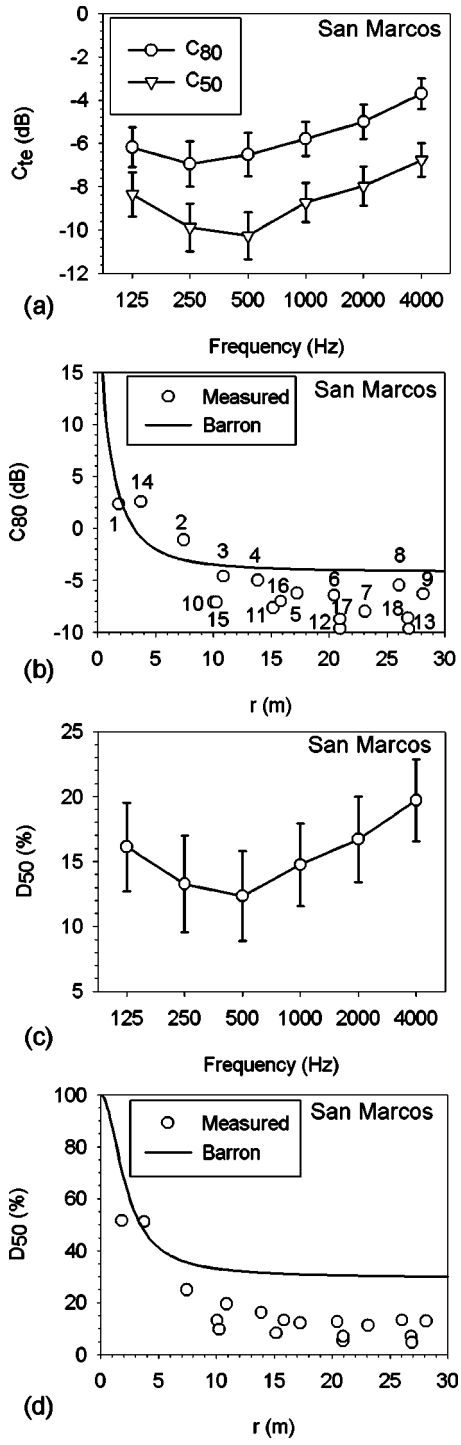

FIG. 12. C_{50} and C_{80} versus frequency (a), C_{80av} versus distance (b), D_{50} versus frequency (c), and D_{50} versus distance (d) for San Marcos church. The measurement points are shown.

reference, the theoretical curve due to Barron's revised theory is also plotted, expressed as

$$C_B = 10 \log\left(\frac{V e^{(0.04r+1.1)/\mathrm{RT}}}{312\mathrm{RT}r^2} + e^{1.1/\mathrm{RT}} - 1 \right). \quad (3)$$

The definition versus frequency and its standard errors are given in Fig. 12(c). Finally, in Fig. 12(d) the weighted definition is presented (in the same way as Marshall[31] proposes for C_{50}, see later) versus source-receiver distance, together with the theoretical curve derived from Barron's revised theory calculated from

$$D_B = 100\% \left(1 - \frac{(31\,200RT/V)e^{(0.04r+0.69)/\mathrm{RT}}}{100/r^2 + (31\,200\mathrm{RT}/V)e^{-0.04r/\mathrm{RT}}} \right). \quad (4)$$

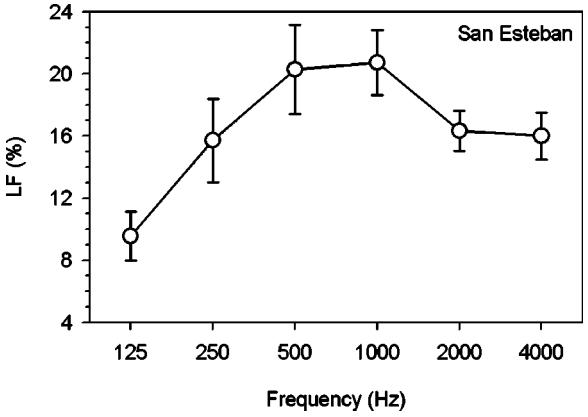

FIG. 13. Lateral energy fraction versus frequency for San Esteban church.

San Marcos church has been chosen as representative of the behavior of the churches, whereby the graphs of the remaining churches have been omitted owing to lack of space although their results appear in Table VI for C_{80} and in Table VII for D_{50}, respectively.

The $C_{50\mathrm{av}}$ (average speech) and $C_{80\mathrm{av}}$ (average music) values correspond to those proposed by Marshall[31] obtained through Eqs. (5), and (6), respectively:

$$C_{50av} = 0.15C_{50}(500\ \mathrm{Hz}) + 0.25C_{50}(1\ \mathrm{kHz}) + 0.35C_{50}(2\ \mathrm{kHz}) + 0.25C_{50}(4\ \mathrm{kHz}), \quad (5)$$

$$C_{80av} = \frac{C_{80}(500\ \mathrm{Hz}) + C_{80}(1\ \mathrm{kHz}) + C_{80}(2\ \mathrm{kHz})}{3}. \quad (6)$$

Spectral behavior is observed in C_{50} and C_{80} for the 12 churches similar to that shown in Fig. 12(a) for San Marcos church, where the minimum values appear at lower frequencies than 1000 Hz.

The graph of the definition versus frequency shows a wider spatial variation of this parameter for all frequencies (via the larger standard error), which classifies this index as significant in the point-to-point spatial variations of acoustic behavior. Although recommended values of the definition do not exist for this typology, the low percentage obtained in all the frequencies reinforces the qualification *poor* for speech intelligibility of the rooms against music, despite these values being higher than those present in other enclosures of ecclesiastic type.[16]

Due to the great correlation among D_{50}, C_{80}, and C_{50}, a very similar tendency is observed in the different measured values of definition against frequency which present a spectral behavior similar to C_{50} and C_{80}.

The data obtained for clarity and definition as a function of source-receiver distance [Figs. 12(b) and (d)] deviate from the theoretical behavior expected from Barron's model expressed through Eqs. (3) and (4), and some stronger attenuations with distance are obtained. This greater attenuation in

TABLE VII. Spatially averaged values of D_{50} (%) (upper row) and their standard errors (lower row) in octave bands for each church.

Frequency	AN	CA	ES	GI	IS	JU	LO	MC	MN	OM	PE	VI	Average
125 Hz	30.1	46.9	36.4	32.6	32.7	35.9	29.5	16.1	29.2	36.4	36.9	41.3	33.7
	4.8	4.9	5.6	4.4	2.6	4.2	4.7	3.4	3.4	4.5	5.2	4.5	4.4
250 Hz	21.8	40.2	25.9	27.7	24.3	25.7	25.2	13.3	26.0	25.3	28.7	28.2	26.0
	4.9	6.0	5.6	4.4	1.9	4.8	5.3	3.7	4.1	5.5	6.3	5.6	4.8
500 Hz	22.5	38.5	24.3	23.5	15.8	24.7	22.5	12.3	24.4	21.2	28.8	22.5	23.4
	5.2	7.8	6.3	5.3	2.0	5.5	5.7	3.4	5.7	5.9	6.3	6.1	5.4
1kHz	26.7	42.1	33.1	27.1	18.6	31.9	29.4	14.8	28.2	22.9	31.6	24.2	27.6
	4.7	6.8	6.2	4.8	2.0	5.4	5.4	3.2	5.3	6.1	6.3	5.4	5.1
2kHz	31.2	43.2	35.8	33.3	20.5	37.4	29.7	16.7	30.6	25.7	33.8	27.1	30.4
	4.9	6.5	6.4	5.1	2.1	5.6	5.5	3.3	5.1	6.2	6.5	5.8	5.3
4kHz	35.0	44.9	38.1	37.4	23.0	41.6	32.4	19.7	34.5	29.6	35.5	29.2	33.4
	5.0	6.9	6.6	5.1	2.2	5.7	5.5	3.2	5.1	6.1	6.6	6.0	5.3

these parameters for distances beyond the acoustic radius depends on frequency.[32] The spectral analysis of these results constitutes part of a later work.

For auditoria the recommended values of C_{80av} should remain within the (−4 dB, +4 dB) interval and the qualification scale given by Marshall[31] allows the intelligibility to be qualified as a function of C_{50av}.

In Fig. 13 the results of the lateral energy fraction as a percentage versus frequency are presented for San Esteban church. The values obtained fall inside an appropriate range for a correct sound sensation, justified by the vicinity of walls which give lateral reflections over the audience. Likewise, these values, whose results are expressed in Table VIII, present great spatial variations since this is a parameter that is intrinsically sensitive to position changes. The recommended value of this parameter uses the average value at frequencies 125, 250, 500, and 1000 Hz,[33] and these results are shown in Table X for all the churches.

Similarly, Barron's equations of both direct sound and of early and late energy density, which are distance dependent and with the consideration of a diffused field, would also allow an equation to be found for the lateral energy fraction versus distance. However, the logic and high dependence of this parameter on position do not provide a clearly defined tendency.

D. Intelligibility

The primordial function of the enclosures analyzed is to provide premises for Catholic worship. In all events related to this use, speech intelligibility is of prime importance. To this end, and with varying results, an electroacoustic sound system has been installed in all the churches. To evaluate the intelligibility with and without a speech reinforcement system, the RASTI index is considered to be highly appropriate. This parameter is also strongly correlated to the D_{50}, the C_{50}, and the EDT as studied in other papers.[22,34]

Figure 14 shows the RASTI index plotted as a function of distance for San Vicente church with the different qualification intervals, universally accepted for auditoria[35] (on the right), and the measurement points identified. Three graphs are highlighted. The first (continuous line) corresponds to the use of the B&K 4225 equipment emitting at ref +10 dB. The second (dotted line) corresponds to the same situation using the reinforcement sound system in its habitual position, with the microphone placed at about 50–60 cm from the emitter. The last graph (dashed line) represents the experiment carried out using MLS signals where a small loudspeaker with directivity similar to the human voice was employed as the emitter.

In only the first experiment graph are the three zones differentiated: the points belonging to the major chapel (○), the central nave, which corresponds to the congregational area (□), and the lateral naves (△); in the other experiments points are omitted to avoid confusion.

The reinforcement systems consist of loudspeakers which have been installed on pillars or lateral walls at 5° to the vertical and generally face the central area in variable numbers in each church (see ground plans, Figs. 2–4).

TABLE VIII. Spatially averaged values of LF (%) (upper row) and their standard errors (lower row) in octave bands for each church.

Frequency	AN	CA	ES	GI	IS	JU	LO	MC	MN	OM	PE	VI	Average
125 Hz	13.2	15.3	9.6	12.6	9.4	9.6	11.7	11.0	12.3	7.3	11.0	11.7	11.2
	1.9	4.5	1.6	2.1	1.5	1.6	2.8	3.5	1.7	1.1	2.4	2.8	2.3
250 Hz	21.0	18.0	15.7	17.1	17.2	18.7	19.8	18.8	15.6	13.4	18.5	10.6	17
	2.7	3.1	2.7	2.7	2.7	2.9	3.6	8.0	2.1	1.8	4.0	2.8	3.3
500 Hz	27.1	24.2	20.3	23.4	26.2	20.5	24.9	16.8	17.6	24.3	20.4	16.1	21.8
	2.9	3.2	2.9	2.6	2.9	2.4	3.2	2.8	2.5	3.5	2.2	2.5	2.8
1 kHz	31.1	24.3	20.7	20.3	28.4	20.2	26.5	19.4	20.8	21.8	22.9	18.2	22.9
	3.0	2.8	2.1	1.6	2.5	2.7	4.2	2.0	2.3	1.9	2.9	2.4	2.5
2 kHz	20.4	17.4	16.3	15.6	20.1	14.6	19.9	16.9	17.8	14.8	16.5	14.3	17.1
	1.5	1.6	1.3	1.0	1.6	1.7	3.1	1.8	2.2	1.7	2.2	2.0	1.8
4 kHz	19.7	19.3	16.0	14.8	18.6	15.3	20.0	19.7	16.4	15.3	17.5	15.7	17.4
	1.5	2.2	1.5	1.0	1.5	1.3	3.1	2.8	1.6	1.6	1.8	1.9	1.8

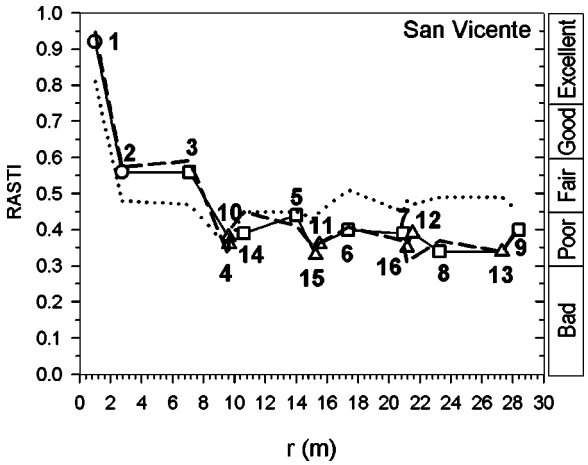

FIG. 14. RASTI as a function of distance for three experiments: B&K ref +10 dB (solid line), B&K ref +10 dB with electroacoustic reinforcement (dotted line), and MLS signals (dashed line), for San Vicente church. Measurement points: (○) major chapel, (□) central nave, and (△) lateral naves.

As can be seen in Fig. 14, the coincidence of solid and dashed lines shows that the emitter used is suitable for measurements with pseudorandom signals, under the considerations previously mentioned in Sec. III. In the congregational seating area and lateral naves, the speech intelligibility of San Vicente church is in the category *poor*, although some fluctuaction exists at several points located in the seating area. The assistance of the electroacoustic system (dotted line) increases the RASTI values in the central and lateral naves by 0.1 on average, which does not cause a jump in the qualification category, in this medium range. On the other hand, the absence of electroacoustic reinforcement in the presbytery leads to a reduction in speech intelligibility for points near the emitter. Analogous behavior has been observed in the other churches whose plotted graphs are omitted due to lack of space.

Figure 15 summarizes the measured RASTI in all the churches surveyed (in ascending alphabetical order), by adjusting the emission level to ref +10 dB for the B&K 4225, both with electroacoustic reinforcement (sound system ''on'') and without (sound system ''off''). The reinforcement system of San Pedro church could not be evaluated due to technical reasons. The results describe the mean values framed by their corresponding maximum and minimum values for each range. The results obtained in the central nave, where the congregational seating is located, are separated from those obtained in the lateral naves.

For the central naves with the absence of electroacoustic reinforcement, eight churches present RASTI values which correspond to a qualification of *poor*. The exceptions are San Pedro, San Lorenzo, and San Julián churches, and especially Santa Catalina church which is in the range of *good* under these conditions. This behavior is attributed to its minor volume and its high degree of decoration, with the presence of lateral chapels, wooden altars, and greater pew zone. These factors also have led this church to be classified in the second group of reverberation times since it has the shortest registered times (Fig. 5).

When the electroacoustic sound system is applied, San

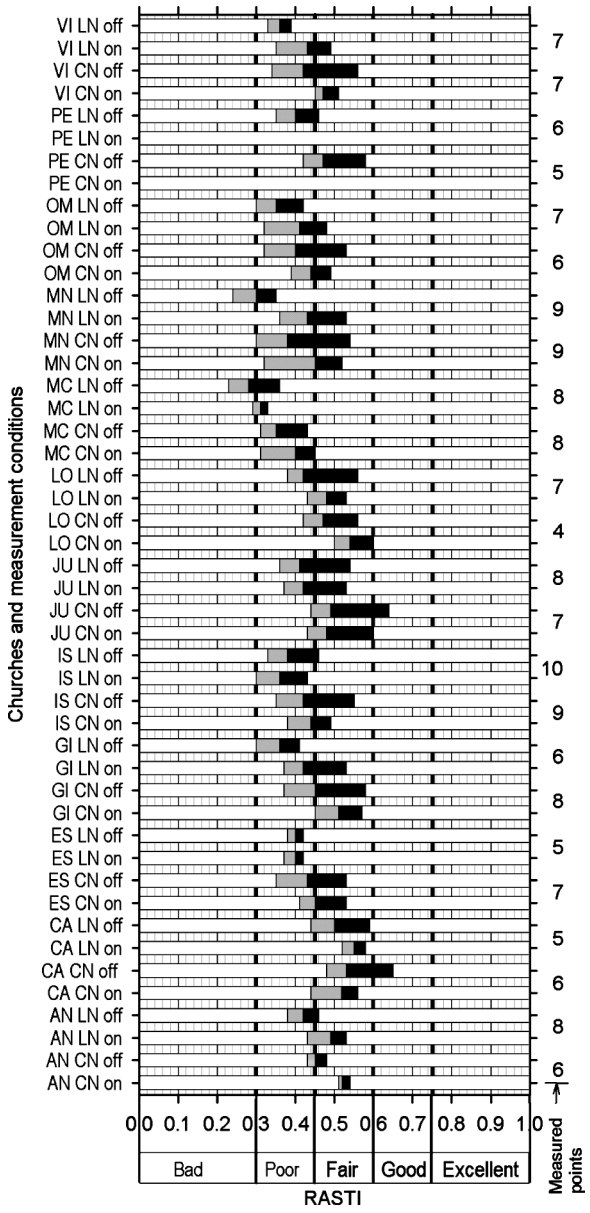

FIG. 15. RASTI range for the churches in the central nave (CN) and in the lateral nave (LN) with electroacoustic system on and off and the corresponding number of receiver positions in each case. Churches are arranged in ascending alphabetical order.

Vicente, San Gil, and San Andrés churches increase their RASTI values toward *fair* conditions. Although most of the remaining churches improve their conditions inside the *poor* range, in some cases the increase of the RASTI values is not significant. As exceptions, in San Julián church and also in Santa Catalina church, the connection of the reinforcement system supposes a decrease in RASTI values, or in other words a setback in intelligibility.

The lateral naves, without an electroacoustic system, register lower mean values (*poor* range) than those corresponding to the central nave, and San Marcos and Santa Marina are even in the *bad* range, which also corresponds to their long reverberation times (Fig. 5).

The application of the electroacoustic system in the lateral naves supposes, in all the churches except San Isidoro, an improvement of the intelligibility conditions. In the case

TABLE IX. Noise rating index for each church.

Church	AN	CA	ES	GI	IS	JU	LO	MC	MN	OM	PE	VI
NR	35	35	40	35	35	30	30	40	40	35	40	40

of San Isidoro, its loudspeakers were directed exclusively toward the congregational area in the central nave and not toward the lateral naves. The churches that have loudspeakers directed toward the lateral naves increase the quality of sound for the congregation in these areas as in the case of San Vicente, San Lorenzo, and San Andrés churches. Of special interest yet again is the case of Santa Catalina, where the disposition of its loudspeakers, which are exclusively located in the lateral naves, provides important reinforcement in the intelligibility within these areas, but lead, as has been pointed out, to a loss of intelligibility in the central nave.

The effectiveness of many of the installed sound reinforcement systems in the churches contributes to a reduction in the variability of RASTI. The most uniform RASTI-intelligibility spatial distributions are in San Andrés (all naves) and San Vicente (central nave), where a greater number of loudspeakers are installed (see Figs. 2–4 ground plans).

These results reflect that a correct application of the electroacoustic system requires careful study, not only in the choice of equipment, but also in its location and orientation, aspects which have not been taken into account in most of the churches studied.

E. Background noise

The spectra measured in each church are of a common form due to the inflow of traffic noise, which is the main source of background noise in almost all the cases. These spectra have provided the expression of the NR (noise rating) index whose results are shown in Table IX.

For ecclesiastic use it is commonly recommended that the index not be greater than 35. In five of the churches this recommendation is exceeded, with a detriment not only for speech intelligibility but also for the long periods of silence which take place in Catholic liturgy.[21] The causes are the lack of hermeticity of apertures and doors, as well as the presence of additional noise from public works due to the continuous rehabilitation of the historical area of the city. The existence of double doors and/or atria in the entrances (see Table II) are efficient in reducing these noise levels.

V. CONCLUSIONS

The architectural heritage concept is being updated to cover both visual and acoustic effects. In this context, assuming the importance of the churches analyzed as a link between Muslim and Christian cultures in the south of Spain, the objective acoustic behavior of these temples has been characterized by means of the most widely used monoaural parameters which describe the acoustics in significant spaces. In this sense the most important monaural parameters have been measured, and are presented here with emphasis on spectral behavior and spatial distribution. This will enable future work of rehabilitation to be assumed while taking acoustic aspects into account. Likewise, since musical events are often staged in these temples, knowledge of their acoustic response may facilitate decision-making as to whether temporary or permanent work should be undertaken in order to mitigate their deficiencies.

Reverberation times show a decrease at high frequencies associated to the porosity of walls, and the widespread increment of absorption at low frequencies shows the presence of a membrane-type absorbent, the most important being the pew zones and the wooden roofs which are the main characteristic of these enclosures. The experimental results deviate from the optimum reverberation times suggested in the bibliography for this type of enclosure.

The acoustic field inside the churches may be considered nondiffuse due to the concentration of absorption in the seating area, the wooden ceiling, and the lateral altars. The distribution of sound levels, center time, clarity, and definition for distances beyond the acoustic radius reveals a shift away from a diffuse acoustic field and that expected from Barron's revised theory for auditoria. In this sense, a greater understanding of the mechanism of the extinction of sound energy density would lead to a semiempirical model for the Mudejar-Gothic churches such as this implemented by Cirillo *et al.*[17] The speech intelligibility with and without a

TABLE X. Acoustic qualifications of each church.

Church	T_S (ms)	C_{80av} (dB)	LF (%)	Music[a]	D_{50} (%)	C_{50av} (dB)	RASTI[b]	Speech	RT (s)	G (dB)	NR
AN	151	−2.32	23	Poor	29.7	−5.48	0.45	Poor-Fair	2.00	9.22	35
CA	104	1.10	20	Fair	42.7	−1.76	0.60	Fair	1.61	9.15	35
ES	136	−0.83	17	Poor	34.0	−3.18	0.43	Poor	2.02	8.50	40
GI	167	−2.14	18	Poor	31.3	−3.70	0.45	Poor-Fair	2.28	7.48	35
IS	189	−4.05	20	Poor	20.0	−6.54	0.42	Poor	2.22	9.33	35
JU	152	−1.29	17	Poor	35.2	−2.56	0.49	Fair	2.28	8.37	30
LO	172	−2.42	21	Poor	29.2	−4.17	0.47	Fair	2.29	7.04	30
MC	269	−5.77	16	Poor	16.3	−8.21	0.35	Poor	3.25	11.50	40
MN	213	−3.03	17	Poor	30.0	−4.48	0.38	Poor	3.09	7.88	40
OM	208	−3.36	17	Poor	25.3	−5.51	0.40	Poor	2.74	7.89	35
PE	148	−1.74	18	Poor	32.9	−3.79	0.47	Fair	2.06	9.47	40
VI	190	−2.87	14	Poor	26.2	−5.14	0.42	Poor	2.48	8.30	40

[a]Auditorium recommended values: $T_S < 140$ ms; -4 dB $\leq C_{80} \leq 4$ dB; LF $> 20\%$.
[b]RASTI values correspond to the central naves with the electroacoustic system off.

sound reinforcement system has been analyzed via the RASTI indices. The low values of clarity for speech index and the low percentage obtained in all frequencies for the definition index reinforce the RASTI qualification *poor* for speech intelligibility. The effectiveness of many of the sound reinforcement systems in the churches is a contribution to a uniform RASTI spatial distribution, more than to an increase in the qualification range for the different areas.

The churches show symmetrical acoustic behavior along the longitudinal axis and the presence of a wooden ceiling is a determining factor for better acoustic conditions since, in San Marcos church where a wooden ceiling is absent, all acoustic parameters present the most adverse values.

In order to globally qualify and summarize the acoustics of each one of these enclosed spaces of worship, the data of all the objective parameters, averaged using the method recommended in Sec. IV, are displayed in Table X. These parameters are directly correlated to the perception of music, on the one hand, and of speech, on the other hand, and hence reverberation time, sound strength, and the noise rating index are given for both perceptions and the consequent qualification of each church.

Regarding the musical aspect, it can be mentioned that San Marcos and those churches of larger volume present reasonable values of the acoustic parameters for organ music (see Table II), while presenting deficiencies in other types of musical representations.

This first analysis suggests typological behavior, which is worth further investigation. Bearing this in mind, the averaged value and spatial dispersion for each parameter and for each frequency have been computed. These values are presented in the last column of each table below the ''Average'' heading. The results are perceived as a basis for further study.

Finally, it is worth emphasizing that the quality of the results of the reverberation times has been checked with computational simulation carried out through the program RAYNOISE[36] and CATT Acoustic[37] (both based on the measured reverberation times). This earlier work on several churches has shown very good agreement between the experimental results and those calculated for all the acoustic parameters specified in their spectral and spatial distributions.

ACKNOWLEDGMENTS

The authors are very grateful to the priests and church managements for allowing the measurements to be carried out. This wok has been partially supported by Spanish MCYT Project No. BIA2003-09306-CO4-02.

[1] A. P. O. Carvalho, ''Influence of architectural features and styles on various acoustical measures in churches,'' Ph.D. dissertation, Univ. of Florida, 1994.
[2] V. Desarnauls and A. P. O. Carvalho, ''Analysis of reverberation time values in churches according to country and architectural style,'' Proceedings of the 17th International Congress on Sound and Vibration, Hong Kong, China, 2–6 July, 2001.
[3] J. J. Sendra and J. Navarro, ''La evolución de las condiciones acústicas en las iglesias: del paleocristiano al tardobarroco'' (''The evolution of acoustic conditions in churches: From early Christian origin to late Baroque''), (Instituto Universitario de Ciencias de la Construcción, Col. Textos de Doctorado, Universidad de Sevilla, 1997).
[4] J. J. Sendra, T. Zamarreño, and J. Navarro, ''Acoustics in churches,'' in *Computational Acoustics in Architecture*, edited by J. Sendra (Witpress, Southampton, 1999), Chap. 6, pp. 133–165.
[5] A. A. Adel, ''Measurement of acoustical characteristics of mosques in Saudi Arabia,'' J. Acoust. Soc. Am. **113**, 1505–1517 (2003).
[6] D. L. Klepper, ''The distributed column sound system at Holy Cross Cathedral, Boston, the reconciliation of speech and music,'' J. Acoust. Soc. Am. **99**, 417–425 (1996).
[7] A. C. Raes and G. Sacerdote, ''Measurement of the acoustical properties of two Roman basilicas,'' J. Acoust. Soc. Am. **25**, 925–961 (1953).
[8] R. Fearn, ''Reverberation in Spanish, English, and French churches,'' J. Sound Vib. **43**, 562–567 (1975).
[9] T. H. Lewers and J. S. Anderson, ''Some acoustical properties of St. Paul's cathedral, London,'' J. Sound Vib. **92**, 285–297 (1984).
[10] M. Recuero and C. Gil, ''Experimental study of the acoustics in the church of the monastery of Santo Domingo de Silos,'' Proceedings of 5th FASE, Thessaloniki, Greece (1985).
[11] R. N. Hammad, ''RASTI measurements of mosques in Amman, Jordan,'' Appl. Acoust. **30**, 335–345 (1990).
[12] M. K. Abdelazeed, R. N. Hammad, and A. A. Mustafa, ''Acoustics of King Abdullah mosque,'' J. Acoust. Soc. Am. **90**, 1441–1445 (1991).
[13] V. Desarnoulds, K. Eggenschwiler, and S. Bossoney, ''Studie zur Raumakustik von Schweizer Kirchen'' (''Acoustic study of Swiss churches''), Proceedings of DAGA, Zürich (1998), pp. 710–711.
[14] A. P. O. Carvalho, ''Relations between rapid speech transmission index (RASTI) and other acoustical and architectural measures in churches,'' Appl. Acoust. **58**, 33–49 (1999).
[15] Z. Karabiber, ''A new approach to an ancient subject: CAHRISMA project,'' on CD-ROM: Garmisch-Partenkirchen, 4–7 July, 7th International Congress on Sound and Vibration, Germany (2000).
[16] A. Magrini and P. Ricciardi, ''An experimental study of acoustical parameters in churches,'' Int. J. Acoust. Vib. **7**, 177–183 (2002).
[17] E. Cirillo and F. Martellota, ''An improved model to predict energy-based acoustic parameters in Apulian-Romanesque churches,'' Appl. Acoust. **64**, 1–23 (2002).
[18] Proceedings of the 17th International Congress on Acoustics, CD-ROM Vol. III (ISBN 88-88387-02-1), Rome, Italy, 2–7 September, 2001.
[19] Proceedings of the Forum Acusticum, CD-ROM (ISBN 84-87985-07-6), Seville, Spain, 16–20 September, 2002.
[20] I. D. Angulo, ''Arquitectura mudéjar sevillana de los siglos XIII, XIV y XV'' (''Sevillian Mudejar architecture in the XIIIth, XIVth and XVth centuries''), Ayuntamiento de Sevilla (1983).
[21] V. Desarnaulds and A. P. O. Carvalho, ''Liturgical conditions of Catholic and Reformed celebrations and their relationship with architectural and acoustical characteristics of churches,'' on CD-ROM: Seville (Spain), 16–20 September, Proceedings of the Forum Acusticum (ISBN 84-87985-07-6) (2002).
[22] M. Galindo, ''La acústica en espacios religiosos católicos: iglesias Gótico-Mudéjares'' (''Acoustics in Catholic worship spaces: Mudejar-Gothic churches''), Ph.D. thesis, Univ. of Seville, Spain, 2003.
[23] T. Houtgast and H. J. M. Steeneken, ''The modulation transfer function in room acoustics as a predictor of speech intelligibility,'' Acustica **28**, 66–73 (1973).
[24] D. Rife, ''Modulation transfer function measurement with maximum-length sequences,'' J. Audio Eng. Soc. **90**, 779–790 (1992).
[25] V. O. Knudsen and C. M. Harris, *Acoustical Design in Architecture*, 5th ed. (Acoustical Society of America, New York, 1998).
[26] L. Cremer, H. A. Müller, and T. J. Schultz, *Principles and Applications of Room Acoustics* (Applied Science, London, 1982), Vol. 1.
[27] E. Mommertz, ''Angle-dependent in-situ measurements of reflection coefficients using a substraction technique,'' Appl. Acoust. **46**, 251–263 (1995).
[28] A. P. O. Carvalho, ''The use of the Sabine and Eyring reverberation time equations to churches,'' Proceedings of the 129th Meeting of the Acoustical Society of America, Washington DC, 30 May–3 June, 1995.
[29] M. Barron and L. J. Lee, ''Energy relations in concert auditoriums I,'' J. Acoust. Soc. Am. **84**, 618–628 (1998).
[30] J. J. Sendra, T. Zamarreño, and J. Navarro, ''An analytical model for evaluating the sound field in Gothic-Mudejar churches,'' in *Computational Acoustics and its Environmental Applications II*, edited by C. A. Brevia, J. Kenny, and R. D. Ciskowski (Computational Mechanics, Southampton, 1997), pp. 139–148.

[31] L. G. Marshall, ''An acoustic measurement program for evaluating auditoriums based on the early/late sound energy ratio,'' J. Acoust. Soc. Am. **96**, 2251–2261 (1994).
[32] M. Galindo, T. Zamarreño, and S. Girón, ''Clarity and definition in Mudejar-Gothic churches,'' J. Build. Acoust. **6**, 1–16 (1999).
[33] Y. W. Lam, ''Acoustics of enclosed spaces,'' Report AE0F3/AE0F4 of University of Salford (1995).
[34] M. Galindo, T. Zamarreño, and S. Girón, ''Speech intelligibility in Mudejar-Gothic churches,'' Acust. Acta Acust. **86**, 381–384 (2000).
[35] T. Houtgast and H. J. M. Steeneken, ''A multi-language evaluation of the RASTI-method for estimating speech intelligibility in auditoria,'' Acustica **54**, 185–199 (1984).
[36] M. Galindo, T. Zamarreño, S. Girón, J. J. Sendra, and J. Navarro, ''Simulated acoustic field in Mudejar-Gothic churches,'' on CD-ROM: Berlin, 14–19 March, Collected Papers, 137th Meeting of the ASA and 2nd Convention of the EAA: Forum Acusticum (ISBN 3-9804568-5-4) (1999).
[37] M. Galindo, T. Zamarreño, and S. Girón, ''Measured acoustic parameters versus predicted ones in two Mudejar-Gothic churches,'' on CD-ROM: Seville (Spain), 16–20 September, Proceedings of the Forum Acusticum (ISBN 84-87985-07-6) (2002).

Acoustic impedance measurements—correction for probe geometry mismatch

N. H. Fletcher,[a] J. Smith, A. Z. Tarnopolsky, and J. Wolfe
School of Physics, University of New South Wales, Sydney 2052, Australia

(Received 28 October 2004; revised 27 January 2005; accepted 2 February 2005)

The effect of evanescent mode generation, due to geometrical mismatch, in acoustic impedance measurements is investigated. The particular geometry considered is that of a impedance probe with an annular flow port and a central microphone, but the techniques are applicable to other geometries. It is found that the imaginary part of the measured impedance error is proportional to frequency, and that the sign of the error is positive for measurements made on tubes with diameter much larger than that of the inlet port, but negative for tubes with diameter close to that of the inlet. The result is a distortion of the measured frequencies of the impedance minima of the duct while the maxima are largely unaffected. There is, in addition, a real resistive component to the error that varies approximately as the square root of the frequency. Experiment confirms the results of the analysis and calculations, and a calibration procedure is proposed that allows impedance probes that have been calibrated on a semi-infinite tube of one diameter to be employed for measurements on components with an inlet duct of some very different diameter. [DOI: 10.1121/1.1879192]

PACS numbers: 43.58.Bh, 43.20.Ye, 43.20.Mv, 43.20.Ks [AJZ] Pages: 2889–2895

I. INTRODUCTION

The measurement of acoustic impedance is of great importance in many branches of the subject, typical cases being the input impedance of mufflers or, in contrast, of musical wind instruments. Most methods involve injecting a known acoustic flow and measuring the resultant acoustic pressure, the only significantly different approach being that using two spaced microphones in a tube leading to the device to be measured so as to evaluate the reflection coefficient. A treatment from the viewpoint of general acoustics has been given by Beranek,[1] and surveys from the more precise viewpoint of musical instrument acoustics by Benade and Ibisi[2] and by Fletcher and Rossing.[3] The resulting analysis is straightforward and the results reliable if the diameter of the impedance head duct through which the flow is injected is equal to the diameter of the inlet to the device under measurement, but such a match is not generally possible. In the case of a significant mismatch of diameters, or in geometry, there is a corresponding error in the measured acoustic impedance. It is the purpose of this note to calculate the effect of this geometrical mismatch and to show how the error can be compensated for by a simple calculation.

In the impedance-measuring heads with which one usually deals, as shown in Fig. 1, the acoustic flow is injected through a high acoustic resistance located coaxially with the pipe inlet to the object being measured, and with either a circular or annular cross-section, the latter having advantages because a very narrow annulus can be less than one viscous diffusion length in width, thus providing a high and nearly frequency-independent acoustic resistance.[4] A small microphone measures the pressure, either at the center of the face of this inlet resistance or sometimes in an asymmetrical manner by being inserted from one side of the duct. The residual area of the pipe inlet is sealed by a flat rigid plate. For simplicity this situation will be idealized in what follows to planar probe geometry and the symmetrical microphone position shown in Fig. 1(a), though it is clearly possible to use the same techniques to calculate more complex geometries. Some such extensions are discussed.

II. EVANESCENT MODES

When a sound wave enters a pipe from a pipe of smaller diameter, localized modes are generated close to the inlet wall in the larger pipe. The effect in the smaller duct can be neglected here, since the injected acoustic flow is assumed to be constant across its whole area in impedance measuring devices. This situation is described by the wave equation in cylindrical polar coordinates,

$$\frac{1}{r}\frac{\partial}{\partial r}\left(r\frac{\partial p}{\partial r}\right)+\frac{1}{r^2}\frac{\partial^2 p}{\partial \phi^2}+\frac{\partial^2 p}{\partial x^2}=\frac{1}{c^2}\frac{\partial^2 p}{\partial t^2}, \tag{1}$$

where p is the acoustic pressure, c is the speed of sound in air, x is the axial coordinate, and r, ϕ are polar coordinates in the cross section. Since it has been assumed that there is no angular variation around the pipe, the coordinate ϕ can be neglected, and the solution has the form

$$p(x,r,t)=\sum_{n=0}^{\infty} A_n J_0(\alpha_n r/R)\exp[j(-k_n x+\omega t)] + B\exp[j(k_0 x+\omega t)], \tag{2}$$

where J_0 is the Bessel function of order zero, ω is the angular frequency of the signal, and A_n, α_n, and k_n are constants to be determined. The A_n are complex amplitudes associated with the injected wave, and the final term with complex am-

[a]Permanent address: Research School of Physical Sciences and Engineering Australian National University, Canberra 0200, Australia. Electronic mail: neville.fletcher@anu.edu.au

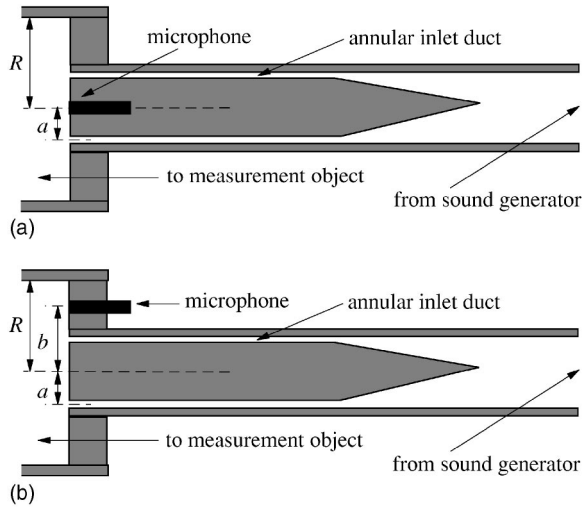

FIG. 1. (a) Geometry of a typical impedance probe connected to a duct of radius R. For the calculation the diameter $2a$ of the annulus that acts as the flow injection port is taken as 7 mm and the microphone diameter as zero. (b) An alternative geometry with the microphone displaced a distance b from the axis of the inlet annulus.

plitude B represents the reflected wave, assumed to be planar, which carries information about the acoustic impedance being measured. Restriction of the frequency range so that higher modes with $n>0$ are all nonpropagating and the returning wave is planar is necessary for the definition of acoustic impedance, since otherwise it would be a multiple-valued function with a different value for each propagating mode.

The values of the quantities α_n are derived from the assumed condition that the walls of the duct are rigid so that, taking the pipe radius to be R, it is required that $\partial p/\partial r=0$ at $r=R$ for each of the modes n. This leads to the condition

$$\left.\frac{dJ_0(\alpha_n r/R)}{dr}\right|_{r=R}=-\frac{\alpha_n}{R}J_1(\alpha_n)=0, \tag{3}$$

and hence[5] to the series of approximate values 3.83, 7.02, 10.17,... for α_n. Substituting (2) back in (1) then leads to the result

$$k_n^2=\left(\frac{\omega}{c}\right)^2-\frac{\alpha_n^2}{R^2}. \tag{4}$$

If the frequency is low enough that $\omega/c<\alpha_n/R$, then k_n becomes imaginary and the corresponding mode is nonpropagating or "evanescent." Such modes are exponentially attenuated along the axis of the pipe and are essentially confined to within an axial distance less than a few times R/α_n, or at most about one pipe-radius from the place where they are generated. In contrast, the plane-wave mode $n=0$, for which $\alpha_0=0$, propagates at all frequencies, although in this case k_0 is still complex because of wall losses along the tube and has the value[4,6]

$$k_0=\omega/c-j\frac{10^{-5}\beta\omega^{1/2}}{R}, \tag{5}$$

where $\beta>1$ is a factor to allow for the nonideal smoothness of the walls. Typically $\beta\approx 3$ for moderately smooth tubes.

In acoustic impedance measurements of the type with which we are concerned here, a one-dimensional plane-wave approximation is assumed in the object being studied, so attention is directed towards the plane wave amplitudes A_0 and B, with the other terms regarded as undesired byproducts of the mismatch between the impedance head and the entry duct. The aim of the present analysis is to identify the contributions of these higher modes and show how they can be corrected for.

To simplify matters, the inlet to the object under test is assumed to be an unobstructed circular tube of radius R with rigid boundaries, at least for a distance away from the measuring plane about equal to its radius. The impedance probe is also assumed to have circular symmetry, and a longitudinal cross section is shown in Fig. 1(a). The flow injection port is assumed to be a narrow annulus of radius a, and the radius of the central microphone diaphragm, assumed to be of very high acoustic impedance, is assumed to be sufficiently small that it can be taken as zero. Geometrical mismatch is then defined in terms of the ratio R/a.

The additional condition imposed by the rigid boundaries at the entry to the pipe is then that

$$\frac{\partial p}{\partial x}=0 \quad \text{if } x=0 \quad \text{and } r\neq a, \tag{6}$$

while the boundary condition across the acoustic flow inlet at $x=0$ requires that

$$v(r)=\frac{U}{2\pi r}\delta(r-a) \tag{7}$$

where U is the total acoustic inlet flow and $\delta(r-a)$ is the Dirac delta function. Now $\partial p/\partial x=-j\omega\rho v$, so that

$$\left.\frac{\partial p}{\partial x}\right|_{x=0}=-j\frac{\omega\rho U}{2\pi a}\delta(r-a). \tag{8}$$

Combining (8) with (2), multiplying by $rJ_0(\alpha_n r/R)$, and integrating from 0 to R then gives

$$k_n A_n M_n-k_0 B M_0\delta_{n,0}=\frac{\omega\rho U}{2\pi}J_0\left(\frac{\alpha_n a}{R}\right), \tag{9}$$

where,[7] since $J_1(\alpha_n)=0$ for all n,

$$M_n=\int_0^R J_0^2\left(\frac{\alpha_n r}{R}\right)r\,dr=\frac{R^2}{2}J_0^2(\alpha_n), \tag{10}$$

and δ_{mn} is the Kronecker delta function which equals 1 if $m=n$ and 0 otherwise. Equation (9) then gives, for the case $n\neq 0$,

$$A_n=\frac{\omega\rho U}{2\pi k_n M_n}J_0\left(\frac{\alpha_n a}{R}\right) \tag{11}$$

and for the case $n=0$.

$$B=A_0-\frac{\omega\rho U}{2\pi k_0 M_0}. \tag{12}$$

Now the measured value of the input impedance is

$$Z_{\text{meas}} = \left.\frac{p}{U}\right|_{x=0,r=0} = \frac{1}{U}\left(\sum_{n=0}^{\infty} A_n + B\right), \tag{13}$$

while the true plane-wave impedance is

$$Z_{\text{true}} = \frac{A_0 + B}{U}. \tag{14}$$

These equations can be combined to give

$$Z_{\text{meas}} = Z_{\text{true}} + \sum_{n=1}^{\infty} \frac{\omega\rho}{2\pi k_n M_n} J_0\left(\frac{\alpha_n a}{R}\right), \tag{15}$$

and this equation will be the basis of the calculations to follow. A rather similar equation could be derived, following the same method, for other probe geometries, as discussed later. Despite the exponential decay of evanescent waves along the measurement axis, it is found by numerical exploration that a large number of modes must be taken into account to ensure smooth convergence. For the calculations to be reported later, 100 modes were included since the computation is quite simple.[8] A reasonable result can, however, be achieved with as few as ten modes.

This analysis is inapplicable at frequencies that are high enough that $k \geqslant \alpha_1 / R$, for then the evanescent modes begin to propagate and higher modes appear in the reflected wave. In practical terms, this occurs in a cylindrical conduit of radius R for frequencies above about $210/R$ Hz, where R is in meters. The analysis also omits consideration of viscous and thermal losses from the evanescent waves at the plane wall terminating the duct at $x=0$. A discussion of this point and an estimate of the form and magnitude of the resistive error is given in Sec. V. While, if the end wall is smooth and rigid, the resistive error contributed by these losses is very small compared with the imaginary part, its inclusion is found in Sec. VII to be necessary to give a complete measurement correction.

It is instructive to write the result (15) in terms of dimensionless parameters. Since the quantities α_n are dimensionless, it follows from (4) that we can write $k_n = R^{-1} f(\omega R/c)$, where the function f can be written down explicitly, while from (10), $M_n \propto R^2$. Thus (15) can be expressed in the form

$$Z_{\text{meas}} = Z_{\text{true}} + \frac{j\rho\omega}{a} G\left(\frac{R}{a}, \frac{\omega a}{c}\right), \tag{16}$$

where the function $G(x,y)$ can be written explicitly. As will be shown below by means of a numerical calculation, the error term $Z_{\text{error}} = Z_{\text{meas}} - Z_{\text{true}}$ in (16) turns out to be almost exactly proportional to frequency over quite a large range of the ratio R/a, which implies that

$$\frac{Z_{\text{error}}}{Z_0(R)} \approx \frac{j\omega a}{c} F\left(\frac{R}{a}\right), \tag{17}$$

where $Z_0(R) = \rho c / \pi R^2$ is the characteristic impedance of the pipe being measured, and the function $F(R/a)$ can be derived from Eqs. (15) and (16) and can be evaluated numerically. The form of this measurement error and its numerical evaluation will be discussed further in Sec. III.

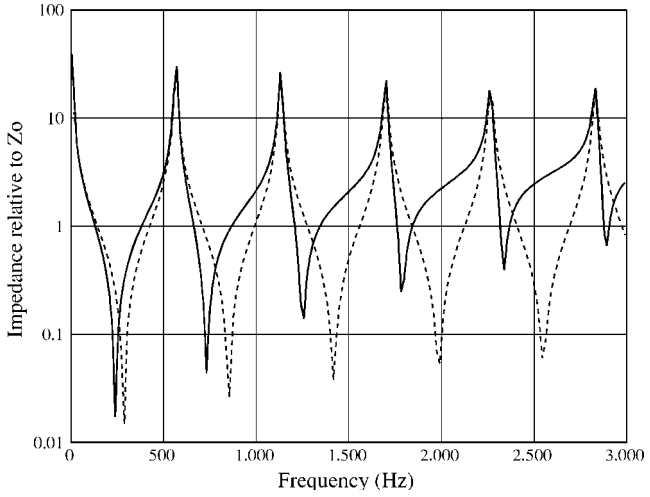

FIG. 2. Calculated magnitude of the impedance for a closed tube of diameter 50 mm and length 300 mm, as would be measured with an annular probe of diameter 7 mm. The broken curve shows the true impedance, assuming a wall loss factor of 3, while the full curve shows the impedance that would be measured.

III. A SPECIFIC EXAMPLE

It is interesting to examine the trend of the calculated results for cases in which the exact solution is known, and an obvious candidate is the simple stopped tube of length L and radius $R > a$, for which the input impedance is known to be

$$Z = -j \frac{\rho c}{\pi R^2} \cot(kL), \tag{18}$$

where wall losses are taken into account as in Eq. (5).

For the specific case calculated, the tube to be measured was assumed to have a diameter of 53 mm and a length of 300 mm, while the input annulus was taken to have a diameter of 7 mm, this being a very substantial mismatch. The wall loss magnification factor β of (5) in the tube being measured is taken to have the value $\beta = 3$, which is fairly typical for tubes of the particular material used. The calculated results for the magnitude of the measured impedance and that of the actual plane-wave impedance are shown in Fig. 2. As will be discussed later, it is necessary to include almost 100 terms in the summation in (15) in order to achieve an accurate result, but this presents no computational difficulty, and indeed a summation with only ten terms gives moderate accuracy. The impedance can readily be split into real and imaginary parts in the calculation if desired. The first higher mode becomes propagating at about 8 kHz in the case of this tube, so the measurement is necessarily limited to significantly below this frequency. Clearly there is a very large discrepancy between the true and measured impedance values even below 3 kHz, so that the measurement in its unadjusted state is of little use unless one is interested simply in the frequencies of the impedance maxima.

Let the acoustic impedance of the device being measured be $Z_{\text{sub}} = R_{\text{sub}} + jX_{\text{sub}}$, with appropriate descriptive subscripts. Then exploration of the reactive part of the measurement error $X_{\text{error}} = X_{\text{meas}} - X_{\text{true}}$ as a function of frequency and of the tube diameter mismatch shows that the error is quite closely proportional to frequency over the frequency

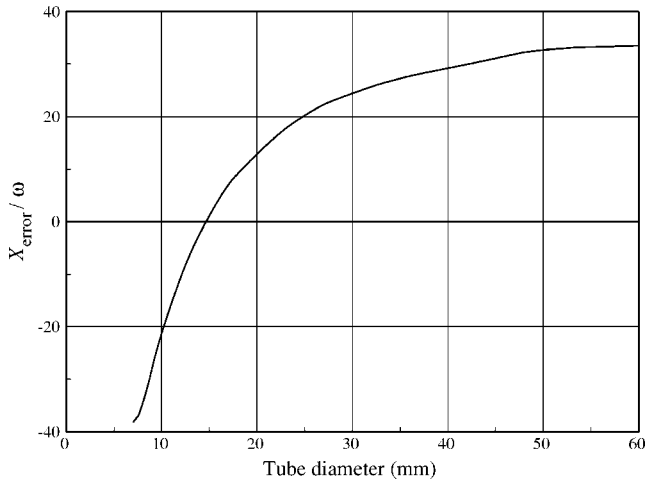

FIG. 3. Calculated frequency-weighted error X_{error}/ω in the imaginary part of the impedance (in units of Pa s^2 m^{-3}) as a function of the diameter of the sample tube, for an annular probe of diameter 7 mm. The real part of the error is smaller by at least a factor of 10.

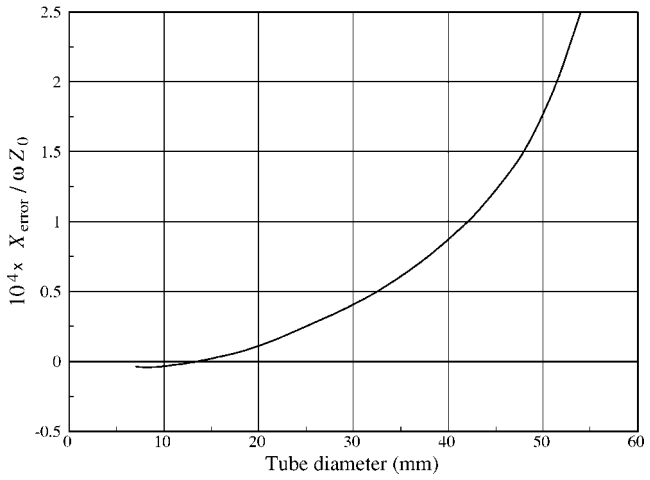

FIG. 4. Calculated frequency-weighted relative error $X_{error}/\omega Z_0$ in the imaginary part of the impedance (in units of seconds) as a function of the diameter of the sample tube for the case of an annular probe diameter of 7 mm. The real part of the error is smaller by at least a factor of 10. Since typically $\omega \sim 10^4\ s^{-1}$, the error is comparable to the value of Z_0 over most of the diameter range shown for frequencies below about 3 kHz. As discussed in the text, this curve is not universal but must be further scaled by a factor $\omega a/c$.

range 0–3 kHz. The deviation from proportionality is negligible for tubes up to 50 mm in diameter, and amounts to only about 5% for a 100-mm tube at 3 kHz. This proportionality to frequency means that, to a good approximation, the impedance error can be thought of as the effect of an inertive impedance jX_{error} in series with the input to the duct being measured. For tube diameters less than about twice that of the inlet annulus, however, the inertance X_{error} is actually negative and is effectively subtracted rather than added.

Exploration of the trend of the error as the diameter mismatch is varied is shown in Fig. 3, where the quantity plotted is X_{error}/ω. For this calculation the contributions of 100 evanescent modes were included in the calculation, since this presents no computational difficulty. If only a much smaller number of modes, say ten, is included, then the curve, while following the same trend as in Fig. 3, exhibits oscillations as a function of tube diameter. The error is almost exactly proportional to frequency over the measurement range 0–3 kHz used, so that the curve in Fig. 3 applies at all frequencies in this range. For large tube diameters, but still below the higher-mode propagation frequency, $X_{error}/\omega \rightarrow 40$ Pa s^2 m^{-3}, which is about equal to the impedance of a short stub tube matching the inlet annulus in diameter and with a length about equal to 0.4 times its radius. This is, as might be expected, comparable to the magnitude of the imaginary part of the radiation impedance for a vibrating circular disc of this size set in an infinite plane baffle. Interestingly, the mismatch error passes cleanly through zero for a tube diameter of about 15 mm, about twice the probe inlet diameter, and then increases in magnitude again, but with a negative sign, for narrower tubes. The reason for this change is that, as the diameter is increased, zeros of the lower-order Bessel functions $J_0(\alpha_n r/R)$ pass successively across the inlet annulus so that their excitation, as seen from the microphone position at $r=0$, shifts from negative to positive. The mode with $n=1$ is particularly important in this connection.

What is important, however, is not the absolute value of the error but rather its magnitude relative to the impedance quantity being measured. A useful measure of this can be reached by dividing the frequency-weighted absolute error X_{error}/ω of Fig. 3 by the characteristic impedance $Z_0(R) = \rho c/\pi R^2$ of the tube being measured. This frequency-weighted relative error $X_{error}/\omega Z_0(R)$ is shown in Fig. 4 as a function of tube radius R. The mismatch range covered is the same as in Fig. 3. From Fig. 4 it is clear that the relative error is small for ducts up to about three times the probe annulus diameter, while for ducts of larger diameter the relative error increases about as the square of the diameter mismatch to the probe. For mismatch ratios larger than about 7 the error is so large that accuracy is severely compromised even after correction. Note incidentally that, from the form of (17), the curve in Fig. 4 is not universal, but must be scaled by a further factor $\omega a/c$.

IV. ALTERNATIVE PROBE GEOMETRIES

The first geometrical variant that should be considered is the assumption made in the previous analysis that the width of the inlet annulus is essentially zero and that the diameter of the microphone is also zero. The first of these assumptions is generally a good approximation, since the diameter of the annulus is typically of order 10 mm while its width is typically only about 0.1 mm. The second assumption is, however, far from being realized in practice, since the microphone diameter is typically about 2 mm, which is an appreciable fraction of the annulus diameter. The effect of this is that, if the probe is connected to a duct of matching diameter for calibration, the contributions of modes for which the first radial zero lies within the radius of the microphone will be very greatly reduced, since positive and negative contributions will be averaged over the microphone surface. Since the sharp minimum in X_{error} shown in Fig. 3 for a microphone of zero diameter in a tube closely matching the probe diameter is largely due to these high-order modes, the impedance correction implied for this situation is actually

exaggerated, typically by as much as a factor of 2. A detailed analysis will not be given here, but essentially it involves integration over the area of the microphone, though to a reasonable approximation a similar result is obtained simply by ignoring the contributions of the higher modes. This matter will be revisited in Sec. VII. As shown in Fig. 4, however, the relative correction for tubes with diameter mismatch less than about a factor of 2 is actually very small, so that the problem is not serious until large mismatches are involved, and a solution for this practical problem is presented in that section.

As an alternative, consider the geometry illustrated in Fig. 1(b), in which the measurement microphone is now offset from the axis defined by the inlet annulus. The analysis of this case proceeds just as before except that allowance must be made for the offset of the microphone. Let us take this offset to be $r=b$ for generality. Equation (13) then becomes

$$Z_{\text{meas}}=\left.\frac{p}{U}\right|_{x=0,r=b}=\frac{1}{U}\left(\sum_{n=0}^{\infty}A_nJ_0\left(\frac{\alpha_n b}{R}\right)+B\right), \tag{19}$$

and (15) becomes

$$Z_{\text{meas}}=Z_{\text{true}}+\sum_{n=1}^{\infty}\frac{\omega\rho}{2\pi k_n M_n}J_0\left(\frac{\alpha_n a}{R}\right)J_0\left(\frac{\alpha_n b}{R}\right). \tag{20}$$

For the particular case in which $b=a$ and the microphone is set at a point upon the inlet annulus, the final term of (20) contains the factor $J_0^2(\alpha_n a/R)$, which is always positive, so that the error term is itself always positive, rather than becoming negative for values of R less than about $3a$, as calculated for the central microphone with $b=0$. Other geometries are similarly easily calculated.

Another probe geometry of interest is that in which the microphone is set forward of the plane of the injection annulus by a small amount δ. Clearly, if $\delta>R$, then most of the evanescent waves will have decayed to negligible amplitude at the microphone position and will not influence the measurement. The impedance that is measured, however, will then not be the true impedance at the inlet port but rather that at the displaced position. While calculation of the necessary correction is possible, its value depends upon the impedance being measured, so that this is not a realistic approach for a general-purpose impedance probe if the diameter mismatch is large.

In real probe geometries, of course, the microphone diameter is not zero, and this must be taken into account by integrating the sensed pressure signal across the microphone area. In most cases this will slightly reduce the value of the necessary correction, since the higher evanescent modes with wavelength smaller than the microphone diameter will have a much reduced effect.

V. RESISTIVE CORRECTION

There is, however, one significant thing that has been omitted from the analysis detailed so far, and that is the possibility of a resistive component to the error contributed by the evanescent modes. Because all the acoustic motion associated with these modes is localized within a distance of about R/α_n of the entry plane, and because there is a significant component of acoustic motion that is tangential to this plane, certain losses are to be expected. The magnitude of these losses should be about inversely proportional to the boundary layer thickness, and should thus vary as $\omega^{1/2}$.

In a formal sense, these effects lead to the arguments of the Bessel functions in Eq. (2) being complex rather than real, but this formal analysis has not been carried out because there will inevitably be a significant correction factor that depends upon the roughness of the surface of the inlet plane, including the microphone, and the possible presence of sharp edges. Since the correction due to this effect is small compared to the reactive component of the error already considered, it will therefore be left as a small adjustable parameter.

VI. APPLICATION TO A CALIBRATED PROBE

Researchers at this laboratory have developed an acoustic impedance probe of the general type shown in Fig. 1, though with several geometrical variations, and have devised a calibration procedure that makes its results very accurate for inlet tubes of specified diameter.[9,10] In the calibration procedure, the probe is connected to an effectively semi-infinite pipe (actually 40–200 m in length, depending upon the pipe diameter, so as to produce an attenuation of about 80 dB in the reflected wave for the frequency range of interest) closely matching it in diameter. The flow annulus is fed with a sound pressure signal made up of a very large number of independently adjustable components with a frequency separation of typically about 2.7 Hz. The response of the computer-controlled pressure measurement system is then adjusted in phase and amplitude so that both these measured quantities are constant over the frequency range of interest. (There are actually some experimental subtleties about this that need not be considered here.) The acoustic volume flow is then taken to be this pressure divided by the characteristic impedance $\rho c/S$ of the effectively semi-infinite calibration tube, and these settings are then used in subsequent measurements. This procedure cancels out all evanescent mode effects as well as all irregularities in phase or amplitude of the injected flow or the microphone response for this tube diameter. Measurements on objects with an input duct closely matching the calibration tube in diameter are therefore highly accurate.

It is clearly impractical to have such very long calibration tubes of all diameters available, so that there are restrictions on the applicability of this calibration technique. If the probe is calibrated on a tube closely matching the inlet annulus in diameter, as is usual, then the calibration procedure effectively adds an inertive impedance in order to cancel out the negative imaginary part of the impedance error shown in Fig. 3. If this calibrated probe is then used to make measurements on an object with a much larger inlet pipe diameter, an additional positive error will be introduced into the imaginary part of the measured impedance. The effect of the correction will then be effectively added to the error. This complication can, however, be largely removed by programming the measurement system to subtract off a positive imaginary impedance of magnitude appropriate to correct for the difference between the errors for the measurement tube and the calibration tube.

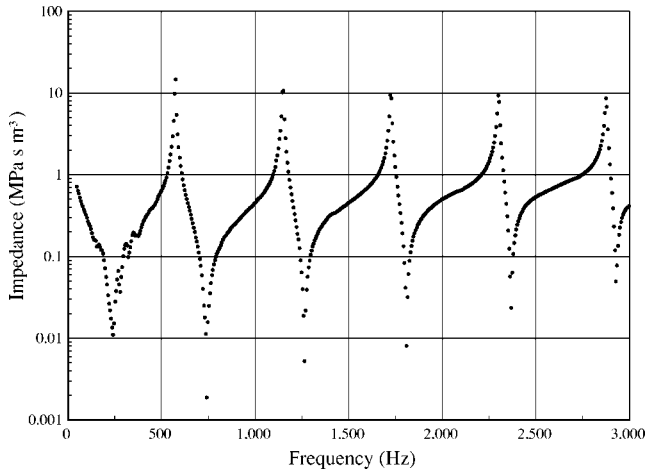

FIG. 5. Measured magnitude, without correction, of the impedance of a stopped tube 300 mm long and 48 mm in diameter, as measured using the impedance probe described, with an inlet annulus diameter of 6.5 mm, calibrated on a tube of diameter 7.8 mm. Individual measurement points are shown.

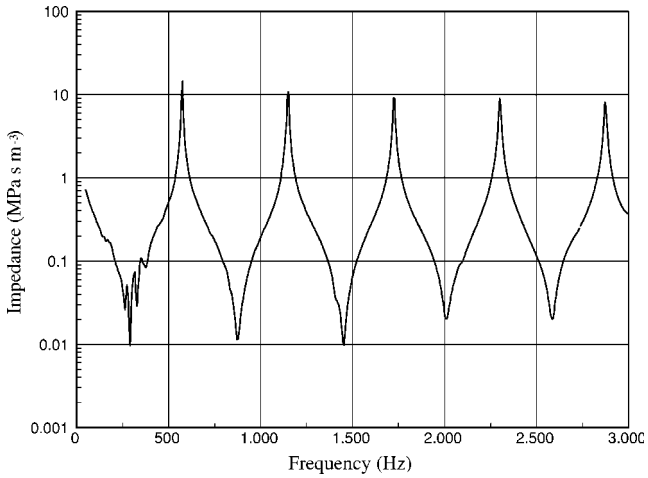

FIG. 6. Measured magnitude of the impedance of the stopped tube of Fig. 5 when corrected by subtracting a series impedance of $(200\omega^{1/2} + 41j\omega)$ Pa s m^{-3}.

Fortunately, the laboratory for which the impedance probe was designed studies the acoustics of musical wind instruments and of the vocal tract, so that only a narrow range of tube diameters is involved, and a set of calibration pipes with appropriate diameters (from 3 to 26 mm) and lengths between 42 and 197 m has been installed without undue expense.

VII. EXPERIMENTAL VERIFICATION

As a check with experiment, an impedance probe with the geometry shown in Fig. 1(a), with inlet annulus mean diameter 6.5 mm and width 0.1 mm and with a centrally located microphone of diameter 1.9 mm was calibrated on a long tube of diameter 7.8 mm, using the procedure previously described.[9,10] When this probe was used to measure the magnitude of the impedance of a rigidly stopped brass pipe of diameter 48 mm and length 300 mm, the results were as shown in Fig. 5. The magnitude and phase of the impedance were measured at each point, and the measurement points are shown in the figure. The characteristic impedance $\rho c/S$ for this pipe is about 0.23 MPa s m^{-3}, and the minima should be located centrally between successive maxima, so that it is clear that the raw measurements are greatly in error. The resemblance of the graph to that calculated in Fig. 2 is clear. The poor signal-to-noise ratio apparent below about 300 Hz is the result of the peculiar measurement configuration chosen for this test. Normally a much smaller mismatch in diameter would have been chosen for the measurement, and the concentric geometry used here for the test transmits a much larger vibration signal to the microphone than does the off-axis geometry normally used in this particular probe.[9,10]

To correct the measurements, the errors for both the calibration tube and the measurement tube must be considered. To further refine the correction, use can be made of the scaling law (17) since the actual diameter of the inlet annulus was 6.5 mm rather than the 7 mm used to calculate Fig. 3. This involves small changes to both the ratio R/a and the factor $\omega a/c$, but these will be neglected here. It is first noted from Fig. 3 that the correction for the calibration pipe is negative, since its diameter is close to that of the inlet annulus. Its value from Fig. 3, which assumed a microphone of zero diameter, is about $-30j\omega$ Pa s m^{-3}. As discussed briefly in Sec. IV, however, the fact that the microphone diameter is actually nearly 2 mm eliminates most of the contribution of modes with $n>10$ so that the real correction is only about half this much, or about $-15j\omega$ Pa s m^{-3}. The large pipe, then, is about seven times the diameter of the annulus, so that the equivalent value of diameter in Fig. 3 is about 45 mm, for which the correction is positive and equal to about $30j\omega$ Pa s m^{-3}. Since the probe was calibrated so as to give zero error on the narrow calibration pipe, it is the difference between the two errors, and thus about $45j\omega$ Pa s m^{-3}, that must be used in correcting the measurement error on the wide pipe. A certain amount of latitude is allowable when making this correction, however, since the effect of nonzero microphone diameter and the slight difference in annulus diameter were only approximately allowed for. A value of $41j\omega$ Pa s m^{-3}, which is quite close to the estimate of $45j\omega$ Pa s m^{-3}, gives a well-corrected result for the frequencies of the impedance minima, as shown in Fig. 6.

If only the imaginary contribution to the correction is considered, however, then the impedance minima are rather shallow, and it is necessary to include the resistive contribution as well. As discussed in Sec. V, it is difficult to estimate the magnitude of this correction, so that trial-and-error is the best approach. In the present case it turns out to be necessary to subtract a resistive correction of $200\omega^{1/2}$ Pa s m^{-3} in order to achieve the appropriate symmetry between impedance maxima and minima, as shown in Fig. 6. Over the frequency range considered, this resistive correction is less than 10% of the inductive correction and affects only the sharpness of the impedance minima.

The correction for the case illustrated in Figs. 5 and 6 is an extreme one, and would not ordinarily be used because the noise in the measurement then becomes noticeable. It would, however, be adequate if an approximate measurement were required and only a narrow probe were available. Rather than relying upon the calculations outlined in the

present paper, however, the best method for determining and applying the necessary correction is probably as follows:

(1) Calibrate the probe in the usual way on a semi-infinite pipe.
(2) Use this calibrated probe to measure the impedance of a stopped pipe with diameter equal to that of the object to be measured and of such a length that it shows several impedance maxima and minima in the proposed measurement range. Record the results. (The maxima will be correct but the minima will be displaced.)
(3) Write a computer program to subtract from the measured impedance a correction $A\omega^{1/2}+jB\omega$, with A and B as real constants and $A>0$, and display the result. Vary the magnitude of B until the minima are as nearly as possible half-way between the maxima; then vary the magnitude of A until the envelope of the minima matches that of the maxima. If a very wide frequency range and/or a very large geometrical mismatch is involved, then the correction can be of the form $A\omega^{1/2}+jB\omega(1+C\omega)$ with $|C\omega|\ll 1$ at the upper frequency limit.
(4) Record this correction and use it to correct all measurements made on devices coupled to the impedance probe through tubes of that diameter.

VIII. CONCLUSIONS

A method has been described that allows calculation of the errors introduced in acoustic impedance measurements when there is a geometrical mismatch, particularly a size mismatch, between the impedance probe and the inlet tube to the device being measured. While this calculation has been carried out for the simplest and most symmetrical geometrical mismatch situations, the methods can clearly be extended to apply to more complex cases, including those in which the microphone is offset both from the axis of the probe and from its inlet plane, or in which the geometry has a symmetry other than circular. Comparison with experiment shows that even quite extreme mismatches in diameter can be corrected for in this way.

This correction approach is not advocated when precise measurements are required, since the experimental noise in the measurements is then exaggerated when the large series inductance is subtracted. For such measurements, a probe of comparable diameter should be used, and this should be calibrated using an effectively infinite pipe closely matching in diameter the input diameter of the object under test.

While this analysis has been performed for the case of an acoustic probe using a high-impedance inlet duct, a very similar result would be obtained for the case of a probe in the form of a standard standing-wave impedance tube. There is, however, an additional complication in this case since the input flow cannot be assumed to be uniform across the whole inlet tube—the influence of evanescent modes within this inlet tube itself must therefore be taken into account.

An ideal design of impedance probe that would overcome these problems would be one in which, instead of using a localized acoustic flow inlet in the form of a very narrow annulus or other convenient geometry, the flow was injected instead through a high-impedance porous-solid plug extending across the whole area of the inlet to the object being measured. Even in this case, however, a calibration procedure using an effectively infinite pipe is desirable in order to compensate for any possible frequency dependence of the flow impedance or of the associated electronic equipment.

[1] L. L. Beranek, *Acoustic Measurements*, revised edition (Acoustical Society of America, New York, 1988), pp. 294–353.
[2] A. H. Benade and M. I. Ibisi, ''Survey of impedance methods and a new piezo-disk-driven impedance head for air columns,'' J. Acoust. Soc. Am. **81**, 1152–1167 (1987).
[3] N. H. Fletcher and T. D. Rossing, *The Physics of Musical Instruments*, 2nd ed. (Springer-Verlag, New York, 1998), pp. 222–223.
[4] J. Backus, ''Input impedance curves for the reed woodwind instruments,'' J. Acoust. Soc. Am. **56**, 1266–1279 (1974).
[5] M. Abramowitz and I. A. Stegun, *Handbook of Mathematical Functions* (National Bureau of Standards, Washington, DC, 1964), p. 411.
[6] A. H. Benade, ''On the propagation of sound waves in a cylindrical conduit,'' J. Acoust. Soc. Am. **44**, 616–623 (1968).
[7] M. Abramowitz and I. A. Stegun, *Handbook of Mathematical Functions* (National Bureau of Standards, Washington, DC, 1964), formula 11.3.34.
[8] W. H. Press, B. P. Flannery, S. A. Teukolsky, and W. T. Vetterling, *Numerical Recipes* (Cambridge U.P., Cambridge, 1986), Sec. 6.4.
[9] J. Wolfe, J. Smith, G. Brielbeck, and F. Stocker, ''A system for real time measurement of acoustic transfer functions,'' Acoust. Aust. **23**, 19–20 (1995).
[10] J. Wolfe, J. Smith, J. Tann, and N. H. Fletcher, ''Acoustic impedance spectra of classical and modern flutes,'' J. Sound Vib. **243**, 127–144 (2001).

Instantaneous frequency decomposition: An application to spectrally sparse sounds with fast frequency modulations

T. J. Gardner[a] and M. O. Magnasco
Laboratory of Mathematical Physics, The Rockefeller University, 1230 York Ave, New York, New York 10021

(Received July 2002; Revised 6 January 2005; accepted 11 January 2005)

Classical time–frequency analysis is based on the amplitude responses of bandpass filters, discarding phase information. Instantaneous frequency analysis, in contrast, is based on the derivatives of these phases. This method of frequency calculation is of interest for its high precision and for reasons of similarity to cochlear encoding of sound. This article describes a methodology for high resolution analysis of sparse sounds, based on instantaneous frequencies. In this method, a comparison between tonotopic and instantaneous frequency information is introduced to select filter positions that are well matched to the signal. Second, a cross-check that compares frequency estimates from neighboring channels is used to optimize filter bandwidth, and to signal the quality of the analysis. These cross-checks lead to an optimal time–frequency representation without requiring any prior information about the signal. When applied to a signal that is sufficiently sparse, the method decomposes the signal into separate time–frequency contours that are tracked with high precision. Alternatively, if the signal is spectrally too dense, neighboring channels generate inconsistent estimates—a feature that allows the method to assess its own validity in particular contexts. Similar optimization principles may be present in cochlear encoding. [DOI: 10.1121/1.1863072]

PACS numbers: 43.60.Ac, 43.60.Hj, 43.58.Ta, 43.64.Bt [ADP] Pages: 2896–2903

I. INTRODUCTION

Time–frequency analysis is a general methodology for representing sound in two dimensions, time and frequency. This is an intuitive representation, evinced by the evolution of the musical score, which since ancient times has shown time horizontally and pitch vertically. Time–frequency analysis is limited by the uncertainty principle: the resolution of frequency measurements is inversely proportional to the resolution of temporal measurements,[1] so the time–frequency plane has a fundamental ''granularity.'' However, while this limit holds for signals drawn from arbitrary ensembles, special classes of signals may have features permitting a higher resolution analysis.

Many methods exist for the analysis of sparse signals, i.e., those composed of a number of well-separated tones with limited amplitude and frequency modulation rates. For example, Greenewalt employed periodicity analysis to great success in his classic study of the acoustics of bird song.[2] One family of methodologies for the analysis of sparse signals is based on the calculation of instantaneous frequencies—the phase derivatives of a complex filter bank.[3–9] Though these methods are capable of representing sparse signals with high precision, they require prior information about the analyzed signal to choose the positions and bandwidth of the filters that contribute to the analysis.[7,8,10] A general method for optimizing these parameters remains an open problem.[11]

Instantaneous frequency decomposition (IFD) provides a methodology for optimizing the parameters of an instantaneous frequency analysis, without reference to any prior information about the analyzed signal. The method consists of two phases: an expansive phase in which the input signal is split through bandpass filtering into a highly *redundant* array of channels, and a contractive phase, in which the redundant channels are checked for agreement, or ''consensus'' and collapsed back together. *Consensus between neighboring channels indicates the quality of the local frequency estimates, and is used to guide optimization of filter bandwidths*. If the signal is sufficiently sparse, the time–frequency representation generated by the IFD will track the individual components of the signal with high precision. If not, poor consensus measures signal the failure of the method.

While our purpose in this article is to describe a practical tool for the high-precision analysis of sparse sounds, it is worthwhile to note its biological motivation. In one of the earliest views of cochlear function, frequency is determined by the spatial, or tonotopic, position of active auditory nerve fibers.[12–14] An alternative form of frequency coding can be found in the phase-locked responses of auditory hair cells;[15] for frequencies below 4 kHz, auditory nerve fibers preferentially initiate action potentials at particular phases of the driving force. Licklider in 1951 suggested that the intervals between phase-locked spikes leads to a second representation of frequency that is independent of the spatial arrangement of auditory fibers.[16] This representation of sound has been experimentally and conceptually supported through neurophysiology,[17,18] psychophysics,[19–21] and functional brain imaging.[22,23] The method of instantaneous frequency decomposition is conceptually related to this spike-interval based coding in the auditory nerve, and provides a rationale for combining tonotopic and phase information in a single analysis, and for comparing frequency estimates from a re-

[a]Current address: MIT E19-528, Cambridge, Massachusetts 02139. Electronic mail: tgardner@mit.edu

 0001-4966/2005/117(5)/2896/8/$22.50

dundant array of phase-locked channels. In this method, cross-checks between tonotopic and phase information determine which filters contribute to the analysis, and comparisons among neighboring channels guide optimization of the analyzing bandwidth. It is possible that similar computations are made in the course of neural auditory processing.[14,24]

II. METHOD

A. Definitions

The continuous Gabor transform, also known as the short-time Fourier transform, is defined in terms of the signal to be analyzed *s*, a windowing function *w*, time *t*, and frequency f[1]:

$$G_w(t,f)=\int s(\tau)w(\tau-t)e^{i2\pi f(\tau-t)}\,d\tau. \tag{1}$$

Gaussian windows are used throughout this article:

$$w=e^{-(t-t_0)^2/\sigma^2}. \tag{2}$$

The temporal spread of this function, Δt, defined in terms of second moments, is $\sqrt{\pi/2}\sigma$, and a complementary relation is found for the frequency spread of its Fourier transform: $\Delta f=(1/\sqrt{2\pi})(1/\sigma)$. Together, they define the uncertainty principle $\Delta f\,\Delta t=1/2$. For all other windowing functions,[1] $\Delta f\Delta t>1/2$. Throughout the text, the term *bandwidth* refers to Δf.

Each frequency f of the Gabor transform provides one ''channel'' in the IFD analysis. In polar form,

$$G_w(t,f)=a_w(t,f)e^{i\phi_w(t,f)}. \tag{3}$$

The *instantaneous frequency* of each channel is defined as

$$f_w^i=\frac{1}{2\pi}\frac{\partial\phi_w(t,f)}{\partial t}. \tag{4}$$

For each channel, instantaneous frequency can be estimated from the local period of oscillation, drawn from intervals between maxima or zero crossings of the signal. In this form, instantaneous frequency is calculated from information homologous to the intervals between phase-locked spikes in the auditory nerve. Instantaneous frequency is calculated analytically as follows:

$$\frac{\partial\phi_w(t,f)}{\partial t}=\frac{\partial\,\mathrm{Im}(\ln(G_w(t,f)))}{\partial t}=\mathrm{Im}\left[\frac{\partial G_w(t,f)/\partial t}{G_w(t,f)}\right]. \tag{5}$$

From this expression, a formula in terms of the windowing function *w* and its derivative w' follows:[7]

$$f_w^i(t,f)=f-\mathrm{Im}\left[\frac{G_{w'}(t,f)}{G_w(t,f)}\right]\frac{1}{2\pi}. \tag{6}$$

The current method is designed for signals that are *tonal*, defined in terms of smooth, time-dependent frequencies $F_k(t)$ and amplitudes $a_k(t)$ as follows:

$$s(t)=\sum_{k=1}^{N}a_k(t)\sin(\phi_k(t)), \tag{7}$$

$$\phi_k(t)=2\pi\int_{\tau=0}^{t}F_k(\tau)d\tau. \tag{8}$$

A signal of this form is *separable* if the Gabor transform, at each time and frequency, receives significant energy from only one tone [one element of the sum in Eq. (7)].[8] Signals analyzed in this method must be *separable*, and must have limited frequency and amplitude modulation rates. For separable signals with sufficiently slow frequency and amplitude modulations, instantaneous frequencies $f_w^i(t,f)$ of a well-chosen bandwidth provide excellent estimates of the frequency contours of the signal, $F_k(t)$. This is demonstrated in the following sections.[5]

We use the term *sparse* to refer to *separable* signals that are modulated slowly enough to be resolved thorough instantaneous frequency analysis. Instantaneous frequency decomposition provides a method for finding the optimum bandwidth of analysis, and estimating $a_k(t)$ and $F_k(t)$, the amplitude and frequency contours of each component. If the method is applied to signals that are not separable, or signals with frequency and amplitude modulations that are too fast, the signal is not resolved, instantaneous frequencies do not track the signal frequencies $F_k(t)$, and the method signals its own error. The following sections illustrate what this means.

One class of *test signals* used in this article consist of a sum of tones with periodic frequency modulations:

$$e^{i\omega_0 t}e^{i(A/\omega)\cos(\omega t)}. \tag{9}$$

Through the Jacobi–Anger expansion, a periodically modulated tone can be represented as a single frequency accompanied by an infinite sum of sidebands:

$$e^{i(A/\omega)\cos(\omega t)}=\sum_{n=-\infty}^{\infty}i^nJ_n\left(\frac{A}{\omega}\right)e^{in\omega t}, \tag{10}$$

where $J_n(z)$ are the Bessel functions of the first kind. This relationship is referred to in the following sections.

B. Instantaneous frequency decomposition

The method of instantaneous frequency decomposition consists of a central processing structure, an outer optimization loop, and a final quality check. The central processing structure computes instantaneous frequencies for channels of a filter bank of fixed bandwidth and applies a cross-check between tonotopic and phase information to determine which filters contribute to the analysis. The optimization loop compares frequency estimates from neighboring channels to generate a measure that we call *consensus*, and uses this measure to optimize the analyzing bandwidth Δf. The quality check uses the same measure of consensus to indicate specific regions of the time–frequency plane where the signal is well resolved, and other regions where high spectral density leads to a failure of the frequency estimates.

1. Raw instantaneous frequency analysis

In the first stage of the analysis, $|G_w(t,f)|$ is computed for each time and a dense set of frequencies, according to Eq. (1), for some initial choice of bandwidth. In this analysis, the distinct values of f are referred to as ''channels.''

Instantaneous frequency representation involves a remapping of the amplitudes $|G_w(t,f)|$ to new positions in the time–frequency plane, namely $(t,f_w^i(t,f))$, where f_w^i is the instantaneous frequency of channel f at time t, calculated

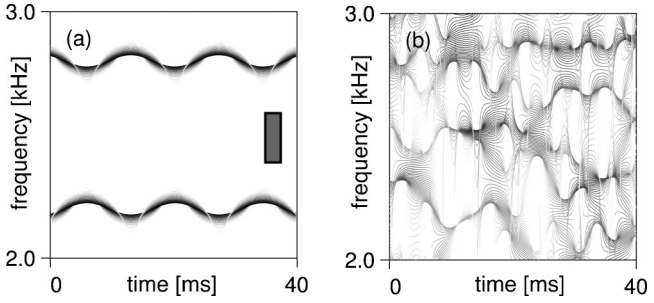

FIG. 1. Raw or unrefined IFD analysis for a two-tone signal (a) and white noise (b). The filter bank contains an independent filter every 10 Hz, each of which has a frequency bandwidth $\Delta f = 220$ Hz. The dimensions of the small rectangle in panel (a) indicate this bandwidth, Δf, and the corresponding temporal resolution of the filter as determined by the uncertainty principle: $\Delta t = 1/2\Delta f$. Pixel intensity is scaled according to the logarithm of power, and ranges over the top 20 dB of signal power.

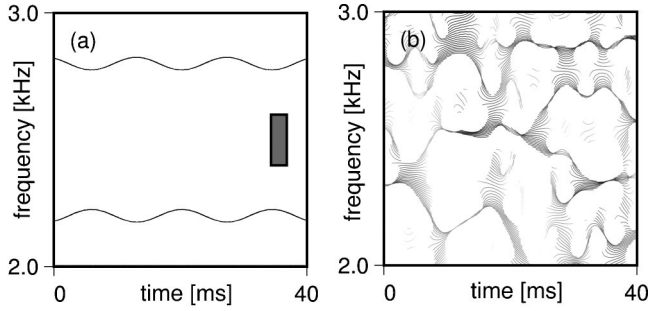

FIG. 2. The single channel tonotopic cross-check improves pitch tracking. The same analysis as in Fig. 1, after applying a locking window $C = \Delta f/2 = 110$ Hz. This cross-check removes frequency lines produced by off-center channels.

from Eq. (6). This first step, the raw instantaneous frequency analysis, has been described in detail elsewhere.[5]

When applied to separable signals with slow modulations, positions (t,f) that are far from the signal tones are mapped onto the signal tones. This is illustrated in the following figure. Figure 1 contains an analysis of two signals according to this remapping rule. The first signal consists of two equal amplitude tones, each of which is frequency modulated with a peak to peak modulation depth of 70 Hz, over a period of 14 ms. The second signal is white noise. The frequency estimates generated from each channel provide one continuous line in each figure. [To avoid confusion, note that in panel (a), many lines overlap, leading to the appearance of a continuous distribution.] For the white noise signal, each channel responds to a slightly different portion of the white-noise spectrum, leading to a spread in frequency contours estimated from neighboring channels. The structure of this web of lines is sensitive to the bandwidth of the filter bank.

2. Tonotopic cross-check

The darkest lines in Fig. 1, panel (a), fall on the correct frequency contours of the signal. The lighter gray lines that deviate from the correct contour are generated by filters whose central frequencies are far from the primary frequencies in the signal. A qualitative explanation of this is as follows: for an unmodulated tone, off-center filters perfectly detect the true frequency, but for modulated tones, off-center filters distort the signal. Modulated signals have a broad frequency spread [Eq. (10)], and off-center filters truncate this broad frequency representation more drastically than centered filters.

The signal representation is improved by establishing a notion of ''jurisdiction'' for each channel. Whenever instantaneous frequency $f_w^i(t,f)$ is far from the center of channel (f), this estimate is discarded. That is, for $|f_w^i(t,f) - f| > C$, the local estimate $f_w^i(t,f)$ does not contribute to the analysis. The constant C we call the *locking window*. When this criterion is applied to a dense array of filters, discarding channels that are not ''in lock'' is no loss, since for each portion of the signal, there is some channel that is positioned correctly. (The number of channels locking onto a single pure tone is the *redundancy* of the filter bank, and in this manuscript redundancies are on the order of 10, so every frequency region is densely covered with similar filters.)

Figure 2 illustrates the effect of applying this criterion to the signals analyzed in Fig. 1. Any instantaneous frequencies coming from outside the locking window $C = \Delta f/2$ are not drawn in the figure. Each panel in this figure contains an equivalent number of channels, but in Fig. 2, panel (a), most channels are excluded by the locking criterion. Those that remain in the analysis condense onto two frequency contours. In contrast, the spread of frequencies in the analysis of the white noise signal [panel (b)] indicates a failure of agreement among neighboring channels, and thus a violation of the central assumption that the signal is sparse. Simple though it may be, this ''blind'' cross-check between tonotopic and phase information significantly improves the analysis of rapidly modulated sparse signals.

C. Bandwidth optimization through consensus

The previous section describes analysis at a fixed bandwidth. To further optimize the analysis, particularly for a signal with unknown properties, this bandwidth must be adjusted to the signal. Figure 3 illustrates the result of various bandwidth choices in the analysis of a two-tone signal. For the standard representation of the signal, the optimum filter width yields Fig. 3, panel (b). For this signal, a range of filter widths around this optimum yield the same time–frequency analysis (not shown). Much wider filter widths as in Fig. 3, panel (a), introduce interactions between the two tones, and much narrower filter widths [(c) and (d)] yield a gradual transition from the modulated tone representation to the sum of sideband representation defined by Eq. (10). In panels (a) and (c), poorly matched filters lead to detailed structures of lines that are sensitive to the precise bandwidth of the analysis—a ''fragile'' representation of the signal.

Bandwidth is optimized by minimizing the linewidth, or *consensus* of the frequency estimates. This optimization can utilize a number of different objective measures of channel consensus. In this article, consensus is defined in terms of the interval between instantaneous frequency estimates from neighboring channels that are ''in lock'' (previous section). Specifically, consensus is the median value of $1/|f_w^i(t,f_a) - f_w^i(t,f_b)|$, where f_a and f_b are center frequencies for neighboring channels that are ''locked'' at time t.

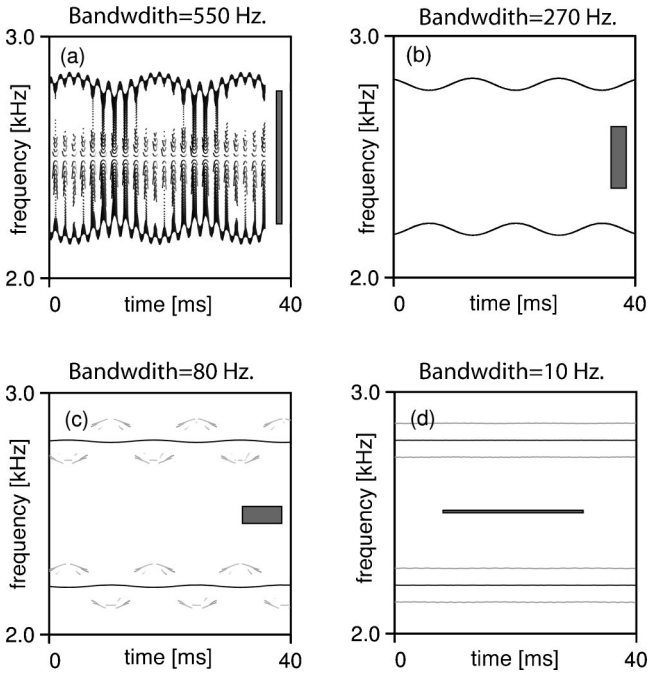

FIG. 3. Instantaneous frequency analysis requires bandwidth optimization. The analysis of a signal consisting of the sum of two frequency modulated tones. One tone is centered at 2.2 kHz, the other at 2.8 kHz. Each tone is modulated with peak to peak variations in frequency of 70 Hz, at a period of 14 ms. The filter bank follows the design used in Fig. 2, but the bandwidth Δf of the filtering (indicated by the gray rectangle in each figure) varies for each panel as follows: (a) 550 Hz; (b) 270 Hz; (c) 80 Hz; (d) 10 Hz. [Each rectangle covers the area defined by Gabor uncertainty, though the rectangle in panel (d) only covers half the actual time scale due to the limited dimensions of the figure.] Filters that are too wide, as in panel (a), introduce interactions among signal components. Filters that are too narrow [panels (c) and (d)] lose temporal resolution.

This measure performs best when frequency estimates with insignificant amplitude are excluded from the calculation of consensus. In practice, information is drawn only from channels whose instantaneous amplitude is greater than the median instantaneous amplitude over all channels.

Figure 4 demonstrates that this measure is maximized at the optimum bandwidth for the signal discussed in Fig. 3. For the sparse signals analyzed in this paper the optimum bandwidth is found at a single, well-defined maximum of this measure of cross-channel consensus. Bandwidth optimization through consensus can, in principle, be generalized to adapt bandwidth separately for different regions of the time–frequency plane.

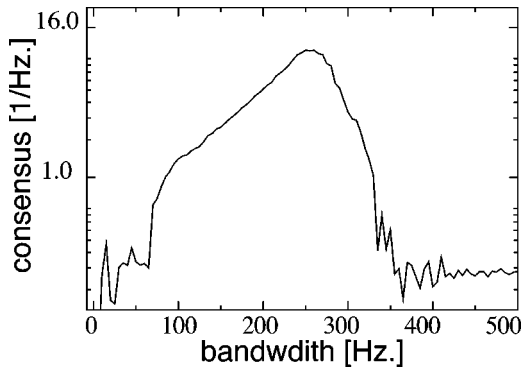

FIG. 4. The optimum bandwidth is derived from the consensus maximum. The cross-channel consensus is plotted as a function of the filter bank bandwidth, for the two-tone signal analyzed in Fig. 3.

D. Quality checks through consensus

This analysis can be applied to sparse sounds—sounds whose tonal components are separable and modulated sufficiently slowly. Fast modulations imply extended frequency representations, so modulated tones with separable center frequencies may nevertheless have significant frequency overlap due to their modulations. To illustrate why fast modulations require wideband analysis, consider a pure tone at frequency ω that is periodically modulated in amplitude at a lower frequency ω_2. This signal, $\cos(\omega t)\cos(\omega_2 t)$ is equivalent to $(1/2)\cos((\omega-\omega_2)t)+(1/2)\cos((\omega+\omega_2)t)$, and to accurately represent it within a single band, a filter centered at ω must have a frequency bandwidth of at least $2\omega_2$.

Similarly, Eq. (10) reveals that a single tone with periodic frequency modulation involves a sum of sidebands with an infinite extent in frequency. Any bandpass filtering will involve truncations of the sum, and the severity of the truncation depends on the center frequency and bandwidth of the filter, as well as the time scale and amplitude of the modulations. If a signal is sparse by our definition, the truncation of frequency modulations at the optimum bandwidth is negligible, and neighboring channels produce very similar results. Alternatively, if the signal is not sparse, truncation is significant, leading to distinct frequency estimates in different channels. For this reason, the magnitude of the cross-channel consensus indicates the degree of error in the analysis.

Figure 5 demonstrates a correlation between cross-channel consensus and frequency error for a family of test signals. Each signal in the set consists of two frequency-modulated tones separated by a fixed interval, as illustrated in Fig. 3. For large intervals between tones and slow modulation rates, the signal is spectrally sparse and can be resolved with the IFD method. For small intervals between tones and fast modulation rates, the tones overlap and error in the analysis increases. To generate the figure, the optimum bandwidth is first determined for each signal by maximizing consensus, as described in the previous section. At the optimum bandwidth, rms error between the known signal content and the IFD estimate is plotted against the median consensus value over the time–frequency plane. When modulation rates are too fast to resolve, consensus measures decrease.

In addition to averaged quality measures, consensus within local regions of the time–frequency plane can indicate well-resolved signal components within a larger analysis. (Even the white noise analysis in Fig. 2 displays what appear to be ''caustics,'' or regions of high agreement between nearby filters, though the overall analysis is characterized by low consensus.)

In summary, consensus between redundant channels is used to guide bandwidth optimization, and to signal the quality of the final analysis. In principle, local consensus measures can be used to find spectrally sparse components within more complex signals, or to adapt a bandwidth separately for different regions of the time–frequency plane.

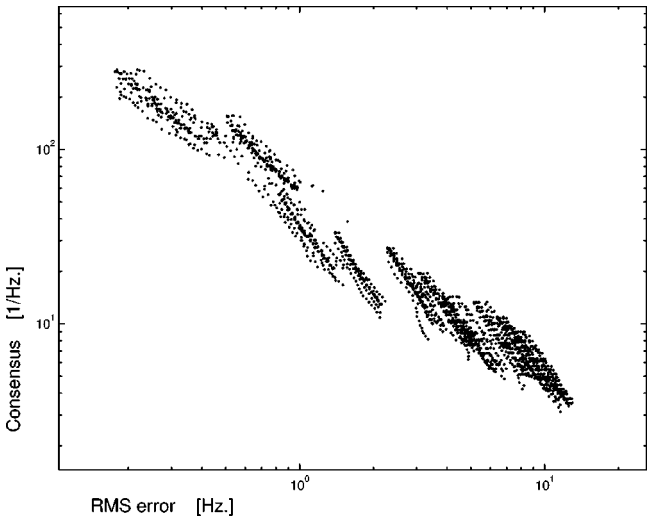

FIG. 5. The consensus measure indicates the degree of error in frequency estimates. Test signals consist of two rapidly modulated tones similar to those illustrated in Fig. 3. The peak to peak modulation depth varies in uniform steps from 100–400 Hz, modulation rate from 20–300 Hz. The interval between the tones is varied in uniform steps from 1200 Hz to 1800 Hz. The analysis employs 500 uniformly spaced channels from 0–3 kHz. The bandwidth is first optimized for each signal, according to the automated procedure described in the text. At the optimum bandwidth, the median value of consensus is plotted against the median error of frequency estimates, based on the known signal content. For the most rapidly modulated signals (3 ms modulation period), the rms error in frequency estimates is only 10 Hz. This precision can be compared with the frequency uncertainty of standard Gabor analysis that must be roughly 300 Hz to accommodate the temporal responses that would resolve 3 ms features.

III. RESOLUTION AND PRECISION

Understanding the limits of the method requires introducing a distinction between *resolution* and *precision*, a distinction well developed in, e.g., microscopy. Precision is the accuracy with which the position of a given object can be computed, while resolution is the smallest distance at which two objects may be discriminated as distinct.

A. Resolution

The IFD analysis requires that the bandwidth of the filters be narrower than the separation between adjacent frequency components. Since the time accuracy of the analysis is inversely proportional to bandwidth, the IFD resolution is constrained by a variant of the Fourier uncertainty relation:

$$\Delta T \, \Delta f_{\min} \geqslant \frac{1}{2}, \tag{11}$$

where $\Delta f_{\min}$ is now the minimum separation between adjacent frequency components, and ΔT the effective time resolution with which frequency changes can be tracked.

The resolution limit of the IFD method can also be described in terms of the maximum modulation rates that can be resolved for a given separation of frequency components. One example of this limit is as follows: for frequency modulations that are faster than the depth of modulation ($A \leqslant \omega$) in Eq. (10), $\Delta f/2$ must be greater than the modulation rate ω, otherwise sidebands of the modulated signal are severely truncated.

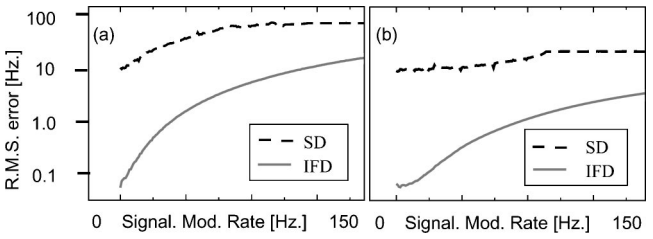

FIG. 6. A comparison of general time–frequency precision based on spectral derivative pitch tracking (SD) with IFD estimates. The rms error in pitch tracking is plotted as a function of the modulation rate of the test signals. The analyzed signal contains modulated tones centered on 1100, 2000, and 2900 Hz. Each tone is independently modulated with fast frequency modulations—200 Hz peak to peak in panel (a) and 40 Hz peak to peak modulations in (b). The optimum time scale of the windowing function in the Fourier analysis was determined and used in this comparison (21 ms). (In the spectral derivative analysis, the windowing functions are prolate spheroidal sequences.) The fixed bandwidth IFD analysis uses Gaussian windows of duration 1.6 ms. The IFD analysis (like many other methods adapted to sparse signals) achieves a pitch tracking precision that can be orders of magnitude sharper than the resolution of general Fourier analysis.

B. Precision

As for other methods specialized for sparse sounds, IFD can achieve high precision in both time and frequency whereas general Fourier analysis is limited by the uncertainty principle. For example, frequency errors for the signals analyzed in Fig. 5 range from less than 1 Hz to 10 Hz, whereas the time scale of modulations in these signals imply a classical frequency uncertainty as high as 300 Hz.

Figure 6 contains an explicit comparison with classical frequency uncertainty for a family of test signals. To produce

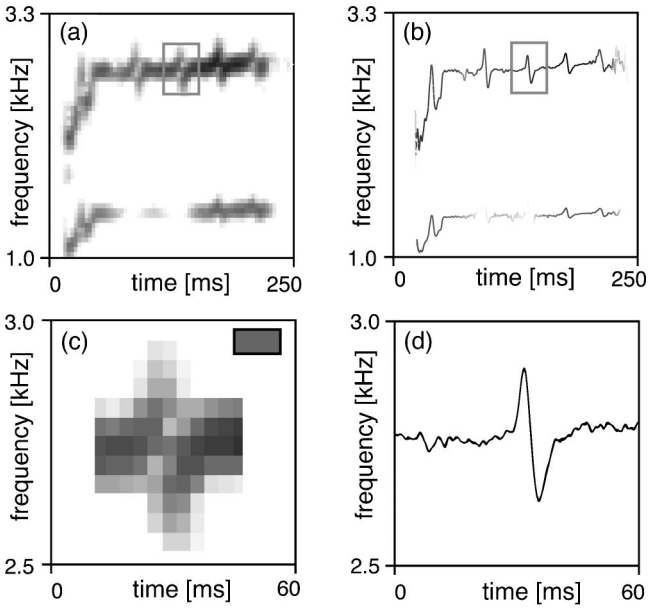

FIG. 7. Vocal illustrations: analysis of a whistle in a canary song. Panel (a) contains a windowed short-time Fourier analysis or sonogram with the following parameters: analyzing window 23 ms, 80% overlap. Panel (b) contains an IFD analysis with channels of bandwidth $\Delta f = 600$ Hz, spaced 20 Hz apart. The locking window for this analysis is $\Delta f/2$. Panels (c) and (d) contain close-up views of a frequency instability in the whistle. Pixel intensities for all four panels were scaled from white (30 dB below the maximum power) to black (maximum power) according to the logarithm of signal power. The fundamental resolution of classical time–frequency analysis ($\Delta f \Delta t > 1/2$) is indicated by the gray rectangle in panel (c).

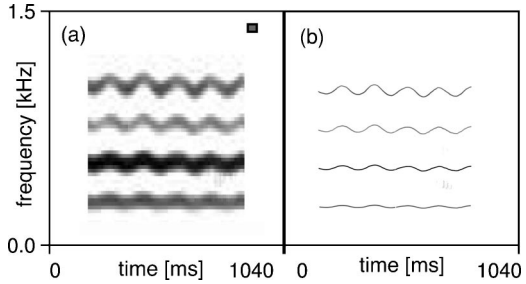

FIG. 8. Vocal illustrations: analysis of a fragment of operatic voice. Panel (a) contains a windowed short-time Fourier analysis using a 42 ms sliding window. Panel (b) contains the instantaneous frequency decomposition, $\Delta f = 70$ Hz. Pixel intensities for both panels are scaled from white (30 dB below the maximum power) to black (maximum power) according to the logarithm of signal power. As in previous figures, the resolution of the uncertainty principle is indicated by the gray rectangle in the figure.

this figure, frequency contours of the test signals are estimated based on either IFD or a short-time Fourier method (zero crossings of multitaper spectral derivatives[25–27]). The rms error in frequency contour estimation was then calculated. Over a range of modulation rates, the IFD analysis at a fixed bandwidth achieves a precision of frequency estimation one or two orders of magnitude sharper than the resolution of general Fourier analysis.

Enhanced resolution for sparse signals is not surprising. Any method specialized for sparse sounds will outperform a more general time–frequency analysis. For specific signal ensembles, specialized applications of Fourier analysis can also outperform the limits of the general method. For example, in the analysis of sparse signals, frequency contours can be more precisely localized by interpolating the Fourier estimates between frequency bins.[28] Comparisons have been made among methods of Fourier interpolation[29,7] and measures of instantaneous frequency. In the vicinity of a spectral peak, instantaneous frequency measures meet or exceed the precision of pitch tracking achieved through Fourier interpolation.[29,7]

Relative to other specialized methods, the primary advantage of the IFD method is the generality conferred by redundancy and cross-check. No information is needed about the analyzed signal to apply the method. If the signal is sufficiently sparse, an optimized analysis is found without reference to the signal character.

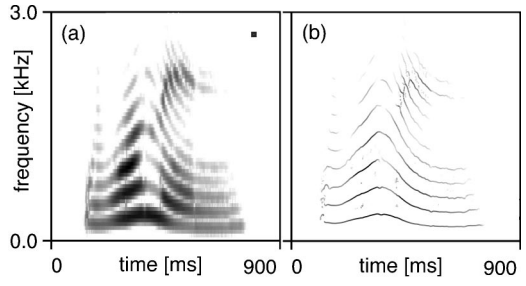

FIG. 9. Vocal illustrations: analysis of the word ''woman.'' Panel (a) contains a windowed short-time Fourier analysis using a 21 ms sliding window. Panel (b) contains the instantaneous frequency decomposition, $\Delta f = 70$ Hz. Pixel intensities for both panels are scaled from white (40 dB below the maximum amplitude) to black (maximum amplitude) according to the log power of the signal.

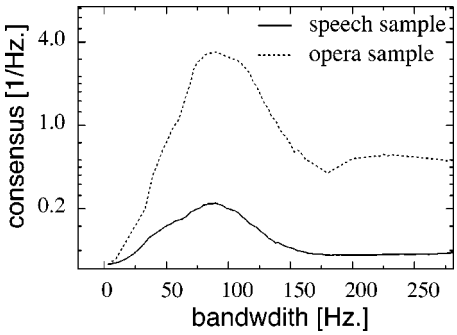

FIG. 10. Consensus properly guides bandwidth selection of the human vocal signals. The cross-channel consensus is plotted as a function of bandwidth, for the fragments of human voice in Fig. 8 and Fig. 9. The optima correspond to bandwidths chosen in the previous figures.

C. Analysis of voice signals

This final section illustrates three applications of the IFD method to the analysis of vocal signals. Figure 7 illustrates a comparison with general time–frequency analysis for a syllable in a canary song. The syllable consists of a sum of tones of very narrow spectral definition. The frequency instabilities of the whistle, expanded in panels (c) and (d), are resolved in detail. The fine structure revealed in tonal bird song is useful for generating more accurate studies of vocal production and perception. In a variety of experiments, birds have demonstrated great acuity for distinguishing fast modulations of high-frequency signals, and thus the structure revealed in a higher resolution analysis is likely to be perceptually relevant.[30,31]

Figure 8 contains an analysis of vibrato from an opera singer's exercises, and Fig. 9 contains an analysis of the word ''woman'' spoken by a female speaker. The relatively low frequency of human voiced sounds results in narrow spacing between the overtones, requiring the use of filters narrowly tuned in frequency to separate the components, and thus a corresponding loss of temporal definition. Even so, in many cases as in Fig. 9, the instantaneous frequency and amplitude for most harmonics can be reliably extracted with high definition. In general, the applicability of the new method to speech analysis is limited to those portions of the signal that are spectrally sparse. Figure 10 illustrates cross-channel consensus as a function of bandwidth for the human vocal signals. In both cases, there is a distinct maximum consensus at the optimum analysis bandwidth.

IV. CONCLUSION

IFD represents sparse signals in time and frequency with high precision through a self-optimized instantaneous frequency analysis. Two aspects of cross-validation are employed to optimize the analysis. The tonotopic cross-check compares tonotopic and phase information within each channel. A filter contributes locally to the analysis only if its center frequency and instantaneous frequency match. In a second cross-check, the consensus of frequency estimates from neighboring channels is used to guide the optimization of analysis bandwidth for a given signal, and to signal the degree of error in the analysis. When applied to sparse signals, the redundant channels of the IFD generate high con-

sensus at the optimum bandwdith, and the analysis splits the signal into component tones, each tracked with high precision. In cases when the IFD method is applied to signals that are spectrally too dense, redundant channels fail to coincide at any bandwidth, signaling the breakdown of the method.

The elements of this analysis may be relevant to auditory processing. Many animal vocalizations contain well-defined pitches that are rapidly modulated, and neural auditory processing has evolved under a need to make demanding distinctions in both time and frequency simultaneously. To achieve an optimum representation of sparse sounds, IFD provides a rationale for integrating information from tonotopic and phase information in the auditory nerve. Cross-checks between spike intervals and the tonotopic position of a fiber could select the fibers with optimal center frequencies. A similar criterion was employed by Srulovicz and Goldstein to explain psychophysical data for the perception of simple unmodulated signals.[24] Second, confidence can be placed on a frequency estimate when different channels with overlapping passbands generate similar spike intervals.[14] Among a redundant set of nerve fibers with varying bandwidths, the cells that form a consensus in their interspike intervals may stand out as salient, preferentially drawing information from channels whose bandwidth was well suited to the local signal content. As early as the cochlear nucleus, there are cells that receive inputs from auditory fibers with a range of center frequencies,[32] thus at this stage of auditory processing or beyond, measures of cross-channel consensus could in principle be implemented.

The method of cross-channel comparison has the potential for high compression and top reconstruction quality at the end stage, but at the computational cost of highly redundant arrays of sensors, and a large number of cross-channel comparisons. Early expansive stages in the neural pathways of hearing and vision[33,34] may serve a similar function: to provide higher accuracy and efficiency not at intermediate stages,[35] but at the far end of the processing pipeline.

ACKNOWLEDGMENTS

The authors would like to thank A. Libchaber, F. Nottebohm, A. J. Hudspeth, and P. P. Mitra for their comments on the manuscript. This work was supported in part by the Burroughs Wellcome Fund.

[1] D. Gabor, ''Theory of communication,'' J. IEE (London), Part 3 **93**, 429–457 (1946).
[2] C. H. Greenewalt, *Bird Song: Acoustics and Physiology* (Smithsonian Institution Press, Washington, 1968).
[3] J. L. Flanagan and R. M. Golden, ''Phase vocoder,'' Bell Syst. Tech. J. **45**, 1493–1500 (1966).
[4] D. Margoliash, ''Acoustic parameters underlying the responses of song-specific neurons in the white-crowned sparrow,'' J. Neurosci. **3**, 1039–1057 (1983).
[5] F. Auger and P. Flandrin, ''Improving the readability of time–frequency and time-scale representations by the reassignment method,'' IEEE Trans. Signal Process. **43**, 1068–1089 (1995).
[6] P. Guillemain and R. Kronland-Martinet, ''Characterization of acoustic signals through continuous linear time–frequency representations,'' Proc. IEEE **84**, 561–585 (1996).
[7] S. Borum and K. Jensen, ''Additive analysis/synthesis using analytically derived windows,'' in *Proceedings of the 2nd International Conference on Digital Audio Effects DAFx-99*, Trondheim, Norway, December 1999, pp. 125–128.
[8] D. J. Nelson, ''Cross-spectral methods for processing speech,'' J. Acoust. Soc. Am. **110**, 2575–2592 (2001).
[9] D. H. Friedman, ''Detection and frequency estimation of narrow-band signals by means of the instantaneous-frequency distribution (IFD),'' in *Spectrum Estimation and Modeling*, 4th Annual ASSP Workshop, Minneapolis, MN, 1988, pp. 71–76.
[10] P. P. Mitra and B. Pesaran, ''Analysis of dynamic brain imaging data,'' Biophys. J. **76**, 691–708 (1999).
[11] I. Daubechies and F. Planchon, ''Adaptive Gabor transforms,'' Appl. Comput. Harmon. Anal. **13**, 1–21 (2002).
[12] H. L. F. Helmholtz, *On the Sensations of Tone as a Physiological Basis for the Theory of Music* (Dover, New York, 1954).
[13] E. F. Evans, ''Auditory processing of complex sounds: an overview,'' Philos. Trans. R. Soc. London, Ser. B **336**, 295–306 (1992).
[14] M. B. Sachs and E. D. Young, ''Representation of steady-state vowels in the temporal aspects of the discharge patterns of populations of auditory nerve fibers,'' J. Acoust. Soc. Am. **66**, 470–479 (1979).
[15] Y. Choe, M. Magnasco, and A. J. Hudspeth, ''A model for amplification of hair-bundle motion by cyclical binding of Ca2+ to mechanoelectrical-transduction channels,'' Proc. Natl. Acad. Sci. U.S.A. **95**, 15321–15326 (1998).
[16] J. C. R. Licklider, ''A duplex theory of pitch perception,'' Experientia **7**, 128–133 (1951).
[17] P. A. Cariani and B. Delgutte, ''Neural correlates of the pitch of complex tones. I. Pitch and pitch salience,'' J. Neurophysiol. **76**, 1698–1716 (1996).
[18] P. A. Cariani and B. Delgutte, ''Neural correlates of the pitch of complex tones. II. Pitch shift, pitch ambiguity, phase invariance, pitch circularity, rate pitch, and the dominance region for pitch,'' J. Neurophysiol. **76**, 1717–1734 (1996).
[19] R. D. Patterson and T. Irino, ''Modeling temporal asymmetry in the auditory system,'' J. Acoust. Soc. Am. **104**, 2967–2979 (1998).
[20] K. Krumbholz, R. D. Patterson, and A. Nobbe, ''Asymmetry of masking between noise and iterated rippled noise: Evidence for time-interval processing in the auditory system,'' J. Acoust. Soc. Am. **110**, 2096–2107 (2001).
[21] L. Wiegrebe, ''Searching for the time constant of neural pitch extraction,'' J. Acoust. Soc. Am. **109**, 1082–1091 (2001).
[22] T. D. Griffiths, C. Büchel, R. S. J. Frackowiak, and R. D. Patterson, ''Analysis of temporal structure in sound by the human brain,'' Nat. Neurosci. **1**, 422–427 (1998).
[23] T. D. Griffiths, S. Uppenkamp, I. Johnsrude, O. Josephs, and R. D. Patterson, ''Encoding of the temporal regularity of sound in the human brainstem,'' Nat. Neurosci. **4**, 633–637 (2001).
[24] P. Srulovicz and J. L. Goldstein, ''A central spectrum model: a synthesis of auditory-nerve timing and place cues in monaural communication of frequency spectrum,'' J. Acoust. Soc. Am. **73**, 1266–1276 (1983).
[25] D. J. Thomson, ''Multitaper analysis of nonstationary and nonlinear time series data,'' in *Nonlinear and Nonstationary Signal Processing*, edited by W. J. Fitzgerald, R. L. Smith, A. T. Walden, and P. C. Young (Cambridge University Press, Cambridge, UK, 2000), Chap. 10, pp. 317–394.
[26] O. Tchernichovski, F. Nottebohm, C. E. Ho, B. Pesaran, and P. P. Mitra, ''A procedure for an automated measurement of song similarity,'' Anim. Behav. **59**, 1167–1176 (2000).
[27] O. Tchernichovski, P. P. Mitra, T. Lints, and F. Nottebohm, ''Dynamics of the vocal imitation process; How a zebra finch learns its song,'' Science **291**, 2564–2569 (2001).
[28] X. Serra, ''Musical sound modeling with sinusoids plus noise,'' in *Musical Signal Processing*, edited by C. Roads, S. T. Pope, A. Piccialli, and G. De Polis (Swets and Zeitlinger, Lisse, the Netherlands, 1997), Chap. 3, pp. 91–122.
[29] F. Keiler and S. Marchand, ''Survey on extraction of sinusoids in stationary sounds,'' in *Proceedings of the 5th International Conference on Digital Audio Effects (DAFx-02)*, Hamburg, Germany, September 2002, pp. 51–58.
[30] S. Amagai, R. J. Dooling, S. Shamma, T. L. Kidd, and B. Lohr, ''Detection of modulation in spectral envelopes and linear-rippled noises by budgerigars (Melop-sittacus undulatus),'' J. Acoust. Soc. Am. **105**, 2029–2035 (1999).

[31] M. L. Dent, R. J. Dooling, and A. S. Pierce, ''Frequency discrimination in budgerigars (Melopsittacus undulatus): effects of tone duration and tonal context,'' J. Acoust. Soc. Am. **107**, 2657–2664 (2000).
[32] G. M. Shepherd, in *The Synaptic Organization of the Brain* (Oxford University Press, Oxford, 1998).
[33] K. L. Chow, ''Numerical estimates of the auditory central nervous system of the rhesus monkey,'' J. Comp. Neurol. **95**, 159–175 (1951).
[34] S. M. Blinkov and I. I. Glezer, *The Human Brain in Figures and Tables; A Quantitative Handbook* (Basic Books, New York, 1968).
[35] J. J. Atick and A. N. Redlich, ''What does the retina know about natural scenes?,'' Neural Comput. **4**, 196–210 (1992); J. Acoust. Soc. Am. **46**, 442–448 (1969).

Adaptive window-length detection of underwater transients using wavelets

Dragana Carevic[a)]
Maritime Operations Division, Defence Science and Technology Organisation, Bldg A-51, HMAS Stirling, Rockingham, 6958, Australia

(Received 26 August 2004; revised 22 February 2005; accepted 22 February 2005)

This paper describes a detection method that adapts to unknown characteristics of the underlying transient signal, such as location, length, and time-frequency content. It applies a set of embedded detectors tuned to a number of signal partitions. The detectors are based on the wavelet theory, whereby two different techniques are examined, one using local Fourier transform and the other using discrete wavelet transform. The detection statistics are computed so as to enable prewhitening of unknown colored noise and to allow for a constant false-alarm rate detection. An adapted segmentation of the signal is next obtained with a goal of finding the largest detection statistics within each segment of the partition. The detectors are tested using several underwater acoustic transient signals buried in ambient sea noise. © *2005 Acoustical Society of America.* [DOI: 10.1121/1.1893270]

PACS numbers: 43.60.Bf, 43.60.Hj, 43.60.Cg [EJS] Pages: 2904–2913

I. INTRODUCTION

In the passive sonar context early detection of a low-noise target can in some cases be accomplished solely based on short-duration acoustic emissions or transients inadvertently emitted by the target. These signals are also important as they may provide information crucial for the correct target identification and localization (Carevic, 2004, 2003). Typical duration of a transient ranges from a few tens of milliseconds to several seconds. Signals are embedded in additive noise and the goal of the detection process is to determine whether the observations belong to a stationary noise distribution or not. For an N-sample temporal data record $\mathbf{x}$ this can be formalized in terms of the binary hypothesis test

$$H_0: x(n) = v(n), \tag{1}$$

$$H_1: x(n) = v(n) + s(n), \quad n = 1,...,N, \tag{2}$$

where $\mathbf{v}$ is a realization of a wide sense stationary noise random process, and $\mathbf{s}$ is a realization of the signal to be detected. The signal is taken to be entirely contained within the processing window of N samples. The detector rejects the null hypothesis H_0 if the detection statistics exceeds the threshold corresponding to a given probability of false alarm (P_{fa}). For the detection problem treated in this paper, it is assumed that shape, duration, time of arrival, and frequency response of the signal are not known.

Detectors usually exploit the notion that a transient signal is a localized burst in time and that its spectrum covers a contiguous frequency band. Signals may also have local oscillatory behavior, thereby yielding high spectral peaks. Many current transient detectors apply an appropriate linear transform, such as wavelet transform (Del Marco and Weiss, 1997; Liu and Fraser-Smith, 2000), Gabor transform (Friedlander and Porat, 1989, 1993), or Fourier transform (Nuttall, 1996, 1997; Streit and Willett, 1999), to the received signal. The transform is expected to match the characteristics of the transient and to condense the signal into a few transform coefficients with large magnitude. In the absence of a transient the distribution of the transform coefficients is spread. Other methods applicable to the detection of underwater acoustic transients involve using higher-order spectra of the received data to compute the detection statistics (Walsh and Delaney, 1995; Pflug *et al.*, 2004, 1992) and techniques based on nonlinear processing of data (Zakarauskas *et al.*, 1991).

Wang and Willett (2001) describe several transient detectors that use discrete Fourier transform (DFT) and discrete wavelet transform (DWT) (Mallat, 1989). These detectors are based on Nuttall's "power-law" detector (Nuttall, 1996). They enable prewhitening of unknown correlated (colored) noise and allow for a constant false-alarm rate (CFAR) detection. These properties are desirable for passive sonar detection where background noise is usually correlated and its statistics may change over time. Besides, these detectors are easy to implement and make minimal assumption about the structure of the transient signal. However, they use windowed signals where the length of the analyzing window is fixed. Consequently, these techniques perform well when the length of the analyzing window is matched to the length of the transient, but when the window length is large as compared to the transient support the performance of the detectors may deteriorate. By contrast, it is assumed that detection performance can be considerably improved by segmenting the signal into parts and by using the detection statistics related only to those segments that are characterized by large transform coefficients. The detection process in this way adjusts to the local characteristics of the signal. Ravier and Amblard (1998) describe one such detector. It uses an adapted local trigonometric transform (Wickerhauser, 1994) to obtain the best signal partition. Noise is taken to be white and Gaussian, and a test based on higher-order statistics is

a)Electronic mail: dragana.carevic@dsto.defence.gov.au

 0001-4966/2005/117(5)/2904/10/$22.50

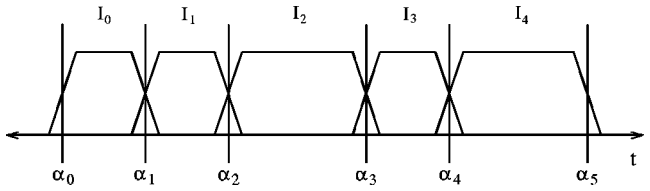

FIG. 1. Partition of line and the corresponding windows for smooth localized orthonormal basis.

applied for transient detection. A disadvantage of this approach is that it cannot handle correlated noise. A different approach to this problem that uses the Wigner distribution is presented by Rao and Taylor (1991).

This paper describes a method that applies a set of embedded transient detectors tuned to a number of signal partitions. The detection statistics are computed using an approach motivated by Wang and Willett (2001). The statistics are combined so as to obtain a best-adapted partition of the signal with the goal of finding the largest detection statistics in each segment. The technique is described in Sec. II. Section III presents experimental results.

II. ADAPTIVE WINDOW-LENGTH TRANSIENT DETECTORS

Similarly as in Wang and Willett (2001), the incoming data stream is divided into blocks of length N. The $L+1$ consecutive data blocks are considered where the $(L+1)$th block is the current block. The L previous data blocks are assumed to be noise only and are used for background normalization. The blocks are processed by using either local Fourier transform (LFT) (Wickerhauser, 1994; Saito, 1999) or the DWT (Mallat, 1989), resulting in two somewhat different detection procedures.

A. LFT-based detectors

The LFT presents a useful time-frequency representation of a signal. It provides a means for expanding the signal into a set of smooth orthonormal bases subordinate to an arbitrary partition (segmentation) of the signal. The bases consist of complex exponential functions smoothly restricted to adjacent overlapping segments. The bases are ''local'' in the sense that they expand the signal only within the particular region of interest. Starting with a partition of the signal into disjoint intervals $\mathbf{R}=\cup_k I_k$, $I_k=(\alpha_k,\alpha_{k+1})$ (see, for example, Fig. 1), the method uses the smooth orthogonal periodization (Wickerhauser, 1994). It first performs windowing of the original signal using smooth, overlapping, compactly supported bump functions or windows placed over each interval. This is followed by folding the windowed segments to the disjoint intervals I_k. Each interval is next locally periodized and separately processed using the standard discrete Fourier transform (DFT). In this way the signal is expended into a set of localized complex exponential functions (also called local Fourier basis). The method ensures that the resulting basis set is orthonormal for $L^2(\mathbf{R})$. Also, the signal decomposition is nonredundant, that is, the number of (complex) transform coefficients is the same as the length of the signal. Since the basis functions are smooth, no discontinuity is created at the segment endpoints.

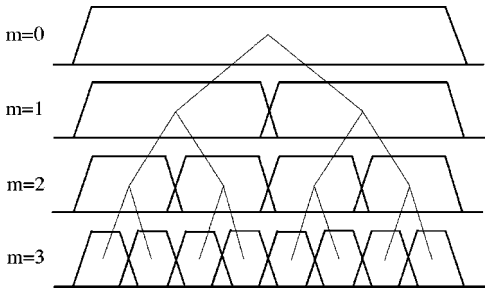

FIG. 2. Organization of localization intervals into a binary tree.

The LFT is applied to a binary tree structured set of intervals yielding a redundant M-level signal decomposition [see Fig. 2, also in Saito (1999) and Coifman and Wickerhauser (1992)]. The length of the segment at the lowest decomposition level $(m=0)$ is dyadic, $N=2^K$, and equal to the block length of the analyzed signal. The intervals at the higher decomposition levels $m=1,2,...,M-1$ are obtained by recursively splitting the segments at lower levels (parent segments) at the midpoint. In this way, at each level $m=0,1,...,M-1$ there are 2^m segments of length $2^{(K-m)}$. Theoretically, the maximum number of decomposition levels is $M=K$, where the segment length at the highest decomposition level is 1. In practical applications $M<K$, and M is chosen with respect to the smallest length of the signal segments of interest. Note that the LFT coefficients can be taken to represent disjoint intervals, since the overlap of the windowed segments can be made relatively small (only a few samples).

Detection statistics are computed for each segment $q=1,2,...,2^m$ at levels $m=0,1,...,M-1$ within the binary tree related to the current [$(L+1)$th] data block. The L previous data blocks are used to estimate the background statistics for normalization. These L blocks are also processed using the M-level LFT. Consider the qth segment at the mth level of decomposition of the ith data block and define $U^{(1)}_{m,q,j,i}=X_{m,q,j,i}$ and $U^{(2)}_{m,q,j,i}=X_{m,q,j-1,i}+X_{m,q,j,i}$, where $X_{m,q,j,i}$, $j=1,2,...,2^{(K-m)}$ is the jth magnitude squared transform coefficient within this segment, and $i=1,2,...,L+1$. Two detection statistics $T^{(1)}_{F_{m,q}}$ and $T^{(2)}_{F_{m,q}}$, for $n=1$, 2, are then defined by

$$T^{(n)}_{F_{m,q}}=\sum_{j=1}^{2^{(K-m)}}\left(\frac{U^{(n)}_{m,q,j,L+1}}{\frac{1}{2^m L}\Sigma_{i=1}^{L}\Sigma_{p=1}^{2^m}U^{(n)}_{m,p,j,i}}\right)^{\nu}. \tag{3}$$

At the level of decomposition $m=0$ there are L background segments that are used for normalization. The statistics computed at this level, $T^{(n)}_{F_{0,1}}$ $n=1$, 2, are the same as those defined in Wang and Willett (2001) [see Eqs. (7) and (8), and Eq. (15) in Wang and Willett (2001)] for the block length 2^K. At the higher levels $m=1,2,...,M-1$ there are $2^m L$ background segments from L previous blocks, that is for $i=1,2,...,L$ and for $q=1,2,...,2^m$. These segments are used to compute detection statistics in all 2^m segments at the mth binary tree level of the current $(L+1)$th block.

The normalization of each component carried out in Eq. (3) prewhitens correlated noise and allows for CFAR detection performance. Also, the detection statistics $T^{(2)}_{F_{m,q}}$ is defined such as to exploit signal contiguity in the frequency domain. The exponent ν in Eq. (3) is an adjustable parameter.

The intention is to find those segments in the binary tree structure that have the largest values of the detection statistics, as this indicates that these segments are best matched by their basis functions. In order to be able to compare the values of $T^{(n)}_{F_{m,q}}$ across the binary tree structure they need to be further normalized to zero mean and unit variance for the noise-only case. This is done by estimating means and variances of noise-only $T^{(n)}_{F_{m,q}}$'s. As can be seen from Eq. (3) the $T^{(n)}_{F_{m,q}}$ for each segment is computed as a sum of random variables (rv) and, in the noise-only case, its distribution depends on the number of the rv's used in the summation (that is, on the length of the underlying segment). So, under the assumption that the noise has a stationary distribution the noise-only $T^{(n)}_{F_{m,q}}$'s related to the segments at the decomposition level m have identical distributions, and their distribution varies across different levels. Using the central limit theorem, Wang and Willett (2001) assume that the detection statistics converge to normal distributions and provide formulas for calculating means and variances of these distributions. In our experiments using simulated and real sea noises it was found that these formulas do not estimate means and variances of the detection statistics across different levels of the decomposition very accurately. A possible reason is that the normal distribution assumption is usually not correct and the formulas in Wang and Willett (2001) are only approximations. Therefore, in this paper means and variances of the noise-only $T^{(n)}_{F_{m,q}}$'s are estimated, for each decomposition level m, using a sufficiently long noise-only section of the input data stream. These values are next used for the normalization of the detection statistics $T^{(n)}_{F_{m,q}}$, $n=1, 2$ for all segments $q=1,2,...,2^m$ at the levels $m=0,1,...,M-1$ of the binary tree. The normalized detection statistics are further processed as described in Sec. II C.

B. DWT-based detectors

Generally, a DWT is computed by recursively convolving the signal with a set of perfect reconstruction paraunitary quadrature mirror filters (qmf) h and g, where h represents a low-pass filter and g is a high-pass filter (Wickerhauser, 1994). The transform consists of a collection of high-pass coefficients representing the detail signal information at a range of resolutions (or scales) and a set of low-pass coefficients capturing the lowest resolution (highest scale) version of the signal. The full DWT of a signal of length $N=2^K$ contains detail coefficients at K scales and the number of low-pass coefficients is 1. As an example, Fig. 3 shows the detail DWT coefficients for the signal of length $N=2^5$ (the entire structure), where the circles denote wavelet coefficients. It can be seen that there are $K=5$ scales, $k=1,...,5$. The number of coefficients at a scale k is $2^{(K-k)}$ and it decreases by factor of 2 from a lower to the next higher scale.

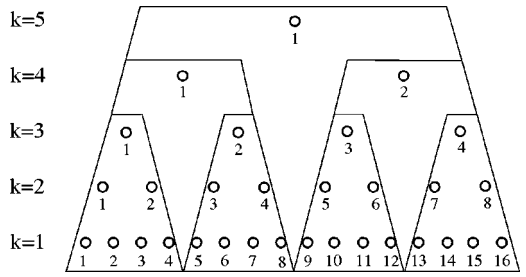

FIG. 3. Organization of the DWT coefficients of localization intervals into a binary tree. Circles represent detail wavelet coefficients. The scales of decomposition are denoted by k.

The usual approach, when processing isolated data blocks of finite length, is to extend the signal beyond the block boundary by either zero padding or by using the signal samples close to the boundary; there are a number of approaches to extending such signals [see, for example, Strang and Nguyen (1996)]. By contrast, in this paper data blocks to be processed are not isolated but belong to an incoming data stream that is assumed to be very long. Consequently, the initial conditions for computing the DWT of the current block can be obtained by carrying over the information resulting from processing the immediately preceding data block. Consider a full (K scale levels) DWT of the block of length 2^K (detail coefficients) computed in this way. It can be shown that this DWT contains within itself the full DWTs of the entire binary tree structured set of intervals obtained by recursive midpoint splitting of the lower-level segments. Each segment DWT at a binary tree level m has $K-m$ scales, and the number of detail coefficients at each scale $k=1,...,K-m$ is 2^{K-k-m}. In our example with the signal of block length $N=2^5$, at the level $m=2$ of the binary tree associated with this signal there are four successive intervals of length 2^3. The grouping of the wavelet coefficients of the original signal that corresponds to the DWT coefficients of each of these intervals or segments is shown in Fig. 3. Each segment DWT has three scales, $k=1, 2, 3$. The DWT coefficients of the first segment, $q=1$, $m=2$ at scale $k=1$ are the detail coefficients indexed by $\{1,2,3,4\}$ at the scale $k=1$ of the original signal DWT. At scale $k=2$ this DWT contains the detail coefficients indexed by $\{1,2\}$ at the scale $k=2$ of the original signal DWT, and at $k=3$ it contains the detail coefficient indexed by $\{1\}$ at scale $k=3$ of the original DWT. Similarly shown is the grouping of the wavelet coefficients that corresponds to the two intervals of length 2^4 at the binary tree level $m=1$. Therefore, the detail DWT coefficients of the nested set of intervals within the binary tree can be obtained simply by rearranging the DWT coefficients computed at the lowest level of the structure, that is, for $m=0$. Note that in this derivation the low-pass DWT coefficients are ignored.

The detection statistics are computed using the DWT coefficients within each segment $q=1,2,...,2^m$ at levels $m=0,1,...,M-1$ of the binary tree related to the current data block. It is assumed that the DWT coefficients of the L immediately preceding noise-only data blocks are also available. Consider the qth segment at the mth level of the ith data block, $i=1,2,...,L+1$. Then, let $Y_{m,q,k,j,i}$ denote the

magnitude-squared DWT coefficient computed for the data within this segment, where $k=1,2,...,K-m$ denotes the DWT scale index and $j=1,2,...,2^{(K-k-m)}$ is the within-scale position index. Next, define $U^{(1)}_{m,q,k,j,i}=Y_{m,q,k,j,i}$ and $U^{(2)}_{m,q,k,j,i}=Y_{m,q,k,j,i}+Y_{m,q,k-1,2j-1,i}+Y_{m,q,k-1,2j,i}$ for $j=1,2,...,2^{K-k-m}$ and $k=P^{(n)}_m,\ldots,K-m$, where $n=1$, 2, and $P^{(1)}_m=1$ and $P^{(2)}_m=2$. The detection statistics $T^{(n)}_{W_{m,q}}$ are then given by

$$T^{(n)}_{W_{m,q}}=\sum_{k=P^{(n)}_m}^{K-m}\sum_{j=1}^{2^{(K-k-m)}}\left(\frac{U^{(n)}_{m,q,k,j,L+1}}{\frac{1}{2^m L}\Sigma_{i=1}^{L}\Sigma_{p=1}^{2^m}U^{(n)}_{m,p,k,j,i}}\right)^{\nu},$$

$$n=1,2. \tag{4}$$

Here, similar to Eq. (3), the statistics are computed using the normalized wavelet coefficients, and $T^{(2)}_{W_{m,q}}$ is defined so as to exploit contiguity of transient signals in the spatial-frequency domain. Also, the detection statistics $T^{(n)}_{W_{0,1}}$ $n=1$, 2 computed at the level $m=0$ are equivalent to those defined by Eq. (18) and Eq. (19) in Wang and Willett (2001), respectively.

All detection statistics computed in this way are again normalized for each decomposition level $m=0,1,...,M-1$ so as to have zero mean and unit variance in the noise-only case. This is done using the means and standard deviations estimated based on a noise-only section of the input data stream.

A disadvantage of the standard (critically sampled) DWT is that it is noninvariant to time shifts of the analyzed signal. The input-signal shifts can generate unpredictable changes in the DWT coefficients that can cause a degradation of the performance of the detectors. Several techniques using best-basis or optimal wavelet design have been proposed to reduce DWT shift sensitivity (Liang and Parks, 1996; Benno and Moura, 1998). An alternative approach is to use complex wavelets to compute the DWT, with the real and imaginary parts of the complex wavelet constituting a Hilbert transform pair. It is argued that, if a transient is present, the real and imaginary part of the complex transform coefficients cannot simultaneously be small and the magnitude of the coefficients should be used for detection (Abry and Flandrin, 1994). Recently Fernandes (2002) proposed a linear projection filter that projects a real-valued signal onto the ''Softy'' space. The filter has the passband over $[0,\pi]$ and stop band over $[-\pi,0]$ so that it retains positive frequencies and suppresses negative frequencies. This projection is then similar to a Hilbert transform of the input signal. The standard DWT is applied to the projected (complex) input signal obtained in this way and as a result complex wavelet coefficients are generated (Fernandes, 2002). This projection-based complex DWT is applied to compute the DWT coefficients in this section.

C. Adapted signal partition

The processing described in Secs. II A and II B results in a set of detectors associated with the binary tree structure of intervals $I_{m,q}$ in Fig. 2. A partition (segmentation) $\cup I_{m_i,q_i}$ of the current data block restricted to $I_{m,q}$, $m=0,1,...,M-1$, $q=1,2,...,2^m$, is next sought, where the union of all segments in the partition $\cup I_{m_i,q_i}$ exhaustively covers the block length 2^K without overlapping, and which (in some sense) provides the largest values of the resulting detection statistics. Denote by $T_{m,q}$ the normalized detection statistics regardless of the method used for its computation [i.e., obtained using either Eq. (3) or Eq. (4)]. Next, assume that $J_{m,q}=\cup I_{n_j,p_j}$ is the segmentation of a given interval $I_{m,q}$ restricted to the intervals $I_{n,p}$, $n=m,\ldots,M-1$ and $p=(n-m+1)q-2^{(n-m)}+1,...,(n-m+1)q$. The collection of intervals $I_{n,p}$ defined in this way is the $(M-m)$-level binary tree structure that originates at $I_{m,q}$. Also, assign by $\{T_{n_j,p_j}\}$ the collection of detection statistics associated with the partition $J_{m,q}$ and define the function $\theta_{m,q}$ as the maximum over $\{T_{n_j,p_j}\}$, i.e., as $\theta_{m,q}=\max\{T_{n_j,p_j}\}$.

A recursive search algorithm is applied to find the best segmentation of the current data block. The algorithm starts with $m=M-1$ and works its way up throughout the whole binary tree structure. In the process it obtains a collection of recursive segmentations $J_{n,q}$ for $n=M-1,...,0$. On initialization $J_{M-1,q}$ is set to the most refined partition in the binary tree structure, $J_{M-1,q}=I_{M-1,q}$ for $q=1,2,...,2^{M-1}$. This also implies that, on initialization, $\theta_{M-1,q}=T_{M-1,q}$. The algorithm proceeds as follows:

$$J_{m-1,q}=\begin{cases} I_{m-1,q} & \text{if } T_{m-1,q}>\max(\theta_{m,2q-1},\theta_{m,2q}),\\ J_{m,2q-1}\oplus J_{m,2q} & \text{otherwise,}\end{cases} \tag{5}$$

and yields the required segmentation $J_{0,1}=\cup I_{m_i,q_i}$. In each recursion $m=M-1,...,1$, the detection statistics of a parent interval $I_{m-1,q}$, $T_{m-1,q}$, is compared to the maxima of the sets of detections statistics related to the partitions of its two children segments, $J_{m,2q-1}$ and $J_{m,2q}$. If the detection statistics of the parent interval is greater than all statistics associated with the children segment partitions, the parent interval is retained in the segmentation in the current recursion. Conversely, if any of the detection statistics that correspond to the partitions of the children segments is greater than that of the parent segment, the parent segment is replaced by the union of the children segment partitions, $J_{m,2q-1}\oplus J_{m,2q}$. A similar algorithm is described in Coifman and Wickerhauser (1992), where the goal was to find the best adapted orthonormal basis for the input signal relative to an entropy-based measure.

Let $\{T_{m_i,q_i}\}$ be the set of detection statistics associated with the final partition $J_{0,1}=\cup I_{m_i,q_i}$. Then, it can be shown that

$$\max_{m_i,q_i}(T_{m_i,q_i})=\max_{m,q}(T_{m,q}),$$

that is, the segment for which the detection statistics is maximal over the entire binary tree structure is included in the best signal partition obtained using Eq. (5).

The values from the set $\{T_{m_i,q_i}\}$ are next assigned to the segments that correspond to the finest partition of the binary tree $I_{M-1,q}$, $q=1,2,...,2^{M-1}$ as follows. The intervals from

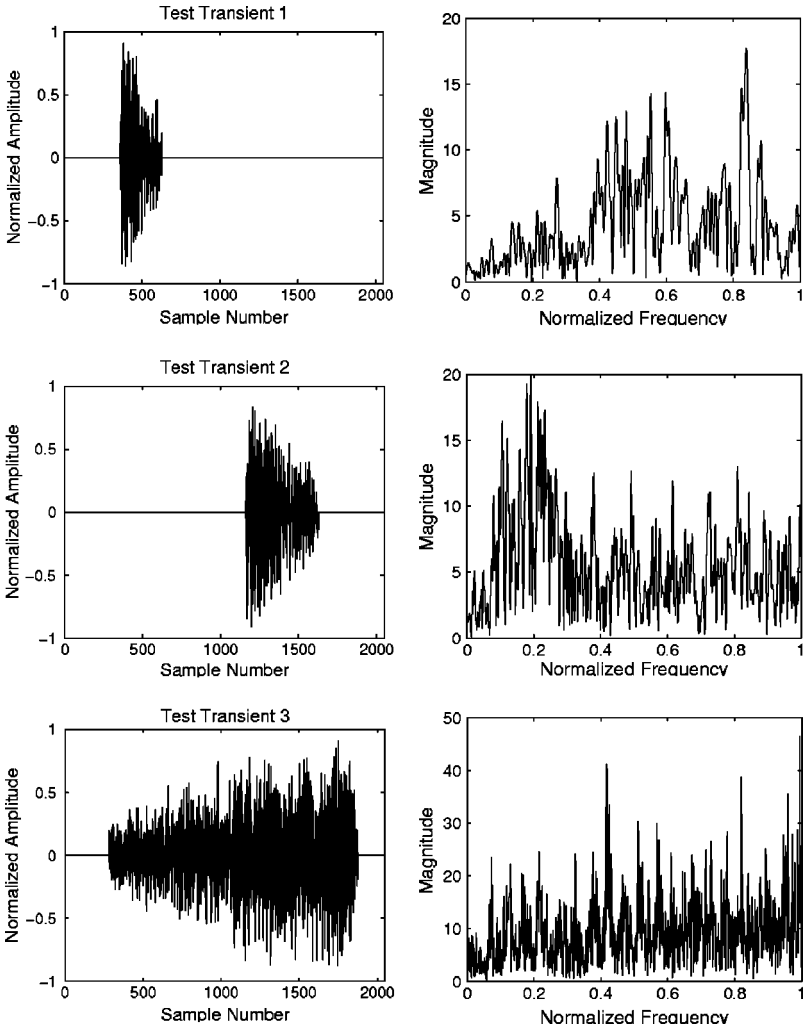

FIG. 4. Test transients used in the experiments. Shown is time series representation (left), and frequency domain representation (right).

the segmentation obtained using Eq. (5) that belong to the set $I_{M-1,q}$, that is, for which $m_i = M-1$, are assigned their respective value T_{m_i,q_i}. Each interval I_{m_i,q_i} for which $m_i < M-1$ is recursively split into halves until the highest level $(M-1)$ is reached. To all segments obtained in this way the same value of the detection statistics is assigned that is equal to the value corresponding to their parent segment. As a result a temporal sequence of detection statistics of the length $2^{(M-1)}$ is obtained. It characterizes the underlying data block and is used for transient detection. Namely, each value of the detection statistics from the sequence, t, is separately compared to a threshold $\mathcal{T}$. The probability that t exceeds the threshold $\mathcal{T}$ for the noise-only data (hypothesis H_0) defines the probability of false alarm P_{fa}, whereas the probability that $t > \mathcal{T}$ when a transient signal is present in the data (hypothesis H_1) is denoted as the probability of detection P_d.

III. DETECTION SIMULATIONS

The performance of the LFT- and DWT-based detectors is evaluated using several underwater acoustic transients that varied in their characteristics regarding both duration and frequency content (see Fig. 4). The transients are real underwater acoustics recordings obtained by using omnidirectional hydrophones. A 40-min-long recording of ambient sea noise is used for the background signal. This signal is not stationary as its amplitude slowly changes throughout the recording. It is divided into blocks of length $N = 2048$ samples, and the transients are inserted into these blocks at different signal-to-noise ratios (SNR). The power spectral density of background noise estimated using 600 overlapping blocks of length 2048 is shown in Fig. 5.

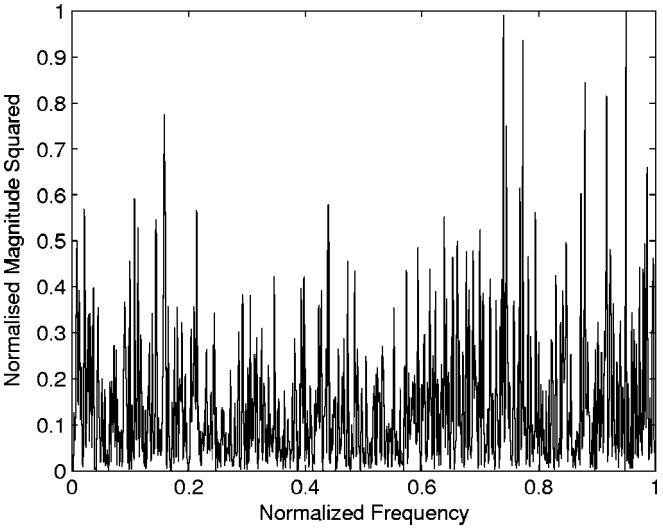

FIG. 5. Power spectral density of background noise estimated using 600 overlapping noise segments of length 2048.

The SNR is defined as the total signal energy divided by the noise energy computed over the support of the transient, that is as

$$\mathrm{SNR} = 10 \log \frac{\Sigma_{k=1}^{K_T} S(k)^2}{\Sigma_{k=1}^{K_T} N(k)^2}, \tag{6}$$

where $S(k)$ are the signal samples, $N(k)$ are noise samples, and $k=1,...,K_T$ is the transient support. The SNR in Eq. (6) is effectively normalized with respect to the signal length. By contrast, Wang and Willett (2001) use *aggregate* SNR defined as the total signal energy divided by the noise variance. This definition gives privileges to the detection of shorter transients as they will have greater magnitudes than the longer signals for the same SNR.

The block length N is chosen so as to be matched to the length of the longest transient that we wish to detect. The detection statistics is computed using $M=5$ level binary tree decomposition. It is assumed that, in some cases, smaller parts of a transient signal may be better matched by the transform basis functions than the entire signal, and that detection performance can be improved by using these segments. Therefore, the length of the smallest segment in the binary tree, i.e., the one that corresponds to the highest decomposition level $M-1$, is set to 128 samples, which is smaller than the length of any of the tested transients. The starting position of each transient within a block is chosen so as not to coincide with the beginning of any subinterval at any level of the binary tree structure and to allow that the entire transient is contained within the block (see Fig. 4).

The number of noise-only data blocks used in Eqs. (3) and (4) for background normalization is set to $L=10$.

Regarding the choice of the exponent ν in Eqs. (3) and (4), the study in Wang and Willett (2001) indicates that, for different block lengths N and output SNRs, and under the assumption that the frequency characteristics of the transient are not known, good values are $1.5<\nu<2$. In our experiments similar results are obtained for both the LFT- and the DWT-based detectors. Therefore, this parameter is set to $\nu=1.7$. Also, several different wavelets with different lengths of the associated filters have been tested. It is found that the performance of the DWT-based detectors does not depend much on the choice of wavelet. This could be expected since the transients in Fig. 4 are noise-like and do not have specific spectral content. We used the Haar wavelet, by which the priority is given to time localization. Besides, the filter that corresponds to the Haar wavelet is short, so that the information carried over from one block of data to the next in the processing of the on-line DWT is minimal. Note that, for the detection of transients that have specific spectral content such as high spectral peaks, a wavelet that is matched to the signal characteristics can be expected to improve detection performance.

In the experiments the total number of data blocks of length $N=2048$ of the sea noise record is $B=9600$. For both LFT- and DWT-based detectors the statistics of the first $0.15\times B$ noise-only blocks are used to estimate means and variances of the detection statistics over different decomposition levels of the binary tree. These estimates are next used to normalize the detection statistics computed for the remaining $0.85\times B$ data blocks.

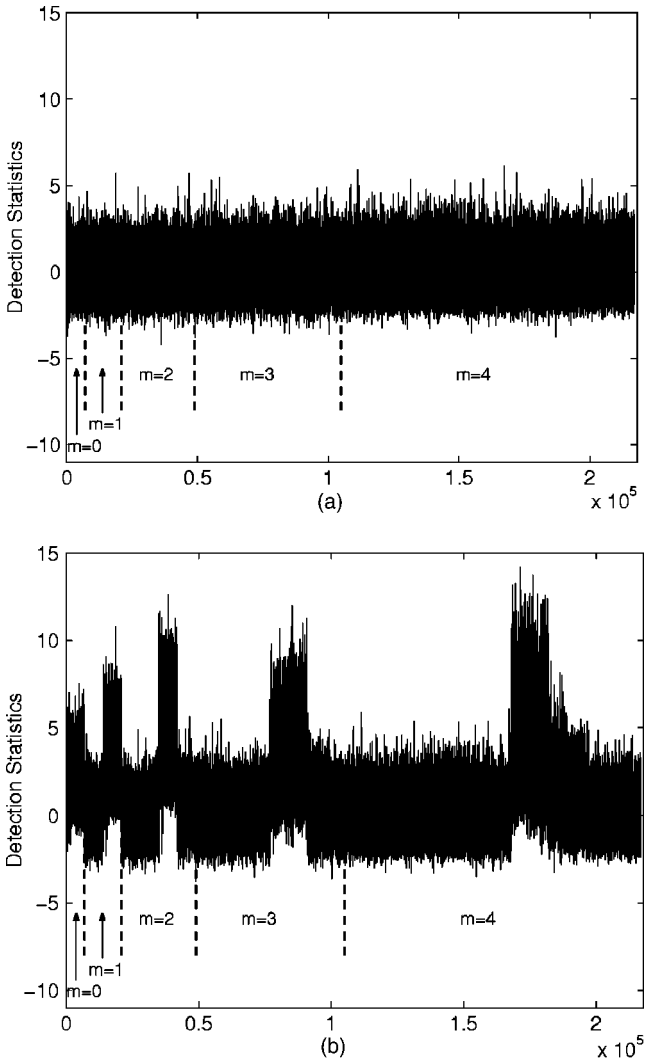

FIG. 6. Normalized detection statistics $T^{(2)}_{W_{m,q}}$ for all segments in the binary tree structure and for all data blocks used in the tests: (a) noise-only case; (b) for the test transient 2 buried in noise at SNR$=-7$ dB.

Figure 6(a) shows the normalized detection statistics $T^{(2)}_{W_{m,q}}$ [see Eq. (4)] for noise-only data computed for all segments in the binary tree structure and for all data blocks used in the tests. The levels of decomposition for which the values $T^{(2)}_{W_{m,q}}$ are computed are shown in the figure. At each level, the statistics computed for the same interval (m,q) within the binary tree over all data blocks are ordered consecutively. It can be seen that the values of the detection statistics for different decomposition levels are approximately correctly normalized and their values can be mutually compared. Figure 6(b) shows the normalized detection statistics $T^{(2)}_{W_{m,q}}$ computed when the test transient 2 is inserted in the ambient noise at -7 dB. Shown are detection statistics for all segments in the binary tree structure and for all data blocks used in the tests. Since the length of the test transient 2 is much smaller than the length of the analyzed data block, the values of the detection statistics computed for the levels of the binary tree $m>0$ that are characterized by shorter data seg-

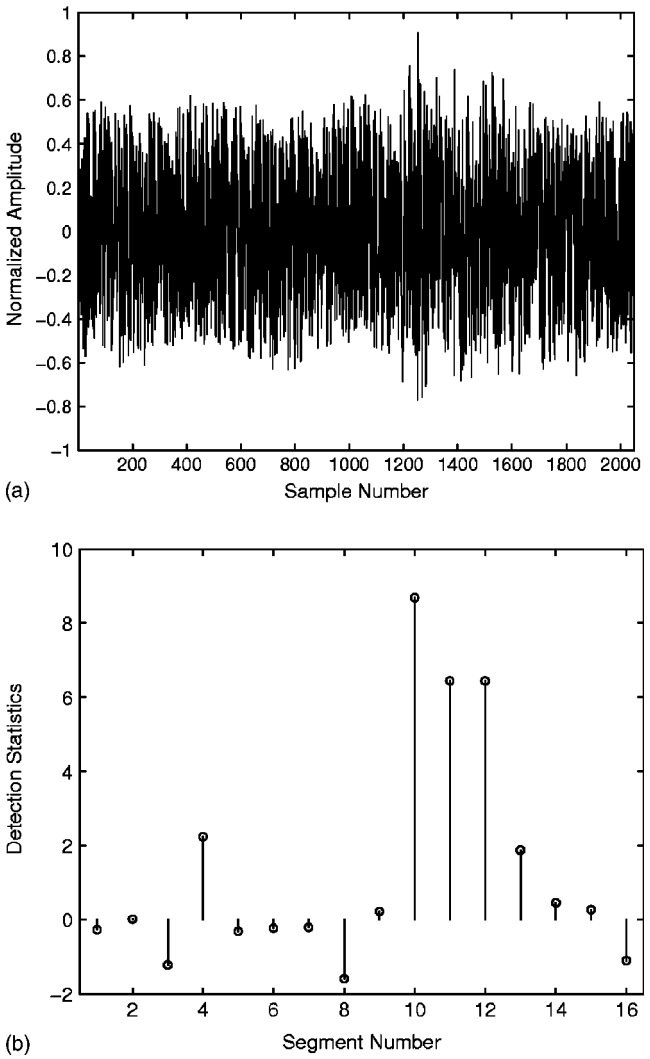

FIG. 7. (a) Test transient 2 in noise at SNR=−7 dB; (b) temporal sequence of detection statistics $T^{(2)}_{W_{m,q}}$ for the signal in (a) obtained using the best-adapted signal partition.

ments (of the length 2^{K-m}) are much greater than those computed for the segment of the length N, that is, at the lowest level of decomposition $m=0$. The reason is that, for $m=0$, the test transient is not well matched by the transform basis functions. Moreover, the content of noise energy in the segment is large as compared to the content of the signal energy. Since the detection statistic is based on the summation of energy over the entire interval, its value is, after the normalization, relatively decreased. By contrast, at the higher levels of decomposition $m>0$ the corresponding basis functions are better adapted to processing this short signal. Note that the position of the largest values of the detection statistics within one decomposition level roughly corresponds to the position of the test transient within the data block (see Fig. 4).

Figure 7(a) shows test transient 2 in noise at SNR=−7 dB. Figure 7(b) shows the temporal sequence of the detection statistics $T^{(2)}_{W_{m,q}}$ resulting after the best-adapted partition of the signal in Fig. 6(a) (see Sec. II C).

A. Probability of detection for the LFT- and DWT-based detectors

In the experiments there is only one occurrence of a transient in each data block. For this reason the transient is considered detected if at least one detection statistics from the temporal sequence obtained by using the best-adapted partition of the data block, restricted to the segments in which resides 90% of the transient energy, is greater than a given threshold. The probability of detection is defined by

$$P_d=\frac{B_d}{B_{\text{tot}}}, \tag{7}$$

where B_d is the number of blocks in which a transient is detected and B_{tot} is the total number of data blocks.

The intention is to use only the segments that contain a significant portion of the transient signal energy to estimate the probability of detection. It can be expected that the segments that enclose the end portion of a transient contain a very small amount of the signal energy and can thus be treated as noise-only. The above definition insures that these segments are not used for the estimation of the probability of transient detection.

B. Probability of false alarm for the LFT- and DWT-based detectors

A false alarm is assumed to occur each time a detection statistics from the temporal sequence resulting from the best-adapted partition of a noise-only data block is greater than a threshold. Therefore, the probability of false alarm is defined as

$$P_{fa}=\frac{\Sigma_{b=1}^{B_{\text{tot}}}N_b}{2^{M-1}B_{\text{tot}}}, \tag{8}$$

where N_b is the number of values in this sequence that are greater than the threshold for the block $b=1,2,...,B_{\text{tot}}$, and M is the number of levels of the binary tree structure of intervals.

C. Detector performance

The performance of the LFT- and DWT-based detectors is evaluated for a number of transients used in this study and is compared to the performance of the DFT- and DWT-based detectors that use fixed window length (Wang and Willett, 2001). The performance of the DFT- and DWT-based detectors in Wang and Willett (2001) is evaluated for the block length $N=2048$. The corresponding detection statistics are computed using the transform coefficients at the level $m=0$ of the binary tree structure as per Eqs. (3) and (4), respectively, i.e., as $T^{(n)}_{F_{0,1}}$ and $T^{(n)}_{W_{0,1}}$ for $n=1$, 2. The results are shown in Figs. 8–10. Figures 8–10(a) show probability of detection P_d of the tested transients as a function of SNR for the probability of false alarm $P_{fa}=10^{-3}$. Figures 8–10(b) show receiver operating characteristics (ROC) evaluated for a fixed SNR specific to each transient.

In Figs. 8–10 the detectors are denoted as follows. The LFT-based detectors are denoted by LFT-T1 for the detection statistics $T^{(1)}_{F_{m,q}}$, and by LFT-T2 for $T^{(2)}_{F_{m,q}}$ in Eq. (3), whereas

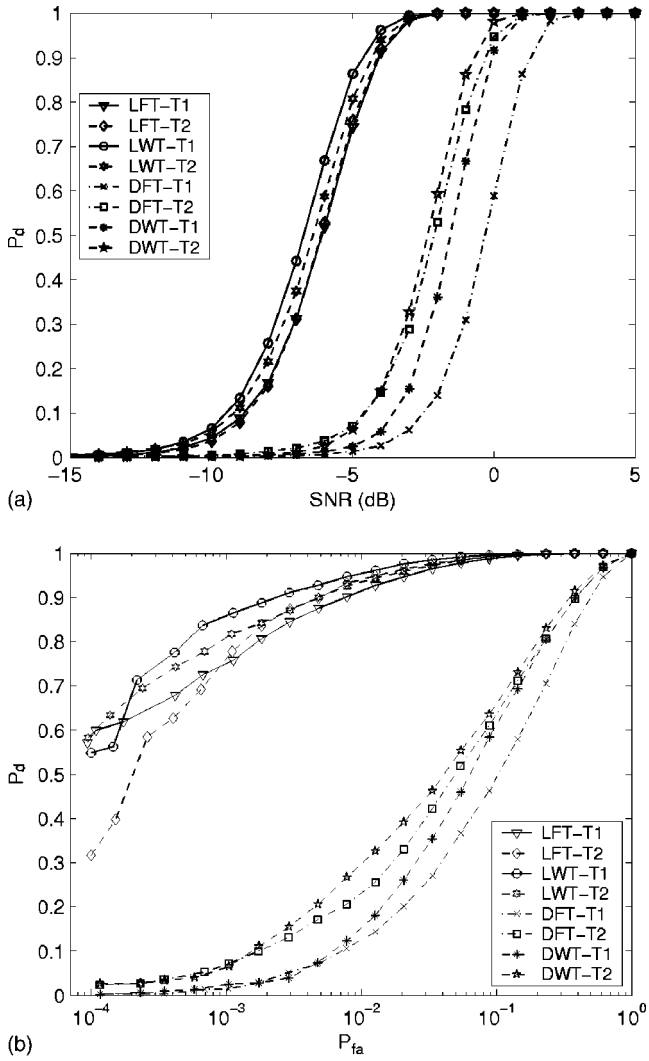

FIG. 8. Performance of detectors for the test transient 1: (a) probability of detection versus SNR for $P_{fa}=10^{-3}$; (b) ROC curves for SNR fixed at -5 dB.

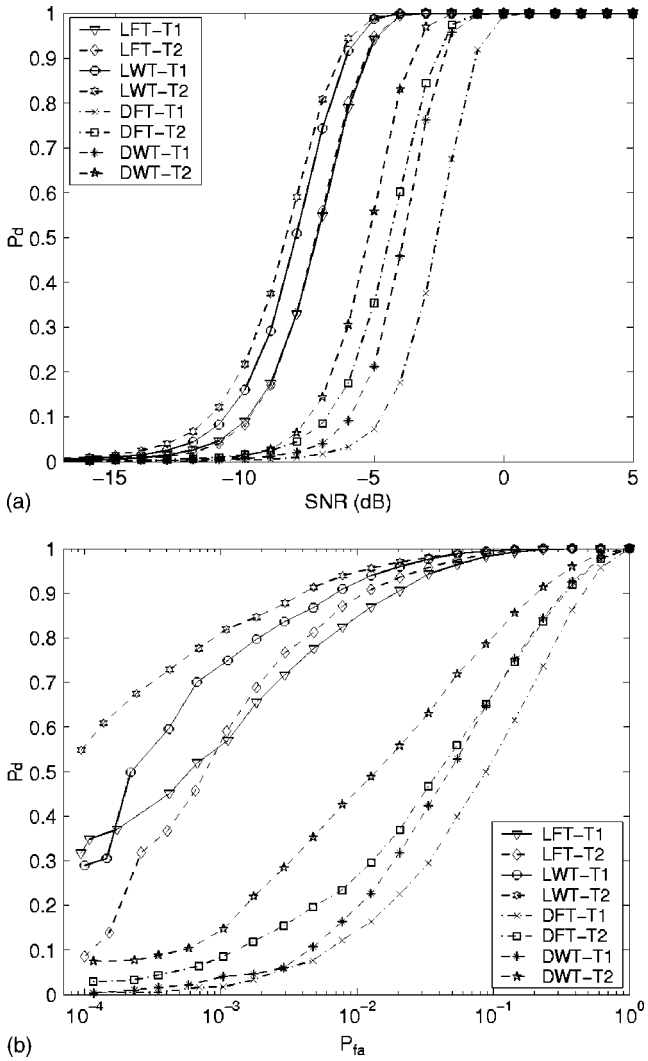

FIG. 9. Performance of detectors for the test transient 2: (a) probability of detection versus SNR for $P_{fa}=10^{-3}$; (b) ROC curves for SNR fixed at -7 dB.

the DWT-based detectors are denoted by LWT-T1 and LWT-T2 for $T^{(1)}_{W_{m,q}}$ and $T^{(2)}_{W_{m,q}}$ in Eq. (4), respectively. The corresponding DFT-based detectors described in Wang and Willett (2001) are denoted by DFT-T1 and DFT-T2 for $T^{(1)}_{F_{0,1}}$ and $T^{(2)}_{F_{0,1}}$, and the DWT-based detectors by DWT-T1 and DWT-T2 for $T^{(1)}_{W_{0,1}}$ and $T^{(2)}_{W_{0,1}}$, respectively.

The results in Figs. 8–10 indicate that adaptive window-length detectors perform better than the standard detectors described in Wang and Willett (2001) for all tested transients. Also, the adaptive window-length detectors using the DWT outperform the LFT-based detectors. For the test transient 1 the LWT-T1 detector gives somewhat better result than that obtained using the detector LWT-T2, whereas, for the test transients 2 and 3, the detector LWT-T2 performs better than the detector LWT-T1. It is interesting to note that the probability of detection as a function of SNR at $P_{fa}=10^{-3}$ for the detectors LFT-T1 and LFT-T2 are almost identical for all tested transients [see Figs. 8–10(a)]. Therefore, for $P_{fa}=10^{-3}$, no advantage is obtained by using the test statistics $T^{(2)}_F$ as compared to the detection statistics $T^{(1)}_F$ in Eq. (3).

In this paper *relative detection gain* (RDG) of adaptive window-length transient detectors is defined as the difference between the SNRs that correspond to the best-performing adaptive detector and to the best-performing detector described in Wang and Willett (2001) evaluated for the probability of detection $P_d=0.5$. The RDG for the test transients used in the experiments for $P_{fa}=10^{-3}$ are measured using the curves shown in Figs. 8–10(a). These RDGs, along with the best-performing adaptive and standard procedure for each transient, are shown in Table I. From these results it can be seen that the RDGs related to the shorter transients are greater than those obtained for the longer transients. This is consistent with our expectation that the performance of the standard detectors (Wang and Willett, 2001) deteriorates when the ratio of the length of the transient to the length of the analyzing data block decreases. By contrast, the proposed detectors choose more appropriate bases for signal decomposition by allowing adaptation to different signal lengths. The RDG decreases for longer transients and is expected to be close to zero when the length of the data block is very close to that of the transient.

From the results in Figs. 8–10, it can also be seen that,

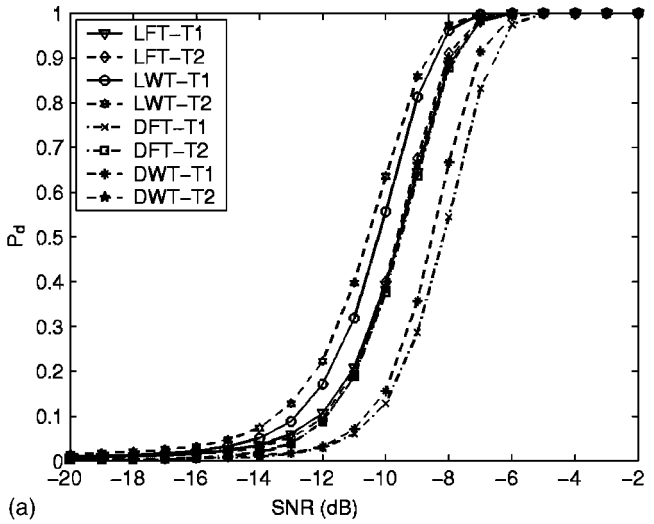

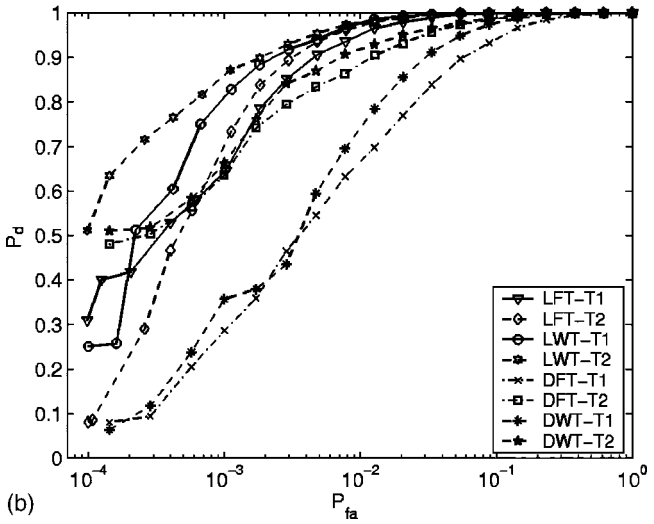

FIG. 10. Performance of detectors for the test transient 3: (a) probability of detection versus SNR for $P_{fa}=10^{-3}$; (b) ROC curves for SNR fixed at -9 dB.

in general and for all tested detectors, shorter transients used in the experiments are detected at greater SNRs as compared to the transients of longer duration. This indicates that, using the tested procedures, shorter transients are harder to detect than the longer ones. Note that in this paper the SNR is defined so as to be independent of the length of the transient. However, it still may depend upon the spectral characteristics of both individual transients and background noise (see Figs. 4 and 5).

IV. CONCLUSION

This paper concerned the detection of acoustic underwater transients of unknown location, length, and time-frequency content. A method that applies a set of embedded transient detectors tuned to a number of signal partitions has been proposed. The detectors are based on the general wavelet theory, whereby two different techniques are examined, the local Fourier transform and the discrete wavelet transform. The detection statistics are computed so as to enable prewhitening of unknown colored noise and to allow for a constant false-alarm rate detection. The statistics are combined so as to obtain a best-adapted partition of the signal with the goal of finding the largest detection statistics in each segment.

The detectors are tested using several underwater acoustic transients buried in ambient sea noise. The results show that the proposed adaptive window-length detectors outperform the detectors with fixed window lengths.

TABLE I. Relative detection gain (RDG) for the test transients for $P_{fa}=10^{-3}$.

Test transient	Best procedure		RDG (dB)
	Adaptive	Standard	
1	LWT-T1	DWT-T2	4.40
2	LWT-T2	DWT-T2	3.13
3	LWT-T2	DWT-T2	1.63

Abry, P., and Flandrin, P. (**1994**). "Multiresolution transient detection," in Proc. IEEE-SP Intern. Symp. Time-Frequency and Time-Scale Analysis (Philadelphia, PA), pp. 225–228.

Benno, S. A., and Moura, J. M. F. (**1998**). "Scaling functions robust to translation," IEEE Trans. Signal Process. **46**, 3269–3281.

Carevic, D. (**2003**). "Robust estimation techniques for target-motion analysis using passively sensed transient signals," IEEE J. Ocean. Eng. **28**, 250–261.

Carevic, D. (**2004**). "Tracking target in cluttered environment using multilateral time-delay measurements," J. Acoust. Soc. Am. **115**, 1198–1206.

Coifman, R. R., and Wickerhauser, M. V. (**1992**). "Entropy-based algorithms for best basis selection," IEEE Trans. Inf. Theory **38**, 713–718.

Del Marco, S., and Weiss, J. (**1997**). "Improved transient signal detection using a wavepacket-based detector with an extended translation-invariant wavelet transform," IEEE Trans. Signal Process. **45**, 841–850.

Fernandes, F. C. (**2002**). "Directional, shift-insensitive, complex wavelet transforms with controllable redundancy," Ph.D. dissertation, Rice University Houston, TX.

Friedlander, B., and Porat, B. (**1989**). "Detection of transient signals by the Gabor representation," IEEE Trans. Acoust., Speech, Signal Process. **37**, 169–180.

Friedlander, B., and Porat, B. (**1993**). "Performance analysis of transient detectors based on a class of linear transforms," IEEE Trans. Inf. Theory **40**, 136–144.

Liang, J., and Parks, T. W. (**1996**). "A translation-invariant wavelet representation algorithm with applications," IEEE Trans. Signal Process. **44**, 225–232.

Liu, T. T., and Fraser-Smith, A. C. (**2000**). "Detection of transients in 1/f noise with the undecimated discrete wavelet transform," IEEE Trans. Signal Process. **48**, 1458–1462.

Mallat, S. G. (**1989**). "A theory of multiresolution signal decomposition: The wavelet representation," IEEE Trans. Pattern Anal. Mach. Intell. **11**, 674–693.

Nuttall, A. (**1996**). "Near-optimum detection performance of power-low processors for random signals of unknown location, structure, extend and arbitrary strength," Naval Undersea Warfare Center Technical Report 11123 (Newport, RI).

Nuttall, A. (**1997**). "Performance of power-low processors with normalization for random signals of unknown structure," Naval Undersea Warfare Center Technical Report 10760 (Newport, RI).

Pflug, L. A., Ioup, G. E., and Ioup, J. W. (**2004**). "Multichannel moment detectors for transients in shallow-water noise," IEEE J. Ocean. Eng. **29**, 157–168.

Pflug, L. A., Ioup, G. E., Ioup, J. W., Barnes, K., Field, R. L., and Rayborn, G. H. (**1992**). "Detection of oscillatory and impulsive transients using higher-order correlations and spectra," J. Acoust. Soc. Am. **91**, 2763–2776.

Rao, P., and Taylor, F. J. (**1991**). "Detection and localization of narrow-band transient signals using the Wigner distribution," J. Acoust. Soc. Am. **90**, 1423–1434.

Ravier, P., and Amblard, P.-O. (**1998**). "Combining an adapted wavelet analysis with fourth-order statistics for transient detection," Signal Process. **70**, 115–128.

Saito, N. (**1999**). ''Local Fourier dictionary: A natural tool for data analysis,'' in Proceedings of SPIE, Wavelet Application in Signal and Image Processing, Vol. 3813, pp. 610–624.
Strang, G., and Nguyen, T. (**1996**). *Wavelets and Filter Banks* (Wellesley-Cambridge Press, Wellesley, MA).
Streit, R., and Willett, P. (**1999**). ''Detection of random transient signals via hyperparameter estimation,'' IEEE Trans. Signal Process. **47**, 1823–1834.
Walsh, D. O., and Delaney, A. (**1995**). ''Detection of transient signals in multipath environment,'' IEEE J. Ocean. Eng. **20**, 131–138.
Wang, Z., and Willett, P. (**2001**). ''All-purpose and plug-in power-law detectors for transient signals,'' IEEE Trans. Signal Process. **49**, 2454–2466.
Wickerhauser, M. V. (**1994**). *Adapted Wavelet Analysis from Theory to Software* (IEEE, Pscataway, NJ).
Zakarauskas, P., Parfitt, C. J., and Thorleifson, J. M. (**1991**). ''Automatic extraction of spring-time Arctic ambient noise transients,'' J. Acoust. Soc. Am. **90**, 470–474.

Application of acoustic reflection tomography to sonar imaging

Brian G. Ferguson[a)]
Maritime Operations Division—Sydney, Defence Science and Technology Organisation, P.O. Box 44, Pyrmont NSW 2009, Australia

Ron J. Wyber
Midspar Systems, 24 Farrer Place, Oyster Bay, NSW 2225, Australia

(Received 28 March 2004; revised 10 November 2004; accepted 14 November 2004)

Computer-aided tomography is a technique for providing a two-dimensional cross-sectional view of a three-dimensional object through the digital processing of many one-dimensional views (or projections) taken at different look directions. In acoustic reflection tomography, insonifying the object and then recording the backscattered signal provides the projection information for a given look direction (or aspect angle). Processing the projection information for all possible aspect angles enables an image to be reconstructed that represents the two-dimensional spatial distribution of the object's acoustic reflectivity function when projected on the imaging plane. The shape of an idealized object, which is an elliptical cylinder, is reconstructed by applying standard backprojection, Radon transform inversion (using both convolution and filtered backprojections), and direct Fourier inversion to simulated projection data. The relative merits of the various reconstruction algorithms are assessed and the resulting shape estimates compared. For bandpass sonar data, however, the wave number components of the acoustic reflectivity function that are outside the passband are absent. This leads to the consideration of image reconstruction for bandpass data. Tomographic image reconstruction is applied to real data collected with an ultra-wideband sonar transducer to form high-resolution acoustic images of various underwater objects when the sonar and object are widely separated.
[DOI: 10.1121/1.1848071]

PACS numbers: 43.60.Gk, 43.60.Lq, 43.60.Pt, 43.20.El [EJS] Pages: 2915–2928

I. INTRODUCTION

Computer-aided tomography (also known as computer-assisted tomography, computerized tomography, computed tomography, or reconstructive tomography) refers to the cross-sectional imaging of an object from either transmission or reflection data by illuminating the object from many different view directions or aspect angles.[1–6] The impact of this noninvasive technique in diagnostic medicine has been revolutionary, since it has enabled the medical profession to view in detail the internal organs of the human body without compromising the safety of the patient. The first medical application utilized x rays to form images of tissues based on their x-ray attenuation coefficient. In recent times, however, medical imaging systems that rely on the principles of computerized tomography have been extended to include other sources such as ultrasound, magnetic resonance, and radioisotopes, where the imaged parameter (or object function) is different in each case. Nonmedical applications of computerized tomography are in the fields of radar, geophysics, radio astronomy, and the nondestructive testing and analysis of structures and materials.

The present application involves the sonar imaging of underwater objects (sea mines). Currently, the acoustic identification of sea mines relies on high-resolution sonar imaging systems that use acoustic lenses to form very narrow beams during pulse transmission and echo reception.[7] Another system has wide beamwidth transmitters and a two-dimensional receive array that uses near-field focused beamforming on receive only to produce a high-resolution three-dimensional sonar image from a single transmission.[8] Since these types of sonars operate at megahertz frequencies, their use is limited to short ranges and requires a remotely operated vehicle to position the sonar close to the object to be imaged, typically within 2–5 m. Newly developed ultra-wideband sonar transducers that operate at mine hunting sonar *detection* frequencies (~100 kHz) with quality factors that approach unity, provide range resolutions of ~1 cm. Coupling this wideband sonar transducer technology with the signal processing for acoustic reflection tomography offers the potential to reconstruct high-resolution images of sea mines at safe standoff distances (100–200 m). Although the application of tomographic reconstruction techniques to sonar imaging has been considered elsewhere,[9,10] the present paper adopts a more systematic approach to the problem. Initially, various tomographic reconstruction algorithms are used to reconstruct the shape of an idealized object (or phantom) using simulated data and their merits assessed. The mathematical representation of each of these algorithms is included as background material to highlight their interrelationship. An important contribution of the paper stems from high-frequency sonar transmissions being bandpass signals, which (unlike absorption tomography) limits the wave number information available for image reconstruction. This prompts the consideration of image reconstruction for bandpass data. Typical images of various exercise mines are re-

a)Electronic mail: brian.ferguson@dsto.defence.gov.au

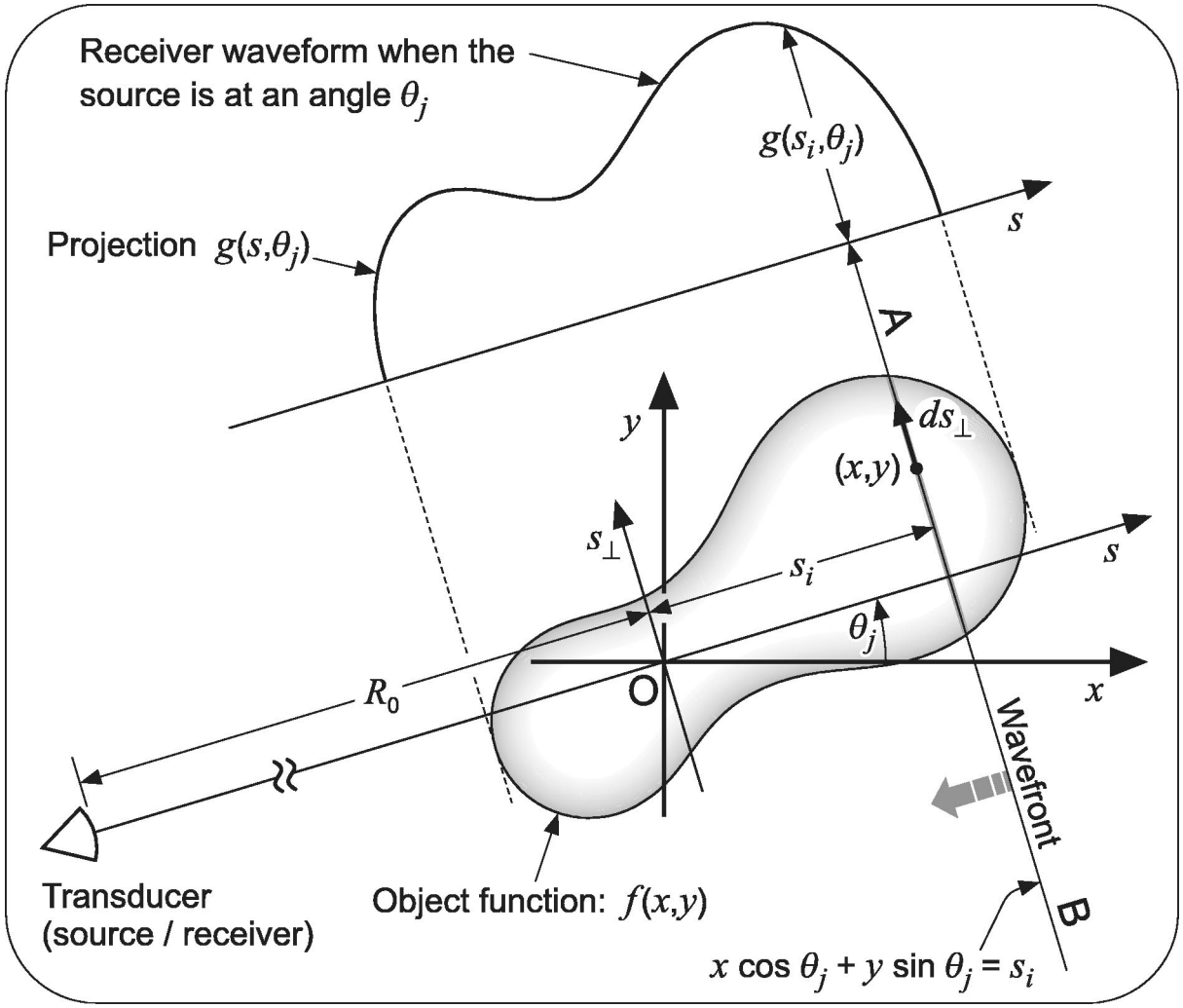

FIG. 1. Plan view of the transducer-object geometry and the projection for an insonification angle of θ_j.

constructed from real wideband sonar data recorded during an experiment in a dam. In the experiment, the sonar transducer and the object were widely separated (by 60 m). Also, the sonar transducer was fixed and each underwater object was rotated about its vertical axis, which enabled the projection data to be recorded for the complete 360° range of viewing angles that are required for tomographic image reconstruction. In an operational system, the sonar would circumnavigate the mine, but this paper provides the preliminary step toward the future application of computerized tomography to the long-range imaging of sea mines and other underwater objects.

II. ACOUSTIC REFLECTION TOMOGRAPHY

For the present monostatic sonar application, the source and receiver are collocated so that, after insonification by the acoustic source, the object scatters some of the energy backwards to the receiver. Consider an idealized case where the insonifying pulse has the properties of a Dirac delta function (zero duration and infinite bandwidth) and there is no acoustic shadowing or absorption within the object. The transducer-object geometry for sonar tomographic imaging is depicted in Fig. 1, where x and y represent a Cartesian coordinate system with the origin O inside the object. The direction of propagation of the sonar transmission is at an angle θ_j to the x axis. The sonar measurement system effectively projects the object's three-dimensional reflectivity function $\rho(x,y,z)$ on the two-dimensional imaging plane (or xy plane) shown in Fig. 1; the z direction is perpendicular to the xy plane. The object function $f(x,y)$ that is reconstructed in acoustic reflection tomography is the two-dimensional spatial distribution of the projected reflectivity function, that is, $f(x,y)=\int_z \rho(x,y,z)dz$. In Fig. 1, the sonar transducer and the object are widely separated so that a planar wave front projected on the imaging (or xy) plane can be represented by the straight line AB, which is defined mathematically by the equation $x\cos\theta_j+y\sin\theta_j=s_i$, where s_i is the perpendicular distance of the line from the origin O. The two-way propagation time for the wave front AB is given by $t_i=t_0+(2s_i/c)$, where c is the speed of sound propagation in the underwater medium and $t_0=2R_0/c$; R_0 is the distance of the origin from the transducer. As the signals backscattered from all of the points along a wave front are in phase, the total signal received at time t_i is found by adding the backscattered signals $f(x,y)$ for values of x and y along the line $x\cos\theta_j+y\sin\theta_j=s_i$. This can be represented mathematically as

$$g(s_i,\theta_j)=\int f(x,y)ds_\perp, \tag{1}$$

where $\int(\cdots)ds_\perp$ denotes integration along the line $x\cos\theta_j+y\sin\theta_j=s_i$. The integral in Eq. (1) is referred to as a *wave front* integral. The set of wave front integrals $g(s_i,\theta_j)$, where $-\infty<s_i<\infty$, forms the function $g(s,\theta_j)$ that defines the projection of $f(x,y)$ for the angle θ_j. Using the inverse Radon transform,[11] or other suitable reconstruction algorithm, an image of the object that is represented by the two-dimensional distribution $f(x,y)$ can be recovered from the projections recorded at all aspect angles θ_j, where $0\leqslant\theta_j<2\pi$.

Note that the sonar provides resolution in the range direction $\vec{s}$ only; there is no spatial resolution in either the cross-range direction $\vec{s}_\perp$ or the vertical direction z since the sonar beam covers the entire object. The spatial resolution in the cross-range direction is achieved by insonifying the object and processing the backscattered signals at *all* aspect angles. Applying a reconstruction algorithm to a complete set of backscattered signal measurements forms a high-resolution two-dimensional reflectivity map of the object.

III. RADON TRANSFORM

The Radon transform of a function $f(x,y)$, denoted as $g(s,\theta)$, is defined as the line integral of $f(x,y)$ along a wave front inclined at an angle θ to the x axis and at a distance s from the origin. Mathematically, it is written as[2]

$$\begin{aligned} g(s,\theta)&=\mathcal{R}f(x,y)\\ &=\int_{-\infty}^{\infty}\int_{-\infty}^{\infty}f(x,y)\,\delta(x\cos\theta+y\sin\theta-s)dx\,dy,\\ -\infty<s<\infty,&\quad 0\leqslant\theta<\pi. \end{aligned} \tag{2}$$

The Radon transform operator, $\mathcal{R}$, is also referred to as the *projection operator*. The function $g(s,\theta)$ is the one-dimensional projection of $f(x,y)$ at an angle θ. In the rotated coordinate system $(s,s_\perp)$—see Fig. 1, where

$$s=x\cos\theta+y\sin\theta,\quad s_\perp=-x\sin\theta+y\cos\theta, \tag{3a}$$

or

$$x=s\cos\theta-s_\perp\sin\theta,\quad y=s\sin\theta+s_\perp\cos\theta, \tag{3b}$$

Eq. (2) can be expressed as[2]

$$g(s,\theta)=\int f(s\cos\theta-s_\perp\sin\theta,s\sin\theta+s_\perp\cos\theta)ds_\perp, \tag{4}$$

for $-\infty<s<\infty$, $0\leqslant\theta<\pi$.

For absorption tomography, the viewing angles are restricted to the range from 0 to π, since viewing the object in the range from π to 2π would provide redundant information as $g(s,\theta)=g(-s,\theta+\pi)$, which is a symmetry property of the Radon transform. This is not the case for reflection tomography where obscuration can lead to part of the object being in an acoustic shadow. Overcoming obscuration effects necessitates insonifying the object at all aspect angles ranging from 0 to 2π. This leads to the formation of a composite projection, which is defined for angles between 0 and π. If, due to shadowing, the projection information is incomplete for a particular aspect angle θ, then the missing information can be extracted from the projection that is obtained by insonifying the object from the opposite side, that is, at an aspect angle of $\theta+\pi$. When obscuration occurs, the composite projection is given by $g(s,\theta)+g(-s,\theta+\pi)$; in the absence of obscuration, it is given by $\{g(s,\theta)+g(-s,\theta+\pi)\}/2$.

The radon transform maps the spatial (x,y) domain to the spatial (s,θ) domain. Each point in (s,θ) space corresponds to a straight line in (x,y) space. Similarly, a fixed point with Cartesian/polar coordinates $(x=r\cos\phi, y=r\sin\phi)$ in the (x,y) plane maps to a sinusoid with locus $s=r\cos(\theta-\phi)$ in the (s,θ) plane.

IV. RECONSTRUCTION ALGORITHMS

A. Phantom

Simulated projection data corresponding to an idealized object (or phantom) are often used in the development and evaluation of reconstruction algorithms. The standard form of reflection tomography derives the two-dimensional reflectivity function of the object by applying the inverse Radon transform to the backscattered signal (or two-dimensional projection function) $g(s,\theta)$. The idealized object considered here is an elliptical cylinder. However, the impulse response of sonar signals backscattered from a rigid elliptical cylinder has a singularity at the elliptical boundary [see Eq. (A1)]. So, for this theoretical example, the preferred approach is to reconstruct the shape of the object rather than its reflectivity function as discussed in the following.

When using an acoustic test signal to insonify a rigid object, it is possible (see Appendix A) to obtain the area function $A(s,\theta)$ by integrating $g(s,\theta)$ twice with respect to s and multiplying the result by -4π. Physically, $A(s,\theta)$ is the area of a vertical slice through the object; the slice is in the same $(zs_\perp)$ plane of the incident wave front, which is perpendicular to the propagation direction $\vec{s}$ of the incident signal. Alternatively, $A(s,\theta)$ can be found by integrating the height function $h(x,y)$ of the object with respect to the variable $s_\perp$, as expressed by the projection equation

$$A(s,\theta)=\int_{s,\theta}h(x,y)ds_\perp=\mathcal{R}h(x,y), \tag{5}$$

where $h(x,y)$ is the height (or thickness) of the object at the point with coordinates (x,y). When the inverse Radon transform is applied to $A(s,\theta)$, the height function $h(x,y)$ of the object is determined. In other words, the inverse Radon transform of $A(s,\theta)$ defines the shape of the object.

The reconstruction of the height function $h(x,y)$ of an elliptical cylinder from the area function $A(s,\theta)$ is considered in the following. The two-dimensional height function $h(x,y)$ is given by

$$h(x,y)=h_0\quad\text{for}\ \frac{x^2}{a^2}+\frac{y^2}{b^2}\leqslant 1,\quad\text{otherwise}\ h(x,y)=0. \tag{6}$$

The area function $A(s,\theta)$ for the elliptical cylinder is given by

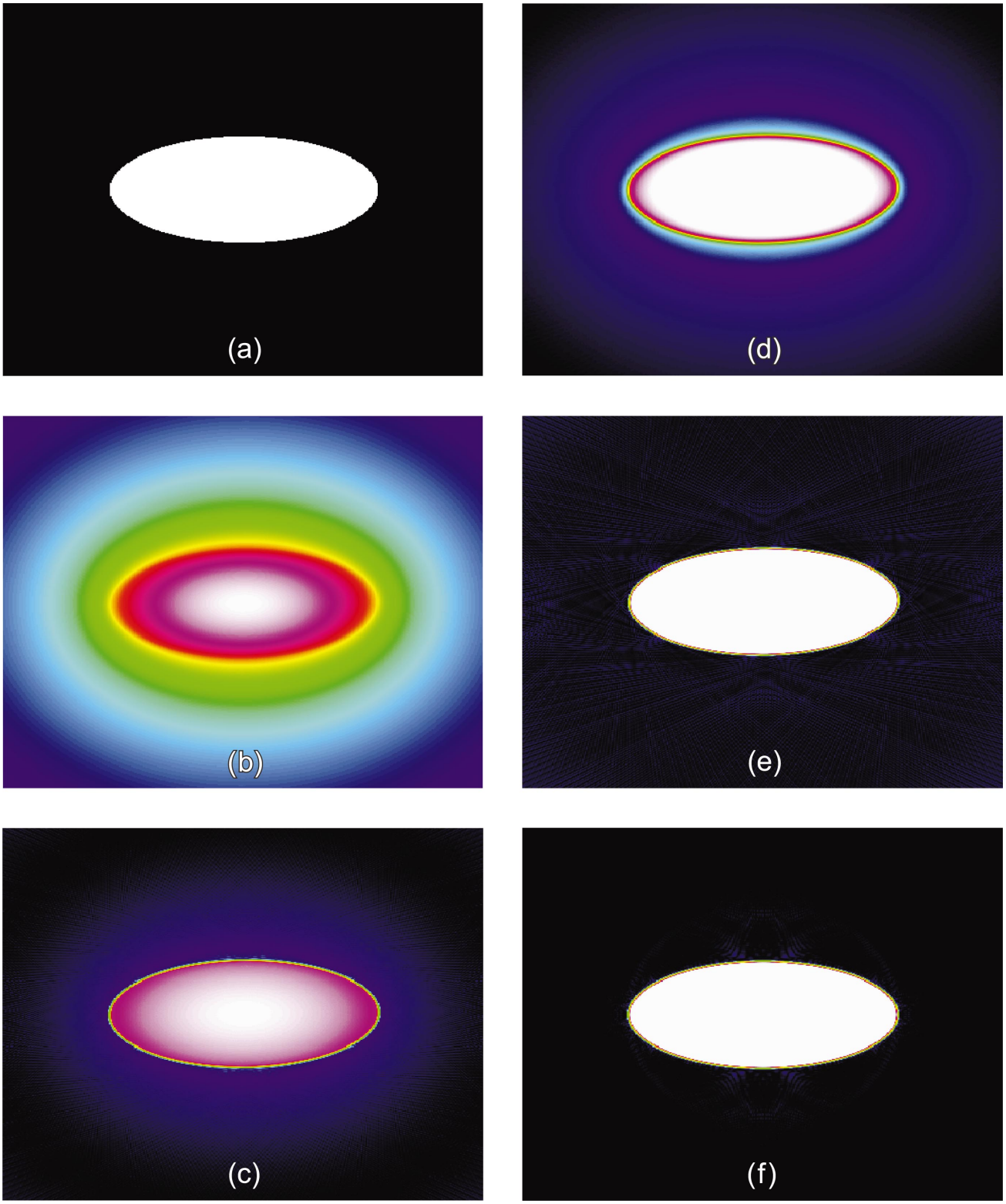

FIG. 2. (a) Plot of the exact object function that defines the shape of an elliptical cylinder. For the remainder, (b)–(f), plot of the object function is estimated by: (b) backprojection; (c) inverse Radon transform using filtered backprojection; (d) inverse Radon transform where the derivative of the projection function is convolved with the impulse response $1/2\pi^2 s$, prior to backprojection; (e) inverse Radon transform where the low-pass filtered projections are convolved with the low-pass filtered impulse response of $-1/2\pi^2 s^2$, prior to backprojection; (f) two-dimensional Fourier reconstruction.

$$A(s,\theta) = \int_{PQ} h(x,y)\,ds_\perp = h_0 \int_{PQ} ds_\perp = h_0 w(s,\theta) = \frac{h_0 2ab\sqrt{s_m^2 - s^2}}{s_m^2}, \quad (7)$$

where $s_m^2 = a^2\cos^2\theta + b^2\sin^2\theta$ and $w(s,\theta)$ is the width of the ellipse at a distance s in the direction $\vec{ds}_\perp$ (which is perpendicular to θ)—see Fig. A1.

Figure 2(a) shows an intensity plot of $h(x,y)$, which reveals the exact shape of the elliptical cylinder; the height

function is constant (h_0) within the region bounded by the ellipse (represented by the white shaded area) and zero outside (black shading). One measure of the quality of a tomographic reconstruction method is its fidelity in matching the exact shape of the object.

B. Backprojection operator

Associated with the Radon transform is the *backprojection operator*, $\mathcal{B}$, that maps a function with (s,θ) coordinates to a function with spatial coordinates (x,y) or (r,ϕ) and is defined as[2]

$$b(x,y)=\mathcal{B}g(s,\theta)=\int_0^{\pi} g(x\cos\theta+y\sin\theta,\theta)d\theta$$

$$=\int_0^{\pi} g(r\cos(\theta-\phi),\theta)d\theta. \tag{8}$$

Backprojection represents the accumulation of the wave front integrals of all the wave fronts that pass through the point with Cartesian coordinates (x,y), or equivalently, with polar coordinates (r,ϕ). The backprojection at (r,ϕ) is also the integration of $g(s,\theta)$ along the sinusoid $s=r\cos(\theta-\phi)$ in the (s,θ) plane. For example, Fig. 2(b) shows the results of applying the backprojection operator to the projection information given by Eq. (7); that is, for the *shape reconstruction* example, $g(s,\theta)=A(s,\theta)$ and $f(x,y)=h(x,y)$. The basic shape of the elliptical cylinder is recovered, but the discontinuity at the boundary is blurred with significant energy leaking into the region where the height function should be zero.

Note that the backprojection operator, $\mathcal{B}$, is *not* the inverse of the projection operator, $\mathcal{R}$; rather $\mathcal{B}$ is the adjoint of $\mathcal{R}$. The backprojected Radon transform can be written as[2]

$$\tilde{f}(x,y)=\mathcal{B}g(s,\theta)=\mathcal{B}\mathcal{R}f(x,y)=f(x,y)*(x^2+y^2)^{-1/2}, \tag{9}$$

where the asterisk $(*)$ denotes the two-dimensional convolution in Cartesian coordinates. The reconstructed function $\tilde{f}(x,y)$ is actually $f(x,y)$ blurred by the point spread function $(x^2+y^2)^{-1/2}$. Since the two-dimensional Fourier transform $\mathcal{F}_2$ of $(x^2+y^2)^{-1/2}$ is $(\xi_x^2+\xi_y^2)^{-1/2}$, the object function $f(x,y)$ can be restored from $\tilde{f}(x,y)$ by a two-dimensional (inverse) filter whose spatial frequency (or wave number) response is $|\xi|=\sqrt{\xi_x^2+\xi_y^2}$, that is,

$$f(x,y)=\mathcal{F}_2^{-1}\{|\xi|\mathcal{F}_2[\mathcal{B}g(s,\theta)]\}, \tag{10}$$

where $\mathcal{F}_2^{-1}$ denotes the two-dimensional inverse Fourier transform operator. For practical purposes, however, the convolution or filtered backprojection methods are preferred for image reconstruction, where the order of the filtering and backprojection operations is reversed, for example, compare Eqs. (10) and (13).

C. Inverse Radon transform

The image reconstruction problem is equivalent to finding the inverse Radon transform of $g(s,\theta)$. Given $g(s,\theta)=\mathcal{R}f(x,y)$, $-\infty<s<\infty$, $0\leqslant\theta<\pi$, its inverse Radon transform is[2] (see Appendix B)

$$f(x,y)=\mathcal{R}^{-1}g(s,\theta)$$

$$=\left(\frac{1}{2\pi^2}\right)\int_0^{\pi}\int_{-\infty}^{\infty}\frac{(\partial g(s,\theta)/\partial s)}{x\cos\theta+y\sin\theta-s}ds\,d\theta. \tag{11}$$

The inverse Radon transform is evaluated using a two-step process. First, each projection $g(s,\theta)$ is filtered by a one-dimensional filter whose frequency response is $|\xi|$. The result, $\tilde{g}_{\xi}(s,\theta)$, is then backprojected to yield $f(x,y)$. If the filtering operation is implemented in the spatial domain, this is referred to as the *convolution backprojection* method. Alternatively, if the filtering operation is implemented in the frequency (or wave number) domain, this is referred to as the *filtered backprojection* method.

D. Convolution backprojection method

The inverse Radon transform can be written as[2] (see Appendix B)

$$f(x,y)=\mathcal{R}^{-1}g(s,\theta)=(1/2\pi)\mathcal{B}\mathcal{H}\mathcal{D}g(s,\theta)$$

$$=\mathcal{B}\left\{\frac{1}{2\pi^2 s}*\frac{\partial g(s,\theta)}{\partial s}\right\}, \tag{12}$$

where $\mathcal{H}$ represents the Hilbert transform operator,[12] $\mathcal{D}$ is the derivative operator,[13] and an asterisk $(*)$ denotes convolution in the spatial domain. Thus the *inverse transform operator* is $\mathcal{R}^{-1}=(1/2\pi)\mathcal{B}\mathcal{H}\mathcal{D}$. Hence, $\mathcal{R}^{-1}$ can be implemented by convolving the differentiated projections $\mathcal{D}g(s,\theta)\equiv\partial g(s,\theta)/\partial\theta$ with $(1/2\pi^2 s)$, then backprojecting the result. Alternatively, $\mathcal{R}^{-1}$ can be implemented by convolving the projections $g(s,\theta)$ with

$$\frac{1}{2\pi}\frac{\partial}{\partial s}\left(\frac{1}{\pi s}\right)=\frac{-1}{2\pi^2 s^2},$$

then backprojecting the result. Since the backprojection operation is required for finding $\mathcal{R}^{-1}$, the reconstructed image pixel at (x,y) requires projections from all directions θ.

E. Filtered backprojection method

Alternatively, the inverse Radon transform can be evaluated by filtering the projections in the Fourier (or wave number) domain and backprojecting the inverse Fourier transform of the result. This implementation is described mathematically by[2] (see Appendix B, Sec. 2)

$$f(x,y)=\mathcal{R}^{-1}g(s,\theta)=\mathcal{B}\mathcal{F}_1^{-1}[|\xi|\mathcal{F}_1 g(s,\theta)]. \tag{13}$$

Thus, prior to implementing the backprojection, the sonar data $g(s,\theta)$ are preprocessed, which involves taking the one-dimensional Fourier transform $\mathcal{F}_1(s\rightarrow\xi)$ of $g(s,\theta)$, multiplying the transform by the modulus of the wave number $|\xi|$, and then taking the inverse Fourier transform $\mathcal{F}_1^{-1}(\xi\rightarrow s)$.

F. Fourier reconstruction methodc

It follows from the projection slice theorem (see Appendix B, Sec. 1) that, given the Fourier transform $\mathcal{F}_1(s\rightarrow\xi)$ of

the projection data $g(s,\theta)$, the object function can be estimated simply by performing a two-dimensional inverse Fourier transform, since

$$f(x,y)=\mathcal{F}_2^{-1}[F(\xi_x,\xi_y)]$$
$$=\mathcal{F}_2^{-1}[F(\xi\cos\theta,\xi\sin\theta)]=\mathcal{F}_2^{-1}[G(\xi,\theta)]$$
$$=\mathcal{F}_2^{-1}[\mathcal{F}_1 g(s,\theta)]. \tag{14}$$

If $G(\xi,\theta)$ was known for all ξ and θ, then $F(\xi_x,\xi_y)$ would be known at all points in the $\xi_x\xi_y$ plane, and so the image (or object function) $f(x,y)$ could be recovered using the two-dimensional inverse Fourier transform:

$$f(x,y)\equiv\int_{-\infty}^{\infty}\int_{-\infty}^{\infty}F(\xi_x,\xi_y)\exp[j2\pi(\xi_x x+\xi_y y)]d\xi_x d\xi_y. \tag{15}$$

V. RESULTS OF DIGITALLY IMPLEMENTING THE RECONSTRUCTION ALGORITHMS

Computerized tomography based on analytic reconstruction methods[3] uses either the inverse Radon transform or the two-dimensional Fourier transform to solve the projection equation: $g(s,\theta)=\int_{s,\theta}f(x,y)ds_\perp$ for $f(x,y)$.

A. Inverse Radon transform

The various forms of the inverse Radon transform are summarized by:

Filtered backprojection

$$\Rightarrow f(x,y)=\mathcal{R}^{-1}g(s,\theta)=\mathcal{B}\mathcal{F}_1^{-1}[|\xi|\mathcal{F}_1 g(s,\theta)], \tag{16a}$$

Convolution backprojection

$$\Rightarrow f(x,y)=\mathcal{R}^{-1}g(s,\theta)=\mathcal{B}\left\{\frac{1}{2\pi^2 s}*\mathcal{D}g(s,\theta)\right\} \tag{16b}$$

$$\Rightarrow f(x,y)=\mathcal{R}^{-1}g(s,\theta)=\mathcal{B}\left\{\frac{-1}{2\pi^2 s^2}*g(s,\theta)\right\}. \tag{16c}$$

When $G(\xi,\theta)$ is known for all ξ and θ, a perfect inverse of the simulated projection information for the elliptical cylinder can be obtained using any form of the inverse Radon transform. However, this is not the case when the reconstruction algorithm is implemented digitally (as in practice). Figures 2(c) and (d) show the results of shape reconstruction of the elliptical cylinder using digital implementations of Eqs. 16(a) and (b), respectively; a similar result (not shown here) to Fig. 2(d) is obtained for the digital implementation of Eq. 16(c). Again, for the *shape reconstruction* example: $g(s,\theta)=A(s,\theta)$ and $f(x,y)=h(x,y)$. The reconstructed shape is imperfect in each case due to the effect of aliasing, which is observed in Figs. 2(c) and (d) as finite intensity values (which, ideally, should be zero) around the periphery of the ellipse.

However, the aliasing problem that arises when functions of infinite extent, specifically $H(\xi)=|\xi|$ and its Fourier transform $h(s)=-1/2\pi^2 s^2$, are sampled at discrete intervals can be avoided by using a low-pass filtering function when computing the filtered projections. The impulse response of the filter need only to have the same spatial frequency bandwidth as the projection data. If the highest spatial frequency of the projections is $\xi_{\max}$, then the low-pass filtered projection at an angle θ is given by

$$\tilde{g}_{\xi,b}(s,\theta)=\int_{-\infty}^{\infty}H_b(\xi)G(\xi,\theta)\exp[j2\pi\xi s]d\xi, \tag{17}$$

where

$$H_b(\xi)=|\xi|b_{\hat{\xi}}(\xi),$$

and

$$b_{\hat{\xi}}(\xi)=1 \text{ when } |\xi|<\xi_{\max} \quad \text{otherwise, } b_{\hat{\xi}}(\xi)=0. \tag{18}$$

The impulse response $h_b(s)$ of the filter $H_b(\xi)=|\xi|b_{\hat{\xi}}(\xi)$ is given by[1]

$$h_b(s)=\int_{-\infty}^{\infty}H_b(\xi)\exp[j2\pi\xi s]d\xi$$
$$=\frac{1}{2\tau_s^2}\mathrm{sinc}(2\alpha)-\frac{1}{4\tau_s^2}[\mathrm{sinc}(\alpha)]^2, \tag{19}$$

where

$$\mathrm{sinc}(\alpha)=\frac{\sin(\alpha)}{\alpha}, \quad \alpha=\frac{\pi s}{2\tau_s}.$$

In accordance with the sampling theorem, there will be no aliasing if the projections $g(s,\theta)$ and impulse response $h_b(s)$ are sampled at intervals of $\tau_s=1/(2\xi_{\max})$. The samples of $h_b(s)$ are given by[1,2]

$$h_b(n\tau_s)=\frac{1}{4\tau_s^2} \quad \text{for } n=0; \tag{20a}$$

$$h_b(n\tau_s)=\frac{-\sin^2(n\pi/2)}{n^2\pi^2\tau_s^2} \quad \text{for } n\neq 0. \tag{20b}$$

From Eq. (20b),

$$h_b(n\tau_s)=0 \text{ for } n \text{ even};$$
$$h_b(n\tau_s)=-1/n^2\pi^2\tau_s^2 \text{ for } n \text{ odd}.$$

The discrete convolution of the sampled projection data $g(m\tau_s,\theta)$ with the discrete impulse response $h_b(n\tau_s)$ is implemented in the frequency domain using the fast Fourier transform. This requires $g(m\tau_s,\theta)$ and $h_b(n\tau_s)$ to be zero padded by a factor of 2 prior to Fourier transformation, so as to minimize the interperiod interference artifacts inherent in periodic (or circular) convolution. This method of implementing the inverse Radon transform greatly reduces the effects of aliasing when the image is reconstructed from the sampled projection data. For example, Fig. 2(e) shows the result of applying this method to reconstruct the shape of the elliptical cylinder; the leakage evident in Figs. 2(c) and (d) has been greatly reduced and the discontinuity that occurs at the boundary of the ellipse is well defined.

B. Fourier reconstruction

The Fourier reconstruction method is implemented by filling the two-dimensional Fourier space with the one-dimensional Fourier transforms of the projections $G(\xi,\theta)$

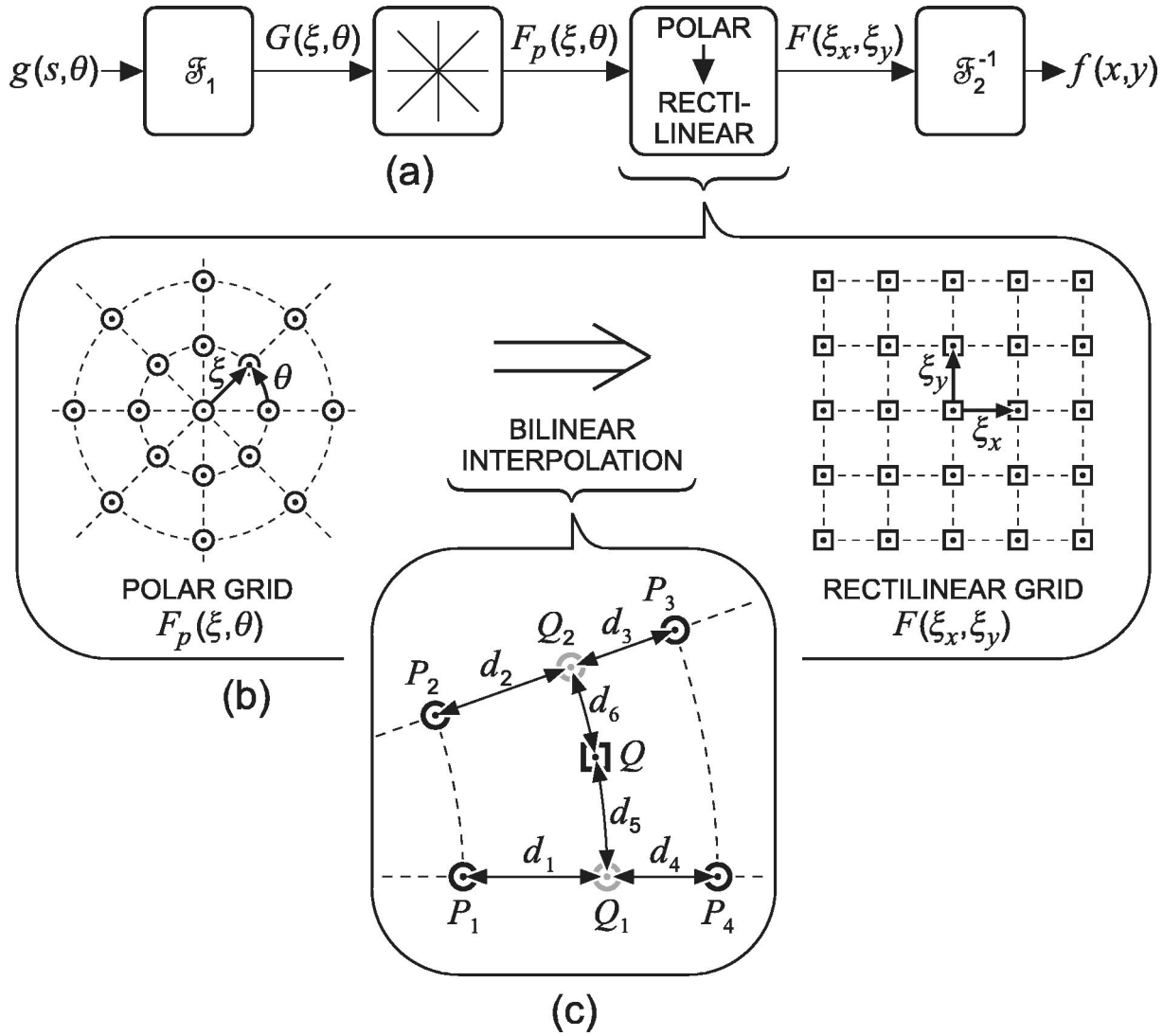

FIG. 3. (a) Fourier reconstruction method for estimating the two-dimensional distribution of the object function. The spatial projection data are windowed and zero padded prior to Fourier transformation. The Fourier space is filled with one-dimensional Fourier transforms of the complete set of projections. Bilinear interpolation is used to map the wave number spectrum from a polar to a rectangular grid, prior to computing a two-dimensional inverse Fourier transform to recover the image. (b) Mapping the wave number data from a polar to a rectangular grid. The Fourier domain data $F_p(\xi,\theta)$ that are available on a polar raster are interpolated using bilinear interpolation to provide estimates of the Fourier coefficients $F(\xi_x,\xi_y)$ on a rectangular raster. (c) Bilinear interpolation at Q using the data from the neighboring points: P_1, P_2, P_3, and P_4.

$=\mathcal{F}_1 g(s,\theta)$, and then converting from a polar raster to a rectangular raster $G(\xi,\theta)\equiv F_p(\xi,\theta)\Rightarrow F(\xi_x,\xi_y)$, prior to taking the two-dimensional inverse Fourier transform $\mathcal{F}_2^{-1}[F(\xi_x,\xi_y)]$—see Fig. 3(a). By taking the projections of an object function at different angles θ_m, $m=1,...,M$ and Fourier transforming each of these projections, the values of $F_p(\xi,\theta)$ can be plotted on radial lines as shown in Fig. 3(b). Since, in practice, only a finite number of projections (M) can be taken, then the Fourier coefficients $F(\xi_x,\xi_y)$ are only known along a finite number of radial lines as depicted in Fig. 3(b). The two-dimensional inverse Fourier transform requires the values of the Fourier coefficients at the uniformly spaced data points of a rectangular grid. Populating the rectangular grid with estimates of the Fourier coefficients is achieved through bilinear interpolation[14] of the radial point data that are available on a polar raster—see Fig. 3(c). Since the density of the radial points becomes sparser as the radial distance from the center of the polar raster increases, the interpolation error increases with radial distance. Figure 4 shows that the radial sampling interval $\delta\xi_r=2\xi_{\max}/N$, where N is the total number of independent wave number sampling points uniformly distributed along a diameter with a spacing of $\delta\xi_r$. Note that N is also the number of sampling points in each projection, where the projections are sampled at intervals of $\tau_s=1/(2\xi_{\max})$ without introducing any aliasing errors. The distance between adjacent sampling points on the periphery of the disc represents the largest azimuthal sampling interval $\delta\xi_\theta=\xi_{\max}\Delta\theta=2\pi\xi_{\max}/M$, where M is the total number of projections that are uniformly distributed over 360° with an angular increment of $\Delta\theta$. A large number of projections is required to reconstruct an image. For example, $M=\pi N$ projections are required for the largest azimuthal sampling interval $\delta\xi_\theta$ to be the same as the radial sampling interval $\delta\xi_r$. When there is an insufficiency of data either through undersampling of the projection data or because not

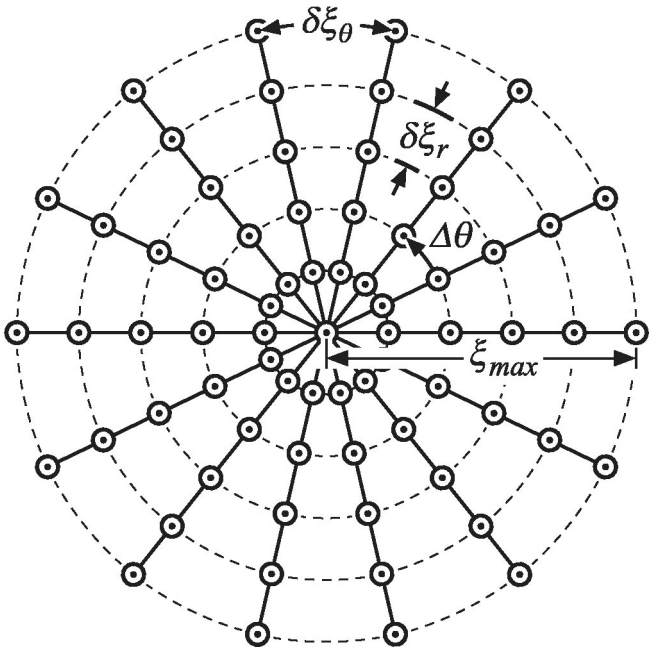

FIG. 4. Diagram showing the radial and azimuthal sampling intervals on a polar raster representation of the wave number data.

enough projections are recorded, errors arise that lead to aliasing distortions of the reconstructed image.

With the digital implementation of the Fourier reconstruction method, the sampled projection data are windowed with a Kaiser–Bessel function and zero padded, prior to the Fourier transformation that computes the discrete components of the wave number spectrum. Windowing is applied to the projection data to minimize the effect of spatial domain truncation that would otherwise lead to spectral leakage in the wave number domain.

The complications generated by the function $|\xi|$ are avoided with the Fourier reconstruction method by mapping the wave number data to a rectangular grid, which automatically compensates for the increasing sparseness of the data as the radial wave number increases. The Fourier reconstruction method is the preferred method that is adopted in this paper for image reconstruction from projections. For example, Fig. 2(f) shows the shape of the elliptical cylinder formed by the Fourier reconstruction method.

VI. RECONSTRUCTION WITH BANDPASS DATA

The above-presented formulation assumes the transmitted signal is an impulse, that is, $g(s,\theta)$ is the impulse response of the imaging system at the look direction θ. However, in practice, high-frequency sonars transmit bandpass signals. In this case, the projection at the look direction θ is given by $g(s,\theta)*p(s)$, where $p(s)$ is the transmitted signal. To demonstrate the effect of bandpass signals on tomographic reconstruction, simulated data for the elliptical cylinder are bandpass filtered (by applying a Kaiser–Bessel filter in the wave number domain). In the following examples, the bandwidth $\xi_b = 0.4\xi_0$, where ξ_0 is the center frequency. The filtered wave number response at a projection angle θ is given by

$$G_{\mathrm{bp}}(\xi,\theta) = G(\xi,\theta)H_{\mathrm{bp}}(\xi) = G(\xi,\theta)\{H_{\mathrm{lp}}(\xi)*([\,\delta(\xi-\xi_0) + \delta(\xi+\xi_0)]/2)\}, \tag{21}$$

where $H_{\mathrm{bp}}(\xi)$ and $H_{\mathrm{lp}}(\xi)$ denote the transfer functions of bandpass and low-pass wave number filters (respectively). The inverse wave number transform of Eq. (21) gives the spatial response

$$g_{\mathrm{bp}}(s,\theta) = g(s,\theta)*h_{\mathrm{bp}}(s) = g(s,\theta)*\{h_{\mathrm{lp}}(s)\cos(2\pi\xi_0 s)\}, \tag{22}$$

where $h_{\mathrm{bp}}(s) \Leftrightarrow H_{\mathrm{bp}}(\xi)$ and $h_{\mathrm{lp}}(s) \Leftrightarrow H_{\mathrm{lp}}(\xi)$.

The shape that is formed by processing the bandpass data is shown in Fig. 5(a). The bandpass filter removes the low spatial frequency components associated with the interior of the cylinder. The shape is dominated by the high spatial frequency components associated with the discontinuity at the boundary. The bandpass filter also removes higher spatial frequency components, which results in smearing of the reconstructed image. The oscillation observed in the image is due to the bandpass nature of the data. This oscillation is removed by first eliminating the negative frequency components to form the analytic signal, $g_+(s,\theta)$, or preenvelope of $g_{\mathrm{bp}}(s,\theta)$, which is given by

$$g_+(s,\theta) = g_{\mathrm{bp}}(s,\theta) + j\mathcal{H}\{g_{\mathrm{bp}}(s,\theta)\} = g_\alpha(s,\theta)\exp(j2\pi\xi_0 s), \tag{23}$$

where $g_\alpha(s,\theta)$ is the complex envelope that is equal to a frequency-shifted version of the analytic signal; the complex envelope is a complex low-pass signal.[15] Figure 5(b) shows $a(x,y)$, which is the estimate of the height function, $h(x,y)$, formed by processing the magnitude of the complex envelope, $|g_\alpha(s,\theta)|$, or equivalently, the magnitude of the analytic signal, $|g_+(s,\theta)|$. Although the oscillation has been suppressed, there is a strong response associated with the discontinuity at the edge of the cylinder. The interior of the cylinder is dished because its flat shape cannot be adequately represented in the absence of the low spatial frequency components. The use of the magnitude of the complex envelope tends to smear the boundary defined by the discontinuity, thus degrading the estimate of the shape function.

A postprocessing method, which proved useful when applied to real data (see Sec. VII), finds the gradient of the reconstructed object function; this approach is similar to applying a high-pass filter to the reconstructed object function. The gradient is given by

$$a_{\mathrm{grad}}(x,y) = \{(\partial a(x,y)/\partial x)^2 + (\partial a(x,y)/\partial y)^2\}^{1/2}. \tag{24}$$

The derivative $\partial a(x,y)/\partial x$ is formed by first taking the Fourier transform with respect to x of the reconstructed object function. The transformed data are then multiplied by[16] $j2\pi\xi_x$ prior to taking the inverse transform with respect to ξ_x, where ξ_x is the wave number in the x direction. Repeating the same operations with respect to y forms the derivative $\partial a(x,y)/\partial y$. The estimate $a_{\mathrm{grad}}(x,y)$ that is formed by combining these two derivatives in accordance with Eq. (24) is shown in Fig. 5(c).

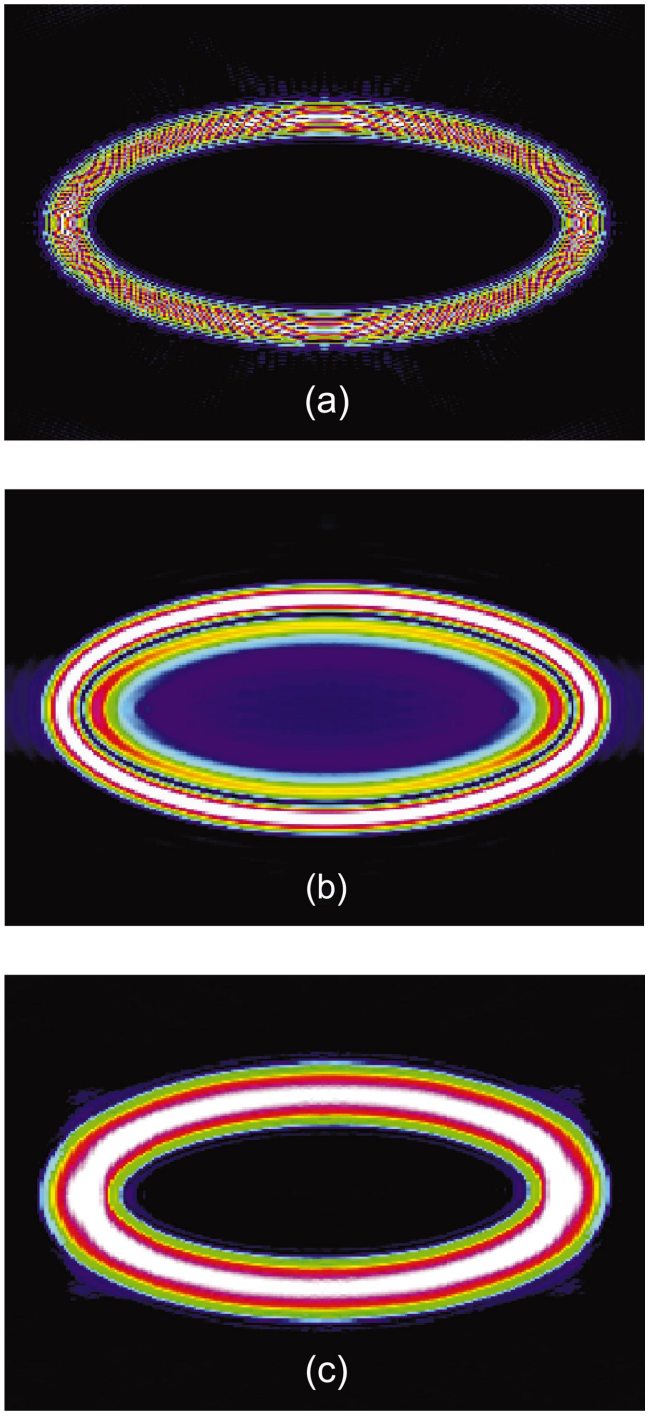

FIG. 5. (a) Fourier reconstruction of the shape of an elliptical cylinder using bandpass filtered data: $g_{\mathrm{bp}}(s,\theta)=\{g(s,\theta)\}*\{h_{\mathrm{lp}}(s)\cos(2\pi\xi_0 s)\}$. (b) Similar to (a) but for $|g_{\alpha}(s,\theta)|$, which is equivalent to the modulus of the analytic signal. (c) Image showing the two-dimensional spatial distribution of $a_{\mathrm{grad}}(x,y)=\{(\partial a(x,y)/\partial x)^2+(\partial a(x,y)/\partial y)^2\}^{1/2}$, where $a(x,y)$ is the amplitude of a point (pixel) with coordinates (x,y) for the image shown in (b).

VII. IMAGE RECONSTRUCTIONS USING REAL SONAR DATA

A monostatic sonar experiment was conducted in a dam to reconstruct the images of three different objects (exercise mines). A distance of 60 m separated the sonar and object to be imaged. The wideband sonar transducer had a bandwidth of 100 kHz and a center frequency of 150 kHz. The transducer was fixed and the object rotated through one complete revolution. The transmitted sonar signals consisted of linear period modulation (LPM) wave forms of 16 ms duration and the processing of the received signals involved pulse compression, band shifting to base band, and alignment to compensate for lateral motion (translation) between the source and the object. Note that LPM is also commonly referred to as hyperbolic frequency modulation.[17]

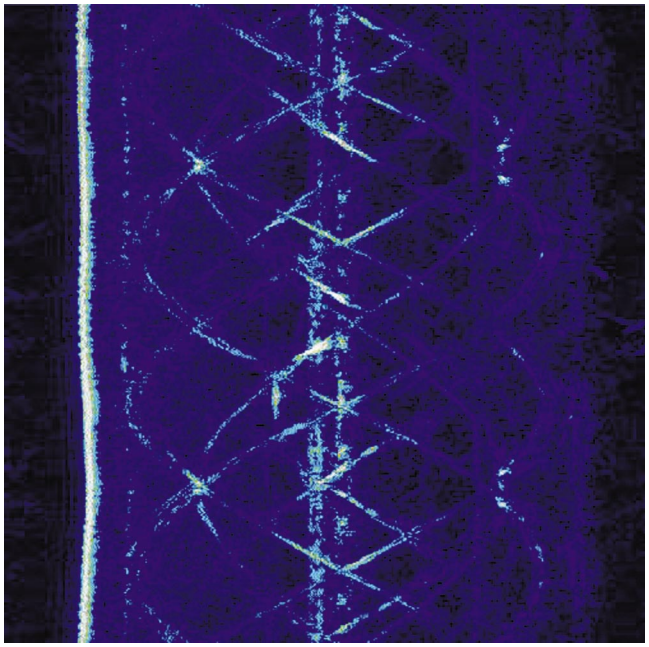

FIG. 6. Intensity plot of the measured projection data $g(s,\theta)$ for the first object; s is the abscissa and θ is the ordinate.

When applying the principles of computerized tomography to reconstruct a reflectivity map using sonar signals reflected from real objects, there is a paucity of information that is measured from the shadow side of the object. A set of projections is synthesized that includes information from both sides of the object by combining the signals received from insonification positions that are displaced by 180°. This requires compensation for time reversal and delay, which can be applied as part of the preprocessing.

Figure 6 shows an intensity plot of the received sonar signal from the first object, which (after transformation of the time variable to the spatial variable: $ct/2\rightarrow s$) is equivalent to the variation of the spatial impulse response as a function of s (horizontal axis) and θ (vertical axis). The aspect angle (or angle of insonification θ) was measured using the difference in the time of arrival of the received signal at two spatially separated hydrophones attached to wire cables that suspended the object in the underwater medium during its rotation. Approximately 1000 views of each object were recorded during its rotation with the angular increment $\Delta\theta$ between projections being 0.35°. Two distinct types of features can be identified in Fig. 6: those tracing a sinusoidal pattern in the display are point reflectors which are visible over a wide range of aspect angles and the other features are due to specular reflections for which the reflecting surface is normal to the incident wave. The positions of the reflectors with this (latter) property are aspect angle dependent. For

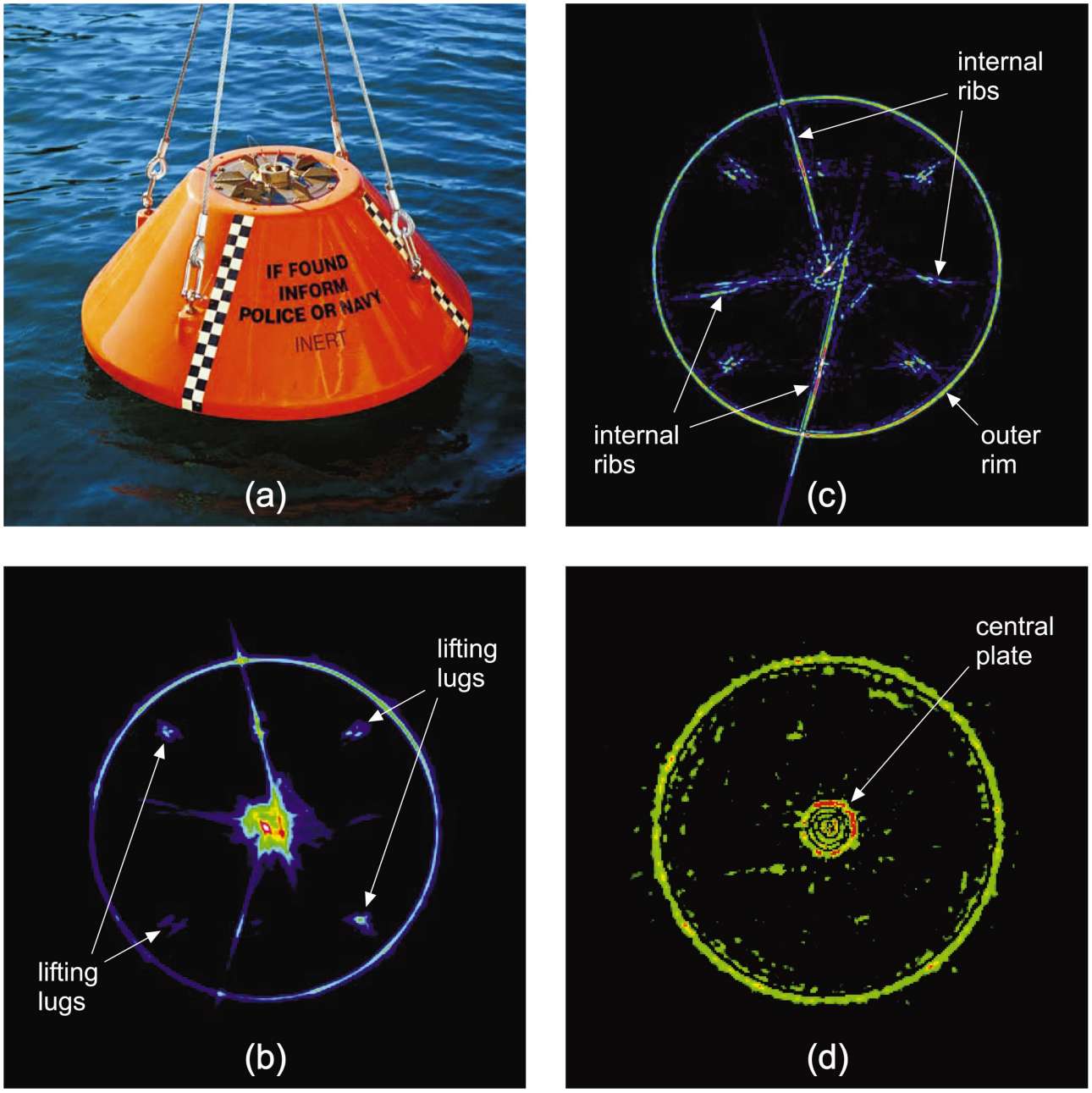

FIG. 7. (a) Optical image of the first object. (b) Acoustic image reconstructed from backprojection of the 150 kHz sonar data shown in Fig. 6. (c) Image formed using the Fourier reconstruction method for the 150 kHz sonar data. (d) Similar to (c) but for the 40 kHz sonar data.

this particular object, the arrival time of the specular reflections is (approximately) constant, which is indicative of a radially symmetric object; this was not the case for the other two objects that were imaged in the experiment.

Figure 7(a) shows a photograph of the object, which is a fiberglass exercise mine shaped as a truncated cone of height 0.5 m with the diameter of the base being 1 m. The acoustic images that are displayed subsequently are analogous to viewing the object from above, that is, the acoustic image is a plan view of the object. Figure 7(b) shows the image formed by backprojecting the projection data shown in Fig. 6; the mathematical representation of the backprojection operation is $b(x,y)=\mathcal{B}g(s,\theta)$—see Eq. (8). Note that backprojection is equivalent to synthetic aperture sonar processing when the synthetic aperture is a circle with a known center position; the function $b(x,y)$ is then the estimate of the reflectivity function. In this image, the discrete scattering points represented by the four lifting lugs are prominent as is the specular reflection from the boundary that coincides with the outer rim of the object. Other acoustic highlights are observed at the center of the circle (which is associated with the end plate mounted on the top surface of the truncated cone) and between the lifting lug highlights (which correspond to the internal ribs of the exercise mine). Figure 7(c) shows the image formed by the Fourier reconstruction method. The acoustic image shows the projection of the object's geometrical shape and acoustic highlights on the imaging plane. The experiment was repeated using another low frequency wideband sonar transducer for which the center frequency and bandwidth were both 40 kHz. The tomogra-

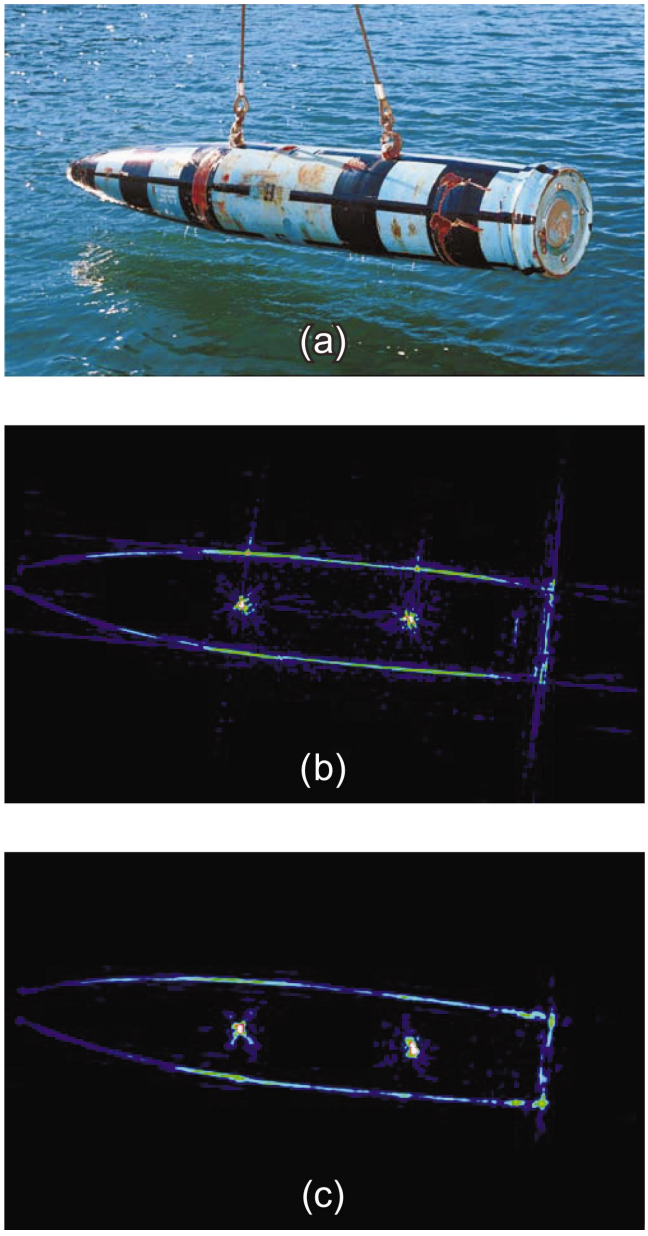

FIG. 8. (a) Optical image of the second object. (b) Image formed using the Fourier reconstruction method for the 150 kHz sonar data. (c) Similar to (b) but for the 40 kHz sonar data.

phic image is shown in Fig. 7(d). Both images reveal the radially symmetric shape of the object but the prominence of the acoustic highlights is different.

A photograph of the second object, which is a 2000 lb bomb, is shown in Fig. 8(a). The tomographic images reconstructed from high-frequency bandpass sonar data using the Fourier reconstruction method are shown in Fig. 8(b) for the 150 kHz transducer and Fig. 8(c) for the 40 kHz transducer.

Figure 9(a) is a photograph of the third object, which is a smaller (500 lb) bomb equipped with four fins that form an air-brake when it is dropped from an aircraft. The acoustic image (not shown here) formed by Fourier reconstruction had a very large dynamic range due to the corner reflectors formed by the fins, which produced leakage that obscured the shape of the bomb. Only the nose of the bomb was discernible from the bright background, which blanked out the rest of the bomb. A postprocessing method that computes the gradient of the image formed by Fourier reconstruction enables the shape of the bomb and the fins to be observed. Figure 9(b) shows the two-dimensional spatial gradient function $a_{\text{grad}}(x,y)$ of the Fourier reconstructed image $a(x,y)$ for the 150 kHz sonar data. The image shows a plan view of the fins and the outline of the bomb's geometrical shape. This image gradient approach provides a representation that enables this object to be recognized.

VIII. CONCLUSIONS

Tomographic imaging deals with reconstructing the image of an object from its projections measured at all angles. The principles of computerized tomography are applicable to high-resolution sonar imaging of underwater objects. Rather than using inverse Radon transform methods that involve either filtered or convolution backprojection, the two-dimensional Fourier reconstruction method is preferred for acoustic image formation. The image that is reconstructed using high-frequency bandpass sonar data shows the outline of the object's geometrical shape and the relative positions of any acoustic highlights. Since the acoustic information is projected on the imaging plane, the reconstructed image represents a plan view of the object.

ACKNOWLEDGMENTS

The authors gratefully acknowledge the contributions to this paper of the Maritime Operations Division's High-Frequency Sonar Trials Team: John Shaw, Gary Speechley, Chris Halliday, Jane Cleary, Ross Susic, Neil Tavener, Mark Savage, and Adrian Head. Also, the authors acknowledge the technical discussions on acoustic backscattering with Dr. Stuart Anstee and sonar signal processing with Dr. Kam Lo; both are with the Defense Science and Technology Organization (Sydney). This research was supported by the Australian Defense Organization's Capability Technology Demonstrator Program (DMO Project SEA 1436) for an advanced mine hunting sonar system.

APPENDIX A: THE SONAR SIGNAL REFLECTED FROM AN ELLIPTICAL CYLINDER

The impulse response for electromagnetic plane waves backscattered from perfectly conducting objects can be estimated using physical optics.[18] By analogy, the impulse response wave forms of sonar signals backscattered from perfectly rigid objects can be readily predicted. Consider a rigid elliptical cylinder of height $z=h$. The signal received by a monostatic sonar as it circumnavigates the object in the xy plane is given by

$$g(s,\theta) = -\frac{1}{4\pi}\frac{\partial^2 A(s,\theta)}{\partial s^2} = \frac{-h}{4\pi}\frac{\partial^2 w(s,\theta)}{\partial s^2}$$

$$= \frac{h}{2\pi}\frac{ab}{(s_m^2 - s^2)^{3/2}}, \quad |s| < s_m$$

$$= 0, \quad |s| \geqslant s_m \tag{A1}$$

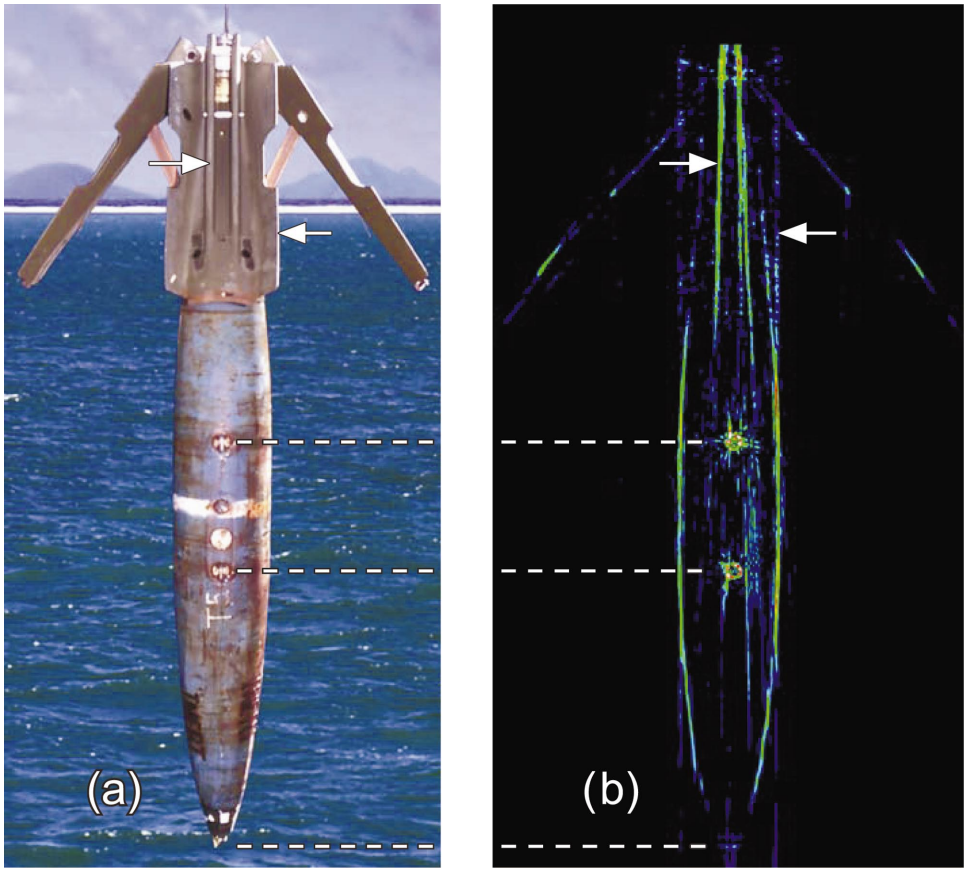

FIG. 9. (a) Optical image of the third object. (b) Image showing the two-dimensional spatial gradient function $a_{\text{grad}}(x,y)$ for the 150 kHz sonar data.

where $s_m^2 = a^2 \cos^2\theta + b^2 \sin^2\theta$, $A(s,\theta)$ is the area of the scatterer surface normal to the incident wave and $w(s,\theta)$ is a cross-sectional width of the object. In Fig. A1, $w(s,\theta)$ is the distance between the points P and Q along the wave front; it is the length of the segment of the wave front that intercepts the object and is given by

$$w(s,\theta) = \frac{2ab\sqrt{s_m^2 - s^2}}{s_m^2}. \tag{A2}$$

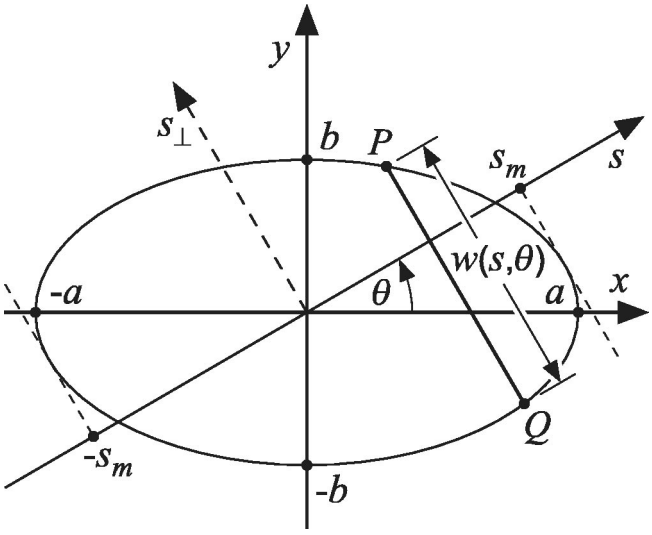

FIG. A1. Geometry of the ellipse.

APPENDIX B: MATHEMATICAL FRAMEWORK FOR COMPUTERIZED TOMOGRAPHY

1. Projection slice theorem

The projection slice theorem[2] (also known as the Fourier slice theorem) summarizes the fundamental relationship between the two-dimensional Fourier transform of an object function and the one-dimensional Fourier transform of its Radon transform and provides the theoretical basis for the various image reconstruction algorithms. The one-dimensional Fourier transform with respect to s of the projection $g(s,\theta)$ is equal to the central slice, at the angle θ, of the two-dimensional Fourier transform of the object function $f(x,y)$, that is, if $g(s,\theta) \Leftrightarrow G(\xi,\theta)$, then

$$G(\xi,\theta) = F_p(\xi,\theta) \equiv F(\xi_x = \xi\cos\theta, \xi_y = \xi\sin\theta).$$

Proof: By definition,

$$G(\xi,\theta) \equiv \int_{-\infty}^{\infty} g(s,\theta)\exp(-j2\pi\xi s)\,ds.$$

Using Eq. (4),

$$G(\xi,\theta) = \int_{-\infty}^{\infty}\int_{-\infty}^{\infty} f(s\cos\theta - s_\perp \sin\theta, s\sin\theta + s_\perp\cos\theta)\exp(-j2\pi\xi s)\,ds\,ds_\perp.$$

Using Eq. (3a) for the coordinate transformation: $(s,s_\perp) \Rightarrow (x,y)$,

$$G(\xi,\theta)=\int_{-\infty}^{\infty}\int_{-\infty}^{\infty}f(x,y)\exp[-j2\pi(x\xi\cos\theta + y\xi\sin\theta)]dx\,dy \equiv F(\xi\cos\theta,\xi\sin\theta)$$

or

$$G(\xi,\theta)=\int_{-\infty}^{\infty}\int_{-\infty}^{\infty}f(x,y)\exp[-j2\pi(\xi_x x+\xi_y y)]dx\,dy \equiv F(\xi_x,\xi_y).$$

2. Inverse Radon transform theorem

The two-dimensional inverse Fourier transform is defined as

$$f(x,y)\equiv\int_{-\infty}^{\infty}\int_{-\infty}^{\infty}F(\xi_x,\xi_y)\exp[j2\pi(\xi_x x+\xi_y y)]d\xi_x d\xi_y,$$

or, in polar coordinates,[19]

$$f(x,y)\equiv\int_0^{2\pi}\int_0^{\infty}F_p(\xi,\theta)\times\exp[j2\pi\xi(x\cos\theta+y\sin\theta)]\xi d\xi d\theta.$$

Changing the limits of integration, allowing ξ to be negative, restricting $\theta\in(0,\pi)$ and noting,

$$F_p(\xi,\theta)=G(\xi,\theta),\quad F_p(\xi,\theta+\pi)=G(-\xi,\theta),$$

then

$$f(x,y)=\int_0^{\pi}\left\{\int_{-\infty}^{\infty}|\xi|G(\xi,\theta)\times\exp[j2\pi\xi(x\cos\theta+y\sin\theta)]d\xi\right\}d\theta,$$

$$f(x,y)=\int_0^{\pi}\left\{\int_{-\infty}^{\infty}|\xi|G(\xi,\theta)\exp[j2\pi\xi s]d\xi\right\}d\theta = \int_0^{\pi}\tilde{g}_{\xi}(s,\theta)d\theta,$$

where

$$\tilde{g}_{\xi}(s,\theta)=\int_{-\infty}^{\infty}|\xi|G(\xi,\theta)\exp[j2\pi\xi s]d\xi = \mathcal{F}_1^{-1}[|\xi|G(\xi,\theta)].$$

Writing $|\xi|G(\xi,\theta)$ as $\xi G(\xi,\theta)\mathrm{sgn}(\xi)$ and applying the convolution theorem, gives

$$\tilde{g}_{\xi}(s,\theta)=[\mathcal{F}_1^{-1}\{\xi G(\xi,\theta)\}]*[\mathcal{F}_1^{-1}\{\mathrm{sgn}(\xi)\}] = \left[\frac{[(\partial g(s,\theta)/\partial s)]}{j2\pi}\right]*\left(\frac{-1}{j\pi s}\right)$$

and so,

$$\tilde{g}_{\xi}(s,\theta)=\left(\frac{1}{2\pi^2}\right)\int_{-\infty}^{\infty}\left[\frac{\partial g(s',\theta)}{\partial s'}\right]\frac{1}{s-s'}ds' = \frac{1}{2\pi}\mathcal{H}\left\{\frac{\partial g(s,\theta)}{\partial s}\right\}.$$

Finally,

$$f(x,y)=\int_0^{\pi}\tilde{g}_{\xi}(s,\theta)d\theta = \int_0^{\pi}\left(\frac{1}{2\pi^2}\right)\int_{-\infty}^{\infty}\left[\frac{\partial g(s',\theta)}{\partial s'}\right]\frac{1}{s-s'}ds'd\theta,$$

and so,

$$f(x,y)=\mathcal{R}^{-1}g(s,\theta) = \left(\frac{1}{2\pi^2}\right)\int_0^{\pi}\int_{-\infty}^{\infty}\frac{[(\partial g(s,\theta)/\partial s)]}{x\cos\theta+y\sin\theta-s}ds\,d\theta.$$

Given $g(s,\theta)=\mathcal{R}f(x,y)$, $-\infty<s<\infty$, $0\leqslant\theta<\pi$, its inverse Radon transform is

$$f(x,y)=\mathcal{R}^{-1}g(s,\theta) = \left(\frac{1}{2\pi^2}\right)\int_0^{\pi}\int_{-\infty}^{\infty}\frac{[(\partial g(s,\theta)/\partial s)]}{x\cos\theta+y\sin\theta-s}ds\,d\theta = \left(\frac{1}{2\pi}\right)\mathcal{B}\mathcal{H}\mathcal{D}g(s,\theta).$$

Note that $\tilde{g}_{\xi}(s,\theta)$ is the Hilbert transform of

$$\left(\frac{1}{2\pi}\right)\frac{\partial g(s,\theta)}{\partial s}\ \text{ for each }\ \theta.$$

Other forms of the inverse Radon transform are given by:

Filter backprojection

$$\Rightarrow f(x,y)=\mathcal{R}^{-1}g(s,\theta)=\mathcal{B}\mathcal{F}_1^{-1}[|\xi|\mathcal{F}_1 g(s,\theta)].$$

Convolution backprojection

$$\Rightarrow f(x,y)=\mathcal{R}^{-1}g(s,\theta)=\mathcal{B}\{\mathcal{F}_1^{-1}|\xi|*g(s,\theta)\},$$

that is

$$f(x,y)=\mathcal{B}\left\{\frac{-1}{2\pi^2 s^2}*g(s,\theta)\right\},$$

or

$$f(x,y)=\mathcal{B}\left\{\frac{-1}{2\pi^2 s}*\mathcal{D}g(s,\theta)\right\}.$$

Note:

$$\mathcal{F}_1^{-1}|\xi|=\mathcal{F}_1^{-1}\{(j\xi)(-j\,\mathrm{sgn}\,\xi)\}=\frac{1}{2\pi}\frac{\partial}{\partial s}\left(\frac{1}{\pi s}\right)=\frac{-1}{2\pi^2 s^2}.$$

[1] A. C. Kak and M. Slaney, *Principles of Computerized Tomographic Imaging* (IEEE Press, New York, 1988).

[2] A. K. Jain, *Fundamentals of Digital Image Processing* (Prentice-Hall, Englewood Cliffs, NJ, 1989).

[3] R. A. Brooks and G. Di Chiro, "Principles of computer assisted tomography (CAT) in radiographic and radio isotopic imaging," Phys. Med. Biol. **21**, 689–732 (1976).
[4] A. C. Kak, "Computerized tomography with X-ray, emission and ultrasound sources," Proc. IEEE **67**, 472–499 (1979).
[5] G. T. Herman, *Image Reconstruction from Projections—The Fundamentals of Computerized Tomography* (Academic, New York, 1980).
[6] M. Soumekh, *Synthetic Aperture Radar Signal Processing* (Wiley, New York, 1999).
[7] E. Belcher, B. Matsuyama, and G. Trimble, "Object identification with acoustic lenses," Proceedings OCEANS 2001, Honolulu, HI, 2001, Vol. 1, pp. 6–11.
[8] R. Vesetas and G. Manzie, "AMI: A 3-D imaging sonar for mine identification in turbid waters," Proceedings OCEANS 2001, Honolulu, HI, 2001, Vol. 1, pp. 12–20.
[9] Y. Doisy, "Application of tomographic reconstruction to target identification," Undersea Defence Technology '88, London, 433–438 (1988).
[10] P. H. Pidsley, R. A. Smith, and G. L. Davies, "Reconstruction of sonar images using computerized tomography," IEE Colloquium on Recent Developments in Radar and Sonar Imaging Systems, 4/1—9 (1995).
[11] Note that $g(s,\theta)=\int_{s,\theta} f(x,y)ds_{\perp}$ is equivalent to the Radon transform of the function $f(x,y)$.
[12] The *Hilbert transform* of a function $\sigma(t)$ is defined as $\mathcal{H}\sigma(t)=\sigma(s)*(1/\pi s)=(1/\pi)\int_{-\infty}^{\infty}[\sigma(s')/s-s']ds'$.
[13] The *derivative operator* is defined as $\mathcal{D}\sigma(s)=\partial\sigma(s)/\partial s$.
[14] In Fig. 3(c), the value $F(Q)$ for the point Q on the rectangular grid is calculated using bilinear interpolation of the known values $F(P_1)$, $F(P_2)$, $F(P_3)$, and $F(P_4)$ of the neighboring radial data points P_1, P_2, P_3 and P_4 on the polar grid: $F(Q)=[F(Q_1)d_6+F(Q_2)d_5]/(d_5+d_6)$, where $F(Q_1)=[F(P_1)d_4+F(P_4)d_1]/(d_1+d_4)$ and $F(Q_2)=[F(P_2)d_3+F(P_3)d_2]/(d_2+d_3)$.
[15] S. Haykin, *Communication Systems*, 3rd ed (Wiley, New York, 1994).
[16] Differentiation of a spatial domain function, $g(s)$, has the effect of multiplying its Fourier transform, $G(\xi)$, by the factor $j2\pi\xi$. Assuming that the Fourier transform of the higher-order derivatives exists, then $(d^n/ds^n)g(s)\Leftrightarrow(j2\pi\xi)^nG(\xi)$, where $\Leftrightarrow$ denotes a Fourier transform pair.
[17] M. I. Skolnik, *Introduction to Radar Systems*, 3rd ed. (McGraw-Hill, New York, 2001).
[18] E. M. Kennaugh and D. L. Moffatt, "Transient and impulse response approximations," Proc. IEEE **53**, 893–901 (1965).
[19] The Jacobian for the coordinate transformation: $(\xi_x,\xi_y)\Rightarrow(\xi,\theta)$ is equal to ξ.

Hilbert space inverse wave imaging in a planar multilayer environment

Sean K. Lehman[a)]
Lawrence Livermore National Laboratory, L-154, 7000 East Avenue, Livermore, California 94550

(Received 10 November 2004; revised 26 January 2005; accepted 1 February 2005)

Most diffraction tomography (DT) algorithms use a homogeneous Green function (GF) regardless of the medium being imaged. This choice is usually motivated by practical considerations: analytic inversions in standard geometries (Cartesian, spherical, etc.) are significantly simplified by the use of a homogeneous GF, estimating a nonhomogeneous GF can be very difficult, as can incorporating a nonhomogeneous GF into standard DT algorithms. Devaney has circumvented these issues by developing a purely numerical DT inversion algorithm [A. J. Devaney and M. Dennison, Inverse Probl. **19**, 855–870 (2003)] that is independent of measurement system geometry, number of frequencies used in the reconstruction, and GF. A planar multilayer GF has been developed for use in Devaney's ''Hilbert space'' algorithm and used in a proof-of-principle nondestructive evaluation (NDE) experiment to image noninvasively a flaw in an aluminum/copper planar multilayer medium using data collected from an ultrasonic measurement system. The data were collected in a multistatic method with no beamforming: all focusing through the multilayer was performed mathematically ''after-the-fact,'' that is, after the data were collected. [DOI: 10.1121/1.1879172]

PACS numbers: 43.60.Pt, 43.60.Ac, 43.35.Zc [ELS] Pages: 2929–2936

I. INTRODUCTION

Most diffraction tomography (DT) algorithms use a homogeneous Green function (GF) regardless of the medium being imaged. This choice is motivated by practical considerations: analytic inversions in ''nice'' (planar, circular, spherical, etc.) geometries are significantly simplified by the use of a homogeneous GF which has convenient decompositions in those coordinate systems, and, estimating a nonhomogeneous GF and incorporating it into standard DT algorithms can be very difficult if not mathematically impossible. Devaney has circumvented these issues by developing a purely numerical DT inversion algorithm[1] that is independent of measurement system geometry, number of frequencies used in the reconstruction, and GF. It is based upon a projection operator interpretation of the forward scattering integral. The projection constitutes a Hilbert space mapping from a *continuous object space* to a *discrete measurement space*. The algorithm is described in detail in Refs. 1 and 2 where it was shown to be successful in reconstructing synthetic data from an annular outwardly directed measurement system. The mathematics of the algorithm decompose the forward scattering operator into its singular value/vector spectrum in a manner similar to that used by Prada *et al*. for the time reversal operator.[3,4]

Here, we apply the Hilbert space algorithm to a planar multilayer domain with the goal of inverting a reflection mode multistatic ultrasonic data set. To this end, we developed a scalar planar multilayer GF. Our GF solution is not new. Complete and detailed planar multilayer GF solutions have been previously derived for many applications.[5–8] We do not, however, require the accuracy of these solutions since our reconstructions are limited by measurement noise and limited data. Additionally, we explicitly filter out evanescent field information since it is, for practical purposes, unusable at the propagation dimensions of our problem. We do require a model that accounts for the reverberation and multipath scattering within and between layers. We also require computational speed since our multilayer GF must be computed repeatedly over all combinations of transducers and frequencies.

The combination of the Hilbert space algorithm with the planar multilayer GF has successfully imaged a hole, the ''flaw,'' in the copper layer of an aluminum/copper multilayer. The data were collected using a 5-MHz linear ultrasonic array in a multistatic method whereby each transmitter sequentially launched the primary field into the medium and the scattered field was measured at all receivers. No beamforming was performed during data collection: we accounted for the multilayer nature of the medium, mathematically, through the multilayer GF, ''after-the-fact,'' that is, after the data were collected.

In most nondestructive evaluation (NDE) cases, prior knowledge of the internal structure of a part under evaluation is known via design or manufacturing specification. Thus, for NDE purposes, it is reasonable that the individual medium layer material properties and specifications are well known and understood. In this case, the inverse wave imaging is used to identify deviations from how the medium was assembled or built (the ''as built'' versus the ''as designed'' problem). Although we apply the algorithm to an NDE problem, it is sufficiently general to be applicable to any scalar wave tomographic imaging in a planar multilayer environment such as walls, civil structures, or a layered earth.

We review the derivation of the Hilbert space inverse wave algorithm in the next section. We summarize the devel-

a)Electronic mail: lehman2@llnl.gov

opment of our planar multilayer Green function in Sec. III. The results are presented in Sec. IV for simulated and experimental data sets on the aluminum/copper multilayer. Our conclusions are in Sec. V.

II. HILBERT SPACE INVERSE WAVE ALGORITHM

The Hilbert space inverse wave (HSIW) algorithm[1,2] interprets the forward scattering operator as a mapping from a continuous, real, object space to a discrete measurement space consisting of the discrete transceiver locations and, optionally, the discrete frequencies at which the measured data are collected. We summarize the HSIW algorithm here; details are presented in the references.

The forward scattering process is described by

$$\psi^{scat}(\mathbf{R}_m^r,\mathbf{R}_n^t,\omega)=k_0^2(\omega)\int d\mathbf{r}G_0(\mathbf{R}_m^r,\mathbf{r},\omega)o(\mathbf{r})\psi(\mathbf{r},\mathbf{R}_n^t\omega), \tag{1}$$

where $\psi^{scat}(\mathbf{R}_m^r,\mathbf{R}_n^t\omega)$ is the *scattered* field measured at the *m*th receiver resulting from the *n*th source; $\psi(\mathbf{r},\mathbf{R}_n^t,\omega)$ is the *total* field resulting from the *n*th source; $\mathbf{R}_m^r$ is the receiver location; $\mathbf{R}_n^t$ is the source location; ω is temporal frequency; $k_0(\omega)$ is the background wave number defined as ω/c_0; c_0 is the background velocity; $G_0(\mathbf{R}_m^r,\mathbf{r},\omega)$ is the homogeneous background Green function; $o(\mathbf{r})$ is the object function to be imaged, defined as $(k^2(\mathbf{r})/k_0^2(\omega))-1$; and $k(\mathbf{r})$ is the object function wave number.

The total field appearing under the integral of Eq. (1) is the sum of the incident and scattered fields. In many instances it is possible to replace the total field by the incident field using the Born approximation.[9,10] This permits the development of a linearized inversion of the integral. We assume the incident field is due to a point source located at $\mathbf{R}_n^t$:

$$\psi^{inc}(\mathbf{r},\mathbf{R}_n^t,\omega)=P(\omega)G(\mathbf{r},\mathbf{R}_n^t,\omega), \tag{2}$$

where $P(\omega)$ is the spectrum of the incident pulse. Substituting Eq. (2) into Eq. (1), we arrive at our forward, distorted Born approximation, scattering model:

$$\psi_B^{scat}(\mathbf{R}_m^r,\mathbf{R}_n^t,\omega_l)$$
$$=P(\omega_l)k_0^2(\omega_l)\int d\mathbf{r}G_0(\mathbf{R}_m^r,\mathbf{r},\omega_l)o(\mathbf{r})G(\mathbf{r},\mathbf{R}_n^t,\omega_l), \tag{3}$$

where the *B* subscript indicates the approximation. As all the measured data will be discretized on a digital computer, we have explicitly discretized the frequencies at which the data are collected via ω_l, where $l=0,1,...,N_f-1$, and N_f is the number of frequencies in the pulse band width.

The HSIW interprets Eq. (3) as a mapping from a *continuous object space* to a *discrete measurement space*. The object space is the physical $\mathbf{r}$ space of the object function. The measurement space consists of the discrete transducer locations and temporal frequencies at which the scattered data are measured. The scattering operator projects the object onto the measurement space. To formulate explicitly Eq. (3) as a projection operator, we define the forward propagation or projection kernel as

$$\Pi^*(\mathbf{r})\equiv P(\omega_l)k_0^2(\omega_l)G_0(\mathbf{R}_m^r,\mathbf{r},\omega_l)G(\mathbf{r},\mathbf{R}_n^t,\omega_l), \tag{4}$$

where $\Pi(\mathbf{r})$ is a $J\equiv(N_{\mathrm{src}}\times N_{\mathrm{rcv}}\times N_f)$ element column vector, N_{src} is the number of sources, and N_{rcv} is the number of receivers. Mathematically, the projection is represented as an inner product between the object function and the kernel via

$$D=\int d\mathbf{r}\Pi^*(\mathbf{r})o(\mathbf{r})\equiv\langle\Pi,o\rangle, \tag{5}$$

where D is a J element column vector of measured data values at each source, receiver, and frequency combination; the asterisk $(*)$ indicates complex conjugation; and the inner product is with respect to the real object space, $\mathbf{r}$. Symbolically, we define the forward scattering operator, K, as

$$K[\,\cdot\,]\equiv\int d\mathbf{r}\Pi^*(\mathbf{r})[\,\cdot\,]. \tag{6}$$

Using the mathematics of linear algebra, it is shown[1,2] the inverse of Eq. (6), which reconstructs the object function, is

$$\hat{o}(\mathbf{r})=\sum_{j=0}^{J-1}\frac{1}{\sigma_j^2}\Pi^T(\mathbf{r})u_ju_j^\dagger D, \tag{7}$$

where σ_j and u_j are the singular values and measurement space singular vectors of K, respectively. Explicitly, these are defined by the normal equations of the singular system:

$$Kv_j(\mathbf{r})=\sigma_ju_j, \tag{8}$$

$$K^\dagger u_j=\sigma_jv_j(\mathbf{r}), \tag{9}$$

where the u_j span the measured data space and the $v_j(\mathbf{r})$ span the object space. The measurement system is inherently ill-posed due to the limited aperture of the measurement system that only measures part of the scattered field, and due to the loss of the evanescent field information. Thus, a subset of the singular values must be rejected: they carry no useful object information and must not be used in the reconstruction of Eq. (7). A decision must be made on the number of singular values/vectors to use. We have chosen to use the *best rank N* approximation. We compute the ratio

$$R(N)=\frac{\Sigma_{j=0}^{N-1}\sigma_j^2}{\Sigma_{j=0}^{J-1}\sigma_j^2}, \tag{10}$$

where we assume the singular values are arranged from smallest to largest: $\sigma_0^2\leqslant\sigma_1^2\leqslant\cdots\leqslant\sigma_{J-1}^2$. Plotting $R(N)$, we graphically identify the point at which the function starts to rise rapidly. The index of the singular value at which this occurs we label as J_0. With this value determined, our final reconstruction is

$$\hat{o}(\mathbf{r})=\sum_{j=J_0}^{J-1}\frac{1}{\sigma_j^2}\Pi^T(\mathbf{r})u_ju_j^\dagger D. \tag{11}$$

Our experience reconstructing both simulated and experimentally collected scattered field data have shown that this criterion works consistently well.

The HSIW algorithm versatility lies in its ability to form reconstructions using any geometrical transducer configuration and any number of frequencies. It requires only the Green functions of Eq. (4). For the current case of interest, we take $G_0(\mathbf{r},\mathbf{r}',\omega)$ to be the free space Green function,

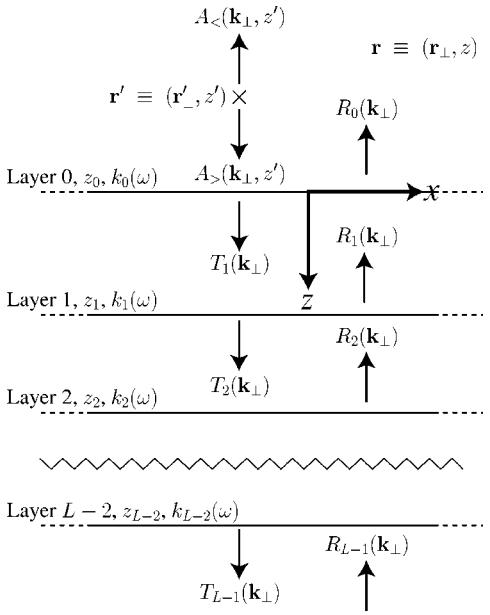

FIG. 1. Multilayer geometry in the planar Fourier domain. There are $\{l\}_{l=0}^{L-1}$ layers. The source is located at $z' \leqslant z_0$.

$$G_0(\mathbf{r},\mathbf{r}',\omega) = \begin{cases} \dfrac{i}{4} H_0^{(1)}(k_0(\omega)|\mathbf{r}-\mathbf{r}'|), & 2\mathrm{D}, \\ \dfrac{1}{4\pi|\mathbf{r}-\mathbf{r}'|} e^{ik_0(\omega)|\mathbf{r}-\mathbf{r}'|}, & 3\mathrm{D}, \end{cases} \tag{12}$$

which is used to propagate a field from a point within the medium to the receiver. For $G(\mathbf{r},\mathbf{r}',\omega)$, we use a multilayer Green function which permits us to propagate a field from a transducer through the layers to a point within the medium. This enables us to focus ''after-the-fact,'' that is, after the data have been collected without the use of beam forming, on targets within the multilayer structure. We develop our Green function in the next section.

III. MATHEMATICAL STATEMENT OF THE PLANAR MULTILAYER PROBLEM

Consider the planar multilayer geometry of Fig. 1. Each layer is identified by its bottom boundary, z_l. The top most layer, layer 0, is defined by z_0. We assume the source is located on or above the top layer. The wave number associated with each layer is $k_l(\omega) \equiv \omega/c_l$, where c_l is the wave field propagation velocity and ω is the temporal radial frequency. We wish to solve the Green function equation,

$$[\nabla^2 + k^2(z)] G(\mathbf{r},\mathbf{r}',\omega) = -\delta(\mathbf{r}-\mathbf{r}'), \tag{13}$$

where the depth-dependent wave number, $k(z)$, is given by

$$k(z) = \begin{cases} k_0(\omega), & z \leqslant z_0, \\ k_1(\omega), & z_0 < z \leqslant z_1, \\ \vdots & \\ k_{L-2}(\omega), & z_{L-3} < z \leqslant z_{L-2}, \\ k_{L-1}(\omega), & z > z_{L-2}, \end{cases} \tag{14}$$

the source location is $\mathbf{r}' \leqslant z_0$ (that is, located on or above the top layer), and $G(\mathbf{r},\mathbf{r}',\omega)$ is the planar multilayer Green function to be determined (for this section, the ω dependence is implicit). Following a method similar to Chap. 4 of Ref. 5 we separate the coordinate system into *planar* and *perpendicular* components, $\mathbf{r} \equiv (\mathbf{r}_\perp, z)$ and $\mathbf{r}' \equiv (\mathbf{r}'_\perp, z')$, and perform a planar Fourier transform (PFT) of Eq. (13) along the planar, $\mathbf{r}_\perp$, coordinate using the transform pair,

$$\tilde{\psi}(\mathbf{k}_\perp, z) = \int d\mathbf{r}_\perp \psi(\mathbf{r}_\perp, z) e^{-i\mathbf{k}_\perp \cdot \mathbf{r}_\perp}, \tag{15}$$

$$\psi(\mathbf{r}_\perp, z) = \frac{1}{(2\pi)^n} \int d\mathbf{k}_\perp \tilde{\psi}(\mathbf{k}_\perp, z) e^{i\mathbf{k}_\perp \cdot \mathbf{r}_\perp}, \tag{16}$$

where n is the dimensionality of the problem, to achieve

$$[\partial_z^2 + k^2(z) - |\mathbf{k}_\perp|^2] \tilde{G}(\mathbf{k}_\perp, z; \mathbf{r}'_\perp, z'; \omega) = -e^{-i\mathbf{k}_\perp \cdot \mathbf{r}'_\perp} \delta(z-z'). \tag{17}$$

Equation (17) is a one-dimensional ordinary differential equation in z. We simplify the notation by defining

$$\gamma_l^2 \equiv k_l(z)^2 - |\mathbf{k}_\perp|^2, \tag{18}$$

$$w(\mathbf{r}'_\perp) \equiv e^{-i\mathbf{k}_\perp \cdot \mathbf{r}'_\perp}, \tag{19}$$

where the z dependence in γ_n is implicit. With these definitions, the equation to be solved reads

$$[\partial_z^2 + \gamma_l^2] \tilde{G}(\mathbf{k}_\perp, z; \mathbf{r}'_\perp, z'; \omega) = w(\mathbf{r}'_\perp) \delta(z-z'). \tag{20}$$

In Secs. III A–C, we develop the solution Eq. (20) following a technique similar to that used by DiNapoli and Deavenport[6] although we use planar Cartesian rather than polar coordinates. The solution is derived analytically but computed numerically. A numerical inverse PFT is used to compute $G(\mathbf{r},\mathbf{r}',\omega)$ from $\tilde{G}(\mathbf{k}_\perp, z; \mathbf{r}'_\perp, z'; \omega)$. We develop the full solution by dividing the problem into three parts:

(1) We solve the problem of two layers with a source in Sec. III A.
(2) We develop the solution between two arbitrary source-free layers in Sec. III B.
(3) We combine these two solutions in Sec. III C to achieve the full multilayer solution.

A. Two layers with a source

The solution to Eq. (20) in the top two layers is

$$\tilde{G}(\mathbf{k}_\perp, z; \mathbf{r}'_\perp, z'; \omega) = \begin{cases} A_<(\mathbf{k}_\perp, z') e^{-i\gamma_0 z}, & z < z', \\ A_>(\mathbf{k}_\perp, z') e^{i\gamma_0 z} + R_0(\mathbf{k}_\perp) e^{-i\gamma_0 z}, & z' < z \leqslant z_0, \\ T_1(\mathbf{k}_\perp) e^{i\gamma_1 z} + R_1(\mathbf{k}_\perp) e^{-i\gamma_1 z}, & z > z_0, \end{cases} \tag{21}$$

where $A_<(\mathbf{k}_\perp, z')$ and $A_>(\mathbf{k}_\perp, z')$ are the point source field coefficients, $R_0(\mathbf{k}_\perp)$ is the layer 0 reflection coefficient, and $T_1(\mathbf{k}_\perp)$ and $R_1(\mathbf{k}_\perp)$ are the layer 1 transmission and reflection coefficients, respectively. $R_1(\mathbf{k}_\perp)$ is included for completeness, were there *only* two layers, $R_1(\mathbf{k}_\perp) \equiv 0$. Equation (21) has five coefficients to be determined [$A_<(\mathbf{k}_\perp, z')$, $A_>(\mathbf{k}_\perp, z')$, $R_0(\mathbf{k}_\perp)$, $T_1(\mathbf{k}_\perp)$, and $R_1(\mathbf{k}_\perp)$]. We impose field boundary conditions (BC) about the source location and z_0 interface to solve for the coefficients. The conditions are

- Continuity of $G(\mathbf{k}_\perp, z; \mathbf{r}'_\perp, z'; \omega)$ about the source location $z = z'$;
- Step discontinuity of $\partial_z G(\mathbf{k}_\perp, z; \mathbf{r}'_\perp, z'; \omega)$ about the source location $z = z'$;
- Continuity of $G(\mathbf{k}_\perp, z; \mathbf{r}'_\perp, z'; \omega)$ at the layer interface, $z = z_0$;
- Continuity of $\partial_z G(\mathbf{k}_\perp, z; \mathbf{r}'_\perp, z'; \omega)$ at the layer interface, $z = z_0$.

Applying the BC and simplifying, we arrive at the following matrix relationship between the transmission and reflection coefficients of each layer:

$$v_1 = U_1^{-1}(z_0) U_0(z_0) v_0, \tag{22}$$

where

$$U_0(z_0) \equiv \begin{bmatrix} \frac{i}{2\gamma_0} w(\mathbf{r}'_\perp) e^{i\gamma_0(z_0 - z')} & e^{-i\gamma_0 z_0} \\ \frac{i}{2} w(\mathbf{r}'_\perp) e^{i\gamma_0(z_0 - z')} & -\gamma_0 e^{-i\gamma_0 z_0} \end{bmatrix}, \tag{23}$$

$$v_0 \equiv \begin{bmatrix} 1 \\ R_0(\mathbf{k}_\perp) \end{bmatrix}, \tag{24}$$

$$U_l(z) \equiv \begin{bmatrix} e^{i\gamma_l z} & e^{-i\gamma_l z} \\ \gamma_l e^{i\gamma_l z} & -\gamma_l e^{-i\gamma_l z} \end{bmatrix}, \tag{25}$$

$$v_l \equiv \begin{bmatrix} T_l(\mathbf{k}_\perp) \\ R_l(\mathbf{k}_\perp) \end{bmatrix}. \tag{26}$$

Thus, given the boundary conditions, v_0, at the top layer (layer 0), we may solve for the layer 1 coefficients via Eq. (22).

B. Solution between two source-free layers

In a source-free region, Eq. (20) reduces to

$$[\partial_z^2 + \gamma_l^2] \tilde{G}(\mathbf{k}_\perp, z; \mathbf{r}'_\perp; z'; \omega) = 0. \tag{27}$$

The solution is

$$\tilde{G}(\mathbf{k}_\perp, z; \mathbf{r}'_\perp, z'; \omega) = \begin{cases} T_l(\mathbf{k}_\perp) e^{i\gamma_l z} + R_l(\mathbf{k}_\perp) e^{-i\gamma_l z}, & z_{l-1} < z \leqslant z_l, \\ T_{l+1}(\mathbf{k}_\perp) e^{i\gamma_{l+1} z} + R_{l+1}(\mathbf{k}_\perp) e^{-i\gamma_{l+1} z}, & z_l < z \leqslant z_{l+1}. \end{cases} \tag{28}$$

Imposing continuity in the field and its derivative (there is no source within this region), we arrive at the relationship between the layer coefficients:

$$v_{l+1} = U_{l+1}^{-1}(z_l) U_l(z_l) v_l, \tag{29}$$

where we have used the definitions of Eqs. (25) and (26). Equation (29) gives us a method for computing the transmission and reflection coefficients for the $(l+1)$th layer given those in the lth layer. In the next section we combine the results from this and the previous section to derive the full, multilayer Green function.

C. Full multilayer solution

Let there be L layers labeled from $[0, L-1]$ as shown in Fig. 1. The full multilayer solution Green function which is a solution to Eq. (20) is

$$\tilde{G}(\mathbf{k}_\perp, z; \mathbf{r}'_\perp, z'; \omega) = \begin{cases} A_<(\mathbf{k}_\perp, z') e^{-i\gamma_0 z}, & z < z', \\ A_>(\mathbf{k}_\perp, z') e^{i\gamma_0 z} + R_0(\mathbf{k}_\perp) e^{-i\gamma_0 z}, & z' < z \leqslant z_0, \\ T_1(\mathbf{k}_\perp) e^{i\gamma_1 z} + R_1(\mathbf{k}_\perp) e^{-i\gamma_1 z}, & z_0 < z \leqslant z_1, \\ T_2(\mathbf{k}_\perp) e^{i\gamma_2 z} + R_2(\mathbf{k}_\perp) e^{-i\gamma_2 z}, & z_1 < z \leqslant z_2, \\ \vdots \\ T_{L-1}(\mathbf{k}_\perp) e^{i\gamma_{L-1} z} + R_{L-1}(\mathbf{k}_\perp) e^{-i\gamma_{L-1} z}, & z > z_{L-1}. \end{cases} \tag{30}$$

The coefficients, $A_<(\mathbf{k}_\perp, z')$, $A_>(\mathbf{k}_\perp, z')$, $\{R_l(\mathbf{k}_\perp)\}_{l=1}^{L-1}$, and $\{T_l(\mathbf{k}_\perp)\}_{l=0}^{L}$, are to be determined. $A_<(\mathbf{k}_\perp, z')$ and $A_>(\mathbf{k}_\perp, z')$ are solved by matching the Green function and step discontinuity of its derivative about the source point, z'. They are found to be

$$A_>(\mathbf{k}_\perp, z') = \frac{i}{2\gamma_0} w(\mathbf{r}'_\perp) e^{-i\gamma_0 z'}, \tag{31}$$

$$A_<(\mathbf{k}_\perp, z') = R_0(\mathbf{k}_\perp) + \frac{i}{2\gamma_0} w(\mathbf{r}'_\perp) e^{i\gamma_0 z'}. \tag{32}$$

$R_0(\mathbf{k}_\perp)$ and $T_{L-1}(\mathbf{k}_\perp)$ are set by the top and bottom layer boundary conditions (BCs) imposed on Eq. (20). Those BCs are

$$v_0 = \begin{bmatrix} 1 \\ R_0(\mathbf{k}_\perp) \end{bmatrix} \quad \text{for the top layer,} \tag{33}$$

$$v_{L-1} = \begin{cases} \begin{bmatrix} T_{L-1}(\mathbf{k}_\perp) \\ 0 \end{bmatrix} & \text{for an infinite or nonreflecting bottom layer,} \\ \begin{bmatrix} T_{L-1}(\mathbf{k}_\perp) \\ T_{L-1}(\mathbf{k}_\perp) \end{bmatrix} & \text{for a perfectly reflecting bottom layer.} \end{cases} \tag{34}$$

The matching conditions for each layer are

$$\begin{aligned} &U_0(z_0) v_0 = U_1(z_0) v_1, \\ &U_1(z_1) v_1 = U_2(z_1) v_2, \\ &U_2(z_2) v_2 = U_3(z_2) v_3, \\ &\vdots \\ &U_{L-2}(z_{L-2}) v_{L-2} = U_{L-1}(z_{L-2}) v_{L-1}. \end{aligned} \tag{35}$$

Eliminating all but the top and bottom coefficients of Eqs. (35), we find

$$v_0 = U_0^{-1}(z_0) U_1(z_0) U_1^{-1}(z_1) U_2(z_1) U_2^{-1}(z_2) \times U_3(z_2) \cdots U_{L-2}^{-1}(z_{L-2}) U_{L-1}(z_{L-2}) v_{L-1}. \tag{36}$$

We simplify the notation by defining

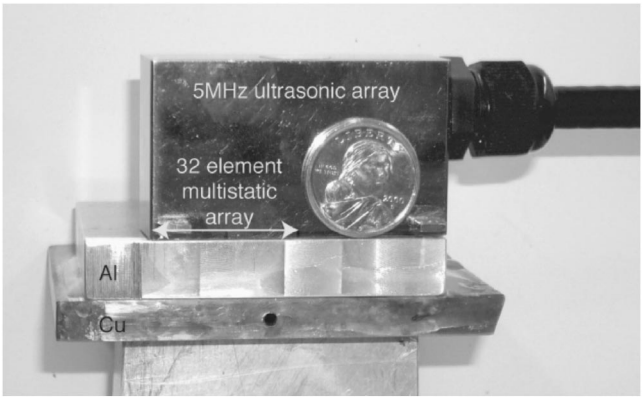

FIG. 2. Aluminum/copper photograph. The aluminum bar below the copper layer is a support for the photograph and was not present during the data collection.

$$\mathcal{H} \equiv U_0^{-1}(z_0)U_1(z_0)U_1^{-1}(z_1)U_2(z_1)U_2^{-1}(z_2) \times U_3(z_2)\cdots U_{L-2}^{-1}(z_{L-2})U_{L-1}(z_{L-2}), \tag{37}$$

and expressing Eq. (36) as

$$v_0 = \mathcal{H} v_{L-1}. \tag{38}$$

Solving Eq. (38) for $R_0(\mathbf{k}_\perp)$ and $T_{L-1}(\mathbf{k}_\perp)$ determines v_0 and v_{L-1}. The remaining coefficients are then calculated using Eq. (29).

1. Solution for infinite bottom layer

For an infinite bottom layer there is no reflection. Thus we set $R_{L-1}(\mathbf{k}_\perp)=0$, reducing Eq. (38) to

$$\underbrace{\begin{bmatrix} 1 \\ R_0(\mathbf{k}_\perp) \end{bmatrix}}_{v_0} = \underbrace{\begin{bmatrix} \mathcal{H}_{11} & \mathcal{H}_{12} \\ \mathcal{H}_{21} & \mathcal{H}_{22} \end{bmatrix}}_{\mathcal{H}} \underbrace{\begin{bmatrix} T_{L-1}(\mathbf{k}_\perp) \\ 0 \end{bmatrix}}_{v_{L-1}}, \tag{39}$$

which yields

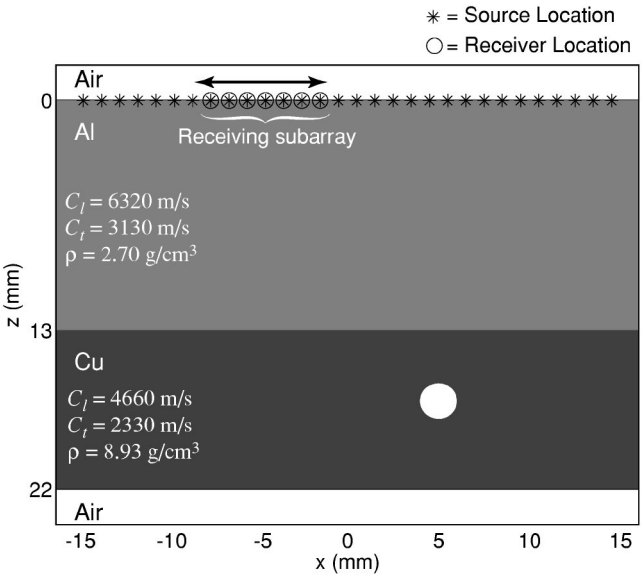

FIG. 3. Air/aluminum/copper/air multilayer simulation geometry.

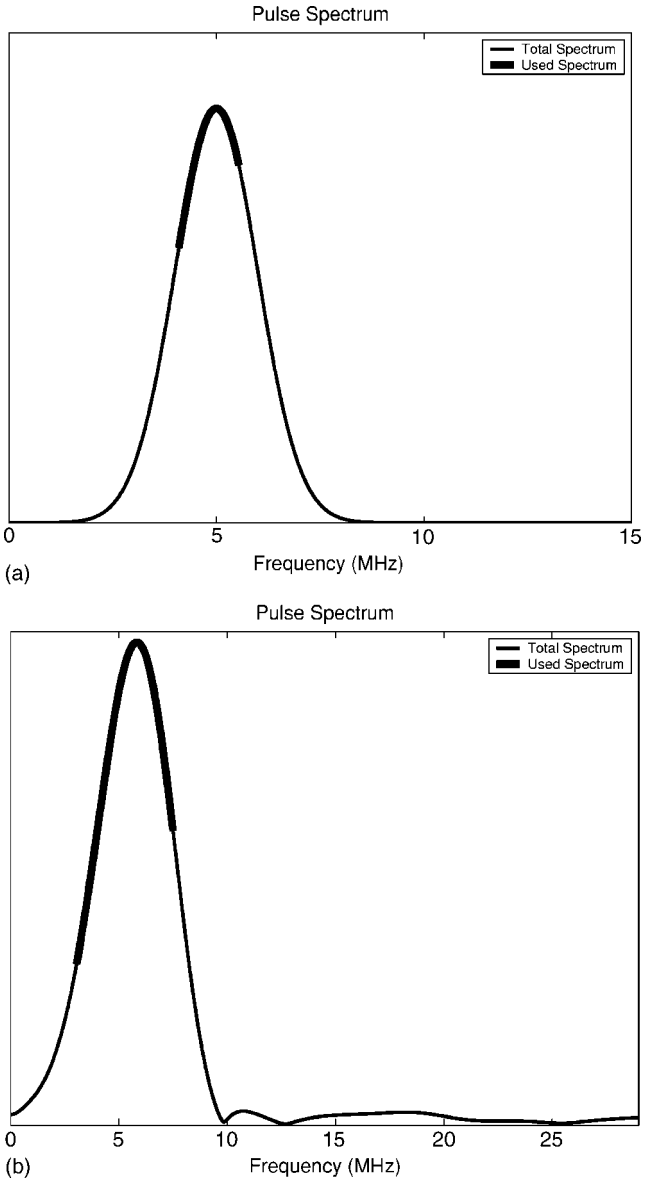

FIG. 4. Spectrum of 5-MHz, five-cycle, Gaussian windowed sine spectrum magnitude used in (a) the FDTD simulation and (b) the experiment. The highlighted parts of the curves show the 58 discrete frequencies used in the reconstructions.

$$T_{L-1}(\mathbf{k}_\perp) = \frac{1}{\mathcal{H}_{11}}, \tag{40}$$

$$R_0(\mathbf{k}_\perp) = \frac{\mathcal{H}_{21}}{\mathcal{H}_{11}} \tag{41}$$

as solution.

2. Solution for perfectly reflecting bottom layer

For a perfectly reflecting bottom layer, the reflection and transmission coefficients are identical. We set $R_{L-1}(\mathbf{k}_\perp) = T_{L-1}(\mathbf{k}_\perp)$, reducing Eq. (38) to

$$\begin{bmatrix} 1 \\ R_0(\mathbf{k}_\perp) \end{bmatrix} = \begin{bmatrix} \mathcal{H}_{11} & \mathcal{H}_{12} \\ \mathcal{H}_{21} & \mathcal{H}_{22} \end{bmatrix} \begin{bmatrix} T_{L-1}(\mathbf{k}_\perp) \\ T_{L-1}(\mathbf{k}_\perp) \end{bmatrix}, \tag{42}$$

which yields

FIG. 5. Full aperture and subaperture processing. (a) In full aperture processing, the time series measured at all receivers are processed together. (b) In subaperture processing, the data from a shifting subarray consisting of a transmitter/receiver surrounded by an equal number of receivers are processed together.

$$T_{L-1}(\mathbf{k}_\perp) = \frac{1}{\mathcal{H}_{11}+\mathcal{H}_{12}}, \tag{43}$$

$$R_0(\mathbf{k}_\perp) = \frac{\mathcal{H}_{21}+\mathcal{H}_{22}}{\mathcal{H}_{11}+\mathcal{H}_{12}}. \tag{44}$$

as solution.

D. Practical considerations for evanescent fields

In anticipation of working with multilayer parts whose layer thicknesses are many wavelengths, we explicitly filter out the evanescent field information prior to performing an inverse planar Fourier transform of Eq. (30). Explicitly, we compute

$$G_{\mathrm{LP}}(\mathbf{r},\mathbf{r}',\omega) = \mathcal{F}^{-1}_{\mathrm{PFT}}\{\tilde{G}(\mathbf{k}_\perp,z;\mathbf{r}'_\perp,z';\omega)h_l(\mathbf{k}_\perp)\}, \tag{45}$$

where $h_l(\mathbf{k}_\perp)$ is a depth-dependent Hanning window whose width is proportional to the propagating spatial cutoff frequency $k_l(\omega)$ of the lth layer, $\mathcal{F}^{-1}_{\mathrm{PFT}}\{\cdot\}$ is the inverse planar Fourier transform of Eq. (16), and the "LP" subscript on the Green function indicates that the Green function has been low-pass filtered. Referring to Eq. (4), we set

$$G(\mathbf{r},\mathbf{R}^t_n,\omega) = G_{\mathrm{LP}}(\mathbf{r},\mathbf{R}^t_n,\omega).$$

This is motivated by the exponentially decaying nature of the evanescent field which, when back-propagated in the presence of noise (measurement and numerical), results in instabilities. Additionally, as the field propagates from the source down through successive layers, we do not propagate fields that have been cut off in higher layers to subsequent layers, even if they can support those spatial field frequencies. Explicitly, if

$$k_l(\omega) > k_{l-1}(\omega),$$

we only propagate spatial frequencies up to $k_{l-1}(\omega)$ for all subsequent layers until a layer with a lower cutoff is encountered.

In Sec. II, we reviewed the inversion algorithm. In Sec. III, we summarized the derivation of the planar multilayer Green function to be used in the inversion algorithm. In the following sections, we apply our planar multilayer inversion algorithm to simulated and experimental data.

IV. EXPERIMENTAL SETUP AND FULL WAVE SIMULATION

The experimental setup consisted of a 32-element 5-MHz ultrasonic array. The transducers had a 1-mm pitch and served as both sources and receivers. The measured data were fully multistatic in that each source successively launched the incident field into the medium and the scattered field was recorded at all receivers. No beamforming was performed during the data collection, nor did we account for the multilayer structure of the medium.

The part under evaluation was an aluminum block epoxy bonded onto a copper block. The aluminum layer was 13 mm thick; the copper layer was 9 mm thick. A "defect" in the form of a 1-mm radius hole was drilled into the middle of the copper layer. The experimental aluminum/copper multilayer setup is pictured in Fig. 2. Due to the finite length of the measurement hardware's input buffer, we did not start recording the backscattered field until 1.7 μs after the launch of the source. We wanted to ensure we recorded the reflection from the bottom of the copper layer as well as the reverberation within each layer. The 1.7-μs delay corresponds approximately to 5 mm of two-way travel time into the aluminum layer (assuming a longitudinal propagation velocity of 6300 m/s). This is important because it dictates the vertical extent over which we may reconstruct the experimental data.

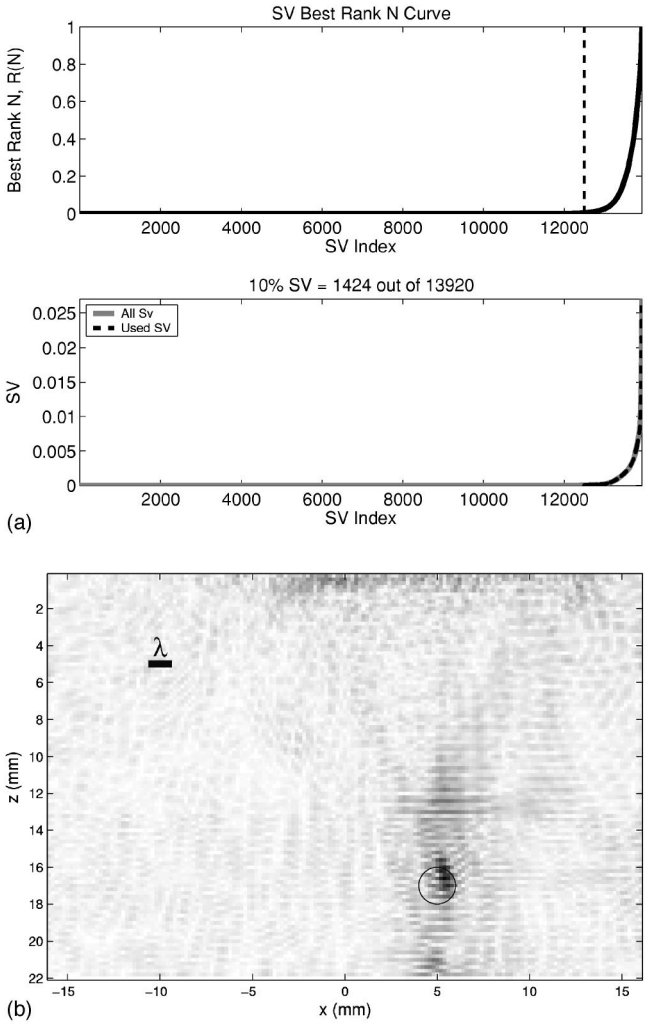

FIG. 6. Reconstruction of simulated data set. (a) The top plot shows the best rank N approximation of Eq. (10). The dashed line shows the threshold below which none of the singular values were used in the reconstruction of Eq. (11). The bottom plot shows the actual singular value distribution. (b) The reconstruction. The circle superposed on the image shows the true location of the flaw. The λ metric is the wavelength of the field in the top, aluminum, layer at $f_0=5$ MHz.

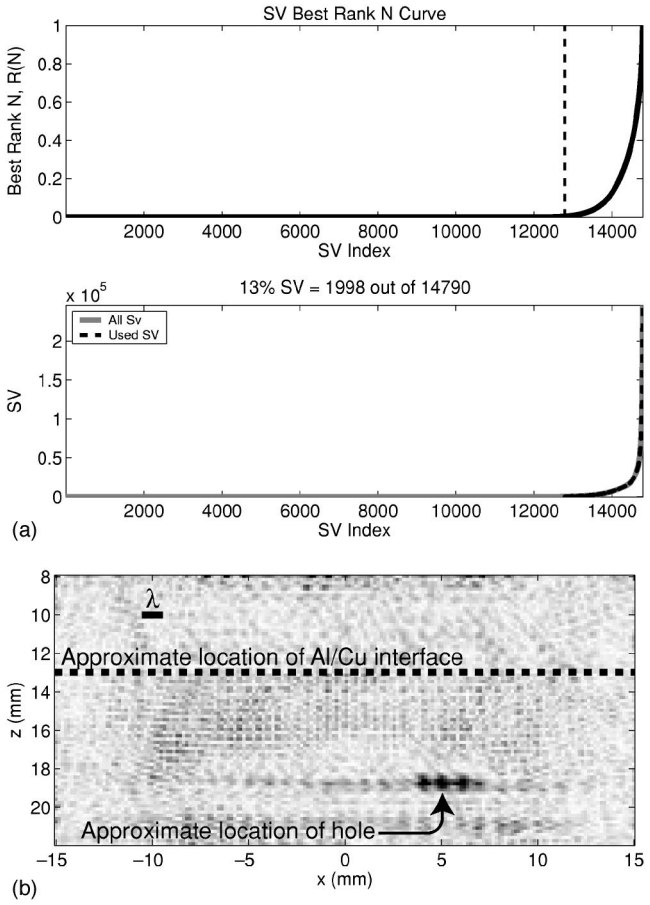

FIG. 7. Reconstruction of experimental data set. (a) The top plot shows the best rank N approximation of Eq. (10). The dashed line shows the threshold below which none of the singular values were used in the reconstruction of Eq. (11). The bottom plot shows the actual singular value distribution. (b) The reconstruction. The arrow superposed on the image shows the approximate location of the flaw. The λ metric is the wavelength of the field in the top, aluminum, layer at $f_0=5$ MHz.

In conjunction with the experiment, we performed a two-dimensional finite-difference time-domain (FDTD) simulation of the setup using E3D, an explicit 2D/3D elastic wave propagation code developed at Lawrence Livermore National Laboratory.[11–16] The code simulates full wave scattering and requires as inputs a longitudinal velocity distribution, a transverse velocity distribution, and a density distribution.

The FDTD simulation domain, shown in Fig. 3, consisted of four layers: air, aluminum, copper, air. The physical parameters assigned to aluminum/copper layers, required by E3D, are shown in the graphic. An air-filled hole with a radius of 1 mm was inserted 4 mm below the aluminum/copper interface.

Both the simulation and experiment used a Gaussian windowed sine as incident pulse:

$$p(t)=\sin(\omega_0 t)e^{-t^2/(2\sigma^2)}, \tag{46}$$

where $\omega_0 \equiv 2\pi f_0$, $\sigma \equiv N_{\mathrm{cyc}}/\omega_0$, and N_{cyc} is the number of cycles in the pulse. We used $f_0=5$ MHz and five cycles. The pulse spectrum magnitude is shown in Fig. 4 for both the simulated and experimental data sets. The highlighted regions of the curves show the 58 discrete frequencies used in the reconstructions. As discussed in Ref. 2, the Hilbert space algorithm is computationally intensive and demanding upon computer storage. Thus, we were unable to use the full pass band of the pulse spectrum in our reconstructions. The Green function computed for the HSIW algorithm consisted of an air/aluminum/copper/air multilayer.

In processing both the experimental and simulated data, we discovered that shear (transverse) waves, which are not modeled in the theory of Secs. II and III, corrupted the reconstructions when we used the entire 32-element aperture. This was caused by late-arriving shear waves at receivers distant from the source. In order to filter out these slower moving shear waves, we processed the data using successive, overlapping *subapertures* rather than the *full aperture*.

In full aperture processing [refer to Fig. 5(a)], the time series measured at *all* receivers are used for each transmitter. Scattered field time series seen at receivers farther removed from the transmitter contained both the pressure (longitudinal) waves and later arriving shear waves. As the latter were

not included in the models, they corrupted the reconstructions.

In subaperture processing, we formed subarrays consisting of a central transmitter/receiver surrounded by equal numbers of receivers as shown in Fig. 5(b). By sequentially indexing the subarray over to the next transmitter/receiver, the entire data set was processed. In this manner, we succeeded in spatially reducing the shear wave corruption of the reconstruction algorithm. We wish to emphasize that the subaperture processing was performed after the data were collected.

The reconstructions are presented in Figs. 6 and 7 for the simulated and experimental data sets, respectively. The top plot of Fig. 6(a) shows the best rank N curve of Eq. (10) used for thresholding the singular values; the bottom shows the actual singular value distribution. Using the best rank N criterion, we determined the top 10% of the singular values should be used in the reconstruction in Fig. 6(b). The flaw is clearly visible and correctly located.

Figure 7 shows the results for the experimental data set. In this case, the top 13% of the singular values were used. The reconstruction of Fig. 7 shows excellent localization and contrast of the flaw. We note the vertical extent of the reconstruction starts at 8 mm into the aluminum block. This conservatively accounts for the 1.7-μs delay in recording the backscattered field.

V. CONCLUSIONS

We developed a scalar planar multilayer Green function for use in the Hilbert space inverse wave tomographic algorithm and used the latter to image a flaw in an aluminum/copper multilayer. We demonstrated our ability to focus successfully through the multilayer medium ''after-the-fact,'' that is, after the data have been collected in a multistatic manner without beamforming or taking into account, during data collection, the multilayer nature of the part.

In most nondestructive evaluation (NDE) cases, prior knowledge of the integral structure of a part under evaluation is known via blueprints or other manufacturing specification. Thus, for NDE purposes, it is reasonable that the individual medium layer material properties and specifications are well known and understood. In this case, the inverse wave imaging is used to identify deviations from how the medium was assembled or built. This is the ''as-built'' versus the ''as-designed'' problem. This algorithm can also be used to determine and track the aging of parts. We hope to develop spherical and cylindrical multilayer Green functions for other NDE applications.

ACKNOWLEDGMENTS

We wish to thank Professor Anthony J. Devaney of Northeastern University in Boston for numerous discussions on the Hilbert space method and the planar multilayer Green function development. We thank Dr. Karl A. Fisher of Lawrence Livermore National Laboratory for collecting and explaining the multistatic data. This work was performed under the auspices of the U.S. Department of Energy by University of California, Lawrence Livermore National Laboratory under Contract W-7405-Eng-48.

[1] A. J. Devaney and M. Dennison, ''Inverse scattering in inhomogeneous background media,'' Inverse Probl. **19**, 855–870 (2003).
[2] S. K. Lehman and S. J. Norton, ''Radial reflection diffraction tomography,'' J. Acoust. Soc. Am. **116**, 2158–2172 (2004).
[3] C. Prada, S. Manneville, D. Spoliansky, and M. Fink, ''Decomposition of the time reversal operator: Detection and selective focusing on two scatterers,'' J. Acoust. Soc. Am. **99**, 2067–2076 (1996).
[4] C. Prada, M. Tanter, and M. Fink, ''Flaw detection in solid with the D.O.R.T. method,'' Proc.-IEEE Ultrason. Symp. **1**, 679–683 (1997).
[5] L. M. Brekhovskikh, *Waves in Layered Media* (Academic, New York, 1960) (translated from the Russian by David Lieberman).
[6] F. R. DiNapoli and R. L. Deavenport, ''Theoretical and numerical Green's function field solution in a plane multilayer medium,'' J. Acoust. Soc. Am. **67**, 92–105 (1980).
[7] D. L. Folds and C. D. Loggins, ''Transmission and reflection of ultrasonic waves in layered media,'' J. Acoust. Soc. Am. **62**, 1102–1109 (1977).
[8] H. Schmidt and J. Glattetre, ''A fast field model for three-dimensional wave propagation in stratified environments based on the global matrix method,'' J. Acoust. Soc. Am. **78**, 2105–2114 (1985).
[9] A. C. Kak and M. Slaney, *Principles of Computerized Tomographic Imaging* (IEEE, 1988).
[10] M. Born and E. Wolf, *Principles of Optics*, 7th ed. (Cambridge U.P. Cambridge, 1999).
[11] A. R. Levander, ''Fourth-order finite-difference p-sv seismograms,'' Geophysics **53**, 1425–1436 (1988).
[12] S. Larsen and J. Grieger, ''Elastic modeling initiative, part III: 3-D computational modeling,'' Soc. Expl. Geophys. Conf. Proc. **68**, 1803–1806 (1998).
[13] S. Larsen, M. Antolik *et al.*, ''3D simulations of scenario earthquakes in the San Francisco Bay area,'' EOS Trans. Am. Geophys. Union **78**, 487 (1997).
[14] R. Madariaga, ''Dynamics of an expanding circular fault,'' Bull. Seismol. Soc. Am. **66**(3), 639–666 (1976).
[15] J. Virieux, ''P-SV wave propagation in heterogeneous media: Velocity-stress finite-difference method,'' Geophysics **51**(4), 889–901 (1986).
[16] S. Larsen and D. Harris, ''Seismic wave propagation through a low-velocity nuclear rubble zone,'' Technical report, Lawrence Livermore National Laboratory (1993).

Optimal nonlocal boundary control of the wide-angle parabolic equation for inversion of a waveguide acoustic field[a)]

Matthias Meyer[b)] and Jean-Pierre Hermand[c)]
Université Libre de Bruxelles, Department of Optics and Acoustics, Avenue F.-D. Roosevelt, 50—CP 194/05, B-1050 Brussels, Belgium

(Received 22 September 2004; revised 2 February 2005; accepted 7 February 2005)

This paper applies the concept of optimal boundary control for solving inverse problems in shallow water acoustics. To treat the controllability problem, a continuous analytic adjoint model is derived for the Claerbout wide-angle parabolic equation (PE) using a generalized nonlocal impedance boundary condition at the water-bottom interface. While the potential of adjoint methodology has been recently demonstrated for ocean acoustic tomography, this approach combines the advantages of exact transparent boundary conditions for the wide-angle PE with the concept of adjoint-based optimal control. In contrast to meta-heuristic approaches the inversion procedure itself is directly controlled by the waveguide physics and, in a numerical implementation based on conjugate gradient optimization, many fewer iterations are required for assessment of an environment that is supported by the underlying subbottom model. Furthermore, since regularization schemes are particularly important to enhance the performance of full-field acoustic inversion, special attention is devoted to the application of penalization methods to the adjoint optimization formalism. Regularization incorporates additional information about the desired solution in order to stabilize ill-posed inverse problems and identify useful solutions, a feature that is of particular importance for inversion of field data sampled on a vertical receiver array in the presence of measurement noise and modeling uncertainty. Results with test data show that the acoustic field and the bottom properties embedded in the control parameters can be efficiently retrieved. [DOI: 10.1121/1.1880872]

PACS numbers: 43.60.Pt, 43.60.Rw, 43.30.Bp [EJS] Pages: 2937–2948

I. INTRODUCTION

Within the last decade a number of papers have addressed the problem of *impedance, transparent* or *nonlocal boundary conditions* for the parabolic equation (PE) in underwater acoustic propagation and investigated their application for various PE solvers.[1] The treatment of transparent boundary conditions is of particular importance also for PE methods in electromagnetic wave propagation.[2,3] The efficiency of acoustic propagation predictions can be improved significantly through the use of nonlocal boundary conditions (NLBCs), which serve to restrict the computational grid to regions of prime importance by representing the field behavior in a known ocean subbottom as a nonlocal boundary condition imposed at the water-bottom interface. Papadakis *et al.*[4,5] first introduced a NLBC that exactly transforms the semi-infinite PE problem to an equivalent one in a bounded domain. Papadakis' method requires the evaluation of a spectral integral (Neuman-to-Dirichlet map) whose integrand is inversely proportional to the impedance of the subbottom medium. Earlier, also Marcus[6] developed a generalized impedance boundary condition (GIBC) in order to eliminate the need for a false bottom in PE finite difference schemes. Based on Papadakis' analytic approach Arnold and Ehrhardt[7] constructed a new discrete transparent boundary condition (DTBC) for a Crank-Nicholson finite difference discretization of the wide-angle parabolic equation (WAPE), while Mikhin[8] proposed a Z transformation of the discrete PE to obtain NLBCs for higher-order Padé approximations. Yevick and Thomson[9] recently derived an alternative procedure for obtaining NLBCs directly from the *z*-space Crank-Nicholson solvers for both Tappert's narrow-angle and Claerbout's wide-angle PEs. In contrast to spectral-based NLBC methods, which require the evaluation of an integral transform from wave number space to physical space, their algorithm is carried out entirely in the physical domain.

This paper develops an optimal boundary control approach for the wide-angle PE based on the nonlocal boundary conditions formulated by Yevick and Thomson,[9] thereby extending the earlier work in Ref. 16. The corresponding physical context is to determine the impedance boundary condition of the ocean bottom from acoustic and oceanographic field data. To solve this boundary controllability problem the continuous adjoint of a Claerbout wide-angle PE system is derived analytically. As an adjoint-based optimization the proposed method is complementary to the adjoint approaches that were introduced recently in ocean acoustic tomography[10,11] and in inverse scattering.[12,13] The latter[13] contains an in-depth comparison of three different adjoint formulations for computing Fréchet derivatives, the conven-

[a)]Portions of this work were presented at the 7th European Conference on Underwater Acoustics, 5–8 July 2004, Delft, The Netherlands, and at the 2nd Workshop for Acoustic Inversion Methods and Experiments for Assessment of the Shallow Water Environment, 28–30 June 2004, Ischia, Italy.

[b)]Electronic address: mmeyer@ulb.ac.be
[c)]Electronic address: jhermand@ulb.ac.be This work was done at the Royal Netherlands Naval College, Postbus 10000, 1780 CA Den Helder, The Netherlands.

tional adjoint method, the Lagrange multiplier method and an integral equation formulation which is based on the Lippmann-Schwinger integral equation approach. While Hursky *et al.*[10] derive a discrete adjoint approach for the standard PE for inversion of sound speed variations due to internal tides, an analytic normal mode-based adjoint is used by Thode[11,14] to invert for three-dimensional sound speed perturbations. Norton[12] treats the case of an acoustically hard scattering object and seeks to reconstruct the shape of its boundary by means of an iterative adjoint approach. Since there is no acoustic penetration into the object, the common boundary condition that has to be satisfied is that the normal component of the particle velocity vanishes on the boundary of the scatterer.

The present paper appends a state-of-the-art impedance boundary condition and extends the adjoint approach for Tappert's small-angle PE[10,15,16] to Claerbout's wide-angle approximation while solving the problem analytically in the continuous domain. The NLBC to be determined ensures the continuity of the pressure and vertical particle velocity across the ocean-bottom interface and accounts for both jump discontinuities in the medium properties and the radiation condition. Especially the use of exact discrete NLBCs[7–9] renders the treatment of the bottom in finite-difference PE solvers more accurately and, what is more, the computational domain can thus be restricted exclusively to the water column, where related measurements of the acoustic field are available. Both the direct and the adjoint PE models are discretized on a finite difference (FD) grid and implemented in an efficient inversion scheme based on conjugate gradient. Further, the application of penalization methods to the proposed adjoint-based inversion approach is investigated. Regularization incorporates additional information about the desired solution to stabilize ill-posed inverse problems and identify useful solutions. Regularization techniques are especially valuable to obtain meaningful solutions when some of the parameters are ill determined by least-squares methods, in particular when the number of parameters is larger than the number of available measurements or the measurements are contaminated by noise.[17] This capability is of particular interest for improving full-field acoustic inversion in the assessment of a shallow water environment where field data are recorded on a non-fully-populated array, and measurement noise and modeling uncertainty are ever present.

The paper proceeds as follows. Sections II A and II B formally introduce the concept of adjoint modeling and briefly review the Claerbout wide-angle PE. Section II C generalizes the Yevick and Thomson formulation of the NLBC for control purposes and Sec. II D derives the corresponding tangent linear model of the wide-angle PE system. The latter is required for the derivation of the analytic adjoint whose main steps are outlined in Sec. III. Details of the FD discretization and numerical implementation in an iterative inversion scheme are given in Sec. III A followed by Sec. III B that presents representative example results selected from benchmark tests. Section IV A considers the application of penalization methods to the adjoint optimization and formally derives both the standard and general forms of regularization for the wide-angle PE adjoint. Section IV B then discusses how the so-called *L-curve* criterion can be used to determine the optimal regularization parameter. Section V presents inversion results obtained from synthetic acoustic fields in two different environments. The first test aims to determine the effectiveness of regularization in its general form when the field is sampled on a vertical array in place of on the FD vertical grid. The second test deals with a more complex acoustic field synthesized from environmental data collected during geoacoustic inversion experiments in the Mediterranean. Section VI concludes by discussing the advantages and limitations of WAPE-adjoint-based inversion and the possible extensions of this work.

II. OPTIMAL CONTROL AND ADJOINT MODELING

In comparison with the discrete Lagrange multiplier method in Ref. 10 and the perturbative Green's function method in Ref. 11, the presented optimal boundary control approach belongs to the category of variational methods. In fact, the adjoint expressions (Born approximation) applied in Refs. 10 and 11 can equally be derived using variational methods, as is shown in Ref. 13.

Originally, the concept of optimal control theory was presented in Refs. 18 and 19 and is also referred to as Hilbert uniqueness method (HUM). Adjoint models nowadays are being used for data assimilation, model tuning, and sensitivity analysis in several fields, among which meteorology, oceanography, and seismics are the most common.[20–26] The adjoint approach is also being applied as optimal design method in computational fluid dynamics, particularly for aeronautical applications.[27,28]

Closely related boundary control problems in other disciplines of physics are, e.g., the exact boundary controllability for the heat equation[29] and for Burgers' equation.[30]

A. Adjoint formalism

Consider a dynamical physical system and a model G describing this system and suppose that the model yields a solution ν corresponding to a set of observations. The least-squares cost function J quantifies the model data-fit.[31] With E, F Hilbert spaces and $\mathbb{R}$ the real number space,

$$\begin{aligned} &J: F \to \mathbb{R}, \\ &\nu \mapsto J(\nu). \end{aligned} \tag{1}$$

If the model is further manipulated by a set of control variables χ,

$$\begin{aligned} &G: E \to F, \\ &\chi \mapsto \nu = G(\chi), \end{aligned} \tag{2}$$

the gradient of the cost function with respect to these control variables can be evaluated using the definition of the adjoint operator as follows

$$\nabla_\chi J = G'^* \nabla_\nu J. \tag{3}$$

In mathematical terms Eq. (3) represents the multidimensional analog of the derivative of a composite function. The linear operator G' is the so-called tangent linear model (TLM) and its adjoint G'^* represents the adjoint model. $\nabla_\nu J$ is the residual norm of the measured-predicted acoustic field

which can be interpreted as a forcing function of the adjoint model. The adjoint model G'^* in Eq. (3) thus produces corrections to the respective model inputs that caused the mismatch between the observations and model predictions. It provides gradient information, which can be used to efficiently minimize the cost function in Eq. (1) with respect to the control variables χ.

Other common notations in this context are also the *Fréchet derivative* and the *environmental pressure derivative*. In this respect, Refs. 13, 21, 22, and 28 give a good overview of the equivalent adjoint approaches.

B. Wide-angle PE

Using the adjoint formalism presented in the previous section, the chosen numerical model G is the wide-angle PE due to Claerbout.[32,33] Following the notation of Refs. 9 and 34, the one-way propagation equation treated here is valid for a medium with varying density $\rho(z)$ in a region $0<z<z_b$ between the surface $(z=0)$ and bottom $(z=z_b)$ of a stratified ocean with sound speed and absorption designated by $c(z)$ and $\alpha(z)$, respectively. Since range-varying waveguides can often be modeled as a sequence of range-independent sections, there is no loss of generality in restricting ρ, c, and α in this way. Substitution of the [1,1]-Padé approximation for the pseudo-differential operator $\sqrt{1+X}$, with

$$X=N^2-1+k_0^{-2}\rho\frac{\partial}{\partial z}\left(\rho^{-1}\frac{\partial}{\partial z}\right), \tag{4}$$

$N(z)=n(z)[1+i\alpha(z)]$, and $n(z)=c_0/c(z)$ into the one-way evolution equation

$$\frac{\partial\psi}{\partial r}=ik_0\{-1+\sqrt{1+X}\}\psi \tag{5}$$

yields Claerbout's rational-linear PE

$$2ik_0\left[1+\frac{1}{4}(n^2-1)\right]\psi_r+\psi_{zz}+k_0^2(n^2-1)\psi+\frac{i}{2k_0}\psi_{zz,r}=0. \tag{6}$$

For a given reference wave number $k_0=\omega/c_0$, the field ψ therein can be related to the complex pressure P according to

$$P(r,z)=\frac{\psi(r,z)\exp(ik_0r)}{\sqrt{k_0r}}. \tag{7}$$

C. Nonlocal boundary condition and optimal control

The control variables χ defined in Eq. (2) are determined by Yevick and Thomson's[9] nonlocal impedance boundary condition at the water-bottom interface, which categorizes the presented approach as an optimal boundary control method for the wide-angle PE.

Yevick and Thomson derive a formula for the wave field at range $r+\Delta r$ in terms of the known field at the previously calculated range values from 0 to r by expanding the approximate vertical wave number operator for the downgoing field in powers of the translation operator $R=\exp(-\Delta r\partial_r)$. The z-space vertical wave number operator for the Claerbout wide-angle approximation is given by

$$\Gamma_1^2=k_0^2\left(N_b^2-1+\nu^2\frac{1-R}{1+R}\left[1+\frac{1}{4}\nu^2\frac{1-R}{1+R}\right]^{-1}\right), \tag{8}$$

where $\nu^2=4i/k_0\Delta r$, and the subscript b indicates the bottom. The authors obtain the required impedance boundary condition

$$\left\{\frac{\partial}{\partial z}-i\left(\frac{\rho_w}{\rho_b}\right)\Gamma_1\right\}\psi(r+\Delta r,z_b)=0. \tag{9}$$

This equation accounts for the total impedance jump (sound speed, attenuation, and density) encountered by waves that cross the lower boundary of the waveguide. Expanding Γ_1 in a power series of R yields a numerically tractable, nonlocal representation of Eq. (9). This is readily accomplished by obtaining the Taylor series for the numerator and denominator separately and then convolving the coefficients. Dividing the interval $0\rightarrow r+\Delta r$ into $L+1$ intervals of width Δr and applying the definition of R yields

$$\left[\frac{\partial}{\partial z}-i\beta\right]\psi[(L+1)\Delta r,z_b]=i\beta\sum_{j=1}^{L+1}g_{1,j}\psi[(L+1-j)\Delta r,z_b], \tag{10}$$

where[35]

$$\beta=\frac{\rho_w}{\rho_b}k_0\sqrt{\frac{(N^2-1)\left(1+\frac{1}{4}\nu^2\right)+\nu^2}{\left(1+\frac{1}{4}\nu^2\right)}}. \tag{11}$$

The right-hand side of Eq. (10) solely depends on the known values of the field along the boundary. This equation allows the boundary value of the acoustic field at a given range-propagation step to be determined in terms of the history of boundary-field values for all previous range steps. The simple analytic nature of this operational procedure, which does not require the evaluation of the inverse Fourier transform of the reciprocal of the impedance spectral function as in Papadakis' method, allows it to be applied to the presented boundary control problem in a straightforward way ($z_b=H$):

$$\psi_z(r)-i\beta\psi(r)|_{z=H}=\beta F(r). \tag{12}$$

D. Calculating the directional derivative

To summarize, the system of the wide-angle PE model including a Dirichlet boundary condition at the surface, an analytical Greene's source term,[36] and the generalized nonlocal boundary condition (NLBC) at the bottom can be described as follows:

$$\begin{aligned}
&2ik_0\left[1+\frac{1}{4}(n^2-1)\right]\psi_r+\psi_{zz}+k_0^2(n^2-1)\psi+\frac{i}{2k_0}\psi_{zz,r}=0,\\
&\psi(r,z=0)=0,\\
&\psi(r=0,z)=S(z),\\
&\text{NLBC}\quad \psi_z(r)-i\beta\psi(r)|_{z=H}=\beta F(r).
\end{aligned} \tag{13}$$

The control χ and its respective variation ϕ each consist of a complex two-element vector, $\chi=[\beta,F]$, $\phi=[b,f]$. For-

mulating the wide-angle PE system for both $\psi(\chi+\xi\phi)$ and $\psi(\chi)$ with $\xi\in\mathbb{R}$, subtraction and subsequent division by ξ gives for $\xi\to 0$ with $w=d\psi/d\xi$ the corresponding WAPE tangent linear model (TLM) in Eq. (16). With regard to the NLBC in the wide-angle PE system, formulating the fourth equation for $\psi(\chi+\xi\phi)$ and $\psi(\chi)$ yields

$$\begin{aligned}&\psi_z(\chi+\xi\phi)-i(\beta+\xi b)\psi(\chi+\xi\phi)=(\beta+\xi b)(F+\xi f),\\&\psi_z(\chi)-i\beta\psi(\chi)=\beta F.\end{aligned}\tag{14}$$

Subtraction of these two equations and subsequent division by ξ gives for $\xi\to 0$ again with $w=d\psi/d\xi$ the corresponding tangent linear NLBC,

$$w_z-i\beta w-ib\psi=\beta f+bF,\tag{15}$$

and the complete tangent linear system reads

$$\begin{aligned}&2ik_0\left[1+\frac{1}{4}(n^2-1)\right]w_r+w_{zz}+k_0^2(n^2-1)w+\frac{i}{2k_0}w_{zz,r}=0,\\&w(r=0,z)=0,\\&w(r,z=0)=0,\\&\text{NLBC}\quad w_z(r)-i\beta w(r)-ib\psi(r)-\beta f(r)-bF(r)\big|_{z=H}=0.\end{aligned}\tag{16}$$

Using the TLM for the derivation of the adjoint wide-angle PE in the next section theoretically corresponds to applying the Born approximation as in Ref. 11 to estimate the derivative of the acoustic field with respect to the control parameter χ.

III. DERIVATION OF THE WIDE-ANGLE PE ADJOINT MODEL

With the cost function as a measure for the fit between the observed ψ_{obs} and predicted ψ fields at the range $r=R$,

$$J(\chi)=\frac{1}{2}\int_{z=0}^{H}|\psi(\chi,R,z)-\psi_{obs}(R,z)|^2\,dz,\tag{17}$$

and the choice of an appropriate inner product[37] $\langle\cdot,\cdot\rangle$, the aim is to use the TLM derived in Eq. (16) in order to evaluate $J'(\chi,\phi)$ and finally get an expression for $\nabla J(\phi)$:

$$\begin{aligned}J'(\chi,\phi)&=\int_{z,r=R}\langle\psi-\psi_{obs},w\rangle dz\\&=\int_{r,z=H}\langle\nabla J(\phi),\phi\rangle dr.\end{aligned}\tag{18}$$

Here the derivative $J'(\chi,\phi)$ is first expressed in the space of the observations and, in the last part, in the (dual) space of the controls. In order to calculate the adjoint G'^* as introduced formally in Eq. (3) the scalar product of the wide-angle TLM PE and the newly introduced adjoint variable p can be written as

$$\int\int_{z,r}\left\langle 2ik_0\left[1+\frac{1}{4}(n^2-1)\right]w_r+w_{zz}+k_0^2(n^2-1)w+\frac{i}{2k_0}w_{zz,r},p\right\rangle dr\,dz=0.\tag{19}$$

By partial integration and repeated use of Stokes' theorem, appropriate conditions for the adjoint variable p have to be identified in order to simplify the integral equation such that the remainder can be expressed in a form similar to Eq. (18). The scalar product in Eq. (19) is first subdivided into four separate terms.

$$\int\int_{z,r}\left\langle 2ik_0\left[1+\frac{1}{4}(n^2-1)\right]w_r,p\right\rangle+\langle w_{zz},p\rangle+\langle k_0^2(n^2-1)w,p\rangle+\left\langle\frac{i}{2k_0}w_{zz,r},p\right\rangle dr\,dz=0.\tag{20}$$

Introducing $\eta=[1+1/4(n^2-1)]$ and integrating by parts, the first of them gives

$$2k_0\int\int_{z,r}\langle i\eta w_r,p\rangle dr\,dz=2k_0\left(\left[\int_z\langle i\eta w,p\rangle dz\right]_{r=0}^{r=R}-\int\int_{z,r}\langle i\eta w,p_r\rangle dr\,dz\right).\tag{21}$$

Using the initial condition $w(r=0,z)=0$ of the TLM in Eq. (16) and further transforming yields

$$2k_0\int\int_{z,r}\langle i\eta w_r,p\rangle dr\,dz=\int_{z,r=R}\langle w,-2ik_0\eta p\rangle dz+\int\int_{z,r}\langle w,2ik_0\eta p_r\rangle dr\,dz.\tag{22}$$

Together with the three double integral terms resulting from a similar treatment of the remaining terms in Eq. (20), the double integral term on the rhs of Eq. (22) forms the adjoint of the wide-angle PE. The single integral term on the rhs of Eq. (22) contributes to the implicit adjoint initial condition at range $r=R$. The conditions for the adjoint field p, thus identified

$$\begin{aligned}&2ik_0\left[1+\frac{1}{4}(n^2-1)\right]p_r+p_{zz}+k_0^2(n^2-1)p+\frac{i}{2k_0}p_{zz,r}=0,\\&p(r,z=0)=0,\\&-2ik_0\left[1+\frac{1}{4}(n^2-1)\right]p(z)-\frac{i}{2k_0}p_{zz}(z)\Big|_{r=R}\\&\quad=\psi(z)-\psi_{obs}(z)|_{r=R},\end{aligned}\tag{23}$$

simplify Eq. (19) in such a way that sorting the remaining terms from Eq. (19) by integration region results in

$$\int_{z,r=R}\langle w,\psi-\psi_{obs}\rangle+\int_{r,z=H}\langle w_z,p\rangle-\langle w,p_z\rangle dr+\cdots$$
$$+\frac{1}{2k_0}\int_{r,z=H}-\langle iw_z,p_r\rangle+\langle iw,p_{r,z}\rangle+\cdots$$
$$+\frac{1}{2k_0}(\langle iw_z,p\rangle_{z=H,r=R}-\langle iw,p_z\rangle_{z=H,r=R})=0. \quad (24)$$

Finally, substitution of the respective TLM boundary condition $w_z=\beta f+bF+i\beta w+ib\psi$ into all instances of w_z in the surface integrals along the bottom completes the adjoint WAPE system with

$$\left[1+\frac{i}{2k_0}\frac{\partial}{\partial r}\right](p_z(r)+i\overline{\beta}p(r))|_{z=H}=0 \quad (25)$$

and leads to the following formula for the gradient of the cost function

$$\nabla J=\left[\begin{array}{c}(i\overline{\psi}(r)-\overline{F}(r))\left(p(r)+\frac{i}{2k_0}p_r(r)\right)\\ -\overline{\beta}\left(p(r)+\frac{i}{2k_0}p_r(r)\right)\end{array}\right]_{z=H}. \quad (26)$$

The resulting wide-angle PE adjoint equation which governs the behavior of the adjoint field p is equivalent to the direct model but backwards in space and contains a complex transparent boundary condition at $z=H$ and an implicit adjoint initial condition at range $r=R$. In contrast to Refs. 10, 11, and 14, where the adjoint field was created by using the phase-conjugated (time-reversed) error residual at each receiver as an acoustic source; this interpretation is not valid for the adjoint wide-angle PE anymore. The Neumann adjoint starter condition at $r=R$ in Eq. (23) replaces the simple adjoint Dirichlet condition at $r=R$ in the former cases. The gradient in Eq. (26), which involves both the direct field ψ and its adjoint p, is finally used in an iterative method described in the following section.

A. Numerical implementation

The finite difference implementation of the direct problem given in Eq. (13) is a standard Crank-Nicholson scheme whereas the discrete formulation of the adjoint system including the implicit adjoint starter condition in Eq. (23) and the transparent boundary condition in Eq. (25) requires a separate treatment of the first range step. Starting from range $r=R$ requires an implicit backward-centered (BW-CT) Euler method before proceeding with the standard Crank-Nicholson scheme. With regard to the iterative optimization strategy, conjugate gradient methods are generally known to perform better than, e.g., steepest descent or fixed point iteration and, especially for problems with a large number of unknowns, they are often superior also to Newton-type methods. For minimization of the cost function in Eq. (17), a conjugate gradient optimization scheme[16,38] of Polak-Ribière type with soft line search is implemented which uses the analytic gradient derived in Eq. (26) at each iteration.

B. Example results

A test case is considered to demonstrate the numerical implementation of the optimal nonlocal boundary control for wide-angle PE. The selected case provides performance results that are representative of the adjoint-based approach developed in this paper. The results are shown in Figs. 1 and 2.

The test environment is a range-independent, shallow-water waveguide with an isospeed water column of 1520 $\mathrm{m\,s^{-1}}$, a water depth of 135 m, and a half-space bottom. The test measurement consists of a monochromatic acoustic field with a frequency of 500 Hz generated by a Greene's sound source at the depth of 93 m; the field is observed over the entire water column at the range of 1 km [Fig. 1(b)].

Both true and initial fields were generated on a sampling grid of 512 points in both range and depth by using the NLBC for the wide-angle PE given in Eq. (10). The true NLBCs were calculated for a hard reflecting bottom (sand) with a compression speed of 1600 $\mathrm{m\,s^{-1}}$, a sound attenuation of 0.5 $\mathrm{dB\,\lambda^{-1}}$, and a bulk density of 1.8 $\mathrm{g\,cm^{-3}}$. The initial NLBCs were set to correspond to a soft absorbing bottom (clay) with a lower compression speed of 1505 $\mathrm{m\,s^{-1}}$. The same holds for the true and initial controls F versus range while the corresponding range-independent controls β were obtained from Eq. (11); F and β are complex-valued.

Even though in Fig. 1 the initial field (a) is seen to be quite different from the true field (b), already after six iterations the reconstructed field at range $R=1$ km agrees well with the true one as indicated by the convergence of the cost function in Fig. 2(a). Due to rigorous stopping criteria that were set for the conjugate gradient optimization, the process carried on until iteration number 16. Adjoint-based inversion of the field observed at the single range $R=1$ km [Fig. 2(d)] produces a reconstructed field that is nearly identical to the true one not only at that range but at all range and depth [Fig. 1(c)]. The overall error[39] across range and depth is reduced from initially $>50\%$ to $<5\%$ upon completion of the process [Fig. 2(b)]. Likewise, the control parameter F in Fig. 2(c) is well retrieved at all ranges [Fig. 2(c)]. The control β is constant with respect to range and is recovered with an overall error of $<1\%$. The initial and true β values were respectively $0.9026+0.6955i$ and $0.8489+0.7379i$.

Runs for other source frequencies and depths and for different initial conditions showed similar behavior.

The results show that adjoint-based optimal control of the wide-angle PE in combination with conjugate gradient optimization accelerates drastically the convergence of matched-field inversion when compared to the conventional. Based on tests made for other constellations, the above results can be considered as representative of the performance of this approach provided that the environment is supported by the underlying bottom model.

IV. REGULARIZATION OF THE ADJOINT-BASED OPTIMIZATION

The theoretical basis for solving ill-posed problems by means of regularization methods as introduced by Tikhonov in 1963 is well developed, at least for linear equations. In a

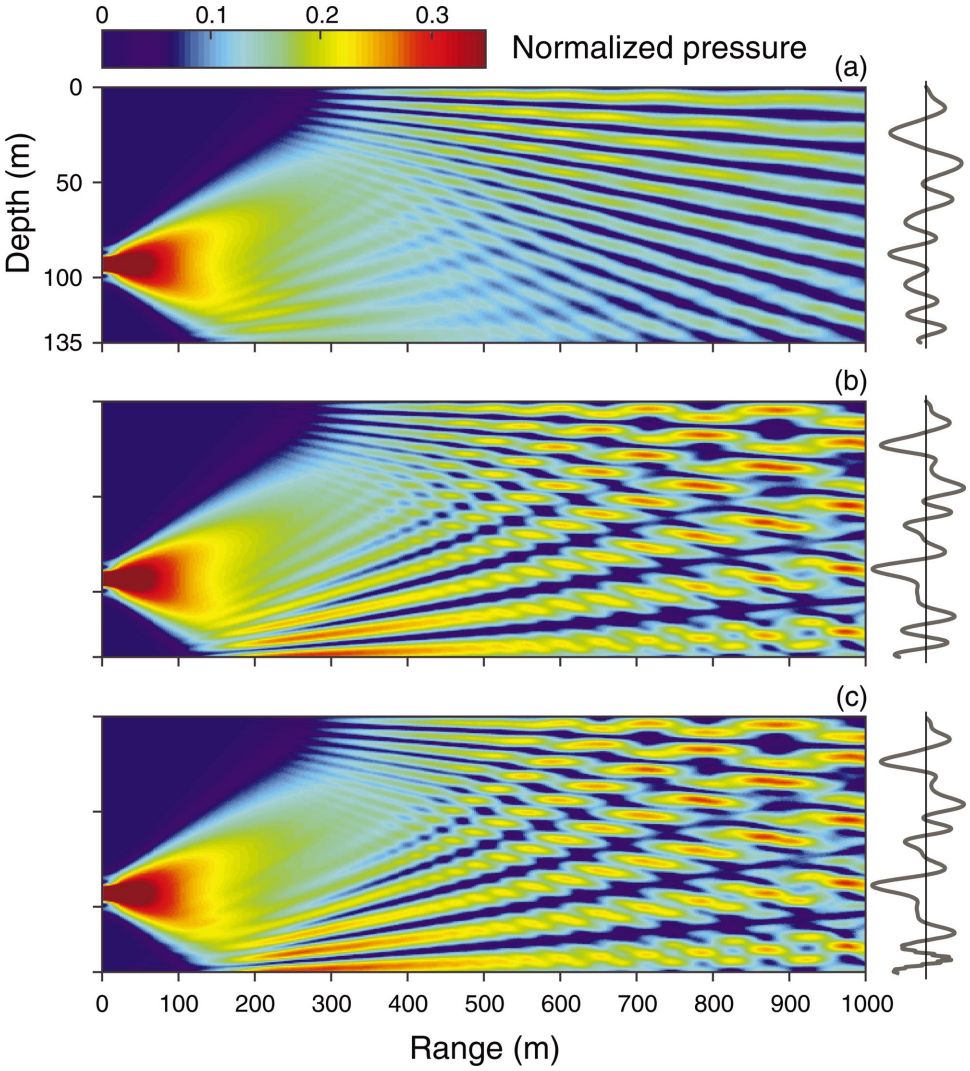

FIG. 1. (Color) Example results of optimal NLBC control for the WAPE. Left: (a) initial, (b) true and (c) inverted acoustic pressure fields. The color scale represents the modulus of the complex-valued ψ, normalized to unity. Right: imaginary part of ψ at range $R=1$ km. The source frequency is 500 Hz and the source depth is 93 m. The receivers are equispaced over the entire water column; their number is 512.

real world, large-scale 2-D or 3-D problems involving large sparse coefficient matrices, the classical Tikhonov's regularization becomes impracticable because the sparsity of the matrices is destroyed. For an iterative numerical model describing a complex nonlinear system or optimization problem an explicit closed-form single matrix representation is difficult to obtain. As a theoretical solution based on, e.g., the generalized SVD of the regularization problem, is often out of reach, computing regularized solutions is mainly based on general heuristics and more practical reasoning. This is particularly true in areas such as medical imaging, seismic inversion, and signal processing.[40–45]

Adding a constraint term to the mean-square error functional of an ill-conditioned inverse problem can, e.g., penalize large variations of the control or emphasize smoother solutions. Regularization of this kind is designed to mitigate ill conditioning in the inversion or to force uniqueness in an underdetermined problem. For example such an approach was proposed for shape reconstruction in inverse scattering.[13]

A. Standard and general form of regularization

A side constraint is imposed on the optimal nonlocal boundary control of the Claerbout wide-angle PE model.

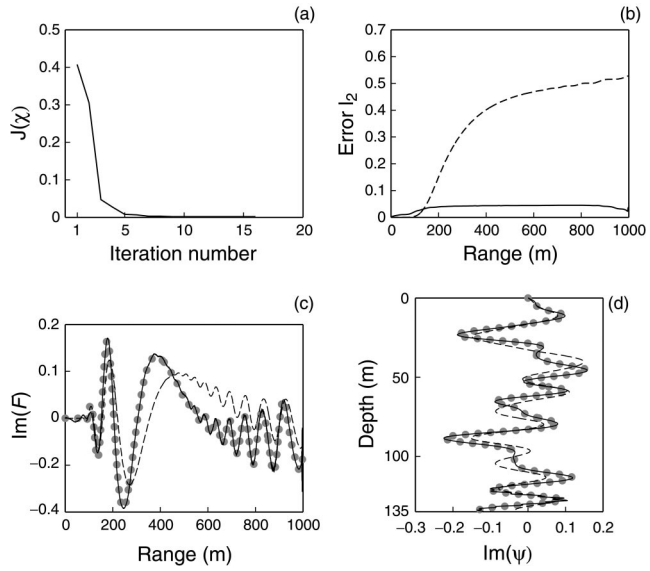

FIG. 2. Example results of optimal NLBC control for the WAPE. (a) Convergence of the algorithm versus iteration number. (b) Relative error between the initial and true acoustic pressure fields (dashed), and between the calculated and true fields (solid). (c) Comparison of the initial (dashed, black), true (dots, gray), and inverted (solid, black) control parameter F versus range. (d) Same as (c) for the field versus depth at the range of 1 km. Only the imaginary parts of F and ψ are shown; the real parts behaved similarly.

This is achieved by augmenting the cost function into a weighted combination of the residual norm of the measured-predicted acoustic fields and the side constraint. The cost function introduced in Eq. (17) is modified to read

$$J(\chi)=\frac{1}{2}\int_{z=0}^{H}|\psi(\chi,R,z)-\psi_{obs}(R,z)|^2\,dz + \frac{1}{2}\alpha\int_{r=0,z=H}^{R}|C(\chi)|^2\,dr, \tag{27}$$

where $C(\chi)$ is a penalty function of the NLBC control $\chi=[\beta,F]$ and α is a non-negative parameter that controls the weight given to the minimization of the side constraint relative to that of the residual. The most common notations in the literature on functional analysis are the so-called *regularization operator* L with α (or k) as the corresponding *regularization parameter*. The principle is to find the regularized control χ_{reg} that provides at the same time a small residual and a moderate value of the penalty function. This regularized control should not be too far from the desired optimal control χ_{opt} of the unperturbed problem that underlies the perturbated one.

Writing the augmented cost function as $J=J_1+J_2$ the resulting gradient is composed of $\nabla J=\nabla J_1+\nabla J_2$, i.e., working through the derivation of ∇J as in Sec. III with the extended cost function yields an additive term for the gradient. In doing so the added regularization term turns out to have no impact on the formulation of the adjoint model itself. In the following the extension to the gradient of the augmented cost function will be determined for two different penalty functions. In an approach which is usually referred to as the *standard form* of regularization, the penalty function C is defined as

$$C(\chi)=\chi(r), \tag{28}$$

which corresponds to the case of an identity regularization operator ($L=I$). Deriving the gradient for the augmented cost function again with $g(\xi)=J_2(\chi+\xi\phi)$ gives

$$J_2'(\chi,\phi)=g'(\xi)|_{\xi=0} = \alpha\int_{r,z=H}\left\langle \chi+\xi\phi,\frac{d}{d\xi}(\chi+\xi\phi)\right\rangle dr. \tag{29}$$

Comparing with $J'(\chi,\phi)=g'(0)=\int_{r,z=H}\langle\nabla J(\phi),\phi\rangle dr$, one can identify $\nabla J_2=\alpha\chi$ to obtain the overall gradient

$$\nabla J=\left[\begin{array}{c}(i\overline{\psi}(r)-\overline{F}(r))\left(p(r)+\dfrac{i}{2k_0}p_r(r)\right)\\ -\overline{\beta}\left(p(r)+\dfrac{i}{2k_0}p_r(r)\right)\end{array}\right]_{z=H}+\alpha\chi(r). \tag{30}$$

With regard to the *general form* of regularization ($L\neq I$), mostly linear differential regularization operators are applied. Choosing a corresponding penalty function

$$C(\chi)=\frac{d}{dr}\chi(r) \tag{31}$$

and applying a similar derivation as above gives

$$\begin{aligned}g'(\xi)&=\alpha\int_{r,z=H}\left\langle\frac{d}{dr}(\chi+\xi\phi),\frac{d^2}{d\xi dr}(\chi+\xi\phi)\right\rangle dr\\ &=\alpha\int_{r,z=H}\frac{d}{dr}\left\langle\frac{d}{dr}(\chi+\xi\phi),\phi\right\rangle - \left\langle\frac{d^2}{dr^2}(\chi+\xi\phi),\phi\right\rangle dr\\ &=\alpha\left[\left\langle\frac{d}{dr}(\chi+\xi\phi),\phi\right\rangle\right]_{r=0}^{r=R} - \alpha\int_{r,z=H}\left\langle\frac{d^2}{dr^2}(\chi+\xi\phi),\phi\right\rangle dr.\end{aligned} \tag{32}$$

Again by comparing with $J'(\chi,\phi)=g'(0)=\int_{r,z=H}\langle\nabla J(\phi),\phi\rangle dr$ and by assuming[46]

$$\frac{d}{dr}\chi\bigg|_{r=R}=\frac{d}{dr}\chi\bigg|_{r=0}=0, \tag{33}$$

one can identify $\nabla J_2=-\alpha(d^2/dr^2)\chi$ and obtain for the overall gradient

$$\nabla J=\left[\begin{array}{c}(i\overline{\psi}(r)-\overline{F}(r))\left(p(r)+\dfrac{i}{2k_0}p_r(r)\right)\\ -\overline{\beta}\left(p(r)+\dfrac{i}{2k_0}p_r(r)\right)\end{array}\right]_{z=H} - \alpha\frac{d^2}{dr^2}\chi(r). \tag{34}$$

In the following the main focus is laid on the general regularization approach which was found to be more appropriate for the underlying problem. For example, noisy components in the data lead to rough oscillations in the controls which in turn are aptly penalized by the differential regularization operator in Eq. (31); standard regularization with an identity regularization operator as defined in Eq. (28) solely penalizes large values of the control χ and is therefore not affected to the same degree by an oscillatory behavior of the controls. The true controls are sufficiently smooth to justify the use of a differential regularization operator.

B. Regularization parameter choice

In the absence of reliable *a priori* error level information or convergence results the so-called *L-curve* criterion is a heuristic approach to determine the optimal regularization parameter α. It is based on a logarithmic representation of the penalization term of the regularized solution versus the corresponding residual term as a function of the regularization parameter. For discrete ill-posed problems, the curve when displayed on a log-log scale has almost always a characteristic "L" shape with a marked corner separating its vertical and the horizontal parts.[40,41]

Although there is no rigorous proof of the universal validity of this approach, an optimal choice for α is made by picking the value that generates the penalty-residual pair at

the point of maximum curvature, i.e., the elbow in the L-curve. The model corresponding to this particular solution then yields the regularized inversion results.

V. NLBC INVERSION RESULTS

Inversion results are presented for two study cases. The first case focuses on the regularized inversion of an acoustic field sampled on a vertical array for the same waveguide as in Sec. III B. The second case deals with the application of optimal NLBC control to a realistic scenario based on experiments in Mediterranean shallow waters.

A. Regularized optimization

The effect of regularization on the adjoint optimization scheme is investigated for the case of a discrete set of receiving points $\{X_m | m=1,...,M\}$ in place of the dense vertical sampling of the FD grid. Considering a vertical receiver array at the range $r=R$, $X_m=X(R,z_m)$, the observed field $\psi_{obs}(R,z)$ becomes

$$\psi_{obs}(R,z)=\sum_{m=1}^{M}\psi_{obs}(R,z)\,\delta(z-z_m) \tag{35}$$

and the cost function reduces to

$$\begin{aligned} J(\Psi)&=\frac{1}{2}\int_{z=0}^{H}\sum_{m=1}^{M} w_m|\psi(\Psi,R,z) \\ &\quad -\psi_{obs}(R,z)|^2\delta(z-z_m)dz \\ &=\frac{1}{2}\sum_{m=1}^{M} w_m|\psi(\Psi,R,z_m)-\psi_{obs}(R,z_m)|^2. \end{aligned} \tag{36}$$

The test involves the same source and environmental parameters as those in Sec. III B to allow comparison of the previous nonregularized solution and the one obtained with the general form of regularization. For this example we choose equidistantly spaced receiver depths spanning the entire water column and a uniform weighting, i.e., $w_m=1$. With respect to the test case in Sec. III B, the spacing is reduced by a factor of 16, i.e., from 0.26 m ($\lambda/12$) to 4.2 m (1.4λ). For reference, Fig. 3 shows nonregularized inversion results, i.e., the regularization parameter α in the augmented cost function Eq. (27) is set to zero. For comparison, a curve of the penalization term versus iteration number is displayed together with the residual norm in Fig. 3(a) even though it does not affect the optimization process since $\alpha=0$.

The residual term in the cost function, which measures the mismatch between the true and inverted fields at the 32 receiver depths and range $r=R$, vanishes after six iterations as for the 512-receiver case. However, the penalization term increases significantly with iteration number, thereby indicating a nonsmooth behavior of the control parameters. Even though the reconstructed field at the 32 depths of the array agrees very well with the true one [Fig. 3(d)], the relative error[39] versus range calculated over the FD grid [Fig. 3(b)] and the high-frequency oscillations of the control F versus range [Fig. 3(c)] indicate a nonoptimal solution which is due to nonuniqueness of the underdetermined optimization problem.

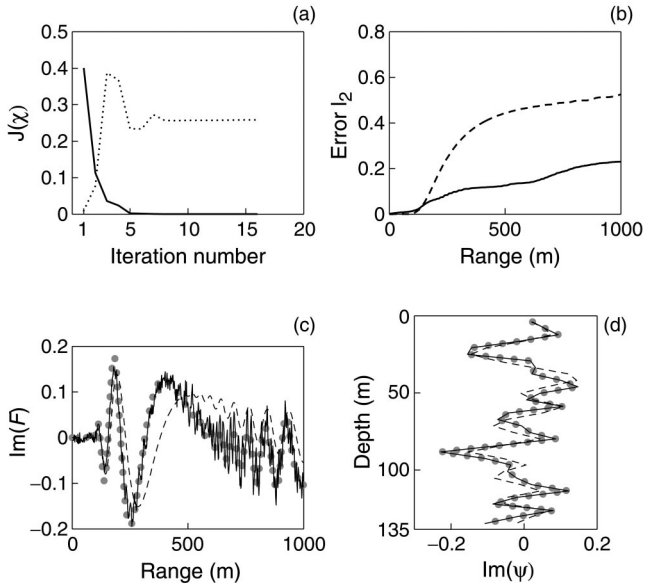

FIG. 3. Nonregularized inversion results with a vertical array of 32 receivers. Convergence of the algorithm versus iteration number: residual norm (solid) and penalization term (dashed). (b) Relative error between the initial and the true fields (dashed), and between the calculated and the true fields (solid). (c) and (d) Comparison of the initial (dashed, black), the true (dots, gray), and the inverted (solid, black) imaginary parts of the control parameter F versus range and the pressure field versus depth at 1-km range.

The *L-curve* criterion described in Sec. IV B is applied to find the optimal regularization parameter α in Eq. (27). The inversion process is repeated for different values of α and the penalization term obtained for each regularized solution is plotted versus the corresponding residual term on a log-log scale. Here, 17 values of α between 0 and 1 were used. The point of maximum curvature in the *L-curve* (Fig. 4) represents the best compromise between the minimization of the penalty term and of the residual norm. The corresponding value $\alpha=0.05$ yields the regularized control χ_{reg} that provides at the same time a small residual and a moderate value of the penalty function. As a matter of fact, Fig. 5 shows that with the regularized controls the penalization and residual terms are equally optimized around the sixth iteration.

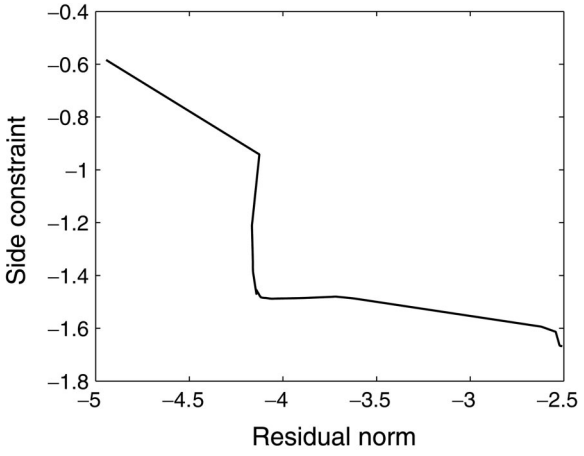

FIG. 4. Optimal choice of the regularization parameter. L-curve in log-log scale. The corresponding inversion results are shown in Fig. 5.

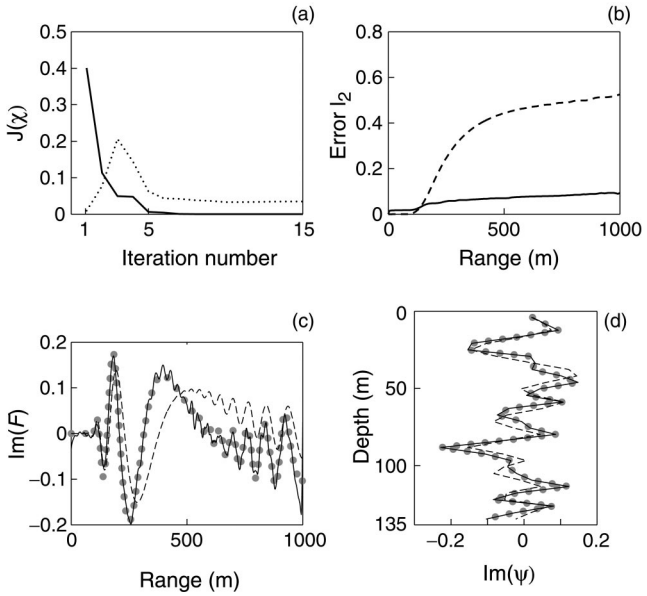

FIG. 5. Regularized inversion results for a vertical array of 32 receivers. The regularization parameter $\alpha=0.05$. See the caption of Fig. 3.

The relative error[39] versus range [Fig. 5(b)] is significantly reduced and the control F versus range [Fig. 5(c)] behaves smoothly. Sixteen iterations are sufficient to recover the field with an error over all range and depth of less than 8% compared to the 23% of the nonregularized results [Fig. 3(d)].

The acoustic field inverted from 512 receiver depths in Sec. III B and the one inverted from 32 depths are compared in Fig. 6, showing that proper regularization of a perturbed problem can give results that are quite close to the unperturbed ones. Including additional information about the desired controls such as smoothness thus stabilizes the underlying ill-posed problem and helps identifying meaningful solutions, but, clearly, even with regularization, the solution of an ill-posed problem has limited accuracy.

B. South Elba environment

WAPE-adjoint-based inversion was also assessed on more complex acoustic fields synthesized from ocean sound speed profiles and subbottom acoustic properties collected in real environments. Here the chosen example is based on simulations of the YELLOW SHARK 94 experiments, south of the island of Elba, Italy, using environmental parameters available from previous full-field inversions of acoustic data, and from an oceanographic survey with a towed-oscillating CTD profiler.[47,48]

The site is modeled as in Ref. 49 and consists of a water column with average depth 113.1 m on top of a 7.5-m-thick clay sediment layer with a compression-speed gradient ($\rho=1.5$ g cm^{-3}, $c=1470$ m s^{-1}, $g=2$ s^{-1}, $\alpha=0.03$ dB λ^{-1}), and a homogeneous fluid half-space modeling a silty-clay sediment ($\rho=1.8$ g cm^{-3}, $c=1530$ m s^{-1}, $\alpha=0.15$ dB λ^{-1}).

The source depth is set to 69.2 m as in one of the ex-

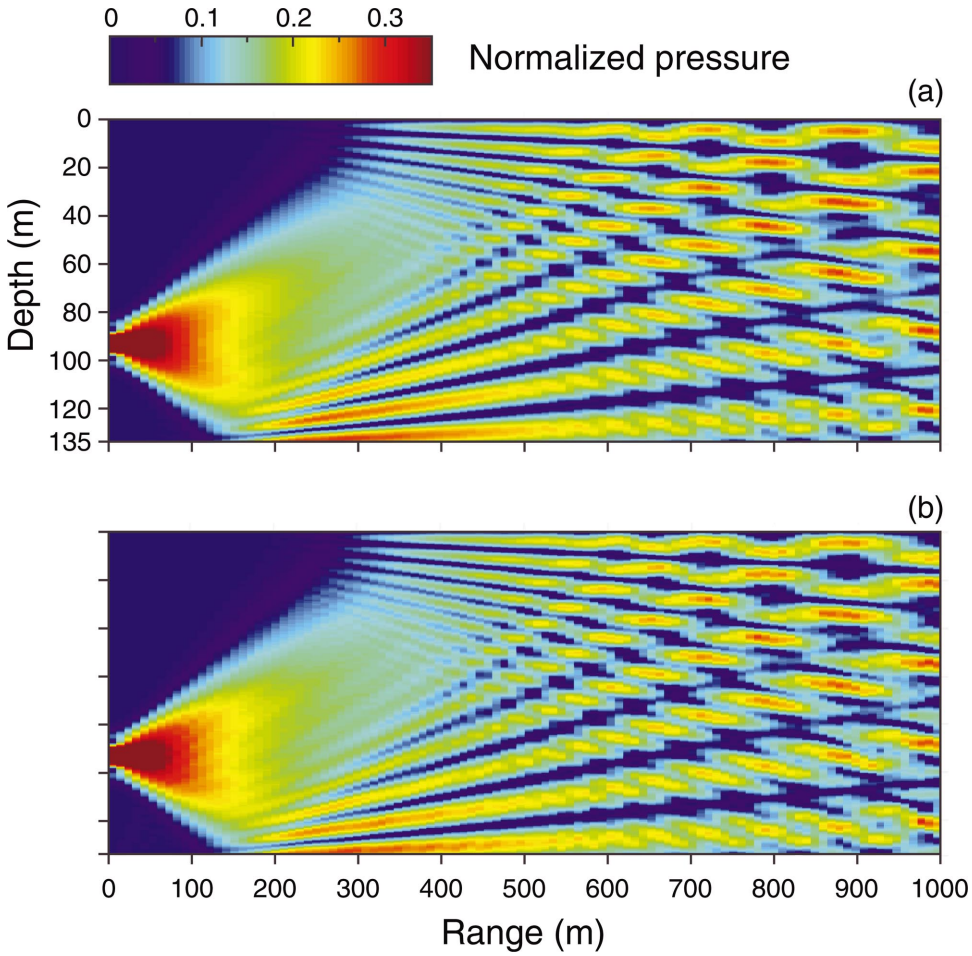

FIG. 6. (Color) Comparison of reconstructed fields from WAPE adjoint-based inversion: (a) nonregularized solution for the 512 receiver depths of the FD grid and (b) regularized solution for the 32 receiver depths of a vertical array.

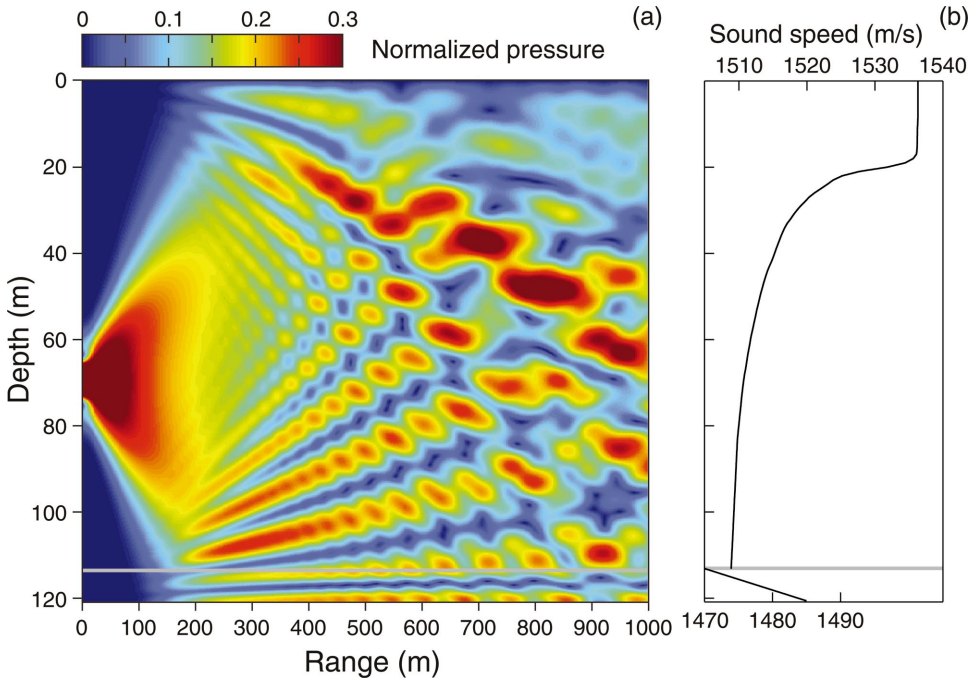

FIG. 7. (Color) South Elba environment. (a) Acoustic pressure field generated with the wide-angle PE using NLBC calculated from measurement of the subbottom properties. The color scale represents the modulus of the complex-valued ψ, normalized to unity. (b) Range-average sound speed profile of the water column and sediment layer used for the modeling. The upper and lower scales refer to water and sediment, respectively.

perimental runs[47] and the source frequency is set to 500 Hz as for the previous test case of Secs. III B and V A. The range average of the sound speed profiles measured during one of the experimental runs is used for the modeling; it is strongly downward refracting as seen in Fig. 7(b). The acoustic field has been generated accordingly on a sampling grid of 512 points in both range and depth using Claerbout's wide-angle PE and the NLBC as described above [Fig. 7(a)].

For the inversion the low-absorbing sediment layer was assumed to be known while the NLBCs associated with the layer-subbottom interface were inverted. For the initial conditions a sand bottom was assumed with a much higher compression speed and sound attenuation ($c=1575\,\mathrm{m\,s^{-1}}$, $\alpha=1$ $\mathrm{dB\,\lambda^{-1}}$).

The performance of the adjoint-based optimization (Fig. 8) is comparable to the previous cases presented in Secs. III B and V A. Again the convergence of the cost function in Fig. 8(a) indicates that already after a couple of iterations the reconstructed field at range $R=1$ km agrees very well with the true one. Upon completion of the process the field obtained at range $R=1$ km [Fig. 8(d)], as well as over the whole section [Fig. 8(b)] and the control parameter F versus range [Fig. 8(c)] correspond to their true counterparts.

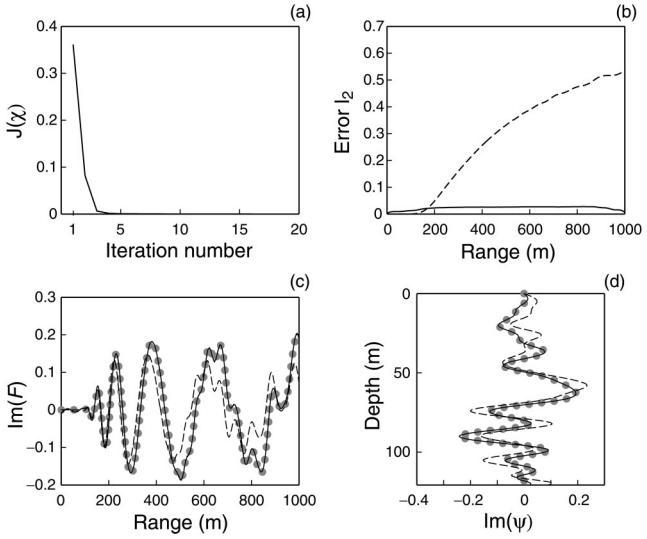

FIG. 8. Inversion results for the South Elba environment. Optimal control of the subbottom NLBC for the WAPE. See the caption of Fig. 3.

Other runs with different initial bottom conditions, e.g., $c=1650\,\mathrm{m\,s^{-1}}$ and $\alpha=0.8$ $\mathrm{dB\,\lambda^{-1}}$, gave nearly identical inversion results and always after a few iterations (not shown).

VI. CONCLUSION AND PERSPECTIVE

A continuous analytical adjoint approach has been developed for a propagation model that is physically realistic for solving a class of inverse problems in shallow water acoustics. The presented approach combines exact nonlocal boundary conditions with an optimal control method based on the analytical derivation of the adjoint of a Claerbout wide-angle PE. Furthermore, the application of regularization to the adjoint optimization has been investigated and analytic gradient extensions have been derived for standard and linear differential regularization operators. The obtained derivations are especially suited for implementation in gradient-based optimization schemes since they are expressed in closed form. They also provide benchmark solutions for validating automatic differentiation tools that are being used to construct adjoint codes directly from computational codes of forward propagation modeling.

Both the wide-angle PE and its adjoint have been implemented numerically in an inversion scheme using a Polak-Ribière-type conjugate gradient optimization, which at each iteration uses analytic gradient information. The implemented optimization algorithm increases the convergence rate and robustness with respect to local optimization ones that have been previously applied to adjoint modeling, e.g., fixed point or steepest descent iteration.

Results with synthesized acoustic fields including those from the South Elba test environment have demonstrated the ability of the adjoint-based optimal control method to invert for the nonlocal impedance boundary conditions and to converge after a couple of iterations, typically less than ten. Moreover, regularization methods have been applied to deal with field data sampled on a vertical receiver array. Regularization will also be important to mitigate the detrimental effects of measurement noise and modeling uncertainty. Regularized adjoint inversion has been shown to produce promising results, but still the studied cases of 32 receiver depths at frequencies lower than 1 kHz represent a sufficiently dense vertical sampling of the acoustic field. Further reducing the number of array elements or, more generally, the number of available measurements with respect to the number of unknown parameters results in ill-determined parameters.

Sparse array geometry will require a generalization of the WAPE-adjoint-based approach to a joint optimization across multiple frequencies. Otherwise, even for the case of ill-posed inverse problems with suboptimal solutions, the very small number of iterations required for minimization of the cost function still allows for multiple initializations of the inversion process or the implementation within a hybrid optimization scheme. If used standalone, one can invert for environmental properties that are supported by the wide-angle PE model and the nonlocal boundary conditions that are presently used in our formulation. Possible extensions of this adjoint boundary control approach can, e.g., incorporate more sophisticated NLBC formulations for a sloping boundary,[50] for an elastic bottom,[4,5] or even for bottom types with linear depth dependence of the refraction index and for simple quasi-stratified bottoms.[3,51]

Work is ongoing to test the adjoint approach on experimental acoustic data with the aim to invert for physical properties of the ocean bottom. For this purpose, it is possible to introduce additional controls and *a posteriori* extract the geoacoustic parameters embedded in the inverted nonlocal impedance boundary conditions. For example, by introducing the density ρ_b itself as a third control in Eqs. (11) and (12), respectively, the remaining unknown parameters c and α can be determined from the equation system formed by the real and imaginary parts of β.

Currently, the state of the art for solving inverse problems in ocean acoustics is mostly represented by a meta-heuristic[52] approach to the global optimization of ocean or bottom parameters. Geoacoustic inversion methods have been shown to produce valuable results in the real world, but still they require a significant amount of computing power which depends on environmental complexity, experimental arrangement, acoustic transmission parameters, optimization algorithms, etc. The alternative approach that has been presented here is fundamentally different in the sense that the ''inversion procedure'' itself is directly linked to the underlying waveguide physics and, most importantly, is extremely fast, thereby realizing a functional tradeoff between resolution and run time. Adjoint acoustic modeling has recently been shown to be a valuable methodology for both ocean tomography and inverse scattering. The presented approach, either used standalone or integrated in a hybrid inversion scheme, is a first step in extending the methodology to geoacoustic inversion through optimal control of the nonlocal boundary conditions of a wide-angle PE.

ACKNOWLEDGMENTS

The authors wish to thank David J. Thomson, DRDC Atlantic, for his helpful collaboration on nonlocal boundary conditions in wide-angle PE modeling. Special thanks also to Craig Carthel, NURC, for fruitful discussions on the numerical implementation of the WAPE optimal boundary control. For the regularization part the authors gratefully acknowledge the correspondence with Per Christian Hansen, Technical University of Denmark. The authors are greatly indebted to Jean-Claude Le Gac, EPSHOM, for sharing results and programming code for narrow-angle PE control, Mark Asch, LAMFA, Université de Picardie Jules Verne, for the advice during the mathematical derivation of the WAPE adjoint, and Frans Absil, RNLNC, for the help during the manuscript preparation. The YELLOW SHARK 94 experimental data were kindly supplied by NURC. The research is funded by the Royal Netherlands Navy (RNLN) and the Service Hydrographique et Océanographique de la Marine (EPSHOM), France, under the REA and SIGMAA projects (Contract Nos. 631.380026.01 and CA/2004/03/CMO) in the framework of the Joint Research Project AO-BUOY REA with the NATO Undersea Research Center (NURC), Italy. The study contributes to the AQUATERRA Integrated Project funded by the European 6th Framework Program (European Commission, Contract No. 505428-GOCE).

[1] D. Lee, A. D. Pierce, and E. C. Shang, ''Parabolic equation development in the twentieth century,'' J. Comput. Acoust. **8**(4), 527–637 (2000).
[2] M. Levy, *Parabolic Equation Methods for Electromagnetic Wave Propagation*, Electromagnetic Waves Series (IEE, London, 2000).
[3] M. Levy, ''Transparent boundary conditions for parabolic equation solutions of radiowave propagation problems,'' IEEE Trans. Antennas Propag. **45**, 66–72 (1997).
[4] J. S. Papadakis, M. I. Taroudakis, P. J. Papadakis, and B. Mayfield, ''A new method for a realistic treatment of the sea bottom in the parabolic approximation,'' J. Acoust. Soc. Am. **92**, 2030–2038 (1992).
[5] J. S. Papadakis, ''Exact, nonreflecting boundary conditions for parabolic-type approximations in underwater acoustics,'' J. Comput. Acoust. **2**, 83–98 (1994).
[6] S. W. Marcus, ''A generalized impedance method for application of the parabolic approximation to underwater acoustics,'' J. Acoust. Soc. Am. **90**, 391–398 (1991).
[7] A. Arnold and M. Ehrhardt, ''Discrete transparent boundary conditions for wide angle parabolic equations in underwater acoustics,'' J. Comput. Phys. **145**(2), 611–638 (1998).
[8] D. Mikhin, ''Exact discrete nonlocal boundary conditions for high-order Padé parabolic equations,'' J. Acoust. Soc. Am. **116**, 2864–2875 (2004).
[9] D. Yevick and D. J. Thomson, ''Nonlocal boundary conditions for finite-difference parabolic equation solvers,'' J. Acoust. Soc. Am. **106**, 143–150 (1999).
[10] P. Hursky, M. B. Porter, W. S. Hodgkiss, and W. A. Kuperman, ''Adjoint modeling for acoustic inversion,'' J. Acoust. Soc. Am. **115**, 607–619 (2004).
[11] A. Thode, ''The derivative of a waveguide acoustic field with respect to a three-dimensional sound speed perturbation,'' J. Acoust. Soc. Am. **115**, 2824–2833 (2004).
[12] S. J. Norton, ''Iterative algorithms for computing the shape of a hard scattering object: Computing the shape derivative,'' J. Acoust. Soc. Am. **116**, 1002–1008 (2004).
[13] S. J. Norton, ''Iterative inverse scattering algorithms: Methods of computing Fréchet derivatives,'' J. Acoust. Soc. Am. **106**, 2653–2660 (1999).

[14] A. Thode and K. Kim, ''Multiple-order derivatives of a waveguide acoustic field with respect to sound speed, density, and frequency,'' J. Acoust. Soc. Am. **116**, 3370–3383 (2004).
[15] M. Asch, J.-C. Le Gac, and P. Helluy, ''An adjoint method for geoacoustic inversions,'' in *Proceedings of the 2nd Conference on Inverse Problems, Control and Shape Optimization*, Carthage, Tunisia (2002).
[16] J.-C. Le Gac, Y. Stephan, M. Asch, P. Helluy, and J.-P. Hermand, ''A variational approach for geoacoustic inversion using adjoint modeling of a PE approximation model with non local impedance boundary conditions,'' in *Theoretical and Computational Acoustics 2003*, edited by A. Tolstoy, Y. C. Teng, and E. C. Shang (World Scientific, Singapore, 2004), pp. 254–263.
[17] H. W. Engl, M. Hanke, and A. Neubauer, *Regularization of Inverse Problems* (Kluwer Academic, Dordrecht, 1999).
[18] J. L. Lions, *Optimal Control of Systems Governed by Partial Differential Equations*, Vol. 170 of *A series of comprehensive studies in mathematics* (Springer Verlag, New York, 1971).
[19] J. L. Lions, ''Exact controllability, stabilization and pertubations for distributed systems,'' SIAM Rev. **30**, 71–86 (1988).
[20] M. S. Zhdanov, *Geophysical Inverse Theory and Regularization Problems*, No. 36 in *Methods in geochemistry and geophysics* (Elsevier, Amsterdam, 2002).
[21] P. R. Gillivray and D. W. Oldenburg, ''Methods for calculating Fréchet derivatives and sensitivities for the non-linear inverse problem: A comparative study,'' Geophys. Prospect. **38**, 499–524 (1990).
[22] A. Tarantola, ''Inversion of seismic reflection data in the acoustic approximation,'' Geophysics **49**, 1259–1266 (1984).
[23] A. Tarantola, *Inverse Problem Theory: Methods for data fitting and model parameter estimation* (Elsevier, New York, 1987).
[24] Z. Sirkes and E. Tziperman, ''Finite difference of adjoint or adjoint of finite difference,'' Mon. Weather Rev. **125**, 3373–3378 (1997).
[25] R. M. Errico, ''What is an adjoint model?'' Bull. Am. Meteorol. Soc. **78**, 2577–2591 (1997).
[26] A. Kirsch, *An Introduction to the Mathematical Theory of Inverse Problems*, Vol. 120 of *Applied Mathematical Sciences* (Springer, New York, 1996).
[27] M. B. Giles and N. A. Pierce, ''Analytic adjoint solutions for the quasi 1d Euler equations,'' J. Fluid Mech. **426**, 327–345 (2001).
[28] M. B. Giles and N. A. Pierce, ''An introduction to the adjoint approach to design,'' Flow, Turbul. Combust. **65**, 393–415 (2000).
[29] C. Carthel, R. Glowinski, and J. L. Lions, ''On exact and approximate boundary controllabilities for the heat equation: A numerical approach,'' J. Optim. Theory Appl. **82**(3), 429–484 (1994).
[30] Y. Leredde, J.-M. Lellouche, J.-L. Devenon, and I. Dekeyser, ''On initial, boundary conditions and viscosity coefficient control for Burgers' equation,'' Int. J. Numer. Methods Fluids **28**, 113–128 (1998).
[31] R. Giering and T. Kaminski, ''Recipes for adjoint code construction,'' ACM Trans. Math. Softw. **24**(4), 437–474 (1998).
[32] F. Jensen, W. Kuperman, M. Porter, and H. Schmidt, *Computational Ocean Acoustics* (American Institute of Physics, New York, 1994), pp. xvi and 612.
[33] J. Claerbout, ''Coarse grid calculations of waves in inhomogeneous media with application to delineation of complicated seismic structure,'' Geophysics **35**, 407–418 (1970).
[34] D. Yevick and D. J. Thomson, ''Impedance-matched absorbers for finite-difference parabolic equation algorithms,'' J. Acoust. Soc. Am. **107**, 1226–1234 (2000).
[35] The expression for the parameter β is not provided explicitly in Ref. 9 for the case of a wide-angle PE. However, the result obtained here has been approved via correspondence with the authors.
[36] The analytical Greene's starter is given as[32] $\psi(r=0,z)=\sqrt{k_0}[1.4467-0.4201k_0^2(z-z_0)^2]\exp(-k_0^2(z-z_0)^2/3.0512)$.
[37] The real-valued inner product $\langle\cdot,\cdot\rangle$ used here is defined in accordance with Refs. 15 and 16 as $\langle z_1,z_2\rangle=\mathrm{Re}(z_1\overline{z_2})$ where z_1, $z_2\in\mathbb{C}$ and $\overline{z_2}$ indicates complex conjugation of z_2.
[38] P. E. Frandsen, K. Jonasson, H. B. Nielsen, and O. Tingleff, ''Unconstrained optimization,'' Lecture note IMM-LEC-2, Technical University of Denmark.
[39] The relative error between the inverted (initial) and the true field is calculated as an 12 norm according to the following formula $errorL2(r_j)=\sqrt{\Sigma_i|\psi_{true}(z_i,r_j)-\psi_{calc}(z_i,r_j)|^2}/\sqrt{\Sigma_i|\psi_{true}(z_i,r_j)|^2}$.
[40] P. C. Hansen, *Rank-deficient and Discrete Ill-posed Problems* (SIAM, Philadelphia, 1998).
[41] M. Hanke and P. C. Hansen, ''Regularization methods for large-scale problems,'' Surv. Math. Ind. **3**, 253–315 (1993).
[42] A. Neumaier, ''Solving ill-conditioned and singular linear systems: A tutorial on regularization,'' SIAM Rev. **40**, 636–666 (1998).
[43] M. Hanke and T. Raus, ''A general heuristic for choosing the regularization parameter in ill-posed problems,'' SIAM J. Sci. Comput. (USA) **17**, 956–972 (1996).
[44] M. Huyer and A. Neumaier, ''A new exact penalty function,'' SIAM J. Optim. **13**(4), 1141–1158 (2003).
[45] A. Neumaier, ''Complete search in continuous global optimization and constraint satisfaction,'' in *Acta Numerica 2004*, edited by A. Iserles (Cambridge U.P., Cambridge, 2004).
[46] With an approach similar to Ref. 13, i.e., outside the region of interest $\chi(r)=\chi_0$, $r\leqslant 0$, $\chi(r)=\chi_1$, $r\geqslant R$ and allowing the domain of integration to expand to infinity, one gets $[(d/dr)\chi=0, r\notin]0,R[]$.
[47] J.-P. Hermand and P. Gerstoft, ''Inversion of broad-band multitone acoustic data from the YELLOW SHARK summer experiments,'' IEEE J. Ocean. Eng. **21**(4), 324–346 (1996).
[48] J.-P. Hermand, ''Broad-band geoacoustic inversion in shallow water from waveguide impulse response measurements on a single hydrophone: theory and experimental results,'' IEEE J. Ocean. Eng. **24**(1), 41–66 (1999).
[49] C. W. Holland, J.-P. Hermand, and S. Dosso, ''Fine-grained sediment geoacoustic properties from remote acoustic measurements,'' in *Proceedings of the 7th European Conference on Underwater Acoustics, ECUA 2004*, Delft, The Netherlands (2004), pp. 677–684.
[50] J. S. Papadakis and B. Pelloni, ''A method for the treatment of a sloping sea bottom in the parabolic approximation,'' J. Comput. Acoust. **4**(1), 89–100 (1996).
[51] A. V. Popov, ''Accurate modeling of transparent boundaries in quasi-optics,'' Radio Sci. **31**(6), 1781–1790 (1996).
[52] S. Voss, S. Martello, I. Osman, and C. Roucairol, *Meta-Heuristics: Advances and Trends in Local Search Paradigms for Optimization* (Springer, New York, 1998).

Dispersion-based short-time Fourier transform applied to dispersive wave analysis

Jin-Chul Hong, Kyung Ho Sun, and Yoon Young Kim[a)]
School of Mechanical and Aerospace Engineering and National Creative Research Initiatives Center for Multiscale Design, Seoul National University, Shinlim-Dong, San 56-1, Kwanak-Gu, Seoul 151-742, Korea

(Received 22 October 2004; revised 18 February 2005; accepted 21 February 2005)

Although time-frequency analysis is effective for characterizing dispersive wave signals, the time-frequency tilings of most conventional analysis methods do not take into account dispersion phenomena. An adaptive time-frequency analysis method is introduced whose time-frequency tiling is determined with respect to the wave dispersion characteristics. In the dispersion-based time-frequency tiling, each time-frequency atom is adaptively rotated in the time-frequency plane, depending on the local wave dispersion. Although this idea can be useful in various problems, its application to the analysis of dispersive wave signals has not been made. In this work, the adaptive time-frequency method was applied to the analysis of dispersive elastic waves measured in waveguide experiments and a theoretical investigation on its time-frequency resolution was presented. The time-frequency resolution of the proposed transform was then compared with that of the standard short-time Fourier transform to show its effectiveness in dealing with dispersive wave signals. In addition, to facilitate the adaptive time-frequency analysis of experimentally measured signals whose dispersion relations are not known, an iterative scheme for determining the relationships was developed. The validity of the present approach in dealing with dispersive waves was verified experimentally. [DOI: 10.1121/1.1893265]

PACS numbers: 43.60.Hj, 43.60.Mn, 43.20.Hq [EJS] Pages: 2949–2960

I. INTRODUCTION

Dispersion is a unique phenomenon that is often observed in guided-wave propagation.[1,2] Time-frequency analysis has been used effectively in the characterization of the time-varying spectral components of dispersive waves. The short-time Fourier transform (STFT)[3] and the continuous wavelet transform (CWT)[4,5] are commonly used for the time-frequency analysis of dispersive waves. Figures 1(a) and (b) show a comparison of the time-frequency tilings of the STFT and CWT, respectively. The time-frequency resolution achieved by the STFT is independent of the location in the time-frequency plane. Therefore, the STFT may be inappropriate for analysis of dispersive waves, whose spectral components vary rapidly in time. On the other hand, the CWT allows frequency-adaptive time-frequency tiling so that the CWT can characterize some class of dispersive wave modes more accurately.[6] To achieve better time-frequency resolution, various modifications of the STFT and CWT based on the optimal windowing[7–10] or adaptive ideas[11–13] have been developed.

Although conventional or modified time-frequency analysis methods such as the STFT and CWT have been used for the analysis of dispersive waves, their time-frequency tilings do not consider the dispersion effect explicitly. If the dispersion effect of a wave is not so small, it will be difficult to extract time-varying signal pattern. However, the time-frequency tilings of the conventional STFT and CWT are not time varying. Thus, these methods can have some limitations in identifying accurately the time-varying aspects of dispersive waves.

The objective of this work is to present an adaptive time-frequency analysis method, whose time-frequency tiling depends on the dispersion characteristics of the wave signal to be analyzed. The method is based on the chirplet transform[14,15] which allows a generalized time-frequency tiling including chirping factors in time or frequency domain. Due to the chirping property, the chirplet transform gives more accurate estimation of instantaneous frequency of given signals.[16] Although the chirping idea can be important for the analysis of time-varying pattered signals, its application to the analysis of dispersive waves has not been reported.

As shown in Fig. 1(c), the dispersion-based time-frequency tiling is performed by adaptively rotating each of the analysis atoms in the time-frequency plane with respect to the wave dispersion relationship. Thus it can be more suitable for representing local variations of dispersive waves. Another important contribution of this work is the theoretical analysis of the time-frequency resolution of the present adaptive method. Its time-frequency resolution was compared with that of the standard short-time Fourier transform. To facilitate our adaptive method for the analysis of experimentally measured signals whose dispersion relations are unknown, an iterative scheme for determining the relationships was also developed. To check the effectiveness of the present adaptive time-frequency method, i.e., the key role of rotating time-frequency tiling for improving time-frequency localization, numerical investigations and experiments were carried out on flexural waves in a plate, and on longitudinal waves in a rod.

[a)]Author to whom correspondence should be addressed. Electronic mail: yykim@snu.ac.kr

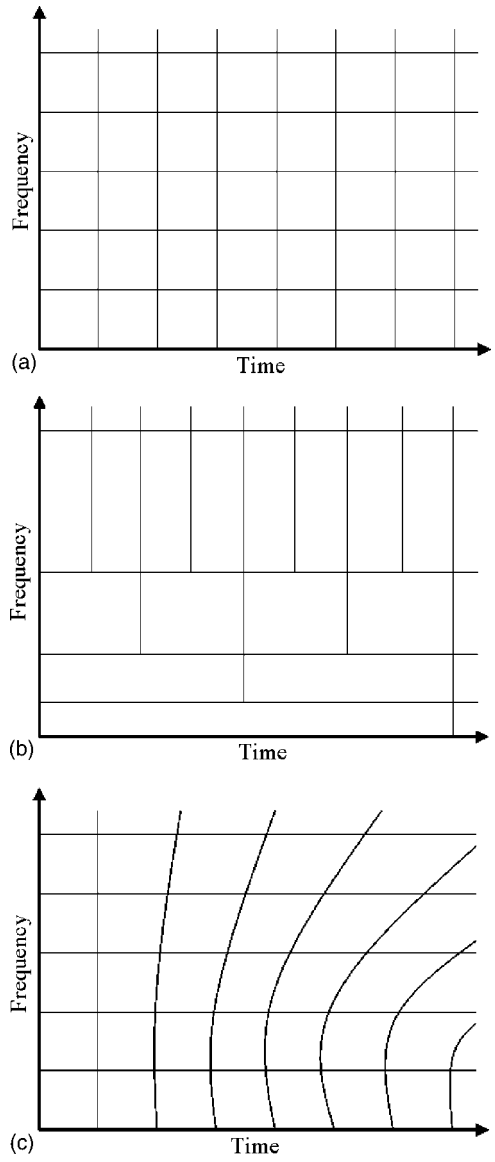

FIG. 1. A comparison of time-frequency tilings. (a) Short-time Fourier transform, (b) continuous wavelet transform, and (c) dispersion-based short-time Fourier transform.

II. DISPERSION-BASED SHORT-TIME FOURIER TRANSFORM

We will begin this section by defining the dispersion-based short-time Fourier transform, and then we will introduce the procedure for estimating the dispersion relationship of a wave under consideration. Finally, its time-frequency resolution will be investigated theoretically, and compared with the resolution achieved using the short-time Fourier transform (STFT).

A. Dispersion-based STFT

Because the dispersion-based STFT (D-STFT) is comparable with the standard STFT, we will first provide a definition of the STFT. For a square-integrable function $f(t)$, its short-time Fourier transform Sf is defined as[3]

$$Sf(u,\xi)=\int_{-\infty}^{\infty} f(t)\overline{g}_{(s,u,\xi)}(t)\,dt$$

$$=\int_{-\infty}^{\infty} f(t)\,\frac{1}{\sqrt{s}}g\left(\frac{t-u}{s}\right)e^{-i\xi t}\,dt, \tag{1a}$$

$$g_{(s,u,\xi)}(t)=\frac{1}{\sqrt{s}}g\left(\frac{t-u}{s}\right)e^{i\xi t}, \tag{1b}$$

where the window function $g(t)$ is selected as the Gaussian window function $g(t)=\pi^{-1/4}e^{-t^2/2}$ and $\overline{g}$ denotes the complex conjugate of g. The parameter s determines the size of the Gaussian window. Because the time and frequency spread of the analyzing function $g_{(s,u,\xi)}(t)$ are independent of the time-frequency location (u,ξ), the STFT has the same resolution across the entire time-frequency plane.

The dispersion-based STFT, D-STFT, is defined using a basis function that includes a new parameter, d, as

$$Df(u,\xi)=\int_{-\infty}^{\infty} f(t)\overline{g}_{(s,u,\xi,d)}(t)\,dt$$

$$=\int_{-\infty}^{\infty} f(t)\left[\frac{1}{\sqrt{s}}g\left(\frac{t-u}{s}\right)*(id)^{-1/2}e^{-i(t^2/2d)}\right]$$

$$\times e^{-i\xi t}\,dt, \tag{2a}$$

$$g_{(s,u,\xi,d)}(t)=\left[\frac{1}{\sqrt{s}}g\left(\frac{t-u}{s}\right)*(-id)^{-1/2}e^{i(t^2/2d)}\right]e^{i\xi t}, \tag{2b}$$

where the symbol $(*)$ in Eq. (2b) denotes the convolution operator, and the parameter d determines the amount of rotation of the time-frequency box in (u,ξ),

$$d=d(u,\xi)=\frac{\Delta u}{\Delta \xi}. \tag{3}$$

The physical meaning of Eq. (2b) can be clearly revealed in the frequency domain, as Eq. (2b) can be expressed as

$$G_{(s,u,\xi,d)}(\omega)=\sqrt{s}G[s(\omega-\xi)]e^{-iu(\omega-\xi)}\cdot e^{-i\,(d/2)(\omega-\xi)^2}$$

$$=\sqrt{s}G[s(\omega-\xi)]e^{-i[u(\omega-\xi)+(d/2)(\omega-\xi)^2]}, \tag{4}$$

where $G(\omega)$ is the Fourier transform of the Gaussian window $g(t)$. Thus, the group delay of the basis function of Eq. (2b) in the time-frequency plane is given by

$$\tau(\omega)=\frac{d}{d\omega}\left[u(\omega-\xi)+\frac{d}{2}(\omega-\xi)^2\right]=u+d(\omega-\xi). \tag{5}$$

Equation (5) implies that the time-frequency box in (u,ξ), using the basis function of Eq. (2b), can be obtained by rotating or shearing the time-frequency box of the standard STFT, using the parameter $d(u,\xi)$. Therefore, if each parameter of $d(u,\xi)$ is chosen with respect to the local wave dispersion, then the resulting time-frequency tiling will correspond with the entire wave dispersion behavior. Because the basis function of Eq. (2b) is similar to that of the standard

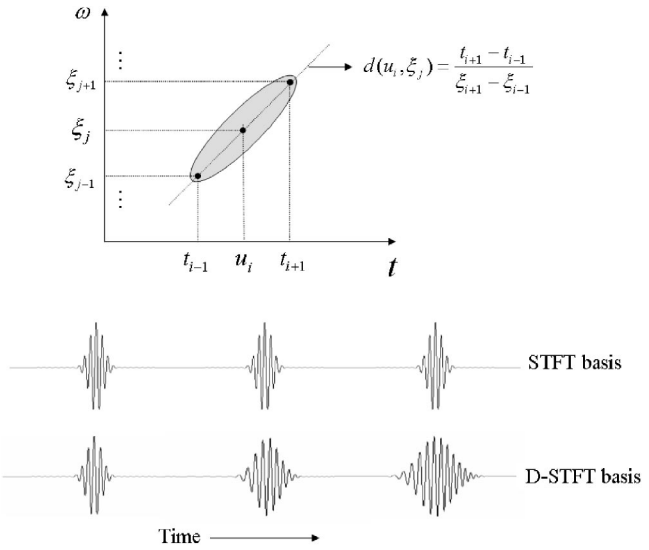

FIG. 2. The determination of the rotating parameter $d(u_i,\xi_j)$ for the given dispersion relationship.

STFT, except for the rotating parameter $d(u,\xi)$ based on the wave dispersion, the transform may be called the dispersion-based short-time Fourier transform (D-STFT).

To use the D-STFT, a procedure connecting each of the rotating parameters $d(u,\xi)$ to the given dispersion relationship is required, and this is graphically illustrated in Fig. 2. To determine $d(u,\xi)$ in (u,ξ), we need to consider a uniformly sampled time-frequency location (u_i,ξ_j) [where u_i $(i=1,2,...,m)$ are the sampled times, and ξ_j $(j=1,2,...,n)$ are the frequencies of interest]. To utilize the dispersion relationship, we assume an experimentally given group velocity, C_g. If the spectral component corresponding to ξ_j is measured at $t=u_i$ (assumed to be incident at $t=0$), then the traveling distance can be expressed as

$$D=C_g(\xi_j)\cdot u_i. \tag{6}$$

Then, t_{i-1} and t_{i+1} denote the arrival times of the neighboring spectral components belonging to ξ_{j-1} and ξ_{j+1}, and are given by

$$t_{i-1}=\frac{D}{C_g(\xi_{j-1})}, \quad t_{i+1}=\frac{D}{C_g(\xi_{j+1})}. \tag{7}$$

Thus, using Eqs. (3) and (7), we can determine the rotating parameter $d(u_i,\xi_j)$ in (u_i,ξ_j) from

$$d(u_i,\xi_j)=\frac{\Delta t}{\Delta\omega}=\frac{t_{i+1}-t_{i-1}}{\xi_{j+1}-\xi_{j-1}}$$
$$=\frac{[D/C_g(\xi_{i+1})-D/C_g(\xi_{i-1})]}{\xi_{j+1}-\xi_{j-1}}. \tag{8}$$

Because the rotating parameter $d(u_i,\xi_j)$ in Eq. (8) is linked to the local wave dispersion in the time-frequency location (u_i,ξ_j), the resulting time-frequency tiling can be very close to the entire wave dispersion.

In Fig. 2, the basis functions of the D-STFT for several time locations at a given frequency are compared conceptually to those of the standard STFT. Because the basis functions of the present transform are time varying and disperse as time passes, they can be more suitable for representing local variations of dispersive waves.

B. Estimation of the dispersion relationship for dispersion-based STFT

To facilitate the dispersion-based STFT, the dispersion relationship of a wave within a waveguide must be known in advance. However, in general, the dispersion relationship is not known in actual situations, and so a procedure for accurately determining the dispersion relationship is required. In this subsection, we will develop a time-frequency-based procedure for experimentally estimating the dispersion relationship of a wave to be analyzed. Although the frequency domain method[17,18] seems to be simpler, the proposed time-frequency method can give more accurate estimation results due to its adaptation property.

The proposed strategy is an iterative estimation scheme of the dispersion relationship, where the dispersion relationship is estimated iteratively by the D-STFT using the initially determined dispersion relationship by the STFT (see Fig. 3). To estimate the dispersion relationship, the STFT of the measured wave signal is first carried out. The dispersion relationship or the frequency-dependent group velocity, $C_g(\omega)$, of the wave can be determined from the traveling distance and arrival time of the wave, as extracted using ridge analysis. In general, since the performance of the STFT is strongly influenced by the window size, s, of the basis function that controls the time-frequency localization properties, it is very important to choose the optimum window size, s_{op}, for a given signal.[10] Thus, to find the optimum value of s, the Shannon entropy cost,[19] which can measure the energy localization in the time-frequency plane, was employed.

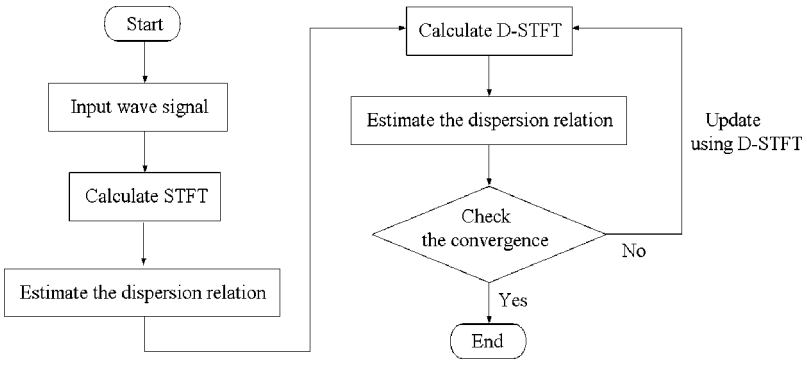

FIG. 3. Proposed iterative scheme for estimation of the dispersion relationship.

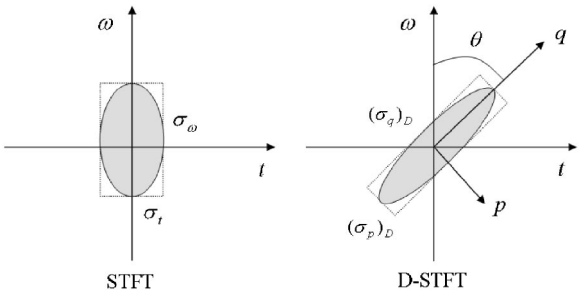

FIG. 4. A comparison of the time-frequency box in the STFT and D-STFT.

To evaluate the Shannon entropy cost for the spectrogram $|S(u,\xi)|^2$ defined in the time-frequency plane, we used a sampled version of $|S(u,\xi)|^2$ which is defined as

$$A_{i,j}=|S(u_i,\xi_i)|^2 \quad (i=1,...,m, j=1,...,n). \tag{9}$$

If the values of $A_{i,j}$ are known, then the two-dimensional Shannon entropy cost can be defined as

$$C(E)=-\sum_j \sum_i \left(\frac{A_{i,j}}{\Sigma_i\Sigma_j A_{i,j}}\right)\log\left(\frac{A_{i,j}}{\Sigma_i\Sigma_j A_{i,j}}\right), \tag{10}$$

where $E=\{A_{i,j}\}_{1\leqslant i\leqslant m,1\leqslant j\leqslant n}$. Then, the optimum window size s_{op} that maximizes the time-frequency energy localization can be determined by minimizing the entropy cost of Eq. (10):

$$s_{op}=\arg\min_s C(E). \tag{11}$$

To find s_{op} in Eq. (11), we interpolate $C(E)$ using a polynomial function of s and minimize the function with respect to s. The ridges extracted from the STFT with s_{op}, which mean the wave arrival times, can be used for determining the initial group velocity C_g.

After finding the initial group velocity using the optimum STFT, the initially estimated group velocity is used in the D-STFT. Then, the group velocity is updated from the resulting D-STFT. The D-STFT is repeatedly used until the group velocity agrees with the convergence criterion $R(k)$ for a prescribed small value ε,

$$R(k)=\frac{\Sigma_j|C_g(\xi_j)_{k+1}-C_g(\xi_j)_k|}{\Sigma_j|C_g(\xi_j)_k|}<\varepsilon, \tag{12}$$

where j denotes the index of the considered frequency ξ and k is the number of iterations. To provide $d(u_i,\xi_j)$ for the D-STFT application in the regions where there is no strong ridge, the group velocity curve estimated is extrapolated by third-order polynomials. The converged group velocity C_g is utilized for determining the rotating parameter $d(u_i,\xi_j)$ in an arbitrary time-frequency location (u_i,ξ_j). Note that the proposed estimation method can be also effectively used for estimating the dispersion relationship in arbitrary waveguides.

C. Time-frequency resolution of dispersion-based STFT

To show the effectiveness of the dispersion-based STFT, its time-frequency resolution was investigated theoretically and compared with that of the standard STFT. For a normalized function, $f(t)$ ($\|f(t)\|^2=\int_{-\infty}^{\infty}|f(t)|^2=1$), its time and frequency resolution (or spread) are defined by

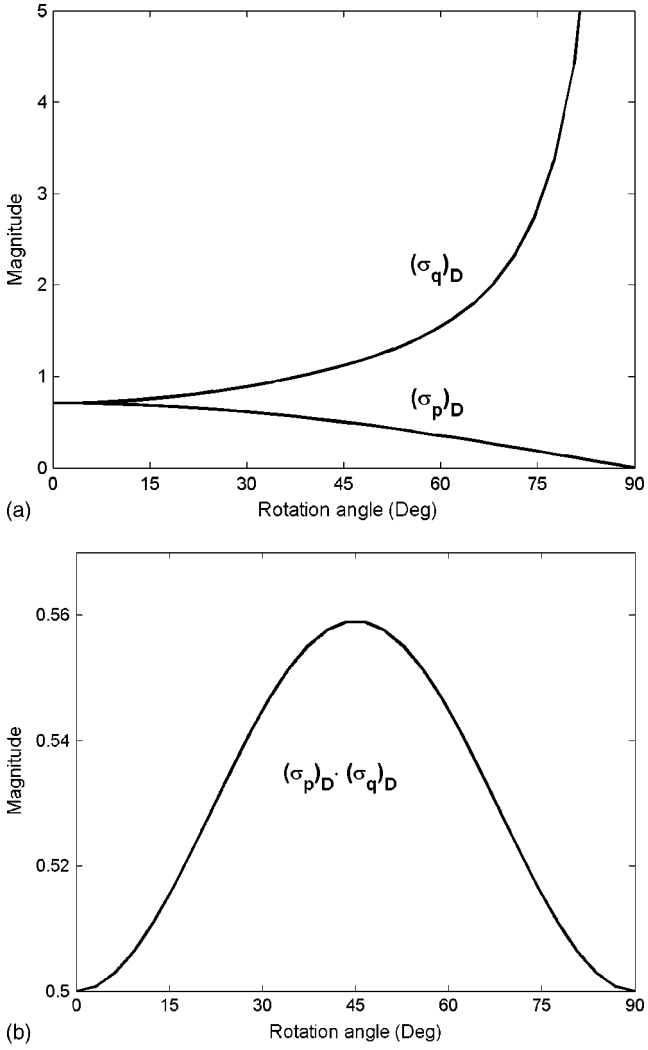

FIG. 5. The resolutions for the p and q rotational axes. (a) Variation of $(\sigma_p)_D$ and $(\sigma_q)_D$ for the rotation angles used, and (b) variation of $(\sigma_p)_D \cdot(\sigma_q)_D$ for the rotation angles used.

$$\sigma_t^2=\int_{-\infty}^{\infty} t^2|f(t)|^2dt, \tag{13a}$$

$$\sigma_\omega^2=\int_{-\infty}^{\infty} \omega^2|\hat{f}(\omega)|^2d\omega, \tag{13b}$$

where $\hat{f}(\omega)$ is the Fourier transform of $f(t)$. To evaluate $|f(t)|^2$ and $|\hat{f}(\omega)|^2$, we employed the following marginal theorem of the Wigner-Ville distribution (WVD):

$$\int_{-\infty}^{\infty} W_f(t,\omega)dt=|\hat{f}(\omega)|^2, \tag{14a}$$

$$\int_{-\infty}^{\infty} W_f(t,\omega)d\omega=|f(t)|^2, \tag{14b}$$

where $W_f(t,\omega)$, the Wigner-Ville distribution of $f(t)$, is defined as

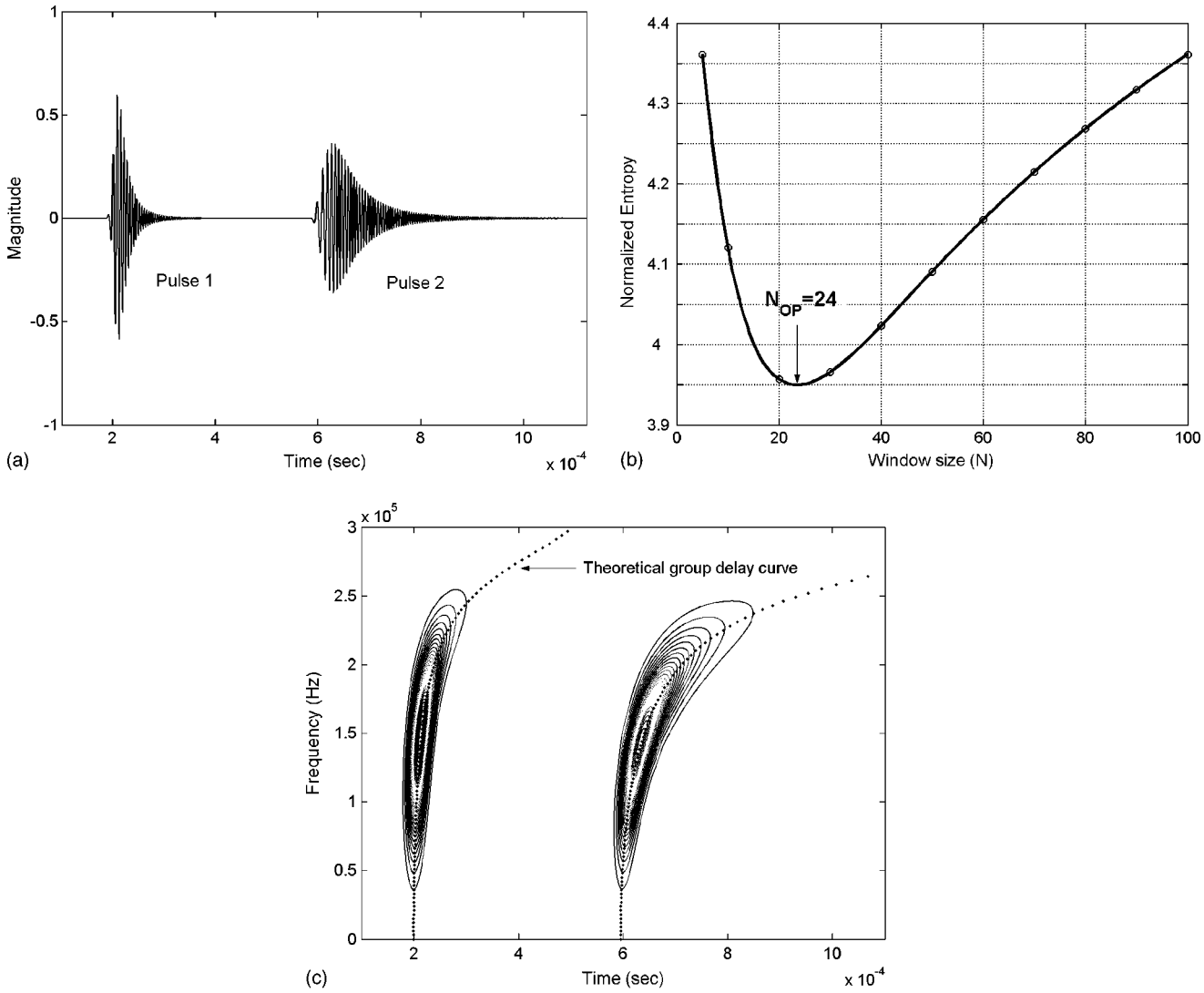

FIG. 6. The absolute values of the STFT of a simulated pulse signal. (a) The simulated pulse signal, (b) entropy cost variation, and (c) the STFT (of absolute values) with $N_{op}=24$ of the simulated pulse signal.

$$W_f(t,\omega)=\frac{1}{2\pi}\int_{-\infty}^{\infty} f\left(t+\frac{\tau}{2}\right) f^*\left(t-\frac{\tau}{2}\right) e^{-i\omega\tau}\, d\tau. \qquad (15)$$

As shown in Fig. 4, because the time-frequency box of the D-STFT rotates in the time-frequency plane, the resolutions for the rotated axes, $(\sigma_p)_D$ and $(\sigma_q)_D$, play a key role in explaining the time-frequency localization properties of our transform. Thus, we focused on resolutions for the rotated axes in the time-frequency plane.

We began with the WVD of the basis function of the standard STFT given in Eq. (1b). Here, the time translation u, and the modulated frequency ξ, can be set to zero without loss of generality. Then, the WVD of the STFT-basis function is calculated as

$$W_{g_{(s,u=0,\xi=0)}}(t,\omega)=2\exp\left(-\frac{t^2}{s^2}-s^2\omega^2\right). \qquad (16)$$

Thus, substituting Eq. (16) into the marginal theorem of Eq. (14b) yields

$$\int_{-\infty}^{\infty} W_{g_{(s,u=0,\xi=0)}}(t,\omega)\,d\omega=|g_{(s,u=0,\xi=0)}(t)|^2 =\frac{1}{\sqrt{\pi}s}e^{-t^2/s^2}. \qquad (17)$$

Therefore, the time spread σ_t of the basis function becomes

$$\sigma_t^2=\int_{-\infty}^{\infty} t^2|g_{(s,u=0,\xi=0)}|^2 dt=\frac{1}{2}s^2. \qquad (18)$$

Likewise, the frequency-spread σ_ω is calculated as

$$\sigma_\omega^2=\int_{-\infty}^{\infty}\omega^2|G_{(s,u=0,\xi=0)}(\omega)|^2 d\omega=\frac{1}{2s^2}, \qquad (19)$$

where $G_{(s,u=0,\xi=0)}(\omega)$ denotes the Fourier transform of $g_{(s,u=0,\xi=0)}(t)$. From Eqs. (18) and (19), the well-known uncertainty principle for the STFT-basis function, $\sigma_t\cdot\sigma_\omega=\frac{1}{2}$, is verified.

The above procedures can be applied to the basis function of the D-STFT given in Eq. (2b) to find the resolutions

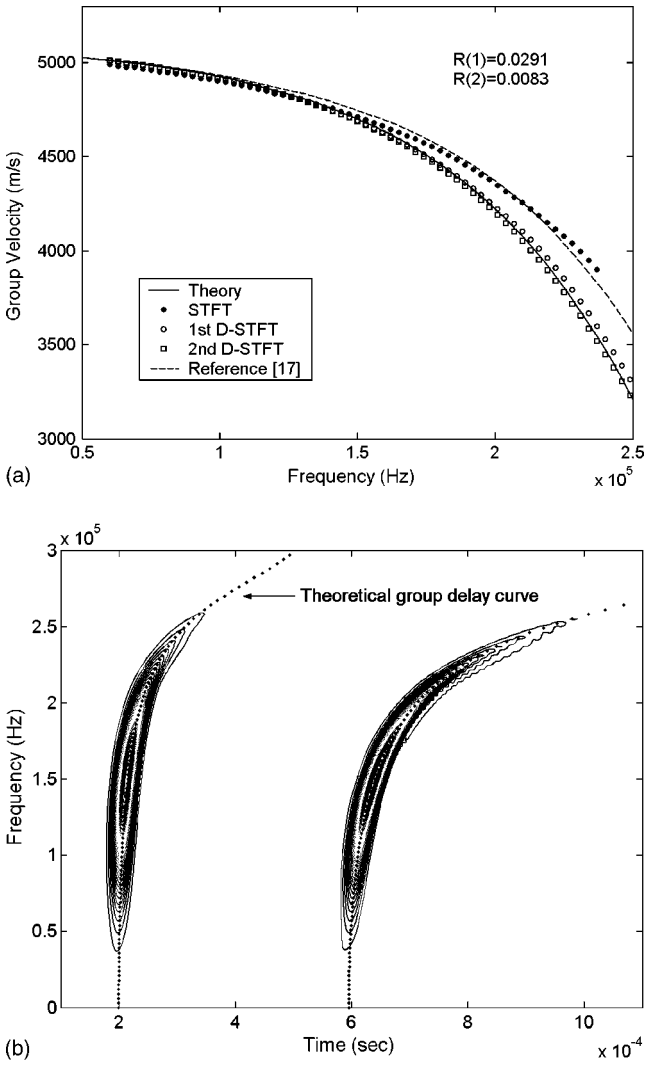

FIG. 7. The absolute values of the D-STFT of a simulated pulse signal. (a) Estimation of the dispersion relationship and (b) the D-STFT(of absolute values) of the simulated pulse signal.

for rotated axes $(\sigma_p)_D$ and $(\sigma_q)_D$. The Wigner-Ville distribution for the basis function of the D-STFT can be expressed from Eqs. (5) and (16) as

$$W_{g_{(s,u=0,\xi=0,d)}}(t,\omega)=2\exp\left(-\frac{(t-d\omega)^2}{s^2}-s^2\omega^2\right). \quad (20)$$

As in Eq. (16), the parameters u and ξ are assumed to be zero. To find the resolutions for the rotated axes p and q, the following well-known coordinate-rotation transforms were carried out:

$$t=p\cos\theta+q\sin\theta,$$
$$\omega=-p\sin\theta+q\cos\theta. \quad (21)$$

Then, from the coordinate transforms of Eq. (21), $W_{g_{(s,u=0,\xi=0,d)}}(t,\omega)$ of Eq. (20) can be replaced by $W_{g_{(s,u=0,\xi=0,d)}}(p,q)$ for the rotated axes p and q. The marginal theorem of Eq. (14b) for $W_{g_{(s,u=0,\xi=0,d)}}(p,q)$ yields

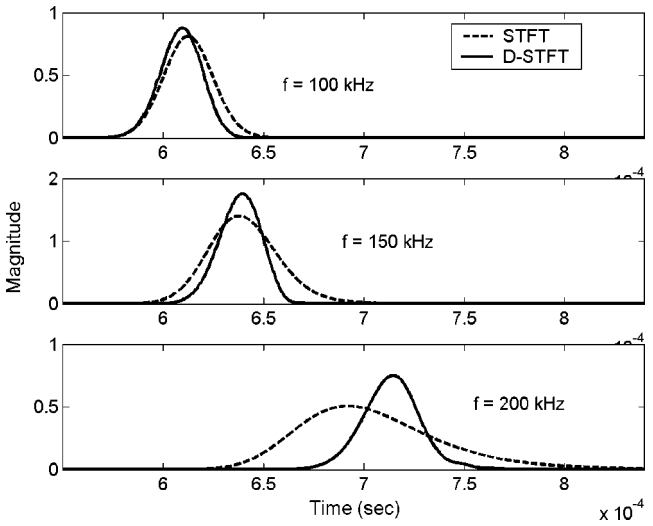

FIG. 8. The magnitudes at frequencies of 100, 150, and 200 kHz for the STFT and D-STFT of the second pulse shown in Fig. 6(a).

$$\int_{-\infty}^{\infty}W_{g_{(s,u=0,\xi=0,d)}}(p,q)dq=|g(p)|^2$$
$$=\frac{1}{(\sqrt{\pi}\cos\theta)s}\exp\left(-\frac{p^2}{s^2\cos^2\theta}\right), \quad (22)$$

where $g(p)$ means the function defined according to the p axis and $\theta=\tan^{-1}d$ denotes the rotation angle as shown in Fig. 4. Thus, the resolution for the p axis is calculated as

$$(\sigma_p)_D^2=\int_{-\infty}^{\infty}p^2|g(p)|^2dp=\frac{1}{2}s^2\cos^2\theta. \quad (23)$$

Likewise, the marginal theorem of Eq. (14a) for $W_{g_{(s,u=0,\xi=0,d)}}(p,q)$ is given by

$$\int_{-\infty}^{\infty}W_{g_{(s,u=0,\xi=0,d)}}(p,q)dp$$
$$=|G(q)|^2=\frac{\exp(-s^2q^2/(\sec^2\theta+s^4\sin^2\theta))}{\sqrt{\pi((\sec^2\theta+s^4\sin^2\theta)/s^2)}}, \quad (24)$$

where $G(q)$ is the function defined according to the q axis. Then, the resolution for the q axis is expressed as

$$(\sigma_q)_D^2=\int_{-\infty}^{\infty}q^2|G(q)|^2dq=\frac{\sec^2\theta+s^4\sin^2\theta}{2s^2}. \quad (25)$$

As can be seen from Eqs. (23) and (25), the resolutions $(\sigma_p)_D$ and $(\sigma_q)_D$ depend on the rotation angle θ determined from the local wave dispersion.

Figures 5(a) and 5(b) show plots of the resolutions for rotated axes $(\sigma_p)_D$ and $(\sigma_q)_D$, and the resolution box size $(\sigma_p)_D\cdot(\sigma_q)_D$ as a function of the rotation angle θ for $s=1$. As can be seen from Fig. 5(b), the resolution box size of the D-STFT seems to be slightly larger than that of the standard STFT $(\sigma_t\cdot\sigma_\omega=\frac{1}{2})$. However, as the axes rotate with respect to the wave dispersion, the resolution for the p axis, $(\sigma_p)_D$ becomes much better than the resolution σ_t in the STFT $(\sigma_t=1/\sqrt{2})$. This higher resolution of $(\sigma_p)_D$ plays an impor-

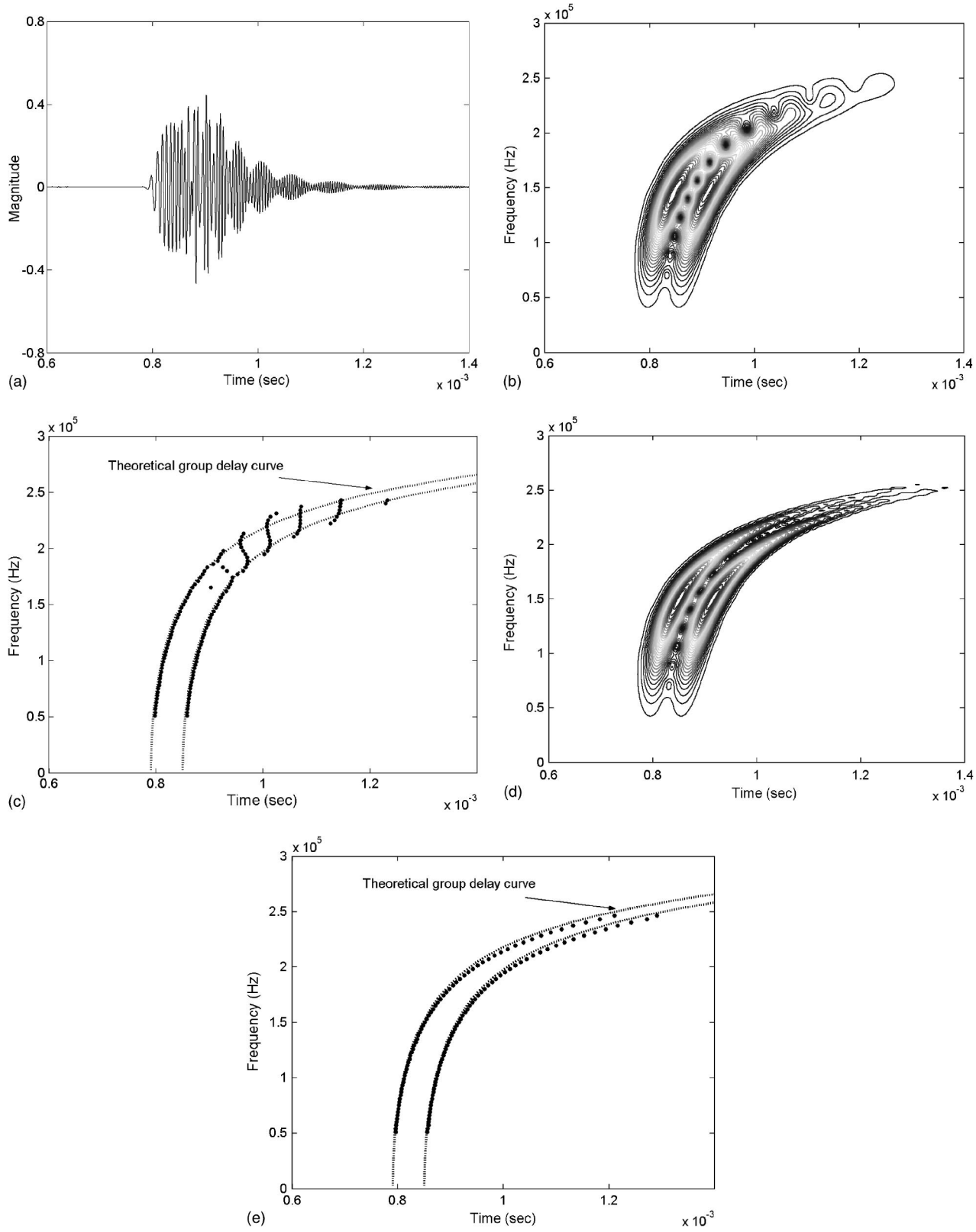

FIG. 9. The absolute values of the STFT and D-STFT of an overlapping pulse signal. (a) The simulated overlapping pulse signal, (b) the absolute values of the STFT of the signal in (a), (c) ridges extracted from the STFT, (d) its D-STFT, and (e) ridges extracted from the absolute values of the D-STFT.

tant role in accurately pinpointing the wave arrivals. As a consequence, the dispersion-based STFT yields an excellent time-frequency localization in the analysis of some dispersive waves.

III. NUMERICAL INVESTIGATION

This section begins with a discussion on the wave signal generation for numerical tests, and then the proposed method for the estimation of the dispersion relationship is proven for

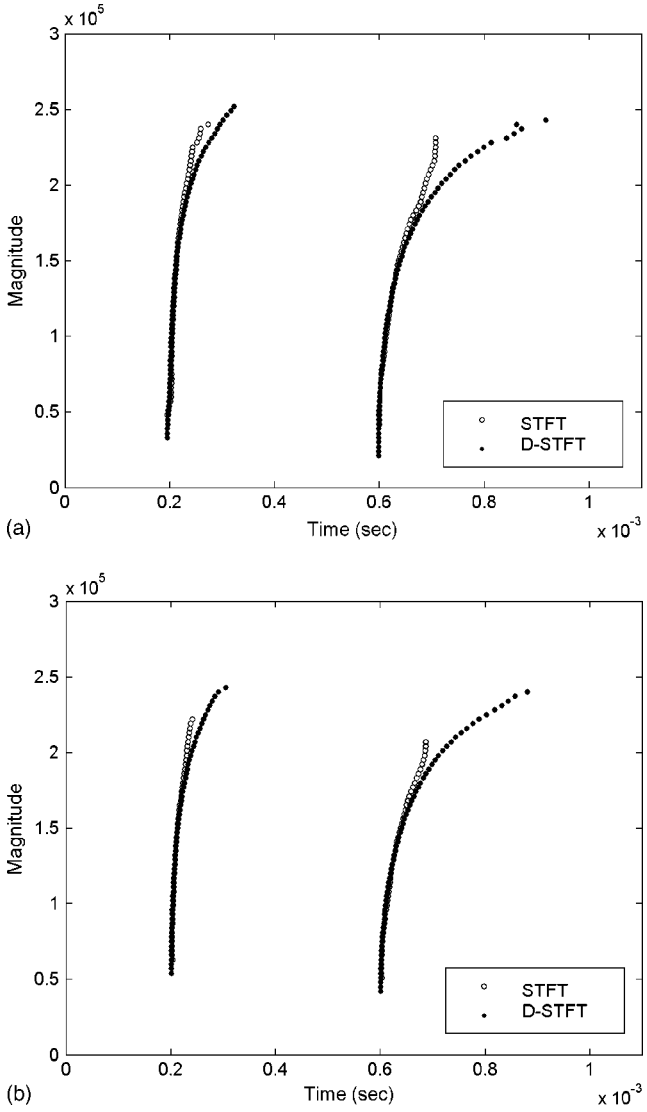

FIG. 10. Ridges extracted from the absolute values of the STFT and D-STFT of the noisy simulated pulse signals.

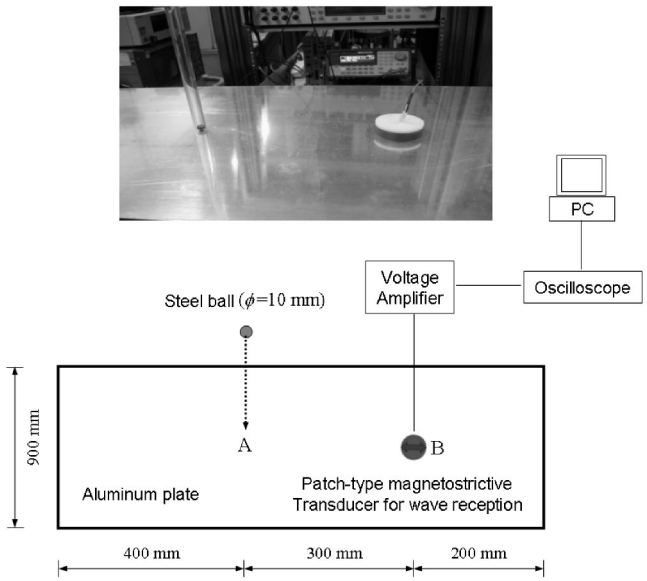

FIG. 11. The experimental setup used to generate a flexural wave in a plate.

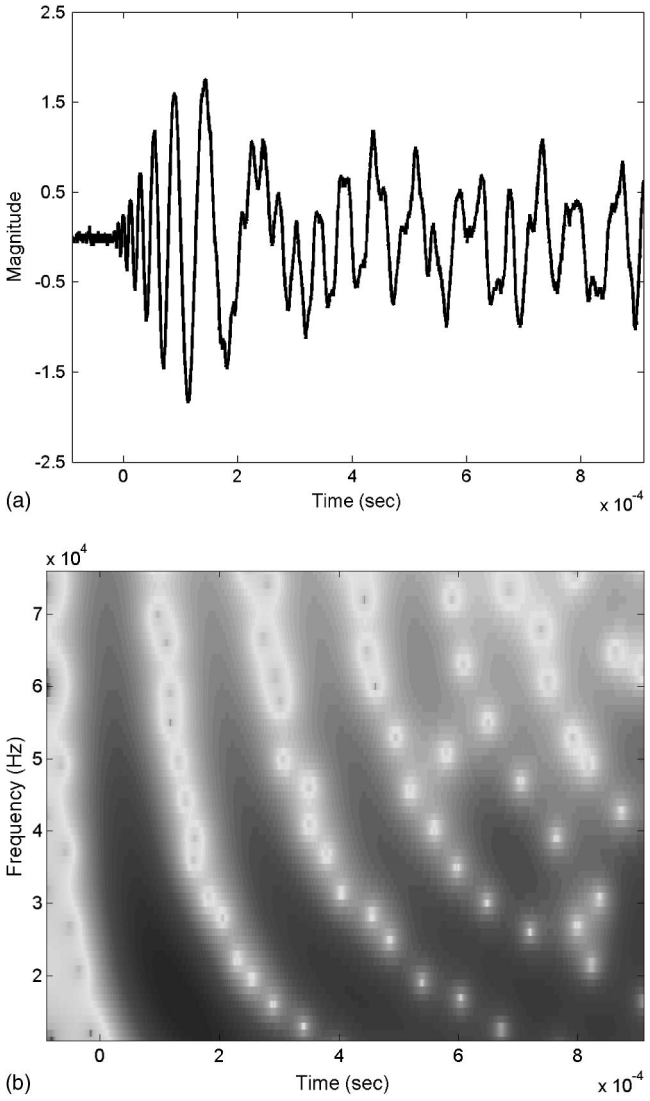

FIG. 12. The STFT of the measured flexural wave signal. (a) The measured flexural wave signal and (b) the absolute values of the STFT of the measured flexural wave signal.

a simulated dispersive wave signal. Finally, the characteristics of the dispersion-based STFT are examined for some critical issues.

A. Wave signal generation for numerical tests

Let us assume that a frequency-modulated Gaussian pulse $s(x=0,t)\equiv s_{in}(t)$ is generated at the point $x=0$ by a transducer, and propagates along a waveguide. In the frequency domain, this pulse can be expressed as its Fourier transform,

$$S(0,\omega)\equiv S_{in}(\omega)=\int_{-\infty}^{\infty} s_{in}(t)e^{-j\omega t}\,dt. \tag{26}$$

When the propagating pulse arrivals at the point $x=x_0$, then $S_{in}(\omega)$ will be shifted in phase by $e^{-jk(\omega)x_0}$, where $k(\omega)$ denotes the frequency-dependent wave number. If $k(\omega)$ is known, then the Fourier transform $S(x_0,\omega)$ of the pulse measured at point $x=x_0$ can be written as

$$S(x_0,\omega)=S_{in}(\omega)e^{-jk(\omega)x_0}. \tag{27}$$

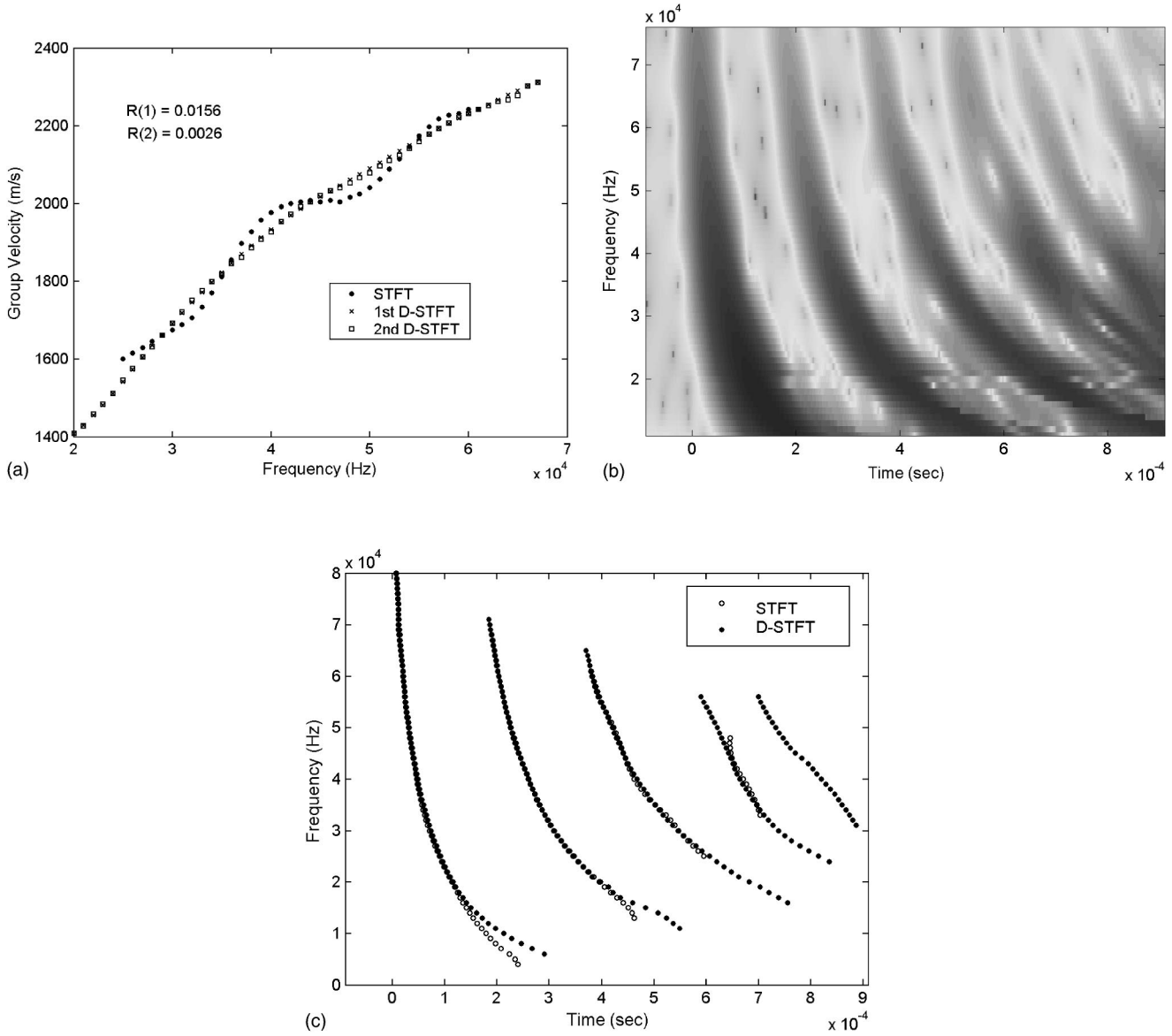

FIG. 13. The D-STFT of the measured flexural wave signal. (a) An estimation of the dispersion relationship, (b) the absolute values of the D-STFT of the measured flexural wave signal, and (c) a comparison of the ridges extracted from the absolute values of the STFT and D-STFT of the measured flexural wave signal.

Consequently, the time-domain signal $s(x_0,t)$ measured at point $x=x_0$ can be obtained from the inverse Fourier transform as

$$s(x_0,t)=\frac{1}{2\pi}\int_{-\infty}^{\infty}[S_{in}(\omega)e^{-jk(\omega)x_0}]e^{j\omega t}\,d\omega. \tag{28}$$

Equation (28) was used to build the wave signals at arbitrary locations for numerical tests. The wave number $k(\omega)$ or the group velocity $C_g(\omega)$ used was based on the well-known Pochhammer-Chree equation in rods.[20,21] The mode considered belongs to the lowest longitudinal $L(0,1)$ mode in a rod with diameter$=10$ mm, Young's modulus $E=209$ GPa, and Poisson's ratio $\nu=0.3$.

B. Estimation of dispersion relationship

This subsection provides a discussion on the validation of the performance of our proposed method for the estimation of the dispersion relationship. To demonstrate this, the estimation of the dispersion relationship for a narrow-band wave signal centered at 150 kHz was carried out. Figure 6(a) shows the simulated signal generated using Eq. (28), which is a composite of dispersive pulses having traveling distances of 1 and 3 m.

For the simulated signal shown in Fig. 6(a), the STFT with various window sizes was performed, and the optimal window size s_{op} was found using the entropy-based method. Figure 6(b) shows the variation of entropy costs, and Fig. 6(c) shows the STFT of the simulated signal with the optimal window size $N_{op}=24$. Here, the window size s was replaced by $N\Delta t$ (where the sampling time, Δt, was $\Delta t=2\times10^{-7}$ s). To evaluate the group velocity $C_g(\omega)$ from this STFT data, the wave arrival times $\tau(\omega)$ were extracted using the ridge analysis of the STFT data. In calculating the group velocity $C_g(\omega)$, the following formula defined between two pulses was used

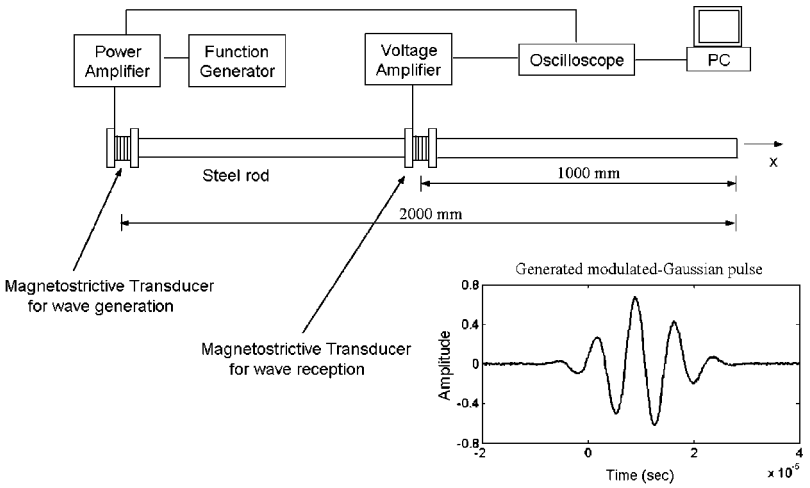

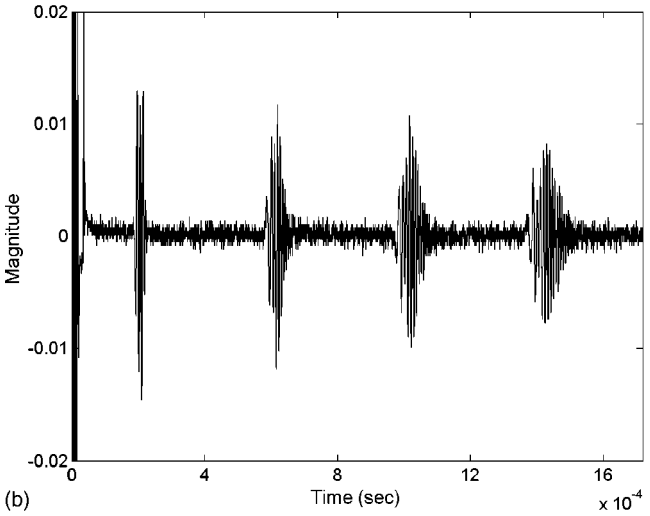

FIG. 14. The experimental setup used to generate a longitudinal wave in a rod. (a) The experimental setup and (b) the measured longitudinal wave signal.

$$C_g(\omega) = \frac{D_{\text{pulse2}} - D_{\text{pulse1}}}{\tau_{\text{pulse2}}(\omega) - \tau_{\text{pulse1}}(\omega)}, \tag{29}$$

where D_{pulse} is the pulse traveling distance. [The formula in Eq. (29) is easier to use than $D_{\text{pulse}}/\tau_{\text{pulse}}$ because no attention needs to be paid to the triggering time.]

The group velocity $C_g(\omega)$, calculated using Eq. (29), was used for the first D-STFT calculation, and then the D-STFT was repeatedly performed until the estimated group velocity $C_g(\omega)$ met the convergence criterion of Eq. (12) for $\varepsilon = 0.01$. In Fig. 7(a), the estimated group velocities $C_g(\omega)$, according to the iterations, are compared with the exact group velocities from the Pochhammer-Chree equation. As can be seen in Fig. 7(a), as the number of iterations increased, the estimated group velocity approached the exact group velocity. The group velocity after the second iteration, where the convergence criterion of Eq. (12) was met, was very close to the exact group velocity. The estimated result by the method of Sachse and Pao[17] is also compared in Fig. 7(a). The proposed D-STFT method gave a more accurate result than the method of Sachse and Pao[17] over a wide frequency range. Figure 7(b) shows a plot of the D-STFT using the final determined group velocity. This final estimated group velocity was utilized in further numerical tests.

C. Characteristics of dispersion-based STFT

Because the time-frequency tiling of the dispersion-based STFT is based on the wave dispersion relationship, it can allow excellent time-frequency localization. In this subsection, the performance of the D-STFT is compared with that of the standard STFT method for some critical issues.

To show the high time-frequency localization properties of the D-STFT, the second pulse within the simulated wave signal of Fig. 6(a) was considered. In Fig. 8, the shape and magnitude of the STFT and D-STFT data at frequencies of 100, 150, and 200 kHz are compared. As can be seen in Fig. 8, the D-STFT gives a higher energy localization. In addition, the magnitudes calculated using the D-STFT are much larger than those calculated using the STFT, because the basis functions of the D-STFT are more correlated with the local variation of the dispersive wave.

To further examine the effectiveness of the D-STFT, a pulse-overlap situation was taken into account. Pulse-overlap is often observed when the propagating pulses are dispersed. This situation was numerically realized by synthesizing dispersive pulses with traveling distances of 4 and 4.3 m. Figure 9 compares the results of the STFT and D-STFT for the simulated signal. When the D-STFT was applied, the ridges denoting the pulse arrival were clearly separated. This high

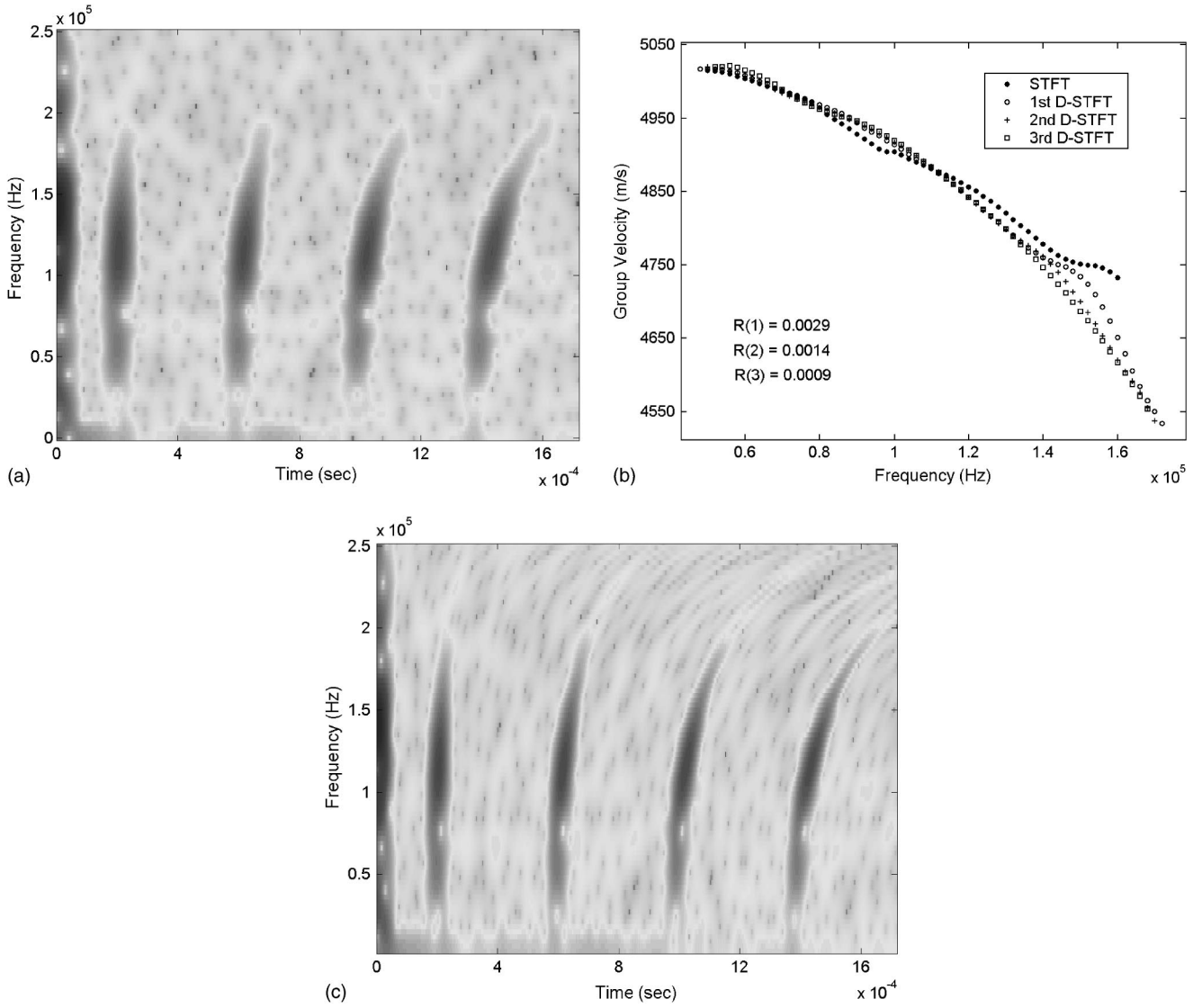

FIG. 15. A comparison of the STFT and D-STFT of the measured longitudinal wave signal. (a) The absolute values of the STFT of the measured longitudinal wave signal, (b) an estimation of the dispersion relationship, and (c) the absolute values of the D-STFT of the measured longitudinal wave signal.

resolution can be explained using Eq. (23). When multiple ridges overlap, the D-STFT, like other approaches, has difficulties in distinguishing the ridges near the overlaps.

Finally, the effect of noise on the performance of the present adaptive time-frequency method was investigated. To this end, the signal shown in Fig. 6(a) was used as the underlying signal $f(t)$, which was then corrupted by a Gaussian noise, $n(t)$. The signal-to-noise ratio (SNR) of the simulated noisy signal was defined as

$$\mathrm{SNR} = 10 \log_{10} \frac{\Sigma_i |f(t_i)|^2}{\Sigma_i |n(t_i)|^2} (\mathrm{dB}). \tag{30}$$

Figures 10(a) and (b) show the transformed results for the noisy signal having SNR=4 and 1 dB, respectively. The ridges describing the pulse arrival are more clearly extracted by the D-STFT than those extracted using the STFT. This is because the wave-dependent time-frequency tiling yields a better time-frequency energy localization.

IV. EXPERIMENTAL VERIFICATION

In this section, the performance of the dispersion-based STFT is examined experimentally, and the proposed approach for the estimation of the dispersion relationship is applied to some dispersive wave signals. The dispersive waves considered were the flexural waves in a plate (A_0 mode) and the longitudinal waves in a rod ($L(0,1)$ mode).

A. Case I: Flexural wave in a plate

Figure 11 shows the experiment setup employed in the experiments on flexural waves in a plate. In this experimental setup, a simple supported aluminum plate with a thickness of 3 mm was excited by the impact of a steel ball dropped at the point A. The generated flexural wave was measured at location B using a patch-type magnetostrictive transducer[22,23] at a sampling frequency of 2.5 MHz.

The signal shown in Fig. 12(a) is the measured flexural wave. The transformed result using the STFT with an optimal window size for the measured wave signal is plotted in

Fig. 12(b), where successive wave arrivals (or ridges) are observed, because of reflections from both ends of the plate. To determine the group velocity of the flexural wave, our proposed method for the estimation of the dispersion relationship was applied, where the arrival times of the first and second ridges were used to estimate the group velocity.

Figure 13(a) shows the estimated group velocity satisfying the convergence criterion of Eq. (12) for $\varepsilon = 0.01$. The final estimated group velocity was used in the D-STFT calculations of the measured flexural wave signal. Figure 13(b) shows the transformed results using the D-STFT, and the ridges extracted from the transformed result are compared with those from the STFT in Fig. 13(c). The successive wave arrivals are clearly seen using the D-STFT, because of its high time-frequency localization. The effectiveness of the present adaptive time-frequency method is again confirmed by the results shown in Fig. 13.

B. Case II: Longitudinal wave in a rod

The dispersion-based STFT was applied to longitudinal waves in a rod. Figure 14(a) shows a schematic diagram of the experimental setup employed, and Fig. 14(b) shows the measured longitudinal wave signals from the experiment. The transformed result from the STFT using the optimum window size for the measured wave signal is plotted Fig. 15(a). Figure 15(b) shows a comparison of the estimated group velocities according to iteration using the first and second ridges, where the convergence criterion of $\varepsilon = 0.001$ was employed. The D-STFT calculation of the measured wave signal using the converged group velocity is plotted in Fig. 15(c).

V. CONCLUSIONS

The dispersion-based STFT method was applied to dispersive wave analysis. To utilize this method, an iterative scheme for estimating the dispersion relationship was developed. Theoretical investigations on the time-frequency resolution show that the present method provides a better time-frequency localization than the standard STFT, because its time-frequency tiling depends highly on the dispersion characteristics of the guided wave. From numerical and experimental tests, the effectiveness of the present method in dealing with dispersive waves was verified.

[1] P. Cawley and D. Alleyne, ''The use of Lamb waves for the long range inspection of large structures,'' Ultrasonics **34**, 287–290 (1996).
[2] T. Ghosh, T. Kundu, and P. Karpur, ''Efficient use of Lamb modes for detecting defects in large plates,'' Ultrasonics **36**, 791–801 (1998).
[3] D. Gabor, ''Theory of communication,'' J. IEE **93**, 429–457 (1946).
[4] I. Daubechies, *Ten Lectures on Wavelets* (SIAM, Philadelphia, 1992).
[5] S. Mallat, *A Wavelet Tour of Signal Processing* (Academic, New York, 1998).
[6] Y. Y. Kim and E. H. Kim, ''Effectiveness of the continuous wavelet transform in the analysis of some dispersive elastic waves,'' J. Acoust. Soc. Am. **110**, 86–94 (2001).
[7] D. L. Jones and T. W. Park, ''A high resolution data-adaptive time-frequency representation,'' IEEE Trans. Acoust., Speech, Signal Process. **38**, 2127–2135 (1990).
[8] X. Sun and Z. Bao, ''Adaptive spectrogram for time-frequency signal analysis,'' in Proceedings of 8th IEEE Signal Processing Workshop on Statistical Signal and Array Processing (1996), pp. 460–463.
[9] G. Jones and B. Boashash, ''Window matching in the time-frequency plane and the adaptive spectrogram,'' Proceedings of the IEEE-SP International Symposium on Time-Frequency and Time-Scale Analysis (1992), pp. 87–90.
[10] J.-C. Hong and Y. Y. Kim, ''The determination of the optimal Gabor wavelet shape for the best time-frequency localization using the entropy concept,'' Exp. Mech. **44**, 387–395 (2004).
[11] S. Mallat and Z. Zhang, ''Matching pursuits with time-frequency dictionaries,'' IEEE Trans. Signal Process. **41**, 3397–3415 (1993).
[12] F. Auger and P. Flandrin, ''Improving the readability of time-frequency and time-scale representations by the reassignment method,'' IEEE Trans. Signal Process. **43**, 1068–1089 (1995).
[13] M. Niethammer, L. J. Jacobs, J. Qu, and J. Jarzynski, ''Time-frequency representations of Lamb waves,'' J. Acoust. Soc. Am. **109**, 1841–1847 (2001).
[14] S. Mann and S. Haykin, ''The chirplet transform: Physical considerations,'' IEEE Trans. Signal Process. **43**, 2745–2761 (1995).
[15] R. G. Baraniuk and D. L. Jones, ''Wigner-based formulation of the chirplet transform,'' IEEE Trans. Signal Process. **44**, 3129–3135 (1996).
[16] L. Angrisani and M. D'Arco, ''A measurement method based on a modified version of the chirplet transform for instantaneous frequency estimation,'' IEEE Trans. Instrum. Meas. **51**, 704–711 (2002).
[17] W. Sachse and Y. Pao, ''On the determination of phase and group velocities of dispersive waves in solids,'' J. Appl. Phys. **49**, 4320–4327 (1978).
[18] T. Pialucha, C. C. H. Guyott, and P. Cawley, ''Amplitude spectrum method for the measurement of phase velocity,'' Ultrasonics **27**, 270–279 (1989).
[19] C. Shannon, ''A mathematical theory of communication,'' Bell Syst. Tech. J. **27**, 379–656 (1948).
[20] J. Miklowitz, *Elastic Waves and Waveguides* (North-Holland, New York, 1978).
[21] K. F. Graff, *Wave Motion in Elastic Solids* (Ohio State U. P., Columbus, 1999).
[22] H. Kwun and K. A. Bartel, ''Magnetostrictive sensor technology and its applications,'' Ultrasonics **36**, 171–178 (1998).
[23] Y. Y. Kim, S. H. Cho, K. H. Sun, and J. S. Lee, ''Orientation-adjustable patch-type magnetostrictive ultrasonic transducer for plates,'' Proceedings of the 5th European Magnetic Sensors and Actuators Conference, T-O.6.

Exploring interaction effects in two-component gas mixtures using orthogonal signal correction of ultrasound pulses

Johan E. Carlson[a] and Pär-Erik Martinsson
EISLAB, Department of Computer Science and Electrical Engineering, Luleå University of Technology, SE-971 87 Luleå, Sweden

(Received 1 October 2004; revised 24 February 2005; accepted 28 February 2005)

Within Sweden and the EU, an increased use of biogas gas and natural gas is encouraged to decrease emission of carbon dioxide. To support more effective manufacturing, distribution, and consumption of energy gases, new methods for the measurement of the calorimetric value or the gas composition are needed. This paper presents a method to extract and visualize variations in ultrasound pulse shape, caused by interaction effects between the constituents of a two-component gas mixture. The method is based on a combination of *principal component analysis* and *orthogonal signal correction*. Pulse-echo ultrasound experiments on mixtures of oxygen and ethane in the concentration range from 20% to 80% ethane show that the extracted information could be correlated with the molar fraction of ethane in the mixture.
[DOI: 10.1121/1.1893565]

PACS numbers: 43.60.-c, 43.20.Ye, 43.35.Yb [YHB] Pages: 2961–2968

I. INTRODUCTION

Natural gas and biogas contain mixtures of several gases, with the major component being methane. Other components are ethane, hydrogen, and other higher order hydrocarbons (such as propane, butane, etc.). Sometimes the gas also contains small, but highly undesired, fractions of oxygen or water vapor. Water and oxygen are both corrosive and can cause severe damage to the pipeline systems. Therefore, knowledge and methods for monitoring the amount of undesired impurities in the gas are important.

Furthermore, with the use of different sources of gas (i.e., different gas fields) the energy content of the gas delivered to customers may vary considerably. Variations of as much as 20% can occur.[1] It is of interest to both provider and customer to know the composition of such gas mixtures, since this determines the energy content (calorimetric value) and, thus, the combustion properties and the monetary value of the gas.

Today, the energy content of gases is measured using either gas chromatography or calorimetry. Both methods are accurate, but require samples of the gas to be removed and analyzed separately, which makes them relatively slow. They are also rather expensive. Because of this, the existing techniques are not suitable for on-line measurement at the customer side of the distribution line.

In conjunction with flow meters the temperature and pressure are measured in order to relate the operating flow conditions to a reference condition. Given the calorimetric value at the reference condition, the energy content can be measured on-line, during operation. However, this approach assumes that the composition of the flow is constant. New methods for on-line measurement of the calorimetric value have been investigated by, for example, Jaeschke *et al.*[2,3] Jaeschke modified the technique by adding measurement of relative permittivity, speed of sound, and CO_2 molar fraction as input to a correlation model in order to improve the accuracy of the energy content estimate.

In this study, we investigate what information that can be extracted from the shape of ultrasound pulses that propagated through the gas. Today, ultrasonic flow meters are used to measure the volume flow, and a method that does not require many additional sensors would be attractive. With the approach presented here, the data available in a conventional flow meter are processed to extract information about the gas composition.

Typically, both the speed of sound and the attenuation of sound within a gas vary with temperature, frequency, pressure, etc. Hence, both these properties can help to monitor changes in experimental conditions. This has recently been studied in both theory and experiments by Dain and Lueptow,[4,5] Martinsson,[6] and Townsend and Meador.[7]

The frequency dependence of the attenuation is fairly easy to measure, but the speed of sound is much more difficult.[8] Both of these affect the shape of the received pulse.

Figure 1 shows three pulses obtained using the experimental setup described in Sec. IV A. The first pulse was measured in pure oxygen, the second in pure ethane, and the third in a mixture of the two, containing molar fraction of 40% of ethane. As the figure shows, there is a small change in pulse shape between pure oxygen and ethane. It is, however, more difficult to notice how this changes when gases are mixed. The pulses in Fig. 1 have been normalized and aligned in time for the purpose of showing differences in shape. The remaining differences in pulse shape are caused by frequency-dependent attenuation and dispersion.

In this paper, we develop a subspace-based filter that can be used to suppress variations in pulse shape originating from the pure gases, hence, leaving only variations originating from interaction effects between the constituent gases. The filter is based on a principle known as *orthogonal signal*

[a]Electronic mail: johan.carlson@csee.ltu.se

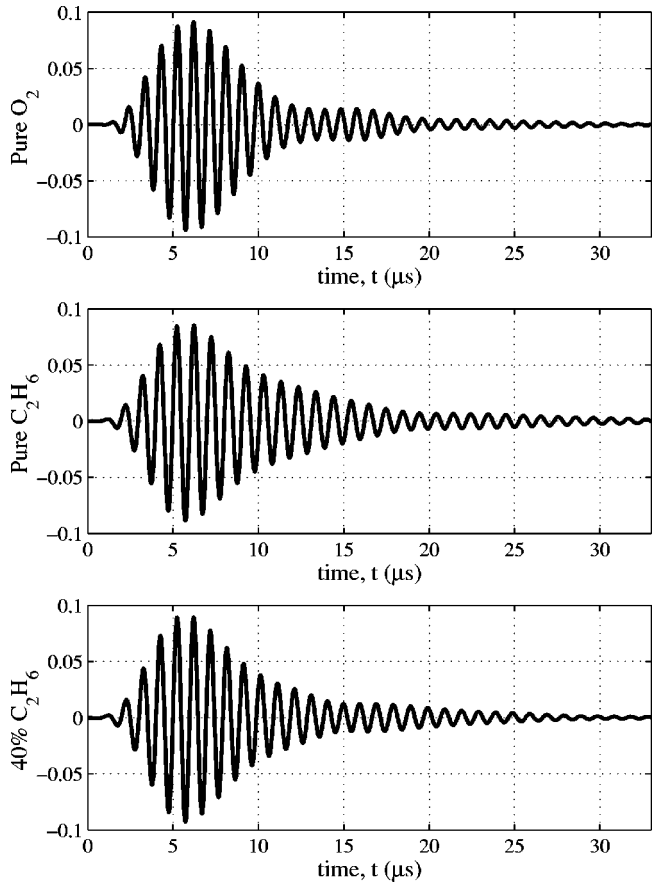

FIG. 1. Example of pulses measured in pure oxygen, pure ethane, and a mixture with a molar fraction of 40% ethane, all measured at a static pressure of 5.0 bar. The temperature was 20 °C. The pulses have been normalized to unit energy and aligned in time.

correction (OSC).[9] Pulses measured in a mixture will be affected by the pure gases and by the inter gas interaction effects. These interaction effects are much smaller than the individual effects of the constituent gases, but highly interesting when the goal is to study the composition of a mixture. The OSC filter is implemented as a projection matrix that projects the measured pulses in gas mixtures onto the orthogonal complement of a basis spanning the experimental variation caused by the pure gases. The remaining experimental variation is then analyzed using *principal component analysis* (PCA).[10] The work presented herein is an extension of the results presented at a recent conference.[11]

The method is evaluated with experiments on pure oxygen (O_2), pure ethane (C_2H_6), and mixtures of the two for molar fractions of ethane in the range of 20%–80%. The results show that the remaining variation can be explained by one principal component, which correlates well with the molar fraction of ethane.

II. NOTATION

We will use bold capital letters (e.g., $\mathbf{X}$) to denote matrices, and small bold letters to denote column vectors (e.g., $\mathbf{x}_i$, for column i of the matrix $\mathbf{X}$). Scalars and matrix row and column indices are denoted with small nonbold (italic) characters (e.g., i, k, n). For example, the first column of the matrix $\mathbf{X}$ is denoted $\mathbf{x}_1$. Matrix transpose is denoted with ^{T}. The notation $x[n]$ denotes the nth element of a vector.

III. THEORY

Any experimentally observed data, x, is composed of two parts: ξ, which is a systematic part, and ε, which is a random noise part, such that $x=\xi+\varepsilon$.

Principal component analysis (PCA)[10] is a well-established tool for analyzing and modeling multivariate data. The central idea is to reduce the dimensionality of a data set consisting of a large number of interrelated variables, but at the same time preserving as much as possible of the systematic experimental variation, ξ, in the data. Figure 2 illustrates the principle for a simple case where a three-dimensional data set is projected onto a two-dimensional subspace.

In order to analyze the shape of ultrasound pulses by PCA, we need to represent them in matrix form. Let $x_i[n]$ $(n=1,...,N)$ be a sampled version of an ultrasound pulse and let $\mathbf{x}_i$ be the column vector representation of the same pulse. Now each measured pulse can be seen as a point in an N-dimensional space. For each of the different experimental settings, a new vector is obtained, and in order to analyze the whole set by PCA, they are stored as columns of a matrix, $\mathbf{X}$.

In the experiments (see Sec. IV), we have two data sets, the first containing pulse-echo measurements of pure oxygen and pure ethane, and the second containing measurements on mixtures of the two. If the effects of oxygen and ethane were to add linearly when mixing the two, the dimensionality of the data set would not increase. That is, the same set of principal components would describe the experimental variation in both data sets. If, however, there are any interaction effects between the gases in the mixture, we would need some additional components to describe these (i.e., the dimensionality of the data set is increased). Now, if the interaction effects are small, which they most likely will be when

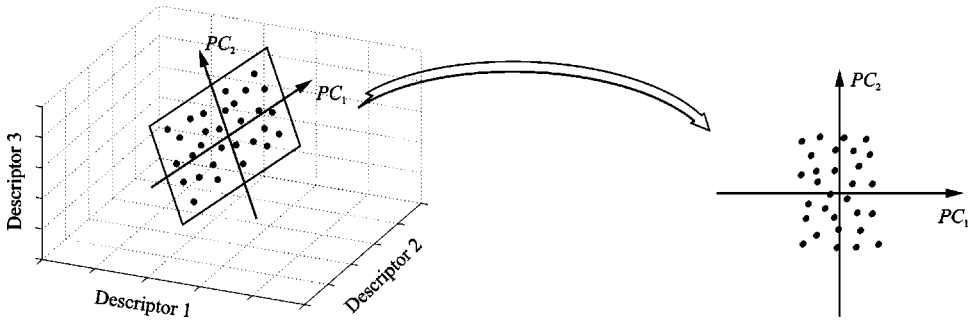

FIG. 2. Schematic description of how PCA reduces the dimensionality of a data set.

the molar fraction is small, they will be practically drowned by the effects of the pure gases. If the goal is to extract the effects of mixing gases, we need some method to remove the effects originating from the pure gases. The way we approach this problem is by *orthogonal signal correction* (OSC).[9]

First, a PCA is performed on measurements on pure gases. This results in a set of components that explain the variations in pulse shape caused by the pure gases, for the different experimental conditions. The pulses measured in gas mixtures will vary due to the individual constituents, but also due to interaction effects between the gases. The OSC process can be seen as a filter that removes the effects of the pure gases from the mixture data, leaving a data set that is uncorrelated (orthogonal) to the measurements in pure gases. The remaining variations in pulse shape originate from interaction effects between the constituent gases.

For this to work, the data set has to be preprocessed to remove the effect of propagation delay and scalar attenuation. This information is, of course, still accessible, but by normalizing the pulses, we do not *a priori* assess any greater statistical significance to any of the measured pulses. Pulses measured in different gas compositions will have a different propagation delay, because of variations in sound velocity. If the delays are not compensated for, this will result in an apparent increase in dimensionality of the data set (i.e., more principal components are needed). This is accomplished by aligning all pulses with respect to one of the measurements (e.g., the first column in the matrix containing all pulses).

The next subsection describes the preprocessing of the ultrasound pulses, and Sec. III B then describes the OSC and the PCA.

A. Preprocessing

The pre-processing consists of two steps:

(1) Normalizing the pulses to unit energy, thus removing the effect of a scalar attenuation due to the propagation distance.
(2) Aligning the pulses in time and thereby removing the effect of changes in propagation delay through the medium, and the effect of any sampling jitter caused by the digitizing hardware.

1. Normalizing

The normalized pulse, $\mathbf{x}_i$, is calculated as

$$\mathbf{x}_i = \frac{\overline{\mathbf{x}_i}}{\sqrt{\overline{\mathbf{x}_i^T \mathbf{x}_i}}}, \tag{1}$$

where $\overline{\mathbf{x}_i}$ denotes the vector containing a sampled version of the pulse, before normalizing.

2. Aligning pulses

Aligning the pulses consists of two steps:

(1) Estimate time-of-flight differences between pulses, with an accuracy of fractions of the sampling time.
(2) Align pulses according to the estimated time-of-flight difference.

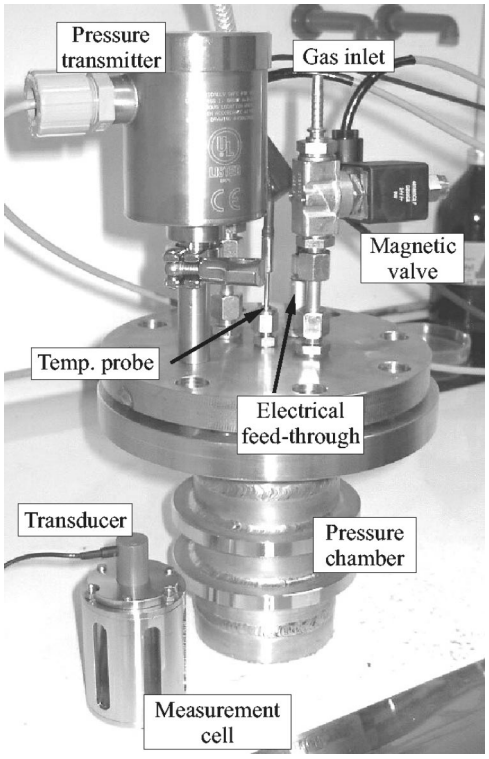

FIG. 3. Description of the measurement cell and the pulse-echo scheme. In this paper the first echo, as indicated in the figure, is analyzed.

In this paper we consider only changes in pulse shape of an ultrasound echo that propagated back and forth through the volume of gas (see Fig. 3). Because we only use the first echo (as indicated in Fig. 3), we do not measure speed of sound and attenuation explicitly, but rather changes in pulse shape caused by frequency-dependent attenuation and speed of sound. However, when the experimental conditions change, the time-of-flight through the gas will also vary. The set of echoes recorded for the different measurement configurations are therefore aligned, with respect to one of the echoes (e.g., the first measurement).

The reason for aligning and normalizing is to better reveal any changes in pulse shape. As a consequence of these changes, it becomes difficult to determine time-of-flight differences, since techniques for this are based on the assumption that the *only* differences between the pulses are a time-of-flight difference and possibly a scalar attenuation.

As a best-effort attempt, we use the analytic cross-correlation technique proposed by Marple[12] to estimate the time-of-flight differences in whole samples (i.e., an integer multiple of the sampling time of the system). Marple's method uses the maximum of the envelope of the cross-correlation function, instead of the cross-correlation function itself. The result is an estimate that is less sensitive to small changes in pulse shape than the standard cross-correlation method, since the envelope is much less sensitive to phase shifts. The details of this method are left out since they are very well described in the original paper by Marple.

A cross-correlation technique will result in an estimate of the time-of-flight difference as a multiple of the sampling time. Variations in propagation speed or jitter in the digitizing hardware can, however, result in delays on a subsample

level (i.e., fractions of the sampling time). To further improve the performance of the PCA, the time-of-flight difference estimates are therefore refined using the estimator proposed by Grennberg and Sandell.[13] This estimator has been shown to work especially well for narrow-band pulses, and for small delays.

Aligning the pulses according to an integer delay (i.e., a multiple of the sampling time) is straightforward, but to shift pulses a fraction of the sampling time, we need to use some interpolation scheme. In this work we have chosen the method of Lagrange interpolation,[14] since this can be implemented as a simple linear filter. Let the original pulse be $\overline{x_i}[n]$. Then, the shifted pulse, $x_i[n]$, is given by

$$x_i[n]=\overline{x_i}[n]*h_l[n,\theta], \tag{2}$$

where θ is the time-of-flight difference, $*$ denotes the convolution, and $h_l[n,\theta]$ is the impulse response of the interpolation filter, according to Lagrange's interpolation formula. For a three-point interpolation, the impulse response is given by

$$h_l[n,\theta]=\begin{cases}\frac{1}{2}\theta(\theta-1), & n=0.\\ (1-\theta^2), & n=1,\\ \frac{1}{2}\theta(\theta+1), & n=2.\end{cases} \tag{3}$$

B. Orthogonal signal correction

After the preprocessing, we are left with a set of measurements that essentially vary only in pulse shape. This section describes the remaining steps of the analysis:

(1) Find a basis for the experimental variation caused by the pure gases (PCA), for different static pressures.
(2) Project the measurements of mixtures onto the orthogonal complement of the basis determined in step 1 (OSC).
(3) Find a new basis for the remaining experimental variation (PCA).

Let $\mathbf{X}_0$ be a matrix where the columns are pulses measured in pure oxygen (O_2) and pure ethane (C_2H_6), for different pressures. Let $\mathbf{X}_1$ be the matrix with columns corresponding to pulses measured in mixtures of the gases, each representing different molar fractions of ethane, also for different static pressures.

Finding a basis for the experimental variation spanned by the columns of $\mathbf{X}_0$ means determining the principal components (PCs) of $\mathbf{X}_0$. In this paper, the PCA is implemented using *singular value decomposition* (SVD).[15] With the SVD, any rank r matrix $\mathbf{X}_0$ can be factored as

$$\mathbf{X}_0=\mathbf{U}_0\mathbf{S}_0\mathbf{V}_0^T, \tag{4}$$

where the columns of $\mathbf{U}_0$ and $\mathbf{V}_0$ are the unit-norm eigenvectors of $\mathbf{X}_0\mathbf{X}_0^T$ and $\mathbf{X}_0^T\mathbf{X}_0$, respectively. The nonzero diagonal elements, σ_i of $\mathbf{S}_0$ are the square-roots of the eigenvalues of $\mathbf{X}_0\mathbf{X}_0^T$ and $\mathbf{X}_0^T\mathbf{X}_0$, sorted so that $\sigma_1\geqslant\sigma_2\geqslant\cdots\geqslant\sigma_r$. This can be seen as a change of basis, where the new basis for the columns of $\mathbf{X}_0$ is given by the columns of $\mathbf{U}_0$ (also called *principal components* or *loading vectors*), and the weights for the new basis (*scores*) are given by the columns of $\mathbf{S}_0\mathbf{V}_0^T$.

The change of basis means that all pulses (columns of $\mathbf{X}_0$) can now be represented as a linear combination of the columns in $\mathbf{U}_0$, using the weights in $\mathbf{S}_0\mathbf{V}_0^T$, i.e.,

$$\mathbf{x}_i=\mathbf{u}_1\sigma_1 v_{i1}+\mathbf{u}_2\sigma_2 v_{i2}+\cdots+\mathbf{u}_r\sigma_r v_{ir}, \tag{5}$$

where r is the rank of $\mathbf{X}_0$. If fewer components than r are used, this yields an optimal low-rank approximation of $\mathbf{X}_0$ (in a least-squares sense). This property is what is used when approximating a data set with a small number of principal components.

To examine how much of the total experimental variation (in %) each principal component explains, we study the scaled singular values, since the singular value σ_i is proportional to the experimental variation in the direction of the ith principal component.[10] Let $\overline{\sigma_i}$ be scaled versions of the r nonzero singular values σ_i:

$$\overline{\sigma_i^2}=100\frac{\sigma_i^2}{\Sigma_{k=1}^{r}\sigma_k^2}. \tag{6}$$

Now, if the effects of the constituent gases were to add linearly, the same set of principal components (columns of $\mathbf{U}_0$) would also span the variations in pulse shape caused by the gas mixtures. That is, the columns of $\mathbf{X}_1$ could all be written as linear combinations of the columns of $\mathbf{U}_0$. If this is not the case, the interaction effects can be extracted from $\mathbf{X}_1$ by projecting onto the orthogonal complement of $\mathbf{X}_0$ as

$$\tilde{\mathbf{X}}_1=\mathbf{\Pi}_{\mathbf{x}_0}^{\perp}\mathbf{X}_1, \tag{7}$$

where the projection matrix $\mathbf{\Pi}_{\mathbf{x}_0}^{\perp}$ is given by[15]

$$\mathbf{\Pi}_{\mathbf{x}_0}^{\perp}=\mathbf{I}-\hat{\mathbf{U}}_0(\hat{\mathbf{U}}_0^T\hat{\mathbf{U}}_0)^{-1}\hat{\mathbf{U}}_0^T, \tag{8}$$

where $\hat{\mathbf{U}}_0$ is the matrix consisting of the n ($n<r$) most significant components of $\mathbf{U}_0$. This is determined by looking at the cumulative sum of the scaled singular values from Eq. (6). Since the columns of $\hat{\mathbf{U}}_0$ are by construction orthonormal,[15] Eq. (8) simplifies to

$$\mathbf{\Pi}_{\mathbf{x}_0}^{\perp}=\mathbf{I}-\hat{\mathbf{U}}_0\hat{\mathbf{U}}_0^T. \tag{9}$$

A basis for the interaction effects is then given by the principal components of $\tilde{\mathbf{X}}_1$, given by the columns of $\tilde{\mathbf{U}}_1$, in

$$\tilde{\mathbf{X}}_1=\tilde{\mathbf{U}}_1\tilde{\mathbf{S}}_1\tilde{\mathbf{V}}_1^T. \tag{10}$$

In other words, we can say that the columns of $\tilde{\mathbf{U}}_1$ form a basis for the experimental variation that remains after removing the contribution of the pure gases. The matrix $\mathbf{\Pi}_{\mathbf{x}_0}^{\perp}$ in Eq. (9) projects the data in $\mathbf{X}_1$ onto a smaller subspace, orthogonal to the subspace spanned by $\hat{\mathbf{U}}_0$. This is why this process is called *orthogonal signal correction*.[9]

C. Summary of the algorithm

The analysis principle described in the previous sections can be summarized as follows:

(1) Store all pulses as columns of the matrix $\overline{\mathbf{X}}$.
(2) Normalize and align the pulses in $\mathbf{X}$ as described in Sec. III A in order to obtain $\mathbf{X}_0$.

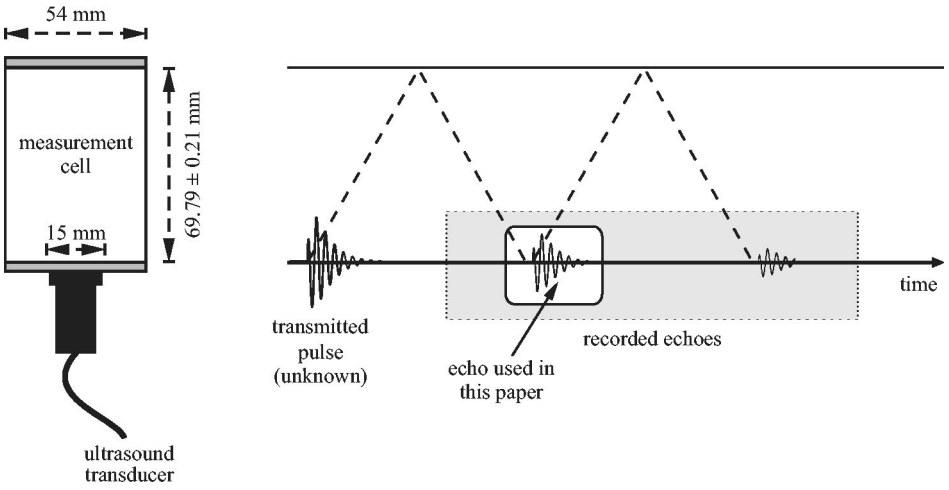

FIG. 4. The measurement equipment. All measurements were performed in a pressure chamber. The pressure was varied between 1.54 and 7.4 bar. The air transducer has a center frequency of 1 MHz.

(3) Calculate principal components ($\mathbf{U}_0$) of the pure gases using Eq. (4).
(4) Remove the effect of the pure gases from the gas mixture using Eq. (7).
(5) Determine the principal components, $\tilde{\mathbf{U}}_1$, of the remaining variation ($\tilde{\mathbf{X}}_1$) using Eq. (10).

IV. EXPERIMENTS

A. Setup

A pulse echo scheme was used to acquire ultrasound pulses that propagated through the gas mixtures. The acoustic properties of interest vary with frequency, f, and pressure, P. In fact, it is the frequency to pressure ratio, f/P, which is the appropriate scale to use.[4] The temperature and frequency dependence of sound velocity and acoustic attenuation have previously been investigated by, for example, Martinsson,[6] Lueptow,[4,5] and Bhatia.[16] There are two ways to vary the f/P ratio in a pulse echo system. Transducers of different center frequency can be used for a fixed pressure, or one transducer can be used while the pressure is changed. The latter of the two principles was chosen for the work in this paper. A 1-MHz air transducer was used. The effective diameter of the transducer was 15 mm (cf. Fig. 3). Diffraction losses were assumed to be negligible, since the pulse-echo measurements are in the near-field region of the transducer.[17]

A custom-built pressure chamber (see Fig. 4) was used to achieve different static pressures. The pressure was varied between 1.54 to 7.4 bar in 12 steps for each gas. Since the attenuation in ethane is extremely high at low pressures and high frequencies, we were limited to make measurements at higher pressure for that particular gas (above 1.86 bar).

The pressure in the chamber was measured with an *ANDERSON TPP Pressure Transmitter* with a range of up to 13.6 bar above atmospheric zero. The transmitter has an accuracy of approximately 30 mbar. This includes the combined effects of linearity, hysteresis, and repeatability.

The transducer was mounted on a stainless steel measurement cell, as seen in the lower left corner of Fig. 4. The measurement cell was then immersed into the pressure chamber. Figure 3 shows the details of the measurement cell. For all calculations in this paper, only the first of the recorded echoes was used, as indicated in the figure. The whole setup was then placed in a temperature controlled chamber (*Heraeus Vötsch HT4010*), where the temperature was kept constant at the desired temperature.

To excite and receive acoustic pulses from the transducer, a *Panametrics Pulser/Receiver Model 5072* was used. For the transmitting mode, the pulser/receiver was set to deliver maximum energy to the transducer, which corresponds to a short voltage impulse with 360-V amplitude, corresponding to an excitation energy of 104 μJ. In receive mode, the signals are amplified 20 dB.

All pulses were sampled at 100 MHz with an 8-bit *Tektronix TDS 724*, 1-GHz digitizing oscilloscope. For each experimental setting, 50 signals were recorded and transferred to a PC, where they were averaged and further processed (see Sec. III A).

For each measurement, the temperature was recorded using an encapsulated PT100 sensor mounted through the wall of the pressure chamber.

The transducer used was originally designed for operation in air which has an acoustic impedance $Z_{\text{air}} = 4154\,\text{Pa}\cdot\text{s/m}$ (at $T = 20\,^{\circ}\text{C}$ and $P = 1$ bar). Since the acoustic impedance of the gases used are different from air, the transducer will not operate at its optimal performance, and consequently not transmit as much power as desirable.

B. Results

The first set of experiments was with pure ethane and pure oxygen, at 20 °C, for pressures of 1.54–7.4 bar. This resulted in 12 measurements of ethane and 12 of oxygen. After aligning and normalizing, as described in Sec. III A, all 24 were stored as columns of the matrix $\mathbf{X}_0$. The second set of experiments was with mixtures of ethane and oxygen, for molar fractions of 20%, 40%, 60%, and 80%, for the same pressure range, also at 20 °C. In total $4\times12=48$ experiments were made on the mixtures. These pulses were aligned and normalized and stored as columns of the matrix $\mathbf{X}_1$.

Looking at the cumulative sum of the squares of the scaled singular values (cf. Fig. 5), $\overline{\sigma_i^2}$, of $\mathbf{X}_0$ we see that the first three components are enough to describe approximately 99% of the total experimental variation. The rest of the components are assumed to represent mainly noise. Figure 6 shows the corresponding *principal components*, $\mathbf{u}_i$ (i

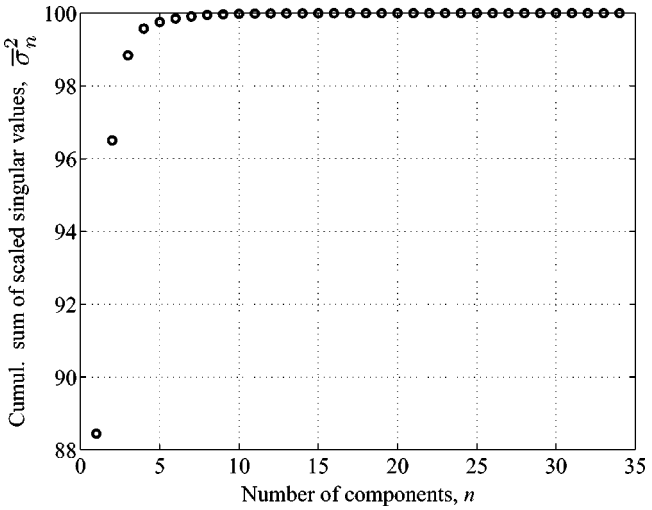

FIG. 5. Cumulative sum of the singular values, $\overline{\sigma_n^2}$, of $\mathbf{X}_0$ (i.e., eigenvalues of $\mathbf{X}_0^T\mathbf{X}_0$), describing the amount of experimental variation explained as components are added to the model [see Eq. (6)]. Note that the first three components are enough to describe approximately 99% of the total variation.

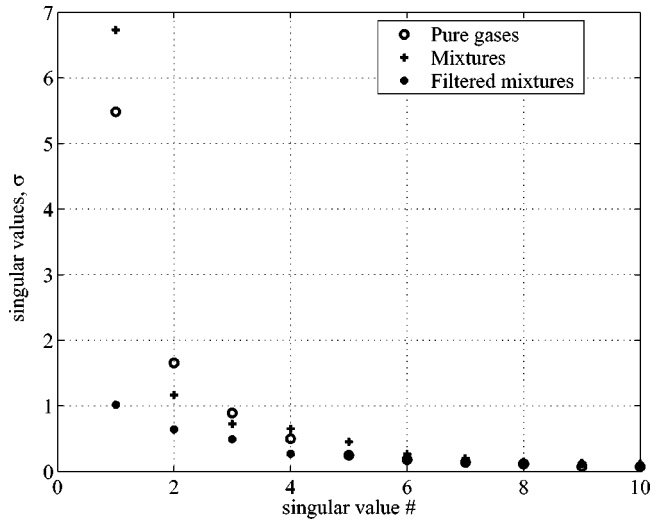

FIG. 7. Singular values of the pure gases ($\mathbf{X}_0$), the mixtures $\mathbf{X}_1$, and the mixtures after projection $\tilde{\mathbf{X}}_1$. It is clear that the pure gases contribute to most of the variation. The filtering reveals the relatively small interaction effects.

$=1,2,3$). Since these three components account for approximately 99% of the experimental variation, this means all measured pulses can be accurately approximated as a linear combination of these, as given by Eq. (5).

Following the steps described in Sec. III C, we obtain the *score matrix*, $\tilde{\mathbf{S}}_1\tilde{\mathbf{V}}_1^T$, and the *loading matrix*, $\tilde{\mathbf{U}}_1$.

The data set for the gas mixtures was then filtered using the OSC filter given by Eq. (7). In order to study how much systematic variation that remains after the OSC filter was applied, a PCA was performed on $\tilde{\mathbf{X}}_1$. From Fig. 7 we see that the remaining variation is significantly smaller. Determining the significance of these components is more difficult, since the singular values do not vary as much as for the unfiltered mixtures. There are two possible reasons for this:

(1) The components contain mainly noise.
(2) All components contain important variation.

The second is not likely, since we know already that approximately 98% of the original variation has been removed. To determine whether the remaining components represent any systematic variation, we need to study the scores associated with each of the components. In Fig. 8 these are shown for the first component. These show a clear interdependence with the physical variables of interest (i.e., f/P ratio and molar fraction). Studying the scores of the other components did not show the same systematic relationship to the molar fraction, and therefore no figures of this have been included in the paper.

Determining the number of necessary principal components can be done in several ways. In this paper we deter-

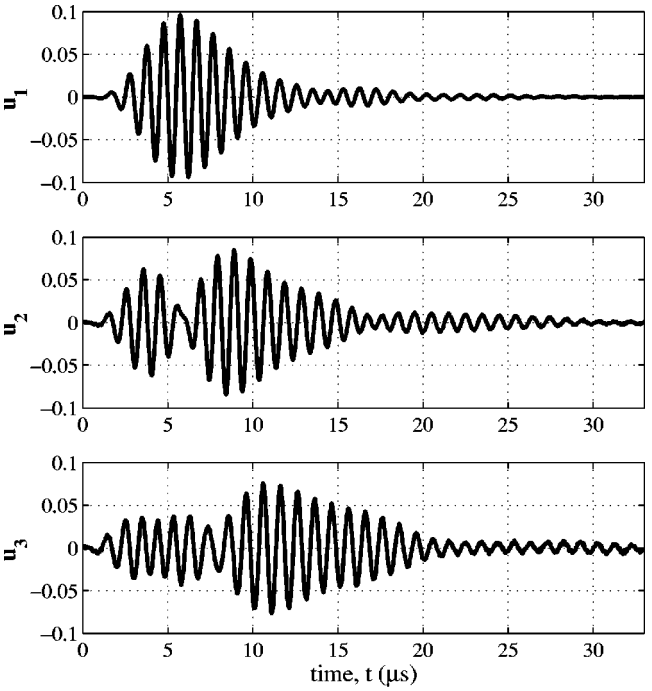

FIG. 6. First three loading vectors, $\mathbf{u}_1$, $\mathbf{u}_2$, $\mathbf{u}_3$, representing approximately 99% of the total experimental variation.

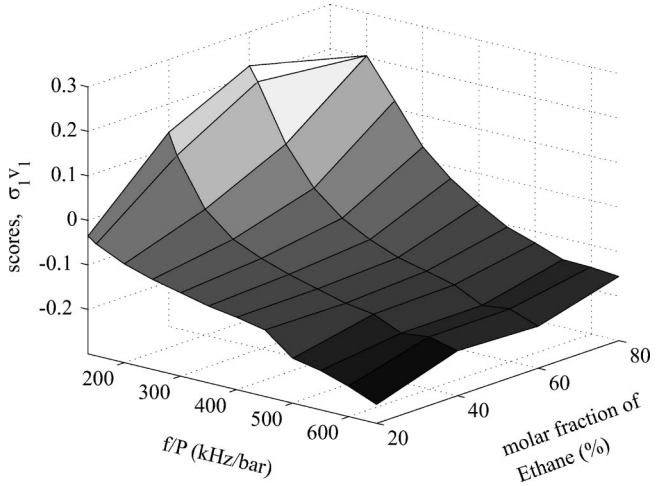

FIG. 8. Scores (coefficients), $\tilde{\mathbf{v}}_1\sigma_1$, of the first principal component of the filtered data set as a function of frequency to pressure ratio and molar fraction of ethane.

mined this by looking at how many components are needed to capture >98% of the experimental variation, using Eq. (6). Depending on the purpose of the analysis (e.g., regression or classification) other methods such as cross validation[18] or the Akaike information criterion[19] could be used.

In Fig. 7 it appears that for the mixtures some of the singular values are smaller than the corresponding values for the pure gases, and vice versa. Some questions were raised whether this contradicts the conclusion that the pure gases contribute to most of the systematic variation. The pure gases and the mixtures are two different data sets, and the intrinsic structures of these sets may vary, and thus the relative size of the singular values can differ. Looking at the singular values of the filtered mixtures, it is, however, clear that most of the variation has been removed. The remaining set is uncorrelated with the pure gases and the conclusion, and thus the remaining variation is due to noise and intergas interaction effects.

Figure 8 shows the *scores* (or coefficients) $\tilde{\mathbf{v}}_1\sigma_1$ of the first component for the filtered mixture data as function of frequency to pressure ratio (f/P) and molar fraction of ethane. For high f/P values (i.e., low static pressures), the acoustic attenuation is very high, and the signal-to-noise-ratio (SNR) drops. For these f/P values, the intergas interaction effects are almost drowned by the experimental noise, and thus become difficult to extract. This can be seen in Fig. 8 as the surface levels out, i.e., the scores describe mainly noise. For higher SNR, there is visible interdependence between the molar fraction of ethane and the scores of the first principal component. To estimate molar fractions, the surface in Fig. 8 could be modeled as a function of the frequency to pressure ratio and molar fraction.

V. DISCUSSION

A first step towards a physical model of a complex system is to identify variables that affect the experimental variation. The methodology described in this paper helps revealing small, but highly interesting properties of gas mixtures, related to intergas interaction effects. The results in Fig. 8 show that these properties vary with the physical properties of interest. It is reasonable to believe that the changes in pulse shape are due to dispersion and frequency-dependent attenuation. For some individual gas components, these effects are predictable using physical models. It is, however, much more difficult to describe the physics of the interaction effects. The focus of this paper is to show that these effects can be observed from measured data, but we have not yet attempted to describe the underlying physical processes. Although the surface in Fig. 8 could be modeled empirically, a good physical model would be more attractive. Current research focuses on studying these phenomena, but to date it is not possible to draw any conclusions regarding this. The physical principles of wave propagation in gases are described in detail elsewhere, and since we do not use the physical models here, these details have been left out. The interested reader is referred to the work by Dain and Lueptow[4,5] or the classic by Bhatia.[16] A challenging problem for future research is to find means of extracting systematic variation from observed data that can be used to estimate parameters in physical models.

In this paper we have only considered a two-component gas mixture. The long-term goal is to develop method for on-line measurement of the energy content of energy gases. In practice, these are always mixtures of more than two gases. Although molar fractions would enable us to calculate the energy content, it might be easier to quantify the energy content directly, using the same methodology as described in this paper.

In Sec. III A, we mention the importance of aligning the pulses in time before processing. If this is not done, the time delays will cause the apparent increase in dimensionality of the data set. Compensating for the time delays is, however, rather difficult. The change in pulse shape that we are interested in extracting is also a source of error when we try to estimate the time delays. The reason for this is that the time delay between pulses with different shape is not well defined. This is a well-understood problem that future research will have to address (see Ref. 20 and references therein).

It should also be mentioned that, except for the methodology described here, it is also possible to run a PCA directly on a matrix containing measurements on both pure gases and gas mixtures. The principal components obtained by this procedure also contain information about the gas composition.[21] The OSC principle does, however, better isolate the specific interaction effects caused by mixing the gases.

VI. CONCLUSIONS

In this paper we have described how OSC and PCA can be used to extract information from ultrasound pulses that vary with the molar fractions of ethane in an ethane/oxygen mixture. OSC enables us to describe variations in pulse shape caused by interaction effects between the gases that cannot be described by the pure gases alone. The OSC can be interpreted as a subspace-based filtering process that removes experimental variation described by the pure gases, thus revealing the intergas interaction effects. These effects are significantly smaller than the effects of the pure gases and, as indicated by Fig. 1, very difficult to estimate from the measured pulses directly. The variation remaining after OSC filtering was analyzed with PCA, and the results show that one principal component is sufficient to describe most of the interaction effects, and that this shows a visible interdependence with the molar fraction of ethane in the two-component gas mixture.

ACKNOWLEDGMENTS

The authors wish to express their sincerest gratitude toward Professor Anders Grennberg and to Professor Rolf Carlson, for their valuable input, and to Professor Jerker Delsing, for supporting this work. Generous grants from the *Kempe Foundation* and *Swedish Energy Agency* are also gratefully acknowledged. Finally, the authors like to thank the reviewers for their valuable comments leading to significant improvements of the manuscript.

[1] J. Delsing and I. Blom, ''On-Line Measurements of Energy Content of Bio Gas and Natural Gas Mixtures,'' Technical Report No. ISSN: 0282-3772, Lund Institute of Technology (unpublished).
[2] M. Jaeschke, ''Thermodynamic research improves energy measurement of natural gas,'' Thermochim. Acta **382**, 37–45 (2002).
[3] M. Jaeschke, P. Schley, and R. J. van Rossmalen, ''Thermodynamic research improves energy measurement in natural gas,'' Int. J. Thermophys. **23**(4), 1013–1031 (2002).
[4] Y. Dain and R. M. Lueptow, ''Acoustic attenuation in three-component gas mixtures—theory,'' J. Acoust. Soc. Am. **109**, 1955–1964 (2001).
[5] Y. Dain and R. M. Lueptow, ''Acoustic attenuation in three-component gas mixtures—Results,'' J. Acoust. Soc. Am. **110**, 2974–2979 (2001).
[6] P.-E. Martinsson and J. Delsing, ''Ultrasonic Measurements of Molecular Relaxation in Ethane and Carbon Monoxide,'' in *Proc. IEEE Int. Ultrason. Symp.* (IEEE, Munich, Germany, 2002), pp. 494–499.
[7] L. W. Townsend and W. E. Meador, ''Vibrational relaxation and sound absorption and dispersion in binary mixtures of gases,'' J. Acoust. Soc. Am. **99**, 920–925 (1995).
[8] J. E. Carlson, F. Sjöberg, and P.-E. Martinsson, ''A Noise-Tolerant Group Delay Estimator Applied to Dispersion Measurement in Gases,'' in *Proc. IEEE Int. Ultrason. Symp.* (IEEE, Honolulu, HI, 2003), pp. 254–257.
[9] S. Wold, H. Antti, F. Lindgren, and J. Öman, ''Orthogonal Signal Correction of Near-Infrared Spectra,'' Chemom. Intell. Lab. Syst. **44**, 175–185 (1998).
[10] I. T. Jolliffe, *Principal Component Analysis*, 2nd ed. (Springer Verlag, New York, 2002).
[11] J. E. Carlson and P.-E. Martinsson, ''Ultrasonic Measurement of Molar Fractions in Gas Mixtures by Orthogonal Signal Correction,'' in *Proc. IEEE Int. Ultrason. Symp.* (IEEE, Montréal, Canada, 2004), pp. 821–825.
[12] S. L. Marple, Jr., ''Estimating Group Delay and Phase Delay via Discrete-Time ''Analytic'' Cross-Correlation,'' IEEE Trans. Signal Process. **47**(9), 2604–2607 (1999).
[13] A. Grennberg and M. Sandell, ''Estimation of Subsample Time Delay Differences in Narrowband Ultrasonic Echoes Using the Hilbert Transform Correlation,'' IEEE Trans. Ultrason. Ferroelectr. Freq. Control **41**(5), 588–595 (1994).
[14] *Handbook of Mathematical Functions With Formulas, Graphs, and Mathematical Tables, Dover Books on Advanced Mathematics*, 8th ed., edited by M. Abramowitz and I. A. Stegun (Dover, New York, 1972).
[15] G. Strang, *Linear Algebra and its Applications*, 3rd ed. (Harcourt Brace Jovanovich, San Diego, 1986).
[16] A. B. Bhatia, *Ultrasonic Absorption—An Introduction to the Theory of Sound Absorption and Dispersion in Gases, Liquids and Solids* (Dover, New York, 1985).
[17] G. S. Kino, *Acoustic Waves: Devices, Imaging, and Analog Signal Processing* (Prentice-Hall, Englewood Cliffs, NJ, 1987).
[18] J. Shao, ''Linear model order selection by cross-validation,'' J. Am. Stat. Assoc. **88**(422), 486–494 (1993).
[19] H. Akaike, ''A new look at statistical model identification,'' IEEE Trans. Autom. Control **19**, 716–723 (1974).
[20] R. L. Trousil, K. R. Waters, and J. G. Miller, ''Experimental validation of the use of Kramers-Kronig relations to eliminate the phase sheet ambiguity in broadband phase spectroscopy,'' J. Acoust. Soc. Am. **109**(5), 2236–2244 (2001).
[21] P.-E. Martinsson and J. E. Carlson, ''Investigating the Feasibility of Using Principal Component Analysis for Ultrasonic Classification of Gas Mixtures,'' in *Proc. IEEE Int. Ultrason. Symp.* (IEEE, Honolulu, HI, 2003), pp. 1396–1399.

Distortion product otoacoustic emissions for hearing threshold estimation and differentiation between middle-ear and cochlear disorders in neonates

Thomas Janssen,[a] Daniel D. Gehr, Annette Klein, and Jörg Müller
Hals-Nasen-Ohrenklinik, Technische Universität München, Ismaningerstraße 22, D-81675 Munich, Germany

(Received 19 July 2004; revised 3 December 2004; accepted for publication 3 December 2004)

Our aim in the present study was to apply extrapolated DPOAE I/O-functions [J. Acoust. Soc. Am. **111**, 1810–1818 (2002); **113**, 3275–3284 (2003)] in neonates in order to investigate their ability to estimate hearing thresholds and to differentiate between middle-ear and cochlear disorders. DPOAEs were measured in neonates after birth (mean age = 3.2 days) and 4 weeks later (follow-up) at 11 test frequencies between f2 = 1.5 and 8 kHz and compared to that found in normal hearing subjects and cochlear hearing loss patients. On average, in a single ear hearing threshold estimation was possible at about 2/3 of the test frequencies. A sufficient test performance of the approach is therefore suggested. Thresholds were higher at the first measurement compared to that found at the follow-up measurement. Since thresholds varied with frequency, transitory middle ear dysfunction due to amniotic fluid instead of cochlear immaturity is suggested to be the cause for the change in thresholds. DPOAE behavior in the neonate ears differed from that found in the cochlear hearing loss ears. From a simple model it was concluded that the difference between the estimated DPOAE threshold and the DPOAE detection threshold is able to differentiate between sound conductive and cochlear hearing loss. [DOI: 10.1121/1.1853101]

PACS numbers: 43.64.Jb Pages: 2969–2979

I. INTRODUCTION

When stimulated by two tones of neighboring frequencies, outer hair cells evoke intermodulation distortions in cochlear micromechanics and fluid which can be measured acoustically by means of a microphone in the outer ear canal and are referred to as distortion product otoacoustic emissions (DPOAEs). In humans, the $2f_1$-f_2 DPOAE has the highest amplitude, hence the highest signal-to-noise ratio, and is therefore primarily used for clinical diagnostics.

Two main requirements have to be met when using DPOAEs as a probe for monitoring the loss of cochlear sensitivity and loss of compression across frequency. First, a primary tone level setting has to be applied that accounts for the different compression of the two primary tones at the DPOAE generation site (the f_2-place) in the cochlea (Whitehead *et al.*, 1995; Janssen *et al.*, 1995a, b; Kummer *et al.*, 2000). When using such a level setting (''scissor'' paradigm; Sec. III), the level and frequency of the higher primary tone (L_2 and f_2) are decisive for DPOAE generation. Thus, when plotting the DPOAE level L_{dp} as a function of L_2 (DPOAE I/O-function) DPOAEs reflect the compressive cochlear sound processing at the f_2-place (Boege and Janssen, 2002) known from measurements of basilar membrane motion in animal experiments (Ruggero *et al.*, 1997).

Second, DPOAEs have to be measured at close-to-threshold primary tone levels which is difficult due to a low signal-to-noise ratio. Therefore, when plotting the DPOAE level L_{dp} as a function of f_2 (DPOAE-gram), the DPOAEs often do not reflect audiometric hearing thresholds.

The way out of this dilemma is the estimation of DPOAEs at threshold by extrapolating DPOAE I/O-functions. When using the scissor paradigm for eliciting DPOAEs a logarithmic dependency of the DPOAE level L_{dp} on the primary tone level L_2 is present. The logarithmic dependency results in a linear dependency between the DPOAE sound pressure p_{dp} and the primary tone sound pressure level L_2. Thus, in a semi-logarithmic plot DPOAE data can easily be fitted by linear regression analysis. In doing this, the intersection point of the regression line with the primary tone level axis L_2 at $p_{dp} = 0$ Pa can then be used as an estimate of the DPOAE level at threshold L_{dpth} (Boege and Janssen, 2002). In patients suffering from cochlear hearing loss, the estimated DPOAE level at threshold and the audiometric pure-tone threshold was found to be significantly correlated (Boege and Janssen, 2002; Gorga *et al.*, 2003).

Besides the estimation of pure-tone thresholds, DPOAE I/O-functions provide an additional measure, i.e., the slope of the I/O-function which is able to estimate cochlear compression. This was shown for guinea pigs in which the outer hair cells were impaired using acute furosemide intoxication (Mills and Rubel, 1996) and for human cochlear hearing loss ears (Janssen *et al.*, 1995a, b, 1998; Kummer *et al.*, 2000; Dorn *et al.*, 2001; Boege and Janssen, 2002; Neely *et al.*, 2003). In these studies the slope of the DPOAE I/O-function increased with increasing hearing loss revealing a loss of compression of outer hair cell amplifiers.

Due to the linear sound processing of the middle ear, one can assume that the DPOAE growth behavior remains to a great extent unaltered with a sound conduction dysfunction. In fact, when inducing a middle ear dysfunction by

[a]Electronic mail: T.Janssen@lrz.tum.de

filling the bulla with physiological saline solution in guinea pigs, the slope of the DPOAE I/O-functions was not significantly affected revealing normal compressive sound processing. In contrast, when the guinea pigs were exposed to noise the slope of the DPOAE I/O-function did differ significantly from that found before noise exposure (Gehr *et al.*, 2004). These findings suggest DPOAE I/O-functions to allow a differentiation between middle and inner ear dysfunction.

Our purpose in the present study was to apply extrapolated DPOAE I/O-functions in neonates in order to find out whether and to what extent this new method is able to estimate hearing thresholds and to differentiate between sound conductive and cochlear hearing loss under hearing screening conditions.

II. METHODS

A. Subjects

There were no selection criteria for participation in the study. The study was performed under realistic test conditions since DPOAE measurements were conducted either in the neonatal care unit (first measurement) or at the baby's home (follow-up). In total, 127 ears from 103 babies were investigated (first measurement). In 8 ears measurements had to be stopped because the babies woke up. In one ear neither ATEOAEs nor DPOAEs could be found. DPOAE measurements were conducted immediately after universal newborn hearing screening (UNHS) using ATEOAE. In most of the babies only one ear was measured in order to not stress the babies unnecessarily. Thus, the population of the present study consisted of 118 ears of 93 babies. The age varied from 27 hours to 10 days (mean age=3.2 days). Postconceptional age ranged between 36 weeks and 41 weeks. These ears are referred to as the neonate group. DPOAE measurements were performed in a quiet room of the neonatal care unit in the gynecological hospital of the *Technische Universität München* during spontaneous sleep. Most of the parents did not agree in a second measurement. Thus, from the 93 neonates only 16 babies (21 ears) were tested in a follow-up study at least four weeks after the birth at their parents' home. These ears are referred to as the follow-up neonate group. DPOAEs were measured after feeding during natural sleep. A quiet room was chosen and the babies were lying in their cradle.

For comparison DPOAEs were measured in 26 ears of 14 adults with normal hearing (7 females, 7 males, mean age=24.7 years) and in 189 ears of 98 patients suffering from cochlear hearing loss. According to pure-tone audiometry the hearing loss of the normal hearing subjects was equal to or lower than 15 dB in the examined frequency range. Audiometric hearing thresholds of the cochlear hearing loss ears were sampled in five groups ranging from -5 dB HL to 40 dB HL, the step being 10 dB (group 1: -5 and 0 dB HL, group 2: 5 and 10 dB HL, group 3: 15 and 20 dB HL, group 4: 25 and 30 dB HL, and group 5: 35 and 40 dB HL). Please note that group 1 and 2 does not mean normally hearing ears. In these ears normal thresholds were found at some frequencies only. The classification was done because it is believed that a cochlear hearing loss ear is not normal, even if its audiometric thresholds are normal within a limited cochlear region. Middle ear and retrocochlear disorders were excluded by tympanometry and auditory brainstem responses. Measurements were performed in a sound-insulated booth while normal hearing subjects and patients, respectively, were seated in a comfortable recliner.

B. DPOAE measurements, DPOAE threshold and compression estimates

DPOAE measurements were conducted by using DP2000 (Starkey)/ER-10C (Etymotic-Research) instrumentation at eleven f_2-frequencies (1.5, 2, 2.5, 3, 3.5, 4, 4.5, 5, 6, 7 and 8 kHz) beginning with the highest one. However, for establishing hearing loss classes in the cochlear hearing loss ears only audiometer frequencies (1.5, 2, 3, 4, 6, and 8 kHz) were considered. The f_2/f_1 ratio was 1.2 for all f_2. DPOAEs were recorded at up to ten different primary tone levels per frequency. The primary tone levels L_1 and L_2 were set according to the "scissor" paradigm equation $L_1=0.4\,L_2+39$ dB (Janssen *et al.*, 1995a, b; Kummer *et al.*, 2000). This level setting was used to account for the nonlinear interaction of the two primaries at the DPOAE generation site at the f_2 place. L_2 was set to a maximum of 65 dB SPL and was decreased in 5 dB steps to a minimum of 20 dB SPL. The maximum averaging time for recording DPOAEs was 4 seconds. Artifact rejection was performed by comparing different buffers. In doing this, the noise floor could be reduced. After an average time of 2 seconds a subtotal was established. If the signal-to-noise ratio was higher than 20 dB the measurement was stopped and the DPOAE was accepted to be valid. If the signal-to-noise ratio was lower than 20 dB after 2 seconds the measurement was continued for another 2 seconds. In this case DPOAEs were accepted as valid for a signal-to-noise ratio exceeding 6 dB. In doing this, measuring time could be considerably reduced. The test time per ear amounted up to about 8 minutes (at 11 frequencies and 10 levels). Parameter setting, measurements, and data analysis were performed automatically.

Linear extrapolation lines were fitted to the discrete DPOAE data given in sound pressure p_{dp}. This linear fitting procedure was established as a tool for objective hearing threshold estimation by Boege and Janssen (2002) and was confirmed and improved by further studies (Gorga *et al.*, 2003; Oswald and Janssen, 2003). Extrapolation curves are shown exemplarily in Fig. 3, later. The estimated DPOAE threshold level L_{dpth} was defined as the stimulus level L_2 at which the linear extrapolation equals $p_{\mathrm{dp}}=0$ Pa. The slope $s\,(L_2)$ of the extrapolated DPOAE I/O-functions in a logarithmic plot was calculated according to the equation $s\,(L_2)=20/\ln 10\;\,(a/(aL_2+b))$ with $p_{\mathrm{dp}}=aL_2+b$ (regression line). The DPOAE compression $k\,(L_2)$ is the reciprocal value of the slope $s\,(L_2)^{-1}$. The criteria for accepting an I/O-function as valid were as follows: (i) I/O-functions had to consist of at least three successive data points, (ii) the coefficient of determination r^2 for the linear regression had to be higher than 0.8, and (iii) the slope of the linear regression line had to be positive.

Before each DPOAE measurement in-the-ear calibration (Whitehead *et al.*, 1995) was performed in order to reduce

TABLE I. DPOAE threshold level L_{dpth} (dB SPL), compression k (at $L_2=55$ dB SPL), and number of ears where criteria for estimating the DPOAE-threshold from extrapolated DPOAE I/O-functions were fullfilled (see Sec. II) for the normal hearing adult, neonate, follow-up neonate, and cochlear hearing loss groups across f_2-frequencies (mean, ±SD). Additionally, the noise floor level L_{nf} (mean, ±SD) for the normal hearing adult, neonate, and follow-up neonate groups across f_2-frequencies is listed (number of ears is identical with that indicated at the DPOAE threshold level L_{dpth} line).

$f2$ (kHz)	1.5	2.0	2.5	3.0	3.5	4.0	4.5	5.0	6.0	7.0	8.0
$L_{\text{dpt,.norm}}$	18.9±9.0	17.6±15.8	14.8±7.6	10.8±11.4	11.2±6.7	10.6±13.7	11.5±11.4	16.0±14.0	25.1±8.3	31.3±8.9	31.9±9.0
26 ears	$n=24$	$n=24$	$n=24$	$n=21$	$n=25$	$n=25$	$n=25$	$n=26$	$n=25$	$n=25$	$n=17$
$L_{\text{dpth,15–20HL}}$	26.6±8.7	27.0±16.1		25.7±13.1		21.6±15.7			32.5±13.1		39.8±10.9
	$n=13/21$	$n=23/37$		$n=16/29$		$n=29/31$			$n=40/56$		$n=7/42$
$L_{\text{dpth,25–30HL}}$	32.2±12.5	21.7±7.2		38.8±6.5		34.1±8.6			41.3±7.6		17.4
	$n=5/7$	$n=3/8$		$n=6/10$		$n=14/18$			$n=16/35$		$n=1/18$
$L_{\text{dpth,35–40HL}}$				42.3±4.9		41.3±5.9			42.5±7.6		42.4
				$n=7/14$		$n=9/15$			$n=4/17$		$n=1/18$
$L_{\text{dpt,.neonate}}$	24.6±11.0	27.0±9.0	23.6±11.1	25.7±9.3	18.9±8.7	21.0±8.9	21.1±9.0	24.3±9.4	29.5±9.8	32.7±9.7	36.0±8.3
118 ears	$n=39$	$n=56$	$n=54$	$n=53$	$n=49$	$n=65$	$n=87$	$n=88$	$n=88$	$n=85$	$n=78$
$L_{\text{dpth,follow-up}}$	21.2±12.4	24.0±21.1	19.0±12.2	17.9±14.8	13.2±10.6	13.3±12.8	19.6±12.2	17.9±12.2	23.4±8.1	27.8±10.1	33.8±6.9
21 ears	$n=7$	$n=9$	$n=9$	$n=9$	$n=10$	$n=14$	$n=16$	$n=19$	$n=17$	$n=16$	$n=16$
k_{norm}	4.2±1.0	4.3±1.8	4.6±0.9	5.1±1.3	5.0±0.8	5.1±1.6	5.0±1.3	4.5±1.6	3.4±1.0	2.7±1.0	2.7±1.0
$k_{\text{15–20HL}}$	3.3±1.0	3.2±1.8		3.4±1.5		3.8±1.8			2.6±1.5		1.7±1.3
$k_{\text{25–30HL}}$	2.6±1.4	3.7		1.8±0.7		2.4±1.0			1.6±0.9		4.3
$k_{\text{35–40HL}}$				1.5±0.6		1.6±0.7			1.4±0.9		1.5
k_{neonate}	3.5±1.3	3.2±1.0	3.6±1.3	3.4±1.1	4.2±1.0	3.9±1.0	3.9±1.0	3.5±1.1	2.9±1.1	2.6±1.1	2.2±1.0
$k_{\text{follow-up}}$	3.9±1.4	3.6±2.4	4.1±1.4	4.3±1.7	4.8±1.2	4.8±1.5	4.1±1.4	4.3±1.4	3.6±1.0	3.1±1.2	2.4±0.8
$L_{\text{nf,norm}}$	−14.3±1.9	−16.8±2.0	−19.9±2.8	−20.5±2.7	−19.9±2.9	−20.9±3.1	−21.9±3.2	−21.8±3.1	−21.4±3.1	−19.1±3.4	−18.1±3.0
$L_{\text{nf,neonate}}$	−3.1±7.2	−7.6±6.2	−10.7±6.5	−9.8±6.8	−14.8±5.4	−14.6±6.0	−15.3±5.2	−13.8±4.7	−13.3±4.2	−13.6±4.9	−14.4±4.0
$L_{\text{nf,follow-up}}$	2.6±9.7	−4.5±8.0	−10.8±6.4	−9.3±7.3	−10.8±6.5	−11.9±6.6	−15.0±5.6	−13.2±5.3	−14.7±4.5	−12.3±5.4	−13.2±4.4

the influence of outer ear canal resonance. As ear canal geometry and size interindividually vary, the adequate stimulus for eliciting DPOAEs, i.e., the sound pressure measured at the ear drum differs notably from the sound pressure measured at the tip of the sound probe (which is decisive for the stimulus setting). No method was applied in advance to take into account this standing wave effect. Consequences will be discussed below. Software for measuring DPOAEs and analyzing the data was custom made using MATLAB (Mathworks). Statistical tests (t-test, Kruskal–Wallis, Mann–Whitney) were performed using SPSS software (SPSS Inc.).

It should be noted that DPOAE measurements in the neonates, the normal hearing subjects, and the cochlear hearing loss patients were done by using the same measuring system and the same parameter settings.

III. RESULTS

A. Test performance

In the normal hearing subject sample (26 ears) hearing threshold estimation could be performed in almost all ears at most test frequencies [e.g., 21/26 (80%, minimum) at 3 kHz, 26/26 (maximum) at 5 kHz], with the exception of $f_2=8$ kHz, where in only 17 ears (65.4%) the criteria for extrapolation (see Sec. II) were fullfilled. In contrast, in the neonate group (118 ears) the percentage of ears in which hearing threshold estimation could be yielded was lower [e.g., 88/118 (74,6 %) at 5 kHz], especially at the lower test frequencies [e.g., 39/118 (33.1 %) at 1.5 kHz], which can be attributed to the higher noise floor. Similar percentages were obtained in the follow-up neonate group (Table I).

The mean noise floor level varied across frequency from −14.3 dB SPL (at 1.5 kHz) to −21.8 dB SPL (at 5 kHz) in the normal hearing subjects, from −3.1 dB SPL (at 1.5 kHz) to −15.3 dB SPL (at 4.5 kHz) in the neonates, and from 2.6 dB SPL (at 1.5 kHz) to −15.0 dB SPL (at 4.5 kHz) in the follow-up neonates (Table I). The higher noise floor level in the neonates, especially at low test frequencies, can be attributed to the fact that the measurements in the neonates were performed at the hospital or at the baby's home, whereas the measurements in the normal hearing subjects were performed in a booth.

At $f_2=8$ kHz, the percentage was nearly the same [78/118 (66.1%)] in the neonates compared to that found in the normal hearing subject sample (65.4%). This can be attributed to the fact that the neonates exhibited higher emission levels at the high test frequencies compared to that found in the ears of the normal hearing subject sample (see Fig. 1).

The percentage of cochlear hearing loss ears in which the hearing threshold estimation could be achieved varied with frequency and hearing loss. The percentage was lowest at $f_2=8$ kHz. The best performance was at $f_2=3$, 4 and 6 kHz (Table I).

B. DPOAE-grams and DPOAE I/O-functions in neonates, normal hearing subjects, and patients with cochlear hearing loss

Figure 1 shows the DPOAE-grams obtained in the neonate group, the follow-up neonate group (upper panels), the normal hearing subject sample, and the 15–20 dB cochlear hearing loss samples (lower panels). The DPOAE level L_{dp} found in the follow-up neonate group is considerably higher compared to that found in the neonate group, predominantly for mid and high frequencies. When comparing the DPOAE-grams of the normal hearing subject sample to that of the neonate group the DPOAE level L_{dp} differed most in the low and the high frequency region, especially at 8 kHz. In both

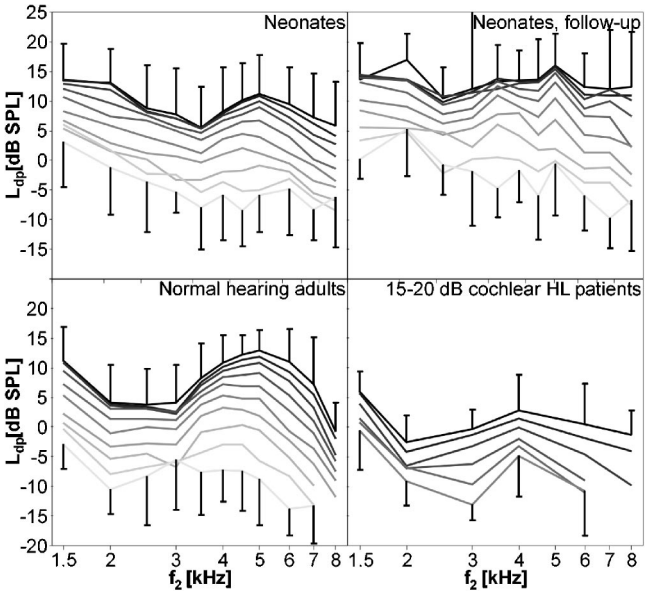

FIG. 1. Mean DPOAE-grams for four different experimental populations: neonates, follow-up neonates, normal hearing adults and a group of patients with a cochlear hearing loss of 15 and 20 dB HL. DPOAE-grams are plotted for all primary tone levels decreasing from $L_2=65$ dB SPL (black line) to $L_2=20$ dB SPL (light gray line, in the first three plots). In the cochlear HL group DPOAEs could only be recorded down to $L_2=40$ dB SPL. Standard deviations are shown for the highest and lowest possible L_2.

neonate ears and normal hearing adult ears DPOAE-grams were close together at high and more separated at low primary tone levels revealing compressive DPOAE growth. In contrast to that, DPOAE-grams of the 15–20 dB cochlear hearing loss ears exhibited lower DPOAE levels and were more separated. The standard deviation of the DPOAE level at the highest did not differ much from that at the lowest primary tone level. The 6 dB signal-to-noise criteria is therefore supposed to be strong enough for ensuring reliable DPOAE measurements.

For a better visualization of the DPOAE growth behavior, DPOAE data are plotted in the form of DPOAE I/O-functions for the neonate group, the follow-up neonate group, and the normal hearing subject sample (Fig. 2, left panel) as well as for the cochlear hearing loss samples (Fig. 2, right panel). The DPOAE level was averaged across f_2 for all subjects. The DPOAE level L_{dp} of the neonate group was lower compared to that found in the follow-up neonate

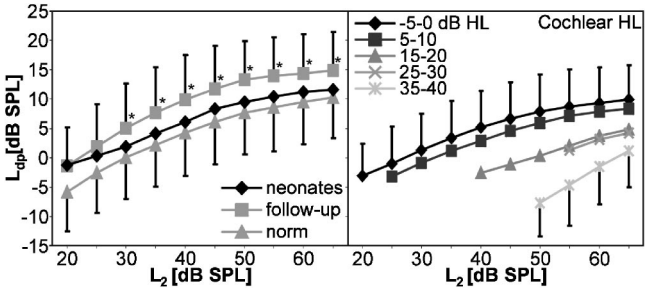

FIG. 2. *Left*: mean DPOAE I/O-functions across all f_2-frequencies for neonates, follow-up neonates and normal hearing adults are plotted. *: $p<0.05$ (t-test). *Right*: mean DPOAE I/O-functions across all f_2-frequencies for different cochlear hearing loss populations. An increase of the slope of the I/O-functions can be seen with increasing HL.

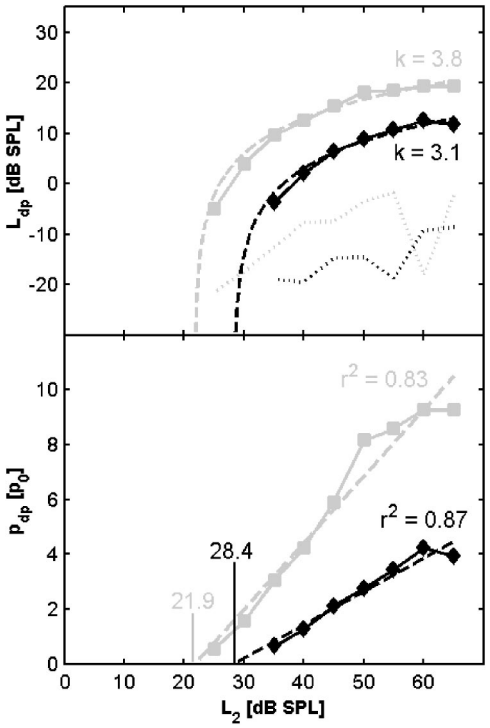

FIG. 3. DPOAE I/O-functions shown in logarithmic (*top*) and semilogarithmic (*bottom*) scale for one neonate at $f_2=4$ kHz: early measurement (black diamonds) and the respective follow-up measurement (gray squares). Extrapolation of the DPOAE I/O-function using linear regression analysis yields the L_{dpth} values at the intersection point between linear regression line and abscissa in the lower panel. Compression k is calculated at $L_2=55$ dB SPL of the extrapolated I/O-function. Dotted lines in the top panel show noise floor. The coefficient of determination r^2 is displayed for each regression line.

group. On average, across L_2, the difference amounted to 2.8 dB. The difference between the neonates and the normal hearing subjects amounted to 2.5 dB, the difference between the follow-up neonates and the normal hearing subjects to 5.3 dB. The DPOAE level of the follow-up neonates differed significantly from that of the neonates and the normal hearing subjects (with the exception at $L_2=20$ and 25 dB for the follow-up neonates). The neonate group (despite the lower DPOAE level), the follow-up neonate group, and the normal hearing subject sample exhibited similar DPOAE growth behavior. In contrast, the DPOAE I/O-functions of the cochlear hearing loss ears exhibited a continuous increase of the slope of the I/O-function with increasing hearing loss (Fig. 2, right panel).

C. DPOAE threshold and compression estimates—Normal hearing versus neonatal hearing and cochlear hearing loss

The linear fitting procedure for estimating the DPOAE threshold level is shown in Fig. 3. The upper panel exemplarily plots I/O-functions at $f_2=4$ kHz in a logarithmic scale (L_{dp} across L_2). They stem from the same neonate ear obtained after birth and 4 weeks later. The lower panel plots the same data in a semilogarithmic scale (p_{dp} across L_2). The intersection point between the linear regression line (dashed line in the lower panel of Fig. 3) and the primary tone level axis ($p_{\mathrm{dp}}=0$ Pa) served as the DPOAE threshold

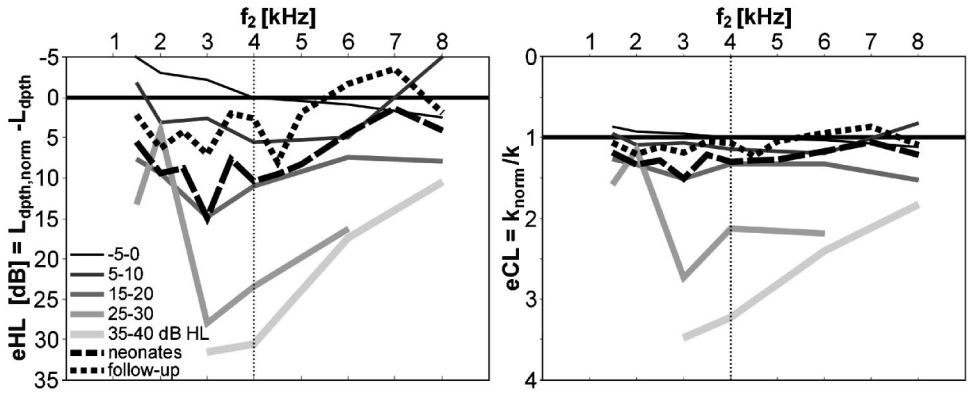

FIG. 4. *Left*: Estimated hearing loss (eHL) in audiogram form. Mean L_{dpth} of the different HL classes and the two neonate groups is normalized with mean $L_{\mathrm{dpth,norm}}$ of the normal hearing subject sample at the respective frequencies. The curves of the two neonate groups fit well between those of HL classes -5 and 0 and 15 and 20 dB HL. *Right*: estimated compression loss (eCL) in audiogram form. Mean k of the different HL classes and the two neonate groups is normalized with mean k_{norm} of the normal hearing subject sample at the respective frequencies. A ratio of eCL$=1$ represents normal hearing. Again, the curves of the two neonate groups fit well between those of HL classes -5 and 0 and 15 and 20 dB HL.

level estimate. The estimated DPOAE threshold level for the first measurement amounted to $L_{\mathrm{dpth,neonate}}=28.4$ dB SPL and for the follow-up measurement to $L_{\mathrm{dpth,follow\text{-}up}}=21.9$ SPL. The dashed lines in the upper panel of Fig. 3 shows the regression lines presented in the logarithmic scale. The compression k calculated at $L_2=55$ dB of the extrapolated I/O-function was smaller in the first measurement compared to that of the follow-up measurement ($k_{\mathrm{neonate}}=3.1$ dB/dB, $k_{\mathrm{follow\text{-}up}}=3.8$ dB/dB).

Figure 4 (left panel) plots the estimated DPOAE threshold for the neonate group and the cochlear hearing loss samples relatively to the normal hearing subject sample across f_2. For example, at $f_2=4$ kHz, the such estimated hearing loss eHL amounted to $L_{\mathrm{dpth,norm}}-L_{\mathrm{dph,follow\text{-}up}}=2.7$ dB for the follow-up neonate ears and to $L_{\mathrm{dpth,norm}}-L_{\mathrm{dpth,neonate}}=10.4$ dB for the early postnatal neonate ears. The estimated hearing loss for the cochlear hearing loss samples amounted to $L_{\mathrm{dpth,norm}}-L_{\mathrm{dpth,HL}}=0.1$ dB for the $-5-0$ dB HL sample, 5.6 dB for the 5–10 dB HL sample, 10.9 dB for the 15–20 dB HL, 23.5 dB for the 25–30 dB HL sample, and 30.6 dB for the 35–40 dB HL sample. When comparing the estimated hearing loss eHL and the behavioral hearing loss HL in the cochlear hearing loss ears, an underestimation of the hearing loss was obvious. Its degree varied with frequency and amount of hearing loss. The estimation error (HL–eHL) was lowest in the mid-frequency region and highest in the high and low frequency regions. The rationale for presenting the data following a clinical audiogram form was to allow an overview on changes between the different groups as well as on frequency and hearing loss specific changes within one group.

Figure 4 (right panel) plots the estimated DPOAE compression k (L_2) calculated at $L_2=55$ dB for the two neonate groups and the cochlear hearing loss samples relatively to that of the normal hearing subject sample (k_{norm}) across f_2. In the following the compression ratio k_{norm}/k is referred to as the estimated compression loss eCL. For example, at $f_2=4$ kHz, eCL amounted to $k_{\mathrm{norm}}/k_{\mathrm{neonate}}=1.3$ for the neonate ears and to $k_{\mathrm{norm}}/k_{\mathrm{follow\text{-}up}}=1.1$ for the follow-up neonate ears, to $k_{\mathrm{norm}}/k_{\mathrm{HL}}=1.0$ (for -5 and 0 dB HL), 1.1 (for 5 and 10 dB HL), 1.3 (15 and 20 dB HL), 2.1 (25 and 30 dB HL), and 3.2 (for 35 and 40 dB HL) for the cochlear hearing loss samples. That means compression in the neonates was lower compared to that of the follow-up neonates. Compression of the neonates was quite similar to that of the 15–20 dB cochlear hearing loss sample. Only in cochlear hearing loss ears with hearing losses exceeding 20 dB a considerably higher compression loss was found.

The t-test was used to determine the statistical difference between the groups. This was done for $f_2=4$ kHz only. In the cochlear hearing loss ears, the estimated hearing loss eHL differed significantly ($p<0.05$) in all groups with the exception of the respective neighboring groups (-5 and 0 dB HL/5 and 10 dB HL, 5 and 10 dB HL/15 and 20 dB HL, etc.). In the neonate and follow-up neonate ears, the estimated hearing loss eHL differed significantly, however, the estimated compression loss eCL did not. The estimated compression loss eCL differed significantly ($p<0.05$) in all cochlear hearing loss groups with the exception of $-5-0$ dB HL/5–10 dB HL and 5–10 dB HL/15–20 dB HL.

The fact that k decreased with increasing cochlear hearing loss suggests the compression to provide an additional measure for quantifying cochlear hearing loss and for differentiating between sound conductive and cochlear hearing loss, at least for the mid frequency range. To test this, compression k (L_2) was calculated at $L_2=65$, 60, 55, 50, and 45 dB SPL for the different groups (Fig. 5). With increasing cochlear hearing loss the compression decreased quite lin-

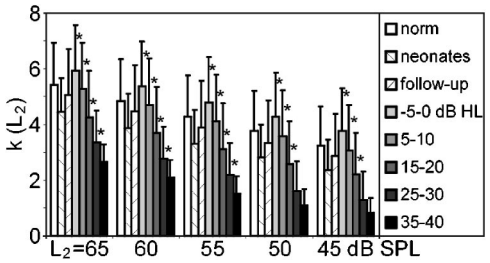

FIG. 5. Mean (+SD) compression k calculated at various points (L_2) of the extrapolated I/O-functions for neonates, follow-up neonates, normal hearing adults and the different groups of the cochlear hearing loss population. k decreases with increasing HL. *: $p<0.05$ (Mann–Whitney).

earily. This was true for all L_2. The standard deviation was quite similar across hearing loss class and L_2.

The Mann–Whitney test was used to determine the statistical difference of the DPOAE compression k in the cochlear hearing loss groups. When comparing neighboring cochlear hearing loss groups, k differed significantly (with the exception of the 35–40 dB HL group at $L_2=45$ and 50 dB SPL). Thus, k is suggested to provide a quantitative measure for assessing cochlear compression.

Mean DPOAE compression k in the neonate, the follow-up neonate, and the norm group were within the range of the $-5-10$ dB HL and 15–20 dB HL cochlear hearing loss groups and it was significantly lower ($p<0.001$) when compared to the cochlear hearing loss groups exceeding 15–20 dB HL. In view of a differentiation between transitory sound conductive and persisting cochlear hearing loss in neonates this is an important finding.

Table I presents the mean and standard deviation of the estimated DPOAE threshold level L_{dpth} and the DPOAE compression k for the neonate, follow-up neonate, normal hearing, and cochlear hearing loss ears.

D. Modeling DPOAE I/O-functions in sound conductive and cochlear hearing loss

For a better understanding of the different DPOAE behavior in sound conductive and cochlear hearing loss ears and hence for developing a strategy for differentiating between middle ear and cochlear disorders, a simple model was used (Fig. 6). In that model a sound conductive hearing loss (A, B, and C) was simulated by shifting the normal hearing reference DPOAE I/O-function (which was adopted from the DPOAE I/O-function of the normal hearing subject sample at 4 kHz, where the average estimated DPOAE threshold level amounted to 10.6 dB SPL (see Table I) to the same degree on the L_2-axis (representing the damping of the primary tone levels) as well as on the L_{dp}-axis (representing the damping of the DPOAE). The shift on the L_2-axis in the logarithmic plot (A, B, and C in the upper panel of Fig. 6) resulted in a shift of the intersection point of the I/O-function in the semilogarithmic plot and hence in a change of the estimated DPOAE threshold level (being 20, 30, and 40 dB SPL corresponding to a hearing loss of 10, 20, und 30 dB HL with the normal hearing I/O-function as a reference; see A, B, and C in the lower panel of Fig. 6). Furthermore, it resulted in an increase of the slope at a fixed L_2 level. In contrast, the shift on the L_{dp}-axis did neither change the estimated DPOAE threshold level nor the slope. However, it resulted in a significant decrease of the L_{dp} level also at high primary tone levels.

For simulating DPOAE behavior in cochlear hearing loss, I/O-functions were used which were modeled on extrapolated DPOAE I/O-functions from the cochlear hearing loss ears of the study (a, b, and c in the upper panel of Fig. 6) resulting in an estimated DPOAE threshold level of 20, 30, and 40 dB SPL corresponding to a hearing loss of 10, 20, und 30 dB HL (a, b, and c in the lower panel of Fig. 6). The slope at a fixed L_2 level increased with increasing hearing loss. In comparison to the sound conductive hearing loss

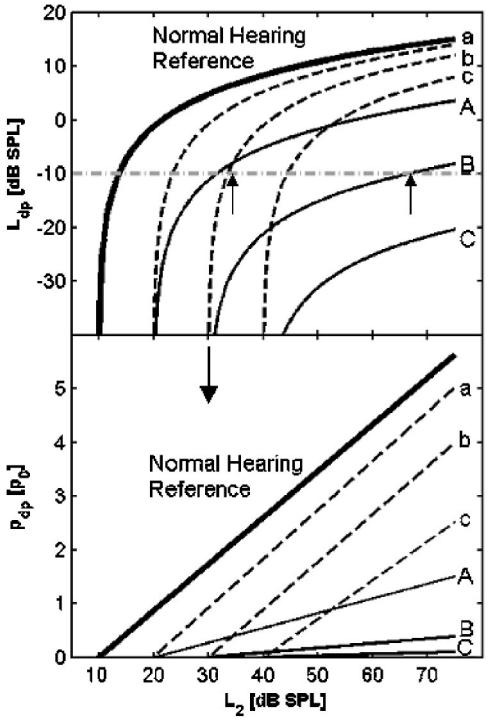

FIG. 6. DPOAE model functions simulating cochlear and middle ear disorders shown in logarithmic (*top*) and semilogarithmic scale (*bottom*). The thick solid line represents a normal hearing reference subject with an estimated DPOAE threshold level of 10 dB SPL. Solid curves A, B, C represent 10, 20, 30 dB HL sound conductive hearing loss. Dashed curves a, b, c represent 10, 20, 30 dB HL cochlear hearing loss. The horizontal line in the upper panel indicates the DPOAE detection threshold (noise level $+6$ dB), which is typical for measurements in neonates under screening conditions at $f_2=4$ kHz (see Table I). Thin arrows indicate the different DPOAE detection thresholds; thick arrows indicate the common estimated hearing threshold in the case of the 20 dB HL cochlear and the 20 dB HL sound conductive hearing loss.

I/O-functions (A, B, C) the shift on the L_{dp}-axis of the cochlear hearing loss I/O-functions (a, b, c) was considerably lower (Fig. 6, upper panel).

To summarize, in both middle-ear and cochlear disorder, an increase of hearing loss resulted in an increase of the slope of the I/O-functions at a certain fixed L_2 level, even if the reasons of the change in slope are of a different nature. In sound conductive hearing loss there was a shift of the I/O-function along the L_2-axis which shifts the fixed point at which the slope is calculated to lower L_2 levels. In contrast, the increase in slope in cochlear hearing loss was suggested to be a result of a change in the nonlinear compressive sound processing of outer hair cell amplifiers. The main difference between sound conductive and cochlear hearing loss can thus be found in the absolute magnitude of DPOAE level L_{dp}, especially at the higher primary tone levels. In sound conductive hearing loss, the shift on the L_{dp}-axis was much higher compared to that one in cochlear hearing loss. When comparing the 30 dB HL I/O-functions of the sound conductive and the cochlear hearing loss a difference in the DPOAE level of almost 30 dB was evident (compare C and c in Fig. 6, upper panel). In contrast, the slope was nearly the same in both conditions. This was also true for the 10 and 20 dB HL I/O-functions (compare A and a, and B and b in Fig. 6, upper panel). That means the slope of the I/O-function in the model

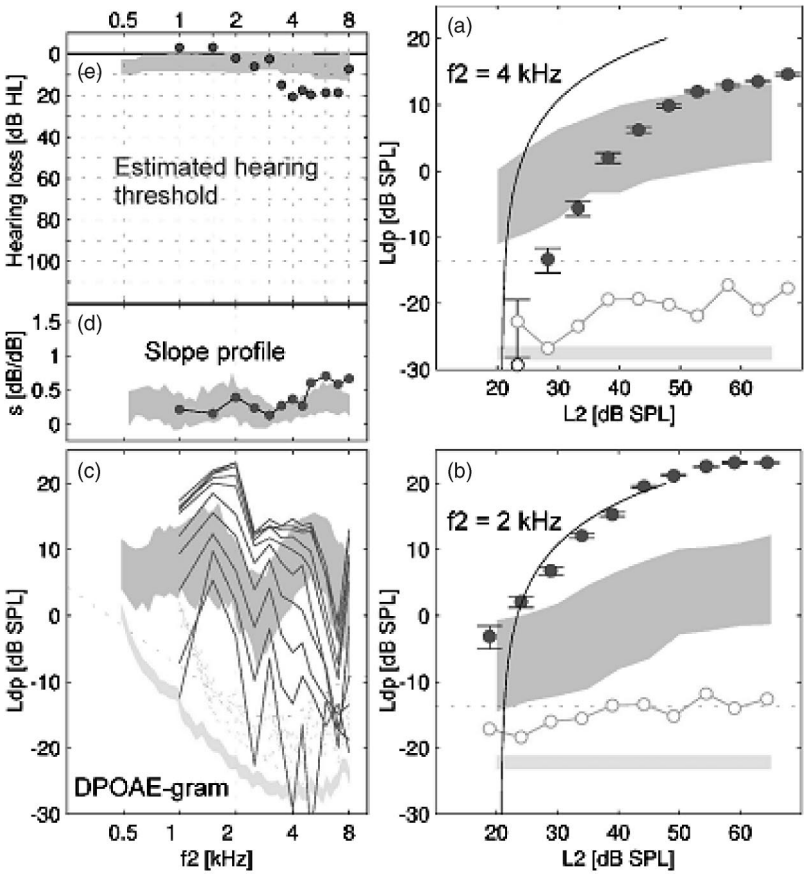

FIG. 7. Case example of a newborn (3 days old). DPOAE I/O-functions at 4 (a) and 2 kHz (b). DPOAE-grams for the 10 primary tone levels [from 20 to 65 dB SPL (L_2)] and slope of the DPOAE I/O-functions are plotted in panels c and d. The estimated hearing threshold derived from extrapolated DPOAE I/O-functions (see the intersection between the extrapolated I/O-function and L_2-axis in a and b of Fig. 7) are shown in panel e. Shaded areas show normative data (standard deviation of the normal hearing subject sample). In panels a and b the noise floor is indicated by circles, in panel c by dotted lines. The bottom gray area in panel c indicates a typical noise floor in the booth where measurements in normal hearing subjects and patients with cochlear hearing loss were performed.

does not allow a differentiation between sound conductive and cochlear hearing loss of the same degree.

In the model, the DPOAE level at a 20 dB HL sound conductive hearing loss amounted only to -10 dB SPL at the highest L_2 (see B in the upper panel of Fig. 6). Supposing a noise floor level of -14 dB SPL which corresponds to the noise floor level found in the neonates around 4 kHz (see Table I) and a SNR exceeding 6 dB, a reliable DPOAE measurement would be possible if the DPOAE level exceeds -10 dB SPL. This DPOAE detection threshold is indicated in Fig. 6. Under this condition, in the presence of a 20 dB HL sound conductive hearing loss DPOAEs would be measurable only at the highest L_2 resulting in a high difference between the estimated DPOAE threshold and the DPOAE detection threshold level (see arrows in Fig. 6). In contrast, the DPOAE level of the 20 dB HL cochlear hearing loss amounted to almost 10 dB SPL at the highest L_2 in the model (see b in the upper panel of Fig. 6). Thus, despite the 20 dB HL cochlear hearing loss a reliable DPOAE measurement would be achieved at L_2 down to almost 30 dB SPL resulting in a small difference between the estimated DPOAE threshold and the DPOAE detection threshold level (see arrows in Fig. 6). At a 30 dB HL sound conductive hearing loss the DPOAE level was below the DPOAE detection threshold (see C in Fig. 6). In contrast, at a 30 dB HL cochlear hearing loss (see c) the detection threshold level and the estimated DPOAE threshold level (which is 40 dB SPL) hardly differed. Even at a 40 dB HL cochlear hearing loss the difference between the estimated DPOAE threshold and the DPOAE detection threshold level was very small. Thus, the difference of the two measures can be considered as a means for differentiating between sound conductive and cochlear hearing loss.

E. Frequency specific DPOAE behavior in the neonates

DPOAE data of a single neonate ear (3 days old) demonstrates that the DPOAE level and the estimated hearing threshold considerably vary with frequency. The DPOAE-grams (see c in Fig. 7c) were close together at the higher (upper curves) and more separated at the lower primary tone levels (lower curves) revealing normal compressive cochlear sound processing. The DPOAE level was lower at the higher test-frequencies (around 4 kHz) compared to that found at the lower test-frequencies (around 2 kHz). When comparing the DPOAE I/O-functions at 2 and 4 kHz a considerable change in the DPOAE level was obvious, the difference being almost 10 dB. However, both I/O-functions exhibited the same compressive shape.

The downward shift of the DPOAE I/O-function and the change in the DPOAE level were comparable with that found in the model in the case of the simulated sound conductive hearing loss (see B in Fig. 6). However, when comparing the neonate DPOAE I/O-functions with that of the model in the case of a 10 dB cochlear hearing loss, a complete different I/O behavior was obvious since the DPOAE level only slightly decreased in the high primary tone level range (see a in Fig. 6). This was quite different from that found in the neonate ear where a difference in DPOAE level of almost 10

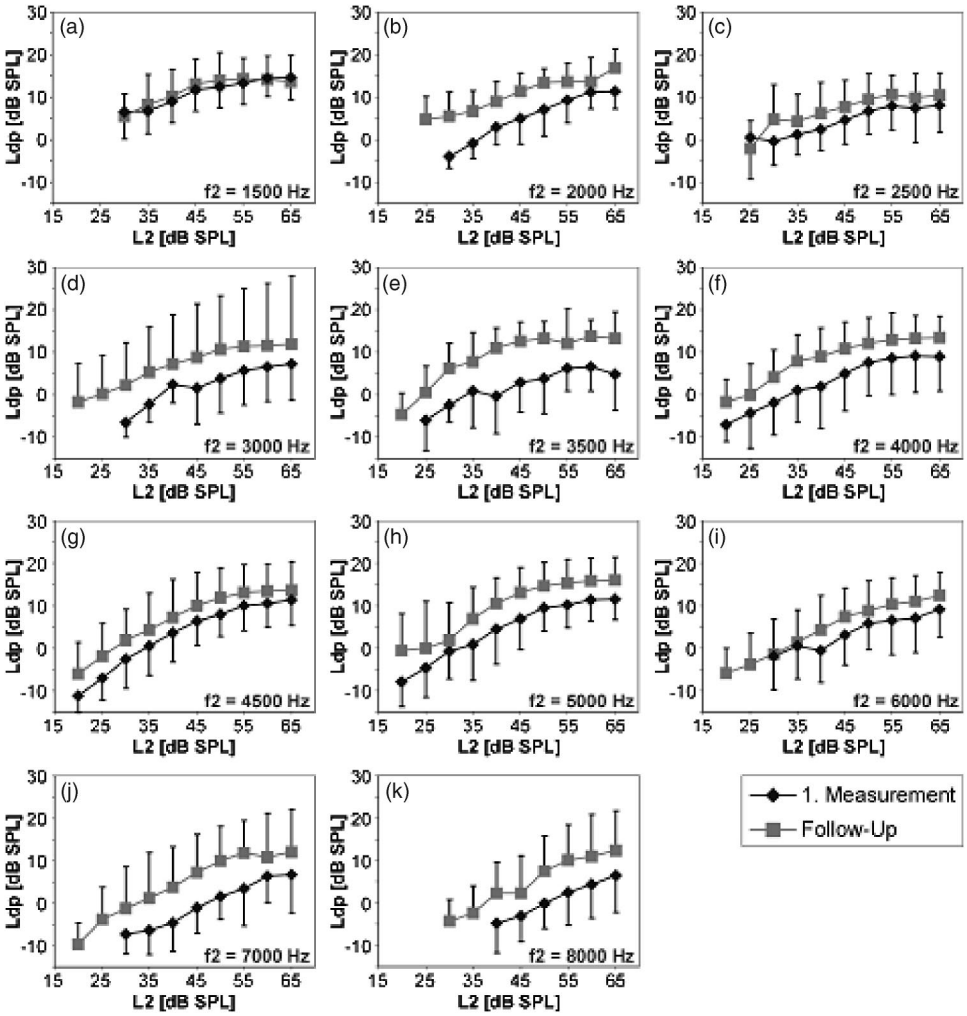

FIG. 8. DPOAE I/O-functions of the first and follow-up measurement in the neonate ears (number of ears across frequency; see Table I). The mean DPOAE level is indicated by diamonds and squares for the first and follow-up measurement, respectively. Error bars show the standard deviation.

dB was present in the entire primary tone level range. The slight increase in slope for test-frequencies above 4 kHz (see d in Fig. 7d) was compatible with the findings of the model where a slight change in the slope was present in the case of the sound conductive hearing loss.

Figure 8 shows mean and standard deviation of the DPOAE level obtained in the 21 follow-up neonate ears during the first and second measurement. At $f_2 = 1.5$ kHz there was no difference in the DPOAE level. At the other test frequencies the DPOAE level differed considerably, being lower in the early postnatal period (compare the first and follow-up measurements in Fig. 8). The highest difference in the DPOAE level was found at $f_2 = 3.5$ kHz and amounted to almost 10 dB at $L_2 = 65$ dB SPL. As in the single neonate ear, the average DPOAE level in the pooled data obtained in the first measurement was highest at the lowest test frequency and decreased almost continuously with increasing test frequency (compare c in Fig. 7 and in a,b,...,k in Fig. 8). In contrast, the follow-up data exhibited a DPOAE level which was almost independent of the test frequency being around 10 dB SPL at $L_2 = 65$ (see Fig. 8, follow-up measurement).

In the pooled data, there was a clear downward shift when comparing the I/O-functions obtained in the follow-up and first measurement. This DPOAE behavior corresponds to that found in the model in the case of the sound conductive hearing loss, where a considerable decrease in the DPOAE level was obvious nearly independent of the primary tone level. (compare A of Fig. 6 and b,...,k of Fig. 8). The frequency specific change in the DPOAE level observed in the early postnatal period, the downward shift of the I/O-functions along the L_{dp}-axis, and the increase of the DPOAE level in the follow-up measurement indicate a transitory sound conductive hearing loss during the early postnatal period.

IV. DISCUSSION

In the present study we addressed the question of whether extrapolated DPOAE I/O-functions are able to estimate hearing loss and to differentiate between middle ear and cochlear disorders in neonates. The main findings were (i) variation of the DPOAE level with test frequency was higher in the normal hearing adult subjects compared to that in the neonate ears; (ii) the DPOAE level was smaller and estimated hearing thresholds were higher during the early postnatal period compared to that found in the follow-up measurement four weeks later; (iii) the DPOAE level varied with test frequeny in the early postnatal period and was almost independent of test frequency in the follow-up measurement; (iv) from a simple model it could be derived that DPOAE I/O-functions in the presence of a sound conductive

hearing loss differed considerably from that which was found in the presence of a cochlear hearing loss; and (v) hearing threshold estimation under hearing secreening conditions was possible in a single ear at about 2/3 of the test frequencies on average.

The higher variation of DPOAE level with test frequency in the normal hearing ears in comparison to the neonate ears can be attributed to calibration errors. The sound probe cannot be positioned near the ear drum. Thus, due to standing waves, the sound pressure at the tip of the sound probe can differ considerably to that measured at the ear drum, especially in outer ear canals with huge lengths, and especially for frequencies in the λ/4 and λ/2 range (see Siegel 1994). As a consequence, suboptimal primary tone stimulation occurred, especially in the adult subjects with the huge ear canal length resulting in DPOAE I/O-functions which do not reflect cochlear nonlinearity and hence do not estimate hearing threshold with a sufficient accuracy. The fact that the variation of the DPOAE level (Fig. 1, normal hearing adults) and the underestimation of the hearing threshold (Fig. 4, cochlear hearing loss patients) was highest in the λ/4 and λ/2 range ($f_2=3$ and 8 kHz) speaks for this assumption. Thus, for improving hearing threshold estimation in the low and high frequency range, the stimulus calibration has to be improved.

What might be the reason for the increase in DPOAE level and the decrease in the estimated hearing threshold when comparing the DPOAE measures obtained in the early postnatal period (mean age 3,2 days) and 4 weeks later? A change in the outer ear canal volume can be excluded since the ear canal volume should be larger in the follow-up neonate ears than in the neonate ears. Consequently, the DPOAE level should decrease and not increase. The lower DPOAE level in the neonate ears is therefore suggested to be caused by other impacts, i.e., sound conductive hearing loss or cochlear maturation.

According to previous literature, DPOAEs of term-born neonates appear to be adult-like. This is true for various parameters like e.g. DPOAE phase delays (Eggermont *et al.*, 1996), shape of I/O-functions, suppression tuning, and growth (Abdala, 1998, 2001). However, in more recent publications several differences between neonates (term-born and premature) and adults are reported. Especially, premature neonates show non-adult-like behavior of DPOAE suppression growth and tuning, and linearized I/O-functions (Abdala, 2000, 2003; Abdala and Chatterjee, 2003). These differences led to the assumption that the cochlear amplifier maturates closely around term birth or in the first months of postnatal life. The analysis of optimum f_2/f_1 ratios for DPOAE measurements (Brown *et al.*, 2000; Vento *et al.*, 2004) may also give information about cochlear maturation, but these data should not be overrated, because of problems with calibration and the different sizes of outer ear canals between various age groups. Mills and Rubel (1998) measured DPOAE I/O-functions in gerbils aged 15 days after birth to adult and reported cochlear amplifier gain to be increased with age at very high frequencies only (>40 kHz). Because of the high-frequency hearing capabilities of this species conclusions from that should not be drawn for cochlear maturation in human neonates.

It is known from the literature that any manipulation of the middle ear results in a change of the DPOAE level. For example, when changing the middle ear's stiffness by changing the atmospheric pressure (Osterhamel *et al.*, 1993; Hauser *et al.*, 1993; Zheng *et al.*, 1997) or changing the middle ear's mass by filling the bulla with fluid or during otitis media with effusion (Ueda *et al.*, 1998; Topolska *et al.*, 2000) the DPOAE level is reported to decrease. Priner *et al.* (2003) recorded DPOAEs in newborn guinea pigs and reported increasing DPOAE levels from birth until the fourth day of life. This increase in the DPOAE level was accompanied by reduced amounts of residual amniotic fluid in the bulla. Gehr *et al.* (2004) simulated middle ear effusion by filling the bulla of guinea pigs with saline solution (0.1 ml) and found a clear downward shift of DPOAE functions with the slope being hardly affected. Moreover, they compared the slope of the such treated guinea pigs with that of guinea pigs which were exposed to white noise with a level of 115 dB SPL for 2.5 h on two consecutive days and found the slope to be significantly increased. The common result of the studies was that increasing stiffness affects the low, whereas increasing mass affects the high test frequencies. When considering the middle ear as a mechanical resonator, where vibration amplitude is decreased at high frequencies when mass is increased and vibration amplitude is decreased at low frequencies when stiffness is increased, these results are not surprising.

Thus, increased middle ear mass due to amniotic fluid and/or increased stiffness due to Eustachian tube dysfunction are suggested to be the most likely reasons for the observed hearing loss in the neonate group of the present study. Increasing mass and stiffness would affect both high and low frequencies. That means the change in hearing threshold is not restricted to the high frequency range. This could be an explanation for the findings of the pooled data (see Fig. 8) which showed a decrease in the DPOAE level in a broader frequency range compared to that observed in the single neonate ear (see Fig. 7). Also, the clear downward shift of the DPOAE I/O-function (see Figs. 7 and 8) which is typical for a sound conductive hearing loss (see model, Fig. 6) speaks for the presence of a sound conductive hearing loss and against cochlear maturation. Please note that the model and practical experience have shown that the DPOAE level is considerably lower in sound conductive hearing loss (because there is a damping of the stimulus *and* a reduction of the DPOAE response) in comparison to that in cochlear hearing loss (where there is only a reduction of the DPOAE response). As a consequence, in sound conduction hearing loss exceeding 20 dB HL (when assuming a DPOAE detection threshold of -10 dB SPL) no DPOAEs would be measurable, whereas in cochlear hearing loss DPOAEs would be measurable at up to a hearing loss of 40 dB HL and more.

DPOAEs in sound conductive and cochlear hearing loss of the same degree exhibited similar compression [see model (Fig. 6) and data (Figs. 4, 5)] and hence a differentiation between middle ear and cochlear disorders by means of DPOAE compression only seems not possible. However, it

should be emphazised that this is a hypothetical outcome. Please note that the findings of the animal experiment (Gehr *et al.*, 2004) exhibited no significant change in the slope of the DPOAE I/O-functions when comparing the data of the filled and unfilled bulla of the guinea pig. The contradicting findings of the model and the measuring data make a search for an additional measure necessary. A suited candidate might be the difference between the estimated DPOAE threshold (which is the intersection point between the extrapolated DPOAE I/O-functions with the L_2-axis) and the DPOAE detection threshold (which is the lowest primary tone level at which a valid DPOAE is measurable).

In cochlear hearing loss the estimated DPOAE and the DPOAE detection thresholds were close together, whereas in sound conductive hearing loss the two measures differed highly (see arrows in Fig. 6). Thus, from the model the difference of the two measures is suggested to be a means for differentiating between sound conductive and cochlear hearing loss. To our knowledge, there is no study in the literature, which compares the DPOAE behavior in sound conductive and cochlear hearing loss ears, neither in neonates nor in children or adults. Thus, further studies will have to find out whether a differentiation between sound conductive and cochlear hearing loss by means of DPOAEs might be possible.

The fact that the compression differed significantly in the different cochlear hearing loss groups (see Fig. 5) suggests the compression (respectively slope) to be an additional measure (besides the DPOAE level and the estimated DPOAE threshold) for quantitatively assessing hearing loss.

In the normal hearing subject sample hearing threshold estimation could be performed in almost all ears at most test frequencies. In the neonates, the percentage of ears in which hearing threshold estimation could be achieved was lower, which can be attributed to the higher noise levels (see Table I). Gorga *et al.* (2000) described DPOAE and noise levels in a huge neonate collective ($n=2348$) for a frequency range between 1 and 4 kHz and for two stimulus intensities ($L_1/L_2=65/50$ dB SPL, $L_1/L_2=75/75$ dB SPL) and reported an increasing noise level with frequency (about -10 dB SPL at $f_2=4$ kHz and 0 dB SPL at $f_2=1.5$ kHz), resulting in the most favorable SNRs at 3 and 4 kHz. The mean noise level in the neonates of the present study was lower compared to that of the Gorga *et al.* study (e.g., -14.6 dB SPL at $f_2=4$ kHz and -3.1 dB SPL at $f_2=1.5$ kHz). Moreover, in the present study, high test frequencies exhibited noise levels which were similar to that found at $f_2=4$ kHz (e.g., -13.3 dB SPL at $f_2=6$ kHz, -14.6 dB SPL at $f_2=8$ kHz). That means that in neonates, favorable SNRs can be achieved in the high frequency region also. This is in contrast to the normal hearing adults in which the DPOAE levels considerably decreased (due to standing wave problems) and hence favorable SNRs could not be achieved at test frequencies above 6 kHz (see Fig. 1). At low test frequencies the noise level was higher (-3.7 dB SPL at $f_2=1.5$ kHz, -7.6 dB SPL at $f_2=2$ kHz) and the DPOAE level was similar to that of the normal hearing adults making measurement less reliable. A possible explanation for the lower noise levels found in the present study compared to that of the Gorga *et al.* study may be the fact that artifact rejection was conducted during the measurement by comparing different buffers.

The variation of the DPOAE and noise level was reflected in the percentage of ears in which hearing threshold estimation across frequency was possible. In the normal hearing adult ears (in which the noise level varied between -14.3 and -21.9 dB SPL) in almost all ears criteria for threshold estimation was fullfilled at all test frequencies with the exception at $f_2=8$ kHz (due to the low DPOAE level) where the percentage was only 65.4%. In the neonates the percentage of ears in which hearing threshold estimation was possible varied between 33.1% and 74.6% across frequency being highest at mid and high test frequencies. On average, in a single neonate ear the approach enabled hearing threshold estimation at about 2/3 of the test frequencies. Thus, it is true that test performance in the neonates was lower compared to that of the adults, but with respect to the worse environmental conditions sufficient test performance of the approach under hearing screening conditions is suggested. It should be emphasized that Table I does not list the number of ears in which valid DPOAEs could be measured but rather the number of ears in which hearing threshold estimation could be performed by extrapolating the DPOAE I/O-functions fullfilling extrapolation criteria (see Sec. II).

In view of an application in newborn hearing screening protocols where a fast measurement procedure is required, the measurement strategy of the present study has to be modified. There are two ways to shorten the test time. First, reducing the number of test frequencies (e.g., $f_2=1.5$, 2, 3, 4, 6 kHz). Assuming an average time of 4 seconds per DPOAE and 5 test frequencies, the maximum test time for estimating the hearing threshold would amount to 200 seconds (at 10 primary tone levels). Second, varying the primary tone level from low to high and stopping the measuring procedure if a valid DPOAE response is present at a defined low primary tone level (e.g., $L_2=25$ dB SPL). At these frequencies the recording of DPOAE I/O-functions would then not be necessary and the hearing threshold could be considered as normal. In doing this the measuring time would then depend on the type and the degree of the hearing loss. The minimum test time would amount to 20 seconds in a normal ear in which a valid response is present at the defined low primary tone level. The implementation of stopping rules, noise-floor dependent averaging time, repetition of measurement in the case of a change in the noise level of a definded amount would improve the performance of the method. Nowadays technology is able to implement the method on a handheld device. Thus, on bed use of the approach would be possible.

V. CONCLUSION

The presented method enables a quantitative and frequency specific assessment of hearing loss in neonates under hearing screening conditions. Moreover, due to the different DPOAE behavior in sound conductive and cochlear hearing loss, the detection of sound conductive hearing loss caused by residual amniotic fluid and/or Eustachian tube dysfunction might be possible. The detection of a transitory sound conductive hearing loss can help to reduce the false refer rate

during early postnatal hearing screening. Considering the fact that most of the babies with refer responses do have a transitory sound conductive hearing loss, cost intensive audiological diagnostics could be avoided when applying the new method in newborn hearing screening. The method could also provide an alternative test in pre-school and school hearing screening where behavioral audiometric tests are commonly used as well as a quick test for assessing hearing loss in children during ENT examination. However, calibration of the sound pressure level in the outer ear canal needs to be improved for yielding a more defined acoustic stimulation and hence reducing errors in hearing threshold estimation. For a better test performance, especially in the low frequency range, methods for improving the signal-to-noise ratio have to be developed.

ACKNOWLEDGMENTS

The authors thank the staff of the gynecological hospital, especially Dr. Zimmermann, all participating test persons, and the babies' parents for their patience and support. The work was supported by Deutsche Forschungsgemeinschaft, DFG Ja 597/6. Also, thanks to the reviewers for improving the manuscript.

Abdala, C. (**1998**). ''A developmental study of distortion product otoacoustic emission (2f1-f2) suppression in humans,'' Hear. Res. **121**, 125–138.

Abdala, C. (**2000**). ''Distortion product otoacoustic emission (2f1-f2) amplitude growth in human adults and neonates,'' J. Acoust. Soc. Am. **107**, 446–456.

Abdala, C. (**2001**). ''Maturation of the human cochlear amplifier: Distortion product otoacoustic emission suppression tuning curves recorded at low and high primary tone levels,'' J. Acoust. Soc. Am. **110**, 1465–1476.

Abdala, C. (**2003**). ''A longitudinal study of distortion product otoacoustic emission ipsilateral suppression and input/output characteristics in human neonates,'' J. Acoust. Soc. Am. **114**, 3239–3250.

Abdala, C., and Chatterjee, M. (**2003**). ''Maturation of cochlear nonlinearity as measured by distortion product otoacoustic emission suppression growth in humans,'' J. Acoust. Soc. Am. **114**, 932–943.

Boege, P., and Janssen, T. (**2002**). ''Pure-tone threshold estimation from extrapolated distortion product otoacoustic emission I/O-functions in normal and cochlear hearing loss ears,'' J. Acoust. Soc. Am. **111**, 1810–1818.

Brown, D. K., Bowman, D. M., and Kimberley, B. P. (**2000**). ''The effects of maturation and stimulus parameters on the optimal f2/f1 ratio of the 2f1-f2 distortion product otoacoustic emission in neonates,'' Hear. Res. **145**, 17–24.

Dorn, P. A., Konrad-Martin, D., Neely, S. T., Keefe, D. H., Cyr, E., and Gorga, M. P. (**2001**). ''Distortion product otoacoustic emission input/output functions in normal-hearing and hearing-impaired human ears,'' J. Acoust. Soc. Am. **110**, 3119–3131.

Eggermont, J. J., Brown, D. K., Ponton, C. W., and Kimberley, B. P. (**1996**). ''Comparison of distortion product otoacoustic emission (DPOAE) and auditory brain stem response (ABR) traveling wave delay measurements suggests frequency-specific synapse maturation,'' Ear Hear. **17**, 386–394.

Gehr, D. D., Janssen, T., Michaelis, C. E., Deingruber, K., and Lamm, K. (**2004**). ''Middle ear and cochlear disorders result in different DPOAE growth behaviour: implications for the differentiation of sound conductive and cochlear hearing loss,'' Hear. Res. **193**, 9–19.

Gorga, M. P., Norton, S. J., Sininger, Y. S., Cone-Wesson, B., Folsom, R. C., Vohr, B. R., Widen, J. E., and Neely, S. T. (**2000**). ''Identification of neonatal hearing impairment: distortion product otoacoustic emissions during the perinatal period,'' Ear Hear. **21**, 400–424.

Gorga, M. P., Neeley, S. T., Dorn, P. A., and Hoover, B. M. (**2003**). ''Further efforts to predict pure-tone thresholds from distortion product otoacoustic emission input/output functions,'' J. Acoust. Soc. Am. **113**, 3275–3284.

Hauser, R., Probst, R., and Harris, F. P. (**1993**). ''Effects of atmospheric pressure variation on spontaneous, transiently evoked, and distortion product otoacoustic emissions in normal human ears,'' Hear. Res. **69**, 133–145.

Janssen, T., Kummer, P., and Arnold, W. (**1995a**). ''Wachstumsverhalten der distorsionsproduktemissionen bei kochleären hörstörungen'' (''DPOAE growth behavior in cochlear hearing loss''), Otorhinolaryngol. NOVA **5**, 34–46.

Janssen, T., Kummer, P., and Arnold, W. (**1995b**). ''Wachstumsverhalten der distorsionsproduktemissionen bei normaler hörfunktion'' (''DPOAE growth behavior in normal hearing''), Otorhinolaryngol. NOVA **5**, 211–222.

Janssen, T., Kummer, P., and Arnold, W. (**1998**). ''Growth behavior of the 2f1-f2 distortion product otoacoustic emission in tinnitus,'' J. Acoust. Soc. Am. **103**, 3418–3430.

Kummer, P., Janssen, T., Hulin, P., and Arnold, W. (**2000**). ''Optimal L1-L2 primary tone level separation remains independent of test frequency in humans,'' Hear. Res. **146**, 47–56.

Mills, D. M., and Rubel, E. D. (**1996**). ''Development of the cochlear amplifier,'' J. Acoust. Soc. Am. **100**, 428–441.

Mills, D. M., and Rubel, E. D. (**1998**). ''Development of the base of the cochlea: place code shift in the gerbil,'' Hear. Res. **122**, 82–96.

Neely, S. T., Gorga, M. P., and Dorn, P. A. (**2003**). ''Cochlear compression estimates from measurements of distortion-product otoacoustic emissions,'' J. Acoust. Soc. Am. **114**, 1499–1507.

Osterhammel, P. A., Nielsen, L. H., and Rasmussen, A. N. (**1993**). ''Distortion product otoacoustic emissions. The influence of the middle ear transmission,'' Scand. Audiol. **22**, 111–116.

Oswald, J. A., and Janssen, T. (**2003**). ''Weighted DPOAE input/output-functions: a tool for automatic assessment of hearing loss in clinical application,'' Z. Med. Phys. **13**, 93–98.

Priner, R., Freeman, S., Perez, R., and Sohmer, H. (**2003**). ''The neonate has a temporary conductive hearing loss due to fluid in the middle ear,'' Audiol. Neuro-Otol. **8**, 100–110.

Ruggero, M. A., Rich, N. C., Recio, A., Narayan, S. S., and Robles, L. (**1997**). ''Basilar-membrane responses to tones at the base of the chinchilla cochlea,'' J. Acoust. Soc. Am. **101**, 2151–2163.

Siegel, J. H. (**1994**). ''Ear-canal standing waves and high-frequency sound calibration using otoacoustic emissions probes,'' J. Acoust. Soc. Am. **195**, 2589–2597.

Toploska, M. M., Hassman, E., and Baczek, M. (**2000**). ''The effects of chronic otitis media with effusion on the measurements of distortion products of otoacoustic emissions: presurgical and postsurgical examination,'' Clin. Otolaryngol. **25**, 315–320.

Ueda, H., Nakata, S., and Hoshino, M. (**1998**). ''Effects of effusion in the middle ear and perforation of the tympanic membrane on otoacoustic emissions in guinea pigs,'' Hear. Res. **122**, 41–46.

Vento, B. A., Durrant, J. D., Sabo, D. L., and Boston, J. R. (**2004**). ''Development of f2/f1 ratio functions in humans,'' J. Acoust. Soc. Am. **115**, 2138–2147.

Whitehead, M. L., Stagner, B. B., McCoy, M. J., and Lonsbury-Martin, B. L. (**1995**). ''Dependence of distortion-product otoacoustic emissions on primary levels in normal and impaired ears: II. Asymmetry in the L1, L2 space,'' J. Acoust. Soc. Am. **97**, 2359–2377.

Zheng, Y., Ohyama, K., Hozawa, K., Wada, H., and Takasaka, T. (**1997**). ''Effect of anesthetic agents and middle ear pressure application on distortion product otoacoustic emissions in the gerbil,'' Hear. Res. **112**, 167–174.

Level dependence of distortion-product otoacoustic emissions measured at high frequencies in humans[a),b)]

Laura E. Dreisbach[c)]
School of Speech, Language, and Hearing Sciences, San Diego State University, San Diego, California 92182-1578

Jonathan H. Siegel
School of Communication, Department of Communication Sciences and Disorders, Northwestern University, Evanston, Illinois 60208

(Received 6 October 2004; revised 2 February 2005; accepted 4 February 2005)

Given that high-frequency hearing is most vulnerable to cochlear pathology, it is important to characterize distortion-product otoacoustic emissions (DPOAEs) measured with higher-frequency stimuli in order to utilize these measures in clinical applications. The purpose of this study was to explore the dependence of DPOAE amplitude on the levels of the evoking stimuli at frequencies greater than 8 kHz, and make comparisons with those data that have been extensively measured with lower-frequency stimuli. To accomplish this, DPOAE amplitudes were measured at six different f_2 frequencies (2, 5, 10, 12, 14, and 16 kHz), with a frequency ratio (f_2/f_1) of 1.2, at five fixed levels (30 to 70 dB SPL) of one primary (either f_1 or f_2), while the other primary was varied in level (30 to 70 dB SPL). Generally, the level separation between the two primary tones ($L_1 > L_2$) generating the largest DPOAE amplitude (referred to as the ''optimal level separation'') decreased as the level of the fixed primary increased. Additionally, the optimal level separation was frequency dependent, especially at the lower fixed primary tone levels ($\leqslant$50 dB SPL). In agreement with previous studies, the DPOAE level exhibited greater dependence on L_1 than on L_2. © *2005 Acoustical Society of America.* [DOI: 10.1121/1.1880792]

PACS numbers: 43.64.Jb, 43.64.Ha [BLM] Pages: 2980–2988

I. INTRODUCTION

When two continuous acoustic pure tones of neighboring frequencies are presented simultaneously, acoustic distortion products at frequencies not present in the acoustic stimuli are produced by intermodulation between the primary stimulus tones, and can be detected in the ear canal as distortion product otoacoustic emissions (DPOAEs). DPOAEs are due to the nonlinear interaction between the traveling waves of the lower frequency primary tone (f_1) and the higher frequency primary tone (f_2) when they overlap along the basilar membrane (BM). Outer hair cells (OHCs), which are responsible for BM tuning properties (e.g., Ruggero and Rich, 1991) and the sensitivity and frequency selectivity observed in the tips of neural tuning curves (Liberman and Dodds, 1984), are also involved in the generation of DPOAEs, as has been determined with the reduction of DPOAE levels consistent with OHC damage (Brown *et al.*, 1989). Studying the stimulus level dependence of DPOAEs is a useful way to characterize the nonlinear mechanism(s) that generate them.

Input/output (I/O) functions can be derived from direct BM measurements (Ruggero and Rich, 1991; Ruggero *et al.*, 1997). In normal cochleae, when a place on the BM is driven at its characteristic frequency (CF), the response at low stimulus levels is linear and becomes compressive with increasing levels (e.g., Ruggero and Rich, 1991). This same pattern has been reported for DPOAE I/O functions in normal-hearing ears (e.g., Dorn *et al.*, 2001). However, with OHC damage, the BM response at CF exhibits an elevated threshold, reduced compression, and a steeper slope of the I/O function. Similar findings were reported for DPOAE I/O functions following cochlear insults in animals (Norton and Rubel, 1990; Whitehead *et al.*, 1992; Mills *et al.*, 1993; Mills and Rubel, 1994) and in cochlear impaired human ears (Janssen *et al.*, 1998; Kummer *et al.*, 1998; Janssen *et al.*, 2000; Dorn *et al.*, 2001). However, the degree to which DPOAE level dependence reflects BM level dependence at CF remains to be established. Although it is commonly assumed that the emissions are generated at the f_2 place, and thus reflect mechanical activity local to that place, the evidence supporting this assumption is highly speculative. It is not even proven that the emission phenomenon originates in the same mechanism responsible for BM nonlinear behavior. Perhaps the level dependence of DPOAEs reflects both the growth of local generators at fixed locations and the spread of excitation to a broader region of generation as the stimulus level is increased. These points will be addressed further in the discussion. Regardless of how DPOAE level dependence data are interpreted, there is a need for a systematic exploration of the phenomenon, and such data are lacking at stimulus frequencies higher than 8 kHz for humans.

When the level of one primary frequency tone is fixed

[a)]Portions of this work were presented in ''Growth functions of 2 f_1-f_2 distortion-product otoacoustic emissions are similar for stimulus frequencies above and below 10 kHz,'' Proceedings of Association for Research in Otolaryngology, St. Petersburg, Florida, February, 1997.
[b)]The majority of this work was completed in the Department of Communication Sciences and Disorders at Northwestern University, Evanston, IL
[c)]Electronic mail: ldreisba@mail.sdsu.edu

 0001-4966/2005/117(5)/2980/9/$22.50

and the other is varied, the DPOAE level has been found to be more dependent on L_1 than L_2 in both animals (Brown and Gaskill, 1990; Whitehead *et al.*, 1990, 1992; Kössl, 1994) and humans (Gaskill and Brown, 1990; Whitehead *et al.*, 1995b; Abdala, 1996). This relationship varies somewhat with the levels of the stimulus tones and frequency, but the basic features remain the same (Whitehead *et al.*, 1995b). The maximum DPOAE level occurs with L_1 greater than L_2, for L_1 equal to or less than 65 dB SPL (Gaskill and Brown, 1990; Whitehead *et al.*, 1995b; Kummer *et al.*, 2000). When L_1 is varied, the slope of the DPOAE level function is usually greater than 1, while the slope is usually less than 1 when L_2 is varied. For L_1 greater than 65 dB SPL, equal level stimulus tones result in the largest DPOAE level (Whitehead *et al.*, 1995b). Overall, the difference in level (L_1-L_2) between the two primary stimuli required to produce the maximum DPOAE (commonly referred to as the ''optimal'' level separation)[1] decreases with increasing overall stimulus level (Whitehead *et al.*, 1995a; Kummer *et al.*, 2000).

Hauser and Probst (1991), using a fixed L_1 and varied L_2 paradigm in humans, found that the optimal level separation depended on the frequencies of the stimuli. The median level difference (L_2-L_1) ranged from -10 to 0 dB SPL. The maximum DPOAE level was produced with a smaller level difference for 4 kHz versus 1 or 2 kHz. The DPOAE growth function was approximately linear with increasing L_2-L_1, followed by a peak, and then a decline. The slopes of the DPOAE growth functions became steeper with increasing frequency.

Previously, it has been reported that similar, continuous trends in DPOAE behavior with varied stimulus parameters existed throughout the range of human hearing (Dreisbach and Siegel, 2001). Hearing at higher frequencies is most vulnerable to cochlear insults. Often sensorineural hearing loss appears first at high frequencies and becomes more severe, before progressing to lower frequencies (see Ohlemiller and Siegel, 1994). Thus, DPOAEs measured with high-frequency stimuli allow the condition of the basal portion of the human cochlea to be explored and may lead to an improved method for the early detection of high-frequency hearing loss. The purpose of this study was to characterize the level dependence of DPOAEs elicited with high-frequency stimuli (>8 kHz) by examining DPOAE growth functions, with varied levels of the evoking stimuli.

II. METHODS

A. Subjects

Eight subjects (five female, three male) ranging in age from 22 to 32 years participated in the study. All subjects demonstrated normal pure-tone sensitivity (<15 dB HL) between 0.25 and 8 kHz, based on routine clinical audiograms (ANSI, 1996). Each subject reported a negative history of significant ear disease, including noise exposure. The right ear of each subject was tested. The experiment was conducted within a double-walled sound isolation chamber with the subject slightly reclined in a comfortable chair. Each subject's tympanic membrane had to be visualized with the probe assembly positioned at the entrance to the ear canal so that a probe tube could be positioned at the eardrum for calibration purposes. Subjects were not included in the study if their eardrum could not be visualized.

B. Equipment

Calibration using sound-pressure levels measured at the eardrum was used to avoid calibration artifacts for stimulus frequencies above 2 to 3 kHz due to standing waves (Siegel, 1994; Dreisbach and Siegel, 2001; Siegel, 2002). For a comparison of DPOAE results obtained with the traditional calibration measurement at the entrance to the ear canal versus calibration at the eardrum, refer to Dreisbach and Siegel (2001). To perform measurements based on eardrum sound-pressure level calibrations, a custom-made version of the Etymotic Research ER-10 (ER-10S) emission probe that allowed the visual placement of a probe tube at the eardrum with the emission probe in place was used for the measurement of DPOAEs.

This custom emission probe had three stainless-steel tubes passing through the body. The first stainless-steel tube was used for sound delivery. Two high-frequency drivers (Radio Shack super tweeters #40-1310B), as modified by Chan *et al.* (1993), produced signals that were mixed passively before being output through this one common sound delivery tube. A silicone rubber probe tube (Etymotic Research ER7-14C), connected to an Etymotic Research ER-7C probe microphone, was passed through the second stainless-steel guide tube to position the probe tube near the eardrum. It should be noted that the ER-7C microphone was only used for calibration purposes, not for collecting the emission data, because its relatively high noise floor is unsuitable for measuring otoacoustic emissions. A 1-mm-o.d. endoscope (Electro FiberOptics Corp.), which was inserted into the ear canal through the third stainless-steel guide tube, was used to visually assess the position of the probe tube. The endoscope formed a clear image of the eardrum and probe tube from a distance of 10–15 mm from the eardrum. Under visual control, the probe tube was carefully advanced until the subject reported contact with the eardrum, and was then withdrawn slightly. Refer to Dreisbach and Siegel (2001) for a schematic of the custom emission probe used in this study.

An optimal placement of the probe tube at the eardrum was considered to be one in which there were no obvious pressure nulls in the frequency response measured by the probe tube below 20 kHz due to reflections from the eardrum (Dreisbach and Siegel, 2001). If quarter-wave pressure nulls were measured in the range of interest with the probe tube microphone, the probe tube was repositioned, usually by advancing it further, until the pressure nulls were no longer evident.

A stainless-steel rod, which extended from the back of the emission probe, supported by a modified impedance probe headband, stabilized the entire assembly. A slight inward pressure was applied to the end of the rod. With this arrangement, relative movements of the probe and the head were small, even if the subject moved. Calibration procedures were completed prior to and following data acquisi-

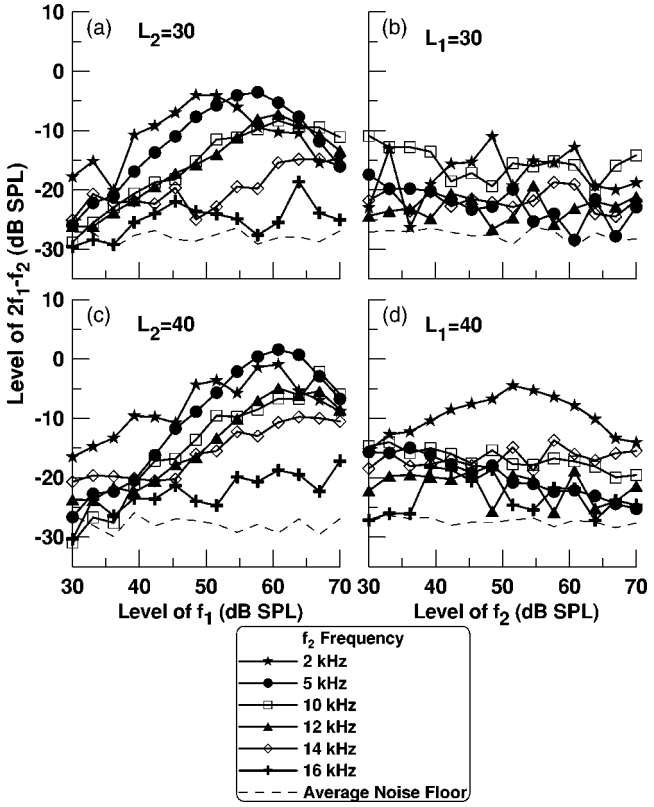

FIG. 1. DPOAE growth functions are illustrated for different stimulus frequencies with either L_2 (a), (c) or L_1 (b), (d) fixed at 30 or 40 dB SPL, respectively, while the other primary level is being increased. The rate of growth for all stimulus frequencies tested is steeper for increasing L_1 with L_2 fixed than for increasing L_2 with L_1 fixed.

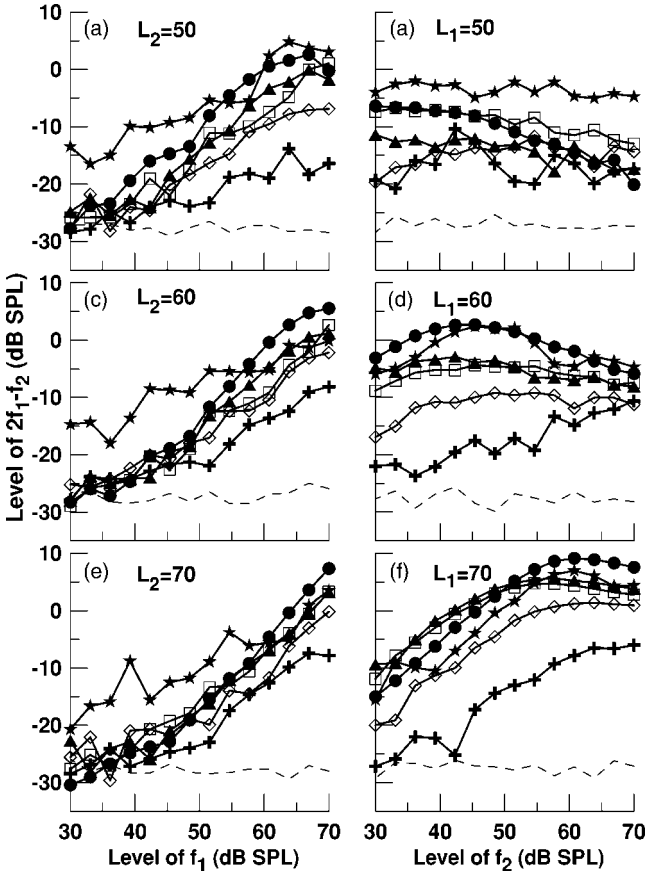

FIG. 2. The same as Fig. 1 except for fixed levels (either L_2 or L_1) of 50, 60, or 70 dB SPL.

tion. Calibrations during the entire experimental session were invariant, which proved excellent stability of the measurements.

Intermodulation distortion of the system at $2f_1-f_2$ was measured in a cavity that approximated the dimensions of the occluded ear canal to verify that a signal measured in the ear canal was an emission, and not an artifact of the equipment. Intermodulation distortion products were found to be at least 80 dB below the stimulus levels for the stimulus conditions used in this study.

C. Procedures

EMAV (Neely and Liu, 1993) software, using the Ariel DSP-16+ digital signal-processing board, was used to collect emission data. The sample rate was 50 kHz. The stimulus calibration portion of the emission data collection used the probe tube microphone, positioned at the tympanic membrane. This procedure assured that stimulus levels were well controlled at the eardrum. Emission data were collected with the emission probe microphone positioned at the entrance to the ear canal.

The EMAV software sampled the ear canal sound pressure in 40.96-ms time windows, accumulated these samples into two interleaved buffers (sample A and sample B), and averaged each buffer in the time domain. The two subaverages were then subtracted (A−B) and fast Fourier transformed to provide an estimate of the noise floor. The grand average [(A+B)/2] was transformed to compute the amplitudes and phases of stimulus tones and distortion products present in the ear canal. Sampling occurred for a minimum of 4 seconds or longer until one of two stopping rules was met: The noise floor at the distortion product frequency was less than −20 dB SPL or until 4 s of artifact-free sampling had been averaged.

The effect of using varied unequal stimulus levels (L_1 varied while L_2 was fixed and vice versa) on the $2f_1-f_2$ level was explored for six f_2 frequencies (2, 5, 10, 12, 14, and 16 kHz). The stimulus frequency ratio (f_2/f_1) was 1.2. L_1 was held constant at 70, 60, 50, 40, and 30 dB SPL, while L_2 was varied for each L_1 from 70 to 30 dB SPL in 3-dB steps. The procedure was repeated holding L_2 constant and varying L_1 over an identical range.

III. RESULTS

Data shown in all figures represent averaged responses from the subjects. Figures 1 and 2 represent growth functions for different stimulus frequencies with either L_1 or L_2 fixed, while the other primary level is varied. The levels of the fixed primary tone are 30 and 40 dB SPL (Fig. 1) and 50, 60, and 70 dB SPL (Fig. 2). As the level of the varied tone increases, the $2f_1-f_2$ level initially grows, may saturate, but typically declines. The pattern of growth depends on which of the stimulus tones is varied and on the level of the fixed tone. For all fixed levels except 70 dB SPL [Figs. 2(e) and

(f)], the rate of growth for all stimulus frequencies tested is steeper when L_1 is varied [Figs. 1(a) and (c), 2(a) and (c)] than when L_2 is varied [Figs. 1(b) and (d), 2(b) and (d)]. The level of $2f_1-f_2$ is almost independent of L_2 in most cases. The maximum DPOAE level occurs with $L_1>L_2$ for a varied L_1 and fixed L_2 [Figs. 1(a) and (c), 2(a) and (c)]. This is also true for a fixed L_1 and varied L_2 [Figs. 1(b) and (d), 2(b) and (d)]. However, the emission level reached a clear maximum only for higher levels of the fixed stimulus ($L_1=50$ and 60 dB SPL). At lower levels of the fixed stimulus (i.e., $L_1=30$ and 40 dB SPL), a clear maximum was not evident.

With L_2 fixed at 70 dB SPL and L_1 varied [Fig. 2(e)], the DPOAE level continuously increases until the primary levels are comparable, whereas with L_1 fixed at 70 dB SPL and L_2 varied [Fig. 2(f)], the emission level increases, reaches a maximum, and then either saturates or declines with further increases in L_2. This means that in order to generate the largest DPOAE level, L_2 must always be less than or equal to the fixed L_1 of 70 dB SPL for all frequencies tested.

Although level dependence is similar for all the frequencies examined, it should be noted that the DPOAE level at 16 kHz was generally the lowest, no matter which stimulus level was varied (Figs. 1 and 2).

Table I summarizes the average optimal level separation of the stimuli ($L_1>L_2$) for the fixed L_2 conditions for individual subjects across the different frequencies. Additionally, the number of subjects where a maximum $2f_1-f_2$ level could be identified contributing to the average and the standard error of the mean are indicated for each frequency examined. The majority of the subjects produced an identifiable maximum $2f_1-f_2$ level at all levels tested for frequencies of 5, 10, 12, and 14 kHz. At 2 and 16 kHz, fewer subjects had an identifiable maximum $2f_1-f_2$ level, especially at the lowest fixed level ($L_2=30$ dB SPL). The optimal level separation decreases as the fixed level of f_2 increases. Generally, for a fixed $L_2=30$, 40, or 50 dB SPL [Figs. 1(a) and (c), 2(a)], the maximum DPOAE level occurs at greater level separations as the frequencies of the stimulus tones are increased, up to 14 kHz. However, at 16 kHz the optimal level separation is more similar to what was seen at the lower frequencies (2 and 5 kHz). For a fixed $L_2=60$ dB SPL [Fig. 2(c)], the optimal level separation was essentially similar across all frequencies tested, whereas approximately equal-level stimuli were optimal for a fixed $L_2=70$ dB SPL [Fig. 2(e)].

Figures 3(a) and (c) illustrate a rate of growth of around 1 dB/dB to a maximum and decline with increasing L_1 for most of the range of fixed levels of f_2 for both 14 and 2 kHz, respectively. The maximum emission level increased with higher levels of the fixed stimulus tone and was always reached when L_1 was greater than L_2, with the exception of a fixed level of 70 dB SPL in which equal-level stimuli were optimal. Figures 3(b) and (d) illustrate shallower growth with L_2 varied, except when L_2 was 70 dB SPL. The patterns illustrated in Fig. 3 were similar for all other frequencies tested.

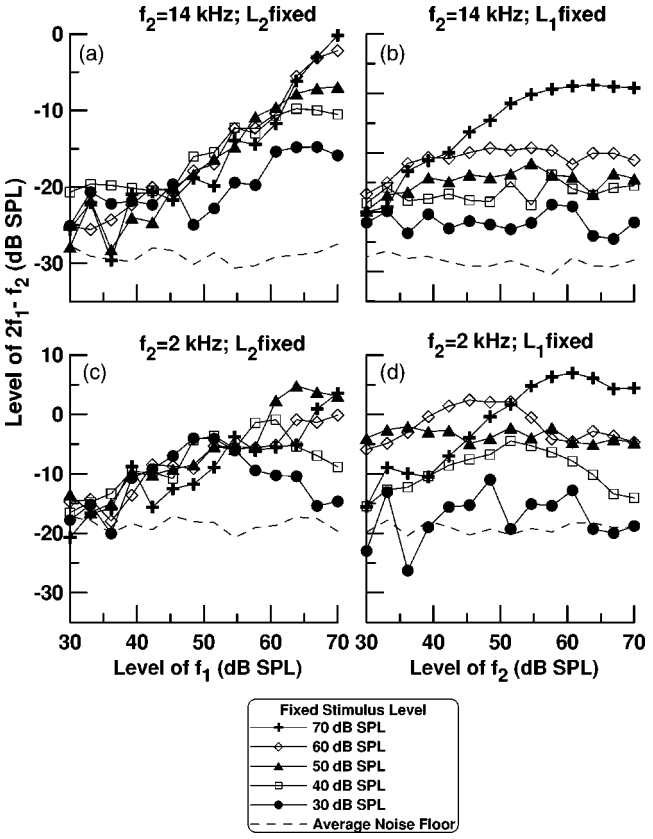

FIG. 3. Emission levels measured with varied L_1 and fixed L_2. (a) and (c) illustrate a rate of growth of around 1 dB/dB to a maximum and decline with increasing L_1 for most of the range of constant levels of L_2 for both 14 and 2 kHz, respectively. For higher fixed levels of L_2 the emission level grows monotonically over the entire range of L_1. The maximum emission level increased with higher levels of the fixed stimulus. The maximum emission level was seen when L_1 was greater than L_2. Emission levels measured with varied L_2 and fixed L_1 (b) and (d) illustrate shallower growth with varied L_2, with the exception at 70 dB SPL. There was typically little dependence on L_2 over the entire range of L_1, except when the fixed stimulus was 70 dB SPL.

TABLE I. The average optimal level separation for individual subjects, where L_1 is increased relative to a fixed L_2 for the different frequencies tested; n = number of subjects where a maximum DPOAE could be defined, sem = standard error of the mean, $L_1=(0.4L_2+39)-L_2$ (dB SPL) = formula proposed by Kummer *et al.* (1998) to calculate optimal level separations of the primary frequencies for measurement of DPOAEs in humans.

Fixed L_2							10			12			14			16			$L_1=(0.4L_2+39)$
(dB SPL)	2 kHz	**n**	sem	5 kHz	**n**	sem	kHz	**n**	sem	kHz	**n**	sem	kHz	**n**	sem	kHz	**n**	sem	$-L_2$ (dB SPL)
30	22	4	2.61	26	8	1.36	29	7	3.85	31	8	1.5	30	6	4.05	23	3	4.35	21
40	19	6	1.98	21	8	0.64	23	8	3.67	25	8	1.16	24	7	1.81	21	5	3.83	15
50	16	5	1.00	14	8	1.35	15	8	3.94	17	8	1.18	16	8	1.57	11	7	3.99	9
60	4	7	2.79	8	8	1.38	6	8	3.98	8	8	1.05	8	8	1.16	8	6	1.35	3
70	−2	6	1.15	0	8	0.00	0	8	0.00	0	8	0.00	−1	8	0.70	−1	7	0.79	−3

IV. DISCUSSION

The Etymōtic Research ER10S microphone system used in this study allowed us to characterize the level dependence of DPOAEs at low as well as high frequencies exceeding 8 kHz. The addition of an endoscope to the measurement system allowed a probe tube microphone to be placed near the eardrum under visual control. Calibration for DPOAE measurement systems is typically performed at the emission probe inlet at the entrance to the ear canal. Using the probe tube at the eardrum for calibration allowed better control over the stimulus levels. By more accurately controlling eardrum sound-pressure levels across the whole range of frequencies examined, interpretation of the trends in the emission data was facilitated. Previously, the effects of calibration errors have been demonstrated clearly (Dreisbach and Siegel, 2001).

A. Level dependence is similar for high- and low-frequency stimuli

In the current study, when varying one stimulus level relative to the other, the dependence of the level of the $2f_1-f_2$ otoacoustic emission on the levels of the stimuli is similar for f_2 frequencies from 2 to 16 kHz (Fig. 3). However, it was noted that the DPOAE levels obtained at 16 kHz were consistently lower in comparison to all other frequencies examined. This difference could be related to the fact that the f_1, f_2 interaction region is nearing the basal end of the cochlea and is therefore by necessity becoming more restricted. Alternately, this may indicate that the most basal region is less nonlinear. As reported by others, the DPOAE level is more strongly dependent on L_1 than L_2 (Gaskill and Brown, 1990; Hauser and Probst, 1991; Rasmussen *et al.*, 1993; Whitehead *et al.*, 1995b; Abdala, 1996; Kummer *et al.*, 2000). The only exception in our data was when L_1 was fixed at 70 dB SPL. For most conditions with $L_1>L_2$ the DPOAE level is almost independent of L_2, at least for $L_2>30$ dB SPL. There is presumably greater dependence on L_2 at lower levels of f_2, as reported by Dorn *et al.* (2001), though we have not studied the range $L_2<30$ dB SPL.

Separating the sources contributing to the measured DPOAE in the ear canal were not attempted in this study. Mauermann and Kollmeier (2004) showed that the contribution from the $2f_1-f_2$ site is not negligible, especially at low stimulus levels. These results were consistent with those reported by Konrad-Martin *et al.* (2001). The $2f_1-f_2$ place source may have contributed variability to the measured DPOAE I/O functions but probably did not disturb the general trends.

While there are similarities in DPOAE level dependence and BM I/O functions for a tone at CF (e.g., Boege and Janssen, 2002), interpreting emission I/O data is complicated by a number of unknowns, which will be discussed in Sec. C. For these reasons we are reluctant to speculate why the DPOAE level is more strongly dependent on L_1 than L_2.

Overall, the level dependence on the evoking stimuli is similar for low- and high-frequency DPOAEs. This implies that the biological process responsible for generating DPOAEs is the same for both low- and high-frequency eliciting tones, as previously concluded (Dreisbach and Siegel, 2001). Thus, DPOAEs elicited with high-frequency stimuli have the potential to be used in clinical applications, as is currently the practice when DPOAEs are evoked with low-frequency stimuli. In the current study only subjects where the eardrum could be visualized for calibration purposes were included. This was done to allow optical placement of a probe tube near the eardrum in an attempt to maintain better control over the eliciting stimulus levels to more accurately characterize DPOAE level dependence at higher frequencies. In clinical applications for high-frequency DPOAE measurements, reasonably accurate calibration at high frequencies may not require placing a probe tube near the eardrum.

B. Level separation generating the largest DPOAE amplitudes

The maximum level of the DPOAE is measured with $L_1>L_2$ for most stimulus frequencies and levels, at which a maximum could be defined in our data (see Table I). The only exception was with a fixed L_2 of 70 dB SPL, where approximately equal-level stimuli were optimal. In agreement with previous reports using lower-frequency stimuli, the optimal level separation is minimal at higher intensities and increases as the level of the fixed primary tone is decreased (Gaskill and Brown, 1990; Whitehead *et al.*, 1995b; Kummer *et al.*, 2000). At lower levels of the fixed primary tone, there is greater variability in our data of the optimal stimulus level separation across frequency. The greatest level separation of the primary tones at fixed levels of L_2 equal 30, 40, and 50 dB SPL, generating the largest emission occurred at 12 kHz. At lower and higher frequencies, the optimal level separation of the evoking stimuli decreased gradually as you deviated further from 12 kHz. At higher levels of the fixed stimulus (i.e., 60 and 70 dB SPL), the optimal stimulus levels were more nearly equal for all frequencies tested.

DPOAE amplitude level dependence on the evoking stimuli has been widely reported (Gaskill and Brown, 1990; Hauser and Probst, 1991; Rasmussen *et al.*, 1993). From this literature an optimal level separation for different frequencies and fixed levels of one of the primary tones has been approximated using linear fits. Whitehead *et al.* (1995b) determined the optimum value of L_1 for any fixed L_2 by fitting their data to the linear equation $L_1=aL_2+(1-a)b$, where a was approximately 0.5 dB/dB and b was approximately 90 dB SPL, for the local maximum occurring at 2 kHz. From their data set examining frequencies between 1 and 8 kHz, these authors concluded that a is relatively constant across frequency but the value of b varied between 65 and 85 dB SPL with frequency (Whitehead *et al.*, 1995a). Kummer *et al.* (1998) derived a linear fit, $L_1=aL_2+b$ dB ($a=0.4$ and $b=39$), from the data of Gaskill and Brown (1990) to approximate stimulus conditions that would generate the largest DPOAE. This linear fit proposed by Kummer *et al.* produced insignificant differences in the optimal level separation across frequency (1 to 8 kHz), varied by less than 5 dB, with restrictions only at the boundaries of this frequency range (Kummer *et al.*, 2000).

From our data we determined the level of f_1 generating the largest DPOAE for different fixed levels of f_2 (30, 40, 50, 60, and 70 dB SPL) across different f_2 frequencies (2 to

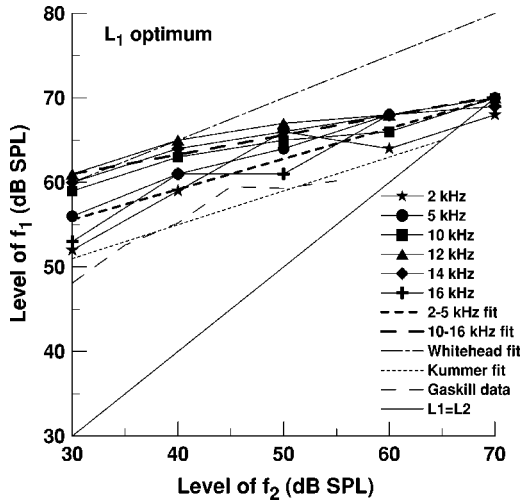

FIG. 4. The level of f_1 that produces the largest DPOAE amplitude for different fixed levels of f_2 is plotted for frequencies between 2 and 16 kHz. The solid symbols and lines represent data that are the averages for individual subjects. The lines representing the 2–5-kHz fit and the 10–16-kHz fit are $L_1=0.36L_2+44.8$ dB and $L_1=0.23L_2+54.1$ dB, respectively, for the data from the current study. The line representing the Whitehead fit is $L_1=aL_2+(1-a)b$, where a was approximately 0.5 dB/dB and b was approximately 90 dB SPL (Whitehead *et al.*, 1995a). The line representing the Kummer fit is $L_1=0.4L_2+39$ dB (Kummer *et al.*, 1998). The Gaskill data line is the optimal stimulus level separations for different fixed levels of f_2 averaged across frequency (Gaskill and Brown, 1990).

16 kHz) (Table I). We also compared our results with the linear fits of Kummer *et al.* (1998) and Whitehead *et al.* (1995a) for optimal stimulus level separations for frequencies between 1 and 8 kHz. These comparisons can be seen in Fig. 4. Using the parameters proposed by Kummer *et al.* (1998, 2000) and Whitehead *et al.* (1995a), the linear fits underestimate and overestimate, respectively, the optimal level separation data reported in this study. Also, in Fig. 4 there is a line representing $L_1=L_2$ and data from Gaskill and Brown (1990) averaged across frequency. From this figure and the data in Table I, the greatest variability in the optimal stimulus level separation is seen at a fixed level of $L_2=30$ dB SPL for the different frequencies examined. This variability in the optimal stimulus level separation across frequency decreases as the level of the fixed stimulus (L_2) increases.

Using the more general linear fit proposed by Kummer *et al.*, $L_1=aL_2+b$ dB, we determined the values for a and b to best fit the data reported here. These values can be found in Table II for each of the different frequencies and collapsed across frequency region (low- and high frequencies). The fits for the lower and higher frequencies can also be seen in Fig. 4.

TABLE II. The a and b values used to calculate the linear fit, $L_1=(aL_2+b)$ dB, for the optimal level separations for each of the primary frequencies examined in this study. Additionally, values for a and b are provided for the best linear fit when collapsed across frequency (low and high).

Frequency (kHz)	a	b
2	0.37	43.3
5	0.35	46.3
10	0.25	52.1
12	0.21	55.7
14	0.22	54.4
16	0.39	42.9
2–5	0.36	44.8
10–16	0.23	54.1

Our sample size ($N=8$) was smaller than those studied by Kummer *et al.* (1998) ($N=20$), but similar to that of Gaskill and Brown (1990) ($N=5$) and Whitehead *et al.* (1995a) ($N=8$). Thus, sample size does not appear to account for the discrepancies found between the optimal stimulus level separations for the different frequencies studied. Differing calibration procedures could account for the differences found between these studies, but this should only be consistent for f_1 frequencies near 4 or 12 kHz ($f_2=5$ or 14 kHz, respectively) (Siegel, 1994, 2002) and differences were found for all frequencies tested. It is unclear what is causing the discrepancies between our optimal stimulus level separations and the values predicted by proposed fits for frequencies up to 8 kHz (Whitehead *et al.*, 1995a; Kummer *et al.*, 1998).

Dorn *et al.* (2001) measured DPOAE I/O functions in normal-hearing ears from 1 to 8 kHz and found when using an optimal stimulus level separation, similar to those proposed by Whitehead *et al.* (1995a) and Kummer *et al.* (1998), that the data at 8 kHz were different from other frequencies at low and moderate levels. They suggested that the level separation they used at 8 kHz was possibly nonoptimal. Based on the data in the current study, this is quite likely the case given that the only conditions that were within 5 dB of the proposed equation by Kummer *et al.* at the higher frequencies were for fixed levels of 60 and 70 dB SPL.

C. General concerns about interpreting DPOAE I/O data

When interpreting the stimulus level dependence of DPOAE, it is usually assumed that the emission is initially generated in a restricted region close to the f_2 place by the same active nonlinear process, the cochlear amplifier, which is invoked to account for the level-dependent nonlinear behavior of the BM. If this were the case, then interpreting DPOAE I/O functions would be a relatively simple matter. However, while there are similarities in DPOAE I/O functions and BM I/O functions for a tone at CF, there are reasons to question whether they are directly related.

One of the most important issues is the extent to which DPOAEs reflect BM nonlinearity. A direct link between DPOAE and BM nonlinearity is strongly disputed by recent evidence that the hair cell transducer generates DPOAEs in ears in which the cochlear amplifier, and thus BM nonlinearity, has been eliminated (Mom *et al.*, 2001; Liberman *et al.*, 2004; Carvalho *et al.*, 2004). The level-dependent growth of the BM vibrations must influence the level dependence of DPOAEs, but the transducer nonlinearity is likely to generate contributions to emissions far outside the relatively restricted cochlear region of the cochlear amplifier (Cody, 1992) in both normal and pathological ears.

Evidence for an extended nonlinear interaction region for moderate-level two-tone stimuli, presumably related to the transducer, comes from population studies of auditory-

nerve fibers (Kim *et al.*, 1979; Kim, 1980; Kim *et al.*, 1980; Siegel *et al.*, 1982). The presence of large Fourier components at intermodulation-distortion frequencies in the period histograms of single auditory-nerve fibers, ranging up to several octaves in CF, demonstrates the simultaneous presence of the two stimulating tones over this large cochlear region with sufficient amplitude to drive hair cell transducers into the nonlinear region of their displacement versus conductance relation. The extent of the nonlinear interaction region expands dramatically as the level of the stimulating tones is raised. The displacement of the stereocilia for CF tones enters the nonlinear range of the transducer approximately at neural threshold, so it is logical to infer that the transducer nonlinearity contributes to DPOAE generation even at the lowest stimulus levels typical of emission measurements. A similar conclusion was reached by Liberman and colleagues (2004). It may also be inferred that the DPOAE I/O functions reflect not only the saturating characteristic of the BM, but also the spatial expansion of the nonlinear interaction region with increasing stimulus level.

The evidence just cited conflicts with the common belief that the f_2 place is the dominant generation site for DPOAEs, based largely on iso-suppression tuning curve data (e.g., Brown and Kemp, 1984; Harris *et al.*, 1992; Kummer *et al.*, 1995; Abdala *et al.*, 1996; Abdala, 2001; Gorga *et al.*, 2003). But, even if iso-suppression contours accurately identified the dominant locus for emission generation at the threshold for suppression, it is a large assumption that the extent of the generation region remains the same at higher stimulus levels. Iso-suppression tuning curve data are not well suited to quantifying the relative contributions of different cochlear regions because a single region emitting somewhat more strongly than other regions can prevent the criterion from being met despite complete suppression of smaller, but significant sources at other locations. Kemp (2002, p. 43) has noted the difficulties in interpreting suppression tuning curves because ''...both the suppressor and the source involve a spatial distribution of excitation. The change induced by the suppressor may in some circumstances be indicative of the mechanical tuning present in the region of the source; in other circumstances it may not...'' Vector decomposition techniques (i.e., Kemp and Brown, 1983; Heitmann *et al.*, 1998; Siegel *et al.*, 1998; Talmadge *et al.*, 1999; Kalluri and Shera, 2001) or interference response area measurements (e.g., Martin *et al.*, 1998a, b) allow quantitative comparisons of sources from different regions, yet, aside from the Martin group, there has been little application of these techniques to address this issue.

Several aspects of reported DPOAE suppression tuning curves do not appear to support the conventional interpretations. Iso-suppression tuning curves become broader as the criterion is reduced, both for DPOAEs (Brown and Kemp, 1984; Kummer *et al.*, 1995) and for SFOAEs (Kemp and Chum, 1980). Kemp attributed this broadening to suppression of emission generators located basal to the tone used to evoke SFOAEs, and the same reasoning can be invoked for the similar trend in DPOAE suppression tuning curves. A serious concern is that DPOAE suppression tuning curves do not broaden consistently as expected in the presence of hearing loss that is known to result in reduced frequency selectivity of the BM (Martin *et al.*, 1998a; Howard *et al.*, 2002, 2003).

There has been relatively little other investigation or consideration of the extent of the region of nonlinear interaction between the primary stimulus tones interaction. Direct evidence for DPOAE emission generators basal to the f_2 place comes from animal experiments using interference tones (Martin *et al.*, 1998a, b, 2003). Even if the emission were generated over a finite cochlear distance around the f_2 place, it is hard to imagine how the net emission from this region measured in the ear canal could reflect with any accuracy the response to a single tone at CF from a single measurement point along the BM. This uncertainty arises from the fact that the relative phase of the responses to the two primary tones must be changing, so that local contributions from the generation region must experience partial cancellation. Kemp (summarized in Kemp, 2002) has long considered otoacoustic emissions as the product of spatially distributed hair cell generators. Additionally, the emission measured in the ear canal is the result of uncanceled contributions from the array of hair cells, determined by the spatial excitation patterns evoked by the stimuli. These alternate views have yet to be evaluated critically. Further complicating the picture is the demonstration that part of the emission arises near the place of the distortion frequency (Kemp and Brown, 1983; Heitmann *et al.*, 1998; Siegel *et al.*, 1998; Talmadge *et al.*, 1999; Kalluri and Shera, 2001; Mauermann and Kollmeier, 2004).

Yet another complexity arises from the Lukashkin and Russell (1998, Lukashkin *et al.*, 2002) exploration of a transducer model which demonstrates that changes in the operating point of the transducer function can strongly affect the level dependence of intermodulation distortion, including the appearance of nonmonotonic behavior. Whether the operating point of the nonlinearity that generates DPOAEs depends on stimulus level or cochlear location is not known.

All of these factors may contribute to the dependence of DPOAE level on the levels of the stimuli, but also relate to the more general question of how to interpret otoacoustic emissions. Clarifying these and other issues will undoubtedly lead to an improvement in applying otoacoustic emissions to the clinical setting.

V. SUMMARY

DPOAE level dependence is similar for low- and high frequencies. For fixed stimulus levels (L_2) less than 70 dB SPL and $f_2/f_1=1.2$, L_1 should always be greater than L_2 to generate the largest DPOAE across f_2 frequencies from 2 to 16 kHz. As the fixed stimulus level (L_2) decreases, the difference increases between the stimulus tones that generate the largest DPOAE amplitude. Proposed optimal stimulus level separation fits (e.g., Kummer *et al.*, 1998) do not necessarily produce the largest DPOAE for higher frequencies at low and moderate levels of the fixed stimulus tone. The best fit for the optimal stimulus level separation at high frequencies in this study would be $L_1=0.23L_2+54.1$ dB.

ACKNOWLEDGMENTS

This work was supported by NIH Grant R01 DC02021. We are grateful to Etymotic Research and Electro FiberOptics Corp. for building the customized devices. We would like to acknowledge Peter Torre III for his insightful editorial comments during the preparation of this manuscript. We would also like to thank two anonymous reviewers for their helpful suggestions on an earlier version of this manuscript.

[1]We adopt this common terminology in the interest of avoiding confusion. While sensitivity of detecting changes in DPOAEs due to hearing loss is increased when L_2 is lowered well below that commonly used (Sutton *et al.*, 1994; Whitehead *et al.*, 1995a; 1995b), there has been no systematic study of which ''standard'' condition should be used to ''optimize'' the detection of hearing loss as a routine procedure. If there is an appropriate use of the term ''optimum,'' this certainly would be one, but it is very different from describing a local maximum in emission levels in normal ears, as is done in this study, as being optimal. Stimulus level differences different from this optimal number may in principle prove beneficial for addressing other practical or theoretical issues.

Abdala, C. (**1996**). ''Distortion product otoacoustic emission ($2f_1-f_2$) amplitude as a function of f_2/f_1 frequency ratio and primary tone level separation in human adults and neonates,'' J. Acoust. Soc. Am. **100**, 3726–3740.

Abdala, C. (**2001**). ''Maturation of the human cochlear amplifier: Distortion product otoacoustic emission suppression tuning curves recorded at low and high primary tone levels,'' J. Acoust. Soc. Am. **110**, 1465–1476.

Abdala, C., Sininger, Y. S., Ekelid, M., and Zeng, F. G. (**1996**). ''Distortion product otoacoustic emission suppression tuning curves in human adults and neonates,'' Hear. Res. **98**, 38–53.

ANSI (**1996**). ANSI 53, 6-1996, ''Specifications for Audiometers'' (American National Standards Institute, New York).

Boege, P., and Janssen, T. (**2002**). ''Pure-tone threshold estimation from extrapolated distortion product otoacoustic emission I/O functions in normal and cochlear hearing loss ears,'' J. Acoust. Soc. Am. **111**, 1810–1818.

Brown, A. M., and Gaskill, S. A. (**1990**). ''Measurement of acoustic distortion reveals underlying similarities between human and rodent mechanical responses,'' J. Acoust. Soc. Am. **88**, 840–849.

Brown, A. M., and Kemp, D. T. (**1984**). ''Suppressibility of the $2f_1-f_2$ stimulated acoustic emissions in gerbil and man,'' Hear. Res. **13**, 29–37.

Brown, A. M., McDowell, B., and Forge, A. (**1989**). ''Effects of chronic gentamicin treatment on hair cells can be monitored using acoustic distortion products,'' Hear. Res. **42**, 143–156.

Carvalho, S., Mom, T., Gilain, L., and Avan, P. (**2004**). ''Frequency specificity of distortion-product otoacoustic emissions produced by high-level tones despite inefficient cochlear electromechanical feedback,'' J. Acoust. Soc. Am. **116**, 1639–1648.

Chan, C. K., Musicant, A. D., and Hind, J. E. (**1993**). ''An insert earphone system for delivery of spectrally shaped signals for physiological studies,'' J. Acoust. Soc. Am. **93**, 1496–1501.

Cody, A. R. (**1992**). ''Acoustic lesions in the mammalian cochlea: Implications for the spatial distribution of the 'active process,' '' Hear. Res. **62**, 166–172.

Dorn, P. A., Konrad-Martin, D., Neely, S. T., Keefe, D. H., Cyr, E., and Gorga, M. P. (**2001**). ''Distortion product otoacoustic emission input/output functions in normal-hearing and hearing-impaired human ears,'' J. Acoust. Soc. Am. **110**, 3119–3131.

Dreisbach, L. E., and Siegel, J. H. (**2001**). ''Distortion-product otoacoustic emissions measured at high frequencies in humans,'' J. Acoust. Soc. Am. **110**, 2456–2469.

Gaskill, S. A., and Brown, A. M. (**1990**). ''The behavior of the acoustic distortion product, $2f1-f2$, from the human ear and its relation to auditory sensitivity,'' J. Acoust. Soc. Am. **88**, 821–839.

Gorga, M. P., Neely, S. T., Dierking, D. M., Dorn, P. A., Hoover, B. M., and Fitzpatrick, D. F. (**2003**). ''Distortion product otoacoustic emission suppression tuning curves in normal-hearing and hearing-impaired human ears,'' J. Acoust. Soc. Am. **114**, 263–278.

Harris, F. P., Probst, R., and Xu, L. (**1992**). ''Suppression of the $2f1-f2$ otoacoustic emission in humans,'' Hear. Res. **64**, 133–141.

Hauser, R., and Probst, R. (**1991**). ''The influence of systematic primary-tone level variation L_2-L_1 on the acoustic distortion product emission $2f_1-f_2$ in normal human ears,'' J. Acoust. Soc. Am. **89**, 280–286.

Heitmann, J., Waldmann, B., Schnitzler, H. U., Plinkert, P. K., and Zenner, H. P. (**1998**). ''Suppression growth functions of DPOAE with a suppressor near f_1-f_2 depends on DP fine structure—evidence for two generations sites of DPOAE,'' J. Acoust. Soc. Am. **103**, 1527–1531.

Howard, M. A., Stagner, B. B., Foster, P. K., Lonsbury-Martin, B. L., and Martin, G. K. (**2003**). ''Suppression tuning in noise-exposed rabbits,'' J. Acoust. Soc. Am. **114**, 279–293.

Howard, M. A., Stagner, B. B., Lonsbury-Martin, B. L., and Martin, G. K. (**2002**). ''Effects of reversible noise exposure on the suppression tuning of rabbit distortion-product otoacoustic emissions,'' J. Acoust. Soc. Am. **111**, 285–296.

Janssen, T., Boege, P., Oestreicher, E., and Arnold, W. (**2000**). ''Tinnitus and $2f1-f2$ distortion product otoacoustic emissions following salicylate overdose,'' J. Acoust. Soc. Am. **107**, 1790–1792.

Janssen, T., Kummer, P., and Arnold, W. (**1998**). ''Growth behavior of the $2f1-f2$ distortion product otoacoustic emission in tinnitus,'' J. Acoust. Soc. Am. **103**, 3418–3430.

Kalluri, R., and Shera, C. (**2001**). ''Distortion-product source unmixing: A test of the two-mechanism model for DPOAE generation,'' J. Acoust. Soc. Am. **109**, 622–637.

Kemp, D. T. (**2002**). ''Exploring cochlear status with otoacoustic emissions. The potential for new clinical applications,'' in *Otoacoustic Emissions: Clinical Applications*, 2nd ed., edited by M. S. Robinette and T. J. Glattke (Thieme, New York), pp. 1–45.

Kemp, D. T., and Brown, A. M. (**1983**). ''An integrated view of cochlear mechanical nonlinearities observable from the ear canal,'' in *Mechanics of Hearing*, edited by E. de Boer and M. A. Viergever (Delft, The Netherlands), pp. 75–82.

Kemp, D. T., and Chum, R. A. (**1980**). ''Observations on the generation mechanism of stimulus frequency acoustic emissions—two tone suppression,'' in *Psychophysical, Physiological and Behavioral Studies in Hearing*, edited by G. van den Brink and F. A. Bilsen (Delft, The Netherlands), pp. 35–42.

Kim, D. O. (**1980**). ''Cochlear mechanics: Implications of electrophysiological and acoustical observations,'' Hear. Res. **2**, 297–317.

Kim, D. O., Molnar, C. E., and Matthews, J. W. (**1980**). ''Cochlear mechanics: Nonlinear behavior in two-tone responses as reflected in cochlear-nerve-fiber responses and in ear-canal sound pressure,'' J. Acoust. Soc. Am. **67**, 1704–1721.

Kim, D. O., Siegel, J. H., and Molnar, C. E. (**1979**). ''Cochlear nonlinear phenomena in two-tone responses,'' Scand. Audiol. Suppl. **9**, 63–81.

Konrad-Martin, D., Neely, S. T., Keefe, D. H., Dorn, P. A., and Gorga, M. P. (**2001**). ''Sources of distortion product otoacoustic emissions revealed by suppression experiments and inverse fast Fourier transforms in normal ears,'' J. Acoust. Soc. Am. **109**, 2862–2879.

Kössl, M. (**1994**). ''Otoacoustic emissions from the cochlea of 'The constant frequency' bats, *Pteronotus parnelli and Rhinolophus rouxi*,'' Hear. Res. **72**, 59–72.

Kummer, P., Janssen, T., and Arnold, W. (**1995**). ''Suppression tuning characteristics of the $2f1-f2$ distortion-product otoacoustic emission in humans,'' J. Acoust. Soc. Am. **98**, 197–210.

Kummer, P., Janssen, Y., and Arnold, W. (**1998**). ''The level and growth behavior of the $2f1-f2$ distortion product otoacoustic emission and its relationship to auditory sensitivity in normal hearing and cochlear hearing loss,'' J. Acoust. Soc. Am. **103**, 3431–3444.

Kummer, P., Janssen, Y., Hulin, P., and Arnold, W. (**2000**). ''Optimal L_1-L_2 primary tone level separation remains independent of test frequency in humans,'' Hear. Res. **146**, 47–56.

Liberman, M. C., and Dodds, L. W. (**1984**). ''Single-neuron labeling and chronic cochlear pathology. III. Stereocilia damage and alterations of threshold tuning curves,'' Hear. Res. **16**, 55–74.

Liberman, M. C., Zuo, J., and Guinan, Jr., J. J. (**2004**). ''Otoacoustic emissions without somatic motility: Can stereocilia mechanics drive the mammalian cochlea?,'' J. Acoust. Soc. Am. **116**, 1649–1655.

Lukashkin, A. N., Lukashkin, V. A., and Russell, I. J. (**2002**). ''One source for distortion product otoacoustic emissions generated by low- and high-level primaries,'' J. Acoust. Soc. Am. **111**, 2740–2748.

Lukashkin, A. N., and Russell, I. J. (**1998**). ''A descriptive model of the receptor potential nonlinearities generated by the hair cell mechanoelectrical transducer,'' J. Acoust. Soc. Am. **103**, 973–980.

Martin, G. K., Jassir, D., Stagner, B. B., and Lonsbury-Martin, B. L. (**1998a**). ''Effects of loop diuretics on the suppression tuning of distortion-product otoacoustic emissions in rabbits,'' J. Acoust. Soc. Am. **104**, 972–983.

Martin, G. K., Jassir, D., Stagner, B. B., Whitehead, M. L., and Lonsbury-Martin, B. L. (**1998b**). ''Locus of generation for the 2 $f1-f2$ vs 2 $f2-f1$ distortion-product otoacoustic emissions in normal-hearing humans revealed by suppression tuning, onset latencies, and amplitude correlations,'' J. Acoust. Soc. Am. **103**, 1957–1971.

Martin, G. K., Villasuso, E. I., Stagner, B. B., and Lonsbury-Martin, B. L. (**2003**). ''Suppression and enhancement of distortion-product otoacoustic emissions by interference tones above $f(2)$. II. Findings in humans,'' Hear. Res. **177**, 111–122.

Mauermann, M., and Kollmeier, B. (**2004**). ''Distortion product otoacoustic emission (DPOAE) input/output functions and the influence of the second DPOAE source,'' J. Acoust. Soc. Am. **116**, 2199–2212.

Mills, D. M., Norton, S. J., and Rubel, E. W. (**1993**). ''Vulnerability and adaptation of distortion-product otoacoustic emissions to endocochlear potential variation,'' J. Acoust. Soc. Am. **94**, 2108–2122.

Mills, D. M., and Rubel, E. W. (**1994**). ''Variation of distortion product otoacoustic emissions with furosemide injection,'' Hear. Res. **77**, 183–199.

Mom, T., Bonfils, P., Gilain, L., and Avan, P. (**2001**). ''Origin of cubic difference tones generated by high-intensity stimuli: Effect of ischemia and auditory fatigue on the gerbil cochlea,'' J. Acoust. Soc. Am. **110**, 1477–1488.

Neely, S. T., and Liu, Z. (**1993**). ''EMAV: Otoacoustic emission averager,'' Tech Memo No. 17 (Boys Town National Research Hospital, Omaha).

Norton S. J., and Rubel, E. W. (**1990**). ''Active and passive ADP components in mammalian and avian ears,'' in *Mechanics and Biophysics of Hearing*, edited by P. Dallos, C. D. Geisler, J. W. Matthews, M. A. Ruggero, and C. R. Steele (Springer, New York), pp. 219–226.

Ohlemiller, K. K., and Siegel, J. H. (**1994**). ''Cochlear basal and apical differences reflected in the effects of cooling on responses of single auditory nerve fibers,'' Hear. Res. **80**, 174–190.

Rasmussen, A. N., Popelka, G. R., Osterhammel, P. A., and Nielsen, L. H. (**1993**). ''Clinical significance of relative probe-tone levels on distortion product otoacoustic emissions,'' Scand. Audiol. **22**, 223–229.

Ruggero, M. A., and Rich, N. C. (**1991**). ''Furosemide alters organ of corti mechanics: Evidence for feedback of outer hair cells upon the basilar membrane,'' J. Neurosci. **11**, 1057–1067.

Ruggero, M. A., Rich, N. C., Recio, A., Narayan, S. S., and Robles, L. (**1997**). ''Basilar-membrane responses to tones at the base of the chinchilla cochlea,'' J. Acoust. Soc. Am. **101**, 2151–2163.

Siegel, J. H. (**1994**). ''Ear-canal standing waves and high-frequency sound calibration using otoacoustic emission probes,'' J. Acoust. Soc. Am. **95**, 2589–2597.

Siegel, J. H. (**2002**). ''Calibrating otoacoustic emission probes,'' in *Otoacoustic Emissions: Clinical Applications*, 2nd ed., edited by M. S. Robinette and T. J. Glattke (Thieme, New York), pp. 416– 441.

Siegel, J. H., Dreisbach, L. E., Neely, S. T., and Spear, W. S. (**1998**). ''Vector decomposition of distortion-product otoacoustic emission sources in humans,'' Assoc. for Res. Otolaryngol. Abst. **21**, 87.

Siegel, J. H., Kim, D. O., and Molnar, C. E. (**1982**). ''Effects of altering organ of Corti on cochlear distortion products $f2-f1$ and 2 $f1-f2$,'' J. Neurophysiol. **47**, 303–328.

Sutton, L. A., Lonsbury-Martin, B. L., Martin, G. K., and Whitehead, M. L. (**1994**). ''Sensitivity of distortion-product otoacoustic emissions in humans to tonal over-exposure: time course of recovery and effects of lowering L2,'' Hear Res. **75**(1–2), 161–174.

Talmadge, C. L., Long, G. R., Tubis, A., and Dhar, S. (**1999**). ''Experimental confirmation of the two-source interference model for the fine structure of distortion product otoacoustic emissions,'' J. Acoust. Soc. Am. **105**, 275–292.

Whitehead, M. L., Lonsbury-Martin, B. L., and Martin, G. K. (**1990**). ''Actively and passively generated acoustic distortion at 2 f_1-f_2 in rabbits,'' in *Mechanics and Biophysics of Hearing*, edited by P. Dallos, C. D. Geisler, J. W. Matthews, M. A. Ruggero, and C. R. Steele (Springer, New York), pp. 243–250.

Whitehead, M. L., Lonsbury-Martin, B. L., and Martin, G. K. (**1992**). ''Evidence for two discrete sources of 2 f_1-f_2 distortion-product otoacoustic emission in rabbit. I. Differential dependence on stimulus parameters,'' J. Acoust. Soc. Am. **91**, 1587–1607.

Whitehead, M. L., McCoy, M. J., Lonsbury-Martin, B. L., and Martin, G. K. (**1995a**). ''Dependence of distortion-product otoacoustic emissions on primary levels in normal and impaired ears. I. Effects of decreasing L_2 below L_1,'' J. Acoust. Soc. Am. **97**, 2346–2358.

Whitehead, M. L., Stagner, B. B., McCoy, M. J., Lonsbury-Martin, B. L., and Martin, G. K. (**1995b**). ''Dependence of distortion-product otoacoustic emissions on primary levels in normal and impaired ears. II. Asymmetry in L_1, L_2 space,'' J. Acoust. Soc. Am. **97**, 2359–2377.

Using the short-time correlation coefficient to compare transient- and derived, noise-evoked otoacoustic emission temporal waveforms

James M. Harte[a] and Stephen J. Elliott
Institute of Sound and Vibration Research, University of Southampton, University Road, Southampton, Hampshire, SO17 1BJ, United Kingdom

(Received 20 December 2004; revised 22 February 2005; accepted 22 February 2005)

Transient-evoked otoacoustic emissions (TEOAEs) and derived, noise-evoked otoacoustic emissions (derived-NEOAEs) were measured in seven normally hearing subjects. The evoked OAEs were all recorded at three excitation levels chosen to ensure that the OAE level curve compressive region was reached. The short-time correlation coefficient (STCC) was used to compare the OAE waveforms at different excitation levels, and thus estimate the time over which the response exceeds the noise level. The short-time correlation for TEOAEs is significant for longer than it is for NEOAEs, particularly in some individuals, and the STCC allows this to be quantified. This suggests that derived NEOAEs do not display the highly synchronized dominant frequencies often seen in TEOAEs. This has been confirmed by examining the derived frequency responses for the two types of excitation. Conventional TEOAEs thus appear to measure a combination of two conceptually different processes, while NEOAEs measure just one. © *2005 Acoustical Society of America.*
[DOI: 10.1121/1.1893285]

PACS numbers: 43.64.Jb, 43.64.Yp, 43.64.Bt [BLM] Pages: 2989–2998

I. INTRODUCTION

The human auditory system is known to contain various nonlinearities; one source is commonly believed to be a feedback loop within the cochlea, often described as the ''active process.'' This was first postulated by Gold (1948), whose theory stated that to account for the high-frequency selectivity the filters in the cochlear must be active. This mechanism sharpens the response of the auditory filters, with the potential to oscillate if too much energy is fed into them. As well as compressing the dynamic range of the cochlear response, the active process is also believed to give rise to otoacoustic emissions (OAEs), first demonstrated by Kemp (1978).

The vast majority of normally hearing adults (~98%) has measurable transient- or click-evoked otoacoustic emissions (TEOAEs or CEOAEs) (Probst *et al.*, 1991). When click stimuli are used, the majority of ears shows emission spectra containing several discrete frequencies, which are known as dominant frequencies. These dominant frequencies may be spontaneous otoacoustic emissions (SOAEs), synchronized by the transient stimuli so that they become ''long'' TEOAEs. Alternatively, they may also be generated by oscillations at specific frequency places that are only present when evoked, but relatively weakly damped (Probst *et al.*, 1991). SOAEs are often thought of as a consequence of particular locations on the cochlear having active mechanisms in a region of instability.

Maat *et al.* (1994, 2000) demonstrated that otoacoustic emissions may also be elicited by noise excitation signals. They have suggested that a derived noise-evoked OAE is fundamentally linked with transient-evoked OAEs (TEOAEs) via the first-order cross-correlation function.

It is believed that OAEs are a consequence of the nonlinearity in the basilar-membrane (BM) vibration response to acoustic stimulation. OAEs thus demonstrate similar nonlinear behavior to that seen on the BM. Growth relationships for OAEs have been well documented, in particular for TEOAEs; Kemp (1978), Wit and Ritsma (1979), Probst *et al.* (1986), and Zwicker (1983) have all shown linear growth in output for low stimulus level, while a compressive nonlinear region is observed at higher levels.

This paper presents a comparison of transient- and derived, noise-evoked OAE temporal waveforms, evoked by stimuli ensuring the compressive region of the BM is excited. Derived NEOAEs are obtained via spectral density estimates and a normalized first-order frequency response function. This method is closely linked with that of Maat *et al.* (2000), and related to the earlier work on reverse correlation functions (revcor) by de Boer and de Jongh (1978). This paper shows that the noise stimuli do not elicit the synchronous dominant frequencies observed in TEOAEs. The short-time correlation coefficient is defined and used to quantify this difference, which is particularly strong in some individuals.

II. EXPERIMENTAL METHODS

The transient- and noise-evoked OAEs were recorded from seven normally hearing subjects. An Otodynamics general-purpose OAE probe (SGS type containing Knowles EM3046 and ED1913 transducers) was used with a Cambridge Electronic Design μ1401 data acquisition system. The μ1401 used 12-bit precision yielding a dynamic range of ≈72 dB before averaging, deemed adequate for these experiments. A sample rate of 40 kHz was used and down-sampled off-line to 20 kHz. The output from the microphone was

[a]Electronic mail: jmh@isvr.soton.ac.uk

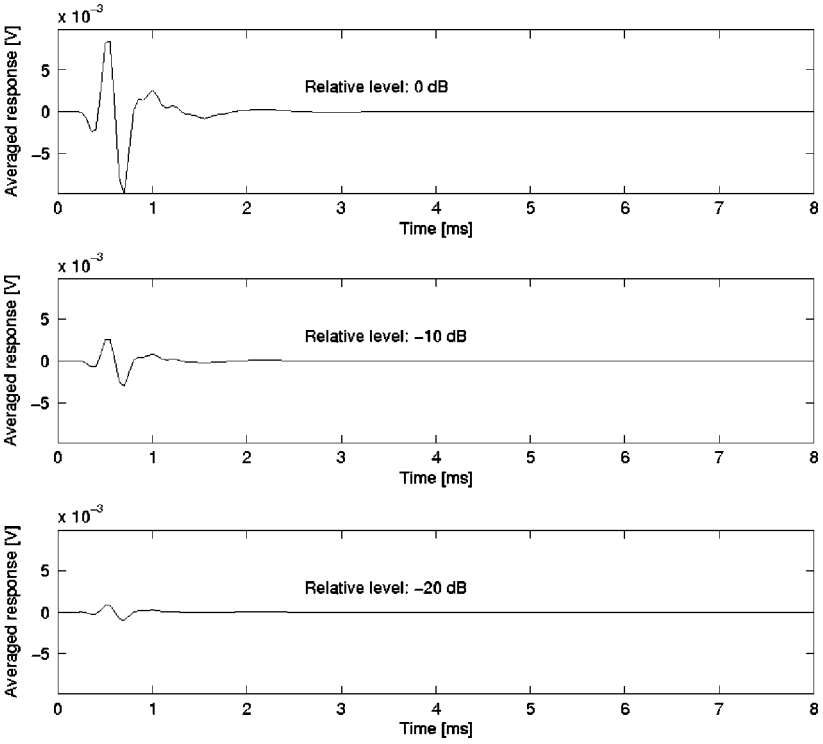

FIG. 1. Short-latency transient responses to clicks for three excitation levels, for IEC711 coupler.

routed through low-pass and high-pass Kemo digital filters with cutoff frequencies of 0.7 and 6 kHz, respectively.

Two sets of stimuli were presented to each subject. The first was a series of clicks of 100-μs duration. Three series were played, with maximum peak equivalent sound-pressure levels (pe SPL) of 72, 62, and 52 dB, respectively, and a repetition rate of $\approx$10 Hz. A total of 2048 sets of click responses was recorded, and $\approx$10% discarded via an off-line artifact rejection template before averaging. The temporal window for each TEOAE was 102.4 ms, or 2048 samples. The second set of stimuli was a series of three Gaussian-distributed random data sets with a bandwidth 0–6 kHz. Each of these had a reference equivalent threshold sound-pressure level (RETSPL) [see EN ISO 389-2 (1997)] of 73 dB and the others 63 and 53 dB, respectively. Approximately 3.5 min of data were recorded at each level of excitation. All the spectral estimators used in the analysis used blocks of 2048 samples to ensure the same spectral resolution as with the TEOAE case.

This paper presents results for two cases, subjects 1 and 2, who were chosen to illustrate subjects with short- and long-duration TEOAEs. The click and noise stimuli have been described in terms of pe SPL and RETSPL, respectively. The highest level is referred to as level 1 and used as a reference point for the others, i.e., level 2 is at -10 dB and level 3 at -20 dB relative to level 1. The levels chosen for the click and noise stimuli are not directly comparable, but the stimuli were sufficiently intense to excite the compressive region of the basilar-membrane response.

A. Passive coupler results

The experiment was initially performed using an ear simulator (IEC711), to give a linear comparison with the human subject results. For illustration purposes only the responses to the transient time series are shown, since identical results were obtained by processing noise-evoked data.

Two regions of the temporal waveforms are defined, the short- and long-latency responses. The short–long latency transition is defined as the region before the coupler linear response descends into the acquisition noise floor, and is at least 40 dB below the largest magnitude response (Probst *et al.*, 1991), to ensure that the average OAE will dominate the waveform after this point. This short–long latency transition was used as an empirical measure of the separation for the human subject cases. The short-latency response corresponds to the linear response of the transducers, outer- and middle ears. The long-latency response is the nonlinear OAE of cochlear origin.

Figure 1 shows the short-latency transient response measured in the coupler, for the three different excitation levels. The short-latency responses in Fig. 1 behave linearly by reducing in 10-dB steps, as the excitation level is decreased by 10-dB pe SPL. Quantifying this linear relationship has been achieved via a relative level calculated numerically, and shown in the figures, defined to be

$$L_{n,\mathrm{rel}}\ (\mathrm{dB}) = 20\log_{10}\left[\frac{\sigma_{y_n}}{\sigma_{y1}}\right], \tag{1}$$

where σ_{y_n} is the rms level of the level n transient response, $y_n(t)$.

The long-latency transient response after 8 ms is very small, of the order of numerical residue or noise. The transition from short–long latency $\tau_T = 8$ ms is long when compared with the results of other authors [see Probst *et al.* (1991) for a review]. It can be explained in terms of the bandpass filters used in the data acquisition system, a pair of Kemo fourth-order Butterworth filters. In the frequency do-

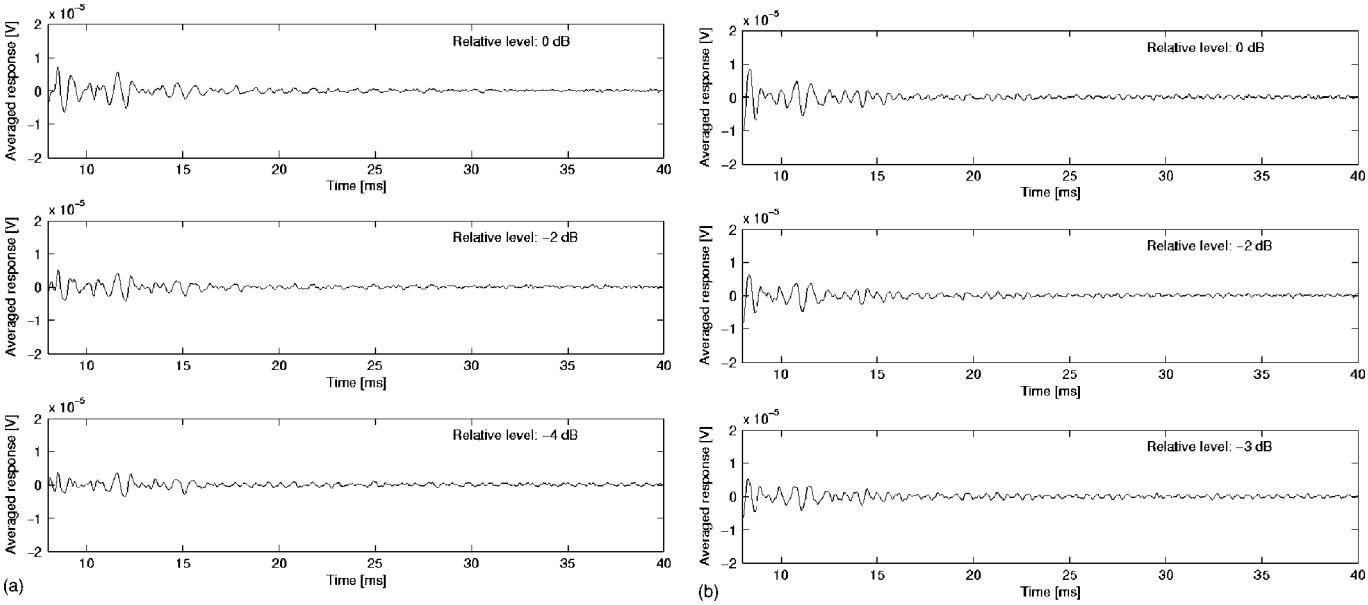

FIG. 2. Long-latency transient responses for three excitation levels, for subject 1 (a) left and (b) right ears, for periodic click excitation.

main these have a sharp 48-dB/octave roll-off, and in the time domain this corresponds to an impulse response with an effective duration of 6–8 ms. Thus, it is necessary to remove this from both the noise- and click-processed and averaged time series, respectively. This will potentially remove the initial long-latency component of the OAE, and the frequency components with shorter latencies (i.e., higher frequencies) will not be present in the OAEs recorded here.

Any OAE level curves derived from these experiments will be dominated by OAE components with very long duration, i.e., lightly damped. This would slightly bias the level curve toward greater compression, as it is known the longer latency OAEs tend to demonstrate more compression (Probst *et al.*, 1991).

III. TRANSIENT-EVOKED OTOACOUSTIC EMISSIONS

Figures 2(a) and (b) show the long-latency component of the click response for the left and right ears of subject 1, respectively. Also shown in these two figures are measurements of the overall output level, relative to the response elicited by the highest level of excitation, calculated from the mean-square value of the responses. However, the left ear has relative levels of 0, −2, and −4 dB for relative input levels of 0, −10, and −20 dB, which are compressive. The right ear follows a similar pattern with $L_{y1,\mathrm{rel}}=0$ dB, $L_{y2,\mathrm{rel}}=-2$ dB, and $L_{y3,\mathrm{rel}}=-3$ dB.

Subject 2, whose left- and right-ear long-latency transient results are shown in Figs. 3(a) and (b), respectively, shows some different characteristics from subject 1. The re-

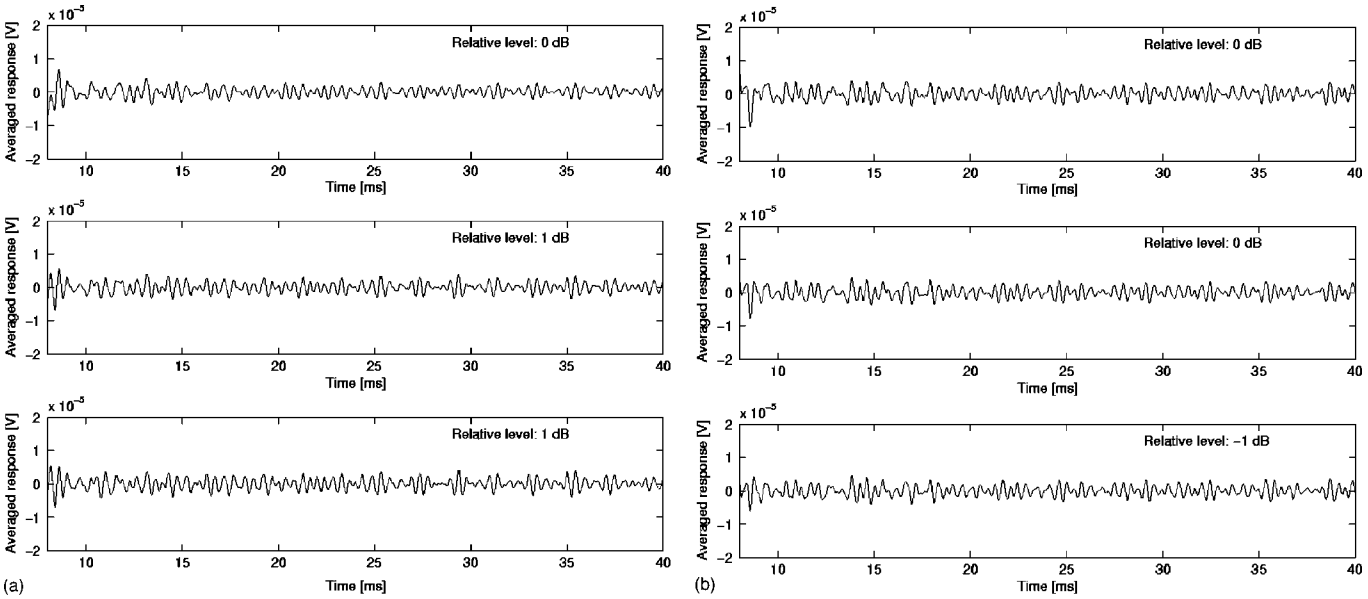

FIG. 3. Long-latency transient responses for three excitation levels, for subject 2 (a) left and (b) right ears, for periodic click excitation.

sults do not appear to have a decaying characteristic on this time scale. This is thought to be due to a synchronization of spontaneous OAEs (SOAEs) with the click frequency. In the literature, very long latency TEOAE responses of this kind are often referred to as synchronous spontaneous otoacoustic emissions (SSOAEs) (Konrad-Martin and Keefe, 2003; Wilson, 1980). A beating effect is observed in Figs. 3(a) and (b) due to multiple sinusoidal components with closely spaced fundamentals. Very strong compression or saturation of the long-latency response is apparent from the relative output levels.

Of the seven subjects successfully tested in this study, three were observed to have very strong synchronous responses for the click stimuli.

IV. NOISE-EVOKED OTOACOUSTIC EMISSIONS

Derived noise-evoked otoacoustic emissions are obtained by processing the random signal recorded in the ear canal as a result of noise excitation. In the experiment, band-limited excitation of 0–6-kHz Gaussian-distributed noise was used. The method chosen to produce the derived NEOAE was via the H_1 estimator (Bendat and Piersol, 1966) defined as $S_{xy}(j\omega)/S_{xx}(\omega)$, i.e., the ratio of the input–output cross-spectral density to the input power-spectral density function. The input power-spectral density was flat in the band 0–6 kHz, and had a roll-off defined by the order of the low-pass filter used to generate the data set. Thus, the response of $1/S_{xx}(\omega)$ is dominated by noise at high frequencies, distorting the results. For this reason a regularized H_1 estimator was used to obtain the derived NEOAE

$$\hat{H}_1(j\omega)=\frac{S_{xy}(j\omega)}{S_{xx}(\omega)+\varepsilon_n}. \tag{2}$$

The regularization constant, ε_n, will bias the H_1 estimator in the absence of noise so that

$$\hat{H}_1(j\omega)=H_1(j\omega)\cdot\frac{S_{xx}(\omega)}{S_{xx}(\omega)+\varepsilon_n}. \tag{3}$$

The bias, defined as the ratio $\hat{H}_1(j\omega)/H_1(j\omega)$, only has an effect when the input power spectral density for a given frequency is small compared to ε_n. The values of ε_n were chosen to be $\varepsilon_1=1\times10^{-4}$, $\varepsilon_2=1\times10^{-5}$, and $\varepsilon_3=1\times10^{-6}$ for each subject, thus producing the same degree of regularization bias across the different excitation levels.

To obtain the calculated output spectra, the frequency response estimates obtained by the regularized H_1 estimator need to be rescaled by the excitation level

$$H_{n,r}(j\omega)=\sigma_{x_n}\cdot\hat{H}_{1,n}(j\omega), \tag{4}$$

where σ_{x_n}[1] is the rms value of the excitation signal. In order to compare the results with the TEOAE waveforms, the calculated response to impulses is calculated by first correctly ordering the calculated output spectrum as a two-sided spectrum, with the negative frequency components being the complex conjugate of the positive frequency, i.e., a conjugate even function

$$G(j\omega)=G^*(-j\omega), \tag{5}$$

where $G(jw)$ is some two-sided spectrum and * denotes complex conjugation. This constraint will ensure that the inverse Fourier transform, which produces the desired calculated response to impulses, will be real valued (Randall, 1987). Note that very careful ordering of the frequency bins is required; if not, then there is potential for leakage in the temporal bins. The inverse Fourier transform of the derived spectrum is then taken to give the calculated response to an impulse

$$h_{n,r}(t)=\sigma_{x_n}\int_{-\infty}^{\infty}\hat{H}_{n,r}(j\omega)e^{j\omega t}d\omega. \tag{6}$$

A detailed discussion on the properties of the estimator for the derived NEOAE is beyond the scope of this paper; see Harte (2004) and future publications.

Figures 4(a) and (b) show the long-latency calculated response to impulses, the derived NEOAE, for the left- and right ears of subject 1. The relative levels of output for all three input levels are compressive, as expected. The form of the long-latency responses calculated from the noise data is similar to that measured with transients [Figs. 2(a) and (b)] for this subject, up to around 15 ms. The noise floor on these responses appears to be greater for high-level inputs than it is for low-level inputs. For a nonlinear system, varying the input by some gain or scale factor does not yield an equivalent factor in the output from the system, as it does not possess the homogeneity property of linear systems. Assuming the nonlinear system is compressive and level dependent, changing the input scale will result in a compressed scale factor on the output. Thus, as excitation level increases, the frequency response function estimate will reduce in magnitude, with the noise floor remaining fixed. Rescaling with the input level results in derived NEOAEs with greater noise on the higher excitation level estimates. This is due to the compressive nature of the nonlinearity; a detailed discussion is found in Harte (2004) and will be addressed in future publications.

The left- and right ears for subject 2 have the calculated long-latency responses shown in Figs. 5(a) and (b). Neither ear appears to show dominant frequencies of synchronized SOAEs; hence, their long-term behavior is quite different from those measured with a periodic sequence of clicks, as shown in Figs. 3(a) and (b).

V. SHORT-TIME CORRELATION COEFFICIENT

The correlation coefficient, $\rho(\tau)$, of the random variables X and Y, is defined to be

$$\rho(\tau)=\frac{cov[X,Y]}{\sigma_X\sigma_Y}, \tag{7}$$

where $cov[X,Y]=E[(x-\mu_x)(y-\mu_y)]$; see Mood *et al.* (1974). The correlation coefficient is a dimensionless measure of the linear relationship between X and Y, and lies in the range $-1\leqslant\rho_{X,Y}\leqslant1$.

This linear measure can be extended to nonstationary time series, via the time-varying correlation coefficient, $\Psi_{xy}(t_w,\mu)$, which is the correlation coefficient across two time series calculated using a moving windowing function.

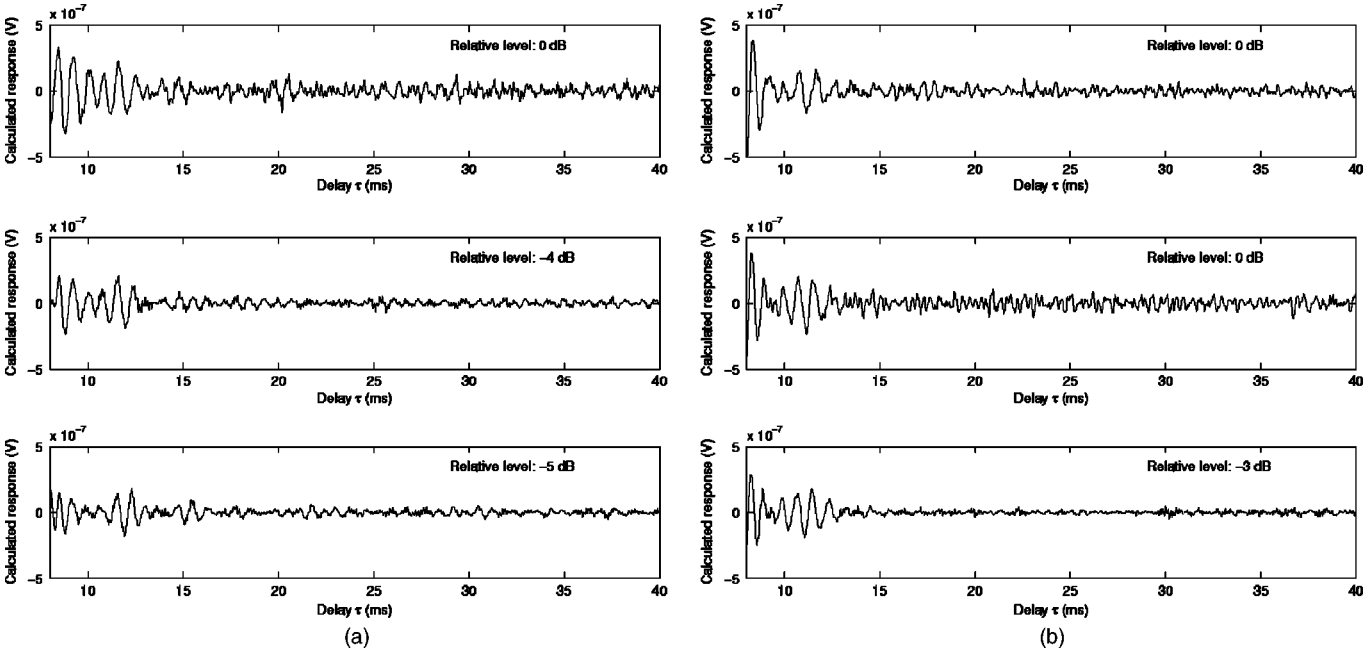

FIG. 4. Long-latency calculated response to impulses for subject 1 (a) left and (b) right ears, for the three different excitation levels, with noise excitation.

Evaluating this at zero lag ($\mu=0$) gives a one-dimensional representation that represents the instantaneous correlation between two signals, denoted here as the short-time correlation coefficient (STCC), $\psi_{xy}(t_w)=\Psi_{xy}(t_w,0)$. This is given by

$$\psi_{xy}(t_w)=\frac{\Sigma[w(t)x(t)y(t)]}{\sqrt{\Sigma[w(t)x(t)]^2\cdot\Sigma[w(t)y(t)]^2}}, \tag{8}$$

where the summation is over all discrete $t=n\Delta$ and $w(t)$ is a moving window function, which is here defined to be the ''boxcar'' function

$$w(t)=1, \quad \text{for } t_1\leqslant t\leqslant t_2,$$
$$=0, \quad \text{for } t\geqslant t_2 \quad \text{and} \quad t\leqslant t_1. \tag{9}$$

The time index, centered in the windowing function, is defined to be $t_w=(t_2+t_1)/2$. By using the window function rather than instantaneous time, t, an estimate which is more robust to noise is obtained. An inherent trade-off exists in such a measure between potential bias and random error. Too long a window and features of the correlation coefficient over time will be ''smeared out,'' even though random fluctuations are reduced. Thus, a compromise for window length must be reached. In this study a window of 128 samples, or

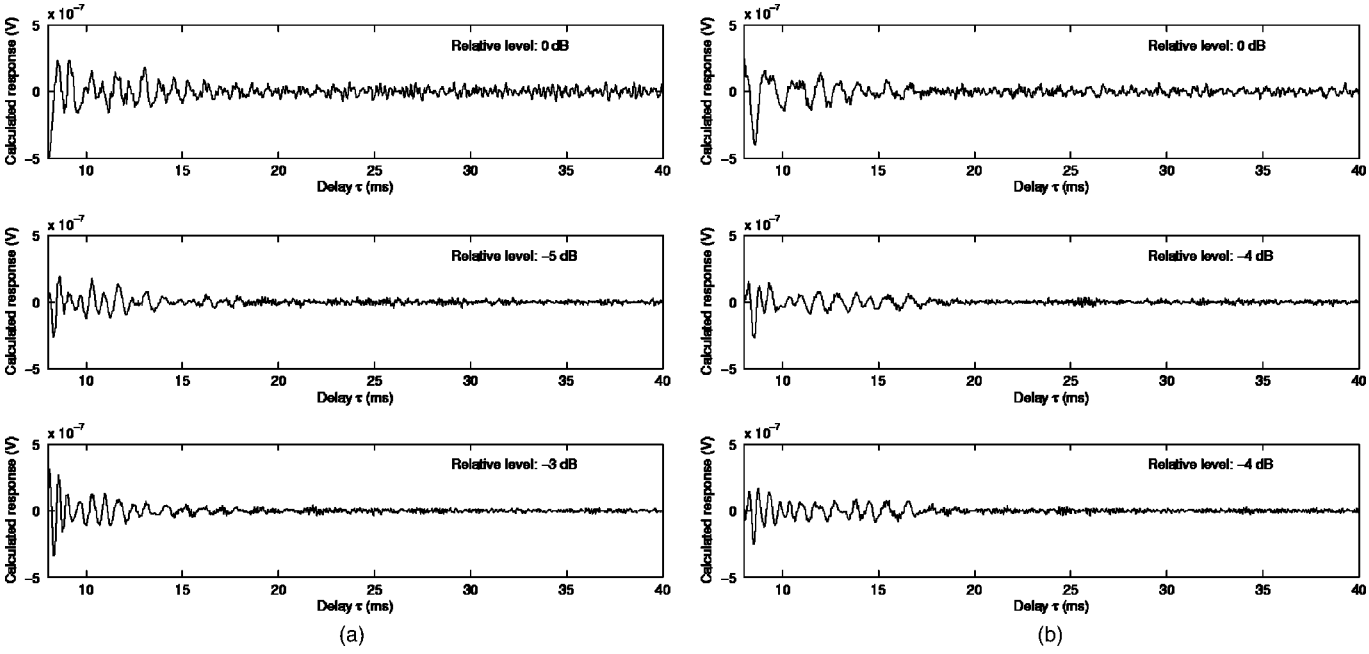

FIG. 5. Long-latency calculated response to impulses for subject 2 (a) left and (b) right ears, for the three different excitation levels, with noise excitation.

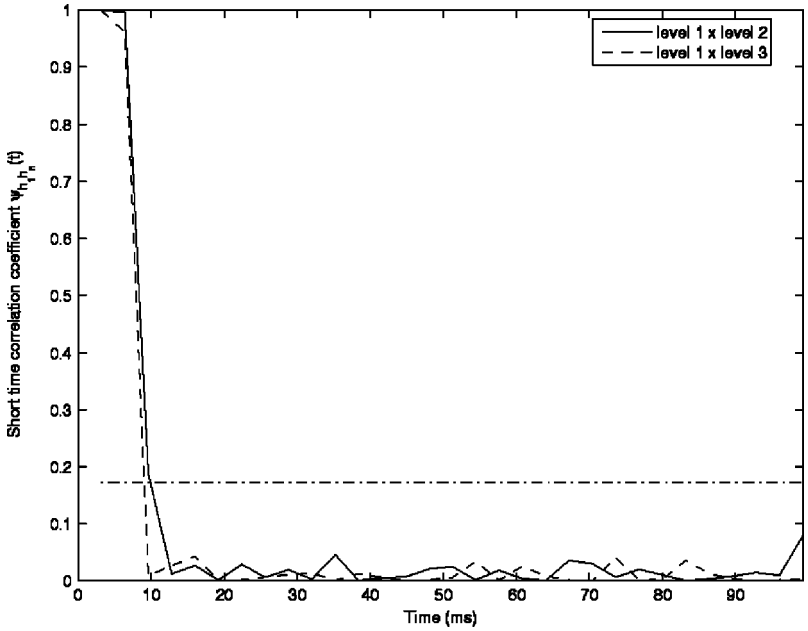

FIG. 6. Short-time correlation coefficients (STCC) for the transient response data for the IEC711 coupler. The solid line shows the STCC for the level 1 and level 2 transient responses, the dashed line the STCC for the level 1 and level 3 responses. The dot-dashed line shows the 95% confidence limits for the 128-sample window.

6.4 ms at a sampling frequency $f_s = 20\,\text{kHz}$, was chosen. This choice encompasses most of the short-latency response of the transient time series; thus, in theory, this linear section should yield an STCC of 1. In order to get better temporal resolution for the STCC, a 50% overlap on the window was used.

The STCC calculated by comparing the level 1 and level 2 responses for the passive coupler data is shown in the solid curve of Fig. 6, with the level 1 and level 3 STCC given by the dashed curve. The figure also shows the 95% confidence limit[2] on the window used. The STCC is close to unity up to about 7 ms, then rapidly decays away when the noise in the measurements becomes greater than the signals.

A. Transient-evoked otoacoustic emissions

The short-time correlation coefficients were calculated for the transient responses for the two subjects. The STCCs for the left- and right ears of subject 1 are shown in Figs. 7(a) and (b), respectively. The solid and dashed curves of Fig. 7(a) show similar results, demonstrating a strong correlation between the level 1 and 2 and level 1 and 3 TEOAE up to a latency of 25–30 ms. This can be understood by examining the averaged long-latency transient response time series, Fig. 2(a), although the different time scales of the two plots should be noted. The time series shows a maximum amplitude response around 12–14 ms; within this window one would expect the STCC to be strong. Outside of this, the TEOAE decays rapidly, leaving what appears to be noise. Figure 7(b) shows the results of the subject's right ear for which a slightly longer time series was recorded; see Fig. 2(b). The STCC for the ear exists above the 95% confidence limit up to around 40–45 ms. The two STCCs for each ear comparing the different level TEOAE time series are very

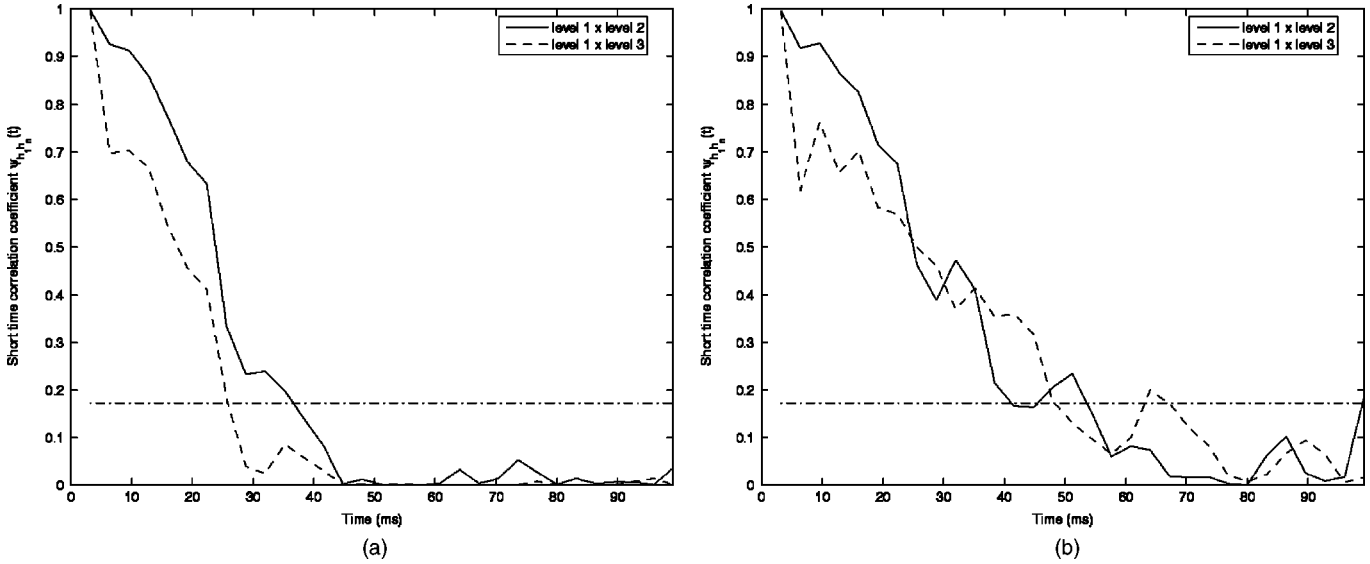

FIG. 7. STCC from the TEOAE waveforms for (a) left and (b) right ears for subject 1. The solid line shows the STCC for the level 1 and level 2 transient responses, the dashed line the STCC for the level 1 and level 3 responses. The dot-dashed line shows the 95% confidence limits for the 128-sample window.

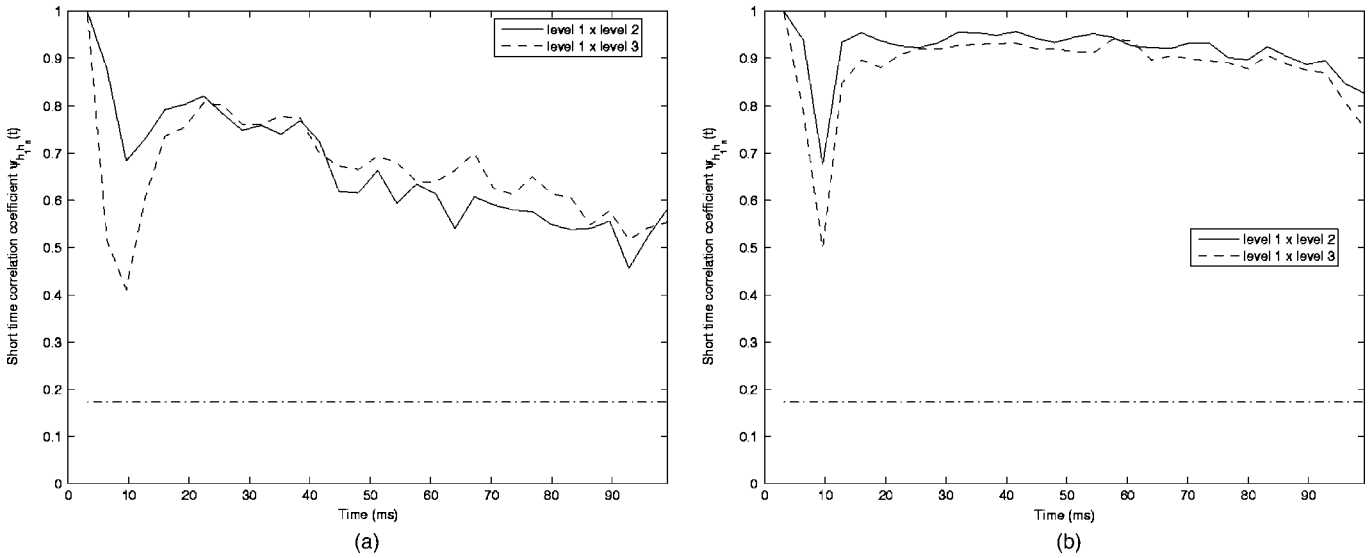

FIG. 8. STCC from the TEOAE waveforms for (a) left and (b) right ears for subject 2. The solid line shows the STCC for the level 1 and level 2 transient responses, the dashed line the STCC for the level 1 and level 3 responses. The dot-dashed line shows the 95% confidence limits for the 128-sample window.

similar. This implies that the latencies for different frequency components of the TEOAEs at high excitation levels do not in fact vary with level.

In contrast to this, the results for subject 2, shown in Figs. 3(a) and (b), appear to have strong dominant frequencies. The TEOAE has a very long response, which is also shown in the STCC for the left- and right ears, as plotted in Figs. 8(a) and (b), where the responses at different levels are strongly correlated over the whole recording window, up to 102.4 ms. Note that a dip occurs in the STCC around 10 ms, i.e., after the decay of the linear ring or short-latency TEOAE response, but before the very highly correlated long-latency region takes over in both ears. It is believed this is due to the settling time for the synchronized SOAEs to dominate the time series, i.e., the cancellation into the noise floor of the rapidly decaying linear transient response. There exist some differences in the left- and right ears of the STCC figures. In particular, the STCC for the right ear seems to remain at a constant value, while the STCC for the left ear has a slow decay.

B. Noise-evoked otoacoustic emissions

The STCCs for the calculated impulse response of subject 1, calculated from noise-evoked data, are shown in Figs. 9(a) and (b). The results are similar to those obtained from the transient OAEs, Figs. 7(a) and (b), but show a somewhat quicker decay with time.

The STCC plots for subject 2, Figs. 10(a) and (b), however, are strikingly different from those obtained from the transient OAEs, Figs. 8(a) and (b). The decay is much faster, and the long-term correlation, which was thought to be due to synchronization of the spontaneous OAEs to the averaging window by the periodic impulse train, is not present. The

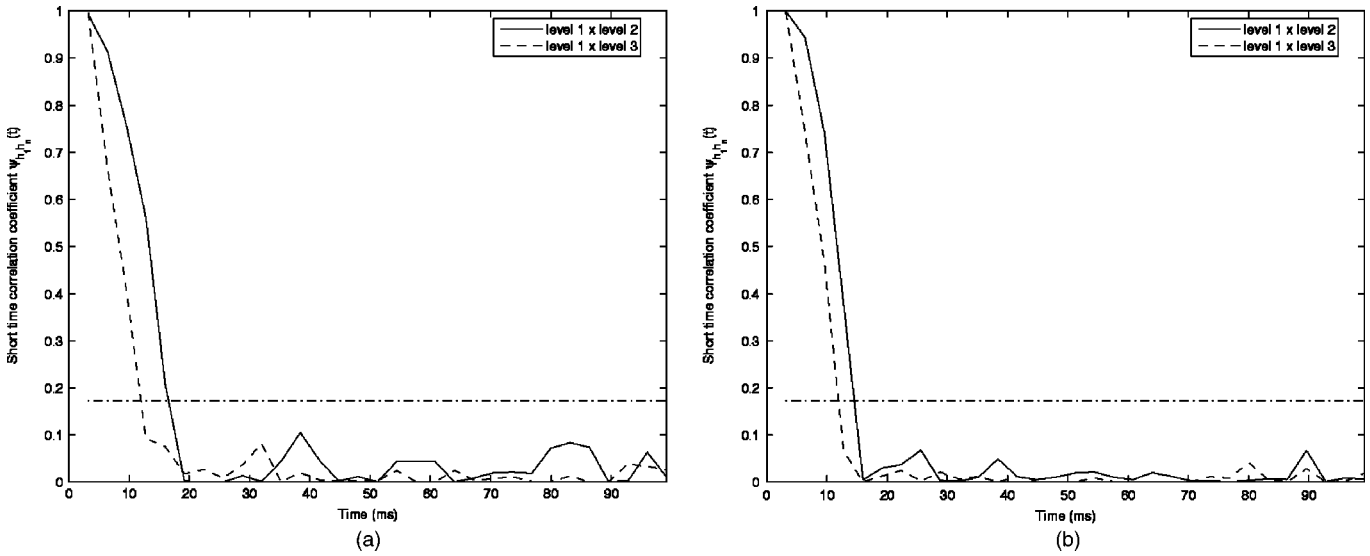

FIG. 9. STCC from the derived-NEOAE waveforms for subject 1 (a) left and (b) right ears. The solid line shows the STCC for the level 1 and level 2 transient responses, the dashed line the STCC for the level 1 and level 3 responses. The dot-dashed line shows the 95% confidence limits for the 128-sample window.

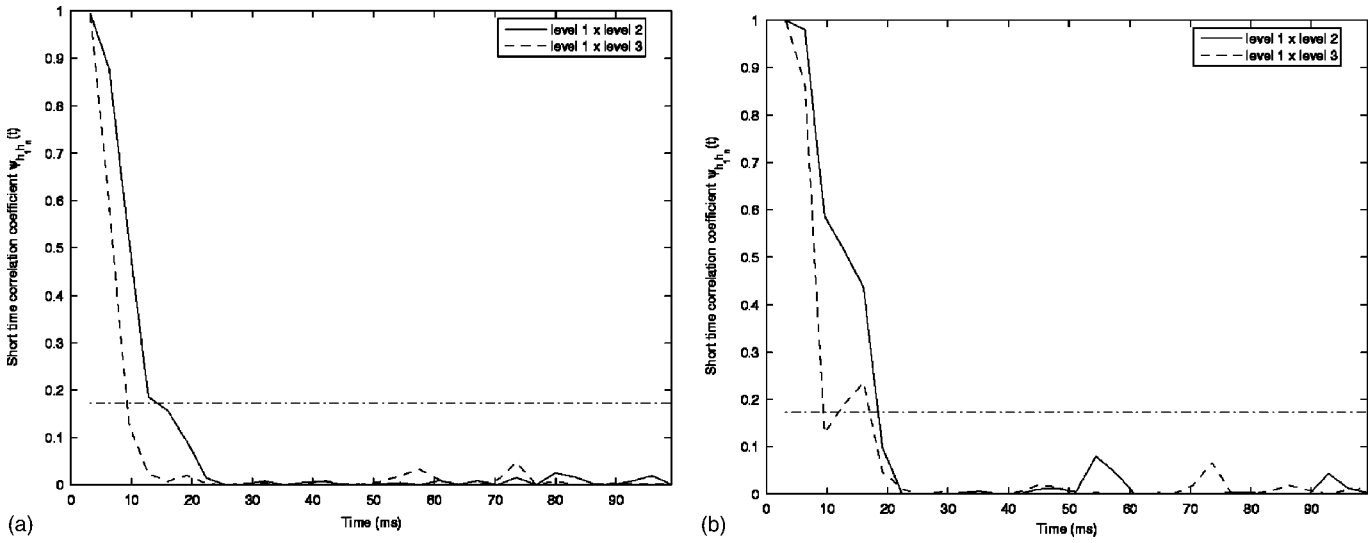

FIG. 10. STCC from the derived-NEOAE waveforms for subject 2 (a) left and (b) right ears. The solid line shows the STCC for the level 1 and level 2 transient responses, the dashed line the STCC for the level 1 and level 3 responses. The dot-dashed line shows the 95% confidence limits for the 128-sample window.

time scales over which the noise-derived responses are correlated are similar for both subjects.

If one were to compute the STCC between derived NEOAEs and TEOAEs, strong correlation would be observed for the linear short latency and the initial few milliseconds of the long-latency response. This would then drop when the SSOAE begins to dominate the TEOAE time series. This provides a quantitative measure of the similarity of both OAE time series; however, it does not demonstrate any new information over existing plots; therefore, these figures have not been included here.

VI. FREQUENCY RESPONSE FUNCTIONS FOR TEOAE AND DERIVED NEOAE

Figures 11(a) and (b) show the measured frequency response (spectrum of output divided by spectrum of input), within the band 0.7–3 kHz, of the derived long-latency response of subject 1 for both the transient- and noise-evoked OAEs at three different input levels. The transfer functions have only been shown up to 3 kHz, as above this little energy was observed in both the TEOAEs and the derived NEOAEs. This is thought to be due to discarding the first 8 ms of the time series used to obtain the transfer functions. This has the effect of potentially removing the shorter latency OAE components, and also results in a steep slope on the phase response. The magnitude of the derived long-latency frequency response is clearly a function of the input level in both cases, indicating a nonlinear response. The relationship is compressive, since the lowest excitation level produces the highest magnitude frequency response function for the long-latency response.

The calculated frequency response is not the same when measured with clicks or with noise. The sharp peak recorded in the transient excited response at about 1.91 kHz is missing from the noise response, for example. These differences are even more pronounced in other subjects in which the

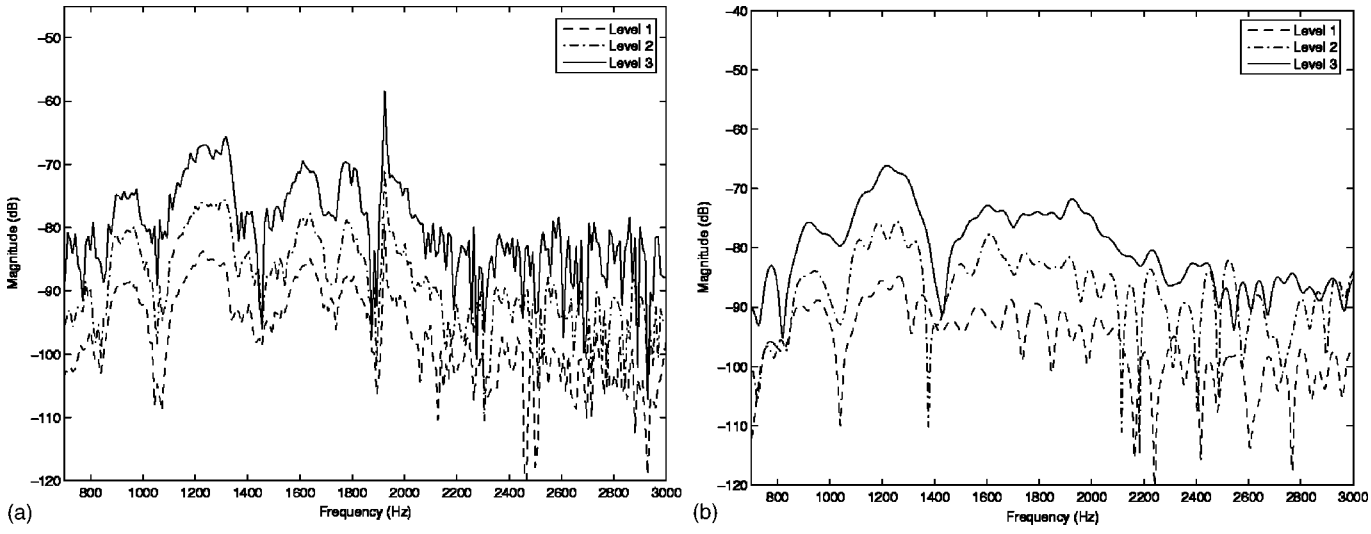

FIG. 11. Derived frequency response for the long-latency part of the transient response calculated with (a) transient and (b) noise stimuli, for the right ear of subject 1.

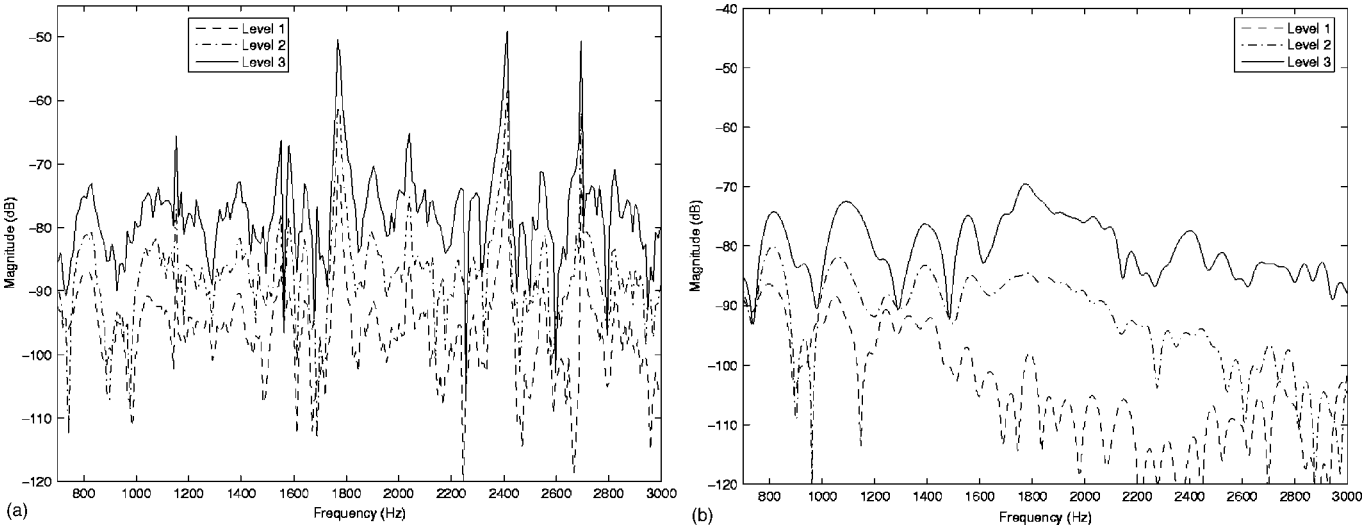

FIG. 12. Derived frequency response for the long-latency part of the transient response calculated with (a) transient and (b) noise stimuli, for the right ear of subject 2.

transient-evoked OAEs showed multiple sharp spectral lines due to the very long transient response, for example in Figs. 12(a) and (b), for the right ear of subject 2. There thus appears to be a relatively smooth, underlying frequency response to the OAE, which has similar compressive properties whether calculated from transient or noise data, but for periodic click excitation this is supplemented by narrow-band components associated with synchronized spontaneous emissions.

The fine structure in the broadband OAE component of Figs. 11(a) and (b) is similar within the frequency range examined. The derived NEOAE appears smoother; however, both spectra were obtained with the same number of samples in the time domain, hence equivalent spectral resolution. The fine structure of the broadband component at different excitation levels in Figs. 12(a) and (b) is not as easy to interpret. The derived NEOAE appear similar, omitting the SSOAE spectral peaks of the TEOAEs. At frequencies above around 1.6 kHz the magnitude for the level 1 and 2 derived NEOAE drops about 10 dB below that of the TEOAE; however, some of the broadband fine structure does remain upon closer examination.

The derived frequency response for the click stimuli also offers an interesting observation around the synchronized spontaneous otoacoustic emission (SSOAE) peaks. Namely, at frequencies lower than the SSOAE or dominant frequency there is a dip in the broadband component which is not present in the noise stimuli cases. For example, subject 1 has an SSOAE at approximately 1.91 kHz and a dip in the broadband response below this with a bandwidth of the order of 50 Hz. Thus, it appears that the presence of the SSOAE frequency somehow suppresses the underlying mechanisms more apically in the cochlea. One can speculate that this observed phenomenon is related to broader SOAE suppression. For example, Murphy *et al.* (1995a) examine the dynamic aspects of the suppression of SOAEs by pulsed external tones. They used a Van der Pol oscillator driven by an external tone as an interpretive model. Murphy *et al.* (1995b) extended their model to include a second Van der Pol oscillator acting on the first primary one. They noted that the second oscillator, in the steady state, suppressed the first oscillator. When a high enough external suppressor tone of sufficiently high frequency is added, the second oscillator is suppressed and the primary oscillator is released from suppression. This qualitatively represented observed experimental data. It is conceivable to adopt that approach here, and in light of this, it is possible to predict that applying a constant suppressor tone alongside the periodic transient stimuli should suppress the SSOAE, and the broadband response should be restored.

VII. CONCLUSIONS

A simple experiment was carried out on human subjects to record transient- and derived noise-evoked otoacoustic emissions. A passive coupler was used as a test cavity to define the short-long latency cutoff, τ_T. Sections III and IV presented the TEOAE and NEOAE results for the same two human subjects, deemed to be illustrative of the overall subject pool.

The short-time correlation coefficient (STCC) was defined to quantify the relationship between the waveforms of the TEOAEs and derived NEOAEs recorded at different excitation levels. For the two human subject cases, the STCC clearly demonstrated the differences between the two types of TEOAEs. The first subject had a TEOAE duration between 30–40 ms. The second subject, with the very strong dominant frequencies, demonstrated correlation between the responses measured at different levels that extended for the whole 102.4-ms window used in the analysis. The STCCs for the derived-NEOAE results did not exceed 15–20 ms for either subject. An important finding was that the duration of the long-latency response derived from the noise data was much shorter than that obtained using the transient excitation for subjects with a particularly long transient-evoked OAE, which was thought to be due to the absence of synchronized spontaneous OAEs. Further support for this argument is obtained from the normalized frequency response plots of the

TEOAE and derived NEOAE. The TEOAE frequency responses show sharp peaks in the magnitude, corresponding to ''dominant frequencies;'' this is lacking in the derived-NEOAE frequency response plot. A similar observation was made by Maat *et al.* (2000), who commented on their NEOAEs or first-order polynomial correlations functions not displaying the very long ''synchronized'' response of the TEOAE results.

It appears that the periodic click excitation and synchronous averaging commonly used to measure the TEOAE can synchronize long-term and potentially spontaneous OAEs for these subjects and artificially extend the measured transient response. The random nature of the noise stimulus does not excite the cochlea in the same way, and these long oscillations are not observed. Conventional TEOAEs thus measure a combination of two conceptually different processes: synchronized spontaneous OAEs and evoked OAEs, while NEOAEs measure just the evoked response. The difference in these processes is believed by the authors to lie in the active mechanism responsible for the cochlear compressive nonlinearity. The specific form this mechanism takes is still open to debate, though it is often thought of as a series of tuned oscillators with some form of positive feedback or energy source (Duke and Jülicher, 2003). The evoked OAE is believed to occur by the normal compressive response and impedance mismatch reflection along the BM length (Kemp and Knight, 2000). The fluctuation and fine structure of the broadband response are caused by local changes in the impedance and potentially the tuned oscillator properties. The SSOAEs occur when one of the tuned oscillators is poised too close to instability (Eguíluz *et al.*, 2000) or is conditionally unstable, and its response can be easily synchronized to an external stimulus (Nayfeh and Mook, 1995).

It is believed that the random nature of the eliciting stimulus for NEOAEs prevents the synchronization observed for periodic click stimuli. By recording TEOAEs with irregular or randomly spaced click stimuli, the synchronous ringing seen in normal TEOAE recording could potentially be disrupted.

ACKNOWLEDGMENTS

This work was jointly funded under the EPSRC doctoral training scheme and a Marie Curie Research Fellowship via the European Doctorate in Sound and Vibration Studies. The authors would also like to thank Mark Lutman for his helpful comments.

[1]Where $\sigma_{x_n} = \sqrt{\sum_{m=1}^{M} x(m)_n^2 / M}$, and M is the total number of samples.

[2]The 95% confidence limit ($\approx$3 standard deviations) is given by $\lambda_{95} = 1.95/\sqrt{N}$, where N is the number of samples in the estimate. See Billings and Zhu (1994).

Bendat, J. S., and Piersol, A. G. (**1966**). *Measurement and Analysis of Random Data* (Wiley, New York).

Billings, S. A., and Zhu, Q. M. (**1994**). ''Nonlinear model validation using correlation tests,'' Int. J. Control **60**, 1107–1120.

de Boer, E., and de Jongh, H. R. (**1978**). ''On cochlear encoding: Potentialities and limitations of the reverse-correlation technique,'' J. Acoust. Soc. Am. **64**, 1386–1391.

Duke, T., and Jülicher, F. (**2003**). ''Active traveling wave in the cochlea,'' Phys. Rev. Lett. **90**, 158101–158101.

Eguíluz, V. M., Ospeck, M., Chose, Y., Hudspeth, A. J., and Magnasco, M. O. (**2000**). ''Essential nonlinearities in hearing,'' Phys. Rev. Lett. **84**, 5232–5235.

EN ISO 389-2 ((**1997**)), ''Acoustics—Reference zero for the calibration of audiometric equipment. Part 2. Reference equivalent threshold sound-pressure levels for pure tone and insert earphones,'' British Standards Institute.

Gold, T. (**1948**). ''Hearing. II. The physical basis of the action of the cochlea,'' Proc. R. Soc. London, Ser. B **135**, 492–498.

Harte, J. M. (**2004**). ''Nonlinear identification for otoacoustic emissions,'' University of Southampton, Institute of Sound and Vibration Research, Ph.D. thesis.

Kemp, D. T. (**1978**). ''Stimulated acoustic emissions from within the human auditory system,'' J. Acoust. Soc. Am. **64**, 1386–1391.

Kemp, D. T., and Knight, R. D. (**2000**). ''Indications of different DPOAE mechanisms from a detailed f_1, f_2 area study,'' J. Acoust. Soc. Am. **107**, 457–473.

Konrad-Martin, D., and Keefe, D. H. (**2003**). ''Time-frequency analysis of transient-evoked stimulus-frequency and distortion-product otoacoustic emissions: Testing cochlear model predictions,'' J. Acoust. Soc. Am. **114**, 2021–2043.

Maat, B., van Dijk, P., and Wit, H. P. (**1994**). ''Noise Evoked Otoacoustic Emissions; Just Another Way of Measuring?,'' in *Advances in Otoacoustic Emissions—Vol II—Recording Techniques for Otoacoustic Emissions*, edited by A. R. D. Thornton and F. Grandori (Casa Editrice Stefanoni, Lecco).

Maat, B., Wit, H. P., and van Dijk, P. (**2000**). ''Noise-evoked otoacoustic emissions in humans,'' J. Acoust. Soc. Am. **108**, 2272–2280.

Mood, A. M., Graybill, F. A., and Boes, D. C. (**1974**). *Introduction to the Theory of Statistics* (McGraw-Hill International Editions, New York).

Murphy, W. J., Tubis, A., Talmadge, C. L., and Long, G. R. (**1995a**). ''Relaxation dynamics of spontaneous otoacoustic emissions perturbed by external tones. I. Response to pulsed single-tone suppressors,'' J. Acoust. Soc. Am. **97**, 3702–3710.

Murphy, W. J., Tubis, A., Talmadge, C. L., and Long, G. R. (**1995b**). ''Relaxation dynamics of spontaneous otoacoustic emissions perturbed by external tones. II. Suppression of interacting emissions,'' J. Acoust. Soc. Am. **97**, 3711–3720.

Nayfeh, A. H., and Mook, D. T. (**1995**). *Nonlinear Oscillations* (Wiley, New York).

Probst, R., Lonsbury-Martin, B. L., and Martin, G. K. (**1991**). ''A review of otoacoustic emissions,'' J. Acoust. Soc. Am. **89**, 2027–2067.

Probst, R., Coats, A. C., Martin, G. K., and Lonsbury-Martin, B. L. (**1986**). ''Spontaneous, click-, and toneburst-evoked otoacoustic emissions from normal ears,'' Hear. Res. **21**, 261–275.

Randall, R. B. (**1987**). *Frequency Analysis* (Bruel & Kjaer, Copenhagen).

Wilson, J. P. (**1980**). ''Evidence for a cochlear origin for acoustic re-emissions, threshold fine structure and tonal tinnitus,'' Hear. Res. **2**, 233–252.

Wit, H. P., and Ritsma, R. J. (**1979**). ''Stimulated acoustic emissions from the human ear,'' J. Acoust. Soc. Am. **66**, 911–913.

Zwicker, E. (**1983**). ''Delayed evoked oto-acoustic emissions and their suppression by Gaussian-shaped pressure impulses,'' Hear. Res. **11**, 359–371.

Two-tone distortion in intracochlear pressure

Wei Dong[a] and Elizabeth S. Olson
Columbia University, Department of Otolaryngology, Head and Neck Surgery, P & S 11-452, 630 W. 168th Street, New York, New York 10032

(Received 2 December 2004; revised 4 February 2005; accepted 4 February 2005)

Two-tone distortion was measured in the intracochlear pressure in the base of the gerbil cochlea, close to the sensory tissue, where the local motions and forces of the organ of Corti can be detected. The measurements probe both the underlying nonlinear process that generates two-tone distortion, and the filtering and spreading of the distortion products. Some of our findings are as follows: (1) The observations were consistent with previous observations of two-tone distortion in BM motion [J. Neurophysiol. **77**, 2385–2399 (1997); J. Neurophysiol. **78**, 261–270 (1997)]. (2) Frequency sweeps show distortion product tuning and phase-versus-frequency behavior that is similar, but not identical, to single tone tuning. (3) The decay of distortion products with distance from the basilar membrane confirms the feasibility that they could drive the stapes by a direct fluid route, as proposed by Ren [Nat. Neurosci. **7**, 333–334 (2004)]. (4) The phases of the distortion products within a single family (the group of distortion products generated by a single primary pair) in some cases alternated between 0° and 180° when referenced to the phases of the primaries. This behavior is predicted by a simple compressive nonlinearity.
[DOI: 10.1121/1.1880812]

PACS numbers: 43.64.Kc, 43.64.Bt [BLM] Pages: 2999–3015

I. INTRODUCTION

Normal cochlear operation relies upon cell-based forces that greatly boost the cochlea's response at low-to-moderate stimulus levels. The cell-based forces are not linearly related to the stimulus and they introduce distortion into the cochlear response (reviewed in Ruggero, 1993). The response to a two-tone stimulus, in addition to the primary stimulus frequencies, contains frequency components at $f_1-n(f_2-f_1)$ and $f_2+n(f_2-f_1)$, where n is a positive integer. Other frequencies are also present in the response, but the f_1-, $f_2+n(f_2-f_1)$ components form a prominent family of distortion components (distortion products, or DPs) that flank the primaries. Two-tone distortion has been measured and studied at many levels of the auditory system: perceptual (e.g., Goldstein, 1967; Zurek and Sachs, 1979), neural (e.g., Kim *et al.*, 1980), in auditory emissions (e.g., Kemp, 1978; Probst *et al.*, 1991) and in basilar membrane (BM) motion (Robles *et al.*, 1997; Cooper and Rhode, 1997). Two-tone distortion in intracochlear pressure was measured close to the cochlear wall by Magnan *et al.* (1997) and Avan *et al.* (1998).

For a given two-tone combination, the distortion is produced within the region of the organ of Corti (OC) where the responses to the two tones overlap (Smoorenburg, 1972; Kim *et al.*, 1980; Siegel *et al.*, 1982; Robles *et al.*, 1997). The DPs, once present, will be filtered by the cochlea's mechanics. Therefore, the local response at a particular DP frequency has been shaped by three processes: the cochlear-mechanical filtering of the primaries, the distortion generation process, and finally the cochlear–mechanical filtering of the DP.

This contribution examines two-tone distortion in the intracochlear pressure close to the BM. Measurements were made at a region that is tuned to ~20 kHz, in turn one of the gerbil cochlea. The experimental design and analysis were guided by two basic objectives: to better understand the underlying nonlinear process that generates the distortion, and to describe the spreading and filtering of the distortion products following their generation. Both these objectives were served with a stimulus protocol in which either f_2, f_1 or $2f_1-f_2$ were set at the BF of our sensor recording position. The localization of the generation process, and the longitudinal propagation of DPs were explored by measuring how the $2f_1-f_2$ and $2f_2-f_1$ DPs varied with the primary ratio and level. Vertical spreading was explored by measuring the decay of these DPs with the distance from the BM towards the cochlear wall. A second stimulus protocol, detailed frequency sweeps with a low f_2/f_1 ratio, was used to measure the filtering of DPs. Finally, the nonlinear process underlying distortion generation was explored by analyzing the relative phases and magnitudes of components within DP families.

The pressure close to the BM is closely akin to BM motion. More concretely, fluid pressure gradients (spatial derivatives) are approximately proportional to fluid acceleration, and close to the BM, the fluid and BM are expected to move together. With single-tone stimuli, Olson (2001) used fluid pressure differences to derive BM velocity. The frequency tuning of the BM motion and of the fluid pressure close to the BM were similar to each other in the region of the BF peak and similar to BM motion tuning measured by others (reviewed in Robles and Ruggero, 2001). In line with this, the two-tone pressure responses measured close to the BM were similar to two-tone responses observed in BM motion (Robles *et al.*, 1997; Cooper and Rhode, 1997). BM motion is closer than cochlear pressure to stereocilia motion, and BM motion measurements are more valuable than pressure measurements in that respect. However, measurements

[a]Electronic mail: wd2015@columbia.edu, eao2004@columbia.edu

of pressure complement those of motion, and are able to probe particular aspects of cochlear mechanics that are not accessible with measurements of sensory tissue motion. For example, the spatial variation of DP pressure within the cochlea is useful for exploring how DPs get out of the cochlea to give rise to cochlear emissions, and the analysis of families of pressure DPs is useful for understanding the nonlinear force.

Several theoretical studies have explored the properties of the two-tone DPs that arise from a compressive nonlinearity [Engebretson and Eldredge, 1968; Fahey, 1989; Fahey *et al.*, 2000; the series by Lukashkin *et al.* (1998, 1999, 2002)]. Similarly, in this contribution a simple nonlinear model is used to better understand the intracochlear distortion we measure.

Although we do not report here on cochlear emissions, the studies here are related to the study of emissions. Several direct experimental examinations of the link between emitted and introcochlear two-tone DPs (measured in intracochlear pressure or sensory tissue motion) have been performed (Magnan *et al.*, 1997; Naryanan *et al.*, 1998; Avan *et al.*, 1998; Cooper and Shera, 2004; Ren, 2004).

II. METHODS

A brief description of methods is here; details have been published (Olson, 1998, 2001).

A. Animal

The measurements were made in gerbils stimulated with one or two tones via a speaker coupled to the ear canal. Intracochlear pressure was measured by inserting specialized pressure sensors into the cochlear scalae through small holes that were hand-drilled through the bony wall of the cochlea. Pressure measurements in the scala tympani (ST) were made in the first turn of the cochlea where the BF was approximately 20 kHz. In ST the pressure was measured at a series of distances from the BM. The pressure in the scala vestibuli (SV) just next to the stapes was measured, either simultaneously with the ST measurement or after most of the ST data had been collected.

The animal was deeply anesthetized throughout the experiment and overdosed with anesthetic at the end of it. A tracheotomy was performed to maintain a patent airway. The animal core temperature was maintained at $\sim 37\,^{\circ}\mathrm{C}$ using a thermostatically controlled heating blanket. An electrode at the round window measured the compound action potential (CAP) response of the auditory nerve to tone pips, as a monitor of cochlear health (Johnstone *et al.*, 1979). The care and use of the animals were approved by the Institutional Animal Care and Use Committee of Columbia University.

B. Sensor

The pressure sensor consists of a glass capillary with inner and outer diameters 100 and 170 μm, tipped with a gold-coated polymer diaphragm. Light from a light-emitting diode is delivered via a fiber optic threaded into the capillary, and reflects from the diaphragm. The amount of light returning to the fiber optic for transmission to a photodetector varies linearly with the pressure-induced motion of the diaphragm (Hu *et al.*, 1992). As has been described previously, the sensors are calibrated individually by submerging them a known distance beneath the surface of a vial of water that is shaken with a known acceleration (Bruel and Kjaer model 4290). This produces a known pressure at the position of the sensor. The sensitivity of the sensors is approximately flat (within 3 or 4 dB) up to at least 40 kHz. The sensor sensitivity is usually ~ -30 dB V/80 dB SPL, but it varies between usable sensors from ~ -20 to -40 dB V/80 dB SPL. The noise level is set by shot noise in the photodetector at a level of ~ -60 dB V; it depends on the quantity of light returning to the photodetector and also varies slightly with different sensors. In some cases the sensor stability was good with very little before/after experiment change, but changes of 6–10 dB were also common. The changes are due to the fragility and vulnerability of the sensitive membrane. The sensitivity changes are frequency independent—the sensitivity remains flat with frequency, just at a different level.

The presence of the sensor close to the BM might perturb cochlear mechanics. In Olson (2001) the perturbation was shown to be small but sometimes measurable, by producing small changes in the CAP response.

Sensor positioning in ST can influence the measurements. The sensor was aimed to face the basilar membrane based on extracochlear landmarks and the degree of actual centering varies among experiments.

Based on our evaluation, the sensors operate linearly and do not introduce distortion. The stiffness of the sensor in theory is primarily due to the stiffness of the air gap between the membrane and optic fiber, with a value of $\sim 1-2$ Pa/nm (Olson, 1998). This stiffness is linear. Another stiffness, of similar size (theoretically slightly smaller) as the air gap stiffness, is the bending stiffness of the membrane. When driving at 80 dB SPL, the intracochlear pressure is ~ 110 dB, corresponding to ~ 6 Pa. This would produce $\sim 3-6$ nm motion of the sensitive membrane. The thickness of the membrane is $\sim 1\,\mu$m, so the motion is a small fraction ($\sim 0.5\%$) of the membrane thickness. At extremely high stimulus levels (large enough to produce intracochlear pressures of 130 dB and above) the motion will be large enough that the membrane's stiffness might begin to become nonlinear. [This nonlinearity is due to the geometry, not stretching the membrane material beyond its elastic limit (Timoshenko, 1959; Gummer *et al.*, 1981).] Several observations rule out the membrane as producing the distortion measured here: (1) DPs could be measured even when one of the primaries was very small (which happened when a primary was nulled due to a slow-wave, fast-wave cancellation); (2) the size of the DPs decreased with the distance from the BM even when the primaries were in the fast-wave frequency region and did not decrease with distance; (3) in general, the DPs were larger close to the sensory tissue in the ST than they were in the SV, even when the primaries were of similar size in the two scalae. Figure 1 illustrates point (3). It shows the response in SV to two equal-intensity tones of 80 dB SPL in the ear canal. Any distortion is beneath the noise level, which is 60 dB beneath the level of the two tones. This specific case was taken from a cochlea that was not in excellent condition

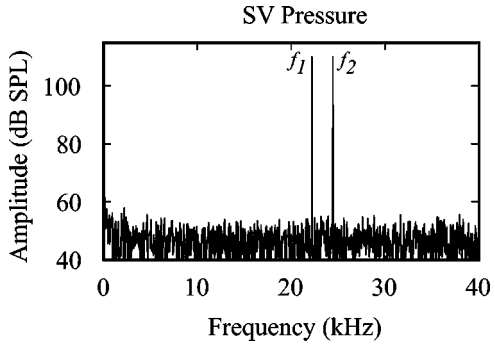

FIG. 1. Absence of system distortion. These data show the SV pressure response measured next to the stapes with two equal-intensity tones of 80 dB SPL delivered to the ear canal ($f_1=22.2$ kHz, $f_2=24.5$ kHz, $f_2/f_1=1.1$). This specific case was a cochlea (E2) that was not in excellent condition and these data do not reflect a general lack of measurable distortion in SV. The purpose of the figure is to illustrate the lack of mechanical distortion in the sensor and sound system.

(based on the degree of compression in the single-tone responses and CAP thresholds) and these data do not reflect a general lack of measurable distortion in SV. The purpose of Fig. 1 is to illustrate the lack of mechanical distortion in the sensor and sound system.

C. Stimuli

Stimuli were single or two pure tones, 1–2 seconds in duration. Stimulation levels refer to the sound pressure level of each tone in the ear canal. Two-tone stimuli were generated digitally (TDT system II or III) and delivered via a closed system by a single Radio Shack tweeter. Two-tone DPs measured in a cavity were at least 70 dB less than the primaries when the primary level was 100 dB SPL.

The frequencies of the two tones were either swept from low to high with a fixed ratio, or were set so that f_1, f_2 or $2f_1-f_2$ was equal to the BF at the recording position, at different ratios. Figure 2 illustrates the stimulus pattern on the BM, showing a cartoon of a two-tone excitation pattern for a stimulus level of 50 dB SPL. The $2f_1-f_2=$BF condition is shown in the left panel, the $f_1=$BF condition in the middle and the $f_2=$BF condition on the right. Upper panels illustrate a small f_2/f_1 ratio (1.05), the lower panels a relatively large ratio (1.25). When the ratio is small, there is almost a complete overlap of the response to the two primary tones, and a substantial overlap of the DPs as well. At the ratio of 1.25, which is the highest ratio used, the overlap is much less. The basal overlapping region will be broader at higher stimulus levels. For example, Kim *et al.*'s (1980) Fig. 2 indicates a large degree of basal overlap at levels of 64 and 74 dB SPL.

D. Analytical methods

The pressure responses were time averaged and analyzed via Fourier transform offline using MATLAB.

A discussion of phase requires a suitable reference phase. For single-tone measurements, the phase reference is typically the phase of the stimulus: of stapes motion, or ear canal pressure or SV pressure close to the stapes, for example. However, the DP frequencies are not present in the stimulus and such a convenient reference does not exist. In many two-tone studies the stimulus is set so that the primary phases both$=0°$ in the ear canal, and then the phase reference can be taken to be $0°$. In our studies we either reference the DPs to the SV pressure measured near the stapes or to the local ST pressure. These primary phases generally are not $0°$. In order to find a suitable reference phase for each DP

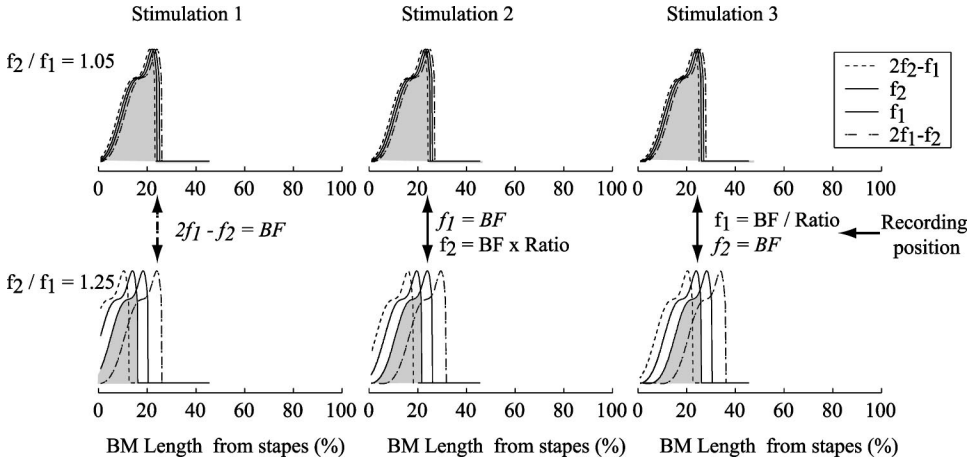

FIG. 2. Cartoon of a two-tone excitation pattern for frequencies around BF. A cartoon of the responses to single tones of frequency f_1, f_2 and two distortion component frequencies gives an idea of the degree of overlap of these excitation patterns, and their longitudinal position relative to the recording position. The patterns are shown for two different f_2/f_1 ratios. The excitation patterns of f_1 and f_2 are shown as solid lines, of $2f_1-f_2$ and $2f_2-f_1$ as dotted lines. The $2f_1-f_2=$BF condition is shown in the left panel, the $f_1=$BF in the middle and the $f_2=$BF condition on the right. Upper panels illustrate a small f_2/f_1 ratio (1.05), the lower panels a relatively large ratio (1.25). [Regarding the construction of the cartoon: The excitation patterns are based on single-tone frequency sweep data at a stimulus level of 50 dB SPL from animal W43, after smoothing and eliminating the fast-wave plateau. To transform the frequency response to a spatial excitation pattern we used the assumption (scaling symmetry) that the tuning Q of the BM is similar at different frequencies. We then generated a family of responses, with each member peaking at a different frequency and corresponding to a different longitudinal location along the cochlea. The longitudinal locations were determined using the place-frequency map of the gerbil cochlea (Muller, 1996). The family of response curves was used to read off the response to a single frequency at different longitudinal locations, generating the plot of response versus position, the "excitation pattern" of the response. This is a standard transformation used in cochlear models, e.g. Geisler and Cai (1996).]

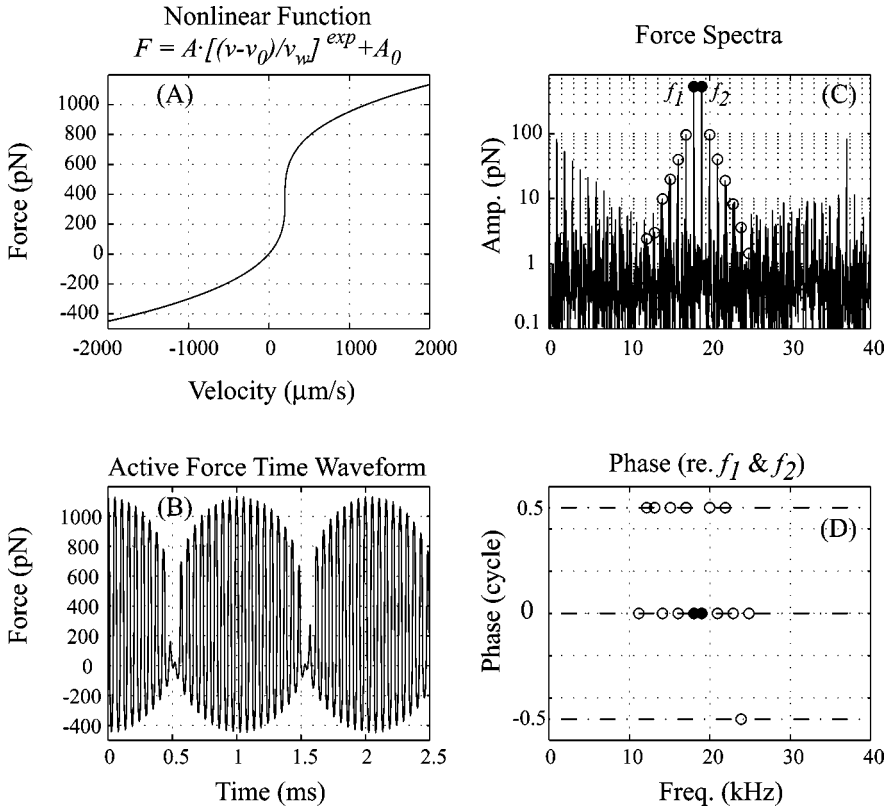

FIG. 3. Characteristics of two-tone distortion components produced by a simple compressive nonlinearity. (a) The nonlinear function is a simple compressive nonlinearity, offset to increase its generality and be more similar to OHC input–output curves (Kros *et al.*, 1995). For illustrative purposes, the nonlinearity takes velocity as an input and outputs force, but these specific inputs and outputs are not important to the general results. The parameters used in the nonlinear function are exp=1/3, $A=63$ pN, $v_w=1$ μm/s, $v_0=200$ μm/s and $A_0=370$ pN. (b) The output of the nonlinearity in the time domain for a two-tone input with amplitudes $L_1=L_2=1000$ μm/s. (c) The same output in a frequency domain amplitude plot shows the characteristic stair–step response. The two-tone distortion products at frequencies $f_1+n(f_2-f_1)$ (n an integer) are circled. (d) The frequency domain phases of the two-tone distortion products $f_1+n(f_2-f_1)$ referred to the phases of the output at the primary frequencies in the combination $\phi_1+n(\phi_2-\phi_1)$. The phases, so referenced, are always 0° or 180° (i.e., 0 or 0.5 cycle.) Note that −0.5 and 0.5 cycle are the same phase.

we use some basic rules about nonlinear system responses. A brief mathematical interlude follows, which provides a background for understanding the phase reference.

The instantaneous nonlinear system response of an input signal of the form $[A\cos(a)+B\cos(b)]$, where a and b have the form $\omega t+\phi$, (a, b=phases, ω=radial frequency, ϕ=phase offset), will output a waveform composed of components whose phases are combinations of the input phases. The particular combinations can be found by first expanding the nonlinear process in a power series. After the input signal is processed by the nonlinearity, the resultant output series is again expanded using cosine rules (Duifhuis, 1989). Following these two expansions a nonlinear process might be found to produce a component with a phase of, for example, $2a-b$. The frequency of this component is $2\omega_a-\omega_b$ and the phase offset is $2\phi_a-\phi_b$. The nonlinearity will produce DPs whose phase offsets, when referenced to the primary phase offsets in the same combination as the combination of primary frequencies in the DP frequency, are 0° (or 180° to allow for interpreting a DP coefficient with a negative sign via phase). (Usually the ''phase offset'' is referred to as the ''phase,'' and this convention is followed in the rest of the paper.) More discussion along these lines is in Weiss and Leong (1985), who analyzed the harmonic output of a compressive nonlinearity when the input was a pure tone.

Because this concept is important to the analysis of our data, we illustrate it with a simple model. Figure 3 shows the family of DPs produced by running a two-tone stimulus through an instantaneous compressive nonlinearity. The nonlinearity was conceived as a BM velocity-to-OHC force transducer, based on the results that in a macromechanical sense the active force has the character of a (negative) resistance (Kolston, 2000; de Boer and Nuttall, 2000; Shera, 2001), at least at frequencies close to the peak [Fig. 3(a)]. However, this aspect of the nonlinearity is not critical; the important aspect is that an input (which could be anything—displacement, velocity, current, voltage, etc.) gives rise to an instantaneous output (force, displacement, voltage, etc.) that scales compressively with the input. The functional form of the nonlinearity we use in our model is included in the figure. The output of the nonlinearity for a two-tone $L_1=L_2$ input is shown in Fig. 3(b) (time domain) and 3(c) (frequency domain amplitudes). In Fig. 3(d), the frequency domain phases of the DPs are plotted. The phases were referred to the phases of the output at the primary frequencies, in the combination as described above. (For example, the phase of the DP at the frequency of $3f_1-4f_2$ was referenced to the phase $3\phi_1-4\phi_2$.) The amplitude of the DP family forms a symmetric stair–step response. The phases are either 0° or 180° (0 or ±0.5 cycles) and in general the phase alternates

between these two values. The precise functional form of the nonlinearity is not critical to these aspects of the output. For example, nonlinearities that more closely mimic the measured form of the OHC displacement-current transducer, or are steeper or shallower functions, give similar results. On the other hand, the pattern is not absolute: offsets in the nonlinear function can produce changes, for example, single DPs might be greatly reduced. Sometimes the neat alternation between 0° and 180° falters, as observed in Fig. 3. We will see the stair–step DPs in many of our results, similar to the distortion families shown in Robles *et al.* (1997). More complicated distortion families are typically seen in cochlear emissions (Kemp and Brown, 1983), likely because the whole cochlea participates in generating and propagating those. When L_1 or L_2 is increased in value, predictable changes in the stair–step pattern occur, based on the simple nonlinear system response (Engebretson and Eldredge, 1968; Fahey *et al.*, 2000). Most notably, an increase in L_2 is expected to cause decreases in the low-side DPs, and an increases in L_1 is expected to cause decreases in the high-side DPs. The size of the low-side DPs as L_1 becomes greater than L_2, and of the high-side DPs as L_2 becomes greater than L_1 can be an increase or a decrease, depending on the particular L_1, L_2 sizes with respect to the parameters of the nonlinearity. Offsets of the nonlinearity can lead to level-dependent notches (Fahey *et al.*, 2000; Lukashkin *et al.*, 2002).

In our experiment the input of the nonlinearity (perhaps stereocilia displacement?) is not accessible, and instead we use either the primary members of the local ST pressure DP family, or the SV primary pressures (measured near the stapes) to construct the reference. It is useful to consider these references: Define Φ_{dt} and Φ_{dv} as the phase of a DP measured in the ST pressure close to the BM and referenced to ST or SV pressure primaries. The DP will have frequency $f_1+n(f_2-f_1)$, where n is a positive or negative integer. ($n=$ the DP number, except $n=0$, $n=1$ correspond not to the DPs but the primaries and $n=2$ is the first high-side DP, $2f_2-f_1$. $n=-1$ is the first low-side DP, $2f_1-f_2$.) The referenced phase of each DP is found as

$$\Phi_{dt\_n}=\phi_{dt\_n}-\{\phi_{t1}+n(\phi_{t2}-\phi_{t1})\} \quad \text{(ST reference)}, \quad (1)$$

$$\Phi_{dv\_n}=\phi_{dt\_n}-\{\phi_{v1}+n(\phi_{v2}-\phi_{v1})\} \quad \text{(SV reference)}. \quad (2)$$

(ϕ_{dt_n} is the phase of the DP of number n measured close to the sensory tissue in ST, ϕ_{t1} and ϕ_{t2} are the phases of ST primaries 1 and 2, and ϕ_{v1} and ϕ_{v2} are the phases of SV primaries 1 and 2.)

The distortion referenced to the SV pressure at the stapes can be rewritten in terms of Φ_{dt}:

$$\Phi_{dv\_n}=\Phi_{dt\_n}+(\phi_{t1}-\phi_{v1})+n\{(\phi_{t2}-\phi_{v2})-(\phi_{t1}-\phi_{v1})\}. \quad (3)$$

The third term, $n\{(\phi_{t2}-\phi_{v2})-(\phi_{t1}-\phi_{v1})\}$, is equal to n times the difference in the traveling wave phase of the two primaries. This difference will be small for a low primary ratio, and in that case the third term will be small. Then the first two terms of the expression, $\Phi_{dv\_n}=\Phi_{dt\_n}+(\phi_{t1}-\phi_{v1})$, show that the phase of the distortion referenced to the SV phase can be interpreted as the phase of the distortion referenced to ST phase plus the single-tone traveling wave phase $(\phi_{t1}-\phi_{v1})$. The phase of the distortion referenced to ST phase will reflect the relationship between the ST pressure and the nonlinear force and will be influenced by whether the measured distortion was locally generated, or traveled from a more apical or basal location. What the data reveal about these relationships will be discussed below.

III. RESULTS AND DISCUSSION

Results from five animals (W34, W43, W45, E1 and W48) are shown in this contribution, and others showed similar results. In the experiments reported here the intracochlear pressure responses to pure tones in ST close to the BM were compressively nonlinear at frequencies close to the BF and the responses remained stable for several hours. The two-tone data from these preparations were consistent with each other, although not every dimension of the measurement (frequency sweep, variation with distance from BM, etc.) was made in every animal. The CAP thresholds of these animals were healthy following the initial surgery: ~30–40 dB SPL at 20 kHz, ~20–30 dB SPL at the most sensitive frequencies (~1–16 kHz) and increasing steeply for frequencies above 30 kHz. The shape of this CAP threshold tuning curve is similar to the behavioral threshold curve for a gerbil (Ryan, 1976) but elevated by ~20 dB, likely due to the different categories of measurement (Muller, 1996). Making the holes to the cochlea is the most invasive and potentially damaging step of the procedure and the experiments reported here were selected because this step was accomplished without substantial CAP threshold elevation. In several animals in order to minimize early damage the SV hole was not made until after most of the ST data had been collected. Then the SV hole was made and SV pressure close to the stapes measured, primarily to provide a phase reference. Thresholds in W43 and W48 were elevated by 5 dB at frequencies around 20 kHz after making the ST hole, and in W48 were elevated by 30 dB after several hours of experimentation with both ST and SV holes. Thresholds in E1 were elevated by 15 dB at frequencies around 20 kHz after making the ST and SV holes. Thresholds in W45 were not available after making the ST hole due to failure of the CAP electrode, but the single tone responses remained compressively nonlinear throughout the experiment.

A. Observations on single-tone responses

The responses to single-tone stimuli are described briefly below. These responses preface our description of two-tone responses by providing a review of the basic pressure response in healthy cochleae. Intracochlear pressure responses to single-tone stimuli are described in more detail in Olson (1998, 1999, 2001).

Figure 4(a) shows the spatial variations in the ST pressure close to the BM in response to 50 dB SPL stimuli (Animal W43). Spatial pressure variations are proportional to fluid acceleration. At frequencies close to the pressure peak,

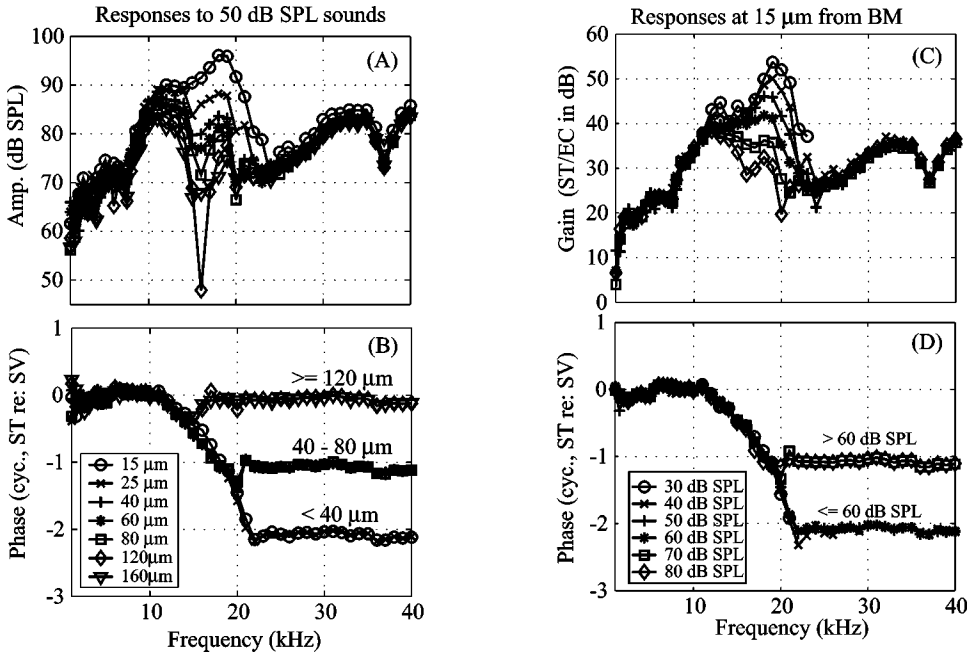

FIG. 4. Single-tone tuning characteristics in ST in the first turn of the gerbil cochlea (W43). (a), (b) ST pressure amplitude and phase (relative to the pressure in SV close to the stapes) with a stimulus level in the ear canal of 50 dB SPL, measured over the range of distances from the BM indicated in the legend. Spatial pressure variations indicate fluid motion. (c) (d) ST pressure measured 15 μm from the BM, with the stimulus level varying from 30 to 80 dB SPL in the ear canal. Pressure amplitude gain (ST pressure/ear canal pressure, expressed in dB) and phase relative to the SV pressure. The greatest total phase change in the pressure is roughly two cycles due to the domination of the fast-wave pressure at frequencies somewhat above the peak. The legend indicates the sound pressure levels in the ear canal. The pressure scales nonlinearly with stimulus level in the region of the peak.

the large spatial variations in pressure (from one curve to the next) reflect the large fluid (and therefore BM) motions at these frequencies. At frequencies below the peak the pressure comes down, and the spatial variations are small. The large pressure value above the peak is due to the cochlear fast wave, and the very small spatial variations at frequencies above the peak reflect the small motions at those frequencies. As a brief review of the fast wave: when the stapes plunges in and out of the cochlea, the pressure difference in cochlear fluid between ST and SV vibrates the OC. The OC responds elastically, initiating the cochlear traveling wave—the ''slow wave.'' Because of the compressibility of the fluid, the excitation of the cochlea by the stapes also gives rise to a (much smaller) compressional fluid motion—a sound wave, known as the ''fast-wave.'' Peterson and Bogart (1950) discussed the fast and slow waves quantitatively in a one-dimensional (1-D) cochlear model. 2-D and 3-D models show that evanescent modes are also present. The evanescent modes are like the fast wave in being closely tied to the stapes motion but like the slow wave because they are associated with bulk, noncompressional fluid motion (Steele and Taber, 1979; Watts, 2000). These modes are generally small.

Returning to the results of Fig. 4(a): close to the BM (within $\sim$30 μm) at frequencies below and through the BF ($\sim$19 kHz), and more so at low stimulus levels, the slow wave is substantially larger than the fast wave and a frequency sweep traces out the familiar basal-turn tuning curve, amplitude, and phase, of the cochlear traveling wave (Robles and Ruggero, 2001). This is apparent in the 15 μm position of Fig. 4(a) at frequencies below 23 kHz. Somewhat above the BF (frequencies greater than $\sim$22 kHz) the vibration is dominated by the fast wave, which is apparent in the plateau in both amplitude and phase. The spatial variations in pressure identify the frequency regions of relatively large fluid motion as beginning about an octave below the BF peak and ending about a quarter octave above it. Notches can arise due to fast-wave/slow-wave cancellation, most prominently in Fig. 4(a) at 16 kHz, 120 μm. The fluid pressures associated with the slow wave decrease as they spread into the cochlear fluid and the phase accumulation decreases with distance away from the sensory tissue, until it causes only a small ripple in the phase ($\sim$15 kHz region at 120, 160 μm positions) on the ''background'' fluid pressure of the fast wave. (Note that even close to the BM the pressure phase accumulates less in the pressure than it does in BM motion (Robles and Ruggero, 2001). The relatively small phase accumulation can be simply understood as being due to the relatively large fast-wave pressure, which dominates the traveling wave pressure at frequencies somewhat above the peak. Fast-wave pressure is comparable in size to slow-wave pressure, but fast-wave motion is much smaller than slow-wave motion.)

Figures 4(c) and 4(d) show a frequency sweep, amplitude gain (amplitude relative to stimulus level) and phase, in the same animal at a distance 15 μm from the BM and at stimulus levels between 30 and 80 dB. The amplitude gain close to the BF increased by 21 dB as the stimulus level decreased over this range. The boosting of the response at low levels is apparent in the region of the peak; at frequencies above and below the peak the response scaled linearly. Figure 5 shows frequency sweeps of the pressure in ST at 25 μm from the BM at different sound pressure levels from animal W45. [This figure is just like Figs. 4(c) and 4(d) in a

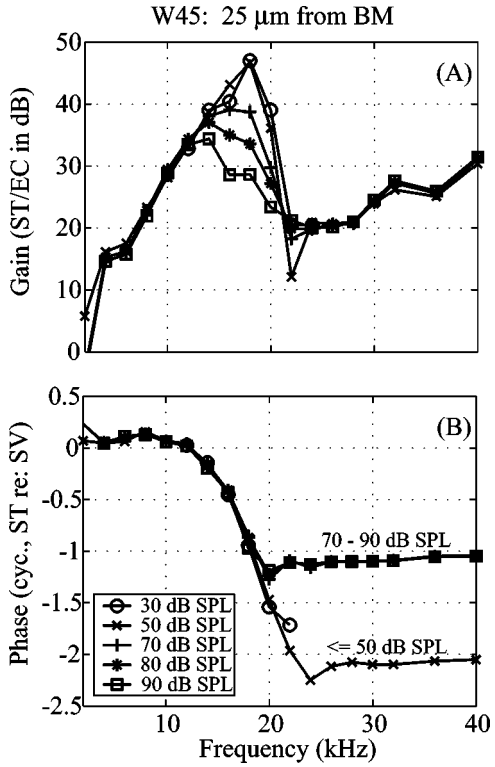

FIG. 5. Single-tone tuning characteristics in ST in the first turn of the gerbil cochlea (W45, 25 μm from BM). ST pressure with stimulus levels of 30 to 90 dB SPL in the ear canal. Two-tone results from this animal are used to illustrate several of the studies. (a) Pressure amplitude gain relative to SPL in the ear canal. (b) Phase relative to the pressure responses in SV near the stapes.

different animal.] The gain of the cochlear amplifier is 18 dB between 50 and 90 dB SPL. Results from this animal and position are used to illustrate several of our two-tone observations.

B. Introduction to observations on two-tone distortion

Figure 6 introduces the two-tone pressure data, showing two-tone distortion measurements in the frequency domain. The results are from the 25 μm position of animal W45 at stimulus levels ($L_1=L_2$) of 60 and 80 dB SPL. The upper panels show results when f_2 and f_1 were chosen such that $2f_1-f_2=\mathrm{BF}$ ($\sim$18 kHz), the lower panels such that $f_2=\mathrm{BF}$. The component at BF is circled. The level and number of DPs increased with the stimulus sound pressure level. A family of DPs was present with the smaller ratio, with the stair–step shape predicted in Fig. 3. The center-of-weight of the family shifted from the low side to the high side when the primaries shifted from a little above BF ($2f_1-f_2=\mathrm{BF}$) to a little below BF ($f_2=\mathrm{BF}$) in frequency, indicating that the members of the DP family were subsequently filtered by the cochlea's single-tone tuning. We will return to this in Fig. 9. With the larger ratio (1.15) only low-side DPs were present for the $2f_1-f_2=\mathrm{BF}$ condition, likely because the distortion was generated further basal (at the f_2, f_1 overlap region) and the high-side DPs were filtered from the recording position by the sharp high frequency cut-off of the cochlea's single-tone tuning.

The $2f_1-f_2$ response was a few dB greater than the f_1 response when it was at the BF [Fig. 6(c)], at the ratio of 1.15 and the stimulus level of 60 dB SPL. In the BM motion measurements of Robles *et al.* (1997) at a ratio of 1.25 and measuring at the $2f_1-f_2$ position, it was shown that the $2f_1-f_2$ DP could be present when f_2 was beneath the noise floor, and even when both f_2 and f_1 were beneath the noise floor. This was a conclusive observation that the DP was produced at a distant location and traveled to the measurement position. In our experiments, the background fast-wave pressure obscures such an observation. The primary frequen-

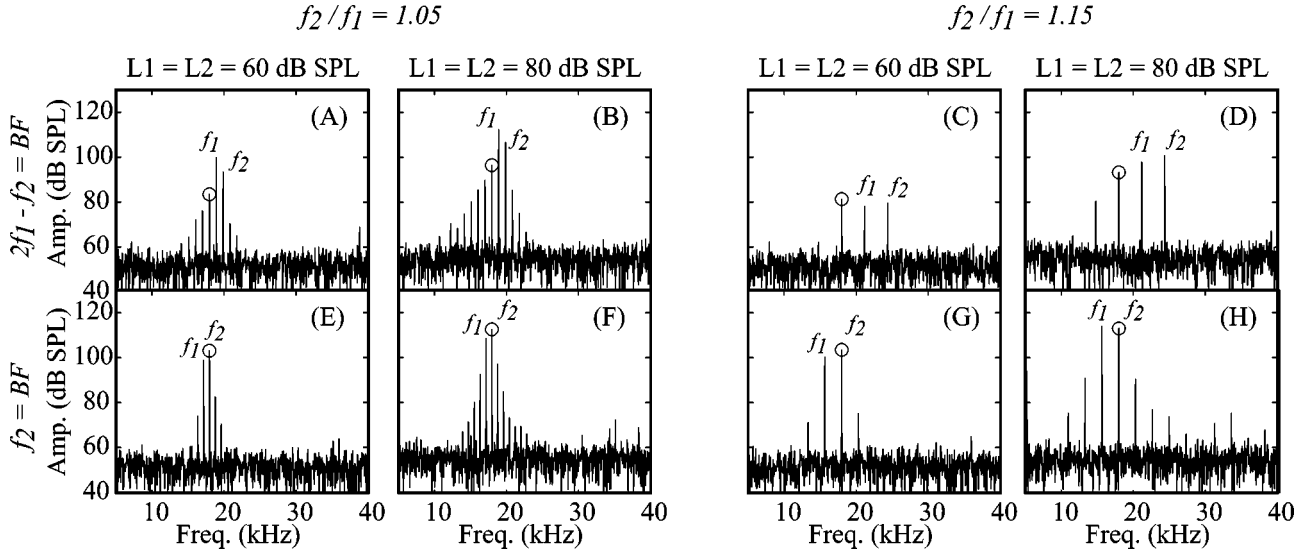

FIG. 6. Two-tone pressure responses in ST in the frequency domain (W45, 25 μm from BM). The stimulus was two equal-intensity primary tones of 60 or 80 dB SPL in the ear canal. The upper panels show the results (amplitude of the response spectrum in dB SPL) when f_1 and f_2 were chosen such that $2f_1-f_2=\mathrm{BF}$ ($\sim$18 kHz), with $f_2/f_1=1.05$ (a), (b) and $f_2/f_1=1.15$ (c), (d). The lower panels show the results when f_2 was chosen such that $f_2=\mathrm{BF}$, with $f_2/f_1=1.05$ (e), (f) and $f_2/f_1=1.15$ (g), (h). The component at BF is circled. With the low-ratio stimulus a stair–step distortion product family is observed, as predicted by the simple nonlinearity of Fig. 3. At the larger ratio relatively fewer distortion components are visible. For $f_2/f_1=1.15$ and $2f_1-f_2=\mathrm{BF}$, it can be seen by referring to Figs. 4 and 5 that f_2 and f_1 are in the fast-wave dominated region where BM velocity (reflected in pressure gradients) is small while the ''background'' fast-wave pressure is large.

cies at the ratio of 1.15 are 21 kHz and 24.4 kHz. The single-tone results of Fig. 5 illustrate that these frequencies were above the peak, in the fast-wave frequency region.

It is interesting to consider what the motion responses (or pressure response without the background fast wave) are in the time domain: A two-tone stimulus produces an amplitude-modulated beating pattern, with the envelope at the difference frequency, f_2-f_1. When the upper primary tone is well above the local BF, the beating envelope of the motion response would not be maintained in a linear cochlea, because only the lower frequency primary would be present in the motion. In contrast, in a healthy, nonlinear cochlea, because of the large $2f_1-f_2$ DP, the beating envelope would be maintained farther down the cochlea. A chain of nonlinear interactions might keep the envelope going. [For that matter, the f_2-f_1 component itself can be present in the nonlinear mechanical response (Kim *et al.*, 1980; Cooper and Rhode, 1997.)]

The observations shown here and below use stimulus levels of 60–90 dB SPL. Although these levels are relatively high, the two-tone distortion measured is nevertheless attributed to nonlinearity in the cochlea's active OHC force. To verify the physiological basis of the two-tone distortion, we measured it pre- and post-mortem in ST pressure close to the BM, at a stimulus level of $L_1=L_2=80$ dB. We found that DPs that were 30 dB out of the noise just pre-mortem had dropped below the noise level one half hour post-mortem. Avan *et al.* (2003) and Lukashkin *et al.* (2002) have argued that high and low level distortion likely arises from the same source. The studies by Avan et al. as well as studies reviewed in Kiang *et al.* (1986), and others, have identified the OHC as the source of cochlear nonlinearity. Referring to the single-tone data of Figs. 4 and 5, the response is compressive over the 60–80 or 90 dB SPL stimulus levels. In a compressively nonlinear cochlea at very high stimulus levels the response at the *primary* frequencies scales almost linearly. However, this does not mean that the response is ''linear'' at those levels, since distortion caused by the saturation of the nonlinear force will still be present. The relatively high-stimulus-level distortion is emphasized here simply because the whole family of DPs could be studied; at stimulus levels below 60 dB sometimes only the $2f_1-f_2$ DP emerged from the noise, and below 50 dB even it could not be detected. Two-tone distortion in BM motion was detectable at lower stimulus levels (Robles *et al.*, 1997; Cooper and Rhode, 1997), most certainly due to a lower noise floor.

Several characteristics of the two-tone distortion are illustrated and discussed in the sections that follow. We show variations with distance from the BM (illustrated in Fig. 7), variations with primary ratio (Fig. 8) and DP tuning (Figs. 9–12). Finally, in Fig. 13 we return to individual distortion families to discuss the DP phase.

C. Two-tone distortion: Variations with distance from the BM

Two-tone distortion is produced in the organ of Corti. The resulting distorted motion of the BM will produce fluid motions that spread into the cochlear fluid. Like the pressure field close to a speaker, this pressure disturbance will have a near-field and a far-field component, with the distance at which the near-field dominates $\sim$ the dimension of the source. Figure 7 shows how the ST primary and $2f_1-f_2$ and $2f_2-f_1$ DP amplitude [Figs. 7(a)–7(c)] and phase [Figs. 7(d)–7(e)] vary with distance from the BM. Measurements were made approximately every 20 μm up to a 200 μm depth. Results from two animals are shown in Fig. 7, and are designated by the subscripts *i* (E1) and *ii* (W34). Figures 7(g)–7(i) use these results to find how the fluid velocity varies with distance from the BM. Fluid velocity was calculated from pairs of pressure measurements at adjacent positions as $v_{\text{fluid}}\approx(i/\omega\rho)\nabla p$ where ω is the angular frequency and ρ is the fluid density (Olson, 1998). The results shown are with an equal-intensity stimulus level of 80 dB SPL, and results at 60 dB SPL were similar. The primary ratio was 1.1 for animal E1 and 1.05 for animal W34. Within each three panel set [e.g., Figs. 7(a)–7(c)], the left panel corresponds to stimulus conditions such that $2f_1-f_2$ is equal to the BF of the recording position (where BF was chosen based on the low-stimulus-level single-tone responses), the middle panel corresponds to stimulus conditions such that $f_1=$BF and the right panel corresponds to stimulus conditions such that $f_2=$BF. Several aspects of these data are notable. Most obvious is that the primaries fall off less rapidly than the DPs. In general, both DPs drop steadily, in some cases reaching the noise level, whereas the primaries level off. The level off in the primaries is due to the background cochlear fast-wave pressure that basically fills the cochlea, as discussed above. Bii and Cii show a 20 dB notch in the response of one of the primaries, presumably due to a fast-wave/slow-wave cancellation. The DPs were unperturbed by the notches that occurred in the primaries. This immunity is reassuring, as it confirms that the distortion was not generated by the pressure sensor.

We were interested in using the variations in fluid pressure and fluid velocity amplitude with depth to explore the hypothesis that the $2f_2-f_1$ DP would decay differently with distance from the BM than the $2f_1-f_2$ DP. This hypothesis was based on the idea that $2f_1-f_2$ is generated in a part of the cochlea where it is able to produce its own traveling wave, whereas the $2f_2-f_1$ DP is generated in a region slightly apical of its own BF place, and would therefore be a nonpropagating disturbance. A nonpropagating disturbance might be expected to decay with distance differently than a traveling wave disturbance. As a background to this expectation: In 2-D models of the cochlea the penetration (decay) depth of the wave in the fluid is proportional to wavelength (de Boer, 1984). However, the results from a previous study (Olson, 1999) showed that the 2-D model penetration prediction was not borne out for the response to single tones. In that study the penetration depth was found to be approximately equal for tone frequencies corresponding to a wide range of traveling wave wavelength. The interpretation of those results was that the decay with depth was influenced more by the finite width of the BM than by the wavelength. If the width is the governing feature of penetration depth, then the penetration of DPs and primaries might be able to identify a multimodal BM motion. Investigations of BM motion have shown that the electrically evoked BM motion is

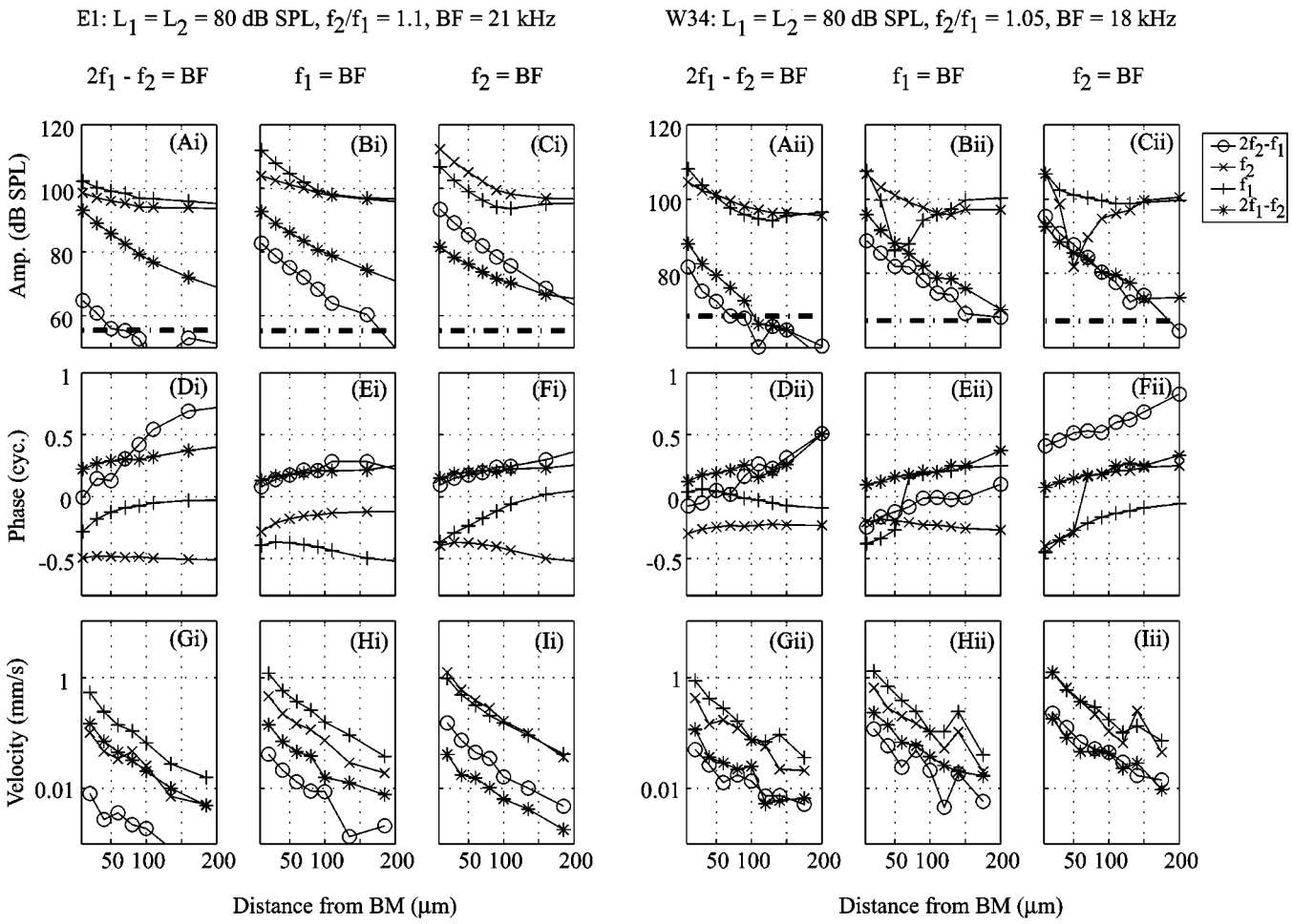

FIG. 7. Spatial variations of ST pressure primaries and DPs (W34, E1). f_1, f_2 and the $2f_1-f_2$ and $2f_2-f_1$ DPs are shown as a function of distance from the BM. Results from two animals are shown; E1 , with BF 21 kHz, is labeled with subscript *i* and W34, with BF 18 kHz, is labeled with subscript *ii*. Dashed lines indicate the noise floor. Both of the primaries were set at 80 dB SPL, with $f_2/f_1=1.1$ for E1 and $f_2/f_1=1.05$ for W34. The upper panels (a)–(c) show the pressure amplitudes, the middle panels (d)–(f) show the phase (not referenced to anything—only the changes with distance are meaningful) and the lower panels (g)–(i) show the fluid velocity amplitude (the component in the direction perpendicular to the pressure sensor's approach) derived from the amplitude and phase data. Within each three panel set the primary frequencies are varied such that $2f_1-f_2=$BF (a), (d), (g), $f_1=$BF (b), (e), (h) and $f_2=$BF (c), (f), (i). The pressure primaries, but not the pressure DPs, exhibit plateaus and notches in amplitude that are attributed to the fast-wave and fast-wave/slow-wave cancellation. The fluid velocities of the primaries and the fluid velocities of the DPs fall-off similarly with distance from the BM.

bimodal across the width of the BM (Xue *et al.*, 1995; Nuttal *et al.*, 1999). In contrast, the response to single-tone acoustic stimulation has usually been found to be unimodal across the width of the BM (Cooper, 2000; Rhode and Recio, 2000), with the exception being the near-BF results of Nilsen and Russell (1999). The active force that gives rise to DPs might, like the electrically elicited motion, produce a bimodal disturbance across the BM. In the same way that the pressure decays more rapidly from a dipole source than from a monopole source (Beranek, 1993), the decay from a bimodal disturbance would be more rapid than from a unimodal disturbance. A DP that is based on a bimodal disturbance that does not propagate (high-frequency-side DP) would be expected to decay more rapidly in the fluid than components that launch or are associated with a traveling wave (the primaries and low-frequency-side DPs). The fluid velocity [Figs. 7(g)–7(i)] is more useful than pressure for this comparison since the fast wave is effectively canceled out when taking the pressure differences to find fluid velocity; then the primaries can be included in the comparison. In general, the $2f_1-f_2$, $2f_2-f_1$, and f_1 and f_2 components all have a similar falloff in fluid velocity [Figs. 7(g)–7(i), i and ii]. The similar decays of primary and high- and low-side DP velocity reported here support the idea that the width of the BM is the governing dimension for penetration, and does not give any indication that these different components have different mode shapes.

The phase data plotted in Fig. 7 are not referenced to anything so only the variations with distance are meaningful, not the absolute values. [Elsewhere in this paper the DP phases are referenced to either ST or SV primary phases. For this figure, it made more sense to plot the unreferenced phase and concentrate on variations with distance because the stimuli (f_1, f_2, their phases) were identical for all the data within a panel.] The primary components change smoothly, and little, except in the region of a notch [ii of Figs. 7(e) and 7(f)] where expected 180° interference jumps are observed. All the DPs have a gradual phase increase with distance that can be as large as 1/3 of a cycle, 120°, over the 200 micrometers of measurement. In a 2-D, short-wave cochlear model, phase variation with depth is related to an amplitude decrease or increase in the direction of wave travel. [See the

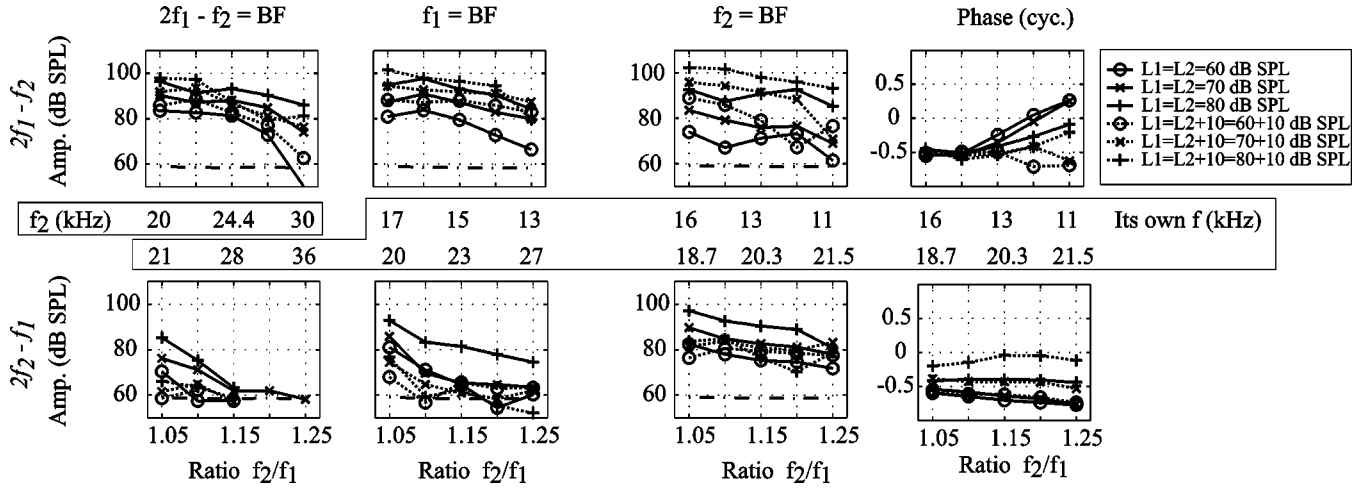

FIG. 8. Dependence of ST pressure DPs $2f_1-f_2$ and $2f_2-f_1$ on primary frequencies and f_2/f_1 ratio (W45, 25 μm from BM). $L_1=L_2$ (solid lines) and $L_1=L_2+10$ (dotted lines) were the stimulus levels used, with $L_2=60$, 70 and 80 dB SPL. The upper panels show the pressure response at $2f_1-f_2$; the lower panels show the response at $2f_2-f_1$. The ratio is on the x axis of these plots and DP amplitude (in dB SPL) is on the y axis except for the far right panels, which plot the DP phase. The left panels show the case in which $2f_1-f_2$ was at the BF (18 kHz). To the right of those is the case in which $f_1=$BF, and then the case in which $f_2=$BF. The phase plots on the right also correspond to the case $f_2=$BF. (The phase is referenced to the ST pressure primaries. Only the $f_2=$BF phases are shown as then both primaries are slow-wave dominated, which is necessary to make this referencing meaningful.) In order to emphasize the influence of the DP frequency on the trends we find, the DP frequency, $2f_1-f_2$ or $2f_2-f_1$ is indicated on a secondary axis in the center of the plot. For the case in which $2f_1-f_2=$BF, the f_2 frequency is indicated on this axis.

discussion of the solution to Laplace's equation ($\nabla^2 p=0$) in a 2-D fluid in de Boer, 1984.] However, given the inability of the 2-D model to predict amplitude variations, a 3-D model is probably also required to interpret the phase.

The decay-with-depth of DP pressure is related to the question of whether the distortion reaches the stapes through the fluid pressure (as opposed to/in addition to a reverse traveling wave on the OC) to generate emissions. The DPs decay steadily over the 200 micrometers in depth that they were measured, to become pressures that are 20–30 dB smaller than they were close to the BM. At this point, the distortions were in some cases dropping beneath the noise level of our system at ~50 dB SPL ($2f_2-f_1$ in Figs. 7(a)i and 7(c)i), although in other cases they are at ~ a 70 dB SPL level [$2f_1-f_2$ in all panels but ii of Fig. 7(a)]. The stapes is about 1 mm distant from the recording position. Extrapolating the data of Fig. 7, the emissions will be reduced at least another 20–30 dB over a distance of 1 mm, to levels of ~20–50 dB SPL. Reverse transmission through the gerbil middle ear probably produces about 20–30 dB of attenuation. This is based on measurements in a guinea pig (Magnan *et al.*, 1997), and the ~30 dB gain of forward transmission (Olson, 1998). Therefore, it is feasible that the distortion pressure would be large enough at the stapes to generate measurable emissions by this route. Studies by Ren (2004) showed a fast stimulation of the stapes by the $2f_1-f_2$ DP, presumably through the fluid pressure. Further work is required to understand the relative contributions of the direct fluid route and reverse-traveling-wave route to cochlear emissions.

D. Two-tone distortion: Variations with primary ratio around BF

Figure 8 shows the DPs as a function of ratio of the primaries. Results from W45 are shown, at a distance 25 μm from the BM. $L_1=L_2$ and $L_1=L_2+10$ were the stimulus levels used, with $L_2=60$, 70 and 80 dB. The ratio is on the x axis of these plots, and the DP amplitude (in dB SPL) is on the y axis, except for the far right panels, which plot the DP phase (relative to the primaries measured in ST) for the $f_2=$BF stimulus condition. The left panels show the case in which $2f_1-f_2$ was at the BF (18 kHz). To the right of those is the case in which $f_1=$BF, and then the case in which $f_2=$BF. The upper panels show $2f_1-f_2$; the lower panels show $2f_2-f_1$. Referring to Fig. 2, as the ratio increases, the region of primary overlap decreases. The distance between the DP best places and the overlap position also increases. In order to clarify the relationship between the BF and the frequencies at play, the DP frequency, $2f_1-f_2$ or $2f_2-f_1$, corresponding to the ratios, are indicated in the center of the plot. For the case where $2f_1-f_2=$BF, the f_2 frequency is indicated on this axis.

(1) $2f_1-f_2=$BF (left column). The high-side, $2f_2-f_1$ DP (lower panel) decreased very rapidly with an increase in ratio. Compared to the $2f_2-f_1$ DP, the amplitude of $2f_1-f_2$ (upper panel) decreased much less rapidly with an increase in ratio. However, at the lowest stimulus level (60 dB), this DP did decrease rapidly for ratios above 1.15. This decrease and its level dependence agree with results of other investigators (Cooper and Rhode, 1997; Robles *et al.*, 1997). The effect of raising L_1 level so that $L_1=L_2+10$ was a general decrease of the high side $2f_2-f_1$ DP. This is the expected behavior of the nonlinearity, following the discussion of Fig. 3.

The rapid decline in the high-side DP with increasing ratio is likely due to the combined effects of decreasing overlap region and single-tone filtering. The $2f_2-f_1$ DP's best-place was basal to the cut-off frequency of the recording location, increasingly so as the ratio increased. The gradual decline in $2f_1-f_2$ with ratio can

only be due to the decrease in the overlap region because, in contrast to the $2f_2-f_1$ DP, the $2f_1-f_2$ DP's best place was at the recording position.

(2) f_2=BF (right two columns). In this case the observation place was approximately at the distortion generation site, assuming that the generation site is where f_1 and f_2 responses spatially overlap and are both large. The $2f_2-f_1$ DP decreased slowly with the increase in ratio. The amplitude of the $2f_1-f_2$ DP had a zig–zag shape as the ratio increased. The $2f_2-f_1$ phase changed little with ratio compared with the $2f_1-f_2$ phase, which changed smoothly by almost a cycle as ratio increased from 1.05 to 1.25. When L_1 was increased so that $L_1=L_2+10$ dB, the high-side DP decreased as expected, following the discussion of Fig. 3. Another effect of raising the level of L_1 was that the high-side DP became almost unchanging with ratio. The low side $2f_1-f_2$ DP increased when L_1 increased. Its zig–zag shape was diminished, being replaced by a gradual decline with ratio, and the phase flattened out.

$2f_2-f_1$ is expected to be mainly a nonpropagating disturbance because its best place is basal to the recording position. In contrast, once generated, the $2f_1-f_2$ can travel apically towards its own best place. The measured $2f_1-f_2$ could be a summation of the local nonlinear generator component and a reflection component from close to the $2f_1-f_2$ best place (Brown *et al.*, 1996; Talmadge *et al.*, 1999). In line with this, the zig–zag amplitude variation of $2f_1-f_2$ with ratio is suggestive of interference. In this conceptual framework, the ''smoothing'' effect (on the amplitude and phase of the $2f_1-f_2$ DP) of raising the L_1 level relative to L_2 suggests that the generator component dominated the reflection component under those stimulus conditions (Mauermann and Kollmeier, 2004). The increasing phase with ratio for the $L_1=L_2$ condition reinforces the idea that the $2f_1-f_2$ DP is in part arising from a distant location. As Fig. 3 showed, a phase of a half cycle is expected for both the $2f_1-f_2$ and $2f_2-f_1$ DPs, at the output of a simple nonlinearity. The phase of the $2f_1-f_2$ DP gradually departed from the half cycle phase as the ratio is increased. This gradual departure might be due to the DP, or some fraction of it, being nonlocally generated. This might be the reflection component of the distortion, from the region of the $2f_1-f_2$ best place. The $2f_2-f_1$ DPs do not depart from the half cycle phase very much as the ratio is increased, suggesting that this distortion was dominated by a local nonlinear generator component.

(3) f_1=BF (second column from the left). In this case the observation place was between the f_2 best place and the $2f_1-f_2$ best place. At the low ratio of 1.05, the amplitudes of $2f_1-f_2$ and $2f_2-f_1$ were nearly the same. At the higher ratio the $2f_2-f_1$ DP dropped off rapidly, but not as rapidly as when $2f_1-f_2$ was at BF. The $2f_1-f_2$ DP actually increased with ratio ($L_1=L_2$ condition) when the ratio increased from 1.05 to 1.1 but then decreased steadily. For $L_1=L_2+10$ dB, the high-side DP again had the expected general decrease, and the low-side DP's most significant change was that it changed to monotonically decreasing with increase in ratio.

Considering all three recording conditions (BF=f_1, f_2 or $2f_1-f_2$) the $2f_2-f_1$ DP in general decreased with ratio. This is probably mostly due to the fact that its frequency was above the local BF, increasingly so as the ratio increased. The decreasing overlap region might also play a role, although this seems to be relatively minor, based on the very gradual decline with ratio in the f_2=BF case. At lower SPL, overlap effects would likely be greater. The $2f_1-f_2$ DP did not drop with ratio (at least up to $f_2/f_1=1.25$) for the f_2=BF condition. Both the f_2=BF and f_1=BF conditions showed nonmonotonic changes with ratio. High-side suppression of the DP by f_1 might account for the reduced size of the $2f_1-f_2$ DP at the lowest ratio in the f_1=BF condition (Cooper and Rhode, 1997), but high-side suppression cannot account for the zig–zag pattern of the f_2=BF case. This behavior is more easily explained by interference between different components (nonlinear generator and reflection) of the $2f_1-f_2$ DP (e.g., Talmadge *et al.*, 1999).

E. Two-tone distortion: Frequency sweeps at fixed ratio

Figures 9–12 show two-tone frequency sweep responses measured close to the BM at a ratio of 1.05 (animals W45 and W48). Figure 2 shows that the responses to the two primaries overlap a great deal with such a low ratio. As the primary frequencies are swept, this tightly overlapping pattern sweeps from apical to basal of the recording site. Figure 9 shows a series of distortion families in response to $L_1=L_2=80$ dB SPL primaries, at the frequencies indicated above the plots (W45, 25 μm from BM). The BF was $\sim$18 kHz, indicated by an arrow in the plots. The characteristics of the distortion families are governed by both the local nonlinear response (which in general will produce stair–steps of DPs on either side of the primaries) and the single-tone tuning of both the primaries and the DPs. As the primaries sweep closer to the BF frequency the families of DPs grow. The influence of single-tone tuning of the DPs can be seen by comparing Fig. 9(c), whose primaries are just below the BF, to Fig. 9(d), whose primaries are just above the BF. The distortion family is weighted towards the high side in Fig. 9(c), towards the low-side in Fig. 9(d). [For completeness, the low-frequency primary is slightly bigger than the high-frequency primary in Fig. 9(d), which would also tend to shift the weight of the distortion family to the low side in this case.] Figure 9(e), with primaries even farther above the BF, shows a strong influence of single-tone tuning of the DPs. The center-of-mass of the distortion family is shifted left from the primaries, and is centered on the 18 kHz BF. The stair–steps shaping around the primaries is still apparent, however, in that the $2f_1-f_2$ DP is relatively large even though it is well above the BF. Referring to Fig. 5, the primaries in Fig. 9(e) are in the fast-wave dominant region; the slow-wave portions of the responses are expected to be small. It is likely that the whole DP family of Fig. 9(e) was generated basal to the recording position, where the slow-wave primary responses were large, with a primary-centered

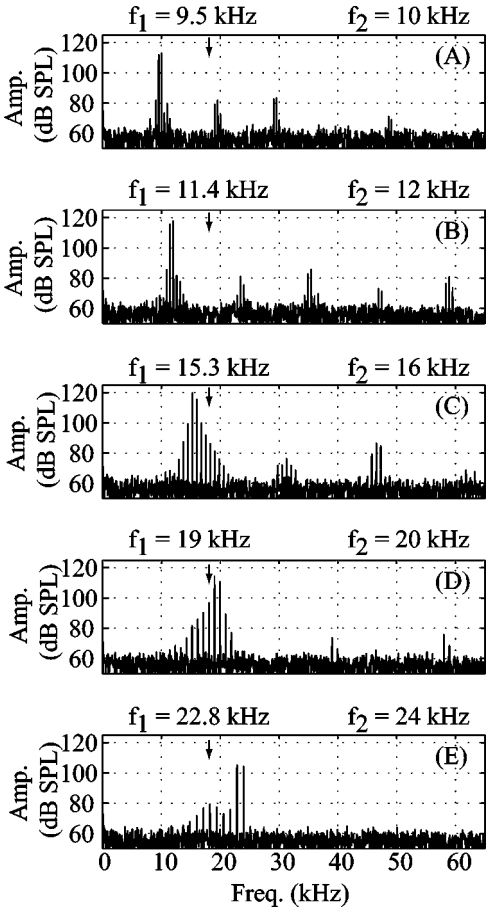

FIG. 9. ST pressure DP families as frequency varies (W45, 25 μm from BM). A series of distortion families generated in response to $L_1=L_2=80$ dB SPL primaries of a range of frequencies. The f_2/f_1 ratio was fixed at 1.05 and the primary frequencies are indicated above the plots. An arrow indicates the 18 kHz BF in each plot.

stair–step shape. Traveling to the recording position, the DP family was filtered by single-tone tuning, and arrived with the observed up–down–up shape. At lower frequencies the family of DPs is relatively less orderly [Figs. 9(a) and 9(b)] perhaps due to interference between locally generated and apically generated distortion. Although the primary frequencies in these panels would peak well apical of the recording site, the harmonic distortion in evidence indicates that some amount of nonlinear distortion was produced locally at these frequencies (Olson, 2004).

Figures 10–12 plot the amplitudes and phases of responses such as those in Fig. 9, sorted by DP. The DPs are plotted relative to their own frequencies. Figure 10 shows data from animal W45 (25 μm from BM), ratio=1.05, and levels ($L_1=L_2$) of 60, 70 and 80 dB SPL. Fig. 11 is similar with $L_1=L_2+10$. Figure 12 shows results from another animal (W48, 10 μm from BM), ratio 1.05, $L_1=L_2=80$. The single-tone primary responses are also included as a reference, at levels of 30, 50 and 70 dB for W45 and 50 and 60 for W48. The tuning of the single-tones reflects the basic cochlear mechanical filtering.

The phases of the DPs are plotted both relative to the ST primaries (recorded along with the DP family) and the SV primaries (recorded near the stapes), as discussed in Sec. II. The ST phase reference is only used when the primary frequencies were low enough that the primaries were in the slow-wave region. The ST-referenced phases are interesting when they are close to 0° or 180°. As Fig. 3 showed, these phases are predicted for the output of an instantaneous nonlinearity that is local to the recording site. Relatively large departures from 0° or 180° might signify that the distortion generation site was not local and small departures might be due to local filtering. The SV-referenced plots include the ST single-tone responses referenced to the SV primaries, which shows the familiar traveling wave phase accumulation. These plots illustrate clearly the frequency regions in which the DP phase-frequency behavior is similar to the ST single-tone phases (consistent with distortion generation local to the measurement location) and regions in which the DP phases depart from the single-tone phases (suggesting distortion generation distant from the measurement location).

The main observation from Figs. 10–12 is that the DPs are tuned quite similarly to the primaries, both in amplitude and in phase. The tuning of the $2f_1-f_2$ amplitude is in agreement with the observations of Robles *et al.* (1997). There are several secondary observations.

(1) The low-side DPs (e.g., $2f_1-f_2$ and $3f_1-2f_2$) are tuned particularly similarly to the single tones. This suggests that the single-tone tuning that precedes distortion generation, and subsequent single-tone tuning of the DPs that follows distortion generation together tune the DP as though it had been a single tone from the start.

(2) The tuning of the high-side DPs (e.g., $2f_2-f_1$ and $3f_2-2f_1$) is slightly offset in frequency compared to the primaries (most prominently in Fig. 12, but also in Fig. 10). In fact, the tuning of the high-side DPs is more similar to the single-tone tuning when the DPs are plotted vs f_2, rather than their own frequency. This suggests that the high-side DPs cannot make as much use of single-tone tuning after being generated as the low-side DPs, and the single-tone tuning of f_2 that preceded distortion generation has a lot to do with the tuning of the high-side DPs. The high-side DPs (especially Fig. 10) have tuning that is more symmetric than either single-tone or low-side DP tuning: The low-frequency slope is steeper, the high-frequency slope is less steep than with single-tone tuning. The contrast between low- and high-side DP tuning reinforces the observation from perceptual studies that low-side DPs cause a single-tone-like cochlear response, whereas high-side DPs do not (Goldstein, 1967; Zurek and Sachs, 1979).

(3) Looking at the phase responses plotted versus the SV phase in Fig. 10: At frequencies in the broad vicinity of the BF (18 kHz), the $3f_2-2f_1$ and $3f_1-2f_2$ DP phases lie nearly on top of the primary phases, whereas the $2f_2-f_1$ and $2f_1-f_2$ DP phases are offset vertically by about a half cycle. When referenced to ST phase, the alternating phases between 0° and 180° are very clear. A similar thing is apparent in Fig. 11, and in Fig. 12 as well, although less robustly. This is predicted for the output of a simple compressive nonlinearity. The 180°

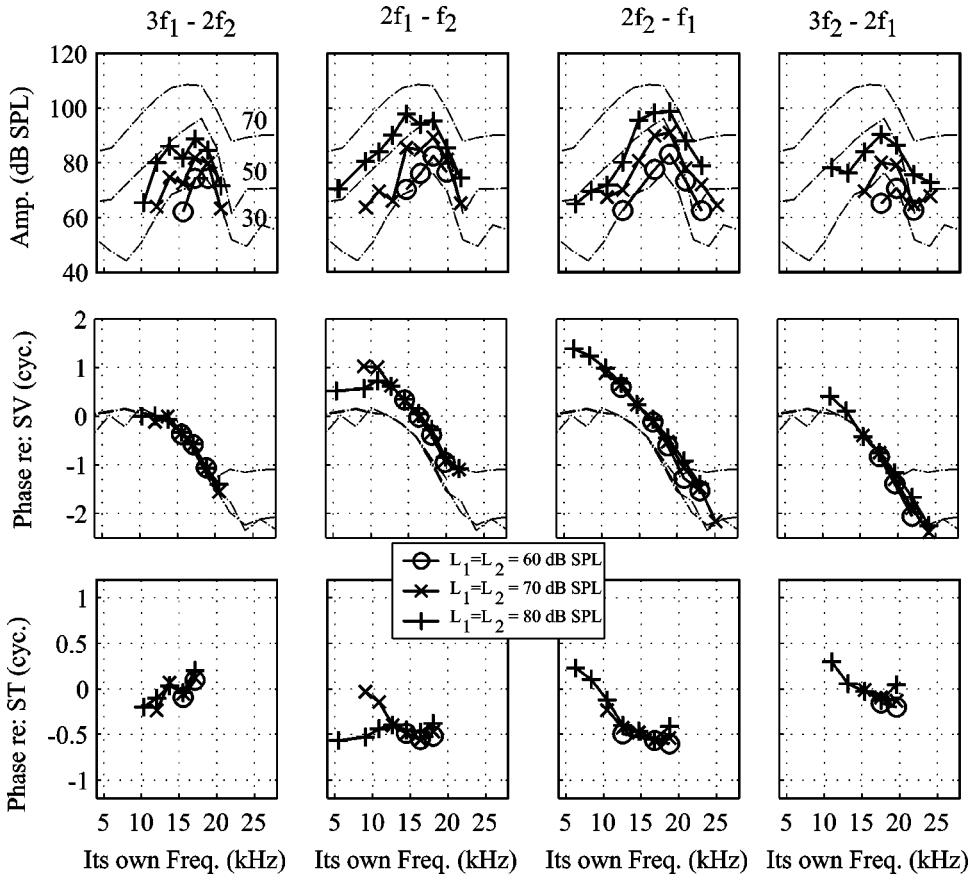

FIG. 10. Distortion product tuning in ST with equal-intensity two-tone stimulus (W45, 25 μm from BM). The stimulus tone levels were both either 60 (circles), 70 (crosses) or 80 dB SPL (pluses) with a fixed frequency ratio of 1.05. The upper panels show how the amplitude (dB SPL) of $3f_2-2f_1$, $2f_2-f_1$, $2f_1-f_2$ and $3f_1-2f_2$ vary with frequency. Each DP is plotted versus its own frequency. Single-tone tuning at 30, 50 and 70 dB SPL are shown (dotted-dashed lines) for a comparison. The middle panels show the DP phases relative to the SV primaries. The bottom panels show the DP phases relative to the ST primaries.

phase can be interpreted as the sign of the DP coefficient being negative for the $2f_1-f_2$ and $2f_2-f_1$ DPs, as discussed in Fig. 3.

(4) Going from Fig. 10 to Fig. 11, the L_1 level was raised 10 dB relative to the L_2 level. (Details on the level dependence of the $2f_1-f_2$ DP in BM motion are in Cooper and Rhode, 1997.) This led to a reduction in the level of the high-side DPs. For example, the $3f_2-2f_1$ DP column from Fig. 10 is not included in Fig. 11 because the DP was nearly missing for the $L_1=L_2+10$ condition. This can be accounted for to a large degree by the action of the nonlinearity. As discussed above (Fig. 3), the processing of a two-tone stimulus by a compressive nonlinearity produces high-side DPs that are reduced, compared to the $L_1=L_2$ condition, when L_1 becomes greater than L_2 (Engebretson and Eldredge, 1968). However, there is a frequency region around 12–15 kHz in which the $2f_2-f_1$ response got bigger when $L_1=L_2+10$ and $L_2=80$ dB. These responses were likely arising from slightly further apical, near the f_2 place where the responses to f_1 and f_2 were nearly equal when $L_1=L_2+10$. In support of this, the bimodal response at this level suggests that more than one component of distortion is present (apically generated plus locally generated). The possibility for an apical generation site when the frequency is somewhat less than the BF will be reinforced by the discussion of phase just below.

(5) Considering the $2f_2-f_1$ DP and 70 dB $2f_1-f_2$ DP in Fig. 10, the phase of the distortion in the below-BF 6–15 kHz region had a phase-frequency slope that was much

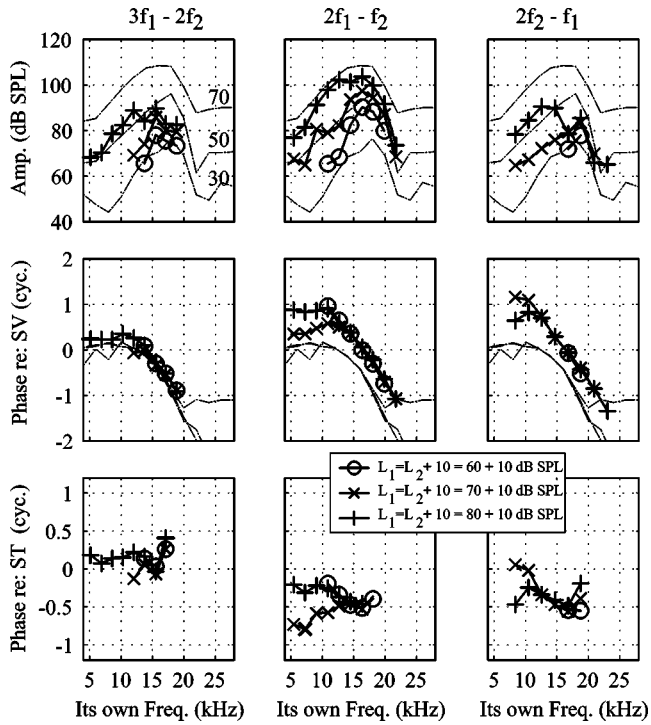

FIG. 11. Distortion product tuning in ST with unequal-intensity two-tone stimulus (W45, 25 μm from BM). As in Fig. 10 except $L_1=L_2+10$ dB. The $3f_2-2f_1$ DP is not shown with these stimulus levels because it was in the noise at most frequencies.

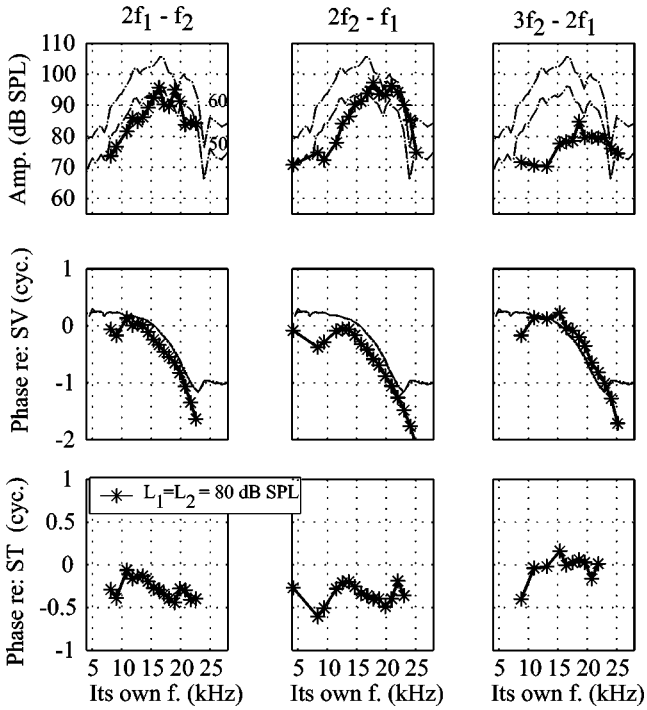

FIG. 12. Distortion product tuning in ST with equal-intensity two-tone stimulus (W48, 10 μm from BM). The primary tone levels were both 80 dB SPL with a fixed frequency ratio of 1.05. These data were from animal W48, with BF ~21 kHz, and were recorded at a distance 10 μm from the BM. The upper panels show how the amplitude (dB SPL) of $3f_2-2f_1$, $2f_2-f_1$, $2f_1-f_2$ and $3f_1-2f_2$ vary with frequency. Each DP is plotted versus its own frequency. Single tone tuning at 50 and 60 dB SPL are shown (dotted–dash lines) for a comparison. The middle panels show the DP phases relative to the SV primaries. The bottom panels show the DP phases relative to the ST primaries.

steeper than the primary phase in this frequency region. The slope indicates a delay that was similar to the delay of the single tones (and DPs) in the BF region. When referenced to ST, this is the frequency region for which the phase smoothly departs from a fixed -0.5 cycle phase. Perhaps these DPs were generated further apical, closer to their own BF places. If they were reflected from a fixed position, the slowing of the traveling wave as the best place was approached would mean a longer travel time and predict the steeper phase-frequency slope (as discussed in Shera and Guinan, 1999). However, if the wave traveled *both to and from* its own BF place as a cochlear traveling wave, its delay time should be about two times the delay of the local BF primary (twice the slope), which was not observed. On the other hand, if the distortion were generated from a nonlinear generator region that moved as the frequency swept, the phase would not be expected to change at all–the slope would be zero (Shera and Guinan, 1999). In summary, in a vague way the 6–15 kHz phase data suggest that the distortion was generated further apical, but the specific behavior is not that expected of either a generator or reflection component. Finally, it should be noted that the phase is not sampled densely enough to be certain of its slope, and more data points might reveal the steep slope that is predicted for a reflection component. When the L_1 level was raised 10 dB in Fig. 11, the steep-sloped low-frequency region of the $2f_1-f_2$ phases became less evident. This suggests that an effect of raising the L_1 level was to cause the local $2f_1-f_2$ DP to gain strength relative to the apical-generated $2f_1-f_2$ DP, as was also suggested in the discussion of Fig. 8.

F. Two-tone distortion: Phase of the distortion within single families

The emission literature includes reports of level-dependent 180° phase jumps (e.g., Mills, 2002) which have been interpreted as being due to either interference between two components or to the level dependence of the nonlinearity's output (Lukashkin and Russell, 1999). Here, we extend these observations of phase differences by describing the absolute phase of ST pressure DPs within families. One of the most striking aspects of the data was the phase of the DPs, referenced to the phase of the primaries: For conditions in which the primaries were close to the BF and the ratio was low, this phase was 180° for the $2f_1-f_2$ and $2f_2-f_1$ DP and 0° for the $3f_2-2f_1$ and $3f_1-2f_2$ DP (Figs. 8, 10–12). We would like to understand the significance of the 0°/180° phase. We look for this significance through both the abstract mathematics of a compressive nonlinearity and the concrete physics of the cochlea's mechanics. In order to illustrate the discussion, in Fig. 13 three distortion families are shown for the conditions $f_1=$BF, $f_2=$BF and $2f_1-f_2=$BF, measured

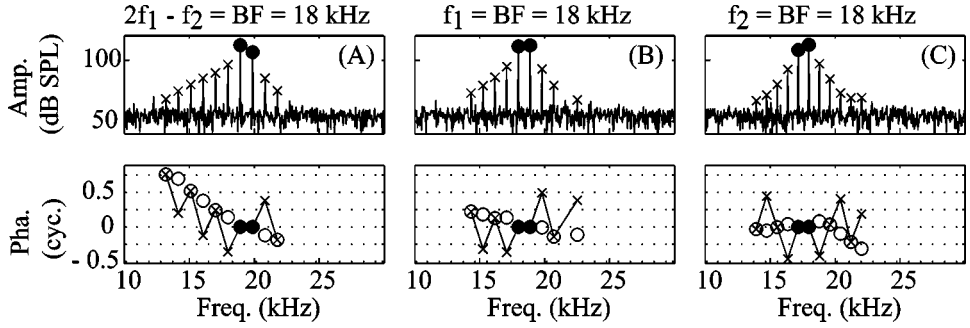

FIG. 13. DP family amplitudes and phases (W45, 25 μm from BM). A two-tone stimulus with $L_1=L_2=80$ dB SPL and f_2/f_1 ratio=1.05 generated a family of DPs, as shown in the upper panels. The primary frequencies were such that $2f_1-f_2=$BF (left panels), $f_1=$BF (middle), and $f_2=$BF (right). The DP phases, referenced to the primary phases, are presented in the lower panels as crosses. The phases basically alternate in phase between 0° and 180° degrees, with sometimes a superimposed slope. In order to better visualize the slope, the phases that alternated by 180° have been also plotted as empty circles, with 180° subtracted or added.

in ST pressure close to the BM (W45, 25 μm from BM, $f_2/f_1=1.05$). The phase is shown relative to the primaries, as described in the analytic section of the methods, and the primary phases when so referenced, automatically $=0°$. The unfilled dots represent data points that have 180° added or subtracted and were included to clarify the slopes of phase-vs-distortion number. (This replotting is based on the idea that 180° phases arise due to the coefficient of a given DP being negative.)

In the $f_2=$BF plots, the phase of the low-side DPs up to $5f_1-4f_2$ are seen (4 DPs) and they all follow the 0°/180° pattern. Five high-side DPs are seen. While the first two of these follow the 0°/180° pattern, the remaining three have a downward slope superimposed on the pattern. This downward slope, superimposed on a 0°/180° pattern, is true of the low- and high-side DPs of the $2f_1-f_2=$BF condition, and the low-side DPs of the $f_1=$BF condition. The high-side DPs of the $f_1=$BF condition are nearly missing the 3rd DP $(4f_2-3f_1)$ and the 4th DP has a phase of ~180° when a phase of 0° is expected had the phases strictly alternated. The general trends in the data bring up two questions: why the 0°/180° phase pattern, and why the superimposed slope? Some related findings in the data that has been presented, for example in Fig. 10 the smooth departure from 180° of the $2f_1-f_2$ phase at low frequencies, have been addressed already, and were attributed to non-local distortion generation sites.

Figure 3 and its discussion showed that the 0°/180° phase is a predicted behavior for the DP output of a simple compressive nonlinearity. However, the ST pressure is not the direct output of the nonlinearity, the active force is. In order to understand the significance of the ST DP phase, we need to consider the relationship between the active force and the ST pressure. At the output of the active force, the phase of the DP of number n, and thus distortion frequency $f_1+n(f_2-f_1)$, would have the form[1]

$$\phi_{da\_n}=\{\phi_{a1}+n(\phi_{a2}-\phi_{a1})\} \tag{4}$$

This follows from Sec. II. The "a" in the subscripts denotes "active," meaning the site of the nonlinearity. As discussed in Sec. II, the phase of a ST DP relative to the ST primaries (what is plotted in Figs. 10–13) is given by Eq. (1), which is rewritten here:

$$\Phi_{dt\_n}=\phi_{dt\_n}-\{\phi_{t1}+n(\phi_{t2}-\phi_{t1})\}. \tag{1}$$

Equation (1) can be re-expressed using Eq. (4):

$$\Phi_{dt\_n}=(\phi_{dt\_n}-\phi_{da\_n})-\{(\phi_{t1}-\phi_{a1})+n[(\phi_{t2}-\phi_{a2})-(\phi_{t1}-\phi_{a1})]\}. \tag{5}$$

Using Eq. (5) to understand the data in Fig. 13: we just noted that the $2f_1-f_2=$BF data, as well as the $f_1=$BF data (low-side) depart from the 0°/180° pattern with a superimposed slope. This can probably be accounted for with the third term in Eq. (5), $n[(\phi_{t2}-\phi_{a2})-(\phi_{t1}-\phi_{a1})]$, as this is a term whose absolute value will grow linearly with n (the number of the DP) just as the data do. The $[(\phi_{t2}-\phi_{a2})-(\phi_{t1}-\phi_{a1})]$ part of the term, which would determine the size of the slope, measures the difference in the phase difference between the f_2 primary ST pressure and f_2 primary active force, and the f_1 primary ST pressure and f_1 active force. The individual differences, e.g., $(\phi_{t2}-\phi_{a2})$, are not expected to be zero. For example, the active force is in phase with BM velocity in many cochlear models (in order to inject energy into the motion) whereas the ST pressure is primarily in phase with acceleration (e.g., using Figs. 14 and 15 in Olson, 2001). In that case, $(\phi_{t2}-\phi_{a2})$ might be ~90°. However, by the same reasoning, $(\phi_{t1}-\phi_{a1})\sim 90°$, and the difference $[(\phi_{t2}-\phi_{a2})-(\phi_{t1}-\phi_{a1})]$ is expected to be 0°. The fact that we observe a linearly growing phase with n means that $(\phi_{t2}-\phi_{a2})\neq(\phi_{t1}-\phi_{a1})$. This inequality could have several causes. Thinking of a local mechanism—perhaps $(\phi_{t2}-\phi_{a2})\neq(\phi_{t1}-\phi_{a1})$ because the active force is filtered—for example, maybe for stimulation at frequency f_1 the active force is still pumping energy into the wave and is primarily in phase with velocity, but at f_2 has shifted phase to let the wave drop off. Then $[(\phi_{t2}-\phi_{a2})-(\phi_{t1}-\phi_{a1})]\neq 0°$. Or, more mundanely, perhaps the fast-wave pressure is influencing the measured ST pressures unequally: f_2 more than f_1, most likely. That would also lead to $[(\phi_{t2}-\phi_{a2})-(\phi_{t1}-\phi_{a1})]\neq 0$, and a resultant superimposed slope. The latter explanation gains credibility with the observation that the slope is biggest for the $2f_1-f_2=$BF condition (both f_1 and f_2 above the BF, getting into fast-wave territory) and the slope is nearly zero for the $f_2=$BF condition (where f_2 and f_1 are safely lower than the fast-wave-dominated region).

Therefore, the basis for the superimposed slope can be understood, and might be interesting (if it is due to active force filtering), or not so interesting (if it is due to the fast wave). But we still have terms in Eq. (5) that need to be examined to understand the 0°/180° phase. These terms are $(\phi_{dt\_n}-\phi_{da\_n})-(\phi_{t1}-\phi_{a1})$. Together the two terms measure the difference in the phase difference between DP ST pressure and the DP active force, and the f_1 primary ST pressure and f_1 active force. As discussed above, the difference $(\phi_{t1}-\phi_{a1})$ is not expected to be zero, and again reviewing the simple case, if ST pressure is proportional to acceleration and active force to velocity, $(\phi_{t1}-\phi_{a1})\sim 90°$. Now, the DP pressure in ST is also likely to be proportional to acceleration, because we have seen from Fig. 7 that the distortion creates fluid motion. If the disturbance sets up its own traveling wave, the disturbance will be the right size (wavelength) so that the pressure will naturally balance the restoring force in the BM. Then the active force at the DP frequency will be devoted to counteracting resistance, and $(\phi_{dt\_n}-\phi_{da\_n})$ will also ~90°. Therefore, and in general, when the distortion is locally generated, and sets up a traveling wave of its own, we could expect that $(\phi_{dt\_n}-\phi_{da\_n})=(\phi_{t1}-\phi_{a1})$, and $(\phi_{dt\_n}-\phi_{da\_n})-(\phi_{t1}-\phi_{a1})=0$. And that could explain why the low-side and lower high-side distortion in the $f_2=$BF case have phases of 0° or 180° and the higher high-side DPs, which are higher in frequency than the BF and so might be less successful in setting up traveling waves, depart from a phase of 0° or 180°.

Therefore, both the 0°/180° phase pattern, and the superimposed slopes can be understood in simple terms. At the

heart of the understanding, and the first assumption, is that $\phi_{da\_n}=\{\phi_{a1}+n(\phi_{a2}-\phi_{a1})\}$ [Eq. (4)]. This came out of considering the nonlinearity as instantaneous—the nonlinearity is a function that relates input to output without delay. But what would be the phase predicted if the nonlinearity were not instantaneous (by acoustic standards)? In other words, has the 0°/180° phase pattern *proven* that the nonlinearity is, or sometimes is, essentially instantaneous? This is the subject of future work.

IV. SUMMARY

We studied two-tone DPs in intracochlear pressure with two basic stimulus sets. In the first stimulus set, stimuli with frequencies around the BF were used to explore the spreading and filtering of DPs in the cochlea. These studies emphasized the $2f_1-f_2$ and $2f_2-f_1$ DPs. Ratio, stimulus level and location in the scala relative to the BM were variables in these measurements. In the second stimulus set, two tones with fixed, low ratio and frequencies that swept over a wide range were used to explore the tuning of several members of the DP family. Both sets of stimuli allowed us to explore the relationship between distortion products and primaries within a single DP family, informing our understanding of the nonlinearity that gives rise to the distortion.

To summarize the results, at low ratio and for primaries in the frequency region of the BF, DP families were produced with the stair–step pattern that is the expected output of a simple, instantaneous nonlinearity. When the primary frequencies were shifted away from the BF, the subsequent tuning of the families by the cochlea's single tone tuning became evident. This was emphasized in the DP-by-DP plots of Figs. 10–12, which showed tuning quite similar to the single tone tuning, particularly for the low-side DPs. This held true for both the amplitude and the phase-vs-frequency behavior of the DPs when plotted relative to the SV primaries (measured near the stapes). At primary frequencies somewhat below the BF, both the amplitude and phase of the DPs sometimes behaved as though they had been generated apical of the recording position, closer to their own BF places.

Variations with f_2/f_1 ratio depended strongly on the relationship between the distortion frequency and the BF. At the 80 dB stimulus level, the effect of reduced overlap due to a wide f_2/f_1 ratio had a relatively small effect, although at the lower stimulus level of 60 dB the reduced overlap had a larger effect, as expected. When $f_2=$BF, the variation with ratio was nonmonotonic, perhaps due to the vector summation of different DP components (reflection/generator).

The DPs fell off rapidly with distance from the BM, but not so rapidly to rule out this route of stapes excitation for generating DP emissions. The measurements here do not address the relative size of through- the-fluid and reverse-traveling-wave stapes excitation. Although it was not described here, the distortion measured in SV close to the stapes in healthy preparations can be quite large. Future studies of SV pressure close to the stapes, coupled with measurements of ear canal emissions and ST pressure, will help sort out this aspect of the emission process. It is notable that the DP pressure close to the BM sometimes underwent large phase variations with distance, which will make the sorting out more challenging. Measurements of Ren (2004) along these lines (BM motion, emission, stapes motion) indicated that the stapes DP motion preceded the BM DP motion. His interesting finding bears repeating and further understanding.

The significance of the 0°/180° phase pattern was explored in some detail, and it was understood as being the expected behavior for a particular condition: that of a local and instantaneous nonlinearity that produces a DP that itself sets up a traveling wave. When the primary frequencies were somewhat lower than the BF, the phase departed from the pattern in a manner that could be attributed to a more apical (as opposed to local) generation spot. Very high-side DPs departed from the 0°/180° pattern in Fig. 13(c), perhaps because they were of too high a frequency to set up traveling waves at the measurement position.

The most striking aspects of the data were the frequency sweeps, showing the degree to which DPs can be tuned as though they were single-tone stimuli, and the 0°/180° pattern of the DP phase.

ACKNOWLEDGMENTS

The authors are grateful to the two JASA reviewers and Ombeline de La Rochefoucauld, Shyam Khanna, and Nigel Cooper for helpful comments on the manuscript, and to Glenis Long for helpful discussions. This work was funded by Grant No. R01 DC03130 from the NIH/NIDCD.

[1]Note that in this simple thought model, the overall distortion is considered to be small, so the input to the nonlinearity is only composed of the two stimulus frequencies. Obviously, when operating in a ''closed loop,'' that input is distorted itself. If the distortion at the input is large enough its effect will modify these simple predictions.

Avan, P., Magnan, P., Smurzynski, J., Probst, R., and Dancer, A. (**1998**). ''Direct evidence of cubic difference tone propagation by intracochlear acoustic pressure measurements in the guinea-pig,'' Eur. J. Neurosci. **10**, 1764–1770.

Avan, P., Bonfils, P., Gilain, L., and Mom, T. (**2003**). ''Physiopathological significance of distortion-product emissions at $2f_1-f_2$ produced by high-versus low-level stimuli,'' J. Acoust. Soc. Am. **113**, 430–441.

Beranek, L. L. (**1993**). *Acoustics* (Acoustical Society of America, New York).

Brown, A. M., Harris, F. P., and Beveridge, H. A. (**1996**). ''Two sources of acoustic distortion products from the human cochlea,'' J. Acoust. Soc. Am. **100**, 3260–3267.

Cooper, N. P. (**2000**). ''Radial variation in the vibration of the cochlear partition,'' in Recent Developments in Auditory Mechanics, edited by H. Wada, T. Takasaka, K. Ikeda, K. Ohyama, and T. Koike (World Scientific, Singapore), pp. 109–115.

Cooper, N. P., and Rhode, W. S. (**1997**). ''Mechanical responses to two-tone DPs in the apical and basal turns of the mammalian cochlea,'' J. Neurophysiol. **78**, 261–270.

Cooper, N. P., and Shera, C. A. (**2004**). ''Backward-traveling waves in the cochlea?'' Abstract #1008 from the Midwinter Meeting of the Association for Research in Otolaryngology.

de Boer, E. (**1984**). ''Auditory physics. Physical principles in hearing theory. II,'' Phys. Rep. **105**, 141–226.

de Boer, E., and Nuttall, A. L. (**2000**). ''The mechanical waveform of the basilar membrane. III. Intensity effects,'' J. Acoust. Soc. Am. **107**, 1497–1507.

Duifhis, H. (**1989**). ''Power law nonlinearities: A review of some less familiar properties,'' in *Cochlear Mechanisms: Structure, Function and Models*, edited by J. P. Wilson and D. T. Kemp (Plenum, New York), pp. 395–403.

Engebretson, A. M., and Eldredge, D. H. (**1968**). ''Model for the nonlinear characteristics of cochlear potentials,'' J. Acoust. Soc. Am. **44**, 548–554.
Fahey, P. F. (**1989**). ''DP responses of saturating nonlinearities,'' in *Cochlear Mechanisms: Structure, Function and Models*, edited by J. P. Wilson and D. T. Kemp (Plenum, New York), pp. 405–412.
Fahey, P. F., Stagner, B. B., Lonsbury-Martin, B. L., and Martin, G. K. (**2000**). ''Nonlinear interactions that could explain DP interference response areas,'' J. Acoust. Soc. Am. **108**, 1786–1802.
Geisler, C. D., and Cai, Y. (**1996**). ''Relationship between frequency-tuning and spatial-tuning curves in the mammalian cochlea,'' J. Acoust. Soc. Am. **99**, 1550–1555.
Goldstein, J. L. (**1967**). ''Auditory nonlinearity,'' J. Acoust. Soc. Am. **41**, 676–689.
Gummer, A. W., Johnstone, B. M., and Armstrong, N. J. (**1981**). ''Direct measurement of basilar membrane stiffness in the guinea pig,'' J. Acoust. Soc. Am. **70**, 1298–1309.
Hu, A., Cuomo, F. W., and Zuckerwar, A. J. (**1992**). ''Theoretical and experimental study of a fiber optic microphone,'' J. Acoust. Soc. Am. **91**, 3049–3056.
Johnstone, J. R., Alder, V. A., Johnstone, B. M., Robertson, D., and Yates, D. K. (**1979**). ''Cochlear action potential threshold and single unit thresholds,'' J. Acoust. Soc. Am. **65**, 254–257.
Kemp, D. T. (**1978**). ''Stimulated acoustic emissions from within the human auditory system,'' J. Acoust. Soc. Am. **64**, 1386–1391.
Kemp, D. T., and Brown, A. M. (**1983**). ''An integrated view of cochlear mechanical nonlinearities observable from the ear canal,'' in *Mechanics of Hearing*, edited by E. de Boer and M. A. Viergever (Martinus Nijhoff, Delft), pp. 75–82.
Kiang, N. Y. S., Liberman, M. C., Sewell, W. F., and Guinan, J. J. (**1986**). ''Single unit clues to cochlear mechanisms,'' Hear. Res. **22**, 171–182.
Kim, D. O., Molnar, C. E., and Mattews, J. W. (**1980**). ''Cochlear mechanics: Nonlinear behavior in two-tone responses as reflected in cochlear-nerve-fiber responses and in ear-canal sound pressure,'' J. Acoust. Soc. Am. **67**, 1704–1721.
Kolston, P. J. (**2000**). ''The importance of phase data and model dimensionality to cochlear mechanics.'' Hear. Res. **145**(1-2), 25–36.
Kros, C. J., Lennan, G. W. T., and Richardson, G. P. (**1995**). ''Transducer currents and bundle movements in outer hair cells of neonatal mice,'' in *Active Hearing*, edited by A. Flock, D. Ottoson, and M. Ulfendahl (Elsevier Science, Amsterdam), pp. 113–125.
Lukashkin, A. N., and Russell, I. J. (**1998**). ''A descriptive model of the receptor potential nonlinearities generated by the hair cell mechanoelectrical transducer,'' J. Acoust. Soc. Am. **103**, 973–980.
Lukashkin, A. N., and Russell, I. J. (**1999**). ''Analysis of the f_2-f_1 and $2f_1-f_2$ distortion components generated by the hair cell mechanoelectrical transducer: Dependence on the amplitudes of the primaries and feedback gain,'' J. Acoust. Soc. Am. **106**, 2661–2668.
Lukashkin, A. N., Lukashkina, V. A., and Russell, I. J. (**2002**). ''One source for DP otoacoustic emissions generated by low- and high-level primaries,'' J. Acoust. Soc. Am. **111**, 2740–2748.
Magnan, P., Avan, P., Dancer, A., Smurzynski, J., and Probst, R. (**1997**). ''Reverse middle-ear transfer function in the guinea pig measured with cubic difference tones,'' Hear. Res. **107**, 41–45.
Mauermann, M., and Kollmeier, B. (**2004**). ''Distortion product otoacoustic emission (DPOAE) input/output functions and the influence of the second DPOAE source,'' J. Acoust. Soc. Am. **116**, 2199–2212.
Mills, D. M. (**2002**). ''Interpretation of standard distortion product otoacoustic emission measurements in light of the complete parametric response,'' J. Acoust. Soc. Am. **112**, 1545–1560.
Muller, M. (**1996**). ''The cochlear place-frequency map of the adult and developing mongolian gerbil,'' Hear. Res. **94**, 148–156.
Naryanan, S. S., Recio, A., and Ruggero, M. A. (**1998**). ''Cubic DPs at the basilar membrane and in the ear canal of chinchilla,'' Abstract #181 from the Midwinter Meeting of the Association for Research in Otolaryngology.
Nilsen, K. E., and Russell, I. J. (**1999**). ''Timing of cochlear feedback: spatial and temporal representation of a tone across the basilar membrane,'' Nat. Neurosci. **2**, 642–648.
Nuttall, A. L., Guo, M., and Ren, T. (**1999**). ''The radial pattern of basilar membrane motion evoked by electrical stimulation of the cochlea,'' Hear. Res. **131**, 39–46.
Olson, E. S. (**1998**). ''Observing middle and inner ear mechanics with novel intracochlear pressure sensors,'' J. Acoust. Soc. Am. **103**, 3445–3463.
Olson, E. S. (**1999**). ''Direct measurement of intracochlear pressure waves,'' Nature (London) **402**, 526–529.
Olson, E. S. (**2001**). ''Intracochlear pressure measurements related to cochlear tuning,'' J. Acoust. Soc. Am. **110**, 349–367.
Olson, E. S. (**2004**). ''Harmonic distortion in intracochlear pressure and its analysis to explore the cochlear amplifier,'' J. Acoust. Soc. Am. **115**, 1230–1241.
Peterson, L. C., and Bogart, B. P. (**1950**). ''A dynamical theory of the cochlea,'' J. Acoust. Soc. Am. **22**, 369–381.
Probst, R., Lonsbury-Martin, B., and Martin, G. (**1991**). ''A review of otoacoustic emissions,'' J. Acoust. Soc. Am. **89**, 2027–2067.
Ren, T. (**2004**). ''Reverse propagation of sound in the gerbil cochlea,'' Nat. Neurosci. **7**, 333–334.
Rhode, W. S., and Recio, A. (**2000**). ''Study of mechanical motions in the basal region of the chinchilla cochlea,'' J. Acoust. Soc. Am. **107**, 3317–3332.
Robles, L., Ruggero, M. A., and Rich, N. C. (**1997**). ''Two-tone distortion on the basilar membrane of the chinchilla cochlea,'' J. Neurophysiol. **77**, 2385–2399.
Robles, L., and Ruggero, M. A. (**2001**). ''Mechanics of the mammalian cochlea,'' Physiol. Rev. **81**, 1305–1352.
Ruggero, M. A. (**1993**). ''Distortion in those good harmonics,'' Curr. Biol. **3**, 755–758.
Ryan, A. (**1976**). ''Hearing sensitivity of the mongolian gerbil, Meriones unguiculatus,'' J. Acoust. Soc. Am. **59**, 1222–1226.
Shera, C., and Guinan, J. J., Jr. (**1999**). ''Evoked otoacoustic emissions arise by two fundamentally different mechanisms: A taxonomy for mammalian OAEs,'' J. Acoust. Soc. Am. **105**, 782–798.
Shera, C. (**2001**). ''Intensity-invariance of fine time structure in basilar-membrane click responses: Implications for cochlear mechanics,'' J. Acoust. Soc. Am. **110**, 332–348.
Siegel, J. H., Kim, D. O., and Molnar, C. E. (**1982**). ''Effects of altering organ of Corti on cochlear DPs f_2-f_1 and $2f_1-f_2$,'' J. Neurophysiol. **47**, 303–328.
Smoorenburg, G. F. (**1972**). ''Combination tones and their origin,'' J. Acoust. Soc. Am. **52**, 615–632.
Steele, C. R., and Taber, L. A. (**1979**). ''Comparison of WKB calculations and experimental results for three-dimensional cochlear models,'' J. Acoust. Soc. Am. **65**, 1007–1018.
Talmadge, C. R., Long, G. R., Tubis, A., and Dhar, S. (**1999**). ''Experimental confirmation of the two-source interference model for the fine structure of distortion product otoacoustic emissions,'' J. Acoust. Soc. Am. **105**, 275–292.
Timoshenko, S. (**1959**). *Theory of Plates and Shells* (McGraw Hill, New York).
Watts, L. (**2000**). ''The mode-coupling Liouville-Green approximation for a two-dimensional cochlear model,'' J. Acoust. Soc. Am. **108**, 2266–2271.
Weiss, T. F., and Leong, R. (**1985**). ''A model for signal transmission in an ear having hair cells with free-standing stereocilia. IV. Mechanoelectric transduction stage,'' Hear. Res. **20**, 175–195.
Xue, S., Mountain, D. C. and Hubbard, A. E. (**1995**). ''Electrically evoked basilar membrane motion.'' J. Acoust. Soc. Am. **97**, 3030–3041.
Zurek, P. M., and Sachs, R. M. (**1979**). ''Combination tones at frequencies greater than the primary tones,'' Science **205**, 600–602.

The effects of neural synchronization and peripheral compression on the acoustic-reflex threshold[a)]

Matthias Müller-Wehlau[b)]
Medizinische Physik, Universität Oldenburg, D-26111 Oldenburg, Germany

Manfred Mauermann
Medizinische Physik, Universität Oldenburg, D-26111 Oldenburg, Germany

Torsten Dau
Centre for Applied Hearing Research, Ørsted·DTU, Technical University of Denmark, DK-2800 Lyngby, Denmark

Birger Kollmeier
Medizinische Physik, Universität Oldenburg, D-26111 Oldenburg, Germany

(Received 29 June 2004; revised 14 January 2005; accepted 18 January 2005)

This study investigates the acoustic reflex threshold (ART) dependency on stimulus phase utilizing low-level reflex audiometry [Neumann *et al.*, Audiol. Neuro-Otol. **1**, 359–369 (1996)]. The goal is to obtain optimal broadband stimuli for elicitation of the acoustic reflex and to obtain objective determinations of cochlear hearing loss. Three types of tone complexes with different phase characteristics were investigated: A stimulus that compensates for basilar-membrane dispersion, thus causing a large overall neural synchrony (basilar-membrane tone complex—BMTC), the temporally inversed stimulus (iBMTC), and random-phase tone complexes (rTC). The ARTs were measured in eight normal-hearing and six hearing-impaired subjects. Five different conditions of peak amplitude and stimulus repetition rate were used for each stimulus type. The results of the present study suggest that the ART is influenced by at least two different factors: (a) the degree of synchrony of neural activity across frequency, and (b) the fast-acting compression mechanism in the cochlea that is reduced in the case of a sensorineural hearing loss. The results allow a clear distinction of the two subjects groups based on the different ART for the utilized types and conditions of the stimuli. These differences might be useful for objective recruitment detection in clinical diagnostics. [DOI: 10.1121/1.1867932]

PACS numbers: 43.66.Nm, 43.64.Ri, 43.64.Ha, 43.64.Jb [BLM] Pages: 3016–3027

I. INTRODUCTION

The acoustic reflex is a contraction of the middle-ear muscles induced by an intense auditory stimulus. Stimulation on either the ipsi- or the contralateral side should result in bilateral muscle contraction in a normal system. Investigations indicate that the main purpose of the reflex is to serve as an attenuator for low-frequency body noise (Simmons, 1964; Katz, 1977; Gelfand, 1998). It is believed that, of the two middle-ear muscles in humans, only the stapedius muscle contracts in response to sound as an acoustic reflex (Borg, 1973; Jerger and Northern, 1980). The reflex elicitation is normally measured acoustically by means of the middle ear's impedance change due to the middle-ear muscle contraction and hence the stiffening of the ossicular chain (Metz, 1951; Lilly, 1984). Detection of the reflex elicitation and assessment of its parameters are commonly used for clinical diagnostics of the hearing system. Deviations of the acoustic reflex threshold, for example, are used as an indicator for neural lesions affecting any portion of the reflex arc central to the cochlea (Clemis, 1984). The pure-tone ART remains almost unaffected by sensorineural hearing loss up to 60 dB (Metz, 1951; Kawase *et al.*, 1997). Generally, the ART decreases with increasing bandwidth of the stimulus eliciting the reflex (Gorga *et al.*, 1980), similarly to the effect of loudness summation in perception. In cases of severe sensorineural or conductive hearing loss, the ART often exceeds the maximal stimulus level of 100 dB HL applied by most impedance bridges. Lower detection thresholds would be preferable, e.g., to make ART measurements usable in subjects with acute auditory damage.

The main goal of the current study was to find an optimal broadband stimulus for low-level elicitation of the ART. Therefore, we adapted a stimulus that is optimized for the measurement of auditory brainstem responses (ABR). Dau *et al.* (2000) demonstrated a significant gain of wave-V amplitude of ABR compared to click stimuli by using a phase-optimized chirp stimulus (BMchirp) that compensates for basilar-membrane travel-time differences across frequency, and thus results in a highly synchronized neural excitation. The gain of neural synchronization is reflected in higher stations of the neuronal pathway like the ventral cochlear nuclei (VCN) and the superior olivary complex (SO), where discharge timing is correlated with cochlear partition motion (Shore *et al.*, 1987; Scherg and Cramon, 1985). A stimulus

[a)]Parts of this study were presented at the 27th Midwinter Research Meeting of the Association for Research in Otolaryngology 2004 in Daytona Beach, Florida [Müller-Wehlau *et al.*, Abstract No. 913, p. 309].

[b)]Author to whom correspondence should be addressed. Electronic mail: wehlau@uni-oldenburg.de

very similar to the chirp stimulus that was optimized for ABR measurements was tested here to reduce the ART. This seems reasonable since the afferent component of the neural pathway of the acoustic reflex can be assumed to follow almost the same path as the sources of ABR. The reflex arc comprises, among other stations, the auditory nerve (N. VIII), the VCN, and the medial nucleus of the SO, before it turns back via the facial nerve (N. VII) to the ear. Therefore, a larger excitation of certain nuclei involved in ABR measurements due to the use of phase-optimized stimulation may be accompanied by a reduction of the ART. The hypothesis tested in the present study was that the chirp stimulus suggested by Dau *et al.*, or a variant of it, may represent an ideal stimulus also for ART measurement due to the increased synchrony of the neuronal excitation. In the following, we refer to this chirp stimulus as the BMchirp. Instead of using single BMchirps, specifically designed tone complexes were used in the present study. These basilar-membrane tone complexes (BMTC) have essentially the same phase characteristics as the original BMchirps, but allow an easier analysis of the residual signal for reflex detection than the original chirps. In addition to the measurements using the BMTC stimuli, corresponding measurements were done with the temporally inverted BMTC tone complexes (iBMTC). The expectation was that the gain due to neural synchronization using the BMTC stimuli would result in a low ART, while the excitation would be highly desynchronized using the iBMTC stimuli, thus resulting in a much higher ART. As a reference, a set of noise-like stimuli was tested consisting of tone complexes with the same magnitude spectrum as the BMTC and iBMTC but with random phase components. Compared to the former stimuli these random-phase tone complexes (rTC) were expected to produce an ART that lies between those obtained with the BMTC and the iBMTC.

However, other aspects besides neural synchronization may also be important for ART determination. For example, effects of peripheral compression due to the different internal representations of the stimuli on the BM may play a role. Kubli *et al.* (2000) measured the acoustic reflex with positive and negative Schroeder-phase tone complexes (Schroeder, 1970). They explained the differences of ART for these two types of stimuli by the different internal representations at the output of cochlear filtering. The internally stronger modulated positive Schroeder-phase stimuli (S+) are supposed to be more affected by fast-acting compression on the BM—thus resulting in increased ARTs—than the negative Schroeder-phase stimuli (S−), which produce a flat internal envelope. In several psychoacoustical detection experiments (e.g., Kohlrausch and Sander, 1995; Lentz and Leek, 2001; Oxenham and Dau, 2001, 2004; Summers and Leek, 1998), the differences of internal representations produced by the Schroeder tone complexes with opposing phase have also been investigated. In these studies, modified Schroeder-phase harmonic tone complexes with different phase curvature showed a different efficiency in masking according to their different temporal modulation within the local auditory filters. These different internal representations are presumably also affected by the compressive characteristics of the BM processing and result in perceptional differences (e.g., Carlyon and Datta, 1997; Summers and Leek, 1998; Oxenham and Dau, 2004). A further variable affecting the ART could be the influence of temporal integration of the stimulus. Although various studies have investigated factors that act as a trigger that elicit the acoustic reflex (Kawase *et al.*, 1998; 1997; Gorga *et al.*, 1980), it is not entirely clear whether signal information is integrated within a certain time frame, or whether the peak amplitude, power, or loudness of the stimulus is appropriate to describe the internal threshold of ART elicitation. In order to test the role of temporal integration and peripheral compression in the current study, the peak-to-rms ratio was varied within a stimulus time frame of about 100 ms. In addition, experiments were carried out in normal-hearing (NH) and hearing-impaired (HI) subjects to investigate the influence of the compressive mechanisms on the BM.

II. MEASUREMENT PARADIGMS AND DATA ANALYSIS

A. Low-level reflex audiometry (LLRA)

To obtain improved ART measurements, i.e., low ART thresholds, we use a method suggested by Neumann *et al.* (1996), called low-level-reflex audiometry (LLRA). For tone pulses, this method is more sensitive than the conventional paradigm (Tolsdorf *et al.*, 2004). Also, the short stimulation time used in this method is more comfortable for the subjects than the stimulation used in the common method. This is especially important since the acoustical stimulation in this study was carried out with levels up to 103 dB SPL. The LLRA uses the same measurement paradigm and equipment as typically employed for the recording of otoacoustic emissions. In this method, rather than using two signals at different frequencies (the evoking stimulus and a continuous test tone—mostly at 226 Hz) as commonly used, a stimulus consisting of two identical short pulses is used to elicit and detect the reflex [see Figs. 1(a) and (d)]. The technique is based on the following principles: If the reflex is elicited during the first stimulus pulse and holds, the eardrum impedance has changed during the presentation of the second pulse. This change of impedance causes a difference between the recorded time signal of the first and second pulse within the sealed ear canal. Since the change in impedance due to the acoustic reflex has a latency of some tens of milliseconds, the second tone pulse is presented after a sufficiently long time following the first, thus leading to a maximal difference of the measured ear-canal response between these two pulses. The difference signal, or the residual of the ear-canal signal, recorded during the presentation of the two tone pulses, is analyzed to indicate the elicitation of the acoustic reflex.

Without an impedance change of the eardrum, i.e., if the first stimulus pulse elicits no reflex, the recorded ear-canal signal is almost the same during both pulses [Fig. 1(b)]. Thus, the spectrum of the difference signal mainly reflects the physiological noise and the noise of the measurement system [Fig. 1(c)]. In the case of an elicited reflex [Fig. 1(e)], the spectrum of the residual shows the frequency components of the stimulus signal [Fig. 1(f)]. The existence of these

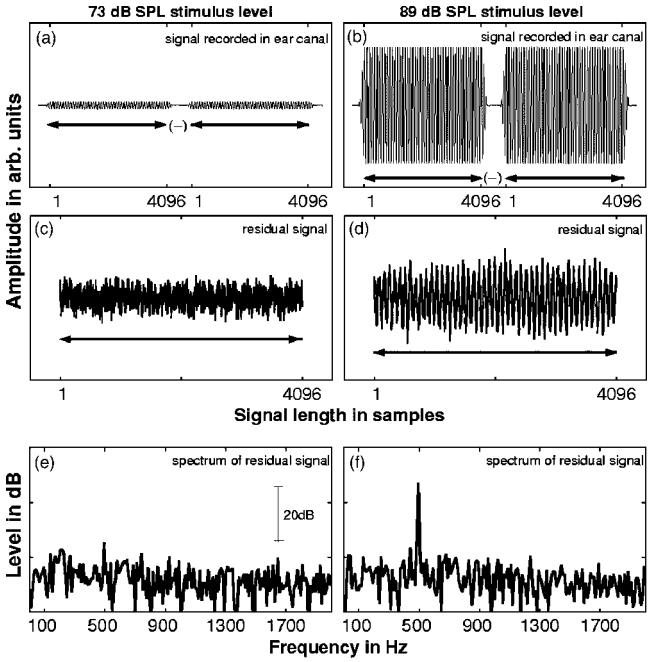

FIG. 1. Illustration of the low-level reflex audiometry (LLRA) method shown for a sinusoidal signal of 500 Hz at two different stimulus levels. The signal consists of two identical pulses of approximately 93 ms (4096 samples) duration, separated by a small gap of 10 ms, and is presented via an OAE probe. The reflex will change the middle ear's reflective properties during the presentation of the stimulus pair, thus changing the recorded signal [(a) and (d)]. By subtracting the two stimulus pulses from each other, the residual signal is obtained [panels (b) and (e)]. If the stimulus level is high enough to elicit the acoustic reflex, the residual is constituted by the stimulus signal as seen in the power spectrum (f). Otherwise the residual is dominated by noise components (g). The residual spectra are shown only for better illustration of the residual properties. The reflex elicitation is detected by means of the phase coherence of an appropriate frequency component in successive presentations.

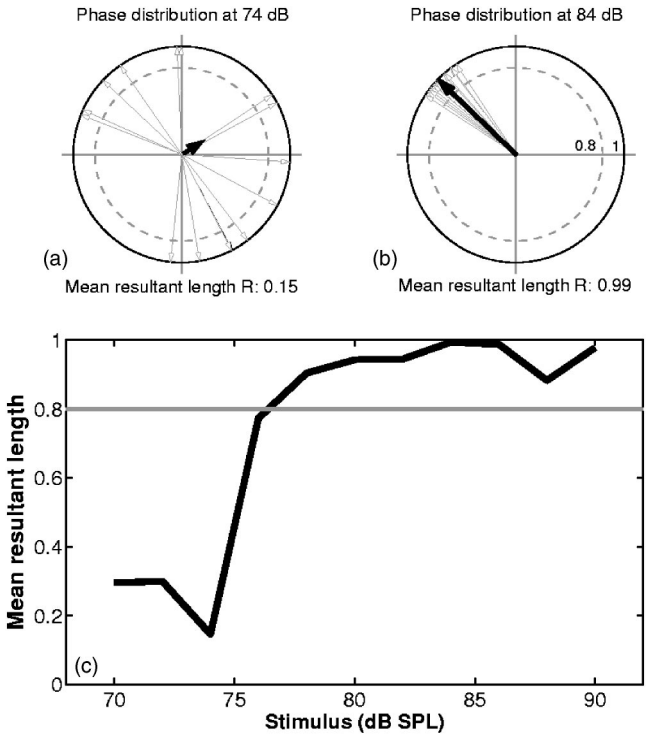

FIG. 2. Phase coherence as a measure of the reflex elicitation: For low stimulus levels the phase of the residual for a number of successive presentations (gray open arrows) is not coherent [panel (a) at 74-dB SPL stimulus level]. Thus, the mean phase vector [black arrow in the panels (a) and (b)] and hence the mean resultant length are small. If the reflex is present during the stimulation, the phase becomes more coherent [panel (b)]. The dashed circle with radius 0.8 in (a) and (b) indicates the threshold condition for the reflex detection. If the length of the mean phase vector is larger than the radius of this circle, i.e., if the mean resultant length R is larger than 0.8, the reflex is considered as elicited. The development of the mean resultant length depending on the stimulus level is shown in panel (c) with the threshold value marked by the gray line, which corresponds to the dashed circles in panels (a) and (b).

frequency components indicates the elicited reflex.

A reliable detection of the stimulus component(s) within the residual signal is essential for the correct detection of the acoustic reflex. Further criteria are needed, especially at higher stimulation levels (close to the limit of the experimental setup), to distinguish between difference components due to the acoustic reflex and physiological or system artifacts. The low-level reflex measurement (Neumann, 1997) utilized for this study was supplemented with a different threshold criterion (see below), since the original criterion used was shown not to be sufficiently reliable (Müller-Wehlau *et al.*, 2002).

B. Analysis methods and ART criterion

The analysis method originally suggested by Neumann *et al.* (1996) is based mainly on a signal-to-noise criterion for the frequency component(s) of the stimulus within the magnitude spectrum of the residual signal, and a further rejection criterion to account for system distortion. However, at higher stimulus levels this method sometimes indicated an ipsilateral acoustic reflex due to artifacts such as heartbeat, even in cochear implant (CI) patients with complete hearing loss and the CI turned off (from our own unpublished data). In the current study, the threshold criterion was based on a coherence synchrony measure (CSM), which is a highly accurate statistical indicator in signal detection (Valdes *et al.*, 1997). The CSM takes the reproducibility of n repetitive measurements (in this study $n=16$) as the criterion to detect the elicited reflex. The CSM is similar to the Rayleigh test of circular uniformity (Mardia, 1972) and can be considered as a measure of phase coherence calculated only from the phase values of a selected frequency component from n successive measurements without considering the amplitude of the signal spectral component. The threshold criterion is given by the mean resultant length R, i.e., the absolute value of the vectorial mean of the normalized phase vectors for a selected frequency component from n consecutive measurement intervals. This method takes into account that successive stimulations demonstrate fast stabilization of their phase values if the stimulus level is high enough to elicit the reflex, thus resulting in highly coherent phase values. This results in a small vectorial mean of the phase vectors, i.e., a small value of R [see Fig. 2(a)] if the phases from consecutive measurement intervals of the selected frequency component are randomly distributed. In contrast, similar phase values of consecutive residuals result in a value of R close to 1 [see Fig. 2(b)]. The mean resultant length R can be computed from the phase values $\theta_i = \theta_1, \ldots, \theta_n$ of the selected frequency components by

$$R = \left| \frac{1}{n} \sum_{i=1}^{n} r_i \right|, \quad \text{with} \quad r_i = \cos\theta_i + i \sin\theta_i . \tag{1}$$

Depending on the phase coherence, the mean resultant length can take values between 0 and 1. If the resultant length is higher than (an empirically found value of) $R \geqslant 0.8$, the reflex is assumed to be elicited (see Fig. 2). This value for R is higher than those commonly used for signal detection in noise by the Rayleigh test.[1] This higher R value represents therefore a more conservative criterion for the reflex elicitation, and meets the fact that ambient factors give rise to small differences in the recorded microphone signal, thus resulting in the presence of spectral components even if the reflex is not present.

Additional artifact suppression was used by rejecting all single measurements whose individual residual amplitude at the selected frequency component was not within a 6-dB margin of the median of all measurements at the respective stimulus level.

The statistical evaluation in the present study was based only on the analysis at one frequency (close to 1000 Hz). A detailed examination of the evaluation frequency by using broadband stimuli showed that between 500 and 1500 Hz the reflex detection does not depend on the selected frequency component. Within this frequency band the change in middle-ear impedance is relatively large, resulting in a clear residual signal if the reflex is elicited. At lower frequencies the phase coherence is more affected by ambient low-frequency noise, while there are broad frequency bands with a strongly reduced change in impedance at higher frequencies.[2]

C. Stimuli

All stimuli consisted of two identical signal frames (see Fig. 1) with frequency components between 100 and 8000 Hz and 4096 samples in length. Since the sampling frequency was 44.1 kHz, the duration, T, of a single stimulus frame was 92.88 ms. The frequency components were adjusted to the signal length, i.e., the exact frequencies were chosen to be multiples of the fast Fourier transform (FFT) base frequency, $1/T$. ARTs were measured for three different types of stimuli. Since our data analysis requires that an appropriate frequency component is presented during the stimulation, all signals used in the experiments were chosen as tone complexes. Twenty samples of Hanning-shaped ramps were added at the beginning and the end of each 4096-sample-long stimulus plateau. Two stimulus frames were separated by a 50-ms gap to be used as a stimulus signal by the LLRA method. Presentations of this frame pair were 1.15 s apart to allow the reflex to decay before subsequent stimulations. In optimization measurements for the LLRA, these settings were found to result in largest residual signals (from our own unpublished data).

1. Tone complexes compensating for cochlear delay across frequency

These stimuli, referred to as the basilar-membrane tone complexes (BMTC) in the following, were generated by adding frequency components with phases that hypothetically compensate for the BM travel-time differences between the different spectral components contained in the stimulus. The stimulus generation was based on the computation of the ''approximate'' chirp stimulus as defined in Dau *et al.* (2000) that was optimized for ABR recordings. According to Dau *et al.* (2000), the propagation time required for the calculation of the respective phase values was estimated using the cochlea model proposed by de Boer (1980) and the frequency-place transformation suggested by Greenwood (1990).

The phase of each frequency component of the tone complex was chosen as follows: The instantaneous phase, φ_{inst}, of the original BMchirp was calculated for the time $t = t_{\text{fs}}$ when the instantaneous frequency of the BMchirp equals the frequency, f_s, of the selected tone complex component. The starting phase, φ_0, for the frequency component at time $t = 0$ was computed such that this component has the phase φ_{m} at the time $t = t_{\text{fs}}$. By superimposing the components with a frequency spacing corresponding to the base frequency of the selected time frame, the respective time signal of a single chirp with flat spectral envelope is achieved [see Figs. 3(c) and (f)].

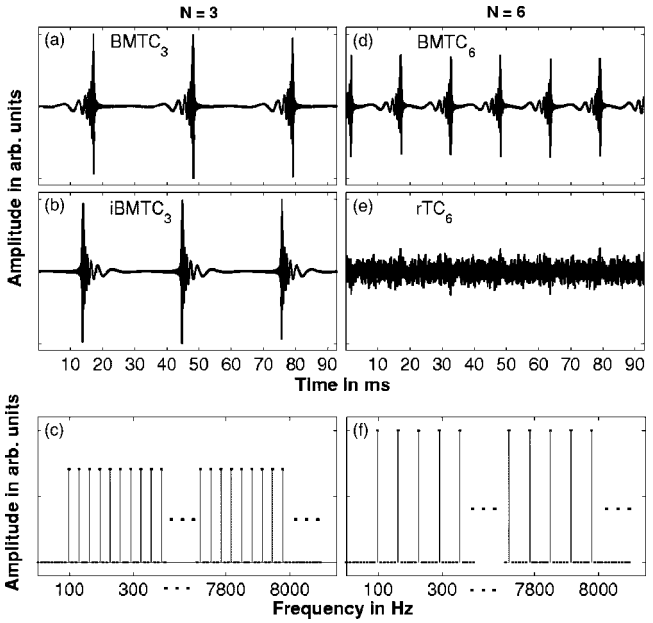

FIG. 3. Stimulus signals: $BMTC_3$ (a), $iBMTC_3$ (b), $BMTC_6$ (d), and rTC_6 (e). All signals are scaled to the same rms level and exhibit a flat spectral envelope with a varied number of contained frequency components. By adding frequency components that are separated by a multiple of the FFT base frequency apart, the number of chirp periods within the time frame is altered without changing the general temporal shape of the successive chirp. The amplitude spectra shown in panels (c) and (f) correspond to the stimuli shown in panels (a) and (b), and (d) and (e), respectively.

2. Temporally inverted tone complexes

The second class of stimuli was generated by temporally inverting the BMTC stimuli. In the following, these stimuli are referred to as the inverted basilar-membrane tone complexes [iBMTC; see Fig. 3(b)]. The expectation was that, by

inverting the BMTC stimulus, the amount of neuronal excitation would be highly desynchronized, thus leading to an increased ART.

3. Random-phase tone complexes

Corresponding measurements were also obtained with a third tone complex with identical magnitude spectrum but random phases of the components, referred to as the random tone complexes [rTC; Fig. 3(e)]. The rTC stimulus for one measurement was generated with respect to one uniformly distributed random phase vector. To exclude incidental compression or synchronization effects due to this certain random phase vector, the measurements were carried out for three rTCs generated with different sets of the random phases.

4. Number of chirp periods per frame—frequency spacing

The BMTC and iBMTC stimuli, comprising frequency components with a spacing equal to the FFT base frequency, exhibit one chirp within the stimulating time frame. Doubling the frequency spacing gives rise to a time signal exhibiting two chirp periods within the time frame of about 100 ms. Further increase of the spacing by a factor N results in an increasing number of N ''overlapping'' chirps in the time domain. In the following, the number N of the chirps used in a certain stimulus is indicated by an index in the stimulus name [e.g., $BMTC_3$ for a BMTC stimulus comprising three chirps per recording frame; see Figs. 3(a), (b), and (c)]. The same notation is used for the rTC stimuli, although the recurring structure in the time domain is not as clearly seen as for the chirp stimuli.

At a fixed rms value, the number of chirp periods (N) and hence the peak-to-rms ratio was varied [compare Figs. 3(a), (d), and (e)] in order to investigate possible summation and compression effects within one stimulus frame. The duration of the original BMchirp for the frequency range used in the current study is 10.4 ms (Dau *et al.*, 2000). We refer to this chirp length as the effective BMchirp duration. Using a maximum number of $N=7$ successive chirps within a stimulus frame of about 100 ms avoids a significant overlap of the chirps within the effective duration. Therefore, interactions of successive chirp periods in the same BM regions within the stimulation can be mostly excluded.

D. Detection of middle-ear muscle reflex versus detection of medial olivocochlear efferent reflex

In general, we assume that the difference of the recorded signals during the two stimulation intervals is mainly due to a contraction of the middle-ear muscle (MEM). In normal-hearing subjects it is conceivable that the residual signal is affected as well by the medial olivocochlear (MOC) efferent reflex. Thereby, the MOC reflex needs to cause a change of a stimulus frequency otoacoustic emission (SFOAE) that is elicited by the probe stimulus (Guinan *et al.*, 2003). Analogous to the difference of the two stimulation intervals due to the MEM, this would result in a residual signal. The residual signals in HI subjects should not be affected by the MOC anyway, since no or only weak SFOAE can be expected for flat hearing losses of about 50 dB. Even in the NH subjects we expect no relevant effect of the MOC reflex on the residual signal, since the stimuli used here are either noise- or chirp-like with a high sweep rate. Although these types of stimuli are appropriate to elicit the MOC reflex, both are unlikely to generate a sufficiently stable SFOAE to allow the detection of the MOC reflex in the residual signal. This holds especially for the noise-like rTC signals. Guinan *et al.* (2003) described the detection of MOC/MEM reflexes based on the change of an SFOAE evoked by a continuous sinusoid. They pointed out that, for a residual signal dominated by the MOC reflex, a rotating phase (i.e., a long group delay) is expected, as known from SFOAE, while for a MEM-dominated residual signal a short group delay can be assumed. An offline analysis of the phase characteristic of the residual signal was performed at the ART level to test for a relevant influence of the MOC on the residual signal and thus on the acoustic reflex detection. This was done for rTC and BMTC at $N=3$ measurements in normal-hearing subjects. BMTC and rTC showed the lowest thresholds and, for $N=3$, the spacing of the frequency components is sufficiently close (ca. 30 Hz) to allow a reliable phase analysis across frequency.

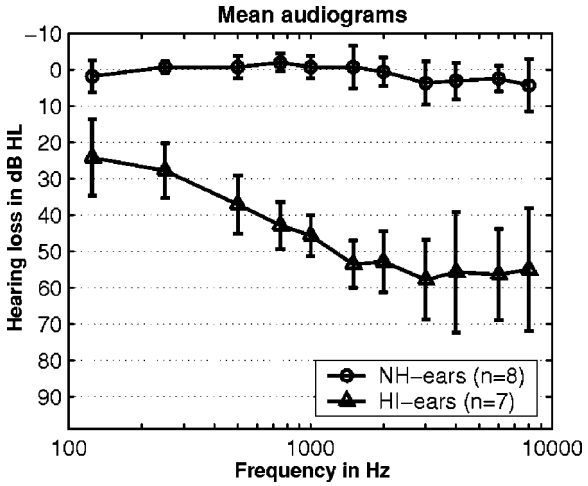

FIG. 4. Average hearing levels for NH subjects (circles) and HI subjects (triangles). The error bars represent the standard deviation of the mean thresholds across subjects.

III. EXPERIMENTAL METHODS

A. Subjects

Eight normal-hearing (NH) subjects (five female, three male) aged between 23 and 32 (average 28 years) with hearing thresholds better than 15 dB HL, and six hearing-impaired (HI) subjects (four female, two male) aged between 38 and 67 (average 54 years) with flat, sensorineural hearing loss participated in this study (see Fig. 4). The NH subject group had no known history of audiological diseases.

The HI subjects were chosen under the assumption that the compressive nonlinearity on the BM will be greatly reduced in these subjects. The ARTs, in response to broadband stimulation, can be expected to be elevated to some degree depending on the hearing loss. The members of the HI sub-

ject group were restricted to subjects with a flat, moderate hearing loss of approximately 50 dB. The subject LP was measured on both sides so that for this group a total of seven measurements was performed.

An audiological examination was carried out on all subjects, including reflex audiometry with a standard impedance audiometer (Grason-Stadler GSI33). The reflex threshold was ascertained by a well-established method in order to make sure that the subjects showed ARTs below 100 dB HL. Subjects showing no conventionally measured ARTs within this range were excluded from further measurements since the experimental setup was limited to stimulus levels of 103 dB SPL. The limitation in sound levels was due to both technical reasons and the goal to restrict the exposure of the subjects to high-level sound over the estimated measurement period of up to 2 h for the full range of experiments conducted. Furthermore, subjects with tympanograms showing only small changes (<0.3 ml) in compliance were also excluded since the LLRA equipment provides no pressure equalization. No abnormally large changes in compliance (>2 ml) have been observed within the subject groups.

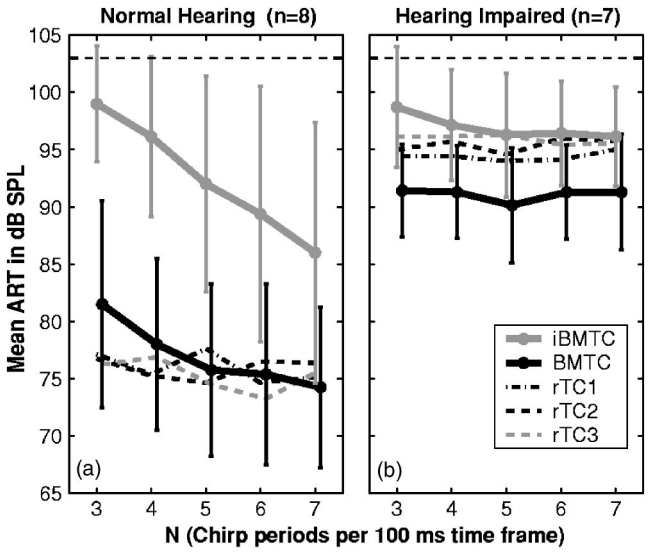

FIG. 5. Mean acoustic reflex thresholds (ART) for NH [Panel (a)] and HI listeners [Panel (b)]. The dashed horizontal line at 103 dB SPL indicates the maximal applied stimulus level. The error bars indicate the interindividual standard deviation of the respective ART measurement. For the reason of clarity, no error bars are given for the three rTC-type stimuli.

B. Setup

The whole measurement was PC based and implemented in a customized program. The level of the signal was digitally controlled and varied on the PC. A digital I/O-card (RME DIGI 96) in the PC was used for the replay of the stimulus signal, which was transmitted via an external DA/AD converter (RME ADI 8 DS) to a headphone buffer (TDT HB6) to drive the probe speaker (Otodynamics ILO BT-type OAE probe). The signal in the ear canal was recorded with an inserted probe microphone (Otodynamics ILO BT-type OAE probe) linked via a connection box that provided the required bias voltage. The microphone signal was amplified by an external low-noise amplifier (Stanford Research SR560) and then directed to the AD converter. The microphone chain was calibrated according to Siegel (2002) using a Bruel & Kjaer type 4192 microphone capsule as reference. The output path including the probe's speakers was calibrated using an artificial ear for insert earphones (Bruel & Kjaer 4157) and a broadband (150–10 000-Hz) calibration signal with flat temporal envelope. The transfer function obtained by this calibration procedure was used to calculate a phase invariant overlap-add filter to correct the stimuli for the frequency response of the output system. No individual correction or in-the-ear calibration was performed.

Before each measurement, the fit of the OAE probe in the individual ear was tested online by presenting a broadband signal and recording with the OAE probe in the sealed ear canal. The spectrum of the recorded signal was displayed in comparison to a reference spectrum obtained in the artificial ear (Bruel & Kjaer 4157) with the same procedure. The fitting of the probe in the individual ear canal was altered to obtain a sufficient correspondence between the reference and the current spectrum.

C. Measurement

An automatic measurement mode was used to assert the reflex threshold starting at medium stimulus levels and subsequently increasing or decreasing the level depending on the reflex detection. After each reversal, the increment/decrement was reduced from 6 dB in the beginning down to 1 dB after the final reversal. Depending on the direction of the level change, either the first or the last measured point where the reflex could successfully be detected after the final reversal was taken as the acoustic reflex threshold. The automatic mode utilized a range of 50 to 103 dB SPL. No reflex threshold was recorded if the reflex could not be detected for three successive measurements at the maximal stimulus level of 103 dB SPL. Since the resulting ARTs were expected to depend on the stimulus type, the starting levels of the automatic algorithm were different for the respective stimuli. All measurements took place inside a sound-attenuating hearing booth (IAC 1203) where the subjects rested in a chair and were allowed to read. Each stimulus was presented 16 times for each of the measured presentation levels. The measurement took approximately 20 min for each of the five stimuli (each for $N=3$ to $N=7$). Therefore, all measurements in one subject were performed in a single session of about 2-h duration.

IV. RESULTS

The results were similar within each of the two subject groups, but differed significantly between the two groups ($p<0.005$).[3] Mean data are shown in Fig. 5.

A. ARTs in normal-hearing subjects

The NH subjects all exhibit significantly lower ARTs for the BMTC stimuli compared to the iBMTC stimuli. The acoustic reflex thresholds of these two stimuli show a clear

dependency on the number of chirps, N, within the stimulus time frame. Paired-samples t-tests reveal the significant decrease of the ARTs with increasing N for both stimuli.[4] This is the case for the BMTC stimuli, where mean thresholds decrease from 81.5 to 74.3 dB SPL, and more pronounced for the iBMTC stimuli with mean thresholds dropping from 98.6 to 86 dB SPL, thus resulting in a convergence that can be generally observed in the NH group. Surprisingly, the ARTs for the rTC stimuli are equal to or even lower than those obtained for the BMTC signals. Two-sided paired-samples t-tests show significantly lower ARTs in response to the rTC stimuli for $N=3$ chirp periods within the time frame for rTC_1 and rTC_3, but no significant difference between any rTC stimulus and BMTC for $N=7$. It can also be observed that the rTC stimulus type does not show a dependency on N with the mean thresholds nearly constant around 76 dB SPL.[5] As expected, all three stimuli of the rTC type with different random phase vectors lead to the same ART.

The characteristics of the ARTs for the different stimulus types were similar among all NH subjects, although the absolute ART levels values for the same stimuli varied between the subjects. In some cases, differences of the ART for the respective stimuli between two NH subjects were up to 15 dB. This difference was also observed for acoustic reflex thresholds measured at 500 and 1000 Hz with a standard procedure (GSI 33 impedance audiometer). If the thresholds in response to the BMTC stimuli were elevated, it was not always possible to assert the threshold for the iBMTC signals due to the limitation of the presentation levels. This was the case for three of the eight NH subjects. In cases where the iBMTC threshold could not be determined, the ART was assumed to be 1 dB higher than the maximal tested stimulation level of 103 dB for statistical analysis. Therefore, the mean values of the iBMTC thresholds, as shown in Fig. 5, are most likely underestimated to some extent. This holds especially for stimuli comprising a low number of chirps within the stimulating time frame, where the resulting thresholds were particularly high for this stimulus type.

Due to the differences in the absolute ART levels, the interindividual standard deviation seen in Fig. 5 for the BMTC and iBMTC thresholds is quite large. Nevertheless, the key properties exhibited by this subject group, i.e. (i) the large difference between the ARTs for the BMTC and iBMTC stimuli; (ii) the dependency of these ARTs on the frequency spacing; and (iii) the low thresholds resulting from the rTC-stimuli, are the same for all subjects of the NH group.

B. ARTs in hearing-impaired subjects

For the HI subjects (right panel of Fig. 5), the ARTs for the BMTC stimuli are also significantly lower than the ARTs obtained by stimulation with iBMTCs. However, the threshold differences between these stimuli are distinctly smaller[3] than for the NH subjects, and range from 8 dB for $N=3$ to 5 dB for $N=7$. Second, in contrast to the NH subjects, no significant difference of the mean ARTs can be found as a function of N, either for the BMTC or the iBMTC stimulus.[6] The mean difference of ART between $N=3$ and $N=7$ for iBMTC stimuli in the HI group is only 2.5 dB (98.6 dB for $N=3$, and 96.1 dB for $N=7$) compared to 12.6 dB in NH subjects. The mean ART in the HI subjects for the BMTC stimuli are nearly independent of N (about 91 dB SPL), while the NH subject group showed a significant[3] decrease of 7.2 dB with increasing N.

Even though the BMTC thresholds found in the HI subjects were elevated compared to the NH subjects, it was possible, with one exception, to assert all ARTs for the iBMTC stimuli in this subject group.

As for the NH subjects, the three rTC stimuli led to essentially the same ART, independent of the frequency spacing and the random vector used for the generation. However, the BMTC thresholds found for the HI were lower than those found for the rTC stimuli, in contrast to the results of the NH group.

For one subject (LP) of the HI group, the pure-tone hearing thresholds for the right ear were about 15 dB lower than for the left ear. A difference of the ARTs for the respective signals can be observed between the two sides, with slightly elevated thresholds for all stimuli on the worse side compared to the thresholds measured in the better ear [compare Figs. 7(a) and (b)]. It can also be observed that the threshold difference between the BMTC and the iBMTC becomes smaller and the dependency on N less pronounced, especially of the iBMTC on the worse ear.

Basic ART characteristics for all subjects are summarized in Table I as the ART T of rTC stimuli (for $N=3$), the difference D between the ART from rTC and iBMTC stimuli (for $N=3$), and the decrease G of ARTs for iBMTC from $N=3$ to $N=7$ (for illustration, see also Fig. 8).

C. Detection of middle-ear muscle reflex versus detection of medial olivocochlear efferent reflex

In order to exclude possible effects of the MOC on the acoustic reflex detection, the phase characteristics of the residual signal across frequency were investigated. All normal-hearing subjects exhibited a constant phase across frequency at threshold levels, indicating that the residual signals are clearly dominated by the MEM contraction (Guinan *et al.*, 2003). This corresponds to the findings of Guinan *et al.* (2003), who found that for elicitor levels of 65 dB SPL or higher, the residual signal is either MEM dominated or a mixture of MEM and MOC.

Furthermore, to exclude the possible influence of spontaneous otoacoustic emission (SOAE) that might be triggered by the stimulus and thereby obscure the ART, we conducted an offline examination of the residual signal at several frequencies between 500 and 1500 Hz using the analysis method mentioned above. This examination did not show the frequency specificity that could be expected if the residual signal was caused by SOAE. All frequencies within certain bands were equally appropriate to detect the reflex, indicating that the residual signal was caused by the impedance change resulting from the MEM contraction.

TABLE I. Comparison of the individual difference D between ARTs for rTC and iBMTC stimuli and the difference G of the ARTs for iBMTC stimuli between $iBMTC_3$ and $iBMTC_7$ (see Fig. 8). The ART T of the rTC stimuli for each subject were calculated with respect to the mean ART of the three rTC type stimuli. No ART for the iBMTC at $N=3$ could be obtained for the subjects indicated by the asterisk (*). In these cases the ART for the $iBMTC_3$ stimulus are approximated from the slope of the remaining iBMTC thresholds. This was not possible for subject JJ, where only the $iBMTC_7$ threshold could be measured. The D value for this subject is estimated from the difference between the mean rTC thresholds and an assumed iBMTC threshold of 104 dB SPL.

NH subjects					HI subjects				
Subject	$D1$ (dB)	$D2$ (dB)	G (dB)	T (dB)	Subject	$D1$ (dB)	$D2$ (dB)	G (dB)	T (dB)
NJ	23	−4	16	68	FR	0	4	2	91
MM	34	−7	32	67	BU	2	13	−1	100
OM*	26	−4	12	78	FD	1	5	−3	92
SA	21	1	14	73	FW*	10	−2	7	94
JJ*	18	−4	⋯	86	WW	−1	8	2	97
KA*	18	−11	16	86	LP (better ear)	8	2	7	94
BS	16	−1	14	82	LP (worse ear)	4	2	4	99
LA	22	−9	10	74					

V. DISCUSSION

A. Mechanisms affecting the acoustic reflex thresholds

The idea behind the generation of the stimuli used in the present study was based on the hypothesis that the reflex threshold is related to the amount of synchronized neural excitation produced by the respective activating stimulus. The experimental results found in the current study partially support this hypothesis. The data also suggest that peripheral compression strongly influences the results for the different stimuli. In all HI subjects, the ''optimized'' BMTC produced the lowest ARTs [see Figs. 6(c) and (d)]. The ARTs obtained with the noise-like rTC stimuli decreased with decreasing hearing loss [Figs. 7(b) and (a)] and obtained values slightly below those for the BMTC stimuli [Figs. 6(a) and (b)] in the NH subjects. This effect and several of the other key observations in the data are discussed in the following. A detailed modeling of the effects was beyond the scope of the study. However, we have attempted to at least qualitatively explain the results based on the different aspects associated with cochlear processing.

1. Excitation characteristics of the different stimuli

The BMTC were designed to compensate for BM dispersion. Ideally, these stimuli produce a maximum amount of excitation across frequency at a particular point in time. In a nonideal case, e.g., if the sweep rate of the chirp does not exactly compensate the delay line characteristic of the cochlea, a relatively broadband synchronized excitation still can be expected that moves in the apical or basal direction. The summation of excitation for the BMTC across all frequency bands as a function of time results in a peaky, i.e., temporally highly modulated ''spectral summation response,'' with the maximum at the time when each auditory filter reaches its maximal excitation. The BMTC are trains of up-chirps, with the instantaneous frequency of each single chirp moving from low to high frequencies. A relatively flat temporal response (slowly increasing and decreasing in time) in each *single* (local) auditory filter can be expected for up-chirps since the stimulus phase curvature has the same sign as the curvature of the phase transfer function of the BM, at least at medium to high frequencies (see, e.g., Smith *et al.*, 1986; Shera, 2001; Oxenham and Dau, 2001, 2004). The temporally inversed iBMTC are trains of down-chirps. A relatively narrow-band BM excitation can be expected at each point in time for a single chirp that moves apically in time, similar to the excitation of a click but moving slower in the apical direction. The spectral summation across frequency will result in a flat response as a function of time (only shaped by the spectral sensitivity of the cochlea and the frequency characteristic of ear canal and middle ear). In contrast to the stimulation with BMTC, not all filters contribute simultaneously; instead, only a few adjacent filters will

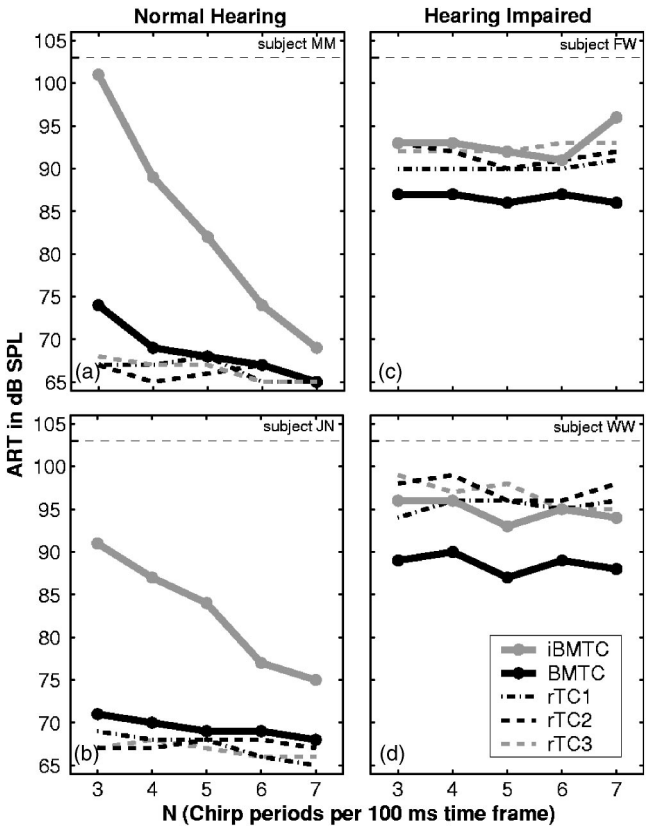

FIG. 6. Examples of ARTs measured for two individual NH [panels (a) and (b)] and two individual HI subjects [panels (c) and (d)].

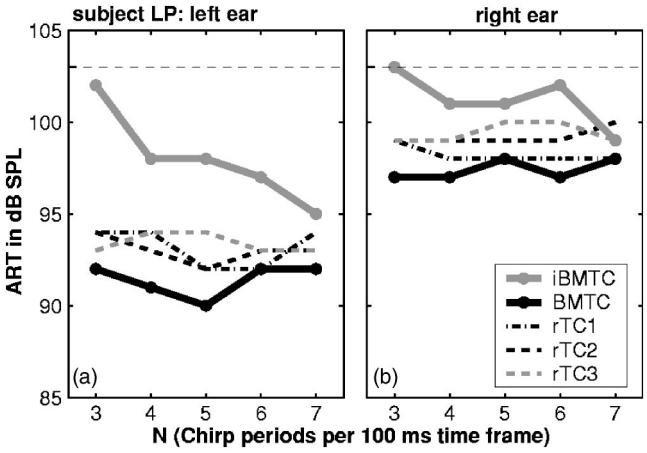

FIG. 7. Examples of the ART characteristic for different degrees of hearing loss. Subject LP showed a general difference in hearing thresholds of about 15 dB between the left (a) and right ear (b). Accordingly, the ART characteristics are different for both ears, with the better ear (a) showing attributes that can also be found in NH listeners. This indicates sufficient sensitivity to utilize this method as an indicator for the loss of BM compression that is associated with OHC damage.

contribute significantly to the spectral summation response at each point in time. From the perspective of the individual auditory filters, a relatively peaky, temporally more modulated response can be expected at the output, since the phase curvature of the down-chirps has the opposite sign as the curvature of (most of) the cochlear phase transfer functions (see, e.g., Oxenham and Dau, 2001). Finally, the rTC stimuli are tone complexes with random phases. These noise-like stimuli are expected to produce a spectrally flat response during the whole stimulation period.

2. Spectral summation and temporal integration

Overall, the acoustic reflex elicitation seems related to the overall spectrally summed cochlear (neural) excitation within a certain time window.[7] The observation that the ARTs in response to $BMTC_3$ and $BMTC_6$ in hearing-impaired subjects are at the same rms level allows a rough estimation of the minimal integration time constant, assuming that nonlinear effects are strongly reduced or absent in the HI subjects. The spectrally summed excitation for $BMTC_6$ comprises two smaller peaks for every peak in the $BMTC_3$ output signal. In order to obtain the same reflex threshold for $BMTC_3$ and $BMTC_6$ (as seen in the HI subjects), the temporally integrated activity/excitation must be the same for the two stimuli. This would be achieved by an integration time window of at least 30 ms, sufficient to include a full chirp of the $BMTC_3$ stimulus and at least two peaks of the spectrally summed cochlear excitation related to two consecutive chirps of the $BMTC_6$ stimulus. However, the criterion for reflex elicitation is not clear. A simple energy summation cannot explain the ART differences between BMTC and iBMTC stimuli. Instead, the differences could possibly be explained by assuming a peak integrator that sums up only contributions of the spectral summation response that exceed an internal threshold. The peaks in the spectral summation response of the BMTCs due to their higher synchronized excitation on the BM exceed this internal threshold at lower stimulus levels than the iBMTC and rTC with their flat temporal envelope of the spectral summation response. However, since the relative amount of excitation that is cut off by the internal threshold increases with decreasing stimulus amplitudes, and since the stimulus amplitude decreases with increasing N while keeping the rms level constant, this model would lead to the prediction of slightly increasing ARTs with N. Thus, for a more detailed model further aspects of processing have to be taken into account.

3. The influence of neural synchronization on the acoustic reflex

Nevertheless, it is reasonable to assume that the ''gain'' obtained with the BMTCs in the HI subjects, reflected in their lower ARTs relative to iBMTC and rTC stimulation [Fig. 5(b)], can be ascribed mainly to the higher neural synchronization. Similar to the explanations for the higher responses in ABR and MEG measurements using BM chirps (Dau, 2003; Rupp *et al.*, 2002), this can be explained by the higher peakiness of the spectral summation response as a function of time. Although derived from a passive BM model, BMTC or BM chirps have so far been tested only in NH subjects (e.g., Dau, 2003). It is not clear whether the improvement obtained with the BM chirp in NH subjects can be expected to hold for HI subjects. A broadening of the BM filters, i.e., a loss of tuning of the BM filters in the HI subjects, may cause a reduction in BM travel time and thus a change of the neural synchronization effect by the stimuli. In turn, it might be that the greater differences between the ARTs for BMTC and iBMTC stimuli, as observed in the NH subjects compared to the HI group [compare Figs. 5(a) and (b)], might reflect the better suitability of the stimuli for compensating the travel-time differences in the healthy cochlea.

4. The influence of cochlear compression on acoustic reflex thresholds

However, with increasing hearing loss the ARTs for the rTC stimuli show a stronger reduction than for the BMTC/iBMTC stimuli. This observation can hardly be explained by a change of the dispersive properties of the BM. Timing effects should not strongly affect these noise-like rTC stimuli, whereas the gain of the spectrally summed activity for the other stimuli is probably influenced strongly by the fast-acting compression in the peripheral auditory system. As is known, e.g., from models of loudness, it is generally assumed that the input from a broadband stimulus to each auditory filter is compressed separately before being summed up across frequencies. Thus, a broadband BM excitation will lead to a higher overall output in comparison to a narrowband excitation. Zwicker and Fastl (1999) describe spectral loudness summation of up to 20 dB in NH subjects for broadband noises centered at 4 kHz, while nearly no loudness summation was found in HI subjects. Thus, the difference of loudness summation between NH and HI subjects is in the order of the gain observed here for the ARTs from the noise-like rTC stimuli in NH subjects in comparison to HI subjects. Although BMTC, iBMTC, and rTC show the same

long-term spectrum, they possess different BM excitations in time. The iBMTC is assumed to produce a high local excitation at each point in time and therefore obtain less gain (maybe almost no gain) from a fast-acting compressive nonlinearity in comparison to the excitation caused by BMTC or rTC which is spread across multiple auditory filters at each time. In each auditory filter, the iBMTCs are expected to produce the peakiest response in time, the BMTCs are assumed to show only a slightly modulated temporal excitation, and the excitation of the rTCs in each local filter will be almost flat in time as well. Assuming an almost instantaneous compression, this will lead to a further gain of the rTC from nonlinear compression in comparison to BMTC and especially iBMTC, since a series of instantaneously compressed low-amplitude excitations will result in a higher integrated output than the respective excitation with only a few higher peaks.

Another observation, the decrease of the ARTs for BMTC and iBMTC with N that can be observed in the NH subject group, also cannot be associated with a change in neural synchronization, since the phase characteristics for the single chirps are kept constant with increasing N.[8] Similar to the decrease in the absolute rTC thresholds, this observation might also be explained by the effects of peripheral compression. Both BMTC and iBMTC produce a temporally defined excitation in each local BM filter. Assuming a static power-law compression in the local cochlear filters, the sum of the compressed output for three excitations with a given amplitude resulting from a $BMTC_3$ elicitor would be smaller than that of six excitations evoked by a $BMTC_6$ stimulus at the same overall rms level.[9] Furthermore, the decrease of ARTs with N might be related to an interaction of successive stimuli on the BM. Especially for the narrow-band excitation of the iBMTC, slowly moving along the cochlear partition, it can be assumed that, for higher N, the excitation of the preceding chirp is still moving towards the apex while the excitation of the current chirp is starting at the base of the cochlea. In the case of a compressive cochlear nonlinearity, the output for lower-level inputs to many filters will exceed the output from a single filter with a respectively higher input, and thus result in lower ARTs. This effect would be more pronounced for the iBMTCs than for the BMTCs, since the iBMTCs are expected to produce a narrow-band excitation slowly moving from the base to the apex in contrast to a synchronized (already) broadband BM excitation from the BMTC. A presumed reduction in travel time on the BM for the damaged cochlear might result in a reduced effect in the HI subject group, leading to no or only a slight dependency on N for these subjects.

Overall, assuming a different gain of neural synchronization for the different stimuli in combination with a major effect of a fast-acting cochlear nonlinearity (in NH subjects) on the observed effects of ART for the different stimuli gives the qualitatively most consistent view on the data. Most HI subjects with severe hearing loss have a strongly reduced compression. In these subjects [see Figs. 6(c) and (d)], the observed effects are dominated by the gain of neural synchronization. There is no ART decrease with increasing N, and the ART from the rTC stimuli is similar to or slightly below the iBMTC stimuli. The peakier overall excitation of the BMTC might be used by a mechanism based on a peak integrator to obtain lower ARTs. With decreasing hearing loss and increasing influence of a nonlinear compression, the ARTs of the rTC stimuli are shifted towards the ARTs of the BMTC stimuli, which are also reduced [see Fig. 7(b)], and even the decrease of the ARTs with increasing N becomes observable for the iBMTC stimuli [see Fig. 7(a) and Figs. 6(b) and (a)]. Thus, besides the absolute ARTs, the differences between the ARTs for different stimuli might be used to improve the value of ART measurements as a screening tool in clinical diagnostics. For example, the difference G for ART from iBMTC stimuli at $N=3$ and $N=6$ or the differences $D1$ and $D2$ between the ARTs of iBMTC, BMTC, and rTC might be useful to indicate a loss of compression.

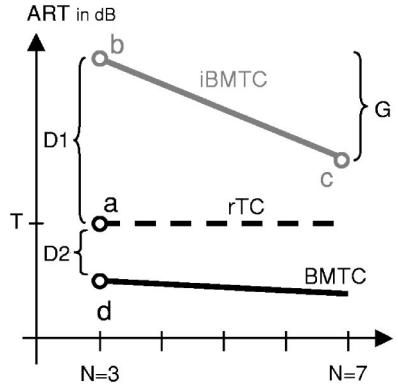

FIG. 8. Illustration of ART characteristics T, $D1$, $D2$, G as given in Table I for all subjects obtained from ART measurements at only four different stimulus conditions (a,b,c,d). T is the ART for an rTC stimulus at $N=3$ given by measurement point a. $D1$ (b–a) is given by the ART difference for an rTC and the iBMTC stimulus at $N=3$ and $D2$ (d–a) as the difference for an rTC and the BMTC, respectively. Finally, G (b–c) gives the ART difference for iBMTC stimuli at $N=3$ and $N=7$.

B. Prediction of hearing status and clinical applications

Besides the absolute thresholds like the threshold T for the rTC (see Fig. 8, Table I), other characteristics of the ART allow for a clear distinction between NH and HI subjects, such as (1) the decrease for ART especially for iBMTC, but also for BMTC, stimulation in NH subjects with increasing N (indicated by G—see Fig. 8, Table I), while no dependency was found for the HI subjects, and (2) larger ART differences between diverse stimuli types. Thus, appropriate criteria to distinguish between NH and HI subjects may be given by the ART differences $D1$ and $D2$ (see Fig. 8 and Table I). $D1$ is the difference between an rTC_3 and the $iBMTC_3$ stimulus, which shows a significant reduction from 22.3 dB in NH subjects to 3.5 dB in the HI subjects.[10] The difference $D2$ between rTC_3 and $BMTC_3$ is negative for most NH subjects and is positive for most HI subjects—probably closely related to an increasing loss of compression. Additionally, the difference G between ARTs from iBMTC stimuli for $N=3$ and $N=7$ allows a clear distinction between NH and HI subjects (see Fig. 8 and Table I). A high sensitivity of the ART differences, e.g., $D1$, with respect to hearing loss and loss of compression may be indicated by the

results from subject LP (see Fig. 7). This subject showed an almost parallel shift of hearing thresholds across frequency of about 15 dB between the two ears that is clearly reflected in different values of T, $D1$, $D2$, and G (see Table I). Therefore, the additional consideration of ART differences for different stimuli beside the evaluation of absolute thresholds may allow a more reliable prediction of hearing impairment than using absolute ARTs alone. Overall, based on the data from this limited group of subjects, the differences of $D1$, $D2$, G, or T in NH and HI subjects for the specially designed stimuli in this study may offer the opportunity to utilize the measurement of ARTs for the objective prediction of hearing loss and recruitment or for hearing-aid fitting in young or uncooperative patients.

Earlier studies showed that a close relationship of the mean ART and the uncomfortable level (UCL) might exist. However, the prediction of the UCL based on the ART measurement will be inaccurate because of the high intersubject variability (review in Olsen, 1999a; Olsen 1999b, c, Margolis and Popelka, 1975; Kawase *et al.*, 1997). As opposed to these studies where loudness and ART were compared directly, the present results suggest a comparison of the differences of ARTs for appropriate stimuli (e.g., BMTC, rTC vs iBMTC) that are differently affected by cochlear compression. Thus, the large intersubject variability might be reduced if the ART differences for special stimuli are considered, rather than the absolute thresholds alone. Based on this limited group of subjects, the derived measures $D1$, $D2$, G, and the ART T for the rTC stimuli give at least a set of highly significant screening indicators to distinguish between NH and HI subjects (see Table I). Further studies will have to investigate if a classification of the individual hearing loss or even a quantitative prediction can be obtained by combining the different indicators in a larger group of subjects with different shapes and types of hearing loss. Another point of interest is to find stimuli with similar properties but higher frequency specificity than the ones used here.

VI. SUMMARY AND OUTLOOK

(i) A clear effect of neural synchronization on acoustic reflex threshold [using the low-level reflex audiometry according to Neumann *et al.* (1996)] can be observed when comparing results obtained from BMTC and iBMTC stimuli. Therefore, the acoustic reflex threshold is strongly affected by the phase properties of the stimulus and thus by the dispersive characteristics of the cochlea. The results suggest that the ART depends on the amount of synchronized neural excitation integrated across frequency.

(ii) The large difference in ART obtained with the different stimuli used here (BMTC, iBMTC, and rTC stimuli) as well as the large difference between normal and hearing-impaired subjects can be explained qualitatively by assuming a compressive nonlinearity as typically found in BM input–output functions of normally functioning cochleae. However, in order to obtain a more quantitative understanding of the cochlear mechanisms that contribute to elicitation of the ART, modeling work is needed in future studies.

(iii) Besides the absolute ART values, there are several other indicators of hearing loss in our (limited) group of subjects like the differences ($D1$ and $D2$) of the acoustic-reflex thresholds for rTC_3 and $iBMTC_3$ or $BMTC_3$ stimuli, respectively. The clear distinctions between the two subject groups by the derived measures $D1$, $D2$, and G in combination with absolute ART may improve the use of acoustic reflex threshold measurements as an objective predictor of a loss of cochlear compression. Further studies are required to validate these measures as a clinical tool.

(iv) The online-analysis method might be improved in future studies by incorporating a multifrequency evaluation. This might be useful to reduce the total number of consecutive stimulus presentations and consequently in measurement time without a decrease in statistical significance. Furthermore, this approach can provide additional artifact suppression with regard to the MOC efferent reflex by considering the change in group delay across frequencies. However, utilizing more than one frequency for the evaluation corresponds with an increase of the number, n, of phase values as long as all used frequencies are equally appropriate. Therefore, no relevant difference in the detection threshold, i.e., in the sensitivity of the method, can be expected.

ACKNOWLEDGMENTS

This study was supported by Deutsche Forschungsgemeinschaft, DFG Ko 942/11-3. We want to thank Jesko Verhey for fruitful discussions about compression. We gratefully acknowledge the two anonymous reviewers for their valuable comments on the manuscript.

[1]The critical value typically used for the detection of a sinusoid in noise for 16 repetitions $R_0(16,0.001)$ is 0.63 (Mardia, 1972). Here, we use the more conservative empirically established reflex elicition threshold value of $R_0 = 0.8$.

[2]In some subjects at higher frequencies, the ART would have been detected even at lower levels while no reflex would have been detected in other subjects at these frequencies. Around 1000 Hz appears to be a frequency region of a reliable impedance change across all subjects.

[3]The comparison of the iBMTC/BMTC difference for both subject groups using the Wilcoxon, Mann, and Whitney U-test for independent samples ($U = 3.5 < 6 = U_{8;7;.005}$).

[4]The single-sided paired-samples t-test revealed significant ART differences for both stimuli under all conditions except for the ARTs in response to $BMTC_6$ compared to $BMTC_7$.

[5]Paired-samples t-tests reveal no significant differences between $N = 3$ and $N = 7$ for any of the rTC-type stimuli.

[6]A paired-sample t-test between the thresholds in response to $iBMTC_3/iBMTC_7$ and $BMTC_3/BMTC_7$ revealed no significant difference between these ART pairs. Therefore, a systematic dependency of the ARTs on N can be rejected for these stimuli in the HI subject group. However, a complete pair comparison reveals single deviations from a constant threshold across N. The ART for $iBMTC_3$, for example, are significantly higher compared to $iBMTC_{4,5}$ and $_6$. For the BMTC stimuli, the ART in response to $BMTC_5$ was significantly lower compared to $BMTC_6$ and $_7$.

[7]This might be some kind of leaky integrator. However, this is subject to a more detailed modeling and will not be discussed here.

[8]This is different from the characteristic known for Schroeder-phase tone complexes. An increase of the repetition rate, i.e., of the fundamental frequency f_0 in Schroeder-phase tone complexes, means by definition a

change in sweep rate or phase curvature as well. This is not the case for the BMTC and iBMTC. An increase of f_0 results simply in an increasing number of consecutive chirps within the stimulus duration. Thus, for the BMTC/iBMTC the phase characteristic of each chirp is kept almost constant as long as $1/f_0$ does not exceed an ''effective chirp duration'' of about 10 ms. For higher f_0 the chirps are shifted into one another.

[9]For example, with an amplitude reduced by a factor of 0.71. Thus, a reduction of approximately 2 dB from $N=3$ to $N=6$ could be expected for an exponent of 0.3, while no effect can be expected for the HI subject assuming negligible compression and therefore an exponent close to 1.

[10]The comparison of the iBMTC/mean(rTC) difference for both subject groups using the Willcoxon, Mann, and Whitney U-test for independent samples demonstrates a significant reduction of this difference in the HI listeners ($p<0.001: U=0<2=U_{8;7;0.001}$).

Borg, E. (**1973**). ''On the neural organization of the acoustic middle ear reflex. A physiological and anatomical study,'' Brain Res. **49**, 101–123.

Carlyon, R. P., and Datta, A. J. (**1997**). ''Masking period patterns of Schroeder-phase complexes: Effects of level, number of components, and phase of flanking components,'' J. Acoust. Soc. Am. **101(6)**, 3648–3657.

Clemis, J. D. (**1984**). ''Acoustic reflex testing in otoneurology,'' Otolaryngol.-Head Neck Surg. **92**, 141–144.

Dau, T., Wegner, O., Mellert, V., and Kollmeier, B. (**2000**). ''Auditory brainstem responses with optimized chirp signals compensating basilar-membrane dispersion,'' J. Acoust. Soc. Am. **107**, 1530–1540.

Dau, T. (**2003**). ''The importance of cochlear processing for the formation of auditory brainstem and frequency following responses,'' J. Acoust. Soc. Am. **113**, 936–50.

de Boer, E. (**1980**). ''Auditory physics. Physical principles in hearing theory I,'' Phys. Rep. **62**, 87–174.

Gelfand, S. A. (**1998**). *Hearing—An Introduction to Psychological and Physiological Acoustics* (Dekker, New York).

Gorga, M. P., Lilly, D. J., and Lenth, R. V. (**1980**). ''Effect of signal bandwidth upon threshold of the acoustic reflex and upon loudness,'' Audiology **19**, 277–292.

Greenwood, D. D. (**1990**). ''A cochlear frequency position function for several species—29 years later,'' J. Acoust. Soc. Am. **87**, 2592–2605.

Guinan, J. J. J., Bradford, C. B., Lilaonitkul, W., and Aharonson, V. (**2003**). ''Medial olivocochlear efferent reflex in humans: Otoacoustic emission (OAE) measurement issues and the advantage of stimulus frequency OAEs,'' J. Assoc. Res. Otolaryng **4**, 521–540.

Jerger, J., and Northern, J. L. (**1980**). *Clinical Impedance Audiometry* (Thieme, Stuttgart, New York).

Katz, J. (**1977**). *Handbook of Clinical Audiology* (Lippincott Williams & Wilkins, Philadelphia).

Kawase, T., Hidaka, H., Ikeda, K., Hashimoto, S., and Takasaka, T. (**1998**). ''Acoustic reflex thresholds and loudness in patients with unilateral hearing losses,'' Eur. Arch. Otorhinolaryngol. **255**, 7–11.

Kawase, T., Hidaka, H., and Takasaka, T. (**1997**). ''Frequency summation observed in the human acoustic reflex,'' Hear. Res. **108**, 37–45.

Kohlrausch, A., and Sander, A. (**1995**). ''Phase effects in masking related to dispersion in the inner ear II. Masking period patterns of short targets,'' J. Acoust. Soc. Am. **97**, 1817–1829.

Kubli, L., Dreisbach, L., Leek, M., and Lentz, J. (**2000**). ''Acoustic reflexes to Schroeder-phase harmonic complexes in normal-hearing and hearing-impaired individuals,'' Assoc. Res. Otolaryngol. Abs. **599**, 173(A).

Lentz, J. J., and Leek, M. R. (**2001**). ''Psychophysical estimates of cochlear phase response: Masking by harmonic complexes,'' J. Assoc. Res. Otolaryng. **2**, 408–422.

Lilly, D. J. (**1984**). *Evaluation of the Response Time of Acoustic-immittance Instruments. The Acoustic Reflex*, edited by S. Silman (Academic, New York), pp. 102–135.

Mardia, K. V. (**1972**). *Statistics of Directional Data* (Academic, London, New York).

Margolis, R. H., and Popelka, G. R.. (**1975**). ''Loudness and the acoustic reflex,'' J. Acoust. Soc. Am. **58**, 1330–1332.

Metz, O. (**1951**). ''Studies on the contraction of the tympanic muscles as indicated by changes in the impedance of the ear,'' Acta Oto-Laryngol. **39**, 397–405.

Müller-Wehlau, M., Mauermann, M., and Kollmeier, B. (**2002**). ''Auswertealgorithmen zur Niedrigpegel-Reflexaudiometrie'' [Evaluation algorithm for the low level reflex audiometry]. Fortschr. Akustik-DAGA 2002 (Ed) 52–53.

Neumann, J. (**1997**). *Recording Techniques, Theory and Audiological Application of Otoacoustic Emissions*. (BIS-Verlag Oldenburg).

Neumann, J., Uppenkamp, S., and Kollmeier, B. (**1996**). ''Detection of the acoustic reflex below 80 dB HL,'' Audiol. Neuro-Otol. **1**, 359–369.

Olsen, S. Ø. (**1999a**). ''The relationship between the uncomfortable loudness level and the acoustic reflex threshold for pure tones in normally hearing and impaired listeners—A meta-analysis,'' Audiology **38**, 61–68.

Olsen, S. Ø, Rassmussen, A. N., Nielsen, L.H., and Borgkvist, B. V. (**1999b**). ''The acoustic reflex threshold: not predictive for loudness perception in normally-hearing subjects,'' Audiology **38**, 303–307

Olsen, S. Ø, Rassmussen, A. N., Nielsen, L. H., and Borgkvist, B. V. (**1999c**). ''The relationship between the acoustic reflex threshold and levels of loudness categories in hearing-impaired listeners,'' Audiology **38**, 308–311.

Oxenham, A., and Dau, T. (**2001**). ''Phase effects in masking in normal-hearing and hearing-impaired listeners,'' J. Acoust. Soc. Am. **110**, 3169–3177.

Oxenham, A., and Dau, T. (**2004**). ''Masker phase effects in normal-hearing and hearing-impaired listeners: Evidence for peripheral compression at low signal frequencies,'' J. Acoust. Soc. Am. **116(4)**, 2248–2257.

Rupp, A., Uppenkamp, S., Gutschalk, A., Beucker, R., Patterson, R. D., Dau, T., and Scherg, M. (**2002**). ''The representation of peripheral neural activity in the middle-latency evoked field of primary auditory cortex in humans,'' Hear. Res. **174**, 19–31.

Scherg, M., and von Cramon, D. (**1985**). ''A new interpretation of the generators of BAEP waves I–V: Results of a spatio-temporal dipole model,'' Electroencephalogr. Clin. Neurophysiol. **62(4)**, 290–299.

Schroeder, M. R. (**1970**). ''Synthesis of low-peak-factor and binary sequences with low autocorrelation,'' IEEE Trans. Inf. Theory **IT-16**, 85–95.

Shera, C. A. (**2001**). ''Frequency glides in click responses of the basilar membrane and auditory nerve: Their scaling behavior and origin in traveling-wave dispersion,'' J. Acoust. Soc. Am. **109(5)**, 2023–2034.

Shore, S. E., Clopton, B. M., and Au, Y. N. (**1987**). ''Unit response in ventral cochlear nucleus reflect cochlear coding of rapid frequency sweeps,'' J. Acoust. Soc. Am. **82**, 471–478.

Siegel, J. H. (**2002**). ''Calibrating otoacoustic emission probes,'' in *Otoacoustic Emissions—Clinical Applications*, edited by M. S. Robinette and T. J. Glattke (Thieme, New York, Stuttgart), pp. 416–441.

Simmons, F. B. (**1964**). ''Perceptual theories of middle ear muscle function,'' Ann. Otol. Rhinol. Laryngol. **73**, 724–739.

Smith, B. K., Sieben, U. K., Kohlrausch, A., and Schroeder, M. R. (**1986**). ''Phase effects in masking related to dispersion in the inner ear,'' J. Acoust. Soc. Am. **80(6)**, 1631–1637.

Summers, V., and Leek, M. R. (**1998**). ''Masking of tones and speech by Schroeder-phase harmonic complexes in normally hearing and hearing impaired listeners,'' Hear. Res. **118**, 139–150.

Tolsdorf, B., Münscher, A., Maier, H., Plotz, K., Müller-Wehlau, M., Mauermann, M., Baumann, U., and Leuwer, R. (**2004**). ''Clinical evaluation of low level acoustic reflex audiometry,'' Assoc. Res. Otolaryngol. Abs. **27**, 34(A).

Valdes, J. L., Perez-Abalo, M. C., Martin, V., Savio, G., Sierra, C., Rodriguez, E., and Lins, O. (**1997**). ''Comparison of Statistical Indicators for the Automatic Detection of 80 Hz Auditory Steady State Responses,'' Ear Hear. **18(5)**, 420–429.

Zwicker, E., and Fastl, H. (**1999**). *Psychoacoustics: Facts and Models* (Springer, Berlin).

Comparing different estimates of cochlear compression in listeners with normal and impaired hearing[a)]

Peninah S. Rosengard,[b)] Andrew J. Oxenham, and Louis D. Braida
Harvard-MIT Division of Health Sciences and Technology, Speech and Hearing Bioscience and Technology Program, Cambridge, Massachusetts 02139 and Research Laboratory of Electronics, Massachusetts Institute of Technology, Cambridge, Massachusetts 02139

(Received 16 October 2004; revised 16 January 2005; accepted 9 February 2005)

A loss of cochlear compression may underlie many of the difficulties experienced by hearing-impaired listeners. Two behavioral forward-masking paradigms that have been used to estimate the magnitude of cochlear compression are growth of masking (GOM) and temporal masking (TM). The aim of this study was to determine whether these two measures produce within-subjects results that are consistent across a range of signal frequencies and, if so, to compare them in terms of reliability or efficiency. GOM and TM functions were measured in a group of five normal-hearing and five hearing-impaired listeners at signal frequencies of 1000, 2000, and 4000 Hz. Compression values were derived from the masking data and confidence intervals were constructed around these estimates. Both measures produced comparable estimates of compression, but both measures have distinct advantages and disadvantages, so that the more appropriate measure depends on factors such as the frequency region of interest and the degree of hearing loss. Because of the long testing times needed, neither measure is suitable for clinical use in its current form. [DOI: 10.1121/1.1883367]

PACS numbers: 43.66.Ba, 43.66.Dc, 43.66.Sr, 43.66.Mk [GDK] Pages: 3028–3041

I. INTRODUCTION

Physiological studies of the healthy mammalian cochlea have shown that the response of the basilar membrane is highly compressive for tones presented at characteristic frequency (Rhode and Robles, 1974; Robles *et al.*, 1986; Murugasu and Russell, 1995; Ruggero *et al.*, 1997; Russell and Nilsen, 1997; Rhode and Recio, 2000). A loss of this nonlinearity may underlie many of the difficulties experienced by hearing-impaired listeners: abnormal loudness growth, reduced frequency selectivity, reduced rate of decay of forward masking, and larger-than-normal gap-detection thresholds in narrow-band noise can all be accounted for by a loss or reduction of compression on the basilar membrane (Yates, 1990; Glasberg and Moore, 1992; Oxenham and Moore, 1997; Oxenham and Bacon, 2003). A reliable behavioral measure of cochlear compression may therefore be of clinical value.

Forward masking of tonal signals is one psychophysical method that has been used in human listeners to derive estimates of the magnitude of cochlear compression. Forward masking lends itself to estimating cochlear response because the nonsimultaneous presentation of the masker and signal eliminates concerns regarding possible nonlinear peripheral interactions, such as suppression. The compression values derived from such measures tend to be quantitatively similar to those obtained using physiological techniques in animals (e.g., Oxenham and Plack, 1997; Rosen *et al.*, 1998; Baker *et al.*, 1998; Glasberg *et al.*, 1999; Hicks and Bacon, 1999; Plack and Oxenham, 2000; Wojtczak *et al.*, 2001; Nelson *et al.*, 2001; Moore *et al.*, 2002; Lopez-Poveda *et al.*, 2003; Plack and Drga, 2003).

The two most commonly used forward-masking techniques for estimating compression are growth of masking (GOM) (e.g., Oxenham and Plack, 1997) and temporal masking (TM) (e.g., Nelson *et al.*, 2001). Both paradigms derive compression values by comparing off-frequency masker levels (i.e., masker frequency less than or equal to 0.6 times signal frequency) with on-frequency masker levels (i.e., masker frequency equal to signal frequency). In line with the available physiological data (usually taken from the base of the cochlea) it is assumed that basilar membrane compression is limited to frequencies around the characteristic frequency and that the response to a tone half an octave or more below characteristic frequency is approximately linear (Yates *et al.*, 1990; Ruggero *et al.*, 1997). While this assumption is probably valid for high characteristic frequencies, some recent physiological and psychophysical studies have questioned its validity at low characteristic frequencies (e.g., Rhode and Cooper, 1996; Oxenham and Dau, 2001, 2004; Lopez-Poveda *et al.*, 2003; Plack and Drga, 2003). For the details of further assumptions, see Oxenham and Plack (1997) and Nelson *et al.* (2001).

In the case of GOM, masker levels necessary to just mask a signal are measured at several fixed signal levels. The slope of a GOM function is thought to reflect relative differences in the response of the basilar membrane to the masker and signal at the place on the basilar membrane where the signal is detected. For on-frequency maskers when both the signal and the masker are nearly equal in level, the GOM function has a slope roughly equal to one, presumably because both the signal and masker are subjected to similar

[a)]Portions of this work were presented at the Association for Research in Otolaryngology Midwinter Meeting, Daytona Beach, FL, February 2003.
[b)]Electronic mail: peninah@mit.edu

amounts of compression. Off-frequency masking produces functions with a slope less than one, especially at medium signal levels, because the response to the signal is compressed while the response to the masker is not. The ratio of the slopes of straight lines fit to the off- and on-frequency data, for a given signal frequency, provides an estimate of the magnitude of compression.

In the case of TM, masker levels necessary to just mask a fixed low sensation level signal are measured as a function of the time delay between the offset of the masker and the onset of the signal. For the on-frequency masker, the change in masker level as a function of delay is thought to reflect the effects of compression and the more central recovery from forward masking; for the off-frequency masker, which is assumed to be processed linearly, the function should reflect only the recovery from forward masking, which is known to be independent of masker frequency (e.g., Nelson and Pavlov, 1989). Thus, the effects of compression and decay of the response to the masker can be separated by plotting off-frequency masker levels as a function of on-frequency masker levels, paired according to signal delay (Nelson *et al.*, 2001; Lopez-Poveda *et al.*, 2003; Plack and Drga, 2003). The resulting function can be viewed as a derived basilar membrane input-output function.

Despite these procedural differences, both GOM and TM purport to measure the same thing, namely basilar membrane compression. However, no study has yet made a direct comparison of the two methods in the same listeners. Such a comparison is of interest for at least two reasons. First, it tests the assumption that the two techniques do indeed provide estimates of the same underlying phenomenon; second, it allows a direct comparison of the two measures in terms of efficiency and reliability. In the current study, GOM and TM curves were measured in five normal-hearing listeners (experiment I) and five hearing-impaired listeners (experiment II).

II. EXPERIMENT I: NORMAL-HEARING LISTENERS

A. Methods

1. Stimuli and procedure

GOM and TM curves were measured at signal frequencies (f_s) of 1, 2, and 4 kHz with an on-frequency ($f_m = f_s$) and off-frequency ($f_m = 0.55 f_s$) forward masker. Both the signal and masker tones were gated with raised-cosine ramps of 5 ms in the 1- and 2-kHz signal frequency conditions and 2.5 ms in the 4-kHz condition. The signal and the masker had steady-state portions of 0 and 100 ms, respectively.

In the GOM paradigm, the level of a forward masker needed to just mask the signal was measured as a function of signal level (50, 55, 60, 65, 70, and 75 dB SPL). These signal levels were selected because this is the level region where the maximum amount of compression is expected (e.g., Oxenham and Plack, 1997). The silent interval between masker offset and signal onset (i.e., signal delay) was 0 ms, defined in terms of the zero-points in the envelope. In order to limit the effects of off-frequency listening, an ipsilateral background noise was presented at a spectrum level 40 dB below the level of the signal. It is important to ensure that the level of the background noise is not intense enough to mask the signal itself. At the specified spectrum level, the highest signal level (75 dB SPL) was at least 20 dB above the simultaneous masked threshold of the signal measured in the background noise alone. The bandwidth of the high-pass background noise was 6 kHz with a lower cutoff frequency of $1.2 f_s$. To avoid detection of the signal in the contralateral ear, a contralateral masking noise was presented at an overall level 20 dB below the level of the signal, with a pass band extending from $0.8 f_s$ to $1.2 f_s$. Both the ipsilateral and contralateral noises were gated on 50 ms before masker onset and gated off 50 ms after signal offset.

In the TM paradigm, the level of a forward masker needed to mask a 10 dB SL signal was measured as function of signal delay (10 to 100 ms at 10-ms intervals). This range of signal delays was selected to ensure that on-frequency masked thresholds would be measured in the level region where maximum compression is expected (i.e., 50 to 75 dB). No background noises were presented in either ear; the signal level was always so low that neither off-frequency listening nor detection in the contralateral ear was deemed likely.

All stimuli were generated digitally and played out via a soundcard (LynxStudio LynxOne) with 24-bit resolution and a sampling frequency of 32 kHz. The stimuli were then routed to a programmable attenuator (TDT PA4) and headphone buffer (TDT HB6) before being presented to the listener via Sennheiser HD 580 headphones. Listeners were seated in a double-walled sound-treated room. A trial consisted of three observation intervals, separated by interstimulus intervals of 500 ms. The masker was presented in all three intervals and the signal was randomly presented in one of the three intervals. Thresholds were tracked using a two-up one-down adaptive procedure that estimates the masker level at the 70.7% correct point on the psychometric function (Levitt, 1971). In the adaptive procedure, the masker level was initially varied with a step size of 8 dB. After the first two level reversals, the step size was reduced to 4 dB and after an additional two reversals to 2 dB. The threshold estimate was taken as the mean of the last eight reversals with a 2-dB step size. The maximum allowable masker level was set at 102 dB SPL; if the tracking procedure attempted to exceed this level more than six times, the run was aborted. Thresholds are only reported for conditions that resulted in no aborted runs. For the GOM data, which involved six data points per curve, each reported threshold is the mean of at least four estimates. When the standard deviation of four estimates exceeded 4 dB, an additional two estimates were made and the mean of all six estimates was recorded as threshold. Approximately 50% of the reported GOM thresholds are the mean of six estimates. The TM data involved more data points per curve (up to ten), so initially only two estimates per condition were made. However, the standard deviation of the two estimates exceeded 4 dB in about 80% of the conditions; in those cases an additional two estimates were made and the mean of all four estimates was recorded as threshold. Thus, on average, GOM and TM involved about 30 and 36 runs per curve, respectively, for each listener. Data collection did not begin until a listener had a minimum of 4 h of practice with each of the two experimen-

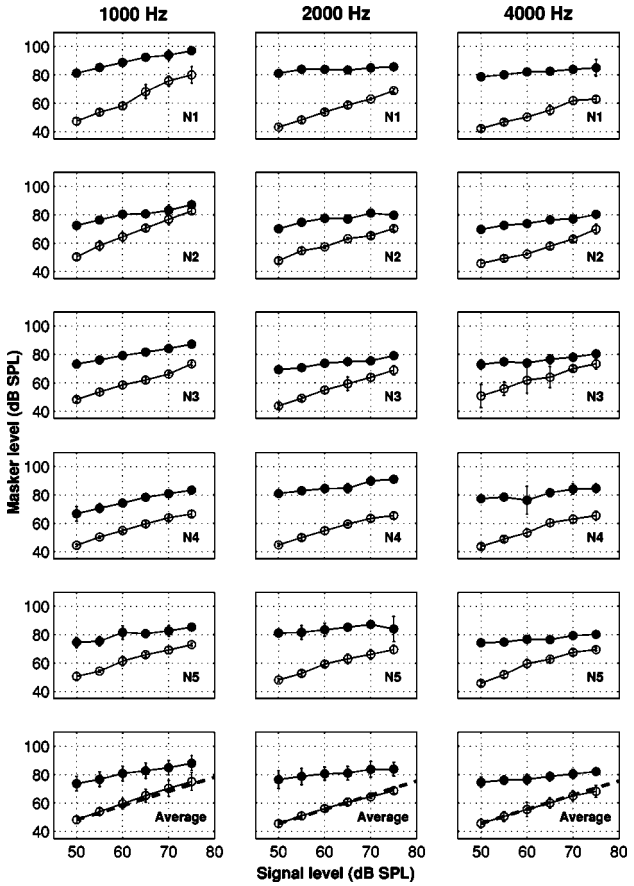

FIG. 1. GOM functions measured at signal frequencies of 1, 2, or 4 kHz for normal-hearing listeners in experiment I. Each row represents a different subject or the mean data. Filled symbols represent off-frequency masked thresholds and open symbols represent on-frequency masked thresholds. Error bars represent ±1 standard deviation. The dotted lines plotted in the bottom row represent a straight line with a slope of one.

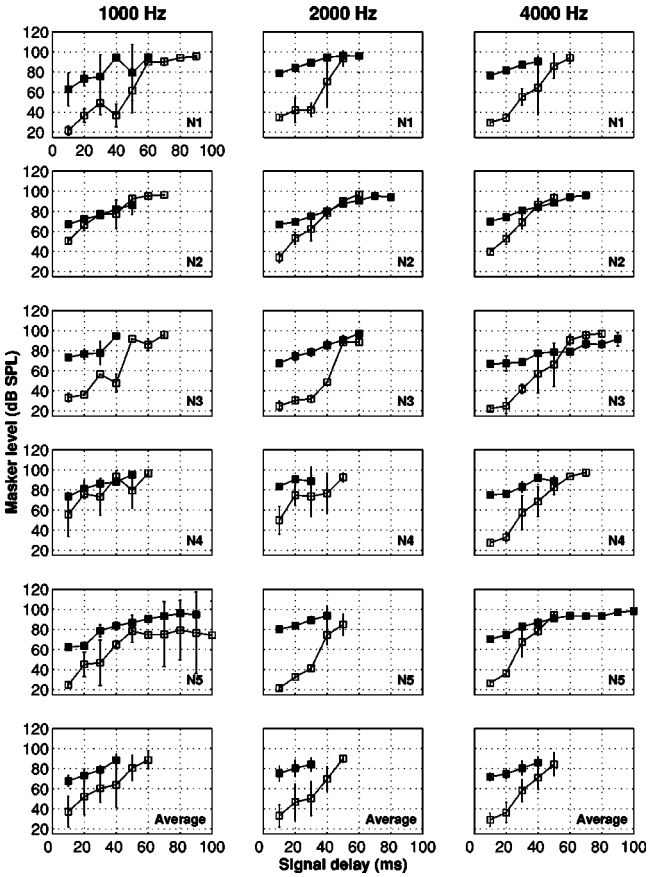

FIG. 2. TM curves measured at signal frequencies of 1, 2, or 4 kHz for normal-hearing listeners in experiment I. Each row represents a different subject or the mean data. Filled symbols represent off-frequency masked thresholds and open symbols represent on-frequency masked thresholds. Error bars represent ±1 standard deviation.

tal paradigms. The order of presentation of the experimental paradigms was randomized across subjects. Testing was completed for all conditions of a given paradigm before testing with the other paradigm began. Listeners N1, N2, and N5 were tested first with GOM while listeners N3 and N4 were tested first with the TM paradigm. The presentation of signal frequency conditions was also randomized within a masking paradigm.

2. Subjects

GOM and TM curves were measured in five normal-hearing listeners who ranged in age from 18 to 32 years. Listeners were verified as having absolute thresholds better than 20 dB HL (ANSI, 1996) for octave frequencies between 250 and 8000 Hz. Listeners were recruited from the M.I.T. student population and were compensated monetarily for their time. Test sessions typically lasted for 2 h (including breaks) and listeners were tested two to three times per week. The total testing time per listener was about 45 h.

B. Results

GOM curves are shown in Fig. 1 and TM curves are shown in Fig. 2 for signal frequencies of 1, 2, and 4 kHz. Each row corresponds to a different listener, and the final row shows the mean data. Mean thresholds are reported only for conditions where data were available for all five listeners. On- and off-frequency masked thresholds are plotted with open and filled symbols, respectively. Error bars represent ±1 standard deviation. As can be seen, within-subject standard deviations across measurements were generally larger for the TM data, particularly in the on-frequency masking condition.

The GOM data (Fig. 1) show that, in agreement with previous studies, the slope of the off-frequency masker functions is in most cases much less than unity, while the slope of the on-frequency masker functions is close to unity (e.g., Oxenham and Plack, 1997). The dashed line shown with mean data (Fig. 1; bottom row) represents a straight line with a unity slope.

Also in agreement with previous studies, the TM data (Fig. 2) show that masker levels increased with signal delay, and the rate of increase differed for the on- and off-frequency masking data (e.g., Nelson *et al.*, 2001; Lopez-Poveda *et al.*, 2003; Plack and Drga, 2003). In most cases, the slope of the on-frequency curve varies over the range of time intervals measured, and there is a region of the on-frequency masking curve that is substantially steeper than the off-frequency masking curve. For the off-frequency conditions, the slope of a given curve tends to be more constant, although there may be a trend for the slope to become shallower at the highest levels. Plack *et al.* (2004) found a similar, and significant,

trend for the slope of the off-frequency masking curve to become shallower at higher masker levels (and larger masker-signal intervals) for their 4-kHz signal frequency (2.2-kHz masker). Although such a trend seems to exist in some of our data, it failed to reach significance, either with a simple correlation of off-frequency masker slope and masker level ($R=-0.18$; $p=0.34$), or with an attempt to find a quadratic component to the regression ($p>0.05$).

There is also a trend for the off-frequency curves to become shallower with increasing signal frequency. The mean slope of the off-frequency masking functions is 0.39 (s.e.=0.04) at a signal frequency of 4 kHz, 0.43 (s.e.=0.05) at 2 kHz, and 0.53 (s.e.=0.04) at 1 kHz. This feature has been reported before (Lopez-Poveda *et al.*, 2003; Plack and Drga, 2003) and is discussed further below.

C. Estimating compression values

In the following sections, compression values are derived from the TM and GOM data, and results from the two paradigms are compared. In previous studies (Nelson *et al.*, 2001; Plack and Drga, 2003), third-order polynomials were found to provide relatively good fits to the data, although in some cases the minimum derivative was a negative number (Plack and Drga, 2003). Recently, Plack *et al.* (2004) suggested fitting the data with a multiphase (i.e., three-segment) linear regression function. With this method, the slopes of the lower and upper segments are fixed at unity and a straight line is fit to the middle segment. The horizontal distance, in dB, between the upper and lower segments can be used to estimate the maximum gain applied by the cochlear active mechanism, if it assumed that the gain at high levels (in the upper segment) is zero (see Plack *et al.*, 2004, for details). An alternative to a generic polynomial is a function that is specifically designed to capture certain features of the basilar membrane input-output function, such as the more compressive mid-level region. The sum of a linear and a sigmoidal function (LS) has been used in a number of studies (e.g., Moore *et al.*, 1996; Oxenham and Moore, 1997; Glasberg and Moore, 2000). In this study, we use a version of this that describes the basilar membrane response (R) for a given input level (L) as

$$R=0.9L+A+B(1-(1/(1+\exp(-0.05(L-50))))), \quad (1)$$

where

$$A=-0.0894G_{\max}+V+10.894, \quad (2)$$

$$B=1.1789G_{\max}-11.789, \quad (3)$$

and where $G_{\max}$ determines the maximum gain (in dB) applied by the active mechanism. The slope of the response curve at very low and very high input levels is nearly linear, as defined by the constant 0.9, and varies slightly with level. The compressive middle region of the function spans the range of input levels between about 20 to 80 dB, the midpoint of which is defined by the constant 50 (in dB SPL). The value of $G_{\max}$ is a free parameter that is allowed to vary to provide the best fit to the data. The free parameter V allows a vertical shift of the function. The values of A and B are specified so that the calculated basilar membrane response is 100 dB for $L=100$ dB and $V=0$. The minimum of the function's first derivative can be used as an estimate of the maximum compression. Here we use all these approaches in deriving compression estimates from the first experiment.

1. Temporal masking

Estimating compression values from TM curves typically involves the interim step of deriving a basilar membrane response curve by plotting off-frequency masker levels as a function of on-frequency masker levels. The fact that off-frequency curves tend to become shallower with increasing signal frequency has been interpreted as evidence that off-frequency curves only reflect truly linear processing of the masker at high signal frequencies (Lopez-Poveda *et al.*, 2003; Plack and Drga, 2003). At lower characteristic frequencies, compression may be applied not only to on-frequency but also to off-frequency stimuli, making the assumption of linear processing of the off-frequency masker invalid. This was taken into account in our analysis by fitting a straight line to the 4-kHz off-frequency masker levels ($f_m=2.2$ kHz) for each subject, and using that as the linear reference against which to plot the on-frequency masker data, as suggested by Lopez-Poveda *et al.* (2003).

Basilar membrane response curves derived from the TM data are shown in Fig. 3. Each row represents a different listener and the final row shows the mean data. Each symbol represents an off-frequency masker level ($f_m=2.2$ kHz) plotted as a function of on-frequency masker level ($f_m=f_s$), paired by signal delay. Using a higher frequency off-frequency masker eliminates the need to rely on the assumption that compression is frequency specific in more apical basilar membrane regions. Using a straight line fit to the off-frequency data, as opposed to the raw data itself, allows $f_m=2.2$ kHz thresholds to be used as the linear reference even for signal frequency conditions where on-frequency masked thresholds were obtained for a greater number of signal delays.

Plotted with a solid line in Fig. 3 is the LS function, fit to the data using a least-squares approach. $G_{\max}$ and V were allowed to vary as free parameters; for every estimated value of $G_{\max}$, the value of V that produced the best fit to the data was determined. The values of $G_{\max}$ and V that minimized the sum of squared errors for the predicted masked levels were accepted as the final parameter values. The resulting LS function was evaluated and is plotted as a solid line in Fig. 3. The Matlab functions *nlinfit* and *fminsearch* were used to generate the fitted function.

Using an approach similar to Plack *et al.* (2004), a multiphase regression function was also fit to the TM data and is plotted with a dotted line in Fig. 3. The lower breakpoint (LBP), upper breakpoint (UBP), lower segment intercept (LI), and slope of the middle segment (MS) were allowed to vary as free parameters. The slope of the lower and upper segments was fixed at 1. The fitting function (*nlinfit*) was constrained so that the middle segment contained a minimum of three data points. The resulting least-squares, three-segment function was evaluated. In general, the sum of squared errors associated with the multiphase regression

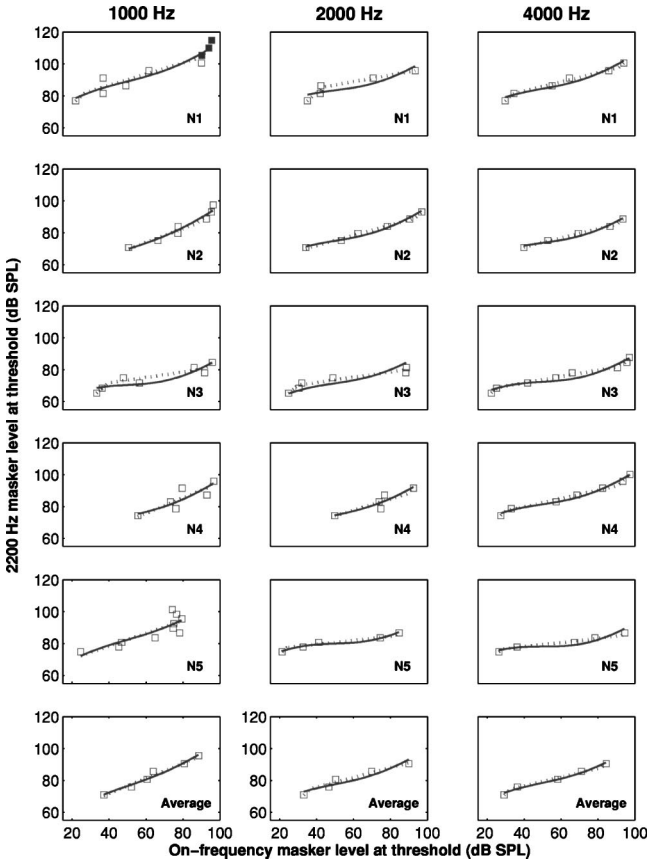

FIG. 3. Basilar membrane response curves derived from TM data for normal-hearing listeners in experiment I. Each row represents a different subject or the mean data. The LS function fit to the data is plotted as a solid line. The multiphase regression function is plotted as a dashed line. A straight line fit to the off-frequency TM curve measured at $f_m = 2.2$ kHz was used as the linear reference.

function was considerably smaller than the LS function, although this may simply reflect the fact that the multiphase regression function has twice as many free parameters as the LS function.

The minimum of the first derivative of each LS function plotted in Fig. 3 is shown in the right-hand column of Table I. Also shown in Table I are minimum slope values for the TM data using a straight line fit to the off-frequency masker levels ($f_m = 0.55 f_s$) as the linear reference. The minimum slope value for each of the multiphase regression functions plotted in Fig. 3 is shown in the right-hand column of Table II. Minimum slope values derived from the TM data using off-frequency masker levels ($f_m = 0.55 f_s$, rather than $f_m = 2.2$ kHz) as the linear references are also shown in Table II. This allows a more direct comparison with the GOM data, where it is not possible to use the same high off-frequency reference for all signal frequencies.

Minimum slope values derived from the TM data were analyzed using a three-factor repeated-measures analysis of variance (fixed effects), using signal frequency (1, 2, or 4 kHz), fitting function (LS or multiphase regression), and linear reference ($f_m = 0.55 f_s$ or $f_m = 2.2$ kHz) as within-subject factors. Here and throughout this paper, p values less than 0.05 are considered significant. The results showed a significant main effect of signal frequency [$F(2,8) = 15.44$, $p = 0.002$] and fitting function [$F(1,4) = 65.47$, $p = 0.001$]. There was no main effect of linear reference [$F(21,4) = 2.64$, $p = 0.18$], but the interaction between signal frequency and linear reference was significant [$F(2,8) = 7.39$, $p = 0.02$]. *Posthoc* Fisher's LSD tests showed a significant ($p < 0.05$) difference between slope values at $f_s = 1$ kHz vs. $f_s = 2$ kHz or 4 kHz. There was also a significant ($p < 0.05$) difference between slope values at $f_s = 1$ kHz using $f_m = 0.55 f_s$ as the linear reference vs. $f_m = 2.2$ kHz.

TABLE I. Estimates of compression calculated from the LS function fit to basilar membrane response curves derived from GOM and TM data, for each signal frequency in experiment I. Values in the "Mean" rows show parameters fitted to the mean data, only including points for which values from all five subjects were available.

Subject	GOM	TM Reference $= 0.55 f_s$	TM Reference $= 2.2$ kHz
		$f_s = 1000$ Hz	
N1	0.38	0.39	0.29
N2	0.32	0.43	0.37
N3	0.54	0.38	0.07
N4	0.75	0.36	0.25
N5	0.43	0.56	0.34
Mean	0.48	0.42	0.26
		$f_s = 2000$ Hz	
N1	0.11	0.07	0.15
N2	0.41	0.19	0.19
N3	0.35	0.23	0.04
N4	0.45	0.06	0.25
N5	0.19	0.15	0.04
Mean	0.30	0.14	0.13
		$f_s = 4000$ Hz	
N1	0.26	0.21	0.21
N2	0.37	0.16	0.16
N3	0.24	0.07	0.07
N4	0.35	0.18	0.18
N5	0.20	0.01	0.01
Mean	0.28	0.13	0.13

The significant effect of fitting function reflects, at least in part, the fact that the LS-function estimate is the slope value at the *point* where the derivative of the function reaches its minimum. In contrast, by definition the slope of the linear regression analysis is defined over at least three data points and thus represents the average slope over a larger region of the level range.

The significant interaction between linear reference and signal frequency suggests that the choice of linear reference is an important factor only for signal frequencies less than 2 kHz. This is consistent with the finding of Lopez-Poveda *et al.* (2003) that the slope of off-frequency TM curves was constant for signal frequencies greater than or equal to 2 kHz. *Posthoc* analysis (Fisher's LSD test) also showed that even when $f_m = 2.2$ kHz was used as the linear reference, slope values at a signal frequency of 1 kHz (average across subjects $= 0.31$ dB/dB) were still significantly larger than values at $f_s = 2$ kHz (average $= 0.18$ dB/dB) or 4 kHz (average $= 0.18$ dB/dB). This finding, suggesting that compression is reduced at lower frequencies, is in contrast to results reported by Lopez-Poveda *et al.* (2003) and Plack and Drga (2003), who found equal compression at low and high frequencies. It

TABLE II. Estimates of compression calculated from the ratio of slopes of the GOM data and from the multiphase regression function fit to basilar membrane response curves derived from the TM data in experiment I. GOM slope values at $f_s = 6$ kHz are from experiment IA. Values in the "Mean" rows show parameters fitted to the mean data, only including points for which values from all five subjects were available.

Subject	GOM Slope ratio	TM Reference $= 0.55 f_s$	TM Reference $= 2.2$ kHz
		$f_s = 1000$ Hz	
N1	0.46	0.42	0.35
N2	0.42	0.46	0.42
N3	0.58	0.40	0.17
N4	0.75	0.54	0.46
N5	0.47	0.60	0.40
Mean	0.53	0.48	0.36
		$f_s = 2000$ Hz	
N1	0.14	0.18	0.21
N2	0.44	0.32	0.32
N3	0.37	0.22	0.16
N4	0.48	0.22	0.35
N5	0.22	0.20	0.13
Mean	0.33	0.23	0.23
		$f_s = 4000$ Hz	
N1	0.28	0.29	0.29
N2	0.41	0.27	0.27
N3	0.32	0.20	0.20
N4	0.37	0.26	0.26
N5	0.25	0.13	0.13
Mean	0.33	0.23	0.23
		$f_s = 6000$ Hz	
N1	0.28	⋯	⋯
N2	0.18	⋯	⋯
N3	0.22	⋯	⋯
N4	0.16	⋯	⋯
N5	0.09	⋯	⋯
Mean	0.19	⋯	⋯

is not clear what accounts for this discrepancy, although it may in part be traced back to the results of listeners N2 and N4. For these listeners the TM curves at 1 kHz start at a fairly high level, meaning that the data may not include the most compressive regions of their data.

2. Growth of masking

The magnitude of compression was estimated from the GOM data (see Fig. 1) by calculating the ratio of the slopes of straight lines fit to off- and on-frequency masker levels. In contrast to the TM paradigm, it is not possible to use the high-frequency off-frequency masker curves as a linear reference, and so all comparisons involve the off-frequency masker at $f_m = 0.55 f_s$. Slope values are shown in Table II. As the data generally fell on a single straight line in the level region tested (50–75 dB SPL), calculating the ratio of the slopes is essentially equivalent to fitting the derived basilar membrane response curve with the three-segment multiphase linear regression function.

Basilar membrane response curves were also derived from the GOM data by plotting off-frequency data as a function of on-frequency data, paired by signal level. The resulting curves were fit with the LS function and minimum slope values are shown in Table I. A comparison of values in Tables I and II indicates that both methods of deriving estimates of compression from GOM data produce similar results.

3. Comparisons of TM and GOM estimates of compression

One goal of this study was to determine whether the GOM and TM paradigms produce consistent intrasubject slope estimates. To address this question, minimum slope values derived from the LS function were analyzed using a two-factor repeated-measures analysis of variance (fixed effects), using masking paradigm (GOM or TM) and signal frequency (1, 2, or 4 kHz) as within-subject factors. In the most comparable conditions, when $f_m = 0.55 f_s$ was used as the linear reference for each TM signal frequency condition, results showed a significant main effect of signal frequency [$F(2,8) = 16.29$, $p = 0.002$]. There was a trend towards a main effect of masking paradigm, although it failed to reach significance [$F(1,4) = 5.76$, $p = 0.07$]. This (nonsignificant) trend reflects the fact that the TM estimates tended to be lower (stronger compression) than the GOM estimates. The interaction between masking paradigm and signal frequency was not significant [$F(2,8) = 1.08$, $p = 0.39$]. An identical pattern of results, in terms of significant differences and interactions, was found for compression values derived from the GOM data using the slope ratios and from the TM data using the multiphase regression functions. The result from the ANOVA showing no significant difference in the compression estimates between the two paradigms is supported by the fact that the correlation between the two measures was significant (Pearson correlation coefficient of 0.54; $p = 0.039$).

Significant differences between the two paradigms did arise if the comparison was made between GOM and TM with a linear reference of $f_m = 2.2$ kHz. This is expected because, as noted above, the same difference was found between the two TM measures, $f_m = 2.2$ kHz and $f_m = 0.55 f_s$, with the latter probably underestimating compression, due to the failure of the assumption that the off-frequency response is linear.

Test reliability was examined by constructing 0.95 confidence intervals around $G_{\max}$ values used to calculate the minimum slope values reported in Table I for individual listeners. The Matlab function *nlparci* was used to determine the confidence interval for a given value of $G_{\max}$ (i.e., nonlinear least-squares parameter estimate) using the residuals and the Jacobian matrix (an analog of the X matrix in the standard linear regression model) at the solution (Table III). A two-factor repeated-measures analysis of variance (fixed effects), using paradigm (GOM and TM) and signal frequency (1, 2, or 4 kHz) as within-subject factors, showed a significant main effect of paradigm [$F(1,4) = 10.03$, $p = 0.03$]. The effect of signal frequency [$F(2,8) = 3.67$, $p = 0.07$] and the interaction of paradigm and signal frequency [$F(2,8) = 2.25$, $p = 0.17$] were not significant. Given that both paradigms involved measuring a similar number of data points, this finding suggests that the GOM paradigm provides a less variable measure than TM.

TABLE III. The mean width of 0.95 confidence intervals around compression estimates derived from individual normal-hearing listeners' GOM and TM data in experiment I, using the LS function. The confidence intervals (CI) were constructed using the Jacobian matrix at the solution to the function.

	Width of CI	
Signal frequency (kHz)	GOM	TM
1	0.06	0.31
2	0.06	0.16
4	0.07	0.11

4. Possible effects of "confusion"

For forward masking with brief masker-signal intervals, researchers have often found evidence for ''confusion,'' where signal thresholds are elevated because listeners have difficulty distinguishing the signal from the offset of the masker (e.g., Neff, 1985). Nelson *et al.* (2001) addressed this in their study of TM curves and found that, although some thresholds were changed by the presence of a cue tone (designed to eliminate confusion), their estimates of compression were unchanged. We completed pilot experiments on several listeners with and without cue tones. We found that, after considerable practice, there were no substantial changes, either in individual thresholds, or in estimates of compression. Thus, we conclude that the present data are unlikely to be contaminated by effects of confusion.

D. Discussion

TM and GOM paradigms produced comparable estimates of basilar membrane compression, although there was a trend towards TM estimates being more compressive than GOM estimates. To the extent that a difference is present, it may be due in part to the fact that the signal level for the TM curves is always 10 dB SL, whereas the signal level from the GOM curves was as high as 75 dB SPL. This highlights an important difference between the two measures: For TM, the use of a fixed signal level ensures that the listener is using the same place or the same limited frequency region on the basilar membrane to detect the signal, regardless of masker level. For GOM, where signal level is varied, the place used to detect the signal will probably be different at high levels than at low levels because the peak of the traveling wave shifts as a function of level (e.g., McFadden, 1986; Moore *et al.*, 2002). Since the growth in the peak of the traveling wave is more linear than the growth at the place with a characteristic frequency equal to the signal, it follows that the GOM paradigm may underestimate compression, particularly at high levels. Thus, the TM paradigm may be thought of as measuring the response function to a signal at the (invariant) *characteristic* frequency, whereas the GOM paradigm may measure something closer to the response function to a signal at the *best* frequency, the place of which varies with level.

The difference in compression estimates between the two fitting procedures (linear regression versus LS function) is not surprising, given that the LS compression value is based on a single point in the function, whereas the regression value is based on an average across a level range of at least 10 dB. In fact, when the LS slope is averaged over a similar level range, the values for the two paradigms become much more comparable.

There is, however, a theoretical reason to question the use of the LS function. In a study of hearing loss and basilar membrane compression, Plack *et al.* (2004) have reported that the maximum gain applied by the active mechanism and the magnitude of maximum compression on the basilar membrane are not statistically correlated. The original LS function assumes that these two auditory functions are intimately related; the value of $G_{\max}$ (i.e., y intercept) is equal to the maximum gain and determines the minimum slope of the fitted function. While the LS function, with the inclusion of the V parameter that shifts on the entire function along the y axis, decouples the two auditory functions to some extent, they still cannot be viewed as being completely independent of one another; the range of input levels over which compression applies and maximum gain are still coupled.

In summary, both GOM and TM paradigms produce similar behavioral estimates of basilar membrane compression when comparable fitting techniques are used. Both GOM and TM ($f_m = 0.55 f_s$) paradigms probably underestimate compression at signal frequencies below 2 kHz, presumably because the assumption of a linear response to the off-frequency masker is violated. This can be remedied with TM by using a high-frequency linear off-frequency reference curve ($f_m = 2.2$ kHz), but cannot be remedied with GOM (Lopez-Poveda *et al.*, 2003). Finally, for given measurement effort, estimates using GOM provide less variable estimates of compression, with confidence intervals nearly half those found for the TM data. However, this comes at the expense of biased estimates at lower signal frequencies.

III. EXPERIMENT IA

Slope values derived from GOM functions measured in experiment I tend to decrease with increasing signal frequency (see Table II). In agreement with other psychoacoustic studies, results from experiment I suggest that a lack of frequency specificity of the compression mechanism may account for the substantially larger slope values at $f_s = 1$ kHz. However, even at signal frequencies of 2000 and 4000 Hz there are several slope values that exceed 0.3 dB/dB. This finding is somewhat puzzling given that other studies using GOM have measured compression values of around 0.2 or less at a signal frequency of 6000 Hz (Oxenham and Plack, 1997; Nelson *et al.*, 2001). The purpose of the current experiment was to determine if the observed trend for slope values to decrease continues at higher signal frequencies, approaching a value of 0.2 dB/dB across listeners at 6 kHz.

A. Methods

Stimuli and procedure

GOM functions were measured at $f_s = 6$ kHz in the same five normal-hearing listeners who participated in experiment I. Stimulus parameters and experimental procedures were identical to those used in experiment I, except that the signal and masker tones were gated with raised-cosine ramps of 2 ms, and that the ipsilateral background noise was presented

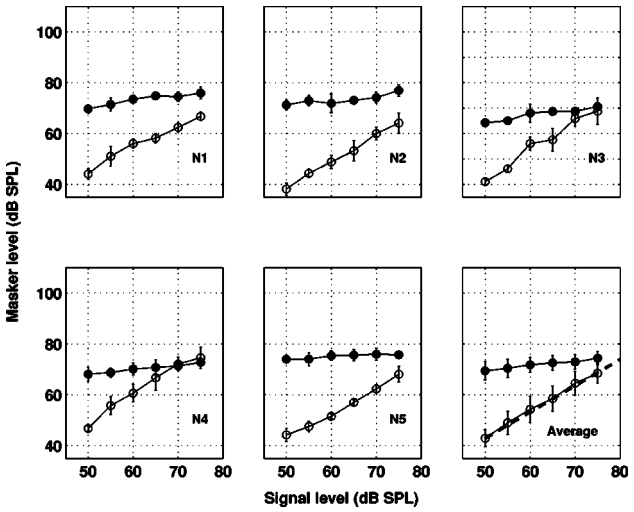

FIG. 4. GOM functions measured at a signal frequency of 6 kHz for normal-hearing listeners in experiment IA. Each panel represents a different subject or the mean data. Filled symbols represent off-frequency masked thresholds and open symbols represent on-frequency masked thresholds. Error bars represent ±1 standard deviation. The dotted line plotted in the bottom panel titled "Average" represents a straight line with a slope of one.

at a spectrum level 45 dB below the level of the signal. These modifications were made to replicate as closely as possible the parameters used by Oxenham and Plack (1997).

B. Results

Results are shown in Fig. 4. Each panel corresponds to a different listener, with the last panel showing the mean data. On-frequency masked thresholds are plotted with open symbols and off-frequency masked thresholds are plotted with filled symbols. Error bars represent ±1 standard deviation. The ratio of the slopes of straight lines fit to the off- and on-frequency data are shown in Table II. The slope values for most listeners continue to decrease with increasing signal frequency. Furthermore, all slope values measured at $f_s = 6$ kHz are less than 0.3 dB/dB. A single-factor repeated measures analysis of variance (fixed effects), using signal frequency (1, 2, 4, or 6 kHz) as a within-subject factor, was performed to determine the significance of observed differences. Results showed a significant main effect of signal frequency [$F(3,12) = 11.39$, $p = 0.001$]. A test of within-subject (linear) contrasts was also significant [$F(1,4) = 18.34$, $p = 0.01$]. These findings are indicative of a systematic increase in compression estimates as a function of signal frequency.

C. Discussion

The slope values measured at $f_s = 6$ kHz are in good agreement with earlier GOM studies (e.g., Oxenham and Plack, 1997; Nelson *et al.*, 2001). Previous studies using GOM at low signal frequencies that have measured slope values exceeding the range of 0.2 to 0.3 dB/dB either failed to prevent off-frequency listening and/or used simultaneous masking (e.g., Stelmachowicz *et al.*, 1987; Hicks and Bacon, 1999; Moore *et al.*, 1999). As mentioned above, the most likely explanation for the apparently decreasing compression exponent with decreasing signal frequency is not that on-frequency compression decreases, but that off-frequency compression increases as the compression itself becomes less frequency selective. This interpretation is consistent with an increasing body of literature (Lopez-Poveda *et al.*, 2003; Plack and Drga, 2003; Oxenham and Dau, 2004). Where our data remain unclear is the point at which the off-frequency response begins to become more compressive: our GOM data suggest that this may be as high as 6 kHz, whereas other data suggest that the point may only be reached between 1 and 2 kHz (Lopez-Poveda *et al.*, 2003).

One potential reason might relate to our use of a very short temporal gap between the masker and signal in GOM, which could in principle result in physical overlap between the masker and signal in the auditory periphery. This might result in effective simultaneous masking, which in turn might reduce the estimated compression. Arguing against this is the fact that no such overlap has been found in the past for frequencies of 1 kHz and above (Vogten, 1978; Shailer and Moore, 1987; Carlyon, 1988). Another possible explanation is that the larger slope values observed at 2000 and 4000 Hz are indicative of (subclinical) cochlear damage. Again, this explanation seems unlikely given that participants were young listeners with audiometrically normal hearing. Furthermore, using methods similar to Shera *et al.* (2002), we measured auditory filter shapes at 1, 2, and 4 kHz in these same listeners. This particular notched-noise paradigm more closely resembles the procedures used in the measurement of neural tuning curves (i.e., near-threshold signal levels, non-simultaneous masking, and constant signal level), and, as such, is thought to be a sensitive and accurate behavioral measure of cochlear tuning. Filter equivalent rectangular bandwidths derived from our listeners' data fell within the normal range observed by Shera *et al.* (2002). Thus, we have no entirely satisfactory explanation of the seemingly continuous increase in estimated compression across the range of frequencies tested here, in contrast to the relatively constant estimates found in previous studies (Plack and Oxenham, 2000; Lopez-Poveda *et al.*, 2003).

IV. EXPERIMENT II: HEARING-IMPAIRED LISTENERS

As discussed in the Introduction, a reliable measure of cochlear compression may be of clinical value because a loss or reduction of compression may explain many of the perceptual difficulties experienced by hearing-impaired listeners. Results from experiment I suggest that GOM produces less variable estimates of compression in listeners with normal hearing at the expense of underestimating compression at lower signal frequencies. While neither GOM nor TM in their present forms are suitable for clinical use because of lengthy test times, the purpose of the following experiment was to determine which of the two masking paradigms is better suited for listeners with impaired hearing.

A. Methods

1. Stimuli and procedure

GOM and TM curves were measured in five hearing-impaired listeners. Stimulus parameters and experimental procedures were identical to those used in experiment I with the following exceptions:

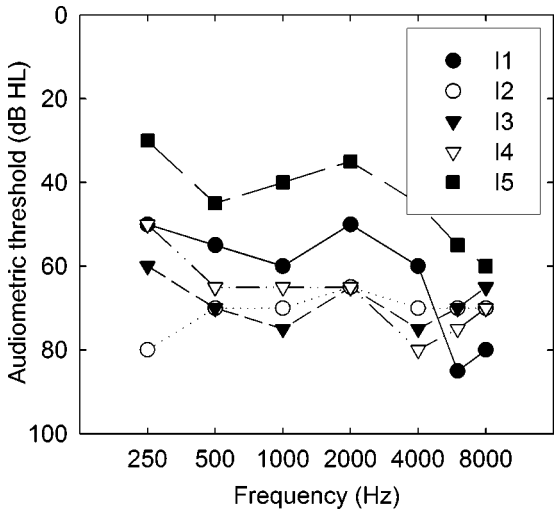

FIG. 5. Audiometric thresholds of the ear tested for each hearing-impaired subject in experiment II.

(1) For GOM functions, the signal was presented at levels between 5 dB SL and the upper limit of maximum comfort, in 5-dB intervals. For most listeners, the signal levels tested were considerably higher than those tested in the group of normal-hearing listeners. Absolute thresholds were measured at the beginning of each test session to verify that the signal was audible.
(2) For TM curves, the signal was presented at 5 dB SL (instead of the 10 dB SL used in experiment I). This facilitated measurements at a greater number of signal delays than would have otherwise been possible. Absolute thresholds were measured at the beginning of each test session to verify that the signal was audible.
(3) With the exception of listener I4, GOM and TM curves were measured at signal frequencies of 1, 2, and 4 kHz. In the case of listener I4, thresholds were measured at 1, 2, and 3 kHz because of the severity of his hearing loss at 4 kHz.

2. Subjects

Five hearing-impaired listeners with relatively flat audiometric thresholds between 500 and 4000 Hz were included as subjects in experiment II. Absolute thresholds and (presumed) etiology of each listener's hearing loss are shown in Fig. 5 and Table IV, respectively. Listeners were recruited from a large audiology clinic in the Boston area and were compensated monetarily for their time. Test sessions typically lasted for 2 h (including breaks) and listeners were tested two to three times per week.

TABLE IV. Presumed etiology of each hearing-impaired subject's hearing loss.

Subject	Ear tested	Etiology
I1	left	Meniere's
I2	left	unknown, congenital
I3	right	Norrie disease
I4	right	unknown
I5	right	presbycusis

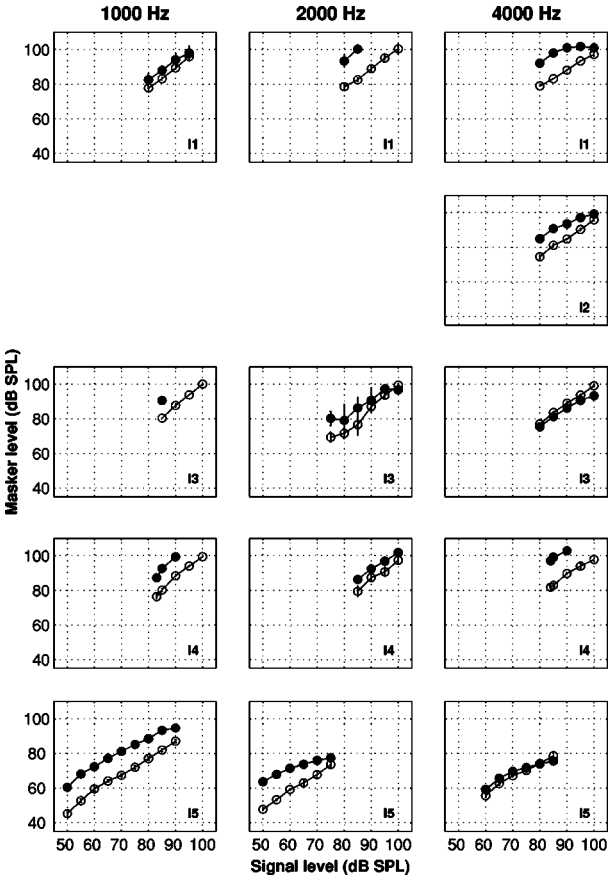

FIG. 6. GOM functions measured at signal frequencies of 1, 2, or 4 kHz for hearing-impaired listeners in experiment II. Each row represents a different subject. Filled symbols represent off-frequency masked thresholds and open symbols represent on-frequency masked thresholds. Error bars represent ±1 standard deviation.

B. Results

Results for the hearing-impaired listeners are shown in Figs. 6 (GOM) and 7 (TM). Each row corresponds to a different listener. On- and off-frequency masked thresholds are plotted with open and filled symbols, respectively. Error bars represent ±1 standard deviation. Due to maximum level discomfort issues and the output limitation of 102 dB SPL, on- and off-frequency masked thresholds could not be collected in all listeners in every condition. For example, neither GOM nor TM curves could be measured in listener I2 at a signal frequency of 1 kHz, as the signal remained detectable at the highest allowable masker level.

With the exception of listener I5, TM thresholds varied little with increasing signal delay. This is in contrast to the listeners tested in experiment I and previously described findings regarding normal-hearing listeners (e.g., Nelson *et al.*, 2001). Reduced rate of decay for forward masking in impaired listeners has been attributed to reduced compression on the basilar membrane (e.g., Glasberg and Moore, 1992; Oxenham and Moore, 1997). However, this hypothesis can only be applied to on-frequency masking data, which is thought to reflect both compression of the masker and decay of the internal representation of the masker. Off-frequency TM curves (particularly at higher frequencies) should only reflect decay of the masker and so should not be affected by

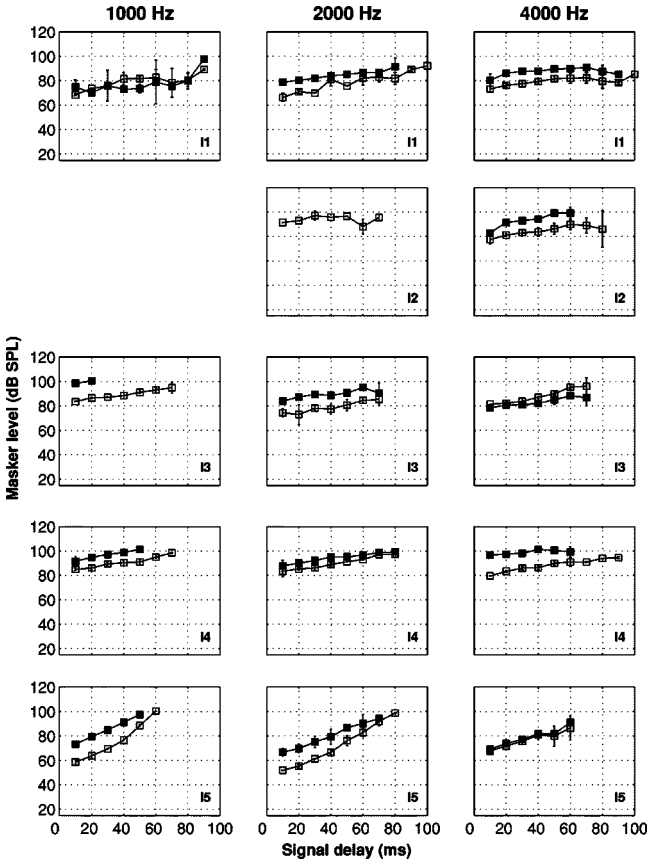

FIG. 7. TM curves measured at signal frequencies of 1, 2, or 4 kHz for hearing-impaired listeners in experiment II. Each row represents a different subject. Filled symbols represent off-frequency masked thresholds and open symbols represent on-frequency masked thresholds. Error bars represent ±1 standard deviation.

a loss of or reduction in the magnitude of basilar membrane compression. Plotting masker threshold in dB SPL as a function of masker-signal delay (ms) and excluding the data of listener I5, the mean slope of the off-frequency masking curve for each signal frequency was 0.17 (s.e.=0.07) at 4 kHz, 0.15 (s.e.=0.01) at 2 kHz, and 0.23 (s.e.=0.02) at 1 kHz. These values are less than half the slope values measured in the normal-hearing listeners. Slope values for listener I5, who had the mildest hearing loss, were close to normal: 0.39 at 4 kHz, 0.48 at 2 kHz, and 0.60 at 1 kHz. These findings suggest either the presence of a true temporal processing deficit unrelated to the effects of cochlear compression or loss of compression (cochlear or more central) that is not restricted to on-frequency stimuli. A similar effect has been found by Plack *et al.* (2004) in more mildly impaired listeners. However, in contrast to their results, the shallower slopes found here seem unlikely to result simply from the somewhat higher masker levels used with the hearing-impaired listeners. The range of levels used was fairly similar across the two groups and, furthermore, no correlation was found between masker level and off-frequency TM slope for the normal-hearing listeners.

For listener I1, higher on-frequency masker levels were needed to just mask the 1-kHz signal for the 0-ms delay condition (GOM paradigm) than for the 10-ms delay condition (TM paradigm) (compare leftmost open data points in Figs. 6 and 7 for listener I1, 1-kHz signal condition). While it is not unusual to find little or no change in threshold with initial increases in forward masking interval with impaired listeners (e.g., Glasberg *et al.*, 1987), increases are less common. The difference may be related to the context in which the conditions were run: in GOM the gap was always 0 ms, and so listeners had ample opportunity to build a perceptual ''template,'' whereas in TM the gaps changed from run to run, perhaps making the detection process in some listeners less ''optimal.''

C. Estimating compression values

Basilar membrane response curves derived from the TM data are shown in Fig. 8. Each row corresponds to a different listener. A straight line fit to the 2.2-kHz masking curve (i.e., off-frequency masking curve measured in the 4-kHz signal condition) was used as the linear reference for all conditions. For listener I4, the 3-kHz signal off-frequency (i.e., 1.65-kHz) masking curve was used as the linear reference. The LS function and the multiphase regression function were fit to the response curves and are shown by the solid and dashed lines, respectively. Minimum slope values derived from the fitted functions are shown in Tables V and VI. As was sometimes the case with the normal-hearing listeners in experiment I, the choice of fitting function sometimes produced substantially different compression values for the same data set. In some conditions, both functions produced implausibly small (as well as a few negative) values. The LS function may be particularly unsuited to dealing with basilar membrane response curves measured in listeners with more severe hearing loss, because the equation defines the function's compressive region to be between 20 and 80 dB and assumes a linear response for input levels exceeding 80 dB. In some listeners the majority of data points fall well above 80 dB and the derived response functions are rather shallow (for example, see listener I4 in Fig. 8). In such cases, the LS function produces minimum (or negative) slope values for input levels that are below the range over which data could be collected. In all cases, however, the slope values quoted in the tables correspond to the minimum values that occurred *within* the range of levels actually measured for a given listener.

Further examination of Fig. 8 highlights a potential difficulty in using the TM paradigm for estimating compression in impaired listeners, regardless of which fitting function is used. Because of the extremely shallow slopes of the TM curves, the derived input-output function poorly describes the response of the basilar membrane, as most of the data points are clustered in one small region. In principle it would be possible to carefully choose masker-signal intervals to span a wider range of masker levels. However, this would require extensive individual pilot testing, which would further increase the duration of the already very long experiment. In contrast, the GOM technique measures compression over a range of levels that is determined by the signal level, which is one of the experimental parameters.

The slope ratios of the GOM functions (see Table VI) seem to produce compression estimates that are generally consistent with peripheral-based hearing loss (e.g., Ruggero

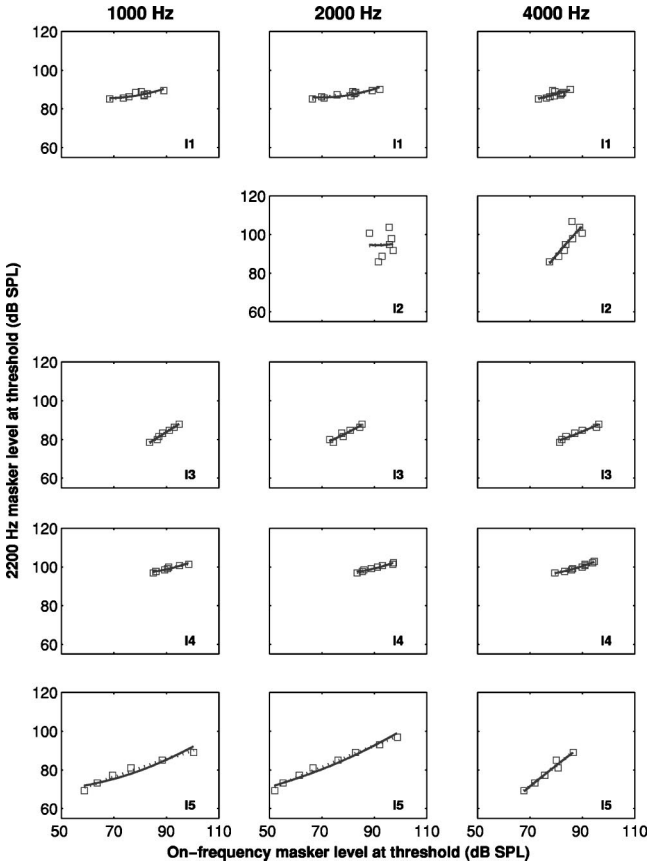

FIG. 8. Basilar membrane response curves derived from TM data for hearing-impaired listeners in experiment II. Each row represents a different subject. The LS function fit to the data is plotted as a solid line. The multiphase regression function is plotted as a dashed line. A straight line fit to the off-frequency TM curve measured at $f_m = 2.2$ kHz was used as the linear reference.

et al., 1996; Oxenham and Moore, 1995), even in listeners with severe hearing loss. However, because of level discomfort issues, the number of GOM thresholds that could be measured was sometimes small. Furthermore, for listeners who demonstrate compression values that approach normal, the issue of the compression's frequency specificity is a factor at lower signal frequencies. For example, compare compression values for listener I5 derived from GOM and TM curves at a signal frequency of 1 kHz. While the minimum slope derived from the TM data (using $f_m = 2.2$ kHz) is close to normal, the GOM slope ratio approached unity. However, if $f_m = 0.55 f_s$ is used as the linear reference for the derived basilar membrane response curve, compression values calculated using the two forward-masking paradigms are more similar (0.62 using the LS function and 0.70 using the regression function). As was the case with normal-hearing listeners in experiment I, this finding suggests that the GOM paradigm may not produce accurate estimates of compression at lower signal frequencies, possibly because of a more extensive compressive region at these characteristic frequencies.

Using a TM paradigm, Plack *et al.* (2004) observed that maximum compression in many listeners with mild to moderate hearing loss approaches normal values, albeit over a reduced range of input levels. In contrast, most of our listeners showed more linearized response functions throughout the level range. This may reflect the fact that our listeners were more severely impaired, and so had less (or no) residual cochlear amplification. It may also be due to the more restricted range of threshold levels that could be measured. An exception to this is seen in listener I5's TM data at $f_s = 1$ kHz (see Fig. 8, bottom left-hand panel). The multiphase regression function fit to the derived basilar membrane response curve indicated the presence of a compressive region between about 60 and 100 dB, with a minimum slope value of 0.46 dB/dB. Examination of the GOM functions also suggests the presence of a reduced region of compression for listener I1 at $f_s = 4$ kHz (see Fig. 6, upper right-hand panel).

To allow a more direct comparison between the TM and GOM data, the LS function and the multiphase regression function were fit to response curves derived from the GOM data by plotting off-frequency masker levels as a function of on-frequency masker levels, paired according to signal level. Whenever possible the actual off-frequency data points were used. In cases where the number of on-frequency data points exceeded the number of off-frequency points, a straight line fit to the off-frequency data was used. Compression values are shown in Table V (column 1) and Table VI (column 2). For listener I4, the multiphase regression function could not be used for signal frequencies of 1000 and 2000 Hz because the number of data points did not exceed the number of parameters in the fitting function. For listener I1 at $f_s = 4$ kHz, the multiphase regression function indicated the presence of a compressive region between about 90 and 100 dB, with a minimum slope value of -0.2 dB/dB. While this slope value is implausible, it does suggest the presence of compressive activity at this frequency. Furthermore, the results of the regression function indicate that calculating the

TABLE V. Estimates of compression calculated from the LS function fit to basilar membrane response curves derived from GOM and TM data, for each signal frequency in experiment II. Dashed lines indicate conditions where estimates could not be calculated due to an insufficient number of thresholds.

Subject	GOM	TM Reference $= 0.55 f_s$	TM Reference $= 2.2$ kHz
		$f_s = 1000$ Hz	
I1	0.85	0.80	0.02
I2	⋯	⋯	⋯
I3	⋯	1.20	0.85
I4	1.3	1.1	−0.18
I5	0.83	0.62	0.25
		$f_s = 2000$ Hz	
I1	1.40[a]	0.42	−0.07
I2	⋯	⋯	0.01
I3	0.48	0.50	0.66
I4	0.85	0.67	0.18
I5	0.51	0.61	0.43
		$f_s = 4000$ Hz	
I1	0.31	0.27	0.27
I2	0.58	1.70	1.70
I3	0.80	0.45	0.45
I4	0.82	0.24	0.24
I5	0.66	1.10	1.10

[a]Based on two data points.

TABLE VI. Estimates of compression calculated from the ratio of slopes of the GOM data and from the multiphase regression function fit to basilar membrane response curves derived from GOM data and TM data in experiment II. Dashed lines indicate conditions where estimates could not be calculated due to an insufficient number of thresholds.

Subject	GOM Slope ratio	GOM-multiphase regression function Reference $=0.55f_s$	TM-multiphase regression function Reference $=0.55f_s$	TM-multiphase regression function Reference $=2.2$ kHz
		$f_s=1000$ Hz		
I1	0.86	⋯	0.82	0.21
I2	⋯	⋯	⋯	⋯
I3	⋯	⋯	1.30[a]	0.86
I4	1.06	⋯	1.04	0.33
I5	0.85	0.83	0.70	0.46
		$f_s=2000$ Hz		
I1	1.25[a]	1.34[a]	0.54	0.19
I2	⋯	⋯	⋯	0.10
I3	0.63	0.44	0.56	0.69
I4	0.85	⋯	0.74	0.36
I5	0.54	0.48	0.67	0.56
		$f_s=4000$ Hz		
I1	0.46	−0.20	0.37	0.37
I2	0.67	0.67	1.55	1.55
I3	0.84	0.75	0.55	0.55
I4	0.86	0.70	0.36	0.36
I5	0.71	0.70	1.07	1.07

[a]Based on two data points.

slope ratio from single straight-line fits to the entire data range would underestimate the magnitude of compression.

Consistent with the results from the normal-hearing listeners, there was no *systematic* difference between compression estimates from GOM and TM when the $0.55f_s$ reference was used (paired *t*-test: $t=0.5$; $p=0.6$). However, in contrast to the results from the normal-hearing listeners, there was no significant correlation between the two measures ($R=0.03$; $p=0.9$). This suggests that either or both measures may not produce results that are reliable enough to distinguish between different listeners. TM seems to produce more scattered results, with some slope estimates being greater than one (suggesting expansion) and others implying strong compression, whereas the GOM estimates tend more generally to imply less-than-normal compression, which is expected based on the degree of hearing loss. However, without independent physiological confirmation it is not possible to say which measure is more accurate in absolute terms.

Test reliability of the GOM and TM paradigms was examined by constructing 0.95 confidence intervals around minimum slope values derived from the LS function using the Jacobian matrix at the solution (Table VII). While the statistical significance of differences in confidence interval width could not be easily assessed due to an unequal number of estimates across the different conditions (GOM and TM curves could not be measured in all listeners at every signal frequency), TM confidence intervals were slightly smaller at 1 kHz but more than twice as large at 2 and 4 kHz. This is similar in trend to the results from normal-hearing listeners, showing that GOM tends to produce less variable estimates of compression.

TABLE VII. The mean width of 0.95 confidence intervals around compression estimates derived from individual hearing-impaired GOM and TM data in experiment II, using the LS function. The confidence intervals were constructed using the Jacobian matrix at the solution to the function.

Signal frequency (kHz)	Width of CI	
	GOM	TM
1	0.19	0.17
2	0.21	0.50
4	0.11	0.23

In summary, hearing-impaired listeners showed shallower on- and off-frequency TM curves than normal-hearing listeners. The shallower off-frequency curves may indicate a reduction in temporal acuity or the presence (in normal hearing) of substantial off-frequency compression, even at 4 kHz. The resulting basilar membrane compression estimates indicated a general loss of compression, in line with that found in earlier studies (e.g., Oxenham and Plack, 1997). In contrast to the results from more mildly impaired listeners (Plack *et al.*, 2004), there was generally no level region in which normal compression was observed. TM curves produced more variable estimates of compression, which were often difficult to interpret, due to the very restricted range of masker levels covered. This could be remedied by using a wider range of masker-signal temporal gaps, but at the cost of even longer testing times.

V. CONCLUSIONS

The main purpose of this study was to determine whether GOM and TM produce within-subject estimates of compression that are consistent across a range of signal frequencies, and which of the two paradigms is a more efficient

measure. Results from normal-hearing listeners in experiment I suggest that while GOM is a less variable measure of compression (i.e., smaller confidence intervals for a similar number of data points), it may also underestimate compression at 1 kHz (and possibly at higher frequencies), most likely due to the reduced frequency specificity of compression in more apical regions (e.g., Plack and Drga, 2003). In the TM paradigm, this concern can be addressed by using a high-frequency off-frequency masking function as the linear reference for all signal frequencies. The two fitting procedures (LS and multiphase regression) produced somewhat different estimates of compression, but this could be ascribed to the different level ranges over which the estimates were valid. LS was considered less desirable because of its implicit assumption that cochlear gain is related to the maximum amount of compression.

The limitations of the LS function were further highlighted in the results of experiment II, which showed that the function failed to capture the trends in the data from the hearing-impaired listeners. Again, the GOM function produced less variable estimates of compression overall, with the caveat that the results may not be accurate at low signal frequencies.

Experiment II produced unexpected results in that the off-frequency TM curves were shallower than normal for the hearing-impaired listeners. Further work will be required to decide whether this reflects a general temporal deficit or whether some other mechanism, such as a non-frequency-specific compression, can account for the effect.

In summary, the advantages of GOM are as follows:

(i) It provides relatively stable estimates of compression: GOM confidence intervals were generally smaller than those for TM.
(ii) The level range over which compression is estimated can be defined in advance, without the need for pilot testing: For TM curves, either a large range of masker-signal intervals must be tested to ensure that the level range of interest is covered, or pilot testing must be undertaken.

The advantages of the TM paradigm are as follows:

(i) It uses a low signal level, which avoids issues related to off-frequency listening and the basal shift of the traveling wave. The issue with off-frequency listening in GOM may be particularly difficult with hearing-impaired listeners, where it may be difficult to ensure off-frequency masking without inadvertently producing on-frequency interference.
(ii) It is possible to estimate compression at low signal frequencies by using off-frequency masking curves from higher signal frequencies: with GOM, compression estimates at lower signal frequencies may be biased and there is no obvious way to compensate for it.

In their current forms, neither paradigm is clinically useful, because of the very long testing times required to derive a full function. However, it remains possible that an abbreviated version can be developed, in which compression over a very limited level range is targeted.

ACKNOWLEDGMENTS

This work was supported by NIH Grant Nos. R01 DC 00117 and R01 DC 03909, and NIH Training Grant No. 5T32 DC 00038. We thank Dr. Chris Halpin for valuable input regarding the design of this study and for help with subject recruitment. The comments by Dr. Chris Plack and an anonymous reviewer greatly improved the manuscript.

ANSI (**1996**). ANSI S3.6-1996. *Specification for Audiometers* (American National Standards Institute, New York).
Baker, R. J., Rosen, S., and Darling, A. (**1998**). ''An efficient characterization of human auditory filtering across level and frequency that is also physiologically reasonable,'' in *Psychophysical and Physiological Advances in Hearing*, edited by A. R. Palmer, A. Rees, Q. Summerfield, and R. Meddis (Whurr, London).
Carlyon, R. P. (**1988**). ''The development and decline of forward masking,'' Hear. Res. **32**, 65–79.
Glasberg, B. R., and Moore, B. C. J. (**1992**). ''Effects of envelope fluctuations on gap detection,'' Hear. Res. **64**, 81–92.
Glasberg, B. R., and Moore, B. C. J. (**2000**). ''Frequency selectivity as a function of level and frequency measured with uniformly exciting notched noise,'' J. Acoust. Soc. Am. **108**, 2318–2328.
Glasberg, B. R., Moore, B. C. J., and Bacon, S. P. (**1987**). ''Gap detection and masking in hearing-impaired and normal-hearing subjects,'' J. Acoust. Soc. Am. **81**, 1546–1556.
Glasberg, B. R., Moore, B. C. J., and Stone, M. A. (**1999**). ''Modeling changes in frequency selectivity with level,'' in *Psychophysics, Physiology and Models of Hearing*, edited by T. Dau, V. Hohman, and B. Kollmeier (World Scientific, Singapore).
Hicks, M. L., and Bacon, S. P. (**1999**). ''Psychophysical measures of auditory nonlinearties as a function of frequency in individuals with normal hearing,'' J. Acoust. Soc. Am. **105**, 326–338.
Levitt, H. (**1971**). ''Transformed up-down methods in psychoacoustics,'' J. Acoust. Soc. Am. **49**, 467–477.
Lopez-Poveda, E. A., Plack, C. J., and Meddis, R. (**2003**). ''Cochlear nonlinearity between 500 and 8000 Hz in listeners with normal hearing,'' J. Acoust. Soc. Am. **113**, 951–960.
McFadden, D. (**1986**). ''The curious half octave shift: Evidence for a basalward migration of the travelling-wave envelope with increasing intensity,'' in *Basic and Applied Aspects of Noise-Induced Hearing Loss*, edited by R. J. Salvi, D. Henderson, R. P. Hamernik, and V. Colletti (Plenum, New York).
Moore, B. C. J., Alcantara, J. I., and Glasberg, B. R. (**2002**). ''Behavioural measurements of level-dependent shifts in the vibration pattern on the basilar membrane,'' Hear. Res. **163**, 101–110.
Moore, B. C. J., Peters, R. W., and Glasberg, B. R. (**1996**). ''Detection of decrements and increments in sinusoids at high overall levels,'' J. Acoust. Soc. Am. **99**, 3669–3677.
Moore, B. C. J., Vickers, D. A., Plack, C. J., and Oxenham, A. J. (**1999**). ''Interrelationship between different psychoacoustic measures assumed to be related to the cochlear active mechanism,'' J. Acoust. Soc. Am. **106**, 2761–2778.
Murugasu, E., and Russell, I. J. (**1995**). ''Salicylate ototoxicity: The effects on basilar membrane displacement, cochlear microphonics, and neural responses in the basal turn of the guinea pig cochlea,'' Aud. Neurosci. **1**, 139–150.
Neff, D. L. (**1985**). ''Stimulus parameters governing confusion effects in forward masking,'' J. Acoust. Soc. Am. **78**, 1966–1976.
Nelson, D. A., and Pavlov, R. (**1989**). ''Auditory time constants for off-frequency forward masking in normal-hearing and hearing-impaired listeners,'' J. Speech Hear. Res. **32**, 298–306.
Nelson, D. A., Schroder, A. C., and Wojtczak, M. (**2001**). ''A new procedure for measuring peripheral compression in normal-hearing and hearing-impaired listeners,'' J. Acoust. Soc. Am. **110**, 2045–2064.
Oxenham, A. J., and Bacon, S. P. (**2003**). ''Cochlear compression: Perceptual measures and implications for normal and impaired hearing,'' Ear Hear. **24**, 352–366.

Oxenham, A. J., and Dau, T. (**2001**). ''Toward a measure of auditory-filter phase response,'' J. Acoust. Soc. Am. **110**, 3169–3178.
Oxenham, A. J., and Dau, T. (**2004**). ''Masker phase effects in normal-hearing and hearing-impaired listeners: Evidence for peripheral compression at low signal frequencies,'' J. Acoust. Soc. Am. **116**, 2248–2257.
Oxenham, A. J., and Moore, B. C. J. (**1995**). ''Additivity of masking in normally hearing and hearing-impaired subjects,'' J. Acoust. Soc. Am. **98**, 1921–1934.
Oxenham, A. J., and Moore, B. C. J. (**1997**). ''Modeling the effects of peripheral nonlinearity in listeners with normal and impaired hearing,'' in *Modeling Sensorineural Hearing Loss*, edited by W. Jesteadt (Erlbaum, Hillsdale, NJ), pp. 273–288.
Oxenham, A. J., and Plack, C. J. (**1997**). ''A behavioral measure of basilar membrane nonlinearity in listeners with normal and impaired hearing,'' J. Acoust. Soc. Am. **101**, 3666–3675.
Plack, C. J., and Drga, V. (**2003**). ''Psychophysical evidence for auditory compression at low characteristic frequencies,'' J. Acoust. Soc. Am. **113**, 1574–1586.
Plack, C. J., and Oxenham, A. J. (**2000**). ''Basilar membrane nonlinearity estimated by in a mouse model of Norrie disease,'' J. Neurosci. **22**, 4286–4292.
Plack, C. J., Drga, V., and Lopez-Poveda, E. A. (**2004**). ''Inferred basilar-membrane response functions for listeners with mild to moderate sensorineural hearing loss,'' J. Acoust. Soc. Am. **115**, 1684–1695.
Rhode, W. S., and Cooper, N. P. (**1996**). ''Nonlinear mechanics in the apical turn of the chinchilla cochlea in vivo,'' Aud. Neurosci. **3**, 101–121.
Rhode, W. S., and Recio, A. (**2000**). ''Study of mechanical motions in the basal region of the chinchilla cochlea,'' J. Acoust. Soc. Am. **107**, 3317–3332.
Rhode, W. S., and Robles, L. (**1974**). ''Evidence from Mossbauer experiments for nonlinear vibration in the cochlea,'' J. Acoust. Soc. Am. **55**, 588–596.
Robles, L., Ruggero, M. A., and Rich, N. C. (**1986**). ''Basilar membrane mechanics at the base of the chinchilla cochlea. I. Input-output functions, tuning curves, and phase responses,'' J. Acoust. Soc. Am. **80**, 1364–1374.
Rosen, S., Baker, R. J., and Darling, A. (**1998**). ''Auditory filter nonlinearity at 2 kHz in normal hearing listeners,'' J. Acoust. Soc. Am. **103**, 2539–2550.
Ruggero, M. A., Rich, N. C., Robles, L., and Recio, A. (**1996**). ''The effects of acoustic overstimulation, other cochlear injury and death on basilar membrane responses to sound,'' in *Effects of Noise on Hearing: Vth International Symposium*, edited by R. J. Salvi, A. Axelsson, D. Henderson, and R. Hamernik (Thieme Medical, Stockholm).
Ruggero, M. A., Rich, N. C., Recio, A., Narayan, S. S., and Robles, L. (**1997**). ''Basilar membrane responses to tones at the base of the chinchilla cochlea,'' J. Acoust. Soc. Am. **101**, 2151–2163.
Russell, I. J., and Nilsen, K. E. (**1997**). ''The location of the cochlear amplifier: Spatial representation of a single tone on the guinea pig basilar membrane,'' Proc. Natl. Acad. Sci. U.S.A. **94**, 2660–2664.
Shailer, M. J., and Moore, B. C. J. (**1987**). ''Gap detection and the auditory filter: Phase effects using sinusoidal stimuli,'' J. Acoust. Soc. Am. **81**, 1110–1117.
Shera, C. A., Guinan, J. J., and Oxenham, A. J. (**2002**). ''Revised estimates of human cochlear tuning from otoacoustic and behavioral measurements,'' Proc. Natl. Acad. Sci. U.S.A. **99**, 3318–3323.
Stelmachowicz, P. G., Lewis, D. E., Larson, L. L., and Jesteadt, W. (**1987**). ''Growth of masking as a measure of response growth in hearing-impaired listeners,'' J. Acoust. Soc. Am. **81**, 1881–1887.
Vogten, L. L. M. (**1978**). ''Low-level pure-tone masking: A comparison of 'tuning curves' obtained with simultaneous and forward masking,'' J. Acoust. Soc. Am. **63**, 1520–1527.
Wojtczak, M., Schroder, A. C., Kong, Y.-Y., and Nelson, D. A. (**2001**). ''The effect of basilar membrane nonlinearity on the shapes of masking period patters in normal and impaired hearing,'' J. Acoust. Soc. Am. **109**, 1571–1586.
Yates, G. K. (**1990**). ''Basilar membrane nonlinearity and its influence on auditory nerve rate-intensity functions,'' Hear. Res. **50**, 145–162.
Yates, G. K., Winter, I. M., and Robertson, D. (**1990**). ''Basilar membrane nonlinearity determines auditory nerve rate-intensity functions and cochlear dynamic range,'' Hear. Res. **45**, 203–220.

Detection, direction discrimination, and off-frequency interference of center-frequency modulations and glides for vowel formants

J. Lyzenga and R. P. Carlyon
MRC Cognition and Brain Sciences Unit, 15 Chaucer Road, Cambridge CB2 2EF, United Kingdom

(Received 27 January 2004; revised 8 February 2005; accepted 8 February 2005)

Vowels are mainly classified by the positions of peaks in their frequency spectra, the formants. For normal-hearing subjects, change detection and direction discrimination were measured for linear glides in the center frequency (CF) of formantlike sounds. A CF rove was used to prevent subjects from using either the start or end points of the glides as cues. In addition, change detection and starting-phase (start-direction) discrimination were measured for similar stimuli with a sinusoidal 5-Hz formant-frequency modulation. The stimuli consisted of single formants generated using a number of different stimulus parameters including fundamental frequency, spectral slope, frequency region, and position of the formant relative to the harmonic spectrum. The change detection thresholds were in good agreement with the predictions of a model which analyzed and combined the effects of place-of-excitation and temporal cues. For most stimuli, thresholds were approximately equal for change detection and start-direction discrimination. Exceptions were found for stimuli that consisted of only one or two harmonics. In a separate experiment, it was shown that change detection and start-direction discrimination of linear and sinusoidal formant-frequency modulations were impaired by off-frequency frequency-modulated interferers. This frequency modulation detection interference was larger for formants with shallow than for those with steep spectral slopes. [DOI: 10.1121/1.1882943]

PACS numbers: 43.66.Fe, 43.66.Mk, 43.71.Es [NFV] Pages: 3042–3053

I. INTRODUCTION

The vowels of natural speech are characterized by the positions of their formants, i.e., the peaks in their spectral envelopes. During production, these formants often change their positions depending on the character of preceding and following consonants (coarticulation, e.g., Fletcher, 1953) or vowels (forming diphthongs). Previously, we measured the detection of center-frequency modulation of formants in a monaural (Lyzenga and Carlyon, 1999) and a binaural (Lyzenga and Carlyon, 2000) paradigm using formantlike complex tones. The results of those studies shed light on the cues that listeners use to detect formant frequency changes, and on how these cues vary as a function of the spectral shape and fundamental frequency (F_0) of the formant in question. It was concluded that, for the majority of stimuli, the detection of formant frequency changes was based on place-of-excitation cues, while for less formantlike stimuli, with just one or two large partials, detection was frequently based on changes in the modulation depth and sometimes on changes in the temporal fine structure.

Perhaps more importantly, the results of Lyzenga and Carlyon (1999) showed that the detection of a formant frequency change can be disrupted by modulations applied to a simultaneously presented formant in a remote frequency region. In contrast, unmodulated formants did not affect performance. This demonstrated that the phenomenon of frequency modulation detection interference (FMDI), previously studied for pure-tone carriers (Wilson *et al.*, 1990; Moore *et al.*, 1991; Carlyon, 1994; Gockel and Carlyon, 2000), could disrupt modulation processing for more speechlike stimuli. Furthermore, for formants whose spectral envelopes were shallow enough to encompass several harmonics, FMDI was greater when the target and the ''interfering'' formant had the same, rather than a different, F_0. Combined with the finding that some FMDI occurred when the interferer was presented contralaterally to the target (Lyzenga and Carlyon, 2000), this suggested that FMDI occurred at a rather central stage of auditory processing. The existence of such FMDI could affect speech perception. For example, cues related to the aforementioned coarticulation may be disrupted by other frequency changes occurring in competing speech or, possibly, even by formant changes occurring in the same speech signal.

In our previous studies, the center frequency (F_C) of a formant was changed in a sinusoidal manner, where each stimulus contained approximately one modulation cycle. Here, we extend the types of formant changes used in those studies to linear FM, which more closely resembles the formant glides that occur in natural speech. Since it is often more important in speech perception to identify the direction of formant changes than to detect a change, we also included a task in which we measured direction discrimination for linear formant changes and starting-phase, or start-direction, discrimination for FM in which the modulator was a single cycle of a sinusoid. In the remainder of this article, we will refer to both tasks as ''direction discrimination.'' The detection thresholds for sinusoidal and linear FM will be denoted using the acronym FMT, whereas the direction discrimination thresholds will be denoted ''direction FMTs (dFMTs).''

Detection of linear frequency glides in pure tones has been investigated in a number of studies (Sergeant and Har-

 0001-4966/2005/117(5)/3042/12/$22.50

ris, 1962; Nábělek and Hirsh, 1969; Tsumara *et al.*, 1973; Tyler *et al.*, 1983; Dooley and Moore, 1988; Madden and Fire, 1996, 1997). Dooley and Moore (1988) found that place-of-excitation models could not completely account for their data, but they did not have conclusive evidence against such models either. Consistent with our earlier conclusions based on formant stimuli with shallow slopes, Madden and Fire (1996, 1997) argued that place models could account for their data. In the present study we compare detection thresholds for linear formant glides with changes in place of excitation, modulation depth, and temporal fine structure to assess the relative importance of these cues. Madden and Fire also argued that the frequency rove they used is essential to prevent subjects from using the frequency difference between the end-point of the first glide and the start of the second glide as a cue. For that reason, we used a frequency rove of ± 160 Hz for the linear formant glide conditions of the present study. No frequency roving was used for the sinusoidal formant modulations, which, unlike linear FM, produced initial and final instantaneous frequencies that were nearly equal.

II. EXPERIMENT 1: DETECTION OF SINUSOIDAL AND LINEAR FM

A. Stimuli

The stimuli were band-limited harmonic tones that resembled vowel formants. The band-limiting filters had triangular spectral envelopes, on a log-log scale, and a slope of either 50 or 200 dB/oct. They were located in either a LOW region (near 500 Hz), a MID region (near 1500 Hz), or a HIGH region (near 3000 Hz). When unmodulated, the center frequencies of the formants were located either at a harmonic or mid-way between two adjacent harmonics, denoted in the figures as /|\ and /||\, respectively. The formants had a fundamental (F_0) of either 80 or 240 Hz. All frequency components of the complexes started in sine phase. Stimulus duration was 200 ms (excluding 25-ms raised-cosine ramps). The spectra of the unmodulated stimuli with a slope of 200 dB/oct are shown in Fig. 1. Some examples of waveforms of stimuli with very different temporal characters are shown in Fig. 2.

For the 80-Hz fundamental and center frequencies coinciding with a harmonic the center frequencies were 480, 1440, and 2960 Hz, for the LOW, MID, and HIGH regions, respectively. When the center frequency was placed between two harmonics, these frequencies were 520, 1560, and 3000 Hz, respectively. For the 240-Hz fundamental, the center frequencies coinciding with a harmonic were 480, 1440, and 2880 Hz, and those placed between two harmonics were 600, 1560, and 3000 Hz. We used a formant-frequency rove of ± 160 Hz for the linear formant glide conditions, which translates into rove spans of, on average, 62.1%, 21.4%, and 10.8% for the regions LOW, MID, and HIGH, respectively. To create a linear increase in the center frequency of a stimulus, the center frequency of the triangular filter was varied linearly over the full 250-ms stimulus duration, thus resulting in a linear movement of the center frequency of the spectral envelope, while the constituent frequency components only changed in level. To modulate the center frequencies of the stimuli in a sinusoidal manner, the same scheme was applied using a sinusoidal 5-Hz modulation of the center frequency of the triangular filter, thus resulting in a single modulation cycle during the 200-ms maximum-level part of the stimuli.

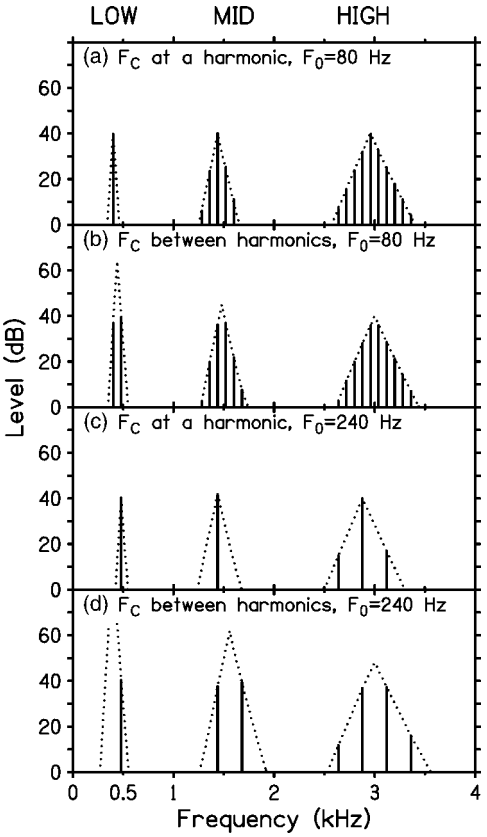

FIG. 1. Examples of stimulus spectra with a 200-dB/oct slope. The dotted lines represent the spectral envelopes. From left to right, each panel shows stimuli in the LOW, MID, and HIGH regions. In panels (a) and (b) the stimuli have an 80-Hz F_0 and in panels (c) and (d) the F_0 is 240 Hz. In panels (a) and (c) the center frequencies coincide with a harmonic and in panels (b) and (d) they are in between two harmonics.

The stimulus waveforms were computed digitally off-line with 16-bit resolution and stored on disk. Each stimulus was generated by calculating its spectral envelope as a function of time, after which all frequency components (with fixed frequency) were added to the stimulus with their calculated time-varying amplitudes. In this way, the formant-frequency changes resulted in amplitude changes of the components, where these changes were in antiphase for components on the lower- and the higher-frequency sides of the formant. On the spectral skirts, components were included down to a level of at least 50 dB below that of the largest one. A set of signals, needed for the determination of one FMT or dFMT, consisted of a steady reference sound with center frequency F_C and 23 targets with an increasingly large center frequency change. The target zero-to-peak frequency change ranged from 0.0125% to 25.6% in 22 steps of a factor $\sqrt{2}$.

In all conditions, a continuous pink noise was present at a spectrum level of 0 dB (*re* 20 μPa) at 1 kHz. For each subject, we measured the detection thresholds for all reference stimuli in the pink noise background. The stimuli were

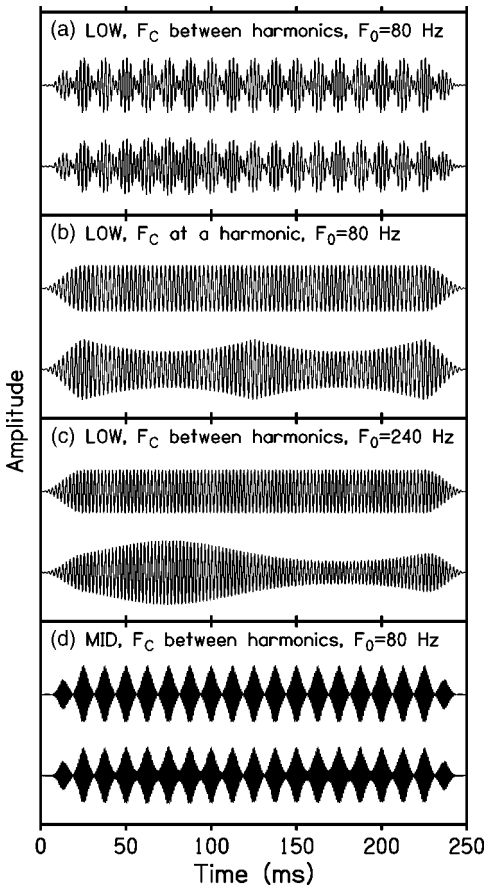

FIG. 2. Four examples of waveforms of formants having 200-dB/oct slopes. The upper trace of each panel contains the unmodulated waveform and the lower trace contains the waveform sinusoidally modulated at a depth of approximately two times detection threshold. The corresponding spectra for the unmodulated waveforms in panels (a)–(d) can be found in Fig. 2 as LOW of panel (b), LOW of panel (a), LOW of panel (d), and MID of panel (b), respectively. In comparison with the unmodulated waveforms, the modulated waveform in panel (a) shows an FM nature, those in panels (b) and (c) show a pure AM nature, and the one in panel (d) only differs from the unmodulated waveform near the minima of the temporal envelope (which is associated with a "beating cue").

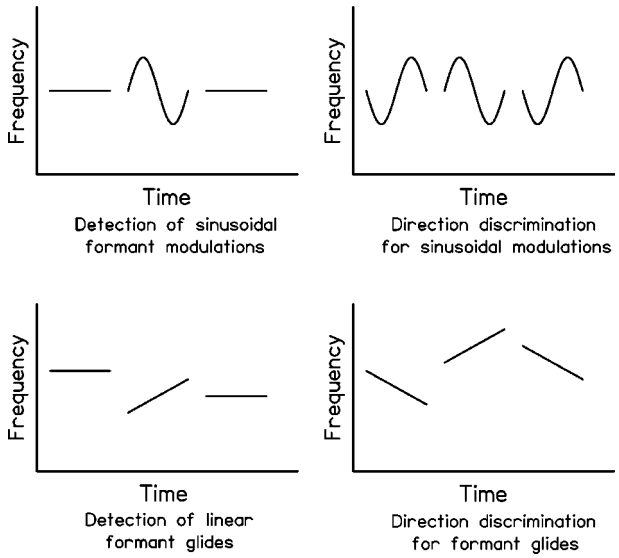

FIG. 3. Examples of the formant frequency relations between a reference and two target tones for a set of stimuli with a sinusoidal formant modulation in the top row, and with a formant glide with frequency roving in the bottom row. The left column depicts the frequency-change detection task, and the right column depicts the direction-discrimination task. The formant frequency relations are shown for the central, maximum amplitude, 200-ms sections of the stimuli.

presented at a level of 30 dB above their thresholds in the pink noise. [For two subjects, these presentation levels were compared to threshold measurements in quiet for all reference stimuli; on average they were found to represent sensation levels of 46.2 dB SL (SD=4.3) and 47.0 dB SL (SD =3.7) for the stimuli with slopes of 50 and 200 dB/oct, respectively]. In the experiments, the stimulus waveforms were retrieved by a PC and converted to analog signals using a 16-bit DAC (CED 1401 plus) at a sample rate of 40 kHz. The waveforms were low-pass filtered at 17.2 kHz (3-dB-down point, Kemo VBF/25.01, slope=100 dB/oct). Attenuation and mixing were performed by computer-controlled attenuators and a mixer (Tucker-Davis Technologies PA4 & SM3). All stimuli were presented monaurally through the right earpiece of Sennheiser HD414 headphones. They were checked using an HP 3561A spectrum analyzer.

B. Procedure and subjects

FMTs and dFMTs for sinusoidal and linear FM of the center frequencies of synthetic formants were measured using a three-interval, three-alternative forced-choice (3I, 3AFC) paradigm and an adaptive procedure. Each FMT estimation was started with the maximum modulation range. After four correct responses, the modulation range was decreased. It was also decreased after one incorrect combined with five correct responses, or after two incorrect combined with six correct responses. The combination of three incorrect and six correct responses led to a test repetition at the same modulation range. After four incorrect responses, the modulation range was increased. The trials were repeated until one of these conditions was met, after which the modulation range was adapted accordingly and the next set of trials performed. This procedure converged on the 63%-correct point of the psychometric function, which, in the absence of response bias, corresponds to $d'=1$ for a 3I, 3AFC procedure; it is described in more detail by Lyzenga and Carlyon (1999). For the change-detection task, two of the three tone intervals contained the stationary reference formant and the remaining interval contained the sinusoidal or linear FM. For the direction-discrimination task, two intervals contained formant changes in one direction and the signal interval contained a change in the opposite direction. In both tasks, the modulation in the signal interval either started in sine phase (for sinusoidal FM) or increased in frequency (for linear FM). For each task, Fig. 3 shows examples of stimulus sequences with the second interval being the signal interval, which was randomly chosen during the measurements. (Note the frequency rove that is present for the linear but not the sinusoidal FM.) The silent interval between the tone intervals was 400 ms. Normal-hearing subjects were asked to identify the interval containing the odd tone. Immediate feedback was given. The different stimulus conditions were presented in a randomized order. Three subjects, with

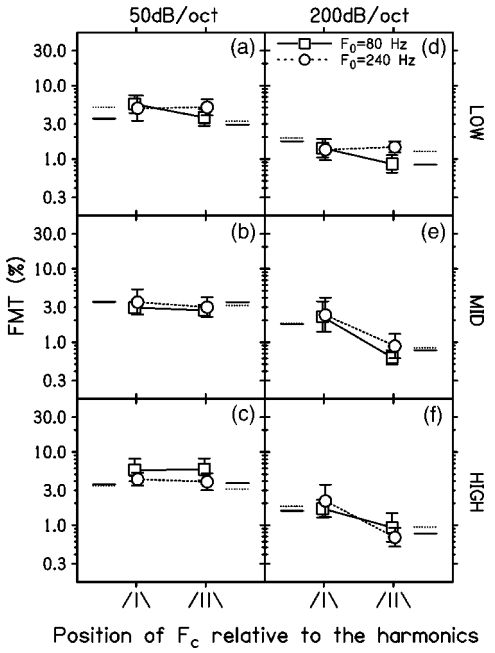

FIG. 4. FMTs for sinusoidal formant-frequency modulations, plotted as zero-to-peak differences. The squares and the circles denote the 80- and 240-Hz F_0, respectively. The left and right columns show the data for the 50- and 200-dB/oct slopes, respectively. From top to bottom the data for the frequency regions LOW, MID, and HIGH are displayed. The error bars indicate the standard deviations over three subjects. Model predictions are shown by the horizontal bars on the far left and right of each panel.

ages between 30 and 37, participated for the sinusoidal FM. Two of them (aged 30 and 31), and a new subject (aged 31), participated for the linear FM.

C. Results

1. FM detection

The FMTs found for sinusoidal FM, expressed as peak-to-peak FM depths, are plotted by the open symbols in Fig. 4. They were almost identical to those found for the same stimuli in our earlier study on FMTs for formants (Lyzenga and Carlyon, 1999, Fig. 4).[1] In general, they are smaller for the steep than for the shallow slopes and do not strongly depend on F_0. The short line segment at the side of the symbols shows the predictions of a hybrid model based on the use of changes in place of excitation, modulation depth, and temporal fine structure of the stimuli. The model is the same as was used in Lyzenga and Carlyon (1999), but for the present data the optimal least-squares fit was achieved using a slightly smaller threshold for the place cue than was used in that study. In short, the first stage of the model consists of a bank of linear filters whose outputs are analyzed in the next stages; from their levels excitation patterns are generated and compared between stimulus intervals (place cues); from their temporal envelopes changes in the depth of the slow ($\leqslant$10 Hz) amplitude modulation of the stimuli that occur between stimulus intervals are determined (AM cues); cues associated with fast amplitude modulations at the rate of the fundamental (80 or 240 Hz), that result from within-channel interactions of components, are derived from peaks in the second derivatives of their temporal envelopes (beating cues). The details of the model, including the applied detection thresholds, are described in the Appendix. The left two data columns of Table I show which cue dominated the predicted threshold for each stimulus conditions. For the shallow slope, Table I shows that the dominant cue was a place cue, while for the steep slope different cues dominated, depending on the F_0 and on whether the formant frequency coincided with a harmonic.

The FMTs for the linear FM are shown in Fig. 5, along with the predictions of the hybrid model. These model prediction were calculated using the central reference and target stimuli, thus ignoring the frequency rove. Because the rove blurred the distinction between formants centered on one harmonic and those falling between two harmonics, predictions that differ between these two cases should be treated with some caution. To achieve the optimal least-squares fit,

TABLE I. For each stimulus condition for sinusoidal and linear FM, the cue that dominated the predicted threshold of the hybrid model is indicated. Place-of-excitation cues are indicated by "P," AM cues by "A," and beating cues by "B." For one condition the place and the modulation-depth changes contributed in nearly equal amounts (within 10% of each other); this is indicated by "C."

			Sinusoidal FM		Linear FM	
			Slope		Slope	
F_0	Frequency region	F_C position	50 dB/oct	200 dB/oct	50 dB/oct	200 dB/oct
80 Hz	LOW	/|	P	A	P	A
		/||	P	P	P	P
	MID	/|	P	A	P	A
		/||	P	B	P	P
	HIGH	/|	P	A	P	P
		/||	P	B	P	P
240 Hz	LOW	/|	C	A	P	A
		/||	P	A	P	A
	MID	/|	P	A	P	A
		/||	P	P	P	P
	HIGH	/|	P	A	P	A
		/||	P	P	P	P

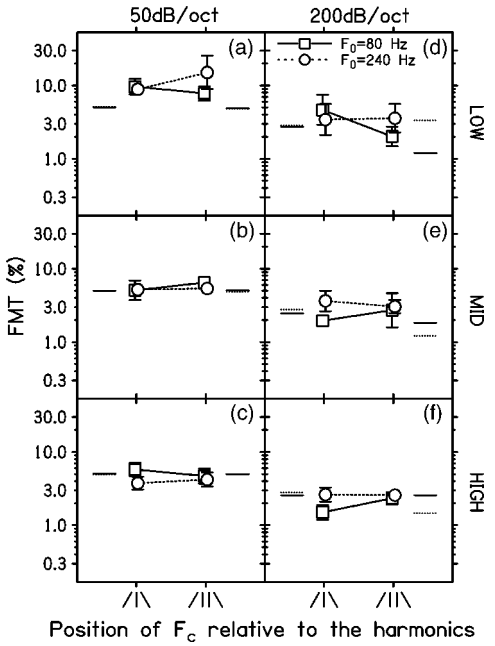

FIG. 5. As in Fig. 4 but for linear formant-frequency glides. The FMTs are plotted as peak-to-peak differences.

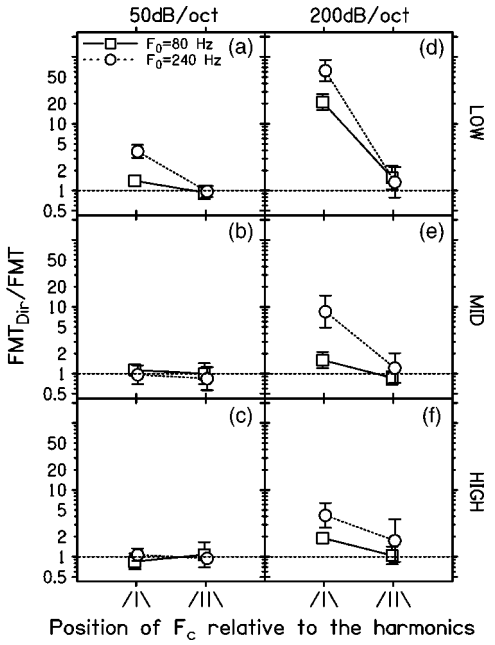

FIG. 6. The ratio between the direction-discrimination FMTs and the detection FMTs for stimuli with a sinusoidal formant modulation. Both thresholds were expressed as the peak-to-peak change in the targets. The format of this figure and the meaning of the symbol shape is the same as for Fig. 4.

the thresholds for both the place cue and the modulation-depth cue had to be increased by 31% relative to the values used for the sinusoidal FM, while the beating cue had to be discounted. The applied frequency roves were 62.1%, 21.8%, and 10.8% for frequency regions LOW, MID, and HIGH, respectively. For most conditions, the FMTs are a ratio of 4 or more smaller than the frequency rove, and, therefore, it is unlikely that information from the start and end points of the formant glides will have affected them. Only the FMTs in Fig. 5(c) are roughly two times smaller than the rove, so information from the start and end points of the formant glides could, in theory, have affected them. However, because these conditions were presented at random through the measurement series, they occurred at arbitrary times in the context of a majority of trials for which start and end points were not a valid cue. This will have made it very hard for the listeners to use these erratic and small cues, and makes it rather unlikely they will have been of any material assistance during the experiment.

Figures 4 and 5 show a reasonably good fit between the model predictions and the FMTs for sinusoidal and linear FM. Overall, the FMTs are larger for the linear FM than for the sinusoidal FM. This increase is fairly constant over a large portion of the stimulus conditions, which is corroborated by the 31% threshold increase for the place and modulation-depth cues that was necessary to obtain the optimal fit between model predictions and FMTs for linear FM. On the other hand, one aspect of the results for the sinusoidal FM is not reflected in the data for the linear FM. For the sinusoidal FM we found an effect of center-frequency position in the MID and HIGH regions for the 200-dB/oct slope [Figs. 4(e) and (f)]; FMTs are smaller for center frequencies between harmonics than for center frequencies coinciding with a harmonic. This is not seen for the linear FM [Figs. 5(e) and (f)]. For the conditions with a center frequency positioned between two harmonics and an 80-Hz F_0, Table I shows [in accordance with Lyzenga and Carlyon (1999)] that a beating cue was involved for the sinusoidal FM but not for the linear FM. When unmodulated, these stimuli consist essentially of two equal-amplitude harmonics, producing an envelope that beats at a rate equal to F_0 [cf. Fig. 2(a)]. As the formant center frequency moves towards one of the harmonics adjacent to it, the depth of the beating is reduced, providing a cue to the FM. However, for the condition with linear FM, the overall formant frequency was randomized from presentation to presentation, and so did not always fall mid-way between two harmonics. As a result, the beating cue would have been less useful in this condition, and this may account for the poorer performance with linear FM. A similar argument may apply for the 240-Hz F_0. Because of the frequency rove used for the linear FM, the center frequency did not always fall mid-way between two harmonics. So, any perceptual advantages that this condition may have offered (in agreement with the model results) will have been disturbed, which would then lead to poorer performance for the linear FM. In general, the results and model suggest that temporal cues are more labile than place-of-excitation, and it is the ''place'' cues that are likely to prove most useful in real-life situations.

2. FM direction discrimination

The ratios between the dFMTs and the FMTs for sinusoidal modulators are shown in Fig. 6. For many stimuli this ratio was close to unity. This may seem surprising because, at a given time into each modulation, the instantaneous difference in formant frequency between the standards and target will be twice as great in the starting-phase-discrimination task as in the FM-detection task [see Figs. 3(a) and (b)]. The

fact that the dFMT was not lower than the FMT suggests that listeners were not able to make use of that extra information and that they relied on judgments of the presence and direction of modulation in each stimulus interval. In turn, this suggests that listeners were able to identify the starting direction of a modulation as soon as they were able to detect that modulation. To test for the effects of the different stimulus conditions, we performed a five-way repeated-measures analysis of variance (task$\times$F$_0$$\times$slope$\times$center-frequency region$\times$center-frequency position) on the logarithmic transform of the individual thresholds. This ANOVA showed significant effects of F$_0$ ($F_{(1,2)}=32.0$, $p<0.05$), slope ($F_{(1,2)}=137.8$, $p<0.01$), center-frequency region ($F_{(1,2)}=21.3$, $p<0.05$), and center-frequency position ($F_{(1,2)}=139.7$, $p<0.01$), but no significant effect of task ($F_{(1,2)}=8.15$, $p=0.10$). However, significant effects involving task did show up in two two-way interactions [task$\times$center-frequency region: $F_{(2,4)}=158.8$, $p<0.001$; task$\times$center-frequency position: $F_{(1,2)}=106.5$, $p<0.01$], in three three-way interactions (task$\times$F$_0$$\times$center-frequency position: $F_{(1,2)}=158.0$, $p<0.01$; task$\times$slope$\times$center-frequency position: $F_{(1,2)}=549.3$, $p\leqslant 0.002$; task$\times$center-frequency region$\times$center-frequency position: $F_{(1,2)}=323.7$), $p\leqslant 0.002$, and even in a significant four-way interaction (task$\times$slope$\times$center-frequency region$\times$center-frequency position: $F_{(2,4)}=12.5$, $p<0.02$).[2]

The fact that the factor ''task'' interacted with other main effects reflects the fact that, for a small subset of conditions, dFMTs were in fact *larger* than FMTs. This was mainly seen for stimuli with a steep slope and a center frequency coinciding with a harmonic. These stimuli all had one large central component, and the 5-Hz FM caused the amplitude to decrease twice per period, once for the positive frequency excursion and once for the negative frequency excursion, thus resulting in a 10-Hz amplitude modulation [an example of such a stimulus is shown in Fig. 2(b)]. For these stimuli, changing the direction of the modulation does not change the envelope of the waveform until the modulations are so large that the condition of the single stimulus component is no longer met (i.e., the formant frequency may move to a position closer to an adjacent harmonic). The FM depths at which these conditions were no longer met are greater at higher F$_0$'s, and, correspondingly, the ratios shown in Fig. 6 are indeed higher at 240 Hz than at 80 Hz.

Analogous ratios are shown for the linear FM in Fig. 7. As with the sinusoidal modulations, the ratio was found to be near unity for most stimuli. This was corroborated by a similar five-way repeated-measures analysis of variance on the logarithmic transform of the individual thresholds as was performed for the sinusoidal FM. The ANOVA showed significant effects of F$_0$ ($F_{(1,2)}=29.2$, $p<0.05$) and center-frequency region ($F_{(1,2)}=65.2$, $p<0.01$); the effect of task just failed to reach significance ($F_{(1,2)}=12.1$, $p=0.07$). There were, however, significant interactions involving the factor task: two two-way interactions (task$\times$slope: $F_{(1,2)}=91.4$, $p<0.02$; task$\times$center-frequency region: $F_{(2,4)}=285.8$, $p<0.001$) and two three-way interactions (task$\times$F$_0$$\times$slope: $F_{(1,2)}=41.6$, $p<0.05$; task$\times$slope$\times$center-frequency region: $F_{(1,2)}=48.7$, $p<0.02$). So, as

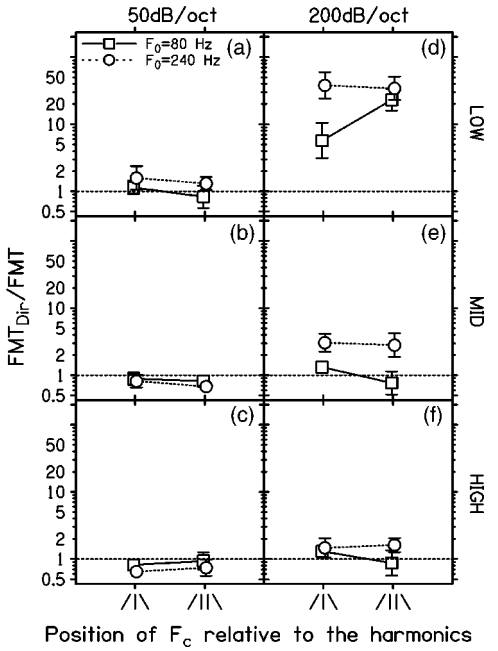

FIG. 7. As in Fig. 5 but for linear formant-frequency glides.

was found for the sinusoidal formant modulations, the effect of task by itself was not significant, but it was involved in several significant interactions.

The interactions involving ''task'' reflect the fact that, again, direction discrimination was much harder than change detection for only a subset of stimuli. As with the sinusoidal modulations, these higher ratios occurred primarily for stimuli in which only one or two components fall within the passband of the filter. However, the frequency rove used with the linear FM makes the distinction between a filter centered on a single component and one falling midway between two components less relevant than for sinusoidal FM, and elevations are observed for both stimulus classes. In addition, the reason for the elevation appears to be slightly different. For the linear FM in the standard interval, there were one or two components present. The exact number varied from standard to standard, depending on the value of the random frequency rove. Nevertheless, for each standard stimulus, the pattern of amplitude modulation (AM) was constant throughout. The signal could thus be detected via a change in the depth of AM produced by the glide in the filter center frequency—this produced either an increase in depth, if the filter moved from being centered on a single harmonic (/|\) to between two harmonics (/||\), or a decrease if it moved from (/||\) to (/|\). For the direction-discrimination task, however, this cue was not available, because the frequency rove randomized the direction of the change in AM depth. Under these circumstances, subjects may have been forced to use place-of-excitation cues, which themselves are unreliable because, when only a small number of components fall within the formant filter, shifts in F$_C$ cause components to ''drop out'' of either end of the filter, producing marked variations in the shape of the excitation pattern. As a result, dFMTs can be very high. For example, with an F$_0$ of 240 Hz in the LOW region [Fig 7(d)], dFMTs are approximately 30 times higher than the FMT, which is itself around 3% [Fig. 5(d)].

In summary, thresholds for the discrimination of differences in the phase of sinusoidal FM or the direction of linear FM were usually similar to those for FM detection. There were a few instances where the discrimination thresholds were higher, but this could be attributed to specific stimuli allowing subjects to perform the FM detection task without encoding the formant frequency *per se*. In those cases, FM detection could be achieved by identifying changes in the pattern of AM at the output of one or more auditory filters.

III. EXPERIMENT 2: FM DETECTION/DISCRIMINATION INTERFERENCE

A. Method

The method of stimulus generation was in most respects identical to that used for experiment 1. For the FMDI measurements of experiment 2, the signals and interferers were chosen in the MID and the HIGH regions, respectively, and only center frequencies coinciding with a harmonic were used. Signals and interferers had either equal or different F_0's of 80 or 240 Hz, and they always had identical slopes of 50 or 200 dB/oct. This subset of formants was chosen on the basis of the results of Lyzenga and Carlyon (1999) for the detection of sinusoidal FM, so as to use stimuli that had produced a substantial FMDI in that study. The interferers and signals were also chosen such that the cues used to detect the FM were, based on arguments presented in that study, usually the same for the signals and the interferers (most were ''place cues'' based on the detection of shifts in hypothetical excitation patterns).

As Lyzenga and Carlyon (1999) showed that unmodulated interferers did not affect thresholds, we only use modulated interferers in the present study. To facilitate easy comparison with the results of the earlier studies (Lyzenga and Carlyon, 1999, 2000), we chose the same 10-Hz modulation-rate for the interferers, along with the 5-Hz rate for the signals, as were used in those studies. These rates were used for the detection and discrimination of sinusoidal FM. Therefore, during the central 200 ms (when the stimulus level was constant), signals contained one modulation cycle and interferers contained two cycles. The FM applied to the signals had a starting phase of 0° or 180° at the start of the maximum level part, depending on condition, and the FM applied to the interferers had a starting phase of 0° at the start of the maximum level part. To maximize the likelihood of FMDI being observed, the extent of the interferers' FM was set to a large value, equal to four times the detection threshold (at $d'=1$) for the interferer in question, based on the FMTs for a 5-Hz modulation rate obtained in experiment 1.[3] For the detection and discrimination of linear FM, the interferer was an up glide on half of all trials and a down glide on the other half, but was always the same in the three intervals of each trial. This direction was chosen at random. The extent of the interferer's glide was set to four times the detection threshold (at $d'=1$) for the interferer in question, based on the FMTs for a linear (upward) modulation obtained in experiment 1.

The presentation levels of the reference signals and interferers were 30 dB above their thresholds in the background pink noise (we checked the thresholds in quiet for the stimuli with a 50-dB/oct spectral slope, and found them to be 46 ± 6 dB lower than the levels of the stimuli used in the experiments, when averaged across all four listeners). In the conditions with interferers, we inserted a narrow-band noise between the signals and the interferers. The narrow-band noise was generated by bandpass filtering (Kemo VBF/25.03, slope=48 dB/oct) white noise (TDT WG1) to have a center frequency of 2150 Hz and a 10-dB bandwidth of 200 Hz, which is somewhat smaller than the critical bandwidth at this center frequency (Scharf, 1970). Its spectrum level at 2150 Hz was 17 dB, which was 20 dB higher than that of the pink noise at 2150 Hz. The narrow-band noise was added to mask any within-channel effects in the excitation slopes of the signals and the interferers, such as beating of a signal and an interferer component that lie very close in frequency. A second strategy for preventing such interference effects was to have their fundamentals at integer multiples (either 1 or 3) of each other. In this way, the occurrence of beating between very closely spaced signal and interferer components could be avoided. The frequency spectra of the two signal/interferer combinations with identical fundamentals, including the background noise spectrum, are shown in Fig. 8. The measurement procedures were identical to those of experiment 1. The same two subject groups were used for the sinusoidal and linear formant changes as in experiment 1, so that individual FMDI ratios could be evaluated.

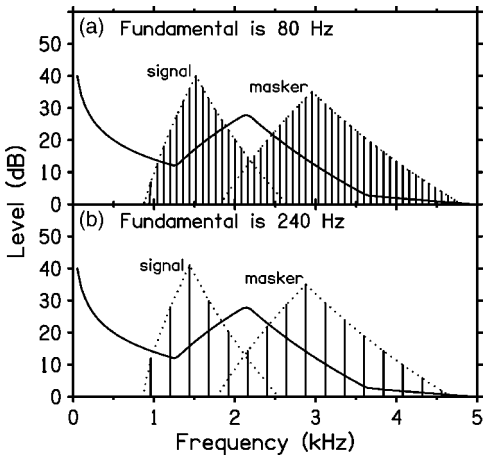

FIG. 8. The solid lines depict the spectra of the background noise bands in relation to the spectra of the signal/interferer combinations (vertical solid lines and dotted lines) for F_0's of 80 Hz (top panel) and 240 Hz (bottom panel). The bandwidth of this spectral analysis is 47.8 Hz. Between 1 and 4 kHz, the width of the auditory filter is larger than 48 Hz (Glasberg and Moore, 1990). Therefore, after auditory filtering the level of the noise will have been slightly larger relative to the complexes than is depicted.

B. Results

The amount of FMDI was defined as the ratio of the FMT or dFMT obtained for a given formant in the presence and in the absence of an interferer. The top half of Fig. 9 shows these ratios for sinusoidal FM, with the results for the change-detection task in the top row, and those for the direction-discrimination task in the second row. The bottom half of Fig. 9 displays the results for the linear FM, with the change-detection results in the third row, and direction-discrimination results in the bottom row. It can be seen that

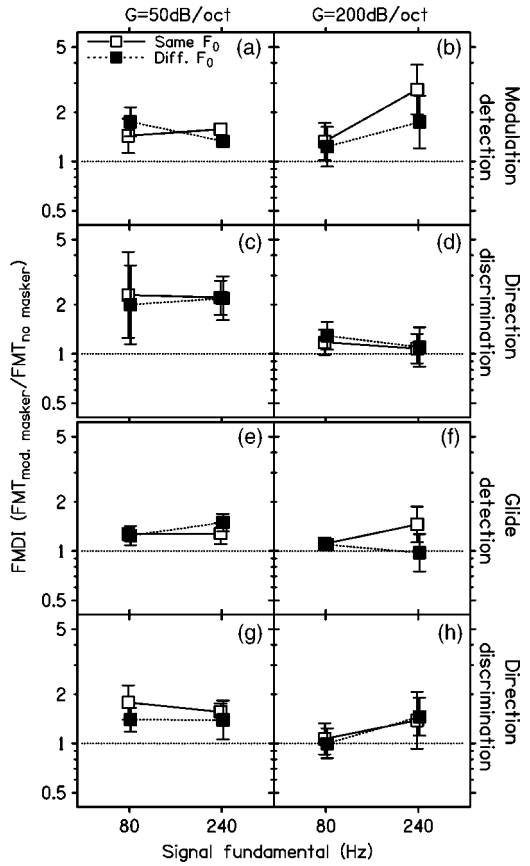

FIG. 9. Mean FMDI for stimuli in the MID region with modulated interferers located in the HIGH region. The left and right columns show the data for the 50- and 200-dB/oct slope, respectively. The open and filled squares display data for stimuli and maskers with identical and different F_0,'s respectively. The error bars indicate the standard deviations over three subjects.

the ratio was greater than one for the majority of the conditions, indicating the presence of significant amounts of FMDI. A significant effect of interferer configuration was found using a one-way mixed-model repeated-measures ANOVA with a three-level factor for interferer configuration (interferer absent, present with same F_0 as target, present with different F_0 than target) on the logarithmic transform of the individual FMTs and dFMTs (interferer configuration: $F_{(2,4)}=15.76$, $p<0.02$). The left-hand column of Fig. 9 shows that FMDI occurred consistently for the shallow slope, while the results for the steep slope in the right-hand column are less consistent. This observation was confirmed by performing a five-way ANOVA (task$\times F_0\times$slope $\times$interferer $F_0\times$center-frequency shape: modulation or glide) on the differences between the logarithmically transformed FMTs and dFMTs for conditions with and without interferers. The only significant main effect was an effect of the formant slopes on FMDI ($F_{(1,2)}=19.5$, $p<0.05$). The ANOVA also showed a significant three-way interaction (task$\times$slope$\times$interferer F_0: $F_{(1,2)}=21.4$, $p<0.05$) and a significant four-way interaction (task$\times F_0\times$slope $\times$center-frequency shape: $F_{(1,2)}=34.3$, $p<0.05$). From the Bonferroni-corrected estimated means, FMDI was found to be significantly larger for formants with shallow slopes than for those with steep slopes (on average: 1.54 vs. 1.24, $p<0.05$). On average, FMDI was slightly larger for formant modulations (1.51) than for formant glides (1.26), but this effect was not significant ($p=0.32$). As found by Lyzenga and Carlyon (1999), FMDI was slightly larger for interferers with the same fundamental than for those with a different fundamental than the signals (on average: 1.43 vs. 1.33). However, possibly connected with the small number of conditions in the present study as compared to the previous one (16 vs. 40), this effect failed to reach significance in the present data ($p=0.16$).

IV. DISCUSSION

A. Center-frequency modulation detection and direction discrimination

In this study, we measured detection of sinusoidal and linear FM, and, with the aid of a hybrid model, we were able to identify a range of cues that might have been used to perform these tasks (Table I). In most cases, the results are consistent with the use of place-of-excitation cues. But for some stimuli, consisting of a small number of components, listeners appeared to have used changes in the depth of the slow ($\leqslant 10$ Hz) amplitude modulation of the stimuli (AM cues) and, for the sinusoidal FM, cues associated with fast amplitude modulations at the rate of the fundamental (80 or 240 Hz) caused by within-channel interactions of components (beating cues). For the linear FM the thresholds used in the model were 31% larger than were used for the sinusoidal FM, reflecting the larger FMTs for linear FM. This increase in threshold probably reflects the extra uncertainty that the frequency rove added to the conditions with linear FM, but may also reflect a reduced effective frequency glide. Because of the start and stop tapering of the stimuli, the start and end frequencies of the linear glides, as they were used in the model calculations, were never actually reached. This can be expected to reduce the effective extent of the glides by approximately 10% to 20%. Furthermore, the frequency extremes that are present in the stimuli are very short lived. As a consequence, the perceived extent of the glide will have been somewhat smaller than the physical frequency change. This effect would have been less marked for sinusoidal modulations, in which the time spent close to the frequency extremes is greater (Hartmann and Klein, 1980). From the present data, these two factors cannot be teased apart. The modeling effort identified candidates for the forms of processing listeners may perform in the present conditions of low uncertainty. For more natural stimuli, there are two reasons why rather subtle AM and beating cues are probably less useful than the more robust place of excitation cues. First, subtle waveform changes are likely to be disturbed by listening conditions such as the presence of reflections and, second, these waveform changes do not explicitly encode the directions of formant changes (which are useful for speech perception). Place of excitation cues do not entail these problems and, in accordance with the results for the shallow slope, may therefore be the more likely candidates for natural stimuli and listening conditions.

For both sinusoidal and linear FM, direction-discrimination thresholds were very close to the detection thresholds for a majority of the conditions, but, as discussed

in Sec. III B, there were a few exceptions where direction (and starting-phase) discrimination thresholds were higher. For both the sinusoidal and the linear FM these exceptions occurred mainly for conditions associated with an AM detection cue. For the linear FM, all exceptions occurred for stimuli with a modulation structure that was symmetrical in time, giving a useful cue for the detection task but not for the direction-discrimination task. For the linear FM, we roved overall frequency, which required subjects to ''abstract'' information about the way in which F_C was changing throughout each stimulus. The effect of the rove was to lessen the utility of cues related to AM in the temporal envelope, not least because it meant that in no condition did the standard or signal fall consistently either on a single harmonic or between two harmonics. We therefore believe that the dFMTs reported here mainly reflect listeners' use of place-of-excitation cues.

B. Center-frequency modulation-detection interference

FMDI was found under many conditions comprising both types of formant changes (modulations and glides) and both tasks (change detection and direction discrimination of formant changes). It was found to be somewhat larger for formant modulations than for linear formant glides, but that difference did not reach significance. The novel finding of the existence of FMDI for *direction discrimination* of formant changes allows us to extend the original conclusions concerning the existence of FMDI for the *detection* of formant changes (Lyzenga and Carlyon, 1999) to conditions a step closer to real speech, where it is usually more important to be able to track the direction of a formant change than simply to detect that change. So, these results suggest that FMDI can affect speech perception in the presence of competing speakers when listeners need to trace the dynamics of formant positions to retrieve information concerning coarticulation or diphthongs.

The amount of FMDI did not depend on the nature of the task, so for both detection and discrimination of formant changes, listeners' performance can be disturbed by sounds that can be present in competing speech. Work on formant center-frequency discrimination indicates that combined formant changes in the same vowel can have a positive effect on detection thresholds (Mermelstein, 1978; Hawks, 1994; Lyzenga and Horst, 1998). In all these studies, thresholds were found to be lower for parallel formant changes of two or more formants than they were when one formant changed while the others were held fixed. So, for coherent formant changes, across-channel information can be combined to the advantage of the listener. On the other hand, in the identification of modulation, across-channel information does not always seem to be processed optimally; when one of two simultaneous tones is amplitude modulated, subjects may be able to detect the AM, but they may fail to identify which tone is the modulated one [Sheft and Yost (1989) and Hall and Grose (1991)—but see Moore and Bacon (1993) for the case of multi-component stimuli]. These findings are now supplemented with the finding that ''confusing'' formant changes can degrade performance in formant-change detection and identification tasks, which could well be a result of the same across-channel mechanisms.

The present results may have implications for speech perception and speech-perception models. First, the existence of FMDI for formants could affect perception of coarticulation cues, as formants change their positions near the start and end of a vowel to make natural transitions to and from its surrounding vowels or consonants. As indicated by the present results, the perceptual changes associated with different formant changes in the same vowel may disrupt each other. In addition, it is likely that processing of such information can be disrupted by formant changes occurring in competing speech. A second observation concerns the missing-formant problem in vowel-perception models (for an overview, see Rosner and Pickering, 1994). For high values of F_0 and for narrow formants, the positions of formant peaks often do not occur near a spectral component, which leads to the loss of information about the precise formant position, and possibly even to no clear cue for the existence of a formant. Formant perception models are susceptible to such ''missing formant'' problems. Recently, more and more sophisticated and insightful models have been proposed to deal with this problem (e.g., de Cheveigné and Kawahara, 1999; Hillenbrand and Houde, 2003). de Cheveigné and Kawahara (1999) proposed a missing-data pattern-recognition model. To prevent a missing formant from corrupting the pattern matching involved in the evaluation of the nature of a vowel, this model ignores such missing formant information by using F_0-dependent weighting functions. Hillenbrand and Houde (2003) introduced a narrow-band pattern-matching model with which they could classify vowels in spoken utterances. In this model disruptive effects from missing formants were avoided using a spectral flooring function that focused attention on spectral peaks while ignoring missing formant information. The present data show that, in particular, dFMTs can increase dramatically for such badly defined formants. Hence it appears that the auditory system cannot extract the formant frequencies for such stimuli, and that it is extremely unlikely that the approach of reducing the influence of such formants on pattern-matching (de Cheveigné and Kawahara, 1999; Hillenbrand and Houde; 2003) will be surpassed by a hereto unknown feature of the auditory system. Hence, under such circumstances, it seems that listeners will just miss some formant information and will have to make up for it using the natural redundancy of speech.

V. CONCLUSIONS

FMTs were somewhat larger for linear than for sinusoidal formant-frequency modulations. This can be attributed partly to the frequency rove used for the conditions with linear FM, and partly to a reduced ''effective'' perceptual extent of linear formant glides due to the tapering of the stimuli and the short-lived frequency extremes.

The FMTs for sinusoidal and linear FM could be well described by a model that separately evaluated and combined the contributions of place cues, modulation-depth cues, and beating cues. The modulation-depth and beating cues were

only useful for a minority of conditions, and did not reliably encode the direction of any frequency change. Our results and model suggest that, for most natural listening conditions, listeners use place-of-excitation cues to encode dynamic changes in formant frequency.

For all stimuli that had enough components to present listeners with information concerning formant position and bandwidth (as will usually be the case with natural formants), the dFMTs were almost equal to the FMTs. This indicates that listeners were not able to use the doubled formant-frequency difference between standard and target offered by the direction-discrimination task relative to the detection task.

FMDI was found under conditions with both sinusoidal and linear FM. The amount of FMDI did not appear to depend on the nature of the task (FM detection versus direction discrimination) or on the F_0 of the modulated formant. Hence FMDI occurs for a wide range of stimuli, including those similar to formant transitions in real speech, and for tasks that require subjects to extract formant frequency and track the way in which it changes over time.

ACKNOWLEDGMENTS

This research was funded by the Wellcome Trust and by Grant no. GR/N64861/01 from the Engineering and Physical Sciences Research Council (U.K.). The authors wish to express their thanks to Brian Moore and Chris Plack whose insightful suggestions helped improve the paper.

APPENDIX: MODEL DESCRIPTIONS

1. The hybrid model

To ensure a clear link with the earlier applications of the model, we used a model implementation that was as close as possible to the hybrid model used by Lyzenga and Carlyon (1999). It encompasses three underlying models: a modified place model, an amplitude-modulation depth model, and a beating detector. Below, these three models are described in detail. In generating the combined d' values, we assumed that d' is proportional to the modulation range (Lyzenga and Carlyon, 1999), and that listeners combine them as independent variables (square root of sum of squares). The thresholds used in the three models underlying the hybrid model were chosen to produce least squared errors between predictions and data (see below for these threshold values). The decision variable, generated by each model, was divided by the corresponding threshold value to transform it into a predicted d' value. Next the resultant d' values of the three models were combined into a single predicted d' value of the hybrid model. This combined d' was then compared with a threshold of 1. If the combined d' was larger than one, the whole procedure was repeated for a smaller modulation depth; if it was smaller than one, it was repeated for a larger modulation depth. This exercise was continued until the predicted d' deviated less than 1% from unity, after which the last used modulation depth was taken as the predicted FMT or dFMT.

2. The modified place model

The first model in the combination is a modified place model in which hypothetical excitation patterns for two sounds are compared, and when these patterns differ by more than a certain threshold value, the two sounds are considered to be perceptually discriminable. It was developed to predict jnd's for steady stimuli, and it was slightly adapted for use with the present formant FM tasks. The most important adaptations were the introduction of two ''looks'' at each stimulus and an increase in threshold value. The frequency rove used for the linear FM was disregarded in the models; only the stimuli in the center of the roving range were used in calculating threshold predictions. It can be expected that the increased stimulus uncertainty of the frequency rove will have increased the thresholds somewhat; this is not accounted for in the model and should be kept in mind when interpreting these predictions. Furthermore, because the rove blurred the distinction between formants centered on one harmonic and those falling between two harmonics, predictions where different cues dominate for these two cases should be treated with caution.

A detailed description of the modified place model is given by Lyzenga and Horst (1997). In short, the model consists of a linear filter bank followed by a detector of level differences. The filter bank consists of 3400 Roex (rounded exponential) filters with a Q of 5 (Patterson and Moore, 1986). The spacing of the center frequencies of these filters is logarithmic above, and linear below, 800 Hz. To form an excitation pattern, the outputs of the filters of all channels are squared, integrated over the stimulus duration, and converted to a level in dB. As a representation of the absolute threshold, a noise floor with a power of 1 (i.e., a level of 0 dB) is added to the output power of each filter before it is converted to dB. A level-difference detector compares the excitation patterns for two tones. This detector ignores overall-level cues: the excitation levels of the presented tones are roughly equalized (by matching their overall levels), after which the maximum positive excitation difference and the absolute value of the largest negative difference are summed, and, lastly, this sum is compared with a detection threshold. This model was developed for use in frequency discrimination experiments and was applied to the present FMTs by assuming that subjects can detect modulation as soon as they can perceive a difference between two well-chosen ''looks'' at a stimulus. For sinusoidal FM, these looks were chosen at the maximum positive and negative center frequency excursion of the (single) modulation cycle of the stimulus. For linear FM these looks were chosen at the start and end points of the frequency glides. However, the duration of these looks (i.e., the time the frequency excursions are near their maximum) is much shorter than the total stimulus duration. Since frequency discrimination deteriorates for short stimulus durations (Moore, 1973), we expected to need larger detection thresholds than in the original settings of the model. We found we needed increases of about a factor of 3 to 4, which is roughly in agreement with the increase in the data between the frequency discrimination task (jnd's) and the modulation detection task (FMTs). In the original model a 2-dB detection threshold was used. For the present task we found that a

5.6-dB (31% larger at 7.3 dB for the linear FM) threshold produced the smallest deviations from the data when this model formed part of the hybrid model (on its own the optimal threshold would have been 3.2 dB for sinusoidal FM and 5.7 dB for linear FM).

3. The amplitude-modulation detection model

The second model is based on the perception of amplitude-modulation depth differences. For this model we assumed that subjects compare the slow amplitude modulations of the targets of each trial with the absence of any slow AM in the reference tone [e.g., Figs. 2(b) and (c)]. In this model the detection of AM in the temporal envelopes of complex stimuli is related to that for pure tones by filtering the complex stimuli with a hypothetical auditory filter and comparing the resulting modulation depths in the auditory channels to AM detection thresholds for pure tones.

The first stage of the amplitude-modulation detection model was the same Roex filter bank of the modified place model. In the channel located at the center frequency of the stimulus, and those at the positions of the two largest components, we calculated the temporal envelope of the filtered stimuli using the Hilbert transform. For the rates of 5 and 10 Hz, we calculated the modulation depths from the Fourier transform of the envelopes. The AM was considered to be detectable when one of the modulation depths found in this way was larger than a threshold value. To account for the fact that either one or two cycles were present in the stimuli, we used different thresholds for the 5- and 10-Hz modulation rates. The expected FMT was determined with the described algorithm by finding the smallest center frequency modulation range of the target that gave rise to an AM depth equal to the corresponding threshold. For all but one stimulus the largest modulation depths occurred in one of the channels at the frequency of the largest components. For the remaining stimulus (which had unresolved partials), the channel at the center frequency of the stimulus gave the largest modulation depth [the square on the right of Fig. 4(f)]. When applying the AM detection model in the hybrid model, the optimal threshold values for the 5- and 10-Hz modulation rates were found to be 45% and 25%, respectively, to predictthe sinusoidal FM data [as in Lyzenga and Carlyon (1999)]. For the linear FM these thresholds needed to be increased by 31%. The threshold values for the sinusoidal FM are in good agreement with thresholds found by Lee and Bacon (1997). For a 10-Hz rate and a 200-ms stimulus duration they found a threshold of 30%. Viemeister (1979) found similar but slightly smaller values. In his ''gated carrier'' condition, stimuli had a total duration of 250 ms. For 4-, 8-, and 16-Hz rates he found detection thresholds for m of approximately 0.2, 0.11, and 0.10, respectively. Interpolating between these values for rates of 5 and 10 Hz, we would find m values of 0.18 and 0.11, which would correspond to depths of 30% and 20%, respectively.

4. The beating detector

The present stimuli often showed fast amplitude modulations at the rate of the fundamental (80 or 240 Hz), which were disregarded in the AM detection model. They were used in the third model, based on the detection of within-channel interactions of components. This model assumes that two sounds are perceptually discriminable when (after auditory filtering) one sound shows beating while the other does not. It will be referred to as the ''beating detector'' model.

A detailed description of this beating detector model is given as the ''temporal model'' by Lyzenga and Horst (1997). As with the AM-detection model, it is based on changes in the temporal envelope of the stimuli. However, the limiting case for the AM-detection model is a 100% modulation depth, whereas within-channel beating represents depths of over 100%. For such depths the temporal envelope touches down to zero at a steep rather than at a shallow angle (as would be the case for 100% AM), producing sharp direction turnings in this envelope [see Fig. 2(d), upper trace], and sudden 180° phase transitions in the temporal fine structure. The beating detector is based on the sharpness of the zero crossings in the temporal envelope, since this is easier to quantify than the abruptness of the corresponding phase reversal, but the model is thought to represent both consequences of beating. The sharpness of the turning in the temporal envelope depends strongly on the relative levels of the unresolved partials of a stimulus. So, for the present stimuli with unresolved components, the 5-Hz center frequency modulation may produce a cue in fluctuations of roughness or beating. In short, the model works as follows: the stimuli are filtered with a simulated auditory filter bank consisting of Roex filters with a Q of 5, whose frequency characteristics were given a phase relation with an exponential shape as shown in Fig. 8 of Lyzenga and Horst (1997). In the channel at the center frequency of the stimulus, the Hilbert transform is used to calculate the temporal envelope, after which its second-order derivative is calculated. When sharp zero crossings are present in the temporal envelope, peaks can be found in the second-order derivative of the reference tone. When a large peak is present, the center frequency modulation range is located for which this peak is reduced to a certain fraction of its original value. The corresponding modulation range is then taken as the expected FMT. This model has been adapted for application in the present study, where the sharpness of the zero crossings in the stimuli is a quantity that changes over time. It now uses the average sharpness of the zero crossings (i.e., the average peak values in the second-order derivative). The optimal threshold was found to be a reduction of the average peak to 15% of its original value [as used by Lyzenga and Carlyon (1999)] [a 33% threshold was used by Lyzenga and Horst (1997)].

[1]The thresholds presented by Lyzenga and Carlyon (1999) are defined in terms of the zero-peak FM excursion and should be doubled when comparing to the peak-peak thresholds described here.

[2]Further significant interactions were: two way: $F_0 \times$ slope: $F_{(1,2)}=50.1$, $p<0.02$; slope $\times$ center-frequency region: $F_{(2,4)}=41.0$, $p\leqslant 0.002$; slope $\times$ center-frequency position: $F_{(1,2)}=370.3$, $p<0.005$; center-frequency region $\times$ center-frequency position: $F_{(2,4)}=14.0$, $p<0.02$, and three way: $F_0 \times$ slope $\times$ center-frequency region: $F_{(1,2)}=20.9$, $p<0.05$.

[3]For a 10-Hz rate, detection thresholds would have been slightly smaller than for the 5-Hz rate (Lee and Bacon, 1997), but this difference would be constant across conditions.

Carlyon, R. P. (**1994**). ''Further evidence against an across-frequency mechanism specific to the detection of frequency modulation (FM) incoherence between resolved frequency components,'' J. Acoust. Soc. Am. **95**, 949–961.
de Cheveigné, A., and Kawahara, H. (**1999**). ''Missing-data model of vowel identification,'' J. Acoust. Soc. Am. **105**, 3497–3508.
Dooley, G. J., and Moore, B. C. J. (**1988**). ''Detection of linear frequency glides as a function of frequency and duration,'' J. Acoust. Soc. Am. **84**, 2045–2057.
Fletcher, H. (**1953**). *Speech and Hearing in Communication*, edited by J. B. Allen, (ASA, New York, 1995) pp. 60–61.
Glasberg, B. R., and Moore, B. C. J. (**1990**). ''Derivation of auditory filter shapes from notched-noise data,'' J. Speech Hear. Res. **47**, 103–138.
Gockel, H., and Carlyon, R. P. (**2000**). ''Frequency modulation detection interference produced by asynchronous and nonsimultaneous maskers,'' J. Acoust. Soc. Am. **104**, 3534–3545.
Hall, W. H., and Grose, J. H. (**1991**). ''Some effects of auditory grouping factors on modulation detection interference (MDI),'' J. Acoust. Soc. Am. **90**, 3028–3035.
Hartmann, W. M., and Klein, M. A. (**1980**). ''Theory of frequency modulation detection for low modulation frequencies,'' J. Acoust. Soc. Am. **67**, 935–946.
Hawks, J. W. (**1994**). ''Difference limens for formant patterns of vowel sounds,'' J. Acoust. Soc. Am. **95**, 1074–1084.
Hillenbrand, J. M., and Houde, R. A. (**2003**). ''A narrow band pattern-matching model of vowel perception,'' J. Acoust. Soc. Am. **113**, 1044–1055.
Lee, J., and Bacon, S. P. (**1997**). ''Amplitude modulation depth discrimination of a sinusoidal carrier: Effect of stimulus duration,'' J. Acoust. Soc. Am. **101**, 3688–3693.
Lyzenga, J., and Carlyon, R. P. (**1999**). ''Center frequency modulation detection for harmonic complexes resembling vowel formants and its interference by off-frequency maskers,'' J. Acoust. Soc. Am. **105**, 2792–2806.
Lyzenga, J., and Carlyon, R. P. (**2000**). ''Binaural effects in center-frequency modulation detection interference for vowel formants,'' J. Acoust. Soc. Am. **108**, 753–759.
Lyzenga, J., and Horst, J. W. (**1997**). ''Frequency discrimination of stylized synthetic vowels with a single formant,'' J. Acoust. Soc. Am. **102**, 1755–1767.
Lyzenga, J., and Horst, J. W. (**1998**). ''Frequency discrimination of stylized synthetic vowels with two formants,'' J. Acoust. Soc. Am. **104**, 2956–2966.
Madden, J. P., and Fire, K. M. (**1996**). ''Detection and discrimination of gliding tones as a function of frequency transition and center frequency,'' J. Acoust. Soc. Am. **100**, 3754–3760.
Madden, J. P., and Fire, K. M. (**1997**). ''Detection and discrimination of frequency glides as a function of direction, duration, frequency span, and center frequency,'' J. Acoust. Soc. Am. **102**, 2920–2924.
Mermelstein, P. (**1978**). ''Difference limens for formant frequencies of steady-state and consonant-bound vowels,'' J. Acoust. Soc. Am. **63**, 572–580.
Moore, B. C. J. (**1973**). ''Frequency difference limens for short-duration tones,'' J. Acoust. Soc. Am. **54**, 610–619.
Moore, B. C. J., and Bacon, S. P. (**1993**). ''Detection and identification of a single modulated component in a complex sound,'' J. Acoust. Soc. Am. **94**, 759–768.
Moore, B. C. J., Glasberg, B. R., Gaunt, T., and Child, T. (**1991**). ''Across-channel masking of changes in modulation depth for amplitude- and frequency-modulated signals,'' Q. J. Exp. Psychol. A **43**, 327–347.
Náběl̆ek, I., and Hirsh, I. J. (**1969**). ''On the discrimination of frequency transitions,'' J. Acoust. Soc. Am. **45**, 1510–1519.
Patterson, R. D., and Moore, B. C. J. (**1986**). ''Auditory filters and excitation patterns as representations of frequency resolution,'' in *Frequency Selectivity in Hearing*, edited by B. C. J. Moore (Academic, London), pp. 123–177.
Rosner, B. S., and Pickering, J. B. (**1994**). *Vowel Perception and Production* (Oxford U. P., Oxford).
Scharf, B., (**1970**). ''Critical bands,'' in *Foundation of Modern Auditory Theory*, edited by J. V. Tobias (Academic, New York), Vol. 1, pp. 159–202.
Sergeant, R. L., and Harris, J. D. (**1962**). ''Sensitivity to unidirectional frequency modulation,'' J. Acoust. Soc. Am. **34**, 1625–1628.
Sheft, S., and Yost, W. A. (**1989**). ''Detection and recognition of amplitude modulation with tonal carriers,'' J. Acoust. Soc. Am. **85**, S121.
Tsumara, T., Sone, T., and Nimura, T. (**1973**). ''Auditory detection of frequency transition,'' J. Acoust. Soc. Am. **53**, 17–25.
Tyler, R. S., Wood, E. J., and Fernandes, M. (**1983**). ''Frequency resolution and discrimination of constant and dynamic tones in normal and hearing-impaired listeners,'' J. Acoust. Soc. Am. **74**, 1190–1199.
Viemeister, N. F. (**1979**). ''Temporal modulation transfer functions based upon modulation thresholds,'' J. Acoust. Soc. Am. **66**, 1364–1380.
Wilson, A. S., Hall, J. W., and Grose, J. H. (**1990**). ''Detection of frequency modulation (FM) in the presence of a second FM tone,'' J. Acoust. Soc. Am. **88**, 1333–1338.

Pitch strength of regular-interval click trains with different length "runs" of regular intervals

William A. Yost, Dan Mapes-Riordan, William Shofner, Raymond Dye, and Stanley Sheft
Parmly Hearing Institute, Loyola University Chicago, Chicago, Illinois 60626

(Received 31 August 2004; revised 11 January 2005; accepted 11 January 2005)

Click trains were generated with first- and second-order statistics following Kaernbach and Demany [J. Acoust. Soc. Am. **104**, 2298–2306 (1998)]. First-order intervals are between successive clicks, while second-order intervals are those between every other click. Click trains were generated with a repeating alternation of fixed and random intervals which produce a pitch at the reciprocal of the duration of the fixed interval. The intervals were then randomly shuffled and compared to the unshuffled, alternating click trains in pitch-strength comparison experiments. In almost all comparisons for the first-order interval stimuli, the shuffled-interval click trains had a stronger pitch strength than the unshuffled-interval click trains. The shuffled-interval click trains only produced stronger pitches for second-order interval stimuli when the click trains were unfiltered. Several experimental conditions and an analysis of runs of regular and random intervals in these click trains suggest that the auditory system is sensitive to runs of regular intervals in a stimulus that contains a mix of regular and random intervals. These results indicate that fine-structure regularity plays a more important role in pitch perception than randomness, and that the long-term autocorrelation function or spectra of these click trains are not good predictors of pitch strength. © *2005 Acoustical Society of America.* [DOI: 10.1121/1.1863712]

PACS numbers: 43.66 Hg, 43.66 Mk, 43.66 Ba [RAL] Pages: 3054–3068

I. INTRODUCTION

Several recent papers (Kaernbach and Demany, 1998; Kaernbach and Bering, 2001; Pressnitzer *et al.*, 2002, 2004, and Yost *et al.*, 2005) have studied the pitch perception of click trains in which the statistics of the intervals between the clicks have been manipulated in several ways. A major feature of these investigations has been the study of first- and second-order intervals. A first-order interval is the interval between successive clicks, while a second-order interval is the interval between every other click. These studies have shown that the auditory system is not as sensitive to second-order as it is to first-order intervals, and in some cases a second-order-interval click train cannot be discriminated from a click train in which all of the intervals are randomly determined. The major features of the autocorrelation analysis used to account for the pitch and pitch strength of complex stimuli are insensitive to the order of the intervals of a click train. Thus, if the auditory system uses mechanisms like autocorrelation to process these click trains, performance should be the same for first- and second-order click trains. Since the data indicate differences in performance, these results suggest that autocorrelation may not be the appropriate mechanism for modeling the auditory processing of regular-interval stimuli (RIS; see Yost, 1998; and Licklider, 1951, Meddis and O'Mard, 1997; Yost, 1996a and 1996b).

The current paper demonstrates another aspect of the statistics of regular-interval click trains that presents a challenge to using the long-term autocorrelation function or long-term spectrum as a model for auditory processing of RIS click trains. In the previous work on first- and second-order click trains, the click trains contain a repeating series of intervals of fixed and random intervals. For instance, the first-order click train may consist of a fixed interval, **k**, of duration **d**, followed by two intervals whose durations are each randomly determined, **x**. This **kxx** sequence is repeated back-to-back many times to construct a first-order regular-interval click train. In this paper, these intervals in this base **kxx** click train were randomly shuffled so that the resulting shuffled click train could have longer runs of **k** or **x** intervals than existed in the base click train, where there is a repeating run of one **k** and two **x**'s. Since all of the intervals are still preserved in the shuffled click train, the major features of the long-term autocorrelation functions and the long-term spectra of the shuffled and unshuffled (base) click train are the same. That is, the temporal lag at which the major peak in the long-term autocorrelation function occurs and its normalized height remains the same for the shuffled and the unshuffled click trains, and the spectral ripples seen in the long-term spectra associated with these stimuli are similar for the shuffled and the unshuffled click trains. However, the perceived pitch strength of the shuffled click train is often stronger than that of the base or unshuffled click train, indicating that these long-term autocorrelation function or spectral features cannot explain the pitch-strength differences. The experiments of this paper explore several aspects of the pitch-strength differences between shuffled and unshuffled regular-interval click trains.

II. EXPERIMENT I—SHUFFLED VERSUS UNSHUFFLED FIRST-ORDER CLICK TRAINS

A. Methods

1. Stimuli

Click-train RIS sounds are sequences of interclick interval (ICI) values, each value representing the duration between the prior and current click. Random-interval click

 0001-4966/2005/117(5)/3054/15/$22.50

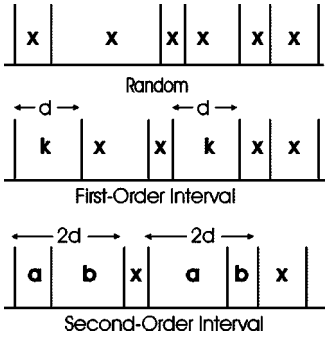

FIG. 1. RIS click trains; top: random intervals (**x**), middle: first-order intervals (**kxx**), bottom: second-order intervals (**abx**), **d** is mean duration.

trains were created using the same method employed by Kaernbach and Demany (1998) by randomly assigning each ICI a duration from a uniform distribution between zero and twice the mean ICI (**d** ms) with a resolution of 25 μ s. No more than two consecutive ICIs could be larger or smaller than **d**. This was done by Kaernbach and Demany to prevent the occurrence of long sequences of short- or long-duration ICIs which could result in a timbre cue.

First-order ICI sequences were created from random ICI sequences by replacing every third random ICI with a regular interval equal to **d**. These ICI sequences have been termed "**kxx**" by Kaernbach and Demany (1998), where **k** represents the regular interval of duration **d** and **x** represents intervals of random duration. The normalized autocorrelation functions for **kxx** stimuli have a major peak (AC1) at **d**, and the height of AC1 is equal to 0.33 for the **kxx** stimuli. In general the height of AC1 for any such regular-interval stimulus is equal to the number of **k** intervals divided by the sum of the number of **k** and **x** intervals (e.g., for **kxxx**, the height of AC1 is 0.25). The spectra of such stimuli have spectral peaks spaced at 1/**d** and the depth of the peak-to-valley ratio of these spectral peaks is proportional to the ratio of the number of the **k** to the number of the **k**+**x** intervals (i.e., to AC1).

Figure 1 provides a schematic example of a random-order interval (**xxx**...) click train and a first-order interval (**kxx**...) and a second-order interval (**abx**..., to be described later in experiment II) click train. Figure 2 shows the summary autocorrelograms of the **kxx** and **abx** wideband stimuli generated when $d=2$ ms (**kxx**) and $2d=4$ ms (**abx**), and Fig. 3 shows the auditory spectra of these same two stimuli. The summary autocorrelograms were computed according to Meddis and Hewitt (1991) and used by Patterson, Allerhand, and Giguere (1995) and Yost, Patterson, and Sheft (1996). They are generated using a gamma-tone filter bank and the Meddis hair cell to simulate the biomechanical properties of the inner ear and the neural activity in auditory-nerve fibers (tuned channels) and then forming the autocorrelation function for each tuned channel (the autocorrelogram). The summary autocorrelogram is the sum of the autocorrelogram across all tuned channels shown as a function of autocorrelation lag (ms). As for the autocorrelation function itself, the locations of the largest peaks in the summary autocorrelogram are used to account for pitch and the relative heights of these peaks for pitch strength (see Meddis and Hewitt, 1991).

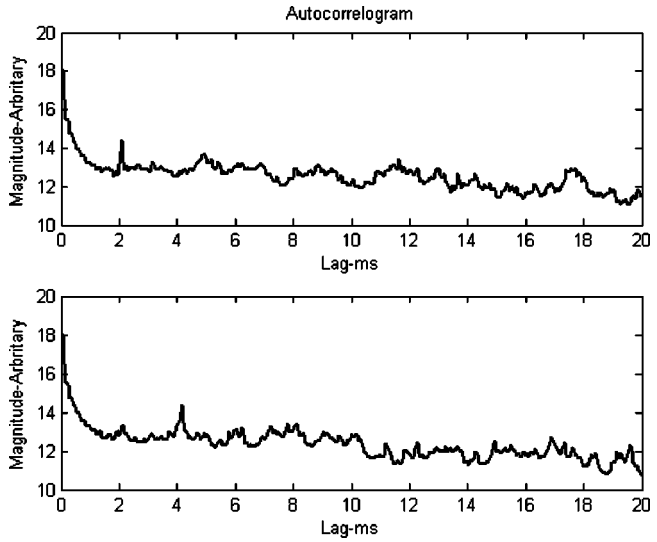

FIG. 2. Autocorrelograms for an auditory model are shown for the first-order interval (**kxx**) stimulus with **d**=2 ms (top panel) and the second-order interval (**abx**) stimulus with 2**d**=4 ms. The peaks at lags of 2 ms (top panel) and 4 ms (bottom panel) indicate the most prominent regularity in these stimuli as might be preserved in the auditory periphery.

The auditory spectra (see Patterson, Allerhand, and Giguere, 1995) were computed by summing simulated neural activity across time for each tuned channel and displaying the summed simulated neural activity for each tuned channel as a function of frequency (i.e., the center frequency of each gamma-tone filter). The auditory spectra reveal the resolved spectral ripple in the low frequencies for the two types of click trains. These figures suggest that both the spectral ripple and the autocorrelations of these stimuli are likely to be preserved within the peripheral auditory system.

The amplitudes of the clicks were identical and were adjusted to create a click train with a spectrum level[1] of 30 dB SPL. Each stimulus was temporally windowed using a 5-ms squared cosine function. The duration of **d** was 1, 2, 4,

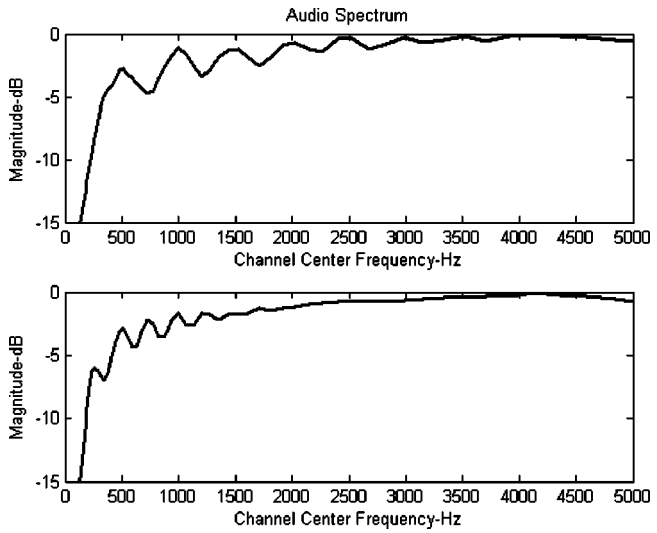

FIG. 3. Auditory spectra for an auditory model are shown for the first-order interval (**kxx**) stimulus with **d**=2 ms (top panel) and the second-order interval (abx) stimulus with 2d=4 ms. The spectral ripple in the low frequencies indicates resolved harmonics as might be preserved in the auditory periphery.

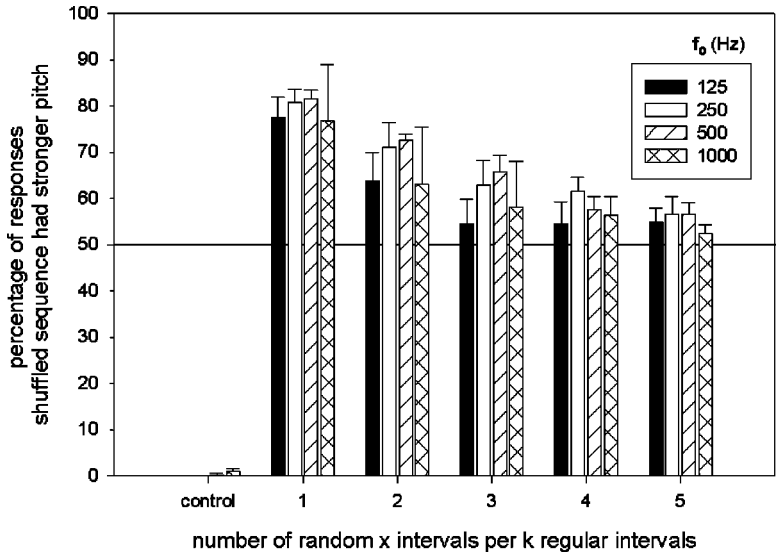

FIG. 4. Ordered (unshuffled) vs shuffled click-train RIS pitch strength comparisons for wideband stimuli, first-order intervals, total duration 500 ms. Bars are mean percentage of four listeners; error bars are standard errors.

or 8 ms, resulting in fundamental frequencies, $\mathbf{f_0}$, of 1000, 500, 250, or 125 Hz ($\mathbf{f_0}$ is the reciprocal of **d**), respectively.

Different ordered click-train conditions were run with a different number of random **x** ICIs per single regular **k** ICI (**kx**, **kxx**, **k**3**x**, **k**4**x**, **k**5**x**). A control condition was also run in which completely random (**xxx**...) interval stimuli were compared to completely regular (**kkk**...) interval stimuli. Total stimulus duration for all stimuli was 500 ms.

On each trial after an ordered click train was generated, a randomly *shuffled* version of this ordered click train was created to make the two stimuli for the pitch-strength discrimination task. A shuffled click train was generated by randomly shuffling the intervals of the ordered click train generated for that trial. That is, rather than having a string of **kxxkxxkxxkxx**... intervals, these intervals were randomly resampled and something like **xkkkxxxxkxxx**... may have been generated as the shuffled version. Note that the major features of the spectrum and autocorrelation function of the long-term (computed over the full 500 ms of the stimulus) click trains are the same for the shuffled-click train as for the unshuffled ordered-click.

All stimuli were delivered to listeners via Tucker Davis Technology (TDT) system II D/A converters at 40-kHz sample rate. These wideband stimuli were low-pass filtered with 4-pole filters with 15-kHz cutoff frequencies to eliminate aliasing. Stimuli were delivered diotically over Sennheiser headphones to listeners seated in a double-walled soundproof room.

2. Procedure

Pitch-strength comparisons were measured using a 2AFC task; one of the stimuli was the ordered click train and the other a shuffled version using the same set of ICIs. Listeners were asked to pick the stimuli that had the stronger pitch strength. A 300-ms silent gap was inserted between stimuli. No feedback of any type was provided.

Five conditions were run with different ratios of random **x** intervals per single regular **k** interval (**kx**, **kxx**, **k**3**x**, **k**4**x**, **k**5**x**). In a control condition a purely regular-interval click train (**kkkk**...) was compared to a purely random-interval click train (**xxxx**...) with the same mean click rate. Thus, there were six different conditions at each value of **d** creating a total of 24 conditions.

A block of trials consisted of all of the six different random-to-regular ratio conditions at a single **d** value. Twenty trials were run at each ratio condition, resulting in 120 trials per block. Trials were randomly selected without replacement in each block. A block of 120 trials was repeated ten times throughout the course of the experiment, resulting in 100 trials per condition for each listener.

3. Listeners

Four normal-hearing paid listeners participated in experiment I. They were all college undergraduate students between the ages of 19 and 35 who reported normal hearing. In a typical day, each listener ran approximately seven randomly assigned blocks of trials over a 90-min period. The first block of trials from each listener each day was considered practice and was not included in the final results.

B. Results

The overall results of experiment I are shown in Fig. 4 as the percentage of trials the shuffled sequence was judged to have the stronger pitch strength. The results of the control conditions are presented as the percentage of trials the purely random-interval sequence (**xxx**...) was judged to have a stronger pitch strength than the purely regular-interval sequence (**kkk**...). The 50% line in Fig. 4 represents equal pitch strength. Only the mean results are presented since the individual results were similar to each other.

Figure 4 shows that approximately 80% of the time, shuffled **kx** stimuli were judged to have a stronger pitch strength than its ordered counterpart. This percentage decreases with increasing number of random intervals. Note that there is also a small fundamental frequency ($\mathbf{f_0}$) effect in that there is a small increase in pitch-strength preference for shuffled stimuli with fundamental frequencies 250 and 500 Hz. This tendency is consistent with other RIS pitch experiments (Yost and Hill, 1978) that show a higher pitch saliency in this range of fundamental frequencies (200–666 Hz).

C. Discussion

Given that shuffling ICIs does not change the number of regular intervals in click train RIS, why does its pitch strength increase? The most likely reason is that shuffling creates ''clumps'' or ''runs'' of consecutive regular **k** ICIs. It is these multiple instances of regular ICIs that are the probable cause of an increase in pitch strength. This suggests that pitch strength is based on short-term temporal regularity in a waveform rather than the overall temporal regularity in an entire waveform. However, it is important to point out that shuffling also creates multiple instances of consecutive random ICIs. Thus, pitch strength is more than just the average of a short-term temporal detector. Since shuffled stimuli contain portions of increased *and* decreased temporal regularity, the average of the short-term temporal regularity is the same as a measure of overall temporal regularity. Thus, the auditory system seems to place increased importance on runs of regular intervals over runs of random intervals. Consider the case of the **kx** stimuli in which the probability of runs of **k** ICIs is equal to that of runs of **x** ICIs in the shuffled click trains, yet shuffled click trains are almost always judged to have a stronger pitch saliency than the unshuffled click trains where the runs of **k** and **x** are always one each. The longer runs of random intervals seem to be weighted far less than runs of regular intervals when pitch strength is computed. This asymmetry in the perception of runs of regular intervals vs runs of random intervals is consistent with the notion that listeners are tuned to perceive temporal regularities in sound, rather than the lack of regularity (randomness).

When there is a run of fixed intervals (where **d** is the duration of each **k** fixed interval), the autocorrelation function may have a major peak at a lag of **d** and at integer multiples of **d**. The normalized height of the peak at **d** is the greatest and the height of the autocorrelation peaks at lags of the integer multiples of **d** decrease. For instance, a **kkkx** repeating stimulus with **d**=2 ms, will have a major autocorrelation peak at a lag of 2 ms with a peak height of 0.75 (3/4), a peak at a lag of 4 ms (2**d**) with a peak height of 0.50 (2/4), and a peak at 6 ms (3**d**) with a peak height of 0.25 (1/4). In general, if there are **m** consecutive **k** intervals each of duration **d** and **p** consecutive random (**x**) intervals of random durations, then the autocorrelation function has peaks at lags of **nd**, where **n**=1,2,...,**m**; and the normalized height of the peak at **nd** is $(\mathbf{m}-\mathbf{n}+1)/(\mathbf{m}+\mathbf{p})$.

Thus, when there are runs of **k**'s in the entire shuffled click trains that are longer than in the unshuffled click trains, it is possible that the correlation associated with the lags at the higher integer multiples of the delay, **d**, could be the basis for the increased pitch strength of the shuffled click trains. For instance, for a **kx** base stimulus, many runs of **kkx** in the shuffled stimulus could produce an autocorrelation function for the entire stimulus with peaks at lags **d** and 2**d** (assuming the duration of the **k** intervals is **d**). The peak at lag **d** could have a normalized height of 0.67 and that at lag 2**d** could have a normalized height of 0.33. It could be that the higher peak at the lag of **d** and/or the peak at lag 2**d** ''reinforces'' that at **d** to produce the greater pitch strength for the shuffled click train.

There are several reasons why these correlations at the longer lags probably do not account for the increased pitch strength of the shuffled click trains if the entire waveform is considered. First, in the work on other RIS conditions, especially iterated rippled noise, there is little evidence that peaks at integer multiples of **d** influence either the pitch or pitch strength of these RIS sounds (see Yost, Patterson, and Sheft, 1996; Yost, 1996a, b). That is, these studies indicate that only the first peak at **d** influences pitch and pitch strength. Second, recall that if one computes the average autocorrelation function over the entire stimulus, the autocorrelation peaks are the same for the shuffled and the unshuffled stimulus. Thus, any additional autocorrelation peaks at higher lags would have to result from stimulus presentations in which there is a strong deviation from the average. If there were a large number of trials in which long runs of regular intervals (**k**) occurred for the shuffled conditions, then these trials might be the ones influencing the increased pitch strength as a result of the peaks at lag **d** and its higher integer multiples. Since approximately 80% of the trials (see Fig. 4) appear to produce a stronger pitch for the shuffled stimulus, one would expect that the proportion of trials with runs of **k** intervals sufficiently long to produce autocorrelation peaks at long lags would also occur in the range of 80%. Table (IV) in the Appendix indicates the mean number of times (and the standard deviations) out of 240 intervals that one might expect long runs of **k**'s to occur. These numbers are too few to produce very many trials in which the autocorrelation functions have noticeable peaks at long lags. In a separate simulation, in a run of 1000 independent generations of a 500-ms shuffled version of a **kx** stimulus, only 198 of them (19.8%) produced a measurable autocorrelation peak at 2**d**, 7.8% produced a measurable autocorrelation peak at 3**d**, and there were no measurable peaks at 4**d** that were above the noise floor (note that half of the intervals are always **k**'s; thus, the peak at lag **d** was measurable on all trials). Thus, it is unlikely that autocorrelation functions associated with the entire waveform could account for the shuffled/unshuffled pitch-strength differences. Therefore, it is likely that some other aspect of the consecutive runs of regular intervals (i.e., a short-term statistic) is the basis for the increased pitch strength associated with the shuffled click trains.

These results have been discussed in terms of the autocorrelation function of these stimuli largely because it has been successful in accounting for the pitch strength of these types of complex stimuli. However, since these click trains are wideband they have several resolved harmonics as indicated in Fig. 3. The height of AC1 is proportional to the spectral peak-to-valley ratio in the spectral ripple of these click trains. Thus, some aspect of the peak-to-valley ratio could also be used to account for the pitch-strength judgments, and AC1 could be seen as one way to quantify the peak-to-valley ratio, since no other spectral measure of pitch strength has been proposed (note that the autocorrelation function is the Fourier transform of the power spectrum; see Wightman, 1973, for a discussion of this fact as it pertains to complex pitch processing). Runs of regular intervals would produce momentary spectral ripples in the running spectra of these click trains (whereas runs of random intervals would produce momentary largely flat, but randomly varying, spec-

TABLE I. Summary of test conditions in Experiment II.

order	**x/k** ratios	Fundamental frequency $\mathbf{f_0}$ (Hz)	mean interval duration **d** (ms)	high-pass cutoff frequency (kHz)		
				Wideband	$8\mathbf{f_0}$	$16\mathbf{f_0}$
1	0-to-5	125	8	⋯	1	2
1	0-to-5	250	4	⋯	2	4
1	0-to-5	500	2	⋯	4	8
1	0-to-5	1000	1	⋯	8	15
2	0-to-5	125	4	⋯	1	2
2	0-to-5	250	2	⋯	2	4
2	0-to-5	500	1	⋯	4	8
2	0-to-5	1000	0.5	⋯	8	15

tral structure). Thus, short-term resolved spectral ripples could be a basis for the increased pitch strength for the shuffled wideband click trains.

It should also be pointed out that the strength of the pitch decreases as the number of random intervals increase (e.g., **kx** has a much stronger pitch than **k4x**). The **k5x** stimulus contained the largest number of random (**x**) intervals which yielded a detectable pitch. Thus, part of the decline in the increased strength of the pitch of the shuffled click trains over the unshuffled click trains with increasing number of **x**'s is probably due to an overall decrease in pitch strength.

III. EXPERIMENT II—EFFECTS OF INTERVAL ORDER AND HIGH-PASS FILTERING

The stimuli in experiment I were broadband and involved only first-order intervals. Thus, the results could be based on spectral processing of the resolved spectral peaks of the broadband first-order click train rather than temporal processing that might be based on mechanisms like autocorrelation. High-pass filtering the click trains so that the spectral peaks (spaced at 1/**d**) are not resolved allowed us to more directly test temporal processing of these click trains. We were also interested to know if the shuffled–unshuffled pitch-strength difference that occurred for the first-order interval click trains of experiment I would occur for second-order interval click trains.

A. Methods

1. Stimuli

The first-order interval click train stimuli were generated the same way as in experiment I. Second-orderICI sequences were created from the random ICI sequences by replacing the first two of every three random ICIs with ICIs whose sum was 2**d**. The duration of the first of the three intervals, denoted **a**, was randomly drawn from a uniform distribution between zero and 2**d**. The duration of the second interval, denoted **b**, was set equal to 2**d**-**a**. Thus, the sequences contained second-order regular intervals of duration $\mathbf{a}+\mathbf{b}=2\mathbf{d}$. These sequences have been termed "**abx**" by Kaernbach and Demany. RIS sounds created from **abx** ICI sequences also have a mean AC1 peak height of 0.33 at delay 2**d**. As mentioned in experiment I, the AC1 peak height corresponds to the proportion of regular intervals to the total number of intervals in the stimuli. The spectra of **abx** stimuli have spectral peaks at 1/2**d**, where the spectral peak-to-valley ratio is proportional to the ratio of the number **ab** to the number of $\mathbf{ab}+\mathbf{x}$ intervals (refer to Figs. 1–3).

Shuffled click trains were generated in experiment II in the same way they were in experiment I. That is, once a first- or second-order interval click train was generated for a particular trial the intervals were shuffled by randomly resampling the intervals of the base stimulus (**k** for the first-order interval stimuli and an "**ab**" pair for the second-order interval stimuli). That is, the pairing of any "**a**" and "**b**" interval that was generated in each instance for the base, unshuffled stimuli remained paired after the shuffling (e.g., if an unshuffled **a** interval of 3 ms was paired with a **b** interval of 1 ms, this same 3-ms–1-ms **ab** pairing remained in the shuffled click train). The shuffled and unshuffled (base) click trains were then compared using the same pitch-strength discrimination task used in experiment I. The same stimulus levels, durations, and values of **d** used in experiment I were used in experiment II.

In the filtered conditions, the high-pass filter cutoff frequencies were 8 and 16 times the fundamental frequency $\mathbf{f_0}$ ($8\mathbf{f_0}$ and $16\mathbf{f_0}$), based on the type of analysis shown in Fig. 3. During the high-pass filter conditions, a low-pass filtered Gaussian noise was added to the signal to mask lower frequency distortion components so that they could not be used as a discrimination cue. The low-pass filter cutoff frequency was one half of an octave below the high-pass cutoff frequency of the click trains. The spectrum level[1] of the masking noise was 20 dB, 10 dB below the spectrum level of the click train stimuli. The relationship between order, fundamental frequency $\mathbf{f_0}$, mean interval duration **d**, and high-pass cutoff frequency is summarized in Table I. Note that since the maximum cutoff frequency of the TDT PF1 module is 15 kHz, the cutoff frequency for the 1000-Hz fundamental frequency, $16\mathbf{f_0}$ high-pass filtered condition was actually 15 kHz instead of 16 kHz.

Also, as in experiment I a control set of stimuli was used in which for the first-order interval conditions, a completely fixed-interval sequence (**kkk**...) was compared to a completely random-interval sequence (**xxx**...). For the second-order interval conditions, a fixed sequence of second-order intervals (**ababab**...) was compared to the completely random-interval sequence (**xxx**...). Again, each "**a**" interval ($\mathbf{a}+\mathbf{b}=\mathbf{d}$) in each "**ab**" pairing was chosen at random.

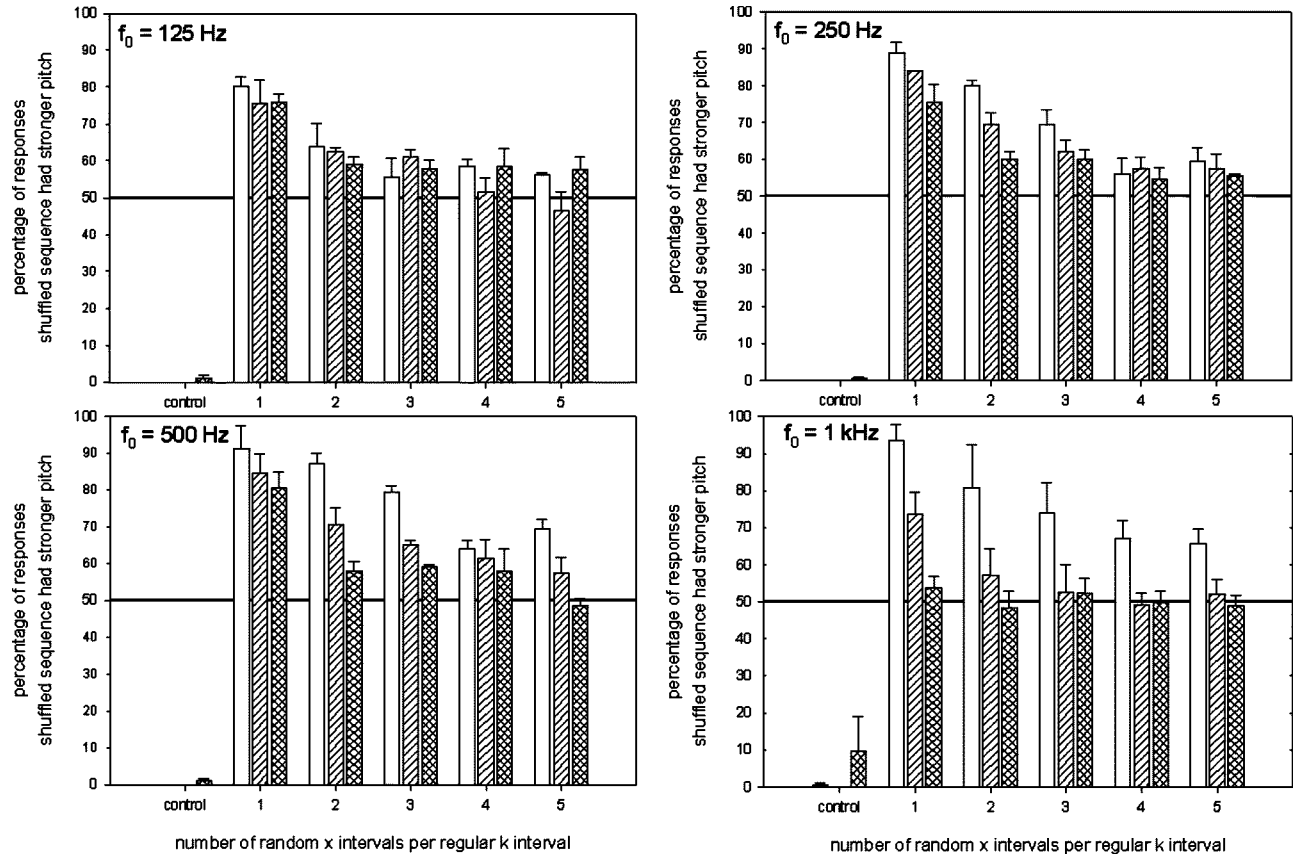

FIG. 5. Ordered (unshuffled) vs shuffled click-train RIS pitch strength comparisons first-order **kxx**-type stimuli for three filter conditions. Bars are mean percentage of four listeners; error bars are standard errors. The left open bars represent the wideband conditions, the middle single-hashed bars represent the high-pass filtered condition at $8\mathbf{f_0}$, and the right double-hashed bars represent the high-pass filtered condition at $16\mathbf{f_0}$.

2. Procedure

The experimental procedure was similar to the procedure in experiment I. The primary difference was the inclusion of high-pass-filtered and second-order regular-interval conditions. One hundred and forty-four different conditions were tested. A block of trials was run at a single fundamental frequency ($\mathbf{f_0}$=125, 250, 500, or 1000 Hz) and a single order (first or second). Each block of trials contained three subblocks, each consisting of the three high-pass-filter conditions (wideband, $8\mathbf{f_0}$, $16\mathbf{f_0}$). The order of the subblocks always began with wideband conditions, then $8\mathbf{f_0}$, and finally $16\mathbf{f_0}$ trials. This was done to provide listeners a clear impression of the pitch in the initial wideband stimulus trials in an attempt to maximize performance in the high-pass-filter conditions. Trials within each subblock were randomly drawn without replacement from ten replicates of all of the six different random-to-regular ratio conditions. A complete block of 180 trials was repeated five times throughout the course of the experiment, resulting in 50 trials per condition for each listener.

3. Listeners

The same four listeners who participated in experiment I also participated in experiment II. The first block of trials from each listener each day was considered practice and was not included in the final results.

B. Results

The overall results of first- and second-order conditions in experiment II are shown in Figs. 5 and 6, respectively. Each of the panels presents the results at a single fundamental frequency and order. The results are presented as the percentage of trials the shuffled sequence was judged to have a stronger pitch strength than the ordered (unshuffled) stimuli. The results of the control conditions are presented as the percentage of trials the random sequences were judged to have the greater pitch strength. The 50% line represents equal pitch strength. Only the overall results are presented since the individual results were similar to each other.

1. First-order interval results

Overall, the wideband conditions in experiment II reveal the same trends exhibited in experiment I (see Fig. 4); a decline in preference for shuffled stimuli as the random to regular ratio increases, and largest preferences for the 250- and 500-Hz fundamental frequencies ($\mathbf{f_0}$). However, in nearly all of the conditions there is an increase in choosing the shuffled stimuli as having the stronger pitch strength in experiment II as compared to experiment I. The amount of increase is as much as 17%. The average increase across all conditions is 8%. This increase from experiment I could be due to an overall effect of experience listening to these stimuli, since the same listeners were used in each experiment. Note that most of the increase occurred in the higher

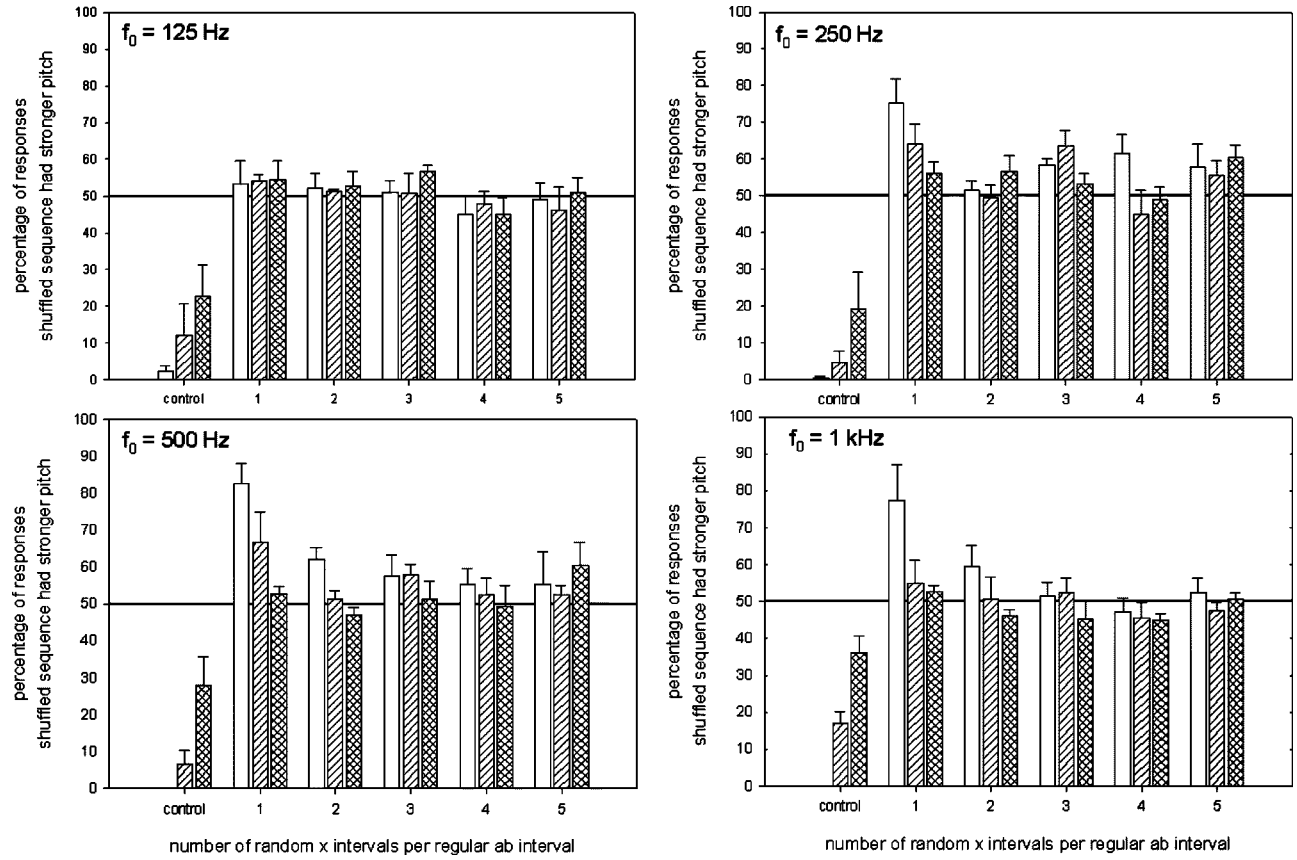

FIG. 6. Ordered (unshuffled) vs shuffled click-train RIS pitch strength comparisons second-order **abx**-type stimuli for three filter conditions. Bars are mean percentage of four listeners; error bars are standard errors. The left open bars represent the wideband conditions, the middle single-hashed bars represent the high-pass filtered condition at $8\mathbf{f_0}$, and the right double-hashed bars represent the high-pass filtered condition at $16\mathbf{f_0}$.

fundamental frequency conditions; there was relatively little change in the $\mathbf{f_0}=125$ Hz conditions. Also recall that no feedback was provided in either experiment I or II, so it is unlikely that the listeners ''learned'' anything specific based on feedbacked training.

Considering first-order stimuli, Fig. 5 shows that increasing the high-pass filter cutoff frequency decreased the preference for shuffled stimuli over unshuffled at a given fundamental frequency ($\mathbf{f_0}$) and random-to-regular interval ratio. In addition, the change in preference with high-pass cutoff frequency increased with fundamental frequency ($\mathbf{f_0}$). This suggests that frequency effects are a function of the actual cutoff frequency rather than its relationship to the fundamental frequency. This is expected at the most extreme cutoff frequency (15 kHz) in the $\mathbf{f_0}=1$-kHz condition since not much of the stimuli remains at this high cutoff frequency. The results confirm this since all of the 15-kHz high-pass filter conditions show no preference between shuffled and ordered stimuli. Note the nonzero percentage (10%) in the control condition (**kkk**... vs **xxx**...) at the 15-kHz high-pass filter condition, indicating listeners are beginning to experience difficulty in differentiating completely random and completely regular ICIs at this high cutoff frequency.

2. Second-order interval results

The second-order results are shown in Fig. 6. These results are striking in comparison to the first-order results. Note that there is relatively little difference in pitch strength between the shuffled and unshuffled stimuli in nearly all of the second-order conditions. None of the $\mathbf{f_0}=125$-Hz conditions show a preference in pitch strength. In addition, none of the conditions that were either high-pass filtered or have a random-to-regular interval ratio greater than 1.0 shows a strong preference in pitch strength. The only conditions that show a preference for shuffled stimuli greater than 70% of the time are the wideband, **abx** second-order conditions with fundamental frequencies ($\mathbf{f_0}$) of 250, 500, and 1000 Hz.

The control conditions give an indication of the difficulty in distinguishing second-order pitch-strength differences. Recall that, in the control conditions, maximal periodic second-order click trains were compared with completely random click trains. These conditions were trivially easy in the first-order conditions; although it was still possible with second-order regular intervals, the increase from 0% in the high-pass filtered conditions indicates some confusion in distinguishing the two stimuli in terms of pitch strength.

C. Discussion

In terms of pitch strength, shuffled second-order regular intervals are harder to distinguish than shuffled first-order regular intervals. It was suggested earlier that the reason shuffled first-order regular intervals have a stronger pitch strength is that shuffling increases the likelihood of multiple instances of consecutive regular intervals. The results of this

TABLE II. The relationship between first- and second-order stimuli in experiment 2 in terms of the percentage of regular intervals in an ICI sequence.

First-order condition	Equivalent second-order condition	Percentage of regular intervals (%), (AC1*100%)
kx	None	50
kxx	**abx**	33
kxxx	**abxx**	25
kxxxx	**abxxx**	20
kxxxxx	**abxxxx**	17
None	**abxxxxx**	14

experiment suggest that consecutive second-order regular intervals do not have the same ability to increase pitch strength as consecutive first-order regular intervals.

In terms of the total number of regular intervals in a complete ICI sequence, first-order **kxx** stimuli are equivalent to second-order **abx** stimuli with 33% of the total intervals being regular intervals. This relationship between order and number of random intervals per regular interval is summarized in Table II. Note that the percentage of regular intervals also corresponds to the AC1 peak height of the stimuli. Despite these statistics, shuffling the intervals of first-order interval stimuli can increase pitch strength for most conditions, whereas shuffling the intervals of second-order interval stimuli only increases pitch strength for some of the wideband conditions.

The results of the second-order high-pass filter conditions indicate the importance of resolved harmonics in creating a salient pitch strength when only second-order regular intervals are present. This result is in contrast to first-order results in Fig. 5, which shows that shuffled first-order intervals do not require resolved harmonics to produce a preference for shuffled stimuli having the stronger pitch strength. The results of the control conditions further substantiate the importance of resolved harmonics in generating pitch strength with second-order intervals. In these conditions, listeners begin to have difficulty distinguishing even extreme differences in the temporal regularity of second-order stimuli when the resolved harmonics are removed, whereas they had much less difficulty in the corresponding first-order conditions.

However, note that the pitch-strength preference for the shuffled second-order-interval stimuli even in the wideband case is less than the pitch-strength preference for the shuffled stimulus in the first-order-interval conditions. If the pitch-strength judgments were based entirely on the spectra of these stimuli, then one would expect that the pitch-strength preferences for the shuffled-over the unshuffled stimuli would be the same for both first- and second-order wideband click trains, since the main spectral features are also the same for the first- and second-order click trains (e.g., the location of the spectral peaks and their overall spectral peak to valley ratios; see Fig. 3). Thus, while having resolved spectral structure appears to be important for processing second-order-interval stimuli in these experiments, the temporal statistics of how the clicks are presented also influences the perception of pitch strength.

The need for resolved harmonics in second-order stimuli for generating a large pitch strength mirrors the regular- vs random-interval discrimination performance differences between first- and second-order stimuli in experiment II. Recall in experiment II that there was a decrease in second-order-interval discrimination performance as compared to first-order performance, especially when the resolved harmonics were removed. This suggests that regular-interval vs random-interval discrimination performance is largely based on the pitch strength generated by regular intervals, and that second-order click train RIS generate a pitch only if they contain spectral energy in resolved channels.

These results are also consistent with those from Yost *et al.* (2005) in which the ability of listeners to discriminate second-order interval click trains from random-order interval click trains was lower than their ability to discriminate first-order-interval click trains from their random-order interval comparisons. That is, the Yost *et al.* study showed that, for all conditions except an 8-kHz high-pass condition, second-order intervals could be discriminated from their random-order interval noise foils. However, performance was always less than for the discrimination of first-order intervals from their random-order-interval noise foils. Those data indicated that the pitch strength of second-order-interval stimuli is less than that for first-order-interval stimuli, which is consistent with the results of the present experiment.

IV. EXPERIMENT III—ORDERED CLICK-TRAIN PITCH-STRENGTH COMPARISONS

Further pitch-strength comparison experiments were conducted to investigate the importance of consecutive regular intervals. In these experiments the exact number of consecutive regular intervals was controlled by only using first-order-interval click-train RIS. The purpose of these experiments was to study the number of consecutive regular intervals as predictors of pitch strength in click-train RIS. This was accomplished by creating stimuli with lower autocorrelation peak height (AC1), but that also have more consecutive regular intervals than the other compared stimuli. Recall that the AC1 peak height is equal to the number of regular **k** intervals divided by the total number of regular **k** and random **x** intervals. In the first set of trials, the pitch strength of **kx** stimuli with an AC1 peak height of 0.5 was compared to stimuli with a lower AC1 peak height (0.33) but consisted of multiple consecutive regular **k** intervals (e.g., 2**k**4**x**). In a second set of trials, 4**k**8**x** stimuli with an AC1 peak height (0.33) were compared to stimuli with higher AC1 peak height (0.5) but fewer multiple consecutive regular **k** intervals (e.g., **kx**).

Since the click trains were not high-pass filtered in these experiments, pitch strength could be based on the resolved components in the spectra of these sounds. However, a measure of the spectrum of the complex-pitch stimuli has not been developed that relates to pitch strength in the same way that the AC1 is related to pitch strength (see Yost, 1996a, and Shofner and Selas, 2002). As AC1 increases so does the peak-to-valley ratio of the spectral ripple of these sounds. Thus, changes in AC1 can also serve to indicate the relative changes in the peak-to-valley ratio of the ripples in the spec-

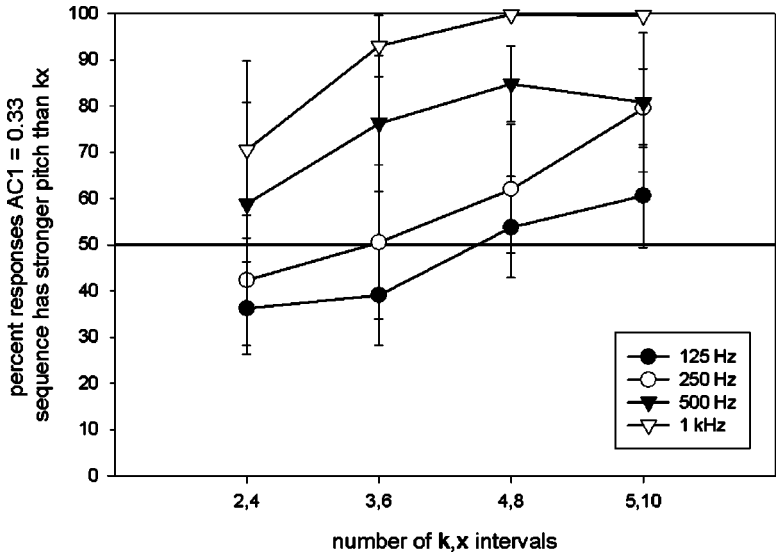

FIG. 7. Ordered (unshuffled) click-train RIS pitch strength comparisons. **kx** vs 2**k**4**x**, 3**k**6**x**, 4**k**8**x**, 5**k**10**x** wideband stimuli. Bars are mean percentage of four listeners; error bars are standard errors.

tra of these click trains. Thus, our attempt in these experiments was to determine how AC1, either as an indicator of the percent of regular intervals or as an indicator of the spectral peak-to-valley ratio in these click trains, or both, interacted with runs of regular intervals in determining pitch-strength judgments.

A. Methods

1. Stimuli

The stimuli were generated in a manner similar to that in experiment I. The primary difference was that only ordered stimuli were compared to each other, i.e., none of the stimuli was shuffled. Different conditions were run comparing ordered click-train RIS sounds with different numbers of random **x** and regular **k** ICIs. The total duration of each stimulus was 500 ms. Stimuli were not high-pass filtered. All other stimulus conditions were identical to those used in experiment I.

2. Procedure

Pitch-strength comparisons were measured using a 2AFC task; one stimulus was the standard and the other an ordered stimulus with a different AC1 peak height made up from a different proportion of regular and random intervals. Listeners were asked to pick the stimuli that had the stronger pitch strength. All other conditions were the same as in experiments I and II, including the fact that no feedback was provided.

Regular ICIs with fundamental frequencies ($\mathbf{f_0}$) of 125, 250, 500, and 1000 Hz were used. In the first set of trials, the standard stimulus was ordered **kx** click trains (AC1 = 0.5) and was paired with ordered 2**k**4**x**, 3**k**6**x**, 4**k**8**x**, or 5**k**10**x** click trains (AC1 = 0.33). In the second set of trials, the standard stimulus was ordered 4**k**8**x** click trains (AC1 = 0.33) and was paired with ordered **kx**, 2**k**2**x**, 3**k**3**x**, or 4**k**4**x** click trains (AC1 = 0.5).

A block of trials consisted of the four different pairings at a single fundamental frequency. Ten trials were run at each condition, resulting in 40 trials per block. Listeners ran four blocks of trials without a break. Trials were randomly selected without replacement in each block. A block of 40 trials was repeated five times throughout the experiment, resulting in 50 trials per condition for each listener. Three of the four listeners who participated in experiment II also participated in this experiment.

B. Results and discussion

The overall results of the first condition of experiment III are shown in Fig. 7. The results are presented as the percentage of trials the target stimuli (AC1 = 0.33) were judged to have a stronger pitch strength than the standard **kx** stimuli (AC1 = 0.5). The 50% line in Fig. 7 represents equal pitch strength. Figure 7 shows that, when $\mathbf{f_0}$ is equal to 1000 and 500 Hz, only two consecutive regular intervals were required to make the pitch strength greater than the standard stimuli which had a higher AC1 peak height. At $\mathbf{f_0}$ equal to 250 and 125 Hz, four consecutive regular intervals were required for the mean pitch strength to be stronger than the standard stimuli.

The overall results of the second set of conditions are shown in Fig. 8. The results are presented as the percentage of trials the target stimuli (AC1 = 0.5) were judged to have a stronger pitch strength than the standard 4**k**8**x** stimuli (AC1 = 0.33). Note that the **kx** condition in the second set of trials is the same as the 4**k**8**x** condition in the first set of trials. The results, although not identical, show the same trend. Figure 8 shows that three consecutive regular intervals can have a larger pitch strength than four consecutive regular intervals if the proportion of regular intervals is 0.5 as compared to 0.33. The change in pitch strength is most striking for the 500- and 1000-Hz fundamental frequency conditions which show an abrupt change in preference from the 2**k**2**x** to the 3**k**3**x** conditions.

However, note in Fig. 8 that the 4,4 (**4k4x**) condition has the same number of **k**'s as the comparison stimulus of (**4k8x**), yet the **4k4x** click train is judged to have the stronger pitch strength. If the number of consecutive **k**'s were the only variable affecting pitch strength, these two stimuli should have been judged equal in pitch strength. In this case, it appears as if the fact that the **4k4x** click train has a higher

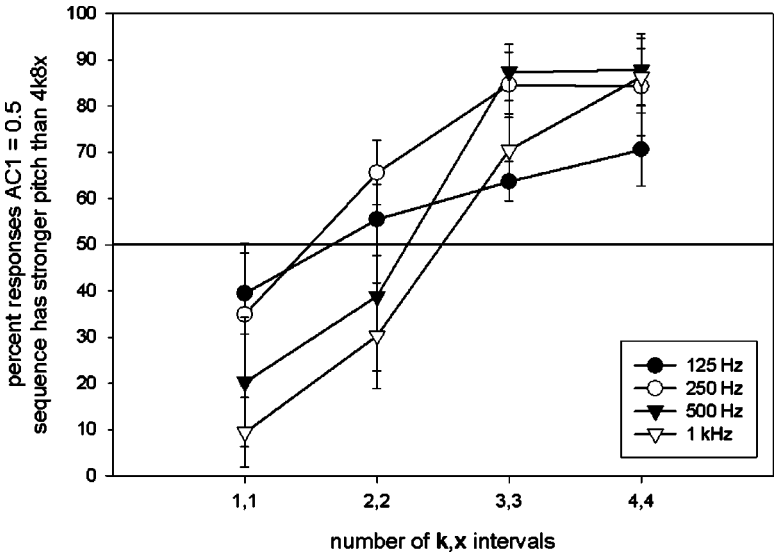

FIG. 8. Ordered (unshuffled) click-train RIS pitch strength comparisons. 4**k8x** vs **kx**, 2**k**2**x**, 3**k**3**x**, 4**k**4**x**, wideband stimuli. Bars are mean percentage of four listeners; error bars are standard errors.

AC1 peak (0.5 as compared to 0.33) led listeners to judge it stronger in pitch. This suggests that pitch strength is both a function of the number of consecutive **k**'s and the ratio of the number **k**'s to the number of **k**'s and **x**'s (i.e., the height of AC1, or spectral peak-to-valley ratio).

In the case of these unshuffled click trains of experiment III, the autocorrelation functions will have peaks at lags at integer multiples of **d** (see the discussion in experiment I concerning multiple peaks in these types of autocorrelation functions). Thus, click trains with longer runs of **k**'s will have more peaks in the autocorrelation function than click trains with shorter runs. Thus, it is possible that one of the reasons that the pitch of stimuli with longer runs of **k**'s is judged stronger is due to the influence of the autocorrelation function peaks at long lags on the perception of pitch strength. However, as was pointed out in experiment I, other studies have failed to show that the peaks at lags that are integer multiples of **d** have any influence on either the pitch or the pitch strength of RIS sounds.

The results of the ordered click-train RIS pitch-strength comparisons confirm the importance of consecutive regular intervals in determining the pitch strength of these stimuli. The data also show that the pitch strength of these stimuli is a function of the number of consecutive regular intervals *and* AC1 peak height (either as an indicator of temporal regularity or of spectral peak-to-valley ratio) of the overall stimulus.

V. EXPERIMENT IV—PITCH STRENGTH RATINGS FOR SHUFFLED CLICK TRAINS

An additional set of trials was run comparing the pitch strength between shuffled ICI click-train RIS with different ratios of random-to-regular intervals. Experiment IV was conducted to allow us to estimate the number of consecutive regular intervals that might be sufficient to increase the pitch strength of the shuffled click train over that of the unshuffled click train. Some of the results from experiment III suggest that 2–4 consecutive regular intervals might be sufficient to increase the pitch strength of a first-order RIS click train.

A. Method

The experimental approach and listeners were identical to experiment I. Regular ICIs with mean interval durations **d** equal to 8, 4, 2, and 1 ms were used. The stimulus set was all **x**'s, **k**4**x**, **k**3**x**, **k**2**x**, **kx**, and all **k**'s. Stimuli were paired with each other, making for 15 different pairings at each value of **d**. A block of randomly chosen trials (without replacement) consisted of a set of 10 replicates of all of 15 different pairings at a single **d** value. These blocks of 150 trials were repeated five times, resulting in 50 trials per pairing for each listener. The three listeners who participated in the experiment III also participated in this experiment.

B. Results

The overall results are tabulated in the preference matrices in Table III. The number in each cell represents the number of times the pitch strength of the row stimuli was judged to be stronger than the pitch strength of the column stimuli.

1. Pitch-strength ratings using Bradley–Terry rating method

The data in Table III were used to construct relative pitch strength ratings using the Bradley–Terry rating method for paired comparisons (see Bradley, 1984; David, 1988). Separate pitch-strength ratings were created at each value of **d**. The Bradley–Terry rating method is an iterative procedure that converts a matrix of paired-comparison preference totals to a relative rating for each stimuli on a scale between zero and 1. For the data in Table III, the ratings converged to four decimal accuracy in 500 iterations. The obtained pitch strength ratings are illustrated in Fig. 9.

As expected, Fig. 9 shows that the pitch-strength estimates based on the Bradley–Terry procedure for the control conditions (all **x**'s and all **k**'s) are near zero and 1, respectively. Note that the relative pitch strength for all of the noncontrol conditions is less than 0.1. This suggests that these stimuli were relatively weak in pitch strength and that they would need more regular intervals than random intervals (e.g., 4**k**1**x**) to have a pitch strength rating greater than 0.5. It

TABLE III. Preference table for shuffled stimuli pairings. Each cell is the total number of preferences (out of 200) for the row stimuli over the column stimuli. The last column is the sum of each row representing the total number of preferences (out of 1000) for that stimuli throughout the experiment.

			Stimuli					Total preferences out of 1000
d	8 ms	All **k**'s	**kx**	**kxx**	**k3x**	**k4x**	All **x**'s	
	All **k**'s		198	196	200	198	194	986
	kx	2		157	170	188	188	705
	kxx	4	43		127	146	154	474
	k3x	0	30	73		106	154	363
	k4x	2	12	54	94		124	286
	All **x**'s	6	12	46	46	76		186
d	4 ms	All**k**'s	**kx**	**kxx**	**k3x**	**k4x**	All**x**'s	
	All **k**'s		194	198	200	198	200	990
	kx	6		155	174	179	190	704
	kxx	2	45		135	163	174	519
	k3x	0	26	65		124	168	383
	k4x	2	21	37	76		148	284
	All **x**'s	0	10	26	32	52		120
d	2 ms	All**k**'s	**kx**	**kxx**	**k3x**	**k4x**	All**x**'s	
	All **k**'s		184	198	200	200	200	982
	kx	16		174	182	188	186	746
	kxx	2	26		150	183	188	549
	k3x	0	18	50		137	176	381
	k4x	0	12	17	63		162	254
	All **x**'s	0	14	12	24	38		88
d	1 ms	All**k**'s	**kx**	**kxx**	**k3x**	**k4x**	All**x**'s	
	All **k**'s		186	200	200	198	200	984
	kx	14		176	190	196	200	776
	kxx	0	24		162	187	194	567
	k3x	0	10	38		122	172	342
	k4x	2	4	13	78		166	263
	All **x**'s	0	0	6	28	34		68

is expected that if such stimuli were included that the pitch strength lines would resemble the familiar "S-shaped" curves of paired-comparison psychometric functions. The current stimulus set seems to only include conditions representing the bottom portion of the "S."

2. Statistical analysis of consecutive regular intervals in shuffled ICI sequences

The previous experiments using shuffled ICI sequence have shown that

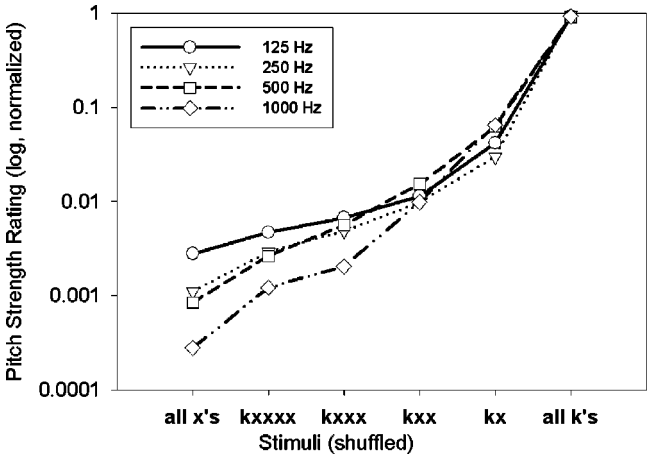

FIG. 9. Pitch strength ratings of shuffled click-train RIS based on Bradley–Terry model, average of four listeners.

(1) A shuffled ICI sequence can exhibit a higher pitch strength as compared to its unshuffled counterpart; and
(2) The pitch strength of shuffled ICI sequences increases with increasing proportion of regular intervals.

These results suggest that the pitch strength in these stimuli is largely determined by multiple occurrences of runs of consecutive regular intervals. The question arises as to what size(s) of runs determine(s) pitch strength. One way to determine the importance of regular interval run size on pitch strength is to analyze the expected number of runs of different sizes in shuffled ICI sequences and to compare these statistics to the pitch strength ratings determined above in experiment IV. Both empirical and analytical solutions for the expected numbers of runs of a given size were derived. The details of these statistical analyses are given in the Appendix.

The asymptotic solution for large numbers of ICIs given in Eq. (A2) was used to compare the run statistics to the pitch-strength ratings illustrated in Fig. 9. These data for the noncontrol conditions are replotted in Fig. 10 along with curves proportional to the expected number of consecutive runs of size 1, 2, 3, 4, and 5. Figure 10 shows that only the runs of size 2, 3, and 4 match the curvature of the pitch-strength ratings, as appears consistent with some of the results from experiment III.

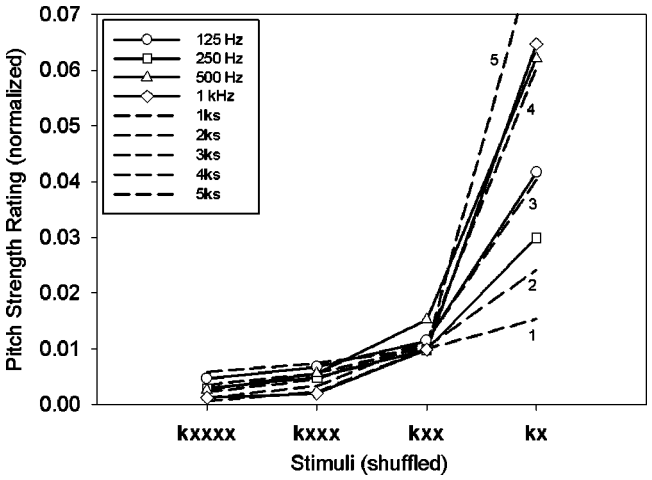

FIG. 10. Pitch strength ratings from Fig. 9 and curves based on statistics of the expected number of consecutive regular intervals of different sizes.

Another way to appreciate the importance of run size is to determine at what size the expected number of large runs in ICI sequences is less than 1. For example, consider the **d**=2-ms regular-interval condition that contains 240 total ICIs. Using Eq. (A2), it can be shown that the expected number of runs of size 8 is less than 1 for shuffled **kx** stimuli. The same is true for runs of size 6, 5, and 4 for **kxx**, **k**3**x**, and **k**4**x** stimuli, respectively. One would not expect pitch to be based on events that occur less than once per trial.[2]

One must be careful not to make too strong predictions when comparing run statistics and pitch-strength rating data. For example, Fig. 9 suggests that the pitch strength of **d** =1- and 2-ms shuffled click trains are based on four consecutive intervals and the **d**=8-ms data are based on three consecutive intervals. However, the auditory system may not rely on only a single run size. It must also be remembered that ordered click-train RIS sounds contain no consecutive regular intervals and yet still have pitches. Also, recall that some of the results of experiment III suggested that consecutive runs of two or three regular intervals may be sufficient to increase the pitch strength of first-order interval click trains. In summary, comparing regular-interval run statistics to shuffled ICI sequences and their corresponding pitch-strength ratings suggests that runs of sizes of only two or three consecutive regular intervals may be all that is required in some conditions for shuffled ICI sequences to impart a stronger pitch strength than ordered ICI sequences. However, additional research will be necessary to obtain a more accurate estimate of the minimum run of regular intervals that influence pitch strength.

VI. CONCLUSIONS

In almost all of the conditions considered in this paper the results depended on **d** (or equivalently, $\mathbf{f_0}$). It is important to point out that the timbre of these sounds changes significantly as a function of **d**. When **d** is long (e.g., 8 ms), the average duration between clicks is long, and the click train has a ''rattling timbre'' as discussed by Kaernbach and Demany (1998), and when the duration is near its longest possible value ($\sim$16 ms), an ''interruption'' can be perceived (although this occurs very infrequently). At short durations (e.g., **d**=1 ms), the timbre is much more like that of a continuous noise. As pointed out previously, the pitch strength of RIS sounds (e.g., the pitch strength of iterated rippled noise, Yost and Hill, 1978) also changes with **d**, such that most studies indicate that the pitch strength at **d**'s of 8 and 1 ms ($\mathbf{f_0}$'s of 125 and 1000 Hz) is lower than at 2 and 4 ms, where the pitch strength has been measured to be about the same. The pitch strength of these click trains must be made in comparison to the overall timbre of the sounds in that there are two percepts associated with these RIS sounds; the base timbre and the pitch that ''arises'' from the base timbre (see Patterson *et al.*, 1996). There are times in which the weakest pitch strength measured seems to be associated with delays of 1 and 8 ms (e.g., Fig. 4); while in some cases (Figs. 7 and 8), the pitch strength at **d**=1 ms seems to be the strongest. In general, the data for **d**=2 and 4 ms appear to be similar. We do not have a clear understanding of why the pitch strength changes as it does with **d** across the conditions of this study. We do believe that the normally low-pitch strength associated with a delay of 8 ms coupled with the rattling nature of its timbre conspire to lower its pitch strength in almost all cases.

Shuffled first-order click trains have runs of regular intervals and as a consequence they are perceived as having higher pitch strength than unshuffled first-order click trains with shorter runs of regular intervals. These results also appear when the stimuli are high-pass filtered so that the spectral peaks associated with these stimuli cannot be resolved, though the pitch-strength differences between shuffled and unshuffled click train becomes smaller as the cutoff frequency of the filters increases. Shuffled second-order click trains are judged to have higher pitch strength than the unshuffled second-order click train only in the broadband conditions when the spectral peaks are resolvable.

Current autocorrelation models based on the long-term autocorrelation functions cannot account for the data of this study as explained in experiment I, nor could spectral models which are based on the long-term spectrum. Wiegrebe and colleagues (Wiegrebe, Hirsch, and Patterson, 1999; Wiegrebe *et al.*, 1998) applied a short-term autocorrelation model to account for the pitch strength of an RIS sound generated by repeating short segments of frozen noise samples. The pitch strength was a nonlinear transform of the height of AC1 as suggested by Yost (1996a) and Shofner and Selas (2002). A similar short-term autocorrelation function analysis in which pitch strength is nonlinearly related to the height of AC1 can qualitatively account for the wideband, first-order-interval click-train pitch-strength discrimination data of experiment I and, to some extent, the high-pass filtered conditions seen in experiment II. However, this model would predict the same results for the second-order-interval pitch-strength discriminations (experiment II) as it would for the first-order intervals. Since the results of experiment II show that this is not the case, this short-term autocorrelation analysis does not appear as a model that could be used to account for some of the key data described in this paper. It appears as if the type of model (either spectral or temporal) that might account for

the data of these experiments is one based on a short-term statistic that is most sensitive to first-order intervals in a waveform.

These data also conflict in some ways with studies that have shown that complex pitch processing is sluggish in that it appears to take perhaps hundreds of milliseconds for the pitch strength of complex sounds to reach maximal saliency (Yost, 1980; Buunen, 1980; Wiegrebe, 2001). The results of the current paper and that of Wiegrebe *et al.* (1998) indicate that pitch strength can be influenced by short-duration changes in the regularity of the sound. These results may not be contradictory in that maximal pitch strength or the best estimate of pitch may require considerable time for processing, but short-term changes can change pitch strength independent of whether or not the pitch is maximal in pitch strength or if the most accurate estimate of the pitch has been achieved.

The fact that runs of regular intervals seem to effect the perception of pitch more than runs of random intervals appears to suggest that the auditory system is more influenced by regularity than randomness. If the suggestion in this paper that a change of only two or three consecutive regular intervals influences pitch-strength judgments, this perhaps implies that the auditory system is very sensitive to the regularity in a complex sound.

ACKNOWLEDGMENTS

This research was supported by a program project grant from the National Institutes of Deafness and other Communication Disorders (NIDCD) and more recently by an NIDCD grant to Dr. Yost, and was part of Dr. Dan Mapes-Riordan's Ph.D. dissertation.

APPENDIX: DETERMINING THE PROBABILITY OF RUNS OF DIFFERENT LENGTHS

Determining the expected number of runs of regular **k** intervals of a given size in a shuffled ICI sequence consisting of a known number of regular **k** and random **x** intervals is a problem known in the field of probability and statistics as *run* or *clump* analysis (e.g., Godbole and Papastavridis, 1994). This problem is identical to finding, for example, the number of runs of red cards of a certain value in a shuffled deck of playing cards with the proportion of red and black cards being variable and cards being drawn *without* replacement. The distributions of sampling without replacement are known as *hypergeometric* distributions, whereas sampling *with* replacement is known as binomial or Bernoulli distribution (see Johnson and Kotz, 1977).

In determining the statistics of runs, care must be taken to define how runs are counted. Runs can be defined as overlapping or nonoverlapping, and contiguous or noncontiguous. For example, if overlapping runs are counted, the sequence **kkkk** contains one run of length 4, two runs of length 3, three runs of length 2, and four runs of length 1. If only nonoverlapping runs are counted, then the above sequence contains one run of length 4, one run of length 3, two runs of length 2, and four runs of length 1. If runs are further restricted to be nonoverlapping and noncontiguous, then the number of runs of length 2 is reduced to 1, and the number of runs of length 1 is reduced to 2. Note that the number of nonoverlapping runs of a given size is always less than the number of overlapping runs of the same size except for the endpoint conditions consisting of runs of size 1 and n**k** (n**k** is the total number of **k**'s in the entire ICI sequence). In these cases, the number of overlapping and nonoverlapping runs is equal. The statistics of overlapping runs were used (except where noted) for relating the statistics of consecutive regular intervals in an ICI sequence to the perception of pitch strength in these click-train RIS.

A literature search turned up no analytical solution for the distribution of numbers of overlapping runs of a given size in a shuffled sequence. The closest known solution is given by Godbole (1990) for the distribution of nonoverlapping runs. As an alternative, a computer program was written that exhaustively searches all permutations of a given sequence of **k**'s and **x**'s (represented by 1's and 0's) and tallies the number of runs of every size. Unfortunately, this program was limited to a maximum ICI sequence length of 32 intervals. The ICI sequence lengths in the shuffled ICI sequence experiments were 60, 120, 240, and 480 intervals. A program for exhaustively searching ICI sequences longer than 32 intervals was not undertaken given the exponentially increasing calculation time for computing the distributions for these sequence lengths. However, the program was used to verify the analytical and empirical solutions given below.

Given equal numbers of regular **k** intervals (n**k**) and random **x** intervals (n**x**) in an ICI sequence, the expected number of **k** runs of size m in a shuffled sequence of these intervals is given (without proof) in Eq. (A1) below.

$$
\begin{aligned}
E\{m\} &= 0; \quad nk < m \\
&= \frac{nk+1}{\binom{nk+nx}{nk}}; \quad nk = m \\
&= \frac{\dfrac{(nk-m+1)(nk-m+2)}{2}}{\dfrac{\binom{2m}{m}}{m+1} + (nk-m)\cdot 2^{(m-2)}}; \quad nk > m
\end{aligned}
\tag{A1}
$$

Equation (A1) is only applicable for equal numbers of regular and random ICIs (n**k**=n**x**). An empirical approach was taken to determine the run statistics for conditions with differing numbers of regular and random intervals. This was accomplished by constructing the desired ICI sequence and repeatingly shuffling it and tallying the number of runs of different sizes. The results for the **d**=2-ms regular-interval condition (240 total ICIs) using 10 000 random permutations are given in Table IV.

An examination of the empirical results in Table IV indicates that the expected number of consecutive regular intervals of a given size resembles a binomial distribution. This is expected given that the results of sampling without replacement converge to the solution with replacement (binomial distribution) as the total number of intervals increases. This asymptotic solution for the expected number of con-

TABLE IV. The results of 10 000 random permutations of an ICI sequence containing 240 total intervals of varying proportion of regular-to-random intervals (columns). The top half of the table are the mean number of consecutive regular intervals of size 2–13 (rows) and the bottom half are the corresponding standard deviations.

Mean number of consecutive intervals of run length (m)	Shuffled stimulus				
	kx	**kxx**	**kxxx**	**kxxxx**	**kxxxxx**
2	59.4701	26.3466	14.7555	9.3882	6.5023
3	29.3299	8.5552	3.5791	1.8147	1.0284
4	14.4066	2.746	0.8574	0.3427	0.1637
5	7.0305	0.8788	0.1989	0.0657	0.0271
6	3.4167	0.28	0.0461	0.0117	0.0039
7	1.644	0.0886	0.0096	0.002	0.0005
8	0.7856	0.0275	0.0022	0.0001	0
9	0.3702	0.0092	0.0006	0	0
10	0.1763	0.002	0.0001	0	0
11	0.0845	0.0003	0	0	0
12	0.0409	0	0	0	0
13	0.0202	0	0	0	0
Standard deviation of number of consecutive intervals of run length (m)					
2	3.9038	3.4606	2.877	2.4882	2.12
3	4.7836	2.9818	1.9953	1.4501	1.0914
4	4.3859	2.0007	1.0971	0.6783	0.4651
5	3.5808	1.2296	0.5515	0.3003	0.1886
6	2.725	0.7128	0.2645	0.1264	0.0699
7	1.9942	0.4054	0.1237	0.0469	0.0224
8	1.4306	0.2235	0.06	0.01	0
9	1.0101	0.1171	0.0283	0	0
10	0.7084	0.051	0.01	0	0
11	0.4994	0.0173	0	0	0
12	0.3564	0	0	0	0
13	0.2585	0	0	0	0

secutive regular intervals of size m in a sequence of ICIs made up of n**k** regular intervals and n**x** random intervals is given in Eq. (A2).

$$E\{m\} \approx (nk-1)\left(\frac{nk-1}{nk+nx-2}\right)^{m-1}. \quad \text{(A2)}$$

[1]Since the spectra of many of the stimuli are ''rippled'' rather than ''flat,'' spectrum level was computed for all stimuli as the total power of the stimulus divided by the bandwidth, which for the broadband conditions was 15 kHz. Thus, the spectral peaks for those stimuli with rippled spectra are greater than the stated spectrum level.

[2]The statistical results are shown for the expected number of *overlapping* consecutive intervals. If *nonoverlapping* interval statistics are used, then runs of size 3, 4, and 5 best match the pitch strength ratings. Refer to the Appendix for a more detailed discussion on the differences between the statistics of overlapping and nonoverlapping runs.

Bradley, R. A. (**1984**). ''Paired comparisons: Some basic procedures and examples,'' in *Handbook of Statistics*, edited by P. R. Krishnaiah and P. K. Sen (Elsevier, New York), Vol. 4.

Buunen, T. J. F. (**1980**). ''The effect of stimulus duration on the prominence of pitch,'' in *International Symposium in Hearing*, edited by G. van den Brink and F. A. Bilsen (Delft University Press, Delft), pp. 374–379.

David, H. A. (**1988**). *The Method of Paired Comparisons* (Oxford, New York), pp. 61–63.

Godbole, A. P. (**1990**). ''On hypergeometric and related distributions of order k,'' Commun. Stat: Theory Meth. **19**, 1291–1301.

Godbole, A. P., and Papastavridis, S., editors (**1994**). *Runs and Patterns in Probability: Selected Papers* (Kluwer, Boston).

Johnson, N. L., and Kotz, S. (**1977**). *Urn Models and Their Application* (Wiley, New York).

Kaernbach, C., and Demany, L. (**1998**). ''Psychophysical evidence against the autocorrelation theory of auditory temporal processing,'' J. Acoust. Soc. Am. **104**, 2298–2306.

Kaernbach, C., and Bering, C. (**2001**). ''Exploring the temporal mechanisms involved in the pitch of unresolved harmonics,'' J. Acoust. Soc. Am. **110**, 1039–1048.

Licklider, J. C. R. (**1951**). ''A duplex theory of pitch perception,'' Experientia **7**, 128–133.

Meddis, R., and Hewitt, M. J. (**1991**). ''Virtual pitch and phase sensitivity of a computer model of the auditory periphery. I Pitch identification,'' J. Acoust. Soc. Am. **89**, 2866–2882.

Meddis, R., and O'Mard, L. (**1997**). ''A unitary model of pitch perception,'' J. Acoust. Soc. Am. **102**, 1811–1820.

Patterson, R. D., Allerhand, M., and Giguere, C. (**1995**). ''Time-domain modeling of peripheral auditory processing: A modular architecture and a software platform,'' J. Acoust. Soc. Am. **98**, 1890–1894.

Patterson, R. D., Handel, S., Yost, W. A., and Datta, J. (**1996**). ''The relative strength of tone and noise components in iterated rippled noise,'' J. Acoust. Soc. Am. **100**, 3286–3294.

Pressnitzer, D., de Cheveigné, A., and Winter, I. M. (**2002**). ''Perceptual pitch shift for sounds with similar waveform autocorrelation,'' ARLO **3**, 1–6.

Pressnitzer, D., de Cheveigné, A., and Winter, I. M. (**2004**). ''Physiological correlates of the perceptual pitch shift for sounds with similar autocorrelation,'' ARLO **5**, 1–6.

Shofner, W. P., and Selas, G. (**2002**). ''Pitch strength and Stevens' power law,'' Percept. Psychophys. **64**, 437–450.

Wiegrebe, L. (**2001**). ''Searching for the time constant of neural pitch extraction,'' J. Acoust. Soc. Am. **109**, 1082–1091.

Wiegrebe, L., Hirsch, H. S., and Patterson, R. D. (**1999**). ''Time constants of pitch processing arising from auditory filtering,'' J. Acoust. Soc. Am. **105**, 1234.

Wiegrebe, L., Patterson, R. D., Demany, L., and Carlyon, R. P. (**1998**). ''Temporal dynamics of pitch strength in regular interval noises,'' J. Acoust. Soc. Am. **104**, 2307–2313.

Wightman, F. L. (**1973**). ''Pitch and stimulus fine structure,'' J. Acoust. Soc. Am. **54**, 397–406.

Yost, W. A. (**1980**). ''Temporal Aspects of Ripple Noise and Other Complex Stimuli,'' in *International Symposium in Hearing*, edited by G. van den Brink and F. A. Bilsen (Delft University Press, Deflt), pp. 367–374.

Yost, W. A. (**1996a**). ''Pitch of iterated rippled noise,'' J. Acoust. Soc. Am. **100**, 511–518.
Yost, W. A. (**1996b**). ''Pitch strength of iterated rippled noise,'' J. Acoust. Soc. Am. **100**, 329–3335.
Yost, W. A. (**1998**). ''Auditory processing of sounds with temporal regularity: Auditory processing of regular interval stimuli,'' in *Psychophysical and Physiological Advances in Hearing, Proceedings of the 11th International Symposium on Hearing*, edited by A. R. Palmer, A. Rees, A. Q. Summerfield, and R. Meddis (Whurr, London).
Yost, W. A., and Hill, R. (**1978**). ''Strength of the pitches associated with ripple noise,'' J. Acoust. Soc. Am. **64**, 485–492.
Yost, W. A., Mapes-Riordan, D., Dye, R., Sheft, S., and Shofner, W. (**2005**). ''Discrimination of first- and second-order regular intervals from random intervals as a function of highpass filter cutoff frequency,'' J. Acoust. Soc. Am. **117**, 59–62.
Yost, W. A., Patterson, R. D., and Sheft, S. (**1996**). ''A time domain description for the pitch strength of iterated ripple noise,'' J. Acoust. Soc. Am. **99**, 1066–1078.

The spatial unmasking of speech: evidence for within-channel processing of interaural time delay

Barrie A. Edmonds and John F. Culling
School of Psychology, Cardiff University, Tower Building, Park Place, Cardiff, CF10 3AT, United Kingdom

(Received 1 September 2004; revised 3 February 2005; accepted 4 February 2005)

Across-frequency processing by common interaural time delay (ITD) in spatial unmasking was investigated by measuring speech reception thresholds (SRTs) for high- and low-frequency bands of target speech presented against concurrent speech or a noise masker. Experiment 1 indicated that presenting one of these target bands with an ITD of $+500$ μs and the other with zero ITD (like the masker) provided some release from masking, but full binaural advantage was only measured when both target bands were given an ITD of $+500$ μs. Experiment 2 showed that full binaural advantage could also be achieved when the high- and low-frequency bands were presented with ITDs of equal but opposite magnitude (± 500 μs). In experiment 3, the masker was also split into high- and low-frequency bands with ITDs of equal but opposite magnitude (± 500 μs). The ITD of the low-frequency target band matched that of the high-frequency masking band and vice versa. SRTs indicated that, as long as the target and masker differed in ITD within each frequency band, full binaural advantage could be achieved. These results suggest that the mechanism underlying spatial unmasking exploits differences in ITD independently within each frequency channel. [DOI: 10.1121/1.1880752]

PACS numbers: 43.66.Pn, 43.66.Dc [AK] Pages: 3069–3078

I. INTRODUCTION

The masked threshold of speech is lower when it is spatially separated from its masker than when the two sounds share a common direction. This effect is called the binaural intelligibility level difference (BILD). The BILD has been described as being dependent on improvements in the audibility of the target speech arising from differences in interaural level difference (ILD) and interaural time delay (ITD) between the two sounds (Bronkhorst and Plomp, 1988; Zurek, 1992). This paper focuses on the binaural gain in intelligibility associated with ITD (e.g., Schubert, 1956; Levitt and Rabiner, 1967a) and how ITD is exploited by the auditory system to bring about release from masking. Three experiments are reported in which we tested for the importance of providing a common ITD across different frequency regions to the BILD.

The effect of spatial separation on the segregation of sounds has also been described in terms of selective attention (e.g., Hirsh, 1950; Broadbent, 1954; Darwin and Hukin, 1999; Freyman *et al.*, 1999; Darwin and Hukin, 2000; Freyman *et al.*, 2001, 2004). That is, it is thought that focusing one's attention on the perceived location of the desired speech might aid the formation and perceptual segregation of the target as an auditory event from that of a masking sound. The relationship between lateralization and binaural detection of sounds has been an open question for many years (e.g., Hirsh, 1948; Licklider, 1948; Hafter *et al.*, 1969); a number of investigations have considered the relative importance of spatial location in the segregation of sounds compared to other cues (Bregman, 1990; Kubovy and Van Valkenburg, 2001; Neuhoff, 2003). Given that ITD contributes to both the perceived lateral position of a sound source (Rayleigh, 1876, 1907) and to binaural unmasking, it is tempting to suggest that the latter is dependent on the former. However, two lines of evidence suggest that this is not the case.

First, the perceived location of a sound can be disrupted without any significant effect on binaural release from masking (Licklider, 1948; Carhart *et al.*, 1967, 1968; 1969; Edmonds and Culling, in press). For example, the masked threshold of speech heard against a masker with zero ITD (and therefore perceived centrally) is lower for target speech presented out of phase at the two ears (perceived to be diffusely located) than for target speech that has a fixed ITD and is heard to be clearly lateralized. In addition, theories of speech intelligibility for spatially separated sounds (e.g., Levitt and Rabiner, 1967b; Zurek, 1992) predict improvements in the masked threshold of target speech as a function of binaural unmasking rather than perceived location.

Second, ITD has been demonstrated to be a relatively weak cue for the segregation of competing sounds. For instance, Hukin and Darwin (1995) showed that a single harmonic could be segregated from other harmonics in a vowel sound if its onset time was altered but not if it was given a different ITD. That is, despite the harmonic having a different ITD from the rest of the vowel sound, listeners group the lone harmonic with the other components of the vowel. In addition, listeners do not appear to exploit ITD when grouping sounds across frequency (Culling and Summerfield, 1995) unless they are given considerable amounts of training (Drennan *et al.*, 2003). Culling and Summerfield (1995) presented listeners with four formant-like noise bands (i.e., their frequencies approximated the first and second formants of speech) which could give rise to the perception of two whispered vowel sounds. They found that listeners were unable to correctly identify (with above-chance performance) the two vowels if presented with different ITDs, but could do so

when the two vowels were presented to different ears. Consequently, it has been argued that the auditory system ignores spatial correspondences between different frequency channels, preferring to exploit within-channel interaural differences between concurrent sounds (Culling and Summerfield, 1995; Akeroyd, 2004).

There are a number of models that describe how ITD might be exploited for binaural unmasking (for an overview see Colburn and Durlach, 1978; Blauert, 1983); however, the two most well known are vector theory (Jeffress, 1972) and the equalization-cancellation (E-C) model (Durlach, 1960; 1963; 1972; Breebaart *et al.*, 2001). The Jeffress model assumes that ITD is exploited by a binaural processor consisting of a series of frequency-dependent coincidence detectors connected by delay lines. The auditory system is thought to be able to compare the activity of this binaural processor over a range of interaural delays in order to perform a cross correlation of the input at the two ears. Durlach's model assumes that, if the target sound and its masker are spatially separated, then it should be possible to apply a set of transformations to the signal such that the noise can be eliminated. For instance, when the target has a different ITD from that of the masker, equalization can be achieved by applying an internal delay in order to compensate for the interaural configuration of the noise.[1] The noise can then be canceled from the binaural signal by subtracting the now-equalized target and masker waveforms from one another in order to deliver an improved signal-to-noise ratio. Consequently, the model accurately predicts that the optimal case for binaural unmasking in a given critical band (e.g., the detection of a tone in noise) is when the tone is presented out of phase at the two ears and the noise is presented in phase at the two ears.

Culling and Summerfield (1995) proposed an elaboration of Durlach's model, the modified equalization-cancellation (mE-C), in order to account for the apparent indifference of the auditory system to ITD across frequency for the grouping of sounds. They suggested that, as the grouping of sounds across frequency does not appear to be constrained by spatial correspondences between different frequency channels, then the equalization step of spatial unmasking must be free to use the best ITD within each frequency channel. Subsequently, the mE-C model has been used to explain the results of a number of binaural phenomena (Culling and Summerfield, 1995; Culling, 1998; Culling *et al.* 1998). More recently, Akeroyd (2004) looked for evidence of this within-channel mechanism in the binaural unmasking of complex tones against a broadband masker. Akeroyd found that, even when each component of a harmonic complex was presented with a different ITD, detection of the complex was undiminished. These results suggest that the decision mechanism responsible for choosing the best delay in the equalization process is free to do so independently within each frequency channel.

This paper investigates whether a channel-independent mechanism for exploiting ITD (such as that assumed in the mE-C model) can account for the binaural gains in the intelligibility of speech in noise associated with spatial separation. In particular, the importance of a common ITD to the BILD was tested by presenting listeners with target stimuli that had different ITDs at different frequencies. Three experiments were conducted to explore various strategies for selecting and canceling competing sounds (i.e., target speech heard against either competing speech or a broadband-noise masker) across frequency using ITD; the BILDs measured suggest that the auditory system is able to exploit ITD independently within each frequency channel.

II. GENERAL METHODS

A. Participants

Cardiff University psychology undergraduate students were recruited and awarded course credit in return for their participation. All participants reported normal hearing and spoke English as their first language. Each participant was a naive listener (i.e., they had little or no previous experience in tests of auditory perception) and contributed data to only one experiment in a single session lasting approximately 45 min.

B. Stimuli

Stimuli were presented to the listener using a TDT AP2 array processor via a TDT psychoacoustics rig (DD1, FT6, PA4, HB6) through Sennheiser HD 590 headphones in a single-walled IAC sound-attenuating booth. Sentences from the MIT recordings of the speaker CW reading the Harvard Sentence Lists (IEEE, 1969) were used as target items. The masker was either a sentence from the speaker DA (again from MIT recordings of the Harvard sentence lists) or Brown noise (i.e., a broadband noise with a 6-dB/octave spectral roll-off). Brown noise produces greater energetic masking for low frequencies than for higher frequencies, and roughly approximates the low-frequency emphasis of speech.

C. High- and low-pass filters

In order to test for the importance of a common ITD across frequency, stimuli were spectrally divided into high- and low-pass filtered frequency bands. This manipulation allowed the high- and low-frequency regions of the signal to be configured independently of each other (i.e., given different ITDs). By doing this, the effect of spatial separation on the intelligibility of speech in different frequency regions could be tested.

In experiments 1, 2, and 3, the stimuli were presented as a pair of high- and low-pass filtered frequency bands using 512-point FIR filters with linear phase and >1000 dB/octave cutoffs. The high- and low-frequency bands were separated by a 1-ERB (equivalent rectangular bandwidth) (Moore and Glasberg, 1983) gap centered at splitting frequencies of 750 and 1500 Hz in experiment 1 and 750, 1500, and 3000 Hz in experiments 2 and 3 (see Table I for a summary of the exact filter cutoffs). This gap prevented energy in frequency channels close to the splitting frequency from creating a confounding interaural interaction.

TABLE I. Summary of the upper and lower cutoff frequencies used to spectrally divide the stimuli about a given splitting frequency. The low-frequency band was created by low-pass filtering the stimuli at a cutoff frequency of $\frac{1}{2}$ of the equivalent rectangular bandwidth below the splitting frequency. The high-frequency band was created by high-pass filtering the stimuli at a cutoff frequency of $\frac{1}{2}$ of the equivalent rectangular bandwidth above the splitting frequency.

Splitting frequency (Hz)	Low-pass cutoff (Hz)	High-pass cutoff (Hz)
3000 (experiments 2 and 3)	2821	3186
1500 (all experiments)	1409	1592
750 (all experiments)	700	802

D. Procedure

Speech reception thresholds (SRTs) were measured for each participant in all conditions. The SRT is the masked level in dB of the target speech for a criterion level of understanding. In this case, it was measured for the report of keywords from the target sentence with an accuracy of 50%. The SRT measurement was implemented using the 1-up/1-down adaptive threshold method described by Plomp and Mimpen (1979). Participants were presented with ten trials for each experimental condition; in order to eliminate the effects of order of presentation and of variations in the difficulty of the target materials the conditions were rotated around the different speech materials for successive participants. That is, each participant heard all the target/masker speech materials in the same order; only the order of the conditions was changed. SRTs were also measured for two practice conditions consisting of only monaural stimuli so that listeners could familiarize themselves with the experimental procedure; thresholds for these practice stimuli are not reported.

For the first trial in each condition, the target speech was presented at a very low level (−28 dB) compared to that of the masking sound. A message presented via a computer terminal, viewed through the booth window, prompted the listener to either enter a transcript (using a computer keyboard located inside the booth) or to replay the stimulus. If the participant replayed the stimulus the level of the target speech was increased by 4 dB. The first trial could be replayed in this way until it was loud enough to be judged partially intelligible by the listener (i.e., they felt they could hear approximately half the sentence). At this point, the participant entered a transcript of the words that they thought they had heard. Next, the correct transcript for the current target sentence was displayed on the computer terminal just below the participant's response. This reference transcript contained five keywords (presented in upper case—nonkeywords were presented in lower case). The participant was then prompted to enter the number of keywords that he/she had correctly identified (scoring 0–5). The procedure then entered a second phase in which the stimulus was played only once before the participant was required to transcribe the target sentence.

In the second phase, a fresh target sentence was presented on each of the remaining trials (i.e., trials 2–10) and the level of the target speech for each of these trials was dependent on the listener's reported accuracy in the previous trial. If the participant reported transcribing two or fewer keywords correctly on one trial, the level of the target on the next trial was increased by 2 dB; otherwise, the level of the target was decreased by 2 dB. After all ten trials had been presented, the SRT was determined to be the mean presentation level used for the last seven trials (i.e., trials 3–10) and what would have been the 11th trial.

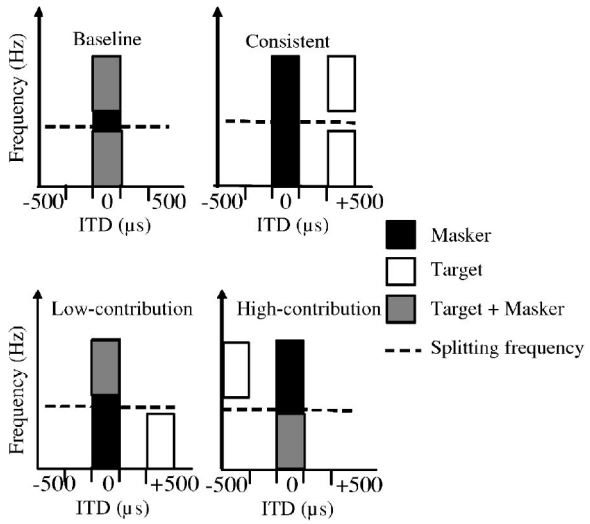

FIG. 1. A schematic illustration of the ITD configurations of experiment 1: Stimuli are represented as high- and low-pass filtered frequency bands presented at distinct ITDs. Target speech bands are depicted in white with black outline, masker bands are depicted in black, and regions that have both target and masker sharing a common ITD are shown in gray. The splitting frequency used to divide the high- and low-pass bands (750 or 1500 Hz) is shown as a dashed line.

III. EXPERIMENT 1

Experiment 1 was a preliminary experiment to establish the importance of both high and low frequencies to speech intelligibility in our experimental paradigm. Its purpose was to ascertain the binaural gain in intelligibility for different frequency regions of target speech. In order to do this we employed a method similar to that of Levitt and Rabiner (1967a). Levitt and Rabiner tested for the importance of different frequency regions of single words heard against a broadband Gaussian noise in binaural release from masking using interaural phase opposition. Here, we measured the binaural advantage due to ITD for high- and low-frequency regions of sentences heard against either a Brown-noise or competing-speech masker.

A. Design

SRTs for target speech presented against a concurrent masker with zero ITD were measured in eight conditions: 2 splitting frequencies (750 and 1500 Hz)×4 ITD configurations (see Fig. 1): *baseline* (both high and low frequencies at zero ITD); *consistent* (both high and low frequencies with +500-μs ITD); *high-contribution* (high frequencies were presented with 500-μs ITD while low frequencies were presented with no ITD); and *low-contribution* (low frequencies were presented with 500-μs ITD while high frequencies were presented with no ITD). Experiment 1 was completed

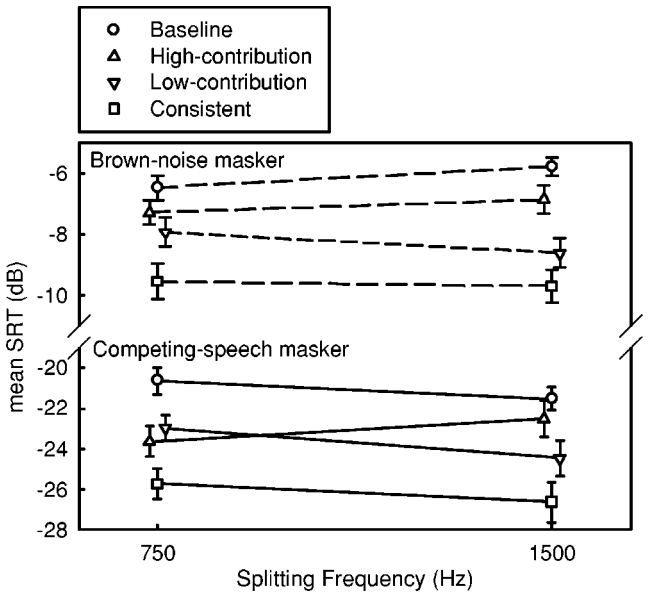

FIG. 2. Mean SRTs of the baseline (circles), high-contribution (upward triangles), low-contribution (downward triangles), and consistent (squares) ITD configurations of experiment 1 for two groups of listeners (Brown-noise masker, dashed lines; competing-speech masker, solid lines). Error bars show standard error. Plots for the high-contribution and low-contribution condition SRTs are offset along the *x* axis in order to improve visibility of the error bars.

by two groups of participants. SRTs were measured for target speech presented against a Brown-noise masker in experiment 1a (16 participants) and against competing speech in experiment 1b (24 participants).

B. Results and discussion

Figure 2 shows the pattern of SRTs for each condition against Brown-noise (dashed lines) and competing-speech (solid lines) maskers. The baseline condition has the highest SRTs in both groups and the consistent condition the lowest; the high-contribution and low-contribution condition SRTs were intermediate. This result suggests that both the high- and low-frequency regions of the target speech were required in order to achieve full binaural advantage (as measured in the consistent condition). Although the pattern of thresholds measured against both types of masker were very similar, the SRTs measured against the competing-speech masker were approximately 12 dB lower (i.e., speech intelligibility was better against competing speech than against the Brown noise).

A two-way repeated-measures analysis of variance (ANOVA) was performed on the SRTs of experiment 1a, and no effect of splitting frequency or interaction between ITD configuration (baseline, high-contribution, low-contribution, and consistent) and splitting frequency (750 and 1500 Hz) was found. However, there was a significant main effect of ITD configuration [$F(3,15)=34.90$, $p<0.001$]. Tukey pairwise tests showed that the comparison of baseline vs high contribution was not significantly different. However, significant differences were found for other comparisons: baseline vs consistent ($q=13.65$, $p<0.001$), baseline vs low contribution ($q=8.37$, $p<0.001$), high contribution vs consistent ($q=9.95$, $p<0.001$), high contribution vs low contribution ($q=4.67$, $p<0.05$), and low contribution vs consistent ($q=5.28$, $p<0.05$).

For experiment 1b, a two-way repeated-measures ANOVA revealed that there was no main effect of splitting frequency, nor was there a significant interaction with ITD configuration, but there was a significant main effect of ITD configuration [$F(3,23)=17.71$, $p<0.001$]. Tukey HSD tests for the pairwise comparisons of the ITD configurations showed that the comparison of high contribution vs low contribution was not significantly different. However, significant differences were found for all other comparisons: baseline vs consistent ($q=10.21$, $p<0.001$), baseline vs low contribution ($q=5.27$, $p<0.05$), baseline vs high contribution ($q=4.00$, $p<0.05$), high contribution vs consistent ($q=6.21$, $p<0.001$), and low contribution vs consistent ($q=4.94$, $p<0.05$).

A number of researchers have explored the importance of different frequency regions on the intelligibility of speech (e.g., Schubert and Schultz, 1962; Levitt and Rabiner, 1967a) and have typically found that binaural unmasking for detection is largely dependent upon interaural phase differences in the low-frequency (e.g., <1000 Hz) region. Experiment 1 tested for the importance of high- and low-frequency bands of target speech to the BILD at two splitting frequencies, and found that neither band alone (i.e., when presented with a different ITD to that of the masker) was sufficient to produce full binaural advantage. SRTs measured in the consistent ITD configuration were lower than those measured for the high-contribution and low-contribution conditions. However, the low-contribution configuration tended to produce lower thresholds than the high-contribution configuration, especially when combined with a splitting frequency of 1500 Hz.

As noted above, thresholds measured against the competing-speech masker were substantially lower than those measured against the Brown-noise masker. Indeed, these thresholds are much lower than those reported in previous studies that have investigated the effects of spatial separation on speech intelligibility which reported SRTs in the region of −20 dB for stimuli with similar spatial configurations (e.g., Hawley *et al.*, 2004). However, it should be noted that in the current study the competing voice was that of a second male talker and not, as in many other studies, the same talker as the target voice. This is likely to have provided the listener with any number of other cues, arising from differences between the two voices, upon which segregation could be based.

IV. EXPERIMENT 2

Experiment 2 was designed to investigate the importance of common ITD for binaural unmasking. Specifically, we investigated the effect of across-frequency consistency in ITD on the intelligibility of target speech. In order to do this we presented listeners with stimuli that had been manipulated so that different frequency regions of the target speech had either the same or opposing ITDs. If the auditory system is able to exploit ITD independently within each frequency channel, then presenting high- and low-frequency bands of the target speech with different ITDs should have no effect

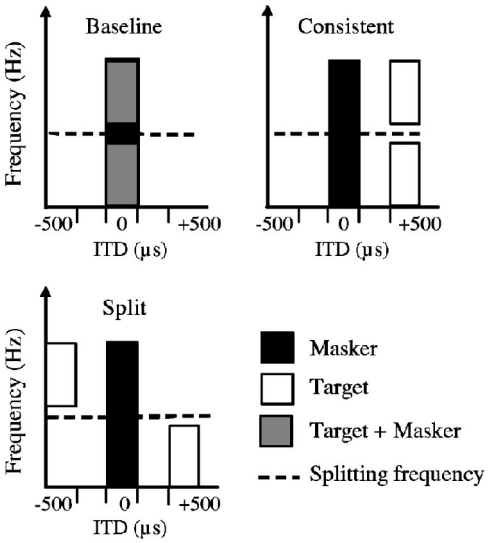

FIG. 3. A schematic illustration of the ITD configurations of experiment 2. Stimuli are represented in high- and low-pass bands presented at distinct ITDs. Target speech bands are depicted in white with black outline, masker bands are depicted in black, and regions that have both target and masker sharing a common ITD are shown in gray. The splitting frequency used to divide the high- and low-pass bands (750, 1500, or 3000 Hz) is shown as a dotted line.

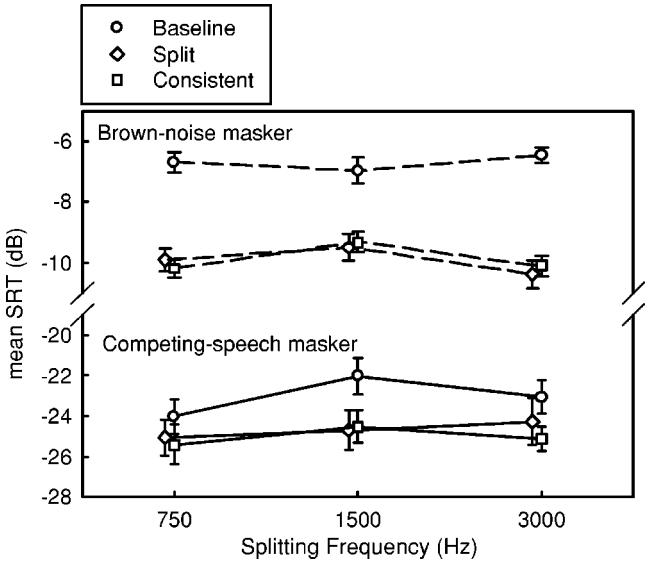

FIG. 4. Mean SRTs of the baseline (circles), split (diamonds), and consistent (squares) ITD configurations of experiment 2 for two groups of listeners (Brown-noise masker, dashed lines; competing-speech masker, solid lines). Error bars show standard error. Plots for the split condition SRTs are offset along the *x* axis in order to improve visibility of the error bars.

on speech intelligibility. Alternatively, if the BILD is dependent on a strategy involving the selection of information at a common ITD across frequency, then one might predict that speech intelligibility in such a condition would be disrupted, as listeners would be constrained to selecting only one of the two possible target speech bands.

A. Design

SRTs were measured for target speech split into a pair of high- and low-pass filtered frequency bands against a concurrent masker over nine conditions: 3 splitting frequencies (3000, 1500, and 750 Hz)×3 ITD configurations (see Fig. 3). The baseline and consistent conditions from experiment 1 were reused and joined by a third condition: *split* (high frequencies were presented with a +500-μs ITD and low-frequencies were presented with a −500-μs ITD). Experiment 2 was completed by two new groups of participants. SRTs were measured for target speech presented against a Brown-noise masker in experiment 2a (18 participants) and against competing speech in experiment 2b (18 participants).

B. Results and discussion

Figure 4 shows that SRTs were poorest (highest) in the baseline condition, but improved in the consistent and split conditions giving a BILD of approximately 3–4 dB in experiments 2a and 2b. Again, the SRTs measured against the competing-speech masker (solid lines) were approximately 12 dB lower than those obtained against the Brown-noise masker (dashed lines), but the pattern of results for both groups was similar.

A two-way repeated-measures ANOVA was performed on the SRTs, with two within-subject factors (ITD configuration, three levels; splitting frequency, three levels). For experiment 2a, there was no main effect of splitting frequency and no statistically significant interaction between ITD configuration and splitting frequency, but there was a significant main effect of ITD configuration [$F(2,17)=109.91$, $p<0.001$]. Tukey HSD pairwise tests showed that the comparison of consistent vs split was not significantly different. However, significant differences were found for the baseline vs split ($q=18.31$, $p<0.001$) and baseline vs consistent ($q=18.00$, $p<0.001$) comparisons.

For experiment 2b, a two-way ANOVA with repeated measures found no main effect of splitting frequency and no statistically significant interaction with ITD, but there was a main effect of ITD configuration [$F(2,17)=5.23$, $p<0.05$]. Tukey HSD pairwise tests showed that the comparison of consistent vs split was not significantly different. However, significant differences were found for comparisons between baseline vs split ($q=3.53$, $p<0.05$) and baseline vs consistent ($q=4.29$, $p<0.05$).

The results of experiment 2 indicate that the intelligibility of masked speech does not require the target speech to be presented with an ITD consistent with a particular direction across different frequency regions in order for full binaural advantage to be achieved. ITD can be exploited to recover target speech at high and low frequencies even when the ITDs of these frequency bands indicate sources in different hemifields. Consequently, it is argued that listeners do not group information across frequency at a common ITD. Rather, the contribution of the target speech bands presented with opposing ITDs to the BILD suggests that listeners were able to exploit ITD within each frequency band independently. However, there are two alternative explanations that might also account for the BILDs observed in this experiment.

First, one might argue that the SRTs measured in the split condition reflect the contribution of both high and low frequencies, but not their simultaneous contributions. One

could imagine, for example, an attention-switching mechanism which allows the auditory system to select information from different locations over time. Second, one might suggest that, rather than selecting sounds with a fixed ITD across frequency, the auditory system simply cancels interfering sounds at a fixed ITD. Consequently, presenting the high- and low-frequency regions of the target speech with opposing ITDs would have little effect on the unmasking process. These issues were addressed in experiment 3.

V. EXPERIMENT 3

The results of experiment 1 demonstrated that recovery of both the high- and low-frequency target bands is required in order to obtain full binaural advantage. Furthermore, experiment 2 showed that listeners could exploit differences in ITD between target speech and a concurrent masker even when different frequency bands of the target speech were presented with different ITDs. It was suggested that this indicated that the auditory system is able to exploit differences in ITD between the target and the masker within each frequency channel independently. However, while the results of experiment 2 suggest that the auditory system is not constrained to select information at a particular ITD, the result was inconclusive in other respects. First, it was difficult to determine whether different frequency regions of a target sound presented with different ITDs contribute to binaural unmasking simultaneously or whether their contributions are pooled together over time. Second, experiment 2 did not consider what role the ITD of the masking sound might have had in the unmasking process. Consequently, experiment 3 was designed to test whether a common ITD could be used to drive either: (i) an attention-switching mechanism for selecting target speech presented with different ITDs at different frequencies, or (ii) a mechanism that cancels at a fixed internal delay rather than selecting the target speech.

Speech intelligibility was measured for a *swapped* ITD configuration (i.e., the ITD of the target at low frequencies matched that of the masker at high frequencies and vice versa). When the target and masker have their ITDs in the high-frequency and low-frequency regions swapped, it should not be possible to integrate information across frequency at a common ITD without recovering a mixture of target and masker. No amount of attention switching in this condition will remove the presence of the masker. Furthermore, it should be impossible to selectively cancel out the masker across frequency in the swapped condition, as any target speech with the same ITD as the masker will also be canceled. Consequently, if the auditory system is restricted to the exploitation of a common ITD across frequency, then speech intelligibility should suffer in the swapped ITD configuration (i.e., SRTs for the swapped ITD configuration should be markedly higher than those measured for the consistent ITD configuration). However, if the SRTs measured under consistent and swapped conditions are indistinguishable, then a strategy for exploiting within-channel differences in ITD independent of frequency will be supported.

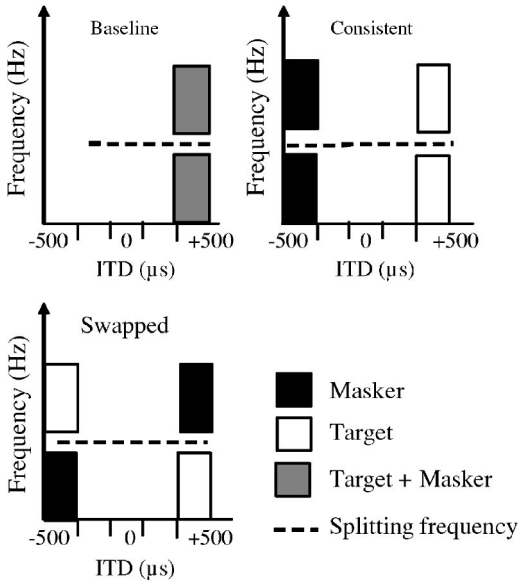

FIG. 5. A schematic illustration of the ITD configurations of experiment 3. Stimuli are represented in high- and low-pass bands presented at distinct ITDs. Target speech bands are depicted in white with black outline, masker bands are depicted in black, and regions that have both target and masker sharing a common ITD are shown in gray. The splitting frequency used to divide the high- and low-pass bands (750, 1500, and 3000 Hz) is shown as a dotted line.

A. Design

In experiment 3, both the target speech and the masker were presented as a pair of high- and low-pass bands separated by splitting frequencies of 750, 1500, or 3000 Hz. SRTs were measured for three configurations (see Fig. 5) of target and masker ITDs: baseline (both target and masker were presented with a $+500$-μs ITD), consistent (the target speech was presented with a $+500$-μs ITD while the masker was presented with a -500-μs ITD), and swapped (the high-frequency target speech band and the low-frequency masker band were presented with a -500-μs ITD while the low-frequency target speech band and the high-frequency masker band were presented with a $+500$-μs ITD). Two new groups of nine listeners took part in this study. SRTs were measured for target speech presented against a Brown-noise masker in experiment 3a and against competing speech in experiment 3b.

B. Results and discussion

Figure 6 shows the mean SRTs for the two groups of listeners in experiment 3. Intelligibility was poorest for the baseline condition, but improved in the consistent and swapped conditions, giving a BILDs of approximately 4 dB for the Brown-noise masker (dashed lines) and competing-speech masker (solid lines) groups. Again, thresholds were lower and more variable (i.e., larger error bars) against competing speech than against Brown noise

A two-way repeated-measures ANOVA was performed on the SRTs of experiment 3a and showed a significant main effect of ITD [$F(2,8)=60.57$, $p<0.001$] and of splitting frequency [$F(2,8)=6.35$, $p<0.05$]. Tukey pairwise tests showed that the following comparisons were not signifi-

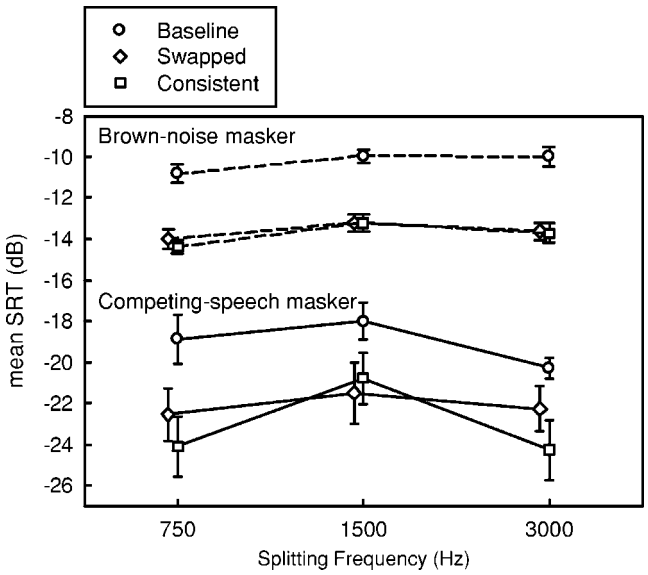

FIG. 6. Mean SRTs of the baseline (circles), swapped (diamonds), and consistent (squares) ITD configurations of experiment 3 for two groups of listeners (Brown-noise masker, dashed lines; competing-speech masker, solid lines). Error bars show standard error. Plots for the swapped condition SRTs are offset along the *x* axis in order to improve visibility of the error bars.

cantly different: swapped vs consistent, 1500 vs 3000 Hz, and 3000 vs 750 Hz. However, significant differences were found for all other comparisons: baseline vs consistent ($q=13.80$, $p<0.001$), baseline vs swapped ($q=13.14$, $p<0.001$), and 750 vs 1500 Hz ($q=4.95$, $p<0.05$).

Statistical analyses (two-way repeated measures ANOVA) of experiment 3b indicated that there was no effect of splitting frequency. However, ITD configuration yielded a significant effect [$F(2,8)=7.35$, $p<0.05$]. Tukey HSD comparisons showed that the SRTs of the swapped and consistent conditions were not significantly different, but differences were found for baseline vs consistent ($q=5.19$, $p<0.05$) and baseline vs swapped ($q=3.96$, $p<0.05$).

Experiment 3 was designed to test whether listeners simply make use of the best ITD within each frequency channel to segregate a target sentence from its masker or whether they use some strategy that is dependent on the lateralization of sounds (i.e., requiring a common ITD across all frequency channels). The swapped condition was crucial to this test as participants were presented with the target and masker at each ITD. The viability of two strategies for exploiting a common ITD for the segregation of concurrent sounds was evaluated and found lacking. Neither attention switching nor cancellation by common ITD provides a suitable explanation of the data. If participants had employed either of these strategies then the SRTs measured for the swapped condition would have been much higher than those measured in the consistent condition. However, SRTs were found to be equivalent in consistent and swapped conditions, suggesting that listeners make use of differences in ITD between target and masker within each frequency channel independently rather than by selectively grouping or canceling information at one ITD across all frequency channels.

VI. GENERAL DISCUSSION

In this paper we explored the binaural gain in speech intelligibility arising from differences in ITD between target speech and a single concurrent masker. Three experiments were conducted to test whether the segregation of spatially separated sounds is dependent on the consistency of ITD across different frequency bands; in particular, whether or not the binaural gain in speech intelligibility was constrained to the exploitation of a single ITD across frequency. Participants were presented with high- and low-frequency regions of target speech and a masker of either Brown noise or competing speech under a number of binaural configurations. It was found that as long as the target and masker had a different ITD in each frequency channel, the size of the BILD was unaffected.

A. Within-channel processing of ITD

The primary aim of this investigation was to determine how ITD is exploited by the binaural system in order to segregate target speech from a concurrent masker. This issue was addressed in experiments 2 and 3. These experiments were designed to test which of a number of strategies for segregating spatially separated sounds best described the SRTs measured for high- and low-frequency regions of target speech presented in a number of binaural configurations. In particular, we were interested in determining (i) whether the segregation of target speech from a concurrent but spatially separated masker was dependent on the exploitation of a common ITD for selecting or canceling sound elements across frequency, or (ii) whether the auditory system was free to choose the best ITD within each frequency channel in order to improve the audibility of the target.

In experiment 2, the target speech was split into high- and low-frequency regions each with a different ITD. It established that binaural advantage could be achieved even when the high- and low-frequency regions of the target speech were given ITDs of equal but opposite magnitude. This suggests that the auditory system is not constrained to select information at a particular ITD across frequency, as doing so would have resulted in a BILD based on the contribution of only the high frequencies or only the low frequencies. We suggested that the most likely interpretation was that listeners were able to exploit the difference in ITD between the target and masker for both the high frequencies and the low frequencies simultaneously. However, at least two other alternatives exist.

First, it is possible for the BILDs of experiment 2 to be explained by the exploitation of a common ITD in order to cancel the masker rather than select the target. The recovery of target speech from a concurrent masker is often implemented in computational models of spatial unmasking by subtracting the masking sound from the compound waveform (e.g., Durlach's E-C model and beamforming techniques for automatic speech recognition). A similar procedure has been proposed to describe the existence of the pitch percept(s) that listeners experience when presented with dichotically delayed noises (Bilsen and Goldstein, 1974).

Second, this experiment did not rule out the possibility that listeners might be able to switch the focus of their atten-

tion from one moment to the next (i.e., in order to piece together the contributions of the high- and low-frequency bands of target speech over time). Peissig and Kollmeier (1997) discussed the possibility of an attention-switching strategy as a mechanism for improving speech intelligibility against multiple masking sounds. However, rather than suggesting that this mechanism selects target speech, they suggested that the binaural system employs this strategy for canceling multiple maskers. Because the waveform of speech is modulated, when multiple voices are presented concurrently there will be, at any time, instantaneous differences between these envelopes that produce differences in the signal-to-noise ratio. They suggested that the auditory system is able to exploit these spectro-temporal gaps in order to cancel the most intense competing voice at a given point in time. By doing so, this process is able to produce gains in the intelligibility of the target speech presented in a stimulus containing multiple speech sources arriving from different directions. However, Hawley *et al.* (2004) recently cast doubt upon the effectiveness of this attention-switching strategy by investigating the effects of speech-spectrum-shaped noises modulated by the temporal envelope of the target on the BILD. Such maskers provided listeners with the same opportunities for exploiting spectro-temporal gaps as a competing-speech masker. If attention switching is a viable strategy for canceling the masker(s) in such a situation, then one might expect the intelligibility of target speech heard against each type of masker to be comparable, but this was not the case. SRTs indicated that listeners received greater benefit from spatial separation when either speech or reversed-speech maskers were used rather than speech-shaped or speech-modulated noise maskers.

Experiment 3 was designed to address the three questions left open in experiment 2. First, whether a common ITD is used to cancel the masker across frequency. Second, whether listeners can exploit different ITDs at different moments in time (i.e., attention switching). Third, whether the auditory system is free to exploit the best ITD within each frequency channel. In order to test for the importance of these strategies to the BILD, we devised a condition (i.e., swapped ITD) in which support for either of the first two strategies would result in a detriment in speech intelligibility, while if the BILD was unaffected by such a binaural configuration this would provide support for the third proposition (i.e., a within-channel mechanism). As the SRT for this swapped-ITD condition was indistinguishable from that of the consistent condition, we suggest that the auditory system is free to choose the best ITD within each frequency channel in order to maximize the audibility of target speech against a concurrent masker. Consequently, this result appears to support Culling and Summerfield's (1995) mE-C model. At the same time, this experiment also supports the dissociation between perceived location and the effects of spatial separation on speech intelligibility (e.g., Licklider, 1948; Carhart *et al.*, 1967, 1968; 1969). Previously, the relationship between perceived location and spatial unmasking was confounded by the fact that, while one of the sounds was diffusely located, the other was clearly localized. That being the case, one might argue that full binaural advantage can be achieved under such conditions by either selecting a clearly localized target or by canceling a clearly localized masker (i.e., the perceived location of the other sound is largely irrelevant). Experiment 3, on the other hand, provided a control for the dissociation of perceived location and spatial unmasking. By ensuring that different portions of target speech and masker were presented with the same ITD, it was not possible to extract information residing at one ITD (i.e., at one spatial location) across frequency in order to either select the target or cancel the masking sound.

B. Informational masking

A number of studies have attempted to distinguish the effects of different types of sounds as maskers. In particular, a distinction has been made between energetic maskers and informational maskers (Pollack, 1975; Watson *et al.*, 1976) depending on which stage in the segregation process the interference takes place (Kidd *et al.*, 1994). Interference at peripheral stages of processing is described as energetic masking (i.e., the target and masker both contain energy at the same critical bands). On the other hand, informational maskers cause interference at some higher level of processing (i.e., uncertainty at the decision stage prevents the target and masker from being perceptually segregated). Consequently, it has been suggested that informational masking can produce an excess of masking (i.e., in addition to any energetic masking caused by the interfering sound). Furthermore, it has been suggested that the spatial separation or apparent spatial separation of two sounds can provide a release from informational masking (Freyman *et al.*, 1999; Brungart, 2001; Brungart *et al.*, 2001; Freyman *et al.*, 2001, 2004).

It is possible to consider both competing speech and Brown noise as energetic maskers. Competing speech can also be considered to be an informational masker, as it might produce interference at a number of levels other than at the peripheral level (e.g., semantically, syntactically, or similarity of pitch). Given that all three of the experiments reported in this paper were conducted against both a Brown-noise masker and competing speech, one might expect to see some evidence for informational masking or release from informational masking in the SRTs that we measured. In particular, one might expect some additional improvements in speech intelligibility against the competing-speech masker due to spatial separation that are not evident in the thresholds measured for target speech presented against Brown noise. However, while these experiments certainly demonstrate a difference in the amount of masking produced by Brown noise and competing speech, it is difficult to describe this effect in terms of informational masking for two reasons.

First, the SRTs measured against competing speech were consistently lower (in the region of 12 dB) than those measured for target speech heard against the Brown-noise masker. Furthermore, the difference between competing-speech and Brown-noise interference was probably underestimated here because Brown noise has much of its energy at very low frequencies which might have limited the degree to which it masked the target speech. This effect likely reflects the difference in energetic masking afforded by each of the

maskers. Brown noise is a purely energetic masker, while the competing-speech materials contained natural pauses and spectro-temporal gaps which might have reduced the amount of energetic masking produced. Whether or not this effect also reflects any informational masking is difficult to determine. What remains clear, however, is that the competing-speech maskers were less effective than a purely energetic Brown noise.

Second, there was no masker-dependent additional release from masking due to the perceived spatial separation of the target speech from the masking sound. While there was greater variance in SRTs measured against the competing-speech masker than against the Brown-noise masker, the BILDs for the corresponding conditions do not provide any direct evidence for informational masking. The difference between consistent and baseline condition SRTs was roughly the same for both speech and noise maskers. However, it is possible that the effects of informational masking on speech intelligibility in these experiments were confounded by other factors that also contribute to the SRT (e.g., pitch differences between the two voices) and no doubt warrant further investigation in order to control for these effects. Nonetheless, it is difficult to conclude that there is any evidence of informational masking or release from informational masking due to spatial separation from these data.

C. Conclusion

While the exploitation of a common ITD might be necessary for sound localization/lateralization (Stern *et al.*, 1988; Shackleton *et al.*, 1992), the results of the experiments described in this paper suggest that this is not the case for binaural unmasking. Here, we have demonstrated that the masked threshold of speech cannot be explained by selecting or canceling information at a common ITD across frequency. Rather, the process responsible for binaural unmasking appears to exploit ITD independently within each frequency channel. Consequently, this result supports previous accounts of the BILD that suggest binaural unmasking is indifferent to the perceived direction of sounds (Carhart *et al.*, 1968; Edmonds and Culling, in press).

ACKNOWLEDGMENT

Work supported by the UK EPSRC (Grants GR/M96155 and GR/S11794).

[1]If the target and masking sounds have different ILDs equalization can also be achieved by applying an internal level adjustment.

Akeroyd, M. A. (**2004**). ''The across frequency independence of equalization of interaural time delay in the equalization-cancellation model of binaural unmasking,'' J. Acoust. Soc. Am. **116**, 1135–1148.

Bilsen, F. A., and Goldstein, J. L. (**1974**). ''Pitch of dichotically delayed noise and its possible spectral basis,'' J. Acoust. Soc. Am. **55**, 292–296.

Blauert, J. (**1983**). *Spatial Hearing—The Psychophysics of Human Sound Source Localization* (MIT Press, Cambridge).

Breebaart, J., van de Par, S., and Kohlrausch, A. (**2001**). ''Binaural processing model based on contralateral inhibition. I. Model structure,'' J. Acoust. Soc. Am. **110**, 1074–1088.

Bregman, A. (**1990**). *Auditory Scene Analysis: The Perceptual Organization of Sound* (MIT Press, Cambridge).

Broadbent, D. E. (**1954**). ''The role of auditory localization in attention and memory span,'' J. Exp. Psychol. **47**, 191–196.

Bronkhorst, A. W., and Plomp, R. (**1988**). ''The effect of head-induced interaural time and level differences on speech intelligibility in noise,'' J. Acoust. Soc. Am. **83**, 1508–1516.

Brungart, D. S. (**2001**). ''Informational and energetic masking effects in the perception of two simultaneous talkers,'' J. Acoust. Soc. Am. **109**, 1101–1109.

Brungart, D. S., Simpson, B. D., Ericson, M. A., and Scott, K. R. (**2001**). ''Informational and energetic masking effects in the perception of multiple simultaneous talkers,'' J. Acoust. Soc. Am. **110**, 2527–2538.

Carhart, R., Tillman, T. W., and Greetis, E. S. (**1969**). ''Release from multiple maskers: Effects of interaural time disparities,'' J. Acoust. Soc. Am. **45**, 411–418.

Carhart, R., Tillman, T. W., and Johnson, K. R. (**1967**). ''Release of masking for speech through interaural time delay,'' J. Acoust. Soc. Am. **42**, 124–138.

Carhart, R., Tillman, T. W., and Johnson, K. R. (**1968**). ''Effects of interaural time delays on masking by two competing signals,'' J. Acoust. Soc. Am. **43**, 1223–1230.

Colburn, H. S., and Durlach, N. I. (**1978**). ''Models of binaural interaction,'' in *Handbook of Perception*, edited by E. C. Carterette and M. P. Friedman (Academic, New York), pp. 467–518.

Culling, J. F. (**1998**). ''Dichotic pitches as illusions of binaural unmasking. II. The Fourcin pitch and the dichotic repetition pitch,'' J. Acoust. Soc. Am. **103**, 3527–3539.

Culling, J. F., and Summerfield, Q. (**1995**). ''Perceptual separation of concurrent speech sounds: Absence of across-frequency grouping by common interaural delay,'' J. Acoust. Soc. Am. **98**, 785–797.

Culling, J. F., Summerfield, A. Q., and Marshall, D. H. (**1998**). ''Dichotic pitches as illusions of binaural unmasking: I. Huggins' pitch and the 'binaural edge pitch,''' J. Acoust. Soc. Am. **103**, 3509–3526.

Darwin, C. J., and Hukin, R. W. (**1999**). ''Auditory objects of attention: The role of interaural time differences,'' J. Exp. Psychol. Hum. Percept. Perform. **25**, 617–629.

Darwin, C. J., and Hukin, R. W. (**2000**). ''Effectiveness of spatial cues, prosody, and talker characteristics in selective attention,'' J. Acoust. Soc. Am. **107**, 970–977.

Drennan, W. R., Gatehouse, S., and Lever, C. (**2003**). ''Perceptual segregation of competing speech sounds: The role of spatial location,'' J. Acoust. Soc. Am. **114**, 2178–2189.

Durlach, N. I. (**1960**). ''Note on the equalization and cancellation theory of binaural masking level differences,'' J. Acoust. Soc. Am. **32**, 1075–1076.

Durlach, N. I. (**1963**). ''Equalization and cancellation model of binaural masking-level differences,'' J. Acoust. Soc. Am. **35**, 1206–1218.

Durlach, N. I. (**1972**). ''Binaural signal detection: Equalization and cancellation theory,'' in *Foundations of Modern Auditory Theory*, edited by J. V. Tobias (Academic, New York), pp. 369–462.

Edmonds, B. A., and Culling, J. F. (**in press**). ''The role of head-related time and level cues in the unmasking of speech in noise and competing speech,'' Acta Acust. Acust.: special issue on spatial and binaural hearing.

Freyman, R. L., Balakrishnan, U., and Helfer, K. S. (**2001**). ''Spatial release from informational masking in speech recognition,'' J. Acoust. Soc. Am. **109**, 2112–2122.

Freyman, R. L., Balakrishnan, U., and Helfer, K. S. (**2004**). ''Effect of number of masking talkers and auditory priming on informational masking in speech recognition,'' J. Acoust. Soc. Am. **115**, 2246–2256.

Freyman, R. L., Helfer, K. S., McCall, D. D., and Clifton, R. K. (**1999**). ''The role of perceived spatial separation in the unmasking of speech,'' J. Acoust. Soc. Am. **106**, 3578–3588.

Hafter, E. R., Bourbon, W. T., Blocker, A. S., and Tucker, A. (**1969**). ''A direct comparison between lateralization and detection under conditions of antiphasic masking,'' J. Acoust. Soc. Am. **46**, 1452–1457.

Hawley, M. L., Litovsky, R. Y., and Culling, J. F. (**2004**). ''The benefit of binaural hearing in a cocktail party: Effect of location and type of interferer,'' J. Acoust. Soc. Am. **115**, 833–843.

Hirsh, I. J. (**1948**). ''The influence of interaural phase on interaural summation and inhibition,'' J. Acoust. Soc. Am. **20**, 536–544.

Hirsh, I. J. (**1950**). ''The relation between localization and intelligibility,'' J. Acoust. Soc. Am. **22**, 196–200.

Hukin, R. W., and Darwin, C. J. (**1995**). ''Effects of contralateral presentation and of interaural time differences in segregating a harmonic from a vowel,'' J. Acoust. Soc. Am. **98**, 1380–1387.

IEEE (**1969**). ''IEEE recommended practice for speech quality measurements,'' IEEE Trans. Audio Electroacoust. **17**, 225–246.
Jeffress, L. A. (**1972**). ''Binaural signal detection: Vector theory,'' in *Foundations of Modern Auditory Theory*, edited by J. V. Tobias (Academic, New York).
Kidd, G. J., Mason, C. R., Deliwala, P. S., and Woods, W. S. (**1994**). ''Reducing informational masking by sound segregation,'' J. Acoust. Soc. Am. **95**, 3475–3480.
Kubovy, M., and Van Valkenburg, D. (**2001**). ''Auditory and visual objects,'' Cognition **80**, 97–126.
Levitt, H., and Rabiner, L. R. (**1967a**). ''Binaural release from masking for speech and gain in intelligibility,'' J. Acoust. Soc. Am. **42**, 601–608.
Levitt, H., and Rabiner, L. R. (**1967b**). ''Predicting binaural gain in intelligibility and release from masking for speech,'' J. Acoust. Soc. Am. **42**, 820–829.
Licklider, J. C. R. (**1948**). ''The influence of interaural phase relations upon the masking of speech by white noise,'' J. Acoust. Soc. Am. **20**, 150–159.
Moore, B. C., and Glasberg, B. R. (**1983**). ''Suggested formulae for calculating auditory-filter bandwidths and excitatory patterns,'' J. Acoust. Soc. Am. **74**, 750–753.
Neuhoff, J. G. (**2003**). ''Pitch variation is unnecessary (and sometimes insufficient) for the formation of auditory objects,'' Cognition **87**, 219–224.
Peissig, J., and Kollmeier, B. (**1997**). ''Directivity of binaural noise reduction in spatial multiple noise-source arrangements for normal and impaired listeners,'' J. Acoust. Soc. Am. **101**, 1660–1670.
Plomp, R., and Mimpen, A. M. (**1979**). ''Improving the reliability of testing the speech-reception threshold for sentences,'' Audiology **18**, 43–52.
Pollack, I. (**1975**). ''Auditory informational masking,'' J. Acoust. Soc. Am. **57**, S5.
Rayleigh, L. (**1876**). ''On perception of the direction of a source of sound,'' Nature (London) **14**, 32–33.
Rayleigh, L. (**1907**). ''On our perception of sound direction,'' Philos. Mag. **8**, 214–232.
Schubert, E. D. (**1956**). ''Some preliminary experiments on binaural time delay and intelligibility,'' J. Acoust. Soc. Am. **28**, 895–901.
Schubert, E. D., and Schultz, M. C. (**1962**). ''Some aspects of binaural signal selection,'' J. Acoust. Soc. Am. **34**, 844–849.
Shackleton, T. M., Meddis, R., and Hewitt, M. J. (**1992**). ''Across-frequency integration in a model of lateralization,'' J. Acoust. Soc. Am. **91**, 2276–2279.
Stern, M. R., Zeiberg, A. S., and Trahiotis, C. (**1988**). ''Lateralization of complex binaural stimuli: A weighted image model,'' J. Acoust. Soc. Am. **84**, 156–165.
Watson, C. S., Kelly, W. J., and Wroton, H. W. (**1976**). ''Factors in the discrimination of tonal patterns. II. Selective attention and learning under various levels of uncertainty,'' J. Acoust. Soc. Am. **60**, 1176–1186.
Zurek, P. M. (**1992**). ''Binaural advantages and directional effects in speech intelligibility,'' in *Acoustical Factors Affecting Hearing Aid Performance*, edited by G. A. Studebaker and I. Hochberg (Allyn and Bacon, Boston), pp. 255–276.

Observer weighting strategies in interaural time-difference discrimination and monaural level discrimination for a multi-tone complex

Raymond H. Dye, Jr.
Parmly Hearing Institute, Loyola University of Chicago, Chicago, Illinois 60626

Mark A. Stellmack
Department of Psychology, University of Minnesota, Minneapolis, Minnesota 55455

Noah F. Jurcin
Parmly Hearing Institute, Loyola University of Chicago, Chicago, Illinois 60626

(Received 1 October 2003; revised 30 December 2004; accepted 5 January 2005)

Two experiments measured listeners' abilities to weight information from different components in a complex of 553, 753, and 953 Hz. The goal was to determine whether or not the ability to adjust perceptual weights generalized across tasks. Weights were measured by binary logistic regression between stimulus values that were sampled from Gaussian distributions and listeners' responses. The first task was interaural time discrimination in which listeners judged the laterality of the target component. The second task was monaural level discrimination in which listeners indicated whether the level of the target component decreased or increased across two intervals. For both experiments, each of the three components served as the target. Ten listeners participated in both experiments. The results showed that those individuals who adjusted perceptual weights in the interaural time experiment could also do so in the monaural level discrimination task. The fact that the same individuals appeared to be analytic in both tasks is an indication that the weights measure the ability to attend to a particular region of the spectrum while ignoring other spectral regions. [DOI: 10.1121/1.1861832]

PACS numbers: 43.66.Pn, 43.66.Mk [AK] Pages: 3079–3090

I. INTRODUCTION

In real-world listening situations in which multiple frequency components are present, a listener might wish to combine information across frequency or to attend to a particular frequency component while ignoring others. When a listener combines information across a number of frequencies, the listener is said to be processing the spectrum synthetically. When, on the other hand, the listener selectively utilizes information at one frequency component while effectively ignoring other components, the listener is said to be listening analytically. This distinction between analytic and synthetic listening dates back to Helmholtz (1859), and has been revived in the writings of Bregman (1990).

The extent to which a listener processes a stimulus synthetically or analytically can be described by a weighting function which estimates the relative weight given to individual stimulus elements in a given listening task. Several procedures for measuring weighting functions have been described in the literature (Berg, 1989; Richards and Zhu, 1994; Dye *et al.*, 1994; Lutfi, 1995). Although the specifics of the various procedures differ, computation of the relative weights is generally based on the extent to which the listener's trial-by-trial responses are related to trial-by-trial variation in the parameter values of the individual stimulus elements.

The issue addressed in the current paper is whether one's ability to be analytic in one auditory task generalizes to other auditory tasks. The two tasks we have used are monaural level discrimination and binaural interaural time discrimination, since considerable individual differences have been reported in the tendency to process these two cues either synthetically or analytically. The principle question is whether listeners who tend to be analytic in one task are also analytic in the other. Are some listeners simply better at focusing attention on the target frequencies while ignoring the distracting ones? A secondary question concerns the manner in which relative weights are distributed across the frequency domain. For cases in which analytic listening is impossible, do the same components tend to be weighted heavily for the two tasks? To address these two questions, it was important that the frequency range be the same for the two tasks. First, the manner in which individuals weigh monaural level differences and then interaural time differences will be reviewed.

Stellmack *et al.* (1997) presented three components to adults and preschool children under conditions in which listeners were instructed to attend to either the 250-, 1000-, or 4000-Hz component (in separate blocks of trials) while ignoring the other two. The ''correct'' interval was defined as the one in which the target component had the higher level and listeners were instructed to choose the interval in which the target component was ''louder.'' In these conditions, the listener could maximize percent correct by basing responses solely on the level change across intervals of the target component while ignoring the other (distractor) components. It was found that adults generally were able to alter their weighting strategy appropriately depending upon which

component was defined as the target while the children tended to apply the same synthetic weighting strategy regardless of which component was the target. There were substantial individual differences, though, and some adult listeners also failed to alter their weighting strategy appropriately as the target component changed.

In a companion paper, Willihnganz *et al.* (1997) estimated the weighting functions of adult and preschool listeners in a level-discrimination task in which listeners were required to listen synthetically in order to achieve optimal performance. Stimuli consisted of the same three components as before (250, 1000, and 4000 Hz). The levels of each component for each interval were chosen randomly and independently from a Gaussian distribution with a mean of 62 dB SPL and a standard deviation of 1–9 dB. The standard deviation was chosen individually for each listener such that 70%–80% correct performance was achieved. Listeners were instructed to choose the ''louder'' interval, which was defined as the interval containing the larger mean level in dB SPL. Thus, in order to maximize percent correct, the optimal strategy would be to weight level information equally in all three stimulus components. In general, weighting functions differed across all preschool and adult listeners with few listeners displaying the optimal weighting strategy.

In a similar study, Doherty and Lutfi (1999) found that in a level-discrimination task both normal-hearing and hearing-impaired adult listeners varied their weighting strategies and generally gave greatest weight to the cued target component in a six-component complex (consecutive octave frequencies from 250 to 8000 Hz). There were, however, large individual differences in the ability to give the target the greatest weight, particularly when it was an intermediate (as opposed to an edge) frequency. In a companion paper in which synthetic listening was required on the part of listeners, Doherty and Lutfi (1996) found that normal listeners gave slightly more weight to the lower and higher frequencies of the same six-octave complex, deemphasizing intermediate frequencies. The data showed that hearing-impaired listeners consistently allotted the greatest weight to the frequencies falling on the sloping region of their hearing loss.

Kortekaas *et al.* (2003) asked listeners to detect a level increment in a multi-component complex consisting of 3, 7, 15, or 24 components. The complexes in their study had a spacing of one bark (critical band) unit, and were centered at 1600 Hz. In one experimental task, all components were incremented by an equal amount (in dB) in the signal interval. An additional random jitter was imposed on the overall level of each component in order to permit the computation of the relative weight given to each component. In this synthetic listening task, listeners could maximize percent correct by weighting all components equally. While nearly equal weight was given to all components, there was a general tendency to give slightly greater weight to the highest-two-to-four frequency components. The authors posited that the highest frequencies received more weight because of a tendency for higher frequencies to suppress lower frequency components (e.g., Moore and Glasberg, 1982). In a second task, the amount by which each component was incremented in level was varied such that the magnitude of the increment increased with increasing frequency. As a result, higher frequency components provided more information to allow listeners to perform the task. Listeners could maximize percent correct by giving weight to the level information in all components but the optimal weighting strategy is one in which the weight increases with increasing frequency. Generally, it was found that listeners did not vary the weight given to individual components when it was advantageous to do so. It should be noted that listeners were not informed of the variation in increment across frequencies and that it would be beneficial to base their responses more heavily on the higher-frequency components.

In a design similar to that described above for monaural level discrimination, Stellmack and Lutfi (1996) examined the weighting strategies adopted by listeners in an analytic binaural listening task. On each trial, listeners were presented with a cue tone followed by a single listening interval that contained a three-component complex (553, 753, and 953 Hz). The cue tone consisted of a diotic presentation of one of the three components in the complex. In the listening interval, a nonzero interaural difference of time (IDT) was chosen randomly and independently for each component from a discrete, rectangular distribution with a mean of zero. IDTs were ongoing delays, since the waveforms at the two ears were gated simultaneously. Listeners were instructed to attend to the cued component and to indicate whether the intracranial image associated with that component in the listening interval appeared to be to the left or right of the midline. In order to maximize percent correct, listeners had to give maximum weight to the target component and no weight to the distractor components. The data showed that the weighting strategy of only one of the six listeners (the first author of that paper) varied across conditions such that whichever component was defined as the target was given greatest weight. The remaining listeners generally gave equal weight to all three components or slightly greater weight to the highest frequency component regardless of which was cued as the target. It appeared that it was possible for listeners to vary their weighting strategy as the demands of the task dictated, but it was more difficult for less experienced listeners to do so.

Dye *et al.* (1996) ran conditions with two-component complexes in which either the target or the distractor was fixed at 753 Hz while the other component varied from 353 to 1153 Hz. The task was identical to the one used by Stellmack and Lutfi (1996). Only two of the eight listeners gave appropriate weight to the target when the target and distractor were spectrally remote, while the two frequencies were weighted about equally when the target and distractor were within 50 Hz of one another. The other six listeners consistently gave more weight to the higher of the two frequencies regardless of which was designated as the target. Weights were derived from the slope of the best linear boundary between left and right responses. One possible explanation for the high-frequency dominance that one observes for judgments based on IDT is that they are determined by wide band composite cross-correlation of the summed two- or three-component waveforms (Sayers and Cherry, 1957; Shackleton

et al. 1992; Dye *et al.* 1996). The cross-correlation function of a periodic waveform is given by

$$\sum_{i=1}^{N} C_{Li}C_{Ri}\cos(2\pi f_i\tau+\delta_{Li}-\delta_R i), \quad (1)$$

where N is the number of components, C_{Li} and C_{Ri} are the rms values of the ith component at the left and right ears, respectively, and $\delta_{\mathrm{Li}}-\delta_{\mathrm{Ri}}$ is the interaural phase difference of the ith component (Lee, 1960). This function is periodic at the inverse of the greatest common divisor of the component frequencies, which is a full second for the studies of Dye *et al.* and Stellmack and Lutfi (since inharmonic complexes were used). The location of the peak in the composite cross-correlation function is more strongly influenced by the higher of the frequencies contained in the signal.

Interestingly, there is evidence from an analogous experiment that employed interaural differences of level (Dye, 1997) for low-frequency dominance. In this study, the target component was always presented at 753 Hz while the distractor was varied from 253 to 2753 Hz. Of the four listeners, two appeared ''analytic'' as long as the two components were at least 50 Hz apart. The other two always gave more weight to the lower frequency as long as the two components were within 400–500 Hz of one another (regardless of which was designated as the target). For wider separations, equal weight was given to the two components (753 and 2753 Hz in the extreme case). These last two listeners were characterized as spectrally synthetic. This pattern of low-frequency dominance is consistent with the upward spread of activation, and suggests that high-frequency dominance is not a general property of binaural processing.

While the adult listeners in the monaural listening tasks of Stellmack *et al.* (1997) were much more likely to vary their weighting strategy appropriately than the listeners in the binaural task of Stellmack and Lutfi (1996), it is possible that the difference in the frequency spacing of the components in the two experiments was a crucial factor. The components in the binaural task were much more closely spaced in frequency, which may have made it more difficult for listeners to perceptually segregate the target component from the distractors. It is possible that the same degree of interference would be seen in the monaural level discrimination task if the components had the same frequency spacing.

The goal of the present paper is to assess the weighting strategies used by listeners in two different listening tasks that utilize the same three frequency components. In one task, listeners performed a replication of the three-component, analytic IDT-discrimination task of Stellmack and Lutfi (1996) that was described above. In a separate set of conditions, listeners performed an analytic, monaural intensity-discrimination task similar to that of Stellmack *et al.* (1997). In both cases, the components were 553, 753, and 953 Hz. In separate blocks of trials, listeners were cued to one of the three components as the target. In order to maximize percent correct, it was necessary for listeners to vary their weighting strategy accordingly. Additional synthetic listening tasks were run in the binaural and monaural conditions in which correct responses were based on the mean value across components of the parameter of interest (either IDT or monaural level). In these conditions, listeners could maximize percent correct by weighting all three components equally. The monaural and binaural listening tasks in and of themselves presumably depend upon very different auditory mechanisms and, as such, there is no *a priori* reason to assume that the weighting strategies will be similar across the two tasks. This experiment addresses the question of whether the weighting strategy utilized by a listener is specific to a particular type of listening task or whether it reflects a listener's general ability to listen synthetically or analytically as necessary across a variety of listening tasks. As in previous studies, it was found that only a small subset of the listeners were able to vary their weighting strategy appropriately for the different listening tasks. In general, those who did so for the binaural task were most likely to do so for the monaural task as well.

II. METHODS

A. Procedure

Each trial consisted of the presentation of a cue followed by the presentation of three-tone signals to be judged. For the interaural time discrimination task, the cue was contained during the first interval and consisted of a diotic presentation of the target frequency to mark the intracranial midline and to cue the listener to the pitch of the target. For the level discrimination task, the first two intervals contained cues. The first interval provided a monaural (left ear) presentation of the target frequency to cue the listener to the pitch of the target. The second cue interval presented the three components to the left ear such that all three components had a level of 57 dB SPL. This interval served to indicate to the listener the reference level of the target component, in the context of two other components. Listeners found it impossible to judge the level of a single frequency with the same component presented as part of a three-tone complex, thus necessitating this second cue interval.

For the interaural time discrimination task, the second interval presented the to-be-judged stimulus. It consisted of a three-tone complex consisting of 553, 753, and 953 Hz, with the level of each component at 57 dB SPL. On each trial, the interaural differences of time (IDTs) of the three components were independently selected from a Gaussian distribution having a mean of 0 μs and a standard deviation of 50 μs. The interaural delays were ongoing delays, since the waveforms at the two ears were gated simultaneously. Participants were instructed to indicate by pressing one of two keys on a keyboard the laterality (left versus right) of the *target component* compared to the intracranial midline as marked by the cue tone presented during the first interval. Listeners were told to ignore the two distractor components. Visual feedback that indicated whether the target frequency led to the left channel or to the right channel was presented on a monitor after each trial.

For the monaural level discrimination task, the third interval presented the to-be-judged stimulus. It consisted of three-tone complexes of 553, 753, and 953 Hz presented to the left ear, with the level of each of the three components chosen from a Gaussian distribution with a mean of 57 dB

and a standard deviation of 3 dB. The task for the listener was to attend to the target frequency, indicating whether its level in interval 2 or 3 was greater by pressing one of two keys on a keyboard. They were told to ignore the two distractor components. Visual feedback that indicated whether the target frequency had been increased or decreased during the third interval was presented on a monitor after each trial.

For both tasks, separate conditions were run in which the target was 553, 753, or 953 Hz, with the other two frequencies serving as distractors. All stimulus intervals that comprised a trial were 200 ms in duration and were separated by 350 ms. The starting phases of the three components were randomized during the two intervals. During the to-be-judged interval, the target and distractors were gated simultaneously with 10-ms $\cos^2$ gating functions. All stimulus differences were limited to within ± 2.5 standard deviations of 0.0 (± 125 μs for interaural time discrimination and ± 7.5 dB for monaural level discrimination). Data were gathered in blocks of 100 trials. Before each block of trials, subjects were allowed to listen to practice trials, which were identical to those presented during the experimental session (with target and distractor values varying from trial to trial). When ready, the listeners initiated a block of test trials. During the interaural time discrimination trials, listeners were instructed to adjust the position of the headphones during practice trials so that the diotic cue tone sounded intracranially centered. Fifteen hundred trials were run for each of the three different target frequencies. Which component served as the target was fixed until all 1500 judgments were obtained for that condition. All data from the interaural time task were collected prior to the initiation of monaural level discrimination. The order that the three different conditions were run was randomly determined for each listener. Data were collected in sessions that lasted approximately 1.25 h, during which each listener made 600–800 target judgments.

As a last condition for the interaural time discrimination task, listeners were given a set of 1500 trials during which they were to respond according to the ''composite'' lateral position, with feedback based upon the interaural difference of time averaged across frequency. Similarly, listeners were given a set of 1500 judgments of ''composite'' level, with feedback consistent with the average level (in dB) of the three components at the end of the monaural level discrimination experiment.

B. Stimulus generation and presentation

Signals were generated digitally on IBM-compatible PCs interfaced to Tucker Davis Technologies (TDT) systems. The digital signals were converted to analog waveforms at a rate of 20 kHz per channel by 16-bit digital-to-analog converters (TDT DD1). The signals were low-pass filtered by matched pairs of programmable filters (TDT PF1) set to 7.5 kHz for signal reconstruction. The final levels of the signals were adjusted with attenuators (TDT PA4) before being led to stereo headphone buffers (TDT HB6), which were used to drive Sennheiser 520 headphones. For the monaural level task, signals were presented to the left earphone only. Listeners were seated in a sound-attenuating chamber.

C. Participants and training

Three of the listeners were the authors of this paper: S1–S3. Eight were undergraduates at Loyola University Chicago who were paid an hourly wage for their participation (S3–S10). Seven (S1–S5, S8, and S10) had participated in other lateralization experiments, while the other three (S6, S7, and S9) had participated in other psychoacoustical experiments. Three were males (S1–S3) and seven were females (S4–S10). Except for S1 and S2, the listeners were in their early 20s; S1 was in his early 30s and S2 was in his mid 40s. All data were collected for the lateralization of tones before any subject judged the level of target components. Prior to data collection, all listeners received at least 10 h of training during which they lateralized low-frequency tones. Before the level discrimination task, they were given another 10 h of training during which they judged the level in isolation as well as in the presence of other components.

D. Data analysis

Three quantities were computed for each target condition. First, weights were obtained from binary logistic regressions (Hosmer and Lemeshow, 1989) for which responses were treated as a binary variable (coded as 0 and 1) and the interaural delays/levels of the three components were used as predictor variables (covariates, X_i).[1] The estimated probability of a ''1'' response given covariates X_1, X_2, and X_3 is expressed as

$$P(response=1|X_1,X_2,X_3) = \frac{\exp(\alpha+\beta_1X_1+\beta_2X_2+\beta_3X_3)}{1+\exp(\alpha+\beta_1X_1+\beta_2X_2+\beta_3X_3)}. \quad (2)$$

The dependent variable in logistic regression is the logit, the natural log of the likelihood ratio,

$$\ln\left[\frac{P(response=1|X_1,X_2,X_3)}{P(response=0|X_1,X_2,X_3)}\right]. \quad (3)$$

Much like linear regression, logistic regression gives each predictor variable a coefficient, β_f, that assesses the contribution to the variability in the dependent variable. In this instance, however, the coefficients reflect the change in log likelihood as the covariate changes one unit. β_f's were found using SPSS 11.01, which uses an iterative procedure that yields maximum likelihood estimation of parameters. β_f's were then converted into normalized weights:

$$\omega_f=\frac{\beta_f}{|\beta_{553}|+|\beta_{753}|+|\beta_{953}|} \quad \text{for} \quad f=553,\ 753,\ \text{and}\ 953\ \text{Hz}. \quad (4)$$

Note that β_f is normalized by the sum of the absolute values of the three coefficients. This ensures that the weights will not exceed 1.0 in the event that one or more of the coefficients is negative. To test the significance of weights, the β_f's were evaluated with the Wald test statistic to determine if they were statistically different from 0.0 ($p<0.05$). In the figures, the weights associated with coefficients that were not statistically different from 0.0 are plotted as open symbols. It

should be noted that one logistic regression was carried out for each condition on the two types of trials (left versus right; softer versus louder), since the stimulus variable (interaural difference of time; intensity) was sampled from one distribution. Berg (1989) derived weights separately for the two types of trials, but then his two types of trials were sampled from distributions having different mean values.

The second measure computed was simple proportion correct [P(Correct)]. This is the proportion of responses consistent with the information carried by the target frequency. The third measure computed was the proportion of responses accurately predicted [P(Accounted)] for a model that assumes the decision variable used in the task to be a linearly weighted (ω_i) combination of information (X_i, either an interaural difference of time or a level change) at each frequency,

$$DV = \sum_{i=1}^{3} \omega_i X_i, \tag{5}$$

where the ω_i's are the listeners' weights computed as described above.[2]

One response is predicted if the computed decision variable is negative (''left'' in the IDT task, ''quieter'' in the level task) and the other response is predicted if the computed decision variable is positive. For the interaural delay conditions, the stimulus variable was taken as the actual interaural delay of each component (in μs) during the second interval. In the case of the level discrimination task, the stimulus variable (X_i) was computed as the difference in dB between intervals 2 and 3.

III. RESULTS

Figure 1 shows the component weights from conditions in which low-frequency tones were to be lateralized on the basis of interaural delay. Keep in mind that optimal performance would be obtained in the analytic tasks if the normalized weights for the target frequency were 1.0 and the distractor weights were 0.0. Weights that were not significantly different from 0.0 are plotted as open symbols. Of the 120 component weights represented in the figure, only one was not significantly different from 0.0 (for S1, the 953-Hz component when 553 Hz served as the target). For the synthetic condition, best performance would be obtained if the weights given to each of the frequency components were equal to one another (0.333). The first four panels show the results for four listeners who adjusted their weighting strategy to be consistent with the demands of the task, although the four listeners did not do so to the same extent. The first two (S1 and S2) gave the target frequency more weight than either of the two distractor components. S3 and S4 behaved similarly, both failing to give the 753-Hz target the greatest weight when it was the target. S3 gave the greatest weight to the 953-Hz component, while S4 gave the greatest weight to 553 Hz. The other six listeners showed no ability to adjust their weights. S5–S9 gave greatest weight to the highest frequency regardless of which component served as the target. S10 gave nearly equal weight to the three components regardless of which component served as the target. For listeners S5–S10, the weights obtained for the synthetic condition were indistinguishable from those obtained in the other three conditions. In summary, only four of the ten listeners appear to be spectrally analytic in their use of interaural delays. Only two (S1 and S2) showed evidence of being able to adjust their weights in a manner consistent with the demands of the listening task, e.g., gave greater weight to the component that served as the target.

Table I shows the proportion of responses accounted for by the weighted average model [P(Accounted) from Eq. (5)], along with the proportion of correct responses [P(Correct)]. Notice that the first two listeners, the ones who made spectrally analytic judgments about the interaural delays of components show the smallest discrepancy between proportion correct and the proportion of responses accounted for by the weighted average model. After all, when a listener gives no weight to the two distractor frequencies, the two proportions, P(Correct) and P(Accounted), converge. However, if listeners give significant weight to information carried by nontarget components so that the decision variable is a weighted combination of information from the three components, then P(Accounted) should exceed P(Correct). Listeners 3–10 all show larger differences between P(Correct) and P(Accounted), with P(Accounted) the larger of the two. In order to ascertain whether the differences between P(Correct) and P(Accounted) were statistically significant, a series of four correlated groups *t*-tests were carried out, one for each listening condition (553, 753, and 953 Hz, and synthetic listening). All statistical results are given for P(Accounted) and P(Correct) that have been arcsine transformed in order to normalize variances (Collett, 1991). For cases in which 553, 753, and 953 Hz served as targets, the differences between P(Accounted) and P(Correct) were significant [$t(9)=4.45$, 8.11, and 5.64, respectively, all $p<0.01$]. Finally, when participants were instructed to combine information across the three components (synthetic condition), the difference between P(Accounted) and P(Correct) was also significant [$t(9)=3.80$, $p<0.01$].

Figure 2 shows the weights for the level discrimination task for the same ten observers (the subject numbers are the same across conditions). S1–S3 and S6 appear to be the only listeners able to adjust the manner in which the sources of monaural level information were weighted. None of the other seven listeners appeared to be able to differentially weight level information, although caution must be exercised in the interpretation of these weights. Table II shows P(Correct) and P(Accounted) for the ten listeners in the monaural level-discrimination task. One can see that listeners generally performed worse in the monaural level task than in the interaural time task (compare Tables I and II). Only S1 and S3 ever obtained performance better than 80% correct. The mean proportion correct (across the ten listeners and all four conditions) was only 0.64 and the mean proportion of responses accounted for by the weights was only 0.68. The comparable numbers from the interaural time discrimination task were 0.71 and 0.78, respectively. Even though P(Accounted)'s were generally lower, we wanted to assess the contribution of nontarget components to judgments by testing the differences between P(Accounted) and P(Correct). Once again,

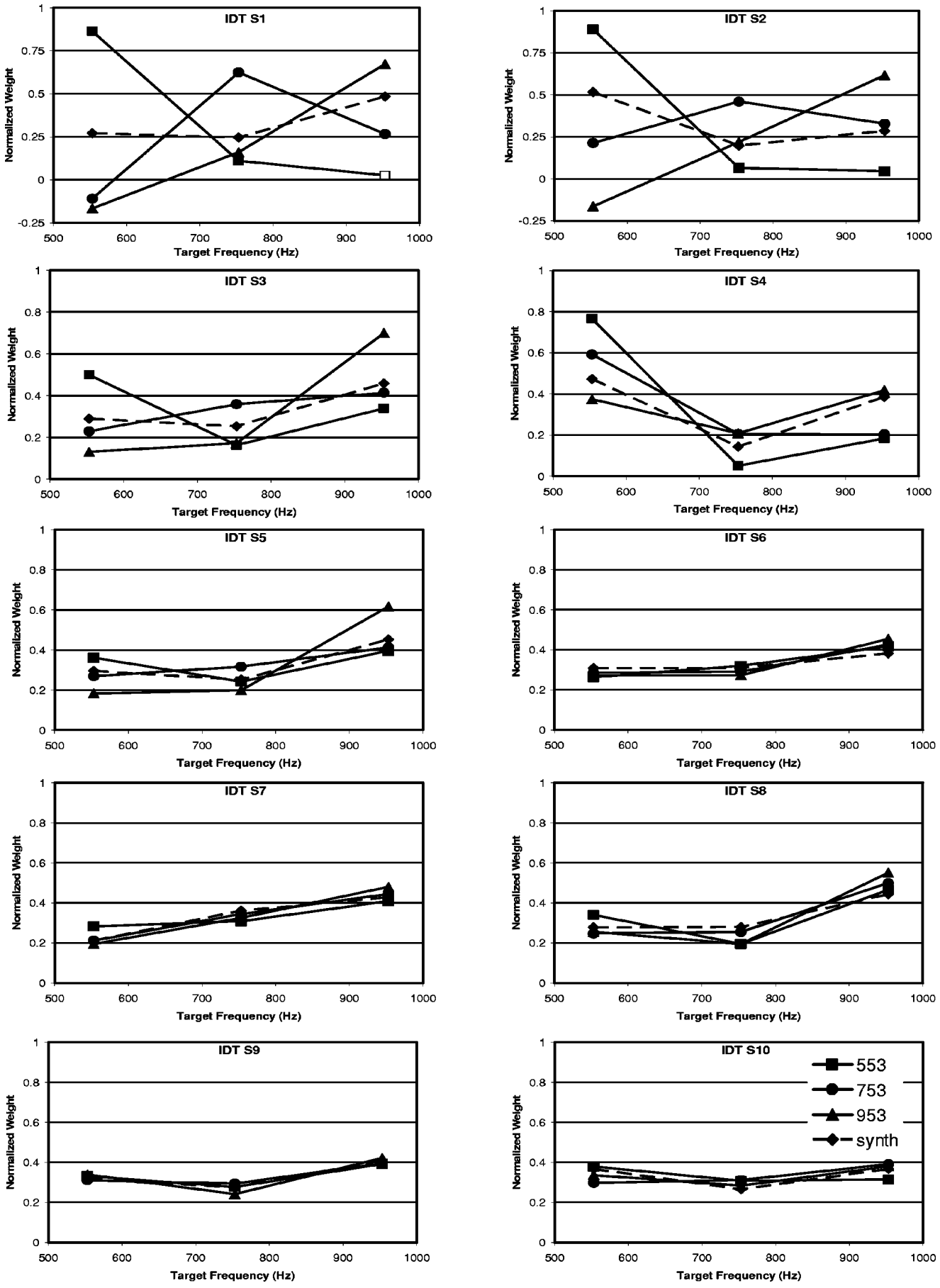

FIG. 1. Normalized weight is shown as a function of frequency for the four different interaural time listening conditions. All weights are significantly different from 0.0 at the 5% level except those plotted as open symbols. Data are presented for each individual participant.

TABLE I. The proportion correct and proportion of responses predicted from the weights are shown for the interaural time discrimination task.

	IDT	P(Correct)	P(Accounted)
S1	553	0.890	0.900
	753	0.800	0.840
	953	0.810	0.850
	Synth	0.820	0.840
S2	553	0.848	0.850
	753	0.620	0.664
	953	0.670	0.687
	Synth	0.790	0.836
S3	553	0.730	0.797
	753	0.640	0.757
	953	0.820	0.839
	Synth	0.840	0.844
S4	553	0.800	0.803
	753	0.590	0.765
	953	0.640	0.715
	Synth	0.770	0.803
S5	553	0.640	0.745
	753	0.610	0.729
	953	0.750	0.784
	Synth	0.730	0.746
S6	553	0.600	0.775
	753	0.620	0.769
	953	0.660	0.711
	Synth	0.810	0.815
S7	553	0.590	0.704
	753	0.650	0.758
	953	0.710	0.766
	Synth	0.720	0.724
S8	553	0.620	0.750
	753	0.620	0.793
	953	0.690	0.729
	Synth	0.850	0.869
S9	553	0.670	0.819
	753	0.650	0.815
	953	0.700	0.803
	Synth	0.810	0.819
S10	553	0.670	0.810
	753	0.630	0.769
	953	0.670	0.772
	Synth	0.790	0.800

correlated groups *t*-tests were performed on arcsine transformed P(Accounted) and P(Correct). The differences between P(Accounted) and P(Correct) were significant for all three analytic listening conditions [$t(9)=4.29$, 4.25, and 2.76 for target frequencies of 553, 753, and 953 Hz, respectively, all $p<0.05$]. The difference between P(Accounted) and P(Correct) for the synthetic condition was also significant [$t(9)=3.64$, $p<0.05$].

In order to compare the ability of listeners to adjust weights in the two tasks, various metrics for capturing this ability were considered. The one that will be used is the average normalized weight given to the target component, $\overline{\omega_T}$. The weights for the synthetic condition were not used in this analysis. As an example, imagine an observer who is generally able to adjust the weights appropriately, giving a weight of 0.7 to the target component regardless of which frequency served as the target. Assume the other two components are given equal weight (0.15, in this case). This observer would have an average target weight of 0.7 when averaged across the 553-, 753-, and 953-Hz conditions. On the other hand, an observer who applies a single weighting strategy in all conditions, regardless of the particular pattern of weights, will have an average target weight of 0.333. As such, the average target weight reflects the extent to which an observer varies weighting strategy across conditions. Thus, $\overline{\omega_T}$'s were computed for the interaural time discrimination task and for the monaural intensity discrimination task. These are presented in Table III. Note that the participants who had high average target weights for the interaural time discrimination task also have them for the monaural level task (S1–S3). S4 was generally more analytic in the interaural time task, while S6 was more analytic in the monaural level task. The Pearson *r* between the average weights in the two tasks was 0.70 ($N=10$, $p<0.02$). It can safely be said that listeners who were spectrally analytic in one task were spectrally analytic in the other task.

Of the five listeners who were not able to adjust their weights in either task (S5 and S7–S10), there was qualitative agreement across the two tasks for S5, S7, and S9. These three listeners tended to give greater weight to the highest frequency component in both IDT and monaural level discrimination tasks. S10 showed this same tendency in the monaural level task, but not the IDT task (in which she gave equal weight to the three components). S8 showed the largest differences in weighting strategies between the two tasks, displaying high-frequency dominance in the IDT task and low-frequency dominance in the monaural level task.

IV. DISCUSSION

The findings (Figs. 1 and 2) show that listeners who are able to adjust perceptual weights for the individual components in the task involving interaural time discrimination are generally the ones who can do so in the task involving monaural level discrimination. This is confirmed by the significant positive correlation between $\overline{\omega_T}$'s obtained for interaural time and monaural level discrimination. Optimal performance in all of the conditions in which maximal weight should be given to the target and no weight given to the distractors can only be obtained if listeners are able to ''hear out'' the target component, perceptually segregating it from the other concurrent frequencies. In the case of interaural time discrimination, this requires identifying the frequency of the target component and then determining whether its intracranial position is to the left or right of the midline. In monaural level discrimination, one must identify the frequency of the target (as marked by interval one) and then indicate whether its level increases or decreases between intervals 2 and 3. Both of these tasks require ''analytic listening.''

For both interaural time and monaural level discrimination, performance was measured for conditions in which listeners were asked to perform the tasks ''synthetically.'' This can be accomplished in two ways. First, the listener could extract independent information from each of the three com-

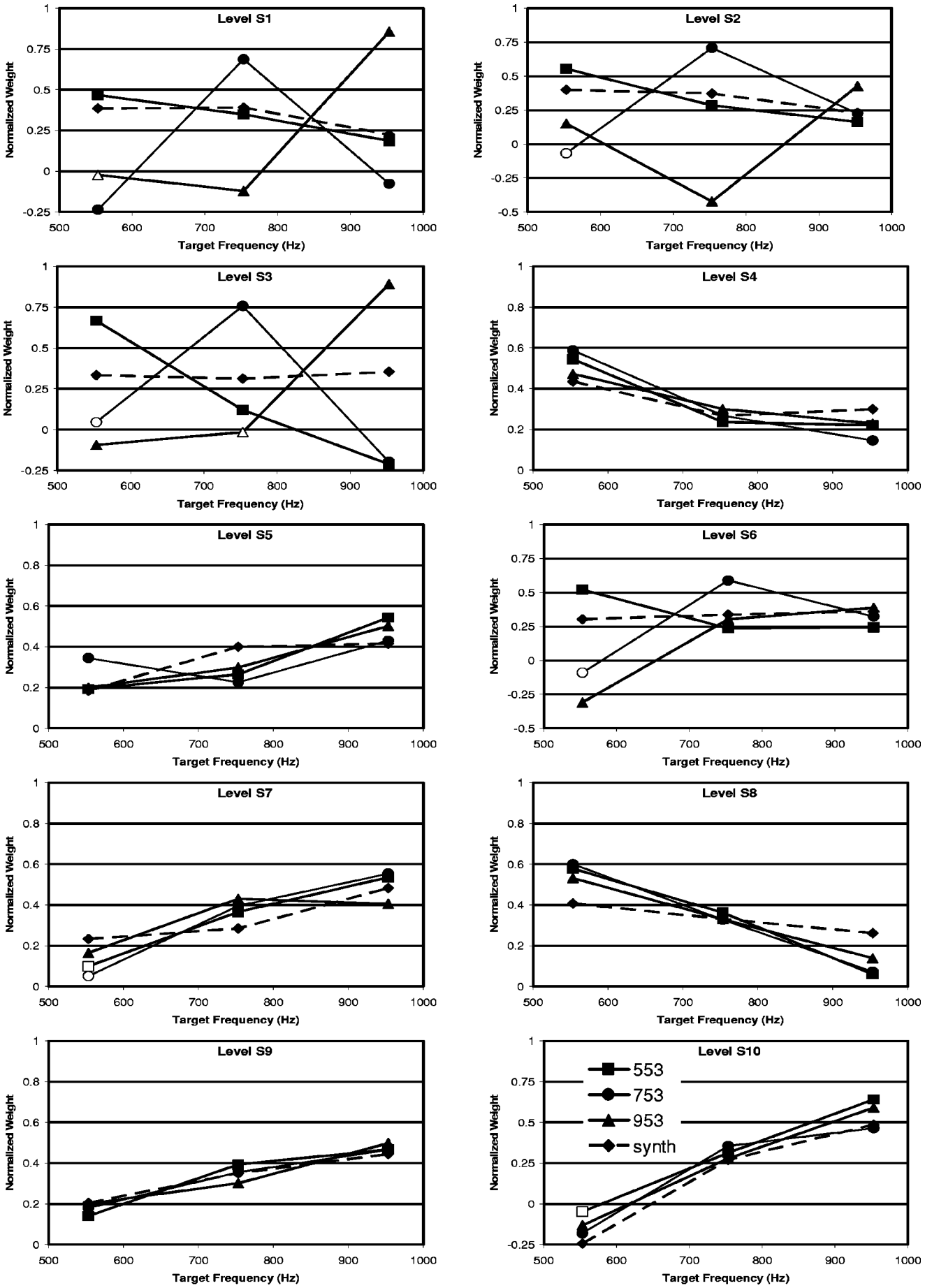

FIG. 2. Normalized weight is shown as a function of frequency for the four different monaural level listening conditions. All weights are significantly different from 0.0 at the 5% level except those plotted as open symbols. Data are presented for each individual participant.

TABLE II. The proportion correct and proportion of responses predicted from the weights are shown for the monaural level discrimination task.

	Level	P(Correct)	P(Accounted)
S1	553	0.693	0.781
	753	0.833	0.852
	953	0.820	0.820
	Synth	0.843	0.861
S2	553	0.731	0.790
	753	0.706	0.709
	953	0.650	0.740
	Synth	0.755	0.770
S3	553	0.740	0.754
	753	0.730	0.755
	953	0.860	0.861
	Synth	0.810	0.815
S4	553	0.660	0.688
	753	0.543	0.600
	953	0.570	0.704
	Synth	0.650	0.654
S5	553	0.530	0.614
	753	0.530	0.619
	953	0.570	0.579
	Synth	0.640	0.651
S6	553	0.580	0.598
	753	0.590	0.613
	953	0.550	0.600
	Synth	0.600	0.600
S7	553	0.530	0.645
	753	0.520	0.641
	953	0.560	0.645
	Synth	0.570	0.618
S8	553	0.700	0.751
	753	0.600	0.745
	953	0.540	0.745
	Synth	0.730	0.733
S9	553	0.520	0.614
	753	0.570	0.627
	953	0.610	0.620
	Synth	0.600	0.615
S10	553	0.480	0.694
	753	0.580	0.656
	953	0.660	0.669
	Synth	0.670	0.717

ponents, and then compute an average value, using the mean as the decision variable. A second possibility is that the listener simply performs ''wideband'' listening, computing the interaural delay of the composite waveform in the interaural time task, or computing the total power of the signals in the monaural level task. These two possibilities are reminiscent of Ashby and Townsend's (1986) distinction between decisional and perceptual integrality.

The fact that the same individuals appear to be analytic in both tasks (when the conditions demand it) is an indication that the weights are most likely measuring the ability to attend to a particular region of the spectrum (ignoring other portions). Bregman (1990) has written that attention is ''strongly biased toward listening to streams,'' but that ''we are capable, with effort and with practice, of listening to individual features of sounds...'' (p. 138). Since the three frequencies were gated simultaneously, there was probably little basis for segregation of the individual components. Our results show that individuals differ considerably in their abilities to attend to individual spectral components (features) of complex sounds. Much of the discussion that follows is an attempt to identify factors that have been found to promote analytic listening.

TABLE III. Average target weights are computed for each of the ten participants.

	IDT	Level
S1	0.720	0.669
S2	0.655	0.562
S3	0.518	0.772
S4	0.463	0.347
S5	0.432	0.307
S6	0.336	0.499
S7	0.369	0.300
S8	0.382	0.348
S9	0.349	0.331
S10	0.357	0.299

Darwin and Hukin (1998, 1999) have argued that interaural differences of time are weak cues for inducing perceptual segregation, but may enhance segregation based on other stimulus cues (e.g., onset asynchrony). Studies of lateralization of low-frequency tones on the basis of IDT have found that only a minority of listeners is capable of judging the laterality of one component independent of concurrent components. Dye *et al.* (1996) found 2 of 8, while Stellmack and Lutfi (1996) found 1 of 6, compared to 4 of 10 in the current study.

It is interesting to note that several studies from the mid-1960s found evidence of analytic processing of IDTs for multiple component complexes (Sayers, 1964; Toole and Sayers, 1965). For instance, Toole and Sayers (1965) asked observers to judge the lateral position of individual components comprising a complex as a function of the interaural delay. Even when as little as 20 Hz (600 and 620 Hz) separated components, the trajectories were cyclic with the period of the to-be-judged component. Even for harmonic complexes with a fundamental frequency of 167 Hz, their observers were able to track trajectories of up to the fifth or sixth harmonic. The attention of the observers was directed to particular harmonics by, at the listener's request, presenting the target frequency alone. These studies were all carried out with stimuli that remained on until judgments were made. This contrasts with the 200-ms signals used by Stellmack and Lutfi (1996), Dye *et al.* (1996), and the current study. Dye *et al.* (1994) found that most listeners gave greater weight to the target frequency as the duration of the two-tone complex (753-Hz target, 553-Hz distractor) was extended out to 400 ms. Perhaps the fact that Toole and Sayers used continuous stimuli explains why their listeners were generally more analytic than those in studies that used limited duration stimuli.

Blauert (1978) has argued that experienced listeners tend to hear dichotic stimuli analytically, while those with less experience hear fused intracranial images. He presented

critical-band wide noises centered at 540 and 840 Hz along with a third band at a variable frequency. All three bands had the same interaural delay, either 200 or 400 μs. As the variable band was increased in frequency beyond 1500 Hz, experienced listeners heard it out as a separate auditory event with an intracranial image that was closer to the midline. Inexperienced listeners described a single, spatially extended image to which they could ascribe an average displacement. Thus, it appears that experience and training also contribute to the ability to listen to binaural stimuli analytically. S1 and S2, two of the participants who were spectrally analytic in both tasks in the current study, were the most experienced listeners in the study. S4, who tended to be analytic in the interaural time discrimination study, had participated in three prior lateralization studies. S3, a listener who was analytic in both tasks, had participated in one prior lateralization experiment.

Stellmack *et al.* (1997) and Doherty and Lutfi (1999) have reported that some adult listeners were able to adjust perceptual weights in monaural level discrimination tasks in which analytic listening was required. Most relevant to the current experiment are those conditions in which Stellmack *et al.*'s listeners were presented all three components (250, 1000, and 4000 Hz) at the same mean level. Two of the five listeners gave greatest weight to whichever component served as the target and two more gave the target frequency the greatest weight in some conditions but not others. Particularly difficult was the case in which central component of 1000 Hz served as the target. The fifth listener essentially gave equal weight to all three components regardless of which served as the target. All five of the pre-school age children in the experiment gave the three components equal weight regardless of which served as the target. Doherty and Lutfi (1999) also found listeners somewhat able to weight the target frequency highest in a level discrimination task (250, 500, 1000, 2000, 4000, 8000 Hz, with 250, 1000, and 4000 Hz serving as the targets). Of their 15 normal-hearing listeners, all gave greatest weight to the 250-Hz target, but only six gave maximum weight to the target in all three target conditions. Two gave nearly equal weight to all six components regardless of which frequency served as the target. The current study, which cued the target frequency on every trial, identified four of ten listeners as giving maximal weight to the target component in all three analytic listening conditions.

Neither Stellmack *et al.* (1997) nor Doherty and Lutfi (1999) cued the target frequency on each trial. Instead, to acquaint listeners with the target frequency, Doherty and Lutfi presented a series of 100 trials consisting of the target component alone before each new target frequency was introduced.[3] Stellmack *et al.* (1997) afforded their listeners the opportunity to manipulate the stimuli during practice to allow familiarization with the target frequency.

Kortekaas *et al.* (2003) found that none of their four listeners were able to adjust perceptual weights between a condition in which all components should be weighted equally and one in which the weights should increase with frequency. Kortekaas *et al.* used 3-, 7-, 15-, and 24-component complexes in which the frequency spacing was equal in critical band (bark) units. The complexes were centered at 11.5 barks (1600 Hz). In one set of conditions, the average levels of all components were equal, and listeners should have given equal weight to all components. However, listeners tended to give greater weight to the highest two-to-four components for most conditions. For complexes with large numbers of components (15 and 24), there was a tendency for some of the listeners to give greater weight to the lower frequencies. With 7 or 15 components, conditions were run in which the average level difference increased progressively with barks, such that

$$\Delta L(z) = \Delta L_o \cdot k^{(z-z1)}, \tag{6}$$

where $\Delta L(z)$ is the level increment (in dB) for the component at bark z, ΔL_o is the nominal level increment, and z_1 is the bark of the lowest component frequency in the complex. As such, the level average level increment for the highest component was a factor of 1.78 greater than that of the lowest frequency component for 7-component complexes and a factor of about 3.8 greater for 15-component complexes. While Kortekaas *et al.* (2003) anticipated listeners being able to change their weighting patterns to accommodate the greater magnitude of level changes at higher frequencies, no such changes were found. It should be noted that their listeners (except for the first author) were not aware of this level manipulation. Furthermore, the general tendency to give the higher-frequency components greater weight when the average increments across the spectrum were equal would tend to make finding the effect of such a subtle manipulation difficult or impossible. Kortekaas *et al.* emphasized the ability of listeners to *combine* information across critical bands, and that this last manipulation cannot really be viewed as promoting analytic listening.

In summary, the factors that appear to promote analytic listening are (1) experience and training and (2) familiarity with the target component. The second of these factors can be promoted either by explicit trial-by-trial cuing (as was done in the current experiments) or by allowing the participants the opportunity to hear the target frequency in isolation (a 1a Doherty and Lutfi, 1999). Blauert (1983, p. 322) warned that these would be key in allowing listeners to report the properties of multiple concurrent auditory events.

Another task in which analytic versus synthetic listening strategies are thought to play a role is in informational masking paradigms. Substantial amounts of informational masking have been created through the introduction of trial-to-trial variability in the acoustic stimulus, especially with regard to the spectral characteristics of the maskers. It has been proposed that informational masking is due to a failure of listeners to focus attention on the target signal, instead basing responses on the uninformative maskers (Leek *et al.*, 1991; Kidd *et al.*, 1994; Neff, 1995; Wright and Saberi, 1999; and Oh and Lutfi, 2000). In support of this claim, Richards *et al.* (2002) and Tang and Richards (2003) measured informational masking and weighting functions for a group of listeners and found a tendency for those displaying nonoptimal weighting strategies (i.e., giving significant weight to nonsignal frequencies) to show larger amounts of informational masking. Alexander and Lutfi (2004) have

looked explicitly at this relationship, finding that higher levels of weighting efficiency[4] yield lower amounts of informational masking.

Oxenham *et al.* (2003) found that musicians showed less informational masking than nonmusicians, arguing that part of musical training involves learning to perceptually segregate the melodic line. As such, individuals with a higher level of musical training would be better able to listen analytically in the multitone masking conditions than nonmusicians. Of our three listeners who were able to adjust perceptual weights in both the interaural time and monaural level tasks, only one had extensive musical training. Two of the seven remaining listeners were practicing musicians at the time that the experiment was performed, and studied piano through their mid-teens. As a consequence, differences in musical training do not appear to account for the individual differences found in the current study.

Neff *et al.* (1996) claim that males show less informational masking than do females. Of our ten participants, three were male. They happen to be the three who were analytic in both interaural time and monaural level discrimination tasks. If one believes that superiority in conditions with multiple maskers is due to a tendency to process stimuli analytically, this is consistent with Neff *et al.*'s findings. It should be noted that Oxenham *et al.* (2003) found no effect of gender in their study.

Durlach *et al.* (2003) have recently demonstrated that reducing target-masker similarity reduces the amount of informational masking. They performed a series of five experiments in which a tonal target signal was detected against a multitone masker whose frequency components varied randomly from trial to trial. For each of the five experiments, the signal was a 1000-Hz tone and the maskers were eight components chosen randomly (on a logarithmic frequency scale) between 200 and 5000 Hz with a protected region of 800–1200 Hz around the signal. In each of the experiments, conditions were run in which the signal was ''similar'' (S) or ''dissimilar'' (D) to the maskers to promote grouping or segregation. Two of their five observers showed significant S-D differences in four of the five experiments, one showed significant S-D differences in three, and two showed significant S-D differences in only one. They conclude that there were ''large intersubject differences in susceptibility to informational masking'' with ''substantial, but far from perfect, intrasubject consistency...'' (Durlach *et al.*, 2003, p. 378).

We know of no other studies in psychoacoustics that have examined weighting functions from different tasks. While we find large individual differences in weighting patterns, the main finding of our study is that individuals who were able to adjust their perceptual weights in an interaural time discrimination task were also able to do so in monaural level tasks. Lutfi *et al.* (2003) found that individual differences in informational masking can be explained by a single factor. They speculate that this factor is the ''attentional bandwidth,'' the number of independent auditory filters that contribute to the decision variable. The data from the current study argue that one's ability to adjust and restrict this ''attentional bandwidth'' generalizes across psychophysical tasks.

ACKNOWLEDGMENTS

We would like to thank our colleagues at the Parmly Hearing Institute for their support and advice while carrying out these experiments. We would also like to thank Armin Kohlrausch and two anonymous reviewers for their careful reading of earlier versions and many constructive comments. This work was supported by a grant from NIDCD (Program Project Grant No. DC000293).

[1]Logistic regression is recommended by statisticians when one is attempting to predict a dichotomous dependent variable, since it makes no assumptions regarding the distributions of the predictor variables (Hosmer and Lemeshow, 1989). Frankly, it was recommended by an anonymous reviewer who was concerned about the low levels of performance for the monaural level task. Weights were computed in earlier drafts via point-biserial correlations (Lutfi, 1995), and they did not differ substantially from those computed via binary logistic regression. Those derived from logistic regression, however, tended to allow us to predict a higher proportion of responses, particularly for the monaural level discrimination task. This was particularly true for S7.

[2]Occasionally logistic regression would return a significant constant, α. When one runs a logistic regression in SPSS, a classification table is generated that shows the proportion of correct classifications predicted from α, β_{553}, β_{753}, and β_{953}. Instead of using this proportion as P(Accounted), we chose to drop the constant term and simply use the β_f's to make this computation. In the 80 binary logistic regressions that were performed, the percentage of responses correctly predicted from SPSS classification table, which included the constant, were never more that 1% greater than the percentage of responses predicted from the weights alone [100 $\times$P(Accounted)].

[3]Doherty and Lutfi also selected the target level from one of two distributions, separated by a level difference yielding $d=1.0$. The fact that the target component was presented at a greater average level during one interval should have enhanced the ability of listeners to perform the task analytically.

[4]Alexander and Lutfi (2004) first determined the root-mean-square (rms) of the difference between the obtained normalized weights and the normalized weights of an ideal observer who gives a weight of 1.0 to the signal frequency and weights of 0.0 to all other components. Weighting efficiency was defined as $1-$rms.

Alexander, J. M., and Lutfi, R. A. (**2004**). ''Informational masking in hearing-impaired and normal-hearing listeners: Sensation level and decision weights,'' J. Acoust. Soc. Am. **116**, 2234–2247.

Ashby, F. G., and Townsend, J. T. (**1986**). ''Varieties of perceptual independence,'' Psychol. Rev. **93**, 154–179.

Berg, B. G. (**1989**). ''Analysis of weights in multiple observation tasks,'' J. Acoust. Soc. Am. **86**, 1743–1746.

Blauert, J. (**1978**). ''Some aspects of three-dimensional hearing in rooms,'' in *Proceedings, Meeting of the Federated Acoustical Societies of Europe*, Warsaw, Vol. 3, pp. 65–68.

Blauert, J. (**1983**). *Spatial Hearing: The Psychophysics of Human Sound Localization* (MIT, Cambridge, MA).

Bregman, A. S. (**1990**). *Auditory Scene Analysis: The Perceptual Organization of Sound* (MIT, Cambridge, MA).

Collett, D. (**1991**). *Modeling Binary Data* (Chapman & Hall, London).

Darwin, C. J., and Hukin, R. W. (**1998**). ''Perceptual segregation of a harmonic from a vowel by interaural time difference in conjunction with mistuning and onset asynchrony,'' J. Acoust. Soc. Am. **103**, 1080–1084.

Darwin, C. J., and Hukin, R. W. (**1999**). ''Auditory objects of attention: The role of interaural time differences,'' J. Exp. Psychol. Hum. Percept. Perform. **25**, 617–629.

Doherty, K. A., and Lutfi, R. A. (**1996**). ''Spectral weights for overall level discrimination in listeners with sensorineural hearing loss,'' J. Acoust. Soc. Am. **99**, 1053–1058.

Doherty, K. A., and Lutfi, R. A. (**1999**). ''Level discrimination of single tones in a multitone complex by normal-hearing and hearing-impaired listeners,'' J. Acoust. Soc. Am. **105**, 1831–1840.

Durlach, N. I., Mason, C. R., Shinn-Cunningham, B. G., Arbogast, T. L., Colburn, H. S., and Kidd, Jr., G. (**2003**). ''Informational masking: Coun-

teracting the effects of stimulus uncertainty by decreasing target-masker similarity,'' J. Acoust. Soc. Am. **114**, 368–379.
Dye, R. H. (**1997**). ''The relative contributions of targets and distractors in judgments of laterality based on interaural differences of level,'' in *Binaural and Spatial Hearing in Real and Virtual Environments*, edited by R. H. Gilkey and T. R. Anderson (Erlbaum, Hillsdale, NJ).
Dye, R. H., Stellmack, M. A., Grange, A. N., and Yost, W. A. (**1996**). ''The effect of distractor frequency on judgments of target laterality based on interaural delays,'' J. Acoust. Soc. Am. **99**, 1096–1107.
Dye, R. H., Yost, W. A., Stellmack, M. A., and Sheft, S. (**1994**). ''Stimulus classification procedure for assessing the extent to which binaural processing is spectrally analytic or synthetic,'' J. Acoust. Soc. Am. **96**, 2720–2730.
Helmholtz, H. von (**1859**). *On the Sensations of Tone as a Physiological Basis for the Theory of Music* (2nd English edition, translated by A. J. Ellis, 1885); reprinted (Dover, New York, 1954).
Hosmer, D. W., and Lemeshow, S. (**1989**). *Applied Logistic Regression* (Wiley, New York).
Kidd, Jr., G., Mason, C. R., Deliwala, P. S., Woods, W. S., and Colburn, H. S. (**1994**). ''Reducing informational masking by sound segregation,'' J. Acoust. Soc. Am. **95**, 3475–3480.
Kortekaas, R., Buus, S., and Florentine, M. (**2003**). ''Perceptual weights in auditory level discrimination,'' J. Acoust. Soc. Am. **113**, 3306–3322.
Lee, Y. W. (**1960**). *Statistical Theory of Communication* (Wiley, New York).
Leek, M., Brown, M. E., and Dorman, M. F. (**1991**). ''Informational masking and auditory attention,'' Percept. Psychophys. **50**, 205–214.
Lutfi, R. A. (**1995**). ''Correlation coefficients and correlation ratios as estimates of observer weights in multiple-observation tasks,'' J. Acoust. Soc. Am. **97**, 1333–1334.
Lutfi, R. A., Kistler, D. J., Oh, E. L., Wightman, F. L., and Callahan, M. R. (**2003**). ''One factor underlies individual differences in auditory informational masking within and across age groups,'' Percept. Psychophys. **63**, 396–406.
Moore, B. C. J., and Glasberg, B. R. (**1982**). ''Interpreting the role of suppression in psychophysical tuning curves,'' J. Acoust. Soc. Am. **72**, 1374–1379.
Neff, D. L. (**1995**). ''Signal properties that reduce masking by simultaneous, random-frequency maskers,'' J. Acoust. Soc. Am. **98**, 1909–1920.
Neff, D. L., Kessler, C. J., and Dethlefs, T. M. (**1996**). ''Sex differences in simultaneous masking with random-frequency maskers,'' J. Acoust. Soc. Am. **100**, 2547–2550.
Oh, E. L., and Lutfi, R. A. (**2000**). ''Effect of masker harmonicity on informational masking,'' J. Acoust. Soc. Am. **108**, 706–709.
Oxenham, A. J., Fligor, B. J., Mason, C. R., and Kidd, Jr., G. (**2003**). ''Informational masking and musical training,'' J. Acoust. Soc. Am. **114**, 1543–1549.
Richards, V. M., and Zhu, S. (**1994**). ''Relative estimates of combination weights, decision criteria, and internal noise based on correlation coefficients,'' J. Acoust. Soc. Am. **95**, 423–434.
Richards, V. M., Tang, Z., and Kidd, Jr., G. D. (**2002**). ''Informational masking with small set sizes,'' J. Acoust. Soc. Am. **111**, 1359–1366.
Sayers, B. McA. (**1964**). ''Acoustic-image lateralization judgments with binaural tones,'' J. Acoust. Soc. Am. **36**, 923–926.
Sayers, B. McA., and Cherry, E. C. (**1957**). ''Mechanism of binaural fusion in the hearing of speech,'' J. Acoust. Soc. Am. **29**, 973–987.
Shackleton, T. M., Meddis, R., and Hewitt, M. J. (**1992**). ''Across frequency integration in a model of lateralization,'' J. Acoust. Soc. Am. **91**, 2276–2279.
Stellmack, M. A., and Lutfi, R. A. (**1996**). ''Observer weighting of concurrent binaural information,'' J. Acoust. Soc. Am. **99**, 579–587.
Stellmack, M. A., Willihnganz, M. S., Lutfi, R. A., and Wightman, F. L. (**1997**). ''Spectral weights in level discrimination by preschool children: Analytic listening conditions,'' J. Acoust. Soc. Am. **101**, 2811–2821.
Tang, Z., and Richards, V. M. (**2003**). ''Examination of a linear model in an informational masking study,'' J. Acoust. Soc. Am. **114**, 361–367.
Toole, F. E., and Sayers, B. McA. (**1965**). ''Lateralization judgments and the nature of binaural acoustic images,'' J. Acoust. Soc. Am. **37**, 319–324.
Willihnganz, M. S., Stellmack, M. A., Lutfi, R. A., and Wightman, F. L. (**1997**). ''Spectral weights in level discrimination by preschool children: Synthetic listening conditions,'' J. Acoust. Soc. Am. **101**, 2803–2810.
Wright, B. A., and Saberi, K. (**1999**). ''Strategies used to detect auditory signals in small sets of random maskers,'' J. Acoust. Soc. Am. **105**, 1765–1775.

Speech intelligibility and spatial release from masking in young children[a)]

Ruth Y. Litovsky[b)]
Waisman Center, University of Wisconsin—Madison, 1500 Highland Avenue, Madison, Wisconsin 53705

(Received 13 August 2003; accepted for publication 27 January 2005)

Children between the ages of 4 and 7 and adults were tested in free field on speech intelligibility using a four-alternative forced choice paradigm with spondees. Target speech was presented from front (0°); speech or modulated speech-shaped-noise competitors were either in front or on the right (90°). Speech reception thresholds were measured adaptively using a three-down/one-up algorithm. The primary difference between children and adults was seen in elevated thresholds in children in quiet and in all masked conditions. For both age groups, masking was greater with the speech-noise versus speech competitor and with two versus one competitor(s). Masking was also greater when the competitors were located in *front* compared with the *right*. The amount of masking did not differ across the two age groups. Spatial release from masking was similar in the two age groups, except for in the one-speech condition, when it was greater in children than adults. These findings suggest that, similar to adults, young children are able to utilize spatial and/or head shadow cues to segregate sounds in noisy environments. The potential utility of the measures used here for studying hearing-impaired children is also discussed. [DOI: 10.1121/1.1873913]

PACS numbers: 43.66.Pn, 43.66.Qp, 43.71.Ft [AK] Pages: 3091–3099

I. INTRODUCTION

Children spend numerous hours every day in complex auditory environments, such as classrooms, where multiple sounds that vary in content and direction typically co-occur. In addition to voices of adults and children, instructional aids, environmental sounds, and reverberation are standard aspects of acoustic environments in classrooms. Some work indicates that children learn best in relatively quiet environments, and often have difficulty hearing speech in the presence of distracting sounds (Crandell, 1993; Yacullo and Hawkins, 1987; Papso and Blood, 1989). Psychophysical studies in which stimuli were presented over headphones have shown that, compared with adults, preschool listeners exhibit poorer attentional selectivity on auditory tasks (e.g., Stellmack *et al.*, 1997; Oh *et al.*, 2001) and reduced unmasking for tone detection under dichotic conditions (Wightman *et al.*, 2003; Hall *et al.*, 2004).

Also under headphones, it has been found that in the presence of two-talker maskers speech reception thresholds are higher in children than adults, and for both age groups thresholds are higher in the presence of two-talker maskers than with speech-shaped noise maskers (Hall *et al.*, 2002). Headphone stimulus presentation is limited, however, because spatial cues that are known to be important for sound segregation in realistic environments are missing. Studies with adults have shown that the ability to segregate target speech from competing speech and/or noise is determined by a complex set of auditory computations that involve both monaural and binaural processes (Hawley *et al.*, 1999, 2004; Bronkhorst, 2000; Culling *et al.*, 2004). Spatial cues in particular play a key role in facilitating source segregation. Speech intelligibility improves by up to 12 dB when the target speech and competing sounds are spatially separated, resulting in ''spatial release from masking'' (Plomp and Mimpen, 1981; Bronkhorst and Plomp, 1992; Nilsson *et al.*, 1994; Koehnke and Besing, 1996; Peissig and Kollmeier, 1997; Hawley *et al.*, 1999, 2004; Shinn-Cunningham *et al.*, 2001; Litovsky *et al.*, 2002).

The extent to which children demonstrate spatial release from masking for speech is poorly understood. Of particular interest in the present study is the effect of number of maskers, as well as their content, on the extent to which young children experience spatial release from masking. In adult listeners spatial release from masking is especially large for multiple (two or more) maskers that carry linguistic content or context (i.e., speech or reversed speech), and relatively small for a single, nonspeech masker such as speech-shaped noise [Hawley *et al.*, (2004); see also Bronkhorst (2000) for review]. The authors of those works have concluded that release from masking as provided by spatial cues is particularly effective when the auditory environment is complex. The concept of ''informational masking'' has been invoked to explain this phenomenon, whereby, in the presence of maskers that are harder to ignore, spatial cues become important for sound source segregation. In this case, maskers that are multiple in number and/or that carry information resembling that contained in the target result in greater spatial release from masking (e.g., Brungart 2001; Freyman *et al.*, 2001; Arbogast *et al.*, 2002; Durlach *et al.*, 2003).

Several studies have reported that speech masking in children depends on the masker type (Papso and Blood,

[a)]Select portions of these data were presented at the 143rd Meeting of the Acoustical Society of America, Pittsburgh, PA, and at the 24th Meeting of the Association for Research in Otolaryngology, Tampa, FL.

[b)]Electronic mail: litovsky@waisman.wisc.edu

TABLE I. List of conditions tested for children (nine subjects per condition).

Group	No. of competitors	Age range (years. months±SD)	Competitor type	Conditions
1	1	5.4±1.1	Speech	Quiet, 1 front, 1 right
2	1	5.6±1.2	Speech-noise	Quiet, 1 front, 1 right
3	2	5.8±1	Speech	Quiet, 2 front, 2 right
4	2	5.6±1	Speech-noise	Quiet, 2 front, 2 right

1989; Hall *et al.*, 2002, 2004). However, the effect of number and spatial cues, and the possible contribution of these stimulus parameters to spatial release from masking, remain poorly understood. Binaural abilities in children are adultlike on measures of binaural masking level differences (Nozza *et al.*, 1988; Moore *et al.*, 1991) and minimum audible angle (Litovsky, 1997). Since spatial cues are known to play a key role in speech understanding for adults, it is important to understand how young children comprehend speech in realistic, multi-source acoustic environments, and the conditions that enable them to benefit from spatial cues. The research paradigm used here may ultimately also be useful in evaluating performance of hearing-impaired children. Noisy environments are particularly problematic for children with a history of otitis media (e.g., Hall *et al.*, 2003; Moore *et al.*, 2003; Roberts *et al.*, 2004) and for hearing aid and cochlear implant users (e.g., Dawson *et al.*, 2004; Eisenberg *et al.*, 2004; Litovsky *et al.*, 2004). Because the important task of hearing speech in noise can be a daily struggle for many of these children, ultimately their performance on these measures can assist with diagnosis and fitting strategies.

In the present study the task involved a four-alternative forced-choice (4AFC) word discrimination paradigm. Subjects selected a picture that matched the speech target from an array of four pictures that appeared on a computer monitor. Other tests such as the HINT-C (Nilsson *et al.*, 1994) may be usable for measuring speech intelligibility in noise in children as young as 6 years, but are difficult to implement with younger children. The test protocol described here was specifically designed to enable the study of speech intelligibility in noise in children as young as 4 years old, an age at which many children begin to spend a significant number of hours in noisy environments such as preschool classrooms.

II. METHODS

A. Subjects

A total of 36 volunteer children were recruited from local public schools and the general community (14 males and 22 females), and all subjects completed testing on the three required conditions. Subjects ranged in age from 4.5 to 7.5 years (average and standard deviation=5.5±1 years; see also Table I).[1] All were native speakers of English with no known auditory dysfunction or other cognitive disorders. According to the parents' report, none of the children were on medication or had known illness or ear infections on the day of testing, and none of the children had a known history of hearing loss. Total testing time for each listener was approximately 45 min.

Nine paid adult volunteers, with normal hearing as verified by standard audiometric testing for frequencies between 250 and 8000 Hz, and English as their first language, were also tested. Since testing was much less time consuming with adults than with children, a within-subject design was used whereby each subject participated in all conditions that pertained to the four groups of children.

B. Testing chamber, materials apparatus

Testing was conducted in a single-walled sound booth (3.6×4 m) with carpeting. This room had a reverberation time (T_{60})=250 ms and ambient noise levels averaging 35 dB SPL. During testing, subjects were always seated in the center of the room, with loudspeakers (Radio Shack Minimus 7) placed at 15.24 cm above ear level for children (ear level for adults) and at a distance of 1.67 m from the center of the subject's head. All stimuli were prerecorded, digitized, and stored on a laptop computer (Winbook). In the one-competitor conditions, the target and competing sound were fed to separate channels of a two-channel soundcard (Digigram VX Pocket), amplified (Crown D-75), and presented to separate loudspeakers. When both target and competitor were presented from the front position, the speakers were placed next to one another, with their centers at ±2°, with their medial walls nearly touching. Each loudspeaker subtended 4° in the horizontal dimension, hence strictly speaking, speakers were separated by 4°. In the two-competitor condition, when both occurred from the front, they were presented from the same loudspeaker. Target stimulus selection, level controls, and output as well as response acquisition were achieved using Matlab. A picture book containing four target pictures per page was placed on a small table in front of the subject.

C. Stimuli

Stimuli consisted of *target words* and *competing sentences*. Targets comprised a closed set of 25 spondaic words from CID W-1 obtained from Auditech and spoken by a male talker. Although a larger set of words is available, the subset chosen for the present study consisted of words that were easily represented with a visual illustration and readily recognized as such during pilot testing of 20, 4 to 5 year-old children (a list of the target words used is shown in the Appendix). The root-mean-square levels were equalized for all target words using Matlab software. The competitors were either speech or modulated speech-shaped noise. Competing sentences were taken from the Harvard IEEE list (Rothauser *et al.*, 1969) and recorded with a female voice. Examples of sentences are ''Glue the sheet to the dark blue background,''

''Two blue fish swam in the tank,'' and ''The meal was cooked before the bell rang.'' Ten such sentences were used, and these were presented in a random order during testing. Speech-noise was made based on the ten competitor sentences and also played in a random order during testing. These interferers were filtered to match the long-term spectrum of the speech competitors, calculated for each talker separately. The noise samples were scaled to the same root-mean-square value and cut to the same length as the matching speech competitor. The envelope was then extracted from the speech competitor and was used to modulate the noise tokens, giving the same coarse temporal structure as the speech. The envelope of running speech was extracted using a method similar to that described by Festen and Plomp (1990) in which a rectified version of the waveform is low-pass filtered. A first-order Butterworth low-pass filter was used with a 3-dB cutoff at 40 Hz.

D. Design

The target words were always presented from the front (0°). Competitors were presented from either front or side (90°). Four groups of children with nine subjects per group were tested (see Table I). The side condition was always with competitor(s) on the right. Each child subject was randomly assigned to a group that was tested on one combination of type (speech or speech-noise) and number (1 or 2) of competitor(s). The subject was then tested on three conditions: (1) *quiet*: no competitor(s), (2) *front*: target and competitor(s) in front, and (3) *right*: target in front and competitor(s) at 90° on the right; the order of conditions was randomized using a Latin-square design. For the adult group, testing was conducted in a single 2-h session, with the order of the nine conditions randomized for each listener.

For each condition one adaptive track was measured. When two competitors were presented they were of the same type, but different samples were used for the two sources; in the two-speech conditions the same female voice was presented, speaking two different sentences, and in the two-speech-noise conditions two different segments of the noise were presented.

E. Familiarization

The present study was not aimed at testing children's vocabulary, but rather their speech intelligibility for known words. The 25 words were selected from the spondee list after pilot testing indicated that 20, 4 to 5 year-old children were either familiar with the words or could easily ascertain their meaning after one presentation. For each of the 25 words a commissioned artist-drawn picture was used to visually represent the meaning of the word. Prior to testing, subjects underwent a familiarization session (approximately 5 min in duration) in which they were presented with the picture-word combinations and tested to insure that they associated each of the pictures with their intended auditory target.

F. Speech reception threshold estimation

The test involved a single interval 4AFC discrimination procedure. On each trial, the child viewed a set of four pictures from the set of 25 picture-word matches. A word matching one of the pictures was randomly selected and presented from the front speaker. A leading phrase such as ''Point to the picture of the...'' or ''Where is the...'' preceded each target word. The child was asked to select the picture matching the heard word, and to guess if not sure or if the word was not audible. The randomization process ensured that for every subject, on average, all 25 words were selected an equal number of times. The experimenter entered the child's response into the computer. Following correct responses, feedback was provided in the form of 3-s musical clips from popular children's music. Approximately 20 clips were digitized and stored on the computer, and randomly selected on correct-feedback trials. Following incorrect responses, feedback was provided in the form of a brief phrase such as ''Let's try another one'' or ''That must have been difficult.'' Five such phrases were digitized and stored on the computer, and randomly selected on incorrect-feedback trials.

An adaptive tracking method was used to vary the level of the target signal, such that correct responses result in level decrement and incorrect responses result in level increment. The algorithm includes the following rules: (1) Level is initially reduced in steps of 8 dB, until the first incorrect response. (2) Following the first incorrect response a three-down/one-up rule is used, whereby level is decremented following three consecutive correct responses and level is incremented following a single incorrect response. (3) Following each reversal the step size is halved. (4) The minimum step size is 2 dB. (5) A step size that has been used twice in a row in the same direction is doubled. For instance, if the level was decreased from 40 to 36 (step=4) and then again from 36 to 32 (step=4), continued decrease in level would result in the next level being 24 (step=8). (6) After three consecutive incorrect responses a ''probe'' trial is presented at the original level of 60 dB. If the probe results in a correct response the algorithm resumes at the last trial before the probe was presented. If more than three consecutive probes are required, testing is terminated and the subject's data are not included in the final sample. (7) Testing is terminated following five reversals.

For each subject, speech-reception-thresholds (SRTs) were measured for each condition. At the start of each SRT measurement, the level of the target was initially 60 dB SPL. When competitors were present (non-*quiet* conditions), the level of each competitor was fixed at 60 dB SPL, such that the overall level of the competitors was increased by approximately 3 dB when two competitors were presented compared with the one-competitor conditions. Thus, the adaptive track began with a signal-to-noise ratio of 0 dB in the one-competitor cases and −3 dB in the two-competitor cases.

Results were analyzed using a constrained maximum-likelihood method of parameter estimation outlined by Wichmann and Hill (2001a, b). All the data from each experimental run for each participant were fit to a logistic function.

Thresholds were calculated by taking the inverse of the function at a specific probability level. In our 4AFC task, using an adaptive three-down/one-up procedure, the lower bound of the psychometric function was fixed at the level of chance performance, 0.25, and the threshold level corresponded to the point on the psychometric function where performance was approximately 79.4% correct. Biased estimates of threshold can occur. Bias can be introduced by the sampling scheme used and lapses in listener attention. Wichmann and Hill (2001a, b) demonstrated that bias associated with lapses was easily overcome by introducing a highly constrained parameter to control the upper bound of the psychometric function. This approach was used to assess our data. The upper bound of the psychometric function was constrained within a narrow range (0.06) as suggested by Wichmann and Hill (2001b). As the authors suggest, under some circumstances, bias introduced by the sampling scheme may be more problematic to avoid even when a hundred trials are obtained per level visited. The possibility of biased threshold estimates due to our sampling scheme was assessed by comparing the thresholds obtained using the constrained maximum-likelihood method with traditional threshold estimates based on the last three reversals in each experimental run. A repeated measured *t*-test on quiet thresholds for the 36 children tested revealed no statistically significant difference between the estimated threshold values obtained using the ML approach versus the traditional approach [$t(35)=1.37$, $p>0.05$, two tailed].

III. RESULTS

SRTs were statistically analyzed for the children groups using a mixed-design analysis of variance (ANOVA) with two between-subjects variables (number of competitors, competitor type) and one within-subjects variable (condition). Significant main effects of number [$F(1,32)=4.05$; $p<0.05$] and condition [$F(2,32)=119.57$, $p<0.0001$] were found, but there was no effect of type. Significant interactions were found for condition with number [$F(2,64)=66.50$; $p<0.03$] and condition with type [$F(2,64)=162.01$; $p<0.001$]. Scheffe's *posthoc* contrasts (significance value $p<0.05$) showed that SRTs in *quiet* were significantly lower than SRTs in either *front* or *right*. Children tested with two competitors had significantly higher SRTs than those tested with one competitor for the *front* and *right* conditions (further comparisons between *front* and *right* are described below with regard to spatial release from masking). Finally, for reasons that are not clear, SRTs on the quiet conditions were lower in the two speech-noise groups than in the groups tested with the speech competitors. Adult data were analyzed with a one-way ANOVA for the nine conditions, which revealed a significant main effect [$F(8,8)=3.77$; $p<0.05$]. Scheffe's *posthoc* contrasts [$F(8,8);Fp<0.01$] revealed that *quiet* SRTs were lower than SRTs on all other conditions. Child and adult SRTs were compared with independent *t*-tests for each of the nine conditions; since the *quiet* condition was tested for each of the child groups, a total of 12 comparisons were conducted. The Bonferroni adjustment for multiple comparisons as described by Uitenbroek (1997) was applied (df=16, criterion of $t>3.34$ and $p<0.004$). Significant differences were found for all 12 comparisons, suggesting that adults' SRTs were lower than those of children for all conditions tested.

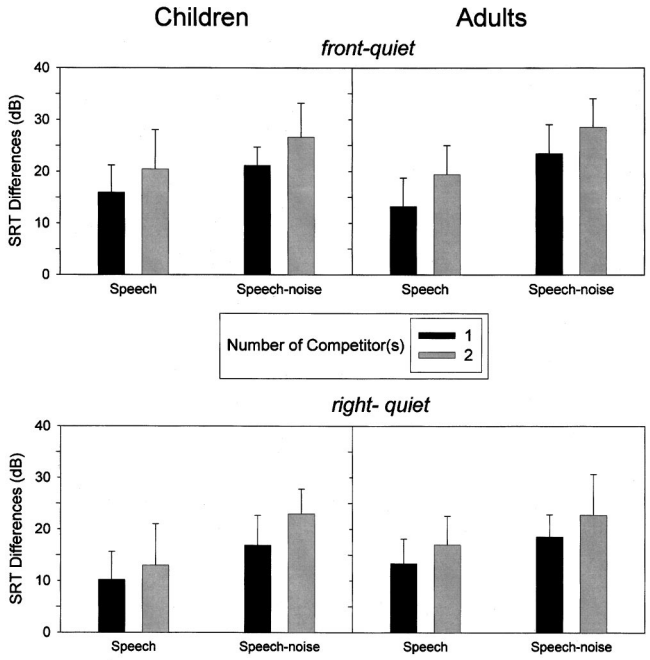

FIG. 1. Average (±SD, dB SPL) differences between speech reception thresholds (SRTs) in the masked and quiet conditions. Data are plotted for *front* (top panels) and *right* (bottom panels) conditions, for children (left panels) and adults (right panels). Each panel compares difference values for the speech and speech-noise competitors when the number of competitor(s) was either one (black bars) or two (gray bars).

Figure 1 shows group means (±SD) for masking (differences between masked and quiet SRTs). For each subject masking amounts for front and right were obtained by subtracting *quiet* SRTs from *front* and *right* SRTs, respectively. To place the masking values into context, average (±SD) SRTs for all groups and conditions are listed in Table II. Statistical analyses on the amount of masking for the child groups were conducted with a three-way mixed-design ANOVA treating condition (*front minus quiet*, *right minus quiet*) as the within-subjects variable and competitor type and number as the between-subjects variables. A significant effect of condition [$F(1,32)=29.13$; $p<0.0001$] suggests

TABLE II. Mean (±SD) speech reception thresholds (in dB SPL)[a]

Group	Quiet	Front	Right
Children			
1 speech	26.02(3.81)	41.81 (6.31)	36.64 (6.48)
2 speech	27.32(5.25)	47.75 (6.30)	40.33 (6.29)
1 speech-noise	23.25(5.56)	44.37 (6.50)	40.13 (3.89)
2 speech-noise	21.45(3.3)	48.01 (2.07)	44.41 (7.18)
Adults			
1 speech	3.84(3.18)	16.71 (5.66)	16.86 (3.84)
2 speech		23.35 (4.41)	20.43 (4.01)
1 speech-noise		27.39 (5.28)	22.25 (4.82)
2 speech-noise		32.82 (4.40)	27.60 (8.65)

[a]It is important to recall that each child was tested on three conditions (quiet, front, right) for one masker type, and that each adult was tested on all nine conditions, hence only one entry in Table II for adult quiet thresholds.

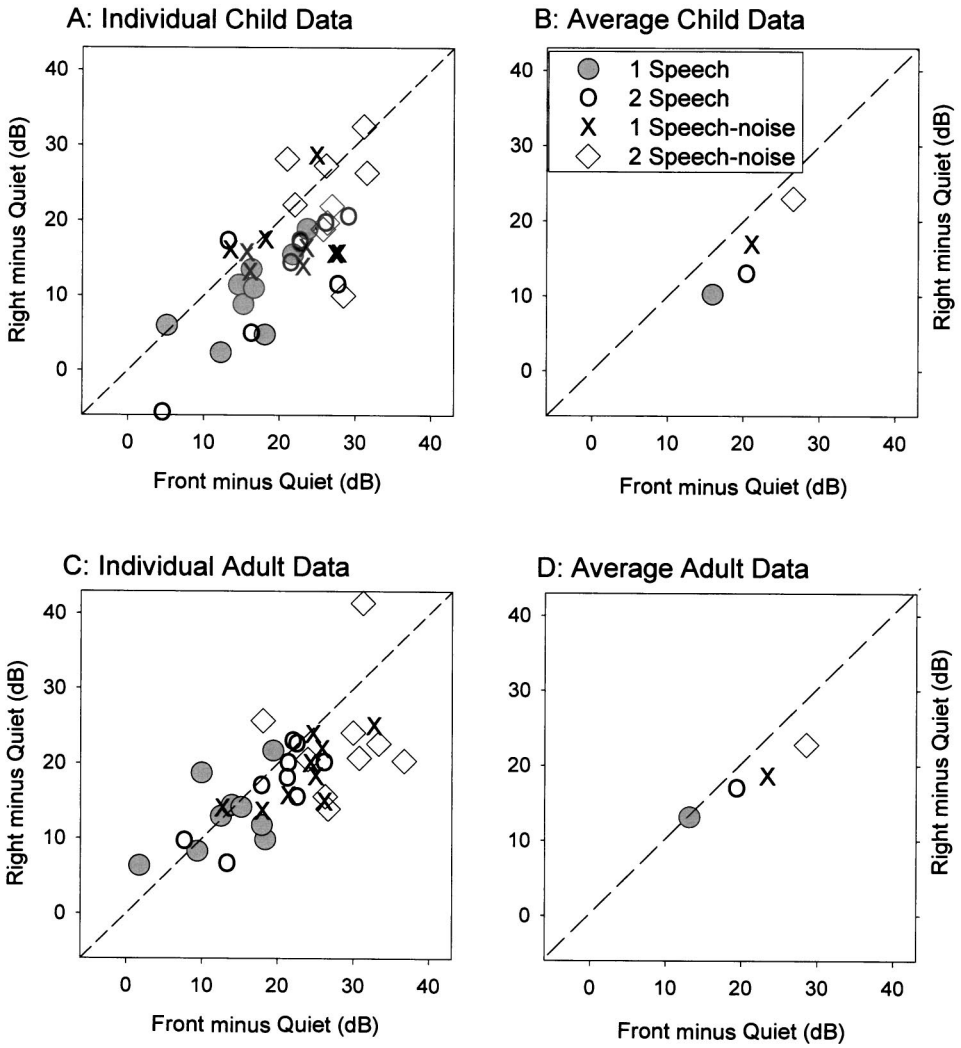

FIG. 2. Masking amounts (differences between masked and quiet thresholds) for the *Right minus Quiet* conditions are plotted vs. *Front minus Quiet* conditions. Panels (A) and (C) show data for children and adults, respectively; each symbol denotes data from an individual subject, and the four different symbols refer to the type/number combination of competitor(s). The diagonal lines denote equality between the two variables. Panels (B) and (D) show average group data from (A) and (C), respectively, for the four conditions tested.

that masking in the *front minus quiet* condition was higher than in *right minus quiet*. Significant effects of type [$F(1,32)=15.51$; $p<0.0001$] and number [$F(1,32)=6.95$; $p<0.013$] further suggest that masking was greater for two competitors than one, and greater for the speech-noise competitor compared with speech. There were no significant interactions. For the adult subjects, a three-way repeated measures ANOVA (condition×type×number) suggested, similar to the children, that masking was greater in the *front* versus *right* conditions [$F(1,8)=27.72$; $p<0.001$], greater with speech-noise than speech [$F(1,8)=30.72$; $p<0.001$] and greater for two compared with one competitor [$F(1,8)=16.71$; $p<0.004$]. Masking data for child and adult groups were compared with independent *t*-tests for each competitor location/type/number combination, and the Bonferroni correction for eight comparisons was applied (Uitenbroek, 1997). None of the comparisons yielded a significant difference in masking between the child and adult groups, and none of the interactions were significant.

Spatial release from masking was defined as the difference between front masking (*front minus quiet*) and right masking (*right minus quiet*). Figure 2 shows individual points for *right minus quiet* plotted versus *front minus quiet* for all subjects and conditions tested. If no spatial release from masking occurred, the points would be expected to fall along the diagonal. Points falling below the diagonal would be indicative of spatial release from masking. Alternatively, points falling above the diagonal would represent cases in which thresholds were higher when the competitors were on the right rather than in front. The majority of individual data points in Fig. 2 are below the diagonal, and average points for all but one group are also indicative of spatial release from masking.

Figure 3 summarizes the findings for spatial release from masking. For children, group average values are between 3.6 and 7.5 dB; the overall average for all 36 children is 5.25 dB. For adults, group averages range from 0 to 5.2 dB with an overall average of 3.34 dB. Children's data were analyzed with a two-way between-subjects ANOVA (type ×number), revealing no significant main effects or interactions. This lack of an effect may not surprising given the large intersubject variability, which is notable in Fig. 3(A); while some children had spatial release from masking values greater than 10 dB, other children had values near 0, and a small number had negative values. Adult data were analyzed with a two-way repeated measures ANOVA (type×number), also revealing no significant effects or interactions. Finally,

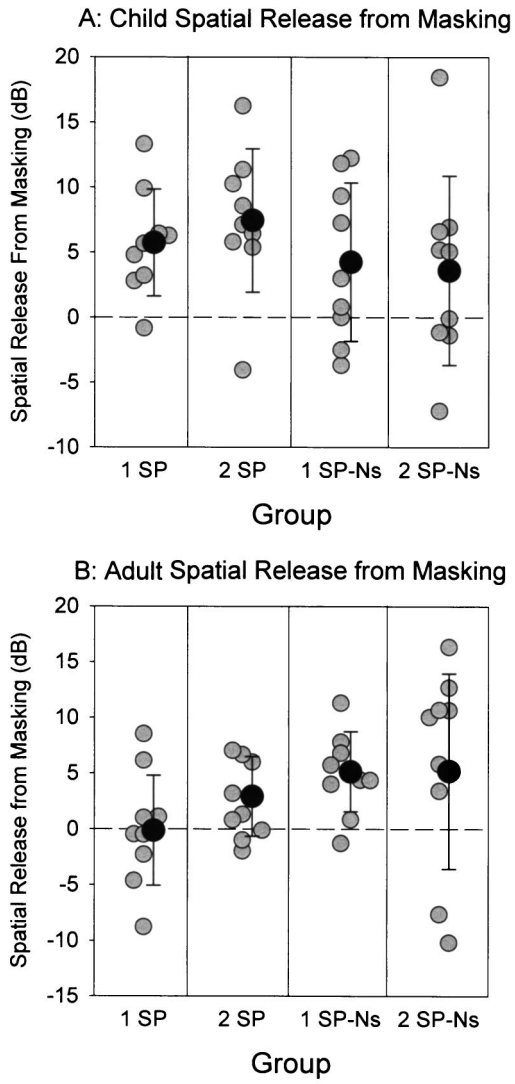

FIG. 3. Spatial release from masking values are shown for children and adults in panels (A) and (B), respectively. Each panel shows values grouped by competitor type/number condition (on the *x*-axis labels SP and Sp-Ns refer to the speech and speech-noise conditions, respectively). Individual values appear in gray circles, and group averages (±SD) are shown in black circles. When necessary to avoid overlap of data points, in some cases there was a slight shifting along the *x* axis.

to compare spatial release from masking for children and adults independent *t*-tests were conducted for each type/number combination, with the Bonferroni correction for four contrasts applied (Uitenbroek, 1997). The only significant difference between groups was for the one-speech competitor condition, in which the average spatial release from masking in adults is 0, compared with an average value of 5.7 for the child group.

IV. DISCUSSION

Speech intelligibility in quiet and in the presence of competing sounds and the ability to benefit from spatial separation of the speech and competitor(s) were investigated in children and adults. Although extensively studied in adults, to date this area of research has been minimal in children. This study may therefore be helpful towards improving our understanding of children's ability to hear and learn in noisy and reverberant environments, especially given that such abilities are known to be compromised compared with abilities measured under quiet condition (e.g., ANSI, 2002; Yacullo and Hawkins, 1987; Knecht *et al.*, 2002). The results can be summarized as follows: (1) Adults' SRTs were lower than those of the children for all conditions. (2) For both age groups masking was significantly greater with speech-noise than with speech and with two competitors compared with one. (3) The amount of masking did not differ across the two age groups. (4) The amount of spatial release from masking was similar for children and adults on all but one condition. (5) The number or type of competitor did not affect the size of spatial release from masking for either age group.

A. SRTs and masking amount

The primary age difference was that of higher SRTs in children than adults, in quiet and in all masked conditions. This age effect is consistent with existing developmental psychoacoustic literature, which has shown that children ages 4 to 7 typically have higher tone detection thresholds compared with adults (e.g., Buss *et al.*, 1999; Oh *et al.*, 2001). Similarly, recognition of spondee words such as those used here in temporally modulated noise has been shown to produce higher thresholds in 5 to 10 year-old children than in adults (Hall *et al.*, 2002).

The age effect found here can be attributed to a combination of peripheral and central mechanisms. Peripherally, frequency resolution is highly similar to that of adults by 5 years of age (Allen *et al.*, 1989; Hall and Grose, 1991; Veloso *et al.*, 1990). However, young children appear to integrate auditory information over a greater number of auditory channels than adults, suggesting that their ability to extract auditory cues, and in the present study to identify target words at low signal levels, is likely to be still developing (e.g., Hall *et al.*, 1997; Buss *et al.*, 1999; Hartley *et al.*, 2000; Oh *et al.*, 2001). Immaturity of central auditory processes and the adoption of listening strategies that are non-optimal or less efficient than adults (Allen and Wightman, 1994; Lutfi *et al.*, 2003) may have also affected SRTs. Finally, differences in thresholds may represent age-related differences in the ability to take advantage of hearing partial word segments and to ''fill in'' the remainder of the target word. Anecdotal reports from adults suggest that they relied heavily on this strategy at low signal levels. The ability to adopt this strategy can most likely be attributed to adults' having more experience and better-developed language skills, including the ability to parse phonetic, semantic, and lexical aspects of speech (Fletcher and MacWhinney, 1995).

Of interest is the lack of an age effect for the amount of masking. Previous studies have typically shown that adults experience reduced masking compared with children (e.g., Buss *et al.*, 1999; Oh *et al.*, 2001; Papso and Blood, 1989; Hall *et al.*, 2002). Although this explanation may not be entirely satisfying, the lack of an age-related masking effect may be attributed to the task itself. In the current study, using the 4AFC task, *quiet* thresholds were extremely low in adults. In contrast, adults tested on the same measure using identical stimuli, but with a 25AFC did not reveal such low

SRTs in *quiet*, but continued to show lower masked SRTs. The amount of masking in the 25AFC task was therefore lower in adults than children (Johnstone and Litovsky, 2005). When increasing task difficulty for adults, a more realistic story with regard to age-related masking differences may emerge, suggesting the importance of equating for difficulty of the task when comparing perceptual abilities across age groups.

B. Competitor type

SRTs did not differ for the two types of competitors for children, but were higher with speech-noise than speech for the adults, which may be in part due to greater statistical power in the adult within-subjects comparisons. For both age groups, masking was greater with speech-noise than speech. These findings are consistent with other findings in adults in a one-masker paradigm, whereby greater amounts of masking were reported in the presence of speech-noise compared with speech (e.g., Hawley *et al.*, 2004). This has been attributed to greater amounts of overlap in the energies of the speech-noise masker and the target, resulting in the reduction of F0 discrimination. However, in previous work, as the number of maskers increased, speech became a more potent masker, an explanation involving informational masking and linguistic interference from multiple speech maskers was invoked to account for the increased interference from speech (e.g., Bronkhorst, 2000; Hawley *et al.*, 2004). Here, there was no interaction of type and number of competitors, which may be explained by stimulus differences across studies. Studies such as those of Hawley *et al.* (2004) typically use male voices for both the target and competitors, whereas here the target was a male voice and the competitor was spoken by a female. The differences in voice pitch, quality, and ongoing F0 differences provided a robust cue for source segregation in the presence of speech competitors, regardless of the number of competitors. The speech-noise competitor, having momentary dips in amplitude but no ongoing changes in frequency, served as a more potent masker whose effect was greater than that of speech. With same-gender competitors it is highly likely that speech would have produced masking at least as great, if not larger than the speech-noise competitor (e.g., Brungart *et al.*, 2001). Finally, the differences in masking amounts for the child groups may be accounted for by the fact that, for reasons that are not entirely clear, but probably due to random variation within the population, SRTs on the quiet conditions were lower in the two speech-noisé groups than in the groups tested with the speech competitors.

C. Number of competitors

For both children and adults, masking was significantly greater for two compared with one competitor(s), and the interactions of number with location (front versus right) were not significant. Averaged over all competitor types and numbers, the addition of a second competing sound resulted in increased masking of 4.7 dB for children and 4.8 for adults. Two interpretations can be considered here. First, in the presence of competitors with envelope modulations such as those used here, listeners may be better able to take advantage of the modulations and ''listen in the gaps'' in the presence of a single competitor. As a second competitor is added the signal contains fewer gaps, thereby decreasing opportunities of ''gap listening'' (e.g., Festen and Plomp, 1990; Hawley *et al.*, 2004). Second, consider the possible role of ''informational'' masking. In recent years this term has been used extensively in the auditory literature to explain masking phenomena that cannot be attributed solely to peripheral auditory mechanisms (e.g., Neff and Green, 1987; Lutfi, 1990; Kidd *et al.*, 2003). In the speech intelligibility literature, one of the conditions under which informational masking has been thought to occur is when the addition of a second masker elevates thresholds by more than the 3 dB expected simply from the added energy in the presence of a second masker (e.g., Brungart *et al.*, 2001; Hawley *et al.*, 2004; Durlach *et al.*, 2003). This threshold elevation may result from the increased complexity of the listening environment, possibly due to uncertainty on the part of the listener as to what aspects of the stimulus to ignore and what aspects to pay attention to. Although difficult to evaluate numerically, this component of masking may have been present here to some extent, and more direct tests of the effect in children would be important to pursue in future studies.

D. Spatial release from masking

Measures of spatial release from masking did not statistically differ across age groups, nor were there effects of competitor type and number. The only effect was the lack of spatial release from masking in the one-speech condition in adults, compared with 5.7 dB in children. The adult data differ from other free field studies in adults, in which spatial release from masking for speech was reported to be at least 3 dB for a single competing talker and as high as 12 dB for multiple talkers (Bronkhorst, 2000; Hawley *et al.*, 2004). The lack of release from masking found here with the one-speech competitor is likely due to the nature of the task and stimuli; the use of a fairly easy 4AFC task in combination with different-gender talkers for the target and competitor most likely created a relatively simple listening situation for adults.

Spatial cues are thought to be especially useful in challenging conditions when nonspatial cues are difficult to access (Peissig and Kollmeier, 1997; Bronkhorst, 2000; Durlach *et al.*, 2003; Freyman *et al.*, 2004). In the adult group tested here, spatial cues were beneficial in the conditions that created greater amounts of *front* masking (two-speech, one-speech-noise and two-speech-noise). The lack of a location effect in the one-speech condition is likely due to the general ease of listening to spondees when the competitor consists of a single, different-gender talker. In that condition, spatial cues did not help to reduce masking in the *right* condition, since masking was already relatively small in that condition. In contrast with adults, in children the one-speech *front* condition did present a challenging situation, probably because children are less able to take advantage of the different-gender competitor to hear the target speech. Thus, spatial cues were indeed relevant to the children so as to produce a robust improvement in the *right* condition com-

pared with the *front*. These findings suggest that, while tasks that are more complex, using sentence material and/or same-gender stimuli may be more appropriate for measuring spatial release from masking in adults, the task used here is a good tool for measuring the ability of young children to negotiate complex auditory environments.

The finding that, overall, spatial release from masking in children is similar to that in adults is consistent with work showing that preschool-age children perform similar to adults on measures of binaural masking level differences (Nozza *et al.*, 1988; Moore *et al.*, 1991) and minimum audible angle [Litovsky (1997); for review see Litovsky and Ashmead (1997)]. This finding implies that for a simple closed-set task young children are able to utilize spatial and/or head shadow cues to the same extent as adults in order to segregate sounds in noisy environments. That is not to say that children would be expected to perform similar to adults on all measures of speech intelligibility in noise. Given recent findings that children exhibit poorer attentional selectivity on auditory tasks (e.g., Oh *et al.*, 2001), and reduced unmasking for tone detection under dichotic conditions (Wightman *et al.*, 2003; Hall *et al.*, 2004), the possibility remains that age differences would be seen under more demanding conditions, such as an open-set test or with same-gender target and competitors. Those differences, however, would not be attributable to age-dependent binaural abilities, but rather to other central processes such as auditory attention.

E. Conclusions

Young children require higher signal levels than adults to identify spondees in a simple 4AFC task, and these age-related differences may be mediated by both peripheral and central auditory processes. The fact that young children can benefit from spatial separation of the target speech and competing sources suggests that in a complex acoustic environment, such as a noisy classroom, they might find it easier to attain information if the source of interest is spatially segregated from noise sources. Although, the extent to which this is true with real-world sounds may depend on duration, complexity and type of sounds, and the demand on attentional resources that various sounds may require. Finally, the test used here (developed by Litovsky, 2003) is designed to also be used in pediatric clinical settings where young children are often fitted with hearing aids or cochlear implants, with little knowledge about the efficacy of the fittings in noisy environments. This test may offer a way to evaluate the abilities in children with hearing aids and cochlear implants to function in noisy environments, and may, for example, be useful in assessing the extent to which children obtain a benefit from bilateral fitting strategies (Litovsky *et al.*, 2004).

ACKNOWLEDGMENTS

The author is grateful to Aarti Dalal and Gerald Ng for assistance with programming and data collection, and to Patti Johnstone and Shelly Godar for helping with data analysis. The author is also grateful to Dr. Joseph Hall for initially suggesting the use of spondees in a forced choice paradigm, and to Dr. Adelbert Bronkhorst and an anonymous reviewer for helpful suggestions during the review process. This work was supported by NIDCD (Grant Nos. DC00100 and DC0055469), National Organization for Hearing Research, and the Deafness Research Foundation. Portions of the data were collected while R. Litovsky was at Boston University, Hearing Research Center.

APPENDIX: LIST OF SPONDEE WORDS USED IN THE PRESENT EXPERIMENT

Hotdog
Ice Cream
Birdnest
Cowboy
Dollhouse
Barnyard
Scarecrow
Railroad
Sidewalk
Rainbow
Cupcake
Birthday
Airplane
Eyebrow
Shoelace
Toothbrush
Hairbrush
Highchair
Necktie
Playground
Football
Baseball
Bluejay
Bathtub
Bedroom

[1]The lower limit of 4.5 years is slightly conservative, and was based on pilot testing which suggested that by that age all children were familiar with the majority of the target words. The upper limit of 7.5 is somewhat smaller than the 10-year limit used in a number of other works (e.g., Oh *et al.*, 2001; Hall *et al.*, 2002), but similar to that used in studies on auditory attention in young children, in which there do not appear to be developmental effects within the age range (e.g., Stellmack *et al.*, 1997; Oh *et al.*, 2001).

Allen, P., and Wightman, F. (**1994**). ''Psychometric functions for children's detection of tones in noise,'' J. Speech Hear. Res. **37**, 205–215.
Allen, P., Wightman, F., Kistler, D., and Dolan, T. (**1989**). ''Frequency resolution in children,'' J. Speech Hear. Res. **32**, 317–322.
American National Standards Institute (**2002**). ''Standard for acoustical characteristics of classrooms in the United States,'' ANSI—S12.60.
Arbogast, T. L., Mason, C. R., and Kidd, G. (**2002**). ''The effect of spatial separation on informational and energetic masking of speech,'' J. Acoust. Soc. Am. **112**, 2086–2098.
Bronkhorst, A. (**2000**). ''The cocktail party phenomenon: A review of research on speech intelligibility in multiple-talker conditions,'' Acta. Acust. Acust. **86**, 117–128.
Bronkhorst, A. W., and Plomp, R. (**1992**). ''Effect of multiple speechlike maskers on binaural speech recognition in normal and impaired hearing,'' J. Acoust. Soc. Am. **92**, 3132–3139.
Brungart, D. S., Simpson, B. D., Ericson, M. A., and Scott, K. R. (**2001**). ''Informational and energetic masking effects in the perception of multiple talkers,'' J. Acoust. Soc. Am. **110**, 2527–2538.

Buss, E., Hall, III, J. W., Grose, J. H., and Dev, M. B. (**1999**). ''Development of adult-like performance in backward, simultaneous, and forward masking,'' J. Speech Lang. Hear. Res. **42**, 844–849.
Crandell, C. C. (**1993**). ''Speech recognition in noise by children with minimal degrees of sensorineural hearing loss,'' Ear Hear. **14**, 210–216.
Culling, J. F., Hawley, M. L., and Litovsky, R. Y. (**2004**). ''The role of head-induced interaural time and level differences in the speech reception threshold for multiple interfering sound sources,'' J. Acoust. Soc. Am. **116**, 1057–1065.
Dawson, P. W., Decker, J. A., and Psarros, C. E. (**2004**). ''Optimizing dynamic range in children using the nucleus cochlear implant,'' Ear Hear. **25**, 230–241.
Durlach, N. I., Mason, C. R., Shinn-Cunningham, B. G., Arbogast, T. L., Colburn, H. S., and Kidd, Jr., G. (**2003**). ''Informational masking: counteracting the effects of stimulus uncertainty by decreasing target-masker similarity,'' J. Acoust. Soc. Am. **114**, 368–379.
Eisenberg, L. S., Kirk, K. I., Martinez, A. S., Ying, E. A., and Miyamoto, R. T. (**2004**). ''Communication abilities of children with aided residual hearing: comparison with cochlear implant users,'' Arch. Otolaryngol. Head Neck Surg. **130**, 563–569.
Festen, J. M., and Plomp, R. (**1990**). ''Effects of fluctuating noise and interfering speech on the speech-reception threshold for impaired and normal hearing,'' J. Acoust. Soc. Am. **88**, 1725–1736.
Fletcher, P., and MacWhinney, B. (**1995**). *Handbook of Child Language* (Blackwell, Oxford, UK).
Freyman, R. L., Balakrishnan, U., and Helfer, K. S. (**2001**). ''Spatial release from informational masking in speech recognition,'' J. Acoust. Soc. Am. **109**, 2112–2122.
Freyman, R. L., Balakrishnan, U., and Helfer, K. S. (**2004**). ''Effect of number of masking talkers and auditory priming on informational masking in speech recognition,'' J. Acoust. Soc. Am. **115**, 2246–2256.
Hall, J. W., Buss, E., Grose, J. H., and Dev, M. B. (**2004**). ''Developmental effects in the masking-level difference,'' J. Speech Lang. Hear. Res. **47**, 13–20.
Hall, III, J. W., and Grose, J. H. (**1991**). ''Notched-noise measures of frequency selectivity in adults and children using fixed-masker-level and fixed-signal-level presentation,'' J. Speech Hear. Res. **34**, 651–60.
Hall, III, J. W., Grose, J. H., and Dev, M. B. (**1997**). ''Auditory development in complex tasks of comodulation masking release,'' J. Speech Lang. Hear. Res. **40**, 946–954.
Hall, III, J. W., Grose, J. H., Buss, E., and Dev, M. B. (**2002**). ''Spondee recognition in a two-talker masker and a speech-shaped noise masker in adults and children,'' Ear Hear. **23**, 159–165.
Hall, III, J. W., Grose, J. H., Buss, E., Dev, M. B., Drake, A. F., and Pillsbury, H. C. (**2003**). ''The effect of otitis media with effusion on perceptual masking,'' Arch. Otolaryngol. Head Neck Surg. **129**, 1056–1062.
Hartley, D. E., Wright, B. A., Hogan, S. C., and Moore, D. R. (**2000**). ''Age-related improvements in auditory backward and simultaneous masking in 6- to 10-year-old children,'' J. Speech Lang. Hear. Res. **43**, 1402–1415.
Hawley, M. L., Litovsky, R. Y., and Colburn, H. S. (**1999**). ''Speech intelligibility and localization in complex environments,'' J. Acoust. Soc. Am. **105**, 3436–3448.
Hawley, M. L., Litovsky, R. Y., and Culling, J. F. (**2004**). ''The benefit of binaural hearing in a cocktail party: Effect of location and type of interferer,'' J. Acoust. Soc. Am. **115**, 833–843.
Johnstone, P., and Litovsky, R. Y. (**2005**). ''Speech intelligibility and spatial release from masking in children and adults for various types of interfering sounds,'' J. Acoust. Soc. Am. (in press).
Kidd, Jr., G., Mason, C. R., and Richards, V. M. (**2003**). ''Multiple bursts, multiple looks, and stream coherence in the release from informational masking,'' J. Acoust. Soc. Am. **114**, 2835–2845.
Koehnke, J., and Besing, J. M. (**1996**). ''A procedure note for testing speech intelligibility in a virtual listening environment,'' Ear Hear. **17**, 211–217.
Knecht, H. A., Nelson, P. B., Whitelaw, G. M., and Feth, L. L. (**2002**). ''Background noise levels and reverberation times in unoccupied classrooms: predictions and measurements,'' Am. J. Audiol. **11**, 65–71.
Litovsky, R. (**1997**). ''Developmental changes in the precedence effect: Estimates of Minimal Audible Angle,'' J. Acoust. Soc. Am. **102**, 1739–1745.
Litovsky, R. (**2003**). ''Method and system for rapid and reliable testing of speech intelligibility in children,'' U.S. Patent No. 6,584,440.
Litovsky, R., and Ashmead, D. (**1997**). ''Developmental aspects of binaural and spatial hearing,'' in *Binaural and Spatial Hearing*, edited by R. H. Gilkey and T. R. Anderson (Earlbaum, Hillsdale, NJ), pp. 571–592.
Litovsky, R. Y., Fligor, B., and Tramo, M. (**2002**). ''Functional role of the human inferior colliculus in binaural hearing,'' Hear. Res. **165**, 177–188.
Litovsky, R. Y., Parkinson, A., Arcaroli, J., Peters, R., Lake, J., Johnstone, P., and Yu, G. (**2004**). ''Bilateral cochlear implants in adults and children,'' Arch. Otolaryngol. Head Neck Surg. **130**, 648–655.
Lutfi, R. A. (**1990**). ''How much masking is informational masking?'' J. Acoust. Soc. Am. **88**, 2607–2610.
Lutfi, R. A., Kistler, D. J., Oh, E. L., Wightman, F. L., and Callahan, M. R. (**2003**). ''One factor underlies individual differences in auditory informational masking within and across age groups,'' Percept. Psychophys. **65**, 396–406.
Moore, D. R., Hutchings, M., and Meyer, S. (**1991**). ''Binaural masking level differences in children with a history of otitis media,'' Audiology **30**, 91–101.
Moore, D. R., Hartley, D. E., and Hogan, S. C. (**2003**). ''Effects of otitis media with effusion (OME) on central auditory function,'' Int. J. Pediatr. Otorhinolaryngol. **67**, S63–S67.
Neff, D. L., and Green, D. M. (**1987**). ''Masking produced by spectral uncertainty with multicomponent maskers,'' Percept. Psychophys. **41**, 409–415.
Nilsson, M., Soli, S. D., and Sullivan, J. A. (**1994**). ''Development of the Hearing in Noise Test for the measurement of speech reception thresholds in quiet and in noise,'' J. Acoust. Soc. Am. **95**, 1085–1099.
Nozza, R. J., Wagner, E. F., and Crandell, M. A. (**1988**). ''Binaural release from masking for a speech sound in infants, preschoolers, and adults,'' J. Speech Hear. Res. **31**, 212–218.
Oh, E. L., Wightman, F., and Lutfi, R. A. (**2001**). ''Children's detection of pure-tone signals with random multiple maskers,'' J. Acoust. Soc. Am. **109**, 2888–2895.
Papso, C. F., and Blood, I. M. (**1989**). ''Word recognition skills of children and adults in background noise,'' Ear Hear. **10**, 337–338.
Peissig, J., and Kollmeier, B. (**1997**). ''Directivity of binaural noise reduction in spatial multiple noise-source arrangements for normal and impaired listeners,'' J. Acoust. Soc. Am. **101**, 1660–1670.
Plomp, R., and Mimpen, A. M. (**1981**). ''Effect of the orientation of the speaker's head and the azimuth on a noise source on the speech reception threshold for sentences,'' Acustica **48**, 325–328.
Roberts, J., Hunter, L., Gravel, J., Rosenfeld, R., Berman, S., Haggard, M., Hall, III, J., Lannon, C., Moore, D., Vernon-Feagans, L., and Wallace, I. (**2004**). ''Otitis media, hearing loss, and language learning: controversies and current research,'' J. Dev. Behav. Pediatr. **25**, 110–122.
Rothauser, E. H., Chapman, W. D., Guttman, N., Nordby, K. S., Silbiger, H. R., Urbanek, G. E., and Weinstock, M. (**1969**). ''IEEE Recommended Practice for Speech Quality Measurements,'' IEEE Trans. Audio Electroacoust. **17**, 227–246.
Shinn-Cunningham, B. G., Schickler, J., Kopco, N., and Litovsky, R. (**2001**). ''Spatial unmasking of nearby speech sources in a simulated anechoic environment,'' J. Acoust. Soc. Am. **110**, 1118–1129.
Stellmack, M. A., Willihnganz, M. S., Wightman, F. L., and Lutfi, R. A. (**1997**). ''Spectral weights in level discrimination by preschool children: analytic listening conditions,'' J. Acoust. Soc. Am. **101**, 2811–2821.
Uitenbroek, D. G. (**1997**). ''SISA Binomial,'' Southampton: D. G. Uitenbroek. Retrieved 1 January, 2004, from the World Wide Web: http://home.clara.net/sisa/binomial.htm.
Veloso, K., Hall, III, J. W., and Grose, J. H. (**1990**). ''Frequency selectivity and comodulation masking release in adults and in 6-year-old children,'' J. Speech Hear. Res. **33**, 96–102.
Wichmann, F. A., and Hill, N. J. (**2001a**). ''The psychometric function: I. Fitting, sampling, and goodness of fit,'' Percept. Psychophys. **63**, 1293–1313.
Wichmann, F. A., and Hill, N. J. (**2001b**). ''The psychometric function: II. Bootstrap-based confidence intervals and sampling,'' Percept. Psychophys. **63**, 1314–1329.
Wightman, F. L., Callahan, M. R., Lutfi, R. A., Kistler, D. J., and Oh, E. (**2003**). ''Children's detection of pure-tone signals: informational masking with contralateral maskers,'' J. Acoust. Soc. Am. **113**, 3297–3305.
Yacullo, W. S., and Hawkins, D. B. (**1987**). ''Speech recognition in noise and reverberation by school-age children,'' Audiology **26**, 235–246.

Localizing nearby sound sources in a classroom: Binaural room impulse responses[a)]

Barbara G. Shinn-Cunningham[b)]
Boston University Hearing Research Center and Departments of Cognitive and Neural Systems and Biomedical Engineering, 677 Beacon Street, Boston, Massachusetts 02215

Norbert Kopco
Boston University Hearing Research Center and Department of Cognitive and Neural Systems, 677 Beacon Street, Boston, Massachusetts 02215

Tara J. Martin
Boston University Hearing Research Center, 677 Beacon Street, Boston, Massachusetts 02215

(Received 15 December 2003; revised 26 January 2005; accepted 27 January 2005)

Binaural room impulse responses (BRIRs) were measured in a classroom for sources at different azimuths and distances (up to 1 m) relative to a manikin located in four positions in a classroom. When the listener is far from all walls, reverberant energy distorts signal magnitude and phase independently at each frequency, altering monaural spectral cues, interaural phase differences, and interaural level differences. For the tested conditions, systematic distortion (comb-filtering) from an early intense reflection is only evident when a listener is very close to a wall, and then only in the ear facing the wall. Especially for a nearby source, interaural cues grow less reliable with increasing source laterality and monaural spectral cues are less reliable in the ear farther from the sound source. Reverberation reduces the magnitude of interaural level differences at all frequencies; however, the direct-sound interaural time difference can still be recovered from the BRIRs measured in these experiments. Results suggest that bias and variability in sound localization behavior may vary systematically with listener location in a room as well as source location relative to the listener, even for nearby sources where there is relatively little reverberant energy. [DOI: 10.1121/1.1872572]

PACS numbers: 43.66.Qp, 43.66.Pn, 43.55.-n, 43.55.Br [AK] Pages: 3100–3115

I. INTRODUCTION

Spatial acoustic cues are important for many tasks, ranging from locating a sound source (e.g., see Middlebrooks and Green, 1991) to detecting and understanding one source in the presence of competing sources from other locations (e.g., see Bronkhorst, 2000; Ebata, 2003). A great deal of research effort in the field of psychoacoustics has gone into measuring and analyzing head-related impulse responses (HRIRs; the impulse response from source to the listener's ears for sources presented in anechoic space) to gain insight into the acoustic cues underlying these important behavioral functions (e.g., see Wightman and Kistler, 1989; Shaw, 1997; Algazi *et al.*, 1999; Brungart and Rabinowitz, 1999; Kulkarni and Colburn, 2004) and to allow simulation of realistic binaural signals (e.g., Middlebrooks, 1999; Begault *et al.*, 2001; Macpherson and Middlebrooks, 2002; Culling *et al.*, 2003; Kidd *et al.*, 2005).

The reverberation present in everyday settings influences auditory perception and behavior in both positive and negative ways. Reverberation can provide listeners with a cue for sound source distance (e.g., see Mershon *et al.*, 1989; Naguib, 1995; Bronkhorst and Houtgast, 1999; Shinn-Cunningham, 2000a; Zahorik, 2002a, b), allow listeners to estimate properties of the environment (e.g., see Bradley and Soulodre, 1995; Bech, 1998b, a; Torres *et al.*, 2001; Shinn-Cunningham and Ram, 2003), and improve the subjective realism and externalization of virtual auditory space simulations (e.g., see Durlach *et al.*, 1992; Begault *et al.*, 2001). Reverberant energy also influences speech intelligibility; early reflections (occurring within 50–80 ms of the direct sound) generally increase the audibility of a speech source without degrading intelligibility (e.g., see Bradley *et al.*, 1999, 2003), whereas later reflections smear out the temporal information in the speech waveform and decrease intelligibility (e.g., see Bradley, 1986; Nabelek *et al.*, 1989; Bradley *et al.*, 1999; Bistafa and Bradley, 2000). Both early and late reflections cause interaural decorrelation that can degrade the accuracy of directional localization (Hartmann, 1983; Hartmann and Rakerd, 1999; Hartmann *et al.*, 1999; Shinn-Cunningham, 2000b; Kopco and Shinn-Cunningham, 2002) and the ability to detect and understand one source in the presence of a statistically stationary competing sound source from another location (Plomp, 1976; Zurek, 1993; Culling *et al.*, 1994; Shinn-Cunningham, 2002; Devore and Shinn-Cunningham, 2003; Zurek *et al.*, 2004). Similarly, early and late reflections are known to have a large impact on the impressions of source width and envelopment (e.g., see Barron, 2001). Despite the importance of reverberant energy on nearly all aspects of auditory perception, few studies have

[a)]Portions of this work were presented at the 2001 Mid-Winter Meeting of the Association for Research in Otolaryngology.
[b)]Electronic mail: shinn@cns.bu.edu

analyzed how reverberant energy affects the spatial acoustic cues reaching a listener.

In the field of architectural acoustics, there have been a number of studies of how auditoria and other large echoic spaces influence various aspects of the signals reaching a listener's ears (e.g., see Kleiner *et al.*, 1993; Bradley, 1996; Hidaka and Beranek, 2000; Nishihara *et al.*, 2001; Torres *et al.*, 2001; Okano, 2002). Similarly, there are some studies of the behavioral impact of reverberation (e.g., see Berkley, 1980; Bradley, 1986; Nabelek *et al.*, 1989; Culling *et al.*, 1994; Hartmann and Rakerd, 1999; Hodgson, 1999; Darwin and Hukin, 2000; Culling *et al.*, 2003). Statistics comparing the relative energy in the early and late portions of room impulse responses (e.g., the clarity index C_{80}) summarize how reverberant energy affects the subjective experience of listening to music or understanding speech in a particular space (e.g., see Hidaka and Beranek, 2000). However, there are relatively few studies of the effects of room reflections on spatial and binaural acoustic cues or how these effects vary with listener location in the room (although see de Vries *et al.*, 2001; Hartmann *et al.*, 2005). The current study analyzes some of the properties of acoustic spatial cues present in binaural room impulse responses (BRIRs; the impulse responses from a sound source to the ears of a listener located in a room) measured in an ordinary classroom. The goal of this study is to begin to quantify how acoustic spatial cues are affected by reverberant energy as a function of the listener's location in a room and the source location relative to the listener.

Most previous studies of HRIRs have focused on measurements made at distances of a meter or more, where the only effect of source distance is an overall change in gain. For these cases, interaural time differences (ITDs) and interaural level differences (ILDs) in the signals reaching the ears resolve source location to within a ''cone of confusion.'' However, for nearby sources (within a meter of the listener), interaural level differences increase and ILDs provide distance information (Duda and Martens, 1998; Brungart and Rabinowitz, 1999). For nearby sources, interaural differences resolve source location to within a ''torus of confusion'' (Shinn-Cunningham *et al.*, 2000) and spectral content can resolve source position within a torus of confusion (i.e., in the up/down, front/back dimensions; Asano *et al.*, 1990; Butler and Humanski, 1992; Wightman and Kistler, 1997; Vliegen and van Opstal, 2004). Because the acoustics of such situations differ from those normally studied, sound localization, source detection, and signal understanding differ when sources are nearby compared to the more commonly studied ''distant source'' conditions (e.g., see Brungart and Durlach, 1999; Shinn-Cunningham, 2000b; Shinn-Cunningham *et al.*, 2001; Shinn-Cunningham, 2002; Kopco and Shinn-Cunningham, 2003). Given that many important, everyday events (e.g., a personal conversation) involve sources relatively near the listener, it is important to understand what spatial acoustic cues arise for nearby sources in reverberant environments.

For nearby sources, small changes in the source location relative to the listener can cause considerably larger changes in the direct-sound energy reaching the ears than for more distant sources and the direct-sound level at the two ears can be very different (e.g., see Brungart and Rabinowitz, 1999; Shinn-Cunningham *et al.*, 2000; Kopco and Shinn-Cunningham, 2003). As a result, the interaction between source location and the effects of reverberation will be maximized when sources are near the listener, even though the overall influence of reverberant energy will be smaller than for more distant sources. Furthermore, analysis of how the effect of room reflections varies with source location for nearby sources can provide insights into what will happen for more distant sources, given that the main effect of increasing source distance beyond one meter is to reduce the direct sound level and increase the relative strength of reverberant energy at the ears.

The current analyses examine how listener location in a room and source location of nearby sources influence BRIRs in one example classroom. The specific room, source locations relative to the listener, and listener locations considered were chosen for two reasons: to (1) explore how the acoustics within a specific room can vary as the listener is moved within the room (e.g., ranging from a listener positioned far from any reflecting surfaces to the most extreme situation, where the listener is seated in the corner of the room) and (2) gain insight into results of related behavioral studies examining the effects of reverberation on perception for sources near a listener that were performed in or simulated the same space analyzed here.[1] While future papers will address how the acoustics of the classroom influence perception and behavior, the current analysis focuses on the effects reverberation can have on different aspects of the spatial cues present in BRIRs. The long-term goal of these efforts is to tease apart which aspects of the perceptual consequences of room reverberation are predicted directly from acoustic effects and which arise from interactions between properties of the signals at the ears and auditory processing.

The following analyses show that in the frequency domain, anechoic head-related transfer functions (HRTFs) vary relatively smoothly with frequency in both phase and magnitude compared to the frequency-to-frequency variability of binaural room transfer functions (BRTFs), a fact that reflects the complex interactions between the direct sound and reflected energy that arise in a room. Whereas anechoic head-related impulse responses are nearly equal to the impulse responses obtained by minimum-phase reconstruction from the magnitude of the HRTF plus a delay related to the travel time to the ear (i.e., phase information in the HRTF is relatively unimportant for reproducing the proper HRIR except for an overall group delay; e.g., see Kistler and Wightman, 1991), the phase information in a BRTF is critical. In a room, each reflection may boost or reduce the energy in a particular frequency of the direct sound, depending upon the exact timing of the reflection and whether it adds in or out of phase with the preceding energy at a given frequency. In addition, if the frequency content of a sound source fluctuates with time, the interaction between direct and reflected energy in a room will also vary over time in ways that depend in detail on the spectro-temporal structure of the source signal and of the BRTF. This complexity is reflected in the frequency-to-

frequency fluctuations in the BRTF magnitude and phase, which can be quite large.

Given the relatively smoothly varying nature of anechoic HRTFs with frequency, small short-term spectral fluctuations in a broadband source signal (e.g., over the course of tens to hundreds of milliseconds, such as are commonly found in speech and music) have only modest effects on the spatial cues reaching a listener in anechoic space. Furthermore, analyzing the spatial cues in a frequency-smoothed anechoic HRTF (e.g., smoothing HRTFs over a critical band of frequencies) provides a reasonable summary of the spatial cues that an arbitrary HRTF-filtered source is likely to contain.

In contrast, and as a direct result of the spectro-temporal complexity of a typical BRIR, even small fluctuations in a sound source's frequency content with time can cause large temporal variations in the spatial cues observed in the BRTF-filtered signal. The exact manner in which the reflected energy in the BRIR will affect spatial cues depends very strongly on both the spectral and temporal properties of a stimulus. For instance, a pure tone signal that is turned on in a room will rapidly converge to a steady-state magnitude and phase value at each ear, with the magnitudes and phases depending only on the left- and right-ear BRTF magnitudes and phases at the tone frequency. Thus, the interaural differences caused by a pure tone in a room will rapidly converge to values that are constant over time. However, a signal with more bandwidth will contain fluctuations in its short-term spectrum. As the short-term signal frequency content varies over time, the way in which the short-term magnitude and phase spectra of the signals reaching each ear are affected by room reverberation will change and evolve dynamically, depending on the spectro-temporal content of the source (including the relative phases of different frequency components of the input) and how it interacts with the reflected energy. Because this interaction is different at the two ears, interaural parameters will also fluctuate over time. This complexity makes it impossible to predict what spatial cues will be present in a room unless the source is specified.

Rather than analyzing what spatial cues will be present in the signals reaching a listener's ears for a specific stimulus, the current analysis examines aspects of BRIRs/BRTFs that are related to the ways in which short-term spatial cues will be influenced by reverberant room energy. For instance, the size of frequency-to-frequency fluctuations in the BRTF magnitude and phase is related to how strongly the spatial cues reaching the ears of a listener in the room depend on the short-term spectro-temporal content of the source. Thus, frequency-to-frequency variability in BRTFs is related to the variability in spatial cues likely to be observed (e.g., at the output of a peripheral auditory nerve) across samples for independent tokens of finite-length broadband noise signals and across time for an ongoing broadband signal. Conversely, the expected value of different spatial cues in the signals reaching a listener's ears (averaged across independent signal tokens or across time) is closely related to properties of the BRTF averaged across frequency (e.g., across a critical band). Thus, in order to gain insight into how reverberant energy will tend to affect across-time variability in spatial cues for broadband sources, we consider frequency-to-frequency variations in the BRTFs as a function of listener location and source position, a property that (as discussed below) depends primarily on the energy ratio of late reverberation to direct sound and early reflections in the BRTFs. In order to gain insight into how reverberant energy influences average spatial properties of the signals reaching the ears, we compare frequency-smoothed BRTFs to comparable anechoic transfer functions as a function of listener and source position in the room.

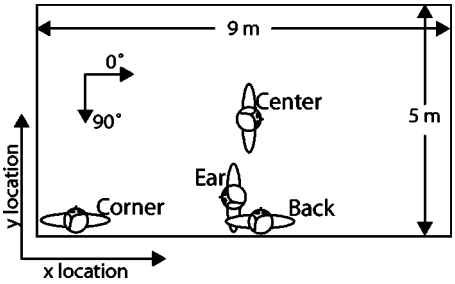

FIG. 1. Schematic showing the rough orientation and location of the KEMAR manikin in the classroom when measurements were made for the four listener locations (see Table I for more detailed descriptions of different listener locations).

II. METHODS

BRIRs were measured on a Knowles Electronics Manikin for Acoustic Research (KEMAR) for 21 different source locations relative to KEMAR, consisting of all combinations of seven source azimuths (0°, 15°, 30°, 45°, 60°, 75°, and 90°) to the right of the listener and three source distances (0.15, 0.40, and 1 m). All measurements were taken with the sound source in the horizontal plane containing the ears [e.g., at zero elevation relative to the listener; see Brown (2000) for more detail]. Measurements were taken with KEMAR seated on a tall wooden stool with his ears approximately 1.5 m above the floor at four different locations in a classroom (shown schematically in Fig. 1 and described in detail in Table I), henceforth called *center, back, ear*, and *corner*. To isolate the influence of reverberant energy on acoustic spatial cues, *pseudo-anechoic* measurements were generated by time-windowing the *center* BRIRs[2] and analyzing only the portion corresponding to the direct sound impulse response (see below).

In order to estimate measurement reliability, all measurements (21 source locations×4 listener locations) were repeated on three separate occasions, with the equipment

TABLE I. Approximate orientation and location of the KEMAR manikin in the classroom when measurements were made for the four listener locations (see Fig. 1 for definition of orientation angle and *x*-*y* axes).

Listener location	Orientation	*X* location (m)	*Y* location (m)
Center/ Anechoic	0°	4.5	2.5
Back	−90°	4.5	0.5
Ear	180°	4.5	0.5
Corner	−90°	0.5	0.5

TABLE II. Number of usable measurement repetitions (of three measurements performed) obtained in each source-listener configuration. Bold numbers highlight configurations for which fewer than three repetitions were usable. (Note that fewer reliable measures were obtained in the *corner* configuration because measurements were repeated three times in the order *center, back, ear,* and *corner,* and one of the two microphones malfunctioned at the end of the final measurement sequence.)

Listener location	Source distance (m)	Source azimuth						
		0°	15°	30°	45°	60°	75°	90°
Center/ Anechoic	0.15	3	3	3	3	3	**2**	3
	0.40	3	3	3	3	3	3	3
	1	3	3	3	3	3	3	3
Back	0.15	3	3	3	3	3	3	3
	0.40	3	3	3	3	3	3	3
	1	3	3	3	3	3	3	3
Ear	0.15	3	3	3	3	3	3	3
	0.40	3	3	3	3	3	3	3
	1	3	3	3	3	3	3	3
Corner	0.15	3	3	**2**	**2**	3	3	3
	0.40	**2**	**2**	**2**	**2**	**2**	**2**	**1**
	1	**2**	**2**	**2**	**2**	**2**	**2**	**2**

taken down and reassembled in between measurement sessions. For 18 of the 84 source-listener configurations, technical problems rendered some of the measurements unusable; Table II details the number of useful repetitions available for each source-listener configuration.

The classroom dimensions were roughly $5\times9\times3.5$ m. The room was carpeted and had hard concrete walls on three sides; the remaining (9-m-long) wall was constructed from a sound-absorptive partition. Acoustic tiles covered the ceiling. Few acoustically hard objects were in the room during the measurements (two small tables along the short wall and a collapsible ping-pong table, which was folded in half and oriented vertically, parallel to and near the long hard wall). The broadband T_{60} of the room was estimated from the measured BRIRs using the method formulated by Schroeder (Schroeder, 1965), as implemented by Brown in a Matlab function available at the Mathworks web site (Brown, 2002). For the *center* location, these estimates did not vary dramatically with source location or distance. The mean of the estimates in the *center* condition (across both ears, all source directions and all source distances) was 565 ms (standard deviation 24 ms). The means (and standard deviations) of the estimates of T_{60} from BRIRs were relatively robust with changes in listener location with mean (and standard deviation) values of 581 ms (28 ms), 585 ms (17 ms), and 619 ms (33 ms) for the *back*, *left*, and *corner* locations, respectively.

BRIRs were measured by concatenating two identical 32 767-long maximum length sequences (MLS; Rife and Vanderkooy, 1989; Vanderkooy, 1994) generated using a 44.1-kHz sampling rate. This MLS signal was sent to a Tucker-Davis Technologies (TDT) D/A converter (PD1), which drove a Crown amplifier connected to a Bose minicube loudspeaker. Prior to each measurement, the Bose loudspeaker was hand-positioned by the experimenter to be at the correct location (e.g., at the desired direction and distance relative to KEMAR, oriented to face the manikin). Miniature microphones (Knowles FG-3329c) mounted in earplugs and inserted into the entrance of KEMAR's ear canals measured the raw acoustic responses to the MLS. Microphone outputs drove a custom-built microphone amplifier connected to a TDT A/D converter (TDT PD1). For each BRIR measurement, the MLS was presented and the response measured ten times. The ten time-domain measurements were then averaged to obtain the final MLS response.

In order to achieve the best possible signal-to-noise ratio for each measurement, the maximum sound source level that did not cause clipping was found by trial and error for each source position and listener location. Signals were then presented roughly 5 dB below the clipping level.

Offline, the average measured response to the MLS was cross-correlated with the original sequence to obtain a raw estimate of a 743-ms-long BRIR (see also Kopco and Shinn-Cunningham, 2003). Each raw BRIR was digitally filtered to remove energy below 100 Hz and above 20 kHz. Visual inspection of the raw BRIRs verified that the first-arriving reflection in every one of the *center* conditions (off the floor) arrives between 9.75 and 11 ms from the start of the measurement (no earlier than 5 ms after the direct sound reaches the ears), as predicted from geometrical calculations. Ten-ms-long, *pseudo-anechoic* BRIRs were generated by multiplying the *center* BRIRs by a time window that was flat (equal to 1.0) up to 9 ms, with a 1-ms-long cosine-squared fall time from 9 to 10 ms, effectively removing all reverberant energy from the *center* BRIRs.

The measured BRIRs contain not only the transfer characteristics of the head and room, but also characteristics of the sound delivery and measurement system. Calibration measurements were taken of the impulse responses to the left and right microphones in the center of the room (without a listener present, orienting the Bose loudspeaker to point towards the microphones) using the same procedures described above (time-windowing out all reverberant energy). Results showed that the system magnitude response is smooth and equal in the two microphones, with a gentle low-pass characteristic (decreasing smoothly by approximately 10 dB from 200 Hz to 20 kHz). Ideally, BRIRs would be postcompensated to remove the transfer characteristics of the sound delivery and recording system by inverse filtering. However, because (1) the distortion due to the measurement system was small, (2) for the main comparisons of interest in the current study (i.e., comparisons across source position re: KEMAR and listener location in the room), any such filtering would have no effect, and (3) such compensation could introduce additional errors into the estimated BRIRs (e.g., if the error in the estimated compensation filter was of the same magnitude or greater than the compensation itself), no postcompensation was used in the reported measurements.

Calibration measurements established that the useful dynamic range in the BRIRs was at least 40 dB for all frequencies from 200 Hz to 20 kHz and that the exponentially decreasing energy in each of the BRIRs was in the electrical/acoustical noise floor by 700 ms. In order to reduce extraneous noise in the measurements, the 0.1–20-kHz bandpass-filtered BRIRs were multiplied by a 743-ms-long time window with a 50-ms-long cosine-squared fall time

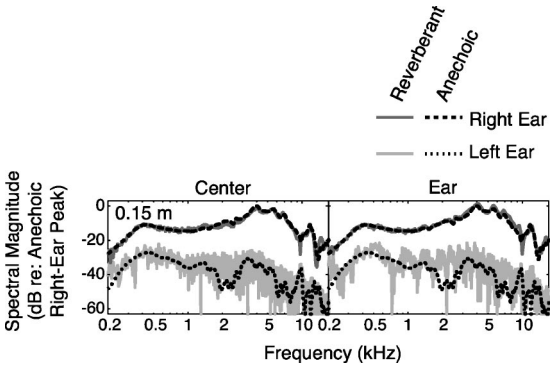

FIG. 2. Magnitude spectra of sample room transfer functions with the source at 90° azimuth, 1 m distance (*re*: KEMAR). Results for the right- and left-ear signals are shown in dark gray and light gray, respectively. Dashed lines show *pseudo-anechoic* results (derived from an independent set of *center* measurements). Results for the *center* and *ear* listener locations are shown in the left and right panels, respectively.

(from 693 to 743 ms) to produce the final BRIRs analyzed below.[3]

The current measurements quantify how source location relative to the listener and listener location in the room affect the spatial acoustic cues in BRIRs for an ordinary room. The study does not exhaustively explore what happens in arbitrary rooms, for arbitrary sound sources. For instance, because the Bose mini-cube speaker is not omni-directional, it was always oriented to face the listener. Altering the orientation or model of the loudspeaker would alter both the direct sound level reaching the listener and the energy in and pattern of the reflections.[4] Similarly, while there was nothing extraordinary about the classroom in which the measurements were taken, other rooms would yield different measurements. However, these results can be extrapolated to predict effects in other rooms by considering the statistics of reverberant energy in these other spaces. As described in Sec. I, because of the significant frequency-to-frequency variation in the BRTF phase and magnitude functions, the way in which reverberant energy distorts spatial cues for a particular source depends critically on the spectro-temporal content of the source. The current analyses explore how source location and listener location can alter different aspects of the BRIRs that relate to the magnitude of the effects of reverberant energy on the mean and variability in spatial cues likely to be observed for broadband sound sources. While in this sense the current results are specific (e.g., to the particular equipment, classroom, listener locations, etc.), the current results are similar to what would happen in these other settings. Finally, because the room measured here has been used in a number of behavioral studies, the specific details of this study may give insight into how reverberant energy influences perception in a range of tasks.

III. RESULTS

A. Example binaural room impulse responses

Figure 2 plots the magnitude spectra of BRIRs for a 0.15-m, 90° source for the *center* and *ear* conditions (left and right panels, respectively) to demonstrate the effects of diffuse reverberation and of an early, intense reflection. The two panels show left- (light gray) and right-ear (dark gray) results from one of the repeated measurements as well as *pseudo-anechoic* results (black dashed lines) from a different *center* measurement. The spectral levels in each plot are normalized to the maximum peak in the right-ear *pseudo-anechoic* measurement.

Comparison of the right- and left-ear *pseudo-anechoic* results (black dashed lines) shows the large ILDs that arise for lateral sources very near the listener (see Brungart and Rabinowitz, 1999; Shinn-Cunningham *et al.*, 2000). The *pseudo-anechoic* results also show characteristic notches and peaks in the received spectral level, features important for signaling source location within a torus of confusion (e.g., see Butler and Belendiuk, 1977).

In the *center* conditions (left panel), the only obvious effects of the reverberant energy can be attributed to diffuse reverberant energy (adding frequency-to-frequency variability; filling in spectral notches; increasing the total energy in the shadowed, left ear). These effects increase as the direct-sound energy decreases, increasing in both ears with source distance, and increasing at the ear on the far side of the head as the source moves laterally.

In the *ear* results for the left-ear spectrum (gray plot in the right panel) there are systematic peaks and valleys consistent with frequency-dependent summation and cancellation of the initial direct sound and the prominent left-wall reflection. These notches are spaced by roughly 480 Hz, starting at 240 Hz, and the autocorrelation of the left-ear BRIR has a prominent peak at 2.1 ms (not shown), consistent with an intense early reflection off the left wall that reaches the left ear 2.1 ms after the direct sound. In all of the BRIRs, the exact timing of, intensity of, and interaural differences in any early reflection depend on source azimuth and distance, as predicted from geometrical considerations. For instance, as source azimuth increases, the delay between the direct sound and the left-ear reflection in the *ear* and *corner* conditions increases and the relative magnitude of the left-ear direct sound decreases. For all tested source locations, the left-ear spectra of the *ear* and *corner* conditions have pronounced comb filtering whose notch frequencies and notch depths vary with the relative timing and intensity of the early reflection. However, there is no pronounced comb filtering in any of the right-ear magnitude spectra for any of the source locations in the *ear* and *corner* conditions; similarly, there is no prominent comb filtering in either ear in the *back* conditions, despite the proximity of the back wall.

B. Effects of reverberant energy on spectral magnitude

The FFT of each left- and right-ear impulse response was analyzed as a function of source and listener location. Summary statistics were computed to demonstrate how source distance, source direction, and listener location influenced the spectral magnitude of the signals reaching the listener.

1. Frequency-to-frequency fluctuations

Random, late-arriving reverberation tends to add frequency-to-frequency variability to the BRTF magnitude.

With such variability in the BRTF magnitude, the gain of the effective room filter acting at any point in time varies with the signal content at that time. Thus, whenever a signal has nonstationary spectro-temporal content, spatial cues in the signals at the ears will tend to vary, and the amount of fluctuation will be related to the variability in the BRTF from frequency to frequency. To characterize how such across-frequency variability depends on listener and source configuration in a room, the average size of the magnitude fluctuations in the BRTF (per Hz) were computed and then averaged across frequency. For each of the source locations (*re*: KEMAR) and listener locations in the room, this summary statistic was then averaged across the repeated measurements.

The BRTF can be thought of as a sum of direct sound, early echoes, and random late-arriving reverberation. Posed in this way, the random fluctuations in the BRTF magnitude as a function of frequency can be attributed primarily to reverberation. Statistical room acoustic analysis predicts that the mean spacing between adjacent maxima in the magnitude response of a room transfer function is approximately $3.91/T_{60}$ (e.g., see Schroeder and Kuttruff, 1962). Furthermore, the average dB change from a local maximum to an adjacent minimum should equal 10 dB (e.g., see Schroeder, 1987). For the current room with $T_{60}=565$ ms, statistical room acoustics analysis thus predicts that the late-arriving reverberation will have fluctuations of approximately 2.9 dB/Hz (i.e., 20 dB of fluctuation from peak to adjacent peak, which is, on average, 6.9 Hz away). Our measurements contain both direct sound and early reflections that vary relatively smoothly with frequency. As a result, the overall size of the fluctuations in the BRTF magnitude should vary between roughly 2.9 dB/Hz (if the reverberant energy dominates the total energy in the BRTF) down to almost no variation (when the reverberant energy is negligible compared to the sum of the energies in the direct sound and early reflections).

Variability in the right ear (not shown) was relatively small (at most less than 0.5 dB/frequency sample for sources straight ahead of the listener at 1 m), decreased slightly with source laterality, increased slightly with source distance, and was essentially identical for all listener locations in the room. The effect on the left ear, which generally received less direct sound energy than the right ear for all of the tested source locations, was greater overall and varied with source laterality, source distance, and listener location in the room.

Figure 3(a) plots the across-measurement mean of the absolute spectral magnitude change per Hz in the left-ear magnitude spectra and, where defined, the across-measurement standard deviation. Within each panel, results for each of the four listener locations in the room (dashed lines) and the *pseudo-anechoic* (solid line) results are shown as a function of source azimuth. Each row gives results for a different source distance.

Fluctuations in the *pseudo-anechoic* results [solid black lines in Fig. 3(a)] are essentially zero and independent of source direction and distance, as predicted. Variations in left-ear spectral energy increase with source azimuth for all listener locations in the room [in Fig. 3(a), values increase from left to right] as expected, as the direct-sound energy at the left ear decreases with source azimuth. Looking within each panel in Fig. 3(a), the average fluctuation is greatest for the *center* and *back* conditions (dark dashed lines) and much smaller for the *ear* and *corner* conditions (light-gray dashed lines).

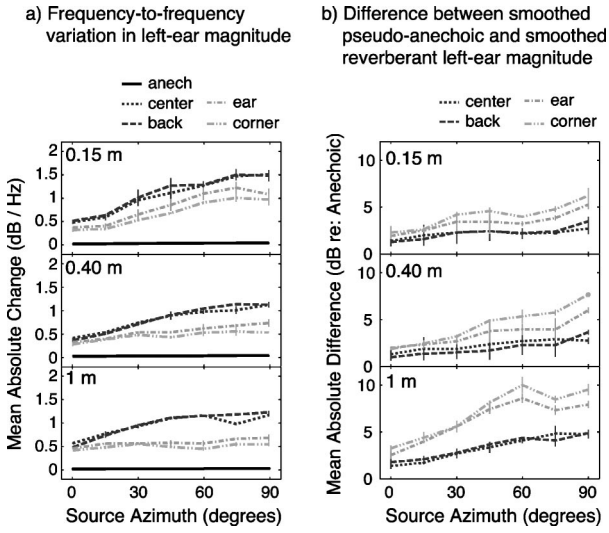

FIG. 3. Effect of reverberant energy on left-ear magnitude spectra. (a) Mean change in spectral magnitude per Hz as a function of source azimuth, calculated by taking the mean of the absolute values of the derivative of each measurement in dB per Hz, then calculating the mean across repeated measures. (b) Mean absolute difference between energy in smoothed third-octave bands of reverberant and *pseudo-anechoic* transfer functions as a function of source azimuth, calculated by computing the absolute value of the difference of the energy falling within each third-octave band of the reverberant and *pseudo-anechoic* transfer functions, calculating the mean across frequency bands, then calculating the mean across the three repeated measures. In both (a) and (b), error bars show the across-repetition standard deviation (where defined) and each row gives results for a different distance from source to listener (0.15, 0.40, and 1 m from top to bottom). Results within each panel correspond to different listener locations in the room.

The late portions of the left-ear results for the 0.15-m sources contain relatively more measurement noise than the other measurements (see footnote 3). Therefore, the average spectral fluctuation is slightly greater for the nearest source than the more distant sources [compare results in the top panel of Fig. 3(a) to those in the middle and bottom panels]. When the effect of the measurement noise is factored out,[5] the magnitude of the frequency-to-frequency variations is roughly constant with increasing source distance. The maximum mean fluctuation in the BRTFs is on the order of 2 dB.

Because the magnitude of the BRTF fluctuations is directly related to the proportion of late-arriving energy making up each impulse response, the values analyzed here should be inversely correlated with standard room-acoustics metrics such as the clarity index, which computes the ratio of early-to-late energy in a room impulse response. C_{80} (the ratio of the energy in the first 80 ms of the impulse response over the energy in the remaining portion of the impulse response) was computed for each BRIR. The mean of this value was then computed across repeated measurements for each ear and each spatial configuration.

Table III gives the mean values of C_{80} for the various measurements. As expected, C_{80} decreases with source dis-

TABLE III. Mean clarity index C_{80} (in dB) averaged across the repeated measurements for each of the BRTFs. (Note that the clarity index is infinite, by definition, for the *anechoic* conditions.)

Ear	Listener location	Source distance (m)	Source azimuth						
			0°	15°	30°	45°	60°	75°	90°
Left	Center	0.15	22.9	21.5	16.8	16.7	16.0	13.7	10.9
		0.40	23.2	20.3	17.3	16.5	15.3	14.5	11.5
		1	18.3	15.2	13.0	12.0	11.1	10.8	10.2
	Back	0.15	22.9	20.8	17.1	17.3	16.4	14.2	11.1
		0.40	24.1	21.0	17.8	17.0	15.9	15.7	12.7
		1	19.5	15.8	14.0	12.7	12.2	11.2	9.4
	Ear	0.15	23.4	21.8	18.1	18.0	16.7	12.3	11.9
		0.40	24.2	22.6	20.1	20.2	18.7	16.9	15.5
		1	20.0	19.0	18.0	18.3	18.0	14.7	15.7
	Corner	0.15	25.3	22.4	18.6	19.6	17.5	15.1	12.3
		0.40	25.7	22.4	21.3	21.2	20.1	19.3	18.5
		1	21.6	20.2	19.4	19.7	19.3	16.8	17.8
Right	Center	0.15	23.5	26.6	31.2	34.1	36.3	36.9	39.3
		0.4	25.3	27.2	29.9	31.3	32.2	33.1	33.7
		1	18.6	20.5	22.1	22.8	23.3	23.0	23.0
	Back	0.15	23.1	25.4	30.9	34.7	35.8	36.3	40.1
		0.40	24.6	27.2	30.0	32.3	33.1	33.9	33.3
		1	19.0	21.1	22.8	24.0	24.0	24.1	23.7
	Ear	0.15	25.0	26.8	31.5	34.8	37.3	37.2	39.4
		0.40	24.7	26.6	29.6	32.0	32.9	33.9	34.2
		1	18.7	20.1	22.2	22.9	23.6	23.4	23.6
	Corner	0.15	24.1	25.9	31.8	35.0	37.7	35.8	38.2
		0.40	25.9	29.4	32.5	33.1	33.8	34.6	34.9
		1	20.2	21.9	23.1	24.1	23.8	23.9	23.8

tance in both ears. For the right ear, C_{80} increases with azimuth, whereas C_{80} decreases with azimuth in the left ear. Room location has little effect on the right ear results; however, the left-ear C_{80} is smaller in the *center* and *back* conditions than in the *ear* and *corner* conditions (where early reflections are more prominent); this difference is most pronounced at the greatest distance.

The correlation between C_{80} and the frequency-to-frequency variability (modified to remove measurement noise as discussed above) was calculated for the 168 independent measurements (2 ears, 4 room conditions, 3 distances, and 7 azimuths). As predicted, these measures are inversely correlated. The correlation coefficient was -0.89 (i.e., roughly 80% of the variance in C_{80} can be accounted for by knowing the frequency-to-frequency variability in the BRTF magnitude and vice versa).

2. Distortion of frequency-smoothed magnitude

If reverberant energy alters the BRTF magnitude averaged over a critical band, the mean spectral content of the BRTF-filtered source will be altered. Whereas frequency-to-frequency fluctuations in the BRTF magnitude can cause temporal fluctuations in the neural excitation pattern caused by a broadband source, systematic distortions of the BRTF magnitude (averaged over a critical band) will alter the mean excitation pattern. To quantify such systematic spectral distortion arising from reverberant energy, the BRTF magnitude was first smoothed over frequency and then compared to *pseudo-anechoic* results. The energy falling within third-octave wide energy bands (center frequencies spanning 0.2–20 kHz) was computed for each measurement in order to estimate how the average rate of a corresponding auditory nerve fiber would be influenced by the reverberant energy for an ongoing broadband stimulus. For each reverberant measurement, the smoothed spectral level was subtracted from the level of a smoothed *pseudo-anechoic* measurement (independent of the *center* result used for a given calculation). The absolute value of the difference between smoothed reverberant and *pseudo-anechoic* results was computed for each third-octave band and then averaged over center frequency. This statistic was then averaged across the independent repeated measures for each source direction, source distance, and listener location.

The mean effect on the right-ear spectra (not shown) is very small (2.4 dB or less) and does not vary significantly with room location, source direction, or source distance. Figure 3(b) plots the across-measurement mean absolute difference between the smoothed reverberant and *pseudo-anechoic* spectra for the left ear (including, where defined, the across-measurement standard deviation). Within each panel, results for each of the listener locations are shown as a function of source azimuth (measured relative to KEMAR's median sagittal plane). Each row gives results for a different source distance.

The effect of the reverberant energy on the left-ear spectra increases for all listener locations in the room as the source moves to the right. For the conditions with an early left-wall reflection [the *ear* and *corner* conditions; light gray results in Fig. 3(b)], the difference between the reverberant and *pseudo-anechoic* smoothed spectra is larger and in-

creases more rapidly with azimuth than in the other conditions [i.e., light gray dashed lines are above and steeper than the dark gray dashed lines in Fig. 3(b)]. The effects of reverberation on the *corner* magnitude spectrum are consistently larger than on the *ear* magnitude spectrum [in Fig. 3(b), the double-dot-dashed light gray line is above or equals the single-dot-dashed light gray line]. With increasing source distance, differences across the listener locations increase [e.g., the separation between the light and dark gray results in the left column increases as one looks from the top to the bottom panels in Fig. 3(b)].

3. Discussion

Whereas local frequency-to-frequency fluctuations in the spectral magnitude are biggest in conditions where diffuse reverberant energy is relatively more important [i.e., in the *center* and *back* conditions; dark gray lines in Fig. 3(a)], systematic deviations between the frequency-smoothed *pseudo-anechoic* and frequency-smoothed reverberant magnitude spectra are largest in the cases where there is a sufficiently strong early reflection to cause comb-filtering of the spectrum [i.e., in the *ear* and *corner* conditions shown by light gray lines in Fig. 3(b)]. Similarly, while source azimuth has the greatest effect on frequency-to-frequency variability in conditions dominated by diffuse reverberant energy (*center* and *back*; dark gray lines in Fig. 3(a); conditions producing the smallest values of C_{80}), azimuth has the greatest influence on changes in the smoothed spectral shape for conditions with an early intense reflection [*ear* and *corner*; light gray lines in Fig. 3(b)]. Overall, these results show that frequency-to-frequency variability in the BRTF magnitude spectra [Fig. 3(a)] depends primarily on the strength of the diffuse reverberant energy relative to the sum of the direct-sound energy and the energy in any early reflection (such as those present in the left ear for the *ear* and *corner* measurements). In contrast, systematic distortion of spectral shape cues depends primarily on the energy in any early intense reflections relative to the direct-sound energy. The location of the listener in the room alters the intensity of any early reflections reaching the listener and, therefore, influences both frequency-to-frequency variability and systematic spectral distortion.

As discussed in the Introduction, frequency-to-frequency variability in the BRTF is related to the across-stimulus-token and across-time fluctuations likely to be observed in a BRTF-filtered sound source. In contrast, systematic deviations between frequency-smoothed BRTFs and their anechoic counterparts are related to how the expected value of the received spectral shape will be affected by the reverberant energy in a room. Because perception of spectral shape is important for judging the location of a source within a cone or torus of confusion, both spectral variability and mean spectral distortion may influence sound localization by listeners in rooms. Frequency-to-frequency variability may reduce the reliability with which the expected spectral shape can be extracted from a finite-length broadband stimulus, and thus might increase variability in judging source location (either across time or across stimulus tokens). In contrast, systematic distortion of spectral cues may induce localization bias, as it will tend to alter the mean perceived spectral shape (again, averaged across time for a long-duration stimulus or across tokens for shorter stimuli). Thus, the way in which reverberant energy influences sound localization in the up/down dimension may depend on the listener location in a room, with token-to-token response variability largest in conditions where the random reverberation energy is largest, and response bias largest in conditions where a listener is near a reflecting surface.

The frequency-to-frequency variability discussed in this section is directly related to the relative energy in the late-arriving, reverberant energy compared to the sum of the earlier portions of the room impulse responses, As a result, this metric is inversely correlated with such common room-acoustics metrics as C_{80} (which is commonly used to summarize the subjective influence of room acoustics on listening to music) and D_{50} (which is predicts the effect of reverberant energy on speech quality in rooms). One advantage of examining the current metric rather than either of these metrics is that it does not depend on making any one choice about what time window should constitute ''early'' and ''late'' portions of the room transfer function.

C. Interaural level differences

1. ILDs in binaural room transfer functions

As with monaural spectral cues, reverberant energy will alter the across-time mean of and variability in ILD cues. Reverberant energy will cause frequency-to-frequency fluctuations in the ILD that are directly related to the monaural frequency-to-frequency fluctuations discussed in the previous section. Such fluctuations, in turn, will cause temporal fluctuations in the short-term ILD observed through any critical band filter for broadband stimuli. Because the influence of reverberant energy on monaural spectral level is larger in the ear far from the source than the near ear, the overall effect of reverberant energy on frequency-to-frequency variability in the ILD increases with source laterality and with the relative level of diffuse reverberant energy (i.e., ILD variability over frequency is inversely correlated with C_{80}).

To quantify how reverberant energy alters the expected ILD for broadband sources, the energy falling within third-octave wide energy bands from 200 Hz to 20 kHz was computed for the left- and right-ear BRTFs for each measurement. These values were subtracted to estimate the ILD in the room response filters as a function of frequency and then averaged across the independent repeated measures for each center frequency, source direction, source distance, and listener location.

Figure 4 plots the across-measurement mean ILD in the smoothed BRIR spectra and, where defined, the across-measurement standard deviation as a function of the center frequency of the third-octave bands. Within each panel, the ILDs are shown for each of the four listener locations in the room (dashed lines) and for an independent *pseudo-anechoic* BRIR (solid line). Each row gives results for a different

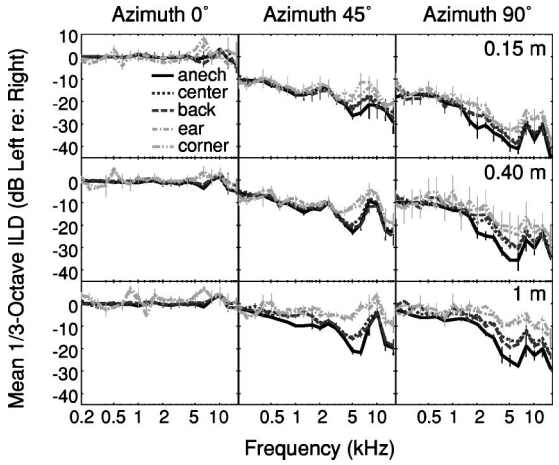

FIG. 4. Mean interaural level differences in the binaural room transfer functions as a function of frequency. Each point was calculated by computing the energy in each third-octave band of the transfer functions, taking the absolute value of the difference between the left- and right-ear values, then averaging these values across the independent repeated measures for each condition. Error bars show the across-repetition standard deviation (where defined). Results within each panel correspond to different listener locations in the room. Results are shown for sources at 0°, 45°, and 90° azimuth (left, middle, and right columns, respectively). Each row gives results for a different source distance (0.15, 0.40, and 1 m in the top, middle, and bottom row, respectively).

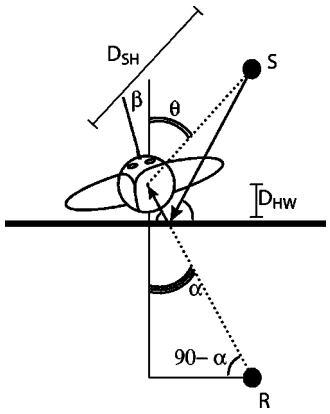

FIG. 5. Schematic diagram showing the source (S) and effective location of the back-wall reflection (R) for the *back* condition. The direct-sound path is shown by the black dashed line, arriving from angle θ relative to a line perpendicular to the wall. The reflection path is shown by solid black lines. The point R shows the effective location of the back-wall reflection (see Allen and Berkley, 1979). The angle of the reflection is given by α. The distance from source to the center of the head is given by D_{SH} and the distance from the center of the head to the wall is given by D_{HW}. When the listener's interaural axis is parallel to the wall (β is zero), the lateral angles (relative to the listener's median sagittal plane) for the arrival direction of S and R equal θ and α, respectively.

source distance. The left, middle, and right columns show results for sources at azimuth angles of 0°, 45°, and 90°, respectively.

For the source directly in front of the listener (left-hand column of Fig. 4), the ILD is very small at all frequencies. However, for the conditions in which the left ear receives an early intense reflection, there are small but consistent ILDs at some low to mid frequencies (a consequence of comb-filtering effects in the left-ear magnitude spectra for the *ear* and *corner* conditions; at higher frequencies, third-octave smoothing hides any comb-filtering and the only consistent effect is a boost in the left-ear energy from the early reflection in the left ear, which causes a slightly positive ILD). Around 6 kHz, there is a modest notch in the direct-sound spectrum that is symmetrical at the two ears for the 0° source location shown in Fig. 4. However, for conditions with a strong left-wall reflection, the left-ear notch is filled in more than in the right ear, producing a small but consistent positive ILD near 6 kHz.

Reverberant energy decreases the magnitude of ILDs and the size of this effect depends on the listener location in the room. In general, the ILD magnitude is smallest for the conditions with early intense reflections (light gray, dashed lines corresponding to the *ear* and *corner* conditions in Fig. 4), intermediate for the conditions with relatively diffuse reverberant energy (dark gray, dashed lines corresponding to the *center* and *back* conditions), and largest for the *pseudo-anechoic* results (solid dark lines). For instance, for the 1-m, 45° source the *pseudo-anechoic* ILD is nearly −20 dB at 5 kHz (solid line in the bottom middle panel of Fig. 4), roughly −12 dB for the *center* and *back* conditions (dark gray dashed lines), and only around −5 dB for the *ear* and *corner* conditions (light gray dashed lines). The effect of reverberant energy on the ILD increases with source distance (e.g., decreasing the ILD magnitude by as much as 20 dB for a 1-m, 90° source in the bottom right panel of Fig. 4, but at most by 10 dB for the 0.15-m, 90° source in the top right panel).

2. Discussion

The impact of reverberant energy on ILDs is dominated by the effect of reverberation on the signals at the ear that is farther from the source. With increasing source distance, reverberant energy tends to increase the energy in the (left) shadowed ear, thereby decreasing the ILD. As the source moves to the right side of the head, reverberant energy causes a relatively larger change in the total energy reaching the left ear and the ILD magnitude decreases by a larger amount. For the *ear* and *corner* conditions, the early intense reflection reaching the left ear off of the nearby left wall adds significantly more energy to the left ear than to the right ear, which receives a head-shadowed version of this early wall reflection. Thus, for these conditions, the ILD magnitude decreases even more due to reverberant energy (particularly at the largest source distances) than for the reverberant conditions where diffuse energy is more dominant.

The similarity between *center* and *back* results can be partially explained by considering the geometry when the listener is near a wall. Figure 5 shows a schematic diagram of this situation. A source S reflects off the back wall (see black lines with arrows), producing a reflection that is roughly equivalent to a phantom source at location R [see Allen and Berkley (1979) for a description of this sort of geometric approximation]. For this geometry, the angle between the arrival direction of the sound source and a line perpendicular to the wall (θ) and the angle between the arrival direction of the reflection and the same reference (α) are related by

$$\alpha = \tan^{-1}\left[\frac{D_{SH}\sin\theta}{2D_{HW}+D_{SH}\cos\theta}\right]. \quad (1)$$

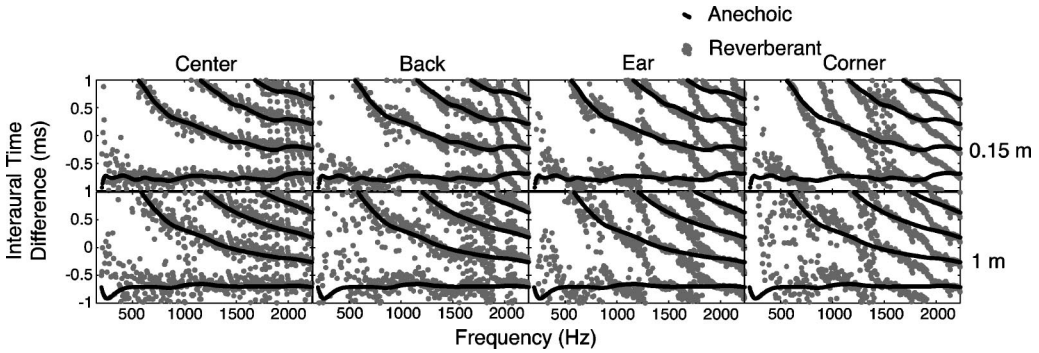

FIG. 6. Interaural time differences in sample room transfer functions with the source at 90° azimuth (*re*: KEMAR) as a function of frequency (shown up to 2.2 kHz). Values were calculated by subtracting the phase of the left- and right-ear transfer functions at each frequency, then dividing by frequency. For each frequency, multiple values are plotted, corresponding to all possible shifts of the ITD by integer multiples of the period (a pure, frequency-independent ITD would give rise to a horizontal line at the true ITD value). Gray points show results for the reverberant conditions. For comparison, black points show *pseudo-anechoic* measurements (derived from an independent set of *center* measurements). Each column shows results for one of the four listener locations in the room. The top and bottom rows give results for distances of 0.15 and 1 m, respectively.

The smaller the distance between listener and wall (D_{HW}) and the greater the distance from source to listener (D_{SH}), the more similar θ and α become. In addition, the difference between θ and α approaches 0 as θ approaches 0. When the listener's interaural axis is oriented parallel to the wall as in the *back* condition (i.e., when β in the figure is zero), θ equals the lateral angle of the direct sound and α equals the lateral angle of the reflection. Thus, when the listener is oriented with his interaural axis parallel to a nearby wall, both the direct sound and the early reflection produce nearly identical interaural differences. As the listener rotates (as the magnitude of β increases from zero), the lateral angle of the direct and phantom sources become increasing disparate, reaching an extreme when the listener has one ear towards the wall (e.g., β is $-90°$, as in the *ear* and *corner* conditions) when the source is directly to one side of the listener (θ is 0°) and the phantom source is on the exact opposite side of the listener. As a result, early reflections in the *back* condition produce significantly less interaural distortion than the early reflections in the *ear* and *corner* conditions.

To the extent that the magnitude of the ILD influences perception of source laterality, sound sources may be systematically perceived as closer to the median sagittal plane in a room than in anechoic space, as the expected ILD magnitude is generally smaller in a room. Furthermore, any such systematic localization bias would be greatest in conditions where the listener is oriented with one ear facing a wall (such as the *ear* and *corner* conditions).

In addition to reducing the average ILD magnitude, diffuse reverberant energy increases the frequency-to-frequency variation in ILDs by introducing frequency-to-frequency variability in monaural spectral levels [e.g., see Fig. 3(a)]. Thus, ILD cues will tend to vary with the short-term spectral content of a source in the presence of diffuse reverberant energy.

Although low-frequency ILD cues [below 3 kHz; see Brungart (1999)] convey source distance for nearby sources, low-frequency ILD cues are less influenced by ordinary room reverberation than are ILDs in the mid to high frequencies (compare results above and below 3 kHz in Fig. 4). Thus, distance perception of nearby sources may be robust in a room, especially given that reverberant energy provides additional distance information to listeners (Mershon *et al.*, 1989).

D. Interaural time differences

1. ITDs in BRTFs as a function of frequency

Frequency-to-frequency variation in ITD cues in BRTFs will cause temporal variability in the ITD cues reaching a listener for a broadband sound presented in a room. Figure 6 compares the ITDs in the reverberant and *pseudo-anechoic* conditions for a source at 90°, plotted as a function of frequency for the low to mid frequencies (200 Hz to 2.2 kHz, frequencies for which the ITD is thought to be most salient). Each plot in Fig. 6 was generated from one individual BRTF measurement. Rather than trying to extract the ''true'' ITD at each frequency, only the phase-wrapped IPD, denoted by $\phi_{\mathrm{mod}(2\pi)}$, was computed: the phases of the left and right BRTFs at each frequency were subtracted and set to an equivalent value modulo 2π. In order to account for the inherent interaural phase ambiguity in $\phi_{\mathrm{mod}(2\pi)}$, at each frequency f a vector of possible IPDs was generated by calculating $\phi_{\mathrm{mod}(2\pi)}+2\pi k$ for all integer values of k. The resulting values were divided by $2\pi f$ to generate multiple ITD values consistent with the observed IPD at each frequency. Figure 6 plots these ITD values as a function of frequency when the sound is 90° to the right of the listener's head. In each panel, gray symbols correspond to the reverberant results and black symbols correspond to *pseudo-anechoic* results. The *pseudo-anechoic* results in each row are identical and derived from an independent *center* measurement to make across-listener-location comparisons ''fair.'' The top and bottom rows give results for 0.15- and 1-m sources, respectively. Each column shows results for one listener location.

All *pseudo-anechoic* plots (black symbols, repeated in each column) contain a roughly horizontal line, consistent with an ITD that is nearly the same at all frequencies. This ITD value is approximately -750 μs for the 90° locations shown, independent of source distance. The other ITD values

consistent with the IPD at each frequency form stereotypically curved lines in the ITD-frequency plots (see, for example, Stern and Trahiotis, 1995).

Looking first at the results for the *center* condition (left column), the relatively diffuse reverberant energy causes small distortions of the ITD that appear to be random and independent from frequency to frequency (i.e., in the left-hand column results, the gray symbols fall near, but randomly scattered around, the black *pseudo-anechoic* results). The amount of distortion caused by the reverberant energy increases with source distance (deviations between the gray symbols and *pseudo-anechoic* results are larger in the bottom left panel than in the top left panel of Fig. 6).

Results for the *back* condition (second column from left) are similar, except that deviations from *pseudo-anechoic* results are greater than for the *center* condition. For a sound source at 90°, the back-wall reflection arrives from a different lateral angle than the direct sound [e.g., roughly 70° for the 1-m source; see Eq. (1)], thus altering the ITD cues reaching the ears. Furthermore, the distortion of the ITD cues varies systematically with frequency (see the upper panel in the second column of Fig. 6), a sign that part of the distortion of ITD cues is from a distinct reflection, rather than diffuse reverberant energy.

Results for the *ear* and *corner* conditions (third and fourth columns in Fig. 6) show prominent, systematic deviations from *pseudo-anechoic* ITD results. For example, for the 0.15-m source in the *ear* condition (top panel of third column), the reverberant results (gray symbols) nearly match the *pseudo-anechoic* results (black symbols) at 500 Hz, but are consistently above the *pseudo-anechoic* results just below 500 Hz and below the *pseudo-anechoic* results just above 500 Hz. With increasing source distance, the distortion caused by reverberant energy grows (e.g., compare the top and bottom panels in the third column). Indeed, the panel showing the 1-m source in the *ear* condition (gray symbols, bottom panel in the third column) shows a striking pattern of negatively sloped lines, without any obvious horizontal line; in other words, there is no single ITD in the plotted range that is consistent across frequency.

2. Cross-correlation analysis

Frequency-to-frequency variability in the ITDs contained in BRTFs influences how short-term ITD cues in a broadband sound source will vary. However, analysis of such variability does not address whether reverberant energy causes a change in the mean ITD. In this section, we compute a broadband cross-correlation of the left- and right-ear BRIRs to investigate whether reverberation causes systematic distortions of ITD information. This analysis is closely related to analysis of the interaural cross-correlation commonly employed in room acoustics studies to summarize the interaural decorrelation caused by room reflections (e.g., see de Vries *et al.*, 2001). Although neural computation of ITD information is performed by computing the narrow-band cross correlation within each critical band as a continuous time function, the broadband cross-correlation function is essentially a weighted average of narrow-band cross-correlation functions when the weighting of each constituent frequency band is proportional to the energy in that band [see Shinn-Cunningham and Kawakyu (2003) for analysis of short-term, narrow-band cross-correlation results and how across-time integration affects ITD estimation from reverberant signals]. As such, the broadband analysis shown here provides a simple summary of the extent to which ITD cues in a room can provide useful information about source laterality.[6]

To quantify the effects of reverberant energy on ITD cues, the normalized cross-correlation of the low-to-mid-frequency portion of the left- and right-ear impulse responses was calculated. For each measurement, the left- and right-ear impulse responses were low-pass filtered with a cutoff frequency of 3 kHz (note that the upper-frequency cutoff has little influence on the results we will present; 3 kHz was chosen in order to focus analysis on the low-to-mid frequency region in which ITD cues are thought most salient). The normalized cross-correlation function $x(\tau)$ was then computed as

$$x(\tau) = \frac{\Sigma_n l[n] r[n-\tau]}{\sqrt{\Sigma_n l^2[n] \Sigma_m r^2[m]}}, \tag{2}$$

where $l[n]$ and $r[n]$ are the low-pass filtered left- and right-ear impulse responses, respectively. This normalized cross-correlation function takes on its largest value at the time delay τ that best aligns the left and right ear signals. For each measurement, the largest peak of $x(\tau)$, $p_{\max}$, was found along with the corresponding time delay, $\tau_{\max}$. Because the largest such peak might fall outside the plausible range of ITD values for a sound in anechoic space, the largest peak within the limited range of $[-1,1]$ ms was also found ($p_{\lim}$) along with the corresponding interaural time delay ($\tau_{\lim}$).

Figure 7 plots the values of $\tau_{\lim}$ and $\tau_{\max}$ [Figs. 7(a) and (b), respectively] and the normalized peak amplitudes $p_{\lim}$ and $p_{\max}$ [Figs. 7(c) and (d), respectively] as functions of the source azimuth. Results for the three source distances are shown in individual panels; results within each panel show different listener locations in the room. Lines show the across-repeated-measurement mean and symbols show individual measurement results.

In all the panels of Fig. 7(a), the peak ITD magnitude increases from roughly 0 to roughly 750 μs as the azimuth ranges from 0° to 90°. Despite the strong distortion of ITD information by reverberation (see Fig. 6), $\tau_{\lim}$ is essentially unaffected by reverberant energy: in all three panels of Fig. 7(a), results for all listener locations fall on top of *pseudo-anechoic* results. In other words, despite the frequency-to-frequency fluctuation in the ITD, integrating information across frequency (e.g., by calculating the broadband cross-correlation from 200 Hz to 3 kHz) gives a reliable ITD estimate when the range of candidate ITD values is limited.

Results in Fig. 7(b) show that $\tau_{\max}$ equals $\tau_{\lim}$ for all cases in which there are no prominent early reflections (i.e., for the *pseudo-anechoic, center,* and *back* conditions; see solid and dashed dark lines). However, for the conditions with an early reflection (the *ear* and *corner* conditions, shown by light results), the largest overall peak in the normalized cross-correlation function does not always fall

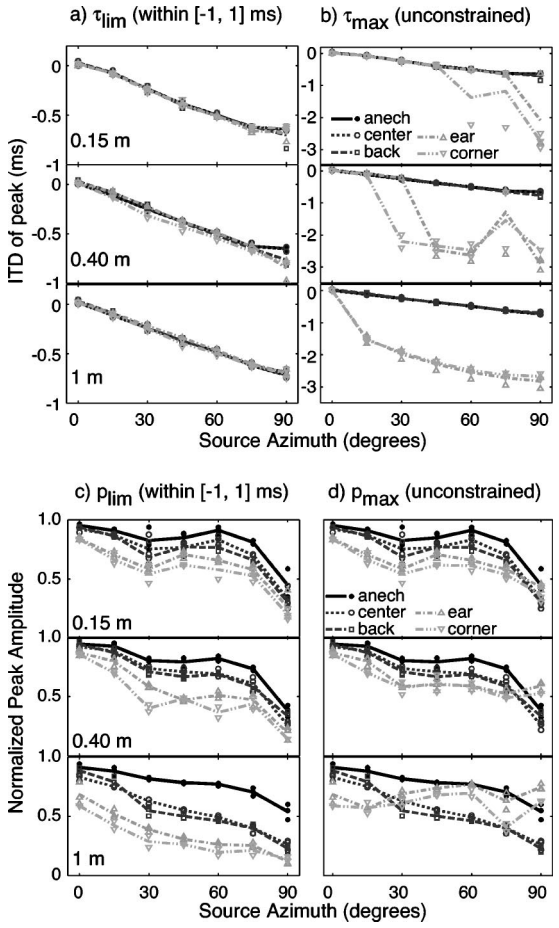

FIG. 7. ITD and normalized height of the peak in the broadband cross-correlation function of left- and right-ear impulse responses as a function of source azimuth. (a) ITD of largest peak within the physiologically plausible range of interaural time differences (−1 to +1 ms). (b) ITD of the largest overall park (without limiting the ITD range). (c) Peak height within the physiologically plausible range of interaural time differences (−1 to +1 ms). (d) Height of the largest overall peak (without limiting the ITD range). Lines show the across repetition average for each listener location in the room. Results for each independent repeated measurement are plotted as symbols. Each row gives results for a different distance from source to listener (0.15, 0.40, and 1 m in the top, middle, and bottom rows, respectively).

within the plausible range. The likelihood that $\tau_{\max}$ differs from $\tau_{\lim}$ increases with increasing source azimuth and with increasing source distance. For instance, the number of *ear* and *corner* measurements (light gray results) with implausible peaks is largest in the bottom panel of Fig. 7(b) and increases from left to right in the panel.

Figure 7(c) shows that for all source distances, $p_{\lim}$ decreases with increasing source laterality (in all panels, $p_{\lim}$ decreases from left to right) and with increasing source distance ($p_{\lim}$ decreases from top panel to bottom panel). Whereas $\tau_{\lim}$ does not vary with listener location in the room, $p_{\lim}$ varies dramatically: in general, $p_{\lim}$ is largest for the *pseudo-anechoic* results (solid black line), intermediate for the *center* and *back* conditions (dark gray results), and smallest for the *ear* and *corner* conditions (light gray results). Differences between the different listener locations also increase with source distance. In fact, for the most-distant sources tested [bottom panel of Fig. 7(c)], even though $\tau_{\lim}$ is essentially unaffected by reverberation [see Fig. 7(a)], $p_{\lim}$ for the *ear* and *corner* conditions is very small (less than 0.4 for sources beyond 15° to the right of the listener).

Figure 7(d) plots $p_{\max}$ for the various source positions and listener locations. For listener locations in which there is no prominent early reflection, $p_{\max}$ always equals $p_{\lim}$, independent of source azimuth and distance [i.e., the solid and dashed dark line results are identical in Figs. 7(c) and (d)]. For the nearest sources [top panel in Fig. 7(d)], the peak amplitude is essentially unchanged when the peak ITD value is unrestricted; only for the sources at 90° are there differences between $p_{\max}$ and $p_{\lim}$, and only then for the *ear* and *corner* conditions (compare the rightmost light gray points in the top panels of Figs. 7(c) and (d)]. With increasing source distance, however, $p_{\max}$ in the *ear* and *corner* conditions changes dramatically. For the intermediate source distance, $p_{\max}$ for the *ear* and *corner* conditions decreases as the source azimuth moves from 0° to 30°, but then changes very little as the source angle changes from 30° to 90° [light gray results in the middle panel of Fig. 7(d)]. For the most distant source in the listener locations for which there is an early left-wall reflection, $p_{\max}$ actually increases as the source azimuth changes from 0° to 90° [light gray results in the bottom panel of Fig. 7(d)].

3. Discussion

Because monaural phase distortion is larger in the ear that receives less direct sound energy, ITD distortion depends most strongly on the phase distortion in the far ear, increasing with source laterality as well as source distance. For listener locations in which there is an early reflection from the left wall, the pattern of ITD as a function of frequency is grossly distorted, even when the source is very near the listener's head.

The small but consistent difference in ITD distortion in the *center* and *back* conditions can be partially explained by the geometry of these listening conditions. The early back-wall reflection causes ITD cues that are identical to those in the direct sound when the source is directly in front of the listener [see Fig. 5 and Eq. (1)]. Thus, for the 0° source angle, the distortion of ITD by reverberation is smaller in the *back* condition than the *center* condition. As the source azimuth increases, the back-wall reflection's lateral angle no longer exactly matches the direct-sound lateral angle [particularly for the smallest source distance; see Eq. (1)], and the ITD deviation in the *back* condition grows rapidly with source azimuth.

Whereas the ITD information in any specific frequency may be dramatically distorted, in the broadband cross-correlation function there is a local ITD peak corresponding to the direct-sound path. These results show that even when there is an early intense reflection, knowledge of the range of ''true'' ITDs and integration of information across frequency enables accurate estimation of the sound source lateral angle. Behaviorally, the distortion of ITD cues by reverberant energy may increase variability in judgments of source laterality across different stimulus tokens. However, because the ITD of the direct sound can be recovered with sufficient

across-frequency integration, laterality judgments based on ITD cues may not show any large bias, regardless of the location of the listener in the room.

IV. SUMMARY AND GENERAL DISCUSSION

This study examines the effects of source distance, source angle, and listener location on the distortion of spatial cues in BRIRs by reverberant energy when sources are nearby a listener in an ordinary room. All of these factors have a significant impact on the form and size of the distortion caused by reverberant energy. This kind of analysis is important for understanding both how reverberant energy alters the statistics of acoustic attributes in the signals reaching a listener (e.g., cues for source direction and for source content) and how reverberant energy can provide information to the listener (e.g., about source distance and the acoustic environment).

Room reflections alter the magnitude spectra of BRIRs by causing random frequency-to-frequency variation; filling in spectral notches; increasing the overall energy, particularly in the ear receiving less direct-sound energy; and, in some cases, generating comb-filter distortion. As source laterality increases, all of these effects become more pronounced at the far ear and smaller at the ear on the near side of the head. While the random variations in spectral content are greatest when most of the reverberant energy is diffuse (*center* and *back* conditions), the systematic distortions of spectral content are greatest when there is a prominent early reflection (*ear* and *corner* conditions).

Spectral magnitude distortion degrades the cues important for resolving source location within a particular torus of confusion. Such spectral distortion is much greater in the far ear than the ear near the source. This observation may explain why listeners give more perceptual weight to spectral shape cues in the near ear when the left- and right-ear spectra are pitted against one another (Morimoto, 2001): in many ordinary (reverberant) environments, the near-ear spectral cues are relatively more reliable than the far-ear cues.

In all cases, reverberation tends to reduce ILDs, especially when the source is relatively far from the listener. For the source locations tested in this study, the reduction of ILDs is especially pronounced when there is an early reflection from the side (i.e., in the *ear* and *corner* conditions). Furthermore, diffuse reverberant energy adds frequency-to-frequency variability in ILD cues. To the extent that listeners use ILD cues to judge source laterality, reverberant energy may therefore induce systematic localization bias, with listeners perceiving sources nearer the median sagittal plane than the true source location, as well as increase variability in judgments of source laterality.

ITD information becomes more distorted by reverberant energy as the source moves away from the median sagittal plane and as source distance increases. Distortion from reverberant energy can cause quite severe interaural decorrelation (e.g., significantly decreasing the amplitude of the ''true'' peak in the normalized cross correlation). Nonetheless, the ITD of the direct sound can still be extracted from the BRIR by combining ITD information across frequency [accomplished in the current analysis by computing a broadband cross correlation; however, see also Shinn-Cunningham and Kawakyu (2003) for a more physiologically motivated analysis of what ITD information can be extracted in a reverberant setting when considering short-term ITD cues arising within critical bands] and restricting the range of ITD values to those that are plausible. In fact, psychophysical tests and theoretical studies suggest that although ITD is computed independently within a critical frequency band, listeners integrate ITD information across frequency when judging source laterality (e.g., see Trahiotis and Stern, 1989; Buell and Hafter, 1991). Perhaps as a result of such across-frequency integration, listeners are able to make reasonable judgments of source laterality of broadband sounds in some reverberant settings (e.g., see Hartmann, 1983; Shinn-Cunningham, 2000b).

The current results suggest that for many aspects of BRIRs, the most important differences that arise from changing listener location in a room can be ascribed to the presence or absence of an early reflection arriving from the side of the head that is opposite the direct sound (i.e., such as arises in the current results in *ear* and *corner* conditions). The strength of any early reflections depends strongly on the listener location in the room and more modestly on the source location relative to the listener. Only when the listener is positioned with one ear facing a nearby wall is the initial reflection sufficiently strong (and from a sufficiently different direction than the direct sound) to cause any systematic distortion of spatial acoustic cues. In the current measurements, reflections from a wall behind the listener (i.e., in the *back* condition) do not cause obvious comb-filtering spectral distortions. Furthermore, the interaural differences in the early reflection from a back wall tend to reinforce rather than distort the interaural cues in the direct sound. As a result, current results from the *back* condition are comparable to those of the *center* condition and unlike those from the *ear* and *corner* conditions for nearly all of the statistics examined.

The acoustic similarity of many spatial cues in the *center* and *back* conditions is consistent with results of a recent behavioral study that examined the ability of trained listeners to identify the four listener locations in the room when listening to stimuli simulating different source and listener configurations using the BRIRs analyzed here (Shinn-Cunningham and Ram, 2003). In this study, listeners were given blocks of trials in which the simulated source location of a random token of noise was fixed relative to the listener, but the simulated listener location in the room varied from trial to trial. The listener's task was to *identify* which of the listener locations was simulated on each trial (i.e., listeners had to categorize the room location while ignoring trial-to-trial variability caused by variations in the noise tokens presented). Listeners generally did not confuse listener locations in which there was an early reflection from the left (the *ear* and *corner* conditions) with stimuli in which there was no such reflection (the *center* and *back* conditions), but were very likely to confuse the *ear* and *corner* stimuli (mislabeling an *ear* trial as a *corner* trial and vice versa) and to confuse *center* and *back* stimuli (although listeners might have been able to *discriminate* between these stimuli, especially if

the noise token had been held constant across trials).

The current analyses may underestimate the effects of reverberation in an ordinary classroom, as the source distance was 1 m or less in all of the conditions considered here. In fact, results show that even for these conditions, where the source is very close to the listener, the effects of reverberation can be quite prominent. These results shed light on the ways in which source location relative to the listener (including source distance) and listener location in the room interact with the effects of reverberation to influence the signals reaching a listener. Of course, many other factors can alter the pattern of direct and/or reverberant energy reaching the listener, including, among other things, room properties (volume, dimensions, and surface properties), source directivity, and source orientation. However, many of the results from this study are applicable to other environments and source-listener configurations that give rise to similar relative levels of direct-sound, early reflection, and reverberant energy. Similarly, the current analyses focus on steady-state properties in the BRIRs and do not directly address how the spectro-temporal content of a sound source interacts with properties of the room or how reverberant energy builds up and decays over time. Instead, these results examine different properties of BRIRs that can influence the mean and variability in spatial cues received by a listener in a room and show how these properties vary with source and listener position.

V. CONCLUSIONS

Measurements of binaural room impulse responses in the classroom studied here demonstrate a number of important principles governing how reverberant energy will distort the spatial acoustic cues reaching the ears of the listener. Some of these principles, which will also apply in other acoustic settings, are listed here:

(1) Especially for sources near the listener, the listener location in a room and the source position relative to the listener influence how reverberant energy distorts and degrades spatial acoustic cues. Systematic distortions are most prominent when a listener is oriented with one ear toward a wall. Reverberant energy influences signals more at the ear farther from the source than at the near ear, particularly when a source is nearby the listener. Spectral cues are more reliable in the near ear than the ear farther from the source, and interaural cues become less reliable with source laterality.
(2) Interaural level differences are systematically reduced by reverberant energy, such that the mapping between the expected ILD (as a function of frequency) and the laterality of a sound source presented in reverberant space depends on acoustic properties of the environment as well as on the location of the listener in the environment.
(3) For moderate levels of reverberation (such as observed here), the ITD in the direct sound can be reliably extracted in reverberant signals by integrating interaural cues across frequency and restricting the estimated ITD to a plausible range of values.
(4) Reverberant energy may have different effects on sound localization in the left/right, up/down, and distance dimensions. Judgments of source laterality may be biased in a room because reverberant energy reduces ILD magnitude; additionally, because reverberation causes temporal fluctuations in both short-term ITD and ILD cues, laterality judgments may show greater token-to-token variability in a room than in anechoic space. Similarly, judgment of the up/down direction of a source may be biased because reverberant energy tends to alter the mean spectral shape of the signals reaching the listener. Finally, distance judgments may be more accurate in a room than in anechoic space, as low-frequency ILD cues that arise for nearby lateral sources are robust to the effects of reverberation and reverberant energy may provide additional distance cues.

ACKNOWLEDGMENTS

This work was supported in part by AFOSR Grant No. F49620-98-1-0108 and the Alfred P. Sloan Foundation. Steve Colburn, Armin Kohlrausch, and two anonymous reviewers provided very helpful and careful comments that vastly improved the manuscript.

[1]Sound localization of human listeners has been studied in the same room, using the same listener locations and a similar range of source locations relative to the listener (e.g., see Santarelli, 2000; Shinn-Cunningham, 2000b; Kopco and Shinn-Cunningham, 2002). The BRIRs analyzed here also have been used in headphone-based experiments investigating how reverberation influences various aspects of perception (e.g., Shinn-Cunningham *et al.*, 2002; Devore and Shinn-Cunningham, 2003; Shinn-Cunningham and Ram, 2003; Shinn-Cunningham, 2004). Researchers interested in obtaining copies of these BRIRs for their own use can contact the first author at shinn@cns.bu.edu

[2]The combination of the source distances relative to KEMAR and the height of KEMAR relative to the floor were chosen to ensure that the initial floor reflection in the *center* position was temporally separated from the direct sound impulse response.

[3]Because the overall level of the MLS measurement signals varied (in order to present signals at the most intense level possible without distortion), the time at which the BRIRs reached the noise floor depended on the location of the source relative to the listener. For the nearest sources, the measurements were taken at a lower overall gain in order to avoid clipping of the direct sound impulse response. As a result, the BRIRs for the 0.15-m distant sources reached the noise floor as much as 150 ms earlier than the BRIRs for sources at 0.40 and 1 m. Because the BRIRs for the 0.15-m sources contain not only reverberation but also additional electro-acoustic noise, the distorting effects of reverberation (compared to the anechoic HRIRs) are, if anything, overestimated in the results presented here. However, the effect of this additional noise was found to be negligible. To validate results, all BRIRs were also processed with a more sophisticated time-windowing scheme. In this scheme, the time at which each measurement reached the noise floor was estimated by determining when the energy in the late portion of the BRIR no longer decayed with time. To approximate the correct exponential decay in the late portions of each BRIR, an appropriate exponentially decaying time envelope (whose decay time constant was determined from estimates of T_{60} for the room) multiplied the late portion of each BRIR from the time at which the measurement hit the noise floor to the end of the BRIR (note that the imposed envelope was longest for the nearest sources). In almost all cases, the results for the original and exponentially windowed BRIRs were indistinguishable. The only analysis for which the exponential window had a noticeable impact was on the summary statistic reported in Fig. 4; see footnote 5.

[4]Comparisons between *pseudo-anechoic* results and theoretical computations (see Kopco and Shinn-Cunningham, 2003) suggest that the radiation pattern of the speaker has little effect on the direct-sound impulse responses. Published specifications (http://www.bose.com/pro/dd/product/main.html) detail the frequency-specific polar radiation patterns for the Bose speaker used. At 8 kHz, the radiation gain is −6 dB relative to the on-axis gain for a direction 40° off axis; at 16 kHz, the −6 dB point occurs

at 20°. Because of this speaker directivity, the direct-to-reverberant energy ratio in our measurements is greater than would be obtained with an omnidirectional point source. However, most natural sources have some directivity; the goal of the current analyses is to explore how source and listener location influence results, not to quantify how reverberation impacts the signals reaching a listener in a room when the source is an ideal point source.

[5]The inclusion of electro-acoustical noise in the late portions of the BRIRs theoretically increased the estimated mean frequency-to-frequency fluctuations in all of the magnitude spectra, but only had a measurable effect on results for left-ear BRIRs for sources at 0.15 m. When an exponential decay was imposed on the late portions of the BRIRs, the mean frequency-to-frequency fluctuations in the left-ear, 0.15-m BRIRs decreased, particularly for sources to the right of the listener (see footnote 3). The maximum spectral fluctuations observed in the left-ear BRIRs for the nearest sources was essentially equal to that observed for the 0.40-m sources, with a maximum between-sample fluctuation for sources at azimuth 90° of approximately 1.1 dB/Hz for *center* and *back* conditions and 0.7 dB/Hz for the *ear* and *corner* conditions. For all other source locations, imposing an exponential decay in the late portion of the BRIR had no noticeable effect.

[6]The broadband cross-correlation analysis shown here essentially predicts the ITD that would be extracted by energy-weighting the narrow-band cross-correlation functions assumed to be available in the brainstem and reporting the peak of this energy-weighted average. However, the peak in the broadband cross-correlation does not always equal the average of the peaks of the narrow-band cross-correlation functions. In other words, this analysis can produce results different than if one first computed the best ITD estimate within a band and then combined these ITD estimates across frequency.

Algazi, V. R., Avendano, C., and Duda, R. O. (**1999**). ''Low-frequency ILD elevation cues,'' J. Acoust. Soc. Am. **106**, 2237.

Allen, J. B., and Berkley, D. A. (**1979**). ''Image method for efficiently simnulating small-room acoustics,'' J. Acoust. Soc. Am. **65**, 943–950.

Asano, F., Suzuki, Y., and Sone, T. (**1990**). ''Role of spectral cues in median plane localization,'' J. Acoust. Soc. Am. **88**, 159–168.

Barron, M. (**2001**). ''Late lateral energy fractions and the envelopment question in concert halls,'' Appl. Acoust. **62(2)**, 185–202.

Bech, S. (**1998a**). ''Spatial aspects of reproduced sound in small rooms,'' J. Acoust. Soc. Am. **103**, 434–445.

Bech, S. (**1998b**). ''Timbral aspects of reproduced sound in small rooms. I,'' J. Acoust. Soc. Am. **97**, 1717–1726.

Begault, D. R., Wenzel, E. M., Lee, A. S., and Anderson, M. R. (**2001**). ''Direct comparison of the impact of head-tracking, reverberation, and individualized head-related transfer functions on the spatial perception of a virtual speech source,'' J. Audio Eng. Soc. **49(10)**, 904–916.

Berkley, D. A. (**1980**). ''Normal listeners in typical rooms: Reverberation perception, simulation, and reduction,'' in *Acoustical Factors Affecting Hearing Aid Performance*, edited by G. A. Studebaker and I. Hochberg (University Park, Baltimore, MD), pp. 3–24.

Bistafa, S. R., and Bradley, J. S. (**2000**). ''Reverberation time and maximum background-noise level for classrooms from a comparative study of speech intelligibility metrics,'' J. Acoust. Soc. Am. **107**, 861–875.

Bradley, J. S. (**1986**). ''Speech intelligibility studies in classrooms,'' J. Acoust. Soc. Am. **80**, 846–854.

Bradley, J. S. (**1996**). ''Some effects of orchestra shells,'' J. Acoust. Soc. Am. **100**, 889–898.

Bradley, J. S., Reich, R. D., and Norcross, S. G. (**1999**). ''On the combined effects of signal-to-noise ratio and room acoustics on speech intelligibility,'' J. Acoust. Soc. Am. **106**, 1820–1828.

Bradley, J. S., Sato, H., and Picard, M. (**2003**). ''On the importance of early reflections for speech in rooms,'' J. Acoust. Soc. Am. **113**, 3233–3244.

Bradley, J. S., and Soulodre, G. A. (**1995**). ''The influence of late arriving energy on spatial impression,'' J. Acoust. Soc. Am. **97**, 2263–2271.

Bronkhorst, A. W. (**2000**). ''The cocktail party phenomenon: A review of research on speech intelligibility in multiple-talker conditions,'' Acustica **86**, 117–128.

Bronkhorst, A. W., and Houtgast, T. (**1999**). ''Auditory distance perception in rooms,'' Nature (London) **397**, 517–520.

Brown, C. (**2002**). T60 Matlab function. 2002.

Brown, T. J. (**2000**). ''Characterization of Acoustic Head-Related Transfer Functions for Nearby Sources,'' in *Electrical Engineering and Computer Science* (MIT, Cambridge, MA).

Brungart, D. S. (**1999**). ''Auditory localization of nearby sources III: Stimulus effects,'' J. Acoust. Soc. Am. **106**, 3589–3602.

Brungart, D. S., and Durlach, N. I. (**1999**). ''Auditory localization of nearby sources. II. Localization of a broadband source in the near field,'' J. Acoust. Soc. Am. **106**, 1956–1968.

Brungart, D. S., and Rabinowitz, W. M. (**1999**). ''Auditory localization of nearby sources I: Head-related transfer functions,'' J. Acoust. Soc. Am. **106**, 1465–1479.

Buell, T. N., and Hafter, E. R. (**1991**). ''Combination of binaural information across frequency bands,'' J. Acoust. Soc. Am. **90**, 1894–1900.

Butler, R. A., and Belendiuk, K. (**1977**). ''Spectral cues utilized in the localization of sound in the median saggital plane,'' J. Acoust. Soc. Am. **61**, 1264–1269.

Butler, R. A., and Humanski, R. A. (**1992**). ''Localization of sound in the vertical plane with and without high-frequency spectral cues,'' Percept. Psychophys. **51**, 182–186.

Culling, J. F., Hodder, K. I., and Toh, C. Y. (**2003**). ''Effects of reverberation on perceptual segregation of competing voices,'' J. Acoust. Soc. Am. **114**, 2871–2876.

Culling, J. F., Summerfield, Q., and Marshall, D. H. (**1994**). ''Effects of simulated reverberation on the use of binaural cues and fundamental-frequency differences for separating concurrent vowels,'' Speech Commun. **14**, 71–95.

Darwin, C. J., and Hukin, R. W. (**2000**). ''Effects of reverberation on spatial, prosodic, and vocaltract size cues to selective attention,'' J. Acoust. Soc. Am. **108**, 335–342.

de Vries, D., Hulsebos, E. M., and Baan, J. (**2001**). ''Spatial fluctuations in measures for spaciousness,'' J. Acoust. Soc. Am. **110**, 947–954.

Devore, S., and Shinn-Cunningham, B. G. (**2003**). ''Perceptual consequences of including reverberation in spatial auditory displays,'' International Conference on Auditory Displays, Boston, MA.

Duda, R. O., and Martens, W. L. (**1998**). ''Range dependence of the response of a spherical head model,'' J. Acoust. Soc. Am. **104**, 3048–3058.

Durlach, N. I., Rigapulos, A., Pang, X. D., Woods, W. S., Kulkarni, A., Colburn, H. S., and Wenzel, E. M. (**1992**). ''On the externalization of auditory images,'' Presence **1**, 251–257.

Ebata, M. (**2003**). ''Spatial unmasking and attention related to the cocktail party problem,'' Acoust. Sci. Technol. **24(3)**, 208–219.

Hartmann, W. M. (**1983**). ''Localization of sound in rooms,'' J. Acoust. Soc. Am. **74**, 1380–1391.

Hartmann, W. M., and Rakerd, B. (**1999**). ''Localization of sound in reverberant spaces,'' J. Acoust. Soc. Am. **105**, 1149.

Hartmann, W. M., Rakerd, B., Gaalaas, J. B., Vander Velde, T., Thorpe, W. R., and Oh, M. M. (**1999**). ''Localization of sound in rooms: Broadband noise,'' Michigan State University.

Hartmann, W. M., Rakerd, B., and Koller, A. (**2005**). ''Binaural coherence in rooms,'' Acust. Acta Acust. (to be published).

Hidaka, T., and Beranek, L. L. (**2000**). ''Objective and subjective evaluations of twenty-three opera houses in Europe, Japan, and the Americas,'' J. Acoust. Soc. Am. **107**, 368–383.

Hodgson, M. (**1999**). ''Experimental investigation of the acoustical characteristics of university classrooms,'' J. Acoust. Soc. Am. **106**, 1810–1819.

Kidd, Jr., G., Mason, C. R., Brughera, A., and Hartmann, W. M. (**2005**). ''The role of reverberation in release from masking due to spatial separation of sources for speech identification,'' Acust. Acta Acust. in press.

Kistler, D. J., and Wightman, F. L. (**1991**). ''A model of head-related transfer fucntions based on principle components analysis and minimum-phase reconstruction,'' J. Acoust. Soc. Am. **91**, 1637–1647.

Kleiner, M., Dalenback, B.-I., and Svensson, P. (**1993**). ''Auralization—An overview,'' J. Audio Eng. Soc. **41**, 861–875.

Kopco, N., and Shinn-Cunningham, B. G. (**2002**). *Auditory localization in rooms: Acoustic analysis and behavior*, 32nd International Acoustics Conference—EAA Symposium, Zvolen, Slovakia.

Kopco, N., and Shinn-Cunningham, B. G. (**2003**). ''Spatial unmasking of nearby pure-tone targets in a simulated anechoic environment,'' J. Acoust. Soc. Am. **114**, 2856–2870.

Kulkarni, A., and Colburn, H. S. (**2004**). ''Infinite-impulse-response models of the head-related transfer function,'' J. Acoust. Soc. Am. **115**, 1714–1728.

Macpherson, E. A., and Middlebrooks, J. C. (**2002**). ''Listener weighting of cues for lateral angle: The duplex theory of sound localization revisited,'' J. Acoust. Soc. Am. **111**, 2219–2236.

Mershon, D. H., Ballenger, W. L., Little, A. D., McMurtry, P. L., and Bucha-

nan, J. L. (**1989**). ''Effects of room reflectance and background noise on perceived auditory distance,'' Perception **18**, 403–416.
Middlebrooks, J. C. (**1999**). ''Virtual localization improved by scaling nonindividualized external-ear transfer functions in frequency,'' J. Acoust. Soc. Am. **106**, 1493–1510.
Middlebrooks, J. C., and Green, D. M. (**1991**). ''Sound localization by human listeners,'' Annu. Rev. Psychol. **42**, 135–159.
Morimoto, M. (**2001**). ''The contribution of two ears to the perception of vertical angle in sagittal planes,'' J. Acoust. Soc. Am. **109**, 1596–1603.
Nabelek, A. K., Letowski, T. R., and Tucker, F. M. (**1989**). ''Reverberant overlap- and self-masking in consonant identification,'' J. Acoust. Soc. Am. **86**, 1259–1265.
Naguib, M. (**1995**). ''Auditory distance assessment of singing cospecifics in Carolina wrens: The role of reverberation and frequency-dependent attenuation,'' Anim. Behav. **50(5)**, 1297–1307.
Nishihara, N., Hidaka, T., and Beranek, L. L. (**2001**). ''Mechanism of sound absorption by seated audience in halls,'' J. Acoust. Soc. Am. **110**, 2398–2411.
Okano, T. (**2002**). ''Judgments of noticeable differences in sound fields of concert halls caused by intensity variations in early reflections,'' J. Acoust. Soc. Am. **111**, 217–229.
Plomp, R. (**1976**). ''Binaural and monaural speech intelligibility of connected discourse in reverberation as a function of azimuth of a single competing sound source (speech or noise),'' Acustica **34**, 200–211.
Rife, D. D., and Vanderkooy, J. (**1989**). ''Transfer-function measurement with maximum-length sequences,'' J. Audio Eng. Soc. **6**, 419–444.
Santarelli, S. (**2000**). ''Auditory Localization of Nearby Sources in Anechoic and Reverberant Environments,'' in *Cognitive and Neural Systems* (Boston Univ., Boston, MA).
Schroeder, M. R. (**1965**). ''New method of measuring reverberation time,'' J. Acoust. Soc. Am. **37**, 409–412.
Schroeder, M. R. (**1987**). ''Statistical parameters of the frequency response curves of large rooms,'' J. Audio Eng. Soc. **35(5)**, 299–305.
Schroeder, M. R., and Kuttruff, K. H. (**1962**). ''On frequency response curves in rooms. Comparison of experimental, theoretical, and Monte Carlo results for the aveage frequency spacing between maxima,'' J. Acoust. Soc. Am. **34**, 76–80.
Shaw, E. A. G. (**1997**). ''Acoustical features of the human external ear,'' in *Binaural and Spatial Hearing in Real and Virtual Environments*, edited by R. Gilkey and T. Anderson (Erlbaum, New York), pp. 25–48.
Shinn-Cunningham, B. (**2004**). ''The perceptual consequences of creating a realistic, reverberant 3-D audio display,'' International Congress on Acoustics, Kyoto, Japan.
Shinn-Cunningham, B., and Kawakyu, K. (**2003**). ''Neural representation of source direction in reverberant space,'' IEEE Workshop on Applications of Signal Processing to Audio and Acoustics, New Paltz, NY.
Shinn-Cunningham, B. G. (**2000a**). ''Distance cues for virtual auditory space,'' IEEE-PCM 2000, Sydney, Australia.
Shinn-Cunningham, B. G. (**2000b**). ''Learning reverberation: Implications for spatial auditory displays,'' International Conference on Auditory Displays, Atlanta, GA.
Shinn-Cunningham, B. G. (**2002**). ''Speech intelligibility, spatial unmasking, and realism in reverberant spatial auditory displays,'' International Conference on Auditory Displays, Kyoto, Japan.
Shinn-Cunningham, B. G., and Ram, S. (**2003**). ''Identifying where you are in a room: Sensitivity to room acoustics,'' International Conference on Auditory Display, Boston, MA.
Shinn-Cunningham, B. G., Constant, S., and Kopco, N. (**2002**). ''Spatial unmasking of speech in simulated anechoic and reverberant rooms,'' 25th mid-Winter meeting of the Association for Research in Otolaryngology, St. Petersburg Beach, FL.
Shinn-Cunningham, B. G., Santarelli, S., and Kopco, N. (**2000**). ''Tori of confusion: binaural localization cues for sources within reach of a listener,'' J. Acoust. Soc. Am. **107**, 1627–1636.
Shinn-Cunningham, B. G., Schickler, J., Kopco, N., and Litovsky, R. (**2001**). ''Spatial unmasking of nearby speech sources in a simulated anechoic environment,'' J. Acoust. Soc. Am. **110**, 1118–1129.
Stern, R. M., and Trahiotis, C. (**1995**). ''Models of binaural interaction,'' in *Hearing*, edited by B. C. J. Moore (Academic, San Diego), pp. 347–386.
Torres, R., Svensson, U. P., and Kleiner, M. (**2001**). ''Computation of edge diffraction for more accurate room auralization,'' J. Acoust. Soc. Am. **109**, 600–610.
Trahiotis, C., and Stern, R. M. (**1989**). ''Lateralization of bands of noise: Effects of bandwidth and differences of interaural time and phase,'' J. Acoust. Soc. Am. **86**, 1285–1293.
Vanderkooy, J. (**1994**). ''Aspects of MLS measuring systems,'' J. Audio Eng. Soc. **42(4)**, 219–231.
Vliegen, J., and van Opstal, A. J. (**2004**). ''The influence of duration and level on human sound localization,'' J. Acoust. Soc. Am. **115**, 1705–1713.
Wightman, F. L., and Kistler, D. J. (**1989**). ''Headphone simulation of free-field listening. I. Stimulus synthesis,'' J. Acoust. Soc. Am. **85**, 858–867.
Wightman, F. L., and Kistler, D. J. (**1997**). ''Monaural sound localization revisited,'' J. Acoust. Soc. Am. **101**, 1050–1063.
Zahorik, P. (**2002a**). ''Assessing auditory distance perception using virtual acoustics,'' J. Acoust. Soc. Am. **111**, 1832–1846.
Zahorik, P. (**2002b**). ''Direct-to-reverberant energy ratio sensitivity,'' J. Acoust. Soc. Am. **112**, 2110–2117.
Zurek, P. M. (**1993**). ''Binaural advantages and directional effects in speech intelligibility,'' in *Acoustical Factors Affecting Hearing Aid Performance*, edited by G. Studebaker and I. Hochberg (College-Hill, Boston, MA).
Zurek, P. M., Freyman, R. L., and Balakrishnan, U. (**2004**). ''Auditory target detection in reverberation,'' J. Acoust. Soc. Am. **115**, 1609–1620.

Reduced order modeling of head related impulse responses for virtual acoustic displays[a)]

D. Wesley Grantham[b)]
Department of Hearing and Speech Sciences, Vanderbilt University Medical Center, Station 17, Nashville, Tennessee 37232-8700

Joel Andrew Willhite and Kenneth D. Frampton[c)]
Department of Mechanical Engineering, Vanderbilt University, VU Station 351592, Nashville, Tennessee 37235-1592

Daniel H. Ashmead
Department of Hearing and Speech Sciences, Vanderbilt University Medical Center, Station 17, Nashville, Tennessee 37232-8700

(Received 10 May 2004; revised 7 February 2005; accepted 8 February 2005)

This study investigated the use of reduced order head related impulse response (HRIR) models to improve the computational efficiency in acoustic virtual displays. State space models of varying order were generated from zero-elevation HRIRs using a singular value decomposition technique. A source identification experiment was conducted under anechoic conditions in which three subjects were required to localize sounds in the front horizontal plane. The sounds were either (1) real sources (emitted by individual loudspeakers in a semi-circular array), (2) virtual sources generated from the original HRIRs, or (3) virtual sources generated using reduced order state space models. All virtual sources were created by simultaneous activation of two loudspeakers at $\pm 30°$ using a virtual source imaging technique based on either the measured or modeled HRIRs. The errors in the perceived direction of the virtual sources generated from the reduced order models were compared to errors in localization using the original HRIRs. The results demonstrate that a very significant reduction in model size can be achieved without significantly affecting the fidelity of the virtual display of horizontally placed sources.
[DOI: 10.1121/1.1882944]

PACS numbers: 43.66.Qp, 43.66.Yw, 43.66.Pn [AK] Pages: 3116–3125

I. INTRODUCTION

The premise of acoustic virtual reality (AVR) is the creation of an illusory sound environment for the listener. Acoustic virtual displays are advantageous in that they have the ability to present information anywhere in a three-dimensional virtual environment (not just the direction of a visual gaze), they allow the ability to discern and switch focus between several different sound sources generated simultaneously, and they can supplement visual displays by allowing the ears to ''point the eyes'' (Wenzel, 1992).

To create a virtual acoustic environment, it is necessary to understand how humans localize sound. An early attempt to explain this was the duplex theory, developed by Lord Rayleigh in the early 1900s (Rayleigh, 1907). The duplex theory suggested that human sound localization was based on two cues that arise from the spatial separation of the ears on the human head: the interaural time delay (ITD) for lower frequencies and the interaural level difference (ILD) for higher frequencies. This theory was formulated to explain localization performance in the horizontal plane, and thus did not incorporate the filtering effects produced by the outer ear, or pinna, that are known to underlie localization performance in the vertical plane (Hebrank and Wright, 1974). Searle *et al.* (1976) have developed a more comprehensive framework for understanding human localization in two dimensions (i.e., in both vertical and horizontal planes), where it is known that localization is mediated by these pinnae filtering effects, along with the effects of the head and torso, as well as interaural difference cues (ITDs and ILDs).

Some recent research has investigated human sound localization using ''virtual'' sound sources. Wightman and Kistler (1989), for example, presented sounds to listeners over headphones and filtered them in such a way that the sounds appeared to come from various arbitrary points in space. To obtain the required filters, transfer functions were carefully measured that related the sound spectrum at a listener's two ear canals to the spectrum of a sound source positioned at many different azimuths and elevations. These so-called head related transfer functions (HRTFs) take into account not only ITDs and ILDs, but also the filtering effects of the pinna, the head, and the torso. The first measurements of HRTFs were published by Wiener and Ross (1946).

The technique employed by Wightman and Kistler involved the presentation of stimuli to subjects via earphones. Another technique of creating virtual sound sources involves

[a)]Portions of this work were presented in ''Reduced order modeling of head related transfer functions for virtual acoustic displays,'' 145th Meeting of the Acoustical Society of America, April 2003, Nashville [J. Acoust. Soc. Am. **113**, 2270 (A)].
[b)]Electronic mail: d.wesley.grantham@vanderbilt.edu
[c)]Author to whom correspondence should be addressed.

the presentation of sounds through two or more fixed loudspeakers at a certain distance from a listener. Early attempts at implementing this type of ''virtual acoustic display'' employed stereophony—that is, the manipulation of amplitude differences between the outputs of two or more loudspeakers in a room with a listener (Bauer, 1961). This led to the ''placement'' of virtual sound sources at any position between the two loudspeakers (see also Nelson *et al.*, 1996). With more sophisticated techniques, one can, with the same two-loudspeaker setup, create a virtual sound source in *any* direction relative to the listener (not just at positions between the two speakers). This can be accomplished by filtering the inputs to the two loudspeakers in such a way that the spectra of the sound signals measured in the listener's two ear canals are the same as those that would be produced by a real source from the desired location. The desired filters may be computed from the HRTFs of the individual listener for sources at the positions of the two loudspeakers and for the specified virtual source position.

However, the filtering process employing HRTFs to create virtual sounds is computationally intensive. In order to address this issue, and create more efficient means of implementing virtual acoustic systems, several investigators have sought to model the HRTFs. One of the earliest efforts was carried out by Kistler and Wightman (1992), who essentially used a Fourier series to curve-fit the HRTFs and then compared subjects' judgments of sound sources produced by the measured and the modeled HRTFs. Kulkarni and Colburn (1998) used a similar Fourier series approach and also included subjective results. Kulkarni and Colburn (2004) continued this work by employing IIR filter modeling techniques. Mackenzie *et al.* (1997) as well as Cheung *et al.* (1998) used modern signal processing techniques to create HRTF models. In each of these cases, the investigators modeled only one HRTF at a time, and then apparently combined them together for a full set. In each case it was noted that individual HRTFs could be modeled with only a very few parameters while retaining mathematical and subjective fidelity. A good review of these and many other HRTF modeling efforts can be found in Huopaniemi *et al.* (1999).

Even with the data reduction effected by such models, modeling the full 3-D set of HRTFs would require hundreds or thousands of parameters. One means of reducing the required number of parameters comes from a fundamental principle of linear systems theory. This principle is that, for multi-input/multi-output systems (such as a full set of HRTFs), all system transfer functions are comprised of a single set of poles (i.e., roots of the denominator). In other words, every transfer function through the system has the same denominator. However, when individual HRTFs are modeled separately (as has been done in each of the previously referenced works), the poles of separate models are typically different. The differences may be small, but the overall model still requires one to keep track of a complete set of poles for each separate transfer function. If the full system transfer functions are modeled simultaneously, then each separate HRTF can be modeled using a common set of poles. This fact was noted by Haneda *et al.* (1999), who developed the ''common-acoustical-pole and zero'' modeling technique. This technique employs optimal filter design and was demonstrated mathematically to result in significant model order reductions while maintaining HRTF accuracy. Georgiou and Kyriakakis (1999) used a singular value decomposition system identification technique, which is capable of modeling all HRTFs simultaneously, resulting in common poles. While these previous two applications demonstrated the ability of exploiting common poles to further reduce model order, they did not demonstrate the subjective accuracy of such models.

The purpose of the work reported here is to create models of HRTFs that are significantly smaller than models previously created. The reduction will be achieved by exploiting common system poles and by employing a system identification technique, based on singular value decomposition, which allows one to further reduce the system order. The effectiveness of such models when used in virtual acoustic displays is demonstrated mathematically and subjectively. Developing such models will result in more efficient filtering processes for creating virtual acoustic sources, particularly for real-time applications. Since the technique to be employed here is applied in the time domain, henceforth we will refer primarily to the time-domain equivalent of the HRTF—namely, the head related impulse response (HRIR). Our approach attempts to improve model reduction efficiency by representing an *entire set* of horizontal plane HRIRs with a single discrete-time state space model (similar to that reported by Georgiou and Kyriakakis, 1999). Models are created of various orders and the mathematical accuracy of these models, as compared to the original HRIRs, is demonstrated. Subjective tests of horizontal-plane sound source localization accuracy were also carried out using real sources and virtual sources based on various order models. The results of these tests demonstrate that quite significant reductions in model size can be achieved while maintaining the subjective accuracy of the virtual display for sound sources in the front horizontal plane.

For the present investigation, emphasis of the modeling efforts and subjective performance is limited to the front horizontal plane, where it is known that interaural differences in time and intensity provide the primary cues underlying human localization performance (e.g., Grantham, 1995). Future investigations are planned to investigate the effectiveness of model reduction in more general cases involving localization in both horizontal and vertical dimensions.

II. THEORY OF ACOUSTIC VIRTUAL REALITY (AVR)

A. AVR and how it works

Consider a two-loudspeaker setup with a listener located at a point forming an equilateral triangle with the speakers, as in Fig. 1. Suppose it is desirable that the source signal *s* appears to originate from a virtual source location which is outside the stereoscope of the speakers relative to the listener (virtual source P in Fig. 1). This can be achieved by properly filtering the signal source *s* with filters F1 and F2 and send-

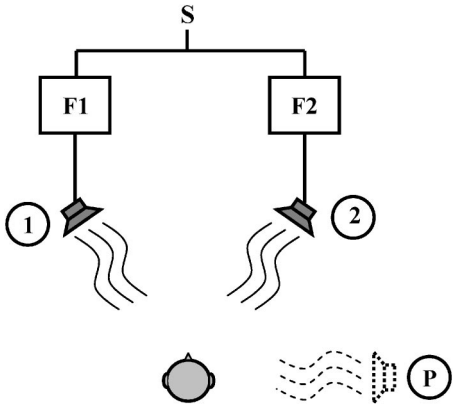

FIG. 1. Virtual acoustic setup using an imaging system with two loudspeakers (1 and 2) positioned at ±30° relative to the subject's head. With appropriate filters F1 and F2, a virtual source can be created that appears to come from an arbitrary direction (indicated by P).

ing those filtered signals to the two loudspeakers (Sakamoto *et al.*, 1981). Appropriate design of filters F1 and F2 is the key to acoustic virtual reality.

The object is for the pressures, $p1$ and $p2$, at the listeners ears to be identical to the pressures that would be heard at the listener's ear if the source actually originated at point P. This implies that the pressures at each ear due to each source must obey the following equations:

$$p_1^L + p_2^L = p_p^L, \quad p_1^R + p_2^R = p_p^R, \tag{1}$$

where p_1, p_2, and p_p are the pressures due to active source 1, active source 2, and the virtual source p, respectively, with superscripts indicating left and right. In words, Eq. (1) says that the active sources must sum at each ear to produce the same pressure as would have been created by a source located at the desired virtual source location.

Now assume that the HRTFs that relate the active speaker outputs and the virtual source output to the left and right ear pressure levels of the listener are known (Fig. 2). The prefilters F1 and F2 can then be determined as follows (Sakamoto *et al.*, 1981):

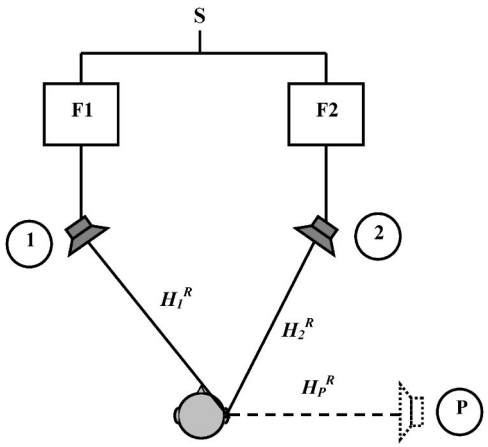

FIG. 2. Illustration of how a virtual stimulus is implemented by using HRTFs from the presentation loudspeaker positions and from the desired virtual position (P). Representations are given for only one of the two ears. See Eqs. (1) and (2).

$$\begin{Bmatrix} F_1 \\ F_2 \end{Bmatrix} = \begin{bmatrix} H_1^L & H_2^R \\ H_2^L & H_1^R \end{bmatrix}^{-1} \begin{Bmatrix} H_P^L \\ H_P^R \end{Bmatrix}, \tag{2}$$

where H_1 and H_2 are HRTFs relating the active speakers to the listener's ears and H_P relates the virtual source to the listeners ears (with superscripts indicating left and right ears).

Applying the prefilters F1 and F2 from Eq. (2) to the source signal at the two ''presentation loudspeakers'' produces identical sound pressure levels at the listener's two ears as a source signal from the virtual source location. Note that the solution process requires inversion of the HRTFs and can become computationally expensive.

The goal of this work is to develop a simpler model of the HRTFs to reduce the complexity of the filtering process. Such a reduction in model size would result in improved performance, particularly for real-time systems. The challenge is to create reduced order models without compromising the perceived accuracy of the virtual acoustic environment. It is important to note that, while most descriptions of AVR are based on HRTF concepts, the approach utilized here is based on HRIRs. However, the transfer functions and impulse response are directly related to each other through the Fourier transform and are therefore equivalent.

B. SVD-based model reduction

A modeling method based on singular value decomposition (SVD) was used to create simplified models of all HRIRs simultaneously. The result is a system whose inputs correspond to the desired azimuths of the virtual sources and whose outputs are the signals heard by the left and right ears. The modeling and experiments conducted here were limited to the horizontal plane azimuths from −90° to +90° in 10° increments. Therefore, the resulting systems have 19 inputs (one for each azimuthal location) and 2 outputs (one for each ear). The HRIRs used to create the state space model were a set measured by Dr. Wightman and provided to the authors by the University of Wisconsin. The full set included measured HRIRs for one individual (identified as SOW) for both ears and for 505 source positions in all directions around the listener. Each impulse response consists of 256 samples, obtained at a 50-kHz sampling rate.

The SVD approach used here is very similar to that used by Georgiou and Kyriakakis (1999), and originally described by Kung (1978) and by Frampton and Clark (1996). The application of this technique to the specific case of HRIR modeling is described below.

Let the left and right ear head related impulse responses for each azimuth in the front hemisphere of the horizontal plane be described as $\mathbf{h}_i^L(kT)$ and $\mathbf{h}_i^R(kT)$, where the superscripts L and R signify left and right ear responses, the subscript i denotes the index of the 19 input azimuths, T is the time increment, and k is the time index. Furthermore, as a matter of mathematical convenience and without loss of generality (Kung, 1978), the original Wightman HRIRs were pre-pended with a single sample of value zero. Therefore, the individual impulse responses now consist of 257 samples.

The HRIRs are arranged to form a matrix-valued impulse response such that

$$\mathbf{h}(kT)=\begin{bmatrix}\mathbf{h}_1^L(kT) & \mathbf{h}_2^L(kT) & \cdots & \mathbf{h}_{19}^L(kT)\\ \mathbf{h}_1^R(kT) & \mathbf{h}_2^R(kT) & \cdots & \mathbf{h}_{19}^R(kT)\end{bmatrix}. \tag{3}$$

In order to make use of the SVD technique the matrix-valued impulse response must be arranged in a block Hankel matrix of the form

$$\mathbf{H}=\begin{bmatrix}\mathbf{h}(T) & \mathbf{h}(2T) & \mathbf{h}(3T) & \cdots & \mathbf{h}\{(N+1)T\}\\ \mathbf{h}(2T) & \mathbf{h}(3T) & \mathbf{h}(4T) & \cdots & 0\\ \mathbf{h}(3T) & \mathbf{h}(4T) & \mathbf{h}(5T) & \cdots & 0\\ \vdots & \vdots & \vdots & \ddots & \vdots\\ \mathbf{h}\{(N+1)T\} & 0 & 0 & \cdots & 0\end{bmatrix}, \tag{4}$$

where $\mathbf{H}$ has dimensions of $m(N+1)\times p(N+1)$, with m being the number of outputs of the system (2 in this case), p being the number of inputs to the system (19 in this case), and N being the number of samples in the HRIRs excluding $\mathbf{h}(0)$ (256 in this case). The singular value decomposition of this block Hankel matrix has the form

$$\mathbf{H}=U\Sigma V^T=\mathbf{U}\mathbf{V}^T, \tag{5}$$

where U is an $m(N+1)\times(N+1)$ orthogonal matrix of the eigenvectors of $\mathbf{H}\mathbf{H}^T$, V is a $p(N+1)\times(N+1)$ orthogonal matrix of the eigenvectors of $\mathbf{H^T}\mathbf{H}$, and the singular value matrix is

$$\Sigma=\mathrm{diag}[\sigma_1\ \ \sigma_2\ \cdots\ \sigma_r\ \ \varepsilon_{r+1}\ \ \varepsilon_{r+2}\ \cdots\ \varepsilon_{N+1}] \tag{6}$$

with the singular values in descending order so that

$$\sigma_1\geqslant\sigma_2\geqslant\cdots\geqslant\sigma_r\geqslant\varepsilon_{r+1}\geqslant\varepsilon_{r+2}\geqslant\cdots\geqslant\varepsilon_{N+1} \tag{7}$$

and

$$\mathbf{U}=U\Sigma^{1/2},\quad \mathbf{V}^T=\Sigma^{1/2}V^T. \tag{8}$$

If the Hankel matrix $\mathbf{H}$ were of rank r, then the singular values $\varepsilon_{r+1},\ldots,\varepsilon_{N+1}$ would be zero. Consequently, for very small values for ε_i compared to the values of σ_i, one could assume the singular values ε_i to be computational noise or redundant poles and infer a rank of approximately r for the Hankel matrix. Thus, the ''fundamental order'' of the system is determined by discarding the insignificant singular values $\varepsilon_{r+1},\ldots,\varepsilon_{N+1}$. Usually, a numerical technique is used to determine the value of r necessary to achieve a particular model error. However, in this study we chose to create reduced models with r equal to 50, 60, 70, 80, 90, 100, 110, 135, 150, 160, 170, 180, 190, 200, 210, 220, and 240. The decision as to the minimum system order necessary to achieve adequate sound localization in the front horizontal plane was determined based on human subject perception data.

The discrete time state-space models generated have the form

$$\begin{aligned}\mathbf{x}[(k+1)T]&=\mathbf{A}\mathbf{x}(kT)+\mathbf{B}\mathbf{u}(kT),\\ \mathbf{y}(kT)&=\mathbf{C}\mathbf{x}(kT)+\mathbf{D}\mathbf{u}(kT),\end{aligned} \tag{9}$$

where T is the time increment and k is the time index. The 19×1 input vector $\mathbf{u}$ is defined by a virtual source signal placed at any of the 19 directional azimuths. The 2×1 output vector $\mathbf{y}$ yields the approximate signal at the left and right ears. The $2r\times1$ state vector $\mathbf{x}$ has no physical significance but is of mathematical construct (Frampton and Clark, 1996).

A realization of the r-order reduced system $(\hat{\mathbf{A}},\hat{\mathbf{B}},\hat{\mathbf{C}},\hat{\mathbf{D}})$ which eliminates the excess states can be obtained by first partitioning the SVD such that

$$\mathbf{H}=\begin{bmatrix}\mathbf{U}_{1,1} & \mathbf{U}_{1,2}\\ \mathbf{U}_{2,1} & \mathbf{U}_{2,2}\\ \vdots & \vdots\\ \mathbf{U}_{N,1} & \mathbf{U}_{N,2}\\ \mathbf{U}_{N+1,1} & \mathbf{U}_{N+1,2}\end{bmatrix}\times\begin{bmatrix}\mathbf{V}_{1,1}^T & \mathbf{V}_{2,1}^T & \cdots & \mathbf{V}_{N,1}^T & \mathbf{V}_{N+1,1}^T\\ \mathbf{V}_{1,2}^T & \mathbf{V}_{2,2}^T & \cdots & \mathbf{V}_{N,2}^T & \mathbf{V}_{N+1,2}^T\end{bmatrix}, \tag{10}$$

where the block matrices $\mathbf{U}_{i,1};\ i=1,2,\ldots,N+1$ are $m\times r$, $\mathbf{U}_{i,2};\ i=1,2,\ldots,N+1$ are $m\times(N+r-1)$, $\mathbf{V}_{i,1};\ i=1,2,\ldots,N+1$ are $p\times r$, and $\mathbf{V}_{i,2};\ i=1,2,\ldots,N+1$ are $p\times(N+r-1)$.

The reduced order state space realization is then defined by

$$\hat{?}=\left(\begin{bmatrix}\mathbf{U}_{1,1}\\ \mathbf{U}_{2,1}\\ \vdots\\ \mathbf{U}_{N,1}\end{bmatrix}^T\begin{bmatrix}\mathbf{U}_{1,1}\\ \mathbf{U}_{2,1}\\ \vdots\\ \mathbf{U}_{N,1}\end{bmatrix}\right)^{-1}\begin{bmatrix}\mathbf{U}_{1,1}\\ \mathbf{U}_{2,1}\\ \vdots\\ \mathbf{U}_{N,1}\end{bmatrix}^T\begin{bmatrix}\mathbf{U}_{2,1}\\ \mathbf{U}_{3,1}\\ \vdots\\ \mathbf{U}_{N+1,1}\end{bmatrix}, \tag{11a}$$

$$\hat{?}=\mathbf{V}_{1,1}^T, \tag{11b}$$

$$\hat{\mathbf{C}}=\mathbf{U}_{1,1}, \tag{11c}$$

$$\hat{\mathbf{D}}=\mathbf{h}(o). \tag{11d}$$

The system defined by $(\hat{\mathbf{A}},\hat{\mathbf{B}},\hat{\mathbf{C}},\hat{\mathbf{D}})$ has a matrix-valued impulse response of the form

$$\mathbf{h}(kT)=\begin{Bmatrix}\hat{\mathbf{D}} & \text{for } k=0,\\ \hat{\mathbf{C}}\hat{\mathbf{A}}^{k-1}\hat{\mathbf{B}} & \text{for } k=1,2,\ldots,N+1.\\ 0 & \text{for } k>N+1\end{Bmatrix}. \tag{12}$$

For the case of the ''full order'' system $(\mathbf{A},\mathbf{B},\mathbf{C},\mathbf{D})$ in which the model is not reduced (i.e., no singular values are thrown away), the matrix-valued impulse response defined in Eq. (12) returns the exact HRIRs used to develop the model. This largest model has 512 states and is twice the length of the original, measured HRIRs. Reduced order systems $(\hat{\mathbf{A}},\hat{\mathbf{B}},\hat{\mathbf{C}},\hat{\mathbf{D}})$ yield matrix-valued impulse responses that are approximations of the original HRIR data.

The effects of the model reduction on the head related filters can be seen in Figs. 3 and 4. Figure 3 plots the HRIR (upper panel) and the magnitude of the HRTF (lower panel) for a source presented from a position of $-50°$ azimuth, measured in the subject's left ear. The solid lines in each panel show the unmodeled functions (i.e., those measured in a real subject's ear and supplied to us by the University of Wisconsin). The dotted lines show the resulting functions

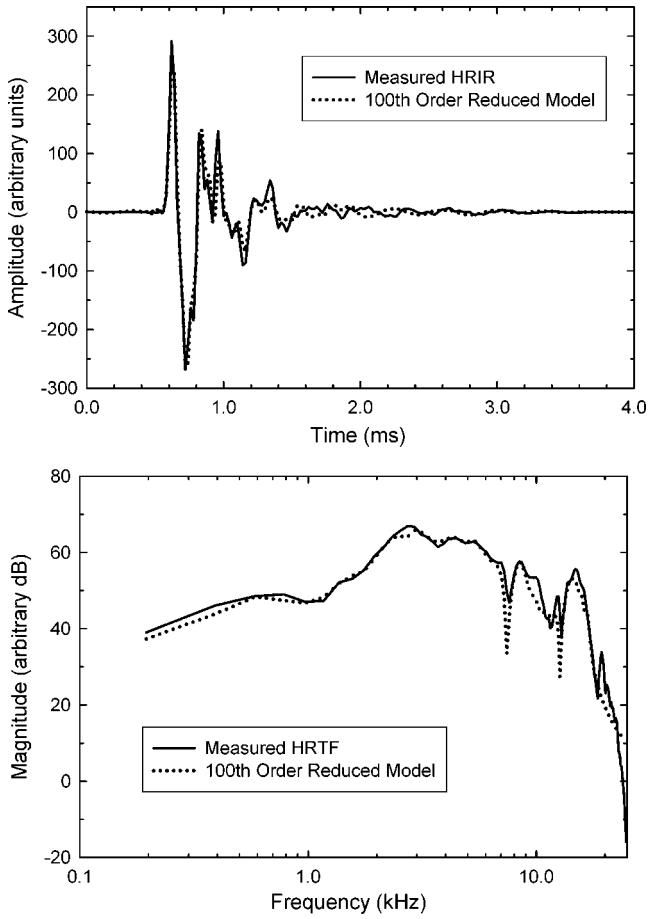

FIG. 3. Upper panel: HRIR for a source from −50° azimuth to subject's left ear. Lower panel: magnitude of the corresponding HRTF. Solid lines indicate the measured functions in a real subject's ear. Dotted lines indicate the functions for a reduced model of 100th order.

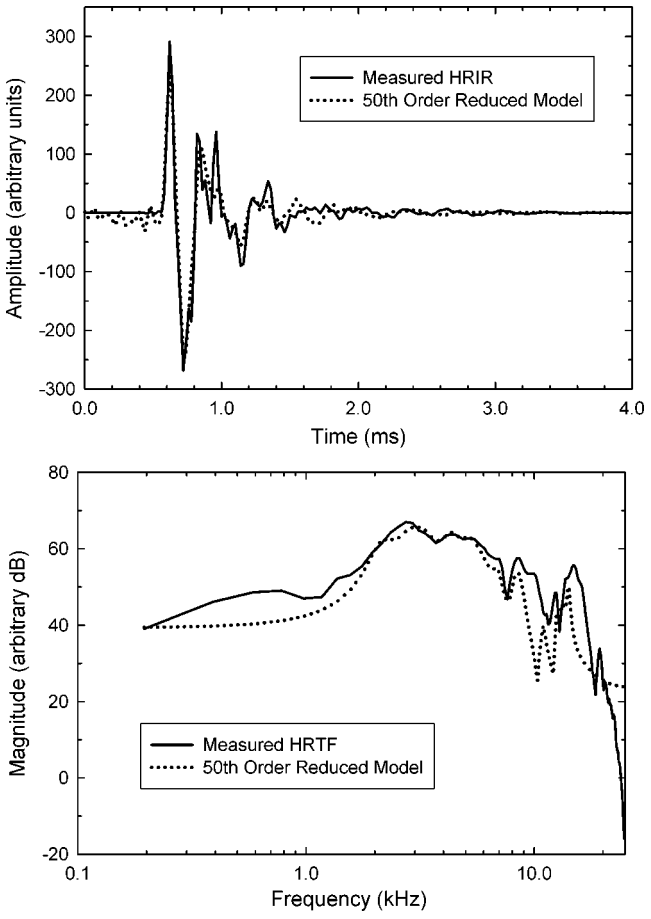

FIG. 4. Upper panel: HRIR for a source from −50° azimuth to subject's left ear. Lower panel: magnitude of the corresponding HRTF. Solid lines indicate the measured functions in a real subject's ear (same as plotted in Fig. 4). Dotted lines indicate the functions for a reduced model of 50th order.

generated by the 100th-order reduced model for the same source position. For the 100th-order reduction, the model functions correspond well with the original functions, especially in the lower frequencies. In Fig. 4, the original HRIR and HRTF functions are replotted (as solid lines) from Fig. 3, and the dotted lines show the 50th-order reduced model functions. In this case, significant deviations between the model and original functions can be seen in both the time and frequency domains.

III. EXPERIMENT: LOCALIZATION OF VIRTUAL SOURCES BASED ON MODELED HRIRs

An experiment was designed and implemented in an anechoic chamber to determine the reduced model of least order that would enable listeners to effectively localize virtual sound sources in the front horizontal plane, as compared to performance with virtual sources created by the original set of HRIRs. As described in Sec. II, the HRIRs (whether modeled or measured) were entered into Eq. (2) to determine the appropriate filters F1 and F2 to produce any particular desired virtual source position.

A. Experimental setup

Tests were conducted in an anechoic chamber with interior dimensions $4\times4\times4$ m^3 (measured between wedge tips) and with a low-frequency cutoff of 125 Hz. A speaker array consisting of 43 loudspeakers was set up at ear-level height in a semi-circle from −89° to +87° in the chamber, with adjacent loudspeakers separated from each other by approximately 4° (Fig. 5). The loudspeakers were clearly labeled with numbers 1 to 43 (starting from the left side). The subject was seated at the center of the arc of speakers, at a distance of 1.8 m from the array, with his head located in the ''sweet spot'' of the array (i.e., so that the head formed an

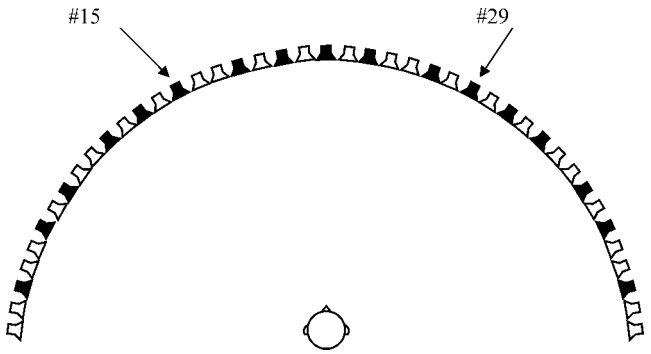

FIG. 5. Loudspeaker array in the anechoic chamber. Only 17 of the 43 loudspeakers (those shown as filled symbols) were employed as the real sources in the localization experiment. Loudspeakers 15 and 29 (at ±30°) were employed to create all virtual sources.

equilateral triangle with loudspeakers 15 and 29—the ''presentation'' loudspeakers). The subject was instructed to maintain an upright, forward orientation; however, no mechanical device was used to hold the subject's head in a fixed position.

B. Procedure

Three males, aged 26–41, with normal hearing bilaterally, were employed as subjects. They were tested individually in experimental sessions lasting 1.0 to 1.5 h (conducted on different days). During an experimental session, five to ten blocks of trials were presented, each of which lasted 5–10 min. Subjects were given a short break between each block, and a longer break after each three to four blocks. Subjects IA and BBH each received three sessions of practice (about 5 h) prior to data collection. Subject PLS (who turned out to have the lowest error scores) only received about 30 min of practice before data collection began. Data collection typically took three to four sessions.

Each block consisted of 68 trials and included three types of stimulus presented in random order: (1) 17 trials using real sources (stimulus from one of the loudspeakers in the array); (2) 17 trials using virtual sources generated using the original HRIRs; and (3) 34 trials that presented virtual sources generated using the reduced order models of 50, 60, 70, 80, 90, 100, 110, 135, 150, 160, 170, 180, 190, 200, 210, 220, and 240th order. The 17 real sources within each block were presented from the 17 loudspeakers shown as filled symbols in Fig. 5 (spanning azimuths from −80° to +80°). All other trials within the block (the 17 virtual sources with the original HRIRs plus the 34 virtual sources with the modeled HRIRs) involved simultaneous activation of loudspeakers 15 and 29 (the ''presentation loudspeakers,'' positioned at ±30° relative to the listener's head). All of these virtual stimuli were presented from virtual azimuths −80° to +80° (in 10° increments).

The stimulus in all cases was a 200-ms broadband noise burst, presented at an SPL of 65 dBA and low-pass filtered at 4 kHz.[1] The duration was restricted to 200 ms to ensure that subjects would not be able to turn their heads toward the perceived location prior to stimulus offset.

The total number of trials presented at each real or virtual azimuth during the course of the experiment depended on the signal type. In the case of the real sources, one trial was presented from each of the 17 sources within each block. Subjects completed a total of 13–17 blocks of trials over the course of the experiment; thus, each subject was presented each real source 13–17 times. Likewise, for the virtual sources based on the original HRIRs, each of the 17 virtual azimuths (−80° to +80°) was presented once within each block, so that each subject received 13–17 presentations from each virtual azimuth.

In the case of the virtual stimuli based on modeled HRIRs, there were typically only two presentations from each virtual azimuth for each reduced model. This was due to the fact that the 34 trials within each block representing the modeled virtual stimuli employed a pseudo-random scheme in which different virtual azimuths were paired with different reduced models. For example, one such pairing (''roster'') is shown in Table I. Within the block of trials that used this pairing, the virtual azimuth of −80° was presented using a 150th-order model (twice), the azimuth at −70°, a 50th-order model (twice), etc. The 34 trials result from each entry in the table being presented twice within the block. There were 17 such rosters, and each one was employed only once for each subject. The construction of the rosters was designed to ensure that the number of presentations at a given virtual azimuth would be equivalent for each of the reduced models over the course of the experiment. Two of the three subjects completed only 13 blocks, with the result that data from some of the modeled stimuli did not have all 17 virtual azimuths represented.

TABLE I. Example of pairings of virtual azimuth and reduced models for a typical block of trials. This was 1 of 17 such rosters, each of which was employed during a single block of trials for each subject. Within a block of trials, each combination shown was presented twice, randomly shuffled with the other types of trials presented within the block.

Virtual azimuth	Model order
−80°	150
−70°	50
−60°	110
−50°	90
−40°	150
−30°	135
−20°	110
−10°	50
0°	50
+10°	50
+20°	150
+30°	90
+40°	135
+50°	90
+60°	150
+70°	150
+80°	110

The subjects were not aware that most of the trials within each block involved virtual stimuli, nor that only a subset of the loudspeaker array was employed in stimulus presentation. For each trial, the subject oriented toward and visually fixated the center loudspeaker (no. 22) and pushed a button when he was ready. The stimulus was presented, at which point the subject was free to rotate in his chair to look at the loudspeaker numbers (the 200-ms duration ensured that the subject did not have time to initiate a head turn prior to stimulus offset). The subject then called out the speaker number from which he perceived the sound to originate. In cases where the subject was not sure where the stimulus came from, or perceived it coming from a position outside the range of loudspeakers on the array, he was instructed to make his best guess about the source location from among the 43 alternatives. The response was entered into the computer by the experimenter sitting in the adjacent control room, listening via an intercom system. Once the response was entered, an LED on the subject's button box indicated that he could proceed to the next stimulus by pressing the button again.

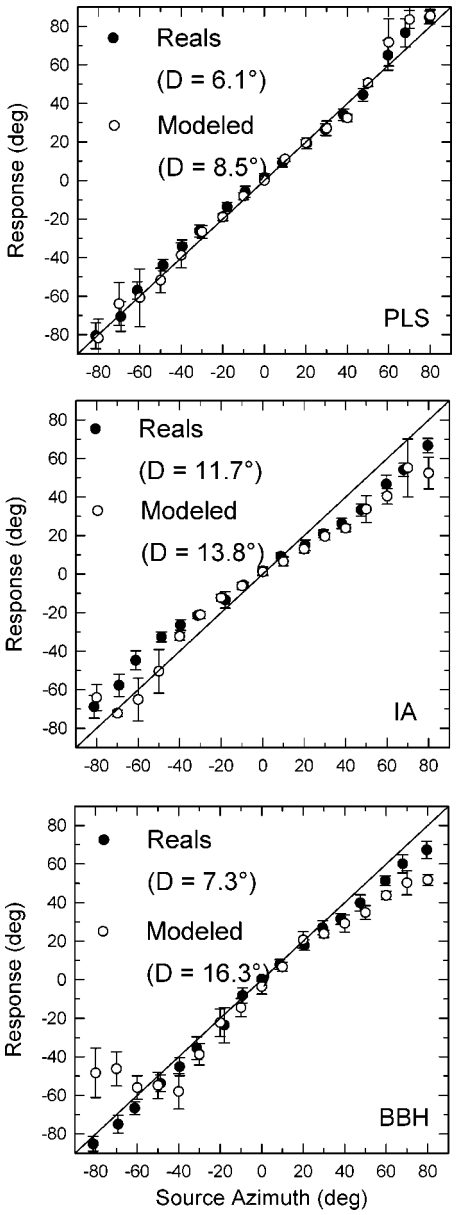

FIG. 6. Localization results for the three subjects (shown in the three panels). Average response azimuth plotted as a function of real or virtual stimulus azimuth, with standard deviations shown across replications (each symbol based on 13–17 responses). Solid symbols show performance for real sources; open symbols show performance for 90–100th-order reduced models (each symbol based on two to four responses). The rms errors are shown for each subject for both conditions.

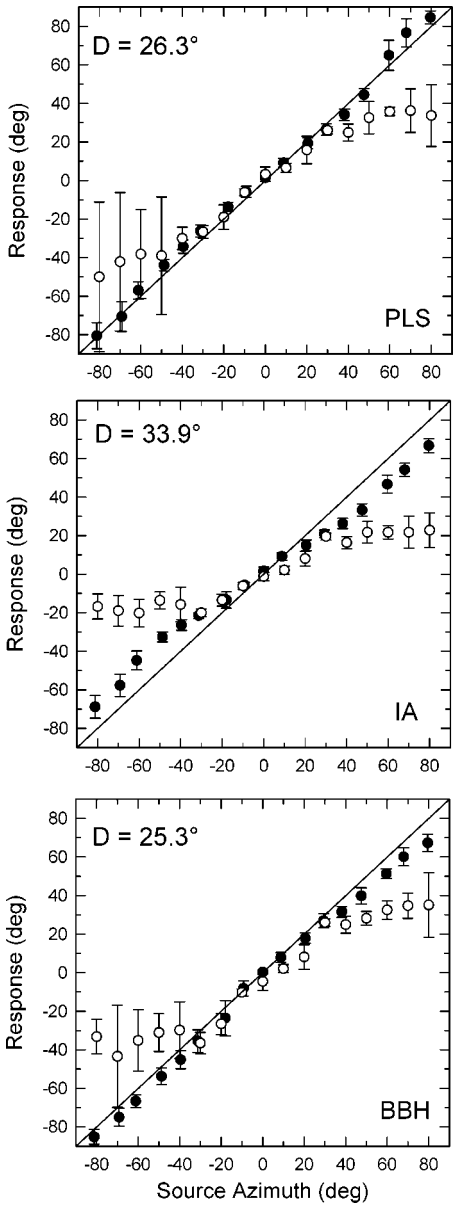

FIG. 7. As in Fig. 6, except open symbols show performance for 70–80th-order reduced model. Solid symbols (for the real sources) are replotted from Fig. 6. The rms error scores are given within each panel for the modeled sources.

C. Results and discussion

Figure 6 shows localization performance for the three subjects (in the three panels). Average response azimuth is plotted versus source azimuth, with error bars showing one standard deviation around the mean. Perfect performance is represented by the diagonal line. The solid data points in each panel show performance for the 17 real sources in the loudspeaker array. As noted in the figure, the rms error (D) for the real sources varied from 6.1° for subject PLS to 11.7° for subject IA.[2] These values are similar to those that have been reported earlier in this type of task with normal-hearing listeners (Vause and Grantham, 1999).

Figure 6 also shows, as open symbols, performance for the virtual stimuli created with the 90th and 100th reduced order models. Note that, in order to increase the number of responses at each virtual azimuth, adjacent orders of the model have been combined in most of the analyses to be reported. For subjects PLS and IA, the rms error for these modeled virtual stimuli is only slightly higher than for the real sources; for the third subject (BBH), the rms error for the virtual sources was more than twice that for the real sources. For all three subjects, the patterns of responses for the higher reduced models (up to the highest order tested: 240) were very similar to those shown here for the 90th–100th reduced order models, indicating that the order can be reduced to this value before significant degradation of localization performance is evident.

When the order of the model is reduced further, performance progressively deteriorates. Figure 7 shows perfor-

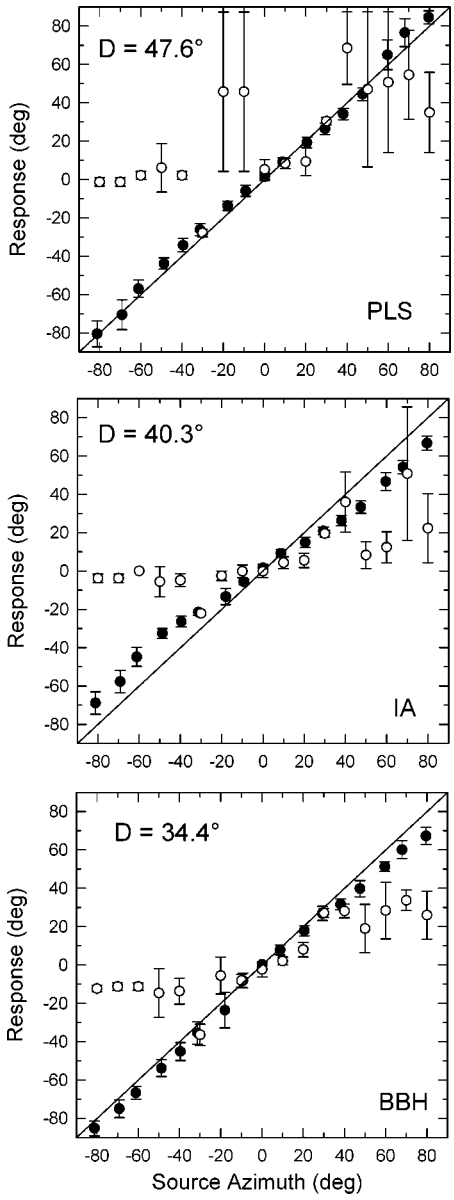

FIG. 8. As in Fig. 6, except open symbols show performance for 50–60th-order reduced model. Solid symbols (for the real sources) are replotted from Fig. 6. The rms error scores are given within each panel for the modeled sources.

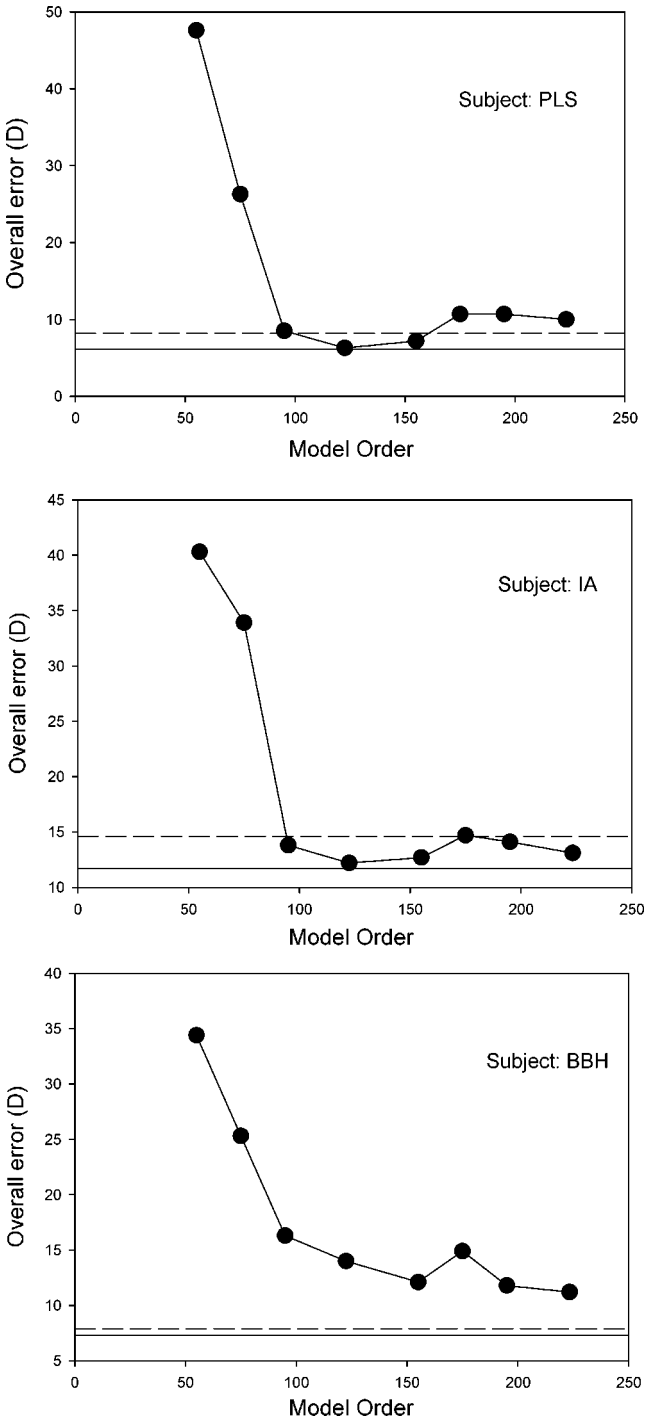

FIG. 9. The rms error for each subject as a function of the order of the reduced model. All points except the last are computed based on two successive orders (i.e., the first point is for orders 50 and 60, the next for orders 70 and 80, etc.). The last point is based on orders 210, 220, and 240. The solid horizontal line in each panel represents subjects' error scores for the real sources, and the dashed horizontal lines represent their error scores for virtual sources produced with unmodeled (measured) HRIRs.

mance for the 70th–80th reduced order models, plotted as open symbols in the same format as in Fig. 6. The solid symbols, depicting performance for the real sources, have been replotted from Fig. 6. It can be seen that with these models all three subjects have particular difficulty localizing sources at the periphery (beyond ±40°): responses are more variable, and tend to be biased toward midline. The rms error measures (shown in the figure) range from 25.3° to 33.9°, three to four times those obtained with the real sources. Finally, for the most severely reduced models (50th–60th reduced order), performance becomes very erratic, especially for virtual sources at the periphery (Fig. 8). The rms error in this case ranges from 34.4° to 47.6°.

The rms localization errors of all of the reduced models created are shown together for each subject in Fig. 9. This figure clearly illustrates the point made earlier: Error rates vary little or none for reduced models of 90th or higher order, but for further reduction in the order of the model, error rate increases substantially. In fact, subjects exposed to sources created by models of 70th order and lower indicated qualitatively that the sound source was either of indistinct origin or that the sound seemed to emanate from a source not located in the array. From Fig. 9, it appears that a state space

TABLE II. Effective order reduction of reduced state space models of HRIRs.

Order Reduction Ration and Effective Order Reduction Ratio			
System order	Order reduction ratio	Effective order	Effective order reduction ratio
512	1.00	78	1.00
240	2.13	55	1.42
150	3.41	44	1.77
135	3.79	43	1.81
110	4.65	36	2.17
100	5.12	32	2.44
90	5.69	26	3.00
80	6.40	24	3.25
70	7.31	20	3.90
60	8.53	16	4.88
50	10.24	12	6.50

model of the set of HRIRs has an approximate effective order of around 90, which is a reduction of order by a factor of about 5.7 (512th order to 90th order).

It is difficult to compare this result directly with previous work but qualitative consistency can be noted. As noted earlier, Georgiou and Kyriakakis (1999) recognized the multi-path advantages of the SVD technique; however they actually modeled each HRTF individually, combined them, and then reduced the overall model. If we presume that this approach is similar to the more direct approach used here, then the reduction by a factor of 5.7 is reasonably consistent with the results of Georgiou and Kyriakakis. It is even more difficult to compare these results directly with those noted in studies using HRTF curve fitting (Kistler and Wightman, 1992; Kulkarni and Colburn, 1998; Mackenzie *et al.*, 1997). This is because the modeling techniques used are very different. However, one can note that in those cases the number of parameters needed to accurately represent a single HRTF was very small (about five to ten parameters per HRTF) compared to the full frequency domain representations.

While the order reduction of 5.7 is a good measure of the reduction in complexity from using the HRTFs in prefiltering, it is important to note that since the source signal was low-pass filtered at 4 kHz, some of the states that were eliminated by order reduction contributed to poles that were above this cutoff and would have been filtered out anyway. To get a better realization of the effective order reduction, the number of poles below the 4 kHz cutoff was compared between the full order (unreduced) model and the reduced order models. A table of these effective reductions is shown in Table II.

The effective order column in Table II lists the number of poles below the 4-kHz cutoff frequency, and the effective order reduction column presents the ratio of the effective orders of the reduced models to the effective order of the unreduced model.

Another effective-order-reduction consideration stems from the fact that initial time delays present in the original HRIRs are modeled as poles located at the origin. Eliminating these initial time delays of the HRIRs—not the interaural delay necessary between the left and right HRIR pairs, but any starting delay common to all of the impulse responses—would reduce the number of poles at the origin and could influence the effective order reduction of the reduced models. A good approach to accommodate the delay was demonstrated by Huopaniemi *et al.* (1999).

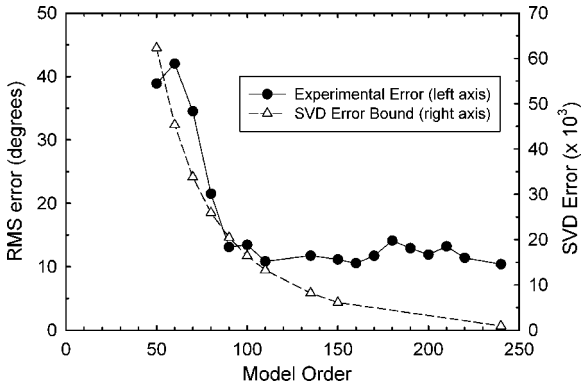

FIG. 10. Solid circles: average rms error for the three subjects (referred to left axis). Open triangles: SVD mathematical error bound (referred to right axis). Both functions are plotted as a function of the order of the reduced model.

A comparison of the mathematical error bounds calculated during the SVD decomposition and the experimental error of the reduced models reinforces the notion of a ''fundamental order'' of the reduced model. Figure 10 shows both the experimental errors (averaged across subjects) and the SVD mathematical error bounds for each model used. The SVD errors are normalized. Note that when the model is reduced beyond 90th order, the mathematical error bound continues to decrease while the experimental localization error tends to stay steady around 8°–10° (which again falls into an acceptable error range for localization using HRIRs to prefilter the data). This ''leveling off'' of localization error implies that for localization in the horizontal plane with sources filtered at 4 kHz, a 90th-order reduced model provides sufficient resolution.

IV. CONCLUSIONS

This work presented a technique for simultaneously modeling numerous HRIRs which takes advantage of the common poles associated with the overall system. The technique is based on the singular value decomposition of the HRIRs and also allows the final model order to be set. Models created in this manner were used in subjective localization tests and the effectiveness of using the reduced models in comparison to full order models was determined for the particular case of localization in the frontal horizontal plane. It was noted that, when simultaneously modeling 17 HRIRs in the horizontal plane, a model that retained only 90 states (as compared to the 512th-order unreduced model) was subjectively as good as the full order system with respect to horizontal plane localization. Future work will address whether the same reduction is applicable for the more general case of localization in three dimensions.

ACKNOWLEDGMENTS

This work was supported by the National Eye Institute under the Bioengineering Research Support Grant No.

5R24EY12894, ''Blind Pedestrians' Access to Complex Intersections'' and by NIDCD Grant No. DC00185, ''Auditory Motion Perception.'' The authors are grateful to Associate Editor Armin Kohlrausch and two anonymous reviewers for constructive comments on earlier versions of this manuscript.

[1]The decision to low-pass filter the stimuli at 4000 Hz was based on pilot work that revealed that most virtual stimuli generated by our computations involving the HRIRs had a spectral peak between 6.0 and 8.0 kHz that resulted in an annoying ''whistle'' sound and that also often created the illusion that the sources were located above the horizontal plane in which the loudspeakers were positioned (although the horizontal-plane component of the perceived location did not appear to be affected). The presence of these prominent spectral peaks reveals some imperfections or limitations in the source imaging technique and/or in the mathematical computations employed to determine the filters (F1 and F2 in Figs. 1 and 2). For example, sharp notches in transfer functions that appear in the denominator may produce unrealistically large peaks in the resultant filters. It remains to be seen whether these imperfections may be overcome by techniques such as employing smoothing algorithms that mimic auditory filter analysis or by appropriate modeling efforts. Since the purpose of the present investigation was to measure the effects on performance of reducing the order of the basic space state model for the simple case of frontal horizontal plane localization, the inclusion of the higher frequencies was deemed not necessary for evaluating the effects of reduction, and the unwanted spectral peaks were thus filtered out.

[2]The rms error D was computed based on azimuthal deviations of responses from the source direction. It thus represents overall error (including both bias and random variability). See Rakerd and Hartmann (1985).

Bauer, B. B. (**1961**). ''Phasor analysis of some stereophonic phenomena,'' J. Acoust. Soc. Am. **33**, 1536–1539.

Cheung, N., Trautmann, S., and Horner, A. (**1998**). ''Head-related transfer function modeling in 3-D sound systems with genetic algorithms,'' J. Audio Eng. Soc. **46**, 531–539.

Frampton, K. D., and Clark, R. L. (**1996**). ''State-space modeling of aerodynamic forces on plate using singular value decomposition,'' AIAA J. **34**, 2627–2630.

Georgiou, P., and Kyriakakis, C. (**1999**). ''Modeling of head related transfer functions for immersive audio using a state-space approach,'' Proceedings of the 33rd IEEE Asilomar Conference, pp. 720–724.

Grantham, D. W. (**1995**). ''Spatial hearing and related phenomena,'' in *Handbook of Perception and Cognition: Hearing*, edited by B. C. J. Moore (Academic, San Diego), pp. 297–345.

Haneda, Y., Makino, S., Kaneda, Y., and Kitawaki, N. (**1999**). ''Common-acoustical-pole and zero modeling of head-related transfer functions,'' IEEE Trans. Speech Audio Process. **7**, 188–196.

Hebrank, J., and Wright, D. (**1974**). ''Spectral cues used in the localization of sound sources on the median plane,'' J. Acoust. Soc. Am. **56**, 1829–1834.

Huopaniemi, J., Zacharov, N., and Karjalainen, M. (**1999**). ''Objective and subjective evaluation of head-related transfer function filter design,'' J. Audio Eng. Soc. **47**, 218–239.

Kistler, D. J., and Wightman, F. L. (**1992**). ''A model of head-related transfer functions based on principal components analysis and minimum-phase reconstruction,'' J. Acoust. Soc. Am. **91**, 1637–1647.

Kulkarni, A., and Colburn, H. S. (**1998**). ''Role of spectral detail in sound-source localization,'' Nature (London) **396**, 747–749.

Kulkarni, A., and Colburn, H. S. (**2004**). ''Infinite-impulse-response models of the head-related transfer function,'' J. Acoust. Soc. Am. **115**, 1714–1728.

Kung, S. (**1978**). ''A new identification and model reduction algorithm via singular value decompositions,'' IEEE 12th Asilomar Conference on Circuits, Systems, and Computers, pp. 705–714.

Mackenzie, J., Huopaniemi, J., Valimaki, V., and Kale, I. (**1997**). ''Low-order modeling of head-related transfer functions using balanced model truncation,'' IEEE Signal Process. Lett. **4**, 39–41.

Nelson, P. A., Orduña-Bustmanta, F., Engler, D., and Hamada, H. (**1996**). ''Experiments on a system for the synthesis of virtual acoustic sources,'' J. Audio Eng. Soc. **44**, 990–1007.

Rakerd, B., and Hartmann, W. M. (**1985**). ''Localization of sound in rooms. II. The effects of a single reflecting surface,'' J. Acoust. Soc. Am. **78**, 524–533.

Rayleigh, L. (**1907**). ''On our perception of sound direction,'' Philos. Mag. **13**, 214–232.

Sakamoto, N., Gotoh, T., Kogure, T., Shimbo, M., and Clegg, A. H. (**1981**). ''Controlling sound-image localization in stereophonic reproduction,'' J. Audio Eng. Soc. **29**, 794–798.

Searle, C. L., Braida, L. D., Davis, M. F., and Colburn, H. S. (**1976**). ''Model for auditory localization,'' J. Acoust. Soc. Am. **60**, 1164–1175.

Vause, N. L., and Grantham, D. W. (**1999**). ''Effects of earplugs and protective headgear on auditory localization ability in the horizontal plane,'' Hum. Factors **41**, 282–294.

Wenzel, E. M. (**1992**). ''Localization in virtual acoustic displays,'' Presence **1**, 80–107.

Wiener, F. M., and Ross, D. A. (**1946**). ''The pressure distribution in the auditory canal in a progressive sound field,'' J. Acoust. Soc. Am. **18**, 401–408.

Wightman, F. L., and Kistler, D. J. (**1989**). ''Headphone simulation of free-field listening. I. Stimulus synthesis,'' J. Acoust. Soc. Am. **85**, 858–867.

Pitch ranking ability of cochlear implant recipients: A comparison of sound-processing strategies

Andrew E. Vandali[a)]
The Cooperative Research Centre for Cochlear Implant and Hearing Aid Innovation, Melbourne, Australia

Catherine Sucher, David J. Tsang, and Colette M. McKay
The Department of Otolaryngology, University of Melbourne, Australia

Jason W. D. Chew
The School of Audiology, University of Melbourne, Australia

Hugh J. McDermott
The Department of Otolaryngology, University of Melbourne, Australia

(Received 5 November 2004; revised 30 January 2005; accepted 31 January 2005)

Pitch ranking of sung vowel stimuli, separated in fundamental frequency (F0) by half an octave, was measured with a group of eleven Nucleus 24 cochlear implant recipients using different sound coding strategies. In three consecutive studies, either two or three different sound coding strategies were compared to the Advanced Combinational Encoder (ACE) strategy. These strategies included Continuous Interleaved Sampling (CIS), Peak Derived Timing (PDT), Modulation Depth Enhancement (MDE), F0 Synchronized ACE (F0Sync), and Multi-channel Envelope Modulation (MEM), the last four being experimental strategies. While pitch ranking results on average were poor compared to those expected for most normal hearing listeners, significantly higher scores were obtained using the MEM, MDE, and F0Sync strategies compared to ACE. These strategies enhanced coding of temporal F0 cues by providing deeper modulation cues to F0 coincidentally in time across all activated electrodes. In the final study, speech recognition tests were also conducted using ACE, CIS, MDE, and MEM. Similar results among all strategies were obtained for word tests in quiet and between ACE and MEM for sentence tests in noise. These findings demonstrate that strategies such as MEM may aid perception of pitch and still adequately code segmental speech features as per existing coding strategies. [DOI: 10.1121/1.1874632]

PACS numbers: 43.66.Ts, 43.66.Hg, 43.64.Me, 43.71.Ky [RAL] Pages: 3126–3138

I. INTRODUCTION

Significant advances in the development of cochlear implant (CI) hardware and software over the last three decades have resulted in improved functional hearing for people with severe to profound deafness. Most postlingually deafened adults are now able to obtain some degree of open-set speech discrimination (Balkany, Hodges, and Luntz, 1996; Staller *et al.*, 1997; Osberger and Fisher, 2001; Anderson, Weichbold, and D'Haese, 2002). However, for speakers of tonal languages, such as Cantonese and Mandarin, in which speaker tone (or voice pitch) is used to convey lexical meaning, speech recognition is less satisfactory (Ciocca *et al.*, 2002; Lee *et al.*, 2002; Barry *et al.*, 2002). These studies have demonstrated poor discrimination by CI users for some tonal contrasts with results at, or marginally above, chance level in many cases. In addition, many CI recipients are unsatisfied with their ability to perceive musical sounds (Gfeller *et al.*, 2000; Leal *et al.*, 2003). Although studies exploring the ability of CI users to perceive different aspects of music have shown that subjects are generally able to perceive rhythmic aspects of musical sounds, pitch, and melody perception as well as instrument identification are more difficult (Gfeller and Lansing, 1991; Gfeller, Turner *et al.*, 2002; Gfeller, Witt, *et al.*, 2002; Leal *et al.*, 2003; Kong *et al.*, 2004). Thus, improved coding of pitch is of substantial importance in tonal language and music perception by users of CIs.

Pitch information can be conveyed by CIs by means of encoding temporal and spectral cues (Townshend *et al.*, 1987; Pijl, 1997; McDermott, 2004; Moore and Carlyon, 2005). The sensation of pitch can be elicited by variation of stimulation rate on a single electrode. Pijl and Schwarz (1995) demonstrated that temporal cues presented in isolation were sufficient for musical pitch and interval perception. However, once the stimulation rate increases beyond approximately 300 Hz, the efficacy of this cue is greatly reduced for the majority of CI users and a wide variability in the ability of individual subjects to utilize rate cues is observed (Tong and Clark, 1985; Townshend *et al.*, 1987; Moore and Carlyon, 2005). Pitch may also be conveyed by periodic fluctuations (modulation) in the amplitude of a train of stimulus pulses (Shannon, 1992; McKay, McDermott, and Clark, 1994; McKay, McDermott, and Clark, 1995; Geurts and Wouters, 2001). In general, the deeper the modulation, the closer the perceived pitch to that of the modulation frequency. However, similar to results observed for the stimulation rate, an upper limit to modulation frequency discrimi-

[a)]Corresponding author: Andrew Vandali, CRC for Cochlear Implant and Hearing Aid Innovation, 384 Albert Street, East Melbourne, 3002 Victoria, Australia. Electronic mail: avandali@bionicear.org

nation of approximately 300 Hz is observed for the majority of CI recipients. The carrier (or stimulation) rate used in sampling the modulation component can also affect pitch perception (McKay *et al.*, 1994; McKay *et al.*, 1995). Results have indicated that the carrier rate must be at least four times the modulation frequency to adequately code it (McKay *et al.*, 1994; Wilson *et al.*, 1997). Pitch can also be affected by interactions between temporal information in the stimulus signal delivered to neighboring electrodes (McKay and McDermott, 1996). Results demonstrated that modulated signals presented at electrodes separated by no more than 3 to 4 mm were perceived as the combined temporal pattern produced by both modulated signals. For greater electrode separations, the pitch was determined by the individual temporal patterns at each electrode. These results are consistent with the spread of electrical current fields (Chatterjee and Shannon, 1998) between neighboring electrodes resulting in the activation of partially overlapping populations of auditory neurons. The implication of these data to coding of complex signals in sound processors is that pitch information derived from amplitude modulation in the stimulus signals may be affected by phase differences between modulation signals at neighboring electrodes (McDermott, 2004). Specifically, out-of-phase modulation information provided at neighboring electrodes can result in reduced or inaccurate temporal pitch information.

Place of electrical stimulation along the cochlea can also be used to convey pitch according to a tonotopic arrangement with basal electrodes generally eliciting a percept of higher pitch than apical electrodes (Busby *et al.*, 1994; Nelson *et al.*, 1995; Busby and Clark, 2000). However, pitch reversals may occur if there is suboptimal electrode placement or variable neural survival within the cochlea. Current spread along the basilar membrane can also affect pitch perception because the population of neurons stimulated cannot be sufficiently focused to a small local population of neurons (Townshend *et al.*, 1987). In addition, the degree of spectral resolution may be limited by the maximum number of channels available in the CI (e.g., 22 for the Nucleus 22 and 24 systems). Finally, pitch may be affected by interactions between temporal and place-related cues to pitch (McKay and McDermott, 1996; McKay, McDermott, and Carlyon, 2000) and by the overall level of the stimuli (Townshend *et al.*, 1987; Pijl, 1997).

Currently available CI sound processing strategies divide the incoming signal into a number of frequency channels using a bank of band-pass filters. The envelope of the signal in each channel is usually estimated, although some strategies utilize the band-pass signals directly. Electrical stimuli are derived from a function of these signals and are used to activate corresponding electrodes within the cochlea using pulsatile stimuli presented at constant stimulation rates, variable rates, or different fixed rates across electrodes depending on the strategy. In some strategies, analog rather than pulsatile stimulation is used. Electrodes are allocated to the frequency channels in a manner consistent with the tonotopic arrangement of the cochlea. In general, spectral cues in the signal are encoded via electrode place whereas temporal envelope cues are coded via amplitude fluctuations in the envelope of the stimulus signal. While it has been found that high levels of speech perception can be achieved via the provision of limited spectral information for both normal-hearing subjects (Shannon *et al.*, 1995) and CI recipients (Skinner *et al.*, 1994; Garnham *et al.*, 2002), such limited information may not be sufficient for satisfactory music and tone perception in CI recipients.

A number of studies have explored pitch perception by CI recipients using strategies designed explicitly to code F0. Jones *et al.* (1995) investigated the use of a strategy that provided F0 timing information on the most apical electrode. Results of several pitch perception tasks did not demonstrate any advantages of this approach. Geurts and Wouters (2001) increased the depth of envelope fluctuations in the channel signals of the Continuous Interleaved Sampling (CIS) strategy (Wilson *et al.*, 1991) and reported that results of F0 discrimination tests using synthetic vowels were not significantly different from those of standard CIS. A more recent study by Green, Faulkner, and Rosen (2004) did however demonstrate that for CIS, the enhancement of temporal cues to F0 could aid the perception of voice pitch in synthetic diphthongal glides. In addition, Geurts and Wouters (2004) demonstrated that a filter bank with sufficient spectral resolution in the F0 frequency region to resolve the frequency of the fundamental could be used to provide place coding cues to F0. In the absence of temporal cues to F0 (by applying a 20-Hz low pass filter to the filter bank envelope signals), this technique provided lower detection thresholds to F0 for synthetic vowel stimuli compared to a conventional filter bank approach. However, when temporal cues to F0 were reintroduced, differences in detection thresholds between filter banks were reduced indicating that the temporal cues also provided some information about F0.

In the present study, five different sound processing strategies were compared to the Advanced Combinational Encoder (ACE) strategy (Vandali *et al.*, 2000) in pitch ranking tests conducted over three consecutive studies. Each of these strategies differed primarily in how they encoded temporal information, although some differences in coding of spectral information also existed. It was hypothesized that by enhancing temporal cues to F0, the improved perception of pitch by CI recipients may be obtained. Speech perception tests were also conducted in the final study to explore possible adverse affects on speech recognition with some of these strategies.

The strategies evaluated in these studies were ACE, CIS, Peak Derived Timing (PDT) (van Hoesel and Tyler, 2003), Modulation Depth Enhancement (MDE), F0 Synchronized ACE (F0Sync), and Multi-channel Envelope Modulation (MEM). The ACE and CIS strategies are both commercially available, whereas PDT, MDE, F0Sync, and MEM are experimental schemes. The CIS strategy generally utilizes fewer band-pass filter bands and electrodes than ACE. The center frequencies of the bands are farther apart which can limit spectral resolution, but conversely they are wider in bandwidth, which may allow higher-frequency temporal envelope cues to be coded. Thus, while the lower spectral resolution may prevent CI users from perceiving fine pitch differences via electrode place cues, temporal envelope cues to

TABLE I. Details of subjects who took part in these studies, including their age in years at the commencement of the study, the number of years they had been implanted at the commencement of the study, the cochlear implant device they were implanted with (CS = Contour System; otherwise straight array), the clinical speech processor and coding strategy they normally used, the stimulation frequency per channel, and the number of channels employed in their clinical map including the frequency allocation table (FAT) which defines the frequency boundaries of the processors band-pass filter bank.

Subject	Age (yr)	Years implanted	Implant	Processor/Strategy	Stimulation frequency (Hz)	Channels (FAT)
S1	59	3	CI24M(CS)	ESPrit3G/SPEAK	250	20 (6)
S2	63	5	CI24M	ESPrit3G/ACE	900	20 (7)
S3	75	1	CI24R (CS)	ESPrit3G/ACE	900	20 (7)
S4	81	4	CI24M	ESPrit24/SPEAK	250	20 (6)
S5	81	2.5	CI24M	ESPrit3G/SPEAK	250	20 (6)
S6	65	3	CI24M	ESPrit3G/SPEAK	250	18 (8)
S7	70	4	CI24M	SPrint/SPEAK	250	20 (6)
S8	82	3	CI24M	SPrint/ACE	900	22 (6)
S9	75	4	CI24R (CS)	ESPrit3G/SPEAK	250	22 (6)
S10	65	5	CI24M	SPrint/ACE	500	17 (11)
S11	71	3	CI24R (CS)	ESPrit3G/ACE	900	20 (8)

pitch may be better encoded. In addition, because CIS usually employs greater separation between activated electrodes, less interaction between electrical current fields and neural population responses to stimuli may occur. This might help to reduce undesirable interactions between out-of-phase modulation information presented at neighboring electrodes, and consequently provide better perception of temporal cues to F0. The PDT strategy codes fine temporal detail in each channel by providing stimuli corresponding in time and amplitude to positive temporal peaks in the band-pass filtered signals. For complex harmonic signals, such as voiced speech and some musical sounds, timing information related to the frequency of individual harmonics in the signal, including that of the fundamental, are coded. This may aid pitch perception if CI recipients are able to utilize this coded information. The MDE, F0Sync, and MEM strategies are modifications of the ACE strategy that were designed to enhance coding of F0 periodicity information in the stimulus signal. These strategies provide deeper modulation cues to F0 than ACE, which may aid perception of the modulation frequency and perhaps pitch. In addition, F0Sync, MEM, and later versions of the MDE strategy provide this periodicity information coincidentally in time across all activated electrodes thereby minimizing phase differences between modulation information in neighboring channels which can be detrimental to the perception of pitch. A comparison between these strategies may provide valuable information regarding the ability of CI recipients to utilize specific pitch cues.

II. METHODS

A. Subjects

Eleven post-lingually deafened adult CI users of the Nucleus CI24 implant system participated in these studies. Their details are summarized in Table I. All were experienced users of the SPEAK (Skinner *et al.*, 1994) or ACE strategy, implemented in the Nucleus SPrint, ESPrit24, or ESPrit3G processor. The stimulation frequency employed in their clinical processor ranged from 250 to 900 pulses per second/channel (pps/ch) and the number of channels/electrodes used ranged from 17 to 22.

B. Sound processing strategies

The six sound processing strategies evaluated in these studies were implemented in a portable, body-worn device, known as SPEAR3,[1] which is used exclusively for research purposes. The strategies shared many common signal-processing techniques and coding parameters. First, the number of channels employed in the ACE, MDE, F0Sync, and MEM strategies were matched to that used in each subject's clinical processor. However for CIS, the number of channels was reduced to 10 (i.e. approximately half the channels used in ACE), and for PDT it was fixed to 19 (due to implementation issues). Second, the number of maxima, which are the channels containing the largest amplitudes that are selected for stimulation, was fixed to 10 for all strategies that select maxima (i.e., ACE, MDE, F0Sync, and MEM). Third, all strategies, except for PDT, employed a group stimulation frequency of 1231 pps/ch. Thus, given that up to 10 channels (maxima) were activated in each stimulation period, the maximum total stimulation frequency possible was 12 310 pps. The stimulation rates used by PDT varied between channels but were limited to a maximum rate of approximately 1400 pps/ch and on average provided a total stimulation frequency of approximately 12 000 pps. Finally, three spectral analysis techniques were utilized: (i) Fast Fourier Transform (FFT); (ii) Complex coefficient Finite Impulse Response (CFIR) band-pass filters (or Hilbert filters); and (iii) Infinite Impulse Response (IIR) band-pass filters. For both the FFT and CFIR filter banks, channel envelope signals were estimated by calculating the magnitude of the complex results returned by these processes. For the IIR filter bank, the band-pass filtered signals were used directly.

1. The ACE strategy

The ACE strategy implemented in the SPEAR3 processor was very similar to that implemented in the Nucleus 24

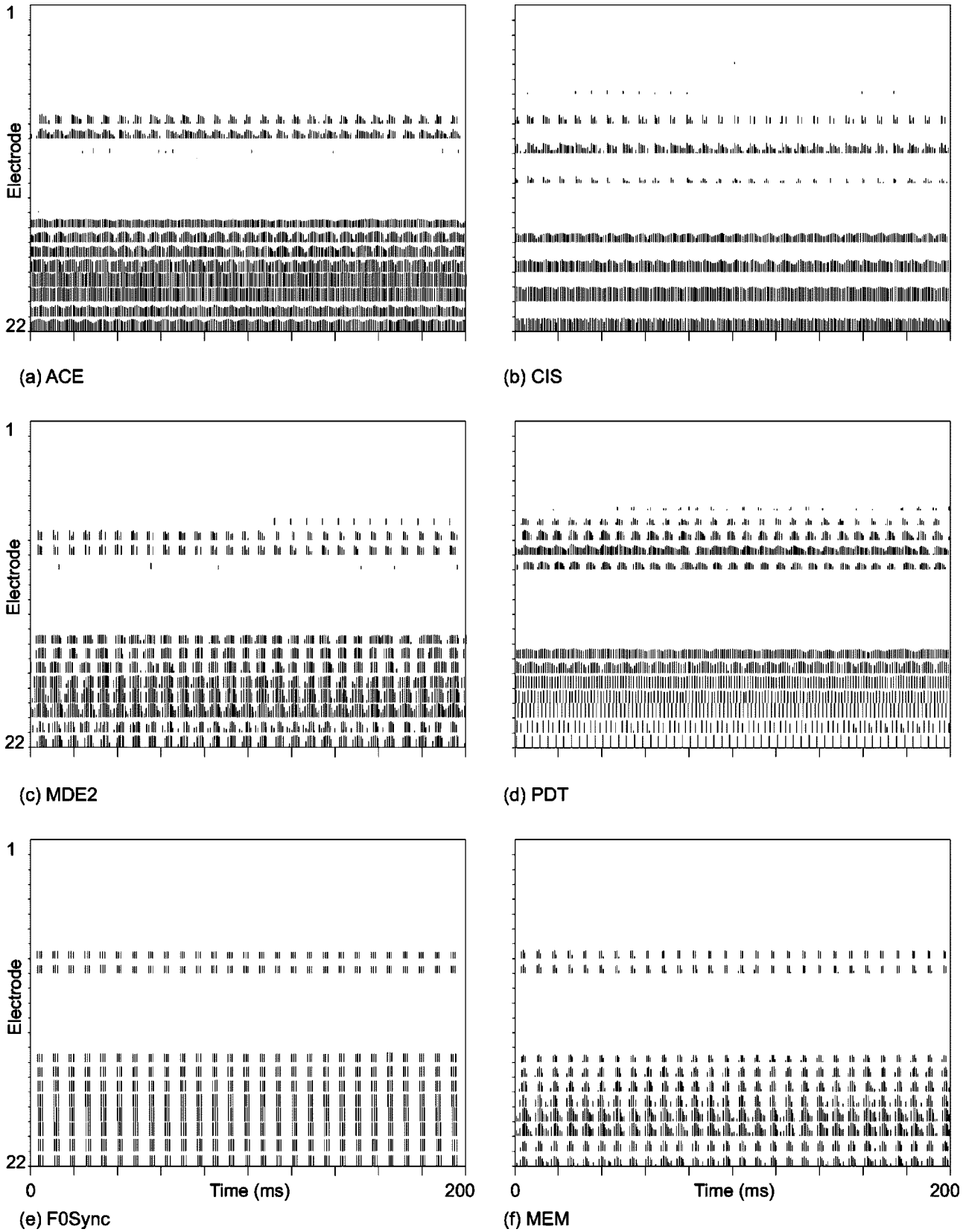

FIG. 1. Stimulus output pattern (electrodogram) recordings for the ACE, CIS, MDE2, PDT, F0Sync, and MEM strategies are shown in panels (a) to (f), respectively, for a 200 ms portion of the C#3 male /a/ vowel used in the pitch ranking tests. For this token, F0≈139 Hz, F1≈600 Hz, F2≈1050 Hz, and F3≈2700 Hz. In each electrogram, time is shown along the abscissa and electrode number along the ordinate. Electrode numbers for the Nucleus 24 implant system begin at 22 for the most-apical electrode, and decrease in number for more-basal electrodes. Each stimulus pulse recorded from the output of the processor is shown as a vertical bar. The height of the vertical bars represent the stimulus intensity in clinical units for which minimum amplitude corresponds to the threshold, and maximum amplitude corresponds to the maximum comfortable loudness level.

system. Most coding parameters of the SPEAR3 ACE strategy emulated those of the Nucleus 24 system precisely. One of two filter bank implementation methods (FFT or CFIR) was used. The method selected was based on the clinical processor that each subject usually wore. Subjects who used the Nucleus SPrint processor were fitted with an FFT filter bank, whereas those who used the Nucleus ESPrit processors were fitted with a CFIR filter bank. This was done so that spectral and temporal characteristics of the implemented filter banks were as similar as practically possible to those of the clinical processors.

To demonstrate the behavior of the strategies, stimulus output patterns, known as electrodograms, which plot the stimulus intensity in each channel over time, were recorded for each strategy and are shown in Fig. 1. The sound signal used in these recordings was a sung vowel taken from the test material used in the pitch-ranking experiment. It can be seen that similar frequency-to-electrode mapping and spectral coding is provided by all strategies, but that temporal coding varies substantially between strategies. For the ACE strategy in Fig. 1(a), it can be seen that temporal modulation (F0 periodicity) coding is provided in the stimulus signal on most of the electrodes, but that the depth of amplitude modulation and the phase relationships between temporal peaks in the stimulus signals do vary substantially across electrodes.

2. The CIS strategy

The CIS strategy implemented in the SPEAR3 processor was very similar to that implemented in the Nucleus 24 system. A 10-channel CFIR band-pass filter bank was used, which provided similar characteristics to that of the ESPrit processors. A CFIR filter bank was chosen because higher frequency temporal information is provided in the channel envelope signals compared to a FFT implementation where the temporal envelope information is limited by the low-pass frequency response of the FFT time window. The band-pass filter bank center frequencies were selected to provide similar frequency-to-electrode mapping to that provided in subjects' clinical maps. However, the reduction in number of electrodes utilized may have introduced some differences in place coding resolution [see Fig. 1(b)]. Like the ACE strategy, CIS provides F0 modulation coding in most channels, but the depth of amplitude modulation and the phase relationships between temporal peaks in the stimulus signals do vary substantially across electrodes.

3. The PDT strategy

In most existing clinical sound processors, fine structure in the input acoustic signal is discarded, and only envelope information is preserved. In contrast, the PDT strategy locates positive peaks in the output from each channel of a band-pass filter bank and stimulates on corresponding electrodes at those times. Although it was designed primarily to preserve temporal fine structure in the signal delivered to bilateral CIs, the application to unilateral systems may also provide benefits. For complex harmonic signals, such as speech, it may convey voice-pitch cues by preserving fine-timing information, particularly in the lower frequency harmonics (up to approximately 1400 Hz). The PDT strategy implemented in this study employed a fixed bank of 19 band-pass filters (6th order IIR) covering a frequency range of 200–7100 Hz. The center frequencies of these filters differed slightly from those which the subjects used in their clinical processors. An example of these differences can be seen by comparing Figs. 1(a) and 1(d). The average stimulation rate on each electrode varied with its filter band center frequency, but was limited to a maximum stimulation rate of approximately 1400 pps/ch. Thus, in apical channels, with center frequencies below approximately 1400 Hz, stimuli accurately coded temporal peaks in the signal. In contrast, for higher frequency channels, some, but not all, of the temporal peaks in the signal were coded. These timing differences across channels can be seen in Fig. 1(d) with the most apical electrode (22) following temporal peaks of the second harmonic and more-basal electrodes coding temporal peaks of higher harmonics (or combinations of them). In cases when multiple harmonics were present in a band-pass filter, F0 envelope modulation can be observed (e.g., electrodes 21, 19, 17).

4. The MDE strategy

The MDE strategy was designed to increase the depth of amplitude modulation in filter-bank channel envelope signals of the ACE strategy. The algorithm operated on modulation frequencies in the range of 80–300 Hz encompassing F0 for nearly all adult males and many females and children. For input signals in which the modulation depth was small and perhaps difficult for subjects to utilize as a cue to the modulation frequency, the algorithm expanded the depth of modulation. For signals in which the modulation depth was large and perhaps sufficiently salient, the modulation depth was not modified. Previous CI psychophysical studies investigating the pitch of sinusoidal amplitude-modulated pulse trains have shown considerable variation between subjects in terms of the modulation depths required for reliable discrimination of pitch (McKay *et al.*, 1995; Geurts and Wouters, 2001). On average, modulation depths ranging from 10% to 40% of the electrical dynamic range were required, although some subjects required depths of almost 100%. Converting these values to the acoustic dynamic range coded by the sound processor, which for the Nucleus 24 system is typically 30 dB, indicates that modulation depths in the acoustic signal of approximately 3 to 12 dB are required on average. Thus, for the algorithm implemented, modulation depths smaller than a specified level, referred to as the knee point, of 6 dB, were expanded using a third-order power function. For modulation depths above this knee point but below an upper limit of 20 dB, a linear expansion function was used. For modulation depths above this upper limit, the modulation depth was not modified. An expansion of the modulation depth was implemented by decreasing the amplitude of temporal minima in the signal while preserving the peak levels (a sliding time window, of duration 10 ms, was employed to track peaks and minima). The modified envelope signals replaced those of the original envelope signals derived from the filter bank and processing continued as per the normal ACE strategy.

The MDE strategy used in studies 2 and 3 (denoted MDE2 and MDE3, respectively) differed from that trialed in

study 1 (denoted MDE1). First, in study 2, a greater expansion of the modulation depth was provided by increasing the knee-point and limit point to 10 and 80 dB, respectively, and the expansion power factor to 7. The increased modulation depth provided by MDE2 compared to ACE can be observed by comparing the electrodograms in Figs. 1(a) and 1(c). In study 3, more conservative expansion was achieved by returning the knee point to 6 dB (as in study 1) and using an expansion power factor of 4 and limit point of 40 dB. Second, for both studies (2 and 3), an additional algorithm was applied to minimize phase differences between periodic modulations in envelope signals across channels. The effect of this phase alignment algorithm can be seen by comparing the location of temporal peaks in Figs. 1(a) and 1(c) for electrodes 17 and 18, in particular. Minimization of the phase difference between channels was achieved using a real-time iterative/feedback procedure. Initially a reference envelope signal (approximately 20 ms long) was constructed by summing the envelope signals across all channels. For each channel a time shift was then determined by finding the time offset between temporal peaks in the channel and reference envelope signals. Time shifts of no more than ± 6 ms were employed. In subsequent iterations, the time-shifted envelope signals were used to construct the reference envelope signal. After three or four iterations, time shifts for each channel converged upon a solution whereby the largest and most periodic temporal peaks in each channel were aligned in time. When summed to produce the reference envelope signal, temporal peaks added constructively so as to reinforce the most periodic information in the input signal, thus providing a good reference signal to which temporal information in subsequent time frames could be aligned. The algorithm did introduce an additional delay of 18 ms (± 6 ms) to the signal path, which may be unacceptable for some CI users (Stone and Moore, 2002).

5. The F0Sync strategy

The F0Sync strategy was designed to provide F0 periodicity information synchronously across all activated electrodes. It utilized similar signal processing to ACE but introduced an additional algorithm to modify the envelope of the stimulus pattern. Essentially, the narrow-band envelope signals estimated by the ACE filter bank were further low-pass filtered using a 50-Hz, second-order LPF, so as to reduce F0 modulation in the envelope signals. Stimulus signals were then derived from these smoothed envelope signals at a stimulation frequency of 1231 pps/ch. A gating algorithm, which could either pass or block the stimulus signal, was employed to gate (modulate) the stimulus signal, using a duty cycle of 33% ON time to 67% OFF time, at a rate corresponding to the F0 frequency. The electrodogram shown in Fig. 1(e) demonstrates the effect of the gating strategy. A real-time F0 estimator was used to provide an ongoing estimate of F0. The F0 estimator was based on the zero-crossing technique employed in the MSP speech processor (Skinner *et al.*, 1991). It employed a 450-Hz LPF to remove signals above the F0 range. This was followed by two identical peak detector/differentiator stages. The peak detectors employed an instantaneous attack time and a decay time constant of 2.2 ms, which effectively acted as a LPF. The differentiators served to sharpen peaks in the low-pass filtered signal and to remove the direct current (dc) component. Finally, an estimate of the F0 period was obtained by measuring the interval between zero crossings in the signal. While this technique may not be optimal for F0 estimation in noisy situations, it was suitable for the material and tests used in these studies.

6. The MEM strategy

Like the F0Sync strategy, the MEM strategy was designed to provide F0 periodicity information synchronously across all activated electrodes. However, rather than employing an F0 estimator, MEM utilized the envelope of the broadband signal (which inherently contains F0 periodicity information) to modulate the level of the filter bank channel signals derived from the ACE strategy. The envelope of the signal was measured by full wave rectifying the broadband signal and then applying a 300-Hz, fourth-order LPF. The modulation depth in the envelope signal was then expanded by applying an 80-Hz, second-order high-pass filter (HPF) which effectively increased the ratio of F0 modulation-to-envelope signal level by removing the dc component. In addition, the low-pass filtered signal (i.e., prior to the HPF) was scaled and added to the output of the HPF stage. This allowed for control of the expansion factor (or increase) applied to the modulation depth. A scaling factor for the LPF output of 0.5 was employed, which for small modulation depths (i.e., below approximately 6 dB), increased the modulation depth by a power of 3 approximately. For higher modulation depths, infinite expansion (i.e., 100% modulation of the electrical dynamic range) was provided. The expanded envelope signal was then half-wave rectified to remove any negative excursion that may have arisen in the filtering/expansion process. The amplitude of the expanded envelope signal was then scaled (normalized) such that its peak level, which was measured using a sliding time window of 12 ms duration, was set to unity relative to the numerical range of the processor. The narrow-band envelope signals estimated by the ACE filter bank were low-pass filtered, using a 50-Hz, second-order LPF. These smoothed narrow-band envelope signals were then multiplied (or modulated) by the normalized F0 envelope signal derived from the broadband signal. Processing then continued as per the normal ACE strategy. An update/stimulation frequency of 1231 pps/ch was employed. It can be seen in Fig. 1(f) that deep modulation in the envelope of the stimulus signals is provided by this technique and that temporal peaks are synchronized in phase across activated electrodes.

C. Strategy fitting

All subjects were initially fitted with the ACE strategy in the SPEAR3 processor using coding parameters equivalent to those used in the subject's clinical processor. The number of maxima selected was fixed to ten and the stimulation rate was set to 1231 pps/ch. Threshold and maximum comfortable loudness levels for electric stimulation on each electrode were then measured for a stimulation rate of 1231 pps. The strategy was then activated so that the subjects could

comment on its clarity and loudness. If necessary, the comfortable and/or threshold stimulation levels were adjusted so that subjects were comfortable with the perception and quality of speech and also comfortable with the loudness of the tokens used in the pitch-ranking tests. Fitting of the other strategies was carried out using similar procedures to those discussed above. In addition, for the CIS strategy the number of electrodes activated was reduced to 10 by removing every second electrode from the map and thus equal spatial separation was maintained between the 10 electrode sites utilized. For the PDT strategy, the number of channels was reduced to 19 by removing basal electrodes from the map. In addition, threshold and comfortable electric stimulation levels were re-measured on each electrode at the stimulation rates appropriate for each channel. For low frequency channels (below 1200 Hz), levels were measured using stimulation rates equal to the center frequency of each channel, which ranged from approximately 270 to 1200 Hz. For higher frequency channels, stimulation rates of 1200 pps/ch were used.

D. Stimuli

The tests conducted in these studies required stimuli in which the voice pitch could be accurately controlled. In addition, it was desirable to employ stimuli that were representative of speech signals rather than synthetic sounds. For these reasons natural vowel stimuli were chosen and produced as sung vowels, rather than spoken vowels, because they allowed for the generation of a broad range of F0s. Two vowels, /a/ and /i/, which differed significantly in spectral shape, were used. Both a male and female singer produced the vowels. For each vowel, four notes were produced, starting from G2 and increasing progressively in half-octave steps to C#3, G3, and C#4 for the male, and C4, F#4, C5, and F#5 for the female. F0s for the four notes were 98, 139, 196, and 277 Hz for the male and 262, 370, 523, and 740 Hz for the female. The vowels were recorded onto digital audio tape (DAT) in a sound-attenuated room in which the singer was located approximately one meter from the recording microphone. The DAT recordings were re-sampled at a frequency of 16 kHz and stored in 16-bit mono-channel wave files using Cool Edit Pro 2.0 software which provided an appropriate 8 kHz antialiasing filter. The tokens were truncated to a duration of 560 ms. Step transients at the onset and offset of the tokens were smoothed by a linear amplitude ramp, of duration 30 ms. All tokens were equalized to a fixed average rms power level. The four tokens for each vowel were combined into three pairs (or F0 intervals) that differed in F0 by half an octave. The three pairs were as follows: G2-C#3, C#3-G3, and G3-C#4 for the male, and C4-F#4, F#4-C5, and C5-F#5 for the female. A 500 ms period of silence was inserted between tokens as the inter-stimulus interval. A second set of combined tokens was also created in which the presentation order for the tokens was reversed. In addition, tokens were randomized in level by 6 dB to reduce the influence of any loudness differences among stimuli on the subjects' ranking of pitch.

E. Evaluation protocol

Three consecutive studies were conducted in which voice-pitch ranking was measured for each subject using ACE and either two or three of the comparison strategies. Subjects were not provided with any take-home strategy experience. Prior to the initial evaluation session, each subject was fitted with ACE and was presented with one block of stimuli from the pitch-ranking test to familiarize them with the procedure. In the final study, speech perception tests were also conducted.

1. Pitch ranking experiment

The pitch ranking tests employed a two-alternative-forced choice procedure in which a pair of tokens, separated in F0 by half an octave, were presented, and the subject was asked to nominate which of the two was higher in pitch (i.e., ''first'' or ''second''). Instructions were given to ignore any variations in loudness. No feedback was provided about the correctness of responses. Separate tests were conducted for each vowel and each singer. However, tests using the stimuli from the female singer were not used in studies 2 and 3. In each test, three F0 intervals (e.g. G2-C#3, C#3-G3, and G3-C#4 for the male tokens) were presented. Data were collected in blocks of 24 presentations, in which eight repetitions of each of the three F0 intervals were presented in random order. The stimulus tokens were played via a high-quality 16-bit sound card and fed directly into the subject's processor via the external audio input socket. The presentation level of the tokens was established by setting the sensitivity of the processor to its recommended (default) level, and adjusting the output level of the sound card so that the subjects reported that the tokens were comfortable in loudness. Once established, this level remained fixed for all tests, subjects, and strategies.

2. Speech perception experiment

The speech perception tests consisted of open-set monosyllabic CNC words (based upon the phoneme set of Peterson and Lehiste, 1962) presented in quiet conditions at 60 dB SPL, and open-set CUNY sentences (Boothroyd, Hanin, and Hnath, 1985) presented at 60 dB SPL in multi-talker babble noise (Auditec, St. Louis, Catalogue No. C146-MT Multitalker) at a signal-to-noise ratio of $+10$ dB. The tests were conducted in a sound-attenuated room using pre-recorded CD material played back via a loudspeaker placed 2.6 m from the subject at an azimuth of zero degrees. The presentation level of the material was measured with a sound-level meter (Simpson Model: 886) using dB A weighting and fast response peak level metering.

3. Evaluation studies

In the first study, five subjects, S1–S5, completed the pitch ranking test using ACE, CIS, PDT, and MDE1. The test was conducted using sung vowel tokens from both singers. For each subject, data were collected over four sessions, using two sessions for each vowel. In each session, all strategies were evaluated, and two blocks of 24 token pairs (3 F0 intervals$\times$8 repeats) for a given vowel were presented

for each singer. Thus, over four sessions, 64 (2 blocks $\times$2 sessions$\times$2 vowels$\times$8 repeats) presentations of each F0 interval and 192 (64$\times$3 F0 intervals) presentations in total for a given singer were provided per strategy to each subject. Each strategy was evaluated twice within session using a fixed counter-balanced order that was repeated between sessions and subjects.

In study 2, three subjects (S1, S6, and S7) completed the pitch ranking test using ACE, MDE2 (with phase alignment), and F0Sync. The test was conducted using sung vowel stimuli from the male singer only. For each subject and strategy, two blocks of 24 token pairs were presented for each vowel per session. Over two sessions, 64 presentations of each F0 interval and 192 presentations in total were provided per strategy to each subject. The order in which the strategies were evaluated was balanced across subjects, using a Latin-square design, and counter-balanced for repeat strategy measures within session. Across sessions, the strategy evaluation order was rotated among subjects.

In the final study, five subjects (S7–S11) completed the pitch ranking test using ACE, CIS, MDE3 (with phase alignment), and MEM. The test was conducted using sung vowel stimuli from the male singer only. For each subject and strategy, one block of 24 token pairs was presented for each vowel per session. Over six sessions, 96 presentations of each F0 interval and 288 presentations in total were provided per strategy to each subject. The order in which the strategies were evaluated within session was balanced as near as possible across subjects (using a incomplete Latin-square design) and rotated among subjects across sessions. Following the completion of the pitch ranking tests, speech perception tests were conducted. Data were collected over two sessions with no take-home strategy experience provided. For the CNC word tests, one list of 50 words was presented per strategy in each session to each subject. For the CUNY sentence tests, two lists of 102 words were presented per strategy in each session to each subject. The strategy evaluation order was balanced as near as possible across subjects and counter-balanced between sessions.

F. Data analysis

For each of the pitch-ranking studies, the total percent correct score for token pairs ranked correctly in pitch for each strategy, subject, session, and (for study 1) singer were calculated by averaging results across vowel and F0 interval within session. Analysis of variance (ANOVA) using a general linear model was performed on the group subject data, using subject as a random factor and strategy and session as fixed factors in the model. For subject data in which ceiling or floor effects were apparent (as confirmed from residual versus fitted value data in the ANOVA), the percentage correct scores for all subjects were transformed using an arcsine-root function. If a significant effect of strategy was observed, then a post-hoc comparison between each strategy and the reference/control strategy (ACE), using a Bonferroni Test, was employed to explore the effect. Because the subject was treated as a random factor in the model, it was not appropriate to explore cross-factor effects involving subject. Thus, the effect of the strategy within subject was explored by performing separate ANOVAs for individual subjects. If a significant effect of strategy was observed, then post-hoc comparisons between each strategy and ACE, using a Bonferroni Test, were conducted. An analysis of variance was also performed on the results of the speech perception tests conducted in study 3. The same analysis model as described above was utilized for a percentage of words, vowels, consonants, and phonemes correct in the CNC word tests, and words correct in the CUNY sentence tests.

The results of the pitch ranking studies were also examined for each strategy by considering the proportion of responses for which the pitch change for each F0 interval was ranked correctly. Separate analyses for each subject, and (for study 1) for each singer were conducted. A two-tailed binomial distribution was used to determine whether the proportion of correctly ranked responses was significantly different from a chance score of 50% (for a significance level of $p=0.05$). Results significantly above chance were classified ''correct,'' those significantly below chance were classified ''reversed,'' and those not significantly different from chance were classified ''chance.''

III. RESULTS

A. Study 1 (pitch ranking)

The results of the pitch ranking test for study 1 are summarized in Figs. 2(a) and 2(b) for stimuli from the male and female singers, respectively. For each strategy, the total percent correct score (averaged across F0 interval and vowel) for token pairs ranked correctly in pitch are shown for each subject as well as for the combined subject group (S1–S5). The analysis of variance performed on the group subject data for the male singer revealed no significant effects for any of the factors examined. Results for the female singer did reveal a significant effect of strategy ($F[3,31]=4.41; p<0.05$). However, post-hoc comparisons found no significant differences between each comparison strategy and ACE. No significant effect of session was observed. An analysis of individual subject results using the male stimuli revealed significant effects of strategy for subjects S2 ($F[3,4]=8.25; p<0.05$) and S5 ($F[3,4]=6.66; p<0.05$). For S5, post-hoc analysis provided no significant differences between each comparison strategy and ACE, but for S2, scores were significantly higher with CIS (63.5%; $p<0.05$) than with ACE (57.3%). A within-subject analysis of variance of results for the female stimuli revealed significant effects of strategy for S3 ($F[3,4]=12.62; p<0.05$) and S4 ($F[3,4]=20.74; p<0.01$). A post-hoc analysis for S3 provided no significant differences between each comparison strategy and ACE, but for S4, scores were significantly higher with ACE (84.9%; $p<0.01$) than with CIS (68.2%).

For each strategy, the results were also examined by considering the proportion of responses for which the pitch of the three F0 intervals, averaged across vowels, were ranked correctly by each subject. The table below the bar graphs in Fig. 2 indicates whether each F0 interval was ranked correctly (white boxes), reversed (black), or at chance level (gray) in pitch for each strategy and subject. In addi-

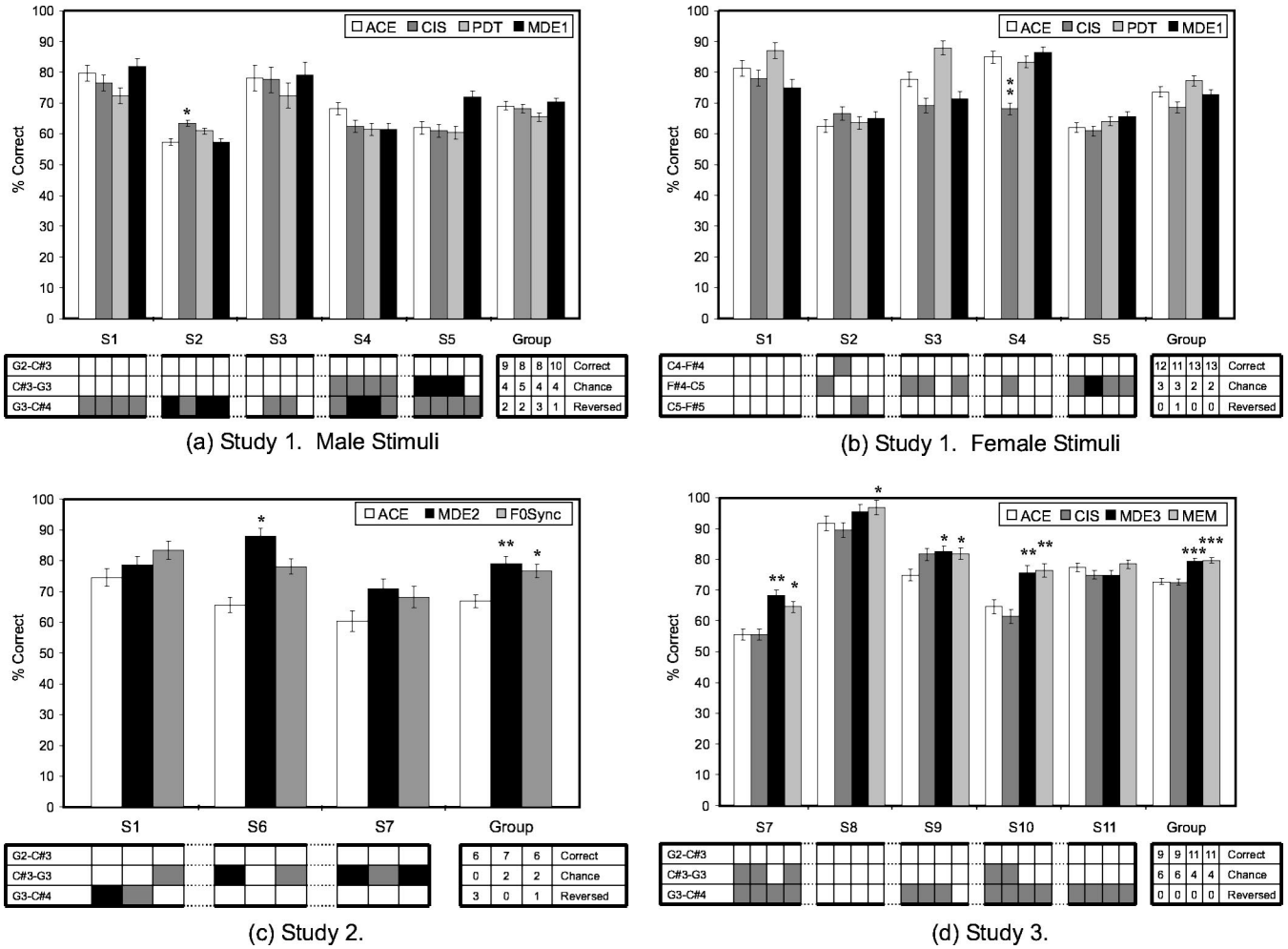

FIG. 2. Results of the pitch ranking tests conducted in studies 1 to 3. Panels (a) and (b) display results, respectively, for the male and female stimuli used in study 1. Panels (c) and (d) display results for studies 2 and 3, respectively. In each panel, the mean percent correct scores for each subject as well as for the subject group are shown. Error bars indicate standard errors of the means and the asterisks indicate significant score differences obtained in comparisons to the reference ACE strategy (* denotes a significance level of $p<0.05$,** $p<0.01$, and*** $p<0.001$). The table below the bar graph summarizes results for the proportion of F0 intervals ranked significantly different from a chance score of 50% according to a two-tailed binomial distribution. For each subject, the table on the left (i.e., below that subject's data in the bar graph) indicates whether each of the three F0 intervals (shown in each row) was ranked correctly (white boxes), reversed (black boxes), or at chance level (gray boxes) for each of the strategies (shown in the corresponding column). For the group subject data, the table on the right (i.e., below the group subject data in the bar graph) indicates the total number of F0 intervals that were ranked correctly, reversed, or at a chance level (rows) for each of the strategies (columns).

tion, the number of F0 intervals ranked correctly, reversed, or at chance level in pitch for each strategy, aggregated across subjects are shown in the table below the group subject scores. For the male stimuli, the number of correctly ranked F0 intervals aggregated across subjects was highest for MDE1 (10 out of 15), followed by ACE (9), CIS (8), and PDT (8). For the female stimuli, the number of correctly ranked intervals was highest for MDE1 (13) and PDT (13), followed by ACE (12) and CIS (11).

B. Study 2 (pitch ranking)

The results of study 2 for subjects S1, S6, and S7 are summarized in Fig. 2(c) in the same way as those presented for study 1. Group mean scores for ACE, MDE2, and F0Sync were 66.8%, 79.2%, and 76.6% respectively. An analysis of variance for group mean scores revealed a significant effect of strategy ($F[2,12]=9.22;p<0.01$). Post-hoc comparisons revealed that scores were significantly higher with MDE2 ($p<0.01$) and F0Sync ($p<0.05$) than with ACE. No significant effect of session was observed. A within-subject analysis of variance revealed a significant effect of strategy for S6 ($F[2,3]=11.12;p<0.05$) and a post-hoc analysis revealed that scores were significantly higher with MDE2 (88.0%; $p<0.05$) than with ACE (65.6%). An analysis of the number of F0 intervals ranked correctly, reversed, or at a chance level aggregated across subjects revealed that MDE2 provided the highest number of correctly ranked intervals (7 out of 9), followed by F0Sync (6) and ACE (6). In addition, no intervals were reversed for MDE2, whereas one was for F0Sync, and three were for ACE.

C. Study 3

1. Pitch ranking

Results of the final study for subjects S7 to S11 are summarized in Fig. 2(d). Group mean scores for ACE, CIS, MDE3, and MEM were 72.8%, 72.6%, 79.4%, and 79.7%,

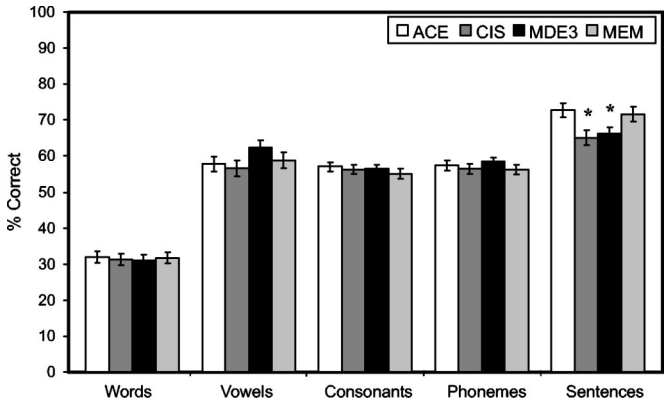

FIG. 3. Results of the speech perception tests conducted in study 3. Group mean scores for the ACE, CIS, MDE3, and MEM strategies are shown for the percentage of words, vowels, consonants, and phonemes correct in the CNC word tests conducted in quiet conditions, and for the percentage of words correct in the CUNY sentence tests conducted in noise. Error bars indicate standard errors of the means and the asterisks indicate significant strategy differences obtained in comparisons to the reference ACE strategy (* denotes a significance level of $p<0.05$,** $p<0.01$, and*** $p<0.001$).

respectively. An analysis of variance for group mean scores revealed a significant effect of strategy ($F[3,107]=17.63; p<0.001$). Post-hoc comparisons revealed that scores were significantly higher with MDE3 ($p<0.001$) and MEM ($p<0.001$) than with ACE. No significant effect of the session was observed. A within-subject analysis of variance revealed significant effects of strategy for S7 ($F[3,20]=7.52; p<0.001$), S8 ($F[3,20]=6.01; p<0.05$), S9 ($F[3,20]=3.75; p<0.05$), and S10 ($F[3,20]=11.42; p<0.001$). For S7, post-hoc strategy comparisons revealed that scores were significantly higher with MDE3 (68.4%; $p<0.01$) and MEM (64.6%; $p<0.05$) than with ACE (55.5%). For S8, scores were significantly higher with MEM (96.9%; $p<0.05$) than with ACE (91.7%). For S9, scores were significantly higher with MDE3 (82.6%; $p<0.05$) and MEM (82.0%; $p<0.05$) than with ACE (75.0%). For S10, scores were significantly higher with MEM (76.4%; $p<0.01$) and MDE3 (75.7%; $p<0.01$) than with ACE (64.6%). An analysis of the number of F0 intervals ranked correctly, reversed, or at chance level aggregated across subjects revealed that MEM and MDE3 provided the highest number of correctly ranked intervals (11 out of 15), followed by ACE (9) and CIS (9). In addition, fewer intervals were ranked at the chance level for MEM and MDE3 compared to ACE and CIS. For all strategies, no intervals were reversed in pitch by any of the subjects.

2. Speech perception

Group subject results for the speech perception tests conducted in study 3 are summarized in Fig. 3. Percent correct scores are provided for each strategy for the CNC word test and the CUNY sentence tests in noise. An analysis of variance for the CNC word tests showed no significant differences between strategies and no session effects. A within-subject analysis of variance for each subject revealed no significant effects of strategy. For the CUNY sentence tests, a significant effect of strategy was observed in the group subject analysis ($F[3,31]=4.08; p<0.05$). Post-hoc comparisons revealed that scores were significantly higher with ACE (72.7%) that with CIS (65.0%; $p<0.05$), and MDE3 (66.1%; $p<0.05$). No significant effect of session was observed. A within-subject analysis of variance revealed a significant effect of strategy for S10 ($F[3,4]=8.07; p<0.05$), however, no significant differences between each comparison strategy and ACE were observed.

IV. DISCUSSION

A. Pitch ranking

Overall, significant strategy benefits in the pitch-ranking tests using the male sung-vowel stimuli were observed for MDE2, MDE3, F0Sync, and MEM compared to ACE. These strategies provided similar electrode place coding to that of ACE, but differed in their coding of temporal information. Temporal coding differed predominantly in two aspects. First, deeper F0 modulation was provided in the envelope of stimulus signals delivered to each activated electrode. This may have provided enhanced cues to F0 periodicity and improved pitch perception. These findings are consistent with results of amplitude modulation studies with CI users, which have demonstrated that deeper modulation generally provides an improved perception of modulation frequency. Second, F0 periodicity information presented across channels was aligned such that temporal peaks in the stimulus signals of each channel occurred coincidently in time. This was done to minimize adverse interactions between temporal information presented at electrodes close to one another, which could affect the perception of temporal pitch. It is speculated that the latter of these two coding differences is most likely responsible for the improved pitch ranking results observed. For instance, results of the first study with MDE1 (which did expand the depth of modulation in the envelope signals of all channels) were not significantly different from those of ACE. Only in studies 2 and 3, in which MDE was modified such that the temporal peaks in each channel were aligned in time across channels, were significant strategy differences found compared with ACE. It would appear that providing similar temporal information to code F0 periodicity at multiple electrode sites, or conversely minimizing phase differences between the temporal information across electrodes, may assist with temporal pitch perception by users of CIs. The provision of relatively deep modulation cues to F0 may also be beneficial, but without coding of synchronous temporal information across electrodes it is insufficient to improve pitch perception.

It is interesting that no significant differences between CIS and ACE were observed for group subject scores in the pitch ranking tests. It was thought that a greater separation between stimulating electrodes might reduce interactions between electrical current fields, and perhaps aid the perception of temporal F0 cues presented across electrodes. In addition, it was anticipated that the use of wider band-pass filters would allow higher-frequency modulation components to be coded in the stimulus signal. The results, however, did not confirm these hypotheses. It may be that the doubling of electrode separation was insufficient to allow for the independent coding of temporal information at each electrode. This is consistent with the results of McKay and McDermott

(1996), which indicated that a separation of 3 to 4 mm (or 4 to 5 electrodes for the Nucleus 22 and 24 systems) was required. Another important factor is that all subjects were experienced users of either ACE or SPEAK, and thus possible benefits to pitch perception arising from temporal coding using CIS may have been offset by slight changes in (or unfamiliar) place coding.

Pitch-ranking results for PDT in study 1 were also not significantly different from those of ACE. As with CIS, slight differences in place coding provided by PDT compared to ACE may have offset any possible benefits to pitch perception provided by PDT. However, it is more likely that lack of subject experience with the strategy, combined with the vastly different form of temporal coding provided by PDT were responsible for the absence of a strategy effect. It may be that, given substantial experience with the strategy, subjects may be able to learn to utilize the temporal information provided by PDT. However, this would require temporal information up to frequencies as high as 1400 Hz to be utilized, which is most likely beyond the ability of many CI recipients. In addition, resolution of different (and out of phase) temporal information presented across nearby electrodes may not be possible.

The F0Sync strategy evaluated in study 2 employed a method of modulating (or gating) the stimulus signals, using a rectangular function, at a frequency equal to an estimate of F0. Results verified the feasibility of this technique in providing pitch cues via coding of F0 periodicity information coincidently across electrodes. These results are consistent with those of a similar strategy described by Green *et al.* (2004) which was recently bought to our attention. However, these approaches rely on reliable estimation of F0 which can be difficult in noisy situations or for polyphonic signals. In addition, in our study subjects described the sound quality as somewhat rough or harsh and unpleasant to listen to. It was thought that the roughness of the sound was related to the use of a rectangular function to modulate the envelope of the stimulus signal. In contrast smoother modulation functions were effectively provided by MDE and MEM. Subjective comments with these strategies were more favorable, although a slight roughness in the sound quality was still reported by some subjects.

In the final study, it is interesting that despite MEM and MDE3 coding deep modulation cues to F0 periodicity coincidently in time across all channels, all subjects except S8 were still not able to correctly pitch rank all F0 intervals, a task which most normal hearing listeners would have little difficulty with. An analysis of results for each interval revealed that for MEM, the lowest interval (G2-C#3) was ranked correctly by all subjects, the middle interval (C#3-G3) was ranked correctly by four of the five subjects, and at chance level by one subject, and the highest interval (G3-C#4) was ranked correctly by two subjects, and at chance level by three subjects. Similar findings were observed for MDE3. An examination of the stimulus signals on each electrode generated by MEM and MDE3 (and in fact by all strategies evaluated excluding F0Sync) for these tokens revealed that the depth of F0 modulation in the stimulus signals decreased with increasing F0, particularly for frequencies above approximately 200 Hz. This might in part explain the trend of decreasing performance with increasing F0. It may also be the case that each subject's ability to use temporal periodicity cues diminished with increasing F0, particularly given that for the male stimuli the highest pitch token (C#4) had an F0 of 277 Hz, which is close to the upper limit of modulation frequency discrimination reported for many CI recipients. In addition, because subjects' clinical processors may have provided poor or misleading temporal cues to F0, such as out-of-phase periodicity coding across channels, subjects may have learned to ignore these cues. Perhaps if greater experience with the experimental strategies was provided they may learn to make better use of periodicity information as a cue to F0.

The above temporal coding limitations are also relevant to the results for the female stimuli used in study1 in which F0 ranged from 262 to 740 Hz. However, despite these F0s being beyond the frequencies that most CI recipients can probably discriminate, and beyond the range of modulation frequencies that were coded by these strategies, mean scores in general were equal to or higher than those obtained using the male stimuli. This would suggest that subjects were using place-coding cues to pitch, given that temporal cues were less salient or unusable for these F0s. In addition, no effect of strategy was observed in the group data for the female stimuli but one case was found for subject S4, in which scores with CIS were significantly lower than ACE. If place cues to pitch were being used by this subject then the reduction in spectral resolution (i.e., the reduced number of electrodes) provided by CIS may have been detrimental for the pitch ranking task. In contrast, the similarity in place-coding cues provided by ACE, PDT, and MDE1 are most likely responsible for the equivocal results obtained for all subjects amongst these strategies. Overall these results and those for the male stimuli were poor compared to those possible with most normal hearing listeners and might be explained by the inconsistent coding of place cues to pitch (McDermott, 2004). Place cues to pitch can vary with both vowel formant frequency and F0. Conflicting place cues to pitch may have been present in the stimuli due to slight adjustment of formant frequencies by the singers when producing different pitch (Loizou, Dorman, and Powell, 1998; Maurer and Landis, 1995). Additionally, under some conditions the average place of stimulation can also vary slightly in a manner that is inconsistent with changes in F0, even when the formant frequencies are fixed. This occurs mainly as a result of inadequate spectral sampling (place coding) of the complex harmonic stimuli. Increasing the spectral/place resolution of the system may be of some benefit provided that CI recipients are able to resolve finer place information. In addition, slight changes in spectral shape (amplitude) can affect selection of spectral maxima, as can nonlinear amplitude processing in the system, such as not coding bands when they fall below some threshold (base) level. Both of these mechanisms can introduce changes in place coding that are inconsistent with changes in F0.

Finally, while the stimuli used in the pitch ranking test were presented via the direct audio input to the processor, the recording of the stimuli was conducted in a sound-attenuated

room and thus some effects of room acoustics, such as resonance and reverberation, were present.[2] In any case, it would be useful to validate the results of these studies by repeating the pitch ranking tests with stimuli presented in the sound field, at least with the most promising strategies.

B. Speech perception

The results of the speech perception tests conducted in the final study showed no significant effect of strategy for the word tests in quiet. A significant effect of strategy was however observed for the sentence in noise test in which scores for CIS and MDE3 were significantly lower than those for ACE. It may be that lack of subject experience with CIS and MDE3 may account for the observed drop in scores especially since all of the subjects normally used either ACE or SPEAK in their own sound processors. For CIS, differences in spectral resolution coding compared to ACE may have affected the outcomes. For MDE3, an examination of the electrodogram recordings for speech in noise indicated that distortions in the amplitude envelope cues coded in each channel, due to adverse effects of the noise signal on the phase alignment algorithm and subsequently the time shift applied to each channel, may have contributed to the reduced scores observed.

For the MEM strategy, the results of these tests were encouraging in that they demonstrated that additional temporal cues to aid pitch perception could be provided without adversely affecting the perception of speech presented in quiet and in noise. Thus, temporal coding techniques of the sort employed by MEM could be utilized to aid tone perception by CI recipients, which might in turn aid speech perception for speakers of tonal languages. However, F0 differences between tonal contrasts in languages such as Cantonese and Mandarin are typically much smaller than those tested in these studies and thus the applicability of these techniques to tonal languages will need further investigation. The perception of vocal sounds in music and perhaps musical appreciation in general may also be advantaged by these approaches, at least for F0s below approximately 300 Hz. However, like tonal language perception, the discrimination of intervals closer in pitch than those tested in these studies are required and thus further exploration is needed.

V. CONCLUSION

While results of the pitch-ranking experiments were not perfect they did demonstrate that significant improvements to pitch perception by CI users were possible via coding of F0 periodicity information in the electrical signal, at least for the male sung vowel stimuli used in these tests. Specifically, improved pitch ranking results for the male stimuli were obtained using MEM, MDE2, MDE3, and F0Sync, which provided deeper modulation cues to F0 coincidentally in time across all activated electrodes. It was speculated that the improved results were more likely a result of the provision of coincident temporal information across electrodes, rather than a provision of deep modulation cues. A detailed analysis of results for each F0 interval for the male stimuli were consistent with findings of previous rate and modulation frequency discrimination studies, which have shown that the efficacy of temporal cues to pitch discrimination diminishes with increasing frequency, with an upper limit of approximately 300 Hz for many recipients. Thus, we can expect that these types of strategies can provide benefits to pitch discrimination when F0 is less than approximately 300 Hz, but for higher F0s, alternative coding techniques such as the use of finer place coding may be required. Finally, the results of speech perception tests using the MEM strategy demonstrated that equivalent results to existing strategies, such as ACE, can be obtained while providing improvements to pitch perception. This indicates that temporal coding techniques employed by strategies such as MEM might be utilized by speakers of tonal languages, in which both segmental speech features and tone are important to perception. However, the question of whether the observed improvements to pitch perception are substantial enough to aid perception of tonal languages is yet to be explored. The same applies to the perception of musical sounds, which might benefit from these techniques, at least for F0s below approximately 300 Hz.

ACKNOWLEDGMENTS

This research was funded by the Cooperative Research Center for Cochlear Implant and Hearing Aid Innovation (CRC HEAR) and the Garnett Passe and Rodney Williams Memorial Foundation. The authors wish to thank the eleven recipients who gave their time to participate in these studies. Thanks also to Richard van Hoesel, Peter Seligman, Brett Swanson, John Heasman, and Valter Ciocca, for their contributions towards the development of strategies used in these studies, to Mark Harrison and Justin Zakis for their work in development of the SPEAR3 research processor, to David MacFarlane and Valerie Looi for producing and editing the sung vowel stimuli, to Graham Hepworth for guidance in statistical analysis of the data, to Robert Cowan for his critique of the manuscript, and to David Nelson, an anonymous reviewer, and Robert Lutfi the associate editor for their review of the manuscript.

[1]The SPEAR3 processor and research system was developed by the Cooperative Research Center for Cochlear Implant and Hearing Aid Innovation. A product brief, ''SPEAR3 Product Brief—3rd Generation Speech Processor for Electrical and Acoustic Research,'' can be obtained from HearWorks, 384 Albert Street, East Melbourne, 3002, Australia, or online from www.hearworks.com.au.

[2]Stimulus output patterns were examined for each F0 interval presented via the direct audio input and via the ear-level microphone in the sound field. F0 Envelope modulation in each channel was found to vary with mode of input but not in a consistent manner (e.g., the modulation depth decreased on some channels and increased on others).

Anderson, I., Weichbold, V., and D'Haese, P. (**2002**). ''Recent results with the MED-EL COMBI 40+ cochlear implant and TEMPO+ behind-the-ear processor,'' Ear Nose Throat J. **81**, 229–233.

Balkany, T., Hodges, A. V., and Luntz, M. (**1996**). ''Update on cochlear implantation,'' Otolaryngol. Clin. North Am. **29**, 277–289.

Barry, J. G., Blamey, P. J., Martin, L. F. A., Lee, K. Y. S., Tang, T., Ming, Y. Y., and van Hasselt, C. A. (**2002**). ''Tone discrimination in Cantonese-speaking children using a cochlear implant,'' Clin. Linguist. Phon. **16**, 79–99.

Boothroyd, A., Hanin, L., and Hnath, T. (**1985**). ''A sentence test of speech perception: reliability, set equivalence, and short term learning (Internal Report RCI 10),'' Speech & Hearing Sciences Research Center, City University of New York.

Busby, P. A., Whitford, L. A., Blamey, P. J., Richardson, L. M., and Clark, G. M. (**1994**). ''Pitch perception for different modes of stimulation using the Cochlear multiple-electrode prosthesis,'' J. Acoust. Soc. Am. **95**, 2658–2669.

Busby, P. A., and Clark, G. M. (**2000**). ''Pitch estimation by early-deafened subjects using a multiple-electrode cochlear implant,'' J. Acoust. Soc. Am. **95**, 2658–2669.

Chatterjee, M., and Shannon, R. V. (**1998**). ''Forward masked excitation patterns in multielectrode electrical stimulation,'' J. Acoust. Soc. Am. **103**, 2565–2572.

Ciocca, V., Francis, A. L., Aisha, R., and Wong, L. (**2002**). ''The perception of Cantonese lexical tones by early-deafened cochlear implantees,'' J. Acoust. Soc. Am. **111**, 2250–2256.

Garnham, C., O'Driscoll, M., Ramsden, And. R., and Saeed, S. (**2002**). ''Speech understanding in noise with a Med-El COMBI 40+ cochlear implant using reduced channel sets,'' Ear Hear. **23**, 540–552.

Geurts, L., and Wouters, J. (**2001**). ''Coding of the fundamental frequency in continuous interleaved sampling processors for cochlear implants,'' J. Acoust. Soc. Am. **109**, 713–726.

Geurts, L., and Wouters, J. (**2004**). ''Better place-coding of the fundamental frequency in cochlear implants,'' J. Acoust. Soc. Am. **115**, 844–852.

Gfeller, K., and Lansing, P. J. (**1991**). ''Melodic, rhythmic, and timbral perception of adult cochlear implant users,'' J. Speech Hear. Res. **34**, 916–920.

Gfeller, K., Christ, A., Knutson, J. F., Witt, S., Murray, K. T., and Tyler, R. S. (**2000**). ''Musical backgrounds, listening habits, and aesthetic enjoyment of adult cochlear implant recipients,'' J. Am. Acad. Audiol **11**, 390–406.

Gfeller, K., Turner, C., Mehr, M., Woodworth, G., Fearn, R., Knutson, J., Witt, S., and Stordahl, J. (**2002**). ''Recognition of familiar melodies by adult cochlear implant recipients and normal-hearing adults,'' Cochlear Implants International **3**, 29–53.

Gfeller, K., Witt, S., Woodworth, G., Mehr, M. A., and Knutson, J. (**2002**). ''Effects of frequency, instrumental family, and cochlear implant type on timbre recognition and appraisal,'' Ann. Otol. Rhinol. Laryngol. **111**(4), 349–356.

Green, T., Faulkner, A., and Rosen, S. (**2004**). ''Enhancing temporal cues to voice pitch in continuous interleaved sampling cochlear implants,'' J. Acoust. Soc. Am. **116**, 2298–2310.

Jones, P. A., McDermott, H. J., Seligman, P. M., and Millar, J. B. (**1995**). ''Coding of voice-source information in the Nucleus cochlear implant system,'' Ann. Otol. Rhinol. Laryngol. **104**, 363–365.

Kong, Y.-Y., Cruz, R., Jones, J. A., and Zeng, F. G. (**2004**). ''Music perception with temporal cues in acoustic and electric hearing,'' Ear Hear. **25**, 173–185.

Leal, M. C., Shin, Y. J., Laborde, M. L., Calmels, M. N., Verges, S., Laugardon, S., Andrieu, S., Deguine, O., and Fraysse, B. (**2003**). ''Music perception in adult cochlear implant recipients,'' Acta Oto-Laryngol. **123**, 826–835.

Lee, K. Y. S., van Hasselt, C. A., Chiu, S. N., and Cheung, D. M. C. (**2002**). ''Cantonese tone perception ability of cochlear implant children in comparison with normal-hearing children,'' Int. J. Pediatric Otorhinolaryngol. **63**, 137–147.

Loizou, P. C., Dorman, M. F., and Powell, V. (**1998**). ''The recognition of vowels produced by men, women, boys, and girls by cochlear implant patients using a six-channel CIS processor,'' J. Acoust. Soc. Am. **103**, 1141–1149.

Maurer, D., and Landis, T. (**1995**). ''F0-dependence, number alteration, and non-systematic behavior of the formants in German vowels,'' Int. J. Neurosci. **83**, 25–44.

McDermott, H. J. (**2004**). ''Music perception with cochlear implants: A review,'' Trends in Amplification **8**, 49–82.

McKay, C. M., McDermott, H. J., and Clark, G. M. (**1994**). ''Pitch percepts associated with amplitude-modulated current pulse trains in cochlear implantees,'' J. Acoust. Soc. Am. **96**, 2664–2673.

McKay, C. M., McDermott, H. J., and Clark, G. M. (**1995**). ''Pitch matching of amplitude-modulated current pulse trains by cochlear implantees: the effect of modulation depth,'' J. Acoust. Soc. Am. **97**, 1777–1785.

McKay, C. M., and McDermott, H. J. (**1996**). ''The perception of temporal patterns for electrical stimulation presented at one or two intracochlear sites,'' J. Acoust. Soc. Am. **100**, 1081–1092.

McKay, C. M., McDermott, H. J., and Carlyon, R. P. (**2000**). ''Place and temporal cues in pitch perception: are they truly independent,'' ARLO **1**, 25–30.

Moore, B. C., and Carlyon, R. P. (**2005**). ''Perception of pitch by people with cochlear hearing loss and by cochlear implant users,'' *Handbook of Auditory Research: Pitch Perception*, edited by C. J. Plack and A. J. Oxenham (Springer-Verlag, New York).

Nelson, D. A., Van Tasell, D. J., Schroder, A. C., Soli, S., and Levine, S. (**1995**). ''Electrode ranking of ''place pitch'' and speech recognition in electrical hearing,'' J. Acoust. Soc. Am. **98**, 1987–1999.

Osberger, M. J., and Fisher, L. (**2001**). ''New directions in speech processing: Patient performance with simultaneous analog stimulation,'' Ann. Otol. Rhinol. Laryngol. **109**, 70–73.

Peterson, G., and Lehiste, I. (**1962**). ''Revised CNC lists for auditory tests,'' J. Speech Hear Disord. **27**, 62–70.

Pijl, S., and Schwarz, D. W. (**1995**). ''Melody recognition and musical interval perception by deaf subjects stimulated with electrical pulse trains through single cochlear implant electrodes,'' J. Acoust. Soc. Am. **98**, 886–895.

Pijl, S. (**1997**). ''Pulse rate matching by cochlear implant patients: effects of loudness randomization and electrode position,'' Ear Hear. **18**, 316–325.

Shannon, R. V. (**1992**). ''Temporal modulation transfer functions in patients with cochlear implants,'' J. Acoust. Soc. Am. **91**, 2156–2164.

Shannon, R. V., Zeng, F. G., Kamath, V., Wygonski, J., and Ekelid, M. (**1995**). ''Speech recognition with primarily temporal cues,'' Science **270**, 303–304.

Skinner, M. W., Holden, L. K., Holden, T. A., Dowell, R. C., Seligman, P. M., Brimacombe, J. A., and Beiter, A. L. (**1991**). ''Performance of postlinguistically deaf adults with the Wearable Speech Processor (WSP III) and the Mini Speech Processor (MSP) of the Nucleus multi-electrode cochlear implant,'' Ear Hear. **12**, 3–22.

Skinner, M. W., Clark, G. M., Whitford, L. A., Seligman, P. A., Staller, S. J., Shipp, D. B., Shallop, J. K., Everingham, C., Menapace, C. M., Arndt, P. L., Antogenelli, T., Brimacombe, J. A., and Beiter, A. L. (**1994**). ''Evaluation of a new spectral peak (SPEAK) coding strategy for the Nucleus 22 channel cochlear implant system,'' Am. J. Otol. **15**, 15–27.

Staller, S. J., Menapace, C., Domico, E., Mills, D., Dowell, R. C., Geers, A., Pijl, S., Hasenstab, S., Justus, M., Bruelli, T., Borton, A. A., and Lemay, M. (**1997**). ''Speech perception abilities of adult and pediatric Nucleus implant recipients using the Spectral Peak (SPEAK) coding strategy,'' Otolaryngol.-Head Neck Surg. **117**, 236–242.

Stone, M. A., and Moore, B. C. J. (**2002**). ''Tolerable hearing-aid delays. II. Estimation of limits imposed during speech production,'' Ear Hear. **23**, 325–338.

Tong, Y. C., and Clark, G. M. (**1985**). ''Absolute identification of electric pulse rates and electrode positions by cochlear implant patients,'' J. Acoust. Soc. Am. **77**, 1881.

Townshend, B., Cotter, N., Van Compernolle, D., and White, R. L. (**1987**). ''Pitch perception by cochlear implant subjects,'' J. Acoust. Soc. Am. **82**, 106–115.

van Hoesel, R. J., and Tyler, R. S. (**2003**). ''Speech perception, localization, and lateralization with bilateral cochlear implants,'' J. Acoust. Soc. Am. **113**, 1617–1630.

Vandali, A. E., Whitford, L. A., Plant, K. L., and Clark, G. M. (**2000**). ''Speech perception as a function of electrical stimulation rate: Using the Nucleus 24 cochlear implant system,'' Ear Hear. **21**, 608–624.

Wilson, B. S., Finley, C. C., Lawson, D. T., Wolford, R. D., Eddington, D. K., and Rabinowitz, W. M. (**1991**). ''Better speech recognition with cochlear implants,'' Nature (London) **352**, 236–238.

Wilson, B., Finley, C., Lawson, D., and Zerbi, M. (**1997**). ''Temporal representations with cochlear implants,'' Am. J. Otol. **18**, s30–s34.

Temporal onset-order discrimination through the tactual sense

Hanfeng Yuan,[a] Charlotte M. Reed, and Nathaniel I. Durlach
Research Laboratory of Electronics, Massachusetts Institute of Technology, Cambridge, Massachusetts 02139

(Received 26 March 2004; revised 21 January 2005; accepted 21 January 2005)

Tactual temporal-onset order thresholds were measured for two sinusoidal vibrations of different frequencies delivered to two separate locations (thumb and index finger) of a multi-finger tactual stimulating device. The frequency delivered to the thumb was fixed at 50 Hz and that to the index finger at 250 Hz. The amplitude and duration of each of the two sinusoidal vibrations were roved independently from trial to trial in a 1-interval, 2AFC procedure. Performance, measured as a function of stimulus-onset asynchrony (SOA), indicated that the temporal-onset-order threshold averaged 34 ms across four subjects. The data were further classified into subsets according to both the amplitude and duration of the two stimuli in each trial of the roving-discrimination paradigm. The results indicated that the amplitude differences of the two stimuli in each trial had a substantial effect on onset-order discrimination, while duration differences generally had little effect. The effects of amplitude differences are explained qualitatively in terms of amplitude latency relationships and stimulus interactions such as temporal masking. Overall, the results not only contribute to an enhanced understanding of the temporal sensitivity of the tactual system but also provide guidelines for the design of tactual aids for hearing-impaired persons. [DOI: 10.1121/1.1869692]

PACS numbers: 43.66.Wv [NFV] Pages: 3139–3148

I. INTRODUCTION

The current research is concerned with the feasibility of encoding temporal cues important to the recognition of speech in tactual displays for persons with profound auditory impairment. In particular, this research is motivated by interest in the tactual presentation of a temporal cue related to voice-onset time (VOT), a parameter that plays an important role in the discrimination of consonantal voicing (Lisker and Abramson, 1964; Zue, 1976). Although voicing carries a high informational load in speech (Grant *et al.*, 1998; Auer and Bernstein, 1996), it is poorly received through lipreading, an important means of obtaining information about speech for many hearing-impaired individuals (Heider and Heider, 1940; Erber, 1974; Walden *et al.*, 1977).

Yuan *et al.* (2004) have demonstrated that a reliable and robust cue to initial consonant voicing can be obtained in real time using amplitude-envelope signals derived from two different filtered bands of speech (e.g., one envelope derived from a lowpass filtered band at 350 Hz and another from a highpass-filtered band at 3000 Hz). Acoustic measurements of the onset-timing difference between the low- and high-frequency envelopes derived from speech syllables indicated a different pattern of envelope-onset asynchrony (EOA) values for initial voiced versus voiceless consonants. For voiceless consonants, the high-frequency envelope tends to precede the low-frequency envelope by roughly 50–200 ms, the specific value depending on the particular consonant. For voiced consonants, on the other hand, the low-frequency envelope may either precede the high-frequency envelope by values ranging from 0–120 ms, or may follow the high-frequency envelope by values as great as 70 ms, depending on the consonant. In general, there is little overlap between the distributions of EOA values for voiced versus voiceless consonants (Yuan *et al.*, 2004). Thus, there is reason to believe that this information, if properly encoded in a tactual display, could provide a useful supplement to lipreading.

Within this general context, our goal in the current study was to measure temporal-onset order thresholds for a particular scheme in which amplitude-envelope information derived from two separate frequency regions of speech was presented to two fingers using two vibrating frequencies. In these experiments, the index finger was always stimulated with a 250-Hz sinewave (I250) and the thumb with a 50-Hz sinewave (T50). Redundant coding of location and vibratory frequency was employed on the basis of previous research suggesting that dimensional redundancy may facilitate performance on a variety of perceptual tasks, including that of tactual temporal-order judgments (Taylor, 1978).

The current study employed a one-interval, two-alternative, forced-choice procedure (1I-2AFC). The subject's task was to determine which of two possible stimulus-onset orders (onset of I250 followed by onset of T50 or *vice versa*) was presented on each trial. (The experiment was conducted using earplugs and masking noise to eliminate any auditory cues arising from the stimulating device or from bone-conducted sound.) The ability to discriminate temporal-onset order for the I250 and T50 signals was measured as a function of stimulus-onset asynchrony (SOA) and threshold was defined as the absolute value of SOA required for performance of $d' = 1$. The current procedure employed roving values of amplitude and duration of each of the two sinusoidal signals presented in each trial. The ranges over which amplitude and duration were roved were selected on the basis of observations of the range of these values observed in the amplitude envelopes of speech signals (Yuan *et al.*, 2004). The data were also classified into subsets according to

[a]Electronic mail: hfyuan@mit.edu

the amplitude and duration of the stimuli in each trial to determine the effects of such differences on performance.

The current research is distinguished from that of previous studies in several ways.

First, this research employs continuous tonal signals to measure temporal onset-order discrimination for tactual stimulation of the fingers. In the tactual modality, most previous studies have employed transient mechanical or electrotactile signals (Hirsh and Sherrick, 1961; Sherrick, 1970; Marks *et al.*, 1982; Shore *et al.*, 2002) or brief vibrotactile patterns (Craig and Baihua, 1990). Because of the transient nature of these stimuli, values of SOA always exceed the signal duration, there is no temporal overlap of the two stimuli presented on a given trial, and both onset and offset cues can enter into judgments of order. Thus, experiments conducted with transient signals provide measurements of *temporal order* discrimination rather than *temporal onset-order* discrimination (which typically involves some temporal overlap of the two stimuli whose onset order is to be discriminated and which eliminate the use of an offset cue). Temporal-order thresholds for brief vibrotactile or electrotactile signals are generally on the order of 20–40 ms (with the exception of electrotactile thresholds on the order of hundreds of ms reported by Marks *et al.*, 1982). The only previous study of which we are aware that is concerned with temporal onset-order judgments through the tactual sense is the unpublished work of Eberhardt *et al.* (1994) concerned with the ability to determine the temporal onset-order of a ''movement'' and a ''vibratory'' signal presented through a haptic display to one finger.

Second, the current study employs the use of roving values of amplitude and duration applied independently to each of the two signals of a trial in order (a) to eliminate potentially confounding cues of offset time, duration, and energy in performing the temporal onset-order task and (b) to provide a more realistic assessment of performance using stimuli designed to approximate those that might arise in a tactual display of speech. Most studies of temporal onset-order discrimination, particularly in audition, have adopted Hirsh's (1959) methodological convention of equating offset times of the two signals whose onset order is to be determined (e.g., see Pastore *et al.*, 1982). In fact, Pastore's (1983) measurements of temporal offset-order discrimination indicate that differences as short as 2–5 ms can be discriminated reliably. The convention of equating offset times of the two signals in a pair, however, introduces differences in their absolute duration and energy which may potentially be confounded with temporal-onset order. No previous study appears to have addressed these methodological issues.

Third, the current procedure permits the examination of the effects of intra-trial differences in amplitude and duration between the two signals presented within a given trial on the ability to discriminate onset order. Based on the relationship between intensity and latency and inter-stimulus masking, it is reasonable to expect that the perceived onset of each of the two signals in a given trial will be affected by both its own amplitude and duration as well as that of the other stimulus. Thus, amplitude/duration imbalances may be expected to affect judgments of onset order.

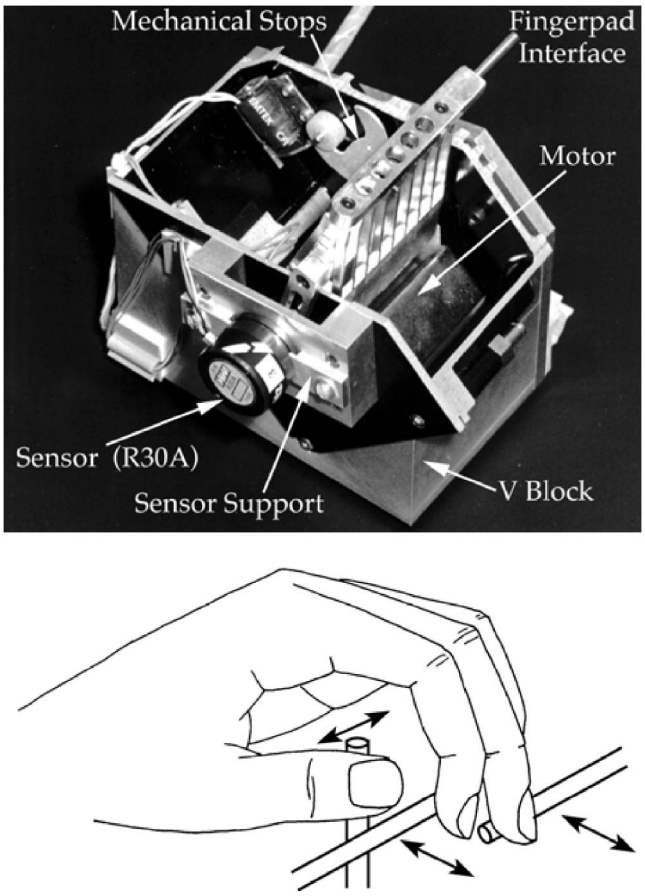

FIG. 1. An illustration of the Tactuator stimulating device. The upper panel is a photograph of one of the three motor assemblies with labeled components. The lower panel is a schematic drawing illustrating finger placement on three vibrating rods of the Tactuator device. (Taken from Tan, 1996.)

II. METHOD

A. Subjects

Four individuals ranging in age from 21 to 32 years (three male and one female) served as subjects in this study. All subjects were screened for tactual threshold detection and temporal-onset order discrimination before participating in the experiments. Hearing testing was conducted through the Audiology Department at the MIT Medical Department to provide a baseline for each subject's hearing level prior to exposure to masking noise. None of the subjects had previous experience in experiments concerned with tactual perception. Subjects were paid for their participation in the study and received periodic incentive bonuses throughout the course of the study.

B. Apparatus

The tactual stimulating device used in the experiments (referred to as the Tactuator—see Fig. 1) was initially developed by Tan (1996) for research with multidimensional tactual stimulation. A complete discussion of this system is provided in Tan (1996) and Tan and Rabinowitz (1996),

including a detailed description of the hardware components, controller components, and performance characteristics of the device. For the current research, the original system was upgraded with a new computer, DSP system, and electronic control system to improve its performance capabilities. A complete description of the characteristics of the modified system is available in Yuan (2003).

The device is a three-finger display capable of presenting a broad range of tactual movement to the passive human fingers. It consists of three mutually perpendicular rods that interface with the thumb, index finger, and middle finger in a manner that allows for a natural hand configuration (see the bottom panel of Fig. 1). A photograph of the motor assembly (with labeled components) associated with one of the rods is provided in the upper panel of Fig. 1. Each rod is driven independently by an actuator that is a head-positioning motor from a Maxtor hard-disk drive. The position of the rod is controlled by an external voltage source to the actuator and is measured by an angular position sensor that is attached to the moving part of each of the three motor assemblies. The rods are capable of moving the fingers, which rest lightly on the rods, in an outward (extension) and inward (flexion) direction relative to a neutral resting position.

The overall performance of the device is well-suited for psychophysical studies of the tactual sensory system. First, the device is capable of delivering frequencies along a continuum from dc to 300 Hz, allowing for stimulation in the kinesthetic (low-frequency) and cutaneous (high-frequency regions), as well as in the mid-frequency range. Second, the range of motion provided by the display for each digit is roughly 26 mm. This range allows the delivery of stimulation at levels from threshold to approximately 50 dB SL throughout the frequency range from dc to 300 Hz. Third, each channel is highly linear, with low harmonic distortion and negligible inter-channel crosstalk. Fourth, loading (resulting from resting a finger lightly on a moving bar of the actuator) does not have a significant effect on the magnitude of the stimulation.

C. Stimuli and procedure

Temporal-onset order discrimination thresholds were measured for stimulation of two fingers (left index finger and left thumb) using two different stimulating frequencies for the two sites. The index finger was always stimulated with a 250-Hz sinusoid (I250) and the thumb was always stimulated with a 50-Hz sinusoid (T50). The experiments employed a one-interval two-alternative forced-choice (1I2AFC) procedure with trial-by-trial correct-answer feedback. One interval (or trial) of the experiment involved the presentation of the stimuli in one of two possible onset orders (with equal *a priori* probabilities): onset of I250 followed by onset of T50 (I250, T50) or onset of T50 followed by onset of I250 (T50, I250). The subject's task was to determine on each trial in which of the two possible onset orders [(I250, T50) or (T50, I250)] the two stimuli were presented, and performance was examined as a function of stimulus-onset asynchrony SOA.

SOA was defined as the time asynchrony between the onset of I250 relative to the onset of T50, i.e., onset time of signal at thumb minus onset time of signal at index finger ($T50_{onset} - I250_{onset}$). The absolute value of SOA was kept constant throughout a given run so that in effect the only aspect of the stimulus that varied during the run (and needed to be judged by the subject on a trial-to-trial basis) was the sign of the SOA.

The experiment was conducted with trial-by-trial roving of both the duration and amplitude of each of the two sinewaves. The value of the duration of the two stimuli in each trial was selected independently from a uniform distribution of the following seven values: 50, 100, 200, 400, 500, 600, 800 ms (leading to $7 \times 7 = 49$ possible duration pairs). Thus, the offset order of the two stimuli on each trial is random, and cannot be used as a cue in the temporal onset-order task. The value of amplitude of the two stimuli in each trial was selected from a uniform distribution of five values of sensation level: 25, 30, 35, 40, and 45 dB SL relative to the average threshold level of each of the two signals (T50 and I250) across subjects S1, S2, and S3.[1] These threshold values (measured using an adaptive 2I2AFC procedure) were 1 dB *re* 1 μ peak for T50 and -19 dB *re* 1 μ peak for I250. The amplitudes of the shorter stimuli (i.e., 50 ms and 100 ms) were compensated for according to a 3 dB/octave rule based on the tactual temporal-integration data of Verrillo (1965). Namely, the amplitude of the 50 ms signals was increased by 6 dB relative to that of stimuli with duration $\geqslant 200$ ms, and the amplitude of the 100 ms signals was increased by 3 dB. Signals were gated on and off with a rise–fall time of 20 ms shaped with a hanning window.

A computer program written in C controlled the generation of the stimuli, the presentation of the stimuli to the Tactuator device, and the recording of subject's responses on a DELL computer. The temporal sequence of events for two representative trials is illustrated in Fig. 2. The upper panel shows stimuli delivered to the thumb through channel 1, and the lower panel shows stimuli delivered to the index finger through channel 2. Sequential events are shown for two full trials (Trial 1 and Trial 2). The onset of each of the two trials is marked by T1 and T4, respectively. The end of each of the two trials is marked by T3 and T6, respectively. On Trial 1, T1 marks the onset of a 250-Hz signal in channel 2 (the index finger), T2 marks the onset of a 50-Hz signal in channel 1 (thumb), and T3 marks the end of the signal in channel 1. The values of the duration and amplitude of each of the two signals are selected randomly and independently from the distributions described previously. Note (as in Trial 2) that it is possible for the signal with an earlier onset to terminate after the second stimulus. In Fig. 2, Trial 1 represents a positive value of SOA, where the onset time for the index finger leads the onset time for the thumb ($T2 - T1 > 0$). Trial 2 illustrates a negative value of SOA, where the onset time for the thumb leads the onset time for the index finger ($T4 - T5 < 0$). During the period from T3 to T4 (that is, the end of one trial to the beginning of the next trial), the following series of events occurs: a prompt is presented for the subject to choose one of the two response codes, the response is stored digitally, the text providing correct-answer feedback is displayed on the monitor, the parameters are computed for the next trial, and finally a prompt is presented for a new

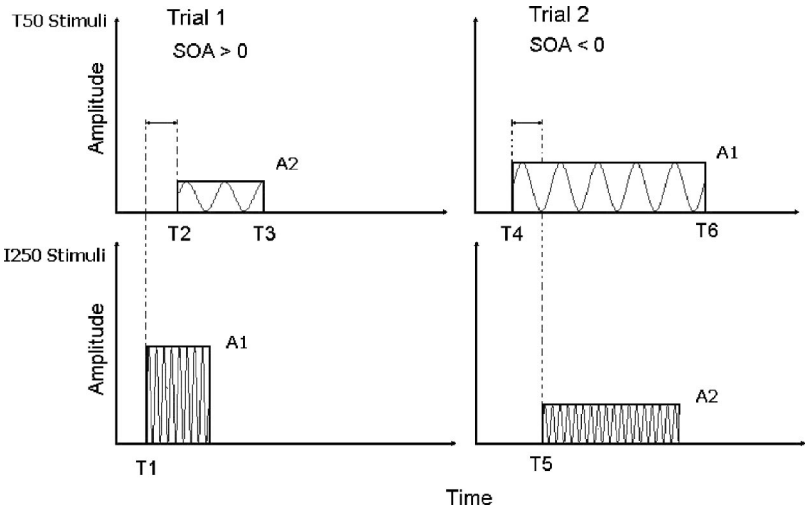

FIG. 2. An illustration of the time line for trials in the temporal-onset order discrimination experiment. The cycles inside the blocks are representative of the two frequencies: 50 Hz (channel 1) and 250 Hz (channel 2).

trial. The duration of this time period varies, depending primarily on the subject's response time.

As stated previously, for any given value of |SOA|, the subject's task was to determine the sign of the SOA. For each subject, performance was measured at six different values of |SOA|. The value of |SOA|, which was fixed within a given run, was selected from a set of nine possible values in the range 5 to 115 ms {5, 10, 25, 40, 55, 70, 85, 100 and 115 ms}. The particular |SOA| values used for each subject were selected on the basis of an initial screening process in which subjects were tested with values of |SOA| in decreasing order. In this initial testing, 2 consecutive 50-trial runs were collected at each |SOA|. Based on a given subject's performance on the initial testing, six values of |SOA| were selected for use in the main experiment to yield performance in the range of roughly 55–90% correct. Five experimental blocks were run using the six values of |SOA| selected for each subject. Within each block, two consecutive 50-trial runs were conducted at each of the six values of |SOA| with the order of the |SOA| chosen at random. On average, the experiment required 6 sessions on 6 different days for each subject.

During the experiment, the subject sat approximately 0.8 meters from the video monitor (DELL Trinitron) and 0.6 meters from the Tactuator, and placed the index finger and the thumb of the left hand on the two corresponding rods of the Tactuator. To eliminate any auditory cues from the vibration of the Tactuator, subjects wore foam earplugs that were designed to provide 30-dB attenuation and also wore earphones that delivered pink masking noise at an overall level of roughly 90 dB SPL. The attenuation and the noise were sufficient to mask any air-conducted sounds arising from the device itself. In addition, the masking noise was deemed sufficient for eliminating any bone-conducted sounds that might arise from the highest levels of stimulation. The subjects were instructed to press "h" if they perceived the order to be (I250, T50), or "l" if they perceived the order to be (T50, I250). They were instructed to guess when they were unsure of the order.

D. Data analysis

For each experimental run and each subject, the results were summarized using two percent-correct scores (one for positive SOA and one for negative SOA) and the signal detection parameters of sensitivity, d', and bias, β (Green and Swets, 1966; Durlach, 1968).[2] The percent-correct scores were averaged over the 10 runs at each SOA and plotted as a function of SOA. Values of d' and β for each subject were calculated from the resulting 2×2 matrices using the assumption that the underlying distributions of sensory events are Gaussian with equal variance. For each subject, these values were computed for each run, averaged over the 10 runs at each value of |SOA|, and plotted as a function of |SOA|. The threshold for temporal-onset order discrimination was defined as the value of |SOA| for which $d'=1$. The data were also classified into subsets according to the amplitude and duration of the two stimuli on a given trial and according to the order in which they were presented (independent of the digit that was stimulated).

III. RESULTS

The results of the temporal-onset order discrimination task for each subject are presented in the upper panel of Fig. 3 for percent-correct performance as a function of SOA, where $\mathrm{SOA}=\mathrm{T50}_{\mathrm{onset}}-\mathrm{I250}_{\mathrm{onset}}$. Positive values of SOA represent conditions where the stimulus to the index finger precedes that to the thumb; negative values represent cases where the thumb leads the index finger. Each point represents the mean of the percent-correct scores over the last ten runs (i.e., 500 trials) for each subject.

The shape of the data curves is similar across subjects, indicating a monotonic increase in performance above and below the value of SOA that produced minimum (near chance) performance. The performance is roughly symmetric about $\mathrm{SOA}=0$ except for S3 (filled circles), for whom it is somewhat asymmetric (performance being better for trials with positive SOA than for trials with negative SOA). The asynchrony required for 71%-correct performance (the average of the absolute values of the two SOA values corresponding to 71%-correct, one for $\mathrm{SOA}>0$, and the other for $\mathrm{SOA}<0$) ranges from 25 ms for the most sensitive subject (S4) to roughly 53 ms for the least sensitive subject (S2).

The means and standard deviations of d' are shown as a function of |SOA| in the bottom left-hand panel of Fig. 3. The data for each subject are well fit by a straight line

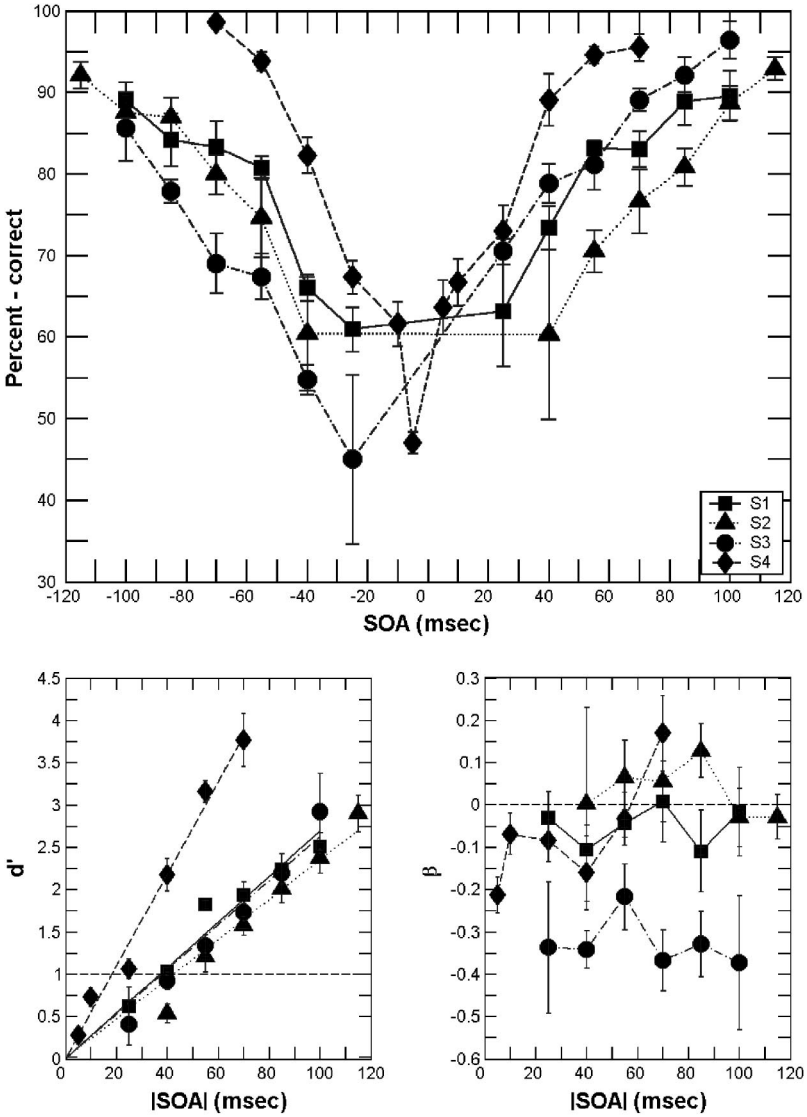

FIG. 3. A summary of results in percent-correct (upper panel), d' (lower left panel), and β (lower right panel). In each panel, data for each subject are represented by different symbols and connecting lines (see the symbol legend). Each data point is the average of 10 50-trial runs; error bars represent ± 1 s.d. In the upper panel, the percent-correct score is plotted as a function of Stimulus-Onset Asynchrony (SOA) in ms. In the lower left and right panels, d' and β, respectively, are plotted as a function of |SOA| in ms.

through the origin using the method of minimum-square-error. Across subjects, the thresholds (defined as the value of |SOA| at which $d'=1$) range from 18 ms to 43 ms, the slopes of the lines range from 0.024 ms^{-1} to 0.055 ms^{-1}, and the correlation coefficients range from 0.971 to 0.996. The specific values of these quantities, as well as the root-mean-square (rms) error of the fits, are shown in Table I for each of the four subjects.

The means and standard deviations of β are shown as a function of |SOA| in the bottom right-hand panel of Fig. 3. Positive bias indicates that the subject has a greater tendency to respond with the order (T50, I250) than to respond with the order (I250, T50), while negative bias indicates the opposite. The bias is negligible for subjects S1, S2, and S4, falling in the range -0.2 and $+0.2$. It is somewhat larger and negative at all |SOA| for S3. This tendency is also reflected in the asymmetry of the percent-correct scores of subject S3 in the upper panel of Fig. 3 (i.e., at the same absolute value of SOA, her performance is always better for trials with positive SOA than for trials with negative SOA).

TABLE I. |SOA| at $d'=1$, slope of the best-fitting line, correlation coefficient of the fit, and rms error of the fit for each of the four subjects.

Subjects	S1	S2	S3	S4
|SOA| (ms) @$d'=1$	37	43	38	18
Slope of d'	0.027	0.024	0.026	0.055
Correlation coefficient	0.971	0.996	0.995	0.992
rms error	0.166	0.188	0.177	0.158

For Fig. 4, the data were classified into categories according to the amplitude differences of the two stimuli in each trial of the roving-discrimination paradigm (see Table II). The amplitude-difference (A_1-A_2), defined as the difference between the amplitude of the stimulus with an earlier onset (A_1) and the amplitude of the stimulus with a later onset (A_2), is calculated for every possible amplitude pairing of the stimuli. The amplitude-difference range (-20 to $+20$ dB SL) was divided into 5 sub-ranges: ($\{-20,-15\}$, $\{-10,-5\}$, $\{0\}$, $\{5, 10\}$, $\{15, 20\}$). Negative values refer to those cases in which a lower-amplitude stimulus was followed by a higher-amplitude stimulus (Low–High) and positive values to the opposite ordering (High–Low). Each amplitude pairing is equally likely; thus, the distribution of each

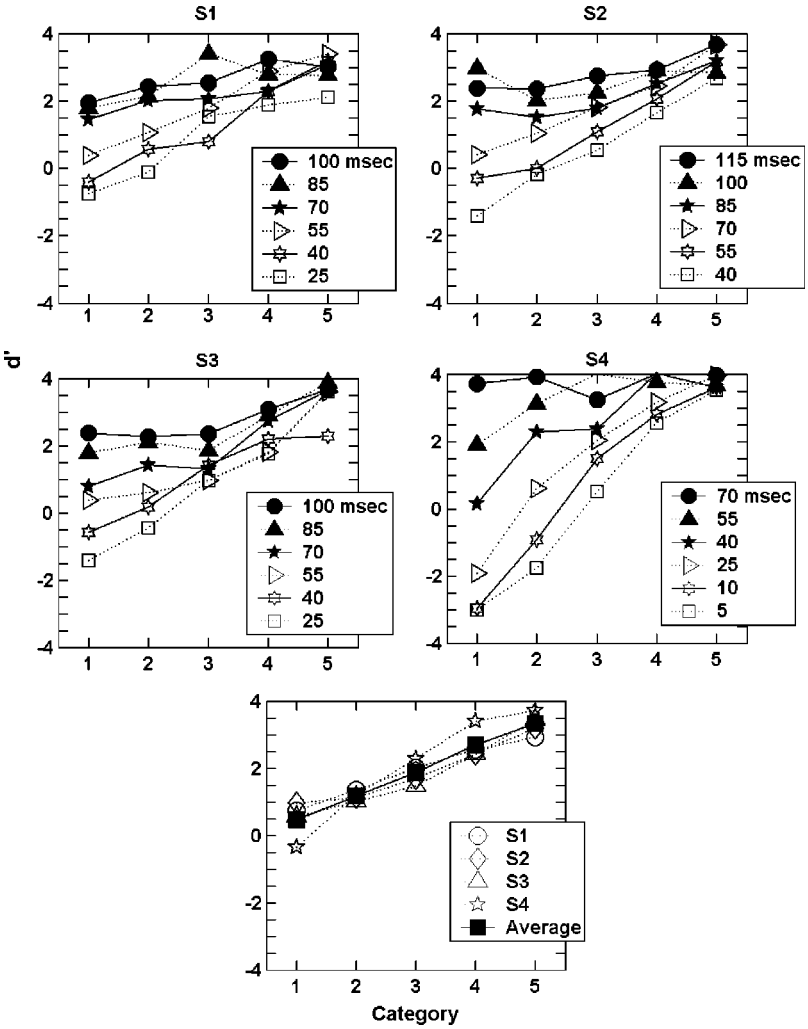

FIG. 4. Sensitivity d' as a function of the category of amplitude difference (A_1-A_2) in dB. See Table II for definitions of Categories 1 through 5. The top four panels show the results for each |SOA| for each of the four subjects. Filled symbols represent the three largest values of |SOA| and unfilled symbols the three smallest values. The bottom panel shows the results averaged across |SOA| for each subject (represented by a different symbol) and the results averaged across both |SOA| and subjects (filled squares).

sub-range is the number of occurrences of each amplitude difference of the sub-ranges divided by 25 (the total number of all possible amplitude difference pairings of the stimuli), shown in Table II.

A 2×2 confusion matrix was derived for each category and each |SOA| and used to calculate d'. The first four panels of Fig. 4 show the dependency of d' on category, with |SOA| as a parameter for each subject. The bottom panel in Fig. 4 shows the results averaged over the value of |SOA|. In general, the results shown in Fig. 4 indicate a tendency for d' to increase with category number (reflecting better performance under High–Low ordering compared to Low–High ordering) as well as with |SOA|, and to increase at a greater rate with category number when the value of |SOA| is small. In addition, when both the category number is small (i.e., the stimulus order is Low–High) and the value of |SOA| is small, there is a tendency for d' to be negative (i.e., for the perceived temporal-onset order to be opposite to the actual order). The values of β averaged across |SOA| for each subject (not shown in Fig. 4) indicate relatively flat bias as a function of category number, ranging from roughly -0.35 to 0.05.

A more detailed breakdown of the effects of amplitude on d' is provided in Fig. 5, where d' is shown as a function of A_1 conditioned on A_2 [panels (a) and (b)] and of A_2 conditioned on A_1 [panels (c) and (d)]. In panels (a) and (c), results are averaged over the three largest |SOA| values tested for each subject. In panels (b) and (d), results are averaged over the three smallest |SOA| values tested for each subject. In panels (a) and (b), performance increases as A_1

TABLE II. Amplitude-difference categories. The second row provides the amplitude differences (A_1-A_2) in each category, where A_1 is the amplitude of the stimulus with an earlier onset and A_2 is the amplitude of the stimulus with a later onset. The third row provides a qualitative description of the amplitude of the stimulus in interval 1 relative to that in interval 2: Low followed by High (Low–High), Equal, or High followed by Low (High–Low). The fourth distribution row (Distribution) gives the frequency of occurrence for each category.

Category	1	2	3	4	5
A_1-A_2	$\{-20,-15\}$	$\{-10,-5\}$	$\{0\}$	$\{5, 10\}$	$\{15, 20\}$
Description	Low–High	Low–High	Equal	High–Low	High–Low
Distribution	3/25	7/25	5/25	7/25	3/25

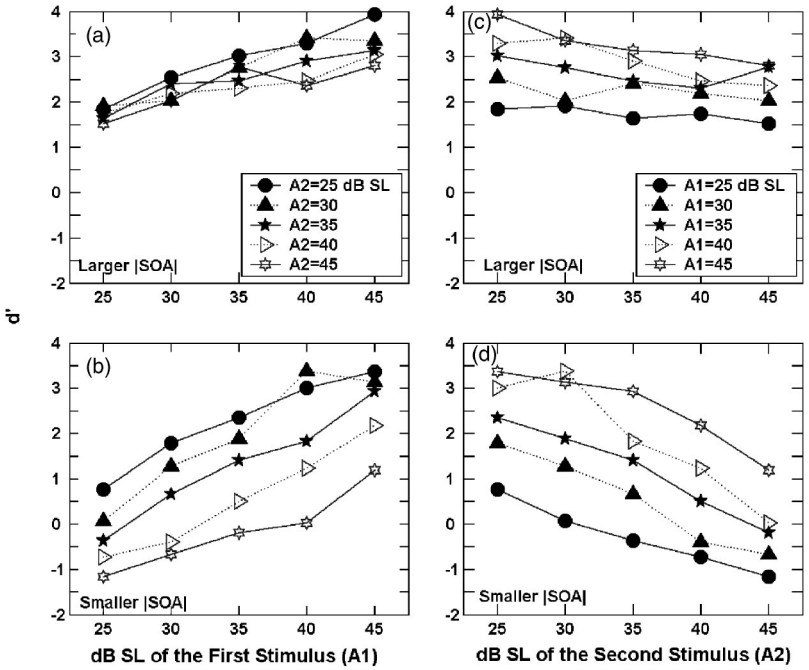

FIG. 5. Sensitivity d' as a function of the amplitude of the earlier-onset stimulus A_1 (in dB SL) [panels (a) and (b)] and of the amplitude of the later-onset stimulus A_2 (in dB SL) [panels (c) and (d)]. Data averaged across the three highest |SOA| values tested for each subject are shown in panels (a) and (c) and averaged across the three smallest |SOA| values are shown in panels (b) and (d). In panels (a) and (b), performance is plotted with A_2 as a parameter. In panels (c) and (d), performance is plotted with A_1 as a parameter.

increases (at each value of A_2) and decreases as A_2 increases. This effect of A_2 on performance is stronger for small |SOA| [panel (b)] than for large |SOA| [panel (a)]. When examined as a function of A_2 [see panels (c) and (d)], performance is shown to decrease as A_2 increases (for each value of A_1) and also to increase as A_1 increases. The effect of A_1 on performance is stronger for small |SOA| [panel (d)] than for large |SOA| [panel (c)]. Furthermore, the effect of A_1 on performance [see panel (c)] appears stronger than the effect of A_2 on performance [see panel (a)] for large |SOA|.

The effects of the duration of the two successive stimuli on each trial on performance, which were analyzed in a similar manner, were minimal. Three subjects (S1, S2, and S4) showed no change in d' or β across differences in duration. Subject 3 demonstrated a tendency for decreased performance only when the duration of the first stimulus exceeded that of the second stimulus by at least 300 ms. The amplitude adjustment applied to the two shortest-duration signals is likely to have contributed to the negligible effects of duration.

IV. DISCUSSION

The tactual temporal onset-order thresholds ($d'=1$) ranged from 18 ms to 43 ms (averaging 34 ms) across the four subjects. These results are similar in magnitude to those obtained in previous studies of tactual temporal order employing brief or transient stimuli (Hirsh and Sherrick, 1961; Sherrick, 1970; Craig and Baihua, 1990; Shore *et al.*, 2002), where results are typically in the range of roughly 20–40 ms.

In the remainder of this discussion, we briefly address the following issues. First, we (a) examine the results of integrating the data on human discrimination of temporal onset-order obtained in this experiment with estimation of the discrimination performance of an ideal observer (with perfect temporal onset-order resolution) operating on our two-channel display for voicing contrasts in real speech sounds (Yuan *et al.*, 2004), and then (b) compare these integrated results to the discrimination capabilities of humans operating on essentially the same materials (Yuan, 2003). Second, we explore the extent to which our results on the effects of amplitude differences are consistent with previous results on the relation of amplitude to latency and on temporal masking. Third and finally, we comment on our use of redundant encoding in the display and on the use of the specific carrier frequencies 50 Hz and 250 Hz for the two stimulation sites.

A. Effect of limited temporal-onset-order resolution on detection of voicing

In a previous paper (Yuan *et al.*, 2004), we computed the values of d' that would be obtained for voicing detection by an ideal receiver using the same display processing as that assumed in the current paper (i.e., the input to the ideal receiver is assumed to be identical to the input to the tactual stimulator) when faced with a corpus of monosyllabic material composed of 16 initial consonants subdivided into 8 voiced-voiceless pairs, 3 vowels, 2 speakers, and 10 utterances/speaker. In this computation, the only limitation on performance is that imposed by the variability in the articulation of the test syllables (as seen at the output of the display processing). Obviously, when this ideal receiver is replaced by the human tactual system with its limited temporal-onset-order resolution, performance in voicing detection is degraded. The values of d' for the ideal receiver operating on the 8 voicing contrasts at the output of the display, together with the corresponding degraded values of d' that result from including the limited temporal-onset-order resolution measured in the present paper, are shown in the first two rows of Table III.[3] For comparison purposes, the third row of Table III shows the results previously obtained by humans in essentially the same voicing detection task (Yuan, 2003). The only differences between the materials used in the human test and the materials used for the ideal

TABLE III. Calculation of performance in d' for each of 8 voicing contrasts (and for the mean across these contrasts) for a 2I, 2AFC procedure. Measurements are provided for the case of an ideal observer with infinite temporal resolution (IO), for the case of an ideal observer with limited temporal resolution of 34 ms (IO-Lim), and for the case of human observers (HO). The d' scores of HO are mean results over the four subjects tested.

		Consonant pair								
		/p-b/	/t-d/	/k-g/	/tʃ-dʒ/	/f-v/	/θ-ð/	/s-z/	/ʃ-ʒ/	Mean
d'	IO	5.1	8.1	6.8	3.9	3.5	4.0	13.0	10.6	6.9
	IO-Lim	3.1	4.1	3.5	2.5	3.1	3.8	8.2	7.2	4.4
	HO	2.5	3.0	2.9	1.7	2.1	3.1	2.9	3.3	2.7

receiver computation are the number of vowel contexts (i.e., 3 vowels vs 16 vowels). As can be seen by examining the results shown in Table III, imposing a limitation on the temporal-onset-order resolution of the ideal observer leads to a reduction in mean sensitivity by a factor of roughly 1.6 (although the reduction varies substantially as a function of the contrast). The mean performance of the limited ideal receiver is nevertheless higher than that obtained with human observers (again by a factor of roughly 1.6), despite the fact that the human data were obtained with less variability in the stimulus set (because of the reduction in number of vowel contexts). This comparison indicates that, in addition to limitations imposed by temporal resolution, other imperfections in human processing (e.g., related to memory and attention) lead to significant degradations in human performance.

B. Roving amplitude effects

Amplitude differences between the successive stimuli of a given trial had a clear and consistent effect on performance (see Figs. 4 and 5). The average d' obtained using a paradigm employing roving values of amplitude and duration, however, is similar to that obtained in a paradigm with fixed values.[4] Thus, the effects of amplitude imbalances appear to cancel out when only mean d' is computed across trials using the roving paradigm.

The major effects of amplitude differences observed in Figs. 4 and 5 are consistent with a simple intensity–latency hypothesis predicting an inverse relation between stimulus amplitude and perceived onset time (e.g., see a review of the auditory literature contained in Scharf, 1978). Both the systematic improvement in performance with an increase in A_1 [see panels (a) and (b) of Fig. 5] and the higher levels of performance observed for larger positive values of A_1-A_2 (see Fig. 4) are easily explained in terms of an earlier perceived onset of the more intense leading stimulus (resulting in a correct decision regarding temporal onset order). In the cases of lower levels of improvement noted for $A_1<A_2$ and for a decrease in performance with increasing A_2, an earlier perceived onset of the lagging stimulus will lead to an incorrect judgment of onset order. Physiological data offer support for the intensity–latency hypothesis in the somatosensory system in view of the finding of decreased latency of the onset of neuronal firings as the stimulus amplitude is increased (e.g., see Wilent and Contreras, 2004). In addition, the population of activated nerve fibers increases in proportion to stimulus amplitude (Johnson, 1974) and a range of conduction velocities is observed across these fibers (Johnson *et al.*, 2000). Thus, a high-amplitude stimulus has a greater probability of activating a fast-conducting neuron and evoking an earlier response than does a low-amplitude stimulus.

More subtle effects observed in the data [in panels (a) and (c) of Fig. 5] demonstrate that the effects of A_1 are more potent than those of A_2 in terms of both the slope and the spread of the functions. Such effects are not accounted for by an intensity–latency hypothesis, but may be explained in terms of interactions between the two stimuli on a given trial. In particular, forward masking has a longer effective time range of several hundreds of ms, while backward masking decays much faster with an effective range on the order of tens of ms (Sherrick, 1964; Weisenberger, 1994).

Several previous studies have also included some examination of amplitude effects on temporal order judgments. Pastore (1983) studied the effect of intensity variations between two different tones in an auditory stimulus-offset asynchrony judgment task. One of the tones was fixed at 70 dB and the other tone was presented at 50, 60, or 70 dB (with data collected separately at each intensity pairing). No effects of intensity variation were noted at any of the four durations studied; however, the data were not analyzed in terms of amplitude differences based on signal order. Sherrick (1970) investigated the effect of small intensity differences (on the order of 3 dB) in a tactual temporal-order task involving two different sites of transient mechanical stimulation separated by 10 or 20 cm along the length of one thigh. Thresholds, which ranged from 30 to 40 ms for both separations, were not greatly affected by level imbalances examined as a function of stimulus order. Craig and Baihua (1990) examined the effect of intensity differences on temporal-order thresholds for two distinct 16-ms vibrotactile patterns using two values of intensity (with a difference of roughly 6 dB) that could be assigned to each member of a stimulus pair (resulting in four possible intensity pairings that were equally likely to occur on any given trial). Different patterns of results were obtained for experiments conducted with same-site stimulation compared to ipsilateral (stimulation of two different fingers on the same hand) and bilateral stimulation. At short values of SOA in the same-site condition, the lowest thresholds were observed when the lower intensity was assigned to the leading stimulus of a given pair and the highest thresholds for the opposite ordering. This result is in the opposite direction both to that observed under the Craig and Baihua (1990) ipsilateral and bilateral conditions and in the results of the current study. The trend observed in the same-site data of Craig and Baihua

(1990), however, was also noted by Bachman *et al.* (2004) in a visual study of temporal order. These cases demonstrate a tendency to attribute recency to the more salient stimulus of a pair. In the visual case, these effects may be related to stronger effects of backward compared to forward masking.

Van Doren *et al.* (1990) observed that gap-detection ability for vibrotactile stimuli was strongly related to stimulus intensity. For sinusoidal signals, gap-detection thresholds ranged from 115 ms at a level of 5 dB SL to roughly 8 ms at a level of 25 dB SL. In the current study, although amplitude *differences* had a strong effect on performance, the performance does not appear to depend on the *absolute* intensity level of the two stimuli in a trial. Performance was roughly comparable for cases of $A_1 = A_2$ at each of the five levels of stimulation employed here (as can be seen in Fig. 5). This result differs from that obtained by Van Doren *et al.* (1990) in a gap-detection task with vibrotactile stimuli presented to the thenar eminence. Temporal-onset order thresholds in the current study (obtained for signals in the range of 25 to 45 dB SL) were several orders of magnitude higher than the gap-detection threshold at 25 dB SL (the highest level reported by Van Doren *et al.*, 1990). This comparison suggests that gap-detection ability is likely to reflect a more peripheral level of sensory processing than does the ability to resolve temporal-onset order.

C. Redundant encoding and choice of stimulating frequencies

The measurements reported here were obtained with stimuli that employed redundant coding of site and frequency such that the thumb was always stimulated with 50 Hz (T50) and the index finger at 250 Hz (I250). Dimensional redundancy was deliberately selected as a coding strategy for enhancing the perception of temporal onset order. A set of corollary measurements was obtained to examine the effects of such redundant coding on temporal-onset-order resolution. These results were obtained on four subjects (one of whom also participated in the original study) using the same general procedures as described for the main experiment. Three conditions were tested: (1) the original condition employing redundant stimulation (T50, I250); (2) a two-site condition employing 55 Hz stimulation at both the thumb and index finger (T55, I55); and (3) a same-site condition employing 50 Hz and 250 Hz at the index finger (I50, I250). Averaged over subjects, thresholds were 50.4 ms for condition (1), 53.4 ms for condition (2), and 62.9 ms for condition (3). Thus, the use of two separate sites appears to be advantageous as opposed to one site of stimulation, but the use of different frequencies at different sites does not lead to significantly improved performance. This result suggests that frequency need not be tied to the site of stimulation and instead may be used to encode information along some other parameter of speech.

Taylor (1978) investigated dimensional redundancy in the processing of vibrotactile temporal order for sequences of three stimuli presented at a duration of 120 ms and SOA of 120 ms. Three conditions were studied: (1) *P*—three values of frequency (50, 150, 450 Hz) balanced for perceived amplitude at the index finger; (2) *S*—one frequency (450 Hz) at three fingers (index, middle, ring) balanced for perceived amplitude at the three locations; and (3) *SP*—redundant frequency-site pairings as follows: 50 Hz at the ring finger, 150 Hz at the middle finger, and 450 Hz at the index finger. Note that chance performance is 1/6 in each condition. The average percent-correct score was 33% for condition (1), 42% for condition (2), and 52% for condition (3). Thus, judgments based on site discrimination were better than those based on frequency discrimination, and the redundant condition improved scores by roughly 10–20 percentage points. This same general trend was observed in our temporal onset-order results in that performance on the basis of site alone was superior to that based on frequency alone. Taylor (1978), however, observed redundancy effects for both frequency and site of stimulation in his more complex task of temporal order identification of three-stimulus sequences compared to our observation of a redundancy effect only for frequency for the simpler temporal onset-order discrimination task.

The particular pair of frequencies (50 and 250 Hz) employed in the experiment may have had an effect on the thresholds reported here. These frequencies were selected to be highly discriminable and to allow for a minimum of 2.5 complete sinusoidal cycles at the shortest duration (50 ms). The interaction between these two frequencies may have an effect on the temporal-order threshold. Further research is warranted on the development of optimal encoding schemes for temporal onset asynchrony, including the effects of site of stimulation (e.g., single-finger versus two-finger displays) and frequency separation of the stimulus pair.

ACKNOWLEDGMENTS

This research was supported by Research Grant No. R01-DC00126 from the National Institute on Deafness and Other Communication Disorders, National Institutes of Health.

[1]Subject 4 entered the experiment at a later date. This subject's thresholds for T50 and I250 were within 3 dB of the average thresholds across S1, S2, and S3.

[2]The calculation of percent correct, d', and β, are based on the 2×2 confusion matrix $\left[\begin{smallmatrix} N_{11} & N_{12} \\ N_{21} & N_{22} \end{smallmatrix}\right]$ obtained from each experimental run. The two percent-correct scores are the two ratios: $N_{11}/(N_{11}+N_{12})$ and $N_{22}/(N_{21}+N_{22})$, respectively. The values of d' and β are also determined by these ratios. Thus, the two percent-correct scores of each run contain exactly the same information as d' and β.

[3]Yuan *et al.* (2004) obtained the distribution of the difference between the envelope-onset asynchronies (EOAs) of each of the eight pairs of voiced–voiceless consonants and their cumulative distributions by a simulation procedure. Each of these cumulative distributions was fit as a Gaussian distribution. Using the mean (M) and standard deviation (σ) of the fits for each distribution, signal-detection theory was applied to estimate performance of (1) an ideal observer with unlimited temporal-onset-order resolution and (2) the same observer with a limited temporal-onset-order resolution of 34 ms.

[4]Additional data were obtained on one subject to compare performance under trial-to-trial roving of amplitude and duration to that obtained with a fixed value of amplitude and duration (Parachuru, 2003). The roving condition was identical to that employed in the current experiment. The fixed condition employed a signal level of 35 dB SPL and a base duration of 400 ms (with equalization of the offset time of the two stimuli presented on a given trial). Threshold values in terms of SOA for 70%-correct were roughly 55 ms for the roving condition and 53 ms for the fixed condition.

Auer, E. T., and Bernstein, L. E. (**1996**). ''Lipreading supplemented by voice fundamental frequency: To what extent does the addition of voicing increase lexical uniqueness for the lipreader?,'' in *ICSLP'96 Proc.*, Philadelphia, PA, 3–6 October 1996, pp. 86–93.
Bachmann, T., Poder, E., and Luiga, I. (**2004**). ''Illusory reversal of temporal order: the bias to report a dimmer stimulus as the first,'' Vision Res. **44**, 241–246.
Durlach, N. I. (1968). *A Decision Model for Psychophysics*, Communication Biophysics Group, Research Laboratory of Electronics, MIT, MA.
Craig, J. C., and Baihua, X. (**1990**). ''Temporal order and tactile patterns,'' Percept. Psychophys. **47**, 22–34.
Erber, N. P. (**1974**). ''Visual perception of speech by deaf children—recent developments and continuing needs,'' J. Acoust. Soc. Am. **39**, 178–185.
Eberhardt, S. P., Bernstein, L. E., Barac-Cikoja, D., Coulter, D. C., and Jordan, J. (**1994**). ''Inducing dynamic haptic perception by the hand: System description and some results,'' *Proceedings of the ASME Dynamic Systems and Control Division*, Vol. 1, pp. 345–351.
Grant, K. W., Walden, B. E., and Seitz, P. F. (**1998**). ''Auditory-visual speech recognition by hearing-impaired subjects: Consonant recognition, sentence recognition, and auditory–visual integration,'' J. Acoust. Soc. Am. **103**, 2677–2690.
Green, D. M., and Swets, J. A. (**1966**). *Signal Detection Theory and Psychophysics* (Wiley, New York).
Heider, F., and Heider, G. M. (**1940**). ''An experimental investigation of lipreading,'' Psychol. Monogr. **52**, 124–133.
Hirsh, I. J. (**1959**). ''Auditory perception of temporal order,'' J. Acoust. Soc. Am. **31**, 759–767.
Hirsh, I. J., and Sherrick, C. E. (**1961**). ''Perceived order in different sensory modalities,'' J. Exp. Psychol. **62**, 423–432.
Johnson, K. O. (**1974**). ''Reconstruction of population response to a vibratory stimulus in quickly adapting mechanoreceptive afferent fiber population innervating glabrous skin of the monkey,'' J. Neurophysiol. **37**, 48–72.
Johnson, K. O, Yoshioka, T., and Vega-Bermudez, F. (**2000**). ''Tactile functions of mechanoreceptive afferents innervating the hand,'' J. Clin. Neurophysiol. **17**, 539–558.
Lisker, L., and Abramson, A. S. (**1964**). ''A cross-language study of voicing in initial stops: Acoustical measurements,'' Word **20**, 384–422.
Marks, L. E., Girvin, J. P., O'Keefe, M. D., Ning, P., Quest, D. O., Antunes, J. L., and Dobelle, W. H. (**1982**). ''Electrocutaneous stimulations 3: the perception of temporal-order,'' Percept. Psychophys. **32**, 537–541.
Parachuru, L. (**2003**). ''Temporal-order discrimination through the tactual sense: effects of variations in signal amplitude and duration,'' Undergraduate thesis paper, Massachusetts Institute of Technology, Cambridge, MA.
Pastore, R. E., Harris, L. B., and Kaplan, J. K. (**1982**). ''Temporal order identification: Some parameter dependencies,'' J. Acoust. Soc. Am. **71**, 430–436.
Pastore, R. E. (**1983**). ''Temporal order judgment of auditory stimulus offset,'' Percept. Psychophys. **33**, 54–62.
Scharf, B. (**1978**). *Loudness*, in *Handbook of Perception, Vol. IV.*, edited E. C. Carterette and M. P. Friedman (Academic, New York), pp. 187–242.
Sherrick, C. E. (**1964**). ''Effects of double simultaneous stimulation of skin,'' Am. J. Psychol. **77**, 42–53.
Sherrick, C. E. (**1970**). ''Temporal ordering of events in haptic space,'' IEEE Trans. Man-Machine Syst. **MMS-11**, 25–28.
Shore, D. I., Spry, E., and Spence, C. (**2002**). ''Confusing the mind by crossing the hands,'' Brain Res. Cognit. Brain Res. **14**, 153–163.
Taylor, B. (**1978**). ''Dimensional redundancy in the processing of vibrotactile temporal order,'' Ph.D. dissertation, Princeton University, Princeton, NJ.
Tan, H. Z. (**1996**). ''Information transmission with a multi-finger tactual display,'' Ph.D. dissertation, Massachusetts Institute of Technology, Cambridge, MA.
Tan, H. Z., and Rabinowitz, W. M. (**1996**). ''A new multi-finger tactual display,'' *Proceedings of the Dynamic Systems and Control Division*, DSC-Vol. 58, pp. 515–522.
Van Doren, C. L., Gescheider, G. A., and Verillo, R. T. (**1990**). ''Vibrotactile temporal gap detection as a function of age,'' J. Acoust. Soc. Am. **87**, 2201–2206.
Verrillo, R. T. (**1965**). ''Temporal summation in vibrotactile sensitivity,'' J. Acoust. Soc. Am. **37**, 843–846.
Walden, B. E., Prosek, R. A., Montgomery, A. A., Scherr, C. K., and Jones, C. J. (**1977**). ''Effects of training on visual recognition of consonants,'' J. Speech Hear. Res. **20**, 130–145.
Weisenberger, J. (**1994**). ''Vibrotactile temporal masking: Effects of multiple maskers,'' J. Acoust. Soc. Am. **95**, 2213–2220.
Wilent, W. B., and Contreras, D. (**2004**). ''Synaptic responses to whisker deflections in rat barrel cortex as a function of cortical layer and stimulus intensity,'' J. Neurosci. **24**, 3985–3998.
Yuan, H. F. (**2003**). ''Tactual display of consonant voicing to supplement lipreading,'' Ph.D. dissertation, Massachusetts Institute of Technology, Cambridge, MA.
Yuan, H. F., Reed, C. M., and Durlach, N. I. (**2004**). ''Envelope-onset asynchrony as a cue to voicing in initial English consonants,'' J. Acoust. Soc. Am. **116**, 3156–3167.
Zue, V. W. (**1976**). ''Acoustic characteristics of stop consonants: a controlled study,'' Ph.D. dissertation, Massachusetts Institute of Technology, Cambridge, MA.

Auditory perception of sound source velocity

Tomasz Kaczmarek[a)]
Institute of Acoustics, Adam Mickiewicz University, Umultowska 85, 61-114 Poznan, Poland

(Received 27 November 2003; revised 7 February 2005; accepted 7 February 2005)

In this study we investigate the perception of the velocity of linearly moving sound sources passing in front of a listener. The binaural simulation of motion used in two psychoacoustical experiments includes changes in the overall sound pressure level, the Doppler effect, and changes in interaural time differences. These changes are considered as cues for the perception of velocity. The present experiments are an extension of the experiments performed by Lutfi and Wang [J. Acoust. Soc. Am. **106**, 919–928 (1999)]. The results of Experiment I show that the differential velocity threshold is independent of the reference velocity (10, 20, 30, and 40 m/s), varying across listeners from 1.5 to 4.6 m/s. In Experiment II, a method based on the successive elimination of cues in compared pairs of signals was employed to estimate the weights of potential cues for velocity discrimination. The magnitudes of all underlying cues at thresholds are reported. The experimental results show the subject's preference for the Doppler cue and a weakest sensitivity to the cue related with interaural time differences. Finally, it was found that spatial differences in the source location at the endpoints of the motion trajectory are not a significant factor in the velocity discrimination task. © *2005 Acoustical Society of America.* [DOI: 10.1121/1.1880832]

PACS numbers: 43.66.−x, 43.66.Lj, 43.66.Qp, 43.66.Ba [AK] Pages: 3149–3156

I. INTRODUCTION

In most previous studies that have investigated the nature of motion perception mechanisms, circularly moving sound sources have been employed. Some of these studies are summarized by Grantham (1997) and Perrot and Strybel (1997). However, in many cases sound is generated by a linearly moving sound source that passes by the listener. The motion of the source in this case produces changes in frequency (due to the Doppler effect) and in the overall sound pressure level (due to the distance variations). Moreover, in these cases, binaural cues, such as interaural time differences (ITD) and interaural level differences (ILD) change in different ways to those cases involving circular motion.

One of the most important abilities in the detection of motion is the perception of source velocity. The discrimination of an angular velocity has been investigated in previous studies by Altman and Viskov (1977), Grantham (1986), and Carlile and Best (2002). In the first two studies, ILD and ITD were the only cues for velocity discrimination, while in the third study head-related transfer functions (HRTF) were also used to simulate motion. In the most recent study, Carlile and Best (2002) showed that for circularly moving targets, differential velocity thresholds were strongly affected by the construction of a presentation interval. Carlile and Best used three different stimulus conditions. In the first condition, both reference and comparison stimuli were centered on the midline, and the stimulus duration was randomized such that the distance traversed by the source was jittered and unrelated to its velocity. In the second condition, stimuli were still centered, but duration was held at a constant value. Thus, the faster stimulus traveled a greater distance and a spatial offset was available at the endpoints. In the last condition, stimuli were ''anchored'' on a common starting point, and hence the spatial offset at the endpoints was doubled for a given velocity pair. In this study, differential thresholds for velocity in the first condition were largest. In the second condition thresholds were reduced by about 25%, while in the last condition thresholds were reduced by about 50%. These results show that the differences in signals at the end points of the motion trajectory are a significant factor in the perception of an angular velocity. Such a relationship has not been directly tested with a linearly moving sound source.

According to the author's knowledge, only three studies by Rosenblum *et al.* (1987), Lutfi and Wang (1994) and Lutfi and Wang (1999) have investigated the perception of a linearly moving sound source. Only the last two studies investigated perception of the velocity. In the most recent study by Lutfi and Wang (1999), three cues to simulate motion over headphones were used: changes in ITD, changes in the overall sound pressure level, and changes in the frequency. They obtained the differential velocity thresholds for two values of the reference velocity: 10 and 50 m/s. The thresholds for these velocities were 2.4 and 3.1 m/s respectively.

The experiments presented in this paper are designed to be an extension of the study of the motion cues for linear trajectories, as begun by Lutfi and Wang (1999). Our primary goal in the present study is the measurement of the differential velocity thresholds for a range of reference velocities; reporting the magnitudes of the underlying cues at thresholds; and the investigation of the weighting of potential cues to velocity discrimination, employing a different technique from that used by Lutfi and Wang.

There are two main differences between Lutfi and Wang (1999) and the present study. The first difference relates to the stimulus presentation method. In particular, in the Lutfi

[a)]Address correspondence to Tomasz Kaczmarek, Institute of Acoustics, Adam Mickiewicz University, Ul. Umultowska 85, 61-114 Poznan, Poland. Telephone number: +48 61 8295105; fax number: +48 61 8295123; electronic mail: tomek@spl.ia.amu.edu.pl

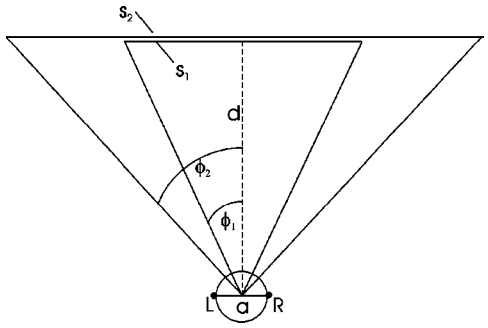

FIG. 1. Geometry of the source presentation pattern. S_1, S_2—trajectories of the reference and comparison source. The source passes the listener's head in the middle of the observation interval at the distance d. ϕ_1 and ϕ_2 are locations of the reference and comparison source at the endpoints of the motion trajectory respectively. The difference in length between S1 and S2 results from differences in velocities.

and Wang experiments the starting points of both reference and comparison stimuli were the same (with one exception: when the distance of the reference stimulus from the observer was randomized). Moreover, starting points were set in such a way that the reference stimulus always ended its trajectory at the same position (45° to the right), regardless of the reference velocity. This construction of the reference system provided the same change in total angular displacement, for a given value of the velocity discrimination threshold, independent of the reference velocity. In this reference system, the end point of the source trajectory provided the same differences in intensity and ITD regardless of the reference velocity. There were no differences in these cues at the start point. Moreover, these differences at the end point were sufficiently large to be potentially effective cues in the velocity discrimination task. Differences in the overall sound pressure level at the end point of the trajectory were approximately 3 dB and 110 μs for ITD. These values significantly exceed the just-noticeable differences (JND) in sound pressure level (which is 1 dB, according to Jesteadt *et al.*, 1977), and in ITD (which is approximately 30 μs for the 200 Hz tone, according to Klumpp and Eady, 1956). The differences in frequency due to the Doppler effect were available at both end points of the sound source trajectory, although the differences at the end point of the trajectory were larger and dependent on a reference velocity. For both reference velocities investigated by Lutfi and Wang, differences in frequency at the end points were 0.9% and 2.3% for velocities 10 and 50 m/s, respectively. These values significantly exceeded the just noticeable differences in frequency of 0.3% (according to Wier *et al.*, 1977). The stimulus condition used in the Lutfi and Wang (1999) study is similar to the condition described as condition 3 by Carlile and Best (2002) (in the case of circular motion).

In the present study, a presentation method, similar to the Carlile and Best second condition was used. A stimulus condition such as this leads to the minimization of differences in cues at the end points of the presentation interval. The geometry of such a presentation interval is presented in Fig. 1.

The point of closest approach is always in the middle of the observation interval, for both a reference and a comparison sound source. For such a construction of the observation interval, locations of the reference (ϕ_1) and comparison (ϕ_2) sources at the end points of the motion trajectory can be calculated as

$$\phi_1 = \arctan\left(\frac{\nu_1 \cdot t}{2 \cdot d}\right), \quad \phi_2 = \arctan\left(\frac{\nu_2 \cdot t}{2 \cdot d}\right), \tag{1}$$

where ν_1 and ν_2 are velocities of the reference and comparison sources, respectively, d is the distance from the trajectory, and t is total duration of the observation interval. For the observation conditions defined above, the difference in the source location at the end points of the motion trajectory $\Delta\phi$ is

$$\Delta\phi = \phi_2 - \phi_1. \tag{2}$$

If one denotes the differential velocity thresholds as $\Delta\nu$, then ν_2 in Eq. (1) can be replaced by $\nu_1 + \Delta\nu$. Let us also assume that duration of the motion (t) is constant. In a situation with increasing reference velocity, constant $\Delta\nu$ will correspond to a decreasing location shift at the end points of the trajectory. A decreasing $\Delta\phi$ value means that differences in total angular displacement will also decrease. With regard to the model of a moving sound source described in the next section, it can be also shown that with increasing reference velocity the differences in sound pressure levels at the end points of the trajectory also decrease. One can expect an increase of thresholds with the reference velocity, if the differences in cues at the trajectory end points are a significant factor in perception of the velocity of a linearly moving sound source.

The difference in the time courses of three acoustic cues calculated for the stimuli presentation method used in Lutfi and Wang (1999) and the present study are shown in Fig. 2. In this figure, time courses of the overall sound pressure level, frequency, and ITD are plotted for a reference stimulus that moves with a velocity of 10 m/s. For this particular reference velocity, time courses of all cues for the reference source are identical (for both presentation methods) and are plotted as a single solid curve. For comparison stimulus (moving with a velocity of 13 m/s), time courses of cues corresponding to Lutfi and Wang conditions are plotted as a dotted line. Thus, the solid and dotted curves represent a situation where the starting points of both sources were the same. Finally, the dashed curves represent the conditions used in the present study. Thus, the solid and dashed curves represent a situation where the sources were centered at the midline. This 3 m/s difference in velocity refers to the previously obtained threshold for velocity by Lutfi and Wang (1999).

The second difference between these two studies lies in the technique of investigating the weighting of the potential cues to the velocity discrimination. Lutfi and Wang measured relative weights by adding some ambiguities to cues in such a way that each cue indicated a slightly different velocity. Then "the weights given to each of the three acoustic cues were estimated from correlations of the listeners responses with these small independent perturbations imposed on cues from trial to trial" (cited from Lutfi and Wang, 1999). The

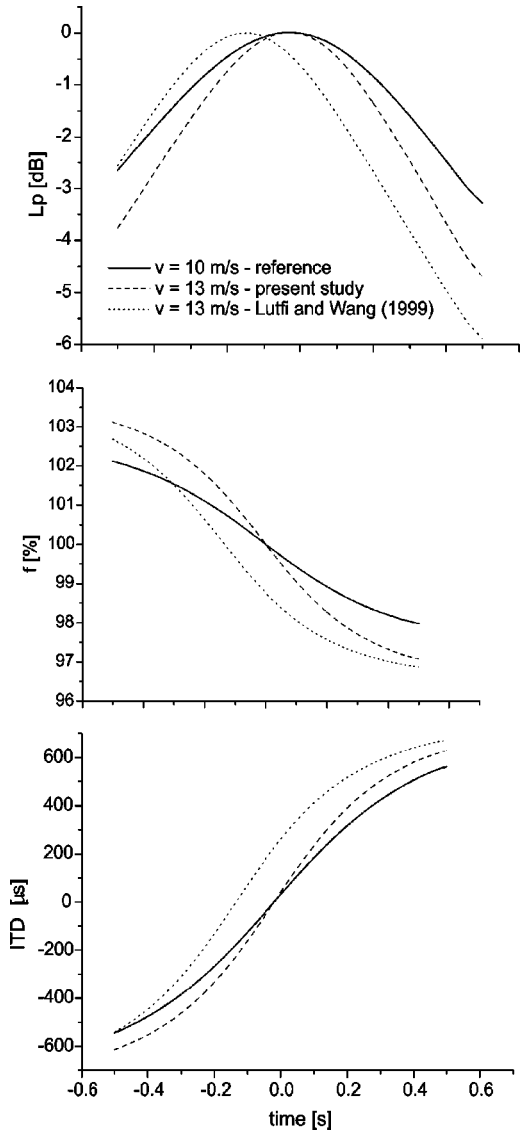

FIG. 2. Time patterns of sound pressure level, frequency and ITD due to the source motion. The solid curve corresponds to a reference velocity of 10 m/s. The dotted curve represents the comparison velocity 13 m/s and corresponds to Lutfi and Wang conditions. Finally, the dashed curves also represent the comparison velocity of 13 m/s, but in this case represents conditions used in the present study.

most preferred cue in the perception of velocity was the Doppler effect. The second cue was the overall sound pressure level. ITD was a less weighted cue.

The method proposed in the present study is based on the successive elimination of cues from compared pairs of signals. A given cue is considered as being eliminated when it corresponds to the same velocity in both compared signals. Cue weights can be obtained by a comparison of the differential velocity thresholds for the reference condition in which all cues are available with conditions in which a different cue (or cues) is eliminated. When only one cue indicates a different velocity, the weight of this particular cue is considered to be inversely proportional to the increment in a difference velocity threshold. This method will be described in detail later in the paper. The main advantage of this method is the possibility of relating the change in the velocity threshold to a single cue magnitude calculated for that

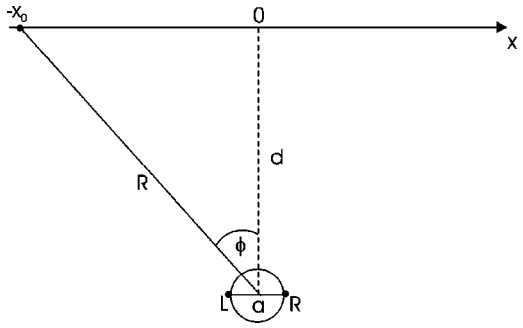

FIG. 3. Geometry of motion. *L*, *R*—left and right ear, *a*—diameter of the head, *d*—distance between head and motion trajectory, v—velocity of sound source, x_0—starting point of the source. ϕ describes the angular location of the source.

threshold. This magnitude can be then related to the just noticeable differences for that cue.

In the present study, two psychoacoustic experiments were performed. In Experiment I the differential velocity thresholds for four reference velocities were obtained. In Experiment II the differential velocity thresholds were assessed at different cue conditions. In both experiments listeners assessed differences in the velocity of a moving sound source based on changes in the overall sound pressure level, changes in frequency, and in ITD. As shown in Fig. 2 (solid and dashed curves), maximal differences in these parameters occur at the end points of the time interval. These differences can be used as three cues to describe changes in the perceived velocity of the moving sound source. The first is related to maximal differences in the overall sound pressure level (denoted as ΔL), the second cue is connected with maximal differences in frequencies (denoted as a Δf) and the third with ITD (denoted as a ΔITD). Having defined the cues, one can approach the cue analyses for different reference velocities.

II. MODEL OF A MOVING SOUND SOURCE

The simulation used in the present study assumes a spherical model of the head. The motion of the sound source along a straight line, placed 5 m from the listener's head, is considered. A free field is assumed. The convection effect described by Morse and Ingard (1986) is used in the simulation of the sound field. The air absorption and the interaural level difference (ILD) are not taken into account. According to Kuhn and Guernsey (1983), the ILD can be neglected for stimuli with frequencies below 1600 Hz. In the present study, the synthesis method proposed by Jenison *et al.* (1998) is used to simulate the motion of the sound source. Making use of the above assumptions and the geometry of motion (Fig. 3), the parameters of an acoustical wave at a point on either side of a sphere can be obtained. Changes in the overall sound pressure level, frequency, and ITD can be calculated. These changes are potential cues for the detection of changes in the parameters of motion.

For a nonmoving sound source emitting a sinusoidal wave, sound pressure at the receiver located in the middle of the head (see Fig. 3) can be defined as follows:

$$p(t) = A \sin(\omega(t)), \tag{3}$$

where A is amplitude and $\omega(t)$ is the instantaneous phase. If we assume that the source is of a frequency f, the instantaneous phase $\omega(t)$ can be then expressed as follows:

$$\omega(t)=2\pi ft. \tag{4}$$

When we consider a source motion along a linear trajectory (Fig. 3), then A in Eq. (3) and f in Eq. (4) will vary over time. One can easily find functions that describe their temporal variations based on geometrical relations. Taking into account the convection effect described by Morse and Ingard (1986) for a point source, the changes in amplitude over time can be approximated as follows:

$$A(t)=\frac{\eta}{R(t)}\left[1+\frac{\nu}{c}\sin(\phi(t))\right]^{-2}, \tag{5}$$

where η is a constant related to the acoustical power of the source and the air impedance, c is the speed of the sound, ν is the velocity of the sound source, $R(t)$ is the instantaneous distance between the source and the center of the head, and $\phi(t)$ is the instantaneous angle defined in Fig. 3. The expression in brackets approximates changes in the amplitude due to the convection effect (for more details see Morse and Ingard, 1986). The Doppler frequency changes can be described as follows:

$$f(t)=\frac{f_0}{1+\frac{\nu}{c}\sin(\phi(t))}, \tag{6}$$

where f_0 is the nominal frequency of the source. Regarding Eq. (3), instantaneous frequency can be also defined as

$$f(t)=\frac{1}{2\pi}\frac{d\omega(t)}{dt}. \tag{7}$$

By substituting Eq. (6) to Eq. (7), integration of Eq. (7) yields the instantaneous phase $\omega(t)$ as

$$\omega(t)=2\pi f_0\int\frac{1}{1+\frac{\nu}{c}\sin(\phi(t))}dt. \tag{8}$$

One can define acoustical pressure at each of the two ears (in the present model represented by points on either side of the sphere—see Fig. 3) by adding the phase shifts related to interaural time difference (ITD) between the left and right ear. According to Kuhn (1977), ITD can be approximated by the following function:

$$\mathrm{ITD}(t)=\frac{3a}{c}\sin(\phi(t)), \tag{9}$$

where a is the average radius of the head (8.5 cm). Using Eq. (6) and Eq. (9) phase shift between the ears can be defined as follows:

$$\omega_{\mathrm{ITD}}(t)=2\pi f(t)\mathrm{ITD}(t). \tag{10}$$

Thus, instantaneous sound pressure at points on either side of the sphere (which represent left and right ear), $p_L(t)$ and $p_R(t)$, is given by

$$\begin{aligned} p_L(t)&=A(t)\cdot\sin\left(\omega(t)-\frac{\omega_{\mathrm{ITD}}(t)}{2}\right),\\ p_R(t)&=A(t)\cdot\sin\left(\omega(t)+\frac{\omega_{\mathrm{ITD}}(t)}{2}\right). \end{aligned} \tag{11}$$

The time courses of $A(t)$, $f(t)$, and $\mathrm{ITD}(t)$ for the sound sources traveling at velocities of 10 (solid curve) and 13 m/s (dashed curve) are shown in Fig. 2.

III. EXPERIMENT I

In Experiment I, differential thresholds for a change in velocity are assessed for four reference velocities of a standard sound source: 10, 20, 30, and 40 m/s.

A. Stimuli and equipment

The stimuli in Experiment I are binaural signals simulating the passing of a moving sound source according to the model described in the previous section. The simulation was carried out in a Matlab environment. A sound source emitted a 200 Hz sinusoidal wave (in the experiments by Lutfi and Wang, 1999, the source signal consisted of the first five harmonics of a 100 Hz tone). The distance from the trajectory of motion to the center of the listener's head was set to 5 m, as in the Lutfi and Wang experiments. Each stimulus had duration of 1 s, as in the Lutfi and Wang study. The point of closest approach was always in the middle of the presentation interval ($t=0.5$ s). Since duration was constant, for 10 m/s the standard source moved along a trajectory of 10 m (moving from 5 m left to 5 m right or in the opposite direction) while for 40 m/s it moved 40 m (moving from 20 m left to 20 m right or in the opposite direction).

The direction of motion between different pairs was random so as to avoid any adaptation to stimuli moving repeatedly in one direction (see Grantham, 1998). However, the direction within a compared pair (reference and comparison stimuli) was the same in all experiments. In the Lutfi and Wang experiments the stimulus always moved from left to right. The maximum overall sound pressure level at the point of closest approach was 80 dB. The level was calibrated by using a PEQ IV.1 programmable equalizer from HEAD acoustics. The experiments were controlled by computer. Stimuli were sent from a PC equipped with an RME DIGI 96/8 PAD sound card to the PEQ IV.1 through an AES/EBU digital output. D/A conversion was made by the PEQ IV.1 with 16 bits resolution and 44 100 Hz sampling frequency. The PEQ IV.1 served also as a headphone amplifier. The stimuli were presented via Sennheiser HD600 headphones, which were individually calibrated by HEAD acoustics. Stimuli were presented to the listener in a specially designed sound attenuated chamber. The computer was placed outside the chamber during the experimental sessions. Only the computer screen and mouse were placed inside to enable the collection of the subject's responses.

B. Subjects

Eight listeners participated in Experiment I, five females (JW,MC,JK,PP,ZL) and three males (AP,KK,PM). The listeners were between 20–25 years old. All were students of the

Faculty of Physics, Adam Mickiewicz University. All listeners qualified as having normal hearing (normal hearing was defined as audiometric threshold of 20 dB HL or better for the frequency range from 250 to 8000 Hz, ANSI, 1996) and were paid for their participation. Listeners had no previous experience in motion detection and source localization experiments.

C. Procedure

The thresholds were obtained by using a two-down, one-up adaptive procedure. A two alternative forced choice procedure (2AFC) was used. The thresholds estimated a 70.7% correct discrimination level. The initial velocity of the comparison stimulus was 30 m/s higher than the standard velocity. The velocity of the comparison stimulus was decreased after two successive correct responses, and increased after one incorrect response. Multiplicative steps were used to track the threshold. Initially a big step was used, equal to 1.5, and after reaching the second reversal point, the step value was changed to 1.25. Each run was continued until 12 reversal points were reached. The first four reversals from each run were not taken into account. The run length was no longer than 6 min. Typically, five runs in one day were carried out with rest intervals. Finally, each threshold was calculated as a mean of four runs. A standard and a target stimulus were presented in pairs. Subjects were asked to choose which of the two sound sources in a pair moved faster.

D. Results and discussion

The results of Experiment I are the differential velocity thresholds obtained for four reference velocities of a sound source, 10, 20, 30, and 40 m/s, respectively. Statistically significant differences between subjects were found [$F(7,128) = 40.4$; $p < 0.000\,01$]. The individual results obtained for each subject are shown in Fig. 4. The dotted lines in the Fig. 4 represent a range of thresholds obtained by Lutfi and Wang (1999).

There are no statistically significant differences between different velocities [$F(3,21) = 1.7$; $p > 0.2$] hence the average threshold for each subject could be calculated. The average thresholds for eight listeners are also presented in Fig. 4.

The three acoustic cues for motion (ΔL, Δf, and ΔITD) were calculated for each obtained threshold for a given velocity (see Tables I, II, and III). ΔL was calculated only at the end point of the source trajectory, because ΔL at the start point was between 85% and 88% of ΔL at the end point in all cases.

The differences in source locations at the end point of motion trajectory—$\Delta\phi$, calculated for all thresholds obtained in Experiment I are shown in Fig. 5.

The results of Experiment I show that differential velocity thresholds are independent of the reference velocity in the range of 10–40 m/s. The mean value of the threshold obtained in this experiment varies across subjects from 1.5 to 4.6 m/s. This result agrees with the values reported in earlier studies by Lutfi and Wang (1999) for velocities 10 and 50 m/s (2.4–3.1 m/s). When the thresholds obtained in Experiment I are expressed as differences in stimulus location at the end points of the motion trajectory, they are different for each velocity (see Fig. 5). These differences generally decrease with increasing velocity and for velocities above 10 m/s are smaller than 4°. A comparison of the end point differences with those obtained by Lutfi and Wang (1999), which were within the range of 11° to 14°, suggests that these differences do not provide any additional cues for the perception of velocity. This suggests that perception of the end point displacement angle is not a factor in the discrimination of the velocity of the linearly moving sources.

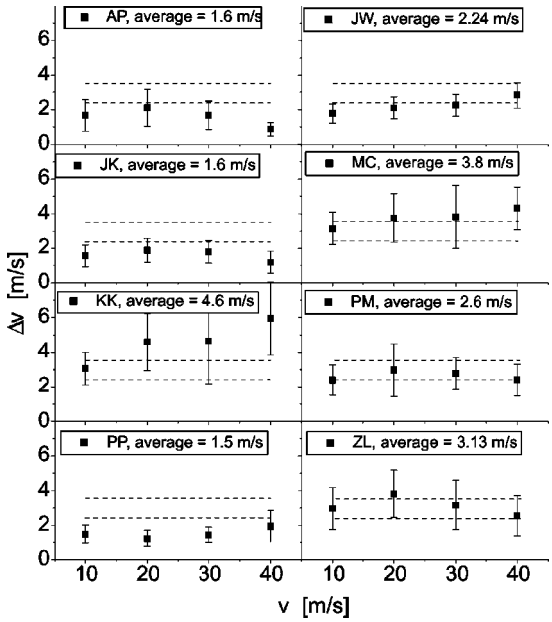

FIG. 4. Results of Experiment I. Differential velocity thresholds obtained for 8 subjects and four velocity values. Each data point is an arithmetic mean of 4 runs and is plotted with its standard deviation. Horizontal dotted lines represent the range of thresholds from the Lutfi and Wang (1999) experiments.

The analysis of cues for velocity calculated on the basis of the results of Experiment I (Tables I–III) did not allow the weights of each cue to be determined. For example, the Δf value was always above the JND threshold for the discrimination of frequency (which is 0.3%, according to Wier *et al.*, 1977). The ΔL was about the JND value for discrimination

TABLE I. Differences in sound pressure levels at the end points of the sound source trajectory, ΔL, in dB, calculated for thresholds obtained in Experiment I. The average values across all listeners and their standard deviations are shown in the last two rows.

	ΔL [dB]			
Subject	v=10 m/s	v=20 m/s	v=30 m/s	v=40 m/s
A.P.	0.8	0.8	0.5	0.2
J.W.	0.8	0.8	0.7	0.7
J.K.	0.7	0.7	0.5	0.3
M.C.	1.5	1.4	1.1	1.0
K.K.	1.4	1.7	1.3	1.4
P.M.	1.1	1.1	0.8	0.6
P.P.	0.7	0.5	0.4	0.5
Z.L.	1.4	1.4	0.9	0.6
Average	1.1	1.1	0.8	0.7
S.D.	0.3	0.4	0.3	0.4

TABLE II. Differences in frequency at the end points of the sound source trajectory, Δf, in %, calculated for thresholds obtained in Experiment I. The average values across all listeners and their standard deviations are shown in the last two rows.

	Δf (%)			
Subject	ν=10 m/s	ν=20 m/s	ν=30 m/s	ν=40 m/s
A.P.	0.40	0.50	0.39	0.20
J.W.	0.41	0.50	0.51	0.64
J.K.	0.37	0.44	0.42	0.27
M.C.	0.75	0.89	0.88	0.98
K.K.	0.73	1.08	1.06	1.34
P.M.	0.57	0.70	0.64	0.55
P.P.	0.36	0.30	0.34	0.44
Z.L.	0.72	0.90	0.73	0.58
Average	0.5	0.7	0.6	0.6
S.D.	0.2	0.3	0.3	0.4

of a sound pressure level (which is 1 dB, according to Jesteadt *et al.*, 1977). The ΔITD value was below the JND (which is approximately 30 μs for 200 Hz, according to Klumpp and Eady, 1956) for velocities above 10 m/s. Based on the results of Experiment I, listeners could potentially use both cues Δf and ΔL in the velocity discrimination task.

IV. EXPERIMENT II

This experiment was designed to estimate the weights of all cues (ΔL, Δf, and ΔITD). As mentioned in the Introduction, the method presented in this paper is different from that used earlier by Lutfi and Wang (1999). In the pilot experiment, single cues were eliminated from signals to estimate the differential velocity thresholds in the absence of a given cue. The thresholds obtained in this way were expected to be proportional to the weights given to the eliminated cue. However, eliminating only one cue did not allow us to estimate the complete cue weight pattern. The results of this pilot experiment showed the dominant role of the Doppler effect cue (Δf). However, it was not possible to estimate the relative weights given to ΔL and ΔITD, because in each experimental condition these cues were utilized together with the most dominant cue—Δf. This problem was eliminated by leaving only one cue in the compared pair of stimuli during each experimental condition in Experiment II.

TABLE III. Differences in ITD at the end points of sound source trajectory, ΔITD, in μs, calculated for thresholds obtained in Experiment I for each subject. The average values across all listeners and their standard deviations are shown in the last two rows.

	ΔITD [μs]			
Subject	ν=10 m/s	ν=20 m/s	ν=30 m/s	ν=40 m/s
A.P.	30.74	9.83	2.89	0.71
J.W.	32.50	9.79	3.79	2.15
J.K.	28.94	8.79	3.08	0.96
M.C.	52.16	16.04	6.03	3.14
K.K.	51.11	18.73	7.10	4.10
P.M.	41.95	13.20	4.56	1.86
P.P.	27.94	6.11	2.55	1.53
Z.L.	50.05	16.24	5.13	1.97
Average	39.4	12.3	4.4	2.1
S.D.	10.6	4.4	1.6	1.1

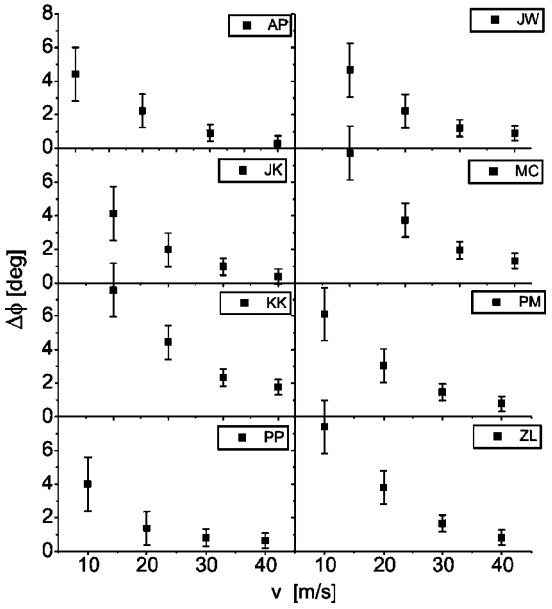

FIG. 5. Differences in source positions at the endpoints of motion trajectory calculated for thresholds obtained in Experiment I for 8 listeners. Each data point is an arithmetic mean of 4 differences and is plotted with its standard deviation.

A. Cue elimination method

Let us assume that two sound sources move with the velocities ν_1 and ν_2. They emit a sine wave with the frequency f (in this example only the left ear will be regarded). The instantaneous pressure at the left ear for these two sources is as follows [Eq. (11)],

$$p_{L1}(t)=A(t,\nu_1)\cdot\sin\left(\omega(t,\nu_1)-\frac{\omega_{\mathrm{ITD}}(t,\nu_1)}{2}\right),$$
$$p_{L2}(t)=A(t,\nu_2)\cdot\sin\left(\omega(t,\nu_2)-\frac{\omega_{\mathrm{ITD}}(t,\nu_2)}{2}\right). \quad (12)$$

Parameters A, ω and ω_{ITD} are time dependent, but they also depend on velocity (Fig. 2). The main idea of this method is to eliminate successively the cues in the compared pairs of stimuli with different velocities. Let us consider the situation when only the cue ΔL is available. In this case, the frequency and interaural time differences for both sources will change in the same way, as presented by Eq. (13):

$$p_{L1}(t)=A(t,\nu_1)\cdot\sin\left(\omega(t,\nu_1)-\frac{\omega_{\mathrm{ITD}}(t,\nu_1)}{2}\right),$$
$$p_{L2}(t)=A(t,\nu_2)\cdot\sin\left(\omega(t,\nu_1)-\frac{\omega_{\mathrm{ITD}}(t,\nu_1)}{2}\right). \quad (13)$$

This means that Δf and ΔITD are zero and these cues are not available to the listener. Only the cue related to the changes in the intensity indicates different velocity. By manipulating the signals in the above way, one can estimate the thresholds obtained in four conditions. Under the first condition all cues are available. Under the three other conditions only one cue is available (ΔL, Δf, and ΔITD). The values of thresholds obtained in this way are taken to be inversely proportional to the weights given to the actually available cue.

TABLE IV. Thresholds $\Delta\nu$ obtained in four conditions employed in Experiment II. All cues were calculated for these thresholds. In the last two rows, average values with their standard deviations are presented.

	all cues available				only ΔL		only Δf		only ΔITD	
listener \Cond.	$\Delta\nu$ [m/s]	ΔL [dB]	Δf [%]	ΔITD [μs]	$\Delta\nu$ [m/s]	ΔL [dB]	$\Delta\nu$ [m/s]	Δf [%]	$\Delta\nu$ [m/s]	ΔITD [μs]
EJ	2.1	0.9	0.6	4.1	5.9	2.4	2.4	0.7	21.5	18.0
GH	3.4	1.5	1.0	6.2	7.0	2.8	3.3	1.0	21.6	18.0
HH	3.3	1.4	1.0	6.0	7.1	2.9	4.4	1.3	10.3	13.1
MW	2.4	1	0.7	4.6	6.0	2.5	2.1	0.6	19.7	17.5
SH	2.8	1.2	0.9	5.3	7.4	3.0	2.8	0.8	20.9	17.8
DJ	2.9	1.3	0.9	5.4	6.2	2.5	3.6	1.1	13.5	15.0
JK	2.5	1.1	0.8	4.8	6.8	2.7	3.5	1.1	20.6	17.8
CJ	3.4	1.5	1.0	6.2	5.8	2.4	3.5	1.1	18.9	17.2
JD	2.7	1.2	0.8	5.1	6.8	2.7	3.4	1.0	21.1	17.9
Average	2.8	1.2	0.9	5.3	6.6	2.7	3.2	1.0	18.7	16.9
S.D.	0.5	0.2	0.1	0.7	0.6	0.2	0.7	0.2	4.0	1.7

B. Stimuli

In Experiment II, the simulated sound source emitted a polychromic signal with a fundamental frequency of 43 Hz and its harmonics up to 1634 Hz. The duration of the stimuli was 2 s. The point of the closest approach was in the middle of the presentation interval ($t=1$ s). Thus, the standard source traversed a path of 40 m with a velocity of 20 m/s (moving from 20 m left to 20 m right or in the opposite direction). Other stimulus presentation details, as well as procedure details, were the same as in Experiment I.

C. Subjects

Nine listeners participated in Experiment II: three females (CJ,JK,JD) and six males (DJ,EJ,GH,HH,MW,SH). The listeners were between 20–25 years old. All were students of the Faculty of Physics, Adam Mickiewicz University. All listeners qualified as having normal hearing (normal hearing was defined as audiometric threshold of 20 dB HL or better for the frequency range from 250 to 8000 Hz; ANSI, 1996) and were paid for their participation. The listeners had no previous experience in motion detection and source localization experiments.

D. Results and discussion

In Experiment II, differential velocity thresholds were obtained only for the reference velocity of 20 m/s, under four experimental conditions. Under the first condition all cues were available. Under each of the other conditions only one cue was available. The acoustic cues calculated for each threshold are shown in Table IV.

A statistical analysis showed significant differences between subjects [$F(8,27)=2.89$; $p<0.018$]. However, this difference was minimal. Highly significant differences between different conditions were found [$F(3,81)=451.4$; $p<0.000\,01$]. The post-hoc Scheffe test performed on these data showed significant differences between all conditions ($p<0.01$), with one exception. The difference between the condition where all cues were available, and the condition where only the Doppler effect was available (only Δf) is statistically insignificant ($p=0.93$).

The results of Experiment II allow the significance of each cue to be classified. In this experiment the lowest threshold values were obtained with the single cue related to the Doppler effect. Thresholds were the highest when only ITD was available. This means that ITD is the least important cue in the perception of a linearly moving sound source. However, it is worth mentioning that with the Doppler effect the differences in frequencies at the end points of the motion trajectory (see Δf in Table IV) are about 1%, which exceed the threshold by about three times (JND for frequency is 0.3%, according to Wier *et al.*, 1977). This value is very similar to the value of Δf in the reference condition (where all cues were available). As far as the ΔL cue is considered as the only available cue, one can find that ΔL is about 2.7 dB (Table IV). This value is also significantly greater than the JND value for perception of the sound pressure level variation (1 dB, according to Jesteadt *et al.*, 1977). Moreover, this value is over 125% higher than the ΔL value for the reference condition. Under the last condition, where only ITD was available, ΔITD was about 16.9 μs. This value is somewhat lower than the JND value for the perception of ITD (30 μs for 200 Hz, according to Klumpp and Eady, 1956). The corresponding average difference in the angular displacement at the end points is about 6.6°. However, any direct comparisons with studies involving circular motion are very difficult, and have to be made with special care. This value is in reasonable agreement with the results obtained by Carlile and Best (2002) where the source offset at the end points calculated for the threshold was in the range of 4°–13°, dependent on the subject. Comparing the results of the reference condition with the results of Experiment I, for the reference velocity 20 m/s, no statistical difference was found [$F(1,15)=0.004$; $p>0.9$] between these two experiments. The different spectrum of stimuli used in both experiments, as well as the different motion duration, did not affect performance.

V. CONCLUSIONS

(1) Human listeners show constant velocity discrimination thresholds for a wide range of the comparison source velocities.
(2) Information provided by the end points of linear motion trajectory are not significant cues in the velocity perception of a linearly moving sound source.
(3) The current cue weighting method, based on successive cue elimination, resulted in a cue weight pattern similar to that obtained by the correlational method used by Lutfi and Wang (1999). In the method proposed here it was possible to refer velocity thresholds to the single cue magnitude, and then analyze it by comparing it with the JND for the quantity related to this cue.
(4) The results suggests that cues provided by linear trajectories (Doppler shift and changes in the overall sound pressure level) receive greater weight than binaural cues (represented here by ITD).

ACKNOWLEDGMENTS

I am grateful to Professor Wesley Grantham, Professor Armin Kohlrausch, and an anonymous reviewer for the many valuable suggestions and insights they provided on earlier versions of this paper. I gratefully acknowledge the help of Professor Anna Preis.

ANSI (**1996**). ANSI S3.6-1996, *Specifications for Audiometers* (American National Standards Institute, New York).

Altman, J. A., and Viskov, D. V. (**1977**). ''Discrimination of perceived movement velocity for fused auditory image in dichotic simulation,'' J. Acoust. Soc. Am. **61**, 816–819.

Carlile, S., and Best, C. (**2002**). ''Discrimination of sound velocity in human listeners,'' J. Acoust. Soc. Am. **111**, 1026–1035.

Grantham, D. W. (**1986**). ''Detection and discrimination of simulated motion of auditory targets in the horizontal plane,'' J. Acoust. Soc. Am. **79**, 1939–1949.

Grantham, D. W. (**1997**). ''Auditory motion perception,'' *Binaural and Spatial Hearing*, edited by R. H. Gilkey and T. R. Andersen (Lawrence Erlbaum, Mahwah, NJ), pp. 295–313.

Grantham, D. W. (**1998**). ''Auditory motion aftereffects in horizontal plane: The effect of spectral region, spatial sector, and spatial richness,'' Acust. Acta Acust. **84**, 337–347.

Jenison, R. L., Nelon, M. F., Reale, R. A., and Brugge, J. F. (**1998**). ''Synthesis of virtual motion in 3D auditory space,'' IEEE Eng. Med. Biol. Mag. **20**, 1096–1100.

Jesteadt, W., Wier, C. C., and Green, D. M. (**1977**). ''Intensity discrimination as a function of frequency and sensation level,'' J. Acoust. Soc. Am. **61**, 169–177.

Klumpp, R. G., and Eady, H. R. (**1956**). ''Some measurements of interaural time difference thresholds,'' J. Acoust. Soc. Am. **28**, 859–860.

Kuhn, G. F. (**1977**). ''Model of the interaural time differences in the azimuthal plane,'' J. Acoust. Soc. Am. **62**, 157–167.

Kuhn, G. F., and Guernsey, R. M. (**1983**). ''Sound pressure distribution about the human head and torso,'' J. Acoust. Soc. Am. **73**, 95–105.

Lutfi, R. A., and Wang, W. (**1994**). ''Thresholds for detection of a change in displacement, velocity, and acceleration of a synthesized sound-emitting source,'' J. Acoust. Soc. Am. **95**, 2897.

Lutfi, R. A., and Wang, W. (**1999**). ''Correlational analisis of cues for the discrimination of auditory motion,'' J. Acoust. Soc. Am. **106**, 919–928.

Morse, P. M., and Ingard, K. U. (**1986**). *Theoretical Acoustics* (Princeton University Press, Princeton, NJ), pp. 718–726.

Perrot, D. R., and Strybel, T. Z. (**1997**). ''Some observations regarding motion without direction,'' *Binaural and Spatial Hearing*, edited by R. H. Gilkey and T. R. Andersen (Lawrence Erlbaum, Mahwah, NJ), pp. 275–294.

Rosenblum, L. D., Carello, C., and Pastore, R. E. (**1987**). ''Relative effectiveness of three stimulus variables for location a moving sound source,'' Perception **16**, 175–186.

Wier, C. C., Jesteadt, W., and Green, D. M. (**1977**). ''Frequency discrimination as a function of frequency and sensation level,'' J. Acoust. Soc. Am. **61**, 178–184.

Sensory and nonsensory influences on children's performance of dichotic pitch perception tasks

Veronica T. Edwards, Deborah E. Giaschi,[a] and Pauline Low
Department of Ophthalmology, University of British Columbia, Vancouver, British Columbia, V6H 3V4, Canada

Dorothy Edgell
Department of Psychology, University of Victoria, and Queen Alexandra Centre for Children's Health, Victoria, British Columbia, V8N 1V7, Canada

(Received 12 December 2003; revised 22 December 2004; accepted 5 January 2005)

Dichotic pitch perception reflects the auditory system's use of binaural cues to perceptually separate different sound sources and to determine the spatial location of sounds. Several studies were conducted to identify factors that influence children's dichotic pitch perception thresholds. An initial study of school children revealed an age-related improvement in thresholds for lateralizing dichotic pitch tones. In subsequent studies potential sensory and nonsensory limitations on young children's performance of dichotic pitch lateralization tasks were examined. A training study showed that with sufficient practice, young children lateralize dichotic pitch stimuli as well as adults, indicating an age difference in perceptual learning of the lateralization task. Changing the task requirements so that young children made a judgment about the pitch of dichotic pitch tones, rather than the spatial location of the tones, also resulted in significantly better thresholds. These findings indicate that nonsensory factors limit young children's performance of dichotic pitch tasks. © *2005 Acoustical Society of America.* [DOI: 10.1121/1.1861599]

PACS numbers: 43.66.−x, 43.66.Pn, 43.66.Qp [AK] Pages: 3157–3164

I. INTRODUCTION

Knowledge of the development of auditory skills is useful for understanding mature auditory function and for identifying auditory impairments during development. The studies reported in this paper were designed to identify factors that influence children's thresholds on dichotic pitch (DP) perception tests. Children's DP perception is of particular interest because of recent evidence that some children with developmental dyslexia have poor DP perception (Dougherty *et al.*, 1998; Edwards *et al.*, 2004).

DP perception, in general, arises when white noise is dichotically presented to both ears with a particular interaural phase relationship. The stimulus at each ear gives no pitch sensation, but disparities between the two ears with binaural presentation lead to the perception of pitch. Historically, dichotic pitch has been studied with a variety of stimuli including: Huggins pitch (Bilsen, 1976; Cramer and Huggins, 1958), Fourcin pitch (Fourcin, 1970), dichotic repetition pitch (Bilsen, 1972), and binaural-edge pitch (Klein and Hartmann, 1981). The stimulus used in this paper is a modification of the multiple-Huggins pitch (Bilsen, 1976; Cramer and Huggins, 1958) that uses interaural time shifts, rather than phase shifts, of a narrow-frequency noise band (Dougherty *et al.*, 1998).

A sound that is to the left of a listener reaches the left ear first and is louder in the left than the right ear. In addition, as the sound source continues to produce sound waves, each crest of these waves will reach the left ear before the right ear. For frequencies with wavelengths greater than the distance between the ears (i.e., below about 1400 Hz), this ongoing interaural time difference (ITD) provides useful cues for localizing sounds. The ongoing ITD also provides cues for segregating sound sources and can be used to create dichotic pitch. When the dichotic noise sources are binaurally fused, the diotic background noise with an ITD of zero appears to originate from the middle of the head. The narrow noise bands with nonzero ITDs can be perceptually segregated from the background noise and are perceived as tones. Each tone is lateralized to a spatial location that depends on its exact ITD value.

The research reported in this paper began with a study of DP perception in 5–16-year-old children (study 1). Thresholds for lateralizing DP tones (i.e., for localizing the tones within the head) were extremely elevated in the youngest age groups and became lower as age increased. There are a number of potential causes of changes in auditory sensitivity as a function of age. For example, auditory thresholds of young children may be affected by a sensory factor, such as immature development of auditory pathways or immature neural processing. Alternatively, immature thresholds might result from age-related differences in nonsensory factors like attention and motivation. Studies 2 and 3 examined the role of sensory and nonsensory factors in the elevated DP thresholds of young children.

II. STUDY 1: DP LATERALIZATION THRESHOLDS OF SCHOOL CHILDREN

The aim of this study was to obtain normative data on DP lateralization for children between the ages of 5 and 16 years.

[a]Electronic mail: giaschi@interchange.ubc.ca

A. Method

1. Participants

Four hundred and thirty-eight children were recruited from six schools in British Columbia. After standard audiometric testing, 37 children were excluded due to elevated hearing thresholds. The criterion for inclusion was a threshold of 25 dB HL or lower in both ears for frequencies of 250, 500, 1000, 2000, 4000 Hz. Data were not obtained for 14 of the youngest children (aged 5–7 years). These children failed to learn the task (6), refused to cooperate (3), or were unwell when tested (5). Due to experimental error or disruptions during testing, data for another 10 children were lost. The final sample was 377 children (192 girls and 185 boys) with an age range of 5 to 16 years.

2. Apparatus

Auditory thresholds were measured using a Beltone 119 audiometer. The DP task was run on a Macintosh Powerbook G3. The stimulus was delivered via the built-in 16-bit, 44.1-kHz stereo sound output through Sennheiser HD265 linear closed headphones, which attenuated much of the environmental noise. The typical environmental noise level was 35 dB A-weighted.

3. Stimulus

The DP stimulus was created using custom C code written by Dougherty (see Dougherty *et al.*, 1998 for a more complete description). Two independent noise sources were generated using a Gaussian-transformed, shuffled Minimal Standard uniform random deviate algorithm (Press *et al.*, 1992). Rectangular filters were applied to one noise source to form a single or complex tone stimulus. For complex tones the filter had two or more rectangular bands corresponding to the peak frequencies in the harmonic complexes. Complementary filters were applied to the other noise source to form a notched background stimulus. Each filtered noise source was then copied and appropriate time shifts were introduced. An ITD of 0 ms was applied to the copies of the background stimuli to produce the percept of noise located in the center of the head. An ITD of ± 0.6 ms was applied to the copies of the tone stimuli to produce the percept of a tone located in either the right or left side of the head. The tone and background stimuli were then summed and low-pass filtered with a 1200-Hz cutoff to reduce the unpleasantness of the noise. The height of the notch filter was adjusted to change the SBR (the signal-to-background amplitude ratio). When expressed in decibels [20*log (SBR)], an SBR of 0 dB represents an amplitude ratio of 1. To keep the resulting monaural spectral power density flat for SBRs of 0 dB or less, the depth of the notches was also adjusted. For SBRs greater than 0 dB there are peaks in the amplitude spectra; therefore, an SBR of zero or less defines the true dichotic pitch region. The peak frequency determines the perceived pitch of the tones. The bandwidth of the frequency bands was 5% of the center frequency.

A trial contained a sequence of tones that formed a melody (330, 660, and 990 Hz; 220, 440, 660, and 880 Hz; 330, 660, and 990 Hz; 440 and 880 Hz. Tones 1 and 4 were presented for 400 ms and tones 2 and 3 were presented for 200 ms, producing a stimulus of 1.2 s. Each stimulus was ramped on and off with a 50-ms half-Gaussian window. The average sound-pressure level was 80 dB.

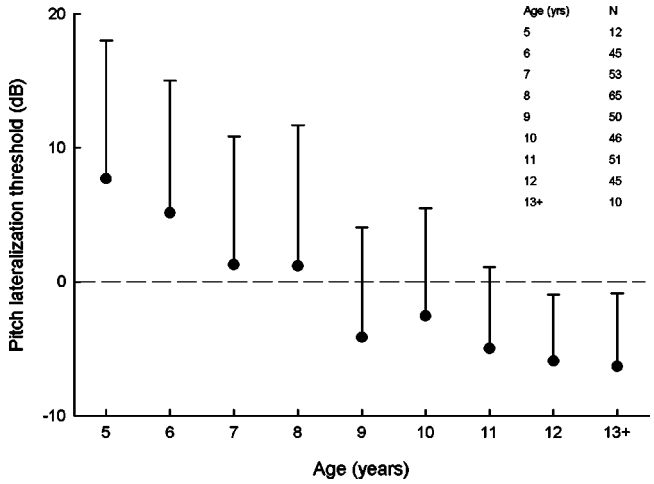

FIG. 1. Mean pitch lateralization thresholds (± 1 SD) as a function of age. Stimuli delivered at SBRs of 0 dB or less (indicated by the dotted line) were truly dichotic.

4. Procedure

A two-down one-up staircase adjusted the SBR. The staircase began with an SBR of 10 dB so that initially the tones were audible monaurally. The SBR was decreased in 6-dB steps until the first response reversal. The step size was then halved on each reversal (3, 1.5, 0.75 dB, etc.) until a minimum step size of 0.05 dB was reached. The step size remained at this minimum level until the staircase ended after 10 reversals or 50 trials.

Testing was conducted in a quiet room at the child's school. The hearing test and the DP lateralization task were completed during separate 15-min sessions. For the DP task children were instructed to report the side of the head where they heard the tones. Older children entered their responses on a game pad; younger children pointed to the left or right side of the head and the experimenter entered the response. Visual feedback was provided after each trial.

Testing began with a 20-trial practice staircase, starting with an SBR of 34 dB. Practice was repeated until the child appeared to understand the task. A full staircase was then completed. Thresholds were estimated by fitting a Weibull function to the data using a maximum-likelihood minimization procedure (Watson, 1979). Threshold was defined as the point of maximum slope on the fitted curve, which occurs at 82% correct in a two-alternative forced-choice procedure (Strasburger, 2001).

B. Results and discussion

Each child's SBR (amplitude ratio) threshold was converted to dB prior to data analyses. DP lateralization thresholds improved with age, as shown in Figure 1. The number of children aged 13–16 years was small; therefore, data for children in this age range were combined. A one-way ANOVA confirmed that the overall age effect was significant [$F(8,368) = 10.32$, $p < 0.001$]. Tamahane's T2 *post hoc* com-

parisons (alpha set at 0.05) revealed significant differences between the thresholds for the 5-year-old children and children aged 11 years and older; between thresholds for the 6-year-old children and children aged 9 years and older; and between thresholds for the 7- and the 8-year-old children and children aged 11 and 12 years. There were no other significant age group differences. Variability was generally high in the younger groups and declined with age. It is typical to find large individual differences between young children of the same age on auditory tasks (Wightman and Allen, 1992).

From 5 to 8 years of age, mean thresholds declined within the range of SBRs that produce a monaural pitch cue; beyond 9 years of age, mean thresholds fell within the dichotic pitch range. The proportion of children with thresholds in the dichotic range was 34% at 5–6 years of age, 59% at 7–8 years of age, 79% at 9–11 years of age, and 92% at 12–16 years of age. From 11 years onward thresholds are in the range of -5 to -6 dB, which is comparable to adult performance (from preliminary data for 20 adults aged 18–34 years, mean SBR threshold $= -5.27$ dB).

III. INTERIM DISCUSSION

Developmental changes in the ability to localize sounds using ITDs or the ability to segregate a signal from noise using ITDs could contribute to the age-related changes in DP lateralization observed in study 1. However, sound localization based on multiple localization cues, as measured by the minimal audible angle, or on ITD cues alone, as measured by lateralization of dichotic clicks, matures before 5 years of age (Ashmead *et al.*, 1991; Litovsky and Ashmead, 1997; Werner and Marean, 1996). Similarly, studies on the binaural masking level difference (BMLD) indicate that the ability to segregate a signal from noise using ITDs matures by 4 years of age (Moore *et al.*, 1991; Nozza *et al.*, 1988). Immature coding of ITDs is therefore not the cause of the elevated DP lateralization thresholds of young children.

A different type of explanation may lie in age-related changes in the physical dimensions of the head. Because young children have smaller heads and so a shorter interaural distance than older children and adults, the maximum ITD they experience is shorter (Knudsen, 1984). Therefore, the 0.6-ms ITD used in study 1, which provides a clear, well-localized sensation of DP in adults (Dougherty *et al.*, 1998), was possibly too long for binaural integration of the inputs in the auditory system of the youngest children, or was not represented in their maps of auditory space. However, based on the average head circumference of 5-year-old children (Hall *et al.*, 1989), a 0.6-ms ITD corresponds with spatial locations of approximately 87 deg from midline for females and 85 deg for males. Thus, the 0.6-ms ITD is within the range of ITDs that 5-year-olds experience naturally.

To ensure the magnitude of the ITD was not the cause of the high DP lateralization thresholds of young children we tested 5-year-olds on ITDs of 0.5 and 0.6 ms. An ITD of 0.5 ms is first encountered around 5 months of age (Clifton *et al.*, 1988) and is therefore well inside the upper limit of ITDs that young children experience naturally. Even so, the children's lateralization thresholds were above an SBR of 0 dB and were not different for the two ITDs.

DP lateralization involves multiple perceptual processes, and immaturity of any component process could cause elevated thresholds. For some auditory tasks, adjusting stimulus parameters to take account of immature processes that are not of interest but that affect task performance reveals mature abilities that are otherwise obscured. For example, young children produce adult-like auditory backward-masking thresholds if the intensity of the stimulus is adjusted to account for relatively poorer intensity discrimination in early childhood (Massaro and Burke, 1991). Similarly, mature BMLD thresholds are produced by young children only when adjustments are made to compensate for age differences in detection thresholds (Nozza *et al.*, 1988).

We modified two aspects of our stimulus to investigate whether poor detection of DP tones is the basis of the elevated lateralization thresholds of young children. First, because detection thresholds of children improve with increasing stimulus duration (Maxon and Hochberg, 1982), we doubled the duration of each DP tone. Second, because in study 1 the thresholds of young children improved in the range of SBRs that produces a monaural pitch cue, it was possible that immature development of detection thresholds in noise was a critical factor. Elevated detection thresholds in noise may reflect immature selective attention (Werner and Marean, 1996). We therefore presented the melody twice on every trial to enhance the probability of a child with poor selective attention detecting the tones. Twenty kindergarten children (ten per condition) were tested on the standard task and a modified version, and neither doubling the duration of the individual tones nor repeating the tone sequence had a significant effect. Several other potential explanations for the age-related effects observed in study 1 were investigated in studies 2 and 3.

IV. STUDY 2: PRACTICE EFFECTS ON YOUNG CHILDREN'S DP LATERALIZATION PERFORMANCE

Perceptual learning effects are seen in young children's performance of auditory perception tasks. For example, Tomblin and Quinn (1983) found that a 5-day training schedule led to significant improvements in the thresholds of 5–6-year-old children on an auditory temporal processing task. Young children's DP lateralization thresholds may show similar improvements from training.

The difference between older and younger children in DP lateralization thresholds might reflect a difference in amount of perceptual learning of the task at the time of threshold measurement. One possibility is that young children have a slower perceptual learning rate than older children. Thus, if all children are tested after a fixed and limited number of practice trials, younger and older children will be performing the task with different amounts of perceptual learning. A slower perceptual learning rate would indicate that younger children require more practice trials than older children require to reach their true threshold level of performance.

If the poor DP lateralization performance of young children is due to a slow rate of perceptual learning, their thresholds should asymptote after sufficient training near the threshold SBR of older children. If a sensory limitation is

contributing to the higher thresholds of young children, their thresholds may still improve with training, but should asymptote at a higher SBR than the threshold SBR of older children.

The purpose of this study was to determine whether young children's performance on the DP lateralization task improves with training. Children were trained over a period of 5 days on an easy-to-hard schedule. Presenting easy discriminations first (i.e., a high SBR in the DP task) is believed to improve performance by enabling the individual to allocate attention to the relevant stimulus dimension (Ahissar, 1999; Goldstone, 1998).

A. Method

1. Participants

Twenty-two children (12 male, 10 female), recruited through daycare programs and community advertisements, took part in the study. They ranged in age from 5.1 to 6.9 years ($M=6.0$ years, SD$=0.5$ years). Each child had normal hearing thresholds for 500 and 1000 Hz and was able to localize pure tones (see below). None had been diagnosed with a developmental disorder.

2. Apparatus and stimulus

Same as study 1.

3. Procedure

The children were tested initially on a localization task to ensure they could (a) localize a left/right sound source and (b) communicate the sound's location by pointing to the appropriate side of the head. The children listened through headphones to three consecutive 1000-Hz sinusoids delivered at 30 dB HL (all children had hearing thresholds of 25 dB or lower for 1000 Hz). There was no background noise. Side of presentation was randomly determined and the child pointed to the ear in which s/he heard the beeps. Blocks of 20 trials were completed until 80% localization accuracy was achieved, which took most children 1–2 blocks.

To make the abstract task of locating a sound source within one's head more tangible for young children, the DP lateralization task was presented as a game. Testing began with a narrated slide show in which the characters were introduced and the game was explained.

The children were assigned to either a training ($n=12$) or no-training ($n=10$) group. Testing for the no-training group was completed in the laboratory and entailed ten learning trials on the DP lateralization task, followed by a staircase run for threshold estimation.

Testing for the training group was completed in kindercare centers attended by the children. Each child was trained on the DP lateralization task for approximately 20 min per day over 5 consecutive days. The training sessions involved the children completing blocks of 20 trials of a fixed SBR. Training began at an SBR of 34 dB for all children and proceeded to more difficult SBR levels (20, 14, 0 dB). For each SBR the children were required to score 80% correct on two blocks before advancing to the next level of difficulty. Individual children therefore progressed through the training phase at different rates and with different amounts of practice across SBRs. Each training session began with the SBR last attempted during the previous session to ensure the 80% criterion was reached or maintained for that level. On day 5 a DP lateralization threshold was measured regardless of whether a child had completed all training levels. To familiarize the child with the staircase procedure, one or two 15-trial staircase runs were completed before a threshold was measured.

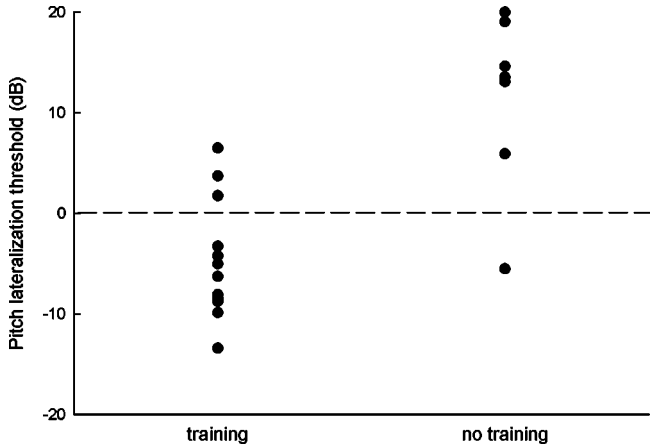

FIG. 2. The effects of training young children on the DP lateralization task. Data points represent individual thresholds (For the untrained group, four children obtained thresholds of 20 dB). Stimuli delivered at SBRs of 0 dB or less (indicated by the dotted line) were truly dichotic.

B. Results and discussion

Reaching the criterion on the training trials required increasingly more training as the SBR declined. The average number of 20-trial training blocks taken to reach criterion was 3 (range: 2–6) for an SBR of 34 dB, 4 (range: 2–8) for an SBR of 20 dB, and 5 (range: 2–12) for an SBR of 14 dB. Only 7/12 children reached the criterion at an SBR of 0 dB before a threshold was measured. Large individual differences in perceptual learning rate are typical (Ahissar, 2001).

Figure 2 shows children's trained and untrained DP lateralization thresholds. Training resulted in lower thresholds and smaller within-group variance for young children. The difference between the thresholds of the trained ($M=-4.62$, SD$=5.93$) and untrained ($M=14.06$, SD$=8.29$) children was statistically significant, $t(20)=6.16$, $p<0.001$. Nine children who underwent training had thresholds in the dichotic range and three had thresholds just outside the dichotic range. Without training, most children had extremely elevated thresholds, with only one of ten children producing a threshold in the dichotic range.

As a consequence of training, young children produced comparable thresholds to the older children in study 1. Due to time constraints, repeated threshold measurements were not made to determine whether each child's performance had approached asymptote. It is therefore possible that the three children whose thresholds were just outside the dichotic range may have continued to improve with further training. It is clear from the present results that most young children are capable of lateralizing DP tones in the absence of monaural cues. The elevated thresholds of young children in the

previous studies were therefore not due to a binaural processing limitation, but can be explained by a slow rate of perceptual learning of the task.

In situations where there are distracting stimuli, such as the noise in the DP task, younger children are generally poorer than older children at differentiating the inputs and ignoring irrelevant information (Gomes *et al.*, 2000). Training from easy to hard discriminations provides an opportunity for individuals to learn to selectively attend to the important stimulus dimensions. There are several dimensions of the DP lateralization task that children might be learning to selectively listen for. Training may lead to an improvement in perceptually segregating the tones from the noise or in determining the spatial location of the tones. The effect of training may also be an improvement in ability to attend to both perceptual dimensions at one time.

V. STUDY 3: ALTERNATIVE METHODS OF MEASURING DP PERCEPTION IN YOUNG CHILDREN

Study 2 demonstrated that young children show a large perceptual learning effect on the DP lateralization task. With training, most young children demonstrated the ability to localize tones in the dichotic range, suggesting that their limitations on the lateralization task arise from nonsensory factors. In this study four different measures of DP perception were examined to see whether young children can demonstrate DP perception without lengthy training.

Several lines of evidence suggest that the lateralization component of the DP task may be a source of task difficulty for young children. First, adults have been found to have higher lateralization thresholds than detection thresholds for some auditory stimuli (Egan and Benson, 1966), suggesting that lateralization tasks may generally be more difficult.

Second, for young children, the lateralization task may be especially difficult because localizing sounds inside one's head is an unfamiliar experience. In everyday experience, sounds originate from an external sound source and produce an externalized sound image. Attending to the location of an external sound source has auditory consequences (i.e., it signals the presence of a sound-emitting object in the environment), whereas attending to the location of an internal sound source is more abstract. Older children may find the task of attending to the location of an internalized sound image less unusual, because they are more likely to have experience listening to auditory stimuli, such as music, through headphones. In general, they will also be more cognitively capable of completing abstract tasks than younger children.

Third, in the training study a child who was unable to localize pure tones or to obtain the 80% correct lateralization criterion at an SBR of 34 dB could reproduce aloud an unfamiliar musical tune created using the DP technique and delivered at an SBR of 0 dB. Thus, although she could not lateralize DP tones, she could demonstrate DP perception on a pitch reproduction task. Whether difficulty lateralizing DP tones is the reason for the elevated thresholds of young children who are able to localize pure tones is unclear, but it is a possibility.

These issues suggest young children may be able to detect DP tones but may have difficulty localizing them. Removing the lateralization dimension of the task will reduce its complexity. Perceptual learning effects are generally larger for more complex tasks (Fine and Jacobs, 2002); thus, without the lateralization aspect the task should require less learning and fewer trials should be required for young children to reach their true threshold level of performance.

Two versions of the DP task that involve pitch identification were examined. Pitch perception for complex tones matures during infancy (Werner and Gray, 1998); thus, pitch perception difficulties are an unlikely source of task difficulty for young children. Two versions that involve lateralization were also examined. One version was the left–right lateralization task used in the previous studies. The other version was a sequence of moving DP tones. This was included to see whether young children are better able to perceive the location of internalized sound images when location can be determined on the basis of relative rather than absolute spatial position.

A. Method

1. Participants

Eleven 5-year-old children ($M = 5.5$ years, SD $= 0.3$ years), seven boys and four girls, were participants. They satisfied the inclusion criteria outlined in study 2, including the criterion for localizing pure tones.

2. Apparatus

Same as study 1.

3. Stimuli

Four versions of the DP task were tested. Each version was disguised as a game in which the child made a decision about an attribute (spatial location, pitch) of the tones. The duration of a trial was 1.2 s in the left–right lateralization version (as described in study 1). For the other versions, the tones were the same duration as the tones in the left–right task; however, 500 ms of noise was added, which increased the entire stimulus duration to 1.7 s. Each sequence began and ended with 100-ms noise and an intertone-interval of 100-ms noise was introduced. The noise was presented diotically and was therefore perceived to be in the center of the head.

a. *Left–right lateralization task*. This was the lateralization task from study 1 in the game format used in study 2.

b. *Lateralization of a moving sound source*. The noise and tones created in study 1 were used in this version. The four tones were presented in temporal sequence, as before; however, each tone was presented in a different spatial location to create the percept of a series of tones moving through the head. The spatial position of the tones was adjusted by altering the ITD of the signal. The ITDs used were $+0.6$ (far right), $+0.3$ (midright), -0.3 (midleft), -0.6 ms (far left). On each trial, the tones were presented randomly either from left to right or from right to left. The task was to indicate the direction of motion of the tones.

c. *High–low pitch identification*. For this task there were two sets of tones. Each set comprised four same-frequency single tones presented in temporal sequence. The

frequency of the tones was 400 Hz in one set and 900 Hz in the other (spread was 5% of the central frequency). The spatial location of the tones was either left or right, determined randomly. On each trial, either the higher or the lower frequency tones were presented and the task was to report which set of tones was played. The set of tones (400 or 900 Hz) was determined randomly across trials.

d. *Up–down pitch identification*. This stimulus comprised four single tones presented in temporal sequence on either the left or right side, determined randomly. The tones differed in frequency by at least 150 Hz (400, 575, 750, and 900 Hz), which is larger than the difference limen for young children. For example, Jensen and Neff (1993) found that the difference limen of 4-year-olds for a 440-Hz stimulus is around 70 Hz. By 6 years of age it is as small as 5 Hz. Thus, young children can easily perceive the difference in the pitch of the tones in the present task. The tones were delivered in either ascending or descending order and the task was to report the direction (up/down) of the frequency sweep.

4. Procedure

Testing was conducted in a daycare center over 5 consecutive days. Each child was tested on every version of the DP task by completing one version per day for 4 days. Auditory thresholds were measured on the remaining day. The tone localization task was completed immediately before the left–right DP lateralization task. The order in which the DP tasks were completed was counterbalanced so that practice effects were distributed evenly across conditions. Daily sessions lasted approximately 20 min.

Instructions for each game were given via a narrated slide show. To promote the children's understanding of each task, blocks of ten training trials at an SBR of 20 dB were completed prior to threshold estimation. The number of training trials completed by a child was contingent on performance; training continued until the child obtained 80% correct on a block or completed three blocks. A 15-trial staircase practice run and then a full staircase run followed this.

B. Results and discussion

The children performed differently on the tasks that required a judgment about the frequency of the tones than on the tasks that required a judgment about the spatial location of the tones. On the lateralization tasks, only 2/11 children were able to reach the 80% correct criterion at SBR 20 dB before a threshold was measured. By contrast, all children met the criterion on the pitch identification tasks. The high–low task required the least amount of practice, with 9/11 children reaching the criterion on the first block of 10 trials. On the up–down task, five children obtained the criterion on the first block of trials, with the remaining children taking two or three blocks to become proficient.

Mean thresholds for each task are displayed in Fig. 3. Thresholds on the left–right lateralization task ($M=17.06$, $SD=7.13$) were well above the DP range, consistent with the results of studies 1 and 2. Thresholds were also elevated for discriminating the direction of motion of a sequence of tones ($M=16.54$, $SD=7.30$). For both pitch identification tasks

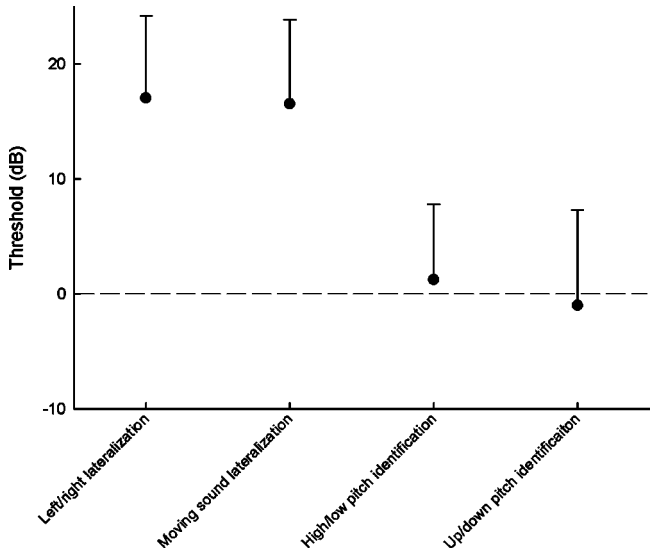

FIG. 3. Mean thresholds (± 1 SD) for 5-year-old children on lateralization and pitch identification tasks. Stimuli delivered at SBRs of 0 dB or less (indicated by the dotted line) were truly dichotic.

thresholds were considerably lower and there was less within-group variability (high–low pitch identification: $M=1.25$, $SD=6.54$ up–down pitch identification: $M=-0.98$, $SD=8.30$). A one-way repeated-measures ANOVA confirmed a significant main effect of task, $F(3,30)=24.80$, $p<0.001$. Newman–Keuls *post hoc* tests indicated significant differences ($p<0.01$) for each pitch task compared to each lateralization task. Thresholds on the pitch tasks were not significantly different from one another and thresholds on the lateralization tasks were not significantly different from one another.

The lower thresholds on the pitch identification tasks are not due to a practice effect because the order for completing the tasks was counterbalanced. The results indicate that pitch identification tasks are more sensitive tests of the DP perception abilities of young children than lateralization tasks. The performance of the children on the practice trials indicates that initial (conceptual or procedural) learning of the task was much more rapid for the pitch measures than for the lateralization measures. This rapid initial learning resulted in the children obtaining relatively low DP thresholds with a limited amount of training. The children's mean thresholds were not in the dichotic range for the high–low task; however, a slightly expanded practice session, incorporating some SBRs less than 20 dB, would likely result in most young children obtaining thresholds in the dichotic range within a single testing session.

The difference between the lateralization and pitch tasks in rate of learning supports the idea that lateralizing DP tones is difficult for young children. One idea was that lateralizing the stationary tones might be difficult because a judgment of the absolute position of the tones is required. However, the children were also poor on the moving tone task, which requires sensitivity to the position of each tone relative to the other tones. Thus, young children seem to be generally unaware of the spatial position of the tones inside the head. This type of difficulty could arise from a lack of familiarity

with localizing internalized sound images; however, studies on the precedence effect have shown that young children are also poor at tracking externalized moving auditory signals (Cranford *et al.*, 1993).

DP lateralization tasks are possibly more difficult for young children than DP pitch tasks because they place greater demands on cognitive processes such as selective attention. Young children may be able to listen selectively in simple listening tasks but have difficulty with more complex listening tasks (Werner and Gray, 1998). The lateralization tasks are more complex than the pitch tasks due to the added processing required to extract location information.

VI. GENERAL DISCUSSION AND CONCLUSIONS

The initial finding in this series of studies was that DP lateralization performance improves during childhood. Among young children there is a lot of variability on the left–right lateralization task and mean SBR thresholds are very high. By 9 years of age most children's thresholds are within the dichotic range, and by 11 years of age thresholds are similar to adult thresholds. The training study results indicate that the basis of the immature task performance of young children is not a sensory limitation, but rather a slow rate of perceptual learning.

From the initial lateralization studies the component of the task that is difficult for young children was not obvious. The difficulty could have been related to segregating the tones from the noise or to identifying the spatial location of the tones. This issue was resolved in the final study, which showed that DP tasks that do not involve localization are relatively easy for young children. Young children obtain low thresholds on pitch identification tasks, indicating that they can isolate the DP tones from the noise. Their difficulty therefore lies in localization and extends to localizing both stationary and moving DP sound sources.

It is surprising that the localization aspect of the task is difficult for young children given that (a) children in studies 2 and 3 could localize monaural, pure tones with 80% accuracy and (b) the ability to lateralize dichotic sounds with greater precision than required in the DP lateralization task is evident early in infancy. However, the DP task is more complex than these other tasks, supporting the conclusion that young children have difficulty in complex listening situations.

The present results argue against an age difference in general attentiveness when completing the tasks. If this was the case, performance of the young children would have been poor on every version of the DP task. Instead, their performance was poor on the lateralization tasks only.

In sum, the ability to perceive dichotic pitch is present from a young age, although young children do not always perform dichotic pitch perception tasks as well as older children and adults because of nonsensory limitations. The effects of nonsensory limitations can be diminished by changing the task demands to reduce the complexity of the processes required for successful task completion or by extended task training.

ACKNOWLEDGMENTS

This research was supported by Grant No. 12-FY00-0175 from the March of Dimes Birth Defects Foundation to D. Giaschi and D. Edgell. We thank Robert Dougherty for providing the DP software. We thank Neil Roach for helpful discussions on the nature of some of the effects observed in these studies. We also thank Pamela Paul, Carolyn Sin, Danielle Prevost, Sandra Bienz, Eleanor To, Tracey Sing and Karen Westerop for assistance with data collection.

Ahissar, M. (**1999**). ''Perceptual learning,'' Curr. Dir. Psychol. Sci. **8**, 124–128.

Ahissar, M. (**2001**). ''Perceptual training: A tool for both modifying the brain and exploring it,'' Proc. Natl. Acad. Sci. U.S.A. **98**, 11842–11843.

Ashmead, D. H., Davis, D. L., Whalen, T., and Odom, R. D. (**1991**). ''Sound localization and sensitivity to interaural time differences in human infants,'' Child Dev. **62**, 1211–1226.

Bilsen, F. A. (**1972**). ''Pitch of dichotically delayed noise,'' in *Hearing Theory*, edited by B. L. Cardozo (I.P.O., Eindhoven), pp. 5–8.

Bilsen, F. A. (**1976**). ''Pronounced binaural pitch phenomenon,'' J. Acoust. Soc. Am. **59**, 467–468.

Clifton, R. K., Gwiazda, J., Bauer, J. A., Clarkson, M. G., and Held, R. M. (**1988**). ''Growth in head size during infancy: Implications for sound localization,'' Dev. Psychol. **24**, 477–483.

Cramer, E. M., and Huggins, W. H. (**1958**). ''Creation of pitch through binaural interaction,'' J. Acoust. Soc. Am. **30**, 413–417.

Cranford, J. L., Morgan, M., Scudder, R., and Moore, C. (**1993**). ''Tracking of moving fused auditory images by children,'' J. Speech Hear. Res. **36**, 424–430.

Dougherty, R. F., Cynader, M. S., Bjornson, B. H., Edgell, D., and Giaschi, D. E. (**1998**). ''Dichotic pitch: A new stimulus distinguishes normal and dyslexic auditory function,'' NeuroReport **9**, 3001–3005.

Edwards, V. T., Giaschi, D. E., Dougherty, R. F., Edgell, D., Bjornson, B. H., Lyons, C., and Douglas, R. M. (**2004**). ''Psychophysical indices of temporal processing abnormalities in children with developmental dyslexia,'' Dev. Neuropsychol. **25**, 321–354.

Egan, J. P., and Benson, W. (**1966**). ''Lateralization of a weak signal presented with correlated and with uncorrelated noise,'' J. Acoust. Soc. Am. **40**, 20–26.

Fine, I., and Jacobs, R. A. (**2002**). ''Comparing perceptual learning across tasks: A review,'' J. Vision. **2**, 190–203.

Fourcin, A. J. (**1970**). ''Central pitch and auditory lateralization,'' in *Frequency Analysis and Periodicity Detection in Hearing*, edited by R. Plomp and G. F. Smoorenburg (Sijthoff, Leiden), pp. 319–328.

Goldstone, R. L. (**1998**). ''Perceptual learning,'' Annu. Rev. Psychol. **49**, 585–612.

Gomes, H., Molholm, S., Christodoulou, C., Ritter, W., and Cowan, N. (**2000**). ''The development of auditory attention in children,'' Front. Biosci. **5**, 108–120.

Hall, J. G., Froster-Iskenius, U. G., and Allanson, J. E. (**1989**). *Handbook of Normal Physical Measurements* (Oxford University Press, New York).

Jensen, J. K., and Neff, D. L. (**1993**). ''Development of basic auditory discrimination in preschool children,'' Psychol. Sci. **4**, 104–107.

Klein, M. A., and Hartmann, W. M. (**1981**). ''Binaural edge pitch,'' J. Acoust. Soc. Am. **70**, 51–61.

Knudsen, E. I. (**1984**). ''The role of auditory experience in the development and maintenance of sound localization,'' Trends Neurosci. **9**, 326–330.

Litovsky, R. Y., and Ashmead, D. H. (**1997**). ''Development of binaural and spatial hearing in infants and children,'' in *Binaural and Spatial Hearing in Real and Virtual Environments*, edited by R. H. Gilkey and T. R. Anderson (Erlbaum, Mahwah, NJ), pp. 571–592.

Massaro, D. W., and Burke, D. (**1991**). ''Perceptual development and auditory backward recognition masking,'' Dev. Psychol. **27**, 85–96.

Maxon, A. B., and Hochberg, I. (**1982**). ''Development of psychoacoustic behavior: Sensitivity and discrimination,'' Ear Hear. **3**, 301–308.

Moore, D. R., Hutchings, M. E., and Meyer, S. E. (**1991**). ''Binaural masking level differences in children with a history of otitis media,'' Audiology **30**, 91–101.

Nozza, R. J., Wagner, E. F., and Crandell, M. A. (**1988**). ''Binaural release from masking for a speech sound in infants, preschoolers, and adults,'' J. Speech Hear. Res. **31**, 212–218.

Oh, E. L., Wightman, F., and Lufti, R. A. (**2001**). ''Children's detection of pure-tone signals with random multitone maskers,'' J. Acoust. Soc. Am. **109**, 2888–2895.
Press, W. H., Teukolsky, S. A., Vetterling, W. T., and Flannery, B. P. (**1992**). *Numerical Recipes in C*, 2nd ed. (Cambridge University Press, Cambridge).
Strasburger, H. (**2001**). ''Converting between measures of slope of the psychometric function,'' Percept. Psychophys. **63**, 1348–1355.
Tomblin, J. B., and Quinn, M. A. (**1983**). ''The contribution of perceptual learning to performance on the repetition task,'' J. Speech Hear. Res. **26**, 369–372.
Watson, A. B. (**1979**). ''Probability summation over time,'' Vision Res. **19**, 515–522.
Werner, L. A., and Gray, L. (**1998**). ''Behavioral studies of hearing development,'' in *Development of the Auditory System*, edited by E. W. Rubel, A. N. Popper, and R. R. Fay (Springer, New York), pp. 12–79.
Werner, L. A., and Marean, G. C. (**1996**). *Human Auditory Development*. (Westview, Boulder, CO).
Wightman, F., and Allen, P. (**1992**). ''Individual differences in auditory capability among preschool children,'' in *Developmental Psychoacoustics*, edited byL. A. Werner and E. W. Rubel (American Psychological Association, Washington, DC), pp. 113–133.

Comparison between distortion product otoacoustic emissions and nerve fiber responses from the basilar papilla of the frog

Sebastiaan W. F. Meenderink[a)]
Department of Otorhinolaryngology and Head & Neck Surgery, University Hospital Maastricht, P.O. Box 5800, 6202 AZ Maastricht, and Institute for Brain and Behavior, Maastricht University, The Netherlands

Pim van Dijk
Department of Otorhinolaryngology, University Hospital Groningen, P.O. Box 30.001, 9700 RB Groningen, and School of Behavioral and Cognitive Neurosciences, University of Groningen, The Netherlands

Peter M. Narins
Department of Physiological Science, University of California, Los Angeles Los Angeles, California 90095-1606

(Received 25 October 2004; revised 21 January 2005; accepted 25 January 2005)

The basilar papilla (BP) is one of the three end organs in the frog inner ear that is sensitive to airborne sound. Its anatomy and physiology are unique among all classes of vertebrates. Essentially, the BP functions as a single auditory filter presumably arising from a mechanically-tuned mechanism. As such, both neural and distortion product otoacoustic emission (DPOAE) tuning may reflect a single mechanical filtering mechanism. Using the Duffing oscillator as a simple model for both neural and DPOAE tuning from the BP, two predictions can be made: [1] the characteristic frequency (CF) of neural tuning and the best frequency (BF) of DPOAE tuning will coincide and [2] the neural tuning curve and DPOAE-audiogram have a similar shape when the neural tuning curve is scaled by a factor of 4 along the *y*-axis. We recorded both neural tuning curves and DPOAE-audiograms from the BP of the leopard frog. These recordings show good agreement with the model predictions when the stimulus tones are related by relatively small stimulus frequency ratios. For larger stimulus frequency ratios, DPOAE recordings clearly deviate from model predictions. These differences are most likely caused by the oversimplified representation of the frog BP by the model. [DOI: 10.1121/1.1871752]

PACS numbers: 43.66.−x, 43.80.−n [BLM] Pages: 3165–3173

I. INTRODUCTION

The anatomy of the inner ear exhibits a high degree of variability across the various classes of vertebrates. Notwithstanding this, the transformation of sound pressure into activity in the auditory nerve ultimately involves the same specialized cells in all vertebrates: hair cells.

In frogs, hair cells that are sensitive to airborne sound are distributed over three anatomically separated papillae, each one most sensitive to a different range of frequencies. The sacculus (S) is sensitive to high-level sounds at very low frequencies. No tonotopic organization has been reported for the frog sacculus. The amphibian papilla (AP), which is most sensitive to the low- and mid-frequencies within the frog hearing range, consists of an elongated strip of hair cells. These cells are directly over the rigid wall of the papillar recess, rather than over a flexible membrane (as in the cochlea). Overlying the AP hair cells is a tectorial membrane. Both the shape of this membrane as well as its position within the papillar recess suggest that it plays an important role in the transduction of sound by hair cells (Lewis and Leverenz, 1983). The papilla exhibits tonotopic organization with the highest (≈1.2 kHz) and lowest (≈0.1 kHz) frequencies being represented caudally and rostrally, respectively (Lewis *et al.*, 1982).

The third hearing organ in the frog is the basilar papilla (BP). This papilla is most sensitive to the highest frequencies within the hearing range of frogs (Feng *et al.*, 1975). In leopard frogs (*Rana pipiens pipiens*) it responds best to sounds of 1.2–2.4 kHz (Ronken, 1991). The anatomy of the BP is unique among all classes of vertebrates (Wever, 1973); it consists of approximately 50–100 hair cells standing directly over the rigid cartilaginous wall of the papillar recess. Almost all of these hair cells are covered by a tectorial membrane. In an individual animal, almost all BP nerve fibers exhibit very similar tuning curves, with characteristic frequencies (CFs) being essentially identical across nerve fibers (Ronken, 1990; Van Dijk *et al.*, 1997). Also, afferent BP fibers are not suppressible (Feng *et al.*, 1975), and the CF of BP fibers do not depend on temperature (Stiebler and Narins, 1990; Van Dijk *et al.*, 1990). Although it is not completely understood how tuning is achieved in this organ, the unique anatomy and physiology of the BP suggest that tuning relies on the mechanical properties of the structures in the papilla, without the contribution of electrical tuning from the hair cells (Smotherman and Narins, 1999).

a)Electronic mail: B.Meenderink@KNO.unimaas.nl

Upon stimulation with two tones that have appropriately chosen frequencies (f_1, f_2) and levels (L_1, L_2), the basilar papilla produces distortion product otoacoustic emissions (DPOAEs; Van Dijk and Manley, 2001). It has been hypothesized that these DPOAEs are the result of the passive nonlinear properties of the anatomical structures (i.e., hair cells, the tectorial membrane) found within this organ (Meenderink and Van Dijk, 2004). So, similar to the nerve, the tuning of DPOAEs seems to be the result of a mechanically tuned filter. Thus, both neural and DPOAE tuning may reflect the same, single auditory filter, with the tuning having a mechanical origin.

Recently, the Duffing oscillator has been used as a simple model for DPOAEs from the BP (Van Dijk and Manley, 2001; Meenderink *et al.*, 2005). These studies show that such a simple model qualitatively describes the dependence of emission amplitude and phase on both absolute (f_1, f_2) and relative (f_2/f_1) stimulus frequencies. In the present study we used the Duffing oscillator as a model for both DPOAEs and neural tuning from the BP. We show that in the model (1) the CF of the frequency threshold curve and the stimulus frequency resulting in a maximum distortion product amplitude coincide. This correlation is independent of the ratio f_2/f_1 used to evoke distortion products; and (2) the shapes of the frequency tuning curves and the DP audiograms are markedly different: the frequency tuning curves are much broader than the DP audiograms. However, when the frequency tuning curves are scaled by a factor of 4 along the *y* axis, the two curves become almost identical in shape.

We tested these two model predictions by obtaining both neural tuning curves and several DPOAE audiograms from the basilar papilla of the leopard frog *R. pipiens pipiens*. When using relatively small stimulus frequency ratios ($f_2/f_1 < 1.16$) during DPOAE recordings, the first model prediction is found. Also, the neural tuning curves are much more broadly tuned than DPOAE audiograms. Scaling of the neural tuning curves by a factor of 4 does render the two curves more similar, although it never results in identically shaped curves. Probably, the theoretical scaling factor of 4 is not applicable to the frog ear, which is most likely caused by the oversimplified representation of the frog BP in the used model.

II. METHODS

A. Animal care

Recordings were made from the left ear of the Northern leopard frog *Rana pipiens pipiens*: $n=9$; body mass: 17.7–31.9 g (mean 24.7 g); snout-vent length: 58.6–78.4 mm (mean: 67.9 mm). Due to the duration of the experiments, nerve fiber recordings were performed the day following the DPOAE recordings. Prior to both DPOAE and nerve fiber recordings the animal was anesthetized by intramuscular injection of sodium pentobarbital (Nembutal: 60 mg/ml; 1.0 μl/g body mass) in one of the hind limbs. If necessary, supplementary anesthesia was administered during the experiments. Recordings were performed inside a sound-attenuating room, with the frog placed on a vibration-isolation table. To prevent dehydration and to facilitate cutaneous respiration during the experiments, the animal was covered by gauze soaked in frog Ringer's solution. At the end of the nerve-fiber experiment, animals were killed by destruction of the central nervous system (double-pith procedure). The "Principles of Care" (NIH publication 85-32, revised 1985) and USA regulations were followed throughout this study, and protocols were approved by the University of California Animal Research Committee.

B. DPOAE recordings

Distortion product otoacoustic emissions (DPOAEs) were recorded using a setup and method described previously (Meenderink *et al.*, 2005). Briefly, after anesthetizing the animal, the open end of a custom-built probe was sealed to the skin surrounding the tympanic membrane using silicone grease. The probe contained two miniature speakers (ER-10C, Etymotic Research) for stimulus delivery and one 1/2 in. condenser microphone (Brüel & Kjær type 4134), connected to a preamplifier (B&K type 2069; 60 dB amplification), for emission recording. In order to evoke DPOAEs, two stimulus tones with frequencies f_1 and f_2 (where $f_1 < f_2$) and levels L_1 and L_2 were played simultaneously, one from each speaker. All DPOAE recordings were made with stimulus levels $L_1 = L_2 = 76$ dB SPL. The stimulus frequency f_1 was systematically increased from 213 to 2774 Hz in approximately 30 Hz steps. This f_1 sweep was repeated 11 times, each sweep with the frequency ratio f_2/f_1 fixed at a different value (f_2/f_1 varied from 1.02 to 1.4, respectively).

The generation of the stimulus tones, as well as the recording of the microphone signal, was controlled by a desktop computer, using software written in Matlab (The Mathworks, Inc.) and Rpvds (Tucker Davis Technologies). This software controlled two separate D/A channels (RP2,TDT) and two programmable attenuators (PA5,TDT) for stimulus generation, and an A/D channel (RP2,TDT) used for recording of the microphone signal.

The two stimulus frequencies were chosen such that they were periodic over the same integer number of sample points. This ensures that the DPOAE frequencies are also periodic over that same number of sample points, resulting in sample blocks in which all frequencies of interest (f_1, f_2, and f_{DPOAE}) are periodic. For each stimulus frequency pair, f_1, f_2, a series of these blocks was recorded. After artifact rejection and averaging of these blocks the levels of the stimulus tones and the DPOAEs were calculated by Fourier analysis.

C. Nerve fiber recordings

The day after the DPOAE recordings, the frog was reanesthetized (using the same dosage of anesthesia as during the DPOAE recordings) in preparation for the recordings from the VIIIth nerve. Before the animal was placed inside the sound-attenuating room, the auditory nerve that innervates the left ear was surgically exposed using a ventral approach (Capranica and Moffat, 1975; Zelick and Narins, 1985). The frog was placed on its back and the lower jaw was retracted to expose the roof of the mouth. After covering the frog with wet gauze, a small hole was drilled on the

lateral side of the brain case, thus exposing the VIIIth nerve and its point of entry into the brain. After surgery, the animal was transferred to the sound-attenuating room to conduct the experiments. For the intracellular recordings from individual nerve fibers, we used conventional glass electrodes filled with 3 M KCL (resulting in an impedance typically>40 MΩ). Under visual control, the tip of the electrode was placed over the surface of the auditory nerve and advanced into the nerve using a remotely driven hydraulic microdrive (Narishige MO-103L). The signal from the electrode was fed through a high input impedance preamplifier (Winston Electronics, Model 1000) and a spike analyzer (Mentor N-750) before being digitized using an A/D converter (DD1,TDT).

Pure-tone stimuli (0.3–5.0 kHz) were generated from a D/A converter (DD1,TDT), set to the correct level using a programmable attenuator (PA4,TDT) and presented to the operated ear through a dynamic speaker (Beyer DT48). This speaker was coupled to the frog ear via a brass housing and a short piece of rubber tubing. A tight seal between the tubing and the skin surrounding the tympanic membrane was obtained using silicone grease. The brass housing also contained a 1/2 in. condenser microphone (Brüel & Kjær type 4134), which was used to calibrate the level of the stimulus tone.

While advancing the electrode through the nerve using the microdrive, the ear was stimulated using short bursts of white noise. As soon as a nerve fiber was encountered, an automated staircase algorithm was used to obtain two frequency threshold curves (FTCs) using an "up–down" threshold-tracking method (Evans, 1979): once from low to high frequencies, and once from high to low frequencies. The automated system consisted of software running on a desktop computer and controlled both stimulus generation and data acquisition. The two FTCs were recorded with a frequency resolution of 40 points/octave and a 1 dB intensity resolution. Their average was calculated and subsequently smoothed using a moving Hanning window (window width =1/8 octave).

III. THEORY: THE DUFFING OSCILLATOR

As a simple model for the basilar papilla, we will consider the Duffing oscillator. This oscillator has been used previously to model distortion product otoacoustic emissions from the BP (Van Dijk and Manley, 2001; Meenderink *et al.*, 2005). Although the Duffing oscillator is an (over)simplification of the basilar papilla mechanics, it models remarkably well the relation between the amplitude and phase of the DPOAE, and the stimulus frequencies f_1 and f_2 (Meenderink *et al.*, 2005). The Duffing oscillator is described by the second-order nonlinear equation,

$$m\ddot{x}+R\dot{x}+k(x)x=F(t), \tag{1}$$

where m is a mass, whose movement is driven by the force $F(t)$. This movement is impeded by both a resistance R, and a nonlinear stiffness $k(x)=k_0(1+x^2/x_0^2)$.

In order to evoke distortion products, the oscillator is driven by a two-tone force,

$$F(t)=A_1\sin(2\pi f_1 t)+A_2\sin(2\pi f_2 t), \tag{2}$$

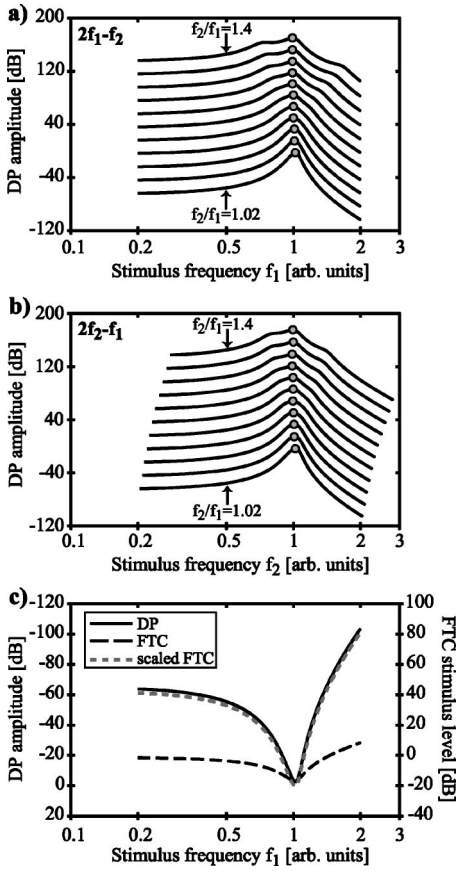

FIG. 1. Tuning properties for distortion products and nerve fiber from a Duffing oscillator model [see Eq. (1)]. Results are for $m=1$, $r=1$, $k_0=4*\pi^2$, $x_0=1$, and $A_1=A_2=1$. (a) The DPOAE amplitude for $2f_1-f_2$ is plotted as a function of f_1. Each curve displays a DP audiogram obtained with a different f_2/f_1. For clarity, the curves are offset by 20 dB, with $f_2/f_1=1.02$ being at the bottom. Successive curves represent data obtained with increasing f_2/f_1, with the curve for $f_2/f_1=1.4$ at the top. The maximum in each DP audiogram is indicated by the filled circles. (b) The same as (a), but for $2f_2-f_1$ plotted as a function of f_2. Each DP audiogram has its maximum when stimulus frequency f_1 (for $2f_1-f_2$) or f_2 (for $2f_2-f_1$) coincides with the resonant frequency of the Duffing oscillator. (c) FTC (black, dashed line) as a function of stimulus frequency. The characteristic frequency (CF) of this curve coincides with the resonant frequency of the oscillator, and as a consequence also with the maximum in the DP audiograms. For comparison, a single DP audiogram ($2f_1-f_2, f_2/f_1=1.02$) is also shown, but with its y axis reversed (black, solid line). It can be seen that the tuning of the FTC is much broader than the tuning of the DP audiogram. This difference is absent when the FTC is scaled by a factor of 4 along the y axis (gray, dashed line). To visually distinguish the DP audiogram from the scaled FTC, the latter is plotted with a small vertical offset.

where A_1 and A_2 are the amplitudes of the two tones at frequencies f_1 and f_2 ($f_2>f_1$), respectively. We calculated distortion products for a range of two-tone combinations: f_1 varied between 0.2 and 2.0 in 0.01 steps, with the normalized resonant frequency being 1, while f_2/f_1 was between 1.02 and 1.4 in steps of 0.01. Figures 1(a), 1(b) show DP amplitude when $m=1$, $r=1$, $k_0=4*\pi^2$, $x_0=1$, and $A_1=A_2=1$. Here, individual lines give DP amplitude, obtained with a fixed-f_2/f_1, as function of stimulus frequency (either f_1 for $2f_1-f_2$, or f_2 for $2f_2-f_1$). It can be seen that for $2f_1-f_2$ [Fig. 1(a)], each DP audiogram has its maximum when f_1 coincides with the resonant frequency of the oscillator, as indicated by the filled circles. In contrast, for $2f_2-f_1$ [Fig. 1(b)], maxima in the different DP audiograms occur when f_2

coincides with the oscillator's resonant frequency (filled circles). Notice that the DP audiograms obtained with relatively large f_2/f_1 exhibit three more or less pronounced lobes, rather than only one single relative maximum. These lobes arise whenever f_1, f_2, or f_{DP} coincide with the resonant frequency of the oscillator, but merge into a single maximum when f_2/f_1 is relatively small.

The Duffing oscillator was also used to model frequency threshold curves (FTCs) in the basilar papilla. A FTC is a function that specifies for each frequency f the corresponding amplitude A required to reach a threshold response in the nerve fiber. Typically, the threshold is defined as an increase in the number of spikes above the spontaneous firing that occurs during a short interval of time. Rather than adding some spike-generator to the model, we will assume that the FTC is inversely proportional to the frequency–response curve of the Duffing oscillator, as expressed by the movement x [Eq. (1)]. This will be approximately true for relatively low stimulus levels, when the growth of the response (i.e., spike rate) with increasing stimulus level is (approximately) linear. The inverted frequency–response function for the Duffing oscillator is shown in Fig. 1(c) (black dashed line) for the same parameters used for the generation of distortion products. The response curve was computed by driving the oscillator by a fixed-amplitude, one-tone force,

$$F(t) = A \sin(2\pi f t), \tag{3}$$

where A and f are the amplitude and the frequency of the stimulus, respectively. The characteristic frequency (CF, i.e., the stimulus frequency that requires the lowest stimulus level A for which movement x reaches the threshold) of the FTC coincides with the resonant frequency ($f=1$) of the oscillator.

In addition to the FTC, Fig. 1(c) also shows a DP audiogram (black solid line; $2f_1-f_2$ obtained with $f_2/f_1=1.02$). To facilitate a graphical comparison between the two, the DP audiogram is plotted with a reversed y axis (the left y axis corresponds to the DP audiogram). The FTC is plotted over the same dB range (right y axis) as the DP audiogram, with its offset chosen to match the minima of the two curves. This shows that the FTC is much more broadly tuned than the DP audiogram. However, when the FTC is scaled by a factor of 4 along the y axis (gray dashed line), its shape becomes almost identical to that of the DP audiogram.

The necessity to scale the FTC by a factor of 4 to make its shape identical to the shape of the inverted DP audiogram can be explained by considering the following example. For a given combination of stimulus tones, let us change stimulus frequency f_1 in such way that the response of the oscillator [as expressed in x in Eq. (1)] to this stimulus tone increases by 1 dB. But this shift of f_1 will also result in a shift of stimulus frequency f_2. When using a small stimulus frequency ratio f_2/f_1, this frequency shift of f_2 will be approximately the same as the shift for f_1. At the same time, the small ratio f_2/f_1 ensures that f_1 and f_2 change over (approximately) the same absolute frequencies. As a consequence, the change in the movement x in response to the f_2 frequency shift will be similar to the change induced by the f_1 frequency shift (i.e., 1 dB). For a power-law nonlinearity, such a 1 dB increase in both of the stimulus tones will result in a distortion product that is increased in amplitude by 3 dB. This alone would give rise to a scaling factor of 3. But the frequency shift of both stimulus tones results in a frequency shift of the DPOAEs as well. Since the generated DPOAEs themselves are part of the response x, they will be filtered accordingly. This filtering, resulting from the frequency shift, also changes the DPOAE amplitude by about 1 dB. Combined, the 3 dB increase (caused by the 1 dB increase from the shift of the stimulus frequencies) and the 1 dB increase (due to the change in DPOAE frequency) result in a scaling factor of 4.

In summary, using the Duffing oscillator as a model for the basilar papilla reveals that the maximum DP amplitude occurs when one of the stimulus tones (f_1 for $2f_1-f_2$ and f_2 for $2f_2-f_1$, respectively) coincides with the CF of the FTC. This is independent of the stimulus frequency ratio f_2/f_1 used. Also, the FTC is much more broadly tuned than the DP audiogram, but this difference is absent when the FTC is scaled by a factor of 4 along the y axis.

IV. RESULTS

Distortion product otoacoustic emissions (DPOAEs) were obtained for a range of stimulus frequencies ($213<f_1<2774$ Hz). As a consequence, DPOAEs were recorded from both the amphibian papilla (AP) and the basilar papilla (BP). It is currently believed that the generation of DPOAEs from both papillae gives rise to the bimodal frequency dependence of emission amplitude in DPOAE audiograms: in the leopard frog, DPOAEs evoked with stimulus frequencies below 1250 Hz presumably arise from the AP, while DPOAEs evoked with higher stimulus frequencies are thought to arise from the BP. Following Van Dijk and Manley (2001), we will refer to emissions from the amphibian papilla as AP-DPOAEs, and those from the basilar papilla as BP-DPOAEs.

The frequency dependence of emission amplitude can be seen in Fig. 2, which shows a series of DPOAE audiograms, each one obtained with a different stimulus frequency ratio f_2/f_1. A relative minimum in emission amplitude is found when either f_1 [for $2f_1-f_2$, Fig. 2(a)] or f_2 [for $2f_2-f_1$, Fig. 2(b)] is approximately 1250 Hz. Both for lower and higher stimulus frequencies, emission amplitude exhibits a relative maximum. The filled circles indicate the maximum DPOAE in the basilar papilla frequency range (stimulus frequencies>1250 Hz) in each DPOAE audiogram. For increasingly larger stimulus frequency ratios f_2/f_1 (successive lines in Fig. 2) it can be seen that this maximum occurs for a fixed stimulus frequency (fixed f_1 for $2f_1-f_2$ and fixed f_2 for $2f_2-f_1$, respectively). Only for the largest stimulus frequency ratios, the maximum BP-DPOAE is found for somewhat lower stimulus frequencies. In the following, we will refer to the stimulus frequency (f_1 for $2f_1-f_2$ and f_2 for $2f_2-f_1$) that results in the maximum BP-DPOAE as the distortion product best frequency BF_{DP}. The term best frequency (BF) is used, rather than characteristic frequency (CF), since DPOAE audiograms are equal-*input* curves. This in contrast to FTCs, which are equal-*output* curves and hence result in characteristic frequencies.

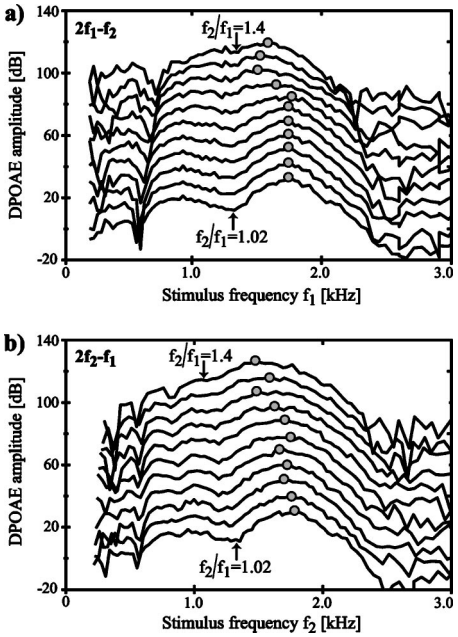

FIG. 2. A series of DPOAE audiograms for (a) $2f_1-f_2$ and (b) $2f_2-f_1$ obtained in one frog. Each DPOAE audiogram was recorded by varying the two stimulus tones while keeping the stimulus frequency ratio constant (i.e., fixed f_2/f_1 sweeps). For clarity, curves are offset by 10 dB with $f_2/f_1=1.02$ at the bottom and $f_2/f_1=1.4$ at the top. The stimulus levels were fixed and constant in all sweeps ($L_1=L_2=76$ dB SPL). Notice that for $2f_1-f_2$ the stimulus frequency f_1 is on the abscissa, while for $2f_2-f_1$ the stimulus frequency f_2 is on the abscissa. All DPOAEs show a bimodal dependence on frequency, with a single relative maximum for frequencies above and below 1250 Hz, respectively. It is currently believed that this reflects DPOAEs from both the amphibian papilla (AP-DPOAE, $f<1250$ Hz) and basilar papilla (BP-DPOAE, $f>1250$ Hz). For the BP-DPOAE, maxima in emission amplitudes are indicated by the filled circles.

The dependence of BF_{DP} on stimulus frequency ratio f_2/f_1 is illustrated in Fig. 3. This figure shows the shift in BF_{DP} (the shift is relative to BF_{DP} for $f_2/f_1=1.02$) as a function of stimulus frequency ratio f_2/f_1, averaged across all frogs. Both for DPOAE at $2f_1-f_2$ ("+," solid line) and $2f_2-f_1$ ("○," dashed line), BF_{DP} remains unchanged for relatively small frequency ratios ($f_2/f_1<1.16$). For increasingly larger ratios, BF_{DP} shifts to increasingly lower frequencies.

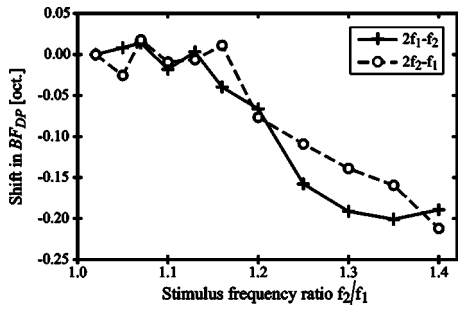

FIG. 3. The stimulus frequency that resulted in the maximum BP-DPOAE (BF_{DP}) as a function of the stimulus frequency ratio f_2/f_1, averaged over all frogs. The BF_{DP} found at $f_2/f_1=1.02$ is taken as a reference, and changes in BF_{DP} are expressed relative to this reference. For neither $2f_1-f_2$ ("+," solid line) nor $2f_2-f_1$ ("○," dashed line) does BF_{DP} change for relatively small stimulus frequency ratios ($f_2/f_1<1.16$). For larger ratios, BF_{DP} shifts toward lower frequencies in both DPOAEs.

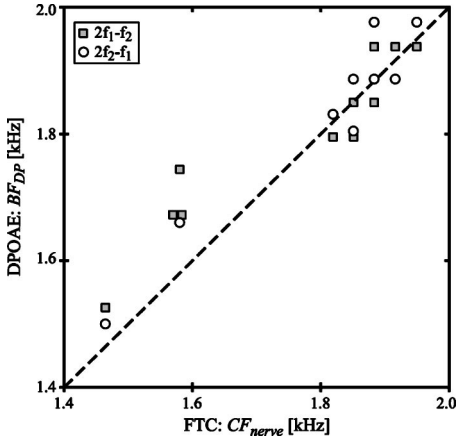

FIG. 4. Scatter plot of the stimulus frequency resulting in the maximum BP-DPOAE amplitude (BF_{DP}) for $f_2/f_1=1.02$ versus the characteristic frequency (CF_{nerve}) of the nerve fiber FTC. For $2f_1-f_2$ (filled "□") BF_{DP} refers to stimulus frequency f_1, while for $2f_2-f_1$ ("○") BF_{DP} refers to stimulus frequency f_2. As a reference, the diagonal dashed line indicates the condition for which $BF_{DP}=CF_{nerve}$.

Besides BP-DPOAEs, we also obtained frequency threshold curves (FTCs) from each frog. To ascertain that a FTC was obtained from a nerve fiber that innervated the basilar papilla, not only CF and the corresponding threshold level (CL) were determined, but also the bandwidth of the tuning curve at 10 dB above CL (i.e., W_{10}). Ronken (1991) showed that W_{10} can be used to discriminate between nerve fibers innervating the AP and the BP, respectively. In our results, nerve fibers that qualified as BP units are those for which W_{10} ranged from 1272 to 2161 Hz, while CFs were between 1464 and 1949 Hz. Besides FTCs from basilar papillar fibers, we also made recordings from nerve fibers that innervated the amphibian papilla and the sacculus, respectively. For the present paper, these recordings were ignored. To distinguish the FTC tuning properties from those calculated for BP-DPOAE, we will add the subscript "nerve" to them.

A graphical comparison between the tuning properties of the FTCs and the DPOAE audiograms (i.e., CF vs BF and a comparison between CL, W_{10}, and $Q_{10}=CF/W_{10}$, respectively) revealed no clear quantitative relation between the two, except when CF and BF were compared (Fig. 4). This figure shows BF_{DP} from DPOAE audiograms obtained with $f_2/f_1=1.02$ against CF_{nerve} from the FTCs, combined for all frogs. Both for DPOAE at $2f_1-f_2$ (filled "□") and $2f_2-f_1$ ("○") the BF_{DP} roughly coincides with the CF_{nerve} of the accompanying FTC.

Figure 5 shows three examples of $2f_1-f_2$ DPOAE audiograms obtained with $f_2/f_1=1.02$ (black, solid line) and FTCs (black, dashed line). Each subplot shows data obtained in one frog. To facilitate a graphical comparison with the FTC, the DPOAE audiogram is plotted with a reversed y axis (the left y axis corresponds to the DPOAE amplitude), while the x axis displays stimulus frequency f_1. The stimulus level range for the FTC (right y axis) was chosen to match the amplitude range used to display the DPOAE audiogram, while the offset was chosen to match the CF of the FTC and the BF of the (reversed) DPOAE audiogram. This is the

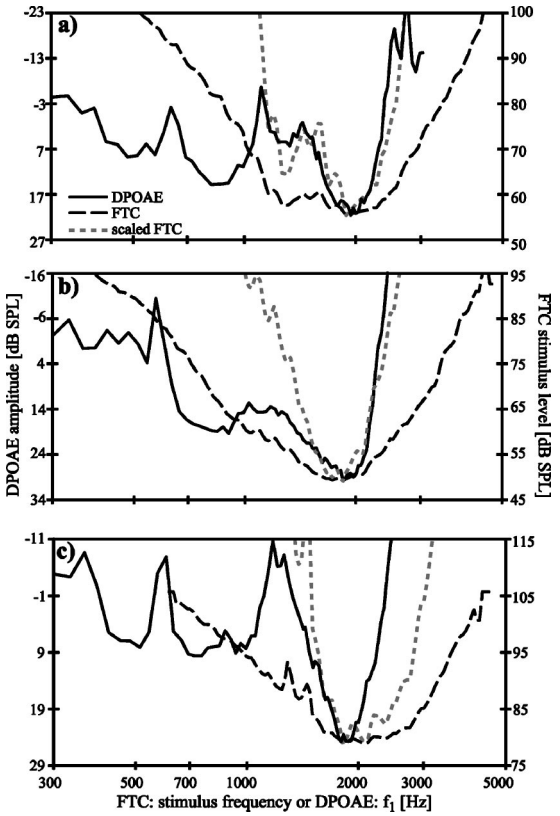

FIG. 5. Examples of FTCs (black; dashed line) and DPOAE audiograms for $2f_1-f_2$ (black, solid line) recorded in three different frogs. DPOAEs were obtained with $f_2/f_1=1.02$. In each panel, the stimulus frequency f_1 for the DPOAE audiograms is indicated on the abscissa, while the left *y* axis shows the DPOAE amplitude. Notice that this axis goes from high to low levels, resulting in a reversed representation of the DPOAE audiogram. The right *y* axis shows the threshold stimulus levels for the FTC. The range of both *y* axes are identical, while the offsets were chosen to match the minima of both curves. In each panel, the gray dashed line is the same FTC, but with its *y* axis scaled by a factor of 4.

same representation as was used in Fig. 1(c). All three subplots show that the CF_{nerve} and the BF_{DP} are almost identical, as was already illustrated in Fig. 4. For frequencies away from CF, the two curves deviate from each other, resulting in a much broader tuning of the FTC compared to the BP-DPOAE. However, when the FTC is scaled by a factor of 4 along its *y* axis (gray dashed lines), the shape of the FTC and the BP-DPOAE become more similar. For frequencies above CF, the two curves either nearly overlap [Figs. 5(a), 5(b)], or are oriented approximately parallel [Fig. 5(c)]. For frequencies below CF, the shape of the FTC and the BP-DPOAE also display similarities. For instance, in the BP-DPOAE of Fig. 5(a), the relative minimum near 1300 Hz coincides with relatively large DPOAEs at the same stimulus frequency f_1. In Figs. 5(b), 5(c) the correspondence between the two curves disappears below about 1500 Hz, presumably due to the contribution of distortion products from the AP.

V. DISCUSSION

In the present study, we reported on both distortion product otoacoustic emissions (DPOAEs) and nerve fiber frequency threshold curves (FTCs) obtained from the frog basilar papilla (BP). We obtained DPOAEs for a range of stimulus frequencies ($213<f_1<2774$ Hz). This range covers frequencies of the highest sensitivity in both the amphibian papilla (AP) and the basilar papilla (BP). It is currently believed that emission-generation in both papillae results in the bimodal frequency dependence in the DPOAE audiograms (Van Dijk and Manley, 2001; Van Dijk *et al.*, 2002; Meenderink and Van Dijk, 2004). This is based on the idea that relative maxima in emission amplitudes arise when the stimulus maximally excites either the AP or the BP. For submaximal stimulation of the papillae, the emission amplitude will be relatively reduced. So, the frequency separation between the two maxima in the DPOAE audiogram would depend on the frequency separation of the highest sensitivity of the AP and the BP. In ranid frogs, the AP gives rise to fibers tuned to frequencies up to 1.5 kHz, while the tuning of the BP varies with frog species. This would result in a species-specific frequency separation of the two relative maxima in the DPOAE audiogram, as is indeed found. For instance, in *Hyla cinerea*, the BP is most sensitive to frequencies of approximately 3.5 kHz (Capranica and Moffat, 1983) and the two relative maxima in the DPOAE audiogram from this species are separated by a frequency range in which no emissions are detected (Van Dijk and Manley, 2001). In the leopard frog, the BP is tuned to lower frequencies, partially overlapping with the frequency range covered by the AP (Ronken, 1991). As a result, DPOAE audiograms show relatively large DPOAE amplitudes in the frequency ranges 500–1200 Hz and 1300–2500 Hz, corresponding to the frequency ranges of the highest sensitivity of the amphibian and the basilar papilla, respectively. In *R. pipiens pipiens* an amplitude notch is often observed in between these two frequency ranges at about 1250 Hz. This suggests that near that frequency, emissions from both papillas may interfere. However, these results strongly support the notion that below and above the notch the DPOAE signal is dominated by a component from either the amphibian or the basilar papilla, respectively.

In the model, DP audiograms obtained with relatively large f_2/f_1 exhibit three more or less pronounced lobes, rather than only a single maximum (Fig. 1). These arise whenever f_1, f_2, or f_{DP} coincides with the resonant frequency of the Duffing oscillator. These three lobes are not immediately apparent in our BP-DPOAE data. Their absence is most likely caused by the relatively broad tuning of the basilar papilla. As a consequence, the frequency ratios f_2/f_1 we used did not result in a frequency separation between the two stimulus tones large enough to separate the three lobes in the DPOAE audiogram. This is similar to why the DP audiograms, obtained with small f_2/f_1, from the model exhibit only a single maximum. The frequency separation between the stimulus tones in relation to the tuning width of the filter is insufficient to separate the three lobes.

The BP is of interest to hearing research, since it functions as a single auditory filter (Ronken, 1990; Van Dijk and Manley, 2001). This property is not found in any other vertebrate hearing organ. In addition, the tuning properties of nerve fiber FTCs and DPOAEs probably are different manifestations of the same mechanical tuning mechanism present

in this papilla, as is implied by the following two considerations (Van Dijk and Manley, 2001): (1) neural tuning of nerve fibers that innervate the basilar papilla presumably originates from a mechanical tuning mechanism (Smotherman and Narins, 1999). Since this papilla lacks a basilar membrane, or an analog structure (hair cells are embedded in the rigid wall of the papillar recess), it is reasonable to assume that the mechanical tuning is the result of the mechanics of the hair bundles and the tectorial membrane; (2) BP-DPOAEs are probably generated by the nonlinear mechanics associated with the basilar papilla hair cells and their overlying tectorial membrane (Meenderink and Van Dijk, 2004). Combining these two considerations, one may conclude that the BP-DPOAEs and the neural FTC very likely reflect the same mechanical filter.

Recently, the Duffing oscillator has been used as a model for DPOAEs from the basilar papilla (Van Dijk and Manley, 2001; Meenderink *et al.*, 2005). These studies show that such a simple model qualitatively describes the dependence of emission amplitude and phase on both absolute (f_1, f_2) and relative (f_2/f_1) stimulus frequencies. Since tuning in nerve fibers from the basilar papilla arises from the same mechanism as the DPOAE, we also used the Duffing oscillator to model nerve fiber frequency threshold curves. These calculations showed several correlations between threshold curves and the tuning properties of the distortion products: (1) distortion product amplitude is maximized whenever the stimulus frequency that is closest to the distortion product frequency (i.e., f_1 for $2f_1-f_2$ and f_2 for $2f_2-f_1$) coincides with the resonant frequency of the oscillator. This is independent of the stimulus frequency ratio f_2/f_1 used [Figs. 1(a), 1(b)]. Also, the characteristic frequency (CF) of the FTC also coincides with the resonant frequency of the oscillator [Fig. 1(c)]. Thus, $CF_{nerve}=BF_{DP}$, independent of the ratio f_2/f_1 used to obtain the DP audiogram. (2) The low- and high-frequency slopes of the DP audiogram are much steeper than those of the FTC. As a consequence, the FTC is much more broadly tuned than the DP audiogram. In the model, this difference in the shape/slope of the two functions is almost absent when the FTC is scaled by a factor of 4 along the *y* axis [Fig. 1(c)]. We will discuss these two model predictions in relation to the BP-DPOAEs and FTCs obtained in the frog.

In the simple model, the FTC is inversely proportional to the amplitude response. Thus, CF_{nerve} will equal the resonant frequency of the model oscillator. At the same time, the DP amplitude is maximized when either f_1 (for $2f_1-f_2$) or f_2 (for $2f_2-f_1$) coincides with the resonant frequency. The combination of these two results gives that $BF_{DP}=CF_{nerve}$, independent of the stimulus frequency ratio f_2/f_1. The scatter plot in Fig. 4 shows that in the frog $BF_{DP}=CF_{nerve}$ for $f_2/f_1=1.02$. As expected from the model, this relation is maintained for increasing f_2/f_1 (as long as $f_2/f_1<1.16$), since BF_{DP} does not change when the stimulus frequency ratio is increased (Fig. 3). However, for larger f_2/f_1 the maxima in the DPOAE audiograms occur for lower stimulus frequencies, i.e., BF_{DP} decreases, and the predicted relation between BF_{DP} and CF_{nerve} is no longer found. This discrepancy between the results and the model may be understood when considering the simplifications made by using the Duffing oscillator as a model for the BP.

The Duffing oscillator is intended to model the mechanics of the tectorial membrane and the hair cell stereovilli of the basilar papilla. The oscillator is a simplification of this system in two respects. First, the Duffing oscillator is a second-order system, containing one stiffness element and one mass. In contrast, the basilar papilla contains between 50–100 hair cells, and the tectorial membrane is a flexible structure with multiple degrees of freedom. This structure presumably behaves as a high-order system, as is confirmed by recordings from primary auditory nerve fibers (Narins and Hillery, 1983; Van Dijk *et al.*, 1994). Second, input–output functions of DPOAEs from the frog ear (Meenderink and Van Dijk, 2004) show that the nonlinear element cannot be as simple as the parabolic stiffness of the Duffing oscillator [Eq. (1)].

The second result from the model is that the filter shapes of the FTC and the DP audiogram are quite different, with the former much more broadly tuned than the latter. In the model, this difference is largely absent when the FTC is scaled by a factor of 4 along the *y* axis.

In qualitative agreement with the model, neural tuning curves are more broadly tuned than DPOAE audiograms. From Fig. 5 it can be seen that the application of a scaling factor of 4 to the recorded FTCs ''improves'' the correspondence between the FTC and the DPOAE audiogram. In the first case [Fig. 5(a)] the scaled FTC closely follows the DPOAE audiogram for frequencies above 1100 Hz. In the second case [Fig. 5(b)] only the tip and the high-frequency slope of the scaled FTC and the DPOAE audiogram coincide. Finally, in the third case [Fig. 5(c)] the tip and part of the low-frequency slopes of both curves coincide.

For frequencies below 1250 Hz, the discrepancy between the (scaled) FTC and the DPOAE audiogram suddenly becomes quite pronounced. This presumably originates from the contribution of the amphibian papilla to the recorded emission signal below this frequency.

The application of a scaling factor of 4 was motivated by the model results. The model includes a cubic nonlinearity, the Duffing stiffness term. Although this may appear to be an expansive nonlinear term, it is actually a compressive nonlinear model: with increasing stimulus level, the stiffness and, consequently, the total impedance of the model rapidly increases.[1] However, we considered the response of the Duffing oscillator at small stimulus amplitudes. Then, the growth of the distortion products is dominated by the cubic nonlinearity, and for fixed stimulus frequencies the DP grows at 3 dB/dB. When simulating FTCs and DP audiograms, the stimulus frequencies are not fixed. As argued in Sec. III, the distortion product itself is also subject to the second-order bandpass character of the oscillator. Consequently, the use of the Duffing oscillator requires a scaling factor of 4.

In frogs, the growth rate of DPOAEs from the BP is close to 2 dB/dB, rather than 3 dB/dB, over a large range of stimulus levels. Only at moderate stimulus intensity, emission levels grow less steep with stimulus amplitude (Meenderink and Van Dijk, 2004). In line with the argument given

in Sec. III, it would be expected that FTCs, scaled by a factor of 3 (i.e. 2+1), would overlap with the DPOAE audiograms. Obviously, both the model and the data presented are not consistent with this expectation. From the rather complex shape of DPOAE input/output functions (Meenderink and Van Dijk, 2004) it follows that the characteristic of the nonlinearity in the ear must be more complex than a simple cubic stiffness term. This would result in a relation between FTCs and DPOAE audiograms that is more complex than described by the Duffing oscillator, also rendering the derivation of the scaling factor more difficult.

Finally, the usefulness of a comparison between details in the shape of a FTC and a DPOAE audiogram is limited by the fact that the former is an iso-output measure and the latter is an iso-input measure. Obtaining both neural and emission responses at a range of input levels may allow for a better comparison between the two quantities.

VI. CONCLUSIONS

We presented both DPOAEs and nerve fiber tuning data from the frog basilar papilla and compared their properties. This comparison is of interest because the BP not only functions as a single auditory filter (Ronken, 1990; Van Dijk and Manley, 2001), it is also believed that both the tuning of nerve fibers FTC) and BP-DPOAEs are the result of the same mechanical filter (Van Dijk and Manley, 2001). As a simple model for such a single auditory filter we used the Duffing oscillator. This model predicts two correlations between the tuning of DPOAEs and neural tuning. (1) The characteristic frequency of the FTC and the best frequency of BP-DPOAEs will coincide ($CF_{nerve}=BF_{DP}$), independent of the ratio f_2/f_1 used during DPOAE recordings, and (2) the shape of the FTC and the BP-DPOAE will be quite different, with the FTC much more broadly tuned compared to the BP-DPOAE. In the model, this difference largely disappears when the FTC is scaled by a factor of 4 along the *y* axis.

To some degree, the results obtained from the frog basilar papilla qualitatively agree with these model predictions. For small stimulus frequency ratios f_2/f_1, the CF_{nerve} and the BF_{DP} were similar. Only for larger f_2/f_1, the first model prediction was no longer found, most likely caused by the oversimplified representation of the BP mechanics in the model. Also in line with model predictions, the shape of the FTC and the DPOAE audiogram were quite different, with the former being much broader tuned than the latter.

In the model, the FTC and the DP audiogram match each other after scaling the FTC by a factor of 4. In the basilar papilla, this scaling procedure results in a partial overlap of these curves. The differences between the scaled FTC and the DPOAE audiogram are not too surprising. The derivation of the scaling factor depends on the nonlinear characteristics of the oscillator. In the model, the relatively small stimulus levels result in a constant scaling factor of 4. In the frog, it seems that the complex nonlinear behavior of the basilar papilla will result in a scaling factor that is not constant, but one that will vary depending on the parameters of the two stimulus tones.

We conclude that the single oscillator model, in which emission and neural tuning result from the same filter, qualitatively describes the behavior of the frog basilar papilla. This supports the idea that this hearing organ functions as a single auditory filter.

ACKNOWLEDGMENTS

We wish to thank Leola Hau for her assistance in the recording of the frequency threshold curves. This work was supported by grants from the Netherlands Organization for Scientific Research (NWO), and the Heinsius Houbolt Foundation to SWFM and PvD, and NIH Grant No. DC-00222 to PMN.

[1]Note that when considering only the nonlinear terms on the left-hand side of Eq. (1), it becomes $x^3/x_0^2=F(t)$. Thus, with $F(t)$ being the "input" and $x(t)$ the "output," the input/output function is compressive: $x(t)=F^{1/3}(t)x_0^{2/3}$. Although this is an oversimplification of the oscillator, it illustrates the oscillator's compressive behavior.

Capranica, R. R., and Moffat, A. J. M. (**1975**). "Selectivity of the peripheral auditory system of spadefoot toads (*Scaphiopus couchii*) for sounds of biological significance," J. Comp. Physiol. **100**, 231–249.

Capranica, R. R., and Moffat, A. J. M. (**1983**). "Neurobehaviourial correlates of sound communication in anurans," in *Advances in Vertebrate Neuroethology*, edited by J. P. Ewert, R. R. Capranica, and D. J. Ingle (Plenum, New York), pp. 701–730.

Evans, E. F. (**1979**). "Single unit studies of mammalian cochlear nerve," in *Auditory Investigations: The Scientific and Technological Basis*, edited by H. A. Beagley (Clarendon, Oxford), pp. 324–367.

Feng, A. S., Narins, P. M., and Capranica, R. R. (**1975**). "Three populations of primary auditory nerve fibers in the bullfrog (*Rana catesbeiana*): Their peripheral origins and frequency sensitivities," J. Comp. Physiol. **100**, 221–229.

Lewis, E. R., and Leverenz, E. L. (**1983**). "Morphological basis for tonotopy in the anuran amphibian papilla," Scan Electron Microsc. **I**, 189–200.

Lewis, E. R., Leverenz, E. L., and Koyama, H. (**1982**). "The tonotopic organization of the bullfrog amphibian papilla, an auditory organ lacking a basilar membrane," J. Comp. Physiol. **145**, 437–445.

Meenderink, S. W. F., Narins, P. M., and Van Dijk, P. (**2005**). "Detailed f_1, f_2 area study of distortion product otoacoustic emissions in the frog," J. Assoc. Res. Otolaryngol. **6**, 37–47.

Meenderink, S. W. F., and Van Dijk, P. (**2004**). "Level dependence of distortion product otoacoustic emissions in the leopard frog, *Rana pipiens pipiens*," Hear. Res. **192**, 107–118.

Narins, P. M., and Hillery, C. M. (**1983**). "Frequency coding in the inner ear of anuran amphibians," in *Hearing—Physiological bases and Psychophysics*, edited by R. Klinke and R. Hartmann (Springer-Verlag, Heidelberg), pp. 70–76.

Ronken, D. A. (**1990**). "Basic properties of auditory-nerve responses from a simple ear: The basilar papilla of the frog," Hear. Res. **47**, 63–82.

Ronken, D. A. (**1991**). "Spike discharge properties that are related to the characteristic frequency of single units in the frog auditory nerve," J. Acoust. Soc. Am. **90**, 2428–2440.

Smotherman, M. S., and Narins, P. M. (**1999**). "Potassium currents in auditory hair cells of the frog basilar papilla," Hear. Res. **132**, 117–130.

Stiebler, I. B., and Narins, P. M. (**1990**). "Temperature-dependence of auditory nerve responses properties in the frog," Hear. Res. **46**, 63–82.

Van Dijk, P., Lewis, E. R., and Wit, H. P. (**1990**). "Temperature effects on auditory nerve fiber response in the americal bullfrog," Hear. Res. **44**, 231–240.

Van Dijk, P., and Manley, G. A. (**2001**). "Distortion product otoacoustic emissions in the tree frog *Hyla cinerea*," Hear. Res. **153**, 14–22.

Van Dijk, P., Mason, M. J., and Narins, P. M. (**2002**). "Distortion product otoacoustic emissions in frogs: correlation with middle and inner ear properties," Hear. Res. **173**, 100–108.

Van Dijk, P., Wit, H. P., and Segenhout, J. M. (**1997**). "Dissecting the frog

inner ear with Gaussian noise. I. Application of high-order Wiener-kernel analysis,'' Hear. Res. **114**, 229–242.
Van Dijk, P., Wit, H. P., Segenhout, J. M., and Tubis, A. (**1994**). ''Wiener kernel analysis of inner ear function in the American bullfrog,'' J. Acoust. Soc. Am. **95**, 904–915.
Wever, E. G. (**1973**). ''The ear and hearing in the frog, *Rana pipiens*,'' J. Morphol. **141**, 461–478.
Zelick, R. D., and Narins, P. M. (**1985**). ''Temporary threshold shift, adaptation, and recovery characteristics in frog auditory nerve fibers,'' Hear. Res. **17**, 161–176.

Medial surface dynamics of an *in vivo* canine vocal fold during phonation

Michael Döllinger,[a] David A. Berry, and Gerald S. Berke
The Laryngeal Dynamics Laboratory, UCLA Division of Head & Neck Surgery, 1000 Veteran Ave. Suite 31-24, Los Angeles, California, 90095-1794

(Received 6 May 2004; revised 25 January 2005; accepted 26 January 2005)

Quantitative measurement of the medial surface dynamics of the vocal folds is important for understanding how sound is generated within the larynx. Building upon previous excised hemilarynx studies, the present study extended the hemilarynx methodology to the *in vivo* canine larynx. Through use of an *in vivo* model, the medial surface dynamics of the vocal fold were examined as a function of active thyroarytenoid muscle contraction. Data were collected using high-speed digital imaging at a sampling frequency of 2000 Hz, and a spatial resolution of 1024 $\times$1024 pixels. Chest-like and fry-like vibrations were observed, but could not be distinguished based on the input stimulation current to the recurrent laryngeal nerve. The subglottal pressure did distinguish the registers, as did an estimate of the thyroarytenoid muscle activity. Upon quantification of the three-dimensional motion, the method of Empirical Eigenfunctions was used to extract the underlying modes of vibration, and to investigate mechanisms of sustained oscillation. Results were compared with previous findings from excised larynx experiments and theoretical models. © *2005 Acoustical Society of America.* [DOI: 10.1121/1.1871772]

PACS numbers: 43.70.Aj, 43.70−h [AL] Pages: 3174–3183

I. INTRODUCTION

Although voice production is a critical component of human communication, the process of voice generation is not well understood, particularly with regard to the voice source. Because of the small size and inaccessibility of the larynx, the possibilities for laryngeal imaging are limited. Most *in vivo* recordings of vocal fold vibration have been performed from a superior aspect using endoscopy.[1–3] From this aspect, it is impossible to quantify the medial surface dynamics of the vocal folds, which describe the opening and closing of the glottis that generates sound. From a superior aspect, it is also impossible to quantify the propagation of the mucosal wave along the medial surface of the folds. Because of these limitations, clinicians usually refer to mucosal wave propagation along the superior surface of the folds, where they see the wave more clearly. Unfortunately, the mucosal wave attenuates quickly upon reaching the superior surface of the folds.

In terms of its influence on voice production, the most critical region of mucosal wave propagation occurs on the medial surface of the vocal folds, where it originates.[4,5] Before reaching the superior surface, the wave travels a relatively long distance along the medial surface, it generates significant tissue vibrations that exhibit geometric and viscoelastic nonlinearities,[6,7] and it couples nonlinearly with other systems, including the opposite vocal fold (e.g., through collision during glottal closure) and sub- and supraglottal systems (e.g., through fluid–structure interactions with the glottal airflow).[8] Indeed, mucosal wave propagation along the medial surface of the folds is governed by a very complex set of dynamics that is only beginning to be understood.[5] The modeling of such complexity is still in its infancy, and requires further quantitative data for validation. Hence, quantification of the medial surface dynamics of the vocal folds holds promise for increasing our understanding of voice production and for supporting computational modeling efforts.[9–11]

Because of the difficulty in imaging the medial surface of the vocal folds, only a few quantitative studies have attempted such imaging.[12–16] However, of these investigations, Berry *et al.*[16] was the only study to image and quantify the medial surface of the vocal folds with sufficient spatial and temporal resolution to enable extraction of the underlying modes of vibration, sometimes referred to as Empirical Eigenfunctions.[17] Such modes have been shown to be helpful for investigating mechanisms of both normal and abnormal voice production.[16,17]

One of the limitations of the previous study of medial surface dynamics was the use of the excised larynx,[16] which neglected the influence of the thyroarytenoid (TA) muscle on vocal fold vibration. With the excised larynx, laryngeal adjustments were implemented through means of external forces. For example, an external force that pulled downward on the thyroarytenoid notch caused the thyroarytenoid cartilage to rock forward on the cricoid cartilage, lengthening the vocal fold. Similarly, an external force that pulled anteriorly on the muscular process caused the arytenoid to rock anteriorly and medially, adducting the vocal process. However, while such external forces can simulate many laryngeal adjustments, they cannot simulate TA contraction. The simultaneous contraction, stiffening, and medial surface bulging of the TA can only occur through active muscular contraction.[18] Muscle shortening and medial surface bulging create a deeper medial surface over which the mucosal wave propagates, impacting the medial surface dynamics of the vocal

[a]Electronic mail: michael.doellinger@gmx.net

 0001-4966/2005/117(5)/3174/10/$22.50

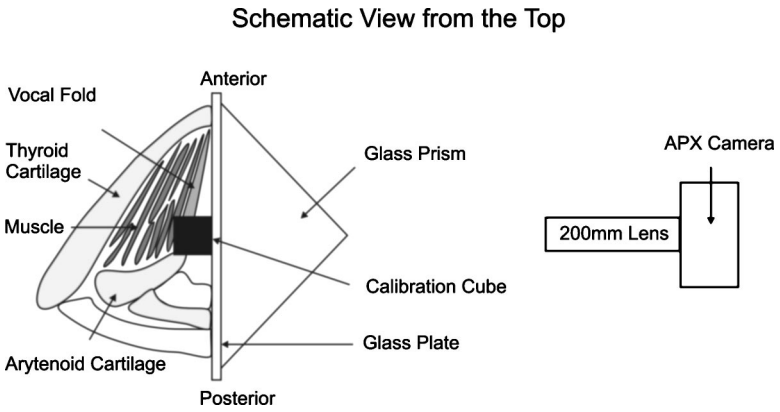

FIG. 1. A schematic representation of the experimental setup from a superior view: The glass plate, situated at the glottal midline, appears as a vertical line in the middle of the picture. The vocal fold and brass calibration cube are situated on the left side of the plate, and the glass prism and high-speed camera are situated on the right.

fold. Increased muscle stiffness may also increase the velocity of the mucosal wave. In addition, TA muscular adjustment is a critical factor influencing vocal registers, such as falsetto and chest.[18] For example, in the chest register, increased TA muscle contraction significantly increases the rate of closure.

On the other hand, the absence of TA muscle contraction simulates a condition of paralysis of the membranous vocal folds, in which the stiffness of the muscle is reduced, approaching the significantly lower stiffness of the cover.[19] In this situation, the vocal folds experience large vertical excursions, reduced mucosal wave velocity, and a relatively gentle closure of the membranous vocal folds. Interestingly, this is the only condition of the membranous glottis that can be simulated in the excised larynx, because the TA is denervated in this model. The inability to model active TA contraction limits the range of glottal conditions that can be investigated in the excised larynx model. The inclusion of the *in vivo* canine laryngeal model broadens the scope of an investigation of the medial surface dynamics of the vocal fold, allowing a more representative range of normal and pathological glottal conditions to be investigated.

Nevertheless, because of the invasive nature of the hemilarynx setup, many technical challenges were involved in adapting it for an *in vivo* study. Hence, the purpose of the present investigation was to demonstrate the viability of the hemilarynx model in quantifying the medial surface dynamics of an *in vivo* canine vocal fold as a function of active contraction of the thyroarytenoid muscle; to extract the underlying modes of vibration; and to investigate mechanisms of sustained oscillation.

II. MATERIAL AND METHODS

A. Experimental setup

The experimental setup in this study was an adaptation of recent work with an excised hemilarynx methodology.[16,20,21] The work was also inspired by previous quantitative imaging of a full excised larynx by Baer,[12] previous excised hemilarynx work by Jiang and Titze,[14] and previous investigations of the *in vivo* canine laryngeal model by Berke *et al.*,[22] and Bielamowicz *et al.*[23]

A male mongrel canine, weighing 25 kg, was selected for the study. The canine was premedicated intramuscularly with acepromazine and buprenex. Over the course of the experiment, halothane ventilation and intravenous pentobaritol was administered to prevent reflexive response to corneal stimulation. Following the experiment, the canine was humanely sacrificed with intravenous *Eutha-6*.

The canine was placed supine on an operating table. A hemilarynx was created through means of a neck dissection and a hemilaryngectomy, which included the removal of half of the hyoid bone. To provide a controlled air supply for phonation, air was insufflated rostrally through a tracheostomy. For the vibration patterns reported in this study, the glottal airflow was held relatively constant at 660 ± 15 ml/s, and the subglottal pressure was varied between 1.2 and 3.7 kPa. The air was heated (37 °C) and humidified using a humidifier (Concha Therm III, Servo-Controlled Heater). The canine was assist-ventilated (Monaghan 300 D/M Ventilator) with 4 L/min O_2 via an endotracheal tube. A schematic representation of the experimental setup is shown in Fig. 1.

So that specific flesh points could be tracked during the experiments, small black monofilament nylon microsutures were placed on the medial surface of the vocal fold (size: 9-0, diameter: 0.034 mm, Ethicon, Inc.). To minimize any disturbance of the natural dynamics, the microsutures were positioned to penetrate only the mucosal epithelium, with a reported thickness of 0.05–0.1 mm.[24] Five columns of microsutures with five microsutures per column were mounted along the medial–superior surface of the vocal fold, where the greatest amplitudes of vibration were expected to occur; see Fig. 2. The distance between the flesh points were 3.1 ± 0.2 mm in the anterior–posterior direction and 2.1 ± 0.2 mm in the vertical direction.

Next, the trachea was mounted over a stainless steel cylindrical tube with an inner diameter of 8 mm. A wedge was mounted within the tube to smoothly channel the airflow beneath the vocal fold. At the top of the tube, a glass plate (width: 61.2 mm, height: 61.1 mm, thickness: 3.2 mm was mounted at the glottal midline; Fig. 1. To eliminate airflow leaks between the vocal fold and the glass plate, strips of gauze, coated with vacuum grease, were inserted between them. The preparation of the experiment took approximately four hours. Following preparation, the experiment itself took less than two hours.

To simultaneously achieve muscle contraction, muscle stiffening, medial surface bulging, and vocal fold adduction, the recurrent laryngeal nerve (RLN) was stimulated using a constant-current nerve stimulator (WR Medical Electronics

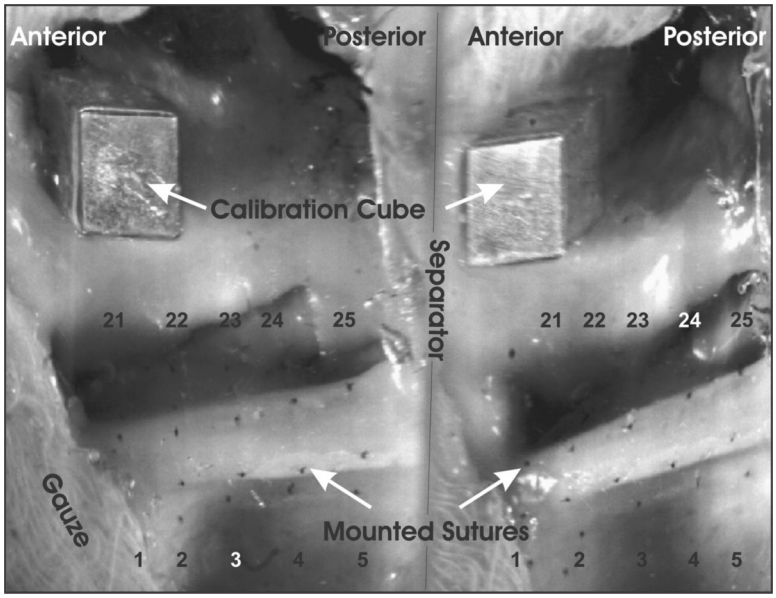

FIG. 2. Split view provided by the prism, as seen through the high-speed camera. Here 25 sutures are enumerated in both views. Above the sutures, the calibration cube is also visible in both views. In both views, the anterior sutures are to the left, and the posterior sutures are to the right. On the lower left side, gauze is visible concealing suture number one.

Co. Model 2SLH, St. Paul, MN). The RLN was stimulated with currents ranging from 0.04–0.08 mA at 80 Hz, with a 1.5 ms pulse duration.[22,23] The superior laryngeal nerve (SLN) was not stimulated. The RLN was isolated 5 cm inferior to the larynx in the tracheoesophageal groove. Custom designed rubber electrodes (monopolar, flexible, conductive neopreme with silicone, and silicone insulation KE45) were applied to the isolated nerve at the most proximal point dissected. Electrical isolation of the nerve was confirmed by direct visualization of the vocal folds during stimulation. The animal required dissection and division of the posterior branch of the RLN to the posterior cricoarytenoid muscle to achieve adduction and modal phonation.

For calibration purposes, a brass cube (5.04 mm $\times$5.04 mm$\times$5.06 mm) was glued to the glass plate superior to the vocal fold. The cube was large enough that one could identify its corners and edges, but small enough to avoid significant disturbance of the glottal airflow (Fig. 1). A right-angle prism was placed against the glass plate, on the side opposite to the vocal fold. The prism yielded two different camera views,[16] which was necessary for the computation of three-dimensional movement.[25] The prism was large enough to yield a view of the entire medial surface of the vocal fold.

The vibrations of the vocal fold were imaged with a high-speed digital camera (Fastcam-Ultima APX, Photron Unlimited, Inc.) with a 200 mm lens (AF MICRO NIKKOR) at a frame rate of 2000 Hz and spatial resolution of 1024 $\times$1024 pixels. Three 150 W lamps (MI-150 Illuminator, Dolan-Jenner, Inc.) served as light sources. The light sources were only applied for a few seconds at a time during imaging to prevent tissue dehydration. Appropriate tissue hydration was further facilitated using a humidified air supply, as already described. The acoustical signal was simultaneously recorded at a distance of 10 cm to the acoustical source with a condenser microphone (Model No. 4193, Brüel & Kjaer Inc.) and digitized at 44.1 kHz. The high-speed recording and the acoustical signal were synchronized through means of an external trigger.

B. Extraction of flesh points

Two primary issues complicated automatic detection of the mounted sutures (i.e., automatic flesh point extraction). First, the sutures on the superior surface of the folds (the top two anterior–posterior rows of sutures) were concealed during portions of the glottal cycle (Fig. 2). Second, the close proximity of the sutures sometimes resulted in overlapping trajectories. Hence, a semi-automatic algorithm was developed, which allowed user intervention to correct possible errors. The algorithm was implemented as follows: First, to increase visibility of the flesh points, all frames were contrast enhanced.[26] Next, for the first five frames, the flesh point positions were selected manually. From these data, the mean values and the variances of each flesh point were computed. In succeeding frames, flesh point positions were determined automatically: a quadratic extrapolation estimated the new flesh point position, a search was performed around this position, with a radius corresponding to the predetermined variance, to locate the cluster of points with the lowest gray values (darkest points). The center of mass of these points was selected as the new flesh point position, and the mean values and variances were appropriately updated. As previously indicated, manual intervention was allowed to correct possible errors.

C. Computation of physical coordinates

To compute the three-dimensional coordinates of the flesh points, at least two two-dimensional camera views were necessary.[25] As in Berry *et al.*,[16] the split view through the prism provided the two camera views (Fig. 2). In the previous hemilarynx study,[16] calibration was performed at the end of the experiment using a Direct Linear Transform (DLT). This method would be inappropriate for the *in vivo* canine, because it would be impossible to keep camera parameters constant across experimental conditions. For example, canine breathing caused lifting and lowering of the chest and the hemilarynx setup (i.e., the prism and the glass plate with

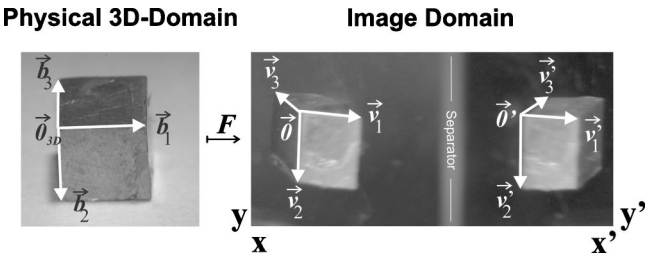

FIG. 3. Schematic representation of the LA method through means of the transformation matrix *F*. The left picture shows the brass cube in the physical domain, while the right picture shows the two camera views through the prism. Both camera views were assumed to preserve parallel projections.

a cube). Stimulating the RLN repositioned the vocal fold at the glass plate. The vocal fold vibrations themselves could potentially induce slight translations of the experimental setup. Also, because of the high sampling rates required to capture laryngeal vibrations, along with the high light intensity, and low *f* stop (i.e., small depth of field), it was often necessary to refocus the camera to maintain sharp focus across experimental conditions.

To deal with the possibility of changing camera parameters, a calibration object (i.e., a brass cube) was present in each imaging frame; see Fig. 2. Because the cube was situated above the vocal fold, an extrapolation had to be performed to compute the physical coordinates of the sutures. This disqualified the use of the DLT,[27–30] which works well under interpolation, but not under extrapolation.[31] Consequently, a linear approximation method (LA method) was implemented. In a recent excised hemilarynx investigation, the LA method yielded a more accurate calibration than the DLT,[20,21] presumably because of the DLT's poor extrapolation performance.

The primary assumption of the LA method was that parallel projections were preserved in the two different camera views. In other words, the parallel edges of the brass cube would remain parallel in both camera views; see Fig. 3. For this assumption to be valid, the camera lens had to be positioned approximately perpendicular to the glass plate (Fig. 1). This assumption was not difficult to satisfy given the relatively small region of interest (e.g., approximately a 1 cm width, 1 cm height, and 0.5 cm depth); Fig. 2. Therefore, any distortions caused by nonparallelism between the camera lens and the glass plate induced only small errors in the mapping to three-dimensional coordinates. Indeed, when parallelism was compromised because of camera orientation, the distortions of the brass cube were immediately apparent in the camera images. As a result, the camera position was refined until the distortions were no longer apparent by mere inspection. The final distortions were quantified using the root-mean-square error.[32] In the recordings to be presented later, the computed linearization error was 9.1%, which was presumably introduced by camera orientation.

Mathematically the LA method may be explained as follows. First, there is a mapping *f* of the three-dimensional physical domain $\mathbb{R}^3$ in a two-dimensional image $\mathbb{R}^2$ (camera view); see Fig. 3. By recording images through a prism, the camera view is split and the image domain can be regarded as two two-dimensional spaces $\mathbb{R}^2\times\mathbb{R}^2$, or as a subspace of $\mathbb{R}^4$. For computational reasons (e.g., matrix inversion), the physical domain was expanded from $\mathbb{R}^3$ to $\mathbb{R}^4$ to yield a mapping: $f:\mathbb{R}^4\mapsto\mathbb{R}^4$. The added fourth dimension in the physical domain served as a dummy dimension. Linear mappings are uniquely determined by the mapping of the basis vectors of the domain. As basis vectors, the three orthogonal directions of the brass cube were chosen, with the origin of the coordinate system at the left upper corner of the cube $\vec{0}_{3\text{-D}}$; see Fig. 3: $\vec{b_1}$, $\vec{b_2}$, $\vec{b_3}$. A fourth orthogonal basis vector, $\vec{b_4}$ was chosen, which spanned the introduced fourth dimension. The basis vectors were mapped by the split camera view (Fig. 3) into

$$\begin{aligned} f(\vec{b_1}) &= (\vec{v}_1,\vec{v}_1') = (x_1,y_1,x_1',y_1'),\\ f(\vec{b_2}) &= (\vec{v}_2,\vec{v}_2') = (x_2,y_2,x_2',y_2'),\\ f(\vec{b_3}) &= (\vec{v}_3,\vec{v}_3') = (x_3,y_3,x_3',y_3')\\ f(\vec{b_4}) &= (0,0,0,y_4'). \end{aligned} \tag{1}$$

The linear mapping *f* from the three-dimensional physical world to the split camera view could now be described by a matrix *F*. Finally, the three-dimensional physical coordinates $\vec{v}_{3\text{-D}}$ of the sutures were computed by multiplying the images coordinates $\vec{v}_{\text{rec}}$ by the inverse matrix F^{-1}:

$$F=\begin{pmatrix} x_1 & x_2 & x_3 & 0\\ y_1 & y_2 & y_3 & 0\\ x_1' & x_2' & x_3' & 0\\ y_1' & y_2' & y_3' & y_4' \end{pmatrix}, \quad \text{with} \quad \vec{v}_{3\text{-D}}=F^{-1}\cdot\vec{v}_{\text{rec}}. \tag{2}$$

For better computational results, the entries of *F* were optimized using the Nelder–Mead Algorithm,[33,34] which has successfully optimized parameters of theoretical models to fit measured vocal fold vibration patterns.[3,35]

D. Data analysis

Because some sutures were not visible during portions of the glottal cycle, not all sutures could be extracted for an analysis. In particular, the two most superior rows (sutures 16–25, Fig. 2), which were placed on the superior surface of the vocal fold, could not be extracted over the entire glottal cycle. Hence, the quantitative investigations for the later reported recording R1 were restricted to sutures No. 1–15 (e.g., the lower three rows), which were placed on the medial surface of the vocal fold. For the other analyzed recording (R2), additionally, sutures no. 1,6,11 were not considered, since the extracted displacements were very small (i.e., 1–2 pixels) and therefore not appropriate for further computation. The analysis was performed over a time period of 100 ms, or 200 frames. The acoustically measured fundamental frequency ranged from 180–220 Hz for chest-like phonation and from 30–80 Hz for fry-like phonation.

Displacements, velocities, and accelerations were computed over the entire medial surface of the vocal fold. To further probe mechanisms of sustained oscillation, Empirical Eigenfunctions (EEF) were also computed. Because EEFs have been described in earlier work,[16,17,36] they will not be explained here in detail. Conceptually, they may be viewed

as the basic building blocks of many simple and complex vibration patterns. In other words, they may be viewed as a decomposition of the vocal fold oscillations into their basic vibratory degrees of freedom. In previous computational studies, essentially constant EEFs explained a variety of periodic and aperiodic vocal fold vibration patterns, which were distinguished primarily by the entrainment (i.e., the same fundamental frequency) or lack of entrainment of the EEFs.[10,17]

III. RESULTS AND DISCUSSION

The hemilarynx model was adapted for the *in vivo* canine, yielding a clear view of the medial surface of the vocal fold, and opening the door for future detailed examination of the influence of the thyroarytenoid muscle on phonation. Improvements to the experimental setup and calibration procedure yielded high quality recordings and quantitative results. In comparison to previous hemilarynx studies, the entire medial surface of the vocal fold was imaged, instead of just one coronal cross section.[16] Furthermore, three-dimensional vibrations were reported in the present investigation, in comparison to previous computational and experimental studies in which only two-dimensional vibrations were reported (e.g., anterior–posterior vibrations were ignored).[10,16,17]

For this *in vivo* hemilarynx, phonation threshold pressure occurred at 1.2 kPa, and phonation was observed across a subglottal pressure range of 1.2–3.7 kPa. Phonation was also observed across a range of RLN stimulation from 0.04–0.08 mA. The original design of this experiment was to report a variety of vibrations as a function of the stimulation current to the RLN. However, this was not a stable input measure with which to differentiate the different vibration patterns. That is, both chest-like and fry-like vibrations were observed across the entire range of current stimulations.

As shown in Nasri *et al.*,[37] the TA stimulation (as measured by electromyography or EMG) is a sigmoidal, or step function of the RLN stimulation current (or voltage). In particular, over a very narrow range of RLN stimulation current, the TA activity varied from 0% to 100% of maximum stimulation. Thus, with only a small amount of input noise, the resultant TA activity may be completely unknown. Perhaps due to this phenomenon, in the present study, the recorded vibration patterns occurred randomly with respect to the input RLN stimulation current.

Nevertheless, the Nasri *et al.*[37] study also reported that robust measures of TA activity (expressed in the percentage of maximum stimulation) could be estimated based on the dynamical range of subglottal pressure. For the present study, the dynamical range of subglottal pressures was 1.2–3.7 kPa. Using the empirical relationship from Nasri *et al.*,[37] periodic, chest-like phonation was observed in the range of 12%–37% of maximum TA stimulation (corresponding to a subglottal pressure of 1.2–2.2 kPa). Fry-like phonation was observed in the range of 37%–100% of maximum TA stimulation (corresponding to a subglottal pressure of 2.2–3.7 kPa), characterized by low fundamental frequencies (30–80 Hz), irregular oscillations, and pulse-like vibrations, with relatively long periods of glottal closure. Within the range of chest-like vibrations, fundamental frequency increased with increasing TA activity. However, beyond a certain threshold of TA activity, fundamental frequency abruptly dropped, resulting in fry-like vibrations. Similar phenomena have been previously observed and predicted.[38–41] For example, it is known that TA activity causes the TA muscle to simultaneously stiffen and contract. If the muscle itself were a significant component of the vibrating tissue (presumably this would be the case in chest voice), as TA activity was increased, the increased stiffness of the TA would result in an increase in the fundamental frequency. Because abrupt jumps between registers (bifurcations) commonly occur for small changes in some input parameter, it is not surprising that an abrupt jump is observed between chest-like and fry-like vibrations for some critical threshold of maximum TA stimulation. However, if the tissue vibrations only occurred in the cover (presumably this would be the case in vocal fry), as TA activity were increased, the contraction of the TA would also shorten the cover, decreasing the stiffness in the cover, and thereby decreasing the fundamental frequency. Future studies will report further details regarding the dynamics of the fry-like vibrations observed in the *in vivo* canine larynx.

TABLE I. The TA stimulation level, the RLN stimulation, the measured subglottal pressure (sP), the applied air flow, and the measured fundamental frequency for the investigated recordings.

Recording	TA stimulation (%)	RLN (mA)	sP (kPa)	Flow (ml/s)	F_0 (Hz)
R1	33	0.07	2.1	650	220
R2	12	0.04	1.6	675	180

In this study, we focus on the details of two chest-like vibrations at 33% (R1) and 12% (R2) of TA activity, respectively. The details regarding these two phonations are summarized in Table I. Exemplarily, the reconstructed physical positions of the sutures for one frame within R1 are illustrated in Fig. 4. For orientation in this figure, glottal airflow initiated inferiorly and proceeded superiorly through the hemiglottis. Zero in the ''lateral'' dimension denoted the glottal midline, or the position of the glass plate. The axis coordinates denoted distances from the chosen origin: the left upper corner of the cube at the glass plate; see Fig. 3. Maximum displacements, velocities and accelerations and decelerations occurred midway between the anterior and posterior extremes of the membranous vocal fold, near the superior extreme of the medial surface (Suture Nos. 12, 13, 14; see Fig. 4), the location where the mucosal wave is expected to have the largest displacement.[5] The largest components of displacements occurred in the lateral direction, and the smallest components occurred in the anterior–posterior direction, as previously reported.[13,42] The sutures with the smallest displacements were near the anterior–inferior edge of the medial surface (Suture Nos. 1, 2; see Fig. 4). For both phonatory utterances, the numerical values of extrema for displacements, velocities, and accelerations are summarized in Table II.

The influence of the 9.1% linearization error of the calibration on the dynamical variables of displacement, velocity, and acceleration was also computed. This was done by recomputing the dynamical variables after randomly varying

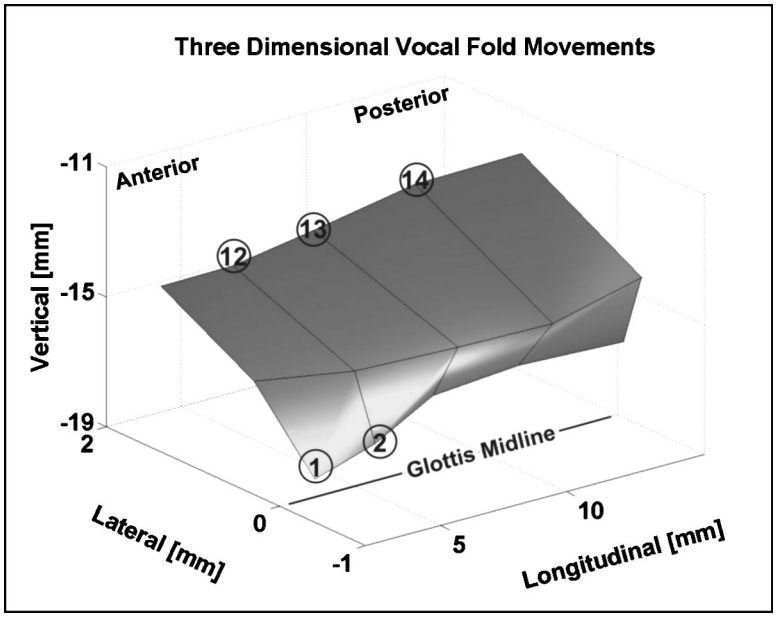

FIG. 4. A three-dimensional reconstruction of the vocal fold. The physical locations of extreme values are denoted by the highlighted sutures. The magnitudes of the corresponding extrema are enumerated in Table II. Zero on the lateral axis corresponds to the glottal midline or the position of the glass plate.

the entries of the mapping matrix F up to 6%, which matched the discrepancy to the former reported calibration error of 3.9%.[20] Across the two examples, the maximum deviations of the maximum displacements due to the increased linearization error were as follows: 0.11 (lateral), 0.07 (vertical), and 0.04 mm (anterior–posterior). The maximum discrepancies were 0.06 mm/ms for maximum velocity, and 0.02 mm/ms^2 for maximum acceleration and deceleration. The stability of the mapping matrix F against small distortions was achieved by using orthogonal basis vectors and an optimized condition number.[20] The condition number reflects the linear independency of the matrix entries. With small condition numbers (i.e., the minimal value is 1) in the mapping matrix F on the order of 3.2–3.6, small disturbances in F resulted in small disturbances in the image.[20]

Empirical Eigenfunctions, or the underlying modes of vibration, were also extracted from the two vibration sequences (see Table III). For R1, the largest EEF (EEF1) captured 69.5% of the energy, the second largest EEF (EEF2) captured 23.6% of the energy, and the third largest EEF (EEF3) 1.6% of the energy. Hence, the two largest EEFs captured 93.1% of the total energy, and the largest three EEFs captured 94.7%. The two dominant eigenfunctions entrained at a fundamental frequency of 220 Hz and the weaker eigenfunction captured the second harmonic at 440 Hz.

For R2, the largest EEF captured 60.2% of the energy, EEF2 captured 33.1% of the energy, and EEF3 2.5% of the energy. Hence, the two largest EEFs captured 93.3% of the total energy, and the largest three EEFs captured 95.8%. The two dominant eigenfunctions entrained at a fundamental frequency of 180 Hz, and the weaker eigenfunction vibrated at an independent frequency of 70 Hz.

At 33% TA activity (R1), the spatial EEFs are displayed in Fig. 5 from a frontal aspect, and in Fig. 6 from a sagittal aspect. In Fig. 5, the three horizontal rows correspond to the three different eigenfunctions EEF1 to EEF3. The five columns correspond to the five vertical columns of sutures on the vocal fold. Zero on the lateral axis indicates the glottal midline. Values larger than zero resulted from computational inaccuracies, which only affect the actual position of the suture, but not the vibrational patterns. Axes are referenced from a chosen origin (i.e., upper left corner of the cube). The arrows indicate the direction of the suture movement. EEF1 captured an alternating convergent/divergent glottis, e.g., the dotted line captured a relatively divergent glottis and the dashed line captured a relatively convergent glottis. Similar to previous studies, the convergent glottis was associated with a relatively elevated vertical position. EEF2 primarily captured the lateral in-phase movements of the medial surface. For EEF3, it was difficult to discern a clear vibration because of the small amplitudes of vibration. Within R2,

TABLE II. The computed extremal values of displacement, velocity, and acceleration, and their positions; see Fig. 4.

	Recording 1 (R1)		Recording 2 (R2)	
	Value	Suture	Value	Suture
Max. displacement longitudinal (mm)	0.32	13	0.28	12
Max. displacement vertical (mm)	1.36	13	1.30	14
Max. displacement lateral (mm)	1.47	13	1.57	13
Min. displacement longitudinal (mm)	0.03	1	0.07	2
Min. displacement vertical (mm)	0.06	1	0.24	2
Min. displacement lateral (mm)	0.02	1	0.20	2
Max. absolute velocity (mm/ms)	1.62	13	1.04	14
Max. absolute acceleration (mm/ms^2)	0.61	13	0.40	14
Max. absolute deceleration (mm/ms^2)	0.58	13	0.38	13,14

TABLE III. Percentage parts of the computed three largest Empirical Eigenfunctions and the corresponding frequencies.

	Recording 1 (R1)		Recording 2 (R2)	
	(%)	Frequency (Hz)	(%)	Frequency (Hz)
EEF1	69.5	220	60.2	180
EEF2	23.6	220	33.1	180
EEF3	1.6	440	2.5	70
Σ	94.7		95.8	

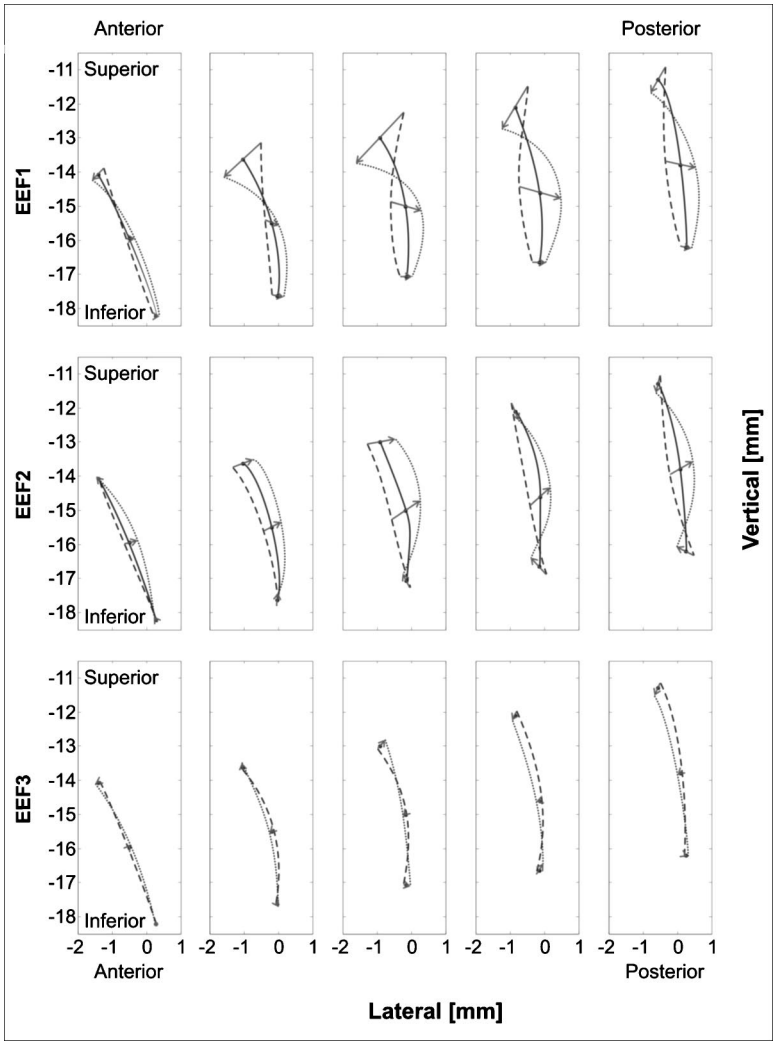

FIG. 5. Empirical Eigenfunctions for R1 (Suture Nos. 1–15): The maximum (dotted line) and minimum (dashed line) projections of the three largest EEFs about the equilibrium position (solid line) from a frontal aspect, for each of the five vertical columns of sutures. Zero on the lateral axis corresponds to the glottal midline. The units are measured from a chosen origin. The arrows indicate the direction of suture movement captured by the illustrated EEF. For EEF3, the mean value (solid line) has been omitted so as not obscure the maximum/minmum projections.

similar vibration and entrainment patterns were observed for EEF1 and EEF2.

While the 9.1% linearization error of the calibration procedure had a small impact on the computation of the dynamical variables, the linearization error had negligible impact on the computation of the eigenfunctions. The eigenvalues, which quantify the energy or the statistical variance captured by the empirical eigenfunctions, deviated by a maximum amount of 0.2% as a result of the linearization error. The dot product of EEF1 computed with and without the additionally induced linearization error was 0.998, also yielding an error of 0.2%. EEF2 yielded identical results. A similar dot product using EEF3 yielded 0.997, or an error of 0.3%. Theses results were consistent with previous reports, which showed that the computation of empirical eigenfunctions was a highly robust procedure, even in the presence of substantial background noise.[43]

Former computational studies[10,17] and experimental studies with excised larynges[16] have yielded similar underlying eigenfunctions for EEF1 and EEF2, with similar entrainment patterns, which are known to be critical for sustained oscillation. For example, the divergent glottis of EEF1 possesses a relatively low intraglottal pressure, while the alternating convergent glottis possesses a relatively high intraglottal pressure.[44] Thus, this eigenfunction correlated strongly with the intraglottal pressure. The elevated position of the convergent glottis was probably induced by the relatively high subglottal pressure associated with that glottal shape. On the other hand, EEF2 captured the net lateral movement of the medial surface.

For the fluid–structure interactions of concern, the transfer of energy from the airflow to the tissue would be optimized if the intraglottal pressure (governed by EEF1) were in-phase with the net lateral velocity of the vocal fold (governed by EEF2). Thus, the entrainment or synchronization of EEF1 and EEF2 would facilitate this transfer of energy, enabling sustained vocal fold oscillations.

Whether EEF1 must capture the alternating convergent/divergent glottal shape or whether it may switch roles with EEF2 is not entirely clear from the experiments to date. The present studies with an *in vivo* larynx, along with all previous computational studies[10,17] have indicated that EEF1 captures the alternating divergent/convergent glottis. On the other hand, in a former excised larynx experiment,[16] EEF1 captured the net lateral movement of the vocal fold, and EEF2 captured the alternating convergent/divergent glottis. So it may be that the roles of EEF1 and EEF2 may be reversed, but that both eigenfunctions are essential for sustained oscillation.

A comparison of the relative strengths of eigenfunctions

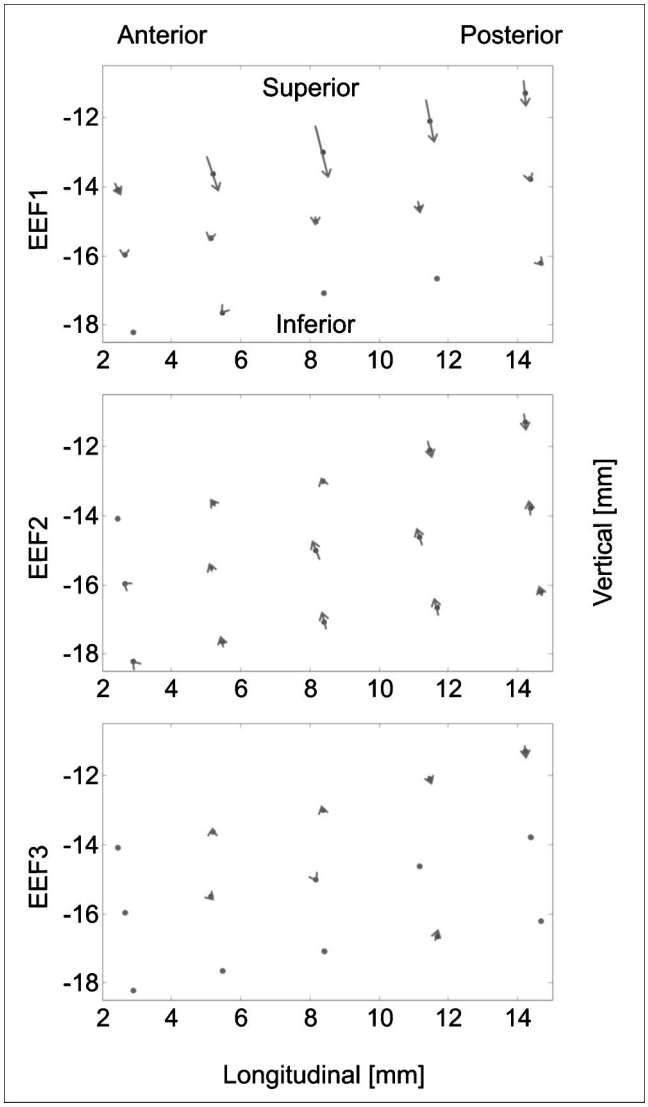

FIG. 6. The three largest EEFs for R1 from a sagittal aspect, for each of the five vertical columns of sutures (Suture Nos. 1–15). The units correspond to a chosen origin (i.e., the left upper corner of the cube). The arrows indicate the direction of the movement. The dots represent the mean values of the suture positions.

in several investigations is also of note. In clinical endoscopic studies of vocal fold vibration,[36] EEF1 captured 97% of the energy for normal phonation. In this study, it is important to note that only lateral movement, or one-dimensional vibrations were analyzed along the anterior–posterior length of the vocal fold. The EEF1 captured a half wavelength of a sinusoid along the anterior–posterior length of the folds, a characteristic feature of normal vocal fold vibration, as observed from a superior view. Higher-order anterior–posterior modes usually only become significant in an irregular voice.[36]

EEFs have also been extracted from finite element models of vocal fold vibration.[10,17] Because anterior–posterior vibrations were neglected in this model, two-dimensional vibrations were analyzed. In these studies, the two largest EEFs captured about 98% of the total energy. In an excised canine larynx experiment (normal phonation), which also reported two-dimensional vibrations (e.g., anterior–posterior vibrations were neglected here as well) the two largest EEFs again, captured 98% of the energy.[16] These results are to be compared with the present three-dimensional study in which the first two eigenfunctions explained about 93% of the energy and the first three eigenfunctions explained about 95% of the energy.

As just mentioned, previous theoretical and experimental studies have neglected anterior–posterior vibrations.[10,16,17] The improved spatial resolution (1024 $\times$1024 pixel) of the high-speed digital camera employed in this investigation enabled the study of full three-dimensional movement, including anterior–posterior vibrations. The results are shown in Fig. 6 from a sagittal view. For EEF1, the vertical movement of the superior row was clearly observable. In the lower two rows, little vertical or longitudinal movement was discernable. However, weak anterior–posterior vibrations did exist. Because EEF2 captured primarily lateral vibrations, both vertical and anterior–posterior vibrations were weak, but on the same order of magnitude. Again for EEF3, no unique behavior was discernable.

IV. CONCLUSIONS

This work reported the three-dimensional medial surface dynamics of an *in vivo* canine vocal fold as a function of RLN stimulation. The RLN stimulation current was not a robust input variable to differentiate the observed vibration patterns. However, an estimate of TA activity did reliably differentiate the vibration types, as did subglottal pressure. It should be noted that RLN innervation stimulates other muscles in addition to the TA, including the PCA (posterior cricoarytenoid), the LCA (lateral cricoarytenoid), and the IA (interarytenoid). However, because the PCA is an abductory muscle that tends to discourage phonation, this branch was clipped for this experiment. In addition, the IA branch was unavoidably clipped with the removal of one vocal fold to implement the hemilarynx procedure. Finally, if the LCA muscle did not adequately adduct the folds to produce phonation, additional external forces are applied to adduct the arytenoid. Thus, in our setup, the TA muscle was the primary muscle and perhaps the only laryngeal muscle dependent solley on RLN innervation.

Nevertheless, in future work, TA activity (or a similar measure such as the complex action potential) should be measured directly, rather than estimated. The hemilarynx methodology, previously designed for the excised larynx, was adapted for an *in vivo* canine larynx with thyroarytenoid muscle contraction. For the larynx in this study, chest-like vibrations were observed in the range of 12%–37% of TA activity (based on the percentage of maximum stimulation). Fry-like vibrations were observed in the range of 37%–100% of TA activity. During the chest-like vibrations, the fundamental frequency increased as a function of increasing TA stimulation. However, beyond a certain threshold in TA stimulation, an abrupt drop in fundamental frequency occurred resulting in fry-like vibration, an expected outcome for high TA and low cricothyroid (CT) stimulation (in the present study, since there was no SLN innervation, there was no presumably stimulation to the CT). This phenomenon could be explained in terms of existing theories of TA

function.[38–41] While the underlying modes of vibration were extracted and mechanisms of sustained oscillation were discussed, some difficulties were encountered (e.g., airflow leakage, and the inability to simultaneously image the superior and medial surfaces of the vocal fold). Nevertheless, areas with high mobility were identified along the medial surface of the vocal fold (Fig. 4). Furthermore, the EEFs were extracted and mechanisms of sustained oscillation were discussed, showing consistency with previous investigations of computational models[10,17] and excised larynx experiments.[16]

Future refinements need to be made in the imaging procedures in order to track sutures simultaneously on both the superior and medial surfaces of the vocal fold, as has been reported for the excised human larynx.[20] Indeed, this task has been implemented with little difficulty on excised human larynx studies, but was presumably more difficult here because of a small vocal lip that sometimes occurs on the canine vocal fold at the junction of the superior–medial surface.[45] Perhaps this difficulty in imaging the canine larynx can be circumvented by replacing the glass prism, with a more flexible set-up using mirrors. Other concerns included sealing airflow leakage in the posterior glottis, and properly hydrating the folds throughout the experiment. Future studies will also explicitly examine the observed fry-like vibrations of the *in vivo* canine vocal fold. Future studies will also covary several input variables, such as both RLN and SLN, which will allow other vocal registers, such as a falsetto, to be observed. It is expected that such studies will further illuminate the mechanisms of vocal production, particularly the poorly understood role of the thyroarytenoid muscle in phonation.[46] Ultimately, it would be desirable to extend these studies to independently estimate the mechanical stresses of the various layers of the vocal fold tissues (including the body, cover, and ligament) as a prelude to predicting tissue dynamics. However, at present, no reliable methods exist to estimate or measure such differential stresses in laryngeal tissue layers.

ACKNOWLEDGMENTS

This work was supported by Grant No. R01 DC03072 from NIH/NIDCD. The authors would also like to thank Norma Antonanzas-Barroso for her helpful comments.

[1] P. Mergell, H. Herzel, and I. Titze, ''Irregular vocal-fold vibration—high speed observation and modelling,'' J. Acoust. Soc. Am. **108**, 2996–3002 (2000).
[2] J. G. Svec, J. Horacek, F. Sram, and J. Vesely, ''Resonance properties of the vocal folds: *In vivo* laryngoscopic investigation of the externally excited laryngeal vibrations,'' J. Acoust. Soc. Am. **108**, 1397–1407 (2000).
[3] M. Döllinger, T. Braunschweig, J. Lohscheller, U. Eysholdt, and U. Hoppe, ''Normal voice production: Computation of driving parameters from endoscopic digital high speed images,'' Methods Inf. Med. **42**, 271–276 (2003).
[4] E. Schönhärl, *Die Stroboskopie in Der Praktischen Laryngologie* (Thieme-Verlag, Stuttgart, 1960).
[5] I. R. Titze, ''Parametrization of the glottal area, glottal flow, and vocal fold contact area,'' J. Acoust. Soc. Am. **75**, 570–580 (1984).
[6] Y. C. Fung, *Biomechanics: Mechanical Properties of Living Tissues* (Springer-Verlag, New York, 1993).
[7] R. Wilhemls-Tricarico, ''Physiological modeling of speech production: methods for modeling soft tissue articulators,'' J. Acoust. Soc. Am. **97**, 3085–3098 (1995).
[8] P. Mergell and H. Herzel, ''Modelling biphonation—the role of the vocal tract,'' Speech Commun. **22**, 141–154 (1997).
[9] M. P. de Vries, H. K. Schutte, and G. J. Verkerke, ''Determination of parameters for lumped parameter models of the vocal folds using a finite-element method approach,'' J. Acoust. Soc. Am. **106**, 3620–3628 (1999).
[10] F. Alipour, D. A. Berry, and I. R. Titze, ''A finite element model of vocal fold vibration,'' J. Acoust. Soc. Am. **108**, 3003–3012 (2000).
[11] E. J. Hunter, I. R. Titze, and F. Alipour, ''A three-dimensional model of vocal fold abduction/adduction,'' J. Acoust. Soc. Am. **115**, 1747–1759 (2004).
[12] T. Baer, ''Investigation of phonation using excised larynges,'' Ph.D. thesis, Massachusetts Institute of Technology, Boston, MA, 1975.
[13] S. Saito, H. Fukuda, S. Kitahira, Y. Tsuzuki, H. Muta, E. Takayama, T. Fujika, N. Kokawa, and K. Makino, ''Pellet tracking in the vocal fold while phonating: experimental study using canine larynges with muscle activity,'' in *Vocal Fold Physiology*, edited by I. R. Titze and R. C. Scherer (Denver Center for the Performing Arts, Denver, CO, 1985), pp. 169–182.
[14] J. J. Jiang and I. R. Titze, ''A methodological study of hemilaryngeal phonation,'' Laryngoscope **103**, 872–882 (1993).
[15] G. M. Gardner, J. Castracane, M. Conerty, and S. M. Parnes, ''Electronic speckle pattern interferometry of the vibrating larynx,'' Ann. Otol. Rhinol. Laryngol. **104**, 5–12 (1995).
[16] D. A. Berry, D. W. Montequin, and N. Tayama, ''High-speed digital imaging of the medial surface of the vocal folds,'' J. Acoust. Soc. Am. **110**, 2539–2545 (2001).
[17] D. A. Berry, H. Herzel, I. R. Titze, and K. Krischer, ''Interpretation of biomechanical simulations of normal and chaotic vocal fold oscillations with empirical eigenfunctions,'' J. Acoust. Soc. Am. **95**, 3595–3604 (1994).
[18] G. S. Berke and B. R. Gerratt, ''Laryngeal biomechanics: An overview of mucosal wave mechanics,'' J. Voice **7**, 123–128 (1993).
[19] F. Alipour-Haghighi and I. R. Titze, ''Elastic models of vocal fold tissues,'' J. Acoust. Soc. Am. **90**, 1326–1331 (1991).
[20] M. Döllinger and D. A. Berry, ''Computation of the three-dimensional medial surface dynamics of the vocal folds,'' J. Biomech. (in press).
[21] M. Döllinger and D. A. Berry, ''Three-dimensional medical surface dynamics of the vocal folds using high-speed digital imaging,'' in *Proceedings of the 26th World Congress of the International Association of Logopedics and Phoniatrics* (Speech Pathology Australia, Melbourne—Australia, 2004), p. CD.
[22] G. S. Berke, D. M. Moore, P. A. Monkewitz, D. G. Hanson, and B. R. Garrett, ''A preliminary study of particle velocity during phonation in an in vivo canine model,'' J. Voice **3**, 306–313 (1989).
[23] S. Bielamowicz, G. S. Berke, J. Kreiman, and B. R. Gerratt, ''Exit jet particle velocity in the in vivo canine laryngeal model with variable nerve stimulation,'' J. Voice **13**, 153–160 (1999).
[24] M. Hirano, ''Structure and vibratory behavior of the vocal folds,'' in *Dynamic Aspects of Speech Production*, edited by M. Sawashima and S. Franklin (Univ. of Tokyo, Tokyo, 1977), pp. 13–30.
[25] Y. I. Abdel-Aziz and H. M. Karara, ''Direct linear transformation from comparator coordinates into object space coordinates in close-range photogrammetry,'' in *Proceedings of the Symposium on Close-Range Photogrammetry* (American Society of Photogrammetry, Falls Church, VA, 1971), pp. 1–18.
[26] J. Lohscheller, M. Döllinger, M. Schuster, U. Eysholdt, and U. Hoppe, '' The laryngectomee substitute voice: Image processing of endoscopic recordings by fusion with acoustic signals,'' Methods Inf. Med. **42**, 277–281 (2003).
[27] N. R. Miller, R. Shapiro, and T. M. McLaughlin, ''A technique for obtaining spatial kinematic parameters of segments of biomechanical systems from cinematographic data,'' J. Biomech. **13**, 535–547 (1980).
[28] H. Hatze, ''High-precision three-dimensional photogrammetric calibration and object reconstruction using a modified DLT-approach,'' J. Biomech. **15**, 11–19 (1988).
[29] L. Chen, C. W. Armstrong, and D. D. Raftopoulos, ''An investigation on the accuracy of three-dimensional space using the Direct Linear Transformation,'' J. Biomech. **27**, 493–500 (1994).
[30] Y. Xunhua and L. Ryd, ''Accuracy analysis for RSA: a computer simulation on 3D marker reconstruction,'' J. Biomech. **30**, 493–498 (2000).
[31] G. A. Wood and R. N. Marshall, ''The accuracy of DLT extrapolation in three-dimensional film analysis,'' J. Biomech. **19**, 781–785 (1986).

[32] A. M. T. Choo and T. R. Oxland, ''Improved RSA accuracy with DLT and balanced calibration marker distributions with an assessment of initial-calibration,'' J. Biomech. **36**, 259–264 (2003).
[33] W. Murray, *Numerical Methods for Unconstrained Optimization* (Academic, London, 1972).
[34] G. Golub and C. V. Loan, *Matrix Computations*, 2nd ed. (The John Hopkins University, Baltimore, MD, 1989).
[35] M. Döllinger, U. Hoppe, F. Hettlich, J. Lohscheller, S. Schuberth, and U. Eysholdt, ''Vocal fold parameter extraction using the two-mass-model,'' IEEE Biomed. Eng. **49**, 773–781 (2002).
[36] J. Neubauer, P. Mergell, U. Eysholdt, and H. Herzel, ''Spatio-temporal analysis of irregular vocal fold oscillations: Biphonation due to desynchronization of spatial modes,'' J. Acoust. Soc. Am. **110**, 3179–3192 (2001).
[37] S. N. Nasri, P. Dulguerov, J. Damrose, M. Ye, J. Kreiman, and G. S. Berke, ''Relation of recurrent laryngeal nerve compound action potential to laryngeal biomechanics,'' Laryngoscope **105**, 639–643 (1995).
[38] M. Hirano, ''Morphological structure of the vocal cord as a vibrator and its variations,'' Folia Phoniatr. **26**, 89–94 (1974).
[39] M. Hirano, ''Phonosurgery: Basic and clinical investigations,'' Otologia (Fukuoka) **21**, 239–440 (1975).
[40] I. R. Titze, J. Jiang, and D. Druker, ''Preliminaries to the body-cover theory of pitch control.,'' J. Voice **1**, 314–319 (1988).
[41] I. R. Titze, *Principles of Voice Production* (Prentice–Hall, Englewood Cliffs, NJ, 1994).
[42] T. Baer, ''Investigation of the phonatory mechanism,'' ASHA Report 11, 1981, pp. 38–47.
[43] K. S. Breuer and L. Sirovich, ''The use of the Karhunen–Loeve procedure for the calculation of linear eigenfunctions,'' J. Comput. Phys. **96**, 277–296 (1991).
[44] I. R. Titze, ''The physics of small-amplitude oscillation of the vocal folds,'' J. Acoust. Soc. Am. **83**, 1536–1551 (1988).
[45] T. Riede, H. Herzel, D. Mehwald, W. Seidner, E. Trumler, G. Böhme, and G. Tembrock, ''Nonlinear phenomena in the natural howling of a dog–wolf mix,'' J. Acoust. Soc. Am. **108**, 1435–1442 (2000).
[46] I. Sanders, Y. Han, J. Wang, and H. Biller, ''Muscle spindles are concentrated in the superior vocalis subcompartment of the human thyroarytenoid muscle,'' J. Voice **12**, 7–16 (1998).

A flow waveform-matched low-dimensional glottal model based on physical knowledge

Carlo Drioli[a)]
Department of Speech, Music and Hearing, Royal Institute of Technology (KTH), Lindstedtsvägen 24, 10044 Stockholm, Sweden

(Received 11 November 2003; revised 30 November 2004; accepted 4 January 2005)

The purpose of this study is to explore the possibility for physically based mathematical models of the voice source to accurately reproduce inverse filtered glottal volume-velocity waveforms. A low-dimensional, self-oscillating model of the glottal source with waveform-matching properties is proposed. The model relies on a lumped mechano-aerodynamic scheme loosely inspired by the one- and multimass lumped models. The vocal folds are represented by a single mechanical resonator and a propagation line which takes into account the vertical phase differences. The vocal-fold displacement is coupled to the glottal flow by means of an aerodynamic driving block which includes a general parametric nonlinear component. The principal characteristics of the flow-induced oscillations are retained, and the overall model is able to match inverse-filtered glottal flow signals. The method offers in principle the possibility of performing transformations of the glottal flow by acting on the physiologically based parameters of the model. This is a desirable property, e.g., for speech synthesis applications. The model was tested on a data set which included inverse-filtered glottal flow waveforms of different characteristics. The results demonstrate the possibility of reproducing natural speech waveforms with high accuracy, and of controlling important characteristics of the synthesis such as pitch.
[DOI: 10.1121/1.1861234]

PACS numbers: 43.70.Bk, 43.70.Aj, 43.72.Ja [DOS] Pages: 3184–3195

I. INTRODUCTION

A wide number of speech analysis, coding, and synthesis techniques adopt today the source-filter model of speech production (Fant, 1960), in which the laryngeal excitation can be reasonably considered independent of vocal tract. In early synthesis schemes, voiced sounds were obtained by convolving an excitation made of impulse-like events with a filter shaping the spectrum toward the desired formant structure. Although synthetic speech was intelligible, the audio quality was often poor and speech sounded unnatural. Since then, new challenges have emerged in speech synthesis technologies. Among these, audio quality of the synthesis, naturalness of speech, speaker-specific synthesis, and rendering of emotions, are topical themes. The glottal source has been recognized to play an important role with respect to the quality of the synthesis (Holmes, 1973; Pinto *et al.*, 1989; Rosenberg, 1971), and speech synthesis schemes and systems relying on extended models of the glottal excitation are now available (Childers and Hu, 1994; Klatt and Klatt, 1990; Meyer *et al.*, 1989; Milenkovic, 1993; Sondhi and Schroeter, 1987). Today, various approaches to glottal excitation modeling have been proposed. A broad classification includes analytical models, in which the glottal pulse is parametrized in terms of analytical functions [the LF model by Fant *et al.* (1985) is a well-known model of this type], and physical models, in which the oscillatory characteristics of the vocal folds are reproduced by numerical discretization of the underlying dynamical process equations [the two-mass model by Ishizaka and Flanagan (1972) is one of the first models of this type]. Applications often require the glottal model to fit observed glottal flow waveforms, e.g., obtained by inverse filtering. While there has been some research dealing with parametric identification of analytical models to match inverse-filtered glottal waveforms (Childers and Ahn, 1995; Childers and Hu, 1994; Fröhlich *et al.*, 2001; Strik, 1998), much less has been devoted to the same problem when physical models are to be used (Meyer *et al.*, 1989; Schroeter and Sondhi, 1992).

Numerical models of the voice source production based on the physiology of the vocal folds have been proposed since 1968 (Flanagan and Landgraf, 1968). The first attempts to simulate the flow-induced oscillations of the vocal folds were based on a lumped-element model made of a single spring–mass oscillator driven by airflow from the lungs. An essential improvement to the one-mass model was proposed by Ishizaka and Flanagan (1972), with their two-mass model (referred to as the IF model from now on). In brief, in the IF model each of the vocal folds is represented by two damped mass–spring systems coupled to each other. In addition, a nonlinear interaction with the airflow is derived from aerodynamic equations describing the pressure drops from lungs to vocal tract. A wide range of variations and improvements has been proposed since the introduction of the original one- and two-mass models (Ishizaka and Flanagan, 1977; Koizumi *et al.*, 1987; Liljencrants, 1991; Titze, 1988). Koizumi *et al.* (1987) have described several variations of the two-mass model devised mainly to provide a better simulation of the mucosal surface wave and vertical phasing. Some of the

[a)]Also at Istituto di Scienze e Tecnologie della Cognizione, Sezione di Padova Fonetica e Dialettologia, Via Anghinoni 10, 35121 Padova, Italy (correspondence address). Electronic mail: drioli@csrf.pd.cnr.it

improvements included were horizontal as well as vertical displacement of masses and time-varying masses dimensions. A more accurate simulation of mucosal surface wave was targeted by Liljencrants (1991) as well, by allowing one mass to rotate around its center of gravity, driven by the pressure gradient in the flow direction. Other authors experimented with lumped models made of a larger number of masses in the attempt to increase the naturalness and accuracy of the model (Titze, 1973). However, the increase of accuracy in the modeling has disadvantages as well, as the growth of computational complexity and the difficulty to fit the model to observed data, due to the large amount of parameters involved. This prevented the physical modeling approach from being extensively adopted in practical applications (such as speech synthesis and coding/compression) in spite of its intrinsic potentialities, and today the principal motivations for physical modeling of the voice source remain the understanding and learning about the phonatory process.

The long-term goal of this research is to design a class of computationally efficient physically based models of the voice production, oriented to speaker-specific and emotional voice synthesis applications, and to model-based speech coding. There are several reasons why the physiological models are potentially interesting for synthesis and coding applications (Schroeter and Sondhi, 1992): many complicated and fast variations in the waveform or in the frequency-domain description are the result of slow variations in the control of the physical quantities and articulators involved in the speech production process. Examples are the transients in the dynamical behavior due to changes in the lung pressure, in the vocal-fold adduction and tension, or in the vocal-tract shape. These fine cues largely contribute to the degree of naturalness of the synthesized or decoded speech. Moreover, the adoption of a dynamical model is in a sense a natural way of interpolating the slowly time-varying control parameters. However, exceptional difficulties in the extraction of the control parameters of complex physical models from the speech signal have prevented these conjectures from being verified.

The complexity of the model inversion (the process of getting the control curves given the target waveform) and the low versatility of most highly accurate physical models, are the principal obstacles to our goal. This article describes a preliminary investigation on a class of source models which combines physical knowledge and data-driven parametric fitting to the aim of reproducing inverse-filtered glottal flow waveforms. The main purpose of this paper is to address the question of whether speech production models based on physical insights are adaptable to match natural speech signals measured from a speaker.

We introduce a waveform-matched mathematical model of the glottis loosely inspired by the myoelastic-aerodynamic theory and the lumped mass–spring paradigm. The principal difference with respect to the original one- and multimass models is the oversimplification of the mechanical resonator and the inclusion of a parametric nonlinear component in the mechano-aerodynamic loop. The design of this component relies on a data-driven identification scheme which allows the model oscillation to be fitted to a target volume-velocity waveform. The principal characteristics of a flow-induced oscillation are maintained. As a result, the necessary stability and transitory behavior can be achieved, while the generic nonlinear term provides for the adaptation to the fine cues of the target flow. The properties of a low-dimensional self-oscillating glottal model are first reviewed, and the improvements introduced to support the data-driven modeling approach are described. The parametric identification of the model and issues concerning the synthesis of voiced sounds are then discussed. The experiment section is finally dedicated to the fitting of different inverse filtered volume-velocity waveforms to the model.

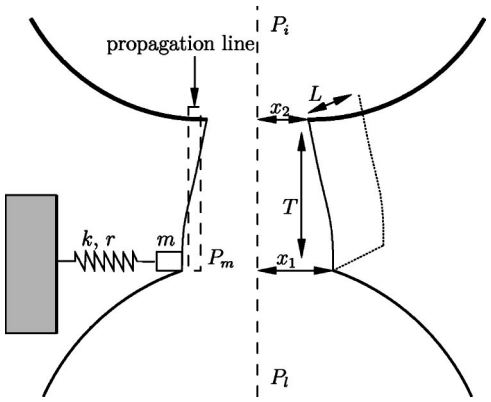

FIG. 1. The one-mass model of the vocal folds.

II. DESCRIPTION OF THE GLOTTAL MODEL

The choice of the glottis model structure is inspired by the lumped multimass paradigm and by the body-cover wave model by Titze (1988). The body-cover model is based on the observation that the vocal folds can be divided into two tissue layer with different mechanical properties: a body layer, made of muscle fibers and ligament fibers, and a cover layer, made of a pliable tissue (the epithelium and the superficial layer) that acts as a sheath around the body layer. Due to its loose connection to the other tissue layers, the cover motion is relatively independent of the body layer. On the basis of these observations, the body-cover model perspective looks at the vocal-fold motion as a surface wave that propagates along the body cover from the bottom of the glottis to the top. In Fig. 1, we reproduced a simplified version of the body-cover model, where a single mass–spring system is provided at the entrance to the glottis, and a transmission line is responsible for the phase delay between the entry and exit to the glottis.[1] A similar one-delayed-mass model has been previously explored by Avanzini *et al.* (2001). It retained the principal characteristics of flow-induced oscillation, despite its simplicity and computational efficiency.

The mechanical system is described by the mass–spring oscillator equation

$$m\ddot{x}_1 + r\dot{x}_1 + kx_1 = F_m, \tag{1}$$

where x_1 is the lateral displacement of the vocal fold at the entrance of the glottis, m, r, and k are, respectively, the mass, damping factor, and stiffness, and F_m is the force that drives

the folds. When the motion of vocal folds is viewed in terms of mucosal waves propagating along the glottis in the direction of the flow, these waves can be described by a one-dimensional equation of the form $\partial^2 x/\partial t^2 = c_f^2 \partial^2 x/\partial z^2$, where z is the distance from the entrance point of the glottis along the vertical axis, $x(z,t)$ is the time-dependent displacement of the fold surface at z, and c_f is the wave velocity on the fold surface (we will assume here a surface-wave velocity of 1 m/s). Using the Taylor series formula to expand its general D'Alembert solution, we have $x(z,t) = x_1(t - z/c_f) = x_1(t) - z\dot{x}_1(t)/c_f$, where $x_1(t) = x(0,t)$ and $\dot{x}_1(t) = \dot{x}(0,t)$ are the displacement and velocity of the folds at entrance of the glottis. If T is the thickness of the folds, the displacement at the exit of the glottis can be expressed as $x_2(t) = x(T,t) = x_1(t) - T\dot{x}_1/c_f$. As usual, a constant $x_0(z)$, denoting the displacement of the folds at rest, is added to the time-varying displacement $x(z,t)$. The area along the z axis of the glottis can then be expressed as $a(z,t) = 2L(x_0(z) + x(z,t)) = 2L(x_0(z) + x_1(t) - z\dot{x}_1(z,t)/c_f)$, where L is the length of the glottis. Furthermore, the areas at entry and exit of the glottis can be, respectively, defined as

$$a_1(t) = 2L(x_{01} + x_1(t)), \tag{2a}$$

$$a_2(t) = 2L(x_{02} + x_1(t) - \tau\dot{x}_1(t)), \tag{2b}$$

where x_{01} and x_{02} are the rest positions of masses at entrance and exit to the glottis, and $\tau = T/c_f$ is the time taken by the wave to propagate from the entrance to the upper end of the glottis.

In multimass models, the driving force acting on each mass is computed from the local pressure, the pressure profile being nonlinear within the glottis. However, this is sometimes simplified, and a mean glottal pressure is used to represent the net driving pressure for the entire vocal tissue (Titze, 1988), or even the assumption that fluid mechanical forces are exerted only on the first mass is made (Pelorson *et al.*, 1994). This is similar to assuming that the other masses are driven uniquely by the displacement of the first one. We assume here that a driving pressure P_m acts only on the first vocal-fold portion at the entrance to the glottis, and is related to the lung pressure P_l by a Bernoulli's relation

$$P_m = f_P(U_g, P_l, x_1) = P_l - \frac{1}{2}\rho\frac{U_g^2}{a_1^2}, \tag{3}$$

where ρ is the density of air, U_g and a_1 are, respectively, the flow and the cross-sectional area of the glottis at entrance.

The driving force, assuming a fixed surface S_m over which the pressure is exerted, is

$$F_m = P_m S_m. \tag{4}$$

We finally assume the flow to be one-dimensional, incompressible, and quasistationary, which leads to the assumption that the flow is independent of the vertical position within the glottis. There is a wide number of possible choices to write simplified formulas for the flow, given the driving lung pressure and the description of the glottis area. The approach we take here is to rely on this term to compensate for all the simplifications made up to now. We use a parametric nonlinear function to relate the displacement of the folds to the airflow through the glottis. With respect to the modeling assumption, this relation can be written as

$$U_g = \mathcal{F}(P_l, x_1, x_2; w_0, w_1, \ldots, w_M), \tag{5}$$

where $w_0, w_1, \ldots, w_M$ are some parameters to be identified to fit the target flow. We will return to the parametric form of the function $\mathcal{F}$ later.

A. Oscillatory properties of the one-mass model

Before getting into the details of data-driven flow modeling, we explore the properties of the low-dimensional one-mass scheme proposed. To this aim we make a simple choice for the function $\mathcal{F}$, i.e., we select a simple model for the flow. A convenient way is to refer to the stationary Bernoulli equation

$$P_l - P_i = \frac{1}{2}\rho\frac{U_g^2}{a^2}, \tag{6}$$

where P_l is the lung pressure, P_i is the vocal-tract input pressure, U_g and a are, respectively, the flow and the area of the glottis. In most parts of the physical models in the literature, this simple formula is refined with several other terms accounting for additional pressure losses, the principal ones being due to the inertness of air, viscosity effects within the glottis, and pressure recovery at the glottis outlet (Pelorson *et al.*, 1994). Equation (6) can be specified for the case where no vocal tract is coupled to the glottis, i.e., when $P_i = 0$, and the glottal area is modeled as the minimum cross-sectional area between the areas at lower and the upper vocal-fold edge, i.e., $a = \min\{a_1, a_2\}$. This implies that the point at which the flow detaches from the glottal wall in the convergent configuration (i.e., $a_1 > a_2$) and in the divergent configuration (i.e., $a_1 \leqslant a_2$) is assumed to be located at the exit and entrance of the glottis, respectively. This simple glottal area model can be further refined by assuming that the flow separation point is located at the exit of the glottis in the case of a convergent glottis, or may move within the glottis, as the folds assume a divergent configuration (Pelorson *et al.*, 1994). In a divergent glottis, the ratio between the glottal area a_s at the point of airflow separation and the minimum glottal area a_1 becomes asymptotically constant, and the approximate relation $a_s = \gamma a_1$ with $\gamma = 1.3$, obtained by Lucero (1999) assuming a linear variation of the glottal area along the glottis, is used here. The flow can hence be computed from Eq. (6) as

$$U_g = \sqrt{\frac{2P_l}{\rho}}\min\{\gamma a_1, a_2\}. \tag{7}$$

Combining this equation with Eqs. (1) and (3), and accounting for the fact that the flow is zero for $a_1 = 0$ (closed glottis), we have the following equation of motion:

$$m\ddot{x} + r\dot{x} + kx = \begin{cases} S_m P_l, & \text{if } a_1 = 0 \\ S_m\left(P_l - P_l\dfrac{\min^2\{\gamma a_1, a_2\}}{a_1^2}\right), & \text{if } a_1 > 0, \end{cases} \tag{8}$$

leading to

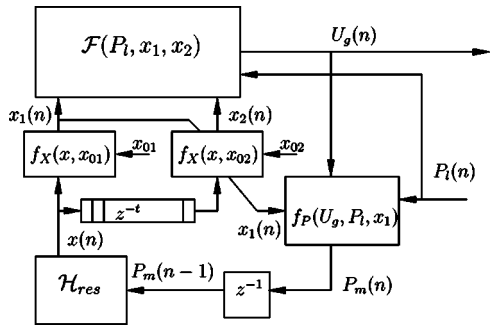

FIG. 2. Block diagram of the discrete-time physically constrained glottis model. U_g is the glottal flow, P_l and P_m denote, respectively, lung pressure and folds driving pressure, x_1 and x_2 denote the displacements of, respectively, the lower and upper edge of the vocal fold. The one-sample delay z^{-1} is necessary to compute the two loops in the scheme.

$$m\ddot{x}+r\dot{x}+kx=\begin{cases} S_m P_l, & \text{if } a_1=0 \\ S_m P_l\left(1-\dfrac{a_2^2}{a_1^2}\right), & \text{if } 0\leqslant a_2\leqslant \gamma a_1 \\ S_m P_l(1-\gamma^2), & \text{if } 0<\gamma a_1<a_2. \end{cases} \quad (9)$$

We note that the driving pressure is a function of glottal geometry, and is smaller during closing glottis ($\gamma a_1<a_2$) than during opening glottis ($\gamma a_1\geqslant a_2$). This supplies the necessary asymmetry in the driving force to allow the onset and maintaining of sustained oscillations even when no vocal tract is coupled (Titze, 1988). A similar description of the flow and of the driving force is found in Stevens (1998) and in Steinecke and Herzel (1995).

A discrete-time version of the system described by the above equations is proposed in Fig. 2 (n denotes here the discrete instant $t_n=n/F_s$, where F_s is the sampling frequency). The mass and spring system is discretized using a series expansion approach (Liljencrants, 1991). This gives a second-order all-pole filter

$$\mathcal{H}_{\text{res}}(z)=\frac{\beta_0}{1+\alpha_1 z^{-1}+\alpha_2 z^{-2}}, \quad (10)$$

with coefficients

$$\alpha_1=-2\exp\left(-\frac{r}{2mF_s}\right)\cos\left(\frac{1}{F_s}\sqrt{\frac{k}{m}-\frac{r^2}{4m^2}}\right), \quad (11)$$

$$\alpha_2=\exp\left(-\frac{r}{mF_s}\right), \quad (12)$$

$$\beta_0=\frac{(1+\alpha_1+\alpha_2)}{k}. \quad (13)$$

When the parameters are set so as to realize a bandpass transfer function, the system behaves as a resonant filter characterized by a resonant frequency

$$f_c=\frac{1}{2\pi}\sqrt{k/m}, \quad (14)$$

and by a quality factor

TABLE I. Parameter values used in the numerical simulation of the glottis model.

Parameter	Value
ρ air density ($\text{kg}\cdot\text{m}^{-3}$)	1.15
m mass (kg)	0.000 17
r damping ($\text{N}\cdot\text{s}\cdot\text{m}^{-1}$)	0.069
k stiffness ($\text{N}\cdot\text{m}^{-1}$)	34
Q filter quality factor	3.3
f_c filter resonant frequency (Hz)	71
L glottal length (m)	0.014
P_l lung pressure ($\text{N}\cdot\text{m}^{-2}$)	300–3000
S_m fold surface (mm^2)	15–60
T fold thickness (mm)	0.06–2
x_{01}, x_{02} rest positions (mm)	0.005–1

$$Q=-\frac{f_c\pi}{F_s\ln(\sqrt{\alpha_2})}. \quad (15)$$

The surface-wave propagation on the vocal fold is approximated with a variable-length delay line, providing a spatial resolution $\Delta l=c_f/F_s$. Therefore, if d is the length of the delay line (in samples), the vocal-fold thickness is $T=d\Delta l$. A sampling frequency F_s of 16 000 Hz, used throughout the paper, gives a spatial resolution Δl of 0.062 mm. The offset x_{01} is summed to the output of the spring–mass system, providing the rest position of the mass. The resultant mass position x_1 is computed as

$$x_1=f_x(x,x_{01})=\begin{cases} x+x_{01}, & \text{if } x>-x_{01} \\ 0, & \text{otherwise.} \end{cases} \quad (16)$$

The same function f_x is used to compute x_2 from the delayed output of the spring–mass system, using x_{02} as the initial position of the upper edge of the fold. Equation (16) implements a rather crude model for the fold collision. A more realistic description, not considered here, should take into account the elastic deformation of fold tissues at collision, as well as the additional flow component due to the fact that folds gradually collide from the lateral side to the middle part, allowing, in the first stage of the collision process, for some air passing through. Finally, we note that not all initial glottis configurations are suited to produce an oscillation. From Eq. (9), it is evident that for an open uniform glottis at rest ($a_1=a_2$), no aerodynamic force can be exerted on the folds, whatever P_l. An initial convergent configuration ($a_1>a_2$) guarantees the start of oscillation and is used in the following. The simulation of the model with the parameters given in Table I produces the results shown in Figs. 3 and 4.

The oscillation properties of this simple one-mass model are in agreement with some relevant phonatory characteristics. The onset of the oscillation is mainly determined by the subglottal pressure P_l and by the rest positions x_{01} and x_{02}. The oscillation frequency is determined mainly by the resonant frequency of the fold model, determined by m, r, and k, but is also influenced by the subglottal pressure. The closed-phase duration is determined mainly by the part of the vocal fold actually involved in the oscillation, i.e., the vocal-fold thickness parameter T. In Fig. 4 it can be seen how a decrease of T produces a decrease in the closed-phase duration [panel (b)], and an increase in T produces an increase of the

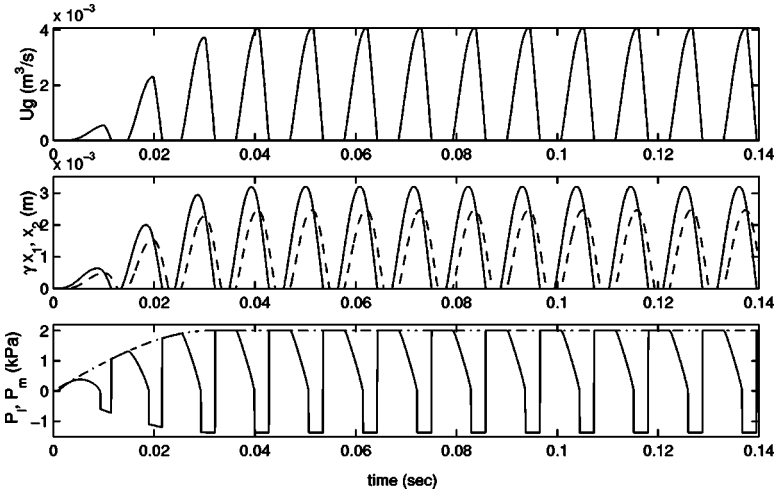

FIG. 3. Simulation of the one-mass model. Upper panel: U_g, middle panel: γx_1 (solid) and x_2 (dashed), lower panel: P_l (dot-dashed) and P_m (solid). The following values were used for the parameters: $P_{l,\max}=2000$ Pa, $x_{01}=0.01$ mm, $x_{02}=0.009$ mm, $T=1.3$ mm ($d=20$ samples), $S_m=42$ mm^2, at a sample rate $F_s=16\,000$ Hz.

closed-phase duration [panel (c)]. The flow waveforms reproduced in these simulations are obviously a rough approximation of a real flow and flow rate waveforms, due to the drastic simplifications. For example, the absence of skewness of the flow with respect to the area function, due to the absence of air inertia since no vocal tract is coupled, is evident. Nonetheless, the simple one-mass model sketched here seems to be provided with the minimal requirements to qualitatively reproduce the flow-induced nonlinear oscillation observed in speech production. It is remarkable that the driving pressure P_m is clearly greater for positive $\dot{x}_1$ (opening of the vocal folds) than for negative $\dot{x}_1$ (closure of the vocal folds), allowing for the onset and sustainment of oscillation even in the absence of vocal-tract coupling.

B. Fitting inverse-filtered glottal flow waveforms with the one-mass model

In this section, the simple one-mass model introduced in the previous section is improved with some extensions which permit approaching the modeling of the flow waveform with a data-driven waveform-matching perspective. The structural extension consists of the definition of a more general flow model, i.e., a parametric function $\mathcal{F}$ is used in place of Eq. (7). Given a target flow waveform obtained by standard inverse-filtering procedures, the parameters of (part of) the model are first adapted in a way that the area function provided by the fold displacement is coherent with the target flow waveform. Then, the parametric model of the flow is designed to transform the area underlying the flow onto the actual flow waveform. An overview of the parametric identification process is given in the following scheme:

(1) Given the flow signal, a feasible lung pressure signal $P_l(n)$ is derived.
(2) Considering the target flow and lung pressure as driving signals, the displacement of the fold edges are computed by running part of the model, i.e., the Bernoulli's term f_P and the mass–spring model $\mathcal{H}_{\text{res}}$ in Fig. 2.
(3) Given the lung pressure and the displacement of the fold edges as input, and the desired flow as output, the set of parameters $\{w_0, w_1, \ldots, w_M\}$ of the flow model $\mathcal{F}(P_l, x_1, x_2; w_0, \ldots, w_M)$ is identified.
(4) Once trained, the system is run with arbitrary control input (within the training range), and the stability of the oscillations is verified.

Items 1 to 3 are referred to as the analysis, or identification, step. Item 4 is referred to as the synthesis step.

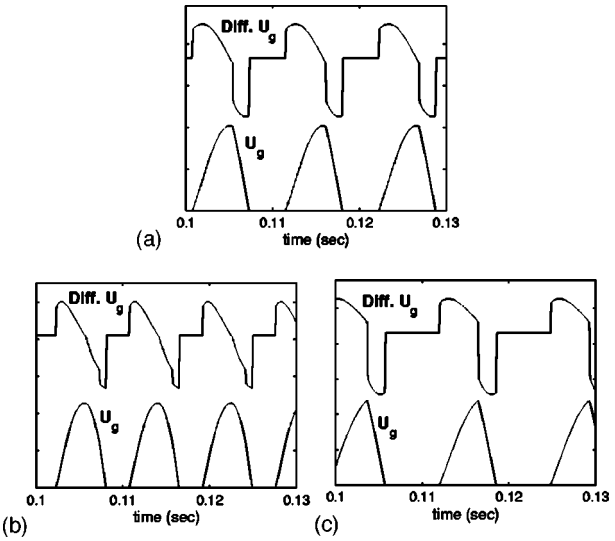

FIG. 4. U_g and $\dot{U}_g$ from the one-mass model (an offset is added to $\dot{U}_g$ for visualization purposes). Panel (a): same as Fig. 3 (detail). Panel (b): $T=0.12$ mm ($d=2$ samples). Panel (c): $T=3.1$ mm ($d=50$ samples). For all cases is $P_{l,\max}=2000$ Pa, $x_{01}=0.01$ mm, and $x_{02}=0.009$ mm.

1. Derivation of lung pressure

The lung pressure is derived from the flow as its magnitude envelope, and normalized to some value feasible for a lung pressure (normally, on the order of 300 to 3000 Pa). The flow waveform is normalized as well, so that the order of magnitude is within a physically acceptable range (10^{-4} to 10^{-3} m^3/s). With these assumptions, we can rely on the values used in Sec. II A for the remaining parameters of the model, to make a first guess on their order of magnitude. Although this procedure provides us with a rather arbitrary lung pressure signal, the result fits our need.

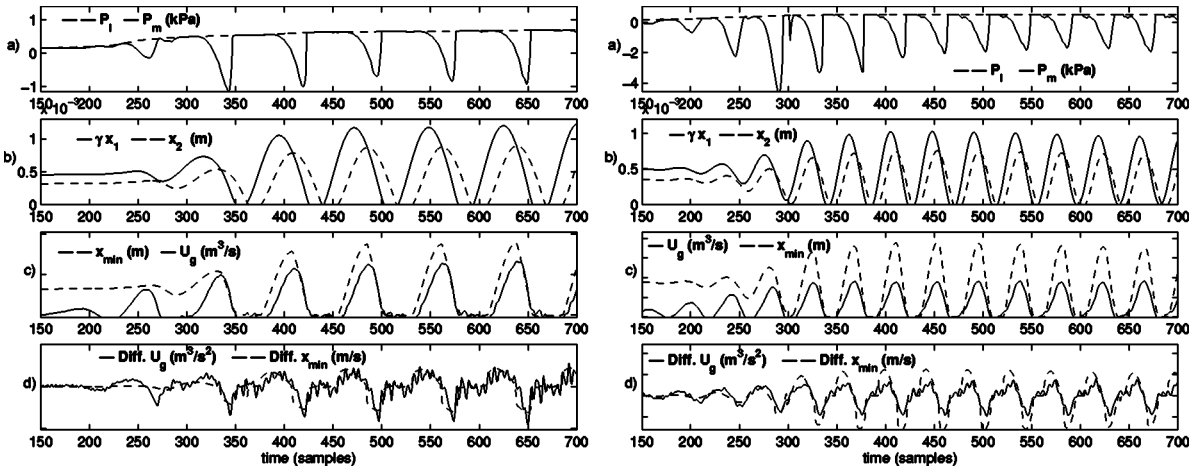

FIG. 5. Tuning of the parameters of the mechanical resonator for a pressed/hyperfunctional voice (left panels, $F_0=210$ Hz) and for a normal voice (right panels, $F_0=372$ Hz). Panel (a): the lung pressure P_l and the driving pressure P_m. Panel (b): fold edges displacements. Panel (c): comparison of the function $x_{\min}=\min\{\gamma x_1, x_2\}$ (proportional to the glottal area function) with the target flow. Panel (d): flow derivative and $x_{\min}$ function derivative.

2. Derivation of the fold driving pressure and area function

The principal concern in the derivation of the driving input to the vocal folds is to reproduce the asymmetry with respect to the adducting and abducting phases. As we have already remarked, the dependence of the driving force on the derivative of the displacement of the vocal tissue is crucial for oscillation. Given the glottal flow U_g, a rough estimate of the aerodynamic driving forces can be constructed relying on the formulation of the driving force due to the Bernoulli's law of kinetic pressure [Eqs. (3) and (4)]. Upon normalization of the lung pressure and flow to values corresponding to the ranges found in the simulations in Sec. II A, the values in Table I can be used as a reference for the physical constants involved. This yields

$$P_m(n)=f_P(U_g(n),P_l(n),x_1(n))$$
$$=P_l(n)-K_bU_g(n)^2/x_1^2(n), \tag{17}$$

where $K_b=\rho/(8L^2)\approx 733$, and

$$F_m(n)=P_m(n)S_m, \tag{18}$$

where $S_m=4.2\cdot 10^{-5}$. Given the time series $P_l(n)$ and $U_g(n)$, we still need to estimate the corresponding fold displacement $x_1(n)$ to compute $P_m(n)$. Hence, we need to operate the simulation of part of the system (referring to the block diagram in Fig. 2, the parts involved are f_P, f_x, and the resonator $\mathcal{H}_{\text{res}}$). A procedure is required here to tune the linear resonator parameters with respect to the characteristics of the target flow. The adaptation of the mechanical analog of the model is performed interactively, following some empirical rules. The resonance frequency of the filter $\mathcal{H}_{\text{res}}$ is initially set equal to the pitch of the flow. The gain of the filter is set in the order of magnitude of $5\cdot 10^{-5}$, in accordance with the values obtained for β_0 in (13). From experiments with the elementary one-mass model introduced in Sec. II A, we know that the quality factor Q of the filter can range within 0.1 and 10. However, a realistic behavior was observed for low values of Q (0.2–4.0, depending on the pitch). High values of Q lead to a highly selective filter, with the consequence that some properties observed in real phonation would be hardly reproduced by the model. For example, the frequency of the oscillation would be poorly affected by changes in the lung pressure, which is in contrast with experimental observations that show a rising of the pitch when the lung pressure increases. Thus, the quality factor Q is initially set at a rather low value and then raised until the function $x_{\min}(n)=\min\{\gamma x_1(n),x_2(n)\}$ (which is a rough estimate of the glottis area) is in phase with the flow. The motivation is that Q affects the phase delay of the second-order filter. Sometimes, especially for low-pitched tones, a lowering of f_c is also required to reach a good phase matching.

The resting position x_{01} is initially set at a value at which the oscillation will start, and at which the displacement of the oscillating mass crosses the zero level (where the collision with the other virtual fold takes place). A convergent configuration of the glottis at rest is assumed by imposing $x_{02}=0.9\cdot x_{01}$. The resting position x_{01} and the delay line length d are then adjusted in order to get the same opening and closing instants for both the flow and the area function. Most of the time, further adjustments of f_c and Q are required at this point to obtain a final good match. At the end of this procedure, the area function is optimally superimposed to the target flow, meaning that the area function and the flow are synchronized and in phase.

Figure 5 shows the result of the iterative tuning for two different voice sources. It can be seen that the driving force computed from the target flow via the Bernoulli's law has the desired qualitative behavior: the driving air pressure P_m is in phase with the velocity of the folds, and the negative peak displacement occurs during the closure of the glottis. This allows us to realize a positive flow of energy from the airflow to the mechanical system during a flow period. The relationship between glottal area and transglottal airflow is an interesting aspect of phonation. This relationship was derived from the model; see Fig. 6. The area/flow plots give a qualitative idea of the skewness of the flow with respect to the area function predicted by the model. The right-end por-

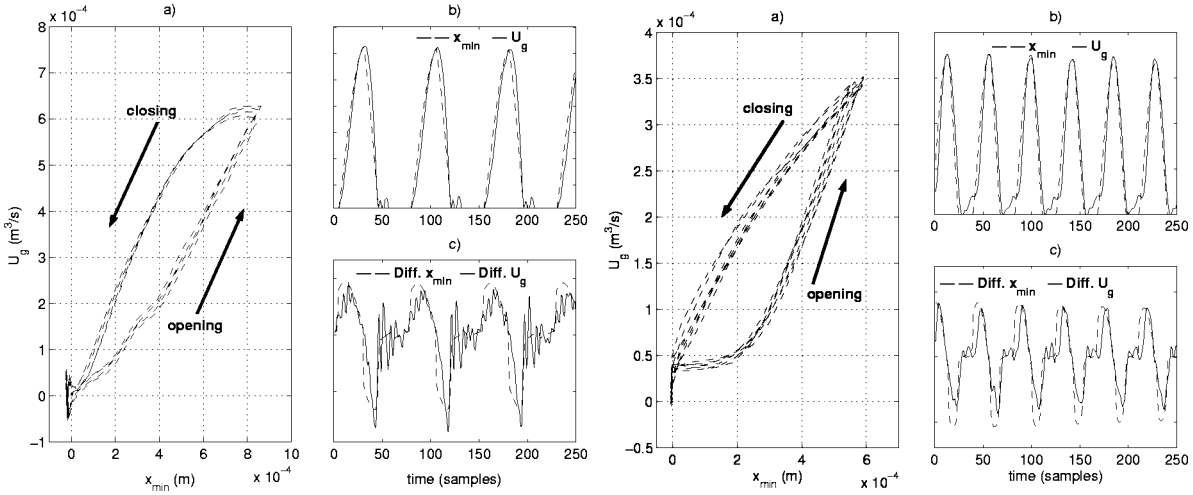

FIG. 6. Area/flow plots: plot of $x_{\min}$ (proportional to the area function) versus the target flow, for the cases in Fig. 5.

tion of the orbits corresponds to the opening of the glottis, where the build-up of the flow is delayed with respect to the increasing area due to the effect of the air inertia. The left-hand portion of the orbits corresponds to the closing of the glottis. In essence the model reproduces the typical behavior observed for normal phonation (Granqvist *et al.*, 2003).

It should be stressed here that the interaction between the vocal tract and the source is not explicitly considered in the model under study. It is known that the acoustic loading due to the vocal-tract coupling is responsible for the skewing of the glottal airflow with respect to the glottal area (Rothenberg and Zahorian, 1977), and for other effects observed in inverse-filtered waveforms (Childers and Wong, 1994). Among these are the ripples superimposed on the opening phase segment of the glottal pulse due to the dissipation of energy from the first formant. In the absence of an explicit term in the flow model relying on physical considerations, all these characteristics are accounted for by the regression model, which mixes together the effects of subglottal and supraglottal acoustic loading with the aerodynamics of the unloaded glottis.

3. Parametric identification of the flow model

So far we have computed the driving force and mass displacement from the airflow and subglottal pressure. To complete the loop, we need a law for the computation of the airflow from the mass displacement and the subglottal pressure. The formula for the flow is now expanded as a regressor-based function of the form

$$U_g(n) = \mathcal{F}(P_l(n), x_1(n), x_2(n); w_0, \ldots, w_M) = \sum_{i=0}^{M} w_i \psi_i(P_l, x_1, x_2), \tag{19}$$

where the w_i are weights to be identified, and $\psi_i(P_l(n-1), x_1(n-1), x_2(n-1))$ are the regressors of the input data. The regressors are functions that can be used to combine the inputs in a nonlinear fashion. Note that the inputs considered here are the lung pressure and fold edges displacement, as suggested by the elementary one-mass model. The choice of the regressors can be made in several ways. Local models, such as Gaussian functions or any other radial basis function, are often used. This approach leads to a model called *radial basis function network* (RBFN) (Chen *et al.*, 1991), used in the field of time-series analysis and modeling. The use of a polynomial expansion of the input leads to a class of NARMAX models (Chen and Billings, 1989), known in the fields of system identification and control. Alternatively, the regressors can be derived on the basis of physical considerations. We follow here an hybrid approach: we use the Bernoulli-based model of the flow [Eq. (7)], and a set of local Gaussian regressors (i.e., an RBFN), to provide a means to reshape the waveform period and to catch the fine details of the inverse filtered waveforms. The resulting set of regressors is

$$\psi_0(P_l, x_1, x_2) = \sqrt{P_l}\,\min\{\gamma x_1, x_2\},$$
$$\psi_j(x_1, x_2) = \exp\left(-\frac{(x_1 - m_{1j})^2 + (x_2 - m_{2j})^2}{\sigma_j^2}\right), \qquad j = 1,\ldots,M, \tag{20}$$

where (m_{1j}, m_{2j}) is the centroid of the jth bidimensional Gaussian kernel, σ_j is the kernel width, and M is the number of Gaussian regressors. All the multiplicative constants in the Bernoulli's regressor have been disregarded, since each regressor will be multiplied by a parameter to be identified. The two-dimensional centroid and width of the Gaussian kernels have to be chosen before the identification procedure. In the following examples, the choice was to limit the kernels to 50 equally spaced and positioned along the 3D trajectory described by one period of the target flow (i.e., the centroids were selected among input pairs (x_1, x_2) from a period in the training set). The width σ of kernels was set in the range $[10^{-4}, 10^{-3}]$.

At this stage of the analysis process, both the input (P_l, x_1, x_2) and the target output U_g of the nonlinear block are available. Hence, the weights in Eq. (19) can be estimated using the following nonlinear identification step: for a given training window of length N, $W_n = [n+1, \ldots, n+N]$, two training data sets are defined as

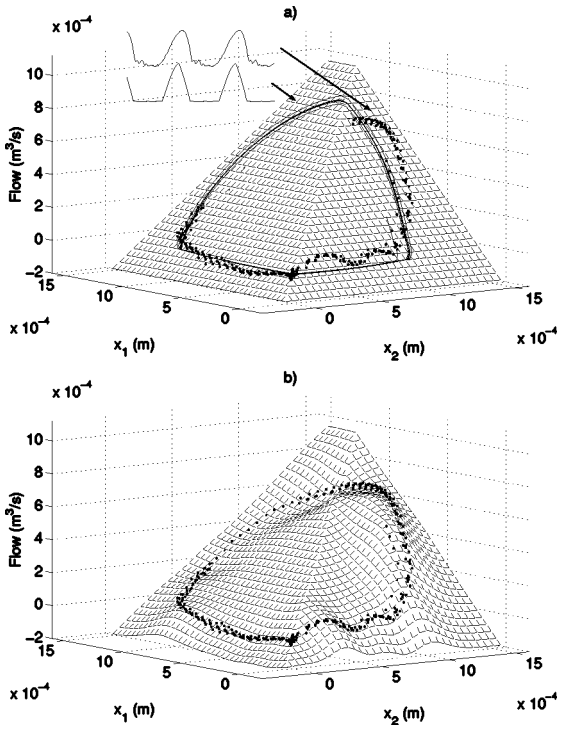

FIG. 7. Result of data-driven flow modeling (same case as Fig. 5, left panels). Panel (a) shows the 3D representation of the simple flow model in (7), for a fixed lung pressure P_l. The flow trajectory from this model (solid lines) and the training data (dotted lines) are also shown. Panel (b) shows the 3D representation of the extended flow model in (19) and (20) after the training procedure. The width σ of all 50 bidimensional Gaussian kernels was set to 0.0005.

$$\mathbf{T}_{U_g} = [U_g(n+1), U_g(n+2), \ldots, U_g(n+N)], \tag{21}$$

$$\mathbf{T}_x = \begin{bmatrix} \psi_0(n+1) & \cdots & \psi_0(n+N) \\ \vdots & \ddots & \vdots \\ \psi_M(n+1) & \cdots & \psi_M(n+N) \end{bmatrix}, \tag{22}$$

where $\psi_i(k) = \psi_i(P_l(k), x_1(k), x_2(k))$, i.e., $\psi_i(k)$ is the output value of the ith regressor at the discrete time k. The data sets in Eqs. (21) and (22) are used to train the regressors in $\mathcal{F}(P_l, x_1, x_2; w_0, \ldots, w_M)$. Specifically, the identification of the weights $\mathbf{w} = [w_0, \ldots, w_M]$ requires the solution of the matrix system

$$\mathbf{w}\mathbf{T}_x = \mathbf{T}_{U_g}. \tag{23}$$

The least-squares solution of Eq. (23) is known to be

$$\mathbf{w} = \mathbf{T}_{U_g}\mathbf{T}_x^{+} = \mathbf{T}_{U_g}(\mathbf{T}_x^T\mathbf{T}_x)^{-1}\mathbf{T}_x^T, \tag{24}$$

where the symbol $+$ denotes the *pseudoinverse* of a matrix, and the superscript T means transposition. Pseudoinversion provides a method to invert nonsquare matrices, and is required in this case since the number of regressors is typically less than the number of samples in one period of the flow waveform.

To better understand the role of the waveform-matched flow model, we provide in Fig. 7 a comparison of the 3D representation of $\mathcal{F}$ before and after the data-driven training of the local Gaussian regressors. It can be seen how the extended flow model (surface in the lower panel) locally adapts to the target data, while globally keeping the underlying structure of the Bernoulli-based flow model (the surface in the upper panel). The underlying bidimensional Gaussians are located along the target trajectory. The smoothness of the surface, which provides desirable interpolation properties, can be tuned by changing the width σ of the kernels (in the example $\sigma = 0.0005$). If we look back at the low-dimensional one-mass model that we started with, the role of the parametric term is to take care of aspects neglected at first, e.g., the nonlinear properties of fold tissues, incompressibility, vertical and horizontal propagation of displacement in the fold, interaction with the vocal tract (skewing of the flow, ripples). In other words, the role of the fudge factors introduced by the parametric term is limited to the fine shaping of the glottal flow waveform, whereas the other parameters relating to the mechanical modeling of the folds are related as much as possible to specific cues of the flow, such as periodicity and open-phase to closed-phase ratio. The attribution of a meaning to the physical or physiological parameters is motivated by the fact that it is desirable to obtain physiologically motivated transformations of the original waveform on the basis of such parameters (e.g., in speech synthesis or speech-processing frameworks): pitch shifting can be obtained by tuning the model of the folds; open-phase duration can be changed by changing the length of the pliable contraction, and so on. On the other hand, no straightforward transformations of the waveform shape can be achieved based on the fudge factors.

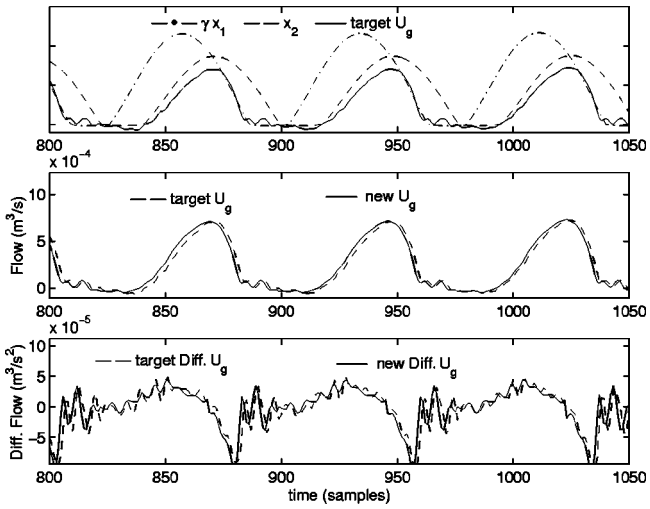

FIG. 8. Open-loop identification result (same case of Fig. 5, left panels). From top to bottom: the fold edges displacement compared to the target flow; the target flow and the reproduced flow (open-loop mode: $\tilde{U}_g$); the target flow rate and the reproduced flow rate (open-loop mode: Diff. $\tilde{U}_g$).

In Fig. 8, the details of the identification for a steady portion are shown (same case of Fig. 5) (the whole training window had a length of 1200 samples).

It is important to note that, even if the identification step appears successful and the reproduction of the flow waveform seems to be highly accurate, these results refer to the situation where the present flow value used to compute the flow at successive time steps comes from the target time series, and is not the result of a previous iteration of the loop.

The system is said to operate in *analysis*, or *open-loop*, mode. We can express this by the equation

$$\tilde{U}_g(n) = \mathcal{M}(\tilde{\mathbf{S}}_n; P_l(n)), \tag{25}$$

where $\mathcal{M}$ is the trained model, and $\tilde{\mathbf{S}}_n$ is the state at time n determined by the past inputs $P_l(k)$, $k=0,...,n-1$, and flow target values $U_g(k)$, $k=0,...,n-1$. The identification error can be defined as $\tilde{e}(n) = \tilde{U}_g(n) - U_g(n)$. In the next section, on the other hand, the autonomous simulation of the system will be addressed: at each successive time sample, only the lung pressure P_l is used as input, and no further correction based on the target flow is applied to the computation of the loop. In this case, the system is said to operate in *closed-loop* mode.

As a final remark, note that here a number of $M=50$ radial basis units was used to represent a waveform frame of length $N=1200$. Thus, the parameters of the fudge factors sum to a total of 202 (centroids plus width plus weights). If we also consider the parameters of the mechanical system, the total number of parameters that represent the frame is less than 210 (the lung pressure is represented by a unique value for each frame, and instantaneous values along the frame are obtained by interpolating adjacent frames). In this sense, the model is compressing the data when run in closed-loop mode.

C. Autonomous oscillations and control of flow characteristics

Once trained, the system is in principle able to autonomously reproduce the flow waveform used in the training, provided that the same input sequence $P_l(n)$ is used, and that the flow reconstruction errors due to the nonlinear flow model remain within a small range. This is usually a major issue, since the iteration of the system without any further correction to the flow can give rise to fast error growth (closed-loop instability). Adopting the same notation introduced in the previous section, the equation for the closed-loop configuration can be written as

$$\hat{U}_g(n) = \mathcal{G}(\hat{\mathbf{S}}_n; P_l(n)), \tag{26}$$

where $\hat{\mathbf{S}}_n$ is the state at time n determined by the past inputs $P_l(k)$, $k=n-1,...,0$, and the flow values $\hat{U}_g(k)$, $k=0,...,n-1$ computed in the previous iterations. Simulation experiments revealed that the trained model is more affected by closed-loop instability the more the open-loop identification is inaccurate. However, this is not a general rule, and the finding of constraints on the flow model that would grant stability is still an open issue.

Physically based models of the vocal folds offer an intuitive interface to control the characteristics of the airflow generated at entrance of the vocal tract. Most parts of the physical parameters in multimass models are univocally related to some acoustic parameter of the flow waveform, e.g., the magnitude of masses and the stiffness of springs determine the pitch of the oscillation. On the other hand, in pure data-driven modeling, such as black-box methods, the cause–effect relations between control input and resulting output are defined during the training phase by the input–output data available. The size of the training data set is fundamental for the accuracy of the model, and transformations of some acoustic parameter outside the range of the data set would have no sense. The hybrid physically based data-driven approach introduced here leads to a different situation: we can train the model, say, on a single pitched target flow waveform, but still rely on the physically inspired part of the model to provide, within a limited extent, for pitch changes.

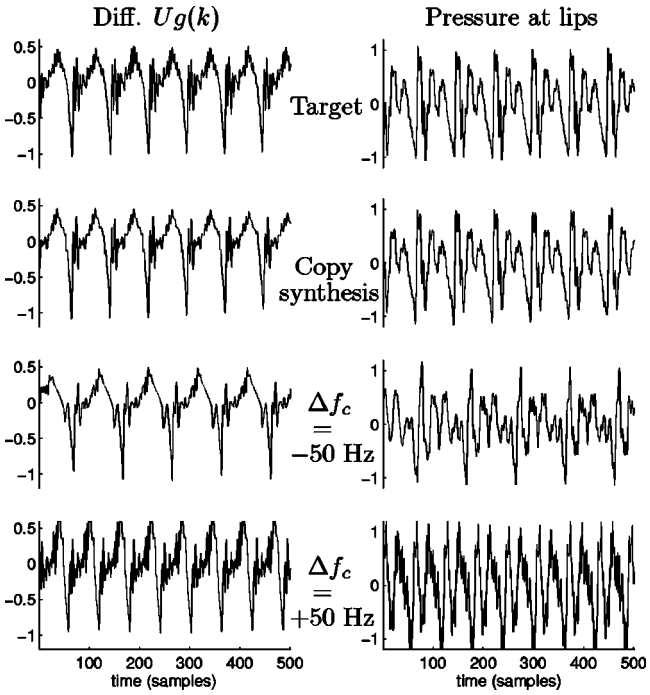

FIG. 9. Closed-loop simulations of the system after training on the target flow in the top panels (differentiated flow is shown, the window length is 31 ms, the pitch of the target flow is 210 Hz). The system was run in closed-loop mode once it reached the steady state. The copy synthesis (2nd panel from top) is obtained by running the glottal model with no changes in the parameter setting. The synthesis with lowered pitch (3rd panel from top) is obtained by lowering the fold resonance frequency parameter f_c by 50 Hz. The synthesis with augmented pitch (bottom panels) was obtained by increasing the fold resonance frequency by 50 Hz. Amplitude range is normalized for the differentiated flow and lip pressure.

Given a model trained with a steady single pitched flow waveform, as is the case considered here, one can expect the model to react to controls accordingly to what the physical insights suggest. Experiments showed that, upon a stable simulation in closed-loop configuration, the model is usually well behaved with respect to pitch and fold resting position changes, while changes in the thickness are more likely to drive the system toward instability. Pitch changes within a range of $\pm 30\%$ usually produce stable oscillations and waveforms with pulse characteristics reasonably similar to the original glottal pulse. Figure 9 shows an example of pitch transformation on a voiced signal. The target flow rate waveform was obtained by inverse filtering the target pressure recorded at lips with a tenth-order all-pole filter. The vocal-tract filter designed during the inverse-filtering process was used to produce the lip pressure signals from the copy and the modified syntheses. It is remarkable that the flow waveform is preserved upon transformations even if no training

TABLE II. Voice source quantification parameters (left) and trained model parameters (right). OQ=open quotient, SQ=speed quotient, CQ=closing quotient, RQ=return quotient; f_c=filter resonant frequency, Q=filter quality factor, x_{01}=mass resting position, T=delay line length, P_l=lung pressure (these values were used to generate the pressure control signal and are the ones actually measured in the acquisition process). The three samples marked with a star are the ones shown in Figs. 10–12.

	Glottal flow parameters					Model parameters				
Voice sample	Orig. pitch (Hz)	OQ	SQ	CQ	RQ	f_c (Hz)	Q	x_{01} (mm)	T (mm)	P_l (Pa)
Male, neutral										
*MN1	104.0	0.66	2.68	0.80	0.03	80.0	0.80	0.005	1.60	500
MN2	127.2	0.56	2.29	0.20	0.02	115.0	0.70	0.005	1.90	800
Male, pressed										
MP1	108.0	0.64	2.24	0.20	0.04	90.0	0.40	0.001	2.10	900
MP2	130.0	0.58	2.65	0.16	0.01	110.0	0.54	0.001	2.10	1400
Female, neutral										
*FN1	207.8	0.75	2.23	0.23	0.09	206	2.0	0.9	0.62	800
*FN2	373.0	0.64	0.81	0.35	0.13	372	10.5	1.0	0.75	1200
Female, pressed										
FP1	210.5	0.61	1.84	0.21	0.05	210	2.0	0.8	0.90	1000
FP2	313.7	0.67	2.30	0.20	0.08	315	5.7	0.8	0.72	1700

data with the final pitch or closed-phase durations were used during the parametric identification. However, the more the pitch is varied from the original pitch used during the training, the more the system dynamics is likely to move away from the original orbit in the 3D surface representing the flow model. To enhance the performance of the system with respect to this point, it would be necessary to improve the parametric identification procedure to extend the training of the flow model to various pitches.

III. EXPERIMENTAL RESULTS

This section is aimed at evaluating the method on several inverse-filtered flow waveforms with different characteristics. The parameters resulting from the training of the model in the different cases are compared and discussed.

A. Speech material and method

The speech material consisted of flow glottograms obtained by inverse filtering of the flow signal recorded at mouth by means of a flow mask (Glottal Enterprises, Syracuse, NY). The subjects, one female and one male, phonated the syllable [pæ] at different pitches and in different modes of phonation. Subglottal pressure was estimated from the oral pressure during the p-occlusion recorded by a pressure transducer attached to a plastic tube, inner diameter 4 mm, that the subject held in the corner of the mouth. The flow and audio signals were recorded on separate channels of a TEAC PCM tape recorder and transferred to sound files, and the inverse filtering was performed using a custom-made computer program.[2] Eight examples of flow glottogram were selected to train the model. In Table II, a set of voice source quantification parameters extracted from the flow and the differentiated flow is shown. The source quantification parameters considered here are the speed quotient SQ (i.e., the ratio of the opening-phase duration T_p to the closing-phase duration T_n), the open quotient OQ (i.e., the ratio of the open phase duration $T_o=T_p+T_n$ to the period), the closing quotient CQ (i.e., the ratio of the closing-phase duration T_n to the period), and the return quotient RQ (i.e., the ratio of the return-phase duration to the period) (Alku and Vilkman, 1996).

For each one of the eight cases, the model was trained according to the two-step procedure introduced in Sec. II B. The lung pressure measured was used to derive a driving pressure signal. For the male samples, a vocal-fold length $L=14$ mm was assumed. This value was reduced to 5 mm for the female samples. After the interactive adaptation of the mechanical analog of the folds, the flow model was identified, and the closed-loop stability of the system was verified.

B. Results and discussion

Table II (right part) shows the mechanical parameters of the one-mass model. Some observations can be made comparing these parameters with the voice source quantification parameters (left part of the table). The resonance frequency of the mass–spring model corresponds to the original pitch of the flow with reasonable accuracy for the female voices, whereas it is slightly lower for the male voices. The quality factor of the filter is higher for higher pitches, reflecting the fact that a female vocal fold is smaller than a male vocal fold [refer to Eq. (15)]. The vocal-fold thickness parameter T models the amount of vocal-fold tissue actually involved in the phonation process, and affects the duration of the closed phase. It is appreciably lower for the training corresponding to female voice sources, reflecting a shorter closed phase (note that similar OQs for different pitches indicate shorter closed phase for higher pitch). The parameter x_{01} models the degree of adduction of the vocal folds and resulted considerably higher for the female samples. Adduction of the vocal folds may affect the speed of the return phase at the closure of vocal folds, which is related to the return quotient RQ. Some coherency of this relation can be seen by comparing the female neutral phonation with the female pressed/hyperfunctional phonation: for the same pitch range, the adduction level is higher (smaller x_{01}) for faster closure (lower RQ).

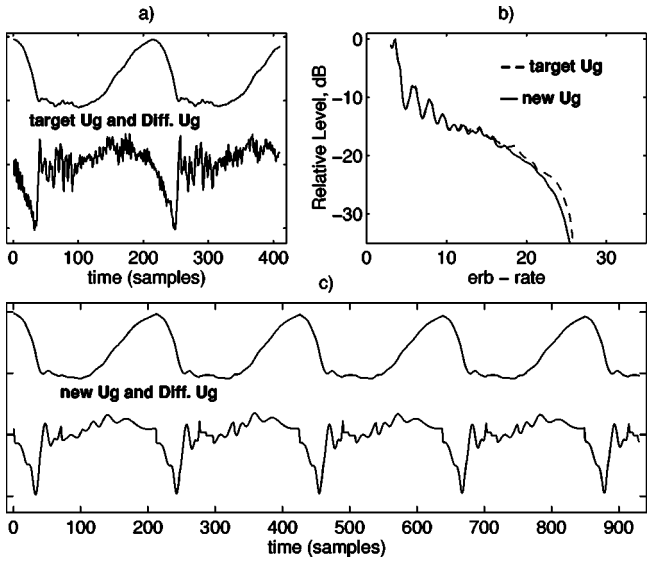

FIG. 10. Target flow [panel (a)] from a male speaker uttering a sustained vowel (MN1, $F_0 = 104$ Hz). Panel (b): comparison of the excitation patterns of the target flow (dashed line) and reproduced flow (continuous line). Panel (c): self-sustained oscillation produced by the model after training (i.e., $\hat{U}_g$ and differentiated $\hat{U}_g$).

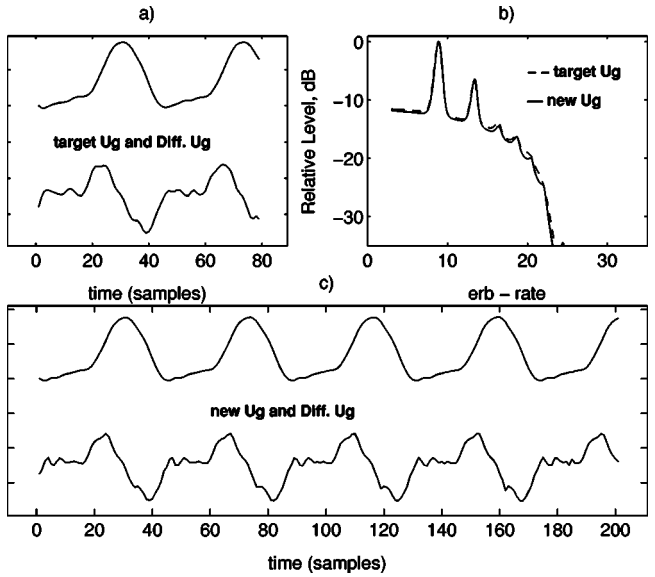

FIG. 12. FN2: the target flow [panel (a)] is from a female speaker uttering a sustained vowel ($F_0 = 372$ Hz). Panel (b): comparison of the excitation patterns of the flow (dashed line: target, continuous line: reproduced). Panel (c): self-sustained oscillation produced by the model after training (i.e., $\hat{U}_g$ and differentiated $\hat{U}_g$).

The highlighting of physiologically founded relations is motivated by the interest in the control perspectives offered by this approach, which can be valuable for applicative perspectives, e.g., speaker-specific or emotive speech synthesis. However, we want to stress the fact that the values of the parameters resulting from the fitting procedure are not intended here to provide an estimation or prediction of the physiology of the speaker.

Figs. 10–12 show the details of the self-oscillation properties of the model after training. The target flow period (upper-left panel), the reproduced flow (lower panel), and the comparison of the two in the frequency domain, are shown for the three cases MN1, FN1, and FN2. The comparison in the frequency domain was made using an auditory excitation pattern representation of the physical spectrum (Moore and Glasberg, 1983); the auditory model transforms the physical spectrum into a pattern of specific loudness as a function of critical band rate, and has previously been found to efficiently predict perceived differences between vowel sounds (Rao *et al.*, 2001).

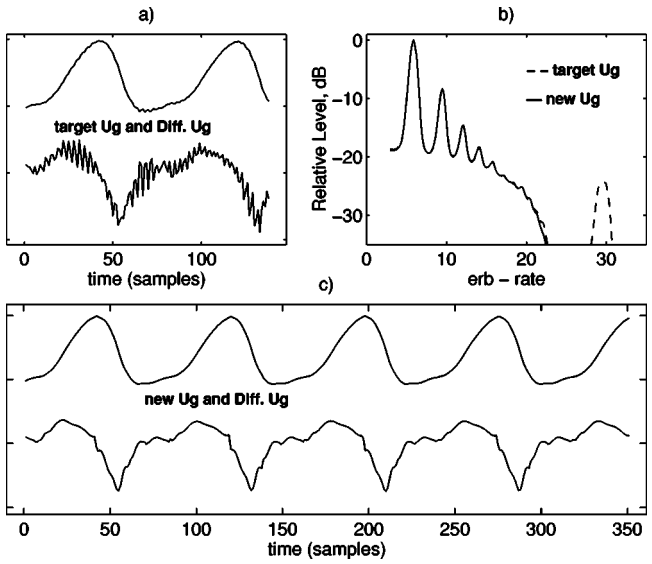

FIG. 11. FN1: the target flow [panel (a)] is from a female speaker uttering a sustained vowel (FN1, $F_0 = 208$ Hz). Panel (b): comparison of the excitation patterns of the target flow (dashed line) and reproduced flow (continuous line). Panel (c): self-sustained oscillation produced by the model after training (i.e., $\hat{U}_g$ and differentiated $\hat{U}_g$). It is evident how the model failed to reproduce the effect of the residual higher formant present in the inverse-filtered flow.

These examples show how the system successfully adapts the parametric flow model so as to fit different flow shapes, while maintaining the original self-oscillatory properties. A good matching of the excitation patterns is observed, at least in the lower part of the ERB scale. The discrepancies in the higher part of the ERB scale were mostly due to the inadequacy of the model in reproducing the residual effect caused by high vocal-tract formants.

IV. CONCLUSIONS

A vocal-fold model based on a one-mass scheme and enhanced with a data-driven identification component was presented. The first part of the paper concerned the exploration of the properties of an oversimplified one-mass model, and it was shown how flow-induced oscillations can be produced with one degree of freedom, even without vocal-tract load, provided that a vertical phase delay is reproduced with a propagation line. The resultant discrete scheme has the advantage of simplicity and of being computationally efficient. The set of control parameters is substantially reduced if compared to the original IF model.

In the second part of the paper, the simple one-mass model was improved with a parametric model of the flow, and a data-driven analysis/synthesis procedure was described

that allows the model to fit to an arbitrary target flow. The training with respect to different flow waveforms demonstrated the versatility of the model, and its potential to represent a wide class of signals. The potentialities of such an approach for speech synthesis have been pointed out by showing examples of controlling the pitch of the model after training.

Finally, the model was trained on a set of voice sources with the aim of highlighting the possible relations between its parameters and the principal characteristics of the flow.

The inversion technique proposed can be applied in principle to any theoretical description of the vocal folds, realistic or not. The advantage of using a physically based description of the vocal folds, as we do here, is that the fitting accuracy provided by the parametric component is coupled with physically consistent dynamical behaviors and control properties. It is relevant to this point that, after training of the fudge factors, the remaining meaningful parameters of the model don't lose their functional role, thus allowing for the control of the synthesis. To fulfill the long-term goals outlined in the introductory sections, i.e., the application to speech synthesis or coding, some points still require investigation: an algorithmic procedure to identify the parameters with physical interpretation is necessary and has to deal with the problem of nonuniqueness of the solution. Moreover, analytical conditions for closed-loop stability after fudge factor parametric identification remain an open issue, and the definition of constraints to account for during training should be addressed.

ACKNOWLEDGMENTS

The author is grateful to Johan Sundberg for providing the glottogram data used throughout the paper and for his many suggestions; and to Sten Ternström for useful discussions and support to this work. The author would also like to thank the reviewers, whose comments and suggestions led to a significantly improved version of the manuscript. This research was supported through the European Community Marie Curie Fellowship No. HPMT-2000-00119.

[1]The terms ''glottal entry'' and ''glottal exit'' refer to the cross-sectional areas defined respectively by the lower and upper edges of the vocal folds, *crossed* by the airflow directed from the subglottal region to the vocal tract.
[2]DECAP, developed at TMH-KTH, Stockholm, by Svante Granqvist.

Alku, P., and Vilkman, E. (**1996**). ''A comparison of glottal voice source quantification parameters in breathy, normal, and pressed phonation of female and male speakers,'' Folia Phoniatr Logop **48**, 240–254.
Avanzini, F., Alku, P., and Karjalainen, M. (**2001**). ''One-delayed-mass model for efficient synthesis of glottal flow,'' Proc. of Eurospeech Conf., pp. 51–54.
Chen, S., and Billings, S. A. (**1989**). ''Representation of non-linear systems: NARMAX model,'' Int. J. Control **49**, 1013–1032.
Chen, S., Cowan, C. F. N., and Grant, P. M. (**1991**). ''Orthogonal least squares learning algorithm for radial basis functions networks,'' IEEE Trans. Neural Netw. **2**, 302–309.
Childers, D., and Ahn, C. (**1995**). ''Modeling the glottal volume-velocity waveform for three voice types,'' J. Acoust. Soc. Am. **97**, 505–519.
Childers, D. G., and Hu, H. T. (**1994**). ''Speech synthesis by glottal excited prediction,'' J. Acoust. Soc. Am. **96**, 2026–2036.
Childers, D. G., and Wong, C. (**1994**). ''Measuring and modeling vocal source–tract interaction,'' IEEE Trans. Biomed. Eng. **41**, 663–671.
Fant, G. (**1960**). *Acoustic theory of speech production* (Mouton The Hague).
Fant, G., Liljencrants, J., and Lin, Q. (**1985**). ''A four-parameter model of glottal flow,'' STL-QPSR, pp. 1–13.
Flanagan, J. L., and Landgraf, L. L. (**1968**). ''Self-oscillating source for vocal-tract synthesizers,'' IEEE Trans. Audio Electroacoust. **AU-16**, 57–64.
Fröhlich, M., Michaelis, D., and Strube, H. W. (**2001**). ''SIM-simultaneous inverse filtering and matching of a glottal flow model for acoustic speech signal,'' J. Acoust. Soc. Am. **110**, 479–488.
Granqvist, S., Hertegård, S., Larsson, H., and Sundberg, J. (**2003**). ''Simultaneous analysis of vocal fold vibrations and transglottal airflow; exploring a new experimental setup,'' J. Voice **17**, 319–330.
Holmes, J. N. (**1973**). ''The influence of the glottal waveform on the naturalness of speech from a parallel formant synthesizer,'' IEEE Trans. Audio Electroacoust. **AU-21**, 298–305.
Ishizaka, K., and Flanagan, J. L. (**1972**). ''Synthesis of voiced sounds from a two-mass model of the vocal cords,'' Bell Syst. Tech. J. **51**, 1233–1268.
Ishizaka, K., and Flanagan, J. L. (**1977**). ''Acoustic properties of longitudinal displacement in vocal cord vibration,'' Bell Syst. Tech. J. **56**, 889–918.
Klatt, D., and Klatt, L. (**1990**). ''Analysis, synthesis, and perception of voice quality variations among female and male talkers,'' J. Acoust. Soc. Am. **87**, 820–857.
Koizumi, T., Taniguchi, S., and Hiromitsu, S. (**1987**). ''Two-mass models of the vocal cords for natural sounding voice synthesis,'' J. Acoust. Soc. Am. **82**, 1179–1192.
Liljencrants, J. (**1991**). ''A translating and rotating mass model of the vocal folds,'' STL-QPSR, pp. 1–18.
Lucero, J. C. (**1999**). ''A theoretical study of the hysteresis phenomenon at vocal fold oscillation onset–offset,'' J. Acoust. Soc. Am. **105**, 423–431.
Meyer, P., Wilhelms, R., and Strube, H. W. (**1989**). ''A quasiarticulatory speech synthesizer for German language running in real time,'' J. Acoust. Soc. Am. **86**, 523–539.
Milenkovic, P. (**1993**). ''Voice source model for continuous control of pitch period,'' J. Acoust. Soc. Am. **93**, 1087–1096.
Moore, B., and Glasberg, B. (**1983**). ''Suggested formulae for calculating auditory-filter bandwidths and excitation patterns,'' J. Acoust. Soc. Am. **74**, 750–753.
Pelorson, X., Hirschberg, A., van Hassel, R. R., and Wijnands, A. P. J. (**1994**). ''Theoretical and experimental study of quasisteady-flow separation within the glottis during phonation. Application to a modified two-mass model,'' J. Acoust. Soc. Am. **96**, 3416–3431.
Pinto, N. B., Childers, D. G., and Lalwani, A. L. (**1989**). ''Formant speech synthesis: Improving production quality,'' IEEE Trans. Acoust., Speech, Signal Process. **ASSP-37**, 1970–1887.
Rao, P., van Dinther, R., Veldhuis, R., and Kohlraush, A. (**2001**). ''A measure for predicting audibility discrimination thresholds for spectral envelope distortions in vowel sounds,'' J. Acoust. Soc. Am. **109**, 2085–2097.
Rosenberg, A. E. (**1971**). ''Effect of glottal pulse shape on the quality of natural vowels,'' J. Acoust. Soc. Am. **49**, 583–590.
Rothenberg, M., and Zahorian, S. (**1977**). ''Nonlinear inverse filtering techniques for estimating the glottal-area waveform,'' J. Acoust. Soc. Am. **61**, 1063–1071.
Schroeter, J., and Sondhi, M. (**1992**). *Advances in Speech Signal Processing* (Dekker, New York), Chap.: ''Speech coding based on physiological models of speech production,'' pp. 231–263.
Sondhi, M. M., and Schroeter, J. (**1987**). ''A hybrid time-frequency domain articulatory speech synthesizer,'' IEEE Trans. Acoust., Speech, Signal Process. **ASSP-35**, 955–967.
Steinecke, I., and Herzel, H. (**1995**). ''Bifurcations in an asymmetric vocal folds model,'' J. Acoust. Soc. Am. **97**, 1874–1884.
Stevens, K. N. (**1999**). *Acoustic Phonetics* (The MIT Press, Cambridge, MA).
Strik, H. (**1998**). ''Automatic parametrization of differentiated glottal flow: Comparing methods by means of synthetic flow pulses,'' J. Acoust. Soc. Am. **103**, 2659–2669.
Titze, I. R. (**1973**). ''The human vocal cords: A mathematical model. I,'' Phonetica **28**, 129–170.
Titze, I. R. (**1988**). ''The physics of small-amplitude oscillations of the vocal folds,'' J. Acoust. Soc. Am. **83**, 1536–1552.

A modeling investigation of articulatory variability and acoustic stability during American English /r/ production

Alfonso Nieto-Castanon[a] and Frank H. Guenther
Department of Cognitive and Neural Systems, Boston University, 677 Beacon Street, Boston, Massachusetts 02215

Joseph S. Perkell
Research Laboratory of Electronics, Massachusetts Institute of Technology, 77 Massachusetts Avenue, Room 36-413, Cambridge, Massachusetts 02139-4307

Hugh D. Curtin
Department of Radiology, Massachusetts Eye and Ear Infirmary, 243 Charles Street, Boston, Massachusetts 02114

(Received 28 December 2004; revised 20 February 2005; accepted 22 February 2005)

This paper investigates the functional relationship between articulatory variability and stability of acoustic cues during American English /r/ production. The analysis of articulatory movement data on seven subjects shows that the extent of intrasubject articulatory variability along any given articulatory direction is strongly and inversely related to a measure of acoustic stability (the extent of acoustic variation that displacing the articulators in this direction would produce). The presence and direction of this relationship is consistent with a speech motor control mechanism that uses a third formant frequency ($F3$) target; i.e., the final articulatory variability is lower for those articulatory directions most relevant to determining the $F3$ value. In contrast, no consistent relationship across speakers and phonetic contexts was found between hypothesized vocal-tract target variables and articulatory variability. Furthermore, simulations of two speakers' productions using the DIVA model of speech production, in conjunction with a novel speaker-specific vocal-tract model derived from magnetic resonance imaging data, mimic the observed range of articulatory gestures for each subject, while exhibiting the same articulatory/acoustic relations as those observed experimentally. Overall these results provide evidence for a common control scheme that utilizes an acoustic, rather than articulatory, target specification for American English /r/. © *2005 Acoustical Society of America.* [DOI: 10.1121/1.1893271]

PACS numbers: 43.70.Bk, 43.70.Jt [AL] Pages: 3196–3212

I. INTRODUCTION

When producing a given phoneme, speakers use a set of articulators (e.g., tongue, jaw, lips) to affect the vocal-tract shape and, ultimately, the characteristics of the resulting acoustic signal. The vocal-tract configuration for the production of a given phoneme is not uniquely defined by phoneme identity. Different speakers will use different articulatory configurations when producing the same phoneme, and often the same speaker will use a range of different articulatory configurations when producing the same phoneme in different contexts. In particular, the American English phoneme /r/ has been associated with a large amount of articulatory variability (Delattre and Freeman, 1968; Westbury *et al.*, 1998; Guenther *et al.*, 1999). While large, the degree of articulatory variability present in natural speech does not seem to hinder phoneme recognition by listeners, and it is often conceptualized as an expression of control mechanisms that make efficient use of a redundant articulatory system. Such efficient use of redundancy in biological motor systems is often referred to as *motor equivalence*.

Current speech movement control theories dealing with the motor equivalence problem can be roughly classified depending on the type of phonemic targets hypothesized (see MacNeilage, 1970, for motivations of a target-based approach to speech motor control theories). The task-dynamic model of Saltzman and Munhall (1989) exemplifies a type of computational model in which phonemic targets are characterized in terms of *tract variables* representing specific aspects of the vocal-tract shape that can be independently controlled by the speech control mechanism (e.g., lip aperture, tongue dorsum constriction location, etc.) In this model, articulatory variability can arise as a consequence of ''blending'' effects from the context phonemes. For example, when producing a /b/ in a VCV context, a full bilabial closure represents the targeted tract variable. Other aspects of the vocal-tract not affecting the targeted tract variable, such as tongue shape, will vary depending on the shape adopted in the production of the leading vowel, while also being subject to anticipatory movements towards the following vowel configuration. In this way, articulatory variability in different phonetic contexts would reflect the interplay between constraints imposed by current and contextual phonemic targets.

The DIVA model (e.g., Guenther *et al.*, 1998; 2003) exemplifies a second type of computational model of speech motor control in which the phonemic targets are characterized in terms of *acoustic/auditory variables*[1] (for example,

[a]Electronic mail: alfnie@bu.edu

 0001-4966/2005/117(5)/3196/17/$22.50

formant frequency descriptors). In this model, the control mechanism moves the articulators in the direction that would bring the formants of the resulting auditory signal closest to the targeted formants, without reference to an explicit vocal-tract shape target. Articulatory variability then arises naturally as a consequence of the many-to-one mapping between the articulatory configurations and the audible acoustic characteristics of the produced sound. In other words, for these models articulatory variability reflects the variety of articulatory configurations that would produce the desired acoustic properties.

Often (e.g., Saltzman and Munhall, 1989; Guenther *et al.*, 1998) the distinction is emphasized between the articulatory configurations (the state of articulatory variables, such as jaw aperture) and the resulting vocal-tract shapes (the state of tract variables, such as tongue dorsum constriction degree). This highlights the redundancy of the speech articulatory system. For example, a particular tongue dorsum constriction degree can be achieved with a relatively low jaw height and a relatively high tongue-body height (relative to the jaw), or a higher jaw height and lower tongue-body height can be used to achieve the same constriction degree. More generally, both articulatory and tract variables represent different coordinate frames that can be used to represent the state of the vocal-tract apparatus (see MacNeilage, 1970, for an introduction to the concept of coordinate systems in speech production). Tract variables represent a more abstract coordinate frame than articulatory variables, since there is a one-to-many relation between tract variables and articulatory variables defined by the geometrical relations among them. In the same way, acoustic or auditory variables (Guenther *et al.*, 1998) can be simply thought of as yet another coordinate frame for the representation of the articulatory state. They also represent a more abstract coordinate frame than articulatory variables, in that there is a one-to-many relation between auditory and articulatory variables. The analysis of variability in articulatory configurations in the production of a given phoneme, similar to the analysis of errors in a pointing task (Carozzo *et al.*, 1999; McIntyre *et al.*, 2000), is a useful approach for uncovering an appropriate coordinate frame for the representation of targets in speech production. We thus believe that the analysis of articulatory variability should serve to direct the definition of motor control models of speech production. Based on this view, the goal of the current paper is twofold: (1) to characterize, in a paradigmatic example of articulatory variability (American English /r/), the extent of articulatory variability in relation to hypothesized target representations (relevant tract and acoustic variables); and (2) to test whether a model of speech motor control based on an acoustic target definition, together with a speaker-specific vocal-tract model, can explain the specificities of the observed articulatory variability in individual speakers. To these ends, we first present new, model-based analyses of electromagnetic midsagittal articulometer (EMMA) data on seven subjects from a previous study (Guenther *et al.*, 1999). These analyses characterize the experimentally observed articulatory variability in relation to hypothesized target variables. We then provide simulation results of an auditory target model controlling the movements of speaker-specific vocal-tract models based on magnetic resonance imaging (MRI) scans of the vocal tracts of two of the seven experimental subjects. The model movements are then compared to those of the modeled speakers. Note that the present study addresses only the production of American English /r/. Several aspects of this paper's methodology (to be described later) are specific to the class of vowel and semivowel productions. The extent to which the presented results generalize to the production of other phoneme classes (in particular, consonants) can only be addressed by further studies.

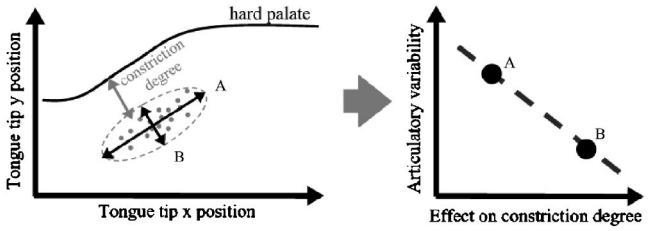

FIG. 1. Schematic example of articulatory variability analysis for a single articulatory measure of interest (tongue tip position). Left: Hypothetical configuration of tongue-tip positions in the production of a phoneme that could be characterized by a tongue tip constriction degree phonemic target. A and B represent the directions of the tongue tip movement resulting from a principal component analysis (PCA) of the tongue-tip articulatory covariance of multiple repetitions. The gray arrow represents the direction of the tongue-tip movement affecting the constriction degree the most. Right: Plot relating the extent of articulatory variability along each of the articulatory directions (A and B) versus the effect that each of these directions has on the hypothetical target variable (constriction degree). The actual analyses performed in this section attempt to provide evidence for several theoretically motivated phonemic target definitions by extending this simple scheme to the case of multiple articulatory measures of interest (indicated by six transducer positions located on the tongue, lips, and jaw of the speakers; see the text for details).

A. Variability analysis rationale

Previous analyses (Guenther *et al.* 1999) showed that articulatory trade-offs during /r/ production act to reduce $F3$ variability. In this paper we attempt to assess this kind of finding in the context of different speech motor control theories by testing the ability of theoretically motivated phonemic target variables to predict the observed variability in articulatory configurations. Our rationale is exemplified in Fig. 1. Let us only consider the movement of the tongue tip in this example. Imagine, during the production of a hypothetical phoneme, the phonemic target consists of accomplishing a given tongue-tip constriction degree (distance between the tongue tip and the hard palate). The expected array of final configurations of the tongue tip for the production of this phoneme would be expected to take the approximate form shown in Fig. 1 left. The axes labeled A and B represent the directions of articulatory movement resulting from a principal component analysis (PCA) of the final articulatory covariance[2] of a number of productions of the phoneme, and the gray arrow characterizes the direction of articulatory movement affecting the degree of the tongue-tip constriction the most. The right side of Fig. 1 plots for each articulatory direction (A and B) their effect on the hypothesized target variable (*effect on constriction degree*) on the x axis, and their extent of *articulatory variability* on the y axis. This plot

schematizes the observation that those articulatory dimensions affecting the target variable the most (B, in this case) would be expected to show a lesser extent of articulatory variability than those dimensions affecting the target variable the least (A). The EMMA analyses in this paper (Sec. II A) extend the simple scheme in this example (with only one transducer reflecting the tongue-tip position) to the case of multiple transducers (six transducers, reflecting tongue, jaw, and lips configurations). The simultaneous analysis of multiple transducers on different articulators allows the articulatory dimensions (12 for each subject) that result from a PCA to characterize complex movements of one or several articulators, such as those described in the literature as trading relations between and within articulators (for example a simultaneous raising of the tongue back and decrease of lip rounding, as in Perkell *et al.*, 1995; or a simultaneous raising of the tongue tip and lowering of the tongue back as in Guenther *et al.*, 1999). As in the example shown here, a functional relationship between the extent of articulatory variability along each of the resulting articulatory dimensions and their associated effect on a hypothesized target variable is taken as indicative of the use of a specific target scheme in the articulatory movement data being analyzed.

In the current article we report the results of analyses of this type performed on the data from each speaker. Subsequent pooling of these results across different speakers allows us to determine whether commonalities exist in the target specification for /r/ across speakers. While we acknowledge that the control strategy for the production of /r/ could be different for different speakers, and the literature has historically emphasized these differences across speakers and phonetic contexts in the articulatory specification of /r/ (e.g., Delattre and Freeman, 1968), our results indicate that commonalities can in fact be found when using an appropriate frame of reference. In particular, we demonstrate that when the articulatory frame of reference is aligned to correspond with important acoustic features, commonalities in the target specification for /r/ are apparent again. These commonalities indicate that a simple control scheme, common across speakers, that utilizes an acoustic production target for /r/ can provide a straightforward and parsimonious explanation for the articulatory variability within and between speakers, whereas control schemes utilizing a common constriction target for /r/ cannot account for the results. To that end the analyses will test both acoustic and tract variables as hypothetical target variables using the methodology outlined above. Note that from these analyses we investigate the possibility of acoustic or tract variables *forming part* of the global target specification for /r/, not whether they fully define it. More complex analyses would be needed to test the possibility of multiple target variables fully defining the target specification for /r/.

B. Modeling and simulations rationale

The analysis of articulatory variability outlined above attempts to identify the nature of the phonemic target for /r/. The results will reveal that there is a great deal more evidence indicative of acoustically defined phonemic targets (in particular one based on $F3$), rather than targets based on vocal-tract variables. Nevertheless, the previous analyses do not explicitly test whether using a common control strategy based on acoustically defined targets is sufficient to explain the variety of articulatory configurations different speakers use in producing /r/. In order to address this issue, in the current article we explicitly simulate the outcome of a control strategy for /r/ production based on acoustic targets. These simulations are performed using specific models of two of our subjects' vocal tracts, so that the results can be directly compared to these subjects' observed articulatory configurations during the production of /r/.

In order to simulate the effect of a common control strategy based on acoustic targets for different speakers, we must first understand for each speaker the relationship between their articulators and the resulting acoustics. There are several reasons why we cannot use the previously obtained EMMA data and acoustic recordings for each subject in order to characterize this relationship. First, independent data pools for modeling and testing are always preferable, as this offers a generally more valid approach to hypothesis testing. Second and equally important, EMMA data have limited potential to characterize the articulatory–acoustic relationship given the relative scarcity of relevant articulatory information, which is limited by the number of available transducers. Articulatory–acoustic mappings obtained from EMMA data are not only less accurate but also lead to limited interpretability, as the researcher is left to speculate the vocal-tract profile from a limited sampling of interpolating points. MRI data, in contrast, provide a more satisfying characterization of vocal-tract morphology. We thus used simultaneous recording of MRI and acoustic data for two subjects to characterize the relationship between each subject's articulatory configurations and the resulting acoustics (see Sec. II B). Then, we simulated the effect of the hypothesized control strategy on each subject's vocal-tract model during the production of /r/ using different leading phonetic contexts, and the modeled results were compared to each subjects' productions (Sec. II C). While this methodology has the added complexity of combining MRI and EMMA data, it is a more valid and informative approach than one based on EMMA data alone. Furthermore, we believe the analyses in these sections not only add an important modeling examination of /r/ production but also contribute to efforts in speech production modeling that addresses speaker-specific behavior, rather than the behavior of an average or idealized speaker.

II. METHODS

A. EMMA data collection and analysis

An EMMA system (Perkell *et al.*, 1992) was used to track the movement of six transducer coils indicating the tongue shape (tongue back, tongue dorsum, and tongue tip), jaw aperture (transducer located on the lower teeth), and lips (upper and lower lip) in the midsagittal plane during the production of /r/ in five different phonetic contexts (''warav,'' ''wabrav,'' ''wavrav,'' ''wagrav,'' ''wadrav'') for seven American English speakers. Each subject repeated each production between two and five times. A directional microphone was used to record the subjects' speech simulta-

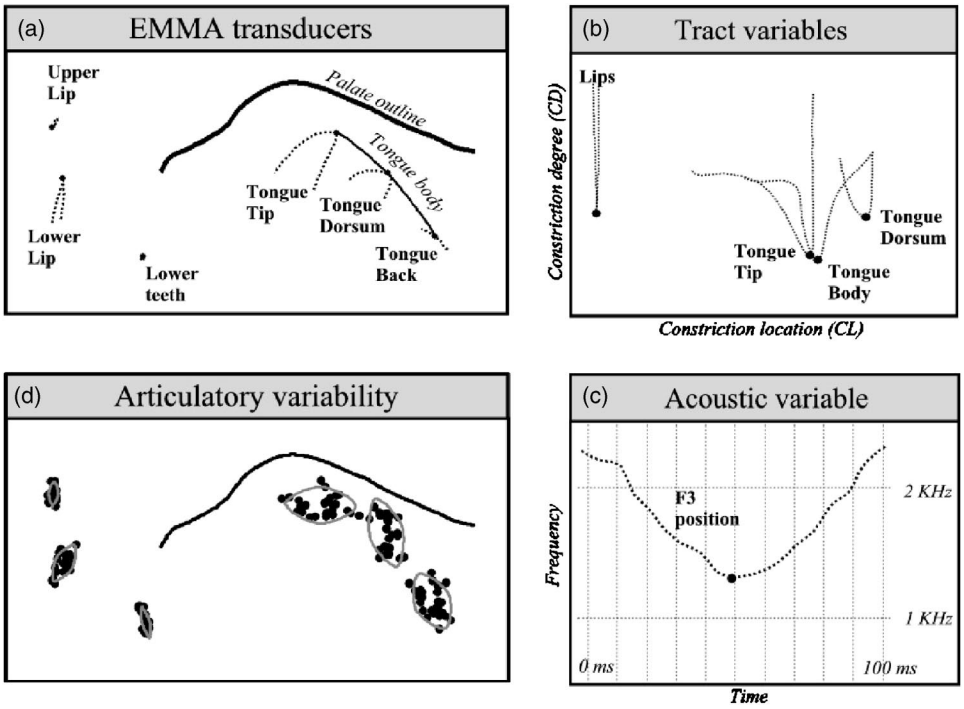

FIG. 2. Main elements in the analysis of EMMA data for each subject. (A). EMMA transducers: Example of the location of the six transducers during production of /r/ in /warav/. Dotted lines represent the trajectories of each transducer. Black dots indicate the center of the /r/ defined from the inflexion point of the tongue-dorsum (see the text for details on alternative definitions of /r/ centers). The line uniting the three tongue transducers was created using a Catmull–Rom spline. (B). Tract variables: Eight variables representing constriction degree and location are derived from the transducer positions to represent four relevant vocal-tract constrictions. Tongue-tip and tongue-dorsum constrictions represent the relative positions of these transducers to the palate outline. A tongue-body constriction was also defined using the relative position of the point on the tongue-body line closest to the palate. The lip constriction represents the relative positions of the two lip transducers (lip aperture and protrusion). (C). Acoustic variable: Trajectory of the third formant ($F3$) around the /r/ center. (D). Articulatory variability: Example of articulatory variability in /r/ production. Ellipsoids represent 95% confidence intervals of each transducer position during the /r/ for a series of /r/ productions in different phonetic contexts. The analyses in this section test the ability of the acoustic variable $F3$ and the eight tract variables defined above to characterize the observed articulatory variability.

neously with the EMMA signals. The details of the methodology are described in Guenther *et al.* (1999). The primary acoustic cue for /r/ is a deep dip in the trajectory of the third formant frequency, or $F3$ (Boyce and Espy-Wilson, 1997; Delattre and Freeman, 1968). The acoustic signal was therefore processed to extract the $F3$ trajectory. An initial definition of the acoustic center of the /r/ was constructed in terms of the time point of the $F3$ minimum. Figure 2 shows the main elements in the analysis of the EMMA data. The plot labeled (A) illustrates the trajectory of the six transducers for a window of 100 ms around the /r/ center during a ''warav'' production, and the plot labeled (C) shows the corresponding $F3$ trajectory.

In addition to the acoustic variable $F3$ [Fig. 2(C)], we defined eight vocal-tract variables reflecting the degree and location of four relevant tongue and lip constrictions [Fig. 2(B)]. *Tongue tip and tongue dorsum constriction degree* were defined as the distance between the hard palate outline and the tongue tip and tongue dorsum transducer positions, respectively. *Tongue tip and tongue dorsum constriction location* were defined as the positions along the hard palate outline of the point closest to each of these transducers. *Lip constriction degree and location* were defined as lip aperture (distance between upper and lower lip transducers) and lip protrusion (average horizontal position of the upper and lower lip transducers), respectively. To accommodate the possibility that the tongue transducers were not optimally located at places of relevant constrictions, we defined an additional tongue constriction by connecting the three tongue transducer locations using a Catmull–Rom spline [shown in Fig. 2(A) as a solid line], and estimating the degree and location of the constriction formed by the point along the resulting tongue outline closest to the hard palate. We call the resulting measures associated with this additional constriction the *tongue-body constriction degree and location*. No tongue back constriction was defined due to the lack of information regarding the pharyngeal wall position for each subject. Based on these constrictions we constructed corresponding articulatory-based definitions for the /r/ centers. These were manually identified as the inflexion point in the trajectories of the four previously defined constrictions (three tongue constrictions and one lip constriction) within a window of 100 ms around the acoustically defined /r/ center. The /r/ centers are indicated in Fig. 2 by dots [in plots (A) and (D) dots indicate the tongue–dorsum /r/ center; in plots (B) and (C) dots indicate the corresponding constriction- or acoustically defined /r/ center]. The articulatory defined /r/ centers occurred on average 7 ms (95% CI [6, 9] milliseconds; $t_{591}=-11.4$; $p<0.001$) before the acoustically defined /r/ centers. Among the articulatory defined centers the main difference was for that defined from the lip constriction. While the lip constriction extreme occurred on average 19 ms (95% CI [16, 22] ms, $t_{147}=-13.7$; $p<0.001$) before the acoustically defined /r/ center, the different tongue con-

strictions were only 4 ms (95% CI [2, 5] ms; $t_{443}=-5.6$; $p<0.001$) before the $F3$ minimum (and approximately at synchrony among them; ANOVA analysis, 7% intergroup variance, $F_2=2.64$; $p=0.07$).

The articulatory data were analyzed in terms of the articulatory variability of the transducer positions [Fig. 2(D)] at the /r/ centers, using as hypothesized target variables the acoustic and tract variables defined above [Figs. 2(B) and (C)]. The details of this analysis follow. Variables associated with transducer positions were normalized independently and separately for each subject in order to appropriately compare across subjects, and also to reduce possibly confounding effects from the different ranges of operation of each of these variables (e.g., the lower teeth transducer showing a smaller range of movement than the tongue transducers). We computed for each subject the articulatory covariance matrix $\mathbf{\Omega}_0$ at the /r/ center. For the analyses involving an acoustic target variable we used the acoustically defined /r/ centers, and for the analyses involving a tract target variable we used the corresponding articulatory defined /r/ centers.

For each subject a principal component analysis of the articulatory covariance led to the definition of a set of 12 vectors or principal articulatory directions $\mathbf{q}_j$ $(j=1,...,12)$ defining a base in the articulatory space. Each of these unit vectors $\mathbf{q}_j$ represents a direction of change of the EMMA positions characterizing the observed articulatory variability. For each articulatory direction j the *percentage of articulatory variability* associated with this direction was computed as

$$\sigma_j \equiv \frac{\mathbf{q}_j^t \cdot \Omega_0 \cdot \mathbf{q}_j}{\Sigma_k \mathbf{q}_k^t \cdot \Omega_0 \cdot \mathbf{q}_k}.$$

Nine target variables were then hypothesized, eight corresponding to tract variables (constriction degree and location for each of the previously defined vocal-tract constrictions) and one corresponding to the acoustic variable $F3$. For each combination of an articulatory direction j and a target variable i, the effect of the articulatory dimension on the target variable was estimated as

$$\lambda_{ij} \equiv \frac{|\mathbf{q}_j^t \cdot \mathbf{X}^+ \cdot \mathbf{y}_i|}{\Sigma_k |\mathbf{q}_k^t \cdot \mathbf{X}^+ \cdot \mathbf{y}_i|}.$$

Here, $\mathbf{y}_i$ is a vector representing the time courses of the target variable i for a window of 10 ms around the /r/ center for all contexts and repetitions, and the matrix $\mathbf{X}^+$ represents the pseudoinverse of a matrix $\mathbf{X}$ containing the corresponding time courses of the transducer positions. The numbers λ_{ij} represent the absolute value of the expected change in the ith target variable associated with moving the articulators along the jth articulatory direction (normalized across all articulatory directions). They can be interpreted as a *percentage load* of the target variable on each of the articulatory dimensions.

We performed two set of analyses on these data, one categorical and one continuous. In the categorical analysis the articulatory dimensions were divided, for each target variable independently, into two sets Θ_i^{small} and Θ_i^{large}, corresponding to the *small-* and *large effect on target variable* dimensions, and each defined as the six dimensions associated with the six lowest or the six largest λ_{ij} values, respectively. We then computed the percentage of articulatory variability associated with small effects on each target variable by combining the variability over of the associated articulatory dimensions: $\sigma_i^{\text{small}} \equiv \Sigma_{j \in \Theta_i^{\text{small}}} \sigma_j$. This leads to a value σ_i^{small} for each subject and for each target variable. Under the null hypothesis (no association between articulatory variability and effect on target variable), the expected percentage of articulatory variability associated with each of these sets would be 50%. We estimated the associated probability level of the observed data using Monte Carlo simulations on randomly defined sets Θ_i^{small}. For collapsing the results across subjects we computed the average of σ_i^{small} for each target variable, and the associated null hypothesis distribution was formed from an equal-weighted mixture of each of the conforming Monte Carlo distributions.

In the continuous analysis we constructed plots relating, for each hypothesized target variable i, the observed articulatory variability along each articulatory direction (σ_j) versus its effect on the target variable (λ_{ij}). The resulting plots were fit using a linear regression on the log variables. R^2 and p values, as well as confidence intervals for the linear fit parameters, are reported in Sec. III.

B. Construction of speaker-specific vocal-tract models

A *speaker-specific vocal-tract model* is a characterization of the range of configurations a speaker's vocal-tract could adopt, together with the acoustic output any configuration would produce under glottal excitation. To estimate the former, a set of 2D MRI midsagittal profiles was acquired for two subjects (the first two subjects in the EMMA experiment) while producing a set of phonemes. To estimate the latter (the associated acoustic outputs), acoustic data were collected at the start of each scan. The following paragraphs describe the data acquisition and the procedure used to interpolate and generalize from the limited available articulatory and acoustic data to other nonobserved configurations. The results provide a simple characterization of the full range of articulatory configurations and acoustic outputs a speaker can produce.

1. Data acquisition

Scans were performed with a 1.5-tesla Siemens scanner using a 14-s TR acquisition, 4-mm midsagittal slice with 256×256 matrix size. Subjects were asked to produce a simple utterance (either a steady-state vowel or a /VC/ sequence) and hold the last phoneme during the 14 s of the image acquisition procedure. Their productions were recorded using a microphone placed in the scanner near the subject's mouth. The MR acquisition started when the subject was holding the last phoneme to allow clear audio recording of their productions prior to the onset of scanner noise. Data for 27 and 15 phoneme productions were acquired for subject 1 and 2, respectively. Productions included several American English vowels (ɛ i æ ʌ uw ɝ ei ow), semivowels (r), fricatives (ʃ s f), nasals (m,n), and stop (p t k b d g) consonant sounds. All utterances were used to

construct the articulatory models. However, since formants could only be reliably extracted for the vowel and semivowel utterances, only these utterances were used to formulate the mapping between articulator configurations and acoustics.

2. Analysis of vocal-tract configurations

Previous approaches to the creation of a parametric description of articulatory movements (e.g. Perrier *et al.*, 1992; Story *et al.*, 1996, 1998) create a grid in the midsagittal plane and obtain the vocal-tract area function from the intersection of this grid with the vocal-tract outline. An articulatory model based directly on a vocal-tract area function representation is, nevertheless, unlikely to produce optimally realistic articulatory movements, given the discontinuity between natural vocal-tract articulator movements and the corresponding area function representation using the grid method. For example, forward movement of the tongue body creates discontinuities in the associated area function changes each time the tongue tip crosses a grid line. These discontinuities are particularly marked when a cavity is formed below the tongue tip, as occurs in some /r/ productions. In this paper we chose to create a parametric definition of the articulator space from a principal component decomposition of the outlines of different vocal-tract segments (tongue, jaw, and lips). In this way the resulting characterization is expected to be both articulatorily meaningful and continuous with respect to movement of the articulators. MR images were inspected visually for movement artifacts, and trials with a large amount of movement were removed from further analyses. In each resulting raw MR image, the region associated with air (vocal cavity and the head exterior) was identified. Pixel intensities were automatically clustered into eight clusters. The idea was to identify the lowest intensity cluster with the regions of air in the midsagittal image. The user then selected a starting point from this air region and a flood-fill algorithm was used to define the air area. Images were manually edited to correct for the cases when the air area comprised multiple disconnected regions (e.g., when the lips were closed). The outline of the resulting air region was then extracted for each image. These vocal-tract outlines were aligned spatially using the hard palate outline to correct for subject movement in the scanner. They were then divided into different segments of interest (tongue body, jaw, lips, hard palate, velum, laryngeal region). Each segment was interpolated by a fixed number of equally spaced 2D points along the identified segment outline. To obtain a simple descriptor of each segment's shape we concatenated both the x- and y coordinates of all the points along a given segment outline. For the present study we concentrated on the effect of tongue, lower lip, and jaw. PCA was applied to each of these shape descriptors to obtain a set of five articulatory components: three for the tongue body, and one each for the jaw and lower lip. The variability in articulatory configurations explained by movements of the jaw was removed prior to the estimation of the tongue and lip principal components in order to remove redundancies in their definition (cf. Maeda, 1990). The resulting set of principal articulatory components was used as a characterization of the range of articulatory configurations the subject could produce. In this way, any articulatory configuration the subject's vocal-tract model could produce was represented by a five-element vector, describing the contribution of each of the five articulatory components to the vocal-tract shape.

3. Analysis of acoustic signals and the articulatory to acoustic mapping

Acoustic recordings of the subject's production of each utterance made while in the MRI scanner (just before the onset of the scanner noise) were analyzed using linear predictive coding (LPC) ($p=26$, $F_s=22$ KHz). The acoustic signal was pre-emphasized with a single delay FIR filter ($a1=0.95$) to reduce the effects due to radiation and the glottal pulse (Wakita, 1973). The first three formant values were extracted for each production.

In order to approximate the vocal-tract articulatory/acoustic mapping, past studies have typically used a transformation from midsagittal cross dimensions to an area function. Then, from acoustic theory the frequency response of a particular vocal-tract shape is computed. In this transformation there are several unknowns that cannot be obtained from simple misagittal MR images, most importantly the midsagittal cross section to area function relationship. Previous models have either fitted these parameters to the subject's acoustic productions (e.g., using a relatively difficult to tune elliptical approximation to the area cross sections; Maeda, 1990) or an elegant but more complex estimation procedure based on multiple 3D volumetric MRI representations of the vocal-tract (Tiede *et al.*, 1996). The collection of 3D volumetric data for multiple phonemes is time-consuming and can suffer from problems in determining the location of the teeth, which do not show up on MR images and thus adversely affect the measured area function. In contrast to this approach, here we use a purely statistical approach characterized by a linear mapping fitting the relationship between the articulatory and formant descriptors for each subject. In this way, the proposed model offers only an approximation to the articulatory–acoustic relationship, but has the advantages of requiring a relatively small amount of MRI and acoustic data for each subject and avoiding the complications derived from the estimation of the area function. The linear mapping best fitting the relationship between articulatory and acoustic components for each subject's data was then estimated using linear regression on the articulatory and acoustic descriptors from vowels and semivowels (nine and six configurations for Subjects 1 and 2, respectively).

The validity of this approach was first estimated by creating a random sample of vocal-tract configurations, and computing the corresponding acoustic outputs using a standard articulatory synthesizer (Maeda, 1990). A random set of 10 000 valid articulatory configurations was created using a normal distribution of the model's articulatory parameters (mean zero, standard deviation one) hard limiting between -3 to 3 standard deviations (the full valid range of articulatory parameters in Maeda's 1990 vocal-tract model). For these data we found a very significant linear relationship ($R^2=0.97$) between the articulatory and formant descriptors. Deviations from linearity were most apparent in extreme configurations (close to a closure). For each articulatory con-

figuration **x** we constructed an approximate measure of percentage extent of closure as $100/k$, where the value k is the minimum value such that the articulatory configuration $x_0 + k(x - x_0)$ would result in a closed vocal-tract configuration ($\mathbf{x}_0$ represents a rest configuration). This measure is 0% for a rest configuration, and 100% for a closed configuration. For this measure we observed that the previously estimated articulatory–acoustic fit provided good approximations ($R^2 > 0.9$) for relatively open configurations ($100/k < 80\%$), but this fit was considerably poorer ($R^2 = 0.65$) for configurations near closure ($100/k > 90\%$). For comparison, average articulatory configurations for /r/ production for Subjects 1 and 2 were reasonably open ($100/k \approx 60\%$). These results indicate that a linear mapping between articulatory and acoustic dimensions is reasonable for our present analysis demands, and in general it is appropriate if the vocal-tract is restricted to nonextreme configurations (e.g., vowels and semivowels). In other words, this methodology would not be appropriate for modeling many consonant productions. As a last validation analysis we estimated the effect that a limited amount of available data points (nine and six configurations for Subjects 1 and 2, respectively) would have in our estimation procedure. The average errors in the estimation parameters (linear regressors) using randomly selected sets of nine and six configurations were found to be relatively low (2% and 11%, respectively, for Subjects 1 and 2).

C. Simulations of /r/ production

The DIVA model (Guenther *et al.*, 1998) was used as a controller for the movement of the speaker-specific vocal-tract articulators to produce an acoustic /r/ target in different phonetic contexts. The DIVA model can be characterized as a derivative controller in the acoustic space. The implementation reduces, at each time point, to iteratively moving the articulators in the articulatory direction that brings the current acoustic output closest to the desired acoustic target. In mathematical terms, the model uses a pseudoinverse of the Jacobian matrix relating articulator movements to their acoustic consequences to move in a straight line (in acoustic space) to the target (see Guenther *et al.*, 1998 for details). While in the complete DIVA model this is accomplished by learning this pseudoinverse transformation through experience (e.g., Guenther *et al.*, 1998), in the current implementation we used an explicit calculation of the pseudoinverse of the articulator-to-acoustic mapping. The articulatory space was defined in terms of the PCA components as described above, and the acoustic space was defined in terms of the first three formants of the spectrum (in Hz). The acoustic target in the model was defined from each subject's own /r/ production formants. To compare the results of the DIVA model simulations to the experimentally obtained EMMA data for each subject, the estimated transducer locations were manually identified on a rest configuration of the modeled speaker-specific vocal tract. The approximate location where the tongue transducers were placed was visually identified following the directives of the original EMMA experimental paradigm, as 1, 2.5, and 5 cm back from the tongue tip. The initial vocal-tract configurations of three phonetic contexts (/ar/, /dr/, and /gr/) were manually edited from the original MRI data to approximate the observed initial transducer configuration (75 ms before $F3$ minimum) in the corresponding contexts for each subject. Simulations of the DIVA model were run starting from these configurations to a ''final'' configuration at the $F3$ minimum for /r/. The estimated direction of movement (difference between the final and starting transducer positions) was compared to the measured transducer movement in the same contexts (correlation coefficients are reported). Finally, using all available MRI configurations as initial vocal-tract configurations (not just the three used for the preceding analyses), additional simulations were run using the same acoustic target for /r/, and the resulting articulatory variability across the model's /r/ productions was determined. On these data we performed articulatory variability analyses similar to those performed on the original EMMA data.

III. RESULTS

A. Predictive relations between hypothetical target variables and articulatory variability

This section deals with the analysis of articulatory movement data in an attempt to show the ability of different phonemic target hypotheses to account for the observed articulatory variability in the production of /r/. In particular, it was expected that the choice of an ''appropriate'' phonemic target would provide good separability of those directions of articulatory movement showing large versus small articulatory variability. The main result shows that, among the hypothesized target variables, the acoustic variable $F3$ provides the best predictions of the articulatory variability in /r/ production. In particular, for any direction of articulatory movement, its effect on the acoustic variable $F3$ is strongly related (for each subject and across subjects) to the extent of articulatory variability along this direction. On the other hand, none of the tract variables tested (corresponding to an articulatory phonemic target representation hypothesis) provides as good predictability across subjects of the articulatory variability in the production of /r/. This section presents these comparative results, and provides a series of analyses describing the observed relationship between effect on $F3$ and articulatory variability.

Figure 3 shows, for each subject, and collapsed across all seven subjects, the percentage of articulatory variability associated with dimensions that have small effects on each of the hypothesized target variables (this percentage of articulatory variability is labeled σ_i^{small} in Sec. II, where i represents each of the hypothesized target variables). Under the null hypothesis (no association between articulatory variability and effect on a target variable) these percentages would be 50%. Higher numbers indicate inverse association between effect on a target variable and articulatory variability, and are taken as indicative of a control strategy utilizing the target variable in the definition of the phonemic target. For example, the articulatory variability for Subject 2 (shown for reference in the left-most column of the figure) shows a tongue-tip distribution similar to that schematized in the example of Fig. 1 (indicating a possible tongue-tip constriction degree target), and the corresponding cell in the table indi-

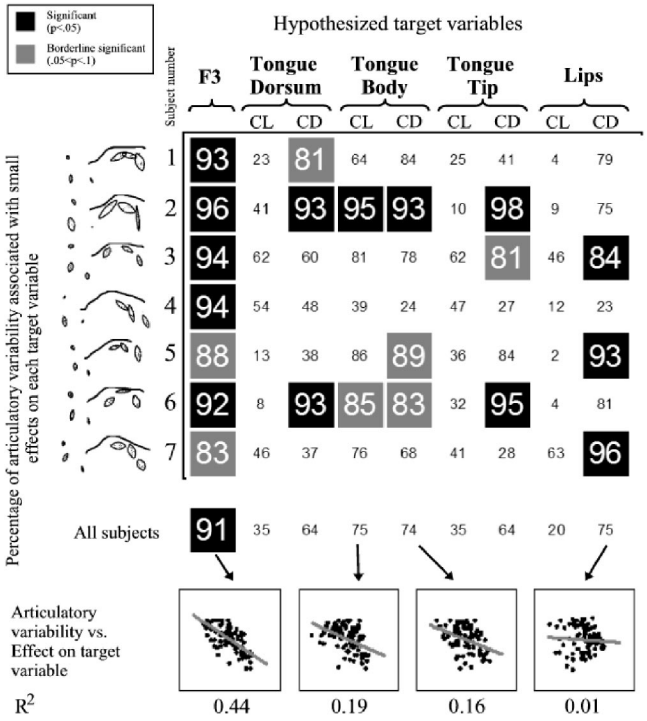

FIG. 3. Relation of hypothetical target variables to articulatory variability during /r/ production. Top: Categorical analyses. Table shows the percentage of articulatory variability associated with small effects on each hypothesized target variable (columns) for each subject (rows), and across all subjects (last row). Statistically significant percentages are highlighted. For reference, plots at the left of the table schematize the shape of the articulatory variability for each subject. Bottom: Continuous analyses. Plots show the relation between each articulatory dimension's variability (abscissa) and its effect on some of the most likely target variables (ordinate). Each dot in the plots represents an articulatory dimension (i.e., a direction of movement of the articulators) for a given subject. Both articulatory variability and effect on target variable are represented in log percentage units.

cates that in fact for this subject a significant amount of articulatory variability (98%) could be associated with this constriction target. While each subject shows indication of one or more possible phonemic targets, the collapsed results across all subjects (*All Subjects row*) indicate that $F3$ is the most consistent phonemic target among the hypothesized variables. Small effects on $F3$ are associated on average with a significant amount of articulatory variability (91%, $p=0.03$). In contrast, small effects on none of the hypothesized tract target variables are found to be significantly associated across subjects ($p>0.21$) with the extent of articulatory variability. Small effects on tongue-body constriction degree and location and lip constriction degree are among the best competing tract variable hypotheses, each associated with about 75% of the articulatory variability (not significantly greater than 50%, $p=0.21$). The plots at the bottom of the figure show the associations between effect on each target variable and articulatory variability in a continuous form. Again, the acoustic target $F3$ is best supported by our data, showing the strongest inverse association ($R^2=0.44$), as expected from a motor control strategy that utilizes $F3$ as a phonemic target.

These results indicate that, among the target variables tested, $F3$ is the most likely target variable that appears consistently across subjects in the production of /r/. In particular, they show that if, for a given subject, deviating from an average /r/ configuration along a given articulatory direction was found to have a relatively large impact on $F3$ (low $F3$ stability), then that subject tended to show little articulatory variability along this articulatory dimension. Conversely, if deviating along a given articulatory direction was found to have relatively little impact on $F3$ (high $F3$ stability), then the subject tended to show a larger amount of articulatory variability along this articulatory dimension. We will refer to this as a *predictive relationship between acoustic stability and articulatory variability*. Figure 4 highlights the continuous (left) and dichotomous (right) description of this relationship. Each dot in the left plot represents an articulatory dimension for a given subject. Their position represents the relative effect of each articulatory dimension on $F3$ (in percentage load, compared to other dimensions for the same

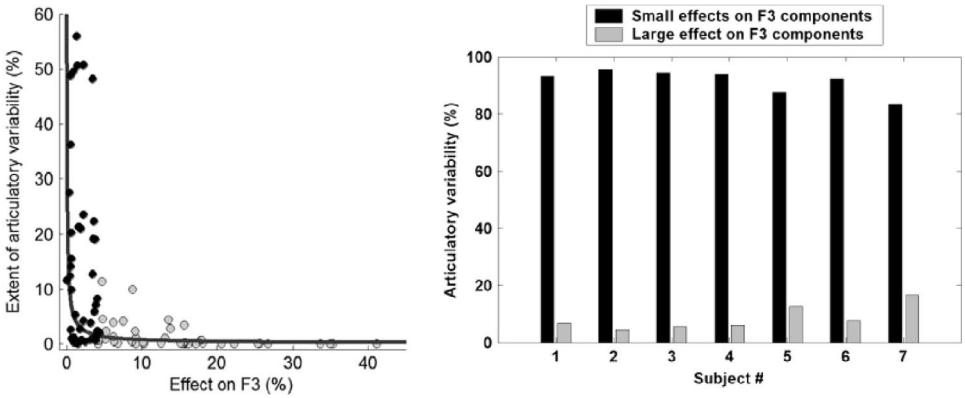

FIG. 4. Predictive relationship between acoustic stability and articulatory variability. Left: The extent of articulatory variability (in percentage of total variability for each subject) vs the effect on third formant frequency (in percentage load for each subject—see the text for details) for all articulatory dimensions for all subjects (each dot represents an articulatory dimension—a direction of movement of the articulators—for a given subject). The thick line represents the inverse relation fit to data (approximating the curve $y=10/x$). Black/gray points represent the articulatory dimensions that, for each subject, would be categorized as small/large effect on $F3$ components. The inverse relation shown in this plot is identified as a *predictive relation between acoustic stability and articulatory variability* Right: Consistency of found articulatory/acoustic relations across subjects. The percentage of articulatory variance associated with large/small effect on $F3$ components is shown for each subject. Under the null hypothesis (articulatory variability not associated with the effect on $F3$) these percentages would be equal (50% each). A strong bias of the articulatory variability towards those articulatory dimensions that have a small effect on $F3$ is apparent in all the experimental subjects.

subject) versus the extent of articulatory variability found along this articulatory dimension (percentage of total variability for each subject). The solid line represents the linear fit on the log variables, which approximates the curve $y = 10/x^{1.2}$ ($F_{1,82}=65.2$; $p<0.001$, 95% confidence intervals [5, 17] and [0.9, 1.5] for the constant in the numerator and the exponent of x, respectively). Dots are colored based on their effect on $F3$, dichotomized to only two equal-sized levels: dark or light dots represent those dimensions that have a small or large effect on $F3$, respectively. The bar plot in Fig. 4 right represents, for each subject, the cumulative variability associated with each of these two levels. We maintain that this relationship is the hallmark of a control mechanism that utilizes an $F3$ target. In computer simulations reported below we validate this claim by simulating a speech control mechanism utilizing an $F3$ target that replicates this relationship.

To assess the statistical significance of the continuous version of the observed predictive relationship between acoustic stability and articulatory variability across subjects, we performed a Monte Carlo test involving replication of all the analysis steps using a series of simulated datasets conforming to a predefined null hypothesis. The null hypothesis represents the case where there is no relation between articulatory variability and acoustic stability. In a worst-case scenario an artifactual relationship could stem solely from measurement noise in the estimation of $F3$. The Monte Carlo dataset consisted of simulated transducer positions at the /r/ center following the same distribution as those observed in our data, and a simulated target variable randomly distributed and independent of the transducer positions. The 95th percentile of the R^2 distribution under this null hypothesis (from 10 000 Monte Carlo simulations) was relatively large ($R^2=0.42$), just below the observed R^2 value from our data ($R^2=0.44$; $p=0.03$). Under this test, only the predictive relationship using the acoustic variable $F3$ survives a 0.05 significant level for the pooled data. For the tract variables the significance level of their predictive relationships is always greater than $p=0.89$. Yet, these are very conservative tests as they do not take into account the observed degree of association between transducer positions and tract variables, which generally indicate a small presence of measurement noise (an average of 89% of the acoustic variable and >95% of each tract variable was linearly associated with the transducer positions). When this is incorporated into the Monte Carlo simulations (by creating a simulated target variable equal to the average transducer position plus a variable amount of independent random noise), the 95th percentile of R^2 under the null hypothesis drops to a value of $R^2=0.03$. Under this more liberal test the predictive relationships using not only $F3$ but also tongue-body constriction location and degree would become statistically significant ($p<0.05$). While the across-subject results need to be interpreted with care, due to the limited amount of subjects in this study, the consistency of the individual subject results together with the Monte Carlo simulations indicate that the observed relation between acoustic stability and articulatory variability is statistically significant beyond possible artifactual causes.

An important source of contextual variability in the current experimental setup is the phonetic context preceding the /r/ production. Articulatory/constriction target models often employ context-dependent articulatory targets (e.g., blended targets in the task-dynamic model of Saltzman and Munhall, 1989), as they are believed to explain the source of articulatory variability. According to these models, in our analyses of articulatory variability, context would be acting as a confounding effect. What we mean by this is that the observed relationship between acoustic stability and articulatory variability could simply be addressing how these context-dependent targets are organized, instead of addressing the target space definition in the speech control strategy. To address this concern, we replicated our original analyses but now explicitly treating context as a confounding effect and removing its effect on the observed articulatory variability by analyzing the intracontext variability in transducer positions. Interestingly, the percentage of *intracontext* articulatory variability associated with small effects on $F3$ was 88% across subjects, very similar to the original 91% of *total* articulatory variability associated with small effects on $F3$. This result was still the only one statistically significant ($p=0.03$) among the tested target variables (next competing tract variable was tongue-body constriction location, 76%; $p=0.15$). What these results indicate is that the observed relationship between acoustic stability and articulatory variability is not an effect of the phonemic context. Furthermore, they indicate that the evidence for tract-variable targets does not significantly improve when considering the effect of the phonetic context on the articulatory variability (i.e., when allowing a different target for each phonetic context). This supports the interpretation of the observed relationship in terms of a motor control mechanism utilizing acoustic targets, rather than one utilizing context-dependent tract-variable targets.

Overall, the positive results in this section highlight a strong and consistent relationship between the acoustic variable $F3$ and articulatory variability. This result is schematized in Fig. 5 to facilitate interpretation. This relationship is consistent with that expected from a control mechanism using an $F3$ target; i.e., the final articulatory variability is lower for those articulatory directions most relevant to determining the $F3$ value (axis A in the plot). Furthermore, this relationship appears both when looking at the total articulatory variability (dotted black ellipsoid) and when looking at the intracontext articulatory variability (dotted gray ellipsoids; the articulatory variability within each of the phonetic contexts tested). These results suggest that an acoustic target motor control mechanism utilizing the same acoustic target across contexts can account for the observed range of articulatory configurations during /r/ production. The next subsection further investigates this assertion with a specific model that utilizes an acoustic target for /r/.

B. Speaker-specific vocal-tract models

For the first two subjects participating in the previous analyses, we constructed from MRI and acoustic data a simple model characterizing the specificities of their vocal tracts and the range of acoustic signals (limited to the first three formant values) that different configurations would produce. PCA of the articulatory configurations led to a set

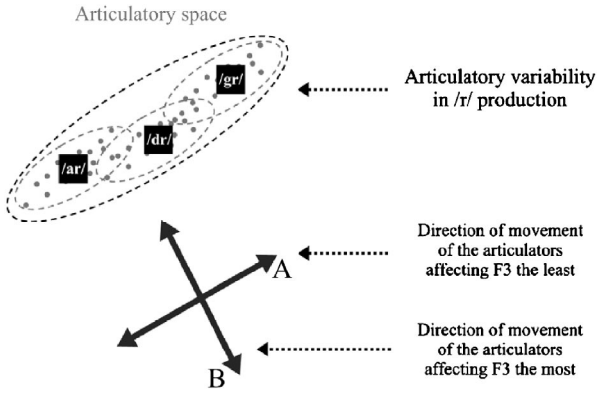

FIG. 5. Diagram summarizing the main results in this section. The plot represents in a schematic way the range of articulatory configurations (dots in the plot) reached in the production of /r/ under different phonetic contexts (black boxes). The main results are (a) An acoustic variable ($F3$) is the best predictor among the phonemic target variables tested for the shape of the articulatory variability in the production of American English /r/. The articulatory variability is maximal along the directions of movement of the articulators associated with small $F3$ changes, and minimal along the directions of movement of the articulators associated with large $F3$ changes. (b) The intracontext articulatory variability (the articulatory variability for each of the phonetic contexts) shows the same association with the effect of $F3$, indicating not the action of a context-dependent target definition, but possibly a common control mechanism utilizing an acoustic phonetic target.

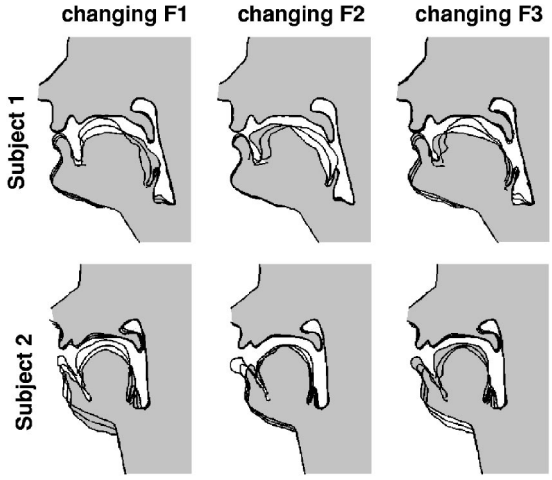

FIG. 6. Characterization of speaker-specific vocal-tract models. Sample movements of the models for Subjects 1 and 2 to change $F1$ (left), $F2$ (center), and $F3$ (right) are shown. For each subject, the deviations from a neutral articulatory configuration necessary to produce an individual change (increase/decrease) in each of the first three formants of the resulting auditory signal is shown in each column (e.g., the first column represents the movements associated with changes in $F1$ while keeping $F2$ and $F3$ constant). The gray area represents the configuration that produces the highest formant value (for the corresponding formant) among the configurations represented.

of five meaningful articulatory components covering 75.4% and 83.7% of the total observed variability in shape for the two subjects, respectively. The jaw component primarily describes the aperture/closure of the mouth, along with the associated lip aperture/closure, and lowering/raising of the tongue body; the three tongue components describe approximately the raising/lowering of the apical and dorsal areas of the tongue and its front/back movement; the lip component describes the frontal extension (protrusion) of the lips (cf. Maeda, 1990; see also Sec. IV). Components derived from other vocal-tract segments (a velum component, describing the opening/closing of the nasal cavity; and a laryngeal component, describing the raising/lowering of the base of the laryngeal region), were estimated but not explicitly used in the simulations presented in this paper (other than any of their movement that was associated with the jaw component). The articulatory to acoustic mapping was then estimated by a linear fit between the articulatory configurations (defined by the positions of each of these five components) and the corresponding acoustic output (defined by the first three formant values measured during the MRI scans). Figure 6 characterizes the resulting mappings by illustrating the movements of the resulting speaker-specific vocal-tract models to achieve changes in $F1$, $F2$, and $F3$. Each column represents for each subject the movement of the articulators, starting from a rest or average configuration, that would be associated with changes in an individual formant. The results are consistent with standard characterizations (Schroeder, 1967; Fant, 1980) of high/low tongue configurations associated with low/high values of $F1$, respectively (left column in Fig. 6), and front/back tongue configurations associated with high/low values of $F2$, respectively (middle column in Fig. 6). At the same time, the resulting vocal-tract models accommodate the specificities of each subject. For example, Subject 2 tended to use lip protrusion more actively to lower $F2$ (see for example Perkell *et al.*, 1993, 1995, where trading relations between lip protrusion and tongue-body raising, argued to stem from their motor equivalence in the control of $F2$, were investigated in the context of /u/ production). With respect to the action on $F3$, Subject 1's movement to decrease $F3$ can be interpreted from an acoustic theory analysis as an increase in the front cavity length together with a decrease of the palatal constriction area, both acting to lower the third formant value. Subject 2 appears to decrease $F3$ primarily by increasing the size of the front cavity.

C. Simulations of /ɹ/ production

A simplified version of the DIVA model (Guenther *et al.*, 1998) was used to control movements of the speaker-specific vocal-tract models for Subjects 1 and 2 while performing /r/ productions in different phonetic contexts. An acoustic /r/ target was defined by its first three formants values ([593, 1238, 1709] Hz for Subject 1, and [376, 1476, 1990] Hz for Subject 2), and the simulations were run starting from articulatory configurations representative of the leading context phonemes (see Sec. II C for details). In order to compare the model simulations to the EMMA data, approximate transducer locations were manually identified (see Sec. II) on each subject-specific vocal-tract model. Acoustic and articulator trajectories for the production of /r/ in the contexts /ar/, /dr/, and /gr/ were then obtained using the DIVA model. These contexts were chosen to represent the full range of articulations seen in the experimental data.

Figure 7 compares the experimentally measured EMMA data (first row) to the simulation results (second row) for each subject, in terms of the direction of movement of the tongue transducers. The initial transducer positions in the simulations is fixed to that obtained from the EMMA data 75 ms before the $F3$ minimum (dashed lines). The results indi-

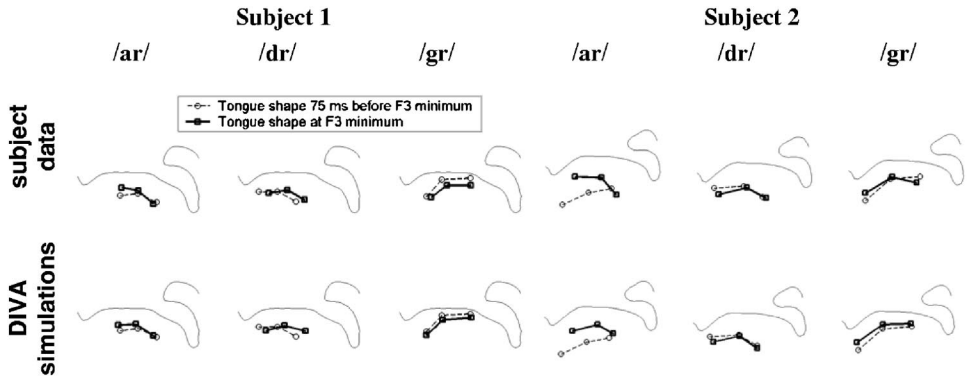

FIG. 7. Simulations of the DIVA model producing /r/ in different leading phonetic contexts. Top row shows the average lingual gestures used by each subject when producing /r/ in the contexts (from left to right) /ar/, /dr/, and /gr/ as measured using electromagnetic midsagittal articulometry (EMMA). Bottom row shows the simulation results using the DIVA model (with a subject-specific acoustically defined target for /r/) in conjunction with each subject-specific vocal-tract model. Dashed lines represent the initial (75 ms before $F3$ minimum) transducer positions, which are fixed to the experimentally observed values in the DIVA simulations. Solid lines represent the final transducer positions (at the $F3$ minimum for /r/). The outline of the hard palate and velum is included for reference. The correlation between the modeled and experimental movement of the tongue (tongue gestures) was $r=+0.86$ and $r=+0.93$ for Subjects 1 and 2, respectively.

cate that the direction of movement estimated using the DIVA model for the three leading phonetic contexts closely approximates the experimentally measured data for both subjects. The correlation between modeled and experimental change in transducer positions (tongue gestures) was $r=+0.86$ and $r=+0.93$ for Subjects 1 and 2, respectively. Qualitatively, the model mimics the range of /r/ configurations used by each subject in the phonetic contexts tested (thick black lines in Fig. 7).

Next, we investigated the ability of an acoustic target speech motor control scheme to predict the emergence of the articulatory/acoustic relationship observed in the experimental data. To that end, we analyzed the /r/ production simulation final articulatory configurations when using a wide range of leading phonetic contexts. All available configurations from the MRI data of each subject were used as starting articulatory positions and the DIVA model was run using the same acoustic /r/ targets as in the preceding simulations. Analysis of the resulting articulatory variability led to the results shown in Fig. 8. For each subject, the five articulatory dimensions show the expected predictive relations between acoustic stability and articulatory variability (Fig. 8 left; cf. the experimental results in Fig. 4, left). The relation between articulatory variability and effect on $F3$ predicted by the model is close to linear in the log variables ($R^2=0.93$), justifying the use of this family of curves when fitting the experimental data. For the simulated data, the linear regression on log variables shows a significant relationship of the form $y=17/x^{0.8}$ between the tested variables despite the limited data ($F_{1,8}=99.8$; $p<0.001$, 95% confidence intervals [10, 28] and [0.6, 1.0] for the constant in the numerator and the exponent of x, respectively). As an additional test, we analyzed the initial articulatory variability (the variability of the contextual articulatory configurations, prior to any movement of the articulators) and confirmed that the articulatory/acoustic relation was not present in the contextual configurations prior to the action of the speech controller ($p>0.39$). This indicates that the relationship resulted from the

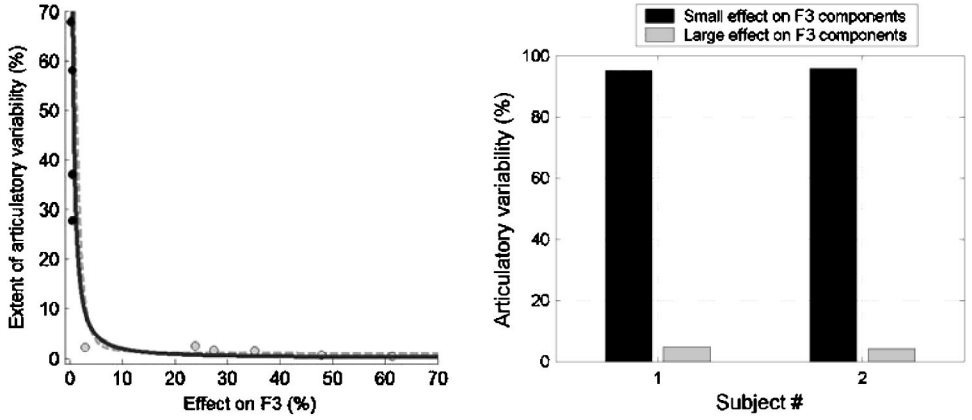

FIG. 8. Simulated articulatory/acoustic relations in /r/ production using the DIVA model (compare to experimental relations in Fig. 4). Left: The extent of final articulatory variability vs the effect on $F3$ for all articulatory dimensions of both subjects' simulations. The solid curve represents the inverse relation fit to these data. The dotted curve represents the expected predictive relation as theoretically derived from the DIVA model (see the Appendix). Black/gray points represent the articulatory dimensions that would be categorized as small/large effect on $F3$ components, respectively. Right: Consistency of simulated articulatory/acoustic relations across subjects. The percentage of articulatory variance in the simulated /r/ productions associated with large/small effect on $F3$ components is shown for each subject. As in the experimental data (see Fig. 4, right), a strong bias of the articulatory variability toward those articulatory dimensions that have a small effect on $F3$ is apparent in both subjects' simulations.

movements produced by the DIVA model. Furthermore, the simulation results mimic the expected relationship as derived theoretically from the DIVA control equations (dotted line in Fig. 8, left; see the Appendix for this derivation). The nature of the inverse relation predicted by the model ($y \propto x^{-0.8}$) was slightly shallower than the one observed in the EMMA data ($y \propto x^{-1.2}$), but the confidence intervals for the two curve parameters overlap as an approximate $y = 10/x$ relation. For completeness, Fig. 8 (right) illustrates the consistency of articulatory/acoustic relations in the simulations across the two subjects (cf. the experimental results in Fig. 4, right). Overall, these results indicate that an acoustic target controller, such as the one used in the present simulations, predicts the relationship between acoustic stability and articulatory variability observed in the experimental data. Furthermore, the DIVA model produces articulatory movements that closely mimic those of a particular speaker when controlling a speaker-specific vocal-tract model.

IV. DISCUSSION

A. On coordinate frames and articulatory dimensions

In target-based speech motor control models, the question of what coordinate frame is used by each model is usually identified with the proposed target representation. The task-dynamic model of Saltzman and Munhall (1989) exemplifies a type of computational model that uses a vocal-tract shape coordinate frame (vocal-tract targets defined by tract variables). The DIVA model (Guenther *et al.*, 1998) exemplifies a computational model that uses an acoustic coordinate frame (targets defined by acoustic variables). While there are many different coordinate frames one could use to represent the articulatory state, a major question for speech production modelers is, what coordinate frame(s) provides a simpler or more parsimonious characterization of behavioral data? In the same way as physical laws can be more readily unveiled when using an appropriate coordinate frame (e.g., planet orbits from an earth-centered vs a sun-centered coordinate frame), for speech production the use of an appropriate coordinate frame should allow the researcher to more clearly expose functional relations in the data. Finally, the ability of different coordinate frames to characterize the available motor speech production behavioral data could direct and facilitate the modeler's enterprise in proposing specific motor control strategies, and in particular it directly relates to the question of appropriate target definitions in target-based motor control schemes.

The behavioral data dealt with in this study is the articulatory variability present in American English /r/ production. Since articulatory variability is a local property (it characterizes the local departures in articulatory configurations from an average configuration) a linear approximation to the articulatory space geometry is appropriate. The issue of coordinate frames, under a linear approximation, becomes the simpler issue of characterization of vector spaces. Under this framework the articulatory space is a multidimensional vector space, and its characterization reduces to the definition of an appropriate base (a set of independent articulatory dimensions, each describing a direction—or vector—in the articulatory space). Different bases would in this way characterize different coordinate frames for the description of the articulatory state. Each of the columns in Fig. 6, for example, describes a different articulatory dimension (i.e., a direction of movement, or vector, in the articulatory space). The three articulatory dimensions in this figure characterize an acoustic coordinate frame (one based on three formant descriptors).

B. Predictive relations between acoustic stability and articulatory variability

A purely empirical approach to describing appropriate coordinate frames for the characterization of articulatory variability in /r/ production could be potentially given by a PCA of the articulatory covariance. This analysis provides the set of independent articulatory dimensions that best (most simply) characterize the observed articulatory variability. Conceptually, these correspond to the articulatory dimensions that offer an optimal separability of the total articulatory variability. In a two-dimensional case, for example, the resulting two articulatory dimensions would correspond to those dimensions associated with the largest and smallest variability, respectively (i.e., there is no one-dimensional subspace comprising more variability than that associated with the first articulatory dimension; equally, there is no one-dimensional subspace comprising less variability than that associated with the second articulatory dimension). A purely empirical approach like this, nevertheless, has potentially limited generalizability; i.e., since articulatory variability is a local property, the characterization resulting from the analysis of /r/ production might not be appropriate for other production examples. Furthermore, the researcher is left to interpret the resulting articulatory dimensions in terms of his/her theoretical constructs.

In this paper we opted for a mixed empirical/theoretical characterization of the observed articulatory variability. In this way, we tested the ability of theoretically motivated articulatory dimensions to offer good separability of the observed variability in articulatory configurations. We feel that this approach has a better chance to generalize to other cases of speech production data, and that it offers a more useful source of information for the development of motor control models of speech production. We also take the view that an account which involves a common control strategy across speakers is preferable to an account that requires different strategies across speakers as it is the more parsimonious account. From this perspective, the relevance of the results presented in the $F3$ column of Fig. 3 is that they show how an articulatory dimension defined by an acoustic property ($F3$, a salient acoustic cue for /r/ perception), offers a good separability of the observed articulatory variability in /r/ production for all subjects tested. In particular, an average of 91% of the articulatory variability concentrates along articulatory dimensions that have a relatively small effect on the third formant ($F3$) value, while only 9% concentrates along articulatory dimensions which have a relatively large impact on $F3$. This result indicates that an acoustically defined articulatory dimension would be a good candidate to enter an appropriate coordinate frame characterization of the presented speech production behavioral data. Furthermore, fol-

lowing the original motivation for searching appropriate coordinate frame characterizations, we showed (Fig. 4) that using an acoustically defined coordinate frame can also be useful for unveiling functional relations in the behavioral data. In particular, we showed that the degree of articulatory variability associated with any particular articulatory dimension is related to the associated extent of change in $F3$ by a linear relationship in the log variables ($R^2=0.44$; $p=0.03$). This relationship is conceptualized as a predictive relation between acoustic stability and articulatory variability. The form of this relationship is again consistent with that expected from a control mechanism using an $F3$ target; i.e., the final articulatory variability is lower for those articulatory dimensions most relevant to determining the $F3$ value.

The previous results show that an acoustic frame of reference can offer a useful characterization of the observed articulatory variability in American English /r/. In terms of the implications of these results for speech production modeling, the results indicate that, while no tract variable dimension was used consistently across speakers for the specification of /r/, all of the subjects showed evidence of an acoustic specification of /r/. The most parsimonious interpretation of these results points to the use of a common control strategy that utilizes acoustic, rather than articulatory, phonemic targets. Note that the results explicitly address the possibility of common acoustic variables *forming part* of the global target specification for /r/, not whether they fully define it. In this way the results indicate that $F3$ is likely to form part of the target specification for /r/, but we would neither claim nor expect it to be the only component in the target specification for this phoneme.

An important issue regarding the observed articulatory/acoustic relations examines the extent to which they favor acoustic target motor control models in contrast to vocal-tract target models. Several results of the present study build a very strong case for the acoustic target hypothesis. First, the results in Fig. 3 indicate that, while the tested acoustic variable ($F3$) shows a significant relation with the extent of articulatory variability (91%; $p=0.03$), making it a potential candidate for a useful articulatory coordinate frame definition, the hypothesized vocal-tract variables fail to show such a relation (less than 75%; $p>0.21$). This negative result addresses mainly the lack of consistency across subjects when hypothesizing tract-variable targets, and also the small evidence for some subjects of any form of tract-variable targets (e.g., Subject 4, although this could be related to the inability of our EMMA data to inform us about possible pharyngeal wall constrictions). Another piece of comparative evidence between acoustic and vocal-tract target hypotheses addresses the possibility of context-dependent effects (context here refers to the phoneme preceding /r/). Our results indicate that the observed articulatory/acoustic relations do not stem solely from the context-dependent articulatory variability, and can be equally observed when focusing on the intracontext articulatory variability (i.e., the articulatory variability resulting from /r/ production in each specific phonetic context). This result again points towards hypotheses that posit the observed trading relations as resulting from the motor control strategy (such as the acoustic target hypothesis), rather than explanations that rely on context-dependent targets (such as the possibility of different articulatory targets for /r/). Last, the possibility of context-dependent articulatory targets was also directly addressed by trying to show predictive relations between tract variables and intracontext articulatory variability. Our failure to observe such relations indicates that using context-dependent articulatory targets does not seem to significantly improve the predictive ability of hypothesized tract variables on the observed articulatory variability. Overall, the results indicate that, for American English /r/, subjects consistently act as though they attempted to produce stable $F3$ configurations. The articulatory variability is reliably minimal along those articulatory dimensions that are important for determining $F3$. No vocal-tract target variable tested offers this level of generalization across subjects. One might argue that, given the linear nature of our analyses, articulatory targets defined as linear combinations of tract variables are completely equivalent to acoustic targets. From this perspective the results simply indicate that, if articulatory targets are being used, they are probably not defined by simple vocal-tract constriction targets but could possibly be defined by nontrivial linear combinations of these variables. Even more specifically, in order to conform to the functional relationship between articulatory variability and acoustic variability observed in this experiment, they could be defined parsimoniously by those linear combinations that best relate to the effect on relevant acoustic cues, as exemplified by $F3$ in the current /r/ production data. Such targets would be in this case more simply characterized as acoustic.

C. Speaker-specific vocal-tract models

The simulation results shown in this paper also indicate that it is possible to construct simple speaker-specific vocal-tract models approximating the specificities of each subject's speech production apparatus from a limited amount of MRI and acoustic data. We were interested in obtaining a simple characterization of the relationship between articulatory configurations and formant positions for two subjects. The model we used is a purely statistical one defined as a simple linear relation between these variables. Compared to physically based models that estimate the area functions and from this calculate the acoustic characteristics, the linear model presented here provides a purely statistical approximation to the true articulatory–acoustic relationship, and as such it offers only an estimation and description (but not a physical explanation) of the articulatory acoustic relationship. However, it has the advantage of requiring only a relatively small amount of MRI and acoustic data for each subject and not requiring an accurate estimation of the area functions (which poses technical difficulties, e.g., the teeth not being portrayed in MR images). A locally linear approximation between articulatory parameters and formant positions is predicted by perturbation theory (Schroeder, 1967; Fant, 1980). Our preliminary validation analyses (see Sec. II B) suggest that this approximation is appropriate ($R^2>0.9$) for a relatively large range of articulatory configurations in our modeled speakers. This implies that approximate speaker-specific vocal-tract models can be estimated using simple linear models with

minimal demands on the amount of necessary data. A detailed analysis of the general accuracy of these models is beyond the scope of this paper. Nevertheless, for Subject 1, for whom we have redundant degrees of freedom to estimate the level of accuracy of the resulting mapping, a significant linear relation between articulatory and formant descriptors was in fact found (general linear model, $R^2=0.90$; $\Gamma_{5,3}=40.0$; $p<0.01$; dof$=4$). The speaker-specific vocal-tract models estimated in this paper are in agreement with standard characterizations of articulatory to acoustic relations (such as the differences between high and low, front and back, tongue configurations) while accommodating the specificities of each subject's vocal tract and their effective articulatory degrees of freedom. We believe the use of subject-specific vocal-tract models, in conjunction with a speaker-independent motor control strategy, is a promising approach to fit the specificities of different subjects' speech movements.

D. Acoustic target model predictions and simulations

Speech motor control models based on acoustic targets posit that the target for production of a phoneme is defined in terms of its acoustic properties, rather than as a specific vocal-tract configuration. In this way the variability in articulator configurations in the production of a given phoneme would reflect the one-to-many relation between the acoustically defined target and the articulatory space (i.e., the range of articulator configurations that are able to produce sounds with equivalent acoustic properties). The DIVA model is an example of such a model. The simulations presented in this paper use this model in conjunction with appropriate speaker-specific vocal-tract models to replicate two of the subjects' articulatory data. Note that while the results of our EMMA study showed evidence of the acoustic specification of /r/ ($F3$ forming part of the production target for /r/), the simulations in this section go beyond that by indicating that an acoustic /r/ target definition (a target defined *only* by acoustic dimensions) can account for the observed data. The simulation results of /r/ production in different leading phonetic contexts (Fig. 7, bottom) mimicked the range of articulatory gestures used by the two subjects being modeled (Fig. 7, top). The correlation between the experimental and modeled tongue gestures was $r=+0.86$ and $r=+0.93$ for Subjects 1 and 2, respectively. Furthermore, the simulated articulatory configurations reached by the DIVA model showed articulatory/acoustic relations (Fig. 8) similar to those found in the experimental data (Fig. 4). In effect, the articulatory variability in the simulations along each articulatory dimension was inversely related to its associated effect on $F3$.

The ability of the DIVA model simulations to fit the specificities of each subject's lingual gestures for the characteristic phonetic contexts tested emphasizes the idea that a relatively wide range of the articulatory variability in /r/ production can be explained by a simple speech motor control scheme using acoustic targets (without the need to appeal to possible multiple articulatory targets). In Fig. 7 top, for example, the tongue tip for each of the subjects moves in different directions for each context, and these directions do not seem to aim at any common lingual configuration. Interestingly, this can be modeled simply as a movement in the articulatory direction that in each case brings the acoustic output closest to a fixed acoustic target. Similarly, as shown by the simulations, the same acoustic target model parsimoniously explains the emergence of predictive relations between acoustic stability and articulatory variability. The expected articulatory/acoustic relation theoretically derived from this model is exemplified in Fig. 8, left (dotted line).

E. Limitations

There are several limitations of this study. First, the study is restricted to the analysis of American English /r/ production. The results presented could only be generalized if the motor control strategy used in speech production, which predicts the emergence of the observed articulatory/acoustic relations, is common across different phonemic targets. Evidence of articulatory trading relations argued to limit acoustic variability in the production of /u/ (Perkell *et al.* 1993) suggests another case where acoustic variables could potentially predict the extent of articulatory variability. It is thus likely that the descriptive ability of the acoustic-target hypothesis generalizes to other vowel and semivowel cases. Whether articulatory- or mixed articulatory/acoustic variables are more instrumental in the description of consonant productions is an issue that could potentially be addressed following a methodology similar to the one presented in this paper. Our expectation would be that the exact nature of the phonemic targets (auditory and/or somatosensory) is learned, and it would depend on the amount of language- and subject-specific allowed variability in these two spaces for that phoneme. Second, the presented articulatory/acoustic relation analyses are restricted to changes in $F3$. While this is an important acoustic cue for /r/ production, it is most probably not the only one. A more complex study showing the form of these relations when multiple acoustic cues are considered could potentially deepen our knowledge on the motor control strategies in speech production. In relation to this issue the simulations presented in this paper use the first three formants as a descriptor of the acoustic /r/ target. The presence of a predictive relationship between $F3$ stability and articulatory variability in the simulations shows that, for these relations to emerge, it is not necessary for the targeted variable to be the sole descriptor of the target coordinate frame. Third, regarding the speaker-specific vocal-tract models, the presented methodology is limited by the linear nature of the analyses involved. The relation between articulatory configurations and the acoustic output is complex. Nevertheless, this relation seems to be well approximated by a linear relation between articulatory and formant descriptors if relatively open configurations (such as vowels and semivowels) are considered. In this way, the validation presented in Sec. II indicates that the appropriateness of the linear model extends for a relatively large proportion of the articulator space (as indicated by the good linear fits between articulatory and acoustic formant descriptors estimated using Maeda's realistic tube model). The proposed speaker-specific vocal-tract models represent a simple first-order approximation to the complexities of the vocal-tract apparatus and the corresponding acous-

tic output. This approximation is especially valid for vowels and semivowels. For the production of consonants different strategies should be investigated. Fourth, regarding the DIVA simulations, this paper does not address how the phonemic targets are learned or transferred between subjects, issues still open to further discussion and research. The DIVA simulations for each subject used an acoustically defined target for /r/ based on his/her own productions. In this way we were simply testing the ability of a single acoustic target for each subject to account for the range of articulatory configurations reached in the production of /r/ in different phonetic contexts. It is possible that some sort of speaker normalization allows each speaker to define acoustic targets that are somehow informed of the actual range of acoustic productions that this speaker can produce. This paper does not attempt to address these issues. More detailed analysis of intersubject differences in vocal-tract morphology and its possible relationship with phonemic target specification could provide very relevant information but is beyond the scope of this paper. Finally, the small number of subjects modeled limits our ability to generalize the model's ability to fit the specificities of each subject's articulatory configurations in different phonetic contexts (cf. Westbury *et al.*, 1998, for a large sample analysis of intersubject articulatory variability in /r/). Our expectation would be that the intersubject variability, assuming a speaker-independent motor control strategy, is mainly affected by differences in vocal-tract morphology, and hence could be accounted for by using appropriate speaker-specific vocal-tract models such as the one presented in this paper.

Future studies using speaker-specific vocal-tract models could in this way help better understand the sources of intersubject variability.

V. SUMMARY

The analysis of articulatory movement data on seven subjects during the production of American English /r/ in different phonetic contexts shows a functional relationship between acoustic stability and articulatory variability. This relation indicates that the extent of articulatory variability along any given articulatory dimension is well predicted by the effect that the articulatory dimension has on a relevant acoustic cue ($F3$): most of the articulatory variability present in the production of American English /r/ is concentrated along articulatory dimensions that produce minimal change in $F3$. Both the presence and direction of the observed relationship are consistent with speech motor control mechanisms utilizing an acoustic ($F3$) target representation. In contrast, no significant relationship was found consistently across subjects between hypothesized vocal-tract target representations and articulatory variability. The combined results indicate that if phonemic targets are being used, they do not seem to be simply defined by constriction variables, but as nontrivial linear combinations of them. Such variables are more parsimoniously defined in terms of an acoustic frame of reference.

The second part of this paper investigated the ability of auditory or acoustic target models to explain the specificities of the range of articulatory gestures observed in the production of American English /r/. Speaker-specific models capturing the specificities of two subjects' vocal tracts were constructed from a combination of MRI and acoustic data. Simulations of the DIVA model (an example of an acoustic target motor control scheme) controlling each speaker-specific vocal-tract model produced articulatory movements that closely mimic those of each speaker. Furthermore, the articulatory configurations realized by this model exhibit similar articulatory/acoustic relations as those observed in the experimental data. The results demonstrate the ability of motor control speech production models utilizing a purely acoustic target representations to mimic central aspects of the experimental articulatory data on a particular example of speech production.

ACKNOWLEDGMENTS

We thank Mark Tiede for his assistance in the collection of MRI data. This research was supported by Grant R01 DC02852 (F. Guenther, PI) from the National Institute on Deafness and Other Communication Disorders. A. Nieto-Castanon and J. Perkell were also supported in part by R01 DC01925 (J. Perkell, PI).

APPENDIX: DERIVATION OF ARTICULATORY/ACOUSTIC RELATION FROM THE MOTOR CONTROL EQUATIONS OF THE DIVA MODEL

In the DIVA model, the differential equation governing the articulator vector $\boldsymbol{x}(t)$ given an acoustic target vector $\boldsymbol{y}$ takes the form

$$\frac{d}{dt}\mathbf{x}(t)=\mathbf{J}^{+}\cdot(\mathbf{y}-\mathbf{f}[\mathbf{x}(t)])-\alpha\cdot\mathbf{\Pi}(\mathbf{J})\cdot\mathbf{x}(t),$$

where $\mathbf{f}(\mathbf{x})$ represents the articulatory to acoustic mapping, $\mathbf{J}$ represents the Jacobian (the multivariate derivative) of this mapping at each point $\mathbf{x}(t)$, $\mathbf{J}^{+}$ and $\Pi(\mathbf{J})$ represent its pseudoinverse and its null space projector operator, respectively, and α is a small factor in the model (relaxation factor) controlling the degree of articulatory relaxation toward a neutral configuration (without loss of generality this is assumed to be $\mathbf{x}=0$). Under a linear approximation of the articulatory to acoustic mapping $[\mathbf{f}(\mathbf{x})=\mathbf{A}\cdot\mathbf{x}]$, and using a regularized form of the pseudoinverse, the explicit form of the previous equation is

$$\begin{aligned}\frac{d}{dt}\mathbf{x}(t)&=\mathbf{A}^{t}\cdot(\mathbf{A}\cdot\mathbf{A}^{t}+\mu\cdot\mathbf{I})^{-1}\cdot[\mathbf{y}-\mathbf{A}\cdot\mathbf{x}(t)]\\&\quad-\alpha\cdot[\mathbf{I}-\mathbf{A}^{t}\cdot(\mathbf{A}\cdot\mathbf{A}^{t}+\mu\cdot\mathbf{I})^{-1}\cdot\mathbf{A}]\cdot\mathbf{x}(t)\\&=\mathbf{A}^{t}\cdot(\mathbf{A}\cdot\mathbf{A}^{t}+\mu\cdot\mathbf{I})^{-1}\cdot[\mathbf{y}-(1-\alpha)\cdot\mathbf{A}\cdot\mathbf{x}(t)]\\&\quad-\alpha\cdot\mathbf{x}(t),\end{aligned}$$

where $\mathbf{A}$ is the linear mapping between the articulatory and acoustic spaces, and μ is a small regularization factor of the pseudoinverse. The solution of this differential equation is the articulatory trajectory $\mathbf{x}(t)$

$$\mathbf{x}(t)=\mathbf{x}_{0}+(\mathbf{I}-e^{-\mathbf{K}\cdot t})\cdot(\mathbf{x}_{\infty}-\mathbf{x}_{0}),$$

$$\mathbf{K}\equiv(1-\alpha)\cdot\mathbf{A}^{t}\cdot(\mathbf{A}\cdot\mathbf{A}^{t}+\mu\cdot\mathbf{I})^{-1}\cdot\mathbf{A}+\alpha\cdot\mathbf{I},$$

where $\mathbf{x}_0$ is the initial articulatory configuration, and $\mathbf{x}_\infty$ is the articulatory configuration that would be reached allowing infinite time ($\mathbf{x}_\infty$ depends on the acoustic target $\mathbf{y}$, and its solution is not relevant to the following discussion). Repeated productions under different initial articulatory configurations will reach, after time T, the articulatory configuration $\mathbf{x}(T)$, following a distribution with average

$$\langle \mathbf{x}(T) \rangle = \mathbf{x}_\infty - e^{-\mathbf{K}\cdot T} \cdot (\mathbf{x}_\infty - \langle \mathbf{x}_0 \rangle),$$

and covariance

$$\mathbf{\Omega}_T = e^{-\mathbf{K}\cdot T} \cdot \mathbf{\Omega}_0 \cdot e^{-\mathbf{K}^t \cdot T},$$

where $\langle \mathbf{x}_0 \rangle$ and $\mathbf{\Omega}_0$ are the average and covariance, respectively, of the initial articulatory configurations. For simplicity, let us assume the distribution of initial articulatory configurations to be normal, with covariance $\sigma_0 \cdot \mathbf{I}$. In this case, the articulatory covariance of the final articulatory configurations takes the form

$$\mathbf{\Omega}_T = \sigma_0 \cdot e^{-2\cdot \mathbf{K}\cdot T}.$$

Let us, finally, define the vector $\mathbf{q}$ to be any eigenvector of the matrix Ω_T (corresponding to one of the articulatory directions resulting from PCA of the final articulatory covariance). The *acoustic effect* of this articulatory direction $\mathbf{q}$ is defined as the associated change in the acoustic vector when moving the articulators along the direction $\mathbf{q}$, and it is computed as $\lambda(\mathbf{q}) \equiv \|\mathbf{A}\cdot\mathbf{q}\|$, and the *articulatory variability* associated with the same articulatory direction $\mathbf{q}$ is computed as $\sigma(\mathbf{q}) \equiv \mathbf{q}^t \cdot \mathbf{\Omega}_T \cdot \mathbf{q}$. Using the definition of the matrices $\mathbf{\Omega}_T$ and $\mathbf{K}$, and noting that their eigenvectors (they are the same for both matrices) will correspond to the right eigenvectors of the matrix $\mathbf{A}$, the articulatory variability $\sigma(\mathbf{q})$ can be expressed, as a function of the acoustic effect $\lambda(\mathbf{q})$, as

$$\sigma(\mathbf{q}) = \sigma_0 \cdot e^{-2\cdot[(1-\alpha)\cdot[(\lambda^2(\mathbf{q}))/(\lambda^2(\mathbf{q})+\mu)]+\alpha]\cdot T}.$$

More simply, the articulatory/acoustic relation predicted from the DIVA equations belongs to the class of functions

$$\sigma(\lambda) \propto \varepsilon^{\lambda^2/(\lambda^2+\mu)},$$

where ε and μ are two small factors. The dashed line in Fig. 8, left is an example of such a function approximating the simulation results ($\varepsilon = 0.01$; $\varepsilon = 0.001$).

[1]The current version of the DIVA model (Guenther, Ghosh, and Nieto-Castanon, 2003) uses a combination of auditory and somatosensory targets. As a result of learning in the model, sounds whose characteristic acoustic signal can be produced with a wide range of articulator shapes end up with primarily auditory targets, while sounds that can only be produced with a consistent somatosensory pattern (e.g., lip tactile information signaling full closure for a bilabial stop) will have both auditory and somatosensory targets. In other words, the model hypothesizes that the exact nature of the target (auditory and/or somatosensory) for a sound will depend on the amount of variability in the two spaces that is allowable for that sound in the infant's native language. In the current article we will deal only with /r/, which we believe to have a primarily auditory target in American English.

[2]The covariance is a multivariate extension of the common univariate concept of variance. Conceptually it characterizes not only the spread or range of each variable but also the level of association between the variables. Numerically it is defined as a symmetric matrix, and the elements in its diagonal correspond to the variance of each of the individual variables. PCA is a common statistical technique for the characterization of multivariate data. Conceptually it is similar to factor analysis. It offers a decomposition of the data in terms of factors or components that successively comprise most of the data variance, and are, in this sense, most explanatory of the data. If the data are normally distributed, forming a rough ellipsoid in an arbitrary multidimensional space, the resulting principal components correspond to the axes defining this ellipsoid. Numerically it is computed as an eigenvector decomposition of the data covariance matrix. See Mardia *et al.* (1979) for a highly detailed exposition of these and other multivariate concepts.

Boyce, S., and Espy-Wilson, C. Y. (**1997**). ''Coarticulatory stability in American English /r/,'' J. Acoust. Soc. Am. **101**, 3741–3753.

Carrozzo, M., Stratta, F., McIntyre, J., and Lacquaniti, F. (**2002**). ''Cognitive allocentric representations of visual space shape pointing errors,'' Exp. Brain Res. **174**(4), 426–436.

Delattre, P., and Freeman, D. C. (**1968**). ''A dialect study of American r's by x-ray motion picture,'' Lingusitics **44**, 29–68.

Fant, G. (**1980**). ''The relations between area functions and the acoustic signal,'' Phonetica **37**(1–2), 55–86.

Guenther, F. H., Ghosh, S.S., and Nieto-Castanon, A. (**2003**). ''A neural model of speech production,'' Proceedings of the 6th International Seminar on Speech Production, Sydney, Australia.

Guenther, F. H., Hampson, M., and Johnson, D. (**1998**). ''A theoretical investigation of reference frames for the planning of speech movements,'' Psychol. Rev. **105**, 611–633.

Guenther, F. H., Espy-Wilson, C. Y., Boyce, S. E., Matthies, M. L., Zandipour, M., and Perkell, J. S. (**1999**). ''Articulatory tradeoffs reduce acoustic variability during American English /r/ production,'' J. Acoust. Soc. Am. **105**(5), 2854–2865.

Maeda, S. (**1990**). ''Compensatory articulation during speech: Evidence from the analysis and synthesis of vocal-tract shapes using an articulatory model,'' in *Speech Production and Speech Modeling*, edited by W.J. Hardcastle and A. Marchal (Kluwer Academic, Boston), pp. 131–149.

Mardia, K. V., Kent, J. T., and Bibby, J. M. (**1979**). *Multivariate Analysis* (Academic, London).

McIntyre, J., Stratta, F., Droulez, J., and Lacquaniti, F. (**2000**). ''Analysis of pointing errors reveals properties of data representations and coordinate transformations within the central nervous system,'' Neural Comput. **2**(12), 2823–2855.

MacNeilage, P. F. (**1970**). ''Motor control of serial ordering of speech,'' Psychol. Rev. **77**(3), 182–196.

Perkell, J., Cohen, M., Svirsky, M., Matthies, M., Garabieta, I., and Jackson, M. (**1992**). ''Electromagnetic midsagittal articulometer (EMMA) systems for transducing speech articulatory movements,'' J. Acoust. Soc. Am. **92**, 3078–3096.

Perkell, J. S., Matthies, M. L., Svirsky, M. A., and Jordan, M. I. (**1993**). ''Trading relations between tongue-body raising and lip rounding in production of the vowel /u/: A pilot 'motor equivalence' study,'' J. Acoust. Soc. Am. **93**(5), 2948–2961.

Perkell, J. S., Matthies, M. L., Svirsky, M. A., and Jordan, M. I. (**1995**). ''Goal-based speech motor control: a theoretical framework and some preliminary data,'' J. Phonetics **23**, 23–35.

Perrier, P., Boe, L. J., and Sock, R. (**1992**). ''Vocal-tract area function estimation from midsagittal dimensions with CT scans and a vocal-tract cast: modeling the transition with two sets of coefficients,'' J. Speech Hear. Res. **35**(1), 53–67.

Saltzman, C., and Munhall, K. G. (**1989**). ''A dynamical approach to gestural patterning in speech production,'' Ecological Psychol. **1**, 333–382.

Schroeder, M. R. (**1967**). ''Determination of the geometry of the human vocal-tract by acoustic measurements,'' J. Acoust. Soc. Am. **41**, 1002–1010.

Story, B. H., Titze, I. R., and Hoffman, E. A. (**1996**). ''Vocal-tract area functions from magnetic resonance imaging,'' J. Acoust. Soc. Am. **100**(1), 537–554.

Story, B. H., Titze, I. R., and Hoffman, E. A. (**1998**). ''Vocal-tract area functions for an adult female speaker based on volumetric imaging,'' J. Acoust. Soc. Am. **104**(1), 471–487.

Tiede, M., Yehia, H., and Vatikiotis-Bateson, E. (**1996**). ''A shape-based approach to vocal-tract area function estimation,'' 4th Speech Production Seminar/ETRW, 41–44.

Wakita, H. (**1973**). ''Direct estimation of the vocal-tract shape by inverse filtering of acoustic speech waveforms,'' IEEE Trans. Audio Electroacoust. **AU-21**(5), 417–427.

Westbury, J. R., Hashi, M., and Lindstrom, M. J. (**1998**). ''Differences among speakers in lingual articulation of American English /r/,'' Speech Commun. **26**, 203–226.

Two-dimensional model of vocal fold vibration for sound synthesis of voice and soprano singing

Seiji Adachi[a] and Jason Yu[b]
ATR Human Information Science Laboratories, 2-2-2 Hikaridai, Keihanna Science City, Kyoto 619-0288 Japan

(Received 2 August 2004; revised 27 December 2004; accepted 3 January 2005)

Voiced sounds were simulated with a computer model of the vocal fold composed of a single mass vibrating both parallel and perpendicular to the airflow. Similarities with the two-mass model are found in the amplitudes of the glottal area and the glottal volume flow velocity, the variation in the volume flow waveform with the vocal tract shape, and the dependence of the oscillation amplitude upon the average opening area of the glottis, among other similar features. A few dissimilarities are also found in the more symmetric glottal and volume flow waveforms in the rising and falling phases. The major improvement of the present model over the two-mass model is that it yields a smooth transition between oscillations with an inductive load and a capacitive load of the vocal tract with no sudden jumps in the vibration frequency. Self-excitation is possible both below and above the first formant frequency of the vocal tract. By taking advantage of the wider continuous frequency range, the two-dimensional model can successfully be applied to the sound synthesis of a high-pitched soprano singing, where the fundamental frequency sometimes exceeds the first formant frequency. [DOI: 10.1121/1.1861592]

PACS numbers: 43.70.Bk, 43.75.Rs [NHF] Pages: 3213–3224

I. INTRODUCTION

Coupling between vocal fold dynamics and vocal tract acoustics attracts our interest in examining the voice quality of various kinds of vocalization. To study this interaction, we need to simulate the entire voice production process. The two-mass model[1] of the vocal folds is widely used for this type of voice synthesis. Several improvements on the model have been devised, such as the three-mass model[2] inspired by the body-cover theory[3] and the translating-rotating-mass model[4] that can directly simulate a mucosal wave with a rotating mass in a simple way. More complex models, such as the 16-mass model[5,6] and the finite element model,[7] have also been proposed. Although simulation of vocal fold vibration is clearly more realistic with a model having a large degree of freedom, a model with a small degree of freedom still has its merits. Such a minimal model highlights the self-excitation mechanism by abstracting the essence from the actual complex vocal fold vibration. The two-mass model has actually been devised as such a minimal model to simulate self-sustained oscillation with a capacitive acoustic load of the vocal tract, which cannot be replicated with the one-mass model.[8]

An acoustic tube generally yields an inductive load in the frequency below a resonance peak, while the load turns out to be capacitive in the frequency above the peak. Therefore, in a normal situation where the fundamental frequency (F0) is lower than the first formant frequency (F1) of the vocal tract, the vocal folds always vibrate with an inductive load. In special cases, however, F0 sometimes exceeds F1 to fall into the capacitive region. In high-pitched soprano singing, F0 enters the range of F1 found in normal speech. The soprano singer then raises F1 as F0 approaches F1 by increasing the jaw opening.[9] As a result, F1 is always tuned close to F0. This tuning is considered to help the singer produce sound with larger intensity. A more recent measurement of the vocal tract resonance[10,11] indicates the same tuning in the middle range of soprano singing. It also shows that F1 cannot be raised above a certain point (roughly 1 kHz), and the order of F0 and F1 is reversed in the high range. These observations imply that the vocal folds should vibrate in the vicinity of the frequency region near F1 where the acoustic load can be both inductive and capacitive.

The two-mass model can simulate self-excited oscillation with a capacitive acoustic load because it can represent the phase difference between the upper and lower parts of the vocal fold. Oscillation is driven by a flow-induced force that becomes larger for a convergent shape of the glottis than for a divergent shape, even though a capacitive load depresses the oscillation. Therefore, it may be possible to simulate a high-pitched singing voice with this model. However, the model has one drawback for this purpose. As the resonance frequency of the vocal fold f_r increases, F0 also increases to approach F1. Near F1, F0 does not increase very much with f_r and becomes smaller than f_r. When F0 meets F1 with a further increase of f_r, it suddenly jumps to a value much larger than f_r. Therefore, it would be very difficult to control the simulated F0 of a soprano singing voice with the two-mass model. This ''repulsive'' characteristic of F0 also contradicts the strategy of the soprano singer to tune F1 to match F0, as reported by Sundberg[9] and Joliveau *et al.*[10,11]

This paper presents a model of vocal fold vibration with an excellent stability of F0 near F1, which the two-mass model fails to demonstrate. This model approximates the vo-

[a]Electronic mail: sadachi@atr.jp
[b]Current address: School of Engineering Science, Simon Fraser University, 8888 University Drive, Burnaby, British Columbia, Canada, V5A 1S6.

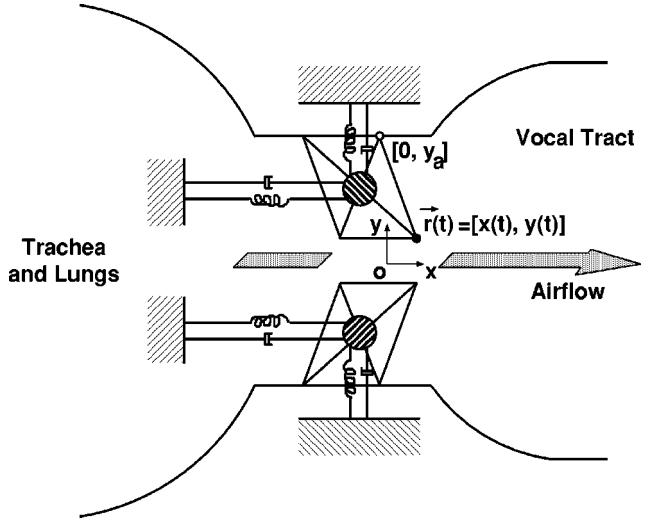

FIG. 1. A schematic diagram of the two-dimensional model of vocal fold vibration. The parallelogram represents the body of the vocal fold. Two sets each of a spring and a damper are attached to the mass located at the center. As the mass moves, the parallelogram is deformed so that the mass keeps its position at the center. Therefore, the vocal fold simultaneously executes both swinging and elastic motions. The two-dimensional position vector $\mathbf{r}(t) = [x(t), y(t)]$ pointing to the upper edge of the vocal fold (marked by a dot) is one of dynamical variables of the entire voice production system. Its coordinate origin (0,0) is on the centerline of the glottis.

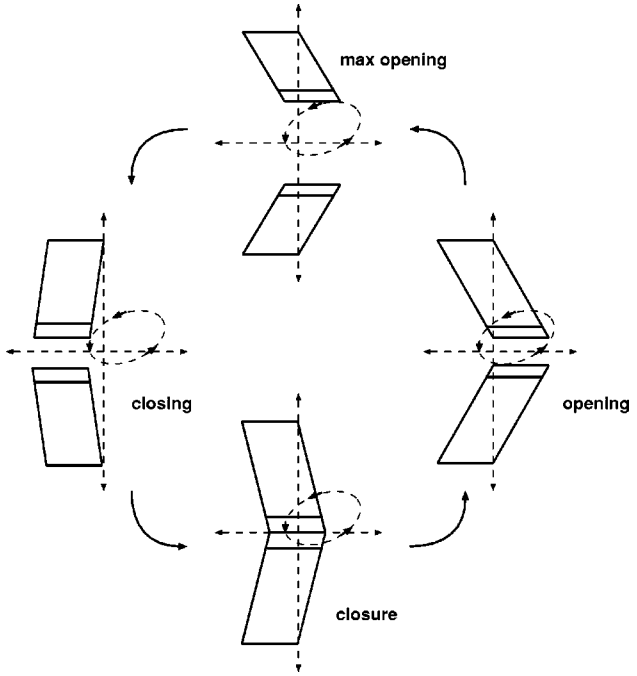

FIG. 2. Motion of vocal folds in four different phases in a single cycle of oscillation. Ellipse represents trajectory of the upper edge of the vocal fold. The glottis retains a rectangular shape and does not move into a convergent or divergent shape.

cal folds as a pair of single masses that can vibrate both parallel and perpendicular to the airflow. Due to the two-dimensional motion of the vocal folds, the model can successfully simulate self-excited oscillation in a wide frequency range on both sides of F1 with no discontinuity of vibration.

II. TWO-DIMENSIONAL MODEL OF VOCAL FOLDS

The proposed model was originally developed to simulate the vibration of a brass player's lips.[12] The model is a combination of two earlier models: the swinging-door model and the transverse model.[13] The former employs a valve (lips or vocal folds) that operates by the pressure difference between the upstream and downstream regions. The latter employs a valve that operates by the Bernoulli pressure generated by a flow passing through the valve aperture. The modeled vocal folds are depicted in Fig. 1. The geometry of the vocal fold is represented by a parallelogram. The upper edge of the vocal fold is marked by a dot and represented by a two-dimensional position vector $\mathbf{r}(t) = [x(t), y(t)]$. The coordinate origin (0,0) is on the centerline of the glottis. The mass M of the vocal fold is assumed to be localized at the center of the parallelogram. Two sets of a spring and a damper are attached to the mass. The springs in the x and y directions are assumed to have the same linear stiffness coefficient, or spring constant, k. Similarly, the two dampers are assumed to have the same resistance coefficient γ. As the mass moves, the parallelogram is deformed so that the mass maintains its position at the center. Therefore, the vocal fold simultaneously executes both swinging and elastic motions, as shown in Fig. 2. In one cycle of oscillation, the glottis retains a rectangular shape and does not move into a convergent or divergent shape. This assumption implies that the present model disregards the effect of a moving separation point of a free jet in the glottis, which is taken into account by the recent two-mass models.[14–16] Forces acting on the vocal fold are illustrated in Fig. 3. These are the resultant Bernoulli force $\mathbf{f}_B(t)$ in the glottis, the force due to the pressure difference $\mathbf{f}_{\Delta p}(t)$, the contact force $\mathbf{f}_C(t)$, and restoring force $\mathbf{f}_R(t)$ from both springs. Figure 3 also shows the lateral dimension (width) w, the length l, and the thickness d of the vocal fold.

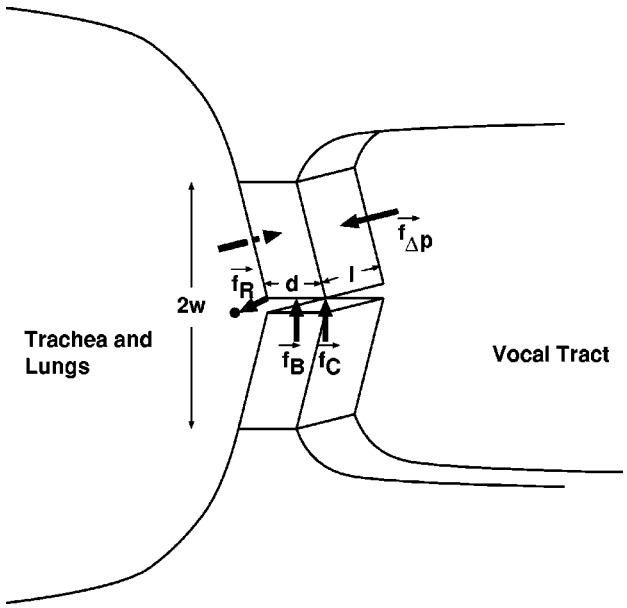

FIG. 3. Forces acting on the vocal fold. These are the resultant Bernoulli force $\mathbf{f}_B(t)$ in the glottis, the force due to the pressure difference $\mathbf{f}_{\Delta p}(t)$, the contact force $\mathbf{f}_C(t)$, and the restoring force $\mathbf{f}_R(t)$ from both springs. The dimensions of the vocal fold are also depicted with length l, thickness d, and width w.

The left and right vocal folds are assumed to vibrate symmetrically. Each vocal fold satisfies the following equation of motion:

$$\frac{1}{2}M\frac{d^2\mathbf{r}(t)}{dt^2}+\frac{1}{2}\gamma\frac{d\mathbf{r}(t)}{dt}=\mathbf{f}_{\mathrm{B}}(t)+\mathbf{f}_{\Delta p}(t)+\mathbf{f}_{\mathrm{C}}(t)+\mathbf{f}_{\mathrm{R}}(t). \tag{1}$$

The factors of $\frac{1}{2}$ in Eq. (1) imply that the acceleration and velocity of the center of the vocal fold are half as much as those of the edge of the vocal fold. The forces $\mathbf{f}_{\mathrm{B}}(t)$, $\mathbf{f}_{\Delta p}(t)$, $\mathbf{f}_{\mathrm{C}}(t)$, and $\mathbf{f}_{\mathrm{R}}(t)$ are written in the x and y components as

$$\mathbf{f}_{\mathrm{B}}(t)=[0,ldp_{\mathrm{g}}(t)], \tag{2}$$

$$\mathbf{f}_{\Delta p}(t)=l(p_0-p(t))\cdot[w-y(t),x(t)], \tag{3}$$

$$\mathbf{f}_{\mathrm{C}}(t)=[0,-ky(t)], \quad \text{if } y(t)<0, \tag{4}$$

$$\mathbf{f}_{\mathrm{R}}(t)=-\tfrac{1}{2}k\cdot[\Delta x(t)(1+\eta\Delta x^2(t)),\Delta y(t)(1+\eta\Delta y^2(t))], \tag{5}$$

where $p_{\mathrm{g}}(t)$ is the pressure in the glottis, p_0 is the subglottal pressure, $p(t)$ is the pressure at the entrance of the vocal tract, $[\Delta x(t),\Delta y(t)]=\mathbf{r}(t)-\mathbf{r}_0$ is a position vector originating from the rest position $\mathbf{r}_0=[x_0,y_0]$, and η is a coefficient representing the nonlinear characteristics of the spring. Equation (4) shows that the contact force is generated during closure of the glottis by another spring having a spring constant the same as k. The resistance coefficient γ is modeled as $\gamma=2\sqrt{Mk}/q$, where q is the quality factor.

The motions along the x and y directions are coupled with each other because the direction of the force in Eq. (3) is not parallel to the air flow but normal to the surface of the vocal fold. The coupling between the x and y motions differentiates the current model from most of the other two-dimensional models, such as those proposed by Liljencrants[4] and Flanagan and Ishizaka.[17] A two-dimensional model proposed by Awrejcewicz[18] includes the coupling between the x and y motions. However, the interaction between the vocal fold and the vocal tract load has not fully been investigated with this model.

III. MODELING VOICE PRODUCTION

To simulate vocal fold vibration with Eq. (1), we have to know the external forces $\mathbf{f}_{\mathrm{B}}(t)$ and $\mathbf{f}_{\Delta p}(t)$, both acting on the vocal folds. These forces are generated by pressure around the glottis, which can be determined by the acoustic response of the vocal tract and fluid dynamics.

The vocal tract has the role of generating pressure $p(t)$ at the entrance of the vocal tract as a response to the incoming volume flow $U(t)$. The acoustic response is characterized by the reflection function $r(t)$ at the entrance of the vocal tract.[19] The Fourier transform of $r(t)$ can be expressed as

$$r(\omega)=\frac{Z_{\mathrm{in}}(\omega)-Z_0}{Z_{\mathrm{in}}(\omega)+Z_0}, \tag{6}$$

where $Z_{\mathrm{in}}(\omega)$ is the input impedance of the vocal tract and $Z_0=\rho c/A_0$ (ρ is air density and c is sound velocity) is the characteristic impedance of the outgoing wave at the entrance of the vocal tract (whose area is A_0). The input impedance $Z_{\mathrm{in}}(\omega)$ as well as the other transfer functions can be calculated from the area function of the vocal tract with the standard method.[20,21] This method takes into account the losses due to the yielding wall, the viscosity and thermal conduction at the vocal tract wall, and the acoustic radiation from the mouth. With the reflection function $r(t)$, we have the following integral equation,

$$p(t)-Z_0U(t)=\int_0^\infty r(s)[p(t-s)+Z_0U(t-s)]ds, \tag{7}$$

which relates the current $p(t)$ and $U(t)$ at time t with the past $p(t-s)$ and $U(t-s)$ at time $t-s$ where $s>0$.

We assume that the flow around the glottis is one-dimensional, incompressible, and quasi-steady. The flow conservation ensures that the volume flow rate $U_{\Delta p}(t)$ due to the transglottal pressure difference is independent of place. The pressure distribution in the contraction region (from the upstream region to the glottis) and in the expansion region (from the glottis to the vocal tract entrance) can be modeled with

$$p_0-p_g(t)=\frac{1}{2}\rho\left(\frac{U_{\Delta p}(t)}{A_g(t)}\right)^2+\frac{\rho d}{A_g(t)}\frac{dU_{\Delta p}}{dt}(t)+\frac{12\mu l^2 d}{A_g^3(t)}U_{\Delta p}(t), \tag{8}$$

$$p_g(t)-p(t)=-\rho U_{\Delta p}^2(t)\left(\frac{1}{A_0A_g(t)}-\frac{1}{A_0^2}\right), \tag{9}$$

where the area of the glottis $A_g(t)=2ly(t)$ for $y(t)>0$ and μ is the shear viscosity coefficient of the air. Equation (8) can be derived from the energy conservation law in the contraction region and from the viscosity effect in the glottis. It can therefore be regarded as an extension of Bernoulli's law. Equation (9) can be derived from the conservation of momentum in the expansion region. For simplicity, the vena-contracta effect at the inlet to the glottis is not considered. Note here again that the glottis is assumed to retain a rectangular shape and does not move into a convergent or divergent shape.

In addition to $U_{\Delta p}(t)$, vocal fold vibration mechanically generates a flow entering the vocal tract. This is equivalent to the volume displaced by the vocal folds per unit time, which becomes

$$U_{\mathrm{mech}}(t)=l\left|[\mathbf{r}(t)-\mathbf{r}_a]\times\frac{d\mathbf{r}(t)}{dt}\right|=l\left\{x(t)\frac{dy(t)}{dt}-\frac{dx(t)}{dt}[y(t)-w]\right\}, \tag{10}$$

with $\mathbf{r}_a=(0,w)$ as the position vector to the axis of the vocal fold. The total volume flow rate entering the vocal tract becomes

$$U(t)=U_{\Delta p}(t)+U_{\mathrm{mech}}(t). \tag{11}$$

During closure of the glottis, Eqs. (8) and (9), derived from the fluid mechanics, do not hold. Instead, we assume that $U_{\Delta p}(t)=0$ and $p_g(t)=0$ in this case.

The four variables $\mathbf{r}(t)$, $p(t)$, $p_g(t)$, and $U(t)$ represent the state of the voice production system at time t. These variables can be simulated in the time domain as follows:

(1) The four variables are all known at any time earlier than the present.
(2) Find the present $\mathbf{r}(t)$ by solving Eq. (1) with the fourth-order Runge–Kutta method.
(3) The present $A_g(t)$ is defined by $A_g(t)=\max\{2ly(t),0\}$.
(4) The present $U_{\text{mech}}(t)$ is calculated from Eq. (10).
(5) By considering Eq. (11), Eq. (7) relates the present $p(t)$ with $U_{\Delta p}(t)$. The sum of Eqs. (8) and (9) also gives us an equation between $p(t)$ and $U_{\Delta p}(t)$. Then, find the present $p(t)$ and $U_{\Delta p}(t)$ by solving these two equations simultaneously.
(6) Obtain the present $U(t)$ from Eq. (11).
(7) Find the present $p_g(t)$ from Eq. (9).
(8) Update time by one step and return to (1).

After finishing the time loop, the output voice sound $p_{\text{out}}(t)$ can be synthesized by convolving the volume flow $U(t)$ with a transfer function of the vocal tract. A flow chart of the voice simulation is shown in Fig. 4.

IV. SIMULATION RESULTS

A. Simulation parameters and physiological constants

Four parameters control the behavior of the two-dimensional vocal fold model: the rest x and y positions of the upper edge of the vocal fold (x_0,y_0), subglottal pressure p_0, and resonance frequency f_r. The physiological constants used in the model are largely referenced from Ishizaka and Flanagan's two-mass vocal fold model:[1] the length of vocal fold $l=14$ mm, the width of vocal fold $w=4.9$ mm, and the thickness of vocal fold $d=3$ mm. The spring constants k of the horizontal and vertical springs are identical and directly proportional to resonance frequency f_r. At $f_r=120$ Hz, the spring constant is set to $k=160$ N/m. Likewise, the mass of the vocal fold is assumed to be inversely proportional to resonance frequency. At $f_r=120$ Hz, the mass is set to $M=0.28$ g. The contact force spring constant h is set to the same value of k. In a preliminary simulation, however, $h=3k$ was assumed as in the simulation of the original two-mass model. This assumption results in a larger duty ratio of the glottal opening (open time to the total period) that is incompatible with that observed in the actual voice production. In other words, the duty ratio can be controlled with this coefficient. The spring nonlinear coefficient of stiffness is $\eta=10\,000$ m^{-2}. The quality factor q is assumed to be 9.0 when $y(t)\geqslant 0$; however, it linearly decreases to 0.9 as $y(t)$ goes to -1 mm. The parameters of the two-dimensional model are listed in Table I. Prior to simulation of the five Japanese vowels, reflection functions were calculated from the vocal tract area functions[22] constructed from three-dimensional cine-MRI data of a male speaker pronouncing the vowels. The calculated F1 and F2 are listed in Table II.

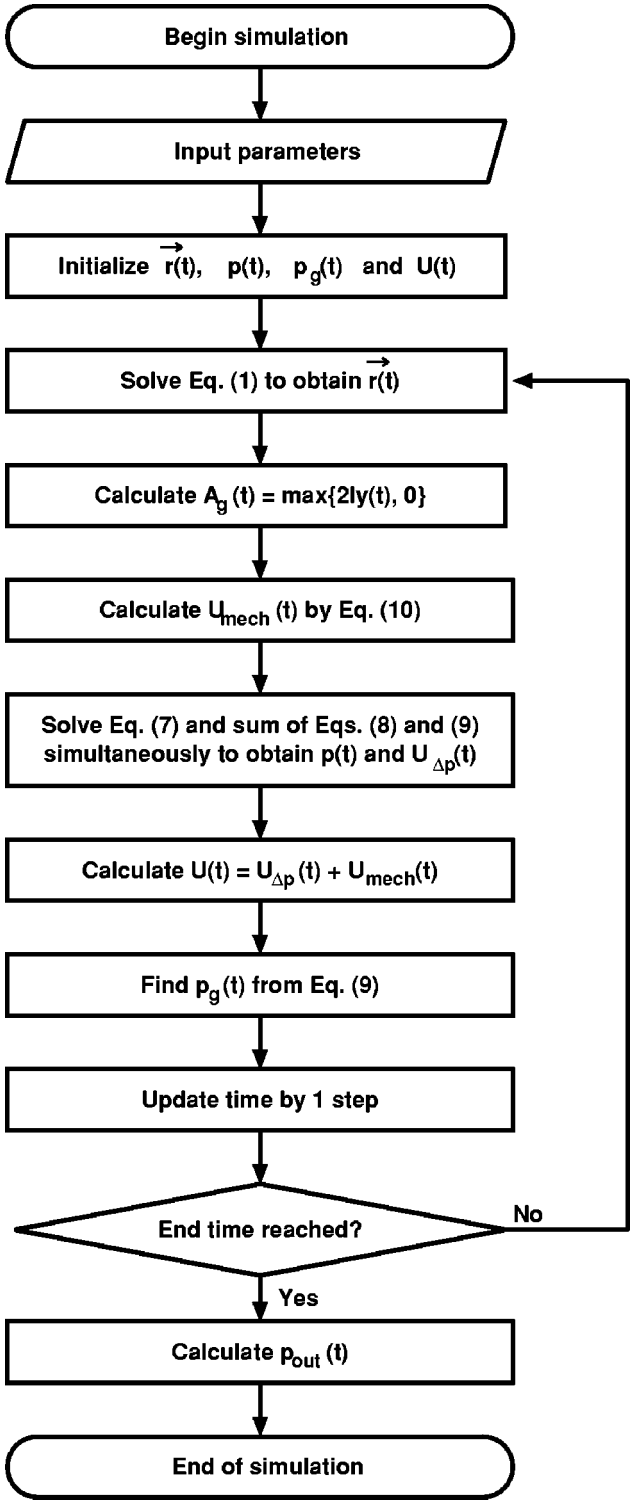

FIG. 4. Flow chart of computer simulation.

B. Waveforms of typical conditions

Figure 5 shows the results of a sound simulation of vowel /e/, where the parameters are set to $x_0=0.2$ mm, $y_0=-0.02$ mm, $p_0=800$ Pa, and $f_r=120$ Hz. In the upper-left panel, the oscillation trajectory of one of the vocal folds is drawn. During the period when $y<0$ mm, the glottis is closed and no air passes through. The duty ratio of the glottal opening (open time to the total period) is 0.68. Although y can be negative, this does not mean that one of the actual

TABLE I. Parameters of the two-dimensional model.

ρ	Air density	1.2 kg/m^3
c	Sound velocity	346.3 m/s
μ	Shear viscosity of air	1.86×10^{-5} kg/s·m
l	Vocal fold length	14 mm
d	Vocal fold thickness	3 mm
w	Vocal fold width	4.9 mm
k	Spring constant	$160\times f_r/120$ N/m $58.6\times f_r/120$ N/m for soprano
M	Vocal fold mass	$0.28\times120/f_r$ g $0.1\times120/f_r$ g for soprano
h	Contact force spring constant	same as k
η	Spring nonlinear coefficient	1.0×10^4 m^{-2}
q	Quality factor	9.0 for $y\geqslant0$, $9.0+8.1y$ for $-1.0\leqslant y<0$ mm 0.9 for $y<-1.0$ mm
(x_0,y_0)	Rest position of vocal fold	typically (0.2, −0.02) mm
p_0	Subglottal pressure	typically 800 Pa
f_r	Vocal fold resonance frequency	typically 120 Hz

vocal folds overlaps with the other. Instead, it means that both the tips of the vocal folds meet at $y=0$. Negative y, however, indicates that the mass located at the center of the vocal fold may come closer to the other with deformation of the vocal fold itself.

The trajectory of the vocal fold has a smooth oval shape, and the oscillation is in the counter-clockwise direction for the upper mass as shown in Fig. 1. This result is in accord with common observations of vocal fold vibration.[23] The glottal area waveform has a symmetric shape in the opening and closing phases. The glottal volume flow waveform shows ripples caused by the resonance of the vocal tract. Asymmetry in the rising and falling phases of the flow is not manifest, as found in the flow simulated with the two-mass model and also assumed by the glottal source model.[24] However, Fourier analysis shows that the oscillation of the volume flow U certainly lags 5.8 deg behind that of the glottal area A_g. This is mainly due to the inductive (inertive) acoustic load of the vocal tract.[25] The inertia of the air passing through the glottis, which is represented in our model by the second term on the right-hand side of Eq. (8), also has an additional but minor effect.

The volume flow of the two-dimensional model lacks the constant zero region within each period that is found in the two-mass model. This is due to the inclusion of a volume flow component $U_{\mathrm{mech}}(t)$ generated by the motion of the vocal folds during oscillation, which creates volume flow even when the glottis is closed. $U_{\mathrm{mech}}(t)$ generally becomes positive in the rising phase of the flow and negative in the falling phase. This probably explains why the asymmetry of $U(t)$ is small in the two-dimensional model.

The pressure waveforms generated by the two-dimensional model resemble those by the two-mass model.

TABLE II. Calculated first (F1) and second (F2) formant frequencies (Hz) of the vocal tracts for five Japanese vowels that are used for simulation.

	/i/	/e/	/a/	/o/	/u/
F1	274.8	477.9	601.0	447.6	310.9
F2	2060	1722	1259	883.1	1272

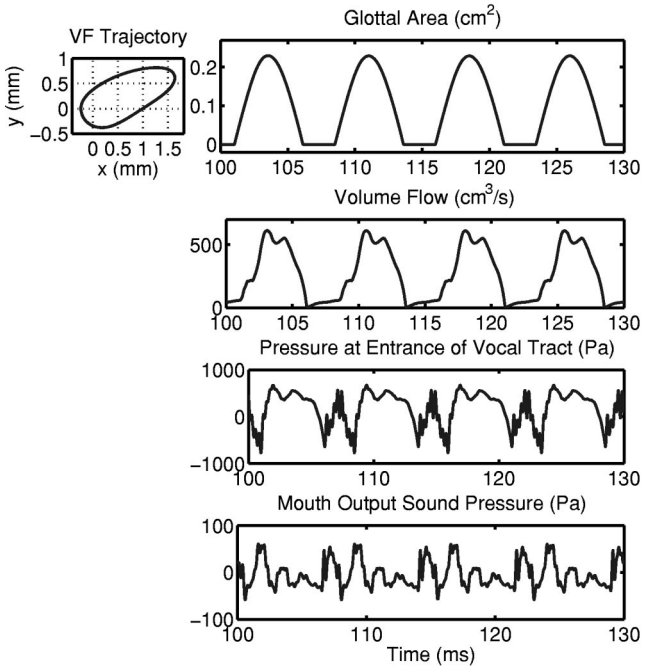

FIG. 5. Simulation results for vowel /e/ showing trajectory of the vocal fold, glottal area, volume flow, pressure at entrance of vocal tract, and output pressure.

The pressure at the entrance of the vocal tract has an oscillation with a high frequency during the phase when the glottis is closed. This is caused by the vocal tract resonances or formants. On the contrary, the pressure has a relatively constant region when the glottis is open. The pressure wave is transmitted to the lip opening with a small delay for the wave to travel through the vocal tract, which is about 0.5 ms. Therefore, output pressure has similar high-frequency oscillation at the closing phase. The pressure waveform at the open phase, however, lacks such a constant region. This is because the low-frequency components are attenuated by a radiation characteristic from the lip opening acting as a high-pass filter.

C. Effect of vocal tract shape

The five Japanese vowels /i/, /e/, /a/, /o/, and /u/ are simulated with the vocal tract shapes obtained from a Japanese male speaker. The values of the simulation parameters are listed in Table III. In determining the values, only y_0 was adjusted so that the duty ratio became 0.68 for all the vowels, while x_0, p_0, and f_r were fixed to the typical values, i.e., $x_0=0.2$ mm, $p_0=800$ Pa, and $f_r=120$ Hz. As seen in the next subsection, the duty ratio is monotonously decreased as

TABLE III. Typical values of the simulation parameters for the five Japanese vowels in speech.

	x_0 (mm)	y_0 (mm)	p_0 (Pa)	f_r (Hz)
/i/	0.2	−0.12	800	120
/e/	0.2	−0.02	800	120
/a/	0.2	−0.02	800	120
/o/	0.2	−0.06	800	120
/u/	0.2	−0.09	800	120

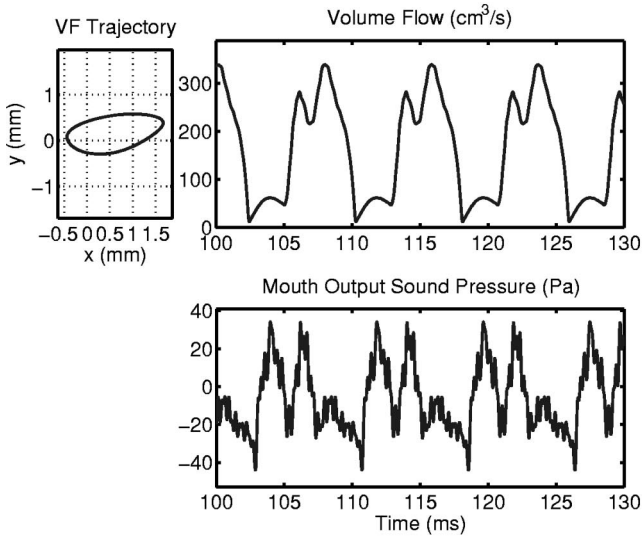

(a) vowel /u/

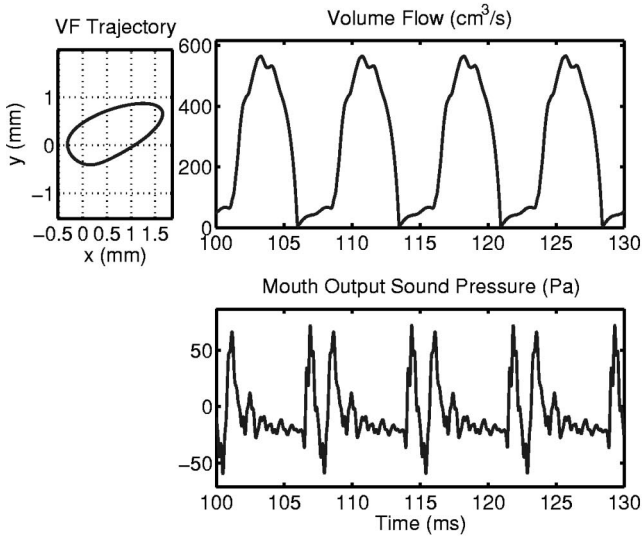

(b) vowel /a/

FIG. 6. Simulation results for (a) vowel /u/ and (b) vowel /a/ showing trajectories of the vocal fold, volume flow, and output sound pressure.

y_0 decreases in a range where oscillation is possible. A smaller y_0 is required for the oscillations of vowels /i/ and /u/. This is because these vowels have low first formants that are attenuated by the yielding wall characteristic of the vocal tract. F0's of the simulated sounds are 126.3, 133.7, 134.1, 130.8, and 127.7 Hz for vowels /i/, /e/, /a/, /o/, and /u/, respectively. The variation in F0 is smaller than that simulated in the one-mass model, but may be larger than that simulated in the two-mass model. The lower F0's of the simulated vowels /i/ and /u/ are probably due to the lower F1's of these vocal tracts. As found in Sec. IV F, F0 is depressed by lower F1 through the coupling between the vocal fold dynamics and vocal tract acoustics.

In Fig. 6, which compares oscillation trajectories, volume flows, and output pressures between vowels /u/ and /a/, one sees that the vocal tract of the model can greatly affect

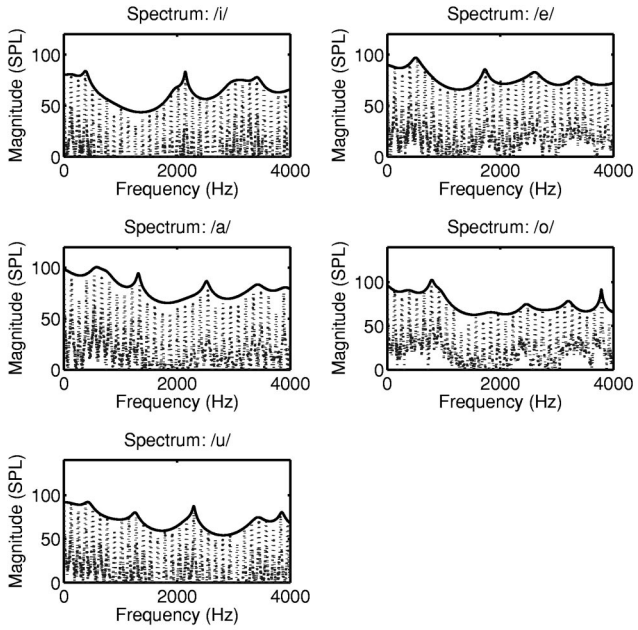

FIG. 7. Simulated sound spectra for vowels /i/, /e/, /a/, /o/, and /u/. The solid lines show the spectrum envelopes estimated by LPC analysis.

the volume flow, as found in the study of the two-mass vocal fold model.[1] The volume flow waveforms differ in shape, the number of "humps," and amplitude depending on which vocal tract shape is used. The shape and size of the vocal fold trajectory slightly differ across the type of vocal tracts, although these differences may be partially attributed to differences in the y_0 parameter used for the vocal tracts. Figure 7 shows the sound spectra of the output pressure for the four vowels /i/, /e/, /a/, /o/, and /u/. These have definite formant structure that contributes to the high quality of the synthesized sounds.

D. Effect of vocal fold rest position

Each vowel has a region of y_0 where oscillation is possible. The regions for vowels /e/, /a/, and /o/ are larger than those for vowels /i/ and /u/. They become larger with larger subglottal pressure p_0. Areas of the oscillation trajectory for vowels /e/ and /u/ are plotted in Fig. 8 as functions of y_0 with different $p_0 = 600$, 800, and 1000 Pa as the parameter. In most of the region of y_0, the size of the oscillation trajectory is compressed in both x and y directions as y_0 decreases, and thus the trajectory area is decreased. When y_0 becomes larger than a certain value, oscillation rapidly dies out. At the boundary, an oscillation with no closure phase may be generated, which provides a more sinusoidal waveform of the glottal volume flow. Such an oscillation for vowel /e/ is marked with a large square in Fig. 8.

The duty ratio is monotonously decreased as y_0 decreases. It ranges approximately from 0.75 to 0.65 except for the oscillation with no closure phase whose duty ratio is 1. The typical oscillations for vowels /e/ and /u/ having duty ratio of 0.68 are marked with a large diamond in Fig. 8. F0 increases with smaller values of y_0. This is because the contact force is generated when y is negative in addition to the restoring force. Decreasing y_0 leads to a larger duty ratio that

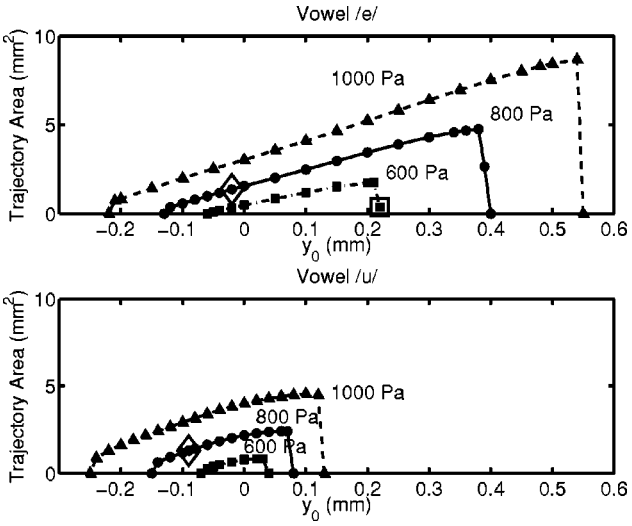

FIG. 8. Areas of the oscillation trajectory for vowels /e/ and /u/ as functions of y_0, the y component of the vocal fold rest position, for different $p_0 = 600$, 800, and 1000 Pa. Vowel /e/ has a wider range of y_0 where oscillation is possible than vowel /u/. The data points marked with a large diamond represent the typical oscillations. The point marked with a large square represents an oscillation with no closure phase.

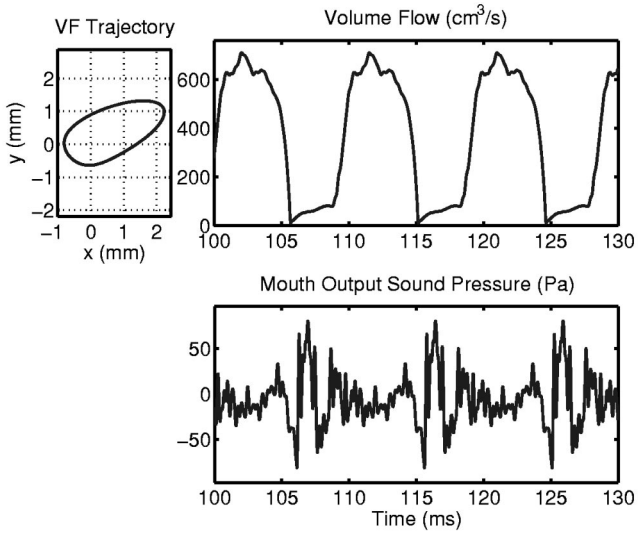

FIG. 9. Waveform for $f_r = 95$ Hz. The generated F0 is 105.3 Hz.

effectively causes increase in the spring constant. In changing y_0, F0 of vowel /e/ varies between 123.4 and 139.1 Hz and F0 of vowel /u/ varies between 118.8 and 131.5 Hz.

The x component of the rest position, x_0, influences the temporal details of the volume flow waveform and can slightly affect the sound frequency. Note that x_0 is the rest position when the subglottal pressure is not given, and it is not equal to the time average of $x(t)$. The time-averaged value $\langle x(t) \rangle$ is always larger than x_0 because the transglottal pressure difference pushes the vocal folds downstream. By holding the other parameters at their typical values, i.e., $y_0 = -0.02$ mm, $p_0 = 800$ Pa, and $f_r = 120$ Hz, the model stops oscillating for values of $x_0 > 3.8$ mm and $x_0 < -0.7$ mm for vowel /e/. Larger values of x_0 tend to generate an oscillation with a larger duty ratio and thus with a lower sound frequency.

E. Effect of vocal fold tension

In our model, the "tension" of the vocal fold is directly related to the resonance frequency f_r. The spring constant k and mass M are functions of f_r and modeled as

$$k = 4\pi^2 a f_r, \quad M = \frac{a}{f_r}, \tag{12}$$

where a is a constant, to give $k = 160$ N/m and $M = 0.28$ g at $f_r = 120$ Hz. Changing f_r gives the same effect as changing the Q parameter in the two-mass model.[1] The simulation result for $f_r = 95$ Hz is shown in Fig. 9. This can be compared with $f_r = 120$ Hz in Fig. 5, which is the simulation result under the typical glottal condition. F0's of the two synthesized samples are 105.3 Hz with $f_r = 95$ Hz and 133.7 Hz with $f_r = 120$ Hz.

Figure 10 shows how F0, the amplitude of the glottal area, and the duty ratio change as functions of f_r. In this experiment, the vocal tract model of vowel /e/ is used with default subglottal pressure $p_0 = 800$ Pa and default rest position $(x_0, y_0) = (0.2, -0.02)$ mm. Although the f_r parameter is defined as the resonance frequency of the spring-mass system, it does not directly correspond to F0, as the vocal folds are usually driven at a frequency higher than their resonance frequency. Instead, the relationship between F0 and the f_r parameter is nearly directly proportional, with an average slope of 1.1 Hz/Hz. This effect is caused by the contact force on the vocal folds when they collide to compress each other. The contact force spring constant adds to the spring constant of the vocal folds upon contact and increases the frequency of the oscillation.

Similar to the two-mass model, variation in the duty ratio with f_r falls into a range between 0.68 and 0.71, which is compatible with the ratio observed for chest voice.[26] The amplitude of the glottal area is monotonously decreased with increasing f_r. This is also similar to the two-mass model. The glottal flow waveform also varies in detail depending on the value of f_r.

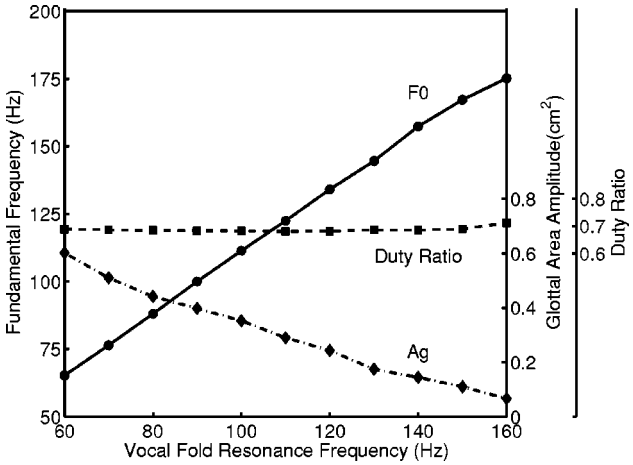

FIG. 10. Sound frequency, the amplitude of glottal area, and the duty ratio of the glottal opening (open time to the total period) as functions of vocal fold resonance frequency, f_r.

TABLE IV. Parameters of the two-mass model.

l	Vocal fold length	14 mm
d_1	Thickness of mass 1	2.5 mm
d_2	Thickness of mass 2	0.5 mm
k_1	Spring constant 1	$111\times f_r/120$ N/m $80\times f_r/120$ N/m for soprano
k_2	Spring constant 2	$0.6\times k_1 m_2/m_1$ $0.3\times k_1 m_2/m_1$ for soprano
k_c	Spring constant b/w two masses	$2.0\times k_1 m_2/m_1$ $1.6\times k_1 m_2/m_1$ for soprano
m_1	Mass 1	$0.18\times 120/f_r$ g $0.13\times 120/f_r$ g for soprano
m_2	Mass 2	$0.045\times 120/f_r$ g $0.025\times 120/f_r$ g for soprano
h_1	Contact force spring constant 1	$3k_1$
h_2	Contact force spring constant 2	$3k_2$
η	Spring non-linear coefficient	1.0×10^4 m^{-2}
q_1	Quality factor for mass 1	10.0 for $x_1 \geqslant 0$ $10.0+9.1x_1$ for $-1.0 \leqslant x_1 < 0$ mm 0.9 for $x_1 < -1.0$ mm
q_2	Quality factor for mass 2	1.667 for $x_2 \geqslant 0$ $1.667+1.042x_2$ for $-1.0 \leqslant x_2 < 0$ mm 0.625 for $x_2 < -1.0$ mm
x_{01}	Rest position of mass 1	typically 0.2 mm
x_{02}	Rest position of mass 2	typically 0.2 mm
p_0	Subglottal pressure	typically 800 Pa
f_r	Vocal fold resonance frequency	typically 120 Hz

F. Behavior under varying acoustic load

An experiment to investigate the effects of acoustic load, identical to the one presented in the two-mass model study, was performed using the two-dimensional model. The first resonance frequency of the acoustic load was lowered into the range of F0, and the magnitude of the input impedance at F0 was increased. This is accomplished by lengthening the vocal tract, a uniform tube 5 cm^2 in cross section, from 20 to 160 cm. The entire length of the tube is regarded as a hard-wall tube without wall vibration effects.

To compare the simulation results between the two models, we constructed a two-mass model with a parameter of the resonance frequency of the vocal fold, which is defined here by

$$f_r = \frac{1}{2\pi}\sqrt{\frac{k_1+k_2}{m_1+m_2}}, \tag{13}$$

where k_1 and k_2 are spring constants attached to masses m_1 and m_2, respectively. Parameters of the two-mass model in this experiment are listed in Table IV. Figure 11 shows the simulation results for the two-mass model and those for the two-dimensional model with two different sets of parameters: One has $(x_0, y_0) = (1.0, 0.1)$ mm, $p_0 = 1050$ Pa, and $f_r = 120$ Hz, and the other has $(x_0, y_0) = (0.2, -0.05)$ mm, $p_0 = 1150$ Pa, and $f_r = 120$ Hz. F0's in both cases of the two-dimensional model decrease more slowly than that of the two-mass model with increasing tube length. When the frequency of the first formant of the vocal tract tube is lowered to the oscillation frequency of the two-mass model, a sharp increase in F0 is observed. The frequency after the jump is the same as that for the 30-cm tube. It gradually decreases again as the tube length is further increased. This result makes control of F0 by vocal fold tension difficult when the acoustic load can shift between inductive and capacitive behaviors.

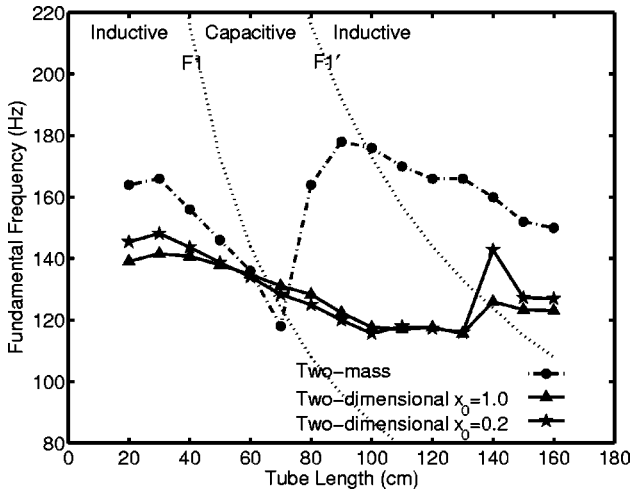

FIG. 11. Variation in F0 with an acoustic load of a uniform tube whose length varies. The solid lines represent the results of the two-dimensional model. The dash-dot line represents the results of the two-mass model. F1 shows the frequency of the first pole of impedance, and F1′ shows the first zero. A jump in F0 occurs in the two-mass model when it crosses the F1 line, whereas no jumps occur in the two-dimensional model across the F1 line.

Neither case for the two-dimensional model has a jump in F0 when crossing between inductive and capacitive impedances. This simplifies control of F0. The F0 decreases smoothly in the capacitive region past the resonance frequency boundary. A jump, however, occurs when the length of the tube reaches 140 cm and the acoustical load becomes inductive again. This experiment on the two-dimensional model implies that the vocal fold has a tendency to oscillate near F1 even if it decreases below F0. As F1 further decreases, the vocal fold becomes unable to continue oscillating at the first resonance. The oscillation frequency, then, jumps to the vicinity of the second resonance of the load.

Comparing Fig. 11 to the F0 measurement of a human subject described in the two-mass model study,[1] one sees that the curves for the two-dimensional model follow more closely the F0 measurements. In particular, the frequency jump in the measurement data does not occur immediately at the tube's first resonance frequency but slightly on the higher side. This behavior is better predicted by the two-dimensional model.

G. Mechanism of self-sustained oscillation

Coupling of the motions along the x and y directions is the key to understanding the reason why the two-dimensional model yields self-sustained oscillation both with an inductive and capacitive vocal tract load. The force due to the pressure difference given by Eq. (3) causes circular motion of the vocal fold. Because it vibrates with a frequency near the resonance frequency, the external force acting on the vocal fold should be in the direction of the velocity. In Eq. (3), the x-component of the force is proportional of w

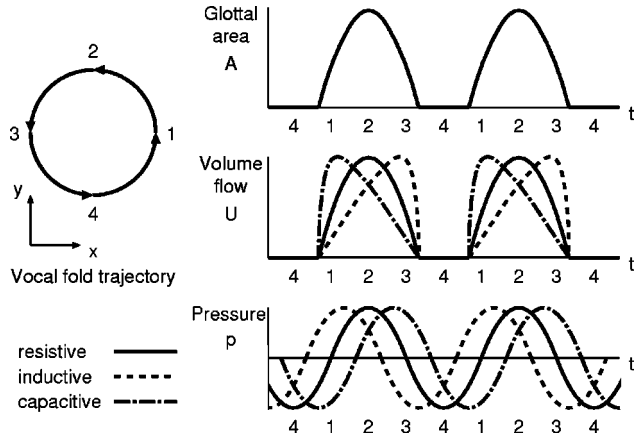

FIG. 12. Schematic vocal fold trajectory and waveforms of glottal area, volume flow, and pressure at the vocal tract entrance. Solid lines are for the case where the acoustic load is resistive (F0≈F1), dashed lines are for the inductive load (F0<F1), and dash-dot lines are for the capacitive load (F0 >F1).

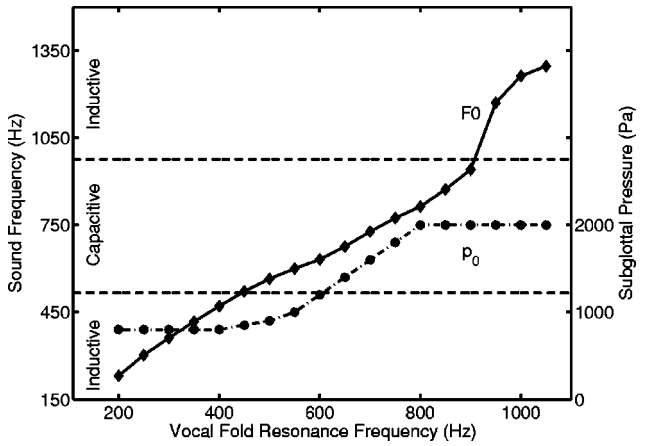

FIG. 13. Variation in F0 with the vocal fold resonance frequency f_r in the straight-tube simulation with the two-dimensional model. As F0 is increased, higher subglottal pressure p_0 is required, and this is plotted with a dash-dot line.

$-y(t)$, and the y-component of the force is proportional to $x(t)$. This implies that this force induces the vocal fold to circulate in the counter-clockwise direction.

The circular motion of the vocal fold is schematically illustrated in Fig. 12. The glottis is maximally opened at phase 2 and completely closed near phase 4. Therefore, a glottal area waveform $A(t)$ shown in the upper-right panel is generated. By assuming this waveform of $A(t)$, it is in principle possible to obtain the volume flow and the pressure waveforms at the entrance of the vocal tract by considering the fluid dynamics at the glottis and the vocal tract resonance. Although this is a difficult task due to the nonlinear characteristic of the fluid dynamics, the volume flow waveform can adequately be estimated by a linearized model.[25] When F0 is well below F1, the vocal tract acoustic load is inductive. In this case, the volume flow $U(t)$ has a waveform with the slower rise and the abrupt fall as indicated by the dashed line in the middle-right panel. (Here, the flow mechanically generated is relatively small and disregarded for simplicity.) Because the phase of pressure $p(t)$ at the vocal tract entrance leads $U(t)$ up to 90 deg, $p(t)$ has a waveform as plotted by the dashed line in the lower-right panel. Assuming the glottal pressure $p_g(t)$ is not very far from $p(t)$, we find $p_g(t)$ pushes the vocal fold at phase 1 and sucks it at phase 3. So, this resultant Bernoulli force given by Eq. (2) is in the same direction of the velocity of the vocal fold and therefore drives the vocal fold oscillation. This is the same mechanism for the one-mass vocal fold model to maintain self-sustained oscillation.

When F0 is close to F1, the vocal tract acoustic load becomes large and resistive. In this case, volume flow and pressure waveforms become symmetrical as indicated by the solid line. In this case, the Bernoulli force does not drive the oscillation because the same force acts on the vocal fold at phases 1 and 3. Instead, $p(t)$ pushes the vocal fold upstream at phase 2 and downstream at phase 4. Namely, the force given by Eq. (3) becomes a driving force. This mechanism works even if the acoustic load becomes capacitive when F0 exceeds F1. The waveforms of volume flow and pressure are depicted in the dash-dot line. Pressure $p(t)$ takes its maximum between phases 2 and 3 and its minimum between phases 4 and 1. This causes a force in the direction of the vocal fold velocity.

V. HIGH-FREQUENCY VOICE SYNTHESIS

The response of the two-dimensional and two-mass models with a capacitive acoustical load was investigated by driving the oscillation frequency to values between the first resonance frequency (F1) and the first antiresonance frequency (F1′). The mass and spring constant of the two-dimensional model were decreased in the following experiments to simulate the female vocal fold. The new values are $M=0.10$ g and $k=58.6$ N/m at 120 Hz. Their relationship with f_r remained unchanged from the previous experiments. Likewise, the masses and spring constants of the two-mass model are also reduced as shown in Table IV.

A. Straight tube load

The two vocal fold models were attached to a cylinder of 17-cm length and 5-cm^2 cross-sectional area. Calculated F1 and F1′ are 516 and 977 Hz, respectively, and the capacitive region lies between F1 and F1′. The models were then driven at the range of the vocal fold resonance frequency f_r, and the sound frequency was measured. When increasing the f_r, the subglottal pressure p_0 should also be increased to obtain self-excitation. This is in accord with the facts that subglottal pressure is increased to produce high-frequency voice and that the range is roughly up to 3 kPa in singing.[27] The other parameters x_0 and y_0 are set to 0.2 and -0.05 mm, respectively, in this experiment. The relationship between sound frequency and f_r for the two-dimensional model is plotted with a solid line in Fig. 13. The relationship for the two-mass model is shown in Fig. 14. In these figures, p_0 change is also plotted with dash-dot lines.

When the sound frequency increases beyond F1, the acoustic load changes from the inductive to capacitive behavior. However, the sound frequency of the two-dimensional model increases smoothly with f_r. Self-excitation is possible in the capacitive region continuously

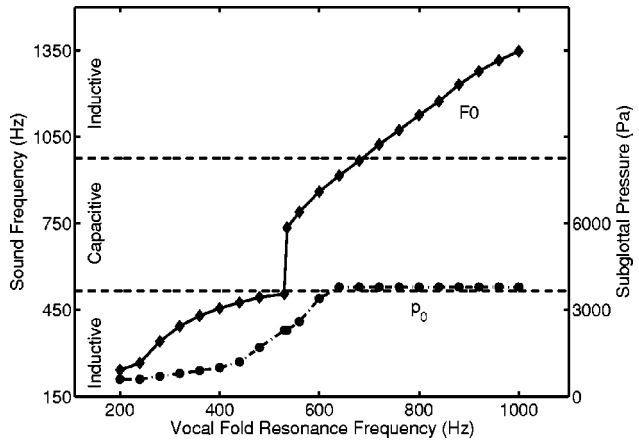

FIG. 14. Variation in F0 with the vocal fold resonance frequency f_r in the straight-tube simulation with the two-mass model.

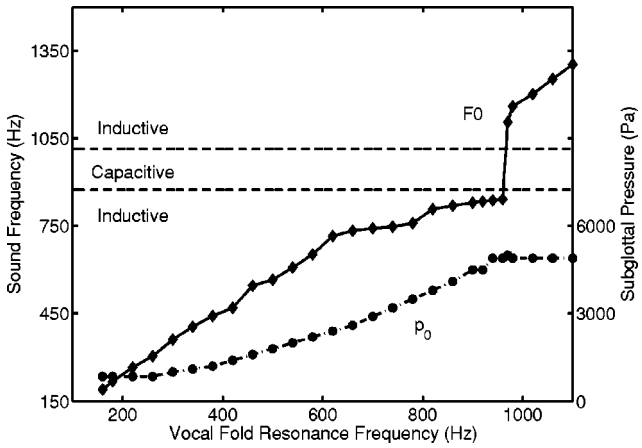

FIG. 16. Variation in F0 with the vocal fold resonance frequency f_r in the /a/ vowel simulation with the two-mass model.

nearly up to F1′. When the sound frequency increases beyond F1′, a frequency jump occurs and the sound is then generated in the second resonance mode of the tube.

On the other hand, the two-mass model has a jump in frequency at F1. The jump covers about the lower half of the capacitive region. Therefore, no self-excitation can be generated between 506 and 735 Hz. After the frequency jump, the relationship between f_r and sound frequency becomes quite linear. Hence, the two-dimensional model is capable of producing a wider continuous range of frequencies for self-excitation than the two-mass model.

B. Vocal tract load

The same experiment as in the previous subsection was performed with an acoustical load of an actual vocal tract. It is of a female speaker pronouncing vowel /a/. The area function of this vocal tract was constructed from MRI data collected with the same method.[22] F1 and F1′ of this vocal tract are calculated to be 874 and 1014 Hz, respectively. The result of the two-dimensional model is shown in Fig. 15. The result of the two-mass models is shown in Fig. 16.

We can observe similarities with the previous experiment. The two-dimensional model is capable of continuing self-excitation beyond F1. The sound frequency increases smoothly over F1 and falls into the capacitive region. When the sound frequency increases further to the antiresonance frequency of the vocal tract, the model has a small jump between 941 and 1037 Hz. This frequency jump reminds us of that observed at the transition from the head register to the whistle register on an ascending glissando sung by a soprano singer.[28] On the other hand, the two-mass model again has a jump in the frequency when it reaches F1. In this case, however, the frequency jump is between 842 and 1106 Hz, and no self-excited oscillation can be generated in the entire capacitive region.

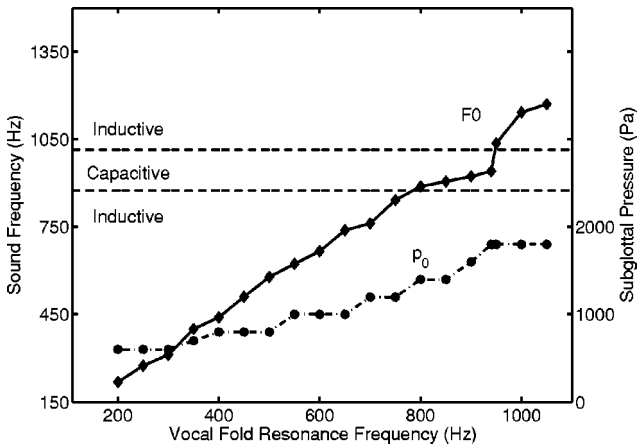

FIG. 15. Variation in F0 with the vocal fold resonance frequency f_r in the /a/ vowel simulation with the two-dimensional model.

C. Simulation of soprano singing

One last experiment was performed to apply the two-dimensional and two-mass models to a simulation of soprano singing. The same vocal tract shape as in the previous experiment is used in this experiment. Tones up to 1400 Hz were simulated using the two models of the vocal fold.

The synthesized sounds from the high-frequency inductive load region sound thin and forced, but the sound qualities are similar between the two models. When F0 passes F1, the synthesized sound can no longer be identified as a vowel because few harmonics are found near the formants. Sometimes, oscillations in the capacitive load region become aperiodic in both models, resulting in an output sound with noise or an unidentifiable pitch in an extreme case. The forced sound quality could be improved by using a vocal tract model of actual soprano singing, but such data were unavailable to us.

Another obvious problem is the sound frequency jump as mentioned previously. With both models we encountered tones on the musical scale in the soprano singing that could not be synthesized. The two-dimensional model is unable to synthesize B5 (988 Hz) and the two-mass model from A5 to C6 (880 to 1047 Hz). All of these tones fall in the range of the respective model's frequency jump shown in Figs. 15 and 16. Furthermore, notes near the endpoints of the frequency jump also presented difficulties, as applying vibrato inevitably shifted the tones up and down the frequency jump, causing a much larger and discontinuous frequency fluctuation compared to normal vibrato.

As an application, the phrase of ''Queen of the Night Aria'' from Mozart's Magic Flute was synthesized by the two models.[29] The two-dimensional model showed no flaw in synthesizing the entire phrase. On the other hand, the two-mass model has difficulty in synthesizing the phrase because in A5, B♭5, and C6 it cannot generate self-excited oscillations of the voice source.

VI. CONCLUSIONS

The two-dimensional model of the vocal fold vibration provides a numerical model to help explain the voice production process. The model is controlled by a few parameters, such as the vocal fold resonance frequency and the subglottal pressure. The output sounds produced by the model using vocal tract shapes for the five Japanese vowels have definite formant structure that contributes to the high quality of the synthesized sounds. By comparing the behavior of the two-dimensional model with that of the widely used two-mass model, similarities are found in the amplitudes of the glottal area and the glottal volume flow velocity, in the variation in the volume flow waveform with the vocal tract shape, and in the dependence of the oscillation amplitude upon the average opening area of the glottis. The response to the change in the vocal fold resonance frequency f_r from 60 to 160 Hz is also the same: F0 linearly changes with f_r and the glottal flow waveform amplitude decreases, while the duty ratio of the glottis remains nearly constant. A few dissimilarities are also found: The glottal area and volume flow have typical waveforms that are more symmetric between the rising and falling phases.

The major improvement of the two-dimensional model over the two-mass model is a smooth transition between oscillations with an inductive load and a capacitive load, with no sudden jumps in the vibration frequency. The two-mass model, on the other hand, demonstrates a jump in the output sound frequency when the type of load changes from inductive to capacitive. Comparing the F0 results measured by Ishizaka and Flanagan on a human subject with varying acoustic load, one sees that the above observation is closer to the behavior of the two-dimensional model, in which F0 changes smoothly across the boundary from inductive to capacitive load but has a jump in F0 further into the capacitive load region.

The relative ease in the control of sound frequency with both inductive and capacitive loads makes the model well suited for simulation of soprano singing, in which F0 can exceed F1 to reach the region of a capacitive load. The two-dimensional model can provide self-excited oscillation in a wide continuous frequency range below and above F1. On the other hand, the two-mass model fails to generate self-excitation in a range just above F1. High-pitched soprano singing can thus be successfully simulated by the two-dimensional model.

The following issues remain for future work. It is necessary to directly measure the vocal fold oscillation during high-pitched singing voice. This would directly test for the presence of the two-dimensional oscillation for high-pitched singing, which has been assumed in this paper. Because the two-dimensional model has been constructed as a functional model, the geometry is somewhat different from that of the actual vocal fold. One way to incorporate the physiological features into the model is to introduce the body-cover concept of vocal fold structure, in the same way that the three-mass model has been developed from the classical two-mass model. The current model is too simple to simulate the phase difference between the upper and lower parts of the vocal folds, which is observed in actual vocal fold vibration. Multi-mass (at least two-mass) representations are needed for this purpose. To simulate the diversity of vocalization, such as pathological voice, it is necessary to consider the degree of freedom along the length of the vocal fold.

ACKNOWLEDGMENT

This research was conducted as part of ''Research on Human Communication'' with funding from the National Institute of Information and Communications Technology (NICT).

[1] K. Ishizaka and J. L. Flanagan, ''Synthesis of voiced sounds from a two-mass model of the vocal cords,'' Bell Syst. Tech. J. **51**(6), 1233–1268 (1972).
[2] B. H. Story and I. R. Titze, ''Voice simulation with a body-cover model of the vocal folds,'' J. Acoust. Soc. Am. **97**, 1249–1260 (1995).
[3] I. R. Titze, ''The physics of small-amplitude oscillation of the vocal folds,'' J. Acoust. Soc. Am. **83**, 1536–1552 (1988).
[4] J. Liljencrants, ''A translating and rotating mass model of the vocal folds,'' STL Quarterly Progress and Status Report, 1, Speech Transmission Laboratory (Royal Institute of Technology (KTH), Stockholm, Sweden, 1991), pp. 1–18.
[5] I. R. Titze, ''The human vocal cords: A mathematical model, part I,'' Phonetica **28**, 129–170 (1973).
[6] I. R. Titze, ''The human vocal cords: A mathematical model, part II,'' Phonetica **29**, 1–21 (1974).
[7] F. Alipour-Haghighi and I. R. Titze, ''Combined simulation of two-dimensional air and vocal fold vibration,'' in *Vocal Fold Physiology: Controlling Complexity and Chaos*, edited by P. Davis and N. Fletcher (Singular, San Diego, 1996), pp. 17–29.
[8] J. L. Flanagan and L. L. Landgraf, ''Self-oscillating source for vocal-tract synthesizers,'' IEEE Trans. Audio Electroacoust. **AU-16**, 57–64 (1968).
[9] J. Sundberg, *The Science of the Singing Voice* (Northern Illinois University Press, DeKalb, 1987), pp. 124–129.
[10] E. Joliveau, J. Smith, and J. Wolfe, ''Tuning of vocal tract resonance by sopranos,'' Nature (London) **427**, 116 (2004).
[11] E. Joliveau, J. Smith, and J. Wolfe, ''Vocal tract resonances in singing: The soprano vice,'' J. Acoust. Soc. Am. **116**, 2434–2439 (2004).
[12] S. Adachi and M. Sato, ''Trumpet sound simulation using a two-dimensional lip vibration model,'' J. Acoust. Soc. Am. **99**, 1200–1209 (1996).
[13] S. Adachi and M. Sato, ''Time-domain simulation of sound production in the brass instrument,'' J. Acoust. Soc. Am. **97**, 3850–3861 (1995).
[14] X. Pelorson, A. Hirschberg, R. R. van Hassel, and A. P. J. Wijnands, ''Theoretical and experimental study of quasisteady-flow separation within the glottis during phonation. Application to a modified two-mass model,'' J. Acoust. Soc. Am. **96**, 3416–3431 (1994).
[15] N. J. C. Lous, G. C. Hofmans, R. N. J. Veldhuis, and A. Hirschberg, ''A symmetrical two-mass vocal-fold model coupled to vocal tract and trachea, with application to prosthesis design,'' Acust. Acta Acust. **84**, 1135–1150 (1998).
[16] D. Sciamarella and C. d'Alessandro, ''On the acoustic sensitivity of a symmetrical two-mass model of the vocal folds to the variation of control parameters,'' Acta Acust. Acust. **90**, 746–761 (2004).
[17] J. L. Flanagan and K. Ishizaka, ''Computer model to characterize the air volume displaced by the vibrating vocal cords,'' J. Acoust. Soc. Am. **63**, 1559–1565 (1978).
[18] J. Awrejcewicz, ''Numerical analysis of the oscillations of human vocal cords,'' Nonlinear Dyn. **2**, 35–52 (1991).

[19] N. H. Fletcher and T. Rossing, *The Physics of Musical Instruments*, 2nd. ed. (Springer-Verlag, New York, 1998), Chap. 8.14, pp. 223–227.
[20] M. M. Sondhi and J. Schroeter, ''A hybrid time-frequency domain articulatory speech synthesizer,'' IEEE Trans. Acoust., Speech, Signal Process. **ASSP-35**, 955–967 (1987).
[21] S. Adachi and M. Yamada, ''An acoustical study of sound production in biphonic singing, Xöömij,'' J. Acoust. Soc. Am. **105**, 2920–2932 (1999).
[22] H. Takemoto, K. Honda, S. Masaki, Y. Shimada, and I. Fujimoto, ''Measurement of temporal changes in vocal tract area function from 3D cine-MRI data,'' submitted to J. Acoust. Soc. Am.
[23] T. Baer, ''Observation of vocal fold vibration: Measurement of excised larynges,'' in *Vocal Folds Physiology*, edited by K. N. Stevens and M. Hirano (Univ. of Tokyo, Tokyo, 1981), pp. 119–133.
[24] A. E. Rosenberg, ''Effect of glottal pulse shape on the quality of natural vowels,'' J. Acoust. Soc. Am. **49**, 583–590 (1971).
[25] M. Rothenberg, ''Acoustic interaction between the glottal source and the vocal tract,'' in *Vocal Folds Physiology*, edited by K. N. Stevens and M. Hirano (Univ. of Tokyo, Tokyo, 1981), pp. 305–323.
[26] I. R. Titze, *Priciples of Voice Production* (Prentice–Hall, Englewood Cliffs, NJ, 1994), pp. 115–116.
[27] J. Sundberg, *The Science of the Singing Voice* (Northern Illinois, University Press, DeKalb, 1987), pp. 35–37.
[28] N. Henrich, B. Boubeau, and M. Castellengo, ''On the use of electroglottography for characterisation of the laryngeal mechanisms,'' Proc. of Stockholm Music Acoustics Conference (2003), pp. 455–458.
[29] http://www.his.atr.jp/~sadachi/MagicFluteDemo/

The effects of tones on speaking frequency and intensity ranges in Mandarin and Min dialects

Sheng H. Chen[a)]
Department of Speech and Hearing Disorders and Sciences, National Taipei College of Nursing, #89, Nei-Chiang Street, Wanhua 108, Taipei, Taiwan

(Received 25 January 2005; accepted for publication 26 January 2005)

The differences of speaking frequency and intensity in different tonal dialects has not been widely investigated. The purposes of this study were (1) to compare the speaking frequency and speaking intensity ranges of Mandarin and Min and (2) to compare the speaking frequency and intensity ranges of Mandarin and Min to those of American English. The subjects were 80 normal Taiwanese adults divided into two dialect groups, Mandarin and Min. The speaking F0, the highest speaking F0, the lowest speaking F0, the maximum range of speaking F0, and the intensity counterpart were obtained from reading in their native dialects. Statistical analysis revealed that Min speakers had a significantly greater maximum range of speaking intensity and a smaller lowest speaking intensity than Mandarin speakers, which indicated tonal effects by speakers of the Min dialect. Moreover, Mandarin and Min speakers had a greater maximum range of speaking F0 and maximum range of speaking intensity than American English speakers. The data may provide an assessment tool for Mandarin speakers and Min speakers.
[DOI: 10.1121/1.1872312]

PACS numbers: 43.70.Gr [AL] Pages: 3225–3230

I. INTRODUCTION

Current theory of speaking frequency and intensity is based mainly on data derived from nontonal English speakers. Dialects related to tonal languages have not been widely investigated. If differences of speaking frequency and intensity are found in different tonal dialects, it is important to establish reference data of that dialect for evaluation of speech and vocal function.

Mandarin and Min are tonal languages of Chinese that are spoken by most people in Taiwan. Mandarin contains four basic tones and Min contains seven basic tones. Each word has one tone. Syllables with different tones convey different meanings (Chao, 1948; Huang, 1990; Ting, 1979). The range of fundamental frequency used in speaking Mandarin mainly depends upon the high-low tone combinations (Chen, 1972), as it also does in Min.

The fundamental frequency of tones in Mandarin has been claimed to be higher than that in Min (Howie, 1976). Although the fundamental frequency pattern of tones in Mandarin was similar to that in Min (Shen, 1989; Tseng, 1990), Mandarin has a higher fundamental frequency in high tone than Min (Huang, 1990). Therefore the total frequency range of tones in Mandarin was suggested to be greater than that in Min, resulting in a greater range of speaking frequency of Mandarin (Huang, 1990).

Nevertheless, information on frequency and intensity in general might lead one to conclude that tonal features of Mandarin and Min may result in a wider speaking frequency range compared to a nontonal language. Chen (1972) investigated the speaking frequency range for native Mandarin and native American English speakers in words and sentences, and found that the speaking frequency range for Chinese Mandarin speakers was 183% to 250% wider than that of American English speakers. This phenomenon was also found in the tonal language of Japanese, in which the variability of speaking fundamental frequency was identified to be greater for Japanese speakers than for American speakers (Yamazawa and Hollien, 1992). Because frequency and intensity are closely related and co-varying with each other (Titze, 1988), these findings suggest the need for a data base of speaking frequency and intensity for tonal dialects.

The purposes of the study are (1) to compare the speaking frequency and speaking intensity ranges of the two different tonal dialects of Mandarin and Min and (2) to compare the speaking frequency and intensity ranges of the tonal dialects of Mandarin and Min to those of the nontonal language of American English.

II. METHOD

A. Subjects

The research subjects were 80 normal Taiwanese young adults equally divided into two dialect groups, Mandarin and Min. Each group consisted of 40 native speakers in which 20 were female and 20 were male.

The mean age of all subjects was 25.7 years with an age range of 21–29 years.

Young adult volunteers from Veterans General Hospital-Taipei, and Yang-Ming University who met the following criteria were selected for study: (1) no history of smoking, heavy drinking, laryngeal surgery, vocal fold pathology, throat problems, hearing impairment, respiratory problems, neurologic problems, or singing training and (2) presented a normal voice condition.

a)Electronic mail: shchen@ntcn.edu.tw

TABLE I. Means and standard deviations of frequency and intensity variables in reading of Mandarin and Min female subjects.

	Mandarin ($n=20$)		Min ($n=20$)	
	Mean	SD	Mean	SD
Speaking fundamental frequency (Hz, ST[a])	196.00 (36.60)	23.06 (1.79)	185.00 (35.80)	23.04 (1.99)
Highest speaking fundamental frequency (Hz, ST)	261.60 (41.30)	21.76 (1.37)	261.60 (41.00)	22.61 (1.50)
Lowest speaking fundamental frequency (Hz, ST)	103.8 (25.70)	30.56 (4.70)	103.8 (25.60)	25.55 (3.68)
Maximum range of speaking fundamental frequency (ST)	15.60	4.08	15.40	3.47
Speaking intensity (dB)	71.50	1.82	70.20	5.63
Highest speaking intensity (dB)	76.00	1.41	76.60	1.47
Lowest speaking intensity (dB)	46.50	8.26	44.70	1.91
Maximum range of speaking intensity (dB)	29.50	3.40	31.90	1.69

[a]ST = semitone.

B. Determination of frequency and intensity data in reading

Frequency and intensity range data were obtained from tasks in reading Mandarin and Min passages. All subjects were instructed to read a passage of their native language at a comfortable frequency and intensity level.

All study procedures were conducted in a sound-treated room with an ambient noise level of 40 dB SPL or less. The subject's voice was recorded with a professional quality cassette tape recorder (Nakamichi Model CR-3) with a unidirectional condenser microphone (Audio-Technica ATM 11). The distance from the microphone to the subject's mouth was 15 cm. A 1000-Hz tone at 80 dB produced 15 cm from the microphone was recorded prior to utterances. This calibration tone served as the reference by which to calculate a sample of vocal intensity in relative dB.

The first and last sentences of each of the passages were deleted for analysis of frequency and intensity. The acoustic waveform of the voice sample was analyzed following digital recording at a sampling rate of 20.0 kHz using Computerized Speech Lab (Kay Model 4300) with frequency extraction and intensity extraction programs.

The frequency value in each frame was converted from Hz to semitones (ST). The 95th percentile of the frequency distribution of the ST for each subject determined their highest speaking fundamental frequency, the lowest speaking fundamental frequency, and the maximum range of speaking fundamental frequency for that subject. Variability of speaking fundamental frequency was measured from the standard deviation of speaking fundamental frequency.

Only voiced frames for intensity values were selected for analysis. The intensity value in each frame was defined as dB SPL. Using the 95th percentile of the frequency distribution of dB SPL for each subject, the highest speaking intensity, the lowest speaking intensity, and the maximum range of speaking intensity for that subject were also determined. Variability of speaking intensity was measured from the standard deviation of speaking intensity.

C. Reliability

Reliability of test-retest procedures of speaking frequency and speaking intensity measurements was determined to be 0.80 with intraclass correlation coefficient.

D. Statistical analysis

A two-factor analysis of variance was used to find the statistical significance of the main effects of dialect and gender, and interaction between dialect and gender in reading.

III. RESULTS

The averaged data on frequency and intensity in reading for the Mandarin and Min subjects of female groups are reported in Table I. The data for the male groups are reported in Table II. Statistical analysis of frequency and intensity variables in reading with two-factor ANOVA is shown in Table III. The ANOVA results revealed that the lowest speaking intensity of the Mandarin group was significantly greater than that of the Min group [$F(1,76)=7.36, P<0.05$], and the maximum range of speaking intensity of the Min group was significantly greater than that of the Mandarin group [$F(1,76)=10.51, P<0.05$]. However, no statistically significant dialect effect was found for any of the frequency variables, speaking intensity, and highest speaking intensity. The speaking fundamental frequency, the highest speaking fundamental frequency, the lowest speaking fundamental frequency, and the maximum range of speaking fundamental frequency of female subjects were significantly greater than those of male subjects [$F(1,76)=543.04, P<0.05$; $F(1,76)=81.55, P<0.05$; $F(1,76)=37.78, P<0.05$; and $F(1,76)=4.61, P<0.05$, respectively]. There was no significant interaction between dialect and gender for any frequency or intensity variables.

Data on maximum range of speaking fundamental frequency and speaking fundamental frequency of this study and studies of the nontonal language of American English for adult females are shown in Table IV. The data for adult males are shown in Table V. Data on maximum range of

TABLE II. Means and standard deviations of frequency and intensity variables in reading of Mandarin and Min male subjects.

	Mandarin ($n=20$)		Min ($n=20$)	
	Mean	SD	Mean	SD
Speaking fundamental frequency (Hz, ST[a])	110.00 (26.50)	16.60 (2.28)	110.00 (26.10)	9.91 (1.41)
Highest speaking fundamental frequency (Hz, ST)	185.00 (35.70)	50.31 (4.26)	174.6 (34.30)	44.26 (3.85)
Lowest speaking fundamental frequency (Hz, ST)	77.70 (20.90)	6.60 (1.29)	82.4 (21.80)	7.30 (1.36)
Maximum range of speaking fundamental frequency (ST)	14.80	4.46	12.50	3.28
Speaking intensity (dB)	69.70	2.50	69.50	3.41
Highest speaking intensity (dB)	75.50	1.76	76.00	1.65
Lowest speaking intensity (dB)	46.20	3.22	45.60	2.25
Maximum range of speaking intensity (dB)	29.30	1.78	30.40	2.26

[a]ST = semitone.

speaking intensity and speaking intensity in this study and studies of the nontonal language of American English for adult females are shown in Table VI. The data on maximum range of speaking intensity for adult males are shown in Table VII.

IV. DISCUSSION

Two significant differences were found between the Mandarin and Min groups. The greater maximum range of speaking intensity for the Min group implies that the Min dialect may have a wider range of intensity change than Mandarin. The smaller lowest speaking intensity for the Min group than for the Mandarin group indicates that more low intensity tones may be observed in the intensity change for the Min group.

In this study, the maximum range of speaking fundamental frequency for female Mandarin and Min speakers was smaller than found by Cowan (1936) and Linke (1953), and for male Mandarin and Min speakers was smaller than reported by Provonost (1942), Snidecor (1943), and Hanley (1951) for nontonal language American English speakers of their comparative genders. However, this measurement for Mandarin and Min speakers of both sexes was greater than that found by other authors for American speakers of their comparative genders (Awan, 1993; Benjamin, 1981; Cowan, 1936; Curry, 1940; Lynch, 1934; Snidecor, 1951). The variability of speaking fundamental frequency for female Mandarin speakers was smaller than the findings of Saxman and Burk (1967), Stoicheff (1981), Brown *et al.* (1991), and Hollien *et al.* (1997), and was greater than reported by Fitch and Holbrook (1970), Hudson and Holbrook (1981), and Fitch

TABLE III. Two-factor ANOVA for frequency and intensity variables in reading of Mandarin and Min female and male groups.

	Gender		Dialect		Gender × Dialect	
	F	*p*	*F*	*p*	*F*	*p*
Speaking fundamental frequency (ST[a])	543.04	<0.0001[b]	1.84	0.178	0.17	0.680
Highest speaking fundamental frequency (ST)	81.55	<0.0001[b]	1.56	0.215	0.65	0.421
Lowest speaking fundamental frequency (ST)	37.78	<0.0001[b]	0.33	0.569	0.51	0.477
Maximum range of speaking fundamental frequency (ST)	4.61	0.034[b]	2.11	0.150	1.49	0.226
Speaking intensity (dB)	2.27	0.136	0.79	0.375	0.50	0.481
Highest speaking intensity (dB)	2.21	0.142	2.21	0.142	0.01	0.944
Lowest speaking intensity (dB)	0.46	0.499	7.36	0.008[b]	1.84	0.178
Maximum range of speaking intensity (dB)	2.40	0.125	10.51	0.001[b]	1.38	0.243

[a]ST = semitone. df = 1 for gender, dialect, and gender × dialect.
[b]$p<0.05$.

TABLE IV. Summary of the present study and previous investigations on maximum range of speaking fundamental frequency and speaking fundamental frequency of adult females.

Investigators	Native language	Mean	SD
Maximum range of speaking fundamental frequency (ST[a])			
Present study	Mandarin	15.60	4.08
Present study	Min	15.40	3.47
Cowan (1936)	English	23.90	···
Snidecor (1951)	English	14.00	···
Linke (1953)	English	18.89	2.46
Benjamin (1981)	English	7.70	1.14
Awan (1993)	English	6.23	2.33
Speaking fundamental frequency (Hz, ST)			
Present study	Mandarin	196.00	23.06 (1.79)
Present study	Min	185.00	23.04 (1.99)
Saxman and Burk (1967)	English	196.34	··· (1.99)
Fitch and Holbrook (1970)	English	217.00	··· (1.70)
Hudson and Holbrook (1981)	English	193.10	18.58 (···)
Stoicheff (1981)	English	224.30	··· (3.06)
Fitch (1990)	English	206.40	15.30 (···)
Brown *et al.* (1991)	English	192.00	··· (2.00)
Hollien *et al.* (1997)	English	198.00	··· (1.94)

[a]ST = semitone.

(1990) for female American speakers. For female Min speakers, this measurement was smaller than that found by Stoicheff (1981) or Brown *et al.* (1991), and was greater than reported by other investigators for female American speakers (Fitch, 1990; Fitch and Holbrook, 1970; Hudson and Holbrook, 1981; Hollien *et al.*, 1997). The variability of speaking fundamental frequency for male Mandarin speakers was smaller than either Hollien and Jackson (1973) or Brown *et al.* (1991) found; however, it was greater than that found by other investigators for male American speakers (Fitch, 1990; Fitch and Holbrook, 1970; Hollien *et al.*, 1997; Horii and Ryan, 1981; Hudson and Holbrook, 1981; Mcintosh, 1939; Ramig and Ringel, 1983). This measurement for male Min speakers was smaller than all findings for male American speakers (Brown *et al.*, 1991; Fitch, 1990; Fitch and Holbrook, 1970; Hollien and Jackson, 1973; Hollien *et al.*, 1997; Horii and Ryan, 1981; Hudson and Holbrook, 1981; Mcintosh, 1939; Ramig and Ringel, 1983).

Although there were no consistent results for the variability of speaking fundamental frequency between Taiwanese in this study and Americans in other studies, the maximum range of speaking fundamental frequency for Taiwanese of both sexes was greater than most findings for Americans. The difference of maximum range of speaking fundamental frequency for the two different language speakers can be explained by the tonal effects of Mandarin and Min. In Mandarin, the frequency range of the four basic tones in words and sentences was reported to be 154% to

TABLE V. Summary of the present study and previous investigations on maximum range of speaking fundamental frequency and speaking fundamental frequency of adult males.

Investigators	Native language	Mean	SD
Maximum range of speaking fundamental frequency (ST[a])			
Present study	Mandarin	14.80	4.46
Present study	Min	12.50	3.28
Lynch (1934)	English	9.32	···
Cowan (1936)	English	9.75	···
Curry (1940)	English	5.50	···
Provonost (1942)	English	17.00	···
Snidecor (1943)	English	16.02	···
Hanley (1951)	English	18.50	2.13
Benjamin (1981)	English	8.70	2.66
Awan (1993)	English	7.34	2.26
Speaking fundamental frequency (Hz, ST)			
Present study	Mandarin	110.00	16.60 (2.28)
Present study	Min	110.00	9.91 (1.41)
Mcintosh (1939)	English	132.00	··· (1.89)
Fitch and Holbrook (1970)	English	116.65	··· (2.11)
Hollien and Jackson (1973)	English	129.40	··· (2.59)
Horii and Ryan (1981)	English	112.00	15.60 (···)
Hudson and Holbrook (1981)	English	110.15	16.21 (···)
Ramig and Ringel (1983)	English	121.93	··· (1.91)
Fitch (1990)	English	112.90	13.60 (···)
Brown *et al.* (1991)	English	118.00	··· (2.60)
Hollien *et al.* (1997)	English	114.00	··· (2.11)

[a]ST = semitone.

258% wider than that of American English (Chen, 1972). Since in this study the maximum range of speaking fundamental frequency of Min in reading was only 0.2 to 2.3 ST less than that of Mandarin, we can expect that the frequency range of tones in the Min dialect would also be much wider than that of American English.

In this study, the maximum range of speaking intensity

TABLE VI. Summary of the present study and previous investigations on maximum range of speaking intensity and speaking intensity of adult females.

Investigators	Native language	Mean	SD
Maximum range of speaking intensity (dB)			
Present study	Mandarin	29.50	3.40
Present study	Min	31.90	1.69
Awan (1993)	English	3.95	0.91
Speaking intensity (dB)			
Present study	Mandarin	71.50	1.82
Present study	Min	70.20	5.63
Brown *et al.* (1993)	English	63.30	3.10

TABLE VII. Summary of the present study and previous investigations on maximum range of speaking intensity of adult males.

Investigators	Native language	Mean	SD
Maximum range of speaking intensity (dB)			
Present study	Mandarin	29.30	1.78
Present study	Min	30.40	2.26
Awan (1993)	English	4.55	1.29

for Mandarin and Min speakers of both sexes was greater than the findings of Awan (1993) for American English speakers of comparative genders. Also, the variability of speaking intensity for female Mandarin and Min speakers was greater than female American speakers (Brown *et al.*, 1993).

The difference of the maximum range of speaking intensity and the variability of speaking intensity between Taiwanese and American English speakers may also be due to the tonal effects of Mandarin and Min. Because the magnitude of vocal intensity was related to the fundamental frequency (Awan, 1991; Gramming *et al.*, 1988; Titze and Sundberg, 1992), the tonal effects of large frequency changes in Mandarin and Min may result in large intensity changes in both dialects. In addition, the tonal effects can be also found in Japanese, because the speaking fundamental frequency variability for Japanese was greater than that for Americans (Yamazawa and Hollien, 1992).

In this study females show higher speaking fundamental frequency, higher highest speaking fundamental frequency, and higher lowest speaking fundamental frequency in reading than males. This effect is due to the fact that females inherently have shorter vocal folds and greater stiffness of the vocal folds resulting in a higher fundamental frequency (Fung, 1981; Hirano, 1983; Titze, 1989).

V. CONCLUSIONS

The difference in speaking frequency and intensity ranges between different tonal dialect's speakers, and between tonal language and nontonal language speakers, underscored the need for normal databases for different dialects.

The data obtained in this study can be used as an assessment tool of speech and voice conditions for Mandarin and Min speakers.

Further investigation of frequency and intensity data in reading across different age groups for Mandarin and Min speakers in Taiwan could provide necessary information for geriatric, middle-aged, and preadolescent patients who have speech and voice disorders. Studies of other tonal languages are also warranted.

ACKNOWLEDGMENTS

The author extends appreciation to Dr. Diane Bless for her guidance in the completion of this project. Also, thanks to Dr. Ray Kent and Dr. Tsai-Fa Cheng for their valuable suggestions. This research was originally completed as part of a doctoral dissertation by the author entitled ''Phonetograms of Normal Taiwanese Young Adults'' at the University of Wisconsin–Madison. This study was supported in part by the Medical Research and Advancement Foundation in Memory of Dr. Chi-Shuen Tsou research funds.

Awan, S.N. (**1991**). ''Phonetographic profiles and F0-SPL characteristics of untrained versus trained vocal groups,'' J. Voice **5**(1), 41–50.

Awan, S.N. (**1993**). ''Superimposition of speaking voice characteristics and phonetograms in untrained and trained vocal groups,'' J. Voice **7**(1), 30–37.

Benjamin, B.J. (**1981**). ''Frequency variability in the aged voice,'' J. Gerontol. **36**(6), 722–726.

Brown, Jr., W.S., Morris, R.J., Hicks, D.M., and Howell, E. (**1993**). ''Phonational profiles of female professional singers and nonsingers,'' J. Acoust. Soc. Am. **7**, 219–226.

Brown, Jr., W.S., Morris, R.J., Hollien, H., and Howell, E. (**1991**). ''Speaking fundamental frequency characteristics as a function of age and professional singing,'' J. Voice **5**(4), 310–315.

Chao, Y.-R. (**1948**). *Mandarin Primer: An Intensive Course in Spoken Chinese* (Harvard U. P., Cambridge).

Chen, G.T. (**1972**). ''A comparative study of pitch range of native speakers of Midwestern English and Mandarin Chinese: An acoustic study,'' doctoral dissertation, University of Wisconsin—Madison, Madison.

Cowan, M. (**1936**). ''Pitch and intensity characteristics of stage speech,'' Arch. Speech **1**, 7–85.

Curry, E. (**1940**). ''The pitch characteristics of the adolescent male voice,'' Speech Monogr. **7**, 48–62.

Fitch, J.L. (**1990**). ''Consistency of fundamental frequency and perturbation in repeated phonations of sustained vowels, reading, and connected speech,'' J. Speech Hear. Disord. **55**, 360–363.

Fitch, J.L., and Holbrook, A. (**1970**). ''Modal vocal fundamental frequency of young adults,'' Arch. Otolaryngol. **92**, 379–382.

Fung Y.C. (**1981**). *Biomechanics* (Springer, New York), pp. 210–211.

Gramming, P., Sundberg, J., Ternstrom, S., Leanderson, R., and Perkins, W.H. (**1988**). ''Relationship between changes in voice pitch and loudness,'' J. Voice **2**(2), 118–126.

Hanley, T.D. (**1951**). ''An analysis of vocal frequency and duration characteristics of selected samples of speech from three American dialect regions,'' Speech Monogr. **18**, 78–93.

Hirano M. (**1983**). ''The structure of the vocal folds,'' in *Vocal Fold Physiology*, edited by K. Stevens and M. Hirano (Univ. of Tokyo, Tokyo), pp. 33–43.

Hollien, H., and Jackson, B. (**1973**). ''Normative data on the speaking fundamental frequency characteristics of young adult males,'' J. Phonetics **1**, 117–120.

Hollien, H., Hollien, P.A., and de Jong, G. (**1997**). ''Effects of three parameters on speaking fundamental frequency,'' J. Acoust. Soc. Am. **102**, 2984–2992.

Horri, Y., and Ryan, W.J. (**1981**). ''Fundamental frequency characteristics and perceived age of adult male speakers,'' Folia Phoniatr. **33**, 227–233.

Howie, J.M. (**1976**). *Acoustical Studies of Mandarin Vowels and Tones* (Cambridge U. P., Cambridge).

Huang, W.-R. (**1990**). *The Study of Tones in Min Dialect in Taiwan* (original publication is in Chinese) (Tzu Li Wan Pao Wen Hua Publisher, Taipei).

Hudson, A.I., and Holbrook, A. (**1981**). ''A study of the reading fundamental vocal frequency of young black adults,'' J. Speech Hear. Res. **24**, 197–201.

Linke, C. (**1953**). ''A study of the pitch characteristics of female voices and their relationship to vocal effectiveness,'' doctoral dissertation, University of Iowa, Iowa City.

Lynch, G.E. (**1934**). ''A phonophotographic study of trained and untrained voices reading factual and dramatic material,'' Arch. Speech **1**, 10–25.

Mcintosh, C. (**1939**). ''A study of the relationship between pitch variability in the voices of superior speakers,'' doctoral dissertation, University of Iowa, Iowa City.

Provonost, G. (**1942**). ''An acoustical study of the habitual and natural pitch levels of superior speakers,'' Speech. Monogr. **9**, 111–123.

Ramig, L.A., and Ringel, R.L. (**1983**). ''Effects of physiological aging on selected acoustic characteristics of voice,'' J. Speech Hear. Res. **26**, 22–30.

Saxman, J.H., and Burk, K.W. (**1967**). ''Speaking fundamental frequency characteristics of middle-aged females,'' Folia Phoniatr. **19**, 167–172.

Shen, X. (**1989**). ''Interplay of the four citation tones and intonation in Mandarin Chinese,'' J. Chin. Linguist. **17**, 61–73.

Snidecor, J.C. (**1943**). ''A comparative study of the pitch and duration characteristics of impromptu speaking and oral reading,'' Speech Monogr. **10**, 50–55.
Snidecor, J.C. (**1951**). ''The pitch and duration characteristics of superior female speakers during oral reading,'' J. Submicrosc. Cytol. **16**, 44–52.
Stoicheff, M.L. (**1981**). ''Speaking fundamental frequency characteristics of nonsmoking female adults,'' J. Speech Hear. Res. **24**, 437–441.
Ting, P.-H. (**1979**). *The Source of Dialects in Taiwan* (original publication is in Chinese) (Shyue Sheng Publisher, Taiwan).
Titze, I.R. (**1988**). ''Regulation of vocal power and efficiency by subglottal pressure and glottal width,'' in *Vocal Fold Physiology: Voice Production, Mechanisms, and Functions*, edited by O. Fujimura (Raven, New York), pp. 227–238.
Titz, I.R. (**1989**). ''Physiologic and acoustic differences between male and female voices,'' J. Acoust. Soc. Am. **85**, 1699–1707.
Titze, I.R., and Sundberg, J. (**1992**). ''Vocal intensity in speakers and singers,'' J. Acoust. Soc. Am. **91**, 2936–2946.
Tseng, C.-Y. (**1990**). *An Acoustic Phonetic Study on Tones in Mandarin Chinese* (Nankang Publisher, Taipei).
Yamazawa, H., and Hollien, H. (**1992**). ''Speaking fundamental frequency patterns of Japanese women,'' Phonetica **49**(2), 128–140.

A parametric model of the vocal tract area function for vowel and consonant simulation[a)]

Brad H. Story[b)]
Speech Acoustics Laboratory, Department of Speech and Hearing Sciences, University of Arizona, Tucson, Arizona 85721

(Received 1 May 2004; revised 20 January 2005; accepted 21 January 2005)

A model of the vocal-tract area function is described that consists of four tiers. The first tier is a vowel substrate defined by a system of spatial eigenmodes and a neutral area function determined from MRI-based vocal-tract data. The input parameters to the first tier are coefficient values that, when multiplied by the appropriate eigenmode and added to the neutral area function, construct a desired vowel. The second tier consists of a consonant shaping function defined along the length of the vocal tract that can be used to modify the vowel substrate such that a constriction is formed. Input parameters consist of the location, area, and range of the constriction. Location and area roughly correspond to the standard phonetic specifications of place and degree of constriction, whereas the range defines the amount of vocal-tract length over which the constriction will influence the tract shape. The third tier allows length modifications for articulatory maneuvers such as lip rounding/spreading and larynx lowering/raising. Finally, the fourth tier provides control of the level of acoustic coupling of the vocal tract to the nasal tract. All parameters can be specified either as static or time varying, which allows for multiple levels of coarticulation or coproduction. [DOI: 10.1121/1.1869752]

PACS numbers: 43.70.−h, 43.70.Bk, 43.71.Es [AL] Pages: 3231–3254

I. INTRODUCTION

During speech production, coordinated movements of the tongue, jaw, lips, and to some degree the larynx, continuously alter the shape of the vocal tract (i.e., pharynx and oral cavity). Movement of the soft palate varies the acoustic coupling of the vocal tract to the nasal passages, and also may slightly change the shape of the upper pharynx. Integrated actions of individual articulators facilitate the creation of time-varying acoustic resonances that transform the sound generated by vocal-fold vibration or turbulence, into the stream of vowels and consonants that comprises speech. Specifically, it is the articulators' collective effect on the variation in cross-sectional area along the length of the vocal tract (i.e., the *area function*) and coupling to the nasal tract, as well as other possible sidebranch cavities, that is most closely related to the pattern of acoustic characteristics expressed in the speech waveform.

Hence, a simplified view of speech production may consist of a tubular system whose cross-sectional area variation, as a function of time, emulates that of a real vocal tract. This view forms the basis of a certain class of speech production models that operate on a parametric representation of the vocal-tract area function, and allow for calculation of corresponding acoustic characteristics. Area function models contrast with ''articulatory'' models in which the positions of individual articulators or some form of vocal-tract shaping components are represented in the midsagittal plane (e.g., Lindblom and Sundberg, 1971; Coker, 1976; Mermelstein, 1973; Maeda, 1990; Dang and Honda, 2004). These are intuitively appealing because of the physiological correlation between model parameters and human articulatory structures, and their ability to replicate observed articulatory movement. As a result, articulatory-type models are well suited for investigating and establishing speech motor control strategies. The relation of the articulatory parameters to the acoustic characteristics is, however, typically mediated by an empirically based conversion of midsagittal cross dimensions to the area function. Hence, control of the detailed vocal-tract shape at the level of cross-sectional area is less direct than with an area function model. A possible exception is a recently developed model that utilizes midsagittally based control parameters, but avoids the cross-dimension transformation to area by generating vocal-tract shapes based on three-dimensional data obtained from MRI (Badin *et al.*, 1998; Badin *et al.*, 2002).

Though admittedly an abstraction of articulatory reality, the area function is the representation that does provide the most direct theoretical connection between vocal-tract shape and resulting acoustic characteristics. A parametric model of the area function is useful for situations in which precise control of the detailed structure of the vocal-tract shape is desired. For example, such a model may have applications in studying source–tract interactions (Ishizaka and Flanagan, 1972; Titze and Story, 1997), investigating relations between vocal-tract structure and acoustic characteristics that are relevant to phonetic categories (e.g., Fant, 1960; Stevens, 1989) and voice quality (Story, Titze, and Hoffman, 2001; Story and Titze, 2002; Story, 2004), and understanding tract length scaling effects (e.g., Nordström, 1977; Goldstein, 1980; Fitch and Giedd, 1999). In addition, an area function model can be an essential component in synthesizing high-quality speech

[a)]A preliminary version of this paper was presented at the 146th Meeting of the Acoustical Society of America.
[b)]Electronic mail: bstory@u.arizona.edu

for presentation to listeners in perceptual tests when vocal-tract variables are the quantities to be manipulated rather than acoustic characteristics. There are also possible technological applications of synthesis based on area functions (Shadle and Damper, 2001; Sondhi, 2002).

The most straightforward form of an area function model (but perhaps the most inefficient) consists of a direct specification of the cross-sectional areas extending from the glottis to the lips. The parameters in this case are simply the areas themselves. Variation over time requires interpolation from one complete area function (representing one phonetic element) to another. In this approach, area data obtained from imaging studies (e.g., Fant, 1960; Narayanan, Alwan, and Haker, 1995; Story, Titze, and Hoffman, 1996; Baer *et al.*, 1991) can be used directly, but the ability to create realistic time-varying vocal-tract shapes (i.e., area functions that did not exist in the original data set) is limited.

Specification of the area function with a small set of physiologically relevant parameters forms the basis for more parsimonious models. Examples are the well-known ''three-parameter'' models (Fant, 1960; Stevens and House, 1955), where the constriction location X_c (distance from glottis or lips to the constriction) and area A_c are specified along with a ratio of the length of the lip opening to its area (l/A). The areas corresponding to the tongue section are determined by a continuous mathematical function (e.g., parabola) constrained by the three parameters. To be more flexible in the variety of shapes that can be generated, these models have been modified in various ways. Atal *et al.* (1978) extended the number of parameters to five, whereas Lin (1990) incorporated separate continuous functions for the back and front cavities.

Another type of area function model was proposed by Mrayati, Carré, and Guérin (1988), where the parameters were derived purely from acoustic considerations. The vocal tract was divided into separate (distinct) regions, each of which has a sensitivity to formant frequency change that is predictably related to an increase or decrease in cross-sectional area of a particular region. To control the first three formant frequencies, the cross-sectional area of eight regions of unequal length must be specified as parameters. This model is perhaps less interpretable than the previous ones in terms of articulation, but is interesting in the sense that sufficient control parameters could be derived in the absence of articulatory knowledge.

An eventual goal of developing a parametric area function model is to accurately reproduce connected speech. That is, speech created by a vocal tract whose shape alternates between those of vowels and consonants or from one vowel to another. Whereas the models discussed previously are most relevant for vowel articulations (consonant characteristics are not specifically parametrized), it is conceivable that they could be modified or extended to create consonant-like vocal-tract shapes (Lin, 1990), perhaps by allowing the minimum area to approach or become zero. Simulation of connected speech would then be carried out by interpolating a sequence of parameter values over the time course of an utterance. A linear sequencing of vowel and consonant events, however, is limited in its representation of coarticulation in natural speech. For instance, a spectrographic study of vowel–consonant–vowel (VCV) syllables led Öhman (1966) to suggest that a consonant gesture (constriction) is superimposed on an underlying vowel substrate. He concluded that ''A VCV utterance of the kind studied here can, accordingly, not be regarded as a linear sequence of three successive gestures.'' The implication is that speech proceeds as a series of independently controlled vowel-to-vowel transitions, interrupted by superposition of consonant perturbations (Fujimura, 1992). Öhman (1967) subsequently proposed a model that allowed for interpolation of the midsagittal cross distance (width) of one vowel shape to another, over the time course of a syllable. Simultaneously, a consonant constriction function was activated to a degree that also varied over the same time course as the vowel component. At each successive point in time, the consonantal function was superimposed on the modeled vowel substrate to produce a composite tract shape. This view contrasts somewhat with that of Kozhevnikov and Chistovich (1965), who suggested that the consonant–vowel syllable (or C_n V, where *n* denotes multiple consonants) is the primary domain over which coarticulation occurs. In other words, the vocal-tract shape for a consonant or consonant cluster is significantly influenced by the articulatory characteristics of the following vowel, but less so due to the preceding vowel. In either case (and based on much research of coarticulatory processes), it is apparent that the vocal-tract shape at any point in time will be affected by the articulatory demands of adjacent vowels and consonants. Hence, an area function model must be capable of representing and combining the influences of consecutive articulatory events.

Öhman's (1966, 1967) paradigm has influenced various control strategies for articulatory and area function types of models. As discussed by Mattingly (1974), Nakata and Mitsuoka (1965), and Ichikawa and Nakata (1968) implemented the idea of superimposing a consonant on a vowel–vowel transition in a rule-based speech synthesizer. Similarly, Båvegård (1995) and Carré and Chennoukh (1995) have both reported vocal-tract area function models where consonant constrictions are superimposed on an interpolation of a vowel-to-vowel transition. In addition, Browman and Goldstein's (1990) development of ''articulatory phonology'' seems also to be motivated, at least in part, by Öhman's work. In their view, speech is produced by a series of overlapping gestures created by activation of ''tract variables'' such as constriction location and degree of the tongue body and tip.

The purpose of this paper is to describe a kinematic model of the vocal-tract area function that is loosely based on Öhman's concept of a vowel substrate and superposition of a consonantal perturbation. The structure of the model is defined by four perturbation ''tiers,''[1] (see Fig. 1) that together generate a composite time-varying area function. The starting point is a ''neutral'' area function, defined as a vocal-tract shape that produces nearly equally spaced formant frequencies. In tier I, deformation patterns extending from glottis to lips perturb the neutral area function into a specific vowel-like shape, thus forming the vowel substrate. A superposition function is generated in tier II that alters the shape

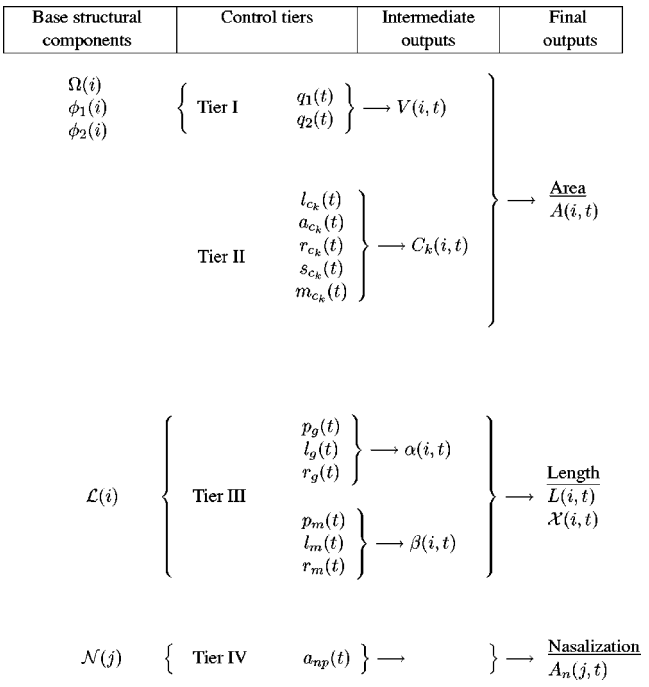

FIG. 1. Diagram of the four-tier area function model. Tier I produces a vowel substrate and tier II generates a superposition function for a consonant. Vocal-tract length changes are generated by tier III, and nasal coupling in tier IV. The ''base structural components'' are dependent only a spatial dimension, whereas the ''final outputs'' are dependent on both space and time.

of the vowel area function in specific regions along the vocal-tract length in order to produce consonantal constrictions. Perturbations of the vocal-tract length can be imposed by tier III, whereas a fourth tier incorporates control of the coupling of the vocal tract to the nasal passages. The parameters within each tier can be time varying; hence, the area function at any instant of time is represented as the combination of the vowel substrate, a superimposed consonantal element, possible lengthening or shortening of various portions of the vocal-tract length, and nasalization. The model is also intended to be flexible enough for easy interchange of components that are characteristic of different speakers. That is, the structure of the underlying vocal tract can be specified independently of the model parameters.

The model is presented here to establish a framework for (1) future studies of the relation between vocal-tract shape and acoustics for connected speech; (2) generating stimuli for perceptual experiments based on manipulation of area function parameters; and (3) eventually producing sentence-level synthetic speech. The specific aim of this paper is limited to a description of the parameters within each of the four tiers and their functional relation to the underlying model. Demonstrations of time-varying area functions and their corresponding acoustic characteristics are also included to verify the concept.

II. AREA FUNCTION MODEL

A schematic representation of the four-tier model is shown in Fig. 1 and descriptions of the components and parameters are given in the Nomenclature. In the first column of the figure are structural components of the vocal tract used to build the foundation of the model. In tiers I and III, these components depend only on the distance from the glottis, as represented by the index *i*, and are modified (by substitution) only if a different speaker's vocal-tract characteristics are desired. The index variable i extends from 1 to N_{vt}, where the area function is assumed to contain N_{vt} cross-sectional areas, concatenated as ''tubelets'' and ordered consecutively from glottis to lips. Similarly, a length function will contain N_{vt} sections representing the length of each tubelet in the area function. Other components of the model contributing to the area or length functions must also contain this same number of sections. Throughout this paper, area functions and associated components contain $N_{vt}=44$ sections.[2] The morphological representation of the nasal tract operates on a different index system *j*, in which the cross-sectional areas are ordered from the point of vocal-tract coupling to the nares.

The control parameters for each tier, shown in the second column of Fig. 1, are used to transform the structural elements (in column 1) into a vocal tract whose shape can be varied over time. Tiers I and II generate time-dependent *area* perturbations in the form of the vowel substrate $V(i,t)$ and consonantal superposition functions $C_k(i,t)$. Together, they produce the composite area function

$$A(i,t)=V(i,t)\prod_{k=1}^{N_c} C_k(i,t) \quad i=[1,N_{vt}], \tag{1}$$

where N_c is the number of consonantal functions. For many cases, only one consonantal function is needed to impose the appropriate constriction. Multiple functions are necessary in cases where simultaneous constrictions may occur. For example, during the production of a consonant cluster such as [sp], there would be a period of time where both the tongue tip and lips are involved in the creation of two separate constrictions. As will be shown in a later section, all C_k's have exactly the same mathematical form, but the control parameters allow for specification of different characteristics of the constriction.

The third tier facilitates *length* perturbations at the glottal and lip ends of the vocal tract. The output is the time-varying composite length function $L(i,t)$, and contains N_{vt} elements representing the length of each tubelet in the area function at a specific instant of time. A cumulative length function $\mathcal{X}$ representing the actual distance from the glottis can be derived from L as

$$\mathcal{X}(i,t)=\sum_{z=1}^{i} L(z,t) \quad i=[1,N_{vt}]. \tag{2}$$

Nasalization is controlled by the fourth tier. At this point, the only parameter is the time-dependent area of the nasal port. It is assigned to a separate tier (rather than embedding it in tiers I or II) to allow acoustic coupling to the nasal tract for either nasal consonant production or nasalization of vowels. Other parameters may be included in the future that more adequately account for the shape of the velopharynx, location of the coupling port, or other changes that may occur during speech production. Additional ''side-branches,'' such as the piriform sinuses and sublingual cavities, also contribute to the overall acoustic character of

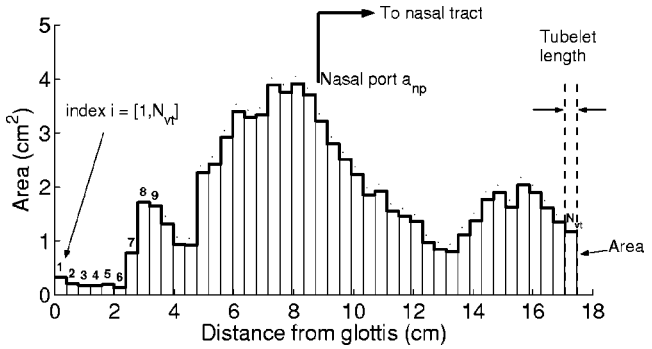

FIG. 2. Example of an area function. It is shown here as a succession of tubelets, denoted by the index *i*, extending from just above the glottis to the lips. Coupling to the nasal passages is indicated by the area a_{np}.

speech. They are not, however, currently included in this model.

An example area function is shown in Fig. 2. It is plotted in stair-step fashion to demonstrate the concatenation of tubelets along the vocal-tract length. Each tubelet has a cross-sectional area as shown by its vertical extent on the *y* axis, and a length as indicated for the *N*th tubelet on the right side of the graph. Note that the index *i* corresponds to the tubelet number; for brevity, these numbers are shown only above the first nine sections. The *x* axis, however, is shown as "distance from the glottis" in units of centimeters, which results from using Eq. (2) to generate the cumulative length function [i.e., $A(i)$ has been plotted against $\mathcal{X}(i)$]. True distance units can be assigned to the *x* axis of the area function and associated perturbation functions, but many of the figures in subsequent sections will simply use *i* as the *x* axis. The nasal coupling location is indicated to be at approximately section 22, or 8.7 cm from the glottis.

It is noted that 14 time-varying control parameters are specified in this model (see column 2 in Fig. 1 and the Nomenclature). Relative to some existing area function models, this is a relatively large number of parameters for which to specify accurate time variations. As will be shown in subsequent sections, however, the parameters do support a precise description of the area function and allow a wide range of flexibility for specifying how the tract shape changes over time. The model has also been designed so that tiers II, III, and IV can be effectively removed, if desired, by setting the parameters to constant values. To model, for example, constant-length, non-nasalized, vowel–vowel transitions, $m_{c_k}(t)$, $L_m(t)$, $L_g(t)$, and $a_{np}(t)$ could be set to zero and all of the other parameters in their respective tiers would become irrelevant, essentially reducing the model to the two parameters in tier I. Similarly, any of tiers II, III, or IV could be utilized independently of the others by providing appropriate parameter values. Eventually some parameters may be found to covary and would not necessarily require a separate specified time variation. For instance, the constriction range $r_{c_j}(t)$ and skewing quotient $s_{c_j}(t)$ are likely to be related to the constriction location $l_{c_j}(t)$; hence, three parameters could perhaps be collapsed into one.

A. Tier I: Vowel substrate

The first tier is based on previous work where a principal components analysis was used to decompose a speaker-specific collection of vowel area functions into a neutral tract shape and a set of basis functions, referred to as *modes* (Story and Titze, 1998). The modes perturb the neutral tract shape according to the following equation:

$$V(i,t)=\frac{\pi}{4}[\Omega(i)+q_1(t)\phi_1(i)+q_2(t)\phi_2(i)]^2$$

$$i=[1,N_{vt}], \tag{3}$$

where the sum of the terms in brackets represents a set of diameters extending from the glottis to the lips. The squaring operation and scaling factor of $\pi/4$ converts the diameters to areas. $\Omega(i)$ is referred to as a neutral diameter function[3] and $\phi_1(i)$ and $\phi_2(i)$ are the modes. The time-dependent parameters $q_1(t)$ and $q_2(t)$ are coefficient values that, when multiplied by the corresponding mode and added to the neutral diameter function as in Eq. (3), construct a desired vowel. The modes have been shown to capture aspects of vowel articulation that allow the model to produce vocal-tract shapes whose acoustic characteristics span a typical $F1-F2$ vowel space (Story and Titze, 1998). Note that when $q_1=q_2=0$, the area function specified as $(\pi/4)\Omega^2(x)$ is expected to produce nearly equally spaced formant frequencies, hence the name "neutral."

This form of the vowel substrate was developed with the assumption that $\Omega(i)$, $\phi_1(i)$, and $\phi_2(i)$ could be derived from an adequate inventory of *any* speaker's vocal-tract area functions. Thus, different speakers' vocal tracts could be modeled by simply interchanging these components. Preliminary data supportive of this assumption were presented in Story (2002), but future analyses of additional MRI-based area function data will need to be performed for verification of the concept, and to provide vowel substrate components for other speakers. The remainder of this paper will utilize the $\Omega(i)$, $\phi_1(i)$, and $\phi_2(i)$ based on MRI-obtained area functions for a single male speaker (Story *et al.*, 1996). They are given in numerical form in Appendix A.

B. Tier II: Consonant perturbation function

The purpose of the second tier is to generate perturbation functions $C_k(i,t)$ that, when multiplied element-by-element with $V(i,t)$, superimpose consonant constrictions on the vowel substrate. The parameters in this tier are the location, area, range, and skewness of the constriction. Location and area roughly correspond to the standard phonetic specifications of place and degree of constriction, whereas the range defines the amount of vocal-tract length over which the constriction will influence the tract shape. The skewness parameter allows for constriction asymmetry along the tract length dimension. An additional parameter is the constriction "magnitude," which is the means by which the constriction is activated or deactivated. Whereas multiple consonant superposition functions $C_k(i,t)$ can be generated [see Fig. 1 and Eq. (1)], they are mathematically identical and their

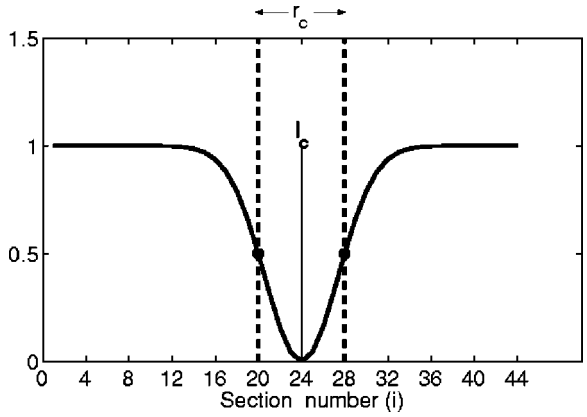

FIG. 3. Example consonantal superposition function $C(i)$ corresponding to Eq. (4). In this case $l_c=24$ and $r_c=8$.

implementation requires only separate specification of the parameters. Hence, only a single constriction will be addressed in the following formulation.

The perturbation has been implemented mathematically with a Gaussian function of the basic form

$$C(i)=1-e^{-\ln(16)[(i-l_c)/r_c]^2}, \tag{4}$$

where l_c is the constriction location. The parameter r_c is the range, and is defined to be the distance between points along the vocal-tract length where the consonant function $C(i)$ is equal to 0.5. This is assured by use of the constant ln (16). In this particular formulation, the parameters must be specified in terms of the index i; however, i could be substituted with $\mathcal{X}(i)$ [Eq. (2)] so they could be specified in actual units of distance. The function will have a value of zero at the point where $i=l_c$, and will asymptotically approach 1.0 on either side of this point. An example is shown in Fig. 3 for the case of $l_c=24$ and $r_c=8$. $C(i)$ is equal to 1 for $i=[1,12]$, after which it decreases continuously and becomes zero at $i=24$ (i.e., $i=l_c$). At locations $i>24$, $C(i)$ gradually increases back to a value of 1. Note that $C(i)=0.5$ at both $i=20$ and $i=28$, due to the range setting of $r_c=8$.

The Gaussian formulation is straightforward to implement and control because it asymptotically returns to the desired value of 1.0 away from the constriction location. Other functions, such as a cosine, can also be used to create the constriction. These, however, require a piecewise concatenation of linear segments with the cosine to complete the function along the entire length of the tract. Also, care must be taken to ensure that a cosine function behaves properly when the constriction location is near the glottal or lip ends. As partial verification, it will be shown in a later section that a Gaussian-based function, superimposed with the vowel substrate, can reasonably approximate consonant area functions obtained directly from imaging experiments.

To accommodate additional parameters for controlling the shape and timing of the constriction, Eq. (4) can be modified to take the form

$$C(i,t)=\begin{cases}1-m_c(t)d_c(t)e^{-\ln(16)([i-l_c(t)]/[r_{cb}(t)])^2} & \text{for } i<l_c(t)\\ 1-m_c(t)d_c(t)e^{-\ln(16)([i-l_c(t)]/[r_{cf}(t)])^2} & \text{for } i>l_c(t).\end{cases} \tag{5}$$

In this equation, $d_c(t)$ is considered to be the "degree" of the constriction, and is determined by the ratio of the desired cross-sectional area $a_c(t)$ at the point of maximal constriction, to the area of the vowel substrate at the location $l_c(t)$ at some specific instant of time. It is calculated by

$$d_c(t)=1-\frac{a_c(t)}{V(l_c(t),t)}. \tag{6}$$

When $a_c(t)$ is equal to zero, $d_c(t)$ will be 1, as was the case implicitly in Eq. (4). But, $a_c(t)$ can also be assigned a value greater than zero to allow for a constriction that does not occlude the vocal tract, as would be necessary for production of fricative and affricate consonants.[4] The parameters $r_{c_b}(t)$ and $r_{c_f}(t)$ in Eq. (5) are determined from the previously defined range $r_c(t)$, *and* a skewing quotient $s_c(t)$

$$r_{c_f}(t)=\frac{s_c(t)r_c(t)}{1+s_c(t)}, \tag{7}$$

$$r_{c_b}(t)=\frac{r_c(t)}{1+s_c(t)}. \tag{8}$$

When $s_c(t)=1$, the total range is distributed equally upstream and downstream of the constriction location, creating a symmetric superposition function. A skewing quotient that is less than or greater than 1 will distribute the specified constriction range asymmetrically around $l_c(t)$, which may be needed to adequately represent some consonant shapes. Shown in Fig. 4 are two examples of $C(i)$ that were generated with different skewing quotients. In both cases, the constriction location is $l_c=24$ and the range was set to $r_c=8$. The first case [Fig. 4(a)] is for a skewing quotient of $s_c=0.3$, where a larger portion of the range is distributed to the downstream side (toward the lip end) of the constriction location. In the second case [Fig. 4(b)], $s_c=3$, and the distribution of the range is reversed; a larger portion of the range is to the upstream side of the constriction location.

The parameter $m_c(t)$ in Eq. (5) is the "magnitude" of the consonant and serves primarily as a timing function to activate and deactivate the consonantal perturbation. In a sense it can be considered a switch, albeit continuous, that allows the constriction to be formed, more or less, depending on its value at a specific point in time. If $m_c(t)=0$, the consonant perturbation is effectively removed because $C(i,t)$ will have a value of 1 over the entire length of the vocal tract, regardless of the other parameter values. In contrast, when $m_c(t)=1$ the cross-sectional area of the constriction specified by $a_c(t)$ is fully realized in the area function. To simulate connected speech at the syllable or word level, $m_c(t)$ would need to continuously vary between zero and 1 to impose and remove consonants at the appropriate instants of time. If $m_c(t)$ is constrained to a maximum value of 1, however, the constriction area will only be realized over

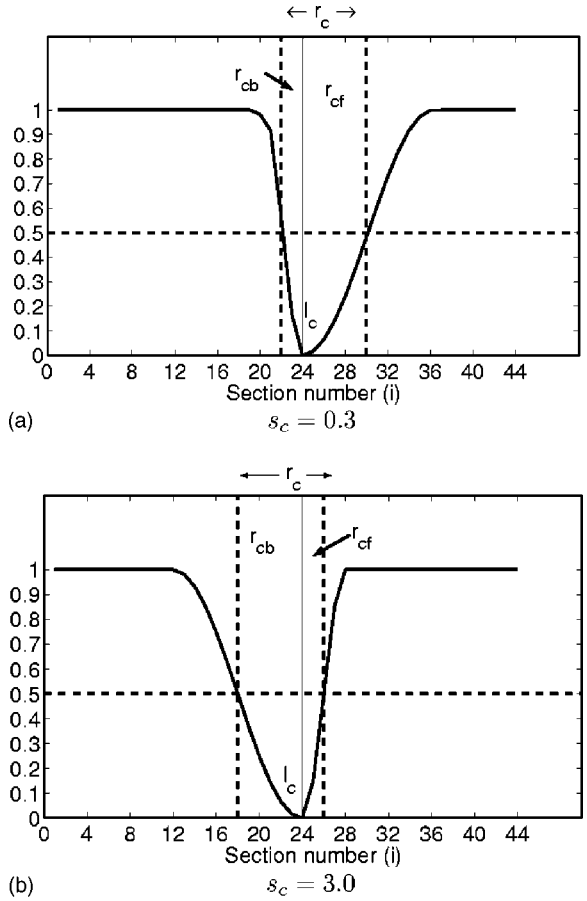

FIG. 4. Demonstration of consonantal superposition functions with asymmetries as specified by the skewing quotient s_c. Both functions were generated with Eq. (5), where $l_c=24$, $a_c=0$, $r_c=8$, and $m_c=1$. (a) Superposition function for $s_c=0.3$. (b) Superposition function for $s_c=3.0$.

a single section along the tract length (i.e., the area of tubelet that is closest to l_c will be zero). For many constriction articulations, an occlusion created by the tongue and lips may consume a larger portion of the tract length than a single tubelet section. Thus, $m_c(t)$ is allowed to exceed 1.0 to force the cross-sectional areas of several consecutive tubelets to be zero, if necessary. With the condition

$$C(i,t)=\max[C(i,t),0], \tag{9}$$

the constriction may be ''spread'' over a greater portion of the vocal-tract length.

An example combination of a single constriction perturbation and vowel substrate is shown in Fig. 5 for a static case (not time dependent). The vowel has been set to the neutral shape $V(i)=(\pi/4)\Omega^2(i)$, and the consonant parameters are, $l_c=24$, $a_c=0$ cm^2, $r_c=8$, $s_c=0.5$, and $m_c=1.1$, where the location and range are specified in terms of the index *i*. The figure contains three plots: the vowel is at the top, the consonant perturbation is in the middle, and the composite area function $A(i)=V(i)C(i)$ is at the bottom. It is observed that $A(i)$ retains the shape of the vowel, except in those sections where the consonant function is less than 1. In these sections the characteristics of both the vowel and the consonant perturbation are expressed in the final output. Note that setting $m_c=1.1$ causes the area to be zero over approximately four sections, effectively spreading the constriction.

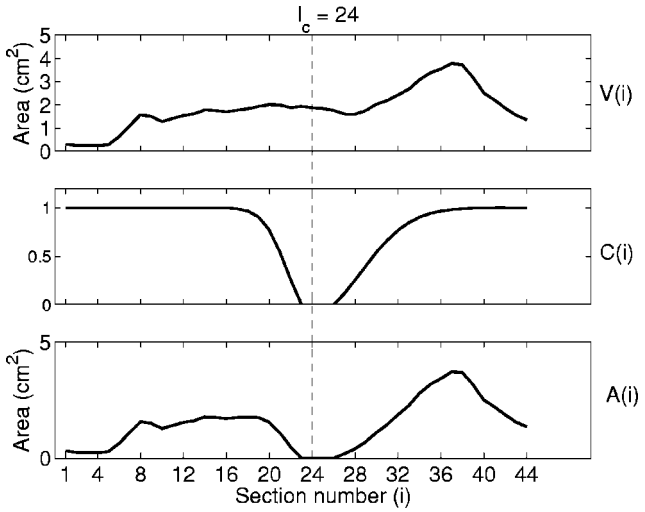

FIG. 5. Combination of the output from tier I and tier II for the case when $q_1=q_2=0$, $l_c=24$, $a_c=0$, $r_c=8$, $s_c=0.5$, and $m_c=1.1$. The top panel shows $V(i)$, the middle panel is $C(i)$, and the bottom panel shows the element-by-element product $A(i)=V(i)C(i)$.

C. Tier III. Length perturbation function

Length modifications are generated in tier III with two superposition functions, similar to those for the consonant constrictions. They are superimposed on a length vector and are designed to either increase or decrease the length of specified portions of the vocal tract.

A nominal or base length vector (length of each tubelet in the area function) consists of N_{vt} *equal* elements

$$\mathcal{L}(i)=\Delta \quad \text{for} \quad i=[1,N_{vt}], \tag{10}$$

where Δ = the tubelet length.[5]

The first function, $\alpha(i,t)$, is intended to produce a length modification near the glottal end of the vocal tract, roughly corresponding to a lowering or raising of the larynx. The function is written as

$$\alpha(i,t)=1+\frac{p_g(t)e^{-K([i-l_g(t)/[2r_g(t)])^2}}{\Delta\Sigma_{i=1}^{N_{vt}}e^{-K([i-l_g(t)]/[2r_g(t)])^2}} \quad i=[1,N_{vt}], \tag{11}$$

where $p_g(t)$ is the amount of larynx lowering ($p_g<0$) or raising ($p_g>0$). The denominator in the second term of the equation is a scaling factor that allows $p_g(t)$ to be specified in actual units of distance (e.g., centimeters). The parameter $l_g(t)$ is the location within the length vector where the length change is centered and maximal. It *must* be specified in terms of the index *i*, much like the constriction location in Eq. (5). The parameter $r_g(t)$ is the number of elements within the length vector over which the length change is distributed. The constant K is set to a value of $2\ln(10\,000)$ to ensure that the length change affects only the number of elements specified by $r_g(t)$. A length perturbation function near the lip end of the vocal tract is needed to represent retraction or protrusion of the lips. Mathematically, this is performed with a function identical to that at the glottal end, except the parameter subscripts are changed. Thus

$$\beta(i,t)=1+\frac{p_m(t)e^{-K([i-l_m(t)]/[2r_m(t)])^2}}{\Delta\Sigma_{i=1}^{N_{vt}}e^{-K([i-l_m(t)]/[2r_m(t)])^2}} \quad i=[1,N_{vt}], \tag{12}$$

where $p_m(t)$ is the amount of lip retraction ($p_m<0$) or protrusion ($p_m>0$) specified in units of distance, $l_m(t)$ is the location where the length change is centered, $r_m(t)$ is the extent over which the length change is distributed, and $K=2\ln(10\,000)$. Typically, the settings for l_g and l_m are 1 and N_{vt}, respectively, so that the maximal length change occurs at the extreme ends of the vocal tract. Equations (11) and (12) are general enough, however, that l_g and l_m can be set to any location along the vocal tract. The perturbed length function is calculated as the product

$$L(i,t)=\mathcal{L}(i)\alpha(i,t)\beta(i,t), \tag{13}$$

resulting in a new length vector with N_{vt} elements, representing modified tubelet lengths.

As a demonstration, length changes of $p_g=-1$ cm at the glottal end, and $p_m=+2.0$ cm at the lip end, were generated with the length perturbation functions. The locations of maximal length change were $l_g=1$ and $l_m=44$, while both r_g and r_m were set equal to 8. The product of $\alpha(i,t)\beta(i,t)$ alone is shown in Fig. 6(a), where it is less than 1 at the glottal end for the decrease in length, equal to 1 from $i=9$ to $i=35$ for no length change, and greater than 1 near the lips to increase the length. The composite length function $L(i,t)$ is plotted in Fig. 6(b). It has an identical shape to that in Fig. 6(a), but the amplitude has been scaled by the nominal length vector. Thus, the plot shows the tubelet length for every element of the length function. The effect of the modified length vector on an area function is shown in Fig. 6(c). It is plotted in stair-step form as a function of distance measured from the *middle* of vocal-tract length, so that the increase or decrease in tubelet length can be easily observed. The lip protrusion can be seen at the right side of the plot, where the length of the lip end of the vocal tract has been increased by 2 cm. The contributions to this overall change come from the gradual length increases of tubelets 36 to 44, where the maximum change is at tubelet 44. The length change at the glottal end can be seen at the left side of Fig. 6(c), where the lengths of tubelets 1 to 8 have been shortened to create the 1 cm reduction in length.

D. Tier IV: Nasalization

As shown previously in Fig. 1, the cross-sectional area of the nasal port is the sole parameter in tier IV. In this simple implementation, it is assumed that the area function of the nasal tract is essentially static (unchanging) during speech production except for the nasal port area $a_{np}(t)$. Other than the first section, the basic cross-sectional area morphology of the nasal tract contained in base function $\mathcal{N}(j)$ (e.g., Dang and Honda, 1994; Story, 1995) will essentially pass unchanged through tier IV to the final output as $A_n(j,t)$. The first section, $A_n(1,t)$, is set equal to the coupling area $a_{np}(t)$ and will be zero, except during production of nasal consonants and nasalized vowels. Although beyond the scope of the present study, cross-sectional area changes in the velopharynx and main vocal tract when the nasal port is open could be more accurately represented by including additional parameters (e.g., Maeda, 1982). Volumetric imaging studies of nasal consonants and nasalized vowels would be an ideal method for providing data to establish the appropriate parametric representation.

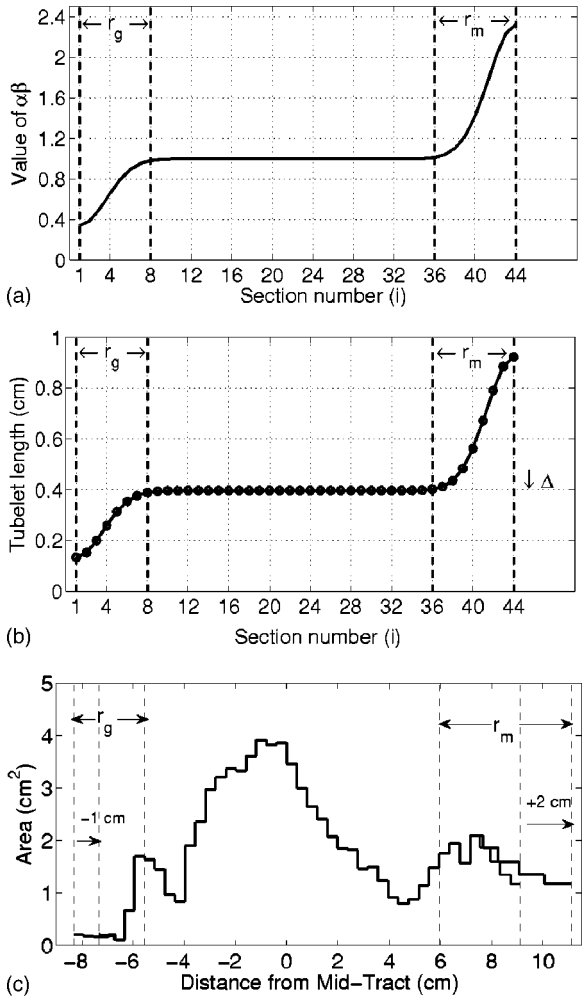

FIG. 6. Example of vocal-tract length change produced by tier III, based on Eqs. (11), (12), and (13). Parameter p_g, representing length change at the glottal end, was -1 cm, and p_m, representing length change at the lip end, was $+2$ cm. The range at both ends (r_g and r_m) was set to be 8 sections. (a) Product of $\alpha(i,t)\beta(i,t)$; (b) length function $L(i,t)$; (c) effect of modified length vector on an area function. The x axis is shown as distance from the center of the vocal-tract length so that length changes at both ends of the vocal tract can be easily observed.

III. STATIC CONSONANTS

A. Stops, nasals, and fricatives

Consonant area functions measured with MRI were reported by Story *et al.* (1996) for the same speaker on which the ''modes'' in Appendix A are based. In addition, four fricative area functions were collected at the same time, but have not been previously published. They are given in numerical form in Appendix B. All were ''static'' consonant shapes because the image acquisition methods required the speaker to maintain a particular vocal-tract configuration for approximately 10 seconds, and repeat it numerous times. Image sets for consonants with an occlusion of the vocal tract were necessarily acquired in their voiceless form, but it is

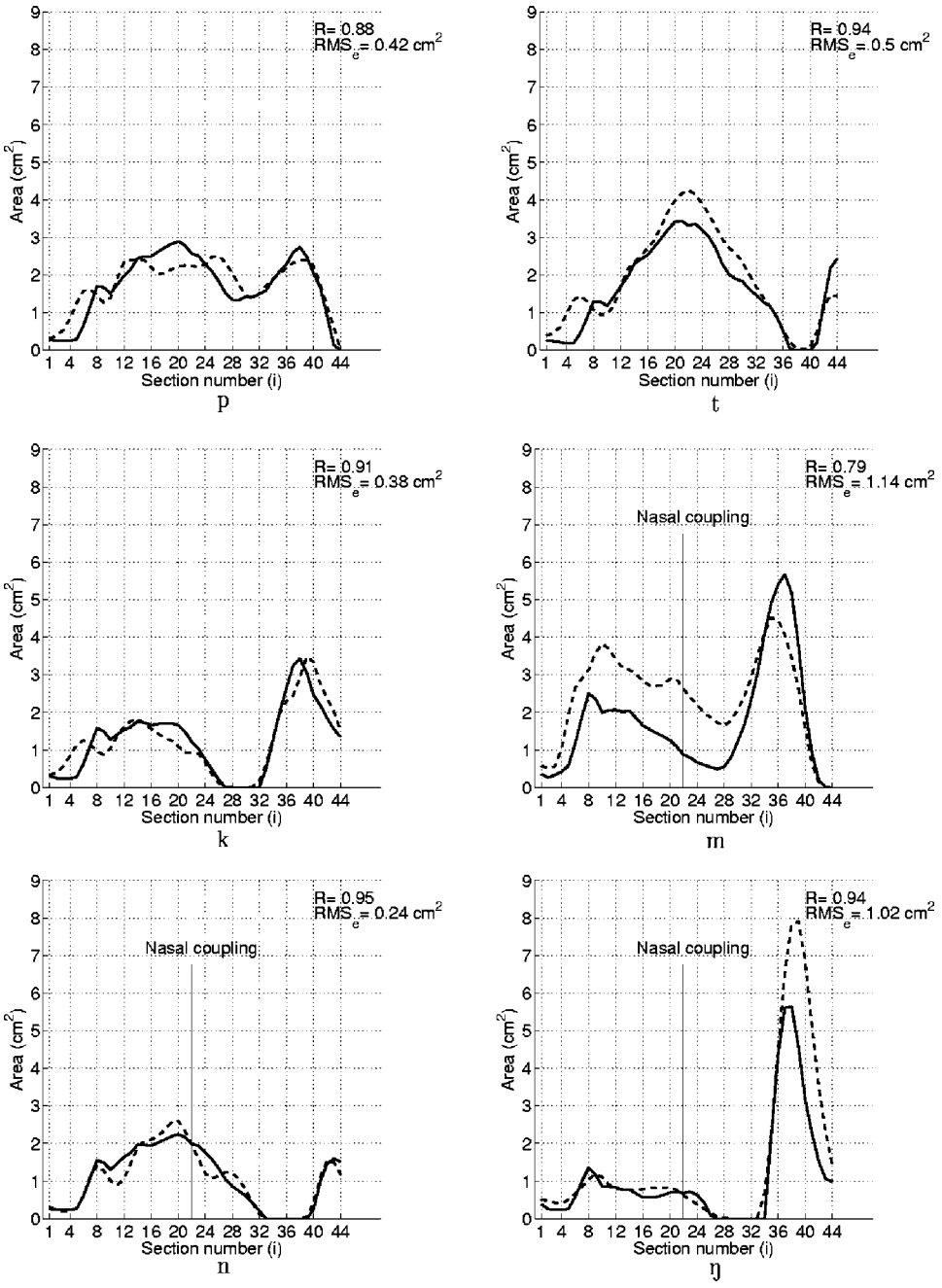

FIG. 7. Comparison of measured area functions (dashed lines) for six consonants with those generated by the area function model (solid lines). In each plot, a correlation coefficient and the rms error is shown at the upper right-hand corner, providing an indication of the fit between measured and modeled area functions. The model parameters for each consonant are given in Table I. For the three nasal consonants, the coupling point between the vocal tract and nasal passages is indicated with a vertical line. Each measured area function shown in this figure has been smoothed prior to fitting the model parameters.

assumed that these tract shapes could be used to guide the synthesis of either a voiced or voiceless consonant. In an attempt to create a neutral vowel context, the speaker was also asked to produce each consonant as if it were preceded and followed by a schwa [ə]. Under these conditions, the resulting area functions do not provide information about coarticulation, but they do specify the constriction location and spatial variations for a variety of consonants. Throughout this section, the measured consonant area functions are used to test the ability of the model described in Sec. II to generate area functions suitable for consonant production. Because the area functions are static, the time dependence of the parameters will be eliminated for the following explanation.

Model parameters for each consonant were first adjusted with an optimization algorithm until a ''best fit'' was determined by minimizing the squared difference between the area functions generated by the model and obtained from measurement. Additional manual tuning was needed to ensure that the portion of the area function dominated by the constriction was fit closely. Comparisons of the original measured and modeled area functions are shown in Figs. 7 and 8. From observation, the fit of the model to the measured consonants appears to be reasonably good, at least in the region of the constrictions. The gross shape in the portions of the area function away from the constrictions also appears well represented in most cases, although there are some large local deviations. For [m] and [f], the model captures the appropriate shape variation along the tract length, but the actual areas were considerably different.

To provide an assessment of the similarity of the area function shape produced by the model parameters relative to

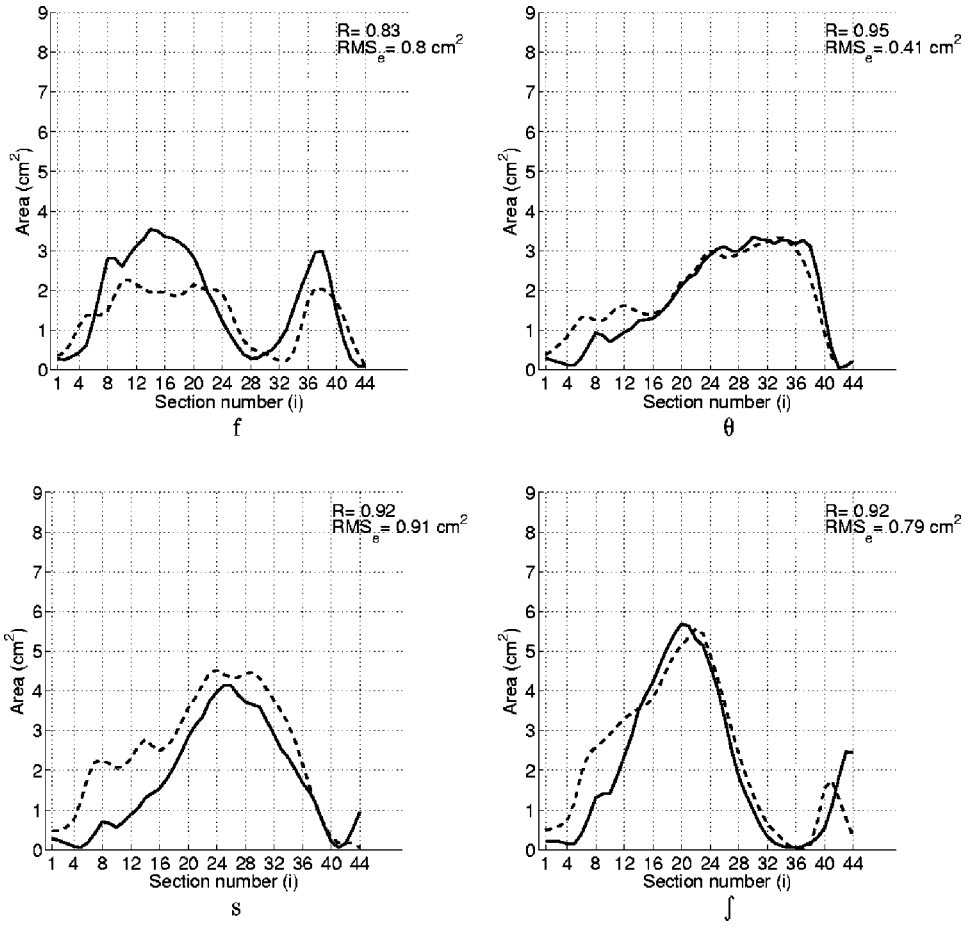

FIG. 8. Comparison of measured area functions (dashed lines) for four fricative consonants with those generated by the area function model (solid lines). Again, in each plot, a correlation coefficient and the rms error is shown at the upper right-hand corner, providing an indication of the fit between measured and modeled area functions. The model parameters for these consonants are also given in Table I and each measured area function shown in this figure has been smoothed prior to fitting the model parameters.

the original measurements, a correlation coefficient (R) was calculated for each pair of measured and modeled area functions. The calculation was performed by dividing the covariance of a given pair of area functions by the product of their standard deviations (e.g., Taylor, 1982). As an indication of the absolute differences in cross-sectional area between each measured and modeled pair of area functions, an rms error was also calculated. The correlation coefficients and rms values are shown at the upper-right side of each plot in Figs. 7 and 8. For seven of the ten consonants $R>0.9$, indicating that the overall shapes of the model-generated area functions were well correlated with the measured versions. The other three consonants generated with the model are somewhat less correlated with $R=0.88$, 0.79, 0.83, for [p], [m], and [f], respectively. The maximum rms error was 1.14 cm^2 for [m], and the minimum was 0.24 cm^2 for [k]. The rms error was generally lowest for the consonants with high correlation coefficients. The exception was [ŋ], for which $R=0.95$ and the rms error was 1.02 cm^2.

Parameter values for each consonant resulting from the optimization process are given in Table I. These data are arranged in three groups consisting of stops, nasals, and fricatives. Within each group they are ordered in terms of their location within the vocal tract. The consonants with a complete occlusion of the vocal tract ([p,t,k,m,n,ŋ]) all required the magnitude setting m_c to be greater than 1. This is to account for the extended region within these area functions where the constriction area a_c is zero. In addition to the

TABLE I. Model parameter values for consonantal area functions.

Consonant	q_1	q_2	l_c (i)	a_c (cm^2)	r_c (i)	s_c	m_c	a_{np} (cm^2)
p	−1.5	0.5	44	0.0	4	1	1.1	0
t	−1.5	2.0	39	0.0	6	1.1	1.3	0
k	0.0	0.0	30	0.0	10	1.5	1.2	0
m	0.0	−3.0	44	0.0	4	1	1.1	1.04
n	−0.5	0.4	38	0.0	11	3	1.3	1.09
ŋ	3.0	−1.0	31	0.0	8	1.5	2.0	1.26
f	−3.0	−2.0	43	0.1	4	1.0	1.0	0
θ	1.0	2.0	42	0.05	9	0.3	1.0	0
s	0.5	3.5	41	0.05	9	0.6	1.0	0
ʃ	−4.0	3.5	36	0.05	11	0.4	1.0	0

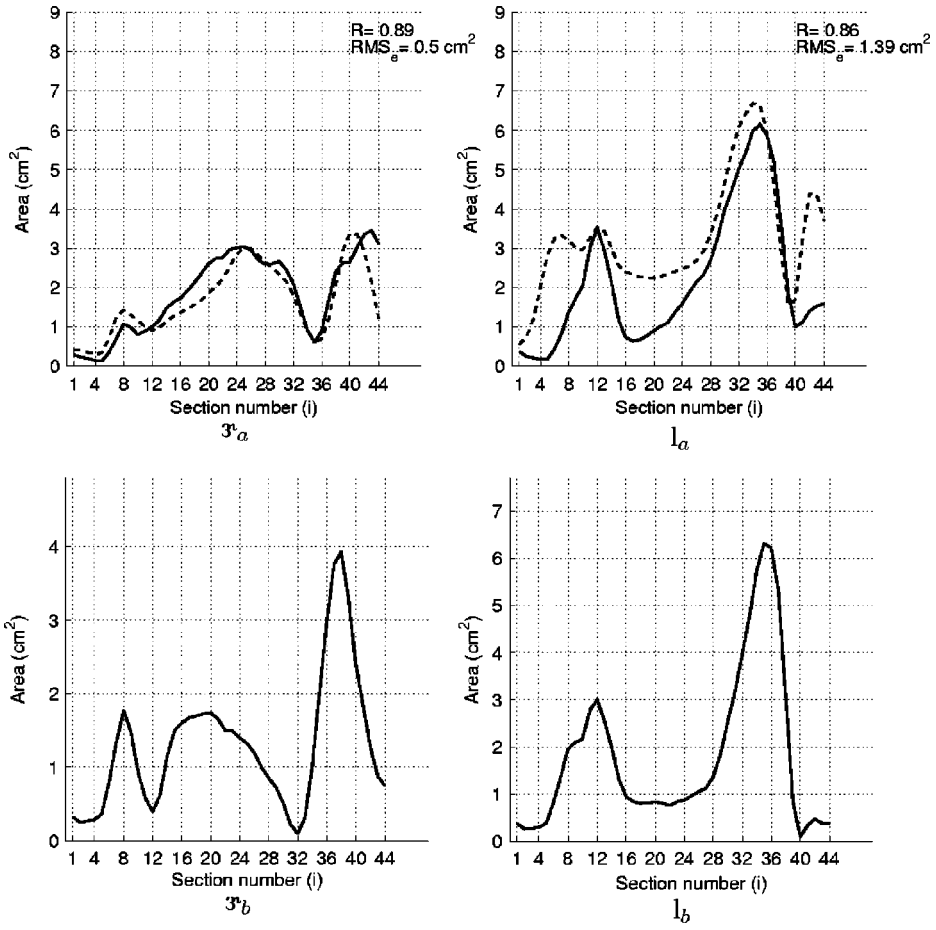

FIG. 9. Area functions for [ɝ] and [l]. Shown in the upper two plots are comparisons of measured area functions (from Story *et al.*, 1996) (dashed lines) to those generated with the area function model (solid lines). In the bottom two plots are model-based area functions that generate acoustic characteristics in line with reported values.

constriction, the nasals also required the nasal coupling a_{np} to be greater than zero. However, a_{np} was not included in the optimization process and the values for it shown in Table I were taken directly from Story *et al.* (1996). For the four fricatives, m_c was equal to 1, and the constriction area was set slightly greater than zero to allow for a narrow orifice connecting the back and front cavities. In general, the range of the constrictions r_c increased as the location was moved from the lips toward the glottis. The exception is in the nasal series where the range of 11 sections for [n] exceeds the 8 sections for [ŋ]. Skewing quotients (s_c) were determined to be 1.0 for the consonants with constriction locations at or near the lips (i.e., [p,m,f]). For the stops and nasals with constriction locations farther back in the vocal tract ([t,k,n,ŋ]), the skewing quotient needed to be greater than 1. In the fricative series the reverse occurred; s_c was less than 1 for all locations posterior to the lips.

If the measured area functions could have been determined from image sets collected during the actual production of a VCV instead of a static posture, q_1 and q_2 should, presumably, have been equal to zero since the speaker was asked to produce each consonant as if it were preceded and followed by a schwa [ə] [roughly equivalent to $(\pi/4)\Omega^2(x)$]. As shown in Table I, however, q_1 and q_2 were set to values different than zero for most of the consonants; only [k] had $q_1=q_2=0$. It must concluded that either the speaker did not accurately produce the consonant configuration within an [əCə] utterance, or these are the shape changes that need to be imposed on an [ə] to accommodate a particular constriction. Nonetheless, the important result is that the consonant perturbation model can generate area functions that are reasonably well matched to those measured from volumetric imaging.

TABLE II. Model parameter values for [ɝ] and [l] area functions. The "a" versions represent the best fit to the measured area functions, where the "b" parameters produce area functions with formant frequencies closer to reported values.

Consonant	q_1	q_2	$[l_{c1},l_{c2}]$ (i)	$[a_{c1},a_{c2}]$ (cm^2)	$[r_{c1},r_{c2}]$ (i)	$[s_{c1},s_{c2}]$	$[m_{c1},m_{c2}]$
ɝ$_a$	0.0	2.0	[12, 35]	[1.0, 0.6]	[4, 4]	[1, 1]	[1, 1]
l$_a$	3.0	0.0	[12, 40]	[3.5, 1.0]	[4, 4]	[1, 1]	[1, 1]
ɝ$_b$	0.0	−1.0	[12, 32]	[0.4, 0.1]	[4, 6]	[1, 1]	[1, 1]
l$_b$	2.0	−2.0	[12, 40]	[3.0, 0.1]	[4, 4]	[1, 1]	[1, 1]

B. Liquids

In addition to the ten consonants discussed previously, Story *et al.* (1996) also reported area functions for static productions of [ɝ] and [l] (for [l], the cross-sectional areas of the two lateral pathways were summed and incorporated into the area function). These were similarly fit with the area function model, but each required two consonant superposition functions to produce an adequate representation of the original. The two upper plots of Fig. 9 show comparisons of the original measured and modeled area functions; the corresponding parameter values are given in the upper part of Table II. For both [ɝ] and [l], the first consonantal function was centered at element 12 and set to areas of 1.0 and 3.5 cm^2, respectively. (The sizes of these cross-sectional areas are large enough that they could be considered consonantal ''settings'' rather than constrictions.) The second constriction for the [ɝ] was centered at element 35 and set to an area of 0.6 cm^2; for [l] a similar constriction was imposed at element 40 with area equal to 1 cm^2. The combination of the two constrictions and the settings of the two vowel substrate parameters given in Table II generates area functions for both consonants that are reasonably close to the originals, as determined both by visual comparison and calculated correlation coefficients of 0.89 for [ɝ] and 0.86 for [l]. The calculated rms error values are also similar to those determined for the previous consonants.

As noted in Story *et al.* (1996), the measured area functions for [ɝ] and [l] produced formant frequency patterns that were not closely representative of those determined from recorded speech. This was primarily due to constriction cross-sectional areas that were too large. Two additional area functions were generated with the area function model that better represent the appropriate acoustic characteristics for these consonants. The parameters are given in the lower part of Table II and the area functions are shown in the bottom two plots of Fig. 9. Specifically, the shift of the second constriction location for [ɝ] to element 32, the change in cross-sectional areas of a_{c1} and a_{c2}, and overall reshaping of the area function with different vowel substrate parameters lowers the third formant ($F3$) from 2.3 kHz for the original to approximately 1.75 kHz, which is more in line with reported values (Peterson and Barney, 1952; Lee, Potamianos, and Narayanan, 1999; Espy-Wilson, 1992). The primary modification for [l] was a decrease in the second constriction area as well as a change in the vowel substrate parameters. These changes combine to increase the third formant frequency from 2.7 kHz for the original area function to about 3 kHz, also similar to reported values (Espy-Wilson, 1992).

It is noted that the area function model ignores the presence and possible effects of lateral pathways for the [l] and sublingual cavities for both [l] and [ɝ] (Espy-Wilson, 1992; Espy-Wilson *et al.*, 2000; Alwan, Narayanan, and Haker, 1997; Narayanan, Alwan, and Haker, 1997). For more accurate representations, the model may eventually need to be augmented with parameters and associated structural components that more closely replicate these differences. In addition, the attempt in this section has been to use the measured area functions as a starting point for the many possible variants of [l] and [ɹ] (Alwan and Haker, 1997; Narayanan and Haker, 1997). This would require a variety of possible settings of the constriction parameters.

The measured area functions used in this section represent only limited instances of consonant production, but they do provide reasonable test cases for assessing the capability of the area function model. The tests demonstrate that the model does have the flexibility to generate realistic area functions within the consonant superposition paradigm and provides parameter values that can be used as a starting point for simulation of consonants.

IV. TIME-VARYING AREA FUNCTIONS

Throughout the description of the area function model in Sec. II, the parameters were shown as time-dependent variables. In this section, a series of time-varying area functions was generated that simulates possible vowel–vowel (VV) and vowel–consonant-vowel (VCV) utterances. For each case, the duration of the utterance was 0.5 s and vocal-tract area variations were accomplished by allowing three parameters to vary with time: two mode coefficients, q_1 and q_2, that create the vowel substrate, and the consonantal magnitude m_c. Other parameters such as the area, location, and

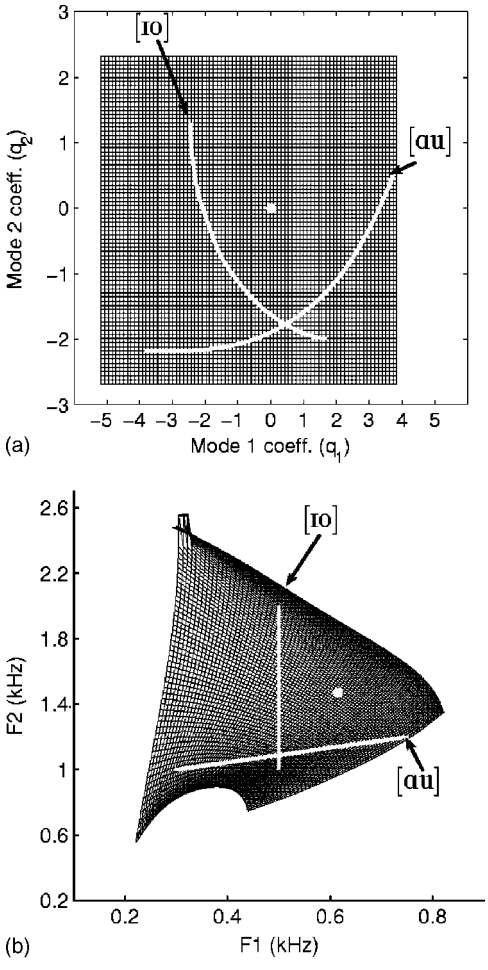

FIG. 10. Mapping between mode coefficients (q_1 and q_2) in (a) and formant frequencies ($F1$ and $F2$) in (b). The curved white lines in the upper plot are the coefficient variations that would produce the corresponding linear formant trajectories for [ɪo] and [au] in the lower plot. The white dot located at $q_1=q_2=0$ in the coefficient plot corresponds to the white dot in the $F1-F2$ plot.

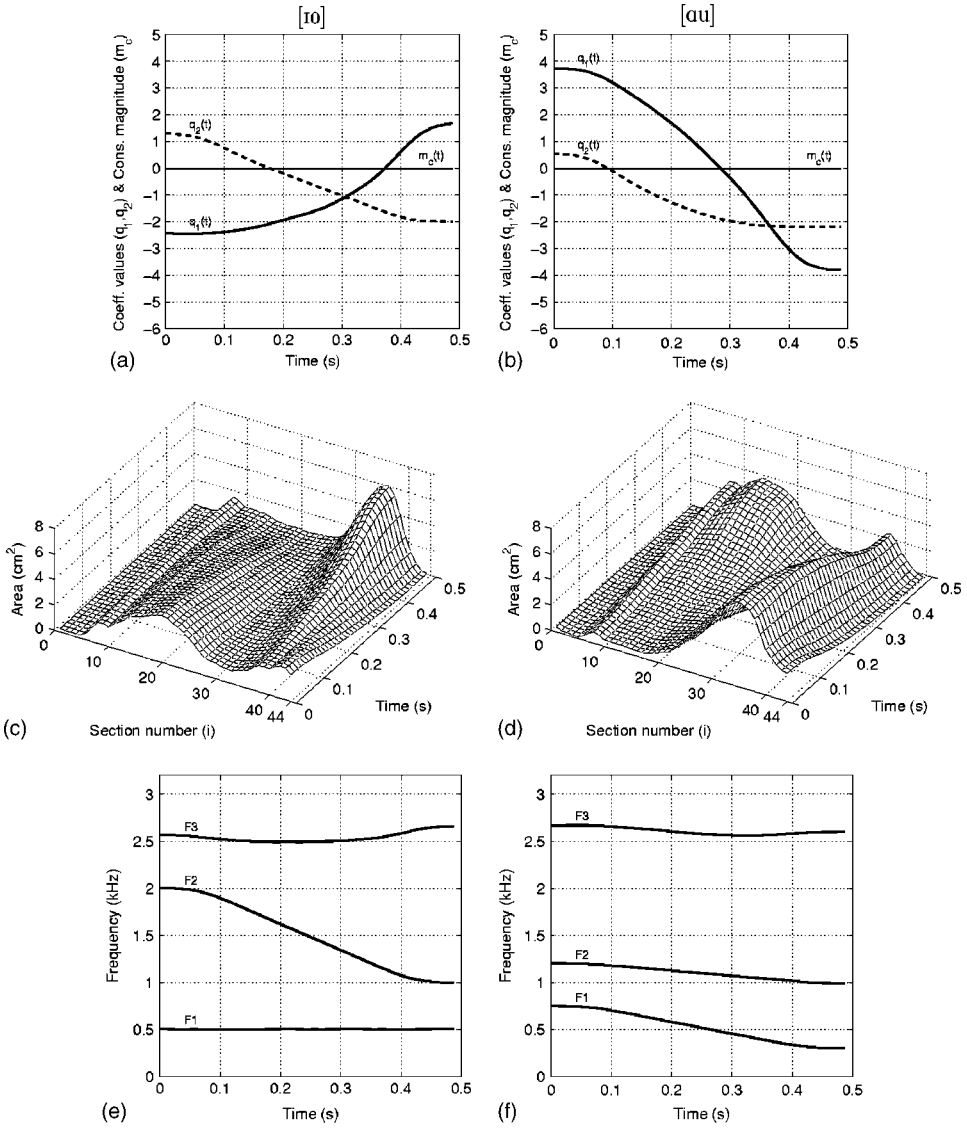

FIG. 11. Area function simulations for two VV transitions. Each *column* of plots shows, in descending order, the time variation of mode coefficients $q_1(t)$ and $q_2(t)$ and consonant magnitude $m_c(t)$ [(a) and (b)], time-varying area functions [(c) and (d)], and time-varying formant frequencies [(e) and (f)]. In the left column the transition is approximately [ɪo], and on the right, [ɑu].

range of the constriction were changed for each case but were held constant over the duration of the simulated utterance. Additional cases are presented that utilize more parameters to simulate a two-consonant cluster (VCCV), vocal-tract length change during a VV transition, and a VCV with a nasal consonant.

A coefficient-to-formant mapping (Story and Titze, 1998, 2002) was used to determine the time variations of the tier I parameters, $q_1(t)$ and $q_2(t)$, that would approximate the VV transitions [ɪo] and [ɑu]. The mapping is shown in Fig. 10. In the upper panel [Fig. 10(a)] is a set of 6400 pairs of q_1 and q_2 coefficients, bounded by the maximum and minimum values given in Table IV. The point where q_1 and q_2 are both equal to zero is indicated with the white dot. The two curves are coefficient trajectories that, when sampled with an appropriate time step ($\Delta T = 0.0125$ for the present examples), can produce time-varying area functions for [ɪo] or [ɑu], respectively. The mesh in Fig. 10(b) is comprised of first and second formant frequencies corresponding to the area functions produced with the coefficient pairs in the upper panel mesh. The straight lines in this figure are $F1-F2$ formant trajectories that correspond to the q_1-q_2 coefficient curves for [ɪo] and [ɑu] in Fig. 10(a). The $F1-F2$ trajectories were deliberately chosen to be linear VV transitions; however, any $F1-F2$ trajectory measured from natural, recorded speech could be mapped to corresponding q_1-q_2 coefficient curves, as long as the formant trajectory remains with the boundaries of the $F1-F2$ space (black mesh) (Story and Titze, 2002). The coefficients $q_1(t)$ and $q_2(t)$ for each vowel transition are shown as functions of time in Figs. 11(a) and (b).

The time variation for the consonantal parameters was generated by a fifth-order polynomial function that produced a "minimum jerk" movement (Hogan, 1982). Other functions such as cosine, damped second-order system, or minimum energy (e.g., Nelson, 1983) could also be used. A minimum jerk transition from one position to another can be specified mathematically as

$$u(t) = u_o + (u_f - u_o)\left(10\left(\frac{t}{T}\right)^3 - 15\left(\frac{t}{T}\right)^4 + 6\left(\frac{t}{T}\right)^5\right) \quad \text{for } 0 \leq t \leq T, \tag{14}$$

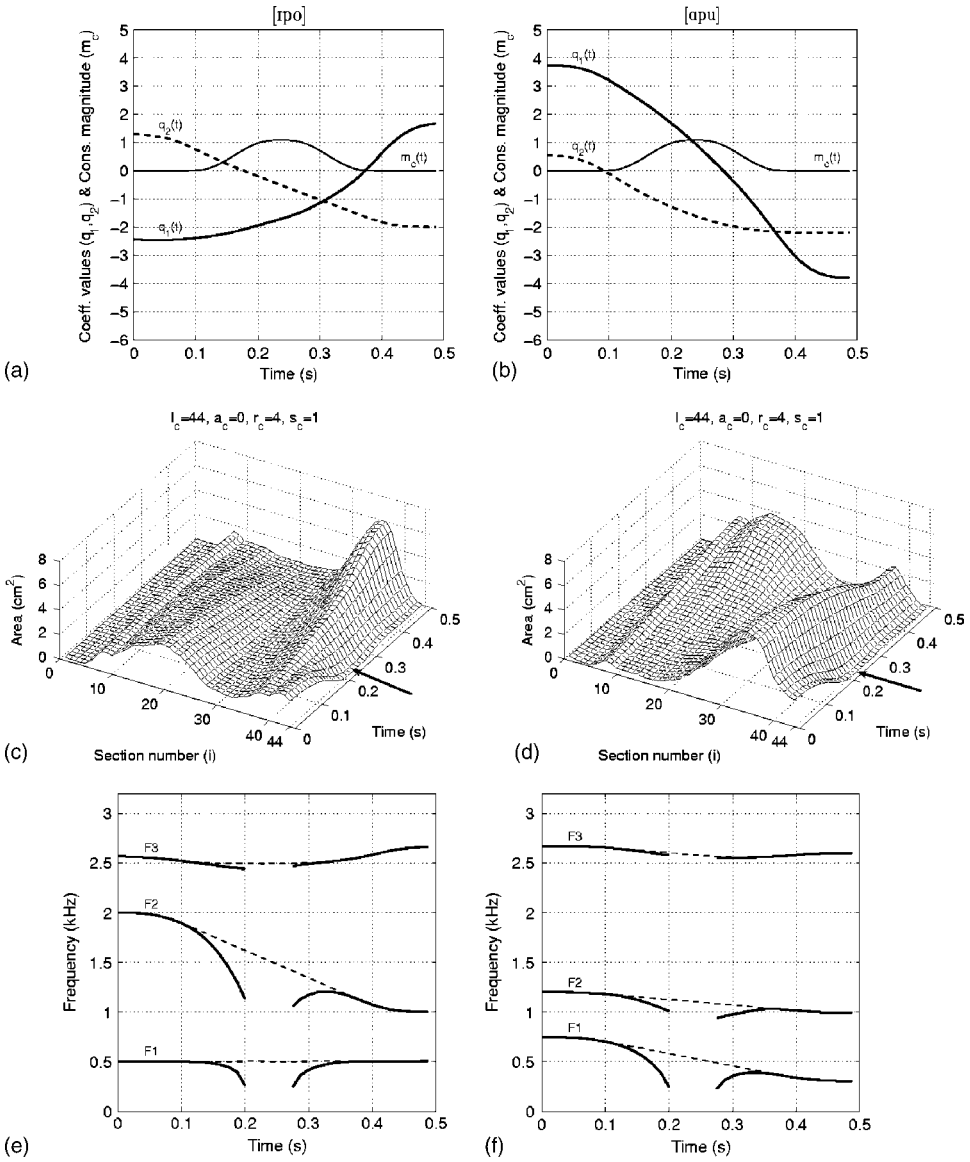

FIG. 12. Area function simulation for two VCVs. In the left column the VCV is approximately [ɪpo], and on the right, [ɑpu]. Shown in descending order are the time variations of mode coefficients $q_1(t)$ and $q_2(t)$ and consonant magnitude $m_c(t)$ [(a) and (b)]. Next are the time-varying area functions [(c) and (d)], where the constant consonantal parameters are shown at the top of the plot, and the point of maximum constriction is indicated with the arrow. Finally, the time-varying formant frequencies are shown at the bottom of the figure [(e) and (f)].

where u_o and u_f are the initial and final positions, respectively, and T is the duration of the movement. Thus, any of the time-varying parameters of the area function model could replace the general variable u, and Eq. (14) would determine its time course of change from one specified value to another. This method of specifying the time variation of parameters is perhaps overly simplistic, but at this point serves the purpose of demonstrating some of the capabilities of the model.

A. VV simulations

The first case is shown in Fig. 11(a), where $q_1(t)$ and $q_2(t)$ initially specify an approximation of the vowel [ɪ] and change over time to values representative of the vowel [o]. Also shown is $m_c(t)$, which is zero across the entire utterance. This means that the consonant tier (tier II) is effectively shut off, and the result is a VV transition. The variation of the area function over time is presented as a three-dimensional plot in Fig. 11(c), where the transition from [ɪ] to [o] can be observed in terms of 40 successive area functions, spaced 0.0125 s apart. For each of the area functions within the [ɪo] transition, a frequency response function was calculated (Sondhi and Schroeter, 1987), and from it the first three formant frequencies were determined with a peak-picking algorithm. Figure 11(e) shows the variation of $F1$, $F2$, and $F3$ over the time course of the vowel transition. The spacing between the first two formants is initially large for the [ɪ]. $F2$ then decreases by about 1 kHz in its transition to [o], while $F1$ remains constant at 0.5 kHz, and $F3$ changes only slightly.

The second column of Fig. 11 presents an analogous case, but with the mode coefficients set to approximate the transition from [ɑ] to [u] [Fig. 11(b)] and $m_c(t)$ is set to zero over the entire utterance. Figures 11(d) and (f) show the time variation of the area function and formant frequencies, respectively. Again, 40 successive area functions are plotted, and the formant frequencies were determined from calculation of the frequency response of each area function. Note that the choice of a linear $F1-F2$ trajectory [see Fig. 10(b)] causes the cross-sectional area at and near the lips to be reduced prior to the formation of the midtract constriction for the [u].

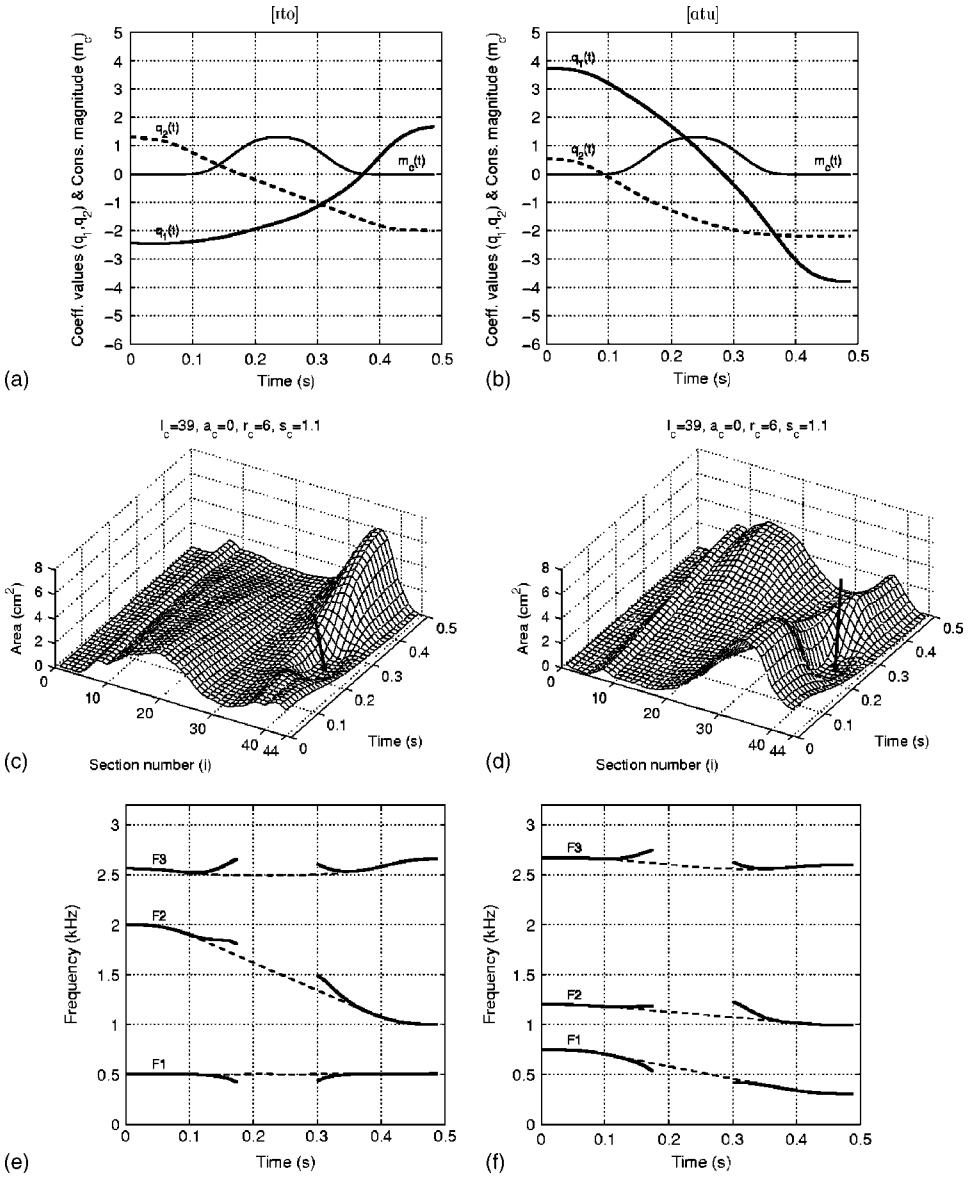

FIG. 13. Area function simulation for two VCVs. In the left column the VCV is approximately [ɪto], and on the right, [ɑtu]. The ordering of the individual plots is identical to those in Fig. 12.

B. VCV simulations

Presented in the next six figures are cases in which the same two vowel substrates shown in Fig. 11 for [ɪo] and [ɑu] were used, but the consonant tier (tier II) was also activated by a nonzero time variation of $m_c(t)$ to produce a VCV. Parameters in tier II were set to approximate the consonants [p,t,k,θ,ɹ] and [l].

Shown in Fig. 12 are two cases where a consonant constriction was imposed at the lips (section 44) with a cross-sectional area of zero, and a range of 4 sections. The time course of $q_1(t)$, $q_2(t)$, and $m_c(t)$ for each case is plotted in Figs. 12(a) and (b). The variations of the mode coefficients are the same as the previous case, but $m_c(t)$ now rises from zero to 1.1 to activate the constriction, and then decreases back to zero to release it. Whereas the choice to have $m_c(t)$ reach its peak 0.25 s into the utterance was arbitrary for these demonstrations, displacing the peak of the consonantal time variation to an earlier or later time point would likely create significant, and potentially interesting, changes in the formant frequency characteristics. In addition, if the goal were to match the formants to a specific production (recording) of the utterance, $m_c(t)$ would likely need to follow some other time course as well.

The parameters displayed at the top of the area function figures [Figs. 12(c) and (d)] were kept constant, and, with the exception of q_1 and q_2, are the same values as those shown in Table I for [p]. The resulting area functions are shown in Figs. 12(c) and (d) and are essentially the same as those in Fig. 11, except in the region near the lip end, where the cross-sectional area is decreased to zero over a time period from approximately 0.2 to 0.27 s. Note that $m_c(t)$ is greater than zero from 0.1 to 0.4 s, but the vocal tract is occluded for only the period of time where $m_c(t)$ is greater than or equal to 1.

The effect of the constriction on the formant frequencies can be seen in Figs. 12(e) and (f). The dashed lines indicate formant variations for the VV transitions of the previous case, whereas the solid lines show the time-varying formant frequencies with the presently imposed constriction. The break in the time course of the formants occurs during the

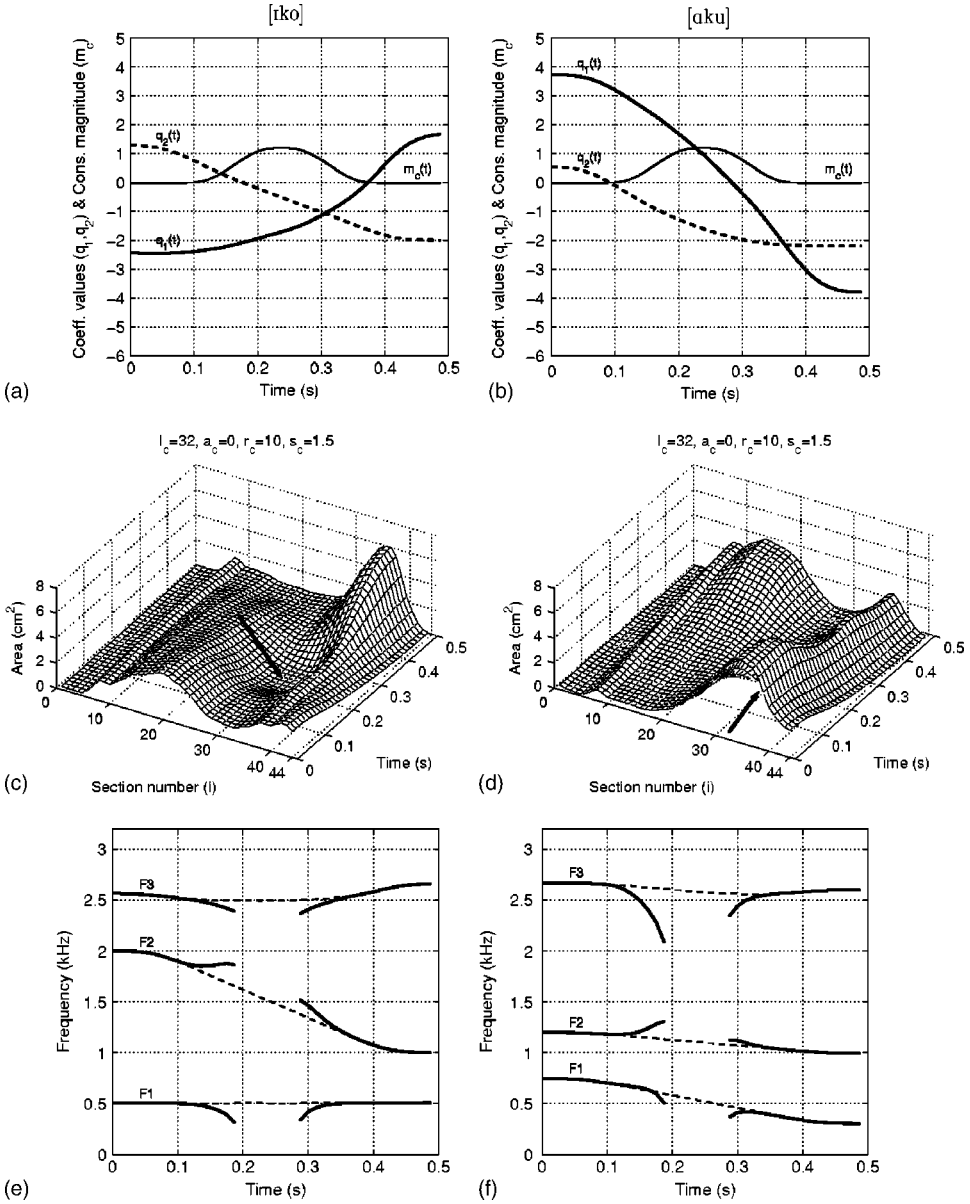

FIG. 14. Area function simulation for two VCVs. In the left column the VCV is approximately [ɪko], and on the right, [ɑku]. The ordering of the individual plots is identical to those in Fig. 12.

period of time in which the vocal tract was fully occluded by the constriction. In both cases, the constriction perturbs all three formant frequencies downward just prior to the occlusion, and upward after its release. Formant characteristics like these for a bilabial consonant are well known (Stevens, 1998) and the figures themselves are reminiscent of those reported by Öhman (1966) for similar initial and final vowels.

Time-varying parameters for the next two cases [Figs. 13(a) and (b)], appear similar to those in the previous figure. The exception is that $m_c(t)$ rises to maximum value of 1.3. More significant, however, are the changes imposed on the constant parameters, where the constriction location is set to section 39, the range is set to 6 sections, and the skewing quotient has been increased to 1.1. These settings are roughly representative of an alveolar stop consonant (see Table I). The constriction can be seen in both time-varying area functions [Figs. 13(c) and (d)] by following element 39 along the time axis, where the occlusion begins at about 0.18 s and is released at 0.3 s. For the case in the left column (≈[ɪto]), the constriction causes $F1$ to decrease by a small amount prior to the vocal-tract occlusion and then it rises following the release of the consonant. During the same time period $F2$ and $F3$ both rise prior to the occlusion and then fall after it is released. The case in the right column (≈[ɑtu]) generates the same directions of formant frequency change, even though the underlying vowel transition is different.

Two simulations of a VCV with an approximation of a velar stop consonant are shown in Fig. 14. The time-varying parameters are, again, nearly identical to the previous cases, but with a maximum value of $m_c(t)=1.2$. The constriction location is at section 32 with a range of 10 sections, and the skewing quotient is set to 1.5. (Note that in Table I, $l_c=30$ was specified for this consonant; in the two vowel contexts used for these demonstrations it was necessary to set $l_c=32$ to produce formant transitions representative of a velar consonant.) The time-varying area function in Fig. 14(c) indicates the constriction forming along the time axis at section 32; the occlusion is indicated by the arrow. In Fig. 14(d), the constriction is more difficult to see because the oral cavity

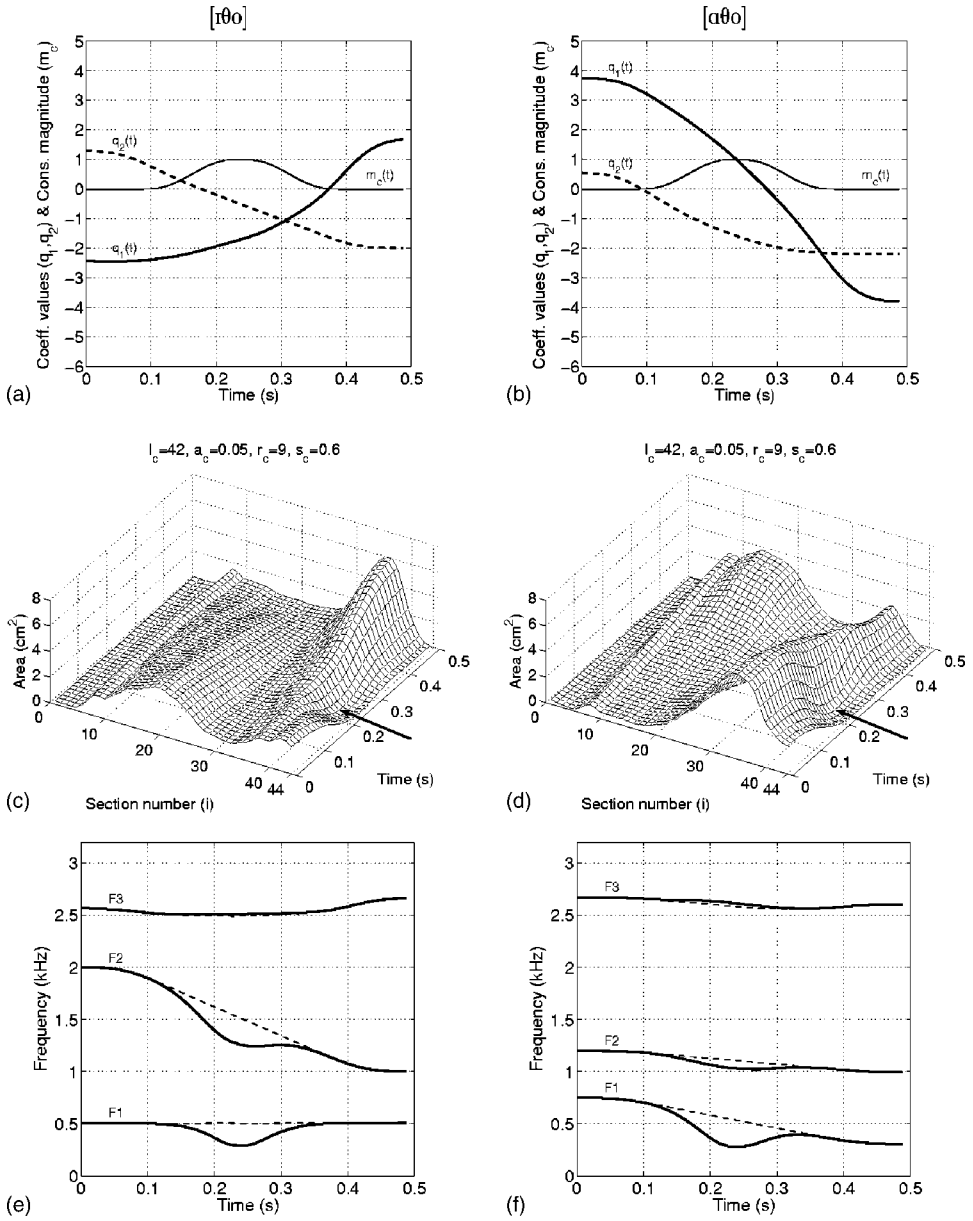

FIG. 15. Area function simulation for two VCVs. In the left column the VCV is approximately [ɪθo], and on the right, [ɑθu]. The ordering of the individual plots is identical to those in Fig. 12.

portion of the vowel area function is expanded in the early stage of the utterance. Following section 32 along the time axis, however, indicates a depression in the area function that occurs at about 0.19 s. Figure 14(e) shows the time-varying characteristics of $F1$, $F2$, and $F3$ for [ɪko], where $F1$ and $F3$ both fall prior to the occlusion and rise after its release. $F2$ exhibits the opposite behavior, rising during the onset of the consonant and falling as it is released. The formant characteristics are similar for [ɑku] [Fig. 14(f)], at least in terms of the direction of change for each formant.

The next two cases contain a constriction area that is nonzero, representative of a fricative consonant. Time-varying parameters are shown in Figs. 15(a) and (b). The consonant magnitude $m_c(t)$ has a maximum value of 1, but, because $a_c = 0.05\ \text{cm}^2$, the minimum area that is achieved during the simulated utterance will be greater than zero. The constriction parameters are taken directly from Table I for the consonant [θ]. The formation of the constriction can be seen along element 42 in the time-varying area function plots [Figs. 15(c) and (d)], and the corresponding formant frequency patterns are displayed in Figs. 15(e) and (f). Because an occlusion does not occur during the time course of the two VCVs, the formant frequencies are continuous. In both cases, $F1$ and $F2$ are perturbed downward in frequency during the presence of the consonant, whereas $F3$ is barely affected. Because the area function is not occluded in this case, the formant frequencies could be calculated over the entire utterance as shown in Figs. 15(e) and (f), but an actual production of [θ] would be unvoiced and a spectrogram would show a discontinuity in the formant frequencies. The present ''simulation'' of the VCV is only of the time-varying area function and the resulting formant frequencies, not speech itself. Hence, the appearance of formants is not affected by the presence or absence of voicing.

Area function simulations that included [ɹ] and [l], are given in Figs. 16 and 17, respectively. The vowel substrate was either [ɪo] or [ɑu], and each consonant require *two* magnitude functions [$m_{c1}(t)$ and $m_{c2}(t)$] that, in this case, both followed the same time course with a maximum value of 1. The constant parameters are those presented in Table II (for

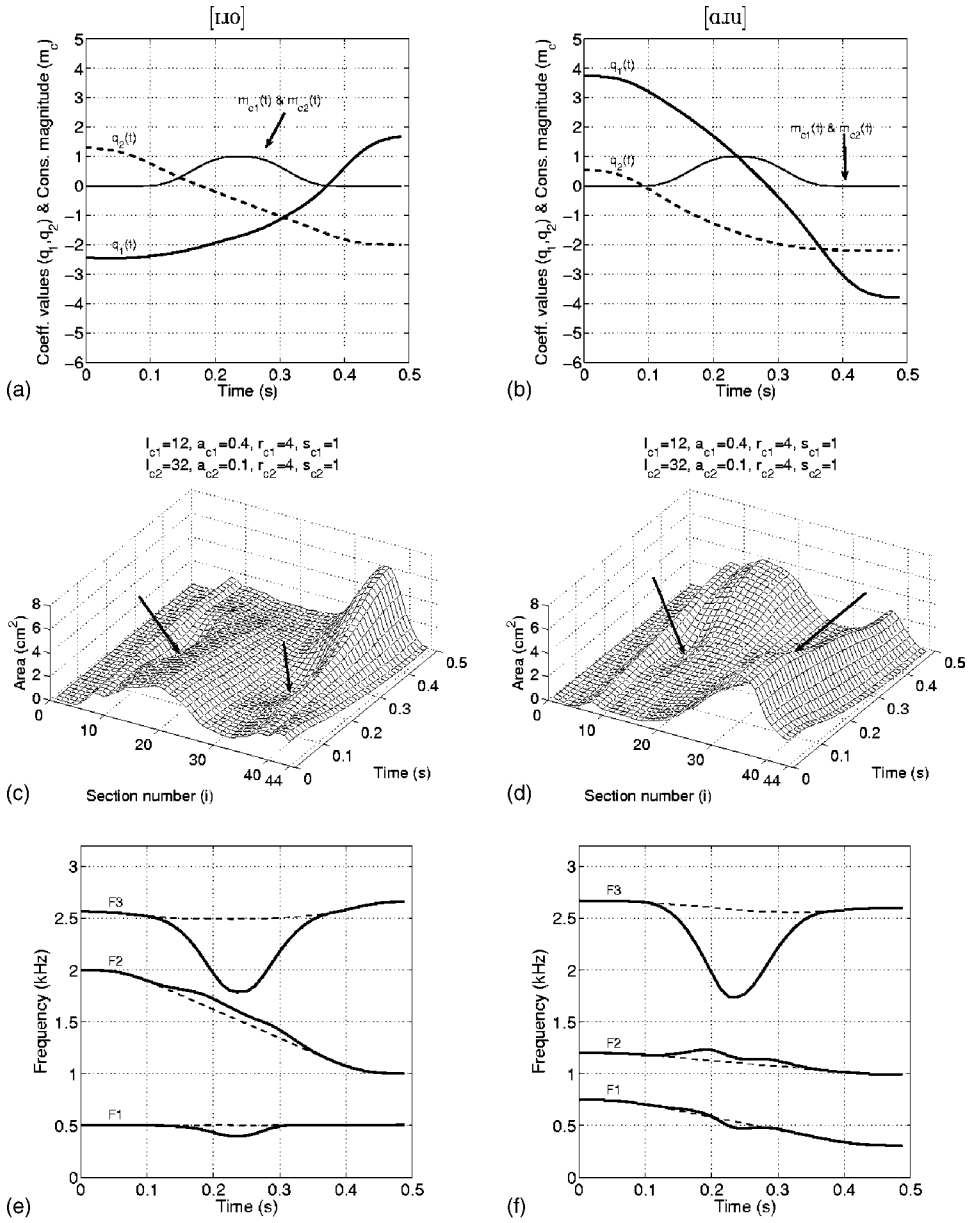

FIG. 16. Area function simulation for two VCVs. In the left column the VCV is approximately [ɪo], and on the right, [ɑɪu]. The ordering of the individual plots is identical to those in Fig. 10. There are, however, two simultaneous constrictions required to produce the [ɹ]. They are each indicated by the arrows and the parameters are specified at the top of the plots in (c) and (d).

the "b" versions) and are shown at the top of the area function plots in each figure. The phonetic symbol [ɹ] is used here because the constriction function creates a time-varying utterance, rather than a sustainable sound such as [ɜ˞].

For the [ɹ], a depression in the time-varying area functions [Figs. 16(c) and (d)] can be seen along the time axis of section 12, most significantly at time 0.25 s. Similarly, at the same point in time, the second constriction can be observed along the time axis of section 32. In either vowel substrate context, the primary effect of the constrictions on the formant frequencies [Figs. 16(e) and 15(f)] is to lower $F3$ by almost 0.8 kHz to bring it momentarily to a value of about 1.77 kHz. In addition, the constrictions perturb $F2$ upward in frequency, whereas $F1$ is perturbed downward.

Area functions for the two simulations with [l] [Figs. 17(c) and (d)] show a slight expansion along the time axis for section 12, opposite of the constrictive effect imposed by the [ɹ] on this same section. At section 40, the second constriction can be seen to take effect during the same time period as the first. In both vowel substrate contexts, the constrictions displace $F3$ upward in frequency, although the pattern of variation over time is different.

C. VCCV simulations

During speech production, two or more consonants may occur consecutively in a cluster without an intervening vowel. For example, in the word /splɪt/, multiple constrictions are rapidly formed and released prior to production of the vowel. Two area function simulations of a two-consonant cluster are presented in Fig. 18. The vowel substrates [Figs. 18(a) and (b)] were again the same [ɪo] and [ɑu] transitions used in all of the previous examples. The two intended consonants superimposed on the vowel substrates were, in sequence, [p] and [ɹ]. Their production requires specification of three constrictions, one for [p] and two for [ɹ], whose parameters will be the same as those in Tables I and II, respectively. The time variation of each constriction magni-

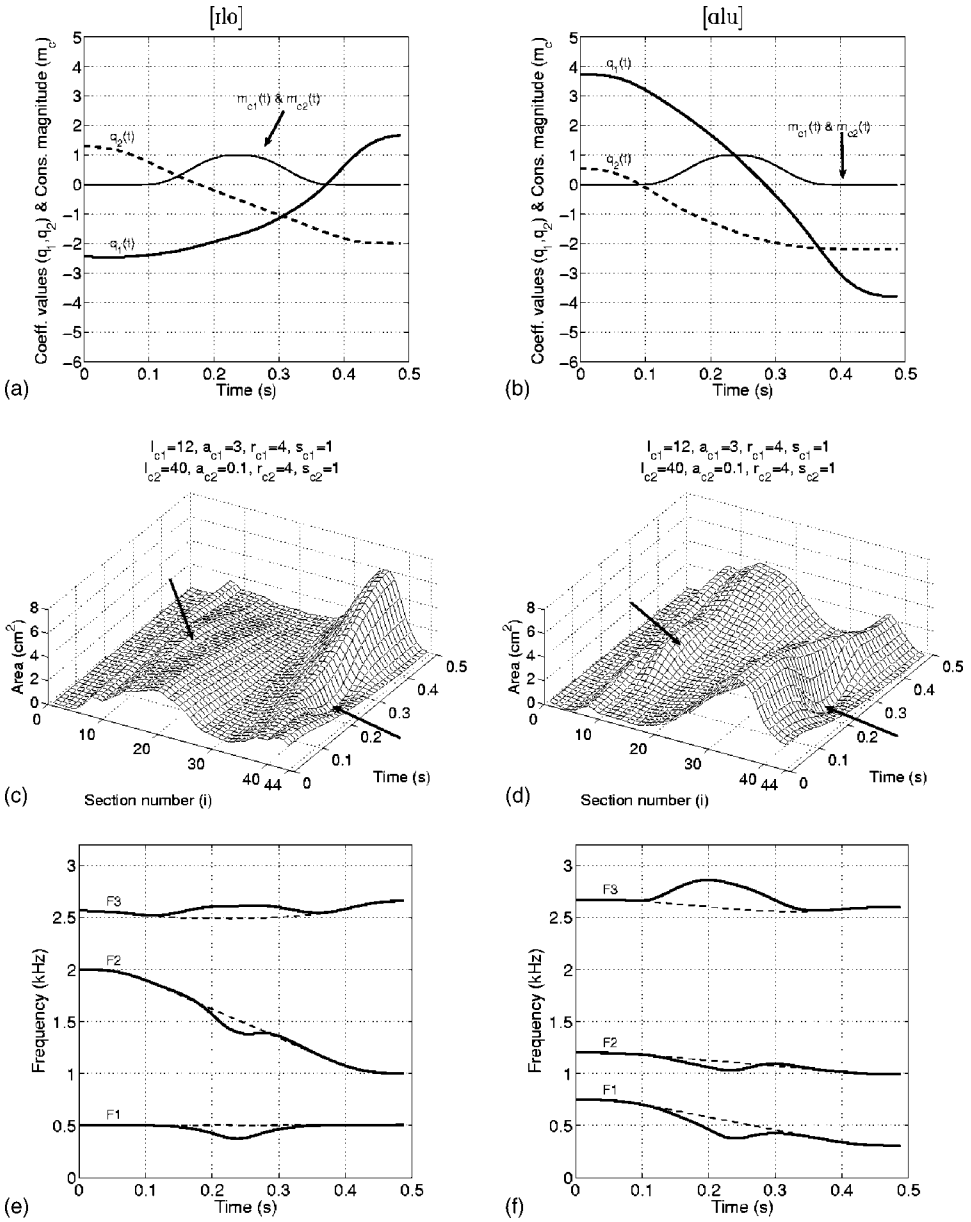

FIG. 17. Area function simulation for two VCV transitions. In the left column the VCV is approximately [ɪlo], and on the right, [ɑlu]. The ordering of the individual plots is identical to those in Fig. 10. Like the previous figure, there are two simultaneous constrictions required to produce the [l]. Again, they are each indicated by the arrows and the parameters are specified at the top of the plots in (c) and (d).

tude is shown in Figs. 18(c) and (d) (these are identical figures but were duplicated to maintain continuity along each column). The magnitude for [p] (solid line) becomes nonzero at 0.08 s, rises to its peak of 1.1 at 0.19 s, and then decreases to zero at 0.33 s. The two constrictions for the [ɹ] follow exactly the same time course as each other, and are identically plotted as the dashed line in the figures. Their magnitudes begin to rise at 0.13 s, which is just slightly delayed relative to the [p] magnitude. The peak occurs at 0.25 s and the constrictions are completely released ($m_{c2}=m_{c3}=0$) at 0.39 s.

The resulting time-varying area functions are shown in Figs. 18(e) and (f), where the three arrows indicate the location and time of each constriction. As dictated by the time course of the constriction magnitudes, there is considerable temporal overlap of the consonants, creating more complex coarticulation than in any of the previous cases. Specifically, the constrictions for the [ɹ] begin to form during production of the [p], and are fully in place just shortly after the occlusion is released.

The formant frequencies for each case [Figs. 18(g) and (h)] are perturbed downward by the [p] constriction, although by different absolute amounts. In the [ɪo] context, $F1$ decreases by 0.25 kHz, while $F2$ drops by 0.8 kHz. The decrease in $F1$ for the [ɑu] context is more than 0.45 kHz, whereas the change in $F2$ is only 0.12 kHz. In both cases, $F3$ drops by about 0.2 kHz. At the point in time when the [p] constriction is released, the vocal tract is nearly configured to produce the [ɹ], and in both cases, the third formants are located at about 1.85 kHz and decrease as the [ɹ] becomes fully expressed in the area function. As the [ɹ] constrictions fade, all of the formants rise to their locations for the final vowel. Most notably is $F3$, which increases in both cases by nearly 0.8 kHz.

D. VV simulations with vocal-tract length change

In this section, a vowel-to-vowel transition is simulated with the area function model while localized changes to the vocal-tract length are simultaneously imposed. A transition

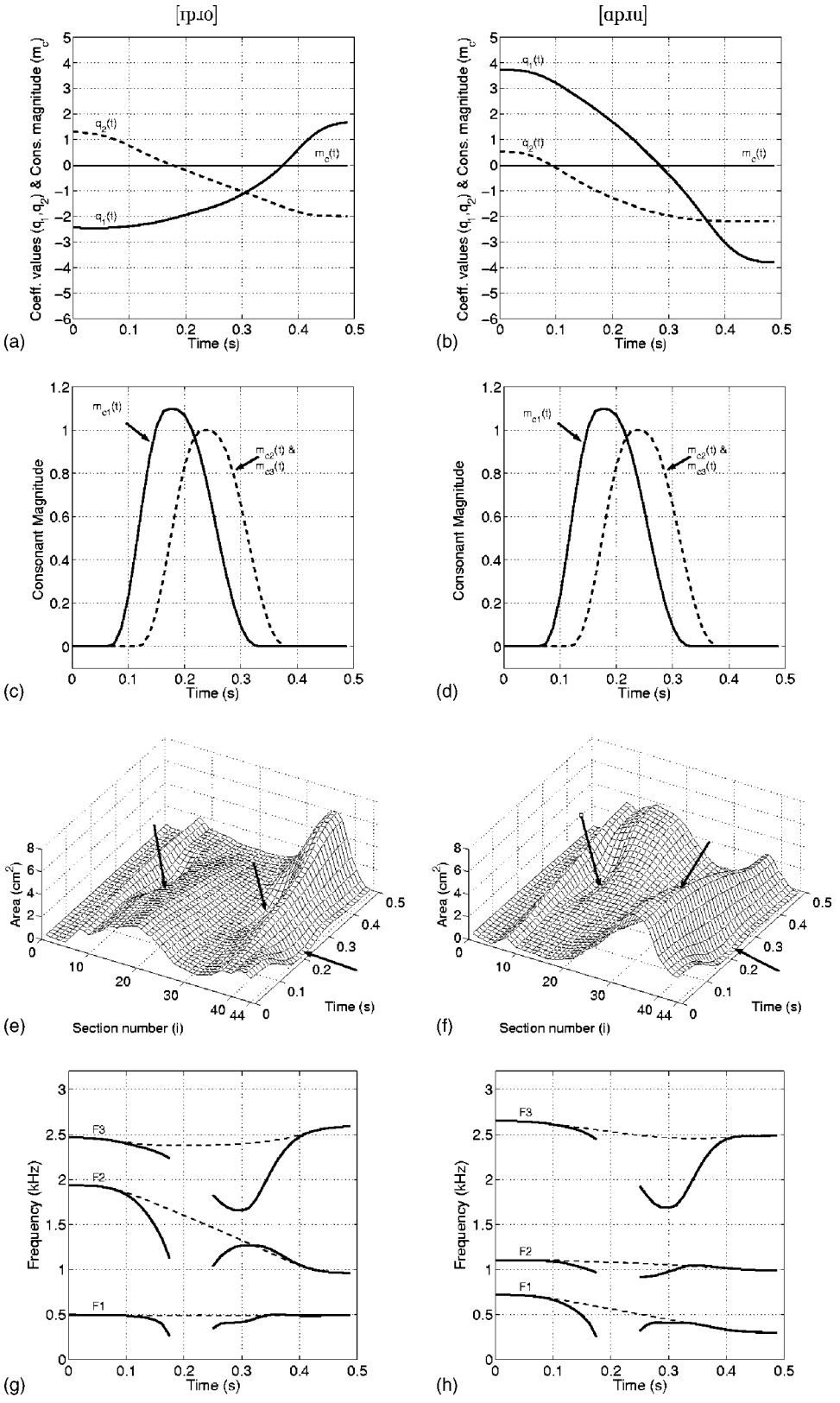

FIG. 18. Area function simulation for two VCCVs. In the left column the VCCV is approximately [ɪɹɪo], and on the right, [ɑɹɪu]. Shown in descending order are the time variations of mode coefficients $q_1(t)$ and $q_2(t)$ [(a) and (b)], and consonant magnitudes for $m_{c1}(t)$, $m_{c2}(t)$, and $m_{c3}(t)$ [(c) and (d)]. Next are the time-varying area functions [(e) and (f)], where the three constrictions imposed during the time course of this utterance are indicated by arrows. Finally, the time-varying formant frequencies are shown at the bottom of the figure [(g) and (h)].

from [ɪ] to [o] was generated that had a duration of 0.5 s and followed a time course dictated by the same mode coefficients as in the previous cases. Length variations were imposed by having $p_g(t)$ and $p_m(t)$ in Eqs. (11) and (12) follow the time courses shown in Fig. 19(a). Initially, $p_g(t)$ was set to -0.5 cm to simulate a shortening at the glottal end of the vocal tract and then was increased to $+0.5$ cm. Similarly, at the lip end $p_m(t)$ was set to initially generate a 1-cm decrease in length, followed by the same amount of increase to lengthen the tract. Figure 19(b) shows the length of each section (tubelet) over the time course of the utterance. Most of the 44 sections are maintained at a constant length throughout, with the exception of the glottal end (near section 1) and lip end (near section 44), which are first short-

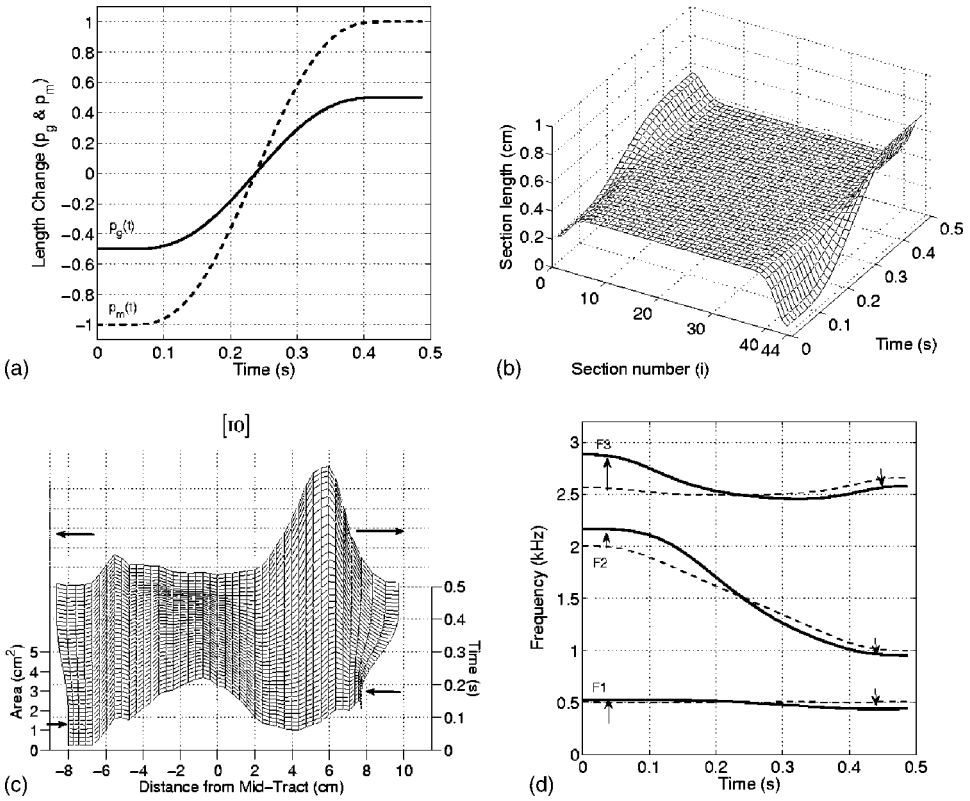

FIG. 19. Area function simulation for a VV transition with simultaneous vocal-tract length change. (a) Time course of the length change specified near the glottis by $p_g(t)$ and near the lips by $p_m(t)$. (b) Time-varying length function [see $L(i,t)$ in Eq. (13)]. (c) Time-varying area function approximating a transition from [ɪ] to [o] with the length changes included. The x axis indicates the distance from the middle of the vocal tract. (d) Time-varying formant frequencies for conditions with the length changes imposed (solid line) and for constant vocal-tract length (dashed line).

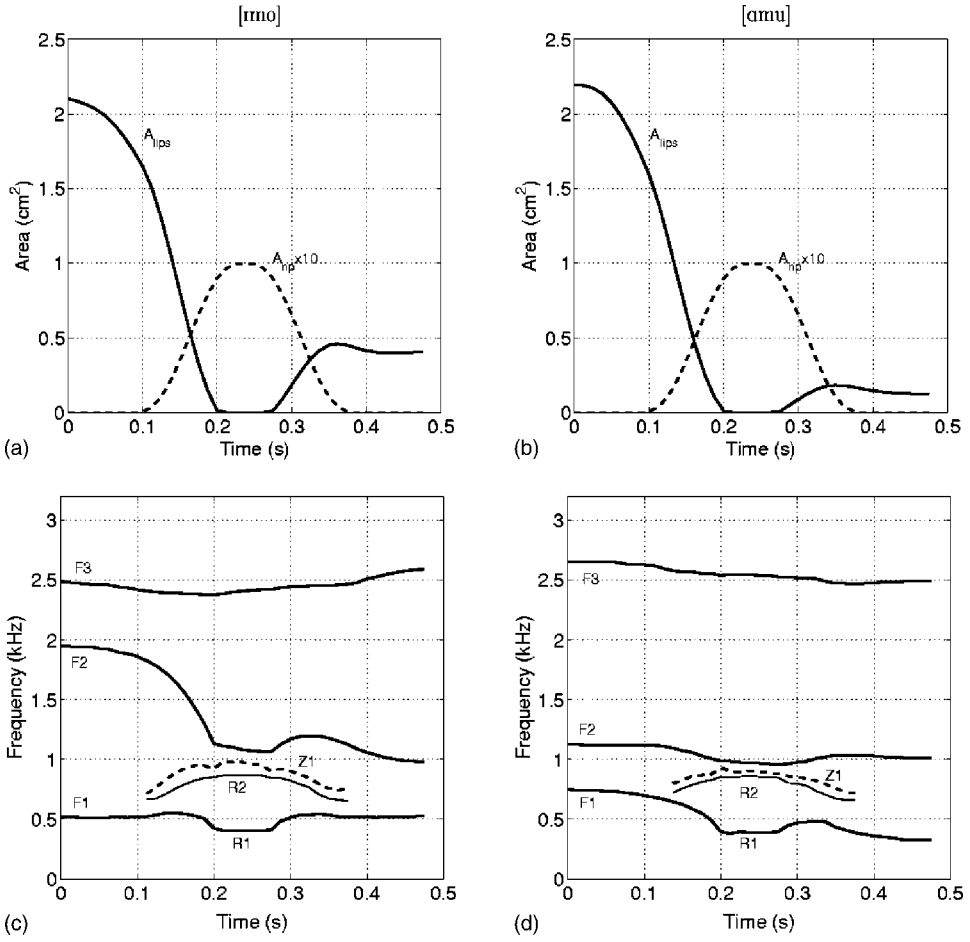

FIG. 20. Simulation of two VCVs with a nasal consonant. The upper plots show the time course of the area change at the lip section (section N_{vt}) (solid) and the nasal coupling area a_{np}, for (a) [ɪmo] and (b) [ɑmu]. The lower plots show the acoustic characteristics for each VCV.

ened and then lengthened over time. The resulting time-varying area function is shown in Fig. 19(c), where the view angle has been set so that the length variations can be observed. The x axis indicates the distance from the middle of the vocal tract, as was used in Fig. 6.

Formant frequencies were determined in the same manner as the previous simulations, except that the length variations were included in the calculations. Resulting time-varying formants are plotted in Fig. 19(d); for comparison, the dashed lines represent formants calculated in the case of constant length. In the initial 0.2 s of the utterance, the shortened tract creates an expected increase in all three formants. At 0.24 s, both $p_g(t)$ and $p_m(t)$ pass through zero, hence, the formants at this point are the same as in the constant length case. As $p_g(t)$ and $p_m(t)$ increase, the three formants are observed to decrease, as expected.

E. VCV simulations with a nasal consonant

The final two simulations were produced with the bilabial nasal consonant [m] imposed on the same [ɪo] and [ɑo] vowel contexts used in the previous examples. The consonant parameters were set to be identical to those for the [ɪpo] and [ɑpu] examples (see Fig. 12), except that the nasal coupling area a_{np} was allowed to be nonzero so that sound could be coupled to the nasal passages. The time variation of a_{np} is shown in Figs. 20(a) and (b), along with the area variation of the lip termination section in the main vocal tract (i.e., area of section N_{vt}). The nasal coupling area begins to increase from 0 cm^2 prior to the occlusion of the vocal tract, and remains nonzero until after the occlusion is released. The maximum area of a_{np} was equal to 0.1 cm^2, but to show the lip area on the same plot, a_{np} was multiplied by 10. The combined resonances of the vocal and nasal tracts, over the time course of the two utterances, are shown in Figs. 20(c) and (d). At the beginning of both [ɪmo] and [ɑmu], only the vocal tract formants ($F1$, $F2$, and $F3$) are present. As soon as a_{np} becomes nonzero, resonances (poles) $R1$ and $R2$ emerge, along with a zero, labeled $Z1$ (notation for the poles and zero during the nasal consonant are the same as in Stevens, 1998). During the time period when the lip section is occluded (from 0.2 to 0.27 s), $R1$ is approximately 0.4 kHz, $R2$ is 0.85 kHz, and $Z1$ is nearly 0.9 kHz. These are roughly in line with expected values for a bilabial nasal consonant (Stevens, 1998).

V. DISCUSSION

The results presented in Secs. III and IV demonstrate that the four-tier parametric model is capable of producing area functions representative of a wide variety of vowels and consonants, in both static and time-varying situations. By itself, the model could be used for studying the relation between the vocal-tract shape and formant frequencies. The separation of the input parameters for the vowel substrate, consonant constriction(s), length variation, and nasalization allows for controlled studies of the effect of each tier alone, or simultaneously. Further, the ''base structural components'' that were specified in Fig. 1 are the only part of the model that is speaker specific. Hence, as data like those given in Appendix A become available for additional speakers, these could be used as the structural components, and the model would represent a different speaker, at least with regard to the underlying physical structure.

As mentioned in the Introduction, the eventual goal of this type of modeling is not only to generate area functions, but to synthesize connected speech. That is, to create an acoustic waveform that would result from wave propagation through the time-varying vocal tract. This requires coupling computational models that simulate both the voice source and propagation of acoustic waves, with the parametric area function model presented here that would specify the vocal-tract shape at any specific point in time. This type of synthesis could provide stimuli to test the effect of various vocal-tract parameters on the perception of speech. For example, the effect of constriction location on the identification of stop consonants could be tested by presenting to listeners, a series of audio samples synthesized with successive changes in l_c (cf. Li and Story, 2003). Through such experiments a connection may be made between vocal-tract shape, acoustics, and perception, rather than just the latter two, which is typical of many speech perception experiments [although this is similar to Stevens' (1989) approach to speech production and perception].

At this point, there are still some significant limitations of the area function model. In particular, specification of the appropriate time course for the parameters is not well established, especially for the parameters in tier II, III, and IV. A next step is to pursue studies that could result in development of mappings between model parameters and acoustic characteristics, similar to that already developed for tier I (see Fig. 10), but would include the parameters for constriction formation, length change, and nasalization. The precise nature of the time variation of the model parameters is also likely to be speaker specific. Hence, the development of such mappings would need to be based on the speech of many speakers.

ACKNOWLEDGMENTS

A preliminary version of this paper was presented at the 146th Meeting of the Acoustical Society of America. This work was supported by NIH R01-DC04789.

NOMENCLATURE Independent variables

N_{vt}	number of x-sect. areas contained in the vocal-tract area function
N_{nt}	number of x-sect. areas contained in the nasal tract area function
N_c	number of consonantal functions
i	index of x-sect areas in an area function of the vocal tract $i=[1,N_{vt}]$
j	index of x-sect areas in an area function of the nasal tract $j=[1,N_{nt}]$
k	index of consonant superposition functions $k=[1,N_c]$
t	time

Base structural components

$\Omega(i)$	mean vocal-tract shape (diameter function)

$\phi_1(i), \phi_2(i)$ area function *modes* (basis functions)
$\mathcal{L}(i)$ nominal (default) length vector (length of each tubelet in an area function)
$\mathcal{N}(j)$ nasal tract area function

Time-varying control parameters

$q_1(t), q_2(t)$ amplitude coefficients for the basis functions
$l_{c_k}(t)$ location (place) of the kth consonant constriction specified as distance from the glottis
$a_{c_k}(t)$ minimum cross-sectional area of the kth consonant constriction
$r_{c_k}(t)$ range of the kth consonant superposition function along the tract length
$s_{c_k}(t)$ skewing quotient of consonant superposition function
$m_{c_k}(t)$ magnitude (activation) of the consonant superposition function
$p_g(t)$ amount of length change at the ''glottal'' end of the vocal tract
$l_g(t)$ location within the length vector $\mathcal{L}(i)$ where the length change p_g is centered
$r_g(t)$ range of the length change p_g
$p_m(t)$ amount of length change at the ''lip'' end of the vocal tract
$l_m(t)$ location within the length vector $\mathcal{L}(i)$ where the length change p_m is centered
$r_m(t)$ range of the length change p_m
$a_{np}(t)$ cross-sectional area of nasal coupling port

Intermediate outputs

$V(i,t)$ time-varying vowel substrate
$C_k(i,t)$ kth time-varying consonantal overlay
$\alpha(i,t)$ vocal tract length modification function for the ''glottal'' end
$\beta(i,t)$ vocal tract length modification function for the ''lip'' end

Final outputs

$A(i,t)$ composite vocal tract area function
$L(i,t)$ composite length (of each tubelet) function
$\mathcal{X}(i,t)$ cumulative length function
$A_n(j,t)$ composite nasal tract area function

APPENDIX A: TIER I STRUCTURAL COMPONENTS

The structural components for the vowel substrate are shown numerically in Table III. The first column is the index i, which denotes successive sections along the length of the vocal tract. Section 1 is located just above the glottis and section 44 at the lips. The other three columns are the neutral diameter function $\Omega(i)$, and the two modes, $\phi_1(i)$ and $\phi_2(i)$, that deform the vocal tract. When multiplied by the corresponding mode and combined with $\Omega(i)$ as specified in Eq. (3), the coefficients in Table IV will produce area functions representative of the indicated vowels.

These data were derived from the vowel area functions reported in Story, Titze, and Hoffman (1996). Each area function was first normalized to the mean vocal-tract length across the vowels, and then a principal components analysis (PCA) was applied to area function set. The ''modes'' are the

TABLE III. Neutral diameter function and two modes that form the vowel substrate in tier I of the area function model. i is an index extending from glottis to lips.

i	$\omega(i)$	$\phi_1(i)$	$\phi_2(i)$
1	0.636	0.018	−0.013
2	0.561	0.001	−0.007
3	0.561	−0.013	−0.029
4	0.550	−0.025	−0.059
5	0.598	−0.036	−0.088
6	0.895	−0.048	−0.108
7	1.187	−0.062	−0.120
8	1.417	−0.076	−0.123
9	1.380	−0.093	−0.118
10	1.273	−0.111	−0.107
11	1.340	−0.130	−0.092
12	1.399	−0.149	−0.075
13	1.433	−0.167	−0.056
14	1.506	−0.183	−0.035
15	1.493	−0.196	−0.014
16	1.473	−0.204	0.008
17	1.499	−0.207	0.032
18	1.529	−0.203	0.057
19	1.567	−0.193	0.084
20	1.601	−0.175	0.111
21	1.591	−0.151	0.138
22	1.547	−0.119	0.164
23	1.570	−0.082	0.188
24	1.546	−0.041	0.206
25	1.532	0.004	0.218
26	1.496	0.051	0.221
27	1.429	0.097	0.214
28	1.425	0.141	0.195
29	1.496	0.181	0.164
30	1.608	0.214	0.121
31	1.668	0.240	0.070
32	1.757	0.257	0.013
33	1.842	0.264	−0.046
34	1.983	0.260	−0.100
35	2.073	0.246	−0.143
36	2.123	0.224	−0.167
37	2.194	0.194	−0.165
38	2.175	0.159	−0.132
39	2.009	0.122	−0.066
40	1.785	0.087	0.031
41	1.675	0.057	0.148
42	1.539	0.038	0.264
43	1.405	0.034	0.346
44	1.312	0.048	0.338

TABLE IV. Mode coefficients that reconstruct the indicated vowels when used with Eq. (3).

Vowel	q_1	q_2
i	−5.176	−2.556
ɪ	−1.092	0.677
ɛ	2.561	3.849
æ	3.471	1.729
ʌ	0.102	−3.565
ɑ	0.981	1.043
ɔ	0.331	2.315
ʊ	0.128	1.356
o	−0.493	−1.910
u	−2.685	−2.065

TABLE V. Area functions for the fricative consonants [f, θ, s, ʃ]. *i* is an index that numbers cross-sectional areas from glottis to lips. The last line indicates the length of each tubelet within the area function.

i	f	θ	s	ʃ
1	0.37	0.39	0.47	0.49
2	0.32	0.40	0.47	0.49
3	0.65	0.76	0.54	0.63
4	1.22	0.71	0.68	0.64
5	1.46	1.10	0.94	0.83
6	1.43	1.50	2.23	2.26
7	1.34	1.34	2.18	2.51
8	1.32	1.23	2.39	2.53
9	1.84	1.15	2.17	2.77
10	2.55	1.34	1.95	2.85
11	2.21	1.72	2.12	3.11
12	2.16	1.65	2.19	3.42
13	2.09	1.52	2.61	3.31
14	1.82	1.50	3.08	3.69
15	2.01	1.32	2.51	3.54
16	1.95	1.42	2.32	3.74
17	1.91	1.49	2.70	4.18
18	1.77	1.49	2.65	4.56
19	1.88	1.94	3.21	4.98
20	2.40	2.41	3.71	5.23
21	2.04	2.29	3.72	5.18
22	1.87	2.37	4.14	5.80
23	2.13	2.99	4.58	5.67
24	2.05	3.09	4.63	4.82
25	1.65	2.98	4.32	4.39
26	1.05	2.75	4.38	3.82
27	0.64	2.82	4.21	2.89
28	0.52	2.96	4.52	2.48
29	0.45	2.95	4.53	1.81
30	0.45	3.13	4.40	1.38
31	0.29	3.24	3.98	0.98
32	0.24	3.13	3.78	0.57
33	0.16	3.36	3.52	0.45
34	0.21	3.43	3.20	0.34
35	1.04	3.21	2.77	0.03
36	1.88	3.08	2.16	0.00
37	2.27	2.82	1.53	0.00
38	2.00	2.39	1.03	0.00
39	1.93	1.75	0.60	0.34
40	1.89	0.90	0.26	2.13
41	1.31	0.09	0.11	1.96
42	0.83	0.00	0.15	1.24
43	0.33	0.09	0.24	0.76
44	0.11	0.22	0.06	0.33
Δ	0.361	0.356	0.353	0.377

two most significant components (in terms of the explained variance) resulting from the PCA (Story and Titze, 1998).

APPENDIX B: AREA FUNCTIONS FOR FRICATIVE CONSONANTS

Four fricative area functions are provided in Table V. These were derived from image sets obtained with magnetic resonance imaging (MRI). These images were collected at the same time as those reported in Story *et al.* (1996), but were not published. The image analysis and determination of the area function were carried out using exactly the same techniques as the previous study. A problem is that the images were acquired in the axial plane. Hence, the detailed structure of the constricted air channels were not well defined, as they may have been with, say, a coronal imaging plane (e.g., Narayan *et al.*, 1995). Thus, they are not adequate to provide information for aerodynamic modeling of turbulence generation (Shadle, 1991; Sinder, 1999), but they do indicate the types of shape information needed for the present area function model.

[1]The term ''tiers'' is used to denote multiple levels of area function control. This is similar, but not identical, to the use of the term by Browman and Goldstein (1990).

[2]Representation of an area function by 44 elements is not a requirement of the general structure of the model. The number derives from the approximate spatial resolution obtained in MRI-based reconstructions of vocal-tract shape (Story *et al.*, 1996). It is also convenient to use 44 elements for simulating speech with acoustic waveguide models because it allows for a sampling frequency of 44.1 kHz when the tract length is approximately 17.5 cm (typical adult male). The formulation of the model, however, is general enough that area functions with any number of elements can be produced.

[3]The symbol Ω is used as a *mathematical* variable describing the ''neutral'' diameter function. It should not be confused with the rarely used *phonetic* symbol [Ω] for a midback rounded vowel (Pullum and Ladusaw, 1996).

[4]It is acknowledged that the details of fricative sound production will not be adequately modeled by a simple constriction of the type proposed here. Rather, it is assumed that a model of turbulent noise generation (e.g., Narayanan, 1995; Sinder, 1999) could be inserted just downstream of the point of minimum area.

[5]For the set of male vocal-tract data used in this paper, $\Delta = 0.396\,825$ cm. Combined with a 44-section area function, the vocal-tract length will be 17.46 cm. It is not suggested that this level of accuracy is required for the tubelet length. Rather, this number originates from the particular type of wave propagation algorithm used by author to synthesize speech (Liljencrants, 1985; Story, 1995), where Δ = speed of sound(c)/2 × sampling frequency (F_s). Choosing $c = 35\,000$ cm/s and $F_s = 44\,100$ Hz, $\Delta = 0.396\,825$.

Alwan, A., Narayanan, S., and Haker, K. (**1997**). ''Toward articulatory-acoustic models for liquid approximants based on MRI and EPG data. II. The rhotics,'' J. Acoust. Soc. Am. **101**, 1078–1089.

Atal, B. S., Chang, J. J., Mathews, M. V., and Tukey, J. W. (**1978**). ''Inversion of articulatory-to-acoustic transformation in the vocal tract by a computer sorting technique,'' J. Acoust. Soc. Am. **63**, 1535–1555.

Badin, P., Bailly, G. Raybaudi, M., and Segebarth, C. (**1998**). ''A three-dimensional linear articulatory model based on MRI data,'' in Proceedings of the 5th International Conf. on Spoken Language Proc., edited by R. H. Mannell and J. Robert-Ribes 2, 417–420.

Badin, P., Bailly, G., Revéret, L., Baciu, M., Segebarth, C., and Savariaux, C. (**2002**). ''Three-dimensional linear articulatory modeling of tongue, lips, and face, based on MRI and video images,'' J. Phonetics **30**, 533–553.

Båvegård, M. (**1995**). ''Introducing a parametric consonantal model to the articulatory speech synthesizer,'' in Proceedings Eurospeech 95, Madrid, Spain, 1857–1860.

Baer, T., Gore, J. C., Gracco, L. C., and Nye, P. W. (**1991**). ''Analysis of vocal tract shape and dimensions using magnetic resonance imaging: Vowels,'' J. Acoust. Soc. Am. **90**, 799–828.

Browman, C., and Goldstein, L. (**1990**). ''Gestural specification using dynamically defined articulatory structures,'' J. Phonetics **18**, 299–320.

Carré, R., and Chennoukh, S. (**1995**). ''Vowel–consonant–vowel modeling by superposition of consonant closure on vowel-to-vowel gestures,'' J. Phonetics **23**, 231–241.

Coker, C. H. (**1976**). ''A model of articulatory dynamics and control,'' Proc. IEEE **64**(4), 452–460.

Dang, J., and Honda, K. (**1994**). ''Morphological and acoustical analysis of the nasal and the paranasal cavities,'' J. Acoust. Soc. Am. **96**, 2088–2100.

Dang, J., and Honda, K. (**2004**). ''Construction and control of a physiological articulatory model,'' J. Acoust. Soc. Am. **115**, 853–870.

Espy-Wilson, C. Y. (**1992**). ''Acoustic measures for linguistic features distinguishing the semivowels /wjrl/ in American English,'' J. Acoust. Soc. Am. **92**, 736–757.

Espy-Wilson, C. Y., Boyce, S. E., Jackson, M., Narayanan, S., and Alwan, A. (**2000**). ''Acoustic modeling of American English /r/,'' J. Acoust. Soc. Am. **108**, 343–356.

Fant, G. (**1960**). *Acoustic Theory of Speech Production* (Mouton, The Hague).
Fitch, W. T., and Giedd, J. (**1999**). ''Morphology and development of the human vocal tract: A study using magnetic resonance imaging,'' J. Acoust. Soc. Am. **106**, 1511–1522.
Fujimura, O. (**1992**). ''Phonology and phonetics—A syllable based model of articulatory organization,'' J. Acoust. Soc. Jpn. **13**, 39–48.
Goldstein, U. G. (**1980**). ''An articulatory model for the vocal tracts of growing children,'' Doctoral dissertation, Department of Electrical Engineering and Computer Science, MIT.
Hogan, N. (**1982**). ''An organizing principle for a class of voluntary movements,'' J. Neurosci. **4**(11), 2745–2754.
Ichikawa, A., and Nakata, K. (**1968**). ''Speech synthesis by rule,'' Reports of the 6th International Congress on Acoustics, edited by Y. Kohasi, Tokyo, International Council of Scientific Unions, 171–1744.
Ishizaka, K., and Flanagan, J. L. (**1972**). ''Synthesis of voiced sounds from a two-mass model of the vocal cords,'' Bell Syst. Tech. J. **51**, 1233–1268.
Kozhevnikov, V. A., and Chistovich, L. A. (**1965**). *Speech: Articulation and Perception* (trans. US Dept. of Commerce, Clearing House for Federal Scientific and Technical Information), No. 30, 543 (Joint Publications Research Service, Washington, D.C.).
Lee, S., Potamianos, A., and Narayanan, S. (**1999**). ''Acoustics of children's speech: Developmental changes of spectral and temporal parameters,'' J. Acoust. Soc. Am. **105**(3), 1455–1468.
Li, K., and Story, B. H. (**2003**). ''An investigation of perceptual tolerance limits of stop constriction regions along the vocal tract,'' J. Acoust. Soc. Am. **114(4) pt 2**, 2337.
Liljencrants, J. (**1985**). ''Speech synthesis with a reflection-type line analog,'' DS dissertation, Dept. of Speech Comm. and Music Acoust., Royal Inst. of Tech., Stockholm, Sweden.
Lin, Q. (**1990**). ''Speech Production Theory and Articulatory Speech Synthesis,'' Doctoral dissertation, Royal Inst. of Tech. (KTH), Stockholm.
Lindblom, B., and Sundberg, J. (**1971**). ''Acoustical consequences of lip, tongue, jaw, and larynx movement,'' J. Acoust. Soc. Am. **4**(2), 1166–1179.
Maeda, S. (**1982**). ''The role of the sinus cavities in the production of nasal vowels,'' in IEEE Proceedings, 911–914.
Maeda, S. (**1990**). ''Compensatory articulation during speech: Evidence from the analysis and synthesis of vocal-tract shapes using an articulatory model,'' in *Speech Production and Speech Modeling*, edited by W. J. Hardcastle and A. Marchal (Kluwer Academic, Dordrecht), pp. 131–149.
Mattingly, I. G. (**1974**). ''Speech synthesis for phonetic and phonological models,'' in *Current Trends in Linguistics*, edited by T. A. Sebeok (Mouton, The Hague), Vol. 12, pp. 2451–2487.
Mermelstein, P. (**1973**). ''Articulatory model for the study of speech production,'' J. Acoust. Soc. Am. **53**(4), 1070–1082.
Mrayati, M., Carré, R., and Guérin, B. (**1988**). ''Distinctive regions and modes: A new theory of speech production,'' Speech Commun. **7**, 257–286.
Nakata, K., and Mitsuoka, T. (**1965**). ''Phonemic transformation and control aspects of synthesis of connected speech,'' J. Radio Res. Labs. **12**, 171–186.
Narayanan, S. S. (**1995**). ''Fricative consonants: An articulatory, acoustic, and systems study,'' Ph.D. thesis, UCLA, Los Angeles, CA.
Narayanan, S., Alwan, A., and Haker, K. (**1997**). ''Toward articulatory-acoustic models for liquid approximants based on MRI and EPG data. I. The laterals,'' J. Acoust. Soc. Am. **101**, 1064–1077.
Narayanan, S. S., and Alwan, A. A. (**1995**). ''An articulatory study of fricative consonants using magnetic resonance imaging,'' J. Acoust. Soc. Am. **98**, 1325–1347.
Nelson, W. L. (**1983**). ''Physical principles of economies of skilled movements,'' Biol. Cybern. **46**, 135–147.
Nordström, P-E. (**1977**). ''Female and infant vocal tracts simulated from male area functions,'' J. Phonetics **5**, 81–92.
Öhman, S. E. G. (**1966**). ''Coarticulation in VCV utterances: Spectrographic measurements,'' J. Acoust. Soc. Am. **39**, 151–168.
Öhman, S. E. G. (**1967**). ''Numerical model of coarticulation,'' J. Acoust. Soc. Am. **41**, 310–320.
Peterson, G. E., and Barney, H. L. (**1952**). ''Control methods used in a study of the vowels,'' J. Acoust. Soc. Am. **24**(2), 175–184.
Pullum, G. K., and Ladusaw, W. A. (**1996**). *Phonetic Symbol Guide* (University of Chicago Press, Chicago), p. 148.
Shadle, C. H. (**1991**). ''The effect of geometry on source mechanisms of fricative consonants,'' J. Acoust. Soc. Am. **19**, 409–424.
Shadle, C. H., and Damper, R. I. (**2001**). ''Prospects for Articulatory Synthesis: A Position Paper,'' in Proceedings of 4th ISCA Workshop on Speech Synthesis, August/September 2001, 121–126, Pitlochry, Scotland.
Sinder, D. J. (**1999**). ''Speech synthesis using an aeroacoustic fricative model,'' Doctoral dissertation, Rutgers University, New Brunswick, NJ.
Sondhi, M. M. (**2002**). ''Articulatory modeling: A possible role in concatenative text-to-speech synthesis,'' Proceedings of IEEE Workshop on Speech Synthesis, 73–78.
Sondhi, M. M., and Schroeter, J. (**1987**). ''A hybrid time–frequency domain articulatory speech synthesizer,'' IEEE Trans. Acoust., Speech, Signal Process. **ASSP-35**(7), 955–967.
Stevens, K. N. (**1989**). ''On the quantal nature of speech,'' J. Phonetics **17**, 3–45.
Stevens, K. N. (**1998**). *Acoustic Phonetics* (MIT Press, Cambridge, MA).
Stevens, K. N., and House, A. S. (**1955**). ''Development of a quantitative description of vowel articulation,'' J. Acoust. Soc. Am. **27**(3), 484–493.
Story, B. H. (**1995**). ''Speech Simulation with an Enhanced Wave-Reflection Model of the Vocal Tract,'' Ph.D. dissertation, University of Iowa.
Story, B. H. (**2002**). ''A parametric area function model of three female vocal tracts based on orthogonal modes,'' Presented at the Acoustical Society Meeting, J. Acoust. Soc. Am. **112(5)**, pt. 2, 2418.
Story, B. H. (**2004**). ''Vowel acoustics for speaking and singing,'' Acust. Acta Acust. **90**(4), 629–640.
Story, B. H., and Titze, I. R. (**1998**). ''Parametrization of vocal tract area functions by empirical orthogonal modes,'' J. Phonetics **26**(3), 223–260.
Story, B. H., and Titze, I. R. (**2002**). ''A preliminary study of voice quality transformation based on modifications to the neutral vocal tract area function,'' J. Phonetics **30**, 485–509.
Story, B. H., Titze, I. R., and Hoffman, E. A. (**1996**). ''Vocal tract area functions from magnetic resonance imaging,'' J. Acoust. Soc. Am. **100**(1), 537–554.
Story, B. H., Titze, I. R., and Hoffman, E. A. (**2001**). ''The relationship of vocal tract shape to three voice qualities,'' J. Acoust. Soc. Am. **109**, 1651–1667.
Taylor, J. R. (**1982**). *An Introduction to Error Analysis* (University Science, Mill Valley, CA).
Titze, I. R., and Story, B. H. (**1997**). ''Acoustic interactions of the voice source with the lower vocal tract,'' J. Acoust. Soc. Am. **101**(4), 2234–2243.

Relative contributions of spectral and temporal cues for phoneme recognition

Li Xu[a)]
School of Hearing, Speech and Language Sciences, Ohio University, Athens, Ohio 45701 and Kresge Hearing Research Institute, Department of Otolaryngology, University of Michigan, Ann Arbor, Michigan 48109

Catherine S. Thompson and Bryan E. Pfingst
Kresge Hearing Research Institute, Department of Otolaryngology, University of Michigan, Ann Arbor, Michigan 48109

(Received 4 May 2004; revised 12 February 2005; accepted 14 February 2005)

Cochlear implants provide users with limited spectral and temporal information. In this study, the amount of spectral and temporal information was systematically varied through simulations of cochlear implant processors using a noise-excited vocoder. Spectral information was controlled by varying the number of channels between 1 and 16, and temporal information was controlled by varying the lowpass cutoff frequencies of the envelope extractors from 1 to 512 Hz. Consonants and vowels processed using those conditions were presented to seven normal-hearing native-English-speaking listeners for identification. The results demonstrated that both spectral and temporal cues were important for consonant and vowel recognition with the spectral cues having a greater effect than the temporal cues for the ranges of numbers of channels and lowpass cutoff frequencies tested. The lowpass cutoff for asymptotic performance in consonant and vowel recognition was 16 and 4 Hz, respectively. The number of channels at which performance plateaued for consonants and vowels was 8 and 12, respectively. Within the above-mentioned ranges of lowpass cutoff frequency and number of channels, the temporal and spectral cues showed a tradeoff for phoneme recognition. Information transfer analyses showed different relative contributions of spectral and temporal cues in the perception of various phonetic/acoustic features. [DOI: 10.1121/1.1886405]

PACS numbers: 43.71.Es, 43.66.Ts [KWG] Pages: 3255–3267

I. INTRODUCTION

Speech signals contain a variety of cues that listeners can use in identifying words. These cues are typically redundant in the sense that all of them can be degraded to various degrees without destroying speech recognition. People using cochlear implants receive a reduced set of speech cues compared to those received by normal-hearing listeners. Speech processors for cochlear implants represent speech information in a variety of ways in the electrical signals delivered to the auditory nerve. Nearly all current commercial cochlear implants use a series of bandpass filters to divide the incoming signals into various frequency-specific components and deliver these to specific regions of the cochlea, based more or less on a correspondence between the frequency range of each filter and the tonotopic organization of the auditory nerve within the cochlea. Often, the signal to each stimulation site is delivered in the form of an amplitude-modulated pulse train for which the modulation frequency carries useful temporal information. Thus, in these processing strategies, spectral information is represented in terms of place of electrical stimulation in the cochlea and temporal information is represented in the temporal waveform of the envelope that amplitude modulates the pulse trains.

It is well known that the spectral information received by cochlear implant users is much poorer than that received by normal-hearing listeners. Friesen *et al.* (2001) and others have shown that perceptually many implanted subjects have a maximum of 7 to 8 functional spectral channels, whereas normal listeners have some 20 to 30. While the temporal information received by the cochlear implant user may be equivalent to that available to the normal-hearing listener in some respects (e.g., Shannon, 1983, 1992), it is not completely normal. The temporal representation in the electrically stimulated deaf listener is probably different from that in a normal-hearing listener due to an abnormally high degree of across-fiber synchrony in the auditory-nerve response to electrical stimulation (Wilson *et al.*, 1997; Rubinstein and Hong, 2003).

Speech recognition is reasonably good for many cochlear implant users despite these limitations, but there is much room for improvement. In a study of 62 subjects, Skinner *et al.* (2002) found that about 1/3 had less than 75% speech recognition for sentences in noise (+10 dB signal-to-noise ratio). At this signal-to-noise ratio, normal-hearing listeners can retain nearly perfect speech recognition. To determine the most promising areas for the improvement of speech recognition, it is important to know the relative con-

[a)]Address correspondence to Dr. Li Xu, School of Hearing, Speech and Language Sciences, Grover Center—W229, Ohio University, Athens, Ohio 45701. Telephone: (740) 593 0310; fax: (740) 593 0287; electronic mail: XuL@ohio.edu

tributions of spectral and temporal information to speech recognition and to determine the extent to which weaknesses in one aspect of perception can be aided by strengths in another. Studies in normal-hearing listeners using acoustic simulations of cochlear prosthesis processing strategies (e.g., Shannon *et al.*, 1995, 1998; Dorman *et al.*, 1997; Loizou *et al.*, 1999) can help define the relative importance of these variables and their interactions, which can then be examined in implanted subjects with various degrees of speech recognition ability. The techniques of acoustic simulations of cochlear prosthesis processing strategies were evolved from the early vocoder technique invented by Dudley in the 1930s (Dudley, 1939; see Schroeder, 1966 for a historic review of the vocoder). This approach has been adopted in a number of previous studies in which the data from normal-hearing subjects listening to simulations were viewed as a potential scenario for the best possible cochlear implant performance (e.g., Dorman *et al.*, 1998, 2000; Fu *et al.*, 1998; Fu and Shannon, 1999, 2000; Loizou *et al.*, 2000; Friesen *et al.*, 2001; Henry and Turner, 2003; Turner *et al.*, 2004; Kong *et al.*, 2004).

Various components of speech depend to different degrees on spectral and temporal cues. Vowel recognition depends in large part on an accurate perception of spectral patterns in the low- and mid-frequency ranges (e.g., 200–2500 Hz). The recognition of some consonants depends on the perception of temporal envelope patterns such as the rise times of the signals. A number of studies have examined the importance of a temporal envelope for speech perception by varying the bandwidth of the envelope or by temporal smearing (Van Tasell *et al.*, 1987; Drullman *et al.*, 1994a, b; Shannon *et al.*, 1995; Fu and Shannon, 2000). Other studies have focused on the required number of spectral channels (Shannon *et al.*, 1995; Dorman *et al.*, 1997; Fu *et al.*, 1998; Loizou *et al.*, 1999). However, few studies have considered the interaction between spectral and temporal envelope cues on speech perception. Shannon *et al.* (2001) demonstrated the relative importance of spectral and temporal resolution by measuring the vowel recognition scores under conditions in which both the number of channels and the envelope cutoff frequency covaried. The authors emphasized that vowel recognition was maintained at high levels when the number of channels was $\geqslant 4$ and when the temporal envelope was lowpass filtered at $\geqslant 20$ Hz. Such results are potentially important and need to be tested in a larger number of subjects, with finer step sizes in both the number of channels and the envelope cutoff frequency, and for both vowel and consonant recognition.

In a previous study (Xu *et al.*, 2002) we examined *lexical-tone perception* in Mandarin Chinese words using noise-excited vocoders while systematically varying both the bandwidth of the temporal envelope (lowpass cutoff frequency of the envelope extractor) and the number of spectral channels available to the listener. We found that both the number of channels and the temporal-envelope bandwidths affected tone perception and that there was a tradeoff between the two cues. This tradeoff occurred when the lowpass cutoff was between 1 and 256 Hz and the number of spectral channels was between 1 and 12.

In the present study we extended this work to examine the perception of American–English consonants and vowels. Our purpose in this study was to determine the relative contributions of spectral and temporal cues and their interactions. An information transmission analysis of the phonetic/acoustic features of the consonants and vowels was further carried out to differentiate the relative contributions of spectral and temporal cues in the perception of various phonetic features. Based on our experience in the previous study (Xu *et al.*, 2002) and data from the literature (e.g., Dorman *et al.*, 1997; Shannon *et al.*, 1995, 1998, 2001; Fu and Shannon, 2000), we selected a range of lowpass cutoff frequencies to include values ranging from 1 to 512 Hz, and the range of the number of channels studied to encompass values from 1 to 16.

II. METHOD

A. Subjects

Seven normal-hearing native-English-speaking listeners (two males and five females, age 22.0 ± 1.8, mean$\pm$s.d.), whose pure-tone averages of either ear were $\leqslant 20$ dB HL for octave frequencies between 250 and 8000 Hz, participated in the study. During screening with original speech materials, consonant and vowel recognition scores were $\geqslant 95\%$ correct for all subjects. The use of human subjects in this study was reviewed and approved by the Institutional Review Boards of the University of Michigan Medical School and Ohio University.

B. Speech test materials

The consonant recognition tests utilized the Shannon *et al.* (1999) consonant stimulus set, consisting of 20 syllables presented in a consonant-/a/ context (ba, cha, da, fa, ga, ja, ka, la, ma, na, pa, ra, sa, sha, ta, tha, va, wa, ya, za). The International Phonetic Alphabet (IPA) symbols for the consonants are /b, tʃ, d, f, g, dʒ, k, l, m, n, p, r, s, ʃ, t, ð, v, w, y, z/. One male (♯3) and one female (♯3) talker were used from the multiple talkers available in these test materials, resulting in 40 tokens for a consonant test. The vowel recognition tests utilized the Hillenbrand *et al.* (1995) vowel stimulus set, consisting of 12 vowels presented in an /h/-vowel-/d/ context (had, hawed, hayed, head, heard, heed, hid, hod, hoed, hood, hud, who'd). The IPA symbols for the vowels are /æ, ɔ, e, ɛ, ɝ, i, ɪ, ɑ, o, ʊ, ʌ, u/. Two male (♯48 and ♯49) and two female (♯39 and ♯44) talkers were used from the multiple talkers available in these test materials, resulting in 48 tokens for a vowel test.

C. Signal processing

Signal processing for acoustic simulations of cochlear implants was performed in MATLAB (MathWorks, Natick, MA). Speech signals were first passed through a bank of sixth-order elliptic bandpass analysis filters. To study effects of the number of channels on the recognition of consonants and vowels, the number of analysis filters was varied between 1 and 16 (1, 2, 3, 4, 6, 8, 12, and 16). The overall bandwidth was 150 to 5500 Hz. The bandwidth and corner

TABLE I. Corner frequencies of analysis filters with various numbers of channels used in the present study.

Number of channels	Corner frequencies (Hz)
1	150; 5500
2	150; 1171; 5500
3	150; 660; 1997; 5500
4	150; 484; 1171; 2586; 5500
6	150; 345; 660; 1171; 1997; 3335; 5500
8	150; 287; 484; 766; 1171; 1751; 2586; 3783; 5500
12	150; 236; 345; 484; 660; 885; 1171; 1535; 1997; 2586; 3335; 4288; 5500
16	150; 212; 287; 377; 484; 612; 766; 950; 1171; 1435; 1752; 2131; 2585; 3130; 3783; 4564; 5500

frequency of each analysis filter was based on an estimated equal distance along the basilar membrane of the cochlea using Greenwood's (1990) formula [frequency $=165.4(10^{0.06x}-1)$, where x is the distance in mm from the apex assuming a basilar–membrane length of 35 mm]. Table I lists the corner frequencies of all numbers of channels studied. Next, the temporal envelope of each analysis band was extracted by half-wave rectification and lowpass filtering (second-order Butterworth). The temporal envelope of each band was then used to modulate a white noise that was bandpassed through the bank of analysis filters that was used earlier to filter the original speech signals. To study the effects of the temporal features on consonant and vowel recognition, the lowpass cutoff frequencies (LPFs) of the lowpass filters were varied between 1 and 512 Hz in 1-octave steps. Finally, the modulated noise bands were summed and the resultant signals were stored on the computer hard disk for presentation.

D. Procedures

The speech signals were presented through a loudspeaker positioned 1 m from the subject at 0° azimuth inside an Acoustic Systems (Model RE2 242S) double-walled sound-attenuating booth. A graphical user interface (GUI) was built to present the consonant and another GUI was built for the vowel tests. In the GUI's, alphabetic representations of the 12 hVd or the 20 CV stimuli were presented in alphabetical order in a grid on a computer screen. The vowels or consonants were presented acoustically in random order and the subject responded after each presentation by pointing the cursor to the appropriate symbol using a computer mouse and clicking on that symbol. Stimuli were presented at ~60 dB (A) measured with a sound-level meter (Brüel and Kjær Type 2231). This level was found to be the most comfortable level for our normal-hearing subjects.

All subjects received about three hours of training in listening to the processed speech materials and in the use of a mouse. The training started with the conditions that had more channels and higher LPFs and progressively moved toward the conditions that had fewer channels and lower LPFs. Feedback was provided during practice.

For the test, there were 80 conditions comprising combinations of 8 number-of-channels conditions (1, 2, 3, 4, 6, 8, 12, and 16 channels) and 10 LPF conditions (1, 2, 4, 8, 16, 32, 64, 128, 256, and 512 Hz). During the tests, the order of the 80 conditions was randomized. When initial testing with all 80 conditions was finished, the tests were administered two more times, each time with a different randomization, resulting in a total of three tests for each condition. To run the 80 conditions three times for the consonant recognition, a total of 9600 responses were collected from each subject (i.e., 40 tokens×80 conditions×3 tests), whereas for the vowel recognition, a total of 11 520 responses (i.e., 48 tokens×80 conditions×3 tests) were collected. It took about 32 h on average for each subject to complete the tests.

E. Data analysis

The Tukey test was used for *post hoc* pairwise comparisons of the phoneme-recognition scores among the dependent variables such as number of channels or LPFs. Significance level was defined as $p<0.05$.

Results were further analyzed for information transmitted for phonetic/acoustic features. For the 20 consonants, classification of the three features (i.e., voice, place of articulation, and manner) was similar to that used by Hornsby and Ricketts (2001). Table II lists the 20 consonants and their classification with regard to the three features. The consonant recognition data were pooled across all seven subjects and a single confusion matrix was created for each condition (i.e., a combination of a particular number of channels and a particular LPF). Matrices of all 80 conditions were then analyzed to determine the percent of conditional information transmitted using the SINFA (Sequential INFormation Analysis) procedure[1] of Wang and Bilger (1973). The SINFA procedure goes through a sequence of iterations (three iterations in our case). The first iteration of SINFA is the same as information transmission analysis described by Miller and Nicely (1955). In subsequent iterations, the feature with the highest percentage of information transmitted in the previous iteration is held constant and remains partialled out. Thus, SINFA helps to eliminate redundancy of specific features in their contribution to phoneme recognition. The 12 vowels used in this study were classified based on three features (duration, F1 frequency, and F2 frequency) quantified by Hillenbrand *et al.* (1995). This classification was similar to that

TABLE II. Classification of consonants by acoustic-phonetic features. Voicing coding: 0=voiceless, 1=voiced. Place coding: 1=labial, 2=dental, 3=alveolar, 4=palatal, 5=back. Manner coding: 1=plosive, 2=fricative, 3=affricate, 4=nasal, 5=glide.

	b	tʃ	d	f	g	dʒ	k	l	m	n	p	r	s	ʃ	t	ð	v	w	y	z
Voicing	1	0	1	0	1	1	0	1	1	1	0	1	0	0	0	1	1	1	1	1
Place	1	4	3	1	5	4	5	3	1	3	1	4	3	4	3	2	1	5	3	3
Manner	1	3	1	2	1	3	1	5	4	4	1	5	2	2	1	2	2	5	5	2

TABLE III. Classification of vowels in the hVd context by acoustic features. Duration coding: 0=short (<220 ms), 1=long (>250 ms). F1 frequency coding: 0=low (<420 Hz), 1=middle (460 to 520 Hz), 2=high (>630 Hz). F2 frequency coding: 0=low (<1030 Hz), 1=middle (1240 to 1450 Hz), 2=high (>1890 Hz).

	æ	ɔ	e	ɛ	ɝ	i	ɪ	ɑ	o	ʊ	ʌ	u
Duration	1	1	1	0	1	1	0	1	1	0	0	1
F1	2	2	1	2	1	0	1	2	1	1	2	0
F2	2	0	1	2	2	2	2	1	0	0	1	0

used by Skinner *et al.* (1996). Table III lists the 12 vowels and their classification with regard to the three features. In a similar manner to the consonant recognition data, the percent of conditional information transmitted was computed using the SINFA procedure (Wang and Bilger, 1973) for the acoustic features of the vowels (Table III) for all the 80 combinations of number of channels and LPF.

The percent correct or percent of information transmitted from the above analysis consisted of matrices of 8×10 (i.e., 8 number-of-channels conditions×10 LPFs). We employed contour plots to illustrate these results. Eight equally distributed contour levels (0—≤12.5%, >12.5—≤25%, >25—≤37.5%, >37.5—≤50%, >50—≤62.5%, >62.5—≤75%, >75—≤87.5%, and >87.5—100%) were chosen for the plots. A contour plot is a standard function of MATLAB software (MathWorks, Natick, MA). Basically, the algorithm scanned the matrix comparing the values of each block of four neighboring elements (i.e., a cell) in the matrix to the contour level values. If a contour level fell within a cell, the algorithm performed a linear interpolation to locate the point at which the contour crossed the edge of the cell. Then, the algorithm connected these points to produce a segment of a contour line (MATLAB, 2002). Finally, the resulting contours at various contour levels were filled using a gray scale.

III. RESULTS

A. Consonant and vowel recognition scores

No differences were found between the scores obtained with female or male speakers; therefore, the results reported here are pooled data for both genders. Group mean results are plotted in Figs. 1–3. Figure 1 plots the phoneme recognition scores as a function of the number of channels for each of the 10 LPF conditions. In general, phoneme recognition improved as a function of the number of channels and such functions were quite similar for both consonants and vowels. For consonant recognition, the improvement was largest between one and six or eight channels with smaller improvement for greater numbers of channels. Results of the *post hoc* statistical analysis are shown in the small panels of Fig. 1. These results confirmed that the consonant recognition scores improved from one to six channels. The differences between six and eight channels were not significant for any degree of temporal information (all $p>0.05$). However, performances with 8 channels were always significantly better than those with 4 channels and performances with 12 and/or 16 channels were usually better than those with 6 channels (Fig. 1). For vowel recognition, the largest improvement usually occurred between 1 and 8 channels and sometimes between 1 and 12 channels. There were no significant improvements from 12 to 16 channels (all $p>0.05$). Interestingly, dramatic improvements in vowel recognition were seen between two and three channels but no significant differences in the vowel recognition scores were found between three and four channels (Fig. 1). This might be due to the frequency bands assigned to these numbers of channels (see Table I) and the distribution of the vowels in the F1–F2 space (Peterson and Barney, 1952; Hillenbrand *et al.*, 1995).

Figure 2 shows the phoneme recognition performance as a function of the lowpass cutoff frequencies from 1 to 512 Hz in octave steps. Different lines plot data for different numbers of channels. The effects of LPFs on consonant recognition depended on the number of channels. Specifically, they depended on whether a single channel or multiple channels were used. In the one-channel condition, the consonant recognition continuously improved from 1 to 512 Hz (but not statistically for 128 Hz and beyond). In contrast, for conditions with multiple channels, the consonant recognition improved only up to 16 Hz. The results of the *post hoc* statistical analysis, as shown in the small panels of Fig. 2, illustrate this dichotomy. For vowel recognition under the one-channel condition, the performance improvement as a function of the LPFs was not apparent, with only the score at LPF of 512 Hz being significantly higher than that at 1 Hz. For conditions with multiple channels, the performance improved slightly as a function of the LPFs and tended to plateau at lower frequencies compared to consonant data. The results of the *post hoc* statistical analysis indicated that no improvement in vowel recognition was seen when the LPF was >4 Hz (with the exception of two- and four-channel conditions in which the performances improved up to 8 Hz) (Fig. 2).

It can be seen from the vertical spread of the lines in Figs. 1 and 2 that the number of channels exerted a more dominant effect on phoneme recognition than did the LPFs, at least in the ranges of numbers of channels and LPFs tested. The mean ranges from the lowest to the highest scores across all LPFs in Fig. 1 were 33.8 and 18.3 percentage points for consonants and vowels, respectively. The mean ranges from the lowest to the highest scores across all numbers of channels in Fig. 2 were 58.6 and 75.9 percentage points for consonants and vowels, respectively. The dominant effect of the number of channels can be seen readily in the contour plots of Fig. 3 in which the phoneme recognition scores are shown by the areas filled using a gray scale with the abscissa and the ordinate representing the number of channels and the LPFs, respectively. Figure 3 also illustrates a tradeoff between the number of channels and the LPFs in phoneme recognition, especially in consonant recognition. The tradeoff is evident when the contour lines in Fig. 3 are more or less parallel to the minor diagonal line. The tradeoff in consonant recognition occurred in the ranges of 1 to 8 or 12 channels and LPFs of 1 to 16 or 32 Hz. For example, to achieve 50%–60% correct consonant recognition with 3 channels, one would need to have a LPF>16 Hz; however, to achieve the same level of performance with 8 to 12 chan-

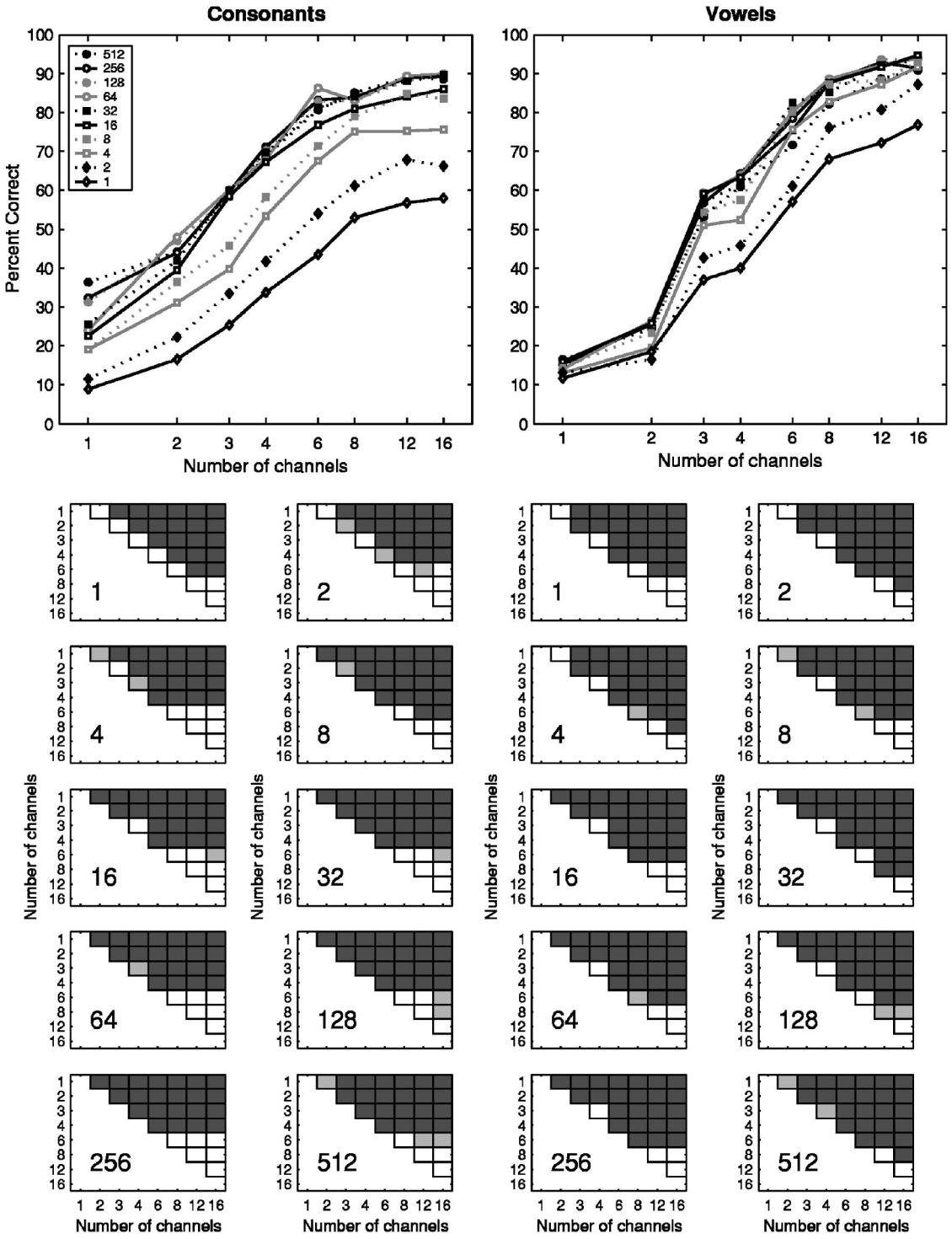

FIG. 1. Phoneme recognition as a function of number of channels. The left and right sides represent data for consonant and vowel recognition, respectively. Data represent the average of all seven subjects. In the upper panels, different lines plot data for different lowpass cutoff frequencies (LPFs) in Hz, as indicated in the figure legend. The lower small panels show the statistical significance of a pairwise comparison of the mean phoneme-recognition scores associated with number of channels, as revealed by the Tukey test. Each of the small panels represents one particular LPF, as indicated by the number (Hz) in the lower left corner of each panel. The light and dark gray squares represent the significance levels at $p<0.05$ and $p<0.01$, respectively. The empty squares represent comparisons not statistically significant.

nels, one could use a LPF as low as 1 Hz (Fig. 3, left). For vowel recognition, some tradeoff between the number of channels and LPFs was observed for LPF$\leqslant$4 Hz and number of channels $\geqslant$4. Vowel recognition was otherwise predominantly determined by the number of channels as long as the LPF was $>$4 Hz (Fig. 3, right).

B. Information analysis

The analysis of perceptual confusions of the consonants and vowels was performed for each of the 80 test conditions using the pooled data from the seven subjects. We caution that, given variability across subjects, the sample size (42

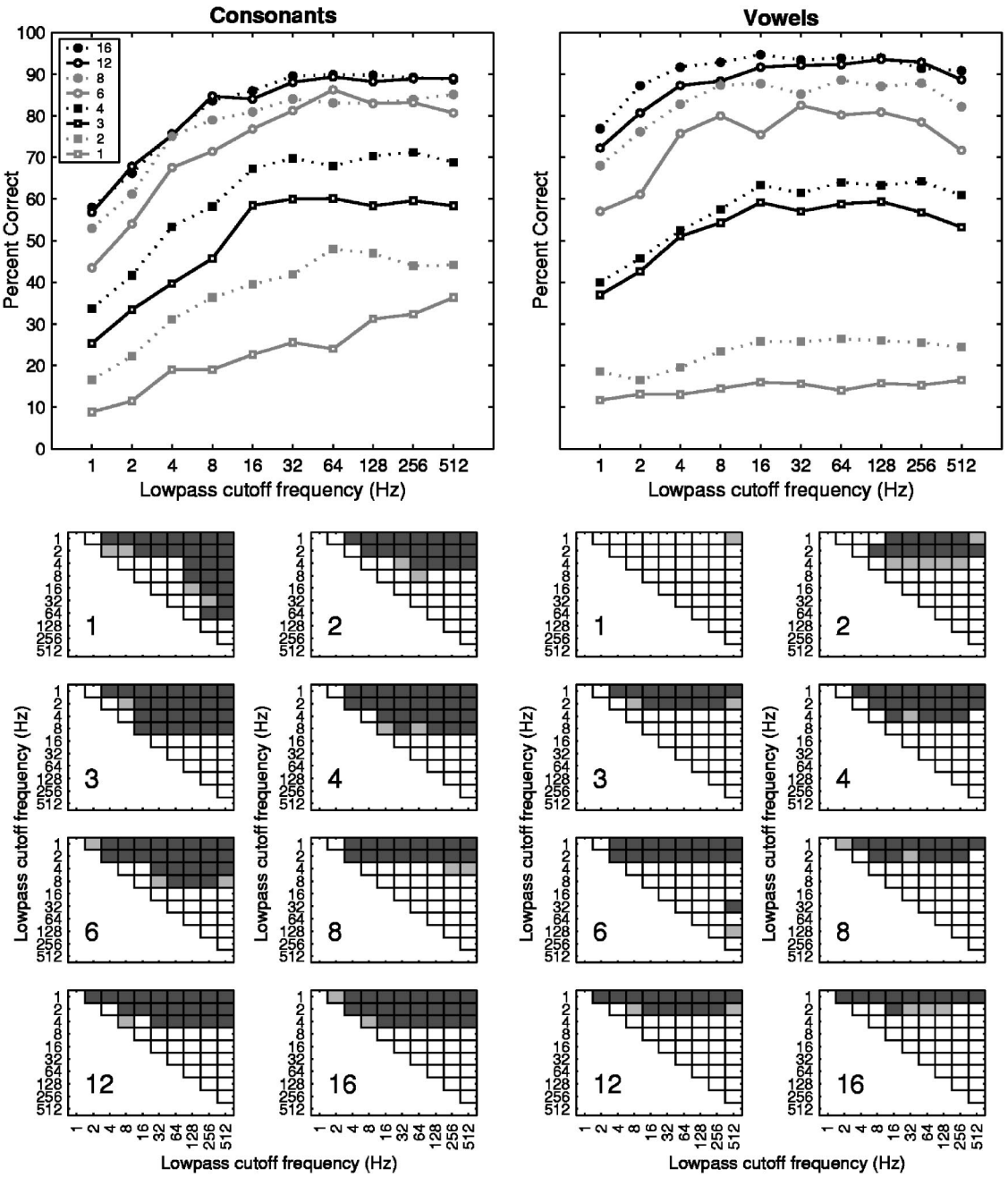

FIG. 2. Phoneme recognition as a function of lowpass cutoff frequencies. The left and right sides represent data for consonant and vowel recognition, respectively. Data represent the average of all seven subjects. In the upper panels, different lines plot data for different numbers of channels, as indicated in the figure legend. The lower small panels show the statistical significance of a pairwise comparison of the mean phoneme-recognition scores associated with lowpass cutoff frequencies, as revealed by the Tukey test. Each of the small panels represents one particular number of channels, as indicated by the number in the lower left corner of each panel. The light and dark gray squares represent the significance levels at $p<0.05$ and $p<0.01$, respectively. The empty squares represent comparisons not statistically significant.

trials for a consonant and 84 trials for a vowel) might still be considered relatively small for the purpose of information analysis. Figure 4 (left) shows the percent of conditional information transmitted for three phonetic features of consonants: voicing, place of articulation, and manner for all the 80 test conditions. The percent of conditional information transmitted is defined as conditional information transmitted (bits) divided by input information for each feature (bits). Figure 4 (right) shows the orders (or iterations) for a feature (voicing, place of articulation, or manner) that was identified and held constant in the SINFA procedure for all the 80 test conditions. Iteration 1 indicates that the information transmitted is the highest when all the three features are analyzed. Iteration 2 indicates that the information transmitted is the higher of the remaining two features when the feature with the highest information is held constant. Iteration 3 indicates that the information transmitted is obtained when the other two features with higher information transmitted are held constant. Thus, to interpret the information analysis data, one should evaluate the results of the percent of conditional information transmitted (Fig. 4, left) and the iterations in which the information transmitted are obtained (Fig. 4, right) in combination.

The right-hand panels of Fig. 4 show the orders (or it-

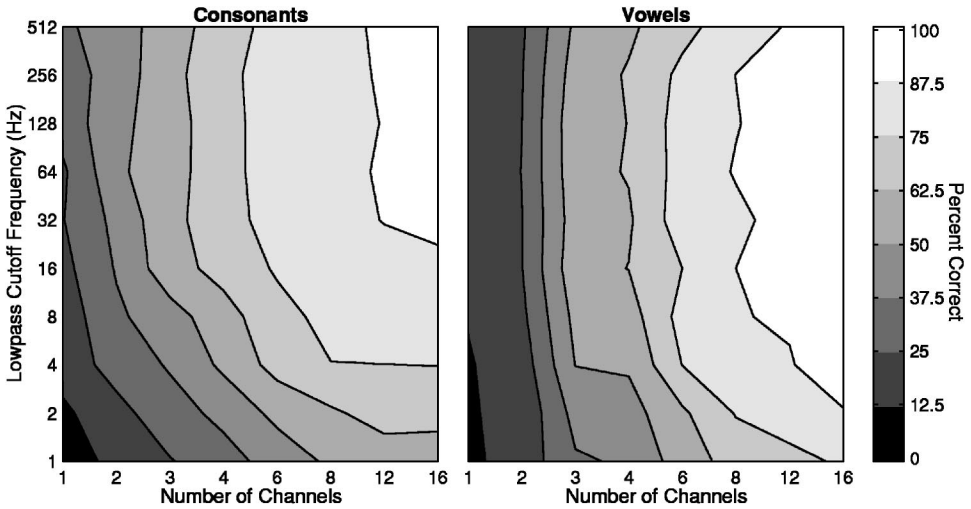

FIG. 3. Phoneme recognition as a function of the number of channels and lowpass cutoff frequency. The left and right panels represent data for consonant and vowel recognition, respectively. In each contour plot, the abscissa and the ordinate represent the number of channels and the lowpass cutoff frequency, respectively. The area that is filled with a particular gray scale represents the phoneme recognition score for a given number of channels and lowpass cutoff frequency. The percent correct represented by the gray scale is indicated by the bar on the right. Data represent the average from all seven subjects.

erations) in which the voicing, place of articulation, and manner features were selected in the SINFA procedure. For example, when the number of channels was >4 and the LPF was >2 Hz, the voicing feature conveyed the greatest amount of information relative to manner and place information. In contrast, when the LPF was 1 or 2 Hz, the voicing feature conveyed the least amount of information, relative to manner and place information, regardless of the number of channels tested. Information transmitted for manner was the highest when the numbers of channels were $\leqslant 4$. Information transmitted for the place of articulation tended to be the smallest among the three features studied (Fig. 4, right). Information transmitted for both manner and voicing depended on both the number of channels and the LPFs (Fig. 4, left). In other words, there was a marked tradeoff in the effects of temporal and spectral cues on transmission of voicing and manner information. On the other hand, information transmitted for the place of articulation predominantly depended on the number of channels with only a slight tradeoff between the number of channels and LPFs when the LPF was $\leqslant 4$ Hz and number of channels $\geqslant 4$ (Fig. 4, left).

The results of the analysis of perceptual confusion of vowels are shown in Fig. 5 in a similar fashion as Fig. 4. Figure 5 (left) plots the percent of conditional information transmitted for three acoustic features of the vowels used in this study: duration, F1 and F2 frequencies. Figure 5 (right) represents the orders (or iterations) for a feature (duration, F1 or F2 frequencies) that was identified and held constant in the SINFA procedure for all the 80 test conditions. Information transmitted for the duration cue was the highest when the LPFs were $\geqslant 4$ Hz for all numbers of channels. When the number of channels was 1 or 2, information transmitted for F2 frequency was higher than that for F1 frequency. However, when the number of channels was $\geqslant 4$, more information was transmitted for F1 than for F2 frequency (Fig. 5, right). In the ranges of the LPFs from 1 to 8 Hz and the number of channels of 1 to 16, the perception of the duration cue showed a tradeoff between the temporal and spectral cues (Fig. 5, left). The ranges in which there was a tradeoff between the temporal and spectral cues for F1 and F2 frequencies were limited to 4 to 16 channels. When the LPFs were greater than 8 Hz, information transmitted for duration, F1 and F2 frequencies was determined by the number of channels (Fig. 5, left).

IV. DISCUSSION

In the present study, we systematically varied the number of channels and the lowpass cutoff frequency for the envelopes of a noise vocoder. Our results confirm many previous observations and provide a clearer view of the interactions of the two independent variables. They also reveal differences in the effects and interactions of these variables that depend on the category of the speech sounds (consonants, vowels, etc.). In the following, we compare our results to previous studies of the effects of spectral and temporal resolution on speech recognition and we discuss the implications of the interaction of spectral and temporal cues.

A. Spectral resolution

Studies using spectral smearing have demonstrated detrimental effects of reduced spectral resolution on speech recognition (e.g., Villchur, 1977; ter Keurs *et al.*, 1992, 1993; Baer and Moore, 1993, 1994; Boothroyd *et al.*, 1996). However, the effect on speech recognition in quiet was hardly noticeable, even for smearing that simulated auditory filters six times broader than normal (Baer and Moore, 1993, 1994). Using a vocoder system, Hill *et al.* (1968) reported that good phoneme recognition ($\sim$70% correct) was obtained with six to eight channels of spectral information. Shannon *et al.* (1995) showed that high levels of speech recognition could be achieved by providing primarily temporal cues in as few as four spectral channels. In recent literature, there are convergent conclusions that only a small number of channels are needed to achieve high-level (i.e., $>$85% correct) speech recognition. The number of channels required for asymptotic

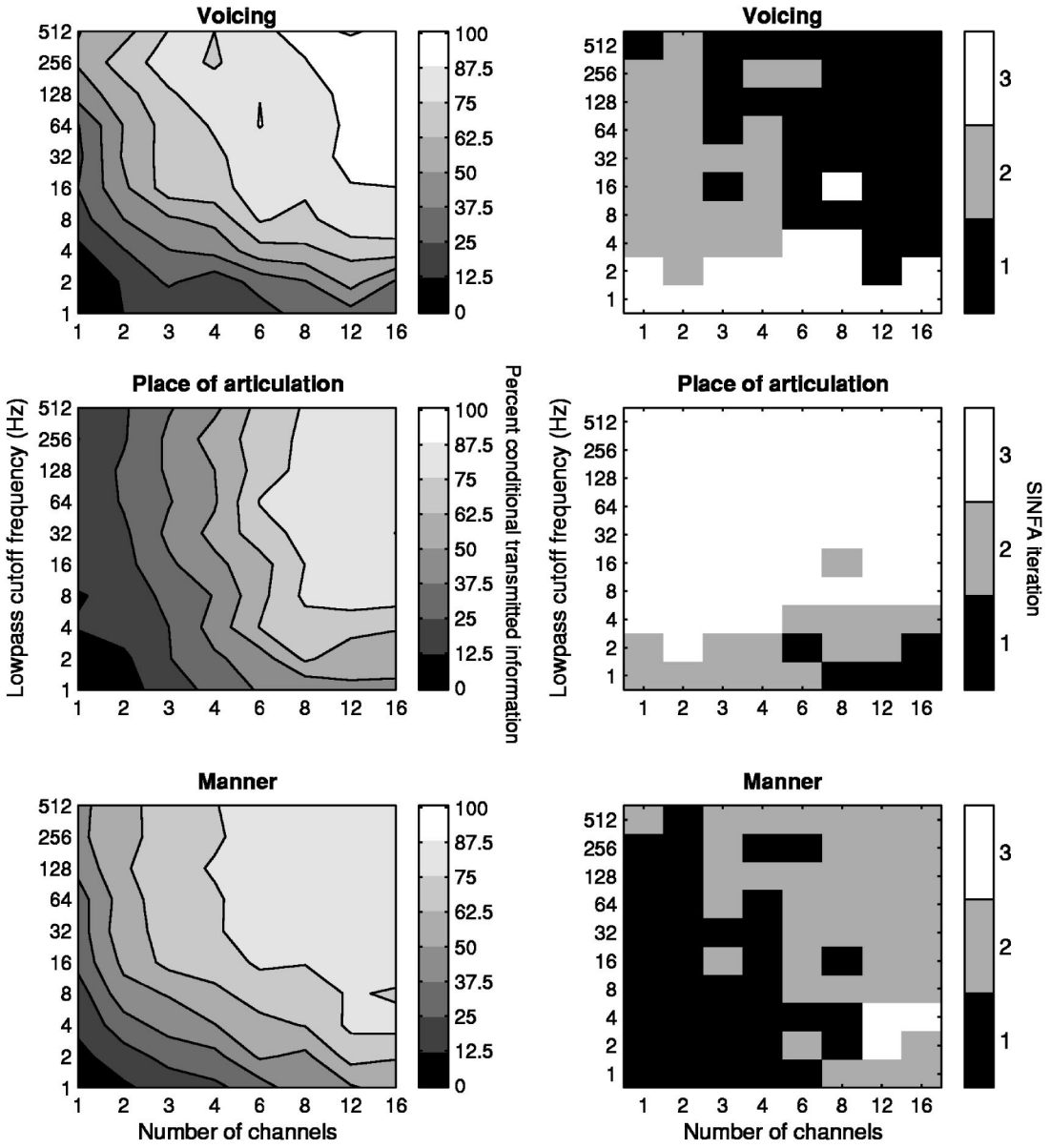

FIG. 4. Left: Percent of conditional information transmitted based on the phonetic features of consonants as a function of number of channels and lowpass cutoff frequency. Right: The iteration in which the information transmitted for each feature was identified in the SINFA procedure. The upper, middle, and lower panels represent data for voicing, place of articulation, and manner, respectively. In each plot, the abscissa and the ordinate represent the number of channels and the lowpass cutoff frequency, respectively. The area that is filled with a particular gray scale represents the percent of conditional information transmitted or the SINFA iteration for a given number of channels and lowpass cutoff frequency. Data analysis was based on pooled confusion matrices of all seven subjects.

speech-recognition performance in quiet varies from four to eight depending on the speech materials (Dorman *et al.*, 1997; Loizou *et al.*, 1999; Xu *et al.*, 2002). The number appeared to be higher for children (Eisenberg *et al.*, 2000). Our present results also indicated that consonant recognition continued to improve from one to six channels and eight channels yielded better performance than four channels (Fig. 1). Although performances with 8 channels were not statistically significantly better than those with 6 channels, performances with 12 or 16 channels were generally better than 6 channels. For vowel recognition, the performance reached a plateau at 12 channels. When the lowpass cutoff frequencies (LPFs) were $\geqslant$4 Hz, the saturation levels were around 90% correct, leaving little room for further improvement. In contrast, the highest consonant recognition was about 80%. This might be due to that consonants inhabit an auditory/acoustic space that is far more multidimensional than that inhabited by vowels. It remains to be tested whether consonant recognition will improve further with increased spectral and temporal information (i.e., more number of channels and higher LPFs). However, such a test can be challenging technically because it is likely that spectral and temporal information is not completely manipulable independently, due to time/bandwidth constraints (Dau *et al.*, 1999).

One of the differences in the results of the present study and those of Shannon *et al.* (1995) warrants discussion. In the Shannon *et al.* (1995) study, subjects reached very high speech-recognition scores with four channels, $\sim$85% correct for consonants and $\sim$95% correct for vowels. In the present study, the best scores at four channels were only 71% correct

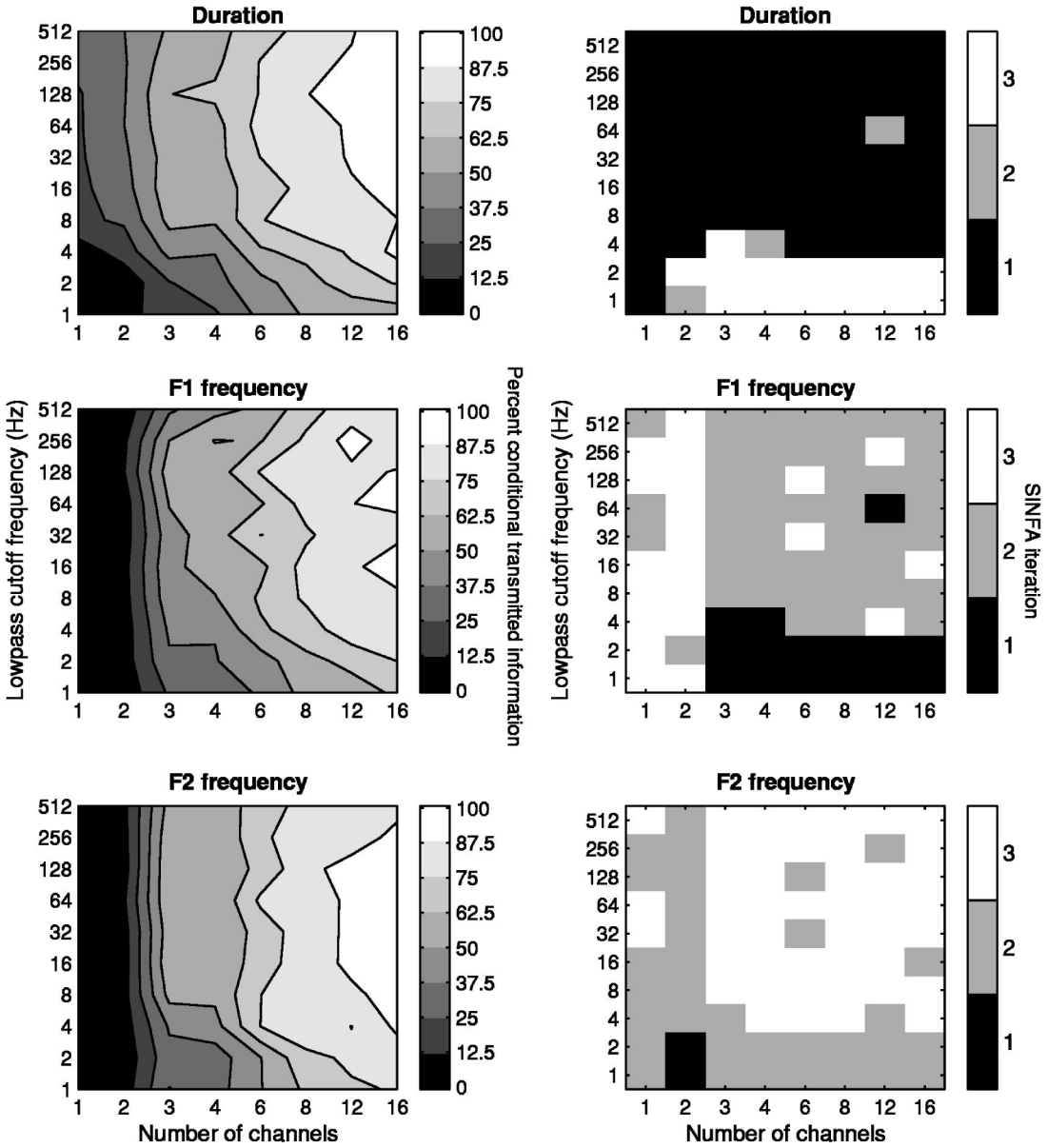

FIG. 5. Left: Percent of conditional information transmitted based on the acoustic features of vowels as a function of number of channels and lowpass cutoff frequencies. Right: The iteration in which the information transmitted for each feature was identified in the SINFA procedure. The upper, middle, and lower panels represent data for duration, F1 frequency, and F2 frequency, respectively. In each plot, the abscissa and the ordinate represent the number of channels and the lowpass cutoff frequencies, respectively. The area that is filled with a particular gray scale represents the percent of conditional information transmitted or the SINFA iteration associated with corresponding numbers of channels and lowpass cutoff frequencies. Data analysis was based on pooled confusion matrices of all seven subjects.

for consonants and 64% correct for vowels. We attribute the difference to the different speech materials used in the tests and amount of training received by the subjects. In Shannon *et al.* (1995), the authors used 16 medial consonants and 8 vowels from one male talker. Their subjects were allowed 8–10 h of practice before testing. In the present study, we used 20 initial consonants recorded by both a male talker and a female talker (Shannon *et al.*, 1999) and 12 vowels recorded by four different talkers (two males and two females) (Hillenbrand *et al.* 1995). Medial consonants are easier to recognize than initial ones, possibly because the vowel to consonant transition that is available in medial consonants is not present in initial consonants. As observed previously by Dorman *et al.* (1997), multiple talkers and more choices of consonants and vowels, as used in the present study, would make the tasks more difficult for the subjects. Furthermore, our subjects received only three hours of training before testing.

It has been shown that under adverse listening conditions, such as in the presence of noise or competing speech, the number of channels required for high-level speech recognition is much larger than under quiet conditions with easy tests. Fu and Shannon (1998) studied phoneme recognition under a variety of signal-to-noise ratios (S/N) and found that the performance with 16 channels (the highest number that was tested) was significantly better than that with 8 channels. Dorman *et al.* (1998) showed that the number of channels for asymptotic performance of sentence recognition in noise was 12 and 20 for +2 dB and −2 dB S/N, respectively. Friesen *et al.* (2001) also showed that the consonant- and vowel-

recognition performance continued to increase up to at least 20 channels in noise conditions.

Data from cochlear implant users have provided evidence that patients can utilize only four to six effective channels (Fishman *et al.*, 1997; Dorman *et al.*, 1998; Fu *et al.*, 1998; Friesen *et al.*, 2001). Some of the better cochlear-implant users exhibited further improvement with seven to ten channels in the presence of background noise (Friesen *et al.*, 2001). The mechanisms underlying the apparent differences in the ability to utilize the spectral information between normal-hearing subjects listening to acoustic simulations and cochlear implant users have not been clearly defined. Friesen *et al.* (2001) proposed that channel interaction and frequency warping in the users' map were two possible reasons. Future efforts to increase the number of effective channels in cochlear-implant users will have the potential to further improve speech perception, especially under conditions with background noise. In cases where it is not possible to increase the number of spectral channels, improvements in temporal resolution might be helpful, as detailed in Secs. IV B and IV C.

B. Temporal resolution

Rosen (1992) partitioned the temporal information in speech into three categories: envelope (2–50 Hz), periodicity (50–500 Hz), and fine structure (500–10 000 Hz). For the most part, fine structure must be represented in a place code. In the present study, we examined the importance of the temporal resolution by modifying the envelope and periodicity cues available through acoustic simulations of cochlear implant processors. For consonant recognition, performance became asymptotic at lowpass cutoff frequencies (LPFs) of about 16 Hz with the exception of the one-channel condition. In the one-channel conditions, the performance showed statistically significant improvement as a function of LPF up to 128 Hz (Fig. 2). For vowel recognition, asymptotic performance was reached at a much lower LPF, i.e., 4 Hz (Fig. 2). For temporal information, a stronger effect on consonant recognition than on vowel recognition was also found in previous studies (Drullman *et al.*, 1994a, 1994b; Fu and Shannon, 2000).

Several studies have demonstrated that speech recognition does not benefit from a LPF that is greater than about 16 to 20 Hz (Drullman *et al.*, 1994a, 1994b; Shannon *et al.*, 1995; Fu and Shannon, 2000). Even though the auditory system with acoustic or electrical stimulation has access to a much higher temporal fluctuation (i.e., about 300–500 Hz), as shown in psychophysical studies (acoustic hearing: Burns and Viemeister, 1976, 1981; Viemeister, 1979; Bacon and Viemeister, 1985; electric hearing: Shannon, 1983, 1992; Zeng, 2002), the listeners may not normally need the full range of the temporal cues for speech recognition. Shannon *et al.* (2001) argued that the speech signal contains a multidimensional and redundant set of cues and that spectral cues are more salient for speech than temporal cues. For the perceptual task, the listeners choose from a smorgasbord of spectral and temporal information in the neural codes (Shannon, 2003). On the other hand, when spectral cues in our study were minimal as in the case of one-channel stimulation, the temporal envelope information at the LPFs as high as 128 Hz made a significant contribution to the consonant recognition (Fig. 2). Van Tasell *et al.* (1987) studied consonant recognition using a one-channel noise band modulated by the speech envelope that was lowpassed at 20, 200, or 2000 Hz. They found that an increasing envelope bandwidth from 20 to 200 Hz significantly improved the subjects' performance, while the further increase from 200 to 2000 Hz did not. Also, the contribution of temporal information to lexical tone perception extends to relatively high LPFs. Temporal fluctuations above 50 Hz are important for extracting periodicity information, as laid out by Rosen (1992). These higher fluctuation rates allow access to information about voicing through a distinction of periodicity versus aperiodicity (a contrast well carried by spectral differences even if there are only two channels), and voice pitch changes. Fu *et al.* (1998) tested tone recognition at LPFs of 50 and 500 Hz and found that the tone recognition scores were around 65% and 80% correct, respectively. We examined lexical-tone recognition for LPFs ranging from 1 to 512 Hz in octave steps and found that tone recognition continuously improved from 1 to 256 Hz for numbers of channels ranging from 1 to 12 (Fig. 7B of Xu *et al.*, 2002). Thus, it is evident that temporal cues are available to subjects up to at least 300 Hz. Evidently, these cues are not needed in all contexts, but they are commonly used when spectral cues are not sufficient, as in the cases of consonant recognition, lexical tone recognition and listening to the processed signals used in cochlear implants when the number of functional channels is small.

C. Interaction or tradeoff between temporal and spectral cues

Given that there seem to be biophysical and physiological limitations on the transmission and reception of both spectral and temporal cues that are important for speech recognition, the tradeoff between these two cues is of high importance to people with cochlear implants. Figure 3 provides a clear view of the interaction between temporal and spectral cues for consonant and vowel recognition in acoustic simulations of implant processors. Both temporal and spectral cues contributed to consonant recognition in this study. These two cues had a tradeoff relation in the range of number of channels between 1 and 12 and LPFs between 1 and 32 Hz. Therefore, to maximize the consonant recognition performance, one would need to provide as much of the spectral and/or temporal information as possible, in the range of interaction. In contrast, the tradeoff between the temporal and spectral cues for vowel recognition was minimal. The spectral cues dominated the vowel recognition as long as the LPF was greater than only 4 Hz.

In a previous study of the relative contribution of temporal and spectral cues for Mandarin tone recognition, we found a tradeoff between the two cues in the ranges of a number of channels between 1 and 12 (the highest tested) and LPFs between 1 and 256 Hz (Xu *et al.*, 2002). Increasing the number of channels gave better access to voice pitch variation because harmonics started to be resolved. The relative strong dependence of tone recognition on the temporal

cues (up to 256 Hz) was probably a unique characteristic of tone recognition. High LPFs permitted the periodicity information in the syllables to pass through the simulations. This could be the reason why high LPFs (e.g., 256 Hz) aided tone recognition.

D. Phonetic/acoustic features and temporal and spectral cues

Van Tasell *et al.* (1987) suggested that both voicing and manner features of consonants could be conveyed by temporal envelope cues. Our results confirmed that in the 1–128 Hz range for voicing and the 1–32 Hz range for manner, LPFs had strong influences on information transmission (Fig. 4). In addition, our results indicated a strong interaction of both temporal and spectral cues for the information transmission of voicing and manner. Fu and Shannon (1999) also showed, in a study of phoneme recognition in cochlear implant users, that nonlinear warping of spectral information had a strong effect on voicing and manner cues. Therefore, it seems that both temporal and spectral cues are important for voicing and manner features of consonants.

In contrast, our data showed that place of articulation relied predominantly on spectral cues (Fig. 4, left), consistent with the acoustic properties of this feature of consonants (Halle *et al.*, 1957; Blumstein and Stevens, 1979; Stevens, 1980). A number of studies have shown that the information transmitted for the place of articulation in cochlear implant users tends to be poorer than that for voicing and manner (Tye-Murray *et al.*, 1992; Tyler and Moore, 1992; Fu and Shannon, 1999, 2000; van Wieringen and Wouters, 1999) when spectral resolution is limited. Our data also demonstrated a similar trend in the normal-hearing subjects listening to acoustic simulations of cochlear implants (Fig. 4, right), where the spectral information was restricted.

For vowel features, we showed that information transmitted for duration cues became important when LPFs were $\geqslant$4 Hz (Fig. 5, right). The syllables we used had a duration of about 200 to 500 ms. When the LPFs were just 1 or 2 Hz, the duration differences between vowels might be smeared. Higher LPFs would have a more clearly marked onset and offset than low LPFs. Also, more pronounced modulation, which accompanies the higher LPFs, could help bind the different frequency channels together based on cross-channel modulation coherence. The fact that information transmitted for F1 and F2 frequencies depended on spectral cues was predictable because both F1 and F2 are features in the spectral domain. Work by Tyler *et al.* (1989), Skinner *et al.* (1996, 1997), and van Wieringen and Wouters (1999) has indicated that some cochlear-implant patients use both F1 and F2 information to help with vowel recognition. Skinner *et al.* (1996) performed sequential information analysis to the vowel recognition data obtained in a group of users of Nucleus devices whose speech-coding strategies were either MPEAK or SPEAK. They found that duration and F2 frequency were the first two features that most information was transmitted and that F1 information was ranked third in their choice of four features. On the other hand, Tyler *et al.* (1992) found in a group of users of Ineraid devices that duration and F1 accounted for nearly 80% of the information transmitted whereas F2 accounted for only a small fraction of the information transmitted. Therefore, despite different implant devices and the speech processing strategies used in the aforementioned studies, it seems that implant patients can utilize F1 cues efficiently whereas an evaluation of the usage of F2 cues has produced mixed results. Our current data from normal-hearing subjects listening to simulations of a CIS-type strategy showed that the order of importance in contribution to vowel recognition was (1) duration, (2) F1, and (3) F2 frequency.

E. Relevance to cochlear implants

It must be recognized that subjects with cochlear implants are not experiencing the same percepts with their implants that normal-hearing subjects experience when listening to the simulated processors. A key difference in normal-hearing and implanted subjects is that the number of auditory neurons available for information transmission is usually much smaller in the implanted subjects. Furthermore, cochlear implants seldom deliver the outputs of individual channels of the processors to exactly the normal tonotopic place for a given output frequency band. Thus, we can reasonably expect that the spectral representation of the acoustic signal is distorted in the cochlear-implant user. The temporal representation of the signal for the implant user is probably also significantly different from that found in a normal-hearing listener. For one thing, across-fiber synchrony to the stimulus is usually much stronger in the electrically stimulated ear. Despite these differences, it seems likely that both spectral and temporal information are available to the implant listener. The relative importance of these two classes of cues for the normal-hearing listener can reasonably be expected to parallel the perceptual needs of the implanted listener and are thus informative as to the relative importance of improving information transmission in these two classes of cues for the cochlear implant user.

V. CONCLUSIONS

Our results have demonstrated that both spectral and temporal cues are important for consonant and vowel recognition. In the ranges of numbers of channels and LPFs tested, the spectral cues exert a greater effect on both consonant and vowel recognition than the temporal cues. The LPF up to 16 Hz is needed for consonant recognition whereas that for vowel recognition is as low as 4 Hz. The number of channels required to reach asymptotic performance for consonant and vowel recognition is 8 and 12, respectively. Within the ranges of the LPF and the number of channels described above, the temporal and spectral cues interact in phoneme recognition, especially for consonants. However, the range within which the interaction occurs is much smaller than that for tone recognition, which we identified in a previous study (Xu *et al.*, 2002). Nonetheless, to reach optimal phoneme recognition, one should maximize the transmission of both temporal and spectral cues. The analysis of information transmitted for phonetic features of consonants revealed that the manner feature contributed to consonant recognition the most in comparison to the place of articulation or voicing

features when the number of channels was ⩽4, whereas the voicing feature conveyed the greatest amount of information when the number of channels was >4 and the LPF was >2 Hz. Information transmitted for both voicing and manner features showed a strong tradeoff in effects of spectral versus temporal cues. The place of articulation feature relied mostly on spectral cues and the percent of information transmitted was relatively low compared to voicing and manner. An analysis of information transmitted for acoustic features of vowels revealed that the duration and F1 cues but not the F2 features contributed substantially to vowel recognition and that the tradeoff between spectral and temporal features was greatest for the duration feature. Future studies of relative contributions of spectral and temporal cues for phoneme recognition in noise conditions and in patients with hearing impairment may provide us with knowledge on how the two cues interact in situations that resemble those faced by cochlear implant patients.

ACKNOWLEDGMENTS

We wish to thank Dr. José Benkí and Dr. Chao-Yang Lee for their comments on earlier versions of the manuscript. We are grateful to Dr. Stuart Rosen and Associate Editor Dr. Ken Grant and an anonymous reviewer for their constructive comments. The work was supported by NIH/NIDCD Grants R01 DC03808 and KHRI Electronics and Computing Core Facilities (P30 DC05188) and Ohio University Research Challenge Awards.

[1]A University College London version of the software for SINFA, called FIX (Feature Information Xfer), is available at http://www.phon.ucl.ac.uk/resource/software.html.

Bacon, S. P., and Viemeister, N. F. (**1985**). ''Temporal modulation transfer functions in normal-hearing and hearing-impaired listeners,'' Audiology **24**, 117–134.

Baer, T., and Moore, B. C. J. (**1993**). ''Effects of spectral smearing on the intelligibility of sentences in noise,'' J. Acoust. Soc. Am. **94**, 1229–1241.

Baer, T., and Moore, B. C. J. (**1994**). ''Effects of spectral smearing on the intelligibility of sentences in the presence of interfering speech,'' J. Acoust. Soc. Am. **95**, 2277–2280.

Blumstein, S. E., and Stevens, K. N. (**1979**). ''Acoustic invariance in speech production: Evidence from measurements of the spectral characteristics of stop consonants,'' J. Acoust. Soc. Am. **66**, 1001–1017.

Boothroyd, A., Mulhearn, B., Gong, J., and Ostroff, J. (**1996**). ''Effects of spectral smearing on phoneme and word recognition,'' J. Acoust. Soc. Am. **100**, 1807–1818.

Burns, E. M., and Viemeister, N. F. (**1976**). ''Nonspectral pitch,'' J. Acoust. Soc. Am. **60**, 863–869.

Burns, E. M., and Viemeister, N. F. (**1981**). ''Played-again SAM: Further observations on the pitch of amplitude-modulated noise,'' J. Acoust. Soc. Am. **70**, 1655–1660.

Dau, T., Verhey, J., and Kohlrausch, A. (**1999**). ''Intrinsic envelope fluctuations and modulation-detection thresholds for narrow-band noise carriers,'' J. Acoust. Soc. Am. **106**, 2752–2760.

Dorman, M. F., Loizou, P. C., Fitzke, J., and Tu, Z. (**1998**). ''The recognition of sentences in noise by normal-hearing listeners using simulations of cochlear-implant signal processors with 6–20 channels,'' J. Acoust. Soc. Am. **104**, 3583–3585.

Dorman, M. F., Loizou, P. C., Fitzke, J., and Tu, Z. (**2000**). ''Recognition of monosyllabic words by cochlear implant patients and by normal-hearing subjects listening to words processed through cochlear implant signal processing strategies,'' Ann. Otol. Rhinol. Laryngol. Suppl. **109**, 64–66.

Dorman, M. F., Loizou, P. C., and Rainey, D. (**1997**). ''Speech intelligibility as a function of the number of channels of stimulation for signal processors using sine-wave and noise-band outputs,'' J. Acoust. Soc. Am. **102**, 2403–2411.

Drullman, R., Festen, J. M., and Plomp, R. (**1994a**). ''Effect of temporal envelope smearing on speech perception,'' J. Acoust. Soc. Am. **95**, 1053–1064.

Drullman, R., Festen, J. M., and Plomp, R. (**1994b**). ''Effect of reducing slow temporal modulations on speech reception,'' J. Acoust. Soc. Am. **95**, 2670–2680.

Dudley, H. (**1939**). ''Remaking speech,'' J. Acoust. Soc. Am. **11**, 169–177.

Eisenberg, L. S., Shannon, R. V., Martinez, A. S., Wygonski, J., and Boothroyd, A. (**2000**). ''Speech recognition with reduced spectral cues as a function of age,'' J. Acoust. Soc. Am. **107**, 2704–2710.

Fishman, K. E., Shannon, R. V., and Slattery, W. H. (**1997**). ''Speech recognition as a function of the number of electrodes used in the SPEAK cochlear implant speech processor,'' J. Speech Lang. Hear. Res. **40**, 1201–1215.

Friesen, L. M., Shannon, R. V., Baskent, D., and Wang, X. (**2001**). ''Speech recognition in noise as a function of the number of spectral channels: Comparison of acoustic hearing and cochlear implants,'' J. Acoust. Soc. Am. **110**, 1150–1163.

Fu, Q.-J., and Shannon, R. V. (**1999**). ''Effects of electrode location and spacing on phoneme recognition with the Nucleus-22 cochlear implant,'' Ear Hear. **20**, 321–331.

Fu, Q.-J., and Shannon, R. V. (**2000**). ''Effect of stimulation rate on phoneme recognition by Nucleus-22 cochlear implant listeners,'' J. Acoust. Soc. Am. **107**, 589–597.

Fu, Q.-J., Shannon, R. V., and Wang, X. (**1998**). ''Effects of noise and spectral resolution on vowel and consonant recognition: Acoustic and electric hearing,'' J. Acoust. Soc. Am. **104**, 3586–3596.

Greenwood, D. D. (**1990**). ''A cochlear frequency-position function for several species—29 years later,'' J. Acoust. Soc. Am. **87**, 2592–2605.

Halle, M., Hughes, G. W., and Radley, J.-P. A. (**1957**). ''Acoustic properties of stop consonants,'' J. Acoust. Soc. Am. **29**, 107–116.

Henry, B. A., and Turner, C. W. (**2003**). ''The resolution of complex spectral patterns by cochlear implant and normal-hearing listeners,'' J. Acoust. Soc. Am. **113**, 2861–2873.

Hill, F. J., McRae, L. P., and McClellan, R. P. (**1968**). ''Speech recognition as a function of channel capacity in a discrete set of channels,'' J. Acoust. Soc. Am. **44**, 13–18.

Hillenbrand, J., Getty, L. A., Clark, M. J., and Wheeler, K. (**1995**). ''Acoustic characteristics of American English vowels,'' J. Acoust. Soc. Am. **97**, 3099–3111.

Hornsby, B. W. Y., and Ricketts, T. A. (**2001**). ''The effects of compression ratio, signal-to-noise ratio, and level on speech recognition in normal-hearing listeners,'' J. Acoust. Soc. Am. **109**, 2964–2973.

Kong, Y.-Y., Cruz, R., Jones, J. A., and Zeng, F.-G. (**2004**). ''Music perception with temporal cues in acoustic and electric hearing,'' Ear Hear. **25**, 173–185.

Loizou, P. C., Dorman, M., Poroy, O., and Spahr, T. (**2000**). ''Speech recognition by normal-hearing and cochlear implant listeners as a function of intensity resolution,'' J. Acoust. Soc. Am. **108**, 2377–2387.

Loizou, P. C., Dorman, M., and Tu, Z. (**1999**). ''On the number of channels needed to understand speech,'' J. Acoust. Soc. Am. **106**, 2097–2103.

MATLAB (**2002**). ''The language of technical computing,'' The MathWorks, Inc., Natick, MA.

Miller, G. A., and Nicely, P. E. (**1955**). ''An analysis of perceptual confusions among some English consonants,'' J. Acoust. Soc. Am. **27**, 338–352.

Peterson, G. E., and Barney, H. L. (**1952**). ''Control methods used in a study of the vowels,'' J. Acoust. Soc. Am. **24**, 175–184.

Rosen, S. (**1992**). ''Temporal information in speech: Acoustic, auditory and linguistic aspects,'' Philos. Trans. R. Soc. London, Ser. B **336**, 367–373.

Rubinstein, J. T., and Hong, R. (**2003**). ''Signal coding in cochlear implants: Exploiting stochastic effects of electrical stimulation,'' Ann. Otol. Rhinol. Laryngol. **112**, 14–19.

Schroeder, M. R. (**1966**). ''Vocoders: Analysis and synthesis of speech,'' Proc. IEEE **54**, 352–366.

Shannon, R. V. (**1983**). ''Multichannel electrical stimulation of the auditory nerve in man,'' I. basic psychophysics. Hear. Res. **11**, 157–189.

Shannon, R. V. (**1992**). ''Temporal modulation transfer functions in patients with cochlear implants,'' J. Acoust. Soc. Am. **91**, 2156–2164.

Shannon, R. V. (**2003**). ''The auditory smorgasbord: Perceptual use of temporal neural information,'' Assoc. Res. Otolaryngol. Abs. **26**, 2.

Shannon, R. V., Fu, Q.-J., Wang, X., Galvin, J., and Wygonski, J. (**2001**). ''Critical cues for auditory pattern recognition in speech: Implications for cochlear implant speech processor design,'' *Physiological and Psychological Bases of Auditory Function*, Proceedings of the 12th International Symposium on Hearing, edited by A. J. M. Houtsma, A. Kohlrausch, V. F. Prijs, and R. Schoonhoven (Shaker Publishing BV, Maastricht, NL).
Shannon, R. V., Jensvold, A., Padilla, M., Robert, M. E., and Wang, X. (**1999**). ''Consonant recordings for speech testing,'' J. Acoust. Soc. Am. **106**, L71–74.
Shannon, R. V., Zeng, F.-G., Kamath, V., Wygonski, J., and Ekelid, M. (**1995**). ''Speech recognition with primarily temporal cues,'' Science **270**, 303–304.
Shannon, R. V., Zeng, F.-G., and Wygonski, J. (**1998**). ''Speech recognition with altered spectral distribution of envelope cues,'' J. Acoust. Soc. Am. **104**, 2467–2476.
Skinner, M. W., Arndt, P. L., and Staller, S. J. (**2002**). ''Nucleus 24 advanced encoder conversion study: Performance vs preference,'' Ear Hear. **23**, 2S–25S.
Skinner, M. W., Fourakis, M. S., Holden, T. A., Holden, L. K., and Demorest, M. E. (**1996**). ''Identification of speech by cochlear implant recipients with the multipeak (MPEAK) and spectral peak (SPEAK) speech coding strategies: I. Vowels,'' Ear Hear. **17**, 182–197.
Skinner, M. W., Holden, L. K., Holden, T. A., Demorest, M. E., and Fourakis, M. S. (**1997**). ''Speech recognition at simulated soft, conversational, and raised-to-loud vocal efforts by adults with cochlear implants,'' J. Acoust. Soc. Am. **101**, 3766–3782.
Stevens, K. N. (**1980**). ''Acoustic correlates of some phonetic categories,'' J. Acoust. Soc. Am. **68**, 836–842.
ter Keurs, M., Festen, J. M., and Plomp, R. (**1992**). ''Effect of spectral envelope smearing on speech reception I,'' J. Acoust. Soc. Am. **91**, 2872–2880.
ter Keurs, M., Festen, J. M., and Plomp, R. (**1993**). ''Effect of spectral envelope smearing on speech reception. II,'' J. Acoust. Soc. Am. **93**, 1547–1552.
Turner, C. W., Gantz, B. J., Vidal, C., Behrens, A., and Henry, B. A. (**2004**). ''Speech recognition in noise for cochlear implant listeners: Benefits of residual acoustic hearing,'' J. Acoust. Soc. Am. **115**, 1729–1735.
Tye-Murray, N., Tyler, R. S., Woodworth, G. G., and Gantz, B. J. (**1992**). ''Performance over time with a Nucleus or Ineraid cochlear implant,'' Ear Hear. **13**, 200–209.
Tyler, R. S., Tye-Murray, N., and Otto, S. R. (**1989**). ''The recognition of vowels differing by a single formant by cochlear-implant subjects,'' J. Acoust. Soc. Am. **86**, 2107–2112.
Tyler, R. S., and Moore, B. C. J. (**1992**). ''Consonant recognition by some of the better cochlear-implant patients,'' J. Acoust. Soc. Am. **92**, 3068–3077.
Tyler, R. S., Preece, J. P., Lansing, C. R., and Gantz, B. J. (**1992**). ''Natural vowel perception by patients with the Ineraid cochlear implant,'' Audiol. **31**, 228–239.
Van Tasell, D. J., Soli, S. D., Kirby, V. M., and Widin, G. P. (**1987**). ''Speech waveform envelope cues for consonant recognition,'' J. Acoust. Soc. Am. **82**, 1152–1161.
van Wieringen, A., and Wouters, J. (**1999**). ''Natural vowel and consonant recognition by Laura cochlear implantees,'' Ear Hear. **20**, 89–103.
Villchur, E. (**1977**). ''Electronic models to simulate the effect of sensory distortions on speech perception by the deaf,'' J. Acoust. Soc. Am. **62**, 665–674.
Viemeister, N. F. (**1979**). ''Temporal modulation transfer functions based upon modulation thresholds,'' J. Acoust. Soc. Am. **66**, 1364–1380.
Wang, M. D., and Bilger, R. C. (**1973**). ''Consonant confusions in noise: A study of perceptual features,'' J. Acoust. Soc. Am. **54**, 1248–1266.
Xu, L., Tsai, Y., and Pfingst, B. E. (**2002**). ''Features of stimulation affecting tonal-speech perception: Implications for cochlear prostheses,'' J. Acoust. Soc. Am. **112**, 247–258.
Wilson, B. S., Finley, C. C., Lawson, D. T., and Zerbi, M. (**1997**). ''Temporal representations with cochlear implants,'' Am. J. Otol. **18**, S30–34.
Zeng, F.-G. (**2002**). ''Temporal pitch in electric hearing,'' Hear. Res. **174**, 101–106.

The effect of inharmonic partials on pitch of piano tones[a)]

Brian E. Anderson[b)] and William J. Strong
Department of Physics and Astronomy, N-283 ESC, Brigham Young University, Provo, Utah 84602

(Received 4 November 2004; revised 17 January 2005; accepted 8 February 2005)

Piano tones have partials whose frequencies are sharp relative to harmonic values. A listening test was conducted to determine the effect of inharmonicity on pitch for piano tones in the lowest three octaves of a piano. Nine real tones from the lowest three octaves of a piano were analyzed to obtain frequencies, relative amplitudes, and decay rates of their partials. Synthetic inharmonic tones were produced from these results. Synthetic harmonic tones, each with a twelfth of a semitone increase in the fundamental, were also produced. A jury of 21 listeners matched the pitch of each synthetic inharmonic tone to one of the synthetic harmonic tones. The effect of the inharmonicity on pitch was determined from an average of the listeners' results. For the nine synthetic piano tones studied, pitch increase ranged from approximately two and a half semitones at low fundamental frequencies to an eighth of a semitone at higher fundamental frequencies. © *2005 Acoustical Society of America.*
[DOI: 10.1121/1.1882963]

PACS numbers: 43.75.Cd, 43.66.Hg [ADP] Pages: 3268–3272

I. INTRODUCTION

Several studies have investigated various subjective behaviors of complex inharmonic pianolike tones. Fletcher *et al.* (1962) found, through subjective testing, that inharmonicity in piano tones contributes a sense of warmth. In 1983, Peters *et al.* (1983) had listeners match components in complex harmonic pianolike tones to a single sine wave to determine the effect on pitch. Moore *et al.* (1985a) found, through subjective testing, that a complex tone consisting of one slightly mistuned partial resulted in a linear residue pitch shift for small mistunings. Moore *et al.* (1985b) also used this type of subjective testing to determine detection thresholds and the importance of each partial. They suggested that inharmonicity is audible for lower piano tones. Moore *et al.* (1993) determined listeners' psychoacoustic abilities to hear individual partials in inharmonic complex tones. Conklin (1996) wrote a series of tutorial papers, the third of which is a summary of research investigations on the subject of inharmonicity. Rocchesso *et al.* (1999) studied ''The influence of accurate reproduction of inharmonicity on the perceived quality of piano tones.'' And most recently, Galembo *et al.* (2001) determined the perceived effect of having various kinds of starting phases for synthetic tones.

This study investigates the effect of inharmonicity on pitch by having listeners match complex inharmonic pianolike tones (based on measured tones) to complex harmonic pianolike tones (based on ideal string theory). Nine piano tones from a standard upright piano were recorded and analyzed. The analysis determined various parameters for as many partials as could be resolved for each of the nine-recorded tones. From this analysis, a synthetic inharmonic tone and a set of harmonic tones with different fundamental frequencies were produced for each of the nine tones. A jury of listeners matched each synthetic inharmonic tone to one of the synthetic harmonic tones among the corresponding set. The effect of inharmonicity on pitch was determined from the average fundamental frequency of harmonic tones matched to an inharmonic tone.

II. TONE GENERATION

A. Recording

In order to study the effects of inharmonicity, a readily available Yamaha Upright Piano (P22 L. OAK) was used for the study. A Larson Davis 2540 pressure microphone was used with a Larson Davis 900B Preamplifier. The 900B preamplifier was then connected to a Larson Davis 2200C Microphone Power Supply and Instrumentation Amplifier. The output of the 2200C went into an Aphex Amplifier 124A. A Panasonic DAT recorder was used to record the output signal from the amplifier.

The recording was done in a large classroom that had been acoustically treated to reduce reverberation. Recordings were done at times when ambient levels could be maintained without interruptions. With this recording environment and the recording setup, it was possible to maintain an overall S/N ratio of at least 30 dB. The Yamaha Upright Piano has a removable cover that allowed for better exposure of the soundboard on the player's side of the piano. The microphone was placed about 6 in. from the soundboard.

Tones were recorded in the lower three octaves of the piano where the effects of inharmonicity are greater. Nine tones (A0, C1, E1, A1, C2, E2, A2, C3, and E3) were individually played and recorded. An effort was made to strike each piano key with the same amount of force. Tones were recorded until their overall sound pressure level decayed to the level of ambient noise in the room. The resulting recorded tones had durations ranging from 10 to 15 s. Finally, the tones recorded on the DAT were digitally transferred onto a CD.

[a)]Portions of this work (preliminary results) were presented in ''The effect of inharmonic partials on pitch of piano tones,'' 143rd Meeting: Acoustical Society of America, Pittsburgh, PA, June 2002.

[b)]Present address: Graduate Program in Acoustics, The Pennsylvania State University, P.O. Box 30, State College, PA 16802. Electronic mail: bea3@email.byu.edu

 0001-4966/2005/117(5)/3268/5/$22.50

B. Analysis

The tones were played on a CD player whose output was directly connected to the input of a Hewlett-Packard dynamic signal analyzer and analyzed in order to obtain the desired partial frequencies. Some of the piano tones had as many as 56 resolvable partials that were obtained in the analysis. In this analysis, it was assumed that the partial frequency values remained constant over time, which, from the tones' spectrograms, proved to be a valid assumption.

The recorded tones were then imported into MATLAB for further analysis. The resolvable frequency values of the partials obtained from the dynamic signal analyzer were used in the MATLAB analysis. The analysis determined the relative initial amplitudes and decay rates for as many partials as could be resolved for each of the nine-recorded tones. An attack portion was also determined for each tone analyzed. Fourier analysis was used to determine the amplitude of each partial, over the period of the fundamental frequency, repeated for 10 s. A linear curve fit was applied to a logarithmic representation of the amplitude versus time data for each partial, from which the initial amplitude and decay rate were obtained. The attack portion of each recorded tone was determined as the time it took from the onset of the tone to reach peak amplitude. The initial phase ϕ_n for each partial was assigned a random value between 0 and 2π. The results of the analysis for each of the nine tones consisted of frequencies of the partials, f_n, amplitudes of the partials, A_n, decay rates of the partials, δ_n, and initial phases, ϕ_n.

C. Synthesis

Based on the analysis, a synthetic inharmonic tone was produced for each of the nine tones analyzed. Each synthetic inharmonic tone was generated based on the following equation,

$$y_{\text{inharmonic}} = A_n e^{-\delta_n t} \sin(2\pi f_n t + \phi_n), \tag{1}$$

where the variables are the results from the analysis.

A series of 10 to 30 harmonic tones was generated for comparison with each inharmonic tone. Partial frequencies of the harmonic tones were integer multiples of the fundamental. Each synthetic harmonic tone was generated based on the following equation,

$$y_{\text{harmonic}} = A_n e^{-\delta_n t} \sin(2\pi n f_1 t + \phi_n), \tag{2}$$

where the variables, with the exception of the fundamental frequency f_1, are results from the analysis. The fundamental frequency for each harmonic tone in the series was incremented in a ratio of 1.005 (approximately a twelfth of a semitone).

A linearly increasing (from zero to the maximum amplitude) attack portion, determined from the analysis procedure, was applied to each synthetic tone. For each of the synthetic harmonic piano tones, an audio CD track was created consisting of the corresponding synthetic inharmonic tone presented first followed by the synthetic harmonic tone. Much of the synthesis procedure was chosen based on previous work done by Anderson (2002).

TABLE I. Curve-fitted inharmonicity coefficients for each of the nine measured piano tones.

Piano note	Inharmonicity coefficient
A0	0.000 453
C1	0.000 319
E1	0.000 231
A1	0.000 144
C2	0.000 130
E2	0.000 108
A2	0.000 111
C3	0.000 129
E3	0.000 110

D. Inharmonicity coefficient

In 1964, Fletcher published a theoretical derivation of an equation governing the shift in partial frequencies of piano strings due to the inherent stiffness in piano strings. Fletcher (1964) gave the following equation for predicting partial frequencies once the fundamental frequency, which itself is affected by the stiffness, is known:

$$f_n = n f_1 \left[\frac{(1 + Bn^2)}{(1 + B)} \right]^{1/2}, \tag{3}$$

where B represents the inharmonicity coefficient. Using this equation, an estimate for the inharmonicity coefficient was determined, using the method of least squares, for each of the nine measured tones.

The least-squares curve fit for the inharmonicity coefficient included a heavier weighting on the lower partials. For the nth partial, the least squares error weighting $W(n)$ is computed as

$$W(n) = N + 1 - n, \tag{4}$$

where N is the total number of partials for the given tone. The resulting weighting is a linearly decreasing function. The results for the curve fitted B values may be found in Table I. Each curve fit result represented the increasing partial frequency values fairly accurately, with a slight tendency to underestimate the lower partials and overestimate the higher partials. The B values were determined in order to investigate the correlation between the pitch shift due to inharmonicity and the inharmonicity coefficient for each measured piano tone.

III. METHOD

A. Subjects

Twenty-one subjects volunteered from among the Physics 167 ''Descriptive Acoustics of Music and Speech'' course offered at Brigham Young University. Students who participated in the study were given extra credit towards their grade in that course. The average age of participants was 20.7 years, with 76% female; 33% had taken a recent hearing test. Participants had an average of 6.6 years of piano playing experience, with an average of 9.1 years total musical instrument experience. Table II shows the data for the listeners, listed according to piano playing experience.

TABLE II. Data for volunteer listeners who participated in inharmonicity perceptual study.

Listener rank	Age (years)	Sex	Taken recent hearing test	Years experience playing the piano	Total years of musical experience
1	21	F	N	15	15
2	20	F	N	15	15
3	20	F	N	14	14
4	20	F	Y	13	13
5	19	F	N	12	12
6	20	F	Y	11	11
7	24	F	N	10	10+
8	19	F	N	10	10
9	20	F	N	8	10
10	22	M	N	6	12
11	19	F	N	6	8
12	20	F	Y	5	8
13	17	F	Y	5	8
14	18	F	Y	5	7
15	20	F	Y	2	5
16	20	F	Y	1	8
17	22	M	N	0	13
18	24	M	N	0	10+
19	25	M	N	0.5	0.5
20	25	M	N	0	3
21	19	F	N	0	0
Average	20.7	76% F	33% Y	6.6	9.1

B. Stimuli

Listeners were given an audio CD player and a set of Sony Studio Monitor/Dynamic Stereo Headphones (model MDR-7506) to playback the tone pairs. Listeners set the volume levels according to their comfort levels. Listeners were placed in a quiet, isolated, semi-anechoic chamber facility located at Brigham Young University. Listeners were free to listen to tone pair CD tracks in any order they chose and as many times as needed. Each listener was instructed to try and find a tone pair, for each of the nine sets, that they perceived as having the closest pitch match. If no match was found among a given set of tone pairs, they were instructed to indicate whether the harmonic tones needed to be higher or lower in pitch in order to find a match; these responses were not included in further analysis.

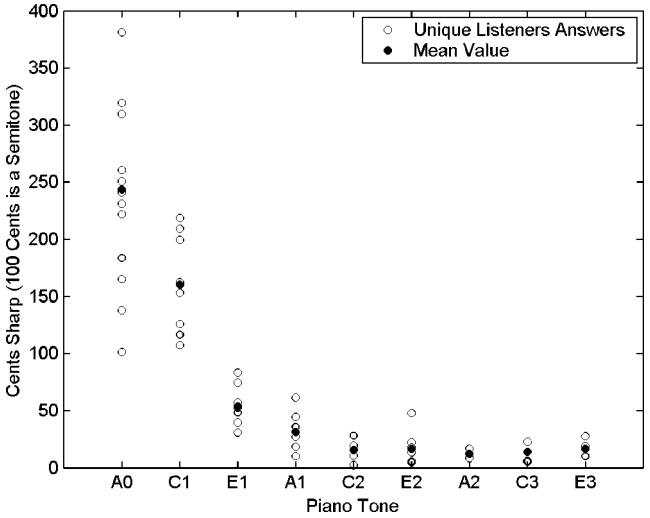

FIG. 1. Results for pitch matching study. Open circles represent unique listeners' answers and closed circles represent the average match for each piano tone set.

IV. RESULTS

Figure 1 shows a scatter plot of individual responses and their average for each tone. (Overlapping individual responses are not apparent in the figure.) The average pitch shift due to inharmonicity was greater in lower frequency piano tones. It can also be seen that the spread or deviation is much greater for lower tones. Table III tabulates the average results of the listening tests. Table III also shows deviation values.

In order to compare the listeners' results for the perceived shift in pitch due to inharmonicity with the least squares fitted values for the inharmonicity coefficients, each set of results was normalized by their respective mean value. A plot of the two normalized sets of results may be found in Fig. 2. Also contained in Fig. 2 is a plot of the normalized relative standard deviation of listeners' results.

A plot of the average perceived cents sharp values divided by the fitted inharmonicity coefficients versus fundamental frequency results in an exponentially decreasing function. This function was least squares curve fitted to an equation of exponential form with an added offset constant.

TABLE III. Average results of listening tests. The actual fundamental and the average matched fundamental frequency values are given in Hertz. Standard deviation values are determined from the matched fundamental frequency values. The relative standard deviation values are defined as the standard deviation values divided by their respective mean values (then multiplied by 100 to represent a percentage).

Piano note	Actual fundamental (Hz)	Average perceived fundamental (Hz)	Cents sharp ((Ratio−1)/0.059)	Standard deviation (Hz)	Relative standard deviation
A0	26.750	30.597	243.8	13.71	44.81
C1	32.125	35.161	160.2	3.39	9.63
E1	40.375	41.649	53.5	3.29	7.89
A1	54.125	55.131	31.5	2.53	4.59
C2	64.500	65.094	15.6	1.99	3.06
E2	81.375	82.162	16.4	2.21	2.69
A2	108.625	109.416	12.3	1.15	1.05
C3	128.500	129.559	14.0	1.27	0.98
E3	163.250	164.830	16.4	1.76	1.07

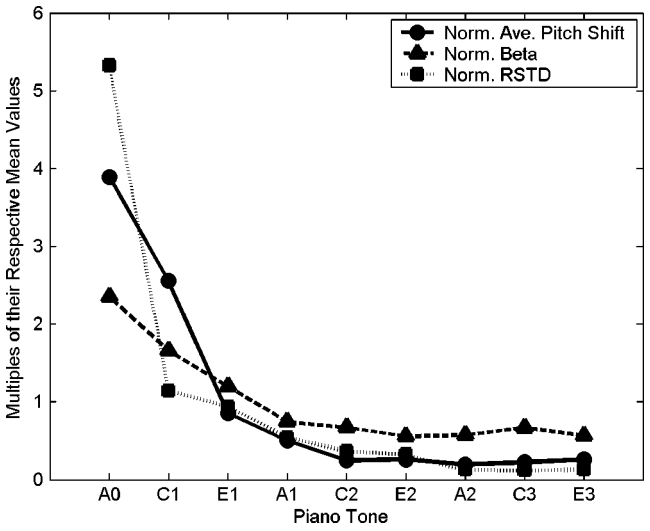

FIG. 2. Normalized average results for pitch matching study, normalized results for inharmonicity coefficient determination, and normalized relative standard deviation results. A value of 1.0 on this plot represents the average value for each data set.

The resulting coefficients for the curve fit resulted in the following equation,

$$\text{CentsSharp} = B[271 \times \exp(-0.0681 \times f) + 12.5] \times 10\,000, \quad (5)$$

where CentsSharp is the perceived cents sharp value, B is the inharmonicity coefficient, and f is frequency in Hz. Figure 3 shows the average cents sharp values divided by the fitted inharmonicity coefficients versus fundamental frequency, along with the optimum exponential curve fit result. The "error bars" represent the standard deviation among listeners' results. It should be noted that for frequencies above around 60 Hz, the relationship between the perceived cents sharp value and the inharmonicity coefficient becomes equivalent to a linear relationship according to the following equation,

$$\text{CentsSharp}(f > 60 \text{ Hz}) = 125\,000 \times B. \quad (6)$$

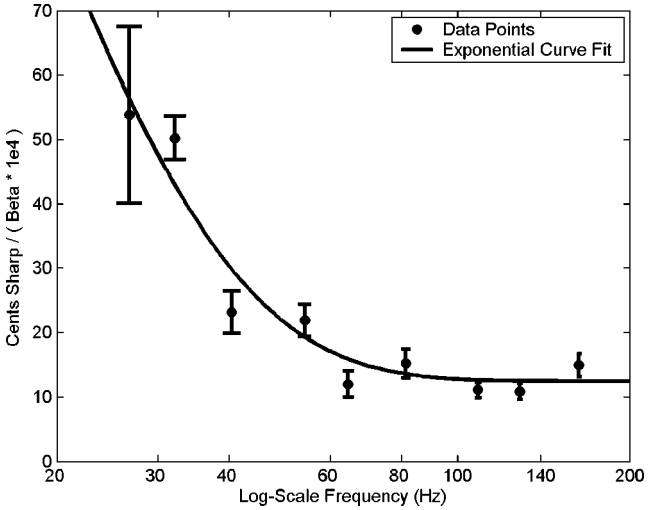

FIG. 3. Filled circles represent average perceived cents sharp values divided by the curve fitted inharmonicity coefficients (scaled by 10 000). The solid line represents the least-squares exponential curve fit to the filled circle values. The "error bars" represent the standard deviation among listeners' results.

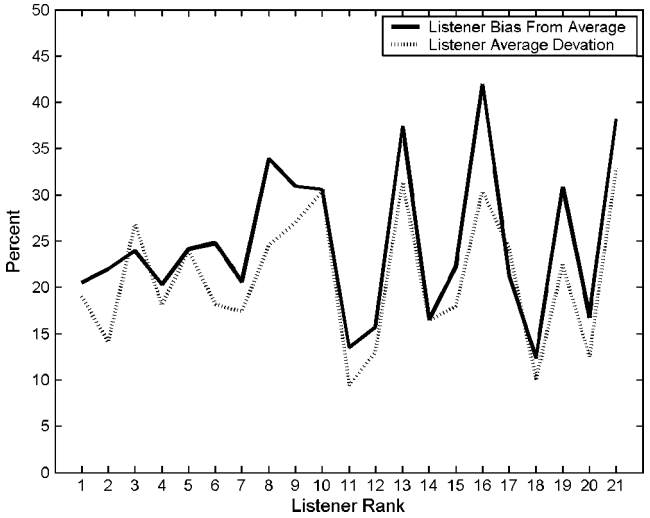

FIG. 4. Comparison across individual listeners of average listener's bias deviation from the average responses and average, across all nine piano tones, listener's relative standard deviation of bias values.

An analysis of each individual listener's results was done in order to determine the dependence on listeners' musical experience. The absolute value of the bias "error," between each listener's answer and the average value for the given tone, was determined. These values were then averaged across the nine piano tone sets for each listener to determine an average bias error value (relative to the average answers) for the given listener. The standard deviation of the bias errors was also determined and averaged across each listener to create a relative standard deviation value. A plot of the bias results and the deviation results may be found in Fig. 4.

V. DISCUSSION

From Fig. 2 it is apparent that the average amount of pitch shift perceived by the jury of listeners is strongly correlated with the inharmonicity coefficient values in the upper seven piano tones studied (E1, A1, C2, E2, A2, C3, and E3). For the lower two piano tones, A0 and C1, the increase in pitch shift relative to the increase in inharmonicity rises significantly.

This study also found an increase in deviation of listeners' perceived matching results for lower fundamental frequency piano tones. This might have some explanation in the well-known psychoacoustic phenomenon that pitch perception ability decreases at lower frequencies.

It was intuitively compelling to find that a given listener's ability to find a pitch match did not depend on their piano musical training. Any given listener tended to have relatively equal probability of perceiving the average of the total listener's pitch matches.

VI. CONCLUSIONS

The perceived pitch due to inharmonicity in piano tones correlated with the inharmonicity coefficient for a given piano tone, although the correlation was less pronounced for the lowest two tones. The deviation among listeners' pitch matches increased at lower frequencies and showed correla-

tion with pitch shift. A given listeners' musical experience of playing the piano did not correlate with the ability to perceptually match piano tones.

The correlation between the pitch shift and the inharmonicity coefficient for the higher frequency piano tones should not be a surprising result. The significant rise in the pitch shift trend relative to the inharmonicity coefficient values for the lowest two tones, however, is a surprising result. The increased pitch shift found in the lower two piano tones should be further studied and extended to the entire lowest octave on a piano (roughly A0 to G♯1). The pitch shift found in piano tone A0 was determined to be nearly 250 cents, two and a half steps, or two and a half semitones.

ACKNOWLEDGMENTS

Portions of this project were supported by the Brigham Young University Acoustics Research Endowment Fund and by the Brigham Young University Physics and Astronomy Department. Thanks are also due to Michael Thompson, who helped on the project while at Brigham Young University.

Anderson, B. E. (**2002**). ''The effect of inharmonic partials on pitch of piano tones,'' J. Acoust. Soc. Am. **111**, 2394.

Conklin, Jr., H. A. (**1996**). ''Design and tone in the mechanoacoustic piano. Part III. Piano strings and scale design,'' J. Acoust. Soc. Am. **100**, 1286–1298.

Fletcher, H. (**1964**). ''Normal vibration frequencies of a stiff piano string,'' J. Acoust. Soc. Am. **36**, 203–209.

Fletcher, H., Blackham, E. D., and Stratton, R. (**1962**). ''Quality of piano tones,'' J. Acoust. Soc. Am. **34**, 749–761.

Galembo, A., Askenfelt, A., Cuddy, L. L., and Russo, F. A. (**2001**). ''Effects of relative phases on pitch and timbre in the piano bass range,'' J. Acoust. Soc. Am. **110**, 1649–1666.

Moore, B. C. J., and Ohgushi, K. (**1993**). ''Audibility of partials in inharmonic complex tones,'' J. Acoust. Soc. Am. **93**, 452–461.

Moore, B. C. J., Glasberg, B. R., and Peters, R. W. (**1985a**). ''Relative dominance of individual partials in determining the pitch of complex tones,'' J. Acoust. Soc. Am. **77**, 1853–1860.

Moore, B. C. J., Peters, R. W., and Glasberg, B. R. (**1985b**). ''Thresholds for the detection of inharmonicity in complex tones,'' J. Acoust. Soc. Am. **77**, 1861–1867.

Peters, R. W., Moore, B. C. J., and Glasberg, B. R. (**1983**). ''Pitch of components of complex tones,'' J. Acoust. Soc. Am. **73**, 924–929.

Rocchesso, D., and Scalcon, F. (**1999**). ''Bandwidth of perceived inharmonicity for physical modeling of dispersive strings,'' IEEE Trans. Speech Audio Process. **7**, 597–601.

A theoretical study of the feasibility of acoustical tweezers: Ray acoustics approach

Jungwoo Lee
Department of Biomedical Engineering, University of Southern California, Los Angeles, California 90089

Kanglyeol Ha
Department of Physics, Pukyong National University, Pusan, Korea

K. Kirk Shung
Department of Biomedical Engineering, University of Southern California, Los Angeles, California 90089

(Received 30 September 2004; revised 21 January 2005; accepted 12 February 2005)

The optical tweezer has been found to have many biomedical applications in trapping macromolecules and cells. For the trapping mechanism, there has to be a sharp spatial change in axial optical intensity and the particle size must be much greater than the wavelength. Similar phenomenon may exist in acoustics. This work was undertaken to demonstrate theoretically that it is possible to acoustically trap particles near the focal point where most of the acoustic energy is concentrated if certain conditions are met. Acoustic force exerted on a fluid particle in ultrasonic fields is analyzed in a ray acoustics regime where the wavelength of acoustic beam is much smaller than the size of the particle. In order to apply the acoustical tweezer to manipulating macromolecules and cells whose size is in the order of a few microns or less, a prerequisite is that the ultrasound wavelength has to be much smaller than a few microns. In this paper, the analysis is therefore based on the field pattern produced by a strongly focused 100 MHz ultrasonic transducer with Gaussian intensity distribution. For the realization of acoustic trapping, negative axial radiation force has to be generated to pull a particle towards a focus. The fat particle considered for acoustic trapping in this paper has an acoustic impedance of 1.4 MRayls. The magnitude of the acoustic axial radiation force that has been calculated as the size of the fat particle is varied from 8λ to 14λ. In addition, both Fresnel coefficients at various positions are also calculated to assess the interaction of reflection and refraction and their relative contribution to the effect of the acoustical tweezer. The simulation results show that the feasibility of the acoustical tweezer depends on both the degree of acoustic impedance mismatch and the degree of focusing relative to the particle size. [DOI: 10.1121/1.1886387]

PACS numbers: 43.80.Gx, 43.80.Jz [FD] Pages: 3273–3280

I. INTRODUCTION

Optical tweezers provide a unique means of noninvasive dynamic control of particles in the size range of tens of nanometers to tens of micrometers, such as bacteria, viruses, living cells, and motor molecules. With a strongly focused laser beam neutral dielectric objects can be pulled towards a focus where photon energy reaches the maximum level by forces that are created when refraction takes place at the boundary between the particle and the surrounding medium. Radiation pressure is given rise to by momentum transfer from photons to objects according to the law of conservation of momentum. The scattering force originated from reflection is proportional to optical intensity and points in the direction of the incident light. The gradient force arising from refraction is proportional to the gradient of intensity and points in the direction of the intensity gradient. The latter plays a more important role in the trapping than does the former since optical trapping by optical tweezers only appears when the latter dominates over the former. For successful implementation of optical tweezers in practice, it is required to have a comprehensive knowledge of both how it works and how optical radiation forces interact. In this paper, the concept of optical trapping or tweezer will be introduced at first. Based on the results drawn from the optical case, the mathematical formulation for acoustical tweezers will be developed. Finally, the numerical simulation results are provided and further analysis and discussion are given.

II. OPTICAL TWEEZER

In this section the underlying principles of optical tweezers will be discussed in detail. Optical tweezers,[1–6] also known as the single beam gradient traps, was first proposed by Ashkin, who found the phenomenon of atomic trapping using a laser and many applications. It can manipulate and trap micron-sized objects with focused laser beams in the vicinity of focal points. The laser is highly focused to the diffraction limited spot using a high numerical aperture microscope objective. Particles that can be trapped are dielectric spheres such as polystyrene, latex, cellular organelles, and so forth. They are electrically neutral and transparent ones having a larger refractive index than that of their surrounding medium. In order to fully understand what makes the phenomenon feasible, the fundamental physics involved in light will be described.

Light, an electromagnetic wave, can be considered as a series of photons propagating through a medium. Each of

them carries certain amount of momentum corresponding to the equation

$$P = \frac{h}{\lambda}, \tag{1}$$

where P is momentum and h is Planck's constant; λ is the wavelength of light. As they travel and interact with objects, momentum transfer occurs between photons and objects. The force delivered to the objects from this momentum is usually called radiation force. It plays an essential role in determining the properties of optical tweezers that are clearly determined by forces exerted on trapped particles among other things. Here, for the sake of simplicity, it is assumed that the particles are of a spherical shape, the size of which is measured by the diameter. The reason of making this assumption will be discussed later. In trapping a particle whose diameter D is larger than or close to λ, it is said to be in the Mie regime while if D is much smaller than λ, it is in the Rayleigh regime.

For analyzing the former, ray optics approximation may be used, whereas a dipole model, also called an electromagnetic model, may be used for the latter. For a particle with a diameter in between these two regimes there are very few well-established approaches. Among various models, a theory proposed by Tlusty[7] appears to best fit experimental results of optical forces in that regime. As mentioned earlier, the shape of an object is one of the critical factors to affect the behavior of optical trapping. In a previous study,[6] a significant conclusion was drawn that the particle shape is of more importance in the event of trapping Mie particles than Rayleigh particles. In the Mie regime, both the magnitude and direction of the force are dependent on the particle shape. For particles in the Rayleigh regime that behave like dipoles, only the magnitude of force is influenced by the particle shape. Therefore the particle is assumed to have a spherical shape with a diameter much greater than the wavelength throughout the paper. Because we will employ the concept of single beam gradient trapping[5] to model the acoustical tweezer for a Mie particle using the field generated by an ultrasonic transducer, only the Mie regime will be reviewed.

Suppose a neutral and transparent sphere is suspended in a medium like water and its homogeneous refractive index is higher than that of the surrounding medium. As an optical ray impinging on an interface between two media, the momentum transfer occurs between them and results in radiation force. Figure 1 illustrates how radiation forces denoted by F are produced by a pair of rays represented by "a" and "b" on a particle in a focused Gaussian intensity distribution. Assume that there is negligible reflection occurring along the surface. All of the rays are refracted through the object. Their directions are graphically deduced by vector subtraction of the outgoing momentum from the incident one, as shown in Fig. 1. They are decomposed into two types of components known as scattering and gradient forces in an orthogonal way to each other. The former arising from reflection is proportional to optical intensity and in the direction of the incident ray. On the other hand, the latter caused by refraction has two components, perpendicular and parallel

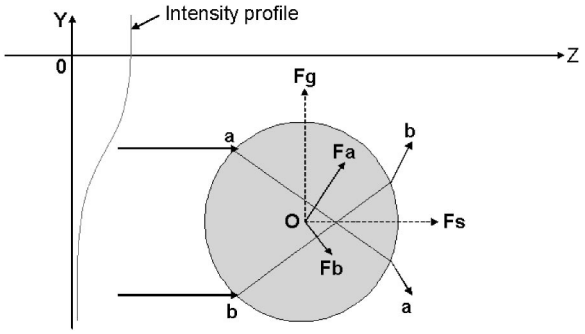

FIG. 1. Application of radiation pressure on a transparent sphere by momentum exchange between a pair of rays and an object with a given intensity profile of the optical field. The scattering force F_s is in the direction of the incident ray while the gradient force F_g is in the direction of the intensity gradient. F_a is the net force that is the sum of the scattering and the gradient forces produced by a corresponding ray "a." F_b is also calculated for a ray "b" in the same way.

to the optical axis, and is proportional to an optical intensity gradient towards the direction of increasing intensity.

With a sphere located off the beam axis the asymmetric intensity distribution around it creates an imbalance between F_a and F_b. In other words F_a driven by higher intensity overcomes F_b at a lower intensity. Eventually a sphere moves transversely towards the beam axis. Figure 2 shows a schematic diagram of two incident light beams "a" and "b" symmetrically positioned about its center exerting radiation forces on it. In a similar manner to Fig. 1, the resultant restoring forces "F_a" and "F_b" guide it towards a focus in the absence of other forces such as radiometric force that can be avoided by using transparent objects. This is how optical tweezer or single beam gradient trap works. It is possible only when the gradient force pulling an object toward a focus is greater than the scattering force pushing it away from a focus.

The complete quantitative description of the total force on a sphere is based on a ray optics approach and given by the following expressions:[8]

$$F_s = \frac{nP}{c}\left\{1 + R\cos 2\theta_i - \frac{T^2[\cos(2\theta_i - 2\theta_r) + R\cos 2\theta_i]}{1 + R^2 + 2R\cos 2\theta_r}\right\}, \tag{2}$$

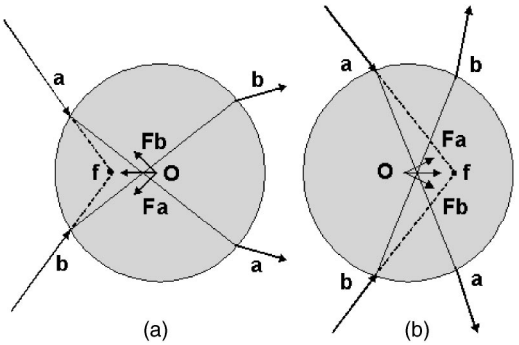

FIG. 2. Generation of restoring forces F_a and F_b pulling a particle back into a focus f. The particles are located either (a) beyond focus or (b) before focus.

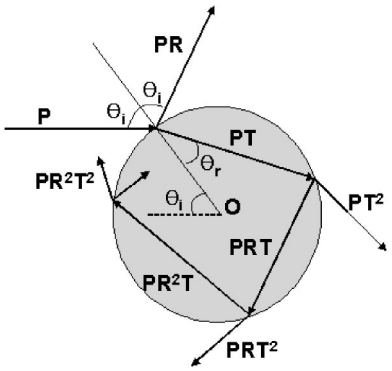

FIG. 3. Configuration for the calculation of radiation force on a sphere. An incident ray of power P leads to successive multiple reflections and refractions to occur after impinging on it. R and T are the Fresnel reflection and transmission coefficients, respectively; θ_i and θ_r are the angles of incidence and refraction, respectively.

$$F_g = \frac{nP}{c}\left\{ R\sin 2\theta_i - \frac{T^2[\sin(2\theta_i - 2\theta_r) + R\sin 2\theta_i]}{1 + R^2 + 2R\cos 2\theta_r} \right\}, \tag{3}$$

where P and n are the power for a single ray and the refractive index of surrounding medium; R and T are the Fresnel reflection and transmission coefficients, respectively; θ_i and θ_r are the angles of incidence and refraction, respectively; c is the speed of light. The averaged Fresnel reflection and transmission coefficients for two linear polarizations are described as follows:[9]

$$R = \frac{1}{2}\left\{ \left(\frac{\tan(\theta_i - \theta_r)}{\tan(\theta_i + \theta_r)} \right)^2 + \left(\frac{\sin(\theta_i - \theta_r)}{\sin(\theta_i + \theta_r)} \right)^2 \right\}, \tag{4}$$

$$T = 1 - R. \tag{5}$$

Figure 3 depicts the schematic diagram used to calculate the total radiation force acting on the sphere. It shows that the successively reflected and refracted rays contribute to the radiation force on a sphere that is the sum of the two force components given in Eqs. (2) and (3) over individual incident rays. For efficient trapping it requires that the size of the sphere covers a significant portion of a highly focused beam and the incident beam have a high convergence angle at the edge of the beam.

III. ACOUSTICAL TWEEZER

An analogy to an optical tweezer in the Mie regime where particle size is larger than the wavelength of light can be found in acoustics. The development of the acoustical tweezer to perform the function of acoustic trapping of particles much larger than the wavelength may be feasible with a highly focused ultrasonic transducer with a sharp intensity variation in the lateral direction. The term acoustical tweezer or trapping implies the spatial control of small particles by an acoustic wave. It allows the precise localization of a particle at a desired position. The first study of the idea of acoustical tweezers was done by Wu *et al.*[10] who demonstrated that a stable force potential well could be formed by using two collimated 3.5 MHz focused ultrasonic beams propagating in opposite directions. Kushibiki *et al.*[11,12] developed a line-focus-beam acoustic microscopy system to measure the propagation characteristics, viz., phase velocity and attenuation of leaky surface acoustic waves excited on the water-loaded specimen surface. However, acoustic trapping with a single beam has never been investigated. In order to be able to do so it is crucial to understand whether it is possible to generate sufficient acoustic radiation force[13,14] to pull a small object towards a focal point. The following theoretical analysis was therefore undertaken to shed light on the magnitude of radiation forces that can be produced on a sphere under the conditions specified for single beam optical trapping. Although all effects should be considered for a complete analysis, acoustic streaming, attenuation, and gravitational force have been neglected in the paper for the sake of simplicity in a first attempt at interrogating this phenomenon.

For the consideration of trapping of biological particles such as cells and macromolecules, the beam of a high frequency (100 MHz) highly focused ultrasonic transducer with small F number which has a sharp Gaussian intensity distribution was assumed. A small F number ensures a tight focus. At high frequencies, attenuation may emerge as an important issue. To avoid severe attenuation proportional to the square of center frequency for a homogeneous medium such as water, the focal point should be located as close to the transducer as possible. These considerations necessitate the use of a small F-number transducer. Small F-number highly focused high frequency single element transducers can be fabricated by a hot pressing technique.[15,16] In this paper the object under consideration for acoustic trapping is assumed to be a fat particle having a spherical shape. The rationale for this is three-fold. The particle should be homogeneous and has similar acoustic properties to water in a way that refraction takes place more dominantly than reflection. Even so, it is inevitable to have total reflection occur when the incident angle is greater than the critical angle. From Snell's law it is known that when the speed of sound in the object is lower than that in the surrounding medium there is no total reflection.

Fat has a sound velocity lower than that of water[17] and almost the same acoustic impedance as that of water minimizing reflection to the level beneficial to acoustical trapping. In other words, if there is significant difference in their acoustic impedances, a large portion of the incident beam entering the object will be reflected along its surface. It was mentioned earlier that reflection plays a critical role in producing scattering forces pushing the particle in the direction of beam propagation. For a simplified treatment of the problem, only the axial component of the acoustic radiation force is considered. The formulation to be used for the force calculation is modified from the optical counterpart.[8,18,9,19] The axial force can be computed from a surface integration of acoustic intensity I. The Gaussian distributed intensity in the y direction is given by

$$I = \frac{P}{w(z)^2}\exp\left[\frac{-2y^2}{w(z)^2}\right], \tag{6}$$

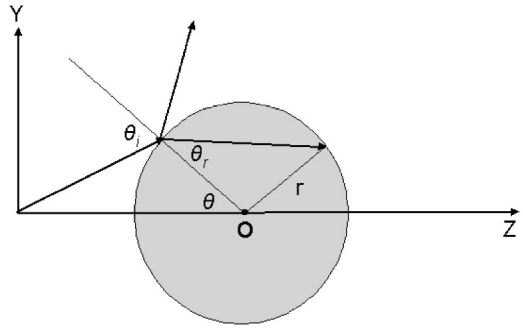

FIG. 4. Notation of angular parameters used to calculate the axial radiation force exerted on a sphere. θ_i and θ_r are the incident and the refracted angles. θ is the angle between the beam axis and a point where the incident ray impinges on the sphere.

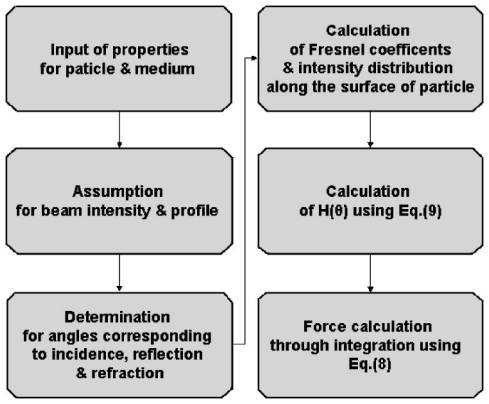

FIG. 5. Flow chart of calculation procedure for axial radiation force.

$$w(z)=w_0\sqrt{1+\left(\frac{\lambda z}{\pi w_0^2}\right)^2}, \tag{7}$$

where $w(z)$ and w_0 are the beam widths at z and at a focal point, respectively.

One can find the axial radiation force from

$$F_z=\frac{1}{c_w}\int_S I\cdot ds=\frac{P}{c_w}\int \frac{r^2}{w(z)^2}\exp\left[\frac{-2y^2}{w(z)^2}\right]H(\theta)d\theta, \tag{8}$$

$$H(\theta)=\cos\theta_i\sin\theta\left\{\cos(\theta_i-\theta)+R\cos(\theta_i+\theta)-\frac{T^2[\cos(\theta_i-2\theta_r+\theta)+R\cos(\theta_i+\theta)]}{1+R^2+2R\cos 2\theta_r}\right\}, \tag{9}$$

where r and c_w are the radius of the sphere and the speed of sound in water, respectively; θ, θ_i, and θ_r are the angles indicated in Fig. 4. $H(\theta)$ decides the fractional ratio of acoustic radiation force applied on the sphere for a given initial force P/c_w. As individual rays interact with the sphere the integration in Eq. (8) with respect to those corresponding θ's must be performed. In acoustics Fresnel reflection coefficient R and transmission coefficient T of a flat interface between two media of acoustic impedances Z_1 and Z_2 are given by

$$R=\left|\frac{Z_2/\cos\alpha_2-Z_1/\cos\alpha_1}{Z_2/\cos\alpha_2+Z_1/\cos\alpha_1}\right|^2, \tag{10}$$

$$T=1-R, \tag{11}$$

where α_1 and α_2 are the incident and transmitted angles. Hence, the resultant acoustic radiation force is mostly affected by the incident angle and the acoustic impedances of the surrounding fluid and the sphere. The calculation is performed with Eqs. (6) through (11) and the numerical procedure is shown in Fig. 5.

IV. RESULTS

In order to determine the specific conditions under which acoustic trapping occurs, Eqs. (8) and (9) are employed to integrate axial radiation forces of individual acoustic rays to find the net axial force acted on an object suspended in water with acoustic impedance of 1.5 MRayls. From Figs. 6 through 10 the simulation results are displayed. It is assumed that the speed of sound in water is 1500 m/s. At 100 MHz, ultrasound wavelength is 15 μm. For the ray acoustics to be valid, the size of an object should be at least 10 times as large as the wavelength, which is 150 μm. For a sphere placed on the beam axis as shown in Fig. 4, the net force on the sphere was calculated as functions of sound speed in the sphere, sphere size, beam width, sphere mass density, and axial location of the object. As the diameter of the sphere is varied from 8λ to 14λ, the net axial radiation forces along beam axis for two different beam widths are plotted in Figs. 6 and 7 where the vertical axis is the net radiation force in the z direction in Newtons and the horizontal axis is the axial distance from the focus in mm.

For implementing the idea of an acoustical tweezer, it is crucial to obtain a negative radiation force that generates a backward movement pulling the particle towards the focus. These plots show under which conditions it is more likely to produce a negative radiation force in the axial direction. As θ specified in Fig. 4 changes, the values of $H(\theta)$ and Fresnel coefficients at different locations are presented in Figs. 8 through 10, making it clearer which one among reflection and refraction contributes more to the effect of an acoustical tweezer. As mentioned in the previous section, now that $H(\theta)$ completely describes higher order internal multiple reflection and refraction, it would be the one function that could be used to predict the magnitude of acoustic radiation force per individual ray. Once this distribution is known, it becomes straightforward to determine whether the particle can be attracted towards a focus or not.

It is seen that the axial distance between two peaks in magnitude of force becomes larger as the size of the object increases for both cases. The beam width (w_0) at the focal point which is determined by the acoustic intensity profile in the y direction affects the axial force a great deal. For $w_0=15\,\mu$m the axial force changes more sharply than does a less focused beam at $w_0=45\,\mu$m. For a fixed size of the object the two local maxima are positioned farther away from each other in a broader beam. As the beam becomes narrower, the magnitude of axial force at the local minimum near the focus decreases in comparison with a broader beam. Moreover, for a tightly focused beam it does not change much independently of the particle size. In Fig. 6 the speed

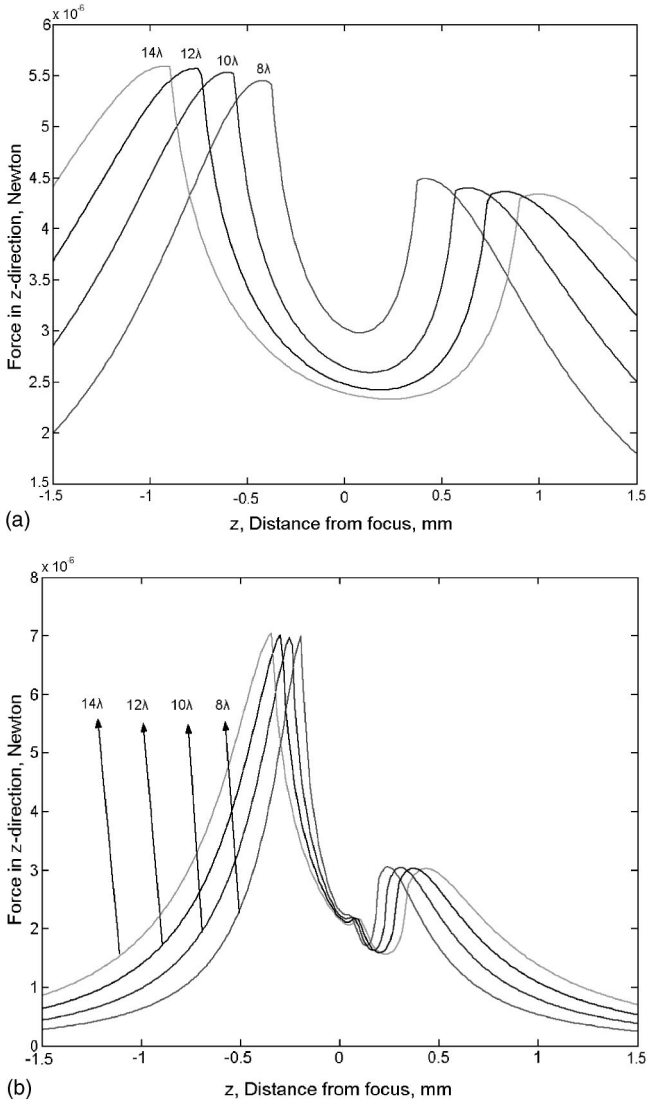

FIG. 6. Axial radiation force along the beam axis as a function of diameter. (a) Beamwidth $(w_0)=3\lambda=45\ \mu$m. (b) Beamwidth $(w_0)=\lambda=15\ \mu$m. In this case acoustic impedance for the object is 1.2 MRayls. For both cases the density is set to be 950 kg/m^3. Sound speeds of the surrounding medium and the sphere are 1500 and 1300 m/s.

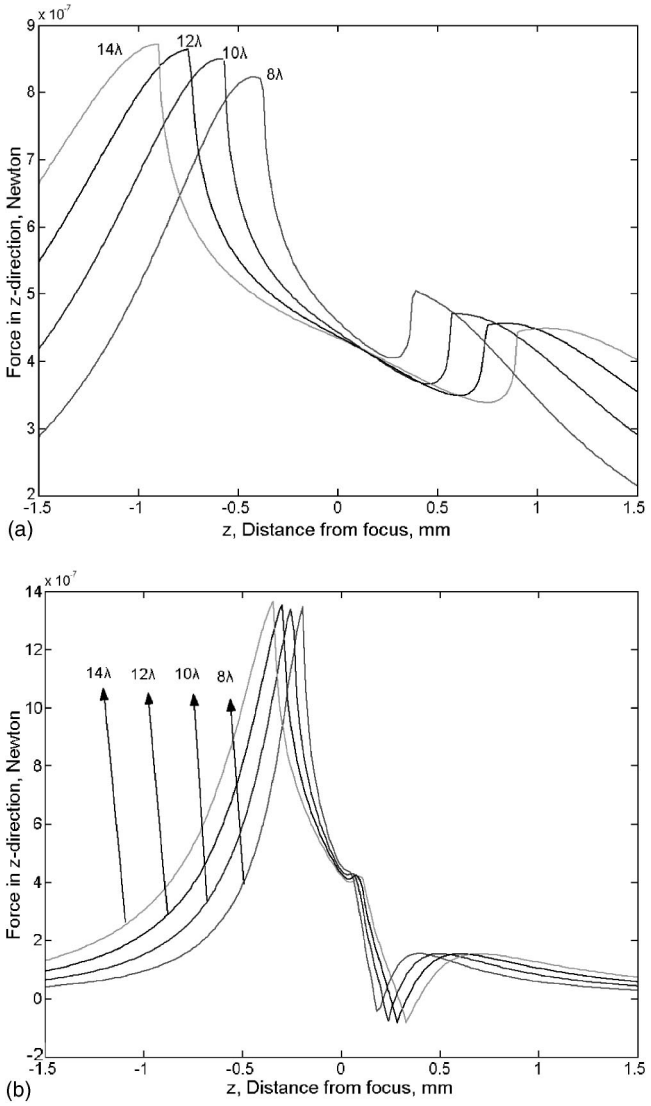

FIG. 7. Axial radiation force along the beam axis with variation of diameters. (a) Beamwidth $(w_0)=3\lambda=45\ \mu$m. (b) Beamwidth $(w_0)=\lambda=15\ \mu$m. Acoustic impedance of the object is 1.4 MRayls. The same as Fig. 6 with the exception that the sound velocity of the particle=1450 m/s.

of sound and density for the sphere are assumed to be 1300 m/s and 950 kg/m^3, respectively. Its acoustic impedance is therefore equal to 1.2 MRayls. The difference in acoustic impedance between water and the object is 20%. Note that all of the magnitude of the axial forces is positive or in the positive z direction everywhere. However, as the difference in acoustic impedance between water and the object is reduced, the results show that it is possible to produce a negative axial radiation force adequate for acoustic trapping, illustrated in Fig. 7.

Now the beam width is assumed to be 15 μm which corresponds to one wavelength and the acoustic impedance of the particle is set to be 1.4 MRayls. The diameter of the fat particle is varied from 8λ to 14λ. Although in Fig. 7(a) two peaks are located at approximately the same positions as they do in Fig. 6(a), Fig. 7(b) shows that a negative axial force in the negative z direction toward the transducer is generated near the focus. In addition, the local minimum shifts to the right side as the size of the sphere is increased. Thus it becomes apparent that the acoustic impedance mismatch between water and the object may result in quite a distinct behavior for acoustic trapping. In the latter example the acoustic impedance mismatch is only about 6.7%. Even with an ideal acoustic impedance match the net force on the object may still be in the forward direction due to the broader beam waist. This problem is alleviated if a more tightly focused beam is used. As compared with the result in Fig. 7(a), Fig. 7(b) illustrates that a more highly focused beam can create a negative radiation force and lead to attractive movement of the particle towards a focus.

As far as the magnitude of radiation force is concerned, the comparison with the magnitude of gravitational force on a particle provides a reference as to how strongly the radiation force can be generated with an acoustical tweezer. For a spherical object with the radius of 75 μm and a density of 950 kg/m^3, the gravitational force on the object is 1.6×10^{-8} N. As shown in Fig. 7(b), the maximum magnitude

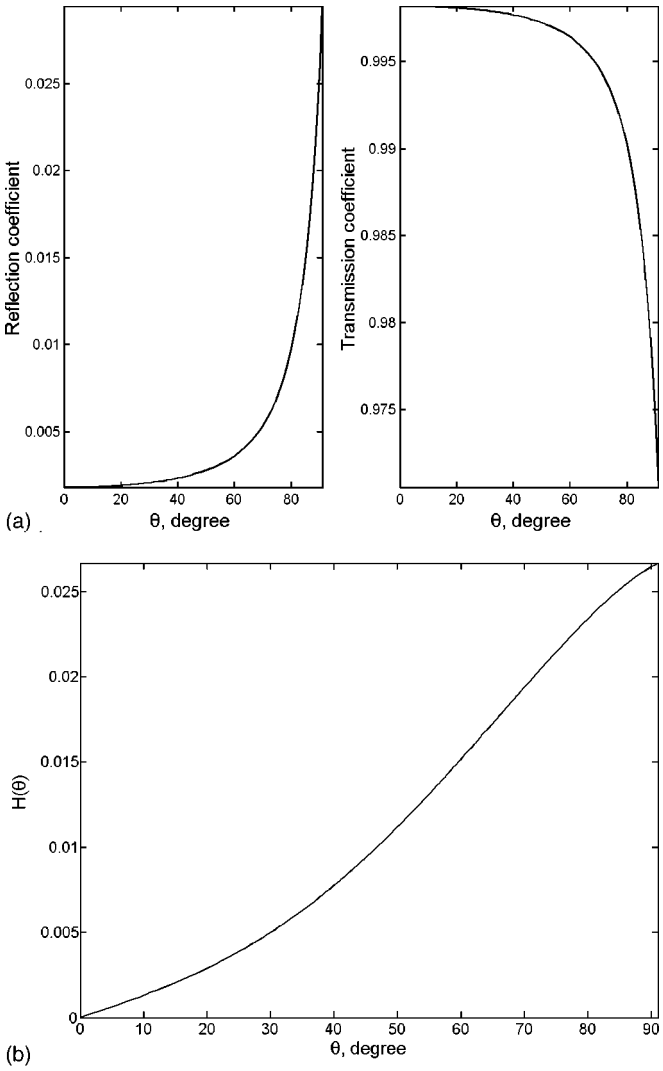

FIG. 8. The characteristics of reflection and refraction along the surface of fat tissue for beamwidth λ. (a) Fresnel reflection and transmission coefficients at $z=-330\ \mu$m. (b) $H(\theta)$ factor versus θ at $z=-330\ \mu$m.

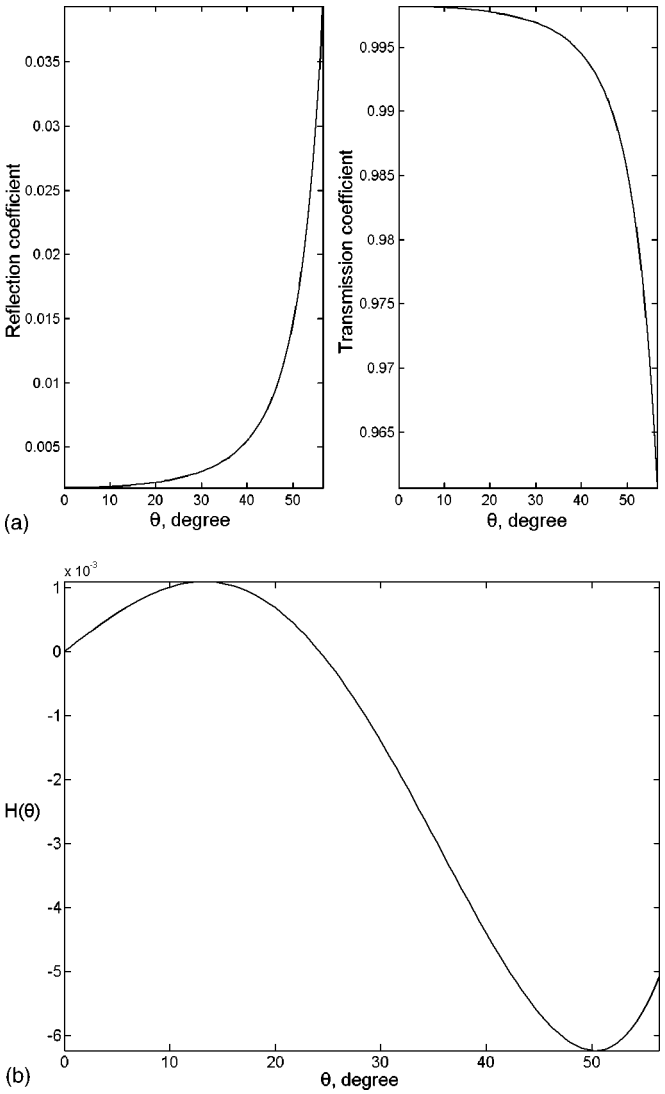

FIG. 9. The characteristics of reflection and refraction along the surface of fat tissue for beamwidth λ. (a) Fresnel reflection and transmission coefficients at $z=330\ \mu$m. (b) $H(\theta)$ factor versus θ at $z=330\ \mu$m.

of axial radiation force is 1.3×10^{-6} N. For given conditions, therefore, the magnitude of radiation force is nearly up to 81 times as large as that of the gravitational force. From Figs. 8 through 10 the characteristics of Fresnel coefficients are shown as θ is varied along the surface of the particle, depicting how reflection and refraction would interact with each other and affect acoustic trapping. The relative behavior of refraction and reflection along the surface where ultrasonic beam impinges on the fat particle, which is placed out of trapping area, is shown in Fig. 8(a), where the horizontal axis denotes the angle θ. For a fat sphere with a diameter of 210 μm at $z=-330\ \mu$m, their Fresnel coefficients are calculated and plotted along the front interface between the two media.

In Fig. 8(b), as described in Eq. (9), $H(\theta)$ is depicted versus θ at z$=-330\ \mu$m. The values for the force in the graph are all positive. Thus the resultant axial force ends up pushing a fat particle away from an ultrasonic source. The maximum incident angle with respect to the horizontal axis is 91°. If the particle is placed in a trapping region at $z=330\ \mu$m, a quite different behavior is observed, as shown in Fig. 9. As opposed to the result in Fig. 8, most values of $H(\theta)$ factors are negative so that they can induce an attractive radiation force toward the focus. In comparison with the previous case the maximum incident angle is 57°. Hence the distribution of the angles is narrower than in the previous example. Finally, Fig. 10 provides the result for the particle at $z=750\ \mu$m. The findings so far indicate that a combination of strong focus and well-tuned acoustic impedance match may make the development of acoustical tweezers for trapping molecules and cells a reality. Further analysis will be followed in the next section.

V. DISCUSSION

The feasibility of the development of acoustical tweezers is demonstrated in this paper by analyzing the axial radiation force under particular conditions. Here our analysis is aimed to show that negative axial force may occur beyond focal point. It will be shown later that different choices of parameters lead to distinct behavior of acoustic trapping. Numerical data are tabulated in Table I where they specify the maximum trapping force, the axial position at the maximum

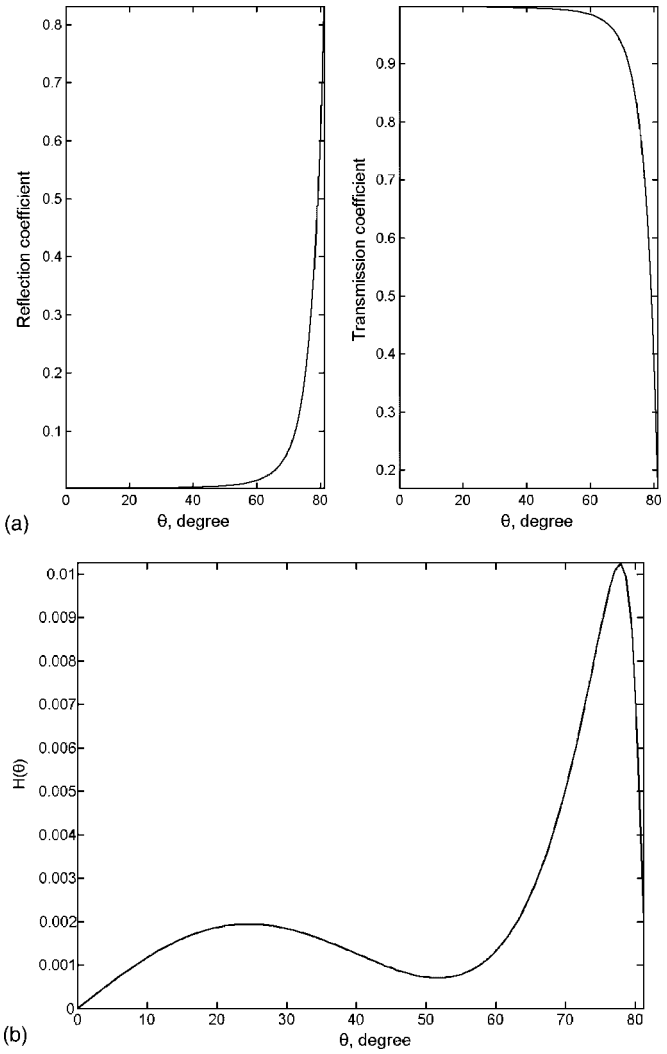

FIG. 10. The characteristics of reflection and refraction along the surface of fat tissue for beamwidth λ. (a) Fresnel reflection and transmission coefficients at z=750 μm. (b) H(θ) factor versus θ at $z=750$ μm.

force, and the range over which tweezer effect occurs, respectively. As shown in Table I acoustic trapping can be found in different regions with different strengths of force. The tweezer range denotes the axial distance along which fat tissue is expected to move towards the focus located at $z=0$. It is quite interesting to see that as the size becomes bigger the axial range for appropriate trapping increases, and so does the negative trapping force, except for 210 μm.

As mentioned before, the tweezer phenomenon typically relies on the intensity gradient force that is affected by refraction rather than the scattering force influenced by reflection.[8] Thus this phenomenon can be better understood

TABLE I. Summarized data by simulation where the beamwidth (w_0) is $\lambda=15$ μm and the acoustic impedance of the object is 1.4 MRayls.

Diameter (μm)	Max. trapping force (10^{-8} N)	Max. trapping point (μm)	Tweezer range (μm)
120	−4	180	170–210
150	−7.5	240	210–273
180	−8.2	290	250–330
210	−8	330	292–391

if the interactions of these forces with the fat tissue are examined in more detail. From Figs. 8 to 10 those interactions are quantitatively described. It is well known that the magnitudes of Fresnel coefficients are dependent on orientation when the incident beam is not normal to the interface between two media.[20] Since a strongly focused beam converges into the focus and diverges rapidly beyond it, the variation is more evident especially at large angles that correspond to the upper portions of spherical fat as shown in Fig. 8(a). Due to the intrinsic feature of fat tissue the refraction takes place more dominantly than does the reflection. The values in Fig. 8(b) are all positive. Thus the resultant axial force gives rise to pushing the particle away from the ultrasonic source. The maximum incident angle with respect to the horizontal axis is 91°. The reason is that the object is located at a point where the ultrasonic beam either converges or diverges rapidly.

It is also intriguing to note that as the beam goes to the edge of the particle the influence of reflection begins to take over that of refraction. This indicates that the incident beam is concentrated on a certain part of the particle near the axis, making a more pivotal contribution to the attractive force. In addition, the contribution should be mostly ascribed to transmission or refraction. This finding suggests that for efficient trapping it would be better off to have transmission occurring on axis i.e., small θ. In Fig. 10 a situation where the object is located far from a trapping region again is considered. The substantial difference from other results lies not only in the distribution of the values of $H(\theta)$ but also in the relative magnitude of those Fresnel coefficients. As shown in Fig. 10(a), it is clear that the reflection coefficient is not negligible, unlike former cases. For the similar reason shown in Fig. 8(a), the scattering force is applied on fat tissue in the direction of beam propagation. Note that the maximum incident angle in this case is 81°, which is larger than 57° in the tweezer range.

From the results given in Figs. 8 to 10, it is plausible that for an acoustical tweezer the particle should be positioned at a region which satisfies the condition that the incident beam is concentrated in a limited angular range centered around the axis. Typically, no matter how strongly the beam is focused, the tweezer effect is hardly realized in front of the focal point with given conditions above. The more focused beam makes the intensity distribution change more abruptly especially around the focal point, giving rise to a high intensity gradient large enough to bring the particle towards the focus. The numerical results presented in the above examples clearly indicate that whether it is possible to trap a particle is determined primarily by both the degree of acoustic impedance mismatch and the degree of focusing relative to the particle size.

VI. CONCLUSION

Utilizing the ray acoustics approach, the acoustic radiation force in the axial direction was calculated. As a counterpart of the optical tweezer, the possible existence of acoustical tweezing or trapping using a highly focused high frequency ultrasonic beam with a Gaussian intensity distribution was demonstrated by the results from a simulation of

the axial radiation force exerted on fat tissue suspended in water. For a better understanding of the distinct behavior of the tweezer effect, various parameters such as the size of the particle, the beam width at focus, the axial position, the frequency of ultrasound, and the acoustic impedance mismatch between the suspended particle and the surrounding medium were considered. It is shown that an acoustical tweezer can be successfully implemented if the particle material and beam characteristics meet certain specifications. The results show that acoustic trapping can occur only within a very limited range around a focal point, especially beyond it. Minimizing the reflection associated with the scattering force and maintaining an appreciable amount of refraction related to the gradient force is one of the most essential elements for the realization of an acoustical tweezer.

ACKNOWLEDGMENT

This work has been supported by NIH Grant No. P41-EB2182.

[1] A. Ashkin, ''Acceleration and trapping of particles by radiation pressure,'' Phys. Rev. Lett. **24**, 156–159 (1970).
[2] A. Ashkin, ''Optical levitation,'' Appl. Phys. Lett. **19**, 283–285 (1971).
[3] A. Ashkin, ''Trapping of atoms by resonance radiation pressure,'' Phys. Rev. Lett. **40**, 729–732 (1978).
[4] A. Ashkin, ''Applications of laser radiation pressure,'' Science **210**, 1081–1088 (1980).
[5] A. Ashkin, J. M. Dziedzic, J. E. Bjorkholm, and S. Chu, ''Observation of a single-beam gradient force optical trap for dielectric particles,'' Opt. Lett. **11**, 288–290 (1986).
[6] A. Ashkin, ''Optical trapping and manipulation of neutral particles using lasers,'' Proc. Natl. Acad. Sci. U.S.A. **94**, 4853–4860 (1997).
[7] T. Tlusty, A. Meller, and R. Bar-Ziv, ''Optical gradient forces of strongly localized fields,'' Phys. Rev. Lett. **81**, 1738–1741 (1998).
[8] A. Ashkin, ''Forces of a single beam gradient laser trap on a dielectric sphere in the ray optics regime,'' Biophys. J. **61**, 569–582 (1992).
[9] S. Nemoto and H. Togo, ''Axial force acting on a dielectric sphere in a focused laser beam,'' Appl. Opt. **37**, 6386–6394 (1998).
[10] J. Wu, ''Acoustical tweezers,'' J. Acoust. Soc. Am. **89**, 2140–2143 (1991).
[11] J.-I. Kushibiki and M. Arakawa, ''A method for calibrating the line-focus-beam acoustic microscopy system,'' IEEE Trans. Ultrason. Ferroelectr. Freq. Control **45**, 421–430 (1998).
[12] J.-I. Kushibiki, Y. Ono, Y. Ohashi, and M. Arakawa, ''Development of the line-focus-beam ultrasonic material characterization system,'' IEEE Trans. Ultrason. Ferroelectr. Freq. Control **49**, 99–113 (2002).
[13] K. Yasuda and T. Kamakura, ''Acoustic radiation force on micrometer-size particles,'' Appl. Phys. Lett. **71**, 1771–1773 (1997).
[14] A. A. Doinikov, ''Acoustic radiation force on a spherical particle in a viscous heat-conducting fluid. I. General formula,'' J. Acoust. Soc. Am. **101**, 713–721 (1997).
[15] G. R. Lockwood, D. H. Turnbull, and F. S. Foster, ''Fabrication of high frequency spherically shaped ceramic transducers,'' IEEE Trans. Ultrason. Ferroelectr. Freq. Control **41**, 231–235 (1994).
[16] K. A. Snook, J. Zhao, C. H. F. Alves, J. M. Cannata, W. Chen, R. J. Meyers, T. A. Ritter, and K. K. Shung, ''Design, fabrication and evaluation of high frequency, single element transducers incorporating different materials,'' IEEE Trans. Ultrason. Ferroelectr. Freq. Control **49**, 169–176 (2002).
[17] H. P. Schwan, *Biological Engineering* (McGraw Hill, New York, 1969).
[18] E. Sidick, S. D. Collins, and A. Knoesen, ''Trapping forces in a multiple-beam fiber-optic trap,'' Appl. Opt. **36**, 6423–6433 (1997).
[19] T. C. Bakker Schut, G. Hesselink, B. G. de Grooth, and J. Greve, ''Experimental and theoretical investigations on the validity of the geometrical optics model for calculating the stability of optical traps,'' Cytometry **12**, 479–485 (1991).
[20] L. E. Kinsler, A. R. Frey, A. B. Coppens, and J. V. Sanders, *Fundamentals of Acoustics*, 4th ed. (Wiley, New York, 2000).

Effect of pulse characteristics on temperature rise due to ultrasound absorption at a bone/soft-tissue interface

Matthew R. Myers[a)]
Center for Devices and Radiological Health, HFZ-170, U.S. Food and Drug Administration, Rockville, Maryland 20852

(Received 3 September 2004; revised 1 February 2005; accepted 2 February 2005)

The transient temperature rise at a bone/soft-tissue interface is an important quantity in the safety evaluation of procedures involving trains of high-intensity ultrasound pulses. Mathematical models based upon the time-averaged intensity of the pulse train can provide rapid estimates of the temperature rise, but are known to underestimate the temperature rise during the on-time of the pulse. This paper extends a previous analytical model to account for pulse shape, and provides error estimates for simulations employing time-averaged intensities. A simple analytic expression for the interface temperature that accounts for both bone and soft-tissue properties is provided. The analytic expression agrees well with temperature rise predictions based upon the finite-element method, when the insonation time is large compared to the pulse repetition period. In this case of large relative insonation time, the pulse shape is found to be inconsequential. © *2005 Acoustical Society of America.* [DOI: 10.1121/1.1879232]

PACS numbers: 43.80.Gx, 43.35.Wa [FD] Pages: 3281–3287

I. INTRODUCTION

The absorption of ultrasound at a bone/soft-tissue interface poses a significant safety concern, as the high absorption of ultrasound in bone can produce large temperature rises in nearby sensitive tissues such as nerves. In a previous paper (Myers 2004; hereafter referred to as M04), a model was developed to estimate the temperature rise near the interface. The model retains the analytic simplicity of point-source models (Nyborg, 1988), yet allows for different material properties in the bone and soft-tissue media. Simple analytical models such as that in M04 are useful for elucidating the functional dependence of critical process parameters, as well as for incorporating into safety standards.

The model presented in M04 computes the transient temperature rise based upon a time-averaged intensity. Herman and Harris (2002) note that approaches employing temporal-average intensities can underestimate the temperature rise during the on-time of pulses currently used in radiation-force imaging. This paper extends the model of M04 to account for the temporal shape of the pulse train, rather than basing the analysis upon a temporal-average intensity.

As in M04, a Laplace-transform approach is employed to solve the heat-conduction equation in the bone and soft-tissue. Attention is eventually restricted to the interface temperature, allowing derivation of a closed-form expression for the temperature rise that does not require the ''high attenuation'' assumption made in M04. The only requirement is that the observation time be large compared to the repetition period for the pulse train. The solution is developed in two stages: first for a rectangular pulse train to illustrate the role played by the various time scales, and subsequently for a general pulse train.

The following section presents the assumptions of the model and develops solutions for the rectangular and general-shape pulses. In Sec. III, model predictions are compared with those of a finite-element approach using parameter values appropriate for radiation-force imaging (Palmeri and Nightingale, 2004). The final section discusses the error incurred by basing calculations upon a time-averaged intensity.

II. METHOD

The assumptions contained in the model are discussed in M04 and Sec. IV of this paper. Here we simply present the features of the model and extend the theory to treat time-varying intensities.

We consider an ultrasound beam of uniform cross section incident from a soft-tissue medium onto a bone surface, with the beam axis perpendicular to the bone surface. The soft-tissue and bone media are assumed to be semi-infinite and separated by a planar interface. The simplified geometric model is shown in Fig. 1.

The intensity of the beam transmitted into the bone is given by $i(t)$. The attenuation within the bone may be described in terms of an intensity attenuation coefficient μ, with attenuation length $1/\mu$. (Since heating is related to intensity gradients, it is convenient in the algebraic manipulations to retain the somewhat archaic intensity coefficient μ. Final results will be reexpressed in terms of an amplitude attenuation coefficient.) Attenuation in the soft tissue is neglected; this simplification is discussed in Sec. IV. Heat generated through attenuation of the ultrasound beam in the bone is transferred via conduction in both media.

After a brief derivation of the general temperature-rise equation, we will restrict our attention to the interface $x=0$. As discussed in M04, the interface is the location of maximum temperature rise in the soft tissue, and close to the location of maximum temperature rise in bone, when the

a)Electronic mail: matthew.myers@fda.hhs.gov

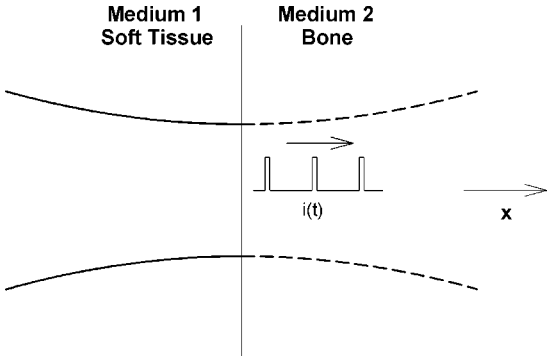

FIG. 1. Ultrasound pulse incident upon planar interface between soft-tissue and bone. Transmitted intensity is denoted by $i(t)$.

beam is focused upon the interface. The interface restriction, which allows for closed-form expression of the temperature-rise results, is discussed further in Sec. IV.

Under the assumptions just described, the temperature rise T within soft tissue (medium 1) is determined by axial diffusion of heat away from the interface:

$$\frac{\partial T_1}{\partial t}-\kappa_1\frac{\partial^2 T_1}{\partial x^2}=0, \tag{1}$$

where x denotes axial distance measured from the interface, t is time, and κ is the thermal diffusivity. In bone (medium 2) ultrasound absorption is significant along with axial diffusion, and the temperature is described by

$$\frac{\partial T_2}{\partial t}-\kappa_2\frac{\partial^2 T_2}{\partial x^2}=\frac{\mu i(t)}{\rho_2 c_2}e^{-\mu x}, \tag{2}$$

where ρ is the density and c is the specific heat. The boundary conditions include continuity of temperature and heat flux across the interface:

$$T_1(0,t)=T_2(0,t), \tag{3}$$

$$k_1\frac{\partial T_1}{\partial x}(0,t)=k_2\frac{\partial T_2}{\partial x}(0,t). \tag{4}$$

Here $k=\kappa\rho c$ is the thermal conductivity.

A. Rectangular pulse

We consider a time-varying intensity in the form of rectangular pulse, as shown in Fig. 2. The peak intensity is given by i_0, the pulse width by Δ, and the pulse repetition period by t_p. In typical applications, $t_p \gg \Delta$ (Nightingale *et al.*, 2001; Walker, 1999, Palmeri and Nightingale, 2004).

To solve the system of equations (1)–(4), we employ a Laplace transform in time. The Laplace transform of $i(t)$ is

$$\frac{i_0}{\lambda}\frac{1-e^{-\lambda\Delta}}{1-e^{-\lambda t_p}}. \tag{5}$$

We transform (1) and (2), solve the resulting ordinary differential equations, then require that the solutions far from the interface ($x=\pm\infty$) decay to zero. After enforcing the transformed versions of (3) and (4), we obtain the following solution for the temperature rise in the bone:

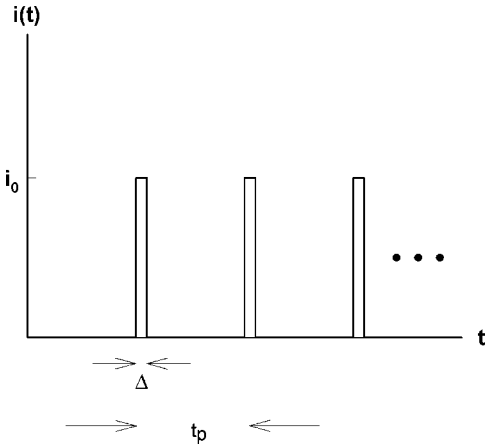

FIG. 2. Characteristics of the rectangular pulse train.

$$T_2=\frac{\mu i_0}{2\pi i\rho_2 c_2}\int_C \frac{d\lambda e^{\lambda t}}{\lambda(\lambda-\mu^2\kappa_2)}\frac{1-e^{-\lambda\Delta}}{1-e^{-\lambda t_p}} \times\left\{e^{-\mu x}-\frac{1+\mu(k_2/k_1)\sqrt{\kappa_1/\lambda}}{1+(k_2/k_1)\sqrt{\kappa_1/\kappa_2}}e^{-\sqrt{\lambda/\kappa_2}x}\right\}. \tag{6}$$

The inversion contour C in the complex λ plane is shown in Fig. 3. The dots along the imaginary axis in Fig. 3 represent the first-order poles at

$$\lambda_n=\frac{2\pi n i}{t_p}, \quad n=\pm 1,\pm 2,\ldots. \tag{7}$$

(The singularity at $\lambda=\kappa_2\mu^2$ is removable.)

We now restrict attention to the interface by setting $x=0$. We also drop the subscript "2" indicating the bone medium, since temperature is continuous across the interface. We next close the contour in the left half-plane, along the dashed contour shown in Fig. 3. The singular behavior at the origin is treated using a circle of small radius ϵ; we momen-

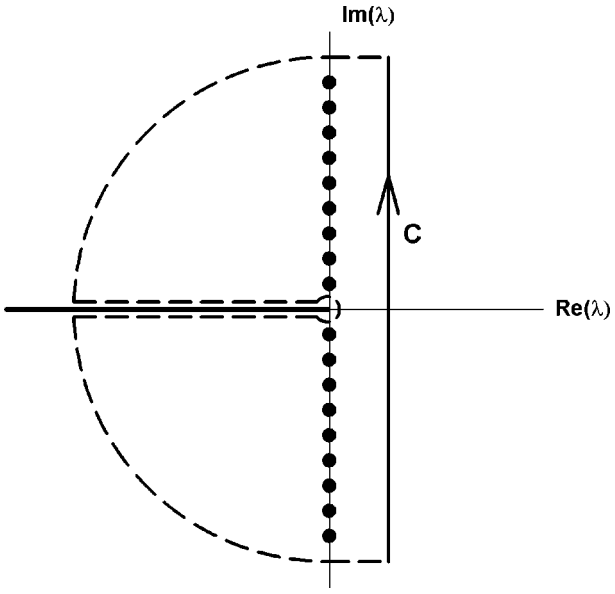

FIG. 3. Inversion contours for the Laplace transform solution, in the complex λ plane. Dots denote poles at $\lambda=\pm 2n\pi i/t_p$.

tarily defer the limiting process. After including the contributions from the integrals along the top and bottom of the branch cut, we obtain

$$T_2=\lim_{\epsilon\to 0}\frac{i_0}{\mu k_2}\left[-\frac{\Delta}{t_p}+S_\epsilon+S_c\right]+2\pi i\sum \text{ residues}, \tag{8}$$

$$S_\epsilon=\frac{1}{2\pi(1+\beta)}\int_{-\pi}^{\pi}\left(1+\frac{\mu\beta}{\sqrt{\epsilon/\kappa_2}e^{i\theta/2}}\right)\times\left(\frac{1-e^{-\epsilon\Delta e^{i\theta}}}{1-e^{-\epsilon t_p e^{i\theta}}}\right)d\theta, \tag{9}$$

$$S_c=\frac{-\beta(\mu^2\kappa_2 t)^{3/2}}{\pi(1+\beta)}\int_{\epsilon t}^{\infty}\frac{e^{-s}}{s^{3/2}(s+\mu^2\kappa_2 t)}\frac{1-e^{-s\Delta/t}}{1-e^{-st_p/t}}ds. \tag{10}$$

Here

$$\beta=\frac{k_2}{k_1}\sqrt{\frac{\kappa_1}{\kappa_2}}=\sqrt{\frac{k_2\rho_2c_2}{k_1\rho_1c_1}}. \tag{11}$$

The residues in (8) arise from the singularities prescribed by (7).

We now assume that the observation time is long compared to the repetition period, i.e., $t\gg t_p$. The condition $t\gg\Delta$ is also required, but since Δ is normally small relative to t_p, this condition is more easily satisfied. After using $t\gg t_p$ in (10), we obtain

$$S_c=\frac{-\beta(\mu^2\kappa_2 t)^{3/2}}{\pi(1+\beta)}\frac{\Delta}{t_p}\int_{\epsilon t}^{\infty}\frac{e^{-s}ds}{s^{3/2}(s+\mu^2\kappa_2 t)}. \tag{12}$$

We next integrate by parts (raising the power of s to $-\frac{1}{2}$) and combine with (9) while setting ϵ to zero. By performing several changes of variable and utilizing

$$\int_0^\infty\frac{s^{-1/2}e^{-s}}{s+b}ds=\pi b^{-1/2}e^b\,\text{erfc}(\sqrt{b}), \tag{13}$$

where erfc represents the complementary error function (Abramowitz and Stegun, 1972), we transform (8) to

$$T=\frac{i_0}{\mu k_2}\frac{\Delta}{t_p}\frac{\beta}{1+\beta}\left[-1+\frac{2M}{\sqrt{\pi}}+e^{M^2}\,\text{erfc}(M)\right]+2\pi i\sum \text{ residues}, \tag{14}$$

where, as in M04,

$$M=(\mu^2\kappa_2 t)^{1/2}. \tag{15}$$

M represents the distance diffused by heat in time t divided by the ultrasound attenuation length.

The residual contribution to (14) is obtained by computing the residue (Carrier *et al.*, 1966) of the integrand in (6) at the singularities given in (7). To simplify the resulting series, we note that using the representative values $\mu=1\ \text{mm}^{-1}$, $\kappa_2=1\ \text{mm}^2/\text{s}$, and $t_p=10^{-4}\ \text{s}$ (M04; Nightingale *et al.*, 2001) gives $\mu^2\kappa_2 t_p\ll 1$. Hence $\mu^2\kappa_2 t_p\ll 2n\pi$, $n=1,2,...$, is easily satisfied in typical ultrasound applications, and the residue series may be written

$$T_p=\frac{-\mu i_0\beta t_p}{4\rho_2c_2\pi^2(1+\beta)}\sum_{n=\pm1,\pm2,...}\frac{e^{2n\pi it/t_p}(1-e^{-2n\pi i\Delta/t_p})}{n^2}. \tag{16}$$

We have labeled the residue sum with the subscript "p" to indicate that it constitutes the periodic portion of the temperature rise T. Using

$$\sum_1^\infty\frac{\cos(kx)}{k^2}=\frac{\pi^2}{6}-\frac{\pi x}{2}+\frac{x^2}{4},\quad 0\leqslant x\leqslant 2\pi \tag{17}$$

(Gradshteyn and Ryzhik, 1980), (16) can be expressed as

$$T_p=\frac{\mu i_0\Delta\beta}{2\rho_2c_2(1+\beta)}\left(-1+\frac{2t'}{\Delta}-\frac{2t'}{t_p}+\frac{\Delta}{t_p}\right),\quad 0\leqslant t'\leqslant\Delta$$
$$=\frac{\mu i_0\Delta\beta}{2\rho_2c_2(1+\beta)}\left(1-\frac{2t'}{t_p}+\frac{\Delta}{t_p}\right),\quad \Delta\leqslant t'\leqslant t_p. \tag{18}$$

Here t' is the time measured from the beginning of the pulse of interest, e.g., for the kth pulse of the pulse train,

$$t=(k-1)t_p+t'. \tag{19}$$

Thus the triangular temperature variation in (18) is repeated with period t_p.

B. General pulse shape

We now consider a general pulse train $i(t)$ with pulse repetition period t_p. The Laplace transform for the general pulse is given by

$$\frac{I_p(\lambda)}{1-e^{-\lambda t_p}}, \tag{20}$$

where

$$I_p=\int_0^{t_p}e^{-\lambda t}i(t)dt. \tag{21}$$

The general expression for the temperature rise, derived in an identical manner to (5), is

$$T_2=\frac{\mu}{2\pi i\rho_2c_2}\int_C\frac{d\lambda e^{\lambda t}}{(\lambda-\mu^2\kappa_2)}\frac{I_p(\lambda)}{1-e^{-\lambda t_p}}\times\left\{e^{-\mu x}-\frac{1+\mu(k_2/k_1)\sqrt{\kappa_1/\lambda}}{1+(k_2/k_1)\sqrt{\kappa_1/\kappa_2}}e^{-\sqrt{\lambda/\kappa_2}x}\right\}. \tag{22}$$

It can be seen from (21) that I_p is analytic in the λ plane, and hence the singularities of (22) are the same as those of (6), i.e., those given in (7).

The general form of S_ϵ, corresponding to (9) for the rectangular pulse, contains the term $I_p(\epsilon e^{i\theta})$, which becomes $I_p(0)$ as $\epsilon\to 0$. Likewise, in the general form of S_c [analogous to (10)], the integrand is dominated by the region near $s=0$, and $I_p(s/t)$ may be approximated by $I_p(0)$ to the desired order of accuracy. (Accuracy of this approximation is discussed in Sec. IV.) From (21), it can be seen that the quantity $I_p(0)$ is the time-averaged (over the period t_p) intensity times the repetition period t_p. Upon substituting $t_p\bar{i}$ for $I_p(0)$ in S_ϵ and S_c, where $\bar{i}$ denotes the average intensity,

and again using (13), we obtain the following general form for the nonperiodic part of the temperature rise:

$$T_{np}=\frac{\bar{i}}{\mu k_2}\frac{\beta}{1+\beta}\left[-1+\frac{2M}{\sqrt{\pi}}+e^{M^2}\,\mathrm{erfc}(M)\right]. \tag{23}$$

Since the integrands in (6) and (22) contain the same singularities [Eq. (7)], the periodic part of the temperature rise in the general case is also obtained by summing the residues at the λ_n values. Again assuming $\mu^2\kappa_2 t_p \ll 2n\pi$, the residue series may be written

$$T_p=\frac{-\mu i_0 \beta t_p}{4\rho_2 c_2 \pi^2(1+\beta)}\sum_{n=\pm1,\pm2,\ldots}\frac{e^{2n\pi i t/t_p}\lambda_n I_p(\lambda_n)}{n^2}. \tag{24}$$

After using the definitions of I_p in (21) and λ_n in (7), switching the order of summation and integration, and using

$$\sum_1^\infty \frac{\sin(kx)}{k}=\frac{\pi}{2}-\frac{x}{2},\quad 0\leqslant x\leqslant 2\pi \tag{25}$$

(Gradshteyn and Ryzhik, 1980), we obtain

$$T_p=\frac{\mu\beta}{2\rho_2 c_2(1+\beta)}\int_0^{t_p} i(\tau)\left(1-\frac{2t}{t_p}+\frac{2\tau}{t_p}\right)d\tau \quad (0<t-\tau<t_p). \tag{26}$$

For a rectangular pulse train, (26) reduces to (18).

III. RESULTS

To evaluate the accuracy of the present model, the analytical results were compared to a finite-element solution to Eqs. (1)–(4). Of particular interest was the error in approximating the full temperature field with T_{np}. In terms of the more commonly used amplitude attenuation coefficient $\alpha=\mu/2$, T_{np} may be reexpressed as

$$T_{np}=\frac{\bar{i}}{2\alpha k_2}\frac{\beta}{1+\beta}\left[-1+\frac{2M}{\sqrt{\pi}}+e^{M^2}\,\mathrm{erfc}(M)\right] \tag{27}$$

with

$$\beta=\frac{k_2}{k_1}\sqrt{\frac{\kappa_1}{\kappa_2}}=\sqrt{\frac{k_2\rho_2 c_2}{k_1\rho_1 c_1}}\quad\text{and}\quad M=(4\alpha^2\kappa_2 t)^{1/2}. \tag{28}$$

Physical properties of the media coincide with those used in M04. Values of density, heat capacity, and thermal conductivity for the soft-tissue and bone media are $[\rho_1,c_1,k_1]=[1000\ \mathrm{kg/m^3},4000\ \mathrm{J/(kg\,K)},0.6\ \mathrm{W/(m\,K)}]$; $[\rho_2,c_2,k_2]=[1700\ \mathrm{kg/m^3},1600\ \mathrm{J/(kg\,K)},2.3\ \mathrm{W/(m\,K)}]$. The resulting thermal diffusivities for soft tissue and cortical bone are $\kappa_1=0.15\times10^{-6}\ \mathrm{m^2/s}$ and $\kappa_2=0.85\times10^{-6}\ \mathrm{m^2/s}$. The dimensionless parameter β attains a value of 1.6.

A pulse train resembling that used by Palmeri and Nightingale (2004) to characterize single-location radiation-force imaging was used in the simulations. The pulse train begins with a sequence of 5-MHz oscillations having a $\sin^2$ intensity profile, for a duration of $\Delta=20\ \mu\mathrm{s}$. The oscillations are followed by an off-time of 180 μs, so that $t_p=200\ \mu\mathrm{s}$ and the effective duty cycle is 10%. The first pulse of the train can thus be written

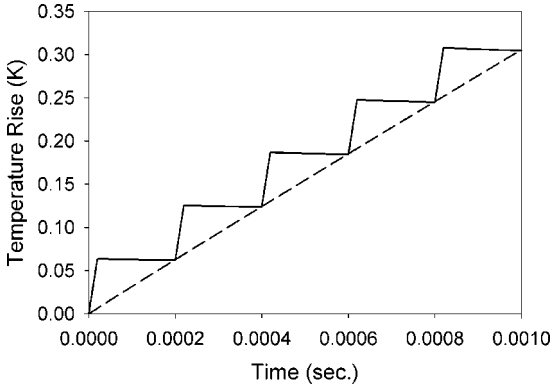

FIG. 4. Transient temperature rise due to a pulse train having a $\sin^2$ profile incident upon a bone/soft-tissue interface. Frequency of sinusoidal oscillations is 5 MHz. Transmitted time-averaged intensity is 70 W/cm^2. On-time of pulse $\Delta=20\ \mu\mathrm{s}$; pulse repetition period $t_p=200\ \mu\mathrm{s}$. Solid line: finite-element calculation using full pulse train. Dashed line: Eq. (27), and finite-element calculation based upon time-averaged intensity.

$$i=i_s\sin^2(2\pi f t),\quad t\leqslant\Delta$$
$$=0,\qquad \Delta\leqslant t\leqslant t_p \tag{29}$$

($f=5$ MHz). A similar form [with t replaced by t' (19)] holds for subsequent pulses in the train. Graphically, each rectangular pulse in Fig. 2 is replaced by a sequence of 200 humps with maximum intensity i_s. The peak intensity i_s was taken to be 1400 W/cm^2. The intensity averaged over a single pulse is then 700 W/cm^2, and the intensity $\bar{i}$ averaged over the repetition period is 70 W/cm^2. These transmitted intensity values correspond to an incident pulse train of pulse-averaged intensity 1000 W/cm^2 (Palmeri and Nightingale, 2004) incident upon the interface, with a transmission coefficient of 0.7 (M04). Figure 2, with $i_0=700\ \mathrm{W/cm^2}$, represents a square-wave approximation to the $\sin^2$ pulse train. The actual $\sin^2$ profile was used in the calculations. Based upon the discussion in M04, the attenuation was taken to be $\mu=2\ \mathrm{mm^{-1}}$, appropriate for 5 MHz.

Finite-element calculations were performed using the above material properties and pulse shape in the FIDAP (Fluent Inc., Lebanon, NH) commercial code. A mesh containing 32 000 nodes in the x direction was employed. Computation time to simulate temperature rise was approximately 1 h (on an IBM RS6000/44P workstation) for each 200-μs pulse of the train. The rather large computation time was required to resolve the 5-MHz variations. Also computed via the finite-element method was the temperature rise due to a steady source having an intensity equal 70 W/cm^2, the time-averaged intensity of the pulse train.

The temperature rise computed using the finite-element method with the intensity profile in (29) is plotted in Fig. 4 (solid line). A sharp, essentially linear temperature rise can be observed during the on-time of the pulse ($t\leqslant\Delta$), followed by a period of nearly constant temperature during the off-time. The dashed line in Fig. 4 represents the nonperiodic temperature rise T_{np} given by (27), with $\bar{i}=70\ \mathrm{W/cm^2}$. Also, to within 0.1%, the dashed line represents the finite-element prediction of the temperature rise due to the 70 W/cm^2 steady source. The temperature rise predicted by (27) is less than or equal to the finite-element calculation employing the unsteady $\sin^2$ source at all times.

IV. DISCUSSION

The values plotted in Fig. 4 represent relatively small temperature rises. However, appreciably larger application times are possible in radiation-force imaging (Walker, 1999); the larger number of pulses would lead to larger temperature rises. A larger number of pulses would also produce a nonlinear shape in the temperature-rise curve; a bending over of the plots is just starting to occur during the fifth cycle of Fig. 4.

Plotted on a much finer time scale, the steep portions of the step profile in Fig. 4 would display a very slight modulation due to the $\sin^2$ intensity variation. Practically speaking, however, the details of the pulse train are unimportant. Since the on-time in radiation-force imaging is typically too short for conduction effects to occur, the steep temperature increase during the on-time is linear and proportional to the pulse-averaged intensity. This fact was verified through additional finite-element calculations using other pulse shapes (including the rectangular shape of Fig. 2) having the same on-time and pulse averaged intensity. The step profile of Fig. 4 was reproduced to within plotting accuracy.

Given the simplicity of (27), it is attractive to use it to estimate the temperature rise occurring due to absorption of ultrasound pulse trains at an interface. However, it can be seen from Fig. 4 that T_{np} does not provide a conservative estimate of the actual temperature rise, and from a safety standpoint it is important to estimate the error in the approximation.

T_{np} is derived from the exact result [Eq. (6)] for the temperature rise using a large time ($t \gg t_p$) approximation, as well as by neglecting the periodic residue series T_p [Eq. (26)]. The first term neglected in the expansion of (10) [and the generalized form containing $I(\lambda)$] for $t \gg t_p$ is of magnitude t_p/t smaller than the terms retained in (27), and hence we anticipate an error of magnitude t_p/t. Similarly, by using a small-M approximation in (27) and dividing the result into (26) [and approximating the integral in (26) by $t_p \bar{i}$], we find that T_p/T_{np} is proportional to t_p/t. Comparison of T_{np} with finite-element calculations over a range of times up to 2000 cycles in duration also showed that the error in estimating the actual temperature rise by T_{np} was of magnitude t_p/t. Indeed, the maximum difference between T_{np} and the finite-element value during the fifth cycle in Fig. 4 is approximately $\frac{1}{5}$.

Making the $t \gg t_p$ approximation in (10) (and its generalized form) and retaining only the first term resulted in an expression for T_{np} that is identical to that applicable to a steady source with intensity $\bar{i}$. This can be verified by setting the function $i(t)$ in (21) equal to the constant $\bar{i}$ and continuing without making any approximations regarding the relative sizes of t and t_p. Thus, the plot of T_{np} in Fig. 4 (dashed line) coincided with the finite-element calculation based upon a time-invariant intensity of magnitude $\bar{i}$. In light of the above comments regarding the accuracy of T_{np}, it may also be said that approximating the actual intensity with its temporal average results in a temperature rise estimate that has a relative error of roughly t_p/t.

The biological effect of approximating the actual temperature rise by T_{np} can be estimated using equivalent dose theory (Sapareto and Dewey, 1984; Miller and Zeskin, 1989). As noted by Herman and Harris (2002), the time in minutes for adverse effects to occur may be written as

$$t_{adv} = 0.5^{(T-43)}, \tag{30}$$

where T and the threshold temperature 43 are measured in degrees Celsius. As is also noted by Herman and Harris (2002), it must be recognized that the validity of the thermal-dose theory has not been verified for very short exposure times. If we rewrite the temperature T as $T_{np} + \delta T$, where δT is the error associated with approximating the actual temperature with T_{np} [Eq. (23) or (27)], then the time for adverse biological effects to occur is off by a factor of

$$f = 0.5^{\delta T}, \tag{31}$$

when T is approximated by T_{np}. Using the error estimate $\delta T \approx (t_p/t) T_{np}$ proposed above, along with the small-time expansion

$$T_{np} \sim \frac{\mu \bar{i}}{\rho_2 c_2} \frac{\beta}{1+\beta} t \tag{32}$$

of (23), yields the factor

$$f = 0.5^{\mu \bar{i} \beta t_p / (\rho_2 c_2 (1+\beta))}. \tag{33}$$

This expression, which requires that the ultrasound exposure time be small enough that the increase in T_{np} with time be approximately linear (Fig. 4), is independent of time. Hence, while the relative error (between T and T_{np}) decreases with time, the biological consequence of any difference in temperature increases in a commensurate manner. After inserting the material properties and pulse-train characteristics from Sec. III, we find that $f \approx 0.95$. Thus, approximating the temperature T by T_{np} produces an estimate for the adverse-event time that is too high by about 5%. Alternatively, it can be said that under the conditions considered, pulse heating reduces the time to tissue damage by about 5% relative to heating with a constant source of the same time-averaged intensity.

The periodic temperature variation (26) can be included into the solution with only a moderate increase in complexity, since (26) can be decomposed into two relatively simple terms, one proportional to $\bar{i}$ and one involving an integral of $\tau i(\tau)$. The integral might require numerical integration for some pulse shapes. In the case of the rectangular pulse train, the triangular pulses defined by (18) increase the temperature at the beginning of the pulse period and decrease it at the end of the period. This effectively increases the accuracy of T_{np} at the beginning of the period and decreases it at the end. Thus while T_p adds a realistic oscillation to the monotonic temperature profile of (27) (Fig. 4), the accuracy of (27) averaged over a period is not enhanced, and in the interest of simplicity T_p was neglected. The accuracy of (27) for moderate values of t_p/t would be increased by including higher-order (in t_p/t) terms in the expansion of the generalized form of (10). This would bring in additional features of the pulse train beyond the average intensity. The final expression for the temperature rise would in general be complicated, however.

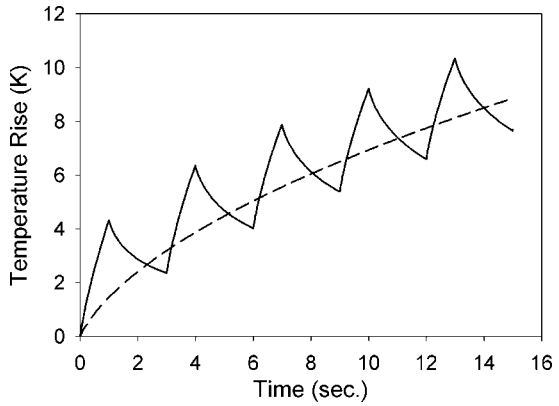

FIG. 5. Transient temperature rise due to a rectangular pulse train with longer pulse repetition period. Transmitted time-averaged intensity is 1 W/cm^2. On-time of pulse=1.0 s; pulse repetition period=3 s. Solid line: finite-element calculation using full pulse train. Dashed line: Eq. (27), and finite-element calculation based upon time-averaged intensity.

Expressions (18) and (26) for T_p, and the error estimates based upon them, were derived under the assumption that $\mu^2\kappa_2 t_p$ is small. That is, the distance diffused by heat during a pulse repetition period is small compared to the ultrasound attenuation length. It is interesting to examine the accuracy of (23) [or (27)] under circumstances where appreciable heat conduction occurs during a pulse repetition period. A finite-element simulation was performed using the values $\Delta=1$ s, $t_p=3$ s, and $\mu=1.2$ mm^{-1} (3 MHz frequency). Here $\mu^2\kappa_2 t_p$ is 3.7 and $\mu^2\kappa_2\Delta$ is 1.2. The resulting temperature-rise trace is shown in Fig. 5. The effect of heat conduction can be seen in the nonlinear behavior during both the on and off portions of the pulse train. The periodic variations in the transient temperature are larger than those in Fig. 4, but a significant part of the variation now resides below the variation predicted by (23) (dashed line in Fig. 5). Thus in this example the relative error associated with estimating the temperature rise by (23) is comparable to the error for the small $\mu^2\kappa_2 t_p$ case (Fig. 4) and is of magnitude t_p/t. For extremely large values of $\mu^2\kappa_2 t_p$ (e.g., the temperature rise decays to zero during the off time), the error estimate would become dependent upon $\mu^2\kappa_2 t_p$ as well as t_p/t, but these cases are unlikely to occur in practice.

To understand the role played by two separate sets of material properties, we examine (23) in the limit of small and large $M=(\mu^2\kappa_2 t)^{1/2}$. As indicated earlier, the small M regime results when the time of interest is small compared to the time required for heat to diffuse an ultrasound attenuation length, and is thus more applicable to lower ultrasound frequencies. For small M, (23) reduces to

$$T_{np}\sim\frac{\mu\bar{i}}{\rho_2 c_2}\frac{\beta}{1+\beta}t. \tag{34}$$

This expression can be thought of as the temperature rise due to a source of strength $\mu\bar{i}\beta/(1+\beta)$, immediately after heating when conduction can be neglected (Herman and Harris, 2002). Hence, the role of the distinct media separated by the interface is to reduce the absorbed intensity by a factor $\beta/(1+\beta)$ relative to the value for a pure bone medium. For bone and soft-tissue media, $\beta/(1+\beta)\approx 0.6$. Equation (34) may also be thought of as the temperature rise just after heating in a single medium having density times heat capacity ($=\rho c$) 60% larger than that of bone. The plot in Fig. 4 displays the linear growth with time characteristic of the low M regime.

For large M, where the distance diffused by heat in time t is large compared to the ultrasound attenuation length, (23) expanded to one term simplifies to the leading term of the asymptotic series of M04:

$$T_{np}=\frac{\bar{i}}{\frac{1}{2}(\sqrt{k_1\rho_1 c_1}+\sqrt{k_2\rho_2 c_2})}\sqrt{\frac{t}{\pi}}. \tag{35}$$

As discussed in M04, (35) is an extension of the "heated disk" model (Nyborg, 1988) to a two-layered medium. The heated disk may be thought of as embedded in a single, effective medium for which the square root of the thermal properties is equal to the average of the square roots for the bone and soft-tissue media. The analysis of this paper demonstrates that the generalized heated-disk model is appropriate for pulse trains provided $M\gg 1$ and $t\gg t_p$. The square root dependence upon time is manifested during the larger times considered in Fig. 5.

The limitations of the present model coincide with those of the bone/soft-tissue interface model developed in M04. These limitations are discussed in M04, and include the requirement that the beam width be small compared to the radii of curvature of the bone surface, yet larger than the distance diffused by heat during the time of interest. The ultrasound beam is also required to be normally incident upon the interface.

The present model restricts attention to the interface temperature, which represents the maximum temperature in the soft-tissue but not in the bone. For large values of M, i.e., when the distance diffused by heat over the time of interest is large compared to the ultrasound attenuation length, the results in M04 showed that the maximum temperature in bone occurs about one-half of an attenuation length away from the interface. While the present model does not provide temperature information beyond the interface, it is not restricted to large values of M.

The effect of neglecting absorption in the soft-tissue medium, as is done in the present formulation, is worth discussing quantitatively. Finite-element simulations similar to those leading to Fig. 4 were repeated while accounting for absorption (of incident and reflected waves) in the soft-tissue medium. A transmission coefficient of 0.7 and reflection coefficient of 0.3 were used. The largest value of absorption in soft tissue considered by Palmeri and Nightingale (2004), 1.5 dB/cm/MHz was assumed. The pulse characteristics and other material properties were identical to those listed in Sec. III. The axial temperature profile at the end of the application ($t=1$ msec) is plotted in Fig. 6, for the cases where soft-tissue absorption is included (dashed line) and when it is neglected (solid line). The interface temperature and temperature in the bone are affected little by energy absorption in the soft tissue. However, the temperature even a slight distance into the soft tissue is not accurately predicted when

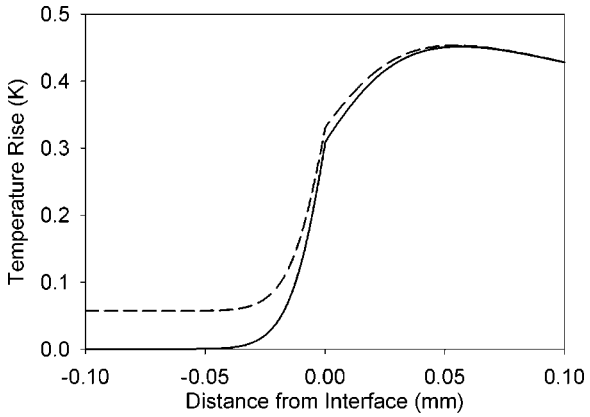

FIG. 6. Finite-element predictions of the temperature profile near the bone/soft-tissue interface, for the $\sin^2$ pulse train of Fig. 4, at the end of the application ($t = 0.001$ s). Solid line: heat generation in soft-tissue ignored. Dashed line: heat generation in soft tissue included.

absorption in soft-tissue is ignored. This error decreases somewhat with increasing time following insonation, as the heat from the bone is conducted further into the soft-tissue medium. The temperature rise in soft tissue due to this conduction can exceed that due to the original heat generation in the soft tissue. Still, the present model is most useful for providing an upper bound (i.e., the interface temperature) for the temperature rise within the soft-tissue medium. Neglecting heat generation in the soft-tissue medium allows the simplicity and ease of computation of the model to be maintained without sacrificing accuracy of the interface temperature prediction.

V. CONCLUSION

This paper analyzes the temperature rise occurring when an ultrasound pulse train is incident upon a soft-tissue/bone interface. The error involved in simulating the transient temperature rise using a time-averaged intensity is shown to be of magnitude t_p/t, t being the time and t_p the pulse repetition period. To within this error, Eq. (27) provides a rapid estimate of the transient temperature rise while accounting for the separate physical properties of the bone and soft-tissue media.

ACKNOWLEDGMENTS

The author wishes to thank Bruce Herman and Gerald Harris of the US FDA/CDRH for suggesting this problem, providing valuable references, and engaging in interesting discussions of the results. The author is also grateful to a reviewer for suggesting the thermal-dose analysis.

Abramowitz, M., and Stegun, I. A. (**1972**). *Handbook of Mathematical Functions* (Dover, New York).

Carrier, G. F., Krook, M., and Pearson, C. E. (**1966**). *Functions of a Complex Variable* (McGraw–Hill, New York).

Gradshteyn, I. S., and Ryzhik, I. M. (**1980**). *Table of Integrals, Series, and Products* (Academic, Orlando, FL).

Herman, B. A., and Harris, G. R. (**2002**). ''Models and regulatory considerations for transient temperature rise during diagnostic ultrasound pulses,'' Ultrasound Med. Biol. **28**, 1217–1224.

Miller, M. W., and Ziskin, M. C. (**1989**). ''Biological consequences of hyperthermia,'' Ultrasound Med. Biol. **15**, 707–722.

Myers, M. R. (**2004**). ''Transient temperature rise due to ultrasound absorption at a bone/soft-tissue interface,'' J. Acoust. Soc. Am. **115**, 2887–2891.

Nightingale, K. R., Palmeri, M. L., Nightingale, R. W., and Trahey, G. E. (**2001**). ''On the feasibility of remote palpation using acoustic radiation force,'' J. Acoust. Soc. Am. **110**, 625–634.

Nyborg, W. L. (**1988**). ''Solutions of the bio-heat transfer equation,'' Phys. Med. Biol. **33**, 785–792.

Palmeri, M. L., and Nightingale, R. W. (**2004**). ''On the Thermal Effects Associated with Radiation Force Imaging of Soft Tissue,'' IEEE Trans. Ultrason. Ferroelectr. Freq. Control **51**, 551–565.

Sapareto, S. A., and Dewey, W. C. (**1984**). ''Thermal dose determination in cancer therapy,'' Int. J. Radiat. Oncol., Biol., Phys. **10**, 787–800.

Walker, W. F. (**1999**). ''Internal deformation of a uniform elastic solid by acoustic radiation force,'' J. Acoust. Soc. Am. **105**, 2508–2518.

Echolocation signals of the free-ranging Yangtze finless porpoise (*Neophocaena phocaenoides asiaeorientialis*)

Songhai Li and Kexiong Wang
Institute of Hydrobiology, The Chinese Academy of Sciences, Wuhan, 430072, People's Republic of China and Graduate School of the Chinese Academy of Sciences, Beijing, 100039, People's Republic of China

Ding Wang[a)]
Institute of Hydrobiology, The Chinese Academy of Sciences, Wuhan, 430072, People's Republic of China

Tomonari Akamatsu
National Research Institute of Fisheries Engineering, Fisheries Research Agency, Ebidai, Hasaki, Kashima, Ibaraki 314-0421, Japan

(Received 14 September 2004; revised 3 February 2005; accepted 8 February 2005)

This paper describes the high-frequency echolocation signals from free-ranging Yangtze finless porpoise in the Tian-e-zhou Baiji National Natural Reserve in Hubei Province, China. Signal analysis showed that the Yangtze finless porpoise clicks are typical high-frequency narrow-band (relative width of the frequency spectrum $Q=6.6\pm1.56$, $N=548$) ultrasonic pulses. The peak frequencies of the typical clicks range from 87 to 145 kHz with an average of 125 ± 6.92 kHz. The durations range from 30 to 122 μs with an average of 68 ± 14.12 μs. The characteristics of the signals are similar to those of other members of the Phocoenidae as well as the distantly related delphinids, *Cephalorhynchus spp*. Comparison of these signals to those of the baiji (*Lipotes vexillifer*), who occupies habitat similar to that of the Yangtze finless porpoise, showed that the peak frequencies of clicks produced by the Yangtze finless porpoise are remarkably higher than those produced by the baiji. Difference in peak frequency between the two species is probably linked to the different size of preferred prey fish. Clear double-pulse and multi-pulse reverberation structures of clicks are noticed, and there is no indication of any low-frequency (<70 kHz) components during the recording period. [DOI: 10.1121/1.1882945]

PACS numbers: 43.80.Ka [WA] Pages: 3288–3296

I. INTRODUCTION

The capabilities of sophisticated echolocation systems have been fully demonstrated by many captive odontocetes (Au, 1993). The acoustical characteristic and target detection performance by echolocation were primarily measured and demonstrated in physically restricted dolphins, and little is known about the actual use of echolocation in the natural habitats of odontocetes (Au, 1993). There are many unstudied aspects of odontocete sonar use in the wild, such as adaptation of echolocation signals to environmental range and noise constraints, the ecological and ethological significance of echolocation use, the scanning range of echolocation to detect a target, diurnal cycles in the odontocetes' phonation, correlation between the abundance of a population and the number of calls of the odontocetes, the advantage of eavesdropping by the animals who do not phonate, and so on (Au, 1993). To answer such questions, above all we need to know the basic acoustical characteristics of echolocation clicks emitted by free-ranging odontocetes.

Since some acoustic behavioral differences have been found between riverine and inshore populations of one odontocete species, *Sotalia*, a hypothesis was proposed that inshore odontocete species emit a bi-component sonar signal with a low-frequency component to detect long-distance targets, and the riverine odontocete species only emits high-frequency unimodal sonar signals which are suitable for functioning in a turbid, muddy, and short-range environment (Kamminga and Wiersma, 1981; Kamminga *et al.*, 1983, 1993). According to this supposition one would expect the Yangtze finless porpoise (*Neophocaena phocaenoides asiaeorientialis*), who is a riverine subspecies, to emit high-frequency unimodal sonar signals.

Odontocete species can be divided into two categories according to their echolocation signal characteristics (Au, 1997). The species in the first category produce both long-duration, frequency-modulated tonal sounds (known as whistles) and ultrasonic pulse sounds (known as clicks). The clicks are broadband and short (<100 μs), often with the energy peak, or one of the energy peaks, below 70 kHz. The species in the second category are known to produce only pulsed signals. Their pulsed signals are narrow band and of long duration (>125 μs), with the energy peak at approximately 110 kHz. Because the acoustic categories of odontocete may reflect similarities and differences of species in ecology and anatomy, it is worthwhile to determine whether the division is the same for all odontocete species, and to which category each species belongs. Though there are some data about the finless porpoise (*Neophocaena phocaenoides*)

[a)]Author to whom correspondence should be addressed. Electronic mail: wangd@ihb.ac.cn

vocalizations (Mizue *et al.*, 1968; Pilleri *et al.*, 1980; Kamminga *et al.*, 1986, 1996; Wang, 1996; Nakahara *et al.*, 1997; Akamatsu *et al.*, 1998; Goold and Jefferson, 2002), interpretation of some results was limited by the equipment used. Some of the studies were also limited to captive animals, and some had no detailed description and analysis of the characteristics of echolocation signals of the porpoise. A description of echolocation ranges of the Yangtze finless porpoise and the baiji (*Lipotes vexillifer*) (Akamatsu *et al.*, 1998) describes some acoustic differences between the characteristics of echolocation signals of the two species, but there was no functional interpretation of the differences.

In the present study, we used a broadband recording system to record and analyze the characteristics of the echolocation signals of free-ranging Yangtze finless porpoise. Our objectives here are to (1) describe the full time and frequency properties of echolocation signals of the population in the wild; (2) test the hypotheses of the high-frequency unimodel sonar signals of the riverine population of odontocete species and the acoustic categories of odontocete; and (3) provide some suppositions about the evolutionary mechanisms of the acoustic characteristics of odontocete.

II. MATERIALS AND METHODS

A. Subjects

The finless porpoise species investigated in this study lives in the Tian-e-zhou Baiji National Natural Reserve, an oxbow that is an old course of the Yangtze River in Shishou, Hubei, China. The area is 21 km in length, 1 to 2 km in width, and 20 m in maximum depth. Establishment of this oxbow as a reserve for protection of baiji and Yangtze finless porpoise was approved by the Chinese central government in 1992, and the Yangtze finless porpoise was introduced into the oxbow in 1990 (Wang *et al.*, 2000; Zhang *et al.*, 1995). There were 19 animals in the reserve during this study. Observations showed that the behavior and ecology of the porpoises in the oxbow are similar and comparable to those of porpoises in the Yangtze River (Wei *et al.*, 2002).

B. Data recording and analysis

During October to November 2003, the porpoises were followed by a 9-m, small wood boat with an outboard diesel powered engine. We occasionally stationed to wait for the occurrence of the animals and try recording. A less-intrusive distance (>100 m) was maintained when following the animals. Behavior sampling and recording took place when the animals were within 300 m of the boat.

Underwater sound recordings were made with a hydrophone (OKI ST1020, sensitivity -180 dB *re*: 1 V/μPa $+12/-3$ dB, up to 150 kHz; the sensitivity declines in company with the increase of frequency from 100 to 150 kHz, and when the frequency is 125 kHz the sensitivity is approximately -180 dB *re*: 1 V/μPa $+5$ dB), an underwater sound level meter (OKI SW1020), and a digital data recorder (Sony PCHB244, with a flat frequency response from dc to 147 kHz within 3 dB; see Akamatsu *et al.*, 1998). The whole sound recording system is able to record signals with frequency up to 147 kHz. Because the signals of other members of the Phocoenidae do not have frequency over 150 kHz (Møhl and Andersen, 1973; Kamminga and Wiersma, 1981; Kamminga, 1988), this system should be sufficient to receive and store the echolocation signals of the investigated animals.

Sound analysis was performed using a PC-based signal processing system, the SIGNAL/RTS™ (Version 3.0, July, 1996, American Engineering Design) software. The signals that were replayed from the data recorder with a speed half that of the recording were digitized by a 12-bit Data Translation-2821G A/D board with a sampling frequency of 200 kHz (i.e., the original recorded signals were sampled with a sampling frequency of 400 kHz). The peak frequency and amplitude of the clicks progressively diminish, and the signals in the time domain become progressively distorted when clicks depart from the on-axis transmission beam (Au, 1993). Therefore, the subsequent analysis of each click in the randomly selected click trains, which have high signal-to-noise ratio, was performed on the click train with the highest recorded amplitude and decent envelope to increase the chance that the analyzed clicks were recorded from the on-axis transmission beam (Schotten *et al.*, 2003; Madsen *et al.*, 2004). First, using the built-in cursor option, we manually selected the click that had the highest recorded amplitude and the smoothest envelope from a randomly selected click train having high signal-to-noise ratio. Because some reverberations often followed and even overlapped with the click itself, it is necessary to make a subjective decision to differentiate the actual click, which has a clear sinusoidal waveshape and is smoothly enveloped, from the reverberations. After manual selection of the analyzed click, the following click characteristics were calculated by using waveform and spectrum whenever necessary (Au, 1993): signal duration (Δt, time between two points at which the click oscillations rose from the background noise and descended into the background noise, or inflexion formed by reverberation), peak frequency (f_p, frequency of maximum energy), 3-dB bandwidth (Δf, width of the frequency band between the two points that are 3 dB lower than the maximum amplitude of a spectrum), number of cycles in one click (n), relative width of the frequency spectra ($Q = f_p/\Delta f$), and time-bandwidth product ($\Delta t \times \Delta f$). Because of uncertainties of the position of animals with respect to the hydrophone, it is impossible to accurately estimate the source level of clicks. All the click characteristics were fed into Excel software and STATISTICA software to be analyzed.

III. RESULTS

A. Qualitative description of echolocation signals

From 20 October to 20 November 2003, 26 h of underwater signal recordings of the free-ranging Yangtze finless porpoise were acquired, which resulted in approximately 15 h of signal recordings that have high signal-to-noise ratio and have been selected for detailed analysis.

Various examples of click waveforms are presented in Fig. 1. As can be seen, the signal-to-noise ratio is very high, which enables the onset and end of the pulse to be estimated accurately. It should be noted that nearly all of the clicks

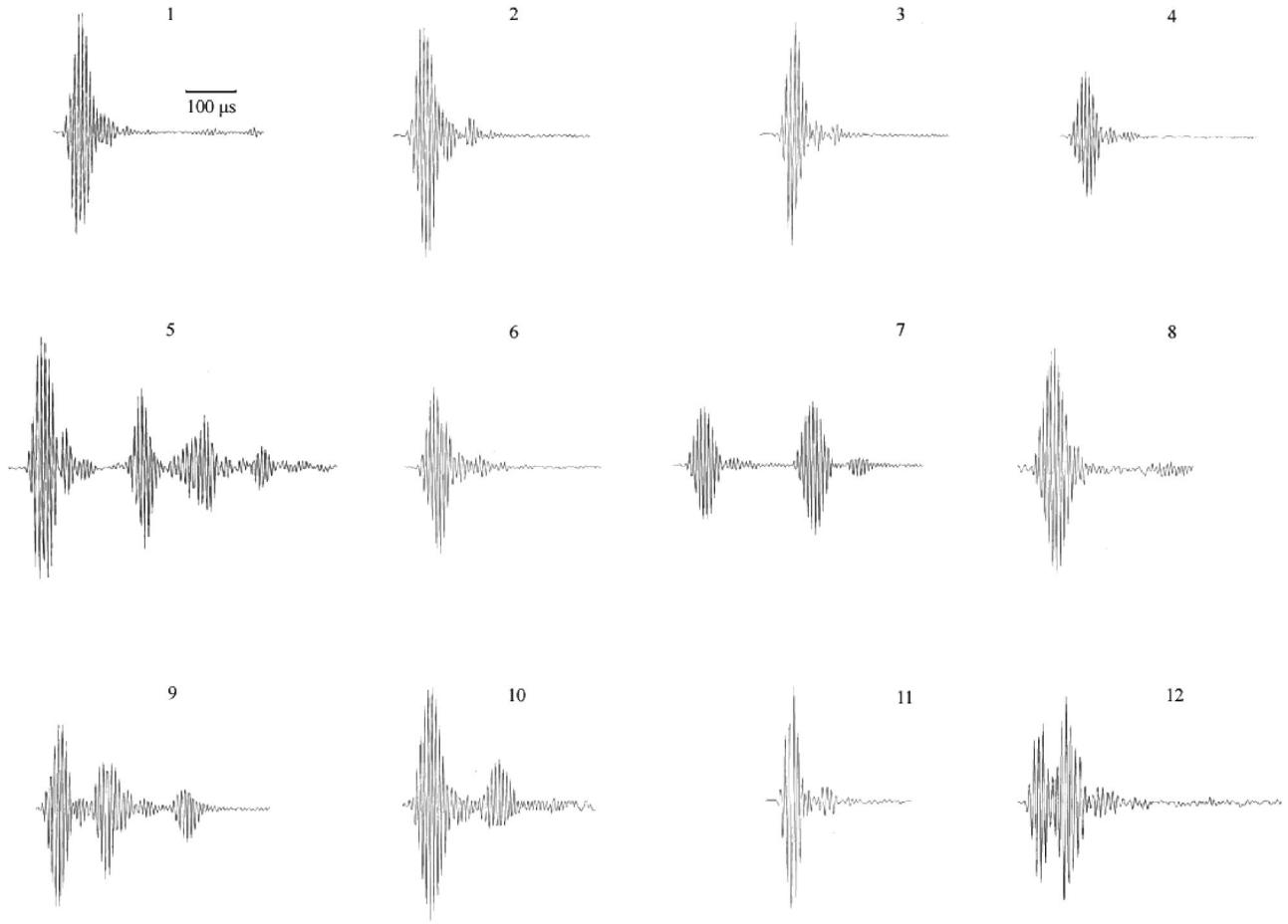

FIG. 1. Examples of the free-ranging Yangtze finless porpoise click waveforms.

have a basic waveshape that has a smooth envelope followed by some reverberations.

Three typical types of clicks are shown in Fig. 2 with the signal waveforms on the left and the frequency spectra on the right. The spectra plots show an obvious sharp peak, which indicates high peak frequencies and relative narrow 3-dB bandwidth. After comparing the waveforms and the spectra, it is not difficult to see that the signal with the greater number of cycles has the higher peak frequency and narrower 3-dB bandwidth.

A middle part of a click train and 20 consecutive pulses of the train are plotted in Fig. 3. Note that the 20 successive pulses that are plotted from left to right and from top to bottom in Fig. 3(b) have a very similar waveform structure, including the interpulse intervals and the difference of amplitude between the first and the second part, with the second part of the time waveform consistently having a higher amplitude than the first.

B. The time and frequency characteristics of echolocation signals

Means, standard deviations, and ranges of the calculated click characteristics of 548 clicks from randomly selected click trains are presented in Table I. Note that the analyzed signals have a high peak frequency ($f_p = 125 \pm 6.92$ kHz), narrow 3-dB bandwidth ($\Delta f = 20 \pm 4.24$ kHz), short signal durations ($\Delta t = 68 \pm 14.12$ μs), and low time-bandwidth product ($\Delta t \times \Delta f = 1.31 \pm 0.11$).

Histograms of signal durations, peak frequencies, and 3-dB bandwidth of the clicks are shown in Fig. 4. Over 75% of the analyzed clicks have signal durations between 50 and 80 μs, less than 3% of the signals have durations longer than 100 μs, and only 0.55% have durations less than 40 μs. The most preferred signal duration for this species is between 60 and 70 μs.

The peak frequency histograms indicate that more than 90% of the clicks have peak frequencies between 115 and 135 kHz. Less than 4% have peak frequencies over 135 kHz, and only 2% of signals have peak frequencies lower than 100 kHz. The animals appear to have a preference for peak frequency range between 125 and 135 kHz.

The 3-dB bandwidth histograms indicate that about 80% of the signals have a bandwidth between 15 and 25 kHz, and only 0.18% and 0.73 of the signals have bandwidths narrower than 10 and wider than 35 kHz, respectively.

The number of cycles as a function of peak frequency is plotted in Fig. 5(a), the 3-dB bandwidth as a function of peak frequency is plotted in Fig. 5(b), and the signal duration as a function of peak frequency is plotted in Fig. 5(c). Each scatter plot is shown along with a linear regression line (Fig. 5) ($p < 0.01$, linear-test).

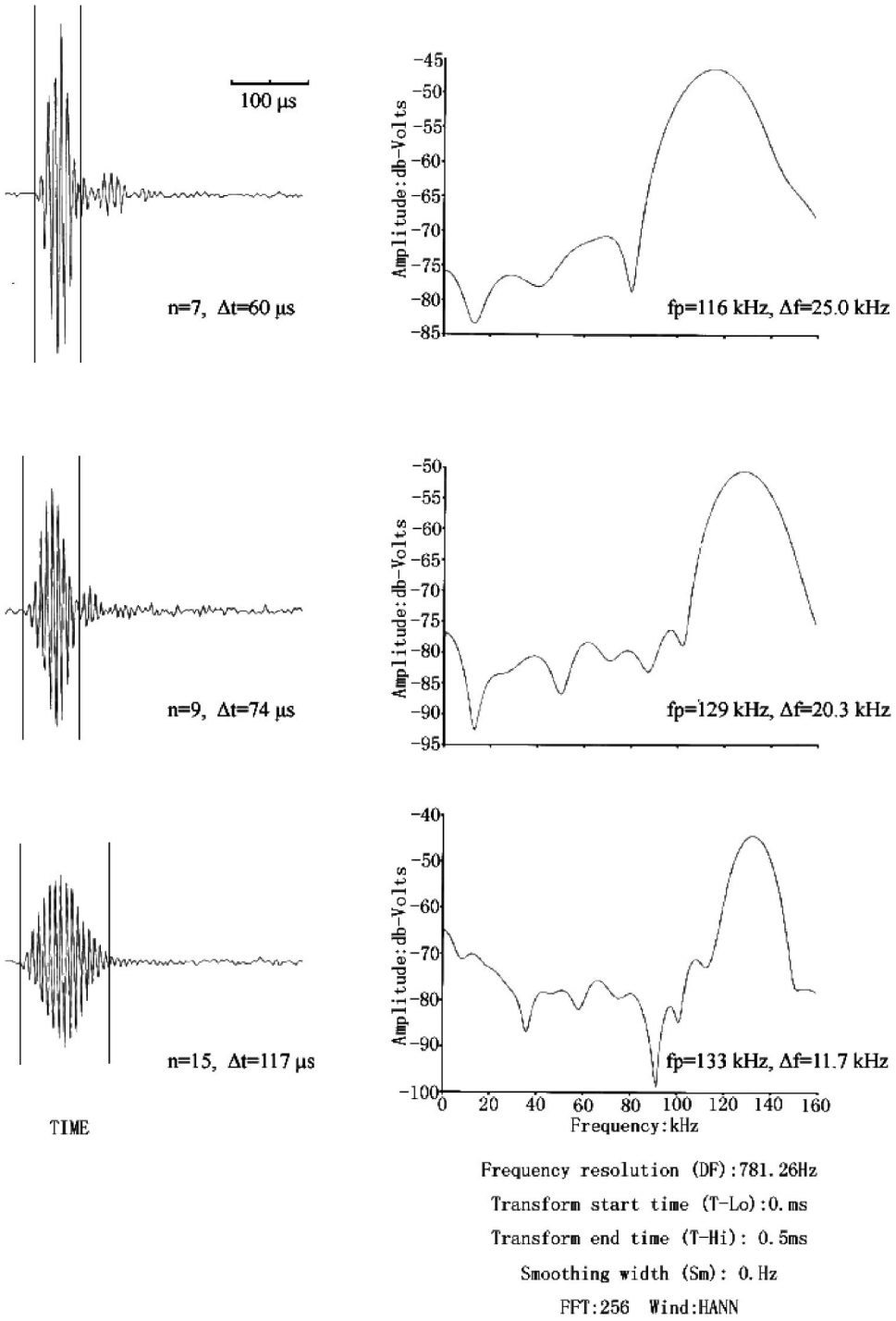

FIG. 2. Waveforms and frequency spectra of three typical types of clicks emitted by the free-ranging Yangtze finless porpoise in the Tian-e-zhou Reserve. "n" represents the number of cycles in one click, "Δt" represents the time between two points at which the click oscillations rose from the background noise and descended into the background noise or inflexion formed by reverberation, "f_p" represents the frequency of maximum energy, and "Δf" represents the width of the frequency band between the two points that are 3 dB lower than the maximum amplitude of a spectrum.

The relation $\Delta t \times \Delta f$ is plotted in Fig. 6, together with the theoretical lower bound $\Delta t \times \Delta f = 1$. A very distinct approximation that follows the bound is presented for all clicks.

IV. DISCUSSION AND CONCLUSIONS

Because of the uncertainty of the position of animals with respect to the hydrophone in the wild, it is impossible to directly know which clicks are on-axis and which are off-axis with the echolocation beam. However, the fact that the analysis was performed on the clicks with the highest recorded amplitude and decent envelope increases the chance that the analyzed clicks were recorded from the on-axis transmission beam (Schotten *et al.*, 2003; Madsen *et al.*, 2004). Also, the obtained waveform structures (Fig. 1) and distribution of parameters (Fig. 4) of the analyzed clicks were similar to the characteristics of on-axis echolocation signals (Au, 1993). Therefore, we feel quite confident to say that most of the analyzed clicks are on-axis or near to on-axis transmission beam, and can be used to represent the characteristics of echolocation signals of the investigated animals.

The Yangtze finless porpoise clicks have waveforms (Fig. 1) that are very similar to those of coastal populations of the species (Kamminga *et al.*, 1986; Kamminga, 1988; Goold and Jefferson, 2002) and other members of the Phocoenidae (Dubrovskii *et al.*, 1971; Møhl and Andersen, 1973;

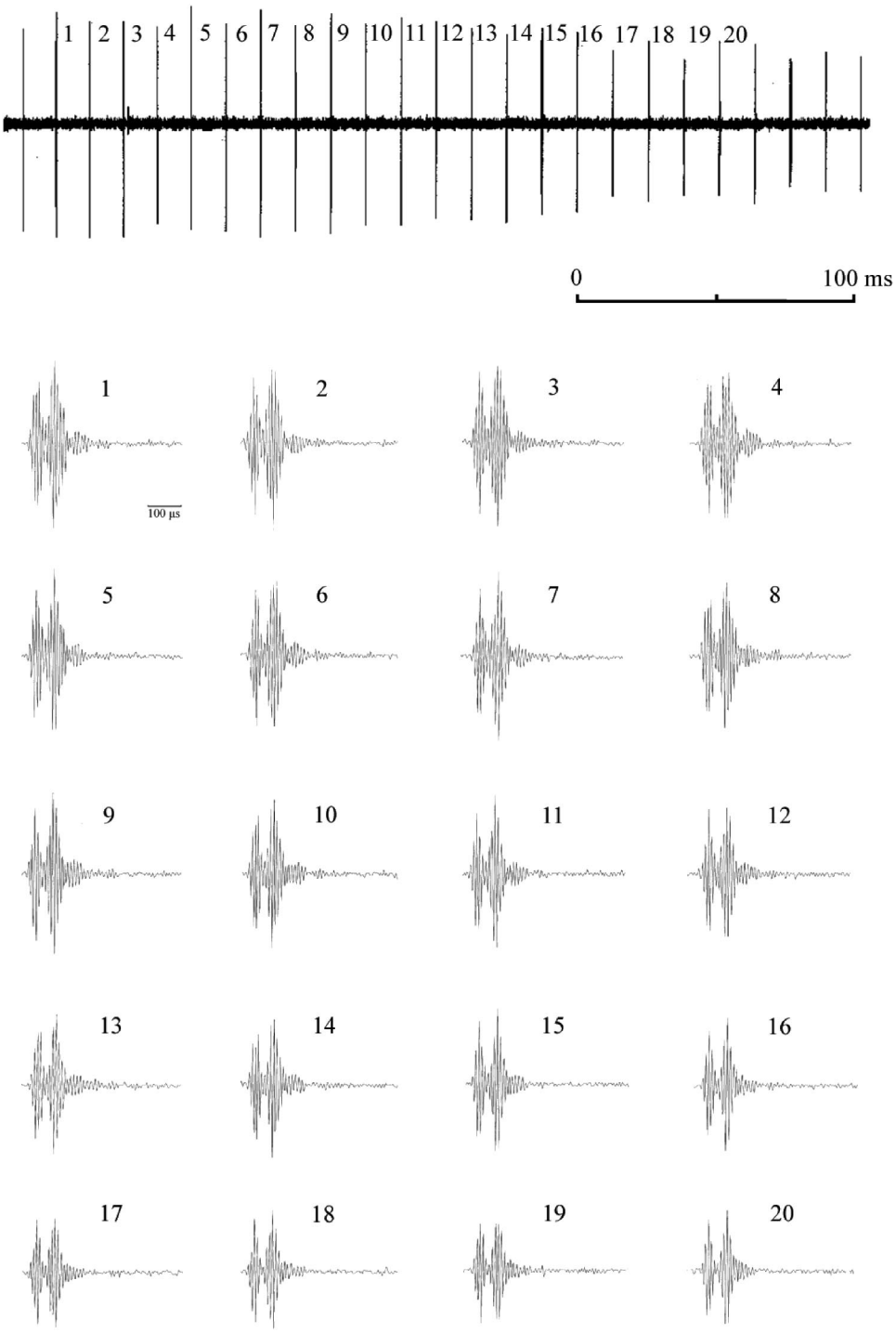

FIG. 3. The middle part of a click train (a) and sequence of successive pulses (b). Note the transition points, interval, and difference of amplitude between the first and the second part.

TABLE I. Calculated click characteristics, including f_p (frequency of maximum energy), Δf (width of the frequency band between the two points that are 3 dB lower than the maximum amplitude of a spectrum), Δt (time between two points at which the click oscillations rose from the background noise, and descended into the background noise or inflexion formed by reverberation), n (number of cycles in one click), Q (relative width of the frequency spectra), and $\Delta t \times \Delta f$ (time-bandwidth product) for 548 analyzed clicks of the free-ranging Yangtze finless porpoise.

	f_p (kHz)	Δf (kHz)	Δt (μs)	n	Q	$\Delta t \times \Delta f$
Mean	125	20.0	68	8	6.6	1.31
s. d.	6.92	4.24	14.12	1.94	1.56	0.11
Range	87–145	9.3–41.9	30–122	4–16	3.0–12.5	1.00–1.68

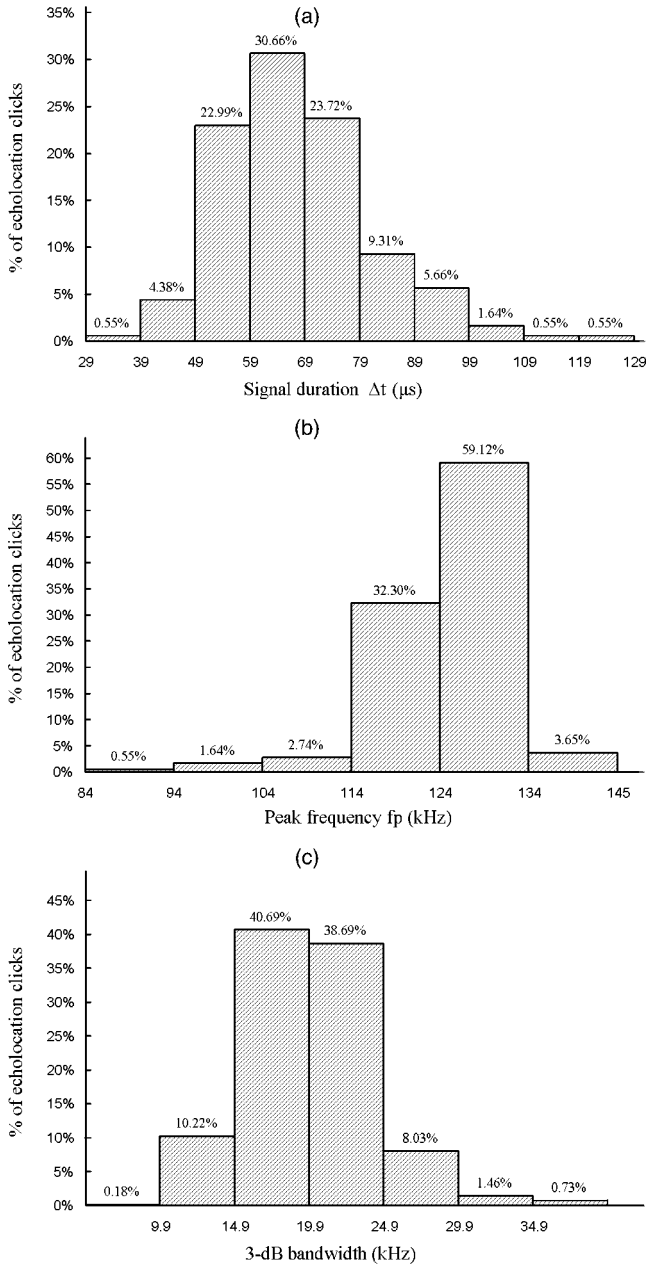

FIG. 4. Histograms of the distribution of signal duration Δt (a), peak frequency f_p (b), and 3-dB bandwidth Δf (c) of the 548 analyzed clicks of the free-ranging Yangtze finless porpoise.

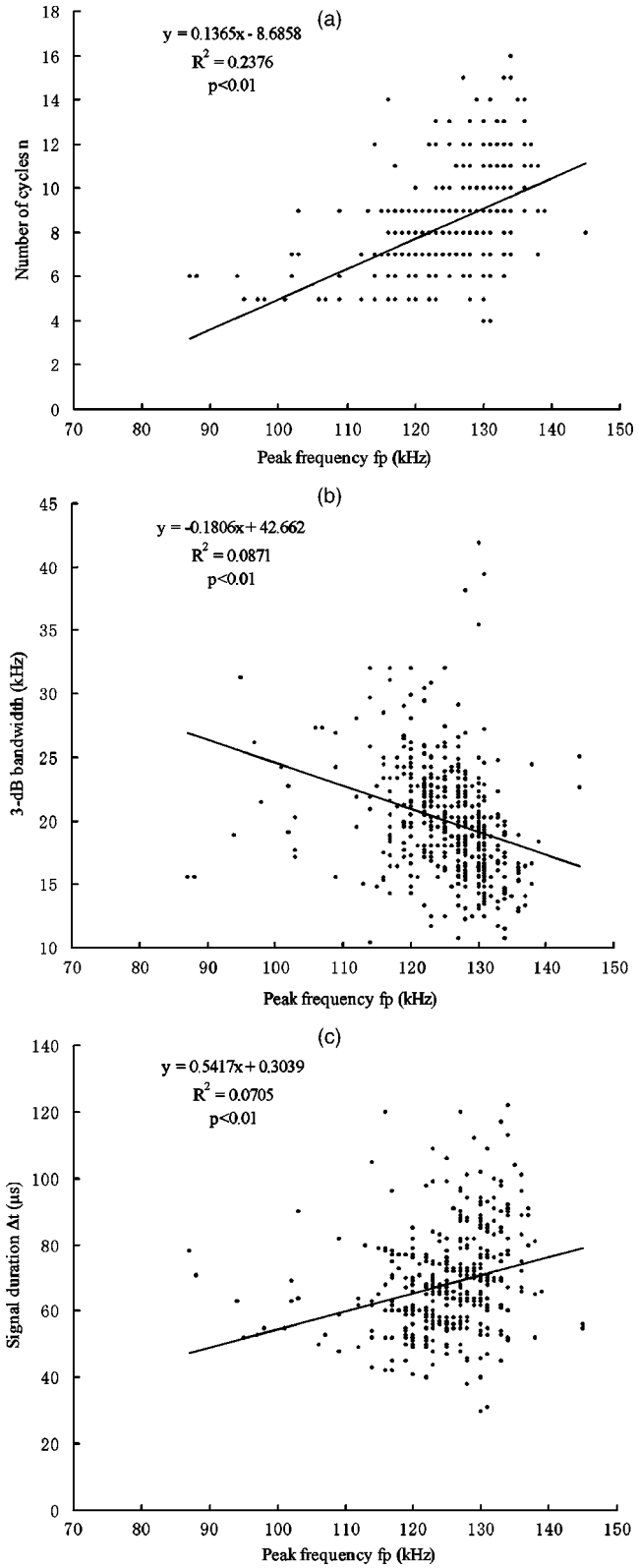

FIG. 5. Scatter plots of number of cycles n versus peak frequency f_p (a), 3-dB bandwidth Δf versus peak frequency f_p (b), and signal duration Δt versus peak frequency f_p (c). The equation of the least square linear regression line through the data, its correlation coefficient, and the p value are indicated in the up left corner of each plot.

Awbrey *et al.*, 1979; Kamminga and Wiersma, 1981; Evans and Awbrey, 1988; Kamminga, 1988; Silber, 1991), as well as the distantly related delphinids, *Cephalorhynchus spp*. (Watkins and Schevill, 1980; Kamminga and Wiersma, 1982; Dziedzic and De Buffrenil, 1989). The waveforms are markedly different from those of the baiji, which occupies the same habitat in the middle and lower reaches of the Yangtze River as the Yangtze finless porpoise (Xiao and Jing, 1989; Akamatsu *et al.*, 1998; Nakamura and Akamatsu, 2003).

The clicks of the Yangtze finless porpoise, as depicted in Figs. 1, 2 and 3(b), often have double-pulse or multi-pulse waveform structures, a phenomenon that has been previously reported and discussed in the clicks of *Sotalia* (Norris *et al.*, 1972), *Tursiops* (Norris *et al.*, 1966), and *Cephalorhynchus* (Kamminga and Wiersma, 1981). Because the animal-hydrophone geometry cannot be ascertained in the wild using one hydrophone, it is difficult to discern whether the double-pulse and multi-pulse waveform structures are being emitted by the animal, or whether the structures are the result

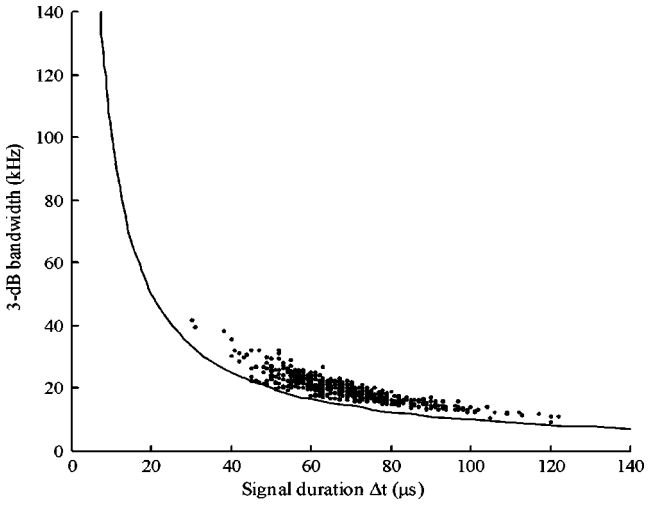

FIG. 6. The uncertainty product of signal duration Δt and 3-dB bandwidth Δf plotted for an ensemble of 548 pulses from randomly chosen pulse trains. The solid line indicates the bound of $\Delta t \times \Delta f = 1$.

of surface or bottom reflections (Au, 1993). Fortunately, tens of consecutive, nearly identical multi-pulse clicks have often been recorded from moving Yangtze finless porpoises in this study. Twenty consecutive clicks are shown as an example in Fig. 3(b). It is nearly impossible that the multi-pulse is from several animals since the interpulse interval is almost consistent among the consecutive multiple clicks, as shown in Fig. 3(b). However, since the moving speed of the Yangtze finless porpoises is usually lower than 5 m/s (Yang and Chen, 1996), the change in animal-hydrophone geometry during the duration of one click train seems not to be enough to observably alter the double-pulse and multi-pulse waveform structures—if we suppose that the double-pulse and multi-pulse waveform structures are the result of surface or bottom reflections. Therefore, the possibility that the multi-pulse click structures are the result of surface or bottom reflections cannot be excluded. Meanwhile, it should also be noted that the second part of the time waveform has a higher amplitude than the first part in the double-pulse structure [Fig. 3(b)]. This phenomenon of double-pulse and multi-pulse waveform structures deserves further investigation.

There is no low-frequency component (<70 kHz) found in our data as expected. There was no direct evidence to indicate that the coastal population of finless porpoise would have echolocation clicks with a low-frequency component (Kamminga *et al.*, 1986; Goold and Jefferson, 2002), and, when only considering the riverine population of this species, the hypothesized difference in frequency components between riverine and coastal populations in one odontocete species (Kamminga *et al.*, 1983) is further supported.

The clicks recorded from the investigated animals are typical high-frequency ($f_p = 125 \pm 6.92$ kHz, $N = 548$), narrow-band ($\Delta f = 20.0 \pm 4.24$ kHz, $N = 548$; $Q = 6.6 \pm 1.56$, $N = 548$) signals that are similar to clicks emitted by nonwhistling dolphin species. The signal durations ($\Delta t = 68 \pm 14.12$ μs, $N = 548$) are obviously shorter than the expected value of greater than 125 μs (Au, 1997). Therefore, one should exercise caution about the hypothesis of the division of odontocetes into two acoustic categories based on the differences of the echolocation signal characteristics (Au, 1997).

As echolocation abilities with frequency lower than 10 kHz may occur in pinnipeds (Poulter and Jennings, 1969; Renouf *et al.*, 1980; Awbrey *et al.*, 2003), aves (Fullard *et al.*, 1993; Bradbury and Vehrencamp, 1998), and even humans (Rice *et al.*, 1965; Arias and Ramos, 1997), "high-frequency sound is not essential for echolocation" (see Herzing and dos Santos, 2003). Then why does the Yangtze finless porpoise, as well as some other odontocetes, use such high-frequency echolocation signals to detect and navigate? Many scientists have attributed this to environmental pressures and evolutionary results. But how this ability evolved and which environmental factors were the main stimulators are important areas still open to investigation.

After inspection and elaborate study of many clicks of the free-ranging Yangtze finless porpoise, the resemblance to the acoustic signals (especially waveform structure and click peak frequency) of other members of the Phocoenidae, as well as the distantly related delphinids, *Cephalorhynchus spp*., became increasingly apparent. The habitats of other members of the Phocoenidae and *Cephalorhynchus spp*. are in coastal regions (Dubrovskii *et al.*, 1971; Kamminga *et al.*, 1986), some of which possess turbid, muddy, and short-range environments analogous to the Yangtze River. It does not then come as a surprise that the signal waveform structure and peak frequency of these species are confirmed to match closely with those of the Yangtze finless porpoise. However, a striking difference is found when comparing the waveform and spectrum of clicks of the baiji, a species occupying the same habitat as the Yangtze finless porpoise, to those characteristics of clicks of the Yangtze finless porpoise.

The signal of the Yangtze finless porpoise has a markedly higher peak frequency than that of the baiji (Xiao and Jing, 1989; Akamatsu *et al.*, 1998; Nakamura and Akamatsu, 2003). One explanation is that the two odontocete species use different frequencies so that their echolocation signals do not overlap and interfere with or mask each other. Alternatively, the size of food of the baiji is larger than that of the Yangtze finless porpoise (Chen *et al.*, 1997, pp. 135–136, 183–184, 233). Only those individuals that have echolocation signals with a peak frequency matching the size of their preferable food can accurately detect and track prey, in order to acquire enough food to increase their chance of survival. To accurately detect smaller food targets in turbid, muddy environments, the Yangtze finless porpoise, through evolutionary refinement over millions of years, may have adopted a higher frequency signal with smaller wavelength to match the smaller sized food. The size of food may therefore be an important stimulative factor of the evolution of the high-frequency echolocation signals.

According to this hypothesis, odontecetes occupying similar habitats and preferring comparable size of food should have clicks with similar peak frequencies. To test such a hypothesis, much more data from different odontocete species and quantitative relationships between peak frequency and size of food are needed. On the other hand, because the high-frequency sound is able to compete with the low-frequency noisy environment, to detect the target more

accurately, the differences of peak frequency of the echolocation signals of baiji and Yangtze finless porpoise may be an important reason for the differing health of these two species' populations. The baiji is in severe danger, but the Yangtze finless porpoise still maintains a population consisting of many individuals (Wang *et al.*, 2000).

Our results suggest that several basic signal parameters, including the peak frequency, the number of cycles, 3-dB bandwidth, and signal duration, are interrelated in a complex relationship (Fig. 5, $p<0.01$, linear-test) in spite of the fact that some of them have a relatively low r^2 value [Figs. 5(b) and 5(c)].

The regression line in Fig. 5(a) suggested that the number of cycles in a click is positively related to the peak frequency. As the peak frequency increases, the number of cycles of a click also increases. From the regression line in Fig. 5(b) we can see that the 3-dB bandwidth has a weak linear relationship to the peak frequency with an r^2 value of only 0.0871. However, this plot shows a trend that the 3-dB bandwidth decreases with the ascending peak frequency. This result contradicts previous results where a linear, increasing relationship between bandwidth and frequency was shown in the echolocation signals of wild Atlantic spotted dolphin (*Stenella frontalis*) (Au and Herzing, 2003), Spinner dolphins (*S. longirostris*), and Pantropical spotted dolphins (*S. attenuata*) (Schotten *et al.*, 2003). The difference might indicate an interspecific variation in the relationship between bandwidth and frequency. Because of the uncertainty product of signal duration and 3-dB bandwidth, there is a reverse relationship between the signal duration and 3-dB bandwidth (Fig. 6). Therefore, the signal duration will tend to increase in concert with the increase of the peak frequency with a low r^2 value [Fig. 5(c)].

A relatively large range of signal parameters has been observed (Table I). The variation might be related to different behavioral contexts, or to the manner in which the recordings were made. For example, the size, age, and behavior of the individual might influence the value of signal parameters. Many efforts have been introduced to reduce the presence of off-axis signals, but the misrepresentations of clicks due to the uncertain position of vocalizing animals is inevitable when recordings are obtained in the wild using one hydrophone. The misrepresentations of clicks may also have affected the relationship between the acoustic parameters, which has a low r^2 value (Fig. 5). Much more work needs to be done, and more refined equipment needs to be introduced, to resolve these existing questions.

ACKNOWLEDGMENTS

The authors are grateful for the help and assistance provided by Zhuo Wei, Benfang Yu, Qingzhong Zhao, Xianfeng Zhang, Weiwei Dong, Xianyan Wang, Jianqiang Xiao, Junhong Xia, Zheng Guo, Jingsong Zheng, and Zeliang Ding during the field signal recordings. We would also like to express our appreciation to Professor Alexander Ya. Supin, Professor Vladimir V. Popov, Dr. Peter T. Madsen, Dr. Whitlow W. L. Au, and two reviewers for their valuable comments and revision on this manuscript. We thank Alison Stimpert of the Zoology Department, University of Hawaii, for her editorial effort. This research was supported by Chinese Academy of Sciences (CAS) and Institute of Hydrobiology, CAS (Nos. KSCX2-SW-118 and 220103) and Program for Promotion of Basic Research Activities for Innovative Biosciences of Japan.

Akamatsu, T., Wang, D., Nakamura, K., and Wang, K. (**1998**). ''Echolocation range of captive and free-ranging baiji (*Lipotes vexillifer*), finless porpoise (*Neophocaena phocaenoides*), and bottlenose dolphin (*Tursiops truncatus*),'' J. Acoust. Soc. Am. **104**, 2511–2516.

Arias, C., and Ramos, O. A. (**1997**). ''Psychoacoustic tests for the study of human echolocation ability,'' Appl. Acoust. **51**, 399–419.

Au, W. W. L. (**1993**). *The Sonar of Dolphins* (Springer-Verlag, New York).

Au, W. W. L. (**1997**). ''Echolocation in dolphins with a dolphin-bat comparison,'' Bioacoustics **8**, 137–162.

Au, W. W. L., and Herzing, D. L. (**2003**). ''Echolocation signals of wild Atlantic spotted dolphin (*Stenella frontalis*),'' J. Acoust. Soc. Am. **113**, 598–604.

Awbrey, F. T., Thomas, J. A., and Evans, W. E. (**2003**). ''Ultrasonic underwater sounds from a captive Leopard seal (*Hydrurga leptonyx*),'' in *Echolocation in Bats and Dolphins*, edited by J. Thomas, C. F. Moss, and M. Vater (Univ. of Chicago, Chicago), pp. 535–541.

Awbrey, F. T., Norris, J. C., Hubbard, A. B., and Evans, W. E. (**1979**). ''The bioacoustics of the Dall porpoise—salmon net interaction,'' Hubbs-Sea World Research Institute Technical Report 79–120.

Bradbury, J. W., and Vehrencamp, S. L. (**1998**). *Principles of Animal Communication* (Sinauer, Sunderland, MA).

Chen, P., Liu, R., Wang, D., and Zhang, X. (**1997**). *Biology, Rearing and Conservation of Baiji* (Science, Baijing).

Dubrovskii, N. A., Krasnov, P. S., and Titov, A. A. (**1971**). ''On the emission of echolocation-signals by the Azov sea harbor porpoise,'' Sov. Phys. Acoust. **16**, 444–448.

Dziedzic, A., and De Buffrenil, V. (**1989**). ''Acoustic signals of the Commerson's dolphin, *Cephalorhynchus commersonii*, in the Kerguelen Islands,'' J. Mammal. **70**, 449–452.

Evans, W. E., and Awbrey, F. T. (**1988**). ''Natural history aspects of marine mammal echolocation: feeding strategies and habitat,'' in *Animal Sonar, Process and Performance*, edited by P. E. Nachtigall and P. W. B. Moore (Plenum, New York), pp. 521–534.

Fullard, J. H., Barclay, R. M. R., and Thomas, D. W. (**1993**). ''Echolocation in free-flying atiu swiftlets (*Aerodramus sawtelli*),'' Biotropica **25**, 334–339.

Goold, J. C., and Jefferson, T. A. (**2002**). ''Acoustic signals from free-ranging Finless porpoises (*Neophocaena phocaenoides*) in the waters around Hong Kong,'' Raffles Bull. Zool., Suppl. **10**, 131–139.

Herzing, D. L., and dos Santos, M. E. (**2003**). ''Functional aspects of echolocation in dolphins,'' in *Echolocation in Bats and Dolphins*, edited by J. Thomas, C. F. Moss and M. Vater (Univ. of Chicago, Chicago), pp. 386–393.

Kamminga, C. (**1988**). ''Echolocation signal types of odontocetes,'' in *Animal Sonar, Process and Performance*, edited by P. E. Nachtigall and P. W. B. Moore (Plenum, New York), pp. 9–22.

Kamminga, C., and Wiersma, H. (**1981**). ''Investigations on Cetacean Sonar II. Acoustical similarities and differences in odontocete sonar signals,'' Aquat. Mamm. **8**, 41–62.

Kamminga, C., and Wiersma, H. (**1982**). ''Investigations on Cetacean Sonar V. The true nature of the sonar sound of *Cephalorhynchus commersonii*,'' Aquat. Mamm. **9**, 95–104.

Kamminga, C., Cohen Stuart, A. B., and Silber, G. K. (**1996**). ''Investigations on cetacean sonar XI: Intrinsic comparison of the wave shapes of some members of the Phocoenidae family,'' Aquat. Mamm. **22**, 45–55.

Kamminga, C., Kataoka, T., and Engelsma, F. J. (**1986**). ''Investigations on cetacean sonar VII. Underwater sounds of *Neophocaena phocaenoides* of the Japanese coastal population,'' Aquat. Mamm. **12**, 52–60.

Kamminga, C., Wiersma, H., and Dudok van Heel, W. H. (**1983**). ''Sonar sounds in *Orcaella brevirostris* of the Mahakam River, East Kalimantan, Indonesia; the first descriptions of the acoustic behaviour,'' Aquat. Mamm. **10**, 83–95.

Kamminga, C., Van Hove, M. T., Engelsma, F. J., and Terry, R. P. (**1993**). ''Investigations on Cetacean Sonar X: A comparative analysis of underwater echolocation clicks of *Inia* spp. And *Sotalia* spp.,'' Aquat. Mamm. **19**, 31–43.

Madsen, P. T., Kerr, I., and Payne, R. (**2004**). ''Echolocation clicks of two free-ranging, oceanic delphinids with different food preferences: false killer whales *Pseudorca crassidens* and Risso's dolphins *Grampus griseus*,'' J. Exp. Biol. **207**, 1811–1823.

Mizue, K., Takemura, A., and Nakasai, K. (**1968**). ''Studies on the little toothed whales in the west sea area of Kyusyu-XV. Underwater sound of the Chinese finless porpoise caught in the Japanese coastal sea,'' Bull. Faculty Fisheries, Nagasaki Univ. **25**, 25–32.

Møhl, B., and Andersen, S. (**1973**). ''Echolocation: high frequency component in the click of the harbour porpoise (*Phocoena phocoena* L.),'' J. Acoust. Soc. Am. **54**, 1368–1373.

Nakahara, F., Takemura, A., Koido, T., and Hiruda, H. (**1997**). ''Target discrimination by an echolocating Finless porpoise, *Neophocaena phocaenoides*,'' Marine Mammal Sci. **133**, 639–649.

Nakamura, K., and Akamatsu, T. (**2003**). ''Comparison of click characteristics among odontocete species,'' in *Echolocation in Bats and Dolphins*, edited by J. Thomas, C. F. Moss, and M. Vater (Univ. of Chicago Press, Chicago), pp. 36–40.

Norris, K. S., Evans, W. E., and Turner, R. N. (**1966**). ''Echolocation in an Atlantic bottlenose porpoise during discrimination,'' in *Animal Sonar System*, edited by R.-G. Busnel (Plenum, New York), Vol. I, pp. 409–447.

Norris, K. S., Harvey, G. W., Burzell, L. A., and Krishna Kartha, T. D. (**1972**). ''Sound production in the freshwater porpoises *Sotalia cf fluviatilis* GERVAIS and DEVILLE and *Inia geoffrensis* Blainville, in the Rio Negro, Brazil,'' in *Investigations on cetacean*, edited by G. Pilleri, Bern, Vol. IV, pp. 251–262.

Pilleri, G., Zbinden, K., and Kraus, C. (**1980**). ''Characteristics of the sonar system of cetaceans with pterygoschis. Directional properties of the sonar system of *Neophocaena phocaenoides* and *Phocoena phocoena* (Phocoenidae),'' Invest. Cetacea. **11**, 157–188.

Poulter, T. C., and Jennings, R. A. (**1969**). ''Sonar discrimination ability of the California sea lion, *Zalophus californianus*,'' Proc. California Acad. Sci. **36**, 381–389.

Renouf, D., Galway, G., and Gaborko, L. (**1980**). ''Evidence for echolocation in harbour seals,'' J. Mar. Biol. Assoc. U.K. **60**, 1039–1042.

Rice, C. E., Felnstein, S. H., and Schusterman, R. J. (**1965**). ''Echo detection ability of the blind: Size and distance factors,'' J. Exp. Psychol. **70**, 246–251.

Schotten, M., Au, W. W. L., Lammers, M. O., and Aubauer, R. (**2003**). ''Echolocation recordings and localization of wild-spinner dolphins (*Stenella longirostris*) and pantropical spotted dolphins (*Stenella attenuata*) using a four hydrophone array,'' in *Echolocation in Bats and Dolphins*, edited by J. Thomas, C. F. Moss, and M. Vater (Univ. of Chicago, Chicago), pp. 393–400.

Silber, G. K. (**1991**). ''Acoustic signals of the Vaquita (*Phocoena sinus*),'' Aquat. Mamm. **17**, 130–133.

Wang, D. (**1996**). ''A preliminary study on sound and acoustic behavior of the Yangtze River finless porpoise, *Neophocaena phocaenoides*,'' Acta Hydrobiol. Sinica. **20**, 127–133.

Wang, D., Liu, R., Zhang, X., Yang, J., Wei, Z., Zhao, Q., and Wang, X. (**2000**). ''Status and conservation of the Yangtze finless porpoises,'' in *Biology and Conservation of Freshwater Cetaceans in Asia.Occas. Pap*, edited by R. R. Reeves, B. D. Smith, and T. Kasuya, IUCN Spec. Surv. Commun. Vol. 23, pp. 81–85.

Watkins, W. A., and Schevill, W. E. (**1980**). ''Characteristic features of the underwater sounds of *Cephalorhynchus commersonii*,'' J. Mammal. **61**, 738–740.

Wei, Z., Wang, D., Kuang, X., Wang, K., Wang, X., Xiao, J., Zhao, Q., and Zhang, X. (**2002**). ''Observations on behavior and ecology of the Yangtze finless porpoise (*Neophocaena phocaenoides asiaeorientalis*) group at Tian-e-Zhou oxbow of the Yangtze River,'' Raffles Bull. Zool., Suppl. **10**, 97–103.

Xiao, Y., and Jing, R. (**1989**). ''Underwater acoustic signals of the baiji, *Lipotes vexillifer*,'' in *Biology and Conservation of the River Dolphin*, edited by W. F. Perrin, R. L. Brownell, Jr., K. Zhou, and J. Liu, IUCN Spec. Surv. Commn. (Gland, Switzerland), pp. 129–136.

Yang, J., and Chen, P. (**1996**). ''Movement and behavior of finless porpoise (*Neophocaena phocaenoides asiaeorientialis*) at Swan oxbow, Hubei province,'' Acta Hydrobiol. Sinica. **20**, 32–40.

Zhang, X., Wei, Z., Wang, X., Yang, J., and Chen, P. (**1995**). ''Studies on the feasibility of establishment of a semi-natural reserve at Tian-e-Zhou (Swan) oxbow for baiji, *Lipotes vexillifer*,'' Acta Hydrobiol. Sinica. **19**, 110–123.

Sound production by North Atlantic right whales (*Eubalaena glacialis*) in surface active groups

Susan E. Parks[a] and Peter L. Tyack
Woods Hole Oceanographic Institution, Woods Hole, Massachusetts 02543

(Received 11 August 2004; revised 19 January 2005; accepted 8 February 2005)

The surface active group (SAG) is the most commonly observed surface social behavior of North Atlantic right whales. Recordings were made from 52 SAGs in the Bay of Fundy, Canada between July and September, from 1999 to 2002. The call types recorded from these groups were similar to those described previously for Southern right whales (*Eubalaena australis*), with six major call types being termed scream, gunshot, blow, upcall, warble, and downcall. The percentage of total calls of each call type depended on the group size and composition. The most common call type recorded was the scream call. The scream calls were produced by the focal female in a SAG. Production of other sound types can be attributed to whales other than the focal female, with gunshot and upcalls produced by males, and warble calls produced by female calves. The source levels for these sounds range from 137 to 162 dB rms *re* 1 μPa-m for tonal calls and 174 to 192 dB rms for broadband gunshot sounds.
[DOI: 10.1121/1.1882946]

PACS numbers: 43.80.Ka [WA] Pages: 3297–3306

I. INTRODUCTION

Little is known about the acoustic behavior of the North Atlantic right whale (*Eubalaena glacialis*). Sounds produced by many baleen whale species have been recorded and described in the past 40 years (Tyack and Clark, 2000), but relatively few studies have attempted to link sound production with behavioral observations to address the functional significance of these sounds. The notable exceptions to this are the humpback whale (*Megaptera novaeangliae*) and the Southern right whale (*Eubalaena australis*). Studies of humpback whales have demonstrated differences in sound production during different behavioral contexts such as the feeding calls in Alaska (D'Vincent *et al.*, 1985) versus song and competitive group sounds on the breeding grounds (Helweg *et al.*, 1992; Payne and McVay, 1971; Silber, 1986; Tyack and Whitehead, 1983). Researchers have also found gender differences in sound production, showing that song is produced by male whales (Darling and Bérubé, 2001; Winn and Winn, 1978).

Several studies have described sound production in the Southern right whale (Clark, 1982, 1983, 1984; Cummings *et al.*, 1972; Payne and Payne, 1971; Saayman and Tayler, 1973). Clark showed that different call types were associated with different levels of activity. Up, down, and constant calls were associated primarily with swimming or mild activity, while high, hybrid, and pulsive calls were the predominant signals produced in fully active and sexually active groups (Clark, 1983). Additional playback experiments demonstrated the right whale's ability to discriminate the sounds of right whales from those of other whale species (Clark and Clark, 1980).

Some of the earliest reports of North Atlantic right whale sound production describe low-frequency signals of feeding right whales (Schevill *et al.*, 1962; Schevill and Watkins, 1962). These publications gave a few examples of sounds with few details about the behavior accompanying the sound production. More recently, several studies have attempted to characterize the call rate, frequency range and source level of sound production by the North Atlantic right whale (Clark, 1999; Matthews *et al.*, 2001; Vanderlaan *et al.*, 2003). One study has compared sound production of the North Atlantic right whale to sounds recorded from the Southern right whale (Wright, 2001).

For this study a distinct, easily detected behavioral context, the surface active group or SAG, was selected for detailed acoustic characterization. A SAG is described as two or more whales (up to 35 observed) interacting at the surface with frequent physical contact (Kraus and Hatch, 2001). This general definition encompasses three types of interactions in Southern right whales described by Clark (1983) as mild, full, and sexual activity. In the Bay of Fundy, Canada, the composition of SAGs commonly involves a single female at the center of the group, referred to as the focal female, surrounded by multiple males (Kraus and Hatch, 2001). However, SAGs have variable composition, including all-male and all-female groups, and it is possible that different kinds of social grouping involving significantly different behavioral interactions have been grouped into a single SAG category. Sound production by whales in these groups may make it possible to distinguish different kinds of SAGs. For example, Clark (1983) provides evidence in Southern right whales that the upcall was absent from all recordings from groups labeled as sexually active (Clark, 1983). In this study, recordings were made from North Atlantic right whale SAGs in the Bay of Fundy, Canada in an attempt to provide a comprehensive description of the sounds associated with these groups.

[a]Current address: Cornell University Bioacoustics Research Program, 159 Sapsucker Woods Road, Ithaca, New York 14850.

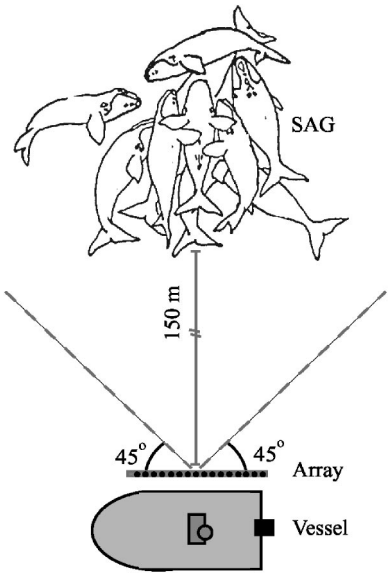

FIG. 1. Position of the vessel during array recording. The vessel was positioned with the SAG between 150 and 300 m away, with the whales centered perpendicular to the axis of the array. The surface currents and wind would push the vessel at a rate of 0.5–3 knots over the surface. The vessel was positioned so that it would drift away from the SAG, preventing the array from being pushed under the boat or the boat drifting too close to the whales. Frequent repositioning was necessary to keep this approximate position for observations. Whales in figure adapted from Kraus and Hatch (2001).

II. METHODS

Recordings and behavioral observations were made from July to September in the Bay of Fundy, Canada, east of Grand Manan Island from 1999 to 2002. Single hydrophone recordings and synchronous hydrophone/video recordings were made opportunistically from four platforms from 1999 to 2002. In 2002, recordings were also made with a 15-channel hydrophone array, allowing determination of angle of arrival of the calls. The recording platforms were the R/V *Nereid* (1999–2001), a 9-m inboard motor vessel operated by the New England Aquarium; the R/V *Song of the Whale* (2000), a 14-m motor sailor operated by the International Fund for Animal Welfare (IFAW); the R/V *Bonita* (2000–2001), a 5-m rigid hull inflatable from the New England Aquarium; and the R/V *Stellwagen* (2001), a 21-m inboard motor vessel chartered by the Woods Hole Oceanographic Institution. A single dedicated platform, the R/V *Callisto*, a 7-m outboard from the New England Aquarium, was used in 2002.

Most recordings were made in sea states $\leqslant 3$. Groups were approached to obtain photographs of whales in the group before recordings commenced. The times of arrival and departure of whales to and from the SAG were noted and new whales were photographed when they joined the SAG. Recordings in all years were made with the vessel positioned between 50 and 500 m from a SAG with the engine shut down for the recordings. For array recordings, the vessel was initially positioned with the SAG directly abeam of the center of the array at a range of about 150 m (Fig. 1). If the SAG approached the vessel too closely or the vessel drifted more than 500 m from the SAG, recording was suspended and the engine was started to reposition the vessel.

A recording session included a series of continuous recordings of a single SAG which were interrupted when the vessel had to reposition for stationary hydrophone deployments. The duration of the recordings from 1999 to 2001 was dependent upon the schedule of the platform. In 2002, recordings were made from the first sighting of the SAG until the end of the SAG or until sea state or light conditions necessitated return to shore.

A. Recording equipment

1. Single hydrophone

Single hydrophone recordings were made with a Hi-Tech HTI-94-SSQ hydrophone (frequency response: 50 Hz to 20 kHz$\pm$0.5 dB) into a TASCAM DA-P1 DAT recorder (frequency response 20 Hz to 20 kHz$\pm$0.5 dB) or a Sony DCR TRV-900 mini-DV handheld video camcorder both sampling at 44.1 kHz. The hydrophone was deployed at depths ranging from $\sim$5 m for the video hydrophone and $\sim$10 m for the DAT recordings to allow for quick retrieval when whales approached the vessel too closely.

2. Hydrophone array

The array recording system consisted of a 3.75-m rigid linear array of 15 Benthos AQ-2TS hydrophones with custom pre-amps with 40 dB gain. The array design and pre-amps were based on an array design developed for use with killer whales (*Orcinus orca*) (Miller and Tyack, 1998). The hydrophones were evenly spaced 0.25 m apart and mounted on a 1-in.-diam PVC pipe cut in half length wise and encased in a 5-m mineral-oil-filled plastic tube. The array was manually deployed at 5-m depth off the side of a stationary vessel. The array was suspended from three positions (front, center, and end) with foam spar buoys made of pipe insulation to maintain the vertical position of the array in the water during behavioral observations.

The signal from each hydrophone was acquired through a 15-channel, single-ended, computer programmable, band-pass filter with adjustable corner frequencies and gain designed by R. B. MacCurdy, an electrical engineer at the Bioacoustic Research Program at Cornell University (CUBRP). The signals from the 15 channels were digitized with a National Instruments PCMCIA DAQCard-6062E (12 bit 500 kS/s sampling) in a Dell Latitude C610 laptop using the program Chickadee developed by John Bart at CUBRP. Sounds for all channels were acquired at an 8-kHz sampling rate.

Beamforming was carried out in the field as data were collected to determine the bearing to sound sources during behavioral observations. The beamforming software, the CUBRP Time-Delay Beamformer developed by K. Dunsmore and K. Fristrup at CUBRP, used acoustic data from four hydrophones in the array. This software has been used in a previous study of finback whale (*Balaenoptera physalus*) vocalizations (Croll *et al.*, 2002). The same software was used

for later processing of saved files to confirm that observed bearings to whales and the calculated bearings to the sounds agreed.

B. Behavioral observations

1. Photo identification

Individual North Atlantic right whales can be reliably identified by unique patterns of callosity, roughened patches of skin on the head (Kraus *et al.*, 1986). Photographs were taken of callosity and scar patterns with a 35-mm camera (Canon EOS Rebel and 5) using a 100–300-mm lens. Photographs were taken of each whale present in the groups to identify individuals. To determine the age and sex of individuals in each group, photographs were compared to the North Atlantic right whale catalog maintained by the New England Aquarium right whale research group in Boston, MA (Hamilton and Martin, 1999).

2. Video recordings

Video of SAG behavior was collected during most underwater acoustic recording sessions. A hydrophone signal was recorded directly into the video camera when feasible. Microphone input to the second audio channel on the video camera served as the primary documentation of systematic observer comments on behavior. Behavioral observations included group size, relative location and behavior of the focal animal in the SAG, and bearing and range to the center of the SAG from the vessel. Video recordings of SAGs were used for audio transcription of observer comments, to aid in the identification of individuals with poor quality 35-mm photographs, and to document the behavior of particular individuals. The behavior of the focal whale during sound production events was analyzed to determine if the focal whale was breathing at the same time that particular sounds were being produced.

3. Bearing and range measurements

Bearing (in degrees) and range (in meters) were taken to SAGs and specific individuals separated from the group during 2002 hydrophone array recordings. This allowed comparison of array bearing of whale sounds to the location of individual whales relative to the array. Bearings were measured using a digital KVH Datascope (0.1° resolution, $\pm 0.5°$ accuracy) and range was measured with a Leica LRF 800 (± 1-m accuracy) laser range finder.

C. Data analysis

1. Sound classification

Sounds recorded from North Atlantic right whales were labeled as one of the following sound types based on aural similarity to categories described for Southern right whales: scream [corresponding to high, hybrid, and pulsive calls (Clark, 1983)], gunshot [corresponding to Underwater Slap sounds (Clark, 1983)], blow, upcall, and downcall. Note that the blow sound refers to an underwater sound produced occasionally during exhalation. The high, hybrid, and pulsive calls were grouped together under one label to simplify analysis. These three call types are less stereotyped than the other classes of calls. The gradation of these three call types, as described by Clark (1982, 1983), Wright (2001), and Parks (2003a), makes it particularly difficult to separate them. There was an additional class of sound, labeled warble, which consisted of screamlike calls that were higher in pitch and stuttered. Warble calls quavered in aural quality and only were recorded when calves were present.

Acoustic recordings were digitized into .aif files using Cool Edit Pro v1.2 (Syntrillium, now incorporated into Adobe Audition). Recordings were acquired at a 44.1-kHz, 16-bit sampling rate. Each whale sound detected in the recordings was extracted and saved as a separate file using Matlab 6.5 (Mathworks, Inc. 2002) browsing software developed by the CUBRP. Spectrograms of extracted whale sounds were visually inspected and compared to classifications of sound types described in Clark (1982). Measurements were made from visual inspection of spectrograms [44.1 kHz sampling, 1024 fast Fourier transform (FFT), Hamming window, 75% overlap] of the sounds to determine duration, fundamental frequency, peak frequency, and highest detectable frequency.

The type and proportion of call types were analyzed as a function of group composition. Counts of the six major call types were made for each recorded SAG, and these counts were sorted by the six known group compositions to determine if call types can be used to predict group composition, or distinguish between distinct behavioral states that may appear the same from surface observations. A Pearson's chi-squared test was carried out on the resulting table. Bootstrapping was performed to assess the validity of the chi-square results due to small sample size for some call types. For the bootstrap analysis, chi-square values for 200 000 randomly generated tables sampled with replacement and which met the assumption of independence were compared to the original table (Legendre and Legendre, 1998).

2. Call timing

The scream is the main call type and evidence suggests that all screams are produced by a single individual in SAGs. The interval between the start of two successive sounds was used to determine the intercall interval (ICI). The production of screams was characterized by bouts of high sound production separated by long periods of silence, indicating that these calls are produced in bouts. Log-survivorship analysis was carried out to determine the bout criterion interval (BCI) (Janik and Slater, 1998; Martin and Bateson, 1993; Slater and Lester, 1982). This is a graphical method used to determine the minimum interval separating bouts of behavioral events, defined as the BCI (Martin and Bateson, 1993). The mean and standard deviation for within-bout and between-bout intervals were calculated using the BCI.

These intercall measurements are strongly influenced by the duration of recording. For example, the longer between-bout intervals were only detectable in longer recording sessions. The correlation between intercall interval and recording duration was measured for scream calls. The number of scream calls produced per minute (CPM) was measured in an attempt to standardize measurements between SAG record-

ings of varying duration. This method allowed for detection of periodic bouts of very high call rates that are missed by the analyses of within-bout intercall intervals that are averaged over the entire recording. This contrasts to other methods of calculating call rate that total up the number of sounds and divide by the total time of a recording (Howard and Young, 1998). The CPM rate of screams was calculated for each SAG. Differences in ICI and CPM were compared to differences in group size and composition.

3. Individual sound production

The identification of which whale produces a particular sound can add to our understanding of interactions between individuals in SAGs. There would be different predictions for group function if (1) the female produces all the sounds in the group and males are silent, (2) males produce all the sounds in the groups and females are silent, or (3) both males and females produce the sounds in the groups. Array data from 2002 were used to determine individual sound production from whales slightly separated from the core group of the SAG. In the SAG itself whales were in body contact so that it was not possible to distinguish individual sound production. Video data were analyzed to determine if the focal animal was breathing when screams or gunshots were produced. The precise sound production mechanism is not known for any baleen whale, but there have been no known observations of whales vocalizing during respiration in this and previous studies of right whales (Clark, 1982). It is likely that calls cannot be produced simultaneously with an exhalation in right whales because opening the blow holes would result in loss of the pressurization likely needed to produce the sound or to get the laryngeal sac to expand to transmit the sound (J. Reidenberg, personal communication). If baleen whales cannot generate internally produced sounds during exhalation, then correlation of sound production with breathing of the focal whale serves as another test for whether the focal produced the sound.

4. Source level

Received level was measured for sounds recorded from whales at a known distance from the hydrophone based on relative bearing information from array recordings and laser range to the whale at that bearing to estimate the source level for different call types. The position of the whale was determined using the beamformer to determine bearing to the sound source and using a Leica LRG 800 laser range finder to measure range to the whale at that bearing at the surface. For the scream and gunshot sounds, the range was to a whale in the center of the SAG and the range could be ± 5 m to the position of the whale producing the sound within the SAG. The hydrophone used for these recordings was a factory calibrated Hi-Tech HTI-94-SSQ hydrophone. The recordings were made on a Sony DA-P1 DAT (44.1-kHz sampling) recorder with a fixed input gain setting. The signals were band pass filtered (50 Hz to 10 kHz). Received level (RL) measurements were made using custom written scripts in Matlab 6.5 (Mathworks, Inc. 2002). The RL at the hydrophone was calculated relative to a calibration signal with a known 3-kHz rms voltage level recorded directly into the DAT recorder. Peak-to-peak (p-p) sound pressure level (dB p-p *re*: 1 μPa) was given by the p-p amplitude difference between the signal and the p-p value of the calibration signal. The rms sound pressure level (dB rms *re*: 1 μPa) was calculated by taking the root of the mean pressure squared in a time window T. This duration T was defined by the sample fraction that generates 90% of the total cumulative energy in a window including the sound pulse (Madsen *et al.*, 2004). Source level (SL) and transmission loss (TL) were estimated for the RL of recorded calls by $\mathrm{SL}=\mathrm{RL}+\mathrm{TL}$, where $\mathrm{TL}=20\log(\mathrm{range})$ under the assumption of spherical spreading (Urick, 1983). The maximum range for SL measurements was 200 m while the average water depth was 180 m. Absorption had negligible effect (<1 dB) on the TL at the ranges (<300 m) and frequency (<10 kHz) in these measurements and was omitted from the calculation of TL. The hydrophone was deployed at a depth of 5–10 m since the whales producing the sounds were at or near the surface during sound production. The calculated source levels (SLs) are reported in the results.

III. RESULTS

Acoustic recordings of 52 SAGs were made between 1999 and 2002, with durations of 2–132 mins. A total of 3435 sounds with high signal-to-noise ratio were selected for analysis from the recordings. The group size ranged from 2 to 15 whales. Six types of SAGs were recorded including groups with male-female pairs ($N=3$), one female with multiple males ($N=11$), multiple females with multiple males ($N=8$), all males ($N=1$), at least one calf ($N=9$), and at least one pregnant female ($N=4$). For recordings from the remaining 16 SAGs the identity or sex of at least one individual could not be determined. No groups composed of only female whales were observed.

A. Sound classification

1. Call types defined

Whale sounds recorded from SAGs were assigned to six classes based on differences in frequency, duration and/or individual responsible for sound production as described in the methods. These six classes correspond to those reported in Clark (1982, 1983). The classes defined in order of number of occurrences were screams, gunshots, blows, upcalls, warbles, and downcalls. The number of calls recorded for each class and the characteristics of these sounds are described in Table I. The corresponding call types described by Clark (1982) for Southern right whales are also included in the table. Spectrograms of each call type are shown in Fig. 2. Figure 3 illustrates the diversity of scream calls recorded from one SAG.

2. Call type by group composition

Table II shows the total counts of call types by SAG type and the resulting deviations [(Observed-Expected)/Expected] for each class of sound for different group compositions ($X^2=848$, $p=0.000\,02$, bootstrap $p=<0.0001$). The scream calls dominate the call types in groups with fe-

TABLE I. Call types recorded in SAGs in the Bay of Fundy. The number of each call type and the duration, fundamental, peak, and maximum detected frequency are listed. For each measurement, mean± SD and range of values are presented. The related Southern right whale call types, as defined by Clark (1982, 1983), are also listed.

Sound class	*N*	Duration (s)	Minimum frequency (kHz)	Peak frequency (kHz)	Maximum frequency (kHz)	Southern right whale types
Scream	2217	Mean: 1.02± 0.46 Range: 0.22–4.55	Mean: 0.42± 0.21 Range: 0.15–1.05	Mean: 0.93± 0.60 Range: 0.13–4.10	Mean: 6.03± 2.94 Range: 2.28–18.95	High, hybrid, and pulsive calls
Gunshot	545	Mean: 0.07± 0.04 Range: 0.01–0.17	Mean: 0.15± 0.17 Range: 0.02–0.51	Mean: 1.19± 1.05 Range: 0.02–11.51	Mean: 15.59± 6.63 Range: 2.99–21.92	Underwater slaps
Blow	315	Mean: 0.76± 0.25 Range: 0.33–1.82	Mean: 0.24± 0.17 Range: 0.02–1.07	Mean: 1.64± 0.89 Range: 0.16–6.13	Mean: 8.58± 3.48 Range: 0.91–20.37	Blows
Upcall	211	Mean: 0.99± 0.35 Range: 0.45–2.08	Mean: 0.08± 0.04 Range: 0.05–0.16	Mean: 0.19± 0.05 Range: 0.11–0.51	Mean: 3.14± 2.96 Range: 0.25–11.23	Up call
Warble	61	Mean: 1.47± 0.78 Range: 0.43–4.77	Mean: 0.47± 0.25 Range: 0.21–1.11	Mean: 1.44± 0.48 Range: 0.34–2.24	Mean: 8.41± 4.20 Range: 2.91–19.77	Hybrid calls
Downcall	40	Mean: 0.73± 0.28 Range: 0.26–1.80	Mean: 0.28± 0.11 Range: 0.02–0.51	Mean: 0.39± 0.12 Range: 0.14–0.64	Mean: 1.54± 2.15 Range: 0.25–10.50	Down calls

males and multiple males but were absent in the all-male group. Scream production was almost equal to gunshot sound production in the male-female pairs. The warble calls were only heard when calves were present, and primarily upcalls and gunshots were heard in the all-male group and one suspected all-male group with a calf. Upcalls were recorded in several different group compositions. These groups include the SAGs that would fit Clark's (1983) definition of sexually active such as the groups with a single female flanked by multiple males in which upcalls were absent in Southern right whales. The context in which upcalls were commonly produced will be discussed further in the individual sound production section.

B. Call timing

1. Intercall intervals (ICI)

Timing of scream call production in SAGs was measured from 42 of the 52 SAG recording sessions. The ten recording sessions omitted from this analysis either had no continuous recording longer than 1 min in duration, high background noise making determination of call production difficult, or no calls recorded during the observation period of the SAG. A total of 2319 scream calls were inspected for this analysis, with the total number of screams from each discrete SAG recording ranging from 2 to 381 (mean= 51,

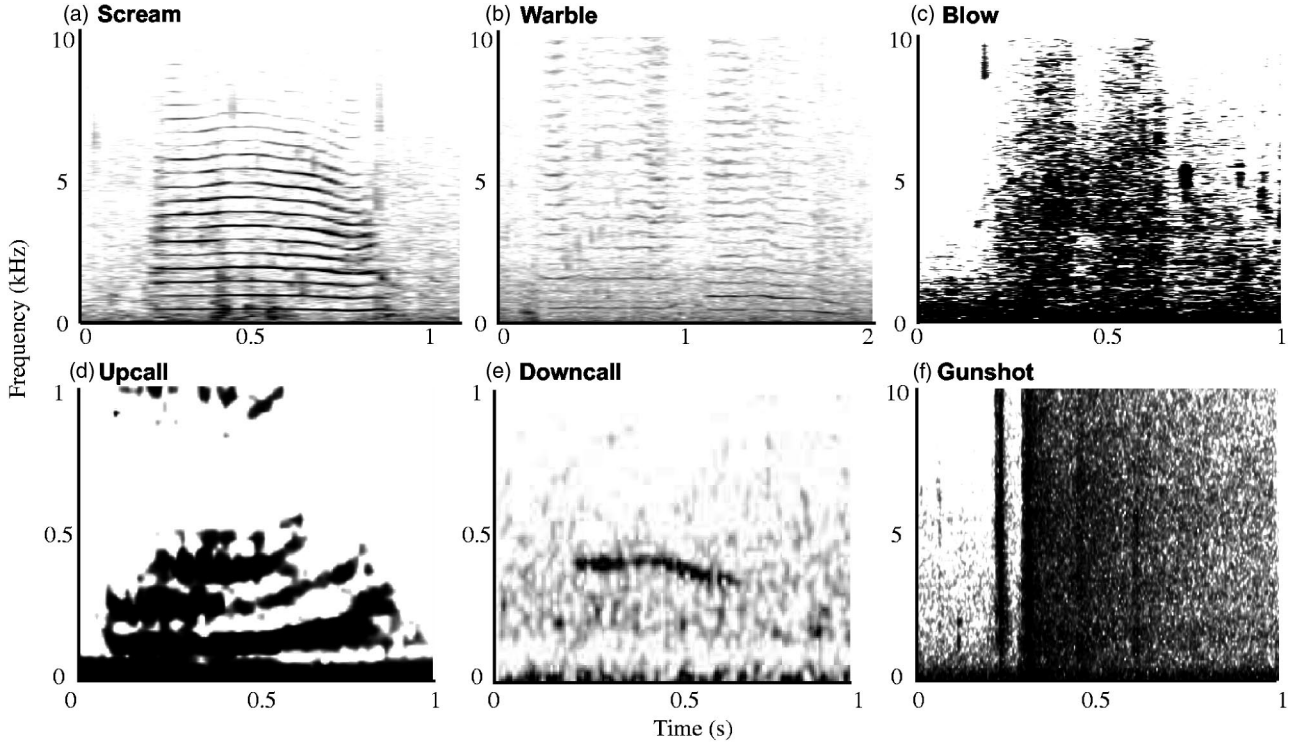

FIG. 2. Spectrograms of the six call types described in Table I: (a) scream, (b) warble, (c) blow, (d) upcall, (e) downcall, and (f) gunshot. The *x* axes are time (s) and the *y* axes are frequency (kHz). Note the different time and frequency scales for different call types. Analysis resolution= 28 Hz and 5.8 ms for (a)–(e). Analysis resolution= 112 Hz and 2.9 ms for (f).

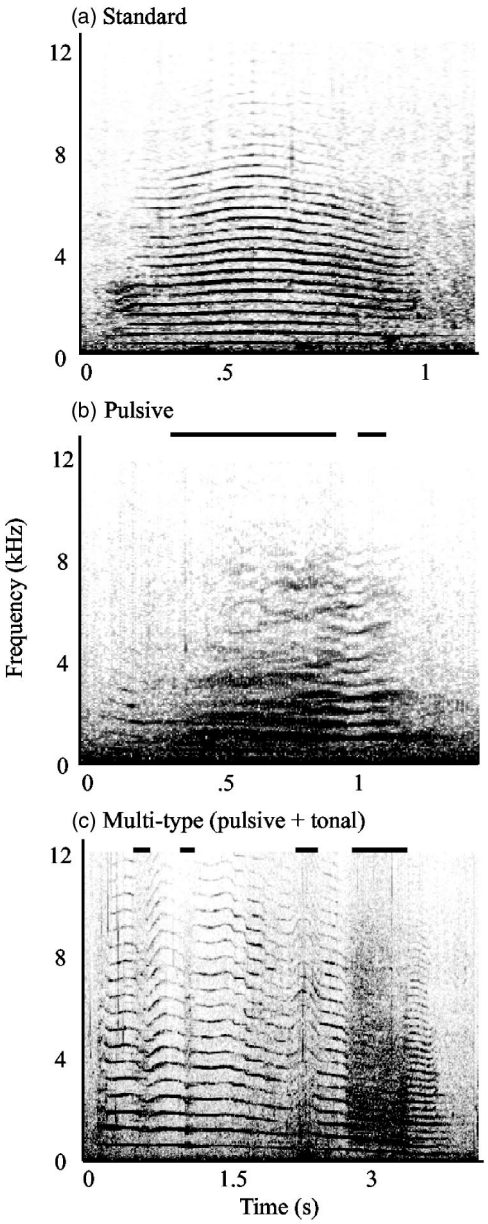

FIG. 3. Diversity of scream calls produced within a single SAG by the same individual. (a) A standard scream call, tonal with clear harmonic structure, approximately 1 s in duration. (b) A pulsive scream call with ''nonlinear'' modulation of harmonics marked with black bars above the spectrogram. (c) Long scream with a combination of tonal and pulsive elements, with the pulsive elements marked by black bars above the spectrogram. The *x* axes are time (s) and the *y* axes are frequency (kHz). Note the different time scales for different call types (analysis resolution 28 Hz, 5.8 ms).

SD=56). Scream calls were characterized by periods of high rates of sound production interrupted by periods of silence. ICIs for screams ranged from 0 to 4592 s.

The log survivorship analysis resulted in a bout criterion interval (BCI) for screams=90 s (Fig. 4). The mean ICI for screams within a bout was 11 ± 15 s ($n=2214$, range $<1-90$ s, median=5) and the mean ICI for screams between bouts was 283 ± 507 s ($n=107$, range 94–4952 s, median=181). The correlation between the maximum ICI and the duration of the recordings resulted in linear and logarithmic correlation values of 0.38 and 0.48, respectively. Figure 5 shows a plot of the maximum ICI for each recording versus the recording duration.

2. Calls per minute (CPM)

Call rate analysis (CPM) was carried out on 927 min of SAG recordings to determine maximum sustained rates of sound production, which can be missed in the intercall interval (ICI) analysis. This shift in emphasis, from the duration between sounds (ICI) to the clustering of sound production (CPM), may be more important for discriminating between group compositions than the absolute timing of each sound produced. The number of minutes of recording analyzed from each SAG ranged from 2 to 130 min (mean =18 min). The number of screams ranged from 0 to 20 calls/minute.

3. Call timing related to group size

Calculations of the mean ICI within bouts, the minimum and mean between bout intervals, and the maximum CPM rate were compared to group size for each SAG. The correlations were not statistically significant for any of these parameters ($r=-0.076$ for mean interscream interval versus group size).

C. Individual sound production

1. Array data

Array recordings were made of seven SAGs in 2002. The duration, signal-to-noise ratio, and number of calls recorded in each session varied. Calibration recordings of passing vessels yielded a range of bearings from 3° to 15° to the known sound source. As a result, during whale recordings, a separation of at least 20° between individuals was considered necessary to assign a call type confidently to a particular individual. This conservative approach was selected to minimize the possibility of incorrectly assigning call types to individuals.

Separations of the focal female by more than 10° from the SAG were never observed while the array was in the water and recording. It was not possible to assign scream call production exclusively to the female in the SAG from the array recordings. Bearings to scream calls were always corresponded to the position of the focal female and screams never occurred when the female was away from the SAG, therefore it is likely that the females are exclusively producing these sounds. Bearings to gunshot sounds were only from the direction of the SAG. Therefore, males and/or females may be producing these sounds in the groups. The bearings to blow sounds were easily linked to visible exhalation of a whale and were produced both by the focal female and other whales present in the group.

Upcall production coincided on five occasions with the separation of an adult male from the SAG. Array bearings to the sound coincided with the location of the male on each occasion. Males produced upcalls when approaching a SAG for the first time and during searching behaviors when the focal female left the group. On two occasions when calves were present in the group, males were seen to stay close to the calf while the calf's mother (the focal female) was on a dive. Upcalls were recorded in both these incidents, and it is unclear whether the calf or the male produced the calls because the two whales were too close together.

TABLE II. (a) Table showing total counts of call type by SAG type from observations. (b) Table showing X^2 deviations by cell for the table of counts of call types versus SAG composition. The cells with |deviations| >1.5 are italicized, indicating larger deviations from the expected values.

Group type	*n*	Screams	Gunshots	Upcalls	Blows	Warbles	Downcalls
(a)							
All male	1	0	40	6	0	0	4
Calf	7	365	127	82	75	62	0
Multiple females	8	212	69	29	45	0	22
One female	9	471	37	10	47	0	1
Male-female pair	3	108	1	0	12	0	1
Pregnant	4	221	39	1	34	0	0
Unknown	12	1041	163	32	109	0	2

Group type	Screams	Gunshots	Upcalls	Blows	Warbles	Downcalls
(b)						
All male	−1.00	*4.72*	*1.55*	−1.00	−1.00	*6.04*
Calf	−0.26	0.30	*1.50*	0.14	*3.88*	−1.00
Multiple females	−0.19	0.33	0.67	0.29	−1.00	*5.98*
One female	0.19	−0.52	−0.62	−0.11	−1.00	−0.79
Male-female pair	0.27	−0.94	−1.00	0.06	−1.00	−0.02
Pregnant	0.07	−0.04	−0.93	0.24	−1.00	−1.00
Unknown	0.11	−0.12	−0.48	−0.13	−1.00	−0.82

Two bearings were obtained to warbles corresponding to the position of a calf alone at the surface while the other whales in the SAG were on a dive. Warble sounds have only been heard in SAGs with female calves present, and these bearing data confirm that calves do produce these sounds. The aural quality of these warbles is generally higher in pitch than most scream calls, often longer in duration and broken up with many stuttering pauses in the sound production of what appears to be a single call unit.

2. Video data

The number of screams and gunshots produced simultaneously with the focal female breathing were counted for 348 min of SAG video recordings with hydrophone input. The focal female was observed to breathe 232 times and a total of 815 screams and 107 gunshot sounds were recorded. There were no instances of the focal female breathing simultaneously with scream production but there were 31 instances of the focal female breathing when gunshot sounds were being produced. Both males and females were observed breathing simultaneously with the occurrence of underwater blow sounds.

D. Source level

The received levels (p-p and rms) of 59 right whale sounds (31 screams, 12 gunshot, 10 Blows, 3 upcalls, and 3 warbles) were measured with ranges to the whales between 40 and 200 m, with an average distance of 88 m. Table III summarizes the calculated source level measurement for all whale sounds. The source levels for these sounds range from 137 to 162 dB rms *re* 1 μPa-m for tonal calls and 174 to 192 dB rms for broadband gunshot sounds.

IV. DISCUSSION

A. Sound classification

Sound production is common in the surface active groups (SAGs) of the North Atlantic right whale. No calls were recorded in 3 of the 52 recording sessions, but in each

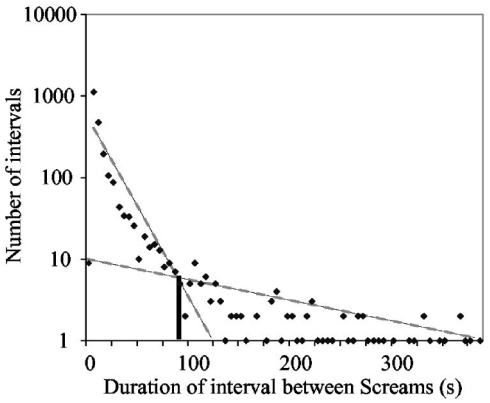

FIG. 4. Log survivorship plot of intercall interval between screams. Dashed lines indicate the approximate slope for two parts of the curve. The black solid line indicates the bout criterion interval value determined from the intersection of the two slope lines.

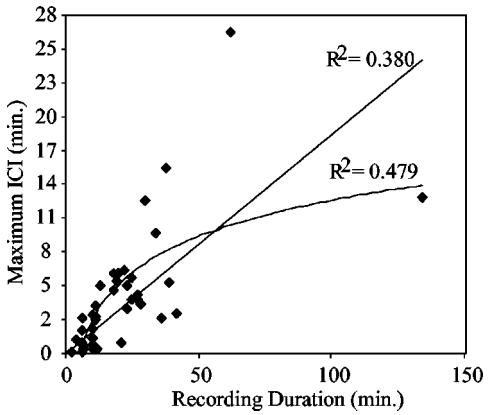

FIG. 5. Correlation of the maximum observed intercall interval versus recording duration for scream calls. Both linear and logarithmic regressions and r^2 values are included in each plot.

TABLE III. Calculated SL for five sound types all measured as dB *re* 1 μPa-m from 50 Hz to 10 kHz. *N* = number of measurements; SL = calculated source level (p-p|rms).

Broadband	Screams (p-p|rms)	Warbles (p-p|rms)	Gunshot (p-p|rms)	Upcalls (p-p|rms)	Blows (p-p|rms)
N	31	3	12	3	10
Minimum SL	155|137	161|144	182|155	164|147	154|137
Maximum SL	175|162	165|145	201|192	168|154	166|149
Mean	164|149	163|145	191|183	166|150	162|144
SD	5|8	2|1	5|5	2|4	4|4

of these cases the SAG was already breaking up when recording began. Whale sounds were grouped into discrete classes based on previous classification studies of right whale calls (Clark, 1982, 1983) and the evidence that they were associated with specific classes of individuals (e.g., warbles made by calves). The two dominant types of whale sounds recorded from SAGs were the scream call and the gunshot sound. The recordings made in this study were consistent with previous reports of female production of scream calls (Kraus and Hatch, 2001; Parks, 2003b). However, the analyses presented here of these recordings indicate that several distinct types of sounds were produced in the SAGs by several different age-sex classes.

B. Call timing

Call timing in SAGs is highly variable. Screams are produced in bouts separated by periods of silence. These bouts of screaming are not regular in duration within particular SAGs, and the interbout periods of silence vary considerably in duration. These periods of silence often occur when the focal female is on a dive, even if other whales are still active at the surface. The maximum ICI versus recording duration indicates that longer maximum ICIs are detected in longer recordings. These results indicate that a larger sample of longer duration recordings should be collected in future studies to more accurately determine the bout intervals.

Call per minute (CPM) results indicate periods of high rates of calling that are missed when averaging intercall intervals over an entire bout. The rates of scream call production do not vary with group size. This observation is consistent with the hypothesis that screams are produced by a single focal female as the call rate is not correlated with the number of whales present in the group.

C. Individual sound production

The data on individual sound production add a new dimension to our understanding of into the interactions taking place within the SAGs. The publication on SAGs by Kraus and Hatch (2001) gives the impression that the focal female may be the only whale producing sounds in the group. While this study supports the idea that the focal female is responsible for production of the scream calls, it is clear that other whales in the group produce some classes of sounds.

1. Scream calls

Array data collected in 2002 showed that the bearings for all recorded cases of screams pointed to the SAG. Therefore, whales probably seldom produce these calls when they are separated from the group. Unfortunately, no separations of the focal female from the rest of the group of more than 10° were documented during array recordings. It is therefore not possible to assign the scream calls to only the female from the array results. Inspection of focal female behavior in SAGs from video recordings indicates that the female was never seen breathing when a scream was produced in the group. While the mechanism for sound production in baleen whales is still unknown, it is believed that it involves the respiratory pathway. This would prevent production of all sounds other than blows while breathing. Kraus and Hatch (2001) reported similar results, never observing focal females breathing when sounds were recorded. Overlapped scream calls of similar intensity were recorded on two occasions in this study. In both cases, the overlapped scream calls were heard when two females were present near the center of the group, and the identity of the focal female was unclear. In both cases, one of the females eventually departed, and no further overlapped screams were heard. These cumulative results are consistent with the hypothesis that a female whale produces the scream calls.

2. Gunshot sounds

Lone adult right whale males produce the gunshot sound in stereotyped displays (Parks, 2003a). Array data collected in 2002 showed that the bearings for all recorded cases of gunshots in SAGs pointed to the SAG. Gunshot sounds were produced on 31 occasions when the focal female was seen breathing, indicating that some other whale in the SAG produced this sound. Gunshot sounds were recorded from the only all-male SAG recorded. These results indicate that males produce the gunshot sounds heard in the groups. These observations do not rule out the possibility of gunshot sound production by the female, but confirm that males do produce this sound on many occasions in these groups.

3. Upcalls

Upcalls were recorded in 22 of the 52 SAGs. Though the percentage of total calls represented by upcalls was always low, this call type was commonly recorded from SAGs. Array data in 2002 confirmed that these upcalls are produced by males while swimming into a SAG for the first time or while alone at the surface when the focal female was on a dive. These observations are consistent with recordings and video made from SAGs without the array in the water. On several occasions, loud upcalls were recorded while males were at the surface and the focal female was on a dive or after the focal female departed the group. The males showed

indications that they may be searching for the female during the production of these sounds as they tended to stay in the general location of the last position of the SAG but would swim slowly back and forth through the area. It is possible that males use this call to announce their presence to the female or other members of the group.

4. Warbles

Warble sounds have not been previously described for North Atlantic right whales. Warble sounds were only recorded when calves were present in the SAG. Array bearings in 2002 provided evidence that calves produce this sound as bearings were obtained to a calf alone at the surface while warble sounds were being produced and all other whales in the SAG were on a dive. These warble sounds were only recorded in two of nine SAGs with calves. In both cases in which the warble call was detected, the calf was female. In the three instances of calves in SAGs without recorded warbles, one calf was female and two calves were male. Only 14 total sounds were recorded during the brief observation of the SAG with a female calf that produced no warbles. The sex or identity of the calves from the remaining four groups was unknown. If SAGs play a role in reproduction, then the presence of females with their calves in SAGs is surprising as North Atlantic right whales have at least a 2-year interval between calves with the current mean interval at 5 years (Kraus *et al.*, 2001). These sounds may represent practice of SAG behavior on the part of a female calf. Perhaps during the first summer after birth the mothers intentionally form SAGs to give their calves experience with the groups. Both male and female offspring could benefit from this experience.

D. Source level

The source level of the sounds produced by North Atlantic right whales in SAGs here are in agreement with previous reports of source level for Southern right whales (Richardson *et al.*, 1995). The directionality of sound production by right whales is unknown and the orientation of the whale to the hydrophone may have influenced the measurements presented here. Masking from ships is a cause for concern because there is considerable overlap of the frequency range of vessel noise and the frequency range of right whale vocalizations (Richardson *et al.*, 1995).

The description of the sounds produced in SAGs and the identification of individuals producing the sound will have multiple applications. Females produce scream calls, males produce gunshot sounds and upcalls, and calves produce warbles. It is clear that, except for the warble call, there is no diagnostic sound type for different SAG compositions. It is possible that these different types of sounds represent different motivations on the part of individual whales. For example, if gunshot sounds represent agonistic interactions between males, it follows that a larger number of these sounds will be heard in contexts when the rate of agonistic interations is higher, for example when more males are present in a single group. Further studies of sound production in these groups are warranted, to provide more details on sound production by individual whales in SAGs and ultimately to provide insight into the behavioral significance of these groups and the sounds associated with their formation and occurrence.

ACKNOWLEDGMENTS

The data used in this paper were collected with the assistance of numerous research staff and volunteers. Sincere thanks to everyone involved in the data collection, particularly the New England Aquarium right whale research group and the International Fund for Animal Welfare (IFAW) crew of the *Song of the Whale*. K. Fristrup and V. Starczak provided statistical advice. P Madsen assisted with RL measurements. C. Clark and two anonymous reviewers provided helpful suggestions which improved this manuscript. Funding for the fieldwork was provided by IFAW, Northeast Consortium (UNH), the National Fish and Wildlife Foundation, the U.S. National Marine Fisheries Service (NMFS), the Reinhart Coastal Research Center, and the Packard Foundation. S. Parks was supported in part by a NDSEG Fellowship. This research was conducted under U.S. permit NMFS No. 1014 and was approved by the WHOI Institutional Animal Care and Use Committee. This is Contribution No. 11199 of the Woods Hole Oceanographic Institution.

Clark, C. W. (**1982**). ''The acoustic repertoire of the southern right whale, a quantitative analysis,'' Anim. Behav. **30**, 1060–1071.

Clark, C. W. (**1983**). ''Acoustic communication and behavior of the southern right whale,'' in *Communication and Behavior of Whales*, American Association for the Advancement of Science Selected Symposium 76, edited by R. S. Payne (Westview, Boulder, CO.), pp. 163–198.

Clark, C. W. (**1984**). ''Acoustic communication and behavior of southern right whales, *Eubalaena australis*,'' Nat. Geo. Soc. Res. Rep. **17**, 897–907.

Clark, C. W. (**1999**). ''The application of autonomous seafloor acoustic recorders for monitoring right whales,'' *Abstract. North Atlantic Right Whale Consortium Meeting*, Boston, MA.

Clark, C. W., and Clark, J. M. (**1980**). ''Sound playback experiments with southern right whales (*Eubalaena australis*),'' Science **207**, 663–665.

Croll, D. A., Clark, C. W., Acevedo, A., Tershy, B., Flores, S., Gedamke, J., and Urban, J. (**2002**). ''Only male fin whales sing loud songs,'' Nature (London) **417**, 809.

Cummings, W. C., Fish, J., and Thompson, P. (**1972**). ''Sound production and other behavior of southern right whales, *Eubalaena glacialis*,'' Trans. San Diego Soc. of Nat. Hist. **17**, 1–14.

Darling, J. E., and Bérubé, M. (**2001**). ''Interactions of singing humpback whales with other males,'' Marine Mammal Sci. **17**, 570–584.

D'Vincent, C. G., Nilson, R. M., and Hanna, R. E. (**1985**). ''Vocalization and coordinated feeding behavior of the humpback whale in southeastern Alaska,'' Sci. Rep. Whales Res. Inst., Vol. 36.

Hamilton, P. K., and Martin, S. M. (**1999**). ''A catalog of identified right whales from the Western North Atlantic: 1935 to 1997,'' New England Aquarium, Central Wharf, Boston.

Helweg, D. A., Frankel, A. S., Mobley, J. R., and Herman, L. M. (**1992**). ''Humpback whale song: our current understanding,'' in *Marine Mammal Sensory Systems*, edited by J. A. Thomas, R. A. Kastelein, and A. Y. Supin (Plenum, New York), pp. 459–483.

Howard, R. D., and Young, J. R. (**1998**). ''Individual variation in male vocal traits and female mating preferences in *Bufo americanus*,'' Anim. Behav. **55**, 1165–1179.

Janik, V. M., and Slater, P. J. B. (**1998**). ''Context-specific use suggests that bottlenose dolphin signature whistles are cohesion calls,'' Anim. Behav. **56**, 829–838.

Kraus, S. D., and Hatch, J. J. (**2001**). ''Mating strategies in the North Atlantic right whale (*Eubalaena glacialis*).'' J. Cet. Res. Man. (Spec. Iss. 2) 237–244.

Kraus, S. D., Hamilton, P. K., Kenney, R. D., Knowlton, A. R., and Slay, C. K. (**2001**). ''Reproductive parameters of the North Atlantic right whale,'' J. Cet. Res. Man. (Spec. Iss. 2) 231–236.

Kraus, S. D., Moore, K. E., Price, C. A., Crone, M. J., Watkins, W. A., Winn, H. E., and Prescott, J. H. (**1986**). ''The use of photographs to identify individual North Atlantic right whales (*Eubalaena glacialis*),'' Rep. Int. Whal. Commn (Spec. Iss. 10) 145–151.

Legendre, P., and Legendre, L. (**1998**). *Numerical Ecology* (Elsevier, Amsterdam), p. 853.

Madsen, P. T., Kerr, I., and Payne, R. (**2004**). ''Source parameter estimates of echolocation clicks from wild pygmy killer whales (*Feresa attenuata*) (L),'' J. Acoust. Soc. Am. **116**, 1909–1912.

Martin, P., and Bateson, P. (**1993**). *Measuring Behaviour: An introductory guide* (Cambridge U. P., Cambridge), p. 222.

Matthews, J. N., Brown, S., Gillespie, D., Johnson, M., McLanaghan, R., Moscrop, A., Nowacek, D., Leaper, R., Lewis, T., and Tyack, P. (**2001**). ''Vocalisation rates of the North Atlantic right whale (*Eubalaena glacialis*),'' J. Cet. Res. Manage. **3**, 271–282.

Miller, P. J., and Tyack, P. L. (**1998**). ''A small towed beamforming array to identify vocalizing *resident* killer whales (*Orcinus orca*) concurrent with focal behavioral observations,'' Deep-Sea Res., Part II **45**, 1389–1405.

Parks, S. E. (**2003a**). ''Acoustic communication in the North Atlantic right whale (*Eubalaena glacialis*),'' Ph.D. thesis, MIT-WHOI Joint Program in Oceanography, Woods Hole, MA.

Parks, S. E. (**2003b**). ''Response of North Atlantic right whales (*Eubalaena glacialis*) to playback of calls recorded from surface active groups in both the North and South Atlantic,'' Marine Mammal Sci. **19**, 563–580.

Payne, R. S., and McVay, S. (**1971**). ''Songs of humpback whales,'' Science **173**, 585–597.

Payne, R. S., and Payne, K. (**1971**). ''Underwater sounds of southern right whales,'' Zoologica (N.Y.) **58**, 159–165.

Richardson, W. J., Greene, C. R. Jr., Malme, C. I., and Thomson, D. H. (**1995**). *Marine Mammals and Noise* (Academic, San Diego).

Saayman, G. S., and Tayler, C. K. (**1973**). ''Some behavior patterns of the southern right whale, *Eubalaena australis*,'' Z. Saugetierk. **38**, 172–183.

Schevill, W. E., and Watkins, W. A. (**1962**). ''Whale and porpoise voices: a phonograph record,'' Woods Hole Oceanographic Institution, Woods Hole, MA.

Schevill, W. E., Backus, R. H., and Hersey, J. B. (**1962**). ''Sound production by marine animals,'' in *Bioacoustics*, edited by M. N. Hill (Wiley, New York), pp. 540–566.

Silber, G. K. (**1986**). ''The relationship of social vocalizations to surface behavior and aggression in the Hawaiian humpback whale (*Megaptera novaeangliae*),'' Can. J. Zool. **64**, 2075–2080.

Slater, P. J. B., and Lester, N. P. (**1982**). ''Minimising errors in splitting behaviour into bouts,'' Behaviour **79**, 153–161.

Tyack, P., and Whitehead, H. (**1983**). ''Male competition in large groups of wintering humpback whales,'' Behaviour **83**, 132–154.

Tyack, P. L., and Clark, C. W. (**2000**). ''Communication and acoustic behavior of dolphins and whales,'' in *Hearing by Whales and Dolphins*, edited by W. W. L. Au, A. N. Popper, and R. R. Fay (Springer-Verlag, New York), pp. 156–224.

Urick, R, J. (**1983**). ''Principles of underwater sound.'' (Peninsula Publishing, Los Altos, CA).

Vanderlaan, A. S. M., Hay, A. E., and Taggart, C. T. (**2003**). ''Characterization of North Atlantic Right-Whale (*Eublalaena glacialis*) Sounds in the Bay of Fundy,'' IEEE J. Ocean. Eng. **28**, 164–173.

Winn, H. E., and Winn, L. K. (**1978**). ''The song of the humpback whale *Megaptera novaeangliae* in the West Indies,'' Mar. Biol. (Berlin) **47**, 97–114.

Wright, D. R. (**2001**). ''Categorization of northern right whale, *Eubalaena glacialis*, sound,'' M.A. thesis, Boston University, Boston, MA.

Optimization of angular and frequency compounding in ultrasonic attenuation estimations

Haifeng Tu,[a] James A. Zagzebski, Anthony L. Gerig, Quan Chen, Ernest L. Madsen, and Timothy J. Hall

Department of Medical Physics, University of Wisconsin—Madison, 1300 University Avenue, Room 1530, Madison, Wisconsin 53706

(Received 21 October 2004; revised 31 January 2005; accepted 2 February 2005)

Previous reports have shown that the variance in ultrasound attenuation measurements is reduced when spatial and frequency compounding were applied in data acquisition and analysis. This paper investigates factors affecting the efficiency of compound attenuation imaging methods. A theoretical expression is derived that predicts the correlation between attenuation versus frequency slope (β) estimates as a function of the increment between measurement frequencies (Δf) and the angular separation between beam lines ($\Delta\theta$). Theoretical results are compared with those from attenuation measurements on tissue-mimicking phantoms and from simulation data. Both predictions and measurement results show that the correlation between β estimates as a function of (Δf) is independent of the length of the radio frequency (rf) data segment over which β is derived. However, it decreases with an increase in the length of the data segment used in power spectra estimates. In contrast, the correlation between β estimates as a function of $\Delta\theta$ decreases when the rf data segment length is longer or the frequency of the signal is higher. © *2005 Acoustical Society of America.* [DOI: 10.1121/1.1879212]

PACS numbers: 43.80.Vj, 43.80.Qf [FD] Pages: 3307–3318

LIST OF SYMBOLS

α	attenuation coefficient (dB/cm)
α_{f_i}	attenuation coefficient at frequency f_i
a_m	coefficient related with least square process
β	attenuation coefficient versus frequency slope ($\beta=\alpha/f$)
β''	attenuation coefficient versus frequency slope after spatial and frequency compounding
β_{f_i}	attenuation coefficient versus frequency slope at frequency f_i ($\beta_{f_i}=\alpha_{f_i}/f_i$)
$\beta_{\theta_i}(f_k)$	attenuation coefficient versus frequency slope at angle θ_i and frequency f_k
β_{θ_i}	attenuation coefficient versus frequency slope at angle θ_i, $\beta_{\theta_i}=\Sigma_{k=1}^{n_f}\beta_{\theta_i}(f_k)/n_f$
b	distance between the center of apertures
BSC	backscatter coefficient
$\mathrm{cov}(\beta_{f_i},\beta_{f_j})$	covariance between β_{f_i} and β_{f_j}
D	aperture
f	frequency
Δf	frequency separation between successive frequencies at which β values are calculated
θ	the angle between the beam axes
φ	the half angle between the beam axes
k	inverse of signal-to-noise ratio SNR ($k=1/\mathrm{SNR}$)
$l_{\min}$	minimum gating coordinate
$l_{\max}$	maximum gating coordinate
m	spatial index of independent power spectra estimate involved in α derivation
n	the number of independent power spectra estimates over Z
n_c	the number of partially correlated angular beam lines
n_f	the number of partially correlated frequency components
N	the number of independent A-lines used in power spectra estimates
N_c	the effective number of independent angular beam lines
N_f	the effective number of independent frequency components
$\sigma_{\alpha_{f_i}}$	standard deviation of α_{f_i}
$\sigma_{\beta_{f_i}}$	standard deviation of β_{f_i}
$\sigma_{\beta_{\theta_i}(f_k)}$	standard deviation of $\beta_{\theta_i}(f_k)$
σ''_β	standard deviation of β after spatial and frequency compounding
$\rho(\beta_{f_i},\beta_{f_j})$	correlation between β_{f_i} and β_{f_j}
$\rho(\beta_{\theta_i},\beta_{\theta_j})$	correlation between β_{θ_i} and β_{θ_j}
$\rho(\beta_{\theta_i}(f_k),\beta_{\theta_j}(f_k))$	correlation between $\beta_{\theta_i}(f_k)$ and $\beta_{\theta_j}(f_k)$
S_{f_i}	periodogram spectral estimate at frequencies f_i
$S_{f_i}^m$	mth periodogram spectral estimate at frequencies f_i
$S_{\theta_i}(f_k)$	periodogram spectral estimate at angles θ_i and frequency f_k
$S_{\theta_i}^m(f_k)$	mth periodogram spectral estimate at angles θ_i and frequency f_k
$\rho(S_{f_i},S_{f_j})$	correlation between S_{f_i} and S_{f_j}

[a]Electronic mail: htu@wisc.edu

$\rho(S^m_{f_i}, S^m_{f_j})$ correlation between $S^m_{f_i}$ and $S^m_{f_j}$

$\rho(S_{\theta_i}(f_k), S_{\theta_j}(f_k))$ correlation between $S_{\theta_i}(f_k)$ and $S_{\theta_j}(f_k)$

$\rho_{1,2}(f_k)$ correlation between Fourier transformed segments whose squared modulus is $\rho(S_{\theta_i}(f_k), S_{\theta_j}(f_k))$

$\rho(S^m_{\theta_i}(f_k), S^m_{\theta_j}(f_k))$ correlation between $S^m_{\theta_i}(f_k)$ and $S^m_{\theta_j}(f_k)$

RS ratio of power spectra from the sample to the reference

S power spectra

T length of gating window applied in power spectra estimates

$p(t)$ gating window applied in periodogram spectral estimates

$p(x,y,f)$ point spread function at frequency f

z depth

z_0 focal distance

Z length of the rf data segment over which a value of β is computed

λ wavelength

$\Delta\Omega_{1,2}$ volume for integration

I. INTRODUCTION

Objectively determined ultrasound attenuation values in tissues could provide useful information about disease in various sites, including the liver,[1,2] breast,[3,4] myocardium,[5] and human aorta.[6] Many methods based on pulse echo techniques have been proposed for estimating the attenuation coefficient. In general, they can be classified as either time domain methods[7–10] or frequency domain methods.[11–14]

Except for work by Walach *et al.*, determination of such values in small, localized regions identified on ultrasound B-mode images or the production of attenuation images are rarely reported. This is partially because of the requirement for large data segments to achieve statistically precise results. We have reported a method[15] which effectively decreases variance in attenuation estimations made over small volumes of tissue. The method uses spatial angular and frequency compounding in the data acquisition and analysis. A reference phantom is applied to account for imaging system dependencies of echo signals. Results demonstrate an effective reduction of the variance in attenuation versus frequency slope ($\beta = \alpha/f$) measurements when compounding is applied versus when no compounding is used. Low-frequency attenuation images of a 3-cm-diam cylinder with 0.3-dB/cm/MHz β contrast in a phantom demonstrated the accuracy and precision of this technique.[15]

In this paper, we further investigate factors affecting the efficiency of spatial angular and frequency compounding through studies of variance reduction in attenuation estimations. A theoretical expression is derived that predicts the correlation between β estimates as a function of the increment between measurement frequencies and the angular separation between beam lines. Theoretical results are compared with those from β measurements on tissue mimicking phantoms using beam steering with a linear array and from simulation data computed for situations where a transducer rotates around its transmit focus. Various factors affecting the decorrelation rate are discussed. The results can be used to optimize spatial angular and frequency compounding schemes in attenuation versus frequency slope derivations.

II. THEORY

A. The reference phantom method (RPM)

The reference phantom method developed by Yao *et al.*[13] is used for attenuation and backscatter estimations. In this method, the echo signal intensity from a sample is compared to the signal intensity at the same depth from a reference phantom, whose attenuation and backscatter properties are known. The reference phantom data are acquired using the same transducer and system settings used for acquiring echo data from the sample. For a gated radio frequency (rf) signal, $\mathrm{RS}(f,z)$, the ratio of the power spectrum from the sample to that from the reference at frequency f and depth z can be expressed as[13]

$$\mathrm{RS}(f,z) = \frac{S_s(f,z)}{S_r(f,z)} = \frac{\mathrm{BSC}_s(f)}{\mathrm{BSC}_r(f)} e^{-4(\alpha_s(f)-\alpha_r(f))z}, \tag{1}$$

where the S's are power spectra; subscripts s and r refer to the sample and reference, respectively; the BSCs are backscatter coefficients; and α's are sample and reference phantom attenuation coefficients at f.

After a least squares line-fit of the curve $\ln(\mathrm{RS}(f,z))$ versus depth, z, the slope is proportional to the difference between the sample and reference attenuation coefficients. Since the latter is known, this provides the attenuation coefficient of the sample. For a uniform sample, the zero depth intercept yields the ratio of the sample and reference backscatter coefficients.

Assume the attenuation in the sample is linearly proportional to the frequency, which is approximately true in tissue for frequencies in the range of 1 to 10 MHz. Thus,

$$\alpha(f) = \beta f. \tag{2}$$

The attenuation coefficient versus frequency slope, β (dB/cm/MHz), is a useful attenuation parameter, and it will be used throughout our study.

B. Role of spatial angular and frequency compounding

Local attenuation estimations are limited by the large variance due to the presence of statistical fluctuations in the backscattered signals. An analysis of the statistical uncertainty of attenuation values derived using the reference phantom method has been presented by Yao *et al.*[16] Generally, the power spectra in Eq. (1) are estimated using data from multiple beam lines acquired from the sample and the reference. The standard deviation of the attenuation coefficient at frequency f_i, $\sigma_{\alpha_{f_i}}$, is related to the uncertainty of the slope

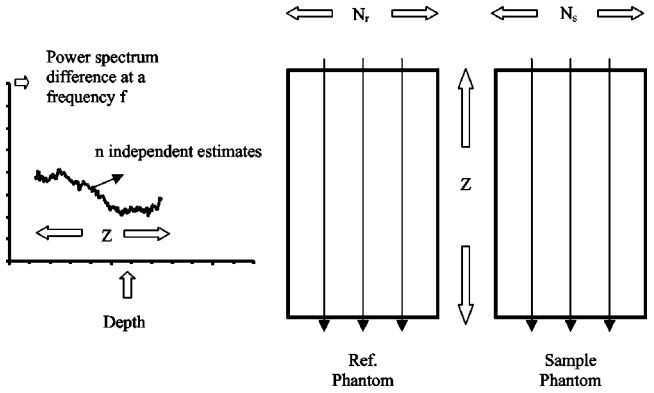

FIG. 1. Data acquisition and processing using a reference phantom to determine attenuation over a region whose axial length is Z. Independent echo signal segments from N_s beam lines in the sample and N_r beam lines in the reference are involved. Adapted from Ref. 15.

calculation of $\ln(\mathrm{RS}(f,z))$ vs. z when the measured values exhibit statistical fluctuations. Results show that $\sigma_{\alpha_{f_i}}$ is given by (see Fig. 1)

$$\sigma_{\alpha_{f_i}} = \frac{7.52k\sqrt{N_s+N_r}}{\sqrt{(n+1)/(n-1)}\sqrt{n}Z\sqrt{N_sN_r}}\,(\mathrm{dB/cm}), \tag{3}$$

where N_r and N_s are the number of independent acoustical lines over which echo data are acquired and analyzed from the reference and the sample, respectively; Z is the length of the rf data segment over which the least squares analysis is applied; n is the number of independent power spectral estimates over the interval Z ($n \geqslant 3$); and the factor k is the inverse of the "signal-to-noise ratio," that is, the mean of the signal intensity to its standard deviation. This ratio is 1 if Rayleigh statistics apply.[17] Since n is proportional to Z, the uncertainty is inversely proportional to the $\frac{3}{2}$ power of the length of the data segments for large n. This expression is different from Yao's original expression because here independent power spectral estimates are modeled as discrete, uniformly spaced data points instead of continuous data points.

One means to decrease the uncertainty in attenuation coefficient estimations without excessively expanding the region over which the estimation is done is to apply spatial angular compounding. Spatial angular compounding during echo data acquisition has proven to be an effective technique for reducing speckle noise to improve B-mode image quality.[18] The method has only recently been used to improve quantitative ultrasound images.[15,19] Another method to decrease errors in these estimations is to average attenuation coefficients derived from different frequency components of the echo signal spectrum. This technique called "frequency compounding" has also been applied to reduce speckle in ultrasound images.[20,21] In the case of attenuation imaging, it has been found advantageous to apply frequency compounding in estimations of β, the attenuation coefficient versus frequency slope defined in Eq. (2).[15]

The statistical uncertainty of estimations of the attenuation coefficient versus frequency slope (β) when both spatial and frequency compounding are applied can be described using the following expression:[15]

$$\sigma''_{\beta} = \frac{1}{\sqrt{N_c}} \cdot \frac{1}{N_f} \cdot \sqrt{\sum_{i=1}^{n_f} \sigma^2_{\beta_{f_i}}}, \tag{4}$$

where σ''_{β} is the standard deviation of the attenuation coefficient versus frequency slope β'', after spatial angular and frequency compounding, and $\sigma_{\beta_{f_i}}$ is the standard deviation of β at frequency f_i, given by $\sigma_{\beta_{f_i}} = (1/f_i)\,\sigma_{\alpha_{f_i}}$. N_f in Eq. (4) is the effective number of independent frequency components used in the attenuation versus frequency slope estimation, and N_c is the effective number[22] of independent beam lines used for spatial angular compounding. n_f is the number of compounded frequency components, which may be partially correlated.

As shown by Eq. (4), increasing N_f or N_c promotes lower standard deviations. Thus, effective use of the signal frequency bandwidth as well as the angular window available for compounding requires knowledge of correlations amongst frequency and amongst angular estimates. With this information, it would be possible to increase the frequency separation between chosen frequency components, as well as the angular separation among the selected beam lines, so that near maximum reduction in σ''_{β} can be achieved using a relatively small number of frequency components or angular beam lines, saving time in data acquisition and processing. Sec. II C 3 outlines a theory that predicts these correlations.

C. Attenuation estimate correlation

1. Correlation between β estimates as a function of the increment between measurement frequencies

Suppose n_f is the total number of (partially correlated) frequency components compounded. Thus, N_f, the effective number of independent frequency components is associated with n_f, the actual number of frequency components used, through the following relation,[15]

$$N_f = \frac{n_f}{\sqrt{1+(\Sigma_{i\neq j}^{n_f}\sigma_{\beta_{f_i}}\sigma_{\beta_{f_j}}\rho(\beta_{f_i},\beta_{f_j}))/\Sigma_{i=1}^{n_f}\sigma^2_{\beta_{f_i}}}} = \frac{n_f}{\delta}, \tag{5}$$

where, $\sigma^2_{\beta_{f_i}}$ is the variance of the attenuation versus frequency slope estimate at frequency f_i, $\delta = \sqrt{1+(\Sigma_{i\neq j}^{n_f}\sigma_{\beta_{f_i}}\sigma_{\beta_{f_j}}\rho(\beta_{f_i},\beta_{f_j}))/\Sigma_{i=1}^{n_f}\sigma^2_{\beta_{f_i}}}$, and $\rho(\beta_{f_i},\beta_{f_j})$ is the correlation between the attenuation versus frequency slopes, estimated at frequencies f_i and f_j. Knowledge of $\rho(\beta_{f_i},\beta_{f_j})$ is the key to increasing the efficiency of frequency compounding in attenuation variance reduction.

Since β is derived from power spectral estimates, it is natural to look for $\rho(\beta_{f_i},\beta_{f_j})$ through the correlation between spectral estimates at frequencies f_i and f_j. We have developed a theory that approximates $\rho(S_{f_i},S_{f_j})$, the correlation between periodogram spectral estimates at any two frequencies, f_i and f_j (see Appendix A). This is given by

$$\rho(S_{f_i},S_{f_j}) = |FT(|p(t)|^2)_{\Delta f}|^2, \tag{6}$$

where $p(t)$ is a gating window applied to the rf data in the periodogram spectral estimates, and $\Delta f=|f_j-f_i|$. Thus $\rho(S_{f_i},S_{f_j})$ only depends on Δf and the length of the gating window T.

It is possible to derive $\rho(\beta_{f_i},\beta_{f_j})$ from $\rho(S_{f_i},S_{f_j})$, and this will be described in Sec. II C 3.

2. Correlation between β estimates as a function of the angular separation between beam lines

N_c, the effective number of independent signals used for spatial angular compounding, can be associated with n_c, the actual number of angular signals used, through the following relation:

$$\frac{1}{N_c}=\frac{1}{n_c}+\sum_{i\neq j}^{n_c}\rho(\beta_{\theta_i},\beta_{\theta_j}) \tag{7}$$

where $\rho(\beta_{\theta_i},\beta_{\theta_j})$ is the correlation between attenuation coefficient versus frequency slopes β_{θ_i}, β_{θ_j} at two angular positions θ_i and θ_j $(i\neq j)$, derived after frequency compounding.[15] $(\beta_\theta=(\Sigma_{k=1}^{n_f}\beta_\theta(f_k))/n_f$, where $\beta_\theta(f_k)$ is the attenuation versus frequency slope estimated at angle θ and frequency f_k. The geometry is illustrated in Fig. 2. This correlation can be estimated as (see Appendix B)

$$\rho(\beta_{\theta_i},\beta_{\theta_j})=\frac{\sum_{k=1}^{n_f}(1/f_k^2)\,\rho(\beta_{\theta_i}(f_k),\beta_{\theta_j}(f_k))}{\delta^2\sum_{k=1}^{n_f}(1/f_k^2)}, \tag{8}$$

where f_k is the kth frequency component used in frequency compounding and δ was defined previously. Therefore, $\rho(\beta_{\theta_i}(f_k),\beta_{\theta_j}(f_k))$, the correlation between attenuation coefficient versus frequency slopes, estimated at angles θ_i and θ_j for frequency f_k, is the critical information needed to increase the efficiency of spatial angular compounding in attenuation variance reduction.

To derive $\rho(\beta_{\theta_i}(f_k),\beta_{\theta_j}(f_k))$, we start with the correlation between power spectral estimates at angular position θ_i and θ_j, and at frequency f_k. Gerig and Chen[23] describe a model for the correlation between periodogram spectral estimates for rf data acquired at angular positions θ_i and θ_j (see Fig. 2). In this setup, positions 1 and 2 are locations of an aperture interrogating the same region but from different angles. The region is assumed to be centered at the focal

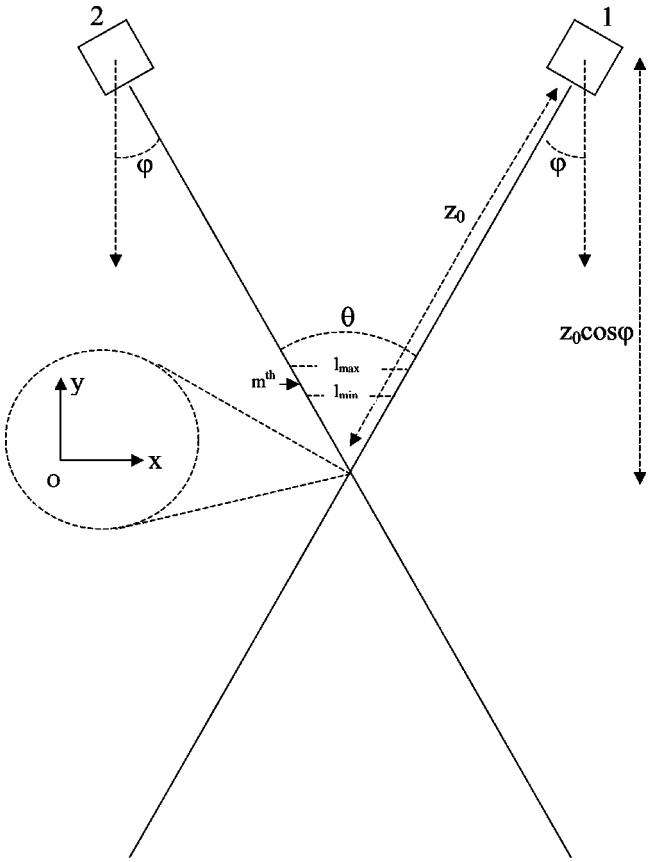

FIG. 2. The coordinate system used in deriving the spectral correlation between rf data from angled beam lines. Adapted from Ref. 23.

distance, z_0, which will be taken as the origin of the coordinate system. θ is the angle between the beam axes, and φ is its half angle; b is the distance between the centers of the apertures, which is also given by $b=2z_0\sin\varphi$. $\Delta\Omega_{1,2}$ is the volume contributing to the echo data, where the x direction extends to the edges of the beam and the y direction is bounded by the position and length of the rf data segment. Then, $\rho(S_{\theta_i}(f_k),S_{\theta_j}(f_k))$, the correlation between periodogram spectral estimates at angular position θ_i and θ_j for frequency f_k, is[23]

$$\rho(S_{\theta_i}(f_k),S_{\theta_j}(f_k))=|\rho_{1,2}(f_k)|^2, \tag{9}$$

where $\rho_{1,2}(f_k)$ is the corresponding correlation between Fourier transformed segments. The latter can be written as

$$\rho_{1,2}(f_k)\approx\frac{\int_{\Delta\Omega_{1,2}}dxdyp(x\cos\varphi-y\sin\varphi,x\sin\varphi+y\cos\varphi,f_k)p(x\cos\varphi+y\sin\varphi,-x\sin\varphi+y\cos\varphi,f_k)}{\int_{\Delta\Omega_{1,2}}dxdyp^2(x,y,f_k)}$$
$$\times\frac{e^{2ik(\sqrt{(x-b/2)^2+(z_0\cos\varphi-y)^2}-\sqrt{(x+b/2)^2+(z_0\cos\varphi-y)^2})}\{1/[(x-b/2)^2+(z_0\cos\varphi-y)^2]1/[(x+b/2)^2+(z_0\cos\varphi-y)^2]\}}{1/[x^2+(z_0-y)^2]^2}. \tag{10}$$

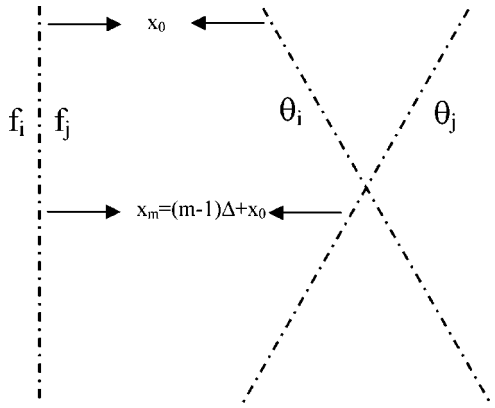

FIG. 3. Sketches to help illustrate derivation of Eqs. (11) and (12) in Appendix C. Dots stand for independent spectral estimate points. The left panel depicts the situation in Eq. (11), while the right panel is for Eq. (12).

In this expression, $p(x,y,f)$ is the point spread function, with $\varphi=\theta/2=|\theta_j-\theta_i|/2$. [Gerig *et al.* use ω in place of f_k. They use subscripts 1 and 2 for θ_i and θ_j, and they use $\rho_s(\omega)$ rather than $\rho(S_{\theta_i}(f_k),S_{\theta_j}(f_k))$.]

Similar to Sec. C II 1, it is possible to associate $\rho(\beta_{\theta_i}(f_k),\beta_{\theta_j}(f_k))$ with $\rho(S_{\theta_i}(f_k),S_{\theta_j}(f_k))$, which is the correlation between periodogram spectral estimates at angular positions θ_i and θ_j at frequency f_k. This will be explained in the next section.

3. Relation between attenuation versus frequency slope correlations and correlation among rf signal power spectra

The efficiency of compounding in attenuation variance reduction depends on the correlation between β estimates as a function of (1) the increment between analysis frequencies, $\rho(\beta_{f_i},\beta_{f_j})$, and (2) the angular separation between beam lines, $\rho(\beta_{\theta_i}(f_k),\beta_{\theta_j}(f_k))$.

Regardless of whether the problem involves correlations between the attenuation versus frequency slope at two frequencies (for a fixed angle) or at two angular positions (for a fixed frequency), it is essentially the same problem associating an attenuation correlation with a corresponding power spectra correlation. That is, the correlation between the attenuation versus frequency slope at positions 1 and 2 can be associated with the power spectra correlation at these positions through a common process, be it for two frequencies or two spatial angular positions (see Appendix C and Fig. 3). Let $\rho(S_{f_i},S_{f_j})$ be the correlation between sample power spectral estimates at frequencies f_i and f_j, and let $\rho(S_{\theta_i}(f_k),S_{\theta_j}(f_k))$ be the correlation of the same quantity as a function of the angular separation between beam lines. This is expressed by the following equations:

$$\rho(\beta_{f_i},\beta_{f_j})=\frac{12}{(n-1)n(n+1)}\sum_{m=1}^{n}a_m^2\rho(S_{f_i}^m,S_{f_j}^m) \tag{11}$$

and

$$\rho(\beta_{\theta_i}(f_k),\beta_{\theta_j}(f_k))=\frac{12}{(n-1)n(n+1)}\sum_{m=1}^{n}a_m^2\rho(S_{\theta_i}^m(f_k),S_{\theta_j}^m(f_k)) \tag{12}$$

where $a_m=m-n/2-\frac{1}{2}$ and $\Sigma_{m=1}^{n}a_m^2=(n-1)n(n+1)/12$ if the attenuation coefficient over region Z is obtained using a least squares method to derive the slope of the log of the power spectrum versus depth. m is a spatial index designating independent power spectral estimates at different depths, and n is the total number of independent estimates within Z, the same as in Eq. (3) (see Appendix C).

It is clear that $\rho(S_{f_i},S_{f_j})$ only depends on Δf and the length of the window T, and it is independent of the index m. Thus, $\rho(\beta_{f_i},\beta_{f_j})$, the correlation between attenuation coefficient versus frequency slopes estimated at two frequencies f_i and f_j, is obtained from

$$\rho(\beta_{f_i},\beta_{f_j})=\rho(S_{f_i},S_{f_j})\frac{12}{(n-1)n(n+1)}\sum_{m=1}^{n}a_m^2$$
$$=\rho(S_{f_i},S_{f_j})=|FT(|p(t)|^2)_{\Delta f}|^2. \tag{13}$$

$\rho(S_{\theta_i}^m(f_k),S_{\theta_j}^m(f_k))$ can be derived from Eqs. (9) and (10), by integrating in the region $\Delta\Omega_{1,2}^m$ where echo data for the mth corresponding periodogram spectral estimate originate. Therefore, $\rho(\beta_{\theta_i}(f_k),\beta_{\theta_j}(f_k))$ can be estimated from Eq. (12) with the knowledge of $\rho(S_{\theta_i}^m(f_k),S_{\theta_j}^m(f_k))$.

III. METHOD

A. Correlation between β estimates as a function of the increment between measurement frequencies

To test Eq. (13), a uniform phantom with 0.5 dB/cm/MHz attenuation was used. The same phantom was used both as a sample and a reference by scanning different regions to assure independent data. A VFX13-5 linear array transducer on a Siemens Antares scanner (Siemens Medical Solutions, Ultrasound Division, Mountain View, CA, USA) was used to acquire the data. A single transmit focus set at a depth of 3 cm was used. The scanner is equipped with a research interface, providing raw beam line data in a radio frequency format as well as header data indicating beam position, frequency, etc. The sampling frequency was 40 MHz, and the line density was 50 lines/cm.

Eleven rf data sets, each consisting a frame of echo data across the entire field of view of the probe, were acquired. The number of acoustic lines acquired in each frame is 192. The transducer was translated in the elevational direction between sets. The translation step was larger than the elevational dimension of the transducer, so that all rf data sets can be regarded as independent because different portions of the phantom were isonified. One data set served as a reference, and the remaining ten sets were taken as samples.

Analysis was done by computing the attenuation coefficient versus frequency slope for segments of individual beam lines whose length, Z, was either 2.16 or 2.77 cm, centered at the 3-cm transmit focal depth. Echo data from within each segment were first divided into subsegments defined by 4-μs

rectangular gating windows (3 mm), with no overlap. For each window, the spectrum was computed by taking the Fourier transform. A rectangular window with no overlap ensured accurate gating of the rf data and independence of power spectral estimates over the segment, as required in our theoretical analysis. Then, Eq. (13) changes to

$$\rho(\beta_{f_i},\beta_{f_j})=\mathrm{sinc}^2(T\Delta f), \tag{14}$$

where T is 4 μs and $\Delta f=|f_j-f_i|$.

In the case of the data from the reference, power spectral values at a given measurement depth were averaged over all 192 beam lines to provide a reference spectra at each depth, with low variability. $\alpha(f)$ was then calculated for each segment by fitting a straight line to the spectral values versus depth, as discussed after Eq. (1). Then attenuation versus frequency slopes ($\beta=\alpha/f$) at frequencies over a range from 6 to 14 MHz were calculated for the segment. One hundred ninety-two such parallel segments from the sample were available for each rf data set.

Correlation between β as a function of the increment between measurement frequencies was calculated for each rf data set using the following formula:

$$\text{Correlation}=\frac{\langle[\beta_{f_i}-\text{mean}(\beta_{f_i})]\cdot[\beta_{f_j}-\text{mean}(\beta_{f_j})]\rangle}{\sigma_{\beta_{f_i}}\cdot\sigma_{\beta_{f_j}}}, \tag{15}$$

where, as defined before, β_{f_i} is the attenuation coefficient versus frequency slope at frequency f_i, and β_{f_j} is the same quantity evaluated at frequency f_j. There are 192 pairs of β_{f_i}, and β_{f_j} for each sample rf data set. Mean (β_{f_i}) and mean (β_{f_j}) are their mean values, and $\sigma_{\beta_{f_i}}$, $\sigma_{\beta_{f_j}}$ are their standard deviations; here $\langle ... \rangle$ stands for the expected value.

Correlation values from frequency pairs that have the same frequency separation, Δf, were averaged to get final correlation values for one independent sample rf data set. In the end, the mean values of these ten independent correlation results from the ten rf data sets were taken as the experimental values, and error bars were calculated by calculating the standard deviation. Theoretical values were obtained from Eq. (14).

B. Correlation between β estimates as a function of the angular separation between beam lines

The accuracy of Eq. (12) was explored using simulated data because key information, including the dynamic aperture of transducers on the scanner, was not available and because simulation code can provide ideal rf data at specified beam angles. Using a simulation program,[25] rf echo signals were modeled for a linear array transducer interrogating a medium containing randomly distributed scatterers. The scatterer size of polystyrene beads applied in the simulation was 50 μm, and the scatterer number density was 9.7 per cubic millimeter, assuring that Rayleigh statistics apply. The linear array consists of elements of size 0.15 mm by 10 mm, with a center-to-center distance of 0.2 mm. Signals for each beam line were assumed to be formed using rf echo data from 75 consecutive elements, for a 1.5-cm aperture. Each of ten independent sample data sets simulated contained 180 lines, with each beam line rotated 0.5° from the previous, yielding a minimum angle of 0° and a maximum of 89.5° between pairs of beam lines. The focus was set at 3 cm from the transducer surface. A reference data set was also simulated, containing 400 lines. The power spectra at each depth within this set were averaged to provide reference spectra. For convenience, the attenuation of the sample was set to be zero while the reference attenuation was assumed in the model to be 0.5 dB/cm/MHz. The speed of sound in both media was set to be 1540 m/s. Neither apodization, dynamic receive focus, nor dynamic aperture were used.

Assume, for the sake of simplicity, the point-spread function for the system is adequately represented by a sinc squared function and the amplitude of the field does not vary significantly near the transmit focus. Equation 10 changes to

$$\rho_{1,2}(f_k)\approx\frac{\int_{\Delta\Omega_{1,2}}dxdy\ \mathrm{sinc}^2[(D/z_0\lambda)(x\cos\varphi-y\sin\varphi)]\mathrm{sinc}^2[(D/z_0\lambda)(x\cos\varphi+y\sin\varphi)]e^{2ik(\sqrt{(x-b/2)^2+(z_0\cos\varphi-y)^2}-\sqrt{(x+b/2)^2+(z_0\cos\varphi-y)^2})}}{\int_{\Delta\Omega_{1,2}}dxdy\ \mathrm{sinc}^4(Dx/z_0\lambda)}. \tag{16}$$

To derive $\rho(S^m_{\theta_i}(f_k),S^m_{\theta_j}(f_k))$ so that Eq. (12) can be solved, integration in Eq. (16) has to be made in the region $\Delta\Omega^m_{1,2}$ where scatterers contributing to the mth corresponding periodogram spectral estimate exist. The integration limits in the y direction were approximated roughly by setting them according to the coordinate along the y axis: $y_{\min}=l_{\min}\cos\varphi$ and $y_{\max}=l_{\max}\cos\varphi$. $l_{\min}$ is the minimum rectangular gating coordinate of the mth subsegment along the beam line, while $l_{\max}$ is the maximum gating coordinate (see Fig. 2). As in Sec. C 1, a 4-μs rectangular gating window (3 mm) with no overlap was used in the periodogram spectral estimates. In addition, as mentioned before, integration in the x direction was bounded by the edges of the beam.

For frequency f_k, attenuation coefficient versus frequency slopes over a specified region of each angled beam line were computed. Not losing generality, segments of each line, centered at the focus, were chosen as these regions. Correlation between attenuation versus frequency slope estimates as a function of the angular separation between beam lines was obtained for each of the ten independent sample data sets in a similar manner as described in Eq. (15). The difference is that in this case $\beta_{\theta_i}(f_k)$ and $\beta_{\theta_j}(f_k)$, the attenuation coefficient versus frequency slopes estimated at angles θ_i and θ_j for frequency f_k, replace β_{f_i} and β_{f_j} in Eq. (15). Their standard deviations $\sigma_{\beta_{\theta_i}(f_k)}$ and $\sigma_{\beta_{\theta_i}(f_k)}$ replace $\sigma_{\beta_{f_i}}$ and $\sigma_{\beta_{f_j}}$ in the same equation. The mean value of these ten independent correlation results from the ten independent

sample data sets was calculated. Theoretical values were obtained from Eq. (12).

IV. RESULTS

A. Correlation between β estimates as a function of the increment between measurement frequencies: Measurement data

Correlations between β estimates as a function of the increment between measurement frequencies (Δf) were calculated for rf data segments of length 2.16 and 2.77 cm. Results are shown in Figs. 4(a). (2.16 cm) and (b) (2.77 cm). Here experimental values are labeled as dots with error bars, while theoretical values calculated using Eq. (14) are plotted as solid lines. Error bars display $\pm$ one standard deviation of the ten independent correlation estimates in each case. For both data segment lengths, experimental values appear to match well with theoretical values in the general trend, although discrepancies are noted in the magnitude of the decorrelation rate. These are discussed in Sec. V. Both experimental and theoretical results indicate that the data segment length is not a factor in the correlation between β estimates at different measurement frequencies. An approximate 0.2-MHz increment between frequencies at which β results are obtained yields completely uncorrelated data when the length of the gating window used, T, is 4 μs.

B. Correlation between β estimates as a function of the angular separation between beam lines: Simulated data

Correlations between attenuation versus frequency slopes at different beam angles were computed for simulated data derived using center frequencies of 3, 5, and 7 MHz. In each case, a 50% bandwidth was represented in the simulation. For each simulated data set, the correlation between β values estimated at different angular separations between beam lines ($\Delta\theta$) was obtained for both 2.16- and 2.77-cm rf data segments. Results are shown in Fig. 5 (2.16 cm) and Fig. 6 (2.77 cm) for the three different center frequencies. Values from simulations are labeled as dots with error bars, while theoretical values are plotted as solid lines. Again, error bars display $\pm$ one standard deviation of the ten independent correlation estimates in each situation. In all situations, the agreement in the general trend between experimental values and theoretical values is good; i.e., it can be seen from both simulation data and theory that the higher the frequency is, the faster is the decorrelation between β estimates as a function of the angular separation between beam lines. A similar statement can be made regarding the effect of data length, namely, attenuation computed over longer segments decorrelates faster with angle. For the situation simulated at 3.5 MHz, the angular increment needed for the attenuation estimates to achieve 0.5 decorrelation is around 2° for the 2.16-cm data segment and 1.6° for the 2.77-cm segment. At 5 MHz, the values are 1.5° for 2.16 cm and 1.2° for 2.77 cm, while at 7 MHz, they are 1.1° for 2.16-cm segments and 0.8° for 2.77-cm segments.

V. DISCUSSION

The theoretical expressions derived in this paper predict the correlation between β estimates as a function of increment between measurement frequencies and angular separation between beam lines. Predictions are found to match experimental results in the general trend of the curves, as noted in the results. However, small deviations between predictions and measurement results are also noticed in Figs. 4–6. Part of the deviation may be contributed by the error propagation assumption used in deriving the theoretical expressions. We associated the covariance of the sample-to-reference power spectrum ratio with the covariance of its logarithm form [Appendix C, Eqs. (C8) and (C12)] in an approximate partial derivative relation. Nevertheless, these theoretical curves give a good approximation to the decorrelation rate in attenuation estimations for incremental changes in beam angle and analysis frequency.

In the frequency compounding method, from Eq. (14), the correlation between β estimates as a function of increment between measurement frequencies is dependent on the length of the gating window, T. The longer T is, the more independent frequency components there are within the bandwidth of the transducer, making N_f in Eq. (4) larger. On the other hand, the longer T is, the smaller will be n, the number of independent spectral estimates over the interval Z, tending to make $\sigma_{\beta_{f_i}}$ in Eq. (4) larger because $\sigma_{\alpha_{f_i}}$ would be larger [see Eq. (3)]. Therefore, according to Eq. (4), there is no apparent difference in terms of reducing the variance of β between long or short gating windows, for the power spectra estimates, provided that the length of the gating window is long enough to make stable attenuation estimates at different frequencies over the spectrum. Yao[26] pointed out that for a Blackman-Harris window, 4 μs is needed for stable attenuation estimates around 5 MHz. Also, because the correlation between β estimates as a function of increment between measurement frequencies is independent of the length of the rf data segment over which attenuation is computed, frequency compounding will have an advantage in local attenuation estimations where data lengths are short.

In angular compounding, the correlation between β estimates as a function of angular separation between beam lines is dependent on both the frequency of the signal and the length of the rf data segment over which the attenuation value is derived. Figures 5 and 6 illustrate that the higher the frequency or the longer the data segment is, the faster the decorrelation with beam angle is. Thus it is a good strategy to include more high-frequency components to get more independent angular estimates, as shown by Eq. (8). The effect of data length on the decorrelation between β estimates puts an adverse effect on attempts to improve resolution in local attenuation estimations where it would be desirable to keep data lengths short. The efficacy of angular compounding in variance reduction of attenuation estimations is limited due to this effect.

To verify Eq. (12), the point spread function was taken to behave as a sinc-squared function, and the field amplitude was assumed to vary insignificantly for sample data sets near the transmit focus, so that the calculation of Eq. (10) could

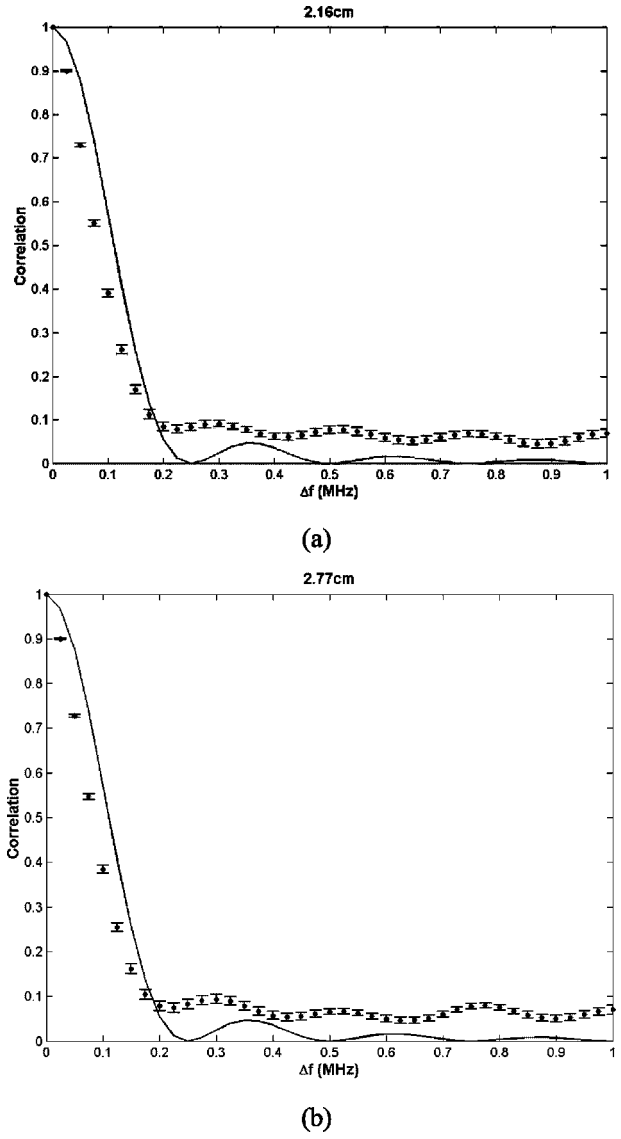

FIG. 4. Correlation between the attenuation versus frequency slope as a function of the increment between measurement frequencies for an echo data segment of length (a) 2.16 cm and (b) 2.77 cm. Solid lines are theoretical values, and dots with error bars are the results of phantom experiments.

be simplified to Eq. (16). The assumption is generally good near the focal region of a transducer, although it may not represent the actual acoustic field at points away from the focus of a real transducer. However, during the design of a compounding scheme for any particular aperture and depth, a numerical calculation can be done using Eq. (10) with detailed knowledge of the acoustic field.

Our theoretical result is based on a model that a single acoustic line is rotated around a common center. Caution must be taken, therefore, on use of these results if multiple acoustic lines [$N_s \neq 1$ in Eq. (3)] are used to get an averaged spectrum before computing the attenuation. If spectra from several beam lines are averaged, the region in which scatterers contribute to the averaged spectrum will be wider than the region which contributes to the spectrum for a single acoustic line. Thus, the overlap between rotating acoustic fields will be larger in the averaged spectrum case than for the case where the spectrum is derived from rf data acquired

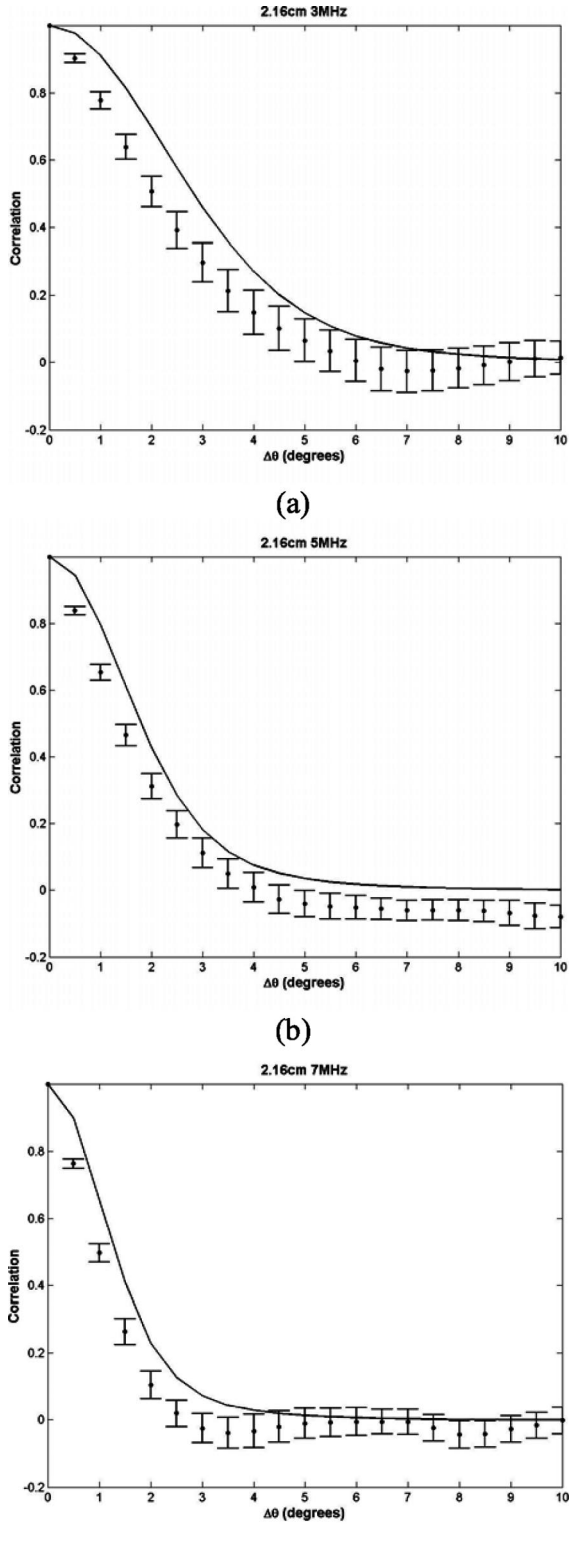

FIG. 5. Correlation between the attenuation versus frequency slope as a function of the angular separation between beam lines for a data segment of length 2.16 cm at frequencies of (a) 3 MHz, (b) 5 MHz, and (c) 7 MHz. Solid lines are theoretical values, and dots with error bars are the results of simulation experiments.

over a single acoustic line if the angle rotated is the same. Therefore, the spectral decorrelation as a function of angular separation between beam lines will be slower when multiple acoustic lines are used to get an averaged spectrum, and so

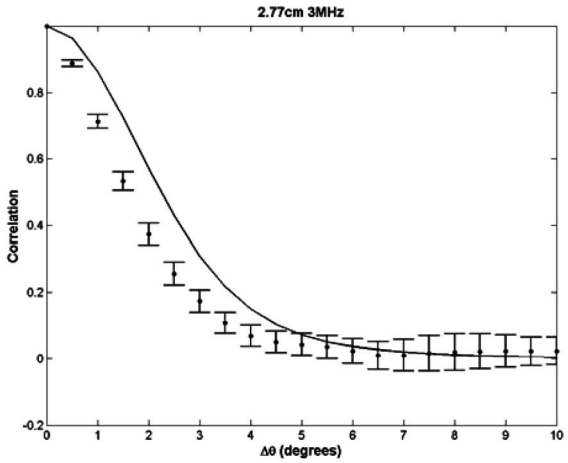

(a)

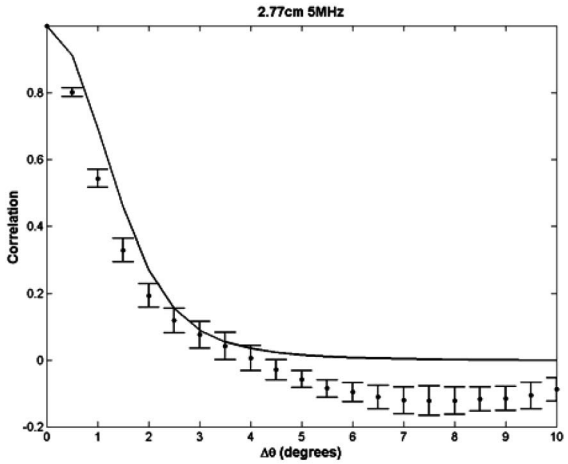

(b)

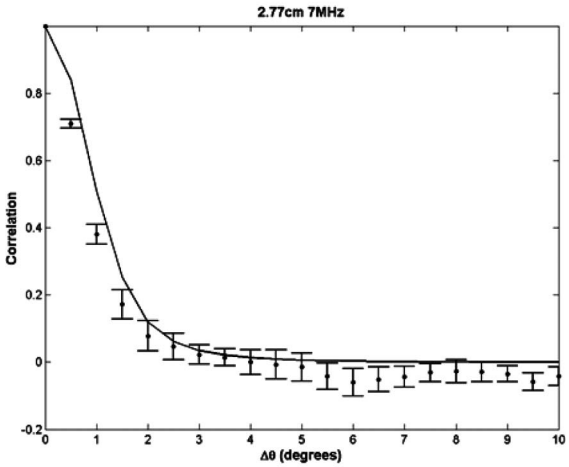

(c)

FIG. 6. Correlation between the attenuation versus frequency slope as a function of the angular separation between beam lines for a data segment of length 2.77 cm, at frequencies of (a) 3 MHz, (b) 5 MHz, and (c) 7 MHz. Solid lines are theoretical values, and dots with error bars are the results of simulation experiments.

will the attenuation decorrelation. Since frequency compounding does not have this effect when using averaged spectra from adjacent lines, it will have an advantage over spatial angular compounding in this case.

Our compounding algorithm is just one type of possible compounding methods that could be applied in attenuation estimations. Other approaches, for example, spectra compounding instead of parameter compounding, may be effective as well. For any real system, noise has to be incorporated into the model when considering an optimized compounding scheme. Still, this study sheds light on a path towards reliable local attenuation estimations. It is, in general, difficult to determine the dependencies of attenuation estimate correlations upon systematic parameters analytically. With simplified conditions such as those applied in the solution of our theoretical model, we are able to show the efficiency of angular or frequency compounding for different system parameters, such as the angular separation between compounded beam lines or the increment between compounded frequencies. With these relations, directions are given for choosing the best scheme for attenuation estimations with the smallest variance.

VI. CONCLUSION

Theoretical expressions for the correlation between attenuation versus frequency slope estimates generated for the same tissue location but using different frequency components or from different angles of incidence have been derived. Predicted results were compared with measurements from phantoms and with simulation data, respectively. Both predictions and measurement results show that the correlation between β estimates as a function of increment between measurement frequencies is independent of the length of the rf data segment over which the attenuation versus frequency slope is derived. However, it decreases with an increase in length of the gating window used in power spectra estimates. In contrast, the correlation between β estimates as a function of angular separation between beam lines does depend on the rf data segment length; it also depends on the frequency of the signal over which the attenuation versus frequency slope is computed. The higher the frequency and the longer the data segment, the faster the decorrelation will be. The relationships for correlation among β estimates can be used to optimize spatial angular and frequency compounding schemes in attenuation versus frequency slope measurements.

ACKNOWLEDGMENTS

This work was supported in part by NIH Grant Nos. R21EB002722 and R21EB003853.

APPENDIX A: CORRELATION BETWEEN PERIODOGRAM VALUES

The signal $V(t)$, gated by a window $p(t)$ with its center at t_0, is

$$V_g(t) = V(t)p(t-t_0). \tag{A1}$$

The value of its Fourier transform at frequency f_i is

$$V_g(f_i,t_0)=e^{-if_it_0}\int v(f)P(f_i-f)e^{ift_0}\,df, \tag{A2}$$

where $v(f)=\mathrm{FT}(V(t))$ and $P(f)=\mathrm{FT}(p(t))$.

At another frequency f_j, we have

$$V_g(f_j,t_0)=e^{-if_jt_0}\int v(f')P(f_j-f')e^{if't_0}\,df', \tag{A3}$$

Thus, the autocorrelation between the two Fourier transforms is

$$\rho=\langle V_g(f_i,t_0)V_g^*(f_j,t_0)\rangle\approx Ce^{-i(f_i-f_j)t_0}\mathrm{FT}(|p(t)|^2)_{\Delta f}. \tag{A4}$$

Here C is a constant absorbed into the normalization, $\Delta f=|f_j-f_i|$, $\langle ...\rangle$ means the expected value, and use is made of the fact that $p(t)$ and $P(f)$ are even functions.

Thus, the correlation between periodogram spectral estimates is

$$\rho(S_{f_i},S_{f_j})=|\rho|^2=|\mathrm{FT}(|p(t)|^2)_{\Delta f}|^2. \tag{A5}$$

APPENDIX B: ATTENUATION CORRELATIONS FOR DATA AT TWO ANGULAR POSITIONS

In our frequency compounding algorithm, the attenuation coefficients versus frequency slopes at angular positions θ_i and θ_j $(i\neq j)$ are given by

$$\beta_{\theta_i}=\frac{\Sigma_{k=1}^{n_f}\beta_{\theta_i}(f_k)}{n_f} \quad \text{and} \quad \beta_{\theta_j}=\frac{\Sigma_{k'=1}^{n_f}\beta_{\theta_j}(f_{k'})}{n_f}, \tag{B1}$$

where n_f is the number of frequency components used in frequency compounding. The variance of these two variables, $\mathrm{cov}(\beta_{\theta_i},\beta_{\theta_j})$, may be written as

$$\begin{aligned}\mathrm{cov}(\beta_{\theta_i},\beta_{\theta_j})&=\frac{1}{n_f^2}\mathrm{cov}\left(\sum_{k=1}^{n_f}\beta_{\theta_i}(f_k),\sum_{k'=1}^{n_f}\beta_{\theta_j}(f_{k'})\right)\\&=\frac{1}{n_f^2}\sum_{k=1}^{n_f}\mathrm{cov}(\beta_{\theta_i}(f_k),\beta_{\theta_j}(f_k)).\end{aligned} \tag{B2}$$

The second equal sign in Eq. (B2) is established because we assume that the covariance between β estimates made at two different angles is negligible unless those estimates are made at the same frequency, i.e., $\mathrm{cov}(\beta_{\theta_i}(f_k),\beta_{\theta_j}(f_{k'}))=0$ when $k'\neq k$. Using $\sigma_{\beta_{\theta_i}}=\sigma_{\beta_{\theta_j}}=\sigma_{\beta_\theta}=(1/N_f)\sqrt{\Sigma_{k=1}^{n_f}\sigma_{\beta_{f_k}}^2}=(\delta/n_f)\sqrt{\Sigma_{k=1}^{n_f}\sigma_{\beta_{f_k}}^2}$, in which σ_{β_θ} is the variance of the attenuation coefficient versus frequency slope estimate after frequency compounding but before spatial angular compounding, we write

$$\begin{aligned}\rho(\beta_{\theta_i},\beta_{\theta_j})&=\frac{\mathrm{cov}(\beta_{\theta_i},\beta_{\theta_j})}{\sigma_{\beta_{\theta_i}}\sigma_{\beta_{\theta_j}}}\\&=\frac{\Sigma_{k=1}^{n_f}\mathrm{cov}(\beta_{\theta_i}(f_k),\beta_{\theta_j}(f_k))}{\delta^2\Sigma_{k=1}^{n_f}\sigma_{\beta_{f_k}}^2}\\&=\frac{\Sigma_{k=1}^{n_f}\sigma_{\beta_{f_k}}^2\rho(\beta_{\theta_i}(f_k),\beta_{\theta_j}(f_k))}{\delta^2\Sigma_{k=1}^{n_f}\sigma_{\beta_{f_k}}^2}.\end{aligned} \tag{B3}$$

Since $\sigma_{\beta_{f_k}}=\sigma_{\alpha_{f_k}}/f_k$ and $\sigma_{\alpha_{f_k}}$ can be approximated as being independent of f_k [see Eq. (3) in the main text], we have

$$\rho(\beta_{\theta_i},\beta_{\theta_j})\approx\frac{\Sigma_{k=1}^{n_f}(1/f_k^2)\,\rho(\beta_{\theta_i}(f_k),\beta_{\theta_j}(f_k))}{\delta^2\Sigma_{k=1}^{n_f}(1/f_k^2)}. \tag{B4}$$

APPENDIX C: ATTENUATION CORRELATIONS RESULTING FROM CORRELATIONS IN POWER SPECTRA

The reference phantom method to derive β, the attenuation coefficient versus frequency slope, is carried out by applying a least squares algorithm to fit the log difference between a sample and a reference power spectral estimate at a given frequency versus the depth. The slope of this fit is proportional to the difference between the attenuation coefficient of the sample and that of the reference. With the known attenuation of the reference, the attenuation coefficient of the sample can be estimated. That value divided by the given frequency is the attenuation coefficient versus frequency slope, β.

Let β be the least squares slope fitted from the natural log difference between the sample and the reference power spectral estimate versus the depth, and let $\Delta\alpha$ be the difference between the attenuation coefficient of the sample and that of the reference at a chosen frequency:

$$\Delta\alpha=-b/4\times 8.68\ \ (\mathrm{dB/cm}). \tag{C1}$$

Here 8.68 is the conversion factor from nepers/cm to dB/cm. The correlation between the attenuation coefficient versus frequency slope, β, at positions 1 and 2 would be

$$\rho(\beta_1,\beta_2)=\rho(\alpha_1,\alpha_2)=\rho(b_1,b_2). \tag{C2}$$

Let x_m be the position of the mth independent power spectral estimate used to calculate the slope b at a specified frequency, and let Δ be the separation between these uniformly spaced data points. y_m is the mth value of the logged difference between the sample and reference power spectral estimates at different depths for that frequency. Thus $y_m=\ln S_m-\ln S_m^r=\ln RS_m$, where $(\mathrm{RS})_m$ is the ratio of the sample power spectrum to the reference power spectrum at point m. $m=1,...,n$, where n is the total number of independent power spectrum estimates along the data segment whose length is Z. In Fig. 3, the left panel depicts the situation described by Eq. (11), while the right panel corresponds to Eq. (12):

$$x_m=(m-1)\Delta+x_0. \tag{C3}$$

According to Bevington,[24]

$$b=\frac{1}{\Delta'}\left(n\sum x_m y_m-\sum x_m\sum y_m\right) \tag{C4}$$

in which $\Delta'=n\Sigma x_m^2-(\Sigma x_m)^2$. Inserting (C3) into (C4), we have

$$b=\frac{1}{\Delta'}n\Delta\sum_{m=1}^{n} a_m y_m, \tag{C5}$$

in which $a_m=m-n/2-1/2$ and $\Sigma_{m=1}^{n}a_m^2=(n-1)n(n+1)/12$.

Thus, we have

$$\begin{aligned}\mathrm{cov}(b_1,b_2)&=\frac{1}{\Delta'^2}n^2\Delta^2\mathrm{cov}\left(\sum_{u=1}^{n} a_{1u}y_{1u},\sum_{v=1}^{n} a_{2v}y_{2v}\right)\\&=\frac{1}{\Delta'^2}n^2\Delta^2\sum_{u=1}^{n}\sum_{v=1}^{n} a_{1u}a_{2v}\mathrm{cov}(y_{1u},y_{2v}).\end{aligned} \tag{C6}$$

It is reasonable to suppose that when $u\neq v$, covariance between y_u and y_v at two different positions 1, 2 is negligible, i.e., $\mathrm{cov}(y_{1u},y_{2v})=0$, when $1\neq 2$, and $u\neq v$. Also we have $\mathrm{cov}(y_{1u},y_{2v})=0$, when $1=2$, but $u\neq v$. The latter is because of the assumption that data points are independent. Thus, we have

$$\mathrm{cov}(b_1,b_2)=\frac{1}{\Delta'^2}n^2\Delta^2\sum_{m=1}^{n} a_m^2\mathrm{cov}(y_{1m},y_{2m}). \tag{C7}$$

Assume the following assumption holds for the error propagation from the ratio of the sample to reference power spectrum to its logged form,

$$\begin{aligned}\mathrm{cov}(y_{1m},y_{2m})&=\frac{\partial y_{1m}}{\partial \mathrm{RS}_{1m}}\frac{\partial y_{2m}}{\partial \mathrm{RS}_{2m}}\mathrm{cov}(\mathrm{RS}_{1m},\mathrm{RS}_{2m})\\&=\frac{1}{\mathrm{RS}_{1m}}\frac{1}{\mathrm{RS}_{2m}}\sigma_{\mathrm{RS}_{1m}}\sigma_{\mathrm{RS}_{2m}}\rho(\mathrm{RS}_{1m},\mathrm{RS}_{2m}).\end{aligned} \tag{C8}$$

And, from Ref. 25,

$$\begin{aligned}\sigma_{\mathrm{RS}_m}^2&=\left(\frac{\partial \mathrm{RS}_m}{\partial\overline{S_m^r}}\right)^2\mathrm{var}(\overline{S_m^r})+\left(\frac{\partial \mathrm{RS}_m}{\partial\overline{S_m}}\right)^2\mathrm{var}(\overline{S_m})\\&=\frac{N_S+N_r}{N_S N_r}\mathrm{RS}_m^2.\end{aligned} \tag{C9}$$

The relation $\mathrm{var}(S)=S^2$ is used in the above equation.[26] N_s and N_r represent the number of sample and reference waveforms used to calculate the spectra, respectively.

Combining Eqs. (C7)–(C9),

$$\mathrm{cov}(b_1,b_2)=\frac{N_s+N_r}{N_s N_r}\frac{1}{\Delta'^2}n^2\Delta^2\sum_{m=1}^{n} a_m^2\rho(\mathrm{RS}_{1m},\mathrm{RS}_{2m}). \tag{C10}$$

Assuming $\sigma_{y_m}=\sigma_y$ for all m, we have $\sigma_b^2=n\,\sigma_y^2/\Delta'$, so

$$\sigma_{b_1}\sigma_{b_2}=\frac{n}{\Delta'}\sigma_{y_1}\sigma_{y_2}. \tag{C11}$$

Similar to (C8) and (C9),

$$\sigma_{y_1}^2=\sigma_{y_2}^2=\sigma_y^2=\left(\frac{\partial y}{\partial \mathrm{RS}}\right)^2\sigma_{\mathrm{RS}}^2=\frac{N_s+N_r}{N_s N_r}. \tag{C12}$$

Combining (C2) and (C10)–(C12),

$$\rho(\beta_1,\beta_2)=\rho(b_1,b_2)=\frac{1}{\Delta'}n\Delta^2\sum_{m=1}^{n} a_m^2\rho(\mathrm{RS}_{1m},\mathrm{RS}_{2m}). \tag{C13}$$

Many reference signals are averaged to form the reference spectrum. Thus the variance of the reference spectrum can be deemed to be very small,

$$\rho(\mathrm{RS}_{1m},\mathrm{RS}_{2m})=\rho(S_{1m},S_{2m}) \tag{C14}$$

and

$$\Delta'=n\Sigma x_m^2-\left(\sum x_m\right)^2=n(n-1)\sigma_x^2=\frac{(n+1)n^2}{12(n-1)}Z^2. \tag{C15}$$

The last equality in Eq. (C15) was established because for n uniformly spaced points on a one-dimensional number axis spread over a distance of Z, $\sigma_x^2=[n(n+1)/12(n-1)^2]Z^2$. Notice that $Z=(n-1)\Delta$. Thus (C13) turns to

$$\rho(\beta_1,\beta_2)=\frac{12}{(n-1)n(n+1)}\sum_{m=1}^{n} a_m^2\rho(S_{1m},S_{2m}). \tag{C16}$$

[1] R. Kuc, "Clinical application of an ultrasound attenuation coefficient estimation technique for liver pathology characterization," IEEE Trans. Biomed. Eng. **27**, 312–319 (1980).

[2] Z. F. Lu, J. A. Zagzebski, and F. T. Lee, "Ultrasound backscatter and attenuation in human liver with diffuse disease," Ultrasound Med. Biol. **25**, 1047–1054 (1999).

[3] A. T. Stavros, D. Thickman, C. L. Rapp, M. A. Dennis, S. H. Parker, and G. A. Sisney, "Solid breast nodules: use of sonography to distinguish between benign and malignant lesions," Radiology **196**, 123–134 (1995).

[4] P. M. Lamb, N. M. Perry, S. J. Vinnicombe, and C. A. Wells, "Correlation between ultrasound characteristics, mammographic findings and histological grade in patients with invasive ductal carcinoma of the breast," Clin. Radiol. **55**, 40–44 (2000).

[5] J. G. Miller, J. E. Perez, J. G. Mottley, E. I. Madaras, P. H. Johnston, E. D. Blodgett, L. J. Thomas III, and B. E. Sobel, "Myocardial tissue characterization: an approach based on quantitative backscatter and attenuation," Proc.-IEEE Ultrason. Symp. **83**, 782–793 (1983).

[6] S. L. Bridal, P. Fornes, P. Bruneval, and G. Berger, "Parametric (intergrated backscatter and attenuation) images constructed using backscattered radio frequency signals (25-56 MHz) from human aorte in vitro," Ultrasound Med. Biol. **23**, 215–229 (1997).

[7] S. W. Flax, N. J. Pelc, G. H. Glover, F. D. Gutmann, and M. McLachlan, "Spectral Characterization and Attenuation Measurements in Ultrasound," Ultrason. Imaging **5**, 95–116 (1983).

[8] P. He and J. F. Greenleaf, "Application of stochastic-analysis to ultrasonic echoes—estimation of attenuation and tissue heterogeneity from peaks of echo envelope," J. Acoust. Soc. Am. **79**, 526–534 (1986).

[9] E. Walach, A. Shmulewitz, Y. Itzchak, and Z. Heyman, "Local tissue attenuation images based on pulse-echo ultrasound scans," IEEE Trans. Biomed. Eng. **36**, 211–221 (1989).

[10] B. S. Knipp, J. A. Zagzebski, T. A. Wilson, F. Dong, and E. L. Madsen, "Attenuation and backscatter estimation using video signal analysis applied to B-mode images," Ultrason. Imaging **19**, 221–233 (1997).

[11] R. Kuc and M. Schwartz, "Estimating the acoustic attenuation coefficient

slope for liver from reflected ultrasound signals,'' IEEE Trans. Sonics Ultrason. **SU-26**, 353–362 (1979).
[12] M. J. T. M. Cloostermans and J. M. Thijssen, ''A beam corrected estimation of the frequency dependent attenuation of biological tissues from backscattered ultrasound,'' Ultrason. Imaging **5**, 136–147 (1983).
[13] L. X. Yao, J. A. Zagzebski, and E. L. Madsen, ''Backscatter coefficient measurements using a reference phantom to extract depth-dependent instrumentation factors,'' Ultrason. Imaging **12**, 58–70 (1990).
[14] M. Fink, F. Hottier, and J. F. Cardoso, ''Ultrasonic signal processing for in vivo attenuation measurement: Short time Fourier analysis,'' Ultrason. Imaging **5**, 117–135 (1983).
[15] H. Tu, T. Varghese, E. L. Madsen, Q. Chen, and J. A. Zagzebski, ''Ultrasound attenuation imaging using compound acquistion and processing,'' Ultrason. Imaging **25**, 245–261 (2003).
[16] L. X. Yao, J. A. Zagzebski, and E. L. Madsen, ''Statistical uncertainty inultrasonic backscatter and attenuation coefficients determined with a reference phantom,'' Ultrasound Med. Biol. **17**, 187–194 (1991).
[17] R. F. Wagner, S. W. Smith, J. M. Sandrick, and H. Lopez, ''Statistics of speckle in ultrasound B-scans,'' IEEE Trans. Sonics Ultrason. **30**, 156–163 (1983).
[18] R. R. Entrekin, B. A. Porter, H. H. Sillesen, A. D. Wong, P. L. Cooperberg, and C. H. Fix, ''Real-time spatial compound imaging: application to breast, vascular, and musculoskeletal ultrasound,'' Semin Ultrasound CT MR **22**, 50–64 (2001).
[19] A. L. Gerig, T. Varghese, and J. A. Zagzebski, ''Improved parametric imaging of scatterer size estimates using angular compounding,'' IEEE Trans. Ultrason. Ferroelectr. Freq. Control **51**, 708–715 (2004).
[20] P. A. Magnin, O. T. von Ramm, and F. L. Thurstone, ''Frequency compounding for speckle contrast reduction in phased-array Images,'' Ultrason. Imaging **4**, 267–281 (1982).
[21] G. E. Trahey, J. W. Allison, S. W. Smith, and O. T. von Ramm, ''A quantitative approach to speckle reduction via frequency compounding,'' Ultrason. Imaging **8**, 151–164 (1986).
[22] M. O'Donnell and S. D. Silverstein, ''Optimum displacement for compound image generation in medical ultrasound,'' IEEE Trans. Ultrason. Ferroelectr. Freq. Control **35**, 470–476 (1988).
[23] A. L. Gerig, Q. Chen, and J. A. Zagzebski, ''Correlation of ultrasonic scatterer size estimates for the statistical analysis and optimization of angular compounding,'' J. Acoust. Soc. Am. **116**, 1832–1841 (2004).
[24] P. R. Bevington and D. K. Robinson, *Data Reduction and Error Analysis for the Physical Sciences*, 2nd ed. (McGraw-Hill, New York, 1992).
[25] A. L. Gerig, J. A. Zagzebski, and T. Varghese, ''Statistics of ultrasonic scatterer size estimation with a reference phantom,'' J. Acoust. Soc. Am. **113**, 3430–3437 (2002).
[26] P. Chaturvedi and M. F. Insana, ''Error bounds on ultrasonic scatter size estimates,'' J. Acoust. Soc. Am. **100**, 392–399 (1996).

Comparison of measurements of phase velocity in human calcaneus to Biot theory

Keith A. Wear[a)]
U.S. Food and Drug Administration, Center for Devices and Radiological Health, HFZ-140, 12720 Twinbrook Parkway, Rockville, Maryland 20852

Andres Laib
SCANCO Medical AG, Auenring 6-8, CH-8303 Bassersdorf, Switzerland

Angela P. Stuber and James C. Reynolds
National Institutes of Health Clinical Center, Bethesda, Maryland 20892
SCANCO Medical AG, Auenring 6-8, CH-8303 Bassersdorf, Switzerland

(Received 22 September 2004; revised 9 February 2005; accepted 12 February 2005)

Biot's theory for elastic propagation in porous media has previously been shown to be useful for modeling the dependence of phase velocity on porosity in bovine cancellous bone *in vitro*. In the present study, Biot's theory is applied to measurements of porosity-dependent phase velocity in 53 human calcanea *in vitro*. Porosity was measured using microcomputed tomography for some samples ($n=23$) and estimated based on bone mineral densitometry for the remaining samples ($n=30$). The phase velocity at 500 kHz was measured in a water tank using a through-transmission technique. Biot's theory performed well for the prediction of the dependence of sound speed on porosity. The trend was quasilinear, but both the theory and experiment show similar slight curvature. The root mean square error (RMSE) of predicted versus measured sound speed was 15.8 m/s. © *2005 Acoustical Society of America.* [DOI: 10.1121/1.1886388]

PACS numbers: 43.80-Qf [FD] Pages: 3319–3324

I. INTRODUCTION

Motivated by geophysical applications, Biot developed a theory for elastic propagation in porous media (Biot 1956a, 1956b, 1956c, 1962, 1963). As reviewed by Haire and Langton (1999), Biot's theory has been applied by several investigators to model propagation in bovine cancellous bone, with more success in the prediction of velocity than attenuation.

The mathematics of Biot theory is thoroughly reviewed in the references given previously. Briefly, Biot considered a porous solid frame filled with a fluid. An ultrasound wave propagating through the composite loses energy due to friction between the frame and the fluid. Biot obtained a quadratic equation for longitudinal phase velocity, based on the material properties of the two media and the mechanical properties of the frame structure. The two solutions correspond to so-called ''fast'' and ''slow'' waves. These two waves correspond to the solid and fluid moving in phase and out of phase, respectively.

Previous efforts have compared Biot's predictions to measurements in bovine cancellous bone. Williams (1992) measured the dependence of longitudinal velocity on porosity in tibia *in vitro* and found good agreement with Biot's predictions. Williams measured fast wave velocity in the direction parallel to the predominant trabecular orientation. Hosokawa and Otani (1997, 1998) measured velocity in femoral distal epiphysis *in vitro* in both parallel and perpendicular orientations. In the parallel orientation, they observed distinct fast and slow longitudinal waves, both with porosity-dependent velocities commensurate with Biot's predictions. In the perpendicular orientation, in which fast and slow waves converge into a single wave, their measurements also matched theory. Mohamed *et al.* (2003) also reported good agreement between Biot theory and measurements of fast and slow waves in tibia *in vitro*. Hughes *et al.* (2003) argued that while both types of waves are observable *in vitro*, conditions required for slow wave propagation are not as easily attained *in vivo*, in which water is replaced by marrow, at typical diagnostic frequencies. (In addition, it is difficult to achieve propagation parallel to the trabeculae *in vivo*, which also complicates separation of the two types of waves.) Lee *et al.* (2003) successfully applied the modified Biot–Attenborough model to predict measurements of velocity and attenuation in tibia.

In this report we describe a comparison of porosity-dependent phase velocity in human calcaneus with Biot's theory.

II. METHODS

A. Bone specimens

Data from two sets of human calcaneus samples were used. Direct estimates of porosity, obtained using micro computed tomography (micro CT), were performed for one set ($n=23$). For the other set ($n=30$), micro CT measurements were not available. For these samples, porosity was estimated from dual energy x-ray absorptiometry (DEXA) measurements (see later).

The calcaneus samples (both genders, ages unknown) were defatted using a trichloro-ethylene solution as described

a)Electronic mail: Kaw@cdrh.fda.gov

TABLE I. Model parameters.

Parameter	Source	Value	Reference
Density of trabecular bone material	Various human	1.8 g/cm^3	Keaveny, 1993
Density of fluid (water)		1 g/cm^3	
Young's modulus of trabecular bone material	Human tibia	8.3 GPa	Rho, 1993
Bulk modulus of fluid (water)		2.2 GPa	Williams, 1992
Poisson's ratio for trabecular bone material	Many bones and bone-like materials	0.3	Grenoble, 1972
Poisson's ratio for skeletal frame	Bovine tibia	0.23	Williams, 1989 Hosokawa, 1998 and Otani
s, where tortuosity$=1-s(1-1/\beta)$ and $\beta=$porosity		0.25	Williams, 1992
Exponent m, where $E_b=E_sV_f^m$, $E_s=$Young's modulus of trabecular bone material, $E_b=$Young's modulus of skeletal frame, and $V_f=$volume fraction of bone.		Obtained by curve fitting	

previously (Wear, 2000a). The lateral cortical layers were sliced off leaving two parallel surfaces with direct access to trabecular bone. The thicknesses of the samples varied from 12 to 21 mm. In order to remove air bubbles, the samples were vacuum degassed underwater in a desiccator. After vacuum, samples were allowed to thermally equilibrate to room temperature prior to ultrasonic interrogation. Ultrasonic measurements were performed in distilled water at room temperature. The temperature was measured for each experiment and ranged between 19.1 °C and 21.2 °C. The relative orientation between the ultrasound beam and the calcanea was the same as with *in vivo* measurements performed with commercial bone sonometers, in which sound propagates in the mediolateral (or lateromedial) direction.

B. Microcomputed tomography

3D reconstructions for one set ($n=23$) of cancellous bone samples were generated using micro CT (Ruegsegger *et al.*, 1996). A desktop fan-beam micro CT scanner (Scanco μCT 40) situated at Scanco Medical AG in Bassersdorf, Switzerland was used. It utilized a microfocus x-ray source with 7 μm spot size, 70 kVp, 8 W (114 μA). The detector was a CCD array containing 2048 X 64 elements with a 24 μm pitch. The resolution was 8 μm (10% Modulation Transfer Function). Quantitative microstructural properties were extracted from the 3D datasets using methods of Hildebrand and co-workers (Hildebrand and Ruegsegger, 1995). Measurements of the ratio of bone volume to total volume (BV/TV) were performed on each of the 23 calcaneal specimens. The voxel size (nominal resolution) was 5 microns. 300 transverse slices (9 mm) were acquired from each specimen. From these 300 slices, a complete (square) cross region was taken, resulting in a volume of interest of about $12\times12\times9$ mm for each bone sample.

C. Bone densitometry

Micro CT data were not available for all samples. For some samples ($n=30$) bone mineral density (BMD) was measured using a Hologic QDR 2000 dual energy x-ray absorptiometry (DEXA) system operating in single beam mode. Areal density was determined for central regions of interest (ROIs) so that cortical bone was excluded. (Although, as mentioned above, lateral cortical plates were removed, some cortical bone remained around the peripheries of the samples. See Wear, 2000b, Fig. 1.) The cross sections of the regions of interest were rectangular. The regions of interest were drawn to approximate ultrasound interrogation regions in the central parts of the specimens. Duplicate measurements were performed on each specimen. The average coefficient of variation for the duplicate areal density determinations was 1.6%. The average areal density (g/cm^2) was divided by the thickness of each sample to give the so-called ''apparent density'' of the skeletal frame (g/cm^3).

The porosities of the samples were estimated as follows. The apparent density d_b of the skeletal frame is equal to $(1-\beta)\,d_s$, where β is the porosity and d_s is the density of the trabecular bone material. Porosities were computed from the DEXA measurements of apparent density d_b and an assumed value for $d_s-1.8$ g/cm^3 for human trabecular bone (see Table I).

The assumption of constant density of the trabecular material was not a serious shortcoming because, as with other investigations (McKelvie and Palmer, 1991; Williams, 1992; Hosokawa and Otani, 1997; Hosokawa and Otani, 1998; Mohamed *et al.*, 2003), a constant value of trabecular material density was assumed for computations of Biot's theoretical model anyway.

Some investigators have used Archimedes' principle to estimate the porosity of trabecular bone samples (Hosokawa and Otani, 1997; Hosokawa and Otani, 1998; Mohamed *et al.*, 2003). For applications in calcaneus, there are two main limitations to this approach. One limitation is that it is difficult to control the degree of water saturation of the bone. Archimedes' principle works well for substances that do not soak up water (e.g., rocks), but is not as reliable for substances that do (e.g., sponges). Trabecular bone lies somewhere in between these two extremes. The second limitation is an imprecise registration of tissue volumes corresponding to ultrasound and density measurements. Ultrasonic mea-

surements are typically made in the central regions of bone samples. The bone sample is typically larger than the beam cross section in order to ensure that all received ultrasound passes through, rather than around, the bone. Archimedes' method measures the trabecular volume of the entire bone sample and therefore produces a weighted average of density within the region of interest (the central part) and density of regions not interrogated with ultrasound (the periphery). This is problematic for bones like the calcaneus that are quite heterogeneous. The advantage of DEXA is that a desired region of the bone, which corresponds closely to the ultrasonic interrogation region, may be isolated for density measurement.

D. Ultrasonic methods

Biot theory predicts phase velocity. The phase velocity of propagating wave, c_p, is a function of angular frequency, ω, and is given by (Morse and Ingard, 1986, and Duck, 1990)

$$c_p(\omega)=\frac{\omega}{k(\omega)}, \tag{1}$$

where $\omega=2\pi f$, f is frequency, $k=2\pi/\lambda$, and λ is wavelength. The relationship between phase velocity and group velocity of a broadband pulse, c_g, is given by (Morse and Ingard, 1986, and Duck, 1990)

$$c_g=\frac{c_{pc}}{1-\dfrac{\omega_c}{c_{pc}}\left(\dfrac{\partial c_p}{\partial\omega}\right)_{\omega=\omega_c}}, \tag{2}$$

where c_{pc} is the phase velocity at the center frequency, ω_c.

Phase velocity may be computed using Eq. (2) and measurements of group velocity if the dispersion of the medium, $\partial c_p/\partial f=(2\pi)^{-1}\partial c_p/\partial\omega$, is known. Dispersion, $\partial c_p/\partial f$, was assumed to be -26.25 m/s per MHz, which is the average value of measurements in human calcaneus reported by four groups (Nicholson *et al.*, 1996; Strelitzki and Evans, 1996; Droin *et al.*, 1998; Wear, 2000a).

To measure group velocity, bone samples were interrogated in a water tank using a pair of coaxially aligned Panametrics (Waltham, MA) 1 in. diameter, focused (focal length=1.5 in.), broadband transducers with center frequencies of 500 kHz. Using Fourier-based (Wear, 2004) and non-Fourier-based (Wear, 2000b) models for diffraction, as reported previously, it was possible to establish that the beam cross section was smaller than the cross-sectional areas of the bone samples. A Panametrics 5800 pulser/receiver was used. Received ultrasound signals were digitized (8 bit, 10 MHz) using a LeCroy (Chestnut Ridge, NY) 9310C Dual 400 MHz oscilloscope and stored on computer (via GPIB) for off-line analysis.

Arrival times of received broadband pulses were measured with and without the sample in the water path. Group velocity, c_g, was computed from

$$c_g=\frac{c_w}{1+\dfrac{c_w\Delta t}{d}}, \tag{3}$$

where d is the thickness of the bone sample, Δt is the difference in arrival times (bone sample present versus bone sample absent), and c_w is the temperature-dependent speed of sound in distilled water given by (Kaye and Laby, 1973)

$$c_w=1402.9+4.835T-0.047\,016T^2+0.000\,127\,25T^3 \text{ m/s}, \tag{4}$$

where T is the temperature in degrees Celsius (measured with a digital thermometer). Each arrival time was computed as follows. First, the digitized received pulse was bandpass filtered (400–800 kHz). Then the signal envelope was computed using the Hilbert transform. The point in time corresponding to the maximum signal envelope was taken to be the arrival time. Because of frequency-dependent attenuation, other commonly used markers that are not at the center of the pulse (such as zero crossings or the leading edge of the pulse) can produce substantial errors in estimates of group velocity (Wear, 2000c; Waters *et al.*, 2005).

These substitution techniques can potentially exhibit appreciable error if the speed of sound differs substantially between the sample and the reference (Kaufman *et al.*, 1995). Apparently, the sound speed in calcaneus, ranging approximately from 1475 m/s to 1650 m/s (Droin *et al.*, 1998), is sufficiently close to that of distilled water at room temperature, 1487 m/s (Kaye and Laby, 1973), that diffraction-related errors may be ignored for an experimental geometry such as the one used here (Droin *et al.*, 1998).

E. Model parameters

Biot's theory requires several input parameters to describe the material and structural properties of the solid and fluid media. Table I shows values used in the present study. Values for human cancellous bone were used when available.

The value for (wet) tissue density (d_s) for human trabecular bone material has been reported by several researchers to lie within the range of 1.6 to 2.0 g/cm^3 (Keaveny and Hayes, 1993). A value of 1.8 g/cm^3 was chosen for the present study.

Rho *et al.* (1993) pointed out that the range of measurements of Young's modulus for human trabecular bone material measured by bending tests is 3.2–7.8 GPa while that measured by buckling and ultrasound is 8.7–12.7 GPa. They argued that the former method tends to underestimate while the latter method tends to overestimate Young's modulus. They concluded that the actual value is likely to lie near the upper end of the former range or the lower end of the latter range. Following this reasoning, a compromised value of 8.3 GPa was chosen for the present study. Admittedly, there is considerable uncertainty associated with this parameter.

Poisson's ratio is near 0.3 for a wide variety of bones and bone-like materials (Grenoble, 1972). Poisson's ratio for the skeletal frame (as opposed to the trabecular bone material) was taken from the measurements of Williams and Johnson (1989) on bovine tibia. Following Williams (1992) and Hosokawa and Otani (1998), the value of s, where tortuosity$=1-s(1-1/\beta)$ and $\beta=$porosity, was taken to be 0.25. Williams chose this value to be consistent with Biot's predictions for hydrodynamic flow in tubes of circular cross

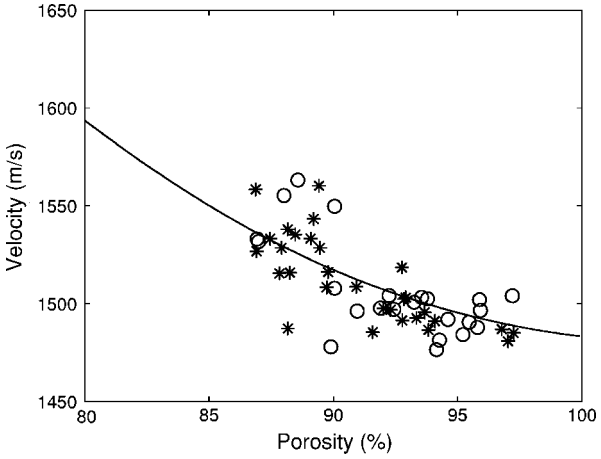

FIG. 1. Phase velocity versus porosity for the human calcaneus samples. The solid curve is the prediction from Biot theory. The samples for which porosity was directly measured (using micro CT) are denoted by circles ($n=23$). The samples for which porosity was indirectly measured (using DEXA) are denoted by asterisks ($n=30$). The Young's modulus (E_s) for the solid bone material was assumed to be 8.3 GPa. (See Sec. II E.)

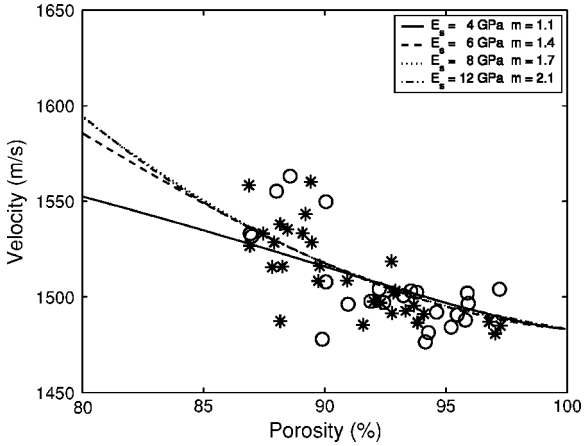

FIG. 2. Biot theory for phase velocity versus porosity for 4 different values for Young's modulus (E_s) for the solid bone material.

sections and random orientations. This value seems to work consistently well for cancellous bone (Williams, 1992; Hosokawa and Otani, 1997; Hosokawa and Otani, 1998).

Following Williams (1992) and Hosokawa and Otani (1998), the value for the exponent m, where $E_b = E_s V_f^m$, E_s = Young's modulus of trabecular bone material, E_b = Young's modulus of skeletal frame, and V_f = volume fraction of bone, was a free parameter to be optimized by curve fitting.

III. RESULTS

Figure 1 shows velocity versus porosity for the 53 human calcaneus samples. The solid curve shows the prediction of Biot's theory. The samples for which porosity was directly measured (using micro CT) are denoted by circles ($n=23$). The samples for which porosity was indirectly measured (using DEXA) are denoted by asterisks ($n=30$). Values for the exponent m (see Sec. II E) obtained by curve fitting were 1.73 ($n=23$, micro CT subset), 1.76 ($n=30$, DEXA subset), and 1.75 (all 53 samples taken together). The root mean square errors of the curve fits were 16.91 m/s ($n=23$, micro CT subset), 14.8 m/s ($n=30$, DEXA subset), and 15.81 m/s (all 53 samples taken together).

IV. DISCUSSION

Biot's theory performs moderately well for the prediction of the dependence of longitudinal phase velocity on porosity in human calcaneus *in vitro*. The trend is quasilinear but both the theory and experiment show a similar slight curvature.

Two factors make the comparison of Biot's theory with measurements more difficult in the present study on human calcaneus than in previous studies in bovine femur or tibia. First, the range of porosities found in the present study in human calcaneus (86%–98%) is considerably narrower than that found in bovine cancellous bone: about 65%–92% (Williams, 1992), about 70%–90% (Hosokawa and Otani, 1997 and 1998), and 21%–67% (Mohamed *et al.*, 2003). Second, the previous studies in bovine cancellous bones were performed on specimens with relatively consistent trabecular orientation (see, for example, Hosokawa and Otani, 1998, Fig. 1). Due to heterogeneity and complex loading patterns on the human calcaneus, trabecular structure was less regular in the present study. This led to a greater range of velocities observed at a given porosity, manifested as scatter in Fig. 1. Such a degree of scatter (a band of velocity measurements up to 50 m/s wide) is commonly encountered in human trabecular bone *in vitro*. (See, for example, Laugier *et al.*, 1997, Fig. 4, and Alves *et al.*, 1996, Fig. 5.)

The experimental dependence of phase velocity on porosity was similar for the two sets of calcanea. (Compare circles with asterisks in Fig. 1.) In addition, curve fitting of Biot theory (with exponent m as the free parameter, see Sec. II E Table I) yielded essentially identical values for both datasets: 1.73 ($n=23$) and 1.76 ($n=30$). This similarity provides further justification for the indirect method of porosity estimation (described above in Sec. II C) based on the assumption of constant material density.

The value for exponent m obtained (by curve fitting) using all 53 calcaneus specimens of 1.75 is somewhat less than that obtained by Hosokawa and Otani (1998) of 2.14 for bovine femoral distal epiphysis for propagation perpendicular to the predominant trabecular orientation. For propagation in the parallel direction, Williams (1992) obtained $m=1.23$ while Hosokawa and Otani (1998) obtained $m=1.46$. For reasons given above, the organization of trabeculae may not be as consistent in human calcaneus as bovine femur or tibia. This could explain why the value of m measured in the present study is between the perpendicular and parallel extremes reported for bovine cancellous bone.

As mentioned above in Sec. II E, there is considerable uncertainty regarding the value of the Young's modulus for the trabecular bone material (E_s). Therefore, it is appropriate to investigate the sensitivity of the theoretical fit to the assumed value for E_s. Figure 2 shows minimum RMSE fits of Biot theory (with exponent m as the free parameter) to the data for four different assumed values for E_s spanning the range of measurements reported in the literature. The four

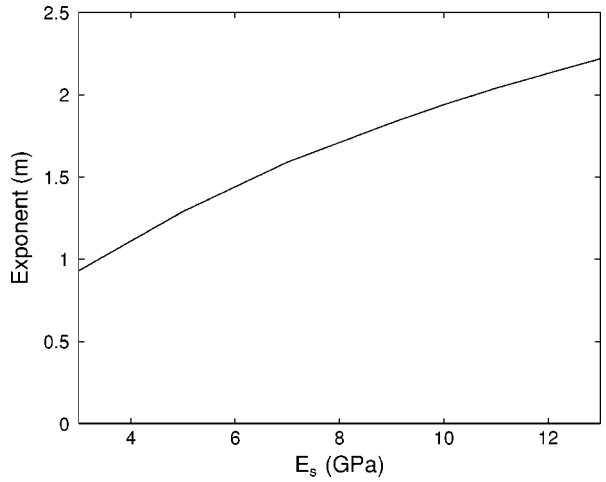

FIG. 3. The exponent m for the minimum RMSE Biot theory fit to experimental data as a function of Young's modulus (E_s) for the solid bone material. (See Sec. IV.)

fits conform to the data comparably well over the range of porosities investigated. Figure 3 shows the approximately linear dependence of the optimum value for m on the assumed value for E_s. The optimum value (in a minimum RMSE sense) for m increases by approximately 0.13 for every 1 GPa increase in E_s.

As pointed out by Hughes *et al.* (1999), two limitations of Biot's model are that (1) it depends on a great number of parameters that are not known with high certainty, and (2) it does not allow for anisotropy. This second factor contradicts the Hans *et al.* (1999) measurements of anisotropy of sound velocity in human trabecular lumbar spine ($c=1715$, 1662, and 1676 m/s in axial, sagittal, and coronal orientations, respectively). To overcome these limitations of the Biot model, Hughes *et al.* introduced the application of the so-called stratified model (Schoenberg, 1984) to the characterization of cancellous bone, in which bone is represented as a periodic array of bone-marrow layers. Hughes *et al.* found good agreement between theoretical predictions and experimental measurements of the angular dependence of phase velocities in bovine tibial and femoral epiphyses. Padilla and Laugier (2000) used the stratified model to predict conditions under which the slow wave is observable. Their results were consistent with measurements reported by Hughes *et al.* Wear (2001) showed that the stratified model successfully predicts negative dispersion in layered polystyrene–water phantoms and in human calcanea. Wear also found, however, that predictions of absolute phase velocity derived from the stratified model were too dependent upon assumed values for material and structural properties to be of much practical value. Lin *et al.* (2001) successfully used the stratified model to predict the dependences of velocity and attenuation on porosity in sheep femoral trabecular bone. Kaczmarek *et al.* (2002) applied the stratified model to the study of bovine femoral cancellous bone in the high frequency limit. Although the stratified model predicts many empirical observations, its alternating layer structure is a crude approximation, at best, to cancellous bone. While the Biot model is isotropic and less parsimonious than the stratified model, it more closely accommodates the physical porous structure of cancellous bone. Each model has its relative merits.

Lee *et al.* (2003) reported success in applying the modified Biot–Attenborough (MBA) model to not only velocity but also dispersion and attenuation in bovine cancellous tibia. It is conceivable that this refinement to the Biot theory could more accurately model phase velocity in human calcaneus. However, it is improbable that this could be proven with the present dataset. Because of the scatter in the data (particularly at lower porosities), it is unlikely that any plausible (i.e., relatively smooth) model function could produce a dramatic decrease in RMSE compared with the Biot model (see Fig. 2). In addition, the MBA model requires two fitting parameters (referred to as s_2 and s_3) that are unknown for human calcaneus. Therefore the more parsimonious Biot model was used in the present study rather than the MBA model.

Due to a more complex trabecular structure and a narrower range of porosities, it is more difficult to assess the compatibility of Biot's theory with human calcaneus than bovine femur or tibia. Nevertheless, Biot's theory performs reasonably well in predicting the dependence of phase velocity on porosity in human calcaneus.

ACKNOWLEDGMENTS

The Food and Drug Administration Office of Women's Health provided funding for this work.

Alves, J. M., Xu, W., Lin, D., Siffert, R. S., Ryaby, J. T., and Kaufman, J. J. (**1996**). "Ultrasonic assessment of human and bovine trabecular bone: a comparison study," IEEE Trans. Biomed. Eng. **43**, 249–258.

Biot, M. A. (**1956a**). "Theory of propagation of elastic waves in a fluid saturated porous solid I. Low frequency range," J. Acoust. Soc. Am. **28**, 168–178.

Biot, M. A. (**1956b**). "Theory of propagation of elastic waves in a fluid saturated porous solid II. High frequency range," J. Acoust. Soc. Am. **28**, 179–191.

Biot, M. A. (**1956c**). "Theory of deformation of a porous viscoelastic anisotropic solid," J. Appl. Phys. **27**, 459–467.

Biot, M. A. (**1962**). "Generalized theory of acoustic propagation in porous dissipative media," J. Acoust. Soc. Am. **34**, 1254–1264.

Biot, M. A. (**1963**). "Mechanics of deformation and acoustic propagation inporous media," J. Appl. Phys. **33**, 1482–1498.

Droin, P., Berger, G., and Laugier, P. (**1998**). "Velocity dispersion of acoustic waves in cancellous bone," IEEE Trans. Ultrason. Ferroelectr. Freq. Control **45**, 581–592.

Duck, F. A. (**1990**). *Physical Properties of Tissue* (University Press, Cambridge, UK).

Grenoble, D. E., Katz, J. L., Dunn, K. L., Gilmore, R. S., and Murty, K. L. (**1972**). "The elastic properties of hard tissues and apatites," J. Biomed. Mater. Res. **6**, 221–233.

Haire, T. J., and Langton, C. M. (**1999**). "Biot theory: A review of its application to ultrasound propagation through cancellous bone," Bone (N.Y.) **24**, 291–295.

Hans, D., Wu, C., Njeh, C. F., Zhao, S., Augat, P., Newitt, D., Link, T., Lu, Y., Majumdar, S., and Genant, H. K. (**1999**). "Ultrasound velocity of trabecular cubes reflects mainly bone density and elasticity," Calcif. Tissue Int. **64**, 18–23.

Hildebrand, T., and Ruegsegger, P. (**1995**). "A new method for the model-independent assessment of thickness in three-dimensional images," J. Microsc. **185**, 67–75.

Hosokawa, A., and Otani, T. (**1997**). "Ultrasonic wave propagation in bovine cancellous bone," J. Acoust. Soc. Am. **101**, 558–562.

Hosokawa, A., and Otani, T. (**1998**). "Acoustic anisotropy in bovine cancellous bone," J. Acoust. Soc. Am. **103**, 2718–2722.

Hughes, E. R., Leighton, T. G., Petley, G. W., and White, P. R. (**1999**). ''Ultrasonic propagation in cancellous bone: a new stratified model,'' Ultrasound Med. Biol. **25**, 811–821.
Hughes, E. R., Leighton, T. G., Petley, G. W., White, P. R., and Chivers, R. C. (**2003**). ''Estimation of critical and viscous frequencies for Biot theory in cancellous bone,'' Ultrasonics **41**, 365–368.
Kaczmarek, M., Kubik, J., and Pakula, M. (**2002**). ''Short ultrasonic waves in cancellous bone,'' Ultrasonics **40**, 95–100.
Kaufman, J. J., Xu, W., Chiabrera, A. E., and Siffert, R. S. (**1995**). ''Diffraction effects in insertion mode estimation of ultrasonic group velocity,'' IEEE Trans. Ultrason. Ferroelectr. Freq. Control **42**, 232–242.
Kaye, G. W. C., and Laby, T. H. (**1973**). *Table of Physical and Chemical Constants* (Longman, London, UK).
Keaveny, T. M., and Hayes, W. C. (**1993**). ''A 20-year perspective on the mechanical preoperties of trabecular bone,'' Trans. ASME, J. Appl. Mech. **115**, 534–542.
Laugier, P., Droin, P., Laval-Jeantet, A. M., and Berger, G. (**1997**). ''In vitro assessment of the relationship between acoustic properties and bone mass density of the calcaneus by comparison of ultrasound parametric imaging and quantitative computed tomography,'' Bone (N.Y.) **20**, 157–165.
Lee, K. I., Roh, H., and Yoon, S. W. (**2003**). ''Acoustic wave propagation in bovine cancellous bone: Application of the modified Biot-Attenborough model,'' J. Acoust. Soc. Am. **114**, 2284–2293.
Lin, W., Qin, Y. X., and Rubin, C. (**2001**). ''Ultrasonic wave propagation in trabecualr bone predicted by the stratified model,'' Ann. Biomed. Eng. **29**, 781–790.
McKelvie, M. L., and Palmer, S. B. (**1991**). ''The interaction of ultrasound with cancellous bone,'' Phys. Med. Biol. **36**, 1331–1340.
Mohamed, M. M., Shaat, L. T., and Mahmoud, A. N. (**2003**). ''Propagation of ultrasonic waves through demineralized cancellous bone,'' IEEE Trans. Ultrason. Ferroelectr. Freq. Control **50**, 279–288.
Morse, P. M., and Ingard, K. U. (**1986**). *Theoretical Acoustics*. (University Press, Princeton, NJ), Chapt. 9.
Nicholson, P. H. F., Lowet, G., Langto, C. M., Dequeker, J., and Van der Perre, G. (**1996**). ''Comparison of time-domain and frequency-domain approaches to ultrasonic velocity measurements in trabecular bone,'' Phys. Med. Biol. **41**, 2421–2435.
Padilla, F., and Laugier, P. (**2000**). ''Phase and group velocities of fast and slow compressional waves in trabecular bone,'' J. Acoust. Soc. Am. **108**, 1949–1952.
Rho, J. Y., Ashman, R. B., and Turner, C. H. (**1993**). ''Young's modulus of trabecular and cortical bone material: ultrasonic and microtensile measurements,'' J. Biomech. **26**, 111–119.
Ruegsegger, P., Koller, B., and Muller, R. (**1996**). ''A microtomographic system for the nondestructive evaluation of bone architecture,'' Calcif. Tissue Int. **58**, 24–29.
Schoenberg, M. (**1984**). ''Wave propagation in alternating solid and fluid layers,'' Wave Motion **6**, 303–320.
Strelitzki, R., and Evans, J. A. (**1996**). ''On the measurement of the velocity of ultrasound in the os calcis using short pulses,'' Eur. J. Ultrasound **4**, 205–213.
Waters, K. R., Hoffmeister, B. K., and Javarone, J. A. (**2005**). ''Application of the Kramers–Kronig relations to measurements of attenuation and dispersion in cancellous bone,'' *Proceedings of the 2004 IEEE Ultrasonic Symposium*.
Wear, K. A. (**2000a**). ''Measurements of phase velocity and group velocity in human calcaneus,'' Ultrasound Med. Biol. **26**, 641–646.
Wear, K. A. (**2000b**). ''Anisotropy of ultrasonic backscatter and attenuation from human calcaneus: Implications for relative roles of absorption and scattering in determining attenuation,'' J. Acoust. Soc. Am. **107**, 3474–3479.
Wear, K. A. (**2000c**). ''The effects of frequency-dependent attenuation and dispersion on sound speed measurements: applications in human trabecular bone,'' IEEE Trans. Ultrason. Ferroelectr. Freq. Control **47**, 265–273.
Wear, K. A. (**2001**). ''A stratified model to predict dispersion in trabecular bone,'' IEEE Trans. Ultrason. Ferroelectr. Freq. Control **48**, 1079–1083.
Wear, K. A. (**2004**). ''Measurement of dependence of backscatter coefficient from cylinders on frequency and diameter using focused transducers—with applications in trabecular bone,'' J. Acoust. Soc. Am. **115**, 66–72.
Williams, J. L., and Johnson, W. J. H. (**1989**). ''Elastic constants of composites formed from PMMA bone cement and anisotropic bovine tibial cancellous bone,'' J. Biomech. **22**, 673–682.
Williams, J. L. (**1992**). ''Ultrasonic wave propagation in cancellous and cortical bone: predictions of some experimental results by Biot's theory,'' J. Acoust. Soc. Am. **92**, 1106–1112.

Off-axis sonar beam pattern of free-ranging finless porpoises measured by a stereo pulse event data logger

Tomonari Akamatsu[a)]
National Research Institute of Fisheries Engineering, Fisheries Research Agency, Japan

Ding Wang and Kexiong Wang
Institute of Hydrobiology, The Chinese Academy of Sciences, Wuhan 430072, People's Republic of China

(Received 3 September 2004; revised 8 February 2005; accepted 22 February 2005)

The off-axis sonar beam patterns of eight free-ranging finless porpoises were measured using attached data logger systems. The transmitted sound pressure level at each beam angle was calculated from the animal's body angle, the water surface echo level, and the swimming depth. The beam pattern of the off-axis signals between 45° and 115° (where 0° corresponds to the on-axis direction) was nearly constant. The sound pressure level of the off-axis signals reached 162 dB *re* 1 μPa peak-to-peak. The surface echo level received at the animal was over 140 dB, much higher than the auditory threshold level of small odontocetes. Finless porpoises are estimated to be able to receive the surface echoes of off-axis signals even at 50-m depth. Shallow water systems (less than 50-m depth) are the dominant habitat of both oceanic and freshwater populations of this species. Surface echoes may provide porpoises not only with diving depth information but also with information about surface direction and location of obstacles (including prey items) outside the on-axis sector of the sonar beam.
[DOI: 10.1121/1.1893325]

PACS numbers: 43.80.-n, 43.80.Ka, 43.66.Gf, 43.80.Ev [WA] Pages: 3325–3330

I. INTRODUCTION

The sonar beam of dolphins and porpoises is known to be highly directional (Norris and Evans, 1967; Au *et al.*, 1978; Au, 1980; Au *et al.*, 1986, 1987, 1995, 1999). A beam-focusing system of sonar signals has been proposed for the head region of dolphins and porpoises wherein the skull reflects sounds ahead while the melon organ focuses the sound beam (Au, 1993). This model is supported by numerical simulations of sound propagation (Aroyan *et al.*, 1992). The focused beam of odontocete sonar is advantageous in that it allows animals to concentrate sound energy ahead for the long-range detection of prey. Directional beams have a better signal-to-noise ratio than do omni-directional beams. As top predators in the oceans and rivers, toothed whales use signals produced in a directional beam to assist in the early detection of remote prey items. The sonar range of odontocetes such as finless porpoises *Neophocaena phocaenoides* and baiji *Lipotes vexillifer* is estimated to reach several tens of meters in open water systems (Akamatsu *et al.*, 1998).

It is also known that the off-axis beam of odontocete sonar is of sufficient intensity to be recorded (Au, 1980). However, the function of these off-axis signals has not been investigated. In bats, sonar signals are used not only for prey capture but also for acoustic scene analysis (Moss and Surlykke, 2001). Off-axis sonar signals in odontocetes might be used for environmental recognition. The scanning sector of an off-axis beam is wider than that of an on-axis beam. Obstacles outside the on-axis beam sector could be detected by receiving off-axis beam echoes. Whether odontocetes can receive echoes of off-axis beams from obstacles in the wild has not been investigated.

Moreover, the sound beam pattern of dolphins and porpoises has not been measured under free-ranging conditions except for white-beaked dolphin *Lagenorhynchus albirostris* (Rasmussen *et al.*, 2004). The relative body angle and the distance between the sound source and the hydrophone must be measured to determine the beam pattern. These experimental constraints made measurements of the beam pattern possible only in controlled captive environments, otherwise several criteria are needed to determine the relative direction of an animal to the hydrophone (Rasmussen *et al.*, 2004). The source level of the sonar signals is highly dependent on the echolocation tasks (Au, 1980; Au and Benoit-Bird, 2003). In the open water and under free-ranging conditions, the off-axis beam intensity is potentially different from that observed in captivity, as wild dolphins and porpoises have the complicated task of detecting remote prey.

Using a stereo acoustic data logger, we measured the ultrasonic pulse intensity of sonar signals and echoes from the water surface that are received at the body of the free-ranging Yangtze finless porpoise (*Neophocaena phocaenoides asiaeorientalis*) in an open water system. The off-axis sonar beam pattern was calculated for eight free-ranging animals. We show that the water surface echoes of off-axis signals are sufficient intensity for reception by finless porpoises in their habitat.

II. MATERIALS AND METHODS

A. Study site and animals

The experimental site was an oxbow lake of the Yangtze River, Hubei, China (29.30–29.37′N,112.13–112.48′E).

a)Electronic mail: akamatsu@affrc.go.jp

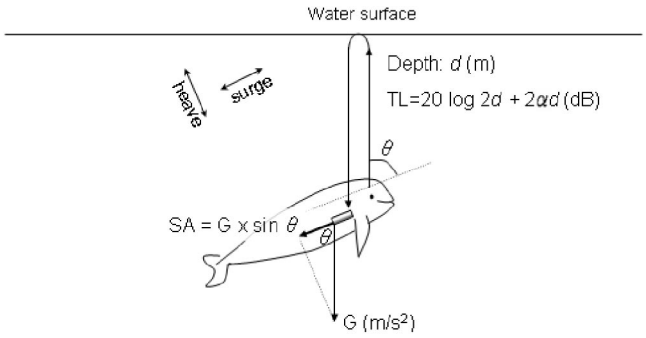

FIG. 1. Measurements of body angle and the off-axis beam intensity. The ''surge'' and ''heave'' directions of the animal are indicated in the upper left inset. The body angle can be calculated by the surging body acceleration (SA) and the gravity force (G). The water surface echo of the off-axis sound was received by the acoustic data logger attached to the side of the animal. Spherical propagation was assumed in calculating the transmission loss (TL) of the sound during the round trip to the water surface. The absorption coefficient α is also included in the transmission loss.

This was an old course of the Yangtze River, 1–2 km in width and 21 km in length. The maximum depth was approximately 20 m, which occurred along the outer bank of the hoop-shaped lake; most of the lake was shallower than 10 m. The main stream of the river inundates the oxbow during the rainy season. The underwater visibility is less than 1 m owing to turbidity. Finless porpoises in this reserve reproduce annually without supplementary feeding by humans (Wei *et al.*, 2002). The environment of this oxbow is considered to be quite similar to that of the main stream of the Yangtze River (Zhang *et al.*, 1995).

All animals used in this experiment were safely captured in October 2003 and temporally housed in an enclosure ($\sim 30 \times 60$ m with a maximum depth of 3.5 m) established in an inlet adjacent to the oxbow. They were maintained in this enclosure for at least 24 h for the alleviation of stress levels prior to release.

B. Data logger systems and attachment

An acoustic data logger (W20-AS, Little Leonardo, Japan) was used to measure the sound pressure levels of sonar signals. The data logger could record the intensity of ultrasonic pulse events over 129 dB *re* 1 μPa peak to peak level up to 2000 times in a second, and its dynamic range was 31 dB. The data logger had directional sensitivity (see later discussion and Fig. 5) similar to the directional hearing of dolphins and porpoises; thus the detection threshold of the data logger at the on-axis direction (0°) was 129 dB compared with 140 dB when the sound came from a 90° off-axis direction. Because of the contamination of internal thermal noise of the data logger system, a relatively higher detection threshold of 129 dB was intentionally employed compared with the audible threshold level of dolphins and porpoises.

A behavior data logger (PD2GT, Little Leonardo, Japan) was simultaneously used to measure the body angle. In the behavior data logger, an accelerometer with two axes measured the surging and heaving body acceleration, including static gravity force. The surging and heaving acceleration could be converted to the pitch and roll angle of the animal's body (Fig. 1). For example, one gravity force of surging acceleration corresponded to a vertical ascent in which the body angle was perpendicular to the water surface, while a horizontal body direction was indicated by zero surging acceleration. To eliminate the higher frequency components of accelerations caused by body vibrations, moving averages of acceleration over 100-ms time intervals were used. The dynamic range of the acceleration measurement was $\pm$five gravity force with 10-bit resolution. The behavioral data logger also recorded the swimming depth and speed and the experienced water temperature.

The acoustic and behavior data loggers were attached on both sides of eight animals by suction cups (Product No. 40-1525-0, Canadian Tire Co. Ltd., Canada). This attachment methodology was simple and less invasive. Each data logger was assembled with a suction cup, a float (expanded polyvinyl chloride Klegecell No. 55, pressure resistant to 8 atm, Kaneka Co. Ltd., Japan), and a transmitter (MM130, Advanced Telemetry Systems, USA). After the experiment, the drag force of the two data logger systems was measured in the experimental towing tank at the National Research Institute of Fisheries Engineering, Japan. The drag force was found to be less than 60 gram-force at the cruising speed of finless porpoises (0.89 m/s).

C. Data analysis

The acoustic data logger recorded direct-path signals from the sound source as well as water surface reflections. The direct-path signal traveled to the acoustic data logger directly from the sound source under the blow hole of the animal (Cranford *et al.*, 1996). The water surface echo is the reflected off-axis signal which is transmitted upward from the animal. The water surface echo delay from the direct-path signal should be identical to the two-way sound travel duration between the animal's depth and the surface. Only pulses delayed within ± 1 ms from the calculated delay time according to the animal's depth were used for the analysis. This means that we accepted an error of ± 75 cm in depth ($\sim$ half the body length of the animals). Echoes received within 1 m of the water surface were also excluded to avoid noise contamination during respiratory splashing. The water surface echo level was scaled by the directional sensitivity of the acoustic data logger, using the body angle simultaneously measured by the behavior data logger. Assuming spherical sound propagation and flat water surface, the transmission loss during the round trip between the animal and the water surface was $20 \log 2d\,(\mathrm{dB}) + 2\alpha d$, where d is the swimming depth and α is the absorption coefficient, respectively (Fig. 1). The absorption coefficient at the sonar frequency of 140 kHz in finless porpoises (Akamatsu *et al.*, 1998) is no more than 0.04 dB/m (Urick, 1983). We calculated the sound pressure level of the transmitted off-axis signal at 1 m from the animal by adding the water surface echo level and the transmission loss.

To calculate the beam pattern, a source level of the on-axis signal was needed as a reference. The acoustic data logger was fixed on the animal's body, and the sound travel distance of the direct-path signal was therefore constant. The received sound pressure level of the direct-path signal was considered to be in proportion to the source level of the sonar

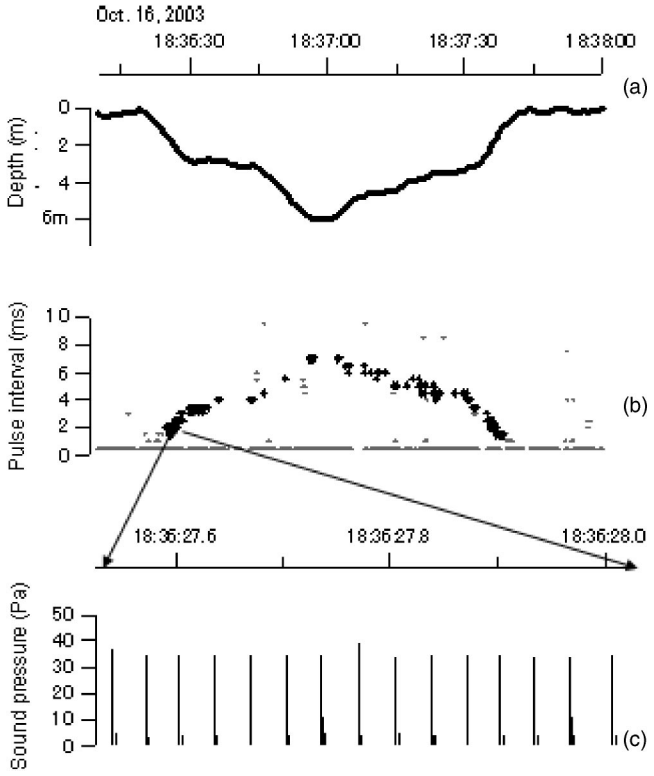

FIG. 2. The depth profile (a), the echo delay (b), and recorded samples of pulse events (c). The echo delay (b) is in proportion with the swimming depth (a) since the round trip time to the surface by underwater sound corresponds to the sound source depth. Especially in shallow water swimming depth, many echoes associated with the sonar signals as shown in double pulse structure in (c).

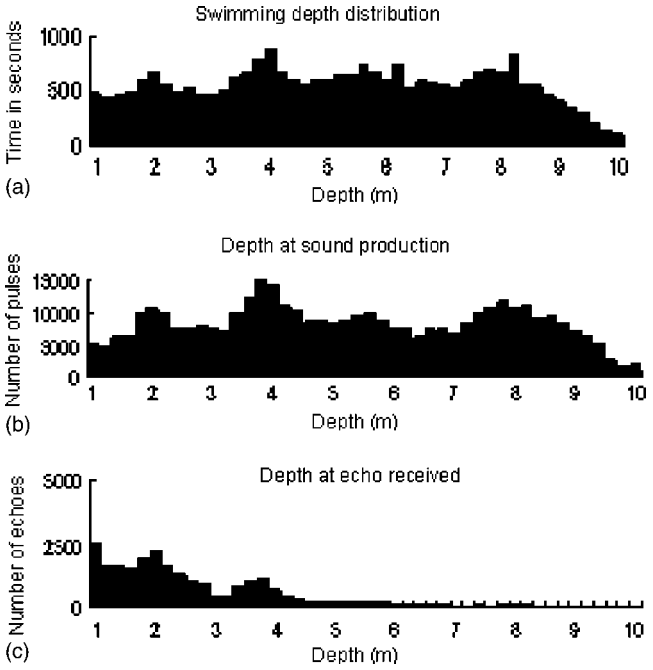

FIG. 3. The time that animals spent at each depth (a), the number of recorded direct-path signals at each depth (b), and the number of recorded echoes at each depth (c). The number of echoes decreased quickly as depth increased.

signals. Using the intensity of the direct-path signal as a reference, we calculated the relative intensity of the off-axis sound pressure level at 1 m from the animal (hereafter termed the ''relative beam intensity''). Finally, we obtained the off-axis sonar beam pattern indicated by the relative beam intensity for each body angle of the eight finless porpoises.

III. RESULTS

All the acoustic and behavior data logger systems were retrieved within 3 days of release. They remained attached to the animals for 13.1 h on average and for a maximum of 36.8 h. The period of simultaneous attachment of both the acoustic and behavior data loggers for each individual was 8.75 h on average. During the experiment, the water surface of the lake was almost flat, with no waves. Such a calm condition happens often in the dry season. Assuming negligible reflection loss at the surface, the transmission loss during the round trip between the animal and the water surface was estimated as the spherical propagation, as previously indicated.

An example dive profile and the received echo delay of an animal (serial no. 8) are given in Fig. 2. In this case, the animal dove for 80 s and reached 6 m in depth [Fig. 2(a)]. Most of the interpulse intervals were interpreted as surface echoes (bold dots) during the entire dive bout [Fig. 2(b)]. Many double pulses were observed [Fig. 2(c)], and the intrapulse interval within the double pulses corresponded to the calculated delay time.

The examination of all recorded dive statistics for porpoise 8 shows that this individual dived to depths of up to 10 m [Fig. 3(a)]. The simultaneous recording of dive behavior and sonar signals revealed that the porpoise produced sonar signals at all depths [Fig. 3(b)]. This animal spent relatively longer time periods at 2-, 4-, and 8-m depth and produced many pulses at these depths. The number of pulses per second at each depth was fairly consistent (mean 14.3 pulses/second, standard deviation 2.3). This finless porpoise used sonar almost continuously with relatively constant sensing effort at each swimming depth. However, surface echoes were frequently received by the acoustic data logger at depths of less than 6 m and were rarely received deeper than 6 m [Fig. 3(c)].

The animal swam horizontally most of the time but occasionally rolled (Fig. 4). The surging acceleration clearly peaked at ~ 0 [Fig. 4(a), black line], indicating that the animal mostly swam horizontally. The heaving acceleration ranged from -10 to $+15\ \mathrm{m/s^2}$ [Fig. 4(a), gray line]. The negative gravity force ($-9.8\ \mathrm{m/s^2}$) of the heaving acceleration corresponded to the animal swimming in a supine posture. The heaving acceleration of this individual shows that the animal sometimes rolled.

The examination of the body acceleration data measured only when surface echoes were received by the acoustic data logger reveals the absence of negative heaving acceleration [Fig. 4(b), gray line]. This means that the animal was swimming with its dorsal side uppermost when the surface echoes were detected. The surface echoes were not received during

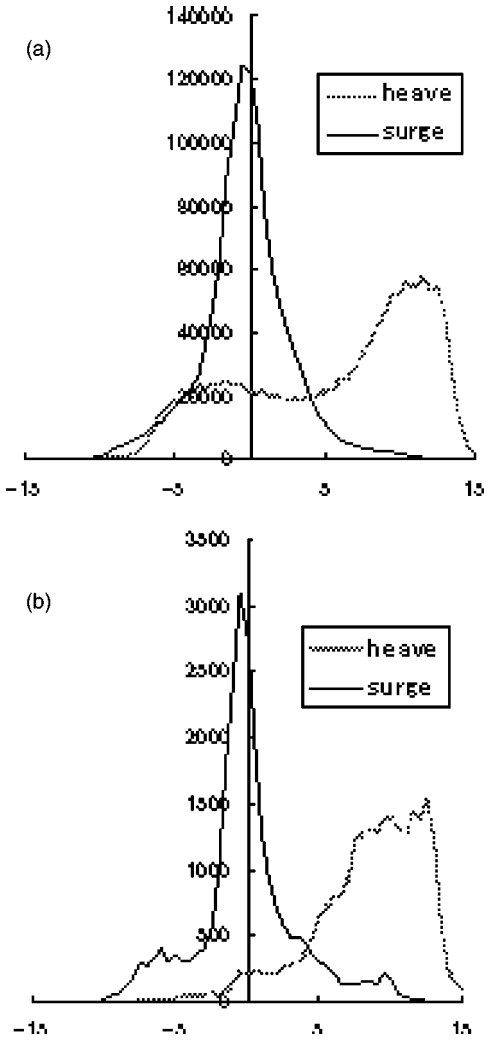

FIG. 4. The number of surging and heaving body accelerations during the entire observation period of animal 8 (a). The number of body accelerations only when surface echoes received is indicated in (b). The distribution of heaving acceleration when surface echo received (b) is positively biased relative to the distribution of (a), indicating that echoes were mostly received during swimming dorsal side uppermost.

swimming in a supine posture. These trends were also observed in the other seven experimental animals.

The off-axis beam pattern could be calculated for a limited range of angles because of the small sample size of near-vertical ascents and the directional sensitivity of the acoustic data logger. As shown in Fig. 4, we observed a very small number of events in which positive and negative gravity force occurred at $\pm 9.8\ \mathrm{m/s^2}$ during surging acceleration. This means that the porpoises rarely ascended or descended in near-vertical postures, and this limited the availability of surface echo data from on-axis signals. When surface echoes were received, porpoise body angles were almost always within 45°–135° degrees (Fig. 5, black circles; 90° is horizontal). Additionally, the directional sensitivity of the acoustic data logger (Fig. 5, white circles) did not allow the reception of off-axis signals at greater than 120°. Over 120°, the detection threshold of the acoustic data logger was close to the thermal noise level of the electric circuit in the logger (dotted line). Therefore, the off-axis beam pattern was calculated between 45° and 120° (this angle range is shown as an arrow in Fig. 5).

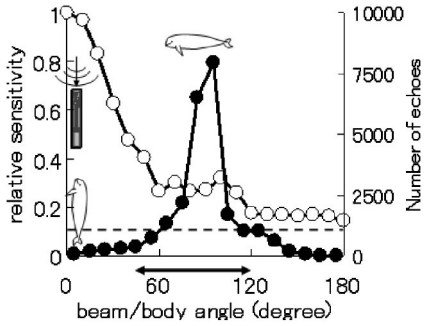

FIG. 5. Directional sensitivity of the acoustic data logger (white circles, left) and the number of received echoes at each body angle (black circles, right). The dotted line indicates the internal electric noise level of the acoustic data logger. As illustrated in the left side of the figure, the data logger is most sensitive when receiving sound coming from 0° (from the front). However, many echoes were received during horizontal swimming (body angle of 90°), and quite a few echoes were received during nearly vertical ascents (0°) and descents (180°).

The averaged off-axis beam pattern of eight finless porpoises for every 10° bin of the body axis is indicated in Fig. 6. The off-axis beam pattern was almost constant across the entire range of this angle.

IV. DISCUSSION

The off-axis sonar beam pattern of free-ranging finless porpoises was obtained by using pulse event recorders attached to the animals. We see three major methodological advantages to our approach. First, there is no need to train animals to be stationed at a fixed point. The body angle was changed by the animal itself, and the intensity of the off-axis beams could be obtained from the water surface echo. Second, the sound pressure level of free-ranging animals can be obtained from the body angle information. The animals could swim freely, thereby enabling the measurement of sonar beam patterns of finless porpoises in the open water system. Third, this method does not require a relatively expensive multi-channel hydrophone system to measure beam patterns.

Many water surface reflections of off-axis signals were beyond the detection threshold level of the acoustic data logger (140 dB *re* 1 μPa, peak-to-peak at 90° of beam angle) during horizontal swimming. The surface echo could be received by the acoustic data logger as deep as 6 m [Fig. 3(c)]. The propagation loss during the round trip from 6 m in depth

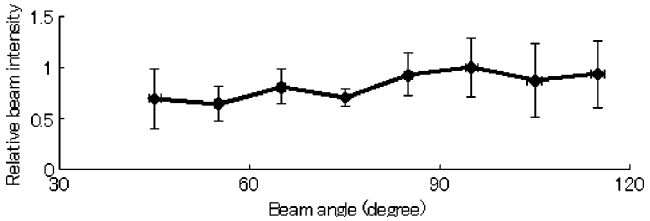

FIG. 6. Off-axis beam pattern of eight finless porpoises. The ordinate shows the relative beam intensity, and the value at 95° is set at 1 as the reference point.

to the surface was 22 dB. During the round trip to the surface, the absorption is estimated to be 0.48 dB which is negligible comparing with 22 dB. Therefore, the source level of the off-axis signal upward (90°) from the horizontally swimming animal was a maximum of 162 dB which is the summation of 140 dB echo level and 22 dB propagation attenuation. Comparing between Fig. 3(b) and (c), approximately half of the transmitted sound associated with surface echo at 1-m depth. This suggests that half of the off-axis sounds have over 146 dB source levels which is the summation of 140 and 6 dB propagation attenuation to the surface from 1-m depth. The lower echoes are out of the dynamic range of the data logger. Therefore, average source level of off-axis signals could not be estimated. Instead, 146 dB seems to be a fair indicator of the ordinary source level of the off-axis beam of finless porpoises.

Finless porpoises are distributed in shallow waters within the Asian continental shelf. An aerial survey of finless porpoises in Japanese waters revealed that they were found in waters shallower than 50-m depth (Shirakihara *et al.*, 1994). They are suggested to have a bottom preference (Akamatsu *et al.*, 2002), possibly for prey capture purposes. They produce sonar signals frequently (Akamatsu *et al.*, 2000), and the echolocation performance of a finless porpoise in target discrimination is reported to be similar to that of a bottlenose dolphin, *Tursiops truncatus* (Nakahara *et al.*, 1997). The finless porpoise belongs to the same family as the harbor porpoise (*Phocoena phocoena*), in which the auditory threshold level is less than 70 dB (Andersen, 1970).

A finless porpoise with an auditory threshold level of 70 dB that is swimming at 50-m depth therefore receives off-axis signal surface echoes at a calculated level of 118 dB (40 dB propagation loss and 4 dB absoption), which is 48 dB higher than the potential auditory threshold level of finless porpoises. This means that finless porpoises are considered to receive surface echoes of off-axis signals with a sufficient signal-to-noise ratio at depths of up to 50 m.

Finless porpoises in our study almost always produced sonar signals, at any depth [Fig. 3(b)]. The maximum depth of the present study area was 20 m, and the maximum transmission loss during the round trip from the lake bed to the surface is 34 dB including 2 dB aborsption loss. Under these circumstances, the echo level received at the animal would be 128 dB. This means that finless porpoises in shallow water environments such as those of the present study can probably receive water surface echoes at all times.

Finless porpoises swam horizontally and dorsal side up when receiving the echoes [Fig. 4(b)]. Therefore, the beam pattern obtained in the present study is on the vertical plane of the dorsal side. Surface echoes could not be received when the animal was swimming in a supine posture. This suggests that the sonar beam of finless porpoises does not propagate ventrally. The upper jaw is a candidate insulator of sound propagated downward from the source. This also suggests that an off-axis sonar beam shadow area might exist on the ventral side of the animal.

The off-axis beam pattern is relatively constant at any measured direction (Fig. 6). Finless porpoises possibly recognize not only a target ahead but also other obstacles within the off-axis beam sector. The sonar of porpoises might have wider coverage than formerly expected. For example, a 10-cm body length clupeoid fish is estimated to have a target strength of -51.9 dB at 38 kHz, according to the formula presented by Foote (1987). The target strength of fish has a slightly negative relationship with the sound frequency. The change of the averaged target strength varies within a few dB in the wide frequency range (Sawada, 2002). Additionally, we should note that the off-axis sonar beam transmitted upward from the porpoise is projected to the ventral side of a fish, but usually the target strength of the fish is measured from the dorsal side. Besides these differences of conditions, we will use the estimated target strength by Foote's formula as an approximate value hereafter. If the fish is 3 m above a finless porpoise, the transmission loss during round trip is 19 dB, making the estimated echo level received by the animal 91 dB, which is still 21 dB above the potential auditory threshold level of a finless porpoise. From a physical point of view, the off-axis beam could be used by finless porpoises for prey and environmental cognition.

An advantage of interpreting the acoustical cues of surface echoes is that not only the depth but also the surface direction can be recognized. As shown in Fig. 4(a), finless porpoises sometimes roll during swimming in a turbid water system. During such a complicated body angle orientation, the directional cue of the surface may aid self-positioning in an environment in which visual cues are less effective. The 162-dB source level of off-axis signals is high enough to allow the bimodal use of sonar. The porpoise detects long-range targets using the on-axis beam and may recognize the environment and other targets out of the on-axis beam sector through off-axis signals. An ''acoustical sidelong glance'' is therefore considered to be physically possible with the use of sonar by finless porpoises.

ACKNOWLEDGMENTS

The authors would like to acknowledge X. Zhang, Q. Zhao, Z. Wei, X. Wang, B. Yu (IHCAS), Y. Naito, K. Sato, A. Kato (NIPR), H. Tanaka (Kyoto University), M. Suzuki (Little Leonardo), H. Muramoto (Marine Micro Technology), N. Sugiyama (Suruga Denshi Co. Ltd.), K. Oota (Intertec Co. Ltd.), A. Matsuda, S. Suzuki, K. Sawada (NRIFE), M. Nakamura, H. Hiruda (Marine World Uminonakamichi), S. Numata, T. Sakai (Oarai Aruarium), T. Tobayama, M. Soichi, H. Katsumata (Kamogawa Sea Wolrd), T. Shinke (System Intech), and A. Zielinski. The Institute of Hydrobiology of the Chinese Academy of Sciences, the Field Station of Tian-e-zhou Baiji Nature Reserve, the National Institute of Polar Research of Japan, Kamogawa Sea World, Marine World Umino Nakamichi, Oarai Aquarium, Little Leonardo Co. Ltd., Marine Micro Technology Co. Ltd., Japan Techno Mate Co. Ltd., OKI Sea Tech Co. Ltd., and Tamai Environment System Co. Ltd. greatly supported our experiments. This research was supported by the Bio-oriented Technology Research Advancement Institution (BRAIN) Promotion of Basic Research Activities for Innovative Biosciences, the Chinese Academy of Sciences (CAS) (No. KSCX2-SW-118), and the Institute of Hydrobiology, CAS (220103).

Akamatsu, T., Wang, D., Nakamura, K., and Wang, K. (**1998**). ''Echolocation range of captive and free-ranging baiji (*Lipotes vexillifer*), finless porpoise (*Neophocaena phocaenoides*), and bottlenose dolphin (*Tursiops truncatus*),'' J. Acoust. Soc. Am. **104**, 2511–2516.

Akamatsu, T., Wang, D., Wang, K., and Naito, Y. (**2000**). ''A method for individual identification of echolocation signals in free-ranging finless porpoises carrying data loggers,'' J. Acoust. Soc. Am. **108**, 1353–1356.

Akamatsu, T., Wang, D., Wang, K., Wei, Z., Zhao, Q., and Naito, Y. (**2002**). ''Diving behavior of freshwater finless porpoises (*Neophocaena phocaenoides*) in an oxbow of the Yangtze River, China,'' ICES J. Mar. Sci. **59**, 438–443.

Andersen, S. (**1970**). ''Auditory sensitivity of the harbour porpoise *Phocoena phocoena*,'' in *Investigations on Cetacea*, edited by G. Pilleri, Vol. II (Hirnanatomisches Institut, Berlin), pp. 255–259.

Aroyan, J. L., Cranford, T. W., Kent, J., and Norris, K. S. (**1992**). ''Computer modeling of acoustic beam formation in *Delphinus delphis*,'' J. Acoust. Soc. Am. **92**, 2539–2545.

Au, W. W. L. (**1980**). ''Echolocation signals of the Atlantic bottlenose dolphin *Tursiops truncatus* in open waters,'' in *Animal Sonar Systems*, edited by R. G. Busnel and J. F. Fish (Plenum, New York), pp. 251–282.

Au, W. W. L. (**1993**). *The Sonar of Dolphins* (Springer, New York), pp. 1–277.

Au, W. W. L., and Benoit-Bird, K. J. (**2003**). ''Automatic gain control in the echolocation system of dolphins,'' Nature (London) **423**, 861–863.

Au, W. W. L., Floyd, R. W., and Haun, J. E. (**1978**). ''Propagation of Atlantic bottlenose dolphin echolocation signals,'' J. Acoust. Soc. Am. **64**, 411–422.

Au, W. W. L., Moore, P. W. B., and Pawloski, D. (**1986**). ''Echolocation transmitting beam of the Atlantic bottlenose dolphin,'' J. Acoust. Soc. Am. **80**, 688–691.

Au, W. W. L., Penner, R. H., and Turl, C. W. (**1987**). ''Propagation of beluga echolocation signals,'' J. Acoust. Soc. Am. **82**, 807–813.

Au, W. W. L., Kastelein, R. A., Rippe, T., and Schooneman, N. M. (**1999**). ''Transmission beam pattern and echolocation signals of a harbor porpoise (*Phocoena phocoena*),'' J. Acoust. Soc. Am. **106**, 3699–3705.

Au, W. W. L., Pawloski, J. L., Nachtigall, P. E., Blonz, M., and Gisiner, R. C. (**1995**). ''Echolocation signals and transmission beam pattern of a false killer whale *Pseudorca crassidens*,'' J. Acoust. Soc. Am. **98**, 51–59.

Cranford, T. W., Amundin, M., and Norris, K. S. (**1996**). ''Functional morphology and homology in the odontocete nasal complex: implications for sound generation,'' J. Morphol. **228**, 223–285.

Foote, K. G. (**1987**). ''Fish target strengths for use in echo integrator surveys,'' J. Acoust. Soc. Am. **82**, 981–987.

Moss, C. F., and Surlykke, A. (**2001**), ''Auditory scene analysis by echolocation in bats,'' J. Acoust. Soc. Am. **110**, 2207–2226.

Nakahara, F., Akira, T., Koido, T., and Hirud, H. (**1997**). ''Target discrimination by an echolocating finless porpoise, *Neophocaena phocaenoides*,'' Marine Mammal Sci. **13**, 639–649.

Norris, K. S., and Evans, W. E. (**1967**). ''Directionality of echolocation clicks in the rough-tooth porpoise, *Steno bredanensis* (Lesson),'' *Marine Bio Acoustics*, edited by W. N. Tavolga (Pergamon, Oxford), pp. 305–316.

Rasmussen, M. H., Wahlberg, M., and Miller, L. A. (**2004**). ''Estimated transmission beam pattern of clicks recorded from free-ranging white-beaked dolphins (*Lagenorhynchus albirostris*),'' J. Acoust. Soc. Am. **116**, 1826–1831.

Sawada, K. (**2002**). ''Study on the precise estimation of the target strength of fish,'' Bulle. of Fishe. Rese. Agency **2**, 47–122 (in Japanese).

Shirakihara, M., Shirakihara, K., and Takemura, A. (**1994**). ''Distribution and seasonal density of the finless porpoise *Neophocaena phocaenoides* in the coastal waters of western Kyushu, Japan,'' Fishe. Scie. **60**, 41–46.

Urick, R. J. (**1983**). *Principles of Underwater Sound*, 3rd ed. (McGraw-Hill, New York), p. 423.

Wei, Z., Wang, D., Kuang, X., Wang, K., Wang, X., Xiao, J., Zhao, Q., and Zhang, X. (**2002**). ''Observations on behavior and ecology of the Yangtze finless porpoise (*Neophocaena phocaenoides asiaeorientalis*) group at Tian-e-Zhou Oxbow of the Yangtze River,'' Raffles Bull. of Zool., Suppl. **10**, 97–103.

Zhang, X., Wei, Z., Wang, X., Yang, J., and Chen, P. (**1995**). ''Studies on the feasibility of establishment of a semi-natural reserve at Tian-e-zhou (swan) oxbow for baiji, *Lipotes vexillifer*,'' Acta Hydrobiol. Sinica **19**, 110–123.